FRONTIERS IN MATERIALS: RISING STARS

EDITED BY: N. M. Pugno, D. Cazorla-Amoros, J.-S. Chen, G.-L. Song, S. A. Akbar, L. Wondraczek, A. Pegoretti, S.-B. Choi, J. L. Provis, J. P. Chu, K. Kordas and L. Dai

PUBLISHED IN: Frontiers in Materials

frontiers Research Topics

frontiers

ISSN 1664-8714
ISBN 978-2-88963-581-8
DOI 10.3389/978-2-88963-581-8

About Frontiers

Frontiers is more than just an open-access publisher of scholarly articles: it is a pioneering approach to the world of academia, radically improving the way scholarly research is managed. The grand vision of Frontiers is a world where all people have an equal opportunity to seek, share and generate knowledge. Frontiers provides immediate and permanent online open access to all its publications, but this alone is not enough to realize our grand goals.

Frontiers Journal Series

The Frontiers Journal Series is a multi-tier and interdisciplinary set of open-access, online journals, promising a paradigm shift from the current review, selection and dissemination processes in academic publishing. All Frontiers journals are driven by researchers for researchers; therefore, they constitute a service to the scholarly community. At the same time, the Frontiers Journal Series operates on a revolutionary invention, the tiered publishing system, initially addressing specific communities of scholars, and gradually climbing up to broader public understanding, thus serving the interests of the lay society, too.

Dedication to Quality

Each Frontiers article is a landmark of the highest quality, thanks to genuinely collaborative interactions between authors and review editors, who include some of the world's best academicians. Research must be certified by peers before entering a stream of knowledge that may eventually reach the public - and shape society; therefore, Frontiers only applies the most rigorous and unbiased reviews.
Frontiers revolutionizes research publishing by freely delivering the most outstanding research, evaluated with no bias from both the academic and social point of view. By applying the most advanced information technologies, Frontiers is catapulting scholarly publishing into a new generation.

What are Frontiers Research Topics?

Frontiers Research Topics are very popular trademarks of the Frontiers Journals Series: they are collections of at least ten articles, all centered on a particular subject. With their unique mix of varied contributions from Original Research to Review Articles, Frontiers Research Topics unify the most influential researchers, the latest key findings and historical advances in a hot research area! Find out more on how to host your own Frontiers Research Topic or contribute to one as an author by contacting the Frontiers Editorial Office: researchtopics@frontiersin.org

FRONTIERS IN MATERIALS: RISING STARS

Cover image: 24Novembers/Shutterstock.com

The *Frontiers in Materials* Editorial Office team are delighted to present the inaugural "Frontiers in Materials: Rising Stars" article collection, showcasing the high-quality work of internationally recognized researchers in the early stages of their independent careers.

All Rising Star researchers featured within this collection were individually nominated by the Journal's Chief Editors in recognition of their potential to influence the

future directions in their respective fields. The work presented here highlights the diversity of research performed across the entire breadth of the materials science and engineering field, and presents advances in theory, experiment and methodology with applications to compelling problems.

This Editorial features the corresponding author(s) of each paper published within this important collection, ordered by section alphabetically, highlighting them as the great researchers of the future.

The *Frontiers in Materials* Editorial Office team would like to thank each researcher who contributed their work to this collection. We would also like to personally thank our Chief Editors for their exemplary leadership of this article collection; their strong support and passion for this important, community-driven collection has ensured its success and global impact.

Laurent Mathey, PhD
Journal Development Manager

Citation: Pugno, N. M., Cazorla-Amoros, D., Chen, J.-S., Song, G.-L., Akbar, S. A., Wondraczek, L., Pegoretti, A., Choi, S.-B., Provis, J. L., Chu, J. P., Kordas, K., Dai, L., eds. (2020). Frontiers in Materials: Rising Stars. Lausanne: Frontiers Media SA. doi: 10.3389/978-2-88963-581-8

Table of Contents

CARBON BASED MATERIALS

COLLOIDAL MATERIALS AND INTERFACES

ENVIRONMENTAL MATERIALS

FUNCTIONAL CERAMICS

GLASS SCIENCE

MECHANICS OF MATERIALS

POLYMERIC AND COMPOSITE MATERIALS

SMART MATERIALS

STRUCTURAL MATERIALS

TRANSLATIONAL MATERIALS SCIENCE

Carbon Based Materials

Raul Berenguer

Dr Raul Berenguer is an Associate Researcher at the Materials Institute (IUMA) of the University of Alicante. In 2010, he obtained his PhD in the field of Material Science and Applied Electrochemistry at the University of Alicante, Spain. He joined the Institute of Multidisciplinary Research for Advanced Materials at Tohoku University (2010-2012, the Chemical Engineering Department at the University of Málaga (2012-2015), the Materials Institute (IUMA) of the University of Alicante (2015-2017), and the Bioelectrogenesis group at the Institute IMDEA Water (2018) as a post-doc. He recently received a "Ramón y Cajal" grant and his current interests include the development of electrode materials for wastewater treatment, microbial electrochemical technologies, or energy storage/conversion.

Francisco José García Mateos

Dr Francisco José García Mateos completed a BSc in Industrial Engineering at the University of Málaga in Spain in 2010, and a MSc degree in Advanced Chemistry at the same institution in 2011. He obtained his PhD in Chemical Engineering at UMA in 2017 with the thesis entitled "Preparation of carbon based submicrometric fibers for energy and environmental applications", supervised by Prof. Cordero and Prof. Rodríguez-Mirasol. During his PhD studies, he completed a short research stay with the "Materiales Carbonosos y Medio Ambiente (MCMA)" group at the University of Alicante (Spain).

He joined the "Tecnología de Residuos y Medio Ambiente (TERMA)" group in 2009. His research focuses on the valorization of biomass and industrial waste for the preparation of submicrometric carbon-based fibers, using an electrospinning technique, as well as the design and preparation of electrodes based on metallic, metal oxides, and carbon materials, for their utilization in adsorption, heterogeneous catalysis, and energy storage processes.

Hongying Hou

Prof. Dr Hongying Hou, an ACS member and reviewer for some international journals, acquired her doctorate in 2009 and worked as a Post doctorate researcher in France between 2010 and 2012. Her research interests are mainly focused on electrochemistry and new energy materials including fuel cells and lithium ion batteries. To date, she has published 33 papers and holds two patents. Her published work includes two review articles published in ChemSusChem and the Journal of Membrane Sciences, both of which achieved great academic impact. In March 2012, she joined the Kunming University of Science and Technology as a high-level talent in China and became a Professor in 2013.

Miriam Navlani-García

Dr Miriam Navlani-García received her PhD in Material Science from Alicante University (Spain) under the supervision of Prof. Diego Cazorla-Amorós in 2014. In 2015, she moved to Osaka University, Japan, where she worked as a Specially Appointed Assistant Professor in the Division of Materials and Manufacturing Science, within the research group of Professor Hiromi Yamashita. In 2017 she was a recipient of a JSPS Postdoctoral Fellowship for Overseas Researchers (Standard) awarded by the Japan Society for the Promotion of Science. She was recently awarded a Postdoctoral Fellowship for researchers with international experience (Plan GenT, Generalitat Valenciana) and she is currently developing her research activities in the Carbon Materials and Environment group at the University Materials Institute of Alicante (IUMA). Her research interests focus on the development of nanocatalysts and photocatalysts for environmental applications, mainly hydrogen purification and production.

Khanin Nueangnoraj

Dr Khanin Nueangnoraj is currently an Assistant Professor at the School of Bio-Chemical Engineering and Technology, Sirindhorn International Institute of Technology (SIIT), Thammasat University, Thailand. He obtained his PhD in 2013 from Tohoku University, Japan. His research interests include structural control of carbon materials with novel structures through a template approach, surface functionalization of carbon materials, electrochemical capacitors, and hybrid energy storage systems.

Martin Oschatz

Dr Martin Oschatz studied Chemistry at the Technische Universität Dresden, Germany. He carried out his PhD studies in the group of Stefan Kaskel and graduated in April 2015 summa cum laude. In 2013 he pursued a research stay with Gleb Yushin at the Georgia Institute of Technology, Atlanta, USA. After a postdoctoral stay at Utrecht University, Netherlands in the group of Krijn de Jong, Martin joined the Colloid Chemistry department of Markus Antonietti at the MPI of Colloids and Interfaces, Germany in November 2016 supported by a Liebig grant of the German Chemical Industry Fund. Since April 2019, he has been working as a Professor (by proxy) for inorganic chemistry at the University of Potsdam, Germany. His research focusses on nanostructured carbon materials for energy and environmental applications.

Takafumi Ishii

Takafumi Ishii received his PhD in 2014 from Tohoku University, Sendai, Japan. He also received A Research Encouragement Award from the Institute of Multidisciplinary Research for Advanced Material" while completing his PhD After obtaining his degree, he was employed as an assistant Professor at Gunma University, Japan. His research interests include the surface chemistry of carbon materials, nano carbons, and carbon catalysts. he is particularly devoted to analyzing the chemical structure of the carbon surface by means of temperature programmed desorption techniques.

Olli Pitkänen

MSc Olli Pitkänen graduated as MSc in electrical engineering in 2010 from the University of Oulu, Finland. After a few years in the industry and university laboratory work, he began to pursue his PhD degree in 2015 and defended his thesis in 2019. His background is in electronics, materials science, and microfabrication. His research has been focused on applications of carbon-based nanomaterials, energy storage and sensors, while the topic of his PhD studies focused on on-device synthesis of carbon nanotube structures.

Ramiro Ruiz Rosas

Ramiro Ruiz Rosas is an Associate Professor of Chemical Engineering at the University of Málaga. He obtained his PhD from the University of Málaga in 2012. He completed research stays at Penn State University, Universidade Nova de Lisboa and the Institute of Multidisciplinary Research for Advanced Materials of Tohoku University. In 2012 he joined the MCMA group at the Materials Institute of the University of Alicante, as a postdoctoral researcher. Since 2018 he is a member of the TERMA group at the University of Malaga. His research interests focus on the preparation and use of advanced carbon materials from lignocellulosic wastes (Hierarchical porous carbons, heteroatom doped activated carbons, templated carbons, carbon molecular sieves, carbon monoliths and porous electrospun carbon fibers) and their use as adsorbents, catalysts, and electrodes in environmental protection and energy storage/generation applications. He has published more than 50 articles in international reviewed journals, four book chapters, and holds 2 patents.

David Salinas-Torres

David Salinas-Torres obtained his PhD. degree in Material Science in 2014 from Alicante University, Spain under the supervision of Prof. Cazorla-Amorós and Prof. Morallón. He moved to the *Université de Liège* and joined the group of Prof. Job where he developed the project focused on the design of N-containing carbon-based materials for their application as electrodes in energy storage devices. He then worked as a Specially Appointed Assistant Professor in the Division of Materials and Manufacturing Science, Graduate School of Engineering, Osaka University. After that, he was granted a JSPS Postdoctoral Fellowship for Research in Japan. He was awarded a "*Juan de la Cierva*" contract from the Spanish government and he is currently developing his research in the Group of Electrocatalysis and Polymer Electrochemistry (GEPE), within the University Materials Institute of Alicante. His current research focuses on the synthesis of carbon-based materials from biomass for their use in energy storage devices.

frontiers in Materials

ORIGINAL RESEARCH
published: 04 June 2019
doi: 10.3389/fmats.2019.00130

Oxidation of Different Microporous Carbons by Chemical and Electrochemical Methods

Raúl Berenguer and Emilia Morallón*

Instituto Universitario de Materiales, Departamento Química Física, Universidad de Alicante (UA), Alicante, Spain

The functionalization of high surface area microporous carbon materials by oxidative treatments receives great interest for multiple applications. The micropore structure of the material and the oxidation method could play an important role in the process. In this work, we analyze and compare the effects of liquid-phase chemical and alternative electrochemical oxidation treatments in the textural and chemical properties of four microporous carbon materials, namely a granular-, cloth-, and powder-like activated carbon (AC) and a powdery zeolite templated carbon (ZTC). Particularly, we provide new data on oxidation kinetics and changes on microporosity and surface chemistry of various microporous carbons. Characterization techniques reveal that the extent, textural changes, and selectivity of the oxidation greatly depend on the type of microporous material and the oxidation method. The incorporation of surface oxygen groups (SOGs) generally causes a more-or-less significant decrease in the measured micropore volume and the specific surface area. In the studied ACs, the extent of oxidation and BET surface area reduction augment with their micropore volume, and the textural changes seem to be governed by the micropore blockage by SOGs. The disordered microporous structure of these materials is then quite robust toward oxidation, but its heterogeneity may contribute to the lack of selectivity during this process. By contrast, the regular micropore framework of the ZTC is rapidly destroyed even under soft oxidizing conditions, but it is proposed to promote certain selectivity during oxidation. The high reactivity and structural fragility of ZTC are assigned to the weak interconnections and large number of exposed edge sites in its structure. Our results demonstrate the fast oxidation rate of chemical treatments under different conditions, especially in the case of ZTC, what is proposed to restrict the control and to limit the oxidizability and selectivity of these functionalization processes. Contrarily, the electrochemical treatments are proved to better control the kinetics of oxidative functionalization, what may explain the observed higher efficiency and selectivity for SOGs introduction and the minimization of degradation in fragile microporous structures.

Keywords: microporous carbons, chemical oxidation, electrochemical oxidation, functionalization, oxidation kinetics, selectivity

OPEN ACCESS

Edited by:
Jie-Sheng Chen,
Shanghai Jiao Tong University, China

Reviewed by:
Fotios K. Katsaros,
National Centre of Scientific Research Demokritos, Greece
Stanisław Biniak,
Nicolaus Copernicus University in Torun, Poland

****Correspondence:***
Raúl Berenguer
raul.berenguer@ua.es

Specialty section:
This article was submitted to Carbon-Based Materials, a section of the journal Frontiers in Materials

Received: *15 March 2019*
Accepted: *16 May 2019*
Published: *04 June 2019*

Citation:
Berenguer R and Morallón E (2019) Oxidation of Different Microporous Carbons by Chemical and Electrochemical Methods. Front. Mater. 6:130. doi: 10.3389/fmats.2019.00130

INTRODUCTION

Microporous carbon materials with pores of < 2 nm diameter and high specific surface area (up to 4,000 m^2/g) receive great interest for multiple applications, such as gas storage and purification (Bottani and Tascón, 2008; Linares-Solano et al., 2008; Tascón, 2012), catalysis (Rodriguez-Reinoso, 1998; Serp and Figueiredo, 2009), wastewater treatment (Radovic et al., 2000; Bottani and Tascón, 2008; Tascón, 2012), energy storage and conversion (Bottani and Tascón, 2008; Beguin and Frackowiak, 2009; Nishihara and Kyotani, 2012), etc. For these applications, the micropore structure (volume, pore-size distribution, ordered/disordered arrangement, interconnectivity, shape, wall thickness, etc. of micropores) becomes crucial. Moreover, the use of oxidative post-treatments to adjust the number and type of oxygen surface groups (SOGs) in these materials could be very important for their optimization in some of these applications. Nevertheless, the control on the extent and selectivity of the oxidation processes is complex and their possible effects on the textural properties must be considered.

Microporosity features are mainly determined by the precursor and preparation method. Activated carbons (ACs) constitute the most widely known family of microporous carbons. In these materials, microporosity mainly develops as spaces among disordered aromatic sheets and small graphitic domains formed upon heating (Rodríguez-Reinoso and Molina-Sabio, 1998; Molina-Sabio and Rodríguez-Reinoso, 2004) and/or by carbon oxidation to CO or CO_2, depending on the activation method (Rodríguez-Reinoso and Molina-Sabio, 1998; Molina-Sabio and Rodríguez-Reinoso, 2004; Linares-Solano et al., 2008). Another family of microporous carbons are the so-called zeolite-templated carbons (ZTCs) obtained by using zeolite as a sacrificial template (Ma et al., 2000; Nishihara and Kyotani, 2018). Unlike ACs, ZTCs exhibit an ordered micropore framework of curved and single-layer graphene coming from the zeolite channels.

The oxidation of microporous ACs has been largely studied in the past. The effect of multiple different oxidation methods and conditions on their properties and applications was analyzed (Shen et al., 2008; Daud and Houshamnd, 2010; Jaramillo et al., 2010; Rivera-Utrilla et al., 2011; Thakur and Thakur, 2016). So far, liquid-phase chemical oxidation by using H_2O_2, HNO_3 or $(NH_4)_2S_2O_8$ has been the most studied oxidative method (Otake and Jenkins, 1993; Moreno-Castilla et al., 1995, 1997, 1998, 2000; De la Puente et al., 1997; Gil et al., 1997; Mangun et al., 1999; Pradhan and Sandle, 1999; El-Sayed and Bandosz, 2001; Shim et al., 2001; Strelko and Malik, 2002; El-Hendawy, 2003; Li et al., 2003, 2011; Houshmand et al., 2011; Ternero-Hidalgo et al., 2016). It has been claimed that the oxidation degree of microporous ACs can be easily controlled by adjusting the oxidation parameters, i.e., treatment time, concentration, and temperature of common oxidants (HNO_3 or $(NH_4)_2S_2O_8$) (Moreno-Castilla et al., 1997; Houshmand et al., 2011). These treatments generally cause a decrease in specific surface area and micropore volume, which becomes more significant with an increasing degree of activation in the oxidized material (Moreno-Castilla et al., 1995, 1997, 2000). While some authors suggest that the decrease in textural properties is due to a blockage by SOGs at the entry of the micropores (Moreno-Castilla et al., 1995, 1997; Pradhan and Sandle, 1999; Li et al., 2003; Maroto-Valer et al., 2004; Szymanski et al., 2004; Houshmand et al., 2011), others claim their destruction by the oxidation reaction (Moreno-Castilla et al., 1995, 1997, 1998; Pradhan and Sandle, 1999; Li et al., 2003). These disparities have been attributed to the distinct oxidation method and differences in the micropore texture, thickness of micropore walls, etc. of the oxidized material. And reciprocally, it has been proposed that the porosity of the material plays an important role in the rate of fixation of SOGs (Moreno-Castilla et al., 1997).

Other conventional treatments of microporous ACs are based on gas-phase chemical oxidation at middle/high temperature (García et al., 1998; Figueiredo et al., 1999; Boudou et al., 2000; Gómez-Serrano et al., 2002; Álvarez et al., 2005). Although high oxidation degrees can be reached with these processes, they generally cause significant textural modification. By contrast, electrochemical oxidative treatments at room temperature have been proposed as promising advantageous alternatives (Kinoshita, 1988; Berenguer et al., 2009, 2012, 2013a,b; Tabti et al., 2013; González-Gaitán et al., 2015; Vujković et al., 2018). We previously carried out systematic studies on the electrochemical oxidation of various carbon materials (Berenguer et al., 2009, 2012, 2013a,b; Tabti et al., 2013). For a microporous AC, preliminary results suggested that the kinetics for SOGs generation through electrochemical oxidation are more controllable than with chemical treatments, without significantly affecting its textural properties (Berenguer et al., 2012).

The oxidation of ZTCs, however, remains practically unexplored (Berenguer et al., 2013a,b; Vujković et al., 2018). In a pioneer work, it was found that, compared to chemical treatments, the electrochemical method enabled to better retain the original microporous structure of the ZTC during SOGs incorporation (Berenguer et al., 2013a). Moreover, from variations in CO/CO_2 ratios it was proposed that the electrochemical oxidation involves a less aggressive and more controlled oxidation than the chemical one (Berenguer et al., 2013b). Although a better controllability of the oxidation kinetics was proposed to explain these phenomena, no kinetics studies were carried out.

It can be deduced from literature, hence, that not only the oxidative method but also the micropore structure of the oxidized material seem to play an important role on the reactivity and effects of the oxidation processes. Among the vast literature, however, few investigations compare the effect of different oxidation methods on a given carbon material (Otake and Jenkins, 1993; Figueiredo et al., 1999; Li et al., 2003; Houshmand et al., 2011; Berenguer et al., 2012, 2013a) and very few deal with the influence of the different micropore structure of the material when oxidized by a specific method (Moreno-Castilla et al., 1997; El-Sayed and Bandosz, 2001). To the knowledge of the authors, there are no investigations analyzing both effects at the same time. Remarkably, studies on the kinetics and controllability of the different oxidation reactions are lacking. In this work, various carbon materials with disordered (three distinct ACs) and ordered (a ZTC)

microporous structure have been oxidized by conventional liquid-phase chemical and alternative electrochemical oxidation methods. The chemical and textural properties of the different materials, before and after oxidation, have been analyzed by various techniques. For these materials, the effects of the different oxidative treatments on the oxidation degree, changes on the microporous texture and the selectivity toward SOGs introduction have been studied. Furthermore, the kinetics of the different oxidative functionalizations have been analyzed. Finally, the effects of the different oxidative methods have been correlated with their kinetics and the microporous structure of the distinct materials.

MATERIALS AND METHODS

Materials

Four different carbon materials were used for this study: (i) the granular activated carbon (GAC) was supplied by Waterlink Suctliffe Carbons (207 A, pH_{PZC} = 9, Mesh: 12 × 20) and it is referred to as *W*; (ii) the activated carbon cloth (ACC) was provided by MAST Carbon (C-TEX27, pH_{PZC} = 6.5) and denoted as *EX*; (iii) the powdery activated carbon (PAC), designated as *A,* was prepared by chemical activation of an anthracite with KOH as reported elsewhere (Lozano-Castelló et al., 2001). For that, a physical mixture of KOH:anthracite = 3:1 was heated at 5°C/min up to 740°C, and kept at this temperature for 1 h, under a 6,000 mL/min flow of N_2; and (iv) the zeolite templated carbon (*ZTC*) was synthesized by using a zeolite Y template (Na-form, SiO_2/Al_2O_3 = 5.6, from Tosoh Co. Ltd.) as previously described (Ma et al., 2000). The main textural and chemical properties of these materials are collected in **Table 1**.

Oxidation Methods

Chemical Oxidative Functionalization

The chemical oxidation of the different ACs and the ZTC was performed with HNO_3, H_2O_2, and/or $(NH_4)_2S_2O_8$, under different conditions, as reported before (Berenguer et al., 2012, 2013a). The nomenclature of the chemically-oxidized materials includes the name of the carbon material (*W*, *EX*, *A*, *ZTC*); the letters N, H, or S referring to the used oxidizing agent (HNO_3, H_2O_2, and $(NH_4)_2S_2O_8$, respectively); a number indicating their concentration (%); a number or the letter R (room temperature) related to the temperature of the experiments (°C); and finally, the treatment time (h or min).

TABLE 1 | Textural and chemical properties of the studied microporous materials.

Material	S_{BET} (m^2/g)	VN_2 (cm^3/g)	VCO_2 (cm^3/g)	CO_2 (μmol/g)	CO (μmol/g)	O (μmol/g)
W	875	0.37	0.29	393	418	1,204
EX	1,130	0.48	0.39	665	1,370	2,700
A	3,130	1.26	0.74	946	2,861	4,753
ZTC	3,650	1.54	1.00	286	2,644	3,216

Electrochemical Oxidative Functionalization

The electrochemical oxidation of the different ACs was carried out in a filter-press electrochemical cell (Berenguer et al., 2009, 2012; Tabti et al., 2013), whereas the ZTC was assembled into a paste to be electrooxidized in a conventional three-electrode cell (Berenguer et al., 2013a). The different materials were galvanostatically treated at RT in 1 M NaOH, 2 wt% NaCl or 1 M H_2SO_4 aqueous electrolytes under different conditions. The nomenclature of the electrochemically-oxidized materials comprises the name of the carbon material (*W*, *EX*, *A*, *ZTC*); a number indicating the applied current; the abbreviations OH^-, Cl^-, or H^+, related to the NaOH, NaCl, and H_2SO_4 electrolytes, respectively; and finally, the treatment time.

Characterization and Parameters

Prior to their characterization, the functionalized materials were washed with abundant distilled water, vacuum-filtered, and dried at 110°C overnight.

Porous Texture Characterization

The textural properties of the materials before and after oxidation were analyzed by N_2 adsorption-desorption at −196°C and CO_2 adsorption at 0°C. The different ACs were analyzed in an Autosorb-6 system (Quantrachrome Corporation) after vacuum out-gassing at 250°C for 4 h, while the *ZTC* samples were characterized in a BEL Japan analyzer (BELSORP-mini) after out-gassing at 150°C under vacuum for 6 h. The apparent surface area (S_{BET}) was determined by the Brunauer–Emmett–Teller (BET) method using the data of N_2 adsorption branch in the P/P_0 range of 0.01–0.05. The total volumes of micropores (VN_2) (d < 2 nm) and narrowest micropores (VCO_2) (d < 0.7 nm) were calculated from the Dubinin–Radushkevich (DR) equation applied to N_2 (in the range 0.005 < P/P0 < 0.17) and CO_2 adsorption isotherms, respectively (Arenillas et al., 2004). The good fitting of the N_2 and CO_2 adsorption data to the DR equation validated the application of this method for the different microporous materials. Pore size distributions were derived by density functional theory (DFT), applying the QSDFT model to the adsorption branch for the analysis of the geometrically and chemically disordered (slit/cylindrical/sphere) micro-/meso-pores of ACs; and the NLDFT equilibrium model of carbon slit pores for the *ZTC* samples. Moreover, the changes on *ZTC* structural order were followed by X-ray diffraction (XRD-6100, Shimadzu) using a Cu-Kα radiation (λ = 1.541 Å) generated at 30 kV and 20 mA.

Particularly, in this work, the change on BET surface area was calculated as:

$$\Delta S_{BET} = S_{BET_{OX}} - S_{BET_0}$$

or, relatively, as the loss (%) of BET surface area:

$$\%S_{BET}\ loss = \frac{\Delta S_{BET}}{S_{BET_0}} \times 100$$

where, $SBET_0$ and $SBET_{OX}$ are the specific surface area of the material before and after oxidation, respectively. As it is

explained below, changes on the S_{BET} of the studied materials are unequivocally attributed to changes on micropore volume.

Surface Chemistry Characterization

The concentration and type of SOGs was characterized by Temperature-Programmed Desorption (TPD) experiments and X-Ray Photoelectron Spectroscopy (XPS). Nevertheless, other techniques, like titration methods, water adsorption, infrared spectroscopy, etc., could have been also used. For the different ACs, the TPDs were performed at 20°C/min up to 950°C under a He flow (100 mL/min) in a SDT 2960 Simultaneous equipment (TA Instruments) coupled to a MSC 200 mass spectrometer (Thermostar, Balzers). The *ZTC* samples were heated up to 1,000°C (2°C/min), and kept at this temperature for 1 h, under a He flow, and the CO_2, and CO evolved gasses were analyzed with a micro gas chromatograph (Varian 490-GC). The XPS analysis was carried out by using a VG-Microtech Multilab electron analyzer and an unmonochromatized Mg-Kα (1253.6 eV) radiation at base pressure of 5×10^{-10} mbar. Photoelectrons were collected at a pass energy of 50 eV and the binding energies (BE) were referenced against the main C1s line at 284.5 eV.

The number of SOGs introduced by a given oxidation method was calculated from TPD measurements by subtraction as:

$$\Delta O = O_{OX} - O_0$$

where, O_0 and O_{OX} are the total oxygen evolved ($O = 2CO_2 + CO$) calculated from the TPD-profiles of the material before and after oxidation, respectively. From this parameter, the change on BET surface area relative to SOGs incorporation was calculated as $\Delta S_{BET}/\Delta O$.

RESULTS AND DISCUSSION

Oxidation Degree and Textural Properties Changes by Chemical Treatments

The studied carbon materials were oxidized by different chemical or electrochemical methods (see experimental section). **Figure 1** represents the increment of SOGs (ΔO) caused by different oxidation treatments vs. the variation of specific surface area (ΔS_{BET}) determined for the studied materials. The increment of SOGs (ΔO) can be associated to the oxidizability of the material and/or the efficacy of the oxidative treatment and conditions. Although ΔS_{BET} was arbitrarily represented as positive, a decrease in the measured S_{BET} was found in all cases, so a higher ΔS_{BET} value was characteristic of a larger decrease in specific surface area. Given the lineal dependence of ΔS_{BET} with the change on the micropore volume (ΔVN_2) (see section Analysis of Textural Changes), changes on ΔS_{BET} can be directly attributed to variations of the micropore volume determined from N_2 adsorption-desorption isotherms.

Chemical Oxidation of the ACs

As it can be observed in the figure, the extent of both the oxidation degree and decrease in surface area greatly depends on different aspects. The RT-treatment of the W ($SBET_0 = 875$ m^2/g) with different oxidizing reagents for 2 h (inlet of **Figure 1**) enables to introduce a maximum of 3,000 μmolO/g in the case of $(NH_4)_2S_2O_8$, which is even more effective than 65 wt% HNO_3 (ΔO = 2,200 μmolO/g) and much than H_2O_2. When the reaction time is prolonged up to 24 h with $(NH_4)_2S_2O_8$, a maximal increment of 5,000 μmolO/g is observed. These results indicate that the chemical oxidation may be faster at the beginning, so that its rate decreases with time (**Figure 2A**). Such a kinetic behavior can be observed also in other ACs reported in literature (Moreno-Castilla et al., 1997; Houshmand et al., 2011; **Figure 2A**) and was associated to the uncontrollability of chemical oxidation (Berenguer et al., 2012). The main consequence is that significantly long times are needed to reach significant oxidation degrees, so that further functionalization of this material by this method and conditions becomes complex and restricted.

On the other hand, none of these treatments produced significant changes on the surface area (a detailed analysis of the textural properties is presented in section Analysis of Textural Changes). In particular, a maximal 4.5% loss in surface area was observed in the case of 65 wt% HNO_3, this being a very low relative decrease of surface area by SOGs gain (0.02 m^2/μmolO).

Quite similar results were found for the chemical oxidation of *EX* under similar conditions (not shown in **Figure 1**), although in this case both the attained oxidation degrees and the observed changes on surface area were slightly higher (ΔO = 6700 μmolO/g and 13% loss in surface area for *EX*-S-24 h). This could be explained by the slightly larger micropore volume and surface area of this material (see **Table 1**), which could result in a greater concentration of reactive edge sites (Arenillas et al., 2004) and larger oxidations (ΔO) (Moreno-Castilla et al., 1995, 1997, 2000; Mangun et al., 1999). For example, in only 1 h a RT-treatment of activated carbon fibers (ACFs) ($SBET_0 = 1390$ m^2/g) with concentrated HNO_3 resulted in larger oxidation degrees (ΔO = 5420 μmolO/g) and surface area losses (6.8%) (Mangun et al., 1999) than a 2 h-similar-treatment of the studied *W*. Moreover, such effects of the surface area at RT were also observed and systematically studied, with other reagents [H_2O_2 and $(NH_4)_2S_2O_8$], by Moreno-Castilla et al. (1995, 1997, 2000).

However, these authors found that the ACs prepared from olive stones display lower oxidative reactivity than those obtained from almond shells (Moreno-Castilla et al., 1995, 1997, 2000). Hence, not only the textural properties but also the nature of the precursor or other features (wettability, dimensions, conformation, mesoporosity, wall thickness, electrical conductivity in the case of electrochemical oxidation, etc.), may affect the reactivity of the material.

The increased reactivity with the development of textural properties was confirmed for the powdery AC, sample *A*, which presents around triple micropore volume and surface area than previous materials (**Table 1**). As it can be seen in **Figure 1**, ca. 5,770 μmolO/g can be introduced after 3 h-oxidation with 65 wt% HNO_3 (*A*-N65-R-3h) and the surface area considerable decreases in a 19.1%. Thus, the relative decrease of surface area by SOGs gain ($\Delta S_{BET}/\Delta O$) increases to ca. 0.10 m^2/μmolO. Nevertheless, the finer particle size of this powdery material

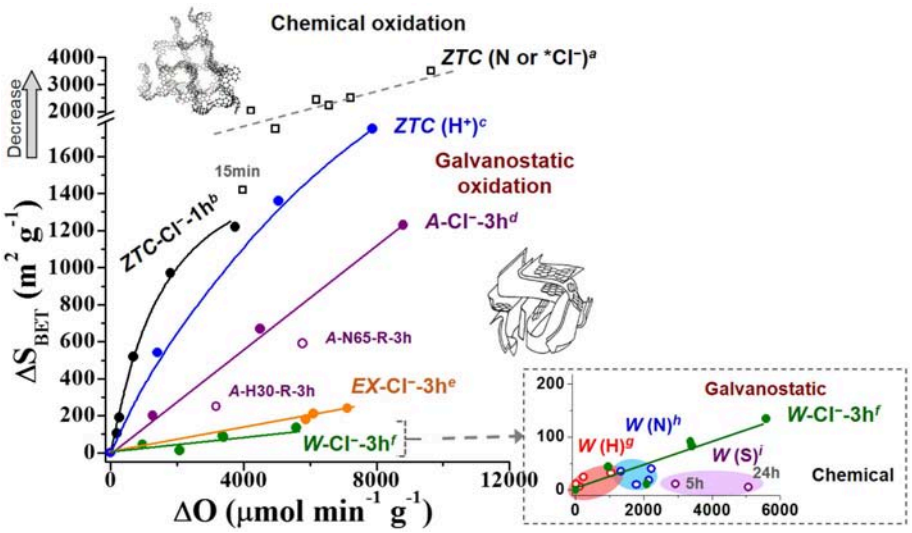

FIGURE 1 | Extent of oxidation (ΔO) and surface area variation (decrease) caused by most common chemical reagents in liquid phase [H_2O_2, HNO_3, and $(NH_4)_2S_2O_8$] and different galvanostatic treatments at different conditions on the studied microporous materials. The carbonaceous structures of the *ZTC* and the ACs are adapted from Nishihara et al. (2009) and Rodríguez-Reinoso and Molina-Sabio (1998), respectively. Note: (*Cl^-) refers to the too strong electrochemical conditions for the oxidation of *ZTC* (≥ 50 mA in NaCl) at which their oxidizing power approaches those of chemical treatments. Oxidation conditions: *a*: 30–60 wt% HNO_3, R−80°C,15 min-2 h; *a**: 50 mA, 3–7 h; *b*: 2–20 mA; *c*: 2–5 mA, 1–36 h; *d*,*e*,*f*: 0.2–1.0 A; *g*: 10–33 wt% H_2O_2, 2 h; *h*: 23-65 wt% HNO_3, 2 h; *i*: $(NH_4)_2S_2O_8$-saturated 1 M H_2SO_4 solution.

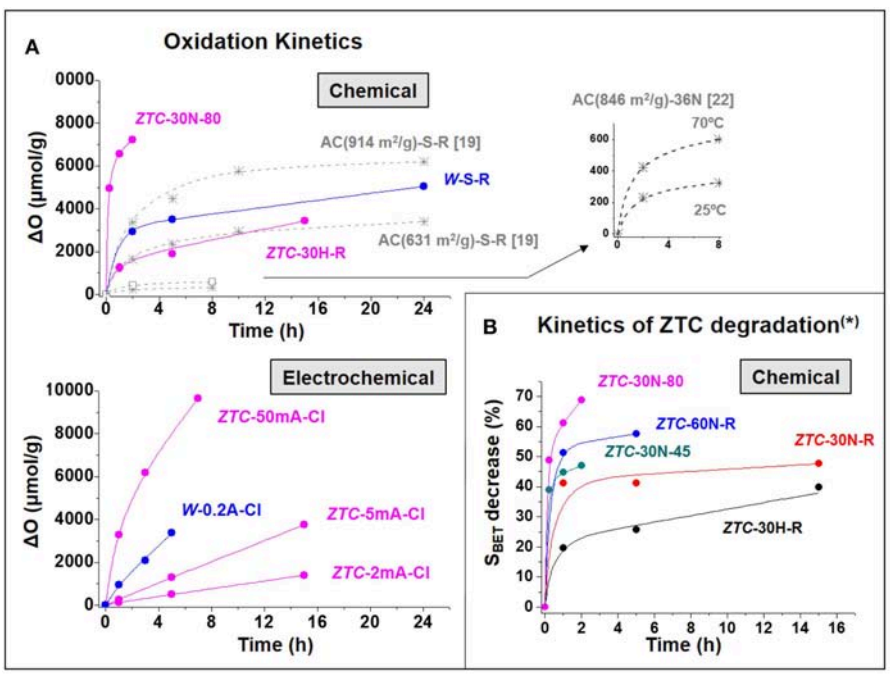

FIGURE 2 | (A) Evolution of the oxidation degree upon time (oxidation kinetics) of various studied and referenced materials functionalized by chemical or electrochemical methods; **(B)** Evolution upon time of the loss in surface area (associated to structural degradation (*) in section Analysis of Textural Changes) of *ZTC* functionalized by different chemical methods.

compared to the previous ones, favoring the contact with the oxidizing agents, may also have a strong influence on its greater oxidizability.

It is well-known that the oxidation degree of ACs reached by the chemical method can be further increased in the range ΔO = 5,000–12,000 μmolO/g, respectively by raising the temperature,

concentration and/or acidity of the reagent (Moreno-Castilla et al., 1995; Mangun et al., 1999; Ternero-Hidalgo et al., 2016). However, these treatments parallelly caused more severe textural modifications, with a decrease in surface area between 10 and 50%. As it can be deduced from literature data (see **Figure 2A** the data of Houshmand et al., 2011), for ACs the kinetics of chemical oxidation greatly increases with such stronger oxidizing conditions.

Chemical Oxidation of the ZTC

Unlike the case of ACs, the *ZTC* experiences a comparable SOGs introduction but a much more marked reduction of surface area when exposed even at much softer oxidizing chemical conditions (see some examples in the upper part of **Figure 1**). For example, in only 15 min (45°C) or 1 h (room temperature) the oxidation of *ZTC* with 30 wt% HNO_3 introduces 4,000–5,000 μmolO/g, but its surface area decreases in more than 1,400 m^2/g. These effects suppose a 39–41% loss in S_{BET} and a considerable enhancement of the relative variation of S_{BET} to 0.30–0.40 m^2/μmolO (for 30 wt% HNO_3). It can be inferred beforehand (see details on section Oxidation Methods) that this loss in surface area is associated to the destruction of the ordered microporous framework of this material, so it is referred to as structural and/or textural degradation. Hence, chemical treatments at RT produce severe damage in the extraordinary textural properties of *ZTC*.

Moreover, in this case it is easier to induce further functionalization by simply extending treatment time, temperature or reagent concentration, but any increment in SOGs gives rise to further textural decline. For example, boiling 30 w% HNO_3 (80°C) can introduce 5,000–7,200 μmolO/g in only 15 min−2 h of treatment, but it causes a 50–70% loss of S_{BET}. Another interesting feature is that the chemical oxidation reaction of *ZTC* is very fast, even in the case of 30 wt% H_2O_2 at RT, the softest conditions studied (**Figure 2A**). Such oxidation kinetics are greatly accelerated at stronger conditions (see for example the results of boiling 30 wt% HNO_3 in **Figure 2A**). As a result, the degradation of *ZTC* properties under chemical conditions is remarkably fast. **Figure 2B** shows that above 40 % of the initial S_{BET} of *ZTC* is lost within the 1 h of treatment with HNO_3 under different conditions. This stresses the extraordinarily high reactivity and fragility of this material toward chemical functionalization, which may be unacceptable for the potential application of these materials with designed unique nanostructure.

Analysis of Textural Changes

The microporosity of the different materials before and after oxidative treatments was analyzed by gas adsorption techniques. **Figure 3** compares the N_2 adsorption-desorption isotherms of the pristine *W*, *A,* and *ZTC* (see their textural parameters in **Table 1**) with those of representative oxidized samples. The isotherm of *EX* (figure not shown) was quite similar to that of *W* (Zakaria, 2014). For the oxidized ACs, examples of materials obtained by electrochemical treatments have been considered because they cause higher oxidation degrees (see section Electrochemical Oxidation: Greater Controllability at Room Temperature), what may help to discern more clear effects. The isotherms for W and A samples are a combination of type I and IV (Lozano-Castelló et al., 2009). In fact, the good correlation between the volume of micropores and the specific surface area of the many samples oxidized under different conditions (**Figure 4A**) confirms the microporous nature of all the oxidized materials considered in this work (Mangun et al., 1999; Strelko and Malik, 2002; Szymanski et al., 2004). Nevertheless, the hysteresis loops observed in the isotherms of *W* and the relatively open elbows at low pressures in the isotherms of *A*, and their oxidized derivatives, indicates the presence of some mesopores in these (combination of Type I and Type IV isotherms) materials. As explained below, this mesoporosity is also evident in the derived PSDs.

Particularly, the *A* material contains ca. 3-fold larger micropore (VN_2) and narrow micropore (VCO_2) volumes than the *W* (**Table 1**), but they show quite similar micropore size distribution. From the derived PSD graphs (**Figure 3**) it can be inferred that most micropores in *W* and *A* materials are 1.10 and 1.05 nm in diameter, respectively, together with a certain concentration of wider micropores and some mesopores, mainly in the case of *A*, ranging between 1.30 and 2.10 nm. Another difference is that *W* contains a larger concentration of different mesopores with diameters (maximum population) of 3.80, 4.60, and 6.70 nm, whereas *A* only contains some mesopores of ca. 3.40 nm. On the other hand, *ZTC* presents even a higher micropore volume with a narrower PSD, thus most pores ranging between 1.10 and 1.30 nm. Nevertheless, the large micropore volume determined by CO_2 adsorption (**Table 1**) may point out the presence of narrower zones, i.e., neck-like interconnections between successive larger cavities. This texture agrees with the 3D-arranged graphenic framework of interconnected 1.2 nm-micropores coming from the templated zeolite Y (Nishihara et al., 2009).

As shown in **Figure 3**, the shape of isotherms for the oxidized microporous materials is quite similar to that of the pristine materials. The main difference is the decrease in the volume of N_2 adsorbed. The VN_2 decrease was generally observed for the different oxidized materials, but its extent depended on the oxidation treatment, like the case of S_{BET} (**Figure 1**, in agreement with their linear relationship, **Figure 4A**). Moreover, the shape of the PSDs is also well-conserved after oxidation, although a slight shift of the main peak in the PSD toward smaller diameters (maximum at 1.00 nm) can be observed for the *W*. These features indicate that, despite the micropore volume decreases, the micropore structure is not significantly affected by the oxidative treatments (at least that of supermicropores, $0.7 < d < 2$ nm) (Mangun et al., 1999; El-Sayed and Bandosz, 2001; Shim et al., 2001; Strelko and Malik, 2002; Maroto-Valer et al., 2004). In the same line, the volume of narrower micropores ($d < 0.7$ nm), deduced from CO_2 adsorption isotherms (not shown), also decreased to a different extent after the different oxidative treatments.

Further information was deduced from the changes on both the wider and narrower micropores. **Figure 4B** depicts the VN_2/VCO_2 ratio vs. the change on specific surface area. For the *W* and *EX* materials, the VN_2/VCO_2 ratio remains practically

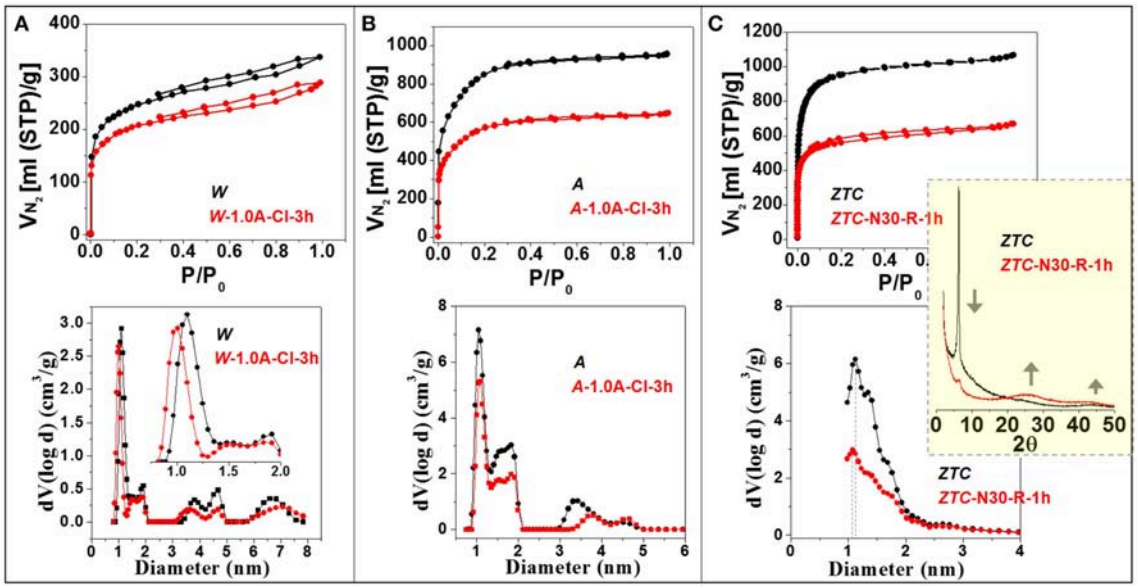

FIGURE 3 | N_2 adsorption-desorption isotherms at −196°C and the DFT-derived pore size distributions of the studied *W* **(A)**, *A* **(B),** and *ZTC* **(C)** microporous materials compared to those of a representative highly-oxidized material obtained after 3 h-treatment at 1.0 A in 2 wt% NaCl **(A,B)** or 1 h-oxidation with 30 wt% HNO_3 **(C)** at room temperature. Inlet of **(C)**: X-ray diffractograms of *ZTC* before and after oxidation.

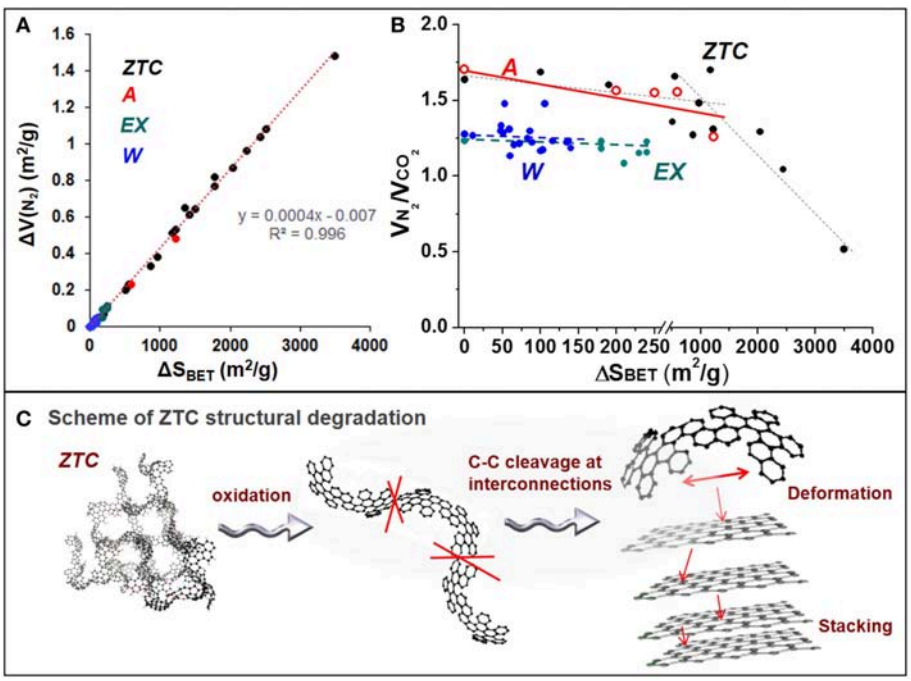

FIGURE 4 | (A) Relation between the change in specific surface area (ΔS_{BET}) and that in the micropore volume ($\Delta V(N_2)$); and **(B)** evolution of the VN_2/VCO_2 ratio with the change in specific surface area, for the differently oxidized materials prepared for this study. **(C)** Proposed mechanism for the breakdown of ZTC structure (adapted from Nishihara et al., 2009) after different oxidative treatments.

constant with the extent of S_{BET} decrease. Contrarily, in the case of *A* and *ZTC* the ratio clearly decreases, and, for the later material starts to decrease more rapidly after certain S_{BET} decrease is reached. Particularly, for the most oxidized *A* sample in this study (*A*-1.0A-Cl-3h), the VN_2/VCO_2 ratio is decreased in ca. 25%, and ca 35–70% for the most oxidized *ZTC* samples.

The similar isotherms and PSDs and nearly constant VN_2/VCO_2 ratios observed, independently of the extent of S_{BET} decrease, for the differently oxidized *W* materials suggest that the decrease in their micropore volume after oxidation may be assigned to a pore blockage by the created SOGs and/or split molecules; and/or electrostatic repulsion of N_2 probe molecules (Moreno-Castilla et al., 1995; Pradhan and Sandle, 1999; Li et al., 2003; Maroto-Valer et al., 2004; Szymanski et al., 2004; Houshmand et al., 2011). Given the constant VN_2/VCO_2 ratios, it may equally affect to wider and narrower micropores. The slight narrowing (shift in PSD) of the most abundant micropores in *W* may be in line with the proposed surface blockage, suggesting that there are N_2 molecules that may be able to pass also through the partially blocked (narrower) micropores. Because it is not destroyed, the micropore structure in these materials may be highly tough toward oxidation.

In the case of sample *A*, the large S_{BET} decrease with the oxidation degree (**Figure 1**) might be also explained by surface blockage, at least this could be similarly deduced from the results of **Figure 3**. In this case a shift in the maximum of PSD is not observed probably because these predominant micropores are narrower from the beginning (maximum at 1.05 nm). However, the decrease in the VN_2/VCO_2 ratio with the extent of oxidation found for *A* could be indicative of other phenomena, like a favored blockage and/or the destruction of wider micropores (VN_2). It has been proposed that the destruction of micropores by breakage of surface C-C bonds can result in the formation of narrower (Gil et al., 1997; El-Sayed and Bandosz, 2001) or wider (Moreno-Castilla et al., 1995, 1997; Pradhan and Sandle, 1999; El-Hendawy, 2003) ones. The much larger relative decrease in VN_2 than in VCO_2 (for this sample the relative variation of both types of micropores $\Delta VN_2/\Delta VCO_2 = 4$), and the fact that no mesopores are generated (see PSD in **Figure 3**), seem to neglect the possibility of micropore destruction. Hence, the idea of a favored blockage of wider micropores seems to gain strength. This could be explained by considering that the sample *A* contains a larger volume and proportion of pores between 1.30 and 2.10 nm than *W* (compare PSD of samples *A* and *W* in **Figure 3**). Thus, despite blocking the entrance of N_2 (of slightly bigger size than CO_2 and presenting more interactions with SOGs), some of the more-opened micropores in the sample *A* could permit the entrance of CO_2, thus, observing a decrease in the VN_2/VCO_2 ratio.

It is noteworthy to mention that other parameters, like the mesoporosity (which may affect the reaction kinetics) and the wall thickness (which can lead to the collapse of the pore structure) could be crucial in the oxidation of microporous carbons. However, the low mesoporosity and the neglected micropore destruction in the studied ACs suggest that these features may not be significant in the observed oxidative behaviors.

The variation of the textural properties of the *ZTC* upon oxidation deserves a special discussion. A detailed analysis of the effect of different oxidation treatments on *ZTC* structural properties was previously carried out (Berenguer et al., 2013a,b). **Figure 3C** shows that, besides a decrease in the adsorption of N_2, the oxidation of *ZTC* (1 h-treatment with 30 wt% HNO_3 in this example) entails a marked reduction in the intensity of its characteristic (111) X-ray diffraction peak. Considering that this peak comes from the *ZTC* regular structure derived from zeolite Y, the decreased intensity or disappearance of this peak evidence the destruction of *ZTC* structure by oxidative treatments. Another exclusive feature of this degradation is the conversion of the 3D arrangement of graphenic layers into a stacked 2D structure, as confirmed by the evolution of the two broad diffraction peaks around 25 and 45° characteristic of graphitic structures. These results suggest that the breakage of *ZTC* gives rise to graphenic fragments that can be stacked. Considering the molecular structure of *ZTC* (Nishihara et al., 2009), it is proposed that the breakage may occur by C-C cleavage at linking/interconnecting points among cavities, where the graphenic layers are thinner, as schematized in **Figure 4C**. Once fragmented, the wall cavities (the larger graphenic parts in *ZTC* structure) might be deformed into planar forms able to be stacked.

The destruction of ZTC structure at its very thin interconnecting points among graphenic layers may be the reason explaining the high fragility of this unique microporous structure. In fact, ordered mesoporous carbons (OMCs) with different wall and/or connector thickness and surface area were found differently affected by the chemical treatments (Lu et al., 2005; Vinu et al., 2007; Bazuła et al., 2008). For example, it has been reported that a soft treatment with 30 wt% H_2O_2 (Lu et al., 2005) or 53 wt% HNO_3 (Bazuła et al., 2008) at RT causes, in few minutes, structural collapse of the CMK-5 carbon framework, as deduced from XRD characterization. This high reactivity was attributed to the unique structure of this material, comprised of porous interconnected tubes of very thin carbon walls (2–3 nm) (Lu et al., 2005; Bazuła et al., 2008). Bazula et al. had to work under low HNO_3 concentrations (4.5–18 wt %) to functionalize this type of materials ($SBET_0$ = 1,389–1,846 m^2/g) (Bazuła et al., 2008). Nevertheless, the temperature was raised to 80°C to generate high oxidation degrees (ΔO = 5,300–10,250 μmolO/g) in 3 h, producing S_{BET} losses of 11–35 % associated to the structure breakdown. On the other hand, unlike tubular OMCs, rod-like CMK-3 carbons with thicker walls and connectors showed increased stability toward oxidative functionalization (Vinu et al., 2007; Bazuła et al., 2008). Such a high fragility exhibited by CMK-5 and CMK-3 OMCs resembles that of the ZTC and it was attributed to C-C cleavage on the links between adjacent tubular or rod-like structures, respectively (Lu et al., 2005; Bazuła et al., 2008). Moreover, these studies showed that the oxidation of these OMCs leads to the formation of small organic molecules and a substantial weight loss; and, whenever the whole structure is not collapsed, the N_2 isotherms of the materials were quite similar shape to those of pristine materials. All these similarities between the oxidative behavior of OMCs and that of *ZTC* support the proposed degradation mechanism and fragility reasons.

Nevertheless, the high reactivity of *ZTC* may not be exclusively related to a weak interconnectivity in its 3D microporous structure. In this sense, the preparation of a mesoporous graphene-based framework, by replication of the outer surface of Al_2O_3 nanoparticles, resulted in a continuous 3D structure

with a minimal number of edge sites (Nishihara et al., 2016). This unique material realized both a large surface area (1,940 m^2/g) and an extraordinarily high stability against oxidation. Hence, another crucial aspect involved in the reactivity and fragility of the studied ZTC may be the large number of exposed edge sites, associated to the very small graphenic layers and/or incomplete replication of the Y zeolite channels in this material (Nishihara et al., 2009), as well as its thin (single layer) wall thickness (Vinu et al., 2007; Bazuła et al., 2008).

Electrochemical Oxidation: Greater Controllability at Room Temperature

Sections Chemical Oxidation of the ACs and Chemical Oxidation of the ZTC have evidenced the limitations of chemical treatments to control the oxidation of carbon materials. **Figure 1** compiles the effects of various electrochemical oxidative treatments on the properties of the studied carbon materials. As it can be observed in this figure, the different materials exhibit variable fragility toward electrochemical oxidation, but remarkable differences can be observed when compared with chemical treatments.

The anodic treatment in NaCl at enough-high currents enables, at room temperature and in short time, to greatly enhance the oxidation degree of the ACs. Particularly, strong electrochemical oxidizing conditions, polarization at 1.0 A, introduced in 3 h a larger amount of SOGs ($\Delta O = 5{,}600$ μmolO/g for *W* and 7,150 μmolO/g for *EX*) than chemical oxidation with $(NH_4)_2S_2O_8$ in 24 h (ca. 5,000 μmolO/g for *W* and 6,700 μmolO/g for *EX*). Similar results are obtained when considered other ACs, like *A* (see for example CO_2-like TPD profiles of *A*-oxidized samples in **Figure 5A**) or other reagents (see for example CO-like TPD profiles of *W*-oxidized samples in **Figure 5B**).

It was previously demonstrated that the oxidation degree introduced on ACs by electrochemical methods can be easily adjusted, without the need of working at higher temperatures or using highly corrosive reagents, by the suitable choice of the applied current and treatment time (Berenguer et al., 2009, 2012). For example, it was found that similar oxidation degrees can be reached when the W is treated at 500 mA for 3 h than when it is oxidized at 200 mA for 5 h (Berenguer et al., 2012). The choice of these parameters may be strongly affected by the reactivity of the material, but also by its dimensions, morphology, and configuration, which may determine their effective polarization in the electrochemical cells and the contribution of direct and/or indirect oxidation mechanisms (Berenguer et al., 2013a). Furthermore, apart from current and time, the electrolyte also plays a key role. For instance, in Cl^- solutions, the anodic generation of Cl_2 and other oxidants can produce, through the indirect mechanism, larger functionalization than in NaOH or H_2SO_4. Thus, the concentration of oxidants during treatments in NaCl can be so high that the oxidizing conditions become even harder than those of chemical treatments, explaining the observed greater oxidation efficiency (**Figure 5A**). Considering all these facts, enough high anodic currents (usually above 200 mA) are necessary to cause similar or larger oxidation degrees than chemical treatments, and specifically in the case of ACs in the form of particles or cloths, which are not completely fixed to/contacting the current collector (i.e., when direct electrooxidation is less important).

Figure 5C represents the SOGs gain and S_{BET} decrease, after similar electro-oxidation treatments, as a function of micropore volume of the studied ACs. It can be observed that the extent of oxidation and induced textural changes in the studied ACs augment with their micropore volume. This trend observed for the electrochemical method agrees with those found in literature and hereby presented for the chemical oxidation of ACs. Respect to the textural properties of the ACs, the extent of S_{BET}-decrease with the oxidation degree seems to be independent of the oxidative method. Thus, the decrease in surface area may be better correlated with the extent of oxidation (**Figure 5D**), so a larger S_{BET} decrease is generally observed for the more efficient electrochemical treatments (inlet of **Figure 1**). This fact is in line with the blockage of micropores as the main mechanism affecting the textural properties of oxidized ACs (see section Analysis of Textural Changes).

In the case of the *ZTC*, both the higher reactivity and the optimum polarization that is achieved by using ZTC-pastes (see experimental section) involves the use of lower currents for electrooxidation experiments. **Figure 1** shows that under different conditions the electrochemical oxidation allows to fill the gap of properties that are difficult to obtain by uncontrolled chemical treatments. For example, short (1 h) oxidation times in NaCl at current between 2 and 20 mA (*ZTC*-Cl- curve) permit to reach lower oxidation degrees that are rapidly overcome during fast chemical treatments. On the other hand, long treatments (15–36 h) in H_2SO_4 at low current (2–5 mA) (*ZTC*-H+- curve) enable to reach similar or larger oxidation degrees to those of most oxidizing chemicals but with considerably lower S_{BET} losses. The effect on the textural properties is shown in the **Figure 5E**. The figure shows that for a similar oxidation degree of 5,100 μmolO/g, the *ZTC* oxidized at 5 mA for 15 in H_2SO_4 maintains a larger volume of micropores (larger volume of N_2 adsorbed at low pressures in the isotherm) than the sample treated with 30 wt% HNO_3 for 1 h, both at RT. This greater microporosity in the electro-oxidized sample agrees with the higher intensity of the X-ray diffraction peak related to the long-range microporous ordering from the Y zeolite template. In this sense, **Figure 5F** demonstrates that at low currents, the extent of structural degradation of ZTC (decrease in the intensity of 111-X-ray peak) can be gradually controlled just by adjusting the treatment time. Hence, the considerably higher oxidation degrees with lesser structural degradation in *ZTC* reached by extending the treatment time of low-current anodic oxidations in H_2SO_4 suggests that these are the most suitable conditions to functionalize *ZTC*. Similar conclusions were reached from the analysis of the modification of CO/CO_2 ratios after the different oxidative treatments (Berenguer et al., 2012, 2013a,b).

Apart from all these effects, to talk about the controllability of the oxidative treatments is necessary to analyze the kinetics of the process. As it can be observed in **Figure 2A**, the linear or almost linear (gradual) evolutions of the oxidation degree with time, for different microporous materials and under quite different electrochemical conditions, are indicative of a

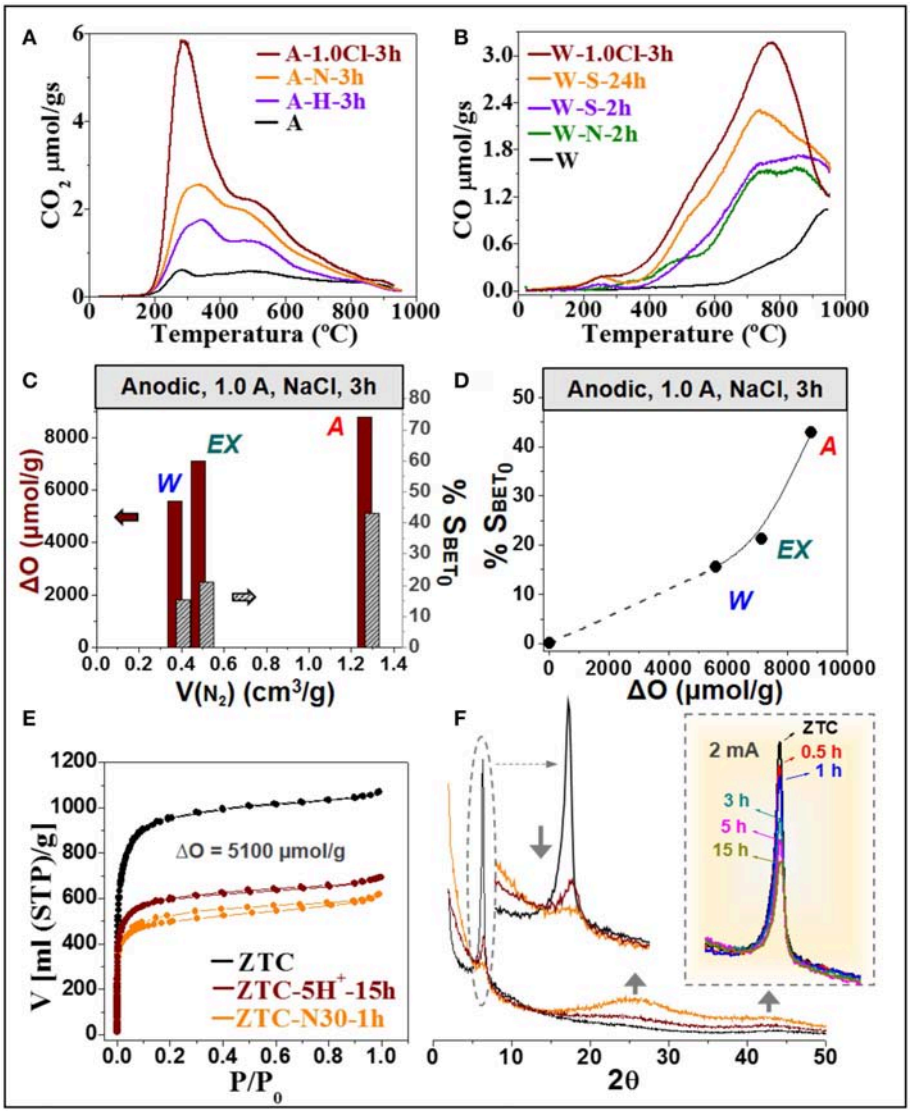

FIGURE 5 | (A,B) Comparison of CO_2-like (for *A* sample) **(A)**, and CO-like (for *W* sample) **(B)** TPD profiles of samples oxidized under different chemical or electrochemical conditions; **(C,D)** Influence of the micropore volume of the studied ACs ($V(N_2)$) in the SOGs gain (ΔO) and S_{BET} decrease ($\%SBET_0$) **(C)**, and relation between this SOGs gain and S_{BET} decrease **(D)** for a given anodic oxidation treatment (1.0 A, in NaCl, 3 h); **(E,F)** Comparison of N_2 adsorption-desorption isotherms (−196°C) **(E)**, and X-ray diffractograms **(F)** of the *ZTC* before and after chemical and electrochemical oxidation treatments with similar efficiency ($\Delta O = 5100$ µmolO/g). Inlet of **(F)** example of the high control on the structural degradation (111-X-ray characteristic peak of the *ZTC*) achieved by electrochemical oxidation in NaCl at low current densities.

controlled oxidation process. The slope of these linear trends is related to the kinetics of the oxidation processes. One of the main consequences of this behavior is that the oxidation kinetics remain approximately constant for a given set of experimental conditions (at least during the analyzed periods of time). Moreover, **Figure 2A** also shows that the modification of these electrochemical parameters (current, time, electrolyte) enables to adjust the slope of the linear trend, i.e., the rate of the oxidation reaction. By contrast, chemical oxidation treatments show all (more exaggerated in the case of the *ZTC*) a fast-initial oxidation (high slope) that rapidly slows down (low slope), i.e., a highly variable reaction rate difficult to control. For the ZTC, the consequence of this fast reaction rate is that above 40% of its initial BET surface area is lost just in few minutes, i.e., within the 1 h of chemical oxidation (**Figure 2B**). This indicates that the collapse of ZTC structure during chemical oxidation is remarkably fast.

Interestingly, even at strong electrochemical conditions for *ZTC* (*ZTC*-50 mA-Cl), where the oxidizing conditions are comparable to those of most oxidizing chemical treatments, the rate of *ZTC* electro-oxidation is slower (more controlled) than chemical oxidation with 30 wt% HNO_3 at 80°C (**Figure 2A**).

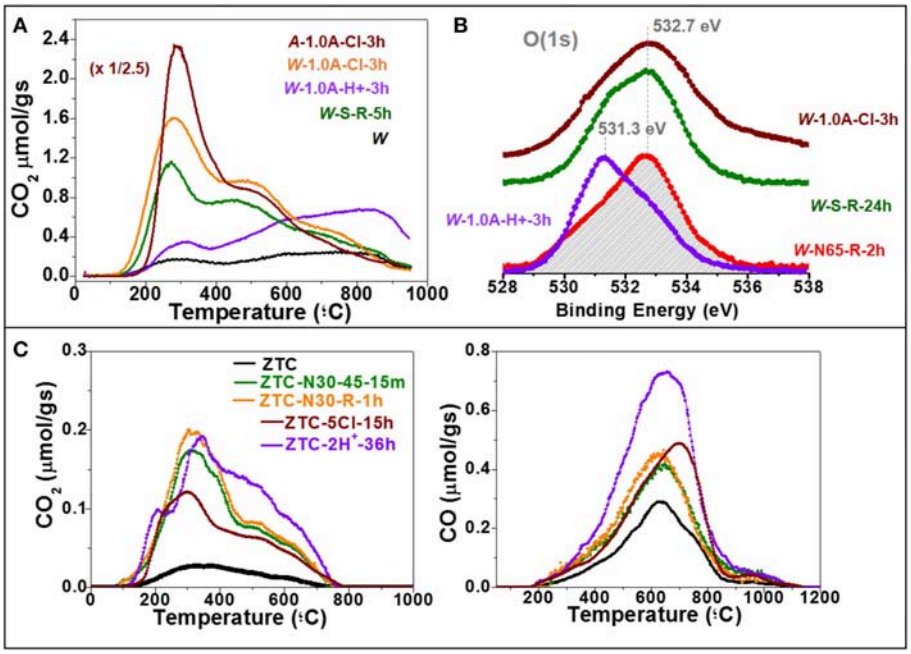

FIGURE 6 | (A) CO_2 evolution from TPD experiments for the original and the chemically- and anodically-treated *W* and *A*; **(B)** O(1s) XPS spectra of the *W* samples oxidized by different chemical and electrochemical methods; **(C)** CO_2 and CO evolution from TPD experiments for the original and the chemically- and anodically-oxidized *ZTC*.

This may be explained by considering that the concentration of reactive species is initially zero and increases in a controlled manner for the NaCl anodic treatment, whereas it is high from the beginning for any chemical oxidation (Berenguer et al., 2012). Another possible consequence of the less controllability of oxidizing conditions is that the chemical oxidation may occur rapidly on the outer surface of the carbon material, just after physical interaction, so that the introduced SOGs could hamper the diffusion of reagent into the inner pores. By contrast, in indirect anodic treatments the reactants may be homogeneously generated in any effectively-polarized micropore impregnated with NaCl. This effect could also contribute to explain the comparatively higher oxidation degrees and greater micropore blockage (during N_2 adsorption-desorption analysis) when the ACs are anodically oxidized in NaCl.

Selectivity

As exposed in the introduction section, among the spectrum of different functionalities, only some specific groups are desired for certain applications. For these applications, hence, the selectivity of the functionalization becomes important. **Figure 6A** compiles the CO_2-evolving TPD profiles of various carbon materials after different effective oxidative treatments ($\Delta O > 3{,}500$ µmolO/g). The chemical oxidation of the *W* with $(NH_4)_2S_2O_8$ (W-S-5 h) mainly increases the CO_2-evolving SOGs with lower thermal stability, i.e., those decomposing at lower temperatures. Particularly, the profile is characterized by two peaks, the most intense with maximum at 275°C and a wider overlapped contribution with maximum at 450°C. These evolutions have been assigned to carboxylic- and lactone-like groups, respectively, on carbon surfaces (Figueiredo et al., 1999). As it can be seen in the figure, the electrochemical oxidation of the GAC in NaCl produces exactly the same CO_2-TPD profile, and the same was observed also for the chemical treatment with 65 wt% HNO_3 (figure not shown). Furthermore, exactly the same CO_2-TPD profiles were also obtained for *A* after electrochemical oxidation in NaCl (**Figure 6A**) and chemical treatments with 65 wt% HNO_3 or H_2O_2 (figures not shown), as well as many other ACs in literature (Otake and Jenkins, 1993; Román-Martínez et al., 1993; Moreno-Castilla et al., 1995, 1997; De la Puente et al., 1997; Figueiredo et al., 1999; Pradhan and Sandle, 1999; Strelko and Malik, 2002; Li et al., 2003; Bleda-Martínez et al., 2006). In particular, different studies on the chemical oxidation of ACs point out that, compared to HNO_3, $(NH_4)_2S_2O_8$ favors the generation of carboxylic groups (Moreno-Castilla et al., 1995, 1997; Vinu et al., 2007). On the other hand, quite similar CO-TPD profiles, with a general increase in the whole temperature range and a shift of the maximum toward lower temperatures, were also obtained for the different materials treated under these conditions.

The results observed by TPD were confirmed by XPS. **Figure 6B** shows the O(1s) XPS spectra of the *W* samples oxidized in 65 wt% HNO_3, $(NH_4)_2S_2O_8$, or anodically in NaCl. As observed, the spectra of the three oxidized samples are centered at the same binding energy (532.7 eV). This suggests that the same type of oxygen bonds prevail in these samples. All these results indicate that, though different in concentration,

the SOGs introduced by the chemical reagents and the anodic treatment in NaCl are of the same nature, stressing the lack of selectivity by these oxidative treatments.

By stark contrast, the GAC samples electrochemically oxidized in H_2SO_4 and NaOH electrolytes, where the electrochemical oxidation may be governed by direct polarization, displayed TPD profiles and XPS spectra with different shape. For example, the anodic oxidation in H_2SO_4 leads to an increase in the most stable CO_2-evolving SOGs (**Figure 6A**) and, accordingly, a remarkable shift in the O(1s) XPS binding energy toward lower binding energies (centered at 531.3 eV) (**Figure 6B**). Hence, by changing the electrolyte the electrochemical oxidation method enables to reach a different selectivity.

In the case of highly-reactive *ZTC*, the oxidation by chemicals or anodically in NaCl at high currents produced a general increase in the whole TPDs, confirming the lack of selectivity. As it can be observed in **Figure 6C**, the relative increase in CO_2-evolving groups was more significant after chemical oxidation ($CO/CO_2 = 2.80–2.90$) than after electro-oxidations at softer conditions in NaCl or H_2SO_4 ($CO/CO_2 = 3.60–5.60$), the later exhibiting a remarkably higher relative increase in CO-evolving groups (sample *ZTC*-2H+-36 h). In addition, this sample treated in H_2SO_4 electrolyte shows a relative larger generation of the most stable CO_2-evolving groups, thus bringing a different selectivity.

The remarkable increase in the CO-profile after electrochemical oxidation in H_2SO_4 was associated to a large generation of quinone-like SOGs (Itoi et al., 2014; Nueangnoraj et al., 2015). Indeed, by controlling the parameters of the electrochemical method, oxidized *ZTC*-derived carbons with ca. 80–90% selectivity toward quinone-like SOGs generation have been obtained. Since such a significant selectivity cannot be achieved in ACs by using similar electrochemical methods, the nature of the material may play also a crucial role. Accordingly, it is hypothesized that the characteristic regular structure of *ZTC* may somehow influence in the incorporation of quinones.

CONCLUSIONS

The results presented in this work clearly show that the efficiency, selectivity and effects on microporous texture associated to the oxidative functionalization depends on the nature of the carbon material and the oxidation method. Independently of the oxidative method, the incorporation of SOGs on ACs decreases the specific surface area by blocking and/or constricting the entry of micropores, while it causes the collapse of the ordered microporous framework of the ZTC. The kinetic analysis indicates that this oxidation reaction for chemical treatments is quite fast and variable, restricting the control of the process. By contrast, by using proper electrolytes, low current and/or extending the treatment time, the electrochemical oxidative method permits at room temperature not only a greater control of the oxidation degree of the microporous carbons, but also to minimize the degradation of the fragile microporous structure of ZTC. Moreover, the electrochemical oxidation enables different selectivity to that provided by chemical methods.

DATA AVAILABILITY

All datasets generated for this study are included in the manuscript.

AUTHOR CONTRIBUTIONS

RB performed the different oxidative experiments, materials characterization and devised the subject of the manuscript. EM greatly contributed to data analyses, results discussion and manuscript preparation.

ACKNOWLEDGMENTS

Financial support from the Spanish Ministerio de Economía y Competitividad and FEDER funds (RYC-2017-23618, MAT2016-76595-R) is gratefully acknowledged.

REFERENCES

Álvarez, P. M., García-Araya, J. F., Beltrán, F. J., Masa, F. J., and Medina, F. (2005). Ozonation of activated carbons: effect on the adsorption of selected phenolic compounds from aqueous solutions. *J. Colloid. Interf. Sci.* 283, 503–512. doi: 10.1016/j.jcis.2004.09.014

Arenillas, A., Rubiera, F., Pevida, C., Ania, C. O., and Pis, J. J. (2004). Relationship between structure and reactivity of carbonaceous materials. *J. Therm. Anal. Cal.* 76, 593–602. doi: 10.1023/B:JTAN.0000028038.34976.83

Bazuła, P. A., Lu, A. H., Nitz, J. J., and Schüth, F. (2008). Surface and pore structure modification of ordered mesoporous carbons via a chemical oxidation approach. *Micropor. Mesopor. Mater.* 108, 266–275. doi: 10.1016/j.micromeso.2007.04.008

Beguin, F., and Frackowiak, E. (2009). *Carbons for Electrochemical Energy Storage and Conversion Systems*. Boca Raton, FL: CRC Press.

Berenguer, R., Marco-Lozar, J. P., Quijada, C., Cazorla-Amorós, D., and Morallón, E. (2009). Effect of electrochemical treatments on the surface chemistry of activated carbon. *Carbon* 47, 1018–1027. doi: 10.1016/j.carbon.2008.12.022

Berenguer, R., Marco-Lozar, J. P., Quijada, C., Cazorla-Amorós, D., and Morallón, E. (2012). A comparison between oxidation of activated carbon by electrochemical and chemical treatments. *Carbon* 50, 1123–1134. doi: 10.1016/j.carbon.2011.10.025

Berenguer, R., Morallón, E., Cazorla-Amorós, D., Nishihara, H., Itoi, H., Ishii, T., et al. (2013b). Tailoring the surface chemistry of zeolite templated carbon by electrochemical methods. *Boletin Del Grupo Espanol Del Carbon* 28, 10–14. Available online at: http://www.gecarbon.org/boletines/articulos/boletinGEC_028-A2.pdf

Berenguer, R., Nishihara, H., Itoi, H., Ishii, T., Morallón, E., Cazorla-Amorós, D., et al. (2013a). Electrochemical generation of O-containing groups in an ordered microporous zeolite-templated carbon. *Carbon* 54, 94–104. doi: 10.1016/j.carbon.2012.11.007

Bleda-Martínez, M. J., Lozano-Castelló, D., Morallón, E., Cazorla-Amorós, D., and Linares-Solano, A. (2006). Chemical and electrochemical characterization of porous carbon materials. *Carbon* 44 2642–2651. doi: 10.1016/j.carbon.2006.04.017

Bottani, E., and Tascón, J. M. D. (2008). *Adsorption by Carbons*. Amsterdam: Elsevier.

Boudou, J. P., Martínez-Alonso, A., and Tascón, J. M. D. (2000). Introduction of acidic groups at the surface of activated carbon by microwave-induced oxygen

plasma at low pressure. *Carbon* 38, 1021–1029. doi: 10.1016/S0008-6223(99)00209-2

Daud, W. M. A. W., and Houshamnd, A. H. (2010). Textural characteristics, surface chemistry and oxidation of activated carbon. *J. Nat. Gas Chem*. 19, 267–279. doi: 10.1016/S1003-9953(09)60066-9

De la Puente, G., Pis, J. J., Menéndez, J. A., and Grange, P. (1997). Thermal stability of oxygenated functions in activated carbons. *J. Anal. Appl. Pyrolysis* 43, 125–138. doi: 10.1016/S0165-2370(97)00060-0

El-Hendawy, A. N. A. (2003). Influence of HNO_3 oxidation on the structure and adsorptive properties of corncob-based activated carbon. *Carbon* 41, 713–722. doi: 10.1016/S0008-6223(03)00029-0

El-Sayed, Y., and Bandosz, T. J. (2001). A study of acetaldehyde adsorption on ACs. *J. Colloid Interface Sci*. 242, 44–51. doi: 10.1006/jcis.2001.7772

Figueiredo, J. L., Pereira, M. F. R., Freitas, M. M. A., and Órfão, J. J. M. (1999). Modification of the surface chemistry of activated carbons. *Carbon* 37, 1379–1389. doi: 10.1016/S0008-6223(98)00333-9

García, A. B., Martínez-Alonso, A., León y León, C. A., and Tascón, J. M. D. (1998). Modification of the surface properties of an activated carbon by oxygen plasma treatment. *Fuel* 77, 61–624. doi: 10.1016/S0016-2361(97)00111-7

Gil, A., de la Puente, G., and Grange, P. (1997). Evidence of textural modifications of an activated carbon on liquid-phase oxidation treatments. *Microporous Mater*. 12, 51–61. doi: 10.1016/S0927-6513(97)00057-6

Gómez-Serrano, V., Álvarez, P. M., Jaramillo, J., and Beltrán, F. J. (2002). Formation of oxygen structures by ozonation of carbonaceous materials prepared from cherry stones. II. kinetic study. *Carbon* 40, 523–529. doi: 10.1016/S0008-6223(01)00142-7

González-Gaitán, C., Ruíz-Rosas, R., Morallón, E., and Cazorla-Amorós, D. (2015). "Electrochemical methods to functionalize carbon materials", in *Chemical Functionalization of Carbon Nanomaterials: Chemistry and Applications*, eds V. K. Thakur and M. K. Thakur (Boca Raton, FL: CRC Press), 231–262.

Houshmand, A., Daud, W. M. A. W., and Shafeeyan, M. S. (2011). Tailoring the surface chemistry of activated carbon by nitric acid: study using response surface method. *Bull. Chem. Soc. Jpn*. 84, 1251–1260. doi: 10.1246/bcsj.20110145

Itoi, H., Nishihara, H., Ishii, T., Nueangnoraj, K., Berenguer, R., and Kyotani, T. (2014). Large pseudocapacitance in quinone-functionalized zeolite templated carbon. *Bull. Chem. Soc. Jpn*. 87, 250–257. doi: 10.1246/bcsj.20130292

Jaramillo, J., Álvarez, P. M., and Gómez-Serrano, V. (2010). Oxidation of activated carbon by dry and wet methods surface chemistry and textural modifications. *Fuel Process. Technol*. 91, 1768–1775. doi: 10.1016/j.fuproc.2010.07.018

Kinoshita, K. (1988). *Carbon: Electrochemical and Physicochemical Properties*. New York, NY: Wiley.

Li, N., Ma, X., Zha, Q., Kim, K., Chen, Y., and Song, C. (2011). Maximizing the number of oxygen-containing functional groups on activated carbon by using ammonium persulfate and improving the temperature-programmed desorption characterization of carbon surface chemistry. *Carbon* 49, 5002–5013. doi: 10.1016/j.carbon.2011.07.015

Li, Y. H., Lee, C. W., and Gullett, B. K. (2003). Importance of activated carbon's oxygen surface functional groups on elemental mercury adsorption. *Fuel* 82, 451–457. doi: 10.1016/S0016-2361(02)00307-1

Linares-Solano, A., Lozano-Castelló, D., Lillo-Ródenas, M. A., and Cazorla-Amorós, D. (2008). "Carbon activation by alkaline hydroxides preparation and reactions, porosity and performance," in *Chemistry and Physics of Carbon, Vol. 30*, ed L. R. Radovic (Boca Raton, FL: CRC Press), 1–62.

Lozano-Castelló, D., Lillo-Ródenas, M. A., Cazorla-Amorós, D., and Linares-Solano, A. (2001). Preparation of activated carbons from Spanish anthracite. I. activation by KOH. *Carbon* 39, 741–749. doi: 10.1016/S0008-6223(00)00185-8

Lozano-Castelló, D., Suárez-García, F., Cazorla-Amorós, D., and Linares-Solano, A. (2009). "Porous texture of carbons," in *Carbons for Electrochemical Energy Storage and Conversion Systems*, eds F. Beguin and E. Frackowiak (Boca Raton, FL: CRC Press), 115–162.

Lu, A. H., Li, W. C., Muratova, N., Spliethoff, B., and Schüth, F. (2005). Evidence for C–C bond cleavage by H_2O_2 in a mesoporous CMK-5 type carbon at room temperature. *Chem. Commun*. 41, 5184–5186. doi: 10.1039/b509300g

Ma, Z. X., Kyotani, T., and Tomita, A. (2000). Preparation of a high surface area microporous carbon having the structural regularity of Y zeolite. *Chem. Commun*. 2, 2365–2366. doi: 10.1039/b006295m

Mangun, C. L., Benak, K. R., Daley, M. A., and Economy, J. (1999). Oxidation of activated carbon fibers: effect on pore size, surface chemistry, and adsorption properties. *Chem. Mater*. 11, 3476–3483. doi: 10.1021/cm990123m

Maroto-Valer, M. M., Dranca, I., Lupascu, T., and Nastas, R. (2004). Effect of adsorbate polarity on thermodesorption profiles from oxidized and metal-impregnated activated carbons. *Carbon* 42, 2655–2659. doi: 10.1016/j.carbon.2004.06.007

Molina-Sabio, M., and Rodríguez-Reinoso, F. (2004). Role of chemical activation in the development of carbon porosity. colloids surf. a physicochem. *Eng. Asp*. 241, 15–25. doi: 10.1016/j.colsurfa.2004.04.007

Moreno-Castilla, C., Carrasco-Marín, F., and Mueden, A. (1997). The creation of acid carbon surfaces by treatment with $(NH_4)_2S_2O_8$. *Carbon* 35, 1619–1626. doi: 10.1016/S0008-6223(97)00121-8

Moreno-Castilla, C., Carrasco-Martín, F., Maldonado-Hodar, F. J., and Rivera-Utrilla, J. (1998). Effects of non-oxidant and oxidant acid treatments on the surface properties of an activated carbon with very low ash content. *Carbon* 36, 145–151. doi: 10.1016/S0008-6223(97)00171-1

Moreno-Castilla, C., Ferro-García, M. A., Joly, J. P., Bautista-Toledo, I., Carrasco-Marín, F., and Rivera-Utrilla, J. (1995). Activated carbon Surface modifications by nitric acid, hydrogen peroxide, and ammonium peroxydisulfate treatments. *Langmuir* 11, 4386–4392. doi: 10.1021/la00011a035

Moreno-Castilla, C., López-Ramón, M. V., and Carrasco-Marín, F. (2000). Changes in surface chemistry of activated carbons by wet oxidation. *Carbon* 38, 1995–2001. doi: 10.1016/S0008-6223(00)00048-8

Nishihara, H., and Kyotani, T. (2012). Templated nanocarbons for energy storage. *Adv. Mater*. 24, 4473–4498. doi: 10.1002/adma.201201715

Nishihara, H., and Kyotani, T. (2018). Zeolite-templated carbons – three-dimensional microporous graphene frameworks. *Chem. Commun*. 54, 5648–5673. doi: 10.1039/C8CC01932K

Nishihara, H., Simura, T., Kobayashi, S., Nomura, K., Berenguer, R., Ito, M., et al. (2016). Stability oxidation-resistant and elastic mesoporous carbon with single-layer graphene walls. *Adv. Funct. Mater*. 26, 6418–6427. doi: 10.1002/adfm.201602459

Nishihara, H., Yang, Q. H., Hou, P. X., Unno, M., Yamauchi, S., Saito, R., et al. (2009). A possible buckybowl-like structure of zeolite templated carbon. *Carbon* 47, 1220–1230. doi: 10.1016/j.carbon.2008.12.040

Nueangnoraj, K., Nishihara, H., Ishii, T., Yamamoto, N., Itoi, H., Berenguer, R., et al. (2015). Pseudocapacitance of zeolite-templated carbon in organic electrolytes. *Energy Storage Mater*. 1, 35–41. doi: 10.1016/j.ensm.2015.08.003

Otake, Y., and Jenkins, R. G. (1993). Characterization of oxygen-containing surface complexes created on a microporous carbon by air and nitric acid treatment. *Carbon* 31, 109–121. doi: 10.1016/0008-6223(93)90163-5

Pradhan, B. K., and Sandle, N. K. (1999). Effect of different oxidizing agent treatments on the surface properties of activated carbons. *Carbon* 37 1323–1332. doi: 10.1016/S0008-6223(98)00328-5

Radovic, L. R., Moreno-Castilla, C., and Rivera-Utrilla, J. (2000). "Carbon materials as adsorbents in aqueous solutions," in *Chemistry and Physics of Carbon, Vol. 27*, ed L. R. Radovic (Boca Raton, FL: CRC Press), 227–405.

Rivera-Utrilla, J., Sánchez-Polo, M., Gómez-Serrano, V., Álvarez, P. M., Alvim-Ferraz, M. C. M., and Dias, J. M. (2011). Activated carbon modifications to enhance its water treatment applications. an overview. *J. Haz. Mater*. 187, 1–23. doi: 10.1016/j.jhazmat.2011.01.033

Rodriguez-Reinoso, F. (1998). The role of carbon materials in heterogeneous catalysis. *Carbon* 36, 159–175. doi: 10.1016/S0008-6223(97)00173-5

Rodríguez-Reinoso, F., and Molina-Sabio, M. (1998). Textural and chemical characterization of microporous carbons. *Adv. Colloid Interface Sci*. 76–77, 271–294. doi: 10.1016/S0001-8686(98)00049-9

Román-Martínez, M. C., Cazorla-Amorós, D., Linares-Solano, A., and Salinas-Martínez de Lecea, C. (1993). TPD and TPR characterization of carbonaceous supports and Pt/C catalysts. *Carbon* 31, 895–902. doi: 10.1016/0008-6223(93)90190-L

Serp, P., and Figueiredo, J. L. (2009). *Carbon Materials for Catalysis*. Hoboken, NJ: John Wiley & Sons, Inc.

Shen, W., Li, Z., and Liu, Y. (2008). Surface chemical functional groups modification of porous carbon. *Recent Pat. Chem. Eng*. 1, 27–40. doi: 10.2174/2211334710801010027

Shim, J. W., Park, S. J., and Ryu,. S. K. (2001). Effect of modification with HNO_3 and NaOH on metal adsorption by pitch-based activated carbon fibers. *Carbon* 39, 1635–1642. doi: 10.1016/S0008-6223(00)00290-6

Strelko, V., and Malik, D. J. (2002). Characterization and metal sorptive properties of oxidized active carbon. *J. Colloid Interface Sci.* 250, 213–220. doi: 10.1006/jcis.2002.8313

Szymanski, G. S., Grzybek, T., and Papp, H. (2004). Influence of nitrogen surface functionalities on the catalytic activity of activated carbon in low temperature SCR of NOx with NH_3. *Catal. Today* 90, 51–59. doi: 10.1016/j.cattod.2004.04.008

Tabti, Z., Berenguer, R., Ruiz-Rosas, R., Quijada, C., Morallón, E., and Cazorla-Amorós, D. (2013). Electrooxidation methods to produce pseudocapacitance-containing porous carbons. *Electrochemistry* 81, 833–839. doi: 10.5796/electrochemistry.81.833

Tascón, J. M. D. (2012). *Novel Carbon Adsorbents*. Amsterdam: Elsevier.

Ternero-Hidalgo, J. J., Rosas, J. M., Palomo, J., Valero-Romero, M. J., Rodríguez-Mirasol, J., and Cordero, T. (2016). Functionalization of activated carbons by HNO_3 treatment: Influence of phosphorus surface groups. *Carbon* 101, 409–419. doi: 10.1016/j.carbon.2016.02.015

Thakur, V. K., and Thakur, M. K. (2016). *Chemical Functionalization of Carbon Nanomaterials: Chemistry and Applications*. Boca Raton, FL: CRC Press.

Vinu, A., Hossian, K. Z., Srinivasu, P., Miyahara, M., Anandan, S., Gokulakrishnan, N., et al. (2007). Carboxy-mesoporous carbon and its excellent adsorption capability for proteins. *J. Mater. Chem.* 17, 1819–1825. doi: 10.1039/b613899c

Vujković, M., Bajuk-Bogdanović, D., Matović L., Stojmenović, M., and Mentus, S. (2018). Mild electrochemical oxidation of zeolite templated carbon in acidic solutions, as a way to boost its charge storage properties in alkaline solutions. *Carbon* 138, 369–378. doi: 10.1016/j.carbon.2018.07.053

Zakaria, T. (2014). *Electroadsorción de Plomo Sobre Carbones Activados en Diferentes Conformaciones: Modificación de la Química Superficial por Métodos Electroquímicos* (dissertation thesis). University of Alicante. Available online at: http://hdl.handle.net/10045/41922

Conflict of Interest Statement: The authors declare that the research was conducted in the absence of any commercial or financial relationships that could be construed as a potential conflict of interest.

frontiers in Materials

REVIEW
published: 24 May 2019
doi: 10.3389/fmats.2019.00114

Controlling the Composition, Morphology, Porosity, and Surface Chemistry of Lignin-Based Electrospun Carbon Materials

Francisco J. García-Mateos, Ramiro Ruiz-Rosas, Juana M. Rosas, José Rodríguez-Mirasol and Tomás Cordero*

Departamento de Ingeniería Química, Facultad de Ciencias, Universidad de Málaga, Andalucía Tech, Málaga, Spain

Electrospinning is a suitable top-down technique for the preparation of polymeric fibers using high voltage electrical fields and solutions of the selected polymer of adequate viscosity and conductivity. The versatility of electrospinning allows accurate control of the morphology and composition of the fibers by a wide combination of operating conditions and small modifications of the spinneret and collector. Alcell lignin, which is extracted from lignocellulosic biomass using organic solvents through Organosolv process, is readily solved in ethanol, producing a solution that matches the requirements of the electrospinning process. This review summarizes the vast collection of carbon materials that can be obtained by processing lignin using electrohydrodynamic forces. The coaxial and triaxial electrospinning setups allow for obtaining fibers with two or more components hierchically arranged, the use of these configurations along with a carefully setting of the operating conditions (distance between needle and collector, voltage, flow rate,…) and the solution properties (conductivity, viscosity,…) facilitates the conformation of lignin into spheres, beaded fibers, straight fibers and fused meshes. All these morphologies can be implemented with solid or hollow bodies (i.e., enabling the production of tubes and hollow spheres) by using a sacrificial templating agent. Phosphoric acid can also be added in small amounts to the lignin solution, shortening the thermostabilization time of the fibers. The porosity of the phosphorus containing carbon fibers can be modified in the last stage of the preparation of carbon fibers by controlled gasification process, owing to the extended oxidation resistance of the P-doped fibers. Fibrillar carbon catalysts can be also obtained by one-pot preparation method, only solving small quantities of metallic salts in the lignin solution. All these carbon materials were successfully tested in different applications such as heterogeneous catalysis, energy storage and environmental protection, confirming that electrospinning is a powerful tool for maximizing the value of lignin as carbon precursor.

Keywords: lignin, electrospinning, H_3PO_4, fiber morphology, fast stabilization, one-post synthesis catalysts, supercapacitors

OPEN ACCESS

Edited by:
Wei Lv,
Tsinghua University, China

Reviewed by:
Huan Li,
University of Adelaide, Australia
Yang Li,
Tianjin University, China

****Correspondence:***
Francisco J. García-Mateos
garciamateos@uma.es

Specialty section:
This article was submitted to Carbon-Based Materials, a section of the journal Frontiers in Materials

Received: *15 February 2019*
Accepted: *07 May 2019*
Published: *24 May 2019*

Citation:
García-Mateos FJ, Ruiz-Rosas R, Rosas JM, Rodríguez-Mirasol J and Cordero T (2019) Controlling the Composition, Morphology, Porosity, and Surface Chemistry of Lignin-Based Electrospun Carbon Materials. Front. Mater. 6:114. doi: 10.3389/fmats.2019.00114

INTRODUCTION

Lignin is one of the three main building blocks of lignocellulosic materials. The lignin structure depends on the feedstock, with softwood, hardwood and other vegetation having different lignin contents, and characteristics. In general, it can be supposed to be a random three-dimensional polymer of phenylpropane units linked together, reason why it is also considered the most abundant source of renewable aromatics on Earth. Industrially, lignin can be produced from different processes, obtaining the corresponding Kraft lignin (KL), Soda lignin, Lignosulphonates (LS), Organosolv lignins (OS), Steam-explosion lignin, and enzymatic hydrolysis lignin (EHL). These lignins also present different chemical structures and properties.

Large scale production of lignin is mainly associated to pulp and paper industry and bioethanol production in wood-to-ethanol biorefineries as by-product. In this context, only around 40% of the generated lignin is needed to cover the internal energy demand of a biorefinery. Apart from this combustion, lignin can be directly used as dispersant, emulsifier, binder, animal feed, and utilized as raw material for the production of synthetic vainillin, but according to Global Lignin Products Market 2017–2021 report "The latest trend gaining momentum in the market is increasing application of lignin in newer applications."[1] In this sense, lignocellulosic biorefineries are looking for opportunities to valorize the lignin by-products in high-value products instead of direct energy production to improve cost-competitiveness.

An important drawback to diversify the application of lignin at an industrial scale is related to the fact that most types of lignin are only soluble in water at alkaline pH and that many of the process to obtain lignin use very harsh conditions. With this regard, the Alcell® pulping process (the most well-known process in the organosolv lignin category) produces lignin soluble in non-toxic organic solvents, such as ethanol, with very low amount of impurities, and more environmentally friendly than others. These properties along with the carbon-rich and high aromatic content of lignin become it a very interesting raw precursor for the preparation of carbon materials with high value added (Rosas et al., 2014).

Among the different options, the preparation of carbon fibers (CFs) from lignin can be considered a very attractive option (Leitten et al., 2002; Frank et al., 2014; Ragauskas et al., 2014; Fang and Smith, 2016). CFs are materials, typically derived from conventional fossil precursors (PAN and pitches), with different advantages such as their low density with a very high strength to weight ratio, high tensile strength, low thermal expansion, high electrical conductivity… Nevertheless, the high manufacture cost, scarcity and growing demand require the look for others raw materials, preferentially less expensive, more abundant and sustainable than PAN and pitches. Specifically, the leading country based on carbon fiber production capacity in 2018 was USA with 45,300 metric tons (MT), followed by Japan, accounting for almost half of the production of USA[2]. However, the high worldwide production rate of carbon fibers is not expected to be enough to meet the demand in 2020, with an estimation of 150,200 MT vs. 129,965 of manufacturing[3]. In this context, the use of lignin as renovable precursor would reduce the manufacture cost of CFs and would also provide an alternative route for lignin valorization (Leitten et al., 2002; Frank et al., 2014; Ragauskas et al., 2014; Fang and Smith, 2016). Specifically, our research group has extensively studied the use of Alcell lignin for this purpose (Lallave et al., 2007; Ruiz-Rosas et al., 2010; Berenguer et al., 2016b; García-Mateos et al., 2017, 2018a).

Generally, the production of lignin CFs implies different steps: (i) purification of lignin and preparation of the spinning solution (if necessary), the low presence of impurities in Alcell lignin and the total solubility in ethanol facilitates this step; (ii) spinning into lignin fibers, which can be carried out by wet-, dry -(Fukuoka, 1969), melt- (Mikawa, 1970), and electrospinning methods (Lallave et al., 2007; Ruiz-Rosas et al., 2010); (iii) oxidative thermostabilization of as-spun lignin fibers to avoid their fusion in subsequent steps, this is one of the key aspects of the manufacture due to the large time required in this step; (iv) carbonization treatment to generate the lignin-based CFs; and finally (v) further treatments in order to enhance their properties for structural and/or functional applications.

Although dry- and wet spinning methods were the firsts used to prepare lignin-based CFs (mid-60s), melt spinning has been the most studied. This last method is based on the extrusion of a fusible lignin, obtaining very homogeneous carbon fibers. The main drawback of melt spinning arises from the very specific lignin properties needed in this method to avoid cross-linking during extrusion, at high stabilization rates. The achievement of these suitable properties is the main objective of the latest research, mainly focused on purification treatments, plasticization with additives, and/or chemically modifications of isolated lignin (Rosas et al., 2014).

Electrospinning is a simple and versatile technique which allows for obtaining lignin-based carbon fibers, using high voltage electrical fields and solutions of the selected polymer of adequate viscosity and conductivity. Most lignin solutions have shown low spinnability, requiring the addition of a plasticizing additive to prevent bead formation and/or electrospray (Dallmeyer et al., 2010, 2014a; Hosseinaei and Baker, 2012). However, our research group has been able to produce lignin based CFs without the incorporation of any spinning-assisted agent, at room temperature and without chemical modifications, reducing the manufacture complexity, time and costs (Lallave et al., 2007; Ruiz-Rosas et al., 2010; Berenguer et al., 2016b; García-Mateos et al., 2017, 2018a). The size of the fibers obtained by this technique ranges from 100 nm to a few microns, what fills the gap between nanofibers prepared by chemical vapor deposition and fibers prepared by conventional extrusion methods. The versatility of electrospinning allows an accurate

[1]https://www.researchandmarkets.com/reports/4403355/global-lignin-products-market-2017-2021

[2]https://www.statista.com/statistics/380549/leading-countries-by-carbon-fiber-production-capacity/

[3]https://www.compositesworld.com/articles/supply-and-demand-advanced-fibers-2016

control of the morphology and composition of the fibers, from which it is possible to obtain pure or doped lignin derived CFs with different heteroatoms, only by adding the corresponding heteroatom to the lignin solution (in this case in ethanol); solid and/or hollow lignin derived CFs, and even ceramic/lignin composite fibers, only with a few modifications of the configuration set-up (coaxial and triaxial configurations).

The main objective of this work consists of demonstrating the different possibilities of carbon materials that can be obtained by processing lignin using electrohydrodynamic forces. The basic of electrospinning are described, as well as the most relevant parameters controlling the morphology and size of the electrospun fibers. In this sense, coaxial, and triaxial electrospinning configurations are highlighted as versatile ways for controlling the structure and composition of electrospun fibers. A review of the contribution to the preparation of lignin fibers/tubes by electrospinning made by our research group is presented, showing examples from our research about the available possibilities for controlling the structure, porosity, surface chemistry, and composition of electrospun carbon fibers. Lastly, we analyze the addition of precursors and porosity promoters in the lignin solution, what allows one-pot synthesis of phosphorus and/or metal-containing carbon fibers. Some applications of electrospun carbon fibers in the field of catalysis, adsorption, and energy storage are also reported as evidences of the advantages of combining lignin, a green carbon precursor, with electrospinning, a versatile top-down nanofiber production method.

ELECTROSPINNING AS A TOOL TO PRODUCE POLYMER, CARBON AND INORGANIC NANOFIBERS

Electrospinning is one of the most suitable techniques for the preparation of continuous polymeric fibers with diameters sizing from a few microns down to a few tens of nanometers. There are different reviews in the recent literature that summarize the main principles of this technique (Huang et al., 2003; Cavaliere et al., 2011; Inagaki et al., 2012; Kenry and Lim, 2017; Xue et al., 2017). Briefly, a highly concentrated solution of the polymer to be spun is prepared using a volatile solvent. This solution is pumped through the spinneret at a fixed flow rate. The spinneret is connected to a high voltage power supply (in the range of kV). A grounded metallic collector is placed at short distance (a few tens of centimeters) from the spinneret. Under the application of a high electric field, the solution exiting the spinneret becomes charged. The interaction between electrohydrodynamic forces (namely the surface tension and the electrostatic repulsion) deforms the droplet at the tip of the spinneret into a conical shape called the Taylor cone. When the applied voltage exceeds the critical value, repulsive forces overcome the surface tension and a micrometric jet of the polymeric solution is ejected from the tip of the Taylor cone and flies toward the grounded collector. The repulsive forces propelling the jet can also generate a whipping or bending instability, enlarging the trajectory from the spinneret to the collector and stretching the jet diameter down to the nanometer scale. Eventually, the liquid jet can break up to form a spray of charged microdrops, in what is known as electrospray (Cloupeau and Prunet-Foch, 1994), a technique with highly interesting applications such as thin film production or drug encapsulation, among many others. Given that the repulsive forces are not strong enough to break the jet in short times, and due to the solvent evaporates at fast rate (owing to a high volatility and a large specific surface area of the jet), solid fibers are formed during the fly deposited at the top of the collector surface. As a result, non-woven mats of nanoscale fibers are formed on the collector. It must be highlighted that certain polymer fibers can be heat treated and transformed into electrospun carbon nanofibers (Inagaki et al., 2012). Moreover, inorganic nanofibers can be also attained by using partially gelated solutions from inorganic alkoxides or by mixing the salt precursors into a polymer solution that would be latter removed by calcining the fiber (Xue et al., 2017).

Parameters Governing the Size and Morphology of Electrospun Fibers

It is important to note that the size of the fibers obtained by electrospinning is independent of the diameter of the nozzle, and it is instead controlled by electrospinning parameters (Gañán-Calvo et al., 1997). In fact, there are parameters related to the solution properties, such as the polymer concentration, the electrical conductivity, the viscosity and the surface tension of the solution, which must be set within a range of adequate values for enabling the electrospinning of the polymer solution (Hohman et al., 2001). Once the spinnable solution is obtained, some other process parameters can be tuned to modify the size and morphology of the nanofibers, like solution flow rate, voltage, nozzle to collector distance, humidity, and temperature. In principle, size of the fiber decreases with polymer concentration (Beachley and Wen, 2009; Inagaki et al., 2012). For polymers showing low conductivity, the electrical conductivity of the solution is usually dictated by the conductivity of the solvent; in such cases, the size of the electrospun fibers decrease with conductivity (Tan et al., 2005). Additives that increase the solution conductivity, like salts or conductive polymers, can be also included and have been proven to decrease fiber size (Son et al., 2004). Other parameters such as feed rate and voltage seem to drive the fiber morphology rather than the fiber diameter (Deitzel et al., 2001), while surface tension and viscosity are related to the polymer concentration, what hinders their actual impact into the fiber diameter. For instance, high viscosity values are known to increase the size of the obtained fibers, but in most cases such high viscosity is achieved by increasing the polymer concentration in the solution (Mit-uppatham et al., 2004). With regard to the morphology, low viscosity, low polymer concentration, high surface tension, and high voltages increase the occurrence of beaded fibers due to the preponderance of surface tension over viscoelasticity of the jet (Fong et al., 1999; Mit-uppatham et al., 2004; Son et al., 2004). Increase of the solution conductivity via the addition of salts can avoid the formation of beaded fibers without increasing the polymer concentration, thus reducing the minimum diameter

of smooth fibers (Fong et al., 1999). Ambient parameters like temperature and humidity modify the evaporation rate of the solvent, and accordingly can improve the spinnability of the solution. However, excessively fast evaporation rate can also dry the solution at the tip of the nozzle, clogging the system after several minutes of operation.

Modification of the Electrospinning Setup: Coaxial and Triaxial Electrospinning

The basic electrospinning setup can be easily customized, what is useful for different purposes (Teo and Ramakrishna, 2006). For instance, melt electrospinning can be used for production of fibers from pure polymers with a better control of fiber alignment and placement (Brown et al., 2016), while needleless electrospinning allows to produce electrospun fibers avoiding the use of syringe pumps (Sabantina et al., 2018). Another variation consists of modifying the collector placement, shape or the ability to rotate. In this sense, the use of rotatory drums is a popular choice, since it allows to impose a predominant fiber orientation on the collected mats (Fennessey and Farris, 2004). Several modifications of the needle and collector placements have been also tested for attaining controllable fiber alignment (Pan et al., 2006).

The spinneret configuration is another source of the flexibility in electrospinning. In this sense, the preparation of electrospun fibers in core-sheath mode with two different materials has been made possible by using two coaxial needles in the spinneret in what is known nowadays as coaxial electrospinning. This setup was first reported by Loscertales et al. (2002) for the encapsulation of liquids, and was later modified for production of silica nanotubes by flowing a partially gelated tetraethyortosilicate (TEOS) solution through the outer needle while feeding a synthetic oil, that served as the template for the hollow core of the tube, through the inner needle (Larsen et al., 2003). Coaxial electrospinning allows to produce a steady compound jet formed by two immiscible liquids that are pumped through the outer and the inner needles. Coaxial electrospinning has remarkable advantages over the conventional setup, such as: (i) hollow fibers can be prepared using a sacrificial solution that is feed through the inner needle; (ii) composite fibers with core-shell structure can be obtained by feeding the outer and inner needle with two different solutions; (iii) it allows the preparation of fibers from a non-spinnable solution by using a spinnable one, which favors the formation of the Taylor cone.

PRODUCTION OF CARBON FIBERS AND TUBES BY ELECTROSPINNING OF LIGNIN SOLUTIONS

The benefits of using lignin as carbon precursor were pointed out in the introduction section. In fact, conventional spinning methods were able to achieve carbon fibers from lignin with sizes ranging in ten of microns. In contrast, electrospinning made possible to produce carbon fibers with sizes below the microns. In 2007, our research group reported for the first time the production of carbon fibers from electrospun lignin fibers (Lallave et al., 2007). For this purpose, Alcell lignin/ethanol solutions of 1/1 weight ratios were prepared. The use of a high concentration of lignin was necessary to get an appropriate viscosity, avoiding the predominance of the Rayleigh instability that leads to early breakage of the jet, producing electrospray.

Unfortunately, a conventional electrospinning setup only operating with the lignin/ethanol solution produced the clogging of the needle tip after a few minutes, stopping the process. The fast evaporation rate of ethanol at the tip of the needle and the high lignin concentration were responsible of this undesired outcome. The use of a coaxial electrospinning was mandatory to get a continuous electrospinning of lignin fibers. In this case, the addition of ethanol through the outer needle compensated the solvent losses at the tip of the needle, allowing to achieve a steady Taylor cone formation. In fact, an adequate selection of the relative flow rate ratios of the ethanol and the lignin solution can be used to tune the morphology obtained on top of the collector surface. **Figure 1** compiles a collection of SEM images obtained by coaxial electrospinning of Alcell lignin/ethanol solutions (0.8:1 weight ratio). These micrographs show the different morphologies that can be obtained by only modifying the ethanol flow rate of the outer needle to values of 30% (**Figure 1A**), 20% (**Figure 1B**), and 10% (**Figure 1C**) of that of the inner needle (lignin solution). The remarkable transition from spheres to beaded fibers and finally solid fibers illustrates the versatility of electrohydrodynamic forces, and specifically of the coaxial electrospinning setup, in controlling the shape of the resulting materials. These morphologies are highly desirable for membrane, controlled drug release and bio-engineering applications (Lannutti et al., 2007; Hu et al., 2014; Ahmed et al., 2015).

Most works regarding the preparation of electrospun lignin fibers reports the use of binders as polyethylene oxide or polyvinyl pyrrolidone (Dallmeyer et al., 2010; Hu and Hsieh, 2013; Wang et al., 2013; Lai et al., 2014). In our case, it must be highlighted that shaping lignin into fibers is attained without the addition of any binder or other type of additive in this method. This enhancement is derived from the suitable properties of Alcell lignin, such as high purity and solubility in ethanol, which enable to reach high lignin concentrations, and hence high viscosity of the solution.

When directly carbonized, lignin fibers melt as soon as their glass transition temperature (Tg) is surpassed. The electrospun Alcell Lignin fibers are submitted to an air treatment at 200°C, which is reached using low heating rates (ca. 5°C/h) to favor the partial oxidation of the lignin chains. This oxidative treatment generates ether groups bridging the lignin polymeric chains. These crosslinking and condensation reactions increase Tg, enabling to obtain carbon fibers on a subsequent treatment under inert atmosphere at temperatures ranging from 600 to 1,000°C (Ruiz-Rosas et al., 2010). Thus, carbonization of the stabilized lignin fibers under inert atmosphere using a heating rate of 10°C/min was successful obtained without deteriorating their morphology and attaining preparation yields as high as 30% at 900°C. Carbonization at such different temperatures rendered carbon fibers with a variety of surface oxygen groups and different micropore volumes and specific surface areas (S_{BET}).

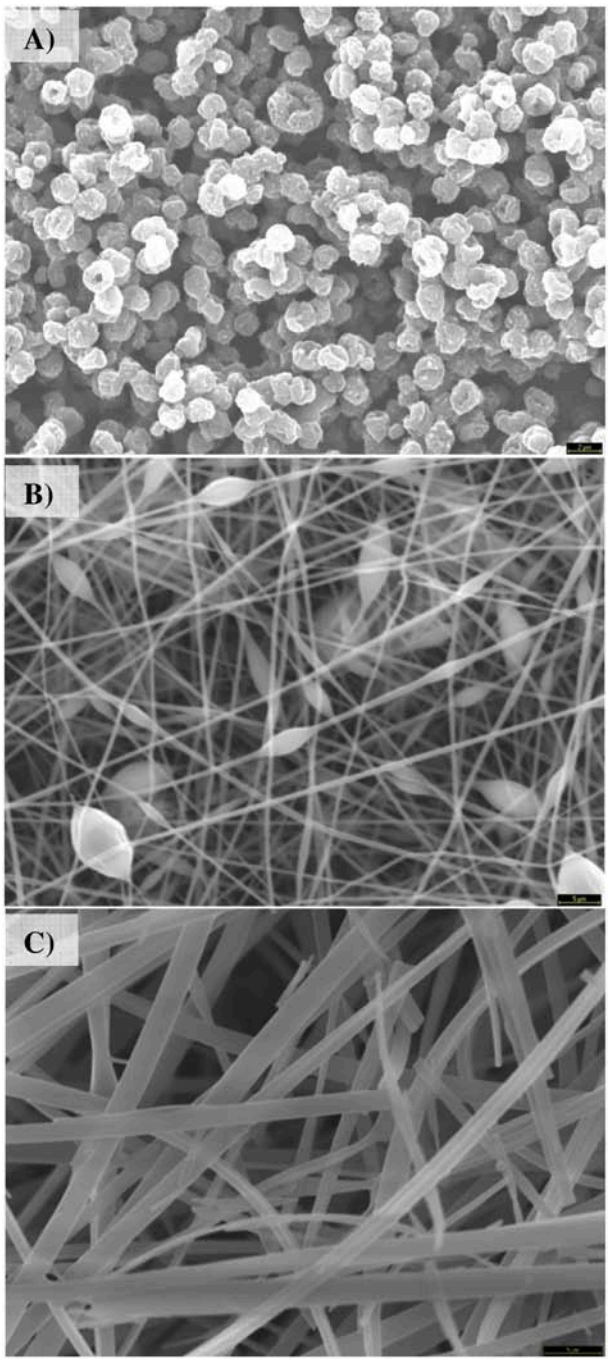

FIGURE 1 | SEM images of lignin **(A)** spheres (scale bar: 2 μm); **(B)** beaded fibers (scale bar: 5 μm); and **(C)** linear fibers (scale bar: 5 μm).

The resulting materials consisted of flexible carbonized mats (thickness of <1 mm). Interestingly, the carbonized fibers show a high development of narrow micropores with sizes around 0.7 nm, as pointed out by the similar micropore volumes obtained by the N_2 adsorption isotherm at −196°C and CO_2 adsorption isotherm at 0°C, without needing additional activation steps. No mesopore volume is developed, and the external surface area, measured by t-plot or α-s method, is in agreement to the geometric surface area of the carbonized fibers. The microporosity generation is related to the high oxygen content of Alcell lignin, which is further increased in the air stabilization treatment. The oxygen surface groups of the stabilized fibers evolve in the form of CO and CO_2 during the thermal treatment, which produces a significant gasification of the carbon fibers. In accordance to a larger removal of oxygen groups at higher carbonization temperatures, the micropore volume and apparent surface area increase with the carbonization temperature from 600 to 900°C, reaching a maximum at ca. 0.4 cm^3/g, with a corresponding S_{BET} of around 1,100 m^2/g. Increasing the carbonization temperature to 1,000°C produces the shrinkage of the porosity, because most of functional oxygen groups are removed at 900°C, easing the stacking and condensation of carbon microcrystallites. The possibility of obtaining highly ordered carbon materials from the direct carbonization of lignin was reported by our research group elsewhere (Rodríguez-Mirasol et al., 1996). In this sense, Raman spectroscopy of the carbonized fibers at relatively high temperature (around 900°C) revealed a low I_D/I_G ratio, indicative of the presence of an incipient graphite-like structural order.

Carbon microtubes are another interesting morphology, due to their improved mass transfer rate, which can be obtained from electrospinning of lignin (Lallave et al., 2007). For this purpose, a tri-axial electrospinning configuration was constructed. **Figure 2** compares the co-axial and tri-axial electrospinning. As can be seen in this figure, the new experimental set-up can be viewed as a modification of the co-axial electrospinning, where a new smaller needle is emplaced inside the old inner needle, allowing to feed a different solution in the core of the lignin solution. A high viscosity solution that is immiscible in ethanol is flown through the new inner needle, so that a compound core/sheath Taylor cone is generated, with the spinnable lignin/ethanol solution flowing as the sheath and pulling from the immiscible solution at the core position. If the innermost compound (i.e., the one in the high viscosity solution) is selectively removed after the fiber collection without compromising the lignin sheath, a hollow lignin fiber (i.e., a lignin tube) will be obtained. Following this scheme, two mineral oils with viscosities of 220 and 1,360 cP, the first one has a viscosity lower than lignin solution, 500 cP, while the latter one has a higher viscosity. These oils were used as the template of the tube cavity and were feed through the inner needle in the core position (Ruiz-Rosas et al., 2009). Since these oils show boiling points over 300°C, and they have a high specific heat that can interfere with the stabilization step, the heating rate of the stabilization treatment was slow down to 3°C/h. The atmosphere of the stabilization step was also modified to include vacuum-air cycles, where vacuum is applied in order to ease the removal of the oils. The stabilized hollow fibers were carbonized in a similar manner to the solid fibers, under inert atmosphere at 900°C using a heating rate of 10°C/min.

The viscosity of the oil played an important role on the resulting morphology of the fibers, as depicted by the SEM and TEM micrographs shown in **Figure 3**. All the materials were obtained fixing the flow rates of the lignin solution, the oil and the ethanol solution to 0.9:0.3:0.1 mL/h, respectively.

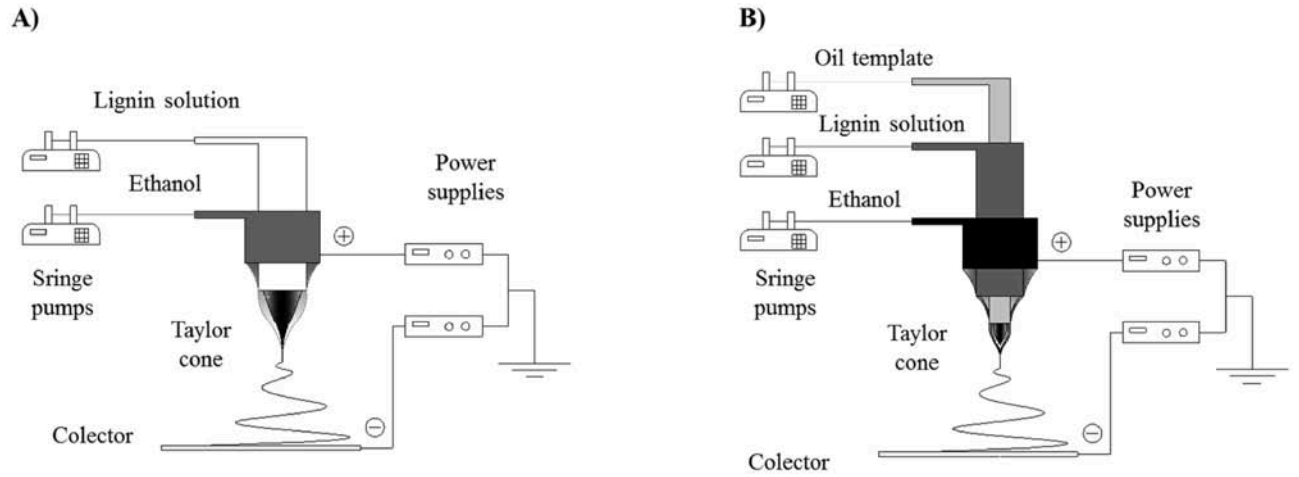

FIGURE 2 | Scheme of **(A)** co-axial and **(B)** tri-axial electrospinning for preparing lignin solid fibers and tubes, respectively.

Nevertheless, the use of a low viscosity oil resulted in carbonized fibers with "bean" morphology, **Figure 3A**, which is different to the classical beaded fibers shown in **Figure 1**. Specifically, when a low viscosity oil is used, lignin solution broke the jet of the oil into drops, which are contained inside the lignin fibers, meanwhile the viscous forces of the high viscosity oil maintain the inner jet intact until the lignin fibers are collected. Differently, the high viscosity oil provided a continuous jet, resulting in smooth hollow fibers, **Figure 3B**. TEM images of the same samples collected in **Figures 3C,D** confirmed the presence of oil encapsulation and continuous hollow carbon fibers, respectively. As in the case of conventional beaded fibers and microspheres, these morphologies could be useful in the fields of membrane science and bio-engineering, where the large and rough surface of bean fibers and the use of a bio-compatible material could be helpful for tissue scaffold applications (Lannutti et al., 2007).

The diameter of the wall of the tube and the size of the cavity of the tube can be easily tuned attending to the flow rate of the high viscosity oil. **Figure 4** shows the effect of increasing the oil flow rate from 0.2 to 0.6 mL/h, keeping constant the lignin solution flow rate at 0.9 mL/h. The size of the cavity increases at the expense of the wall thickness. The external diameter of the carbon tubes also increases with the oil flow rate. These images evidence the accuracy that can be attained in controlling the morphology and size of microsized materials when using this simple technique.

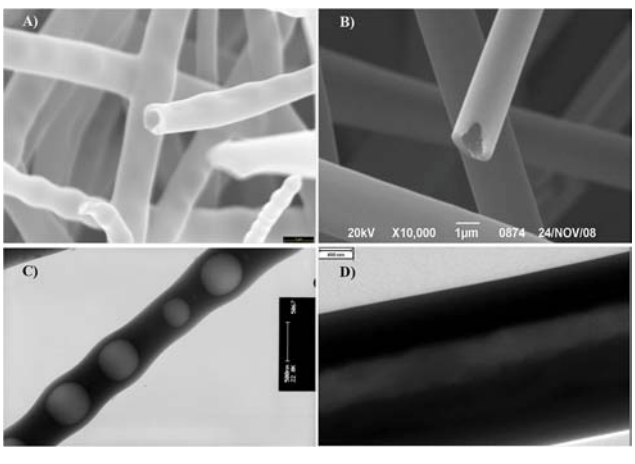

FIGURE 3 | SEM images of carbonized electrospun lignin fibers obtained using **(A)** a low viscosity oil; and **(B)** high viscosity oil. Bar lengths: 1 μm. TEM images of the same carbonized electrospun lignin fibers obtained using **(C)** the low viscosity oil (bar length: 500 nm); and **(D)** the high viscosity oil (bar length: 400 nm).

ELECTROSPUN CARBON FIBERS AS BINDERLESS ELECTRODES OF SUPERCAPACITORS

These promising properties moved us to test the carbonized electrospun lignin fibers as supercapacitor electrodes (Berenguer et al., 2016b). Supercapacitors are energy storage devices showing high power capability, long durability and medium energy density. However, their cost in terms of energy density is still one order of magnitude larger than that of Li-ion batteries (Miller, 2016), and it needs to be decreased for achieving a widespread use, especially in the case of flexible and portable devices. For the latter application, binderless, seamless, and flexible electrodes are preferred. Unfortunately, most of their synthesis procedures are conceived for the use of nanostructured carbon materials, which are expensive and cannot be easily handled and processed into electrodes, increasing the cost of these devices (Wang et al., 2014). The combination of lignin, as carbon source, and electrospinning, as a simple, top-down technique, for the production of binderless and flexibles electrodes could help in delivering lower production costs in this field (Espinoza-Acosta et al., 2018). The carbonized mats prepared at 900°C were cut in the desired shape, soaked in 1 M H_2SO_4 and

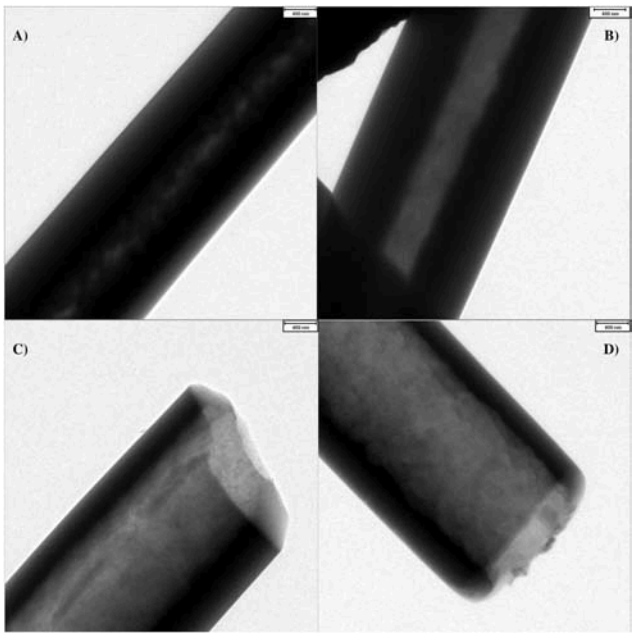

FIGURE 4 | TEM images of carbon fibers obtained from electrospun lignin fibers prepared using an oil flow rate of **(A)** 0.2 mL/h; **(B)** 0.4 mL/h; **(C)** 0.5 mL/h; and **(D)** 0.6 mL/h. Scale bar: 400 nm.

directly attached to the current collectors, acting as binderless, flexible electrodes. The electrochemical characterization by cyclic voltammetry of these lignin-based electrodes revealed 3-electrode capacitance values of ca. 150 F/g, box-shaped cyclic voltammetry, characteristic of capacitive materials, and excellent rate performance when the scan rate was increased from 0.01 up to 1 V/s. The electrochemical stability of the electrodes was also determined, showing a wide potential window (from −0.4 to 1.0 V vs. Ag/AgCl). The good electrical conductivity is related to the structural order observed in Raman spectroscopy and to the high carbon fibers interconnectivity of the electrode. A notable decline in the rate performance of the grinded fibers was observed when the electrochemical response of the grinded carbon mat (losing its binderless and free-standing features) was analyzed. This test was carried out by shaping it into an electrode using the traditional mixture, with conductivity promoter and binder, and showed worse electrochemical performance than binderless interconnected carbon fibers. In view of these promising results, two additional modifications were implemented on the preparation of the carbon mats: (i) improvement of the electrode interconnectivity by doubling the heating rate during the air stabilization, what produces partial melting of the stabilized fibers and increases the electrical conductivity with a negligible impact on the porosity development (ii) one-step physical activation of the carbonized lignin fibers using diluted air atmosphere during their carbonization, increasing the surface area by 40% without additional preparation steps. By combining both modifications, we constructed a symmetric two-electrode supercapacitor showing energy density of 10 Wh/kg and maximum power density of 60 kW/kg in aqueous electrolyte. The high durability of these carbon fibers was demonstrated when the supercapacitor cell was able to be safely loaded and unloaded at 1.3 V using 5 A/g for 100,000 cycles, showing minor degradation of energy and power densities. The performances shown by these carbon mats were close to the highest ever reported for PAN electrospun binderless electrodes, but using a greener carbon precursor and without requesting additional activation steps.

TUNING THE ELECTROSPINNING SOLUTION FOR THE PREPARATION OF LIGNIN-BASED CARBON FIBERS

Attending to the modification of the electrospinnign solution, the addition of stabilizer, porosity development and metal salt precursors to the initial lignin solution was studied. In our research group, we have proposed H_3PO_4 as stabilizing agent as well as chemical agent to activate the carbon fibers. Furthermore, Pt-containing carbon fibers catalysts were prepared by adding Pt-salt precursor to the initial solution.

Addition of H_3PO_4 as Stabilizer and Porosity Development Promoter

As above mentioned, stabilization is a critical step in the preparation of carbon fibers from lignin due to the low glass transition temperature (Tg) of lignin. To increase Tg, crosslinking and condensation reactions have to be favored. For this purpose, the production of ether groups that bridge the lignin polymeric chains have to be produced by oxidation of the fibers. Due to the importance of the stabilization step, the parameters of lignin fibers stabilization have been studied by many authors (Kadla et al., 2002; Braun et al., 2005; Brodin et al., 2011; Norberg et al., 2013). In this sense, Jagtoyen et al. stablished some time ago that cross-linking and condensation reactions occur when H_3PO_4 is mixed with a lignocelullosic material (Jagtoyen and Derbyshire, 1998). Our research group has a vast experience in the preparation of carbon materials from different lignocellulosic raw materials, including lignin, by chemical activation with H_3PO_4 (Gonzalez-Serrano et al., 2004; Rosas et al., 2008; Bedia et al., 2011; Cordero-Lanzac et al., 2018). With the objective to promote the cross linking and condensation reactions and the porosity development, the addition of H_3PO_4 to the lignin/ethanol solution was studied (García-Mateos et al., 2018a). A low amount of H_3PO_4 as stabilizing agent with Alcell lignin and ethanol (weight ratio of H_3PO_4/lignin/ethanol of 0.3/1/1) was mixed. Using similar electrospinning conditions to those reported for pure lignin fibers, a cotton-like mat consisting of non-woven and continuous microsized fibers were obtained on the collector. XPS and TPD measurements show that the electrospinning of H_3PO_4/lignin/ethanol solutions produces more oxidized lignin fibers. For pure lignin fibers, an increase in the oxygen content (from 26 to 32%) after a stabilization step of 100 h is observed. In contrast, for phosphorus-containing lignin fibers, higher oxygen content (around 28%) was obtained after the addition of H_3PO_4 to the initial lignin/ethanol solution. This higher oxygen contents is associated to the presence of

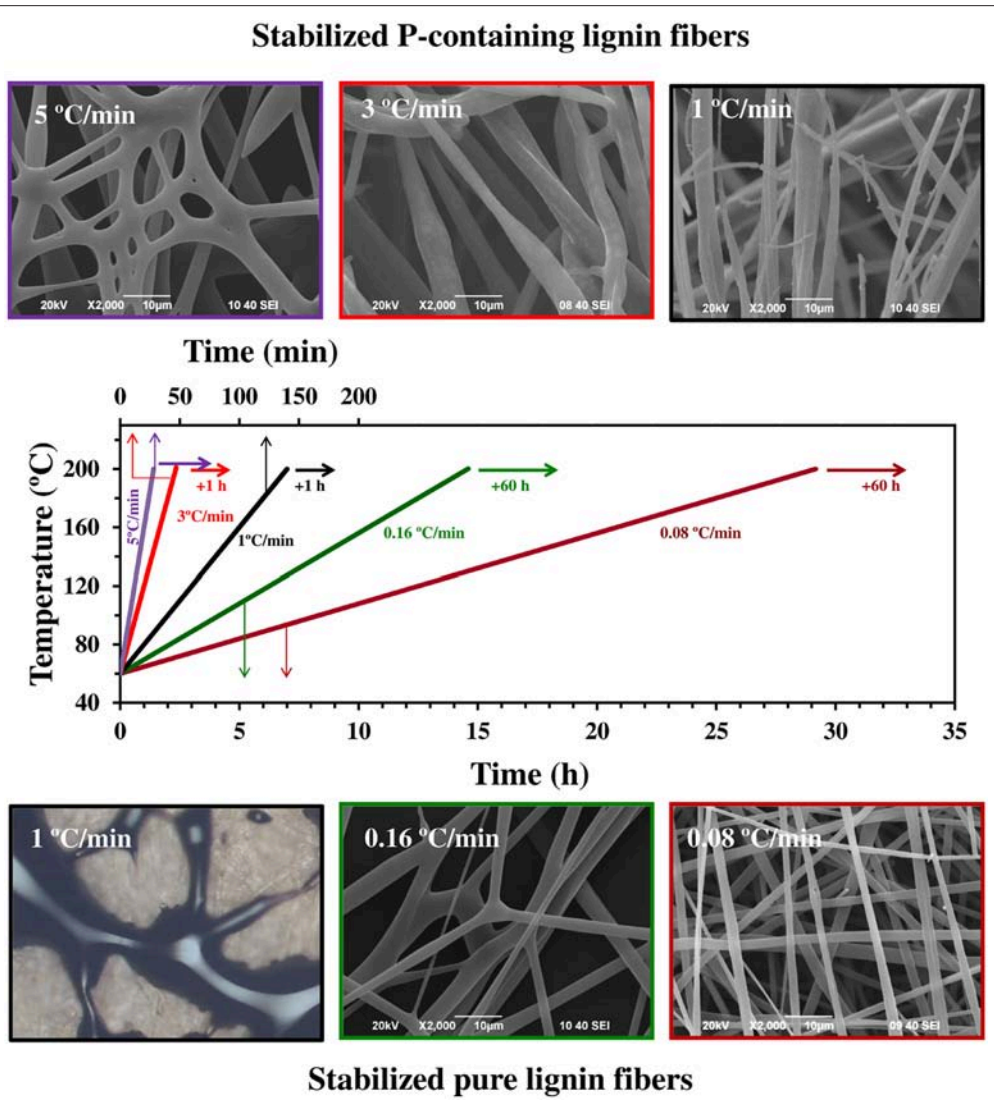

FIGURE 5 | Effect of the heating rate on the stabilization of pure and P-containing lignin fibers.

C-O-P bonds. A further increase of oxygen is observed after stabilization step (29.5%). These bonds seem to be related to the presence of different phosphates (and/or polyphosphates) groups that are responsible of the cross-linking of the polymeric chains of lignin, allowing the air stabilization to be carried out at faster rate. The cross-linking and condensation attained at this stage is sufficient to proceed with the direct carbonization of the lignin fibers (i.e., avoiding the air stabilization step) without melting of the fibers if a low heating rate (1°C/min) is used. **Figure 5** shows the effect of the heating rate in the stabilization of pure and P-containing lignin fibers. For the latest, high heating rates as high as 3°C/min are used without producing the melting of the fibers, while a heating rate of 5°C/min can be employed to provide interconnected lignin fibers. Only relatively short times (1 h) during the isothermal stabilization temperature at 200°C are required when using high heating rates in the stabilization step to complete it, preventing the fusion of the fibers in the next carbonization step at 900°C with a heating rate of 10°C/min. In contrast, much longer times are necessary for pure lignin fibers, during the stabilization step to prevent the fusion. A heating rate of 1°C/min produces the complete fusion of the lignin fibers (**Figure 5**), meanwhile values as low as 0.16°C/min provide interconnected-lignin fibers. In fact, the heating rate is 35 times slower than that for the P-containing lignin fibers (0.08 vs. 3°C/min) and the total stabilization time of the fibers including the isothermal step is 50 times longer than that for the P-containing lignin fibers.

In addition to the advantages shown by H_3PO_4 on the lignin fibers stabilization, some others are also found in the resulting carbonized fibers. First of all, it is known that the preparation of carbon materials by chemical activation with H_3PO_4 increase the preparation yield due to the restriction of

tars formation and the dehydration of the lignin structure (Rosas et al., 2009). A preparation yield around 40 % was found for the preparation of phosphorus carbon fibers at 900°C, being much higher than that obtained for pure carbon fibers (yield = 27%). Microporous carbon fibers were obtained by direct carbonization of pure stabilized lignin fibers with a specific surface area (S_{BET}) of 850 m^2/g. Comparing the micropore volumes obtained from N_2 and CO_2 adsorption at −196 and 0°C, respectively, it is possible to find a relation of V_t^{N2}/V_{DR}^{CO2} of 0.82, which indicates the predominance of narrow microporosity. The chemical composition of pure carbon fibers, obtained by XPS, was 96.3 and 3.7% of carbon and oxygen, respectively. Chemical activation with H_3PO_4 is used to prepare carbon materials with a well-porosity development in the micro-mesopore range, whose results depend on the impregnation ratio and activation temperature (Rosas et al., 2009; Bedia et al., 2011). With the addition of a 30% wt of H_3PO_4 (with respect to lignin) in the lignin solution, carbon fibers with 1,345 m^2/g of specific surface area (S_{BET}) were obtained. For phosphorus containing carbon fibers, a micropore volume of 0.58 cm^3/g is observed from N_2 adsorption isotherm. A lower value of narrow micropore volume (0.412 cm^3/g) was obtained, indicating that the addition of H_3PO_4 widens the microporosity of carbonized fibers. In this case, higher amount of oxygen (7.7 %wt) was detected on the carbon fibers surface due to the presence of C-O-P bonds from the phosphate groups. Furthermore, the presence of thermally stable C-O-P groups on the lignin fibers is responsible for the high oxidation resistance of these materials. This interesting feature allows to selectively gasify with diluted oxygen (3 %v) at temperatures of 900°C, showing carbon fibers with a specific surface area of 2,000 m^2/g. Carbonization in the presence of diluted O_2 develops wider micropores (relation between V_t^{N2}/V_{DR}^{CO2} of 2) and even mesopores ($V_{mesopores}$ 0.107 cm^3/g). As for the surface chemistry of gasified carbon fibers, an increase up to 16 %wt of the oxygen content is detected. Finally, the amount of phosphorus increases from 1.8 to 2.8 %wt, when the fibers are carbonized in presence of diluted oxygen.

The pore size distribution (PSD) of the carbon fibers prepared by direct carbonization, chemical and physical/chemical activation is presented in **Figure 6**. PSDs are drawn from N_2 adsorption data by applying a 2D-NLDFT heterogeneous surface model. The most frequent pore size for carbon fibers prepared by direct carbonization is 5.8 Å. In accordance to the N_2/CO_2 micropore volume ratios, the addition of H_3PO_4 produce carbon fibers with wider porosity after carbonization, shifting the maximum of the PSD to 6.3 Å and delivering the appearance of new micorpores of sizes around 13 Å. In the case of chemical activation in presence of diluted oxygen, a bimodal pore size distribution, with the maximum of pore sizes at 6.8 and 16 Å, is observed.

A brief summary of the fiber diameter (Ø) and specific surface areas of carbon fibers prepared from different types of lignin and experimental conditions is collected in **Table 1**. In general, carbonization of pure lignin fibers produces carbon fibers with a low porosity development, being the surface areas values higher when Alcell lignin is used as raw material. The use of chemical agents in the initial lignin solutions (KOH, NaOH and H_3PO_4) produces an increase in the porosity development. The highest surface area, 2,000 m^2/g, of the carbon fibers prepared in one step (referred to the carbonization/activation step) is obtained when chemical activation is carried out under diluted air flow. Two steps preparation of lignin carbon fibers (marked with * in **Table 1**), consisting of carbonization followed by partial gasification of the fibers, provide carbon fibers with similar apparent surface areas to that obtained by our research group in only one step, only overpassed by those obtained by Lin et al. (2012).

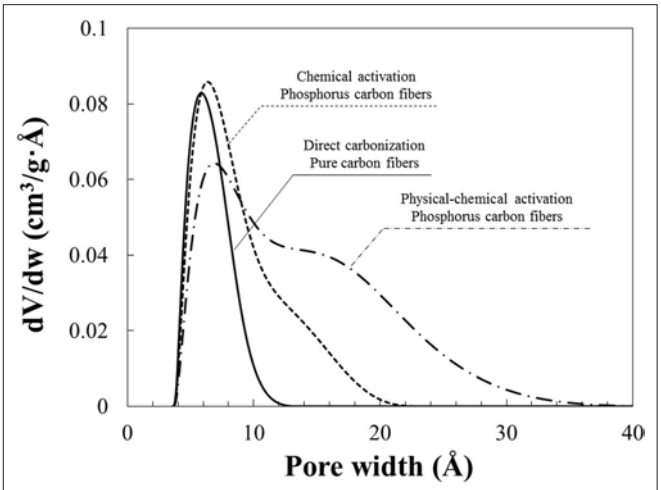

FIGURE 6 | Pore size distribution of carbon fibers prepared by direct carbonization, chemical activation and physical/chemical activation.

The preparation of phosphorus containing carbon fibers has a great importance in catalysis, adsorption and electrochemical applications. For instance, phosphorus containing carbon fibers have been used as catalysts for the alcohol decomposition reaction, which is used to evaluate the acid/basic properties of the catalyst. A positive relationship between the catalyst activity in 2-propanol decomposition and the P content in the carbon fibers was found. The 2-propanol decomposition on the P-containing carbon fibers showed selectivity to propylene of 100%, evidencing the acid character of these carbon fibers. Moreover, the P-containing carbon fibers with the highest P surface amount show similar catalytic activity than that obtained for a commercial acid catalyst (γ-Al_2O_3). On the other hand, when pure carbon fibers were used as catalyst for 2-propanol decomposition, high selectivity to acetone was obtained, suggesting the basic character of these catalysts. In addition, pure carbon fibers showed high oxidation resistance by itself, combusting at temperatures higher than 500°C in presence of oxygen. However, phosphorus containing carbon fibers have even higher oxidation resistance, starting to burnt-off at temperatures near to 525–550°C. P-surface groups, that are thermally stable at high temperature, are the responsible for the increase of the oxidation resistance of these carbon fibers, as previously mentioned (Wu and Radovic, 2006; Rosas et al., 2012; Valero-Romero et al., 2017). The textural properties, physico-chemical properties, morphology and small sizes of these fibers are very attractive to use these materials

TABLE 1 | Specific surface areas of carbon fibers prepared from different types of lignin.

Type of lignin	Fiber preparation method	Carbonization or activation process	Ø (μm)	S_{BET} (m^2/g)	References
Softwood acetic acid lignin	Melt spinning	Carbonization at 1,000°C	–	370	Uraki et al., 2001
Kraft Lignin	Melt spinning	Carbonization at 1,000°C	70	336	Kubo et al., 2007
Alcell lignin	Electrospinning	Carbonization at 900°C	0.8–2	1,195	Ruiz-Rosas et al., 2010
Alkali lignin	Electrospinning	Carbonization at 850°C	–	13	Hu and Hsieh, 2013
Alkali lignin	Electrospinning	Chemical activation with NaOH at 850°C	0.3-0.5	1,444	Hu and Hsieh, 2013
Alkali lignin	Electrospinning	Chemical activation with KOH at 850°C	0.1-0.3	1,407	Hu and Hsieh, 2013
Alcell lignin	Electrospinning	Carbonization at 900°C	–	473	Wang et al., 2013
Kraft lignin	Electrospinning	Carbonization at 1,000°C	0.6	411	Dallmeyer et al., 2014b
Kraft lignin	Electrospinning	Carbonization at 1,000°C	0.6	374	Dallmeyer et al., 2014b
Alkali lignin	Electrospinning	Carbonization at 1,200°C	0.25	580	Lai et al., 2014
Alcell lignin	Electrospinning	Physical activation with diluted oxygen 900°C	1	1,005	Berenguer et al., 2016b
Alcell lignin	Electrospinning	Carbonization at 900°C	1	850	García-Mateos et al., 2018a
Alcell lignin	Electrospinning	Chemical activation with H_3PO_4 at 900°C	2.5	1,348	García-Mateos et al., 2018a
Alcel lignin	Electrospinning	Chemical/physical activation with H_3PO_4/O_2 at 900°C	2.4	2,000	García-Mateos et al., 2018a
Acetic acid lignin	Melt spinning	Physical activation with steam at 900°C*	–	1,250	Uraki et al., 1997
Softwood acetic acid lignin	Melt spinning	Physical activation with steam at 900°C*	20	1,930	Uraki et al., 2001
PEG-lignin	Melt spinning	Physical activation with steam at 900°C*	10	3,060	Lin et al., 2012

**Two-step activated carbon fibers preparation (carbonization and physical activation).*

as adsorbent in liquid phase. Phosphorus carbon fibers present high phenol adsorption capacities, around 180 mg of phenol per gram of adsorbent, with an equilibrium phenol concentration of 25 mg/L at 25°C. Finally, the P-containing carbon fibers were also evaluated as binderless carbon electrodes. We have already mentioned that carbonization at 900°C provides a high structural order and, in consequence, a high electrical conductivity to carbonized lignin fibers (Berenguer et al., 2016b). P-containing carbon fibers also showed promising result in electrochemical applications as supercapacitors, especially duet to their high stability, which allow them to operate safely in wide potential windows for different electrolytes ($\Delta E = 1.6$, 1.65 and 1.9 for H_2SO_4, NaOH, and Na_2SO_4, respectively). Again, the presence of phosphorus groups strongly bonded to the carbon surface improve the electro-oxidation resistance of these materials, probably due to the deactivating effect of these groups in the electrochemical water decomposition reaction (Berenguer et al., 2015).

One-Pot Synthesis Preparation of Metal-Containing Lignin-Based Electrocatalysts

Carbon materials are widely used as catalyst support for the dispersion of metallic nanoparticles acting as the active phase of different catalytic and electrocatalytic reactions (Liu et al., 2004; Cordero-Lanzac et al., 2017). The methodology most commonly used for the preparation of conventional carbon-based catalysts can be divided into different steps (Rosas et al., 2010; Berenguer et al., 2016a); (i) preparation of carbon support, (ii) impregnation with the metallic solution by wet impregnation routes, and (iii) stabilization of the active phase. The use of electrospinning for the preparation of metal-decorated carbon fibers is a new method that simplifies the preparation process of catalysts.

In our research group, we have reported the one-pot preparation of Pt supported lignin-based carbon fibers in a simple way by using electrospinning technique (García-Mateos et al., 2017). In this work, different amounts of platinum acetylacetonate (Pt salt:lignin 0.006 and 0.03) were added to the spinnable lignin/ethanol or H_3PO_4/lignin/ethanol solution with the objective to obtain Pt-containing lignin fibers in one step with low and high Pt content (1 and 5% wt. Pt, respectively, in the final carbon electrocatalysts). After stabilization and carbonization of the H_3PO_4-free carbon fibers, carbon fibers electrocatalysts with well-dispersed platinum nanoparticles were obtained, although the preparation yields decreased with the platinum loading, being between 10 and 30%. This drawback was overcome when phosphoric acid was included in the solution. Similar stabilization and carbonization yields were obtained regardless the amount of platinum acetylacetonate used (yield of 88 and 33% for stabilization and carbonization, respectively). These results can be related with the high activity of Pt for gasification reactions, which are reduced in the case of P-containing lignin fibers, due to the presence of C-O-P groups.

The incorporation of Pt precursor to the lignin solutions has a strong influence on the porous texture of pure carbon fibers. Pure carbon fibers without Pt are microporous materials with a specific surface area of 851 m^2/g. The increase of the Pt content produces a development of the mesoporosity. For the final carbon fibers electrocatalysts with low and high Pt content, specific surface areas of around 760 m^2/g were obtained, but an increase of the external surface area (from 161 to 383 m^2/g) and mesopore volume (from 0.24 to 0.51 cm^3/g) are produced as the Pt content increases. These results are in concordance with the effect of

Pt as gasification promoter. For P-containing carbon fibers the gasification is prevented by the presence of C-O-P groups and a typical isotherm for microporous materials is obtained in all the cases, regardless of the amount of platinum used. Only a slightly increase in the specific surface area is attained as Pt loading increases (from 1,210 to 1,289 m^2/g).

Figure 7 shows the SEM images of the carbon fibers catalysts. It can be appreciated that the addition of different quantities of Pt precursor does not modify the roughness of the carbon fibers.

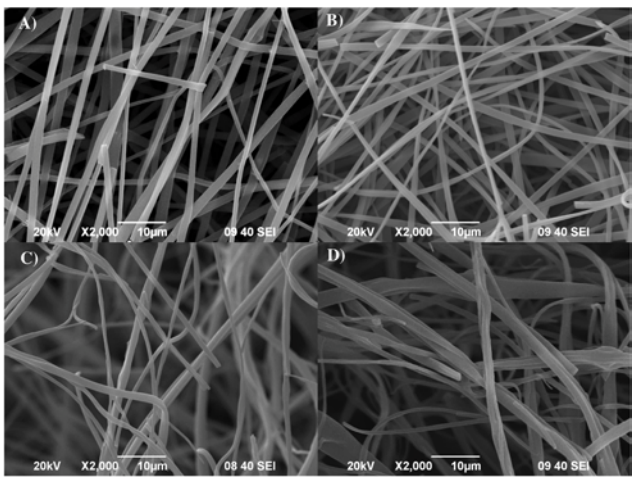

FIGURE 7 | SEM micrographs of **(A,B)** CFs with 1 and 5% of Pt, respectively; and **(C,D)** PCFs with 1 and 5% of Pt, respectively.

The size of the Pt supported carbon fibers catalysts ranged from 0.6 to 1 μm for pure carbon fibers and from 0.6 to 3 μm for P-containing carbon fibers.

TEM images of the Pt-decorated carbon fibers shown in **Figure 8** confirmed the presence of well-dispersed platinum nanoparticles in the carbonized fibers, no matter the addition of phosphoric acid into the starting solution. These results evidence the usefulness of electrospinning in the preparation of metal loaded carbon fibers through a simple procedure. Phosphorus-containing carbon fibers exhibit lower Pt particles sizes and narrower particles sizes distribution than pure carbon fibers (mean particle size of 2.8 and 2.1 nm for low and high Pt content for P-containing carbon fibers, respectively, in front of 5.6 and 9.6 nm for pure carbon fibers).

Another effect related to the addition of phosphoric acid was revealed during the XPS analyses. The chemical surface compositions obtained from XPS are presented in **Figure 9**. They confirmed the presence of carbon, oxygen, platinum and phosphorus (the latest only in the P-containing carbon fibers). On the one hand, the oxygen content remains similar, for carbon fibers without the presence of phosphorus, no matter the platinum concentration. On the other hand, P-containing carbon fibers catalysts show higher values of oxygen than the pure ones. In these materials, the oxygen is taken by C-P-O bonds, when platinum is reduced during the thermal treatment, forming new C-O-P bonds, and so increasing the oxygen concentration.

The Pt concentration were 1.0 and 7.1 %wt for low and high Pt content of pure carbon fibers, being close to the nominal Pt loading of the fiber. The deviation observed for the high Pt content in pure carbon fibers may be related to the gasification

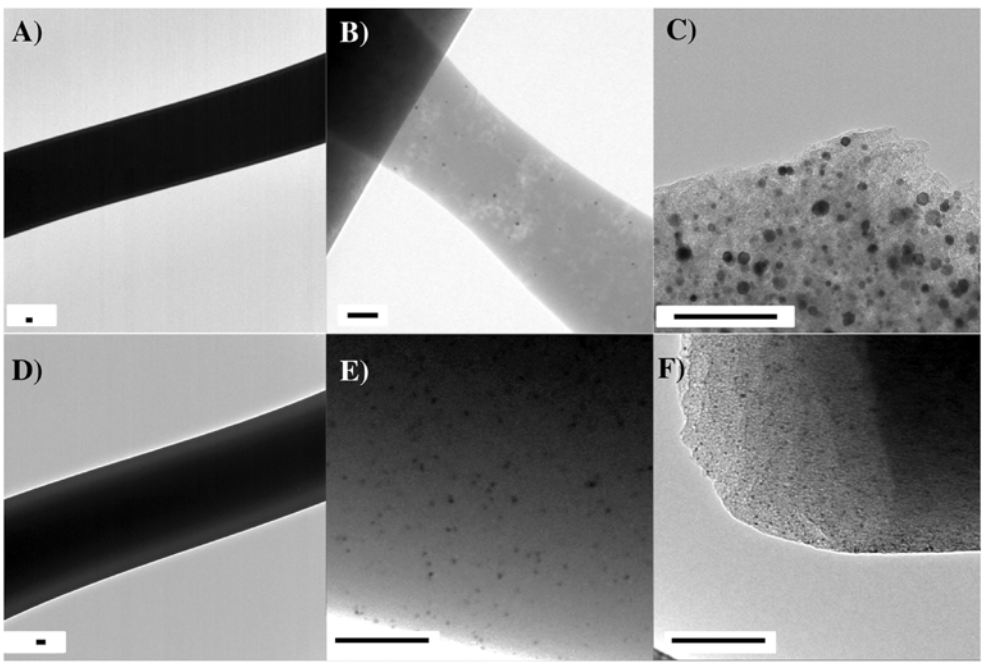

FIGURE 8 | TEM images of Pt-containing carbon fibers **(A–C)** CFs; and **(D–F)** PCFs. Bar scale: 100 nm.

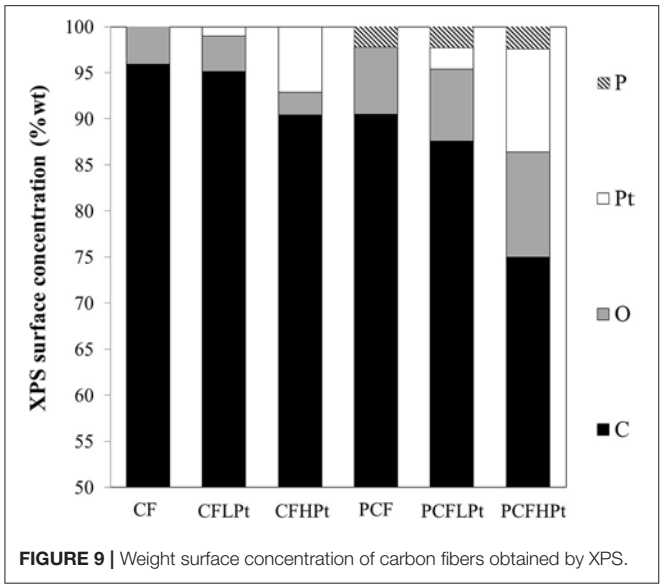

FIGURE 9 | Weight surface concentration of carbon fibers obtained by XPS.

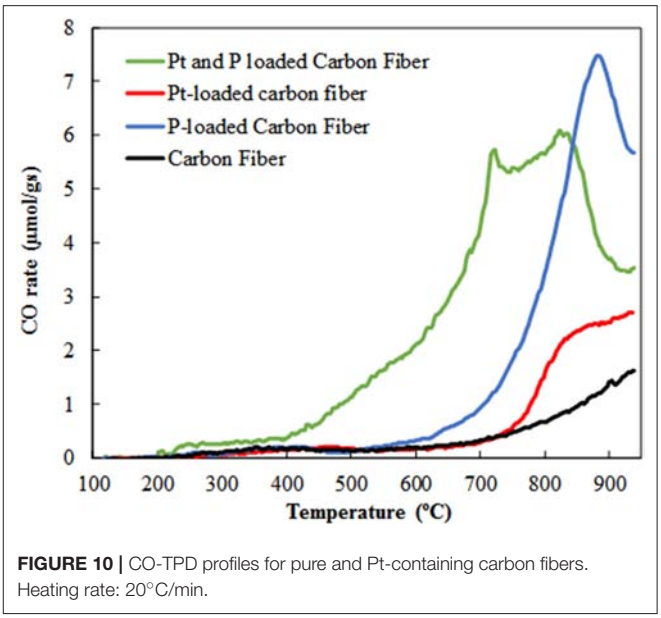

FIGURE 10 | CO-TPD profiles for pure and Pt-containing carbon fibers. Heating rate: 20°C/min.

effect of Pt, which was not considered in the formulation of the lignin/salt/ethanol solution. On the contrary, for phosphorus containing carbon fibers, high values of Pt content were obtained by XPS (2.3 and 11.2 %wt for low and high Pt content). Since XPS technique only analyzes the surface of the fibers (around 20 Å deep), these results indicate that Pt is preferable located on the surface of the fibers. Moreover, the detailed analysis of the XPS spectrum in the Pt4f photoemission region revealed the interaction between the P-anions, which favors the presence of Pt^{2+}, restricting the formation of metallic Pt particles and their subsequent sintering. The concentration of phosphorus in carbon fibers remains constant regardless of the Pt amount.

CO-TPD analyses on **Figure 10** of pure and Pt-contaning carbon fibers confirm that the presence of platinum renders small modifications to the TPD profiles (black and red profiles in **Figure 10**). However, the addition of both platinum precursors and phosphoric acid produce a large increase in the amount of surface oxygen groups (blue and green profiles in **Figure 10**). Furthermore, the CO release associated to the decomposition of the C-O-P bonds from the phosphate groups (peak at ca. 860°C in the blue profile, **Figure 10**) is shifted to 800°C, and the temperature onset of the decomposition of surface oxygen groups is lowered from 600 to 400°C. The decrease in the thermal stability of C-O-P bonds denote the strong interaction between platinum and phosphate groups.

The well-dispersion of all the elements in the carbon fibers was corroborated by EDX mapping showed in **Figure 11**. As was confirmed by XPS, the mean element presented in the carbon fibers is carbon (more intensity of red color) followed by oxygen (green color). In the case of P-containing carbon fibers, phosphorus is well-distributed in all the fibers. Again, a homogeneous dispersion of Pt is found on both carbon fibers, which suggests the feasibility of using electrospinning technique to prepare well-dispersed metal decorated carbon fibers.

Taking into account the well-dispersed Pt nanoparticles on the carbon fibers and their physico-chemical properties, these materials were tested as electrocatalysts for the methanol and ethanol electro-oxidation (MOR and EOR, respectively), reactions of interest for the development of direct alcohol in fuel cells. Owing to their advantageous conformation as continuous carbon cloths, the samples were simply cut in a shape resembling the surface of the collector and attached to it for the electrocatalytic tests. All the analyzed samples showed catalytic activity (i.e., presence of large oxidation peaks at positive potentials during CV measurements in a methanol solution in 0.5 M H_2SO_4), what points out that platinum nanoparticles are reachable by the electrolyte and methanol and active toward the intended reaction. The highest catalytic activity and lower onset potential was obtained for pure carbon fibers with the highest amount of Pt, what could be connected to the presence of a more developed pore structure (easing the access of methanol to the metal nanoparticles) of this sample. This electrocatalyst showed an excellent alcohol electro-oxidation performance, starting to oxidize methanol at 0.40 V vs. Ag/AgCl. The ratio of the forward (I_f) to reverse (I_b) anodic peak current densities was of 1.2, indicating the excellent tolerance of these catalyst toward CO poisoning. The presence of P enhances the resistance toward CO poisoning, but a lower catalytic activity was observed. Durability tests at constant potential of 0.6 V for the most active sample delivered an initial current density value of 495 A/g_{Pt}, with ca. 75% of this value being retained after the first hour of experiment. The electro-activity of the pure carbon fibers with the highest Pt content (the most active one in methanol oxidation) was also evaluated for the ethanol electro-oxidation, obtaining a peak value of current density of 370 A/g_{Pt} in the forward scan at 0.69 V. The exceptional platinum distribution, high dispersion and the excellent charge propagation characteristic of the carbon support due to the high structural order and interconnectivity of the carbon fibers are the responsible for the outstanding performance for methanol and ethanol electro-oxidation.

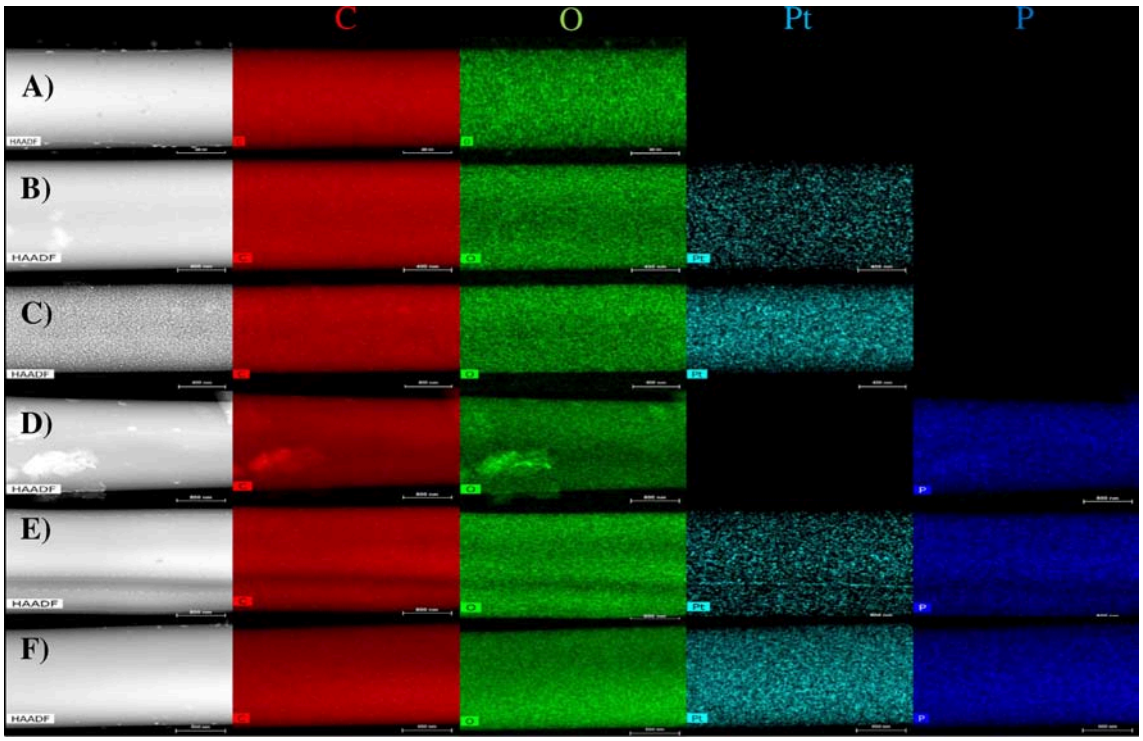

FIGURE 11 | EDX mapping of: free metal, low and high Pt concentration in CFs **(A–C)**, respectively); and PCFs **(D–F)**, respectively).

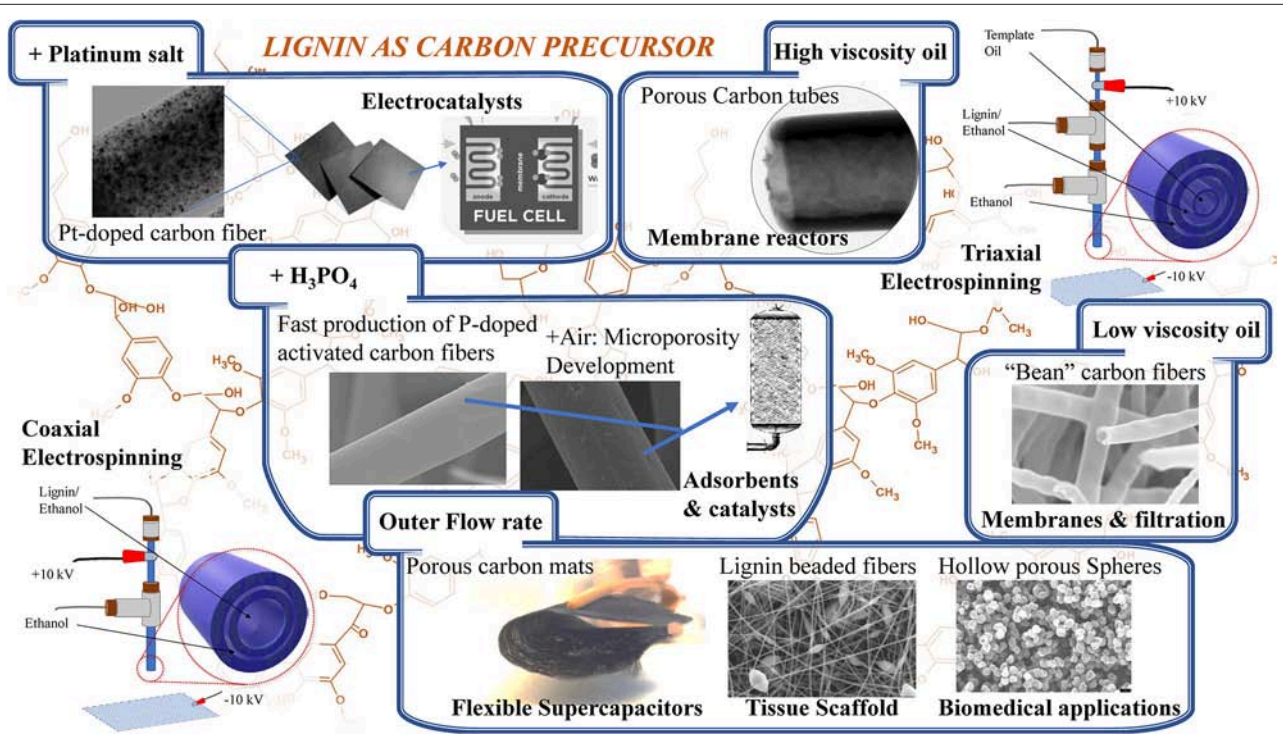

FIGURE 12 | Preparation and potential applications of the electrospun lignin-based carbon forms.

Following the same methodology, our research group is currently working in the preparation of other valuable electrocatalysts using different metals, such as Fe, Co, or Pd, which could replace Pt in the electrodes of fuel cell devices and help to reduce their production costs. Supported metallic nanoparticles are put into the carbon fibers catalyst by adding different nitrates, chlorides and even acetylacetonate metallic salts to the lignin solution. The presence of these salt precursors during the carbonization step results in a development of the mesoporosity, what is desirable for the intended application. The electrochemical characterization in acid and alkaline electrolyte has confirmed that the metal-containing carbon cloths are promising ORR catalysts that could be useful for reducing the amount of noble metals in the electrodes or for allowing the use of non-noble metals as catalysts (García-Mateos et al., 2018b).

Figure 12 summarizes the different possibilities for the modification of the morphology, surface chemistry and porosity of electrospun lignin-based carbons presented in this work along with their potential applications.

CONCLUSIONS

The works herein reviewed highlights the advantages brought by the electrospinning of Alcell lignin/ethanol solutions to the production of porous carbon fibers of a large variety of morphologies and compositions. The use of coaxial spinnerets is the key for enabling a steady production of microsized, solid lignin fibers by the addition of a small amount of ethanol through the external needle. No additives for the modification of the viscosity or the surface tension of the solution are needed owing to the high solubility of Alcell lignin in ethanol. Tuning of the ethanol flow rate in the outer needle leads to the selective production of spheres, beaded, or linear fibers. In addition, triaxial configuration enables to prepare lignin tubes using different oils as templates. Shape and sizes of these tubes can be controlled through the relative outer to inner flow rates. The electrospun lignin fibers are collected as a non-woven mat that can be carbonized to produce flexible microporous carbon sub-microfibers (without further porosity development treatments) after a slow thermooxidative step in air. The connectivity of the mat can be also increased by speeding up the thermostabilization process, leading to partial fusion of the fibers. Moreover, the time required for this treatment is greatly shortened when using a silica-lignin composite that maintain the lignin core within a silica shell, avoiding the melting of the fibers, and also when phosphoric acid is added into the lignin solution, catalyzing the crosslinking of the polymeric structure of lignin. In addition, the latter treatment also leads to porosity development. Partial gasification in diluted air during the carbonization step is another valid method for increasing the porosity of the fibers. Finally, metal nanoparticles can be casted into the carbon fibers by adding the metallic precursor in the lignin solution, enabling the preparation of carbon-supported catalysts in fibrillary morphology in a one-step procedure.

Due to the combination of high chemical and electrochemical resistance, large specific surface area and porosity development, improved mass transfer rate, high electrical conductivity, good metal dispersion and adequate mechanical properties, these carbon fibers are good candidates for being used in several applications. The composition, surface chemistry and porosity of the lignin-based electrospun materials are tuned for the intended application. In this sense, microporous carbon fibers have an outstanding performance as binderless carbon electrodes, while Pt-loaded meso- and microporous carbon fibers are excellent carbon electrocatalysts for methanol oxidation. Phosphorus containing carbon fibers shows high activity as catalysts in alcohol dehydration reactions because of its high surface acidity, while pure carbon fibers have basic character and promote alcohol dehydrogenation reactions. Finally, microporous carbon fibers have shown large adsorption capacities for the removal of pollutants in aqueous phase. In addition, the introduction of surface roughness and the encapsulation of molecules within the carbon fibers, that can be achieved using the triaxial configuration paves the way to their applications as membranes or for controlled drug delivery. All these results confirm that electrospinning of lignin solution is a promising method for the preparation of a large variety of carbon materials in fibrillary morphologies that show excellent performances as porous carbon catalysts, electrocatalysts, electrodes, and adsorbents.

AUTHOR CONTRIBUTIONS

FG-M, RR-R, and JR prepared the manuscript. FG-M prepared the carbon fibers, performed the characterization of samples, the catalytic and adsorption test, and the discussion of these results. RR-R performed the electrochemical characterization. JR, JR-M, and TC developed the synthesis concept. All authors discussed the result and commented on the manuscript.

FUNDING

Ministerio de Economía y Competitividad, Gobierno de España and Fondo Europeo de Desarrollo Regional (FEDER) for CTQ2015-68654-R project.

ACKNOWLEDGMENTS

This work was supported by the Spanish Ministry of Economy and Competitiveness and FEDER (CTQ2015-68654-R).

REFERENCES

Ahmed, F. E., Lalia, B. S., and Hashaikeh, R. (2015). A review on electrospinning for membrane fabrication: challenges and applications. *Desalination* 356, 15–30. doi: 10.1016/j.desal.2014.09.033

Beachley, V., and Wen, X. (2009). Effect of electrospinning parameters on the nanofiber diameter and length. *Mater. Sci. Eng. C* 29, 663–668. doi: 10.1016/j.msec.2008.10.037

Bedia, J., Barrionuevo, R., Rodríguez-Mirasol, J., and Cordero, T. (2011). Ethanol dehydration to ethylene on acid carbon catalysts. *Appl. Catal. B* 103, 302–310. doi: 10.1016/j.apcatb.2011.01.032

Berenguer, R., Fornells, J., García-Mateos, F. J., Guerrero-Pérez, M. O., Rodríguez-Mirasol, J., and Cordero, T. (2016a). Novel synthesis method of porous VPO catalysts with fibrous structure by electrospinning. *Catal. Today* 277, 266–273. doi: 10.1016/j.cattod.2016.03.002

Berenguer, R., García-Mateos, F. J., Ruiz-Rosas, R., Cazorla-Amorós, D., Morallón, E., Rodríguez-Mirasol, J., et al. (2016b). Biomass-derived binderless fibrous carbon electrodes for ultrafast energy storage. *Green Chem.* 18, 1506–1515. doi: 10.1039/C5GC02409A

Berenguer, R., Ruiz-Rosas, R., Gallardo, A., Cazorla-Amorós, D., Morallón, E., Nishihara, H., et al. (2015). Enhanced electro-oxidation resistance of carbon electrodes induced by phosphorus surface groups. *Carbon* 95, 681–689. doi: 10.1016/j.carbon.2015.08.101

Braun, J. L., Holtman, K. M., and Kadla, J. F. (2005). Lignin-based carbon fibers: oxidative thermostabilization of kraft lignin. *Carbon* 43, 385–394. doi: 10.1016/j.carbon.2004.09.027

Brodin, I., Ernstsson, M., Gellerstedt, G., and Sjöholm, E. (2011). Oxidative stabilisation of kraft lignin for carbon fibre production. *Holzforschung* 66, 141–147. doi: 10.1515/HF.2011.133

Brown, T. D., Dalton, P. D., and Hutmacher, D. W. (2016). Melt electrospinning today: An opportune time for an emerging polymer process. *Prog. Polymer Sci.* 56, 116–166. doi: 10.1016/j.progpolymsci.2016.01.001

Cavaliere, S., Subianto, S., Savych, I., Jones, D. J., and Rozière, J. (2011). Electrospinning: designed architectures for energy conversion and storage devices. *Energy Environ. Sci.* 4, 4761–4785. doi: 10.1039/C1EE02201F

Cloupeau, M., and Prunet-Foch, B. (1994). Electrohydrodynamic spraying functioning modes: a critical review. *J. Aerosol Sci.* 25, 1021–1036. doi: 10.1016/0021-8502(94)90199-6

Cordero-Lanzac, T., García-Mateos, F. J., Rosas, J. M., Rodríguez-Mirasol, J., and Cordero, T. (2018). Flexible binderless capacitors based on P- and N-containing fibrous activated carbons from denim cloth waste. *Carbon* 139, 599–608. doi: 10.1016/j.carbon.2018.06.060

Cordero-Lanzac, T., Palos, R., Arandes, J. M., Castaño, P., Rodríguez-Mirasol, J., Cordero, T., et al. (2017). Stability of an acid activated carbon based bifunctional catalyst for the raw bio-oil hydrodeoxygenation. *Appl. Catal. B* 203, 389–399. doi: 10.1016/j.apcatb.2016.10.018

Dallmeyer, I., Ko, F., and Kadla, J. F. (2010). Electrospinning of Technical Lignins for the Production of Fibrous Networks. *J. Wood Chem. Technol.* 30, 315–329. doi: 10.1080/02773813.2010.527782

Dallmeyer, I., Ko, F., and Kadla, J. F. (2014a). Correlation of elongational fluid properties to fiber diameter in electrospinning of softwood kraft lignin solutions. *Ind. Eng. Chem. Res.* 53, 2697–2705. doi: 10.1021/ie403724y

Dallmeyer, I., Lin, L. T., Li, Y., Ko, F., and Kadla, J. F. (2014b). Preparation and characterization of interconnected, kraft lignin-based carbon fibrous materials by electrospinning. *Macromol. Mater. Eng.* 299, 540–551. doi: 10.1002/mame.201300148

Deitzel, J. M., Kleinmeyer, J., Harris, D., and Beck Tan, N. C. (2001). The effect of processing variables on the morphology of electrospun nanofibers and textiles. *Polymer* 42, 261–272. doi: 10.1016/S0032-3861(00)00250-0

Espinoza-Acosta, J. L., Torres-Chávez, P. I., Olmedo-Martínez, J. L., Vega-Rios, A., Flores-Gallardo, S., and Zaragoza-Contreras, E. A. (2018). Lignin in storage and renewable energy applications: a review. *J. Energy Chem.* 27, 1422–1438. doi: 10.1016/j.jechem.2018.02.015

Fang, Z., and Smith, R. L Jr. (2016). *Production of Biofuels and Chemicals from Lignin*. Singapore: Springer. Available online at: //www.springer.com/gp/book/9789811019647 (accessed January 25, 2019).

Fennessey, S. F., and Farris, R. J. (2004). Fabrication of aligned and molecularly oriented electrospun polyacrylonitrile nanofibers and the mechanical behavior of their twisted yarns. *Polymer* 45, 4217–4225. doi: 10.1016/j.polymer.2004.04.001

Fong, H., Chun, I., and Reneker, D. H. (1999). Beaded nanofibers formed during electrospinning. *Polymer* 40, 4585–4592. doi: 10.1016/S0032-3861(99)00068-3

Frank, E., Steudle, L. M., Ingildeev, D., Spörl, J. M., and Buchmeiser, M. R. (2014). Carbon fibers: precursor systems, processing, structure, and properties. *Angew. Chem. Int. Ed.* 53, 5262–5298. doi: 10.1002/anie.201306129

Fukuoka, Y. (1969). Method for producing carbonized lignin fiber. *Jpn. Chem. Q.* 5, 63–66.

Gañán-Calvo, A. M., Dávila, J., and Barrero, A. (1997). Current and droplet size in the electrospraying of liquids. Scaling laws. *J. Aerosol Sci.* 28, 249–275. doi: 10.1016/S0021-8502(96)00433-8

García-Mateos, F. J., Berenguer, R., Valero-Romero, M. J., Rodríguez-Mirasol, J., and Cordero, T. (2018a). Phosphorus functionalization for the rapid preparation of highly nanoporous submicron-diameter carbon fibers by electrospinning of lignin solutions. *J. Mater. Chem. A.* 6, 1219–1233. doi: 10.1039/C7TA08788H

García-Mateos, F. J., Cordero-Lanzac, T., Berenguer, R., Morallón, E., Cazorla-Amorós, D., Rodríguez-Mirasol, J., et al. (2017). Lignin-derived Pt supported carbon (submicron)fiber electrocatalysts for alcohol electro-oxidation. *Appl. Catal. B.* 211, 18–30. doi: 10.1016/j.apcatb.2017.04.008

García-Mateos, F. J., Ruiz-Rosas, R., Ortega, A., Cazorla-Amorós, D., Morallón, E., Rodriguez-Mirasol, J., et al. (2018b). One-pot sinthesys of lignin-based electrospun oxygen reduction reaction electrocatalysts. in *Program and Short Abstracts of the Carbon Conference* (Madrid).

Gonzalez-Serrano, E., Cordero, T., Rodriguez-Mirasol, J., Cotoruelo, L., and Rodriguez, J. J. (2004). Removal of water pollutants with activated carbons prepared from H 3PO4 activation of lignin from kraft black liquors. *Water Res.* 38, 3043–3050. doi: 10.1016/j.watres.2004.04.048

Hohman, M. M., Shin, M., Rutledge, G., and Brenner, M. P. (2001). Electrospinning and electrically forced jets. II. Applications. *Phys. Fluids* 13, 2221–2236. doi: 10.1063/1.1384013

Hosseinaei, Q., and Baker, D. A. (2012). "Electrospun carbon nanofibers from kraft lignin," in *Book of Abstracts of the Fiber Society* (Boston, MA), 7–9.

Hu, S., and Hsieh, Y.-L. (2013). Ultrafine microporous and mesoporous activated carbon fibers from alkali lignin. *J. Mater. Chem. A.* 1, 11279–11288. doi: 10.1039/C3TA12538F

Hu, X., Liu, S., Zhou, G., Huang, Y., Xie, Z., and Jing, X. (2014). Electrospinning of polymeric nanofibers for drug delivery applications. *J. Control. Rel.* 185, 12–21. doi: 10.1016/j.jconrel.2014.04.018

Huang, Z.-M., Zhang, Y.-Z., Kotaki, M., and Ramakrishna, S. (2003). A review on polymer nanofibers by electrospinning and their applications in nanocomposites. *Compos. Sci. Technol.* 63, 2223–2253. doi: 10.1016/S0266-3538(03)00178-7

Inagaki, M., Yang, Y., and Kang, F. (2012). Carbon nanofibers prepared via electrospinning. *Adv. Mater.* 24, 2547–2566. doi: 10.1002/adma.201104940

Jagtoyen, M., and Derbyshire, F. (1998). Activated carbons from yellow poplar and white oak by H3PO4 activation. *Carbon* 36, 1085–1097. doi: 10.1016/S0008-6223(98)00082-7

Kadla, J. F., Kubo, S., Venditti, R. A., Gilbert, R. D., Compere, A. L., and Griffith, W. (2002). Lignin-based carbon fibers for composite fiber applications. *Carbon* 40, 2913–2920. doi: 10.1016/S0008-6223(02)00248-8

Kenry, and Lim, C. T. (2017). Nanofiber technology: current status and emerging developments. *Progress Polymer Sci.* 70, 1–17. doi: 10.1016/j.progpolymsci.2017.03.002

Kubo, S., Yoshida, T., and Kadla, J. F. (2007). Surface Porosity of Lignin/PP Blend Carbon Fibers. *J. Wood Chem. Technol.* 27, 257–271. doi: 10.1080/02773810701702238

Lai, C., Zhou, Z., Zhang, L., Wang, X., Zhou, Q., Zhao, Y., et al. (2014). Free-standing and mechanically flexible mats consisting of electrospun carbon nanofibers made from a natural product of alkali lignin as binder-free electrodes for high-performance supercapacitors. *J. Power Sour.* 247, 134–141. doi: 10.1016/j.jpowsour.2013.08.082

Lallave, M., Bedia, J., Ruiz-Rosas, R., Rodríguez-Mirasol, J., Cordero, T., Otero, J. C., et al. (2007). Filled and hollow carbon nanofibers by coaxial electrospinning of alcell lignin without binder polymers. *Adv. Mater.* 19, 4292–4296. doi: 10.1002/adma.200700963

Lannutti, J., Reneker, D., Ma, T., Tomasko, D., and Farson, D. (2007). Electrospinning for tissue engineering scaffolds. *Mater. Sci. Eng. C* 27, 504–509. doi: 10.1016/j.msec.2006.05.019

Larsen, G., Velarde-Ortiz, R., Minchow, K., Barrero, A., and Loscertales, I. G. (2003). A method for making inorganic and hybrid (organic/inorganic) fibers and vesicles with diameters in the submicrometer and micrometer range via sol–gel chemistry and electrically forced liquid jets. *J. Am. Chem. Soc.* 125, 1154–1155. doi: 10.1021/ja028983i

Leitten, C. F., Griffith, W. L., Compere, A. L., and Shaffer, J. T. (2002). High-Volume, low-cost precursors for carbon fiber production. *SAE Trans.* 111, 727–734. doi: 10.4271/2002-01-1907

Lin, J., Kubo, S., Yamada, T., Koda, K., and Uraki, Y. (2012). Chemical thermostabilization for the preparation of carbon fibers from softwood lignin. *BioResources* 7, 5634–5646. doi: 10.15376/biores.7.4.5634-5646.

Liu, Z., Ling, X. Y., Su, X., and Lee, J. Y. (2004). Carbon-supported Pt and PtRu nanoparticles as catalysts for a direct methanol fuel cell. *J. Phys. Chem. B* 108, 8234–8240. doi: 10.1021/jp04 9422b

Loscertales, I. G., Barrero, A., Guerrero, I., Cortijo, R., Marquez, M., and Gañán-Calvo, A. M. (2002). Micro/Nano encapsulation via electrified coaxial liquid jets. *Science* 295, 1695–1698. doi: 10.1126/science.1067595

Mikawa, S. (1970). Lignin-based carbon fiber. *Chem. Econ. Eng. Rev.* 2, 43–46.

Miller, J. R. (2016). Engineering electrochemical capacitor applications. *J. Power Sour.* 326, 726–735. doi: 10.1016/j.jpowsour.2016.04.020

Mit-uppatham, C., Nithitanakul, M., and Supaphol, P. (2004). Ultrafine electrospun polyamide-6 fibers: effect of solution conditions on morphology and average fiber diameter. *Macromol. Chem. Phys.* 205, 2327–2338. doi: 10.1002/macp.200400225

Norberg, I., Nordström, Y., Drougge, R., Gellerstedt, G., and Sjöholm, E. (2013). A new method for stabilizing softwood kraft lignin fibers for carbon fiber production. *J. Appl. Polymer Sci.* 128, 3824–3830. doi: 10.1002/app.38588

Pan, H., Li, L., Hu, L., and Cui, X. (2006). Continuous aligned polymer fibers produced by a modified electrospinning method. *Polymer* 47, 4901–4904. doi: 10.1016/j.polymer.2006.05.012

Ragauskas, A. J., Beckham, G. T., Biddy, M. J., Chandra, R., Chen, F., Davis, M. F., et al. (2014). Lignin valorization: improving lignin processing in the biorefinery. *Science* 344:1246843. doi: 10.1126/science.1246843

Rodríguez-Mirasol, J., Cordero, T., and Rodríguez, J. J. (1996). High-temperature carbons from kraft lignin. *Carbon* 34, 43–52. doi: 10.1016/0008-6223(95)00133-6

Rosas J. M., Rodríguez-Mirasol, J., and Cordero, T. (2010). NO Reduction on carbon-supported chromium catalysts. *Energy Fuels* 24, 3321–3328. doi: 10.1021/ef901455v

Rosas, J. M., Bedia, J., Rodríguez-Mirasol, J., and Cordero, T. (2008). Preparation of hemp-derived activated carbon monoliths. *Adsorpt. Water Vapor. Indus. Eng. Chem. Res.* 47, 1288–1296. doi: 10.1021/ie070924w

Rosas, J. M., Bedia, J., Rodríguez-Mirasol, J., and Cordero, T. (2009). HEMP-derived activated carbon fibers by chemical activation with phosphoric acid. *Fuel* 88, 19–26. doi: 10.1016/j.fuel.2008.08.004

Rosas, J. M., Berenguer, R., Valero-Romero, M. J., Rodríguez-Mirasol, J., and Cordero, T. (2014). Preparation of different carbon materials by thermochemical conversion of lignin. *Front. Mater.* 1:29. doi: 10.3389/fmats.2014.00029

Rosas, J. M., Ruiz-Rosas, R., Rodríguez-Mirasol, J., and Cordero, T. (2012). Kinetic study of the oxidation resistance of phosphorus-containing activated carbons. *Carbon* 50, 1523–1537. doi: 10.1016/j.carbon.2011. 11.030

Ruiz-Rosas, R., Bedia, J., Barrero, A., Loscertales, I. G., Rodríguez-Mirasol, J., and Cordero, T. (2009). "Lignin-based electrospun carbon submicrotubes and submicroforms," in *Annual World Conference on Carbon 2009* (Biarritz), 14–19.

Ruiz-Rosas, R., Bedia, J., Lallave, M., Loscertales, I. G., Barrero, A., Rodríguez-Mirasol, J., et al. (2010). The production of submicron diameter carbon fibers by the electrospinning of lignin. *Carbon* 48, 696–705. doi: 10.1016/j.carbon.2009.10.014

Sabantina, L., Rodríguez-Cano, M. Á., Klöcker, M., García-Mateos, F. J., Ternero-Hidalgo, J. J., Mamun, A., et al. (2018). Fixing PAN Nanofiber Mats during Stabilization for Carbonization and Creating Novel Metal/Carbon Composites. *Polymers* 10:735. doi: 10.3390/polym10070735

Son, W. K., Youk, J. H., Lee, T. S., and Park, W. H. (2004). The effects of solution properties and polyelectrolyte on electrospinning of ultrafine poly(ethylene oxide) fibers. *Polymer* 45, 2959–2966. doi: 10.1016/j.polymer.2004.03.006

Tan, S.-H., Inai, R., Kotaki, M., and Ramakrishna, S. (2005). Systematic parameter study for ultra-fine fiber fabrication via electrospinning process. *Polymer* 46, 6128–6134. doi: 10.1016/j.polymer.2005.05.068

Teo, W. E., and Ramakrishna, S. (2006). A review on electrospinning design and nanofibre assemblies. *Nanotechnology* 17, R89–R106. doi: 10.1088/0957-4484/17/14/R01

Uraki, Y., Kubo, S., Kurakami, H., and Sano, Y. (1997). Activated carbon fibers from acetic acid lignin. *Holzforschung* 51, 188–192. doi: 10.1515/hfsg.1997.51.2.188

Uraki, Y., Nakatani, A., Kubo, S., and Sano, Y. (2001). Preparation of activated carbon fibers with large specific surface area from softwood acetic acid lignin. *J. Wood Sci.* 47, 465–469. doi: 10.1007/BF00767899

Valero-Romero, M. J., García-Mateos, F. J., Rodríguez-Mirasol, J., and Cordero, T. (2017). Role of surface phosphorus complexes on the oxidation of porous carbons. *Fuel Process. Technol.* 157, 116–126. doi: 10.1016/j.fuproc.2016. 11.014

Wang, S.-X., Yang, L., Stubbs, L. P., Li, X., and He, C. (2013). Lignin-Derived fused electrospun carbon fibrous mats as high performance anode materials for lithium ion batteries. *ACS Appl. Mater. Interfaces* 5, 12275–12282. doi: 10.1021/am4043867

Wang, X., Lu, X., Liu, B., Chen, D., Tong, Y., and Shen, G. (2014). Flexible energy-storage devices: design consideration and recent progress. *Adv. Mater.* 26, 4763–4782. doi: 10.1002/adma.201400910

Wu, X., and Radovic, L. R. (2006). Inhibition of catalytic oxidation of carbon/carbon composites by phosphorus. *Carbon* 44, 141–151. doi: 10.1016/j.carbon.2005.06.038

Xue, J., Xie, J., Liu, W., and Xia, Y. (2017). Electrospun nanofibers: new concepts, materials, and applications. *Acc. Chem. Res.* 50, 1976–1987. doi: 10.1021/acs.accounts.7b00218

Conflict of Interest Statement: The authors declare that the research was conducted in the absence of any commercial or financial relationships that could be construed as a potential conflict of interest.

frontiers in Materials

ORIGINAL RESEARCH
published: 24 April 2019
doi: 10.3389/fmats.2019.00080

Direct and Indirect Recycling Strategies of Expired Oxytetracycline for the Anode Material in Lithium Ion Batteries

Hongying Hou[1], Zhipeng Dai[1], Xianxi Liu[2], Yuan Yao[1], Chengyi Yu[1] and Dongdong Li[1]*

[1] Faculty of Material Science and Engineering, Kunming University of Science and Technology, Kunming, China, [2] Faculty of Mechanical and Electrical Engineering, Kunming University of Science and Technology, Kunming, China

It is well-known that the antibiotics inhibit the wide spread of various infection diseases and guarantee the life safety of many patients. However, various waste antibiotics into the environment also pose the great challenges of the environmental contamination and the ecological poison. Unreasonable disposal of expired antibiotics is one of the main sources of waste antibiotics in the ecological environment. For this reason, in order to focus on the circular economy of such highly refined medical grade chemicals, expired oxytetracycline was recycled for the anode active material in lithium ion batteries (LIBs) by direct and indirect strategies. That is, it was directly used as the anode active material or recycled by two-step carbonization for LIBs anode. Furthermore, the effect of these two strategies on the electrochemical performances was also discussed. Both anode materials showed their individual advantages and high feasibility for LIBs anode. For example, both them delivered the satisfactory Li-storage performances. Additionally, the direct route possessed lower recycling cost and high recovery rate, while the application range of carbon material in the indirect route was broader.

Keywords: expired oxytetracycline, recycling, carbon anode, lithium ion batteries, circular economy

OPEN ACCESS

Edited by:
Jie-Sheng Chen,
Shanghai Jiao Tong University, China

Reviewed by:
Wei Luo,
Tongji University, China
Mataz Alcoutlabi,
The University of Texas Rio Grande Valley, United States
Chunhai Jiang,
Xiamen University of Technology, China

****Correspondence:***
Hongying Hou
hongyinghou@kmust.edu.cn;
hongyinghou@hotmail.com

Specialty section:
This article was submitted to Colloidal Materials and Interfaces, a section of the journal Frontiers in Materials

Received: *13 February 2019*
Accepted: *05 April 2019*
Published: *24 April 2019*

Citation:
Hou H, Dai Z, Liu X, Yao Y, Yu C and Li D (2019) Direct and Indirect Recycling Strategies of Expired Oxytetracycline for the Anode Material in Lithium Ion Batteries. Front. Mater. 6:80. doi: 10.3389/fmats.2019.00080

INTRODUCTION

The development of the mankind has been accompanied by various infection diseases, that is, various lives in the world have suffered from the threats from various infection diseases. Fortunately, the discovery of the antibiotics in the twentieth century defended these lives against the attacks from various infection diseases owing to broad-spectrum antibacterial activity and easy availability. Therefore, massive antibiotics were produced in large scale for the clinic therapy of the infection diseases, and the annual consumption in the world reached about 100,000–200,000 tons (Kummerer, 2009; Wang et al., 2017). Unfortunately, not all the antibiotics can be completely consumed prior to the validity period. Resultantly, about 40% antibiotics are inevitably overdue and surplus. As one of important indicators about the safety and the effectiveness of medicines, the validity period can guarantee the medication safety and avoid the occurrence of the medical accidents with very low probability. So once the antibiotics expire, they can't be continually used for the clinical therapy anymore. Currently, these expired antibiotics generally experience the incineration or landfill. However, such treatments will lead to the waste of useful resources as well as the environment pollutions. It is very difficult to eliminate the antibiotics once they flow into

the natural environment (Wang et al., 2014; Xiong et al., 2017). The antibiotics in the ecological environment would do harm to the creatures and induce the generation of the antibiotic-resistant bacteria, thus making the treatment of the patients more difficult and increasing the mortality (Yan et al., 2013; Sullivan et al., 2017). Therefore, it is urgent to reasonably recycle the expired antibiotics and effectively prevent from their emission into the environment. In fact, for these highly refined medical grade chemicals, the expiration does not always mean the metamorphism. So it is particularly important to pursue the new strategy to exploit the secondary non-medical value for the alternative applications, thereby reducing their damage to the ecological environment.

Since being commercialized in 1991, lithium ion batteries (LIBs) have been widely applied, and many desirable materials have been investigated for the anode active materials in LIBs, such as carbon, Si, Sn, P, alloys, metal oxides, carbonyl compounds, and so on (Ji et al., 2011, 2016; Liang et al., 2012; Agubra et al., 2016, 2017; Zuo et al., 2017; Agrawal et al., 2018). As one kind of common antibiotics with easy availability and broad-spectrum antibacterial activity, oxytetracycline has been widely applied in the clinical therapy since the commercialization in the middle of nineteenth century (Auerbach et al., 2007; Harja and Ciobanu, 2018). Its molecular structure is composed of four fused rigid rings and several functional groups on the rings such as hydroxyl and amino groups, methyl groups, tertiary amine group, and carbonyl groups, as shown in **Scheme 1**. Such a structure would make the direct recycling route possible. For example, carbonyl group possesses the potential electrochemical Li-storage activity, while the skeleton may guarantee the structural stability during the cyclic lithiation/delithiation (Armand et al., 2009; Schon et al., 2016). Meanwhile, considering that organic oxytetracycline contains the abundant carbon element, it should be a suitable carbon precursor and serve as the anode material in LIBs after carbonization. Seemingly, it may be an interesting attempt to reuse expired oxytetracycline as the anode active material in LIBs via the direct or indirect routes.

As mentioned above, the direct recycling strategy as the anode material mainly depends on the electrochemical Li-storage activity of the functional group within the oxytetracycline. However, not all the organic drugs are active to the electrochemical Li-storage. Alternatively, the indirect strategy can make up for this limitation and play an important role in recycling the expired medicines, because quite a few organic drugs contain rich carbon element and can be indirectly applied as LIBs anode after carbonization. Considering that hydrothermal carbonation may facilitate to form the regular morphology with uniform particles size, it could be used to control the morphology during the carbonization of expired oxytetracycline (Titirici and Antonietti, 2009; Tang et al., 2012; Zhang et al., 2012). However, to the best of our knowledges, the corresponding report is still scarce. Herein, such an attempt was made: both the direct and indirect strategies were adopted to recycle the expired oxytetracycline for the anode active material in LIBs, and the effect of different recycling routes was also compared and discussed.

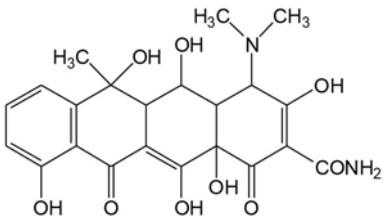

SCHEME 1 | Chemical structural formula of the oxytetracycline.

EXPERIMENTAL

The Recycling of Expired Oxytetracycline Tablets

The expired oxytetracycline tablets (containing more than 90 wt% of oxytetracycline before expiration) were from the household reserve, and the expiration time was half a year. As shown in **Figure 1**, these tablets were recycled by direct and indirect routes, respectively. In the case of the direct recycling strategy, the expired oxytetracycline tables were directly downgraded as the anode active material in LIBs after being ground into the powders. For the indirect route, expired oxytetracycline tables were recycled via hydrothermal carbonization and the subsequent pyrolysis. Firstly, 2.3 g expired oxytetracycline powders were dissolved in 50 mL 0.7 wt% HCl solution and stirred for 0.5 h. Secondly, the resultant yellow solution was heated at 200°C for 5 h in an autoclave as a result of black suspension. Thirdly, the black solid powders were collected from the black suspension and pyrolysed at 800°C for 1 h in N_2 atmosphere. Finally, some black carbon powders were obtained after being cleaned and dried.

Characterization of Microstructure and Morphology

The microstructure and morphology of the samples were characterized by scanning electron microscopy (SEM) (Quanta 200, FEI, USA), energy dispersive X-ray spectroscopy (EDS) (Apollo, EDAX, USA), Fourier transform infrared (FTIR) spectra (Nicolet iS10, USA), X-ray photoelectron spectroscopy (XPS) (K-α+, Thermo Fisher, USA) and X-ray diffraction (XRD) (TTRAX III, Riguku, Japan) with Cu Kα radiation ($\lambda = 1.5406$ Å) at 40 kV and 10°/min, respectively.

Electrochemical Measurements

The electrode slurries were prepared by mixing expired oxytetracycline powders or expired-oxytetracycline-derived carbon powders with acetylene black and polyvinylidene fluoride in mass ratios of 6:3:1 and 8:1:1 in N-methy-2-pyrrolidine, respectively. The anodes were obtained by pasting the slurries onto the single surface of Cu foils and then vacuum dried at 60°C for 12 h, and the corresponding densities of active materials were about 1.2 and 1.5 mg/cm^2, respectively. The electrochemical Li-storage performances were tested by assembling CR2025 coin cells with Li foil and Celgard 2,400 film as the counter electrode and the separator, respectively. The electrolyte was 1 M $LiPF_6$

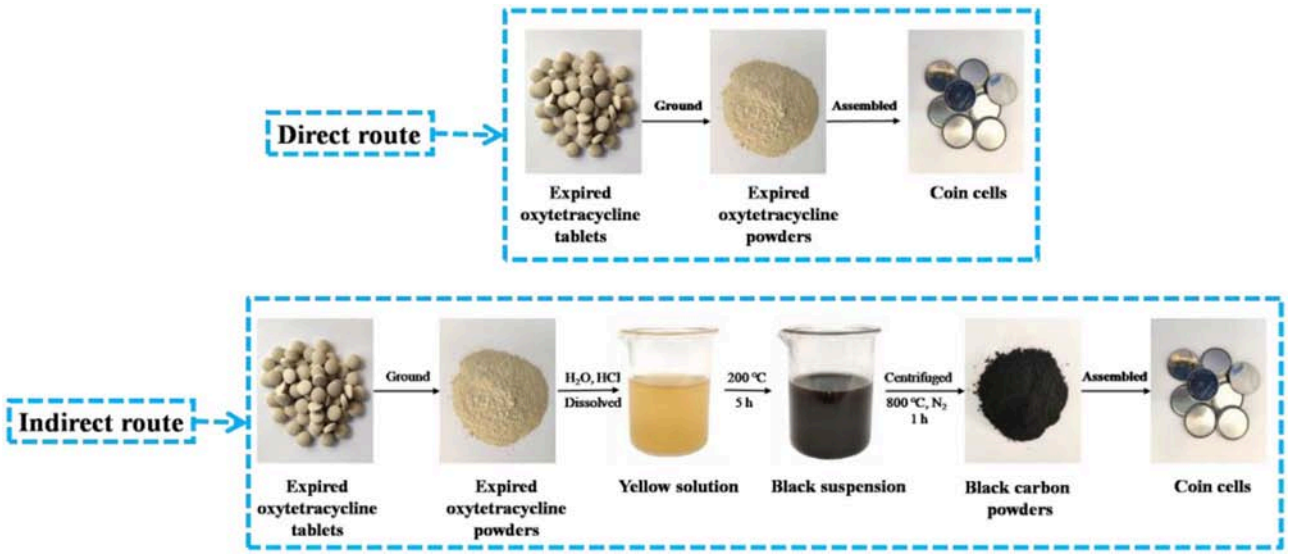

FIGURE 1 | The direct and indirect recycling routes of expired oxytetracycline.

in the mixed ethylene carbonate and diethyl carbonate (1:1 in volume). The voltage ranged from 0.01 V to 3.0 V and the current densities were 50, 100, 200, 400, 800, 1,600, and 2,000 mA/g, respectively. Furthermore, cyclic voltammetry (CV) was performed on an electrochemical workstation (Parstat 4,000, Princeton Applied Research, USA) at 0.2 , 0.4, 0.6, 0.8, and 1.0 mV/s between 0.01 and 3.0 V, and alternative current (AC) impedance was also measured from 0.01 Hz to 10^2 kHz with 10 mV amplitude at open circuit voltage of 1.0 V.

RESULTS AND DISCUSSION

SEM-EDS

SEM images and EDS spectra of the expired oxytetracycline powders and the expired-oxytetracycline-derived carbon powders were shown in **Figure 2**. Prior to two-step carbonization, expired oxytetracycline powders manifested the morphology of irregular microparticles with the diameter of 5.5–11.9 μm, and many smaller particles attached onto the surface of larger ones (in **Figures 2A,B**). Such multi-scale particles may be beneficial for the large electrode/electrolyte interface area and the ionic diffusion. According to EDS spectrum in **Figure 2C**, the main elements in the expired oxytetracycline remained C, N, and O, coinciding with the chemical element composition of oxytetracycline. To be different, after two-step carbonization, the expired-oxytetracycline-derived carbon powders appeared as many regular microspheres with the diameter from about 2.0 μm to hundreds of nanometers, in which some smaller spheres dispersed on the surface or among the gaps of larger microspheres (in **Figures 2D,E**). Only C and O elements were detected in EDS spectrum in **Figure 2F**. Compared with EDS spectrum of the expired oxytetracycline, the peak of C element became stronger, while the peak of O element became weaker, and the signal peak of N element even disappeared, indicating high carbonization degree of expired oxytetracycline.

FTIR Analysis

In order to gain the insight into the micro-structure of the samples, FTIR spectra were also recorded, as shown in **Figure 3**. In the case of expired oxytetracycline, the signal peaks were sharp and ample. In detail, one peak at 3,479 cm^{-1} could be ascribed to the stretching vibration of O-H bond, while three peaks at 1,395, 1,315, and 678 cm^{-1} could be assigned to the bending vibration of O-H bond (Jin et al., 2016; Hou et al., 2018a). One peak at 3,372 cm^{-1} resulted from the stretching vibration of N-H bond, and two peaks at 1,245 and 781 cm^{-1} were due to the bending vibration of N-H bond (Jin et al., 2016; Hou et al., 2018a). Three peaks at 1,650, 1,622, and 1,590 cm^{-1} were attributed to the stretching vibrations of C=O bonds on the amide and the rings (Aristilde et al., 2010; Mahamallik et al., 2015). Two peaks at 1,520 and 1,462 cm^{-1} were ascribed to the stretching vibrations of C=C bond (Hou et al., 2018a). In addition, one peak at 3,082 cm^{-1} was indexed to the stretching vibration of C-H bond, and three peaks at 937, 861, and 839 cm^{-1} were due to the bending vibration of C-H bond (Hou et al., 2018a). Furthermore, three peaks at about 1,125, 1,182, and 1,010 cm^{-1} corresponded to the stretching vibrations of C-N bond, C-O bond, and C-C bond, respectively (Aristilde et al., 2010; Orellana et al., 2010). Seemingly, FTIR spectrum analysis indicated that the main structure in the expired oxytetracycline didn't significantly change. After two-step carbonization, most of the signal peaks disappeared, and only three broad peaks remained at 3,435, 1,618, and 1,060 cm^{-1}, corresponding to the stretching vibrations of O-H bond, C=O bond and C-C/C-O bonds, respectively (Hou et al., 2018b). FTIR result indicated that small amount of residual O-containing functional groups remained even after two-step carbonization, in according with EDS spectrum.

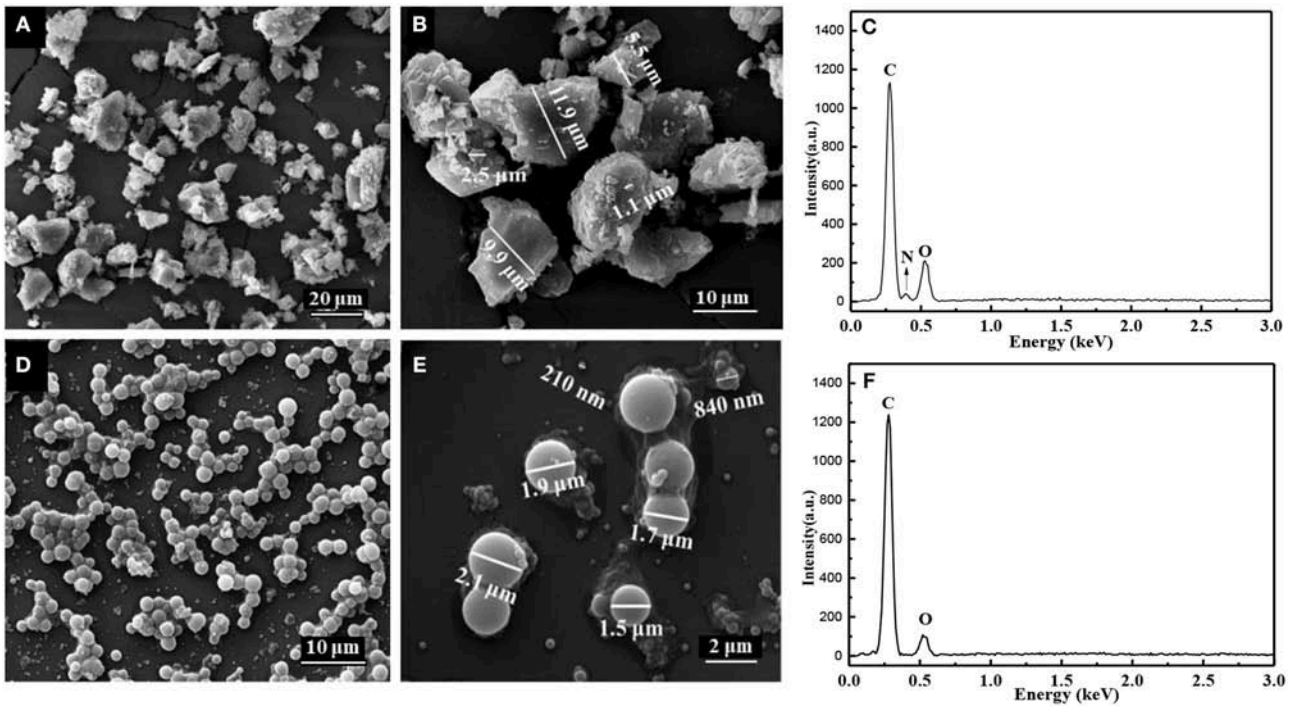

FIGURE 2 | SEM images of **(A,B)** expired oxytetracycline powders and **(D,E)** expired-oxytetracycline-derived carbon powders, and EDS spectra of **(C)** expired oxytetracycline powders and **(F)** expired-oxytetracycline-derived carbon powders.

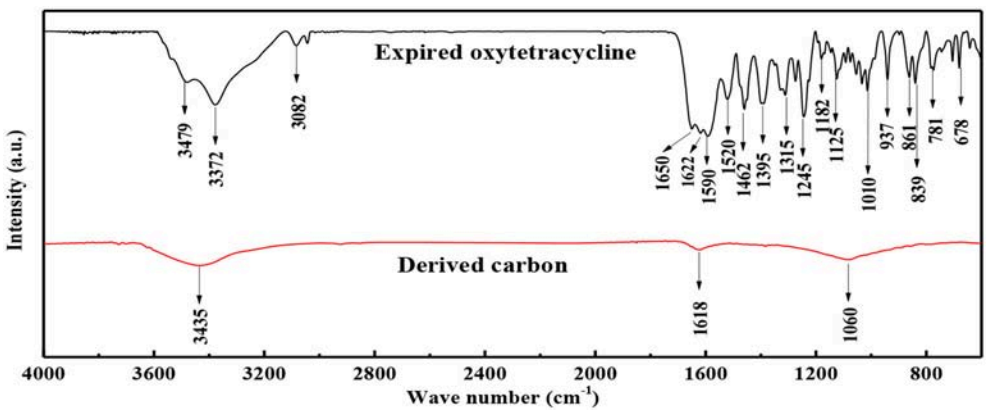

FIGURE 3 | FTIR spectra of expired oxytetracycline and expired-oxytetracycline-derived carbon powders.

XPS Analysis

The binding states of chemical elements in the samples were further studied by XPS technology, as shown in **Figure 4**. In the wide scan spectrum of expired oxytetracycline, the signal peaks at about 285, 399, and 533 eV were indexed to C 1s, N 1s, and O 1s, respectively (**Figure 4A**). After carbonization, only two signal peaks corresponding to C 1s and O 1s still appeared, in which C 1s peak became stronger, while O 1s peak became much weaker and N 1s peak was even absent. Such changes again confirmed the carbonization of expired oxytetracycline, which was consistent with EDS results. Furthermore, these signal peaks can be deconvoluted. In detail, C 1s peak of expired oxytetracycline could be further deconvoluted into four peaks at 284.8, 285.4, 286.4, and 287.9 eV, which were assigned to C-C/C-H, C=C, C-O/C-N and C=O bonds, respectively (**Figure 4B**). N 1s spectrum was divided into two peaks at 399.2 and 401.4 eV, corresponding to C-N and N-H bonds, respectively (**Figure 4C**). O 1s spectrum in **Figure 4D** was fitted into three peaks at 530.8, 531.7, and 532.7 eV, which could be ascribed to O-H, C=O and C-O bonds (Hou et al., 2018a). After carbonization, only three peaks at 284.8 eV (C-C bond), 286.4 eV (C-O bond), and 287.9 eV (C=O bond) were detected in C 1s spectrum, and the

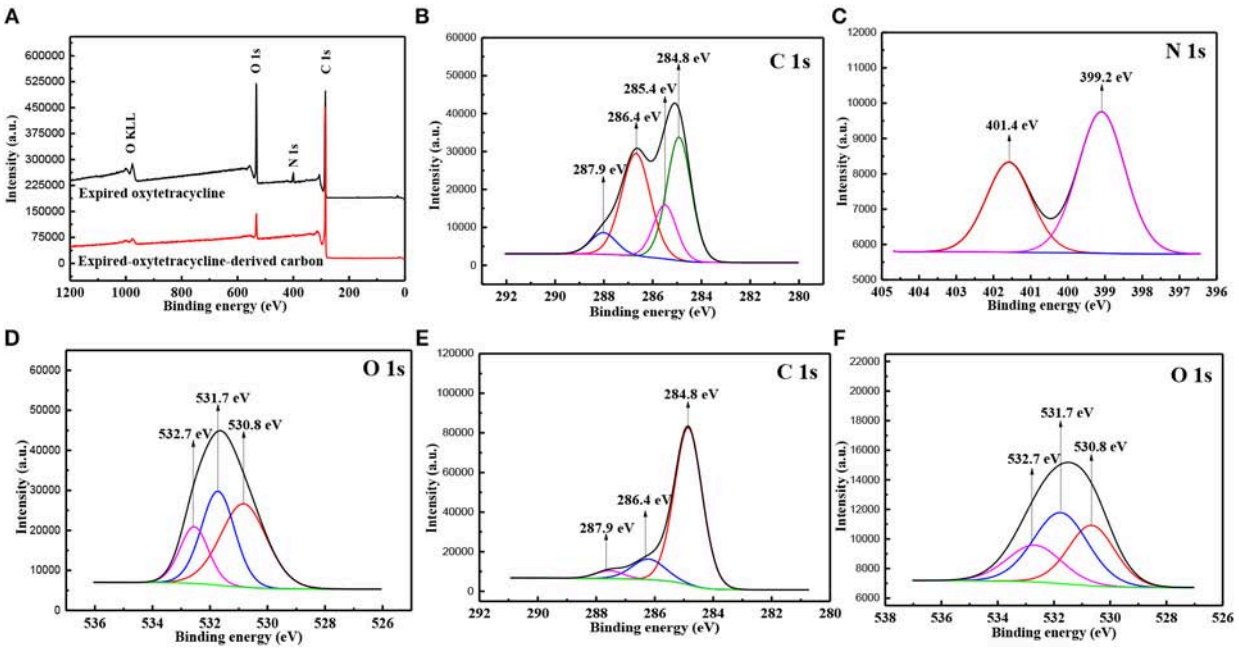

FIGURE 4 | The wide scan XPS spectra **(A)** of expired oxytetracycline and its derived carbon powders, spectra of **(B)** C 1s, **(C)** N 1s and **(D)** O 1s in expired oxytetracycline, and spectra of **(E)** C 1s, **(F)** O 1s in expired-oxytetracycline-derived carbon.

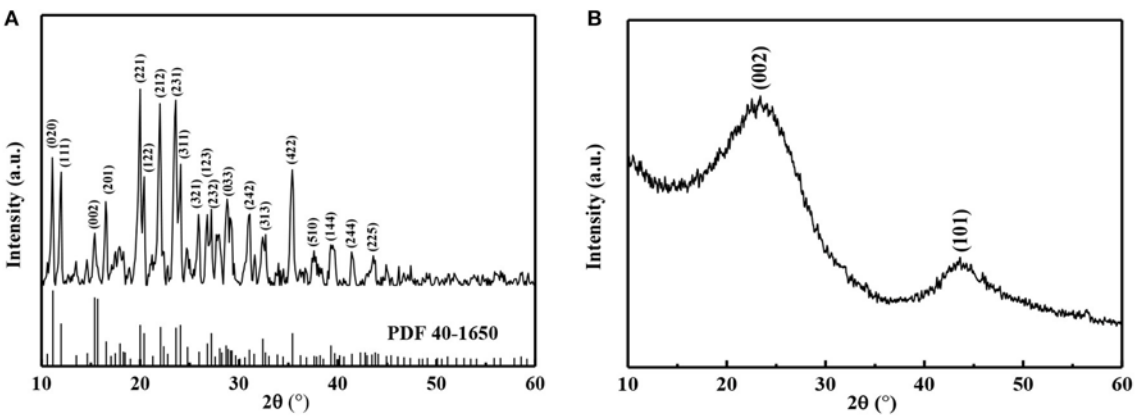

FIGURE 5 | XRD patterns of **(A)** expired oxytetracycline and **(B)** expired-oxytetracycline-derived carbon powders.

peak at 285.4 eV corresponding to C=C bond disappeared, as shown in **Figure 4E**. O 1s spectrum in **Figure 4F** could be also deconvoluted into three peaks similar to the results in **Figure 4D**, except that the peak intensities became weaker. Obviously, the binding states of chemical elements within two samples were further verified by XPS spectra, in good agreement with EDS and FTIR analysis.

XRD Analysis

XRD patterns of two samples were recorded, as shown in **Figure 5**. In the case of XRD pattern of expired oxytetracycline powders, many sharp diffraction peaks were detected, indicating highly crystal structure of the oxytetracycline due to its orderly molecular structure with four linearly annulated rigid six-membered rings (in **Figure 5A**) (Stezowski, 1976; Toro et al., 2007). According to the standard JCPDS card (No. 40-1650), these diffraction peaks at $2\theta = 11.1°$, 11.9°, 15.4°, 16.6°, 20.0°, 20.4°, 22.1°, 23.6°, 24.1°, 25.9°, 26.8°, 27.2°, 28.7°, 31.1°, 32.7°, 35.4°, 37.6°, 39.3°, 41.4° and 43.5° could be assigned to the crystal planes (020), (111), (002), (201), (221), (122), (212), (231), (311), (321), (123), (232), (033), (242), (313), (422), (510), (144), (244), and (225) of the oxytetracycline with $P2_12_12_1$ space group. As for XRD pattern of expired-oxytetracycline-derived carbon powders (**Figure 5B**), two classic diffraction peaks were observed at $2\theta = 23°$ and 43°, corresponding to the reflections of (002) crystal plane of parallel-stacked graphene sheets and

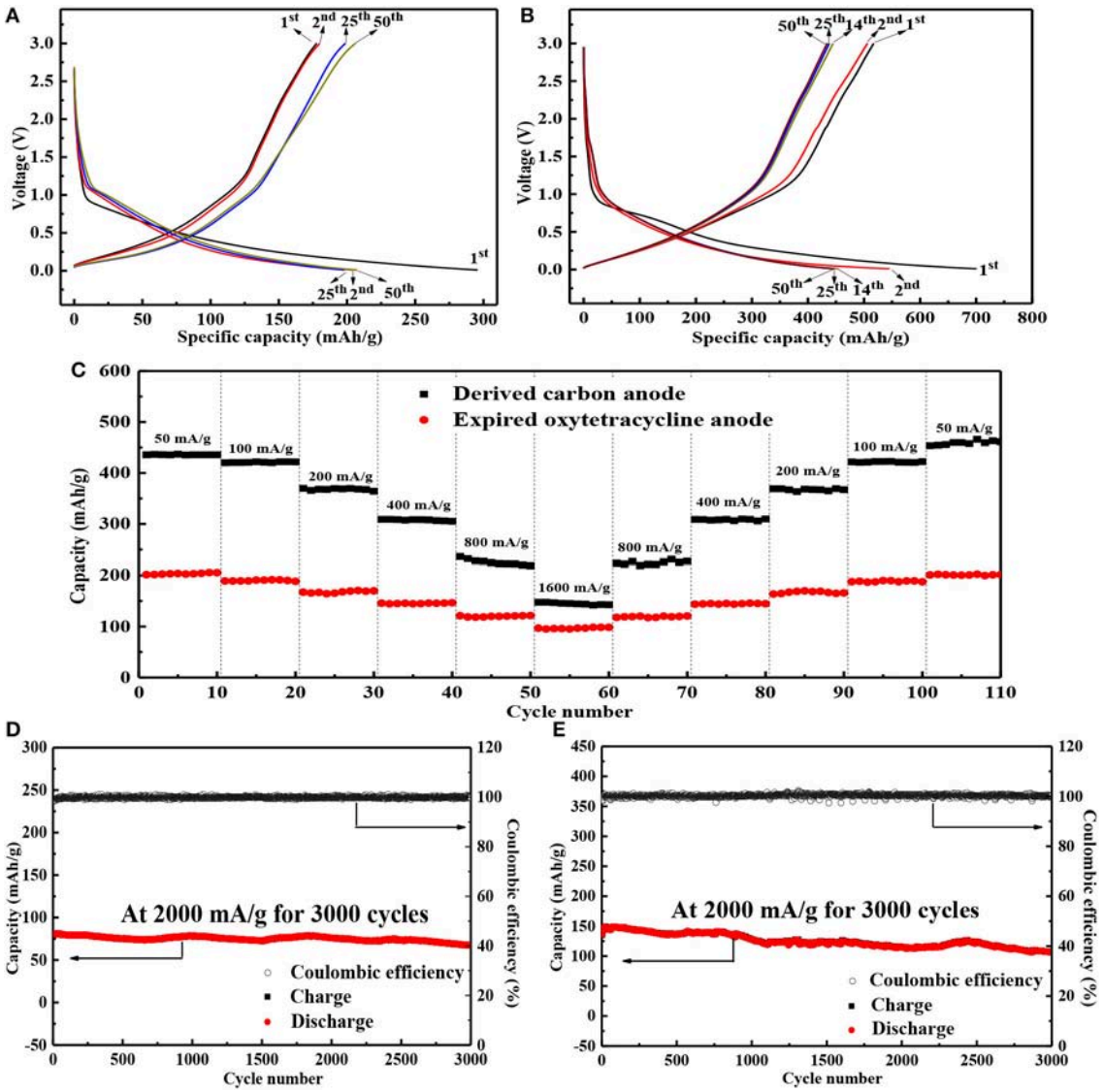

FIGURE 6 | Representative charge/discharge profiles of **(A)** expired oxytetracycline anode and **(B)** expired-oxytetracycline-derived carbon anode at 50 mA/g, **(C)** the rate performances of both anodes and the cyclic performances of **(D)** expired oxytetracycline anode and **(E)** expired-oxytetracycline-derived carbon anode.

(101) crystal plane of sp^2 carbon with the honeycomb structure, respectively (Han et al., 2014; Wu et al., 2016). Additionally, these two diffraction peaks were broad and weak, indicating amorphous structure.

Electrochemical Performances

Charge/Discharge Performances

When the expired oxytetracycline was directly downgraded as the anode active material in LIBs, the initial and second specific charge/discharge capacities were 177.8/295.8 and 180.0/204.4 mAh/g, respectively, as shown in **Figure 6A**. The initial Coulombic efficiency (ICE) and the initial irreversible discharge capacity loss can be calculated as 60.1 and 30.9%, which may be due to the decomposition of the electrolyte and the formation of solid electrolyte interface (SEI) film on the electrode surface during the initial discharging (Armand et al., 2009; Sun et al., 2016). Subsequently, the discharge specific capacity stably maintained at 207.4 mAh/g and the Coulombic efficiency increased above 99.0%, indicating high reversibility and feasibility of the expired oxytetracycline anode. After two-step carbonization, the initial and second charge/discharge capacities of expired-oxytetracycline-derived carbon anode were 517.4/700.2 and 506.1/545.0 mAh/g, respectively (**Figure 6B**). The corresponding ICE and the initial irreversible discharge capacity loss were 73.9 and 22.2 %, respectively, mainly due to the formation of SEI film and the irreversible Li^+ insertion/deinsertion in the spaces of carbon anode during the initial discharge (Elizabeth et al., 2016; Zuniga et al., 2016; Huang et al., 2018). Subsequently, the electrochemical reaction gradually tended to be stable. The profiles almost overlapped

TABLE 1 | The comparison of performances of expired oxytetracycline with other analogous organic anode materials in literatures.

Anode materials	Initial discharge capacity (mAh/g), ICE	Capacity (mAh/g) @ current density (mA/g) for cycles	Literatures
Expired-oxytetracycline	296, 60%	207 @ 50 for 50	This work
Li terephthalate	236, 66%	85 @ 15 for 50	Zhang et al., 2014
Tetralithium 2,5-dihydroxyterephthalic acid	358, 71%	232 @ 24 for 50	Wang et al., 2013b
Dilithium benzenediacrylate	246, 42%	170 @ 12 for 20	Renault et al., 2013

TABLE 2 | The comparison of performances of expired-oxytetracycline-derived carbon with those of other precursors-based carbon anode in literatures.

Carbon matrix precursors	Initial discharge capacity (mAh/g), ICE	Capacity (mAh/g) @ current density (mA/g) for cycles	Literatures
Expired-oxytetracycline	700, 74%	450 @ 50 for 50	This work
Sucrose	906, 52%	315 @ 50 for 100	Agrawal et al., 2018
Rice husk	789, 51%	403 @ 75 for 100	Wang et al., 2013a
Sugarcane bagasse	560, 45%	310 @ 200 for 100	Matsubara et al., 2010

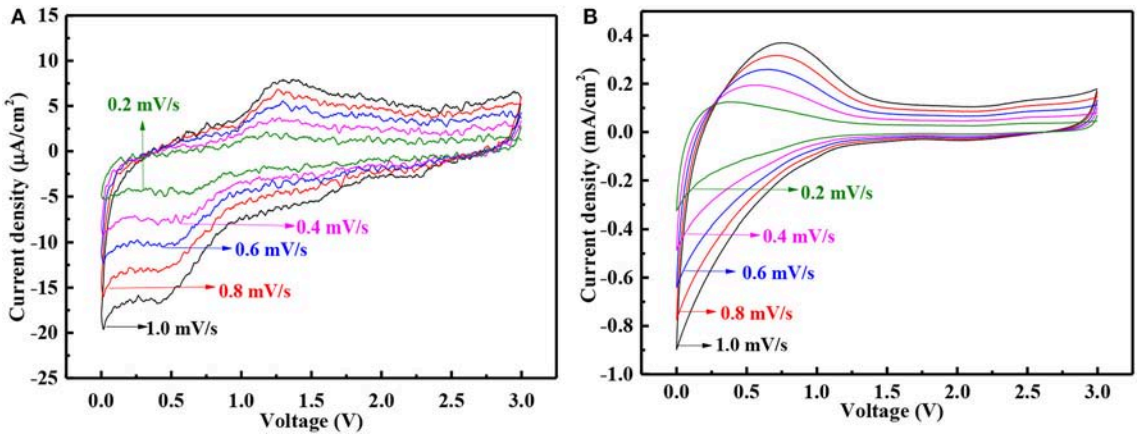

FIGURE 7 | CV curves at different scanning rates of **(A)** expired oxytetracycline anode and **(B)** expired-oxytetracycline-derived carbon anode.

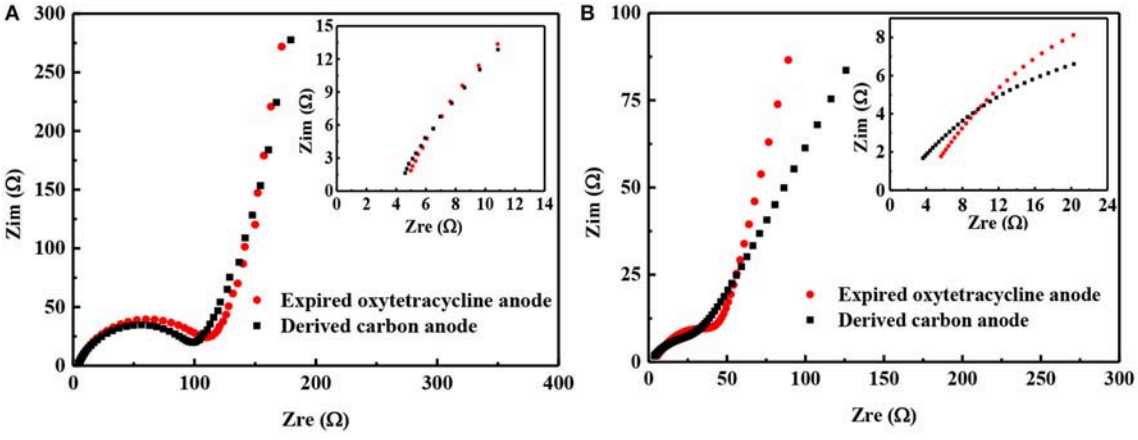

FIGURE 8 | Nyquist plots of two anodes **(A)** before and **(B)** after 500 cycles.

each other from the 14th cycle and the discharge capacities stabilized at 450.3 mAh/g. At the same time, Coulombic efficiency also increased above 97.5%, implying high reversibility of the expired-oxytetracycline-derived carbon anode.

Additionally, both anodes also delivered high rate performances, as shown in **Figure 6C**. For example, when the expired oxytetracycline anode was cycled at the different current densities of 50, 100, 200, 400, 800, and 1,600 mA/g, respectively, the corresponding average reversible specific capacities were 207.4, 188.5, 166.9, 144.5, 119.1, and 96.7 mAh/g; while those of the expired-oxytetracycline-derived carbon anode were about 450.3, 421.1, 367.9, 307.7, 225.3, and 144.8 mAh/g, respectively. With the stepwise decrease of the current density, all the reversible discharge capacities could rapidly restore, demonstrating high tolerance to the large current changes. Moreover, both anodes also exhibited stable cyclic performances even at 2,000 mA/g for 3,000 cycles, as shown in **Figures 6D,E**. In detail, the expired oxytetracycline and expired-oxytetracycline-derived carbon anodes delivered average discharge capacities of 75.1 and 125.3 mAh/g. Meanwhile, the Coulombic efficiency of both anodes could maintain at about 100% during the long-term cycling. Seemingly, both the direct and indirect recycling routes were feasible during the reutilization of expired oxytetracycline. The electrochemical Li-storage performances of expired oxytetracycline anode in the direct strategy were slightly lower than those of carbon anode from the indirect route, but the electrochemical Li-storage capacity was comparable with those of other similar organic anodes in literatures, as listed in **Table 1**; moreover, this recycling strategy was simpler and cheaper, and the recovery was higher (close to 100%). On the other hand, although the indirect route was relatively complicated and expensive, the resultant carbon material possessed wider application range, and its Li-storage performances were also comparable with those of other precursors-based carbon anodes in literatures (**Table 2**). In a word, both recycling strategies possessed their individual advantages.

CV Curves and AC Impedance

In order to further explore the electrochemical reaction mechanism during the charge/discharge, CV curves of two anodes were recorded at different scanning rates, as shown in **Figures 7A,B**. In the case of expired oxytetracycline anode, one couple of redox peaks were detected at 0.5 and 1.2 V, corresponding to the revisable lithiation/delithiation of C=O group, respectively. The possible electrochemical reaction mechanism can be depicted as the following formula (1) (Hou et al., 2018a). Likewise, one couple of redox peaks were also detected in the CV curves of the expired-oxytetracycline-derived carbon anode, but these two peaks appeared at 0 and 0.5 V respectively. In the case of Li-storage mechanism of carbon anode, Li^+ can reversibly intercalate into and deintercalate from the interspaces, so this couple of redox peaks should be attributed to Li^+ insertion/deinsertion in carbon anode structure (Liu et al., 1996; Hou et al., 2018b). With the increase of the scanning rate, all of the peaks became stronger and the peak interval gradually increased. Additionally, compared to the expired oxytetracycline anode, the expired-oxytetracycline-derived carbon anode displayed higher peak current at the same scanning rate possibly attributed to its higher electrical conductivity.

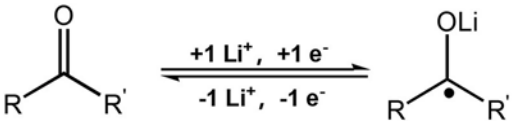

(1)

Finally, the electrochemical impedances of both anodes were also measured before and after 500 cycles. Before cycling, the internal resistance (R_s) and the charge transfer resistance (R_{ct}) of expired-oxytetracycline anode can be estimated as 4.5 and 103.1 Ω, respectively, higher than 4.3 and 94.3 Ω of expired oxytetracycline-derived carbon anode, as shown in **Figure 8A**, (Duan et al., 2016). Higher electrical conductivity, smaller particle size and more regular micro-sphere morphology of the expired-oxytetracycline-derived carbon may be responsible for this difference. After cycling, R_s and R_{ct} of expired oxytetracycline anode decreased to 3.2 and 52.1 Ω, while those of expired-oxytetracycline-derived carbon anode also decreased to 2.3 and 39.8 Ω, respectively, possibly attributed to gradually activation of the anode during the cycling, as shown in the **Figure 8B** (Sun et al., 2018).

CONCLUSIONS

In summary, expired oxytetracycline was recycled for LIBs anode active materials by direct and indirect strategies, respectively. The direct strategy may be limited by the functional group with electrochemical Li-storage activity, but the simplicity, high recovery and low cost were greatly impressed. The indirect strategy need two-step carbonization with high cost and energy consumption, but it was suitable for almost all the expired organic carbon-containing waste drugs, and the resultant carbon material can be applied in more fields such as supercapacitor, LIBs, catalyst support, adsorbent and so on. Seemingly, both routes possessed their individual merits, providing the new strategies to reutilize highly refined medical grade chemicals and delaying the submission of these chemicals into the waste streams.

AUTHOR CONTRIBUTIONS

HH: design experiments and write manuscript; ZD: complete major experiments and analysis data; XL: provide theoretical support; YY, CY, and DL: provide help to complete the experiment.

ACKNOWLEDGMENTS

This work was financially supported by the National Natural Science Foundations of China (Grant No. 51566006 and 51363011), the 46th Scientific Research Foundation for the Returned Overseas Chinese Scholars, State Education Ministry in China (6488-20130039), the 19th Young Academic and Technical Leaders of Yunnan Province (1097-10978240), the Program of High-level Introduced Talent of Yunnan Province (10978125) and the Project of Key Discipline (14078232 and 14078311).

REFERENCES

Agrawal, A., Biswas, K., Srivastava, S., and Ghosh, S. (2018). Effect of N-doping on hard carbon nano-balls as anode for Li-ion battery: improved hydrothermal synthesis and volume expansion study. *J. Solid State Electrochem.* 22, 3443–3455. doi: 10.1007/s10008-018-4044-6

Agubra, V., Zuniga, L., Flores, D., Campos, H., Villarreal, J., and Alcoutlabi, M. (2017). A comparative study on the performance of binary SnO_2/NiO/C and Sn/C composite nanofibers as alternative anode materials for lithium ion batteries. *Electrochim. Acta* 224, 608–621. doi: 10.1016/j.electacta.2016.12.054

Agubra, V., Zuniga, L., Flores, D., Villarreal, J., and Alcoutlabi, M. (2016). Composite nanofibers as advanced materials for Li-ion, Li-O_2 and Li-S batteries. *Electrochim. Acta* 192, 529–550. doi: 10.1016/j.electacta.2016.02.012

Aristilde, L., Marichal, C., Miéhé-Brendlé, J., Lanson, B., and Charlet, L. (2010). Interactions of oxytetracycline with a smectite clay: a spectroscopic study with molecular simulations. *Environ. Sci. Technol.* 44, 7839–7845. doi: 10.1021/es102136y

Armand, M., Grugeon, S., Vezin, H., Laruelle, S., Ribière, P., Poizot, P., et al. (2009). Conjugated dicarboxylate anodes for Li-ion batteries. *Nat. Mater.* 8, 120–125. doi: 10.1038/nmat2372

Auerbach, E. A., Seyfried, E. E., and McMahon, K. D. (2007). Tetracycline resistance genes in activated sludge wastewater treatment plants. *Water Res.* 41, 1143–1151. doi: 10.1016/j.watres.2006.11.04

Duan, J., Hou, H., Liu, X., Liu, S., Liao, Q., and Yao, Y. (2016). High performance PPO/Ti^{3+}/TiO_2NT membrane/electrode for lithium ion battery. *Ceram. Int.* 42, 16611–16618. doi: 10.1016/j.ceramint.2016.07.082

Elizabeth, I., Singh, B. P., Trikha, S., and Gopukumar, S. (2016). Bio-derived hierarchically macro-meso-micro porous carbon anode for lithium/sodium ion batteries. *J. Power Sources* 329 (Supplement C), 412–421. doi: 10.1016/j.jpowsour.2016.08.106

Han, S. W., Jung, D. W., Jeong, J. H., and Oh, E. S. (2014). Effect of pyrolysis temperature on carbon obtained from green tea biomass for superior lithium ion battery anodes. *Chem. Eng. J.* 254, 597–604. doi: 10.1016/j.cej.2014.06.021

Harja, M., and Ciobanu, G. (2018). Studies on adsorption of oxytetracycline from aqueous solutions onto hydroxyapatite. *Sci. Total Environ.* 628, 36–43. doi: 10.1016/j.scitotenv.2018.02.027

Hou, H., Dai, Z., Liu, X., Yao, Y., Liao, Q., Yu, C., et al. (2018a). Reutilization of the expired tetracycline for lithium ion battery anode. *Sci. Total Environ.* 630, 495–501. doi: 10.1016/j.scitotenv.2018.02.126

Hou, H., Yu, C., Liu, X., Yao, Y., Liao, Q., Dai, Z., et al. (2018b). Waste-loofah-derived carbon micro/nano particles for lithium ion battery anode. *Surf. Innovations* 6, 159–166. doi: 10.1680/jsuin.17.00068

Huang, X. D., Zhang, F., Gan, X. F., Huang, Q. A., Yang, J. Z., Lai, P. T., et al. (2018). Electrochemical characteristics of amorphous silicon carbide film as a lithium-ion battery anode. *RSC Adv.*8, 5189–5196. doi: 10.1039/c7ra12463e

Ji, L., Lin, Z., Alcoutlabi, M., and Zhang, X. (2011). Recent developments in nanostructured anode materials for rechargeable lithium-ion batteries. *Energy Environ. Sci.* 4, 2682–2699. doi: 10.1039/c0ee00699h

Ji, L., Meduri, P., Agubra, V., Xiao, X., and Alcoutlabi, M. (2016). Graphene-based nanocomposites for energy storage. *Adv. Energy. Mater.* 6:1502195. doi: 10.1002/aenm.201502159

Jin, X., Qiu, S., Wu, K., Jia, M., Xiong, F., Gu, C., et al. (2016). The effect of Cu^{2+} chelation on the direct photolysis of oxytetracycline: a study assisted by spectroscopy analysis and DFT calculation. *Environ. Pollut.* 214, 831–839. doi: 10.1016/j.envpol.2016.04.084

Kummerer, K. (2009). Antibiotics in the aquatic environment – a review – part I. *Chemosphere* 75, 417–434. doi: 10.1016/j.chemosphere.2008.11.086

Liang, Y., Tao, Z., and Chen, J. (2012). Organic electrode materials for rechargeable lithium batteries. *Adv. Energy Mater.* 2, 742–769. doi: 10.1002/aenm.201100795

Liu, Y., Xue, J., Zheng, T., and Dahn, J. (1996). Mechanism of lithium insertion in hard carbons prepared by pyrolysis of epoxy resins. *Carbon N. Y.* 34, 193–200. doi: 10.1016/0008-6223(96)00177-7

Mahamallik, P., Saha, S., and Pal, A. (2015). Tetracycline degradation in aquatic environment by highly porous MnO_2 nanosheet assembly. *Chem. Eng. J.* 276, 155–165. doi: 10.1016/j.cej.2015.04.064

Matsubara, E., Lala, S., and Rosolen, J. (2010). Lithium storage into carbonaceous materials obtained from sugarcane bagasse. *J. Braz. Chem. Soc.* 21, 1877–1884. doi: 10.1590/S0103-50532010001000012

Orellana, S., Soto, C., and Toral, M. I. (2010). UV–vis, IR and 1H NMR spectroscopic studies and characterization of ionic-pair crystal violet–oxytetracycline. *Spectrochim. Acta Part A* 75, 437–443. doi: 10.1016/j.saa.2009.11.002

Renault, S., Brandell, D., Guatafsson, T., and Edström, K. (2013). Improving the electrochemical performance of organic Li-ion battery electrodes. *Chem. Commun.* 49, 1945–1947. doi: 10.1039/c3cc39065a

Schon, T. B., Mcallister, B. T., Li, P. F., and Seferos, D. S. (2016). The rise of organic electrode materials for energy storage. *Chem. Soc. Rev.* 45, 6345–6404. doi: 10.1039/C6CS00173D

Stezowski, J. J. (1976). Chemical-structural properties of tetracycline derivaties. 1. Molecular structure and conformation of the free base derivatives. *J. Am. Chem. Soc.* 98, 6012–6018. doi: 10.1021/ja00435a039

Sullivan, B. A., Vance, C. C., Gentry, T. J., and Karthikeyan, R. (2017). Effects of chlorination and ultraviolet light on environmental tetracycline-resistant bacteria and tet(W) in water. *J. Environ. Chem. Eng.* 5, 777–784. doi: 10.1016/j.jece.2016.12.052

Sun, X., Shao, C., Zhang, F., Li, Y., Wu, Q., and Yang, Y. (2018). SiC nanofibers as long-life lithium-ion battery anode materials. *Front. Chem.* 6:166. doi: 10.3389/fchem.2018.00166

Sun, Y., Liu, N., and Cui, Y. (2016). Promises and challenges of nanomaterials for lithium-based rechargeable batteries. *Nat. Energy* 1:16071. doi: 10.1038/NENERGY.2016.71

Tang, K., White, R. J., Mu, X., Titirici, M. M., Van Aken, P. A., and Maier, J. (2012). Hollow carbon nanospheres with a high rate capability for lithium-based batteries. *ChemSusChem* 5, 400–403. doi: 10.1002/cssc.201100609

Titirici, M. M., and Antonietti, M. (2009). Chemistry and materials options of sustainable carbon materials made by hydrothermal carbonization. *Chem. Soc. Rev.* 39, 103–116. doi: 10.1039/B819318P

Toro, R., Diaz de Delgado, G., Bahsas, A., and Delgado, J. M. (2007). The presence of polymorphism in oxytetracycline hydrochloride shown by X-ray powder diffraction techniques. *Z. Kristallogr. Suppl.* 26, 563–568. doi: 10.1524/zksu.2007.2007.suppl_26.563

Wang, H., Che, B., Duan, A., Mao, J., Dahlgren, R. A., Zhang, M., et al. (2014). Toxicity evaluation of beta-diketone antibiotics on the development of embryo-larval zebrafish (danio rerio). *Environ. Toxicol.* 29, 1134–1146. doi: 10.1002/tox.21843

Wang, L., Schnepp, Z., and Titirici, M. (2013a). Rice husk-derived carbon anodes for lithium ion batteries. *J. Mater.Chem. A* 1, 5269–5273. doi: 10.1039/c3ta10650k

Wang, S., Wang, L., Zhang, K., Zhu, Z., Tao, Z., and Chen, J. (2013b). Organic $Li_4C_8H_2O_6$ nanosheets for lithium-ion batteries. *Nano Lett.* 13, 4404–4409. doi: 10.1021/nl402239p

Wang, Z., Du, Y., Yang, C., Liu, X., Zhang, J., Li, E., et al. (2017). Occurrence and ecological hazard assessment of selected antibiotics in the surface waters in and around lake Honghu, China. *Sci. Total Environ.* 609, 1423–1432. doi: 10.1016/j.scitotenv.2017.08.009

Wu, J., Zuo, L., Song, Y., Chen, Y., Zhou, R., Chen, S., et al. (2016). Preparation of biomass-derived hierarchically porous carbon/Co_3O_4 nanocomposites as anode materials for lithium-ion batteries. *J. Alloys Compd.* 656, 745–752. doi: 10.1016/j.jallcom.2015.10.063

Xiong, Y., Harb, M., and Hong, P. Y. (2017). Performance and microbial community variations of anaerobic digesters under increasing tetracycline concentrations. *Appl. Microbiol. Biotechnol.* 101, 5505–5517. doi: 10.1007/s00253-017-8253-1

Yan, C., Yang, Y., Zhou, J., Liu, M., Nie, M., Shi, H., et al. (2013). Antibiotics in the surface water of the Yangtze estuary: occurrence, distribution and risk assessment. *Environ. Pollut.* 175, 22–29. doi: 10.1016/j.envpol.2012.12.008

Zhang, H., Deng, Q., Zhou, A., Liu, X., and Li, J. (2014). Porous $Li_2C_8H_4O_4$ coated with N-doped carbon by using CVD as an anode material for Li-ion batteries. *J. Mater. Chem. A* 2, 5696–5702. doi: 10.1039/c3ta14720g

Zhang, M., Yang, H., Liu, Y., Sun, X., Zhang, D., and Xue, D. (2012). Hydrophobic precipitation of carbonaceous spheres from fructose by a hydrothermal process. *Carbon N. Y.* 50, 2155–2161. doi: 10.1016/j.carbon.2012.01.024

Zuniga, L., Agubra, V., Flores, D., Campos, H., Villareal, J., and Alcoutlabi, M. (2016). Multichannel hollow structure for improved electrochemical performance of TiO_2/Carbon composite nanofibers as anodes for lithium ion batteries. *J. Alloys Compd.* 686, 733–743. doi: 10.1016/j.jallcom.2016.06.089

Zuo, X., Zhu, J., Müller-Buschbaum, P., and Cheng, Y. (2017). Silicon based lithium-ion battery anodes: a chronicle perspective review. *Nano Energy* 31, 113–143. doi: 10.1016/j.nanoen.2016.11.013

Conflict of Interest Statement: The authors declare that the research was conducted in the absence of any commercial or financial relationships that could be construed as a potential conflict of interest.

frontiers in Materials

ORIGINAL RESEARCH
published: 31 October 2018
doi: 10.3389/fmats.2018.00063

The Recovery of the Waste Cigarette Butts for N-Doped Carbon Anode in Lithium Ion Battery

Chengyi Yu[1], Hongying Hou[1], Xianxi Liu[2]*, Lina Han[1], Yuan Yao[1], Zhipeng Dai[1] and Dongdong Li[1]*

[1] Faculty of Material Science and Engineering, Kunming University of Science and Technology, Kunming, China, [2] Faculty of Mechanical and Electronic Engineering, Kunming University of Science and Technology, Kunming, China

As one of the common life garbages, about 4.5 trillion waste cigarette butts are produced and randomly discarded every year due to the addiction to the nicotine and the need of the social intercourse. Such a treatment would result in the waste of the resources and the environmental pollution if they weren't reasonably recycled in time. Herein, the waste cigarette butts were recycled in form of N-doped carbon powders with high economic value-added via one-step facile carbonization at 800°C for 2 h in the inert N_2 atmosphere. The waste-cigarette-butts-derived black carbon powders were characterized by scanning electron microscope (SEM), N_2 adsorption/desorption, and X-ray photoelectron spectroscopy (XPS). Furthermore, the corresponding electrochemical performances as the anode in lithium ion battery (LIB) were also investigated by galvanostatic charge/discharge, cyclic voltammetry (CV), and alternating current (AC) impedance. The results suggested that the recycled N-doped waste cigarette butts carbon (WCBC) powders consisted of major carbon and minor residual N-containing and O-containing functional groups, and the corresponding specific surface area was about 1,285 $m^2 \cdot g^{-1}$. Furthermore, the reversible specific discharge capacity was about 528 $mAh \cdot g^{-1}$ for 100 cycles at 25 $mA \cdot g^{-1}$ and about 151 $mAh \cdot g^{-1}$ even at 2,000 $mA \cdot g^{-1}$ for 2,500 cycles. Additionally, full cell performances were also satisfactory, indicating high feasibility. N-doping effect (such as additional active sites and higher electronic conductivity) and the residual O-containing functional groups may be responsible for the satisfactory electrochemical performances, which offered good inspiration and strategy to develop the green energy and circular economy.

Keywords: waste cigarette butts, recovery, N-doped carbon, lithium ion battery, anode

OPEN ACCESS

Edited by:
Jie-Sheng Chen,
Shanghai Jiao Tong University, China

Reviewed by:
Yong Chen,
Hainan University, China
Leszek A. Czepirski,
AGH University of Science and Technology, Poland

***Correspondence:**
Hongying Hou
hongyinghou@kmust.edu.cn
Xianxi Liu
xxiliu@tom.com

Specialty section:
This article was submitted to Carbon-Based Materials, a section of the journal Frontiers in Materials

Received: *20 August 2018*
Accepted: *12 October 2018*
Published: *31 October 2018*

Citation:
Yu C, Hou H, Liu X, Han L, Yao Y, Dai Z and Li D (2018) The Recovery of the Waste Cigarette Butts for N-Doped Carbon Anode in Lithium Ion Battery. Front. Mater. 5:63. doi: 10.3389/fmats.2018.00063

INTRODUCTION

According to the World Health Organization's statistics in 2012, there existed about 1.1 billion smokers in the world (Islami et al., 2015). As is known to all, although the smoking is harmful to the health, it is difficult to quit smoking due to the addiction to the nicotine and the need of the social intercourse, resulting in the production and large accumulation of the countless waste cigarette butts (Jarvis, 2004). It was reported that about 4.5 trillion waste cigarette butts were randomly discarded as one of the common life garbages every year worldwide (Slaughter et al., 2011). The waste cigarette butts are ubiquitous in the environment, as shown in **Figure 1**, which would cause

the environment pollution and the waste of the resources if they weren't reasonably recycled in time. For example, the leachate from the waste cigarette butts can seriously affect the survival of the aquatic organisms, as reported elsewhere (Slaughter et al., 2011).

Generally, one waste cigarette butt consists of three parts: the filter tip, the remnant tobacco and the packing paper (Slaughter et al., 2011). As one main part of the waste cigarette butt, the filter tip is made up of the cellulose acetate, which can protect the smoker by absorbing the various carcinogenic constituents within the cigarette such as the tar, nicotine, hydrogen cyanide, and benzopyrene (Hoffmann and Hoffmann, 1997; Smith and Novotny, 2011). And the packing paper and the remnant tobacco also contain the rich cellulose. Generally, the waste cigarette butts into the environment are subjected to the incineration and the landfill together with other common life garbages, which may result in the waste of the useful resources and the potential environment pollution. Therefore, it is imperative to explore the reasonable reutilization of the waste cigarette butts. Considering that the main component of the waste cigarette

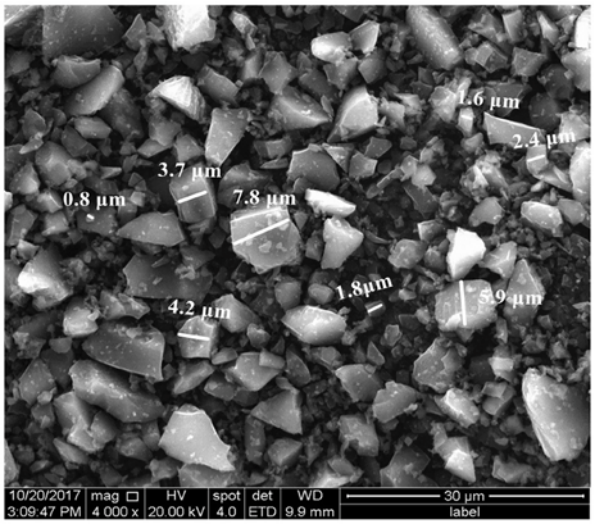

FIGURE 3 | SEM image of N-doped WCBC powders.

FIGURE 1 | The ubiquitous waste cigarette butts in the environment: **(a)** scrap heap, **(b)** tree well, **(c)** street corner, **(d)** puddle, **(e)** roadside and **(f)** wasteland (Guernsey Police, 2013; Woods, 2015).

FIGURE 2 | The recycled procedures of the waste cigarette butts.

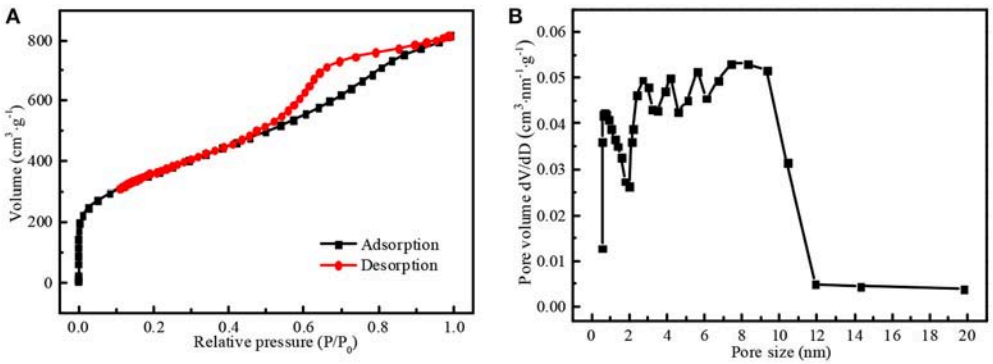

FIGURE 4 | (A) N_2 adsorption/desorption isotherms and **(B)** the pore size distribution curve of N-doped WCBC powders.

butt is the organic carbon-rich cellulose, the waste cigarette butts may be reasonably recycled in the form of high economic value-added carbon powders, which will not only alleviate the potential environmental pollution but also promote the circular economy and the sustainable development. However, there are few reports about the recovery of the waste cigarette butts for the moment.

Currently, some energy storage and conversion devices such as lithium ion battery (LIB), sodium ion battery, fuel cell, and supercapacitor attracted much attention, among which LIB has rapidly captured the market of the portable devices and the electric vehicles due to the long cycle life span and environmental friendliness since its commercialization in 1990s (Li et al., 2014, 2015; Luo et al., 2015; Dai et al., 2016; Liu et al., 2016a; Tie et al., 2018; Yu et al., 2018). As we know, it is the application of carbon-based anode that achieved such a huge success of LIB due to low cost, good electrical conductivity, stable physicochemical property. N-doping can further enhance the electrochemical performances of carbon anode due to the following N-doping effect such as high electrical conductivity, the formation of the structural defects and additional Li-storage active sites (Bulusheva et al., 2011; Song et al., 2014; Zheng et al., 2014). Firstly, N atoms within the graphitic matrix can act as the electron donors and increase the local state density at Fermi level, and thus enhance the electrical conductivity (Royea et al., 2006; Wiggins-Camacho and Stevenson, 2009). Secondly, several different combinations of N with C such as pyridinic N and pyrrolic N may act as the additional active sites for Li-storage (Bhattacharjya et al., 2014). Additionally, N-doping may also induce the formation of some defect spaces for the additional active sites to storage Li^+. For example, it was reported that N-doping can increase the reversible discharge capacity of carbon anode from 250 to 535 mAh·g^{-1} at 20 mA·g^{-1} after 200 cycles (Han et al., 2012). Generally, N-doping of carbon material can be achieved via the hydrothermal route, the ultrasonication or the electrochemistry, among which *in situ* carbonization of N-containing carbon precursors may be preferable because the uniform distribution of N atom can be achieved (Stephan et al., 1994; Saravanan and Kalaiselvi, 2015). Considering that both nicotine and hydrogen cyanide within the waste cigarette butts belong to N-containing compounds, the waste cigarette butts containing the rich cellulose may be a preferable precursor of N-doped carbon material.

Herein, in this work, the waste cigarette butts were recycled by one step facile carbonization at 800°C for 2 h in the inert N_2 atmosphere. Furthermore, N-doped WCBC anode in LIB exhibited high specific capacity and cycling stability. Furthermore, in order to further investigate the feasibility of N-doped WCBC anode, a full cell was also assembled and tested by coupling N-doped WCBC anode with commercial $LiCoO_2$ cathode. It is very instructive to build the bridge between the waste resources and the clean energy materials, especially for the toxic wastes.

EXPERIMENTAL

The Recovery of the Waste Cigarette Butts

After some waste cigarette butts were collected and cleaned, they were recycled in form of black N-doped carbon powders via one step facile carbonization, as shown in **Figure 2**. Briefly, after being cleaned and cut into small pieces, the waste cigarette butts were carbonized at 800°C in a tubular furnace for 2 h at 5°C·min^{-1} under N_2 flow. Then, the obtained black carbon powders were immersed in 10% HCl aqueous solution for 24 h at room temperature to remove the inorganic impurities and then washed with the distilled water. Finally, the clean black carbon powders were obtained after being dried and fully ground.

Structure and Morphology Characterization

The morphology of the sample was probed by SEM (Quanta200 FEI, USA). The corresponding surface area and pore volume were determined by specific surface and pore size analysis instrument (V-Sorb 2800TP Gold APP, China), and the chemical component was characterized by XPS technology on X-ray photoelectron spectrometer (PHI5000 Versaprobe-II ULVAC-PHI, Japan).

Electrochemical Measurements

The procedures to fabricate the electrode and assemble the coin cell were described as follows. Firstly, the electrode slurry was prepared by fully mixing 80 wt% active material, 10 wt% acetylene

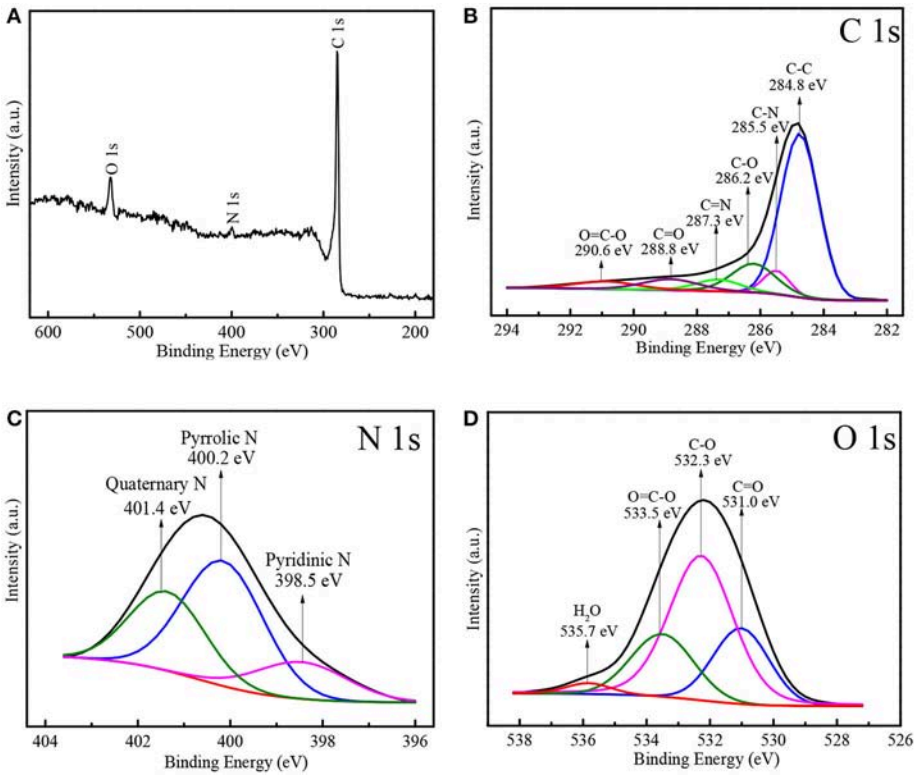

FIGURE 5 | XPS spectra of N-doped WCBC powders: **(A)** the wide scan **(B)** C 1s, **(C)** N 1s, and **(D)** O 1s.

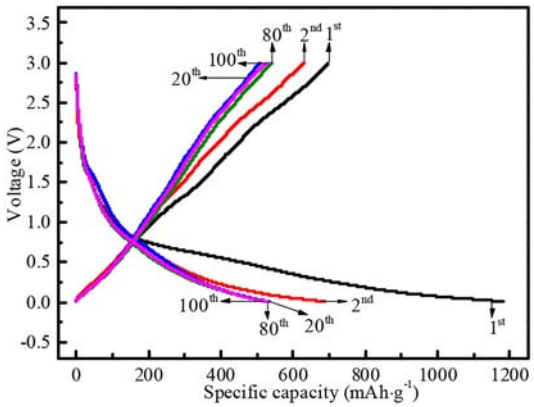

FIGURE 6 | The 1st, 2nd, 20th, 80th, and 100th galvanostatic charge/discharge profiles of N-doped WCBC anode at 25 mA·g^{-1}.

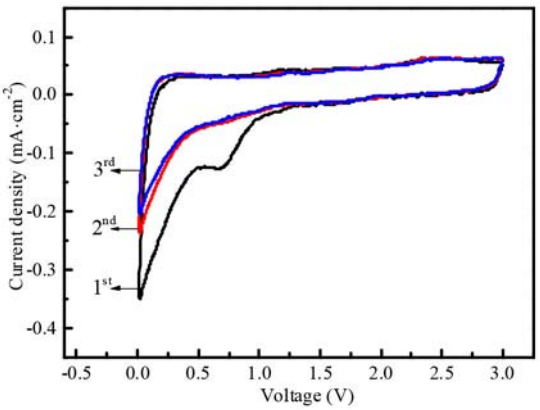

FIGURE 7 | CV curves of N-doped WCBC anode at different cycles.

black, and 10 wt% PVDF binder in N-methyl-2-pyrrolidone. Secondly, N-doped WCBC anode and $LiCoO_2$ cathode can be obtained by coating the electrode slurries onto Cu foil and Fe foil, respectively, and vacuum dried at 60°C for 12 h. The loading densities of N-doped WCBC and $LiCoO_2$ were about 1.1 and about 2.8 mg·cm^{-2}, respectively. CR2032 coin cell was assembled in an argon-filled glove box (Mikrouna Super 1220/750/900), in which N-doped WCBC anode was coupled with the counter electrodes of Li foil and $LiCoO_2$ cathode in half and full cell, respectively, and the electrolyte was 1 M $LiPF_6$ in ethylene carbonate and diethyl carbonate (1:1 in volume), and the commercial porous Celgard 2400 film was the separator (Hou et al., 2018). The coin cell was evaluated by galvanostatic charge/discharge on a battery testing system (Neware CT-3008W, China) at 25, 1,000, and 2,000 mA·g^{-1}. The electrochemical performances were further carried out by cyclic voltammetry (CV) curve (0.01−3.0 V at 0.2 mV·s^{-1}) and AC impedance

(0.01 Hz−100 kHz, 10 mV perturbation) on the electrochemical workstation (Parstat 4000, Princeton Applied Research, USA).

RESULTS AND DISCUSSION

SEM

The micro-morphology of N-doped WCBC powders was probed by SEM, as shown in **Figure 3**. Clearly, N-doped WCBC powders were made up of many irregular micro-particles with the particle size of about 0.8–7.8 μm, which may endow N-doped WCBC powders with high surface area and facilitate the sufficient infiltration of the electrolyte into the electrode (Jiang et al., 2016).

Nitrogen Adsorption/Desorption Analysis

N_2 adsorption/desorption isotherms of N-doped WCBC powders were recorded by static volumetric method (also known as manometric method), which exhibited the features of type IV curve, as shown in **Figure 4A** (Thommes et al., 2015; Qin and Chen, 2017). Specifically, the adsorption volume steeply increased at the range of $P/P_0 < 0.01$ and an obvious hysteresis loop appeared at the range of $P/P_0 > 0.45$, indicating the

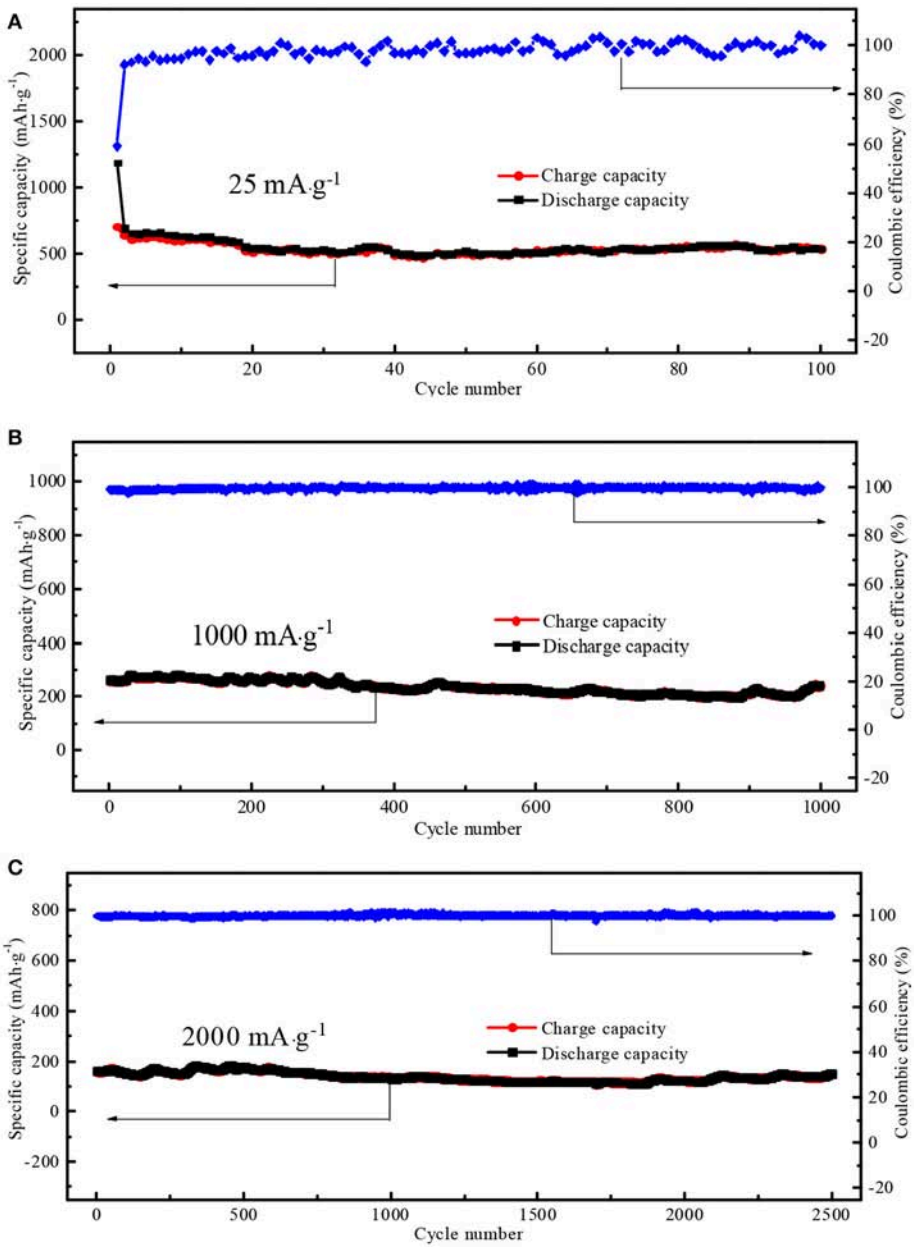

FIGURE 8 | The cycling performances of N-doped WCBC anode at **(A)** 25 mA·g^{-1}, **(B)** 1,000 mA·g^{-1}, and **(C)** 2,000 mA·g^{-1}.

co-existence of the micropores and mesopores (Qin and Chen, 2017). The pore size distribution plots were recorded from the desorption branch of the isotherms based on Barrett-Joyner-Halenda (BJH) model, as shown in **Figure 4B**. There existed five knee points at about 0.7, 2.7, 4.2, 5.6, and 7.3 nm in the pore size distribution curve, again indicating the co-existence of the micropores and the mesopores within N-doped WCBC powders (Hou et al., 2018). Furthermore, the surface area was calculated to be about 1,285 $m^2 \cdot g^{-1}$ according to Brunauer-Emmett-Teller (BET) equation at the range of P/P_0 = 0.05–0.23, higher than that of undoped carbon powders (Hou et al., 2018). No doubt, high specific surface area and multi-scaled pores can enlarge the electrode/electrolyte interface and facilitate the transport of Li^+ (Liu et al., 2016a; Zhang et al., 2017).

XPS Analysis

The fine chemical component of N-doped WCBC was further analyzed by XPS technology. As shown in the wide scan XPS spectrum in **Figure 5A**, three signal peaks were detected at 284.8, 399.6, and 532.0 eV, corresponding to C 1s, N 1s, and O 1s, respectively. The relative atomic percentages of C, N, and O were 90.8, 1.6, and 7.6%, respectively, indicating that N-doped WCBC powders consisted of major carbon and minor N-containing and O-containing functional groups. Furthermore, high resolution C1s spectrum could be deconvoluted into six peaks, among which one strong peak at 284.8 eV was assigned to C–C bond, while other five weak peaks at about 285.5, 286.2, 287.3, 288.8, and 290.6 eV were corresponding to C–N, C–O, C=N, C=O, and O=C-O bonds, respectively (**Figure 5B**) (Li and Xue, 2014; Selvamani et al., 2016; Liu et al., 2018). Moreover, three characteristic peaks were observed at 398.5, 400.2, and 401.4 eV in N1s spectrum in **Figure 5C**, corresponding to pyridinic N, pyrrolic N and quaternary N, respectively (Li and Xue, 2014; Hou et al., 2016). It was reported that pyrrolic N and pyridinic N may offer the additional active sites for Li-storage, thereby enhancing Li-storage capacity (Zheng et al., 2014). In the case of O 1s spectrum in **Figure 5D**, four peaks at 531.0, 532.3, 533.5, and 535.7 eV can be attributed to C=O, C–O, O=C–O, and H_2O, respectively (Saravanan and Kalaiselvi, 2015; Liu et al., 2016b). The residual O-containing functional groups (C=O, C–O, and O=C–O) may also increase the defects, the disorder or the local electron density beneficial for Li-storage, as reported elsewhere (Bhattacharjya et al., 2014). Seemingly, both N-doping and residual O-containing groups may play an important role in improving the electrochemical performances.

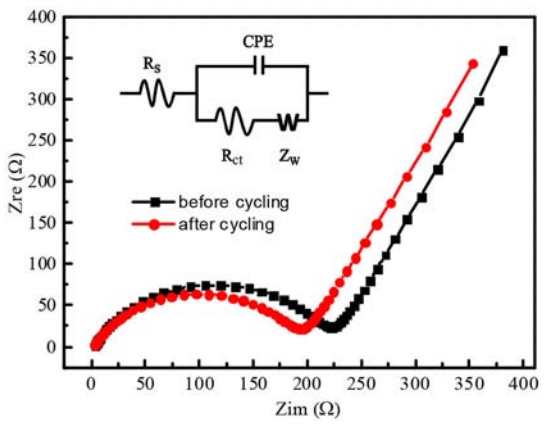

FIGURE 9 | Nyquist plots of N-doped WCBC anode, the inset: the corresponding equivalent circuit.

TABLE 1 | The fitting parameters of the equivalent circuit.

Parameters	Before cycling	After cycling
R_s (Ω)	2.58	2.59
R_{ct} (Ω)	221.30	192.60
Z_w (Ω)	2,233	2,095
i_0 ($mA \cdot cm^{-2}$)	0.10	0.12

Electrochemical Performances

Charge/Discharge Performances

Several representative charge/discharge profiles of N-doped WCBC anode at 25 $mA \cdot g^{-1}$ were shown in **Figure 6**. The corresponding specific discharge capacities at the 2nd, 20th, 80th, and 100th cycles were about 1,182, 686, 532, 531, and 528 $mAh \cdot g^{-1}$, respectively. Although there existed an initial irreversible capacity loss due to the formation of solid electrolyte interface (SEI) film, N-doped WCBC anode began to stably charge /discharge from the 20th cycle, indicating high reversibility (Bhattacharjya et al., 2014). Several possible reasons were responsible for the satisfactory charge/discharge performances: (i) N atoms within carbon matrix may act as the electron donors and increase the local state density at Fermi level, and thus improve the electronic conductivity and the charge transport; (ii) N-doping-induced pyridinic N and pyrrolic N species may provide the additional active sites for Li-storage; (iii) The existences of N and O atoms may also induce the formation of some defects, because the incorporation of the heteroatoms into the graphite-like lattice may promote the formation of some pentagons and thus the distortion of the graphite layer; (iv) the residual O-containing functional groups such as C=O, C–O, and O=C–O may also produce lots of radicals on the electrode surface and thus significantly enhance Li-storage by forming the chemical bonds with Li^+; (v) N-doping and O-containing groups may also induce the pseudo-capacitive Li-storage mechanisms, beneficial for the electrochemical performances; (vi) high specific surface area and multi-scaled pores can also enlarge the electrode/electrolyte interface and facilitate the ionic transport (Royea et al., 2006; Ismagilov et al., 2009; Wiggins-Camacho and Stevenson, 2009; Lee et al., 2011; Wang et al., 2012; Bhattacharjya et al., 2014; Zheng et al., 2014; Saravanan and Kalaiselvi, 2015).

CV Analysis

In order to further monitor the electrochemical behaviors of N-doped WCBC anode, CV measurement was also conducted at the different cycles, as shown in **Figure 7**. At the first cycle, an

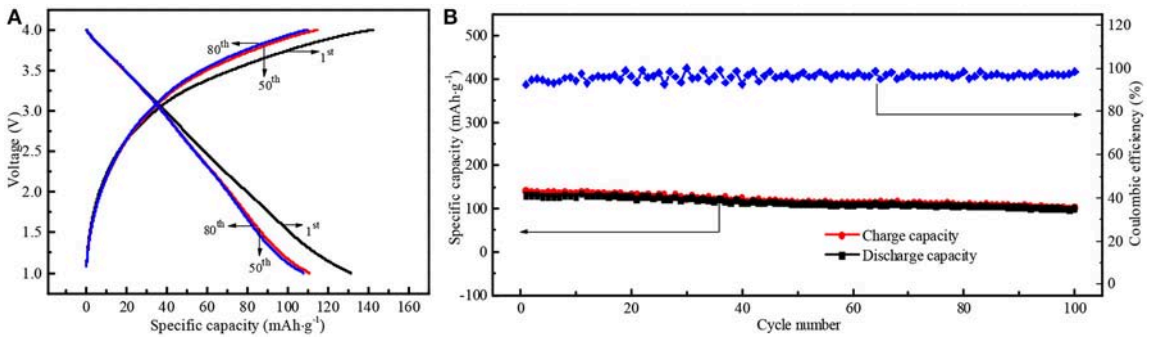

FIGURE 10 | (A) The 1st, 50th, and 80th galvanostatic charge/discharge profiles and **(B)** the cyclic performance of N-doped WCBC/$LiCoO_2$ full cell.

oxidation peak appeared at 0.25 V, while two reduction peaks were also detected at 0 and 0.7 V, respectively. Obviously, the oxidation peak corresponded to Li^+ deinsertion from N-doped WCBC anode, while the reduction peak at 0 V corresponded to Li^+ insertion into N-doped WCBC anode, and another reduction peak at 0.7 V was primarily attributed to the formation of SEI film (Wang et al., 2015; Mullaivananathan et al., 2017; Zhang et al., 2017). Subsequently, the reduction peak at about 0.7 V disappeared, and CV curve at the 2nd cycle almost overlapped with that at the 3rd cycle, indicating high reversibility of N-doped WCBC anode (Hou et al., 2018).

Cycling Performances

The cycling performances of N-doped WCBC anode were also shown in **Figure 8**. On cycling at 25 $mA{\cdot}g^{-1}$ after 100 cycles, a stable discharge capacity of 528 $mAh{\cdot}g^{-1}$ was maintained with 98% Coulombic efficiency (**Figure 8A**). Especially, the reversible discharge capacities remained about 241 and 151 $mAh{\cdot}g^{-1}$ even at 1,000 $mA{\cdot}g^{-1}$ for 1,000 cycles and 2,000 $mA{\cdot}g^{-1}$ for 2,500 cycles, respectively (in **Figure 8B** and **Figure 8C**). The corresponding capacity retentions were 94 and 92%, respectively, while both Coulombic efficiencies were 100%, demonstrating good electrochemical reversibility and long cycle life span of N-doped WCBC anode (Hou et al., 2018).

AC Impedance Analysis

Figure 9 showed Nyquist plots of N-doped WCBC anode before and after the cycling performances, and the corresponding equivalent circuit was also inset. Here, R_s, R_{ct}, CPE, and Z_w stand for the internal resistance, the charge transfer resistance, the double layer capacitance and Warburg impedance, respectively (Meng et al., 2016). After the cycling, R_s didn't change significantly, while R_{ct} and Z_w decreased, indicating that the charge transfer rate increased upon the cycling, as listed in **Table 1**. Additionally, the exchange current density (i_0) can be calculated according to Equation (1) (Elizabeth et al., 2016):

$$i_0 = RT/(nFR_{ct}A) \quad (1)$$

Where R is the ideal gas constant, T is the absolute temperature, F is Faraday constant, and A is the electrode area (about 1.1 cm^2) (Duan et al., 2016). Obviously, i_0 also increased upon the cycling, indicating facile charge transfer rate (Ou et al., 2015).

Full Cell Performances

To further investigate the practical feasibility of N-doped WCBC anode in LIB, a full cell was also assembled by coupling N-doped WCBC anode with commercial $LiCoO_2$ cathode. The 1st, 50th, and 80th galvanostatic charge/discharge profiles at 1.0–4.0 V were shown in **Figure 10A**. At the 1st cycle, the initial discharge capacity and Coulombic efficiency were about 131 $mAh{\cdot}g^{-1}$ and 92%, respectively. Subsequently, the corresponding discharge specific capacity slightly decreased to about 111 $mAh{\cdot}g^{-1}$ at the 50th cycle, close to that at the 80th cycle, indicating good cyclic stability, which was more intuitive and clear in **Figure 10B**. The reversible discharge specific capacity can maintain at 111 $mAh{\cdot}g^{-1}$ with 97% Coulombic efficiency, comparable with that of hard carbon/$LiCoO_2$ full cell in literature (Sun et al., 2007). Obviously, N-doped WCBC/$LiCoO_2$ full cell also exhibited good electrochemical performances, indicating high feasibility of N-doped WCBC anode in LIB.

CONCLUSIONS

In this work, the waste cigarette butts were recycled in form of N-doped carbon powders via one step facile carbonization. To be satisfactory, the resultant N-doped WCBC anode exhibited high reversible capacities of about 528 at 25 $mA{\cdot}g^{-1}$ for 100 cycles and about 151 $mAh{\cdot}g^{-1}$ even at 2,000 $mA{\cdot}g^{-1}$ for 2,500 cycles. N-doping effect such as high electronic conductivity, structural defects and additional active sites may contribute into the satisfactory electrochemical performances. Additionally, high specific surface area and the residual O-containing groups also facilitated high electrochemical performances. These satisfactory electrochemical performances may offer good inspiration and strategy to develop the sustainable energy and circular economy.

AUTHOR CONTRIBUTIONS

HH contributed to the conception and highlighted the scientific value of the study. CY and HH contributed significantly to analysis and manuscript preparation. HH and CY performed the

data analyses and wrote the manuscript. XL, LH, YY, ZD, and DL helped perform the analysis with with constructive discussions.

ACKNOWLEDGMENTS

This work was financially supported by the National Natural Science Foundations of China (Grant No. 51566006 and 51363011), the 46th Scientific Research Foundation for the Returned Overseas Chinese Scholars, State Education Ministry in China (6488-20130039), the 19th Young Academic and Technical Leaders of Yunnan Province (1097-10978240), the Program of High-level Introduced Talent of Yunnan Province (10978125), and the Project of Key Discipline (14078232 and 140 78311).

REFERENCES

Bhattacharjya, D., Park, H. Y., Kim, M. S., Choi, H. S., Inamdar, S. N., and Yu, J. S. (2014). Nitrogen-doped carbon nanoparticles by flame synthesis as anode material for rechargeable lithium-ion batteries. *Langmuir* 30, 318–324. doi: 10.1021/la403366e

Bulusheva, L. G., Okotrub, A. V., Kurenya, A. G., Zhang, H. K., Zhang, H. J., Chen, X. H., et al. (2011). Electrochemical properties of nitrogen-doped carbon nanotube anode in Li-ion batteries. *Carbon* 49, 4013–4023. doi: 10.1016/j.carbon.2011.05.043

Dai, D. M., Li, B., Tang, H. W., Chang, K., Jiang, K., Chang, Z. R., et al. (2016). Simultaneously improved capacity and initial coulombic efficiency of Li-rich cathode $Li[Li_{0.2}Mn_{0.54}Co_{0.13}Ni_{0.13}]O_2$ by enlarging crystal cell from a nanoplate precursor. *J. Power Sources* 307, 665–672. doi: 10.1016/j.jpowsour.2016.01.046

Duan, J. X., Hou, H. Y., Liu, X. X., Liu, S., Liao, Q. S., and Yao, Y. (2016). High performance PPO/Ti^{3+}/TiO_2NT membrane/electrode for lithium ion battery. *Ceram. Int*. 42, 16611–16618. doi: 10.1016/j.ceramint.2016.07.082

Elizabeth, I., Singh, B. P., Trikha, S., and Gopukumar, S. (2016). Bio-derived hierarchically macro-meso-micro porous carbon anode for lithium/sodium ion batteries. *J. Power Sources* 329, 412–421. doi: 10.1016/j.jpowsour.2016.08.106

Guernsey Police (2013). *Guernsey Police Issue Fixed Penalty Notices for Littering*. Available online at: http://www.sustainableguernsey.info/blog/2013/05/guernsey-police-issue-fixed-penalty-notices-for-littering

Han, P. X., Yue, Y. H., Zhang, L. X., Xu, H. X., Liu, Z. H., Zhang, K. J., et al. (2012). Nitrogen-doping of chemically reduced mesocarbon microbead oxide for the improved performance of lithium ion batteries. *Carbon* 50, 1355–1362. doi: 10.1016/j.carbon.2011.11.007

Hoffmann, D., and Hoffmann, I. (1997). The changing cigarette, 1950-1995. *J. Toxicol. Environ. Heal.* 50, 307–364. doi: 10.1080/009841097160393

Hou, H. Y., Liu, X. X., and Peng, J. H. (2016). "New Energe Material: Graphene," in *Graphene Science Handbook*, eds M. Aliofkhazraei, N. Ali, W. I. Milne, C. S. Ozkan, S. Mitura, and J. L. Gervasoni (Boca Raton, FL: CRC), 419–438.

Hou, H. Y., Yu, C. Y., Liu, X. X., Yao, Y., Liao, Q. S., Dai, Z. P., et al. (2018). Waste-loofah-derived carbon micro/nanoparticles for lithium ion battery anode. *Surf. Innov*. 6, 159–166. doi: 10.1680/jsuin.17.00068

Islami, F., Torre, L. A., and Jemal, A. (2015). Global trends of lung cancer mortality and smoking prevalence. *Transl. Lung Cancer Res.* 4, 327–338. doi: 10.3978/j.issn.2218-6751.2015.08.04

Ismagilov, Z. R., Shalagina, A. E., Podyacheva, O. Y., Ischenko, A. V., Kibis, L. S., Boronin, A. I., et al. (2009). Structure and electrical conductivity of nitrogen-doped carbon nanofibers. *Carbon* 47, 1922–1929. doi: 10.1016/j.carbon.2009.02.034

Jarvis, M. J. (2004). Why people smoke. *Brit. Med. J.* 328, 277–279. doi: 10.1136/bmj.328.7434.277

Jiang, Q., Zhang, Z. H., Yin, S. Y., Guo, Z. P., Wang, S. Q., and Feng, C. Q. (2016). Biomass carbon micro/nano-structures derived from ramie fibers and corncobs as anode materials for lithium-ion and sodium-ion batteries. *Appl. Surf. Sci.* 379, 73–82. doi: 10.1016/j.apsusc.2016.03.204

Lee, S. W., Gallant, B. M., Byon, H. R., Hammond, P. T., and Shao-Horn, Y. (2011). Nanostructured carbon-based electrodes: bridging the gap between thin-film lithium-ion batteries and electrochemical capacitors. *Energy Environ. Sci*. 4, 1972–1985. doi: 10.1039/C0EE00642D

Li, B., Li, Y. J., Dai, D. M., Chang, K., Tang, H. W., Chang, Z. R., et al. (2015). Facile and nonradiation pretreated membrane as a high conductive separator for Li-ion batteries. *ACS Appl. Mater. Interfaces* 7, 20184–20189. doi: 10.1021/acsami.5b05718

Li, B., Wei, X. G., Chang, Z. R., Chen, X. N., Yuan, X. Z., and Wang, H. J. (2014). Facile fabrication of $LiMn_2O_4$ microspheres from multi-shell MnO_2 for high-performance lithium-ion batteries. *Mater. Lett*. 135, 75–78. doi: 10.1016/j.matlet.2014.07.117

Li, M., and Xue, J. M. (2014). Integrated synthesis of nitrogen-doped mesoporous carbon from melamine resins with superior performance in supercapacitors. *J. Phys. Chem. C* 118, 2507–2517. doi: 10.1021/jp410198r

Liu, S., Hou, H. Y., Liu, X. X., Duan, J. X., Yao, Y., Liao, Q. S., et al. (2016a). Recycled hierarchical tripod-like CuCl from Cu-PCB waste etchant for lithium ion battery anode. *J. Hazard. Mater*. 324,357–364. doi: 10.1016/j.jhazmat.2016.10.069

Liu, S., Wang, G., Hou, H. Y., Liu, X. X., Duan, J. X., and Liao, Q. S. (2016b). Binder-free combination of large area reduced graphene oxide nanosheets with Cu foil for lithium ion battery anode. *Diam. Relat. Mater*. 68,102–108. doi: 10.1016/j.diamond.2016.06.013

Liu, X. F., Wang, D., Zhang, B. S., Luan, C., Qin, T. T., Zhang, W., et al. (2018). Vertical graphene nanowalls coating of copper current collector for enhancing rate performance of graphite anode of Li ion battery: the merit of optimized interface architecture. *Electrochim. Acta* 268, 234–240. doi: 10.1016/j.electacta.2018.02.004

Luo, J. S., Jensen, A. H., Brooks, N. R., Sniekers, J., Knipper, M., Aili, D., et al. (2015). 1,2,4-Triazolium perfluorobutanesulfonate as an archetypal pure protic organic ionic plastic crystal electrolyte for all-solid-state fuel cells. *Energy Environ. Sci*. 8, 1276–1291. doi: 10.1039/C4EE02280G

Meng, R. J., Hou, H. Y., Liu, X. X., Yan, C. X., Duan, J. X., and Liu, S. (2016). High performance binder-free quaternary composite CuO/Cu/TiO_2NT/Ti anode for lithium ion battery. *Ceram. Int*. 42, 6039–6045. doi: 10.1016/j.ceramint.2015.12.160

Mullaivananathan, V., Sathish, R., and Kalaiselvi, N. (2017). Coir pith derived bio-carbon: demonstration of potential anode behavior in lithium-ion batteries. *Electrochim. Acta* 225, 143–150. doi: 10.1016/j.electacta.2016.12.086

Ou, J. K., Zhang, Y. Z., Chen, L., Zhao, Q., Meng, Y., Guo, Y., et al. (2015). Nitrogen-rich porous carbon derived from biomass as a high performance anode material for lithium ion batteries. *J. Mater. Chem. A* 3, 6534–6541. doi: 10.1039/C4TA06614F

Qin, D., and Chen, S. (2017). A sustainable synthesis of biomass carbon sheets as excellent performance sodium ion batteries anode. *J. Solid State Electrochem*. 21, 1305–1312. doi: 10.1007/s10008-016-3485-z

Royea, W. J., Hamann, T. W., Brunschwig, B. S., and Lewis, N. S. (2006). A comparison between interfacial electron-transfer rate constants at metallic and graphite electrodes. *J. Phys. Chem. B* 110, 19433–19442. doi: 10.1021/jp062141e

Saravanan, K. R., and Kalaiselvi, N. (2015). Nitrogen containing bio-carbon as a potential anode for lithium batteries. *Carbon* 81, 43–53. doi: 10.1016/j.carbon.2014.09.021

Selvamani, V., Ravikumar, R., Suryanarayanan, V., Velayutham, D., and Gopukumar, S. (2016). Garlic peel derived high capacity hierarchical N-doped porous carbon anode for sodium/lithium ion cell. *Electrochim. Acta* 190, 337–345. doi: 10.1016/j.electacta.2016.01.006

Slaughter, E., Gersberg, R. M., Watanabe, K., Rudolph, J., Stransky, C., and Novotny, T. E. (2011). Toxicity of cigarette butts, and their chemical components, to marine and freshwater fish. *Tob. Control* 20, i25–i29. doi: 10.1136/tc.2010.040170

Smith, E. A., and Novotny, T. E. (2011). Whose butt is it? tobacco industry research about smokers and cigarette butt waste. *Tob. Control* 20, i2–i9. doi: 10.1136/tc.2010.040105

Song, H. W., Li, N., Cui, H., and Wang, C. X. (2014). Enhanced storage capability and kinetic processes by pores- and hetero-atoms-riched carbon nanobubbles for lithium-ion and sodium-ion batteries anodes. *Nano Energy* 4, 81–87. doi: 10.1016/j.nanoen.2013.12.017

Stephan, O., Ajayan, P. M., Colliex, C., Redlich, P., Lambert, J. M., Bernier, P., et al. (1994). Doping graphitic and carbon nanotube structures with boron and nitrogen. *Science* 266, 1683–1685. doi: 10.1126/science.266.5191.1683

Sun, H., He, X. M., Ren, J. G., Li, J. J., Jiang, C. Y., and Wan, C. R. (2007). Hard carbon/lithium composite anode materials for Li-ion batteries. *Electrochim. Acta* 52, 4312–4316. doi: 10.1016/j.electacta.2006.12.012

Thommes, M., Kaneko, K., Neimark, A. V., Olivier, J. P., Rodriguez-Reinoso, F., Rouquerol, J., et al. (2015). Physisorption of gases, with special reference to the evaluation of surface area and pore size distribution (IUPAC Technical Report). *Pure Appl. Chem*. 87, 1051–1069. doi: 10.1515/pac-2014-1117

Tie, X. Y., Han, Q. Y., Liang, C. Y., Li, B., Zai, J. T., and Qian, X. F. (2018). Si@SiOx/Graphene nanosheets composite: ball milling synthesis and enhanced lithium storage performance. *Front. Mater*. 4, 1–7. doi: 10.3389/fmats.2017.00047

Wang, F. F., Song, R. R., Song, H. H., Chen, X. H., Zhou, J. S., Ma, Z. K., et al. (2015). Simple synthesis of novel hierarchical porous carbon microspheres and their application to rechargeable lithium-ion batteries. *Carbon* 81, 314–321. doi: 10.1016/j.carbon.2014.09.062

Wang, H. B., Maiyalagan, T., and Wang, X. (2012). Review on recent progress in nitrogen-doped graphene: synthesis, characterization, and its potential applications. *ACS Catal*. 2, 781–794. doi: 10.1021/cs200652y

Wiggins-Camacho, J. D., and Stevenson, K. J. (2009). Effect of nitrogen concentration on capacitance, density of states, electronic conductivity, and morphology of N-doped carbon nanotube electrodes. *J. Phys. Chem. C* 113, 19082–19090. doi: 10.1021/jp907160v

Woods, S. (2015). *Help Local Councils Take Action Against Littering From Vehicles*. Available online at: http://www.slwoods.co.uk/?m=201505

Yu, C. Y., Hou, H. Y., Liu, X. X., Yao, Y., Liao, Q. S., Dai, Z. P., et al. (2018). Old-loofah-derived hard carbon for long cyclicity anode in sodium ion battery. *Int. J. Hydrogen Energy* 43, 3253–3260. doi: 10.1016/j.ijhydene.2017.12.151

Zhang, J. L., Zhang, L. J., Yang, S. L., Li, D. H., Xie, Z. X., Wang, B. B., et al. (2017). Facile strategy to produce N-doped carbon aerogels derived from seaweed for lithium-ion battery anode. *J. Alloys Compd*. 701, 256–261. doi: 10.1016/j.jallcom.2017.01.082

Zheng, F., Yang, Y., and Chen, Q. (2014). High lithium anodic performance of highly nitrogen-doped porous carbon prepared from a metal-organic framework. *Nat. Commun*. 5, 5261–5270. doi: 10.1038/ncomms6261

Conflict of Interest Statement: The authors declare that the research was conducted in the absence of any commercial or financial relationships that could be construed as a potential conflict of interest.

frontiers in Materials

REVIEW
published: 22 March 2019
doi: 10.3389/fmats.2019.00044

New Approaches Toward the Hydrogen Production From Formic Acid Dehydrogenation Over Pd-Based Heterogeneous Catalysts

Miriam Navlani-García[1]*, *Kohsuke Mori*[1,2,3], *David Salinas-Torres*[1], *Yasutaka Kuwahara*[1,3] *and Hiromi Yamashita*[1,3]

[1] Division of Materials and Manufacturing Science, Graduate School of Engineering, Osaka University, 2-1 Yamada-oka, Suita, Osaka, Japan, [2] PRESTO, Japan Science and Technology Agency (JST), Kawaguchi, Japan, [3] Unit of Elements Strategy Initiative for Catalysts & Batteries (ESICB), Kyoto University, Katsura, Kyoto, Japan

The urgency for finding clean energy sources is nowadays latent, and the role of hydrogen in the future of energy is well-recognized. However, there are still various barriers that limit the widespread utilization of hydrogen, which are mainly related to its storage and transportation. Chemical hydrogen storage stands out as a suitable alternative to traditional physical storage methods, and formic acid holds tremendous promise within the molecules studied so far. This review summarizes some of the recent approaches considered in our research group for the preparation of efficient catalysts for the production of hydrogen via dehydrogenation of formic acid by using Pd-based heterogeneous catalysts supported on carbon or carbon-containing materials. Several routes were considered to attain efficient catalysts, from the optimization of the size and composition of the nanoparticles to the modulation of important features of the support, such as the porous texture and nitrogen doping level.

Keywords: hydrogen generation, formic acid, carbon materials, palladium nanoparticles, chemical hydrogen storage

OPEN ACCESS

Edited by:
Ashok K. Sundramoorthy, SRM Institute of Science and Technology, India

Reviewed by:
Rajib Paul, Case Western Reserve University, United States
Yan Jiao, University of Adelaide, Australia
Yang Li, Tianjin University, China

***Correspondence:**
Miriam Navlani-García
miriam@mat.eng.osaka-u.ac.jp; miriam.navlani@ua.es

Specialty section:
This article was submitted to Carbon-Based Materials, a section of the journal Frontiers in Materials

Received: *28 November 2018*
Accepted: *25 February 2019*
Published: *22 March 2019*

Citation:
Navlani-García M, Mori K, Salinas-Torres D, Kuwahara Y and Yamashita H (2019) New Approaches Toward the Hydrogen Production From Formic Acid Dehydrogenation Over Pd-Based Heterogeneous Catalysts. Front. Mater. 6:44. doi: 10.3389/fmats.2019.00044

INTRODUCTION

Energy consumption is closely linked to the world's development, population and living standards. Currently, around 90% of the world's energy supply comes from fossil fuels, but their depletion, global energy consumption growth, and the CO_2 emissions associated with their use are driving the search for alternative and sustainable energy sources. CO_2 is a major greenhouse gas (along with water vapor), and its emission to the atmosphere is responsible for changing the natural greenhouse effect that makes the Earth habitable. The anthropogenic greenhouse effect is giving rise to catastrophic consequences, such as the increase in global temperatures, acidification of the oceans, melting arctic ice, decreased crop yield, human diseases and mortality, and so forth. Since CO_2 generated by the energy sector accounts for about 65% of the total anthropogenic greenhouse gas emissions, it is evident that a massive change in the current energy scenario is necessary to avoid further irreversible environmental impacts (Durmaz, 2018). In this context, it was stated by the Intergovernmental Panel on Climate Change (IPCC) that the use of fossil fuels must be gradually reduced, and the utilization of renewable energy must rise to 80% of the power sector by 2050 to avoid catastrophic climate change. The importance of non-fossil fuels, such as solar, biofuel, wind, geothermal heat, etc., in palliating energy issues has been expressed in countless

studies, but their widespread utilization is still limited because of their relatively high cost and technical difficulties in certai countries (Nguyen and Kakinaka, 2018).

The pivotal role of hydrogen in the future of energy is no longer questionable and, even though it is not naturally available as a ready-to-use molecule but is rather bound up in chemical compounds with other elements, its ideal status as an energy vector stems from its outstanding characteristics. The principal advantages of hydrogen as an energy carrier can be summarized as follows (Graetz, 2009; Rosen and Koohi-Fayegh, 2016):

- It can be manufactured from hydrocarbon and non-hydrocarbon energy sources.
- It can be utilized as a chemical fuel and as a chemical feedstock in a number of industrial processes and transportation.
- It is transportable.
- It is environmentally friendly. The combustion of hydrogen to produce energy ($\Delta H = 120$ kJ g^{-1}) is, unlike the combustion of the commonly used fossil fuels (coal, oil, and natural gas), a C-free reaction.
- In contrast to electricity, hydrogen can be stored in various forms that are usually classified as physical and chemical storage methods.

Nevertheless, safety issues related to its storage and transportation have limited its extensive utilization. However, despite the undesired properties of hydrogen in terms of safety, numerous studies revealed that the danger of hydrogen might not be worse than that shown by other fuels. Still, from a practical standpoint, storing, and transporting a hydrogen storage molecule that can provide hydrogen when required would be a better option than storing and transporting hydrogen in tanks for pressurized hydrogen gas or liquid hydrogen, which require high-pressure systems or high liquefaction energy.

Chemical hydrogen storage, in which hydridic/protonic H is combined with other elements, stands as a safe and more convenient option to the classical physical storage. The search for solid and liquid-state hydrogen storage materials has been the focus of fruitful investigations in the last decades. Examples of some representative hydrogen storage molecules include ammonia borane (NH_3BH_3) (García-Aguilar et al., 2016a; Navlani-García et al., 2016a; Navlani-garcía et al., 2018), ammonia (NH_3) (Lan et al., 2012; Afif et al., 2016), methanol (CH_3OH) (Nielsen et al., 2013; Monney et al., 2014), sodium borohydride ($NaBH_4$) (Chowdhury et al., 2015; Demirci, 2015), magnesium hydride (MgH_2) (Lillo-Ródenas et al., 2008; El-Eskandarany et al., 2016) and formic acid (HCOOH) (Navlani-García et al., 2015a; Mori et al., 2017b; Wu et al., 2017) with hydrogen contents of 19.5, 17.6, 12.6, 10.8, 7.6, and 4.4 wt.% of hydrogen, respectively. However, the practical application of some of these hydrogen storage molecules is greatly limited due to their low kinetics for reversible H_2 adsorption-desorption reactions, thermodynamic stability, low inherent thermal conductivity, high price, and toxicity (Czaun et al., 2014; Zhong et al., 2018).

Formic acid is currently considered one of the most promising candidates. It was identified as a potential hydrogen storage medium 40 years ago (Williams et al., 1978), but increasing interest in the development of catalysts to boost the hydrogen production from formic acid has mainly been generated in the last decade. Among the virtues of formic acid as hydrogen carrier, its high volume of 53 g_{H2} L^{-1} (higher than the 2020 target of 40 g_{H2} L^{-1} for on-board hydrogen storage for light-duty fuel cell vehicles updated by the U. S. Department of Energy (DOE) in May 2017), low-toxicity (median lethal dose, LD50 (oral, rat) value of 1,100 mg kg^{-1}), non-flammability (flash point of 69°C, much higher than that of methanol and gasoline (12 and −40°C, respectively) and biodegradability should be mentioned (Navlani-García et al., 2018a). Furthermore, it is in liquid phase at ambient temperature, which makes its transportation and refueling easy so that its handling could be comparable to that of diesel and gasoline (Enthaler et al., 2010).

It is well-known that formic acid decomposition can take place by dehydration (decarbonylation) and dehydrogenation (decarboxylation), which are represented by the following chemical equations (Eppinger and Huang, 2017):

Dehydration: $HCOOH \leftrightarrow CO + H_2O$; ($\Delta G^\circ = -12.4$ kJ·mol^{-1}, $\Delta H^\circ = 29.2$ kJ·mol^{-1}, and $\Delta S^\circ = 139$ J·mol^{-1}·K^{-1})

Dehydrogenation: $HCOOH \leftrightarrow H_2 + CO_2$; ($\Delta G^\circ = -32.9$ kJ·mol^{-1}, $\Delta H^\circ = 31.2$ kJ·mol^{-1}, and $\Delta S^\circ = 216$ J·mol^{-1}·K^{-1})

The gas mixture generated from the formic acid dehydrogenation reaction can be directly utilized as a feed gas for an H_2/air fuel cell (Loges et al., 2008) so that the dehydration route should be avoided to suppress the formation of CO, which leads to the poisoning of the catalysts used in the fuel cell. Formic acid dehydration can be avoided through highly selective catalysts able to boost its dehydrogenation to generate H_2 and CO_2. It has been reported that the pathway followed in the decomposition of formic acid (by either dehydration or dehydrogenation) is strongly dependent on the catalytic surface, which controls the adsorption of formic acid molecules. It was claimed that large terrace sites tend to adsorb the molecules of formic acid following a bidentate form, which gives raise to the dehydrogenation pathway, while surface-unsaturated sites boost the dehydration pathway (Tedsree et al., 2011).

Besides its intrinsic features, another important aspect of the use of formic acid as a hydrogen storage material is that the CO_2 generated in formic acid dehydrogenation can be subsequently hydrogenated so that formic acid molecules are regenerated in a carbon-free emission process (Fellay et al., 2008; Loges et al., 2008; Enthaler et al., 2010) that can be simply schematized in **Figure 1**.

Williams first reported on the electrochemical reduction of CO_2 to formic acid in 1978 (Williams et al., 1978), and since then interesting investigations have been undertaken by using electrochemical (Lu et al., 2014; Gupta et al., 2016; Zhang et al., 2017b), photoelectrochemical (Lu et al., 2017; Jiang M. et al., 2018), catalytic (Moret et al., 2014; Mori et al., 2018), and photocatalytic (Premkumar and Ramaraj, 1997; Qin G. et al., 2013) approaches. However, despite the ideality of this system, several aspects should be considered to boost the thermodynamically uphill formation of liquid formic acid from gaseous CO_2 and H_2. Usually, the reaction of CO_2 and H_2 is

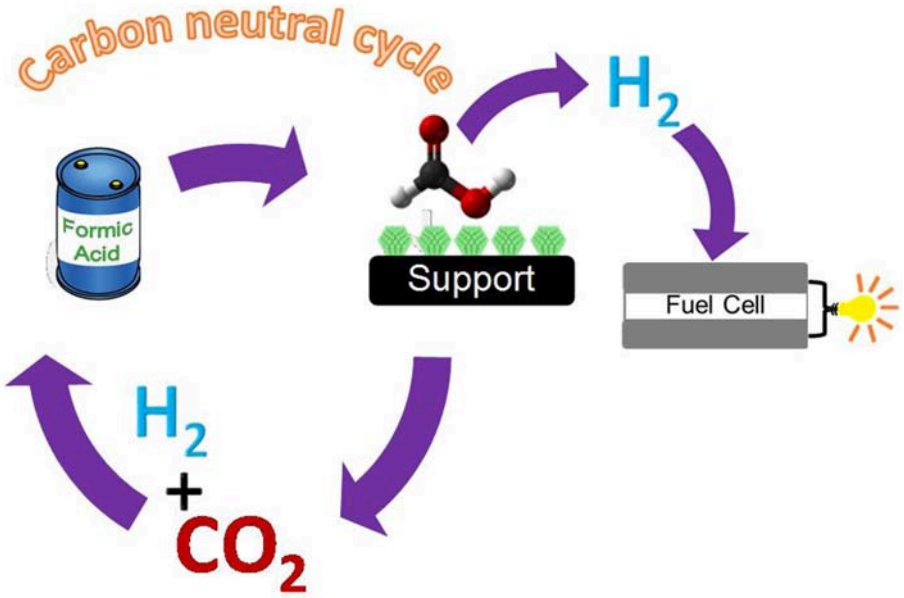

FIGURE 1 | Carbon-neutral energy storage using formic acid as a hydrogen carrier molecule.

through the water gas shift reaction, resulting in the formation of CO and H_2O (Paul et al., 2015; Reddy and Smirniotis, 2015), but the selection of suitable experimental conditions (such as the use of inorganic or organic basis) and an appropriate catalyst might shift the reaction equilibria toward the hydrogenation of CO_2 (Zhu and Xu, 2015).

Since Coffey first reported the decomposition of formic acid over a homogeneous catalytic system in 1967 (Coffey, 1967), many investigations dealing with the preparation of highly active and robust homogeneous catalysts that selectively produce H_2 and CO_2 from formic acid under mild conditions have been documented (Fukuzumi et al., 2008, 2010; Mellmann et al., 2016), including ruthenium (Boddien et al., 2009; Czaun et al., 2014), rhodium (Strauss et al., 1979), iron (Boddien et al., 2010; Zell et al., 2013), and iridium (Bavykina et al., 2015; Czaun et al., 2016; Matsunami et al., 2017) complexes being some of the most representative studied catalysts. However, achieving competitive and selective heterogeneous catalysts under mild conditions is still a difficult task (Enthaler et al., 2010; Grasemann and Laurenczy, 2012).

The investigation of the decomposition of formic acid over heterogeneous catalysts dates back to the 1930s, but in the initial studies the optimization of the catalysts, as well as the measurement of the CO evolved from the formic acid dehydration side reaction, were not deeply considered (Grasemann and Laurenczy, 2012). In that case, the reaction has mainly been studied in the gas phase, and temperatures higher than 100°C (the normal boiling point of formic acid) or the use of an inert carrier gas to dilute formic acid below its saturated vapor pressure were needed, which, from the practical application viewpoint, would constitute additional complexity for the setup used to conduct the reaction test. Then, the development of heterogeneous catalysts for formic acid dehydrogenation in liquid-phase is highly desirable (Zhu and Xu, 2015). The search for an optimum heterogeneous catalyst encompasses the investigation of several active phases, mainly in the form of noble metal nanoparticles, but reports in which non-noble metal nanoparticles are studied can be also found in the literature, approaching this issue from both experimental and theoretical perspectives (Yoo et al., 2014).

Among all the catalysts studied in this application, those based on palladium have been claimed to be very promising alternatives, and they have received great attention not only because they are more tolerant to CO than other metals, but also because relatively high hydrogen conversion and selectivity values have been achieved under moderate temperatures (He and Li, 2016). Thus, the research community interested in formic acid as a hydrogen carrier has devoted tremendous efforts to understand and optimize the Pd-based catalytic systems by enhancing either their performance under mild conditions or their stability and/or durability as well as selectivity. Some of the strategies tackled in this matter include the optimization of the active phase features (in terms of size, composition, structure, and so forth) as well as the impact of the support properties in modulating the final behavior of the catalysts by controlling the metal-support interaction or the acid/base properties. There are a number of supports investigated for this application, including silica (García-Aguilar et al., 2016b; Mori et al., 2017a), zeolites (Navlani-García et al., 2015a), metal-organic frameworks (MOFs) (Wen et al., 2017), etc. Among them, carbon materials are certainly the most extensively investigated so far. The virtues of carbon materials as catalytic support are nowadays recognized and they can be ascribed to unique properties that make them preferable over other common supports such as silica or

TABLE 1 | Representative catalysts based on carbon materials used in the formic acid dehydrogenation reaction.

Catalyst	T (°C)	TOF (h^{-1})	References
Pd/C	25	64	Wang Z.-L. et al., 2012
Pd/mpg-C_3N_4	25	144	Lee et al., 2014
Pd/C	25	304	Jiang et al., 2014
Pd/$CN_{0.25}$	25	752	Bi et al., 2016
Pd/C	25	835	Li J. et al., 2017
Pd/NMC-400	25	913	Sun et al., 2019
Pd/1.0Ti-g-C_3N_4	30	77	Wu et al., 2017
Pd/C	30	228.3	Wang X. et al., 2014
Pd_{IMP}/CNF-HHT	30	563.2	Sanchez et al., 2018
Pd/carbon black	30	1,815	Zhang S. et al., 2017
Pd/N-C	45	645	Jeon et al., 2016
Pd/MSC-30	50	2623	Zhu Q. L. et al., 2014
Pd/C	50	7,959	Zhou et al., 2016
Pd/C nanospheres	60	7,256	Zhu et al., 2015
Pd/N-MSC-30	60	8,414	Li Z. et al., 2017
Ag@Pd/C (1:1)	20	192	Tedsree et al., 2011
Pd_1Ag_6/N-rGO	25	171	Huang et al., 2017
Ag@Pd/N-GCNT	25	413	Nabid et al., 2017
PdAg@g-C_3N_4	25	420	Liu et al., 2019
$Ag_{74}Pd_{26}$/graphene	25	572	Yang et al., 2015
AgPd/C	30	854	Feng et al., 2016
C-$Ag_{42}Pd_{58}$	50	382	Zhang et al., 2013
Ag_9Pd_{91}/g-C_3N_4	50	480	Yao et al., 2017
PdAg/amine-MSC	75	5,638	Masuda et al., 2018
Au_6Pd_4/carbon black	0	635	Wu et al., 2014
AuPd–CeO_2/N-rGO	25	52.9	Wang et al., 2014a
Au@Pd/N–mrGO	25	89.1	Wang et al., 2013b
Pd–Au–Dy/C	92	269	Zhou et al., 2010
$Au_{0.75}Pd_{0.25}$/C–L-7.5	25	718	Cheng et al., 2016
Au_6Pd_4-L-Mg	25	1,120	Wu et al., 2015
$Co_{1.6}Ag_{62.2}Pd_{36.2}$/graphene	25	110	Yang et al., 2016
$Co_{0.30}Au_{0.35}Pd_{0.35}$/C	25	80	Wang et al., 2013a

alumina (Rodríguez-Reinoso, 2010). Among those features, their resistance to basic and acid media, tailored porous structure, controllable hydrophilicity, and the possibility of incorporation of heteroatoms in their structure are of particular interest for the formic acid dehydrogenation reaction. Carbon materials are ideal catalytic support for the present application, not only because they serve as anchoring sites for the metal nanoparticles but also because they can be modified so as to incorporate basic functionalities that can be actively involved in the formic acid dehydrogenation reaction, ultimately resulting in highly performing catalysts.

In order to provide a wide view of the recent breakthroughs achieved by using catalysts based on carbon materials, some representative examples are listed in **Table 1**.

In this review, we address some of the recent studies conducted by our research group toward the design of Pd-based heterogeneous catalysts supported on carbon or carbon-containing materials for the formic acid dehydrogenation reaction in liquid phase.

PD-BASED HETEROGENEOUS CATALYSTS SUPPORTED ON CARBON MATERIALS

As it was previously mentioned, Pd-based catalysts have been claimed to be the most active toward hydrogen production from the formic acid dehydrogenation reaction. Numerous factors, such as morphology of the metallic active phase, composition and architecture of the nanoparticles, metal loading, etc., have already been investigated in an attempt to design efficient heterogeneous catalysts that can be competitive to those generally more active homogeneous systems, while offering the well-known advantages inherent to heterogeneous catalysis. Most of the investigated heterogeneous catalysts studied in this application are carbon-supported systems. Among them, activated carbon is the most extensively used support (Navlani-García et al., 2018a), which is due to its high surface area, which gives the possibility to achieve highly dispersed and well-distributed metal nanoparticles, which are accessible to the molecules involved in the reaction. However, interesting reports on several kinds of carbon materials and carbon-based materials, such as reduced graphene oxide (rGO) (Ping et al., 2013; Yan et al., 2018), graphene nanosheets (Qin Y.-L et al., 2013; Bulut et al., 2018) carbon nanospheres (Zhu et al., 2015; Zhang et al., 2017a), various nitrogen-doped carbon materials [carbon black (Jeon et al., 2016), carbon nanotubes (Podyacheva et al., 2018), carbon xerogels (Navlani-García et al., 2019), carbon nanosheets (Jiang Y. et al., 2018; Zhang et al., 2019)], mesoporous carbon (Masuda et al., 2018), hierarchical porous carbon (Lee et al., 2017), etc.), carbon-based composite supports (Qin et al., 2014), and also carbon-containing structures such as carbon nitride (Cai et al., 2013; Oh, 2016), can be found in the recent literature.

Herein some of the recent investigations performed in our research group will be summarized. The effect of the features of both metal active phase and carbon-based supports on the catalytic performance in the formic acid dehydrogenation reaction were studied in the investigations herein reviewed.

Effect of the Nanoparticle Size

The investigation of the active phase properties in the final catalytic performance is usually the cornerstone of the successful preparation of highly-performing catalysts. Active phases are usually in the form of metal nanoparticles, which tend to display higher catalytic reactivity by virtue of their small sizes and high surface-to-volume ratio and which, in turn, result in the presence of low-coordinated atoms (Xie and Schlücker, 2018). Numerous aspects such as nanoparticle size, shape, and electronic features have already been studied by those researchers tackling the design of catalysts for hydrogen production from the decomposition of formic acid.

Our research group was a pioneer in the investigation of the effect of the nanoparticle size in the decomposition of formic acid by assessing the activity of Pd-based catalysts (Navlani-García et al., 2015b, 2016b). In that study, the commercial activated carbon Shirasagi M (Osaka Gas Chemicals Co. Ltd.) was used as catalytic support. The synthesis of colloidal size-controlled Pd nanoparticles was based on a polyol process by using palladium (II) acetate as a Pd precursor, polyvinylpyrrolidone

(PVP) as a stabilizing agent and ethylene glycol as the solvent and reducing agent. Several experimental parameters, such as PVP/Pd molar ratio as well as synthesis temperature and time were used to tune the final size of the nanoparticles. The as-synthetized colloidal nanoparticles were subsequently loaded on the carbon support and catalysts with an average nanoparticles size ranging from 2.7 to 5.5 nm (2.7, 3.6, 3.9, 4.2, and 5.5 for catalysts Pd/C(1)–(5), respectively) were obtained. All catalysts were thoroughly characterized and the presence of Pd (0) in the nanoparticles was confirmed by X-ray photoelectron (XPS) and X-ray absorption fine structure (XAFS) spectroscopies. The hydrogen production was monitored by gas chromatography while the reaction took place at 30°C. The results of the hydrogen produced after 3 h of reaction as a function of the size of the nanoparticles are summarized in **Figure 2A**. As can be observed in **Figure 2A**, sample Pd/C(3), with an average nanoparticle size of 3.9 nm was the best-performing catalyst among those investigated. The volcano type relationship found between the hydrogen production ability and the size of the nanoparticles in that study was ascribed to the relative proportion of low-coordinated atoms (LC) and high-coordinated atoms (HC) with respect to the total number of surface atoms present in the catalysts. To get further insight into the size-sensitivity observed, we assumed that Pd nanoparticles were cuboctahedral in shape, with a cubic close-packed structure in this size range and the full-shell nanoparticles model was adopted to calculate geometric parameters (Mori et al., 2004) (total surface atoms, LC and HC atoms). Turnover Frequency (TOF) values were calculated on the basis of these specific atoms (see **Figure 2B**). If all the atoms on the nanoparticle surface possess the same catalytic activity toward the hydrogen production, the TOF values calculated on the basis of the surface atoms should be the same regardless of the Pd particle sizes. As a result, TOF values changed by nearly 40% in the investigated size range and the values fell in the following order: Pd/C(3) (3.9 nm) > Pd/C(5) (5.5 nm) > Pd/C(2) (3.6 nm) > Pd/C(4) (4.2 nm) > Pd/C(1) (2.7 nm). Such differences in the normalized TOF values indicated that all the Pd surface sites did not present the same catalytic activity in the formic acid decomposition. Furthermore, the tendencies observed for the TOF values calculated on the basis of LC and HC (see **Figure 2B**) suggested that the formic acid dehydrogenation reaction is "structure-sensitive" and the HC Pd atoms at terrace sites act as the main active species.

Furthermore, a plausible mechanism pathway was proposed (**Figure 3**). According to that mechanism the following reaction steps would take place:—Step I: O-H bond cleavage, providing a proton (H^+), and a palladium-formate (Pd-$[HCOO]^-$) intermediate;—Step II: Pd-$[HCOO]^-$ species undergo C-H bond dissociation, affording a palladium hydride (Pd-$[H]^-$), and CO_2;—Step III: the generation of H_2 along with the regeneration of the Pd species take place after the recombination of Pd-$[H]^-$ with a H^+.

In addition, to get more information about the size sensitivity in the elementary steps of the formic acid dehydrogenation, Kinetic Isotope Effect (KIE) experiments were conducted by monitoring the evolution of the reaction using deuterated formic acid (HCOOD and DCOOH) and the results for each catalyst are listed in **Table 2**. As can be seen, the reaction rate constant ratio (K_H/K_D) with HCOOH and HCOOD were similar for all the samples, suggesting that step I (O-H bond cleavage) was not dependent on the size of the NPs. The much larger K_H/K_Dvalues obtained with HCOOH and DCOOH for all the catalysts suggested that step II (C-H dissociation) was the rate-determining reaction step. K_H/K_D values were well-correlated with the catalytic tendency and the smallest values obtained with sample Pd/C(3) confirmed the best performance displayed by that catalyst.

Subsequent studies also tackled the investigation of the size sensitivity. For instance, Zhang S. et al. (2017) also addressed the effect of Pd nanoparticles size in the formic acid decomposition over carbon-supported catalysts with average sizes ranging from 2.0 to 5.2 nm and using carbon black (Vulcan XC-72R) as support. A capping-free synthetic protocol was then chosen, and the size of the nanoparticles was controlled by means of modifying the pH of the metal precursor, which was achieved with the addition of Na_2CO_3, $NH_3{\cdot}H_2O$, or NaOH. It was also observed that the catalytic performance displayed a volcano-type relationship with the Pd nanoparticle size, with the sample containing an average size of 2.2 nm being the most active among assessed. Following our study on the size-effect investigation (Navlani-García et al., 2016b), the volcano-type tendency observed in that case was also related to the proportion of low coordinated and high coordinated atoms in the nanoparticles. Such a volcano-type tendency for Pd/C catalysts using activated carbon was also observed by Jeon and Chung (2017) by evaluating the activity of catalysts synthesized by several preparation methods [i.e., (i) adsorption of "ready-made" NPs; (ii) Pd precursor adsorption and reduction; (iii) adsorption of the Pd precursor plus deposition and reduction; (iv) Pd precursor ion exchange and reduction; (v) Pd precursor ion exchange, deposition and reduction; (vi) *in situ* metal sol formation and reduction; (vii) *in situ* metal sol formation, deposition and reduction]. Li and co-workers (Li J. et al., 2017) also reported on the effect of the Pd nanoparticles size for the formic acid dehydrogenation reaction by using carbon black (Vulcan XC-72R) as support. In that case, sodium citrate was used as a stabilizer and several Pd precursors to sodium citrate ratios were used so as to obtain Pd nanoparticles with average sizes ranging from 2.1 to 4.5 nm. Under the experimental conditions used in that study, the smallest nanoparticles displayed the best performance among those investigated, which was related to a better dispersion of the nanoparticles and larger proportion of positively charged Pd species. Jin et al. also focused on the effect of the Pd nanoparticles size in their study on Pd/NH_2-KIE-6 catalysts (being KIE-6 a mesoporous silica) (Jin et al., 2018). The control of the nanoparticle size was achieved by means of modifying experimental conditions such as Pd precursor [i.e., palladium (II) nitrate hydrate, palladium (II) acetate, palladium (II) acetylacetonate, and potassium tetrachloropalladate (II)] and the stirring time used in the preparation of the catalysts and nanoparticles, with sizes ranging from 2.0 to 2.8 nm being measured by STEM analysis. In that case, the catalysts synthesized from palladium nitrate displayed the smallest NP size

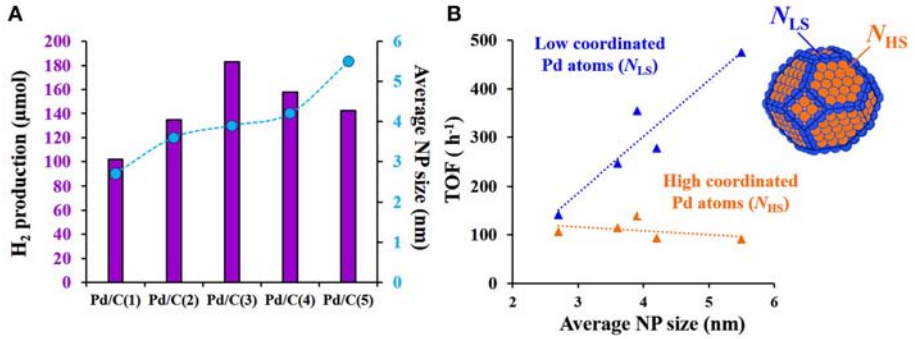

FIGURE 2 | (A) Relationship between H_2 production after 3 h of reaction at 30°C and the average Pd nanoparticles (NP) size; **(B)** Normalized TOF values calculated on the basis of high-coordinated (HC) and low-coordinated (LC) as a function of the average Pd NP size. Adapted with permission from Navlani-García et al. (2016b). Copyright 2016 Wiley.

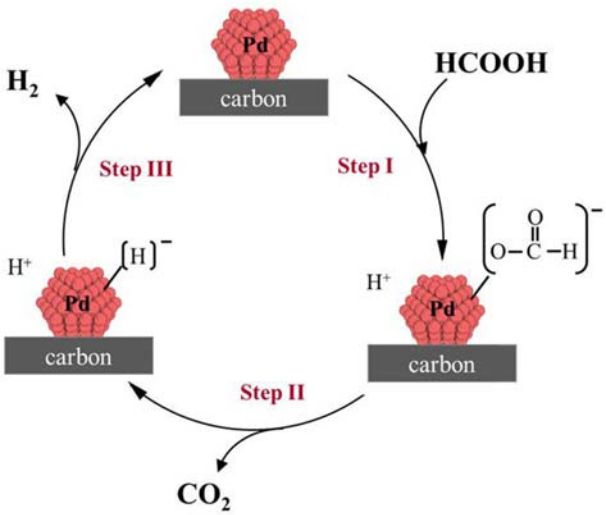

FIGURE 3 | Reaction mechanism proposed for H_2 production from the formic acid dehydrogenation catalyzed by Pd/C catalysts.

TABLE 2 | KIE in the decomposition of formic acid.

Catalyst	Average NP size (nm)[a]	Formic acid	Reaction rate (μmol · min^{-1})	k_H/k_D
		HCOOH	0.64	–
Pd/C(1)	2.7 ± 0.7	HCOOD	0.20	3.13
		DCOOH	0.02	35.20
		HCOOH	1.03	–
Pd/C(2)	3.6 ± 0.8	HCOOD	0.43	2.40
		DCOOH	0.03	32.05
		HCOOH	1.79	–
Pd/C(3)	3.9 ± 0.9	HCOOD	0.78	2.29
		DCOOH	0.17	10.37
		HCOOH	1.80	–
Pd/C(4)	4.2 ± 0.6	HCOOD	1.27	1.42
		DCOOH	0.16	11.02
		HCOOH	1.62	–
Pd/C(5)	5.5 ± 1.6	HCOOD	0.34	4.76
		DCOOH	0.12	13.85

Adapted with permission from Navlani-García et al. (2016b). Copyright 2016 Wiley.
[a] *Average nanoparticle size determined by TEM analysis.*

and, in turn, showed the best performance in the formic acid dehydrogenation reaction.

Effect of the Nanoparticle Composition

As was previously mentioned, most of the heterogeneous catalysts used in the formic acid dehydrogenation reaction are based on Pd nanoparticles. However, Pd monometallic systems often suffer from deactivation caused by the adsorption of reaction intermediates on the surface of the nanoparticles. It was observed that the use of bimetallic or multimetallic systems can greatly palliate such problem and display better performance than the Pd monometallic counterpart. Such enhancement of the catalytic activity and selectivity of the bimetallic and multimetallic systems are usually ascribed to the modification of the Pd electronic density and geometric structure as well as resistance to poisoning intermediates (Zhang et al., 2017a).

Furthermore, the utilization of bimetallic or multimetallic systems has been a widely employed strategy to reduce the cost of the final catalysts, particularly when non-noble metals are used in their compositions. A number of bimetallic and multimetallic heterogeneous catalysts, such as PdNi (Qin Y.-L et al., 2013), PdCu (Mori et al., 2015), PdAu (Huang et al., 2010; Gu et al., 2011; Wen et al., 2017) (Yan et al., 2015), PdAg (Mori et al., 2013; Wang et al., 2014b; Song et al., 2018), NiAuPd (Wang et al., 2014b; Bulut et al., 2018), PdCuCr (Mori et al., 2017b), AuAgPd (Li et al., 2015), CoAuPd (Wang et al., 2013a), etc., have already been reported to be active in the formic acid dehydrogenation reaction. Among them, noble metal-based systems have been so far the most studied, and PdAg-based catalysts have taken pole position in attracting extensive investigations (Mori et al., 2013; Masuda et al., 2018) as they have shown to be one of the most

active catalysts in the formic acid decomposition reaction. Their superior performance is usually ascribed to the efficient charge transfer from Ag to Pd that results in electronically promoted Pd species, which are more active in catalyzing the formic acid dehydrogenation reaction. Since Tedsree et al. first reported on the potential of PdAg catalysts for this application in 2011 (Tedsree et al., 2011), an increasing number of studies on the decomposition of formic acid over PdAg catalysts can be found in the literature. Unlike monometallic catalysts, factors such as composition and configuration of the nanoparticles should be kept in mind while evaluating the performance of bimetallic or multimetallic catalysts. The complexity of these systems usually complicates the proper evaluation of only one aspect such as the composition or size of the bimetallic nanoparticles.

Our research group reported on the screening of carbon-supported PdAg catalysts prepared by loading pre-synthetized PVP-capped nanoparticles on activated carbon (Shirasagi M), in which the composition of the nanoparticles was optimized in terms of Pd/Ag and PVP/metal molar ratios (Navlani-García et al., 2016c).

As in the study of the effect of the size of monometallic Pd catalysts (Navlani-García et al., 2016b), the polyol method was utilized to synthesize colloidal nanoparticles. In this case, the composition of the nanoparticles was carefully controlled by modifying the initial amount of the metal precursors and capping agent (PVP) in the synthesis, so that 12 colloids with fixed Pd concentration, PVP/metal molar ratio of 1/1, 5/1 or 10/1, and Pd/Ag molar ratios of 1/0.5, 1/1, 1/2, and 1/4 were obtained. From these composition-controlled colloids, 12 carbon-supported catalysts were prepared. The catalysts were denoted as PdxAgy/C(z) attending to the composition of the nanoparticles ("x" and "y" related to the Pd/Ag molar ratio, and "z" indicating the PVP/metal molar ratio). The catalytic activity of the samples was assessed by means of gas chromatography by following the hydrogen generated after 3 h of reaction at 30°C, and the results are summarized in **Figure 4**.

All catalysts showed ∼ 100% of selectivity toward the formic acid dehydrogenation reaction so that the generation of CO through formic acid dehydration was suppressed. The catalytic activity was shown to be strongly dependent on the composition of the nanoparticles, both Pd/Ag molar ratio and PVP content. It was observed that the incorporation of Ag in the catalysts greatly enhanced the activity, reaching the optimum activity for those samples with a Pd/Ag of 1/2 for most of the PVP contents. However, the catalytic activity decayed dramatically for those samples with the highest Ag content (Pd/Ag of 1/4). Among all catalysts investigated, sample Pd1Ag2/C(1) was the most active and the beneficial effect from the addition of Ag was also confirmed by the comparison with the Pd monometallic counterpart catalyst (the H_2 production after 3 h of reaction was 266 and 144 μmol for Pd1Ag2/C(1) and Pd/C, respectively, under identical experimental conditions).

Once the best-performing catalyst was identified, its applicability in a large-scale reactor was also checked by using a burette system equipped with a reflux condenser, so that the hydrogen generation could be measured by observing the volume of gas displaced. A reaction rate of 3,000 mL min^{-1} g_{Pd}^{-1} was achieved, confirming the suitability of the studied catalysts. Furthermore, Pd1Ag2/C(1) showed a TOF value of 855 h^{-1} (on the basis of Pd content), which was higher than those values achieved by other bimetallic PdAg catalysts previously reported in the literature (Tedsree et al., 2011; Liu et al., 2016).

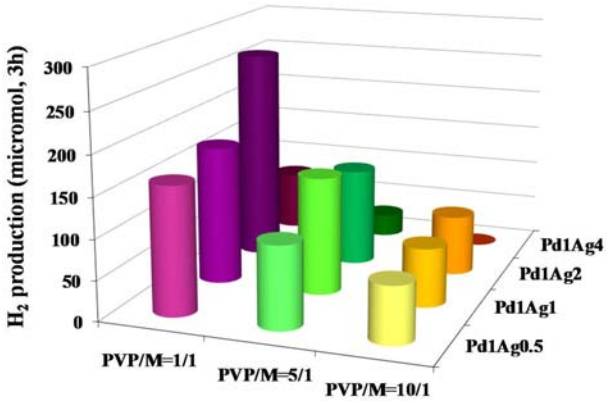

FIGURE 4 | H_2 generated after 3 h of reaction over PdAg/C catalysts with a various composition of the nanoparticles. Adapted with permission from Navlani-García et al. (2016c). Copyright 2016 American Chemical Society.

As for the effect of PVP, it was seen that the catalytic performance decayed as the capping agent content increased, which was initially ascribed to either change in the surface composition of the nanoparticles and electronic effect exerted by the PVP molecules, or changes in the size of the nanoparticles. In order to ascertain the relationship between the composition of the nanoparticles and their activity, the catalysts were thoroughly characterized.

The result of TEM analysis indicated that similar average nanoparticle size was obtained for those catalysts with Pd/Ag of 1/0.5, 1/1, and 1/2, (sizes ranging from 3.0 to 3.9 nm) regardless the PVP content (see **Table 3**). Furthermore, it was shown that the addition of Ag in the nanoparticles resulted in smaller nanoparticles as compared to the Pd monometallic counterpart catalysts. That fact was related to the favored reduction of Pd ions when Ag ions were present, which would lead to a larger number of seeds in the nucleation step and would eventually produce nanoparticles with a smaller size. As for the catalysts with larger Ag content (Pd/Ag of 1/4), the average size of the nanoparticles was larger, particularly in the samples with lower PVP content (5.0, 4.0, and 3.6 nm for Pd1Ag4/C(1), Pd1Ag4/C(5), and Pd1Ag4/C(10) catalysts, respectively). Furthermore, some aggregates were detected in sample Pd1Ag4/C(10), which was ascribed to the high PVP content and concentration of metal precursors used in the synthesis of the corresponding colloid.

HR-TEM analysis was also performed for a representative colloid (Pd1Ag2, with a PVP/metal ratio of 1/1) and the lattice space was measured to be 0.23 nm, between the (111) lattice spacing of fcc (face-centered cubic) Pd (0.224 nm)

TABLE 3 | Particle size determined by TEM analysis (d_{TEM}) for all catalysts.

Sample	d_{TEM} (nm)	Sample	d_{TEM} (nm)
Pd1Ag0.5/C(1)	3.9 ± 0.8	Pd1Ag2/C(1)	3.5 ± 0.9
Pd1Ag0.5/C(5)	3.4 ± 0.7	Pd1Ag2/C(5)	3.0 ± 0.6
Pd1Ag0.5/C(10)	3.4 ± 0.6	Pd1Ag2/C(10)	3.1 ± 0.8
Pd1Ag1/C(1)	3.6 ± 0.9	Pd1Ag4/C(1)	5.0 ± 3.0
Pd1Ag1/C(5)	3.3 ± 0.6	Pd1Ag4/C(5)	4.0 ± 1.1
Pd1Ag1/C(10)	3.4 ± 0.6	Pd1Ag4/C(10)	3.6 ± 1.0

Adapted with permission from Navlani-García et al. (2016c). Copyright 2016 American Chemical Society.

and Ag (0.235 nm), which suggested the presence of alloyed nanoparticles.

The set of catalysts that displayed the highest activity among investigated Pd1Ag2/C samples were characterized by XAFS analysis. As can be seen in **Figure 5**, the Fourier transformation (FT) of k^3-weighted extended X-ray absorption fine structure (EXAFS) spectra of the reference samples (Pd and Ag foils), displayed peaks centered at 2.5 and 2.7 Å, respectively (**Figures 5A,B**), corresponding to metal-metal bonding (Pd-Pd and Ag-Ag, respectively). In the case of the catalysts, those peaks were shifted as compared to the references, confirming the presence of heteroatomic Pd-Ag bonding in the nanoparticles.

The electronic structure of these catalysts was also analyzed by means of XPS and, even though both Pd and Ag were mainly in their metallic form, oxidized forms were also detected. Such species were related to the metal-PVP interaction via C=O groups of the polymer molecules. Then, the presence of Pd(II) and Ag(I) species in the nanoparticles was related to the presence of PVP molecules. Furthermore, the charge transfer from Ag to Pd was also considered. It was observed that such charge transfer was hampered for high PVP content in the nanoparticles, which was due to its capping effect on the Ag species. It was found that the PVP content greatly affected the surface composition of the nanoparticles, as higher Pd/Ag surface ratio was detected as the PVP content in the nanoparticles decreased (surface Pd/Ag ratio of 1.26, 1.20, and 0.78 for Pd1Ag2/C(1), Pd1Ag2/C(5), and Pd1Ag2/C(10), respectively), which was associated with the relative interaction ability of Pd and Ag with the polymer molecules.

In view of the characterization results, the catalytic tendency displayed by the set of samples were discussed. First, it was claimed that the poor performance displayed by the Pd1Ag4 set of catalysts could be due to the aggregation found in those samples. However, that aspect did not determine the tendency observed for the other three sets of catalysts (Pd1Ag0.5, Pd1Ag1, and Pd1Ag2) because of the very similar average nanoparticle size observed in those samples. The detailed characterization of Pd1Ag2/C set of samples by means of XPS analysis revealed that the PVP/metal molar ratio present in the catalysts had an important effect on the features of the catalysts, in terms of surface Pd enrichment in the nanoparticles and electronic density in the Pd atoms which, along with an optimum composition of the nanoparticles (i.e., Pd/Ag molar ratio), were shown to be the determining aspects for controlling the catalytic activity.

Pd-Catalysts Supported on Nitrogen-Doped Carbon Xerogels

Even though the design of catalysts is usually focused on tailoring the active phase features, in terms of nanoparticles size, shape, composition and so forth (García-Aguilar et al., 2016b; Navlani-García et al., 2016b,c), the impact of the support characteristics in the final catalytic performance toward the hydrogen production from the formic acid dehydrogenation reaction has merited several investigations and various approaches, in which either the incorporation of additional functional groups or the intrinsic support features were assessed, can be found in the literature. For instance, the local basicity of the support has been pointed out as an important parameter to enhance the formic acid dehydrogenation reaction, as such basic groups can either influence the final electronic density of metallic active sites or directly participate as hydrogen scavengers (Mori et al., 2014, 2015, 2017a; Masuda et al., 2018). At this point, carbon material-based catalysts have been considered as a promising alternative to attain competitive hydrogen production abilities because their basicity can be easily modified by nitrogen functionalization (Bashkova et al., 2003; Bagreev et al., 2004; Hulicova-Jurcakova et al., 2009). Hence, some experimental studies combined with theoretical calculations have tried to shed some light on the understanding of the nitrogen effect on active sites in the formic acid dehydrogenation reaction. Recently, an interesting study about N-doped mesoporous carbon-supported Pd species demonstrated that the interaction between single isolated Pd^{2+} cations and pyridinic nitrogen groups boosted the formic acid dehydrogenation reaction as compared to the N-free counterpart catalyst (Bulushev et al., 2016b). Furthermore, the nitrogen functionalization present on carbon materials has been found to be anchoring points for metal nanoparticles, which results in small and well-distributed nanoparticles on the surface of the catalysts and enhanced catalytic performances (Jeon et al., 2016).

We recently studied the effect of the nitrogen doping level on the catalytic ability in the formic acid dehydrogenation reaction over Pd-based N-doped carbon catalysts (Navlani-García et al., 2019). To do this, carbon xerogels were chosen as carbon support, in which apart from fixing the nitrogen doping level, the porous texture could also be modulated by modifying the synthesis conditions. The control of the pore texture allowed us to design catalysts that gathered both an accessible porous structure and nitrogen groups, which could facilitate homogenous dispersion of small nanoparticles on the surface of the catalysts. In that study, N-doped carbon xerogels were prepared by a polycondensation method of resorcinol and formaldehyde in the presence of melamine using the same protocol as it was reported in a previous work (Salinas-Torres et al., 2018). All supports were characterized by both N_2 adsorption-desorption isotherms and mercury porosimetry measurements to gain knowledge about the pore texture (see **Table 4**) as well as elemental analysis and XPS to know the nitrogen content and nitrogen functionalities, respectively. The supports were denoted as Pd/aN-CX-b to distinguish the nitrogen doping level (a) and the pore texture (b) in each sample. All supports had micropores related to the gas uptake at low P/P_0 observed in the N_2 isotherms. Moreover, these

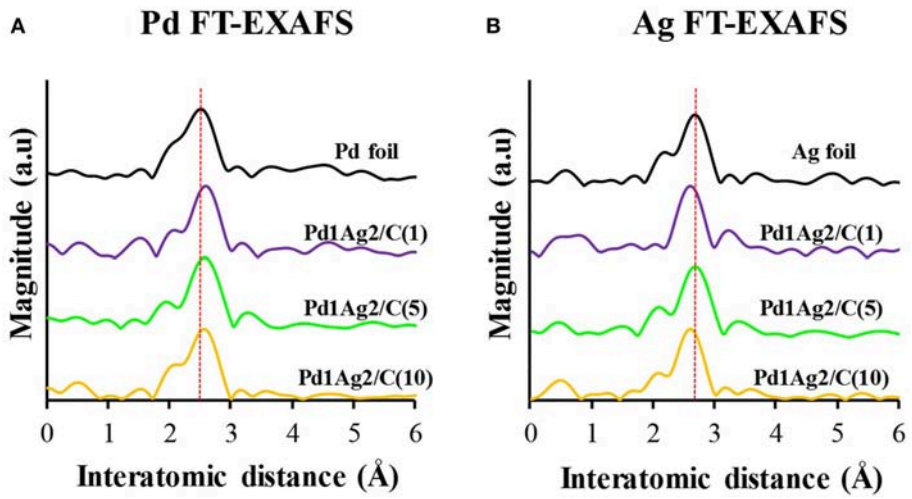

FIGURE 5 | (A) Pd and **(B)** Ag FT-EXAFS spectra of Pd1Ag2/C catalysts prepared using colloids with different PVP/M ratios [Pd1Ag2/C(1), Pd1Ag2/C(5), and Pd1Ag2/C(10)] and reference samples (Pd and Ag foils). Adapted with permission from (Navlani-García et al., 2016c). Copyright 2016 American Chemical Society.

TABLE 4 | Porous texture properties for *N*-doped carbon xerogels supports.

Support	S_{BET} ($m^2\ g^{-1}$)	V_{DR} ($cm^3\ g^{-1}$)	V_V ($cm^3\ g^{-1}$)	Pore size (nm)
CX-meso	726	0.29	1.46	16
2N-CX-meso	545	0.22	0.46	6
4N-CX-meso	590	0.24	0.94	14
4N-CX-macro	587	0.24	1.60	1,180
8N-CX-macro	307	0.13	0.65	–

Adapted with permission from Navlani-García et al. (2019). Copyright 2019 Elsevier.

N-doped carbon xerogels also presented volume of mesopores or macropores as well as different average pore size depending on the precursors' solution selected (**Table 4**).

Subsequently, a wet impregnation method was used to synthesize their Pd-based N-doped carbon catalyst counterparts (Pd/support). Afterwards, the particle size of the as-synthesized catalysts was analyzed by TEM (see **Figure 6**). From the histograms, it was observed that the average nanoparticle size ranged from 2.2 to 3.4 nm for most of the samples. However, Pd/8N-CX-macro micrograph revealed the formation of large nanoparticles with non-regular shapes and with an average nanoparticle size of 8.3 nm, which were not well-distributed on the support. This fact could be associated with both the high concentration of Lewis basic sites and the lowest apparent surface area for 8N-CX-macro support. On the contrary, the rest of the catalysts, which had lower nitrogen content than 8N-CX-macro support, displayed good dispersion of spherical-shaped nanoparticles. It is important to mention that Pd/CX-meso support (*N*-free sample) exhibited the largest average nanoparticle size (3.4 nm), excluding 8N-CX-macro support. Therefore, according to that result, the nitrogen doping level was a crucial parameter to produce both small and well-dispersed nanoparticles, provided that the nitrogen doping level did not surpass a specific amount.

The electronic state of Pd nanoparticles was analyzed by XPS measurements. Taking into account the position of the binding energies of Pd 3d peaks for Pd-based N-doped carbon catalysts compared to the N-free catalyst, the existence of Pd-N interaction was concluded. Regarding the nitrogen groups, XPS spectra for both N-carbon xerogel supports and their Pd-based catalyst counterparts revealed that pyridinic and quaternary *N* groups were the most abundant, although pyrrolic/pyridone nitrogen groups were also observed. X-ray absorption measurements were completed to gain a better understanding of the electronic state of Pd. From EXAFS analysis (see **Figure 7**), it was demonstrated that all catalysts presented Pd in the metallic state (2.5 Å). Furthermore, the peak ascribed to the Pd-N interaction (1.6 Å) was also observed for the N-containing catalysts, with the exception of the Pd/8N-CX-macro catalyst. This weak Pd-N interaction could be attributed to the difficult accessibility of Pd nanoparticles to the nitrogen functionalities due to the low apparent surface area of the Pd/8N-CX-macro catalyst. Furthermore, the less important Pd-N interaction could also be responsible for the larger nanoparticles observed in that sample. The existence of PdO in the samples could not be discarded because the corresponding peak appears at the same interatomic distance as that of the Pd-N bond.

After characterization of all catalysts, the catalytic activity was evaluated by monitoring the gas evolved ($H_2 + CO_2$) in a burette system, immediately after the addition of a solution that consisted of formic acid and sodium formate (molar ratio = 9:1). **Figure 8** depicts the gas generated for all samples as well as the TOF values calculated after 10 min of reaction. It was observed that the catalytic ability in the formic acid dehydrogenation reaction not only depended on the nitrogen doping level, but the pore texture also played a key role in the catalytic performance. For instance, the volume of gas produced by the

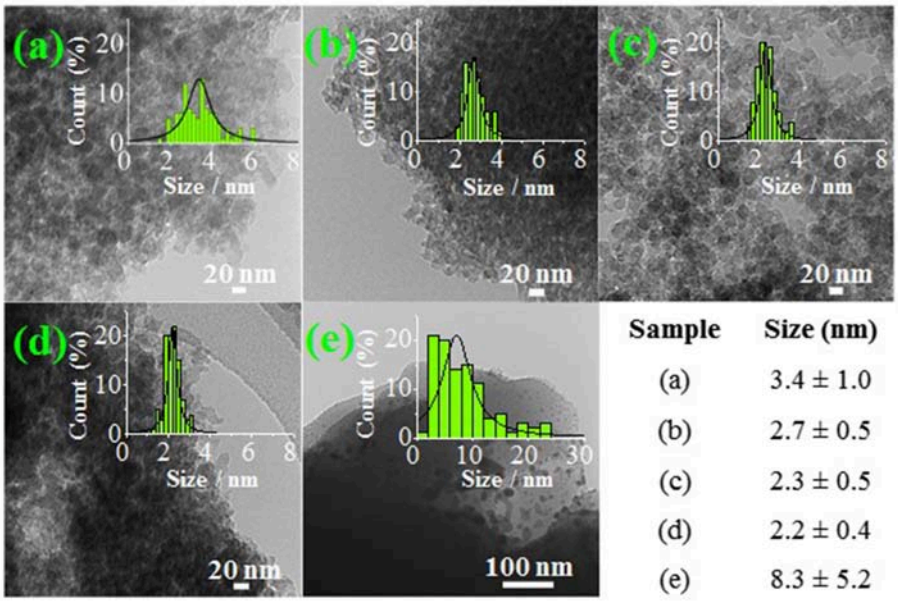

FIGURE 6 | TEM micrographs of catalysts: **(a)** Pd/CX-meso, **(b)** Pd/2N-CX-meso, **(c)** Pd/4N-CX-meso, **(d)** Pd/4N-CX-macro, **(e)** Pd/8N-CX-macro. Adapted with permission from Navlani-García et al. (2019). Copyright 2019 Elsevier.

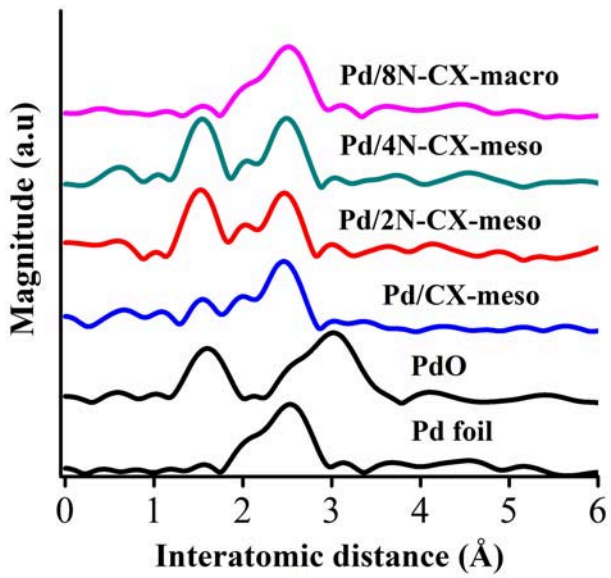

FIGURE 7 | Pd K-edge FT-EXAFS spectra for all catalysts, and Pd foil and PdO as reference samples. Adapted with permission from Navlani-García et al. (2019). Copyright 2019 Elsevier.

Pd/4N-CX-meso catalyst was almost three times that obtained from the Pd/4N-CX-macro. Moreover, despite the fact that the Pd/CX-meso catalyst did not contain nitrogen, it showed almost the same behavior as the Pd/8N-CX-macro catalyst. However, it is important to note that all Pd-based N-doped carbon xerogel catalysts, with the exception of the Pd/8N-CX-macro catalyst, displayed enhanced catalytic performance as compared to the N-free sample. Regarding the catalysts with micro-mesoporous texture and different nitrogen doping level, the Pd/2N-CX-meso catalyst showed poorer catalytic ability in the formic acid dehydrogenation reaction than Pd/4N-CX-meso catalysts, indicating that nitrogen content must be regarded as an important parameter to control the catalytic abilities in the present application. According to the tendency observed, it was concluded that a nitrogen content higher than 4 wt.% favored the formation of larger nanoparticles (8.3 nm) and non-homogenous dispersion on the support, and therefore the catalytic activity in the formic acid dehydrogenation reaction dropped drastically compared to the other Pd-based N-doped carbon catalysts.

In light of these results, it was concluded that the improvement of the catalytic ability could not be only attributed to the nitrogen content, since the Pd electronic state as well as the basicity and the pore texture of the support material should be considered. This is because those factors can influence the interaction with formic acid or reaction intermediates, which in turn is one of the most important aspects involved in the formic acid dehydrogenation reaction (Kim et al., 2018).

Unlikely most of the previous studies reported, it was therein demonstrated that not only was the presence of specific nitrogen functionalities important to achieving high-performing catalysts, but the nitrogen doping level in carbon materials with tuned porosity was also a crucial aspect for attaining good catalytic activities in the formic acid dehydrogenation reaction. A promising initial TOF value of 2,014 h^{-1} on the basis of the total Pd amount was obtained for the most active catalyst among those investigated. These findings could serve as a platform for the design of N-doped carbon materials with controlled porosity and active basic sites in order to foster the catalytic

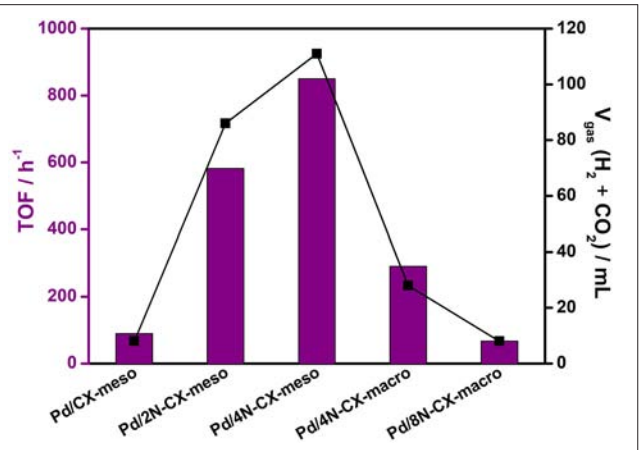

FIGURE 8 | TOF (calculated at 10 min of reaction) and V_{gas} (H_2 + CO_2) generated from the formic acid dehydrogenation reaction (75°C).

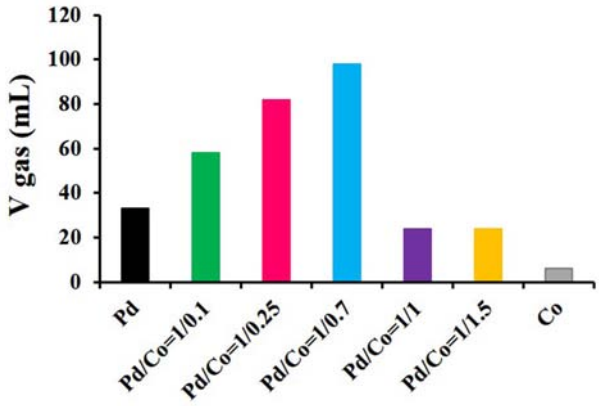

FIGURE 9 | Gas generated after 1 h of reaction at 75°C for the PdCo/g-C_3N_4 set of catalysts along with Pd and Co monometallic counterparts.

performance in the hydrogen generation from the formic acid dehydrogenation reaction.

Pd-Catalysts Supported on Graphitic Carbon Nitride

The latter sections summarized some of our recent studies on carbon-supported catalysts for the formic acid dehydrogenation reaction by using both commercial activated carbon and synthetized nitrogen-doped carbon xerogels. In the present section, our study on carbon nitride-supported catalysts is included because, although the structure and properties of graphitic carbon nitride (g-C_3N_4) significantly differ from those of conventional carbon materials (Inagaki et al., 2019), it could be considered as a C-N-based material analogous to graphite because of its layered structure (Wang et al., 2012). It might also be of interest for those readers interested in carbon-related materials.

Motivated by the promising results obtained in our study on N-doped carbon xerogels (Navlani-García et al., 2019) and other investigations on the impact of the nitrogen functionalization on carbon materials for their use as support in the formic acid dehydrogenation reaction (Bulushev et al., 2016a; Masuda et al., 2018), along with the outstanding role attributed to g-C_3N_4 in stabilizing small metal nanoparticles (Zhu J. et al., 2014; Bhowmik et al., 2015; Wu et al., 2017), our recent study was focused on the development of g-C_3N_4-supported catalysts (Navlani-García et al., 2018b). In that case, PdCo bimetallic nanoparticles with various compositions were used as active phase, while the role of g-C_3N_4 as catalytic support for this application was pointed out by comparison with standard supports based on carbon materials (i.e., carbon black and activated carbon) and oxides (i.e., CeO_2, Al_2O_3, and TiO_2). It should be mentioned that, as it was previously commented, most of the bimetallic or multimetallic Pd-based heterogeneous catalysts used in this application are composed of noble-metal active phases. In the study on PdCo catalysts mentioned above, the incorporation of a non-noble metal element in the catalysts was selected as an interesting strategy to reduce the final cost of the resulting materials.

In order to optimize the composition of the catalysts, g-C_3N_4, previously obtained from thermal decomposition of dicyandiamide, was simultaneous impregnated with different proportions of the precursors of Pd and Co (i.e., Na_2PdCl_4 and $Co(NO_3)_2$) and subsequently reduced with $NaBH_4$, so as to prepare catalysts with fixed Pd loadings and various Pd-to-Co molar ratios of 1/0.1, 1/0.25, 1/0.7, 1/1, and 1/1.5. As in the former study, the performance of the catalysts at 75°C was assessed by monitoring the gas generation (H_2 + CO_2) in a burette system after adding a solution containing formic acid and sodium formate in a molar ratio of 9 to 1 (see **Figure 9**). It was observed that the activity strongly depended on the composition of the nanoparticles and a marked enhancement was evidenced by the bimetallic nanoparticles as compared to the monometallic catalysts, both Pd/g-C_3N_4 and Co/g-C_3N_4. The optimum composition of the nanoparticles among those investigated was found in the PdCo/g-C_3N_4 (1/0.7) catalyst, which showed a TOF value of 1,193 h^{-1}, calculated on the basis of Pd. It was observed that the catalysts with higher Co content were less active in the formic acid dehydrogenation reaction, which was initially ascribed to the Co-rich surface of the nanoparticles and its low activity in the present application.

The best performing catalyst [PdCo/g-C_3N_4(1/0.7)] was compared with various catalysts prepared with the same composition of the metallic active phase (Pd/Co = 1/0.7) and some traditional supports with higher apparent surface area (S_{BET} = 7, 241, 995, 125, 189, and 46 m^2 g^{-1} for g-C_3N_4, carbon black, activated carbon, CeO_2, Al_2O_3, and TiO_2, respectively). The much higher catalytic ability for the formic acid dehydrogenation reaction displayed by PdCo/g-C_3N_4(1/0.7) highlighted the suitability of g-C_3N_4 for the present application because of its role in anchoring the metal nanoparticles and possible direct participation in the dehydrogenation reaction through the nitrogen atoms present on its structure.

To shed some light on the behavior observed in the catalytic systems, detailed characterization of the catalysts was performed by both experimental techniques and density functional theory (DFT) calculations. After confirming the intact structure of the catalysts by XRD analysis and the composition of the nanoparticles by ICP, TEM micrographs were recorded to determine the average nanoparticle size of some of the selected catalysts. The average nanoparticle size was determined to be 3.8, 2.5, 2.3, and 9.1 nm for Pd/g-C_3N_4, PdCo/g-C_3N_4 (1/0.7), PdCo/g-C_3N_4 (1/1), and PdCo/activated carbon (1/0.7), which pointed out the role of both the addition of Co in the nanoparticles and the importance of g-C_3N_4, in the synthesis of small and well-distributed nanoparticles, which ultimately had an impact on the catalytic activity.

XPS analysis was used to investigate the electronic properties of the catalysts. A marked shift toward lower binding energy values was observed in Pd 3d spectra of PdCo/g-C_3N_4 samples as compared to Pd/g-C_3N_4, which was attributed to the presence of electron-rich Pd species in the alloyed PdCo nanoparticles due to the different electronegativity value of both elements (1.9 and 2.2, in Pauling units, for Co and Pd, respectively). It should be mentioned that, according to several studies, such electron-rich Pd species are crucial for catalyzing the formic acid dehydrogenation reaction. For comparison purposes, bimetallic catalysts based on other supports (carbon black, activated carbon, CeO_2, Al_2O_3, and TiO_2) were also analyzed by XPS but in those cases the Pd-Co interaction was not shown to be as obvious as in the case of PdCo/g-C_3N_4, suggesting that the formation of alloyed nanoparticles on those supports might be less favored and that g-C_3N_4 was a suitable catalytic support for the anchoring of metal precursors and subsequent formation of bimetallic nanoparticles.

Furthermore, the charge transfer from Co to Pd found experimentally for the PdCo/g-C_3N_4 catalysts was confirmed by theoretical calculation using DFT analysts with Pd_{43} and $Pd_{22}Co_{21}$ clusters as models of Pd and PdCo nanoparticles, respectively. As is evidenced by the Mulliken atomic charges represented in **Figure 10**, the surface Pd atoms of the PdCo model were negatively charged as compared to those of the monometallic Pd cluster, while Co atoms had a positive charge because of the charge transfer to Pd atoms in the alloyed system.

In addition, XAFS measurements were also conducted to get more information about the PdCo alloying effect and the support-metal interaction through the nitrogen function group of g-C_3N_4 by analyzing some selected PdCo/g-C_3N_4 and PdCo/activated carbon catalysts. FT-EXAFS spectra of the PdCo/g-C_3N_4 catalysts analyzed displayed two main peaks at 1.6 and 2.5 Å, which were related to the presence of Pd-O (and/or Pd-N) and metal Pd-Pd bonds, respectively. Concerning the first peak (at 1.6 Å), it should be mentioned that the features of the catalysts in terms of small nanoparticles size and abundant nitrogen content of the support complicated its assignation to either Pd-N or Pd-O, because both bonds might exist in the samples. It should be mentioned that the Pd-Co bond (∼2.2 Å) could not be clearly detected in the Pd spectrum because the corresponding peak might be overlapping with some other peak, but the contribution of Pd-Co bond was detected in the Co spectra, which appeared along with the contribution of Co-O and Co-Co bonds (located at 1.7 and 2.7 Å, respectively). This once again confirmed the presence of alloyed nanoparticles in the catalysts. Unlike the g-C_3N_4-supported catalysts, such peak assigned to the Pd-Co bond was not observed for the catalyst supported on activated carbon, revealing that alloyed PdCo nanoparticles might not exist in the PdCo/activated carbon catalyst but segregated Pd and Co species might exist instead, which again corroborated the importance of the support in affording alloyed nanoparticles.

At that point of the study, it was determined that the enhanced performance observed by the bimetallic systems, in particular for PdCo/g-C_3N_4 (1/0.7), was due to the positive impact of both features of the nanoparticles (size and distribution of charge in the bimetallic nanoparticles) and support properties. As for the effect of the alloyed system, the profiles of potential energy obtained by DFT calculations using Pd and PdCo clusters confirmed the beneficial effect of the alloyed nanoparticles

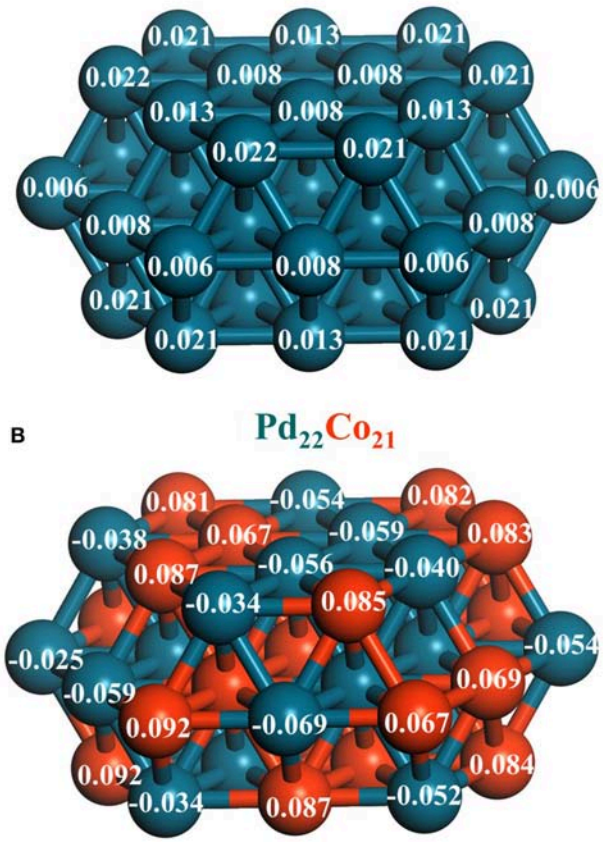

FIGURE 10 | Mulliken atomic charges of **(A)** monometallic cluster (Pd_{43}) and **(B)** bimetallic ($Pd_{22}Co_{21}$) cluster. Adapted with permission from Navlani-García et al. (2018b). Copyright 2018 Elsevier.

in boosting the formic acid dehydrogenation reaction. Such profiles were obtained by using a *trans*-M(O)–M(H-O)-bridged configuration (M = Pd or Co) as starting point (specie designed as I). The reaction steps were determined to be as follows:—Step 1: O-H bond cleavage and formation of $HCOO^-$ (II) via transition state $TS_{I/II}$;—Step 2: isomerization to a *trans*-M(H)–Pd(O)-bridged HCOOH configuration (III) via transition state $TS_{II/III}$;—Step 3: C-H bond dissociation leading to Pd-H species (IV) and CO_2 *via* the transition state $TS_{III/IV}$;—Step 4: H_2 release *via* $TS_{IV/V}$. The profiles of potential energy and energy barriers for each reaction step calculated for monometallic and alloyed catalysts are depicted in **Figure 11**. The energy barriers for Steps 1–4 were calculated to be 44.7, 14.2, 27.8, and 80.3 kcal mol^{-1}, respectively, for the monometallic Pd_{43} cluster and 31.3, 12.25, 14.5, and 65.4 kcal mol^{-1}, respectively, for the $Pd_{22}Co_{21}$ cluster. According to those values, a reduction in the energy barriers in all reaction steps was observed in the presence of the bimetallic system as compared to the monometallic catalyst, being particularly important for the energy barrier of step 3 (C-H bond dissociation), in which a reduction of 48% of the energy barrier calculated for the Pd catalyst was achieved by the bimetallic catalyst. Then, from that result, the positive role of the bimetallic PdCo system in boosting the C-H bond cleavage was pointed out. In addition, the role of the bimetallic system in catalyzing the formic acid dehydrogenation reaction, particularly in assisting the C-H bond dissociation, was confirmed by KIE experiments using HCOOH, HCOOD, and DCOOH.

Then, from all the experimental and theoretical results encompassed in that investigation, it was concluded that the resulting PdCo/g-C_3N_4 catalytic system under study was a good alternative to the traditionally more widely investigated catalysts based on PdAg or PdAu nanoparticles. The selection of an adequate support was crucial to developing small and well-distributed alloyed nanoparticles. Furthermore, it was observed that the composition of the nanoparticles (Pd/Co molar ratio) was a key aspect to control the size of the nanoparticles, as well as the existence of electron

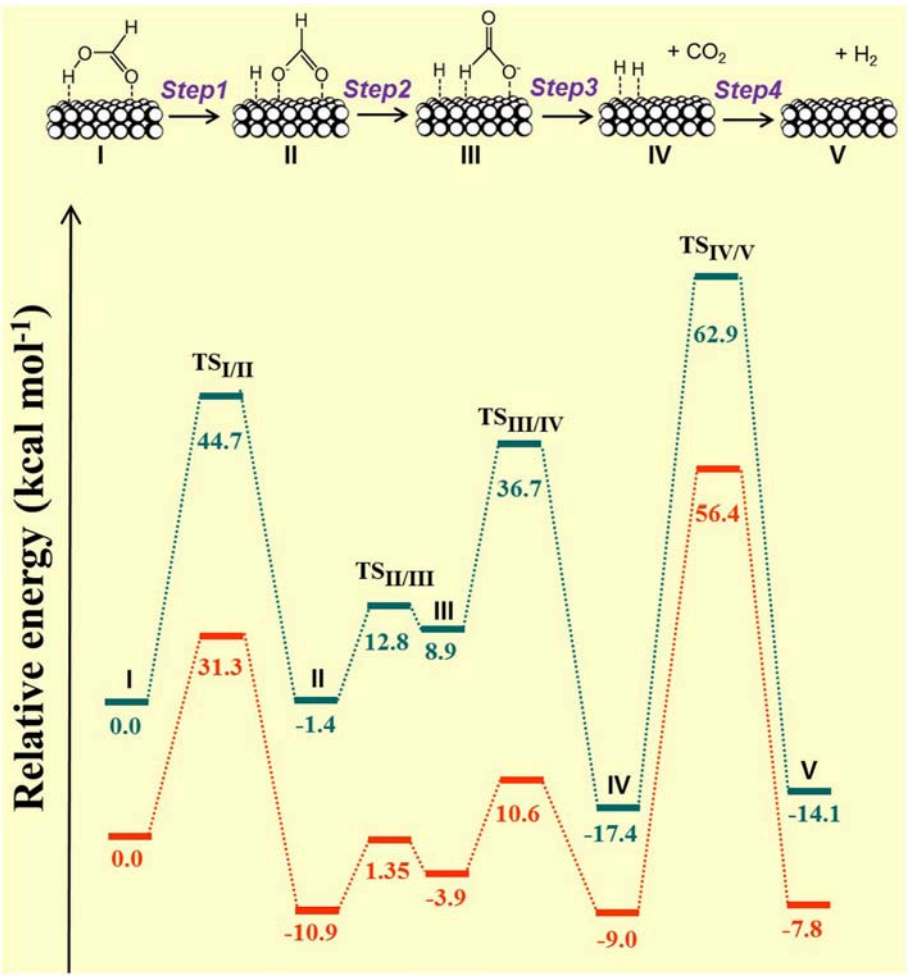

FIGURE 11 | Reaction pathway and profiles of potential energy for the formic acid dehydrogenation reaction catalyzed by Pd monometallic ($Pd_{43,}$ in blue) and bimetallic ($Pd_{22}Co_{21,}$ in orange) clusters. Adapted with permission from Navlani-García et al. (2018b). Copyright 2018 Elsevier.

rich Pd species. The combination of all these features, together with the basicity of the support used, could afford the preparation of efficient and selective catalysts for the formic acid dehydrogenation reaction, achieving a TOF value of 1,193 h^{-1} [for the best-performing catalyst among investigated; PdCo/g-C_3N_4 (1/0.7)] and suppressing the production of undesired CO (<5 ppm). It should be mentioned that such a TOF value is higher than some other g-C_3N_4-based catalysts previously reported in the literature, such as Ag_9Pd_{91}/g-C_3N_4 (TOF of 480 h^{-1} at 50°C) (Yao et al., 2017), Pd/1.0Ti-g-C_3N_4 (TOF of 77 h^{-1} at 30°C) (Wu et al., 2017), or Pd/mpg-C_3N_4 (TOF of 144 h^{-1} at 25°C) (Lee et al., 2014).

CONCLUSIONS AND OUTLOOK

In the present review, some of the investigations recently conducted in our research group tackling the design of efficient catalysts for the production of hydrogen via dehydrogenation of formic acid are summarized. Firstly, in order to contextualize the importance of a such investigation, a brief description of the role of hydrogen in the future energy scenario was highlighted by pointing out the urgency of finding alternatives to fossil fuels, which are currently used as the main source to obtain energy. The importance of chemical hydrogen storage in overcoming the safety drawbacks of physical hydrogen storage was mentioned, and the superiority of formic acid over other hydrogen carrier molecules was justified in the introduction section of the present manuscript. After that, some of our representative investigations on heterogeneous carbon-supported palladium catalysts for the formic acid dehydrogenation reaction in liquid-phase were summarized. In the selected studies herein described, important features of both metal active phase and catalytic supports were investigated in order to find the optimum catalysts under the experimental conditions used in each case. The first study was based on the investigation of the size sensitivity over carbon-supported palladium nanoparticles with sizes ranging from 2.7 to 5.5 nm, from which an optimum average nanoparticle size of 3.9 nm was found under the experimental conditions used in that case. The next step in our investigation was aimed at the optimization of the composition of carbon-supported PdAg catalysts by means of identifying the best-performing Pd/Ag ratio and modulating the surface composition of the nanoparticles by using the assistance of PVP as a capping agent. After that, our study on Pd catalysts supported on nitrogen-doped carbon xerogels was included to highlight the role of the nitrogen functional groups present in carbon materials to achieve efficient catalysis for the studied application. It was found that, aside from the functionalization of the support, its porous structure played a key role in the final catalytic performances. Finally, in an attempt to develop cost-effective materials for this application, PdCo alloyed catalysts were investigated by optimizing the composition of the nanoparticles while using graphitic carbon nitride as the catalytic support. In that case, properties of both metal nanoparticles (size, composition, and presence of electron-rich Pd species) and support (nitrogen functionalities and ability to afford small and well-distributed nanoparticles) were responsible for the efficient performance of the catalysts. All the studies herein summarized exemplified the importance of some of the most representative parameters to be controlled in order to achieve efficient catalysts for the formic acid dehydrogenation reaction.

From our results and those found in the ample literature reporting on the design and preparation of heterogeneous catalysts for the formic acid dehydrogenation reaction, it can be understood that, even though great breakthroughs have recently been achieved in the last years, there is still the possibility for further improvements. It could be envisaged that the stability of the catalysts will be the main issue to be improved in future investigations since this aspect is lacking in most of the systems reported so far, and it is a crucial feature for the practical application of the catalysts. In this respect, modulating the nanoparticle-support interactions could be of great importance in achieving durable catalysts, and the incorporation of an adequate heteroatom doping level in the carbon material structure might be a promising tool. Furthermore, the use of some other carbon materials apart from the most widely investigated activated carbons might help in finding interesting catalytic systems for the present application upon suitable surface functionalization. Optimizing the synthetic procedure so that the porosity of the carbon material support can be fully utilized in anchoring and dispersing the metallic active phase might be another point of interest to achieve active and durable catalysts, and finding a suitable capping agent able to prevent the nanoparticle sintering under reaction conditions while preserving their composition could be envisaged as a promising approach. As for the composition of the metallic active phase, the use of non-noble metal-containing nanoparticles could be expected to be investigated more often in the coming years to find cost-efficient yet active catalysts in formic acid dehydrogenation reaction.

AUTHOR CONTRIBUTIONS

MN-G designed and performed the experiments corresponding to the publications reviewed in the present manuscript, analyzed the results and conceived and wrote the manuscript, KM contributed to the conception of the study and helped with the discussion of the results, DS-T helped with the design and development of the catalysts and contributed to the manuscript writing and revision, YK and HY oversaw the study. All authors approved the manuscript for publication.

ACKNOWLEDGMENTS

We are thankful for the financial support from JST and PRESTO (JPMJPR1544) as well as for Grants-in-Aid for Scientific Research (Nos. 26220911, 25289289, and 26630409, 26620194) from the Japan Society for the Promotion of Science (JSPS) and MEXT and the Elemental Strategy Initiative to Form Core Research Center MN-G (A17F173810) and DS-T (J171015004) thank JSPS for the International Postdoctoral Research Fellowships.

REFERENCES

Afif, A., Radenahmad, N., Cheok, Q., Shams, S., Kim, J. H., and Azad, A. K. (2016). Ammonia-fed fuel cells: a comprehensive review. *Renew. Sustain. Energy Rev.* 60, 822–835. doi: 10.1016/j.rser.2016.01.120

Bagreev, A., Menendez, J. A., Dukhno, I., Tarasenko, Y., and Bandosz, T. J. (2004). Bituminous coal-based activated carbons modified with nitrogen as adsorbents of hydrogen sulfide. *Carbon* 42, 469–476. doi: 10.1016/j.carbon.2003.10.042

Bashkova, S., Bagreev, A., and Bandosz, T. J. (2003). Adsorption/oxidation of CH_3SH on activated carbons containing nitrogen. *Langmuir* 19, 6115–6121. doi: 10.1021/la0300030

Bavykina, A. V., Goesten, M. G., Kapteijn, F., Makkee, M., and Gascon, J. (2015). Efficient production of hydrogen from formic acid using a Covalent Triazine Framework supported molecular catalyst. *ChemSusChem* 8, 809–812. doi: 10.1002/cssc.201403173

Bhowmik, T., Kundu, M. K., and Barman, S. (2015). Ultra small gold nanoparticles-graphitic carbon nitride composite: an efficient catalyst for ultrafast reduction of 4-nitrophenol and removal of organic dyes from water. *RSC Adv.* 5, 38760–38773. doi: 10.1039/C5RA04913J

Bi, Q. Y., Lin, J. D., Liu, Y. M., He, H. Y., Huang, F. Q., and Cao, Y. (2016). Dehydrogenation of formic acid at room temperature: boosting palladium nanoparticle efficiency by coupling with pyridinic-nitrogen-doped carbon. *Angew. Chem. Int. Ed.* 55, 11849–11853. doi: 10.1002/anie.201605961

Boddien, A., Loges, B., Gärtner, F., Torborg, C., Fumino, K., Junge, H., et al. (2010). Iron-catalyzed hydrogen production from formic acid. *J. Am. Chem. Soc.* 132, 8924–8934. doi: 10.1021/ja100925n

Boddien, A., Loges, B., Junge, H., Gärtner, F., Noyes, J. R., and Beller, M. (2009). Continuous hydrogen generation from formic acid. *Adv. Synth. Catal.* 351, 2517–2520. doi: 10.1002/adsc.200900431

Bulushev, D. A., Zacharska, M., Lisitsyn, A. S., Podyacheva, O. Y., Hage, F. S., Ramasse, Q. M., et al. (2016a). Single atoms of Pt-group metals stabilized by N-doped carbon nanofibers for efficient hydrogen production from formic acid. *ACS Catal.* 6, 3442–3451. doi: 10.1021/acscatal.6b00476

Bulushev, D. A., Zacharska, M., Shlyakhova, E. V., Chuvilin, A. L., Guo, Y., Beloshapkin, S., et al. (2016b). Single isolated Pd^{2+} cations supported on N-doped carbon as active sites for hydrogen production from formic acid decomposition. *ACS Catal.* 6, 681–691. doi: 10.1021/acscatal.5b02381

Bulut, A., Yurderi, M., Kaya, M., Aydemir, M., Baysal, A., Durap, F., et al. (2018). Amine-functionalized graphene nanosheet-supported PdAuNi alloy nanoparticles: efficient nanocatalyst for formic acid dehydrogenation. *New J. Chem.* 42, 16103–16114. doi: 10.1039/C8NJ03117G

Cai, Y., Li, X., Zhang, Y., Wei, X., Wang, K., and Chen, J. (2013). Highly efficient dehydrogenation of formic acid over a palladium- angewandte. *Angew. Chem. Int. Ed.* 52, 1–5. doi: 10.1002/anie.201304652

Cheng, J., Gu, X., Sheng, X., Liu, P., and Su, H. (2016). Exceptional size-dependent catalytic activity enhancement in the room-temperature hydrogen generation from formic acid over bimetallic nanoparticles supported by porous carbon. *J. Mater. Chem. A* 4, 1887–1894. doi: 10.1039/c5ta08534a

Chowdhury, A. D., Agnihotri, N., and De, A. (2015). Hydrolysis of sodium borohydride using Ru-Co-PEDOT nanocomposites as catalyst. *Chem. Eng. J.* 264, 531–537. doi: 10.1016/j.cej.2014.11.108

Coffey, R. S. (1967). The decomposition of formic acid catalysed by soluble metal complexes. *Chem. Commun.* 923–924. doi: 10.1039/C1967000923b

Czaun, M., Goeppert, A., Kothandaraman, J., May, R. B., Haiges, R., Prakash, G. K. S., et al. (2014). Formic acid as a hydrogen storage medium: ruthenium-catalyzed generation of hydrogen from formic acid in emulsions. *ACS Catal.* 4, 311–320. doi: 10.1021/cs4007974

Czaun, M., Kothandaraman, J., Goeppert, A., Yang, B., Greenberg, S., May, R. B., et al. (2016). Iridium-catalyzed continuous hydrogen generation from formic acid and its subsequent utilization in a fuel cell: toward a carbon neutral chemical energy storage. *ACS Catal.* 6, 7475–7484. doi: 10.1021/acscatal.6b01605

Demirci, U. B. (2015). The hydrogen cycle with the hydrolysis of sodium borohydride: a statistical approach for highlighting the scientific/technical issues to prioritize in the field. *Int. J. Hydrogen Energy* 40, 2673–2691. doi: 10.1016/j.ijhydene.2014.12.067

Durmaz, T. (2018). The economics of CCS: why have CCS technologies not had an international breakthrough? *Renew. Sustain. Energy Rev.* 95, 328–340. doi: 10.1016/j.rser.2018.07.007

El-Eskandarany, M. S., Shaban, E., and Alsairafi, A. A. (2016). Synergistic dosing effect of TiC/FeCr nanocatalysts on the hydrogenation/dehydrogenation kinetics of nanocrystalline MgH_2 powders. *Energy* 104, 158–170. doi: 10.1016/j.energy.2016.03.104

Enthaler, S., Von Langermann, J., and Schmidt, T. (2010). Carbon dioxide and formic acid - The couple for environmental-friendly hydrogen storage? *Energy Environ. Sci.* 3, 1207–1217. doi: 10.1039/b907569k

Eppinger, J., and Huang, K.-W. (2017). Formic acid as a hydrogen energy carrier. *ACS Energy Lett.* 2, 188–195. doi: 10.1021/acsenergylett.6b00574

Fellay, C., Dyson, P. J., and Laurenczy, G. (2008). A viable hydrogen-storage system based on selective formic acid decomposition with a ruthenium catalyst. *Angew. Chem. Int. Ed.* 47, 3966–3968. doi: 10.1002/anie.200800320

Feng, C., Wang, Y., Gao, S., Shang, N., and Wang, C. (2016). Hydrogen generation at ambient conditions: AgPd bimetal supported on metal-organic framework derived porous carbon as an efficient synergistic catalyst. *Catal. Commun.* 78, 17–21. doi: 10.1016/j.catcom.2016.01.034

Fukuzumi, S., Kobayashi, T., and Suenobu, T. (2008). Efficient catalytic decomposition of formic acid for the selective generation of H_2 and H/D exchange with a water-soluble rhodium complex in aqueous solution. *ChemSusChem* 1, 827–834. doi: 10.1002/cssc.200800147

Fukuzumi, S., Kobayashi, T., and Suenobu, T. (2010). Formic acid acting as an efficient oxygen scavenger in four-electron reduction of oxygen catalyzed by a heterodinuclear iridium-ruthenium complex in water. *J. Am. Chem. Soc.* 132, 11866–11867. doi: 10.1021/ja104486h

García-Aguilar, J., Navlani-García, M., Berenguer-Murcia, Á., Mori, K., Kuwahara, Y., Yamashita, H., et al. (2016a). Enhanced ammonia-borane decomposition by synergistic catalysis using CoPd nanoparticles supported on titano-silicates. *RSC Adv.* 6, 91768–91772. doi: 10.1039/C6RA21302B

García-Aguilar, J., Navlani-García, M., Berenguer-Murcia, Á., Mori, K., Kuwahara, Y., Yamashita, H., et al. (2016b). Evolution of the PVP-Pd surface interaction in nanoparticles through the case study of formic acid decomposition. *Langmuir* 32, 12110–12118. doi: 10.1021/acs.langmuir.6b03149

Graetz, J. (2009). New approaches to hydrogen storage. *Chem. Soc. Rev.* 38, 73–82. doi: 10.1039/b718842k

Grasemann, M., and Laurenczy, G. (2012). Formic acid as a hydrogen source - recent developments and future trends. *Energy Environ. Sci.* 5, 8171. doi: 10.1039/c2ee21928j

Gu, X., Lu, Z. H., Jiang, H. L., Akita, T., and Xu, Q. (2011). Synergistic catalysis of metal-organic framework-immobilized Au-Pd nanoparticles in dehydrogenation of formic acid for chemical hydrogen storage. *J. Am. Chem. Soc.* 133, 11822–11825. doi: 10.1021/ja200122f

Gupta, K., Bersani, M., and Darr, J. A. (2016). Highly efficient electro-reduction of CO2to formic acid by nano-copper. *J. Mater. Chem. A* 4, 13786–13794. doi: 10.1039/c6ta04874a

He, N., and Li, Z. H. (2016). Palladium-atom catalyzed formic acid decomposition and the switch of reaction mechanism with temperature. *Phys. Chem. Chem. Phys.* 18, 10005–10017. doi: 10.1039/c6cp00186f

Huang, Y., Xu, J., Ma, X., Huang, Y., Li, Q., and Qiu, H. (2017). An effective low Pd-loading catalyst for hydrogen generation from formic acid. *Int. J. Hydrogen Energy* 42, 18375–18382. doi: 10.1016/j.ijhydene.2017.04.138

Huang, Y., Zhou, X., Yin, M., Liu, C., and Xing, W. (2010). Novel PdAu@Au/C core-shell catalyst: superior activity and selectivity in formic acid decomposition for hydrogen generation. *Chem. Mater.* 22, 5122–5128. doi: 10.1021/cm101285f

Hulicova-Jurcakova, D., Seredych, M., Lu, G. Q., and Bandosz, T. J. (2009). Combined effect of nitrogen- and oxygen-containing functional groups of microporous activated carbon on its electrochemical performance in supercapacitors. *Adv. Funct. Mater.* 19, 438–447. doi: 10.1002/adfm.200801236

Inagaki, M., Tsumura, T., Kinumoto, T., and Toyoda, M. (2019). Graphitic carbon nitrides (g-C_3N_4) with comparative discussion to carbon materials. *Carbon* 141, 580–607. doi: 10.1016/j.carbon.2018.09.082

Jeon, H.-J., and Chung, Y. M. (2017). Hydrogen production from formic acid dehydrogenation over Pd/C catalysts: effect of metal and support properties on the catalytic performance. *Appl. Catal. B Environ.* 210, 212–222. doi: 10.1016/j.apcatb.2017.03.070

Jeon, M., Han, D. J., Lee, K. S., Choi, S. H., Han, J., Nam, S. W., et al. (2016). Electronically modified Pd catalysts supported on N-doped carbon for the dehydrogenation of formic acid. *Int. J. Hydrogen Energy* 41, 15453–15461. doi: 10.1016/j.ijhydene.2016.04.102

Jiang, K., Xu, K., Zou, S., and Cai, W.-B. (2014). B-doped pd catalyst: boosting room-temperature hydrogen production from formic acid-formate solutions. *J. Am. Chem. Soc.* 136, 4861–4864. doi: 10.1021/ja5008917

Jiang, M., Wu, H., Li, Z., Ji, D., Li, W., Liu, Y., et al. (2018). Highly selective photoelectrochemical conversion of carbon dioxide to formic acid. *ACS Sustain. Chem. Eng.* 6, 82–87. doi: 10.1021/acssuschemeng.7b03272

Jiang, Y., Fan, X., Chen, M., Xiao, X., Zhang, Y., Wang, C., et al. (2018). AuPd nanoparticles anchored on nitrogen-decorated carbon nanosheets with highly efficient and selective catalysis for the dehydrogenation of formic acid. *J. Phys. Chem. C* 122, 4792–4801. doi: 10.1021/acs.jpcc.8b00082

Jin, M. H., Park, J. H., Oh, D., Lee, S. W., Park, J. S., Lee, K. Y., et al. (2018). Pd/NH2-KIE-6 catalysts with exceptional catalytic activity for additive-free formic acid dehydrogenation at room temperature: controlling Pd nanoparticle size by stirring time and types of Pd precursors. *Int. J. Hydrogen Energy* 43, 1451–1458. doi: 10.1016/j.ijhydene.2017.10.117

Kim, Y., Kim, J., and Kim, D. H. (2018). Investigation on the enhanced catalytic activity of a Ni-promoted Pd/C catalyst for formic acid dehydrogenation: effects of preparation methods and Ni/Pd ratios. *RSC Adv.* 8, 2441–2448. doi: 10.1039/c7ra13150j

Lan, R., Irvine, J. T. S., and Tao, S. (2012). Ammonia and related chemicals as potential indirect hydrogen storage materials. *Int. J. Hydrogen Energy* 37, 1482–1494. doi: 10.1016/j.ijhydene.2011.10.004

Lee, D. W., Jin, M. H., Oh, D., Lee, S. W., and Park, J. S. (2017). Straightforward synthesis of hierarchically porous nitrogen-doped carbon via pyrolysis of Chitosan/Urea/KOH mixtures and its application as a support for formic acid dehydrogenation catalysts. *ACS Sustain. Chem. Eng.* 5, 9935–9944. doi: 10.1021/acssuschemeng.7b01888

Lee, J. H., Ryu, J., Kim, J. Y., Nam, S.-W., Han, J. H., Lim, T.-H., et al. (2014). Carbon dioxide mediated, reversible chemical hydrogen storage using a Pd nanocatalyst supported on mesoporous graphitic carbon nitride. *J. Mater. Chem. A* 2, 9490–9495. doi: 10.1039/C4TA01133C

Li, J., Chen, W., Zhao, H., Zheng, X., Wu, L., Pan, H., et al. (2017). Size-dependent catalytic activity over carbon-supported palladium nanoparticles in dehydrogenation of formic acid. *J. Catal.* 352, 371–381. doi: 10.1016/j.jcat.2017.06.007

Li, S. J., Ping, Y., Yan, J. M., Wang, H. L., Wu, M., and Jiang, Q. (2015). Facile synthesis of AgAuPd/graphene with high performance for hydrogen generation from formic acid. *J. Mater. Chem. A* 3, 14535–14538. doi: 10.1039/c5ta03111g

Li, Z., Yang, X., Tsumori, N., Liu, Z., Himeda, Y., Autrey, T., et al. (2017). Tandem nitrogen functionalization of porous carbon: toward immobilizing highly active palladium nanoclusters for dehydrogenation of formic acid. *ACS Catal.* 7, 2720–2724. doi: 10.1021/acscatal.7b00053

Lillo-Ródenas, M. A., Guo, Z. X., Aguey-Zinsou, K. F., Cazorla-Amorós, D., and Linares-Solano, A. (2008). Effects of different carbon materials on MgH_2 decomposition. *Carbon* 46, 126–137. doi: 10.1016/j.carbon.2007.10.033

Liu, H., Liu, X., Yang, W., Shen, M., Geng, S., Yu, C., et al. (2019). Photocatalytic dehydrogenation of formic acid promoted by a superior PdAg@g-C_3N_4 Mott–Schottky heterojunction. *J. Mater. Chem. A.* 7, 2022–2026. doi: 10.1039/C8TA11172C

Liu, J., Lan, L., Li, R., Liu, X., and Wu, C. (2016). Agglomerated Ag-Pd catalyst with performance for hydrogen generation from formic acid at room temperature. *Int. J. Hydrogen Energy* 41, 951–958. doi: 10.1016/j.ijhydene.2015.10.144

Loges, B., Boddien, A., Junge, H., and Beller, M. (2008). Controlled generation of hydrogen from formic acid amine adducts at room temperature and application in H_2/O_2 fuel cells. *Angew. Chem. Int. Ed.* 47, 3962–3965. doi: 10.1002/anie.200705972

Lu, W., Jia, B., Cui, B., Zhang, Y., Yao, K., Zhao, Y., et al. (2017). Efficient photoelectrochemical reduction of carbon dioxide to formic acid: a functionalized ionic liquid as an absorbent and electrolyte. *Angew. Chem. Int. Ed.* 56, 11851–11854. doi: 10.1002/anie.201703977

Lu, X., Leung, D. Y. C., Wang, H., Leung, M. K. H., and Xuan, J. (2014). Electrochemical reduction of carbon dioxide to formic acid. *ChemElectroChem* 1, 836–849. doi: 10.1002/celc.201300206

Masuda, S., Mori, K., Futamura, Y., and Yamashita, H. (2018). PdAg nanoparticles supported on functionalized mesoporous carbon: promotional effect of surface amine groups in reversible hydrogen delivery/storage mediated by formic acid/CO_2. *ACS Catal.* 8, 2277–2285. doi: 10.1021/acscatal.7b04099

Matsunami, A., Kuwata, S., and Kayaki, Y. (2017). A bifunctional iridium catalyst modified for persistent hydrogen generation from formic acid: understanding deactivation via cyclometalation of a 1,2-Diphenylethylenediamine motif. *ACS Catal.* 7, 4479–4484. doi: 10.1021/acscatal.7b01068

Mellmann, D., Sponholz, P., Junge, H., and Beller, M. (2016). Formic acid as a hydrogen storage material-development of homogeneous catalysts for selective hydrogen release. *Chem. Soc. Rev.* 45, 3954–3988. doi: 10.1039/C5CS00618J

Monney, A., Barsch, E., Sponholz, P., Junge, H., Ludwig, R., and Beller, M. (2014). Base-free hydrogen generation from methanol using a bi-catalytic system. *Chem. Commun.* 50, 707–709. doi: 10.1039/c3cc47306f

Moret, S., Dyson, P. J., and Laurenczy, G. (2014). Direct synthesis of formic acid from carbon dioxide by hydrogenation in acidic media. *Nat. Commun.* 5, 1–7. doi: 10.1038/ncomms5017

Mori, K., Dojo, M., and Yamashita, H. (2013). Pd and Pd-Ag nanoparticles within a macroreticular basic resin: an efficient catalyst for hydrogen production from formic acid decomposition. *ACS Catal.* 3, 1114–1119. doi: 10.1021/cs400148n

Mori, K., Hara, T., Mizugaki, T., Ebitani, K., and Kaneda, K. (2004). Hydroxyapatite-supported palladium nanoclusters: a highly active heterogeneous catalyst for selective oxidation of alcohols by use of molecular oxygen. *J. Am. Chem. Soc.* 126, 10657–10666. doi: 10.1021/ja0488683

Mori, K., Kakudo, H., and Yamashita, H. (2014). Creation of nickel-based active species within a macroreticular acidic resin: a noble-metal-free heterogeneous catalyst for visible-light-driven H2evolution from water. *ACS Catal.* 4, 4129–4135. doi: 10.1021/cs501119d

Mori, K., Masuda, S., Tanaka, H., Yoshizawa, K., Che, M., and Yamashita, H. (2017a). Phenylamine-functionalized mesoporous silica supported PdAg nanoparticles: a dual heterogeneous catalyst for formic acid/CO_2-mediated chemical hydrogen delivery/storage. *Chem. Commun.* 53, 4677–4680. doi: 10.1039/c7cc00864c

Mori, K., Naka, K., Masuda, S., Miyawaki, K., and Yamashita, H. (2017b). Palladium copper chromium ternary nanoparticles constructed *in situ* within a basic resin: enhanced activity in the dehydrogenation of formic acid. *ChemCatChem* 9, 3456–3462. doi: 10.1002/cctc.201700595

Mori, K., Sano, T., Kobayashi, H., and Yamashita, H. (2018). Surface engineering of a supported PdAg catalyst for hydrogenation of CO_2 to formic acid: elucidating the active Pd atoms in alloy nanoparticles. *J. Am. Chem. Soc.* 140, 8902–8909. doi: 10.1021/jacs.8b04852

Mori, K., Tanaka, H., Dojo, M., Yoshizawa, K., and Yamashita, H. (2015). Synergic catalysis of PdCu alloy nanoparticles within a macroreticular basic resin for hydrogen production from formic acid. *Chem. A Eur. J.* 21, 12085–12092. doi: 10.1002/chem.201501760

Nabid, M. R., Bide, Y., and Etemadi, B. (2017). Ag@Pd nanoparticles immobilized on a nitrogen-doped graphene carbon nanotube aerogel as a superb catalyst for the dehydrogenation of formic acid. *New J. Chem.* 41, 10773–10779. doi: 10.1039/C7NJ01108C

Navlani-García, M., Martis, M., Lozano-Castelló, D., Cazorla-Amorós, D., Mori, K., and Yamashita, H. (2015a). Investigation of Pd nanoparticles supported on zeolites for hydrogen production from formic acid dehydrogenation. *Catal. Sci. Technol.* 5, 364–371. doi: 10.1039/c4cy00667d

Navlani-García, M., Mori, K., Kuwahara, Y., and Yamashita, H. (2018a). Recent strategies targeting efficient hydrogen production from chemical hydrogen storage materials over carbon-supported catalysts. *NPG Asia Mater.* 10, 277–292. doi: 10.1038/s41427-018-0025-6

Navlani-García, M., Mori, K., Nozaki, A., Kuwahara, Y., and Yamashita, H. (2016a). Highly efficient Ru/carbon catalysts prepared by pyrolysis of supported Ru complex towards the hydrogen production from ammonia borane. *Appl. Catal. A Gen.* 527, 45–52. doi: 10.1016/j.apcata.2016.08.018

Navlani-García, M., Mori, K., Nozaki, A., Kuwahara, Y., and Yamashita, H. (2016b). Investigation of size sensitivity in the hydrogen production from formic acid over carbon-supported Pd nanoparticles. *Chem. Select* 1, 1879–1886. doi: 10.1002/slct.201600559

Navlani-García, M., Mori, K., Nozaki, A., Kuwahara, Y., and Yamashita, H. (2016c). Screening of carbon-supported PdAg nanoparticles in the

hydrogen production from formic acid. *Ind. Eng. Chem. Res.* 55, 7612–7620. doi: 10.1021/acs.iecr.6b01635

Navlani-García, M., Mori, K., Wen, M., Kuwahara, Y., and Yamshita, H. (2015b). Size effect of carbon-supported pd nanoparticles in the hydrogen production from formic acid. *Bull. Chem. Soc. Jpn.* 1370, 78–80. doi: 10.1080/03758397.1955.10857269

Navlani-García, M., Salinas-Torres, D., Mori, K., Kuwahara, Y., and Yamashita, H. (2018b). Enhanced formic acid dehydrogenation by the synergistic alloying effect of PdCo catalysts supported on graphitic carbon nitride. *Int. J. Hydrogen Energy*. doi: 10.1016/j.ijhydene.2018.11.057. [Epub ahead of print].

Navlani-García, M., Salinas-Torres, D., Mori, K., Léonard, A. F., Kuwahara, Y., Job, N., et al. (2019). Insights on palladium decorated nitrogen-doped carbon xerogels for the hydrogen production from formic acid. *Catal. Today* 324, 90–96. doi: 10.1016/j.cattod.2018.06.013

Navlani-garcía, M., Verma, P., Kuwahara, Y., and Kamegawa, T. (2018). Visible-light-enhanced catalytic activity of Ru nanoparticles over carbon modified g-C_3N_4. *J. Photochem. Photobiol. A* 358, 327–333. doi: 10.1016/j.jphotochem.2017.09.007

Nguyen, K. H., and Kakinaka, M. (2018). Renewable energy consumption, carbon emissions, and development stages: some evidence from panel cointegration analysis. *Renew. Energy* 132, 1049–1057. doi: 10.1016/j.renene.2018.08.069

Nielsen, M., Alberico, E., Baumann, W., Drexler, H. J., Junge, H., Gladiali, S., et al. (2013). Low-temperature aqueous-phase methanol dehydrogenation to hydrogen and carbon dioxide. *Nature* 495, 85–89. doi: 10.1038/nature11891

Oh, T. H. (2016). A formic acid hydrogen generator using Pd/C_3N_4 catalyst for mobile proton exchange membrane fuel cell systems. *Energy* 112, 679–685. doi: 10.1016/j.energy.2016.06.096

Paul, R., Reifenberger, R. G., Fisher, T. S., and Zemlyanov, D. Y. (2015). Atomic layer deposition of FeO on Pt(111) by ferrocene adsorption and oxidation. *Chem. Mater.* 27, 5915–5924. doi: 10.1021/acs.chemmater.5b01778

Ping, Y., Yan, J. M., Wang, Z. L., Wang, H. L., and Jiang, Q. (2013). $Ag_{0.1}$-$Pd_{0.9}$/rGO: An efficient catalyst for hydrogen generation from formic acid/sodium formate. *J. Mater. Chem. A* 1, 12188–12191. doi: 10.1039/c3ta12724a

Podyacheva, O. Y., Bulushev, D. A., Suboch, A. N., Svintsitskiy, D. A., Lisitsyn, A. S., Modin, E., et al. (2018). Highly stable single-atom catalyst with ionic Pd active sites supported on N-doped carbon nanotubes for formic acid decomposition. *ChemSusChem* 11, 3724–3727. doi: 10.1002/cssc.201801679

Premkumar, J., and Ramaraj, R. (1997). Photocatalytic reduction of carbon dioxide to formic acid at porphyrin and phthalocyanine adsorbed Nafion membranes. *J. Photochem. Photobiol. A Chem.* 110, 53–58. doi: 10.1016/S1010-6030(97)00156-1

Qin, G., Zhang, Y., Ke, X., Tong, X., Sun, Z., Liang, M., et al. (2013). Photocatalytic reduction of carbon dioxide to formic acid, formaldehyde, and methanol using dye-sensitized TiO_2 film. *Appl. Catal. B Environ.* 129, 59–605. doi: 10.1016/j.apcatb.2012.10.012

Qin, Y., Wang, J., Wu, Y., and Wang, L. (2014). Improved hydrogen production from formic acid under ambient conditions using a PdAu catalyst on a graphene nanosheets–carbon black support. *RSC Adv.* 4, 30068–30073. doi: 10.1039/C4RA05379F

Qin, Y.-L., Wang, J., Meng, F.-Z., Wang, L.-M., and Zhang, X.-B. (2013). Efficient PdNi and PdNi@Pd-catalyzed hydrogen generation via formic acid decomposition at room temperature. *Chem. Commun.* 49, 10028–10030. doi: 10.1039/c3cc46248j

Reddy, G. K., and Smirniotis, P. G. (2015). *Water Gas Shift Reaction: Research Developments and Applications*. Elsevier. doi: 10.1016/C2013-0-09821-0

Rodríguez-Reinoso, F. (2010). The role of carbon materials in heterogeneous catalysis. *Nonlin. Anal. Theory, Methods Appl.* 72, 2658–2683. doi: 10.1016/j.na.2009.11.013

Rosen, M. A., and Koohi-Fayegh, S. (2016). The prospects for hydrogen as an energy carrier: an overview of hydrogen energy and hydrogen energy systems. *Energy, Ecol. Environ.* 1, 10–29. doi: 10.1007/s40974-016-0005-z

Salinas-Torres, D., Léonard, A. F., Stergiopoulos, V., Busby, Y., Pireaux, J. J., and Job, N. (2018). Effect of nitrogen doping on the pore texture of carbon xerogels based on resorcinol-melamine-formaldehyde precursors. *Microporous Mesoporous Mater.* 256, 190–198. doi: 10.1016/j.micromeso.2017.08.004

Sanchez, F., Alotaibi, M. H., Motta, D., Chan-Thaw, C. E., Rakotomahevitra, A., Tabanelli, T., et al. (2018). Hydrogen production from formic acid decomposition in the liquid phase using Pd nanoparticles supported on CNFs with different surface properties. *Sustain. Energy Fuels* 2, 2705–2716. doi: 10.1039/c8se00338f

Song, F. Z., Zhu, Q. L., Yang, X., Zhan, W. W., Pachfule, P., Tsumori, N., et al. (2018). Metal–organic framework templated porous carbon-metal oxide/reduced graphene oxide as superior support of bimetallic nanoparticles for efficient hydrogen generation from formic acid. *Adv. Energy Mater.* 8, 1–5. doi: 10.1002/aenm.201701416

Strauss, S., Whitmire, K., and Shriver, D. (1979). Rhodium (I) catalyzed decomposition of formic acid. *J. Organomet. Chem.* 174, C59–C62. doi: 10.1016/S0022-328X(00)85605-3

Sun, J., Qiu, H., Cao, W., Fu, H., Wan, H., Xu, Z., et al. (2019). Ultrafine Pd particles embedded in nitrogen-enriched mesoporous carbon for efficient H_2 production from formic acid decomposition. *ACS Sustain. Chem. Eng.* 7, 1963–1972. doi: 10.1021/acssuschemeng.8b04130

Tedsree, K., Li, T., Jones, S., Chan, C. W. A., Yu, K. M. K., Bagot, P. A. J., et al. (2011). Hydrogen production from formic acid decomposition at room temperature using a Ag-Pd core-shell nanocatalyst. *Nat. Nanotechnol.* 6, 302–307. doi: 10.1038/nnano.2011.42

Wang, X., Qi, G.-W., Tan, C.-H., Li, Y.-P., Guo, J., Pang, X.-J., et al. (2014). Pd/C nanocatalyst with high turnover frequency for hydrogen generation from the formic acid-formate mixtures. *Int. J. Hydrogen Energy* 39, 837–843. doi: 10.1016/j.ijhydene.2013.10.154

Wang, Y., Wang, X., and Antonietti, M. (2012). Polymeric graphitic carbon nitride as a heterogeneous organocatalyst: from photochemistry to multipurpose catalysis to sustainable chemistry. *Angew. Chem. Int. Ed.* 51, 68–89. doi: 10.1002/anie.201101182

Wang, Z.-L., Ping, Y., Yan, J. M., Wang, H. L., and Jiang, Q. (2014b). Hydrogen generation from formic acid decomposition at room temperature using a NiAuPd alloy nanocatalyst. *Int. J. Hydrogen Energy* 39, 4850–4856. doi: 10.1016/j.ijhydene.2013.12.148

Wang, Z.-L., Yan, J.-M., Wang, H.-L., Ping, Y., and Jiang, Q. (2012). Pd/C synthesized with citric acid: an efficient catalyst for hydrogen generation from formic acid/sodium formate. *Sci. Rep.* 2:598. doi: 10.1038/srep00598

Wang, Z.-L., Yan, J.-M., Zhang, Y.-F., Ping, Y., Wang, H.-L., and Jiang, Q. (2014a). Facile synthesis of nitrogen-doped graphene supported AuPd–CeO_2 nanocomposites with high-performance for hydrogen generation from formic acid at room temperature. *Nanoscale* 6, 3073–3077. doi: 10.1039/C3NR05809C

Wang, Z.-L., Yan, J. M., Ping, Y., Wang, H. L., Zheng, W. T., and Jiang, Q. (2013a). An efficient CoAuPd/C catalyst for hydrogen generation from formic acid at room temperature. *Angew. Chem. Int. Ed.* 52, 4406–4409. doi: 10.1002/anie.201301009

Wang, Z. L., Yan, J. M., Wang, H. L., Ping, Y., and Jiang, Q. (2013b). Au@Pd core-shell nanoclusters growing on nitrogen-doped mildly reduced graphene oxide with enhanced catalytic performance for hydrogen generation from formic acid. *J. Mater. Chem. A* 1, 12721–12725. doi: 10.1039/c3ta12531a

Wen, M., Mori, K., Kuwahara, Y., and Yamashita, H. (2017). Plasmonic Au@Pd nanoparticles supported on a basic metal-organic framework: synergic boosting of H_2 production from formic acid. *ACS Energy Lett.* 2, 1–7. doi: 10.1021/acsenergylett.6b00558

Williams, R., Crandall, R. S., and Bloom, A. (1978). Use of carbon dioxide in energy storage. *Appl. Phys. Lett.* 33, 381–383. doi: 10.1063/1.90403

Wu, S., Yang, F., Sun, P., and Chen, T. (2014). Au–Pd alloy catalyst with high performance for hydrogen generation from formic acid-formate solution at nearly 0 °C. *RSC Adv.* 4, 44500–44503. doi: 10.1039/C4RA08389J

Wu, S., Yang, F., Wang, H., Chen, R., Sun, P., and Chen, T. (2015). Mg^{2+}-assisted low temperature reduction of alloyed AuPd/C: an efficient catalyst for hydrogen generation from formic acid at room temperature. *Chem. Commun.* 51, 10887–10890. doi: 10.1039/C5CC02604K

Wu, Y., Wen, M., Navlani-García, M., Kuwahara, Y., Mori, K., and Yamashita, H. (2017). Palladium nanoparticles supported on titanium doped graphitic carbon nitride for formic acid dehydrogenation. *Chem. Asian J.* 12, 860–867. doi: 10.1002/asia.201700041

Xie, W., and Schlücker, S. (2018). Surface-enhanced Raman spectroscopic detection of molecular chemo- and plasmo-catalysis on noble metal nanoparticles. *Chem. Commun.* 54, 2326–2336. doi: 10.1039/c7cc07951f

Yan, J.-M., Wang, Z.-L., Gu, L., Li, S.-J., Wang, H.-L., Zheng, W.-T., et al. (2015). AuPd-MnO x /MOF-Graphene: an efficient catalyst for hydrogen

production from formic acid at room temperature. *Adv. Energy Mater.* 5:1500107. doi: 10.1002/aenm.201500107

Yan, J. M., Li, S. J., Yi, S. S., Wulan, B. R., Zheng, W. T., and Jiang, Q. (2018). Anchoring and upgrading ultrafine NiPd on room-temperature-synthesized bifunctional NH_2-N-rGO toward low-cost and highly efficient catalysts for selective formic acid dehydrogenation. *Adv. Mater.* 30, 2–9. doi: 10.1002/adma.201703038

Yang, L., Hua, X., Su, J., Luo, W., Chen, S., and Cheng, G. (2015). Highly efficient hydrogen generation from formic acid-sodium formate over monodisperse AgPd nanoparticles at room temperature. *Appl. Catal. B Environ.* 168–169, 423–428. doi: 10.1016/j.apcatb.2015.01.003

Yang, L., Luo, W., and Cheng, G. (2016). Monodisperse CoAgPd nanoparticles assembled on graphene for efficient hydrogen generation from formic acid at room temperature. *Int. J. Hydrogen Energy* 41, 439–446. doi: 10.1016/j.ijhydene.2015.10.074

Yao, F., Li, X., Wan, C., Xu, L., An, Y., Ye, M., et al. (2017). Highly efficient hydrogen release from formic acid using a graphitic carbon nitride-supported AgPd nanoparticle catalyst. *Appl. Surf. Sci.* 426, 605–611. doi: 10.1016/j.apsusc.2017.07.193

Yoo, J. S., Abild-Pedersen, F., Nørskov, J. K., and Studt, F. (2014). Theoretical analysis of transition-metal catalysts for formic acid decomposition. *ACS Catal.* 4, 1226–1233. doi: 10.1021/cs400664z

Zell, T., Butschke, B., Ben-David, Y., and Milstein, D. (2013). Efficient hydrogen liberation from formic acid catalyzed by a well-defined iron pincer complex under mild conditions. *Chem. Eur. J.* 19, 8068–8072. doi: 10.1002/chem.201301383

Zhang, S., Jiang, B., Jiang, K., and Cai, W., Bin (2017). Surfactant-free synthesis of carbon-supported palladium nanoparticles and size-dependent hydrogen production from formic acid-formate solution. *ACS Appl. Mater. Interfaces* 9, 24678–24687. doi: 10.1021/acsami.7b08441

Zhang, S., Metin, Ö., Su, D., and Sun, S. (2013). Monodisperse AgPd alloy nanoparticles and their superior catalysis for the dehydrogenation of formic acid. *Angew. Chem. Int. Ed.* 52, 3681–3684. doi: 10.1002/anie.201300276

Zhang, X., Shang, N., Shang, H., Du, T., Zhou, X., Feng, C., et al. (2019). Nitrogen-decorated porous carbon supported AgPd nanoparticles for boosting hydrogen generation from formic acid. *Energy Technol.* 7, 140–145. doi: 10.1002/ente.201800522

Zhang, X., Shang, N., Zhou, X., Feng, C., Gao, S., Wu, Q., et al. (2017a). AgPd-MnO_x supported on carbon nanospheres: an efficient catalyst for dehydrogenation of formic acid. *New J. Chem.* 41, 3443–3449. doi: 10.1039/c6nj03873e

Zhang, X., Zhao, Y., Hu, S., Gliege, M. E., Liu, Y., Liu, R., et al. (2017b). Electrochemical reduction of carbon dioxide to formic acid in ionic liquid [Emim][$N(CN)_2$]/water system. *Electrochim. Acta* 247, 281–287. doi: 10.1016/j.electacta.2017.06.112

Zhong, H., Iguchi, M., Chatterjee, M., Himeda, Y., Xu, Q., and Kawanami, H. (2018). Formic acid-based liquid organic hydrogen carrier system with heterogeneous catalysts. *Adv. Sustain. Syst.* 2:1700161. doi: 10.1002/adsu.201700161

Zhou, J. P., Zhang, J., Dai, X. H., Wang, X., and Zhang, S. Y. (2016). Formic acid–ammonium formate mixture: a new system with extremely high dehydrogenation activity and capacity. *Int. J. Hydrogen Energy* 41, 22059–22066. doi: 10.1016/j.ijhydene.2016.10.015

Zhou, X., Huang, Y., Liu, C., Liao, J., Lu, T., and Xing, W. (2010). Available hydrogen from formic acid decomposed by rare earth elements promoted Pd-Au/C catalysts at low temperature. *ChemSusChem* 3, 1379–1382. doi: 10.1002/cssc.201000199

Zhu, J., Xiao, P., Li, H., and Carabineiro, A. C. (2014). Graphitic carbon nitride: synthesis, properties, and applications in catalysis. *ACS Appl. Mater. Interfaces* 6, 16449–16465. doi: 10.1021/am502925j

Zhu, Q. L., Tsumori, N., and Xu, Q. (2014). Sodium hydroxide-assisted growth of uniform Pd nanoparticles on nanoporous carbon MSC-30 for efficient and complete dehydrogenation of formic acid under ambient conditions. *Chem. Sci.* 5, 195–199. doi: 10.1039/c3sc52448e

Zhu, Q. L., Tsumori, N., and Xu, Q. (2015). Immobilizing extremely catalytically active palladium nanoparticles to carbon nanospheres: a weakly-capping growth approach. *J. Am. Chem. Soc.* 137, 11743–11748. doi: 10.1021/jacs.5b06707

Zhu, Q. L., and Xu, Q. (2015). Liquid organic and inorganic chemical hydrides for high-capacity hydrogen *storage*. 8, 478–512. doi: 10.1039/c4ee03690e

Conflict of Interest Statement: The authors declare that the research was conducted in the absence of any commercial or financial relationships that could be construed as a potential conflict of interest.

frontiers in Materials

ORIGINAL RESEARCH
published: 16 May 2019
doi: 10.3389/fmats.2019.00104

A Simple "Nano-Templating" Method Using Zeolite Y Toward the Formation of Carbon Schwarzites

Pawan Boonyoung[1], *Takatoshi Kasukabe*[2], *Yasuto Hoshikawa*[2], *Ángel Berenguer-Murcia*[3,4], *Diego Cazorla-Amorós*[3,4], *Bundet Boekfa*[5], *Hirotomo Nishihara*[2], *Takashi Kyotani*[2] *and Khanin Nueangnoraj*[1]*

[1] School of Bio-Chemical Engineering and Technology, Sirindhorn International Institute of Technology, Thammasat University – Rangsit Campus, Pathum Thani, Thailand, [2] Institute of Multidisciplinary Research for Advanced Materials, Tohoku University, Sendai, Japan, [3] Materials Institute, University of Alicante, Alicante, Spain, [4] Department of Inorganic Chemistry, University of Alicante, Alicante, Spain, [5] Department of Chemistry, Faculty of Liberal Arts and Science, Kasetsart University, Kamphaeng Saen Campus, Nakhin Pathom, Thailand

Schwarzites have a three-dimensional sp^2 carbon structure with negative Gaussian curvatures. They can be synthesized through the deposition of carbon by chemical vapor deposition on a zeolite template and may be formed by increasing the amount of carbon. In this research, the amount of carbon deposition was increased by shortening the length of the diffusion pathways of the template through the use of nano-sized zeolite Y (nano-FAU). It was found that significantly larger quantities of carbon could be deposited inside the pores of nano-FAU (40 nm), compared to the micro-sized zeolite Y (300 nm). It is thus confirmed that by shortening the diffusion pathways enables more carbon to infiltrate into the center of the template before the pore channels are blocked, which leads to larger carbon depositions. A low acetylene gas concentration (15% vol in N_2) and a prolonged period for chemical vapor deposition (6 h) is preferable for effectively loading carbon into the template. The obtained carbon replica exhibits the ordered structure derived from zeolite Y with an unprecedented 72 carbon atoms per supercage, of which a model with a structure similar to schwarzite was proposed.

Keywords: zeolite-templated carbon, zeolite Y, nano-template, chemical vapor deposition, schwarzites

OPEN ACCESS

Edited by:
Federico Cesano, University of Turin, Italy

Reviewed by:
Efrem Braun, University of California, Berkeley, United States
Humberto Terrones, Rensselaer Polytechnic Institute, United States

***Correspondence:**
Khanin Nueangnoraj
khanin@siit.tu.ac.th

Specialty section:
This article was submitted to Carbon-Based Materials, a section of the journal Frontiers in Materials

Received: *14 January 2019*
Accepted: *23 April 2019*
Published: *16 May 2019*

Citation:
Boonyoung P, Kasukabe T, Hoshikawa Y, Berenguer-Murci Á, Cazorla-Amorós D, Boekfa B, Nishihara H, Kyotani T and Nueangnoraj K (2019) A Simple "Nano-Templating" Method Using Zeolite Y Toward the Formation of Carbon Schwarzites. Front. Mater. 6:104. doi: 10.3389/fmats.2019.00104

INTRODUCTION

The primal unit of sp^2 carbon, graphene, is a highly versatile material that serves as the base structure of a variety of carbon architectures, such as fullerene (Kroto et al., 1985) and carbon nanotubes (Iijima, 1991). Researchers have shown that the induction of negative Gaussian curvature (Mackay, 1985) onto graphene forms a carbon structure with an open topology (Mackay and Terrones, 1991). This structure enables the construction of a three-dimensional framework, also known as schwarzite (Phillips et al., 1992; Vanderbilt and Tersoff, 1992).

It has been recently reported that the growth of carbon inside the hard porous materials, so-called template carbonization (Kyotani et al., 1997), has successfully synthesized carbons with structures that fits the description of schwarzites (Braun et al., 2018). Zeolite Y (FAU) is a commonly used template material, due to its three-dimensional pore structure, high thermal stability, and large pores (Kyotani et al., 2003; Braun et al., 2018). Conventionally, carbon is loaded into FAU through the use of chemical vapor deposition (CVD) with a carbon-source gas, such as acetylene

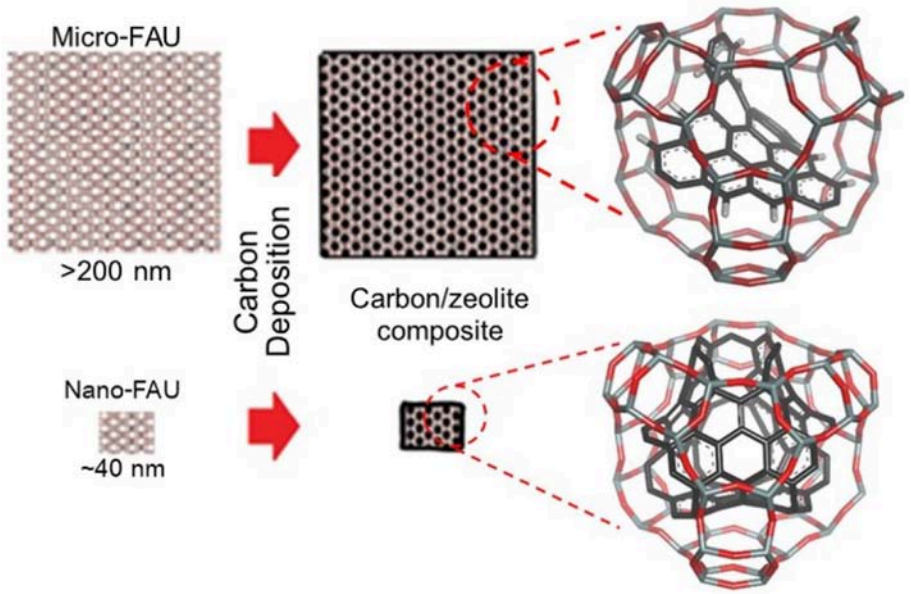

GRAPHICAL ABSTRACT | Possible formation of schwarzites by carbon loading inside the "nano-FAU" in comparison to that loaded inside the "micro-FAU".

(Hou et al., 2005) or propylene (Ma et al., 2000), as illustrated in **Figure 1A**. The carbon prepared from FAU and other zeolites is also known as zeolite-templated carbon (ZTC). Thus far, these materials have shown great potential in energy storage applications (Nishihara and Kyotani, 2012), such as electrochemical capacitors and hydrogen storages, due to their inherently high surface area (Ma et al., 2001) and high electrical conductivity (Lee et al., 2017).

Schwarzites can be formed by increasing the amount of carbon. It has been reported that a low amount of carbon was deposited in FAU (Ma et al., 2000, 2002), which can lead to the carbon structure not fully resembling the pore morphology of FAU [one of which is shown in **Figure 1B** (Nishihara et al., 2018)]. During CVD, the carbon that was deposited inside the template could reduce the size of pore openings, preventing more carbon from infiltrating into the center of the template. Furthermore, carbon deposition on the external surface of FAU can also lead to the formation of graphitic stacking layers (Yang et al., 2006; Nueangnoraj et al., 2013; Choi et al., 2015), which further exacerbates the inability of carbon to enter the template. The deposition of a larger quantity of carbon inside the FAU template would allow the formation of schwarzites.

There have been numerous attempts to increase the amount of carbon deposition inside FAU. The most notables include the use of a pressure-pulsed CVD (P-CVD) (Nueangnoraj et al., 2013) and doping the zeolite template with catalytic ions such as calcium (Kim et al., 2017) and lanthanum (Kim et al., 2016). P-CVD yielded a carbon structure with approximately 63 carbon atoms per supercage of FAU. However, it was observed that a thick layer of graphitic carbon was grown on the external surface of FAU crystals, which caused pore blockages and prevented the deposition of carbon inside the template. In contrast, the introduction of catalytic ions into the FAU framework allowed CVD to be performed at lower temperatures. The lower temperature with catalysis allows the carbon-source gas to crack primarily inside the template. This inhibits the deposition of carbon on the external surface of FAU, and therefore, reduces the formation of graphitic stacking. It was reported that ~80% of the pore channels in La^{3+} catalyzed FAU could be filled with carbon from CVD.

Apart from the methods previously mentioned, there is another parameter affecting the carbon deposition: the diffusion pathway. During CVD, carbon-source gas must diffuse into the pore channels of the template where deposition takes place. This may cause a layer of graphitic carbon to grow near or on the external surface of the zeolite. Therefore, the internal pores of the zeolite get blocked by already-deposited carbon, making it difficult for carbon to diffuse through the pores. Reducing the size of the FAU template proportionately shortens the length of the diffusion pathways, which would allow a greater portion of pore channels to be occupied before carbon is unable to infiltrate into the zeolite. To the best of our knowledge, there has been no investigation of the effects on the carbon deposition from the size of the FAU template. Therefore, in this work, we attempt to use a "nano-FAU" (<100 nm particles) for the deposition of carbon, so-called a "nano-templating" method, toward the formation of carbon schwarzites (**Graphical Abstract**).

EXPERIMENTAL

Preparation of Zeolite Y

Zeolite Y (FAU) was prepared from an aluminosilicate gel with a molar composition of 2.4 $(TMA)_2O$: 0.024 Na_2O: Al_2O_3: 3.4 SiO_2: 370 H_2O, using a slightly modified method

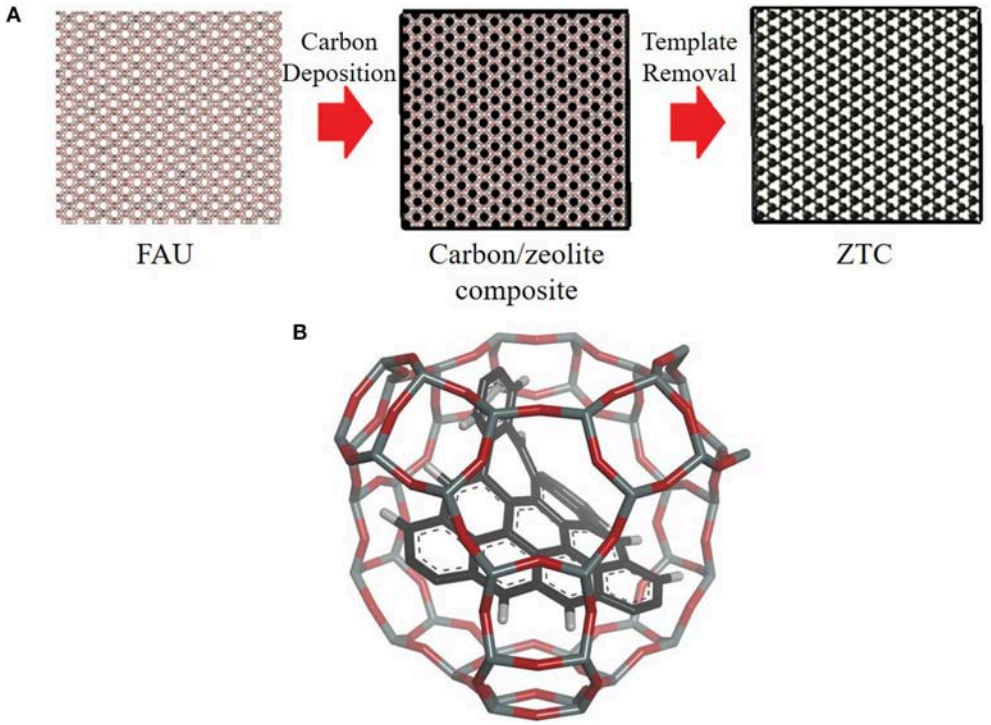

FIGURE 1 | (A) Illustration of chemical vapor deposition on the FAU and **(B)** structural model of the ZTC embedded inside one supercage of FAU, obtained by CVD method on the micro-FAU (Nishihara et al., 2018). Note that the gray and red sticks represent the FAU framework, whereas the black sticks are for the carbons.

reported elsewhere (Morales-Pacheco et al., 2009). The gel was prepared by dissolving sodium hydroxide pellets (Wako Pure Chemical Industries, Ltd.), tetramethylammonium hydroxide pentahydrate ($TMAOH{\cdot}5H_2O$, Wako Pure Chemical Industries, Ltd.), and aluminum isopropoxide (Wako Pure Chemical Industries, Ltd.) in RO water. Tetraethyl orthosilicate (Wako Pure Chemical Industries, Ltd.) was then added dropwise to the clear solution under vigorous stirring. The solution was then left to age for 20 h at room temperature.

The gel was hydrothermally treated in a PTFE vessel within a stainless-steel autoclave at 90 or 130°C for 120 h to crystallize the FAU particles. At the hydrothermal temperature of 90°C, the obtained FAU had an average size of 40 nm, while 300 nm particles were obtained at 130°C. After the hydrothermal treatment, the FAU suspension was immediately centrifuged (41,000 RCF for 30 min at 5°C) and re-dispersed in RO water at least three times to remove alkalinity. Finally, the sample was dried at 105°C, overnight.

Template Carbonization

FAU (0.50 g) was placed into a vertical quartz reactor and heated to 600°C under N_2 flow (150 $ml{\cdot}min^{-1}$) at a heating rate of $5°C{\cdot}min^{-1}$. Continuous chemical vapor deposition (C-CVD) was conducted on the zeolite by acetylene flow in N_2 (150 $ml{\cdot}min^{-1}$) at 600°C. The concentration of acetylene was varied from 15% vol to 35% vol in N_2, and the CVD period was varied from 2 to 6 h. After CVD, the carbon/zeolite composite was heated to 900°C at $5°C{\cdot}min^{-1}$ under 150 $ml{\cdot}min^{-1}$ of N_2, and the heat treatment was performed for another 3 h. The samples are referred to as ZTC40-xx-yy and ZTC300-xx-yy, where xx and yy are the acetylene concentration (% vol in N_2) and CVD time (h), respectively. The obtained carbon/zeolite composite was then washed with hydrofluoric acid (46 wt% HF, Wako Pure Chemical Industries, Ltd.) to remove the template.

Characterizations

The structure of the as-prepared FAU was confirmed using X-ray diffraction (Rigaku Miniflex 600), with a CuK_α source (40 kV and 15 mA). Laser diffraction (Microtrac MT3300EXLL) and SEM (Hitachi S4800) were used to estimate the particle size distribution of the obtained zeolite crystals.

The carbon content of the carbon/zeolite composites was obtained from thermogravimetric analysis (Shimadzu TGA-51) by combusting the samples in air at 800°C with a heating rate of $5°C{\cdot}min^{-1}$. The quantity of ordered carbon was estimated by differentiating the TG data of the liberated carbon, which was combusted in 5% vol O_2 in N_2 at 800°C with a heating rate of $2°C{\cdot}min^{-1}$.

TEM (JEOL JEM-2010) and XRD were employed to confirm the successful replication of FAU pores by the deposited carbon.

Modeling of Carbon

The models of the carbon were generated using the programs Avogadro and Chem3D 17.1. The Merck Molecular Force Field (MMFF94) was employed for the

energy minimization of the developed structure. After that, the semi-empirical algorithm PM6 was used in collaboration with the program MOPAC2016 for the final geometrical optimization. Avogadro and GaussView 5.0 were employed to calculate the energy of the predicted carbon structure.

RESULTS AND DISCUSSIONS

One of the main challenges in preparing the ZTC by CVD on the zeolite is the low carbon deposition inside the template. To increase the amount of carbon deposition, the following approaches were considered:

- Nano-sized FAU particles (40 nm, or nano-FAU) as the template material are used to reduce the length of the diffusion pathways, so that larger amounts of carbon could infiltrate into the center before blockages occur. Micro-sized FAU (>200 nm, or micro-FAU) are used for comparison.
- Acetylene is used as the carbon-source gas due to its small size relative to ethylene and propylene, which would allow for easy diffusion into the template.

Preparation of the Zeolite Template

Once the hydrothermal treatment of the aluminosilicate gel was completed, the FAU crystals were obtained as a white suspension within the gel. Centrifugation and re-dispersion were performed to remove alkalinity from the zeolite. XRD patterns of the obtained crystals were compared with a reference FAU sample (HSZ320NAA, Tosoh Corporation), which confirmed the successful synthesis of FAU particles. Laser diffraction was used to estimate the average particle size of the FAU, which was 40 nm for those hydrothermally treated at 90°C, while the 130°C treated crystals were ∼300 nm (see **Supplementary Material** for details).

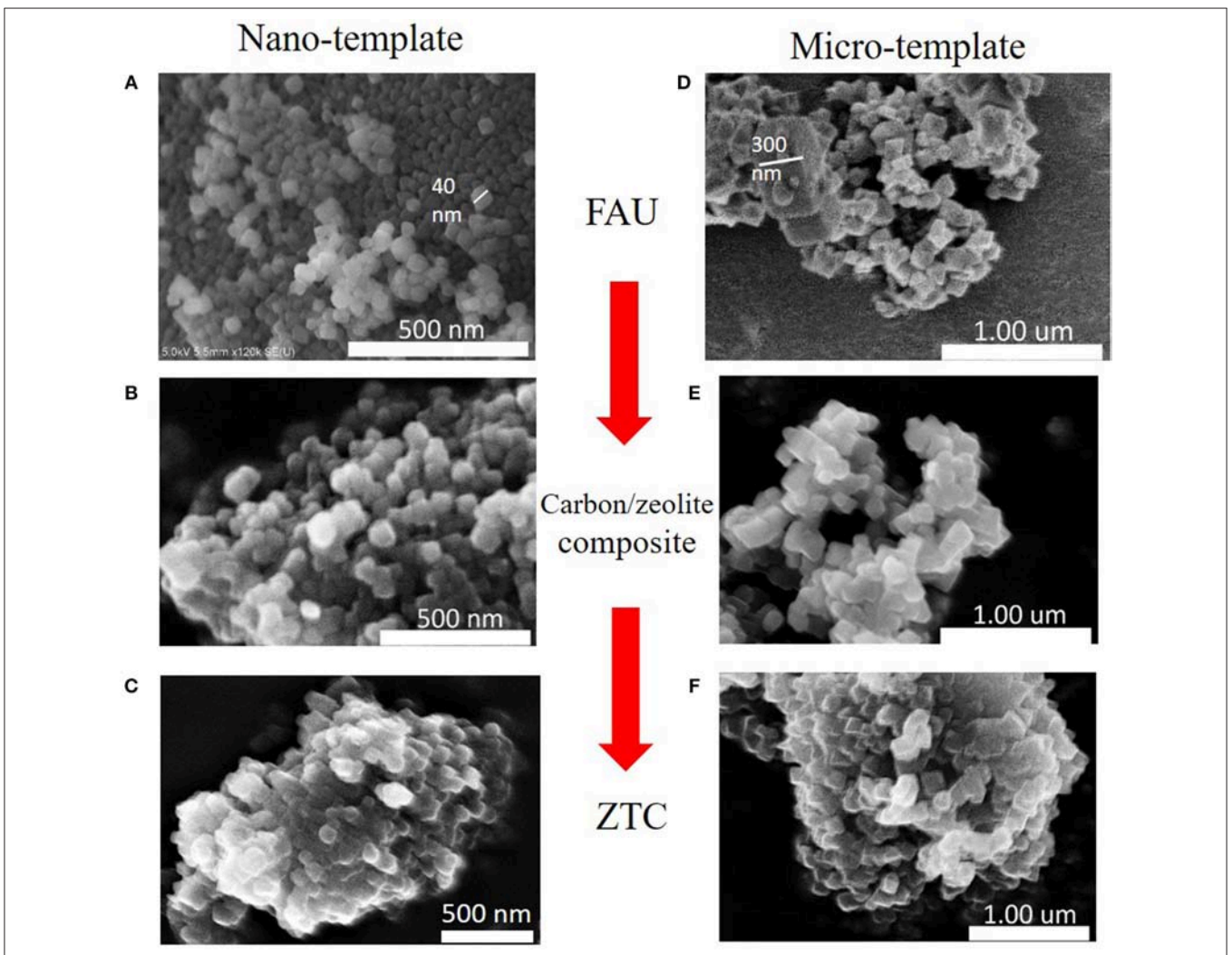

FIGURE 2 | SEM images of the various stages of ZTC preparation; **(A)** 40 nm FAU (nano-FAU), **(B)** carbon/nano-FAU composite, **(C)** liberated ZTC40, **(D)** 300 nm FAU (micro-FAU), **(E)** carbon/micro-FAU composite, and **(F)** liberated ZTC300.

Formation of Zeolite-Templated Carbon

The various stages of ZTC formation, which are the FAU particles, carbon/zeolite composites, and liberated ZTC, are shown in **Figure 2**. It can be seen from **Figures 2A,D** that the FAU particles have approximate sizes of 40 and 150–300 nm, respectively, which are in good agreement with the laser diffraction analysis. After CVD, it is observed that there is little change in the size and morphology of the crystals (**Figures 2B,E**). This suggests that carbon is only deposited onto the zeolite. Finally, after the zeolite template was removed by HF washing (**Figures 2C,F**), the particles of carbon retain their cubic shape, indicating that there was no collapse of the structure.

Confirmation of the Template Replication

XRD patterns (**Figure 3**) of the liberated carbon display a prominent sharp peak at $2\theta = 6.3^{\circ}$, which is at the identical angle of diffraction as found in the FAU. This corresponds to the (111) plane and is calculated to have a d-spacing of 1.4 nm in accordance with Bragg's Law. This supports the claim that carbon has replicated the morphology of the pores in FAU. A small secondary peak could be observed at $2\theta = 18^{\circ}$ in most of the samples. This peak signifies the presence of polyfluoroethylene (PTFE), which likely contaminated the sample during the washing process due to the use of PTFE vessels and filtration membranes. Nevertheless, PTFE is not important in this work and may be neglected.

The XRD patterns of ZTC300-25-4 and ZTC300-35-4 in **Figure 3C** show two distinct broad peaks at approximately $2\theta = 26^{\circ}$ and $2\theta = 44^{\circ}$, which are not present in the FAU. These correspond to the (002) and (10) planes in the graphitic carbon, having a d-spacing of 0.34 and 0.21 nm, respectively. When the XRD plots were magnified, these peaks become visible in all

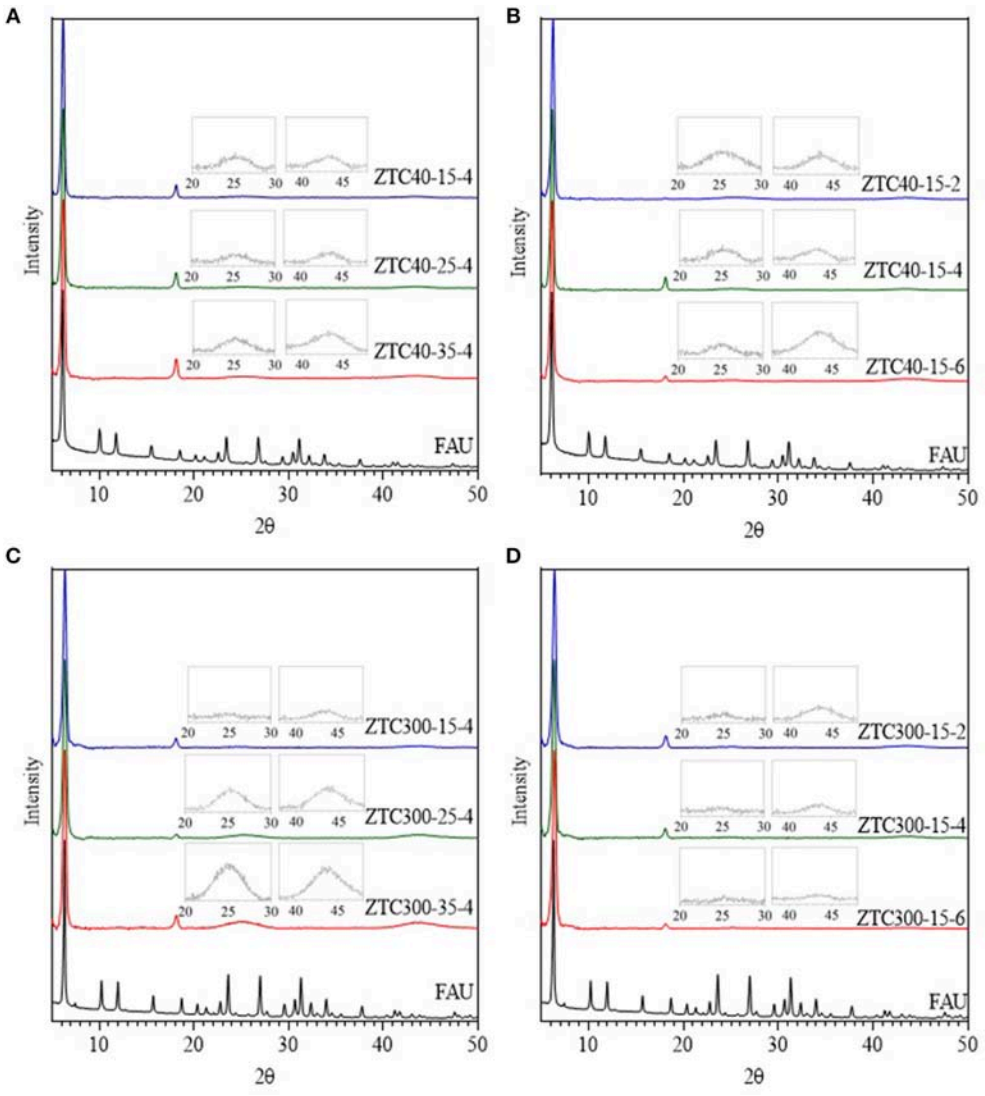

FIGURE 3 | XRD patterns of the liberated carbon at various **(A)** acetylene concentrations and **(B)** CVD times for ZTC40, and at various **(C)** acetylene concentrations and **(D)** CVD times for ZTC300.

ZTC samples. Interestingly, when the acetylene concentration was increased, the intensity of the (002) and (10) planes become more prominent for ZTC produced from 300 nm FAU. However, this effect is diminished when the 40 nm template was used. Therefore, a higher acetylene concentration greatly favors the formation of a graphitic structure on the surface of larger-sized FAUs, which should be avoided as this would cause pore blockage.

TEM images of the liberated carbon display black lines with high uniformity, as shown in **Figure 4**. The periodicity of these ordered lines is ∼1.3 nm, which is similar to the d-spacing in FAU and is in good agreement with the XRD patterns of the liberated carbon. Therefore, it is confirmed that the carbon has successfully replicated the FAU pore structures.

Carbon Content

Carbon Content of the Carbon/Zeolite Composite

Carbon contents in the carbon/zeolite composites were estimated from the thermogravimetric (TG) curves and are listed in **Table 1**. At the lowest acetylene concentration (15% in N_2), carbon/zeolite composites produced from 40 nm FAU have a higher carbon content for all CVD times, compared to those prepared from 300 nm FAU. The ZTC prepared from both sizes of FAU exhibited an increase in carbon content as the CVD time was prolonged from 2 to 6 h. This suggests that the carbon could be consistently deposited into the template. However, as the acetylene concentration increases, only ZTC300 exhibits a large increase in carbon deposition, from 0.56 to 1.02 $g{\cdot}g^{-1}$, whereas ZTC40 increases from 0.72 to 0.75 $g{\cdot}g^{-1}$, which is comparatively small. The 300 nm FAU is, therefore, significantly more susceptible to increases of acetylene concentration. We discuss in detail the formation of different types of carbon after the CVD in the following section.

Quantification of the Ordered Carbon

As the XRD patterns of the carbon replicas indicate the presence of a graphitic structure in addition to an ordered carbon structure, the samples need to be quantified to distinguish such structures. We had previously reported (Nueangnoraj et al., 2013) that these carbons combust at relatively different temperatures, ca. 560°C for the ordered carbon, and at a higher temperature for the stacked graphitic layers. Therefore, differential thermogravimetric (DTG) analysis was applied to estimate the quantity of each carbon structure.

The DTG plots were obtained by differentiating the TG curves of the liberated carbon. A peak fitting program, Fityk (Wojdyr, 2010), was employed to distinguish and separate the two peaks observed (**Figure 5**). The Gaussian and Pearson VII equations were used to fit the first (ordered carbon) and the second (graphitic carbon) peaks, respectively, and to estimate the area under the curves. However, for samples ZTC300-25-4 and ZTC300-35-4, the asymmetric Gaussian and asymmetric Pearson VII equations showed a better fit. The quantity of ordered carbon (W_{inside}) for each ZTC sample was calculated and is listed in **Table 2**.

It is observed that W_{inside} of ZTC40 (prepared from 40 nm FAU) is higher than that of ZTC300 for most of the CVD conditions, except for a CVD time of 2 h, where the carbon contents are equivalent. This supports the hypothesis that short diffusion pathways enable more carbon to easily deposit deep within the template.

Prolonged CVD time is favorable for the deposition of carbon inside both sizes of the FAU, in particular, the nano-FAU. The increase in W_{inside} for ZTC40 as the CVD time was prolonged

TABLE 1 | Total carbon content of the carbon/zeolite composites.

Sample*	W_{total} ($g \cdot g^{-1}$)**	Sample*	W_{total} ($g \cdot g^{-1}$)**
ZTC40-15-2	0.64	ZTC300-15-2	0.50
ZTC40-15-4	0.72	ZTC300-15-4	0.56
ZTC40-15-6	0.76	ZTC300-15-6	0.53
ZTC40-25-4	0.74	ZTC300-25-4	0.76
ZTC40-35-4	0.75	ZTC300-35-4	1.02

*Nomenclature: ZTC [size of FAU (nm) – acetylene concentration (% vol) – CVD time (h)].
**Total weight of carbon as obtained from TGA data (g carbon · g^{-1} zeolite).

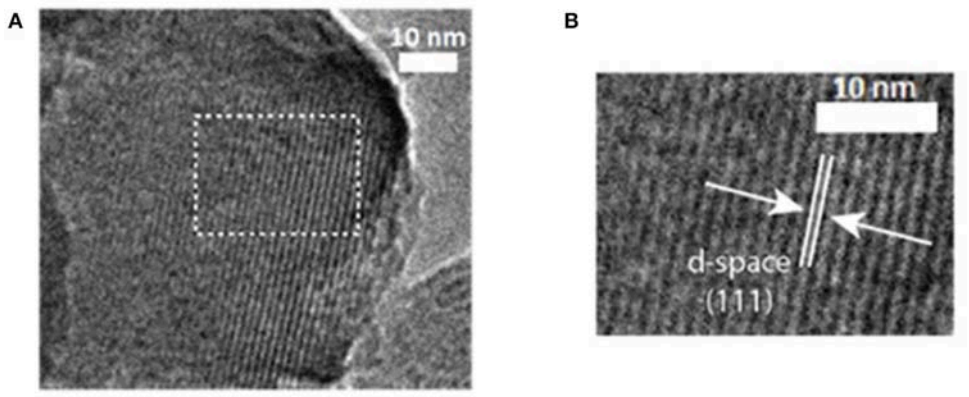

FIGURE 4 | (A) TEM images of ZTC40 showing the periodicity of the ordered carbon and **(B)** magnification of the dashed white box.

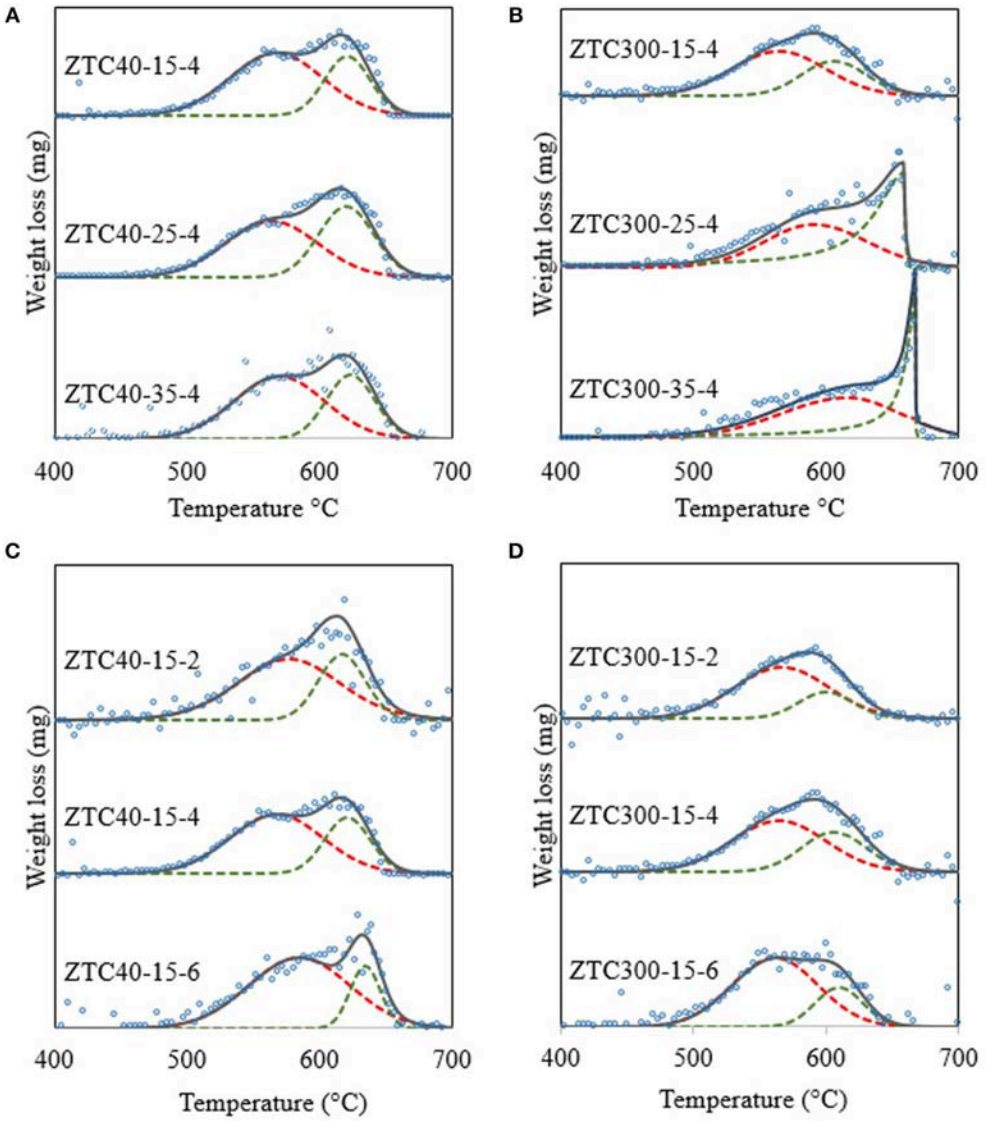

FIGURE 5 | DTG plots and peak fittings for the difference in acetylene concentration on **(A)** ZTC40 **(B)** ZTC300, and the difference in CVD time for **(C)** ZTC40 and **(D)** ZTC300. Open circles show the raw differentiated TG data. Dashed lines represent the peak fittings while the solid lines are the summation of the peak fittings.

from 2 to 6 h was 0.22 $g{\cdot}g^{-1}$, whereas the increase for ZTC300 was only 0.02 $g{\cdot}g^{-1}$. Therefore, a longer CVD time is preferable for the deposition of a larger amount of carbon inside the template. However, we have found that the steady-state has been reached with a CVD time of 12 h (see **Supplementary Material**), and W_{inside} increased to 0.62 $g{\cdot}g^{-1}$.

A high acetylene concentration, in contrast, has a detrimental effect on the carbon loading. W_{inside} for both ZTC40 and ZTC300 decrease as the source-gas concentration was increased. A possible explanation for this phenomenon is as follows. When the source gas concentration increases, carbon would be deposited near the pore entrance or on the external surface of the zeolite. As described earlier, the internal pores of the zeolite would get blocked by already-deposited carbon, making it difficult for carbon to diffuse through the pores. The excess carbon is therefore deposited onto the external surface of FAU, leading to the formation of graphitic stacking layers. This is far more significant for ZTC300 than ZTC40, as the increase in external carbon deposition is from 0.18 to 0.72 $g{\cdot}g^{-1}$. For ZTC40, the graphite content increases from 0.22 to 0.29 $g{\cdot}g^{-1}$, which was calculated by subtracting W_{inside} from the total carbon content. This result is further supported by the XRD patterns shown in **Figure 3**, as the broad (002) and (10) peaks indicate the presence of large quantities of graphitic structures for ZTC300 at high acetylene concentrations.

A low acetylene concentration with a long CVD time is therefore preferable for a large amount of carbon deposition

TABLE 2 | Carbon content that deposited inside the FAU template and the average number of carbon atoms per supercage.

Sample	W_{inside} ($g \cdot g^{-1}$)*	Average number of carbon atoms**	Sample	W_{inside} ($g \cdot g^{-1}$)*	Average number of carbon atoms**
ZTC40-15-2	0.38 ± 0.01	46 ± 2	ZTC300-15-2	0.38 ± 0.02	46 ± 3
ZTC40-15-4	0.50 ± 0.02	60 ± 2	ZTC300-15-4	0.38 ± 0.02	46 ± 2
ZTC40-15-6	0.60 ± 0.03	72 ± 3	ZTC300-15-6	0.40 ± 0.02	48 ± 2
ZTC40-25-4	0.48 ± 0.02	57 ± 2	ZTC300-25-4	0.37 ± 0.01	45 ± 1
ZTC40-35-4	0.46 ± 0.02	55 ± 2	ZTC300-35-4	0.30 ± 0.01	36 ± 1

Weight of carbon inside FAU template—excluding the graphitic layers on the external surface of zeolite (g carbon · g^{-1} zeolite).
**Average number of carbon atoms per supercage of FAU estimated from W_{inside}.*

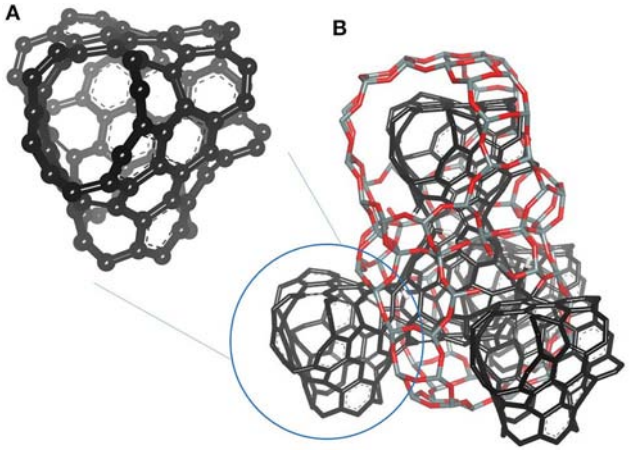

FIGURE 6 | The proposed model of **(A)** single C_{72} unit and **(B)** the framework of C_{72} units connected in a tetrahedral configuration that is embedded inside the FAU framework. Note that the gray and red sticks represent the FAU template, whereas the black sticks are for the carbons.

inside the FAU. ZTC40-15-6 shows the highest W_{inside} of 0.60 $g \cdot g^{-1}$, which corresponds to approximately 72 carbon atoms per supercage of FAU (**Table 2**). This carbon content is competitive to that of the P-CVD method for commercial FAU (particle size >200 nm), where the quantity of carbon deposited inside the template was ∼63 atoms per supercage of FAU. However, this "nano-templating" approach is simpler in practice due to the use of continuous CVD, as opposed to the pulse and vacuum approach of the P-CVD.

Molecular Structure of the Carbon

The hypothetical model for ZTC40-15-6 was drawn using Avogadro with the Merck Molecular Force Field (MMFF94) for energy minimization (Halgren, 1996a,b). The ZTC model was constructed with the following assumptions:

- The model should be able to fit inside the pores of FAU.
- The model is constructed of only carbon hexagons and heptagons.
- The deposition of carbon is fully uniform throughout the template.

Based on the experiment, one supercage of the FAU would contain 72 carbon atoms. We thus assemble these atoms in accordance with the above assumptions, as shown in **Figure 6A**. The one-unit structure of this model (C_{72}, **Figure 6B**) is fitted inside the supercage of FAU and is connected to another 4 units to form the three-dimensional framework. The carbon model was then geometrically optimized with the semi-empirical algorithm PM6 (Stewart, 2007, 2008) using the MOPAC2016 (Stewart, 2016). There are other possibilities to form the models based on the arrangement of polygons (see **Supplementary Material**). However, we proposed the most geometrically stable model as displayed in **Figure 6**. It should be noted that the structure shown in **Figure 6** is built as an average structure. Each unit structure of the real ZTC material is actually diverse and ZTC cannot be defined as a crystal, because its XRD pattern does not show many peaks (**Figure 3**). The atomic coordinates of the average structure shown in **Figure 6** can be found in **Supplementary Material**.

Due to the pore structure of FAU and the presence of carbon heptagons, the model resembles a tetrapod and can form the three-dimensional tetrahedral framework as described earlier. This model fits the description of schwarzites proposed by Braun et al. (2018), and thus, could be one type of schwarzite.

CONCLUSION

Zeolite-templated carbon (ZTC) was successfully synthesized in both 40 and 300 nm FAU. Carbon could be effectively deposited inside the smaller "nano-FAU" rather than the "micro-FAU" because of the shorter diffusion pathways. A longer CVD time is beneficial for the deposition of carbon inside the template. Higher acetylene concentrations during the CVD inhibit the diffusion of carbon inside the FAU and favor the growth of graphitic layers on the external surface of the template. ZTC-40-15-6, which was prepared by using the nano-FAU with the lowest CVD concentration (15% vol in N_2) and longest CVD time (6 h), possesses the largest amount of carbon deposition inside the template (0.60 $g \cdot g^{-1}$). This corresponds to 72 carbon atoms per supercage of FAU, one of the highest to date. A structural model of this carbon was proposed, which can be considered as one type of schwarzite. Furthermore, the amount of carbon deposition is competitive with that of previous studies, such as P-CVD (63 atoms). The "nano-templating" approach is simpler to perform due to the use of continuous CVD. It is possible for the other forms of carbon schwarzites to be synthesized through further refinement of this "nano-templating" approach. This approach can also be combined with other carbon deposition techniques, which could open many possibilities for a new branch of research on novel templated carbon materials.

AUTHOR CONTRIBUTIONS

PB, ÁB-M, DC-A, HN, TKy, and KN contributed conception and design of the study. PB, TKa, and YH performed the experiments.

HN, TKy, and KN analyzed and organized the results. BB contributed in the proposed model. PB wrote the first draft of the manuscript. All authors contributed to manuscript revision, read, and approved the submitted version.

ACKNOWLEDGMENTS

This work was supported by Grant-in-Aid for Scientific Research (A), 17H01042 (HN); the Nano-Macro Materials, Devices and System Research Alliance; and the Network Joint Research Center for Materials and Devices. The support from Sirindhorn International Institute of Technology under the Excellent Thai Student Program (PB) and from the Research Grant for New Scholar (Grant No. MRG6080153) co-funded by the Thailand Research Fund (TRF); the commission on Higher Education, Thailand; and Thammasat University, are also acknowledged.

SUPPLEMENTARY MATERIAL

The Supplementary Material for this article can be found online at: https://www.frontiersin.org/articles/10.3389/fmats.2019.00104/full#supplementary-material

REFERENCES

Braun, E., Lee, Y., Moosavi, S. M., Barthel, S., Mercado, R., Baburin, I. A., et al. (2018). Generating carbon schwarzites via zeolite-templating. *Proc. Natl. Acad. Sci. U.S.A.* 115, E8116–E8124. doi: 10.1073/pnas.1805062115

Choi, S., Kim, H., Lee, S., Wang, Y., Ercan, C., Othman, R., et al. (2015). Large-scale synthesis of high-quality zeolite-templated carbons without depositing external carbon layers. *Chem. Eng. J.* 280, 597–605. doi: 10.1016/j.cej.2015.06.055

Halgren, T. A. (1996a). Merck molecular force field. I. Basis, form, scope, parameterization, and performance of MMFF94. *J. Comput. Chem.* 17, 490–519. doi: 10.1002/(SICI)1096-987X(199604)17:5/6<490::AID-JCC1>3.0.CO;2-P

Halgren, T. A. (1996b). Merck molecular force field. III. Molecular geometries and vibrational frequencies for MMFF94. *J. Comput. Chem.* 17, 553–586. doi: 10.1002/(SICI)1096-987X(199604)17:5/6<553::AID-JCC3>3.0.CO;2-T

Hou, P.-X., Yamazaki, T., Orikasa, H., and Kyotani, T. (2005). An easy method for the synthesis of ordered microporous carbons by the template technique. *Carbon* 43, 2624–2627. doi: 10.1016/j.carbon.2005.05.001

Iijima, S. (1991). Helical microtubules of graphitic carbon. *Nature* 354:56. doi: 10.1038/354056a0

Kim, K., Kwon, Y., Lee, T., Cho, S. J., and Ryoo, R. (2017). Facile large-scale synthesis of three-dimensional graphene-like ordered microporous carbon via ethylene carbonization in CaX zeolite template. *Carbon* 118, 517–523. doi: 10.1016/j.carbon.2017.03.082

Kim, K., Lee, T., Kwon, Y., Seo, Y., Song, J., Park, J. K., et al. (2016). Lanthanum-catalysed synthesis of microporous 3D graphene-like carbons in a zeolite template. *Nature* 535, 131–135. doi: 10.1038/nature18284.

Kroto, H. W., Heath, J. R., O'Brien, S. C., Curl, R. F., and Smalley, R. E. (1985). C60: buckminsterfullerene. *Nature* 318, 162–163.

Kyotani, T., Ma, Z., and Tomita, A. (2003). Template synthesis of novel porous carbons using various types of zeolites. *Carbon* 41, 1451–1459. doi: 10.1016/S0008-6223(03)00090-3

Kyotani, T., Nagai, T., Inoue, S., and Tomita, A. (1997). Formation of new type of porous carbon by carbonization in zeolite nanochannels. *Chem. Mater.* 9, 609–615. doi: 10.1021/cm960430h

Lee, H., Kim, K., Kang, S. H., Kwon, Y., Kim, J. H., Kwon, Y. K., et al. (2017). Extremely high electrical conductance of microporous 3D graphene-like zeolite-templated carbon framework. *Sci. Rep.* 7:11460. doi: 10.1038/s41598-017-11602-5

Ma, Z., Kyotani, T., Liu, Z., Terasaki, O., and Tomita, A. (2001). Very high surface area microporous carbon with a three-dimensional nano-array structure: synthesis and its molecular structure. *Chem. Mater.* 13, 4413–4415. doi: 10.1021/cm010730l

Ma, Z., Kyotani, T., and Tomita, A. (2000). Preparation of a high surface area microporous carbon having the structural regularity of Y zeolite. *Chem. Commun.* 23, 2365–2366. doi: 10.1039/B006295M

Ma, Z., Kyotani, T., and Tomita, A. (2002). Synthesis methods for preparing microporous carbons with a structural regularity of zeolite Y. *Carbon* 40, 2367–2374. doi: 10.1016/S0008-6223(02)00120-3

Mackay, A. L. (1985). Periodic minimal surfaces. *Nature* 314:604. doi: 10.1038/314604a0

Mackay, A. L., and Terrones, H. (1991). Diamond from graphite. *Nature* 352:762. doi: 10.1038/352762a0

Morales-Pacheco, P., Alvarez, F., Bucio, L., and Domínguez, J. M. (2009). Synthesis and structural properties of zeolitic nanocrystals II: FAU-type zeolites. *J. Phys. Chem. C* 113, 2247–2255. doi: 10.1021/jp8070713

Nishihara, H., Fujimoto, H., Itoi, H., Nomura, K., Tanaka, H., Miyahara, M. T., et al. (2018). Graphene-based ordered framework with a diverse range of carbon polygons formed in zeolite nanochannels. *Carbon* 129, 854–862. doi: 10.1016/j.carbon.2017.12.055

Nishihara, H., and Kyotani, T. (2012). Templated nanocarbons for energy storage. *Adv. Mater.* 24, 4473–4498. doi: 10.1002/adma.201201715

Nueangnoraj, K., Nishihara, H., Imai, K., Itoi, H., Ishii, T., Kiguchi, M., et al. (2013). Formation of crosslinked-fullerene-like framework as negative replica of zeolite Y. *Carbon* 62, 455–464. doi: 10.1016/j.carbon.2013.06.033

Phillips, R., Drabold, D. A., Lenosky, T., Adams, G. B., and Sankey, O. F. (1992). Electronic structure of schwarzite. *Phys. Rev. B* 46, 1941–1943.

Stewart, J. J. (2007). Optimization of parameters for semiempirical methods V: modification of NDDO approximations and application to 70 elements. *J. Mol. Model.* 13, 1173–1213. doi: 10.1007/s00894-007-0233-4

Stewart, J. J. (2008). Application of the PM6 method to modeling the solid state. *J. Mol. Model.* 14:499. doi: 10.1007/s00894-008-0299-7

Stewart, J. J. P. (2016). *"MOPAC2016"*. Colorado Springs, CO: Stewart Computational Chemistry.

Vanderbilt, D., and Tersoff, J. (1992). Negative-curvature fullerene analog of C_{60}. *Phys. Rev. Lett.* 68, 511–513.

Wojdyr, M. (2010). Fityk: a general purpose peak-fitting program. *J. Appl. Crystallogr.* 43, 1126–1128. doi: 10.1107/S0021889810030499

Yang, Z., Xia, Y., Sun, X., and Mokaya, R. (2006). Preparation and hydrogen storage properties of zeolite-templated carbon materials nanocast via chemical vapor deposition: effect of the zeolite template and nitrogen doping. *J. Phys. Chem. B* 110, 18424–18431. doi: 10.1021/jp0639849

Conflict of Interest Statement: The authors declare that the research was conducted in the absence of any commercial or financial relationships that could be construed as a potential conflict of interest.

frontiers in Materials

ORIGINAL RESEARCH
published: 24 April 2019
doi: 10.3389/fmats.2019.00065

Effects of Carbon Pore Size on the Contribution of Ionic Liquid Electrolyte Phase Transitions to Energy Storage in Supercapacitors

*Konstantin Schutjajew[1], Runyu Yan[1], Markus Antonietti[1], Christina Roth[2] and Martin Oschatz[1]**

[1] Department of Colloid Chemistry, Max Planck Institute of Colloids and Interfaces, Potsdam, Germany, [2] Institute for Chemistry and Biochemistry, Freie Universität Berlin, Berlin, Germany

Recent research on ionic liquid electrolyte-based supercapacitors indicated the contribution of phase transitions of the electrolytes at high cell voltages to the energy stored. This mechanism can be exploited to significantly increase the energy density of supercapacitors, which up to now remains their major drawback. It was found that these ordering transitions require the presence of mesopores within the carbon electrode materials and that porosity in general is a key factor to trigger them, but details of the mechanism remains unexplained. To get a more profound understanding of this phenomenon, carbon materials with different pore diameters and volumes were synthesized and the effect of those properties on the phase transitions in the ionic liquids was studied by means of cyclic voltammetry. A clear correlation between the peak current and the mesopore volume is revealed and an optimal pore diameter was determined, exceeding which does not improve the phase transition behavior. These findings are useful as guidelines for the rational design of carbon mesopores in order to utilize the new energy storage modes which are neither fully capacitive, nor redox-based.

Keywords: supercapacitors, porous carbon, energy storage, ionic liquids, ordering transitions

OPEN ACCESS

Edited by:
Diego Cazorla-Amoros, University of Alicante, Spain

Reviewed by:
Emilia Morallon, University of Alicante, Spain
Marta Sevilla, Instituto Nacional del Carbón (INCAR), Spain

****Correspondence:***
Martin Oschatz
martin.oschatz@mpikg.mpg.de

Specialty section:
This article was submitted to Carbon-Based Materials, a section of the journal Frontiers in Materials

Received: *23 January 2019*
Accepted: *01 April 2019*
Published: *24 April 2019*

Citation:
Schutjajew K, Yan R, Antonietti M, Roth C and Oschatz M (2019) Effects of Carbon Pore Size on the Contribution of Ionic Liquid Electrolyte Phase Transitions to Energy Storage in Supercapacitors. Front. Mater. 6:65. doi: 10.3389/fmats.2019.00065

INTRODUCTION

The progressing integration of modern technology into daily life has led to an ever increasing energy demand, causing the exploitation of already scarce fossil fuel resources close to their exhaustion and consequently causing extensive damage to the environment. Therefore, renewable energy sources moved into focus as an alternative for a sustainable energy supply on the long run ranging from low energy systems such as communication and individual mobility up to the electric grid mains. The integration of renewables into daily life, especially for public and personal transportation or mobile consumer electronics is a particular challenge. Although the development of the lithium ion battery with high energy storage capacity has led to its widespread application, some inherent drawbacks such as safety issues and environmental concerns raise the demand for safer and more sustainable solutions (Choi et al., 2012; Manthiram, 2017).

The electrical double layer capacitor (EDLC) is a possible supplement to the lithium-ion battery (Simon and Gogotsi, 2008, 2013; González et al., 2016; Salanne et al., 2016). The energy in such devices is traditionally stored via electrostatic adsorption of electrolyte ions to the electrode surface, which results in very high power density and exceptionally long cycle life. On the other hand,

EDLCs can only reach about a tenth of the energy density of lithium-ion batteries. Significant efforts have been invested in increasing the energy density of capacitors by tuning electrolytes, electrode materials, or even coupling the double layer formation to reversible surface redox reactions, but the capacity of battery technology still remains out of reach (Béguin et al., 2014; Borchardt et al., 2014).

More recently, the utilization of so called room-temperature ionic liquids (RTILs) as electrolytes has opened a prospect to solve the problem of the supercapacitors' low energy density (Merlet et al., 2012; Brandt et al., 2013; Macfarlane et al., 2014; Salanne, 2017). This special class of "molten salts" has electrochemical stability windows of more than 4 V, which is very beneficial as the energy stored in a capacitor generally is strongly related to the applied voltage. RTILs are also non-flammable and can be regarded as environmentally less damaging than common solvent-based organic electrolytes. Even more importantly, theoretical, and experimental studies showed that the energy storage mechanism is likely different than the compression double layer present in solvent based electrolytes, because the overall ion density is nearly constant in such electrolytes. They further showed the possibility of a change in coordination geometry of RTILs when confined in a porous carbon environment, triggered by an applied electric potential (Tazi et al., 2010; Kiyohara et al., 2011; Fedorov and Kornyshev, 2014; Rotenberg and Salanne, 2015; Futamura et al., 2017; Yan et al., 2018). These phase transitions may play a crucial role for the conservation of electroneutrality and thus for energy storage in RTIL-based EDLCs (Antonietti et al., 2018). This new mode of energy storage was recently proposed based on a series of experiments on porous carbon materials and the presence of mesopores with diameters as large as the dimensions of a few RTIL ion layers was found to play a particularly important role (Antonietti et al., 2018; Lai et al., 2018; Yan et al., 2018). However, the influence of carbon pore structure and structure of the RTIL on this phenomenon remains still poorly understood.

To address some of those questions, an established hard-templating approach has been employed to synthesize a series of carbon materials with varying porosities (Jun et al., 2000; Postnov et al., 2013). They were employed as electrode materials for cyclic voltammetry experiments within different RTIL electrolytes, namely 1-ethyl-3-methylimidazolium tetrafluoroborate ($EMImBF_4$), 1-butyl-3-methylimidazolium tetrafluoroborate ($BMImBF_4$), and 1-ethyl-3-methylimidazolium bis(trifluoromethylsulfonyl)imide (EMImTFSI). It turned out that irrespectively of the RTIL used the phase transformation was more pronounced in smaller mesopores. Even more, there is a direct correlation between mesopore volume and peak current, corroborating the idea of a phase transition taking place inside the carbon mesopores. This systematic investigation provides profound experimental insights into this mechanism and improves our understanding of the underlying principles.

MATERIALS AND METHODS

Synthesis of the Carbon Materials

Aerosil®*n-m* carbons were synthesized by an incipient wetness impregnation approach using fumed silica Aerosil® 90 and Aerosil® 380 (Evonik Industries AG) as hard templates. A comparable method has previously been described by Jun et al. (2000) and the template has been employed by Postnov et al. (2013). The two template materials are composed of spherical primary particles and differ mainly in particle size, enabling control over pore size in the carbon replicas. The pore volume was adjusted by changing the mass ratio of silica to carbon precursor (sucrose) from 1:1 to 1:2 and 1:4. The variable n in the sample name denotes the template type, while the variable m represents the sucrose/silica mass ratio. In a typical synthesis the corresponding mass of silica precursor was impregnated with a solution of 2 g sucrose and 0.2 g concentrated sulphuric acid in 10 ml water. The mixture was heated at 100°C for 6 h and the temperature was increased to 160°C for another 6 h. The dark brown to black compound was transferred into a porcelain boat and carbonized at 900°C for 2 h at a heating rate of 60 K h^{-1} in a horizontal tube furnace under nitrogen flow. Removal of the template was accomplished by heating the solid to 120°C in 5 M sodium hydroxide aqueous solution overnight under reflux, followed by filtration and washing with ∼2 L water in the cases of carbons Aerosil *n*-2 and Aerosil *n*-4. For carbons with a 1:1 sucrose/silica ratio the template was removed by stirring the carbonization product in 500 ml of a 4 M $[NH_4][F_2H]$ aqueous solution for 3 days, followed by filtration and subsequent washing with a 1:1 ethanol/water mixture and another stirring procedure in $[NH_4][F_2H]$ solution. After a similar filtration and washing sequence a residual template mass as low as 4 % was achieved as indicated by thermogravimetric analysis.

Structural Characterization

N_2 and CO_2 physisorption experiments have been carried out on a Quadrasorb apparatus (Quantachrome Instruments) at −196 and 0°C, respectively. Before each measurement, 40-70 mg of the sample have been degassed under vacuum at 150°C for 20 h. Specific surface areas have been calculated from the N_2 physisorption measurements using the multipoint BET-method ($p/p_0 = 0.05$–0.20). Pore volumes and pore size distributions have been calculated from the adsorption branch of the N_2 isotherms using the quenched solid density functional theory (QSDFT) for N_2 on carbon assuming cylindrical and slit-shaped pores. Pores with a diameter smaller than 1.5 nm have been analyzed by CO_2 adsorption experiments at 0°C, where the pore size distribution was calculated by means of the non-local density functional theory (NLDFT) for CO_2 adsorbed on carbon surfaces.

Thermogravimetric Analysis (TGA) was carried out on a Netzsch TG 209 F1 Iris device in a temperature range between room temperature and 1,000°C at a heating rate of 5 K min^{-1}. Samples were placed in a platinum crucible and subjected to a constant synthetic air flow. Elemental Analysis (EA) was done on a vario microcube CHNS analyzer by Elementar Analysensysteme GmbH.

Raman spectra were measured on a Witec Raman microscope at an excitation wavelength of 532 nm with a power of 4.0 mW. After the substraction of background noise the D, D^2, A and G bands are fitted with a Lorentz function.

X-ray diffraction measurements were performed on a Bruker D8 in Bragg-Brentano geometry in a 2θ range of 10°-70° with a resolution of 0.03°. $Cu_{K\alpha}$ radiation ($\lambda = 1.54$ Å) and a

NaI scintillation detector were used and the sample was placed horizontally on a silicon single crystal sample holder.

Transmission electron microscopy (TEM) characterization was carried out using an EM 912 microscope (Omega/Carl-Zeiss Oberkochen) operating at 120 kV. The samples were prepared by dispersion in ethanol in an ultrasonic bath for 10 min. The dispersion was dropwise applied onto a carbon-coated copper TEM grid and dried at room temperature.

Electrochemical Measurements

The carbon materials were fabricated into free-standing electrodes by mixing them with a polytetrafluoroethylene solution (PTFE, 60% in water, Sigma-Aldrich) in a mass ratio of carbon to PTFE of 9:1. The mixture was dispersed in ethanol and homogenized for several minutes using an ultrasonic bath. The dispersion was poured on a glass plate and mixed with razor blades under air atmosphere, so that upon evaporation of the solvent a substance of a rubber-like consistency was obtained. It was dried for 4 h at 60°C, then placed on an aluminum foil and rolled to a sheet of ∼120 µm thickness (measured with a micrometer caliper) using a commercially available roll mill. Finally, the sheet was punched into freestanding circular electrodes of 10 mm diameter, which were dried at 60°C overnight. The mass of each electrode was determined before each electrochemical measurement.

Cyclic voltammetry (CV) measurements were performed in two-electrode configuration on a Biologic® MPG-2 potentiostat using Swagelok® type cells where the carbon electrodes and the separator (Dreamweaver® Silver 25, 13∼mm diameter) were sandwiched between two platinum current collectors. The areal loading can be found in **Table 1**. The cells were assembled inside a glove box with oxygen and moisture contents below 0.1 ppm. The CV measurements were carried out in potential ranges of 0-5.0 V vs. counter electrode potential at a scan rate of $\nu = 2\,\mathrm{mV\ s^{-1}}$ after the cell resistance was determined by means of electrochemical impedance spectroscopy. In the CV curves the mass specific differential capacitance C_d was plotted instead of the current, which is calculated as follows.

$$C_d = \frac{2I}{\mu\nu}$$

Here I is the measured current in A, μ is the mass of the carbon in one electrode in g, and ν is the scan rate in V s^{-1}. The factor of 2 for the capacitance calculations is left out for the three-electrode measurements. As the electrolytes 1-ethyl-3-methylimidazolium tetrafluoroborate ($EMImBF_4$, >98%, IoLiTec GmbH), 1-butyl-3-methylimidazolim tetrafluoroborate ($BMImBF_4$, >98%, IoLiTec GmbH), and 1-ethyl-3-methylimidazolium bis(trifluoromethylsulfonyl)imide (EMImTFSI, >98%, IoLiTec GmbH) were employed. The RTILs were stored over a molecular sieve (4 Å) in a glove box prior to usage.

Three-electrode cyclic voltammograms were obtained using a custom-built cell, similar to a T-shaped Swagelok cell (see **Figure S1**). The counter electrode consisted of a piece of the same carbon as the working electrode, which was oversized by two to three times. The quasi-reference electrode was prepared by coating a superP-carbon/PTFE solution similar to the one used to fabricate the electrode sheets on a piece of a metal rod following the method of Weingarth et al. The reference potential was 190 ± 10 mV vs. Fc/Fc^+ (Weingarth et al., 2014). To investigate the possible influence of contaminations of the electrolyte, the three-electrode measurements were performed in RTILs of the highest available purity grade ($EMImBF_4$ 99%, $BMImBF_4$ 99%, EMImTFSI 99.5%, all IoLiTec GmbH) which were additionally purified by vacuum drying followed by stirring over previously activated molecular sieve (3 Å) at 60°C for 72 h, according to the method of Gnahm and Kolb (2011).

RESULTS AND DISCUSSION

Characterization of the Carbon Materials

Mesoporous carbon materials were synthesized using a hard templating approach with Aerosil® 90 and Aerosil® 380 as silica templates (**Figure 1**). Those commercially available fumed silicas consist of spherical primary particles that differ in size as well as extent of agglomeration. Aerosil® 90 consists of larger primary particles and has lower specific surface area than Aerosil® 380. The Aerosil® particle size and shape has a significant impact on the resulting carbon pore size, while the template loading influences the pore volume. X-ray diffraction patterns of the carbon samples consist only of two broad peaks at $2\theta = 24°$ and 44°, demonstrating their weakly ordered structure with only minor graphitic stacking which is typical for hard-templated carbon prepared from sucrose under comparable conditions (Oschatz et al., 2014). Only in the cases of Aerosil380-1 and Aerosil90-1 small additional peaks are present at $2\theta = 18°$ (Supplementary Information, **Figure S2**). TGA analysis under air atmosphere shows an ash content of 2–4 wt% for all samples at temperatures above 600°C (**Figure S3**), indicating only minor amounts of residual template. The amount of heteroatoms such as nitrogen or sulfur is negligibly low according to elemental analysis (**Table S1**). The Raman spectra (**Figure S4**) show a D-band close to 1,340 cm^{-1} originating from the breathing mode of the six-fold sp^2-hybridized carbon rings due to the presence of disorder and defects. The width of the D-band allows conclusions about the structural order and extent of these sp^2 rings. The wide D-bands (FWHM between 146 and 171 cm^{-1}) are caused by the abundance of structurally disordered sections. Furthermore, the ordering of the carbons can be evaluated from the ratio of the D- to the G-band (I_D/I_G), which is proportional to the amount of six-membered rings. Its value is similar in all samples between 1.1 and 1.3 and does not show any trend throughout the series. Hence a comparable microstructure (thus also surface chemistry and electric conductivity) of the carbons can be assumed (Osswald et al., 2012; Pawlyta et al., 2015; Oschatz et al., 2016). This result is reasonable in view of the similar carbonization temperatures and carbon precursors applied for the synthesis of all samples.

The porosity was assessed by nitrogen physisorption at −196°C (**Table 1** and **Figure 2**). The shape of the isotherms (**Figure 2A**) can be described as type IV(a) with a H4 type hysteresis according to the IUPAC classification (Thommes et al., 2015). The hysteresis is located at higher relative pressures for Aerosil®-90-templated carbons ($0.7 < p/p_0 < 1.0$) than for

TABLE 1 | BET specific surface area (SSA), total pore volume (V_{tot}), micro-, and mesopore volumes from DFT (V_{micro} and V_{meso}), and Raman data of the Aerosil® templated carbons.

	SSA [$m^2\ g^{-1}$]	DFT pore volume		Mass loading [mg cm^2]	I_D/I_G ratio	FWHM of D-band [cm^{-1}]
		V_{micro} [$cm^3\ g^{-1}$]	V_{meso} [$cm^3\ g^{-1}$]			
Aerosil90-1	891	0.20	1.51	3.9	1.1	171
Aerosil90-2	881	0.25	0.69	5.3	1.2	164
Aerosil90-4	490	0.16	0.36	10.7	1.1	164
Aerosil380-1	1,230	0.17	2.15	2.6	1.1	146
Aerosil380-2	987	0.22	1.05	4.5	1.3	157
Aerosil380-4	567	0.15	0.41	10.5	1.2	157

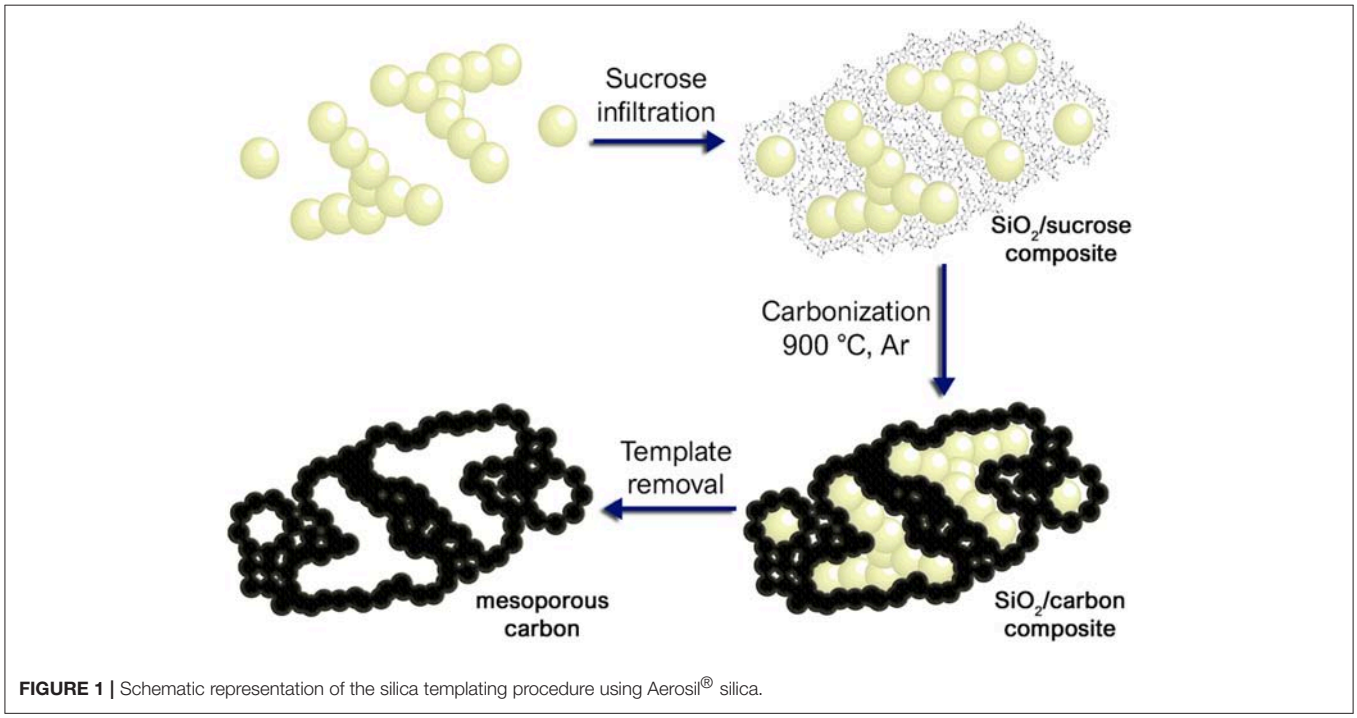

FIGURE 1 | Schematic representation of the silica templating procedure using Aerosil® silica.

Aerosil®-380-templated ones ($0.7 < p/p_0 < 0.9$). This indicates larger mesopores in carbons templated with Aerosil® 90 than in those templated with Aerosil® 380, which is in good accordance with the silica primary particle size. As expected, the pore volume increased with decreasing sucrose loading, while different silica templates led to a comparable pore volume at similar loading. There is a drastic increase of adsorbed nitrogen at relative pressures approaching 1 in the case of Aerosil90-1 and Aerosil380-1, indicating the presence of a high volume of large meso- and macropores. This is because the amount of sucrose is very low compared to that of the template, which prevents the carbon precursor to fully encapsulate the silica and finally leaves the carbons with a high fraction of macropores and external surface area. This is further supported by TEM images (**Figure 3**), where a sponge-like structure with spherical holes corresponding to the size of the silica primary particles can be seen in Aerosil90-1 as well as in Aerosil380-1, and to some extent also in Aerosil90-2 and Aerosil380-2. In contrast, the decreasing template content gives rise to the denser morphology of Aerosil90-4 and Aerosil380-4. In agreement with the gas physisorption experiments, no indications for pore blocking or closed pores are observable in the electron microscopy images of the carbon materials.

As can be seen from the differential PSD of the materials (**Figure 2B**), the mesopore diameters of Aerosil®-380- and Aerosil®-90-templated carbons are centered at around 8 nm and 16 nm, respectively. The cumulative pore volume plot (**Figure 2C**) reveals an increase of the mesopore volume with increasing template content at similar primary particle size. In general, the mesopore volume increases with the increase of the template content, and is comparable for the different kinds of templates, while the micropore (pore diameter <2 nm) volume remains low.

The microporosity of the carbon materials was investigated using CO_2 physisorption at 0°C (**Figure 4**). The isotherms of carbons with similar sucrose/silica ratios are practically identical. Carbons with a silica/sucrose ratio of two feature the highest amount of gas adsorbed, while those with a ratio of four show the

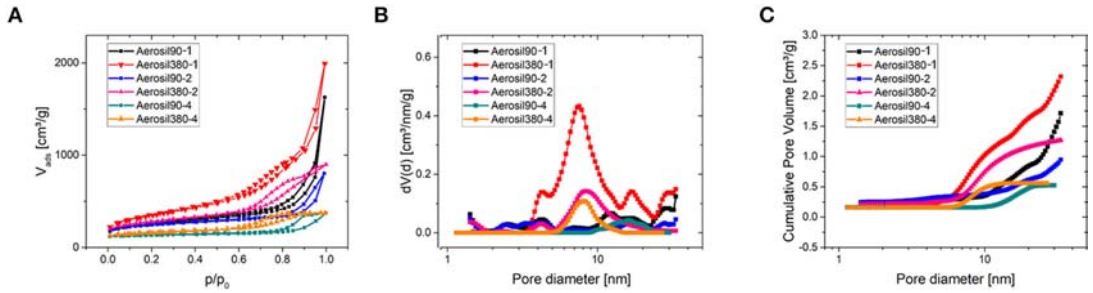

FIGURE 2 | N_2 physisorption measurements at −196°C **(A)** and corresponding differential **(B)** and cumulative **(C)** pore size distributions of Aerosil®-templated carbons.

lowest, with Aerosil*n*-1 carbons in between. In consequence, the same trend can be perceived from the cumulative pore volume plot of the pore size distribution obtained by fitting the isotherms to a NLDFT-kernel. Although the volume of narrow micropores obviously depends on the template content during the synthesis, it is vanishingly low in all samples, so the influence of micropores on the following CV measurements is expected to be negligible.

Investigations of Cooperative Ordering Transitions of Ionic Liquids in Carbon Mesopores With Cyclic Voltammetry

The structure of the electrical double layer in RTILs is fundamentally different from that of a solvent-based electrolyte. In the latter cases an applied potential causes a gathering of ions as "mirror charges" on the surface of the respective electrode and an increasing thickness and compression of the double layer with progressing potential ramp. This mechanism cannot be applied to RTIL-based electrolytes, as they are solely composed of ions without a surrounding dielectric medium (Antonietti et al., 2018). Therefore, the ions exhibit an intrinsic local structuring called *coulombic ordering*, where each ion is surrounded by a shell of counterions and the local density of ions has to be nearly the same on the electrode surface and within the bulk electrolyte. Hence, the charge storage must proceed via local ordering transitions, where ions switch their positions to conform to the applied potential. Those processes are known as *overscreening* at lower voltages, i.e., the overcompensation of the potential due to coulombic ordering, and *crowding*, i.e., the formation of multiple coion layers at the electrode/electrolyte interface due to very high voltages (Bazant et al., 2011; Kondrat et al., 2011). These and related mechanisms are widely accepted in the case of planar metallic electrodes (Fedorov and Kornyshev, 2014; Elbourne et al., 2015; Wen et al., 2015) as well as for microporous systems (Largeot et al., 2008; Futamura et al., 2017). Although they have been proposed also for mesoporous materials (in terms of ordering transitions that can propagate deep into the bulk of the electrolyte instead of being limited to the surface of the electrode materials), detailed understanding is still lacking (Antonietti et al., 2018; Yan et al., 2018).

To deduce a general relationship between the phase transition mechanism and basic mesopore properties such as their diameter and volume, the synthesized carbon materials were subjected to cyclic voltammetry using three different RTILs as electrolytes. The chosen ionic liquids are stable in a voltage window of more than 4.3 V (Zhang et al., 2018) and their decomposition is generally observed upon exceeding this voltage. However, another process seems to overlay with the degradation of the ionic liquid, which is manifested as a peak beginning at ∼3.9 V, for Aerosil90-1 and Aerosil380-1 in EMImTFSI electrolyte (**Figure 5A**). It has recently been shown that the presence of this peak strongly depends on the presence of mesopores (Antonietti et al., 2018; Yan et al., 2018). As a consequence, there is a significant increase in current observable for the highly mesoporous Aerosil®-templated carbon materials. For samples Aerosil*n*-1 and Aerosil*n*-2 the use of different template particle sizes leads to significant differences in the maximum current of the peaks and higher mesopore volumes lead to higher peak currents (**Figures 5A,B**, **Figures S5, S6**). For both pore sizes (i.e., for the Aerosil-90-*m* and the Aerosil-380-*m* series) it can be clearly seen that the maximum peak current scales with the pore volume becoming smaller for materials with higher sucrose content and thus lower pore volume. On the contrary, for samples Aerosil*n*-4 with no apparent difference in mesopore volume the peak height remains rather comparable (**Figure 5C**). In the case of Aerosil*n*-1 carbons with the largest mesopore volumes, the peaks are identical with respect to onset and peak potentials. The same observations hold for the reverse peaks. In Aerosil*n*-2 carbons the peak is sharper and higher for smaller pores, but the area remains approximately the same. The reverse peak is smeared out and does not lie completely within the measurement range for Aerosil90-2.

The onset potential and the peak area are of particular interest here, as the former is related to the enthalpy released or taken up during a physical process and the latter gives an indication about the number of units participating. While no explicit correlation between onset potential and pore diameter can be observed, the peak is generally larger in smaller mesopores. This means that even if the phenomenon behind the peak is not necessarily energetically more favored in smaller pores, it proceeds inside them to a greater extent.

In order to fix the potential at which the peak occurs, CV-measurements were conducted in a three-electrode setup with activated carbon as the quasi-reference electrode. Before each measurement the open circuit potential (OCP) of the cell was

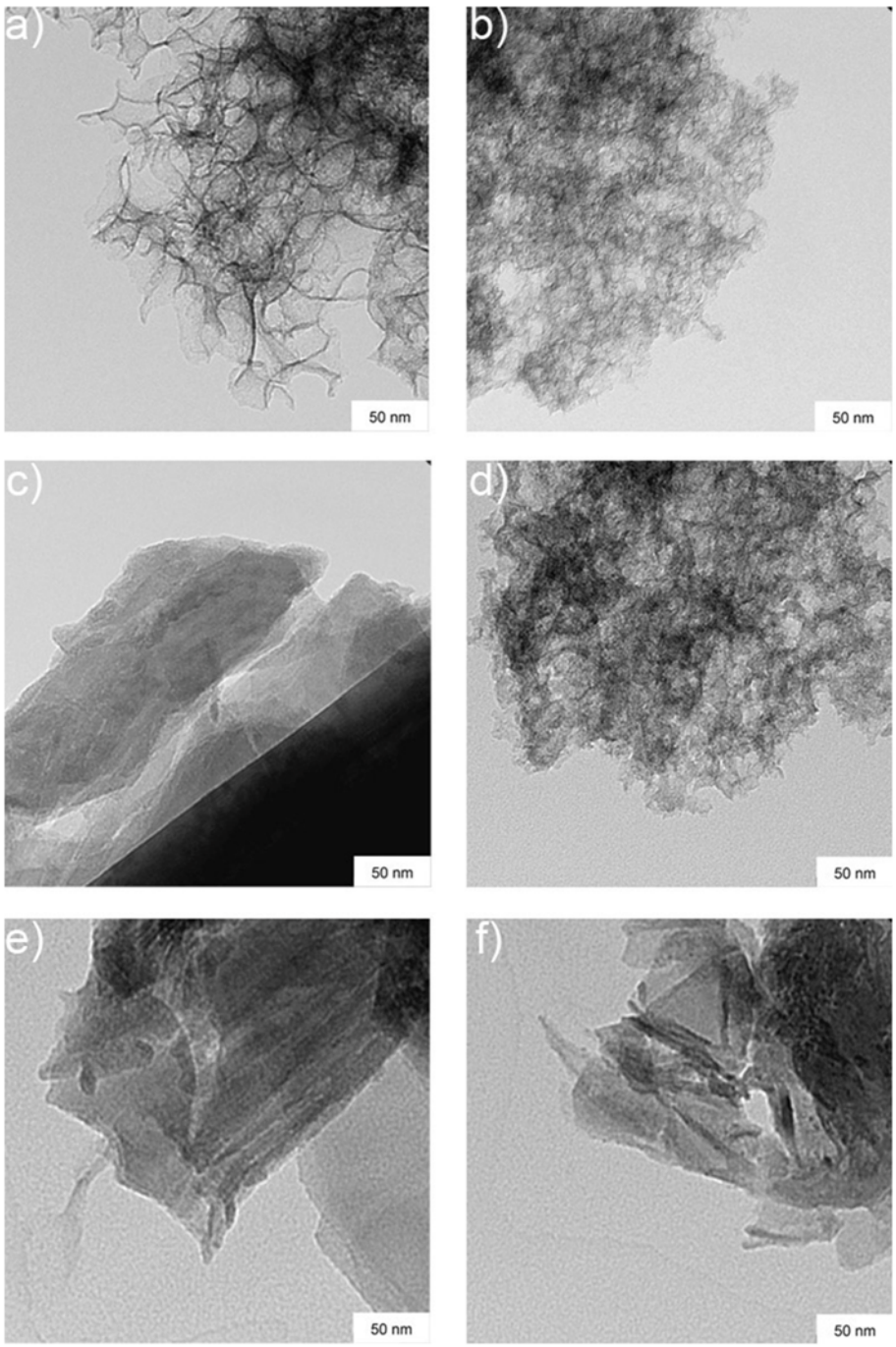

FIGURE 3 | TEM-images of Aerosil®-templated carbons. **(a)** Aerosil90-1, **(b)** Aerosil380-1, **(c)** Aerosil90-2, **(d)** Aerosil380-2, **(e)** Aerosil90-4, and **(f)** Aerosil380-4.

measured and was determined to be close to 0 V. Deviations in the order of a few tens of mVs may be due to the different dimensions of counter and working electrode. To rule out the influence of residues of halide ions and water traces, RTILs of the highest available quality were employed after an additional purification step. The forward peak is located at potentials of 2–3 V vs. activated carbon (AC) in all three investigated RTILs and can be therefore attributed to a phenomenon at the positive electrode (**Figure 6**). The differential capacitance of the peak is significantly higher and narrower with three electrodes due to the precise control of the potential. The reverse peak is furthermore better resolved in the three-electrode measurements and consists of two separate smaller peaks located at +1 and −1 V vs. AC. As the OCP is known to be approximately at 0 V it can be stated

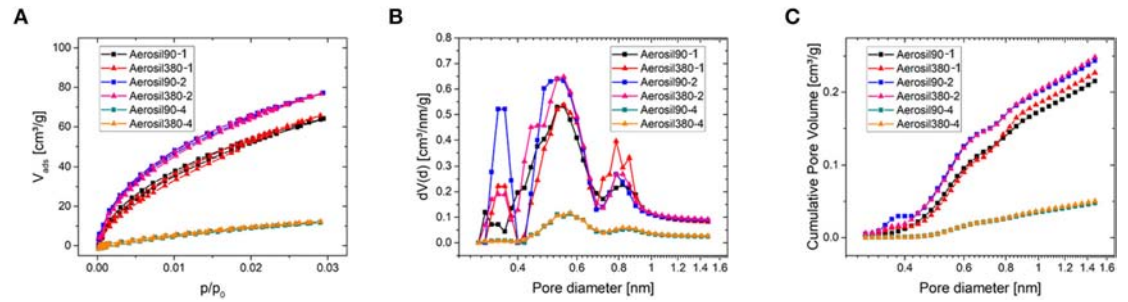

FIGURE 4 | CO_2 physisorption measurements at 0°C **(A)** and corresponding differential **(B)** and cumulative **(C)** pore size distributions of Aerosil®-templated carbons.

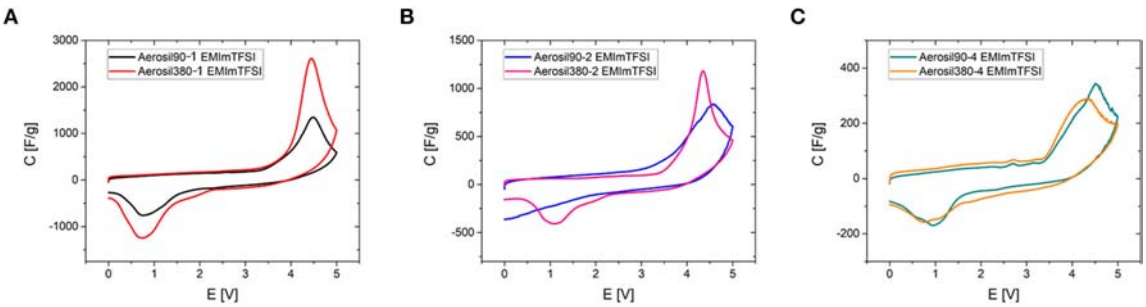

FIGURE 5 | Comparison of cyclic voltammograms of Aerosil® -templated carbons in EMImTFSI depending on pore sizes and pore volumes (0 – 5.0 V, $\nu = 2\,\text{mV s}^{-1}$). **(A)** Aerosil*n*-1, **(B)** Aerosil*n*-2, and **(C)** Aerosil*n*-4.

that the former peak appears at a positive and the latter at a negative polarization of the working electrode. Note that even the combined current of both small reverse peaks does not reach that of the large forward peak, which is most probably due to the fact that in a two-electrode measurement the sum of the currents of the processes at the positive and negative electrodes are recorded. This problem is tackled by the employment of a three-electrode cell in order to avoid any interferences arising from the counter electrode. Except for the deviation of the reverse peak, the two- and three-electrode experiments are in excellent agreement as can be seen for example in **Figure 7** or **Figure S7**, where the CVs from two-and three-electrode setups are shown, which are essentially superimposable. To finally rule out effects of decomposition and to study the behavior at negative polarization, the initial voltage window was extended to negative potentials instead of positive ones (**Figure S8**). The combined results of the study of the working electrode as both the anode and the cathode contain information similar to the measurements of van Aken et al. (2015), in our case considering explicitly the working electrode. It is evident that upon negative polarization rapid and obvious decomposition takes place inherently, which has nothing in common with the processes at positive potentials. Now, that the connection between two- and three-electrode measurements is hereby established most of the further study relies on the results from two-electrode measurements, because the simplicity and practical reliability of the two-electrode cell outweighs the advantages of the three-electrode setup.

Although these ordering transitions would be able to make a significant contribution to the increase of the energy density of supercapacitors, the overlap of the potential at which they significantly contribute to the capacitance with the onset potential of electrochemical electrolyte/electrode degradation currently limits the reversibility of this process. The first seven CV cycles in a potential range of 0-5 V have been measured for Aerosil380-4 with $EMImBF_4$ and EMImTFSI as the electrolyte (**Figure 8**). In the first cycle the CVs are generally of a similar appearance, featuring a constant differential specific capacitance of around $100\,\text{F g}^{-1}$ until ∼3.3 V, which is typical for a predominantly mesoporous supercapacitor electrode material operated in such electrolytes. The current and thus differential capacitance then increases drastically to yield a signal with a peak at ∼4.4 V. The peak is obviously found in addition to the degradation of the electrolyte. On the reverse scan another peak can be measured at a cell voltage of 1.5–1.0 V with a slightly lower peak current. During the following cycles, decay in peak current can be observed in the forward and backward scans (**Figure 8C**). Additionally the peak potential of the backward peak is shifted toward lower voltages in the case of $EMImBF_4$. For EMImTFSI both peaks are much smaller in current and exhibit a significantly different behavior during cycling. The forward signal splits into two peaks in the second cycle, where one appears at lower and one at higher potential by ∼0.5 V. The same happens to the reverse peak. During the subsequent cycles both signals diminish and are no longer present in the seventh iteration. The same CV profiles are observed for the RTILs independent of the pore diameter and volume of the carbon electrode. The comparable peak current of the respective forward and reverse peaks pleads for an at least partial reversibility of the process, while the unusually large peak

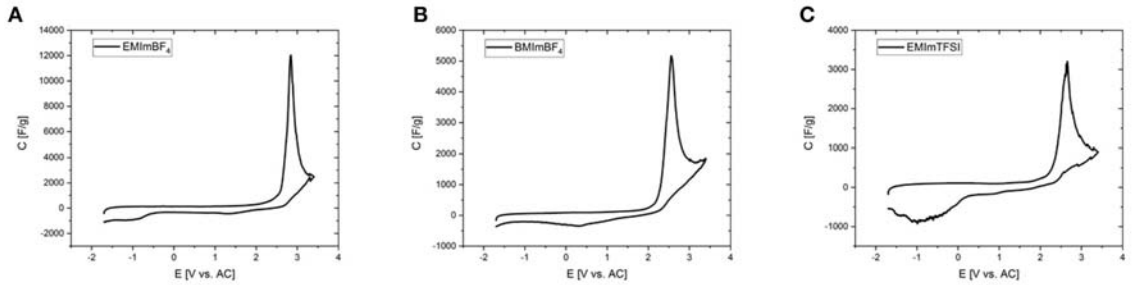

FIGURE 6 | Cyclic voltammograms of the investigated RTILs with Aerosil90-2 as the electrodes in a three-electrode setup (0 – 5.0 V, $\nu = 2\,\text{mV s}^{-1}$). **(A)** $EMImBF_4$, **(B)** $BMImBF_4$, and **(C)** EMImTFSI.

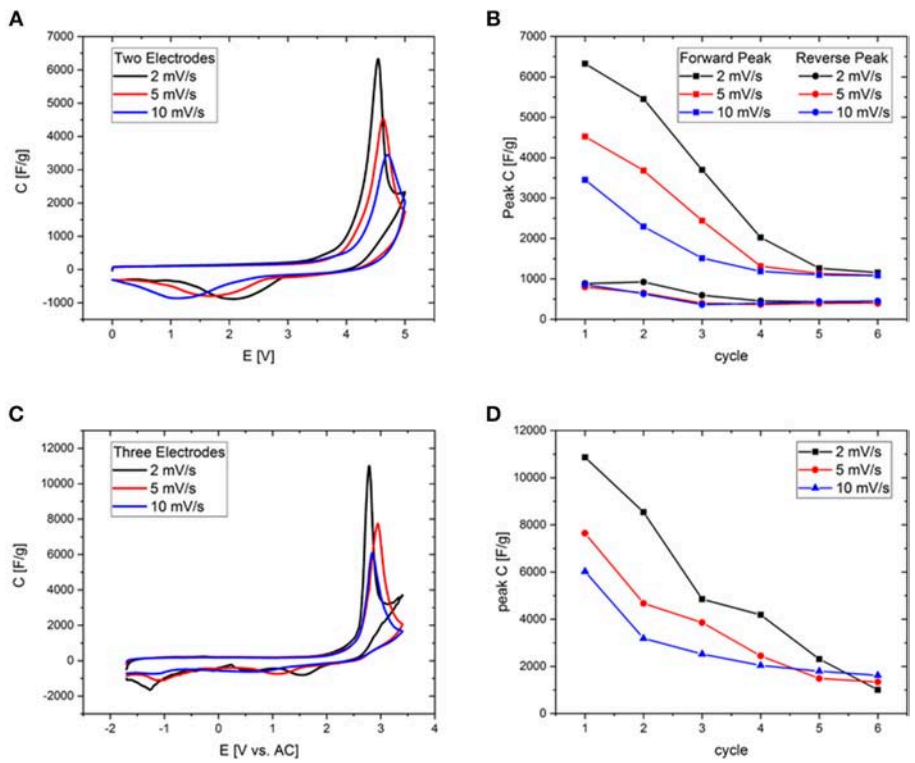

FIGURE 7 | (A,C) Cyclic voltammograms of Aerosil380-1 in $EMImBF_4$ in a potential range of 0–5 V at scan rates of 2, 5, and 10 mV s^{-1}. **(B,D)** Comparison of forward peak current evolution during cycling at different scan rates. **(A,B)** Measured in two-electrode-, **(C,D)** in three-electrode setup.

separation of several volts further count against a classical redox reaction as the origin of the signal. This reversible character shows that it might indeed be possible to use the contribution of these ordering transitions for energy storage also in real world supercapacitor devices. For the phase transitions to be applicable in practice, their occurrence must be decoupled from the unwanted degradation of the electrolyte. In an attempt to study the processes separately from each other, two- and three-electrode measurements have been carried out at different scan rates with Aerosil380-1 in $EMImBF_4$ as the electrolyte. Due to the most probably different reaction rates of the decomposition and phase transition, the two mechanisms should respond in a distinct fashion. The graphs have again been normalized to the scan rate (**Figures 7A,C**) and the results are discussed in terms of differential capacitances. With increasing scan rate the peak height of the forward scan diminishes and the potential is slightly shifted toward more positive values. The large reverse peak is again not observed in the three electrode measurement, but the two small ones can be found in all three CVs and appear at more negative potentials. The behavior of the forward peak during cycling is as well remarkable (**Figure S7**). After the first four cycles at 2 mV s^{-1} the peak differential capacitance already has significantly diminished. While in the two-electrode measurements the peak potential does not alter much, already

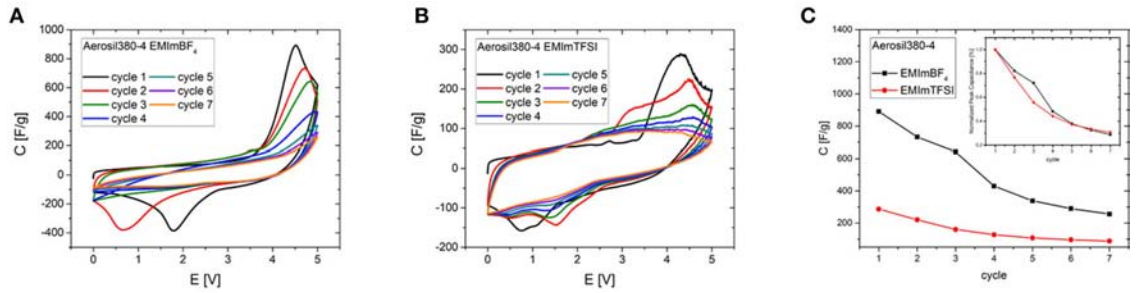

FIGURE 8 | First seven CV cycles of Aerosil380-4 **(A)** in $EMImBF_4$ and **(B)** in EMImTFSI (0-5.0 V, $\nu = 2\,mV\,s^{-1}$) and **(C)** comparison of peak currents during cycling.

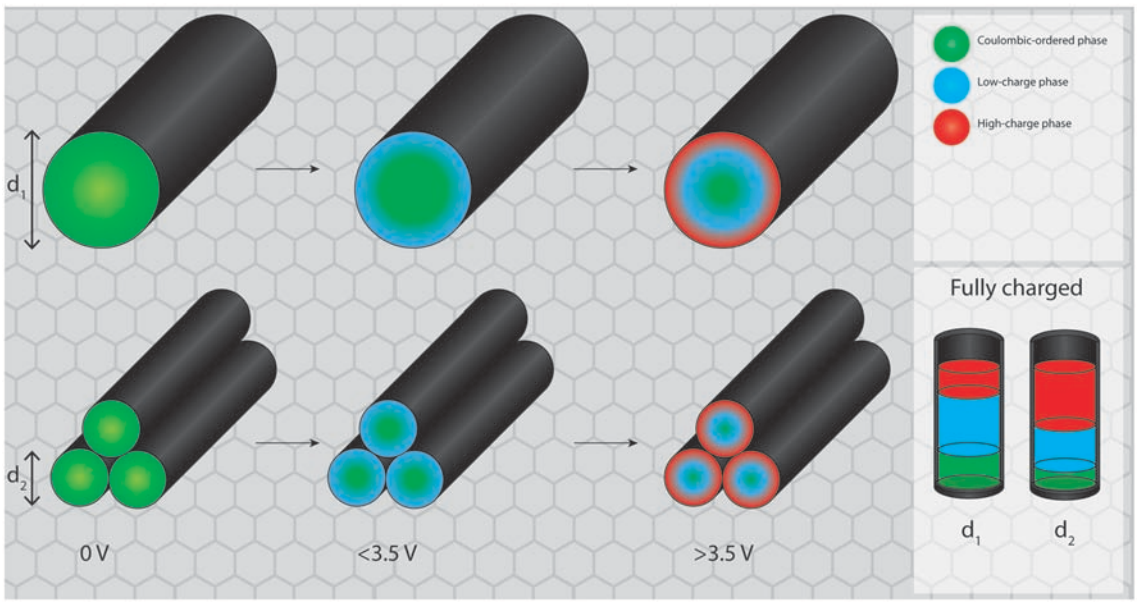

FIGURE 9 | Proposed mechanism for potential induced phase transitions in larger and smaller mesopores. While the total pore volume remains equal for both systems, the fraction of RTIL reorganized into the high charge state is higher in smaller mesopores.

at the fifth and sixth cycles the peak is shifted by almost 1 V to lower potentials in the three electrode setup. At 5 mV s^{-1} already in the second cycle the peak splits in two and at 10 mV s^{-1} the signals maximum monotonously decreases throughout the experiment. If the peak differential capacitances vs. cycle number are compared it becomes apparent that for higher scan rates the decay is less steep and those measurements finally retain slightly higher peak capacitances (**Figures 7B,D**). The reverse peak in the two electrode measurements diminishes and remains constant almost irrespective of the scan rate. Therefore, it is finally necessary to find a way to shift the onset potential of the phase transition to lower values by influencing the nucleation process via the RTIL-surface interactions either by porosity or surface chemistry of the electrode material or by adjusting the properties of the ionic liquid itself.

The analogy to capillary condensation in gas adsorption can be considered here for illustrative purposes with the adsorption potential here corresponding to the electrochemical potential on the electrode surface (**Figure 9**). While on a flat surface the newly formed high-potential RTIL phase (provided that the formation of such a phase is favorable outside of a porous environment) would propagate semi-infinitely into the bulk of the electrolyte, in a porous system the electrode surface at a certain distance is opposed by the other side of the pore wall. Therefore, after the new phase nucleates at the electrode surface, the phase transition proceeds from both pore walls into the center of the pore. The newly formed phase meets somewhere in between the walls, which happens at lower potentials in smaller mesopores. By these means the conversion of the regular RTIL phase into the high-potential phase can be achieved faster in smaller mesopores at equal pore volumes. These results thereby imply that making mesopores even larger will probably not result in a better utilization of the discussed structural rearrangement for energy storage, as the potential required to induce the ordering transitions is apparently independent of the pore size. On the basis of the carbon materials used in the present and in prior

studies, the optimum is most likely located between ∼4 and 10 nm. The reason for the existence of a lower limit of the mesopore size for the phase transition is that a certain amount of RTIL bulk must be accommodated inside of the pore to enable bulk effects.

To emphasize the interplay of pore volume and different RTILs, the CV curves in different RTIL electrolytes are compared (**Figure 10**). The peak obviously scales up with the mesopore volume in all cases and is broader for the same RTIL for the Aerosil-90®-templated carbons which is likely to be a consequence of their broader pore size distribution. This clear correlation between the mesopore volume and the discussed CV peak indicates that the phase transition takes place inside the carbon mesopores. A notable observation can be made in the supercapacitors operated with $EMImBF_4$ electrolyte and Aerosil380-1 and Aerosil-380-2 carbons as the electrode materials (**Figure 10B**). In these cases a clear local minimum in current is observed between the peak caused by the ordering transitions and the current caused by electrolyte degradation which further proves the presence of two overlapping processes in this potential range. Comparing different RTILs in similar materials, the peak is smaller for $BMImBF_4$ (**Figures 10C,D**) as compared to $EMImBF_4$ (**Figures 10A,B**) for both template sizes. Comparing $EMImBF_4$ (**Figures 10A,B**) and EMImTFSI (**Figures 10E,F**), the former is showing higher peak currents. As mentioned above, the peak area indicates the number of chemical

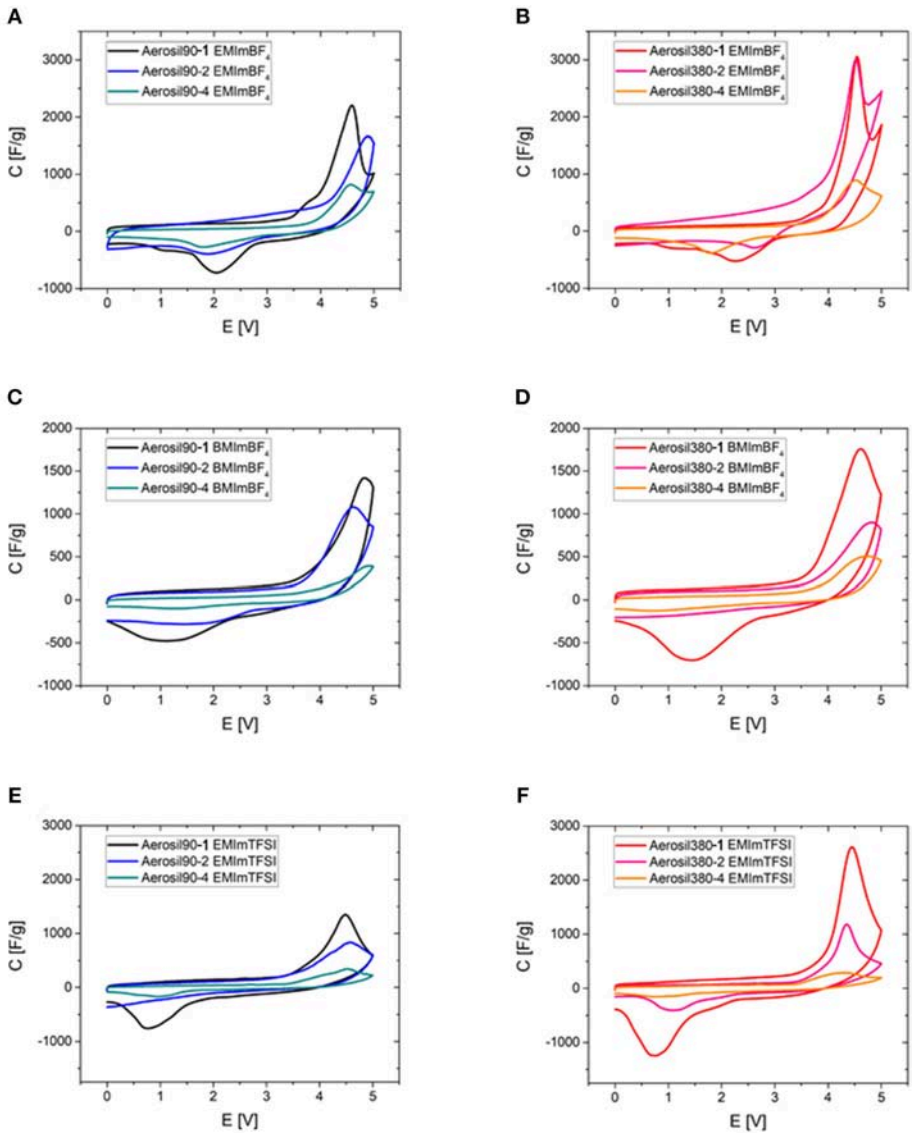

FIGURE 10 | Cyclic voltammograms of Aerosil®-templated carbons of different pore sizes depending on their pore volume in all three investigated ionic liquids (0–5.0 V, $\nu = 2\,mV\,s^{-1}$). **(A)** Aerosil90-*m* $EMImBF_4$, **(B)** Aerosil380-*m* $EMImBF_4$, **(C)** Aerosil90-*m* $BMImBF_4$, **(D)** Aerosil380-*m* $BMImBF_4$, **(E)** Aerosil90-*m* EMImTFSI, and **(F)** Aerosil380-*m* EMImTFSI.

events or, in other words, the number of RTIL ions participating in the ordering transitions in the limited mesopore volume. It appears thus logical that RTILs with smaller ions lead to higher peak areas and maximum peak currents. Finally, it should also be pointed out that from the data shown here it becomes apparent that the current caused by electrolyte decomposition also scales with mesoporosity and surface area. As expected, high mesoporosity will not only allow for an increase of the number of ordering transitions within the bulk of the electrolyte, but also speeds up electrolyte degradation on the carbon electrode surface. The same trend can be observed, when purified RTIL is employed in a three-electrode cell (**Figure S9**).

CONCLUSION

Carbon materials with two prevailing mesopore diameters were synthesized with different mesopore volumes by using silica templates with different primary particle sizes and different ratios between carbon precursor and template. They were used as supercapacitor electrodes to investigate the influence of mesopore structure on the potential-dependent liquid phase transition of RTILs under practically relevant conditions. This phenomenon takes place at the positive electrode of the cell and has obvious similarities with the capillary condensation which is widely known from the field of gas adsorption in mesoporous materials. It is found that the phase-transition peak current is more prominent for carbons with smaller mesopores centered at 8 nm, therefore the rearrangement is concluded to propagate from the pore walls into the bulk electrolyte. A clear correlation to the carbon mesopore volume was found. Higher mesopore volume clearly leads to higher peak areas and currents, indicating that the origin of the peak must indeed be a process inside of the mesopores of the electrode. Because the charge flow is the higher the more ions undergo a phase transition, there is an obvious correlation of peak height and the size of the involved electrolyte ions. These phase transitions are reversible, but as the potential range in which they significantly contribute to capacitance overlaps with the potential range in which electrolyte/electrode system decomposition occurs, decreasing contribution of the phase transition and generally decreased performance of the supercapacitors is observed upon continued cycling. Indications toward the competition between decomposition and the phase transition process have been found and more importantly, the two mechanisms can be separated by application of different scan rates, where the RTIL rearrangement is amplified at higher rates. This property could be beneficial for further applications.

These findings support the presence and contribution of RTIL phase transitions to the energy storage mechanism in supercapacitors and encourage the systematic design of mesopores rather than micropores to enhance the energy density of such devices, by incorporation of new energy storage terms. It is our belief that it is possible to shift the potential needed to utilize this phase change to lower values in order to utilize it more efficiently without electrolyte degradation by controlling the nucleation process of the non-equilibrium phase of the electrolyte by either the properties of RTIL ions or the textural and/or chemical properties of the carbon electrodes.

AUTHOR CONTRIBUTIONS

KS and RY designed and carried out synthetic experiments, analyzed and discussed data, and wrote the paper. MA, CR, and MO designed experiments, discussed data, and wrote the paper.

FUNDING

Financial support by the Max Planck Society is gratefully acknowledged. RY acknowledges financial support from China Scholarship Council.

ACKNOWLEDGMENTS

The authors thankfully acknowledge Antje Völkel for the careful conduction of the thermal analysis and Heike Runge for the assistance during the TEM measurements. The authors would also like to thank Qing Qin for measuring Raman Spectra.

SUPPLEMENTARY MATERIAL

The Supplementary Material for this article can be found online at: https://www.frontiersin.org/articles/10.3389/fmats.2019.00065/full#supplementary-material

REFERENCES

Antonietti, M., Chen, X., Yan, R., and Oschatz, M. (2018). Storing electricity as chemical energy: beyond traditional electrochemistry and double-layer compression. *Energy Environ. Sci.* 11, 3069–3074. doi: 10.1039/C8EE01723A

Bazant, M. Z., Storey, B. D., and Kornyshev, A. A. (2011). Double layer in ionic liquids: overscreening versus crowding. *Phys. Rev. Lett.* 106:046102. doi: 10.1103/PhysRevLett.106.046102

Béguin, F., Presser, V., Balducci, A., and Frackowiak, E. (2014). Carbons and electrolytes for advanced supercapacitors. *Adv. Mater.* 26, 2219–2251. doi: 10.1002/adma.201304137

Borchardt, L., Oschatz, M., and Kaskel, S. (2014). Tailoring porosity in carbon materials for supercapacitor applications. *Mater. Horiz.* 1, 157–168. doi: 10.1039/C3MH00112A

Brandt, A., Pohlmann, S., Varzi, A., Balducci, A., and Passerini, S. (2013). Ionic liquids in supercapacitors. *MRS Bull.* 38, 554–559. doi: 10.1557/mrs.2013.151

Choi, N.-S., Chen, Z., Freunberger, S. A., Ji, X., Sun, Y.-K., Amine, K., et al. (2012). Challenges Facing Lithium Batteries and Electrical Double-Layer Capacitors. *Angew. Chem. Int. Ed.* 51, 9994–10024. doi: 10.1002/anie.201201429

Elbourne, A., Mcdonald, S., Voïchovsky, K., Endres, F., Warr, G. G., and Atkin, R. (2015). Nanostructure of the ionic liquid–graphite stern layer. *ACS Nano* 9, 7608–7620. doi: 10.1021/acsnano.5b02921

Fedorov, M. V., and Kornyshev, A. A. (2014). Ionic liquids at electrified interfaces. *Chem. Rev.* 114, 2978–3036. doi: 10.1021/cr400374x

Futamura, R., Iiyama, T., Takasaki, Y., Gogotsi, Y., Biggs, M. J., Salanne, M., et al. (2017). Partial breaking of the Coulombic ordering of ionic liquids confined in carbon nanopores. *Nat. Mater.* 16, 1225–1232. doi: 10.1038/nmat4974

Gnahm, M., and Kolb, D. M. (2011). The purification of an ionic liquid. *J. Electr. Chem.* 651, 250–252. doi: 10.1016/j.jelechem.2010.11.019

González, A., Goikolea, E., Barrena, J. A., and Mysyk, R. (2016). Review on supercapacitors: technologies and materials. *Renew. Sustain. Energy Rev.* 58, 1189–1206. doi: 10.1016/j.rser.2015.12.249

Jun, S., Joo, S. H., Ryoo, R., Kruk, M., Jaroniec, M., Liu, Z., et al. (2000). Synthesis of new, nanoporous carbon with hexagonally ordered mesostructure. *J. Am. Chem. Soc.* 122, 10712–10713. doi: 10.1021/ja002261e

Kiyohara, K., Sugino, T., and Asaka, K. (2011). Phase transition in porous electrodes. *J. Chem. Phys.* 134:154710. doi: 10.1063/1.3578468

Kondrat, S., Georgi, N., Fedorov, M. V., and Kornyshev, A. A. (2011). A superionic state in nano-porous double-layer capacitors: insights from Monte Carlo simulations. *Phys. Chem. Chem. Phys.* 13, 11359–11366. doi: 10.1039/c1cp20798a

Lai, F., Feng, J., Yan, R., Wang, G.-C., Antonietti, M., and Oschatz, M. (2018). Breaking the limits of ionic liquid-based supercapacitors: mesoporous carbon electrodes functionalized with manganese oxide nanosplotches for dense, stable, and wide-temperature energy storage. *Adv. Funct. Mater.* 28:1801298. doi: 10.1002/adfm.201801298

Largeot, C., Portet, C., Chmiola, J., Taberna, P.-L., Gogotsi, Y., and Simon, P. (2008). Relation between the ion size and pore size for an electric double-layer capacitor. *J. Am. Chem. Soc.* 130, 2730–2731. doi: 10.1021/ja7106178

Macfarlane, D. R., Tachikawa, N., Forsyth, M., Pringle, J. M., Howlett, P. C., Elliott, G. D., et al. (2014). Energy applications of ionic liquids. *Energy Environ. Sci.* 7, 232–250. doi: 10.1039/C3EE42099J

Manthiram, A. (2017). An outlook on lithium ion battery technology. *ACS Central Sci.* 3, 1063–1069. doi: 10.1021/acscentsci.7b00288

Merlet, C., Rotenberg, B., Madden, P. A., Taberna, P.-L., Simon, P., Gogotsi, Y., et al. (2012). On the molecular origin of supercapacitance in nanoporous carbon electrodes. *Nat. Mater.* 11, 306–310. doi: 10.1038/nmat3260

Oschatz, M., Boukhalfa, S., Nickel, W., Lee, J. T., Klosz, S., Borchardt, L., et al. (2014). Kroll-carbons based on silica and alumina templates as high-rate electrode materials in electrochemical double-layer capacitors. *J. Mater. Chem. A* 2, 5131–5139. doi: 10.1039/c3ta14815g

Oschatz, M., Pr,é, P., Dörfler, S., Nickel, W., Beaunier, P., Rouzaud, J.-N., et al. (2016). Nanostructure characterization of carbide-derived carbons by morphological analysis of transmission electron microscopy images combined with physisorption and Raman spectroscopy. *Carbon N. Y.* 105, 314–322. doi: 10.1016/j.carbon.2016.04.041

Osswald, S., Chmiola, J., and Gogotsi, Y. (2012). Structural evolution of carbide-derived carbons upon vacuum annealing. *Carbon N. Y.* 50, 4880–4886. doi: 10.1016/j.carbon.2012.06.016

Pawlyta, M., Rouzaud, J.-N., and Duber, S. (2015). Raman microspectroscopy characterization of carbon blacks: spectral analysis and structural information. *Carbon N. Y.* 84, 479–490. doi: 10.1016/j.carbon.2014.12.030

Postnov, V. N., Peretrukhina, Y. V., and Novikov, A. G. (2013). A porous carbon material prepared by template synthesis using Aerosil. *Russian J. Appl. Chem.* 86, 662–666. doi: 10.1134/S1070427213050091

Rotenberg, B., and Salanne, M. (2015). Structural transitions at ionic liquid interfaces. *J. Phys. Chem. Lett.* 6, 4978–4985. doi: 10.1021/acs.jpclett.5b01889

Salanne, M. (2017). Ionic liquids for supercapacitor applications. *Top. Curr. Chem.* 375:63. doi: 10.1007/s41061-017-0150-7

Salanne, M., Rotenberg, B., Naoi, K., Kaneko, K., Taberna, P. L., Grey, C. P., et al. (2016). Efficient storage mechanisms for building better supercapacitors. *Nat. Energy* 1:16070. doi: 10.1038/nenergy.2016.70

Simon, P., and Gogotsi, Y. (2008). Materials for electrochemical capacitors. *Nat. Mater.* 7, 845–854. doi: 10.1038/nmat2297

Simon, P., and Gogotsi, Y. (2013). Capacitive energy storage in nanostructured carbon–electrolyte systems. *Acc. Chem. Res.* 46, 1094–1103. doi: 10.1021/ar200306b

Tazi, S., Salanne, M., Simon, C., Turq, P., Pounds, M., and Madden, P. A. (2010). Potential-induced ordering transition of the adsorbed layer at the ionic liquid/electrified metal interface. *J. Phys. Chem. B* 114, 8453–8459. doi: 10.1021/jp1030448

Thommes, M., Kaneko, K., Neimark, A. V., Olivier, J. P., Rodriguez-Reinoso, F., Rouquerol, J., et al. (2015). Physisorption of gases, with special reference to the evaluation of surface area and pore size distribution (IUPAC Technical Report). *Pure Appl. Chem.* 87, 1051–1069. doi: 10.1515/pac-2014-1117

van Aken, K. L., Beidaghi, M., and Gogotsi, Y. (2015). Formulation of ionic-liquid electrolyte to expand the voltage window of *supercapacitors*. *Angew. Chem. Int. Ed. Engl.* 54, 4806–4809. doi: 10.1002/anie.201412257

Weingarth, D., Zeiger, M., Jäckel, N., Aslan, M., Feng, G., and Presser, V. (2014). Graphitization as a universal tool to tailor the potential-dependent capacitance of carbon supercapacitors. *Adv. Energy Mater.* 4:1400316. doi: 10.1002/aenm.201400316

Wen, R., Rahn, B., and Magnussen, O. M. (2015). Potential-dependent adlayer structure and dynamics at the ionic Liquid/Au(111) interface: a Molecular-Scale *in situ* Video-STM study. *Angew. Chem. Int. Ed.* 54, 6062–6066. doi: 10.1002/anie.201501715

Yan, R., Antonietti, M., and Oschatz, M. (2018). Toward the experimental understanding of the energy storage mechanism and ion dynamics in ionic liquid based supercapacitors. *Adva. Energy Mater.* 8:1800026. doi: 10.1002/aenm.201800026

Zhang, S., Brahim, S., and Maat, S. (2018). High-voltage operation of binder-free CNT supercapacitors using ionic liquid electrolytes. *J. Mater. Res.* 33, 1179–1188. doi: 10.1557/jmr.2017.455

Conflict of Interest Statement: The authors declare that the research was conducted in the absence of any commercial or financial relationships that could be construed as a potential conflict of interest.

frontiers in Materials

ORIGINAL RESEARCH
published: 04 June 2019
doi: 10.3389/fmats.2019.00129

An Ion-Sensitive Field Effect Transistor Using Metal-Coordinated Zeolite-Templated Carbons as a Three-Dimensional Graphene Nanoribbon Network

*Takafumi Ishii, Akihiro Horiuchi and Jun-ichi Ozaki**

Faculty of Science and Technology, International Research and Education Center for Element Science, Gunma University, Kiryu, Japan

Zeolite template carbon (ZTC) is a carbon material composed of a three-dimensional network of graphene nanoribbons (GNR), and thus, is expected to exhibit electronic characteristics identical to those of GNR. ZTC is capable of doping heteroatoms in its structure, which offers the advantage of controlling its electronic properties by the presence of the heteroatoms. In this study, we prepared heteroatom-doped ZTCs and applied them to an ion-sensitive field effect transistor (ISFET), for investigating the effect of heteroatom doping on its electronic properties. The ISFET characteristics of un-doped ZTC include bipolarity, whereas oxygen-doped ZTC shows p-type semiconductor characteristics, and nitrogen-doped ZTC shows n-type characteristics. Furthermore, copper and nitrogen co-doped ZTC exhibits high sensor sensitivity (the change of electric conductivity reaches up to 50%) as a carbon-based ISFET. As a result of the analytical evaluation, a copper-nitrogen complex is formed in the co-doped ZTC, and the electronic interaction between copper and nitrogen atoms is able to change electrochemically. Owing to the presence of the copper-nitrogen complex, the co-doped ZTC shows specific ISFET characteristics.

Keywords: zeolite-templated carbon, doped carbon, graphene nanoribbon, ion sensor, ISFET

OPEN ACCESS

Edited by:
Wee-Jun Ong,
Xiamen University, Malaysia

Reviewed by:
Shun Mao,
Tongji University, China
Che Azurahanim Che Abdullah,
Putra Malaysia University, Malaysia

****Correspondence:***
Jun-ichi Ozaki
jozaki@gunma-u.ac.jp

Specialty section:
This article was submitted to Carbon-Based Materials, a section of the journal Frontiers in Materials

Received: *28 February 2019*
Accepted: *16 May 2019*
Published: *04 June 2019*

Citation:
Ishii T, Horiuchi A and Ozaki J (2019) An Ion-Sensitive Field Effect Transistor Using Metal-Coordinated Zeolite-Templated Carbons as a Three-Dimensional Graphene Nanoribbon Network. Front. Mater. 6:129. doi: 10.3389/fmats.2019.00129

INTRODUCTION

An ion-sensitive field effect transistor (ISFET) is expected to be a novel sensor device for electrically detecting ions and has been applied to biosensors (Mao et al., 2017; Chen et al., 2018, 2019; Syu et al., 2018), pH sensors (Duroux et al., 1991), etc. Silicon based materials are generally used as the channel material of the ISFET (Martinoia et al., 2005); however, it has an issue in that the sensitivity is lowered by an oxide film formed on its surface. Graphene nanoribbon (GNR) has attracted attention as a channel material to replace silicon (Ahmadi et al., 2016). GNR is a graphene sheet with its width reduced to the order of nanometers. Unlike graphene, GNR shows high sensitivity as a channel material of ISFET because of having a band gap (Zhang and Cui, 2013). The electronic state of GNR is influenced by the edge sites of the graphene sheet and the doping of heteroatoms. This is explained by the localization of π electrons to the edge sites (Bronner et al., 2012) and the electron attraction/donation action (Yu et al., 2010; Wang et al., 2014) in the π electron system

caused by the presence of heteroatoms. These phenomena make it possible to control the electronic properties of GNR such as by managing its band gap formation or changing its Dirac point (Wang et al., 2014). Although GNR is considered to be a promising channel material to overcome the shortcomings of silicon, there are many problems associated with its practical application as an ISFET. For synthesis of GNR, precise and high-cost techniques are required, such as an electron beam lithography (Bai and Huang, 2010) and carbon nanotube incision (Kosynkin et al., 2009). In addition, GNR has a problem in that the current flowing in the channels is too small, even as compared with graphene and silicon, because of its smaller channel area.

We focused on zeolite-templated carbon (ZTC) (Nishihara and Kyotani, 2018) as a novel carbon material for replacing GNR in this study. ZTC is composed of a three-dimensional network of GNR with a width of approximately 1 nm and the pore size is uniform at approximately 1.2 nm (Nishihara and Kyotani, 2018). Because of its three-dimensional network of GNR, ZTC is expected to increase the detected current value in ISFET, while maintaining the same sensitivity as GNR. ZTC does not require expensive processes such as lithography for its synthesis and can be industrially manufactured at a low cost. Moreover, GNR is obtained by a "top-down" approach of chopping graphene, whereas ZTC is prepared by a "bottom-up" approach of template carbonization using a chemical vapor deposition (CVD) method. When doping heteroatoms in GNR, structural geometries are easily changed. However, in the case of ZTC, it is possible to freely select a carbon source for template carbonization, and by using the source containing heteroatoms, doping of heteroatoms can be achieved while the structure is controlled. This means that ZTC has the possibility of developing various electronic properties due to heteroatom-doping. Till date, ZTC has reportedly been applied to electrochemical electrodes (Itoi et al., 2011, 2014, 2016; Berenguer-Murcia et al., 2013; Nueangnoraj et al., 2015) and gas storage materials (Nishihara et al., 2014; Itoi et al., 2017); however, its electronic states or semiconductor characteristics have not been reported. Similar to GNR, if ZTC functions as an ISFET, ZTC can be used as a novel industrially applicable carbon material having GNR characteristics.

In this study, we investigated the possibility of ZTC composed of a GNR three-dimensional network as a novel channel material of graphene for ISFET channel material. ZTC doped with typical and transition metal elements was prepared, and the influence of the presence of these heteroatoms on ISFET characteristics was evaluated. We tried to clarify the principle of the heteroatoms involved in ISFET characteristics of ZTC by investigating the chemical state of them.

EXPERIMENTAL

Sample Preparation

Preparation of ZTC and Oxidized ZTC

ZTC was synthesized using Y-type zeolite (HSZ-320NAA, Na cation type, Tosoh Corp.) as a template. The zeolite was vacuum-dried at 150°C for 48 h. Furfuryl alcohol (FA) was added dropwise to the dried zeolite powder, and then left standing overnight at room temperature under vacuum. After the excess FA was washed with mesitylene approximately 5 times, a FA/zeolite composite was obtained by suction filtration. This composite was heat-treated at 80°C for 48 h under nitrogen flow, and then heat-treated at 150°C for 8 h. Thereafter, the composite was carbonized by heating it to 800°C under nitrogen flow. Propylene (2 vol.% in N_2) was allowed to flow for 4 h while maintaining the temperature at 800°C, and a further carbon source was filled in the zeolite pores to obtain a carbon/zeolite composite. The obtained composite was subjected to wet pulverization treatment in agate mortar with methanol for 30 min. The zeolite template included in the composite was removed with 47 wt. % hydrofluoric acid to obtain a ZTC sample. The obtained ZTC with FA and propylene as a carbon source is named P-ZTC.

For preparing oxygen doped ZTC, P-ZTC was sandwiched between gold mesh electrodes, and an electrochemical oxidation treatment was carried out using a three-electrode cell. A reversible hydrogen electrode (RHE) was used for the reference electrode, Pt was used for the counter electrode, a sample electrode was used for the working electrode, and 0.5 mol L^{-1} H_2SO_4 was used for the electrolyte. The electrochemical oxidation treatment was carried out by maintaining the working electrode potential at 2.5 V vs. the RHE for 200 s. The sample after the electrochemical oxidation is called Ox-ZTC.

Preparation of Nitrogen-Doped ZTC

Acetonitrile (ACN) was added dropwise to the dried zeolite powder, and left standing overnight at room temperature under vacuum. After washing the excess ACN with mesitylene approximately 5 times, an ACN/zeolite composite was obtained by suction filtration. Heat treatment was performed at 60°C for 48 h under a nitrogen flow, and then the ACN was carbonized by heating it to 800°C under a nitrogen flow. While maintaining the temperature of 800°C, ACN (3 vol. % in N_2) was passed for 6 h. The zeolite template was removed by the same operation as P-ZTC to obtain a nitrogen-doped ZTC sample, called N-ZTC.

Preparation of Copper-Doped ZTC

Sodium ions are present as exchange cations for the zeolite used as a template. This exchange cation was ion-exchanged to Cu^{2+} as follows. Ion exchange was carried out by dispersing 5 g of the zeolite in 100 ml of 0.3 mol L^{-1} aqueous solution of $CuCl_2$, and stirring at 90°C for 1 h using a hot stirrer. The ion-exchanged zeolite was suction-filtered and washed with distilled water. The pristine zeolite, a white powder, turns blue by copper ion exchange. Using the prepared ion-exchanged zeolite as a template, a ZTC sample was prepared in the same manner as mentioned in section Preparation of ZTC and oxidized ZTC, and is named Cu-ZTC. Nitrogen-doped ZTC samples were also prepared using the ion-exchanged zeolite as a template according to the method in section Preparation of nitrogen-doped ZTC, and are denoted as Cu-N-ZTC.

Characterization

Structural Analysis

The crystal structures of the prepared ZTC samples were evaluated using X-ray diffraction (XRD, XRD-6100, Cu-Kα, SHIMADZU Corp.). In order to evaluate the specific surface

area and pore structure of the sample, nitrogen adsorption measurement at −196°C was carried out using an automatic surface area analyzer (BELSORP MAX, Microtrac BEL Corp.). As a pretreatment, the sample was heat-treated at 150°C for 2 h under vacuum. From the resulting nitrogen adsorption isotherm, the specific surface area was determined by applying the Brunauer-Emmett-Teller (BET) theory. The range of the BET plot was $P/P_0 = 0.01$ to 0.05. The total pore volume of each sample was obtained from the nitrogen adsorption amount of $P/P_0 = 0.98$. The pore size distribution curves and micropore volumes were obtained by the density functional theory (DFT) and MP methods, respectively. The microstructure and element distribution of the sample were evaluated by high-angle annular dark-field scanning transmission microscopy (STEM-HAADF) and energy dispersive X-ray spectroscopy (EDS) measurement. A single atom analysis electron microscope (JEM-ARM 200 F, JEOL Corp.) was used for the measurement.

Temperature Programmed Desorption

Temperature-programmed desorption (TPD) measurement was carried out to investigate the amount of edge sites and the element composition of the ZTC samples. Approximately 1 mg of the sample was placed in a graphite sample holder and transferred into a TPD apparatus. The inside of the apparatus was evacuated to a 10^{-5} Pa level. The sample was heated up to 1,600°C at a heating rate of 10°C min^{-1} by high frequency induction heating, and the desorbed gases were quantitatively analyzed with a quadrupole mass spectrometer (MPH-100 M, Inficon Co., Ltd.). From the components and amounts of desorbed gases, the amount of edge sites and element composition were determined. The details of TPD measurement have been reported in previous studies (Ishii et al., 2014, 2017a).

X-Ray Photoelectron Spectroscopy

In order to obtain information on the surface chemical state of the sample, X-ray photoelectron spectroscopy (XPS) measurement was carried out using Kratos AXIS NOVA (SHIMADZU Corp.). Al Kα radiation (10 mA, 15 kV) was used as an X-ray source. The charge-up correction was performed by setting the peak position of the C 1 s spectrum to 284.5 eV.

Atomic Absorption Spectrometry

The amount of metal species present in the sample was quantified by atomic absorption analysis (AAS). The sample was incinerated by oxygen plasma treatment and dissolved in 0.5 mol L^{-1} HNO_3 aqueous solution to prepare a measurement solution. The concentration of metal ions in the solution was measured using an atomic absorption spectrophotometer (iCE3300, Thermo Fisher Scientific, Inc.). The amount of metal in the sample was calculated from the determined metal ion concentration.

Work Function Measurement

In order to compare the Fermi level of the sample, a contact potential difference (CPD) was measured using a Kelvin probe (UVH-KP020-50, KP Technology Co., Ltd.), and a work function was also calculated. The sample was filled in a sample base made of aluminum, and measurement was carried out at ambient temperature and atmospheric pressure in the air. Au powder (particle diameter 1–2 μm, 99.99 %, Nilaco Corp.) was used as a reference sample. The work function of Au powder was set to 5.1 eV (Kahn, 2016). The work function of the sample was obtained from the difference between the obtained CPDs for Au and the sample.

Evaluation of Ion Sensing Characteristics

Glassy carbon plates were used for the source and drain electrodes for the ISFET. The ZTC sample was sandwiched between two glassy carbon electrodes and fixed with an acrylic plate and a plastic screw to fabricate a ZTC-ISFET. Carbon black (VXC, VXC72R, Cabot Co., Ltd.) was also evaluated in the same manner, as a reference sample. Activated carbon (YP-50F, Kuraray Chemical Co., Ltd.) was used for the gate electrode. The transistor characteristics of the ISFET in 1 mol L^{-1} HCl aqueous solution were evaluated by a semiconductor characterization system (4200-SCS, KEITHLEY Corp.). The source-drain voltage V_{DS} was fixed to 0.01 V, and the source-gate voltage V_{GS} was applied from −0.5 to 0.5 V with 0.1 V steps. In each V_{GS}, the current flowing between the source and drain electrodes when reaching the ion adsorption equilibrium, I_{DS}, was recorded. When V_{GS} is negative, the change of I_{DS} by V_{GS} is measured with reference to the value of I_{DS} obtained at $V_{GS} = -0.1$ V, and the value of I_{DS} obtained at $V_{GS} = 0.1$ V is also used as a reference in a positive V_{GS} region (as shown in **Figure S1**).

RESULTS AND DISCUSSION

Structural Evaluation of ZTC Samples

Table 1 shows elemental compositions obtained from TPD and AAS measurements of each ZTC sample. The hydrogen contents confirmed in the samples are higher than that of the various carbon materials such as a carbon black (Kashihara et al., 2012; Ishii et al., 2014; Hoshikawa et al., 2016), indicating that the ZTC samples have a large number of edge sites. The hydrogen content of P-ZTC is 16.2%, which is the maximum value in all samples, but the oxygen content is as small as 1 %, indicating that most of the edge sites terminated with hydrogen. The oxygen content of Ox-ZTC subjected to electrochemical oxidation is 3.6%, more than three times that of P-ZTC. As the amount of hydrogen in Ox-ZTC is reduced to approximately 60% of that of

TABLE 1 | Elemental compositions of zeolite-templated carbon (ZTC) samples determined from temperature-programmed desorption (TPD) and atomic absorption analysis (AAS).

Sample	Atomic concentration/%				
	C	N	O	H	*1Cu
P-ZTC	82.8	0	1.0	16.2	0
Ox-ZTC	86.3	0	3.6	10.1	0
N-ZTC	82.8	2.4	3.1	11.7	0
Cu-ZTC	84.9	0	3.0	12.1	0.27
Cu-N-ZTC	82.4	3.0	2.5	12.1	0.04

*1 Cu concentrations were determined by atomic absorption spectrometry.

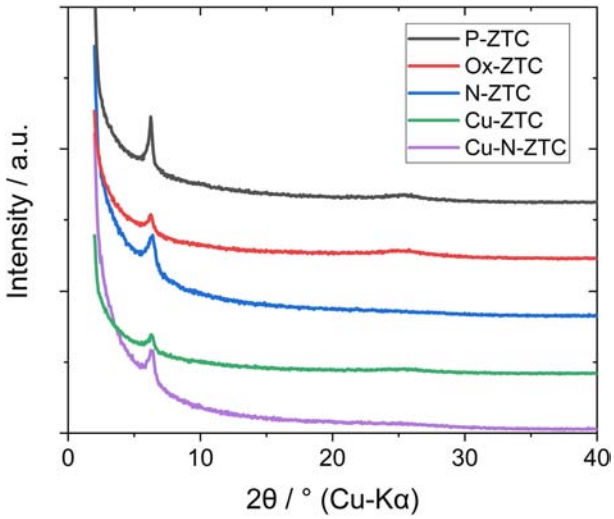

FIGURE 1 | XRD patterns of ZTC samples.

P-ZTC, it is expected that the edge hydrogen is oxidized by the electrochemical oxidation of P-ZTC, and that oxygen-containing functional groups are formed. The nitrogen content of N-ZTC (2.4%) is a common value regarded as a doping amount for nitrogen-doped carbons (Ozaki et al., 2006; Kan-Nari et al., 2010; Deng et al., 2016; Ishii et al., 2017b). In the sample doped with Cu, the presence of Cu was confirmed, although it was a trace amount. The zeolite was removed with hydrofluoric acid while the sample preparation, Cu as confirmed here, is considered to be incorporated in the carbon structure in an insoluble state by the acid.

Figure 1 shows the X-ray diffraction patterns of the ZTC sample obtained from the XRD measurement. A single peak was observed at $2\theta = 6.3^{\circ}$ for all samples, derived from the (111) plane of the zeolite template, showing high structural regularity (Nishihara and Kyotani, 2018). Although the peak of the heteroatom-doped sample is weaker than that of the un-doped sample (P-ZTC), the peak is clearly confirmed in them, indicating that the degradation of structural regularity owing to the doping level is relatively small. The nitrogen adsorption isotherm of the sample and the pore size distribution obtained by the DFT method are shown in **Figure S2**. The obtained isotherms are classified as Type I and indicate that the samples are micro porous carbon with a sharp pore size distribution of approximately 1.2 nm. **Table 2** shows the BET surface area, total pore, and micro pore volumes obtained from the nitrogen adsorption isotherm. The heteroatom-doped samples have a reduced specific surface area as compared to P-ZTC. This decrease in specific surface area is caused by the degradation of the uniform pore structure estimated from the result of XRD. Regarding Cu-N-ZTC, the existing form of Cu was evaluated by STEM-HAADF observation. Element mapping of C, N, O, and Cu of Cu-N-ZTC was performed, as shown in **Figure 2**. From the STEM-HAADF images, it was observed that not only were O and N uniformly dispersed atomically in the sample, but also Cu.

TABLE 2 | Specific surface area and pore volumes of ZTC samples.

Sample	$S_{BET}/m^2\ g^{-1}$	$V_{total}/cm^3\ g^{-1}$	$V_{micro}/cm^3\ g^{-1}$
P-ZTC	4,080	1.93	1.82
Ox-ZTC	2,860	1.35	1.23
N-ZTC	3,620	1.79	1.64
Cu-ZTC	2,130	1.51	0.97
CU-N-ZTC	3,020	1.83	1.57

Ion Sensing Characteristics of P- Ox- and N-ZTCs

Figure 3A shows the results of the V_{GS}-I_{DS} plot of P-ZTC and VXC. When VXC was used as a channel material, I_{DS} showed a constant value without respect to the gate voltage. VXC is considered to be a conductor, because no change in conductivity is observed regardless of the presence or absence of ion adsorption. In contrast, P-ZTC shows a semiconductor characteristic. Its I_{DS} varies with respect to V_{GS}, indicating that P-ZTC shows ISFET characteristics. The ISFET characteristics show bipolarity, and this result is similar to that of GNR (Zhang and Cui, 2013). This means that P-ZTC has the same semiconductor characteristics as GNR. Therefore, ZTC is considered to be composed of aggregates of GNR, and this is also supported by the fact that a large number of edge sites exist in the structure, as shown in **Table 1**. Localization of electrons on this large number of edge sites makes the band gap similar to GNR, and as a result, P-ZTC would show such semiconductor characteristics.

Figure 3B shows the results of the V_{GS}-I_{DS} plot of the heteroatom-doped ZTC samples. P-ZTC showed a slight increase in electrical conductivity in both positive and negative directions, indicating bipolarity, but in Ox-ZTC doped with oxygen, the electric conductivity increases with decreasing V_{GS}. The I_{DS} change (sensing sensitivity) of Ox-ZTC is approximately 8% ($\Delta I_{DS}/\Delta V_{GS} = 16\%/V$) at the maximum, which is close to the reported value when using GNR as a channel material in ISFET (Zhang and Cui, 2013). By contrast, the electrical conductivity of N-ZTC increases with increasing V_{GS}. These results show that doping oxygen to ZTC has p-type semiconductor characteristics and doping nitrogen to ZTC has n-type semiconductor characteristics, indicating that controlling a valence state of ZTC is possible by selection of a doping species.

For a deeper understanding, it is important to consider the factors that changed the ISFET characteristics by the doping of heteroatoms. **Table 3** shows the work function of each sample. The work function is the energy difference between the Fermi level and the vacuum level. The Fermi level becomes low energy as the work function increases. The work function increased and decreased, respectively in Ox-ZTC N-ZTC as compared to un-doped P-ZTC. This means that by doping with oxygen or nitrogen, the Fermi level of ZTC decreased and increased, respectively. The ISFET characteristics of Ox-ZTC and N-ZTC can be explained by the Fermi level. The Fermi level of Ox-ZTC is close to the valence band, while that of N-ZTC is

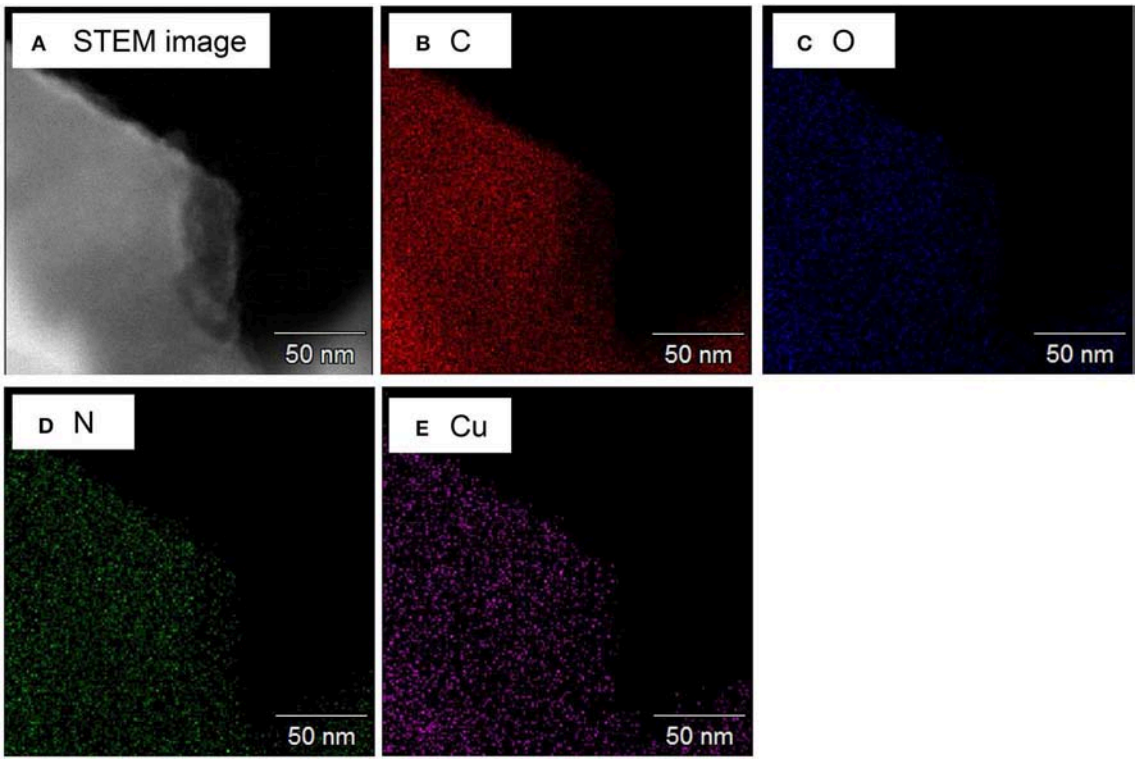

FIGURE 2 | (A) STEM-HAADF images of Cu-N-ZTC and **(B–E)** the elemental mapping for C, O, N, and Cu, respectively.

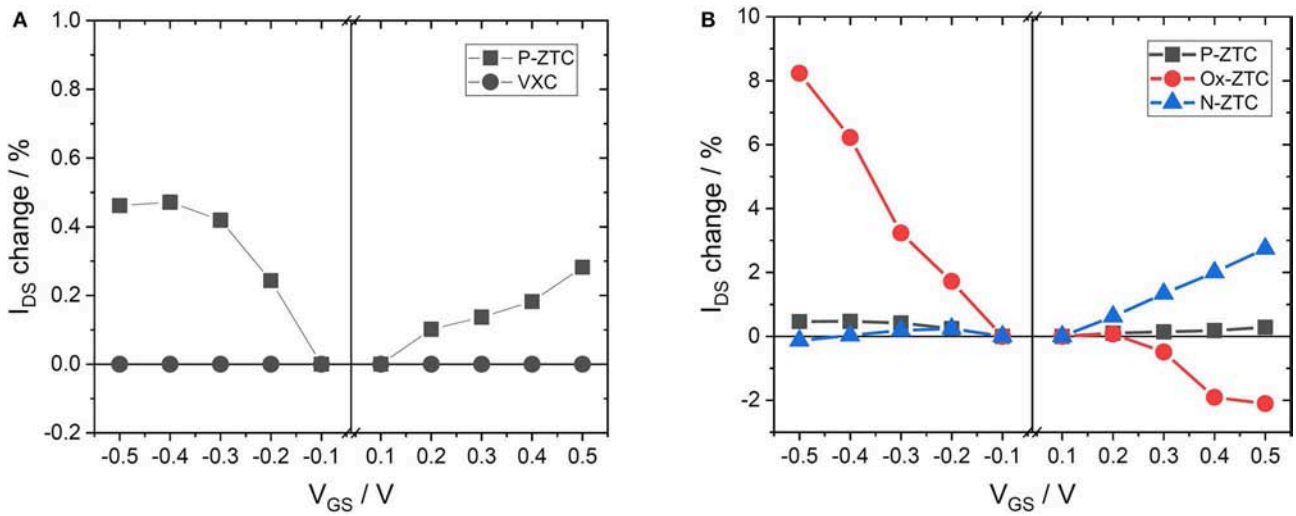

FIGURE 3 | ISFET characteristic curve of **(A)** P-ZTC and VXC and **(B)** Ox-ZTC and N-ZTC.

close to the conduction band, thus the former exhibited p-type semiconductor characteristics and the latter exhibited n-type characteristics. As shown in **Table 1**, it has been confirmed that many oxygen-containing functional groups are formed in Ox-ZTC. The Fermi level would be decreased because of the electron withdrawing ability of oxygen-containing functional groups. For N-ZTC, nitrogen species have different electronic influences on the carbon, owing to its chemical state. Therefore, the chemical state of nitrogen was analyzed from XPS measurement, and the chemical state of nitrogen was examined in more detail by performing peak deconvolution. The N 1s spectrum of N-ZTC follows the classification advocated by Raymundo-Pinero

TABLE 3 | Work function of ZTC samples.

Sample	Work function/eV
P-ZTC	4.56
Ox-ZTC	4.72
N-ZTC	4.28
Cu-N-ZTC	4.69
Au (as reference)	5.10

et al. (2002), i.e., pyridine (398.5 eV), pyrrol/pyridone (400.5 eV), quaternary (401.2 eV) and oxide (402.9 eV). **Figure S3** shows the result of peak deconvolution of the N 1s spectrum of N-ZTC. These four kinds of nitrogen species are present in the same proportions in N-ZTC. According to the study by Wang et al. a doping of quaternary nitrogen promotes n-type semiconductor characteristics, and pyridine-type nitrogen generally promotes p-type characteristics (Wang et al., 2014). However, there is a report that the pyridine present in CVD graphene (Luo et al., 2011) and nanographene (Yan et al., 2007) promotes n-type semiconductor properties, and this effect is considered to be caused by hydrogenation of pyridine-type nitrogen (Schiros et al., 2012). The Fermi level of N-ZTC would be increased because of the influence of quaternary and pyridine-type nitrogen in its structure.

Ion Sensing Characteristics of Cu-Doped ZTCs

Figure 4 shows the results of the V_{GS}-I_{DS} plot of the Cu-doped ZTC samples. The ISFET characteristics of Cu-ZTC were not significantly different from P-ZTC. In contrast, Cu-N-ZTC showed a bipolarity characteristic, and the sensitivity reached approximately 50 % in I_{DS} change ($V_{GS} = -0.5$ V). This ISFET sensitivity is much higher than the reported value of GNR (Zhang and Cui, 2013). As there was a little change in sensing sensitivity with the addition of copper into ZTC, the enhancement of the sensitivity is considered to be caused by the interaction between nitrogen and copper.

In order to investigate the influence on the ZTC by the simultaneous addition of nitrogen and copper, the electronic state was considered from the work function and the chemical state of the heteroatoms in its structure. Despite the nitrogen doping of Cu-N-ZTC, its work function was 4.69 eV (as shown in **Table 3**), which was close to the value of Ox-ZTC. This indicates that the Fermi level was decreased by co-doping nitrogen and copper. The surface chemical states were analyzed from XPS measurement. **Figure 5A** shows the N 1 s spectra of N-ZTC and Cu-N-ZTC. Bimodal peaks were confirmed in both cases. As compared with N-ZTC, Cu-N-ZTC shows that the peak intensity derived from pyridine-type nitrogen on the low-energy side decreases, and the higher energy peak increases. **Figure 5B** shows the Cu 2p spectra of Cu-ZTC and Cu-N-ZTC. In Cu-ZTC, a peak attributable to Cu^{2+} (CuO) near 934.5 eV was confirmed. In contrast, in Cu-N-ZTC, the Cu 2p peak position shifted to a lower-energy side than that in Cu-ZTC, which was attributed to Cu^{+} (932.4 eV).

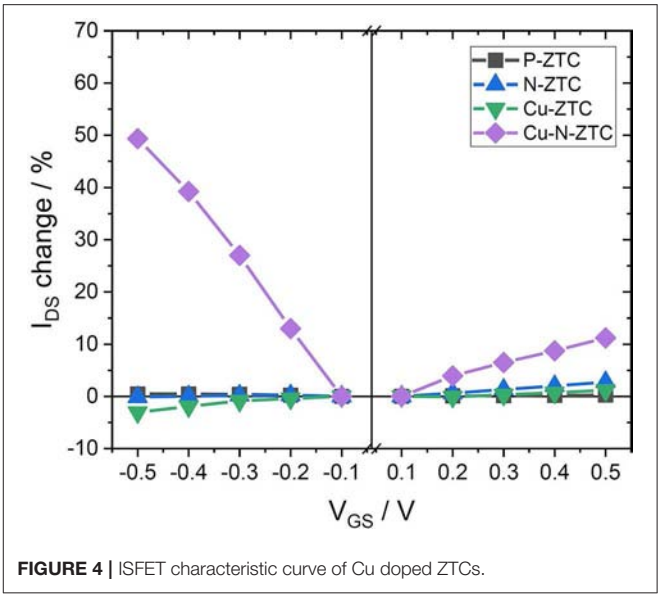

FIGURE 4 | ISFET characteristic curve of Cu doped ZTCs.

Shaozheng and colleagues have reported that the presence of Cu-N bond results in a down shift of the Cu 2p peak from Cu^{2+} to Cu^{+} simultaneously with the upshift of the energy of N 1s peak (Hu et al., 2017). This is consistent with the change in N 1s and the Cu 2p peak energy shift seen in **Figure 5**, suggesting that Cu-N bond present in the structure, and that nitrogen species coordinated with copper ion certainly exist. The peak appeared at 400.5 eV in the N 1s difference spectrum (shown in **Figure 5A**) with attributes of the N species bonding with Cu^{+}. From this complex formation of Cu^{+} and nitrogen, we can explain the decrease of the Fermi level of Cu-N-ZTC. When nitrogen species are coordinated by Cu^{+}, electrons of the ligand nitrogen are attracted to the Cu^{+}. Concomitantly, nitrogen acquires an electron withdrawing ability, and attracts π-electrons on the graphenic structure. From the above discussion, the formation of the complex of nitrogen and Cu^{+} is considered to shift the Fermi level to the lower-energy side.

In the previous section, the formation of coordination of nitrogen and copper showed that the Fermi level moved to the low-energy side. However, considering only the movement of the Fermi level, Cu-N-ZTC should show a p-type semiconductor characteristic that is the same as that in the case of Ox-ZTC. In order to investigate the cause of the exhibited bipolarity shown in Cu-N-ZTC, the effect of electrochemical potential on the state of Cu was evaluated. The electrochemical potential of Cu-N-ZTC was set at a predetermined potential, and the XPS measurement of the sample was immediately started. As the open circuit potential (OCP) of the Cu-N-ZTC is approximately 0.65 V vs. RHE in 1 mol L^{-1} HCl aqueous solution, the potential sweep range was set to 0.4 to 0.9 V vs. RHE. **Figure 6** shows the Cu 2p spectrum of Cu-N-ZTC at OCP, reduction potential (0.4 V vs. RHE), and oxidation potential (0.9 V vs. RHE). The Cu 2p peak shifted by approximately 1 eV from the oxidation state to reduction state, indicating that the chemical state of copper in Cu-N-ZTC varies with the

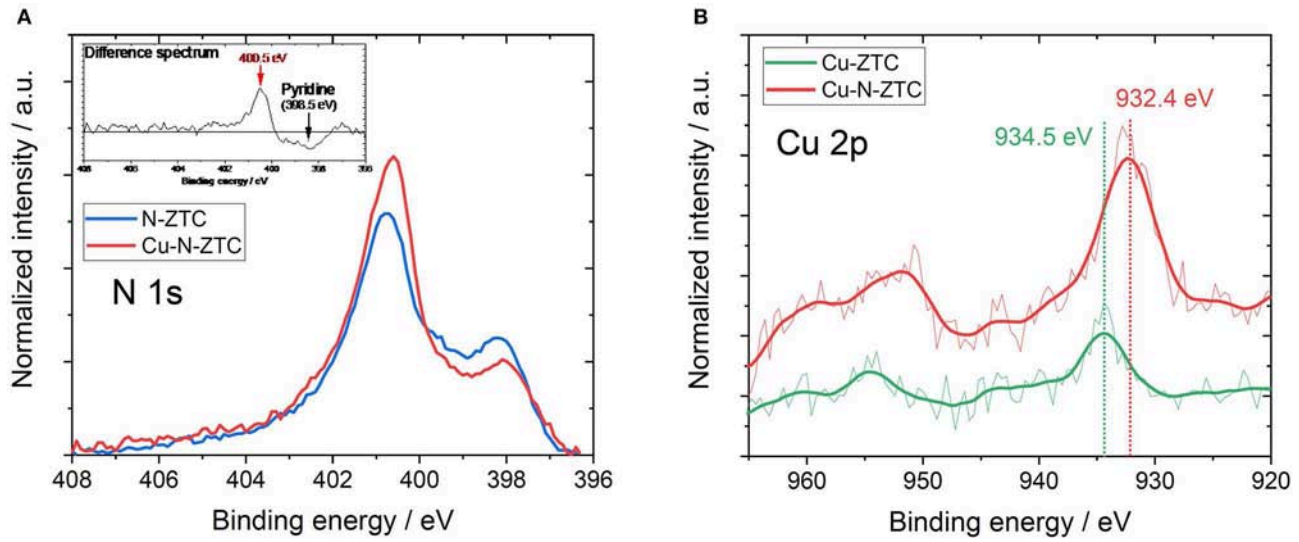

FIGURE 5 | XPS spectra of **(A)** N 1s region and **(B)** Cu 2p region of ZTC samples.

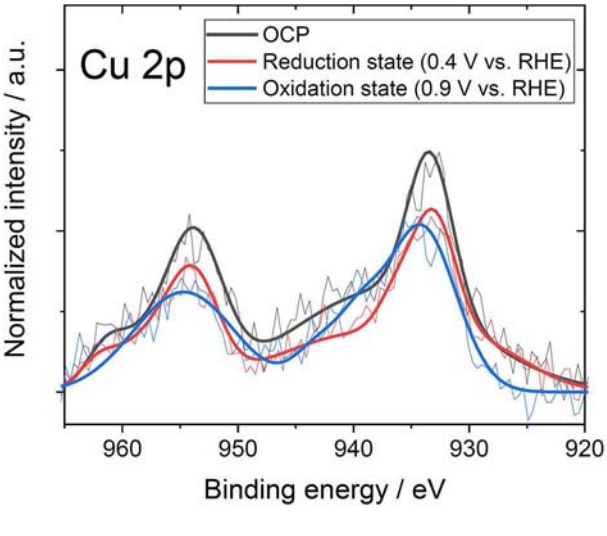

FIGURE 6 | XPS spectra of Cu 2p region for Cu-N-ZTCs being in different redox states.

electrochemical potential, and exists in a redoxable state. The bipolarity characteristics Cu-N-ZTC shown can be explained based on the above electrochemical evaluation. Owing to the changing chemical state of copper along with the V_{GS}, the degree of the electronic distribution between the nitrogen and copper would be changed. This polarization change affects the electron withdrawing ability of the coordination of nitrogen and copper toward π-electrons of carbon, and as a result, induces bipolarity in its ISFET characteristic.

It is conceivable that the sensitivity of Cu-N-ZTC in ISFET is enhanced by physical and chemical effects. In the physical adsorption of ions that is the common case in ISFET, the electron carrier is supplemented with electrostatic force. In contrast, the change of electronic polarization between nitrogen and copper is supposed to chemically supplement the carrier of the π-electron system. The former is a physical field effect, and the latter can be regarded as a chemical change of a functional group. It is considered that Cu-N-ZTC showed high sensing sensitivity owing to the effects of both. From the above considerations, the change in the electronic polarization between nitrogen and copper by the applied V_{GS} causes the bipolarity of the ISFET characteristic and the enhancement of the sensitivity.

CONCLUSION

In this study, we focused on ZTC composed of a three-dimensional network of GNR as an alternative to GNR and evaluated its ISFET characteristics. Various heteroatoms such as oxygen, nitrogen, and copper were doped in the structure of ZTC, and the carbon structure of ZTC was maintained even when doping them. The evaluation of ISFET characteristics of various ZTC samples showed that the un-doped ZTC exhibited bipolar characteristics, whereas the oxygen- and nitrogen-doped samples showed p-type and n-type semiconductor characteristics, respectively. The co-doped sample of Cu and N (Cu-N-ZTC) showed bipolarity as an ISFET characteristic, and exhibited the highest sensitivity. The detailed investigation confirmed that the coordination of nitrogen and copper exists in the structure of Cu-N-ZTC, and the chemical state of copper can be changed by an electrochemical potential. The specific ISFET characteristic of Cu-N-ZTC was explained by the existence of the coordination. Regarding the interaction between carbon and heteroatoms, its essence is quite deep,

and still insufficiently understood. This study recognizes the influence of heteroatoms, and particularly the coordination of nitrogen and copper, on the electronic state of carbon and ISFET characteristics. Furthermore, the manner of interaction between carbon and heteroatoms could be developed based on the evaluation of ISFET characteristics.

DATA AVAILABILITY

All datasets generated for this study are included in the manuscript and/or the **Supplementary Files**.

AUTHOR CONTRIBUTIONS

All authors listed have made a substantial, direct and intellectual contribution to the work, and approved it for publication.

ACKNOWLEDGMENTS

We acknowledge the financial support by Advanced Low Carbon Technology Research and Development Program of the Japan Science and Technology Agency and Ministry of Education, Science, Sports and Culture, Grant-in-Aid for Scientific Research, 18K14312. This work has been also supported by Izumi Science and Technology Foundation. STEM-HAADF measurement was carried out at National Institute for Materials Science (NIMS) Battery Research Platform.

SUPPLEMENTARY MATERIAL

The Supplementary Material for this article can be found online at: https://www.frontiersin.org/articles/10.3389/fmats.2019.00129/full#supplementary-material

REFERENCES

Ahmadi, M. T., Ismail, R., and Anwar, S. (2016). *Handbook of Research on Nanoelectronic Sensor Modeling and Applications*. Hershey, PA: IGI Global.

Bai, J. W., and Huang, Y. (2010). Fabrication and electrical properties of graphene nanoribbons. *Mater. Sci. Eng. R Rep.* 70, 341–353. doi: 10.1016/j.mser.2010.06.019

Berenguer-Murcia, Á., Ruiz-Rosas, R. R., García-Aguilar, J., Nueangnoraj, K., Nishihara, H., Morallón, E., et al. (2013). Binderless thin films of zeolite-templated carbon electrodes useful for electrochemical microcapacitors with ultrahigh rate performance. *Phys. Chem. Chem. Phys.* 15, 10331–10334. doi: 10.1039/c3cp51945g

Bronner, C., Leyssner, F., Stremlau, S., Utecht, M., Saalfrank, P., Klamroth, T., et al. (2012). Electronic structure of a subnanometer wide bottom-up fabricated graphene nanoribbon: End states, band gap, and dispersion. *Phys. Rev. B* 86:085444. doi: 10.1103/PhysRevB.86.085444

Chen, X., Liu, Y., Fang, X., Li, Z., Pu, H., Chang, J., et al. (2019). Ultratrace antibiotic sensing using aptamer/graphene-based field-effect transistors. *Biosens. Bioelectron.* 126, 664–671. doi: 10.1016/j.bios.2018.11.034

Chen, X., Pu, H., Fu, Z., Sui, X., Chang, J., Chen, J., et al. (2018). Real-time and selective detection of nitrates in water using graphene-based field-effect transistor sensors. *Environ. Sci. Nano* 5, 1990–1999. doi: 10.1039/C8EN00588E

Deng, Y. F., Xie, Y., Zou, K. X., and Ji, X. L. (2016). Review on recent advances in nitrogen-doped carbons: preparations and applications in supercapacitors. *J. Mater. Chem. A* 4, 1144–1173. doi: 10.1039/C5TA08620E

Duroux, P., Emde, C., Bauerfeind, P., Francis, C., Grisel, A., Thybaud, L., et al. (1991). The ion sensitive field-effect transistor (Isfet) Ph Electrode - a new sensor for long-term ambulatory Ph monitoring. *Gut* 32, 240–245. doi: 10.1136/gut.32.3.240

Hoshikawa, Y., An, B. G., Kashihara, S., Ishii, T., Ando, M., Fujisawa, S., et al. (2016). Analysis of the interaction between rubber polymer and carbon black surfaces by efficient removal of physisorbed polymer from carbon-rubber composites. *Carbon* 99, 148–156. doi: 10.1016/j.carbon.2015.12.003

Hu, S. Z., Qu, X. Y., Bai, J., Li, P., Li, Q., Wang, F., et al. (2017). Effect of Cu(I)-N active sites on the N-2 photofixation ability over flowerlike copper-doped g-C3N4 prepared via a novel molten salt-assisted microwave process: the experimental and density functional theory simulation analysis. *Acs Sustain. Chem. Eng.* 5, 6863–6872. doi: 10.1021/acssuschemeng.7b01089

Ishii, T., Kaburagi, Y., Yoshida, A., Hishiyama, Y., Oka, H., Setoyama, N., et al. (2017a). Analyses of trace amounts of edge sites in natural graphite, synthetic graphite and high-temperature treated coke for the understanding of their carbon molecular structures. *Carbon* 125, 146–155. doi: 10.1016/j.carbon.2017.09.049

Ishii, T., Kashihara, S., Hoshikawa, Y., Ozaki, J., Kannari, N., Takai, K., et al. (2014). A quantitative analysis of carbon edge sites and an estimation of graphene sheet size in high-temperature treated, non-porous carbons. *Carbon* 80, 135–145. doi: 10.1016/j.carbon.2014.08.048

Ishii, T., Maie, T., Kimura, N., Kobori, Y., Imashiro, Y., and Ozaki, J. (2017b). Enhanced catalytic activity of nanoshell carbon co-doped with boron and nitrogen in the oxygen reduction reaction. *Int. J. Hydrogen Energy* 42, 15489–15496. doi: 10.1016/j.ijhydene.2017.05.003

Itoi, H., Nishihara, H., Ishii, T., Nueangnoraj, K., Berenguer-Betrian, R., and Kyotani, T. (2014). Large pseudocapacitance in quinone-functionalized zeolite-templated carbon. *Bull. Chem. Soc. Japan* 87, 250–257. doi: 10.1246/bcsj.20130292

Itoi, H., Nishihara, H., Kobayashi, S., Ittisanronnachai, S., Ishii, T., Berenguer, R., et al. (2017). Fine dispersion of Pt4-5 subnanoclusters and Pt single atoms over porous carbon supports and their structural analyses with X-ray absorption spectroscopy. *J. Phys. Chem. C* 121, 7892–7902. doi: 10.1021/acs.jpcc.7b00422

Itoi, H., Nishihara, H., Kogure, T., and Kyotani, T. (2011). Three-dimensionally arrayed and mutually connected 1.2-nm nanopores for high-performance electric double layer capacitor. *J. Am. Chem. Soc.* 133, 1165–1167. doi: 10.1021/ja108315p

Itoi, H., Nishihara, H., and Kyotani, T. (2016). Effect of heteroatoms in ordered microporous carbons on their electrochemical capacitance. *Langmuir* 32, 11997–12004. doi: 10.1021/acs.langmuir.6b02667

Kahn, A. (2016). Fermi level, work function and vacuum level. *Mater. Horizons* 3, 7–10. doi: 10.1039/C5MH00160A

Kan-Nari, N., Okamura, S., Fujita, S., Ozaki, J., and Araib, M. (2010). Nitrogen-doped carbon materials prepared by ammoxidation as solid base catalysts for knoevenagel condensation and transesterification reactions. *Adv. Synth. Catal.* 352, 1476–84. doi: 10.1002/adsc.201000029

Kashihara, S., Otani, S., Orikasa, H., Hoshikawa, Y., Ozaki, J., and Kyotani, T. (2012). A quantitative analysis of a trace amount of hydrogen in high temperature heat-treated carbons. *Carbon* 50, 3310–3314. doi: 10.1016/j.carbon.2011.12.029

Kosynkin, D. V., Higginbotham, A. L., Sinitskii, A., Lomeda, J. R., Dimiev, A., Price, B. K., et al. (2009). Longitudinal unzipping of carbon nanotubes to form graphene nanoribbons. *Nature* 458, 872–U875. doi: 10.1038/nature07872

Luo, Z. Q., Lim, S. H., Tian, Z. Q., Shang, J. Z., Lai, L. F., Macdonald, B., et al. (2011). Pyridinic N doped graphene: synthesis, electronic structure, and electrocatalytic property. *J. Mater. Chem.* 21, 8038–8044. doi: 10.1039/c1jm10845j

Mao, S., Chang, J., Pu, H., Lu, G., He, Q., Zhang, H., et al. (2017). Two-dimensional nanomaterial-based field-effect transistors for chemical and biological sensing. *Chem. Soc. Rev.* 46, 6872–6904. doi: 10.1039/C6CS00827E

Martinoia, S., Massobrio, G., and Lorenzellib, L. (2005). Modeling ISFET microsensor and ISFET-based microsystems: a review. *Sens. Actuat. B Chem.* 105, 14–27. doi: 10.1016/S0925-4005(04)00107-8

Nishihara, H., Ittisanronnachai, S., Itoi, H., Li, L. X., Suzuki, K., Nagashima, U., et al. (2014). Experimental and theoretical studies of hydrogen/deuterium spillover on Pt-loaded zeolite-templated carbon. *J. Phys. Chem. C* 118, 9551–9559. doi: 10.1021/jp5016802

Nishihara, H., and Kyotani, T. (2018). Zeolite-templated carbons - three-dimensional microporous graphene frameworks. *Chem. Commun.* 54, 5648–5673. doi: 10.1039/C8CC01932K

Nueangnoraj, K., Nishihara, H., Ishii, T., Yamamoto, N., Itoi, H., Berenguer, R., et al. (2015). Pseudocapacitance of zeolite-templated carbon in organic electrolytes. *Energy Storage Mater.* 1, 35–41. doi: 10.1016/j.ensm.2015.08.003

Ozaki, J., Anahara, T., Kimura, N., and Oya, A. (2006). Simultaneous doping of boron and nitrogen into a carbon to enhance its oxygen reduction activity in proton exchange membrane fuel cells. *Carbon* 44, 3358–3361. doi: 10.1016/j.carbon.2006.08.022

Raymundo-Pinero, E., Cazorla-Amoros, D., Linares-Solano, A., Find, J., Wild, U., and Schlogl, R. (2002). Structural characterization of N-containing activated carbon fibers prepared from a low softening point petroleum pitch and a melamine resin. *Carbon* 40, 597–608. doi: 10.1016/S0008-6223(01)00155-5

Schiros, T., Nordlund, D., Pálová, L., Prezzi, D., Zhao, L., Kim, K. S., et al. (2012). Connecting dopant bond type with electronic structure in N-doped graphene. *Nano Lett.* 12, 4025–4031. doi: 10.1021/nl301409h

Syu, Y. C., Hsu, W. E., and Lin, C. T. (2018). Review-field-effect transistor biosensing: devices and clinical applications. *Ecs J. Solid State Sci. Technol.* 7, Q3196–Q3207. doi: 10.1149/2.0291807jss

Wang, X., Sun, G., Routh, P., Kim, D. H., Huang, W., and Chen, P. (2014). Heteroatom-doped graphene materials: syntheses, properties and applications. *Chem. Soc. Rev.* 43, 7067–7098. doi: 10.1039/C4CS00141A

Yan, Q., Huang, B., Yu, J., Zheng, F., Zang, J., Wu, J., et al. (2007). Intrinsic current-voltage characteristics of graphene nanoribbon transistors and effect of edge doping. *Nano Lett.* 7, 1469–1473. doi: 10.1021/nl070133j

Yu, S. S., Zheng, W. T., and Jiang, Q. (2010). Electronic properties of nitrogen-/boron-doped graphene nanoribbons with armchair edges. *IEEE Trans. Nanotechnol.* 9, 78–81. doi: 10.1109/TNANO.2009.2020797

Zhang, B., and Cui, T. H. (2013). Suspended graphene nanoribbon ion-sensitive field-effect transistors formed by shrink lithography for pH/cancer biomarker sensing. *J. Microelectromech. Syst.* 22, 1140–1146. doi: 10.1109/JMEMS.2013.2254701

Conflict of Interest Statement: The authors declare that the research was conducted in the absence of any commercial or financial relationships that could be construed as a potential conflict of interest.

frontiers in Materials

ORIGINAL RESEARCH
published: 03 May 2019
doi: 10.3389/fmats.2019.00093

Piezoresistive Carbon Foams in Sensing Applications

Krisztian Kordas and Olli Pitkänen*

Microelectronics Research Unit, University of Oulu, Oulu, Finland

Mechanical strain sensing is ubiquitous, found in applications such as heart rate monitoring, analysis of body part motion, vibration of machines, dilatation in buildings and large infrastructure, and so forth. Piezoresistive materials and sensors based on those offer versatile and robust solutions to measure strains and displacements and can be implemented even in acceleration and pressure analyses. In this paper, we overview the most prominent piezoresistive materials, and present a case study on carbon foams as well as on their hierarchical hybrid structures with carbon nanotubes/nanofibers. Our results show highly non-linear electrical resistance and mechanical stress dependence on uniaxial strain in both types of materials up to 50% compression. The Young's moduli increase with compressive strain between 1–65 and 0.1–92 kPa for the foam and hierarchical structure, respectively. The foams have giant gauge factors (up to −1000) with large differential gauge factors (on the scale of −10) and differential pressure sensitivity of 0.016 Pa^{-1} (at 10% strain) making them suitable for detecting both small and large displacements with excellent accuracy of electrical readout as we demonstrate in detecting building wall displacement as well as in monitoring heart rate and flexing of fingers.

Keywords: carbon foams, carbon nanotubes, hybrid structures, piezoresistivity, non-universal conductivity critical exponent, percolation, strain gauges

OPEN ACCESS

Edited by:
Federico Cesano, University of Turin, Italy

Reviewed by:
Senentxu Lanceros-Mendez, University of Minho, Portugal
Jan Macutkevic, Vilnius University, Lithuania

****Correspondence:***
Krisztian Kordas
krisztian.kordas@oulu.fi

Specialty section:
This article was submitted to Carbon-Based Materials, a section of the journal Frontiers in Materials

Received: *30 December 2018*
Accepted: *12 April 2019*
Published: *03 May 2019*

Citation:
Kordas K and Pitkänen O (2019) Piezoresistive Carbon Foams in Sensing Applications. Front. Mater. 6:93. doi: 10.3389/fmats.2019.00093

INTRODUCTION

Electrically conductive and semiconducting materials change their conductivity upon mechanical deformation. The effect is known as piezoresistivity, and can be described by the gauge factor (GF), which shows the relative change of resistance with the applied strain. In a first order approximation, $GF = \frac{\frac{R}{R_0}}{\varepsilon} = \frac{\frac{\rho}{\rho_0}}{\varepsilon} + 1 + 2\nu$, where $\Delta R/R_0$ and $\Delta\rho/\rho_0$ are the relative change of resistance and resistivity, respectively, ε is the mechanical strain and ν is the Poisson's ratio of the material.

In most of the bulk metals (e.g., Al, Au, Cu) and in many crystalline alloys and metallic glass compositions (e.g., constantan, $Cu_{60}Ni_{40}$, $Ni_{68}Si_{15}B_{17}$, $Ni_{80}Cr_{20}$, $Pd_{40}Cu_{30}Ni_{10}P_{20}$), GF is typically ∼2 (Hu et al., 2000; Schweizer, 2005; Yi et al., 2011; Jiang et al., 2015) and thus piezoresistivity may be accounted mainly for the change of geometry (viz. the Poisson's ratio is ∼0.5). However, some metals such as Pt and Ni display much larger GF values (4 and −12, respectively; Schmid et al., 2014 and Yi et al., 2011), which indicates that the deformation-induced change in resistivity has also a role in the piezoresistive effect and shall be taken into account.

In semiconductors, GF can be several orders of magnitude higher than in metals, as piezoresistivity is mainly governed by the strong variation of the materials' resistivity with strain, and thus the geometrical effects may be neglected. When deforming a semiconducting solid, the band structure and the effective mass of carriers also change, which result in their increased or decreased concentration and mobility (depending on the type of majority carriers and whether the strain is compressive or tensile; Bardeen and Shockley, 1950; Kanda, 1991). In the case of common crystalline semiconductors such as p-type Si or Ge, GF has a value of ∼100. Interestingly, for Si nanowires even higher GFs (up to 30-fold, compared to bulk Si) were reported and explained by strain induced carrier mobility change and surface effects (He and Yang, 2006). However, as it was demonstrated later using time-dependent electromechanical measurements, the increased apparent piezoresistive coefficients were actually due to charge trapping and detrapping on the surface of depleted Si, whereas the intrinsic piezoresistvity of the nanostructured material is essentially the same as that of bulk (Milne et al., 2010). Recent studies on semiconducting metal oxide thin films and nanostructures, e.g., on TiO_2 (Fraga et al., 2012), MoO_3 (Wen et al., 2014), and ZnO (Kaps et al., 2017); as well as on layered transition metal dichalcogenides, e.g., MoS_2 (Nayak et al., 2014; Manzeli et al., 2015), $MoSe_2$, WSe_2 (Hosseini et al., 2015), and $PtSe_2$ (Li et al., 2016; Wagner et al., 2018) showed highly strain dependent electronic properties, giving rise to quite high GFs comparable to those of Si and Ge (e.g. 441 for MoO_3 nanobelts, −148 for MoS_2 monolayers or −85 for $PtSe_2$ thin films).

Piezoresistivity in powders of conductive materials has been also studied for quite long time. For instance, the first carbon microphones made nearly 150 years ago exploited the pressure sensitivity of electrical resistance in carbon powders placed between an electrically conductive metal diaphragm and a back-side electrode plate (Hope, 1978). The pressure waves of sound induce vibrations of the thin diaphragm, which then transfers the vibrations to the carbon powder thus varying the intimacy of contacts between the conductive particles resulting in a variation of its overall resistance in synchrony with the waves of the sound. In the compressed carbon powder, the distance between the particles decrease giving rise to a better percolation and higher tunneling probability of electrons thus inducing an apparent piezoresistivity with gauge factors of around 20 (Cunningham and Bibby, 1993). In a similar fashion, powders, films and woven-like fabrics of 1 and 2-dimensional (1D and 2D, respectively) carbon nanoparticles, i.e., single (Gilshteyn and Nasibulin, 2015) and multi-walled nanotubes (Feng et al., 2010; Tadakaluru et al., 2014; Chun et al., 2018), graphene (Bae et al., 2013; Smith et al., 2013; Zhao et al., 2015; Liu X. et al., 2017) and reduced graphene oxide (Kuang et al., 2013; Mi et al., 2017; Xu et al., 2018) show piezoresistive properties. The great benefits of the low dimensional carbon nanostructures are easy formation of entangled thin films and simple transfer onto elastomers enabling excellent strain sensor devices to monitor heart rate, motion of body parts (Chang et al., 2018; Gilshteyn, 2018; Liu Y. et al., 2018; Park et al., 2018) and dilatation/vibrations of buildings as well as other large infrastructure (Schumacher and Thostenson, 2014; Augustin, 2018) among many others (Amjadi et al., 2016).

In contrast to bulk or thin film Au, quite large gauge factors (from 33 to 109) were measured for very thin films (assembled 2–3 particle layers) of monodisperse (12 nm in diameter) 3-mercaptopropionic acid and 6-mercaptohexanoic acid functionalized Au nanoparticles. The unprecedented gauge factors are explained by the easy change of inter-particle distances in the soft mercaptocarboxylic matrix causing considerable variation of tunneling resistances and current paths in the nanoparticle network (Jiang et al., 2015). In fact, percolation and tunneling play crucial roles in the overall piezoresisive behavior of composites with conductive fillers (e.g., carbon or metal nanomaterials) embedded in polymer matrices (Stassi et al., 2014). A large variety of organic as well as inorganic polymer composites with highly diverse mechanical properties was demonstrated in the past years, such as CNTs, carbon filaments, graphene and MXenes e.g., in poly(methyl methacrylate) (Kang et al., 2006), polysulfone (Oliva-Aviles et al., 2011), poly(dimethylsiloxane) (Liu and Choi, 2010; Hou et al., 2013) epoxy (Chiacchiarelli et al., 2013), polyimide (Ma et al., 2017), poly(styrene-butadienestyrene) (Wang et al., 2018), or even in concrete (Chung, 2002). Also polymer blends of conductive and insulating phases were proved as useful strain gauge materials. For instance, solution cast films of polyaniline and styrene-ethylene/butylene-styrene SEBS copolymer were found to bear with piezoresistive character with moderate GFs of ∼2 (Costa et al., 2018); however, electrospun fibers of poly(3,4-ethylenedioxythiophene) poly(styrenesulfonate) and polyvinyl alcohol showed GF up to ∼400 (Liu et al., 2011). Foams of intrinsically conductive materials as well as their polymer composites enrich even further the palette of piezoresistive materials providing new degrees of freedom (e.g., porosity, pore structure) to tune the mechanical and electromechanical properties (Pham et al., 2014; Liu H. et al., 2017; Ke et al., 2018; Liu W. et al., 2018; Yang et al., 2018). Such a good mechanical diversity is particularly important since the optimal transfer of strain or displacement from the object to the sensor device requires soft (or stiff) matrices for large (small) displacements or deformations of soft (stiff) objects. The gauge factors of soft composites is typically low or moderate (between 1 and 10) but allow good analysis of large strains of up to several tens of percentages, whereas hard composites such as those of epoxy or cement have GF values even above 50 (Chiacchiarelli et al., 2013; Yoo et al., 2018) which can be exploited in low strain regimes.

Here, we present and compare soft piezoresistive foams of pyrolyzed polymer foams and their hierarchical structures with carbon nanotubes (CNTs) and nanofibers (CNFs), which display high gauge factors in a large strain window. The fascinating properties pave the road for versatile strain sensing in very different fields that we also demonstrate here. In addition, in an attempt to explain the underlying mechanism of piezoresistive behavior, we analyze the strain dependent conductivity data and highlight the shortcomings of the percolation model for the foam-type 3-dimensional conductive networks.

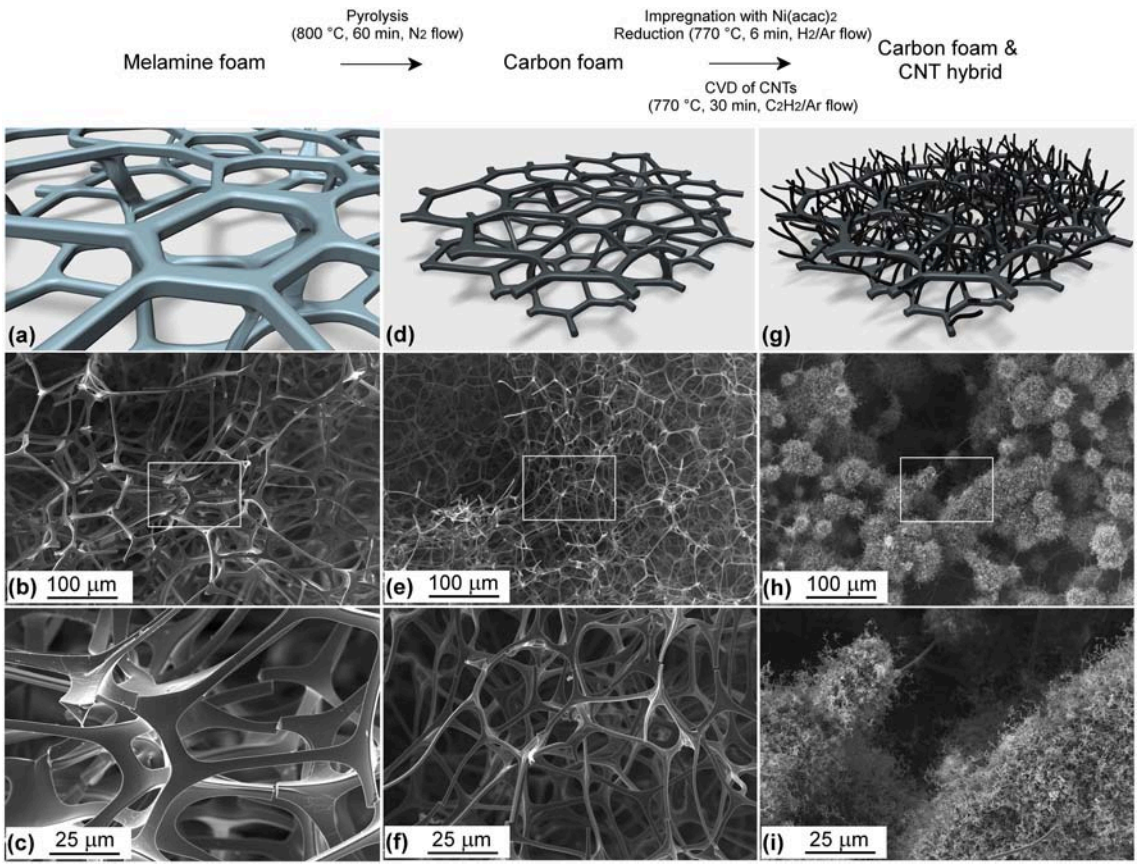

FIGURE 1 | (a,d,g) Schematic drawings of the original open pore structure melamine foam, carbon foam and hierarchical carbon foam and carbon nanotube hybrid, respectively. Panels **(b,e,h)** show low magnification scanning electron micrographs of the corresponding structures. In panels **(c,f,i)** magnified images of the samples are shown as indicated by the corresponding white rectangular selected areas in images **(b,e,g)**.

RESULTS AND DISCUSSION

Structure and Piezoresistive Behavior

Pyrolysis of the melamine foams results in a significant weight loss (∼90%) and volumetric shrinkage (∼90%), while the open-pore structure remains unchanged. After impregnating nickel acetylacetonate and reducing that in H_2 to form Ni nanoparticles in the foams, we grow CNTs/CNFs at 770°C on the catalyst nanoparticles along the skeletal structure by chemical vapor deposition from acetylene precursor. The dimensions of the as-synthesized hierarchical hybrid structures do not decrease any further compared to the parent carbon foams. The CNTs are multi-walled with high concentration of defects as indicated by their curled microstructure. Apart from CNTs, we can also find some CNFs, which emerge from larger Ni catalyst nanoparticle upon the CVD process (**Figures 1A–I**).

Resistance and stress measurements vs. mechanical strain show both the carbon foam and its hierarchical structures with CNTs/CNFs have highly non-linear behavior (**Figures 2A–D**). The Young's moduli of the materials increase with compression between 1–65 kPa and 0.1–92 kPa for the foam and hierarchical structure, respectively. The enormous decrease of resistances being approximately 3-orders of magnitude upon 50% compressive strain for both types of materials make up giant gauge factors $|GF| > 1000$. Even the differential gauge factors calculated as $\frac{dR}{R \cdot d\varepsilon}$ are having values as high as −10 in the low strain regime ($0 < \varepsilon < 0.2$). The differential pressure sensitivity values $\frac{dI}{I \cdot d\sigma}$ are 0.002 and 0.016 Pa^{-1} (at $\varepsilon = 0.1$) for the carbon foam and hierarchical structures, respectively making these materials as promising choices for detecting both small and large displacements with excellent accuracy of electrical resistance readout. The hierarchical structures display pressure sensitivities close those measured for highly complicated laminated multilayer thin films structures of polypyrrole, polyvinyl alcohol nanowires, polyethylene terephthalate, and indium-doped tin oxide (Luo et al., 2017).

Practical Examples of Piezoelectric Strain Sensor Applications

To assess the piezoresistive functionality of the carbon foams in the practice, we mounted their small pieces in three very different environments: between two structurally separate walls in our laboratory building as well as on a human index finger joint and

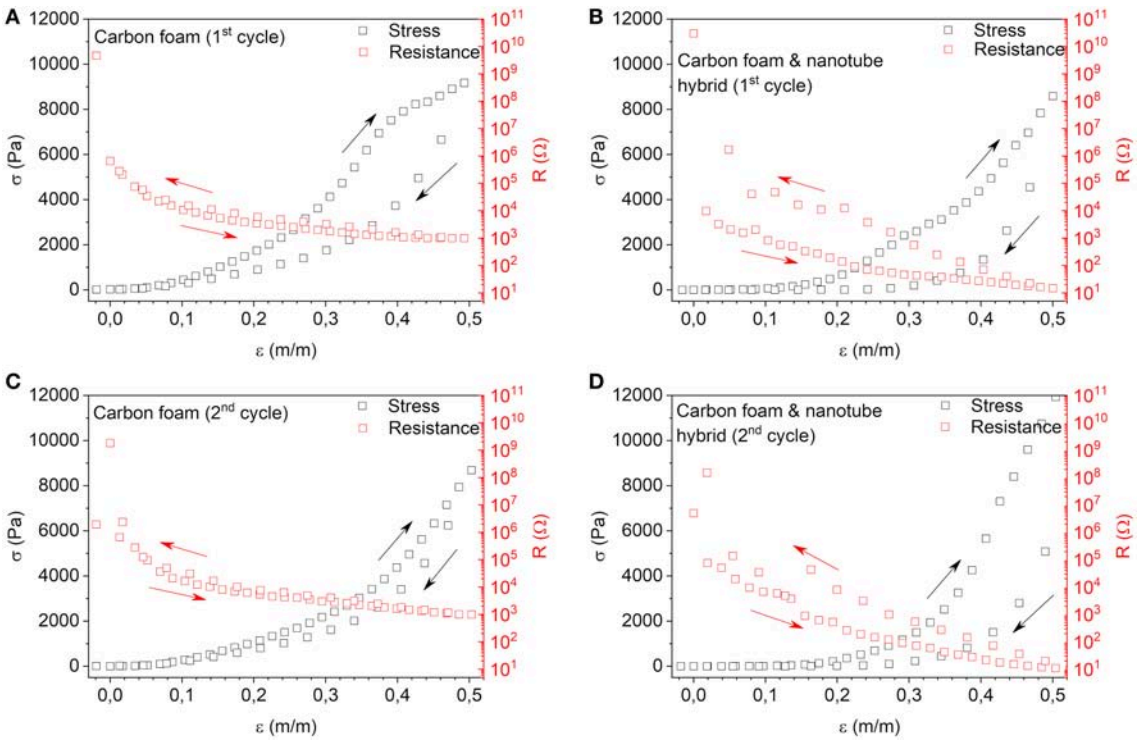

FIGURE 2 | Electrical resistance and mechanical stress as a function of strain for **(A)** carbon foam and **(B)** hierarchical carbon foam and carbon nanotube hybrid structures measured in the first deformation cycle up to ∼50%strain and back to the starting position. Panels **(C,D)** display the measured data obtained in the second deformation cycle for the corresponding specimens. The original dimensions (width × length × height) of the samples are 11.1 × 9.0 × 2.0 mm^3 (carbon foam) and 9.6 × 9.3 × 2.0 mm^3 (carbon foam and nanotube hybrid). The first resistance data point in each plot below 0% strain indicates insufficient contact with the electrodes in the experimental jig.

over the radial artery of a wrist (**Figure 3**). In each experiment, the applied foams were simply sandwiched between aluminum packaging foil slices (acting as electrical contacts) and then pre-stressed to ensure firm fixture of the sensors for the experiments to detect relative motion of the adjacent walls as well as to analyze flexing of the finger and to monitor heart rate, respectively.

The electrical resistance of the carbon foam placed between the two separate building walls (**Figure 3A**) shows a continuous drift, which seems to be independent from the temperature of the sensor (monitored with a thermocouple placed next to it). This is not surprising, since the temperature coefficient of resistance at near room temperature for the foam is about-0.02 deg^{-1} that we calculated from the temperature dependent resistance data published earlier (Pham et al., 2014). On day 4, the monotonic increase of resistance is broken by a significant drop ($\Delta R/R\sim$-0.4) that occurred within a period of 16 h, suggesting a slow but well defined compressive deformation of the sensor. The relative change of resistance corresponds to ∼4% decrease of the length of the sensor from ∼5.0 mm to ∼4.8 mm corresponding to a relative lateral displacement of ∼0.2 mm of the two walls. Motion of buildings is a known phenomenon (Lenczner, 1981), which may be caused by several reasons, including the change of the environment moisture and temperature as well as subsequent variation of the temperature gradients in the ground and building parts. To see whether the change of weather conditions could be responsible for the lateral movement of the two separate walls detected by the sensor, we checked the official outside air temperature measured by a meteorological station ∼5 km from our laboratory. The records show that the outside air temperature has started to drop from -2°C to -10°C about 7 h before the sensor detected the displacement. When the temperature has started to increase again (after ∼16 h), the resistance of the sensor followed that, again with ∼7 h of delay indicating the possible correlation between the outside air temperature and building motion data.

Carbon foams mounted on an index finger and on the radial artery also proved to be feasible for monitoring the corresponding physiological functions. In the former case, the higher degree the finger is flexed, the higher the measured voltage drop is measured over the resistor connected in series with the sensor (**Figure 3B**). This is logical since flexing of the finger compresses the sensor making it more conductive, thus allowing higher currents in the circuit. Even without any particular optimization, already ∼15° flexing angle can be detected well. As for the pulse monitoring sensor, we can clearly follow up the heart beats by simply pressing the foam against the radial artery (**Figure 3C**). Considering the voltage signal variation, measured over a series resistor of 330 Ω, the change of the current in

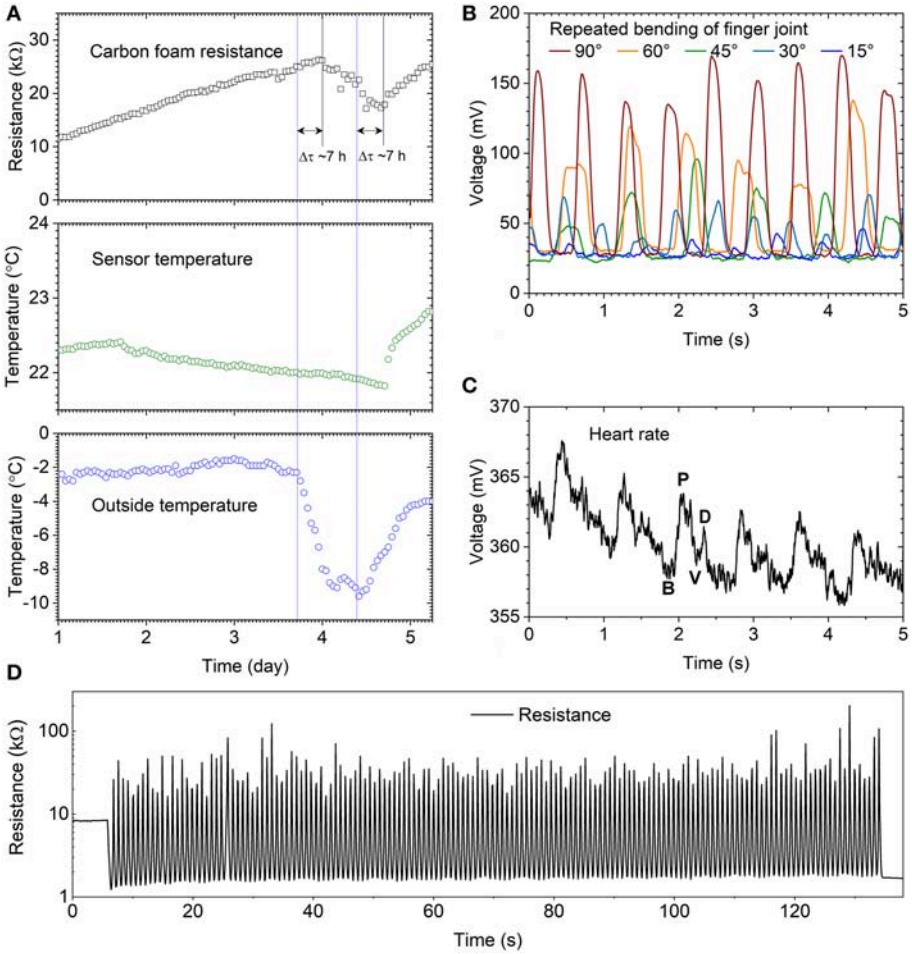

FIGURE 3 | Carbon foam based sensors monitoring displacements with highly diverse nature: **(A)** relative displacement of adjacent building walls constructed on separate concrete foundations, **(B)** repeated flexing of the index finger joint between the middle and proximal phalanges, and **(C)** heart rate monitored on the radial artery (B: base point, P: percussion wave, V: valley and D: dicrotic wave). **(D)** Resistance of a cube shaped foam under mechanical compression cycling (160 repetitions at 30% strain).

the circuit is ∼2%, which corresponds to ∼3% decrease of the sensor device resistance being sufficient to resolve the typical waveform (Chang, 2013) including the percussion wave, dicrotic notch (valley) and dicrotic wave in each pulse.

The foams are not only easy to integrate into very different environments to perform sensing but they also show reliable operation over long period of time as demonstrated in the building wall displacement measurements (**Figure 3A**) and they can stand repeated deformations very well (**Figures 3B–D**). These properties are particularly important in the practice and make the carbon based foams a good challenger of other soft piezoresistive composites of polymers and conductive fillers.

Qualitative Model for the Piezoresistive Behavior of Carbon Based 3-Dimensional Foams

In 2 or 3-dimensional (2D or 3D) networks of nanomaterials, the conduction mechanism has been shown to obey the percolation-tunneling model described by the power function $\kappa = \kappa_0 (c - c_0)^{\alpha}$, where κ is the conductivity, c is the volumetric concentration or areal density of the conductive filler, c_0 is the corresponding critical concentration or density, and α is the critical exponent having a typical (universal) value of around 2 for 3D (Hou et al., 2013) and 1.33 for 2D networks (Hu et al., 2004), respectively. Furthermore, even conductivity of cellular and reticulated vitreous carbon foams derived from self-similar polymer foams (e.g., phenolic-furanic foams, polyurethane templates resorcinol-formaldehyde) have been shown to have power function dependence on the density of structures (Letellier et al., 2017).

To plot our data and see whether it is in line with the percolation model, we first transform the R resistance values to conductivity taking into account the deformation of the foam as: $\kappa = \frac{1}{R}\frac{l(1-\varepsilon)}{A(1+2\nu\epsilon)}$, where l and A are the original sample thickness and cross-section area, ε is the applied strain and ν is the Poisson's ratio considered as 0.3, typical for foams.

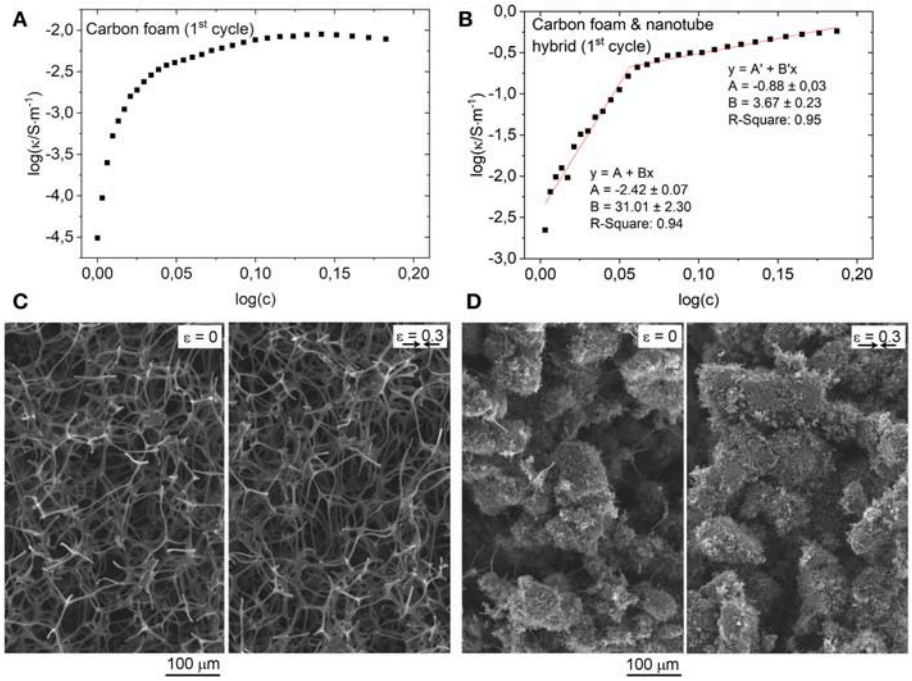

FIGURE 4 | Double logarithmic plots of the electrical conductivity and concentration (strain dependent inverse volume) for **(A)** carbon foam and **(B)** carbon foam and carbon nanotube hybrid structures. The plots are derived from the first compression cycle data of electrical resistance vs. mechanical stress in **Figures 2A,B**. Scanning electron micrographs of **(C)** carbon foam and **(D)** composite foam without and with uniaxial strain.

Similarly, we also transform the strain axes to concentration by taking it as unity at $\varepsilon = 0$ and dividing that with the volume of the deformed sample as: $c = \frac{1}{l(1-\varepsilon)A(1+2\nu\epsilon)}$. After having κ and c, in a double logarithmic plot, a linear fit gives the critical exponent, α. We find that none of the plots may be fitted with a single linear. In the case of the carbon foam, we cannot make any sort of reasonable fit because of the continuously changing slope as shown in **Figure 4A**. For the hybrid sample in **Figure 4B**, we find the data scatters around two linear slopes giving critical exponents 31.0 ± 2.3 (low strain regime $0 < \varepsilon < 0.2$) and 3.7 ± 0.2 (high strains $0.2 < \varepsilon < 0.5$), both being rather high in reference to the universal value of 2 supposed to be valid for random networks of percolating conductors. Accordingly, the very steep function of resistance vs. strain in our carbon foams and hierarchical structures cannot be explained by a simple percolation-tunneling model of conductors placed randomly in a volume. This is actually not completely surprising, since percolated foams are not fulfilling entirely the conditions of the model. Instead of having randomly placed conductors in 3D, the carbon foam made by the pyrolysis of melamine foam is a macroscopically continuous 3D skeleton of a carbon material with poorly ordered sp^2 and sp^3 content, which is likely to follow the multi-phonon hopping transport model as we concluded earlier from temperature dependent electrical conductivity measurements (Pham et al., 2014). Here, we speculate that upon deformation, the stresses in certain volumes of the carbon skeleton change the electronic band structure locally (e.g., by introducing new energy states in the insulating domains of the material and/or changing the Fermi level in the conductive phase) and alter not only the heights of tunneling gaps but also the distances between adjacent conductive regions thus giving rise to a highly complex strain dependent conduction. We have to emphasize here, that stress dependent conduction is not only seen for ordinary semiconducting crystals, but has been shown both theoretically and experimentally for various form of carbon nanomaterials. In the case of carbon nanotubes, band gap opening is common under stress (Martel et al., 1998; Yang and Han, 2000). Further, as it was concluded for sputter deposited amorphous carbon films with both sp^2 and sp^3 carbon content, the piezoresistivity of such material is due to hopping between conductive sp^2 grains in an insulating sp^3 surrounding (Grimaldi et al., 2000; Peiner et al., 2006).

On the other hand, in the case of the carbon foam and nanotube hybrid structure, electrical transport via the CNT network superposes on the one of the skeletal structure, and plays also a role in the overall conduction process. At low strains, the CNT network on the skeleton of the foam is already forming an entangled layer, which is reflected by the relatively high conductivity of the hybrid foam in reference to the carbon foam ($\sim 10^{-2}$ vs. $\sim 10^{-4}$ S/m). Increasing the strain in the hybrid structure until $\varepsilon \sim 20\%$ is improving the conduction in the skeleton as described for the carbon foam. Over ~20% strain, we find a change of the conduction mechanism with a critical exponent of 3.7 ± 0.2 (in contrast to the low strain exponent being 31.0 ± 2.3). Considering the microstructure of the hierarchically structured foam, it is a physically realistic

scenario that strains above ∼20% result in new contacts between the CNT networks located at the adjacent skeletal wires of the carbon foam. To visualize such a phenomenon, we use electron microscopy imaging to analyze how the skeleton structure of the carbon foam as well as the hierarchical structure of the composite foam change under mechanical strain ($\varepsilon = 0.3$). As shown in **Figure 4C**, the skeleton of the carbon foam only deforms without significantly changing the density of the interconnects. On the other hand, upon compression of the carbon nanotube coated composite foam, a more compact structure seems to form, in which the nanotube layers on adjacent skeleton wires can make direct contacts (**Figure 4D**). As such, we can eventually talk about percolation and tunneling in the foam despite the slightly higher critical exponent than the anticipated universal value for 3D network of conductive particles.

In fact, the critical exponent may show non-universal values, usually exceeding the value of 2, as found in carbon-polymer composites and granular metal-oxide networks (Vionnet-Menot et al., 2005; Bauhofer and Kovacs, 2008). The origin of such behavior has been extensively studied during the past years and has been attributed to anisotropy (Celzard and Marêché, 2003) as well as to the statistical distribution of the electrical transport properties of the contacts (Kogut and Straley, 1979; Halperin et al., 1985; Feng et al., 1987). For instance, according to the inverted random-void model (Balberg, 1987, 1998), in which tunneling current flows between conducting spheres placed in an insulating matrix, the critical exponent may be dependent on the mean tunneling distance and can be much higher than 2, if the distribution function of the tunneling distances decays slower than the tunneling decay (Vionnet-Menot et al., 2005). Therefore, these models may give a reasonable explanation why the non-ideal network of contacts between the CNT coated parts of the hybrid foam show the slightly higher critical exponent than the universal value.

CONCLUSIONS

In closing, we studied the piezoresistive behavior of two different types of carbon foam structures, one made by the pyrolysis of an open pore structure melamine foam, and another obtained by growing carbon nanotubes/nanofibers in pores of the first. Both kinds of foams show giant piezoresistive gauge factors ($GF < -1000$) and withstand very large compressive deformations ($\varepsilon \sim 0.5$) that are reversible after the first compression cycle thus enabling versatile strain gauge applications for displacement, deformation, and pressure sensing. The giant piezoresistive gauge factors cannot be explained solely by the classical percolation-tunneling model. The results suggest a more complex mechanism, in which a local variation of the electrical transport behavior in the sp^2-sp^3 hybridized carbon skeleton of the foam takes place due to local stresses upon mechanical deformation.

MATERIALS AND METHODS

The carbon foams were obtained by pyrolyzing melamine foam (BASF, Basotect® W) at 800°C for 60 min in 150 mL/min flow of N_2 similar to that we described earlier (Pham et al., 2014). Heating rates of 15°C/min until 300°C, and 2°C/min from 300 to 800°C were applied. The obtained carbon foams were rinsed and sonicated in de-ionized water and then dried at 70°C overnight to remove any Na^+ impurities enriched on the surface of the skeletal structure we found by XPS in our previous work (Pham et al., 2014). To grow carbon nanotubes in the pores of the foams, the samples were cut into $30 \times 10 \times 5$ mm^3 pieces, impregnated with a solution of nickel acetylacetonate (0.8 g/L in acetone), and then dried in a box furnace at 70°C for 1 h. After decomposing and reducing the Ni precursor to metallic Ni nanoparticles in 2 L/min 15% H_2/Ar flow at 770°C for 6 min, the gas flow was switched for a mixture of C_2H_2 (80 mL/min) and 15% H_2/Ar (70 mL/min, bubbled through a water container) for 30 min.

For the mechanical strain dependent stress and electrical resistance measurements, the synthesized foams were cut into pieces of $\sim 10 \times 10 \times 2$ mm^3 size and then were placed between two parallel copper plates. The lower plate was fixed on a tray of a computer connected weighting scale (Precisa LS 620M), whereas the upper plate was mounted on a computer controlled vertical translation stage. The pressing force was calculated from the measured weight upon compression adjusted by the vertical displacement of the upper copper electrode plate. The as formed circuit was sourced with 5 V DC and the current was measured using a Keithley 2636A SourceMeter.

Measurement of Building Wall Displacement

A rectangular foam cut to a size of $23 \times 5 \times 7$ mm^3 was brought in mechanical contact with Al packaging foil sheets and after being pressed along the 7 mm long side, it was placed in a gap of ∼5 mm between two walls in our laboratory. One of the walls is an ordinary wall of the building, whereas the other one is a part of a vibration-free structure built on a separate and more robust concrete foundation. The resistance of the pre-strained foam was measured with a Fluke 2635A Hydra Series II Data Bucket for over several days. A thermocouple was placed in the proximity of the sensor to monitor the actual temperature of the sensor. For the local temperature outside the building we use the weather data of the Finnish Meteorological Institute collected at a station located ∼5 km from our laboratory building.

Analysis of Finger Joint Flexing

A piece of carbon foam with dimensions of $15 \times 5 \times 3$ mm^3 was equipped with two Al foil slices and then fixed over the joint of proximal and middle phalanges of the index finger using a rubber ring. A resistor of 330 Ω was connected in series to the sensor and the circuit was sourced with 1 V (Agilent E3630A), while the voltage drop over the resistor was using an oscilloscope (Agilent DSO-X 3024A).

Heart Rate Monitoring

The measurement setup is similar to that used in the analysis of finger joint bending but the carbon foam (size of $5 \times 5 \times 5$ mm^3) sandwiched between Al foil pieces was manually pressed against the radial artery with a pressure of ∼15 kPa.

AUTHOR CONTRIBUTIONS

OP designed and performed the experiments. KK and OP analyzed the data and wrote the paper.

FUNDING

The authors acknowledge funding received from the EU H2020 (NewPack), Business Finland (Grelectronics), Academy of Finland (Suplacat), Interreg Nord–Lapin liitto (Flexibla Transparenta Ledande Filmer som Electroder), University of Oulu (more-than-Moore RC and Entity), and Infotech Oulu.

ACKNOWLEDGMENTS

Technical help of Dr. Jussi Putaala and Topias Järvinen are acknowledged. We also thank the support received from the Micro- and Nanotechnology Center, University of Oulu.

REFERENCES

Amjadi, M., Kyung, K. U., Park, I., and Sitti, M. (2016). Stretchable, skin-mountable, and wearable strain sensors and their potential applications: a review. *Adv. Funct. Mater*. 26, 1678–1698. doi: 10.1002/adfm.201504755

Augustin, T. (2018). *Structural Health Monitoring of Carbon Fiber Reinforced Polymers and Carbon Nanotube Modified Adhesive Joints via Electrical Resistance Measurement*. Doctoral thesis, Hamburg University of Technology, Germany.

Bae, S.-H., Lee, Y., Sharma, B. K., Lee, H.-J., and kim, J.-H., Ahn, J.-H. (2013). Graphene-based transparent strain sensor, *Carbon* 51, 236–242. doi: 10.1016/j.carbon.2012.08.048

Balberg, I. (1987). Tunneling and nonuniversal conductivity in composite materials. *Phys. Rev. Lett*. 59, 1305–1308. doi: 10.1103/PhysRevLett.59.1305

Balberg, I. (1998). Limits on the continuum-percolation transport exponents. *Phys. Rev. B* 57, 13351–13354. doi: 10.1103/PhysRevB.57.13351.

Bardeen, J., and Shockley, W. (1950). Deformation potentials and mobilities in non-polar crystals. *Phys. Rev*. 80:72. doi: 10.1103/PhysRev.80.72

Bauhofer, W., and Kovacs, J. Z. (2008). A review and analysis of electrical percolation in carbon nanotube polymer composites. *Comp. Sci. Technol*. 69, 1486–1498. doi: 10.1016/j.compscitech.2008.06.018

Celzard, A., and Marêché, J. F. (2003). Non-universal conductivity critical exponents in anisotropic percolating media: a new interpretation. *Phys. A* 317 305–312. doi: 10.1016/S0378-4371(02)01367-5

Chang, H., Kim, S., Jin, S., Lee, S. W., Yang, G. T., Lee, K. Y., et al. (2018). Ultrasensitive and highly stable resistive pressure sensors with biomaterial-incorporated interfacial layers for wearable health-monitoring and human-machine interfaces. *ACS. Appl. Mater. Interf*. 10, 1067–1076. doi: 10.1021/acsami.7b14048

Chang, S. (2013). The meridian system and mechanism of acupuncture–a comparative review. Part 2: mechanism of acupuncture analgesia. *Taiwan J. Obstet. Gynecol*. 52, 14–24. doi: 10.1016/j.tjog.2013.01.004

Chiacchiarelli, L. M., Rallini, M., Monti, M., Puglia, D., Kenny, J. M., and Torre, L. (2013). The role of irreversible and reversible phenomena in the piezoresistive behavior of graphene epoxy nanocomposites applied to structural health monitoring. *Composite Sci. Technol*. 80, 73–79. doi: 10.1016/j.compscitech.2013.03.009

Chun, S., Son, W., and Choi, C. (2018). Flexible pressure sensors using highly-oriented and free-standing carbon nanotube sheets. *Carbon* 139, 586–592. doi: 10.1016/j.carbon.2018.07.005

Chung, D. D. L. (2002). Piezoresistive cement-based materials for strain sensing. *J. Intell. Mater. Syst. Struct*. 13, 599–609. doi: 10.1106/104538902031861

Costa, P., Oliveira, J., Horta-Romarís, L., Abad, M.-J., Moreira, J. A., Zapiráin, I., et al. (2018). Piezoresistive polymer blends for electromechanical sensor applications. *Comp. Sci. Technol*. 168, 353–362. doi: 10.1016/j.compscitech.2018.10.022

Cunningham, M. J., and Bibby, G. L. (1993). "Measurement and instrumentation," in *Electrical Engineer's Reference Book*, ed G. R. Jones (Oxford: Butterworth-Heinemann Ltd.), 3/39.

Feng, C., Liu, K., Wu, J.-S., Liu, L., Cheng, J.-S., Zhang, Y., et al. (2010). Flexible, stretchable, transparent conducting films made from superaligned carbon nanotubes. *Adv. Funct. Mater*. 20, 885–891. doi: 10.1002/adfm.200901960

Feng, S., Halperin, B. I., and Sen, P. N. (1987). Transport properties of continuum systems near the percolation threshold. *Phys. Rev. B* 35, 197–214. doi: 10.1103/PhysRevB.35.197

Fraga, M. A., Furlan, H., Pessoa, R. S., Rasia, L. A., and Mateus, C. F. R. (2012). Studies on SiC, DLC and TiO2 thin films as piezoresistive sensor materials for high temperature application. *Microsyst. Technol*. 18, 1027–1033. doi: 10.1007/s00542-012-1435-y

Gilshteyn, E. (2018). *Components for Stretchable Electronics Based on Single-Walled Carbon Nanotubes*. Doctoral thesis, Skolkovo Institute of Science and Technology, Russia.

Gilshteyn, E., and Nasibulin, A. G. (2015). "Aerosol synthesized carbon nanotube films for stretchable electronic applications,"in *IEEE 15th International Conference on Nanotechnology (IEEE-NANO) 27-30 July 2015,* Rome, 893–896. doi: 10.1109/NANO.2015.7388758

Grimaldi, C., Ryser, P., and Strässler, S. (2000). Gauge factor of thick film resistors: outcomes of the variable range hopping model. *J. Appl. Phys*. 88, 4164–4169. doi: 10.1063/1.1290738

Halperin, B. I., Feng, S., and Sen, P. N. (1985). Differences between lattice and continuum percolation transport exponents. *Phys. Rev. Lett*. 54, 2391–2394. doi: 10.1103/PhysRevLett.54.2391

He, R., and Yang, P. (2006). Giant piezoresistance effect in silicon nanowires. *Nat. Nanotechnol*. 1, 42–46. doi: 10.1038/nnano.2006.53

Hope, A. (1978). 100 years of microphones. *New Scientist* 78:378.

Hosseini, M., Elahi, M., Pourfath, M., and Esseni, D. (2015). Very large strain gauges based on single layer $MoSe_2$ and WSe_2 for sensing applications. *Appl. Phys. Lett*. 107:253503. doi: 10.1063/1.4937438

Hou, Y., Wang, D. R., Zhang, X. M., Zhao, H., Zha, J. W., and Dang, Z. M. (2013). Positive piezoresistive behavior of electrically conductive alkyl-functionalized graphene/polydimethylsilicone nanocomposites. *J. Mater. Chem. C* 1, 515–521. doi: 10.1039/c2tc00114d

Hu, C., Gao, Y., and Sheng, Z. (2000). The piezoresistance coefficients of copper and copper-nickel alloys. *J. Mater. Sci*. 35, 381–386. doi: 10.1023/A:1004755014553

Hu, L., Hecht, D. S., and Grüner, G. (2004). Percolation in transparent and conducting carbon nanotube networks. *Phys. Rev. B* 4, 2513–2517. doi: 10.1021/nl048435y

Jiang, C. H., Ni, I.-C., Tzeng, S.-D., and Kuo, W. (2015). Nearly isotropic piezoresistive response due to charge detour conduction in nanoparticle thin films. *Sci. Rep*. 5:11939. doi: 10.1038/srep11939

Kanda, Y. (1991). Piezoresistance effect of silicon. *Sens. Actuat. A* 28, 83–91. doi: 10.1016/0924-4247(91)85017-I

Kang, I., Schulz, M. J., Kim, J. H., Shanov, V., and Shi, D. (2006). A carbon nanotube strain sensor for structural health monitoring. *Smart Mater. Struct*. 15, 737–748. doi: 10.1088/0964-1726/15/3/009

Kaps, S., Bhowmick, S., Gröttrup, J., Hrkac, V., Stauffer, D., Guo, H., et al. (2017). Piezoresistive response of quasi-one-dimensional ZnO nanowires using an *in situ* electromechanical device. *ACS Omega* 2, 2985–2993. doi: 10.1021/acsomega.7b00041

Ke, K., Bonab, V. S., Yuan, D., and Manas-Zloczower, I. (2018). Piezoresistive thermoplastic polyurethane nanocomposites with carbon nanostructures. *Carbon* 139, 52–58. doi: 10.1016/j.carbon.2018.06.037

Kogut, P. M., and Straley, J. P. (1979). Distribution-induced non-universality of the percolation conductivity exponents. *J. Phys. C* 12:2151. doi: 10.1088/0022-3719/12/11/023

Kuang, J., Liu, L., Gao, Y., Zhou, D., Chen, Z., Han, B., et al. (2013). A hierarchically structured graphene foam and its potential as a large-scale strain-gauge sensor. *Nanoscale* 5, 12171–12177. doi: 10.1039/c3nr03379a

Lenczner, D. (1981). *Movements in Buildings*, 2nd Edn (Oxford: Pergamon Press), 1–108. doi: 10.1016/C2009-0-06788-9

Letellier, M., Macutkecic, J., Kuzhir, P., Banys, J., Fierro, V., and Celzard, A. (2017). Electromagnetic properties of model vitreous carbon foams. *Carbon* 122, 217–227. doi: 10.1016/j.carbon.2017.06.080

Li, P., Li, L., and Zeng, X. C. (2016). Tuning the electronic properties of monolayer and bilayer $PtSe_2$ via strain engineering. *J. Mater. Chem. A* 4:18922. doi: 10.1039/C6TA08032D

Liu, C. X., and Choi, J. W. (2010). Strain-dependent resistance of PDMS and carbon nanotubes composite microstructures. *IEEE Trans. Nanotechnol.* 9, 590–595. doi: 10.1109/TNANO.2010.2060350

Liu, H., Dong, M., Huang, W., Gao, J., Dai, K., Guo, J., et al. (2017). Lightweight conductive graphene/thermoplastic polyurethane foams with ultrahigh compressibility for piezoresistive sensing. *J. Mater. Chem. C* 5:73. doi: 10.1039/c6tc03713e

Liu, N., Fang, G., Wan, J., Zhou, H., Long, H., and Zhao, X. (2011). Electrospun PEDOT:PSS–PVA nanofiber based ultrahigh-strain sensors with controllable electrical conductivity. *J. Mater. Chem.* 21, 18962–18966. doi: 10.1039/c1jm14491j

Liu, W., Liu, N., Yue, Y., Rao, J., Luo, C., Zhang, H., et al. (2018). A flexible and highly sensitive pressure sensor based on elastic carbon foam. *J. Mater. Chem. C*, 1451–1458. doi: 10.1039/c7tc05228f

Liu, X., Tang, C., Du, X., Xiong, S., Xi, S., Liu, Y., et al. (2017). A highly sensitive graphene woven fabric strain sensor for wearable wireless musical instruments. *Mater. Horiz.* 4, 477–486. doi: 10.1039/c7mh00104e

Liu, Y., Wang, H., Zhao, W., Zhang, M., Qin, H., and Xie, Y. (2018). Flexible, stretchable sensors for wearable health monitoring: sensing mechanisms, materials, fabrication strategies and features. *Sensors* 18:645. doi: 10.3390/s18020645

Luo, C., Liu, N., Zhang, H., Liu, W., Yue, Y., Wang, S., et al. (2017). A new approach for ultrahigh-performance piezoresistive sensor based on wrinkled PPy film with electrospun PVA nanowires as spacer. *Nano Energy* 41, 527–534. doi: 10.1016/j.nanoen.2017.10.007

Ma, Y., Liu, N., Li, L., Hu, X., Zou, Z., Wang, J., et al. (2017). A highly flexible and sensitive piezoresistive sensor based on MXene with greatly changed interlayer distances. *Nat. Comm.* 8:1207. doi: 10.1038/s41467-017-01136-9

Manzeli, S., Allain, A., Ghadimi, A., and Kis, A. (2015). Piezoresistivity and strain-induced band gap tuning in atomically thin MoS_2. *Nano Lett.* 15, 5330–5335. doi: 10.1021/acs.nanolett.5b01689

Martel, R., Schmidt, T., Shea, H. R., Hertel, T., and Avouris, P. H. (1998). Single- and multi-wall carbon nanotube field-effect transistors. *Appl. Phys. Lett.* 73, 2447–2449. doi: 10.1063/1.122477

Mi,. Q., Wang, Q., Zang, S., Mao, G., Zhang, J., and Ren, X. (2017). RGO-coated elastic fibres as wearable strain sensors for full-scale detection of human motions. *Smart Mater. Struct.* 27:015014. doi: 10.1088/1361-665X/aa9aff

Milne, J. S., Rowe, A. C. H., Arscott, S., and Renner, C. H. (2010). Giant piezoresistance effects in silicon nanowires and microwires. *Phys. Rev. Lett.* 105:226802. doi: 10.1103/PhysRevLett.105.226802.

Nayak, A. P., Bhattacharyya, S., Zhu, J., Liu, J., Wu, X., Pandey, T., et al. (2014). Pressure-induced semiconducting to metallic transition in multilayered molybdenum disulphide. *Nat. Commun.* 5:3731. doi: 10.1038/ncomms4731

Oliva-Aviles, A. I., Aviles, F., and Sosa, V. (2011). Electrical and piezoresistive properties of multi-walled carbon nanotube/polymer composite films aligned by an electric field. *Carbon* 49, 2989–2997. doi: 10.1016/j.carbon.2011.03.017

Park, S.-J., Kim, J., Chu, M., and Khine, M. (2018). Flexible piezoresistive pressure sensor using wrinkled carbon nanotube thin films for human physiological signals. *Adv. Mater. Technol.* 3:1700158. doi: 10.1002/admt.201700158

Peiner, E., Tibrewala, A., Bandorf, R., Biehl, S., Lüthje, H., and Doering, L. (2006). Micro force sensor with piezoresistive amorphous carbon strain gauge. *Sens. Actuat. A* 130–131, 75–82. doi: 10.1016/j.sna.2005.11.059

Pham, T. N., Samikannu, A., Kukkola, J., Rautio, A.-R., Pitkänen, O., Dombovari, A., et al. (2014). Industrially benign super-compressible piezoresistive carbon foams with predefined wetting properties: from environmental to electrical applications. *Sci. Rep.* 4:6933. doi: 10.1038/srep06933

Schmid, P., Zarfl, C., Balogh, G., and Schmid, U. (2014). Gauge factor of titanium/platinum thin films up to 350°C. *Proc. Eng.* 87, 172–175. doi: 10.1016/j.proeng.2014.11.611

Schumacher, T., and Thostenson, E. T. (2014). Development of structural carbon nanotube–based sensing composites for concrete structures. *J. Intellig. Mater. Syst. Struct.* 25, 1331–1339. doi: 10.1177/1045389X13505252

Schweizer, T. M. (2005). *Electrical Characterization and Investigation of the Piezoresistive E?ect of PEDOT:PSS Thin films.* Master's thesis, Georgia Institute of Technology, US.

Smith, A. D., Niklaus, F., Paussa, A., Vaziri, S., Fischer, A. C., Sterner, M., et al. (2013). Electromechanical piezoresistive sensing in suspended graphene membranes. *Nano Lett.* 13, 3237–3242. doi: 10.1021/nl401352k

Stassi, S., Cauda, V., Canavese, G., and Pirri, C. F. (2014). Flexible tactile sensing based on piezoresistive composites: a review. *Sensors* 14, 5296–5332. doi: 10.3390/s140305296

Tadakaluru, S., Thongsuwan, W., and Singjai, P. (2014). Stretchable and flexible high-strain sensors made using carbon nanotubes and graphite films on natural rubber. *Sensors* 14, 868–876. doi: 10.3390/s140100868

Vionnet-Menot, S., Grimaldi, C., Maeder, T., Strässler, S., and Ryser, P. (2005). Tunneling-percolation origin of nonuniversality: theory and experiments. *Phys. Rev. B* 71:064201. doi: 10.1103/PhysRevB.71.064201.

Wagner, S., Yim, C., McEvoy, N., Kataria, S., Yokaribas, V., Kuc, A., et al. (2018). Highly sensitive electromechanical piezoresistive pressure sensors based on large-area layered $PtSe_2$ films. *Nano Lett.* 18, 3738–3745. doi: 10.1021/acs.nanolett.8b00928

Wang, X., Meng, S., Tebyetekerwa, M., Li, Y., Pionteck, J., Sun, B., et al. (2018). Highly sensitive and stretchable piezoresistive strain sensor based on conductive poly(styrene-butadiene-styrene)/few layer graphene composite fiber. *Compos. A* 105, 291–299. doi: 10.1016/j.compositesa.2017.11.027

Wen, X., Yang, W., Ding, Y., Niu, S., and Wang, Z. L. (2014). Piezoresistive effect in MoO_3 nanobelts and its application in strain-enhanced oxygen sensors. *Nano Res.* 7, 180–189. doi: 10.1007/s12274-013-0385-8

Xu, M., Qi, J., Li, F., and Zhang, Y. (2018). Highly stretchable strain sensors with reduced graphene oxide sensing liquids for wearable electronics. *Nanoscale* 10, 5264–5271. doi: 10.1039/c7nr09022f

Yang, J., Ye, Y., Li, X., Lü, X., and Checn, R. (2018). Flexible, conductive, and highly pressure-sensitive graphene-polyimide foam for pressure sensor application. *Compos. Sci. Technol.* 164, 187–197. doi: 10.1016/j.compscitech.2018.05.044

Yang, L., and Han, J. (2000). Electronic structure of deformed carbon nanotubes. *Phys. Rev. Lett.* 85, 154–157. doi: 10.1103/PhysRevLett.85.154

Yi, J., Bai, H. Y., Zhao, D. Q., Pan, M. X., and Wang, W. H. (2011). Piezoresistance effect of metallic glassy fibers. *Appl. Phys. Lett.* 98:241917. doi: 10.1063/1.3599843

Yoo, D.-Y., You, I., Youn, H., and Lee, S.-J. (2018). Electrical and piezoresistive properties of cement composites with carbon nanomaterials. *J. Compos. Mater.* 52, 3325–3340. doi: 10.1177/0021998318764809

Zhao, J., Wang, G., Yang, R., Lu, X., Cheng, M., He, C., et al. (2015). Tunable piezoresistivity of nanographene films for strain sensing. *ACS Nano* 9, 1622–1629. doi: 10.1021/nn506341u

Conflict of Interest Statement: The authors declare that the research was conducted in the absence of any commercial or financial relationships that could be construed as a potential conflict of interest.

frontiers in Materials

ORIGINAL RESEARCH
published: 06 June 2019
doi: 10.3389/fmats.2019.00134

About the Role of Porosity and Surface Chemistry of Phosphorus-Containing Activated Carbons in the Removal of Micropollutants

Ramiro Ruiz-Rosas, Francisco J. García-Mateos, María del Carmen Gutiérrez, José Rodríguez-Mirasol and Tomás Cordero*

Departamento de Ingeniería Química, Facultad de Ciencias, Universidad de Málaga, Andalucía Tech, Málaga, Spain

The preparation of phosphorus-containing activated carbons and the effect of their surface chemistry and porosity on the performance as adsorbents of paracetamol are herein reported. A parent activated carbon is prepared by chemical activation of olive stones with phosphoric acid at 500°C and impregnation weight ratio of 3:1. This carbon is thermal treated under inert atmosphere at 900°C, producing porosity shrinkage, loss of 20% of surface area and less oxidized phosphorus groups. In addition, our knowledge about the redox behavior of P-containing groups has allowed the controlled gasification of the parent activated carbon in diluted air atmosphere, developing wide micropores and mesopores, increasing 40% the specific surface area and producing more oxidized phosphorus groups. Adsorption of a model micropollutant, paracetamol, has been conducted over these activated carbons by using diluted aqueous solutions ($<10\,mg\,L^{-1}$). Batch and small-scale column experiments confirmed that the presence of narrow microporosity and surface chemistry compatible with paracetamol improves the adsorption capacity, at the point of overcoming the potential effect of additional microporosity development. Moreover, the presence of a well-developed micro- and mesoporisity combined with a low surface acidity (that increases the affinity of the activated carbon surface and paracetamol) enhances the mass transfer rate of the adsorbent, improving the small-scale column performance parameters. To sum up, this study emphasizes the key role played by surface chemistry on the applicability of P-containing activated carbon as adsorbents. These results also confirm that controlled gasification at high temperatures of P-containing activated carbons is a useful method for improving their behavior in micropollutant abatement.

Keywords: activated carbon, adsorption, water treatment, micropollutant removal, surface chemistry, porosity

OPEN ACCESS

Edited by:
Wei Lv,
Tsinghua University, China

Reviewed by:
Ji-Jun Zou,
Tianjin University, China
Leszek A. Czepirski,
AGH University of Science and Technology, Poland

****Correspondence:***
Ramiro Ruiz-Rosas
ramiro@uma.es

Specialty section:
This article was submitted to Carbon-Based Materials, a section of the journal Frontiers in Materials

Received: *15 February 2019*
Accepted: *21 May 2019*
Published: *06 June 2019*

Citation:
Ruiz-Rosas R, García-Mateos FJ, Gutiérrez MC, Rodríguez-Mirasol J and Cordero T (2019) About the Role of Porosity and Surface Chemistry of Phosphorus-Containing Activated Carbons in the Removal of Micropollutants. Front. Mater. 6:134. doi: 10.3389/fmats.2019.00134

INTRODUCTION

Water is a very important constituent of the ecosystem on the Earth and essential component of life. The current deterioration of water quality is directly related to population growth and a lower availability of water sources. This deterioration is reflected in an increase of micropollutants or emerging pollutants, which presence in water effluents is mainly attributed to their incomplete

removal through conventional methods in wastewater treatment plants (WWTP) (Onesios et al., 2009; Luo et al., 2014; Petrie et al., 2014). Consequently, these compounds are increasingly found in water systems, mainly in surface waters such as rivers, affecting the quality of drinking water supplies (Mailler et al., 2016). Micropollutants are characterized by their wide distribution and low concentration (ppb or ppt), high variety and heterogeneous physicochemical properties. Currently, they are being widely detected and have the potential to generate an environmental impact and have adverse effects on the health of living beings (Estrada-Arriaga et al., 2016). Therefore, WWTPs face great challenges in optimizing technologies to remove, as much as possible, this type of chemical compounds avoiding human health problems and ensuring environmental sustainability (Teodosiu et al., 2018).

Among the wide diversity of viable technologies to remove micropollutants from water, many researchers support that activated carbons adsorption is superior to other methods providing an effective and fast removal of pollutants with low operating cost, simple design and low production of harmful by-products (Rivera-Utrilla et al., 2011; Boehler et al., 2012; Bhatnagar et al., 2013). In fact, the interest for using activated carbons for adsorption has spread into diverse industrial fields such as food, chemical, petroleum, nuclear or pharmaceutical industries among others (Bansal and Goyal, 2005). The environmental and economic advantages of this method are obviously increased when activated carbons are obtained from biomass waste because it is cheap, renewable and available in large quantities (Danish and Ahmad, 2018). Specifically, olive stone, a lignocellulosic biomass waste highly abundant in our region, is a potential precursor of activated carbons (López-González et al., 1980; Rodríguez-Reinoso et al., 1995).

Our research team have lots of experience in the preparation of activated carbons from olive stone (Bedia et al., 2009; García-Mateos et al., 2015), hemp fiber (Rosas et al., 2009), lignin (Rodríguez-Mirasol et al., 1993; Gonzalez-Serrano et al., 1997, 2004; Cotoruelo et al., 2009, 2011) or others biomass waste such as eucalyptus wood (Tancredi et al., 1996), Pinus caribaea sawdust (Márquez-Montesinos et al., 2001) or fruit skin (Marquez-Montesinos et al., 2002; Rosas et al., 2010). We have reported the effects of the activation process with chemicals and physical methods in the porosity and surface chemistry and how they improve the carbon adsorption properties.

The activation process is the preparation stage of activated carbon where pore development takes part, with the available methods being classified either as physical activation or as chemical activation. While physical activation methods result in the preparation of microporous solid with large surface area but poor mass transfer rate, chemical activation methods allow the development of mesoporosity that enhances mass transfer rates of pollutants (Aktaş and Ferhan, 2012). It is important to note that the selected activation temperature and the activating agent in the chemical activation play a key role on the preparation yield as well as on the texture properties and surface chemistry of the resulting activated carbons (Rosas et al., 2012). In this sense, by controlling the activation process, it is possible to generate a wide variety of activated carbons to satisfy the requirements of diverse applications (Rosas et al., 2009). With regard to activated agents, many reagents have been tested; the most widely used are $ZnCl_2$ (Gonzalez-Serrano et al., 1997), H_3PO_4 (Gonzalez-Serrano et al., 2004; Duan et al., 2017), KOH (Li et al., 2017), and NaOH (Kiliç et al., 2012), being $ZnCl_2$ and H_3PO_4 preferred when activating lignocellulosic materials.

Specifically, activation of biomass waste by using phosphoric acid as activating agent is a well-established method that allows the preparation of carbons with higher contribution of the mesoporosity, which enhances mass transfer rates of pollutants. Several studies reported that phosphoric acid promotes the depolymerization of hemicellulose and lignin at low temperature during the chemical activation of lignocellulosic materials, as well as promote cyclation and condensation reactions of the polymeric fragments at medium temperatures. As a consequence, the formation and release of tars and volatiles is restricted during the carbonization process, thus increasing the yield of the remaining solid product (Jagtoyen and Derbyshire, 1998; Rosas et al., 2009). In addition, phosphate and polyphosphate groups form ester linkages through the hydroxyls of cellulose. These phosphorus groups have high thermal stability, crosslinking the polyaromatic units of the charred solid when temperature is increased. Therefore, the subsequent removal of the acid leaves the carbon matrix in an expanded state, with a high pore development structure (Castro et al., 2000; Vernersson et al., 2002; Li et al., 2005).

It is worth noting that the presence of stable phosphorous groups introduced during activation also confers to these carbonaceous solids high surface acidity (Bedia et al., 2010b) and oxidation resistance (Rosas et al., 2012), increasing the possibilities of these materials for applications in catalysis (Bedia et al., 2010a; Hita et al., 2016). The relevance of phosphorous groups on carbon reactivity has been demonstrated for the oxygen-carbon reaction (Valero-Romero et al., 2017) reported that the oxidation of P-containing carbons renders the preferential formation of oxygen-containing P surface groups through the oxidation of C-P to C-O-P bonds. Since C-O-P bonds are thermally stable up to 700°C, the carbon-oxygen reaction is inhibited at lower temperatures. Moreover, thermal treatment at temperatures over 800°C reduces C-O-P to C-P bonds. These redox properties of P groups also vary the carbon electrochemical reactivity (Berenguer et al., 2015) and the manner in which activated carbons are functionalized through organic reactions (Palomo et al., 2017).

Taking into account these considerations, the main aim of this study is to evaluate the role of surface chemistry and porosity of P-containing activating carbons from olive stones on the paracetamol adsorption. Following this purpose, a parent activated carbon is prepared by chemical activation with H_3PO_4. Two new activated carbons have been obtained from the parent activated carbon by thermal treatment at 900°C (i) in inert atmosphere (ii) in diluted air. The three activated carbons are characterized in terms of porous texture, surface chemistry and acidity. Batch and small-scale column adsorption of paracetamol on the three activated carbons are studied. Thermodynamic and kinetic parameters drawn from the batch adsorption experiments allow an accurate prediction of the breakthrough profiles from

the column adsorption. Finally, the relationships between the surface properties of the activated carbons and their performance as adsorbents are discussed.

MATERIALS AND METHODS

Preparation of Activated Carbons

Olive stones (provided by Sociedad Cooperativa Andaluza Olivarera y Frutera San Isidro, Periana) are used as feedstock for the preparation of activated carbons. The raw material is rinsed in water, dried overnight and impregnated with H_3PO_4 (85 wt%, Sigma Aldrich) at 60°C for 24 h. The weight impregnation ratio is set at 3:1 (3 grams of H_3PO_4 per gram of olive stone) in order to produce a high mesopore volume, a desirable feature for liquid phase adsorbents. The impregnated olive stones are placed in a tubular furnace and activated at 500°C at a heating rate of 10°C min^{-1} (holding time: 2 h) under continuous N_2 flow (150 cm^3 STP min^{-1}). The sample is cooled down to room temperature in N_2 and washed with distilled water at 60°C until neutral pH and negative phosphate analysis in the eluate are ensured. The obtained carbon (AC) is dried and weighted in order to determine the yield of the activation process (weight of activated carbon related to weight of raw material, in dry basis). The AC is grinded and sieved (300–100 μm) in order to control the particle size used in the adsorption experiments. In addition, two activated carbons with different porosity and surface chemistry are prepared by thermal treatment of AC at 900°C. The activated carbon labeled as AC-T is obtained under N_2 flow during the treatment, whereas a gasified activated carbon (AC-G) is prepared by feeding diluted air (1% O_2). Heating rate of 10°C min^{-1}, holding time of 5 min and flow rate of 150 cm^3 STP min^{-1} are utilized during the treatment. The sample is cooled down to room temperature in nitrogen in both cases.

Characterization of Activated Carbon

The porous texture of the activated carbons is analyzed by N_2 adsorption-desorption at −196°C and CO_2 adsorption at 0°C in ASAP 2020 equipment (Micromeritics) following the recommendations given by the IUPAC (Thommes et al., 2015). Samples are previously outgassed at 150°C for at least 8 h. From the N_2 isotherm, the apparent surface area (S_{BET}) is determined applying the BET equation, while the micropore volume (V_t) is calculated by using the t-method and the mesopore volume (V_{mes}^{N2}) is evaluated applying the Gurvich rule as the difference between the adsorbed volume of N_2 at a relative pressure of 0.995 and the micropore volume (V_t). From the CO_2 adsorption data, the narrow micropore volume (V_{DR}) is calculated by using the Dubinin-Radushkevich equation. Pore size distribution is obtained from the N_2 adsorption isotherms by using the 2D-NLDFT heterogeneous surface model (Jagiello and Olivier, 2013). Additionally, the mercury intrusion profiles into the pores of the activated carbons prepared in this work have been measured from 0 to 210 MPa with a Hg Micromeritics porosimeter (Autopore IV 9550). Contact angle of 130 degrees and surface tension of 485 dyne cm^{-1} have been considered in the Kelvin equation for the estimation of the pore size from the applied pressure.

The size, shape and texture of the carbon particles are characterized by scanning electron microscopy (SEM). The micrographs are recorded using a JEOL (JSM-6490LV) instrument. A collection of micrographs have been taken in order to determine the average particle size (R_p, m). The density in water of the samples (ρ_p, g cm^{-3}) has been determined by water displacement in a pycnometer using 5 grams of dried sample.

The surface chemistry of the samples is analyzed by X-ray photoelectron spectroscopy (XPS) in a Physical Electronics equipment (5700C model) using Mg kα radiation (1253.6 eV). For detailed study of the peaks, the maximum of the C1s peak was set to 284.5 eV and used as reference to shift the other peaks. P 2p photoemission region has been deconvoluted following the procedure detailed elsewhere (Rosas et al., 2012). CO and CO_2 temperature programmed desorption (TPD) analyses up to 940°C (10°C min^{-1}) under inert flow (150 cm^3 STP min^{-1}) are carried out to determine the amount and type of surface oxygen groups. The gases evolved during the thermal treatment of 100 mg dried sample are analyzed by using specific CO and CO_2 NDIR equipment (Siemens Ultramat 22). The bulk amount of phosphorus in the activated carbons has been determined by analyzing the P content of the ashes obtained by calcination in air at 900°C using inductively coupled plasma optical emission spectrometry (ICP-OES).

The acidity of the samples was evaluated by pyridine chemisorption at 120°C. For this study, 10 mg of dry activated carbon are loaded in a thermobalance (CI instruments) and outgassed at 150°C for 1 h under N_2 flow (150 cm^3 STP min^{-1}). Saturation of the activated carbon is achieved at 120°C feeding pyridine (2% v v^{-1} in N_2) until constant weight. The feeding gas is reverted to pure nitrogen flow in order to remove physically the adsorbed pyridine. The amount of chemisorbed pyridine is stablished as the weight uptake at the end of the experiment.

Adsorption of Paracetamol

Determination of the Adsorption Isotherms

Paracetamol ($C_8H_9NO_2$, purity 99.5%, Sigma-Aldrich, labeled as PA along the text) is selected as a model compound for studying the effect of surface chemistry and porosity of P-containing activated carbons on the adsorption of emergent pollutants. The adsorption isotherm at 25°C has been determined by using batch experiments where 100 mL of PA solutions with different concentrations (1–20 mg L^{-1}) and 10 mg of the different activated carbons are put in contact in stopped glass flasks. Adsorption equilibrium is ensured by keeping the flasks in an orbital incubator (Gallenkamp, model INR-250) at 200 rpm equivalent stirring rate for 10 days. The adsorbate concentrations are determined by UV spectroscopy (λ_{max}: 243 nm) with an UV-Visible (Varian, Model Cary 1E) spectrophotometer. Adsorption capacities in the equilibrium, q_e (mg g^{-1}), are then determined:

$$q_e = \frac{C_0 - C_e}{w} \quad (1)$$

In Equation (1), C_0 and C_e stand for the initial and the equilibrium concentrations (mg L^{-1}) of the adsorbate in solution, and w is the adsorbent dose (g L^{-1}).

The experimental data for PA adsorption at the equilibrium were fitted using different adsorption isotherm models, being the best fitting provided by Langmuir model:

$$q_e = \frac{q_L \cdot K_L \cdot C_e}{1 + K_L \cdot C_e} \quad (2)$$

K_L is the equilibrium constant (L mg^{-1}), usually related to the enthalpy of adsorption, and q_L is the equilibrium concentration of the adsorbate (mg g^{-1}) on the activated carbon corresponding to a complete coverage of the available adsorption sites (i.e., adsorption capacity for the adsorption of a monolayer of the adsorbate).

Kinetic Adsorption

PA kinetic adsorption experiments are carried out in a 250 cm^3 thermostatized batch system equipped with glass stirrer (rotating rate of 300 rpm). An initial PA concentration of 5 mg L^{-1}, solution volume of 150 cm^3 and adsorption temperature of 25°C are used for these experiments. 135 cm^3 of distilled water and 15 mg of the carbon adsorbent are placed into the batch system before starting the experiment for wetting of the activated carbon pores. At the beginning of the experiment, 15 cm^3 of a 50 mg L^{-1} PA solution is poured into the stirred tank. The concentration of the adsorbate is continuously monitored at the batch outlet by UV-vis by using a continuous-flow cell that allows the solution to pass through the spectrometer. The dead volume of the external tubbing and the flow cell is 4 cm^3. The adsorbed amount of PA, q_t (mg g^{-1}), in the kinetic tests is calculated as:

$$q_t = \frac{C_0 - C_t}{w} \quad (3)$$

where C_t (mg L^{-1}) represents the adsorbate concentration in the aqueous phase at a given time. The kinetic results have been fitted to a modified hyperbolic equation (Equation 4) for data smoothing, what eases the determination of the diffusion constants.

$$q_t = \frac{q_m \cdot (a \cdot t)^m}{1 + (a \cdot t)^m} \quad (4)$$

where a (min^{-1}), q_m (mg g^{-1}) and m are empirical parameters. q_m represents the asymptotic q_t (mg g^{-1}) value in the function at the set experimental conditions. Therefore, qt tended to qm at the maximum contact time in the kinetic test.

In this sense, the equation proposed by Vermeulen (1953) (Equation 5) has been used to correlated the diffusion coefficient with time and the obtained data have been fitted by an exponential empirical equation (Equation 6)

$$D_e = \frac{-R_p^2}{\pi^2 t} \mathrm{Ln}\left[1 - \left(\frac{q_t}{q_e}\right)^2\right] \quad (5)$$

$$D_e = b \cdot \exp\left(\frac{c}{t + d}\right) \quad (6)$$

where R_p is the particle radius (m) and b, c and d are empirical parameters.

Combining the hyperbolic equation (Equation 4) with Equation (6) it is possible to obtain an equation correlating the heterogeneous effective diffusion coefficient with the amount of adsorbed PA (Equation 7).

$$D_e = b \cdot \exp\left(\frac{c}{\frac{1}{a}\left(\frac{q_t}{q_m - q_t}\right)^{\frac{1}{m}} + d}\right) \quad (7)$$

Small-Scale Column Adsorption Experiments

In order to analyze the dynamic response of activated carbons in the removal of the selected emerging pollutant, PA, small-scale adsorption columns experiments are performed using 200 mg of dry activated carbon. The activated carbons are packed within a thermostatized glass column (internal diameter of 5 mm) at 25 (± 0.5°C). The column height depends on the bulk density of the tested activated carbons, ranging from 2.8 to 3.4 cm. Before the test is started, the column is backwashed with water for 30 minutes to ensure the removal of trapped air and to fully wet the activated carbon porosity. PA solution (5 mg L^{-1}) is pumped downflow through the column at 6 cm^3 min^{-1} using a peristaltic pump. The breakthrough curves are obtained by continuous monitoring of the column outlet by UV spectrometry. We neglect the impact of axial dispersion effects confirming that the bed-length to particle diameter ratio (L_b/R_p) is larger than 20 in all cases (Raghavan and Ruthven, 1983).

In a previous work, we have reported a mathematical solution to the mass balance of the adsorption column that allows the prediction breakthrough profiles from batch adsorption measurements (García-Mateos et al., 2015). This approach has been also taken in this work to describe the column adsorption of paracetamol over P-containing activated carbons from the results of the batch adsorption experiments. In order to do so, a finite difference method is applied to solve simultaneously the PA mass balances i) along the carbon bed (z-axis) and ii) in the carbon particle (R-axis). Our previous work revealed that for the conditions used in this work, the external mass transfer resistance is much lower than the internal one, so that it is not necessary to include it in the mass balance to provide an accurate prediction of the breakthrough profile. The evaluation of a Peclet (which compares the advective to diffusive transport rates) number of ca. 2000 suggests that axial dispersion can be neglected. Moreover, a linear driving force model along with the assumption of a parabolic concentration profile of PA inside the carbon particles provides a good description of the internal mass transfer rate of the adsorbents. In consequence, the PA mass balances to be solved read as follow:

$$\varepsilon \cdot \frac{\partial C_b}{\partial t} = -v \cdot \frac{\partial C_b}{\partial z} - (1 - \varepsilon)\frac{15 D_e}{{R_p}^2}\rho \cdot (q_b - \overline{q}) \quad (8)$$

$$\frac{\partial \overline{q}}{\partial t} = \frac{15 \cdot D_e}{{R_p}^2} \cdot (q_b - \overline{q}) \quad (9)$$

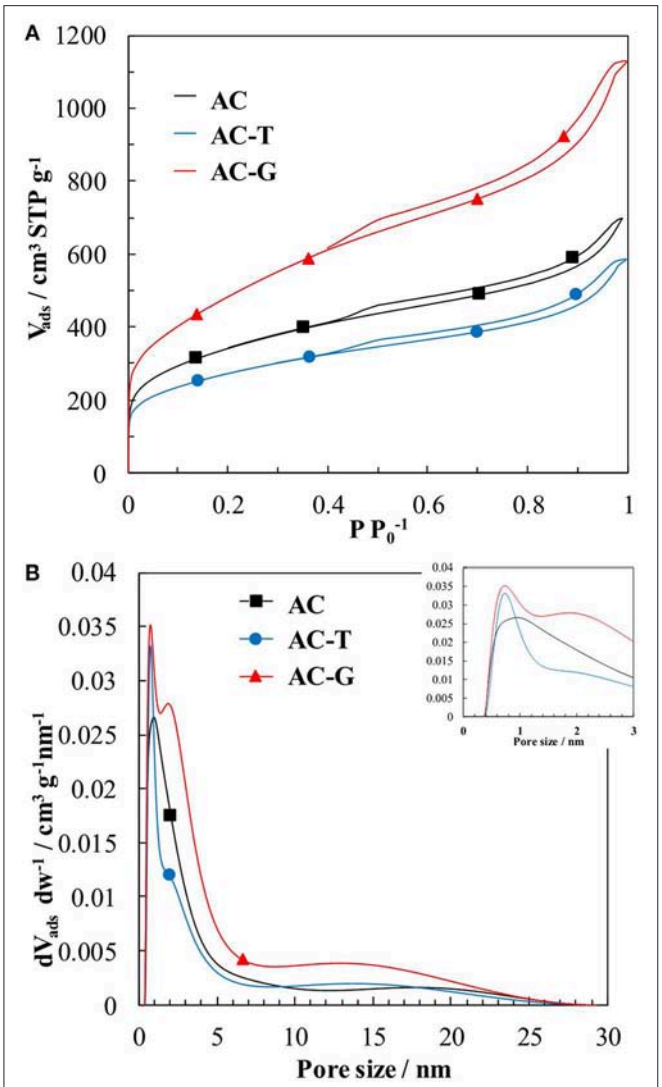

FIGURE 1 | (A) N_2 adsorption-desorption isotherms at −196°C of AC (square dot), AC-T (circle dot), and AC-G (triangle dot). **(B)** NL-DFT pore size distribution (PSD) derived from the N_2 adsorption isotherms.

With v being the linear velocity of the liquid phase flowing through the column, ρ_p being the activated carbon density determined in water and ε being the bed porosity. In it, the diffusion coefficient, D_e, is related to the amount of adsorbed PA, $\overline{q}$, a dependency that is described in Equation (7). On the other hand, the Langmuir adsorption isotherm, Equation 2, and the assumption of the parabolic concentration profile in the carbon particle allows relating the concentration of PA in the bed, C_b, with the amount of PA adsorbed at the surface of the carbon particle at z point, q_b. This allows the estimation of the average amount of adsorbed PA in the carbon porosity, $\overline{q}$, from the solution of the differential in Equation (9). More details regarding the mathematical solution of the mass balance to the adsorption column are provided elsewhere (García-Mateos et al., 2015).

TABLE 1 | Textural properties of activated carbon samples.

Textural parameters		AC	AC-T	AC-G
S_{BET}	$m^2\ g^{-1}$	1235	985	1750
V_{DR}^{CO2}	$cm^3\ g^{-1}$	0.21	0.22	0.30
V_t	$cm^3\ g^{-1}$	0.45	0.36	0.64
V_{me}^{N2}	$cm^3\ g^{-1}$	0.63	0.55	1.10
V_{me}^{Hg}	$cm^3\ g^{-1}$	0.66	0.36	0.51
V_{ma}^{Hg}	$cm^3\ g^{-1}$	0.42	0.19	0.37
ρ_p	$g\ cm^{-3}$	1.050	1.295	0.981
η	(%)	57.7	42.4	19.2
R_p	(μm)	98.7	92.5	82.6

RESULTS AND DISCUSSION

Physicochemical Parameters of Activated Carbons

The textural properties of the activated carbons have been determined by means of N_2 adsorption-desorption isotherms and Hg porosimetry. N_2 adsorption isotherm of the parent AC (**Figure 1A**) reveals a sharp and large N_2 uptake at low relative pressures owing to the presence of micropores, that is followed by a steady increase of adsorbed N_2 amount at medium relative pressures, which can be related to the existence of mesopores (Thommes et al., 2015). The thermal treatments bring noticeable changes on the N_2 adsorption isotherm of AC, which are different depending on the composition of the carrier gas. When performed under inert atmosphere, sample AC-T, the adsorbed volume decreases for all the relative pressures, indicating a porosity shrinkage. Differently, when a slightly oxidative atmosphere is used, sample AC-G, a controlled gasification of AC is achieved, delivering a large increase on the N_2 uptake. The BET surface area, micropore and mesopore volumes derived from these isotherms are compiled in **Table 1**. They confirm the porosity shrinkage previously mentioned for sample AC-T (observed drops of 20% in micropore volume and S_{BET}, and 13% in mesopore volume). In the case of the gasified sample, the surface area and micropore volume increases 40%, while mesopore volume is enlarged 75%. CO_2 adsorption isotherm is used to assess the narrowest microporosity (pore sizes <0.7 nm) (Cazorla-Amorós et al., 1996, 1998). For all activated carbons, the micropore volume measured by N_2 is larger than that measured by CO_2, pointing out the predominance of wide micropores (i.e., pore sizes of 0.7–2.0 nm) in these samples. However, the V_t/V_{DR}^{CO2} ratio decreases in sample AC-T, what is in line with a shrinkage of wide micropores to form narrow micropores. In the case of AC-G, this ratio remains unaltered, probably as a consequence of new wide micropores being formed by gasification of AC.

The evaluation of macro and mesopores volume of the analyzed samples by mercury porosimetry (**Table 1**) shows that AC has the largest macropore (V_{ma}^{Hg}, pore size from 2,500 to 50 nm) and wide mesopores (V_{me}^{Hg}, pore sizes from 6 nm to 50 nm). The thermal treatment produces a shrinkage of both pore

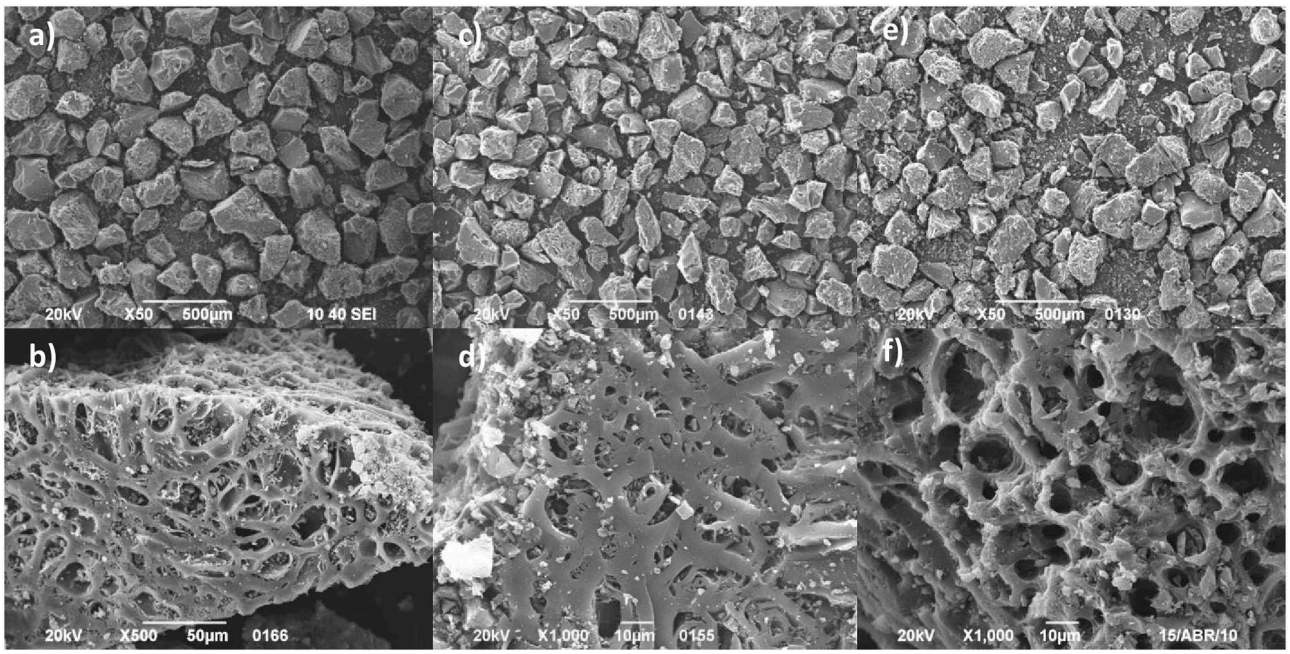

FIGURE 2 | SEM images of **(a,b)** parent activated carbon, AC; **(c,d)** thermal treated activated carbon, AC-T, and **(e,f)** gasified activated carbon, AC-G.

volumes. The pore contraction is larger in the case of AC-T. **Figure 2** shows micrographs of the activated carbon samples at different magnifications. The decrease on these pore volumes seems to be related to a loss of external roughness of the particles, as pointed out by the smoother surface of AC-T and AC-G particles detected by SEM images at higher magnification covered in **Figure 2**. It is worth mentioning that mesopore volume measured from the nitrogen adsorption isotherm is larger than that measured by Hg porosimetry in AC-T and AC-G, pointing out the predominance of narrow mesopores (sizes from 2 to 6 nm) in these samples. The porosity shrinkage after the thermal treatment comes along with an increase of ca. 30% in the density evaluated in water of AC-T, ρ_p on **Table 1**. On the contrary, the development of micro and mesoporosity in AC-G renders a slight decrease of 7% on the density when compared to the parent AC. Finally, the burn-off of AC-G has been estimated from the preparation yields of AC-T (which is taken as the baseline of the gasification treatment) and AC-G, giving a value of 55%.

The pore size distribution curves derived from the N_2 isotherms have been obtained by NL-DFT (Jagiello and Olivier, 2013) and represented in **Figure 1B**. The DFT volumes from the integration of the PSDs are in agreement with the micropores and mesopores volumes obtained from t-method in **Table 1**. The PSD curves show a well-defined micropore distribution centered at 1.2 nm for AC with a long tail falling into the mesopore region, see inset of **Figure 1B**. In the case of AC-T, the shift of the PSD curve to smaller pore sizes (maximum moves to 1.0 nm) points out the shrinkage of the pore size of this sample. On AC-G, a similar shrinkage seems to take place (the same narrow peak centered at 1.0 nm is observed). However, the controlled gasification delivers the formation of wide micropores having an average size of 2 nm.

TABLE 2 | Surface chemistry of the activated carbons.

C	AC	AC-T	AC-G
C_{XPS} (%w)	86.9	85.1	81.5
O_{XPS} (%w)	9.0	8.8	12.1
P_{XPS} (%w)	3.9	5.7	6.2
N_{XPS} (%w)	0.2	0.4	0.2
P_{bulk} (%w)	3.6	4.1	6.4
CO^{TPD} (mmol g^{-1})	1.85	1.41	3.14
CO_2^{TPD} (mmol g^{-1})	0.34	0.16	0.42
Py_{ads} (mmol g^{-1})	1.4	0.9	1.2
Py_{ads} (µmol m^{-2})	1.1	0.9	0.7

As for the mesopore distribution size, comparison between the PSD curves of AC and AC-T confirms the shrinkage of narrow and wide mesopores. This shrinkage is more pronounced in the 2–5 nm size range, what is probably related to the cleavage of polyphosphates bridges that produces the mesoporosity collapse. The mechanism of pore development during phosphoric acid activation of lignocellulosic biomass has been profusely described in the past and can be found elsewhere (Solum et al., 1995; Jagtoyen and Derbyshire, 1998; Rosas et al., 2009). On the contrary, gasification of AC proceeds with the development of mesopores with sizes averaging 13 nm, **Figure 1B**.

The surface chemistry of activated carbons has been analyzed by XPS and TPD. **Table 2** shows the surface weight composition from XPS measurements, and **Figure 3** details the P2p region

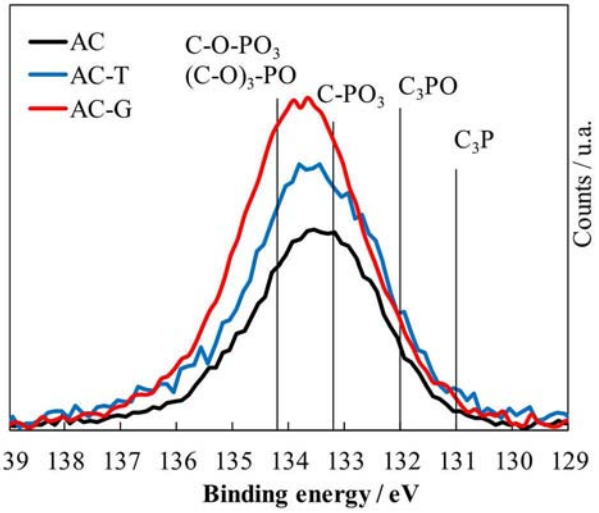

FIGURE 3 | XPS P2p photoemission region of the activated carbons.

of the XPS spectra recorded on the activated carbons. C1s and O1s XPS region as well as the deconvolution of the P2p spectrum are included in the supplementary file for the sake of brevity (**Figures S1, S2** and **Table S1**). The binding energies of P species with different amount of C-O-P, C-P-O and C-P bonds available in the literature have been also marked by vertical lines in **Figure 3** (Bedia et al., 2009; Rosas et al., 2012). The assignation of the XPS binding energies to the presence of these species has been discussed elsewhere (Puziy et al., 2006; Wu and Radovic, 2006; Rosas et al., 2009). A broad peak centered at 133.5 eV is observed in AC, suggesting that the pentavalent phosphorus prevails over the trivalent species (Moulder et al., 1995), what remains true no matter the treatment performed on it. The thermal treatment of AC delivers an increase in P content, **Table 2**, confirming that phosphorus is not lost from the surface of the activated carbon during thermal annealing, and only a minor increase in the presence of C-P-O bonds. Similar outcomes (i.e., reduced impact of thermal treatment in inert atmosphere) after thermal treatment of P-containing carbons can be found in our previous studies (Rosas et al., 2012; Berenguer et al., 2015; García-Mateos et al., 2015; Valero-Romero et al., 2017). Bulk P contents are in agreement with XPS determinations for AC and AC-G, while P seems to be more concentrated on the surface of AC-T ($P_{XPS} > P_{bulk}$). The gasification of AC further increases both P and O content, and slightly shifts the spectrum to higher binding energy, pointing out that the P species distribution is moved toward the presence of more oxidized ones, of the like of $C\text{-}O\text{-}PO_3/(C\text{-}O)_3\text{-}PO$ species, **Figure S2** and **Table S1**.

Table 2 compiles the amount of surface functional groups released as CO and CO_2. CO_2 evolution is traditionally related to the decomposition of surface oxygen groups with acid character, such as carboxylic acid at low temperatures and lactones and anhydrides at intermediate temperatures. The thermal treatment at 900°C removes most of these groups from the surface of AC-T, whereas the presence of oxygen during the preparation of AC-G induces the formation of CO_2 evolving groups, see $\mathbf{CO_2^{TPD}}$ in **Table 2**. Attending to the release of CO_2, AC should be the most acid activated carbon, followed by AC-G and finally by AC-T. When it is expressed in terms of surface area, AC-T would be slightly more acid than AC-G (0.23 μmol CO_2 m^{-2} vs. 0.21 μmol CO_2 m^{-2}, respectively). On the other hand, the CO evolution originates from the presence of neutral or slightly basic groups, such as phenols at intermediate temperatures, and ether, quinones, and carbonyls at high temperatures. It is possible to see that AC-G has the largest amount of CO-type groups, followed by AC and finally by AC-T. In order to clarify the acidity of these carbons, we have utilized pyridine chemisorption method ($\mathbf{Py_{ads}}$, **Table 2**) that has been successfully applied for detailing the acidity of P-containing carbons serving as dehydration catalysts (Bedia et al., 2010c). Acidity was decreased after the thermal treatment, no matter the atmosphere. It is slightly higher for AC-G, although AC-T surpasses AC-G in terms of surface acidity (i.e., adsorbed pyridine divided by specific surface area). In general, oxidation treatments in air are known to deliver minor changes in surface acidity (Bandosz, 2008).

CO and CO_2 TPD profiles are shown in **Figure 4**. In the CO profile, the main feature is the presence of a well-defined peak centered at temperatures around 850°C, **Figure 4A**. This CO evolution has been identified as the thermal decomposition of C-O-P groups, which releases CO (Rosas et al., 2009; Valero-Romero et al., 2017). The maximum of the peak is centered ca. 800°C in the case of AC and it is shifted to 860°C in AC-G and AC-T, reflecting the stabilizing effect of the benzene rings formed during thermal treatment (aromatic condensation reactions) on the C-C bonds that should be broken for the release of CO from the reduction of the C-O-P species. In the case of AC, additional release of small quantities of CO at temperatures from 500 to 750°C can be assigned to the presence of anhydrides (confirmed by the evolution of CO_2 in a temperature range of 450–650°C, **Figure 4B**) and phenols/quinones (that decomposes in the form of CO at temperatures between 650 and 750°C) (Román-Martínez et al., 1993; Figueiredo et al., 1999; Boehm, 2002). Water evolution during TPD from 650 up to 900°C is also detected (H_2O profiles not included for the sake of brevity), what has been proposed to be produced by the condensation of P-OH and saturated C atoms, forming C-P bonds (Valero-Romero et al., 2017). After the thermal treatment at 900°C under inert atmosphere, anhydrides and phenols/quinones are no longer observed, and most of the CO evolution found in sample AC-T is related to the presence of C-O-P species. We have already reported that the C-P bonds formed during the thermal treatment of P-containing activated carbons are prone to reoxidize at fast rate when they are again contacted with air, even at room temperature (Valero-Romero et al., 2017), what explains why the CO evolution related to the presence of C-O-P decomposition is seen in AC-T.

The C-O-P TPD related peaks at high temperature are notoriously increased in AC-G (red profiles in **Figure 4**), confirming the formation of larger numbers of C-O-P bonds in P groups. The amounts of CO and CO_2 released at temperatures >700°C during TPD can be related to the amount of phosphorus on these activated carbons in order to gain

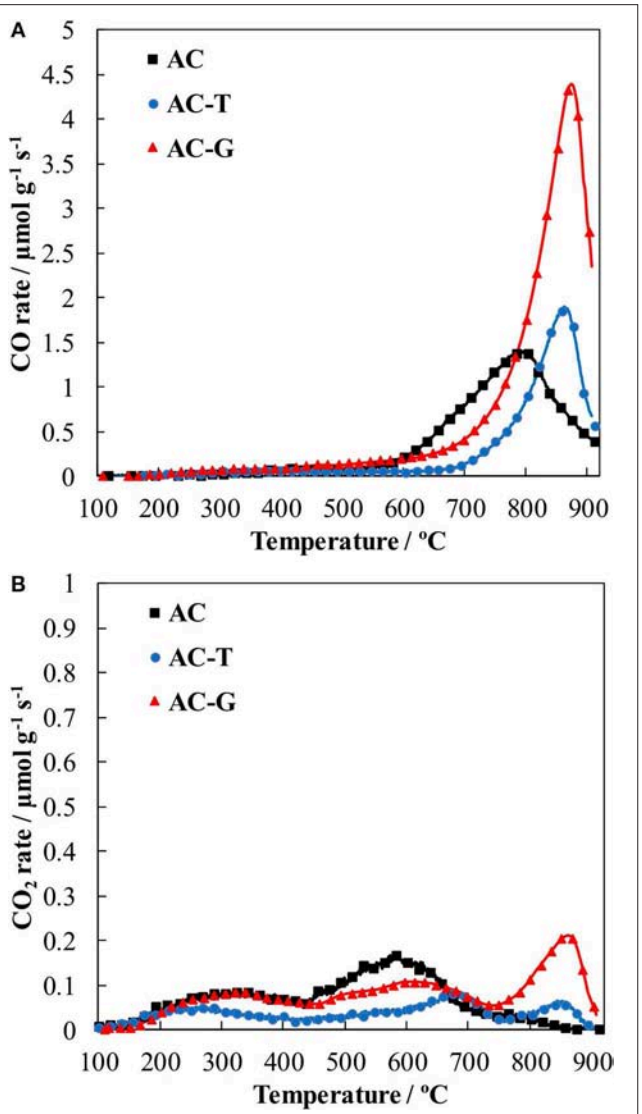

FIGURE 4 | CO **(A)** and CO_2 **(B)** TPD evolution profiles of the prepared activated carbons.

knowledge of the number of C-O-P bonds on these carbons. Ratios of 1.15, 0.75 and 1.50 mmol O_{TPD} $mmol^{-1}$ P_{XPS} (O_{TPD} $=CO_{TPD}+2{\cdot}CO_{2,TPD}$) are obtained for AC, AC-T and AC-G, illustrating that P groups containing one C-O-P bond are more likely found in the former samples, while AC-G may contain P groups with one, two or even three C-O-P bonds. The O/P atomic ratios obtained from XPS for the same samples are 4.2 for AC, 2.8 for AC-T and 3.5 for AC, AC-T and AC-G, respectively. These ratios are higher than those of C-O-P bonds, pointing out that phosphorus can be also forming P=O bonds (and P-OH bonds in the case of AC, as pointed out by the thermal release of H_2O at high temperatures) in all these samples.

Interestingly, a different porosity development was previously reported by our research group in the case of the gasification of a H_3PO_4-activated carbon prepared under similar conditions than AC (Rosas et al., 2012). In that work, mesoporosity was mostly destroyed after the gasification in air of AC until burn-off of 33%, while microporosity was preserved. These differences can be explained by the temperature chosen for the gasification. In the former work, the gasification of AC proceeded at 450°C for 3 h. At that temperature, C-O-P bonds are thermally stable, and gasification rate in air is noticeably hindered with respect to P-free activated carbons due to the slow rate of oxygen chemisorption and spillover over phosphorus groups and subsequent transfer to carbon free sites on the carbon structure. Differently, in this work gasification of AC takes place in diluted air in a non-isothermal heat treatment from room temperature up to 900°C. During the heating of the sample, oxidation of C-P to C-O-P bonds takes place (Rosas et al., 2012), while carbon gasification rate is much lower than before due to the low oxygen pressure. Once temperature surpasses 850°C, cleavage of C-O-P bonds takes part at fast rateline, with the release of CO_2 (g) and the formation of a C'-P bonds, where C' refers to a carbon edge site formed on the loss of the carbon atom on CO_2. C'-P bonds are highly reactive with oxygen, so that C'-O-P bonds are regenerated, enabling a new gasification circle on the carbon surface. Consequently, the gasification of AC is driven by the continuous reduction of phosphate groups by carbon and oxidation of the freshly formed phosphorane groups by oxygen. Since this redox cycle scavenges carbon atoms close to P species during the reduction step, new porosity is formed in a controlled way. This gasification mechanism is presented in **Figure 5**.

Effect of Textural Properties and Surface Chemistry on Paracetamol Adsorption

PA adsorption on AC, AC-T, and AC-G has been studied in order to evaluate the effect of the adsorbent physico-chemical properties (See **Table 1**). The effect of pH ranging from 2 to 10 on the PA adsorption on several activated carbons was evaluated in a previous work, where we found it to be negligible (Cotoruelo et al., 2011), for what adsorption experiments herein reported have been performed at neutral pH. **Figure 6** shows the PA adsorption equilibrium isotherms at 25°C. From these isotherms, it could be concluded the high ability of these carbon adsorbents to remove PA at very low equilibrium concentrations, obtaining large adsorption capacities even at 2 mg L^{-1}. These adsorption isotherms could be classified as a type L of Giles (Giles et al., 1960). The experimental data are correctly described by the equation proposed by Langmuir, whose characteristic parameter values, q_L (Langmuir monolayer adsorption capacity) and K_L (Langmuir adsorption constant) are showed in **Table 3**.

The highest adsorption capacity is found for AC-G, followed by AC-T, with AC showing the lowest value. Although AC has a larger surface area than AC-T, a higher adsorption capacity was attained in AC-T. When q_L values are normalized by S_{BET}, adsorption capacities of 47.8, 99.9, and 61.7 µg m^{-2} are obtained for AC, AC-T and AC-G, respectively. It is known that the adsorption process has a strong relationship with surface area, but the dominant role of the surface chemistry in PA adsorption is out of the question. In this sense, AC-G shows the highest adsorption capacity, but it only shows a

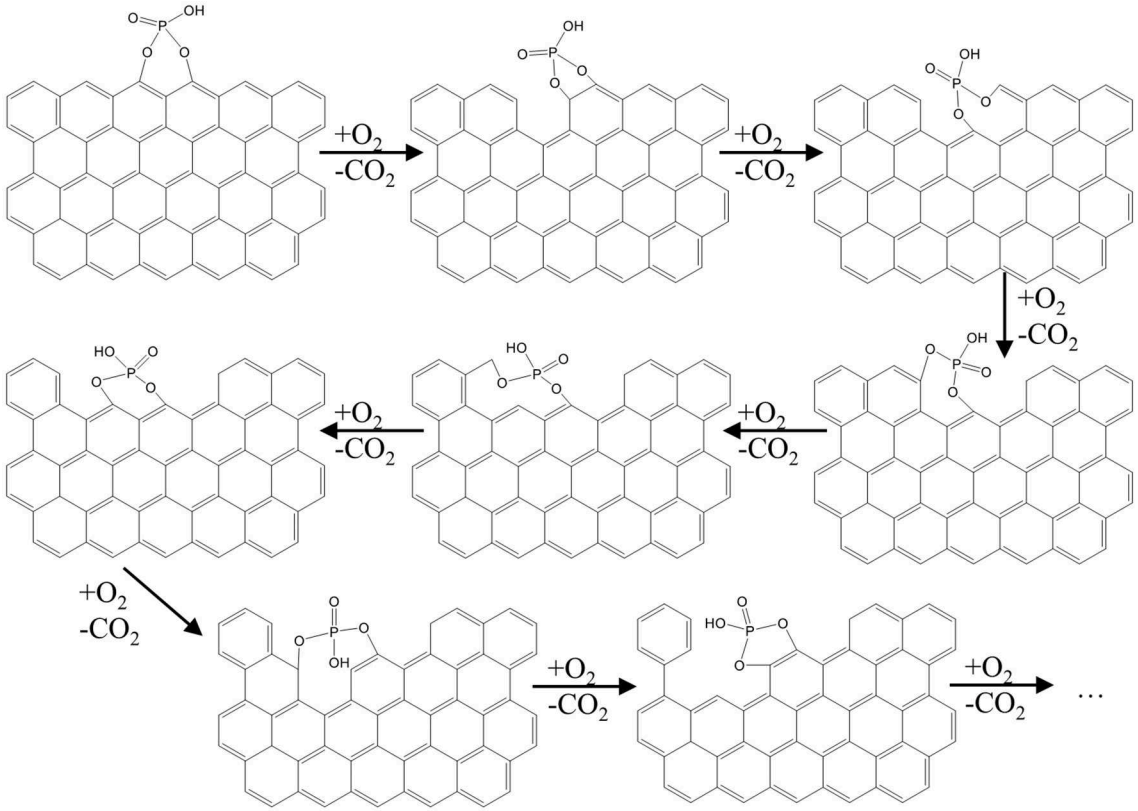

FIGURE 5 | Scheme of a possible gasification mechanism of AC at 900°C.

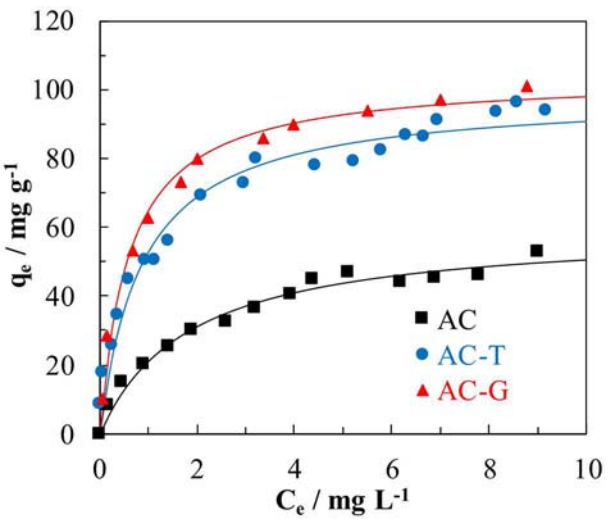

FIGURE 6 | Paracetamol adsorption isotherm at 25°C on AC, AC-T, and AC-G (dots: experimental data; line: Langmuir fitting).

raise in PA adsorption of 10%, despite the increase in 77% of surface area (respect to AC-T). On the one hand, the structure of aromatic molecules, such as PA, is planar, and they show strong π- π dispersion interaction mechanism with basal planes, what increases the affinity of these molecules for the slit-shape, narrowest micropores of activated carbons (Moreno-Castilla, 2004; Rodríguez-Mirasol et al., 2005). The wide micropores developed on AC-G (see **Figure 2b**) do not match the size and shape for the optimum PA adsorption, what explains the minor impact of surface area. On the other hand, it has been known for a long time that increasing the acidity and the hydrophilicity of activated carbons decreases the amount of aromatic molecules adsorbed from aqueous solutions (Moreno-Castilla, 2004). More specifically, some authors have linked the PA adsorption capacity with the acidity of P-containing carbons (Wiśniewski et al., 2011). In this regard, a linear relationship between the Langmuir parameters and the specific acidity (determined as the ratio between the amount of chemisorbed pyridine and S_{BET}) of these samples has been found, **Figure 7**. The agreement is especially relevant in the case of the affinity constant, K_L, confirming that surface acidity governs the interaction between PA and the adsorbents.

The kinetic of PA adsorption results are shown in **Figure 8**, as well as the fitting results using the hyperbolic equation described in Equation 4. The fitting parameters are compiled in **Table 3**. The hyperbolic equation describes correctly the behavior of the experimental data, and the kinetic parameter, q_m, related to the adsorption equilibrium capacity at infinite time is close, for all cases, to the equilibrium capacity, q_e, calculated by Langmuir

TABLE 3 | Langmuir parameters for the paracetamol adsorption at 25°C on the different activated carbons.

Carbon adsorbent	q_L mg g^{-1}	K_L L mg^{-1}	R^2
AC	59.0	0.58	0.977
AC-T	98.4	1.13	0.982
AC-G	108.0	1.50	0.972

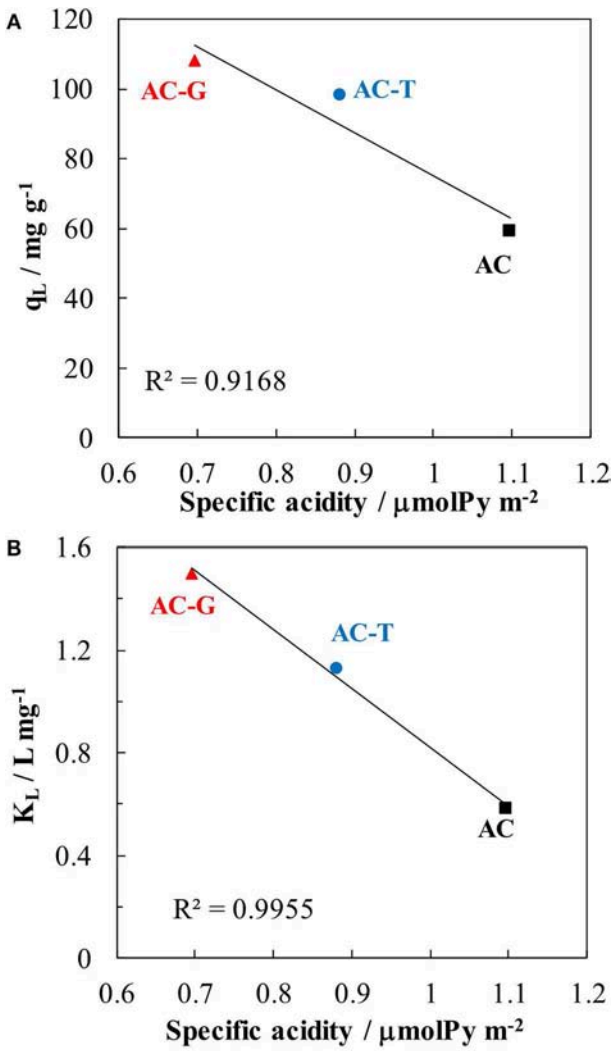

FIGURE 7 | Relationship between paracetamol adsorption capacity and specific acidity **(A)** and paracetamol adsorption equilibrium constant and specific acidity **(B)**.

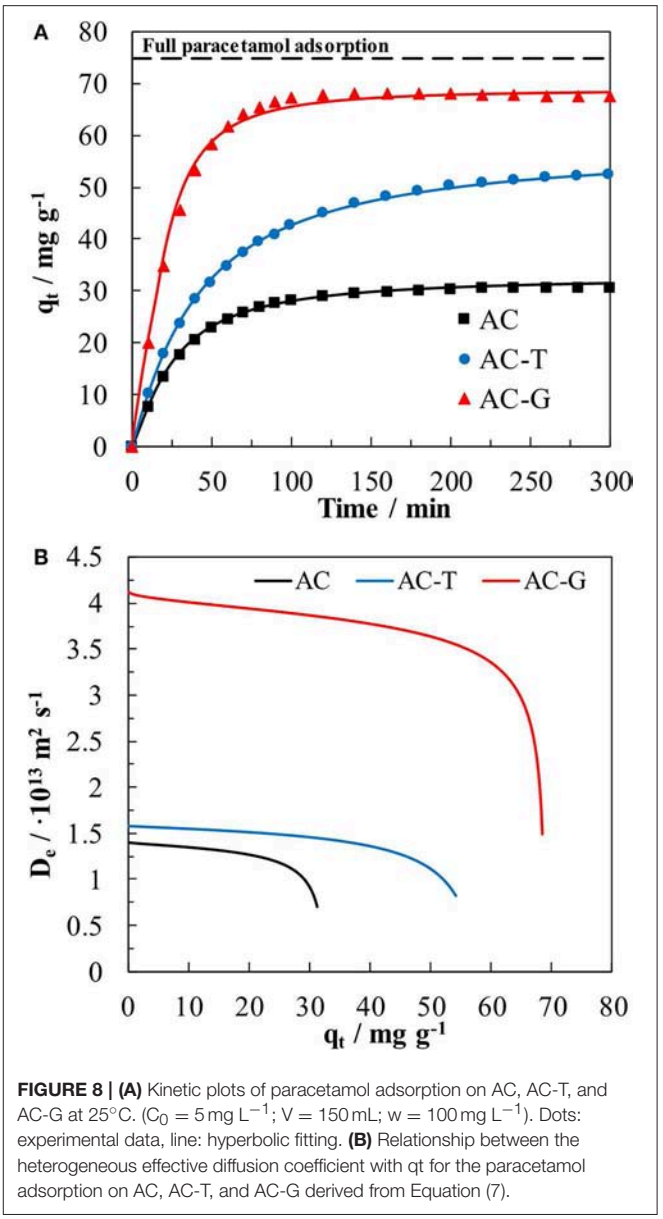

FIGURE 8 | (A) Kinetic plots of paracetamol adsorption on AC, AC-T, and AC-G at 25°C. (C_0 = 5 mg L^{-1}; V = 150 mL; w = 100 mg L^{-1}). Dots: experimental data, line: hyperbolic fitting. **(B)** Relationship between the heterogeneous effective diffusion coefficient with qt for the paracetamol adsorption on AC, AC-T, and AC-G derived from Equation (7).

equation using $Ct_{infinite}$ as equilibrium concentration. As in the equilibrium study, the maximum adsorption capacity was obtained for AC-G adsorbent.

Different steps are differenced in the kinetic adsorption process. At short times, the adsorption rate is faster in the adsorbent showing wider pores (AC and AC-G) owing to the external control of the adsorption process. At intermediate times, the diffusion process becomes internally controlled, with the volume and interconnectivity of mesopore and wide micropores governing the diffusion rate. At this point, the q_t values for AC and AC-G reach near to constant value, an indicative of equilibrium being reached in short times owing to their well-developed meso- and micropore structure, **Table 1**, what increases the internal mass transfer rate of these samples. Contrarily, the heat treatment of AC-T brought a notable porosity shrinkage that reduced the mesoporosity and wide microporosity of this sample. In consequence, the adsorption rate becomes controlled by the diffusion process in the narrowest pores, which have a very slow diffusion rate, and long times are needed to reach the equilibrium for this adsorbent, as depicted in **Figure 8**.

TABLE 4 | Hyperbolic equation and heterogeneous diffusion coefficient parameters obtained from the kinetic study.

Carbon adsorbent	AC	AC-T	AC-G
HYPERBOLIC EQUATION			
a (min^{-1})	0.0388	0.0244	0.0536
q_m ($mg\ g^{-1}$)	32.6	58.0	68.8
m	1.32	1.14	1.78
HETEROGENEOUS DIFFUSION COEFFICIENT			
$b{\cdot}10^{15}$ ($m^2\ s^{-1}$)	4.15	4.73	21.4
c (s)	269758	395161	129769
d (s)	76566	112620	43918

In a previous work (García-Mateos et al., 2015), we defined an heterogeneous effective diffusion coefficient from the kinetic experiments that relies on the amount of adsorbed PA inside the carbon particle, q. A similar procedure has been applied in this work. The obtained parameters from the application of Equation 4 and 6 are compiled in **Table 4**, while the relationship between the heterogeneous diffusivity coefficient and q_t has been plotted in **Figure 8B**. The diffusivity against qt plot corroborates the highest values of the diffusion coefficients are obtained by the carbon adsorbent with the largest porosity development (AC-G). Surprisingly, AC diffusivity coefficient values are lower than those of AC-T, in spite of the presence of a more opened porosity, **Table 1**. This unexpected result can be understood when it is considered that surface diffusion is the main mass transfer mechanism in activated carbons. Since AC shows the less compatible surface chemistry of the tested adsorbents (see the low K_L value in **Table 3**), the surface diffusion rate is negatively impacted by the low affinity between PA and AC surface. Then, the mismatched surface chemistry overcomes the benefits of a well-developed porosity, rendering a large decrease of the effective diffusion coefficient. This result is in agreement with the findings by Błasinski and Kazmierczak (1984) concerning the decrease of surface diffusivity coefficient of p-nitrophenol with the increase of acidity of a series of adsorbents consisting in 14 activated carbons.

Figure 9 shows the breakthrough profiles of PA adsorption on the carbon adsorbents and their solution of the numerical model. All the breakthrough curves have the typical S-shaped curve for column operation with favorable adsorption isotherms (Ruthven, 1984). In those experiments, the value of the capacity adsorption can be determined from the area above the curve. From the breakthrough curves, the bed service time (BST) can be calculated as the time in which the outlet concentration is $C/Ci = 0.05$, where Ci is the concentration of PA in the inlet stream. Another critical parameter for determining the operation and the dynamic response of adsorption on activated carbon is the height of the mass transfer zone (H_{MTZ}), being related to the shape of the curve. A short H_{MTZ} means that most of the adsorption capacity of the carbon bed will be profited when BST is reached. Given that carbon beds have different height owing to the different carbon density, we have included the ratio H_{MTZ} to bed length ($H_{MTZ}\ L_b^{-1}$) for each experiment. All the parameters related to the adsorption in column system are showed in **Table 5**.

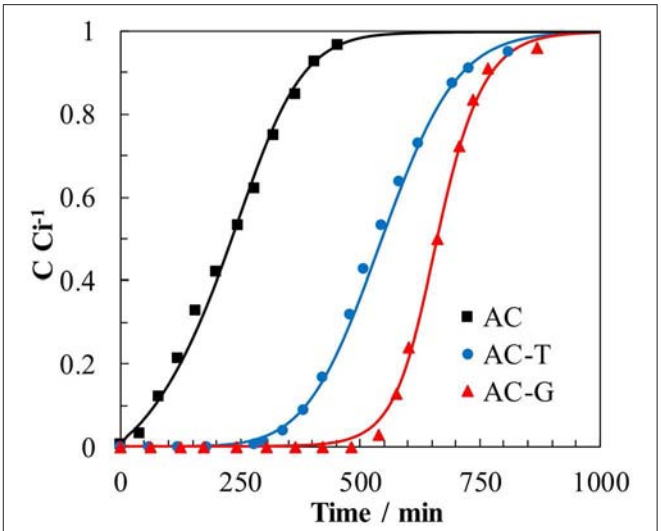

FIGURE 9 | Breakthrough curves in column operation for paracetamol adsorption on AC, AC-T, and AC-G (W: 200 mg, Ci: 5 mg L^{-1}, T: 25°C; Q = 6 mL min^{-1}). Dots: experimental data; lines: prediction from the solution of the mass balance.

TABLE 5 | Breakthrough profile parameters.

Carbon adsorbent	AC		AC-T		AC-G	
	Exp*	MB**	Exp*	MB**	Exp*	MB**
q ($mg\ g^{-1}$)	38.1	39.9	81.1	81.6	100.5	99.7
BST (min)	47	40	354	344	542	530
H_{MTZ} (cm)	2.39	2.46	1.02	1.06	0.54	0.64
$H_{MTZ}\cdot L_b^{-1}$ (%)	74.7	–	37.7	–	15.8	–

*From experimental data.
**Estimated from the mass balance solution.

In our previous work (García-Mateos et al., 2015), we used the adsorption parameters obtained from batch experiences to predict the PA breakthrough curves on small-scale columns. The same approach has been herein implemented. Both the adsorption isotherm parameters obtained from Langmuir equation, **Table 3**, and the relationship between the heterogeneous effective diffusion coefficient and q_t, obtained from Equation (7), are used to solve the mass balance for the adsorption column and for the carbon particles, Equations (8, 9). The good agreement between the predicted breakthrough profiles and the experimental ones in **Figure 9** is worth mentioning. Similar good agreement is seen for the bed performance parameters compiled in **Table 5**, confirming the excellent accuracy provided by this procedure.

It is also remarkable that, in spite of showing only a difference of 23% in the amount of adsorbed PA in full saturation of the carbon bed (qt value on **Table 5**), the bed loaded with AC-G shows a BST 53% higher than its counterpart, AC-T. This is explained by the shorter H_{MTZ} of AC-G. This result brings into light the importance of the gasification process in improving the

mass transfer rate of the P-containing activated carbon, what have been achieved without increasing the surface acidity of the sample (i.e., maintaining a high PA affinity for the surface of AC-G, the activated carbon with the highest value of K_L in **Table 3**). Moreover, the preponderance of surface chemistry over the porosity in PA adsorption on activated carbons is clearly illustrated by the poor AC performance. Even though it would be expectable a higher mass transfer rate in AC owing to its more opened porosity, the low affinity of paracetamol for the surface chemistry of AC sample greatly impedes its adsorption, what hinders the effective surface diffusion rate of this adsorbent. In consequence, mass transfer zone of the bed is much larger than for AC-T, and the BST is severely decreased.

Finally, volumetric capacities (i.e., weight of pollutant retained per volume of the adsorbent bed) are also of importance when designing adsorption columns. Thus, the density values from **Table 1** have been employed for estimating the volumetric performance of AC-T and AC-G. In this sense, the highest PA saturation capacity in volumetric terms is obtained for AC-T, having 105 g per liter of adsorbent in contrast with the 98 g per liter showed by AC-G. Even with the advantage of being a denser solid, AC-T would still show a worse BST than AC-G when working at the same column height owing to the equivalent BST of AC-G being 377 min, which is 10% larger than that of AC-T.

CONCLUSIONS

P-containing activated carbons have been prepared by chemical activation with H_3PO_4 of olive stones at 500°C using an impregnation ratio of 3:1 (parent carbon AC), followed by thermal treatment under inert atmosphere at 900°C (AC-T) or by gasification in diluted air at the same temperature (AC-G). AC-T shows a decrease of S_{BET} of 20%, as well as large porosity shrinkage, loss of oxygen functional groups, decrease of the number of C-O-P species and acidity. On the other hand, microporosity and mesoporosity of AC-G increases 40 and 70%, respectively, while an increase on the quantities of C-O-P species, loss of oxygen functional groups and a lower specific acidity are observed. Controlled gasification by using diluted air at such high temperature has been possible only due to the presence of P groups, which governs the gasification rate and mechanism of these P-containing carbons.

These activated carbons have been used as adsorbents of a model micropollutant, i.e., paracetamol. They all show Langmuir type isotherms and adsorption capacities from 55 to 105 mg g^{-1} at 10 mg L^{-1}. In spite of the large meso- and micropore volumes of the P-containing activated carbon prepared at 500°C, it turns out that adsorption capacity determined in batch experiments is the lowest one, and the adsorption kinetic rate is lower than that of the carbon showing the narrowest pore size distribution, AC-T. This outcome suggests a low affinity between the surface of AC and paracetamol, as pointed out by the low value of the adsorption constant. In addition, the Langmuir adsorption constant and saturation adsorption capacity are linearly related to the surface acidity of the activated carbons. Even though the main micropore size of AC-G does not match the optimum pore size for improving the adsorption of aromatic molecules, it shows the best performance in column adsorption (largest BST and shorter H_{MTZ}) owing to the combination of adequate surface chemistry, large surface area and opened porosity.

In summary, this study provides evidences of the key role played by surface chemistry on the applicability of P-containing activated carbon as adsorbents, and how gasification in diluted air at high temperature produces the most interesting combination of surface chemistry and porosity properties that enhances the performance of such activated carbons for adsorption applications.

DATA AVAILABILITY

The datasets generated for this study are available on request to the corresponding author.

AUTHOR CONTRIBUTIONS

RR-R and FG-M synthesized the materials and with MG prepared the manuscript. Adsorption experiments were performed by FG-M. RR-R performed the characterization of samples and the discussion of the results. JR-M and TC developed the synthesis concept and the adsorption experiments. All authors discussed the result and commented on the manuscript.

ACKNOWLEDGMENTS

This work was supported by the Spanish Ministry of Economy and Competitiveness and FEDER (CTQ2015-68654-R). MCGM gratefully acknowledges the assistance of Spanish Ministry of Economy and Competitiveness through a Juan de la Cierva–Formación fellowship (FJCI-2015-25788).

SUPPLEMENTARY MATERIAL

The Supplementary Material for this article can be found online at: https://www.frontiersin.org/articles/10.3389/fmats.2019.00134/full#supplementary-material

REFERENCES

Aktaş, Ö., and Ferhan, Ç. (2012). "Fundamentals of adsorption onto activated carbon in water and wastewater treatment," in *Activated Carbon for Wastewater Treatment: Integration of Adsorption and Biological Treatment* (Weinheim: WILEY-VCH Verlag GmbH & Co. KGaA), 13–42. doi: 10.1002/9783527639441.ch2

Bandosz, T. J. (2008). "Surface chemistry of carbon materials," in *Carbon Materials for Catalysis*, eds P. Serp and J. L. Figueiredo (Hoboken, NJ: John Wiley & Sons, Inc.), 45–92.

Bansal, R. C., and Goyal, M. (2005). *Activated Carbon Adsorption*. Boca Raton, FL: Taylor & Francis. doi: 10.1201/9781420028812

Bedia, J., Rosas, J. M., Márquez, J., Rodríguez-Mirasol, J., and Cordero, T. (2009). Preparation and characterization of carbon based acid

catalysts for the dehydration of 2-propanol. *Carbon* 47, 286–294. doi: 10.1016/j.carbon.2008.10.008

Bedia, J., Rosas, J. M., Rodríguez-Mirasol, J., and Cordero, T. (2010a). Pd supported on mesoporous activated carbons with high oxidation resistance as catalysts for toluene oxidation. *Appl. Catal. B Environ.* 94, 8–18. doi: 10.1016/j.apcatb.2009.10.015

Bedia, J., Ruiz-Rosas, R., Rodríguez-Mirasol, J., and Cordero, T. (2010b). A kinetic study of 2-propanol dehydration on carbon acid catalysts. *J. Catal.* 271, 33–42. doi: 10.1016/j.jcat.2010.01.023

Bedia, J., Ruiz-Rosas, R., Rodríguez-Mirasol, J., and Cordero, T. (2010c). Kinetic study of the decomposition of 2-butanol on carbon-based acid catalyst. *AIChE J.* 56, 1557–1568. doi: 10.1002/aic.12056

Berenguer, R., Ruiz-Rosas, R., Gallardo, A., Cazorla-Amorós, D., Morallón, E., Nishihara, H., et al. (2015). Enhanced electro-oxidation resistance of carbon electrodes induced by phosphorus surface groups. *Carbon* 95, 681–689. doi: 10.1016/j.carbon.2015.08.101

Bhatnagar, A., Hogland, W., Marques, M., and Sillanpää, M. (2013). An overview of the modification methods of activated carbon for its water treatment applications. *Chem. Eng. J.* 219, 499–511. doi: 10.1016/j.cej.2012.12.038

Błasinski, H., and Kazmierczak, J. (1984). Surface diffusion on active carbon in adsorption from solutions. *Chem. Eng. Commun.* 25, 351–361. doi: 10.1080/00986448408940116

Boehler, M., Zwickenpflug, B., Hollender, J., Ternes, T., Joss, A., and Siegrist, H. (2012). Removal of micropollutants in municipal wastewater treatment plants by powder-activated carbon. *Water Sci. Technol.* 66, 2115–2121. doi: 10.2166/wst.2012.353

Boehm, H. P. (2002). Surface oxides on carbon and their analysis: a critical assessment. *Carbon* 40, 145–149. doi: 10.1016/S0008-6223(01)00165-8

Castro, J. B., Bonelli, P. R., Cerrella, E. G., and Cukierman, A. L. (2000). Phosphoric acid activation of agricultural residues and bagasse from sugar cane: influence of the experimental conditions on adsorption characteristics of activated carbons. *Ind. Eng. Chem. Res.* 39, 4166–4172. doi: 10.1021/ie0002677

Cazorla-Amorós, D., Alcañiz-Monge, J., de la Casa-Lillo, M. A., and Linares-Solano, A. (1998). CO_2 As an adsorptive to characterize carbon molecular sieves and activated carbons. *Langmuir* 14, 4589–4596. doi: 10.1021/la980198p

Cazorla-Amorós, D., Alcañiz-Monge, J., and Linares-Solano, A. (1996). Characterization of activated carbon fibers by CO_2 adsorption. *Langmuir* 12, 2820–2824. doi: 10.1021/la960022s

Cotoruelo, L. M., Marqués, M. D., Leiva, A., Rodríguez-Mirasol, J., and Cordero, T. (2011). Adsorption of oxygen-containing aromatics used in petrochemical, pharmaceutical and food industries by means of lignin based active carbons. *Adsorption* 17, 539–550. doi: 10.1007/s10450-010-9319-x

Cotoruelo, L. M., Marqués, M. D., Rodríguez-Mirasol, J., Rodríguez, J. J., and Cordero, T. (2009). Lignin-based activated carbons for adsorption of sodium dodecylbenzene sulfonate: equilibrium and kinetic studies. *J. Colloid Interface Sci.* 332, 39–45. doi: 10.1016/j.jcis.2008.12.031

Danish, M., and Ahmad, T. (2018). A review on utilization of wood biomass as a sustainable precursor for activated carbon production and application. *Renew. Sustain. Energy Rev.* 87, 1–21. doi: 10.1016/j.rser.2018.02.003

Duan, X., Srinivasakannan, C., Wang, X., Wang, F., and Liu, X. (2017). Synthesis of activated carbon fibers from cotton by microwave induced H3PO4activation. *J. Taiwan Instit. Chem. Eng.* 70, 374–381. doi: 10.1016/j.jtice.2016.10.036

Estrada-Arriaga, E. B., Cortés-Muñoz, J. E., González-Herrera, A., Calderón-Mólgora, C. G., de Lourdes Rivera-Huerta, M., Ramírez-Camperos, E., et al. (2016). Assessment of full-scale biological nutrient removal systems upgraded with physico-chemical processes for the removal of emerging pollutants present in wastewaters from Mexico. *Sci. Total Environ.* 571, 1172–1182. doi: 10.1016/j.scitotenv.2016.07.118

Figueiredo, J. L., Pereira, M. F. R., Freitas, M. M. A., and Órfão, J. J. M. (1999). Modification of the surface chemistry of activated carbons. *Carbon* 37, 1379–1389. doi: 10.1016/S0008-6223(98)00333-9

García-Mateos, F. J., Ruiz-Rosas, R., Marqués, M. D., Cotoruelo, L. M., Rodríguez-Mirasol, J., and Cordero, T. (2015). Removal of paracetamol on biomass-derived activated carbon: modeling the fixed bed breakthrough curves using batch adsorption experiments. *Chemi. Eng. J.* 279, 18–30. doi: 10.1016/j.cej.2015.04.144

Giles, C. H., MacEwan, T. H., Nakhwa, S. N., and Smith, D. (1960). 786. Studies in adsorption. Part XI. A system of classification of solution adsorption isotherms, and its use in diagnosis of adsorption mechanisms and in measurement of specific surface areas of solids. *J. Chem. Soc.* 1960, 3973–3993. doi: 10.1039/jr9600003973

Gonzalez-Serrano, E., Cordero, T., Rodriguez-Mirasol, J., Cotoruelo, L., and Rodriguez, J. J. (2004). Removal of water pollutants with activated carbons prepared from H_3PO_4 activation of lignin from kraft black liquors. *Water Res.* 38, 3043–3050. doi: 10.1016/j.watres.2004.04.048

Gonzalez-Serrano, E., Cordero, T., Rodríguez-Mirasol, J., and Rodríguez, J. J. (1997). Development of porosity upon chemical activation of kraft lignin with $ZnCl_2$. *Ind. Eng. Chem. Res.* 36, 4832–4838. doi: 10.1021/ie970261q

Hita, I., Cordero-Lanzac, T., Gallardo, A., Arandes, J. M., Rodríguez-Mirasol, J., Bilbao, J., et al. (2016). Phosphorus-containing activated carbon as acid support in a bifunctional Pt–Pd catalyst for tire oil hydrocracking. *Catal. Commun.* 78, 48–51. doi: 10.1016/j.catcom.2016.01.035

Jagiello, J., and Olivier, J. P. (2013). 2D-NLDFT adsorption models for carbon slit-shaped pores with surface energetical heterogeneity and geometrical corrugation. *Carbon* 55, 70–80. doi: 10.1016/j.carbon.2012.12.011

Jagtoyen, M., and Derbyshire, F. (1998). Activated carbons from yellow poplar and white oak by H_3PO_4 activation. *Carbon* 36, 1085–1097. doi: 10.1016/S0008-6223(98)00082-7

Kiliç, M., Apaydin-Varol, E., and Pütün, A. E. (2012). Preparation and surface characterization of activated carbons from Euphorbia rigida by chemical activation with $ZnCl_2$, K_2CO_3, NaOH and H_3PO_4. *Appl. Surf. Sci.* 261, 247–254. doi: 10.1016/j.apsusc.2012.07.155

Li, G., Bhosale, S., Tao, S., Bhosale, S., and Fuhrhop, J. H. (2005). Conducting polythiophenes with a broad spectrum of reactive groups. *J. Polym. Sci. A Polym. Chem.* 43, 4547–4558. doi: 10.1002/pola.20928

Li, S., Han, K., Li, J., Li, M., and Lu, C. (2017). Preparation and characterization of super activated carbon produced from gulfweed by KOH activation. *Micropor. Mesopor. Mater.* 243, 291–300. doi: 10.1016/j.micromeso.2017.02.052

López-González, J., de, D., Martínez-Vilchez, F., and Rodríguez-reinoso, F. (1980). Preparation and characterization of active carbons from olive stones. *Carbon* 18, 413–418. doi: 10.1016/0008-6223(80)90033-0

Luo, Y., Guo, W., Ngo, H. H., Nghiem, L. D., Hai, F. I., Zhang, J., et al. (2014). A review on the occurrence of micropollutants in the aquatic environment and their fate and removal during wastewater treatment. *Sci. Total Environ.* 473–474, 619–641. doi: 10.1016/j.scitotenv.2013.12.065

Mailler, R., Gasperi, J., Coquet, Y., Derome, C., Bulet,é, A., Vulliet, E., et al. (2016). Removal of emerging micropollutants from wastewater by activated carbon adsorption: experimental study of different activated carbons and factors influencing the adsorption of micropollutants in wastewater. *J. Environ. Chem. Eng.* 4, 1102–1109. doi: 10.1016/j.jece.2016.01.018

Márquez-Montesinos, F., Cordero, T., Rodríguez-Mirasol, J., and Rodríguez, J. (2001). Powdered activated carbons from Pinus caribaena sawdust. *Sep. Sci. Technol.* 36, 3191–3206. doi: 10.1081/SS-100107767

Marquez-Montesinos, F., Cordero, T., Rodriguez-Mirasol, J., and Rodriguez, J. J. (2002). CO2 and steam gasification of a grapefruit skin char. *Fuel* 81, 423–429. doi: 10.1016/S0016-2361(01)00174-0

Moreno-Castilla, C. (2004). Adsorption of organic molecules from aqueous solutions on carbon materials. *Carbon* 42, 83–94. doi: 10.1016/j.carbon.2003.09.022

Moulder, J. F., Stickle, W. F., Sobol, P. E., and Bomben, K. D. (1995). *Handbook of X-ray Photoelectron Spectroscopy*. Norwalk: PhysicalElectronics Division, Perkin-Elmer Corp.

Onesios, K. M., Yu, J. T., and Bouwer, E. J. (2009). Biodegradation and removal of pharmaceuticals and personal care products in treatment systems: a review. *Biodegradation* 20, 441–466. doi: 10.1007/s10532-008-9237-8

Palomo, J., Ternero-Hidalgo, J. J., Rosas, J. M., Rodríguez-Mirasol, J., and Cordero, T. (2017). Selective nitrogen functionalization of phosphorus-containing activated carbons. *Fuel Process. Technol.* 156, 438–445. doi: 10.1016/j.fuproc.2016.10.006

Petrie, B., Barden, R., and Kasprzyk-Hordern, B. (2014). A review on emerging contaminants in wastewaters and the environment: current knowledge, understudied areas and recommendations for future monitoring. *Water Res.* 72, 3–27. doi: 10.1016/j.watres.2014.08.053

Puziy, A. M., Poddubnaya, O. I., and Ziatdinov, A. M. (2006). On the chemical structure of phosphorus compounds in phosphoric acid-activated carbon. *Appl. Surf. Sci.* 252, 8036–8038. doi: 10.1016/j.apsusc.2005.10.044

Raghavan, N. S., and Ruthven, D. M. (1983). Numerical simulation of a fixed-bed adsorption column by the method of orthogonal collocation. *AIChE J.* 29, 922–925. doi: 10.1002/aic.690290608

Rivera-Utrilla, J., Sánchez-Polo, M., Gómez-Serrano, V., Álvarez, P. M., Alvim-Ferraz, M. C. M., and Dias, J. M. (2011). Activated carbon modifications to enhance its water treatment applications. An overview. *J. Hazard. Mater.* 187, 1–23. doi: 10.1016/j.jhazmat.2011.01.033

Rodríguez-Mirasol, J., Bedia, J., Cordero, T., and Rodríguez, J. J. (2005). Influence of water vapor on the adsorption of VOCs on lignin-based activated carbons. *Sep. Sci. Technol.* 40, 3113–3135. doi: 10.1080/01496390500385277

Rodríguez-Mirasol, J., Cordero, T., and Rodriguez, J. J. (1993). CO_2-reactivity of eucalyptus kraft lignin chars. *Carbon* 31, 53–61. doi: 10.1016/0008-6223(93)90155-4

Rodríguez-Reinoso, F., Molina-Sabio, M., and González, M. T. (1995). The use of steam and CO_2 as activating agents in the preparation of activated carbons. *Carbon* 33, 15–23. doi: 10.1016/0008-6223(94)00100-E

Román-Martínez, M. C., Cazorla-Amorós, D., Linares-Solano, A., and de Lecea, C. S.-M. (1993). Tpd and TPR characterization of carbonaceous supports and Pt/C catalysts. *Carbon* 31, 895–902. doi: 10.1016/0008-6223(93)90190-L

Rosas, J. M., Bedia, J., Rodríguez-Mirasol, J., and Cordero, T. (2009). HEMP-derived activated carbon fibers by chemical activation with phosphoric acid. *Fuel* 88, 19–26. doi: 10.1016/j.fuel.2008.08.004

Rosas, J. M., Bedia, J., Rodríguez-Mirasol, J., and Cordero, T. (2010). On the preparation and characterization of chars and activated carbons from orange skin. *Fuel Process. Technol.* 91, 1345–1354. doi: 10.1016/j.fuproc.2010.05.006

Rosas, J. M., Ruiz-Rosas, R., Rodríguez-Mirasol, J., and Cordero, T. (2012). Kinetic study of the oxidation resistance of phosphorus-containing activated carbons. *Carbon* 50, 1523–1537. doi: 10.1016/j.carbon.2011.11.030

Ruthven, D. M. (1984). *Principles of Adsorption and Adsorption Processes*. New York, NY: John Wiley & Sons.

Solum, M. S., Pugmire, R. J., Jagtoyen, M., and Derbyshire, F. (1995). Evolution of carbon structure in chemically activated wood. *Carbon* 33, 1247–1254. doi: 10.1016/0008-6223(95)00067-N

Tancredi, N., Cordero, T., Rodríguez-Mirasol, J., and Rodríguez, J. J. (1996). Activated carbons from Uruguayan eucalyptus wood. *Fuel* 75, 1701–1706. doi: 10.1016/S0016-2361(96)00168-8

Teodosiu, C., Gilca, A. F., Barjoveanu, G., and Fiore, S. (2018). Emerging pollutants removal through advanced drinking water treatment: a review on processes and environmental performances assessment. *J. Clean. Prod.* 197, 1210–1221. doi: 10.1016/j.jclepro.2018.06.247

Thommes, M., Kaneko, K., Neimark, A. V., Olivier, J. P., Rodriguez-Reinoso, F., Rouquerol, J., et al. (2015). Physisorption of gases, with special reference to the evaluation of surface area and pore size distribution (IUPAC Technical Report). *Pure Appl. Chem.* 87, 1051–1069. doi: 10.1515/pac-2014-1117

Valero-Romero, M. J., García-Mateos, F. J., Rodríguez-Mirasol, J., and Cordero, T. (2017). Role of surface phosphorus complexes on the oxidation of porous carbons. *Fuel Process. Technol.* 157, 116–126. doi: 10.1016/j.fuproc.2016.11.014

Vermeulen, T. (1953). Theory for irreversible and constant-pattern solid diffusion. *Ind. Eng. Chem.* 45, 1664–1670. doi: 10.1021/ie50524a025

Vernersson, T., Bonelli, P. R., Cerrella, E. G., and Cukierman, A. L. (2002). Arundo donax cane as a precursor for activated carbons preparation by phosphoric acid activation. *Bioresour. Technol.* 83, 95–104. doi: 10.1016/S0960-8524(01)00205-X

Wiśniewski, M., Pacholczyk, A., Terzyk, A. P., and Rychlicki, G. (2011). New phosphorus-containing spherical carbon adsorbents as promising materials in drug adsorption and release. *J. Colloid Interface Sci.* 354, 891–894. doi: 10.1016/j.jcis.2010.11.072

Wu, X., and Radovic, L. R. (2006). Inhibition of catalytic oxidation of carbon/carbon composites by phosphorus. *Carbon* 44, 141–151. doi: 10.1016/j.carbon.2005.06.038

Conflict of Interest Statement: The authors declare that the research was conducted in the absence of any commercial or financial relationships that could be construed as a potential conflict of interest.

frontiers in Materials

REVIEW
published: 29 May 2019
doi: 10.3389/fmats.2019.00115

Strategies to Enhance the Performance of Electrochemical Capacitors Based on Carbon Materials

David Salinas-Torres[1,2]*, *Ramiro Ruiz-Rosas*[3], *Emilia Morallón*[2] and *Diego Cazorla-Amorós*[4]

[1] Division of Materials and Manufacturing Science, Graduate School of Engineering, Osaka University, Osaka, Japan, [2] Departamento de Química Física, Instituto Universitario de Materiales, University of Alicante, Alicante, Spain, [3] Departamento de Ingeniería Química, University of Málaga, Málaga, Spain, [4] Departamento de Química Inorgánica, Instituto Universitario de Materiales, University of Alicante, Alicante, Spain

OPEN ACCESS

Edited by:
Ashok K. Sundramoorthy, SRM Institute of Science and Technology, India

Reviewed by:
Thiagarajan Soundappan, Navajo Technical University, United States
Rajib Paul, Case Western Reserve University, United States
Sorin Melinte, Catholic University of Louvain, Belgium

***Correspondence:**
David Salinas-Torres
david@mat.eng.osaka-u.ac.jp;
david.salinas@ua.es

Specialty section:
This article was submitted to Carbon-Based Materials, a section of the journal Frontiers in Materials

Received: 14 January 2019
Accepted: 07 May 2019
Published: 29 May 2019

Citation:
Salinas-Torres D, Ruiz-Rosas R, Morallón E and Cazorla-Amorós D (2019) Strategies to Enhance the Performance of Electrochemical Capacitors Based on Carbon Materials. Front. Mater. 6:115. doi: 10.3389/fmats.2019.00115

The increasing worldwide energy consumption has contributed to both the vast growth of greenhouse emissions from carbon-containing fuels-based sources (coal, petroleum, etc.) and the depletion of the aforementioned sources. Given this scenario, the development of inexpensive and high-performing energy storage devices, which have the least possible environmental impact, is needed. At this point, electrochemical capacitors (ECs) or supercapacitors are a particular alternative or complementary option to batteries and fuel cells (FCs). ECs present high power output and long cycle life, but little power density compared to conventional or Lithium-ion batteries. Therefore, ECs are going to play a pivotal role, not only in portable electronic devices, but also to provide power density in hybrid electric vehicles. Many efforts have been focused on improving the energy output of ECs, although its enhancement keeping the high power density is still the cornerstone of most investigations. Many studies have been conducted toward the development of electrode materials such as metal oxides, conducting polymers or novel carbons. Nevertheless, they have shown important shortcomings to be implemented (i.e., high cost, low electrical conductivity, poor stability, etc.). Recent studies put the spotlight on nitrogen-containing carbon materials as candidates to improve the ECs performance in terms of energy. Optimizing the ECs configuration (asymmetric and hybrid) is another approach reported to tackle the challenge. Additionally, it is important to mention that the design of carbon materials obtained from inexpensive precursors lately attracted the attention of the research community. This review compiles works performed in our research group over the last years. The effect of nitrogen groups present in the carbon network on the capacitance will be reported and the study of asymmetric configuration to enhance de energy density will be discussed, either opening the potential window or by increasing the capacitance. Moreover, a lignin-based ECs will be described as an environmentally friendly approach. Finally, perspective and conceivable research guidelines in order to hurdle the challenges proposed to implement the carbon materials in the field of ECs will be addressed.

Keywords: supercapacitors, N-doped carbon materials, lignin, green chemistry, asymmetric, flexible

INTRODUCTION

The use of energy has helped the development of human civilization and different ways to obtain and to exploit energy have been considered along the history. Nowadays, the authorities have boosted the utilization and development of renewable energies, which have been accompanied by the outstanding advances in energy storage devices to face the decoupling between the energy generation from these renewable technologies and the energy demand. ECs are considered promising devices to store and supply energy efficiently. Unlike conventional capacitors that store energy (a few mF of capacitance) through an electric field, ECs consist of two electrodes generally based on nanostructured porous carbon materials within an electrolyte, in which electrical energy storage on the electrode can occur through two mechanisms. The first one is the formation of the electric double layer (EDL) by adsorption, desorption or ion-exchange of ions at the electrolyte/electrode interface (capacitive process), and the second consists on faradic reactions at the surface of the electrodes (pseudocapacitive process) (Conway, 1999; Simon and Gogotsi, 2008; Brousse et al., 2015). Hence, ECs are classified as electric double-layer capacitors (EDLC) or pseudocapacitors. However, according to the composition of the electrode materials, these are also classified as symmetric, asymmetric or hybrid systems. Even though EC can store much more energy per unit volume/mass than conventional capacitors, it is still not enough so that ECs have to be used in specific applications or combined with other generation and storage systems. Therefore, an important part of the research in the field of ECs is dedicated to enhance the energy density without changing their usual high power output (>10 kW kg^{-1}) and to increase their lifetime.

The maximum energy stored in an EC is given by Equation (1) (that can be applied to EDL capacitors):

$$E_{max} = \frac{1}{2} C V_{max}^2 \quad (1)$$

The improvement in both capacitance (C) and maximum operating cell voltage (V_{max}) results in ECs with high energy density, leading to reliable devices able to deliver high power and to harvest energy quickly. The easiest way to increase the capacitance is to increase specific surface area (SSA) of the electrode.

The maximum power delivered in an EC is expressed as:

$$P_{max} = \frac{V_{max}^2}{4\,ESR} \quad (2)$$

P_{max} depends on the square of cell voltage and the equivalent series resistance (ESR) that encompasses resistive contributions of the ECs components. From Equations (1) and (2), it is clear that voltage has a stronger effect on the performance than capacitance. The capacitance is related to the design of the electrode material, while an increase in the cell voltage is associated with the electrolyte or the device configuration. However, the previous assertion is in fact inaccurate, for instance, it was demonstrated that the tailoring of the surface chemistry of porous carbon materials used as electrodes to increase the capacitance, also extended the maximum operating cell voltage (Bleda-Martínez et al., 2008b; Salinas-Torres et al., 2013; Mostazo-López et al., 2015) and it was also observed that the design of electrolyte to expand the operating voltage resulted in an improvement in terms of specific capacitance (Leyva-García et al., 2016b; Schütter et al., 2016). This correlation between the carbon surface and electrolyte in the formation of EDL was shown in the literature (Deschamps et al., 2013; Forse et al., 2016; Oschatz et al., 2016). Therefore, regardless of the strategy chosen to enhance the ECs performance, the improvement in both capacitance and voltage can occur. Accordingly, it is crucial to study the connection among different parameters (chemical composition, pore structure, interaction electrolyte-surface, etc.) to maximize the EC performance. Since the most used materials in manufacturing electrodes are the nanoporous and nanostructured carbon materials (NCMs), the next sections will be focused on the state-of-the-art of carbon based ECs components (electrode materials and electrolytes) as well as on recent investigation conducted in our research group.

STATE-OF-THE-ART OF EC COMPONENTS

This section includes information about the development of carbon materials and their composites used as electrodes to enhance properties such as capacitance, electrical conductivity as well as new electrolytes with higher operating potential windows, which improve the capacitor performance. Finally, a brief explanation of ECs configurations will be included.

Electrode Materials

It is well-known that NCMs are the most used materials as electrode in ECs, which is due to the combination of high surface area, good electrical conductivity, diversity of structures and a large variety of porous textures. NCMs also present other characteristics, which are not less important, such as high chemical and thermal stability, control of morphology and surface chemistry and wide operating potential range. In addition, from the industrial viewpoint, their non-toxicity, abundance and easy processability make them excellent materials for electrode manufacturing. This section encompasses a summary of the main types of NCMs used as electrode material in ECs, as well as the combination with other electroactive materials.

Outline of the Main Types of NCMs

Activated carbons (ACs) are the conventional carbon materials used as electrodes in commercial ECs because they have specific surface areas larger than 1,000 m^2 g^{-1}, high pore volume, suitable electrical properties and moderate cost (Sevilla and Mokaya, 2014), delivering high capacitance values in both aqueous and organic electrolyte (>200 F g^{-1} and ~120 F g^{-1}, respectively). A way to improve the capacitance would be to increase the SSA. However, the capacitance deviates from the linearity with the SSA at very high SSA (Bleda-Martínez et al., 2010), what can be explained attending to their pore structure. ACs are usually synthesized by chemical or physical activation of carbon precursors (Lozano-Castelló et al., 2001; Bleda-Martínez et al.,

2010; Falco et al., 2013), leading to NCMs that possess an important contribution of narrow micropores (<0.5 nm) and random pore pathways, which hamper the electrolyte ions transport, mainly in organic electrolytes (Fuertes et al., 2004; Liu et al., 2011). For this reason, many works have been addressed to constrain the PSD in the range of mesopores (2–50 nm) and improve the accessibility to the porosity. These are named as ordered mesoporous carbons (OMCs), which are prepared using a hard or soft template (ZnO, SBA-15, copolymer F127, etc.) (Zhou et al., 2003; Li et al., 2007, 2011; Liu et al., 2011; Jiang et al., 2014; Du et al., 2018; Yoshida et al., 2018), and have achieved remarkable electrochemical performance at high current densities, but their relatively low SSA limits the capacitance value. Alternatively, Itoi et al. (2011) used the zeolite Y as template, obtaining a zeolite-templated carbon (ZTC) with interconnected pores and a high SSA (∼3,000 $m^2\ g^{-1}$). In addition, the PSD displayed essentially pores of size of 1.2 nm and exhibited both good gravimetric and volumetric capacitance, attributed to the pore structure matching the radius of naked electrolyte ions, which was in agreement with previous works (Chmiola et al., 2008; Largeot and Portet, 2008). This effect was also observed in the carbide derived-carbons (CDCs) that have pores smaller than 1 nm, leading to an anomalous rise in capacitance (Chmiola et al., 2006). Bearing in mind that micropores enhance the capacitance and meso-macropores facilitate the ion diffusion at high currents, the NCMs with micro-mesopores well-interconnected by macropores would be a promising alternative for ECs (Qie et al., 2013; Valero-Romero et al., 2014). Hierarchical porous carbons (HPCs) fulfill these features and they could achieve ECs with outstanding performance (Wang et al., 2008; Xia et al., 2008; Qie et al., 2013; Li et al., 2014; Ruiz-Rosas et al., 2014; Salinas-Torres et al., 2016). Wang et al. (2008) reported a hierarchical porous graphitic carbon (HPGC) with micropores, mesopores walls, and macropores, which provided a capacitance value larger than 220 Fg^{-1} in 6 M KOH (relatively high in alkaline solution). Moreover, it delivered a two-fold energy and power density values (5.7 Wh Kg^{-1} and 10 kW kg^{-1}) compared to a commercial AC measured at the same conditions and using a two-electrode cell.

There is also an important piece of research on the use of carbon nanotubes (CNTs) which possess a high electrical conductivity, what is very important to reduce ESR in the device. However, their relatively low SSA has hindered their further development in this application because capacitance values are limited in a two electrode cell (<50 F g^{-1}) (Frackowiak et al., 2000, 2002; Lee et al., 2001; Yoon et al., 2004). Therefore, several strategies have focused on increasing the SSA by chemical or electrochemical treatments (Frackowiak et al., 2002; Ye et al., 2005a) or by synthesizing arrays or sponge-like foams which displayed an open porous structure compared to those obtained from CNT films (Futaba et al., 2006; Hsia et al., 2014). Recently, graphene (2D NCM) has also been studied as electrode material in ECs. This material has a theoretical high SSA, high electrical conductivity and the possibility to produce different architectures (Lee J. S. et al., 2013; Yoon et al., 2014; Miller and Outlaw, 2015; Yang et al., 2019). Thus, graphene is a good candidate to prepare binderless electrodes, in which the use of electrical conductivity promotor and even the collector could be avoided. However, the main drawback to make graphene-based ECs is the stacking of graphene sheets that causes an important loss of accessible SSA. Graphene-related materials, mainly reduced graphene oxide (rGO), have also been studied (Yoo et al., 2011; Zhu et al., 2011). Yoo et al. (2011) reported a rGO-based EC with a remarkable energy density 9.7 Wh kg^{-1}, although this value was obtained for electrodes with a very low thickness and its comparison to other NCMs would not be accurate.

Despite the aforementioned progress, many challenges still have to be overcome in the design of carbon-based electrode materials to enhance the capacitance. For this reason, other approaches have also been explored to improve the specific capacitance and electrical conductivity. One of them, taking into account the carbon materials mentioned above, deeps into new structural designs such as mesoporous carbon spheres or carbon nanofiber arrays (Nakamura et al., 2006; Liu et al., 2009, 2010; Wang et al., 2009; Huang et al., 2017), well-aligned free-standing mesoporous carbon nanofibers or CNTs (Esconjauregui et al., 2010; Li et al., 2011; Kang et al., 2013; Yan et al., 2013; Arcila-Velez et al., 2014), interconnected porous carbon fibers (Berenguer et al., 2016), and so on.

Doped NCMs: An Approach to Enhance the Capacitor Performance

The surface functionalization is another strategy to enhance the capacitor performance. NCMs have been modified by introducing various heteroatoms (O, N, S, B, P, Si, etc.) into the carbon network (Hulicova-Jurcakova et al., 2009a; Deng et al., 2015; Liu Z. et al., 2015; Mostazo-López et al., 2015; Xiang et al., 2017; Inagaki et al., 2018). However, nitrogen and oxygen are the most common heteroatoms used to synthesize heteroatom-doped NCMs for their use as electrodes in ECs. Obviously, oxygen has been widely studied because of its inherent presence in the carbon materials. Oxygen functionalities are easily introduced in NCMs by chemical reactions with activating or oxidizing agents. A wide variety of oxygen-containing functionalities can be found in NCMs, such as phenol, carbonyl, ether, carboxylic and quinone groups among others (Figueiredo et al., 1999). Although, it has been established that only quinone groups (CO-type) are electrochemically active in acidic electrolytes (Hsieh and Teng, 2002; Bleda-Martínez et al., 2005; Seredych et al., 2008), the oxygen groups play a key role in the capacitance performance, since they modify the wettability of the surface, the reactivity and the electrical conductivity of the material. Oxygen-functional groups also revealed electrochemical activity in basic electrolyte (Liu et al., 2008; Xu et al., 2015). Xu et al. (2015) reported that a graphitized CDC treated in HNO_3 improved its wettability, which in turn increased its capacitance from 11 to 146 F g^{-1}, showing the important contribution of oxygen-functional groups in the capacitance of the carbon materials. Zhao Y. et al. (2015) reported that a suitable combination of a high amount of oxygen groups (13 wt.%) with porous texture for HPC improved the capacitance in both acid and basic medium. Oxygen groups also show pseudocapacitance in organic electrolyte. In this sense, Nueangnoraj et al. (2015) reported the electrochemical behavior

of ZTC with a high amount of oxygen-functional groups (14.4 wt.%) in organic electrolyte. This large capacitance was related to the redox-active functional groups based on the formation of quinone anion radicals and ether cation radicals.

Concerning the nitrogen-functional groups, they have attracted increasing attention from researchers as good candidates to modify the carbon network because their incorporation can lead to the improvement in electrochemical behavior compared to the pristine NCM mainly because of their contribution to double layer capacitance or pseudocapacitance (Kwon et al., 2009; Yang et al., 2010; Lei et al., 2011; Ornelas et al., 2014; Wei et al., 2016), wettability improvement (Kwon et al., 2009; Yang et al., 2010; Candelaria et al., 2012), stabilizing effect (i.e., decrease of material reactivity) (Salinas-Torres et al., 2015) and electron donor capability (Seredych et al., 2008; Wang et al., 2013). There are many methods to introduce nitrogen-functional groups in NCMs such as reaction with N-containing source (NH_3, urea, NO, etc.), carbonization of a N-containing precursor (melamine, pyridine, etc) and thermal treatment of N-containing precursors infiltrated into a template (Raymundo-Piñero et al., 2002; Xia and Mokaya, 2004; Kruk et al., 2005; Bleda-Martínez et al., 2008a; Inagaki et al., 2010; Nishihara and Kyotani, 2012; Shen and Fan, 2013; Mostazo-López et al., 2015, 2016; Salinas-Torres et al., 2015; Quílez-Bermejo et al., 2017). Using these methods, the most common nitrogen-functional groups generated are pyridine, quaternary N, pyrrole and oxidized N species. It is extensively accepted that pseudocapacitance is related to pyridine or pyrrole groups located at the edges of the graphene layers (Lota et al., 2005; Lei et al., 2011; Su et al., 2011; Ornelas et al., 2014; Wei et al., 2016). While quaternary N and oxidized N species do not produce faradic reactions, their positive charge density can enhance the capacitance and promote the electron transfer (Seredych et al., 2008; Hulicova-Jurcakova et al., 2009b; Wei et al., 2016). Sun et al. (2014) reported a nitrogen-doped porous graphitic carbon (NPGC) with both high SSA of 1,027 $m^2 g^{-1}$ and nitrogen content (7.7 wt%). NPGC presented a high capacitance value in 6 M KOH (293 F g^{-1}) and then, ECs based on NPGC exhibited high energy density value (8.1 Wh kg^{-1}) at a high power density. This outstanding performance was particularly attributed to the nitrogen-functional groups, which improved the wettability, the electrical conductivity and the electron transfer rate. The effect of the nitrogen-functional groups on ECs performance was also reported by Zhao J. et al. (2015). Hierarchical nitrogen-doped carbon nanocages (hNCNCs) were compared to their equivalent sample without nitrogen (hCNCs). The hNCNCs displayed a very high specific capacitance up to 313 F g^{-1} in 6 M KOH and ECs constructed with hNCNCs reached a maximum energy density value of 10.9 W h kg^{-1} while those based on hCNCs exhibited only 7.9 W h kg^{-1}. To a certain extent, the better hNCNCs performance was associated to N-doping that improved the hydrophilicity, which in turns increased both ion-accessible surface and the capacitance. To summarize, nitrogen- functional groups not only enhance the capacitance by faradic reactions but also improve the hydrophilicity and electron transfer rate, which in turn cause the improvement in capacitance performance in ECs.

Regarding other heteroatoms, their effect on the capacitance still remains unclear. However, co-doping processes of some heteroatoms with nitrogen or oxygen-functional groups have shown a synergistic effect (Hulicova-Jurcakova et al., 2009a,c; Wen et al., 2016). Yan et al. (2014) indicated that, despite their low SSA (S_{BET} < 60 $m^2 g^{-1}$), N,P-doped non-porous carbon nanofibers with C-O-P groups and pyrrole-like nitrogen, exhibited a high specific capacitance 224 F g^{-1}, which was related to a synergistic effect in which N-groups delivered a high pseudocapacitance while phosphorus contributed to enhancing the capacitive processes by increasing the wettability. The performance of EC based on N,P-co-doped graphene (G) monoliths was checked by Wen et al. (2016). N/P-Gs were synthesized with different doping level of N and P, leading to a stable EC at 1.6 V in H_2SO_4 and delivering a high energy density value of 11.33 W h kg^{-1}. This value is higher than those obtained from N-doped graphene in the literature (Lee Y. H. et al., 2013), showing that phosphorus groups combined with nitrogen groups cause a synergistic effect. The effect of other co-doping processes (N-S, B-N, etc.) on the electrochemical behavior of the doped-carbon materials has been reported, although studies of the performance of the capacitor in two-electrode cells are scarce (Guo and Gao, 2009; Konno et al., 2010; Tomko et al., 2011; Zhang et al., 2014; Chen C. et al., 2015; Xiang et al., 2017). In view of the above summary on the effect of heteroatoms, it can be concluded that the approach of introducing heteroatoms into the carbon network is a promising method to enhance the energy density in ECs.

NCMs Composites

NCMs have been combined with other electroactive materials such as metal oxides or conducting polymers (CPs) that contribute to the storage of energy through pseudocapacitive processes.

It is well-known that the pseudocapacitance produced by faradic reactions in metal oxides leads to electrode materials with much higher capacitances than those of NCMs. Transition metal oxides (RuO_2, MnO_2, V_2O_5, etc.), spinel oxides ($NiCo_2O_4$ or $MnCo_2O_4$) and Ni/Co hydroxides (Demarconnay et al., 2011; Jiang et al., 2012; Wang et al., 2012; Augustyn et al., 2014) are among the most studied. Regarding RuO_2-based materials, they show extraordinary gravimetric capacitance, making them interesting electrode materials for ECs. The first report about RuO_2-based electrode material in ECs showed a high capacitance (720 F g^{-1}) (Zheng and Jow, 1995). Since then, RuO_2 has widely been studied for their use in ECs (Conway and Pell, 2003; Park et al., 2003; Ye et al., 2005b; Rakhi et al., 2011; Zhang et al., 2011; Huang et al., 2013; Xia et al., 2015). Shen et al. (2016) reported ECs based on RuO_2 nanodots on graphene using ionic liquid as electrolyte, which displayed an energy density of 103 W h kg^{-1} with a potential window of 3.8 V. Metal oxide nanoparticles on graphene were evaluated in alkaline medium by Rakhi et al. (2011) in a two-electrode cell, exhibiting an energy density value of 50.6 Wh kg^{-1} for RuO_2/G. According to these values of energy density, RuO_2 composites are very good candidates as electrode materials, but their price and scarcity hinder their commercialization. At this point, MnO_2 is an

interesting alternative since ECs based on MnO_2/G composites have already exhibited a high energy density value of 33.1 W h kg^{-1} (Rakhi et al., 2011). The combination of RuO_2 with inexpensive metal oxides (such as TiO_2, VO_x, MoO_3, and SnO_2) has been also proposed (Takasu and Murakami, 2000; Sugimoto et al., 2002), leading to RuO_2 composites with a larger SSA that can increase the electrochemical activity. Recently, Ni and Co oxides were evaluated as electrode materials for ECs because they have pseudocapacitance and high electrical conductivity that can also favor the capacitive processes (Faraji and Ani, 2014). In summary, metal oxide-modified NCMs can be considered as promising electrode materials because the faradic reactions and double layer contributions from the metal oxide, combined with the already explained properties of NCMs can lead to enhanced ECs performance (Chen et al., 2018; Lai et al., 2018).

Concerning CPs, polyaniline (PANI), polypyrrole (PPy), polythiophene (PTh), and poly(3,4-ethylenedioxythiophene) (PEDOT), are the most common ones and they have interesting properties that make them suitable materials for their use in ECs. These properties include pseudocapacitance from its redox activity, high electrical conductivity and large electrochemical stability voltage, among others (Snook et al., 2011; Ghosh and Lee, 2012; Wang et al., 2012; Vlad et al., 2016). However, the main drawbacks for their implementation in ECs are their difficult processability and poor mechanical stability of the electrodes due to the changes of volume occurring during the doping/de-doping processes. All this makes necessary the combination of CPs with other materials in order to produce adequate electrodes for ECs. In this sense, NCMs are considered interesting supports to mitigate volume changes and their combination with the most common CPs have already been reported (Snook et al., 2011; Bose et al., 2012; Wang et al., 2012). PPy and PANI are the most studied due to their easy synthesis, environmental stability and low cost (Park and Park, 2002; Gupta and Miura, 2006; Mini et al., 2011). Gupta and Miura (2006) reported SWCNT/PANI composites as excellent electrode material, obtaining a capacitance value of 485 F g^{-1}. Mini et al. (2011) synthesized a PPy thin film on graphene by electropolymerization, obtaining an extraordinary specific capacitance of 1,510 F g^{-1}. As can be seen, the combination of CPs and NCMs is an interesting approach to increase the energy density values through the pseudocapacitance contribution from CPs. In addition, the poor mechanical properties of CPs are improved, which in turn results in an increase in the cycle life of the ECs.

Electrolytes

The electrolytes (salt/solvent) used in ECs can be divided into four groups: organic, aqueous, ionic liquids and solid-state polymer. Organic electrolytes are the most used in commercial ECs because of their high potential stability window (2.5–3.2V). The most used organic electrolyte consists of salts such as triethylmethylamoniumtetrafluoroborate ($TEMABF_4$) or tet raethylammoniumtetrafluroborate ($TEABF_4$) in acetonitrile or propylene carbonate as solvents. However, organic electrolytes present disadvantages such as a high cost, low electrical conductivity, toxicity, and flammability. On the contrary, aqueous electrolytes (H_2SO_4, KOH, or Na_2SO_4) do not have these shortcomings and, even though they exhibit higher specific capacitance and electrical conductivity than those obtained in organic electrolytes, their main drawback is their lower potential stability window (<1.23 V). For this reason, there is an increasing interest in the development of new electrolytes, which may circumvent the shortcomings showed by both organic and aqueous electrolytes. Balducci (2016) indicated the aspects to be considered in the electrolyte design such as large electrochemical stability, high conductivity, low viscosity, high chemical stability, high boiling point and so forth. Ionic liquids, which are composed by an organic cation and an inorganic/organic anion, encompass some of the considerations mentioned above such as low flammability, insignificant volatility, high stability and higher potential stability window (>4 V) (Zhong et al., 2015; Martins et al., 2018). The most studied ILs in ECs are pyrrolidinium and imidazolium cations coupled with anions such as PF_6^-, BF_4^-, or $TFSI^-$. Regarding solid polymer electrolyte, it has both the role of ionic medium and separator. There are many types of solid polymer electrolytes, but the research community has recently been focused on gel polymer electrolytes. They consist of a polymer such as poly-(vinylalcohol) (PVA), or polyethylene oxide (PEO) among others, which is dissolved in aqueous solutions (H_2SO_4, H_3PO_4, etc.) (Choudhury et al., 2009; Fei et al., 2014) and, even though these electrolytes have been claimed as a promising alternative to be used in supercapacitors, they have only been used in specific electronic devices up to date.

Despite the remarkable development in the design of electrolytes so far, strong efforts are being devoted to increase their electrical conductivity and their electrochemical stability, which are key factors in the enhancement on energy density of the ECs.

Device Configuration

The most common classification is based on the composition of electrode material and, although there are some discrepancies to set the borderline among different types of ECs, three configurations are differentiated as follows: (i) symmetric, (ii) asymmetric, and (iii) hybrid. The main features for each configuration will be established in this section along with some specific examples reported in the literature.

Symmetric ECs

This configuration consists of two identical electrodes in terms of chemical composition and mass, regardless of whether both electrodes display a purely capacitive or pseudocapacitive behavior. Most of the symmetric ECs are based on AC in both organic and aqueous electrolytes. Recently, there is an increasing interest in the use of aqueous electrolytes instead of organic ones. The main approach is based on increasing their low working voltage, which is limited by the potentials of water decomposition. To do that, some authors have evaluated the stability of neutral electrolytes such as Na_2SO_4 or Li_2SO_4 (Bichat et al., 2010; Demarconnay et al., 2010; Chen et al., 2018). Bichat et al. (2010) demonstrated that an AC-based symmetric EC using Na_2SO_4 as electrolyte displayed a high stability voltage of

1.6 V and an interesting performance. Later, Gao et al. (2012) reported that AC-based symmetric capacitor using Li_2SO_4 as electrolyte exhibited a high cell voltage of 1.9 V and a good capacitance retention after 10,000 cycles. These high cell voltages are connected to the high overpotential of the negative electrode to electrochemical hydrogen evolution reaction. Therefore, it is essential to develop NCMs with high overpotential values for oxygen and hydrogen evolution reactions in order to broaden the cell voltage.

Asymmetric ECs

Asymmetric supercapacitors are composed of two different electrode materials, one of them with an essentially capacitive behavior, and the other one with pseudocapacitive processes. In addition, ECs based on the same electrode material and different active mass can also be considered as asymmetric configuration (Chae and Chen, 2012; Piñeiro-Prado et al., 2016), regardless of the electrochemical behavior of the electrode material, which can be purely capacitive or pseudocapacitive. The main advantage of these systems is that a small mass balancing causes the unequalization of both positive and negative electrode capacitance values, allowing to expand the available stability potential window for both electrodes and to reach the maximum operating cell voltage.

A wide variety of electrode materials has been used to build asymmetric ECs, although the most common are based on metal oxides, CPs or their composites with NCMs (Demarconnay et al., 2011; Fan et al., 2011; Ou et al., 2015; Kim et al., 2017; Li et al., 2018). Demarconnay et al. (2011) evaluated the maximum cell voltage for an aqueous asymmetric EC constituted by MnO_2/AC, showing a noticeable stability at 2 V. Recently, Ou et al. (2015) reported an asymmetric capacitor based on Na-doped MnO_2 and AC, that had a cell voltage up to 2.4 V. Chen et al. (2011) studied CNT-V_2O_5/AC-based asymmetric EC in organic medium, leading to a high-density energy of 40 W h kg^{-1}. Regarding asymmetric ECs based on CPs, Frackowiak et al. (2006) studied the composites of CNT with CPs (PANI, PPy, PEDOT) in a two-electrode cell, which presented good capacitance values and cell voltages up to 1.8 V. Zhou et al. (2014) indicated that ECs based on aligned CNTs and PEDOT/CNTs in organic medium can reach 4 V of voltage and deliver an outstanding volumetric energy of 82.8 W h L^{-1}.

In summary, this configuration is very promising to enhance the energy density of the capacitors since a suitable selection of electrode materials and a rigorous study of their electrochemical stability limits, will allow us to exploit the entire operating voltage by optimization of mass ratio or composition (Peng et al., 2010; Chae and Chen, 2012).

Hybrid Supercapacitors

Hybrid ECs are those devices that combine a supercapacitor-type electrode and a battery-type one (Chen Y. M. et al., 2015; Yu et al., 2016). Several hybrid systems, such as AC/$MnCo_2S_4$, AC/$NiCo_2S_4$, AC/Co_3S_4 and so on, have been studied. The CPs/NCMs composites as electrodes are also considered by some researchers as battery-type because a large fraction of the charge is stored by faradic reactions. Thus, ECs based on NCMs as negative electrode (capacitor-type) and CPs/NCMs as positive electrode (battery-type) could be classified within this group. Other devices considered as hybrid supercapacitors used redox active electrolyte such as iodide/iodine, bromide/bromine or Fe^{3+}/Fe^{2+} (Frackowiak et al., 2014; Ma et al., 2014; Zhong et al., 2015; Ren et al., 2017). Therefore, the faradic contribution comes from both the electrolyte and the electrode material. For instance, Lota and Frackowiak (2009) reported a supercapacitor consisting of carbon electrodes and iodine-based electrolyte that showed a capacitance value of 125 F g^{-1} at 50 A g^{-1} and a good stability after 10,000 cycles. Undoubtedly, the most important hybrid systems are the ion-lithium capacitors that are based on activated carbon as positive electrode and an intercalation electrode material (graphite, $Li_4Ti_5O_{12}$, etc.) as negative electrode to host lithium ions. LICs can store 5–10 times more energy than conventional supercapacitors and are capable of delivering high power density for a long time (Naoi et al., 2012; Sivakkumar and Pandolfo, 2012; Han et al., 2018).

Along this section, many aspects of how to enhance the EC performance were dealt. Not only the synthesis of NCMs was described, but also different EC configurations were addressed to enhance the EC performance. However, the comparison between different ECs becomes the object of controversy. This is because the important parameters such as power or energy density values are measured at different experimental conditions. In spite of this, a table that summarizes some representative examples of EC based on NCMs can be useful to extract conclusions (see **Table 1**).

ENHANCEMENT OF ELECTROCHEMICAL CAPACITORS PERFORMANCE

This section is dedicated to review some studies related with ECs, which were performed in our research group in order to improve the ECs performance following some of the different approaches mentioned previously. This section is divided in the following four parts:

ECs Based on N-doped Porous Carbon: Stabilizing Effect of N-groups

The role of the nitrogen-functional groups on the electrochemical performance of N-containing porous carbons used as electrode material in ECs has been studied in detail [77]. For this purpose, activated carbon fibers (ACF) were used as carbon source material because of the lower tortuosity of its porosity network compared to other carbon materials. Aniline monomer was adsorbed on the ACF before chemical polymerization to polyaniline which was subsequently carbonized. The ordered structure of the N-containing precursor (i.e., polyaniline) results in the formation of specific type of nitrogen groups after carbonization, which could play a pivotal role in the final performance of these materials used in energy storage applications (Snook et al., 2011; Kim and Park, 2012).

Regarding the preparation of PANI-ACF samples, they were synthesized by a chemical polymerization method described in previous works (Bleda-Martínez et al., 2008a; Salinas-Torres et al., 2012, 2013), obtaining a polyaniline thin film within

TABLE 1 | Overview of EC based on NCMs.

Material	Synthesis	Power	Energy	Remarks	References
Zeolite templated carbon (+) activated carbon (–)	CVD (+) and KOH activation (–)	–	24.5 Wh kg^{-1}	Asymmetric 1.0 M H_2SO_4 V = 1.4 V	Nueangnoraj et al., 2014
Microporous carbon	KOH activation	0.7 kW kg^{-1}	10.9 Wh kg^{-1}	Asymmetric 0.5 M Na_2SO_4 V = 1.8 V	Piñeiro-Prado et al., 2016
Zeolite templated carbon	CVD	23 kW kg^{-1}	5.9 Wh kg^{-1}	Symmetric 1 M H_2SO_4	Mostazo-López et al., 2018
N-Zeolite templated carbon	CVD	98 kW kg^{-1}	7.5 Wh kg^{-1}	Symmetric 1 M H_2SO_4	Mostazo-López et al., 2018
graphene mesosponge	CVD	10 kW kg^{-1}	60 Wh kg^{-1}	Symmetric 1 M Et_3MeNBF_4/PC V = 4.4 V	Nomura et al., 2019
N-Carbon Nanosheets	N-doping of GO	0.111 kW kg^{-1}	86.6 Wh kg^{-1}	Symmetric BMIMPF_6 V = 4.0 V	Li et al., 2017
N,S co-doped carbon nanospheres	pyrolysis of polypyrrole (PPy) and $(NH_4)_2S_2O_8$	0.100 kW kg^{-1}	18.1 Wh kg^{-1}	Symmetric 6 M KOH V = 4.0 V	Xin et al., 2018
N,B co-doped porous carbon nanowires	Electrodeposition of PANI/H_3BO_3 /carbonization	0.200 kW kg^{-1}	22.7 Wh kg^{-1}	Symmetric 1.0 M H_2SO_4 V = 1.6 V	Zhao and Xie, 2018
N-doped activated carbon	Organic routes at mild conditions	0.0612 kW kg^{-1}	14.5 Wh kg^{-1}	Symmetric 1.0 M H_2SO_4 V = 1.4 V	Mostazo-López et al., 2016
N-doped carbon nanocages	MgO template with pyridine/benzene	0.250 kW kg^{-1}	10.9 Wh kg^{-1}	6 M KOH	Zhao J. et al., 2015
CP on aligned CNTs	CVD	269.4 kW kg^{-1}	170.7 Wh kg^{-1}	Asymmetric 2.0 M BMIBF_4/PC V = 4.0 V	Zhou et al., 2014
CNT-V_2O_5/AC-	hydrothermal process	0.210 kW kg^{-1}	40 Wh kg^{-1}	Asymmetric 1 M LiClO4/PC V = 2.7 V	Chen et al., 2011
Metal hidroxide Nanosheets@N-doped CNT	CBD	0.966 kW kg^{-1}	71 Wh kg^{-1}	Asymmetric 2 M KOH	Zhang et al., 2019

the porosity of the ACF with an estimated average thickness of about 0.5 nm. Three different concentrations of aniline monomer were used for aniline adsorption (10, 30, and 70 mM) and a subsequentpolymerization step was performed. Finally, these three different PANI/ACF samples were carbonized at 600 and 800°C by following the method described elsewhere (Salinas-Torres et al., 2015). Porous texture of all samples was characterized by physical adsorption of N_2 at −196 °C, leading to Type I isotherms (typical of microporous solids) and showing an important decrease in the N_2 uptake after PANI loading because of the formation of polyaniline thin film over the surface of the fibers. A small increase in N_2 uptake at low pressures happened after carbonization, although S_{BET} of pristine ACF was not completely recovered.

From the XPS results, it was observed that nitrogen content for ACF/PANI samples dropped after their carbonization. As an example, **Figure 1A** shows the deconvolution of N1s spectra for sample ACF30 and after carbonization. It can be seen some differences between ACF30 and their carbonized counterparts. On the one hand, ACF30 presented the main peak at around 399.5 eV corresponding to neutral amine group (Raymundo-Piñero et al., 2002) and a small peak is located at 402 eV, which is associated to oxidized N species. On the other hand, ACF30-600 exhibited two peaks at different binding energies in comparison to ACF30. One peak appeared at around 398.7 eV related to pyridine groups, while the second peak is centered at 400.5 eV corresponding to pyrrole and pyridone groups (Raymundo-Piñero et al., 2002).

As the temperature increased, both peaks in ACF30-800 become much sharper than those of ACF30-600. The first peak appeared at 398.7 eV and the second shifted to higher binding energies (400.7 eV), which was mainly assigned to pyrrole/pyridone and quaternary N groups. The evolution of nitrogen-functional groups upon heat treatment is in agreement with the carbonization mechanism proposed for PANI (Rozlívková et al., 2011; Kuroki et al., 2013).

After that, symmetric ECs based on these samples were assembled using an Al/Mg-body two-electrode cell and were evaluated in organic electrolyte (1 M; TEMA-BF_4/PC) by a floating test, keeping 3.2 V for 100 h (see **Table 2**).

First, a rate performance study was carried out for all samples and it was noticed that the capacitance values dropped as the current density increases. This decay was sharper in ACF/PANI samples than in the carbonized ones because PANI deposited inside the porosity may hamper the mass transfer rate.

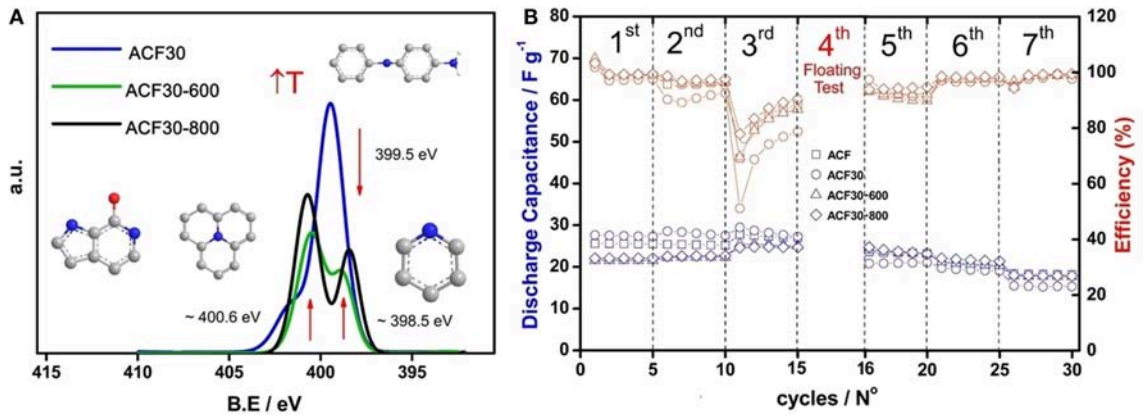

FIGURE 1 | (A) Deconvoluted N1s XPS spectra of ACF30, ACF30-600, and ACF30-800. **(B)** Capacitance performance and efficiency for symmetric ECs based on ACF, ACF30, ACF30-600, and ACF30-800 samples. Electrolyte: 1 M TEMA-BF4/PC.

TABLE 2 | Electrochemical conditions and temperature during the durability test.

Steps	T/°C	V/V	j/mA g $^{-1}$	N° Cycles
1st	40	0–2.5 V	80	1st–5th
2nd	70	0–2.5 V	80	6th–10th
3rd	70	0–3.2 V	80	11th–15th
4th	70	3.2 V*	–	–
5th	70	0–3.2 V	80	16th–20th
6th	70	0–2.5 V	80	21th–25th
7th	40	0–2.5 V	80	26th–30th

**Hold at 3.2 V for 100 h.*

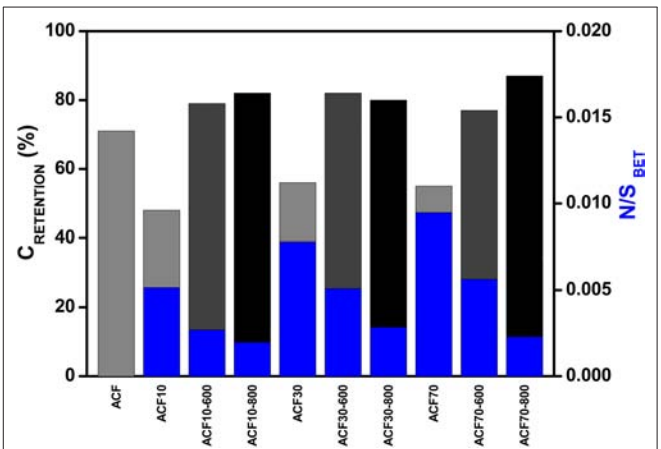

FIGURE 2 | Effect of the nitrogen amount on the capacitance retention (C/Co).

Both coulombic efficiency and capacitance for all symmetric ECs were obtained from the floating test. **Figure 1B** displays the evolution of both capacitance and efficiency during the durability test for symmetric ECs that are based on sample ACF30 and their carbonized counterparts under galvanostatic conditions. ACF-based symmetric EC was also plotted for comparison purposes. At the beginning, coulombic efficiency remained almost constant for all samples. However, the efficiency for ACF30 sample, which had not been carbonized, experienced a moderate fall after increasing the temperature at 70°C because of the polyaniline degradation.

Regarding the discharge capacitance, all samples followed the same trend as coulombic efficiency during the two initial steps. Then, efficiency decreased drastically after increasing the cell voltage up to 3.2 V because of the severe conditions applied, which triggered the decomposition of electrolyte and electrode material, exhibiting the strongest decomposition for ACF30 (non-carbonized sample). At this step, the capacitance diminished slightly for the pristine ACF and ACF30, while the values for the carbonized ones remained constant. After the floating test, it was observed that significant changes happened in terms of the capacitance; ACF30 presented the lowest value, likely due to polyaniline (electrode material) and TEMA-BF_4/PC (electrolyte) degradation. However, carbonized samples and pristine ACF presented the same values in spite of the fact that ACF possesses nearly two-fold SSA as compared to carbonized ones. Thus, the durability test revealed that there was an effect of the nitrogen-functional groups on the capacitance performance. As it was mentioned in the previous section, the insertion of nitrogen into the carbon network enhances the electrical conductivity, the electron transfer rate and improves the stability of the electrode material, decreasing the electrolyte decomposition rate.

In order to elucidate the effect of the N-functional groups on the performance of the N-containing materials, electrochemical characterization, SSA obtained from N_2 adsorption isotherms and XPS data were taken into account. **Figure 2** shows the capacitance retention and nitrogen amount normalized by SSA for all samples. It can be seen that carbonized samples exhibited the highest capacitance retention values, even better than pristine ACF, while ACF/PANI samples showed lower capacitance retention values despite their higher nitrogen content. According to XPS results, PANI- containing ACF presented mainly amine

TABLE 3 | Porous texture and surface chemistry characterization of all samples.

Sample	$S_{BET}/m^2\ g^{-1}$	$V_{DR}\ N_2/cm^3\ g^{-1}$	$V_{DR}\ CO_2/cm^3\ g^{-1}$	$CO/\mu mol\ g^{-1}$	$CO_2/\mu mol\ g^{-1}$
AC	3,310	1.20	0.76	2,250	660
ACH	3,180	1.10	0.70	495	100
CAC	995	0.45	0.41	660	320

groups while carbonized samples showed pyridine and positively charged nitrogen species (pyrrole and quaternary N). Therefore, amine groups present in PANI-containing ACF samples favor the propylene carbonate-ring opening because of their nucleophilic character (Kinage et al., 2011). The carbonate-ring opening is also enhanced by oxygen groups as reported by Cazorla-Amorós et al. (2010). For this reason, ACF showed lower performance than those obtained from carbonized samples, whose N-functionalities provide a stabilizing effect on both the electrolyte and the electrode material. In addition, another parameter obtained from the floating test was the integrated-leakage current, which is related to electrochemical decomposition of the electrolyte or electrode. The smallest integrated-leakage current was displayed by the carbonized samples, confirming the stabilizing effect on the electrolyte or electrode. To conclude, it is demonstrated that specific nitrogen functional groups improve the supercapacitor performance by a remarkable stabilizing effect.

AC/AC-Based Asymmetric EC: Opening the Operating EC Voltage

Asymmetric ECs (in terms of mass configuration) were designed in order to widen the operating voltage using an aqueous electrolyte (Na_2SO_4). Throughout this study, three activated carbons were used: a) ultraporous activated carbon (AC); b) the same one treated in H_2 at 800°C (ACH); c) an activated carbon used in commercial ECs (CAC). Na_2SO_4 was selected because their overpotential for water decomposition is higher than those obtained from both acid and basic electrolytes. In contrast, the pseudocapacitive redox processes, which are associated to the surface chemistry, are mostly suppressed.

Table 3 compiles the porous texture and surface chemistry characterization for all electrode materials. AC and ACH displayed a higher S_{BET} than CAC. Moreover, all samples showed a high development in the microporosity. CAC presented the narrowest PSD according to the difference between $V_{DR}N_2$ and $V_{DR}CO_2$. From surface chemistry results, AC presented the highest amount of oxygen groups, which evolved as CO-type groups (carbonyls, quinone, and phenols) or CO_2-type groups (mainly in carboxylic and lactones) during the thermal treatment (Román-Martínez et al., 1993; Figueiredo et al., 1999; Boehm, 2002). The amount of evolving groups dropped for ACH because most of them were removed by hydrogen treatment, while CAC sample also presented a lower amount of CO-evolving groups than AC. The quantity of CO_2-evolving groups for AC was twice of that for CAC, which were identified mainly as carboxylic groups.

All activated carbons were characterized by cyclic voltammetry (CV) in a three-electrode cell to evaluate their capacitance and the maximum stability potential window in a neutral electrolyte (0.5 M Na_2SO_4) (Fic et al., 2012). The carbon electrodes were prepared with a thickness of 200–300 μm that is similar to the values used in commercial supercapacitors. It is important to note that thickness is a pivotal parameter in the final performance of ECs (Stoller and Ruoff, 2010). The voltammogram for AC exhibited a quasi-rectangular shape related to the electric double layer formation in almost the whole potential window (**Figure 3**). During the negative-going scan, it can be seen that the reduction process appeared at −0.9 V, which corresponds to the hydrogen evolution reaction (Bleda-Martínez et al., 2008b), while during the positive-going scan, the oxidation of the carbon material did not become important up to potentials close to 0.7 V. At this point, the degradation would be severe if the potential remained constant for a long time.

Regarding ACH and CAC, both samples showed electrochemical behavior similar to AC sample. However, in the case of ACH, the hydrogen evolution reaction shifted to more negative potential values and capacitance values were lower than AC because of the increased hydrophobic character produced by the hydrogen treatment. CAC sample also displayed lower values of capacitance than AC.

It is well-known that the positive electrode is completely charged to the upper potential limit before the negative electrode reaches its negative potential limit in symmetric ECs (Peng et al., 2010). Therefore, the design and optimization of an asymmetric capacitor allow us to widen the voltage without affecting the stability of both electrolyte and electrode material. Briefly, the methodology for optimization consisted on assessing the potential limits and the capacitance for both positive electrode and negative one, which must be determined from open circuit potential (E_{OCP}) to the upper potential limit and the lower one, respectively. Then, the mass of one of the electrodes is fixed, while the mass of the second electrode is obtained using Equation (4) (Peng et al., 2010; Chae and Chen, 2012).

$$Q = C_{SP+} \cdot w_{+} \cdot \Delta V_{+} = C_{SP-} \cdot w_{-} \cdot V_{-} \tag{3}$$

Where w_i is the weight of the electrode, C_{SPi} is the gravimetric capacitance of the electrode in the stability potential window and the ΔV_i is the potential window used and is equal to E_i-E_{OCP}. Therefore, after fixing ΔV_+ and ΔV_- from the three-electrode cell characterization, and assuming that the capacitor is completely charged, the mass ratio of the electrodes is determined as follows (Equation 5):

$$w_{+}/w_{-} = C_{SP-} \cdot |\Delta V_{-}| \,/\, (C_{SP+} \cdot |\Delta V_{+}|) \tag{4}$$

Taking into account the potential stability windows and inherent specific capacitance values, asymmetric ECs were built using the carbon materials mentioned above in a two-electrode cell configuration. From the voltammograms of AC sample (**Figure 3**), it was extracted that the open circuit voltage was 0.2 vs. Ag/AgCl, while both the lower potential limit and the upper one were −1 V and 0.8 V vs. Ag/AgCl, respectively. Then, the specific capacitance values from galvanostatic charge-discharge curves at the stability potential windows were determined, obtaining a value of 199 F g^{-1} in the range of −1 to 0.2 V and 131 F g^{-1} between 0.2 to 0.8 V ($\Delta V = 1.8$ V). Finally, the mass ratio was 3 for AC using these capacitance values and the chosen stability potential windows. The same procedure was used for assembling asymmetric ECs based on ACH and CAC in the stability potential window of 1.7 and 2.0 V, respectively.

Finally, asymmetric ECs were analyzed by CV and galvanostatic charge-discharge (GCD) curves to demonstrate the proper operation of the EC in the selected voltage. **Figure 4** shows the Ragone plot for all asymmetric ECs before starting the durability test. It can be seen that the evolution of energy density as power density increases presented different behavior for each EC. AC-based EC showed the highest values of energy density at low power densities. However, its power performance was poorer than that of asymmetric CAC/CAC, which achieved a power density value of 3.8 kW kg^{-1} while the maximum power density for asymmetric AC/AC was 2.3 kW kg^{-1}. Concerning the supercapacitor based on ACH, its power density was also higher than that of AC/AC, despite the lowest energy density showed by ACH/ACH. A higher cell resistance was observed for asymmetric AC/AC compared to asymmetric CAC/CAC. Taking into account that sample CAC has a narrower PSD compared to AC material, which would result in higher ion diffusion resistance inside the pore network, the lower power density for AC/AC capacitor can be due to the lower intrinsic conductivity of the electrode material, which is in agreement with the highest porosity development and higher oxygen content in AC sample. The improvement in the power density of ACH/ACH compared to AC/AC is then due to the enhancement of electrical conductivity in ACH sample as oxygen-functional groups were removed by hydrogen treatment (Bleda-Martínez et al., 2005).

Then, the durability test was performed. It consisted of 10,000 cycles of charge-discharge with a current density of 1 A g^{-1} at the maximum cell voltage suitable for each supercapacitor. From these GCD cycles, parameters related to the capacitor performance were obtained. The capacitance values decreased after 10,000 cycles for AC/AC and CAC/CAC, although the highest drop occurred for the asymmetric AC/AC. Concerning asymmetric ACH/ACH, it would seem that the performance improved after the durability test, although it is not strictly true because in the first 2,000 cycles the capacitance increased up to 34 F g^{-1} from its initial capacitance value and then, it followed the same trend as AC and CAC. This phenomenon was attributed to the increase in the hydrophilic character of the ACH surface during the durability test due to the electrochemical generation of surface oxygen groups, which facilitate the electrolyte diffusion into the accessible porosity and the EDL formation.

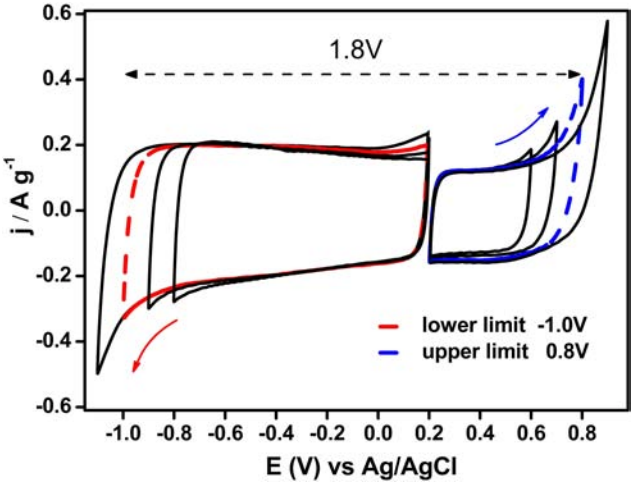

FIGURE 3 | Steady state voltammograms for AC sample from E_{OCP} to both upper and lower limit potential values ($\upsilon = 1$ mV s^{-1}; 0.5 M Na_2SO_4).

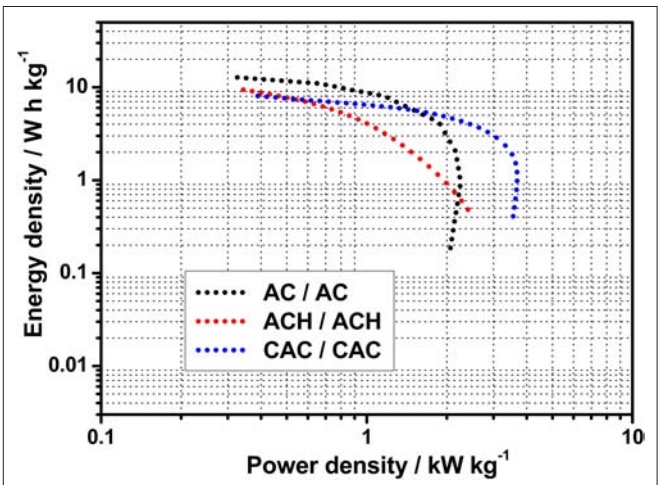

FIGURE 4 | Ragone plot for asymmetric supercapacitors of AC ($\Delta V = 1.8$ V), ACH ($\Delta V = 1.7$ V), and CAC ($\Delta V = 2.0$ V) before durability test.

Regarding the energy and power density values, the asymmetric AC/AC capacitor displayed the highest energy density, while the best performance in terms of durability and power density was presented by asymmetric CAC/CAC, which is in agreement with the low resistance in the device as mentioned above. In addition, energy density values in volumetric basis were calculated because the comparison with other devices is more accurate. Energy densities were 7.3, 4.5, and 6.5 W h L^{-1} for AC/AC, ACH/ACH, and CAC/CAC capacitors, respectively. In conclusion, these values referred to unit volume exceed those obtained from symmetric supercapacitors based on activated carbons in aqueous electrolyte (2.2 Wh L^{-1}) (Simon and Burke, 2008) and, in the case of asymmetric devices based on AC and CAC, they are close to those of symmetric supercapacitors in organic electrolyte (7.6 Wh L^{-1})

(Simon and Burke, 2008) or commercial capacitors (3.2–7.2 Wh L^{-1}) (Simon and Burke, 2008; Gogotsi and Simon, 2011). Therefore, this strategy for designing asymmetric supercapacitors in greener and inexpensive electrolytes could be considered as an outstanding approach to boost the energy density value of the capacitors.

Asymmetric Hybrid Supercapacitor: Enhancement of Capacitance

The capacitance of the carbon-based electrodes can be enhanced using PANI as active material in the electrode together with an AC with high surface area. In this sense, the effect of polyaniline on the capacitance performance of an asymmetric EC in aqueous electrolyte (H_2SO_4) was studied, in which an activated carbon with a high specific surface area (SSA) was used as negative electrode and an activated carbon fiber/PANI composite as the positive one.

The AC was not only selected for its high SSA ($S_{BET} \sim$ 3,000 $m^2\ g^{-1}$) but also for its suitable surface chemistry that contributed to the pseudocapacitance by faradic reactions from CO-type groups (Bleda-Martínez et al., 2006). Additionally, the electrochemical behavior observed in the voltammogram of the material revealed that during the negative-going scan (**Figure 5A**), the hydrogen evolution reaction did not appear up to potential values close to −0.6 V vs. RHE. Therefore, the activated carbon selected possessed a high overpotential for hydrogen evolution reaction, indicating that this activated carbon has a remarkable stability at cathodic reduction potentials that makes it a good candidate as negative electrode. Furthermore, its specific capacitance from GCD experiments was 300 F g^{-1}.

ACF/PANI composite was synthesized by chemical method described in a previous work (Salinas-Torres et al., 2012). The initial concentration of adsorbed monomer was established to have composites with 30 wt.% of aniline monomer inside the porosity. Both voltammograms of ACF and ACF/PANI samples are shown in **Figure 5B** and it can be observed that pristine ACF presented a weak peak centered at 0.60 V vs. RHE during the positive-going scan, which was assigned to surface oxygen groups (Wu et al., 2005). Regarding the ACF/PANI, several redox peaks related to the redox processes of polyaniline were observed, although these are not well-defined and are shifted compared to those obtained from pure polyaniline (Huang et al., 1986). In addition, defects mainly associated to quinone groups cannot be ruled out as consequence of the use of ammonium persulphate as oxidizing agent during the chemical synthesis, which could produce some polyaniline overoxidation (Bleda-Martínez et al., 2008a). Using this methodology, a thin film of polyaniline (0.5 nm) was deposited inside the porosity of the ACF as determined by SAXS (Salinas-Torres et al., 2012), and it did not hinder the ion diffusion inside the porosity considering that the pore size is still sufficiently large (Salinas-Torres et al., 2012). Finally, ACF/PANI sample displayed a specific capacitance of 200 F g^{-1}, showing a 33% increase in capacitance compared to that for the pristine ACF (150 F g^{-1}).

Then, an asymmetric hybrid EC was built, which combined the high SSA and high overpotential for the hydrogen evolution reaction provided by the AC (with a relatively high SSA) and the pseudocapacitance (delivered by PANI deposited on ACF). Before building the asymmetric hybrid EC, the mass ratio of the electrode was optimized to enhance the performance as much as possible by using the mathematical method developed by Snook et al. (2009) to maximize the specific energy density in asymmetric ECS based on CPs. It consisted of fixing the specific capacitance values for both positive electrode (C_+) and negative one (C_-), obtaining the maximum ratio of the active mass according to the Equation (6) and then, the mass of the positive electrode (m_+) was fixed to calculate the mass of negative one (m_-) by using Equation (7):

$$\gamma_{max} = \left(\frac{C_-}{C_+}\right)^{\frac{1}{2}}; \quad (5)$$

$$\gamma_{max} = \frac{m_{(+)}}{m_{(-)}} \quad (6)$$

Additionally, AC-based symmetric EC was assembled for comparison purposes and to demonstrate that asymmetric configuration can be a promising alternative to improve the energy density.

From GCD curves, AC||AC and AC||ACF supercapacitors exhibited a quasi-triangular shape, indicating that bulk faradic processes are negligible and, on the other hand, AC||ACF/PANI showed a distorted triangular shape as consequence of the pseudofaradic processes of PANI. Moreover, the asymmetric AC||ACF/PANI presented a good performance until 2 A g^{-1}.

The evolution of specific capacitance with current density for all supercapacitors at the cell voltage of 1.6 V showed that the capacitance values for AC||ACF/PANI supercapacitor are around 20% higher compared to AC||ACF in the entire range. The evolution of capacitance with the current density for all ECs reveals the ion diffusion problems which are more important with increasing the applied current. The decrease in capacitance is sharper for AC||AC supercapacitor than for both asymmetric capacitors. Moreover, the EC based on AC and ACF/PANI exhibited the best rate performance, which is associated to the faster kinetics for ACF electrodes compared to AC electrodes (Bleda-Martínez et al., 2010). Briefly, AC porosity possesses higher tortuosity than ACF, which explains this electrochemical behavior. Furthermore, the pivotal role of PANI in an asymmetric system was demonstrated because its presence improved the charge transfer and enhanced the total capacitance through the doping-dedoping processes of CP. Additionally, the polyaniline thin film slowed down the oxidation of ACF because the oxygen evolution reaction is probably shifted at more positive potentials, given that the polyaniline oxidation happened at lower potential values.

The specific capacitance for all ECs diminished with cycling. The AC||ACF/PANI capacitor retained more than 80% of the initial value, obtaining an outstanding specific capacitance of 55.3 F g^{-1} after 1,000 cycles. On the contrary, AC-based symmetric EC displayed the lowest specific capacitance after 1,000 cycles despite their initial capacitance, which exceeded the specific capacitance for the AC||ACF supercapacitor, indicating that the AC as electrode material suffered a faster degradation.

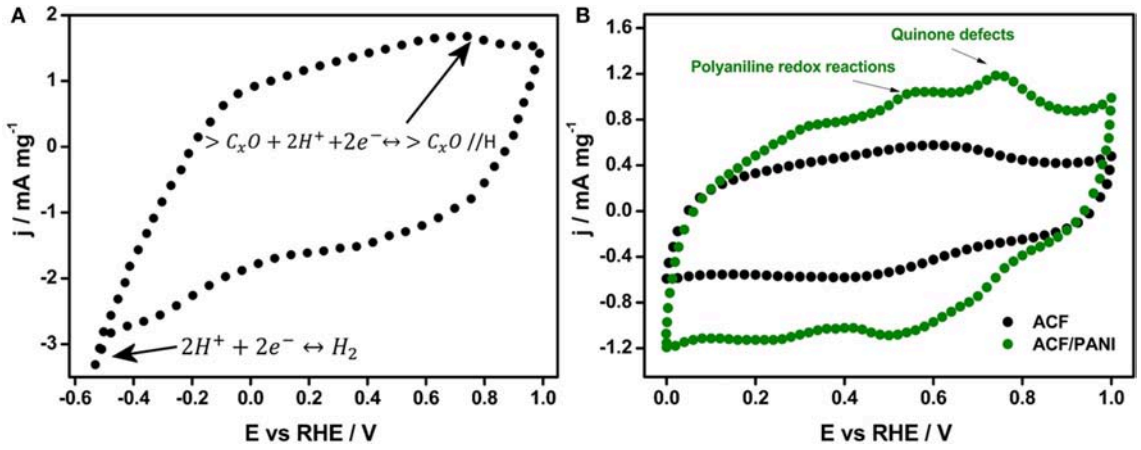

FIGURE 5 | Steady state cyclic voltammograms of: **(A)** AC (negative electrode) and **(B)** ACF/PANI (positive electrode) and pristine ACF in 0.5 M H_2SO_4. Scan rate: 5 mV s^{-1}. Three-electrode cell.

TABLE 4 | P and E obtained for the capacitors at a potential window of 1.6 V in 0.5 M H_2SO_4 as electrolyte.

Device	P_{max} (kW kg^{-1})	P_{max} (kW dm^{-3})	E (W h kg^{-1})	E (W h dm^{-3})	E_{calc} (W h kg^{-1})
AC||AC	0.5	0.1	15.3	2.2	26.7
AC||ACF	1.7	0.3	18.1	2.7	18.2
AC||ACF/PANI	2.1	0.6	20.0	5.7	21.4

Table 4 includes the energy density values for the unpackaged-active material and power density (gravimetric and volumetric basis) as well as the theoretical energy density values using the method described elsewhere (Snook et al., 2009). These theoretical energy density values are close to those obtained experimentally for the asymmetric capacitors, which validates the correct design of the asymmetric EC.

Both power and energy density values increase more than 20% in presence of PANI. The energy and power density values obtained for asymmetric AC||ACF/PANI supercapacitor were close to those obtained in organic electrolyte for supercapacitors based on AC||graphitic carbon (18 W h kg^{-1} and 6.4 kW kg^{-1}) and higher than those obtained in aqueous electrolyte (Simon and Burke, 2008). In addition, the AC||ACF/PANI performance was higher than other previous systems based on PANI or PANI/CM composite (Fusalba et al., 2001; Park and Park, 2002; Meng et al., 2010; Wu et al., 2010), although this comparison is difficult and it could be slightly inaccurate.

On the basis of the results obtained, PANI thin film inside the microporosity of ACF plays a key role in the improvement in power and energy density values of the asymmetric supercapacitors because of redox processes increased the capacitance of the positive electrode. Additionally, PANI film reduced the oxidation of ACF and increased its cycle life, which in turn enhanced the AC||ACF/PANI supercapacitor. This can be considered as an interesting strategy to get advantage of both the high porosity of the porous carbons and the pseudocapacitance of the CP.

EC Using Lignin-Based Porous Carbons: An Environmentally Friendly Approach

This section presents an example of assembling an asymmetric supercapacitor in mass using porous carbons that have been derived from a biomass residue. These porous carbons can be used to design sustainable and inexpensive electrode material. The carbon material selected in this study was lignin-based hierarchical porous carbons (HPCs) synthesized by carbonization of lignin-zeolite mixtures (Valero-Romero et al., 2014). The use of these lignin-based HPCs described by Valero-Romero et al. (2014) was motivated by the environmentally friendly synthesis method, since lignin is one on the most abundant biopolymer in Earth and the use of a zeolite as template to generate porosity allows to avoid chemical activation with corrosive agents. A previous study of these lignin-based HPCs showed an outstanding electrochemical behavior in acidic medium (Ruiz-Rosas et al., 2014). Thus, some of these lignin-based HPCs attained 250 F g^{-1} (three-electrode cell) and showed a relevant capacitance retention at high current densities due to their interconnected porous network.

The preparation of lignin-based HPCs consisted of mixing a lignin solution in ethanol with zeolite Y or BETA according to Valero-Romero et al procedure (Valero-Romero et al., 2014). Samples were named as L-Y-900 and L-B-900 according to the template and temperature used. Their C, O, and N mass surface concentrations were around 84–86, 12–15, and 1–2%, respectively. From **Figure 6A**, it can be observed that the zeolite structure influenced the final porosity. L-Y-900 showed high gas uptake at low relative pressures (micropores) and a small hysteresis loop at a relative pressure of 0.4 (small mesopore volume), while L-B-900 also displayed a high N_2 uptake at low pressures, but its hysteresis loop was larger than L-Y-900 and shifted at relative pressures of 0.7–0.9 (large mesopore volume). For comparison purposes, a commercial activated carbon (ACR)

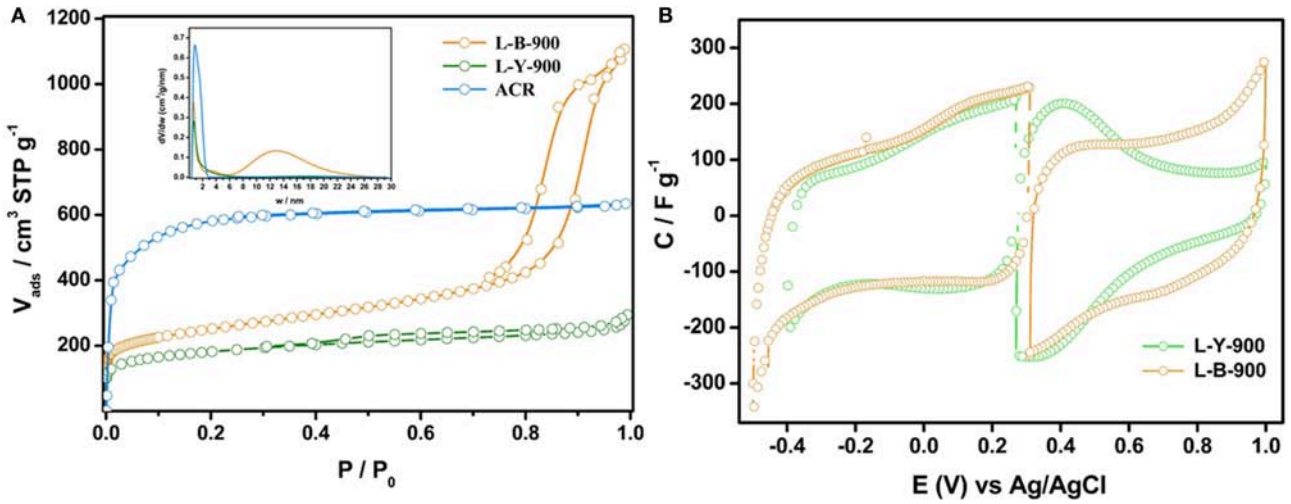

FIGURE 6 | (A) N_2 adsorption-desorption isotherms for all samples (The inset depicts their PSD). **(B)** Steady voltammograms from for both lignin-based HPCs.

was used (mainly microporous). The pore size distribution (inset of **Figure 6A**) confirmed that both lignin-based HPCs possessed a similar volume of micropores and average micropore size. The mesoporosity of L-Y-900 ranged from 2 to 6 nm, while L-B-900 presented a larger size distribution (7–24 nm), which was in agreement with the pore size obtained from TEM images.

Both L-B-900 and L-Y-900 were studied in a three-electrode cell to assess the stability potential window. It must be noted that L-Y-900 has reactive edges sites in its structure, which are susceptible of being electrooxidized (Ruiz-Rosas et al., 2014). Hence, L-Y-900 was previously electrooxidized by CV before building the supercapacitor to stabilize its electrochemical behavior. **Figure 6B** shows the voltammograms from E_{OCP} to the upper and lower potential limits for both samples, which were carefully chosen for the design of the asymmetric supercapacitor.

On the one hand, the voltammogram to negative potential values for L-Y-900 showed a quasi-rectangular shape with some pseudocapacitance contribution close to E_{OCP}, which was assigned to redox processes of CO-evolving oxygen groups (Bleda-Martínez et al., 2005), and a small current at −0.4 V related to the reduction of carbon material (Cheng and Teng, 2003) or the hydrogen evolution reaction (Bleda-Martínez et al., 2008b). On the other hand, the voltammogram of L-Y-900 recorded to positive potentials displayed a broad peak (0.4 V), which was related to the high concentration of electroactive CO-evolving surface oxygen groups (see **Table 5**) (Bleda-Martínez et al., 2005). Moreover, the voltammogram shape was similar to those obtained in acid electrolyte for other templated porous carbons using the zeolite Y (Ania et al., 2007; Itoi et al., 2014). The voltammograms of L-B-900 sample recorded from E_{OCP} to the upper and the lower potential limits showed a lower pseudocapacitance contribution than L-Y-900, which was in agreement with the lower amount of CO-type groups in L-B-900 (see **Table 5**). From GCD curves, specific capacitance values for each lignin-based HPCs electrode was accurately determined and according to their relatively low ohmic drop for both L-Y-900 and L-B-900 at 2 A g^{-1}, it was concluded that these lignin-based HPCs possessed an important connectivity between pores because the ion diffusion was not hampered.

After that, asymmetric supercapacitors based on both L-B-900 and L-Y-900 were built following the procedure shown in section AC/AC-Based Asymmetric EC: Opening the Operating EC Voltage. Moreover, the symmetric counterparts were also assembled as well as a commercial activated carbon-based symmetric supercapacitor (named ACR).

After assembling all symmetric supercapacitors, charge-discharge experiments at different current densities were performed to stabilize the electrochemical behavior. It was observed that the cell resistance was lower in the case of lignin-based HPCs than ACR. It could be indicative of better electrical conductivity and charge transfer, which might be assigned to the specific properties of lignin to produce highly conductive microporous carbon materials (Berenguer et al., 2016). The effect of the lower resistance on the performance was observed in the Ragone plot (**Figure 7**). ACR-based supercapacitor delivered an energy density of 9.9 W h kg^{-1} at 0.53 kW kg^{-1}, while both L-B-900 and L-Y-900 supercapacitors supplied 4.8 and 2.9 W h kg^{-1}, respectively. However, this meaningful difference dropped when higher power output was demanded and the better performance in terms of energy density was presented by HPCs due to their capacitance retention. As the current density was increased from 1 to 64 A g^{-1}, both L-Y-900 and L-B-900 retained 48 and 44% of the initial value, respectively, while the supercapacitor based on ACR lost 77% of the initial capacitance value. This points out the advantages of the interconnected porosity of these HPCs, delivering higher energy density than ACR devices for short discharge times.

Taking into account this maximum voltage for both L-B-900 (1.5 V) and L-Y-900 (1.4 V) as well as the capacitance

TABLE 5 | Porous texture and surface chemistry characterization of all samples.

Sample	SSA/m^2 g^{-1}	V_{DR} N_2/cm^3 g^{-1}	V_{meso}/cm^3 g^{-1}	CO/μmol g^{-1}	CO_2/μmol g^{-1}
L-Y-900	670	0.27	0.10	1,310	470
L-B-900	930	0.36	1.19	800	90
ACR	2,180	0.93	0.06	1,440	380

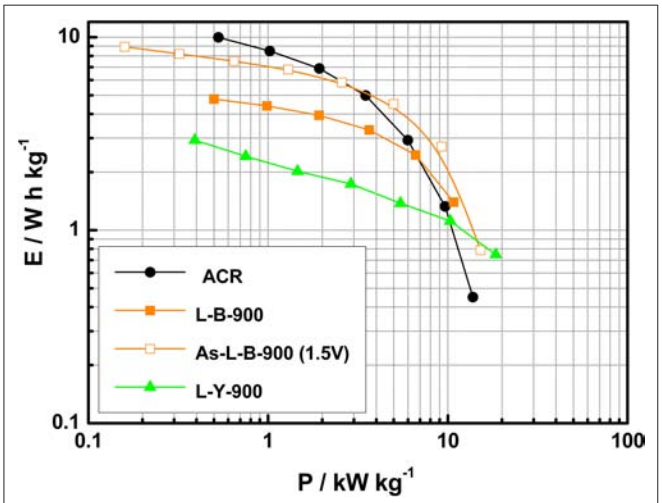

FIGURE 7 | Ragone plot for the symmetric supercapacitors (L-B-900, L-Y-900, ACR, solid dots) at a cell voltage of 1.2 V and the asymmetric based on L-B-900 (hollow dots).

determined by charge-discharge experiments, the mass ratio was optimized to build asymmetric supercapacitors following the method described in section AC/AC-Based Asymmetric EC: Opening the Operating EC Voltage (Peng et al., 2010; Chae and Chen, 2012). The resulting devices demonstrated both a good stability and an improvement in gravimetric capacitance. **Figure 7** shows as an example the Ragone plot for the asymmetric capacitor built with samples L-B-900 working up to 1.5 V. The As-L-B-900 supercapacitor was compared to its symmetric counterpart and the ACR-based symmetric supercapacitor. Even though a higher energy density was delivered by ACR at fixed power density (1.3 kW kg^{-1}), a much better energy efficiency was given by the L-B-900 supercapacitors. Moreover, the energy density increased by 35 and 44% at 1.4 and 1.5 V, respectively, when the asymmetric configuration was used.

Asymmetric L-B-900 improved the energy density delivered, while keeping the high power that is characteristic of using HPCs as electrode materials (see **Figure 7**). The As-L-B-900 working at 1.5 V showed better energy density than ACR from a power density of 3.1 kW kg^{-1}, which was a promising result according to the much lower SSA displayed by L-B-900. Finally, durability tests were performed by charge-discharge at 1 A g^{-1} for 5,000 cycles and it was observed that As-L-B-900 (1.5 V) suffered a noticeable drop in its performance. Given that As-L-B-900 (1.4 V) showed an energy density similar to that obtained at 1.5 V, it was concluded that the most adequate voltage to improve both energy density and stability for As-L-B-900 supercapacitor was 1.4 V. Therefore, this example demonstrates that the mass-balancing of electrodes and the sustainable approach used for the preparation of these electrodes can lead to the production of greener supercapacitors with improved performance.

PERSPECTIVE AND POSSIBLE RESEARCH DIRECTIONS FOR OVERCOMING THE CHALLENGES FOR SPREADING THE USE OF CARBON NANOMATERIALS IN ELECTROCHEMICAL CAPACITORS

In the previous sections, we have illustrated the huge advantages in electrochemical capacitor performance that can be achieved by using carbon nanomaterials as electrodes. However, some important challenges are still to be addressed for widespread utilization of these materials. The most important factor that needs to be improved is the cost. Nowadays, most of the electrode material employed in conventional supercapacitors consists of activated carbon prepared from biomass wastes. The use of low-cost carbon materials is one of the reasons behind the large drop in the price of supercapacitors, which fell below 0.01 $ per farad in 2010 (Conte, 2010). The production cost of such activated carbons is much lower than engineered carbon nanomaterials, and the improvement in the performance cannot compensate such a huge difference.

Chen et al. (2009) in a critical review endorsed the use of supercapacitors for high power and power quality applications and labeled the technical maturity of electrochemical capacitors as developed, but they are also cataloged as expensive devices in terms of the stored energy capacity. Recently, Miller evaluated the current commercial applications of supercapacitors and identified the cost per kWh of a supercapacitor to be roughly 20 times higher than that of Li-ion batteries, and even when considering the power requirement, similar implementation costs for both devices are obtained for these niches applications. Only the long life cycle, reduced volume for equivalent power requirement and safer operation of supercapacitors can explain their ability to replace batteries in these applications (Miller, 2016). At this point, even though nanostructured carbons are the best choice in high power stationary and mobile applications because of their unmatched electrical conductivity and improved ion mobility, their cost could not be assumable unless they are produced using less expensive methods. Nishihara and Kyotani's review on templated nanocarbons concludes with an explicit mention about the high production cost and poor mass-productivity (Nishihara and Kyotani, 2012). They claim that

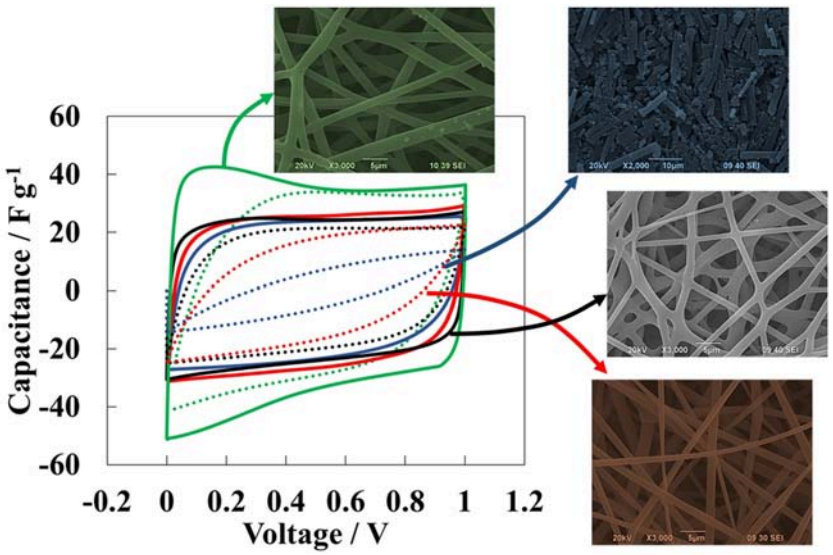

FIGURE 8 | Cyclic voltammetry at 0.1 (solid lines) and 1.0 V s^{-1} (dashed lines) of 2-electrode supercapacitor cells using milled carbon papers electrodes prepared using PTFE as binder and a carbon black as conductivity promoter (blue lines); self-standing carbon paper electrodes (red lines); self-standing and interconnected carbon paper electrodes (black lines); self-standing and interconnected carbon paper electrodes carbonized in 1% air (green lines).

the performance of the templated nanocarbons are actually not superior enough to that of conventional highly porous activated carbons, so that the production cost gap between them cannot be compensated. Salunkhe et al. (2014) also concluded that the production cost is one of the future challenges of nanoarchitectured carbons-based supercapacitors.

Another important issue to reduce the production cost is the processing of the electrodes and cell assembly and match the application requirements. Handling and shaping of nanostructured carbon materials into electrodes are difficult tasks, and novel techniques are currently being developed for facilitate those processes. Also, the development of portable and wearable electronics, and the miniaturization of such devices have experimented a large boost in the last years, and they constitute a niche application where carbon nanomaterials can be the answer for the technical challenges brought by these devices.

As was mentioned, the use of wastes and biomass as precursors is one of the most promising trends for reducing costs of carbon nanomaterials. Dutta et al. (2014) recently reviewed on the production of hierarchical nanostructured carbons from biomass and biopolymers that have an excellent mass transfer and ion mobility, where mesopores act as ion reservoirs and provide high accessibility to micropores, which are responsible for boosting the capacitance of the electrode. This review encompasses the preparation techniques of such carbons (hard-templating or nanocasting, soft-templating, and non-templating routes). Ravi and Vadukumpully (2015) published a review about the use of biomass wastes and other low-cost precursors in the production of CNTs, graphene, quantum dots and so on.

We have recently reported the electrochemical performance of hierarchical porous carbon produced from lignin as carbon source (Ruiz-Rosas et al., 2014). Lignin is one of the most abundant biopolymers in nature and its high availability, reduced cost and a relatively high carbon and aromatic content, make it a suitable precursor for the production of nanostructured carbon materials (Rosas et al., 2014). In this work, the resulting HPCs exhibited interesting electrochemical features such as a high capacitance and an outstanding capacitance retention. The aforementioned results highlight the possibility of "greening" the production of nanostructured porous carbons by choosing inexpensive biomass byproducts as precursors (Ruiz-Rosas et al., 2014; Quesada-Plata et al., 2016).

It is worthy of mention the concept of microcapacitor that arises for fulfilling the requirements of electronic self-powered devices. The use of nanostructured carbon materials in microcapacitors solves the main drawback of the first microcapacitors based on CPs with short cycle life.

Ink printing is one of the most effective techniques for fabricating thin film electrodes from nanostructured carbon. Lawes et al. (2015) reviewed the preparation of energy storage devices using inkjet printing that makes possible to cast electrode materials on large-area flexible substrates. Moreover, through patterning and printing several different layers, the topology of the electrodes could be controlled, allowing the combination of materials for tuning the performance of the supercapacitors. The aforementioned review provides an example about the printing of activated carbon electrodes (Pech et al., 2010), but it is also claimed that in most cases, carbon nanomaterials like CNTs (Kordás et al., 2006) and graphene (Le et al., 2011) are preferred for this technique to achieve controllable thickness lower than 25 μm (Lawes et al., 2015). Other suitable techniques for the production of microcapacitors are selective etching of

TABLE 6 | Summary of NCMs used as electrodes in flexible EC.

Material electrode	Power	Energy	Remarks	References
MXene/rGO	74.4 Wcm^{-3}	32.6 mWh cm^{-3}	3 M H_2SO_4 Stable after 2.10^{-4} cycles	Yan et al., 2017
Porous CF	61 kW kg^{-1}	10 Wh kg^{-1}	1 M H_2SO_4 Precursor: Lignin	Berenguer et al., 2016
NF-doped mesoporous carbon nanofibers (NFMCNFs)	0.248 kW kg^{-1}	8.07 Wh kg^{-1}	1 M H_2SO_4	Na et al., 2017
NiCoP@NiCoP (+) AC (–)	0.750 kW kg^{-1}	34.8 Wh kg^{-1}	3 M KOH Asymmetric V = 1.5	Zhu et al., 2019
N-doped carbon/rGO	4 kW kg^{-1}	20 Wh kg^{-1}	6 M KOH Precursor: cotton	Fan et al., 2017
N-doped AC/Graphene	0.0125 kW kg^{-1}	11.8 W h kg^{-1}	6 M KOH	Xie et al., 2017
MnO_2@ACF	726 μW cm^{-2}	36 μW h cm^{-2}	Electrolyte: carboxymethyl cellulose sodium/Na_2SO_4	Li et al., 2019
MnO_2/rGO (+) MoO_3/rGO (–)	0.0764 Wcm^{-3}	18.2 mWh cm^{-3}	Solid-State EC Fiber-shaped Asymmetric	Ma et al., 2017
Triple heteroatom-doped carbon	0.0459 Wcm^{-3}	0.58 mWh cm^{-3}	Solid-State EC Precursor: Polyimide	Kim et al., 2019
N-carbon/MWCNT	0.072 Wcm^{-3}	0.50 mWh cm^{-3}	Solid-State EC Precursor: Polyimide	Kim et al., 2018
N-doped porous CNF	0.25 kW kg^{-1}	9.20 Wh kg^{-1}	Solid-State Precursor: Polyacrylonitrile/PANI	Miao et al., 2016
RGO/Ni cotton	1.4 Wcm^{-3}	6.1 mWh cm^{-3}	Wire EC PVA/LiCl gel	Liu L. et al., 2015
Vanadium Nitride/CNTs (+) MnO_2/CP/CNTs (–)	270 μW cm^{-2}	96.07 μWh cm^{-2}	Fiber-shaped EC Asymmetric coaxial	Zhang et al., 2017
PANI/CNT/PANI	11,424 μW cm^{-2}	131 μWh cm^{-2}	1 M H_2SO_4 Substrate: activated carbon fiber cloth (ACFC)	Dong et al., 2017
ACF/MnO_2/CNTs	8,028 μW cm^{-2}	11.1 μWh cm^{-2}	6 M KOH Symmetric EC	Dong et al., 2016
Activated carbon textile	0.025 W cm^{-3}	18 mWh cm^{-3}	1 M H_2SO_4 Good mechanical and electrical properties	Lam et al., 2016
MnO_2@carbonized cotton	3.97 W cm^{-3}	5.71 mWh cm^{-3}	V = 1.6 V Stable after 1.10^{-4} cycles	Wang et al., 2019
r-Bi_2O_3/graphene (+) Co_3O_4/graphene (–)	0.690 W cm^{-3}	7.74 mWh cm^{-3}	6 M KOH Asymmetric Substrate: bacterial cellulose	Liu et al., 2017
Graphene nanomesh film (GMF)	3,000 W cm^{-3}	2.3 mWh cm^{-3}	6 M KOH and PVA/KOH polymer	Zhang et al., 2018
Holey rGO film (+) rGO@Fe_3O_4 (–)	25 kW kg^{-1}	148 Wh kg^{-1}	Li-ion EC	Liang et al., 2018
Activated porous carbon	2.29 W cm^{-3}	4.70 mWh cm^{-3}	5 M LiCl Substrate: carbon fiber textile Stable after 25.10^{-3} cycles	Han et al., 2019
Phosphorene/graphene	1.5 W cm^{-3}	11.6 mWh cm^{-3}	Electrolyte: $BMIMPF_6$ V = 3.0 V	Xiao et al., 2017
Sheet-like nanocarbons	35 kW kg^{-1}	51.7 Wh kg^{-1}	Electrolyte: $EMIMBF_4$ V = 3.0 V	Su et al., 2017

titanium carbide substrates (Chmiola et al., 2010), chemical vapor deposition (CVD), laser-induced porous graphene (Gao et al., 2011; Lin et al., 2014) and electrospray of CNT or graphene suspensions (Kim et al., 2006; Tang et al., 2015).

In the case of hard templated carbons, electrophoretic deposition of the template followed by the preparation of the carbon material is an interesting alternative for the production of thin films (Berenguer-Murcia et al., 2013). The capacitance

retention of the powdered sample at high scan rates was lower than that of the ZTC thin film deposited on the carbon collector. Leyva-García et al. (2016a) prepared a binderless thin film made of mesoporous carbon material using a mesoporous silica thin film as hard-template. This process produced a continuous mesoporous carbon thin film having a mean pore size between 2 and 3 nm. The 2-electrode microcapacitor cell based on the amorphous carbon and the composite thin film achieved capacitance values of 5.0 and 3.7 mF cm^{-2} at 5 mA cm^{-2}, respectively. Moreover, full capacitance retention remained after 50,000 cycles. It indicates that electrophoretic deposition or dip-coating of hard templates are promising strategies to prepare binderless thin film of nanostructured carbon materials with outstanding performances.

Kyotani et al. (1997) and Itoi et al. (2011) reported a different approach by preparing a highly microporous ZTC with (S_{BET} ∼ 3,600 m^2 g^{-1}) and a three-dimensional ordered structure consisting of a highly curved graphene layer. It showed improved ion mobility and proneness to be easily electro-oxidized, forming CO-evolving oxygen groups that boosted the pseudocapacitance in acid electrolyte (Nueangnoraj et al., 2014). However, the preparation of a thin film from the powdered form or the replication of this structure is a challenge. The use of electrospray to prepare thin films of superporous ZTC on different substrates with adjustable thicknesses has already been proposed to overcome these hurdles (Rosas et al., 2016).

Among the alternatives encompassed toward the fabrication of supercapacitors, the use of flexible EC is expected to be an outstanding option able to fulfill the requirement to be utilized in countless valuable applications in portable and wearable electronic devices (Chen et al., 2017; Muzaffar et al., 2019). In these systems, the electrode material is usually composed by either a thin film of nanostructured materials or by a binderless, flexible textile electrode (Ye et al., 2018). The electrodes of these devices should be highly conductive and have a large energy density in addition to good mechanical properties.

In this sense, graphene was identified as a unique material for this purpose because of its atom-thick two-dimensional structure (Zhong et al., 2015), what makes graphene sheets easily bendable in the direction normal to its surface, providing it with good flexibility (Wang and Shi, 2015). However, CNTs, CNTs/graphene or carbon microfiber are also an excellent alternative as active phase in these devices (Cheng et al., 2013; Park et al., 2013) as self-standing electrodes in flexible supercapacitors (Zhang et al., 2015).

The two main strategies for their production are (Nyholm et al., 2011; Dubal et al., 2014; Ginting et al., 2018; Heo et al., 2018): (i) to support the active materials (metal oxides or CPs) on flexible substrates (metal sheet, carbon paper or insulating support) from dipping-dry to electrodeposition (Hu et al., 2010; Tang et al., 2015), CVD, electrografting (Aqil et al., 2015), etc. (ii) the fabrication of flexible free-standing films of the active materials (mainly nanostructured carbon materials that act as both the active phase and the current collector). These flexible free-standing films can be attained from fibrillar forms of carbon, such as CNTs, carbon nanofibers and activated carbon microfibers (Shi et al., 2013). Free-standing CNT films can be prepared by methods such as filtration and evaporation, and can be easily transferred to the plastic substrate to pack them into cells.

One of the most suitable methods for the production of free-standing electrodes is electrospinning. Berenguer et al. (2016) recently reported the outstanding performance of seamless carbon electrodes prepared by the electrospinning of lignin solution followed by their air stabilization and carbonization. Carbon fibers of 1 μm in diameter, high structural order and surface areas as high as 1,100 m^2 g^{-1} can be obtained using this method (Lallave et al., 2007). Interestingly, as the heating rate of the stabilization step was increased over the allowable limit, partial melting of the lignin fibers was observed. This resulted in an improved electrical conductivity of the resulting film.

Thus, supercapacitors based on these self-standing paper electrodes made of carbonized electrospun lignin fibers were assessed. Additionally, a supercapacitor based on these self-standing paper was processed using a conventional procedure for what the carbon paper was milled along with a conductivity promoter and a binder. The destruction of such morphology revealed that the fiber morphology is responsible for the remarkable capacitance retention (see **Figure 8**) (Berenguer et al., 2016). Moreover, the interconnection of fibers achieved by partial melting of lignin delivered an improvement in the capacitance retention (solid black voltammogram, **Figure 8**).These results point out that self-standing, flexible electrodes with outstanding performance are achievable using green precursors and alternative techniques as electrospinning.

Some of the most representative breakthroughs achieved in the field of flexible capacitors based on carbon materials are summarized in **Table 6**.

As a summary, supercapacitors are considered as a mature technology. However, their performance needs to be improved in order to expand their potential applications, whereas their costs per Farad and Watt·hour still need to be lowered. In this sense, the use of nanostructured carbon materials could be highly beneficial. Although many challenges are still ahead, expectations are high, and the next years would probably bring a huge development in the commercial implementation of these materials as electrodes of novel forms of supercapacitors.

CONCLUSIONS

Herein we review the recent breakthroughs achieved in the field of supercapacitors. Most researches on EC have been addressed to enhance the energy output by designing the electrode materials, many other issues have been also tackled. In this vein, the search of new electrolytes and the optimization of advanced configurations have been studied. Regarding the electrode materials, N-doped carbon materials have been attracted the attention because the introduction of nitrogen functionalities into the carbon network enhances important properties, such as electrical conductivity, wettability, and the

stability of the material. As for the electrolytes, ionic liquids are being lately studied due to its large electrochemical stability voltage, while aqueous electrolytes have also caught the attention because of the higher capacitance of the electrode materials in this medium in comparison to organic electrolytes. However, the low potential stability window of aqueous electrolytes have motivated the study of new configurations (hybrid and asymmetric) in order to expand the voltage of the devices. In the view of the recent advances in the field of ECs, it can be envisaged that the future direction will be focused on the development of lightweight and flexible electrode materials. At this point, graphene and CNTs are the main alternatives, however, the main shortcoming to reach the target application is the large scale production of ECs based on these carbon materials because of their high cost to produce them. In conclusion, the development of energy-storage devices should consider the performance of the resulting EC as well as the production costs in order to implement these devices in practical applications such as portable electronics or hybrid electric vehicles.

AUTHOR CONTRIBUTIONS

DS-T performed and analyzed the experiments related to the publications summarized in the present review. DS-T conceived and wrote this manuscript. RR-R contributed to the manuscript writing and revision. EM and DC-A contributed to the design and conception of the study and discussion of the results as well as the manuscript writing and revision. All authors approved the manuscript for publication.

FUNDING

We want to acknowledge the financial support by the Ministry of Economy and Competitiveness of Spain (MINECO) and FEDER (CTQ2015-66080-R MINECO/FEDER and MAT2016-76595-R).

ACKNOWLEDGMENTS

DS-T (J171015004) thanks JSPS for the International Postdoctoral Research Fellowships.

REFERENCES

Ania, C. O., Khomenko, V., Raymundo-Piñero, E., Parra, J. B., and Béguin, F. (2007). The large electrochemical capacitance of microporous doped carbon obtained by using a zeolite template. *Adv. Funct. Mater.* 17, 1828–1836. doi: 10.1002/adfm.200600961

Aqil, A., Vlad, A., Piedboeuf, M.-L., Aqil, M., Job, N., Melinte, S., et al. (2015). A new design of organic radical batteries (ORBs): carbon nanotube buckypaper electrode functionalized by electrografting. *Chem. Commun.* 51, 9301–9304. doi: 10.1039/c5cc02420j

Arcila-Velez, M. R., Zhu, J., Childress, A., Karakaya, M., Podila, R., Rao, A. M., et al. (2014). Roll-to-roll synthesis of vertically aligned carbon nanotube electrodes for electrical double layer capacitors. *Nano Energy* 8, 9–16. doi: 10.1016/j.nanoen.2014.05.004

Augustyn, V., Simon, P., and Dunn, B. (2014). Pseudocapacitive oxide materials for high-rate electrochemical energy storage. *Energy Environ. Sci.* 7:1597. doi: 10.1039/c3ee44164d

Balducci, A. (2016). Electrolytes for high voltage electrochemical double layer capacitors: a perspective article. *J. Power Sources* 326, 534–540. doi: 10.1016/j.jpowsour.2016.05.029

Berenguer, R., García-Mateos, F. J., Ruiz-Rosas, R., Cazorla-Amorós, D., Morallón, E., Rodríguez-Mirasol, J., et al. (2016). Biomass-derived binderless fibrous carbon electrodes for ultrafast energy storage. *Green Chem.* 18, 1506–1515. doi: 10.1039/C5GC02409A

Berenguer-Murcia, Á., Ruiz-Rosas, R. R., García-Aguilar, J., Nueangnoraj, K., Nishihara, H., Morallón, E., et al. (2013). Binderless thin films of zeolite-templated carbon electrodes useful for electrochemical microcapacitors with ultrahigh rate performance. *Phys. Chem. Chem. Phys.* 15, 10331–10334. doi: 10.1039/C3CP51945G

Bichat, M. P., Raymundo-Piñero, E., and Béguin, F. (2010). High voltage supercapacitor built with seaweed carbons in neutral aqueous electrolyte. *Carbon* 48, 4351–4361. doi: 10.1016/j.carbon.2010.07.049

Bleda-Martínez, M. J., Lozano-Castelló, D., Cazorla-Amorós, D., and Morallón, E. (2010). Kinetics of double-layer formation: influence of porous structure and pore size distribution. *Energy and Fuels* 24, 3378–3384. doi: 10.1021/ef901521g

Bleda-Martínez, M. J., Lozano-Castelló, D., Morallón, E., Cazorla-Amorós, D., and Linares-Solano, A. (2006). Chemical and electrochemical characterization of porous carbon materials. *Carbon* 44, 2642–2651. doi: 10.1016/j.carbon.2006.04.017

Bleda-Martínez, M. J., Maciá-Agulló, J. A., Lozano-Castelló, D., Morallón, E., Cazorla-Amorós, D., and Linares-Solano, A. (2005). Role of surface chemistry on electric double layer capacitance of carbon materials. *Carbon* 43, 2677–2684. doi: 10.1016/j.carbon.2005.05.027

Bleda-Martínez, M. J., Peng, C., Zhang, S., Chen, G. Z., Morallón, E., and Cazorla-Amorós, D. (2008a). Electrochemical methods to enhance the capacitance in activated carbon/polyaniline composites. *J. Electrochem. Soc.* 155, A672–A678. doi: 10.1149/1.2956969

Bleda-Martínez, M. J., Pérez, J. M., Linares-Solano, A., Morallón, E., and Cazorla-Amorós, D. (2008b). Effect of surface chemistry on electrochemical storage of hydrogen in porous carbon materials. *Carbon* 46, 1053–1059. doi: 10.1016/j.carbon.2008.03.016

Boehm, H. (2002). Surface oxides on carbon and their analysis: a critical assessment. *Carbon* 40, 145–149. doi: 10.1016/S0008-6223(01)00165-8

Bose, S., Kuila, T., Mishra, A. K., Rajasekar, R., Kim, N. H., and Lee, J. H. (2012). Carbon-based nanostructured materials and their composites as supercapacitor electrodes. *J. Mater. Chem.* 22, 767–784. doi: 10.1039/C1JM14468E

Brousse, T., Belanger, D., and Long, J. W. (2015). To be or not to be pseudocapacitive? *J. Electrochem. Soc.* 162, A5185–A5189. doi: 10.1149/2.0201505jes

Candelaria, S. L., Garcia, B. B., Liu, D., and Cao, G. (2012). Nitrogen modification of highly porous carbon for improved supercapacitor performance. *J. Mater. Chem.* 22:9884. doi: 10.1039/C2JM30923H

Cazorla-Amorós, D., Lozano-Castelló, D., Morallón, E., Bleda-Martínez, M. J., Linares-Solano, A., and Shiraishi, S. (2010). Measuring cycle efficiency and capacitance of chemically activated carbons in propylene carbonate. *Carbon* 48, 1451–1456. doi: 10.1016/j.carbon.2009.12.039

Chae, J. H., and Chen, G. Z. (2012). 1.9V aqueous carbon–carbon supercapacitors with unequal electrode capacitances. *Electrochim. Acta* 86, 248–254. doi: 10.1016/j.electacta.2012.07.033

Chen, C., Fan, W., Zhang, Q., Fu, X., and Wu, H. (2015). One-step hydrothermal synthesis of nitrogen and sulfur co-doped graphene for supercapacitors with high electrochemical capacitance performance. *Ionics* 21, 3233–3238. doi: 10.1007/s11581-015-1522-z

Chen, H., Cong, T. N., Yang, W., Tan, C., Li, Y., and Ding, Y. (2009). Progress in electrical energy storage system: a critical review. *Prog. Nat. Sci.* 19, 291–312. doi: 10.1016/j.pnsc.2008.07.014

Chen, X., Paul, R., and Dai, L. (2017). Carbon-based supercapacitors for efficient energy storage. *Natl. Sci. Rev.* 4, 453–489. doi: 10.1093/nsr/nwx009

Chen, Y., Zhang, J., Li, M., Yang, C., Zhang, L., Wang, C., et al. (2018). Strong interface coupling and few-crystalline MnO_2/Reduced graphene oxide composites for supercapacitors with high cycle stability. *Electrochim. Acta* 292, 115–124. doi: 10.1016/j.electacta.2018.09.131

Chen, Y. M., Li, Z., and Lou, X. W. (2015). General formation of $M_xCo_{3-x}S_4$ (M=Ni, Mn, Zn) hollow tubular structures for hybrid supercapacitors. *Angew. Chem. Int. Ed.* 54, 10521–10524. doi: 10.1002/anie.201504349

Chen, Z., Augustyn, V., Wen, J., Zhang, Y., Shen, M., Dunn, B., et al. (2011). High-performance supercapacitors based on intertwined CNT/V_2O_5 nanowire nanocomposites. *Adv. Mater.* 23, 791–795. doi: 10.1002/adma.201003658

Cheng, H., Dong, Z., Hu, C., Zhao, Y., Hu, Y., Qu, L., et al. (2013). Textile electrodes woven by carbon nanotube-graphene hybrid fibers for flexible electrochemical capacitors. *Nanoscale* 5, 3428–3434. doi: 10.1039/C3NR00320E

Cheng, P. Z., and Teng, H. (2003). Electrochemical responses from surface oxides present on HNO3-treated carbons. *Carbon* 41, 2057–2063. doi: 10.1016/S0008-6223(03)00212-4

Chmiola, J., Largeot, C., Taberna, P.-L., Simon, P., and Gogotsi, Y. (2010). Monolithic carbide-derived carbon films for micro-supercapacitors. *Science* 328, 480–483. doi: 10.1126/science.1184126

Chmiola, J., Largeot, C., Taberna, P. L., Simon, P., and Gogotsi, Y. (2008). Desolvation of ions in subnanometer pores and its effect on capacitance and double-layer theory. *Angew. Chemie Int. Ed.* 47, 3392–3395. doi: 10.1002/anie.200704894

Chmiola, J., Yushin, G., Gogotsi, Y., Portet, C., Simon, P., and Taberna, P. L. (2006). Anomalous increase in carbon capacitance at pore sizes less than 1 nanometer. *Science* 313, 1760–1763. doi: 10.1126/science.1132195

Choudhury, N. A., Sampath, S., and Shukla, A. K. (2009). Hydrogel-polymer electrolytes for electrochemical capacitors: an overview. *Energy Environ. Sci.* 2, 55–67. doi: 10.1039/B811217G

Conte, M. (2010). Supercapacitors technical requirements for new applications. *Fuel Cells* 10, 806–818. doi: 10.1002/fuce.201000087

Conway, B. E. (1999). *Electrochemical Supercapacitors*. New York, NY: Plenum Publishers.

Conway, B. E., and Pell, W. G. (2003). Double-layer and pseudocapacitance types of electrochemical capacitors and their applications to the development of hybrid devices. *J. Solid State Electrochem.* 7, 637–644. doi: 10.1007/s10008-003-0395-7

Demarconnay, L., Raymundo-Piñero, E., and Béguin, F. (2010). A symmetric carbon/carbon supercapacitor operating at 1.6 v by using a neutral aqueous solution. *Electrochem. Commun.* 12, 1275–1278. doi: 10.1016/j.elecom.2010.06.036

Demarconnay, L., Raymundo-Piñero, E., and Béguin, F. (2011). Adjustment of electrodes potential window in an asymmetric carbon/MnO_2 supercapacitor. *J. Power Sources* 196, 580–586. doi: 10.1016/j.jpowsour.2010.06.013

Deng, Y., Xie, Y., Zou, K., and Ji, X. (2015). Review on recent advances in nitrogen-doped carbons: preparations and applications in supercapacitors. *J. Mater. Chem. A* 4, 1144–1173. doi: 10.1039/C5TA08620E

Deschamps, M., Gilbert, E., Azais, P., Raymundo-Piñero, E., Ammar, M. R., Simon, P., et al. (2013). Exploring electrolyte organization in supercapacitor electrodes with solid-state NMR. *Nat. Mater.* 12, 351–358. doi: 10.1038/nmat3567

Dong, L., Liang, G., Xu, C., Liu, W., Pan, Z.-Z., Zhou, E., et al. (2017). Multi hierarchical construction-induced superior capacitive performances of flexible electrodes for wearable energy storage. *Nano Energy* 34, 242–248. doi: 10.1016/j.nanoen.2017.02.031

Dong, L., Xu, C., Li, Y., Wu, C., Jiang, B., Yang, Q., et al. (2016). Simultaneous production of high-performance flexible textile electrodes and fiber electrodes for wearable energy storage. *Adv. Mater.* 28, 1675–1681. doi: 10.1002/adma.201504747

Du, J., Liu, L., Hu, Z., Yu, Y., Qin, Y., and Chen, A. (2018). Order mesoporous carbon spheres with precise tunable large pore size by encapsulated self-activation strategy. *Adv. Funct. Mater.* 28:1802332. doi: 10.1002/adfm.201802332

Dubal, D. P., Kim, J. G., Kim, Y., Holze, R., Lokhande, C. D., and Kim, W. B. (2014). Supercapacitors based on flexible substrates: an overview. *Energy Technol.* 2, 325–341. doi: 10.1002/ente.201300144

Dutta, S., Bhaumik, A., and Wu, K. C.-W. (2014). Hierarchically porous carbon derived from polymers and biomass: effect of interconnected pores on energy applications. *Energy Environ. Sci.* 7, 3574–3592. doi: 10.1039/C4EE01075B

Esconjauregui, S., Fouquet, M., Bayer, B. C., Ducati, C., Smajda, R., Hofmann, S., et al. (2010). Growth of ultrahigh density vertically aligned carbon nanotube forests for interconnects. *ACS Nano* 4, 7431–7436. doi: 10.1021/nn1025675

Falco, C., Marco-Lozar, J. P., Salinas-Torres, D., Morallón, E., Cazorla-Amorós, D., Titirici, M. M., et al. (2013). Tailoring the porosity of chemically activated hydrothermal carbons: influence of the precursor and hydrothermal carbonization temperature. *Carbon* 62, 346–355. doi: 10.1016/j.carbon.2013.06.017

Fan, Y.-M., Song, W.-L., Li, X., and Fan, L.-Z. (2017). Assembly of graphene aerogels into the 3D biomass-derived carbon frameworks on conductive substrates for flexible supercapacitors. *Carbon* 111, 658–666. doi: 10.1016/j.carbon.2016.10.056

Fan, Z., Yan, J., Wei, T., Zhi, L., Ning, G., Li, T., et al. (2011). Asymmetric supercapacitors based on graphene/MnO_2 and activated carbon nanofiber electrodes with high power and energy density. *Adv. Funct. Mater.* 21, 2366–2375. doi: 10.1002/adfm.201100058

Faraji, S., and Ani, F. N. (2014). Microwave-assisted synthesis of metal oxide/hydroxide composite electrodes for high power supercapacitors—a review. *J. Power Sources* 263, 338–360. doi: 10.1016/j.jpowsour.2014.03.144

Fei, H., Yang, C., Bao, H., and Wang, G. (2014). Flexible all-solid-state supercapacitors based on graphene/carbon black nanoparticle film electrodes and cross-linked poly(vinyl alcohol)-H_2SO_4 porous gel electrolytes. *J. Power Sources* 266, 488–495. doi: 10.1016/j.jpowsour.2014.05.059

Fic, K., Lota, G., Meller, M., and Frackowiak, E. (2012). Novel insight into neutral medium as electrolyte for high-voltage supercapacitors. *Energy Environ. Sci.* 5, 5842–5850. doi: 10.1039/C1EE02262H

Figueiredo, J. L., Pereira, M. F. R., Freitas, M. M. A., and Órfão, J. J. M. (1999). Modification of the surface chemistry of activated carbons. *Carbon* 37, 1379–1389. doi: 10.1016/S0008-6223(98)00333-9

Forse, A. C., Merlet, C., Griffin, J. M., and Grey, C. P. (2016). New perspectives on the charging mechanisms of supercapacitors. *J. Am. Chem. Soc.* 138, 5731–5744. doi: 10.1021/jacs.6b02115

Frackowiak, E., Delpeux, S., Jurewicz, K., Szostak, K., Cazorla-Amoros, D., and Béguin, F. (2002). Enhanced capacitance of carbon nanotubes through chemical activation. *Chem. Phys. Lett.* 361, 35–41. doi: 10.1016/S0009-2614(02)00684-X

Frackowiak, E., Khomenko, V., Jurewicz, K., Lota, K., and Béguin, F. (2006). Supercapacitors based on conducting polymers/nanotubes composites. *J. Power Sources* 153, 413–418. doi: 10.1016/j.jpowsour.2005.05.030

Frackowiak, E., Meller, M., Menzel, J., Gastol, D., and Fic, K. (2014). Redox-active electrolyte for supercapacitor application. *Faraday Discuss.* 172, 179–198. doi: 10.1039/C4FD00052H

Frackowiak, E., Metenier, K., Bertagna, V., and Béguin, F. (2000). Supercapacitor electrodes from multiwalled carbon nanotubes. *Appl. Phys. Lett.* 77, 2421–2423. doi: 10.1063/1.1290146

Fuertes, A. B., Pico, F., and Rojo, J. M. (2004). Influence of pore structure on electric double-layer capacitance of template mesoporous carbons. *J. Power Sources* 133, 329–336. doi: 10.1016/j.jpowsour.2004.02.013

Fusalba, F., Gouérec, P., Villers, D., and Belanger, D. (2001). Electrochemical characterization of polyaniline in nonaqueous electrolyte and its evaluation as electrode material for electrochemical supercapacitors. *J. Electrochem. Soc.* 148, A1–A6. doi: 10.1149/1.1339036

Futaba, D. N., Hata, K., Yamada, T., Hiraoka, T., Hayamizu, Y., Kakudate, Y., et al. (2006). Shape-engineerable and highly densely packed single-walled carbon nanotubes and their application as super-capacitor electrodes. *Nat. Mater.* 5, 987–994. doi: 10.1038/nmat1782

Gao, Q., Demarconnay, L., Pineroa, E. R., and Beguin, F. (2012). Exploring the large voltage range of carbon/carbon supercapacitors in aqueous lithium sulfate electrolyte. *Energy Environ. Sci.* 5, 9611–9617. doi: 10.1039/C2EE22284A

Gao, W., Singh, N., Song, L., Liu, Z., Reddy, A. L. M., Ci, L., et al. (2011). Direct laser writing of micro-supercapacitors on hydrated graphite oxide films. *Nat. Nanotechnol.* 6:496. doi: 10.1038/nnano.2011.110

Ghosh, A., and Lee, Y. H. (2012). Carbon-based electrochemical capacitors. *ChemSusChem* 5, 480–99. doi: 10.1002/cssc.201100645

Ginting, R. T., Ovhal, M. M., and Kang, J.-W. (2018). A novel design of hybrid transparent electrodes for high performance and ultra-flexible

bifunctional electrochromic-supercapacitors. *Nano Energy* 53, 650–657. doi: 10.1016/j.nanoen.2018.09.016

Gogotsi, Y., and Simon, P. (2011). Materials science. *True performance metrics in electrochemical energy storage. Science* 334, 917–918. doi: 10.1126/science.1213003

Guo, H., and Gao, Q. (2009). Boron and nitrogen co-doped porous carbon and its enhanced properties as supercapacitor. *J. Power Sources* 186, 551–556. doi: 10.1016/j.jpowsour.2008.10.024

Gupta, V., and Miura, N. (2006). Polyaniline/single-wall carbon nanotube (PANI/SWCNT) composites for high performance supercapacitors. *Electrochim. Acta* 52, 1721–1726. doi: 10.1016/j.electacta.2006.01.074

Han, P., Xu, G., Han, X., Zhao, J., Zhou, X., and Cui, G. (2018). Lithium ion capacitors in organic electrolyte system: scientific problems, material development, and key technologies. *Adv. Energy Mater.* 8, 1801243. doi: 10.1002/aenm.201801243

Han, Y., Lu, Y., Shen, S., Zhong, Y., Liu, S., Xia, X., et al. (2019). Enhancing the capacitive storage performance of carbon fiber textile by surface and structural modulation for advanced flexible asymmetric supercapacitors. *Adv. Funct. Mater.* 29:3629. doi: 10.1002/adfm.201806329

Heo, Y.-J., Lee, J. W., Son, Y.-R., Lee, J.-H., Yeo, C. S., Lam, T. D., et al. (2018). Large-scale conductive yarns based on twistable Korean traditional paper (Hanji) for supercapacitor applications: toward high-performance paper supercapacitors. *Adv. Energy Mater.* 8:1854. doi: 10.1002/aenm.201801854

Hsia, B., Marschewski, J., Wang, S., In, J. B., Carraro, C., Poulikakos, D., et al. (2014). Highly flexible, all solid-state micro-supercapacitors from vertically aligned carbon nanotubes. *Nanotechnology* 25:055401. doi: 10.1088/0957-4484/25/5/055401

Hsieh, C.-T., and Teng, H. (2002). Influence of oxygen treatment on electric double-layer capacitance of activated carbon fabrics. *Carbon* 40, 667–674. doi: 10.1016/S0008-6223(01)00182-8

Hu, L., Pasta, M., La Mantia, F., Cui, L., Jeong, S., Deshazer, H. D., et al. (2010). Stretchable, porous, and conductive energy textiles. *Nano Lett.* 10, 708–714. doi: 10.1021/nl903949m

Huang, H. S., Chang, K. H., Suzuki, N., Yamauchi, Y., Hu, C. C., and Wu, K. C. (2013). Evaporation-induced coating of hydrous ruthenium oxide on mesoporous silica nanoparticles to develop high-performance supercapacitors. *Small* 9, 2520–2526. doi: 10.1002/smll.201202786

Huang, J., Wei, J., Xu, Y., Xiao, Y., and Chen, Y. (2017). A pinecone-inspired hierarchical vertically aligned nanosheet array electrode for high-performance asymmetric supercapacitors. *J. Mater. Chem. A* 5, 23349–23360. doi: 10.1039/c7ta07868d

Huang, W., Humphrey, B. D., and MacDiarmid, A. G. (1986). Polyaniline, a novel conducting polymer. Morphology and chemistry of its oxidation and reduction in aqueous electrolytes. *J. Chem. Soc. Faraday Trans. 1 Phys. Chem. Condens. Phases* 82, 2385–2400. doi: 10.1039/F19868202385

Hulicova-Jurcakova, D., Puziy, A. M., Poddubnaya, O. I., Suárez-García, F., Tascón, J. M., and Lu, G. Q. (2009a). Highly stable performance of supercapacitors from phosphorus-enriched carbons. *J. Am. Chem. Soc.* 131, 5026–5027. doi: 10.1021/ja809265m

Hulicova-Jurcakova, D., Seredych, M., Lu, G. Q., and Bandosz, T. J. (2009b). Combined effect of nitrogen- and oxygen-containing functional groups of microporous activated carbon on its electrochemical performance in supercapacitors. *Adv. Funct. Mater.* 19, 438–447. doi: 10.1002/adfm.200801236

Hulicova-Jurcakova, D., Seredych, M., Lu, G. Q., Kodiweera, N. K., Stallworth, P. E., Greenbaum, S., et al. (2009c). Effect of surface phosphorus functionalities of activated carbons containing oxygen and nitrogen on electrochemical capacitance. *Carbon* 47, 1576–1584. doi: 10.1016/j.carbon.2009.02.006

Inagaki, M., Konno, H., and Tanaike, O. (2010). Carbon materials for electrochemical capacitors. *J. Power Sources* 195, 7880–7903. doi: 10.1016/j.jpowsour.2010.06.036

Inagaki, M., Toyoda, M., Soneda, Y., and Morishita, T. (2018). Nitrogen-doped carbon materials. *Carbon* 132, 104–140. doi: 10.1016/j.carbon.2018.02.024

Itoi, H., Nishihara, H., Ishii, T., Nueangnoraj, K., Berenguer-Betrian, R., and Kyotani, T. (2014). Large pseudocapacitance in quinone-functionalized zeolite-templated carbon. *Bull. Chem. Soc. Jpn.* 87, 250–257. doi: 10.1246/bcsj.20130292

Itoi, H., Nishihara, H., Kogure, T., and Kyotani, T. (2011). Three-dimensionally arrayed and mutually connected 1.2-nm nanopores for high-performance electric double layer capacitor. *J. Am. Chem. Soc.* 133, 1165–1167. doi: 10.1021/ja108315p

Jiang, J., Li, Y., Liu, J., Huang, X., Yuan, C., and Lou, X. W. (2012). Recent advances in metal oxide-based electrode architecture design for electrochemical energy storage. *Adv. Mater.* 24, 5166–5180. doi: 10.1002/adma.201202146

Jiang, L., Yan, J., Xue, R., Sun, G., and Yi, B. (2014). Partially graphitized ordered mesoporous carbons for high-rate supercapacitors. *J. Solid State Electrochem.* 18, 2175–2182. doi: 10.1007/s10008-014-2458-3

Kang, E., Jeon, G., and Kim, J. K. (2013). Free-standing, well-aligned ordered mesoporous carbon nanofibers on current collectors for high-power micro-supercapacitors. *Chem. Commun.* 49, 6406–6408. doi: 10.1039/C3CC42436G

Kim, D. K., Bong, S., Jin, X., Seong, K. D., Hwang, M., Kim, N. D., et al. (2019). Facile *in situ* synthesis of multiple-heteroatom-doped carbons derived from polyimide precursors for flexible all-solid-state supercapacitors. *ACS Appl. Mater. Interfaces* 11, 1996–2005. doi: 10.1021/acsami.8b15162

Kim, D. K., Kim, N. D., Park, S.-K., Seong, K.-D., Hwang, M., You, N.-H., et al. (2018). Nitrogen doped carbon derived from polyimide/multiwall carbon nanotube composites for high performance flexible all-solid-state supercapacitors. *J. Power Sources* 380, 55–63. doi: 10.1016/j.jpowsour.2018.01.069

Kim, J. H., Nam, K. W., Ma, S. B., and Kim, K. B. (2006). Fabrication and electrochemical properties of carbon nanotube film electrodes. *Carbon* 44, 1963–1968. doi: 10.1016/j.carbon.2006.02.002

Kim, K.-S., and Park, S.-J. (2012). Easy synthesis of polyaniline-based mesoporous carbons and their high electrochemical performance. *Microporous Mesoporous Mater.* 163, 140–146. doi: 10.1016/j.micromeso.2012.04.047

Kim, M. S., Lim, E., Kim, S., Jo, C., Chun, J., and Lee, J. (2017). General synthesis of N-doped macroporous graphene-encapsulated mesoporous metal oxides and their application as new anode materials for sodium-ion hybrid supercapacitors. *Adv. Funct. Mater.* 27:1603921. doi: 10.1002/adfm.201603921

Kinage, A. K., Upare, P. P., Shivarkar, A. B., and Gupte, S. P. (2011). Highly regio-selective synthesis of β-amino alcohol by reaction with aniline and propylene carbonate in self solvent system over large pore zeolite catalyst. *Green Sustain. Chem.* 1, 76–84. doi: 10.4236/gsc.2011.13013

Konno, H., Ito, T., Ushiro, M., Fushimi, K., and Azumi, K. (2010). High capacitance B/C/N composites for capacitor electrodes synthesized by a simple method. *J. Power Sources* 195, 1739–1746. doi: 10.1016/j.jpowsour.2009.09.072

Kordás, K., Mustonen, T., Tóth, G., Jantunen, H., Lajunen, M., Soldano, C., et al. (2006). Inkjet printing of electrically conductive patterns of carbon nanotubes. *Small* 2, 1021–1025. doi: 10.1002/smll.200600061

Kruk, M., Dufour, B., Celer, E. B., Kowalewski, T., Jaroniec, M., and Matyjaszewski, K. (2005). Synthesis of mesoporous carbons using ordered and disordered mesoporous silica templates and polyacrylonitrile as carbon precursor. *J. Phys. Chem. B* 109, 9216–9225. doi: 10.1021/jp045594x

Kuroki, S., Hosaka, Y., and Yamauchi, C. (2013). A solid-state NMR study of the carbonization of polyaniline. *Carbon* 55, 160–167. doi: 10.1016/j.carbon.2012.12.022

Kwon, T., Nishihara, H., Itoi, H., Yang, Q.-H., and Kyotani, T. (2009). Enhancement mechanism of electrochemical capacitance in nitrogen-/boron-doped carbons with uniform straight nanochannels. *Langmuir* 25, 11961–11968. doi: 10.1021/la901318d

Kyotani, T., Nagai, T., Inoue, S., and Tomita, A. (1997). Formation of new type of porous carbon by carbonization in zeolite nanochannels. *Chem. Mater.* 9, 609–615. doi: 10.1021/cm960430h

Lai, F., Feng, J., Yan, R., Wang, G.-C., Antonietti, M., and Oschatz, M. (2018). Breaking the limits of ionic liquid-based supercapacitors: mesoporous carbon electrodes functionalized with manganese oxide nanosplotches for dense, stable, and wide-temperature energy storage. *Adv. Funct. Mater.* 28:1801298. doi: 10.1002/adfm.201801298

Lallave, M., Bedia, J., Ruiz-Rosas, R., Rodríguez-Mirasol, J., Cordero, T., Otero, J. C., et al. (2007). Filled and hollow carbon nanofibers by coaxial electrospinning of alcell lignin without binder polymers. *Adv. Mater.* 19, 4292–4296. doi: 10.1002/adma.200700963

Lam, D. V., Jo, K., Kim, C.-H., Kim, J.-H., Lee, H.-J., and Lee, S.-M. (2016). Activated carbon textile via chemistry of metal extraction for supercapacitors. *ACS Nano* 10, 11351–11359. doi: 10.1021/acsnano.6b06608

Largeot, C., and Portet, C. (2008). Relation between the ion size and pore size for an electric double-layer capacitor. *J. Am. Chem. Soc.* 130, 2730–2731. doi: 10.1021/ja7106178

Lawes, S., Riese, A., Sun, Q., Cheng, N., and Sun, X. (2015). Printing nanostructured carbon for energy storage and conversion applications. *Carbon* 92, 150–176. doi: 10.1016/j.carbon.2015.04.008

Le, L. T., Ervin, M. H., Qiu, H., Fuchs, B. E., and Lee, W. Y. (2011). Graphene supercapacitor electrodes fabricated by inkjet printing and thermal reduction of graphene oxide. *Electrochem. Commun.* 13, 355–358. doi: 10.1016/j.elecom.2011.01.023

Lee, J. S., Kim, S. I., Yoon, J. C., and Jang, J. H. (2013). Chemical vapor deposition of mesoporous graphene nanoballs for supercapacitor. *ACS Nano* 7, 6047–6055. doi: 10.1021/nn401850z

Lee, S.-W., Park, D. K., Lee, J. K., Ju, J. B., and Sohn, T. W. (2001). Discharge capacitance of electric double layer capacitor with electrodes made of carbon nanotubes directly deposited on SUS304 plates. *Korean J. Chem Eng.* 18, 371–375. doi: 10.1007/BF02699180

Lee, Y. H., Chang, K. H., and Hu, C. C. (2013). Differentiate the pseudocapacitance and double-layer capacitance contributions for nitrogen-doped reduced graphene oxide in acidic and alkaline electrolytes. *J. Power Sources* 227, 300–308. doi: 10.1016/j.jpowsour.2012.11.026

Lei, Z., Christov, N., Zhang, L. L., and Zhao, X. S. (2011). Mesoporous carbon nanospheres with an excellent electrocapacitive performance. *J. Mater. Chem.* 21, 2274–2281. doi: 10.1039/C0JM03322G

Leyva-García, S., Lozano-Castelló, D., Morallón, E., and Cazorla-Amorós, D. (2016a). Silica-templated ordered mesoporous carbon thin films as electrodes for micro-capacitors. *J. Mater. Chem. A* 3, 4570–4579. doi: 10.1039/C5TA10552H

Leyva-García, S., Lozano-Castelló, D., Morallón, E., Vogl, T., Schütter, C., Passerini, S., et al. (2016b). Electrochemical performance of a superporous activated carbon in ionic liquid-based electrolytes. *J. Power Sources* 336, 419–426. doi: 10.1016/j.jpowsour.2016.11.010

Li, H., Liang, J., Li, H., Zheng, X., Tao, Y., Huang, Z. H., et al. (2019). Activated carbon fibers with manganese dioxide coating for flexible fiber supercapacitors with high capacitive performance. *J. Energy Chem.* 31, 95–100. doi: 10.1016/j.jechem.2018.05.008

Li, H.-Q., Luo, J.-Y., Zhou, X.-F., Yu, C.-Z., and Xia, Y.-Y. (2007). An ordered mesoporous carbon with short pore length and its electrochemical performances in supercapacitor applications. *J. Electrochem. Soc.* 154, A731–A736. doi: 10.1149/1.2741198

Li, J., Li, H., Li, J., Wu, G., Shao, Y., Li, Y., et al. (2018). A single-walled carbon nanotubes/poly(3,4-ethylenedioxythiophene)-poly(styrenesulfonate)/copper hexacyanoferrate hybrid film for high-volumetric performance flexible supercapacitors. *J. Power Sources* 386, 96–105. doi: 10.1016/j.jpowsour.2018.03.046

Li, M., Liu, C., Cao, H., Zhao, H., Zhang, Y., and Fan, Z. (2014). KOH self-templating synthesis of three-dimensional hierarchical porous carbon materials for high performance supercapacitors. *J. Mater. Chem. A* 2, 14844–14851. doi: 10.1039/C4TA02167C

Li, S., Yu, C., Yang, J., Zhao, C., Fan, X., Huang, H., et al. (2017). Ultrathin nitrogen-enriched hybrid carbon nanosheets for supercapacitors with ultrahigh rate performance and high energy density. *ChemElectroChem* 4, 369–375. doi: 10.1002/celc.201600614

Li, W., Zhang, F., Dou, Y., Wu, Z., Liu, H., Qian, X., et al. (2011). A self-template strategy for the synthesis of mesoporous carbon nanofibers as advanced supercapacitor electrodes. *Adv. Energy Mater.* 1, 382–386. doi: 10.1002/aenm.201000096

Liang, T., Wang, H., Xu, D., Liao, K., Wang, R., He, B., et al. (2018). High-energy flexible quasi-solid-state lithium-ion capacitors enabled by a freestanding rGO-encapsulated Fe3O4 nanocube anode and a holey rGO film cathode. *Nanoscale* 10, 17814–17823. doi: 10.1039/C8NR04292F

Lin, J., Peng, Z., Liu, Y., Ruiz-Zepeda, F., Ye, R., Samuel, E. L., et al. (2014). Laser-induced porous graphene films from commercial polymers. *Nat. Commun.* 5:6714. doi: 10.1038/ncomms6714

Liu, C.-L., Dong, W., Cao, G., Song, J., Liu, L., and Yang, Y. (2008). Capacitance limits of activated carbon fiber electrodes in aqueous electrolyte. *J. Electrochem. Soc.* 155, F1–F7. doi: 10.1149/1.2799683

Liu, H.-J., Wang, X.-M., Cui, W.-J., Dou, Y.-Q., Zhao, D.-Y., and Xia, Y.-Y. (2010). Highly ordered mesoporous carbon nanofiber arrays from a crab shell biological template and its application in supercapacitors and fuel cells. *J. Mater. Chem.* 20, 4223–4230. doi: 10.1039/B925776D

Liu, H. J., Cui, W. J., Jin, L. H., Wang, C. X., and Xia, Y. Y. (2009). Preparation of three-dimensional ordered mesoporous carbon sphere arrays by a two-step templating route and their application for supercapacitors. *J. Mater. Chem.* 19, 3661–3667. doi: 10.1039/B819820A

Liu, H. J., Wang, J., Wang, C. X., and Xia, Y. Y. (2011). Ordered hierarchical mesoporous/microporous carbon derived from mesoporous titanium-carbide/carbon composites and its electrochemical performance in supercapacitor. *Adv. Energy Mater.* 1, 1101–1108. doi: 10.1002/aenm.201100255

Liu, L., Yu, Y., Yan, C., Li, K., and Zheng, Z. (2015). Wearable energy-dense and power-dense supercapacitor yarns enabled by scalable graphene–metallic textile composite electrodes. *Nat. Commun.* 6:7260. doi: 10.1038/ncomms8260

Liu, R., Ma, L., Niu, G., Li, X., Li, E., Bai, Y., et al. (2017). Oxygen-deficient bismuth oxide/graphene of ultrahigh capacitance as advanced flexible anode for asymmetric supercapacitors. *Adv. Funct. Mater.* 27:1635. doi: 10.1002/adfm.201701635

Liu, Z., Fu, X., Li, M., Wang, F., Wang, Q., Kang, G., et al. (2015). Novel silicon-doped, silicon and nitrogen-codoped carbon nanomaterials with high activity for the oxygen reduction reaction in alkaline medium. *J. Mater. Chem. A* 3, 3289–3293. doi: 10.1039/C4TA05937A

Lota, G., and Frackowiak, E. (2009). Striking capacitance of carbon/iodide interface. *Electrochem. Commun.* 11, 87–90. doi: 10.1016/j.elecom.2008.10.026

Lota, G., Grzyb, B., Machnikowska, H., Machnikowski, J., and Frackowiak, E. (2005). Effect of nitrogen in carbon electrode on the supercapacitor performance. *Chem. Phys. Lett.* 404, 53–58. doi: 10.1016/j.cplett.2005.01.074

Lozano-Castelló, D., Lillo-Ródenas, M. A., Cazorla-Amorós, D., and Linares-Solano, A. (2001). Preparation of activated carbons from Spanish anthracite - I. *Activation by KOH. Carbon* 39, 741–749. doi: 10.1016/S0008-6223(00)00185-8

Ma, G., Li, J., Sun, K., Peng, H., Mu, J., and Lei, Z. (2014). High performance solid-state supercapacitor with PVA-KOH-$K_3[Fe(CN)_6]$ gel polymer as electrolyte and separator. *J. Power Sources* 256, 281–287. doi: 10.1016/j.jpowsour.2014.01.062

Ma, W., Chen, S., Yang, S., Chen, W., Weng, W., Cheng, Y., et al. (2017). Flexible all-solid-state asymmetric supercapacitor based on transition metal oxide nanorods/reduced graphene oxide hybrid fibers with high energy density. *Carbon* 113, 151–158. doi: 10.1016/j.carbon.2016.11.051

Martins, V. L., Rennie, A. J. R., Sanchez-Ramirez, N., Torresi, R. M., and Hall, P. J. (2018). Improved performance of ionic liquid supercapacitors by using tetracyanoborate anions. *ChemElectroChem* 5, 598–604. doi: 10.1002/celc.201701164

Meng, C., Liu, C., Chen, L., Hu, C., and Fan, S. (2010). Highly flexible and all-solid-state paperlike polymer supercapacitors. *Nano Lett.* 10, 4025–4031. doi: 10.1021/nl1019672

Miao, F., Shao, C., Li, X., Wang, K., and Liu, Y. (2016). Flexible solid-state supercapacitors based on freestanding nitrogen-doped porous carbon nanofibers derived from electrospun polyacrylonitrile@polyaniline nanofibers. *J. Mater. Chem. A* 4, 4180–4187. doi: 10.1039/C6TA00015K

Miller, J. R. (2016). Engineering electrochemical capacitor applications. *J. Power Sources* 326, 726–735. doi: 10.1016/j.jpowsour.2016.04.020

Miller, J. R., and Outlaw, R. A. (2015). Vertically-oriented graphene electric double layer capacitor designs. *J. Electrochem. Soc.* 162, A5077–A5082. doi: 10.1149/2.0121505jes

Mini, P. A., Balakrishnan, A., Nair, S. V., and Subramanian, K. R., V (2011). Highly super capacitive electrodes made of graphene/poly(pyrrole). *Chem. Commun.* 47, 5753–5755. doi: 10.1039/c1cc00119a

Mostazo-López, M. J., Ruiz-Rosas, R., Castro-Muñiz, A., Nishihara, H., Kyotani, T., Morallón, E., et al. (2018). Ultraporous nitrogen-doped zeolite-templated carbon for high power density aqueous-based supercapacitors. *Carbon* 129, 510–519. doi: 10.1016/j.carbon.2017.12.050

Mostazo-López, M. J., Ruiz-Rosas, R., Morallón, E., and Cazorla-Amorós, D. (2015). Generation of nitrogen functionalities on activated carbons by amidation reactions and Hofmann rearrangement: chemical and electrochemical characterization. *Carbon* 91, 252–265. doi: 10.1016/j.carbon.2015.04.089

Mostazo-López, M. J., Ruiz-Rosas, R., Morallón, E., and Cazorla-Amorós, D. (2016). Nitrogen doped superporous carbon prepared by a mild method. *Enhancement of supercapacitor performance. Int. J. Hydrogen Energy* 41, 19691–19701. doi: 10.1016/j.ijhydene.2016.03.091

Muzaffar, A., Ahamed, M. B., Deshmukh, K., and Thirumalai, J. (2019). A review on recent advances in hybrid supercapacitors: design, fabrication and applications. *Renew. Sustain. Energy Rev.* 101, 123–145. doi: 10.1016/j.rser.2018.10.026

Na, W., Jun, J., Park, J. W., Lee, G., and Jang, J. (2017). Highly porous carbon nanofibers co-doped with fluorine and nitrogen for outstanding supercapacitor performance. *J. Mater. Chem. A* 5, 17379–17387. doi: 10.1039/C7TA04406B

Nakamura, T., Yamada, Y., and Yano, K. (2006). Three-dimensionally ordered array of nanoporous starburst carbon spheres. *Chem. Lett.* 35, 1436–1437. doi: 10.1246/cl.2006.1436

Naoi, K., Ishimoto, S., Miyamoto, J., and Naoi, W. (2012). Second generation 'nanohybrid supercapacitor': evolution of capacitive energy storage devices. *Energy Environ. Sci.* 5, 9363–9373. doi: 10.1039/C2EE21675B

Nishihara, H., and Kyotani, T. (2012). Templated nanocarbons for energy storage. *Adv. Mater.* 24, 4473–4498. doi: 10.1002/adma.201201715

Nomura, K., Nishihara, H., Kobayashi, N., Asada, T., and Kyotani, T. (2019). 4.4 V supercapacitors based on super-stable mesoporous carbon sheet made of edge-free graphene walls. *Energy Environ. Sci.* doi: 10.1039/C8EE03184C

Nueangnoraj, K., Nishihara, H., Ishii, T., Yamamoto, N., Itoi, H., Berenguer, R., et al. (2015). Pseudocapacitance of zeolite-templated carbon in organic electrolytes. *Energy Storage Mater.* 1, 35–41. doi: 10.1016/j.ensm.2015.08.003

Nueangnoraj, K., Ruiz-Rosas, R., Nishihara, H., Shiraishi, S., Morallón, E., Cazorla-Amorós, D., et al. (2014). Carbon-carbon asymmetric aqueous capacitor by pseudocapacitive positive and stable negative electrodes. *Carbon* 67, 792–794. doi: 10.1016/j.carbon.2013.10.011

Nyholm, L., Nyström, G., Mihranyan, A., and Strømme, M. (2011). Toward flexible polymer and paper-based energy storage devices. *Adv. Mater.* 23, 3751–3769. doi: 10.1002/adma.201004134

Ornelas, O., Sieben, J. M., Ruiz-Rosas, R., Morallón, E., Cazorla-Amorós, D., Geng, J., et al. (2014). On the origin of the high capacitance of nitrogen-containing carbon nanotubes in acidic and alkaline electrolytes. *Chem. Commun.* 50, 11343–11346. doi: 10.1039/C4CC04876H

Oschatz, M., Borchardt, L., Hippauf, F., Nickel, W., Kaskel, S., and Brunner, E. (2016). "Interactions between electrolytes and carbon-based materials—NMR studies on electrical double-layer capacitors, lithium-ion batteries, and fuel cells," in *Annual Reports on NMR Spectroscopy*, ed G. A. Webb (London, UK: Elsevier Ltd.), 237–318. doi: 10.1016/bs.arnmr.2015.08.003

Ou, T.-M., Hsu, C.-T., and Hu, C.-C. (2015). Synthesis and characterization of sodium-doped MnO_2 for the aqueous asymmetric supercapacitor application. *J. Electrochem. Soc.* 162, A5124–A5132. doi: 10.1149/2.0191505jes

Park, J. H., Ko, J. M., and Ok Park, O. (2003). Carbon nanotube/RuO_2 nanocomposite electrodes for supercapacitors. *J. Electrochem. Soc.* 150:A864. doi: 10.1149/1.1576222

Park, J. H., and Park, O. O. (2002). Hybrid electrochemical capacitors based on polyaniline and activated carbon electrodes. *J. Power Sources* 111, 185–190. doi: 10.1016/S0378-7753(02)00304-X

Park, S., Vosguerichian, M., and Bao, Z. (2013). A review of fabrication and applications of carbon nanotube film-based flexible electronics. *Nanoscale* 5, 1727–1752. doi: 10.1039/C3NR33560G

Pech, D., Brunet, M., Taberna, P. L., Simon, P., Fabre, N., Mesnilgrente, F., et al. (2010). Elaboration of a microstructured inkjet-printed carbon electrochemical capacitor. *J. Power Sources* 195, 1266–1269. doi: 10.1016/j.jpowsour.2009.08.085

Peng, C., Zhang, S., Zhou, X., and Chen, G. Z. (2010). Unequalisation of electrode capacitances for enhanced energy capacity in asymmetrical supercapacitors. *Energy Environ. Sci.* 3, 1499–1502. doi: 10.1039/C0EE00228C

Piñeiro-Prado, I., Salinas-Torres, D., Ruiz-Rosas, R., Morallón, E., and Cazorla-Amorós, D. (2016). Design of activated carbon/activated carbon asymmetric capacitors. *Front. Mater.* 3, 1–12. doi: 10.3389/fmats.2016.00016

Qie, L., Chen, W., Xu, H., Xiong, X., Jiang, Y., Zou, F., et al. (2013). Synthesis of functionalized 3D hierarchical porous carbon for high-performance supercapacitors. *Energy Environ. Sci.* 6, 2497–2504. doi: 10.1039/C3EE41638K

Quesada-Plata, F., Ruiz-Rosas, R., Morallón, E., and Cazorla-Amorós, D. (2016). Activated carbons prepared through H_3PO_4-assisted hydrothermal carbonisation from biomass wastes: porous texture and electrochemical performance. *ChemPlusChem* 81, 1349–1359. doi: 10.1002/cplu.201600412

Quílez-Bermejo, J., González-Gaitán, C., Morallón, E., and Cazorla-Amorós, D. (2017). Effect of carbonization conditions of polyaniline on its catalytic activity towards ORR. *Some insights about the nature of the active sites. Carbon* 119, 62–71. doi: 10.1016/j.carbon.2017.04.015

Rakhi, R. B., Chen, W., Cha, D., and Alshareef, H. N. (2011). High performance supercapacitors using metal oxide anchored graphene nanosheet electrodes. *J. Mater. Chem.* 21, 16197. doi: 10.1039/C1JM12963E

Ravi, S., and Vadukumpully, S. (2015). Sustainable carbon nanomaterials: recent advances and its applications in energy and environmental remediation. *J. Environ. Chem. Eng.* 4, 835–856. doi: 10.1016/j.jece.2015.11.026

Raymundo-Piñero, E., Cazorla-Amorós, D., Linares-Solano, A., Find, J., Wild, U., and Schlögl, R. (2002). Structural characterization of N-containing activated carbon fibers prepared from a low softening point petroleum pitch and a melamine resin. *Carbon* 40, 597–608. doi: 10.1016/S0008-6223(01)00155-5

Ren, L., Zhang, G., Yan, Z., Kang, L., Xu, H., Shi, F., et al. (2017). High capacitive property for supercapacitor using Fe^{3+}/Fe^{2+} redox couple additive electrolyte. *Electrochim. Acta* 231, 705–712. doi: 10.1016/j.electacta.2017.02.056

Román-Martínez, M. C., Cazorla-Amorós, D., Linares-Solano, A., and de Lecea, C. S.-M. (1993). TPD and TPR characterization of carbonaceous supports and Pt/C catalysts. *Carbon* 31, 895–902. doi: 10.1016/0008-6223(93)90190-L

Rosas, J. M., Berenguer, R., Valero-Romero, M. J., Rodríguez-Mirasol, J., and Cordero, T. (2014). Preparation of different carbon materials by thermochemical conversion of lignin. *Front. Mater.* 1, 1–17. doi: 10.3389/fmats.2014.00029

Rosas, J. M., Ruiz-Rosas, R. R., Berenguer, R., Cazorla-Amorós, D., Morallon, E., Nishihara, H., et al. (2016). Easy fabrication of superporous zeolite templated carbon electrodes by electrospray on rigid and flexible substrates. *J. Mater. Chem. A* 4610–4618. doi: 10.1039/C6TA00241B

Rozlívková, Z., Trchová, M., Exnerová, M., and Stejskal, J. (2011). The carbonization of granular polyaniline to produce nitrogen-containing carbon. *Synth. Met.* 161, 1122–1129. doi: 10.1016/j.synthmet.2011.03.034

Ruiz-Rosas, R., Valero-Romero, M. J., Salinas-Torres, D., Rodríguez-Mirasol, J., Cordero, T., Morallón, E., et al. (2014). Electrochemical performance of hierarchical porous carbon materials obtained from the infiltration of lignin into zeolite templates. *ChemSusChem* 7, 1458–1467. doi: 10.1002/cssc.201301408

Salinas-Torres, D., Ruiz-Rosas, R., Valero-Romero, M. J., Rodríguez-Mirasol, J., Cordero, T., Morallón, E., et al. (2016). Asymmetric capacitors using lignin-based hierarchical porous carbons. *J. Power Sources* 326, 641–651. doi: 10.1016/j.jpowsour.2016.03.096

Salinas-Torres, D., Shiraishi, S., Morallón, E., and Cazorla-Amorós, D. (2015). Improvement of carbon materials performance by nitrogen functional groups in electrochemical capacitors in organic electrolyte at severe conditions. *Carbon* 82, 205–213. doi: 10.1016/j.carbon.2014.10.064

Salinas-Torres, D., Sieben, J. M., Lozano-Castelló, D., Cazorla-Amorós, D., and Morallón, E. (2013). Asymmetric hybrid capacitors based on activated carbon and activated carbon fibre–PANI electrodes. *Electrochim. Acta* 89, 326–333. doi: 10.1016/j.electacta.2012.11.039

Salinas-Torres, D., Sieben, J. M., Lozano-Castello, D., Morallón, E., Burghammer, M., Riekel, C., et al. (2012). Characterization of activated carbon fiber/polyaniline materials by position-resolved microbeam small-angle X-ray scattering. *Carbon* 50, 1051–1056. doi: 10.1016/j.carbon.2011.10.010

Salunkhe, R. R., Lee, Y. H., Chang, K. H., Li, J. M., Simon, P., Tang, J., et al. (2014). Nanoarchitectured graphene-based supercapacitors for next-generation energy-storage applications. *Chem. A Eur. J.* 20, 13838–13852. doi: 10.1002/chem.201403649

Schütter, C., Husch, T., Viswanathan, V., Passerini, S., Balducci, A., and Korth, M. (2016). Rational design of new electrolyte materials for electrochemical double layer capacitors. *J. Power Sources* 326, 541–548. doi: 10.1016/j.jpowsour.2016.06.022

Seredych, M., Hulicova-Jurcakova, D., Lu, G. Q., and Bandosz, T. J. (2008). Surface functional groups of carbons and the effects of their chemical character, density and accessibility to ions on electrochemical performance. *Carbon* 46, 1475–1488. doi: 10.1016/j.carbon.2008.06.027

Sevilla, M., and Mokaya, R. (2014). Energy storage applications of activated carbons: supercapacitors and hydrogen storage. *Energy Environ. Sci.* 7, 1250–1280. doi: 10.1039/C3EE43525C

Shen, B., Zhang, X., Guo, R., Lang, J., Chen, J., and Yan, X. (2016). Carbon encapsulated RuO2 nano-dots anchoring on graphene as an electrode for asymmetric supercapacitors with ultralong cycle life in an ionic liquid electrolyte. *J. Mater. Chem. A* 4, 8180–8189. doi: 10.1039/C6TA02473D

Shen, W., and Fan, W. (2013). Nitrogen-containing porous carbons: synthesis and application. *J. Mater. Chem. A* 1, 999–1013. doi: 10.1039/C2TA00028H

Shi, S., Xu, C., Yang, C., Li, J., Du, H., Li, B., et al. (2013). Flexible supercapacitors. *Particuology* 11, 371–377. doi: 10.1016/j.partic.2012.12.004

Simon, P., and Burke, A. (2008). Nanostructured carbons: double-layer capacitance and more. *Electrochem. Soc. Interface* 17, 38–43.

Simon, P., and Gogotsi, Y. (2008). Materials for electrochemical capacitors. *Nat. Mater.* 7, 845–854. doi: 10.1038/nmat2297

Sivakkumar, S. R., and Pandolfo, A. G. (2012). Evaluation of lithium-ion capacitors assembled with pre-lithiated graphite anode and activated carbon cathode. *Electrochim. Acta* 65, 280–287. doi: 10.1016/j.electacta.2012.01.076

Snook, G. A., Kao, P., and Best, A. S. (2011). Conducting-polymer-based supercapacitor devices and electrodes. *J. Power Sources* 196, 1–12. doi: 10.1016/j.jpowsour.2010.06.084

Snook, G. A., Wilson, G. J., and Pandolfo, A. G. (2009). Mathematical functions for optimisation of conducting polymer/activated carbon asymmetric supercapacitors. *J. Power Sources* 186, 216–223. doi: 10.1016/j.jpowsour.2008.09.085

Stoller, M. D., and Ruoff, R. S. (2010). Best practice methods for determining an electrode material's performance for ultracapacitors. *Energy Environ. Sci.* 3, 1294–1301. doi: 10.1039/C0EE00074D

Su, F., Poh, C. K., Chen, J. S., Xu, G., Wang, D., Li, Q., et al. (2011). Nitrogen-containing microporous carbon nanospheres with improved capacitive properties. *Energy Environ. Sci.* 4, 717–724. doi: 10.1039/C0EE00277A

Su, H., Zhang, H., Liu, F., Chun, F., Zhang, B., Chu, X., et al. (2017). High power supercapacitors based on hierarchically porous sheet-like nanocarbons with ionic liquid electrolytes. *Chem. Eng. J.* 322, 73–81. doi: 10.1016/j.cej.2017.04.012

Sugimoto, W., Shibutani, T., Murakami, Y., and Takasu, Y. (2002). Charge storage capabilities of rutile-type RuO_2-VO_2 solid solution for electrochemical supercapacitors. *Electrochem. Solid-State Lett.* 5, A170–A172. doi: 10.1149/1.1483155

Sun, L., Tian, C., Fu, Y., Yang, Y., Yin, J., Wang, L., et al. (2014). Nitrogen-doped porous graphitic carbon as an excellent electrode material for advanced supercapacitors. *Chem. A Eur. J.* 20, 564–574. doi: 10.1002/chem.201303345

Takasu, Y., and Murakami, Y. (2000). Design of oxide electrodes with large surface area. *Electrochim. Acta* 45, 4135–4141. doi: 10.1016/S0013-4686(00)00534-X

Tang, H., Yang, C., Lin, Z., Yang, Q., Kang, F., and Wong, C. P. (2015). Electrospray-deposition of graphene electrodes: a simple technique to build high-performance *supercapacitors*. 7, 9133–9139. doi: 10.1039/C5NR00465A

Tomko, T., Rajagopalan, R., Aksoy, P., and Foley, H. C. (2011). Synthesis of boron/nitrogen substituted carbons for aqueous asymmetric capacitors. *Electrochim. Acta* 56, 5369–5375. doi: 10.1016/j.electacta.2011.03.112

Valero-Romero, M. J., Márquez-Franco, E. M., Bedia, J., Rodríguez-Mirasol, J., and Cordero, T. (2014). Hierarchical porous carbons by liquid phase impregnation of zeolite templates with lignin solution. *Microporous Mesoporous Mater.* 196, 68–78. doi: 10.1016/j.micromeso.2014.04.055

Vlad, A., Singh, N., Melinte, S., Gohy, J.-F., and Ajayan, P. M. (2016). Carbon redox-polymer-gel hybrid supercapacitors. *Sci. Rep.* 6:22194. doi: 10.1038/srep22194

Wang, D.-W., Li, F., Liu, M., Lu, G. Q., and Cheng, H.-M. (2008). 3D aperiodic hierarchical porous graphitic carbon material for high-rate electrochemical capacitive energy storage. *Angew. Chem. Int. Ed.* 47, 373–376. doi: 10.1002/anie.200702721

Wang, G., Zhang, L., and Zhang, J. (2012). A review of electrode materials for electrochemical supercapacitors. *Chem. Soc. Rev.* 41, 797–828. doi: 10.1039/C1CS15060J

Wang, K. X., Birjukovs, P., Erts, D., Phelan, R., Morris, M. A., Zhou, H. S., et al. (2009). Synthesis and characterisation of ordered arrays of mesoporous carbon nanofibres. *J. Mater. Chem.* 19, 1331–1338. doi: 10.1039/B817156D

Wang, X., Liu, C.-G., Neff, D., Fulvio, P. F., Mayes, R. T., Zhamu, A., et al. (2013). Nitrogen-enriched ordered mesoporous carbons through direct pyrolysis in ammonia with enhanced capacitive performance. *J. Mater. Chem. A* 1, 7920–7926. doi: 10.1039/c3ta11342f

Wang, X., and Shi, G. (2015). Flexible graphene devices related to energy conversion and storage. *Energy Environ. Sci.* 8, 790–823. doi: 10.1039/C4EE03685A

Wang, Y., Li, X., Wang, Y., Liu, Y., Bai, Y., Liu, R., et al. (2019). High-performance flexible MnO 2 @carbonized cotton textile electrodes for enlarged operating potential window symmetrical supercapacitors. *Electrochim. Acta* 299, 12–18. doi: 10.1016/j.electacta.2018.12.181

Wei, X., Jiang, X., Wei, J., and Gao, S. (2016). Functional groups and pore size distribution do matter to hierarchically porous carbons as high-rate-performance supercapacitors. *Chem. Mater.* 28, 445–458. doi: 10.1021/acs.chemmater.5b02336

Wen, Y., Rufford, T. E., Hulicova-Jurcakova, D., and Wang, L. (2016). Nitrogen and phosphorous co-doped graphene monolith for supercapacitors. *ChemSusChem* 9, 513–520. doi: 10.1002/cssc.201501303

Wu, M., Snook, G. A., Gupta, V., Shaffer, M., Fray, D. J., and Chen, G. Z. (2005). Electrochemical fabrication and capacitance of composite films of carbon nanotubes and polyaniline. *J. Mater. Chem.* 15, 2297–2303. doi: 10.1039/B418835G

Wu, Q., Xu, Y., Yao, Z., Liu, A., and Shi, G. (2010). Supercapacitors based on flexible graphene/polyaniline nanofiber composite films. *ACS Nano* 4, 1963–1970. doi: 10.1021/nn1000035

Xia, C., Chen, W., Wang, X., Hedhili, M. N., Wei, N., and Alshareef, H. N. (2015). Highly stable supercapacitors with conducting polymer core-shell electrodes for energy storage applications. *Adv. Energy Mater.* 5:1805. doi: 10.1002/aenm.201401805

Xia, K., Gao, Q., Jiang, J., and Hu, J. (2008). Hierarchical porous carbons with controlled micropores and mesopores for supercapacitor electrode materials. *Carbon* 46, 1718–1726. doi: 10.1016/j.carbon.2008.07.018

Xia, Y., and Mokaya, R. (2004). Synthesis of ordered mesoporous carbon and nitrogen-doped carbon materials with graphitic pore walls via a simple chemical vapor deposition method. *Adv. Mater.* 16, 1553–1558. doi: 10.1002/adma.200400391

Xiang, S., Yang, X., Lin, X., Chang, C., Que, H., and Li, M. (2017). Nitrogen and sulfur co-doped polyurethane-based porous carbon materials as supercapacitors exhibit excellent electrochemical performance. *J. Solid State Electrochem.* 21, 1457–1465. doi: 10.1007/s10008-017-3505-7

Xiao, H., Wu, Z.-S., Chen, L., Zhou, F., Zheng, S., Ren, W., et al. (2017). One-step device fabrication of phosphorene and graphene interdigital micro-supercapacitors with high energy density. *ACS Nano* 11, 7284–7292. doi: 10.1021/acsnano.7b03288

Xie, Q., Wu, S., Zhang, Y., and Zhao, P. (2017). Nitrogen-enriched flexible porous carbon/graphene composite cloth as free-standing electrodes for high performance aqueous supercapacitors. *J. Electroanal. Chem.* 801, 57–64. doi: 10.1016/j.jelechem.2017.07.031

Xin, G., Wang, M., Zhang, W., Song, J., and Zhang, B. (2018). Preparation of high-capacitance N,S co-doped carbon nanospheres with hierarchical pores as supercapacitors. *Electrochim. Acta* 291, 168–176. doi: 10.1016/j.electacta.2018.08.137

Xu, J., Wu, C., Yan, P., Wang, J., Zhang, R., Zhang, X., et al. (2015). Enhanced electrochemical performance of graphitized carbide-derived carbon in alkaline electrolyte. *Electrochim. Acta* 174, 411–416. doi: 10.1016/j.electacta.2015.06.025

Yan, J., Ren, C. E., Maleski, K., Hatter, C. B., Anasori, B., Urbankowski, P., et al. (2017). Flexible MXene/Graphene films for ultrafast supercapacitors with outstanding volumetric capacitance. *Adv. Funct. Mater.* 27:1264. doi: 10.1002/adfm.201701264

Yan, X., Liu, Y., Fan, X., Jia, X., Yu, Y., and Yang, X. (2014). Nitrogen/phosphorus co-doped nonporous carbon nanofibers for high-performance supercapacitors. *J. Power Sources* 248, 745–751. doi: 10.1016/j.jpowsour.2013.09.129

Yan, Z., Ma, L., Zhu, Y., Lahiri, I., Hahm, M. G., Liu, Z., et al. (2013). Three-dimensional metal-graphene-nanotube multifunctional hybrid materials. *ACS Nano* 7, 58–64. doi: 10.1021/nn3015882

Yang, X., Wu, D., Chen, X., and Fu, R. (2010). Nitrogen-enriched nanocarbons with a 3-D continuous mesopore structure from polyacrylonitrile for supercapacitor application. *J. Phys. Chem. C* 114, 8581–8586. doi: 10.1021/jp101255d

Yang, Z., Tian, J., Yin, Z., Cui, C., Qian, W., and Wei, F. (2019). Carbon nanotube- and graphene-based nanomaterials and applications in high-voltage supercapacitor: a review. *Carbon* 141, 467–480. doi: 10.1016/j.carbon.2018.10.010

Ye, G., Zhu, D., Zhou, Q., Li, D., Zuo, Y., Duan, X., et al. (2018). One-step electrodeposition method to prepare robust flexible pedot-based films for ultra-stable supercapacitors. *ChemElectroChem* 5, 1130–1136. doi: 10.1002/celc.201800099

Ye, J.-S., Liu, X., Cui, H. F., Zhang, W.-D., Sheu, F.-S., and Lim, T. M. (2005a). Electrochemical oxidation of multi-walled carbon nanotubes and its application to electrochemical double layer capacitors. *Electrochem. Commun.* 7, 249–255. doi: 10.1016/j.elecom.2005.01.008

Ye, J. -S., Cui, H. F., Liu, X., Lim, T. M., Zhang, W. De, and Sheu, F. S. (2005b). Preparation and characterization of aligned carbon nanotube-ruthenium oxide nanocomposites for supercapacitors. *Small* 1, 560–565. doi: 10.1002/smll.200400137

Yoo, J. J., Balakrishnan, K., Huang, J., Meunier, V., Sumpter, B. G., and Srivastava, A. (2011). Ultrathin planar graphene supercapacitors. *Nano Lett.* 11, 1423–1427. doi: 10.1021/nl200225j

Yoon, B.-J., Jeong, S.-H., Lee, K.-H., Seok Kim, H., Gyung Park, C., and Hun Han, J. (2004). Electrical properties of electrical double layer capacitors with integrated carbon nanotube electrodes. *Chem. Phys. Lett.* 388, 170–174. doi: 10.1016/j.cplett.2004.02.071

Yoon, Y., Lee, K., Kwon, S., Seo, S., Yoo, H., Kim, S., et al. (2014). Vertical alignments of graphene sheets spatially and densely piled for fast ion diffusion in compact supercapacitors. *ACS Nano* 8, 4580–4590. doi: 10.1021/nn500150j

Yoshida, N., Hirota, Y., Uchida, Y., Asada, T., Kobayashi, N., and Nishiyama, N. (2018). Solvent-free synthesis and KOH activation of mesoporous carbons using resorcinol/Pluronic F127/hexamethylenetetramine mixture and their application to EDLC. *Microporous Mesoporous Mater.* 272, 217–221. doi: 10.1016/j.micromeso.2018.06.028

Yu, X. Y., Yu, L., and Lou, X. W. (2016). Metal sulfide hollow nanostructures for electrochemical energy storage. *Adv. Energy Mater.* 6, 1–14. doi: 10.1002/aenm.201501333

Zhang, B., Kang, F., Tarascon, J.-M., and Kim, J.-K. (2015). Recent advances in electrospun carbon nanofibers and their application in electrochemical energy storage. *Prog. Mater. Sci.* 76, 319–380. doi: 10.1016/j.pmatsci.2015.08.002

Zhang, D., Zheng, L., Ma, Y., Lei, L., Li, Q., Li, Y., et al. (2014). Synthesis of nitrogen- and sulfur-codoped 3D cubic-ordered mesoporous carbon with superior performance in supercapacitors. *ACS Appl. Mater. Interfaces* 6, 2657–2665. doi: 10.1021/am405128j

Zhang, J., Jiang, J., Li, H., and Zhao, X. S. (2011). A high-performance asymmetric supercapacitor fabricated with graphene-based electrodes. *Energy Environ. Sci.* 4, 4009–4015. doi: 10.1039/C1EE01354H

Zhang, Q., Liu, Z., Zhao, B., Cheng, Y., Zhang, L., Wu, H.-H., et al. (2019). Design and understanding of dendritic mixed-metal hydroxide nanosheets@N-doped carbon nanotube array electrode for high-performance asymmetric supercapacitors. *Energy Storage Mater.* 16, 632–645. doi: 10.1016/j.ensm.2018.06.026

Zhang, Q., Wang, X., Pan, Z., Sun, J., Zhao, J., Zhang, J., et al. (2017). Wrapping aligned carbon nanotube composite sheets around vanadium nitride nanowire arrays for asymmetric coaxial fiber-shaped supercapacitors with ultrahigh energy density. *Nano Lett.* 17, 2719–2726. doi: 10.1021/acs.nanolett.7b00854

Zhang, Z., Liu, M., Tian, X., Xu, P., Fu, C., Wang, S., et al. (2018). Scalable fabrication of ultrathin free-standing graphene nanomesh films for flexible ultrafast electrochemical capacitors with AC line-filtering performance. *Nano Energy* 50, 182–191. doi: 10.1016/j.nanoen.2018.05.030

Zhao, J., Lai, H., Lyu, Z., Jiang, Y., Xie, K., Wang, X., et al. (2015). Hydrophilic hierarchical nitrogen-doped carbon nanocages for ultrahigh supercapacitive performance. *Adv. Mater.* 27, 3541–3545. doi: 10.1002/adma.201500945

Zhao, Y., Ran, W., He, J., Song, Y., Zhang, C., Xiong, D. B., et al. (2015). Oxygen-rich hierarchical porous carbon derived from artemia cyst shells with superior electrochemical performance. *ACS Appl. Mater. Interfaces* 7, 1132–1139. doi: 10.1021/am506815f

Zhao, Z., and Xie, Y. (2018). Electrochemical supercapacitor performance of boron and nitrogen co-doped porous carbon nanowires. *J. Power Sources* 400, 264–276. doi: 10.1016/j.jpowsour.2018.08.032

Zheng, J. P., and Jow, T. R. (1995). a new charge storage mechanism for electrochemical capacitors. *J. Electrochem. Soc.* 142, L6–L8. doi: 10.1149/1.2043984

Zhong, C., Deng, Y., Hu, W., Qiao, J., Zhang, L., and Zhang, J. (2015). A review of electrolyte materials and compositions for electrochemical supercapacitors. *Chem. Soc. Rev.* 44, 7484–7539. doi: 10.1039/C5CS00303B

Zhou, H., Zhu, S., Hibino, M., and Honma, I. (2003). Electrochemical capacitance of self-ordered mesoporous carbon. *J. Power Sources* 122, 219–223. doi: 10.1016/S0378-7753(03)00439-7

Zhou, Y., Xu, H., Lachman, N., Ghaffari, M., Wu, S., Liu, Y., et al. (2014). Advanced asymmetric supercapacitor based on conducting polymer and aligned carbon nanotubes with controlled nanomorphology. *Nano Energy* 9, 176–185. doi: 10.1016/j.nanoen.2014.07.007

Zhu, Y., Murali, S., Stoller, M. D., Ganesh, K. J., Cai, W., Ferreira, P. J., et al. (2011). Carbon-based supercapacitors produced by activation of graphene. *Science* 332, 1537–1541. doi: 10.1126/science.1200770

Zhu, Y., Zong, Q., Zhang, Q., Yang, H., Wang, Q., and Wang, H. (2019). Three-dimensional core-shell NiCoP@NiCoP array on carbon cloth for high performance flexible asymmetric supercapacitor. *Electrochim. Acta* 299, 441–450. doi: 10.1016/j.electacta.2019.01.043

Conflict of Interest Statement: The authors declare that the research was conducted in the absence of any commercial or financial relationships that could be construed as a potential conflict of interest.

Colloidal Materials and Interfaces

Li-Na Han

Li-Na Han obtained a MSc degree in chemistry from Jilin University in 2012, and obtained her PhD degree from Shanghai Jiao Tong University in 2016 under the supervision of Professor Jie-Sheng Chen. Since 2016, she worked at the School of Materials Science and Engineering, Kunming University of Science and Technology. Her current scientific interests mainly focus on the following areas: (i) preparation and characterization of functional transition metal compounds (such as TiN, VN, and Co2P), (ii) carbon based materials (heteroatom-doped carbon and carbon-based composite materials), (iii) studying the performance of fuel cells, Zn-air batteries and supercapacitors.

Chunhai Jiang

Dr Chunhai Jiang is a Professor at Xiamen University of Technology. He obtained his PhD degree in materials science and engineering from the Institute of Metal Research, Chinese Academy of Sciences (IMR, CAS) in 2003 under co-supervision of Prof. Guiwen Qiao and Dr Jaimoo Yoo (Korea Institute of Materials Science). Since October 2003, he has worked as a postdoctoral researcher in Dr Hiroaki Kumakura's group at the National Institute for Materials Science (NIMS) in Tsukuba, Japan, in Dr Haoshen Zhou's group at National Institute of Advanced Industrial Science and Technology (AIST) in Tsukuba, Japan, and in Prof. Shixue Dou's group at the University of Wollongong, Australia. In March 2008, he joined IMR, CAS as an associate Professor and moved to Xiamen University of Technology in July 2015. His current research interests lie in functional nanomaterials for energy storage and water cleaning. To date, he has published over 90 peer-reviewed papers and has authorized nine Chinese patents.

Fengqi Lu

Dr Fengqi Lu is an associate research fellow at the Guilin University of Technology (GLUT), Guilin, China. He received his PhD degree from the School of Chemistry and Chemical Engineering at Sun Yat-Sen University (SYSU) in 2013, after he graduated from Yulin Normal University (YNU) and Guangxi Normal University (GXNU) with a BSc and MSc in 2007 and 2010, respectively. His current research interests focus on the design, synthesis, and characterization of functional nanomaterials and the application of energy storage and electrochemical catalyses, such as lithium ion batteries, sodium ion batteries, and electrochemical water splitting.

Andras Sapi

András Sápi is an Assistant Professor of Chemistry in the Department of Applied and Environmental Chemistry, at the University of Szeged. He received his PhD in 2012 in Chemistry. Dr Sápi has published over 70 scientific articles in the field of nanomaterials and material sciences. His research focuses on size controlled metallic nanoparticles and mesoporous metal-oxides, as well as atomic and molecular level investigation of such materials under reaction conditions in heterogeneous catalysis. He is an expert of surface science and catalysis.

Ming Xia

Dr Ming Xia is a Postdoctoral Research Fellow at the Centre for Smart Infrastructure and Digital Construction, Swinburne University of Technology in Melbourne, Australia. He received his MSc and BSc from Tongji University, China, and his PhD from Swinburne University of Technology. His PhD thesis topic focused on the "Investigation of Cementitious Materials for Powder-based 3D Printing" under the supervision of Prof. Jay Sanjayan.

Dr Xia's research interests include 3D concrete printing, and Geopolymer concrete and microstructure characterization of cementitious materials. He looks into innovative approaches to develop Geopolymer and/or Portland cement concrete that can be used in the powder-based 3D concrete printing process for digital construction. Dr Xia is also passionate about implementing research developments for industrial practice to solve challenges faced in 3D concrete printing technology.

frontiers in Materials

ORIGINAL RESEARCH
published: 24 April 2019
doi: 10.3389/fmats.2019.00085

Cobalt Nanoparticles Encapsulated in Nitrogen-Doped Carbon Nanotube as Bifunctional-Catalyst for Rechargeable Zn-Air Batteries

Yang Liu[1,2], *Peng Dong*[2], *Mian Li*[2], *Hao Wu*[1,2], *Chengxu Zhang*[2], *Lina Han*[1,2]* *and Yingjie Zhang*[1,2]*

[1] School of Materials Science and Engineering, Kunming University of Science and Technology, Kunming, China, [2] National and Local Joint Engineering Laboratory for Lithium-ion Batteries and Materials Preparation Technology, Key Laboratory of Advanced Battery Materials of Yunnan Province, Kunming University of Science and Technology, Kunming, China

Developing economic and efficient non-noble-metal electrocatalysts toward oxygen reduction reaction (ORR) and oxygen evolution reaction (OER) is vitally important to improve the performance and economic outlook of alkaline-based rechargeable Zn-air battery technologies. In this work, a nitrogen-doped carbon nanotube encapsulated with metallic cobalt nanoparticles (Co@NC) was synthesized through a facile method and subsequent pyrolysis treatment. The field emission scanning electron microscope (FESEM), high resolution transmission electron microscopy (HRTEM), Raman spectra investigations demonstrate that the presence of Co induces the formation of carbon nanotube during the pyrolysis process and increase degree of graphitization of carbon nanotubes. The electrode activity is assessed by comparing OER with ORR indicators (ΔE). The ΔE value of Co@NC is 0.91 V, which is lower than the commercialized Pt/C (1.1 V) and nitrogen-doped carbon (NC) (1.17 V). The Co@NC-based primary Zn-air battery display an open circuit potential of 1.4 V, a high power density of 137 $mW{\cdot}cm^{-2}$, and outstanding energy density (708.3 $mAh{\cdot}kg_{Zn}^{-1}$ and 868.9 Wh kg_{Zn}^{-1} at 10 $mA{\cdot}cm^{-2}$), which batter than the commercialized Pt/C.

Keywords: bifunctional electrocatalyst, Co@NC, oxygen reduction reaction, oxygen evolution reaction, Zn-air battery

OPEN ACCESS

Edited by:
Jie-Sheng Chen,
Shanghai Jiao Tong University, China

Reviewed by:
Yaobing Wang,
Fujian Institute of Research on the Structure of Matter (CAS), China
Bao Yu Xia,
Huazhong University of Science and Technology, China
Zhang Jianan,
Zhengzhou University, China

***Correspondence:**
Lina Han
hanln2016@163.com
Yingjie Zhang
zyjkmust@126.com

Specialty section:
This article was submitted to Colloidal Materials and Interfaces, a section of the journal Frontiers in Materials

Received: *14 January 2019*
Accepted: *08 April 2019*
Published: *24 April 2019*

Citation:
Liu Y, Dong P, Li M, Wu H, Zhang C, Han L and Zhang Y (2019) Cobalt Nanoparticles Encapsulated in Nitrogen-Doped Carbon Nanotube as Bifunctional-Catalyst for Rechargeable Zn-Air Batteries. Front. Mater. 6:85. doi: 10.3389/fmats.2019.00085

INTRODUCTION

In response to the growing global energy demand and environmental crisis, extensive research has focused on energy conversion and storage devices. It is well-known that oxygen reduction reaction (ORR) and oxygen evolution reaction (OER) play a vital role in various energy storage systems, for instance, metal-air batteries (Park et al., 2016; Feng et al., 2018; Guo et al., 2018a; Wen et al., 2018) and fuel cells (He et al., 2013; Karim et al., 2017).

For this reason, excellent electrochemical performance Zn-air batteries need a bifunctional catalyst, which reveal excellent catalytic performance and stability, for ORR and OER. Traditionally, Platinum is deemed the best catalyst for ORR, while iridium is reputed the greatest catalyst for OER. However, some shortcomings such as exorbitant price, scarcity and poor stability have prohibited their extensive application (Deng et al., 2013; Dong et al., 2016; Tian et al., 2016; Qiao et al., 2017; Si et al., 2017).

To address above issue, various non-precious metal electrocatalyst, including transition metal oxides, transition metal nitrides, various carbon, and metal-free heteroatoms doped carbon were explored (Deng et al., 2015; Tao et al., 2015; Zhou et al., 2015; Cao et al., 2016; Qu et al., 2016, 2017; Yang Z. K. et al., 2016; Guo J. et al., 2017; Mo et al., 2017; Guo et al., 2018b; Liu et al., 2018). Among the various electrocatalysts being developed, CNT can not only improve electron transport, but also maintain and improve the stability of the catalyst under harsh conditions, which due to the metal cobalt encased in carbon nanotubes (Fang et al., 2016a; Guo S. et al., 2017; Sheng et al., 2017). Liu et al. adopted a hybrid strategy to synthesize carbon nanotubes and graphene as the carrier of metallic cobalt, and the catalyst also maintain high catalytic activity and stability under severe acidic conditions. Zheng et al. found that cobalt nanoparticles were wrapped in carbon nanotubes, which could prevent Co nanoparticles from being etched and oxidized in the post-process after pyrolysis, which have a pivotal part in enhancing the electrocatalyst stability to ORR and OER. Deng et al put forward a new idea to synthesize carbon nanotube encapsulated iron as ORR catalyst. In their opinion, the encapsulated metallic Fe can reduce the local work function of the surface carbon, which improve the ORR performance (Deng et al., 2017; Zhe et al., 2017; Zheng et al., 2017; Liu et al., 2018).

Recently, nitrogen-doped carbon nanotube has the potential to replace the metal-free-based electrocatalysts, which is mainly due to the nitrogen induced charge delocalization (Hao et al., 2017). Deng et al. obtained a suite of NCNTs by controlling the pyrolysis temperature of precursor polyaniline (PANI), which achieved the doping of nitrogen atoms into the carbon skeleton at the atomic level. By researching the unique electron configurations of carbon atoms in combination with different nitrogen functional groups, they found that nitrogen doping can provide atomic-level catalytic activity centers for ORR (Deng et al., 2017). Wang et al. developed an economical approach to obtain metallic Co encapsulated in N,S co-doped carbon nanotubes. the porous channels of the carbon skeleton provide more space for the dispersion of cobalt nanoparticles, and the introduction of nitrogen and sulfur into carbon nanotubes can provide more catalytic active sites (Wang et al., 2018). Zehtab et al. synthesized phosphorus functionalized carbon nanotubes (PCNTs) by heat treating CNT-H_3PO_4 at 170°C. The high phosphorus content and high specific surface area of PCNTs provided the corresponding conditions for improving the catalytic activity of ORR (Zehtab et al., 2015).

Recently, effective synthesis strategies are developed to accelerate the intensive research work of transition metal/nitrogen doped carbon nanotubes composites for ORR and OER. Song et al. obtained nitrogen-doped carbon nanotubes encapsulated cobalt nanoparticles catalyst by pyrolysis process, which showing preferable electrocatalytic performance. Li et al. conceived a method to synthesize *in situ*-generated Co@NCNTs derived from MOFs under H_2/Ar atmosphere. Jie et al. published a one-pot pyrolysis method to obtained N-doped carbon nanotubes encapsulated the synthesized nickel-cobalt alloy, which has high catalytic performance. Yang et al. designed a synthetic strategy using $FeCl_3/NH_3$ as the source to obtain Fe-N-C catalyst by heat-treating defective graphene at 950°C. Dilpazir et al. synthesized novel Co nanoparticles immobilized NCNTs on the zeolitic imidazolate framework treated with dicyandiamide (Yang X. et al., 2016; Jie et al., 2017; Li et al., 2017; Song et al., 2017; Dilpazir et al., 2018). However, in these experiments, the introduction of a template or the use of ammonia gas increased the cost and risk of the experiment.

Herein, cobalt acetate tetrahydrate ($Co(Ac)_2{\cdot}4H_2O$), dicyanamide (DCDA) and Poly(ethyleneglycol)-block-poly(propyleneglycol)-block-poly(ethyleneglycol) (P123) were elaborately selected to fabricate cobalt nanoparticles@N-doped carbon nanotubes composites (Co@NC). During the pyrolysis process, dicyanamide not merely do duty for a nitrogen source and carbon source and not only uses its reductivity to form the cobalt nanoparitcles. P123, serve as the main carbon source for the formation carbon nanotube structure under cobalt species inducing effect. In terms of its excellent overall catalytic performance for ORR and OER, the prepared Co@NC electrocatalyst is served as a cathode in rechargeable Zn-air battery and reveals a high specific power density, peak power density and stability, superior to that of the commercialized Pt/C.

EXPERIMENTAL SECTION

Chemicals

Cobalt acetate tetrahydrate ($Co(Ac)_2{\cdot}4H_2O$) was bought from Guangdong Guanghua Sci-Tech Co., Ltd. P123 (Mw = 5,800) and Nafion (5.0 wt %) were obtained from Sigma-Aldrich. Dicyandiamide (DCDA, 99.5%) was purchased from Acros. Concentrated hydrochloric acid (HCl, 37%) was bought from Chengdu Kelong Chemical Co., Ltb. Pt/C catalyst (20% Pt) was obtained from Shanghai Hesen Electric Co., Ltd. All the chemicals were used without further purification.

Synthesis of Co@NC Electrocatalysts

$Co(Ac)_2{\cdot}4H_2O$ and P123 were dissolved with H_2O and HCl in the 200 mL beaker. After stirring at 50°C for 12 h, the DCDA was added. The final molar ratio of $Co(Ac)_2{\cdot}4H_2O$: P123: DCDA: HCl: H_2O in the mixture was 0.003: 0.001: 1: 0.8: 13. Then the solution was dried at 50°C to obtain precursor. The bulk precursor was calcined in a tube furnace under the protection of a N_2 atmosphere. Firstly, it was arised to 400°C at a heating rate of 5°C/min and maintained 1 h, then the temperature further arised to 900°C at the same heating rate and maintained 1 h. In the preparation of the precursor, we performed an experiment without adding a cobalt source under the same synthesis conditions, and the obtained sample was named NC.

Electrochemical Measurements

Electrochemical measurements were performed on a Metrohm Autolab (Swiss Wantong Co. Ltd, Switzerland), using a typical three-electrode device. The rotation ring-disk electrode (RRDE, φ = 5 mm, Swiss Wantong Co., Ltd.) was used as working electrode, Ag/AgCl electrode was used as referode electrode and platinum foil was used as counter electrode. The fabrication of the working electrode was carried out as following: catalyst (5 mg)

was mixed with H_2O (0.8 mL), CH_3CH_2OH (0.2 mL) and Nafion solution (50 μL) in an ultrasonic bath to get evenly dispersed ink.

Then, 10 μL of the ink was dripped onto the glass carbon surface and natural drying at room temperature. The mass loading of catalyst on the surface of glass carbon electrode was 0.24 mg·cm^{-2}. All potentials in this paper are based on reversible hydrogen electrode potentials (RHE): $E_{RHE} = E_{Ag/AgCl} + 0.1976 + 0.0592 \times pH$ (Yang X. et al., 2016).

Cyclic voltammetry (CV) were measured in N_2-saturated or O_2-saturated 0.1 M KOH solution with a sweep rate of 10 mV·s^{-1}. The RDE and RRDE tests were carried out in O_2-saturated 0.1 M KOH solution at 1600 rpm with a scan rate of 10 mV·s^{-1}. The electrochemical impedance spectroscopy (EIS) of catalysts were measured in O_2-saturated KOH with 5 mV amplitude from 100 kHz to 0.01 Hz. NC and Pt/C catalyst were also measured using the same methods for comparison. All of the above electrochemical tests were performed at room temperature.

RESULTS AND DISCUSSION

Material Characterization of the Co@NC

The overall synthetic process of Co@NC is shown in **Figure 1a**. In the first step, nanorod colloid formed by P123 self-assembly in 2 M HCl solution containing amount of Co^{2+}. Secondary, DCDA with rich -NH_2, -NH and -C≡N functional group was added to obtain the precursor. Finally, the bulk precursor was annealed under N_2 atmosphere to obtain Co@NC. During precursor pyrolysis, carbon nanotube formed in the presence of cobalt, and Co^{2+} was reduced to Co nanoparticles encapsulated in carbon nanotube.

Field emission scanning electron microscope (FESEM) and TEM were used to investigate the as-obtained samples microstructure (**Figures 1b–d** and **Figures S2**, **S3**). The low resolution FESEM and TEM image (**Figures S2a**, **S3a**) indicate Co nanoparticles was encapsulated in carbon nanotube successfully, and the particle size of Co nanoparticles is within the scope of 20–100 nm. The width and length of carbon nanotube is about 200 nm and 10 μm, respectively. the interplanar spacing was about 0.203 nm (**Figure 1d**), corresponding to the distance between the (111) planes of cobalt particles. Moreover, cobalt nanoparticles can be observed clearly encapsulated by several graphene layers. The TEM elemental mapping images show an atomically uniform distribution of the C, N and Co elements in prepared Co@NC sample (**Figure 1e**).

XRD patterns of NC and Co@NC were shown in **Figure 2A**, three diffraction peaks at 44.2°, 51.5°, and 75.6° were indexed to the (111), (200), and (220) crystal planes of face-centered (fcc) Co (PDF# 15-0806) (Chen et al., 2016), which suggested that Co^{2+} was induced to cobalt successfully. Beyond that, a broad peak around 26°, corresponding to graphitized carbon (002) diffraction (Hao et al., 2017; Liang et al., 2019). And compared with NC, the C(002) diffraction peak strengthened, indicating the increased graphitization of the carbon in the presence of cobalt nanoparticles (Ai et al., 2018).

Raman measurements were then used to investigate the carbon defects and the degree of graphitization. In **Figure 2B**, two distinct peaks at 1,360 and 1590 cm^{-1} are associated with D and G bands, respectively. The area ratio between D and G bands (S_D/S_G) were calculated as 3.047 and 1.489 for NC and Co@NC, respectively. The results indicate that the existence of cobalt could improve the degree of graphitization, which will have a positive effect on its conductivity and catalytic activity (Dai et al., 2016). Three characteristic peaks of Co were observed around 475.6, 516, and 676 cm^{-1} by Raman spectroscopy, which correspond to classical vibration modes E_g, F_{2g}, and A_{1g} of Co, respectively (Jie et al., 2017; Li et al., 2017).

X-ray photoelectron spectroscopy (XPS) was carried out to analyse the chemical valence state and surface element composition of Co@NC and NC in **Figures 2C,D** and **Figures S6**, **S7**. The survey spectra revealed that NC only contains three elements of C, N, O, and C, N, O, Co were coexistent in Co@NC (**Figure S6**). The specific contents of all elements are summarized in **Table S1**. The high resolution C1s spectrum were deconvoluted into three peaks (**Figure S7a**): C-C (284.6 eV), C-O (285.4 eV), and C=O (286.5 eV) (Dilpazir et al., 2018). The high resolution C1s spectrum (**Figure 2C**) exhibits four types of *N* species at 398.5, 400.1, 401, 403.6 eV, which correspond to pyridinic N, pyrrolic N, graphitic N, and oxidized N (Zhao and Chen, 2015; Fang et al., 2016a; Zhou T. et al., 2017). The content of pyridinic N was also higher than that of the other three nitrogen species in Co@NC, higher content of pyridine N is expected to exhibit superior ORR performance (Wei et al., 2017). As shown in **Figure 2D**, high resolution Co2p spectrum shows two types of Co species at 780.3 and 795.8 eV, corresponding to metallic Co2p3/2 and Co2p1/2 (Zhou L. et al., 2017). This further suggested that Co^{2+} was induced to cobalt successfully used DCDA as reducing agent. The presence of Co^{2+} and Co^{3+} may be due to the oxidation of the surface of the sample exposed to air during the preparation process (Chen et al., 2016). According to the XPS results (Zhou L. et al., 2017), the relative content of Co in the Co@NC sample was calculated to be about 0.91 at%.

Electrochemical Performance for ORR and OER

The ORR catalytic activity of Co@NC and NC were measured by cyclic voltammetry (CV) in N_2-saturated and O_2-saturated 0.1 M KOH solution with a sweep rate of 10 mV·s^{-1}, firstly. The diffusion current density of Co@NC, NC and Pt/C (**Figure S8**) both increases significantly in the case of the introduction of O_2, which indicate the intrinsic ORR catalytic activity of the Co@NC and NC.

To gain further insights into the electrocatalytic behavior of Co@NC and NC toward ORR and OER, LSV curves were acquired in a conentional three-electrode device in the O_2-saturated 0.1 M KOH solution. As observed, Co@NC electrocatalyst has a conspicuous electrocatalytic performance, the onset potential and half-wave potential ($E_{1/2}$) are 0.89 and 0.81 V, respectively, which both higher than NC and IrO_2/C (0.84 V, 0.7 V). Compared with the review results in the literature (**Table S3**), the ORR activity of Co@NC is one of non-precious metal electrocatalysts in alkaline media.

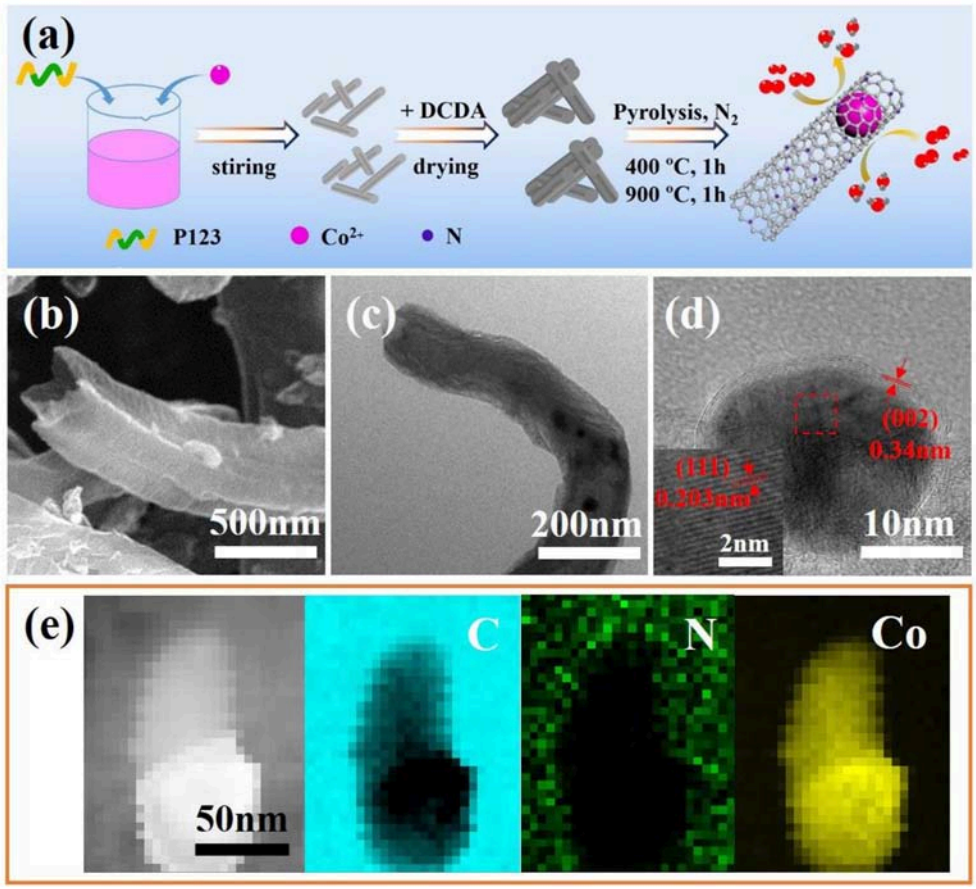

FIGURE 1 | (a) Schematic illustration of the overall synthetic process of Co@NC. **(b)** FESEM, **(c)** Transmission electron microscopy (TEM) and **(d)** HRTEM images of the Co@NC. **(e)** High angle annular dark field-scanning transmission electron microscope (HAADF-STEM) image and the corresponding elemental mapping of the Co@NC.

The Tafel slope was obtained from ORR polarization curves to evaluate the kinetic features of electrocatalysts, as shown in **Figure 3B**. The calculated Tafel slope of Co@NC (71 mV/dec) was close to Pt/C (61 mV/dec) and lower than NC (82 mV/dec) and IrO_2/C (103 mV/dec). The results suggested that the presence of cobalt can improve the degree of graphitization, thus increase the conductivity and decrease the slope of Tafel of Co@NC (Wang et al., 2016).

The catalytic activity of OER is customary assessed by comparing the potential at 10 mA·cm^{-2} (Qiao et al., 2016). As shown in **Figure 3A**, the Co@NC show the OER onset potential (1.47 V) and overpotential (0.5 V), which is comparable to the previously reported catalyst (**Table S3**). In addition, the Tafel slope was also calculated (**Figure 3C**), indicating the OER kinetics of the NC, Co@NC and Pt/C. The lower value of Tafel slope means a higher electrocatalysis performance for the OER. The Tafel slope of Co@NC is 110 mV/dec, lower than NC (163 mV/dec) and Pt/C (291 mV/dec), which suggest that the OER kinetics at Co@NC is faster than the other samples (Qiao et al., 2016). The turnover frequency (TOFs) was calculated to compare intrinsic activity (**Supporting Information**), the TOFs of the Co@NC and NC are 0.117 s^{-1} and 0.214 s^{-1} at an overpotential of 400 mV, respectively, and comparable to the previously reported noble-metal-free electrocatalyst in **Table S3**. Electrode activity can also be assessed by OER and ORR indicators differences ($\Delta E = E_{j=10} - E_{1/2}$), where the $E_{j=10}$ value is the corresponding OER potential at 10 mA·cm^{-2} (Meng et al., 2016). Co@NC shows the lowest ΔE value (0.91 V) compared with NC (1.1 V), Pt/C (1.17 V), and IrO_2/C (0.92 V), confirming the remarkable reversible oxygen electrode characteristics of Co@NC, which directly affects the charge-discharge performance of rechargeable Zn-air batteries (Kashyap and Kurungot, 2018).

To obtain more electrochemical kinetic information, the K-L plots of Co@NC, NC and Pt/C are obtained by K-L equation. **Figure 3D** shows the K-L plots calculated at 0.5 V at different speeds LSV curves. The K-L plots shows a good linearity between j^{-1} and $\omega^{-1/2}$, which indicated that the first-order reaction kinetics is closely related to the concentration of dissolved O_2 (Deng et al., 2017). The electron transfer numbers (n) of Co@NC, NC and Pt/C are calculated to be 3.74, 3.67, and 3.91, respectively, suggesting n is close to 4e$^-$ pathway for ORR (Zhang et al., 2015).

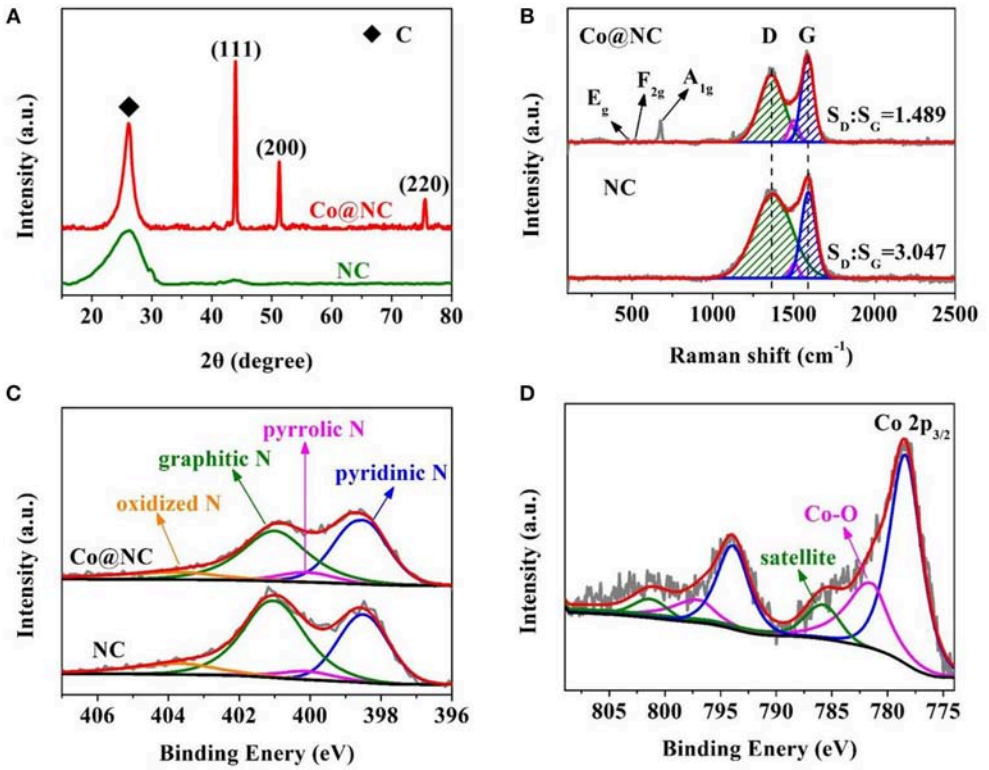

FIGURE 2 | (A) XRD patterns, **(B)** Raman spectra of NC and Co@NC. The high resolution spectrum of **(C)** N1s of NC and Co@NC. **(D)** The high resolution Co2p spectrum of Co@NC.

To further understand the reaction pathways and monitor the formation of peroxide, RRDE tests were carried out accurately calculate the amount of H_2O_2 generated. The proportion of H_2O_2 yield (**Figure S10**) and the electron transfer numbers (**Figure 4B**) of Co@NC, NC and commercial Pt/C were calculated according to disking current density and ring current density (**Figure 4A**). In the case of Co@NC electrocatalyst, the proportion of H_2O_2 yield is lower than 20%, and the n is higher than 3.5, which showed electrocatalytic selectivity was slightly lower than commercial Pt/C, consistenting with K-L plots results. Further suggest that Co@NC ideally performs oxygen reduction via $4e^-$ transfer pathway.

In addition, the stability of Co@NC electrocatalyst is a typical index to evaluate ORR performance, which is of great significance for the safe and stable operation of Zn-air batteries (Park et al., 2016). After accelerating aging process by continuously performing 200 cycles at 10 $mV{\cdot}s^{-1}$, the half-wave potential of Co@NC catalyst was merely 7 mV negative shift and its diffusion current density show no obvious decay (**Figure 4C**), which indicating significant electrochemical stability of Co@NC electrocatalyst. Comparatively speaking, the half-wave potential of NC catalyst has a negative shift of 10 mV and its diffusion current density decreased significantly.

To better understand the catalytic performance of Co@NC and the role played by N and Co, we further probed the active sites. Transition metals are very sensitive to SCN^- ions and can selectively attack the metal centers, impeding their catalytic activity. The ORR activity of Co@NC was re-examined in an electrolyte containing 5 mM KSCN. As shown in **Figure 4D**, we found that the onset potential, half wave potential and limited diffusion current density of Co@NC decreases in the presence of KSCN, suggesting a strong SCN^- ion coordination and blockage of the Co active sites (Amiinu et al., 2018). However, the onset potential, half wave potential and limited diffusion current density of NC was almost unchanged in the presence of SCN^- ions. We believe that both Co NPs and N-doped carbon play an important role in enhancing ORR catalytic performance. For the removal of Co NPs, the as-obtained material was also immersed in 0.5 M H_2SO_4 for 24 h. After washing with deionized water and ethanol for three times, the N-doped CNTs were obtained. As shown in supporting information **Figure S11**, we can know that Co@NC is more electrocatalytically active than N-doped CNTs. This comparison clearly shows that the N-C active site and Co NPs active site existed in Co@NC can significantly improve the catalytic activity (Guo et al., 2018a).

Electrochemical impedance spectroscopy (EIS) showed that the equivalent series resistance of Co@NC was smaller than NC (**Figure S12**), and there was no high frequency semicircle indicating that charge transfer resistance at the NC/electrolyte and Co@NC/electrolyte interface can be ignored, corresponding to a faster reaction rate. This indicates that the Co@NC has higher conductivity than NC, which corresponds to the Raman results.

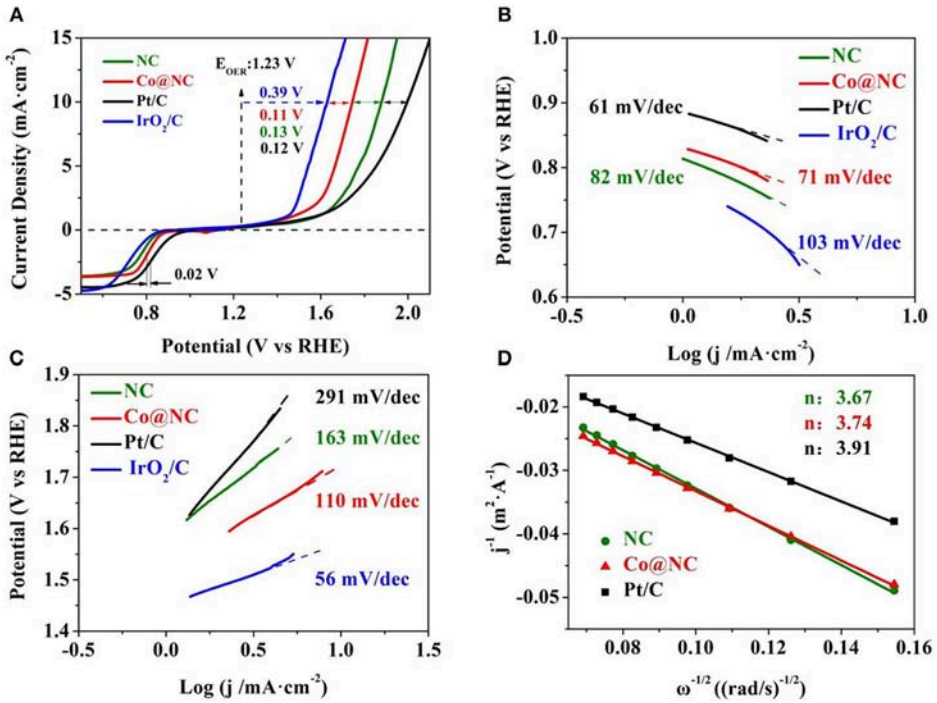

FIGURE 3 | (A) ORR and OER polarezation curves of Co@NC, NC, and Pt/C (electrolyte: O_2-saturated 0.1 M KOH, scan rate: 10 mV·s^{-1}, rotational speed: 1,600 rpm). Tafel plots of Co@NC, NC, Pt/C and IrO_2/C for **(B)** ORR; **(C)** OER. **(D)** Koutecky-Levich (K-L) plots of NC, Co@NC, and Pt/C at 0.5 V.

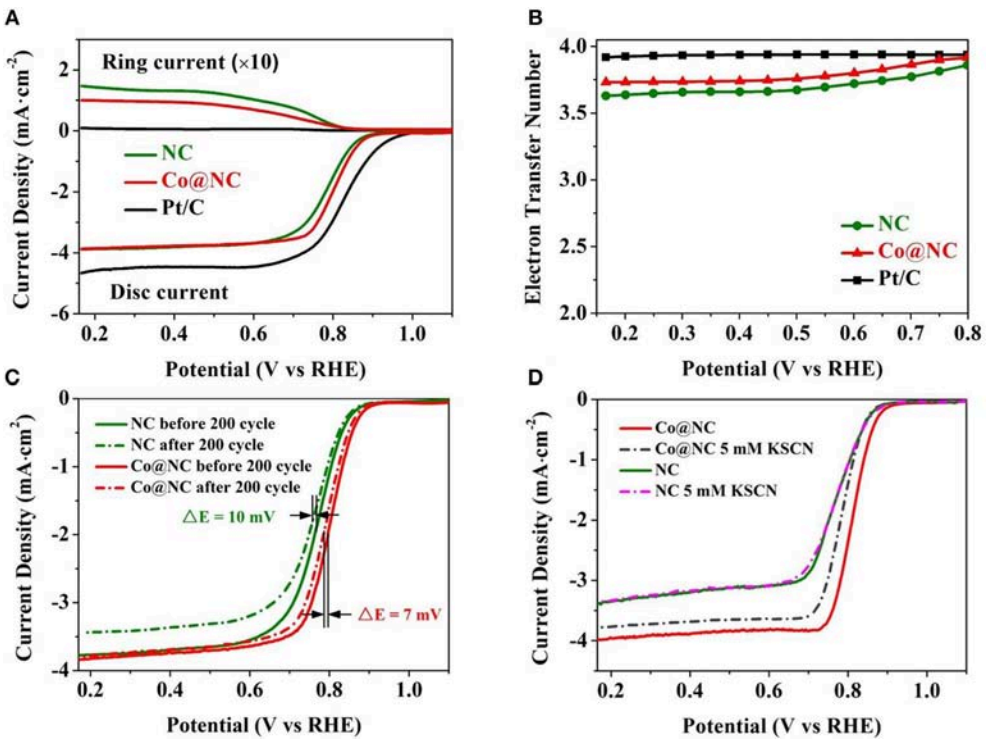

FIGURE 4 | (A) RRDE disk and ring currents recorded. **(B)** Electron transfer number of the Co@NC, NC and Pt/C (electrolyte: O_2-saturated 0.1 M KOH, scan rate: 10 mV·s^{-1}, rotational speed: 1,600 rpm). ORR polarization plots of **(C)** Co@NC and NC before and after continuously 200 cycles (electrolyte: O_2-saturated 0.1 M KOH). **(D)** Effect of KSCN interaction on the catalytic activity of Co@NC and NC.

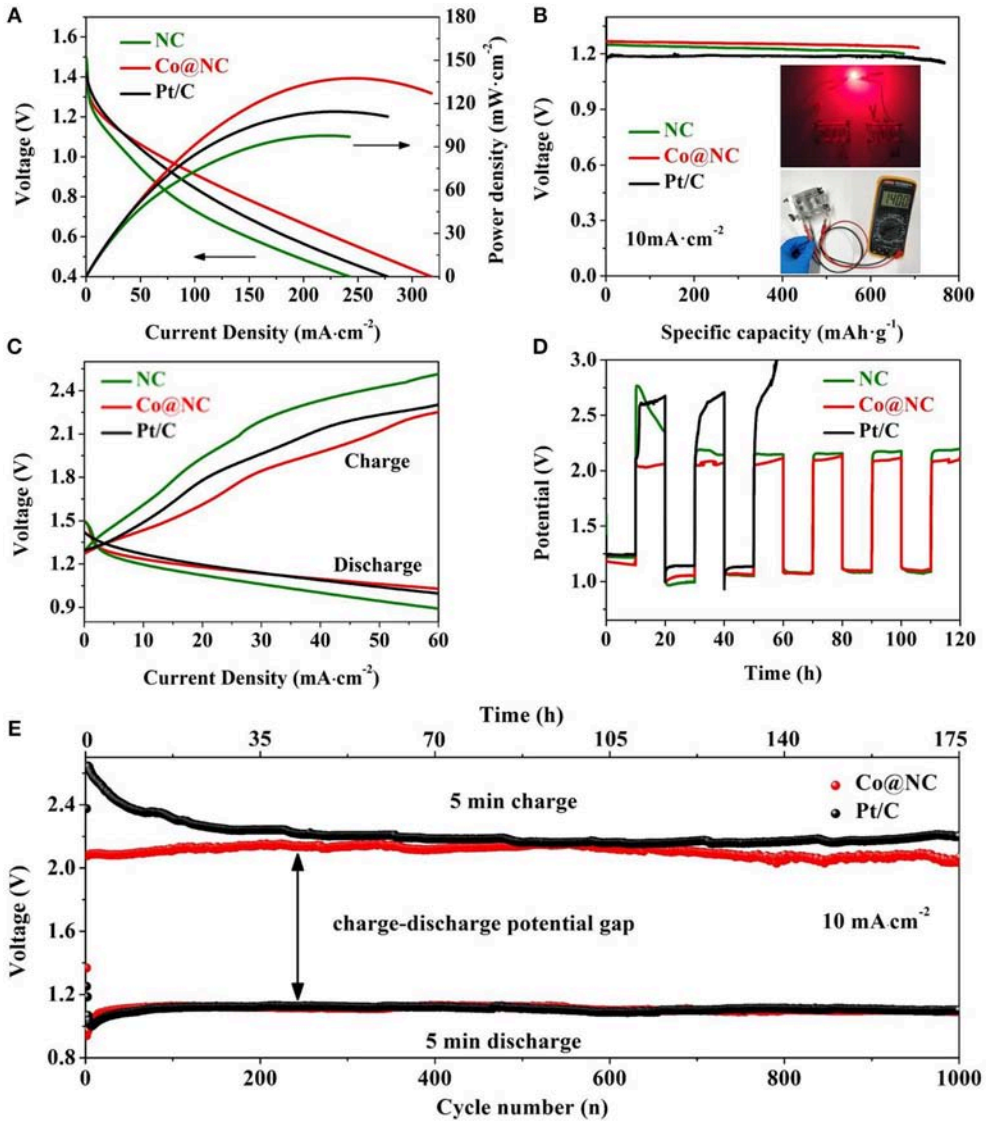

FIGURE 5 | (A) Discharge polarization curves and their corresponding power density curves. **(B)** Typical discharge curves of Co@NC, NC, and Pt/C based Zn-air batteries under continuous discharge until complete consumption of Zn. The illustrations are photograph of the assembled battery with an open-circuit voltage of 1.4 V and red LED powered in series by two rechargeable Zn-air batteries. **(C)** Charge/discharge polarization curves of the Co@NC, NC, and Pt/C catalyst, respectively. **(D)** Galvanostatic charge/discharge test of Co@NC, NC, and Pt/C based Zn-air battery (current density: 10 mA·cm^{-2}, cycle period: 20 h). **(E)** Charge/discharge cycling curves of Co@NC-based battery (current density: 10 mA·cm^{-2}, cycle period: 10 min).

Rechargeable Zn-Air Batteries

Superior bifunctional catalysts can accelerate the process of wide application of Zn-air batteries, and thus Co@NC was synthesized to build a typical Zn-air battery. In which, Co@NC electrocatalyst was loaded on conductive carbon paper (0.5 mg·cm^{-2}), Zn plate and 6 M KOH containing 0.2 M zinc acetate were used as the cathode, anode and electrolyte, respectively. **Figure 5A** presents polarization and power density curves of Co@NC, NC, and Pt/C electrocatalyst, Co@NC electrocatalyst exhibited a higher peak power density (137 mW·cm^{-2}) and a larger current density (246 mA·cm^{-2}) at 0.56 V, both of these are apparently higher than NC and Pt/C. Moreover, the Zn-air battery based on Co@NC electrocatalyst exhibits a large specific capacity of 708.3 mAh·g$_{Zn}^{-1}$ with a discharge platform of 1.27 V at 10 mA·cm^{-2} (**Figure 5B**), which is comparable to the specific capacity of Pt/C (767.1 mAh·g$_{Zn}^{-1}$), but is much larger than the specific capacity of NC (674.9 mAh·g$_{Zn}^{-1}$). By calculation we can also find that the energy density of Co@NC (868.9 mWh·g$_{Zn}^{-1}$) is slightly smaller than Pt/C (892.6 mWh·g$_{Zn}^{-1}$) but higher than NC (829.7 mWh·g$_{Zn}^{-1}$). Two Zn-air batteries were connected in series (**Figure 5B**), which can provide the required working voltage of the light-emitting diode (LED) and illuminate the rad LED in practical application. The results show that the air cathode of Co@NC can significantly improve the performance of the Zn-air battery than the others,

which is attributed to the superior ORR performance of Co@NC catalyst in alkaline medium (Fang et al., 2016b). Furthermore, in the charging process (OER process), Co@NC exhibited higher current density than Pt/C catalyst (**Figure 5C**), corresponding to the OER test result in **Figure 3A**.

Durability is an important indicator for future commercial applications of Zn-air batteries. Therefore, galvabostatic charge and discharge battery cycle were test at 10 $mA{\cdot}cm^{-2}$ in a 20 h cycle period in **Figure 5D**. The Zn-air battery with Co@NC electrocatalyst exhibit superior cycling stability. After 6 discharge/charging cycles, the total time exceeds 120 h, and the discharge/charging overpotential slightly changes. Comparatively speaking, the Zn-air battery based on Pt/C requires higher discharge/charge overpotential and <2 discharge/charge cycles (40 h). Besides that, the stability of Zn-air batteries with Co@NC, NC, and Pt/C catalysts were also evaluated at 10 $mA{\cdot}cm^{-2}$ with a 10 min cycle period (**Figure 5E** and **Figure S13**). It is worth noting that the charge/discharge overpotential (0.93 V) of Co@NC based Zn-air battery decreased slightly after 1,000 cycles. Which is smaller than the Zn-air battery with Pt/C (1.57 V) and NC(1.1 V). Although the Pt/C catalyst shows higher ORR kinetics, the degradation of the catalyst in charging process leads to a decline in continuous cycle activity. Above all, the as-prepared Co@NC electrocatalyst can be considered as a potential and more environmentally friendly catalyst that can be used as a substitute for noble metal catalysts for rechargeable metal-air batteries.

CONCLUSION

In summary, we developed a facile method for fabrication of nitrogen-doped carbon nanotube encapsulated with cobalt nanoparticles. In this process, DCDA and P123 were rational designed as the precursors and reducing agent to construct carbon nanotube and form cobalt nanoparitcles. The degree of graphitization of nitrogen-doped carbon strengthened in the presence of cobalt nanoparticles. The as obtained Co@NC electrocatalyst showed an excellent ORR and OER bifunctional electrocatalytic performance. In addition, the typical two-electrode Zn-air battery based on Co@NC electrocatalyst exhibited higher peak power density, large specific capacity and durability. The results of this paper provide a new strategy for the efficient production of nitrogen-doped carbon nanotube encapsulated cobalt. This method can be used in other energy storage devices, for instance, supercapacitors and fuel cells.

AUTHOR CONTRIBUTIONS

LH conceived the study designed the experiments. YL performed the experiments work, analyzed the data, and wrote the manuscript with the help from LH and YZ. HW performed the FESEM testing. PD, CZ, and ML analyzed the TEM data. All authors approved the manuscript for publication.

FUNDING

This work was supported by the National Natural Science Foundation of China (51802134, 51764029, and 51864024).

SUPPLEMENTARY MATERIAL

The Supplementary Material for this article can be found online at: https://www.frontiersin.org/articles/10.3389/fmats.2019.00085/full#supplementary-material

REFERENCES

Ai, L., Su, J., Wang, M., and Jiang, J. (2018). Bamboo-structured nitrogen-doped carbon nanotube co-encapsulating cobalt and molybdenum carbide nanoparticles: an efficient bifunctional electrocatalyst for overall water splitting. *ACS Sust. Chem. Eng.* 6, 9912–9920. doi: 10.1021/acssuschemeng.8b01120

Amiinu, I. S., Liu, X., Pu, Z., WenqiangLi, Li, Q., Jie, Z., Tang, H., et al. (2018). From 3D ZIF nanocrystals to Co-Nx/C nanorod array electrocatalysts for ORR, OER and Zn-air batteries. *Adv. Funct. Mater.* 28:1704638. doi: 10.1002/adfm.201704638

Cao, X., Zheng, X., Tian, J., Jin, C., Ke, K., and Yang, R. (2016). Cobalt sulfide embedded in porous nitrogen-doped carbon as a bifunctional electrocatalyst for oxygen reduction and evolution reactions. *Electrochim. Acta* 191, 776–783. doi: 10.1016/j.electacta.2016.01.137

Chen, J., Zhou, H., Huang, Y., Yu, H., Huang, F., Zheng, F., et al. (2016). A 3D Co-CN framework as a high performance electrocatalyst for the hydrogen evolution reaction. *RSC Adv.* 6, 42014–42018. doi: 10.1039/C6RA05632F

Dai, X., Li, Z., Ma, Y., Liu, M., Du, K., Su, H., et al. (2016). Metallic cobalt encapsulated in bamboo-like and nitrogen-rich carbonitride nanotubes for hydrogen evolution reaction. *ACS Appl. Mater. Interfaces* 8, 6439–6448. doi: 10.1021/acsami.5b11717

Deng, C., Zhong, H., Li, X., Yao, L., and Zhang, H. (2015). A highly efficient electrocatalyst for oxygen reduction reaction: phosphorus and nitrogen co-doped hierarchically ordered porous carbon derived from an iron-functionalized polymer. *Nanoscale* 8, 1580–1587. doi: 10.1039/C5NR06749A

Deng, D., Yu, L., Chen, X., Wang, G., Jin, L., Pan, X., et al. (2013). Iron Encapsulated within pod-like carbon nanotubes for oxygen reduction reaction. *Angew. Chem. Int. Edit.* 125, 389–393. doi: 10.1002/ange.201204958

Deng, H., Qian, L., Liu, J., and Feng, W. (2017). Active sites for oxygen reduction reaction on nitrogen-doped carbon nanotubes derived from polyaniline. *Carbon N. Y.* 112, 219–229. doi: 10.1016/j.carbon.2016.11.014

Dilpazir, S., He, H., Li, Z., Meng, W., Lu, P., Liu, R., et al. (2018). Cobalt single atoms immobilized N-doped carbon nanotubes for enhanced bifunctional catalysis toward oxygen reduction and oxygen evolution reactions. *ACS Appl. Energy Mater.* 1, 3283–3291. doi: 10.1021/acsaem.8b00490

Dong, S. H., He, D., Jing, W., Yue, L., Yin, P., Xun, H., et al. (2016). Ultrathin icosahedral Pt-enriched nanocage with excellent oxygen reduction reaction activity. *J. Am. Chem. Soc.* 138, 1494–1497. doi: 10.1021/jacs.5b12530

Fang, Y., Li, X., Li, F., Lin, X., Tian, M., Long, X., et al. (2016a). Self-assembly of cobalt-centered metal organic framework and multiwalled carbon nanotubes hybrids as a highly active and corrosion-resistant bifunctional oxygen catalyst. *J. Power Sources* 326, 50–59. doi: 10.1016/j.jpowsour.2016.06.11

Fang, Y., Wang, H., Hao, Y., and Feng, P. (2016b). From chicken feather to nitrogen and sulfur co-doped large surface bio-carbon flocs: an efficient electrocatalyst for oxygen reduction reaction. *Electrochim. Acta* 213, 273–282. doi: 10.1016/j.electacta.2016.07.121

Feng, Z., Wei, M., Jing, S., Chao, J., Yong, L., Bie, S., et al. (2018). Cobalt phosphide microsphere as an efficient bifunctional oxygen catalyst for Li-air batteries. *J Alloy. Compd.* 750, 655–658. doi: 10.1016/j.jallcom.2018.04.070

Guo, J., Niu, Q., Yuan, Y., Maitlo, I., Nie, J., and Ma, G. (2017). Electrospun core-shell nanofibers derived Fe-S/N depoed carbon material for oxygen reduction reaction. *Appl. Surf. Sci.* 416, 118–123. doi: 10.1016/j.apsusc.2017.04.135

Guo, S., Yuan, P., Zhang, J., Jin, P., Sun, H., Lei, K., et al. (2017). Atomic-scaled cobalt encapsulated in P, N-doped carbon sheaths over carbon nanotubes for enhanced oxygen reduction electrocatalysis under acidic and alkaline media. *Chem. Commun.* 53, 9862–9865. doi: 10.1039/C7CC05476A

Guo, Y., Yuan, P., Zhang, J., Hu, Y., Amiinu, I. S., Wang, X., et al. (2018b). Carbon nanosheets containing discrete Co-Nx-By-C active sites for efficient oxygen electrocatalysis and rechargeable Zn-air batteries. *ACS Nano* 12, 1894–1901. doi: 10.1021/acsnano.7b08721

Guo, Y., Yuan, P., Zhang, J., Xia, H., Cheng, F., Zhou, M., et al. (2018a). Co_2P-CoN double active centers confined in N-doped carbon nanotube: heterostructural engineering for trifunctional catalysis toward HER, ORR, OER, and Zn-air batteries driven water splitting. *Adv. Funct. Mater.* 28:1805641. doi: 10.1002/adfm.201805641

Hao, Y., Lu, Z., Zhang, G., Chang, Z., Luo, L., and Sun, X. (2017). Cobalt-embedded nitrogen doped carbon nanotubes as high performance bifunctional oxygen catalysts. *Energy Technol.* 5, 1265–1271. doi: 10.1002/ente.201600559

He, Q., Suraweera, N. S., Joy, D. C., and Keffer, D. J. (2013). Structure of the ionomer film in catalyst layers of proton exchange membrane fuel cells. *J. Phys. Chem. C* 117, 25305–25316. doi: 10.1021/jp408653f

Jie, Y., Zhong, Y., Wei, Z., and Shao, Z. (2017). Facile synthesis of nitrogen-doped carbon nanotubes encapsulating nickel cobalt alloys 3D networks for oxygen evolution reaction in an alkaline solution. *J. Power Sources* 338, 26–33. doi: 10.1016/j.jpowsour.2016.11.023

Karim, N. A., Kamarudin, S. K., and Loh, K. S. (2017). Performance of a novel non-platinum cathode catalyst for direct methanol fuel cells. *Energy Convers. Manag.* 145, 293–307. doi: 10.1016/j.enconman.2017.05.003

Kashyap, V., and Kurungot, S. (2018). Zirconium-substituted cobalt ferrite nanoparticle supported N-doped reduced graphene oxide as an efficient bifunctional electrocatalyst for rechargeable Zn-air battery. *ACS Catal.* 8, 3715–3726. doi: 10.1021/acscatal.7b03823

Li, J. S., Du, B., Lu, Z. H., Meng, Q. T., Sha, J. Q., Li, J. S., et al. (2017). *In situ*-generated Co@nitrogen-doped carbon nanotubes derived from MOFs for efficient hydrogen evolution in both alkaline and acidic conditions. *N. J. Chem.* 41, 10966–10971. doi: 10.1039/C7NJ02334K

Liang, Q., Jin, H., Wang, Z., Xiong, Y., Yuan, S., Zeng, X., et al. (2019). Metal-organic frameworks derived reverse-encapsulation Co-NC@Mo_2C complex for efficient overall water splitting. *Nano Energy* 57, 746–752. doi: 10.1016/j.nanoen.2018.12.060

Liu, Y., Lv, Y., and Cao, D. (2018). Co, N-codoped nanotube/graphene 1D/2D heterostructure for efficient oxygen reduction and hydrogen evolution reactions. *J. Mater. Chem. A* 6, 3926–3932. doi: 10.1039/C7TA11140A

Meng, F., Zhong, H., Bao, D., Yan, J., and Zhang, X. (2016). *In situ* coupling of strung Co_4N and intertwined N-C fibers toward free-standing bifunctional cathode for robust, efficient, and flexible Zn-air batteries. *J. Am. Chem. Soc.* 138, 10226–10231. doi: 10.1021/jacs.6b05046

Mo, Q., Chen, N., Deng, M., Yang, L., and Gao, Q. (2017). Metallic Cobalt@Nitrogen-doped carbon nanocomposites: carbon-shell regulation toward efficient Bi-functional electrocatalysis. *ACS Appl. Mater. Interfaces* 9, 37721–37730. doi: 10.1021/acsami.7b10853

Park, M. G., Lee, D. U., Seo, M. H., Cano, Z. P., and Chen, Z. (2016). 3D Ordered mesoporous bifunctional oxygen catalyst for electrically rechargeable zinc-air batteries. *Small* 12, 2707–2714. doi: 10.1002/smll.201600051

Qiao, X., Jin, J., Fan, H., Li, Y., and Liao, S. (2017). *In situ* growth of cobalt sulfide hollow nanospheres embedded in nitrogen and sulfur co-doped graphene nanoholes as a highly active electrocatalyst for oxygen reduction and evolution. *J. Mater. Chem. A* 5, 12354–12360. doi: 10.1039/C7TA00993C

Qiao, X., Liao, S., Zheng, R., Deng, Y., Song, H., and Du, L. (2016). Cobalt and nitrogen codoped graphene with inserted carbon nanospheres as an efficient bifunctional electrocatalyst for oxygen reduction and evolution. *ACS Sust. Chem. Eng.* 4, 4131–4136. doi: 10.1021/acssuschemeng.6b00451

Qu, K., Zheng, Y., Dai, S., and Qiao, S. Z. (2016). Graphene oxide-polydopamine derived N, S-codoped carbon nanosheets as superior bifunctional electrocatalysts for oxygen reduction and evolution. *Nano Energy* 19, 373–381. doi: 10.1016/j.nanoen.2015.11.027

Qu, K., Zheng, Y., Zhang, X., Davey, K., Dai, S., and Qiao, S. Z. (2017). Promotion of electrocatalytic hydrogen evolution reaction on nitrogen-doped carbon nanosheets with secondary heteroatoms. *ACS. Nano* 11, 7293–7300. doi: 10.1021/acsnano.7b03290

Sheng, J., Wang, L., Deng, L., Zhang, M., He, H., Zeng, K., et al. (2017). A MOF-templated fabrication of hollow Co_4N@N-doped carbon porous nanocages with superior catalytic activity. *ACS Appl. Mater. Interfaces* 10, 7191–7200. doi: 10.1021/acsami.8b00573

Si, C., Zhang, Y., Zhang, C., Gao, H., Ma, W., Lv, L., et al. (2017). Mesoporous nanostructured spinel-type MFe_2O_4 (M = Co, Mn, Ni) oxides as efficient bi-functional electrocatalysts towards oxygen reduction and oxygen evolution. *Electrochim. Acta* 245, 829–838. doi: 10.1016/j.electacta.2017.06.029

Song, A., Wang, Y., Wu, Y., Gang, S., Yin, X., Gao, L., et al. (2017). Facile synthesis of cobalt nanoparticles entirely encapsulated in slim nitrogen-doped carbon nanotubes as oxygen reduction catalyst. *ACS Sust. Chem. Eng.* 5, 3973–3981. doi: 10.1021/acssuschemeng.6b03173

Tao, A., Ge, X., Hor, T. S. A., Goh, F. W. T., Geng, D., Du, G., et al. (2015). Co_3O_4 nanoparticles grown on N-doped Vulcan carbon as a scalable bifunctional electrocatalyst for rechargeable zinc-air batteries. *RSC Adv.* 5, 75773–75780. doi: 10.1039/C5RA11047E

Tian, X., Luo, J., Nan, H., Zou, H., Chen, R., Shu, T., et al. (2016). Transition metal nitride coated with atomic layers of Pt as a low-cost, highly stable electrocatalyst for the oxygen reduction reaction. *J. Am. Chem. Soc.* 138, 1575–1583. doi: 10.1021/jacs.5b11364

Wang, R., Dong, X. Y., Du, J., Zhao, J. Y., and Zang, S. Q. (2018). MOF-derived bifunctional Cu_3P nanoparticles coated by a N, P-codoped carbon shell for hydrogen evolution and oxygen reduction. *Adv. Mater.* 30:1703711. doi: 10.1002/adma.201703711

Wang, Z., Xiao, S., An, Y., Long, X., Zheng, X., Lu, X., et al. (2016). $Co(II)_{1--x}Co(0)_{x/3}Mn(III)_{2x/3}S$ nanoparticles supported on B/N-codoped mesoporous nanocarbon as a bifunctional electrocatalyst of oxygen reduction/evolution for high-performance zinc-air batteries. *ACS Appl. Mater. Interfaces* 8, 13348–13359. doi: 10.1021/acsami.5b12803

Wei, C., Wang, H., Eid, K., Kim, J., Kim, J. H., Alothman, Z. A., et al. (2017). A three-dimensionally structured electrocatalyst: cobal-embedded nitrogen-doped carbon nanotubes/nitrogen-doped reduced graphene oxide hybrid for efficient oxygen reduction. *Chem-Eur. J.* 23, 637–643. doi: 10.1002/chem.201604113

Wen, L., Deng, Y. P., Li, G., Cano, Z. P., Wang, X., Dan, L., et al. (2018). Two-dimensional phosphorus-doped carbon nanosheets with tunable porosity for oxygen reactions in zinc-air batteries. *ACS Catal.* 8, 2464–2472. doi: 10.1021/acscatal.7b02739

Yang, X., Zheng, Y., Yang, J., Shi, W., Zhong, J. H., Zhang, C., et al. (2016). Modeling Fe/N/C catalysts in monolayer graphene. *Acs Catal.* 7, 139–145. doi: 10.1021/acscatal.6b0270

Yang, Z. K., Lin, L., Liu, Y.-N., Zhou, X., Yuan, C.-Z., and Xu, A.-W. (2016). Supramolecular polymers-derived nonmetal N, S-codoped carbon nanosheets for efficient oxygen reduction reaction. *RSC Adv.* 6, 52937–52944. doi: 10.1039/C6RA05523K

Zehtab, Y. A., Fei, H., Ye, R., Wang, G., Tour, J. M., and Sundararaj, U. (2015). Boron/nitrogen co-doped helically unzipped multiwalled carbon nanotubes as efficient electrocatalyst for oxygen reduction. *ACS Appl. Mater. Interfaces* 7, 7786–7794. doi: 10.1021/acsami.5b01067

Zhang, J., Zhao, Z., Xia, Z., and Dai, L. (2015). A metal-free bifunctional electrocatalyst for oxygen reduction and oxygen evolution reactions. *Nat. Nanotechnol.* 10, 444–452. doi: 10.1038/NNANO.2015.48

Zhao, J., and Chen, Z. (2015). Carbon-doped boron nitride nanosheet: an efficient metal-free electrocatalyst for the oxygen reduction reaction. *J. Phys. Chem. C* 119, 26348–26354. doi: 10.1021/acs.jpcc.5b09037

Zhe, W., Peng, S., Hu, Y., Li, L., Tao, Y., Yang, G., et al. (2017). Cobalt nanoparticles encapsulated in carbon nanotube-grafted nitrogen and sulfur co-doped multichannel carbon fibers as efficient bifunctional oxygen electrocatalysts. *J. Mater. Chem. A* 5, 4949–4961. doi: 10.1039/C6TA10291C

Zheng, Y., Jiao, Y., Zhu, Y., Cai, Q., Vasileff, A., Li, L. H., et al. (2017). Molecule-level g-C_3N_4 coordinated transition metals as a new class of

electrocatalysts for oxygen electrode reactions. *J. Am. Chem. Soc.* 139, 3336–3339. doi: 10.1021/jacs.6b13100

Zhou, L., Qu, X., Zheng, D., Tang, H., Liu, D., Qu, D., et al. (2017). Electrochemical hydrogen storage in facile synthesized Co@N-doped carbon nanoparticle composites. *ACS Appl. Mater. Interfaces* 9, 41332–41338. doi: 10.1021/acsami.7b14163

Zhou, T., Zhou, Y., Ma, R., Zhou, Z., Liu, G., Liu, Q., et al. (2017). Nitrogen-doped hollow mesoporous carbon spheres as a highly active and stable metal-free electrocatalyst for oxygen reduction. *Carbon* 114, 177–186. doi: 10.1016/j.carbon.2016.12.011

Zhou, W., Zhou, Y., Yang, L., Huang, J., Ke, Y., Zhou, K., et al. (2015). N-doped carbon-coated cobalt nanorod arrays supported on a titanium mesh as highly active electrocatalysts for hydrogen evolution reaction. *J. Mater. Chem. A* 3, 1915–1919. doi: 10.1039/C4TA06284A

Conflict of Interest Statement: The authors declare that the research was conducted in the absence of any commercial or financial relationships that could be construed as a potential conflict of interest.

frontiers in Materials

ORIGINAL RESEARCH
published: 10 October 2018
doi: 10.3389/fmats.2018.00061

A Sandwich-Structured Hybrid Anode With Nitrogen-Doped Amorphous Carbon Nanoarrays Vertically Anchoring on Graphene Nanoplatelets for High Rate Li Storage

*Zhimin Zou, Limin Wu, Jianwei Chen and Chunhai Jiang**

Fujian Provincial Key Laboratory of Functional Materials and Applications, School of Materials Science and Engineering, Institute of Advanced Energy Materials, Xiamen University of Technology, Xiamen, China

OPEN ACCESS

Edited by:
Jie-Sheng Chen,
Shanghai Jiao Tong University, China

Reviewed by:
Jie Shu,
Ningbo University, China
Yonggang Wang,
Fudan University, China
Mingdeng Wei,
Fuzhou University, China

***Correspondence:**
Chunhai Jiang
chjiang@xmut.edu.cn

Specialty section:
This article was submitted to Colloidal Materials and Interfaces, a section of the journal Frontiers in Materials

Received: *28 August 2018*
Accepted: *20 September 2018*
Published: *10 October 2018*

Citation:
Zou Z, Wu L, Chen J and Jiang C (2018) A Sandwich-Structured Hybrid Anode With Nitrogen-Doped Amorphous Carbon Nanoarrays Vertically Anchoring on Graphene Nanoplatelets for High Rate Li Storage. Front. Mater. 5:61. doi: 10.3389/fmats.2018.00061

Graphene is not an ideal anode material of Li-ion batteries because of its low packing density and low initial Coulombic Efficiency although it shows much higher specific capacity than graphite. Herein, we report a sandwich-structured hybrid anode material which integrates the nitrogen-doped amorphous carbon nanoarrays on both sides of graphene nanoplatelets. The former provides high capacity and excellent rate capability, while the latter stabilizes the cycle performance, both of them brought out outstanding electrochemical properties to the hybrid anode. High discharge capacities of 562 and 217 mA h g^{-1} are obtained at current densities of 0.1 and 3 A g^{-1}, respectively, which are much higher than those of the starting graphene nanoplatelets (404 and 81 mA h g^{-1}, respectively). Moreover, a discharge capacity of 540 mA h g^{-1} is maintained after 300 cycles at 0.5 A g^{-1}, demonstrating an excellent cycle stability. This study provides a facile process to prop up the 2 D graphene nanoplatelets with vertically aligned carbon nanoarrays, which may push forward the application of graphene as anode material of Li-ion batteries because of the avoided aggregation and additional Li storage capacity contributed by the N-doped amorphous carbon.

Keywords: Li-ion batteries, graphene nanoplatelets, anode, composite, rate capability

INTRODUCTION

The rapid development of electric vehicles (EVs) calls for reliable energy storage devices with both high energy and high power densities. Li-ion batteries (LIBs) are currently the most widely used power sources of EVs, but their low energy density is still one major concern of EV manufacturers and customers, as one always hopes to drive as long as possible at a single charge. The inferior energy and power densities of LIBs are majorly determined by the intrinsic characteristics of their electrode materials (Nitta et al., 2015). Taking the state-of-the-art anode material of LIBs, graphite, as an example, it has high reversibility and stable cycle performance, but limited capacity (only 372 mA h g^{-1} theoretically) and rate performance. This makes graphite not an ideal anode material for high power LIBs (Zhang et al., 2014).

The low capacity and poor rate performance of graphite are ascribed to its low number of active sites and narrow lattice space (∼0.335 nm; Striebel et al., 2004). Reducing the thickness of graphite is found effective to improve its specific capacity and rate performance because of the introduction of additional Li-ion storage sites and shortening of the Li-ion diffusion distance. For an instance, ultrathin layered graphite prepared by jet impinging apparatus showed a high reversible capacity of 393 mA h g^{-1}, obviously higher than the 345 mA h g^{-1} of traditional graphite (Chen et al., 2018). As one-atom layer or few-atom layers ultrathin two-dimensional graphite, graphene has shown further increased lithium storage capacity in comparison to ultrathin layered graphite. Specific capacities of 1,175, 1,007, and 842 mA h g^{-1} have been reported on graphene sheets with single, triple and quintuplicate layers, respectively (Tong et al., 2011). However, graphene is not a suitable anode material of commercial LIBs because of its low packing density, large irreversible capacity loss in the first cycle and the capacity fluctuation related to the complex surface chemistry and electrochemical reactions at the electrolyte/electrode interface (Dong et al., 2017). Instead, hybridizing graphene with other high capacity active materials, such as silicon (Assresahegn et al., 2018), metal oxides (Liu et al., 2015; Qiu et al., 2015; Hong et al., 2016; Jiang et al., 2018; Shi et al., 2018; Wang et al., 2018; Zhang et al., 2018), and metal sulfides (Che et al., 2016; Wang et al., 2017), etc., has been the frequently used strategy to develop high performance anode materials.

Besides graphene, amorphous carbons have been recognized as another family of high capacity anode materials of LIBs with specific capacity up to 1,000 mA h g^{-1} (Qie et al., 2012; Li et al., 2013; Dutta et al., 2014). Such a high capacity is ascribed to the additional lithium storage at the interface or defects in amorphous carbons. The small crystalline size and wider interlayer distance may have also speed up the Li^+ ions diffusion within the disordered structure of amorphous carbons, resulting in outstanding rate capability. However, in most studies, amorphous carbon anodes suffer from low initial Coulombic Efficiencies and poor cycle stability due to pulverization of the carbon particles, variations in surface morphology, disordered non-crystallized sites, random lattice structures and contamination from metallic impurities (Wu et al., 1999; Fujimoto, 2010). The severe polarization of amorphous carbon anodes also prevents them from practical applications in LIBs.

Taking the advantages of high stability of graphite and high capacity of amorphous carbons, hybridizing them may yield potential high performance anode materials with both high capacity and high cycle stability. However, such works are so far mainly carried out on graphene or reduced graphene oxide (rGO) substrates. Zhou et al fabricated a three-dimensional carbon-coated graphene anode, which exhibited excellent Na-storage performance, with a high initial discharge capacity of 824 mA h g^{-1} at 50 mA g^{-1} (Zhou et al., 2017). Liu et al prepared a nitrogen-doped carbon/graphene hybrid anode for Na-ion batteries, which showed an excellent rate performance, namely 94 mA h g^{-1} at 5 A g^{-1} (Liu et al., 2016). Xu and coauthors fabricated a hybrid anode with vertically aligned carbon nanotubes growing on few-layer graphene. The obtained electrode exhibited a reversible Li storage capacity of 525 mA h g^{-1} after 1,000 cycles at 0.5 A g^{-1} with Coulombic Efficiency inexcess of 98% (Xu et al., 2018). To date, hybrid anodes based on graphene nanoplatelets and amorphous carbon are rarely reported although the former exhibited more stability and higher packing density than graphene and rGO.

In this work, a sandwich-structured hybrid anode with nitrogen-doped amorphous carbon nanoarrays vertically anchoring on graphene nanoplatelets was prepared by a MnO_2 templated polymerization and post-annealing process (Jiang et al., 2017). The hybrid anode displayed obvious higher specific capacity and rate capability than the starting graphene nanoplatelets for Li storage. The detailed preparation, characterizations and electrochemical performance of the hybrid anode are reported in this paper.

EXPERIMENTAL

Sample Preparation and Characterizations

The chemicals used in this work are analytical grade and used as received. The graphene nanoplatelets (about 6–10 layers) were purchased from Suzhou Tanfeng Graphene Sci. and Tech. Co. Ltd, China. The sandwich-structured hybrid anode material was prepared as follows: 0.05 g graphene nanoplatelets were dispersed in 200 ml ultrapure water holding in a 300 ml glass beaker under magnetic stirring. 0.3 g $KMnO_4$ (Aladdin Chemistry) and 0.6 ml concentrated HCl were added into the beaker in sequence under stirring. The beaker was then sealed tightly by a piece of thin polyethylene film and put into an oil bath holding at 80°C. The magnetic stirring was maintained for another few hours till the purple color of the solution disappeared. With this treatment, vertically aligned birnessite MnO_2 nanosheets were coated on both sides of the graphene nanoplatelets. After filtering and washing with ultrapure water a few times, the product was re-dispersed in 100 ml 0.5 M HCl solution under magnetic stirring. Then, 0.3 ml pyrrole monomer (Aladdin Chemistry) was dropped into the solution slowly. After being stirred for another 3 h, the product was filtered out, washed repeatedly with ultrapure water and dried at 80°C. By this process, the birnessite MnO_2 nanosheets were *in situ* replaced by polypyrrole (PPy) nanoasheets via a redox polymerization reaction. The PPy nanoasheets were finally converted to nitrogen-doped amorphous carbon (NC) nanoarrays by annealing at 500°C for 2 h in flowing nitrogen. To simplify the description, the graphene nanoplatelets and graphene nanoplatelets coated by N-doped amorphous carbon nanoarrays were named as G and GNC, respectively.

The graphene nanoplatelets and resulting samples were characterized by powder X-ray diffraction (XRD, Rigaku MiniFlex600), X-ray photoelectron spectroscopy (XPS, ESCALAB250, Thermo VG), Raman Spectrometer (RM-1000, Renishaw), scanning electronic microscope (SEM, Zeiss Sigma 500), and transmission electronic microscope (TEM, FEI Talos F200s), respectively.

Electrochemical Measurements

Electrochemical performances of the graphene nanoplatelets and the sandwich-structured hybrid anode material were evaluated by coin-type Li-metal half cells. The working electrodes were

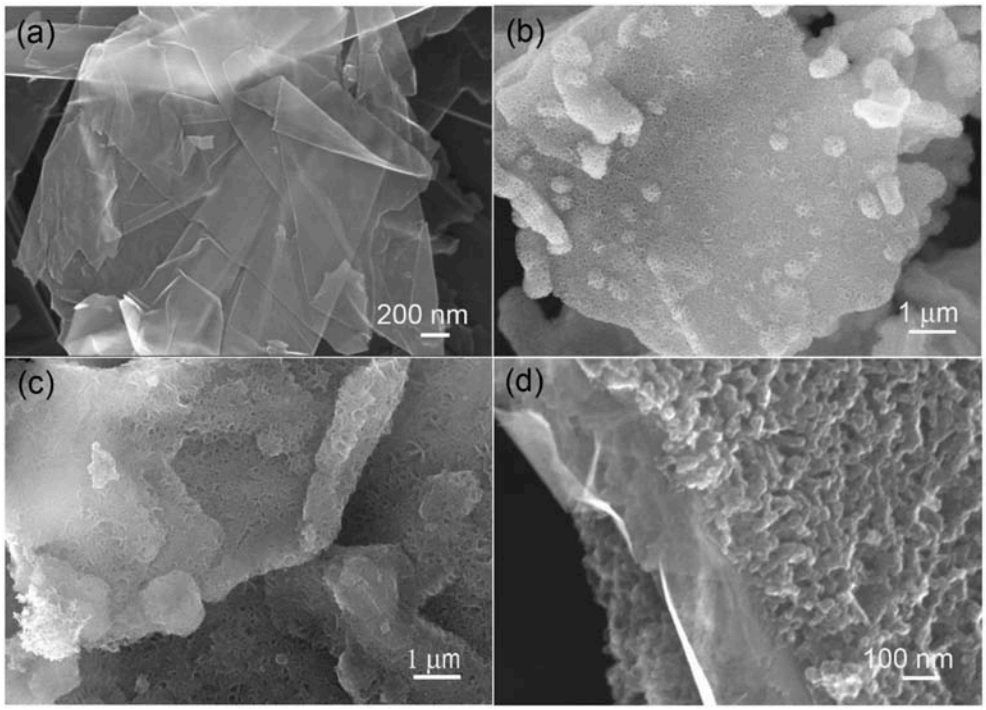

FIGURE 1 | SEM images of the starting graphene nanoplatelets **(a)**, the graphene nanoplatelets coated by birnessite MnO_2 **(b)**, PPy **(c)**, and N-doped amorphous carbon nanoarrays **(d)**.

prepared by mixing 80 w% of the active materials (G and GNC), 10 wt% of acetylene carbon black and 10 wt% of polyvinylidene fluoride binder in N, N-dimethyl pyrrolidone (NMP) solvent and then coated on copper foil by a doctor-blade method. The loading mass of active materials in each electrode was about 0.8–1.0 mg cm^{-2}. The electrolyte was a 1 M solution of $LiPF_6$ dissolved in ethylene carbonate (EC) and dimethyl carbonate (DEC) with a volume ratio of 1:1. The 2025-type coin cells were assembled in an argon filled glove box with lithium metal as the counter electrode and polypropylene membrane (Celgard 2400) as the separator, respectively. Galvonostatic discharge/charge measurements were performed in the voltage range of 0.01–3.0 V (vs. Li/Li^+) using a battery cycler (LAND CT2001A, Wuhan Kingnuo Electronic Co., China). The cyclic voltammetry curves were recorded in the voltage range of 0.01–3.0 V (vs. Li/Li^+) on a CHI660e electrochemical workstation (Chenhua, Shanghai, China) at a scan rate of 0.1 mV s^{-1}. Electrochemical impedance spectra (EIS) were measured on the same electrochemical workstation in a frequency range of 10 MHz to 0.01 Hz with an alternative amplitude of 10 mV.

RESULTS AND DISCUSSION

The microstructures of the starting graphene nanoplatelets and their composites with MnO_2, PPy and N-doped amorphous carbon were examined by SEM at first, as shown in **Figure 1**. From **Figure 1a** it is seen that the starting graphene nanoplatelets are composed of stacked ultrathin layered graphite with planar size from a few to several tens of micrometer squares. After a soft hydrothermal treatment with $KMnO_4$ solution, the graphene nanoplatelets were uniformly coated by vertically aligned MnO_2 nanosheets on both sides (**Figure 1b**). By an *in situ* polymerization process in acidic solution, the MnO_2 nanosheets were replaced by polypyrrole nanosheets (**Figure 1c**). By a low temperature heat treatment at 500°C for 2 h in flowing nitrogen, the PPy nanosheets were converted to N-doped amorphous carbon nanoarrasys, forming a sandwich-structured hybrid material (**Figure 1d**).

The microstructure of the sandwich-structured hybrid material was further characterized by TEM analysis, as shown in **Figure 2**. The bright-field TEM images shown in **Figures 2a,b** at different magnifications indicate that the amorphous carbon nanoarrays vertically grew on both sides of the graphene nanoplatelets. The typical thickness of the sandwich structure is around 300 nm. A HADDF image (**Figure 2c**) clearly reveals that the carbon nanoarrays growing on the thin graphene nanoplatelets are highly porous. The C (**Figure 2d)** and N (**Figure 2e**) element maps of the hybrid material corresponding to image shown in **Figure 2c** demonstrate that the carbon coating layers derived from PPy nanosheets are uniformly doped by nitrogen. This is consistent to the results of our previous publication, i.e., PPy can be converted to N-doped amorphous carbon by low temperature annealing in inert atmosphere (Jiang et al., 2017).

The XRD patterns of the starting graphene nanoplatelets and their composites with MnO_2 and N-doped carbon nanosheests

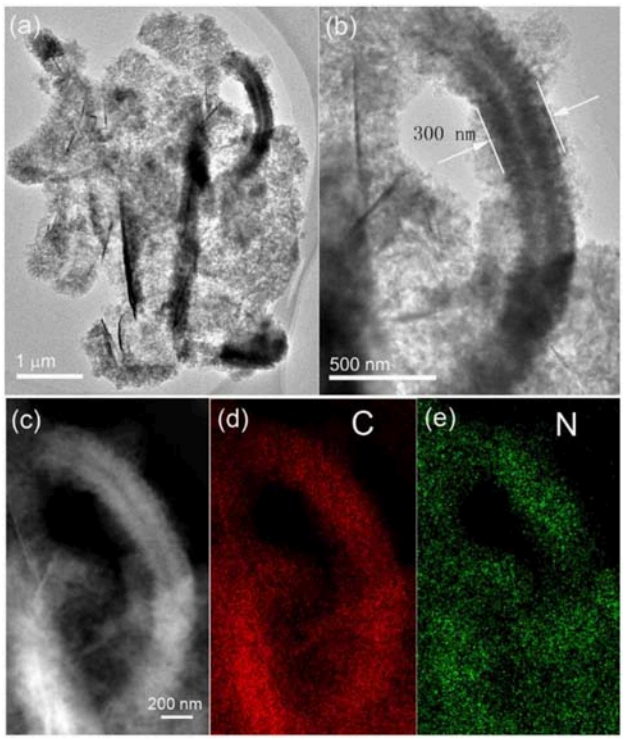

FIGURE 2 | Bright-field TEM images **(a,b)**, HADDF image **(c)** of the sandwich-structured hybrid material, and the element maps of C **(d)**, and N **(e)** corresponding to the figure shown in **(c)**.

are displayed in **Figure 3A**. The XRD pattern of the starting graphene nanoplatelets show the typical (0 0 2) diffraction peak of graphite at $2\theta = 26.4^{\circ}$, indicating that the starting materials are multilayer graphene. After hydrothermal treatment with $KMnO_4$, only weak (0 0 2) diffraction peak of graphite is detected. The sample is fully covered with birnessite MnO_2. In the XRD pattern of GNC, except the strong peak of (0 0 2), there is also a broad diffraction peak at around $2\theta = 26^{\circ}$, indicating the amorphous nature of the obtained N-doped carbon nanoarrays. This result is consistent to our previous report that annealing PPy at a low temperature would result in N-doped amorphous carbon with low graphitization degree (Jiang et al., 2017).

The starting graphene nanoplatelets and GNC sample were further characterized by Raman spectroscopy (**Figure 3B**). The starting graphene nanoplatelets have a weak D band at 1,333 cm^{-1}, a sharp G band at 1,580 cm^{-1} and a broad 2D band at 2,680 cm^{-1}. These characteristic peaks are similar to that of bulk graphite (Liu et al., 2017). This again indicates that the starting materials are multilayer graphene. The GNC shows an overlapped Raman spectrum of the graphene nanoplatelets and the N-doped amorphous carbon produced from PPy. The increased intensity of D band in GNC is related to the disorder introduced by defects or heteroatoms, which further confirms nitrogen doping in the amorous carbon nanoarrays. **Figures 3C,D** show the XPS C1s and N1s core scans of the GNC. As can be seen in **Figure 3C**, the C1s XPS spectrum can be deconvoluted into five different peaks at 284.0, 284.6, 285.2, 286.2, and 289.2 eV, respectively. According to Selvamani et al, 284.0 eV represents the sp^3 C, 284.6 eV corresponds to the sp^2 C=C, and 285.2 eV is related to the combination of sp^3 C and C-N bonding. The 286.2 eV belongs to the pyridinic carbon linked to nitrogen C=N/C=O, and 289.2 eV is associated with O–C=O bonding (Selvamani et al., 2016). The N1s spectrum can also be deconvoluted into pyrrolic N and pyridicnic N (see **Figure 3D**), similar to the results reported in our previous publication (Jiang et al., 2017). In combination with the N clement map in **Figure 2e**, it is evident that the carbon nanoarrays anchoring on the graphene nanoplatelets are uniformly doped by nitrogen.

The electrochemical performances of the starting graphene nanoplatelets and GNC were firstly evaluated by CV measurements at 0.1 mV s^{-1} within a voltage range of 0.01–3 V (vs. Li/Li^+), as shown in **Figure 4A**. The electrode made of graphene nanoplatelets exhibits a typical CV curve of graphite, which includes a reduction peak at around 0.67 V in the first cathodic scan, corresponding to the formation of Solid Electrolyte Interphase (SEI) film, and a pair of sharp redox peaks at 0.01 V/0.25 V in the following cathodic and anodic scan due to the insertion/extraction of Li^+ ions into/from graphite interlayer lattice (Wang and Yoshio, 2001). The redox peaks at about 0.16 V/0.28 V appearing from the second cycle also correspond to lithiation and delithiation processes. The GNC electrode exhibits left shift of the cathodic peak in the first scan and increased voltage gap between the cathodic and anodic scans as compared to that of the graphene nanoplatelets. This should be ascribed to the overlap of CV curves of the N-doped amorphous carbon and the graphene nanoplatelets. The N-doped amorphous carbon has lower Li^+ intercalation potential than graphite, which then has lowered the SEI formation potential. The peak at about 1.38 V in the anodic scan can be assigned to the reaction of Li^+ ions with N-containing functional groups (Jiang et al., 2017). The larger area of CV loop of the GNC electrode suggests that it has higher Li storage capacity.

The rate capability of the G and GNC electrodes are shown in **Figure 4B**. It is clear to see that, at all current densities, GNC exhibits higher specific capacity than the graphene nanoplatelets. For example, the average discharge capacities of GNC at 0.1 (except the first cycle), 0.2, 0.5, 1, 2, and 3 A g^{-1} are about 562, 482, 398, 318, 242, and 217 mA h g^{-1}, respectively, whereas the corresponding values for the graphene nanoplatelets are 404, 372, 324, 252, 135, and 81 mA h g^{-1}, respectively. This indicates that hybridizing N-doped amorphous carbon nanoarrays with graphene nanoplatelets has greatly enhanced the lithium storage capacity of the latter. This is reasonable as the PPy-derived N-doped amorphous carbon possess not only higher capacity but better rate capability than graphite due to the nitrogen doping induced enhancement of electronic conductivity and better wetting of the electrode by electrolyte. The vertically aligned N-doped amorphous carbon nanoarrays might have also facilitated the Li^+ ions transportation within the electrode material, resulting in much improved rate capability. From **Figure 4B** we can also see that, the Coulombic Efficiencies for GNC and the starting graphene nanoplatelets at the first cycle are 60.3 and 72.6%, respectively. The lowered initial Coulombic

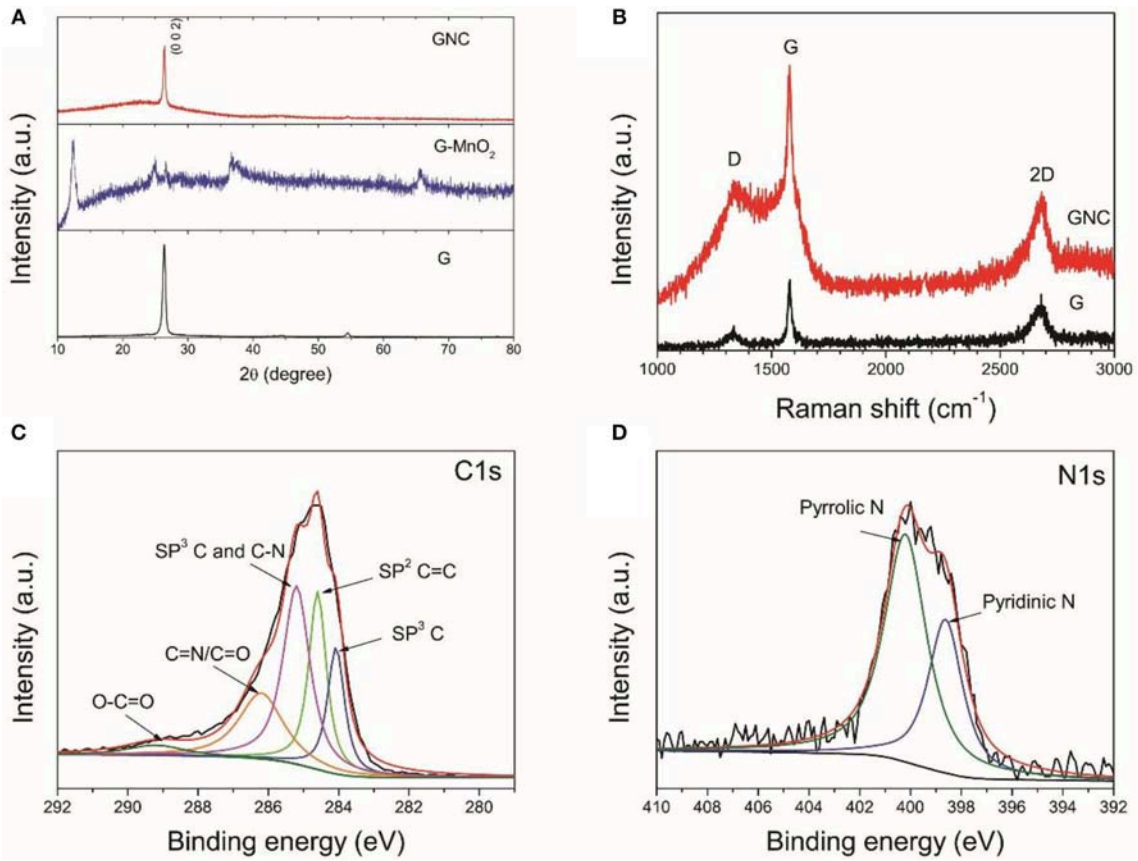

FIGURE 3 | XRD patterns of the starting graphene nanoplatelets and their composite with birnessite MnO_2 and N-doped amorphous carbon **(A)**, the Raman spectra of the starting graphene nanoplatelets and GNC **(B)**, the XPS C1s **(C)**, and N 1s **(D)** core scans of GNC.

Efficiency can be ascribed to the larger irreversible capacity loss of amorphous carbon in the first cycle. Thereafter, the Coulombic Efficiencies of both samples are well-preserved at about 100% at all current densities. This demonstrates that introduction of N-doped amorphous carbon nanoarrays did not degrade the reversibility of the graphene nanoplatelets.

To investigate the origin of the improved capacity in GNC as compared to that of graphene nanoplatelets, typical discharge and charge profiles of G and GNC electrodes measured at different current densities are shown in **Figures 4C,D**, respectively. As seen from the discharge/charge curves in **Figure 4C**, the capacity of the G electrode is mainly contributed by Li^+ storage in the graphite lattice, which is represented by the flat voltage plateau below a certain value, such as 0.25 V at 0.1 A g^{-1}. This Li storage behavior is very similar to that of graphite. The discharge/charge profiles of the GNC electrode show a short voltage plateau and a long sloped region, obviously different from that of graphene nanoplatelets. Such discharge/charge profiles can also be treated as overlap of the discharge/charge curves of the graphene nanoplatelets and the N-doped amorphous carbon nanoarrays. In other words, the Li storage capacity in GNC is contributed by both components. Moreover, as seen in **Figure 4D**, the voltage plateau associated to Li storage in graphite lattice almost disappears at 2 and 3 A g^{-1}. The excellent high rate capacities of GNC anode are almost completely contributed by the sloped region, i.e., by the N-doped amorphous carbon nanoarrays. This convincingly proves that anchoring vertical N-doped amorphous carbon nanoarrays on both sides of graphene nanoplatelets has greatly improved the specific capacity and rate performance of the latter. Such excellent rate performance enables the hybrid material to be a potential anode of high power LIBs.

Figure 5 shows the cycle performances of the graphene nanoplatelets and GNC measured at 0.5 A g^{-1}. It should be pointed out that the vibration of the cycling curves was due to the temperature fluctuation during daylight and night time. It is interesting to note that the specific capacity of the graphene nanoplatelets keeps increasing at the beginning 80 cycles and then maintains at about 260–290 mA h g^{-1}, whereas that of GNC keeps increasing from 420 to about 540 mA h g^{-1} after 300 cycles. The capacity increase of both samples along cycling might be ascribed to gradual activation of the active materials. The Coulombic Efficiencies of both cells are nearly 100%. As reported in our previous work (Jiang et al., 2017), the capacity of N-doped carbon anode derived from PPy would decrease gradually along cycling. The excellent cycle performance of

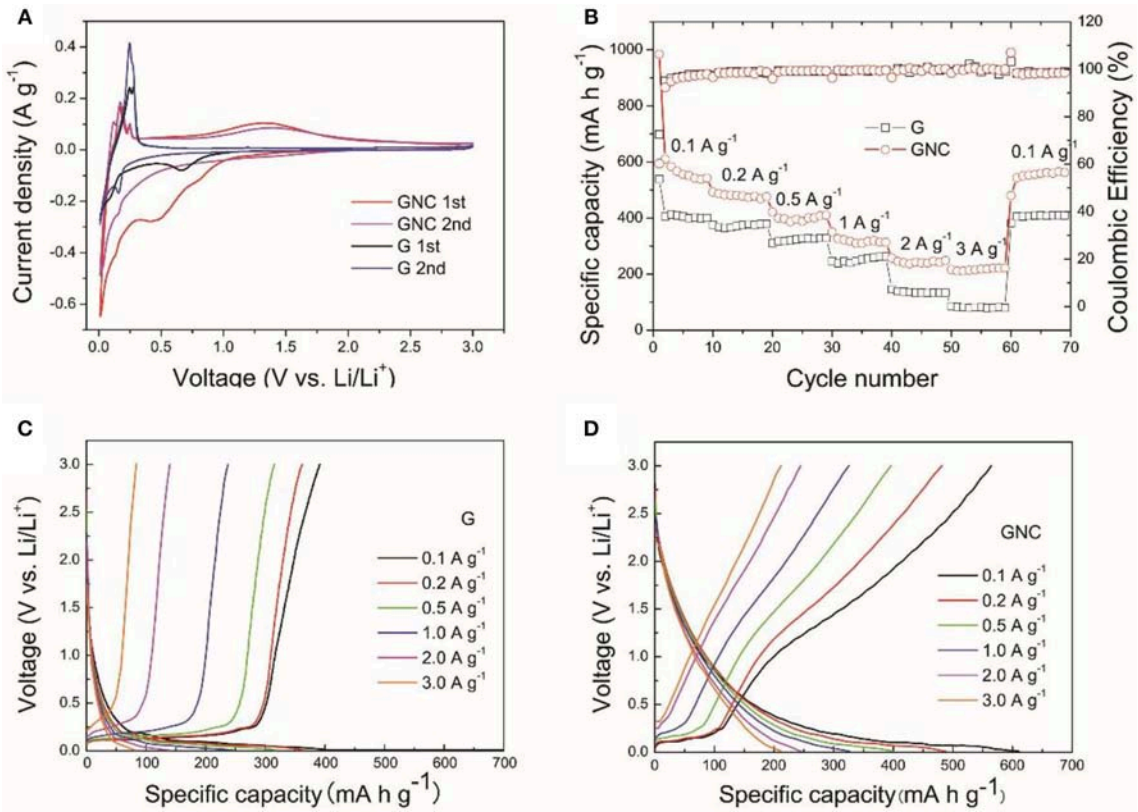

FIGURE 4 | The CV curves measured at a scan rate of 0.1 mV s^{-1} **(A)**, the rate capability **(B)**, the discharge/charge profiles of the G **(C)**, and GNC **(D)** electrodes at different current densities.

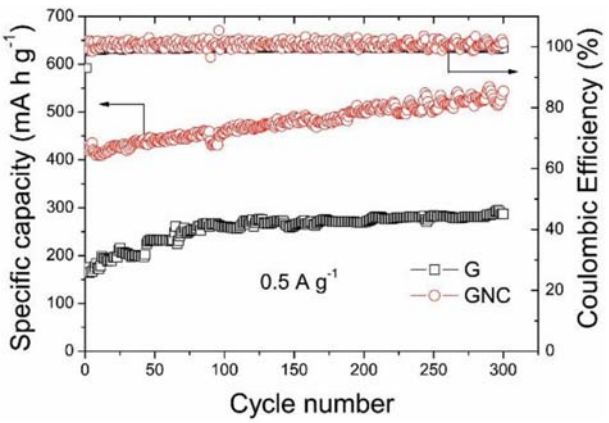

FIGURE 5 | Cycle performances of the graphene nanoplatelets and GNC at 0.5 A g^{-1}.

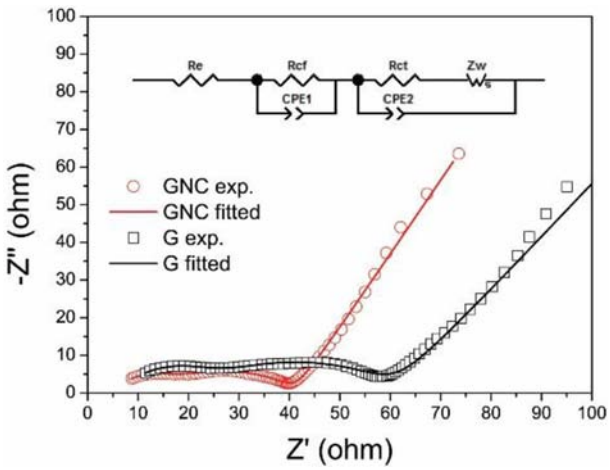

FIGURE 6 | The Nyquist plots of the half cells made from G and GNC.

GNC strongly suggests that the inner graphene nanoplatelets in the sandwich-structured GNC have stabilized the hybrid anode material during the cycling, whereas the vertical N-doped amorphous carbon nanoarrays have provided high capacity and excellent rate performance. These synergistic effects have resulted in the outstanding electrochemical Li storage property of the GNC hybrid anode material.

The electrochemical impedance spectra (EIS) of the G//Li and GNC//Li half cells after the cycling tests were measured at the discharged state (about 0.01 V). The Nyquist plots and the equivalent circuit used for the data fitting are shown in **Figure 6**. Both Nyquist plots show two compressed semicircles in the high and middle-frequency regions, which correspond to the resistance of Li^+ ions penetration through the SEI film (R_{cf})

and the charge transfer resistance between the electrolyte and electrode (R_{ct}), respectively. As fitted by Zview software using eh equivalent circuit shown in **Figure 6** inset, the R_{cf} and R_{ct} values for GNC are 9.75 and 26.62 Ω, respectively, which are much smaller than those of the starting graphene nanoplatelets (16.03 and 39.05 Ω). This clearly indicates that the hybrid anode shows greatly reduced resistance of Li^+ ions transportation through the SEI film and the electrolyte/electrode interface, possibly due to the high electronic conductivity and the ultrathin sheet-like structure of the N-doped amorphous carbon nanoarrays. The reduced charge transfer resistance may also account for the much improved rate capability of the GNC electrode.

CONCLUSION

Graphene itself is not an ideal anode material of Li-ion batteries due to its low packing density and severe aggregation of the ultrathin graphene sheets. In this work, a sandwich-structured hybrid anode was prepared by vertically anchoring nitrogen-doped amorphous carbon nanoarrays on both sides of graphene nanoplatelets. The hybrid anode exhibits high capacity and excellent rate capability as well as stable cycle stability toward Li storage. High average discharge capacities of 562 and 217 mA h g^{-1} were achieved at 0.1 and 3 A g^{-1}, which were much higher than the 404 and 81 mA h g^{-1} of the graphene nanoplatelets. The hybrid anode maintained a discharge capacity of 540 mA h g^{-1} after 300 cycles at 0.5 A g^{-1}, demonstrating an outstanding cycle performance. It was believed that the vertically aligned highly conductive N-doped amorphous carbon nanaoarrays have provided high capacity and excellent rate performance, and the inner graphene nanoplatelets have improved the cycle stability of the hybrid anode material. The results reported here may provide a versatile way to fabricate sandwich-structured hybrid material with N-doped carbon nanoarrays vertically growing on a two-dimensional substrate, hence building up a three-dimensional porous network for enhanced energy storage capacity.

AUTHOR CONTRIBUTIONS

ZZ and CJ proposed the work, performed materials characterizations and wrote the manuscript. LW and JC fabricated the materials and performed LIB testing.

FUNDING

This work is supported by Natural Science Foundation (No. 2016J01746) and Guidance Project (No. 2016H0038), Minjiang Scholarship program (No. 60815002) of Fujian Province, China.

REFERENCES

Assresahegn, B. D., Ossonon, B. D., and Bélanger, D. (2018). Graphene nanosheets and polyacrylic acid grafted silicon composite anode for lithium ion batteries. *J. Power Sources* 391, 41–50. doi: 10.1016/j.jpowsour.2018.03.067

Che, Z., Li, Y., Chen, K., and Wei, M. (2016). Hierarchical MoS2@RGO nanosheets for high performance sodium storage. *J. Power Sources* 331, 50–57. doi: 10.1016/j.jpowsour.2016.08.139

Chen, Z., Liu, Y., Zhang, Y., Shen, F., Yang, G., Wang, L., et al. (2018). Ultrafine layered graphite as an anode material for lithium ion batteries. *Mater. Lett.* 229, 134–137. doi: 10.1016/j.matlet.2018.06.104

Dong, Y., Wu, Z.-S., Ren, W., Cheng, H.-M., and Bao, X. (2017). Graphene: a promising 2D material for electrochemical energy storage. *Sci. Bull.* 62, 724–740. doi: 10.1016/j.scib.2017.04.010

Dutta, S., Bhaumik, A., and Wu, K. C. W. (2014). Hierarchically porous carbon derived from polymers and biomass: effect of interconnected pores on energy applications. *Energy Environ. Sci.* 7, 3574–3592. doi: 10.1039/C4EE01075B

Fujimoto, H. (2010). Development of efficient carbon anode material for a high-power and long-life lithium ion battery. *J. Power Sources* 195, 5019–5024. doi: 10.1016/j.jpowsour.2010.02.005

Hong, Z., Zhou, K., Zhang, J., Huang, Z., and Wei, M. (2016). Self-assembled synthesis of mesocrystalline TiO_2@C-rGO hybrid nanostructures for highly reversible sodium storage. *Crystal Growth Design* 16, 6605–6612. doi: 10.1021/acs.cgd.6b01293

Jiang, C., Wang, J., Chen, Z., Yu, Z., Lin, Z., and Zou, Z. (2017). Nitrogen-doped hierarchical carbon spheres derived from MnO_2-templated spherical polypyrrole as excellent high rate anode of Li-ion batteries. *Electrochim. Acta* 245, 279–286. doi: 10.1016/j.electacta.2017.05.157

Jiang, Y., Yan, X., Mei, P., Zhang, Y., Xiao, W., and Tang, H. (2018). Electrochemical reconstruction induced high electrochemical performance of Co_3O_4/reduced graphene oxide for lithium ion batteries. *J. Alloys Compd.* 764, 80–87. doi: 10.1016/j.jallcom.2018.06.044

Li, J., Yao, R., Bai, J., and Cao, C. (2013). Two-dimensional mesoporous carbon nanosheets as a high-performance anode material for lithium-ion batteries. *ChemPlusChem* 78, 797–800. doi: 10.1002/cplu.201300158

Liu, C., Liu, X., Tan, J., Wang, Q., Wen, H., and Zhang, C. (2017). Nitrogen-doped graphene by all-solid-state ball-milling graphite with urea as a high-power lithium ion battery anode. *J. Power Sources* 342, 157–164. doi: 10.1016/j.jpowsour.2016.11.110

Liu, H., Jia, M., Cao, B., Chen, R., Lv, X., Tang, R., et al. (2016). Nitrogen-doped carbon/graphene hybrid anode material for sodium-ion batteries with excellent rate capability. *J. Power Sources* 319, 195–201. doi: 10.1016/j.jpowsour.2016.04.040

Liu, X., Li, Z., Fei, H., and Wei, M. (2015). Composite of K-doped $(NH_4)_2V_3O_8$/graphene as an anode material for sodium-ion batteries. *Dalton Trans.* 44, 18864–18869. doi: 10.1039/C5DT03239C

Nitta, N., Wu, F., Lee, J. T., and Yushin, G. (2015). Li-ion battery materials: present and future. *Mater. Today* 18, 252–264. doi: 10.1016/j.mattod.2014.10.040

Qie, L., Chen, W. M., Wang, Z. H., Shao, Q. G., Li, X., Yuan, L. X., et al. (2012). Nitrogen-doped porous carbon nanofiber webs as anodes for lithium ion batteries with a superhigh capacity and rate capability. *Adv. Mater.* 24, 2047–2050. doi: 10.1002/adma.201104634

Qiu, H., Zeng, L., Lan, T., Ding, X., and Wei, M. (2015). *In situ* synthesis of GeO_2/reduced graphene oxide composite on Ni foam substrate as a binder-free anode for high-capacity lithium-ion batteries. *J. Mater. Chem. A* 3, 1619–1623. doi: 10.1039/C4TA05212A

Selvamani, V., Ravikumar, R., Suryanarayanan, V., Velayutham, D., and Gopukumar, S. (2016). Garlic peel derived high capacity hierarchical N-doped porous carbon anode for sodium/lithium ion cell. *Electrochim. Acta* 190, 337–345. doi: 10.1016/j.electacta.2016.01.006

Shi, S., Hua, X., and Guo, H. (2018). Microwave-assisted one-pot synthesis of SnC_2O_4/graphene composite anode material for lithium-ion batteries. *Ceram. Int.* 44, 13495–13501. doi: 10.1016/j.ceramint.2018.04.179

Striebel, K. A., Shim, J., Cairns, E. J., Kostecki, R., Lee, Y.-J., Reimer, J., et al. (2004). Diagnostic analysis of electrodes from high-power lithium-ion cells cycled under different conditions. *J. Electrochem. Soc.* 151, A857–A866. doi: 10.1149/1.1710514

Tong, X., Wang, H., Wang, G., Wan, L., Ren, Z., Bai, J., et al. (2011). Controllable synthesis of graphene sheets with different numbers of layers and effect of the number of graphene layers on the specific capacity of anode material in lithium-ion batteries. *J. Solid State Chem.* 184, 982–989. doi: 10.1016/j.jssc.2011.03.004

Wang, H., and Yoshio, M. (2001). Carbon-coated natural graphite prepared by thermal vapor decomposition process, a candidate anode material for lithium-ion battery. *J. Power Sources* 93, 123–129. doi: 10.1016/S0378-7753(00)00552-8

Wang, J., Lin, L., and He, D. (2018). Self-assembly of Fe_2O_3 nanotubes on graphene as an anode material for lithium ion batteries. *J. Alloys Compd.* 750, 871–877. doi: 10.1016/j.jallcom.2018.04.079

Wang, R., Wang, S., Jin, D., Zhang, Y., Cai, Y., Ma, J., et al. (2017). Engineering layer structure of MoS2-graphene composites with robust and fast lithium storage for high-performance Li-ion capacitors. *Energy Storage Mater.* 9, 195–205. doi: 10.1016/j.ensm.2017.07.013

Wu, Y.-P., Wan, C.-R., Jiang, C.-Y., Fang, S.-B., and Jiang, Y.-Y. (1999). Mechanism of lithium storage in low temperature carbon. *Carbon* 37, 1901–1908. doi: 10.1016/S0008-6223(99)00067-6

Xu, J., Han, Z., Wu, J., Song, K., Wu, J., Gao, H., et al. (2018). Synthesis and electrochemical performance of vertical carbon nanotubes on few-layer graphene as an anode material for Li-ion batteries. *Mater. Chem. Phys.* 205, 359–365. doi: 10.1016/j.matchemphys.2017.11.039

Zhang, L., Zhang, M., Wang, Y., Zhang, Z., Kan, G., Wang, C., et al. (2014). Graphitized porous carbon microspheres assembled with carbon black nanoparticles as improved anode materials in Li-ion batteries. *J. Mater. Chem. A* 2, 10161–10168. doi: 10.1039/C4TA00356J

Zhang, W., Xu, T., Liu, Z., Wu, N. L., and Wei, M. (2018). Hierarchical TiO_2-x imbedded with graphene quantum dots for high-performance lithium storage. *Chem. Commun.* 54, 1413–1416. doi: 10.1039/C7CC09406J

Zhou, D., Liu, Y., Song, W.-L., Li, X., Fan, L.-Z., and Deng, Y. (2017). Three-dimensional porous carbon-coated graphene composite as high-stable and long-life anode for sodium-ion batteries. *Chem. Eng. J.* 316, 645–654. doi: 10.1016/j.cej.2017.02.008

Conflict of Interest Statement: The authors declare that the research was conducted in the absence of any commercial or financial relationships that could be construed as a potential conflict of interest.

frontiers in Materials

ORIGINAL RESEARCH
published: 26 February 2019
doi: 10.3389/fmats.2019.00022

Cobalt Phosphate Nanoparticles Embedded Nitrogen and Phosphorus-Codoped Graphene Aerogels as Effective Electrocatalysts for Oxygen Reduction

Li-Li Xuan, Xiao-Jun Liu and Xue Wang**

China-Japan Union Hospital of Jilin University, Changchun, China

OPEN ACCESS

Edited by:
Jie-Sheng Chen,
Shanghai Jiao Tong University, China

Reviewed by:
Bao Yu Xia,
Huazhong University of Science and Technology, China
Yang Hou,
Zhejiang University, China

****Correspondence:***
Xiao-Jun Liu
171020963@qq.com
Xue Wang
349500296@qq.com

Specialty section:
This article was submitted to Colloidal Materials and Interfaces, a section of the journal Frontiers in Materials

Received: *14 November 2018*
Accepted: *05 February 2019*
Published: *26 February 2019*

Citation:
Xuan L-L, Liu X-J and Wang X (2019) Cobalt Phosphate Nanoparticles Embedded Nitrogen and Phosphorus-Codoped Graphene Aerogels as Effective Electrocatalysts for Oxygen Reduction. Front. Mater. 6:22. doi: 10.3389/fmats.2019.00022

Developing cost-efficient and high-performance non-noble metal electrocatalysts for oxygen reduction reaction is of great significance for large-scale commercialization of fuel cells. Here, a novel cobalt phosphate-embedded nitrogen and phosphorus co-doped graphene aerogel [labeled as $Co_3(PO_4)_2$/N,P-GA] is prepared via combination of a facile hydrothermal apporoach with a pyrolysis procedure. The obtained $Co_3(PO_4)_2$/N,P-GA catalysts display excellent catalytic performance in base media, with optimal $Co_3(PO_4)_2$/N,P-GA-900 (the material prepared at pyrolysis temperature of 900°C) showing better catalytic activity for ORR than other as-obtained contrast materials in terms of the onset potential, half-wave potential and diffusion-limiting current density, even superior to the commercial Pt/C catalyst. Furthermore, the $Co_3(PO_4)_2$/N,P-GA also possesses good methanol tolerance and excellent durability. The superior performance of $Co_3(PO_4)_2$/N,P-GA is attributed to the hierachical porous structure, large BET surface area, N,P-codoping, cobalt phosphate-based nanoparticles loaded on graphene nanosheets, and synergistic effects between the doped active species. Therefore, it is expected to replace Pt/C as a promising fuel cell catalyst in alkaline direct methanol fuel cells.

Keywords: cobalt phosphate, graphene aerogel, electrocatalyst, N,P-codoped, oxygen reduction reaction

INTRODUCTION

Fuel cells and metal-air batteries have been identified as clean and efficient energy conversion and storage techniques due to their environmentally-friendly and sustainable features (Ren et al., 2000), in which the electrochemical oxygen reduction reaction (ORR) plays a critical role (Walter et al., 2010; Shao et al., 2012; Katsounaros et al., 2014; Zheng et al., 2014; Dai et al., 2015; Zhang et al., 2015a,b). As an important half-reaction in these energy conversion and storage technologies, ORR is subjected to sluggish kinetics, so using the catalyst to improve the reaction rate is of great significance (Debe, 2012; Chen et al., 2014). At present, the most efficient electrocatalysts for ORR are noble platinum-based catalysts. However, the scarcity and high price of platinum have impeded

their large-scale application in energy conversion and storage techniques. Therefore, it is urgent but remains challenging to develop non-noble catalysts with low cost and high activity for ORR (Hou et al., 2014b; Menezes et al., 2015; Yuan et al., 2015).

In recent years, transition metal phosphates have been aroused wide concern for energy conversion and storage applications due to their catalytic efficiency and high stability (Kim et al., 2007; Kanan and Nocera, 2008; Park et al., 2010; Wang et al., 2011a; Gonzalez-Flores et al., 2015). Among them, Mn(II) and Co(II) phosphates have especially attracted tremendous attention because of their potential as a ORR catalyst (Zhan et al., 2016). However, they have accomplished little success in the recent state of investigation and development because of their high tendency for aggregation and low conductivity. Hence, it is necessary to decorate the metal phosphates nanoparticles with conducting carbon materials in order to improve their catalytic activity (Liang et al., 2013; Mao et al., 2014; Xia et al., 2015; Hu et al., 2016; Zhou et al., 2016). Among these carbonaceous materials, graphene is considered as an ideal carbon substrate due to the special sp^2-hybrid structure, high electrical conductivity, excellent chemical stability, and large specific surface area (Geim and Novoselov, 2007; Wang et al., 2011b; Yang et al., 2011; Yu et al., 2011). The abundance of functional groups on the graphene surface that can serve as the nucleation sites increases the nanoparticle dispersion and decreases the nanoparticle size, resulting in enhanced activity and a greater utilization of the active material (Wang and Dai, 2013; Hou et al., 2014a; Li et al., 2018).

Many studies have been conducted to improve the ORR activity of graphene-based materials by surface modification with heteroatoms (Wang et al., 2012, 2014; Hou et al., 2014b). Particularly, N-doped graphene materials has been widely studied due to their excellent ORR catalytic activity (Wang et al., 2011c; Hibino et al., 2013; Goran et al., 2015). The reason for improving the catalytic activity is that the N atoms incorporated into carbon matrix can create a lot of active sites and change asymmetry spin density and charge density of the carbon lattice (Gong et al., 2009; Jeon et al., 2013; Cheon et al., 2014). Phosphorus (P), another group-V element, possesses the same valance electron number and similar chemical behavior with N (Hu et al., 2014). P has higher electron-donating ability and stronger n-type effect than N, which make it a good candidate as a dopant in graphene (Some et al., 2012). In addition, P has an electronegativity value of 2.19 that is lower than that of N (3.04). The introduction of N and P with different electronegativity into carbon skeleton can effectively increase defect density, creating more reactive sites for ORR (Wang et al., 2012, 2014). More importantly, the synergistic effect between N and P can further enhance the electrocatalytic activity toward ORR (Maria Rosas et al., 2012; Nasini et al., 2014; Ornelas et al., 2014; Razmjooei et al., 2014).

In addition to modifying the graphene surface, the structure of graphene has much effect on the catalytic activity, two-dimensional (2D) graphene sheets easily lead to aggregation and accumulation during drying due to physical interaction, leading to a decrease in specific surface area (Mao et al., 2015; Fu et al., 2016). Assembling 2D graphene into a 3D architectures is an feasible method to overcome the accumulation problem. The 3D graphene aerogel possesses interconnected pore structures, thus providing more exposed reactive sites as well as high rate of mass transfer and electron transport for the heteroatoms-doped graphene-based composites.

Based on discussion above, it is believed that loading transition metal phosphate nanoparticles on heteroatoms-doped graphene aerogels is an effective method to construct highly-efficient ORR catalysts. Benefiting from high conductivity, large specific surface area and heteroatoms doping effect of graphene aerogel, as well as the cooperativity of transition metal phosphates and heteroatoms-doped graphene aerogels, the obtained hybrids are expected to deliver excellent electrocatalytic activity and good stability for ORR. To the best of our knowledge, there are few reports in this aspect (Yuan et al., 2015).

Herein, we report a novel catalyst composed of $Co_3(PO_4)_2$ nanoparticles and the 3D N,P-codoped graphene aerogel ($Co_3(PO_4)_2$/N,P-GA). The hybrid is prepared via a two-step method, consisting of a hydrothermal assembly process and

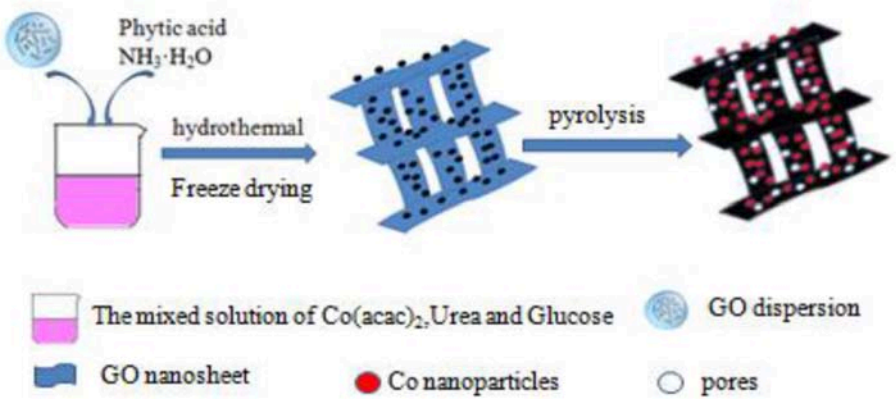

SCHEME 1 | Illustration of preparation of $Co_3(PO_4)_2$/N,P- GA-900.

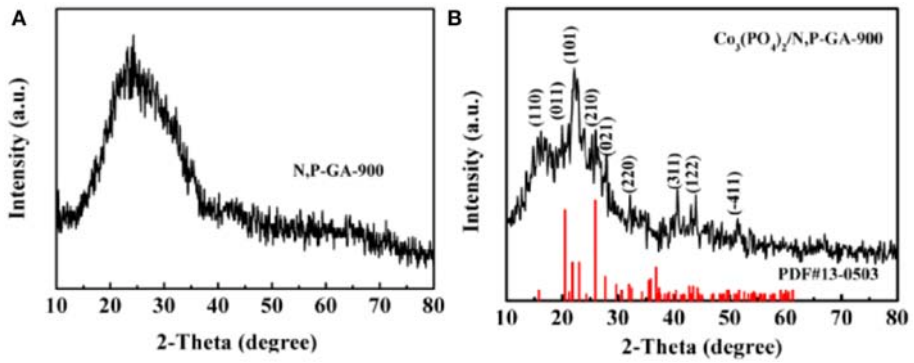

FIGURE 1 | XRD patterns of the **(A)** N,P-GA-900 and **(B)** $Co_3(PO_4)_2$/N,P-GA-900.

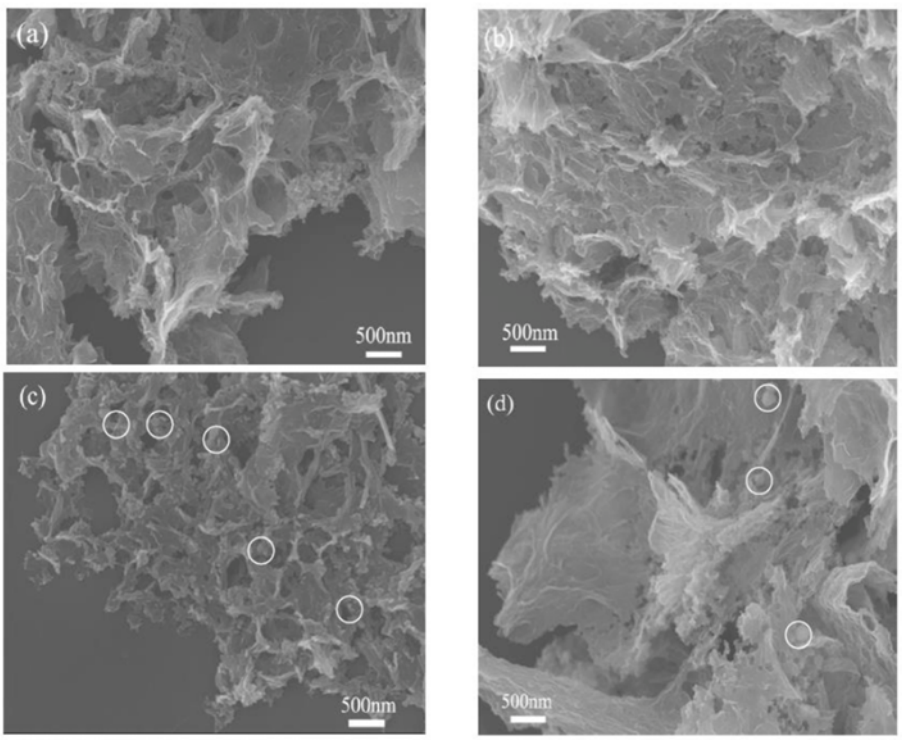

FIGURE 2 | SEM images of **(a)** the N,P-GA-900; **(b)** the $Co_3(PO_4)_2$/N,P-GA-900; **(c)** the Co_2P/P- GA-900; and **(d)** Co/N-GA-900.

subsequent pyrolysis procedure in the Ar atmosphere. The as-obtained $Co_3(PO_4)_2$/N,P-GA-900 (where 900 represents the pyrolysis temperature of 900°C) catalyst displays excellent catalytic activity and good operational stability for ORR, and is expected to substitute the commercial Pt/C as a promising electrocatalyst for ORR.

EXPERIMENTAL SECTION

Materials

Graphite powder was purchased from Beijing Chemical Company (China). Nafion® perfluorinated resin solution (5%) was bought from Sigma-Aldrich. Phytic acid (PA) was purchased from Aladdin Ltd (Shanghai, China). Commercial Pt/C (20 wt% Pt on Vulcan carbon black) catalyst was provided by Alfa Aesar. Ultra-pure water was obtained from a Milli-Q water system. All other reagents were of analytical reagent grade and used directly.

Synthesis of $Co_3(PO_4)_2$/N,P-GA-900

Graphene oxide (GO) was prepared through the modified Hummers' method according to a previous report (Zhang et al., 2014). Typically, GO was dispersed into water to form a suspension (2 mg mL^{-1}) by ultrasonic vibration. Then,

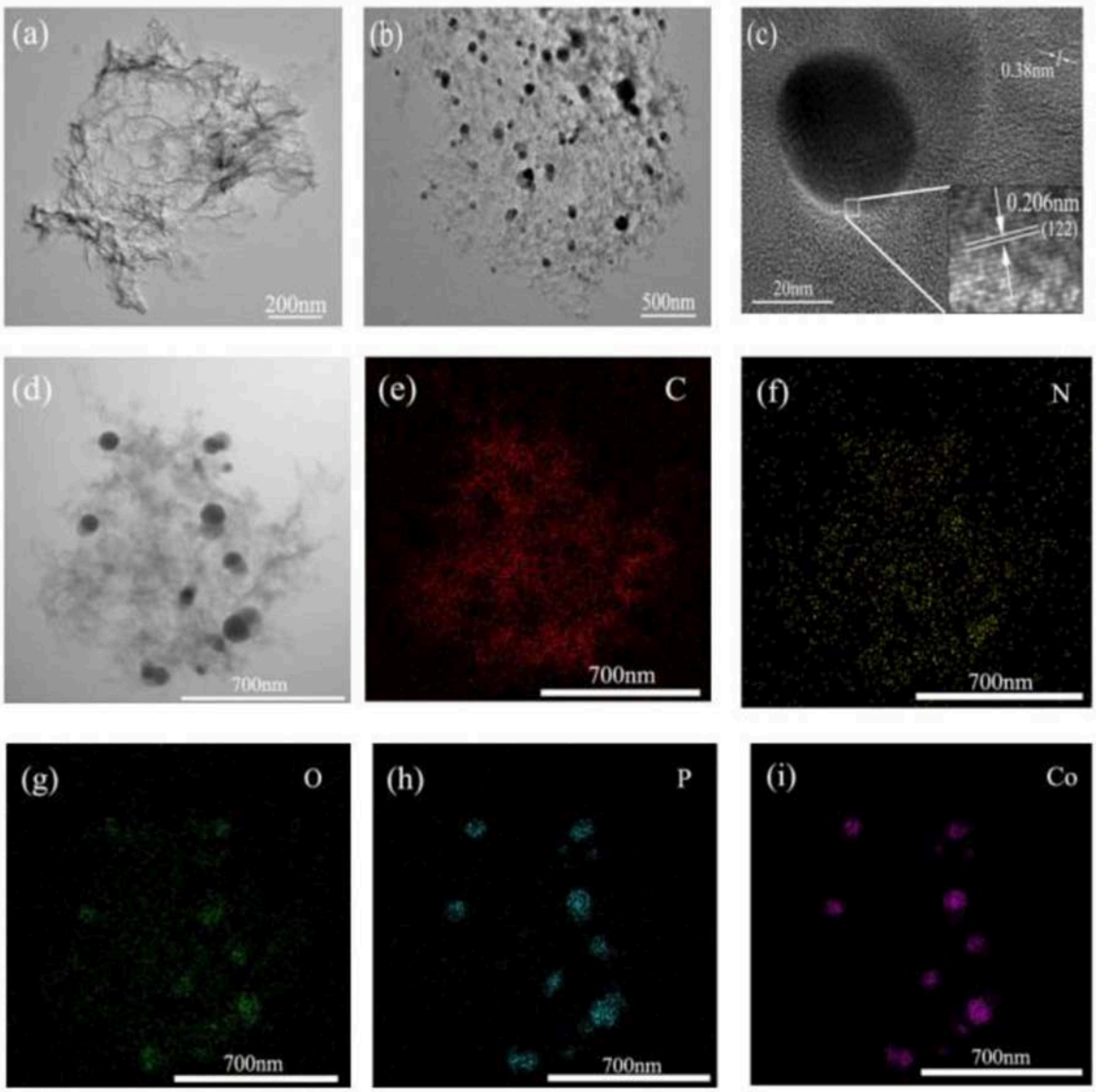

FIGURE 3 | (a) TEM images of N,P-GA-900; **(b–d)** tem IMAGES OF $cO_3(po_4)_2$/n,p-ga-900 AT DIFFERENT MAGNIFICATIONs; **(e–i)** Elemental mappings of C, N, O, P and Co of $Co_3(PO_4)_2$/N,P-GA-900.

cobalt acetate (10 mg), urea (500 mg), and glucose (20 mg) were dissolved in 10 mL water, followed by adding aqueous ammonia into the above solution to adjust solution pH greater than 12. Finally, PA (20 mg) and GO (10 ml, 2 mg mL^{-1}) were added into the above solution. The obtained suspension was sonicated for 1 h, transferred to a 50 mL Teflon-lined stainless autoclave and hydrothermally treated at 180°C for 12 h. After cooling to the ambient temperature, the hydrogel was obtained. The hydrogel was washed with deionized water until neutral pH, followed by freeze-drying to get the aerogel. The as-synthesized aerogel was directly pyrolyzed at the set temperature in a tube furnace in Ar atmosphere for 1 h and the heating rate is 5°C min^{-1}. The corresponding samples pyrolyzed at 700, 800, 900, and 1,000°C were denoted as $Co_3(PO_4)_2$/N,P-GA-700, $Co_3(PO_4)_2$/N,P-GA-800, $Co_3(PO_4)_2$/N,P-GA- 900, $Co_3(PO_4)_2$/N,P-GA-1000, respectively. For comparison, the Co/N-doped graphene aerogel (Co/N-GA-900), Co_2P/P-doped graphene aerogel (Co_2P/P-GA-900), and N,P-doped graphene aerogel (N,P-GA-900) were also prepared by using the same procedures as making $Co_3(PO_4)_2$/N,P-GA-900, but without the presence of PA, urea and $Co(acac)_2$ during the hydrothermal process, respectively.

Characterization

The morphology and microstructure of the catalysts were characterized by using scanning electron microscopy (SEM,

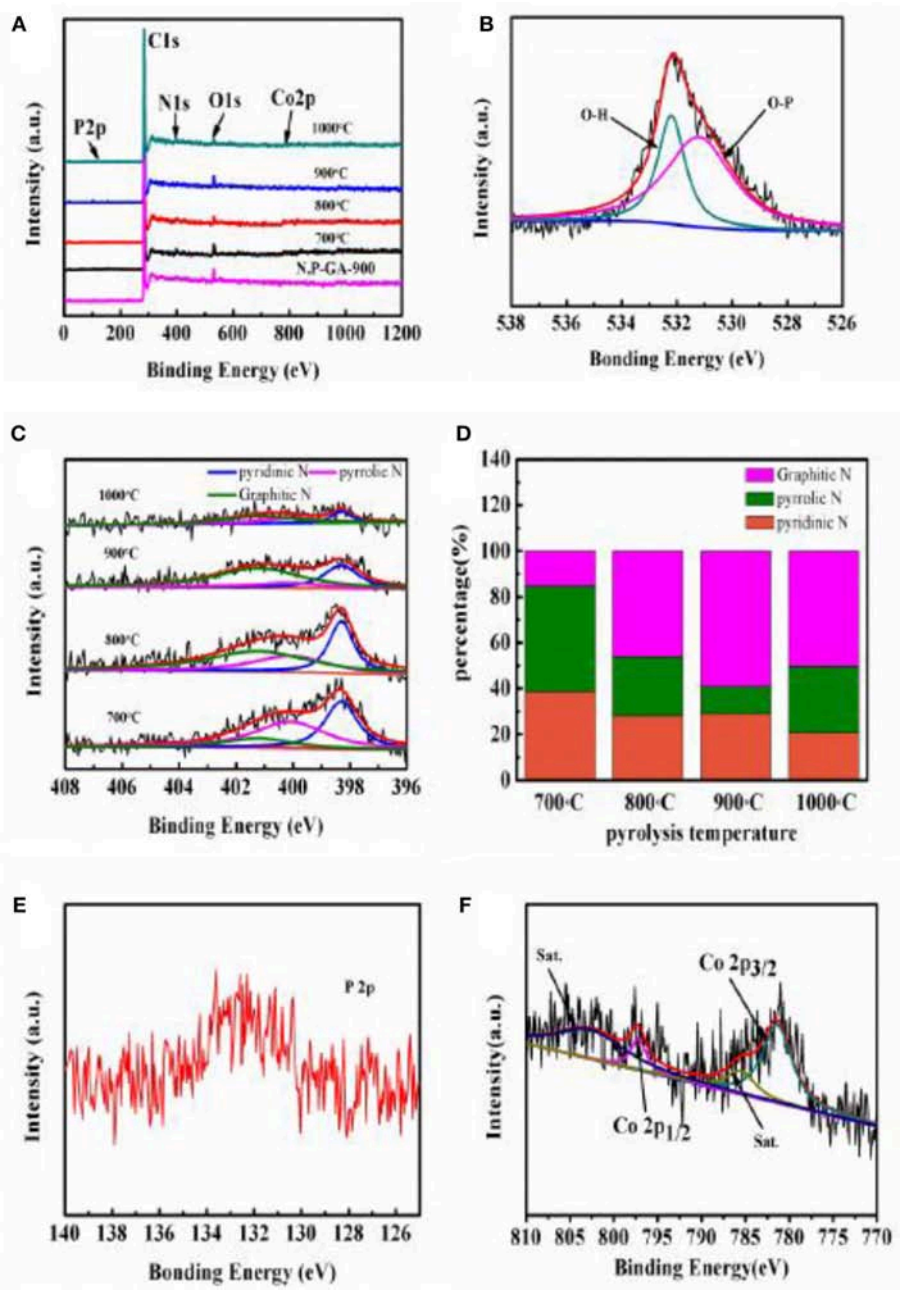

FIGURE 4 | (A) The XPS survey spectra of N,P-GA-900 and $Co_3(PO_4)_2$/N,P-GA at different pyrolysis temperatures; **(B,C,E,F)** High-resolution XPS spectra of O 1s, N 1s, P 2p, and Co 2p of $Co_3(PO_4)_2$/N,P-GA-900; **(D)** The percentage of deconvoluted N 1s species in $Co_3(PO_4)_2$/N,P-GA.

JEOL JSM-6701F operating at an accelerating voltage of 5 kV) and transition electron microscopy (TEM, JEOL-2010 operating at 200 kV) techniques. TEM associated energy-dispersive X-ray (EDX) elemental mapping was obtained from a JEOL-2010 transmission electron microscope operating at 200 kV. The crystal structural information was recorded on a power X-ray diffractometer by using Cu-K_α radiation (RIGAKU, D/MAX2250VB/PC). The specific surface area and pore structure were characterized on a Micromeritics ASAP 2020 surface area and porosity analyzer conducted at 77 K with N_2 as adsorbate. The specific surface areas of the catalysts were evaluated from the nitrogen adsorption/desorption isotherms by utilizing the Brunauer-Emmett-Teller (BET), whereas the pore size distribution curves were obtained from the Barrett-Joyner-Halenda (BJH) method (for mesopores) and the density functional theory (DFT) method (for micropores). The surface chemical composition was measured by X-ray photoelectron spectroscopy (XPS), using an ESCLAB 250 spectrometer with

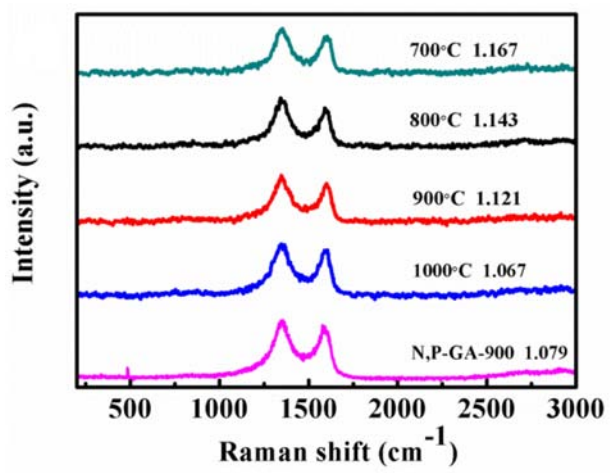

FIGURE 5 | Raman spectra of $Co_3(PO_4)_2$/N,P-GA and N,P-GA-900.

a monochromatized Al K_α X-ray source. Raman spectra were collected on a Lab RAMHR Evolution Raman spectrometer using 532 nm excitation laser.

Electrochemical Test

To research the electrochemical catalytic activity of the as-prepared catalysts, a series of electrochemical tests were conducted on a CHI760E electrochemical workstation assembled with a rotational system with a standard three-electrode glass cell, in which a platinum sheet was served as the counter electrode, saturated calomel electrode (SCE) as the reference electrode and a modified glass carbon electrode as the working electrode. In order to modify the working electrode, 1 mg of the as-prepared catalyst power was dispersed in 1 mL of ethanol and treated by ultrasonic vibration for 2 h, and then 55 uL of the catalyst solution was dropped onto the GCE by a microsyringe. Finally, 1.0 uL of 10% Nafion solution (in ethanol) was placed on the working electrode serving as a protector. After drying at room temperature, the electrocatalyst was loaded on the working electrode with the catalyst loading of around 280 μg cm^{-2}. As a contrast, the commercial Pt/C (20 wt% Pt on Vulcan carbon black) catalyst was used as a reference. All electrochemical tests were proceeded after receiving stable cyclic voltammetry (CV) curves by continuous CV tests. All of the potentials reported in this work were referenced to the reversible hydrogen electrode (RHE) scale according to the Nernst equation ($E_{RHE} = E_{SCE}+0.059pH+0.242$ V).

RESULTS AND DISCUSSION

Characterization of Morphology and Structure

The process for synthesis of the $Co_3(PO_4)_2$/N,P-GA-900 is illustrated in **Scheme 1**. In the first step, phytic acid and GO suspension were successively added to a mixture solution of cobalt acetate, urea and glucose containing aqueous ammonia. Then the mixture was hydrothermally treated to form cobalt-based nanoparticles and make the GO sheets assemble into 3D graphene hydrogel. The gas evolution generated micropores, and graphene was further reduced during the process of pyrolysis.

To identify the crystallographic phases of the as-obtained N,P-GA-900 and $Co_3(PO_4)_2$/N,P-GA-900 catalysts, the X-ray diffraction (XRD) analysis was performed. In **Figure 1**, two composites appear a broad diffraction peak at $2\theta\approx26.0^\circ$, implying the formation of graphitic structure in the hybrids (Liu et al., 2016) For $Co_3(PO_4)_2$/N,P-GA-900, the characteristic diffraction peaks at $2\theta\approx21.9$, 25.9, 27.8, 32.1, 40.6, 44.1, and 51.7° are recognized, corresponding to the (101), (210), (021), (220), (311), (122), and (−411) crystalline facets of $Co_3(PO_4)_2$ (JCPDS No.13-0305, **Figure 1B**), respectively. The XRD results prove the formation of $Co_3(PO_4)_2$ nanocrystals. As exhibited in **Figure S1a**, the specific diffractive peaks of Co_2P/P-GA-900 are easily indexed to Co_2P phase with reference to the standard card (PDF card no.32-0306), which suggests the existence of Co_2P. Besides, the XRD pattern of Co/N-GA-900 composite exhibits the full suite of the characteristic peaks of Co (JCPDS file # 15-0806, **Figure S1b**).

To reveal the morphological and structural information of the obtained catalysts, scanning electron microscopy (SEM) and transmission electron microscopy (TEM) were performed. The N,P-GA-900 exhibits a three-dimensional (3D) crumpled morphology with microsized pores constructed by interconnected GO sheets, which can provide abundant channels for the transportation of ORR-relevant species (**Figure 2a**). For the as-synthesized $Co_3(PO_4)_2$/N,P-GA-900 composite, the nanoparticles loaded on N,P-GA can be clearly seen without obvious aggregation (see **Figure 2b**). The *in-situ* growth of nanoparticles within pore structure of graphene can enhance the interaction between nanoparticles and graphene. Above SEM results definitely validate that the $Co_3(PO_4)_2$/N,P-GA-900 with an interconnected porous network was successfully prepared. Additionally, one can also observe the existence of Co_2P and Co nanoparticles loaded on folded 3D P-doped and N-doped graphene aerogels, respectively (see **Figures 2c,d**).

TEM images (see **Figure 3a**) disclose that the N,P-GA-900 presents crumpled and wrinkle-like structure, in line with those of SEM results. The TEM image and corresponding elemental mappings indicate the presence of C, N, and P in the N,P-GA-900 (**Figure S2**), manifesting that N and P were successfully doped into graphene skeleton. In **Figure 3b**, one can clearly see the nanoparticles distributed on wrinkle-like graphene sheets, and the d-spacing of crystalline lattices is 0.206 nm, which corresponds to the (122) plane of $Co_3(PO_4)_2$ (**Figure 3c**). The measured interplanar distances of graphene are ∼0.38 nm, in accord with the separation of the layers of hexagonal graphite. The EDS elemental mapping shows the presence of C, N, O, P and Co elements (**Figures 3d–i**). Moreover, Co, P as well as O elements are mainly distributed in the area where nanoparticles exist (**Figures 3g–i**). These results suggest that the $Co_3(PO_4)_2$ nanoparticles may have been formed. In addition, the different resolution TEM images of Co_2P/P-GA-900 and Co/N-GA-900 are demonstrated in **Figure S4**. The nanoparticles scattered on graphene sheets can also be observed (**Figures S3a,b**). Obviously,

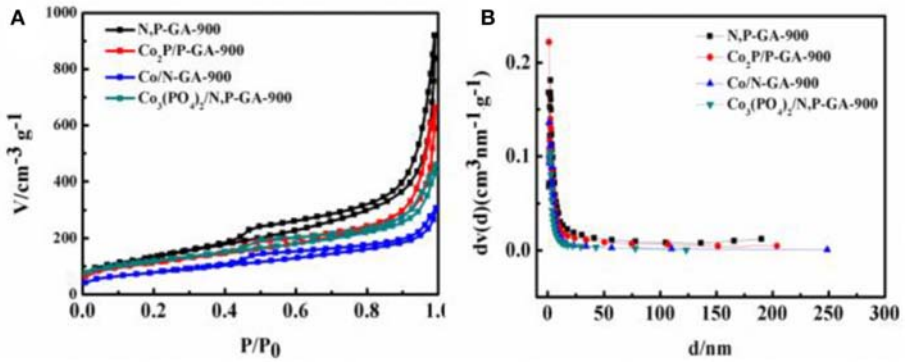

FIGURE 6 | (A) Nitrogen adsorption-desorption isotherms and **(B)** pore size distribution of N,P-GA-900, Co/N-GA-900, Co_2P/P-GA-900, and $Co_3(PO_4)_2$/N,P-GA-900.

TABLE 1 | The pore structure parameters of the as-prepared catalysts.

Sample	SA (m^2g^{-1})	PV (cm^3g^{-1})	PD (nm)
$Co_3(PO_4)_2$/N,P-GA-700	329.3	1.18	14.34
$Co_3(PO_4)_2$/N,P-GA-800	321.2	0.75	9.38
$Co_3(PO_4)_2$/N,P-GA-900	426.3	0.54	5.09
$Co_3(PO_4)_2$/N,P-GA-1000	332.5	1.06	12.76
Co/N-GA-900	288.0	0.48	6.6
Co_2P/P-GA-900	407.1	1.03	10.1
N,P-GA-900	487.6	1.43	11.74

SA, Surface area; PV, Pore volume; PD, Pore diameter.

the lattice fringes with a d-spacing of 0.220 nm are designated to the (121) plane of Co_2P (**Figure S3c**), confirming the formation of Co_2P nanoparticles. Moreover, Co (111) and (200) planes can be clearly observed with the lattice plane spacings of 0.205 and 0.175 nm, respectively (**Figure S3d).**

X-ray photoelectron spectroscopy was further used to evaluate the elemental compositions and bonding states on the catalyst surface. As presented in **Figure 4A**, C, N, O, P, and Co elements are detected from the overall XPS spectra of $Co_3(PO_4)_2$/N,P-GA-900, in agreement with the EDS mapping results. Obviously, the high-resolution O 1s signals are centered at ca. 530.2, 531.9, and 532.8 eV, which are assigned to the Co-O in $Co_3(PO_4)_2$, C-O and C=O in graphene, as displayed in **Figure 4B** (Fei et al., 2015). The high-resolution N 1s spectrum of $Co_3(PO_4)_2$/N,P-GA-900 can be deconvoluted into three signals, different N species at around 398.3, 400.1, and 401.2 eV are assigned to pyridinic N, pyrrolic N and graphitic N, respectively (Shanmugam and Osaka, 2011; Yang et al., 2011). Moreover, the catalysts pyrolyzed at other temperatures have the same nitrogen forms with $Co_3(PO_4)_2$/N,P-GA-900 (**Figure 4C**). The total nitrogen contents of $Co_3(PO_4)_2$/N,P-GA-700, $Co_3(PO_4)_2$/N,P-GA-800, $Co_3(PO_4)_2$/N,P-GA-900 and $Co_3(PO_4)_2$/N,P-GA-1000 are estimated to be 3.84, 3.7, 2.46, and 2.11 at %, respectively. Obviously, the nitrogen contents decrease rapidly at elevated pyrolysis temperatures, which can be attributed to the instability of nitrogen in high temperature (Zhong et al., 2014). However, the percentage content of graphitic N increases gradually due to the conversion of pyridinic N and pyrrolic N to graphitic N at higher annealing temperatures (**Figure 4D**). It is proposed that pyridinic N and graphitic N are the main forms to improve the activity for ORR (Lai et al., 2012), and the former enhances the onset potential whereas the latter increases the limiting current density. Taking the highest total percentage content of pyridinic-N and graphitic-N in the $Co_3(PO_4)_2$/N,P-GA-900 into consideration, it is expected that the as-prepared composite possesses outstanding catalytic performance for oxygen reduction reaction. The information of P 2p spectrum is rendered in **Figure 4E**. The single peak located at 133 eV can be attributed to the phosphate in the composite (Steinmiller and Choi, 2009). The P is introduced by phytic acid, additional P incorporating into N-doped graphene have proven to create more active sites and generate synergistic effects for ORR electrocatalysis (Yang et al., 2012; Jiang et al., 2014).

Co also can be detected from the $Co_3(PO_4)_2$/N,P-GA-900 specimen surface. High-resolution Co 2p spectrum (**Figure 4F**) discloses the binding energies of Co $2p_{3/2}$ and Co $2p_{1/2}$ at 781.4 and 797.2 eV with their corresponding satellite peaks at 787.6 and 802.7 eV, respectively. These binding energies are characteristic of Co(II) in the hybrid material (Zhou et al., 2016). The above observations further demonstrate that the $Co_3(PO_4)_2$ loaded nitrogen and phosphorus-codoped graphene aerogel [$Co_3(PO_4)_2$/N,P-GA] hybrid materials were successfully obtained.

Raman spectroscopy has been widely used to evaluate the degree of graphitization and defect. According to **Figure 5**, the catalysts obtained at different temperatures show two distinct peaks in 1,349 cm^{-1} (D-band) and 1,590 cm^{-1} (G-band), which correspond to the disordered carbon and sp^2 hybridized graphitic carbon, respectively (Zhang et al., 2013). The I_D/I_G proportions of $Co_3(PO_4)_2$/N,P-GA-700, $Co_3(PO_4)_2$/N,P-GA-800, $Co_3(PO_4)_2$/N,P-GA-900, $Co_3(PO_4)_2$/N,P-GA-1000 and N,P-GA-900 are 1.167, 1.143, 1.121, 1.067, and 1.079, respectively. The ratios of I_D to I_G for the $Co_3(PO_4)_2$/N,P-GA decreases with the increase of pyrolysis temperature, which implies that a higher pyrolysis temperature facilitates the

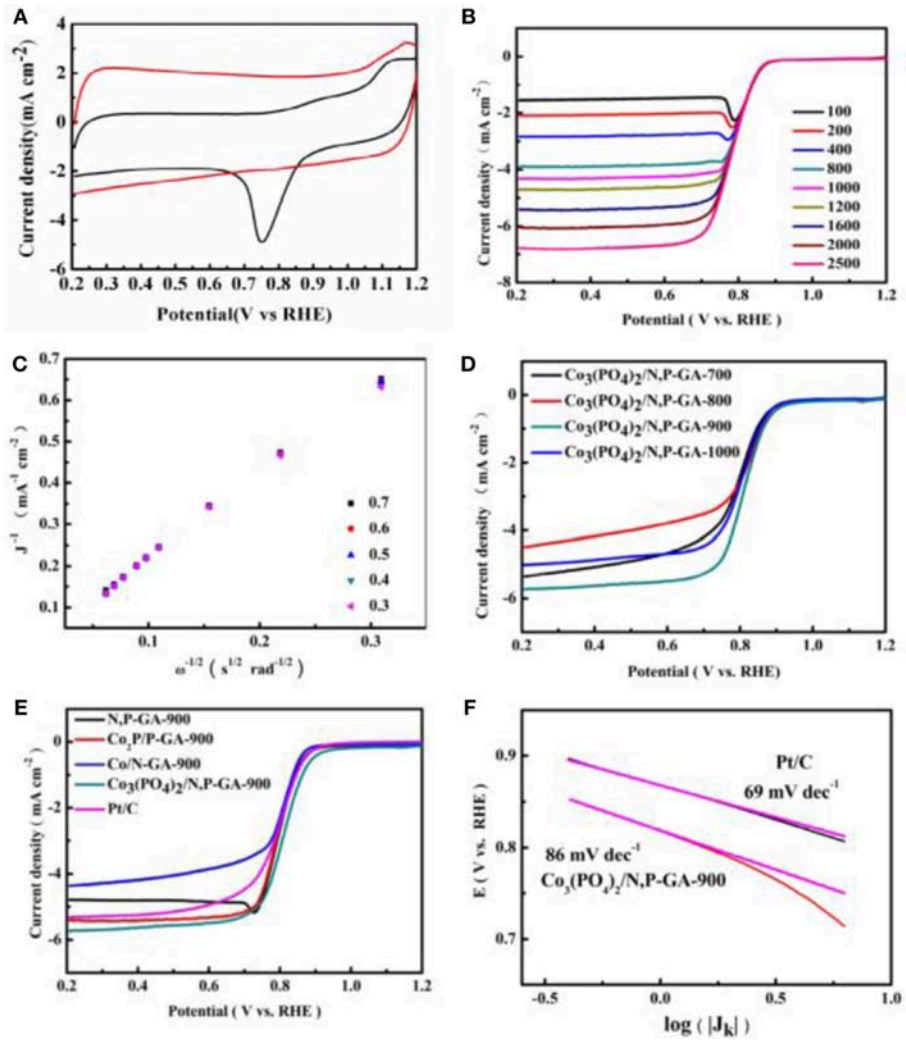

FIGURE 7 | (A) CV curves of the $Co_3(PO_4)_2$/N,P-GA- 900 in N_2- and O_2-saturated 0.1 M KOH at a scan rate of 100 mV s^{-1}; **(B)** LSV curves on $Co_3(PO_4)_2$/N,P-GA-900 in an O_2-saturated 0.1 M KOH with a scan rate of 10 mV s^{-1}; **(C)** The corresponding K-L plots of ORR for $Co_3(PO_4)_2$/N,P- GA-900 catalyst; **(D)** LSV polarization curves of $Co_3(PO_4)_2$/N,P-GA-T (T = 700, 800, 900, and 1,000) in O_2-saturated 0.1 M KOH at a scan rate of 10 mV s^{-1} with the rotating speed of 1,600 rpm; **(E)** LSV polarization curves of$Co_3(PO_4)_2$/N,P-GA-900, Co_2P/P-GA-900, Co/N-GA-900 and Pt/C in O_2-saturated 0.1 M KOH at a scan rate of 10 mV s^{-1} with the rotating speed of 1,600 rpm; **(F)** Tafel plots of $Co_3(PO_4)_2$/N,P-GA-900 and Pt/C in 0.1 M KOH.

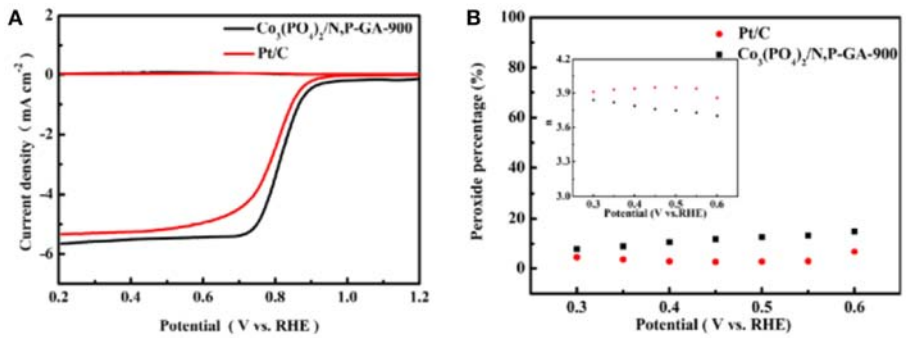

FIGURE 8 | (A) Rotating ring disk electrode (RRDE) measurements of $Co_3(PO_4)_2$/N,P-GA-900 and Pt/C in 0.1 M KOH; **(B)** Peroxide percentage and electron transfer number (inset) at different potentials based on the corresponding RRDE data in **(A)**.

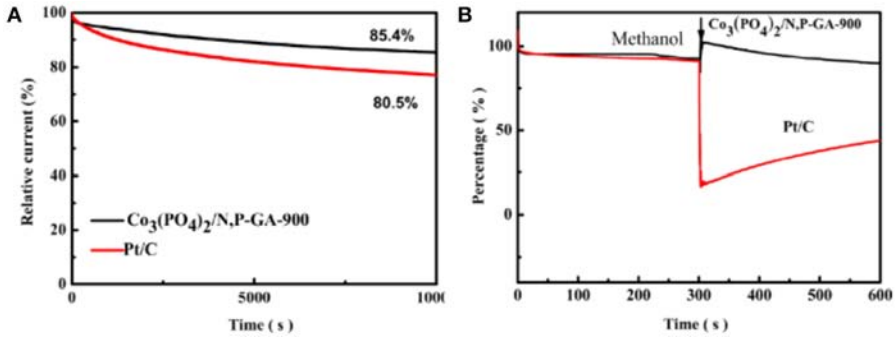

FIGURE 9 | (A) Chronoamperometric curves of $Co_3(PO_4)_2$/N,P-GA-900 and Pt/C in 0.1 M KOH solution saturated with O_2 at a rotating speed of 1,600 rpm and the scan rate of 10 mV s^{-1}; **(B)** Chronoamperometric response for ORR on $Co_3(PO_4)_2$/N,P-GA-900 and Pt/C in O_2-saturated 0.1 M KOH at a rotating speed of 1,600 rpm and the scan rate of 10 mV s^{-1} with 3 M methanol added after 300 s.

generation of more ordered graphitic carbon. High degree of graphitization can improve the electronic conductivity and erosion resistance of the as-obtained composite (Chen et al., 2015). It is worth noting that the I_D/I_G value (1.121) of $Co_3(PO_4)_2$/N,P-GA-900 is larger than that (1.079) of N,P-GA-900, suggesting the introduction of $Co_3(PO_4)_2$ leads to formation of more structure distortion. This result definitely demonstrates that more defects exist in the $Co_3(PO_4)_2$/N,P-GA-900 hybrid.

Brunauer-Emmett-Teller (BET) analysis was used to characterize the specific surface areas, pore sizes and pore volumes for the as-prepared catalysts (**Figures 6A,B**). In **Figure 6A**, the nitrogen adsorption-desorption curve displays a typical type-IV isotherm with a distinct hysteresis loop at the relative pressures (P/P_0) between 0.45 and 1.00, indicating the existence of mesopores in as-prepared $Co_3(PO_4)_2$/N,P-GA-900 catalyst. The pore structure parameters of all as-prepared composites are presented in **Table 1**. It can be seen that the BET surface area of $Co_3(PO_4)_2$/N,P-GA-900 (426.3 m^2 g^{-1}) is distinctly larger than those of Co/N-GA-900 (288.0 m^2 g^{-1}) and Co_2P/P-GA-900 (407.1 m^2 g^{-1}), demonstrating that the N/P co-doping is beneficial for an increase in BET surface area. Besides, $Co_3(PO_4)_2$/N,P-GA-900 possesses the highest specific BET surface area relative to other $Co_3(PO_4)_2$/N,P-GA-T (T = 700, 800, 1,000) counterparts, which is beneficial for the exposure of more active sites. It is worth noting that the BET surface area of $Co_3(PO_4)_2$/N,P-GA-900 is slightly reduced when compared to N,P-GA-900 (487.6 m^2 g^{-1}), which can be attributable to the incorporation of $Co_3(PO_4)_2$ nanoparticles into N,P-GA.

Electrocatalytic Performance for ORR

To evaluate the ORR performance of $Co_3(PO_4)_2$/N,P-GA-900, cyclic voltammetry (CV) curves were firstly recorded to estimate the electrocatalytic activity in O_2-/N_2-saturated 0.1 M KOH solutions. As seen in **Figure 7A**, the $Co_3(PO_4)_2$/N,P-GA-900 shows a palpable cathode reduction peak in an O_2-saturated solution whereas no characteristic peak in a N_2-saturated electrolyte, suggesting the electroactivity of $Co_3(PO_4)_2$/N,P-GA-900 for ORR. Linear sweep voltammetry (LSV) curves of $Co_3(PO_4)_2$/N,P-GA-900 in **Figure 7B** exhibits the limiting current density augment with the increase of rotating speeds from 100 to 2,500 rpm, due to the reduced diffusion distance at higher speeds. The corresponding Koutecky-Levich (K-L) plots show linearity and parallelism, indicating the first-order kinetics relative to the concentration of dissolved oxygen and similar electron transfer numbers (**Figure 7C**). Pyrolysis temperature is a significant factor in affecting active sites, and different pyrolysis temperatures result in different catalytic activities. By changing the pyrolysis temperature (700, 800, 900, and 1,000°C), one can see that the catalyst $Co_3(PO_4)_2$/N,P-GA-900 possesses the best ORR activity in relation to onset potential (E_0), half-wave potential ($E_{1/2}$), and limiting current density (J_L), as shown in **Figure 7D**. Consequently, 900°C is the optimal temperature, and other contrast samples are treated at the same temperature. As displayed in **Figure 7E**, the $Co_3(PO_4)_2$/N,P-GA-900 shows more prominent ORR catalytic activity than that of Co/N-GA-900 and Co_2P/P-GA-900, confirming that the synergistic effect of nitrogen and phosphorus can improve the performance of catalyst. Moreover, $Co_3(PO_4)_2$/N,P-GA-900 exhibits more positive onset potential (0.95 V vs. RHE) than N,P-GA-900 (0.91 V vs. RHE), manifesting that the $Co_3(PO_4)_2$ nanoparticles loaded are also the main active sites in enhancing the ORR activity. Not only that, the E_0 and $E_{1/2}$ of $Co_3(PO_4)_2$/N,P-GA-900 (0.95 V, 0.81 V) approaches to that of the commercial Pt/C (0.95 V, 0.80 V), while its diffusion limiting current density (5.73 mA cm^{-2}) is superior to the benchmark Pt/C (5.33 mA cm^{-2}). These results distinctly suggest that the $Co_3(PO_4)_2$/N,P-GA-900 possesses rapid kinetics process for ORR (**Figure S5** and **Table S1**). The ORR kinetics was also evaluated by Tafel slope (see **Figure 7F**). The $Co_3(PO_4)_2$/N,P-GA-900 catalyst gives a Tafel slope of 86 mV dec^{-1}, close to 20 wt% Pt/C (69 mV dec^{-1}), verifying the similar ORR mechanism of these two catalysts. The outstanding ORR activity of $Co_3(PO_4)_2$/N,P-GA-900 in alkaline media may be attributed to the synergistic effects of the following factors: (1) The particular 3D wrinkle porous architecture is beneficial for exposing more active sites and accelerating the accessibility of oxygen; (2) The insertion of N and P heteroatoms into the carbon skeleton is conductive to an increase in BET

surface area. Additionally, it can trigger charge redistribution and promote the adsorption of oxygen and the reduction reaction on graphene; (3) The $Co_3(PO_4)_2$ inserted into N,P-GA can not only produce more defects, but also improve the ORR activity of the obtained hybrid catalyst; (4) The synergistic coupling between the doped active components conduces to enhance the ORR activity markedly.

The ORR in an alkaline medium can be achieved via two possible pathways: involving a two-electron process to generate H_2O_2/HO_2^-, or the other, a direct four-electron pathway to produce H_2O/OH^-. In order to explore the ORR pathway of the obtained $Co_3(PO_4)_2$/N,P-GA-900, the rotating ring disk electrode (RRDE) experiments were performed. The electron transfer number (n) and percentage of hydrogen peroxide can be calculated according to the following equations (Liu et al., 2013).

$$\%HO_2^- = \frac{200 \times I_R/N}{I_D + I_R/N} \quad (1)$$

$$n = \frac{4 \times I_R/N}{I_D + I_R/N} \quad (2)$$

Where I_D is the disk current, I_R is the ring current, and N (=0.37) is the current collection efficiency of the Pt ring.

The RRDE test results present the disk and ring current density for $Co_3(PO_4)_2$/N,P-GA-900 and Pt/C (**Figure 8A**). **Figure 8B** shows the yield of hydrogen peroxide (H_2O_2%) and the electron transfer number (n) at different potentials for the two catalysts. It can be observed that the percentage of H_2O_2 for $Co_3(PO_4)_2$/N,P-GA-900 is less than 15%, and the calculated electron transfer number is 3.7–3.84 in the potential range of 0.3–0.6 V vs. RHE. These results suggest that the $Co_3(PO_4)_2$/N,P-GA-900 catalyze ORR undergoes a predominant 4e process by reducing O_2 directly to OH^-.

Methanol poisoning and the durability are significant matters challenging the cathode catalysts in current fuel cell devices (Yu et al., 2012; Jin et al., 2014). For estimating the long-term stability of the $Co_3(PO_4)_2$/N,P-GA-900 hybrid, the chronoamperometry test over a period of 10,000 s at 1,600 rpm and 10 mV s^{-1} was conducted (see **Figure 9A**). Remarkably, the current retention of $Co_3(PO_4)_2$/N,P-GA-900 is 85.4%, while Pt/C reserves only 80.5% of its initial current under the same conditions, indicating the better durability of the $Co_3(PO_4)_2$/N,P-GA-900 catalyst relative to Pt/C. In order to explore the selectivity of $Co_3(PO_4)_2$/N,P-GA-900, a methanol crossover test was conducted (**Figure 9B**). Obviously, the $Co_3(PO_4)_2$/N,P-GA-900 hybrid demonstrates almost no distinct current density variation when 3 M methanol is injected, while the current density of the Pt/C decreases sharply under the same operation, manifesting the more excellent methanol tolerance of our as-prepared catalyst than Pt/C.

CONCLUSION

In summary, a novel $Co_3(PO_4)_2$/N,P-GA electrocatalyst for ORR was prepared by a facile two-step method, including a hydrothermal reaction and subsequent pyrolysis treatment. The optimized $Co_3(PO_4)_2$/N,P-GA-900 (where 900 represents the pyrolysis temperature) catalyst displays better ORR activity than the N,P-GA-900, Co/N-GA-900 and Co_2P/P-GA-900, which is ascribed to the synergistic effect between $Co_3(PO_4)_2$ and N,P-GA-900. In addition, the as-obtained $Co_3(PO_4)_2$/N,P-GA-900 also exhibits better operational stability and methanol tolerance than the commercial Pt/C. Therefore, this work may offer the basis to prepare Co,N,P-tridoped graphene aerogel with hierarchical porosity, and provide an unprecedented avenue to design more three-dimensional electrocatalysts as a replacement to noble metals for electrochemical energy conversion and storage devices.

AUTHOR CONTRIBUTIONS

L-LX makes substantial contributions to conception and design. X-JL makes contributions to acquisition of data. XW makes contributions to analysis and interpretation of data.

SUPPLEMENTARY MATERIAL

The Supplementary Material for this article can be found online at: https://www.frontiersin.org/articles/10.3389/fmats.2019.00022/full#supplementary-material

REFERENCES

Chen, S., Duan, J., Jaroniec, M., and Qiao, S. Z. (2014). Nitrogen and oxygen dual-doped carbon hydrogel film as a substrate-free electrode for highly efficient oxygen evolution reaction. *Adv. Mater.* 26, 2925–2930. doi: 10.1002/adma.201305608

Chen, Y. Z., Wang, C., Wu, Z. Y., Xiong, Y., Xu, Q., Yu, S. H., et al. (2015). From bimetallic metal-organic framework to porous carbon: high surface area and multicomponent active dopants for excellent electrocatalysis. *Adv. Mater.* 27, 5010–5016. doi: 10.1002/adma.201502315

Cheon, J. Y., Kim, J. H., Kim, J. H., Goddeti, K. C., Park, J. Y., and Joo, S. H. (2014). Intrinsic relationship between enhanced oxygen reduction reaction activity and nanoscale work function of doped carbons. *J. Am. Chem. Soc.* 136, 8875–8878. doi: 10.1021/ja503557x

Dai, L., Xue, Y., Qu, L., Choi, H. J., and Baek, J. B. (2015). Metal-free catalysts for oxygen reduction reaction. *Chem. Rev.* 115, 4823–4892. doi: 10.1021/cr5003563

Debe, M. K. (2012). Electrocatalyst approaches and challenges for automotive fuel cells. *Nature* 486, 43–51. doi: 10.1038/nature11115

Fei, H., Dong, J., Arellano-Jiménez, M. J., Ye, G., Kim, N. D., Errol, L. G., et al. (2015). Atomic cobalt on nitrogen-doped graphene for hydrogen generation. *Nat. Commun.* 6:8668. doi: 10.1038/ncomms9668

Fu, X., Choi, J. Y., Zamani, P., Jiang, G., Hoque, M. A., Hassan, F. M., et al. (2016). Co-N decorated hierarchically porous graphene aerogel for efficient oxygen reduction reaction in acid. *ACS Appl. Mater. Interfaces* 8, 6488–6495. doi: 10.1021/acsami.5b12746

Geim, A. K., and Novoselov, K. S. (2007). The rise of graphene. *Nat. Mater.* 6, 183–191. doi: 10.1038/nmat1849

Gong, K., Du, F., Xia, Z., Durstock, M., and Dai, L. (2009). Nitrogen-doped carbon nanotube arrays with high electrocatalytic activity for oxygen reduction. *Science* 323, 760–764. doi: 10.1126/science.1168049

Gonzalez-Flores, D., Sanchez, I., Zaharieva, I., Klingan, K., Heidkamp, J., Chernev, P., et al. (2015). Heterogeneous water oxidation: surface activity versus amorphization activation in cobalt phosphate catalysts. *Angew. Chem. Int. Ed.* 54, 2472–2476. doi: 10.1002/anie.201409333

Goran, J. M., Phan, E. N. H., Favela, C. A., and Stevenson, K. J. (2015). H2O2 detection at carbon nanotubes and nitrogen-doped carbon nanotubes: oxidation, reduction, or disproportionation? *Anal. Chem.* 87, 5989–5996. doi: 10.1021/acs.analchem.5b00059

Hibino, T., Kobayashi, K., and Heo, P. (2013). Oxygen reduction reaction over nitrogen-doped graphene oxide cathodes in acid and alkaline fuel cells at intermediate temperatures. *Electrochim. Acta* 112, 82–89. doi: 10.1016/j.electacta.2013.08.101

Hou, Y., Huang, T., Wen, Z., Mao, S., Cui, S., and Chen, J. (2014a). Metal-organic framework-derived nitrogen-doped core-shell-structured porous Fe/Fe_3C@C nanoboxes supported on graphene sheets for efficient oxygen reduction reactions. *Adv. Energy Mater.* 4:1400337. doi: 10.1002/aenm.201400337

Hou, Y., Wen, Z., Cui, S., Ci, S., Mao, S., and Chen, J. (2014b). An advanced nitrogen-doped graphene/cobalt-embedded porous carbon polyhedron hybrid for efficient catalysis of oxygen reduction and water splitting. Adv. *Funct. Mater.* 25, 872–882. doi: 10.1002/adfm.201403657

Hu, H., Han, L., Yu, M., Wang, Z., and Lou, X. W. (2016). Metal-organic-framework-engaged formation of Co nanoparticle-embedded carbon@Co9S8 double-shelled nanocages for efficient oxygen reduction. *Energ. Environ. Sci.* 9, 107–111. doi: 10.1039/C5EE02903A

Hu, Y., Liu, H., Ke, Q., and Wang, J. (2014). Effects of nitrogen doping on supercapacitor performance of a mesoporous carbon electrode produced by a hydrothermal soft-templating process. *J. Mater. Chem. A* 2, 11753–11758. doi: 10.1039/C4TA01269K

Jeon, I. Y., Zhang, S., Zhang, L., Choi, H. J., Seo, J. M., Xia, Z., et al. (2013). Edge-selectively sulfurized graphene nanoplatelets as efficient metal-free electrocatalysts for oxygen reduction reaction: the electron spin effect. *Adv. Mater.* 25, 6138–6145. doi: 10.1002/adma.201302753

Jiang, H., Zhu, Y., Feng, Q., Su, Y., Yang, X., and Li, C. (2014). Nitrogen and phosphorus dual-doped hierarchical porous carbon foams as efficient metal-free electrocatalysts for oxygen reduction reactions. *Chem. Eur. J.* 20, 3106–3112. doi: 10.1002/chem.201304561

Jin, J., Pan, F., Jiang, L., Fu, X., Liang, A., Wei, Z., et al. (2014). Catalyst-free synthesis of crumpled boron and nitrogen co-doped graphite layers with tunable bond structure for oxygen reduction reaction. *ACS Nano* 8, 3313–3321. doi: 10.1021/nn404927n

Kanan, M. W., and Nocera, D. G. (2008). *In situ* formation of an oxygen-evolving catalyst in neutral water containing phosphate and Co2+. *Science* 321, 1072–1075. doi: 10.1126/science.1162018

Katsounaros, I., Cherevko, S., Zeradjanin, A. R., and Mayrhofer, K. J. J. (2014). Oxygen electrochemistry as a cornerstone for sustainable energy conversion. *Angew. Chem. Int. Ed.* 53, 102–121. doi: 10.1002/anie.201306588

Kim, C., Lee, B., Park, Y., Park, B., Lee, J., and Kim, H. (2007). Iron-phosphate/platinum/carbon nanocomposites for enhanced electrocatalytic stability. *Appl. Phys. Lett.* 91, 113101. doi: 10.1063/1.2783035

Lai, L., Potts, J. R., Zhan, D., Wang, L., Poh, C. K., Tang, C., et al. (2012). Exploration of the active center structure of nitrogen-doped graphene-based catalysts for oxygen reduction reaction. *Energ. Environ. Sci.* 5, 7936–7942. doi: 10.1039/c2ee21802j

Li, J., Mao, S., Hou, Y., Lei, L., and Yuan, C. (2018). 3D Edge-enriched Fe_3C@C nanocrystals with a core-shell structure grown on reduced graphene oxide networks for efficient oxygen reduction reaction. *ChemSusChem* 11, 3292–3298. doi: 10.1002/cssc.201801084

Liang, Y., Li, Y., Wang, H., and Dai, H. (2013). Strongly coupled lnorganic/nanocarbon hybrid materials for advanced electrocatalysis. *J. Am. Chem. Soc.* 135, 2013–2036. doi: 10.1021/ja3089923

Liu, Y., Wu, Y. Y., Lv, G. J., Pu, T., He, X. Q., and Cui, L. L. (2013). Iron(II) phthalocyanine covalently functionalized graphene as a highly efficient non-precious-metal catalyst for the oxygen reduction reaction in alkaline media. *Electrochim. Acta* 112, 269–278. doi: 10.1016/j.electacta.2013.08.174

Liu, Z. Q., Cheng, H., Li, N., Ma, T. Y., and Su, Y. Z. (2016). ZnCo2O4 quantum dots anchored on nitrogen-doped carbon nanotubes as reversible oxygen reduction/evolution electrocatalysts. *Adv. Mater.* 28, 3777–3784. doi: 10.1002/adma.201506197

Mao, S., Lu, G., and Chen, J. (2015). Three-dimensional graphene-based composites for energy applications. *Nanoscale* 7, 6924–6943. doi: 10.1039/C4NR06609J

Mao, S., Wen, Z., Huang, T., Hou, Y., and Chen, J. (2014). High-performance bi-functional electrocatalysts of 3D crumpled graphene-cobalt oxide nanohybrids for oxygen reduction and evolution reactions. *Energ. Environ. Sci.* 7, 609–616. doi: 10.1039/C3EE42696C

Maria Rosas, J., Ruiz-Rosas, R., Rodriguez-Mirasol, J., and Cordero, T. (2012). Kinetic study of the oxidation resistance of phosphorus-containing activated carbons. *Carbon N. Y.* 50, 1523–1537. doi: 10.1016/j.carbon.2011.11.030

Menezes, P. W., Indra, A., Gonzalez-Flores, D., Sahraie, N. R., Zaharieva, I., Schwarze, M., et al. (2015). High-performance oxygen redox catalysis with multifunctional cobalt oxide nanochains: morphology-dependent activity. *ACS Catal.* 5, 2017–2027. doi: 10.1021/cs501724v

Nasini, U. B., Bairi, V. G., Ramasahayam, S. K., Bourdo, S. E., Viswanathan, T., and Shaikh, A. U. (2014). Phosphorous and nitrogen dual heteroatom doped mesoporous carbon synthesized via microwave method for supercapacitor application. *J. Power Sources* 250:257–265. doi: 10.1016/j.jpowsour.2013.11.014

Ornelas, O., Sieben, J. M., Ruiz-Rosas, R., Morallon, E., Cazorla-Amoros, D., Geng, J., et al. (2014). On the origin of the high capacitance of nitrogen-containing carbon nanotubes in acidic and alkaline electrolytes. *Chem. Comm.* 50, 11343–11346. doi: 10.1039/C4CC04876H

Park, Y., Lee, B., Kim, C., Kim, J., Nam, S., Oh, Y., et al. (2010). Modification of Gold Catalysis with Aluminum Phosphate for Oxygen-Reduction Reaction. *J. Phys. Chem. C* 114, 3688–3692. doi: 10.1021/jp9103323

Razmjooei, F., Singh, K. P., Song, M. Y., and Yu, J. S. (2014). Enhanced electrocatalytic activity due to additional phosphorous doping in nitrogen and sulfur-doped graphene: a comprehensive study. *Carbon N. Y.* 78:257–267. doi: 10.1016/j.carbon.2014.07.002

Ren, X., Zelenay, P., Thomas, S., Davey, J., and Gottesfeld, S. (2000). Recent advances in direct methanol fuel cells at Los Alamos National Laboratory. *J. Power Sources* 86, 111–116. doi: 10.1016/S0378-7753(99)00407-3

Shanmugam, S., and Osaka, T. (2011). Efficient electrocatalytic oxygen reduction over metal free-nitrogen doped carbon nanocapsules. *Chem. Comm.* 47, 4463–4465. doi: 10.1039/c1cc10361j

Shao, Y., Park, S., Xiao, J., Zhang, J. G., Wang, Y., and Liu, J. (2012). Electrocatalysts for nonaqueous lithium-air batteries: status, challenges, and perspective. *ACS Catal.* 2, 844–857. doi: 10.1021/cs300036v

Some, S., Kim, J., Lee, K., Kulkarni, A., Yoon, Y., Lee, S., et al. (2012). Highly air-stable phosphorus-doped n-type graphene field-effect transistors. *Adv. Mater.* 24, 5481–5486. doi: 10.1002/adma.201202255

Steinmiller, E. M. P., and Choi, K. S. (2009). Photochemical deposition of cobalt-based oxygen evolving catalyst on a semiconductor photoanode for solar oxygen production. *Proc. Natl. Acad. Sci. U.S.A.* 106, 20633–20636. doi: 10.1073/pnas.0910203106

Walter, M. G., Warren, E. L., McKone, J. R., Boettcher, S. W., Mi, Q., Santori, E. A., et al. (2010). Solar water splitting cells. *Chem. Rev.* 110, 6446–6473. doi: 10.1021/cr1002326

Wang, H., and Dai, H. (2013). Strongly coupled inorganic-nano-carbon hybrid materials for energy storage. *Chem. Soc. Rev.* 42, 3088–3113. doi: 10.1039/c2cs35307e

Wang, H., Yang, Y., Liang, Y., Cui, L. F., Casalongue, H. S., Li, Y., et al. (2011a). LiMn1-xFexPO4 nanorods grown on graphene sheets for ultrahigh-rate-performance lithium ion batteries. *Angew. Chem. Int. Ed.* 50, 7364–7368. doi: 10.1002/anie.201103163

Wang, H., Yang, Y., Liang, Y., Robinson, J. T., Li, Y., Jackson, A., et al. (2011b). Graphene-wrapped sulfur particles as a rechargeable lithium-sulfur battery cathode material with high capacity and cycling stability. *Nano Lett.* 11, 2644–2647. doi: 10.1021/nl200658a

Wang, X., Cao, X., Bourgeois, L., Guan, H., Chen, S., Zhong, Y., et al. (2012). N-doped graphene-SnO2 sandwich paper for high-performance lithium-ion batteries. *Adv. Funct. Mater.* 22, 2682–2690. doi: 10.1002/adfm.201103110

Wang, X., Weng, Q., Liu, X., Wang, X., Tang, D. M., Tian, W., et al. (2014). Atomistic origins of high rate capability and capacity of N-doped graphene for lithium storage. *Nano Lett.* 14, 1164–1171. doi: 10.1021/nl4038592

Wang, Z., Jia, R., Zheng, J., Zhao, J., Li, L., Song, J., et al. (2011c). Nitrogen-promoted self-assembly of N-Doped carbon nanotubes and their intrinsic catalysis for oxygen reduction in fuel cells. *ACS Nano* 5, 1677–1684. doi: 10.1021/nn1030127

Xia, W., Zou, R., An, L., Xia, D., and Guo, S. (2015). A metal-organic framework route to *in situ* encapsulation of Co@Co3O4@C core@bishell nanoparticles into a highly ordered porous carbon matrix for oxygen reduction. *Energ. Environ. Sci.* 8, 568–576. doi: 10.1039/C4EE02281E

Yang, D. S., Bhattacharjya, D., Inamdar, S., Park, J., and Yu, J. S. (2012). Phosphorus-doped ordered mesoporous carbons with different lengths as efficient metal-free electrocatalysts for oxygen reduction reaction in alkaline media. *J. Am. Chem. Soc.* 134, 16127–16130. doi: 10.1021/ja306376s

Yang, S., Feng, X., Wang, X., and Muellen, K. (2011). Graphene-based carbon nitride nanosheets as efficient metal-free electrocatalysts for oxygen reduction reactions. *Angew. Chem. Int. Ed.* 50, 5339–5343. doi: 10.1002/anie.201100170

Yu, D., Xue, Y., and Dai, L. (2012). vertically aligned carbon nanotube arrays Co-doped with phosphorus and nitrogen as efficient metal-free electrocatalysts for oxygen reduction. *J. Phys. Chem. Lett.* 3, 2863–2870. doi: 10.1021/jz3011833

Yu, G., Hu, L., Vosgueritchian, M., Wang, H., Xie, X., McDonough, J. R., et al. (2011). Solution-processed graphene/MnO2 nanostructured textiles for high-performance electrochemical capacitors. *Nano Lett.* 11, 2905–2911. doi: 10.1021/nl2013828

Yuan, H., Hou, Y., Wen, Z., Guo, X., Chen, J., and He, Z. (2015). Porous carbon nanosheets codoped with nitrogen and sulfur for oxygen reduction reaction in microbial fuel cells. *ACS Appl. Mater. Interfaces* 7, 18672–18678. doi: 10.1021/acsami.5b05144

Zhan, Y., Lu, M., Yang, S., Xu, C., Liu, Z., and Lee, J. Y. (2016). Activity of transition-metal (manganese, iron, cobalt, and nickel) phosphates for oxygen electrocatalysis in alkaline solution. *ChemCatChem* 8, 372–379. doi: 10.1002/cctc.201500952

Zhang, C., Mahmood, N., Yin, H., Liu, F., and Hou, Y. (2013). Synthesis of phosphorus-doped graphene and its multifunctional applications for oxygen reduction reaction and lithium ion batteries. *Adv. Mater.* 25, 4932–4937. doi: 10.1002/adma.201301870

Zhang, J., Xia, Z., and Dai, L. (2015a). Carbon-based electrocatalysts for advanced energy conversion and storage. *Sci. Adv.* 1:e1500564. doi: 10.1126/sciadv.1500564

Zhang, J., Zhao, Z., Xia, Z., and Dai, L. (2015b). A metal-free bifunctional electrocatalyst for oxygen reduction and oxygen evolution reactions. *Nat. Nanotechnol.* 10, 444–452. doi: 10.1038/nnano.2015.48

Zhang, Q., Li, R., Zhang, M., Zhang, B., and Gou, X. (2014). SnS2/reduced graphene oxide nanocomposites with superior lithium storage performance. *Electrochim. Acta* 115, 425–433. doi: 10.1016/j.electacta.2013.10.193

Zheng, Y., Jiao, Y., Zhu, Y., Li, L. H., Han, Y., Chen, Y., et al. (2014). Hydrogen evolution by a metal-free electrocatalyst. *Nat. Commun.* 5:3783. doi: 10.1038/ncomms4783

Zhong, H. X., Wang, J., Zhang, Y. W., Xu, W. L., Xing, W., Xu, D., et al. (2014). ZIF-8 Derived graphene-based nitrogen-doped porous carbon sheets as highly efficient and durable oxygen reduction electrocatalysts. *Angew. Chem. Int. Ed.* 53, 14235–14239. doi: 10.1002/anie.201408990

Zhou, T., Du, Y., Yin, S., Tian, X., Yang, H., Wang, Xf. (2016). Nitrogen-doped cobalt phosphate@nanocarbon hybrids for efficient electrocatalytic oxygen reduction. *Energ. Environ. Sci.* 9, 2563–2570. doi: 10.1039/C6EE01297C

Conflict of Interest Statement: The authors declare that the research was conducted in the absence of any commercial or financial relationships that could be construed as a potential conflict of interest.

frontiers in Materials

ORIGINAL RESEARCH
published: 13 February 2019
doi: 10.3389/fmats.2019.00001

Encapsulating Mo-Doped TiO_2 Anatase in N-Doped Amorphous Carbon With Excellent Lithium Storage Performances

Ying Xia, Chao Rong, Xiaoyan Yang, Fengqi Lu and Xiaojun Kuang*

MOE Key Laboratory of New Processing Technology for Nonferrous Metal and Materials, Guangxi Universities Key Laboratory of Nonferrous Metal Oxide Electronic Functional Materials and Devices, College of Materials Science and Engineering, Guilin University of Technology, Guilin, China

To improve the capability, cycling stability and rate capacity of anatase TiO_2-based electrode, Mo-doped TiO_2 anatase encapsulated in nitrogen-doped amorphous carbon (denoted for Mo-TiO_2@NC) were synthesized using a facile hydrothermal method followed by a coating with polyaniline (PANI) and heating treatment. When tested as an anode for lithium ion batteries, the Mo-TiO_2@NC electrode showed an initial discharge and charge capacity of 850.7 and 548.3 mAh g^{-1} at a current density of 85 mA g^{-1}, respectively, with a remarkable discharge capacity maintained at 449.2 mAh g^{-1} after 100 cycles. Even at a high current density of 850 mA g^{-1}, a reversible capacity of 154 mAh g^{-1} after 200 cycles was obtained, displaying good rate capacity and long-term cycling stability. The outstanding electrochemical performance of Mo-TiO_2@NC can be attributed to the synergistic effect of aliovalent ions doping and carbon coating.

Keywords: anatase, titanium dioxide, anode materials, lithium-ion batteries, aliovalent ions doped, nitrogen doped carbon

OPEN ACCESS

Edited by:
Kai-Xue Wang,
Shanghai Jiao Tong University, China

Reviewed by:
Kai Zhu,
Harbin Engineering University, China
Shengfu Tong,
Sun Yat-sen University, China
Chunhai Jiang,
Xiamen University of Technology, China

****Correspondence:***
Fengqi Lu
lufengqi@glut.edu.cn.

Specialty section:
This article was submitted to Colloidal Materials and Interfaces, a section of the journal Frontiers in Materials

Received: *30 September 2018*
Accepted: *03 January 2019*
Published: *13 February 2019*

Citation:
Xia Y, Rong C, Yang X, Lu F and Kuang X (2019) Encapsulating Mo-Doped TiO_2 Anatase in N-Doped Amorphous Carbon With Excellent Lithium Storage Performances. Front. Mater. 6:1. doi: 10.3389/fmats.2019.00001

INTRODUCTION

The development of high safety lithium-ion batteries (LIBs) with high powder density, a longer cycle life and at lower cost are necessary to meet the needs of future portable electronics and electric or hybrid electric vehicles (Chen et al., 2013; Reddy et al., 2013; Lü et al., 2016). Because of its low cost, non-toxicity, rich earth content, and negligible volume expansion (<4 % for anatase) during charging and discharging, titanium dioxide (TiO_2) has been considered as a potential anode material of LIBs (Jiang and Zhang, 2013; Wu et al., 2014). Accordingly, diverse crystals of TiO_2, such as anatase, rutile, brookite and bronze, have been studied as anode materials for LIBs (Liu et al., 2015; Yu et al., 2015; Guan et al., 2016), Because of its essential crystal, anatase TiO_2 is considered favorable for lithium ion intercalation/deintercalation, environmental friendliness, low cost and stability, and has been widely investigated as a promising anode material for LIBs (Hyder et al., 2013; Mo et al., 2014; Zhang et al., 2014a). Unfortunately, the lithium storage performance of anatase TiO_2 is not good enough for its practical application, which is mainly derived from a relatively low lithium ion diffusion coefficient and poor electronic conductivity (Wu et al., 2012; Myung et al., 2013).

To solve its intrinsic disadvantage, different strategies have been devoted to improve the lithium ion storage performance, such as compounding with conductive agents to enhance electronic conductivity (Gomes et al., 2013; Wang et al., 2016), reducing particle size to nano-scale to shorten the lithium ion diffusion distance (Hu et al., 2015), and manufacturing mesoporous or porous TiO_2 to increase the electrolyte/electrode contact area (Li et al., 2015, 2016). Furthermore, researchers found that the electrical property of TiO_2 is impressible to aliovalent ions doping in the lattice (Zhang et al., 2012; Zhao et al., 2015). Aliovalent ion doping in the structure of TiO_2 can slightly modify the electronic structure, which can improve the electronic conductivity and facilitate lithium ion diffusivity (Sheppard et al., 2008). When used as electrode materials for LIBs, this doping method not only favors the charge transfer but also creates a defect to provide more space for the storage of lithium ion and provides more channels for lithium ion diffusion (Wang et al., 2010b; Jiao et al., 2013). Wei and his coworkers prepared Nb doped brookite TiO_2 Nano sheets displayed reversible capacities of 119.7 mAh g^{-1} at 5 C after 100 cycles (Liu et al., 2015). Ji and his coworkers reported that Ti^{3+} self-doped dark rutile TiO_2 ultrafine nanorods with durable high-rate capability for LIBs (Chen et al., 2015b). Wang's research group presented that niobium doped mesoporous anatase TiO_2 showed good electrochemical performance with a stable capacity of 160 mAh g^{-1} after 100 cycles (Wang et al., 2010b). Recently, Kim and his coworkers reported that Mo-doped $TiNb_2O_7$ anode material showed excellent high C-rates electrochemical performance, which could be attributed to dope hetero-generous Mo atom increasing electronic conductivity and facilitating lithium ion diffusivity (Song and Kim, 2015). However, few papers reported the Mo-doped TiO_2 materials for application in LIBs. For example, Thi et al. and Zhang et al. showed that Mo-doped anatase TiO_2 exhibited significant capacity, excellent cycle performance and remarkable rate capability, compared with pristine anatase TiO_2, owning to the increase of the electrical conductivity, the decrease of the crystal size and lattice distortion by Mo^{6+} doping (Thi et al., 2014; Zhang et al., 2014b). Notwithstanding these advances, the rational design and facile synthesis of Mo-doped anatase TiO_2-based nanostructures for highly reversible lithium storage still remain a significant challenge.

In this present study, to overcome inferior cycling stability and rate capability of anatase TiO_2-based materials, we prepared Mo-doped TiO_2 anatase encapsulated in nitrogen-doped amorphous carbon (Mo-TiO_2@NC) as anode materials for high performance LIBs. This material was synthesized via a facile hydrothermal method followed by a coating with polyaniline (PANI) and calcination treatment. As expected, the Mo-TiO_2 nanoparticles were homogenously embedded in the nitrogen-doped amorphous carbon. As a result, the obtained Mo-TiO_2@NC materials exhibit high reversible capacity and excellent rate capabilities.

EXPERIMENTAL SECTION

Materials

Tetrabutyl titanate (TBT, $Ti(OC_4H_9)_4$, 99%), hydrogen peroxide (H_2O_2,∼30%), molybdenum powder (Mo, 99.95%), ammonia water ($NH_3{\cdot}H_2O$, 25∼28%), ammonium persulfate (APS, $(NH_4)_2S_2O_8$, 98%), hydrochloric acid (HCl, 36∼38%), aniline ($C_6H_5NH_2$, 99.5%), were purchased from a chemical reagents factory and used without further purification.

Synthesis of Mo-Doped TiO_2

Mo-doped TiO_2 (the Mo/(Mo+Ti) ratio equals to 5 mol%) nanoparticles were synthesis using hydrothermal methods. Firstly, 30 mg of molybdenum powder were dissolved into 4 mL hydrogen peroxide and 24 mL of de-ionized (DI) water under continuous stirring until a clear and yellow solution was obtained, followed by adding 2 mL TBT. After 30 min, 0.5 mL of ammonia water was added and stirred for another 30 min. The reaction solution was then transferred to a Teflon-lined stainless steel autoclave (50 mL) and kept in an electric oven at 180°C for 12 h. The autoclave was removed from the oven and cooled to room temperature naturally. The blue precipitate was washed with DI water and collected via centrifugation several times and then dried at 60°C. As a comparison, the undoped TiO_2 sample was also similarly prepared without adding molybdenum powder.

Synthesis of Mo-TiO_2@NC

The Mo-TiO_2@PANI composite materials were prepared by the *in situ* oxidative polymerization of aniline monomers using ammonium persulfate as an oxidizer. In a typical process, 200 mg of Mo-TiO_2 were dispersed in DI water (150 mL) and ultrasonicated for 2 h. The hydrochloric acid was added to adjust pH and the concentration was 0.15 mol L^{-1}. Four hundred microliter of aniline was then added to the solution. The obtained suspension solution was stirred in an ice bath (0∼5°C). After 30 min, APS with the molar ratio of 1:1.5 (APS: aniline) was added to the suspension and stirred for 8 h in the ice bath. Precipitations were washed several times with DI water and ethanol until a medium solution was obtained and then dried at 60°C. The Mo-TiO_2@PANI nanocomposites were then obtained.

To obtain the Mo-TiO_2@NC, Mo-TiO_2@ PANI nanocomposites were annealed in Ar gas at the temperature of 500°C for 3 h with a heating rate of 2°C min^{-1}. For comparison, Mo-TiO_2 and TiO_2 were also annealed under the same conditions.

Characterizations

The phase of the samples were characterized by X-ray diffraction (XRD) with PANalytical X'pert Power (Holland) using Cu Kα radiation ($\lambda = 1.5418$ Å). Rietveld refinements were performed using Topas-Academic software (Coelho, 2005). The morphologies of as-prepared samples were observed by a field-emission scanning electron microscope (FE-SEM, S4800, Hitachi, Japan), Transmission electron microscopies (TEM, JEM-2010HR, 200 kV) and high-resolution transmission electron microscopies (HRTEM). X-ray photoelectron spectroscopy (XPS) was recorded using a Perkin-Elmer ESCALAB 250Xi, and using C 1s (B. E. 284.8 eV) as a reference. Thermogravimetric analysis (TGA) was carried out by STA8000 analyzer (PerkinElmer, USA), heated from 30 to 850°C in air at a rate of 5°C/min. Raman spectra were tested on a DXR Raman

microscope (Thermo Fisher Scientific DXR) with 633 nm Ar ion laser at 8 mW.

Electrochemical Measurements

The electrochemical properties of the samples were performed by using CR2032-type coin cells. The working electrodes consisted of 70 wt% Mo-TiO_2@NC, 20 wt% carbon (Super-P-Li), and 10 wt% polyvinylidene fluoride (PVDF). The slurry was coated onto Cu foil and then dried under a vacuum at 100°C for 12 h. The CR2032-type coin cells were assembled in an argon-filled glove box [Mikrouna (China) Co., Ltd.] with the moisture and oxygen concentrations below 0.1 ppm. The pure lithium foil was used as the counter and reference electrode. The electrolyte was 1 M $LiPF_6$ in a 50:50 v/v mixture of ethylene carbonate/dimethyl carbonate solution. A micro-porous membrane (Celgard 2400) was used as the separator. The galvanostatic charge-discharge performances were tested at different current densities in the voltage range of 0.01–3 V using a battery testing system (Shenzhen Neware, China). Cyclic voltammogram (CV) and electrochemical impedance spectroscopy (EIS) measurements were tested on an electrochemical workstation (CHI760E, Shanghai Chenhua). All of the tests were measured at room temperature.

RESULTS AND DISCUSSION

The synthesis process of Mo-TiO_2@NC is straightforward, as described in **Scheme 1**. Firstly, Mo-TiO_2 nanoparticles were prepared via hydrothermal method in aqueous solution with TBT as a titanium source and metal molybdenum powder as a molybdenum source. The Mo-TiO_2@PANI was then obtained by *in situ* oxidative polymerization; the Mo-TiO_2@PANI samples

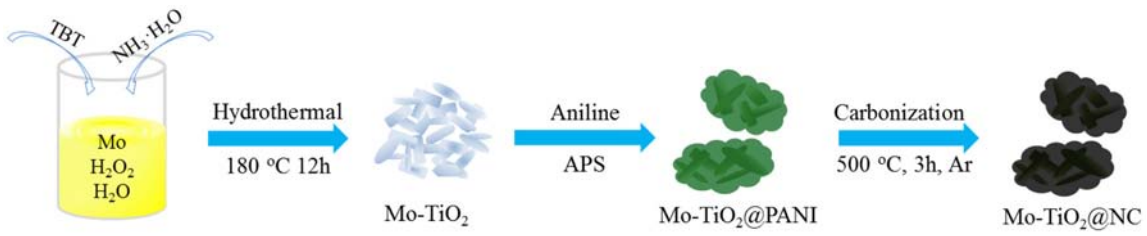

SCHEME 1 | Schematic illustration of the formation of anatase Mo-TiO_2@NC.

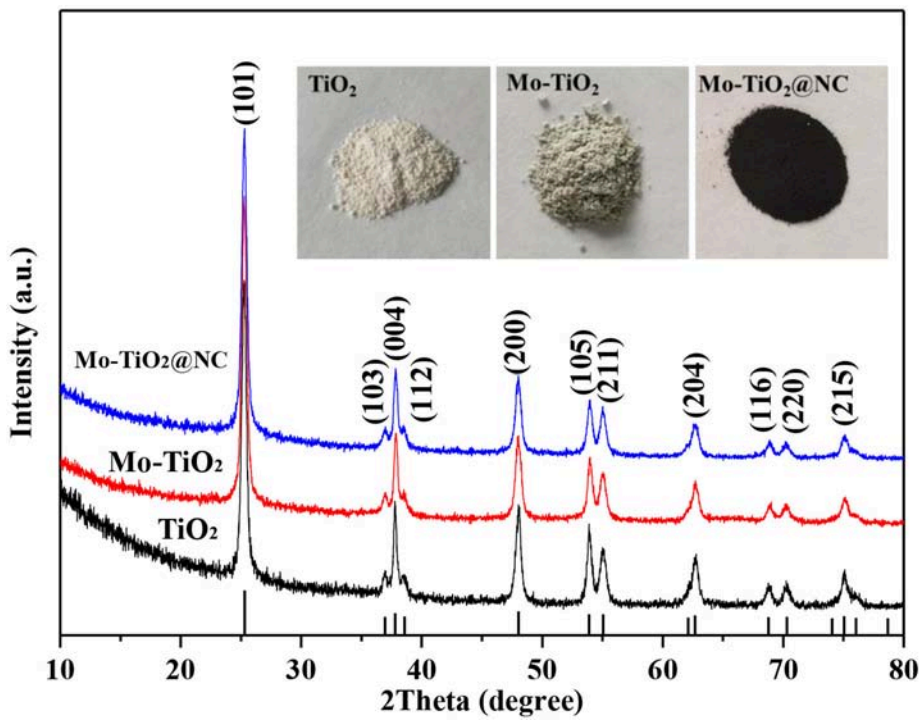

FIGURE 1 | XRD patterns of TiO_2, Mo-TiO_2 and Mo-TiO_2@NC. The lower vertical lines represent the JCPDS card no. 01-84-1285 (anatase). The upper inset maps are the physical photos of TiO_2, Mo-TiO_2, and Mo-TiO_2@NC.

with dark green are different from light blue Mo-TiO_2 samples. To obtain better confirmation of the presence of PANI, Raman spectroscopic investigation was conducted. **Figure S1** shows the Raman spectra of Mo-TiO_2 and Mo-TiO_2@PANI. The Raman spectra show the meaningful structural changes that take place during the oxidative polymerization process from aniline to polyaniline. For Mo-TiO_2@PANI samples, the Raman characteristic peaks at 1,171, 1,349, 1,449, and 1,586 cm^{-1} and can be assigned to the C-H bending vibration of the quinoid ring, C–N and C=N stretching of the bipolaronic structure, and C=C stretching vibration of the benzenoid plan ring, respectively (Wang et al., 2010a). After heating treatment in Ar atmosphere, Mo-TiO_2 nanoparticles encapsulated in nitrogen-doped amorphous carbon were obtained by thermal-induced carbonization of PANI.

The phase of as-obtained samples was measured by X-ray diffraction (XRD). The diffraction peaks showed a XRD pattern of TiO_2, Mo-TiO_2 before annealing treatment, and Mo-TiO_2@PANI could be well-indexed to anatase TiO_2 (PDF#01-084-1285) (**Figure S2**). Diffraction peaks of MoO_3 or other Mo-containing samples were not detected in Mo-doped samples. The light blue Mo-TiO_2 was also different from white TiO_2, indicating that a low molar ratio of Mo was doped into the TiO_2 crystal lattice. For Mo-TiO_2@PANI, there was a broad and weak peak located at about 20°, which indicated the formation of amorphous PANI. After heating treatment, TiO_2 kept its initial white color, while Mo-TiO_2 turned light gray from light blue, and Mo-TiO_2@NC was black color because of existing carbon derived from PANI thermolysis. After heating treatment, the phase composition was also confirmed by XRD. The XRD patterns of TiO_2, Mo-TiO_2 and Mo-TiO_2@NC are shown in **Figure 1**. The diffraction peaks located at 25.26, 36.92, 37.81, 47.96, 53.92, 55.01, 62.83, 68.88, 70.24, 75.04°, corresponding with (101), (103), (004), (200), (105), (211), (204), (116), (220), (215) planes of anatase TiO_2 (PDF#01-084-1285, space group: $I4_1/amd$), respectively. There was no diffraction peak from carbon or graphite, suggesting that amorphous carbon was generated by the thermal decomposition of PANI. Owning to the ionic radius of Mo^{6+} ion (0.062 nm) is very similar to that of the Ti^{4+} ion (0.0605 nm), the Mo^{6+} ion could easily substitute the Ti^{4+} ion in the lattice, which leads to lattice deformation (Štengl and Bakardjieva, 2010). The lattice constants were refined by the Rietveld method with Topas-Academic software. The XRD plots after refinement are in **Figure S3**. The lattice parameters *a*, *c,* and volume (V) are given in **Table 1**. The cell parameter a increased after Mo doping in the lattice as well as an increase in V, while the cell parameter *c* decreased slightly, demonstrating that the Mo elemental has been successfully doped into the lattice of anatase. This is in accordance with the results reported in the literature for Mo doped TiO_2 samples (Štengl and Bakardjieva, 2010; Zhang et al., 2014b). According to the experimental design, the content of Mo is 5 mol%, however, Rietveld refinements of such a low amount of doped element remain challenging. In order to confirm the carbon content of Mo-TiO_2@NC, thermal gravimetric analysis (TGA) were operated in air with a heating rate of 5°C min^{-1} (**Figure S4**). The residual products were anatase phase without other impurity after TGA (**Figure S5**). The weight loss of 2.19% to 800°C of TiO_2 and Mo-TiO_2 can be attributed to the removal of absorbed water molecules. For Mo-TiO_2@NC, the weight loss of 7.75% below 400°C was attributed to the evaporation of absorbed water, and the sharp weight loss from 400 to 800°C showed that the carbon layer in the Mo-TiO_2@NC was oxidized completely. By calculating the TGA results, the carbon content of Mo-TiO_2@NC was estimated to be 37.34 wt%.

TABLE 1 | The lattice parameters and volume of TiO_2, Mo-TiO_2, and Mo-TiO_2@NC.

Sample	*a* (Å)	*c* (Å)	V ($Å^3$)
TiO_2	3.7872 (1)	9.5151 (3)	136.47 (1)
Mo-TiO_2	3.7913 (1)	9.5023 (4)	136.58 (1)
Mo-TiO_2@NC	3.7934 (2)	9.5081 (5)	136.87 (1)

The morphologies of the TiO_2, Mo-TiO_2, and Mo-TiO_2@NC were investigated by field emission scanning electron microscopy (FESEM, **Figures 2a–c**) and transmission electron microscopy (TEM, **Figures 2d–f**). As shown in **Figures 2a,b**, TiO_2 and Mo-TiO_2 have particle morphologies with uniform diameters of 20∼30 nm. Compared with Mo-TiO_2, the external size of Mo-TiO_2@NC composite material increased to 50∼60 nm, and showed irregular shapes, suggesting that carbon layers are coated on the surface of granular Mo-TiO_2. Transmission electron microscopy (TEM) and high-resolution transmission electron microscopy (HRTEM) images in **Figures 2d–i** further study the microstructure of the TiO_2, Mo-TiO_2, and Mo-TiO_2@NC samples. For TiO_2 nanoparticle, the TEM image (**Figure 2d**) shows that the rice-like morphology with a length of 30∼50 nm and a diameter of about 15 nm, and the lattice-resolved HRTEM image in **Figure 2g** shows the interplanar spacing of 3.46 Å belongs to (101) plane of anatase TiO_2. For Mo-TiO_2 nanoparticle, the TEM image in **Figure 2e** also shows that the particle morphologies with uniform diameters of 15 nm and a length of about 30∼40 nm. The two sets d-spacing obtained in **Figure 2h** from HRTEM image is 3.41 Å of Mo-TiO_2, which corresponding to the equivalent crystal planes (101) and (011), respectively. Compared with pristine TiO_2 samples (**Figure 2d**), the morphology of the Mo-TiO_2 samples changes from inhomogeneous rice-like to uniform rectangular shapes, which indicates that substitution of Ti^{4+} by Mo^{6+} in the anatase structure restrains the growth of TiO_2 nanoparticles. The selected-area electron diffraction (SAED) patterns (**Figure 2i**) indicates the Mo-TiO_2 nanoparticles are polycrystalline in nature, all diffraction rings of Mo-TiO_2 (101), (103), (004), (112), (200), and (202) were displayed in the SAED patterns, which can be completely indexed to the anatase TiO_2 phase. The TEM image of Mo-TiO_2@NC, in **Figure 2f**, show that the Mo-TiO_2 particles were conformably coated by carbon shells. Further, the EDS and EDS elemental mapping results of Mo-TiO_2@NC are shown in **Figure S6**. The Mo/(Mo+Ti) ratio equals to 4.86(2) mol% based on the EDS results (**Figure S6a**), which is consistent with the experiment. EDS elemental mappings (**Figure S6b**) are confirmations that the Ti, Mo, C, N, and O elements are uniformly distributed in the Mo-TiO_2@NC. In

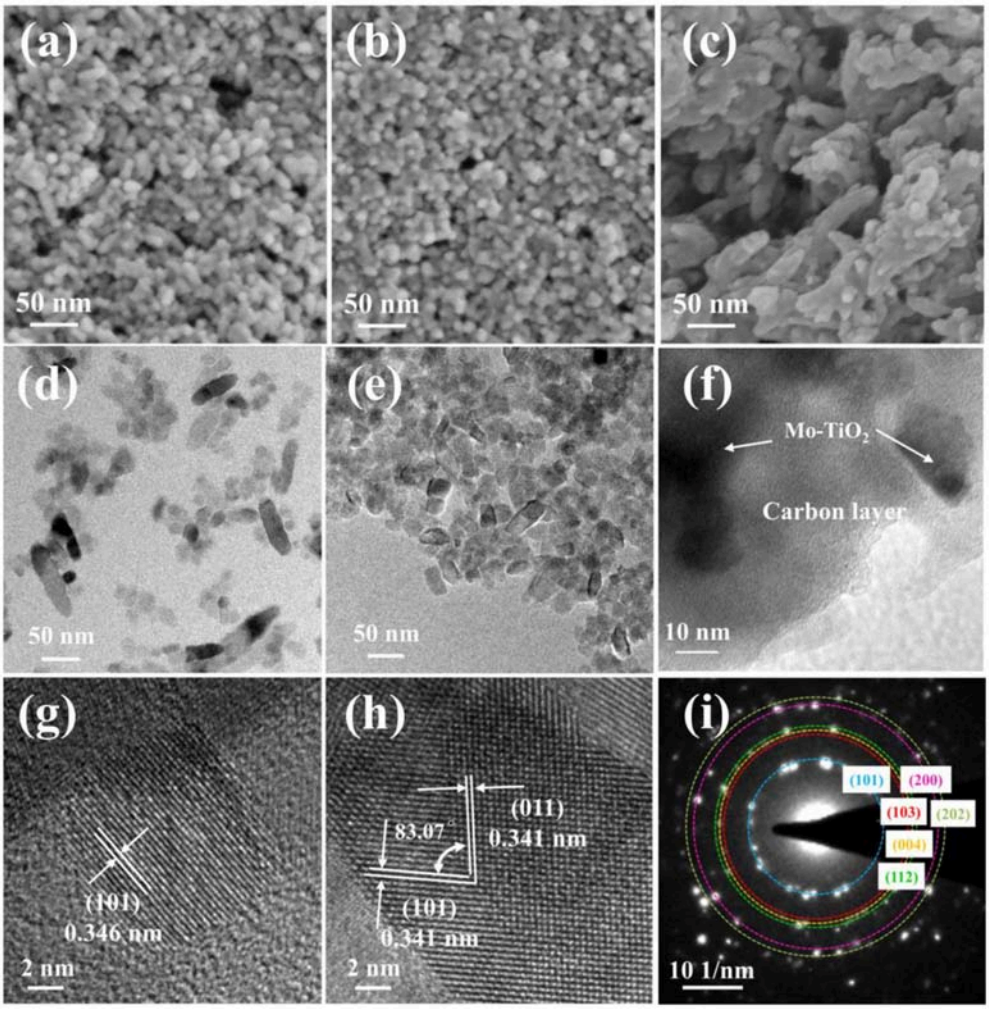

FIGURE 2 | SEM images of TiO_2 **(a)**, Mo-TiO_2 **(b)**, and Mo-TiO_2@NC **(c)**. TEM images of TiO_2 **(d)**, Mo-TiO_2 **(e)**, and Mo-TiO_2@NC **(f)**. HRTEM images of TiO_2 **(g)** and Mo-TiO_2 **(h)**, **(i)** SAED pattern of Mo-TiO_2.

particular, as the energy edge of Au (Mα, 2.123 keV) is close to that of Mo (Lα, 2.293 keV), the EDS elemental mapping of Mo looks a bit bright. Such a shell-core nanostructure can observably improve the electrical conductivity and avoid the reunions of Mo-TiO_2 nanoparticles.

In order to further analyze the chemical environment and valence state of samples, we also performed X-ray photoelectron spectroscopy (XPS) analyses (**Figure 3**). **Figure 3A** shows the XPS survey spectra of TiO_2, Mo-TiO_2, and Mo-TiO_2@NC composites. No trace of Mo peaks can be detected in TiO_2 samples. Compared with pristine TiO_2, typical Mo, Ti, O, C and N signals were all observed in the Mo-TiO_2@NC sample, indicating that the Mo has been successfully innovated into TiO_2 and the N-doped carbon coating. **Figure 3B** shows the high-resolution Ti 2p core-level XPS spectra and the states of the Ti in the samples were determined to be Ti^{4+}. After doping with Mo, the Ti 2p peaks shifted to a lower binding energy, indicating that the atoms were reduced by the charge redistribution (Song and Kim, 2015). A high symmetric peak of Ti 2p means a complete oxidation of Ti (Luo et al., 2014). **Figure 3C** shows the high-resolution Mo 3d core-level XPS spectra, the binding energies of 232.9 eV and 235.99 eV can be ascribed to the feature of Mo^{6+}, while 232.09 eV and 235.1 eV consistent with the existence of Mo^{5+} in the Mo-TiO_2@NC composites (Luo et al., 2012). These results therefore show that the Mo was doped into the lattice of TiO_2 nanoparticle and represented in the state of Mo^{6+} and Mo^{5+} in the Mo-TiO_2@NC samples, thereby when Mo^{6+} and Mo^{5+} replaced the Ti^{4+}, the titanium vacancies formed in the TiO_2 lattice. **Figure 3D** shows the high-resolution O 1s core-level spectrum of TiO_2 and Mo-TiO_2@NC. For pure TiO_2, the O 1s spectrum can be divided into two peaks, the main peak located at about 530.13 eV is attributed to the lattice oxygen in TiO_2, and the small left shoulder peak at about 531.51 eV is contributed to adsorbed oxygen. For Mo-TiO_2@NC, the O 1s XPS spectrum shows three peaks, the first peak located at 530.31 eV corresponds to the formation of Ti-O bond in the

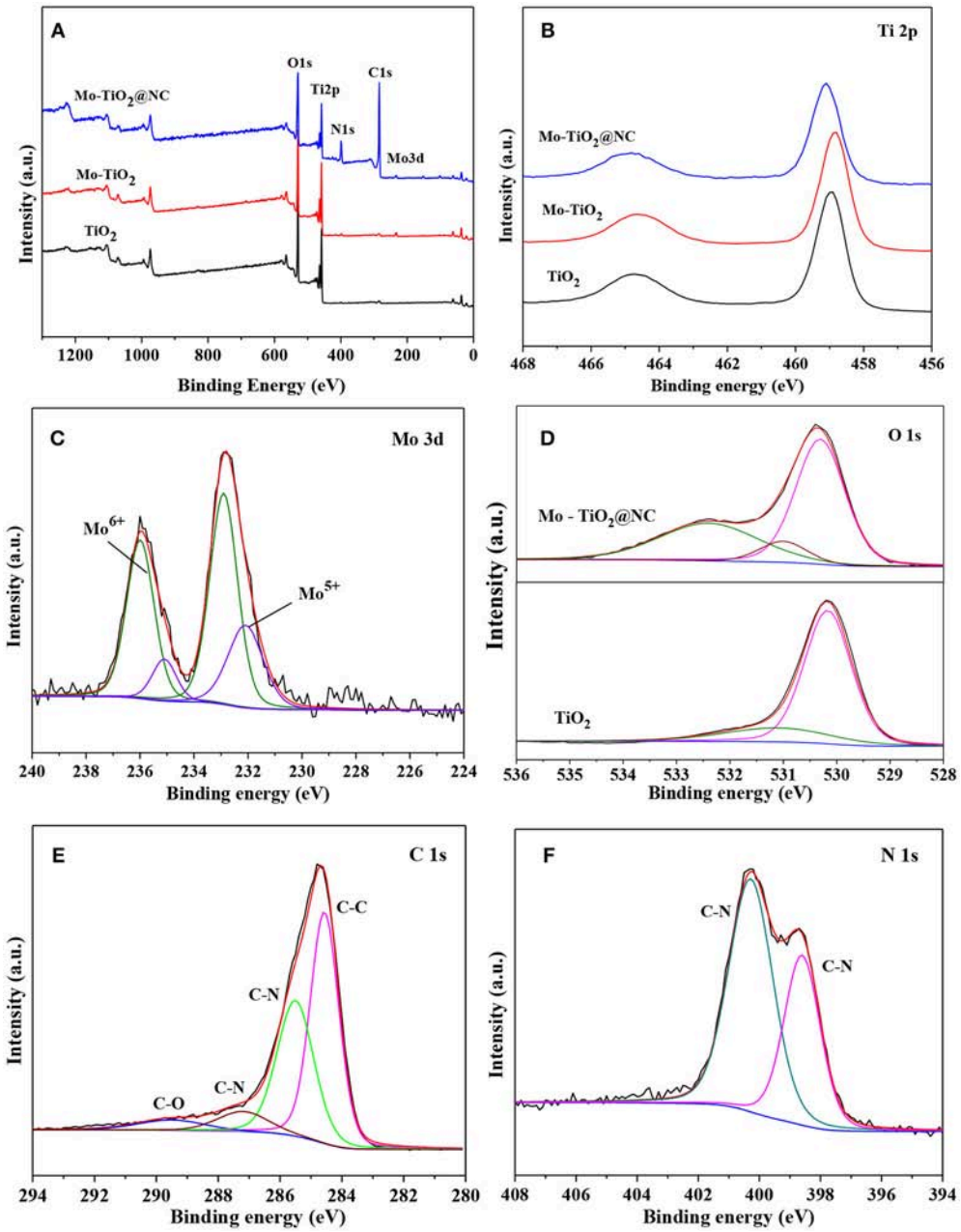

FIGURE 3 | (A) Full XPS spectra of TiO_2 Mo-TiO_2, and Mo-TiO_2@NC, **(B)** Ti 2p XPS spectra of TiO_2 Mo-TiO_2 and Mo-TiO_2@NC, fitted XPS spectra of Mo **(C)**, O **(D)**, C 1s **(E)**, N 1s **(F)** of Mo-TiO_2@NC.

TiO_2 lattice, the second peak at about 531.04 eV consistent with adsorbed oxygen and the last peak at about 532.4 eV only appears in Mo-TiO_2, which is attributed to adsorbed water and hydroxyl groups. The C 1s and N 1s XPS spectra of Mo-TiO_2@NC are shown in **Figures 3E,F**, respectively. The XPS C 1s spectra can decompose to four peaks centered at 284.56, 285.50, 287.2, and 289.5 eV and can be attributed to sp^3 C-C, sp^3 C-N, sp^2 C-N, and C-O bonding, respectively, the results corresponding to the references (Lin et al., 2008). The XPS spectra of N 1s appear at two peaks located at about 398.6 and 400.28 eV and can be attributed to sp^3 C-N and sp^2 C-N bonding, respectively (Lin et al., 2008). The nitrogen doping into the carbon layer could be conducive to improve the electronic conductivity.

ELECTROCHEMICAL PERFORMANCES

The electrochemical properties of the samples after heating treatment were investigated as anode materials for LIBs in the voltage range of 0.01–3.0 V. In previous works of TiO_2-based anode, the voltage window was frequently discharged to 1.0 V.

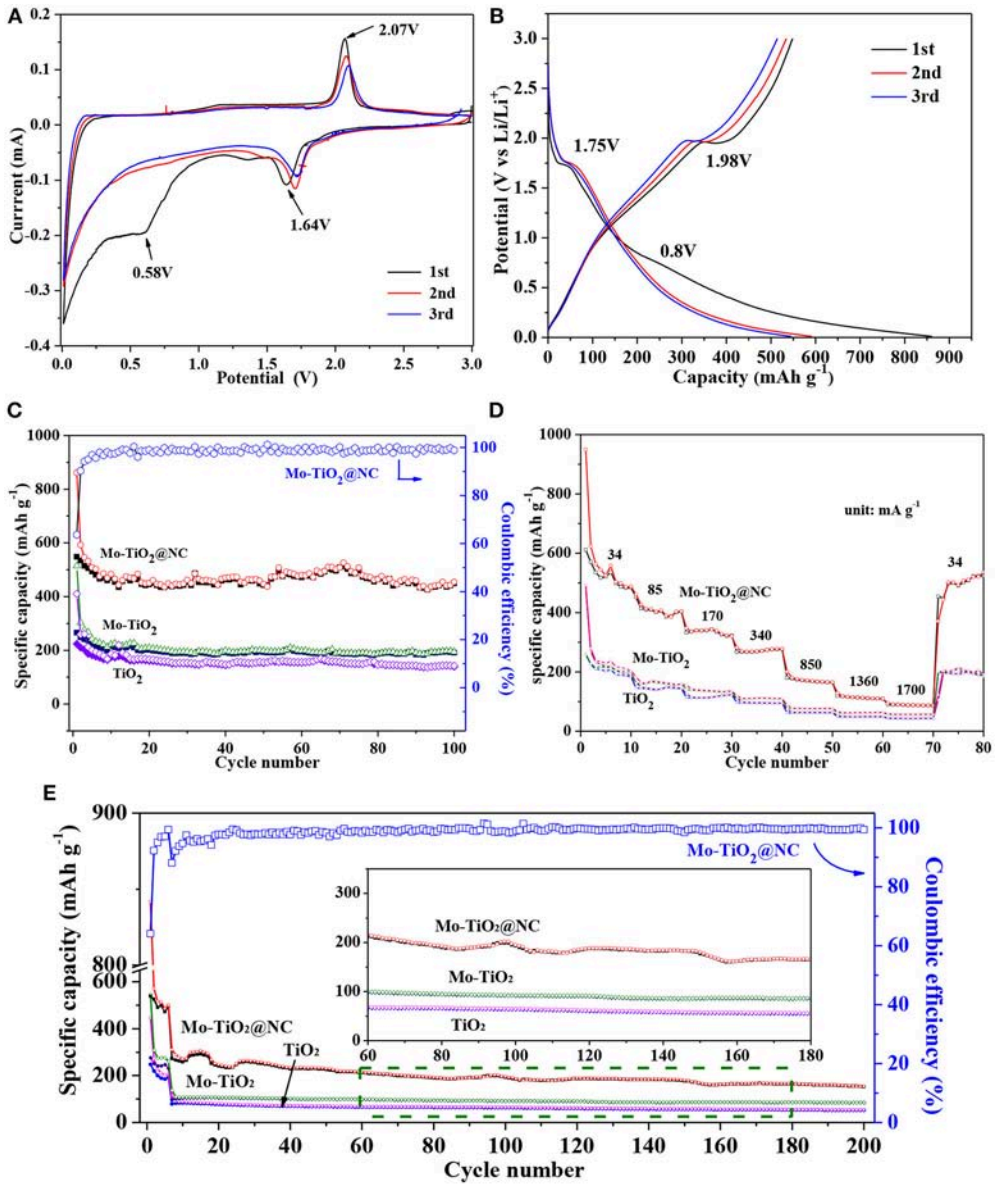

FIGURE 4 | (A) Cyclic voltammograms (CV) curves of the first three cycles of Mo-TiO_2@NC. **(B)** The 1st, 2nd, and 3rd voltages-capacity curves of Mo-TiO_2@NC at a current density of 34 mA g^{-1}. **(C)** Cycle performance of TiO_2, Mo-TiO_2, and Mo-TiO_2@NC at a current density of 34 mA g^{-1}. **(D)** Rate performances of TiO_2, Mo-TiO_2, and Mo-TiO_2@NC electrodes from 34 to 1,700 mA g^{-1}. **(E)** Cycle performance of TiO_2, Mo-TiO_2, and Mo-TiO_2@NC at a current density of 850 mA g^{-1}.

In this work, a voltage window range of 0.01–3.0 V was chosen to consider the contribution of the nitrogen doping carbon layer and the conversion reaction of the Mo^{6+} dopants with Li^+. The electrochemical performances are shown in **Figure 4**. **Figure 4A** show the 1st−3rd cycle CV curves of Mo-TiO_2@NC electrode in the voltage range from 0.01 to 3 V at a scan rate of 0.1 mV s^{-1}. In the first cycle, two reduction peaks can be observed around at 1.64 and 0.58 V. The former reduction peak can be attributed to the lithium insertion in the TiO_2 lattice without phase decomposition (Dong et al., 2016; Xie et al., 2017). The latter peak can be associated with the decomposition of electrolytes and the formation of a solid-electrolyte interphase (SEI) layer in the first cycle (Chen et al., 2011, 2017). From the second cycle, the peak at 0.58 V disappeared, which is consistent with the irreversible capacity loss of the anode (Dong et al., 2016; Chen et al., 2017; Xie et al., 2017). The oxidation peak at 2.07 V can be assigned to the lithium extraction from the TiO_2 lattice (Xu et al., 2007; Zhang et al., 2007; Chen et al., 2015a; Ge et al., 2016). A pair of redox peaks at 1.64 V and 2.1 V for the following two cycles are ascribed to the process of Li^+ insertion and extraction in the TiO_2 lattice [Equation (1)], (Dong et al., 2016; Xie et al., 2017) which is also observed to be highly reversible in

subsequent cycles, certifying that a stable SEI layer is generated on the surface of the coated carbon layer. The electrochemical behavior is consistent with the reported anatase anode electrodes in the literature (Zhao and Shao, 2012; Shen et al., 2013). The CV curves of TiO_2 (**Figure S7a**) and Mo-TiO_2 (**Figure S7b**) are also consistent with the electrochemical behavior of anatase TiO_2. It is interesting that Mo-TiO_2@NC has the smallest voltage difference (0.43 V) between the cathodic and anodic peaks, compared to those of TiO_2 (0.54 V) and Mo-TiO_2 (0.59 V) in the first cycle CV, displaying the lowest polarization of the Mo-TiO_2@NC electrode by hybridizing with Mo-doped and carbon coating.

$$TiO_2 + xLi^+ + xe^- \longleftrightarrow Li_xTiO_2 (0 \le x \le 0.5) \quad (1)$$

Next, the cycle performances of TiO_2, Mo-TiO_2, Mo-TiO_2@NC were investigated. Firstly, the capacity contribution of the carbon layer in the composite was evaluated, the cycle performances of the carbon layer were tested at the current density of 85 and 850 mA g^{-1} as shown in **Figure S8**. The capacity contribution of the carbon layer was ascribed to lithium ion insertion and extraction below 0.5 V. The discharge capacity of the carbon layer was about 195.5 mAh g^{-1} after 30 cycles at 85 mA g^{-1} (**Figure S7a**), indicating that the carbon layer has a rather high contribution to the total capacity at low current density. At high current density of 850 mA g^{-1}, the discharge capacity was about 26.4 mAh g^{-1} after 30 cycles (**Figure S7b**), showing that the contribution of the carbon layer was limited at high current density. Thus, considering the contribution of the carbon layer, the specific capacity was calculated by the total mass for Mo-TiO_2@NC. **Figure 4B** shows the charge-discharge voltage-capacity curves of Mo-TiO_2@NC electrode for the 1st, 2nd, and 3rd cycle at a current density of 85 mA g^{-1}. The two typical discharge plateaus (1.75 and 0.8 V) were apparent at the first cycle, which matches well with the results observed in the CV curves. The initial discharge and charge specific capacities are 860.7 and 548.3 mAh g^{-1}, respectively, with an initial coulombic efficiency of 63.7%. The low coulombic efficiency can be attributed to decomposition of electrolytes and the formation of a SEI layer (Chen et al., 2017; Xie et al., 2017). The 1st, 2nd, and 3rd cycle charge-discharge voltage-capacity curves of TiO_2 and Mo-TiO_2 electrode at a current density of 85 mA g^{-1} are shown in **Figure S7**. As seen in **Figures S7b,c**, the obvious voltage plateaus are in agreement with the CV curves. The cycle performance of TiO_2, Mo-TiO_2, and Mo-TiO_2@NC were performed at a current density of 85 mA g^{-1} (**Figure 4C**). For Mo-TiO_2@NC, a reversible specific capacity up to 449.2 mAh g^{-1} can still be obtained after 100 cycles, which is higher than the specific capacity of Mo-TiO_2 (193.97 mAh g^{-1}) and TiO_2 (142.08 mAh g^{-1}), indicating that the Mo-TiO_2@NC electrode possesses stable electrochemical reversibility. Besides this, from the corresponding coulombic efficiency curve of Mo-TiO_2@NC shown in **Figure 4C**, the columbic efficiency quickly increases to 90.29% at the second cycle and approaches 99% after the third cycle, which reveals the excellent electrochemical reversibility of Mo-TiO_2@NC.

The rate capacities of the TiO_2, Mo-TiO_2, and Mo-TiO_2@NC electrodes were tested by discharging/charging at various current densities from 34 to 1,700 mA g^{-1} (**Figure 4D**). The average discharge capacities of TiO_2 are 242.93, 147.55, 117.76, 97.48, 64.59, 49.86, and 43.41 mAh g^{-1} at rates of 34, 85, 170, 340, 850, 1,360, and 1,700 mA g^{-1}, respectively. The average discharge capacities of Mo-TiO_2 are 255.94, 165.22, 138.85, 112.19, 78.14, 63.34 and 57.3 mAh g^{-1} at rates of 34, 85, 170, 340, 850, 1,360, and 1,700 mA g^{-1}, respectively. By contrast, the Mo-TiO_2@NC electrode showed higher discharge capacities of 574.07, 410.44, 335.74, 273.38, 173.41, 114.47, and 88.68 mAh g^{-1} at different current densities of 34, 85, 170, 340, 850, 1,360, and 1,700 mA g^{-1}, respectively. When the current density came back to 34 mA g^{-1}, the discharge capacity of Mo-TiO_2@NC electrode still remained at 449.2 mAh g^{-1}. Compared with TiO_2 and Mo-TiO_2 electrode, the Mo-TiO_2@NC electrode shows an obvious advantage with a higher discharge capacity and good cycling stability. And the cycle performance of TiO_2, Mo-TiO_2, and Mo-TiO_2@NC were performed at a high current density of 850 mA g^{-1} (**Figure 4E**). After discharging/charging 200 cycles, the reversible specific capacities of TiO_2, Mo-TiO_2, and Mo-TiO_2@NC are 52.89, 85.24, and 154 mAh g^{-1}, respectively. The Mo-TiO_2@NC composites electrode holds the highest reversible

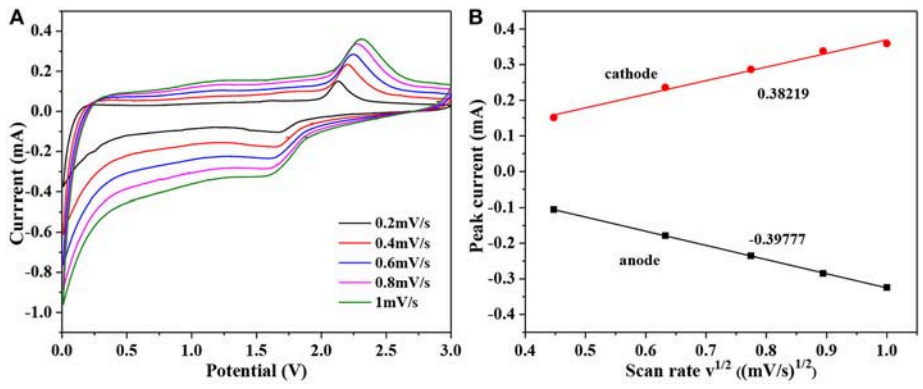

FIGURE 5 | (A) CV curves of Mo-TiO_2@NC at different scan rates: 0.2, 0.4, 0.6, 0.8, and 1 mV s^{-1}. **(B)** The relationship between peak current (i_p) and square root of the scan rate ($v^{1/2}$).

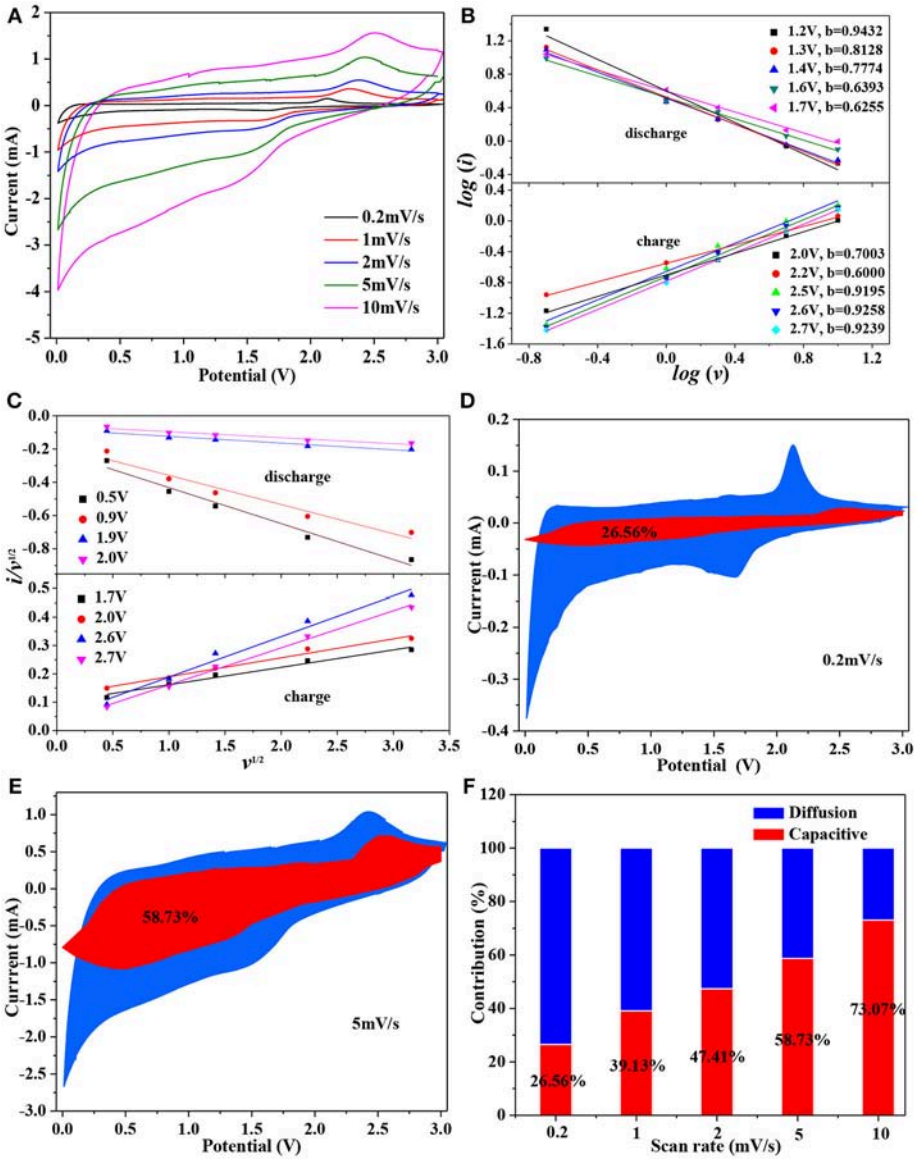

FIGURE 6 | (A) CV curves of Mo-TiO_2@NC at different scan rates; **(B)** the relationship between log i and log *v*; **(C)** the plots of $i(V)/v^{1/2}$ vs. $v^{1/2}$ used for calculating constants k_1 and k_2 at different potentials; capacitive current contribution at different scan rates. **(D)** 0.2 mV/s, **(E)** 5 mV/s; **(F)** the proportion of capacitive current contribution at different scan rates.

capacity. The comparison summarized in **Table S1** shows that the Mo-TiO_2@NC electrode obtains the highest value capacity at low current density, and even at higher current density it was comparable to most other TiO_2-based electrode materials which charge/discharge at low current densities, revealing that the Mo-TiO_2@NC holds potential application in high-energy lithium ion batteries.

The oxidation/reduction or phase transformation process in the electrode reaction can be studied by CV curves, and then the D_{Li}^{+} in the TiO_2 particles can be estimated quantitatively (Rui et al., 2010). **Figure 5A** shows the CV curves at various sweep rates of 0.2, 0.4, 0.6, 0.8, and 1 mV s^{-1}, the area under the curves represents the capacity of electrode. With the increase of scan rates, the intensities and areas of redox peak increase. Furthermore, the value of the oxidation peak and reduction peak have shifted to higher and lower, respectively. It indicates that the irreversible behavior becomes more obvious with the increase of scan rates, especially scan rate at 1 mV s^{-1}. For semi-infinite and finite diffusion, the relationship of the peak current (i_p) and the CV scan rate (v) in the CV curves can be expressed as follow: (Das et al., 2005)

$$i_p = 2.69\times10^5 n^{3/2} A D^{1/2} v^{1/2} \Delta C_o \quad (2)$$

where n is the number of charge-transfer (for Li^+ it is 1), A is the contact area between electrode material and electrolyte solution

(here the area of electrode is 1.13 cm^2), ΔC_o is the change of concentration of Li corresponding to the specific electrochemical reaction [2.34×10^{-2} mol cm^{-3} for $x = 0.5$, calculated from the volume of TiO_2 (142.02 $Å^3$)]. At slow scan rate (<1 mV s^{-1}), an almost linear relationship between peak current (i_p) and squre root of the scan rate ($v^{1/2}$) as displayed in **Figure 5B**. Based on Equation (2) and slope of i_p vs. $v^{1/2}$, the diffusion coefficient can be calculated to be 2.15×10^{-9} cm^2 s^{-1} (anode) and 2.33×10^{-9} cm^2 s^{-1} (cathode). These values are slightly higher than those reported in the literature (Wagemaker et al., 2001; Shen et al., 2013, 2014).

The lithium total storage mechanism mainly includes three parts: the faradaic contribution from the diffusion-controlled Li^+ insertion, the lithium storage mechanism from charge transfers with surface atoms (named as pseudocapacitance effect) and the non-faradaic contribution from double-layer effect (Augustyn et al., 2014; Chao et al., 2016). Furthermore, the capacitive and diffusion effect to the electrode total storage in active materials, described and analyzed by the cyclic voltammetry data at different scan rates, obey the following equation: (Yu et al., 2018)

$$i = av^b \tag{3}$$

Both a and b are the adjustable parameters, the b value can be determined by plotting the slop of *log* (i) vs. *log* (v). There are two boundary conditions of the b-value: $b = 0.5$ and $b = 1.0$. For a b value of 0.5, indicating the current comes mainly from Li^+ intercalation process; while a b value between 0.5 and 1.0, implies that the charge storage is dominated by a mostly contributed by capacitive effect (Yu et al., 2018). **Figure 6A** shows the CV curves for Mo-TiO_2@NC nanocomposites at different scan rates of 0.2, 1, 2, 5, and 10 mV s^{-1} in the voltage range from 0.01 to 3 V, the area under the CV curves represent the total charge storage adding from faradaic and non-faradaic processes. And the b-value can be determined from the slope of the linear plot of *logi* vs. *logv* in **Figure 6B**, which indicates that the lithium storage is controlled by both diffusion and capacity effect processes, and mainly by the pseudocapacitance effect. Thereby, the current response at an any fixed potential can be described as the sum of the pseudocapacitance effect and diffusion-controlled behavior:

$$i(V) = k_1 v + k_2 v^{1/2} \tag{4}$$

To facilitate the analysis, the equation 4 can also be rewritten into the following format:

$$i(V)/v^{1/2} = k_1 v^{1/2} + k_2 \tag{5}$$

where $i(V)$ represent the total current response at any fixed potential V, $k_1 v$, and $k_2 v^{1/2}$ correspond to the current contribution from capacity effects and diffusion controlled intercalation process, respectively., It is key to determine k_1 (slope) and k_2 (intercept) through linear fitting of $i(V)/v^{1/2}$ vs. $v^{1/2}$ (see **Figure 6C**), therefore making it possible to estimate the contribution from Li^+ insertion and capacitive-controlled process at a certain potential. **Figures 6D,E** show the voltage profile from the capacitive current (red region) in the Mo-TiO_2@NC electrode at 0.2 and 5 mV s^{-1}, and the capacitive contribution was 25.56 and 58.73%, respectively. As the scan rate increases, the ratio of capacitive effect ($k_1 v$) contribution further increases (**Figure 6F**). The pseudocapacitive contribution for Mo-TiO_2@NC enlarged to 73.07% at 10 mV s^{-1}, indicating the highest capacitive contribution of the Mo-TiO_2@NC electrode, which could improve its high rate reversible capacity.

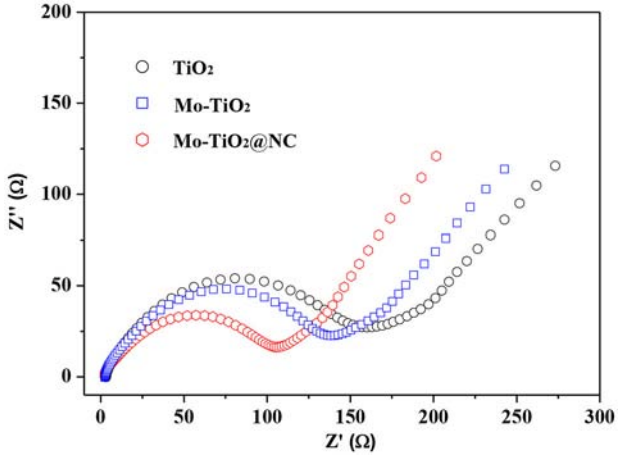

FIGURE 7 | Nyquist plots of TiO_2, Mo-TiO_2, and Mo-TiO_2@NC electrodes before cycling.

To deeply understand the electrode kinetics, electrochemical impedance spectra (EIS) were performed in a frequency range from 10^5 to 0.1 Hz at room temperature. **Figure 7** show the Nyquist plots of TiO_2 Mo-TiO_2 and Mo-TiO_2@NC electrode. All Nyquist plots exhibit a semicircle in the medium-high frequency region and a sloped line in the low frequency region, which indicates that the electrochemical behavior is controlled by both charge transfer and lithium ion diffusion (Manjunatha et al., 2011; Hang et al., 2013). As shown in **Figure 7**, the diameter of the semicircle for Mo-TiO_2 is shorter than that of the pristine TiO_2, indicating a smaller charge-transfer in the former. Owning to the partial substitution of Ti^{4+} with Mo^{6+} ions could create oxygen vacancies, titanium vacancies, or conduction band electrons to compensate for the imbalance in the charge by doping (Kroger and Vink, 1956), thus significantly heightening the electrical conductivity of the electrode, enhancing much easier charge transfer, therefore, reducing the overall internal resistance of the battery. Apparently, after coating with N-doped carbon layer, the Mo-TiO_2@NC has the minimum diameter of the semicircle in the medium-high frequency region. This demonstrates that the Mo-TiO_2@NC electrode has the lowest charge-transfer impedance, which could promote the Li^+ diffusion in the electrode during the lithium ion insertion/extraction process, consequently, improving the electrochemical performances.

Based on the above results, the total capacity of Mo-TiO_2@NC comes from the lithium ion insertion/extraction of Mo-TiO_2 and N-doped carbon layer, as well as the contribution of pseudocapacitance. The excellent electrochemical performance of the obtained Mo-TiO_2@NC as an anode material for LIBs could be attributed to their unique structural features and several possible factors. First, Mo-doping can adjust the electronic

structure of TiO_2 and increase the cell volume, thereby improving the electrical conductivity and accelerating lithium ion diffusion (Thi et al., 2014; Zhang et al., 2014b). Second, Mo-doping in the structure of TiO_2 can generate defects in the structure; these vacancies could act as new sites for lithium ion insertion (Liao et al., 2016). Also, the conversion reaction could occur between Mo with Li, thus increasing the theoretical capacity (Zhang et al., 2014b). Third, the structure of anatase TiO_2 is very stable during charge/discharge process, which could improve the cycle stability (Bauer et al., 2017). Finally, the nitrogen doped carbon layer has relatively high conductivity, which can not only enhance the conductivity and help to form a stable SEI layer during cycling, but also has great contribution to the capacity at low current density (Liu et al., 2017). It is worth noting that the Mo-TiO_2@NC composed of small nanoparticles can short diffusion length in the solid phase for lithium ion and electrons, which further improves the lithium reaction rate (Jiang and Zhang, 2013). These distinct advantages significantly improve the long-term and high-rate performances of the Mo-TiO_2@NC hybrid and make it a very promising anode material for LIBs.

CONCLUSIONS

In summary, Mo-doped anatase TiO_2 coating with nitrogen-doped amorphous carbon layer were obtained using a facile hydrothermal and heat treatment. When used as an anode material, the reversible capacities, cycling performance, and rate capability are significantly improved by Mo doping and carbon coating. The Mo-TiO_2@NC delivers a high reversible capacity of 449.2 at 85 mA g^{-1} after 100 cycles, which is much higher than that of TiO_2 and Mo-TiO_2. Remarkably, a reversible capacity up to 154 mAh g^{-1} is obtained after 200 cycles at 850 mA g^{-1}. The present study show that aliovalent ions doped in the TiO_2 lattice combined with carbon coating is a synergistic effect for enhancing the performance of TiO_2-based electrodes for lithium-ion batteries.

AUTHOR CONTRIBUTIONS

YX and CR conducted the synthesis. YX and XY carried out the characterization and the electrochemical measurements. FL and XK co-wrote the manuscript. All authors discussed the data and commented on the manuscript.

ACKNOWLEDGMENTS

The authors acknowledge financial support from Guangxi Natural Science Foundation (No. 2017GXNSFBA198149). The authors thank Prof. Wenfeng Zhu and Ms. Yuchun Ji for the help on the SEM and EDS experiments, and Ms. Shuyi Mo on the XPS measurement.

SUPPLEMENTARY MATERIAL

The Supplementary Material for this article can be found online at: https://www.frontiersin.org/articles/10.3389/fmats.2019.00001/full#supplementary-material

REFERENCES

Augustyn, V., Simon, P., and Dunn, B. (2014). Pseudocapacitive oxide materials for high-rate electrochemical energy storage. *Energy Environ. Sci.* 7, 1597–1614. doi: 10.1039/c3ee44164d

Bauer, D., Roberts, A. J., Matsumi, N., and Darr, J. A. (2017). Nano-sized Mo- and Nb-doped TiO_2 as anode materials for high energy and high power hybrid Li-ion capacitors. *Nanotechnology*. 28:195403. doi: 10.1088/1361-6528/aa69df

Chao, D., Zhu, C., Yang, P., Xia, X., Liu, J., Wang, J., et al. (2016). Array of nanosheets render ultrafast and high-capacity Na-ion storage by tunable pseudocapacitance. *Nat Commun*. 7:12122. doi: 10.1038/ncomms12122

Chen, J., Archer, L. A., and Lou, X. W. (2011). SnO_2 hollow structures and TiO_2 nanosheets for lithium-ion batteries. *J. Mater. Chem*. 21, 9912–9924. doi: 10.1039/C0JM04163G

Chen, J., Hou, H., Yang, Y., Song, W., Zhang, Y., Yang, X., et al. (2015a). An electrochemically anodic study of anatase TiO_2 tuned through carbon-coating for high-performance lithium-ion battery. *Electrochim. Acta*. 164, 330–336. doi: 10.1016/j.electacta.2015.02.202

Chen, J., Song, W., Hou, H., Zhang, Y., Jing, M., Jia, X., et al. (2015b). Ti^{3+} self-doped dark rutile TiO_2 ultrafine nanorods with durable high-rate capability for lithium-ion batteries. *Adv. Funct. Mater*. 25, 6793–6801. doi: 10.1002/adfm.201502978

Chen, J., Yang, L., Zhang, Z., Fang, S., and Hirano, S. (2013). Mesoporous TiO_2-Sn@C core-shell microspheres for Li-ion batteries. *Chem. Commun.* 49, 2792–2794. doi: 10.1039/c3cc40671g

Chen, Q., Lu, F., Xia, Y., Wang, H., and Kuang, X. (2017). Interlayer expansion of few-layered Mo-doped SnS_2 nanosheets grown on carbon cloth with excellent lithium storage performance for lithium ion batteries. *J. Mater. Chem. A* 5, 4075–4083. doi: 10.1039/c7ta00236j

Coelho, A. A. (2005). *TOPAS Academic V4, Coelho Software*. Brisbane, QLD:Australia.

Das, S. R., Majumder, S. B., and Katiyar, R. S. (2005). Kinetic analysis of the Li^+ ion intercalation behavior of solution derived nano-crystalline lithium manganate thin films. *J. Power Sources*. 139, 261–268. doi: 10.1016/j.jpowsour.2004.06.056

Dong, Y., Yu, M., Wang, Z., Liu, Y., Wang, X., Zhao, Z., et al. (2016). A top-down strategy toward 3D carbon nanosheet frameworks decorated with hollow nanostructures for superior lithium storage. *Adv. Funct. Mater*. 26, 7590–7598. doi: 10.1002/adfm.201603659

Ge, M., Cao, C., Huang, J., Li, S., Chen, Z., Zhang, K.-Q., et al. (2016).A review of one-dimensional TiO_2 nanostructured materials for environmental and energy applications. *J. Mater. Chem. A* 4, 6772–6801. doi: 10.1039/c5ta09323f

Gomes, W. J. A. S., Araújo, D. M., Carvalho, A. J. F., Campana-Filho, S. P., and Huguenin, F. (2013). High lithium ion electroinsertion rate into self-assembled films formed from TiO_2. *J. Phys. Chem. C* 117, 16774–16782. doi: 10.1021/jp404179x

Guan, B., Yu, L., Li, J., and Lou, X. W. (2016). A universal cooperative assembly-directed method for coating of mesoporous TiO_2 nanoshells with enhanced lithium storage properties. *Sci. Adv*. 2:e1501554. doi: 10.1126/sciadv.1501554

Hang, T., Mukoyama, D., Nara, H., Takami, N., Momma, T., and Osaka, T. (2013). Electrochemical impedance spectroscopy analysis for lithium-ion battery using $Li_4Ti_5O_{12}$ anode. *J. Power Sources* 222, 442–447. doi: 10.1016/j.jpowsour.2012.09.010

Hu, H., Yu, L., Gao, X., Lin, Z., and Lou, X. W. (2015). Hierarchical tubular structures constructed from ultrathin TiO2(B) nanosheets for highly reversible lithium storage. *Energy Environ. Sci*. 8, 1480–1483. doi: 10.1039/C5EE00101C

Hyder, M. N., Gallant, B. M., Shah, N. J., Shao-Horn, Y., and Hammond, P. T. (2013). Synthesis of highly stable sub-8 nm TiO_2 nanoparticles and their multilayer Eelectrodes of TiO_2/MWNT for electrochemical applications. *Nano Lett.* 13, 4610–4619. doi: 10.1021/nl401387s

Jiang, C., and Zhang, J. (2013). Nanoengineering titania for high rate lithium storage: a review. *J. Mater. Sci. Technol.* 9, 97–122. doi: 10.1016/j.jmst.2012.11.017

Jiao, W., Li, N., Wang, L., Wen, L., Li, F., Liu, G., et al. (2013). High-rate lithium storage of anatase TiO_2 crystals doped with both nitrogen and sulfur. *Chem. Commun*. 49, 3461–3463. doi: 10.1039/c3cc40568k

Kroger, F. A., and Vink, H. J. (1956). *Solid State Physics.* New York, NY: Academic Press.

Li, W., Liu, J., and Zhao, D. (2016). Mesoporous materials for energy conversion and storage devices. *Nat. Rev. Mater.* 1, 1–17. doi: 10.1038/natrevmats.2016.23

Li, W., Wang, F., Liu, Y., Wang, J., Yang, J., Zhang, L., et al. (2015). General strategy to synthesize uniform mesoporous TiO_2/graphene/mesoporous TiO_2 sandwich-like nanosheets for highly reversible lithium storage. *Nano Lett*. 15, 2186–2193. doi: 10.1021/acs.nanolett.5b00291

Liao, H., Xie, L., Zhang, Y., Qiu, X., Li, S., Huang, Z., et al. (2016). Mo-doped gray anatase TiO_2: lattice expansion for enhanced sodium storage. *Electrochim. Acta* 219, 227–234. doi: 10.1016/j.electacta.2016.10.016

Lin, L., Niu, H., Zhang, M., Song, W., Wang, Z., and Bai, X. (2008). Electron field emission from amorphous carbon with N-doped nanostructures pyrolyzed from polyaniline. *Appl. Surf. Sci.* 254, 7250–7254. doi: 10.1016/j.apsusc.2008.05.347

Liu, Y., Liu, M., Lan, T., Dou, J., and Wei, M. (2015). One-step hydrothermal synthesis of Nb doped brookite TiO_2 nanosheets with enhanced lithium-ion intercalation properties. *J. Mater. Chem. A* 3, 18882–18888. doi: 10.1039/C5TA04870B

Liu, Z., Lu, T., Song, T., Yu, X.-Y., Lou, X. W., and Paik, U. (2017). Structure-designed synthesis of FeS2@C yolk-shell nanoboxes as a high-performance anode for sodium-ion batteries. *Energy Environ. Sci*. 10, 1576–1580. doi: 10.1039/c7ee01100h

Lü, X., Howard, J. W., Chen, A., Zhu, J., Li, S., Wu, G., et al. (2016). Antiperovskite Li_3OCl superionic conductor films for solid-state Li-ion batteries. *Adv. Sci.* 3:1500359. doi: 10.1002/advs.201500359

Luo, S.-Y., Yan, B.-X., and Shen, J. (2012). Enhancement of photoelectric and photocatalytic activities: Mo doped TiO_2 thin films deposited by sputtering. *Thin Solid Films* 522, 361–365. doi: 10.1016/j.tsf.2012.07.121

Luo, S.-Y., Yan, B.-X., and Shen, J. (2014). Direction-regulated electric field implanted in multilayer Mo-TiO_2 films and its contribution to photocatalytic property. *Superlattice Microst*. 75, 927–935. doi: 10.1016/j.spmi.2013.12.009

Manjunatha, H., Mahesh, K. C., Suresh, G. S., and Venkatesha, T. V. (2011). The study of lithium ion de-insertion/insertion in $LiMn_2O_4$ and determination of kinetic parameters in aqueous Li_2SO_4 solution using electrochemical impedance spectroscopy. *Electrochim. Acta* 56, 1439–1446. doi: 10.1016/j.electacta.2010.08.107

Mo, R., Lei, Z., Sun, K., and Rooney, D. (2014). Facile synthesis of anatase TiO_2 quantum-dot/graphene nanosheet composites with enhanced electrochemical performance for lithium-ion batteries. *Adv. Mater.* 26, 2084–2088. doi: 10.1002/adma.201304338

Myung, S. T., Kikuchi, M., Yoon, C. S., Yashiro, H., Kim, S. J., Sun, Y. K., et al. (2013). Black anatase titania enabling ultra-high cycling rates for rechargeable lithium batteries. *Energy Environ. Sci.* 6, 2609–2614. doi: 10.1039/C3EE41960F

Reddy, M. V., Subba Rao, G. V., and Chowdari, B. V. R. (2013). Metal oxides and oxysalts as anode materials for Li-ion batteries. *Chem. Rev*. 113, 5364–5457. doi: 10.1021/cr3001884

Rui, X., Ding, N., Liu, J., Li, C., and Chen, C. (2010), Analysis of the chemical diffusion coefficient of lithium ions in $Li_3V_2(PO_4)_3$ cathode material. *Electrochim. Acta* 55, 2384–2390. doi: 10.1016/j.electacta.2009.11.096

Shen, J., Wang, H., Zhou, Y., Ye, N., Wang, Y., and Wang, L. (2013). Hollow mesoporous frameworks without the annealing process for high-performance lithium–ion batteries: a case for anatase TiO_2. *Chem. Eng. J.* 228, 724–730. doi: 10.1016/j.cej.2013.05.050

Shen, K., Chen, H., Klaver, F., Mulder, F. M., and Wagemaker, M. (2014). Impact of particle size on the non-equilibrium phase transition of lithium-inserted anatase TiO_2. *Chem. Mater*. 26, 1608–1615. doi: 10.1021/cm4037346

Sheppard, L. R., Bak, T., and Nowotny, J. (2008). Electrical properties of niobium-doped titanium dioxide. 3. thermoelectric power. *J. Phys. Chem. C* 112, 611–617. doi: 10.1021/jp0730491

Song, H., and Kim, Y.-T. (2015). A Mo-doped $TiNb_2O_7$ anode for lithium-ion batteries with high rate capability due to charge redistribution. *Chem. Commun.* 51, 9849–9852. doi: 10.1039/c5cc02221e

Štengl, V., and Bakardjieva, S. (2010). Molybdenum-doped anatase and its extraordinary photocatalytic activity in the degradation of orange II in the UV and vis regions, *J. Phys. Chem. C* 114, 19308–19317. doi: 10.1021/jp104271q

Thi, T. V., Rai, A. K., Gim, J., Kim, S., and Kim, J. (2014). Effect of Mo^{6+} doping on electrochemical performance of anatase TiO_2 as a high performance anode material for secondary lithium-ion batteries. *J. Alloy. Comp.* 598, 16–22. doi: 10.1016/j.jallcom.2014.02.019

Wagemaker, M., Van, d,. K. R., Kentgens, A. P., van Well, A. A., and Mulder, F. M. (2001). Two phase morphology limits lithium diffusion in TiO_2 (Anatase): a Li-7 MAS NMR study. *J. Am. Chem. Soc*. 123, 11454–11461. doi: 10.1021/ja0161148

Wang, F., Wang, C., Zhao, Y., Liu, Z., Chang, Z., Fu, L., et al. (2016). A quasi-solid-state Li-ion capacitor based on porous TiO_2 hollow microspheres wrapped with graphene nanosheets. *Small* 12, 6207–6213. doi: 10.1002/smll.201602331

Wang, H., Hao, Q., Yang, X., Lu, L., and Wang, X. (2010a). Nanostructured graphene/polyaniline hybrid material for supercapacitors. *Nanoscale* 2, 2164–2170. doi: 10.1039/c0nr00224k

Wang, Y., Smarsly, B. M., and Djerdj, I. (2010b). Niobium doped TiO_2 with mesoporosity and its application for lithium insertion. *Chem. Mater*. 22, 6624–6631. doi: 10.1021/cm1020977

Wu, H., Chen, J., Hng, H. H., and Lou, X. W. (2012). Nanostructured metal oxide-based materials as advanced anodes for lithium-ion batteries. *Nanoscale* 4, 2526–2542. doi: 10.1039/c2nr11966h

Wu, Q., Xu, J., Yang, X., Lu, F., He, S., Yang, J., et al. (2014). Ultrathin anatase TiO_2 nanosheets embedded with TiO_2-B nanodomains for Lithium-ion storage: capacity enhancement by phase boundaries. *Adv. Energy Mater*. 5:1401756. doi: 10.1002/aenm.201401756

Xie, H., Chen, M., and Wu, L. (2017). Hierarchical TiO_2/SnO_2 hollow spheres coated with graphitized carbon for high-performance electrochemical Li-ion storage. *Small* 13:1604283. doi: 10.1002/smll.201604283

Xu, J., Jia, C., Cao, B., and Zhang, W. F. (2007). Electrochemical properties of anatase TiO_2 nanotubes as an anode material for lithium-ion batteries. *Electrochim. Acta*. 52, 8044–8047. doi: 10.1016/j.electacta.2007.06.077

Yu, Q., Jiang, B., Gao, Y., Li, P., Liu, Z., Suo, G., et al. (2018). Metallic octahedral $CoSe_2$ threaded by N-doped carbon nanotubes: a flexible framework for high-performance potassium-ion batteries. *Adv. Sci.* 5:1800782. doi: 10.1002/advs.201800782

Yu, X., Wu, H., Yu, L., Ma, F., and Lou, X. W. (2015). Rutile TiO_2 submicroboxes with superior lithinm storage properties. *Angew. Chem. Int. Ed*. 54, 4001–4004. doi: 10.1002/anie.201411353

Zhang, G., Wu, H., Song, T., Paik, U., and Lou, X. W. (2014a), TiO_2 hollow spheres composed of highly crystalline nanocrystals exhibit superior lithium storage properties. *Angew. Chem. Int. Ed*. 53, 12590–12593. doi: 10.1002/anie.201406476

Zhang, H., Li, G., An, L., Yan, T., Gao, X., and Zhu, H. (2007). Electrochemical lithium storage of titanate and titania nanotubes and nanorods. *J. Phys. Chem. C* 111, 6143–6148. doi: 10.1021/jp0702595

Zhang, J., Huang, T., Zhang, L., and Yu, A. (2014b). Molybdenum-doped titanium dioxide and its superior lithium storage performance, *J. Phys. Chem. C* 118, 25300–25309. doi: 10.1021/jp506401q

Zhang, R., Elzatahry, A. A., Al-Deyab, S. S., and Zhao, D. (2012). Mesoporous titania: from synthesis to application. *Nano Today* 7, 344–366. doi: 10.1016/j.nantod.2012.06.012

Zhao, B., and Shao, Z. (2012). From paper to paper-like hierarchical anatase TiO_2 film electrode for high-performance lithium-ion batteries. *J. Phys. Chem. C* 116, 17440–17447. doi: 10.1021/jp305744c

Zhao, Z., Tian, J., Sang, Y., Cabot, A., and Liu, H. (2015). Structure, synthesis, and applications of TiO_2 nanobelts. *Adv. Mater.* 27, 2557–2582. doi: 10.1002/adma.201405589

Conflict of Interest Statement: The authors declare that the research was conducted in the absence of any commercial or financial relationships that could be construed as a potential conflict of interest.

frontiers in Materials

ORIGINAL RESEARCH
published: 04 June 2019
doi: 10.3389/fmats.2019.00127

Synergetic of Pt Nanoparticles and H-ZSM-5 Zeolites for Efficient CO_2 Activation: Role of Interfacial Sites in High Activity

András Sápi[1], Upendar Kashaboina[1], Kornélia B. Ábrahámné[1], Juan Fernando Gómez-Pérez[1], Imre Szenti[1], Gyula Halasi[1], János Kiss[2,3], Balázs Nagy[1], Tamás Varga[1], Ákos Kukovecz[1] and Zoltán Kónya[1,3]*

[1] Department of Applied and Environmental Chemistry, Interdisciplinary Excellence Centre, University of Szeged, Szeged, Hungary, [2] Department of Physical Chemistry and Material Science, University of Szeged, Szeged, Hungary, [3] MTA-SZTE Reaction Kinetics and Surface Chemistry Research Group, University of Szeged, Szeged, Hungary

OPEN ACCESS

Edited by:
Alexey A. Sokol, University College London, United Kingdom

Reviewed by:
Andrew Michael Beale, University College London, United Kingdom
Manuel Sánchez-Sánchez, Institute of Catalysis and Petrochemistry (ICP), Spain

***Correspondence:**
András Sápi
sapia@chem.u-szeged.hu

Specialty section:
This article was submitted to Colloidal Materials and Interfaces, a section of the journal Frontiers in Materials

Received: *18 January 2019*
Accepted: *15 May 2019*
Published: *04 June 2019*

Citation:
Sápi A, Kashaboina U, Ábrahámné KB, Gómez-Pérez JF, Szenti I, Halasi G, Kiss J, Nagy B, Varga T, Kukovecz Á and Kónya Z (2019) Synergetic of Pt Nanoparticles and H-ZSM-5 Zeolites for Efficient CO_2 Activation: Role of Interfacial Sites in High Activity. Front. Mater. 6:127. doi: 10.3389/fmats.2019.00127

Catalytic systems prepared by controlled processes play an important role in the utilization of CO_2 via catalytic hydrogenation to produce useful C1 chemicals (such as CO, CH_4, and CH_3OH), which will be vital for forthcoming applications in energy conversion and storage. Size-controlled Pt nanoparticles were prepared by a polyol method and deposited on H-ZSM-5 ($SiO_2/Al_2O_3 = 30$, 80, and 280) zeolite supports. The prepared catalysts were tested for the CO_2 hydrogenation in the temperature range of $T = 473$–873 K and ambient pressure, with $CO_2/H_2 = 1{:}4$. Size-controlled Pt nanoparticles boosted the catalytic activity of the pure H-ZSM-5 zeolites resulted in ∼16 times higher CO_2 consumption rate. The activity were ∼4 times higher and CH_4 selectivity at 873 K was ∼12 times higher over 0.5% Pt/H-ZSM-5 ($SiO_2/Al_2O_3 = 30$) compared to 0.5% Pt/H-ZSM-5 ($SiO_2/Al_2O_3 = 280$). *In-situ* DRIFTS studies assuming the presence of a surface complex in which the CO is perturbed by hydrogen and adsorbes via C-end on Pt but the oxygen tilts to the protons of the zeolite support.

Keywords: CO2 activation, heterogeneous catalysis, zeolites, controlled size Pt, drifts, mechanisms

INTRODUCTION

In recent decades, the industrialization and population growth have resulted in record high atmospheric concentration of greenhouse gases threatening the development of our economy and society (Mikkelsen et al., 2010; International Energy Outlook 2013, 2013). At the same time, the dispute between the increasing energy requirement and declining non-renewable fossil fuel resources could cause a foreseeable crisis to mankind. Carbon dioxide (CO_2) is the second most abundant greenhouse gas after water vapor. The utilization of CO_2 as a C1 building block is an outstanding approach toward decreasing the global CO_2 emissions and additionally initiates a new sustainable direction for producing beneficial feedstock chemicals and fuels (Aresta et al., 2016; Robert, 2016; Wang et al., 2016; Li et al., 2017). CO_2 is a thermodynamically stable molecule where the activation of CO_2 requires significant Gibbs energy input ($\Delta G^{\circ}_{298.15} = -394.4$ kJ·mol^{-1}). In the presence of H_2, the catalytic hydrogenation of CO_2 is a thermodynamically favorable reaction. However, the most important nature of the proposed catalyst for CO_2 conversion is that it should

lower the activation energy barriers in the various reactions of CO_2 with H_2. The key reactions along with their enthalpy and Gibbs energy values are listed below.

Reverse water gas shift reaction (RWGS):

$$CO_2 + H_2 \rightarrow CO + H_2O \quad (1)$$

$$\Delta H_{298\ K} = 41.2\ kJ \times mol^{-1};\ \Delta G_{298\ K} = 28.6\ kJ \times mol^{-1}$$

CO_2 methanation:

$$CO_2 + 4H_2 \rightarrow CH_4 + 2H_2O \quad (2)$$

$$\Delta H_{298\ K} = -252.9\ kJ \times mol^{-1};\ \Delta G_{298\ K} = -113.5\ kJ \times mol^{-1}$$

Methanol formation:

$$CO_2 + 3H_2 \rightarrow CH_3OH + H_2O \quad (3)$$

$$\Delta H_{298\ K} = -49.5\ kJ \times mol^{-1};\ \Delta G_{298\ K} = 3.8\ kJ \times mol^{-1}$$

The catalytic hydrogenation of CO_2 to CO, known as the RWGS reaction (Equation 1), is one of the promising ways to convert CO_2, whereas economize on the utilization of hydrogen compared with other CO_2 hydrogenation reactions (Danjun et al., 2011). In addition to that, the production of CO via RWGS reaction might be the best replacement technique to conventional coal gasification technology, which will become a basis for the future green coal chemistry industry. Particularly, methanation of CO_2 (Equation 2) is also one of the most significant reactions, this reaction can transform the exhausted CO_2 into methane (CH_4), where the formed methane can be recycled for the synthesis of fuel or chemicals (Sakakura et al., 2007; Olah et al., 2009).

Typically, ZSM-5 are used as sorbents and catalyst due to their unique channel structure, thermal stability, acidity, and shape-selective property (Falamaki et al., 1997; Kumar et al., 2002; Cheng et al., 2005; Ismail et al., 2006). Furthermore, the boosting effect of the size-controlled Pt nanoparticles (NPs) on the hydrogenation reaction of CO_2 was extensively studied and was attributed to the active cooperation of the metallic Pt and oxide support (Sápi et al., 2018). In this work, our purpose is to prove that the anchoring of Pt NPs on different ZSM-5 zeolite supports is a favorable heterogeneous hybrid catalyst for the hydrogenation of CO_2 into valuable products.

In their early work, Roman-Martinez and co-workers studied the structure sensitivity of Pt-based catalysts for the hydrogenation of CO_2 (Román-Martínez et al., 1996). Recently, Shyam et al. studied the effect of Pt interaction over different oxide (e.g., SiO_2, TiO_2, etc.) supports (Kattel et al., 2016). It was found that the formation of CO is preferred to that of $HCOO^-$ ion, both kinetically and thermodynamically, indicating that methane can preferably be formed on the Pt-based catalysts. Therefore, when Pt NPs are packed on the zeolite support for hydrogenation of CO_2, the distribution of products is significantly affected due to the long contact time of reactant gases over the catalyst as well as the special pore structure of the zeolites. Particularly, the methanation process of CO_2 ($CO_2 \rightarrow CO \rightarrow CH_4$) involves the formation of CO as an intermediate and CH_4 as the final product. For this reason, constructions of such composites with Pt NPs would be advantageous to find the correlation between CO/CH_4 selectivity and structure sensitivity of the catalyst (Takeguchi et al., 2000; An et al., 2008). Zhan and Zeng also studied a novel sandwich type ZIF-67@Pt@mSiO_2 nanocube catalyst in CO_2 hydrogenation reaction (Zhan and Zeng, 2017). It was reported that CO_2 hydrogenation on Na-modified, Fe-based Fischer-Tropsch catalyst (Wei et al., 2017) and In_2O_3 catalyst (Gao et al., 2017) combined with H-ZSM-5 exhibited excellent selectivity in gasoline, and a CeO_2-Pt@mSiO_2-Co tandem catalyst with two metal-oxide interfaces converted CO_2 to C2–C4 hydrocarbons with 60% selectivity (Xie et al., 2017). Very recently, Zheng et al. developed a highly active catalyst that is a monodispersed spherical Zr-based metal-organic framework catalyst, Pt/Au@Pd@UIO-66, comprising an Au@Pd core-shell encapsulated in a UIO-66 center for the hydrogenation of CO_2 (Zheng et al., 2017).

In this study, 4.5 nm controlled-size Pt nanoparticles were anchored onto the surface of H-ZSM-5 zeolites with different Si/Al ratio and were tested in CO_2 hydrogenation reaction at 723–873 K. Size-controlled Pt nanoparticles boosted the catalytic activity of the pure H-ZSM-5 zeolites resulted in ∼16 times higher CO_2 consumption rate. The activity was ∼4 times higher and CH_4 selectivity at 873 K was ∼12 times higher over 0.5% Pt/H-ZSM-5 ($SiO_2/Al_2O_3 = 30$) compared to 0.5% Pt/H-ZSM-5 ($SiO_2/Al_2O_3 = 280$). *In-situ* DRIFTS studies assuming the presence of a surface complex in which the CO is perturbed by hydrogen and adsorbes via C-end on Pt but the oxygen tilts to the protons of the zeolite support.

EXPERIMENTAL SECTION

Synthesis of the H-ZSM-5 Based Catalysts for CO_2 Hydrogenation Reactions

Synthesis of the H-ZSM-5 Zeolites

All NH_3-ZSM-5 zeolites were purchased from Alfa Aeasar. NH_3-ZSM-5-30 zeolite has a SiO_2:Al_2O_3 molar ratio of 30:1, NH_3-ZSM-5-80 zeolite has a SiO_2:Al_2O_3 molar ratio of 80:1 and NH_3-ZSM-5-280 zeolite has a SiO_2:Al_2O_3 molar ratio of 280:1. All the zeolites were calcined in air at ambient pressure and a temperature of 973 K for 5 h before the investigation and heterogeneous catalytic tests to stabilize the protonated ZSM-5 form. We use the notation H-ZSM-5-30, H-ZSM-5-80, H-ZSM-5-280, respectively, to specify the various calcined zeolites according to their composition.

Synthesis of 4.4 ± 0.6 nm Platinum Nanoparticles

The following method was used for the preparation of 4.4 nm Pt nanoparticles. 41 mg H_2PtCl_4 and 20 mg polyvinylpyrrolidone (PVP, MW = 40.000) were dissolved in 5 ml ethylene-glycol and sonicated for 30 min to get a homogeneous solution. The solution was evacuated and purged with atmospheric pressure argon gas. After three purging cycles, the flask was immersed into an oil bath heated to 473 K under vigorous stirring of the reaction mixture as well as the oil bath. After 120 min of reaction, the flask was cooled down to room temperature. The suspension was precipitated by adding acetone to the mixture. After precipitation, the particles were washed by centrifugation with hexane and re-dispersing in ethanol.

Synthesis of 0.5% Pt-H-ZSM-5 Catalysts

To fabricate the supported catalysts, the proper amount of ethanol suspension of Pt nanoparticles with known Pt concentration (measured with ICP-MS) and the H-ZSM-5 zeolite with different Si/Al ratio after calcination at 973 K were mixed together in ethanol and sonicated in an ultrasonic bath (40 kHz, 80 W) for 3 h. The supported nanoparticles were collected by centrifugation. The products were washed with ethanol three times and subsequently dried at 353 K overnight. H-ZSM-5-30, H-ZSM-5-80, and H-ZSM-5-280 zeolites loaded with Pt nanoparticles are labeled as Pt-H-ZSM-5-30, Pt-H-ZSM-5-80, and Pt-H-ZSM-5-280 according to their SiO_2/Al_2O_3 composition ratio.

Characterization of the ZSM-5 Supports and Pt-H-ZSM-5 Catalysts

The morphology of the support, as well as the dispersion of the Pt nanoparticles over the zeolite supports, was investigated by Transmission Electron Microscopy (TEM, FEI TECNAI G220 X-TWIN operated at 200 kV).

The crystal structure of the NH_3-ZSM-5, as well as the H-ZSM-5, were examined by X-ray Diffraction [XRD, Rigaku MiniFlex II Desktop Diffractometer operated with a Cu Kα source ($\lambda = 0.1542$ nm) at 30 kV and 15 mA].

The surface properties, specific surface area, and pore size distributions were investigated using a Quantachrome NOVA 3000e gas sorption instrument by N_2 adsorption at liquid N_2 temperature. The temperature-programmed desorption (TPD) was carried out in a BELCAT-A apparatus using a reactor (quartz tube with 9 mm outer diameter) that was externally heated. Before the measurements, the catalyst samples were treated in oxygen at 1,073 K for 30 min. Thereafter, the sample was cooled in flowing Ar to room temperature and equilibrated for 15 min. The oxidized sample was flushed with Ar containing 10% H_2, and the reactor was heated linearly at a rate of 20 K·min^{-1} up to 1,373 K. The H_2 consumption was detected by a thermal conductivity detector (TCD). The powders were first out-gassed at 473 K to ensure a clean surface.

Inductively coupled plasma (ICP) mass spectrometry was used for the determination of the metal content in each sample synthesized. The measurements were performed with an "Agilent 7700x" type ICP-MS spectrometer. The sample was previously dissolved in an acidic mixture of HNO_3 and HCl.

In-situ infrared spectroscopy measurements were carried out with an "Agilent Cary-670" FTIR spectrometer equipped with "Harrick Praying Mantis" diffuse reflectance attachment. The sample holder had two BaF_2 windows in the infrared path. The spectrometer was purged with dry nitrogen. The spectrum of the pretreated catalyst was used as a background. At room temperature, a CO_2:H_2 molar ratio of 1:4 was introduced into the DRIFTS cell. The tubes were externally heated to avoid condensation. The catalyst was heated under the reaction feed linearly from room temperature to 773 K, with a heating rate of 20 K·min^{-1} and IR spectra were collected at 50 K intervals. All spectra were recorded between 4,000 and 900 cm^{-1} at a resolution of 2 cm^{-1}. Typically, 32 scans were registered. Due to the short optical path within the DRIFTS cell, the contribution of the reactant gases was negligible, and from the gas phase products, only the most intense features were observable.

TABLE 1 | Parameters based on the N_2 adsorption measurements of the pure H-ZSM-5 zeolites with different SiO_2:Al_2O_3 ratio.

Catalyst	S_{BET} (m^2/g)	V_m (cm^3/g)	V_t (cm^3/g)
H-ZSM-5-30	330.4	0.133	0.24
H-ZSM-5-80	360.3	0.073	0.22
H-ZSM-5-280	350.0	0.063	0.22

S_{BET} is the BET specific surface area.
V_m is the pore volume.
V_t is the total specific pore volume calculated from the volume adsorbed of P/P_0 at 0.98 (the highest measuring point). The N_2 adsorption-desorption method was used to find the specific surface area (S_{BET}) of the materials.

CO_2 Hydrogenation Reaction in the Flow Mode

The hydrogenation of CO_2 was conducted in a fixed-bed down tubular quartz flow reactor at atmospheric pressure. The reactor system was equipped with a programmable temperature controller. A mixture of CO_2/H_2 with a ratio of 1:4 used as the feed. Typically, the catalytic activity tests were carried out using 0.2 g of grinded pelletized catalyst (typically round-shaped pellet with 13 mm diameter and 1–3 mm thickness are pressed under 10 bar, than mortared into 1 um pieces) which was suspended between two quartz wool plugs in the reactor with an inner diameter of 15 mm and the remaining vacant space was filled with quartz beads. Firstly, the catalyst was pretreated with O_2 at 50 mL·min^{-1} at 573 K for 30 min, followed by *in-situ* reduction at the above temperature using H_2 flow for 30 min. Then the reactor was cooled down to 473 K and the reaction was tested in the temperature range of 473–873 K under a mixture of CO_2/H_2 with a ratio of 1:4 and a flow rate of 50 ml/min. The catalyst was heated with 20 K/min upto 873 K than for time-on-stream reaction the temperature was held for another 6 h. Outlet gases were fed into a gas chromatograph (GC 4890D, Agilent) equipped with PORAPAK QS+ S column and the products were analyzed by TCD and FID (Supelco EQUITY−1). Argon was utilized as a carrier gas for the gas chromatograph and hydrogen and synthetic air were used for FID. CO_2 conversion (X_{CO_2}) and product selectivity (S_{prod}) toward to CO and CH_4 and C_2H_4 are defined as follows:

$$X_{CO_2} = \frac{nX_{CO_2}, in - nX_{CO_2},\ out}{nX_{CO_2}, in} \tag{4}$$

$$S_{prod} = \frac{n_{prod,\ out} \times N_C}{nX_{CO_2}, in - nX_{CO_2},\ out} \tag{5}$$

RESULTS AND DISCUSSION

Structural and Textual Properties

In our characterization experiments, the Brunauer-Emmett-Teller (BET) gas adsorption method was used for the determination of surface area of the catalysts. Results for the BET surface area (S_{BET}), and total pore volume (V_t) are

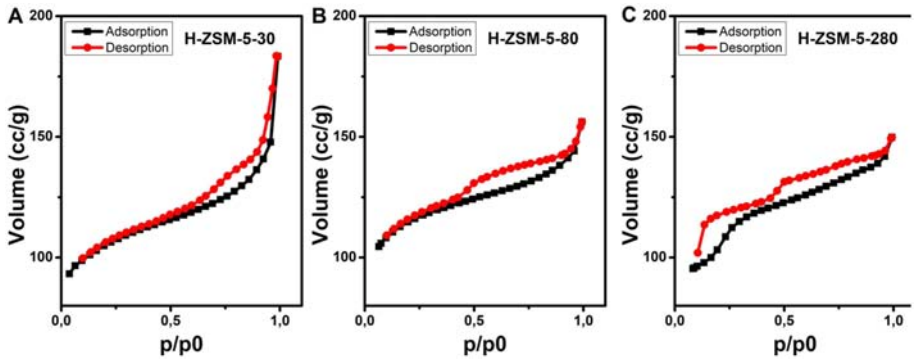

FIGURE 1 | N_2 adsorption-desorption isotherm plot of the pure H-ZSM-5 zeolites. **(A)** H-ZSM-5-30; **(B)** H-ZSM-5-80, **(C)** H-ZSM-5-280.

summarized in **Table 1**. The BET surface area of H-ZSM-5 zeolites, is insensitive to the Si:Al ratio (330.4–360.3 $m^2 \cdot g^{-1}$). However, the pore volume was ∼2 times higher in the case of H-ZSM-5-30 zeolite compared to the other counterparts with higher Si/Al ratio.

Nitrogen adsorption-desorption isotherms of H-ZSM-5 zeolites are presented in **Figure 1**. The hysteresis loop confirms the type-IV behavior (type H2 according to IUPAC classification) (Sing, 1985), which is related to capillary condensation taking place in the mesopores and also 3D interconnectivity of the pores. In the case of H-ZSM-5-30, the largest hysteresis loop was observed at high pressure which is attributed to the large internal void.

Typically, the catalytic hydrogenation of CO_2 depends upon the surface distribution of the acidic-basic sites of the materials. The Brønsted acidic sites can be essential for the activity in the field of catalysis (Zhao et al., 1993) and most of these sites exist within the pore structure of the catalyst.

In the case of the H-ZSM-5 zeolites, the total and Brønsted acidity of the catalysts were measured by TPD of ammonia and the resulted graphs are shown in **Figure 2A**. **Table 2** represents the obtained values of the week and strong acidic sites (from **Figure 2A**) and basic sites (from **Figure 2B**). Two distinct NH_3 or NH^{4+} desorption peaks are observed in all H-ZSM-5 supports. The peaks at 454-481 K and 653-670 K corresponding to weak (physisorbed NH_3) and strongly-bonded Brønsted acid sites, respectively. In the case of the zeolites with lower Si/Al ratio, a higher amount of acidic sites were obtained. Costa et. al. already reported on the acidity of ZSM-5 zeolites, that the acidity depends on the Si/Al ratio and the number of the total acidic sites decreased with the increasing Si/Al ratio (Costa et al., 2000). The ammonium desorption peak temperature increases as the Si/Al ratio decreases. In the case of the weak acidic sites, the ammonia desorption takes place at 454, 476, and 481 K for H-ZSM-5-280, H-ZSM-5-80, and H-ZSM-5-30, respectively. A similar trend was observed in the case of the strong acidic sites (H-ZSM-5-280: 653 K, H-ZSM-5-80: 678 K, H-ZSM-5-30: 670 K), however, the strength of the acidic sites for H-ZSM-5-80 and H-ZSM-5-30 are close to each other.

Thus, increasing the Si/Al ratio the peak corresponding to the weak acidic sites was shifted to lower temperatures, indicating

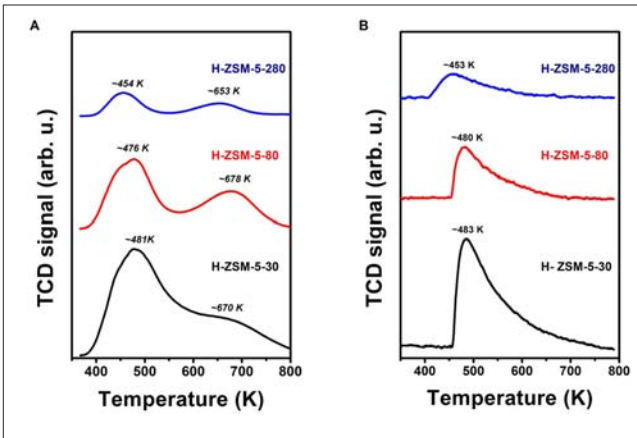

FIGURE 2 | Temperature programmed desorption (TPD) of the H-ZSM-5 catalysts; **(A)** TPD of ammonia, **(B)** TPD of CO_2.

the decreasing strength of such acidic sites. The highest total amount of acid sites was obtained over the H-ZSM-5-30 zeolite (0.75 mmol $NH_3 \cdot g^{-1}$) (Kim et al., 2011) due to the lowest Si/Al ratio and the lowest total number of acidic sites was observed for H-ZSM-5-280 (0.12 mmol $NH_3 \cdot g^{-1}$) due to the high Si/Al ratio. On the other hand, the ratio of the strong/weak acidic sites is the lowest in the case of the H-ZSM-5-30 zeolite. In summary, in the case of the H-ZSM-5-30 support, NH_3-TPD study showed that the acidic site concentration of the zeolite surface, as well as the strength of the sites was the highest, while the distribution of the weak and strong sites showed the lowest ratio of strong/weak sites.

Figure 2B represents the TPD-CO_2 profiles for the various H-ZSM-5 supports. The CO_2 adsorption capacity was the highest for H-ZSM-5-30 and the lowest for H-ZSM-5-280 with the value of 0.167 mmol $CO_2 \cdot g^{-1}$ and 0.041 mmol $CO_2 \cdot g^{-1}$, respectively. Also, the CO_2 desorption temperature is the highest for H-ZSM-5-30. From these results, we can conclude that H-ZSM-5-30 has the strongest basic sites as well as the highest surface concentration of them compared to other H-ZSM-5 zeolites.

N_2, NH_3, and CO_2 adsorption/desorption studies are bringing the following conclusions useful for our system as well as catalytic behavior. The Pt NP dispersion on the surface of the H-ZSM-5

TABLE 2 | Acidity and basicity of NH_3-ZSM-5 catalysts.

Catalyst	Acidity (mmol $NH_3 \cdot g^{-1}$)						Basicity (mmol $CO_2 \cdot g^{-1}$)
	Weak	T (K)	Strong	T (K)	Total	Strong/weak	
H-ZSM-5-30	0.53	481	0.22	670	0.75	0.42	0.167
H-ZSM-5-80	0.26	476	0.20	678	0.46	0.77	0.073
H-ZSM-5-280	0.065	454	0.056	653	0.121	0.86	0.041

supports may depend on the acidic strength of the support: the more acidic is the surface, the less sintering during the reaction maybe expected. However, earlier studies showed that Pt nanoparticles with >5 nm sizes are not showing any sintering under similar reaction conditions (Sápi et al., 2018). It is worth mentioning that the lack of the Brønsted acidic sites over the zeolite supports, the Pt NPs are not stable and consequently might be leading to the formation of their agglomeration over the support. Therefore, high acidic and also more basic zeolites (here: NH_3-ZSM-5-30) may offer higher stability for Pt species as well as different interfacial metal–support interactions (O'Malley et al., 2015). The above trend should be described through the following way; the Pt atom coordinated with a Brønsted proton and with a nearby bridging framework oxygen in the ZSM-5 support. These metal-support interacted sites are good for adsorption of CO_2 and may also offer CO_2 activation leads to higher catalytic activity as well as selectivity toward the desired products.

X-ray diffraction (XRD) patterns of the pure supports are displayed in **Figure 3**. Almost all NH_3-ZSM-5 samples are exhibited the similar diffraction patterns at 2θ angles of 7.9°, 8.8°, 23.1°, and 23.7°, which represent the (011), (020), (051), and (033) planes, respectively (Bin et al., 2014), characteristic for ZSM-5 type zeolites. The insignificant differences between NH_3-ZSM-5-30 and H-ZSM-5-30 samples show that the heat treatment of the samples at 973 K has no effect on the structure of zeolites. On the other hand, we can conclude that the structure of ZSM-5 remains intact at all Si/Al ratio.

Figure 4 shows the TEM images of the Pt-NH_3-ZSM-5 catalysts presented in this study. It is important to say that the polyol based method of Pt nanoparticle synthesis resulted incontrolled-size nanoparticles with a narrow size distribution centered at 4.4 ± 0.6 nm, where the particles have a spherical shape.

The Pt nanoparticles were uniformly dispersed on the H-ZSM-5 zeolites in all three Si/Al ratio cases. The microporous nature and the surface acidity of the ZSM-5 support helps the adsorption of Pt nanoparticles, which in turn improves the interaction between the Pt nanoparticles and the H-ZSM-5 zeolites which also resulted in the development of isolated and well-dispersed Pt nanoparticles on the surface.

Catalytic Hydrogenation of CO_2

H-ZSM-5 catalysts with different Si/Al ratios (30, 80, and 280) as well as their counterparts loaded with 0.5% of 4.4 nm Pt nanoparticles were tested in CO_2 hydrogenation reaction in a flow reactor in the temperature range of 473–873 K at ambient pressure. Before the catalytic tests, the catalysts were pretreated in O_2 at 573 K followed by H_2 reduction at the same temperature.

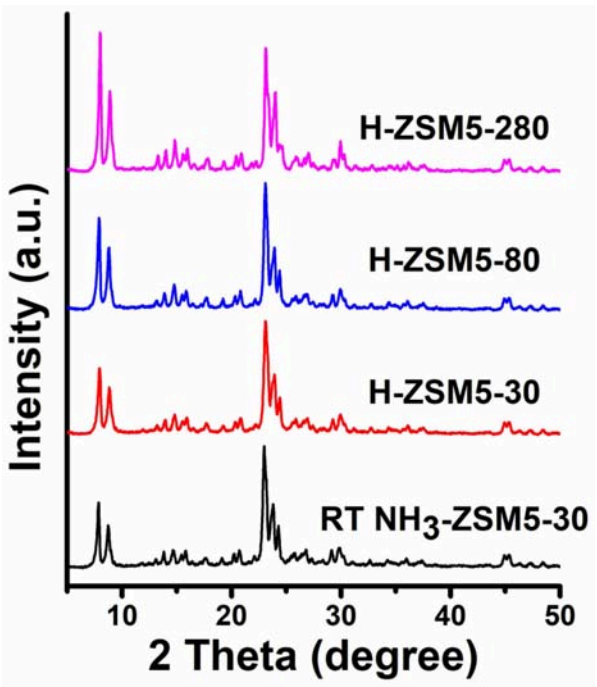

FIGURE 3 | XRD patterns of the NH_3-ZSM-5 catalysts.

Initially, Pt-free H-ZSM-5 supports were tested where we found that the catalysts have slight activity at 723–873 K where the main products were CO, CH_4 as well as C_2H_4 (**Figure 5**). Zeolite with the highest aluminum content (H-ZSM-5-30) showed the highest catalytic activity compared to H-ZSM-5-80 and H-ZSM-5-280 at 723 K. In the case of the H-ZSM-5-80, the lowest catalytic activity was observed. In the case of H-ZSM-5-280, the highest catalytic activity (120 nmol·g^{-1}·s^{-1}) was observed at 873 K, which was ∼2 times higher compared to the activity of H-ZSM-5-30 and that of H-ZSM-5-80. The catalytic activity was 5 times higher in the case of H-ZSM-5-280 at 873 K compared to the activity at 723 K. While catalytic activity was increased in the case of the H-ZSM-5-30 at higher temperature, the increment was not as significant. These unusual phenomena maybe attributed to the investigation at the low conversion regime, as well as the special influence of the different

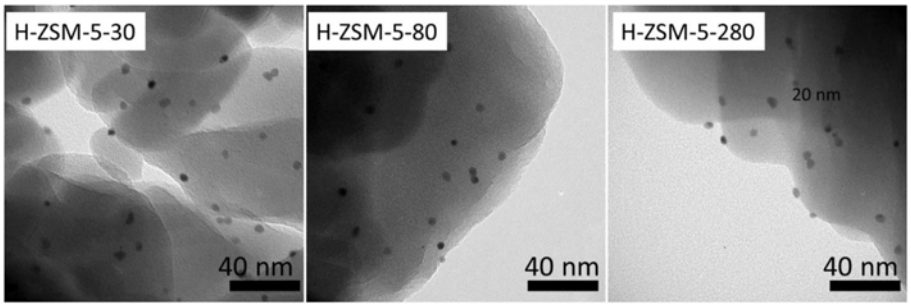

FIGURE 4 | TEM images of H-ZSM-5 zeolite supported 4.4 nm Pt nanoparticles.

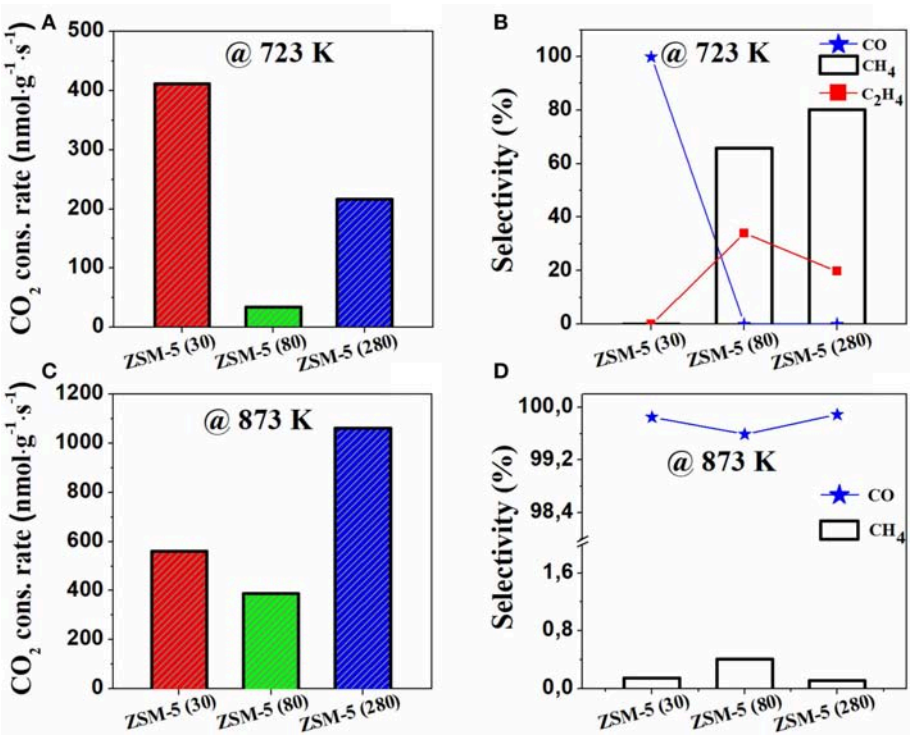

FIGURE 5 | CO_2 consumption rate and distribution of products at 723 and 873 K over Pt-free, H-ZSM-5 zeolites. **(A)** CO_2 consumption rate at 723 K, **(B)** Selectivity at 723 K **(C)** CO_2 consumption rate at 873 K, **(D)** Selectivity at 873 K.

ratio of the weak and strong acidic sites as well as the basic sites developed by NH_3-TPD and CO_2-TPD under these low activity range.

In the case of the Pt-free zeolites, CO, CH_4, and C_2H_4 were formed at 723 K, while only CO and CH_4 was observed at 873 K. H-ZSM-5-280 showed the highest selectivity toward CH_4 (80%) at 723 K compared to H-ZSM-5-30 (2%) and H-ZSM-5-80 (62%). H-ZSM-5-30 produced 100% while there was no CO in the case of H-ZSM-5-80 and H-ZSM-5-280. A significant amount of C_2H_4 was formed in the case of H-ZSM-5-80 (36%) and H-ZSM-5-280 (22%).

At 873 K, CO was the main product in case of the testing of all Pt-free zeolites. While the formation of CH_4 is insignificant, it was observed that H-ZSM-5-80 showed the highest CH_4 selectivity (0.7%) compared to H-ZSM-5-30 (0.25%) and H-ZSM-5-280 (0.2%). It is interesting to note, that H-ZSM-5-80 showed the lowest activity compared to the zeolites with lower or higher Al/Si ratio. As TPD results showed, the concentration and strength of the different acidic and basic sites are crucial for the catalytic activity we believe that in this case, a special synergetic of the ratio, concentration and strength of the active sites needed for high activity.

4.4 nm Pt nanoparticles anchored to the surface of the different H-ZSM-5 catalysts were also tested in CO_2 hydrogenation reactions (**Figure 6**). H-ZSM-5-30 were able to consume CO_2 with a rate of 410 and 580 mmol·g^{-1}·s^{-1} at temperatures of 723 and 873 K, respectively. The consumption rate of CO_2 was enormously increased after the addition of Pt nanoparticles (i.e., Pt-H-ZSM-5-30 performed with a CO_2 consumption rate of 1,630 and 8,130 mmol·g^{-1}·s^{-1} at 723 K

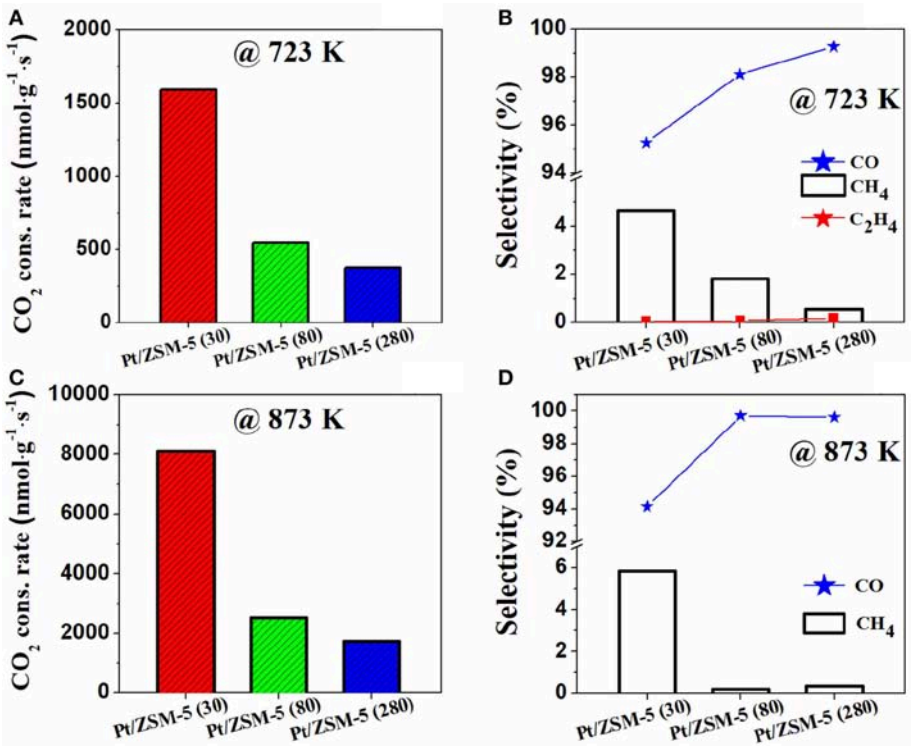

FIGURE 6 | CO_2 consumption rate and distribution of products at 723 and 873 K over 0.5% Pt supported on H-ZSM-5 catalysts. **(A)** CO_2 consumption rate at 723 K, **(B)** Selectivity at 723 K **(C)** CO_2 consumption rate at 873 K, **(D)** Selectivity at 873 K.

and 873 K, respectively). Pt supported on zeolites with lower Si/Al ratio showed higher activity. In the case of Pt-H-ZSM-5-30, the catalytic activity (1,630 mmol·g^{-1}·s^{-1}) was 3 times as well as 4 times higher compared to the activity of Pt-H-ZSM-5-80 (530 mmol·g^{-1}·s^{-1}) and Pt-H-ZSM-5-280 (460 mmol·g^{-1}·s^{-1}), respectively at 723 K. The same trend was observed in the case of activity at 873 K.

For the Pt-H-ZSM-5 catalysts CO and CH_4 was the main product, where a small amount of C_2H_4 was formed only at 723 K. All the Pt-loaded catalysts were more selective to CO than CH_4 at 723 K as well as 873 K. The CH_4 selectivity is low, however, the Pt-H-ZSM-5-30 catalysts show 3-10 times higher methane selectivity compared to the catalysts based on zeolites with higher Si:Al ratio. At 873 K, in the case of the Pt-H-ZSM-5-30 catalyst, the methane selectivity is 20 times higher compared to the Pt-free, H-ZSM-5-30 zeolites.

After we tested the samples upto 873 K, the catalysts were monitored at the same temperature for another 6 h. During the time-on-stream measurements no significant deactivation was observed.

Anchoring of Pt NPs over the H-ZSM-5 zeolites directed to the synthesis of a more active catalyst, where the pores of the zeolite support are appropriate to adsorb the reactant molecules (CO_2 and H_2). Presumably, the Pt NPs are located on the surface as well as in the channels of the zeolites support and the upcoming CO_2 can be captured inside the cage. Then the concentration of CO_2 is much higher near the Pt NP. It is worth mentioning that with increasing the reaction temperature, the methane (hydrocarbon) selectivity decreased and the CO selectivity increased. Therefore, we deliberate that the relatively lower temperature is suitable for obtaining a high yield of methane. The superior performance of Pt-H-ZSM-5-30 can be attributed to its highest Brønsted acidity but also to the formation of homogeneously dispersed Pt NPs over the zeolite support. The resultant composite catalysts are highly active in gas-phase CO_2 hydrogenation, in which the reaction pathway involves (i) a Pt site that might be involved in the formation of CO from CO_2 through the reverse water gas shift reaction and, subsequently, (ii) methanation and or hydrogenation of CO catalyzed by the nearby Brønsted acidic sites. This can be explained by the following way; the edges and corners of the Pt nanoparticles are active sites and kinetically preferred to stimulate the hydrogenation of the CO_2 reaction. The adsorption of CO_2 over the Pt NPs (binding energy $= -0.23$ eV) is the rate-determining step for the overall conversion of CO_2 to CO, CH_4, CH_3OH, and C_2H_4. For a deeper understanding of the mechanisms, high activity and behavior of the catalysts *in-situ* DRIFTS studies were performed and discussed in the following section.

In-situ DRIFTS Studies of the Catalysts Under Reaction Conditions

For heterogeneous catalytic reactions, the exploration of surface species formed during the catalytic processes plays a decisive role in understanding the reaction mechanism. Toward this

goal, DRIFT spectra were monitored at increasing reaction temperatures, in the presence of the reactant mixture/products. The detailed infrared studies were performed on H-ZSM-5-30 for reference state, as well as on Pt-H-ZSM-5-30 and Pt-H-ZSM-5-280 catalysts under reaction conditions (4:1 H_2:CO_2 ratio at 323–773 K) using FTIR spectrometer equipped with diffuse reflectance attachment (**Figures 7**, **8**).

The evaluation of the low wavenumber (1,300–2,000 cm^{-1}) region is difficult, as the zeolites itself has weak absorptions at the region as well as a sharp absorption edge at ∼1,300 cm^{-1}. Although these features should be accounted for by the background spectrum, they might also change as a function of temperature and thus disturb our spectra. Above the frame vibrations of zeolites we obtained relatively weak bands at 1,557 cm^{-1} already at 323 K in the case of H-ZSM-5-20 (**Figure 7A**). These bands can be attributed to the formation of formate ion ($HCOO^-$) from the CO_2 + H_2 reaction mixture, and these are assigned to ν_a(OCO) and ν_s(OCO) vibrations, respectively (Liao et al., 2001; Raskó et al., 2004). When the reaction temperature is increased to 573 K, a new weak peak developed at 1,737 cm^{-1} which can be tentatively assigned to aldehyde like CO stretch (Novák et al., 2002; Sápi et al., 2018). These bands were present up to 873 K, from 673 K peaks for gas phase CO (2,115 and 2,167 cm^{-1}) and methane (3,013 cm^{-1}) showed up (not shown here). It is interesting that when the acidity is decreased by the increasing Si/Al ratio, the formaldehyde-like CO (formyl) decreases, on the surface of Pt-H-ZSM-5-280.

It is very likely, in line with the literature data obtained on different catalysts (Wang et al., 2015; Sápi et al., 2018; László et al., 2019) that the activation of CO_2 on zeolites does not occur basically via direct dissociation to adsorbed CO and O; rather it proceeds through a carboxylate or bicarbonate intermediate, which reacts with adsorbed hydrogen species and formate is produced (Wang et al., 2015; Sápi et al., 2018). The formate intermediate may transform to the formaldehyde form at higher temperatures if a significant number of protons are available:

$$CO^*_{2(a)} + H_{(a)}(OH_{(a)}) \rightarrow (HCO_3^-) \rightarrow HCOO_{(a)} + O_{(a)} \quad (1)$$

$$HCOO_{(a)} + H_{(a)} \rightarrow H_2CO_{(a)} \quad (2)$$

On the other hand, the formate may decompose to methane (Román-Martínez et al., 1996) or CO as was observed on NiO (Sápi et al., 2018), and at higher temperatures, the formaldehyde may transform to gas phase CO on TiO_2 (Raskó et al., 2004):

$$H_2CO_{(a)} \rightarrow CO_{(g)} + 2H_{(a)} \quad (3)$$

On Pt free zeolites the reaction partway strongly depends on acidity and, in harmony with this, on the Si/Al ratio. On less acidity sample this kind of formaldehyde form was not observed on IR spectra. According to catalytic measurements on pure zeolite CO formation was the significant reaction pathway. We may suppose that the CO formation occurs via decomposition of formate:

$$HCOO_{(a)} \rightarrow CO_{(a)} + OH_{(a} \quad (4)$$

At the high Si/Al ratio with less acidic character, the formate may partially decompose via C-O bond breaking and the CH fragments hydrogenate to methane according to RWGS reaction (Wang et al., 2014)

$$HCOO_{(a)} \rightarrow H_2COH_{(a)} \rightarrow H_2C_{(a)} + OH_{(a)} \quad (5)$$

$$H_2C_{(a)} + 2H_{(a)} \rightarrow CH_{4(g)} \quad (6)$$

Ethylene formation was also detected on zeolites with less acidic character (**Figure 5B**). It means that a certain fragment of $CH_{2(a)}$ recombines, and ethylene is formed in a fast coupling reaction step: (Kiricsi et al., 1999)

$$H_2C_{(a)} + CH_{2(a)} \rightarrow C_2H_{4(g)} \quad (7)$$

Adsorbed ethylene or ethylidine were not detected in DRIFTS during the reaction, it means that the ethylene forms in the surface reaction rate determine step.

Pt-H-ZSM-5-30 and Pt-H-ZSM-5-280 catalysts contain more absorption bands during the reaction (**Figures 7B,C**). Peaks for bidentate formate also appeared at 1,553 cm^{-1}, but unfortunately, the symmetric component probably overlaps with the Si-O stretching band. At low-temperature regime (323–573 K) a peak was detected at 1,617 cm^{-1} wich is attributed to monodentate formate (Wang et al., 2015) on Pt-H-ZSM-5-30. This peak may have a bicarbonate component which is the precursor for formate formation (Wang et al., 2015). Formate species is generally accepted as a key intermediate in CO_2 hydrogenation in literature among others on Pt/NiO (Sápi et al., 2018), Pd/Al_2O_3 (Erdöhelyi et al., 1986; Wang et al., 2015), Rh/Al_2O_3 (Solymosi et al., 1980), and Rh/TiO_2. (Novák et al., 2002). We believe that in our case the bidentate form appears on the H-ZSM-5 and monodentate formate on the Pt sites which play also significant role in CO_2 + H_2 reaction. As we demonstrated in **Figure 6B**, the formation of methane drastically increased on Pt containing Pt-H-ZSM-5-30. The methane formation proceeds very probably through formate pathway (Román-Martínez et al., 1996; Wang et al., 2015; Sápi et al., 2018), preferentially on Pt sites:

$$HCOO_{(a)} + H_{(a)} \rightarrow HCOOH_{(a)}{}^* \quad (8)$$

$$HCOOH^* + H_{(a)} \rightarrow H_2COOH_{(a)}{}^* \quad (9)$$

$$H_2COOH_{(a)}{}^* \rightarrow H_nCO_{(a)}{}^* + OH_{(a)} \quad (10)$$

The $H_nCO^*_{(a)}$ (n = 1, 2) intermediates may stabilize on the surface either as adsorbed formaldehyde and decomposes to CO (Equation 3) or decomposes to CH_2 via C-O rupture as it described in Equations 5,6 and finally CH_4 was produced. Carbonyl hydrites, $H_nCO^*_{(a)}$ (n = 1, 2) or with other words hydrogen perturbed adsorbed CO is frequently supposed in CO_2 hydrogenation reactions (Solymosi et al., 1981; Henderson and Worley, 1985; Fisher and Bell, 1996; Wang et al., 2015). This band is usually detected at 1,825–1,840 cm^{-1}. In this structure, it is suggested that CO bonds linearly to noble metal perturbed by hydrogen (Henderson and Worley, 1985; Fisher and Bell, 1996). The frequency shift (∼200 cm^{-1}) comparing to simple linearly bond CO (2,070 cm^{-1}) indicates a weakening in C-O bond. The support for hydrogen-assisted dissociation of CO comes from the observation of methane formation at temperatures lower

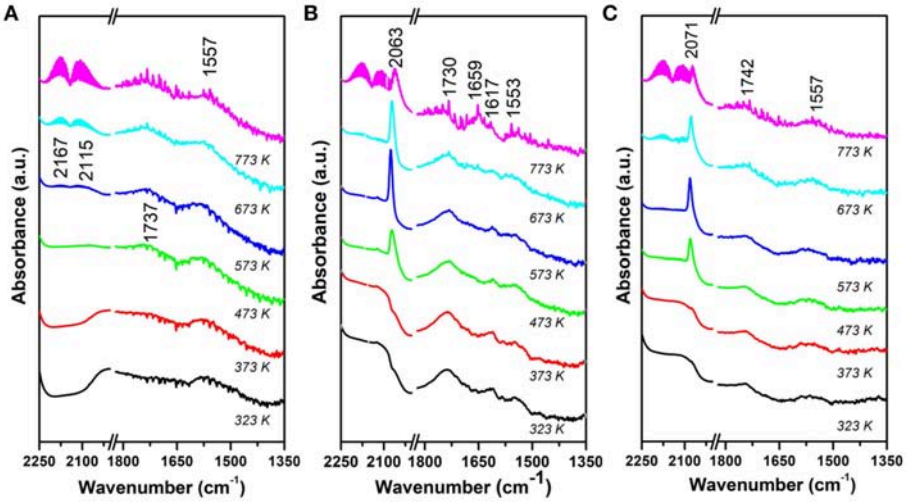

FIGURE 7 | DRIFTS spectra of H-ZSM-5-30 **(A)**, Pt-H-ZSM-5-30 **(B)**, and Pt-H-ZSM-5-280 **(C)** under reaction conditions (CO_2:H_2 = 1:4) at 323–773 K.

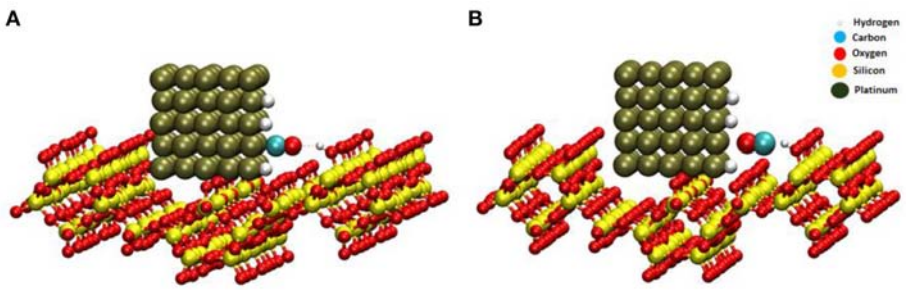

FIGURE 8 | CO adsporbs on the Pt NP via the C end **(A)**, and CO adsorbs to Pt NP via the O end **(B)**.

than those required for dissociation in the absence of hydrogen (Sachtler and Ichikawa, 1986). BOC-MP calculation has also shown that the dissociation of H_nCO, where n = 1, 2, or 3, is energetically more favorable than the direct dissociation of CO on Pd or Pt (Shustorovich and Bell, 1988). We did not detect this wavenumber but we observed further frequency shift in C-O bond (1,730 cm^{-1}) even at 323 K (**Figure 7B**), which indicates a further weakening in C-O bond.

The peak at 1,730 cm^{-1} position may attributable to adsorbed formyl or formaldehyde (CH_2CO) as it was observed on Pt free H-ZSM-5-30 at high temperatures (**Figure 7A**). However, we think that $H_nCO^*_{(a)}$ intermediate could also exist at this wavenumber on Pt-H-ZSM-5-30 from 323 K (**Figure 7B**). For identification of this species, we should mention that band around 1,750 cm^{-1} was observed upon CO adsorption on Co_3O_4(111) film [and at somewhat lower wavenumber on MgO(100) and Fe_3O_4(111)]. The band was attributed to a weakly bound bidentate carbonate which is formed at defect site (Ferstl et al., 2015). However, in our case, this band was not observed during adsorption of CO_2 without hydrogen. We suggest that the CO in this form exists in a surface complex in which the CO is perturbed by hydrogen and adsorbes via C-end on Pt but the oxygen tilts to the proton in zeolites. The other scenario is also imaginable; namely the $H_nCO^*_{(a)}$ bond to zeolite frame and the oxygen tilts to Pt site or hydrogen located on Pt at the interface. These two scenarios are shown in **Figure 8**. Recently, 1,720 cm^{-1} infrared band was observed during the interaction of CO_2 with H_2 on Rh/Al_2O_3. This band was attributed to bridge bonded CO species positioned between Rh and Al atoms from the support. In our study, in the case of the Pt-H-ZSM-5-30, the peak area of the 1,737 cm^{-1} band decreases (**Figure 9A**) while CH_x and CH_3 species were developed with increasing temperature as well as >600 K gas phase methane was detected (**Figure 9C**). However, in the case of Pt-free H-ZSM-5-30, no CO or CH_x was detected only the presence of CH4 at elevated temperature (**Figure 9B**). This phenomena maybe attributed to the fact that, the inclined H-CO species is forming methane at the Pt/H-ZSM-5 interface, however, in the case of the Pt-free catalyst the formate route is favorable.

The inclined, bent configuration plausibly significantly weakens the C-O bond (shifted further to lower wavenumbers) and it could easily break. Low wave number CO (1,770 cm^{-1})

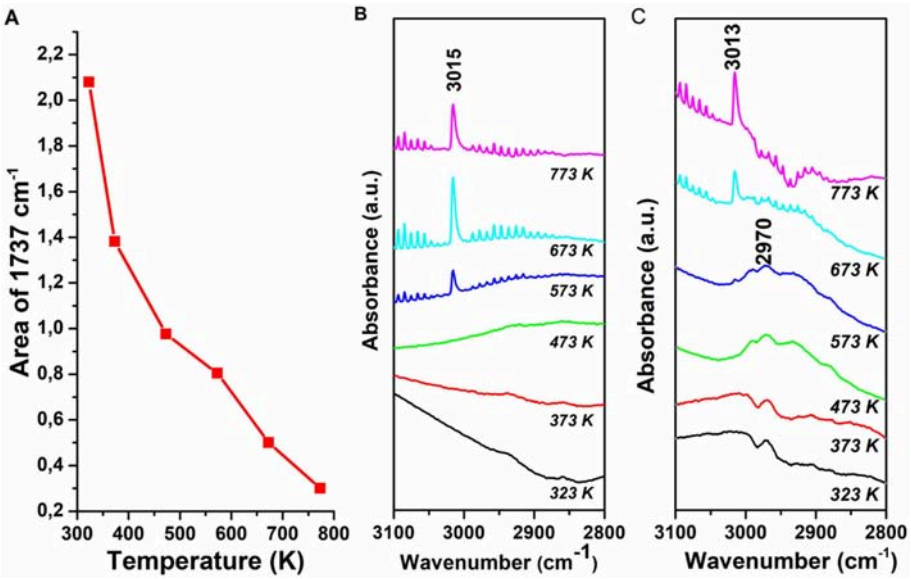

FIGURE 9 | Peak area of the 1,737 cm^{-1} peak region as a function of temperature **(A)**, DRIFTS spectra of H-ZSM-5-30 in CH region **(B)**, DRIFTS spectra of Pt-H-ZSM-5-30 in CH region during reaction condition **(C)**.

was detected under the reaction of $CO_2 + H_2$ on Rh supported on titanates (Tóth et al., 2012). In addition, this unusually low wave number was also observed in CO adsorption on Mn, La, Ce, Fe promoted Rh/SiO_2 (Ichikawa and Fukushima, 1985; Stevenson et al., 1990; Chuang et al., 2005). It was suggested that the oxygen on CO inclined to promoter cations, and enhanced the rupture of C-O bond. On Pt-containing most acidic ZSM-5 we suggest the following further steps in CO_2 hydrogenation (methane formation) where plenty of adsorbed hydrogen is available:

$$H_n(CO)_{(a)}H_{(a)} \rightarrow CH_{n(a)} + OH_{(a)} \quad (11)$$

$$OH_{(a)} + H_{(a)} \rightarrow H_2O_{(g)} \quad (12)$$

On Pt-containing zeolites ethylene formation was not observed (**Figure 6B**), which means that the formed CH species does not recombine but reacts with hydrogen forming methane or further dehydrogenates where carbon is formed causing the deactivation of the catalysts:

$$CH_{n(a)} + H_{(a)} \rightarrow CH_{4(g)} \quad (13)$$

$$CH_{n(a)} \rightarrow C_{(a)} + nH_{(a)} \quad (14)$$

The inclined CO has different structure and stability than that of the linearly adsorbed CO on Pt sites, which appeared at 2,070 cm^{-1} (**Figures 7B,C**) from 573 K. It forms in formate decomposition or in reaction with hydrogen besides formaldehyde/formyl decomposition:

$$HCOO_{(a)} + H_{a)} \rightarrow CO_{(a)} + H_2O \quad (15)$$

The other possible scenario is that CO_2 activated and forms adsorbed CO on Pt sites even at 300 K. This activation process proceeds via formation of negatively charged CO_2 radical and it converts to CO with the help of activated hydrogen (Solymosi et al., 1981; Fisher and Bell, 1996).

The formed adsorbed CO starts to desorb above 600 K. The observed CO position is almost agreed with those detected on Pt-H-ZSM-5 (Rivallan et al., 2010) previously. In that study two bands appeared; one is at 2,095 cm^{-1}, the other is at 2,080–2,050 cm^{-1}. This later peak is ascribed to smaller Pt particles for which CO adsorbs abundantly on less coordinated Pt atoms. The peak at ∼1,730 cm^{-1} (formaldehyde and hydrogen perturbed inclined CO) is present up to 700–800 K. Above 773 K bands appeared at 1,659 cm^{-1} probably due to carbonate which comes from the decomposition of formate and formaldehyde.

CONCLUSION

In summary, we synthesized 4.4 nm Pt nanoparticles with narrow size distribution and these Pt NPs were successfully anchored onto the surfaces of H-ZSM-5 (Si/Al= 30, 80, and 280) supports. The final composite catalysts are firstly explored for the hydrogenation CO_2 at 723 and 873 K temperatures and atmospheric pressure. The characterization results revealed that Pt NPs diffused H-ZSM-5 catalysts have been conceded for its unique property which makes potential candidates for catalytic hydrogenation of CO_2. Comparison with bare H-ZSM-5 catalysts the Pt NP modified composites showed superior catalytic activity. The lower Si/Al ratio composite was showing the highest catalytic activity. The reasons for this high activity as well as CH4 selectivity of 0.5% Pt-H-ZSM-5-30 could be explained by the presence of the CO in a surface complex in which the CO is perturbed by hydrogen and adsorbes

via C-end on Pt but the oxygen tilts to proton in zeolites The other scenario is also imaginable; namely the $H_nCO^*_{(a)}$ bond to zeolite frame and the oxygen tilts to Pt site or hydrogen located on Pt at the interface, where this inclined, bent configuration plausibly significantly weakens the C-O bond being responsible for the high activity and selectivity of methane.

AUTHOR CONTRIBUTIONS

AS, UK, and GH: preparation evaluation article adjustment, catalysis, BET, XRD. KÁ, JK, and IS: DRIFTS studies and mechanism. BN: calculations. TV, JG-P: TEM. ÁK and ZK: support.

ACKNOWLEDGMENTS

UK thank to the University of Szeged, Hungary, for the financial support. This paper was supported by the Hungarian Research Development and Innovation Office through grants NKFIH OTKA PD 120877 of AS. ÁK, GH, and ZK is grateful for the fund of NKFIH (OTKA) K112531 & NN110676, PD 115769, and K120115, respectively. This collaborative research was partially supported by the Széchenyi 2020 program in the framework of GINOP-2.3.2-15-2016-00013 Intelligent materials based on functional surfaces—from syntheses to applications project. The Ministry of Human Capacities through the EFOP-3.6.1-16-2016-00014 and 20391-3/2018/FEKUSTRAT project is also acknowledged.

REFERENCES

An, X., Zuo, Y.-Z., Zhang, Q., Wang, D., and Wang, J.-F. (2008). Dimethyl ether synthesis from CO_2 hydrogenation on a CuO–ZnO–Al_2 O_3 – ZrO_2/HZSM-5 bifunctional catalyst. *Ind. Eng. Chem. Res.* 47, 6547–6554. doi: 10.1021/ie800777t

Aresta, M., Dibenedetto, A., and Quaranta, E. (2016). State of the art and perspectives in catalytic processes for CO_2 conversion into chemicals and fuels: the distinctive contribution of chemical catalysis and biotechnology. *J. Catal.* 343, 2–45. doi: 10.1016/j.jcat.2016.04.003

Bin, F., Song, C., Lv, G., Song, J., Wu, S., and Li, X. (2014). Selective catalytic reduction of nitric oxide with ammonia over zirconium-doped copper/ZSM-5 catalysts. *Appl. Catal. B Environ.* 150–151, 532–543. doi: 10.1016/j.apcatb.2013.12.052

Cheng, Y., Wang, L. J., Li, J. S., Yang, Y. C., and Sun, X. Y. (2005). Preparation and characterization of nanosized ZSM-5 zeolites in the absence of organic template. *Mater. Lett.* 59, 3427–3430. doi: 10.1016/j.matlet.2005.06.008

Chuang, S. S. C., Stevens, R. W., and Khatri, R. (2005). Mechanism of C2+ oxygenate synthesis on Rh catalysts. *Top. Catal.* 32, 225–232. doi: 10.1007/s11244-005-2897-2

Costa, C., Dzikh, I. P., Lopes, J. M., Lemos, F., and Ribeiro, F. R. (2000). Activity-acidity relationship in zeolite ZSM-5. Application of Bronsted- type equations. *J. Mol. Catal. A Chem.* 154, 193–201. doi: 10.1016/S1381-1169(99)00374-X

Danjun, W., Furong, T. A. O., Huahua, Z., Huanling, S., and Lingjun, C. (2011). Preparation of Cu/ZnO/Al2O3 catalyst for CO_2 hydrogenation to methanol by CO_2 assisted aging. *Chinese J. Catal.* 32, 1452–1456. doi: 10.1016/S1872-2067(10)60256-2

Erdöhelyi, A., Pásztor, M., and Solymosi, F. (1986). Catalytic hydrogenation of CO_2 over supported palladium. *J. Catal.* 98, 166–177. doi: 10.1016/0021-9517(86)90306-4

Falamaki, C., Edrissi, M., and Sohrabi, M. (1997). Studies on the crystallization kinetics of zeolite ZSM-5 With 1,6-hexanediol as a structure-directing agent. *Zeolites* 19, 2–5. doi: 10.1016/S0144-2449(97)00025-0

Ferstl, P., Mehl, S., Arman, M. A., Schuler, M., Toghan, A., Laszlo, B., et al. (2015). Adsorption and activation of CO on Co3O4(111) thin films. *J. Phys. Chem. C* 119, 16688–16699. doi: 10.1021/acs.jpcc.5b04145

Fisher, I. A., and Bell, A. T. (1996). A comparative study of CO and CO_2 hydrogenation over Rh/SiO2. *J. Catal.* 162, 54–65. doi: 10.1006/jcat.1996.0259

Gao, P., Li, S., Bu, X., Dang, S., Liu, Z., Wang, H., et al. (2017). Direct conversion of CO_2 into liquid fuels with high selectivity over a bifunctional catalyst. *Nat. Chem.* 9, 1019–1024. doi: 10.1038/nchem.2794

Henderson, M. A., and Worley, S. D. (1985). An infrared study of the hydrogenation of carbon dioxide on supported rhodium catalysts. *J. Phys. Chem.* 89, 1417–1423. doi: 10.1021/j100254a023

Ichikawa, M., and Fukushima, T. (1985). Infrared studies of metal additive effects on carbon monoxide chemisorption modes on silicon dioxide-supported rhodium-manganese, -titanium and iron catalysts. *J. Phys. Chem.* 89, 1564–1567. doi: 10.1021/j100255a003

International Energy Outlook 2013. (2013). *U.S. Energy Information Agency, 2013.*

Ismail, A. A., Mohamed, R. M., Fouad, O. A., and Ibrahim, I. A. (2006). Synthesis of nanosized ZSM-5 using different alumina sources. *Cryst. Res. Technol.* 41, 145–149. doi: 10.1002/crat.200510546

Kattel, S., Yan, B., Chen, J. G., and Liu, P. (2016). CO 2 hydrogenation on Pt, Pt/SiO2 and Pt/TiO2 : importance of synergy between Pt and oxide support. *J. Catal.* 343, 115–126. doi: 10.1016/j.jcat.2015.12.019

Kim, Y. T., Jung, K. D., and Park, E. D. (2011). Gas-phase dehydration of glycerol over silica-alumina catalysts. *Appl. Catal. B Environ.* 107, 177–187. doi: 10.1016/j.apcatb.2011.07.011

Kiricsi, I., Förster, H., Tasi, G., and Nagy, J. B. (1999). Generation, characterization, and transformations of unsaturated carbenium ions in zeolites. *Chem. Rev.* 99, 2085–2114. doi: 10.1021/cr9600767

Kumar, N., Nieminen, V., Demirkan, K., Salmi, T., Murzin, D. Y., and Laine, E. (2002). Effect of synthesis time and mode of stirring on physico-chemical and catalytic properties of ZSM-5 zeolite catalysts. *Appl. Catal. A Gen.* 235, 113–123. doi: 10.1016/S0926-860X(02)00258-2

László, B., Baán, K., Ferencz, Z., Galbács, G., Oszkó, A., Kónya, Z., et al. (2019). Gold size effect in the thermal-induced reaction of CO $_2$ and H $_2$ on titania- and Titanate nanotube-supported gold catalysts. *J. Nanosci. Nanotechnol.* 19, 470–477. doi: 10.1166/jnn.2019.15772

Li, S., Xu, Y., Chen, Y., Li, W., Lin, L., Li, M., et al. (2017). Tuning the selectivity of catalytic carbon dioxide hydrogenation over iridium/cerium oxide catalysts with a strong metal-support interaction. *Angew. Chemie Int. Ed.* 56, 10761–10765. doi: 10.1002/anie.201705002

Liao, L.-F., Wu, W.-C., Chen, C.-Y., and Lin, J.-L. (2001). Photooxidation of formic acid vs formate and ethanol vs ethoxy on TiO2 and effect of adsorbed water on the rates of formate and formic acid photooxidation. *J. Phys. Chem. B* 105, 7678–7685. doi: 10.1021/jp003541j

Mikkelsen, M., Jørgensen, M., and Krebs, F. C. (2010). The teraton challenge. A review of fixation and transformation of carbon dioxide. *Energy Environ. Sci.* 3, 43–81. doi: 10.1039/B912904A

Novák, É., Fodor, K., Szailer, T., Oszkó, A., and Erdöhelyi, A. (2002). CO_2 hydrogenation on Rh/TiO2 previously reduced at different temperatures. *Top. Catal.* 20, 107–117. doi: 10.1023/A:1016359601399

Olah, G. A., Goeppert, A., and Prakash, G. K. S. (2009). *Beyond Oil and Gas: The Methanol Economy, 2nd Edn.* Los Angeles, CA: Wiley-VCH. 1–334.

O'Malley, A. J., Parker, S. F., Chutia, A., Farrow, M. R., Silverwood, I. P., García-Sakai, V., et al. (2015). Room temperature methoxylation in zeolites: insight into a key step of the methanol-to-hydrocarbons process. *Chem. Commun.* 52, 2897–2900. doi: 10.1039/C5CC08956E

Raskó, J., Kecskés, T., and Kiss, J. (2004). Formaldehyde formation in the interaction of HCOOH with Pt supported on TiO2. *J. Catal.* 224, 261–268. doi: 10.1016/j.jcat.2004.03.025

Rivallan, M., Seguin, E., Thomas, S., Lepage, M., Takagi, N., Hirata, H., et al. (2010). Platinum sintering on H-ZSM-5 followed by chemometrics of CO adsorption and 2D pressure-jump IR spectroscopy of adsorbed species. *Angew. Chemie Int. Ed.* 49, 785–789. doi: 10.1002/anie.200905181

Robert, M. (2016). Running the clock: CO $_2$ catalysis in the age of anthropocene. *ACS Energy Lett*. 1, 281–282. doi: 10.1021/acsenergylett.6b00159

Román-Martínez, M. C., Carzorla-Amorós, D., Salinas-Martínez de Lecea, C., and Linares-Solano, A. (1996). Structure sensitivity of CO_2 hydrogenation reaction catalyzed by Pt/carbon catalysts. *Langmuir* 12, 379–385. doi: 10.1021/la950329b

Sachtler, W. M. H., and Ichikawa, M. (1986). Catalytic site requirements for elementary steps in syngas conversion to oxygenates over promoted rhodium. *J. Phys. Chem.* 90, 4752–4758. doi: 10.1021/j100411a009

Sakakura, T., Choi, J.-C., and Yasuda, H. (2007). Transformation of carbon dioxide. *Chem. Rev*. 107, 2365–2387. doi: 10.1021/cr068357u

Sápi, A., Halasi, G., Kiss, J. ,Dobó, D. G., Juhász, K. L., Kolcsár, V. J., et al. (2018). *In-situ* DRIFTS and NAP-XPS exploration of the complexity of CO_2 hydrogenation over size controlled Pt nanoparticles supported on mesoporous NiO. *J. Phys. Chem. C* 122, 5553–5565. doi: 10.1021/acs.jpcc.8b00061

Shustorovich, E., and Bell, A. T. (1988). Analysis of CO hydrogenation pathways using the bond-order-conservation method. *J. Catal.* 113, 341–352. doi: 10.1016/0021-9517(88)90263-1

Sing, K. S. W. (1985). International union of pure commission on colloid and surface chemistry including catalysis-reporting physisorption data for gas/solid systems with special reference to the determination of surface area and porosity. *Pure Appl. Chem.* 57, 603–619. doi: 10.1351/pac198557040603

Solymosi, F., Erdöhelyi, A., and Bánsági, T. (1981). Infrared study of the surface interaction between H_2 and CO_2 over rhodium on various supports. *J. Chem. Soc. Faraday Trans. 1 Phys. Chem. Condens. Phases* 77:2645. doi: 10.1039/f19817702645

Solymosi, F., Erdöhelyi, A., and Kocsis, M. (1980). Surface interaction between H_2 and CO_2 on RhAl2O3, studied by adsorption and infrared spectroscopic measurements. *J. Catal.* 65, 428–436. doi: 10.1016/0021-9517(80)90319-X

Stevenson, S. A., Lisitsyn, A., and Knoezinger, H. (1990). Adsorption of carbon monoxide on manganese-promoted rhodium/silica catalysts as studied by infrared spectroscopy. *J. Phys. Chem.* 94, 1576–1581. doi: 10.1021/j100367a066

Takeguchi, T., Yanagisawa, K., Inui, T., and Inoue, M. (2000). Effect of the property of solid acid upon syngas-to-dimethyl ether conversion on the hybrid catalysts composed of Cu–Zn–Ga and solid acids. *Appl. Catal. A Gen*. 192, 201–209. doi: 10.1016/S0926-860X(99)00343-9

Tóth, M., Kiss, J., Oszkó, A., Pótári, G., László, B., and Erdohely, A. (2012). Hydrogenation of carbon dioxide on Rh, Au and Au–Rh bimetallic clusters supported on titanate nanotubes, nanowires and TiO2. *Top. Catal.* 55, 747–756. doi: 10.1007/s11244-012-9862-7

Wang, H., Sapi, A., Thompson, C. M., Liu, F., Zherebetskyy, D., Krier, J. M., et al. (2014). Dramatically different kinetics and mechanism at solid/liquid and solid/gas interfaces for catalytic isopropanol oxidation over size-controlled platinum nanoparticles. *J. Am. Chem. Soc.* 136, 10515–10520. doi: 10.1021/ja505641r

Wang, X., Shi, H., Kwak, J. H., and Szanyi, J. (2015). Mechanism of CO $_2$ hydrogenation on Pd/Al_2O_3 catalysts: kinetics and transient DRIFTS-MS studies. *ACS Catal.* 5, 6337–6349. doi: 10.1021/acscatal.5b01464

Wang, X., Yang, G., Zhang, J., Chen, S., Wu, Y., Zhang, Q., et al. (2016). Synthesis of isoalkanes over a core (Fe–Zn–Zr)–shell (zeolite) catalyst by CO_2 hydrogenation. *Chem. Commun.* 52, 7352–7355. doi: 10.1039/C6CC01965J

Wei, J., Ge, Q., Yao, R., Wen, Z., Fang, C., Guo, L., et al. (2017). Directly converting CO_2 into a gasoline fuel. *Nat. Commun.* 8:15174. doi: 10.1038/ncomms15174

Xie, C., Chen, C., Yu, Y., Su, J., Li, Y., Somorjai, G. A., et al. (2017). Tandem catalysis for CO_2 hydrogenation to C_2-C_4 hydrocarbons. *Nano Lett.* 17, 3798–3802. doi: 10.1021/acs.nanolett.7b01139

Zhan, G., and Zeng, H. C. (2017). ZIF-67-derived nanoreactors for controlling product selectivity in CO_2 hydrogenation. *ACS Catal.* 7, 7509–7519. doi: 10.1021/acscatal.7b01827

Zhao, Y. X., Bamwenda, G. R., Groten, W. A., and Wojciechowski, B. W. (1993). The chain mechanism in catalytic cracking: the kinetics of 2-methylpentane cracking. *J. Catal.* 140, 243–261. doi: 10.1006/jcat.1993.1081

Zheng, Z., Xu, H., Xu, Z., and Ge, J. (2017). A monodispersed spherical Zr-based metal-organic framework catalyst, Pt/Au@Pd@UIO-66, comprising an Au@Pd core-shell encapsulated in a UIO-66 center and its highly selective CO_2 hydrogenation to produce CO. *Small* 14:1702812. doi: 10.1002/smll.201702812

Conflict of Interest Statement: The authors declare that the research was conducted in the absence of any commercial or financial relationships that could be construed as a potential conflict of interest.

frontiers in Materials

ORIGINAL RESEARCH
published: 04 February 2019
doi: 10.3389/fmats.2019.00005

Citric Acid Modified Bentonite for Congo Red Adsorption

Hanbing Zhang[1,2], *Juan Zhou*[2,3], *Yaseen Muhammad*[2,4], *Rui Tang*[2], *Kun Liu*[1], *Ying Zhu*[1] *and Zhangfa Tong*[2*]

[1] Institute of Environmental Engineering, College of Resources, Environment and Materials, Guangxi University, Nanning, China, [2] Guangxi Key Laboratory of Petrochemical Resource Processing and Process Intensification Technology, School of Chemistry and Chemical Engineering, Guangxi University, Nanning, China, [3] Guangzhou of China Light Industry Engineering Co. Ltd., Guangzhou, China, [4] Institute of Chemical Sciences, University of Peshawar, Peshawar, Pakistan

Raw bentonite (RB) was chemically modified by citric acid (CA) to obtain a low-cost and environment-friendly citric acid incorporated bentonite (CAB) adsorbent, which was applied for the adsorptive removal of Congo Red (CR). The effect of adsorbent dosage, contact time, ionic strength, surfactant, and pH on adsorption was investigated. Adsorption equilibrium data fitted well with Langmuir model while the Langmuir adsorption capacity of CR on CAB reached up to 384 $mg{\cdot}g^{-1}$. Furthermore, CR adsorption on CAB followed pseudo-second kinetic model while intra-particle diffusion was not the only rate-limiting step as determined from intra-particle diffusion model investigation. RB and CAB were characterized by XRD, FT-IR, and BET techniques. A proposed mechanism for the adsorption of CR over CAB suggested the chemical adsorption phenomenon is mainly controlled by chelation, hydrogen bonding, and fixing.

Keywords: citric acid modified bentonite, Congo Red, adsorption model, adsorption mechanism, XRD and FT-IR

OPEN ACCESS

Edited by:
Jie-Sheng Chen,
Shanghai Jiao Tong University, China

Reviewed by:
Zhentao Yu,
Nanjing University, China
Jinyang Zhang,
Neijiang Normal University, China
Binbin Yu,
Yangzhou University, China
Li-Hua Chen,
Wuhan University of Technology, China

***Correspondence:**
Zhangfa Tong
zhftong@sina.com

Specialty section:
This article was submitted to Colloidal Materials and Interfaces, a section of the journal Frontiers in Materials

Received: *27 November 2018*
Accepted: *10 January 2019*
Published: *04 February 2019*

Citation:
Zhang H, Zhou J, Muhammad Y, Tang R, Liu K, Zhu Y and Tong Z (2019) Citric Acid Modified Bentonite for Congo Red Adsorption. Front. Mater. 6:5. doi: 10.3389/fmats.2019.00005

INTRODUCTION

Dyes are widely used in textile, printing, feather, cosmetics, and plastics industries due to their bright colored and washable nature and sunfast feature (Rosa et al., 2018). However, the effluents discharged by these industries contain untreated dyes which can be toxic to human beings and aquatic life and hence their removal from contaminated wastewater is essential. Various methods such as adsorption over activated carbon (Wen et al., 2016), thermolysis, and coagulation (Yen et al., 2017), membrane separation (Cazzorla et al., 2018; Ye et al., 2018), electrochemical decolorization (Xu L. et al., 2018), photocatalytic degradation (Liu et al., 2019), and biological treatment (Banihani et al., 2018) have been widely reported for the removal of organic pollutants. Among these methods, adsorption over activated carbon is envisaged as highly effective technique. However, the high cost of activated carbon restricts its widespread utilization. On the contrary, low-cost adsorbents including acid treated red mud (Toor et al., 2015), sand (Li P. et al., 2018), raw pine and acid treated pine (Schorr et al., 2018), Ashoka leaf (Shivaprakash et al., 2018), sulphuric acid treated Palm flower (Magdalena et al., 2018), hen feathers (Tesfaye et al., 2018), and clay minerals (Shaban et al., 2018) have been investigated for the treatment of dyes containing wastewater.

Researchers are focusing on the applications of clay minerals attributed to their low-cost, abundant outputs, non-toxicity, stability, and ability of ion exchange. In this regard, several clay minerals such as bentonite (Beheshti et al., 2018; Mat et al., 2018), montmorillonite (Mahmoudian et al., 2018), zeolite (Abdelrahman, 2018), and kaolin (Li Y. et al., 2018) have been reported for the removal of dyes from wastewater. Among these, bentonite had received greater attention as adsorbent due to its high adsorption capacity and cost-effective nature. Mudrinic et al. (2018) studied the removal of acid dyes over sulphuric acid activated bentonite with high adsorption capacity. Baytar et al. (2018) studied removal of methylene blue by acid-activated bentonite and raw bentonite where the former was found more efficient than the later. Ding et al. (2018) reported better efficiency of hydrochloric acid treated bentonite than the nascent version for the removal of Congo Red (CR). Araujo et al. (2018) prepared and effectively applied chitosan and hexadecyl trimethyl ammonium bromide modified bentonite (CTS–CTAB-Bent) absorbent for the removal of weak acid scarlet. These reports suggest that inorganic/organic acid treatment can increase the adsorption capacity of bentonite toward various types of dyes. However, the structure of bentonite could readily be destroyed by strong inorganic acid such as sulphuric acid and hydrochloric acid. Meanwhile, the current commonly used organic modifiers for bentonite includes CTAB, polyacrylic acid, and multi amine-containing gemini surfactants (Li W. Y. et al., 2018; Xu Y. et al., 2018). However, the toxicity and cost of these modifiers and complicated modification technology limit their applications in bentonite modification. Therefore, it is essential to find a suitable, mild, environmentally friendly acid to modify bentonite without compromising on the dye removal efficiency.

As a simple and non-toxic organic acid, citric acid (CA) is very cheap and abundant because it can be obtained from natural biomass. In addition, –OH and –COOH groups in CA are not only effective linking groups for loading CA on RB but also good chelating groups for organic dyes and heavy metals removal. In recent years, some CA-modified adsorbents have been reported for the adsorption of dyes and heavy metals (Wang et al., 2017, 2018; Yan et al., 2018). According to the earlier work in our group, CA can not only modify bentonite environmentally-friendly via a moderate and rapid route but also avoid secondary pollution (Zhou et al., 2015). Thus, CA was selected to modify raw bentonite (RB) to obtain CA modified bentonite (CAB) in this study, which was in turn used for the adsorptive removal of CR. The effect of various factors such as adsorbents dosage, contact time, ionic strength, surfactant, and pH was systematically studied. The adsorption data of CAB and RB were evaluated by kinetic models and isotherm models. To get deeper insight into the adsorption mechanism, RB, and CAB were analyzed by X-rays diffraction (XRD), Brunauer, Emmett, and Teller (BET) surface area analysis and Fourier transform infra-red (FT-IR) spectroscopy.

MATERIALS AND METHODS

Materials

RB was obtained from Shanghai Chemical Co., Ltd, China. CR ([1-napthalene sulfonic acid, 3, 3'-(4, 4'-biphenylenebis (azo)) bis (4-amino-) disodium salt]) was a type of indicator having chemical formula of $C_{33}H_{22}N_6Na_2O_6S_2$, and molecular weight of 696.7 g·mol^{-1}, while its structure is given in **Figure 1**. Cationic CTAB, anionic surfactant sodium dodecyl benzene sulfonate (SDBS), and CA were obtained from Sinopharm Chemical Reagent Co., Ltd, China. All the chemicals were of analytical grade and used without further purification.

Preparation of CAB

CAB was prepared by the following procedure: 5 g of RB was dispersed in 50 mL deionized water in a three-necked flask. 2.78 g CA was dissolved in 50 mL deionized water at room temperature in a separating funnel and the solution was dropwise added into RB dispersion. The mixture was agitated on a magnetic stirrer at 323 K for 3 h, filtered, and washed several times with deionized water and dried at 323 K for 24 h. The adsorbent was ground and sieved through 200 mesh size and kept in a dryer till further analysis/use.

Characterizations of RB and CAB Before and After CR Adsorption

RB, CAB, and CR loaded CAB (CR–CAB) were characterized by XRD (D/MAX 2500 V X-ray diffractometer) with Cu Kα radiation in a 2θ range of 4–60° with a scan speed of 5°/min. The specific surface area and average pore size of RB, ACB, and CR–CAB were determined by a Quantachrome NOVA 1200e volumetric nitrogen adsorption apparatus. The functional groups of samples were studied using FT-IR spectrophotometer (Nicolet FT-IR 6700) in a 4,000–500 cm^{-1} region.

CR Adsorption Studies

Batch adsorption experiments for CR onto RB and CAB were performed. One Hundred milliliter CR solution (200 mg·L^{-1}) with different amounts of adsorbents (0.2–2.0 g·L^{-1}) were taken in conical flasks (250 mL) and agitated using a shaking water bath at 150 rpm at 303 K for fixed time duration. The effect of ionic strength and surfactant on CR adsorption was studied under various concentrations of NaCl, $CaCl_2$, CTAB, and SDBS. The pHs of CR solutions within a range 4–11 were adjusted using 0.1 M NaOH and 0.1 M HCl solutions by a STARTER 3C pH-meter. The kinetic studies of CR adsorption were performed by agitating 100 mL CR solution (100–1,200 mg·L^{-1}) in 250 mL conical flask at 303 K for 12 h until reaching equilibrium. The supernatant of CR was tested for change in concentration at different time intervals. The adsorbent was separated from solution by filtration and filtrate was subjected to centrifugation at 5,000 rpm for 10 min. The supernatants were analyzed by a UV-visible spectrophotometer (UV-2550, Shimadzu) at 498 nm.

CR removal efficiency, the amount of CR adsorbed per unit mass of adsorbent and per unit time were calculated using Equations (1–3), respectively.

$$\eta = \frac{C_0 - C_e}{C_0} \times 100\% \quad (1)$$

$$q_e = \frac{C_0 - C_e}{\frac{m}{V}} \quad (2)$$

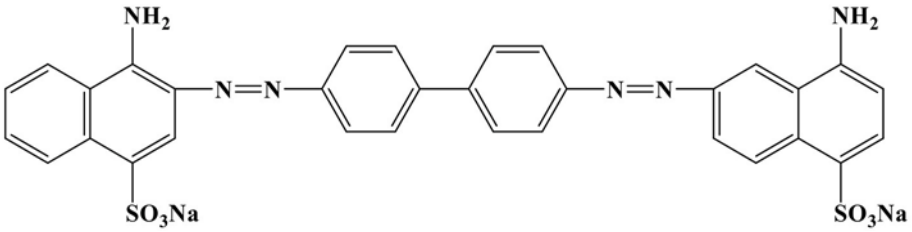

FIGURE 1 | Structure of CR.

$$q_t = \frac{C_0 - C_t}{\frac{m}{V}} \quad (3)$$

where η is the removal efficiency of the adsorbent, q_e, and q_t are the adsorption capacity ($mg{\cdot}g^{-1}$), at equilibrium time and at any given time, respectively. C_0, C_e, and C_t are the concentrations ($mg{\cdot}L^{-1}$), of the dye at initial time, at equilibrium time, and at any given time, respectively. m is the mass (g) of adsorbent and V is the volume (mL) of dye solution.

Adsorption Isotherm Studies

Adsorption isotherm models such as Langmuir (Sha et al., 2018) and Freundlich (Xavier et al., 2018) are commonly used for the fitting of experimental data. Parameters of each model can explain the adsorption mechanisms between the adsorbate and adsorbent. The linear forms of Langmuir and Freundlich models are presented in Equations (4, 5), respectively:

$$\frac{C_e}{q_e} = \frac{1}{q_{\max} K_L} + \frac{C_e}{q_{\max}} \quad (4)$$

$$\ln q_e = \ln K_F + \frac{1}{n} \ln C_e \quad (5)$$

where $q_{\max}$ is the theoretical estimation of maximum adsorption capacity, K_L ($L{\cdot}mg^{-1}$) is the Langmuir isotherm constant related to the energy of adsorbate/adsorbent interaction. K_F ($mg{\cdot}g^{-1}$) and n are the Freundlich constants related to adsorption capacity and adsorption intensity, respectively.

The kinetic models are equations which reflect the relationship of adsorption time and adsorption capacity. Thus, kinetic data from CR adsorption on RB and CAB was evaluated by pseudo-first kinetic model (Bernstein et al., 2018), pseudo-second kinetic model (Bernstein et al., 2018), and intra-particle diffusion model (Olivoalanis et al., 2018) using their linear forms shown by Equations (7–9), respectively.

$$\log(q_e - q_t) = \log q_e - \frac{k_1}{2.303} t \quad (6)$$

$$\frac{t}{q_t} = \frac{1}{k_2 q_e^2} + \frac{1}{q_e} t \quad (7)$$

$$q_t = k_{id} t^{1/2} + I \quad (8)$$

where k_1 (min^{-1}) and k_2 ($g{\cdot}mg^{-1}{\cdot}min^{-1}$) are the rate constants of pseudo-first kinetic model and pseudo-second kinetic model, respectively, at time t (min). k_{id} ($mg{\cdot}g^{-1}{\cdot}min^{-1/2}$) and I ($mg{\cdot}g^{-1}$) are the intra-particle model constants.

RESULTS AND DISCUSSION

Effect of Various Experimental Conditions on CR Adsorption

Effect of Adsorbent Dosage on CR Adsorption

The effect of various dosages of RB and CAB on the removal of CR was tested and the results are compiled in **Figure 2**. The removal of CR increased sharply with increasing dosage of CAB from 0.2 to 1 $g{\cdot}L^{-1}$ and then reached to equilibrium. While for RB, the removal of CR increased gradually over the dosage range, which indicated direct relation between amount of adsorbent and active sites (Fosso et al., 2016). The active adsorption sites increased with increasing adsorbent dosage, which ultimately led to grater CR adsorption. CR removal by RB and CAB increased from 13 to 74% and 30 to 92%, respectively, by increasing adsorbent dosage from 0.2 to 2.0 $g{\cdot}L^{-1}$. However, CR adsorption capacity decreased with increasing adsorbent dosage, which could be attributed to aggregation of adsorption sites with each other resulting in decreasing total surface area available to CR and increase in diffusion path length (Bernstein et al., 2018). In **Figure 2**, the optimum dosage of CAB was 1 $g{\cdot}L^{-1}$ was chosen for onward experiments.

Effect of Contact Time on CR Adsorption

The results for the effect of contact time on CR adsorption by CAB and RB are plotted in **Figure 3**, which suggests that the removal efficiency of CR on both adsorbents increased with increasing contact time from 0 to 90 min and attained equilibrium afterwards. **Figure 3** further suggests that CR removal on RB was only 20% within 5 min which slowly reached to 54% after 450 min. Compared with RB, CAB showed better adsorption capacity for CR i.e., CR removal efficiency by CAB in first 5 min was 45%, which was enhanced to 87% after 120 min. By comparing the CR removal efficiency (87%) by CAB with some literature reports, one can conclude that the newly designed CAB had faster reaction kinetics and hence can be deemed greatly cost effective on industrial level applications (Toor et al., 2015; Tarmizi et al., 2017).

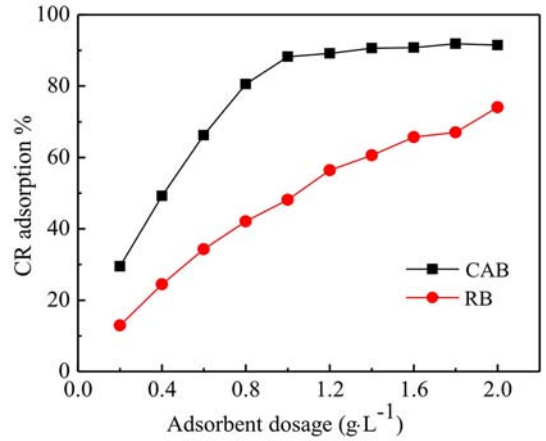

FIGURE 2 | Effect of adsorbent dosage on CR adsorption on RB and CAB.

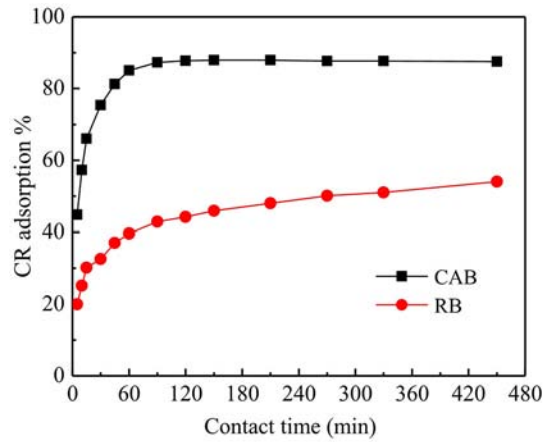

FIGURE 3 | Effect of contact time on CR adsorption on RB and CAB.

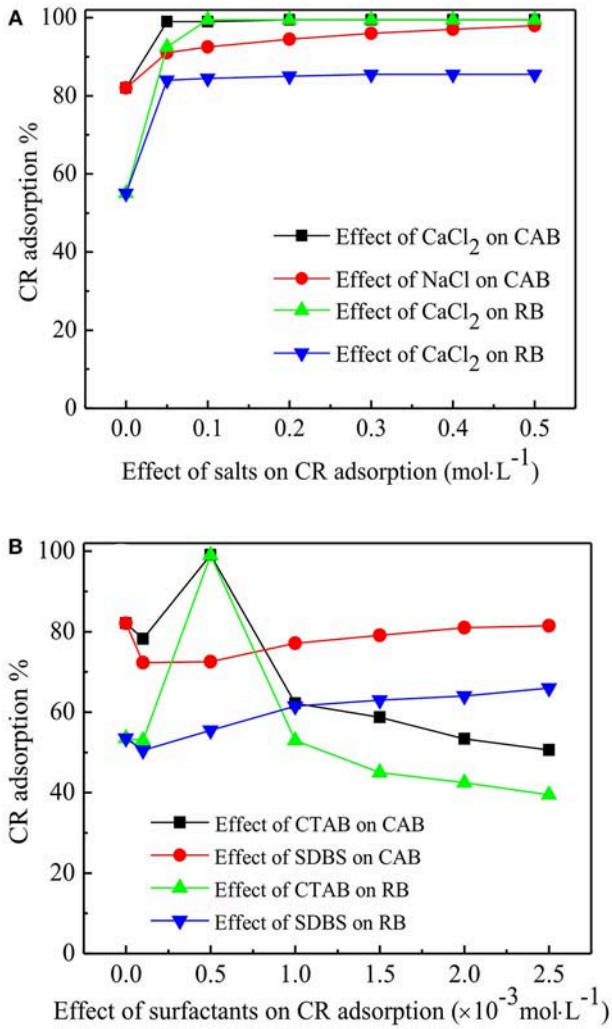

FIGURE 4 | Effect of inorganic salt **(A)** and surfactants **(B)** on CR adsorption on RB and CAB.

Effect of Ionic Strength and Surfactant on CR Adsorption

The effect of NaCl and $CaCl_2$ concentration (0–0.5 mol·L^{-1}) on CR adsorption were studied and the results are compiled in **Figure 4A**. An increase in CR removal was observed by increasing slat concentration of NaCl and $CaCl_2$ from 0 to 0.05 M and became constant onward. The increase in CR removal with increasing salts' concentration could be credited to decrease in the electrostatic repulsion between CR anions, thus accelerating CR aggregation (Lin et al., 2018). In addition, compared with NaCl, higher enhancement in CR removal was observed by the presence of $CaCl_2$, which could be due to the presence of more positive charge on Ca^{2+} than Na^{+}, hence bitterly neutralizing negative charges in aqueous solution. Furthermore, Ca-dye precipitation could occur in CR solution with the existence of Ca^{2+} (Hadjltaief et al., 2018), while the aggregation of CR and Ca-CR precipitation could also be counted toward better CR removal.

Surfactants are widely used in the treatment of dyes, thus the effect of cationic surfactant (CTAB) and anionic surfactant (SDBS) in a concentration range of 0.1 and 2.5 mM, were investigated on CR adsorption. The results compiled in **Figure 4B** suggest that in the presence of 0.5 mM CTAB, a CR removal of up to 99% was achieved on RB and CAB. However, further increase in CTAB concentration led to decrease in CR removal. This could be accredited to the fact that at low CTAB concentration, surfactant monomers firstly adsorbed to adsorbent surface, creating additional positive charges which electrostatically increased CR adsorption (Sham and Notley, 2018). Decrease in CR removal efficiency above critical micelle concentration (CMC) of CTAB was due to micelle formation and dye solubilization (Gorsd et al., 2018; Sham and Notley, 2018). The micelles were formed at high CTAB concentration which solubilized CR molecules, hence preventing CR adsorption. However, researchers (Yao et al., 2012; Gorsd et al., 2018) have

reported far lower residual concentration of CTAB than its CMC when the dye removal efficiency started to decline, which could be attributed to the pore-blocking on the adsorbent surface. **Figure 4B** shows that at a low concentration of SDBS, CR removal decreased slightly, and then ascended gradually on both CAB and RB. Anionic surfactants have been reported to have different influence on different anionic dyes and hence their chemical structures play an important role on dye adsorption (Lee et al., 2018; Zhou et al., 2018).

Effect of pH on CR Adsorption

Figure 5 shows that pH exhibited different effect on CR removal by CAB and RB. CR removal by RB decreased from 76 to 49% with increasing pH, which could be due to the dissociation of sulfonate groups of CR (D-SO_3Na) in aqueous medium producing anionic dye ions (Jia et al., 2018). At low pH, the negative surface of RB was efficiently neutralized by H^+ ions thereby reducing hindrance for the spreading of CR. In addition, electrostatic attraction between RB and the anionic dye ions promote CR adsorption in acidic condition. As pH increased, the number of negatively charged sites on RB increased enhancing the electrostatic repulsion hence hindering CR adsorption. Moreover, the competitions for adsorption active sites occurred between OH^- and anionic dye ions with increasing pH. CR removal by CAB increased with increasing pH from 4 to 6 followed by a decline with further increase in pH. The highest CR removal by RB and CAB was above 83%, which was achieved at neutral and weak acidic pH. The plots of absorbance vs. wavelength for CR adsorption on CAB at various pH (4–11) (**Figure 6**) suggested that the maximum adsorption wavelength of CR (498 nm) barely altered with pH. Hence, CR remained stable within pH 4–11 range and thus CAB removed CR mainly by adsorption.

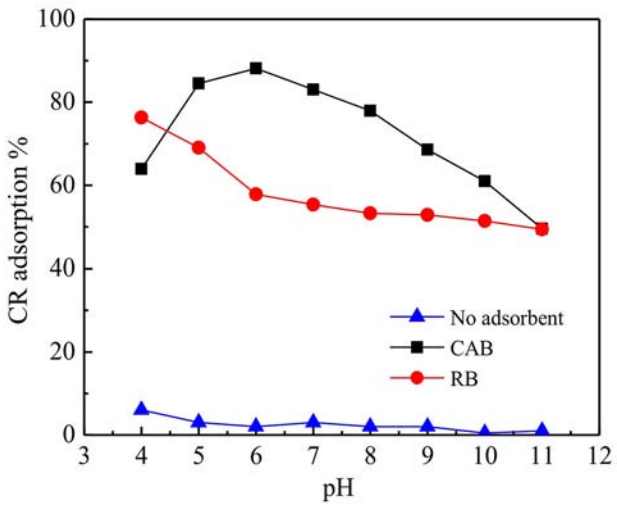

FIGURE 5 | Effect of pH on CR adsorption on RB and CAB.

Adsorption Isotherms

The Langmuir adsorption isotherm is applied for calculating monolayer adsorption with the basic assumption that sorption takes place at specific homogeneous sites within the adsorbent (Xavier et al., 2018). The maximum adsorption capacity (q_m) represents the saturated monolayer adsorption at equilibrium. The Freundlich equation is an empirical equation for describing adsorbate on the heterogeneous surface of the adsorbent. The affinity between the adsorbate and the adsorbent could be indicated by heterogeneous factor, $1/n$. The isotherm parameters are presented in **Table 1**. The saturated adsorption capacities at 303 K for CAB and RB were 384 and 250 $mg{\cdot}g^{-1}$, respectively. The Freundlich parameter, $0 < 1/n < 1$, indicated favorable of CR adsorption on CAB and RB. The correlation coefficient R^2 of Langmuir was 0.99, much higher than that of Freundlich isotherm, indicating better fit of experimental data with the Langmuir model. The preparation conditions and CR adsorption performance of various adsorbents were compared with the present work in **Table 2** (Zhang et al., 2013; Srivastava and Sillanpää, 2016; Huang et al., 2017; Said et al., 2017; Shaba et al., 2017; Shaban et al., 2018). Compared with the traditional methods of clay adsorbents synthesis, present work can considerably shorten the reaction time. Moreover, CAB was prepared under a more moderate pH range using a non-toxic, abundant low-molecular organic acid (CA), which can reduce the adsorbent cost, and avoid secondary pollution. Therefore, this synthesis method of

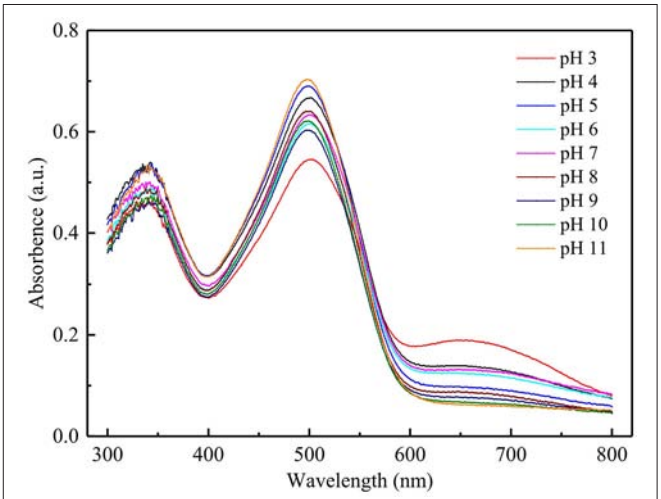

FIGURE 6 | The UV-vis absorbance spectra of CR within experimental pH range.

TABLE 1 | Parameters of isotherm models for CR adsorption on RB and CAB (q_{max}: $mg{\cdot}g^{-1}$, k_L: $L{\cdot}mg^{-1}$, k_f: $mg{\cdot}g^{-1}$).

Adsorbent	Langmuir model			Freundlich model		
	q_m	$K_L \times 10^{-2}$	R^2	K_F	$1/n$	R^2
RB	250	0.71	0.996	19.9	0.362	0.981
CAB	384	255	0.999	59.6	0.294	0.901

CAB was competitive with reported ones. It also noted that CAB removal efficiency was comparable to other adsorbents for CR removal from aqueous solution at lower adsorbent dosage and short equilibrium time. The Langmuir adsorption capacity of CAB for CR was 1.6–19.2 times higher than that of reported literature (malachite@bentonite and bentonite with organometallic $[Fe_3O(OOC_6H_5)_6(H_2O)_3(NO_3).nH_2O]$, respectively) (Srivastava and Sillanpää, 2016; Said et al., 2017). Keeping in mind the enhanced adsorption performance with simple preparation technology and cost effectiveness, CAB could be deemed a promising adsorbent for dyes removal from wastewater.

Adsorption Kinetics

Pseudo-first-order, pseudo-second-order, and intra-particle diffusion models were applied to analyze the kinetics of CR adsorption. The parameters of kinetic models were calculated from the best fitting plots listed in **Table 3**, which suggest that

TABLE 2 | Comparison of preparation conditions and adsorption performance of various adsorbents for CR removal.

Adsorbent	Preparation conditions	Adsorption conditions	Langmuir capacities ($mg \cdot g^{-1}$)	References
Alkaline Ca- bentonite	Modifier: CaO Temperature: 60°C Reaction time: 3 h pH: 10	Dosage: 2.0 $g \cdot L^{-1}$ CR: 100 $mg \cdot L^{-1}$ Time: 2 h pH: 7	149	Zhang et al., 2013
Insertion of bentonite with organometallic $[Fe_3O(OOC_6H_5)_6(H_2O)_3(NO_3).nH_2O]$	Modifier: $[Fe_3O(OOC_6H_5)_6(H_2O)_3(NO_3).nH_2O]$ Room temperature Reaction time: 24 h pH: 10 N_2 protection	Dosage: 0.6 $g \cdot L^{-1}$ CR: 150 $mg \cdot L^{-1}$ Time: 1 h pH: 7	20	Said et al., 2017
CTAB/bentonite	Modifier: CTAB Temperature: 60°C Reaction time: 7 h pH: 7	Dosage: 2.0 $g \cdot L^{-1}$ CR: 300 $mg \cdot L^{-1}$ Time: 1.5 h pH: 8	157	Huang et al., 2017
Malachite@clay	NO modifier Room temperature Reaction time: 2 h pH: 7	Dosage: 2.0 $g \cdot L^{-1}$ CR: 300 $mg \cdot L^{-1}$ Time: 3 h pH: 7	238	Srivastava and Sillanpää, 2016
Bentonite/Zeolite-NaP	NO modifier Temperature: 150°C Reaction time: 6 h pH: 12	Dosage: 0.2 $g \cdot L^{-1}$ CR: 10 $mg \cdot L^{-1}$ Time: 4 h pH: 5	46	Shaban et al., 2018
Inorganic- and organic-modified kaolinite	Modifier: $CTAB/CH_3COONa/Na_3PO_4/Na_2SO_4$ Temperature: 50°C Reaction time: 24 h Non-buffered pH	Dosage: 0.7 $g \cdot L^{-1}$ CR: 100 $mg \cdot L^{-1}$ Time: 2 h pH: 7	149	Shaba et al., 2017
RB	NO modifier Temperature: 60°C Reaction time: 3 h pH: 7	Dosage: 1.0 $g \cdot L^{-1}$ CR: 200 $mg \cdot L^{-1}$ Time: 1.5 h pH: 7	250	Present study
CAB	Modifier: citric acid Temperature: 60°C Reaction time: 3 h pH: 7	Dosage: 1.0 $g \cdot L^{-1}$ CR: 200 $mg \cdot L^{-1}$ Time 1.5 h pH: 6	384	Present study

TABLE 3 | Parameters of kinetic models for CR adsorption on RB and CAB.

Adsorbent	$q_{e,exp}$	Pseudo-first-order model			Pseudo-second-order model			Intra-particle diffusion model		
		$q_{e,cal}$	$k_1 \times 10^{-3}$	R^2	$q_{e,cal}$	$k_2 \times 10^{-4}$	R^2	k_{i2}	I	R^2
RB	107	64.4	9.60	0.901	108	4.64	0.997	1.90	68.1	0.995
CAB	175	14.9	11.2	0.484	178	15.4	1.000	9.90	95.0	0.991

the R^2 of pseudo-second-order kinetic model were higher than the other two models. The calculated q_e values were consistent with the experimental ones, which concluded the better fit of CR adsorption data on RB and CAB to pseudo-second kinetic model.

Normally, the intra-particle diffusion model could be divided into three parts. The first part showed the diffusion of adsorbate to external surface of the adsorbent or boundary layer diffusion. The second part describes the gradual adsorption stage where the intra-particle diffusion rate is considered as the rate-limiting factor, while the last part is the equilibrium stage (Bernstein et al., 2018; Olivoalanis et al., 2018). The fitting plots of q_t vs. $t^{0.5}$ are shown in **Figure 7**. The fitting plots for CR adsorption by CAB could be divided into three parts, hence, three steps involved in the adsorption process, i.e., CR molecules diffused rapidly on the surface of CAB, then penetrated into the interior surface of CAB and reached adsorption equilibrium at last. The adsorption process could be divided into two steps on RB i.e., one for the boundary layer diffusion and the other for the intra-particle diffusion. The plots do not pass through the origin indicating that intra-particle diffusion was involved in the adsorption process, though it was not the only rate-limiting step.

Characterizations of Nascent and CR Loaded Adsorbents

X-ray Diffraction and Pore Structures

Table 4 presents the parameters of basal spacing and pore structures of various samples. Compared with the RB, the specific area of CAB decreased which could be attributed to CA activation resulting in decrease in micro-pores and increase in the number of meso-pores. The pore diameter of CAB was larger than that of RB, which corresponded with the higher reaction rate shown in **Table 3** (Tohdee et al., 2018). The decrease in BET surface area of CR-CAB may be caused by two mechanisms: (1) CR ions may screen CAB surface, which was inaccessible by the nitrogen molecules; (2) CR molecules may have blocked some smaller pores and inhibit the passage of nitrogen molecules into these pores (Mahmoudian et al., 2018). **Table 4** also showed the value of basal spacing of RB, CAB, and CR-CAB. The 2θ of RB at 5.7 was the characteristic basal spacing (d_{001}) of 1.55 nm for calcium bentonite (Zhang et al., 2011). After CA modification, the basal spacing of CAB changed compared with RB. The d_{001} spacing of CR-CAB increased only 0.03 nm which implied CR molecule did not penetrate into CAB interlayer space, i.e., CR adsorption by CAB was mainly controlled by surface adsorption since the molecule dimensions of CR are 3.00 nm wide, 0.73 nm deep, and 0.25 nm thick (Mi et al., 2017).

FT-IR

FT-IR spectra of CAB and RB before and after CR adsorption are shown in **Figure 8**. For RB and CAB, the bands at 1,036 and 524 cm^{-1} were due to Si-O-Si and Si-O-Al (where Al comes from an octahedral cation) stretching peaks, respectively (Brito et al., 2018). The bands at 3,613 and 3,419 cm^{-1} corresponding to –OH stretching vibration of adsorbed water and hydrogen bonding between water molecules and Si-O surface, respectively (Zhang et al., 2014). The new adsorption band in CAB at 1,732 cm^{-1} was assigned to C=O symmetrical stretching, which obviously related to carboxyl groups of CA (Sonia et al., 2018). The main binding modes of CA on bentonite are as follows: (1) Esterification reaction between bentonite and CA. Abundant -OH groups on the surface of RB can react with CA by forming an ester linkage and thus introduce carboxyl groups in CAB

TABLE 4 | Basal spacing, BET surface area, total pore volume, and pore diameter of RB, CAB, and CR-CAB.

Adsorbent	D-spacing (nm)	BET surface area ($m^2 \cdot g^{-1}$)	Total pore volume ($cm^3 \cdot g^{-1}$)	Pore diameter (nm)
RB	1.55	40.1	0.07	8.06
CAB	1.54	16.4	0.06	11.7
CR-CAB	1.57	11.5	0.05	15.5

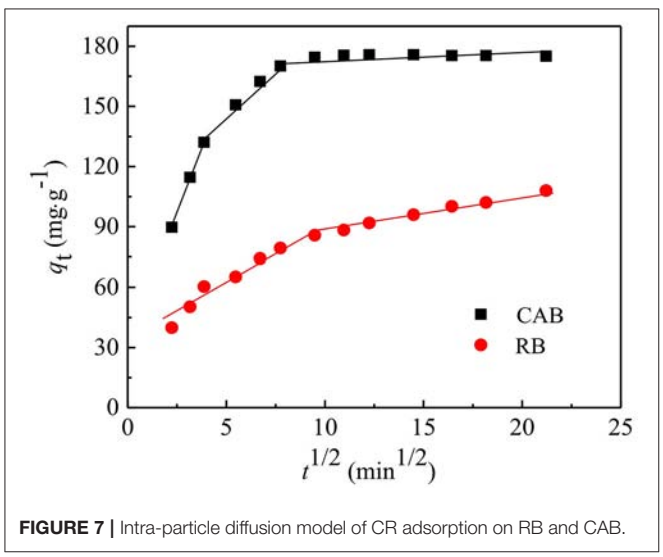

FIGURE 7 | Intra-particle diffusion model of CR adsorption on RB and CAB.

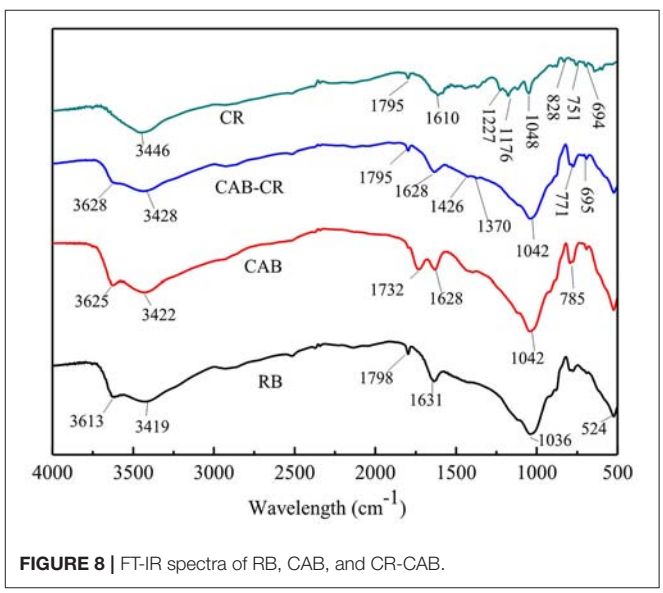

FIGURE 8 | FT-IR spectra of RB, CAB, and CR-CAB.

(**Figure 9**) (El-Sheikh et al., 2018; Liu et al., 2018). (2) Cation exchange reaction between hydrogen ions from CA and the exchange cations (such as Na, Ca, and Mg) in RB interlayer via the following reaction.

$$CA^{n-}—nH^{+} + M^{n+}—\text{Bentonite} \rightarrow M^{n+} + CA—\text{Bentonite} \quad (9)$$

where M and *n* are the exchangeable cation in RB interlayer and the corresponding valence of the cation, respectively. By the cation exchange reaction, CA can bond with RB easily (Bulut et al., 2008; Gong et al., 2018).

The band diminished after CR adsorption and new bands at 1,426 and 1,370 cm^{-1}, which corresponded to symmetric vibration and asymmetric vibration of -COO^{-}, respectively (Rossi et al., 2018). –COOH of CA ionized to give H^{+} and -COO^{-}, and CR ions were protonated by H^{+} ions when CR molecules reached the edge of CAB. Therefore, there existed an electrostatic interaction between the protonated CR ions and negatively charged groups of CAB. The band at 3,446 cm^{-1} corresponded to –N-H- stretching vibration and 1,610 cm^{-1} was assigned to -N=N- stretching in the structure of CR, which diminished after CAB adsorption, while the peaks at 1,176 and 1,048 cm^{-1} assigned to S=O stretching (Sonia et al., 2018) also diminished. Hence, chances of hydrogen bonding or esterification may exist between the functional electronegative groups on CR such as -NH_2, -N=N-, -SO_3, -OH, and -COOH groups of CAB. Therefore, CR adsorption by CAB was a chemical adsorption process and the main active adsorption sites were -NH_2, -N=N-, -SO_3, -OH, and -COOH groups.

Adsorption Mechanism of CR on ACB

The main adsorption mechanism of CAB for CR removal included chelation, hydrogen bonding, and fixation. (1) Good chelating ability toward CR. The -COOH groups of citric acid were not only used as linking groups for coating CA on RB, but also provided active adsorption sites for CR via chelation (**Figure 10**) (Yin et al., 2018). The chelation between –COOH on CAB and -NH_2 on CR has also been confirmed by the FT-IR results analysis. (2) Hydrogen bonding. Abundant -OH groups on CAB can bind with more electronegative groups including -NH_2, -N=N- or -SO_3 on CR and thus form hydrogen bonds (Feng et al., 2017). It is also crucial for CR adsorption on CAB. (3) Fixation is also a principal mechanism for dyes removal by the clay materials. CAB has a number of micropores and mesopores, so CR may diffuse and be fixed into the pore spaces of CAB structure (Zhao et al., 2018). Adsorption kinetics fitting results especially intraparticle diffusion model has confirmed that CR adsorption on CAB involves pore-filling by diffusing. In addition, BET surface area of CAB before and after CR adsorption also indicated that a certain amount of CR was fixed on CAB by physical adsorption.

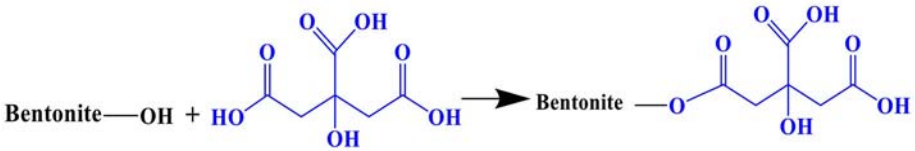

FIGURE 9 | Esterification reaction of bentonite and critic acid.

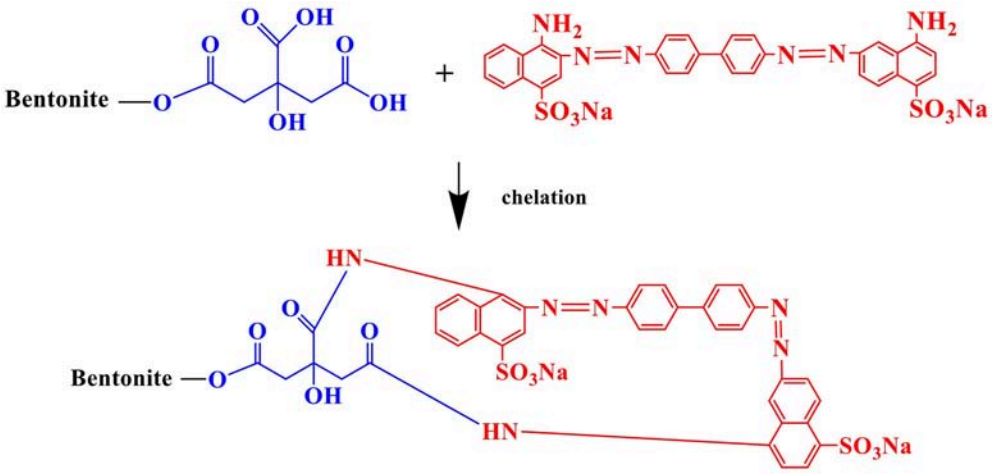

FIGURE 10 | Chelation between CAB and CR.

CONCLUSIONS

In this study, CAB was prepared by modifying RB with CA and its adsorption performance for CR was investigated. Experimental results showed that adsorption capacity of CR on CAB was higher (384 $mg \cdot g^{-1}$) with much faster kinetics than that on RB. In addition, adsorption of CR on RB and CAB was seriously influenced by pH, concentration of NaCl, $CaCl_2$, and CTAB. The isotherm studies revealed that Langmuir model could better describe CR adsorption, while kinetic data best fitted with pseudo-second order model. CR adsorption on CAB was a chemical process including chelation, hydrogen bonding, and fixation, which controlled by the active adsorption sites (–OH and –COOH) of CAB surface. This study credited to the ease and facile synthesis approach for CAB with high adsorption efficiency for CR, can be deemed as a promising approach for industrial waste-water treatments.

AUTHOR CONTRIBUTIONS

HZ conceived and designed the experiments. JZ, RT, and KL contributed through execution and optimization of experiments along with analysis of data. ZT contributed reagents, materials, analysis tools. YM and YZ wrote the paper. All authors have read and approved the final manuscript.

ACKNOWLEDGMENTS

We acknowledge the National Nature Science Foundation of China (Grant No. 21166004 and 21576055) for the financial support.

REFERENCES

Abdelrahman, E. A. (2018). Synthesis of zeolite nanostructures from waste aluminum cans for efficient removal of malachite green dye from aqueous media. *J. Mol. Liq*. 253, 72–82. doi: 10.1016/j.molliq.2018.01.038

Banihani, A., Deery, C., Toumba, J., and Duggal, M. (2018). Effectiveness, costs and patient acceptance of a conventional and a biological treatment approach for carious primary teeth in children. *Caries Res*. 53, 65–75. doi: 10.1159/000487201

Baytar, O., Sahin, O., Saka, C., and Agrak, S. (2018). Characterization of microwave and conventional heating on the pyrolysis of pistachio shells for the adsorption of methylene blue and iodine. *Anal. Lett*. 51, 2205–2220. doi: 10.1080/00032719.2017.1415920

Beheshti, A., Nozarian, K., Ghamari, N., Mayer, P., and Motamedi, H. (2018). Selective high capacity adsorption of Congo Red, luminescence and antibacterial assessment of two new Cadmium(II) coordination polymers. *J. Solid State Chem. France* 258, 618–627. doi: 10.1016/j.jssc.2017.11.035

Bernstein, O. M., Mcgee, T. E., Silzel, L. E., and Silzel, J. W. (2018). Fluorescent pseudorotaxanes of a quinodicarbocyanine dye with gamma cyclodextrin. *Spectrochim Acta A* 189, 202–214. doi: 10.1016/j.saa.2017.07.060

Brito, D. F., Edson, C., Fonseca, G., and Maria, G. (2018). Organophilic bentonites obtained by microwave heating as adsorbents for anionic dyes. *J. Environ. Chem. Engin*. 6, 7080–7090. doi: 10.1016/j.jece.2018.11.006

Bulut, E., Ozacar, M., and Sengil, I. A. (2008). Equilibrium and kinetic data and process design for adsorption of Congo Red onto bentonite. *J. Hazard Mater*. 154, 613–622. doi: 10.1016/j.jhazmat.2007.10.071

Cazzorla, C., Bensi, G., Biasucci, G., Leuzzi, V., Manti, F., Musumeci, A., et al. (2018). Living with phenylketonuria in adulthood: the pku attitude study. *Mol. Genet. Meta*. 16, 39–45. doi: 10.1016/j.ymgmr.2018.06.007

de Araújo M. J. G., Barbosa, R. C., Fook, M., Canedo, E. L., Silva, S., and Medeiros, E. S. (2018). HDPE/Chitosan Blends modified with organobentonite synthesized with quaternary ammonium salt impregnated chitosan. *Materials* 11:291. doi: 10.3390/ma11020291

Ding, S., Sun, Q., Chen, X., Liu, Q., Wang, D., and Lin, J. (2018). Synergistic adsorption of phosphorus by iron in lanthanum modified bentonite (phoslock): new insight into sediment phosphorus immobilization. *Water Res*. 134, 32–43. doi: 10.1016/j.watres.2018.01.055

El-Sheikh, A. H., Fasfous, I. I., Al-Salamin, R. M., and Newman, A. P. (2018). Immobilization of citric acid and magnetite on sawdust for competitive adsorption and extraction of metal ions from environmental waters. *Chem. Eng. J*. 4, 5186–5195. doi: 10.1016/j.jece.2018.08.020

Feng, Y., Liu, Y., Xue, L., Sun, H., Guo, Z., Zhang, Y., et al. (2017). Carboxylic acid functionalized sesame straw: a sustainable cost-effective bioadsorbent with superior dye adsorption capacity. *Bioresource Technol*. 238, 675–683. doi: 10.1016/j.biortech.2017.04.066

Fosso, K., Frans, W., and Fourie, C. L. (2016). Adsorption of Congo Red by surfactant-impregnated bentonite clay. *Desalin Water Treat*. 57, 27663–27671. doi: 10.1080/19443994.2016.1177599

Gong, N., Liu, Y. P., and Huang, R. H. (2018). Simultaneous adsorption of Cu2+ and Acid fuchsin (AF) from aqueous solutions by CMC/bentonite composite. *Int. J. Biol. Macromol*. 115, 580–589. doi: 10.1016/j.ijbiomac.2018.04.075

Gorsd, M. N., Sosa, A. A., Frenzel, R. A., and Pizzio, L. R. (2018). Synthesis and characterization of tungstophosphoric acid-modified mesoporous sponge-like tud-1 materials. *J. Sol. Gel. Sci. Techn*. 87, 204–215. doi: 10.1007/s10971-018-4677-z

Hadjltaief, H. B., Ameur, S. B., Costa, P. D., Zina, M. B., and Galvez, M. E. (2018). Photocatalytic decolorization of cationic and anionic dyes over ZnO nanoparticle immobilized on natural tunisian clay. *Appl. Clay Sci*. 152, 148–157. doi: 10.1016/j.clay.2017.11.008

Huang, Z. H., Li, Y. Z., Chen, W. J., Shi, J. H., and Zhang, Y. X. (2017). Modified bentonite adsorption of organic pollutants of dye wastewater. *Mater. Chem. Phys*. 202, 266–276. doi: 10.1016/j.matchemphys.2017.09.028

Jia, X. J., Wang, J., Wu, J., Teng, W., Zhao, B., and Li, H. (2018). Facile synthesis of $MoO_2/CaSO_4$ composites as highly efficient adsorbents for Congo Red and Rhodamine B. *Rsc Adv*. 8, 1621–1631. doi: 10.1039/C7RA11292K

Lee, W., Yoon, S., Choe, J. K., Lee, M., and Choi, Y. (2018). Anionic surfactant modification of activated carbon for enhancing adsorption of ammonium ion from aqueous solution. *Sci. Total Environ*. 639, 1432–1439. doi: 10.1016/j.scitotenv.2018.05.250

Li, P., Gao, B., Li, A., Hu, L., and Yang, H. (2018). Highly selective adsorption of dyes and arsenate from their aqueous mixtures using a silica-sand/cationized-starch composite. *Micropor. Mesopor. Mat*. 263, 210–219. doi: 10.1016/j.micromeso.2017.12.025

Li, W. Y., Bai, Y. S., Ma, Q. L., Chen, W. J., Wu, M., and Ma, H. Z. (2018). Polyacrylic acid/ctab-bentonite coated filter paper: efficient and rapid removal of anionic and cationic dyes. *Appl. Surf. Sci*. 458, 903–909. doi: 10.1016/j.apsusc.2018.07.169

Li, Y., Meas, A., Shan, S., Yang, R., Gai, X., and Wang, H. (2018). Characterization, isotherm and kinetic data for adsorption of Congo Red and 2-naphthol on different bamboo hydrochars. *Data Brief*. 19, 49–54. doi: 10.1016/j.dib.2018.04.066

Lin, J., Jiang, B., and Zhan, Y. (2018). Effect of pre-treatment of bentonite with sodium and calcium ions on phosphate adsorption onto zirconium-modified bentonite. *J. Environ. Manage*. 217, 183–195. doi: 10.1016/j.jenvman.2018.03.079

Liu, K., Qin, Y. L., Muhammad, Y., Zhu, Y., Tang, R., and Zhang, H. B. (2019). Effect of Fe_3O_4 content and microwave reaction time on the properties of Fe_3O_4/ZnO magnetic nanoparticles. *J. Alloy Compd*. 781, 790–799. doi: 10.1016/j.jallcom.2018.12.085

Liu, X., Xu, L., Liu, Y., and Zhou, W. (2018). Synthesis of citric acid-modified resins and their adsorption properties towards metal ions. *R. Soc. Open Sci.* 8, 167–177. doi: 10.1098/rsos.171667

Magdalena, R., Hassanein, M. M. M., Abdel-Razek, A. G., Kmiecik, D., Siger, A., and Ratusz, K. (2018). Influence of composition on degradation during repeated deep-fat frying of binary and ternary blends of palm, sunflower and soybean oils with health-optimised saturated-to-unsaturated fatty acid ratios. *Int. J. Food Sci. Tech.* 53, 1021–1029. doi: 10.1111/ijfs.13678

Mahmoudian, M., Balkanloo, P. G., and Nozad, E. (2018). A facile method for dye and heavy metal elimination by pH sensitive acid activated montmorillonite/polyethersulfone nanocomposite membrane. *Chin. J. Polym. Sci.* 36, 49–57. doi: 10.1007/s10118-018-2004-3

Mat, S. S. A., Zuber, S. Z. H. S., Rahim, S. K. E. A., Sohaimi, K. S. A., Halim, N. A. A., and Zainudin, N. F. (2018). Malachite green adsorption by spent coffee grounds. *Mater. Sci. Eng.* 318, 12–15.doi: 10.1088/1757-899X/318/1/012015

Mi, J., Gregorich, E. G., Xu, S., Mclaughlin, N. B., Ma, B., and Liu, J. (2017). Effect of bentonite amendment on soil hydraulic parameters and millet crop performance in a semi-arid region. *Field Crop Res.* 212, 107–114. doi: 10.1016/j.fcr.2017.07.009

Mudrinic, T. M., Ajdukovic, M. J., Jovic-Jovicic, N. P., Marinovic S. R., Mojovic, Z. D., Milutinović-Nikolić, A. D., et al. (2018). Al, Fe, Ni-pillared bentonite in the catalytic wet peroxide oxidation of the textile dye acid yellow 99. *React. Kinet. Mech. Cat.* 124, 75–88. doi: 10.1007/s11144-018-1386-0

Olivoalanis, D., Garciareyes, R. B., Alvarez, L. H., and Garciagonzalez, A. (2018). Mechanism of anaerobic bio-reduction of azo dye assisted with lawsone-immobilized activated carbon. *J. Hazard Mater.* 347, 423–430. doi: 10.1016/j.jhazmat.2018.01.019

Rosa, A. D., Elvis, C., Guilherme, L. D., Hedda, S., and Liliana, A. F. (2018). Biosorption of rhodamine B dye from dyeing stones effluents using the green microalgae *Chlorella pyrenoidosa*. *J. Clean. Prod.* 198, 1302–1310. doi: 10.1016/j.jclepro.2018.07.128

Rossi, T. J., Escobedo, J., Santos, C. M. D., Rossi, L. R., Silva, B. P. D., and Pai, E. D. (2018). Global, diffuse and direct solar radiation of the infrared spectrum in botucatu/sp/ brazil. *Renew. Sust. Energy Rev.* 82, 448–459. doi: 10.1016/j.rser.2017.09.030

Said, M., Utami, H. P., and Hayati, F. (2017). Insertion of bentonite with organometallic $[Fe_3O(OOC_6H_5)6(H_2O)_3(NO_3).nH_2O]$ as adsorbent of Congo Red. *IC2MS* 299:012086. doi: 10.1088/1757-899X/299/1/012086

Schorr, D., Blanchet, P., and Essoua, G. G. E. (2018). Glycerol and citric acid treatment of lodgepole pine. *J. Wood Chem. Technol.* 2, 123–136. doi: 10.1080/02773813.2017.1388822

Sha, Z., Luo, X., Liao, X., Wang, S., Wang, Q., and Chen, S. (2018). Preparation and characterization of the inclusion complex of astaxanthin. *J. Korean Phys. Soc.* 72, 1228–1236.

Shaba, M., Sayed, M. I., Mohamed, G., and Zeinab, M. (2017). Adsorption behavior of inorganic- and organic-modified kaolinite for Congo red dye from water, kinetic modeling, and equilibrium studies. *J. Sol-Gel. Sci. Tech.* 81, 421–447. doi: 10.1007/s10971-018-4719-6

Shaban, M., Abukhadra, M. R., Shahien, M. G., and Ibrahim, S. S. (2018). Novel bentonite/zeolite-nap composite efficiently removes methylene blue and Congo Red dyes. *Environ. Chem. Lett.* 2, 275–280. doi: 10.1007/s10311-017-0658-7

Sham, A. Y. W., and Notley, S. M. (2018). Adsorption of organic dyes from aqueous solutions using surfactant exfoliated graphene. *J. Environ. Chem. Eng.* 6, 495–504. doi: 10.1016/j.jece.2017.12.028

Shivaprakash, K. N., Ramesh, B. R., Umashaanker, R., and Dayanandan, S. (2018). Functional trait and community phylogenetic analyses reveal environmental filtering as the major determinant of assembly of tropical forest tree communities in the western ghats biodiversity hotspot in india. *Forest Ecosyst.* 5:25. doi: 10.1186/s40663-018-0144-0

Sonia, J., Ocampo-Pérez, R., Mendoza, M. S., Ramos, R., Azuara, A., and Castillo, N. A. (2018). Walnut shell treated with citric acid and its application as biosorbent in the removal of Zn(II). *J. Water Process Eng.* 25, 45–53. doi: 10.1016/j.jwpe.2018.06.007

Srivastava, V., and Sillanpää, M. (2016). Synthesis of malachite@clay nanocomposite for rapid scavenging of cationic and anionic dyes from synthetic wastewater. *J. Environ. Sci.* 51, 97–110. doi: 10.1016/j.jes.2016.08.011

Tarmizi, T., Risfidian, M., Rohendi, D., and Lesbani, A. (2017). "Kinetic and thermodynamic adsorption studies of congo red on bentonite," in *AIP Conference Proceedings* (Yogyakarta: AIP Publishing), 1823, 020028-1–020028-8. doi: 10.1063/1.4978101

Tesfaye, T., Sithole, B., and Ramjugernath, D. (2018). Valorisation of waste chicken feathers: optimisation of decontamination and pre-treatment with bleaching agents using response surface methodology. *Sustain. Chem. Pharma.* 8, 21–37. doi: 10.1016/j.scp.2018.02.003

Tohdee, K., Kaewsichana, L., and Ullah, A. (2018). Enhancement of adsorption efficiency of heavy metal Cu(II) and Zn(II) onto cationic surfactant modified bentonite. *J. Environ. Chem. Eng.* 6, 2821–2828. doi: 10.1016/j.jece.2018.04.030

Toor, M., Jin, B., Dai, S., and Vimonses, V. (2015). Activating natural bentonite as a cost-effective adsorbent for removal of Congo Red in wastewater. *J. Ind. Eng. Chem.* 21, 653–661. doi: 10.1016/j.jiec.2014.03.033

Wang, H., Qin, X. Y., Li, Z. Y., Zheng, Z. Z., and Fan, T. Y. (2018). Preparation and characterization of citric acid-modified superparamagnetic iron oxide nanoparticles. *J. Peking Univ.* 2, 340–346. doi: 10.3969/j.issn.1671-167X.2018.02.023

Wang, Y. Y., Shi, H. Z., Zhang, H. B., Yu, S. M., Chen, N. H., and Tong. Z. F. (2017). Research on Cr(VI) adsorption with magnetic citric acid bentonite. *J. Chem. Eng. Chin. Univ.* 3, 726–732. doi: 10.3969/j.issn.1003-9015.2017.03.030

Wen, Q., Qiong, H., Yi, Z., Jin, P., and Li, Z. (2016). Microwave-assisted regeneration of spent activated carbon containing zinc acetate and its application for removal of Congo Red. *Desalin Water Treat.* 57, 28496–28511. doi: 10.1080/19443994.2016.1179675

Xavier, A., Adarme, O., Furtado, L. M., Ferreira, G., Da, L. S., and Gil, L. F. (2018). Modeling adsorption of Copper(II), Cobalt(II) and Nickel(II) metal ions from aqueous solution onto a new carboxylated sugarcane bagasse. part II: optimization of monocomponent fixed-bed column adsorption. *J. Colloid Interf. Sci.* 516, 431–445. doi: 10.1016/j.jcis.2018.01.068

Xu, L., Xu, X., Cao, G., Liu, S., Duan, Z., Song, S., et al. (2018). Optimization and assessment of Fe-electrocoagulation for the removal of potentially toxic metals from real smelting wastewater. *J. Environ. Manage.* 218, 129–138. doi: 10.1016/j.jenvman.2018.04.049

Xu, Y., Asim, K. M., Wang, F. Y., Xia, M. Z., and Lei, W. (2018). Novel multi amine-containing gemini surfactant modified montmorillonite as adsorbents for removal of phenols. *Appl. Clay Sci.* 162, 204–213. doi: 10.1016/j.clay.2018.06.023

Yan, J., Lan, G., Qiu, H., Chen, C., Liu, Y., and Du, G. (2018). Adsorption of heavy metals and methylene blue from aqueous solution with citric acid modified peach stone. *Sep. Sci. Technol.* 11, 1678–1688. doi: 10.1080/01496395.2018.1439064

Yao, M., Zhang, X., and Lei, L. (2012). Removal of reactive blue 13 from dyeing wastewater by self-assembled organobentonite in a one-steep progress. *J. Chem. Eng. Data* 57, 1915–1922. doi: 10.1021/je300216e

Ye, W., Lin, J., Borrego, R., Chen, D., Sotto, A., Luis, P., et al. (2018). Advanced desalination of dye/NaCl mixures by a loose nanofiltration membrane for digital ink-jet printing. *Sep. Purif. Technol.* 197, 27–35. doi: 10.1016/j.seppur.2017.12.045

Yen, L., Yee, W., Tze, A., Soon, O., Nabilnah, L., and Li, H. (2017). Degradation reaction of diazo reactive black 5 dye with Copper (II) sulfate catalyst in thermolysis treatment. *Environ. Sci. Pollut. Res. Int.* 25, 7067–7075. doi: 10.1007/s11356-017-1069-9

Yin, Z. C., Wang, Y. L., and San, J. S. (2018). Adsorption behavior of hydroxypropyl guar gum onto montmorillonite and reducing adsorption in the reservoir. *Appl. Clay Sci.* 166, 123–130. doi: 10.1016/j.clay.2018.09.015

Zhang, C., Qi, Y. H., Qian, P., Zhong, M. J., Wang, L., and Yin, H. Z. (2014). Quantum chemical study of the adsorption of water molecules on kaolinite surfaces. *Comput. Theor. Chem.* 1046, 10–19. doi: 10.1016/j.comptc.2014.07.004

Zhang, H. B., Tong, Z. F., Wei, T. Y., and Tang, Y. K. (2011). Removal characteristics of Zn(II) from aqueous solution by alkaline Ca-bentonite. *Desalination* 276, 103–108. doi: 10.1016/j.desal.2011.03.026

Zhang, H. B., Zhang, T. S., Tang, Y. K., Wei, T. Y., Tong, Z. F., and Deng, Z. F. (2013). Adsorption of methylene blue and congo red on alkaline Ca-bentonite. *Fine Chem.* 30, 657–673. doi: 10.13550/j.jxhg.2013.06.026

Zhao, J. B., Zou, Z. D., Ren, R., Sui, X. F., Mao, Z. P., Xu, H., et al. (2018). Chitosan adsorbent reinforced with citric acid modified β-cyclodextrin for highly efficient removal of dyes from reactive dyeing effluents. *Eur. Polym. J.* 108, 212–218. doi: 10.1016/j.eurpolymj.2018.08.044

Zhou, J., Zhang, H. B., Tong, Z. F., Qin, Y. L., Chen, G. H., Song, Z. Y., et al. (2015). Adsorption behavior of methylene blue on citric acid bentonite. *Chinese J. Chem. Eng.* 3, 1057–1061.

Zhou, Y., Yao, S., Ma, Y., Li, G., Huo, Q., and Liu, Y. (2018). An anionic single-walled metal-organic nanotube with an armchair (3,3) topology as an extremely smart adsorbent for the effective and selective adsorption of cationic carcinogenic dyes. *Chem. Commun.* 54:3006. doi: 10.1039/C8CC00542G

Conflict of Interest Statement: The authors declare that the research was conducted in the absence of any commercial or financial relationships that could be construed as a potential conflict of interest.

frontiers in Materials

ORIGINAL RESEARCH
published: 31 October 2018
doi: 10.3389/fmats.2018.00064

Grand Canonical Monte Carlo Simulations of Ethanol Conversion to Propylene Over Zeolite Catalysts

Fangfang Wang, Wei Xia, Longxiang Wang, Junguo Wang, Xiujie Yang and Kun Chen*

State Key Laboratory of Heavy Oil Processing, College of Chemical Engineering, China University of Petroleum (East China), Qingdao, China

The transformation of ethanol to propylene (ETP) was investigated over H-ZSM-5 (40) and H-LEV (40) catalysts. For H-ZSM-5 (40), the propylene yield kept constant at about 20.0% during 8 h. For H-LEV (40), higher initial propylene yield reached 34.0%. However, there is almost no propylene obtained over H-LEV (40) catalyst after 2 h. H-ZSM-5 (40) catalyst exhibited higher stability than H-LEV (40). The lower stability of H-LEV (40) is probably due to coke deposition. The reactant and products adsorption performances in the ethanol conversion reaction over H-ZSM-5 (40) and H-LEV (40) catalysts were studied by Monte Carlo simulations. Results show that the higher adsorption amount of ethanol, ethylene and propylene in H-LEV (40) led to the more difficult desorption of products and higher content of coke deposition.

Keywords: ethanol, propylene, adsorption, zeolite, Grand Canonical Monte Carlo

OPEN ACCESS

Edited by:
Jie-Sheng Chen,
Shanghai Jiao Tong University, China

Reviewed by:
Baowang Lu,
University of Toyama, Toyama, Japan
Shuyan Gao,
Henan Normal University, China
Qiang Wu,
Shanghai University of Electric Power, China

****Correspondence:***
Wei Xia
xiawei@upc.edu.cn

Specialty section:
This article was submitted to Colloidal Materials and Interfaces, a section of the journal Frontiers in Materials

Received: *15 September 2018*
Accepted: *12 October 2018*
Published: *31 October 2018*

Citation:
Wang F, Xia W, Wang L, Wang J, Yang X and Chen K (2018) Grand Canonical Monte Carlo Simulations of Ethanol Conversion to Propylene Over Zeolite Catalysts. Front. Mater. 5:64. doi: 10.3389/fmats.2018.00064

INTRODUCTION

Propylene is one of the most important chemicals, which could obtain from several routes such as steam cracking of naphtha, fluid catalytic cracking (Ren et al., 2006), and MTP (methanol to propylene). These processes depend on the fossil resources and confront environmental problems heavily. Bioethanol is considered to be one of the most prospective renewable resources for the production of ethylene and propylene (Parajuli et al., 2017). Thus, the conversion of ethanol to propylene (ETP) attracts broad attention in the academic and industrial fields (Huangfu et al., 2016; Xia et al., 2017a,b). The research work on the conversion of ETP over zeolite and transition metal oxide catalysts were reviewed by Li. The existing researches show that ZSM-5 is the best candidate for propylene production (Li et al., 2016). Levyne (LEV), which belongs to CHA type zeolite, exhibit the specific shape selectivity for the transformation of methanol or ethanol (Venkatathri and Yoo, 2008; Inoue et al., 2009; Bhawe et al., 2012). The optimum selectivity of ethylene (43.0%) and propylene (32.0%) from methanol over LEV catalysts was reported by Bhawe group (Bhawe et al., 2012). Venkatathri et al. synthesized LEV catalyst and investigated the conversion of methanol to olefin (MTO) over synthesized LEV catalysts. Higher selectivity of light olefins was obtained over LEV than that over SAPO-34 catalyst (Venkatathri and Yoo, 2008). Inoue et al. also reported that 35.8% of C_2H_4 and 34.4% of C_3H_6 were acquired over LEV catalyst for the transformation of ethanol to olefins (Inoue et al., 2009).

The adsorption of reactants and products could influence the catalytic selectivity and stability in the heterogeneous catalytic reaction. However, it is very difficult to interpret the adsorption processes of guest molecules in the host zeolites through only experiment. Molecular simulation is a valuable method to simulate the motion behavior of molecules by theoretical calculation.

Much more particular properties, such as the energy and density distribution of components in zeolite, could also be achieved from the molecular simulation. To investigate the adsorption and diffusion of adsorbate in different porous materials, molecular simulation is widely used (Klemm et al., 1998; Hansen et al., 2005; Navarro et al., 2010). Many researchers have studied the adsorption behavior of different systems in zeolite. Zhang et al. studied gas permeation of propane and propylene across ZSM-5 membranes by a non-equilibrium molecular dynamics technique (Zhang et al., 2003). The adsorption and diffusion behavior of ethanol and water through silicalite membranes was also reported by Yang et al. using molecular simulation method (Yang et al., 2007). Phenol obtained from benzene catalyzed by ZSM-5 type zeolite was investigated by Klemm et al. The strong adsorption of phenol should be inhibited to prevent the formation of coke (Klemm et al., 1998). The adsorption and diffusion were examined regarding the conversion of methanol to ethylene in HZSM-5 (300) and HZSM-5 (30) by (Chatterjee and Chatterjee, 2008). Adsorption amount is the most important physical quantity in the adsorption study. In the process of ETP reaction, the adsorption of reactants and products play an important role. Thus, in order to understand the ZSM-5 and LEV catalytic performance for ETP reaction, it is of great significance to study the adsorption behavior of ethanol and main products. There are a few researches which combined the adsorption of light olefins in zeolite with the product distribution in the process of catalytic reaction (Yang et al., 2007).

Transformation of ETP was systematically investigated over H-ZSM-5 (40) and H-LEV (40) with time-on-stream. Monte Carlo simulations are used to shed light on the effects of zeolite on their adsorption performance in the ETP reaction. The adsorptions of ethanol and light olefins molecules in H-ZSM-5 (40) and H-LEV (40) are calculated by Monte Carlo simulations.

MATERIALS AND METHODS

Catalytic Apparatus and Ethanol Transformation Reaction

The H-LEV and H-ZSM-5 catalysts (Si/Al ratio of 40) were obtained from Zeolyst International, which were calcined in air for 4 h at 873 K. The heating rate is 4.5 K/min. The calcined H-LEV and H-ZSM-5 samples were named H-LEV (40) and H-ZSM-5 (40), respectively. Ethanol (99.5%, Wako) was used without further purification. The ETP reactions were carried out in a fixed-bed quartz tubular reactor at atmospheric pressure. Details of the catalytic reaction process can be found in our previous report (Wang et al., 2018).

A TG/DTA apparatus (SSC/5200 Seiko Instruments) was used to measure the coke deposition (airflow 50 mL/min from 323 to 973 K with a heating rate of 10 K/min). The amounts of coke deposition were calculated as follows:

$$C(wt\%) = (m_{\text{used}} - m_{\text{fresh}}) \times 100\% / m_{\text{used}} \quad (1)$$

Where m_{fresh} and m_{used} were the mass of fresh catalyst and the mass of used catalyst, respectively.

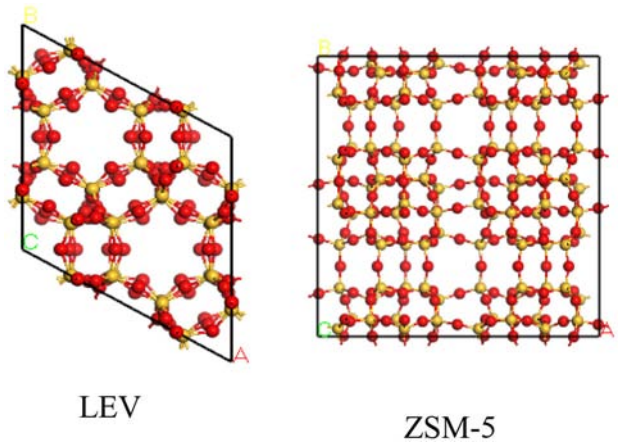

FIGURE 1 | Structures of Lev and ZSM-5. The yellow and red balls denote Si and O atoms, respectively.

Molecular Simulations

The structures of H-LEV (40) and H-ZSM-5 (40) are present in **Figure 1**, which are obtained from International Zeolite Association. Simulations were performed in a simulation box of 2*2*2 unit cell. For ZSM-5 and LEV catalysts, initial frameworks include oxygen and silicon atoms. In order to obtain the structure of Si/Al atomic ratio = 40, some silicon atoms are replaced by aluminum atoms basing on the Lowenstein rule (Jakobtorweihen et al., 2005). H^+ extra-framework cations were used to compensate the negative charge, which was introduced by taking place of Si by Al. Generally, extra-framework cations are located around oxygen atoms neighboring aluminum atoms, therefore, their positions are determined by the location of Al atoms (Beerdsen et al., 2002; Mentzen et al., 2006). Forcite module of Materials Studio 8.0 package was firstly used to geometrically optimize the structure.

The GCMC method is carried out by the sorption module in Materials Studio 8.0 simulation package to simulate the adsorption process. The distribution of movements was 40% exchange, 20% rotation, 20% conformation, and 20% translation in each MC simulation. The COMPASS forcefield was used in this study. The electrostatic and van der Waals potential energy were calculated by the Ewald summation and the atom based technique, respectively. Lennard-Jones potentials were used to present the interactions between atoms. The production steps were set to $2 * 10^6$ and the equilibration steps were set to $2 * 10^6$ Monte Carlo steps. To build a homogeneous solid, periodic boundary conditions are adopted in three directions. A cut-off of 12.5 Å is used to the Lennard–Jones interactions. Ewald sum was used to calculate the long-range electrostatic interactions. The simulated value of heat of adsorption was compared with the experimental ones to check the accuracy of interaction parameters. The calculated isosteric heat of adsorption for ethylene in ZSM-5 is 31.8 KJ·mol^{-1} at 303 K; the available experimental data is 24.0–32.7 KJ·mol^{-1} (Jakobtorweihen et al., 2005). The adsorption isotherms and isosteric heat of ethylene

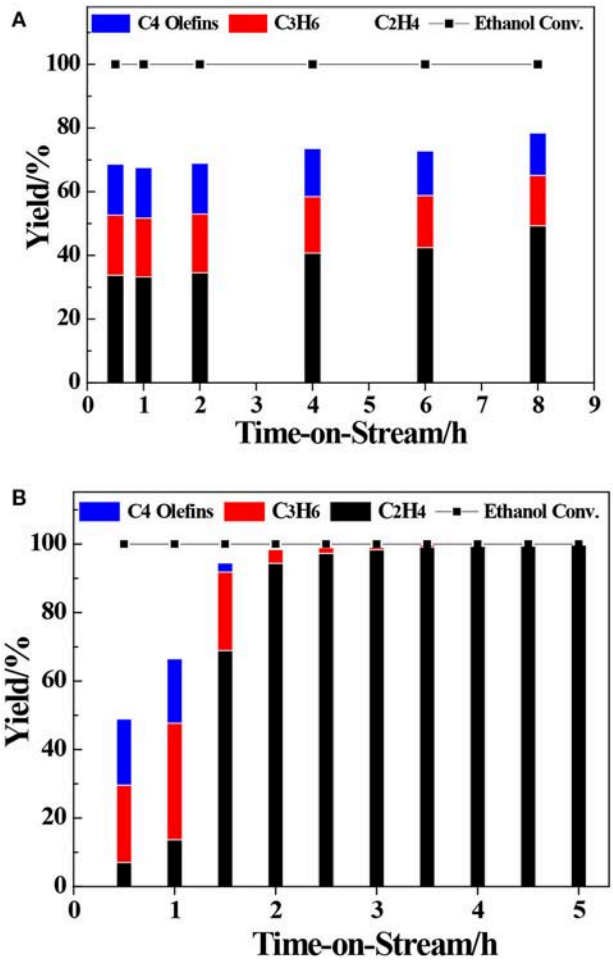

FIGURE 2 | Product distributions of ethanol conversion over ZSM-5 and LEV with time on stream. **(A)** H-ZSM-5 (40), (**B)** H-LEV (40), Reaction conditions: 673 K, 0.1 MPa, W/F = 0.05 g.min.mL^{-1}.

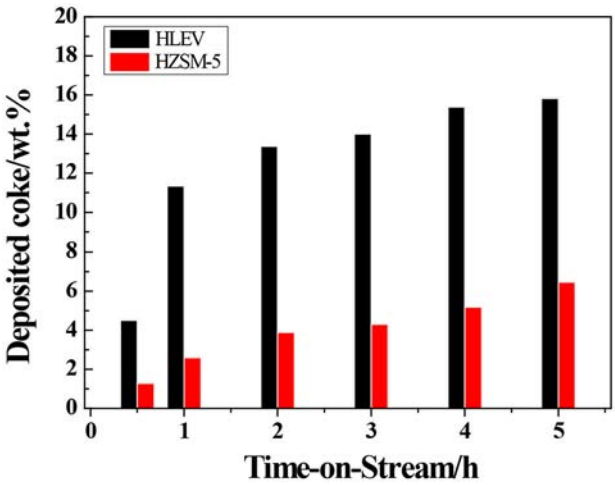

FIGURE 3 | Evolution of coke deposited over H-ZSM-5 (40) and H-LEV (40) with time on stream. Reaction conditions: 673 K, 0.1 MPa, W/F = 0.05 g.min.mL^{-1}.

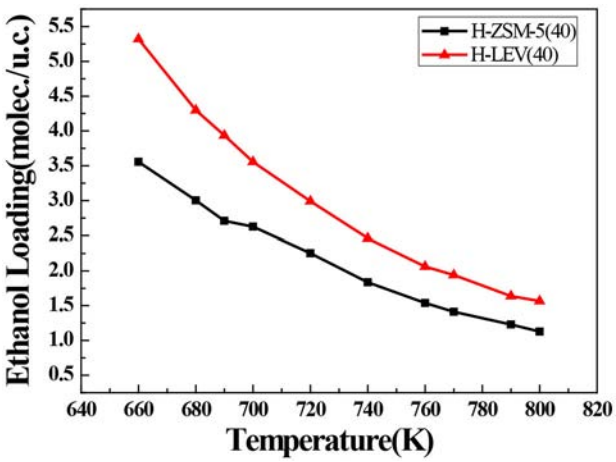

FIGURE 4 | Ethanol adsorption amounts in H-ZSM-5 (40) and H-LEV (40) with different temperatures under 100 kPa.

on ZSM-5 zeolite at 303 K have been calculated to verify the rationality of model construction and simulation parameters.

RESULTS AND DISCUSSION

Catalytic Performance

The transformation reaction of ETP over H-ZSM-5 (40) and H-LEV (40) catalysts were systematically investigated. Catalyst stability results are shown in **Figure 2**. For two catalyst samples, the conversions of ethanol were 100% during the whole time on stream. For H-ZSM-5 (40), the propylene yield gradually decreased from 20.0 to 17.8%. The C4 olefin yield also slowly decreased from 16.0 to 13.2% (as shown in **Figure 2A**). For H-LEV (40), the initial propylene yield reached 34.0% and sharply decreased to 4.0% after 2 h. There is almost no propylene produced after 2 h. The C4 olefins yield sharply decreased from 19.3 to 0.0%, ethylene yield quickly increased from 7.4 to 94.4% with time on stream from 0.5 to 2 h (as shown in **Figure 2B**). The formation of ethylene seems not influenced by catalyst deactivation. It could be explained that ethylene formed at weak acidic sites, and the formation of other products such as propylene requires stronger acidic sites (Aguayo et al., 2002). The production distribution could be strongly affected by the catalyst deactivation, especially coke deposition (Inoue et al., 2009). **Figure 3** shows the different coke deposition content over the two catalysts. As shown in **Figure 3**, the coke deposition content on H-LEV (40) is much higher than that on H-ZSM-5 (40). The coke deposition content of H-LEV (40) increased sharply during 2 h, after that the trend of growth become gentle to steady state with time on stream. Due to the high content of coke deposition on H-LEV (40) at the beginning of reaction, the catalytic performance of H-LEV (40) decreased quickly. It is for this reason that the yield of propylene decreased sharply with time on stream.

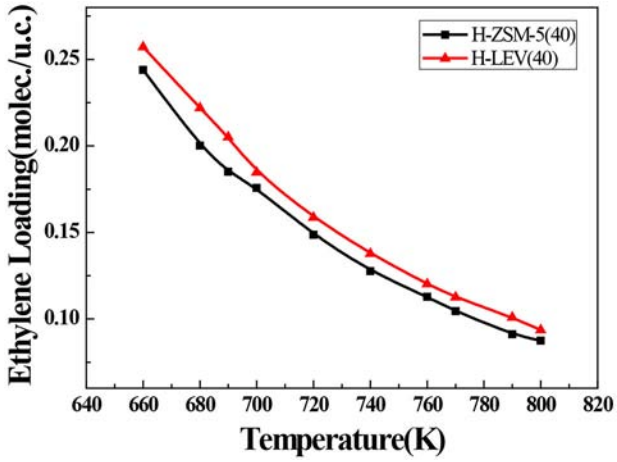

FIGURE 5 | Ethylene adsorption amounts in H-ZSM-5 (40) and H-LEV (40) with different temperatures under 100 kPa.

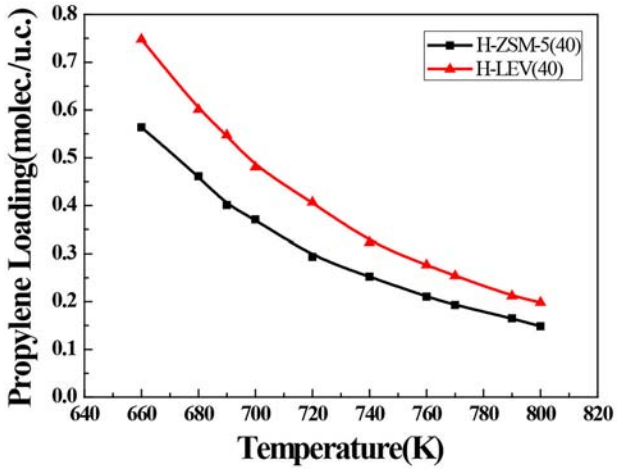

FIGURE 6 | Propylene adsorption amounts in H-ZSM-5 (40) and H-LEV (40) with different temperatures under 100 kPa.

Results of Molecular Simulation

The catalytic performance could be strongly affected by the adsorption of the guest molecule in the host zeolite. Under the same ETP reaction condition, reactant (ethanol) and products (ethylene and propylene) adsorptions in the H-ZSM-5 (40) and H-LEV (40) structure models were investigated through Monte Carlo simulations. The adsorption amounts of ethanol, ethylene, and propylene in zeolites at different temperatures were shown in **Figures 4**, **5**, **6**, respectively. Ethanol, ethylene, and propylene have obvious adsorption on H-ZSM-5 (40) and H-LEV (40) structure models. All of the ethanol, ethylene, and propylene adsorption amounts decreased with increasing of temperature for any one component. According to product of propylene, under certain conditions, higher reaction temperature favors the ETP reaction. As shown in **Figures 4**, **5**, **6**, all of the ethanol, ethylene, and propylene have higher adsorption amounts in H-LEV (40) than that in H-ZSM-5 (40). Under same conditions, the ethanol adsorption capacity on molecular sieves is obviously higher than

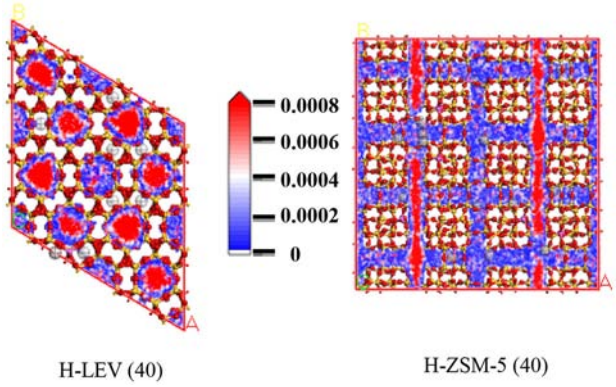

FIGURE 7 | Density distribution of ethanol in H-ZSM-5 (40) and H-LEV (40) under 680 K, 100 kPa.

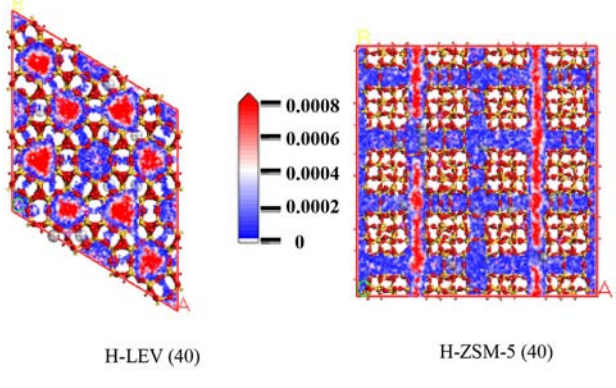

FIGURE 8 | Density distribution of ethylene in H-ZSM-5 (40) and H-LEV (40) under 680 K, 100 kPa.

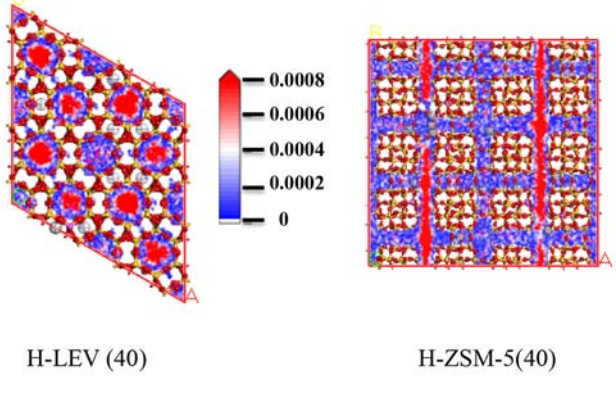

FIGURE 9 | Density distribution of propylene in H-ZSM-5 (40) and H-LEV (40) under 680 K, 100 kPa.

those of ethylene and propylene. This is mainly due to the larger molecular weight of ethanol, the dipole distance is 1.68D, and the greater polarizability. The adsorption amounts of ethanol, ethylene and propylene obviously decreased with temperature increasing over H-ZSM-5 (40) and H-LEV (40). The adsorptive molecules easily break away from intramolecule bound with the increase of molecular energy, thus the amount of adsorption amounts decreased (Smit and Maesen, 2008). Under the same conditions, the order of adsorption amount of ethanol, ethylene, and propylene on molecular sieve is H-LEV (40) > H-ZSM-5 (40). It is favorable for the desorption of reactant and products from H-ZSM-5 (40). Propylene has larger adsorption amount in H-LEV (40) and H-ZSM-5 (40) than ethylene. It is favorable for the desorption of ethylene from H-LEV (40) and H-ZSM-5 (40) than propylene. Therefore, two kinds of zeolite catalysts are all helpful to improve selection of ethylene in ETP reaction. On the H-ZSM-5 (40), the adsorption amounts of products are less than that on H-LEV (40). These products could desorb quickly which restrain the polymerization and dimerization reactions, which is the main reason of coking deposition (Huang et al., 2015). The higher adsorption amount of products in the structure model of H-LEV (40) led to the higher amount of coke deposition, which is the main factor influencing the product distribution.

Figures 7, **8**, **9** show the various density distributions of ethanol, ethylene, and propylene in the model at 680 K, 100 kPa over the two zeolite catalysts, respectively. As shown in **Figures 7**, **8**, **9**, ethanol, ethylene, and propylene mainly adsorbed in straight channel of H-ZSM-5 (40). Ethanol, ethylene, and propylene mainly adsorbed in the 8-membrane ring channels of H-LEV (40). The components are able to fully occupy most of the molecular sieve pore position in 10-membrane ring channel of H-ZSM-5 (40) and 8-membrane ring channel of H-LEV (40). For same component, the distribution probability density in the straight channel is higher than that in the curved channel, and the density is higher in the region closer to the center of channel. Higher adsorption amount of component, higher proportion of red region could be observed in the probability density map.

CONCLUSIONS

In this work, conversions of ETP were systematically carried out on H-ZSM-5 (40) and H-LEV (40). H-LEV (40) exhibited higher propylene yield and lower stability than H-ZSM5 (40) for ETP reaction. The molecular simulation results show that the adsorption of ethanol, ethylene and propylene in H-LEV (40) was stronger that in H-ZSM-5 (40), which led to the difficult desorption of products, high yields of by-products, and coke deposition. A strong adsorption of reactants and products in H-LEV (40) should be depressed to inhibit the coke formation.

AUTHOR CONTRIBUTIONS

WX designed experiments. FW, LW, and JW carried out experiments. FW, XY, and KC analyzed experimental results. FW and WX wrote the manuscript.

ACKNOWLEDGMENTS

This work is a project sponsored by the National Natural Science Foundation of China (Grant 21406269 k, 21502227), Shandong Provincial Natural Science Foundation, China (Grant ZR2014BQ012), Scientific Research Foundation for Returned Scholars, Ministry of Education of China (K1504051C), Shandong Provincial Key Research Program (Grant: 2015GSF121017), the Fundamental Research Funds for the Central Universities (15CX05013A), the International Cooperation and Exchange Fund, China University of Petroleum (East China) (UPCGJ2018010), and the Graduate Innovation Project, China University of Petroleum (East China) (YCX2018047).

REFERENCES

Aguayo, A. T., Gayubo, A. G., Tarrío, A. M., Atutxa, A., and Bilbao, J. (2002). Study of operating variables in the transformation of aqueous ethanol into hydrocarbons on an HZSM-5 zeolite. *J. Chem. Technol. Biotechnol.* 77, 211–216. doi: 10.1002/jctb.540

Beerdsen, E., Smit, B., and Calero, S. (2002). The influence of non-framework sodium cations on the adsorption of alkanes in MFI- and MOR-type zeolites. *J. Phys. Chem. B* 106, 10659–10667. doi: 10.1021/jp026257w

Bhawe, Y., Moliner-Marin, M., Lunn, J. D., Liu, Y., Malek, A., and Davis, M. (2012). Effect of cage size on the selective conversion of methanol to light olefins. *ACS Catal.* 2, 2490–2495. doi: 10.1021/cs300558x

Chatterjee, A., and Chatterjee, M. (2008). Computational designing of gradient type catalytic membrane: application to the conversion of methanol to ethylene. *Mol. Simulat.* 34, 1091–1097. doi: 10.1080/08927020802225848

Hansen, N., Jakobtorweihen, S., and Keil, F. J. (2005). Reactive Monte Carlo and grand-canonical Monte Carlo simulations of the propene metathesis reaction system. *J. Chem. Phys.* 122:164705. doi: 10.1063/1.1884108

Huang, Y., Dong, X., Li, M., and Yu, Y. (2015). A density functional theory study on ethylene formation and conversion over P modified ZSM-5. Catal. *Sci. Technol.* 5, 1093–1105. doi: 10.1039/C4CY01205D

Huangfu, J., Mao, D., Zhai, X., and Guo, Q. (2016). Remarkably enhanced stability of HZSM-5 zeolite co-modified with alkaline and phosphorous for the selective conversion of bio-ethanol to propylene. *Appl. Catal. A* 520, 99–104. doi: 10.1016/j.apcata.2016.04.016

Inoue, T., Itakura, M., Jon, H., Oumi, Y., Takahashi, A., Fujitani, T., et al. (2009). Synthesis of LEV zeolite by interzeolite conversion method and its catalytic performance in ethanol to olefins reaction. *Micropor. Mesopor. Mat.* 122, 149–154. doi: 10.1016/j.micromeso.2009.02.027

Jakobtorweihen, S., Hansen, N., and Keil, F. J. (2005). Molecular simulation of alkene adsorption in zeolites. *Mol. Phys.* 103, 471–489. doi: 10.1080/00268970512331316021

Klemm, E., Wang, J., and Emig, G. (1998). A comparative study of the sorption of benzene and phenol in silicalite, HAlZSM-5 and NaAlZSM-5 by computer simulation. *Micropor. Mesopor. Mat.* 26, 11–21. doi: 10.1016/S1387-1811(98)00203-0

Li, X., Kant, A., He, Y., Thakkar, H. V., Atanga, M. A., Rezaei, F., et al. (2016). Light olefins from renewable resources: selective catalytic dehydration of bioethanol

to propylene over zeolite and transition metal oxide catalysts. *Catal. Today* 276, 62–77. doi: 10.1016/j.cattod.2016.01.038

Mentzen, B. F., Bergeret, G., Emerich, H., and Weber, H. P. (2006). Dehydrated and Cs^+-exchanged MFI zeolites: location and population of Cs^+ FROM *in situ* diffraction data as a function of temperature and degree of exchange. *J. Phys. Chem. B* 110, 97–106. doi: 10.1021/jp055230k

Navarro, M. V., Puértolas, B., García, T., Murillo, R., and Mastral, A. M., Varela-Gandía, F. J., et al. (2010). Experimental and simulated propene isotherms on porous solids. *Appl. Surf. Sci.* 256, 5292–5297. doi: 10.1016/j.apsusc.2009.12.120

Parajuli, R., Knudsen, M. T., Birkved, M., Djomo, S. N., Corona, A., and Dalgaard, T. (2017). Environmental impacts of producing bioethanol and biobased lactic acid from standalone and integrated biorefineries using a consequential and an attributional life cycle assessment approach. *Sci. Total Environ.* 598, 497–512. doi: 10.1016/j.scitotenv.2017.04.087

Ren, T., Patel, M., and Blok, K. (2006). Olefins from conventional and heavy feedstocks: Energy use in steam cracking and alternative processes. *Energy* 31,425–451. doi: 10.1016/j.energy.2005.04.001

Smit, B., and Maesen, T. L. (2008). Molecular simulations of zeolites: adsorption, diffusion, and shape selectivity. *Chem. Rev.* 108, 4125–4184. doi: 10.1021/cr8002642

Venkatathri, N., and Yoo, J. W. (2008). Synthesis, characterization and catalytic properties of a LEV type silicoaluminophosphate molecular sieve, SAPO-35 from aqueous media using aluminium isopropoxide and hexamethyleneimine template. *Appl. Catal. A* 340, 265–270. doi: 10.1016/j.apcata.2008.02.026

Wang, F., Xia, W., Mu, X., and Chen, K. (2018). Experimental and molecular simulation studies on ethanol conversion to propylene over different zeolite catalyst. *Catal. Lett.* 148, 1768–1774. doi: 10.1007/s10562-018-2375-7

Xia, W., Wang, F., Mu, X., Chen, K., Takahashi, A., Nakamura, I., et al. (2017a). Catalytic performance of H-ZSM-5 zeolites for conversion of ethanol or ethylene to propylene: effect of reaction pressure and SiO_2/Al_2O_3 ratio. *Catal. Commun.* 91, 62–66. doi: 10.1016/j.catcom.2016.12.010

Xia, W., Wang, F., Mu, X., Chen, K., Takahashi, A., Nakamura, I., et al. (2017b). Highly selective catalytic conversion of ethanol to propylene over yttrium-modified zirconia catalyst. *Catal. Commun.* 90, 10–13. doi: 10.1016/j.catcom.2016.11.011

Yang, J. Z., Liu, Q. L., and Wang, H.T. (2007). Analyzing adsorption and diffusion behaviors of ethanol/water through silicalite membranes by molecular simulation. *Membr. Sci.* 291, 1–9. doi: 10.1016/j.memsci.2006.12.025

Zhang, Y., Furukawa, S., and Nitta, T. (2003). Computer simulation studies on gas permeation of propane and propylene across ZSM-5 membranes by a non-equilibrium molecular dynamics technique. *Sep. Purif. Technol.* 32, 215–221. doi: 10.1016/S1383-5866(03)00040-6

Conflict of Interest Statement: The authors declare that the research was conducted in the absence of any commercial or financial relationships that could be construed as a potential conflict of interest.

Environmental Materials

Hongbo Cong

Dr Hongbo Cong is currently an Assistant Professor in the Corrosion Engineering program at the University of Akron, Ohio, USA. Prior to joining UAkron, Dr Cong was a senior engineer in the Materials and Corrosion Technology Center at Det Norske Veritas (DNV). He received his PhD and MSc in Materials Science and Engineering from the University of Virginia, Virginia, USA and his B.E. in Materials Science and Engineering from Tsinghua University, Beijing, China. He was the 2011 recipient of the Morris Cohen Award from the Electrochemical Society. His research areas include localized corrosion, corrosion inhibition, corrosion sensors, and environmentally assisted cracking.

Amy Gandy

Amy became a Lecturer in Nuclear Engineering in the Department of Materials Science and Engineering at the University of Sheffield, UK, in September 2015. She was awarded an MPhys in Physics and Space Technology from the University of Salford and holds a PhD in Physics and Materials Science from both Salford and the University of Poitiers, France. Her research focuses on examining radiation-induced damage and recovery mechanisms and gas bubble formation in alloys and poly-crystalline oxide-based materials for nuclear fission and fusion, and she leads an international collaboration between UK and Indian researchers to develop radiation damage resistant alloys for advanced nuclear systems. Her research group is currently developing reduced activation compositionally complex alloys for plasma facing components, and lithium-containing ceramics which are candidates for tritium breeder materials for fusion technology. Amy also works in collaboration with the Culham Centre for Fusion Energy (CCFE) and the National Nuclear Laboratory (NNL).

Ziming Wang

Dr Z.M. Wang is an Associate Professor of the College of Materials, at Xiamen University. He obtained his PhD in materials science from the Institute of Metal Research, Chinese Academy of Sciences, in Shenyang in 2010. After graduating, he worked for the Sinopec group dealing with corrosion problems in CO2-EOR production systems. He moved to Xiamen University and joined the Center for marine materials corrosion and protection in October 2017. His current research mainly focuses on corrosion in multiphase media and the application of corrosion-resistant alloys. He has authored more than 20 peer-reviewed papers.

frontiers in Materials

ORIGINAL RESEARCH
published: 13 February 2019
doi: 10.3389/fmats.2019.00010

CO_2 Corrosion of Low Carbon Steel Under the Joint Effects of Time-Temperature-Salt Concentration

*Shengxi Li, Zhipeng Zeng, Michael A. Harris, Lizeth J. Sánchez and Hongbo Cong**

Department of Chemical and Biomolecular Engineering, Corrosion Engineering program, University of Akron, Akron, OH, United States

The time-dependent effects of temperature and salt (NaCl) concentration on the corrosion behavior of carbon steel in CO_2-saturated environments were explored using various electrochemical techniques coupled with XRD, Raman spectroscopy, and SEM/FIB examinations. At constant salt level, corrosion rate increases, and stabilizes when the temperature is below 60°C. When temperature is higher than 60°C, corrosion rate firstly increases, reaches an apex, and then starts decreasing continuously. The magnitude of the decrease is inversely proportionally to the salt concentration, which is attributed to the microstructure of dual-layer $FeCO_3$ scale. Polarization experiments indicate the anodic process is more affected by salt concentration than temperature while the opposite is true for the cathodic kinetics. Although chloride is not detected in the corrosion scale, it is regarded to have significant influence on the nucleation and growth of $FeCO_3$ and therefore the properties (e.g., thickness and compactness) of the corrosion scales. Lastly, a mechanism is proposed for the evolution of corrosion scales on carbon steel in CO_2 saturated environment as a function of temperature and salt concentration.

Keywords: mild steel, EIS, CO_2 corrosion, chloride effect, temperature effect, corrosion kinetics, corrosion scale

OPEN ACCESS

Edited by:
Guang-Ling Song,
Xiamen University, China

Reviewed by:
Changdong Gu,
Zhejiang University, China
Zhiyong Liu,
University of Science and Technology Beijing, China

****Correspondence:***
Hongbo Cong
hcong@uakron.edu

Specialty section:
This article was submitted to Environmental Materials, a section of the journal Frontiers in Materials

Received: *23 November 2018*
Accepted: *25 January 2019*
Published: *13 February 2019*

Citation:
Li S, Zeng Z, Harris MA, Sánchez LJ and Cong H (2019) CO_2 Corrosion of Low Carbon Steel Under the Joint Effects of Time-Temperature-Salt Concentration. Front. Mater. 6:10. doi: 10.3389/fmats.2019.00010

INTRODUCTION

The corrosion of carbon steel caused by dissolved carbon dioxide (CO_2) has been recognized to pose a serious threat to the oil and gas industry (Jasinski, 1987; Liu et al., 2009a, 2012; Liu F. G. et al., 2009; Zhu et al., 2011; Sun et al., 2012). The carbonic acid (H_2CO_3), in equilibrium with dissolved CO_2, is very corrosive to carbon steel. The failure of equipment in the oil and gas industry caused by CO_2 corrosion often results in great economic loss and catastrophic accidents, which has attracted great attention (de Waard et al., 1991; Liu et al., 2009a,b; Ortega-Sotelo et al., 2011).

The understanding of CO_2 corrosion mechanisms under the effects of many mechanical and environmental factors has been of great interest in the corrosion field. Numerous factors have been investigated to further our understanding on CO_2 corrosion, including temperature (Nesic et al., 1996; Kinsella et al., 1998; Liu F. G. et al., 2009; Zhu et al., 2011), pH (de Waard et al., 1991; Nesic et al., 1996; Linter and Burstein, 1999), partial pressure (Jasinski, 1987; Kinsella et al., 1998; Zhang et al., 2012), and flow rate (Videm and Dugstad, 1987; de Waard et al., 1991; Fang et al., 2013). Temperature, as one of the most important influencing factors in CO_2 corrosion, plays a vital role in the possible formation of corrosion product layer. It is generally believed that, at low temperatures (below 60°C), no protective layer forms on the steel surface because of the high solubility of the

corrosion product iron carbonate ($FeCO_3$). As temperature increases, $FeCO_3$ precipitates from the solution due to the decrease of solubility and forms compact and adherent corrosion product layers on the steel surface (Tang et al., 2003; Shukla and Quraishi, 2009; Porcayo-Calderon et al., 2015). Therefore, corrosion rate generally decreases as the protective corrosion layers form at temperatures above 60°C. Yin et al. (2009) investigated the effect of temperature on the corrosion of carbon steel in CO_2-saturated NaCl environments. They concluded that temperature affected the crystal size and thickness of the corrosion product layer and both high and low temperatures resulted in small amounts of cementite (Fe_3C) and magnetite (Fe_3O_4) in the corrosion product layer. Han et al. (2009) also confirmed Fe_3O_4 and $FeCO_3$ as the dominant species in the corrosion product using X-ray diffraction (XRD) and transmission electron microscopy/energy dispersive X-ray analysis (TEM/EDX).

In recent years, the effect of salt concentration on the CO_2 corrosion of mild steel has also been studied. Liu et al. demonstrated that chloride destroyed the corrosion product films and changed their morphology but had no effect on the composition of the corrosion product (Liu et al., 2014). Mao et al. found that the presence of a small content of chloride could significantly reduce the passivating tendency of carbon steel (Mao et al., 1994). Schmitt et al. reported that increasing chloride could inhibit CO_2 corrosion by decreasing the solubility of CO_2 in solution at room temperature (Schmitt, 2015). Similarly, Nešić et al. found that the corrosion rate of carbon steel in CO_2 and NaCl environment significantly decreased with increasing NaCl concentration from 3 to 25 wt. % (Fang et al., 2013). Han et al. also reported decreased corrosion rates with an increase of salt concentration from 0.5 to 20 wt. % (Han et al., 2011). They proposed a model showing that cathodic reactions were decelerated by NaCl but anodic reactions were not significantly affected. Contrary to Han's model (Han et al., 2011), the potentiodynamic sweep analyses by Nešić et al. showed that both cathodic and anodic processes were slowed down by the increase of salt concentration (Fang et al., 2013). In our recent study of Cl^- concentration on the corrosion behavior of carbon steel at room temperature, the results suggested that corrosion rate increased with decreasing Cl^- concentration (Zeng et al., 2016). Moreover, there was no protective corrosion scale formed at room temperature, and the increasing presence of Cl^- resulted in the formation of more porous and non-protective corrosion product films on carbon steel (Liu et al., 2014; Zeng et al., 2016).

Despite the above-mentioned studies, scarce information is available on how temperature affects the cathodic and anodic kinetics individually and how Cl^- influences the microstructure of the corrosion scale at various temperatures. In this research, we investigated the effect of salt concentration (0.001–10 wt.%) on the corrosion behavior of carbon steels (C1018 and C1010) in CO_2-saturated NaCl solutions at various temperature levels (25 to 80°C). The corrosion rate evolution of C1018 steel was obtained through electrochemical impedance spectroscopy (EIS) and linear polarization resistance (LPR) measurements. The effects of temperature and Cl^- concentration on the anodic and cathodic kinetics were investigated separately by potentiodynamic and potentiostatic polarization experiments using microelectrodes. The surface and cross-sectional morphology of the corrosion scale was examined using scanning electron microscope (SEM) equipped with focused ion beam (FIB). The composition of the corrosion products was obtained using a combination of XRD and Raman spectroscopy. Lastly, a new corrosion scale formation mechanism was proposed based on all the results obtained.

MATERIALS AND METHODS

Materials

Two grades of carbon steels, C1010 and C1018 were used depending on their availability. The nominal chemical composition of the carbon steels has been reported in a previous publication (Zeng et al., 2016). Wire electrodes of alloy C1010 with a diameter of 500 μm (~0.002 cm^2 exposed area) were utilized in the polarization (potentiodynamic and potentiostatic) experiments. Rectangular cuboid electrodes with dimensions of 15 × 10 × 6 mm (~6 cm^2 exposed area) were cut from a C1018 carbon steel bar and tested under naturally corroding conditions. The preparation and assembly of these electrodes has been given in a previous publication (Zeng et al., 2016). Before each test, the specimen was ground successively with 240, 320, and 600 grit silicon carbide (SiC) abrasive papers, rinsed with acetone, isopropanol, deionized (DI) water (18.2 MΩ·cm, MilliQ DQ-3), and Ar-dried.

Electrolytes and Atmosphere

The test solutions with concentrations ranging from 0.001, 0.01, 0.1, 1, to 10 wt.% were made from analytical grade NaCl (Fisher Scientific) and DI water. The test solution was pre-purged with research grade CO_2 (99.9%, Praxair) for at least 1 h before immersing the specimen, and the test system was continuously purged at a lower flow rate to ensure CO_2 saturation throughout the test. The initial solution pH was ~ 4 at room temperature with negligible dependence on NaCl concentration (Zeng et al., 2016). All tests were performed at ambient pressure.

Electrochemical Techniques

A 200 ml jacketed EuroCell (Gamry) was used as the test vessel. Working electrode was either the epoxy embedded C1010 wire electrode or C1018 rectangular cuboid electrode. A graphite rod (Gamry) was used as counter electrode and saturated calomel electrode (SCE, Pine Research) was connected to the cell externally through a luggin capillary and positioned by the working electrode as closely as possible (~1 mm).

The long-term immersion tests were conducted using the rectangular cuboid C1018 steel electrodes for 100 cycles (1 h/cycle) and each cycle contained sequential measurements of 45-min OCP (Open Circuit Potential), 3-min LPR, 2-min OCP, and 10-min EIS. LPR measurements were conducted by polarizing the electrode from −10 to +10 mV with respect to OCP at a scan rate of 0.125 mV/s. EIS measurements were carried out at OCP with an AC excitation amplitude of 10 mV, and frequency range from 10^4 to 10^{-2} Hz.

Anodic and cathodic polarization experiments were performed using the epoxy-embedded C1010 wire electrodes. Before polarization, 1 h OCP measurement was conducted to let the potential of the electrode stabilize. A typical anodic scan started at −30 mV vs. OCP to +1.0 V vs. SCE, while the cathodic scan started at +30 mV vs. OCP to −1.1 V vs. SCE, with a scan rate of 0.167 mV/s. Potentiostatic polarization tests were also conducted at selected potential levels of −0.5 V and −0.8 V vs. SCE using the wire electrodes for 20 h.

The cell temperature was maintained with a circulating water bath (Polyscience) and the effect of temperature was investigated at four levels: 25, 40, 60, and 80°C. All the electrochemical measurements were carried out by using a Solartron Modulab® system.

Microstructural and Compositional Characterization

After long-term immersion, the electrodes were immediately rinsed with DI water and acetone. The surface and cross-sectional morphologies of the corrosion scales were examined by a TESCAN LARA3 field emission SEM coupled with a gallium FIB. The accelerating voltage was 20 kV.

A Rigaku MiniFlex™ II benchtop XRD system equipped with a Cu (Kα) radiation was used for XRD measurements directly from the exposed sample surface. The scans were performed in a 2θ range of 20–80° with a scan speed of 0.02° (2θ)/s.

Raman spectroscopic analysis of the phase composition of the corrosion products was conducted using a Horiba LabRam HR micro Raman spectrometer operated with an air-cooled Nd:YAG laser (532 nm). The laser power (at sample) was approximately 6 mW. The spectra resolution was 4 cm^{-1} and the accumulation time was 120 s.

RESULTS AND DISCUSSION

Effect of Temperature and Cl^- Concentration on the Corrosion Resistance of Carbon Steel

Corrosion Resistance From EIS Measurements

The EIS technique was used to determine both polarization resistance and solution resistance. **Figures 1A,B** show examples of Nyquist and Bode plots of C1018 electrodes in CO_2-saturated 1% NaCl solutions maintained at 40 °C. In the first few hours (0∼10 h), the Nyquist plots (**Figure 1A**) exhibit depressed capacitive semicircles at high to medium frequency, inductive semicircles at low frequency, and another capacitive semicircles at even lower frequency (as marked by arrows in **Figure 1A**). The depressed capacitive semicircles at high to medium frequency are related to the double layer capacitance and charge transfer resistance, while the inductive semicircles at low frequency can be attributed to the adsorption of intermediate corrosion products (Sun et al., 2012), or the relaxation of water-iron species (das Chagas Almeida et al., 2017) on the steel surface. The appearance of this new capacitive semicircle at low frequency is correlated to the formation of initial corrosion product (e.g., $FeCO_3$) on the electrode surface (Sun et al., 2012). This capacitive semicircle gradually disappeared with increasing immersion time, indicating that the initial corrosion product was unable to accumulate in this environment. The corresponding Bode plots (**Figure 1B**) show two time constants, i.e., a high frequency peak and a low frequency valley. The peak with a maximum phase angle increases and shifts to lower frequency with increasing immersion time, which is usually associated with an increase of double layer capacitance (Sun et al., 2012; Zhao and Chen, 2012). In comparison, **Figures 1C,D** show examples of Nyquist and Bode plots of C1018 electrodes in CO_2-saturated 1% NaCl solutions maintained at higher temperature (80°C). It is observed from the inset of **Figure 1C** that, in the first 10 h, the shape of Nyquist plots is similar to that of the plots shown in **Figure 1A** (three semicircles). However, only a high-frequency capacitive semicircle and a low-frequency capacitive semicircle can be found after 30 h. The low-frequency inductive semicircle has disappeared. The corresponding Bode plots show two peaks at both high-frequency and low-frequency ranges. The aperture of phase angles also increases with increasing immersion time, which could be a result of an increased surface coverage leading to a more capacitive surface film (Kinsella et al., 1998; Ortega-Toledo et al., 2011; Sun et al., 2012). The larger diameter of the semi-circle indicates higher corrosion resistance due to the formation of protective corrosion scale at 80°C.

In order to provide an insight into the effect of Cl^- on the formation of corrosion scales, long-term immersion tests were conducted at 80°C in solutions with various salt concentrations (from 0.001 to 10%). As an example, **Figure 2** shows the Nyquist and Bode plots of C1018 steel tested in 0.01% NaCl at 80°C. In the initial stage (<5 h, **Figure 2A**), the acquired Nyquist plot shows a capacitive semicircle at high to medium frequency, an inductive loop and a capacitive semicircles at low frequency, similar to those obtained in 1% NaCl at 80°C (**Figure 1C**). After 30 h, the inductive loop disappears (**Figure 2B**). Another noticeable change in the shape of the Nyquist plot occurs after 60 h, which is characterized by the appearance of a capacitive semicircle at high frequency (**Figure 2B**). Then, the diameters of these capacitive semicircles increase with immersion time, indicating the increase of polarization resistance. At 100 h, the two capacitive semicircles in the range of medium to low frequency nearly overlap (**Figure 2C**). The corresponding Bode plots are shown in **Figure 2D**. Only a high frequency peak and a low frequency capacitive "semi-peak" can be observed before 60 h. In comparison, three peaks can be clearly seen after 60 h (as marked by arrows in **Figure 2D**), indicating that corrosion product films with different microstructures may have formed on the steel surface. In terms of the EIS results that are not shown here, those obtained in the 0.001 and 0.1% NaCl solutions at 80°C are similar to those obtained in the 0.01% NaCl (**Figure 2**), and those from the 10% NaCl solution are similar to those from the 1% NaCl solution (**Figures 1C,D**). Since the shape of the impedance plots changes noticeably with Cl^- concentration, it is reasonable to infer that Cl^- may play a critical role in the microstructure of corrosion scale, as discussed in the following sections.

The EIS results were fitted with different equivalent electrical circuits (ECs) shown in **Figure 3** (Zhu et al., 2011; Sun et al., 2012; Wei et al., 2015). These ECs were proposed based on the EIS characteristics and SEM/FIB characterizations. In these ECs,

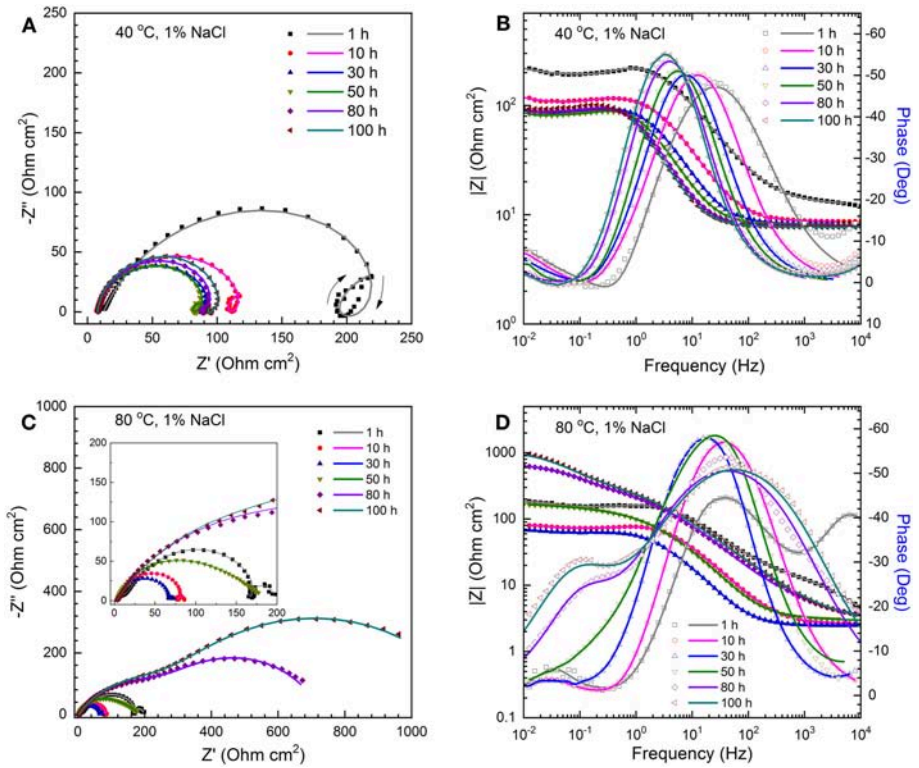

FIGURE 1 | The time-sequenced Nyquist plots **(A,C)** and corresponding Bode plots **(B,D)** for the C1018 steel samples tested in CO_2-saturated 1% NaCl solutions at 40°C **(A,B)** and 80°C **(C,D)**. Scatter plots: measured; solid lines: fitted.

the following elements were considered: solution resistance (R_s), charge transfer resistance (R_t), inductive resistance (R_L), constant phase element (CPE) representing the double layer capacitance, and the resistance of corrosion scale/film (R_f).

The EC in **Figure 3A** has no R_f element and was used for fitting most of the EIS data obtained at 25°C and 40°C because no stable protective corrosion scale formed under these circumstances. Notice that, at 40°C, initial corrosion product actually formed in the early stage of immersion (<10 h) but later dissolved. Therefore, an EC containing the R_f element (**Figure 3B**) was used to analyze the EIS data from the initial stage. At temperature levels of 60 and 80°C, the shape of the obtained EIS spectra varied significantly in different stages of immersion. In general, three stages were identified. In stage I (< 30 h), a protective corrosion scale started to form and partially covered the sample surface, and an EC which includes the elements for this scale (i.e., R_f and CPE2 in **Figure 3B**) was used for curve fitting. In stage II (30–60 h), it is believed that a uniform corrosion scale (inner layer) completely covered the sample surface and resulted in the disappearance of inductance loops in the EIS spectra. Therefore, a new EC without the R_L element (**Figure 3C**) was employed. In stage III (>60 h), $FeCO_3$ crystals gradually formed an additional layer (outer layer). Since the microstructure of this layer was different from the inner layer (SEM/FIB characterizations), it caused additional semicircles at high frequency in the EIS spectra. Therefore, an EC which has elements for both the inner and outer corrosion product layers was used to fit the EIS data in this case (**Figure 3D**). The following equations were used to calculate R_P^{EIS} based on different ECs in **Figure 3**:

$$\mathrm{EC(A)}: \frac{1}{R_P^{EIS}} = \frac{1}{R_t} + \frac{1}{R_L} \quad (1)$$

$$\mathrm{EC(B)}: R_P^{EIS} = \frac{1}{\frac{1}{R_t} + \frac{1}{R_L}} + R_f \quad (2)$$

$$\mathrm{EC(C)}: R_P^{EIS} = R_t + R_f \quad (3)$$

$$\mathrm{EC(D)}: R_P^{EIS} = R_1 + R_2 + R_t \quad (4)$$

Corrosion Resistance From LPR Measurements

The LPR measurements were also conducted to determine the corrosion resistance in conjunction with the EIS measurements. **Figure 4A** shows the evolution of LPR curves (up to 100 h) of C1018 steel in CO_2-saturated 1% NaCl solutions maintained at 40°C. A good linear relationship between polarization ($E–E_{corr}$) and current density is observed. The apparent polarization resistance (R_P^{app}), determined by the slope of the LPR curves, gradually decreases with immersion time up to 30 h (marked by an arrow in **Figure 4A**). After ~ 50 h, the LPR curves overlap, indicating the stabilization of polarization resistance. This result coincides with the finding in a previous work conducted at room temperature (Zeng et al., 2016). In contrast,

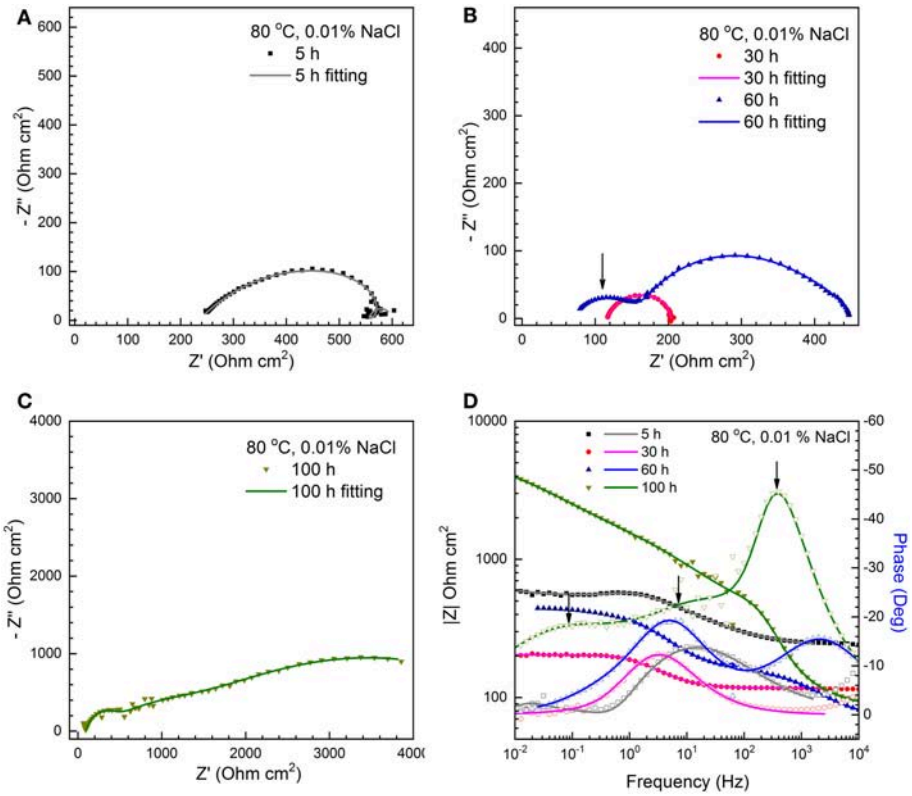

FIGURE 2 | The Nyquist plots **(A–C)** and corresponding Bode plots **(D)** for a C1018 sample tested in 0.01% NaCl with CO_2 saturation at 80°C (scatter plots: measured; solid lines: fitted).

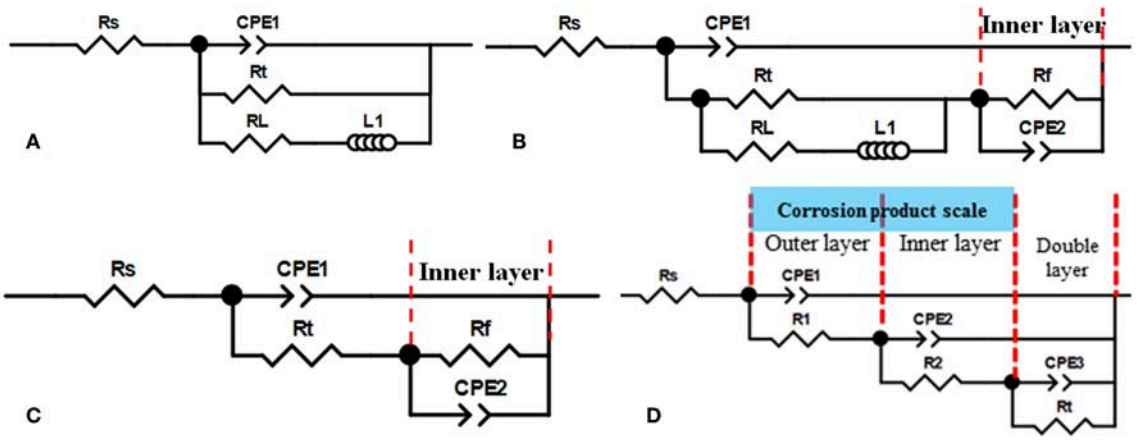

FIGURE 3 | Four equivalent electrical circuits used to fit the EIS curves obtained in different concentration NaCl solutions at different temperature and exposure time. **(A)** no corrosion scale; **(B)** initial formation of corrosion scale; **(C)** complete formation of inner layer; **(D)** dual-layer corrosion product scale.

at 80°C, the slope of the LPR curves decreases initially but starts to increase significantly after 30 h (**Figure 4B**), and relatively high polarization resistance is found after extended immersion (>80 h). **Figure 4C** shows the representative LPR results of C1018 steel in the dilute NaCl solution (0.001%) maintained at 80°C. An initial decrease of polarization resistance up to 30 h is followed by a later increase, similar as those shown in **Figure 4B**. The true polarization resistance (R_P^{LPR}) was obtained by subtracting the solution resistance (R_s by EIS results) from the apparent polarization resistance (R_P^{app}), and then converted to corrosion rates.

The evolution of polarization resistance (R_P) is compared at different temperature levels in 1% NaCl (**Figure 5A**) and different salt concentrations at 80°C (**Figure 5B**). It is evident

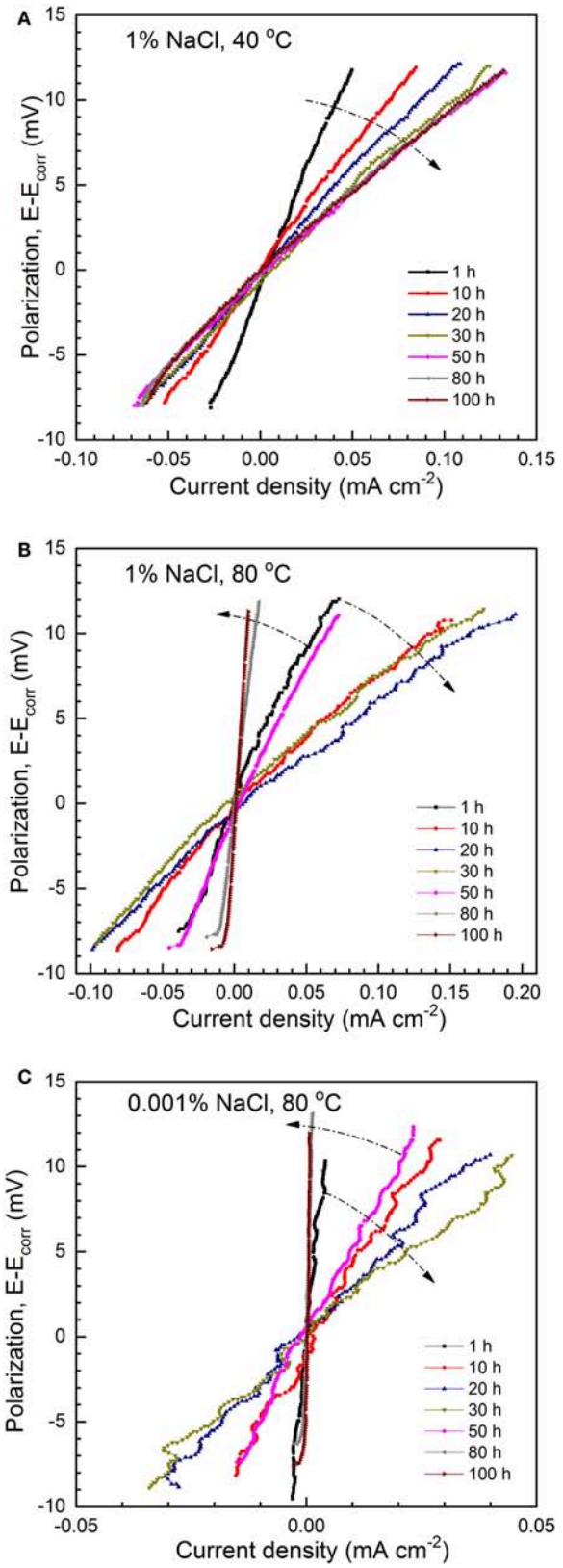

FIGURE 4 | The evolution of LPR curves of C1018 in **(A)** 1% NaCl, 40°C, **(B)** 1% NaCl, 80°C, and **(C)** 0.001% NaCl, 80°C with CO_2 saturation.

that the results from EIS (R_P^{EIS}) and LPR (R_P^{LPR}) agree with each other. The corrosion rates were then determined by Stern-Geary equation, using an average B ($\frac{b_a|b_c|}{2.303(b_a+|b_c|)}$) value of 21 mV. Detailed explanation is provided in a previous publication (Zeng et al., 2016). **Figure 5C** shows the effect of temperature on corrosion rate in 1% NaCl solution. As immersion time increases, the corrosion rate gradually increases and reaches steady state around 30 h. The general trend is that corrosion rate increases with rising temperature at the same exposure time. The highest corrosion rate in 1% NaCl at 80 °C appears in the initial stage of the immersion (10–30 h). Corrosion rate does not change with further immersion at 25 and 40°C. However, after ∼ 80 h at 60°C and 30 h at 80°C, corrosion rate starts decreasing with longer immersion time, which is more noticeable at 80°C. It is projected that the corrosion rate would keep decreasing at 60°C should testing time be prolonged.

Figure 5D presents the effect of Cl^- concentration on corrosion rate at 80°C. The corrosion rate increases initially with time (0–30 h) at all salt concentrations. At ∼30 h, the highest corrosion rate of C1018 steel is reached at the same level (∼0.2–0.3 mA/cm^2) in different Cl^- solutions. After 30 h, corrosion rates start decreasing at all Cl^- concentration levels. The general trend is that corrosion rate increases with increasing salt concentration at the same exposure time. The corrosion rate of the sample tested in 0.001% NaCl at 80°C shows the most significant decrease, possibly due to the formation of more compact and $FeCO_3$-rich corrosion scale at high temperature and low Cl^- concentration. In comparison, the sample in 10% NaCl solution shows the least decrease in corrosion rate after 30 h. It should be noted that the 30 h critical time may be related to the specific experimental setup used in this work, including the size of the electrode.

Microstructure and Morphology of Corrosion Scale

Effect of Temperature on the Corrosion Scale Composition

Figure 6A presents the XRD pattern of the corrosion product on a C1018 steel sample tested in 1% NaCl at 40°C. The diffraction peaks observed at angles of 44.8° and 65.2° can be ascribed to the Fe substrate (JCPDS NO. 87-0722), while the rest of the peaks with low intensity, are in good agreement with Fe_3C (JCPDS NO. 76-1877). **Figure 6B** shows the XRD pattern obtained from a sample tested in 1% NaCl at 80°C. The main corrosion product identified in this environment is $FeCO_3$ (JCPDS NO. 83-1764) with three main diffraction peaks at 25.0°, 32.3°, and 53.4° corresponding to the (012), (104), and (116) planes of $FeCO_3$, respectively. In addition, Fe_2CO_3OH (JCPDS NO. 52-0163) as an intermediate corrosion product was also detected.

Effect of Temperature on the Corrosion Scale Morphology

Figure 7 shows the surface morphology of corrosion scale formed on C1018 steel exposed in CO_2-saturated 1% NaCl solution with different temperatures. At 25°C (**Figure 7a**) and 40°C (**Figure 7b**), typical morphology of Fe_3C (cementite) was

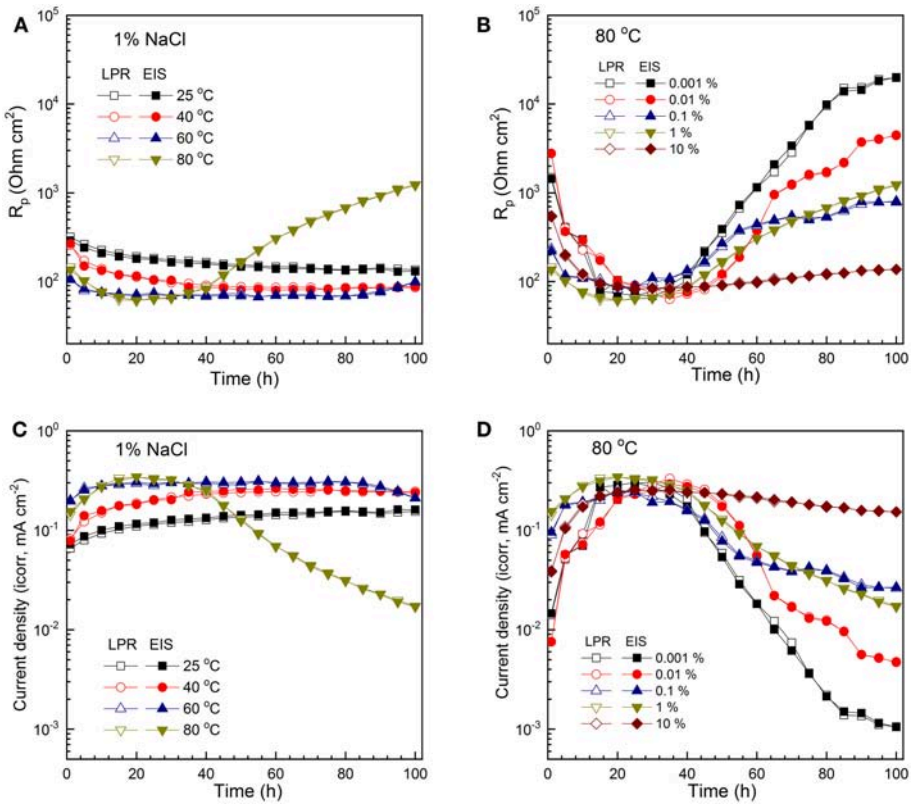

FIGURE 5 | The evolution of R_p **(A)** and corrosion rate **(C)** of C1018 steel in 1% NaCl at various temperature levels, showing the effect of temperature; evolution of R_p **(B)** and corrosion rate **(D)** of C1018 steel in NaCl solutions maintained at 80°C and with varying NaCl concentration, showing the effect of NaCl concentration.

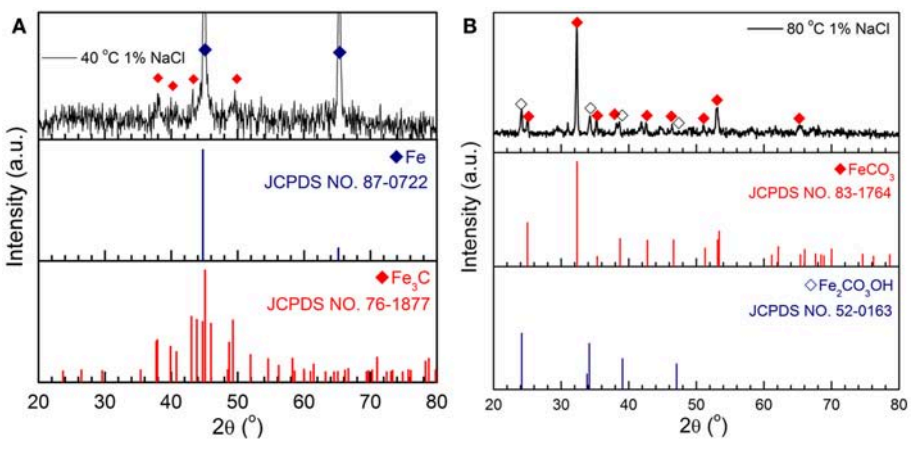

FIGURE 6 | XRD patterns of the corrosion products formed on C1018 steel after 100 h in 1% NaCl at **(A)** 40 and **(B)** 80°C.

observed and no crystalline particles formed on the sample surfaces. In addition, more Fe_3C accumulated on the sample tested at 40°C than that from 25°C, which is correlated to the higher corrosion rate observed at higher temperature (40 vs. 25°C). For the C1018 steel samples tested at 60°C (**Figure 7c**) and 80°C (**Figure 7d**), the morphologies feature the formation of crystalline particles that are uniformly distributed on the surfaces. Two types of $FeCO_3$ are identified to have formed on the steel exposed at 60 and 80°C, one has a cubic structure and the other is of a planar type. Although the corrosion scales formed at 60 and 80°C are believed to be protective, they still contain pores (arrows indication in **Figures 7c,d**) that may act as channels for local corrosion to occur. In addition, the size of the cubic $FeCO_3$ crystalline particles formed at 80°C is larger

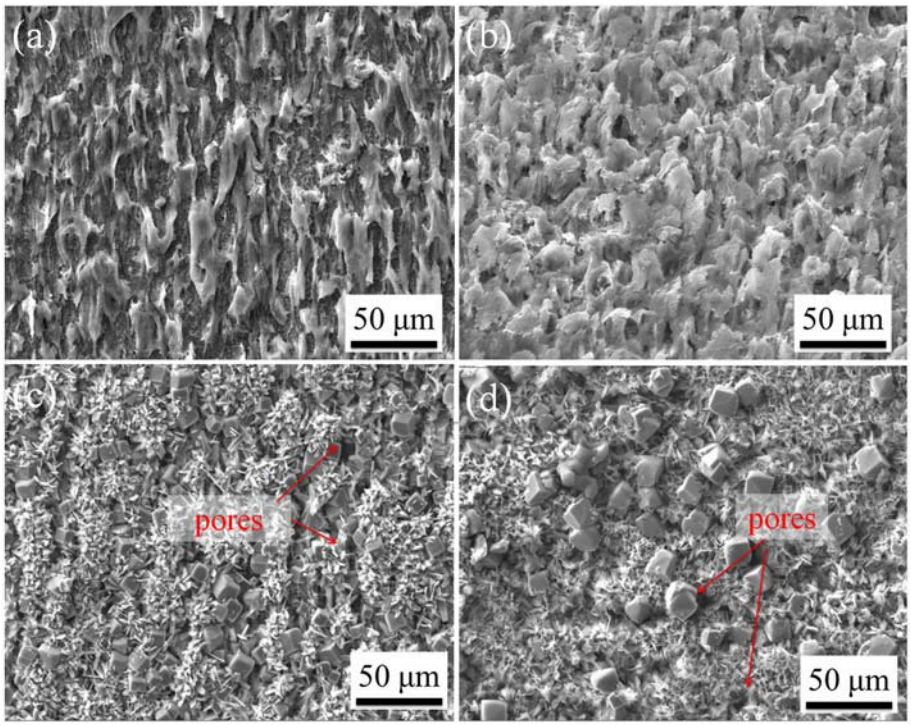

FIGURE 7 | SEM images of C1018 steel sample surfaces after 100 h immersion in 1% NaCl solutions maintained at **(a)** 25°C, **(b)** 40°C, **(c)** 60°C, and **(d)** 80°C.

than those formed at 60°C, indicating the growth of $FeCO_3$ is accelerated at higher temperature.

Figure 8 provides the corresponding cross-sectional morphologies of the corrosion scales formed on C1018 steel tested in CO_2-saturated 1% NaCl solutions with different temperatures. The Fe_3C layer on the sample exposed at 40°C (**Figure 8b**) is thicker and more dense than that on the sample exposed at 25°C (**Figure 8a**). Notice that a relatively large portion of the Fe_3C scale on the sample from 40°C has a lamellar structure, as shown in the inset in **Figure 8b**. **Figures 8c,d** show the morphologies of the corrosion scales formed at 60 and 80°C, which contain both compact regions and porous regions.

Effect of Cl^- Concentration on the Corrosion Scale Morphology

In an attempt to understand the role of Cl^- in the corrosion scale formation, the surface and cross-section of the C1018 steel samples exposed in 0.01 and 10% NaCl solutions at 80°C were further investigated by SEM/FIB and compared. **Figure 9a** shows typical SEM images of the sample tested in 0.01% NaCl solution at 80°C, which shows a uniform corrosion product scale without large pores. A high-magnification SEM image (inset in **Figure 9a**) reveals that the corrosion scale is mainly composed of thin flakes with some cubic particles embedded in it. In comparison, the sample tested in 10% NaCl solution at 80°C has more cubic particles on its surface (**Figure 9b**). Notice that this corrosion scale also has many small holes and cracks underneath the cubic particles. **Figures 9c,d** show the corresponding cross-sectional images of the two samples. It can be clearly seen that the corrosion product films are composed of both outer layer and inner layer. Moreover, the inner layer on the sample tested in 0.01% NaCl (**Figure 9c**) is much more compact than its counterpart in 10% NaCl (**Figure 9d**). In addition, the sample tested in 0.01% NaCl solution has larger planar-shaped crystals and smaller cubic crystals than the sample tested in 10% NaCl. A high-magnification SEM image for the marked region in **Figure 9d** is shown in **Figure 9e**, which indicates that the inner layer of the scale consists of lamellar-structured Fe_3C and $FeCO_3$ particles, as confirmed by Raman spectra in **Figure 9f**. The spectrum from the outer layer (crystal particle layer) has main peaks at 183, 281, 728, 1084, and 1721 cm^{-1}, which can be as assigned to $FeCO_3$ (Li et al., 2015, 2016; Wei et al., 2015). Besides the strong peaks for $FeCO_3$, the spectrum obtained from the inner layer also shows a weak peak at 950 cm^{-1}, possibly due to Fe_3C. Based on the microstructure shown in **Figure 9e**, it is reasonable to hypothesize that, at relatively high Cl^- concentration, lamellar-structured Fe_3C crosslinked with the $FeCO_3$ particles in the initial stage of corrosion to form the porous inner layer, while $FeCO_3$ crystals (both of planar and cubic structures) precipitated from the solution forming the outer layer on the top of the $Fe_3C/FeCO_3$ inner layer. In contrast, the much more compact inner layer in low Cl^- solution significantly reduces corrosion and the formation of $FeCO_3$ crystals (cubic) in the outer layer.

The microstructural characterization of the corrosion scale agrees with the corrosion rate analysis shown in **Figure 5**. At

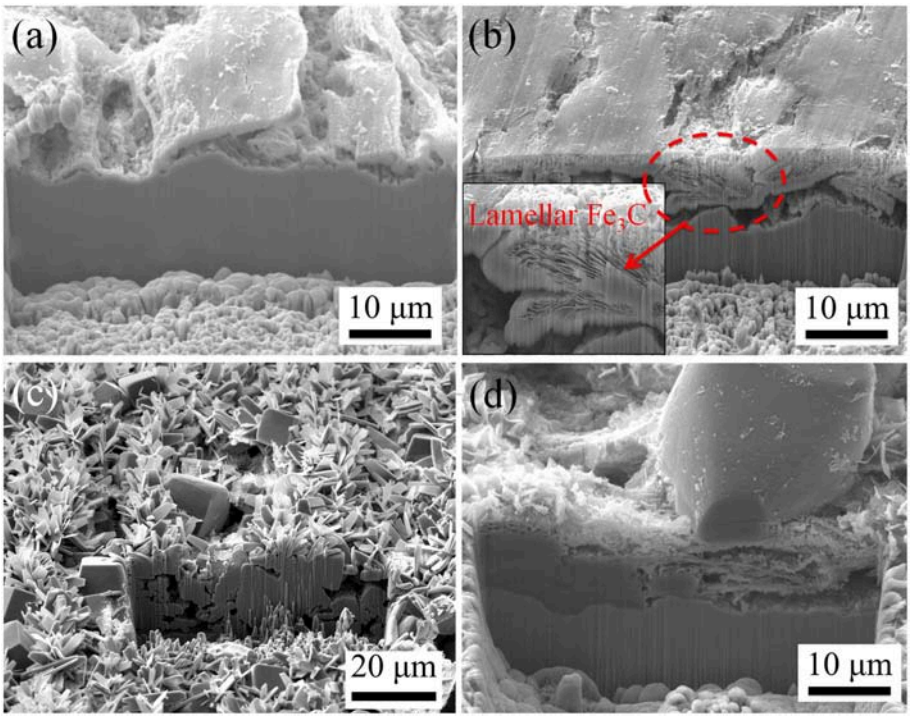

FIGURE 8 | Cross-sectional morphologies of the corrosion product layers on C1018 samples tested in 1% NaCl solutions maintained at **(a)** 25°C, **(b)** 40°C, **(c)** 60°C, and **(d)** 80°C.

relatively low temperature (i.e., 25 and 40°C), the corrosion product layers mainly consist of Fe_3C with minimal presence of $FeCO_3$ and are thus porous and non-protective. As a result, the corrosion rate remains high even after 100 h. The accumulation of more Fe_3C at 40°C compared to 25°C, may further enhance the corrosion rates by serving as strong cathode. In contrast, thick and compact (at least locally) corrosion scales formed on C1018 steel surface exposed at 60 and 80°C, which resulted in the decrease of overall corrosion rate. The high temperature facilitated the precipitation of $FeCO_3$ particles especially at 80°C, which shows larger crystal size and higher density as compared to those formed at 60°C (**Figures 7**, **8**). Lastly, at 80°C, the presence of higher Cl^- concentration interferes with the formation of a compact inner layer and the protectiveness decreases as a result, which suggests the detrimental effect of Cl^- and explains the higher corrosion rate observed (**Figure 5D**).

Effect of Temperature and Cl^- on the Anodic and Cathodic Kinetics

Potentiodynamic and potentiostatic polarization experiments were performed using microelectrodes to further understand the effect of temperature and chloride concentration on the anodic and cathodic kinetics of carbon steel in CO_2-saturated NaCl solutions.

Anodic Kinetics

As shown in **Figure 10**, increasing Cl^- concentration slightly decreases the E_{corr} values at all three temperature levels: (A) 40°C, (B) 60°C, and (C) 80°C, but significantly increases the anodic current density, indicating an acceleration of anodic process by Cl^-. In contrast, at a fixed Cl^- concentration, the anodic current density increases only slightly as the temperature increases from 25 to 80°C (**Figures 10D–F**). Therefore, within the temperature-salt concentration matrix studied here, the anodic process is regarded as Cl^--driven instead of temperature-driven, or the anodic reaction is more sensitive to Cl^- concentration than temperature.

The anodic current density (i_a) can be expressed by the following relationship:

$$i_a = k_a[Cl^-]^{\alpha}[OH^-]^{\gamma}\exp\left(\frac{\beta FE}{RT}\right)\exp\left(-\frac{E_a}{RT}\right) \quad (5)$$

To determine the dependence of i_a on [Cl^-] (i.e., exponent α), current density values at selected constant potential (**Figures 10A–C**) were plotted against chloride concentration at the same temperature (results not shown). A good linear relationship was found for all temperature levels (40°C, 60°C, and 80°C), and the slopes are approximately 0.5 at the same applied potential (e.g., −0.5 V/SCE), i.e.,

$$\left.\frac{\partial \log[i_a]}{\partial \log[Cl^-]}\right|_{E,\,T,\,pH} \cong 0.5 \quad (6)$$

Our previous study on the effect of Cl^- concentration on the anodic kinetics at 25°C showed that Cl^- accelerated

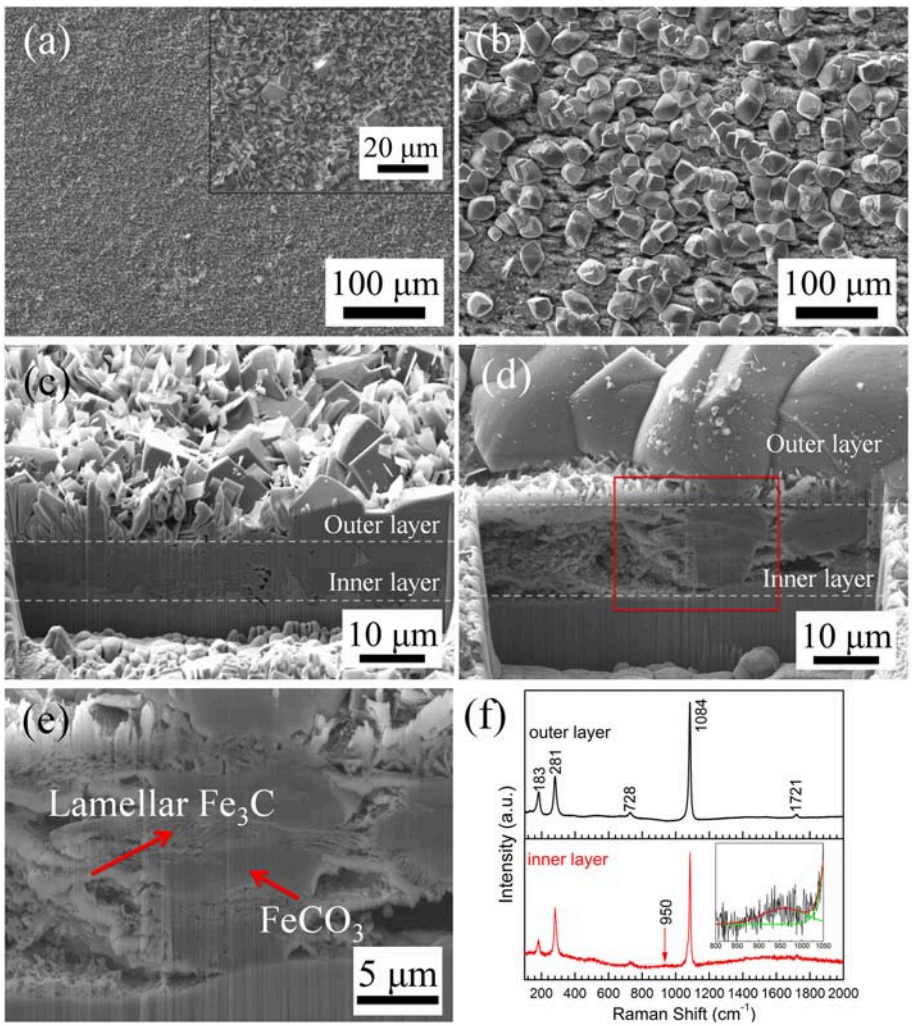

FIGURE 9 | (a) Surface and **(c)** cross-sectional morphologies of C1018 steel sample tested in 0.01% NaCl at 80°C; **(b)** surface and **(d,e)** cross-sectional morphology of C1018 steel sample tested in 10% NaCl solution at 80°C; **(f)** Raman spectra obtained from the inner and outer corrosion product layers.

the anodic reaction with a reaction order of 0.5 (Zeng et al., 2016). At room temperature, the anodic kinetics is dominated by chloride adsorption in concentrated chloride solutions (e.g., 10%) and hydroxyl adsorption in dilute solutions (e.g., 0.001%) (McCafferty and Hackerman, 1972; Burstein and Davies, 1980). The catalytic role of Cl^- in the anodic dissolution of iron has been proposed to form intermediate adsorbed species, such as $FeCl^-_{ads}$ (McCafferty and Hackerman, 1972) and $FeCl(OH)^-_{ads}$ (Wei et al., 2015). In contrast, the formation of $FeOH^-_{ads}$dominates in dilute solutions (McCafferty and Hackerman, 1972). A comparison between **Figure 10D** (0.01%) and **Figure 10F** (10%) clearly indicates two different anodic behaviors. A change in the anodic behavior can be observed from the polarization curves in 0.1% NaCl solution (green circle in **Figure 10A**), which may suggest the transition from predominant hydroxyl adsorption to chloride adsorption. Lastly, it has been reported that CO_2 does not appear to act directly over a free iron surface and there is no competition between water and CO_2 (das Chagas Almeida et al., 2017). The role of HCO_3^- (by dissolved CO_2) can be hypothesized as follows (Burstein and Davies, 1980).

$$HCO_3^- + FeOH_{ads} \rightarrow FeHCO_3^+ \rightarrow FeCO_3 \quad (7)$$

The potentiodynamic polarization results can be approximately dissected into two regions: low applied potential region under charge transfer control and high applied potential under mass transport control. Large current oscillation (one order of magnitude) is observed in the mass transport region, more noticeable at higher temperature and higher salt concentrations. Potentiostatic polarization experiments were then performed to study this oscillating behavior at selected applied potential ($E_{applied} = -0.5$ V/SCE) in 1% NaCl solution with various temperatures and the results are shown in **Figure 11**. It is observed that the current density gradually decreases throughout

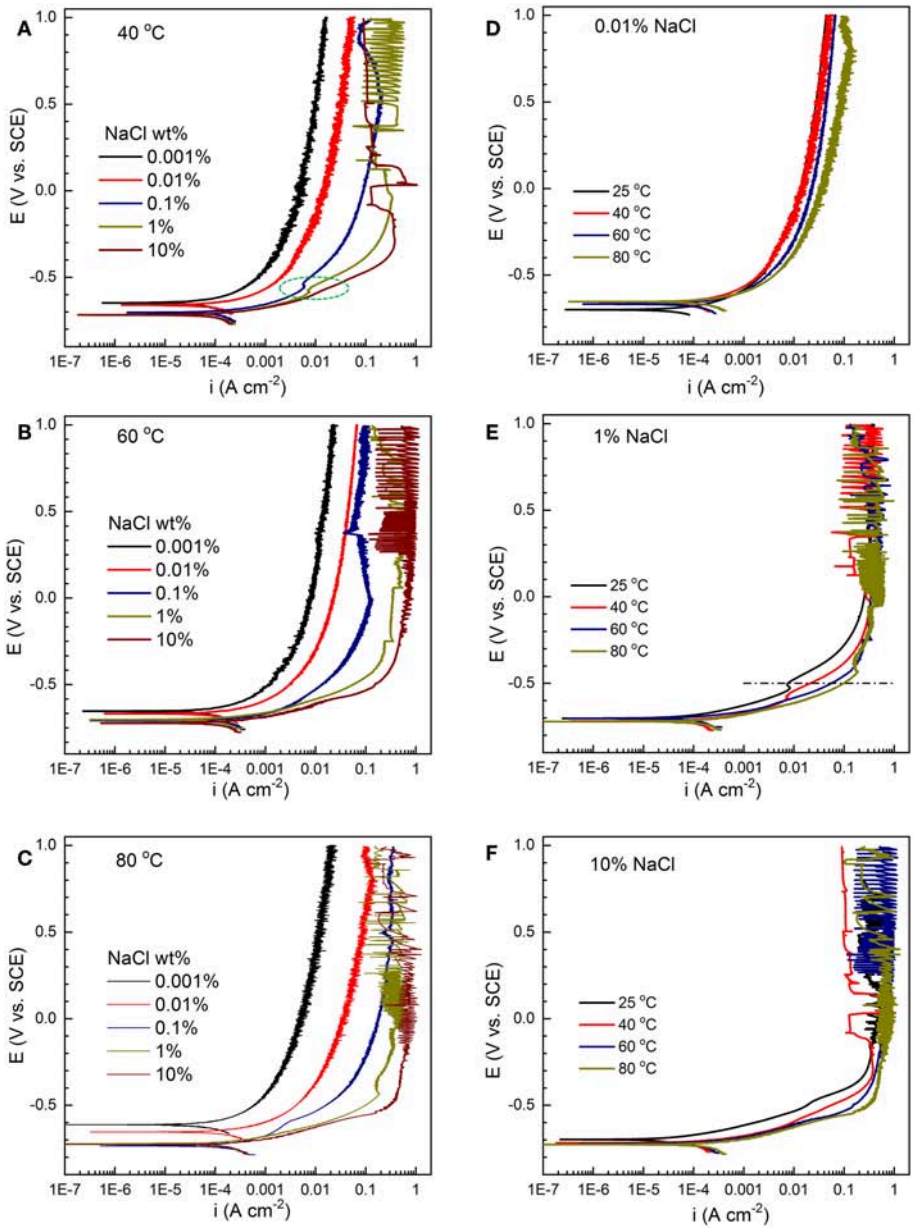

FIGURE 10 | Anodic polarization curves of C1010 steel with varying salt concentration (0.001% to 10%) at constant temperature levels, **(A)** 40°C, **(B)** 60°C, and **(C)** 80°C. Anodic polarization curves with varying temperature (25 to 80°C) at constant salt concentration levels, **(D)** 0.01%, **(E)** 1%, and **(F)** 10%.

the 20-h period at 40°C. In contrast, the current density profiles show periodic oscillations for the samples tested at 60 and 80°C, which feature sharp current peaks and drops. The oscillation amplitude (peak to valley) decreases throughout the 20-h test and upper limit shows similar trend as 40°C. It is hypothesized that the periodic current oscillation is attributed to the precipitation and re-dissolution of corrosion products. The drop of current is due to accumulation of the corrosion product film leading to mass transport control, whereas the rise of current is probably related to the breakdown of film with subsequent active iron dissolution processes (Ma et al., 2003). In addition, the oscillation occurs more frequently at 80°C than 60°C, which may be attributed to faster precipitation rate and lower solubility of $FeCO_3$ at higher temperature (Bénézeth et al., 2009).

Cathodic Kinetics

As shown in **Figures 12A-C**, the cathodic polarization curves show a nearly vertical line in the low overpotential range, indicating that the cathodic process is under mass-transport

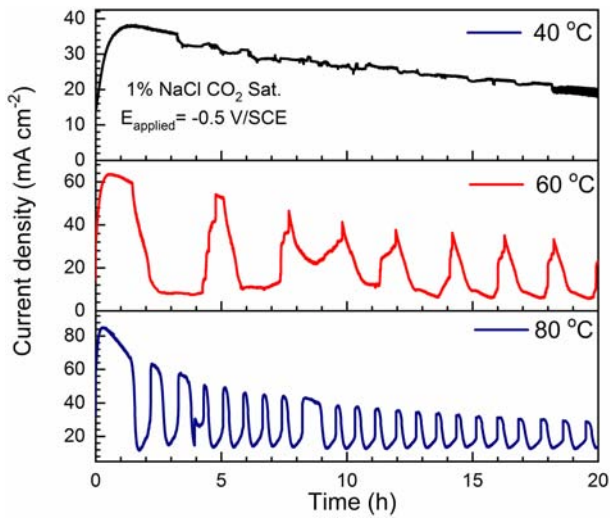

FIGURE 11 | Potentiostatic polarization curves ($E_{applied} = -0.5$ V/SCE) of C1010 steel tested in 1% NaCl with CO_2 saturation for 20 h at different temperature levels, i.e., 40, 60, and 80°C.

control, probably due to H^+ and/or H_2CO_3 reduction (Heuer and Stubbins, 1999; Wu et al., 2004). At more negative potential (below −0.9 V/SCE), water reduction becomes the dominant process (Bonnel et al., 1983; Ogundele and White, 1986). The diffusion-limited cathodic current density is in the range of 0.2–0.6 mA/cm^2 (e.g., at −0.8 V/SCE). It increases slightly with lower Cl^- concentration (Zeng et al., 2016), but overlap is observed. In contrast, the cathodic current density increases significantly with increasing temperature at the constant Cl^- concentration, as demonstrated in **Figures 12D-F**. This suggests that the cathodic reaction is more sensitive to temperature than Cl^- concentration, opposite to the anodic kinetics. In addition, as temperature increases, the cathodic kinetics gradually changes from mass-transport control to mixed charge-transfer/mass transport control.

To better understand the dependence of cathodic kinetics on temperature, potentiostatic polarization experiments were conducted at −0.8 V/SCE in 1% NaCl solutions for 20 h at various temperatures. The result is shown in **Figure 13**. Activation energy (E_a^c) was calculated according to Equation 8 (Tang et al., 2003; Shukla and Quraishi, 2009; Porcayo-Calderon et al., 2015).

$$i_c = k_c exp(-\frac{E_a^c}{RT}) \quad (8)$$

When the stabilized cathodic current densities are plotted vs. temperature (inset in **Figure 13**), the slope yields an activation energy value of 20 kJ mol^{-1}, close to that obtained from the potentiodynamic polarization results at the same potential (i.e., 22 kJ mol^{-1} in **Figure 12E**).

When dissolved in water, CO_2 is hydrated to form carbonic acid, which can be further dissociated to provide hydrogen ions for the cathodic reduction reaction.

$$CO_2 + H_2O \leftrightarrow H_2CO_3 \leftrightarrow H^+ + HCO_3^- \leftrightarrow 2H^+ + CO_3^{2-} \quad (9)$$

The cathodic reactions on carbon steel in CO_2-saturated NaCl solutions have been well-documented by Nešić and co-workers (Nesic et al., 1996), through the possible reduction routes of H^+, H_2CO_3, and/or HCO_3^-. It is suggested that the cathodic limiting current density is strongly related to the CO_2 concentration in the solution (Nesic et al., 1995). It has been confirmed that corrosion rate strongly depends on the solubility of CO_2 (Nesic et al., 1995; Shadley et al., 1998; Liu et al., 2014). Our results also indicate that the peak corrosion rates under freely corroding condition (**Figure 5D**) match the cathodic limiting current densities (**Figure 12**), on the order of 0.3 mA/cm^2.

To evaluate the variation of dissolved CO_2 concentration as a function of temperature and NaCl concentration, calculation was performed using the OLI® stream analyzer and the result is shown in **Figure 14**. At constant temperature levels, the concentration of dissolved CO_2 decreases slightly as the NaCl concentration increases from 0.001 to 1%, but a relatively large drop upon further increase to 10%. Moreover, the decreasing trend becomes less significant as temperature increases from 25 to 80°C (i.e., less salt concentration effect was observed at higher temperature). This offers one possible explanation for the initial increase (30 h) of corrosion rates to approximately the same level at 80°C in all NaCl concentrations (**Figure 5D**). In addition, **Figure 14** also shows the significant decreases of CO_2 solubility with the increase of temperature from 25 to 80°C, more noticeable in more diluted solution. In contrast, cathodic polarization results suggest that the diffusion limiting current density increases with temperature at all NaCl concentrations (**Figure 12D–F**), and corrosion rate increases with temperature in the early stage of immersion (**Figure 5C**). This clearly indicates that CO_2 solubility cannot be used as the sole indicator for cathodic kinetics (Schmitt, 2015). Increasing temperature may accelerate both electrochemical and chemical reactions by promoting transfer process of reactive species or increasing reactive rate coefficient (Yin et al., 2009; Porcayo-Calderon et al., 2015), which dominates over the decreasing solubility of CO_2.

Proposed Mechanism for Corrosion Scale Formation

According to the above-mentioned results and discussion, a possible mechanism for the formation of corrosion scale on carbon steel in CO_2-saturated NaCl solutions is proposed and illustrated in **Figure 15**. Initially, corrosion occurs uniformly in small areas (anodic) with the formation of H_2 bubbles on top of the Fe_3C phase (cathodic) (**Figure 15A**). In this stage, EIS spectra indicate similar corrosion behavior, regardless of salt concentration and temperature. In general, the apparent corrosion rates increase with rising temperature (cathodic kinetics) and salt concentration (anodic kinetics), and gradually increase with time. The dissolution of Fe surrounding the Fe_3C phase exposes more cementite on the sample surface (**Figure 15B**). At the same time, the enrichment and local supersaturation of Fe^{2+} ions at the metal surface facilitates the formation of early corrosion products, for example $FeCO_3$ (**Figure 15C**), as verified by additional semicircles at low frequency in the EIS spectra shown in **Figure 1**. At

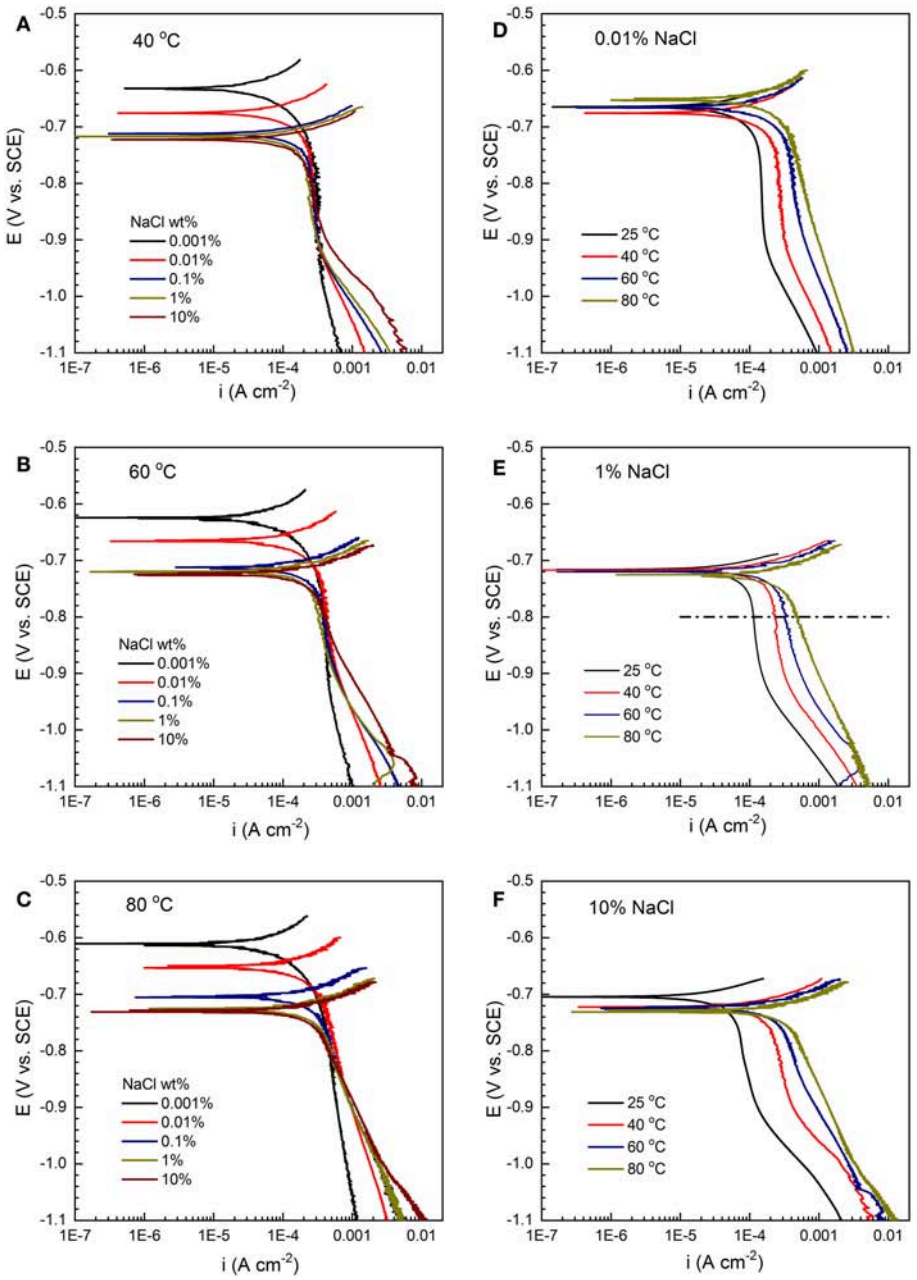

FIGURE 12 | Cathodic polarization curves of C1010 steel with varying salt concentration (0.001% to 10%) at constant temperature levels, **(A)** 40°C, **(B)** 60°C, and **(C)** 80°C. Cathodic polarization curves with varying temperature (25 to 80°C) at constant salt concentration levels, **(D)** 0.01%, **(E)** 1%, and **(F)** 10%.

lower temperature (≤40°C), the initially formed $FeCO_3$ is unstable, and later dissolves due to its high solubility at low temperatures. This results in Fe_3C accumulation on the surface (**Figure 15D**), as confirmed by SEM images in **Figure 7** and XRD results in **Figure 6**. In contrast, $FeCO_3$ is more stable and begins to accumulate on the steel surface at higher temperature (≥60°C), because the corrosion rate increases but the solubility of $FeCO_3$ decreases with increasing temperature (Bénézeth et al., 2009).

It is generally believed that the growth of the $FeCO_3$ film occurs in two steps: nucleation and crystal growth. The growth behavior of crystals is mainly determined by the internal structure of a given crystal (Liu et al., 2012). The carbonate ions (CO_3^{2-}) exhibits planar structure and the bond angle of O-C-O is 120° (Zhong et al., 2013). When Fe^{2+} and CO_3^{2-} combine to form $FeCO_3$ crystal nuclei (stage I), iron and oxygen atoms tend to form Fe-O octahedron between the different planes of CO_3^{2-}. As a result, the germinated $FeCO_3$ prefers

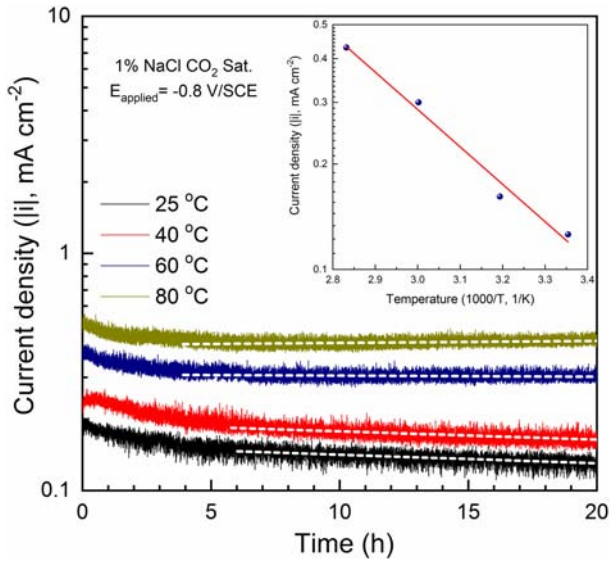

FIGURE 13 | Potentiostatic polarization curves ($E_{applied} = -0.8$ V/SCE) of C1010 steel tested in 1% NaCl with CO_2 saturation at different temperature levels, i.e., 25, 40, 60, and 80°C. Inset: a plot of *i* as a function of *1/T* for the calculation of cathodic activation energy of 20 kJ mol^{-1}.

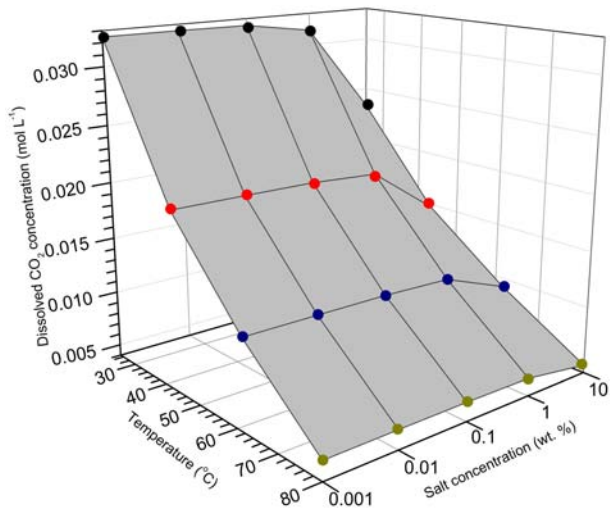

FIGURE 14 | OLI® calculation of CO_2 solubility as a function of NaCl salt concentration and temperature.

to grow in lamellar structure and finally matures to cubic crystal particles according to the Fe^{2+}/CO_3^{2-} concentration (Zhu et al., 2006; Liu et al., 2012; Zhong et al., 2013). In this case, a protective film (inner layer) consisting of a combination of Fe_3C and $FeCO_3$ (planar and crystal structure) is formed (stage II). However, the microstructure of the corrosion scale depends on both temperature and Cl^- concentration. In high salt concentration (1% NaCl and above), the Cl^--accelerated anodic reaction (**Figure 10**) leads to the formation of more porous inner layer (**Figure 9**). As a result, the apparent corrosion rate remains high (**Figure 5**). The higher Fe^{2+} concentration, at least locally, facilitates the formation of cubic form of corrosion products on top of the inner layer (**Figure 15E**). The cubic form of corrosion product is likely a result of dissolution-precipitation process. At the same salt concentration, higher temperature promotes the further nucleation and growth of crystal particles, and therefore, more crystal particles with larger size form (**Figure 15F**). In low salt concentration (0.001 to 0.1%) at 80°C, however, a majority of the steel surface is covered with planar $FeCO_3$ instead of cubic crystal particles (**Figure 15G**). This phenomenon can be probably attributed to the relatively low Cl^- concentrations and slower anodic kinetics (**Figure 10**). Assuming similar availability of CO_3^{2-}, lower Fe^{2+} in dilute NaCl solutions controls the precipitation process and small crystals form uniformly which are further anchored with Fe_3C to create a more compact layer. This form of corrosion product may be a direct reaction by HCO_3^- with surface absorbed species (e.g., $FeOH_{ads}$) through Equation 7. This layer significantly increases the corrosion resistance of carbon steel and slows down further corrosion (**Figure 5**). Therefore, the steel surfaces immersed in dilute NaCl solutions are covered with planar-structured $FeCO_3$ crystals with only a small amount of cubic crystals embedded in them, because the low concentration of Fe^{2+} in the bulk solution limits the growth of $FeCO_3$ to large cubic size. In summary, although Cl^- has no effect on the composition of the corrosion product, its presence and concentration significantly affect the morphology and microstructure of the corrosion scale and therefore the apparent corrosion rate.

CONCLUSIONS

1) In CO_2-saturated NaCl solutions, the corrosion rate of carbon steel increases with temperature during the initial stage of immersion. However, corrosion rate shows a decreasing trend over time at higher temperature (i.e., 60 and 80°C). This is attributed to the formation of protective corrosion scales (i.e., $FeCO_3$), which occurs faster at higher temperature.
2) At constant temperature, the initial corrosion rate of carbon steel increases with salt concentration. After an apex corrosion rate is reached, which is independent of the salt concentration, corrosion rate shows a decreasing trend over time and the magnitude is inversely proportional to the salt concentration.
3) At temperature higher than 60°C, $FeCO_3$ is the dominant corrosion product, with the possible existence of Fe_2CO_3OH. The cross-sectional profile of the corrosion scale shows a dual layer structure with a surface layer consisting of bulk $FeCO_3$ crystals (planar and cubic) and an inner layer of Fe_3C anchored with $FeCO_3$. The thickness and compactness of $FeCO_3$ layer increase from 60 to 80°C. In contrast, the corrosion product formed on carbon steel is mainly Fe_3C at temperature below 60°C.

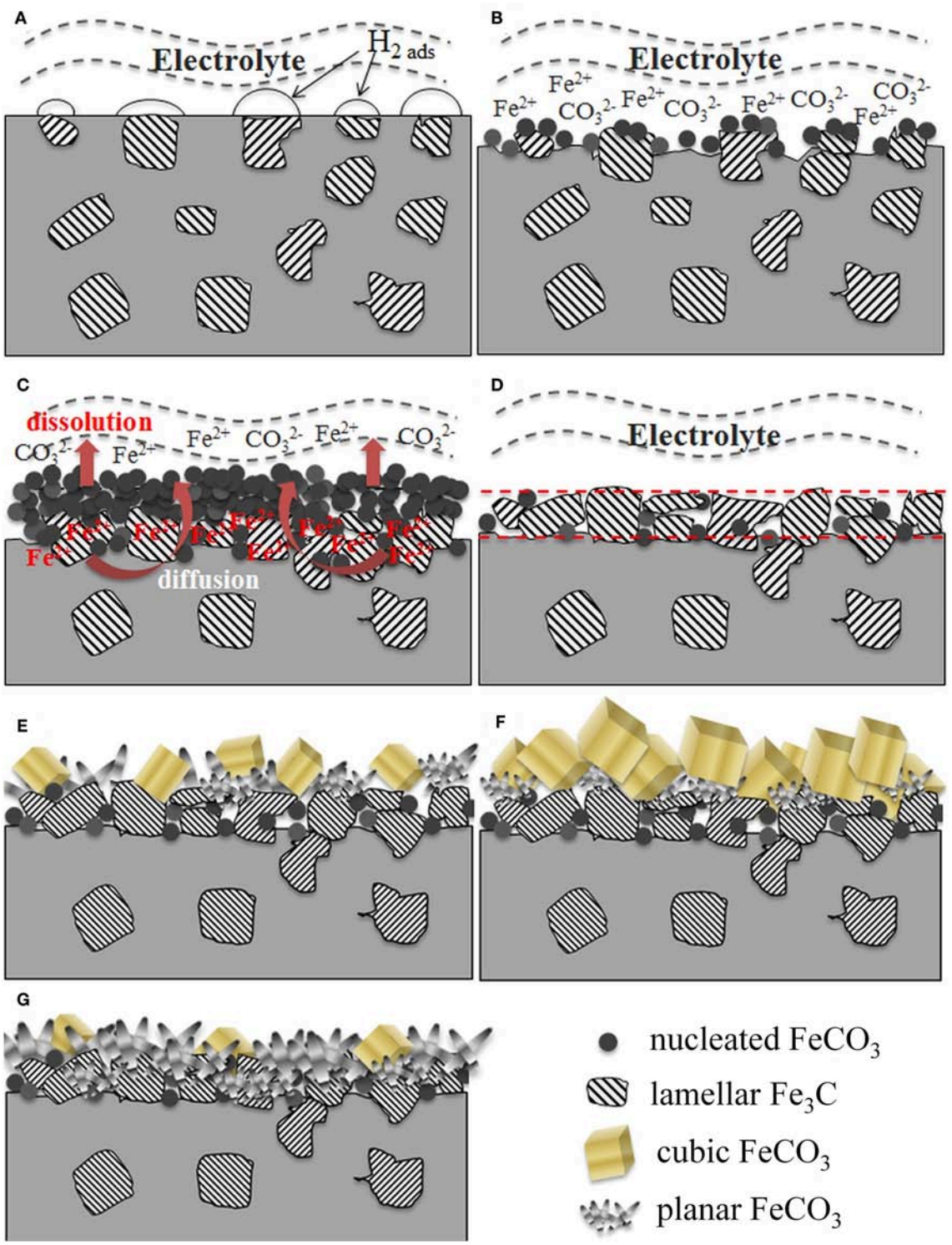

FIGURE 15 | Schematic diagrams showing the formation of corrosion scales on carbon steel immersed in CO_2-saturated NaCl solutions as a function of time, temperature and salt concentration. **(A)** initial corrosion upon immersion; **(B)** early $FeCO_3$ nucleation; **(C)** accumulation of $FeCO_3$; **(D)** accumulation of Fe_3C; **(E)** dual-layer formation; **(F)** growth of cubic $FeCO_3$ in outer layer; **(G)** compact inner layer with planar $FeCO_3$.

4) Cl^- has no effect on the composition of the corrosion product; however, it affects the microstructure of the corrosion scale. In dilute NaCl solutions (0.001%, 0.01%, 0.1%), the nucleation of $FeCO_3$ is fast and occurs uniformly, resulting in a compact inner layer of $FeCO_3$ and an outer layer of crosslinked $FeCO_3$ flakes. However, in concentrated NaCl solutions (1 and 10 %), the adsorption of Cl^- may impede the nucleation of $FeCO_3$, resulting in the growth of large $FeCO_3$ crystals on top of the porous inner layer.
5) The salt concentration has more noticeable effect on the anodic kinetics than temperature. The competition between Cl^- and OH^- affects the anodic reaction rate and more importantly, the protectiveness of the corrosion scale. Periodic precipitation and dissolution of the corrosion scale is inferred to occur at higher temperature and higher applied potential.
6) The cathodic reaction, which is under diffusion control and/or mixed control, is more sensitive to temperature than salt concentration. Theoretical calculation indicates the solubility of CO_2 decreases with increasing temperature, which suggests the enhanced cathodic kinetics at higher temperature is due to other factors.

AUTHOR CONTRIBUTIONS

SL and ZZ conducted electrochemical tests, data analyses and characterizations, and also drafted the manuscript. MH assisted in performing electrochemical tests and LS helped with manuscript preparation. HC supervised the overall research work and finalized the manuscript.

ACKNOWLEDGMENTS

We acknowledge the funding support from the University of Akron.

REFERENCES

Bénézeth, P., Dandurand, J. L., and Harrichoury, J. C. (2009). Solubility product of siderite (FeCO3) as a function of temperature (25–250°C). *Chem. Geol.* 265, 3–12. doi: 10.1016/j.chemgeo.2009.03.015

Bonnel, A., Dabosi, F., Deslouis, C., Duprat, M., Keddam, M., and Tribollet, B. (1983). Corrosion study of a carbon steel in neutral chloride solutions by impedance techniques. *J. Electrochem. Soc.* 130, 753–761. doi: 10.1149/1.2119798

Burstein, G. T., and Davies, D. H. (1980). The effects of anions on the behaviour of scratched iron electrodes in aqueous solutions. *Corrosion Sci.* 20, 1143–1155. doi: 10.1016/0010-938X(80)90145-6

das Chagas Almeida, T., Bandeira, M. C. E., Moreira, R. M., and Mattos, O. R. (2017). New insights on the role of CO2 in the mechanism of carbon steel corrosion. *Corrosion Sci.* 120, 239–250. doi: 10.1016/j.corsci.2017.02.016

de Waard, C., Lotz, U., and Milliams, D. E. (1991). Predicitive model for CO_2 corrosion engineering in wet natural gas pipelines. *Corrosion* 47, 976–985. doi: 10.5006/1.3585212

Fang, H., Brown, B., and Nesic, S. (2013). Sodium chloride concentration effects on general CO_2 corrosion mechanisms. *Corrosion* 69, 297–302. doi: 10.5006/0222

Han, J., Carey, J. W., and Zhang, J. (2011). Effect of sodium chloride on corrosion of mild steel in CO_2-saturated brines. *J. Appl. Electrochem.* 41, 741–749. doi: 10.1007/s10800-011-0290-3

Han, J., Young, D., Colijn, H., Tripathi, A., and Nesic, S. (2009). Chemistry and structure of the passive film on mild steel in CO_2 corrosion environments. *Ind. Eng. Chem. Res.* 48, 6296–6302. doi: 10.1021/ie 801819y

Heuer, J. K., and Stubbins, J. F. (1999). An XPS characterization of $FeCO_3$ films from CO_2 corrosion. *Corrosion Sci.* 41, 1231–1243. doi: 10.1016/S0010-938X(98)00180-2

Jasinski, R. (1987). Corrosion of N80-Type steel by CO_2/water mixtures. *Corrosion* 43, 214–218. doi: 10.5006/1.3583139

Kinsella, B., Tan, Y. J., and Bailey, S. (1998). Electrochemical impedance spectroscopy and surface characterization techniques to study carbon dioxide corrosion product scales. *Corrosion* 54, 835–842. doi: 10.5006/1.32 84803

Li, S., George, R. D., and Hihara, L. H. (2016). Corrosion analysis and characteristics of discarded military munitions in ocean waters. *Corrosion Sci.* 102, 36–43. doi: 10.1016/j.corsci.2015.09.014

Li, S., Kealoha, J., and Hihara, L. H. (2015). "Corrosion of low-carbon steel in seawater/biodiesel mixtures – a study related to the corrosion of fuel tanks in ships," in *Corrosion 2015 Conference and Expo* (Houston, TX: NACE International).

Linter, B. R., and Burstein, G. T. (1999). Reactions of pipeline steels in carbon dioxide solutions. *Corrosion Sci.* 41, 117–139. doi: 10.1016/S0010-938X(98)00104-8

Liu, F. G., Du, M., Zhang, J., and Qiu, M. (2009). Electrochemical behavior of Q235 steel in saltwater saturated with carbon dioxide based on new imidazoline derivative inhibitor. *Corrosion Sci.* 51, 102–109. doi: 10.1016/j.corsci.2008.09.036

Liu, G., Deng, Q., Wang, H., Ng, D. H. L., Kong, M., Cai, W., et al. (2012). Micro/nanostructured [small alpha]-Fe_2O_3 spheres: synthesis, characterization, and structurally enhanced visible-light photocatalytic activity. *J. Mater. Chem.* 22, 9704–9713. doi: 10.1039/C2JM31586F

Liu, Q. Y., Mao, L. J., and Zhou, S. W. (2014). Effects of chloride content on CO_2 corrosion of carbon steel in simulated oil and gas well environments. *Corrosion Sci.* 84, 165–171. doi: 10.1016/j.corsci.2014.03.025

Liu, X., Okafor, P. C., and Zheng, Y. G. (2009a). The inhibition of CO_2 corrosion of N80 mild steel in single liquid phase and liquid/particle two-phase flow by aminoethyl imidazoline derivatives. *Corrosion Sci.* 51, 744–751. doi: 10.1016/j.corsci.2008.12.024

Liu, X., Zheng, Y. G., and Okafor, P. C. (2009b). Carbon dioxide corrosion inhibition of N80 carbon steel in single liquid phase and liquid/particle two-phase flow by hydroxyethyl imidazoline derivatives. *Mater. Corrosion* 60, 507–513. doi: 10.1002/maco.200805133

Ma, H. Y., Yang, C., Li, G. Y., Guo, W. J., Chen, S. H., and Luo, J. L. (2003). Influence of nitrate and chloride ions on the corrosion of iron. *Corrosion* 59, 1112–1119. doi: 10.5006/1.3277530

Mao, X., Liu, X., and Revie, R. W. (1994). Pitting corrosion of pipeline steel in dilute bicarbonate solution with chloride ions. *Corrosion* 50, 651–657. doi: 10.5006/1.3293540

McCafferty, E., and Hackerman, N. (1972). Kinetics of iron corrosion in concentrated acidic chloride solutions. *J. Electrochem. Soc.* 119, 999–1009. doi: 10.1149/1.2404426

Nesic, S., Postlethwaite, J., and Olsen, S. (1996). An electrochemical model for prediction of corrosion of mild steel in aqueous carbon dioxide solutions. *Corrosion* 52, 280–294. doi: 10.5006/1.32 93640

Nesic, S., Pots, B., Postlethwaite, J., and Thevenot, N. (1995). Superposition of diffusion and chemical reaction controlled limiting currents-application to CO_2 corrosion. *J. Corrosion Sci. Eng.* 1.

Ogundele, G. I., and White, W. E. (1986). Some observations on corrosion of carbon steel in aqueous environments containing carbon dioxide. *Corrosion* 42, 71–78. doi: 10.5006/1.3584888

Ortega-Sotelo, D. M., Gonzalez-Rodriguez, J. G., Neri-Flores, M. A., Casales, M., Martinez, L., and Martinez-Villafañe, A. (2011). CO_2 corrosion inhibition of

X-70 pipeline steel by carboxyamido imidazoline. *J. Solid State Electrochem.* 15, 1997–2004. doi: 10.1007/s10008-010-1226-2

Ortega-Toledo, D. M., Gonzalez-Rodriguez, J. G., Casales, M., Martinez, L., and Martinez-Villafañe, A. (2011). CO_2 corrosion inhibition of X-120 pipeline steel by a modified imidazoline under flow conditions. *Corrosion Sci.* 53, 3780–3787. doi: 10.1016/j.corsci.2011.07.028

Porcayo-Calderon, J., Martínez de la Escalera, L. M., Canto, J., Casales-Diaz, M., and Salinas-Bravo, V. M. (2015). Effect of the temperature on the CO_2-corrosion of Ni_3Al. *Int. J. Electrochem. Sci.* 10, 3136–3151.

Schmitt, G. (2015). "Fundamental aspects of CO_2 metal loss corrosion. part ii: influence of different parameters on CO_2 corrosion mechanism," in *Corrosion 2015 Conference and Expo* (Houston, TX: NACE International).

Shadley, J. R., Shirazi, S. A., Dayalan, E., and Rybicki, E. F. (1998). Prediction of erosion-corrosion penetration rate in a carbon dioxide environment with sand. *Corrosion* 54, 972–978. doi: 10.5006/1.3284819

Shukla, S. K., and Quraishi, M. A. (2009). 4-Substituted anilinomethylpropionate: new and efficient corrosion inhibitors for mild steel in hydrochloric acid solution. *Corrosion Sci.* 51, 1990–1997. doi: 10.1016/j.corsci.2009.05.020

Sun, J. B., Zhang, G. A., Liu, W., and Lu, M. X. (2012). The formation mechanism of corrosion scale and electrochemical characteristic of low alloy steel in carbon dioxide-saturated solution. *Corrosion Sci.* 57, 131–138. doi: 10.1016/j.corsci.2011.12.025

Tang, L., Mu, G., and Liu, G. (2003). The effect of neutral red on the corrosion inhibition of cold rolled steel in 1.0 M hydrochloric acid. *Corrosion Sci.* 45, 2251–2262. doi: 10.1016/S0010-938X(03)00046-5

Videm, K., and Dugstad, A. (1987). "Effect of flow rate, pH, Fe^{2+} concentration and steel quality on the CO_2 corrosion of carbon steel," in *Corrosion/87 Conference and Expo* (Houston, TX: NACE International).

Wei, L., Pang, X., Liu, C., and Gao, K. (2015). Formation mechanism and protective property of corrosion product scale on X70 steel under supercritical CO_2 environment. *Corrosion Sci.* 100, 404–420. doi: 10.1016/j.corsci.2015.08.016

Wu, S. L., Cui, Z. D., He, F., Bai, Z. Q., Zhu, S. L., and Yang, X. J. (2004). Characterization of the surface film formed from carbon dioxide corrosion on N80 steel. *Mater. Lett.* 58, 1076–1081. doi: 10.1016/j.matlet.2003.08.020

Yin, Z. F., Feng, Y. R., Zhao, W. Z., Bai, Z. Q., and Lin, G. F. (2009). Effect of temperature on CO_2 corrosion of carbon steel. *Surf. Interface Anal.* 41, 517–523. doi: 10.1002/sia.3057

Zeng, Z., Lillard, R. S., and Cong, H. (2016). Effect of salt concentration on the corrosion behavior of carbon steel in CO_2 environment. *Corrosion* 72, 805–823. doi: 10.5006/1910

Zhang, G. A., Lu, M. X., Qiu, Y. B., Guo, X. P., and Chen, Z. Y. (2012). The relationship between the formation process of corrosion scales and the electrochemical mechanism of carbon steel in high pressure CO_2-containing formation water. *J. Electrochem. Soc.* 159, C393–C402. doi: 10.1149/2.030209jes

Zhao, J., and Chen, G. (2012). The synergistic inhibition effect of oleic-based imidazoline and sodium benzoate on mild steel corrosion in a CO_2-saturated brine solution. *Electrochim. Acta* 69, 247–255. doi: 10.1016/j.electacta.2012.02.101

Zhong, Y., Su, L., Yang, M., Wei, J., and Zhou, Z. (2013). Rambutan-like $FeCO_3$ hollow microspheres: facile preparation and superior lithium storage performances. *ACS Appl. Mater. Interfaces* 5, 11212–11217. doi: 10.1021/am403453r

Zhu, L.-P., Xiao, H.-M., Liu, X.-M., and Fu, S.-Y. (2006). Template-free synthesis and characterization of novel 3D urchin-like [small alpha]-Fe_2O_3 superstructures. *J. Mater. Chem.* 16, 1794–1797. doi: 10.1039/B604378J

Zhu, S. D., Fu, A. Q., Miao, J., Yin, Z. F., Zhou, G. S., and Wei, J. F. (2011). Corrosion of N80 carbon steel in oil field formation water containing CO_2 in the absence and presence of acetic acid. *Corrosion Sci.* 53, 3156–3165. doi: 10.1016/j.corsci.2011.05.059

Conflict of Interest Statement: The authors declare that the research was conducted in the absence of any commercial or financial relationships that could be construed as a potential conflict of interest.

frontiers in Materials

ORIGINAL RESEARCH
published: 28 June 2019
doi: 10.3389/fmats.2019.00146

High Temperature and Ion Implantation-Induced Phase Transformations in Novel Reduced Activation Si-Fe-V-Cr (-Mo) High Entropy Alloys

Amy S. Gandy[1], Bethany Jim[1,2], Gabrielle Coe[1], Dhinisa Patel[1], Liam Hardwick[1], Shavkat Akhmadaliev[3], Nik Reeves-McLaren[1] and Russell Goodall[1]*

[1] Department of Materials Science and Engineering, University of Sheffield, Sheffield, United Kingdom, [2] Department of Materials, University of Oxford, Oxford, United Kingdom, [3] Institute of Ion Beam Physics and Materials Research, Helmholtz-Zentrum Dresden-Rossendorf, Dresden, Germany

OPEN ACCESS

Edited by:
Tadeusz Hryniewicz, Koszalin University of Technology, Poland

Reviewed by:
Gloria Pena Uris, University of Vigo, Spain
Alexander John Knowles, University of Birmingham, United Kingdom

***Correspondence:**
Amy S. Gandy
a.gandy@sheffield.ac.uk

Specialty section:
This article was submitted to Environmental Materials, a section of the journal Frontiers in Materials

Received: *26 February 2019*
Accepted: *07 June 2019*
Published: *28 June 2019*

Citation:
Gandy AS, Jim B, Coe G, Patel D, Hardwick L, Akhmadaliev S, Reeves-McLaren N and Goodall R (2019) High Temperature and Ion Implantation-Induced Phase Transformations in Novel Reduced Activation Si-Fe-V-Cr (-Mo) High Entropy Alloys. Front. Mater. 6:146. doi: 10.3389/fmats.2019.00146

For fusion to be realized as a safe, sustainable source of power, new structural materials need to be developed which can withstand high temperatures and the unique fusion radiation environment. An attractive aspect of fusion is that no long-lived radioactive wastes will be produced, but to achieve this structural materials must comprise reduced activation elements. Compositionally complex alloys (CCAs) (also called high entropy alloys, HEAs) are promising candidates for use in extreme environments, including fusion, but few reported to date have low activation. To address these material challenges, we have produced novel, reduced activation, HEAs by arc-melting, and investigated their thermal stability, and radiation damage resistance using 5 MeV Au^{2+} ion implantation. Whilst the alloys were designed to form single phase BCC, using room temperature and non-ambient *in situ* X-ray diffraction we have revealed the thermodynamically stable structure of these alloys is in fact a sigma phase. We propose that a BCC phase is formed in these alloys, but at high temperatures (>1000°C). A BCC phase was also formed during heavy ion implantation, which we propose to be due to the rapid heating and cooling that occurs during the thermal spike, effectively freezing in the BCC phase produced by an implantation induced phase transformation. The BCC phase was found to have high hardness and a degree of ductility, making these new alloys attractive in the development of reduced activation HEAs for nuclear applications.

Keywords: high entropy alloy (HEA), reduced activation, phase transformation, ion implantation, thermal stability, nuclear, radiation damage

INTRODUCTION

High Entropy Alloys (HEAs), also known as compositionally complex alloys (CCAs), comprise multiple principal elements instead of being based upon one single element, a characteristic of most traditional alloys. As a result of their unique compositions, some HEAs have been reported to exhibit properties such as excellent hardness, high-temperature thermal stability, and resistance to

wear and corrosion (Yeh et al., 2004; Senkov et al., 2013a), although brittle behavior (Salishchev et al., 2014) and low thermal conductivity (Yan et al., 2018) have also been reported, which are undesirable properties for nuclear applications. Suppression of radiation-induced damage accumulation has recently been observed in several HEA systems (Egami et al., 2014; Xia et al., 2015; Zhang et al., 2015; Lu et al., 2016; Kombaiah et al., 2018). The reported superior properties have highlighted CCAs as candidates for applications in extreme environments, such as plasma facing materials (PFMs) in a fusion reactor. PFMs must be able to withstand neutron fluxes higher than in any current nuclear fission reactor, and maintain their properties whilst subjected to high heat loads. Another critical requirement of potential PFMs is that they have low neutron activation and generate only short-lived (<100 years) radionuclides, following removal from the fusion core. Absorption of fusion neutrons by some common constituent CCA elements, such as Co and Ni, results in transmutation and production of long-lived radionuclides (Gorley, 2015). Therefore, new CCAs need to be developed which preserve the excellent mechanical properties and radiation stability, whilst meeting the requirement for low activation. To address this challenge, we have produced and investigated two new HEAs from the systems SiFeCrVMo and SiFeCrV; the first forms a more traditional HEA type alloy, with five components, the latter is a reduced activation version of the system without molybdenum. Mo is not a reduced activation element but we employ both these alloys as examples of novel HEAs, to investigate the high temperature thermal stability and radiation damage resistance that can be achieved.

BCC structured metals have been found to display superior resistance to radiation damage compared to FCC metals. Garner et al. (2000) reported that following fast fission reactor neutron irradiation between 400°C and 550°C in 304L austenitic (FCC) stainless steel and 9–12%Cr ferritic/martensitic (BCC) steels, the void swelling rate per displacements per atom (dpa) was approximately 50 times higher for the FCC stainless steel compared to BCC ferritic/martensitic steels. Furthermore, radiation-induced defect cluster sizes and densities have been found to differ between FCC and BCC alloys. Zinkle and Snead (2014) reported the formation of significantly higher defect cluster densities in FCC austenitic steel compared to BCC ferritic steels, following low-temperature neutron irradiation. It is hypothesized that the formation of fewer, finely dispersed defect clusters in BCC structured alloys may enable greater defect recombination during dynamical and thermal annealing (Zinkle and Snead, 2014). Furthermore, as radiation-induced embrittlement is due to the pinning of dislocations by defect clusters, the production of fewer defect clusters in BCC alloys is expected to suppress radiation-induced embrittlement, thus extending the lifetime of the alloy in operation.

To date, radiation damage studies on CCAs have mainly focused on FCC structured alloys. Zhang et al. (2015) reported that radiation damage resistance in the NiCoFeCr HEA was due to chemical disorder and compositional complexity, which reduces the electron mean free path and thermal conductivity, leading to much slower energy dissipation and, consequently, slower damage accumulation during ion irradiation. However, Egami et al. (2015) using a density functional theory approach, reported that atomic-level stresses and local lattice distortion facilitated amorphisation and subsequent recrystallisation of CoFeNi and NiCoFeCr HEAs, resulting in the "wiping-out" of structural defects. More recently, Owen et al. (2017) used total neutron scattering measurements to determine the lattice strain in the equiatomic CrMnFeCoNi HEA, and reported, contrary to the mechanism proposed by Egami et al. (2015), no clear evidence that the local lattice strain was anomalously large. The irradiation stability in the high activation $Al_xCoCrCuFeNi$ system was investigated by Xia et al. (2015), who observed enhanced irradiation induced swelling in BCC $Al_{1.5}CoCrCuFeNi$, compared to FCC $Al_{0.1}CoCrCuFeNi$, following 3 MeV Au ion implantation, to 50 dpa, at room temperature, a swelling behavior contrary to other BCC alloys (Zinkle and Snead, 2014). It is evident therefore that the link between CCA composition and structure, and their resistance to radiation damage is not well understood.

In this study, the two alloys (from the systems SiFeCrV and SiFeCrVMo) were computationally designed to produce single-phase BCC alloys, in order to further investigate how BCC structured HEAs respond to radiation damage, produced in this work by 5 MeV Au^{2+} ion implantation at room temperature. The thermal stability of the alloys was determined by examining changes in crystal-structure and microstructure, using data collected from bulk and *in-situ* measurements.

MATERIALS AND METHODS

Design of the Alloys

In order to explore further the behavior of CCAs during irradiation, alloys showing new characteristics are required. With the view that such alloys may be employed in plant for nuclear power generation, a procedure was followed, developed for the design of novel brazing filler metals (Snell, 2017) to attempt to create novel alloys which may have future potential for these applications. This approach uses a Python script written in-house to perform calculations across a large number of potential alloy systems and compositions. Initially, elements of potential interest are selected, which here were the set of elements known to have low neutron activation cross section (Cheng, 1989; Gorley, 2015) plus some additional elements adopting body centered cubic structures at room temperature (Mo, Nb). A preponderance of BCC-stable elements was maintained in the list, intended to drive the preferential formation of this structure, but the search was otherwise deliberately quite wide-ranging, to identify and explore alloys which had not previously been the subject of research. From the full list, the script selects combinations of 4 or 5 of these elements, and calculates, for each possible composition with each element present in a quantity between 5 and 40%, the average atomic size mismatch, δ and the enthalpy of mixing, ΔH_{mix}. The average atomic size mismatch, δ is defined as:

$$\delta = 100\sqrt{\sum_{i=1}^{n} c_i\left(1-\frac{r_i}{\bar{r}}\right)^2} \quad (1)$$

where c_i is the atomic fraction of the ith element, r_i is its radius and the average radius is given by:

$$\bar{r} = \sum_{i=1}^{n} c_i r_i \quad (2)$$

The enthalpy of mixing, ΔH_{mix}, is estimated following the method introduced by Miedema (Miedema, 1973a,b), extended to multicomponent systems by using the coefficients (Ω ij) reported in Takeuchi and Inoue (2005) and the equation:

$$\Delta H_{mix} = 4 \sum_{i=1, i<j}^{n} c_i c_j \Omega_{ij} \quad (3)$$

Once these quantities have been determined, they can be used to rank the likely formation of a single phase alloy in each system. In other work on HEAs particular ranges where favorable compositions are more likely to lie are defined (e.g., Ye et al., 2016). However, as in this wide alloy search with multiple different elements the behavior can be very different, and we further wish to identify the most promising alloys. We have therefore elected to apply different criteria, first setting the limits that $0 < \Delta H_{mix} < 5$ kJ/mol, and then, for the alloys that meet this condition, of minimizing the absolute value of the atomic size mismatch.

The method identified the systems of Si-Fe-V-Cr-Mo and Si-Fe-V-Cr with alloys of the specific composition $Si_{0.05}Fe_{0.35}V_{0.16}Cr_{0.35}Mo_{0.09}$ and $Si_{0.06}Fe_{0.38}V_{0.18}Cr_{0.38}$ (atomic percent, at%) as the optimized compositions, based on this approach. As the procedure carries out this optimization on alloys by varying the composition, it is noteworthy, though not surprising, that the alloys are non-equiatomic in composition (of the type described as Complex Concentrated Alloys, CCAs, rather than equiatomic as entropy-maximizing HEAs will be).

While it must be acknowledged that there are other ways of performing these calculations (e.g., the Miedema enthalpy of mixing can be calculated in several different ways (Gallego et al., 1988; Wang et al., 2007) and other criteria which have been successfully used to predict such alloys (e.g., Poletti and Battezzati, 2014; Leong et al., 2017), we have found that these approaches give a good combination of suitable accuracy to facilitate experimentation, and speed of calculation, even in systems containing unusual pairs of elements where, for example, the lack of data preclude the use of CALPHAD. The approach is not a rigorous prediction, and will not successfully predict optimized alloys in all cases, yet it is nevertheless useful to guide early stage experimental work toward systems which have been little considered.

Alloy Production and Characterization

To produce the alloys, elemental Si, Fe, V, Cr, and Mo (purity > 99.5 %) were weighed to obtain the desired stoichiometry, and melted using an argon-backfilled vacuum arc melter (MAM1 Buehler). The alloys were re-melted and flipped five times to improve homogeneity. The $Si_{0.05}Fe_{0.35}V_{0.16}Cr_{0.35}Mo_{0.09}$ alloy composition was produced as a 5 g ingot, and the $Si_{0.06}Fe_{0.38}V_{0.18}Cr_{0.38}$ alloy composition was produced as a 2.5 g ingot. The smaller quantity was better adapted to the size of the arc melting equipment used, though 5g was possible and was used to facilitate greater accuracy in weighing out the small level additions (Si and Mo).

Due to the potential for volatilization of elements during arc melting, quantitative analysis of as-produced alloy compositions was conducted by X-ray fluorescence (XRF) using a PANalytical Zetium spectrometer and PANalytical's Omnian analysis methodology. Small spot mapping was carried out under vacuum with a spot size of 500 μm on a minimum of four random points for each alloy. XRF results were used to calculate an estimate for the theoretical melting temperature (T_m) of the alloys using the rule of mixtures.

The density of the as-cast alloys was determined using a Mettler Toledo NewClassic MF balance, applying the Archimedes method. Vickers hardness measurements were taken from a minimum of three random locations for each as-cast alloy. The measurements were made using a Zwick-Roell Hardness Tester with loads varying from 5 to 30 kg and a dwell time of 10 s. The variation in load was made to ensure the resultant indent was visible through the ×10 magnification view finder without causing significant damage to the sample. A Nikon Eclipse LV150N optical microscope was used to image hardness indents in greater detail.

To investigate thermal stability, the alloys were sectioned and annealed in a tube furnace under a flowing Ar atmosphere, with a Ti getter, for 48 h at either 0.5 T_m or 0.65 T_m (with T_m the estimated value as described above). The samples were heated from room temperature, held at temperature for 48 h, and then slow cooled in the furnace.

X-ray diffraction (XRD) was used to determine the crystal structures of as-cast and thermally annealed samples, using a Bruker D2 Phaser with Cu Kα radiation. Phase analysis used the International Center for Diffraction Data's (ICDD) PDF-4+ database, 2018 edition, and associated SIeve+ software. Lattice parameters were obtained via least squares refinement using STOE's WinX^{POW} software. High temperature XRD (HTXRD) data was used to investigate temperature induced phase transitions in the SiFeVCr HEA. The alloy was first ball milled in a Retzch GmbH Cryomill to powderise the material. The sample was placed in a 50 ml steel grinding jar, with a 25 mm steel ball used as the grinding organ. Milling was performed over a period of 20 min, in 2 min intervals, and a grinding frequency of 25 Hz was used throughout. A final 2 min milling stage with liquid nitrogen cooling was performed, again with a frequency of 25 Hz. Non-ambient X-ray diffraction data were collected from the powdered alloy *in situ*, from 30 to 1000°C under a vacuum of 1.5 × 10^{-5} mbar, using an Anton Paar HTK1200N furnace mounted on a PANalytical X'Pert^3 Powder diffractometer, using Cu Kα radiation and a PIXcel^{1D} detector, in Bragg-Brentano geometry.

Scanning Electron Microscopy (SEM) was used to observe the microstructures and element distribution in all samples, using an Hitachi TM3030 desktop Scanning Electron Microscope (SEM) equipped with a BSE detection system, operating at 15 kV. Energy

TABLE 1 | Measured alloy compositions from XRF and EDX, and melting and annealing temperatures calculated using the rule of mixtures and XRF data.

	Si (at %)	Fe (at %)	V (at %)	Cr (at %)	Mo (at %)	Tm (°C)	0.5 Tm (°C)	0.65 Tm (°C)
SiFeVCrMo (XRF)	2.30 ± 0.11	36.90 ± 0.90	14.79 ± 0.17	35.09 ± 0.39	10.92 ± 0.55	1983	991	1289
SiFeVCrMo (EDX)	5.30 ± 0.10	35.23 ± 1.00	16.60 ± 0.40	35.23 ± 0.90	7.37± 0.40			
SiFeVCr (XRF)	2.16 ± 0.18	42.56 ± 0.48	17.94 ± 0.32	37.33 ± 0.73	0	1963	981	1276
SiFeVCr (EDX)	5.19 ± 0.10	39.69 ± 0.18	18.41 ± 0.18	36.69 ± 0.18	0			

TABLE 2 | Refined structural parameters obtained from standard least squares refinement.

		Tetragonal				BCC		
		Space group	**a (Å)**	**c (Å)**	**V (Å)**	**Space group**	**a (Å)**	**V (Å)**
SiFeVCrMo	As-cast	P42/mnm	8.913 (16)	4.625 (13)	367.5 (6)	$Im\bar{3}m$	3.1486 (10)	31.213 (16)
	0.5 Tm	P42/mnm	8.932 (7)	4.621 (4)	368.7 (6)			
	0.65 Tm	P42/mnm	8.9201 (5)	4.6155 (7)	367.24 (5)	$Im\bar{3}m$	3.1519 (17)	31.31 (3)
SiFeVCr	As-cast	P42/mnm	8.8468 (18)	4.5889 (18)	359.16 (12)	$Im\bar{3}m$	2.8877 (5)	24.081 (7)
	0.5 Tm	P42/mnm	8.858 (4)	4.585 (3)	359.79 (24)			
	0.65 Tm	P42/mnm	8.8525 (9)	4.5867 (5)	359.44 (5)			

Dispersive X-Ray (EDX) analysis was used to obtain elemental maps and spectra.

The as-cast SiFeVCrMo alloy was implanted at room temperature with 5 MeV Au^{2+} ions to a fluence of 5×10^{15} Au^{2+} ions per cm^2 at the Ion Beam Centre in Helmholtz-Zentrum Dresden-Rossendorf, Germany. The implantation was carried out using a scanning beam, the beam spot size was about 3–5 mm on the target, the irradiated area was 50 mm in diameter, and the beam was moved fast by scanning in X and Y directions. The ion flux was approximately 1.6×10^{11} Au^{2+} ions per second per cm^2, and the ion beam current density was about 50 nA/cm^2. Prior to implantation, the sample surface was polished to a mirror finish, first using a range of SiC papers with decreasing grit size, followed by a final polishing stage using colloidal silica. The same method was used to prepare the samples for SEM, XRF and XRD. The implantation induced damage profile was determined using results from the Monte Carlo code SRIM (Ziegler et al., 1985). The calculation type "detailed calculation with full damage cascade" was chosen, a displacement energy, E_d, of 50 eV was set for each element, and the experimentally determined density of 7.2 g/cm^3 was used. Grazing incidence XRD (GI-XRD) was used to determine the crystal structure of the Au^{2+} ion implanted SiFeVCrMo sample. In GI-XRD, the penetration depth of the X-rays can be tuned so as to probe only the near-surface implantation-induced damaged region. The X-ray penetration depth was calculated using linear attenuation theory, from which an incident angle of 1.659° was determined to correspond to a penetration depth up to 500 nm below the surface, allowing the maximum level of damage produced, as calculated using results from the SRIM simulation, to be probed. GI-XRD of the SiFeVCrMo alloy before and after Au^{2+} ion implantation was performed on a PANalytical X'pert^3 diffractometer, using Cu Kα radiation and a PIXcel^{1D} detector in 0D mode.

RESULTS AND DISCUSSION

Phase Analysis

Quantitative analysis, using XRF, was performed on as-cast alloy specimens. Results are presented in **Table 1**, and show reasonable agreement with the targeted alloy compositions, though both alloys are slightly richer in Fe and Cr than anticipated and somewhat Si deficient. From these quantitative results, theoretical melting temperatures were calculated using the rule of mixtures (understanding that this is a very approximate estimation), and used to set the required annealing temperatures (**Table 1**).

Room temperature XRD data were also collected to characterize the phases present in both the as-cast and thermally annealed alloys. The refined structural parameters obtained from least squares refinement are presented in **Table 2**. In as-cast SiFeVCrMo, **Figure 1A**, most observed Bragg reflections could be indexed on a tetragonal unit cell, in the $P4_2/mnm$ space group, with lattice parameters a = 8.913 Å, c = 4.625 Å. A small amount of a secondary BCC phase, in the $Im\bar{3}m$ space group, was also observed, with Bragg peak positions indexing well to Mo, and lattice parameter a = 3.1486 Å, identified in **Figure 1A** by circles. For as-cast SiFeVCr, **Figure 1B**, the predominant phase observed was BCC-type, indexing to the $Im\bar{3}m$ space group, and lattice parameter a = 2.8877 Å. A small amount of secondary tetragonal phase was observed in this sample. This phase, identified by triangles in **Figure 1B**, could also be indexed in the $P4_2/mnm$ space group, with lattice parameter a = 8.8468 Å and c = 4.5889 Å.

For SiFeVCr, XRD data collected following annealing at either 0.5 T_m (981°C) or 0.65 T_m (1276°C), **Figure 2A**, showed predominantly a sigma-type phase. For this alloy, Bragg peaks could be well indexed using a $P4_2/mnm$ unit cell with lattice parameters a = 8.858 Å, c = 4.585 Å for the sample annealed at 0.5 T_m, and a = 8.8525 Å and c = 4.5867 Å for the sample

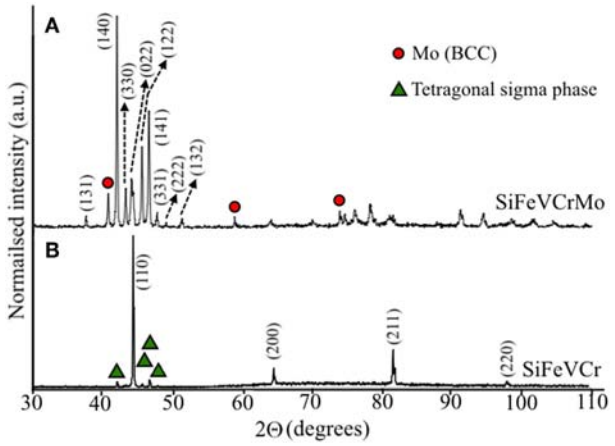

FIGURE 1 | Room temperature XRD patterns from the as-cast SiFeVCrMo **(A)** and SiFeVCr **(B)** samples. The circles indicate peaks attributed to BCC Mo. The triangles indicate peaks attributed to a tetragonal phase.

annealed at 0.65 T_m. There is no evidence of a BCC cell being present following the annealing treatment, and no significant change in either peak position or intensity for samples annealed at either 0.5 T_m or 0.65 T_m.

Similarly, no peaks from a BCC-type phase were observed for the SiFeVCrMo sample annealed at 0.5 T_m (991°C), **Figure 2B**. Peaks could again be indexed using a single tetragonal sigma-type unit cell (space group $P4_2/mnm$), with lattice parameters a = 8.932 Å, c = 4.625 Å. However, after annealing at 0.65 T_m (1289°C) XRD data showed evidence of phase segregation, with the re-emergence of peaks indexed to a Mo-type BCC phase (space group $Im\bar{3}m$, and lattice parameter a = 3.1519 Å), and a significant shifting of peaks from the sigma phase to lower diffraction angles, indicating an increase in the lattice parameters for this phase and most likely a significant change in its composition. In metallic systems, the sigma phase does not have a specific stoichiometry and therefore can exist over a range of compositions (Hall and Algie, 1966). The sample annealed at 0.65 T_m was indexed to the $P4_2/mnm$ space group with lattice parameter a = 8.9291 Å and c = 4.6155 Å.

From these room temperature data, it was unclear whether the BCC or sigma type phases were most thermodynamically stable, or whether one was a high temperature phase that had been quenched in on cooling. Metastability is observed in HEAs, especially in the small scale samples used for research purposes, such as the discovery of precipitation in CoCrFeNiMn when treated at moderate temperatures for extended times (Pickering et al., 2016). The variation in phase assemblages observed in the as-cast alloys here could be due to differential rates of cooling during alloy production. The SiFeVCrMo alloy was produced as a 5 g ingot, while the SiFeVCr alloy was produced as a 2.5 g ingot. Therefore, the smaller SiFeVCr alloy may have cooled more quickly during casting, effectively enabling the quenching in of a high temperature BCC phase.

To further investigate the thermodynamic stability of the phases observed, HTXRD data were collected under vacuum on an as-cast SiFeVCr alloy sample that had been powdered by cryomilling (**Figure 3**). At 30°C, the data could now be indexed on a single BCC type unit cell, space group $Im\bar{3}m$, with no observable peaks from any tetragonal sigma phase present. On heating, such peaks do begin to appear at 400°C, and can indeed be indexed using the $P4_2/mnm$ space group, appearing analogous to the sigma phase found in $FeCr_{0.5}V_{0.5}$ (Martens and Duwez, 1952). Peaks from a third phase, Cr_2O_3, appear on heating from 600°C, suggesting some level of surface oxidation occurring despite the sample being heated under vacuum. The peaks corresponding to the tetragonal phase become more prominent with increasing temperature, though it is difficult to determine whether a complete transformation from BCC to sigma phase occurs, due to the overlap of peaks at around 65°2θ from the BCC phase and Cr_2O_3, and at around 45 and 82°2θ from the BCC and tetragonal phases. There is no evidence of a high temperature tetragonal to BCC phase transition, suggesting that, if it exists, it takes place at temperatures above 1000°C in this alloy.

Non-ambient XRD data collected on subsequent cooling of the alloy from 1000°C show peaks from both sigma and Cr_2O_3 phases are retained to room temperature, with a slight shift in peaks to higher diffraction angles due to thermal contraction (**Figure 4**). As with **Figure 3**, due to overlapping of peaks in **Figure 4**, it is difficult to unambiguously determine whether a BCC phase is present and has been retained at room temperature.

The alloys were designed to form single phase BCC yet results from XRD data show that the thermodynamically stable phase is a sigma phase. This difference between designed and actual structure is due to the nature of the prediction, which is simplistic to give rapid exploration capability, and is primarily concerned with identifying compatible elements capable of mixing and forming a mutual solid solution. By choosing mostly BCC metals as the input, stability in a BCC form, rather than for example FCC, may be expected to dominate (Leong et al., 2017). However, as sigma phase is known to form in the Si-Fe-Cr and Si-Fe-V ternaries (Hall and Algie, 1966) a more stable option exists in this case: the sigma phase is an even lower energy structure, that is not assessed in our predictive calculations.

Mechanical Properties

Table 3 gives the measured densities and Vickers Hardness values of both as-cast alloys, the crystal structures, as determined by room temperature XRD, and the deformation behavior observed surrounding the hardness indent, shown in the optical images in **Figures 5a,b**. Whilst the densities of both alloys are similar, 7.20 ± 0.11 gcm^{-3} for SiFeVCrMo, and 7.09 ± 0.10 gcm^{-3} for SiFeVCr, the SiFeVCrMo alloy was found to be much harder (784 ± 54 HV5, or 7.69 ± 0.53 GPa) than the as-cast SiFeVCr alloy (436 ± 50 HV5, or 4.28 ± 0.49 GPa). The errors in the measurements for both density and hardness is one standard deviation. From these data, and the approximate rule that hardness is three times the yield strength, σ_y of the alloys were estimated to be 2.6 GPa for SiFeVCrMo, and 1.43 GPa for SiFeVCr. The cracks propagating from the edges and corners of the indent in the SiFeVCrMo alloy, shown in **Figure 5a**, are indicative of brittle fracture. By contrast, the deformation of indent edges in the SiFeVCr alloy, shown

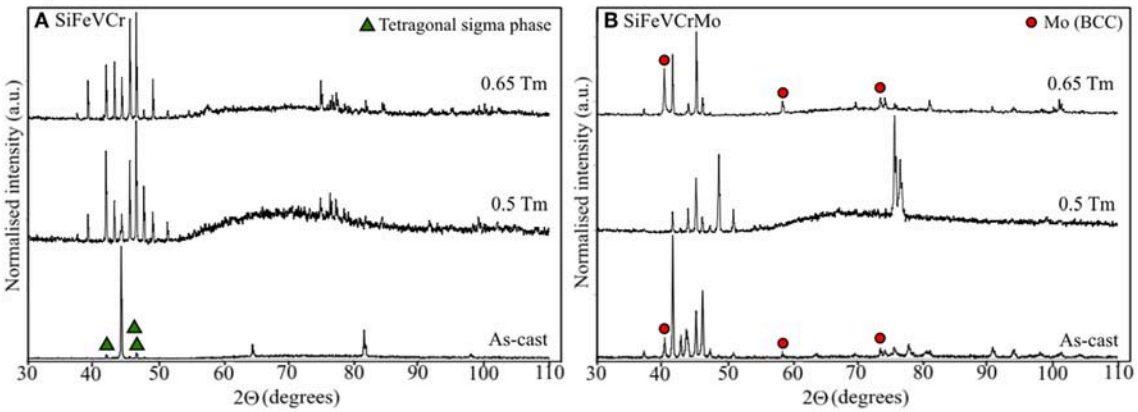

FIGURE 2 | Room temperature XRD patterns from **(A)** the SiFeVCr sample after annealing at 0.5 T_m (981°C) and 0.65 T_m (1276°C) for 48 h, and from **(B)** the SiFeVCrMo sample after annealing at 0.5 T_m (991°C) and 0.65 T_m (1289°C) for 48 h. The circles indicate peaks attributed to BCC Mo and triangles to tetragonal sigma phase.

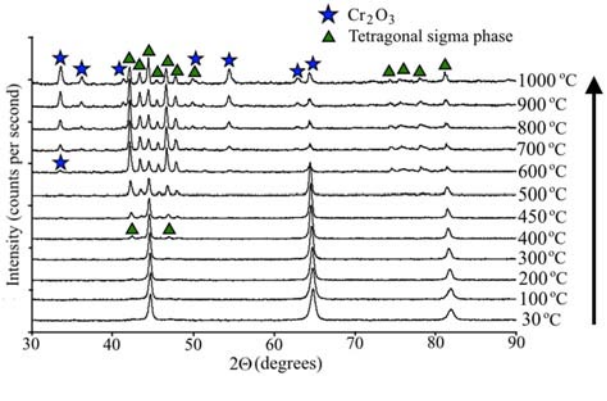

FIGURE 3 | Non-ambient XRD data from FeSiVCr, showing single-phase BCC at room temperature up to 400°C; BCC to tetragonal phase transition from 400°C, and formation of $Cr2O_3$ at 600°C. The triangles indicate peaks attributed to a tetragonal phase, isostructural with $FeCr_{0.5}V_{0.5}$. The stars indicate peaks attributed to Cr_2O_3.

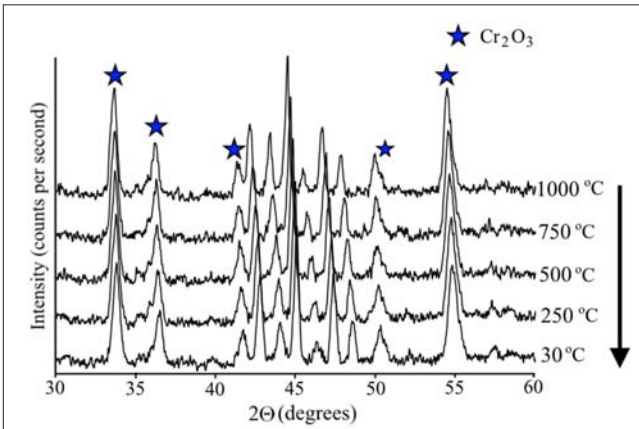

FIGURE 4 | Non-ambient XRD data collected during cooling to room temperature, from 1000°C. Peaks from both sigma and Cr_2O_3 phases are retained in all data.

in **Figure 5b**, suggests ductile deformation during indentation. The sets of parallel lines surrounding the indent in **Figure 5b** are therefore determined to be step edges, resulting from the interaction of dislocations with the surface as they propagate on crystallographic slip planes during loading. The hardness values of both alloys are greater than typical for conventional alloys, but are comparable to other HEAs reported. The hardness and yield stress, at room temperature, of as-cast SiFeVCr (BCC + σ phase) is comparable to the single-phase BCC structured refractory $Al_{0.4}Hf_{0.6}NbTaTiZr$ HEA, (Senkov et al., 2014) as well as to NbTiVZr, $NbTiV_2Zr$, CrNbTiZr and CrNbTiVZr, reported to have very high Vickers microhardness of 3.29 GPa, 2.99 GPa, 4.10 GPa, and 4.72 GPa, respectively, attributed to the presence of disordered BCC solid solutions (Senkov et al., 2013b). The higher hardness of as-cast SiFeVCrMo (σ phase) is comparable to AlCoCrCuFe, which, after Spark Plasma Sintering, comprises an ordered BCC (B2) phase, Cu rich FCC (FCu) phase and a σ phase (Praveen et al., 2012).

Whilst the brittle nature of SiFeVCrMo is undesirable for use as a structural material, the high hardness and ductile behavior of SiFeVCr, as well as it being reduced activation, is promising for the use of this alloy as a plasma facing material. However, the desirable mechanical behavior of SiFeVCr is only observed in the proposed high temperature BCC phase. Further work is required to determine whether the proposed high temperature phase can be stabilized at lower temperatures by, for example, altering the alloy stoichiometry, as has been reported in other HEA systems (Leong et al., 2017). In addition, other mechanical properties, such as toughness, need to be evaluated in order to further develop these alloys.

Microstructure: Morphology and Stoichiometry

To investigate the microstructures and distribution of elements in the as-cast and heat treated alloys, backscattered SEM images

TABLE 3 | Density and Vickers Hardness values of the as-prepared alloys.

	Density (gcm^{-3})	Vickers hardness (HV5)	Crystal structure	Observed deformation behavior
SiFeVCrMo	7.2 ± 0.11	784 ± 54	Tetragonal (σ phase)	Brittle
SiFeVCr	7.09 ± 0.10	436 ± 50	BCC + tetragonal (σ phase)	Ductile

(BSE) and EDX maps and spectra were obtained. **Figures 6–8** show the SEM/EDX data collected on the SiFeVCrMo (**Figures 6**, **7**) and SiFeVCr (**Figure 8**) alloys. The microstructures of the two as-cast alloys (**Figures 6A**, **8A,B**) show some differences, with the SiFeVCr alloy comprising larger, more well defined regions of different contrast. **Figures 6A–C** show the microstructures observed in the as-cast, 0.5 T_m, and 0.65 T_m heat treated SiFeVCrMo alloys, respectively. The contrast in BSE images is due to variations in atomic number, with lighter regions indicating the presence of heavier elements, and darker regions indicative of lighter elements. To aid identification of regions with different contrast, the contrast in the BSE images presented here was enhanced by readjusting gray-scale levels using paint.net. The microstructure of the as-cast alloy (**Figure 6A**) and alloy following annealing at 0.5 T_m (**Figure 6B**) comprises three regions, shown in the image as light gray, dark gray, and black contrast. It is noted that the contrast variation between light and dark gray regions is not as well defined in the 0.5 T_m heat treated alloy compared to the as-cast alloy, suggesting the formation of a more homogenous alloy following annealing. Following annealing at 0.6 T_m (**Figure 6C**), the alloy comprises only two distinct regions, defined here as light gray and black.

To determine the compositions of the different regions, EDX spot maps were collected in each region, using a spot size of diameter 5 μm. The spot size, collection time and magnification were the same for all spectra collected. **Table 4** gives the average compositions of the phases identified by SEM/EDX. For each phase, data was collected from two locations, with the errors quoted being one standard deviation. The crystal structures as determined by XRD are included for reference. Indicative locations from where the EDX data were collected are shown by the circles on each BSE image, with the blue dotted circles indicating light gray regions, the red solid circles indicating dark gray regions, and the green circles with combined dotted and solid lines indicating black regions. In **Figures 6**, **8**, EDX spectra are presented under the alloys from which they were collected, and circles on each spectrum identify the collection region. In **Figure 6**, EDX spectra (d–f) were collected from the light gray regions, (g–i) from the black regions, and (j, k) from the dark gray regions. The Al present in some of the EDX spectra is attributed to contamination during sample preparation where the samples are fixed to an Al sample holder during grinding and polishing.

From the compositional data presented in **Table 4**, no clear relationship between the light and dark gray phases is evident, with variations in compositions observed within the same phase across samples. The EDX data does indicate that both phases are rich in Fe and Cr, relative to the other elements, and it is clear that the black regions in all three alloys (as-cast, 0.5 T_m and 0.65 T_m) are rich in V, relative to the light and dark gray phases. After annealing at 0.6 T_m, the V rich phases grow in size, and form two distinct morphologies, either roughly circular or platelet. **Figure 6L** shows a lower magnification BSE image of the as-cast alloy, which clearly shows regions of light contrast. **Figure 7** shows elemental maps from this region to show the spatial distribution of elements. The light contrast here is attributed to residual Mo, which did not fully alloy during arc melting. Because of this residual Mo, EDX data was collected from both SiFeVCrMo and SiFeVCr, from an area of approximately 200 μm^2, in order to determine the nominal composition of both HEAs. The data is presented in **Table 1**, to compare with XRF data from both alloys. A greater amount of Si is detected by EDX in both HEAs, which we attribute to contamination from the SiC paper used to prepare the sample surfaces for SEM. There is relatively little difference between the concentration of Mo detected by XRF and EDX, suggesting that the random XRF spot maps (with spot size of 500 μm) that were collected from the alloy did not intersect any residual Mo.

The microstructures of the as-cast, 0.5 T_m and 0.65 T_m heat treated SiFeVCr alloys are shown in **Figures 8A,C,D**, respectively. A lower magnification BSE image of the as-cast alloy is given in **Figure 8B**. Similar to the SiFeVCrMo alloy, the as-cast alloy comprises multiple regions of varying contrast, indicative of the formation of an inhomogeneous alloy. Following annealing at 0.5 T_m and 0.65 T_m, the variations in contrast are reduced, suggesting some homogenization occurs during annealing. Small black regions are visible in all three alloys that do not grow in size significantly during annealing. EDX spectra from the lighter gray matrix (e) and (f), and the small black regions (g) and (h), are presented for the 0.5 T_m and 0.65 T_m heat treated SiFeVCr alloys. Quantitative EDX data from all three samples (as-cast, 0.5T_m and 0.65T_m) is presented in **Table 4**. As with the SiFeVCrMo samples, the lighter gray regions comprise all five elements and are rich in Fe and Cr, and the black regions are rich in V relative to the other elements.

The room temperature XRD pattern from the as-cast SiFeVCrMo alloy (**Figure 1A**) and SEM/EDX data suggests that, within the sensitivity of the techniques, a single-phase tetragonal alloy has been produced: whilst extra peaks corresponding to BCC Mo are present, the SEM/EDX data suggests these are attributed to unalloyed Mo. For both SiFeVCrMo and SiFeVCr alloys, whilst the SEM/EDX data show regions of varying contrast indicative of differences in composition, there is no evidence of secondary phases (other than Mo) in the XRD patterns. Sigma phases can form over a range of compositions, therefore it is unsurprising that in SiFeVCrMo and SiFeVCr the structure type remains the same across regions of different compositions, e.g., in both the CrFe-rich and V-rich regions.

Heating the alloys in flowing Ar to 0.5 T_m and 0.65 T_m resulted in some homogonization of the as-cast morphologies. Furthermore, whilst the small V rich phases present in the SiFeVCrMo alloy grew in size and changed morphology, this growth was suppressed in the SiFeVCr alloy, suggesting Mo somehow aids diffusion of V, or reduces the stability of V in the solid solution. Heating BCC SiFeVCr to above 400°C has been shown to provide sufficient thermal energy to facilitate the formation of the stable tetragonal phase. As no higher

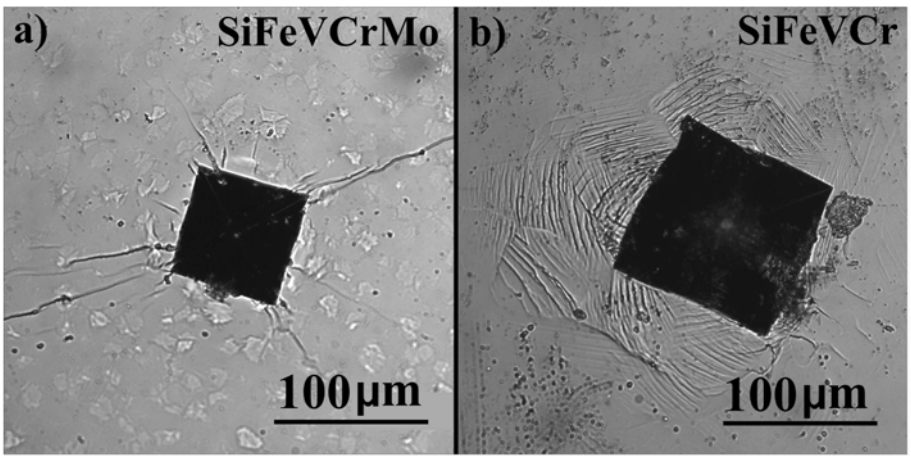

FIGURE 5 | Optical microscope images of indentations following Vickers Hardness testing in the as-cast samples, showing evidence of **(a)** brittle fracture in SiFeVCrMo and **(b)** ductile behavior in SiFeVCr.

temperature tetragonal to BCC phase transition was observed in the HTXRD data, we conclude that this transition, if it exists, occurs at temperatures > 1000°C. The Fe-V, Fe-Si and Fe-Cr binary phase diagrams all show BCC phases at high temperatures. The binary Fe-V phase diagram shows the formation of a BCC phase across the entire compositional range at temperatures greater than 1252°C (Andersson, 1983). In the Fe-rich region of the Fe-Si phase diagram, BCC alloys exist in both ordered (B2 and D03) and disordered (A2) structures (von Goldbeck, 1982a), and in Fe-Cr, the sigma phase transforms into a BCC phase by a congruent reaction BCC ↔ σ at temperatures between 820 and 825°C (von Goldbeck, 1982b; Mikikits-Leitner et al., 2010; Jacob et al., 2018). It has previously been reported that the α (BCC) to σ phase transition, in an Fe-Cr alloy, was time and temperature dependant, with S-shaped kinetic curves indicative of a nucleation and growth process, with maximum transformation rate at 750°C (Baerlecken and Fabritius, 1955). Elements such as Si (Yukawa et al., 1972) and Mo (Kubaschewski, 1982) have been found to accelerate the α to σ phase transition. In this work, peaks corresponding to the sigma phase appear in non-ambient XRD data at 400°C, increase in intensity and become predominant at 600°C, compared to the original BCC phase present, indicative of nucleation and growth of the sigma phase within the BCC matrix. The stability of sigma phase at low temperatures, compared to other reported FeCr alloys, could be due to the addition of Si, V and Mo, reducing the activation energy of sigma phase formation, although it is noted that sigma phase is produced at about 500°C in a 47 wt%Cr alloy, as indicated in the Fe-Cr binary phase diagram.

MeV Au^{2+} Ion Implantation and Grazing Incidence X-Ray Diffraction

The radiation stability of the as-cast SiFeVCrMo alloy was investigated using 5 MeV Au^{2+} ion implantation. In order to design a simplified implantation experiment, this alloy was chosen for implantation as it formed as a single phase tetragonal structure which we have determined to be the stable phase in this alloy system, and had the least amount of V precipitation, compared to the annealed samples. Discrete phases, such as precipitates have been found to alter the radiation damage response of alloys, such as in oxide dispersion strengthened (ODS) steels (Song et al., 2018), where alloys containing nano-particles are produced to improve high temperature mechanical properties of the alloy. The implantation conditions chosen here (5 MeV Au^{2+} ions implanted at room temperature with 5×10^{15} Au $^{2+}$ ions/cm^2) are not representative of the fusion environment, but, in the absence of accessible fusion neutron irradiation facilities, heavy ions are often used as analogs for energetic particles produced during radioactive decay, including transmutation, such as neutrons or alpha-daughter recoil nuclei. Results from the Monte Carlo code SRIM were used to calculate the damage produced by 5 MeV Au^{2+} ion implantation, to a fluence of 5×10^{15} Au ions/cm^2. **Figure 9** shows the damage profile calculated using results from the SRIM simulation. These results indicated that a damaged region extending from the surface to a depth of approximately 900 nm would be produced, with a peak damage of about 30 dpa located at a depth of approximately 400 nm below the surface. GI-XRD was used to determine any ion implantation induced structural modifications up to a depth of approximately 500 nm below the surface of the alloy. **Figure 10A** shows the GI-XRD patterns from the ion implanted sample, with the GI-XRD pattern from the as-cast alloy in **Figure 10B** for comparison. Due to peak broadening due to data collected in grazing incidence, least squares refinement was not performed on the GI-XRD data. However, in agreement with results from room temperature XRD data in **Figure 1A**, and by using the SIeve+ software and ICDD database, the diffraction pattern from the as-cast alloy was found to be analogous to the sigma phase found in $FeCr_{0.5}V_{0.5}$ (Martens and Duwez, 1952). The GI-XRD pattern following heavy ion implantation was determined to be analogous to the BCC structured $Cr_{0.6}Mn_{0.4}$ alloy (Pearson and Hume-Rothery, 1953), which indexes well to the BCC phase in the as-cast SiFeVCr alloy (**Figure 1B**).

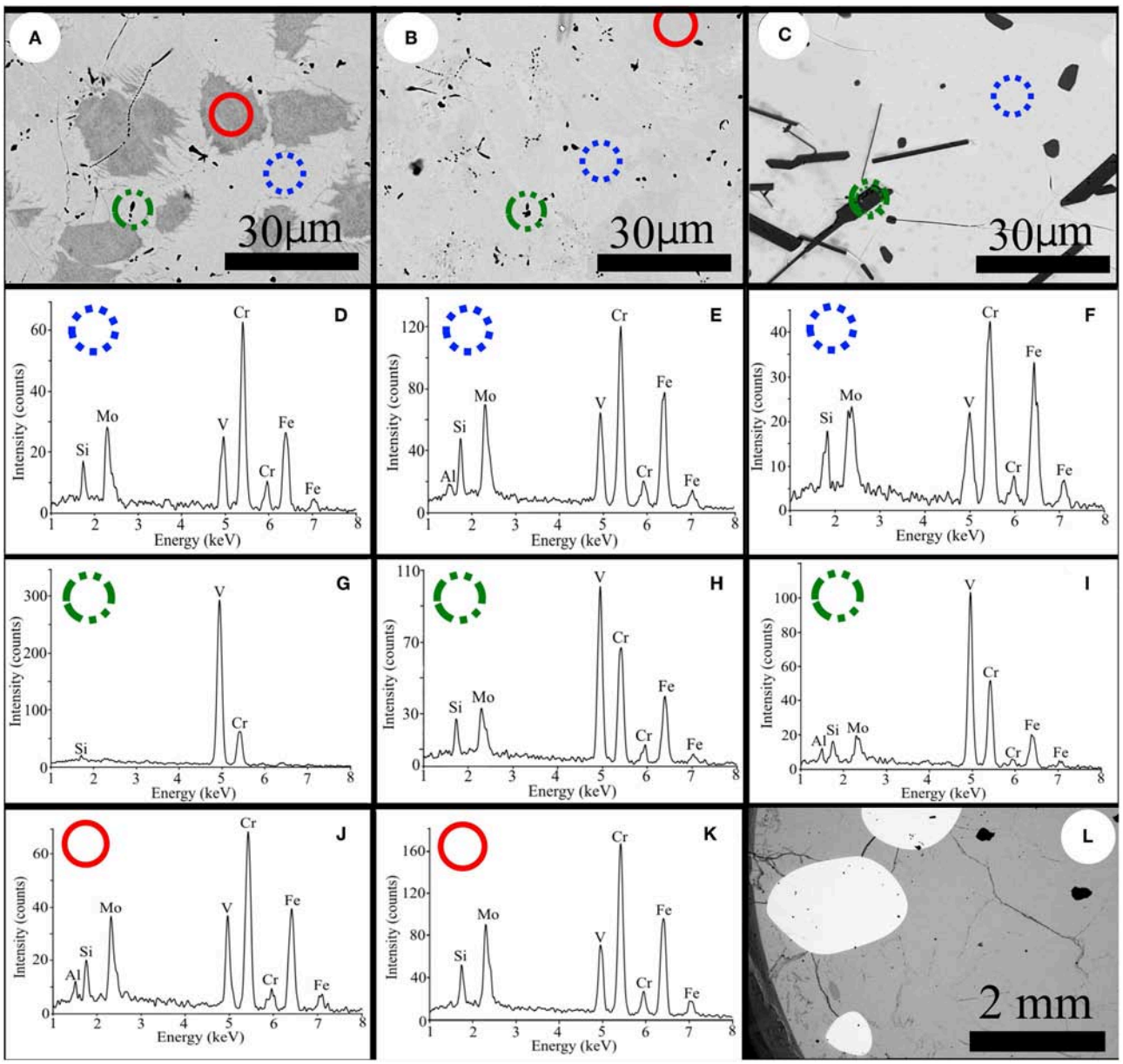

FIGURE 6 | Backscattered electron images of SiFeVCrMo **(A)** as-cast, **(B)** after annealing at 991°C (0.5 T_m) for 48 h, and **(C)** after annealing at 1289°C (0.65 T_m) for 48 h. EDX spectra **(D,G,J)** collected from the as-cast sample, **(E,H,K)** from the sample annealed at 0.5 T_m, and **(F,I)** from the sample annealed at 0.65 T_m. A low magnification image of the as-cast alloy is shown in **(L)**.

During ion implantation, elastic interactions between Au^{2+} ions and atoms in the alloy results in numerous atomic displacements. The displacement energy, E_d, is the energy required to displace an atom from its lattice site by an energetic particle. If the energy transferred from the Au^{2+} ion to an atom in the alloy is greater than E_d, then the atom will be displaced from its position and travel through the lattice. This displaced atom, called the primary knock-on atom (PKA), can go on to displace a significant number of other atoms in the alloy, if it has sufficient energy. Each elastic interaction results in the transference of kinetic energy from the PKA to other atoms, until the PKA and displaced atoms have energy less than E_d. This process is called a collision or displacement cascade, at the end of which the atoms will have insufficient energy to produce further displacements. The final excess kinetic energy is then in the form of lattice vibrations, which results in localized heating of temperatures up to several thousand Kelvin, which lasts a few picoseconds, known as a thermal spike (Skirloa and Demkowicz, 2012). Due to the rapid rate at which this thermal energy dissipates, the damage produced during the thermal spike is quenched in a region surrounding the implanted ion track.

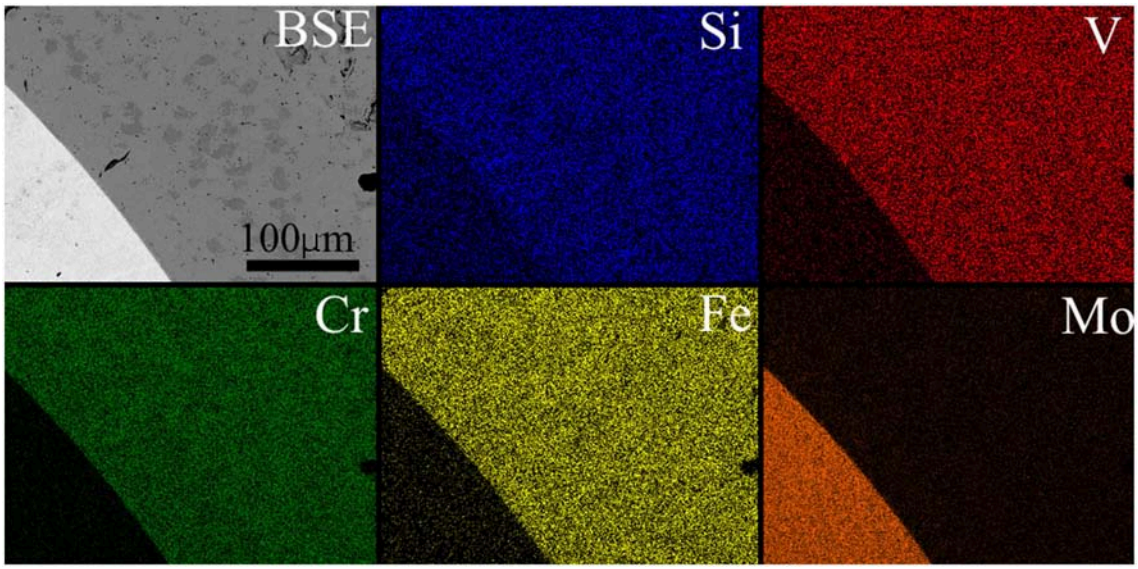

FIGURE 7 | Lower magnification backscattered electron image of as-cast SiFeVCrMo, with elemental maps showing the special distribution of elements.

The resultant implantation induced damage can take many forms, depending on the sample material, implanted ion species and energy, and temperature of the sample during ion implantation. Radiation enhanced diffusion results in phase separation and transformation in many alloys (Doyle et al., 2018), including the formation of a secondary brittle Ni_3Al phase following 5 MeV Ni^+ ion implantation in the Ni-12.8 at%Al solid solution (Rehn, 1982), and can result in stress corrosion cracking in irradiated stainless steel due to Cr diffusion away from grain boundaries (Hackett et al., 2009). During radiation enhanced diffusion, atoms of different atomic sizes can diffuse at different rates and by different mechanisms (vacancy- or interstitially-mediated) leading to the local rearrangement of atoms, and the formation of regions either rich or depleted in certain elements. Due to the local change in composition, solubility limits may be exceeded and the formation of secondary phases occurs. Secondary phase formation has been observed in the $Al_{0.12}$NiCoFeCr HEA following Ni^+ ion implantation at 500°C up to 100 dpa (Kombaiah et al., 2018).

Implantation induced phase transformations have been observed in Ni_2Al_3, following Xe or Ne ion implantation at liquid nitrogen temperatures (Nastasi and Meyer, 1991). Ni_2Al_3 has a trigonal crystal structure, which transforms upon ion implantation to an ordered cubic phase, NiAl, which possess a CsCl structure. The phase transition is reported to be driven by the similarity in the crystal structures, possessed by Ni_2Al_3 and NiAl, and the ordering of Ni vacancies in Ni_2Al_3 and disordering of vacancies in NiAl. Displacement of atoms during ion implantation results in the loss of vacancy ordering, transforming the Ni_2Al_3 in NiAl.

Implantation induced amorphisation has been observed in some metallic systems, including 2 MeV proton irradiated Zr−1.6Sn−0.6Nb−0.2Fe−0.1Cr to a dose of 8.2 dpa (Shen et al., 2014) and $Zr(Fe,Cr)_2$ precipitates in Zircaloy-4, during 2 MeV proton irradiation to 5 dpa at a temperature of 310°C (Zu et al., 2005). Whilst, ion implantation induced amorphisation has not been directly observed in HEAs, it has been proposed as a damage recovery mechanism. Egami et al. (2014) reported that, due to local strain facilitating amorphisation, both local melting and recrystallization occur more easily in HEAs during the thermal spike. They suggest that this rapid recrystallization wipes out implantation induced structural defects, making HEAs radiation damage resistant.

It is clear that ion implantation-induced damage can take on many forms in alloys, e.g., secondary phase formation and phase segregation, crystal structure transformations, and ultimately amorphisation. In absence of any evidence of ion implantation induced amorphisation in SiFeVCrMo, we propose that an implantation induced sigma to BCC phase transition occurred, similar to that seen in Ni_2Al_3, rather than the amorphisation/recryallisation model proposed by Egami et al. The rapid cooling experienced during the thermal spike may have been sufficient to quench in the high temperature BCC phase in SiFeVCrMo, similar to the rapid cooling experienced by the smaller ingot sized SiFeVCr alloy, which formed the metastable BCC phase. Irrespective of the mechanisms governing the ion implantation induced phase transformation, these results suggest that reduced activation HEAs comprising SiFeVCr have the potential to maintain high hardness and ductile behavior (observed here in the BCC phase), at high temperature during ion implantation. There would therefore appear to be great scope for further development of alloys of this type, in this system and others, for applications requiring high resistance to radiation, and thermal stability.

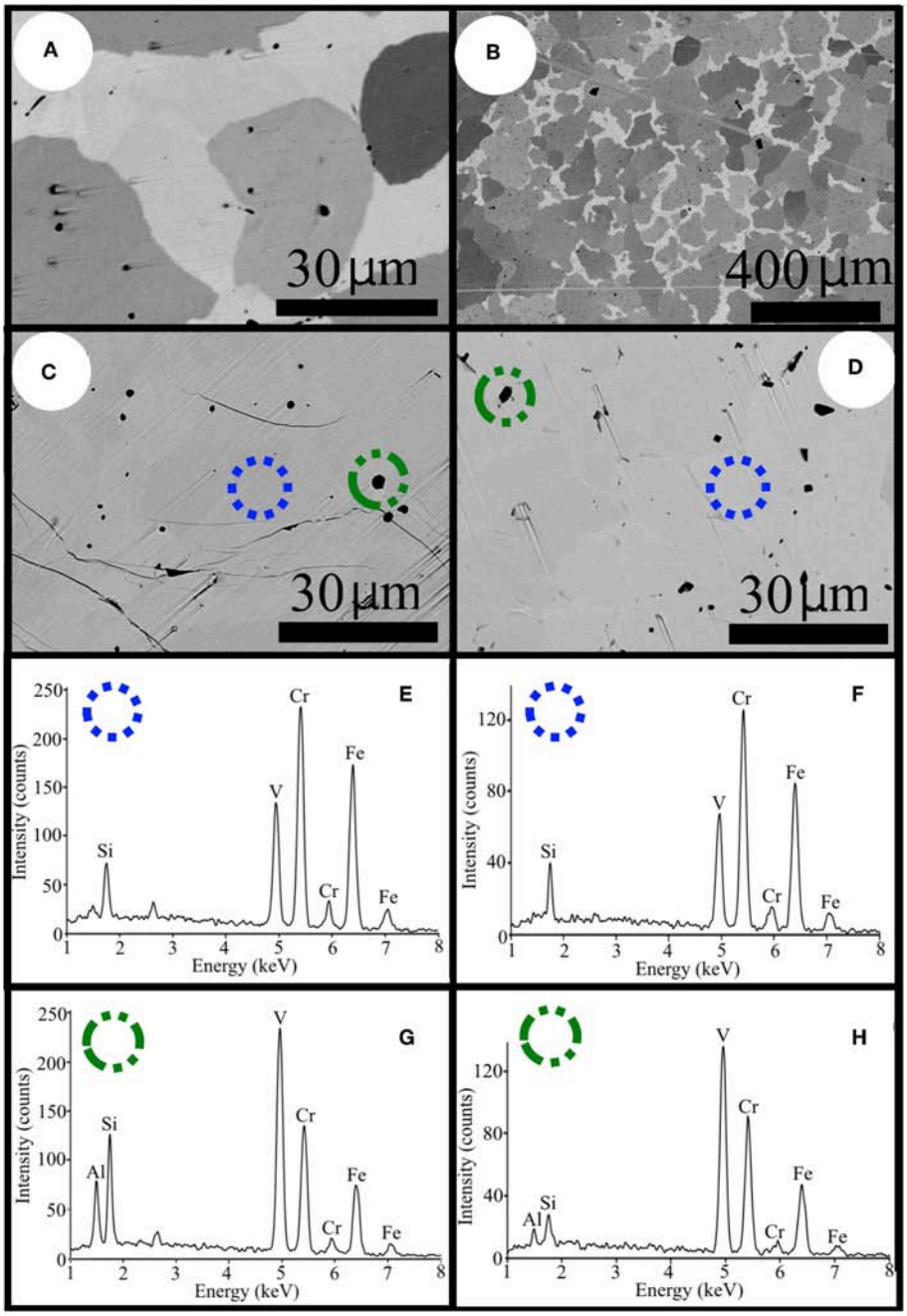

FIGURE 8 | Backscattered electron images of SiFeVCr, **(A,B)** as-cast, **(C)** after annealing at 981°C (0.5 T_m) for 48 h, and **(D)** after annealing at 1276°C (0.65 T_m) for 48 h. EDX spectra **(E,G)** collected from the sample annealed at 0.5 T_m, and **(F,H)** from the sample annealed at 0.65 T_m.

CONCLUSION

The thermal stability and radiation damage resistance of novel high entropy alloys, one comprising solely reduced activation elements, have been examined using 5 MeV Au^{2+} ion implantation, room temperature and *in situ* XRD, and SEM/EDX analysis. It was found that for both alloys the thermodynamically stable structure is a tetragonal sigma phase. A radiation induced sigma to BCC phase transformation was observed in SiFeVCrMo, and a high temperature (>1000°C) σ to BCC phase transformation was proposed for both SiFeVCr and SiFeVCrMo. Rapid cooling during alloy production of SiFeVCr and of the irradiated volume in SiFeVCrMo enabled the BCC phase to be observed in room temperature XRD data. The BCC phase

TABLE 4 | Summary of crystal structures as determined by XRD and phase compositions as determined by SEM/EDX.

SiFeVCrMo	**Composition (at%)**							
	As-cast			**0.5 T_m**			**0.65 T_m**	
	Light gray	**Dark gray**	**Black**	**Light gray**	**Dark gray**	**Black**	**Light gray**	**Black**
Si	5.48 ± 0.53	5.15 ± 1.15	4.05 ± 0.55	4.43 ± 0.38	5.88 ± 0.68	3.78 ± 0.10	5.08 ± 0.43	0.96 ± 0.38
Fe	37.51 ± 0.18	31.01 ± 1.73	26.77 ± 2.38	35.66 ± 1.59	38.40 ± 0.24	25.62 ± 0.70	36.72 ± 0.29	2.60 ± 0.65
V	16.35 ± 1.51	16.32 ± 2.46	39.02 ± 0.90	16.56 ± 0.09	16.41 ± 0.16	37.53 ± 0.90	13.96 ± 0.82	87.68 ± 5.50
Cr	33.93 ± 1.65	40.50 ± 0.47	25.79 ± 0.58	36.89 ± 1.36	32.95 ± 0.76	28.14 ± 0.70	37.26 ± 1.13	8.23 ± 6.68
Mo	6.75 ± 0.18	7.04 ± 0.89	4.38 ± 0.35	6.47 ± 0.71	6.36 ± 0.30	4.92 ± 0.30	7.00 ± 0.40	0.53± 0.14
Crystal structure	Tetragonal (σ phase)			Tetragonal (σ phase)			Tetragonal (σ phase)	

SiFeVCr	**Composition (at%)**						
	As-cast			**0.5 T_m**		**0.65 T_m**	
	Light gray	**Dark gray**	**Darker gray**	**Light gray**	**Black**	**Light gray**	**Black**
Si	6.52 ± 0.28	21.53 ± 0.36	4.38 ± 0.34	5.12 ± 2.03	13.51 ± 2.48	5.38 ± 0.16	3.45 ± 0.30
Fe	40.91 ± 2.09	28.00 ± 1.65	37.07 ± 1.21	42.02 ± 1.62	24.07 ± 5.46	41.32 ± 0.52	26.86 ± 1.61
V	19.10 ± 1.15	29.44 ± 1.73	18.74 ± 1.02	18.27 ± 1.47	41.76 ± 0.45	17.68 ± 0.42	44.56 ± 0.45
Cr	33.48 ± 1.23	19.14 ± 0.28	39.81 ± 0.16	34.60 ± 1.89	20.67 ± 1.27	35.62 ± 0.07	25.13 ± 1.77
Crystal structure	Predominately BCC with some tetragonal (σ phase)			Tetragonal (σ phase)		Tetragonal (σ phase)	

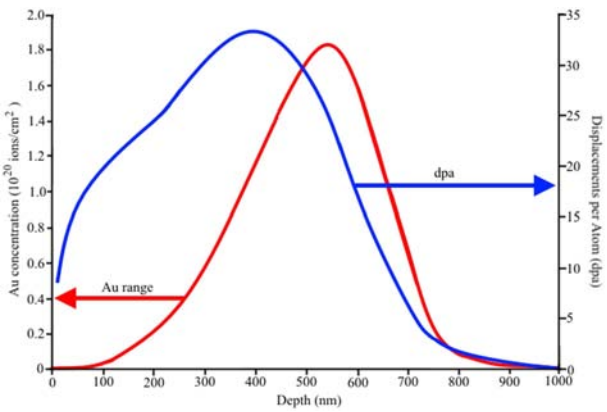

FIGURE 9 | Calculated damage profile, in displacements per atom (dpa), and range of implanted Au^{2+} ions, in ions/cm^2, from SRIM simulation of 5 MeV Au^{2+} ion implantation to a fluence of 5 × 10^{15} Au ions/cm^2.

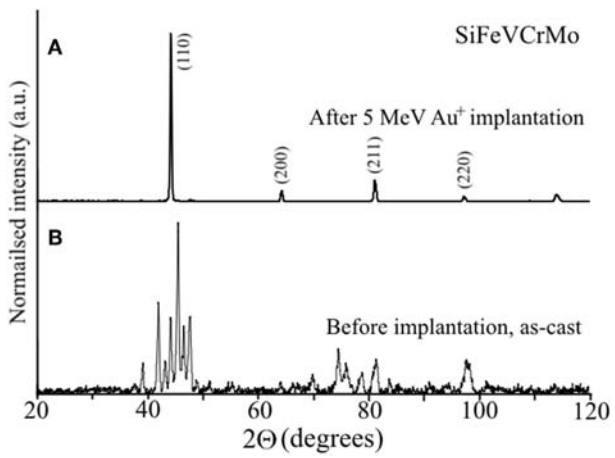

FIGURE 10 | Room temperature grazing incidence XRD patterns from SiFeVCrMo, before **(B)** and after **(A)** room temperature ion implantation with 5 Mev Au^{2+} ions, to a fluence of 5 × 10^{15} Au^{2+} ions/cm^2, showing the transformation from tetragonal to BCC following ion implantation.

was found to have desirable mechanical properties, based on hardness measurements and observation of the indents. As the BCC phase was formed at high temperatures as well as under ion irradiation, these alloys represent promising developments in the search for reduced activation alloys for advanced nuclear systems.

DATA AVAILABILITY

The datasets generated for this study are available on request to the corresponding author.

AUTHOR CONTRIBUTIONS

AG and RG contributed conception and design of the study. DP produced the alloys. GC and BJ undertook sample preparation, SEM and XRD. DP, GC, BJ, and NR-M indexed XRD patterns. NR-M performed the HT-XRD. LH powderised the SiFeVCr sample. SA performed the Au^{2+} ion implantations. AG, RG, NR-M, and LH wrote sections of the manuscript. All authors

contributed to manuscript revision, read and approved the submitted version.

ACKNOWLEDGMENTS

The authors would like to acknowledge the financial support of the EPSRC Centre for Doctoral Training in Advanced Metallic Systems (EP/L016273/1). AG would like to acknowledge funding from EPSRC grant EP/R021864/1. RG would like to acknowledge a Fellowship supported by the Royal Academy of Engineering under the *RAEng/Leverhulme Trust Senior Research Fellowships* scheme. This work has been carried out within the framework of the EUROfusion Consortium and has received funding from the Euratom research and training programme 2014–2018 under grant agreement No 633053. The views and opinions expressed herein do not necessarily reflect those of the European Commission. This research was performed in part at the MIDAS Facility, at the University of Sheffield, which was established with support from the Department of Energy and Climate Change.

REFERENCES

Andersson, J. O. (1983). A thermodynamic evaluation of the iron-vanadium system. *Calphad* 7, 305–315. doi: 10.1016/0364-5916(83)90010-X

Baerlecken, E., and Fabritius, H. (1955). Umwandlungskinetik der Sigma phase in einer Eisen-Chrom-Legierung mit 48% Chrom. *Arch. Eisenhuttenw*. 26, 679–686. doi: 10.1002/srin.195502095

Cheng, E. T. (1989). "Activation cross-sections for safety and environmental assessments of fusion reactors," in *Proceedings of a Specialists Meeting on Neutron Activation Cross Sections for Fission and Fusion Energy Applications* (Argnonne National Laboratory).

Doyle, P. J., Benensky, K. M., and Zinkle, S. J. (2018). Modeling the impact of radiation-enhanced diffusion on implanted ion profiles. *J. Nucl. Mater.* 509, 168–180. doi: 10.1016/j.jnucmat.2018.06.042

Egami, T., Guo, W., Rack, P. D., and Nagase, T. (2014). Irradiation resistance of multicomponent alloys. *Metall. Mater. Trans. A* 45:180. doi: 10.1007/s11661-013-1994-2

Egami, T., Ojha, M., Khorgolkhuu, O., Nicholson, D. M., and Stocks, G. M. (2015). Local electronic effects and irradiation resistance in high-entropy alloys. *JOM* 67, 2345–2349. doi: 10.1007/s11837-015-1579-1

Gallego, L. J., Somoza, J. A., Alonso, J. A., and Lopez, J. M. (1988) Prediction of the glass formation range of transition metal alloys. *J. Phys. F* 18, 2149–2157. doi: 10.1088/0305-4608/18/10/006

Garner, F. A., Toloczko, M. B., and Sencer, B. H. (2000). Comparison of swelling and irradiation creep behavior of fcc-austenitic and bcc-ferritic/martensitic alloys at high neutron exposure. *J. Nucl. Mater*. 276, 123–142. doi: 10.1016/S0022-3115(99)00225-1

Gorley, M. J. (2015). Critical Assessment 12: prospects for reduced activation steel for fusion plant. *Mat. Sci. Technol.* 31, 975–980. doi: 10.1179/1743284714Y.0000000732

Hackett, M. J., Busby, J. T., Miller, M. K., and Was, G. S. (2009). Effects of oversized solutes on radiation-induced segregation in austenitic stainless steels. *J. Nucl. Mater*. 389, 265–278. doi: 10.1016/j.jnucmat.2009.02.010

Hall, E. O., and Algie, S. H. (1966). The sigma phase. *Metallurg. Rev*. 11, 61–88. doi: 10.1179/095066066790138257

Jacob, A., Povoden-Karadeniz, E., and Kozeschnik, E. (2018). Revised thermodynamic description of the Fe-Cr system based on an improved sublattice model of the σ phase. *Calphad* 60, 6–28. doi: 10.1016/j.calphad.2017.10.002

Kombaiah, B., Jin, K., Bei, H., Edmondson, P. D., and Zhang, Y. (2018). Phase stability of single phase Al0.12CrNiFeCo high entropy alloy upon irradiation. *Mater. Design* 160, 1208–1216. doi: 10.1016/j.matdes.2018.11.006

Kubaschewski, O. (1982). *Iron Binary Phase Diagram*. Düsseldorf: Springer Verlag.

Leong, Z., Wróbel, J. S., Dudarev, S. L., Goodall, R., Todd, I., and Nguyen-Manh, D. (2017). The effect of electronic structure on the phases present in high entropy alloys. *Sci. Rep*. 7:39803. doi: 10.1038/srep39803

Lu, C., Niu, L., Chen, N., Jin, K.e., Yang, T., Xiu, P., et al. (2016). Enhancing radiation tolerance by controlling defect mobility and migration pathways in multicomponent single-phase alloys. *Nat. Comms*. 7:13564. doi: 10.1038/ncomms13564

Martens, H., and Duwez, P. E. (1952). Phase relationships in the iron-chromium-vanadium system. *Trans. Am. Soc. Met* 44:484.

Miedema, A. R. (1973a). A simple model for alloys I: rules for the alloying behaviour of transition metals. *Phil. Tech. Rev.* 33, 149–160.

Miedema, A. R. (1973b). A simple model for alloys II: the influence of ionicity and the stability and other physical properties of alloys. *Phil. Tech. Rev*. 33, 196–202.

Mikikits-Leitner, A., Sepiol, B., Leitner, X., Cieślak, J., and Dubiel, S. M. (2010). Investigation of σ-to- α-phase transition in Fe-Cr. *Phys. Rev. B* 82:100101. doi: 10.1103/PhysRevB.82.100101

Nastasi, M., and Meyer, J. W. (1991) Thermodynamics and kinetics of ion-induced phase transformations. *Mat. Sci. Rep*. 6:51. doi: 10.1016/0920-2307(91)90003-6

Owen, L., Pickering, E. J., Playford, H. Y., Stone, H. J., Tucker, M. G., and Jones, N. G. (2017). An assessment of the lattice strain in the CrMnFeCoNi high-entropy alloy. *Acta Mater.* 122, 11–18. doi: 10.1016/j.actamat.2016.09.032

Pearson, W. B., and Hume-Rothery, W. (1953). The constitution of Cr-Mn alloys below 1000 degree C. *J. Inst. Metals* 81, 311–314.

Pickering, E. J., Muñoz-Moreno, R., Stone, H. J., and Jones, N. G. (2016). Precipitation in the equiatomic high-entropy alloy CrMnFeCoNi. *Script. Mater.* 113, 106–109. doi: 10.1016/j.scriptamat.2015.10.025

Poletti, M. G., and Battezzati, L. (2014) Electronic and thermodynamic criteria for the occurrence of High Entropy Alloys in metallic systems. *Acta Mater.* 75, 297–306. doi: 10.1016/j.actamat.2014.04.033

Praveen, S., Murty, B. S., and Kottada, R. S. (2012). Alloying behavior in multicomponent AlCoCrCuFe and NiCoCrCuFe high entropy alloys. *Mater. Sci. Eng. A* 534, 83–89. doi: 10.1016/j.msea.2011.11.044

Rehn, L. E. (1982). "Surface modification and radiation induced segregation," in *Metastable Materials Formation by Ion Implantation*, eds S. T. Picraux and W. J. Choyke (New York, NY: Elsevier Science), 17–33.

Salishchev, G. A., Tikhonovsky, M. A., Shaysultanov, D. G., Stepanov, N. D., Kuznetsov, A. V., Kolodiy, I. V., et al. (2014). Effect of Mn and V on structure and mechanical properties of high-entropy alloys based on CoCrFeNi system. *J. Alloys Compound.* 591, 11–21. doi: 10.1016/j.jallcom.2013.12.210

Senkov, O. N., Senkova, C., Woodward, C., and Miracle, D. B. (2013b). Low-density, refractory multi-principal element alloys of the Cr–Nb–Ti–V–Zr system: microstructure and phase analysis. *Acta Mater*. 61:1545. doi: 10.1016/j.actamat.2012.11.032

Senkov, O. N., Senkova, S. V., Miracle, D. B., and Woodward, C. (2013a). Mechanical properties of low-density, refractory multi-principal element alloys of the Cr–Nb–Ti–V–Zr system. *Mater. Sci. Eng. A* 565, 51–62. doi: 10.1016/j.msea.2012.12.018

Senkov, O. N., Senkova, S. V., and Woodward, C. (2014). Effect of aluminum on the microstructure and properties of two refractory high-entropy alloys. *Acta Mater*. 68, 214–228. doi: 10.1016/j.actamat.2014.01.029

Shen, H. H., Peng, S. M., Xiang, X., Naab, F. N., Sun, K., and Zu, X. T. (2014). Proton irradiation effects on the precipitate in a Zr-1.6Sn-0.6Nb-0.2Fe-0.1Cr alloy. *J. Nucl. Mater*. 452:335. doi: 10.1016/j.jnucmat.2014.05.042

Skirloa, S. A., and Demkowicz, M. J. (2012). The role of thermal spike compactness in radiation-induced disordering and Frenkel pair production in Ni3Al. Script. *Mater.* 67, 724–727. doi: 10.1016/j.scriptamat.2012.06.029

Snell, R. M. (2017). *The Development of Novel Silver Brazing Alloys*. Sheffield: Department of Materials Science and Engineering, The University of Sheffield.

Song, P., Morrall, D., Zhang, Z., Yabuuchi, K., and Kimura, A. (2018). Radiation response of ODS ferritic steels with different oxide

particles under ion-irradiation at 550°C. *J. Nucl. Mater.* 502, 76–85. doi: 10.1016/j.jnucmat.2018.02.007

Takeuchi, A., and Inoue, A. (2005) Classification of bulk metallic glasses by atomic size difference, heat of mixing and period of constituent elements and its application to characterization of the main alloying element. *Mater. Trans.* 46, 2817–2829. doi: 10.2320/matertrans.46.2817

von Goldbeck, O. K. (1982a). "Fe-Si," in *Binary Phase Diagrams* (Berlin, Heidelberg: Springer-Verlag), 136–139.

von Goldbeck, O. K. (1982b). "Fe-Cr," in *Binary Phase Diagrams* (Berlin, Heidelberg: Springer-Verlag), 31–34.

Wang, W. C., Li, J. H., Yan, H. F., and Liu, B. X. (2007). A thermodynamic model proposed for calculating the standard formation enthalpies of ternary alloy systems. *Script. Mater.* 56, 975–978. doi: 10.1016/j.scriptamat.2007.01.044

Xia, S. Q., Yang, X., Yang, T. F., Liu, S., and Zhang, Y. (2015). Irradiation resistance in AlxCoCrFeNi high entropy alloys. *JOM* 67, 2340–2344. doi: 10.1007/s11837-015-1568-4

Yan, J., Liu, F., Ma, G., Gong, B., Zhu, J., Wang, X., et al. (2018). Suppression of the lattice thermal conductivity in NbFeSb-based half-Heusler thermoelectric materials through high entropy effects. *Script. Mater.* 157, 129–134. doi: 10.1016/j.scriptamat.2018.08.008

Ye, Y. F., Wang, Q., Lu, J., Liu, C. T., and Yang, Y. (2016) High-entropy alloy: challenges and prospects. *Mater. Today* 19, 349–362. doi: 10.1016/j.mattod.2015.11.026

Yeh, J. W., Chen, S. K., Lin, S. J., Gan, J. Y., Chin, T. S., Shun, T. T., et al. (2004). Nanostructured high-entropy alloys with multiple principal elements: novel alloy design concepts and outcomes. *Adv. Eng. Mater.* 6, 299–303. doi: 10.1002/adem.200300567

Yukawa, N., Hida, M., Imura, T., Kawamura, M., and Mizuno, Y. (1972). Structure of chromium-rich Cr-Ni, Cr-Fe, Cr-Co, and Cr-Ni-Fe alloy particles made by evaporation in argon. *Metall. Trans.* 3:887. doi: 10.1007/BF02647663

Zhang, Y.,Stocks, G. M., Jin, K., Lu, C., Bei, H., Sales, B. C., et al. (2015). Influence of chemical disorder on energy dissipation and defect evolution in concentrated solid solution alloys. *Nat. Commun.* 6:8736. doi: 10.1038/ncomms9736

Ziegler, J. F., Biersack, J. P., and Littmark, U. (1985). *The Stopping and Range of Ions in Solids*. New York, NY: Pergamon Press. Available online at: http://www.srim.org/

Zinkle, S. J., and Snead, L. L. (2014). Designing radiation resistance in materials for fusion energy. *Annu. Rev. Mater. Res.* 44, 241–267. doi: 10.1146/annurev-matsci-070813-113627

Zu, X. T., Sun, K., Atzmon, M., Wang, L. M., You, L. P., Wan, F. R., et al. (2005). Effect of proton and Ne irradiation on the microstructure of Zircaloy 4. *Philos. Mag.* 85:649. doi: 10.1080/14786430412331320017

Conflict of Interest Statement: The authors declare that the research was conducted in the absence of any commercial or financial relationships that could be construed as a potential conflict of interest.

frontiers in Materials

REVIEW
published: 01 November 2019
doi: 10.3389/fmats.2019.00272

Corrosion Control in CO_2 Enhanced Oil Recovery From a Perspective of Multiphase Fluids

Zi Ming Wang[1]*, *Guang-Ling Song*[1]* and *Jian Zhang*[2]

[1] Center for Marine Materials Corrosion and Protection, College of Materials, Xiamen University, Xiamen, China, [2] Sinopec Energy and Environmental Engineering Co. Ltd, Wuhan, China

Carbon capture and storage (CCS) combined with CO_2-enhanced oil recovery (EOR), has been recently viewed as an economical and effective method for the reduction of carbon emissions. However, corrosion is a challenging issue in the whole chain process of CO_2-EOR production if water presents and mild steel pipeline is used. In this paper, the corrosion risk of pipeline at different stages of CO_2-EOR production is systematically assessed based on a detailed analysis of the fluid characteristics. According to the fluid state of CO_2, water and crude oil, current understandings on the corrosion behavior of steel materials in multiphase flow conditions are reviewed. Furthermore, the intermittent water wetting phenomena and the fluid behavior of water droplets or clusters in an electrolyte/non-electrolyte emulsion are correlated with the steel corrosion performance, providing new insights into the corrosion phenomena. Besides application of corrosion resistant materials and corrosion inhibitors, tailoring of processing parameters, such as enhancing the water entrainment, shortening the water contact time, and reducing the solution corrosivity, is highly recommended as an effective method for corrosion control in aggressive CO_2-EOR production conditions. Based on these, some important future research topics on the corrosion in multiphase fluids are suggested.

Keywords: CCS, CO_2-EOR, multiphase flow corrosion, corrosion mechanism, pipeline

OPEN ACCESS

Edited by:
Wei Gao,
The University of Auckland,
New Zealand

Reviewed by:
Wolfram Fürbeth,
DECHEMA Forschungsinstitut (DFI), Germany
Guangyu Sun,
China University of Petroleum (Huadong), China

***Correspondence:**
Zi Ming Wang
zmwang@xmu.edu.cn
Guang-Ling Song
guangling.song@hotmail.com

Specialty section:
This article was submitted to Environmental Materials, a section of the journal Frontiers in Materials

Received: *20 February 2019*
Accepted: *16 October 2019*
Published: *01 November 2019*

Citation:
Wang ZM, Song G-L and Zhang J (2019) Corrosion Control in CO_2 Enhanced Oil Recovery From a Perspective of Multiphase Fluids. Front. Mater. 6:272. doi: 10.3389/fmats.2019.00272

BACKGROUND

Our daily life is closely relied on the technological advancement of a carbon-based civilization. Over eighty percent of the global energy consumption in 2015 is fossil fuels, i.e., coal (29.2%), crude oil (32.9%), and natural gas (23.8%), from which a direct emission of about 36 billion tons of carbon dioxide has become a great challenge in combating its possible environmental impacts. Carbon Capture and Sequestration (CCS) is one of the most promising ways for reducing the buildup of greenhouse gas emissions in the atmosphere.

Combined with CCS techniques, CO_2 enhanced oil recovery (EOR) has proved to be currently applicable in China for reducing CO_2 emissions (Zhang et al., 2013; Lv et al., 2015). The CO_2-EOR technique may produce a net zero emission of CO_2, as it can store carbon underground during oil production. Therefore, the crude oil comes from CO_2-EOR is generally termed as "carbon negative oil" (Hornafius and Hornafius, 2015). A significant improvement of oil production can be observed with CO_2 injection into reservoirs compared to the conventional water injection production. In a pilot scale CCS-EOR project in Shengli oilfield, the improved efficiency of crude oil is around 8%

and the dynamic ratio of carbon storage in reservoir conditions is around 50% (Lv et al., 2015). It provides a green and economical way to improve oil production in an old oilfield.

However, corrosion is a big concern in operating a CO_2-EOR project, as CO_2 becomes corrosive to steel-based facilities when it meets water. For example, in the CO_2-EOR production section of Shengli oilfield, the presence of a large amount of CO_2 in the production fluids has resulted in an abrupt increase of pipeline leakages within the initial 3 years after the injection of CO_2 into reservoirs (Wang et al., 2015), revealing an averaged corrosion rate of pipeline materials higher than 1.0 mm/y (Zhang J. et al., 2012; Wang Z. M. et al., 2014). According to the field experience from Chevron, the coated tubes can only service for 50 months in CO_2-injection well conditions (IEAGHG, 2010). Similar damage induced by the presence of high partial pressure of CO_2 has also been reported in other CO_2-EOR projects (Tzimas et al., 2005; Singh et al., 2010). The corrosion performance of different materials in CO_2-containing aqueous solutions has been systematically investigated, and some strategies on corrosion control in CCS and CO_2-EOR production have been suggested based on field experiences (Sim et al., 2014b; Wang et al., 2015). The use of corrosion-resistant alloys (CRA) and corrosion inhibitors is regarded as two of the important ways to mitigate corrosion in aggressive CO_2 conditions (IEAGHG, 2010). However, in operating a large-scale CO_2-EOR project, corrosion management should be systematically considered at the design and operation stages, which could significantly minimize the cost. Therefore, the corrosion risk of pipeline materials should be carefully evaluated. In this paper, we summarize the current views on corrosion evaluation and control of the CO_2-containing multiphase flow pipelines in CCS-EOR production, based on which some ideas on corrosion management in the whole chain process of a CCS-EOR project are discussed.

FIELD ANALYSIS

Whole Chain Process

There has been a long history of the trial application of CO_2-EOR technique in oil and gas industry. However, the combination of this technique with CCS was recently adopted. As illustrated in **Figure 1**, the whole chain can be divided into carbon capture, CO_2 transportation, CO_2 injection, and oil production, during which a great portion of CO_2 are permanently stored underground and the other is reutilized in the recycling process. In this whole chain process, CO_2 can be viewed as a feedstock and crude oil is the product. When the net emission of CO_2 is less than zero, i.e., the amount of CO_2 stored underground is larger than that produced after burning the CO_2-EOR crude oil, the crude oil will become "carbon negative."

Currently, corrosion is one of the big concerns for wide application of the CCS-EOR technique, as water may be acidified in a CO_2-containing environment. The presence of crude oil could vastly change the corrosion performance of steel materials, implying that the fluid structure may significantly affect corrosion. Therefore, the state of water and the fluid properties will be highlighted in this paper.

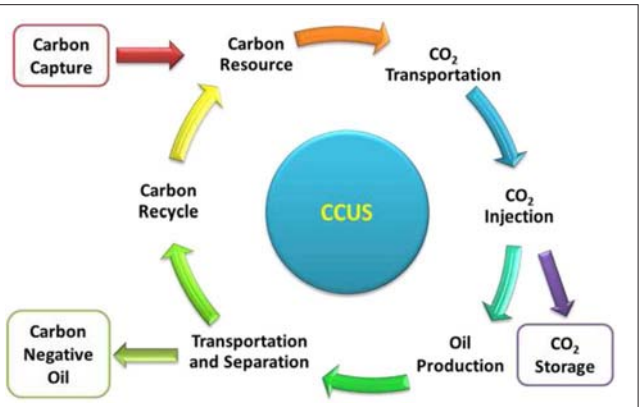

FIGURE 1 | Whole chain process of a CCS-EOR project.

Fluid Properties

Pressure and Temperature

Pressure and temperature are two important parameters that determine the properties of the CO_2-containing fluids, including the state of CO_2 phase, solubility, and pH-values, as well as the properties of crude oils. The diagram of pressure and temperature of CO_2 phase is illustrated in **Figure 2**, where pressure refers to the partial pressure of CO_2. A transitional point at 7.31 MPa and 31.06°C is indicated and the liquid phase, supercritical phase and gas phase of CO_2 are separated by black lines, as labeled in **Figure 2**.

CO_2 can be transported in different states, but a single-phase state is preferred in pipeline for a security reason. Generally, a supercritical phase or a gas phase is selected, since it needs less energy for long-distance transportation. In some cases, CO_2 is liquefied to a small volume and transported by tanks. Liquid CO_2 may also be encountered when CO_2 is transported in a supercritical state, as the failure of the heat-resistant coatings on the outside surface of a pipeline may result in a decrease of temperature below the critical point. Generally, the pressure of CO_2 transportation pipeline is in a range from 5 to 20 MPa. A high pressure can increase the efficiency of transportation. The temperature may vary in a wide range from below 20°C up to 50°C, depending on the heating or cooling conditions.

CO_2 injection may need a pressure higher than 10 MPa at wellhead and the pressure will be further increased with depth from wellhead. As reported in a previous paper (Wang and Song, 2018), at a depth of 3,000 m, the pressure can be higher than 35 MPa, which is certainly determined by the injection rate and the pressure at wellhead. Temperature is closely relied on the depth profile of the ground temperature. According to the field experience in Shengli oilfield, a supercritical state could be kept during continuous injection deeper than 700 m if CO_2 was initially injected in a liquid state. A higher injection rate will push the transitional point to a deeper site in well conditions. The ranges of temperature and pressure of CO_2 fluid in a typical well are schematically shown in **Figure 2**.

In an oil production well, the distributions of pressure and temperature are dependent on well depth. At the wellbore,

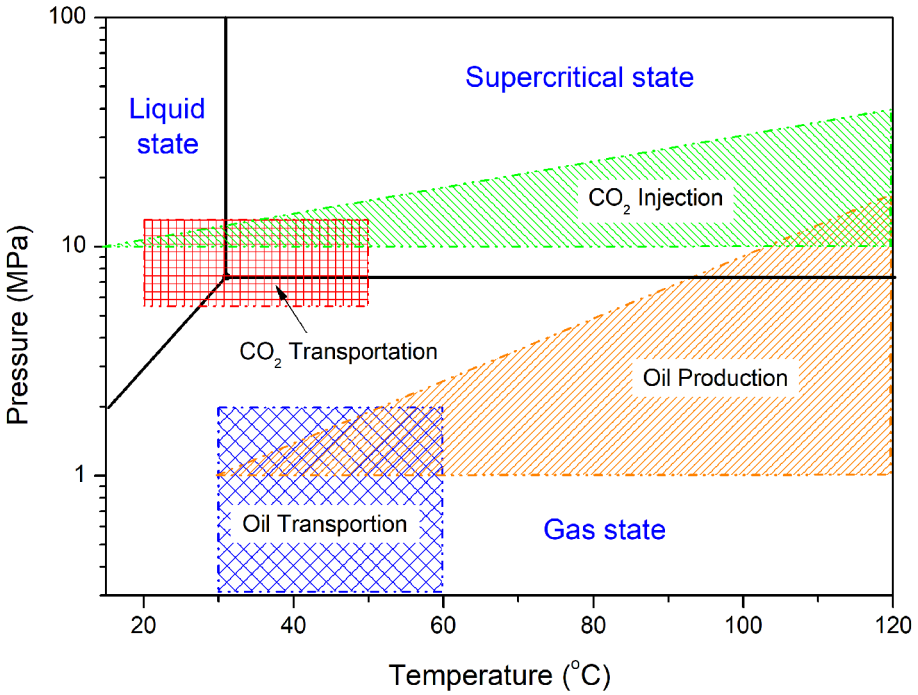

FIGURE 2 | Pressure and temperature diagram in the whole chain process of a CO_2-EOR project.

temperature and pressure reach their highest values, where CO_2 may be in a supercritical or gas state. As flowing from the well bottom to wellhead, both of the pressure and temperature of the fluids gradually decrease. In some cases, temperature may decrease below 30°C at wellhead and pressure below 1.0 MPa. The fluid must be heated and pressurized in the following transportation process. Different from a CO_2 injection well, the fluid in an oil production well is generally a complex mixture of oil, water and gas. In CO_2-EOR production, the content of CO_2 in gas phase can be as high as 70% in volume (Wang et al., 2015).

The oil gathering and transportation system is generally operated at a pressure from 0.3 to 2.0 MPa, relatively low compared to the pressure in well conditions. Its temperature is generally lower than 60°C, but for some highly viscous crude oil it may reach 80°C for obtaining a good fluidity. Therefore, the CO_2-containing aqueous phase in oil transportation pipeline is usually less corrosive than that in oil production well. It is obvious that the flow pattern in a horizontal pipe or a slightly inclined pipe for crude oil transportation is generally different from that in a vertical well tube.

CO_2 Phase

In CO_2 transportation and injection, the state of CO_2 phase is determined by its pressure and temperature. As shown in **Figure 2**, the supercritical state of CO_2 may be widely encountered in the CO_2 transportation, injection, and oil production processes. Depending on the technology of carbon capture and the resource of CO_2, trace amounts of impurity gases may remain in the CO_2 after purification. These impurities generally include water, O_2, SO_x, NO_x, and H_2S. Water is the most common impurity compound in CO_2 during transportation and injection, whose concentration limit is recommended to be <500 ppm. Although these impurities are generally controlled at a very low level, they may affect steel corrosion in water-containing supercritical (SC) CO_2 conditions.

In the oil production and transportation stages, CO_2 gas is mixed with natural gas at a fraction around 30∼70 vol.%, according to the CO_2-EOR production in Sinopec Shengli oilfield (Wang et al., 2015). At the initial stage of injection, the fraction of CO_2 is similar to that of the conventional oil production, as CO_2 has not migrated to the production well. After continuous injection for months, a sharp increase of the fraction of CO_2 can be observed, finally reaching a value around 50∼70% in volume fraction. In this case, besides acidifying the aqueous phase, the large volume of CO_2 gas may also affect the flow patterns.

Water Phase

During CCS and EOR production, water is saturated with CO_2 forming carbonic acid. The pH-value of the aqueous solution is depending on the partial pressure of CO_2 and the temperature, as well as the salinity of solution (Nesic, 2007); a linear relationship can be observed between pH-value and CO_2 pressure. It should be noticed that the diffusion coefficient of CO_2 in water is around 10^{-8} m^2/s in stagnant conditions, according to which it needs several to tens of minutes to diffuse through the bulk solution layer (Grogan et al., 1988; Farajzadeh et al., 2009). However, in a multiphase flow condition the saturation of CO_2 in water can be greatly accelerated owing to the well-known

migration mechanism. It should be noticed that CO_2 corrosion is generally controlled by cathodic reactions, where different kinds of ionic species (such as H^+, HCO_3^-, and even H_2CO_3) would be participated in the reduction process depending on pH-values (Nesic, 2007). The formation of corrosion product layer mainly relies on the local solution chemistry at the vicinity near the steel surface where the concentrations of ferrous ion and CO_3^{2-} are above the solubility limit of $FeCO_3$ for precipitation (Nesic et al., 2004; Ingham et al., 2012; Bian et al., 2015). In turn, the formation of $FeCO_3$ layer will retard the anodic reaction depending on its morphology and protectiveness (Barker et al., 2018). The presence of a trace amount of S^{2-} (Yang et al., 2017) and Ac^- (Amri et al., 2010) ions in aqueous phase can change the formation and the stability of $FeCO_3$ layers.

Crude Oil

Crude oil is a complex mixture of hydrocarbons and it is generally categorized into three types according to its density. A heavy crude oil has an American Petroleum Institute (API) gravity lower than 20, a medium crude oil has an intermediate API gravity of 20–34, while a light crude oil has an API gravity higher than 34. The API gravity is a factor inversely proportional to the density of crude oil. It is generally accepted that heavier oils are more protective than lighter ones with regard to corrosion (De Waard et al., 2003). Another way to classify crude oils is based on the proportions of the organic compounds (Sokolova et al., 1992), such as paraffin, aromatic compounds, and naphthenic compounds. These compounds may have a profound effect on the wettability of crude oil and the chemistry of brine solutions (Efird et al., 2004), thus affecting pipeline corrosion.

The presence of CO_2 may change the properties of crude oil. The solubility of CO_2 in a crude oil is generally many times higher than that in water (Rostami et al., 2017). The incorporation of CO_2 may induce a volume expansion of crude oil (Yang et al., 2013). The viscosity of crude oil vastly decreases with increasing pressure, as more CO_2 and natural gas can be dissolved into crude oil (Freitag, 2018). A beneficial effect of low viscosity has been reported in multiphase flow loop tests (Kanwar, 1994; Jepson and Menezes, 1995) and recently observed in an oil/water alternate wetted condition (Wang et al., 2019a). These observations are particularly interesting for corrosion evaluation under well conditions where the oil viscosity may be vastly changed with temperature and pressure. One should also notice that a lower viscosity may lead to an easier separation of oil and water and it is harmful for the corrosion mitigation in water-in-oil (w/o) emulsions or dispersions.

Solid Particle and Scale Deposition

Besides the oil, water and gas phases, solid particles may also be presented in CO_2-EOR production fluids. The solid phase may come from the reservoir and the precipitation of scales due to variation of brine chemistry. Generally, extremely large (>1 mm) solid particles are rarely observed in the oil and water transportation systems, as a number of filters are equipped on pipeline ahead of a pump. However, in the well conditions or the deep-sea pipeline, where the removal of sand becomes economically unacceptable, erosion corrosion may be encountered (Pouraria et al., 2016). The precipitation of scales on a pipeline surface can be encountered in CO_2-containing fluids, especially in a water treatment system, where the CO_2 partial pressure and pH-value have greatly changed, breaking the balance of brine chemistry. This would produce an under-deposit corrosion problem.

Corrosion Risk Analysis

CO_2 Transportation and Injection

Corrosion can only occur when CO_2 meets water. Therefore, the concentration of water in CO_2 during transportation and injection is generally controlled below a critical value. There are several recommendations according to successful project experiences, as summarized in **Table 1**. For example, a recommended value of H_2O in dense phase CO_2 was 500 ppm in the DYNAMIS project (de Visser et al., 2008). Below this concentration, it was believed that corrosion would not be a problem during CO_2 transportation and injection conditions (Cole et al., 2011; Sandana et al., 2012; Jacobson, 2014). However, in case of CO_2 and water being alternately injected into reservoirs to reduce CO_2 migration, the well tubes may suffer from serious corrosion damage (IEAGHG, 2010). Occasional ingress of water into the transportation pipeline may also induce corrosion.

Another possibility of water ingress is originated from the diffusion of water after injection stops. Theoretically, this takes a few months to form a water saturated CO_2 phase in the well tube usually within a length of several and tens of meters from wellbore, since the diffusion of water in stagnant CO_2 is relatively slow. However, in a long-term sealed well, corrosion induced by water diffusion from the reservoirs must be considered. Even though cement sealing outside the casing pipe is generally believed to be a robust protective layer, it should be borne in mind that CO_2 is actually very corrosive to cement, which has not been widely realized in engineering. After long-term carbonation, the originally protective cement layer might have failed much earlier than expected (Kutchko et al., 2007; Carpenter et al., 2011).

TABLE 1 | Practical recommendation of water concentrations in CO_2 transportation.

Project name	Operation conditions	Recommended water level
Weyburn (Race et al., 2012; Barker et al., 2017)	18.6 and 20.4 MPa	20 ppm
DYNAMIS (de Visser et al., 2008)	Worst case 4°C, 4.0 MPa	500 ppm
Central Basin (Oosterkamp and Ramsen, 2008; Race et al., 2012)	15.1–17.2 MPa	257 ppmw
Sheep Mountain (Oosterkamp and Ramsen, 2008)	Critical 1.7°C, 8.27 MPa	129 ppmw
Snøhvit (Oosterkamp and Ramsen, 2008; Race et al., 2012)	15 MPa, 25°C	50 ppm
Shengli EOR	15°C, 10 MPa	~200 ppm

There are many reported damage cases of CO_2 transportation pipelines and injection well tubes induced by corrosion. According to the CO_2-EOR projects in the United States since 1970s, aggressive corrosion damage has been observed in CO_2 injection wells in a water-alternate-gas (WAG) injection condition, although corrosion resistant alloys and liners were adopted for corrosion protection (IEAGHG, 2010). For CO_2 transportation pipelines, corrosion induced damage at the pipeline bottom has also been encountered in the practical operation in east China, owing to the accumulation of the remaining water in CO_2 phase.

Oil Production Well

The produced fluid is complex and its corrosiveness is determined by many factors, such as the fraction of CO_2, pH-value, states of oil, water content and water chemistry. Different from conventional oil production, the well fluid contains a large fraction of CO_2 in CO_2-EOR production. As estimated from a previous reference (Choi and Nešić, 2011), the pH-value at wellbore condition can be as low as 3.0. A greater depth of the well tube can result in a higher partial pressure of CO_2, which indicates a higher corrosion risk at deeper sites. It should also be noticed that the gas-to-liquid ratio becomes extremely high once a large amount of CO_2 gas is presented in the well tube. It has been reported that the gas-to-liquid ratio could be as high as several hundreds (Wang et al., 2015). Therefore, a highly stirred oil-water-gas three phase flow is a predominant feature of the CO_2-EOR production fluid. A complete mixture of oil and water may reduce the corrosion risk of well tubes (Cai et al., 2012; Wang et al., 2015), owing to the inhibition effect of crude oil on corrosion. As stated above, the viscosity reduction in oil well conditions may also reduce the corrosion risk of well tubes. Moreover, the accumulation of corrosion released ferrous ion in well tube may in return affect corrosion of steel materials (Bian et al., 2015), through formation of a protective iron carbonate layer. All these make the corrosion process extremely complicated.

Oil Gathering and Transportation

The produced fluid is subsequently transported by pipelines to a treatment station for separation. Different from the well condition, the transportation pipeline is generally in a horizontal or inclined direction. Its corrosion risk is highly dependent on the mixing state of oil and water, which is determined by the flow parameters (Sarica and Zhang, 2008; Kee et al., 2014), such as the flow rate, fraction and fluidity of different phases and the pressure and temperature of the system. The settlement of free water at the bottom of pipeline can initiate corrosion (Jiang and Cheng, 2013; Wang Z. L. et al., 2014). A large gas-to-liquid ratio will further complicate the mixing state of oil, water, and gas (Wang et al., 2015), which can also result in a significantly increased actual flow velocity of the liquid phase. On one hand, this may lead to flow-accelerated corrosion if water cannot be completely entrained into the oil phase or erosion-corrosion damage when solid particles are involved in the transportation. On the other hand, a mixture of oil and water may reduce the corrosion at the pipeline bottom, as the water phase may be highly dispersed and thus continuous water wetting of the steel surface is avoided.

Water Treatment

CO_2 cannot be completely removed from water phase after separation of the produced fluid at the treatment station. The partial pressure of CO_2 may be reduced significantly from ∼1.0 MPa or higher to <0.2 MPa, and the dissolved CO_2 gas may evolve from the aqueous phase. However, the left fluid remains corrosive to mild steel. Without the presence of crude oil, the CO_2 containing aqueous fluid can become even more aggressive to steel. It can also be less corrosive as the transportation temperature and pressure are lower than the oil production and transportation systems.

In some cases, alkaline solution may be introduced to neutralize the CO_2 containing solution, further reducing its corrosiveness. However, neutralization of the CO_2 containing fluid may induce a scaling problem, owing to the presence of Ca^{2+} and Mg^{2+} ions. Generally, these scale forming cations are dissolved from the reservoir rocks in CO_2-EOR conditions. Once the salt scale is formed and attached on the inner surface of pipeline, under-deposit corrosion and crevice corrosion will occur, leading to localized corrosion damage of the pipeline in CO_2-containing environments (Zhang et al., 2016). A complicated corrosion product layer may be formed owing to the incorporation of Ca^{2+} and Mg^{2+} cations, which may have improved protectiveness or increased pitting susceptibility (Esmaeely et al., 2013; Tavares et al., 2015). Recently, Shamsa et al. (2019) identified the corrosion products on X65 carbon steel as $Fe_xCa_yCO_3$ in the presence of Ca^{2+} cations. The stoichiometry of $Fe_xCa_yCO_3$ could vary with immersion time. They also pointed out that incorporation of the Ca^{2+} cations in the corrosion product layer may lead to severe localized corrosion damage at a low temperature relevant to oil production (generally below 80°C in the gathering and transportation system).

MULTIPHASE FLOW CORROSION

Single-Phase CO_2

In the temperature range of oil production, completely dry CO_2 is not corrosive to steel. Direct carbonation of steel materials by CO_2 can only occur at a high temperature (Cao et al., 2012). As mentioned above, CO_2 is generally transported and injected into wells in a dense phase state, for example, the supercritical state. The presence of a trace amount of water in the dense phase CO_2 is the origin of corrosion; the formation of CO_2 saturated water layer on steel surface triggers corrosion. In this case, corrosion will be very slight, since this water layer can quickly become saturated with ferrous ion and an iron carbonate layer can be easily formed on the steel surface. The variation of local temperature and pressure is believed to be the primary cause of forming droplets or a water layer on steel surfaces (Choi and Nešić, 2011), just like that in a wet natural gas pipeline. However, CO_2 fluids can have a very high density, vastly different from natural gas. As seen from **Figure 3**, the density of CO_2 can be higher than 800 kg/m^3 in a certain depth in the injection well.

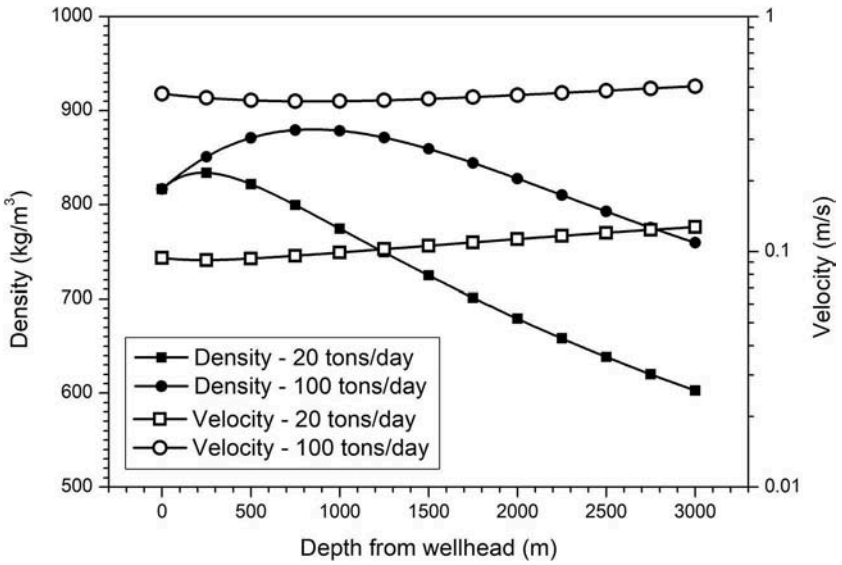

FIGURE 3 | Distribution of density and velocity of CO_2 fluid as a function of well depth at different injection flow rates, which was calculated based on the field condition of an injection well in Shengli oilfield, where the injection temperature and pressure of CO_2 fluid at wellhead were −20°C and 10 MPa, respectively (Wang and Song, 2018).

Therefore, in a flow condition, such a dense-phase CO_2 may behave more like an oil phase rather than a natural gas phase.

Recently, it was found that the corrosion morphology was highly relied on the flow rate and the degree of water saturation (Liu et al., 2018); a higher flow rate and a higher degree of water saturation produced larger corrosion product particles and patches, implying a possible corrosion mechanism related to the direct bombardment of water droplets on steel surfaces and these droplets are likely entrained in the dense CO_2 phase, rather than directly nucleated on steel surfaces. In SC CO_2 fluids, the entrainment of these water-rich clusters (or droplets) is possible and the presence of such water-rich heterogeneities in wet SC CO_2 has been identified by near-infrared spectroscopy (Wang et al., 2013) and radial distribution function method (Glezakou et al., 2010). Above the solubility limit of water in SC CO_2, the water-CO_2 mixture may form stable water-in-SC CO_2 micro-emulsions (Lee et al., 1999). Below the saturation limit, the formation of a weak Lewis acid-base H_2O:CO_2 complex (Thanthiriwatte et al., 2012; Wang et al., 2013) has been reported in SC CO_2 media. As illustrated in **Figure 3**, depending on the flow rate in transportation and injection, the velocity of a CO_2 fluid can be in a wide range from <0.1 to 0.5 m/s or higher. Obviously, decreasing the velocity of CO_2 can reduce the impact of water droplets on steel surface, thus reducing the corrosion risk (Bian et al., 2015). Therefore, to get a high transportation efficiency, pressurizing the CO_2 fluid is better than improving its flow velocity from a corrosion view.

Besides the influence of flow rate and water concentration, it has been reported that some impurity gases may also significantly change the corrosion morphology and increase the corrosion rate. To date, the corrosion performance of steel in presence of trace amounts of O_2 (Xiang et al., 2013; Hua et al., 2014b), SO_x, NO_x (Ayello et al., 2010; Dugstad et al., 2013a), H_2S (Choi et al., 2015; Sun et al., 2016b), and their mixtures (Choi et al., 2010; Dugstad et al., 2013b; Ruhl and Kranzmann, 2013; Xiang et al., 2013) have been extensively investigated. The results show that these impurity gases may greatly change the water limit for triggering corrosion, as they exacerbates corrosion by influencing corrosion products and participating in corrosion processes. However, it should be noticed that the presence of impurities may also change the stability of the water-CO_2 mixture in a supercritical state (Mohitpour et al., 2012). Visualization tests should be conducted to further explore the initial corrosion and water settlement in SC CO_2 environments. This may finally lead to a better management of the corrosion risk in CO_2 transportation and injection pipelines.

Water-CO_2 Slugs

Although CO_2 is dried prior to transportation, water ingress may happen in some occasional conditions. It has been reported that the corrosion rate of mild steel in a dense-phase CO_2-water flowing conditions can be as high as several to tens of mm/y depending on their fluid parameters (Dugstad et al., 2011a; Barker et al., 2017), because the aqueous solution was saturated with high pressure CO_2. There are many experimental results on the corrosion rates and corrosion morphologies of steel materials in high-pressure CO_2 environments (Cui et al., 2006; Cao et al., 2012; Zhang Y. et al., 2012; Hua et al., 2015), from which it can be deduced that the steel materials suffer from severe corrosion attack and the flow can vastly accelerate corrosion (Dugstad et al., 2011a; Wei et al., 2018) in the presence of a bulk volume of water during the transportation of dense-phase CO_2.

In practice, CO_2 and water may also be alternatively injected into wells (Rogers and Grigg, 2001; Lv et al., 2015; Dang et al., 2016). For example, in Shengli oilfield, the water alternating gas (WAG) injection technique is planned to be adopted after a

further verification in the pilot-scale CO_2-EOR project (Lv et al., 2015). This WAG injection process can to some extent retard gas-migration under reservoir conditions (Dugstad et al., 2011b). By adjusting the WAG ratio, a maximum ratio of the oil production to CO_2 injection could be reached (Dai et al., 2014). However, the alternating exposure of the pipe inner wall to water and CO_2 fluids can result in severe corrosion damage. According to field experiences, the water phase may linger for a long time in crevices or dead spots after dry conditions were restored (IEAGHG, 2010), leading to a corrosion problem in aggressive well environments. Temperature and pressure are believed to be the critical factors in corrosion (De Waard et al., 1991), since they directly determine the solubility of water in CO_2 and the pH-value of the water layer (Choi and Nešić, 2011). During the WAG injection process, corrosion occurs when the CO_2 slug begins to drive down the previous water slug, leaving a water layer on the pipe inner wall being acidified by flowing CO_2. Recently, Wang and Song theoretically evaluated the corrosion risk of steel materials in such WAG conditions by assuming that the steel surfaces were periodically exposed to the wet/dry cycles in CO_2 fluids and the corrosion was dependent on the dissolution of CO_2 in the water layer (Wang and Song, 2018). In their simulation work, the time of forming a CO_2 saturated water layer was simiply determined by the diffusion rate of CO_2 through the layer, which was assumed to be very fast and genrally less than several minutes (Grogan et al., 1988; Farajzadeh et al., 2009), having little influence on the overall corrosion performace. Therefore, the long-term corrosion behavior relied on the time for drying the steel surface by flowing "dry" CO_2, and the amount of water absorbed by the "dry" CO_2 fluid was critical for determing corrosion risk, where the "dry" CO_2 meant that the water concentration in CO_2 phase was far below its saturation limit, a shorter drying time meant a less exposure of steel surface to the CO_2 saturated corrosive water, and corrosion was supposed to cease when the water layer was completely absorbed into the CO_2 fluid. In this way, they concluded that the alternate period determined the long-term corrosion performance. The injection rate of CO_2 fluid is another critical factor influencing the distributions of temperature and pressure in well (Lindeberg, 2011; Ruan et al., 2013) and it also affects the drying time of the water layer along the pipe internal wall.

Oil-Water Mixtures

The presence of crude oil may reduce the corrosion risk of CO_2-EOR pipelines. The corrosion performance of pipeline may be influenced by crude oil's physical properties, such as its density (Lotz et al., 1991; De Waard et al., 2003; Papavinasam et al., 2007), viscosity (Kanwar, 1994; Jepson and Menezes, 1995; Papavinasam et al., 2007), conductivity (Craig, 1998), and wettability (Craig, 1996; Smart, 2001; Efird et al., 2004). Recently, Wang and Zhang (2016) summarized four different mechanisms for the inhibition effect of crude oil on corrosion: (1) water entrainment, (2) crude oil wetting, (3) soluble chemical partitioning, and (4) corrosion product layer modification. De Waard et al. (2003) found that heavy oil was less corrosive than light one in an oil-water two-phase flow condition, which could be attributed to the formation of w/o dispersions (Xu, 2007). A simple notion for corrosion risk analysis has been proposed based on the assumption that corrosion would occur only when free water was separated from w/o emulsion during transportation (Wang Z. L. et al., 2014). At some extremely high water cuts, w/o emulsion can also be formed. For example, the experimentally measured emulsion inversion point (EIP) is generally reported to be as high as 70 wt.% (Fingas and Fieldhouse, 2004; Wang Z. L. et al., 2014), which means that a w/o emulsion can be formed at a relatively high water cut under sufficiently stirred conditions. Free water will be separated within a very short period from a w/o dispersed fluid when the flow is slower than a critical velocity (Xu, 2007). In practical oil production, it is hard to completely emulsify the oil-brine mixtures with a very high water concentration. Generally, a w/o emulsion containing <30 wt.% water is relatively stable under flow conditions (Fingas and Fieldhouse, 2004).

The occurrence of corrosion may be related to the droplet behavior in a w/o emulsion or dispersion, and the droplets may grow to larger ones during transportation, leading to the settlement on pipeline bottom. According to Stokes equation, the settlement rate (V_t) of water droplets in a w/o emulsion can be expressed as (Frising et al., 2006),

$$V_t = \frac{d_t^2 g(\rho_w - \rho_0)}{18\mu} \tag{1}$$

where d_t is the mean diameter of droplets at a test condition, g is the gravitational acceleration, ρ_w and ρ_o are the densities of water and oil phases, and μ is the viscosity of oil-water mixtures. It is clear that a larger water droplet is easier to settle down in a lighter oil-water mixture. It should also be noticed that the formation of a stable emulsion may significantly increase the fluid viscosity (Xu, 2007; Wang Z. L. et al., 2014), thus retarding the settlement of water droplets. In practical uses, the theoretical analysis must be verified by the stability of emulsion samples in field conditions. Recently, Paolinelli et al. (2018) examined the correlation of water droplet size distribution with different fluid parameters (flow rate, pressure drop, oil types, and fraction of water) after a globe valve on a pipe flow loop and compared with theoretical analysis, and gave some reasonable hints for the control of water droplets in flow conditions. In this way, before the settlement of water droplets or the formation of water layer at pipeline bottom, corrosion could be totally retarded during the long-distance transportation of oil-water emulsion and a fast transportation could shorten the time from wellhead to treatment station (Wang Z. L. et al., 2014), beneficial for reducing the corrosion risk.

At a higher water cut, where total entrainment of water droplets becomes impossible, the steel surface will be intermittently wetted by water. Flow loop tests indicated that the corrosion rate was retarded under intermittent water wetting conditions compared to continuous water wetting (Li et al., 2006). In a flow condition, the intermittent wetting behavior closely depends on the flow pattern characteristics (Nesic and Carroll, 2003). Several studies have demonstrated that with increasing flow rate, the steel surface can be changed from continuous water wetting to intermittent wetting or even continuous oil wetting (Nesic and Carroll, 2003; Cai et al., 2012),

hence reducing the corrosion risk at the pipeline bottom. The intermittent wetting by oil and water at steel surface has been verified by various sensors in flow loop tests (Fordham et al., 1999; Zong et al., 2010; Luo et al., 2017). Efforts have been made to monitor the wetting and corrosion phenomena by electrochemical noise method in oil-water mixtures (Bouazaze et al., 2005). However, the electrochemical noise signals are much complicated. A quantitative and controllable method is urgently needed for analyzing the dynamic wetting and corrosion phenomena in one test. To further reveal the corrosion phenomena in oil-water intermittent conditions, Wang et al. (2019a) recently proposed an "alternate wetting cell" to record the current signals under anodic polarization with a rotating electrode. With a controllable movement of the oil/water interface relative to electrode, it can simplify the intermittent flow pattern as the alternate wetting of the electrode surface by oil and water, as illustrated in **Figure 4**. The actual wetting state could be presented as a series of oil and water slugs (see **Figure 4A**). Interestingly, there is a delay in the actual oil wetting time (t_{ao}) and the actual water wetting time (t_{aw}), which can be confirmed by the anodic current peaks in **Figure 4B**. The height and width of the current peaks could reflect the corrosion and water wetting on the electrode surface, respectively. Their results indicate that a slow flow and a short alternate period can generate high corrosion mitigation efficiency. The "alternate wetting cell" method provides a possible way to describe the correlation between corrosion and wetting under a controllable manner and a new insight into the corrosion phenomena in a complicated system. It can be used for the evaluation of corrosion inhibitors in an oil-water system (Wang et al., 2019b).

The covering effect of crude oil at the steel surface is widely accepted as the origin for corrosion inhibition. However, a thin layer of crude oil at the steel surface is unstable to prevent corrosion for a long time. For example, Wang Z. L. et al. (2014) observed that a crude oil layer could only persist for about 15 min on a vertically placed steel surface in a stagnant condition. The heterogeneous adsorption of crude oil on steel surface may induce localized corrosion (Sun et al., 2016a). The degree of localized corrosion may be vastly different from the averaged corrosion rate in oil-brine mixed conditions (Choi et al., 1989; Sun et al., 2016a), but this phenomenon and its mechanisms have not been clearly addressed. Some soluble organic compounds in crude oil can also decisively reduce the corrosion rate in a manner like corrosion inhibitors (Efird and Jasinski, 1989; Castillo et al., 2000; Ayello et al., 2013) and they may produce a possible hybrid effect on corrosion products (Mendez et al., 2001; Yang et al., 2014; Taleb et al., 2017).

Oil-Water-Gas/Solid Flow

The multiphase fluids are commonly encountered in CO_2-EOR production, in which a large fraction of CO_2 in the gas phase is involved. Previous efforts were mainly focused on the relationship between corrosion and the flow characteristics of a gas-liquid two-phase flow. Although very limited number of studies have been focused on the corrosion phenomena in CO_2-EOR multiphase flow conditions, the results regarding corrosion in conventional oil production can be employed for reference. For instance, in a slug flow, the corrosion risk of pipelines can be closely related to the superficial gas velocity (Maley, 1997; Kang et al., 1999), slug frequency (Kang et al., 1996; Maley, 1997; Wang et al., 2015), and Froude number (Kang et al., 1996; Chen and Jepson, 1999). Generally, direct visualization is used to determine the flow patterns. Other methods are also widely accepted, for examples, pressure drop (Sotgia et al., 2008), wetting behavior (Cai et al., 2012), and phase density distribution (Hoffmann and Johnson, 2011). Currently, many research institutes have developed multiphase flow loops for corrosion tests (Kouba and Jepson, 1990; Nyborg, 1998; Li et al., 2006; Zheng et al., 2008; Wang et al., 2015). Based on the flow loop tests, the relationship between corrosion and flow characteristics has been built. It was found that a higher slug frequency may increase the corrosion rate of pipelines, owing to a sharp increase in the local wall shear stress (Yang et al., 2010), which was viewed as an important parameter in corrosion (Wang et al., 2002; Zheng et al., 2008). A higher shear stress may enhance the local corrosion kinetics or damage the corrosion products (Schmitt et al., 2000; Li et al., 2016). It was also observed that a higher gas flow rate could reduce the pressure drop and lower the frequency of liquid slugs at a constant liquid velocity (Kang et al., 1999; Villarreal et al., 2006; Wang et al., 2015), thus reducing the corrosion risk.

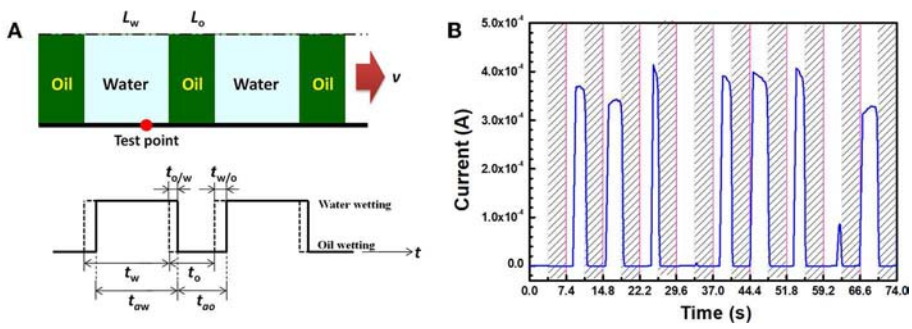

FIGURE 4 | (A) Simplification of intermittent flow pattern as an "alternate slug model" and **(B)** the anodic current transient detected on a rotating disk electrode alternately wetted by oil and water by the "alternate wetting cell" test method (Wang et al., 2019a). In **(A)**, t_w is the time of water slug passing though the test point, $t_{w/o}$ is the time of water-replacing-oil, and $t_{o/w}$ is the time of oil-replacing-water. In **(B)**, the rotation is 600 rpm, the alternate period is 7.4 s for the current response and the applied anodic potential is +100 mV vs. open circuit potential.

In conducting a flow loop experiment, oil and water may be emulsified during a long-term cyclic test if crude oil was used. The heavier the crude oil is, the easier it can be emulsified. At a fixed pump input fraction of oil and water, the entrainment of water in oil phase may increase the actual water fraction of input fluids. It has been reported that a significantly large amount of water can be entrained into the crude oil phase after 3 days of the cycle test in a closed flow loop (Wang and Zhang, 2016). No free water can be separated from the oil-water mixture within a short period after the cyclic test. Emulsification is the main reason for the use of white oil, instead of crude oil, in most multiphase flow loop tests. To overcome the emulsification problem, a multiphase flow loop was built in a treatment station of Shengli oilfield, where the oil, water and gases were separately introduced into the test loop from the production pipelines and then went back to the production system via the output pipeline after corrosion test. The input of oil, water and gas was also driven by pumps and the process was similar to that of a laboratory-scale setup reported previously (Wang et al., 2015). The only difference is that the mixed fluids after going through the corrosion test section directly flows into the oil production system and never goes back to the pipe section for corrosion tests. Using this "open" flow loop system, field corrosion was monitored at the steel pipe bottom. The corrosion rate can be automatically converted from the galvanic current of a commercial corrosion probe, which has been previously used for corrosion monitoring in an oil-water system (Wang Z. L. et al., 2014). A flat sheet of 20# steel was used as the corrosion probe and the diameter of the pipeline was 80 mm. With changing water cut, a series of field conditions can be simulated.

One may notice that CO_2-EOR production fluids generally contain an extremely high fraction of gas phase with a gas-to-liquid ratio over 200, in which CO_2 gas can reach a volume fraction of 70% in the gas phase (Wang et al., 2015). Under such a high gas-to-liquid ratio, oil and water may be strongly stirred during transportation, and corrosion can be reduced once the oil phase reaches the bottom of pipeline. In **Figure 5**, the influence of gas-to-liquid ratio on corrosion was further verified at different water cuts in filed conditions. The corrosion rate initially increased and then decreased after the gas-to-liquid ratio increased to a critical value, depending on the water cuts. A higher water cut generally leads to a transition point at a higher gas-to-liquid ratio. However, when the gas-to-liquid ratio is higher than 20, corrosion will be obviously reduced. The result agrees with the theoretical analysis of corrosion mitigation in oil-water-gas three-phase flow conditions (Wang et al., 2015). This is also consistent with the notion that corrosion can be mitigated in an oil-brine mixed flow by increasing turbulence to generate oil wetting (Wicks and Fraser, 1975; Cai et al., 2012). Under a high pressure, the dissolved gas may reduce the viscosity of crude oil, thus changing the flow pattern and the wetting behavior in pipeline (Luo et al., 2017).

Sand or solid particles in CO_2-EOR fluids may induce erosion or localized corrosion problem. Generally, in the CO_2 injection and water treatment processes, no sand or solid particle is involved. The influence of sand or solid particle on corrosion is usually considered in presence of crude oil. The simulation

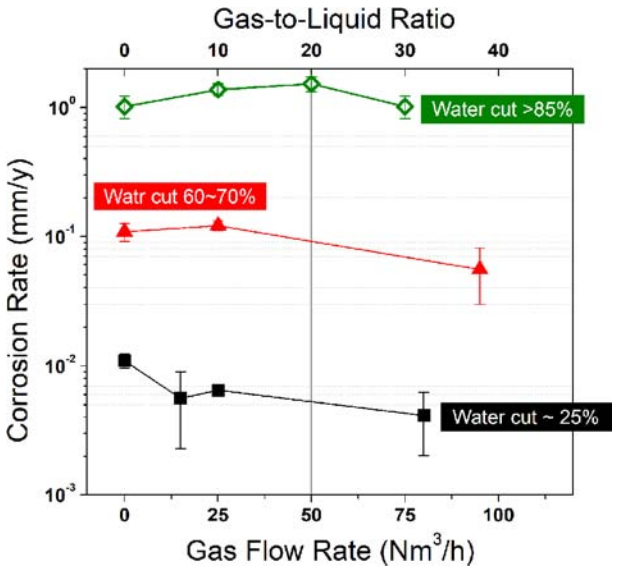

FIGURE 5 | The measured corrosion rate as a function of gas flow rate (or Gas-to-liquid ratio) at different water cuts obtained from the multiphase flow loop test at 0.3 MPa in field condition of Shengli oilfield. The crude oil was heavy oil with a density of 0.92 g/cm^3 at 20°C and a viscosity of 135.3 mPas at the operation temperature of 60°C. The fraction of CO_2 in gas phase was around 50 vol.%. For the present field test, the liquid flow rate was 4.5 m^3/h. The input fluid was controlled by pumps and the water cut was experimentally estimated by on-site sampling of the oil-water mixtures.

work from Landry et al. (2012) suggested that the settlement of solid particles is much easier onto the pipeline bottom and water may also be accumulated around such solid particles forming a locally water-rich environment. In this condition, corrosion may be preferentially initiated around the solid particle (Han et al., 2013). Tang et al. (2008) observed severe erosion-corrosion damage on steel surface and the contribution of erosion was measured to be around 70% in the oil-sand slurry with different sand concentrations. However, Stack and Abdulrahman (2012) reported the movement behavior of sand particles sealed by an oil layer, which produces a weaker impact on steel surface, and thus reduce the mechanical and electrochemical attacks. A further analysis is essential for understanding the corrosion behavior associated with sand particles and crude oils, which will be helpful to the field corrosion management in CO_2-EOR well and deep-sea conditions.

CORRELATING CORROSION WITH FLUID STRUCTURES

Corrosion control in multiphase flow conditions is technically challenging, owing to the complexity of fluid. In CO_2-EOR production, the multiphase flow is generally relevant to an oil-water mixture or a dense phase CO_2 containing a trace amount of water, which attributes to oil production and CO_2 injection, respectively. Here, these two cases can both be termed as water/non-electrolyte mixture. In a previous paper, Liu et al.

(2018) believed that the state of water in SC CO_2 phase might behave like the w/o emulsion or dispersion, where a corrosion mechanism was proposed in SC CO_2 environment regarding the impact of water droplets on steel surfaces. It implies that the density and velocity of water clusters in SC CO_2 phase determine the corrosion morphology. Although the corrosion propagation has not been directly monitored, the observation of different types of corrosion product particles on steel surfaces after autoclave test can verify this microscopic mechanism. Actually, similar circular-shaped corrosion product particles can also be observed on steel surface after corrosion in a w/o emulsion for a short period (e.g., 72 h), as typically illustrated in **Figure 6**. For a longer period, the corrosion product particles may be merged to become large patches, finally forming a layer of $FeCO_3$. It seems that these corrosion product particles are probably originated from the attachment of corrosive water droplets. Presently, the direct links between the sizes of corrosion product particles and water droplets are still not clear. It is interesting that the corrosion morphologies of steel surface are similar in different types of fluids. It is quite possible that the water droplets or clusters present in the w/o emulsion (Wang Z. L. et al., 2014) and the water containing SC CO_2 (McGrail et al., 2009; Thanthiriwatte et al., 2012; Wang et al., 2013) result in the corrosion product particles on steel surfaces. As proposed by Liu et al. (2018) in CO_2 fluid, the flow and wetting behavior of water clusters are the origin of corrosion damage. This mechanism could be extended to interpret the corrosion performance of steel samples in various electrolyte/non-electrolyte mixtures. This provides a new view on corrosion prediction in complex conditions, where water is highly dispersed in a non-conductive fluid.

The similarity in corrosion mechanism could be firstly testified by the dependence of corrosion rate on water concentration. As an example, **Figure 7** illustrates the corrosion rate of steel samples in different mixtures, such as w/o emulsion and water containing SC CO_2, where it presents a linear relationship with water concentration. Such a linear dependence of corrosion rate on water concentration could be found in a wide range of water concentrations, regardless of the experimental conditions, which was also observed in correlating the weight-loss data with water concentrations in a SC CO_2 environment when the water concentration is higher than 1,000 ppmw (Sim et al., 2014a). It also reported that the conductivity of a w/o emulsion presented a linear relationship with water concentrations (Craig, 1998). This may be related to the impact of moving water droplets or clusters on steel surfaces. Generally, a higher water concentration may generate a larger volume of water droplets in mixed fluids (Plasencia et al., 2013). Compared with a SC CO_2 fluid, crude oil can entrain a larger volume of water droplets, and thus the corrosion rate was not significantly increased at high water concentrations. This could be explained by the difference in wettability at steel surface. The oil phase is more effective than the dense CO_2 phase against the adsorption of water droplets on steel surfaces.

In multiphase flow corrosion, the state of fluid structure has not been systematically investigated. Water entrainment and water settlement are the control steps in corrosion. The entrainment of water in crude oil is believed to be beneficial in corrosion mitigation (Wicks and Fraser, 1975; Craig, 1996; De Waard et al., 2003; Cai et al., 2012). Following this idea, methods to stabilize water in SC CO_2 emulsions might also be effective in preventing pipeline corrosion, which has been widely investigated in food and purification industries. However, to date no effort has been made to tailor the SC CO_2 fluid for a corrosion mitigation purpose. If it works, this method can be applied in CO_2 transportation and injection systems.

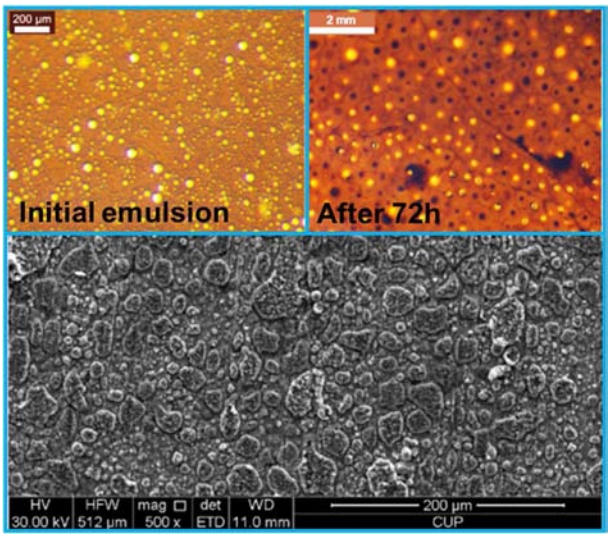

FIGURE 6 | Microscopic images of a water-in-oil emulsion with a water cut of 70 wt.% before and after corrosion test and the corrosion morphology of P110 steel surface after autoclave test for 72 h at a CO_2 pressure of 10 MPa, 80°C. The initial emulsion was prepared by mixing oil and water at a stirring rate of 1,200 rpm in an emulsifier. The "after 72 h" refers to the state of the emulsion after autoclave test. The oil's density is about 0.88 g/cm^3 (Wang Z. L. et al., 2014) and the brine solution is similar to the CO_2-EOR production water in Shengli oilfield (Zhang J. et al., 2012; Wang et al., 2015). The image of emulsions was observed using a stereomicroscope (as described in Wang Z. L. et al., 2014) and the corrosion morphology was detected by a Scanning electron microscope.

CONTROL STRATEGIES

It should be noticed that the operation conditions for CO_2 transportation, injection and oil production are different. As summarized in **Table 2**, their control strategies cannot be the same. Generally speaking, CRAs are most effective, which have been attempted in many projects (IEAGHG, 2010). For example, in a pilot-scale CO_2-EOR project in Shengli oilfield, stainless steels were employed for the CO_2 injection well tubes. There is no doubt that the use of CRAs is a safe choice when we have little knowledge on the corrosion risk of an operation system, but it is economically unacceptable. Coatings and liners are also adopted in CO_2-EOR production wells (IEAGHG, 2010), but there are still challenging problems, such as blistering and detachment in deep well conditions.

Recently, several kinds of corrosion inhibitors were tested in simulated CO_2 injection or transportation conditions (Turgoose

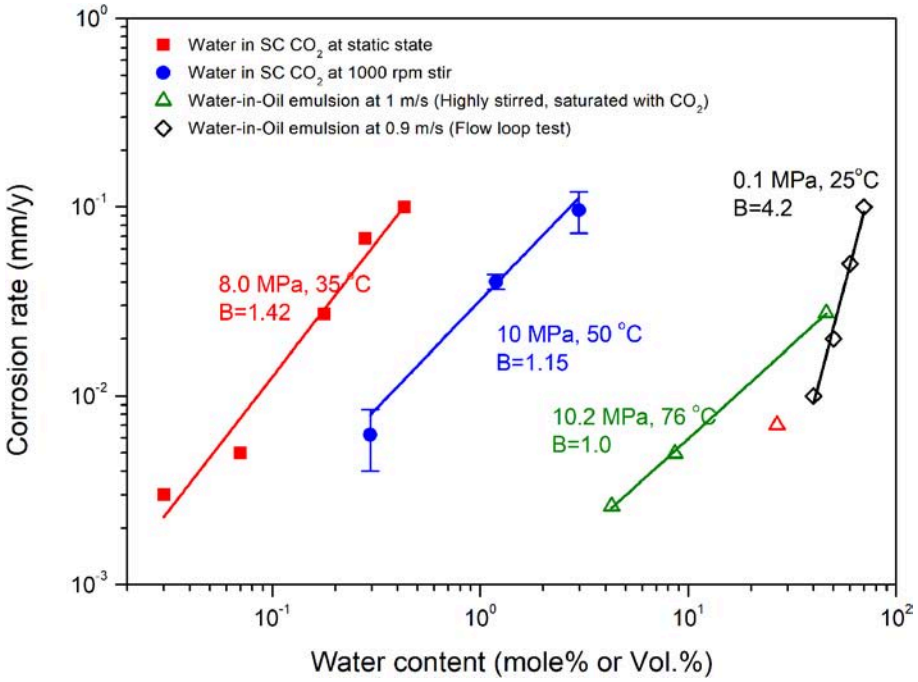

FIGURE 7 | The dependence of corrosion rate on water concentration in different electrolyte/non-electrolyte binary systems. The red solid square and the blue solid circle refer to the corrosion data in SC CO_2 environment according to Hua et al. (2014a) and Liu et al. (2018). The green open triangle and the black open rhombus refer to the corrosion rates in w/o emulsions or mixtures according to Sun et al. (2016a) and Li (2009). B represents the slope of the fitted line of the experimental data points in a log coordinate system.

et al., 2014; Choi et al., 2017; Xiang et al., 2017; Cen et al., 2019), which may theoretically be a reasonable choice in the aggressive environments. However, the corrosion inhibitors should be effective in high temperature conditions. Corrosion inhibitors have also been widely used in water injection systems where CO_2 was involved. The presence of crude oil in the CO_2-EOR production system may poison the inhibitors (Gulbrandsen and Kvarekval, 2007; Horsup et al., 2010), reducing their effectiveness. Therefore, the evaluation of corrosion inhibitors in oil-water mixed fluids becomes critical for the practical inhibitor selection (Li et al., 2014, 2016; Wang et al., 2019b). Presently, there is still lack of effective and applicable methods for the evaluation of corrosion inhibitors in oil-water mixed conditions (ASTM G202−12, 2016), which generally relies on a large-scale multiphase flow loop test (Salama and Brown, 2009; Cai et al., 2012; Wang and Zhang, 2016). Most recently, Wang et al. provided a possible method for the fast evaluation of corrosion inhibitors in oil/water alternate conditions by using a specially designed "Alternate Wetting Cell" (Wang et al., 2019a), with which a kind of ODD corrosion inhibitor has been evaluated to be effective (with a high inhibition efficiency of 99.9%) in oil-water media (Wang et al., 2019b). In a multiphase flow environment containing crude oil, the wettability at the oil/water/pipe interface and the emulsion state might be changed by the addition of a trace amount of organic agents, such as corrosion inhibitors (Foss et al., 2009; Li et al., 2014; Wang et al., 2019b) or some surfactant chemicals (Wang Z. L. et al., 2014; Quej-Ake et al., 2018), finally enhancing or decreasing the corrosion mitigation efficiency of crude oil.

To our knowledge, managing the process parameters is one of the most attractive methods for corrosion control in CO_2-EOR production (Wicks and Fraser, 1975; Kang et al., 1996; Cai et al., 2012; Wang et al., 2015), as it is generally applicable, effective and inexpensive, but the control strategies must be relied on a deep understanding of the corrosion performance and corrosion mechanism of pipeline materials (Store et al., 2011). For example, to avoid corrosion damage of pipelines, CRAs were usually used and water was strictly limited below a very low concentration in an early pilot CO_2-EOR project because of little knowledge on steel corrosion in a dense CO_2 phase. Currently, it is generally believed that corrosion will not be a problem if there is no free water or water droplet settlement on the pipeline bottom. However, the critical water concentration threshold to trigger corrosion can be different, depending on pressure, temperature, flow rate, as well as the concentrations of impurities. Nevertheless, limiting water concentration is still the best choice for corrosion mitigation in CO_2 transportation (Sim et al., 2014b; Barker et al., 2017). It can be deduced from the experimental simulation that pressurizing CO_2 could extend the solubility of water (Wang and Song, 2018) and thus reduce the possibility of water wetting on steel surface. Slowing down the flow rate may reduce the probability of the bombardment of water clusters entrained in dense phase CO_2,

TABLE 2 | Corrosion control strategies in CCS-EOR systems.

	Materials	Corrosion inhibitors	Process control
CO_2 transportation	Mild steel (e.g., 16 Mn)	Effective in highly acidified, high pressure and high temperature conditions. (e.g., Xiang et al., 2017)	Controlling impurity gases (de Visser et al., 2008; Sim et al., 2014b) Limiting water concentration (Sim et al., 2014b) Slowing down flow and pressurizing (Liu et al., 2018)
CO_2 injection	Mild steel (N80, P110) Stainless steel (304SS, 13Cr) Coatings or liners (IEAGHG, 2010)	Injected with water slugs	Reducing water/gas alternate frequency (Wang and Song, 2018)
Oil production	Mild steel (N80, P110) Stainless steels (304SS, 13Cr)	Effective in the presence of oil, such as tailoring wettability (Li et al., 2014; Wang et al., 2019b) and enhancing emulsification (Wang Z. L. et al., 2014).	Not available.
Oil transportation	Mild steel (20#, X52) Stainless steel for valves Liners for separators		Water separation before transportation (Wang Z. L. et al., 2014) Reducing CO_2 partial pressure (Choi and Nešić, 2011) Flow pattern control: a high flow rate, high gas-to-liquid ratio (Cai et al., 2012; Wang et al., 2015) Enhancing emulsification (Wang Z. L. et al., 2014)
Water treatment	Mild steel (20#, X52) Glass fiber reinforced plastics	Effective in CO_2 aqueous environments Adding pH neutralizer	Reducing dissolved CO_2 by N_2 stripping.

The recommended materials are based on the pilot-scale CO_2-EOR project in Shengli oilfield and the reported projects in North American.

and thus decrease the density of iron carbonate particles on steel surface (Liu et al., 2018). In this way, transporting water containing CO_2 at a high pressure and with a slow rate may be helpful for corrosion mitigation. In a WAG CO_2 injection process, reducing the alternate frequency and increasing the injection rate can extend the service lifetime of well tube (Wang and Song, 2018). Obviously, tailoring the processing parameters in CO_2 transportation and injection should be cautious as the environmental variation may totally change the control strategies.

In oil production, if water could be completely entrained into crude oil, corrosion would cease. Therefore, an effective method is to separate free water from crude oil before transportation. It would be safe if crude oil can be transported to the terminal station before de-emulsification and water settlement. In this way, a fast transportation seems to be beneficial. At the same time, a high flow rate stirs the fluid, hindering the deposition of free water. Similarly, a high gas-to-liquid ratio is also recommended to obtain a turbulent state and reduce the wetting of water at pipeline bottom (Wang et al., 2015). These control strategies are relevant to the management of flow patterns of oil, water and gas in pipeline. In some extreme conditions, emulsification of water into oil may be applicable in reducing the corrosion risk during long-distance transportation. It should be noticed that depressurizing may also reduce the corrosiveness of the CO_2-containing fluids, which can be employed in the oil transportation and the water treatment stages.

SUMMARY AND FUTURE IDEAS

In this review, the corrosion of pipeline in CO_2-EOR production is systematically analyzed from a fluid perspective. Firstly, the corrosion risk of pipeline at different stages of CO_2-EOR production was evaluated relevant to the fluid properties. It identified that the presence of water in fluid was the key for triggering corrosion. In CO_2 transportation and injection systems, although water was generally limited well below its saturation limit, the occasional water ingress or the alternate water slug may induce corrosion damage. In oil production and transportation systems, the presence of crude oil may reduce corrosion, while the flow pattern and the mixing state of oil and water were critical for determining the corrosion risk of well tubes and pipelines. In water treatment stage, the scaling problem should be noticed with a reduction in CO_2 partial pressure. After a review of the corrosion behavior of steel materials in multiphase flow conditions according to the fluid states of CO_2, water and crude oil, corrosion was supposed to be correlated with the fluid structure, in which the dependence of the corrosion rate on water concentrations was attributed to the fluid behavior of water droplet or clusters in an electrolyte/non-electrolyte binary system. An alternate wetting test method was introduced for better understanding the corrosion phenomena in oil/water intermittent flow. Finally, the corrosion control strategies were summarized. Besides the application of corrosion resistant materials and corrosion inhibitors, tailoring the processing parameter was suggested to be an attractive method for preventing corrosion in aggressive CO_2-EOR production conditions. For the CO_2 transportation and injection systems, limiting water concentrations, slowing down the flow rate and reducing contact time would be beneficial for corrosion mitigation. For the oil production system, enhancing the water entrainment, increasing the turbulence of flow and mitigating the corrosive environment would be helpful.

Future studies on multiphase flow corrosion associated with CO_2-EOR production should address the flowing issues:

(1) Broadening ideas on corrosion control for aggressive CO_2-saturated oil-water mixed fluids, for example, exploring the possibility of using oil/water alternate slugs to reduce corrosion risk of the pipeline bottom.
(2) Selection of suitable emulsifier agents in water-SC CO_2 environments to extend the water limits for a secure transportation and injection of CO_2.
(3) Deciphering the microscopic origin of corrosion initiation and propagation and their relationship with fluid structure in a binary mixed system.
(4) Developing new electrochemical and analytical methods in badly conductive and harsh environments, such as the water containing SC CO_2 and the oil-water mixtures.

AUTHOR CONTRIBUTIONS

ZW and G-LS wrote and finalized the paper. ZW and JZ collected and analyzed the field data.

FUNDING

This work was supported by the National Science Foundation of China under grant No. 51671163, the Natural Science Foundation of Fujian Province (Grant No. 2019J01031), and part of the experimental work was founded by the Technology Development Project of Shengli Oilfield Company (No. YKD1503).

REFERENCES

Amri, J., Gulbrandsen, E., and Nogueira, R. P. (2010). Propagation and arrest of localized attacks in carbon dioxide corrosion of carbon steel in the presence of acetic acid. *Corrosion* 66:035001. doi: 10.5006/1.3359618

ASTM G202−12 (2016). *Comparison of Laboratory Methodologies to Evaluate Corrosion Inhibitors for Oil and Gas Pipelines*. West Conshohocken: ASTM International.

Ayello, F., Evans, K., Thodla, R., and Sridhar, N. (2010). *Effect of Impurities on Corrosion of Steel in Supercritical CO_2. NACE Corrosion*. San Antonio, TX: NACE International. doi: 10.1115/IPC2010-31053

Ayello, F., Robbins, W., Richter, S., and Nešić, S. (2013). Model compound study of the mitigative effect of crude oil on pipeline corrosion. *Corrosion* 69, 286–296. doi: 10.5006/0631

Barker, R., Burkle, D., Charpentier, T., Thompson, H., and Neville, A. (2018). A review of iron carbonate ($FeCO_3$) formation in the oil and gas industry. *Corrosion Sci.* 142, 312–341. doi: 10.1016/j.corsci.2018.07.021

Barker, R., Hua, Y., and Neville, A. (2017). Internal corrosion of carbon steel pipelines for dense-phase CO_2 transport in carbon capture and storage (CCS)–a review. *Int. Mater. Rev.* 62, 1–31. doi: 10.1080/09506608.2016.1176306

Bian, C., Wang, Z. M., Han, X., Chen, C. F., and Zhang, J. (2015). Electrochemical response of mild steel in ferrous ion enriched and CO_2 saturated solutions. *Corrosion Sci.* 96, 42–51. doi: 10.1016/j.corsci.2015.03.015

Bouazaze, H., Huet, F., and Nogueira, R. P. (2005). A new approach for monitoring corrosion and flow characteristics in oil/brine mixtures. *Electrochim. Acta* 50, 2081–2090. doi: 10.1016/j.electacta.2004.08.051

Cai, J. Y., Li, C., Tang, X. P., Ayello, F., Richter, S., and Nesic, S. (2012). Experimental study of water wetting in oil–water two phase flow—horizontal flow of model oil. *Chem. Eng. Sci.* 73, 334–344. doi: 10.1016/j.ces.2012.01.014

Cao, G., Firouzdor, V., Sridharan, K., Anderson, M., and Allen, T. R. (2012). Corrosion of austenitic alloys in high temperature supercritical carbon dioxide. *Corrosion Sci.* 60, 246–255. doi: 10.1016/j.corsci.2012.03.029

Carpenter, M., Aarnes, J., Coleman, D., and Levett, B. (2011). *Guideline for the Risk Management of Existing Wells at CO_2 Geological Storage Sites*. Det Norske Veritas. DNV Report No. 2011–0448.

Castillo, M., Rincon, H., Duplat, S., Vera, J., and Baron, E. (2000). *Protective Properties of Crude Oils in CO_2 and H_2S Corrosion*. Orlando, FL: NACE International.

Cen, H., Cao, J., Chen, Z., and Guo, X. (2019). 2-Mercaptobenzothiazole as a corrosion inhibitor for carbon steel in supercritical CO_2-H_2O condition. *Appl. Surf. Sci.* 476, 422–434. doi: 10.1016/j.apsusc.2019.01.113

Chen, Y., and Jepson, W. P. (1999). EIS measurement for corrosion monitoring under multiphase flow conditions. *Electrochim. Acta* 44, 4453–4464. doi: 10.1016/S0013-4686(99)00160-7

Choi, H. J., Cepulis, R. L., and Lee, J. B. (1989). Carbon dioxide corrosion of L80 grade tubular in flowing oil-brine two-phase environments. *Corrosion* 45, 943–950. doi: 10.5006/1.3585005

Choi, Y.-S., Hassani, S., Vu, T. N., and Nesic, S. (2015). *Effect of H_2S on the Corrosion Behavior of Pipeline Steels in Supercritical and Liquid CO_2 Environments*. NACE Corrosion. Dallas, TX: NACE International. doi: 10.5006/2026

Choi, Y.-S., Hassani, S., Vu, T. N., Nesic, S., Abas, A. Z. B., Nor, A. M., et al. (2017). *Corrosion Inhibition of Pipeline Steels under Supercritical CO_2 Environment*. NACE Corrosion. New Orleans, LA: NACE International.

Choi, Y.-S., and Nešić, S. (2011). Determining the corrosive potential of CO_2 transport pipeline in high pCO_2-water environments. *Int. J. Greenhouse Gas Control* 5, 788–797. doi: 10.1016/j.ijggc.2010.11.008

Choi, Y. S., Nesic, S., and Young, D. (2010). Effect of impurities on the corrosion behavior of CO_2 transmission pipeline steel in supercritical CO_2-water environments. *Environ. Sci. Technol.* 44, 9233–9238. doi: 10.1021/es102578c

Cole, I. S., Corrigan, P., Sim, S., and Birbilis, N. (2011). Corrosion of pipelines used for CO_2 transport in CCS: Is it a real problem? *Int. J. Greenhouse Gas Control* 5, 749–756. doi: 10.1016/j.ijggc.2011.05.010

Craig, B. (1998). Predicting the conductivity of water-in-oil solutions as a means to estimate corrosiveness. *Corrosion* 54, 657–662. doi: 10.5006/1.3287645

Craig, B. D. (1996). Corrosion in oi/water systems. *Mater. Perform.* 35, 61–62.

Cui, Z. D., Wu, S. L., Zhu, S. L., and Yang, X. J. (2006). Study on corrosion properties of pipelines in simulated produced water saturated with supercritical CO_2. *Appl. Surf. Sci.* 252, 2368–2374. doi: 10.1016/j.apsusc.2005.04.008

Dai, Z., Middleton, R., Hari, V., Fessenden-Rahn, J., Bauman, J., Pawar, R. S.-, et al. (2014). An integrated framework for optimizing CO_2 sequestration and enhanced oil recovery. *Environ. Sci. Technol. Lett.* 1, 49–54. doi: 10.1021/ez4001033

Dang, C., Nghiem, L., Nguyen, N., Chen, Z., and Nguyen, Q. (2016). Evaluation of CO_2 low salinity water-alternating-gas for enhanced oil recovery. *J. Nat. Gas Sci. Eng. A* 35, 237–258. doi: 10.1016/j.jngse.2016.08.018

de Visser, E., Hendriks, C., Barrio, M., Molnvik, M. J., de Koeijer, G., Liljemark, S., et al. (2008). Dynamics CO_2 quality recommendations. *Int. J. Greenhouse Gas Control* 2, 478–484. doi: 10.1016/j.ijggc.2008.04.006

De Waard, C., Lotz, U., and Milliams, D. E. (1991). Predictive model for CO_2 corrosion engineering in wet natural gas pipelines. *Corrosion* 47, 976–985. doi: 10.5006/1.3585212

De Waard, C., Smith, L. M., and Craig, B. D. (2003). *The Influence of Crude Oils on Well Tubing Corrosion Rates*. San Diego, CA: NACE Corrosion.

Dugstad, A., Halseid, M., and Morland, B. (2013a). Effect of SO_2 and NO_2 on corrosion and solid formation in dense phase CO_2 pipelines. *Energy Proc.* 37, 2877–2887. doi: 10.1016/j.egypro.2013.06.173

Dugstad, A., Halseid, M., Morland, B., and Sivertsen, A. O. (2013b). Corrosion in dense phase CO_2 - the impact of depressurisation and accumulation of impurities. *Energy Proc.* 37, 3057–3067. doi: 10.1016/j.egypro.2013.06.192

Dugstad, A., Morland, B., and Clausen, S. (2011a). Corrosion of transport pipelines for CO_2-Effect of water ingress. *Energy Proc.* 4, 3063–3070. doi: 10.1016/j.egypro.2011.02.218

Dugstad, A., Morland, B., and Clausen, S. (2011b). Geochemical investigation of the combined effect of injecting low salinity water and carbon dioxide on carbonate reservoirs. *Energy Proc.* 4, 3063–3070. doi: 10.1016/j.egypro.2014.11.800

Efird, K. D., and Jasinski, R. J. (1989). Effect of the crude oil on corrosion of steel in crude oil/brine production. *Corrosion* 45, 165–171. doi: 10.5006/1.3577835

Efird, K. D., Smith, J. L., Blevins, S. E., and Davis, N. D. (2004). *The Crude Oil Effect on Steel Corrosion Wettability Preference and Brine Chemistry*. NACE Corrosion. Houston, TX: NACE International.

Esmaeely, S. N., Choi, Y. S., Young, D., and Nesic, S. (2013). Effect of calcium on the formation and protectiveness of iron carbonate layer in CO_2 corrosion. *Corrosion* 69, 912–920. doi: 10.5006/0942

Farajzadeh, R., Zitha, P. L. J., and Bruining, J. (2009). Enhanced mass transfer of CO_2 into water: experiment and modeling. *Ind. Eng. Chem. Res.* 48, 6423–6431. doi: 10.1021/ie801521u

Fingas, M., and Fieldhouse, B. (2004). Formation of water-in-oil emulsions and application to oil spill modelling. *J. Hazard. Mater.* 107, 37–50. doi: 10.1016/j.jhazmat.2003.11.008

Fordham, E. J., Ramos, R. T., Holmes, A., Simonian, S. S.-,Huang, M., and Lenn, C. P. (1999). Multi-phase-fluid discrimination with local fibre-optical probes: III. Three-phase flows. *Meas. Sci. Technol.* 10, 1347–1352. doi: 10.1088/0957-0233/10/12/333

Foss, M., Gulbrandsen, E., and Sjoblom, J. (2009). Effect of corrosion inhibitors and oil on carbon dioxide corrosion and wetting of carbon steel with ferrous carbonate deposits. *Corrosion* 65, 3–14. doi: 10.5006/1.3319113

Freitag, N. P. (2018). Similarity of the effect of different dissolved gases on heavy-oil viscosity. *SPE Reserv. Eval. Eng.* 2018:189456. doi: 10.2118/189456-PA

Frising, T., Noik, C., and Dalmazzone, C. (2006). The liquid/liquid sedimentation process: from droplet coalescence to technologically enhanced water/oil emulsion gravity separators: a review. *J. Dispersion Sci. Technol.* 27, 1035–1057. doi: 10.1080/01932690600767098

Glezakou, V.-A., Rousseau, R., Dang, L. X., and McGrail, B. P. (2010). Structure, dynamics and vibrational spectrum of supercritical CO_2 /H_2O mixtures from *ab initio* molecular dynamics as a function of water cluster formation. *Phys. Chem. Chem. Phys.* 12, 8759–8771. doi: 10.1039/b923306g

Grogan, A. T., Pinczewski, V. W., and Ruskauff, G. J. (1988). Diffusion of CO_2 at reservoir conditions: models and measurements. *SPE Reserv. Eng.* 3, 93–102. doi: 10.2118/14897-PA

Gulbrandsen, E., and Kvarekval, J. (2007). Effect of oil-in-water emulsions on the performance of carbon dioxide corrosion inhibitors. *Corrosion* 63, 187–196. doi: 10.5006/1.3278343

Han, D., Jiang, R. J., and Cheng, Y. F. (2013). Mechanism of electrochemical corrosion of carbon steel under deoxygenated water drop and sand deposit. *Electrochim. Acta* 114, 403–408. doi: 10.1016/j.electacta.2013.10.079

Hoffmann, R., and Johnson, G. W. (2011). Measuring phase distribution in high pressure three-phase flow using gamma densitometry. *Flow Meas. Instrument.* 22, 351–359. doi: 10.1016/j.flowmeasinst.2011.02.005

Hornafius, K. Y., and Hornafius, J. S. (2015). Carbon negative oil: a pathway for CO_2 emission reduction goals. *Int. J. Greenhouse Gas Control* 37, 492–503. doi: 10.1016/j.ijggc.2015.04.007

Horsup, D. L., Clark, J. C., Binks, B. P., Fletcher, P. D. L., and Hicks, J. T. (2010). The fate of oilfield corrosion inhibitors in multiphase systems. *Corrosion* 66:036001. doi: 10.5006/1.3359624

Hua, Y., Barker, R., Charpentier, T., Ward, M., and Neville, A. (2015). Relating iron carbonate morphology to corrosion characteristics for water-saturated supercritical CO_2 systems. *J. Supercritical Fluids* 98, 183–193. doi: 10.1016/j.supflu.2014.12.009

Hua, Y., Barker, R., and Neville, A. (2014a). Effect of temperature on the critical water content for general and localised corrosion of X65 carbon steel in the transport of supercritical CO_2. *Int. J. Greenhouse Gas Control* 31, 48–60. doi: 10.1016/j.ijggc.2014.09.026

Hua, Y., Barker, R., and Neville, A. (2014b). Understanding the influence of SO_2 and O_2 on the corrosion of carbon steel in water-saturated supercritical CO_2. *Corrosion* 71, 667–683. doi: 10.5006/1504

IEAGHG (2010). *Corrosion and Selection of Materials for Carbon Capture and Storage*. International Energy Agency. Available online at: https://hub.globalccsinstitute.com/publications/corrosion-and-materials-selection-ccs-systems/overview

Ingham, B., Ko, M., Laycock, N., Burnell, J., Kappen, P., Kimpton, J. A., et al. (2012). *In-situ* synchrotron X-ray diffraction study of scale formation during CO_2 corrosion of carbon steel in sodium and magnesium chloride solutions. *Corrosion Sci.* 56, 96–104. doi: 10.1016/j.corsci.2011.11.017

Jacobson, G. A. (2014). Pipeline corrosion issues related to carbon capture, transportation and storage. *Mater. Perform.* 53, 24–31. Available online at: http://www.materialsperformance.com/articles/material-selection-design/2015/08/pipeline-corrosion-issues-related-to-carbon-capture-transportation-and-storage

Jepson, W. P., and Menezes, R. (1995). *The Effects of Oil Viscosity on Sweet Corrosion in Multiphase Oil, Water/Gas Horizontal Pipelines*. NACE Corrosion. Orlando, FL: NACE International.

Jiang, R. J., and Cheng, Y. F. (2013). Mechanism of electrochemical corrosion of steel under water drop. *Electrochem. Commun.* 35, 8–11. doi: 10.1016/j.elecom.2013.07.019

Kang, C., Jepson, W. P., and Gopal, M. (1999). Effect of drag-reducing agent on slug characteristics in multiphase flow in inclined pipes. *J. Energy Resour. Technol.* 121, 86–90. doi: 10.1115/1.2795073

Kang, C., Wilkens, R. J., and Jepson, W. P. (1996). *The Effect of Slug Frequency on Corrosion in High-Pressure, Inclined Pipelines.* Denver, CO: NACE Corrosion.

Kanwar, S. (1994). *Study and Modeling of Sweet Corrosion of Multiphase Mixtures in a Horizontal Pipeline* (Master's thesis). Ohio University, Athens, OH.

Kee, K. E., Richter, S., Babic, M., and Nesic, S. (2014). *Flow Patterns and Water Wetting in Oil-Water Two Phase Flow - A Flow Loop Study*. NACE-Corrosion. San Antonio, TX: NACE International.

Kouba, G. E., and Jepson, P. (1990). The flow of slugs in horizontal, two-phase pipelines. *J. Energy Resour. Technol.* 112, 20–24. doi: 10.1115/1.2905707

Kutchko, B. G., Strazisar, B. R., Dzombak, D. A., Lowry, G. V., and Thaulow, N. (2007). Degradation of well cement by CO_2 under geologic sequestration conditions. *Environ. Sci. Technol.* 41, 4787–4792. doi: 10.1021/es062828c

Landry, X., Runstedtler, A., Papavinasam, S., and Place, T. D. (2012). Computational fluid dynamics study of solids deposition in heavy oil transmission pipeline. *Corrosion* 68, 904–912. doi: 10.5006/0444

Lee, T. C. Jr., Psathas, P. A., and Johnston, K. P. (1999). Water-in-carbon dioxide emulsions: formation and stability. *Langmuir* 15, 6781–6791. doi: 10.1021/la9903548

Li, C. (2009). *Effect of Corrosion Inhibitor on Water Wetting and Carbon Dioxide Corrosion in Oil-Water Two-Phase Flow* (Ph.D. thesis). Ohio University, Athens, OH.

Li, C., Richter, S., and Nešić, S. (2014). How do inhibitors mitigate corrosion in oil-water two-phase flow beyond lowering the corrosion rate? *Corrosion* 70, 958–966. doi: 10.5006/1057

Li, C., Tang, X. P., Ayello, F., Cai, J. Y., and Nesic, S. (2006). *Experimental Study on Water Wetting and CO_2 Corrosion in Oil-Water Two-Phase Flow.* San Diego, CA: NACE Corrosion.

Li, W., Pots, B. F. M., Brown, B., Kee, K. E., and Nesic, S. (2016). A direct measurement of wall shear stress in multiphase flow - Is it an important parameter in CO_2 corrosion of carbon steel pipelines? *Corrosion Sci.* 110, 35–45. doi: 10.1016/j.corsci.2016.04.008

Lindeberg, E. (2011). Modelling pressure and temperature profile in a CO_2 injection well. *Energy Proc.* 4, 3935–3941. doi: 10.1016/j.egypro.2011.02.332

Liu, A. Q., Bian, C., Wang, Z. M., Han, X., and Zhang, J. (2018). Flow dependence of steel corrosion in supercritical CO_2 environments with different water concentrations. *Corrosion Sci.* 134, 149–161. doi: 10.1016/j.corsci.2018.02.027

Lotz, U. L., Bodegom, V., and Ouwehand, C. (1991). The effect of type of oil or gas condensate on carbonic acid corrosion. *Corrosion* 47, 635–645. doi: 10.5006/1.3585301

Luo, X., Lü, G., Zhang, W., He, L., and Lü, Y. (2017). Flow structure and pressure gradient of extra heavy crude oil-water two phase flow. *Exp. Thermal Fluid Sci.* 82, 174–181. doi: 10.1016/j.expthermflusci.2016.11.015

Lv, G., Li, Q., Wang, S., and Li, X. (2015). Key techniques of reservoir engineering and injection-production process for CO_2 flooding in China's SINOPEC Shengli Oilfield. *J. CO_2 Utilization* 11, 31–40. doi: 10.1016/j.jcou.2014.12.007

Maley, J. (1997). *Slug flow characteristics and corrosion rates in inclined high pressure multiphase flow pipes* (Master degree). Ohio University, Athens, OH.

McGrail, B. P., Schaef, H. T. V., Glezakou, A., Dang, L. X., and Owen, A. T. (2009). Water reactivity in the liquid and supercritical CO_2 phase: has half the story been neglected? *Energy Proc.* 1, 3415–3419. doi: 10.1016/j.egypro.2009.02.131

Mendez, C., Duplat, S., Hernandez, S., and Vera, J. (2001). *On the Mechanism of Corrosion Inhibition by Crude Oils.* Houston, TX: NACE Corrosion.

Mohitpour, M., Seevam, P., Botros, K. K., Rothwell, B., and Ennis, C. (2012). *Chapter 5: Pipeline Transportation of Carbon Dioxide Containing Impurities*. ASME Press. doi: 10.1115/1.859834

Nesic, S. (2007). Key issues related to modelling of internal corrosion of oil and gas pipelines – A review. *Corrosion Sci.* 49, 4308–4338. doi: 10.1016/j.corsci.2007.06.006

Nesic, S., and Carroll, F. (2003). Horizontal rotating cylinder-A compact apparatus for studying the effect of water wetting on carbon dioxide corrosion of mild steel. *Corrosion* 59, 1085–1095. doi: 10.5006/1.3277528

Nesic, S., Xiao, Y., and Pots, B. F. M. (2004). *A Quasi 2-D Localized Corrosion Model*. NACE Corrosion. New Orleans, FL: NACE International.

Nyborg, R. (1998). *Initiation and Growth of Mesa Corrosion Attack During CO_2 Corrosion of Carbon Steel*. NACE Corrosion. San Diego, CA: NACE International.

Oosterkamp, A., and Ramsen, J. (2008). State-of-the-art overview of CO_2 pipeline transport with relevance to offshore pipelines. Polytech Report No.: POL-O-2007-2138-A. Available online at: https://www.researchgate.net/publication/228688545_State-of-the-Art_Overview_of_CO_2_Pipeline_Transport_with_Relevance_to_Offshore_Pipelines

Paolinelli, L. D., Rashedi, A., and Yao, J. (2018). Characterization of droplet sizes in large scale oil-water flow downstream from a globe valve. *Int. J. Multiphase Flow* 99, 132–150. doi: 10.1016/j.ijmultiphaseflow.2017.09.014

Papavinasam, S., Doiron, A., Panneerselvam, T., and Revie, R. W. (2007). Effect of hydrocarbons on the internal corrosion of oil and gas pipelines. *Corrosion* 63, 704–712. doi: 10.5006/1.3278419

Plasencia, J., Pettersen, B., and Nydal, O. J. (2013). Pipe flow of water-in-crude oil emulsions: effective viscosity, inversion point and droplet size distribution. *J. Petrol. Sci. Eng.* 101, 35–43. doi: 10.1016/j.petrol.2012.11.009

Pouraria, H., Seo, J. K., and Paik, J. K. (2016). A numerical study on water wetting associated with the internal corrosion of oil pipelines. *Ocean Eng.* 122, 105–117. doi: 10.1016/j.oceaneng.2016.06.022

Quej-Ake, L. M., Contreras, A., and Aburto, J. (2018). The effect of non-ionic surfactant on the internal corrosion for X52 steel in extra-heavy crude oil-in-water emulsions. *Anti Corrosion Methods Mater.* 65, 234–248. doi: 10.1108/ACMM-03-2017-1770

Race, J. M., Wetenhall, B., Seevam, P. N., and Downie, M. J. (2012). Towards a CO_2 pipeline specification: defining tolerance limits for impurities. *J. Pipeline Eng.* 11, 173–190. Availble online at: https://pureportal.strath.ac.uk/en/publications/towards-a-co2-pipeline-specification-defining-tolerance-limits-fo

Rogers, J. D., and Grigg, R. B. (2001). A literature analysis of the WAG injectivity abnormalities in the CO_2 process. *SPE Reserv. Eval. Eng.* 4, 375–386. doi: 10.2118/73830-PA

Rostami, A., Arabloo, M., Kamari, A., and Mohammadi, A. H. (2017). Modeling of CO_2 solubility in crude oil during carbon dioxide enhanced oil recovery using gene expression programming. *Fuel* 210, 768–782. doi: 10.1016/j.fuel.2017.08.110

Ruan, B., Xu, R., Wei, L., Ouyang, X., Luo, F., and Jiang, P. (2013). Flow and thermal modeling of CO_2 in injection well during geological sequestration. *Int. J. Greenhouse Gas Control* 19, 271–280. doi: 10.1016/j.ijggc.2013.09.006

Ruhl, A. S., and Kranzmann, A. (2013). Investigation of pipeline corrosion in pressurized CO_2 containing impurities. *Energy Proc.* 37, 3131–3136. doi: 10.1016/j.egypro.2013.06.199

Salama, M., and Brown, B. (2009). *Factors Affecting CO_2 Corrosion and Inhibitor Effectiveness Using Multi-phase Flow Loop*. NACE-Corrosion. Atlanta, GA: NACE International.

Sandana, D., Hadden, M., Race, J., and Charles, E. (2012). Transport of gaseous and dense carbon dioxide in pipelines: is there an internal corrosion risk? *J. Pipeline Eng.* 11, 229–238. Available online at: https://pureportal.strath.ac.uk/en/publications/transport-of-gaseous-and-dense-phase-carbon-dioxide-is-there-an-i

Sarica, C., and Zhang, H. (2008). *DOE Final Report: Development of Next Generation Multiphase Pipe Flow Prediction Tools*. Tulsa, OK: The University of Tulsa.

Schmitt, G., Bosch, C., Mueller, M., and Siegmund, G. (2000). *A Probabilistic Model for Flow Induced Localized Corrosion*. NACE Corrosion. Orlando, FL: NACE International: 00049.

Shamsa, A., Barker, R., Hua, Y., Barmatov, E., Hughes, T. L., and Neville, A. (2019). The role of Ca^{2+} ions on Ca/Fe carbonate products on X65 carbon steel in CO_2 corrosion environments at 80 and 150°C. *Corrosion Sci.* 156, 58–70. doi: 10.1016/j.corsci.2019.05.006

Sim, S., Bocher, F., Cole, I. S. X.-,Chen, B., and Birbilis, N. (2014a). Investigating the effect of water content in supercritical CO_2 as relevant to the corrosion of carbon capture and storage pipelines. *Corrosion* 70, 185–195. doi: 10.5006/0944

Sim, S., Cole, I. S., Choi, Y. S., and Birbilis, N. (2014b). A review of the protection strategies against internal corrosion for the safe transport of supercritical CO_2 via steel pipelines for CCS purposes. *Int. J. Greenhouse Gas Control* 29, 185–199. doi: 10.1016/j.ijggc.2014.08.010

Singh, R., Eng, M. S., and Mweldi, I. (2010). "Enhanced oil recovery and CO_2 corrosion a challenge," in *2010 China International Pipeline Forum* (Langfang), 162–171.

Smart, J. S. (2001). Wettability- A major factor in oil and gas system corrosion. *Mater. Perform.* 40, 54–59. Available online at: https://jglobal.jst.go.jp/en/detail?JGLOBAL_ID=200902186387082008&rel=0

Sokolova, I. M., Abryutina, N. N., Punanov, V. G., and Petrov, A. A. (1992). Chemical classification of naphthenic condensates and oils. *Organ. Geochem.* 19, 1–11. doi: 10.1016/0146-6380(92)90023-Q

Sotgia, G., Tartarini, P., and Stalio, E. (2008). Experimental analysis of flow regimes and pressure drop reduction in oil–water mixtures. *Int. J. Multiphase Flow* 34, 1161–1174. doi: 10.1016/j.ijmultiphaseflow.2008.06.001

Stack, M. M., and Abdulrahman, G. H. (2012). Mapping erosion–corrosion of carbon steel in oil–water solutions: effects of velocity and applied potential. *Wear* 274–275, 401–413. doi: 10.1016/j.wear.2011.10.008

Store, M., Passade-Boupat, N., Bonis, M., and Adams, B. (2011). *Inhibitive Properties of Crude Oils: Can We Count on Them?* Houston, TX: NACE Corrosion.

Sun, J., Sun, C., Zhang, G., Zhao, W., and Wang, Y. (2016a). Effect of water cut on the localized corrosion behavior of P110 tube steel in supercritical CO_2/oil/water environment. *Corrosion* 72, 1470–1482. doi: 10.5006/1926

Sun, J. B., Sun, C., Zhang, G. A., Li, X. D., Zhao, W. M., Jiang, T., et al. (2016b). Effect of O_2 and H_2S impurities on the corrosion behavior of X65 steel in water-saturated supercritical CO_2 system. *Corrosion Sci.* 107, 31–40. doi: 10.1016/j.corsci.2016.02.017

Taleb, W., Pessu, F., Wang, C., Charpentier, T., Barker, R., and Neville, A. (2017). Siderite micro-modification for enhanced corrosion protection. *NPJ Mater. Degrad.* 1:13. doi: 10.1038/s41529-017-0014-1

Tang, X., Xu, L. Y., and Cheng, Y. F. (2008). Electrochemical corrosion behavior of X-65 steel in the simulated oil-sand slurry. II: Synergism of erosion and corrosion. *Corrosion Sci.* 50, 1469–1474. doi: 10.1016/j.corsci.2008.01.019

Tavares, L. M., da Costa, E. M., Andrade, J. J. D., Hubler, R., and Huet, B. (2015). Effect of calcium carbonate on low carbon steel corrosion behavior in saline CO_2 high pressure environments. *Appl. Surf. Sci.* 359, 143–152. doi: 10.1016/j.apsusc.2015.10.075

Thanthiriwatte, K. S., Duke, J. R., Jackson, V. E., Felmy, A. R., and Dixon, D. A. (2012). High-level Ab initio predictions of the energetics of $mCO_2 \cdot (H_2O)n$ (n= 1-3, m = 1-12) clusters. *J. Phys. Chem. A* 116,: 9718–9729. doi: 10.1021/jp306594h

Turgoose, S., John, G., Flynn, M., Kadir, A. A., Economopoulos, G., and Dicken, G. (2014). *Corrosion Inhibition in Supercritical Carbon Dioxide Systems Containing Water*. NACE Corrosion. San Antonio, TX: NACE International.

Tzimas, E., Georgakaki, A., Garcia, C. C., and Peteves, S. D. (2005). *Enhanced Oil Recovery Using Carbon Dioxide in the European Energy System*. Petten: Institute for Energy.

Villarreal, J., Laverde, D., and Fuentes, C. (2006). Carbon-steel corrosion in multiphase slug flow and CO_2. *Corrosion Sci.* 48, 2363–2379. doi: 10.1016/j.corsci.2005.09.003

Wang, H., Cai, J., Bosch, C., Jepson, W., and Hong, T. (2002). *Enhanced Mass Transfer and Wall Shear Stress in Multiphase Slug Flow*. Denver, CO: NACE Corrosion.

Wang, Z., Felmy, A. R., Thompson, C. J., Loring, J. S., Joly, A. G., Rosso, K. M., et al. (2013). Near-infrared spectroscopic investigation of water in supercritical CO_2 and the effect of $CaCl_2$. *Fluid Phase Equil.* 338, 155–163. doi: 10.1016/j.fluid.2012.11.012

Wang, Z. L., Zhang, J., Wang, Z. M., Zhou, L., Han, X., Li, Q. F., et al. (2014). Emulsification reducing the corrosion risk of mild steel in oil-brine mixtures. *Corrosion Sci.* 86, 310–317. doi: 10.1016/j.corsci.2014.06.009

Wang, Z. M., Han, X., Zhang, J., and Wang, Z. L. (2014). *In-situ* observation of CO_2 corrosion under high pressure. *Corros. Eng. Sci. Tech.* 49, 352–356. doi: 10.1179/1743278213Y.0000000144

Wang, Z. M., Liu, X. T., Han, X., and Zhang, J. (2015). Managing internal corrosion of mild steel pipelines in CO_2 enhanced oil recovery multiphase flow conditions. *Energy Technol.* 3, 225–233. doi: 10.1002/ente.201402159

Wang, Z. M., Lun, Q. Y., Wang, J., Han, X., Zhang, J., and Song, G. L. (2019a). Corrosion mitigation behavior of an alternately wetted steel electrode in oil/water media. *Corrosion Sci.* 152, 140–152. doi: 10.1016/j.corsci.2019.03.008

Wang, Z. M., and Song, G.-,L. (2018). An Analytical model for the corrosion risk of water alternating gas injection wells in CO_2 enhanced oil recovery. *Adv. Theory Simul.* 1:1800041. doi: 10.1002/adts.201800041

Wang, Z. M., Song, G.-L., Wang, J., Han, X., and Zhang, J. (2019b). *Fast Evaluation of Corrosion Inhibitors Used in Oil/Water Mixed Fluids.* NACE Corrosion. Nashville, TN: NACE International.

Wang, Z. M., and Zhang, J. (2016). Corrosion of multiphase flow pipelines: the impact of crude oil. *Corrosion Rev.* 34, 17–40. doi: 10.1515/corrrev-2015-0053

Wei, L., Pang, X., and Gao, K. (2018). Effect of flow rate on localized corrosion of X70 steel in supercritical CO_2 environments. *Corrosion Sci.* 136, 339–351. doi: 10.1016/j.corsci.2018.03.020

Wicks, M., and Fraser, J. P. (1975). Entrainment of water by flowing oil. *Materials Perform.* 14, 9–12.

Xiang, Y., Long, Z. W., Li, C., Huang, H., and He, X. (2017). Inhibition of N80 steel corrosion in impure supercritical CO_2 and CO_2-saturated aqueous phases by using imino inhibitors. *Int. J. Greenhouse Gas Control* 63, 141–149. doi: 10.1016/j.ijggc.2017.05.010

Xiang, Y., Wang, Z., Xu, M. H., Li, Z., and Ni, W. D. (2013). A mechanistic model for pipeline steel corrosion in supercritical CO_2-SO_2-O_2-H_2O environments. *J. Supercrit. Fluids* 82, 1–12. doi: 10.1016/j.supflu.2013.05.016

Xu, X. X. (2007). Study on oil–water two-phase flow in horizontal pipelines. *J. Petrol. Sci. Eng.* 59, 43–58. doi: 10.1016/j.petrol.2007.03.002

Yang, D. R., Rosas, O., and Castaneda, H. (2014). $FeCO_3$ layer evolution for API 5L X52 steel in carbon dioxide-saturated NaCl brine in the presence of 1-decyl-3-methyrimidazolium chloride. *Corrosion Sci.* 87, 40–50. doi: 10.1016/j.corsci.2014.05.021

Yang, M., Wang, Z. M., Han, X., and Zhang, J. (2017). Corrosion inhibition by the trace amount of sulphide ion in CO_2-saturated brine solutions. *Corrosion Eng. Sci. Technol.* 52, 73–79. doi: 10.1080/1478422X.2016.1216661

Yang, Y., Brown, B., Nesic, S., Gennaro, M. E., and Molinas, B. (2010). *Mechanical Strength and Removal of a Protective Iron Carbonate Layer Formed on Mild Steel in CO_2 Corrosion*. San Antonio, TX: NACE Corrosion.

Yang, Z., Li, M., Peng, B., Lin, M., and Dong, Z. (2013). Volume expansion of CO_2 + oil at near critical and supercritical conditions of CO_2. *Fuel* 112, 283–288. doi: 10.1016/j.fuel.2013.04.037

Zhang, J., Wang, Z. L., Wang, Z. M., and Han, X. (2012). Chemical analysis of the initial corrosion layer on pipeline steels in simulated CO_2-enhanced oil recovery brines. *Corrosion Sci.* 65, 397–404. doi: 10.1016/j.corsci.2012.08.045

Zhang, Y., Pang, X., Qu, S., Li, X., and Gao, K. (2012). Discussion of the CO_2 corrosion mechanism between low partial pressure and supercritical condition. *Corrosion Sci.* 59, 186–197. doi: 10.1016/j.corsci.2012.03.006

Zhang, Y. N., Wang, T. L., Han, X., Wang, Z. M., and Zhang, J. (2016). Corrosion of artificial rock layer covered steel electrodes in a CO_2 environment: the influence of permeability. *Corrosion Sci.* 105, 190–201. doi: 10.1016/j.corsci.2016.01.017

Zhang, Y. Y., Zhang, Y., and Zhang, J. (2013). Environmental impacts of Carbon capture, transmission, enhanced oil recovery and sequestration: an overview. *Environ. Forensics* 14, 301–305. doi: 10.1080/15275922.2013.843616

Zheng, D. H., Che, D. F., and Liu, Y. H. (2008). Experimental investigation on gas–liquid two-phase slug flow enhanced carbon dioxide corrosion in vertical upward pipeline. *Corrosion Sci.* 50, 3005–3020. doi: 10.1016/j.corsci.2008.08.006

Zong, Y.-B., Jin, D. Z.,Wang, Y. Z.,Gao, K., and Wang, C. (2010). Nonlinear dynamic analysis of large diameter inclined oil-water two phase flow pattern. *Int. J. Multiphase Flow* 36, 166–183. doi: 10.1016/j.ijmultiphaseflow.2009.11.006

Conflict of Interest: The authors declare that the research was conducted in the absence of any commercial or financial relationships that could be construed as a potential conflict of interest.

Functional Ceramics

Chang-Mou Wu

Chang-Mou Wu is a Professor in the Department of Materials Science and Engineering at the Taiwan University of Science and Technology. He obtained his PhD in materials science and engineering from the National Sun Yet-Sen University, Taiwan in 1999. He subsequently worked as a scientist for research institutes (Academia Sinica and ChungShan Institute of Science and Technology) and in industry (Optimax). In 2007 he started his teaching and research career at FengChia University. His current research interests focus on functional/smart organic/inorganic nanocomposites, and electrospinning technology and its applications. Dr Wu was Head of the Program of Green Energy Science and Technology at FengChia University from 2009 to 2013. He was secretary general of the Society for the advancement of material and process engineering, (SAMPE, Taiwan Chapter) from 2009 to 2012. His research has received more than 30 awards since 2012, including the best oral presentation award at the 9th ACCM in 2014 and the best poster paper award at the 6th AESP in 2013.

frontiers in Materials

REVIEW
published: 27 March 2019
doi: 10.3389/fmats.2019.00049

Recent Advances in Tungsten-Oxide-Based Materials and Their Applications

Chang-Mou Wu, Saba Naseem, Min-Hui Chou, Jyun-Hong Wang and Ying-Qi Jian*

Department of Materials Science and Engineering, National Taiwan University of Science and Technology, Taipei, Taiwan

Among several active photothermal nanomaterials, tungsten-oxide-based materials have received considerable attention recently because of their ability to absorb near-infrared (NIR) light and their efficient light-to-heat conversion properties. In addition, tungsten-oxide-based materials have an unusual oxygen defect structure and strong local surface plasma resonance (LSPR), which offers strong photoabsorption in a broad wavelength range of the NIR region. In the past, several light-absorbing nanomaterials such as noble metals, polymeric materials, and other inorganic nanomaterials were of interest for their use in photothermal therapy for cancer treatment. In this study, we review the synthesis, properties, and applications of tungsten-oxide-based nanomaterials as a new type of photothermal material. The basic ideas behind photothermal nanomaterial development as well as the factors that influence their structural designs are also discussed in this study. In addition, recent progress in various fields such as NIR light-shielding, pyroelectric, water evaporation, photocatalysis, gas sensors, and energy-related applications for WO_{3-x}- and M_xWO_3-based nanomaterials (including their hybrids) are highlighted. Finally, this review presents promising insights into this rapidly growing field that may inspire additional research leading to practical applications.

Keywords: photothermal conversion, non-stoichiometric tungsten-oxides ($WO_{2.72}$), tungsten bronze (M_xWO_3), water evaporation, photocatalyst

OPEN ACCESS

Edited by:
Sheikh A. Akbar,
The Ohio State University,
United States

Reviewed by:
Rujia Zou,
Donghua University, China
Mukul Pradhan,
National Institute of Technology
Meghalaya, India

****Correspondence:***
Chang-Mou Wu
cmwu@mail.ntust.edu.tw

Specialty section:
This article was submitted to Functional Ceramics, a section of the journal Frontiers in Materials

Received: *03 January 2019*
Accepted: *04 March 2019*
Published: *27 March 2019*

Citation:
Wu C-M, Naseem S, Chou M-H, Wang J-H and Jian Y-Q (2019) Recent Advances in Tungsten-Oxide-Based Materials and Their Applications. Front. Mater. 6:49. doi: 10.3389/fmats.2019.00049

INTRODUCTION

Near-infrared (NIR) irradiation has a broad wavelength in the range of 780–2,500 nm. Fundamentally, nearly half of the energy available on the earth's surface is composed of sunlight that is near-infrared (i.e., greater than 780 nm). Maximizing NIR light for human use has been an interesting topic for scientists. NIR-absorbing photothermal materials (PTMs) have gained research interest because of their attractive light-to-heat behavior. Photothermal conversion is a process in which light energy of a specific wavelength is absorbed and is converted directly into heat. Through light-to-heat conversion, the heat generated can be applied to many fields such as photothermal therapy (Wang et al., 2017a), water evaporation (Wang, 2018), photocatalysis (Wang et al., 2017c), electrochromic devices (Liao et al., 2007), NIR shielding (Li et al., 2016b), and energy-related applications (Liu et al., 2018). PTMs have been used for photothermal ablation (PTA) therapy for the past few decades. Photothermal therapy is used in cancer treatment in which the target tissues are exposed to higher temperatures derived from photothermal properties to destroy abnormal cells (Chen et al., 2013). Yang et al. (2010) studied the *in-vivo* behavior of PEGylated nanographene sheets in tumor-bearing mice by *in-vivo* fluorescence imaging and determined that PEGylated nanographene sheets were extremely effective in *in-vivo* photothermal therapy (PTT).

In recent years, a variety of nanomaterials, noble metal nanomaterials, carbon-based materials, conductive polymers, and semiconductor nanoparticles have been studied for their NIR absorption properties (Lee et al., 2003; Marques, 2013; Zhang et al., 2015a; Wang et al., 2016a,b, 2017b; Riley and Day, 2017; Chen et al., 2018; Xu et al., 2018; Zhenzhen et al., 2018; Zeng et al., 2019).

Non-stoichiometric metal oxides such as WO_{3-x}, MoO_{3-x}, CuS, and TiO_x are of particular interest, as their strong photoabsorption properties in the broad wavelength range of the NIR region make them suitable for various applications (Guo et al., 2011b; Chen et al., 2013; Hu et al., 2016; Yan et al., 2016; Ding et al., 2017). In semiconductor-based materials, light is absorbed to generate electron-hole pairs. In particular, tungsten-oxide-based materials are effective in their utilization of the NIR region. Of these, oxygen-deficient $WO_{2.72}$ have been found to be useful in various applications such as smart windows, electrochromic devices, photothermal therapy, and NIR shielding. Other than photoabsorption properties, WO_x-based materials with large band gaps have attracted a lot of research interest due to their potential uses in optical recording devices (Aoki et al., 2005), field-emission applications (Baek and Yong, 2007) and high-T_c superconductors (Reich et al., 2009). Moreover, tungsten-bronze-type compounds with the general structure of M_xWO_3 ($M_xW^{+6}_{1-x}W^{+5}_xO_3$, where M = Cs, Rb, K, Na, and NH_4) were developed by doping an element that produces a tungsten bronze structure, which in turn exhibits broadband NIR absorption properties (Kim et al., 2012; Li et al., 2016c). The aim of this review is to discuss $WO_{2.72}$, M_xWO_3, and their hybrid-based materials to promote further scientific investigations in this field. The utilization and preparation of common PTMs such as $WO_{2.72}$ and M_xWO_3 are reported and the preparation techniques, photothermal conversion properties, and recent progress in their applications, including those in NIR shielding, water evaporation, pyroelectricity, photocatalysis, energy-related devices, and gas sensors are highlighted.

PHOTOTHERMAL CONVERSION MATERIALS AND THEIR PROPERTIES

The first and foremost requirement of a PTM is that it must have a light-absorption capability. During the last few decades, various PTMs with strong light absorbance have been investigated for wide solar spectra. In the literature, various photothermal nanomaterials have been examined. Because of their NIR responsive properties, the photothermal conversion dynamics of these materials have not been fully explored.

Noble-based metals like Au, Ag, and Pd have been widely studied mainly for applications in cancer therapy. Among them, Au has been investigated for cancer therapy because of its chemical stability, facile synthesis, high quality, high yield, and nontoxicity (Huang and El-Sayed, 2010). The local surface plasma resonance (LSPR) band is much stronger, particularly for noble metals like Au and Ag. Chen et al. (2007) designed a relatively small gold nanocage with an 810-nm dimension using laser-driven PTT. They showed that immuno-gold nanocages strongly absorb at their LSPR peak and thus might be a major factor in reducing the thermal damage threshold. Despite the advantages related to the photothermal effects of noble metals, their relatively high cost and poor photostability at a prolonged laser irradiation have led the research community to explore other alternatives.

Carbon-based nanomaterials are primarily of two types: graphene- and carbon-nanotube (CNT)-based. These have been used in cancer therapy, solar evaporation, and sensor applications (Hashishin and Tamaki, 2008; Lou et al., 2016; Son et al., 2016; Hu et al., 2017). CNTs are best known for their photothermal conversion properties as well as their low cost, light weight, and high stability. Wang et al. (2016b) studied photothermal CNT-based materials and reported a solar thermal conversion efficiency of as high as 82% with bilayered CNT-silica materials. Polymers such as polydopamine was pioneered as a biodegradable PTM (Jiang et al., 2017). Organic polymers such as polypyrrole (Zhang et al., 2015a), polyaniline (PANI) (Huang et al., 2015a), and poly(1,3,5-hexahydro-1,3,5-triazine) (Chen et al., 2018) have been explored for their photothermal properties. Song et al. (2018) reported that hydrophobic $Cu_{12}Sb_4S_{13}$ nanoparticles deposited on a porous cellulose acetate membrane form a photothermal film that could achieve photothermal heating for vapor generation and antibacterial activity simultaneously under light irradiation.

The research on semiconductor materials is rapidly expanding. In addition, studies are being conducted on noble and carbon-based PTMs, which includes copper chalcogenides, Ti_2O_3, MXene- (Ti_3C_2), MoO_{3-x}, and WO_{3-x} (Guo et al., 2012b; Ding et al., 2017; Lin et al., 2017; Wang et al., 2017b; Yan et al., 2017). These semiconductor-based materials are considered to be highly promising candidates, as they offer desirable photothermal conversion efficiencies. Copper chalcogenides are plasmonic-based metal-oxide-type semiconductors that are promising. Some researchers have investigated copper compounds, as they satisfy the efficiency requirement of strong vis-NIR absorption. Tian et al. (2011) synthesized hydrophilic flower-like CuS by using the hydrothermal method and achieved an enhanced absorption ability for a 980-nm laser. Similarly, nanocomposites like Cu_9S_5@SiO_2 (Song et al., 2013), Cu_7S_4 (Song et al., 2014), and CuS (Zhou et al., 2010) nanoparticle have been investigated for potential use in 980-nm laser-driven PTA therapy (Hua et al., 2017). developed porous floating HCuPO-PDMS that exhibited a very high absorption in the vis-NIR band at 808 nm. A photothermal conversion effciency of 41.8% was achieved for solar evaporation by HCuPO due to d-d transition of Cu^{2+}.

In this review, tungsten oxide materials are discussed in more detail with information on preparation and applications of $WO_{2.72}$ and M_xWO_3. WO_3 consists of perovskite units and is one of the most attractive candidates for photothermal conversion because of its suitable band gap (2.62 eV) (Huang et al., 2015b). It is also known for its good optical absorption characteristics under ultraviolet light. However, its photothermal conversion ability in NIR is inferior to that of $WO_{2.72}$. As the NIR absorbent properties of $WO_{2.72}$ have recently received greater attention, the photothermal performance of WO_3 in

other optical regions has also been investigated. The non-stoichiometric properties of $WO_{2.72}$ have been an interesting topic over the past decades. Many forms of WO_{3-x} such as $WO_{2.9}$, $WO_{2.83}$, and $WO_{2.72}$, which generally are blue in color, have also been considered because of their unusual defects; these defects improve the electrical conductivity by a large degree. However, these materials are not soluble in any solvent. With a prolonged time, they can be oxidized to WO_3. Moreover, the low crystallinity of $WO_{2.72}$ may be a concern (Sun et al., 2018). Thus far, the photothermal capabilities of other forms of WO_{3-x} are still unknown. Doping an element in WO_3 produces M_xWO_3, which further enhances the optical absorption in the solar spectrum. M_xWO_3 has also attracted considerable attention because it offers a wide variety of crystal structures and has many interesting attributes such as electrochromic, optical-electrical, and superconductive properties.

Semiconductors such as WO_{3-x} are interesting candidates as LSPR hosts because of their unique characteristic of having an outer d-valence electron. WO_{3-x} is well-known for its non-stoichiometric properties derived from the presence of numerous oxygen vacancies that can narrow the band gap. The new discrete energy bands below the conduction band are created by the oxygen vacancies (Yan et al., 2015; Zheng et al., 2015). The strong NIR absorption properties are induced by LSPR with an intensity comparable to the bandgap absorption and is achieved either by creating oxygen vacancies or by inserting metal ions. The LSPR band in plasmonic nanoparticles is proportional to the square root of the free electron density in the particle. The LSPR is dependent on certain factors such as the particle size, shape, structure, and the dielectric properties of the metal (Huang and El-Sayed, 2008). WO_{3-x} with a band gap of 2.4–3.0 eV are recognized as n-type semiconductors. Heat treatment in a reducing atmosphere is an effective approach to increase the concentration of oxygen vacancies. The dopants contribute electrons and increase the free-electron density in the conduction band. Finally, the LSPR creates an intensive local electric field, which is favorable for many practical applications (a topic to be discussed in the next section). The presence of mixed valence W^{5+} and W^{6+} sites are promising for harvesting NIR light through small polaron absorption and for increasing the electrical conductivity (Wang et al., 2017c). Among the non-stoichiometry tungsten oxides, monoclinic $WO_{2.72}$ (expressed as $W_{18}O_{49}$) has received considerable interest due to its distinctive oxygen defect structure and intense near-infrared photoabsorption.

In our previous study, we demonstrated the photothermal conversion properties of $WO_{2.72}$/polyurethane (PU) nanocomposites using a UV-Vis NIR spectrometer (Chala et al., 2017). The transmittance values of $WO_{2.72}$/PU were found to be 75% in the visible region (400–780 nm). Transmittance of the $WO_{2.72}$/PU nanocomposites in the range of 780–2500 nm was very low (8%), which suggested that the $WO_{2.72}$/PU nanocomposites exhibited stronger NIR absorption (92%) compared to other nanocomposites. This was because of the presence of free electrons or oxygen-vacancy-induced small polarons formed during the reduction process. For comparison, the transmittance spectra of $WO_{2.8}$/PU, WO_3/PU, and WO_2/PU nanocomposites are also shown (**Figure 1A**). The WO_{3-x} phase went through phase transformations during reduction, under a CO atmosphere, and created oxygen vacancies that led to a non-stoichiometric structure. The color of the WO_{3-x} powder varied after reduction at different temperatures (**Figure 1B**). The color changed from yellow to dark blue and to black for WO_3, WO_{3-x}, and WC, respectively. The temperature ΔT rapidly increased for $WO_{2.72}$/PU, $WO_{2.8}$/PU, WO_3/PU, and pure PU to 58.9, 41.9, 30.9, and 9.9 °C after 30 s, respectively (see **Figure 1C**) (Chala et al., 2017). These results suggested that the $WO_{2.72}$/PU nanocomposites exhibit a faster photothermal conversion rate than do $WO_{2.8}$/PU, WO_3/PU, and pure PU. As previously discussed, $WO_{2.72}$ considerable instabilities is the result if a longer time passes in which $WO_{2.72}$ can be oxidized to WO_3. This problem can be overcome by M_xWO_3, as it has similar absorption properties. Chen and Chen (2013) reported the photothermal conversion property of $Cs_{0.33}WO_3$, which exhibited strong characteristic absorption in the NIR region because of free electrons or polarons. It was demonstrated that NIR absorption was considerably enhanced by reducing the particle size or by increasing the particle concentration. In addition, the study reported that it generated a photothermal conversion efficiency of approximately 73% while demonstrating excellent photothermal stability. An effective NIR absorption and photothermal conversion ability was proved, which revealed great potential for practical applications.

PREPARATION OF TUNGSTEN-OXIDE-BASED MATERIALS

In this section, we discuss various preparation methods and the pros and cons of synthesizing nanomaterials including M_xWO_3 and WO_{3-x}. For M_xWO_3, these are summarized in **Table 1**. These include mechanochemical, vapor-phase synthesis, solid phase reaction, inductively coupled thermal plasma, and hydrothermal and solvothermal methods. Hydrothermal and solvothermal methods have been widely adopted because of their easy scalability.

Mechanochemical Method

Mechanochemical techniques like ball-milling or grinding are considered to be candidates for solvent-free synthesis. This method involves a chemical transformation which is induced by mechanical energies such as compression, shearing, or friction.Wang et al. (2003) prepared $Na_{0.88}WO_3$ nanocrystals by grinding the precursor Na pieces and WO_3 powders having an average grain size of 17 nm. Electrical property tests showed that $Na_{0.88}WO_3$ exhibited semiconductor characteristics that might cause lattice distortion of the material as a result of high-energy ball-milling affecting its electrical conductivity. This process has many advantages including the use of low-cost raw materials, simplicity of process, and the ability to obtain fine particles. However, the main limitation is that the chemical reaction must be controlled for air- and moisture-sensitive substances.

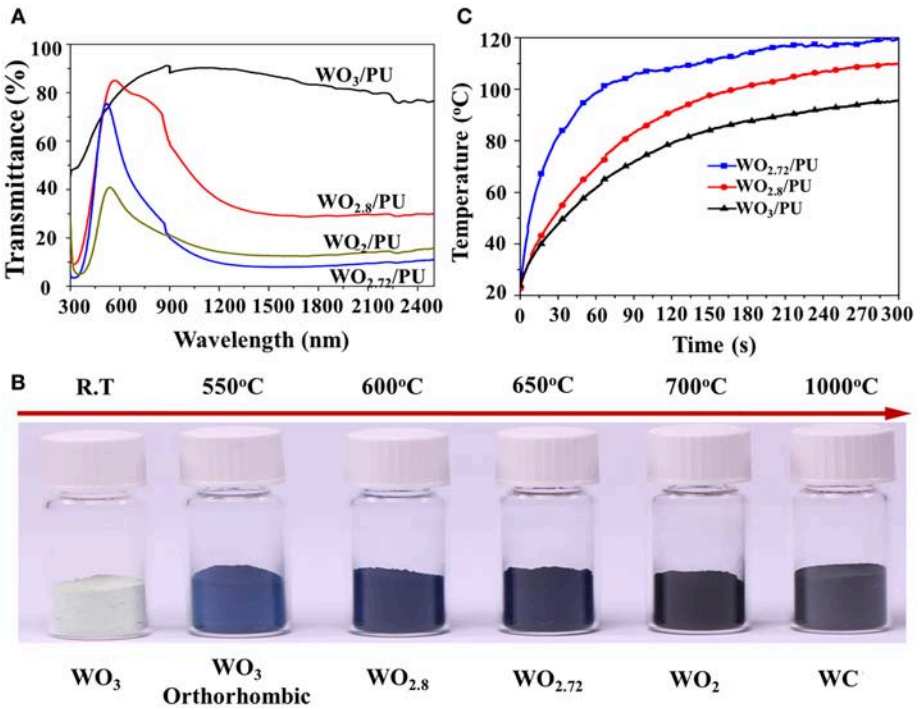

FIGURE 1 | Photothermalconversion properties of $WO_{2.72}$/PU nanocomposites by **(A)** UV-Vis-NIR transmittance spectra, **(B)** variation in the color observed for reduced tungsten oxide powder, and **(C)** the temperature difference WO_3/PU, $WO_{2.8}$/PU, and $WO_{2.72}$/PU with 7 wt % as a function of time under infrared light irradiation. Reproduced with permission (Chala et al., 2017). Copyright 2017, MDPI.

Chemical Vapor Transport

Based on the principles of chemical vapor transport (CVT), volatilization of a solid in the presence of a gaseous reactant (the so-called "transport agent") deposits the solid elsewhere and usually in crystalline form Schmidt et al. (2013). Hussain et al. (1997) employed this method and prepared crystal growth of alkali metal tungsten bronzes M_xWO_{3-x} (M=K, Rb, Cs). Several transport agents were used ($HgCl_2$, $HgBr_2$, Hgl_2, Cl_2, $PtCl_2$), but $HgCl_2$ and $HgBr_2$ were found to be equally efficient as transport agents for growing large crystals of tungsten bronzes. The crystals were grown to 6 mm in length for hexagonal tungsten bronzes. However, the tetragonal tungsten bronzes (M_xWO_3) were prepared at a size of 0.1 mm by using $HgCl_2$ and $HgBr_2$, where x was 0.25. Yet, when $x \geq 0.35$, very little or no transport occurred. The transport rate and crystal size were reduced with increasing alkali metal concentration. These were prepared under isothermal conditions both with and without adding transport agents, which showed nearly identical results. However, the results showed an appreciable transport effect when used as transport agents. Note also that the use of transport agents may cause environmental damage with high-energy consumption.

Solid-Phase Reaction

A solid-phase reaction refers to a process in which a solid reaction occurs between two solids, and a solid product is formed without chemical equilibrium. This technique is simple and requires low-cost equipment. However, it has a slow reaction rate at a high temperature. Preparation of tungsten bronze Cs, Rb, Na, and K have been reported when using the solid-phase reaction method (Lee et al., 2014b). Takeda and Adachi (2007) synthesized hexagonal tungsten bronze (HTB) $Cs_{0.33}WO_3$, $Rb_{0.33}WO_3$ powder and cubic tungsten bronze (CTB) $Na_{0.75}$ WO_3 powder using metal salts mixed with $WO_3{\cdot}NH_3$ as a precursor that reacted at 550°C for 1 h with H_2/N_2 or H_2/Ar. It was then annealed at 800 °C in an N_2 atmosphere for 1 h. $Cs_{0.33}WO_3$, $Rb_{0.33}WO_3$ resulted in strong and broad NIR absorption peaking at approximately 1,500 nm. It was revealed that the HTB phase $M_{0.33}WO_3$ was quite suitable for solar filter applications because of its strong absorption in the NIR range. Moon et al. (2013) demonstrated that quaternary tungsten bronze has better NIR absorption properties in the range of 780 to 1,200 than does tungsten bronze because of the modulated optical response by the quaternary element of sodium.

Inductively Coupled Thermal Plasma Method

Thermal plasma is mainly used as a heat source for the evaporation of solid precursors or decomposition of gaseous precursors. Reactive gases are used as main constituents to form a plasma flame for synthesis of nano-sized materials. Thermal plasma synthesis of M_xWO_3 was reported by Mamak et al. (2010) in which a powder mixture containing a precursor of $(NH_4)_{10}(H_2W_{12}O_{42})$. $4H_2O$ and salt of HCOOCs, Na2CO3,

TABLE 1 | List of the preparation methods for tungsten bronze (M_xWO_3).

Preparation method	Product	Precursor	Process	References
Mechanochemical method	$Na_{0.88}WO_3$ powder	Na pieces, WO_3 powders	At 200 rpm with Ar for 44 h	Wang et al., 2003
Chemical vapor transport	M_xWO_3 crystal (M = Cs, Rb, K)	K_2WO_4, KI, Rb_2WO_4, Cs_2WO_4,	Transport agent: $HgCl_2$, $HgBr_2$, Cl_2	Hussain et al., 1997
Solid phase reaction	M_xWO_3 powder (M = Cs, Rb, Na, K)	$((NH_4)_{10}H_2(W_2O_7)_6$, Cs, Rb, Na, K–salts	Heated at 550°C with H_2/N_2 or H_2/Ar for 1 h Annealing at 800°C with N_2 or Ar for 1 h	Takeda and Adachi, 2007 Lee et al., 2014b Guo et al., 2011a
	$Cs_{0.33}WO_3$ powder $Na_{0.11}Cs_{0.22}WO_3$ powder	$(NH_4)_6W_{12}O_{39}{\cdot}xH_2O$ Cs_2CO_3, Na_2CO_3	Heated at 550°C with H_2/Ar for 1 h Annealed at 800°C with Ar for 1 h	Moon et al., 2013
Inductively coupled thermal plasma method	M_xWO_3 powder M = Cs, Na, K	$(NH_4)_{10}(H_2W_{12}O_{42}){\cdot}4H_2O$, HCOOCs, Na2CO3, K3C6H5O7	Central gas: Ar Sheath gas: H_2	Mamak et al., 2010
Hydrothermal method	$Cs_{0.33}WO_3$	Cs_2WO_4, WO_2, WO_3, H_2O	Heated at 800 °C for 24 h	Okusako et al., 2012
	$K_{0.26}WO_3$ nanorod	K_2WO_4, K_2SO_4, H_2O	Heated at 200°C for 24 h were post-calcine	Wu et al., 2017b
	$(NH_4)_{0.33}WO_3$ nanorod	(NH4)10·4H2O, Ethylene glycol, CH_3COOH	Heated at 200°C for 72 h	Guo et al., 2012a Wu et al., 2017b
	$K_{0.26}WO_3$ nanowire	K_2WO_4, EDA, H_2O	Heated at 250°C for 48 h (Electrostatic-induced)	Liu et al., 2013a
Solvothermal method	$Cs_{0.3}WO_3$ powder	WCl_6, CsOH, Ethanol	Heated at 200°C for 12 h	Liu et al., 2010
	$Cs_{0.32}WO_3$ powder	H_2WO_4, H_2O_2, CsCl, Oleic acid	Heated at 220–280 °C for 4 h	Yao et al., 2018
	$M_{0.33}WO_3$ nanorod (M = Rb, Cs)	WCl_6, RbOH, CsOH Ethanol, CH_3COOH	Heated at 200–240°C for 20 h (Water controlled-release)	Wu et al., 2017b Guo et al., 2010

and K3C6H5O7 in a varied ratio of W and M were used. However, Ar was used as the central gas along with a small amount of H_2 to provide the reducing environment required for the synthesis of M_xWO_3. A mixture of tungsten and alkali salts with low decomposition temperature was used as the precursor. Thermal plasma synthesis has advantages in terms of material handling, raw material cost, and processing throughput. Inductively coupled thermal plasma (ICTP) synthesis has proven to be a unique method for the high throughput production of M_xWO_3, where M = Na, K, and Cs tungsten bronze nanopowders were synthesized at a high purity, using low-cost precursor materials. In general, materials produced by thermal plasma have a favorable optical absorption, high purity, and a tunable composition when using low-cost precursor materials. Major applications include coatings and heat shielding filters, as they exhibit a high extinction coefficient in the NIR region with little effect on transparency or visible color. ICTP is a fast reaction method for high production at low temperatures. It has high potential and can be used extensively in future research.

Hydrothermal Method

The hydrothermal method is simple and versatile for use in the synthesis of inorganic nanomaterials from aqueous solutions under high-temperature and high-pressure conditions. Temperature, pressure, and precursor concentration are the parameters that must be adjusted to the characteristics of nanomaterials. Water is the most commonly used solvent in the hydrothermal process. The water density and the dielectric constant are highly dependent on the temperature and pressure. A drop in the dielectric water constant is closely linked to an increase in temperature and a decrease in pressure. As the dielectric constant of water decreases, the reaction rate is enhanced considerably and thus the nucleation growth of crystals is facilitated. It offers many advantages such as a one-step synthetic procedure, environmental friendliness, production feasibility, good dispersion in solutions, and inexpensive instrumentation. Moreover, this method avoids the use of H_2 and considerably improves safety. However, it induces high-temperature energy consumption. Tungsten bronze such as $Cs_{0.33}WO_3$, $K_{0.26}WO_3$ nanorods and $(NH_4)_{0.33}WO_3$ nanorods have been reported by hydrothermal method. For the preparation of $Cs_{0.33}WO_3$, the precursor Cs_2WO_4, WO_2, WO_3, and distilled water were mixed and heated at 800°C for 24 h (Okusako et al., 2012). $K_{0.26}WO_3$ nanorods were synthesized with K_2WO_4, K_2SO_4, and distilled water at 200°C for 24 h and further post-calcined at 600°C for 2 h under an atmosphere of H_2 (5 vol%)/N_2 (Wu et al., 2017b). For the synthesis of $(NH_4)_{0.33}WO_3$ nanorods, ammonium paratungstate, ethylene glycol, and acetic acid were mixed and heated at 200°C for 72 h (Guo et al., 2012a). Liu et al. (2013a) reported the synthesis of $K_{0.26}WO_3$ nanowires by an electrostatic-induced process using K_2WO_4 as a precursor along with ethylenediamine (EDA) and water. It was heated further in an electric oven at 250°C for 48 h. EDA served as a reducing agent, which is much milder compared to other reducing agents such as $NaBH_4$ (Zhu and Manthiram, 1994) or N_2H_4 (Yang et al., 2003) used in the preparation of

tungsten bronzes. In fact, it is important to note from these preparations that different nanoparticles have different reaction schemes and processing conditions. Therefore, determining the proper chemical reactions with suitable conditions for different nanoparticles is desirable.

Solvothermal Method

The solvothermal method uses ethanol and ethylene glycol instead of water as a solvent to achieve the dual role of solvent and reducing agent. The control variables can be varied by adjusting the solvent type, changing the reaction atmosphere, and using different surfactants, pH, reactant concentration, and filled volume of autoclave. The $Cs_{0.3}WO_3$ powder was synthesized by a normal solvothermal reaction with the precursor of WCl_6, where their metal hydroxides (CsOH) were mixed with ethanol and heated at 200°C for 12 h and further annealed in the NH_3 atmosphere at 500°C for 1 h (Liu et al., 2010). $Cs_{0.32}WO_3$ powder was also synthesized by a H_2WO_4 precursor heated at 220°C for 4 h (Yao et al., 2018). To control the water releasing process, which is based on an esterification reaction between ethanol and acetate acid, monodispersed nanorods of M_xWO_3 (M = Cs and Rb) were produced (Guo et al., 2010; Wu et al., 2017b). An ethanol solution of WCl_6 and CsOH was mixed with CH_3COOH and heated at 200°C for 20 h. In this method, the heat treatment temperature is reduced by replacing it with ethanol as compared to the hydrothermal method. Moreover, the ethanol solvent serves a multifunctional property to control the morphology and to decrease the heat treatment temperature. Thus, it overcomes the high temperature energy consumption using a low temperature. However, comparatively, the hydrothermal method has a reduced environmental impact.

Figure 2 demonstrates different morphologies of $WO_{2.72}$ with the function of reaction time. This shows a morphological evolution from nanoparticles to urchin nanostructures (Su and Lin, 2009; Guo et al., 2012c; Moshofsky and Mokari, 2012). **Table 2** presents a brief summary of the nanostructured $WO_{2.72}$ types that were prepared by CVT and solid-phase reaction. $W/WO_{2.72}$ heterostructures (Liu et al., 2013b) ($WO_{2.72}$ nanowires grown on the side surface of the W whiskers along the radial direction), $WO_{2.72}$ nanoneedles (Jin et al., 2004), $WO_{2.72}$ sub-micro fibers (Liu et al., 2012), and $WO_{2.72}$ tapered needles (Wang et al., 2007) were synthesized using WO_3 as a precursor by a two-step CVT method. In general, the temperature of the furnace was increased from the room temperature to 800–1000°C. $WO_{2.72}$ nanoparticles were reported by the solid-phase reaction method using WCl_6 as a raw material with ethanol (Venables and Brown, 1996; Takeda and Adachi, 2007). Ma et al. (2017) prepared $WO_{2.72}$ nanoparticles using WCl_6 and ethanol with NH_3 solution as a solvent, which was pyrolyzed under air atmosphere. Because ammonia molecules tend to chelate strongly with tungsten ions, they could work as capping agents to hinder particle growth.

A brief summary of the preparation of $WO_{2.72}$ nanostructures by hydrothermal and solvothermal methods are listed in **Table 3**. $WO_{2.72}$ nanorods have been reported by the hydrothermal method using H_2WO_4 and Na_2SO_4 at 160°C for 24 h (Lou and Zeng, 2003). Guo et al. (2011b) reported $WO_{2.72}$ nanorods synthesized hydrothermally by reducing the as-obtained $(NH_4)_xWO_{3+x/2}$ and using sulfate as a capping agent in an atmosphere of H_2 (5 vol%)/N_2 at 500°C for 1 h. The solvothermal method was extensively studied for $WO_{2.72}$ for different nanostructures. $WO_{2.72}$ nanowires were synthesized by a simple solvothermal method using WCl_6 and ethanol solution under 180°C for 10–24 h (Qin et al., 2011b; Xi et al., 2012; Guo et al., 2016). Cetyltrimethylammonium bromide has also been used as a growth-directing agent to fabricate $WO_{2.72}$ nanowires (Li et al., 2016a). Huang et al. (2014a) synthesized $WO_{2.72}$ nanowires by using $WCl_6/NaNO_3$ through NO_3^--mediated assembly. With an increase in the NO_3^- concentration, the uniformity of the $WO_{2.72}$ alignments was enhanced, clearly demonstrating the process of NO_3^--medicated orientation. Li et al. (2016b) fabricated $WO_{2.72}$ nanofibers by using WCl_6 with oleic acid and 2.5 mL tri-n-octylamine under 350°C for 1 h. $WO_{2.72}$ nanowire bundles were synthesized with WCl_6 and propanol solvent at 200°C for 9 h, and the product was annealed in air at 250–450 °C for 2 h (Qin et al., 2011b). A different morphology was reported when varying the annealing temperature from 250 to 550°C. It was found that nanowires remain unchanged by the annealing treatment at 250 and 350°C. However, annealing at 450 and 550 °C induced WO_3 nanobelt-like structures. The Fabrication of mesoporous 1D-$WO_{2.72}$ nanobelts was conducted using a solvothermal method mixed with WO_3, polyvinyl pyrrolidone, and EDA at 180°C for 12 h, calcined at Ar/H_2 atmosphere at 580°C for 3 h (Sun et al., 2016). 3D $WO_{2.72}$ networks were obtained by solvothermally treating WCl_6 in ethanol at 160°C (Bai et al., 2013). The results showed that high precursor concentration contributed to the formation of $WO_{2.72}$ networks. However, when the concentration was further increased, plate-like $WO_{2.72}$ was found at a lower concentration. Sea-urchin-like structures composed of radial nanowires were obtained. $WO_{2.72}$ nanocrystals were synthesized by treating the precursor of WCl_6 and ethanol under 200°C for 24 h (Guo et al., 2012c). The effect of the tungsten precursor on the morphology was investigated in this case. Similar experiments were conducted using mixtures of WCl_6 and tungsten (VI) ethoxide ($W(EtO)_6$) with varied molar ratios, $WO_{2.72}$ nanorods were obtained with sizes ranging from 300 to 600 nm when mixtures of 5 mM $W(EtO)_6$ and 10 mM WCl_6 were used as the tungsten source. However, when equimolar mixtures of $W(EtO)_6$ and WCl_6 (7.5 mM) were used, plate-like particles with sizes of 300–500 nm were obtained. As the concentration of $W(EtO)_6$ was increased to 50 mM, well-defined monodispersed microspheres of 0.5–2 μm diameter were formed. It was suggested this might be because of the rate of water generation from different tungsten sources, and the difference in the hydrolysis behavior between $W(EtO)_6$ and WCl_6 resulted in different morphologies of WO_{3-x}. Mesoporous sphere 3D $WO_{2.72}$ was formed by using WCl_6 as a precursor mixed with solvent ethanol and CH_3COOH at 180°C for 16 h (Huang et al., 2014b; Zhao et al., 2017). At low precursor concentrations, only semi-closed spheres and disordered nanoparticles were formed. At higher concentration, hollow spheres were formed very easily that were bigger and had thicker shells. Only disordered nanoparticles were formed at a low

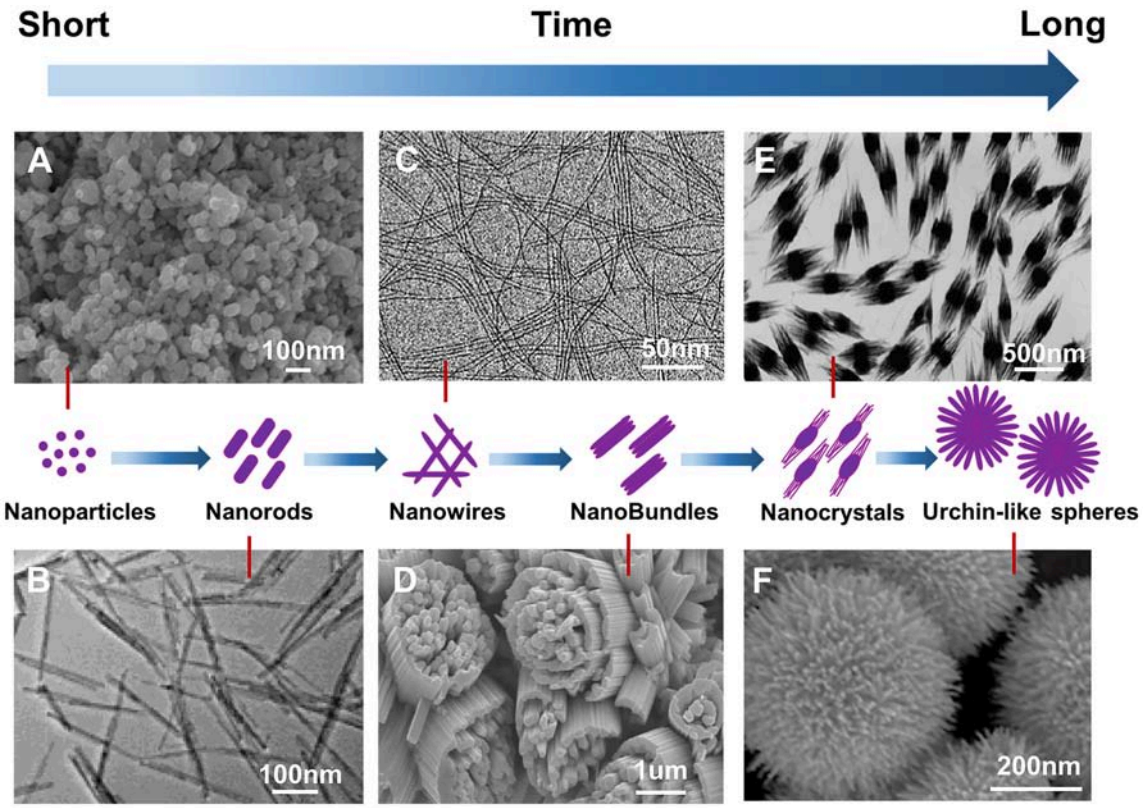

FIGURE 2 | Morphologies of $WO_{2.72}$ prepared with different reaction time. **(A)** nanoparticles, **(B)** nanorods, **(C)** nanowires. Reproduced with permission (Moshofsky and Mokari, 2012). Copyright 2012, Chemistry of Materials. **(D)** nanobundles. Reproduced with permission (Su and Lin, 2009). Copyright 2009, The Journal of Physical Chemistry C. **(E)** nanocrystals. Reproduced with permission (Guo et al., 2012c) Copyright 2012, American chemical society (ACS), and **(F)** urchin-like spheres.

TABLE 2 | Preparations of non-stoichiometric tungsten-oxide ($WO_{2.72}$) by chemical vapor transport and solid phase reaction.

Preparation method	Products	Precursor	Process	References
Chemical vapor transport	$W/WO_{2.72}$ heterostructure	WO_3	Quartz tube:Ar Furnace tube:H_2 Heated at 950°C for 4 h	Liu et al., 2013b
	$WO_{2.72}$ crystal	W	Quartz tube: Ar Furnace tube: N_2	Jin et al., 2004
	$WO_{2.72}$ sub-micro fiber	WO_3	Quartz tube:Ar Heated at 900°C for 4 h	Liu et al., 2012
	$WO_{2.72}$ tapered needle	W powders, $(NO_3)_2.6H_2O$	Quartz tube:argon Heated at 800 for 40 min	Wang et al., 2007
Solid phase reaction	$WO_{2.72}$ nanoparticle	WCl_6, Ethanol	Reduction 550°C with H_2/N_2 for 1 h Heated at 800°C with N_2 or Ar for 1 h	Takeda and Adachi, 2007
			Heated at 650–700°C with H_2 or CO	Venables and Brown, 1996 Chala et al., 2017
		WCl_6, Ethanol, Ammonia solution	Heated at 100°C for 3.5 h WO_3 powders were pyrolyzed under air atmosphere	Ma et al., 2017

temperature (120°C) even when sufficient WCl_6 was provided. This demonstrated that the morphology can be fine-tuned by controlling variables such as time, precursor concentration, and temperature (Guo et al., 2016). synthesized $WO_{2.72}$ urchin-like nanostructures and nanowires by treating WCl_6 with ethanol under 180°C for 10 h. $WO_{2.72}$ nanowires were obtained when the precursor concentration was 0.5 g L^{-1} and the reaction time was 10 h. Control of different morphologies by adjusting the concentration of precursor was discussed in this study. When the precursor concentration increased to 1 g L^{-1}, the

TABLE 3 | Preparations of non-stoichiometric tungsten-oxide ($WO_{2.72}$) by hydrothermal and solvothermal methods.

Preparation method	Products	Precursor	Process	References
Hydrothermal	$WO_{2.72}$ nanorod	$H_2WO_4 \cdot xH_2O$, Na_2SO_4	Heated at 160–200°C for 24 h	Lou and Zeng, 2003
		Na_2WO_4, $(NH_4)_2SO_4$	Heated at 200∘C for 24 h Heated at 500∘C with H_2/N_2 for 1 h	Guo et al., 2011b
Solvothermal process	$WO_{2.72}$ nanowire	WCl_6, Ethanol	Heated at 180°C for 10–24 h	Guo et al., 2016 Xi et al., 2012 Late et al., 2010
		WCl_6, Ethanol, CTAB	Heated at 180°C for 18 h	Li et al., 2016a
		WCl_6, n-propanol, $NaNO_3$	Heated at 200°C for 24 h	Huang et al., 2014a
	$WO_{2.72}$ nanofiber	WCl_6, Oleic acid, Tri-n-octylamine.	Heated at 350°C for 1 h	Li et al., 2016b
	$WO_{2.72}$ nanowire bundle	WCl_6, Propanol	Heated at 200°C for 9 h Annealed at 450°C with air for 2 h	Qin et al., 2011b
	Mesoporous $WO_{2.72}$ nanobelt	WO_3, Polyvinyl pyrrolidone, EDA	Heated at 180°C for 12 h Annealed at 580°C with Ar/H_2 for 3 h	Sun et al., 2016
	$WO_{2.72}$ nanowire network	WCl_6, Ethanol	Heated at 160°C	Bai et al., 2013
	$WO_{2.72}$ nanocrystal	WCl_6, Ethanol	Heated at 200°C for 24 h	Guo et al., 2012c
	Mesoporous $WO_{2.72}$ nanosphere	WCl_6, Ethanol, CH_3COOH	Heated at 180°C for 16 h	Huang et al., 2014b Zhao et al., 2017
	urchin-like $WO_{2.72}$	WCl_6, Ethanol	Heated at 180°C for 10 h	Guo et al., 2016

$WO_{2.72}$ nanowires changed to bundle-like $WO_{2.72}$. When the concentration was further increased to 3 g L^{-1}, a mixture of urchin-like nanostructures and nanowires was obtained. Once the concentration reached 5 g L^{-1}, nanospheres were obtained. The results showed that urchin-like $WO_{2.72}$ nanostructures have a better light harvesting capacity in the IR region than nanowires. The mechanism of different nanostructures proposed as $WO_{2.72}$ nanocrystals would preferably grow in the [010] direction as nanowires. Because the diameter of the nanowires was very small (with a large surface energy), the nanowires became bundle-like $WO_{2.72}$ (thus reducing the surface energy). As a result, bundle-like $WO_{2.72}$ nanostructures continued to be packaged and developed into urchin-like $WO_{2.72}$ nanostructures. Urchins were thus formed and further developed into nanospheres. Zhao et.al reported that $WO_{2.72}$ architectures including nanofibers, nanofiber bundles, and sea urchin-like microspheres were prepared by a template-free solvothermal method that tuned the WCl_6 concentrations (Zhao et al., 2017). In fact, it is important to note from these reports that different nanoparticles have different reaction schemes and processing conditions. Therefore, the proper chemical reactions with suitable conditions for different nanoparticles must be determined. Compared with the methods previously mentioned, solvothermal treatment is a facile, cost-effective, and well-studied liquid-phase technique, which has the capability of producing WO_x with different nanomorphologies.

APPLICATIONS OF TUNGSTEN-OXIDE-BASED MATERIALS

Tungsten-oxide-based materials $WO_{2.72}$, M_xWO_3, and their hybrids have attracted considerable attention in various fields such as heat generation, photocatalysis, and energy-related and gas-sensor applications. These applications are both important and interesting. They are discussed in more detail as follows.

Heat Generation

Heat generation is emerging as a promising technology and one of its important practical applications is in manufacturing polyethylene terephthalate (PET) bottles. An extruder PET preform is heated above its glass transition (Tg) point by IR irradiation so than it can be blown into the required shape. A small amount of WO_3 is incorporated into the PET to reduce the IR irradiation time and thus speed up productivity. The photothermal conversion properties of $WO_{2.7}$ show much greater potential in heat generation. A rise in temperature in a short span of time further reduces the IR irradiation time with $WO_{2.72}$. This could considerably improve the productivity of PET bottles. Considering their potential in harvesting solar energy and in heat conversion, various applications such as thermo/pyroelectricity, water evaporation, and NIR shielding are discussed.

Thermo/Pyroelectricity

Thermoelectric technology has been widely used as a means to convert heat into electrical energy through the Seebeck effect. Pyroelectricity is one of the least-known properties of certain solids and condensed materials. This property pertains to temperature-dependent spontaneous polarization in certain anisotropic solids and refers to the ability of a certain class of materials to generate an electric charge when heated and cooled consecutively. The temperature variations slightly modify the position of atoms within the crystal structure causing effects such as polarization change. The change in polarization creates a voltage across the material. Thus, it can be used

as a thermal-electric converter. However, achieving a high temperature difference in a non-conducted way is difficult. Therefore, it cannot be efficiently used to convert thermal energy into electric energy through a time-dependent temperature variation with spatial uniformity. To this end, PTM $WO_{2.72}$ incorporated within an electrospun pyroelectric polyvinylidene difluoride (PVDF) fiber membrane were prepared. Schematics of the pyroelectric measurement are shown in **Figure 3A**. Here, a higher temperature variation was obtained by irradiating NIR light in an on-off sequence on $WO_{2.72}$/PVDF fiber membranes. This resulted in higher output voltages compared to the fiber membranes without $WO_{2.72}$ (**Figure 3B**) (Wu et al., 2017a). Steady reproducibility of temperature variation and higher output voltages are shown as well. The results demonstrate that the $WO_{2.72}$/PVDF materials can be used for NIR sensing and solar energy harvester applications (Wu et al., 2017a). It is worth noting that hybrids of WO_3 have recently gained attention in thermo/pyroelectric studies. However, $WO_{2.72}$ and M_xWO_3 (their hybrids) are yet to be explored.

Water Evaporation

A solar-driven water evaporation process that utilizes sunlight as a renewable energy resource can be used in numerous practical applications. Such applications include freshwater production, desalination, and distillation (Hua et al., 2017; Shang et al., 2017; Awad et al., 2018; Kim et al., 2018). Solar heating designed as "air-water interface solar heating" has the ability to trap a wide solar spectrum selectively by strengthening the air-water interface (Wang et al., 2017d). However, heat transfer minimizes from interfacial to underlying bulk water. The photothermal layer that induces self-floating on the top of a water surface is deliberately designed as a heat barrier, that introduced interfacial heating in solar thermal applications (Liu et al., 2015; Lou et al., 2016). To include multifunctionality in a single-component material, multilayered materials offer researchers the opportunity to design more practical solutions, as demonstrated in our recent work. We had efficiently utilized $WO_{2.72}$ photothermal materials with polylactic acid (PLA). The photoabsorption properties of these photothermal materials made them suitable for converting light energy to thermal energy (Chala et al., 2018a). These composites were designed as fiber membranes that have a self-floating ability and act as heat barriers at air-water interfaces for light-driven water evaporation. **Figure 4A** shows a schematic of the experimental setup used for this measurement. For $WO_{2.72}$/PLA, a rapid rise of temperature ΔT can be seen from 19.4°C to 44.7°C and then to 75.3°C for over 5 min of irradiation containing 0, 4, and 7 wt% of $WO_{2.72}$ nanoparticles, respectively, as shown in **Figure 4B**. The water evaporation efficiency of the $WO_{2.72}$/PLA fiber membrane containing 7 wt% $WO_{2.72}$ nanoparticles reached 81.39%, which is significantly higher than pure water 39.09% (**Figure 4C**) (Chala et al., 2018a). These distinct properties of $WO_{2.72}$ make it feasible for commercial applications such as steam generation, desalination, and sterilization.

WO_x photothermal materials have been investigated by (Ming et al., 2018) for direct steam generation. In their study, under 1 sun illumination, water and $WOAr_2$ nanofluids reached 34.3°C and 41.0°C, respectively, after 1,800 s. The solar evaporation effciency of 2D defective WO_x nanofluids reached 78.6% compared to that of the water (12.22%). $WO_{2.72}$ and its hybrid recently gained interest for the study of water evaporation. It is worth noting that WO_3 and M_xWO_3 (their hybrids) are still unknown in this field. Therefore, the development of hybrids of photothermal materials in full spectrum solar light has become important in terms of energy conservation and sustainability for photothermal water evaporation, desalination, and steam generation.

NIR Shielding

NIR-shielding materials have received considerable attention for their use in developing transparent solar heat-shielding filters, which can be used for solar control windows in automobiles and buildings. WO_{3-x} and M_xWO_3, $M = Na^+$ (Moon et al., 2013), K^+ (Guo et al., 2011a), Rb^+ (Guo et al., 2011a), Cs^+ (Zeng et al., 2015), and NH_4^+ (Huiyuan et al., 2018) are candidates for such applications. Among the many tungsten materials with a capability of shielding NIR light through absorption mechanism, cesium tungsten oxide (particularly $Cs_{0.33}WO_3$) nanoparticles are considered highly promising materials for transparent solar filter applications. Guo et al. developed $WO_{2.72}$ nanorods coated on a quartz glass. Excellent heat-insulating performance was realized even after the $WO_{2.72}$ nanorods on a quartz glass were irradiated for 1 h, when the inner temperature was increased to only 26.2 °C, which was much lower than the temperatures reached using the quartz glass and indium–tin oxide glass (**Figure 5**) (Guo et al., 2012c). Cs_xWO_3/ZnO composite films were found to be highly efficient for heat insulation because of the excellent NIR shielding properties of Cs_xWO_3 (Wu et al., 2015). These composite films also showed good capacity to block harmful UV lights. The hybrids of WO_3 and M_xWO_3 for NIR shielding applications have been widely studied. However, to the best of our knowledge, $WO_{2.72}$ and its hybrid have yet to be fully explored in this field.

Photocatalysts

Photochemical utilization of solar energy (i.e., photocatalytic degradation of organic pollutants, hydrogen production, photocatalytic reduction of CO_2, and photocatalytic oxidation of alcohols) is being intensively studied (Wang et al., 2017c). Semiconductor materials such as for WO_{3-x} and M_xWO_3 have been widely used in many fields of photocatalysis, including air purification, wastewater treatment, anti-virus sterilization, photolysis of hydrogen and oxygen production, nitrogen oxide fixation, and remediation of crude oil spills. Five photochemical uses of solar energy for WO_x and M_xWO_3 materials are discussed as follows.

Water Oxidation

A water oxidation reaction acquires electrons from the earth's abundant water. An efficient water oxidation catalyst can provide the necessary electrons for proton reduction. However, in terms of effective utilization of solar light, the catalyst design concept requires light absorption characteristics in the visible light range. Water oxidation must meet one major thermodynamic criteria: the valence band (VB) level of a semiconductor should be more

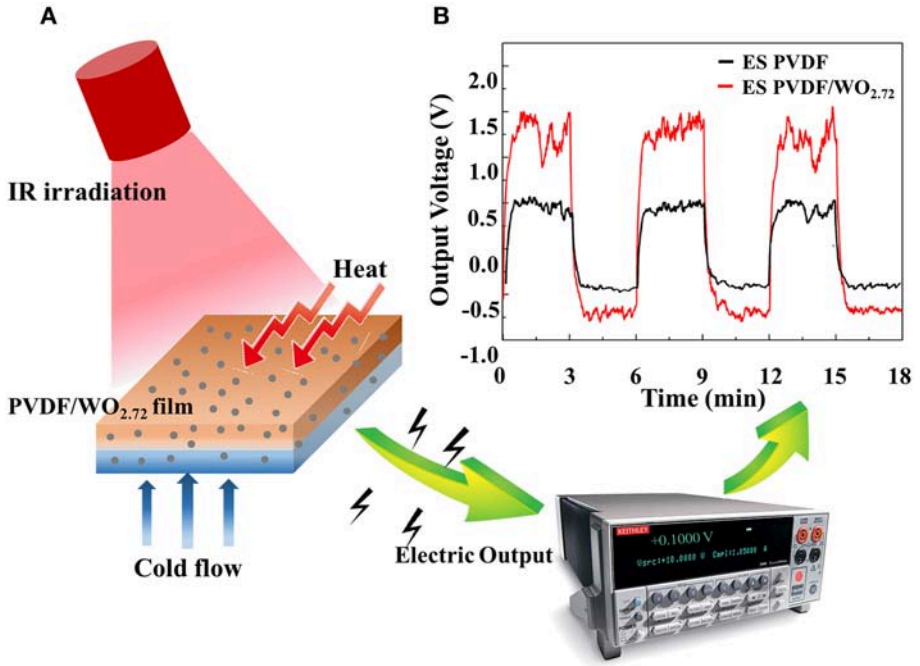

FIGURE 3 | (A) Schematic illustrations of the pyroelectric measurement and **(B)** pyroelectric ability of electrospun PVDF and PVDF/$WO_{2.72}$ in response to the corresponding rate of change in temperature (Wu et al., 2017a).

positive than the standard redox potential of H_2O/O_2 (1.23 eV). The VB potential of WO_{3-x} is located at ca. 3.0 eV, and thus is a promising material for water oxidation application (Wang et al., 2012; Yan et al., 2015).

Reduction of CO_2

Photocatalytic reduction of CO_2 is also a catalyst that is excited in order to generate electrons and holes, which migrate to the surface of the catalyst. Molecules adsorbed on the surface of the catalyst trigger a series of chemical reactions and eventually produce various products such as CH_4, HCOOH, HCHO, and CH_3OH. However, the process of photoreduction of CO_2 is complicated. In particular, the cleavage of C-O bonds and the formation of C-H bonds are complex processes. Xi reported that $WO_{2.72}$ may also enable efficient reduction of CO_2 to obtain CH_4 (Xi et al., 2012).

Hydrogen Production

Photocatalysts may act as reducing and oxidizing agents. They may also decompose water molecules to produce H_2 and O_2. If photocatalysts are to be used to decompose water, their energy band gap (Eg) must be greater than 1.23 eV (<1,000 nm) and less than 3.0 eV (>400 nm) to respond in the visible region (Pihosh et al., 2015). In other words, the semiconductor photocatalyst must have a relatively small band gap (1.23 eV < E_g < 3.0 eV) to absorb as much light as possible for the purpose of photogenerated electrons/holes (Zhang et al., 2018). The results of hydrogen production by photolysis showed that the hydrogen production efficiency of g-C_3N_4 improved considerably after $WO_{2.72}$ was incorporated. The $WO_{2.72}$ (30 wt%)/g-C_3N_4 sample had the highest hydrogen production efficiency (3.69 μmol h^{-1}), which was approximately 4.5 times that of pure g-C_3N_4 (Song et al., 2016).

Degradation of Organic Compounds

The conduction band of WO_3 is slightly higher than the reduction potential of an H_2/H_2O reaction. In addition, its valence band is much higher than the oxidation potential of an H_2O/O_2 reaction, which enables the WO_3 photocatalytic oxidation degradation of many organic compounds such as textile dyes and bacteria contaminants. In addition, WO_3 offers strong stability in an acidic environment, making it promising for treating wastewater that contains organic acids. The oxygen vacancies in WO_{3-x} are helpful for O_2 reduction because of the electron transfer between mixed-valence states. $WO_{2.72}$ exhibits a higher activity than WO_3 in pollutant degradation, and $^{\cdot}O_2^-$ is the major active species for the mineralization of pollutants (Bhuyan et al., 2017). Our research group recently reported on the outstanding photocatalytic activity of hybrid Rb_xWO_3/Ag_3VO_4 degradation of methylene blue (MB) under a full spectrum (UV-VIS-NIR region). The photocatalytic performance was considerably enhanced because of the extended optical absorption in the entire UV-visible-NIR region, efficient separation of electron and hole pairs (e-/h+), and a synergetic effect between Rb_xWO_3 and Ag_3VO_4 (Chala et al., 2018b).

Oxidation of Alcohols

The activated species in the photocatalytic reaction react with the alcohol, and the oxygen in the alcohol allows electrons to fill the holes in the valence band and finally obtain the

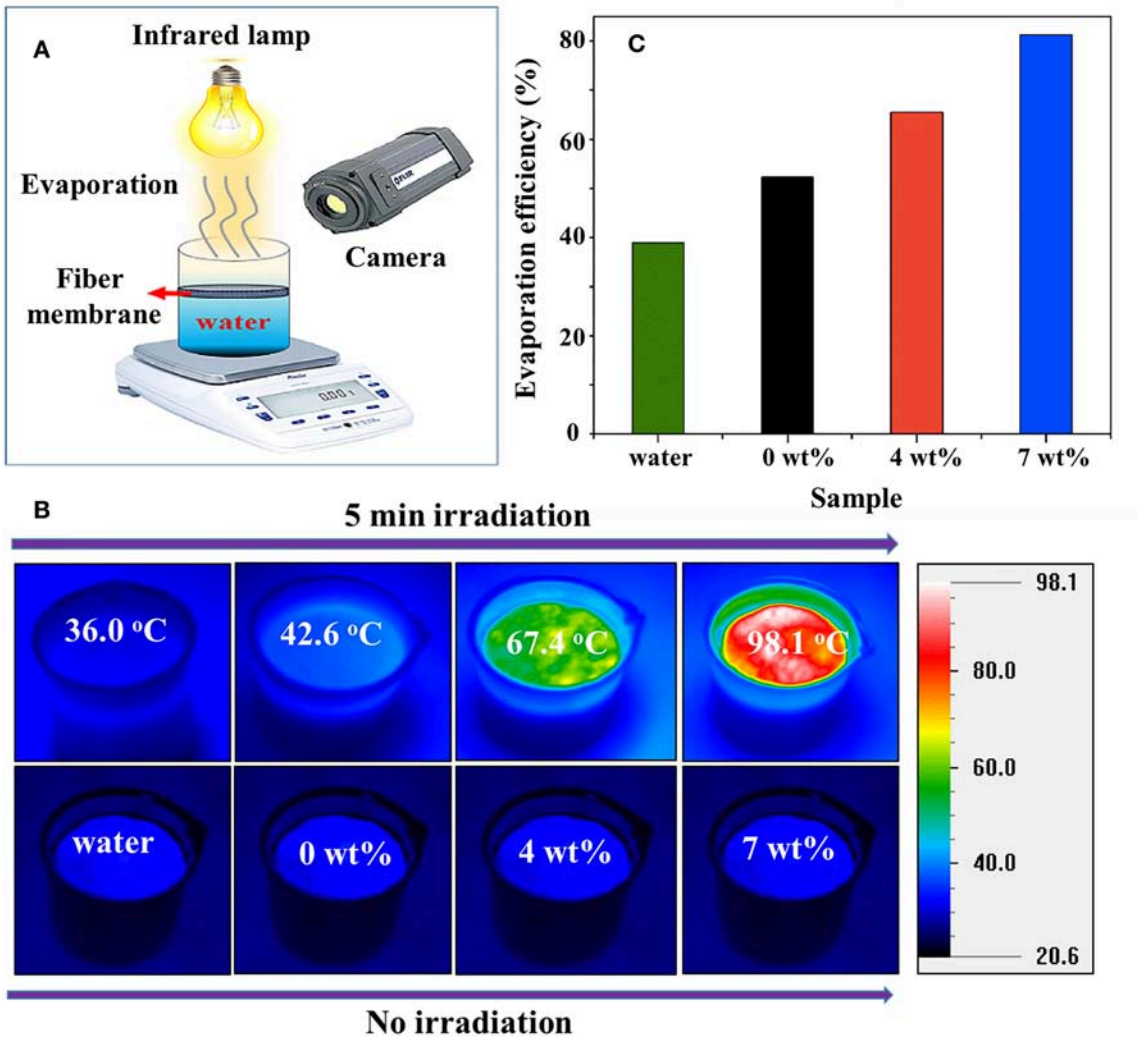

FIGURE 4 | (A) Schematic of water evaporation measurement with $WO_{2.72}$/PLA fiber membrane floating on air-water interface, **(B)** temperature of $WO_{2.72}$/PLA fiber membrane containing 0, 4, and 7 wt% $WO_{2.72}$ nanoparticles floating on water, and **(C)** evaporation efficiency for $WO_{2.72}$/PLA fiber membrane containing 0, 4, and 7 wt% $WO_{2.72}$ nanoparticles. Reproduced with permission (Chala et al., 2018a). Copyright 2018, ACS.

corresponding aldehyde or ketone. The reaction has many advantages. For example, toxic and harmful metal salts do not need to be introduced as oxidants. In addition, it offers mild reaction conditions, minimal equipment requirements, a high conversion rate, and high selectivity. Thus, the photocatalytic oxidation of alcohols offers broad application prospects for the future. $WO_{2.72}$ can be used for the photocatalytic dehydration of isopropanol to propylene (Bai et al., 2013). Three morphologies of $WO_{2.72}$ including rods, urchins, and plates were studied. It was found that urchin-like products performed the best. WO_3 and its hybrid have been widely explored for photocatalysis. Currently, hybrids of $WO_{2.72}$- or M_xWO_3-based materials have received considerable attention for their use in developing solar absorbers capable of broadband absorption in the entire region. These materials must be further explored for photocatalysis.

Energy-Related Applications

WO_3 and WO_{3-x} have more efficient prospects for energy storage devices because of their multiple oxidation states, low price, high intrinsic density, high melting temperatures, and strong mechanical properties. These have been widely studied for supercapacitor electrodes, lithium ion batteries (LIB), and fuel cells. These are discussed in more detail as follows.

Supercapacitors

In the studies on supercapacitors, WO_3 has been shown to suffer from low electrical conductivity because of the presence of oxides (Liu et al., 2018). Partial reduction of WO_{3-x} enhanced the electrical conductivity because of multiple oxidation states (W^{+5} and W^{+6}). It was found to have high capacity and faster performance than other tungsten oxides. Yoon et al. (2011b) synthesized mesoporous WO_{3-x} (m-WO_{3-x}) and

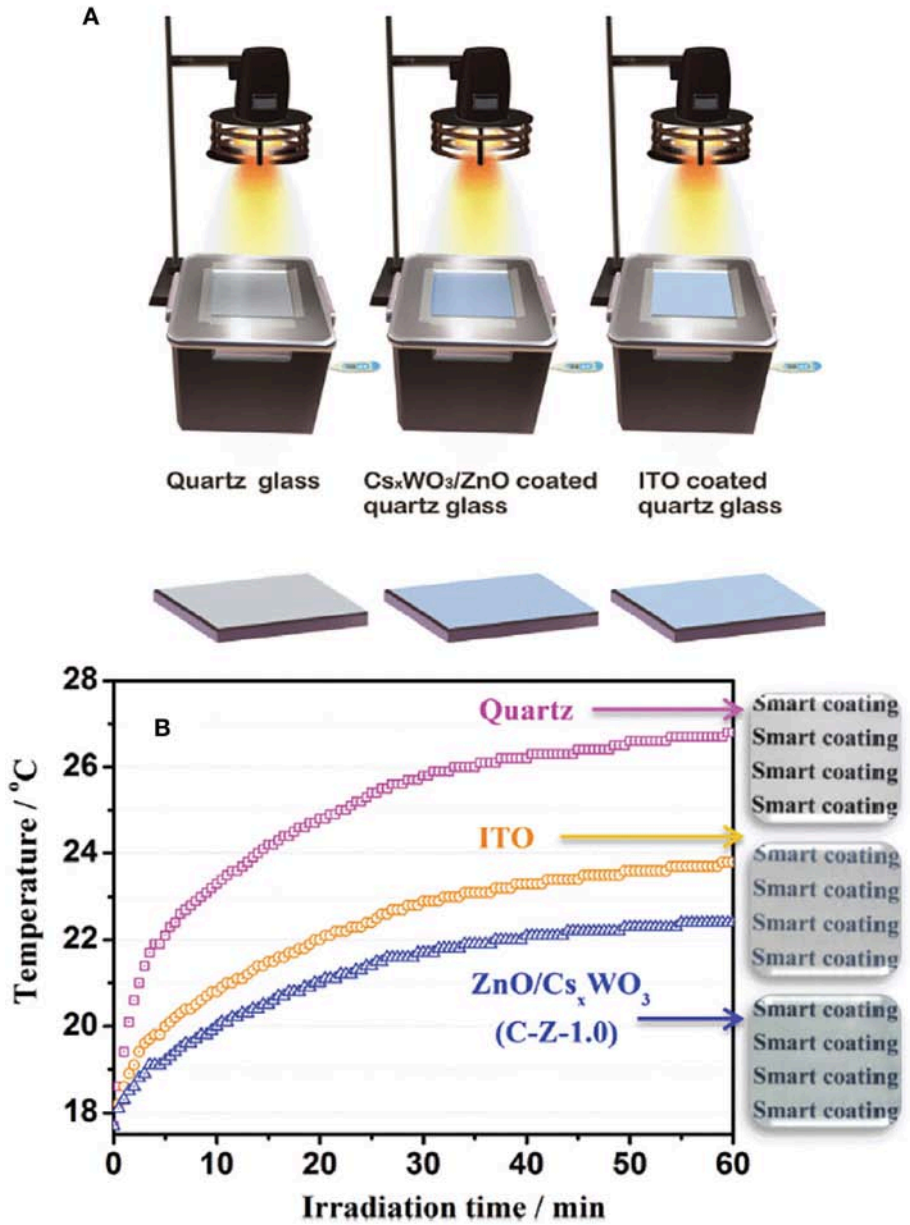

FIGURE 5 | (A) Schematic illustration of the simulated heat ray shielding test using the boxes with facet covered by pure quartz glass, $WO_{2.72}$ nanorods coated on quartz glass and ITO glass under the irradiation of a 50 W halogen lamp, and the temperature changes were determined by an electronic thermometer. **(B)** Time dependence of the temperature in the box. Reproduced with permission (Guo et al., 2012c) Copyright 2012, ACS.

found it had high rate capability and excellent capacitance of 366 μFcm^{-2} and 639 Fcm^{-3}, respectively. Ordered mesoporous WO_{3-x} showed high electrical conductivity of 1.76 S cm^{-1} and highly interconnected ordered pores with a large surface area, making them suitable for use in electrode materials of supercapacitors (Zhou et al., 2013). explored ordered mesoporous carbon/WO_{3-x} nanocomposites. The results revealed excellent rate capability with high volumetric capacity (125 Fcm^{-1}) (Tian et al., 2014). developed a novel smart supercapacitor electrode engraved with a pattern consisting of $WO_{2.72}$ on a PANI background. Both $WO_{2.72}$ and PANI displayed multiple color changes and they operated electrochemically with a widened potential window. The specific capacitance was found to be 302 Fg^{-1} at 10 Ag^{-1} current density, which might appear as a new feature of supercapacitors. Among the various $WO_{x's}$, $WO_{2.72}$ has attracted the most interest because it offers the highest oxygen deficiencies. Moreover, it is the most stable form and possesses good conductivity, making it a promising candidate for supercapacitors (Jung and Kim, 2018; Huang et al., 2019; Li et al., 2019a).

Lithium-Ion Batteries (LIB)

WO_3 has been used as an anode material because it offers a high theoretical capacity, low cost, and environmental friendliness. The only major drawback is its low electrical conductivity, although this has been improved with WO_{3-x} materials. Yoon et al. (2011a) focused on developing high performance anode mesoporous WO_{3-x} using a hard template with high electrical conductivity. The developed material exhibited a high reversible capacity (748 mAh g^{-1}) and a high volumetric capacity (1,500 mAh cm^{-3}) compared to the bulk WO_{3-x}. Lee et al. (2014a) reported that flexible reduced tungsten oxide–carbon composite nanofiber (WO_x-C-NF) films used as anode materials in LIB exhibited a high reversible capacity (481 mA h g^{-1}), stable cycle, and improved rate performance compared to WO_x-C-nano and WO_x-nano electrodes. These studies proved that WO_{3-x} is one of the most promising anode materials for LIB. Recently, WO_{3-x} composites as anode materials for high performance lithium-ion batteries were reported (Zhang et al., 2015b; Yue et al., 2017; Li et al., 2019b). Liu et al. (2017) reported that flower-like WO_3/$CoWO_4$/Co nanostructure electrodes could deliver discharge capacities of 2,435 and 1,074 $mAhg^{-1}$ during the first cycle at current densities of 100 and 200 mAg^{-1} respectively. The pristine WO_3 electrode without cobalt doping exhibited a capacity of 1,151 and 331 $mAhg^{-1}$ at 100 and 200 mAg^{-1} respectively. The hybrids of WO_3 (i.e., WO_3/$CoWO_4$/Co composites used as anode materials) have superior cycling performance as compared to that of WO_3 particles.

Fuel Cells

H_2 fuel has been investigated extensively. Improved catalytic activity and durability are highly desirable for this technology. Here, we focus on the use of WO_{3-x}-based electrocatalysts in fuel cells. Lu et al. (2014) synthesized Pd tetrahedron–tungsten oxide nanosheet hybrids (Pd/$WO_{2.72}$) that enhanced electrocatalytic activity and provided durability for fuel cells. As compared to Pd nanocrystal, Pd/$WO_{2.72}$ hybrids demonstrated not only high activity but also superior stability for the oxygen reduction reaction (ORR) in alkaline solutions. The mass activity of Pd/$WO_{2.72}$ at 0.90 V is 0.216 A mg^{-1}, which is much higher than commercial Pt/C, Pd NPs, and Pd/C. Kang et al. (2010) prepared ordered mesoporous WO_{3-x} by using a hard template and mesostructured WO_{3-x} responsible for its high conductivity. Pt/mesoporous WO_{3-x} exhibited a considerable tolerance to cycling between 0.6 and 1.3 V_{NHE}. It could be used as an ORR catalyst support, thus offering long-term stability. In general, hybrids of WO_3 have been explored widely for energy-related devices in the past few decades. Hybrids of $WO_{2.72}$ in energy applications have also gained attention recently, but M_xWO_3 remain unnoticed.

Gas Sensors

WO_x has oxygen defects in its crystal lattice, which cause the band to bend and enable conductivity. When the material is in contact with oxygen, oxygen absorbs electrons from the surface of the semiconductor to form negative ions, and the surface energy band is bent upward. This results in a decrease in surface electron concentration of the gas sensing material, a decrease in electrical conductivity, and an increase in resistance of the sensor. However, if the gas sensitive material is in contact with the reducing gas, desorption occurs, the surface energy band is lowered, both the electron concentration and electrical conductivity increase, and the resistance value of the sensor decreases.

WO_3 and $WO_{2.72}$ were reported as sensor materials to monitor flammable and toxic gases such as NH_3 (Kim et al., 2005), NO_x (Qin et al., 2011a), H_2 (Boudiba et al., 2010), H_2S (Rout et al., 2008), and SO_x (Godbole et al., 2017). WO_x can also reduce gases such as H_2, CH_4, CO_x (Stankova et al., 2005), and C_2H_5OH (Vallejos et al., 2015). Although $WO_{2.72}$ has the largest oxygen deficiency, it has greater potential in this field (Wang et al., 2018). prepared WO_3 nanorod/sulfonated reduced graphene oxides (WO_3/S-rGO), which showed fast response recovery characteristics at all concentrations of NO_2 gas, indicating its good response and recovery properties for sensor applications. However, the gas sensor of the WO_x still has the disadvantages of poor stability, low selectivity, and a high operating temperature. Therefore, how to reduce the working temperature and improve the selectivity and sensitivity of the detection gas have become the focus of our current research. Composite and metal-hybrid doping have proven effective at improving the sensitivity of WO_x for reducing gases. WO_3 and its hybrid are widely explored for gas sensors and the properties of $WO_{2.72}$ have recently gained attention. However, M_xWO_3 has yet to be fully studied.

CONCLUSION AND FUTURE PROSPECTS

In this study, we summarized the comprehensive progress made in the last few years in the application of tungsten-oxide-based materials. WO_{3-x}, M_xWO_3, and their hybrid materials as interesting research topics, particularly for morphology control and composite construction to enhance optical absorption, charge separation, redox capability, and electrical conductivity. The well-studied liquid-phase technique known as the solvothermal treatment is the most used method alongside the hydrothermal treatment, which is a facile and cost-effective method that can produce WOx with different nanomorphologies. The morphology can be fine-tuned by controlling variables such as time, precursor concentration, and temperature. A critical challenge is to enhance the utilization efficiency by extending the solar spectrum response from the UV to the NIR region. To meet these requirements, hybrids of $WO_{2.72}$ and M_xWO_3 have become important because of their strong photoabsorption ability and intervalence charge properties. A major advantage of this material is the LSPR effect, which may encourage researchers to focus not only on the interesting properties for new applications but also to investigate the many opportunities it offers to improve the efficiency of current applications.

DATA AVAILABILITY

All datasets generated for this study are included in the manuscript and/or the supplementary files.

AUTHOR CONTRIBUTIONS

C-MW performed initial literature search to identify papers, provided relevant information for the text, reviewed final manuscript, and conceptualization. SN contributed to writing the manuscript. M-HC, J-HW, and Y-QJ performed literature search and provided relevant information. All authors approved the final version to be published and agreed to be accountable for all aspects of the work.

ACKNOWLEDGMENTS

The authors are thankful for the partial financial support received from the Ministry of Science and Technology of Taiwan, ROC, under contract numbers: MOST 107-2221-E-011-044.

REFERENCES

Aoki, T., Matsushita, T., Suzuki, A., Tanabe, K., and Okuda, M. (2005). Optical recording characteristics of WO_3 films grown by pulsed laser deposition method. *J. Vacuum Sci. Technol. A* 23, 1325–1330. doi: 10.1116/1.1978891

Awad, F.S., Kiriarachchi, H.D., Abouzeid, K.M., özgürü., and El-Shall, M.S. (2018). Plasmonic graphene polyurethane nanocomposites for efficient solar water desalination. *ACS Appl. Energy Mater.* 1, 976–985. doi: 10.1021/acsaem.8b00109

Baek, Y., and Yong, K. (2007). Controlled growth and characterization of tungsten oxide nanowires using thermal evaporation of WO_3 powder. *J. Phys. Chem. C* 111, 1213–1218. doi: 10.1021/jp0659857

Bai, H., Su, N., Li, W., Zhang, X., Yan, Y., Li, P., et al. (2013). $W_{18}O_{49}$ nanowire networks for catalyzed dehydration of isopropyl alcohol to propylene under visible light. *J. Mater. Chem. A* 1, 6125–6129. doi: 10.1039/c3ta10835j

Bhuyan, B., Paul, B., Dhar, S.S., and Vadivel, S. (2017). Facile hydrothermal synthesis of ultrasmall $W_{18}O_{49}$ nanoparticles and studies of their photocatalytic activity towards degradation of methylene blue. *Mater. Chem. Phys.* 188, 1–7. doi: 10.1016/j.matchemphys.2016.12.035

Boudiba, A., Zhang, C., Navio, C., Bittencourt, C., Snyders, R., and Debliquy, M. (2010). Preparation of highly selective, sensitive and stable hydrogen sensors based on Pd-doped tungsten trioxide. *Proc. Eng.* 5, 180–183. doi: 10.1016/j.proeng.2010.09.077

Chala, T. F., Wu, C.-M., Chou, M.-H., Gebeyehu, M. B., and Cheng, K.-B. (2017). Highly efficient near infrared photothermal conversion properties of reduced tungsten oxide/polyurethane nanocomposites. *Nanomaterials* 7**:**91. doi: 10.3390/nano7070191

Chala, T. F., Wu, C.-M., Chou, M.-H., and Guo, Z.-L. (2018a). Melt electrospun reduced tungsten oxide /polylactic acid fiber membranes as a photothermal material for light-driven interfacial water evaporation. *ACS Appl. Mater. Interfaces* 10, 28955–28962. doi: 10.1021/acsami.8b07434

Chala, T. F., Wu, C.-M., and Motora, K. G. (2018b). *RbxWO3/Ag3VO4 Nanocomposites Towards Efficient Full-Spectrum (UV, Visible, and Near Infrared) Photocatalysis* (Taiwan Institute of Chemical Engineers).

Chen, C.-J., and Chen, D.-H. (2013). Preparation and near-infrared photothermal conversion property of cesium tungsten oxide nanoparticles. *Nanoscale Res. Lett.* 8, 57. doi: 10.1186/1556-276X-8-57

Chen, J., Wang, D., Xi, J., Au, L., Siekkinen, A., Warsen, A., et al. (2007). Immuno gold nanocages with tailored optical properties for targeted photothermal destruction of cancer cells. *Nano Lett.* 7, 1318–1322. doi: 10.1021/nl070345g

Chen, Q., Pei, Z., Xu, Y., Li, Z., Yang, Y., Wei, Y., et al. (2018). A durable monolithic polymer foam for efficient solar steam generation. *Chem. Sci.* 9, 623–628. doi: 10.1039/C7SC02967E

Chen, Z., Wang, Q., Wang, H., Zhang, L., Song, G., Song, L., et al. (2013). Ultrathin PEGylated $W_{18}O_{49}$ nanowires as a new 980 nm-laser-driven photothermal agent for efficient ablation of cancer cells *in vivo*. *Adv. Mater.* 25, 2095–2100. doi: 10.1002/adma.201204616

Ding, D., Huang, W., Song, C., Yan, M., Guo, C., and Liu, S. (2017). Non-stoichiometric MoO_{3-x} quantum dots as a light-harvesting material for interfacial water evaporation. *Chem. Commun.* 53, 6744–6747. doi: 10.1039/C7CC01427A

Godbole, R., Godbole, V. P., and Bhagwat, S. (2017). Surface morphology dependent tungsten oxide thin films as toxic gas sensor. *Mater. Sci. Semicond. Process.* 63, 212–219. doi: 10.1016/j.mssp.2017.02.023

Guo, C., Yin, S., Dong, Q., and Sato, T. (2012a). Simple route to $(NH_4)_xWO_3$ nanorods for near infrared absorption. *Nanoscale* 4, 3394–3398. doi: 10.1039/c2nr30612c

Guo, C., Yin, S., Huang, L., and Sato, T. (2011a). Synthesis of one-dimensional potassium tungsten bronze with excellent near-infrared absorption property. *ACS Appl. Mater. Interfaces* 3, 2794–2799. doi: 10.1021/am200631e

Guo, C., Yin, S., Huang, Y., Dong, Q., and Sato, T. (2011b). Synthesis of $W_{18}O_{49}$ nanorod via ammonium tungsten oxide and its interesting optical properties. *Langmuir* 27, 12172–12178. doi: 10.1021/la202513q

Guo, C., Yin, S., and Sato, T. (2012b). Tungsten oxide-based nanomaterials: morphological-control, properties, and novel applications. *Rev. Adv. Sci. Eng.* 1, 235–263. doi: 10.1166/rase.2012.1016

Guo, C., Yin, S., Yan, M., Kobayashi, M., Kakihana, M., and Sato, T. (2012c). Morphology-controlled synthesis of $W_{18}O_{49}$ nanostructures and their near-infrared absorption properties. *Inorg. Chem.* 51, 4763–4771. doi: 10.1021/ic300049j

Guo, C., Yin, S., Zhang, P., Yan, M., Adachi, K., Chonan, T., et al. (2010). Novel synthesis of homogenous Cs_xWO_3 nanorods with excellent NIR shielding properties by a water controlled-release solvothermal process. *J. Mater. Chem.* 20, 8227–8229. doi: 10.1039/c0jm01972k

Guo, X., Qin, X., Xue, Z., Zhang, C., Sun, X., Hou, J., et al. (2016). Morphology-controlled synthesis of $WO_{2.72}$ nanostructures and their photocatalytic properties. *RSC Adv.* 6, 48537–48542. doi: 10.1039/C6RA08551B

Hashishin, T., and Tamaki, J. (2008). Conductivity-type sensor based on CNT-WO3 composite for NO2 detection. *J. Nanomater.* 2008:31. doi: 10.1155/2008/352854

Hu, X., Xu, W., Zhou, L., Tan, Y., Wang, Y., Zhu, S., et al. (2017). Tailoring graphene oxide-based aerogels for efficient solar steam generation under one sun. *Adv. Mater.* 29**:**1604031. doi: 10.1002/adma.201604031

Hu, X.-S., Shen, Y., Xu, L.-H., Wang, L.-M., Lu, L.-S., and Zhang, Y.-T. (2016). Preparation of flower-like CuS by solvothermal method for photocatalytic, UV protection and EMI shielding applications. *Appl. Surf. Sci.* 385, 162–170. doi: 10.1016/j.apsusc.2016.05.089

Hua, Z., Li, B., Li, L., Yin, X., Chen, K., and Wang, W. (2017). Designing a novel photothermal material of hierarchical microstructured copper phosphate for solar evaporation enhancement. *J. Phys. Chem. C* 121, 60–69. doi: 10.1021/acs.jpcc.6b08975

Huang, S., He, Q., Xu, S., and Wang, L. (2015a). Polyaniline-based photothermal paper sensor for sensitive and selective detection of 2,4,6-trinitrotoluene. *Anal. Chem.* 87, 5451–5456. doi: 10.1021/acs.analchem.5b01078

Huang, W., and El-Sayed, M.A. (2008). Photothermally excited coherent lattice phonon oscillations in plasmonic nanoparticles. *Eur. Phys. J.Spec. Top.* 153, 325–333. doi: 10.1140/epjst/e2008-00456-x

Huang, X., and El-Sayed, M.A. (2010). Gold nanoparticles: optical properties and implementations in cancer diagnosis and photothermal therapy. *J. Adv. Res.* 1, 13–28. doi: 10.1016/j.jare.2010.02.002

Huang, X., Zhang, Z., Li, H., Wang, H., and Ma, T. (2019). *In-situ* growth of nanowire $WO_{2.72}$ on carbon cloth as a binder-free electrode for flexible asymmetric supercapacitors with high performance. *J. Energy Chem.* 29, 58–64. doi: 10.1016/j.jechem.2018.01.024

Huang, Z.-F., Song, J., Pan, L., Jia, X., Li, Z., Zou, J.-J., et al. (2014a). $W_{18}O_{49}$ nanowire alignments with a BiOCl shell as an efficient photocatalyst. *Nanoscale* 6, 8865–8872. doi: 10.1039/C4NR00905C

Huang, Z.-F., Song, J., Pan, L., Lv, F., Wang, Q., Zou, J.-J., et al. (2014b). Mesoporous $W_{18}O_{49}$ hollow spheres as highly active

photocatalysts. *Chem. Commun.* 50, 10959–10962. doi: 10.1039/C4CC02201G

Huang, Z.-F., Song, J., Pan, L., Zhang, X., Wang, L., and Zou, J.-J. (2015b). Tungsten oxides for photocatalysis, electrochemistry, and phototherapy. *Adv. Mater.* 27, 5309–5327. doi: 10.1002/adma.201501217

Huiyuan, L., Hua, L., Yujie, C., and Hezhou, L. (2018). A facile hydrothermal method to synthesize ammonium tungsten bronze nanoplatelets for nir absorption. *IOP Conf. Series Mater. Sci. Eng.* 382:022062. doi: 10.1088/1757-899X/382/2/022062

Hussain, A., Gruehn, R., and Rüscher, C.H. (1997). Crystal growth of alkali metal tungsten brozes M_xWO_3 (M = K, Rb, Cs), and their optical properties. *J. Alloys Compd.* 246, 51–61. doi: 10.1016/S0925-8388(96)02470-X

Jiang, Q., Gholami Derami, H., Ghim, D., Cao, S., Jun, Y.-S., and Singamaneni, S. (2017). Polydopamine-filled bacterial nanocellulose as a biodegradable interfacial photothermal evaporator for highly efficient solar steam generation. *J. Mater. Chem. A* 5, 18397–18402. doi: 10.1039/C7TA04834C

Jin, Y.Z., Zhu, Y.Q., Whitby, R.L., Yao, N., Ma, R., Watts, P.C., et al. (2004). Simple approaches to quality large-scale tungsten oxide nanoneedles. *J. Phys. Chem. B* 108, 15572–15577. doi: 10.1021/jp048596q

Jung, J., and Kim, D.H. (2018). $W_{18}O_{49}$ nanowires assembled on carbon felt for application to supercapacitors. *Appl. Surf. Sci.* 433, 750–755. doi: 10.1016/j.apsusc.2017.10.109

Kang, E., An, S., Yoon, S., Kim, J.K., and Lee, J. (2010). Ordered mesoporous WO_{3-x} possessing electronically conductive framework comparable to carbon framework toward long-term stable cathode supports for fuel cells. *J. Mater. Chem.* 20, 7416–7421. doi: 10.1039/c0jm00227e

Kim, J. Y., Jeong, S. Y., Shin, G. J., Lee, S. K., and Choi, K. H. (2012). Near infrared cut-off characteristics of various perovskite-based composite films. *Appl. Mech. Mater.* 229–231, 2733–2736. doi: 10.4028/www.scientific.net/AMM.229-231.2733

Kim, K., Yu, S., An, C., Kim, S.-W., and Jang, J.-H. (2018). Mesoporous three-dimensional graphene networks for highly efficient solar desalination under 1 sun illumination. *ACS Appl. Mater. Interfaces* 10, 15602–15608. doi: 10.1021/acsami.7b19584

Kim, Y. S., Ha, S.-C., Kim, K., Yang, H., Choi, S.-Y., Kim, Y.T., et al. (2005). Room-temperature semiconductor gas sensor based on non-stoichiometric tungsten oxide nanorod film. *Appl. Phys. Lett.* 86:213105. doi: 10.1063/1.1929872

Late, D. J., Kashid, R. V., Sekhar rout, C., More, M. A., and Joag, D. S. (2010). Low threshold field electron emission from solvothermally synthesized WO2.72 nanowires. *Appl. Phys. A* 98, 751–756. doi: 10.1007/s00339-009-5536-0

Lee, J., Jo, C., Park, B., Hwang, W., Lee, H.I., Yoon, S., et al. (2014a). Simple fabrication of flexible electrodes with high metal-oxide content: electrospun reduced tungsten oxide/carbon nanofibers for lithium ion battery applications. *Nanoscale* 6, 10147–10155. doi: 10.1039/C4NR01033G

Lee, K., Seo, W.S., and Park, J.T. (2003). Synthesis and Optical properties of colloidal tungsten oxide nanorods. *J. Am. Chem. Soc.* 125, 3408–3409. doi: 10.1021/ja034011e

Lee, S. Y., Kim, J. Y., Lee, J. Y., Song, H. J., Lee, S., Choi, K. H., et al. (2014b). Facile fabrication of high-efficiency near-infrared absorption film with tungsten bronze nanoparticle dense layer. *Nanoscale Res. Lett.* 9:294. doi: 10.1186/1556-276X-9-294

Li, B., Shao, X., Liu, T., Shao, L., and Zhang, B. (2016a). Construction of metal/$WO_{2.72}$/rGO ternary nanocomposites with optimized adsorption, photocatalytic and photoelectrochemical properties. *Appl. Catal. B Environ.* 198, 325–333. doi: 10.1016/j.apcatb.2016.06.001

Li, G., Gao, L., Li, L., and Guo, L. (2019a). An electrochromic and self-healing multi-functional supercapacitor based on PANI/nw-WO2.7/Au NPs electrode and hydrogel electrolyte. *J. Alloys Comp.* 786, 40–49. doi: 10.1016/j.jallcom.2018.12.142

Li, G., Wu, G., Guo, C., and Wang, B. (2016b). Fabrication of one-dimensional $W_{18}O_{49}$ nanomaterial for the near infrared shielding. *Mater. Lett.* 169, 227–230. doi: 10.1016/j.matlet.2016.01.094

Li, G., Zhang, S., Guo, C., and Liu, S. (2016c). Absorption and electrochromic modulation of near-infrared light: realized by tungsten suboxide. *Nanoscale* 8, 9861–9868. doi: 10.1039/C5NR09147K

Li, Y., Chang, K., Tang, H., Li, B., Qin, Y., Hou, Y., et al. (2019b). Preparation of oxygen-deficient WO_{3-x} nanosheets and their characterization as anode materials for high-performance Li-ion batteries. *Electrochim. Acta* 298, 640–649. doi: 10.1016/j.electacta.2018.12.137

Liao, C.-C., Chen, F.-R., and Kai, J.-J. (2007). Electrochromic properties of nanocomposite WO_3 films. *Solar Energy Mater. Solar Cells* 91, 1282–1288. doi: 10.1016/j.solmat.2006.11.020

Lin, H., Wang, X., Yu, L., Chen, Y., and Shi, J. (2017). Two-dimensional ultrathin Mxene ceramic nanosheets for photothermal conversion. *Nano Lett.* 17, 384–391. doi: 10.1021/acs.nanolett.6b04339

Liu, G., Wang, S., Nie, Y., Sun, X., Zhang, Y., and Tang, Y. (2013a). Electrostatic-induced synthesis of tungsten bronze nanostructures with excellent photo-to-thermal conversion behavior. *J. Mater. Chem. A* 1, 10120–10129. doi: 10.1039/c3ta11479a

Liu, J., Zhang, Z., Wang, Z., Tang, M., Li, J., Yi, J., et al. (2017). Flower-like WO_3/$CoWO_4$/Co nanostructures as high performance anode for lithium ion batteries. *J. Alloys Compd.* 727, 107–113. doi: 10.1016/j.jallcom.2017.08.057

Liu, J.-X., Ando, Y., Dong, X.-L., Shi, F., Yin, S., Adachi, K., et al. (2010). Microstructure and electrical–optical properties of cesium tungsten oxides synthesized by solvothermal reaction followed by ammonia annealing. *J. Solid State Chem.* 183, 2456–2460. doi: 10.1016/j.jssc.2010.08.017

Liu, X., He, Y., Wang, S., Zhang, Q., and Song, M. (2012). Controllable synthesis and tunable field-emission properties of tungsten oxide sub-micro fibers. *Int. J. Refract. Metals Hard Mater.* 34, 47–52. doi: 10.1016/j.ijrmhm.2012.04.002

Liu, X., Sheng, G., Zhong, M., and Zhou, X. (2018). Dispersed and size-selected WO_3 nanoparticles in carbon aerogel for supercapacitor applications. *Mater. Des.* 141, 220–229. doi: 10.1016/j.matdes.2017.12.038

Liu, X., Song, M., Wang, S., and He, Y. (2013b). Structure and field-emission properties of W/$WO_{2.72}$ heterostructures fabricated by vapor deposition. *Phys. E* 53, 260–265. doi: 10.1016/j.physe.2013.05.017

Liu, Y., Chen, J., Guo, D., Cao, M., and Jiang, L. (2015). Floatable, self-cleaning, and carbon-black-based superhydrophobic gauze for the solar evaporation enhancement at the air–water interface. *ACS Appl. Mater. Interfaces* 7, 13645–13652. doi: 10.1021/acsami.5b03435

Lou, J., Liu, Y., Wang, Z., Zhao, D., Song, C., Wu, J., et al. (2016). Bioinspired multifunctional paper-based rGO composites for solar-driven clean water generation. *ACS Appl. Mater. Interfaces* 8, 14628–14636. doi: 10.1021/acsami.6b04606

Lou, X. W., and Zeng, H. C. (2003). An inorganic route for controlled synthesis of $W_{18}O_{49}$ nanorods and nanofibers in solution. *Inorg. Chem.* 42, 6169–6171. doi: 10.1021/ic034771q

Lu, Y., Jiang, Y., Gao, X., Wang, X., and Chen, W. (2014). Strongly coupled Pd nanotetrahedron/tungsten oxide nanosheet hybrids with enhanced catalytic activity and stability as oxygen reduction electrocatalysts. *J. Am. Chem. Soc.* 136, 11687–11697. doi: 10.1021/ja5041094

Ma, B., Huang, E., Wu, G., Dai, W., Guan, N., and Li, L. (2017). Fabrication of $WO_{2.72}$/RGO nano-composites for enhanced photocatalysis. *RSC Adv.* 7, 2606–2614. doi: 10.1039/C6RA26416F

Mamak, M., Choi, S.Y., Stadler, U., Dolbec, R., Boulos, M., and Petrov, S. (2010). Thermal plasma synthesis of tungsten bronze nanoparticles for near infra-red absorption applications. *J. Mater. Chem.* 20, 9855–9857. doi: 10.1039/c0jm02169e

Marques, M. P. M. (2013). Platinum and palladium polyamine complexes as anticancer agents: the structural factor. *ISRN Spectrosc.* 2013, 1–29. doi: 10.1155/2013/287353

Ming, X., Guo, A., Wang, G., and Wang, X. (2018). Two-dimensional defective tungsten oxide nanosheets as high performance photo-absorbers for efficient solar steam generation. *Solar Energy Mater. Solar Cells* 185, 333–341. doi: 10.1016/j.solmat.2018.05.049

Moon, K., Cho, J.-J., Lee, Y.-B., Yoo, P. J., Bark, C. W., and Park, J. (2013). Near infrared shielding properties of quaternary tungsten bronze nanoparticle $Na_{0.11}Cs_{0.22}WO_3$. *Bull. Korean Chem. Soc.* 34, 731–734. doi: 10.5012/bkcs.2013.34.3.731

Moshofsky, B., and Mokari, T. (2012). Length and diameter control of ultrathin nanowires of substoichiometric tungsten oxide with insights into the growth mechanism. *Chem. Mater.* 25, 1384–1391. doi: 10.1021/cm302015z

Okusako, T., Tokuyama, T., Mikami, K., Nogami, Y., and Hanasaki, N. (2012). Thermoelectric effect in hexagonal tungsten oxides. *J. Phys. Soc. Japan* 81**:**SB028. doi: 10.1143/JPSJS.81SB.SB028

Pihosh, Y., Turkevych, I., Mawatari, K., Uemura, J., Kazoe, Y., Kosar, S., et al. (2015). Photocatalytic generation of hydrogen by core-shell WO_3/$BiVO_4$ nanorods with ultimate water splitting efficiency. *Sci. Rep.* 5**:**11141. doi: 10.1038/srep11141

Qin, Y., Li, X., Wang, F., and Hu, M. (2011a). Solvothermally synthesized tungsten oxide nanowires/nanorods for NO_2 gas sensor applications. *J. Alloys Compd.* 509, 8401–8406. doi: 10.1016/j.jallcom.2011.05.100

Qin, Y., Shen, W., Li, X., and Hu, M. (2011b). Effect of annealing on microstructure and NO_2-sensing properties of tungsten oxide nanowires synthesized by solvothermal method. *Sens. Actuat. B Chem.* 155, 646–652. doi: 10.1016/j.snb.2011.01.024

Reich, S., Leitus, G., Popovitz-Biro, R., Goldbourt, A., and Vega, S. (2009). A Possible 2D H_xWO_3 Superconductor with a T c of 120 K. *J. Superconduct. Novel Magnet.* 22, 343–346. doi: 10.1007/s10948-009-0443-3

Riley, R.S., and Day, E.S. (2017). Gold nanoparticle-mediated photothermal therapy: applications and opportunities for multimodal cancer treatment. *Wiley Interdiscipl. Rev. Nanomed. Nanobiotechnol.* 9**:**e1449. doi: 10.1002/wnan.1449

Rout, C.S., Hegde, M., and Rao, C.N.R. (2008). H_2S sensors based on tungsten oxide nanostructures. *Sens. Actuat. B Chem.* 128, 488–493. doi: 10.1016/j.snb.2007.07.013

Schmidt, P., Binnewies, M., Glaum, R., and Schmidt, M. (2013). "Chemical vapor transport reactions–methods, materials, modeling," in *Advanced Topics on Crystal Growth* (London: InTech), 227–305.

Shang, M., Li, N., Zhang, S., Zhao, T., Zhang, C., Liu, C., et al. (2017). Full-spectrum solar-to-heat conversion membrane with interfacial plasmonic heating ability for high-efficiency desalination of seawater. *ACS Appl. Energy Mater.* 1, 56–61. doi: 10.1021/acsaem.7b00135

Son, K.H., Hong, J.H., and Lee, J.W. (2016). Carbon nanotubes as cancer therapeutic carriers and mediators. *Int. J. Nanomed.* 11, 5163–5185. doi: 10.2147/IJN.S112660

Song, C., Li, T., Guo, W., Gao, Y., Yang, C., Zhang, Q., et al. (2018). Hydrophobic $Cu_{12}Sb_4S_{13}$-deposited photothermal film for interfacial water evaporation and thermal antibacterial activity. *New J. Chem.* 42, 3175–3179. doi: 10.1039/C7NJ04545J

Song, G., Han, L., Zou, W., Xiao, Z., Huang, X., Qin, Z., et al. (2014). A novel photothermal nanocrystals of Cu_7S_4 hollow structure for efficient ablation of cancer cells. *Nano Micro Lett.* 6, 169–177. doi: 10.1007/BF03353781

Song, G., Wang, Q., Wang, Y., Lv, G., Li, C., Zou, R., et al. (2013). A low-toxic multifunctional nanoplatform based on Cu_9S_5@$mSiO_2$ core-shell nanocomposites: combining photothermal- and chemotherapies with infrared thermal imaging for cancer treatment. *Adv. Funct. Mater.* 23, 4281–4292. doi: 10.1002/adfm.201203317

Song, K., Xiao, F., Zhang, L., Yue, F., Liang, X., Wang, J., et al. (2016). $W_{18}O_{49}$ nanowires grown on g-C_3N_4 sheets with enhanced photocatalytic hydrogen evolution activity under visible light. *J. Mol. Catal. A Chem.* 418, 95–102. doi: 10.1016/j.molcata.2016.03.029

Stankova, M., Vilanova, X., Llobet, E., Calderer, J., Bittencourt, C., Pireaux, J., et al. (2005). Influence of the annealing and operating temperatures on the gas-sensing properties of rf sputtered WO_3 thin-film sensors. *Sens. Actuat. B Chem.* 105, 271–277. doi: 10.1016/j.snb.2004.06.009

Su, C.-Y., and Lin, H.-C. (2009). Direct route to tungsten oxide nanorod bundles: microstructures and electro-optical properties. *J. Phys. Chem. C* 113, 4042–4046. doi: 10.1021/jp809458j

Sun, L., Li, Z., Su, R., Wang, Y., Li, Z., Du, B., et al. (2018). Phase-Transition induced conversion into a photothermal material: quasi-metallic $WO_{2.9}$ Nanorods for solar water evaporation and anticancer photothermal therapy. *Angew. Chem. Int. Ed.* 57, 10666–10671. doi: 10.1002/anie.201806611

Sun, Y., Wang, W., Qin, J., Zhao, D., Mao, B., Xiao, Y., et al. (2016). Oxygen vacancy-rich mesoporous $W_{18}O_{49}$ nanobelts with ultrahigh initial Coulombic efficiency toward high-performance lithium storage. *Electrochim. Acta* 187, 329–339. doi: 10.1016/j.electacta.2015.11.064

Takeda, H., and Adachi, K. (2007). Near infrared absorption of tungsten oxide nanoparticle dispersions. *J. Am. Ceram. Soc.* 90, 4059–4061. doi: 10.1111/j.1551-2916.2007.02065.x

Tian, Q., Tang, M., Sun, Y., Zou, R., Chen, Z., Zhu, M., et al. (2011). Hydrophilic flower-like CuS superstructures as an efficient 980 nm laser-driven photothermal agent for ablation of cancer cells. *Adv. Mater.* 23, 3542–3547. doi: 10.1002/adma.201101295

Tian, Y., Cong, S., Su, W., Chen, H., Li, Q., Geng, F., et al. (2014). Synergy of $W_{18}O_{49}$ and polyaniline for smart supercapacitor electrode integrated with energy level indicating functionality. *Nano Lett.* 14, 2150–2156. doi: 10.1021/nl5004448

Vallejos, S., Gràcia, I., Bravo, J., Figueras, E., Hubálek, J., and Cané, C. (2015). Detection of volatile organic compounds using flexible gas sensing devices based on tungsten oxide nanostructures functionalized with Au and Pt nanoparticles. *Talanta* 139, 27–34. doi: 10.1016/j.talanta.2015.02.034

Venables, D.S., and Brown, M.E. (1996). Reduction of tungsten oxides with carbon. part 1: thermal analyses. *Thermochim. Acta* 282, 251–264. doi: 10.1016/0040-6031(95)02814-5

Wang, G., Ling, Y., Wang, H., Yang, X., Wang, C., Zhang, J.Z., et al. (2012). Hydrogen-treated WO_3 nanoflakes show enhanced photostability. *Energy Environ. Sci.* 5, 6180–6187. doi: 10.1039/c2ee03158b

Wang, H.-Q., Hu, P.-F., Zheng, Y., Zhao, Z., Zheng, B., Chang, J., et al. (2017a). Construction of ICG encapsulated $W_{18}O_{49}$@MSN as a fluorescence carrier for real-time tracked photothermal therapy. *Mater. Sci. Eng. C* 80, 102–109. doi: 10.1016/j.msec.2017.05.131

Wang, J., Li, Y., Deng, L., Wei, N., Weng, Y., Dong, S., et al. (2017b). High-performance photothermal conversion of narrow-bandgap Ti_2O_3 nanoparticles. *Adv. Mater.* 29:1603730. doi: 10.1002/adma.201603730

Wang, J., Liu, G., and Du, Y. (2003). Mechanochemical synthesis of sodium tungsten bronze nanocrystalline powders. *Mater. Lett.* 57, 3648–3652. doi: 10.1016/S0167-577X(03)00142-3

Wang, P. (2018). Emerging investigator series: the rise of nano-enabled photothermal materials for water evaporation and clean water production by sunlight. *Environ. Sci. Nano* 5, 1078–1089. doi: 10.1039/C8EN00156A

Wang, S., He, Y., Zou, J., Cao, P., Jiang, Y., Huang, B., et al. (2007). Synthesis of tungsten oxide tapered needles with nanotips. *J. Cryst. Growth* 303, 574–579. doi: 10.1016/j.jcrysgro.2006.11.342

Wang, T., Hao, J., Zheng, S., Sun, Q., Zhang, D., and Wang, Y. (2018). Highly sensitive and rapidly responding room-temperature NO_2 gas sensors based on WO_3 nanorods/sulfonated graphene nanocomposites. *Nano Res.* 11, 791–803. doi: 10.1007/s12274-017-1688-y

Wang, X., Ou, G., Wang, N., and Wu, H. (2016a). Graphene-based recyclable photo-absorbers for high-efficiency seawater desalination. *ACS Appl. Mater. Interfaces* 8, 9194–9199. doi: 10.1021/acsami.6b02071

Wang, X., Wang, F., Sang, Y., and Liu, H. (2017c). Full-spectrum solar-light-activated photocatalysts for light–chemical energy conversion. *Adv. Energy Mater.* 7**:**1700473. doi: 10.1002/aenm.201700473

Wang, Y., Zhang, L., and Wang, P. (2016b). Self-floating carbon nanotube membrane on macroporous silica substrate for highly efficient solar-driven interfacial water evaporation. *ACS Sustain. Chem. Eng.* 4, 1223–1230. doi: 10.1021/acssuschemeng.5b01274

Wang, Z., Ye, Q., Liang, X., Xu, J., Chang, C., Song, C., et al. (2017d). based membranes on silicone floaters for efficient and fast solar-driven interfacial evaporation under one sun. *J. Mater. Chem. A* 5, 16359–16368. doi: 10.1039/C7TA03262E

Wu, C.-M., Chou, M.-H., and Chala, T.F. (2017a). "Pyroelectricity of electrospun polyvinylidene fluoride/tungsten oxide nanofibrous membranes," in *22nd International Conference on Advanced Materials and Nanotechnology* (Osaka, Japan).

Wu, X., Wang, J., Zhang, G., Katsumata, K.-I., Yanagisawa, K., Sato, T., et al. (2017b). Series of M_xWO_3/ZnO (M= K, Rb, NH4) nanocomposites: combination of energy saving and environmental decontamination functions. *Appl. Catal. B Environ.* 201, 128–136. doi: 10.1016/j.apcatb.2016.08.030

Wu, X., Yin, S., Xue, D., Komarneni, S., and Sato, T. (2015). A Cs_xWO_3/ZnO nanocomposite as a smart coating for photocatalytic environmental cleanup and heat insulation. *Nanoscale* 7, 17048–17054. doi: 10.1039/C5NR04452A

Xi, G., Ouyang, S., Li, P., Ye, J., Ma, Q., Su, N., et al. (2012). Ultrathin $W_{18}O_{49}$ nanowires with diameters below 1 nm: synthesis, near-infrared absorption, photoluminescence, and photochemical reduction of carbon dioxide. *Angew. Chem.* 124, 2445–2449. doi: 10.1002/ange.201107681

Xu, X.-Q., Wang, Z., Li, R., He, Y., and Wang, Y. (2018). A degradable and recyclable photothermal conversion polymer. *Chem. A Eur. J.* 24, 9769–9772. doi: 10.1002/chem.201801654

Yan, C., Tian, Q., and Yang, S. (2017). Recent advances in the rational design of copper chalcogenide to enhance the photothermal conversion efficiency for the photothermal ablation of cancer cells. *RSC Adv.* 7, 37887–37897. doi: 10.1039/C7RA05468H

Yan, J., Liu, P., Ma, C., Lin, Z., and Yang, G. (2016). Plasmonic near-touching titanium oxide nanoparticles to realize solar energy harvesting and effective local heating. *Nanoscale* 8, 8826–8838. doi: 10.1039/C6NR01295G

Yan, J., Wang, T., Wu, G., Dai, W., Guan, N., Li, L., et al. (2015). Tungsten oxide single crystal nanosheets for enhanced multichannel solar light harvesting. *Adv. Mater.* 27, 1580–1586. doi: 10.1002/adma.201404792

Yang, K., Zhang, S., Zhang, G., Sun, X., Lee, S.-T., and Liu, Z. (2010). Graphene in mice: ultrahigh *in vivo* tumor uptake and efficient photothermal therapy. *Nano Lett.* 10, 3318–3323. doi: 10.1021/nl100996u

Yang, X.-G., Li, C., Mo, M.-S., Zhan, J.-H., Yu, W.-C., Yan, Y., et al. (2003). Growth of $K_{0.4}WO_3$ whiskers via a pressure-relief-assisted hydrothermal process. *J. Cryst. Growth* 249, 594–599. doi: 10.1016/S0022-0248(02)02323-0

Yao, Y., Zhang, L., Chen, Z., Cao, C., Gao, Y., and Luo, H. (2018). Synthesis of Cs_xWO_3 nanoparticles and their NIR shielding properties. *Ceram. Int.* 44, 13469–13475. doi: 10.1016/j.ceramint.2018.04.158

Yoon, S., Jo, C., Noh, S. Y., Lee, C. W., Song, J. H., and Lee, J. (2011a). Development of a high-performance anode for lithium ion batteries using novel ordered mesoporous tungsten oxide materials with high electrical conductivity. *Phys. Chem. Chem. Phys.* 13, 11060–11066. doi: 10.1039/c1cp20940j

Yoon, S., Kang, E., Kim, J. K., Lee, C. W., and Lee, J. (2011b). Development of high-performance supercapacitor electrodes using novel ordered mesoporous tungsten oxide materials with high electrical conductivity. *Chem. Commun.* 47, 1021–1023. doi: 10.1039/C0CC03594G

Yue, L., Tang, J., Li, F., Xu, N., Zhang, F., Zhang, Q., et al. (2017). Enhanced reversible lithium storage in ultrathin $W_{18}O_{49}$ nanowires entwined Si composite anode. *Mater. Lett.* 187, 118–122. doi: 10.1016/j.matlet.2016.10.093

Zeng, W., Suo, L., Zhang, C., Wu, D., and Zhu, H. (2019). AgI–Ag2S heterostructures for photothermal conversion and solar energy harvesting. *J. Taiwan Inst. Chem. Eng.* 95, 273–280. doi: 10.1016/j.jtice.2018.07.012

Zeng, X., Zhou, Y., Ji, S., Luo, H., Yao, H., Huang, X., et al. (2015). The preparation of a high performance near-infrared shielding Cs_xWO_3/SiO_2 composite resin coating and research on its optical stability under ultraviolet illumination. *J. Mater. Chem. C* 3, 8050–8060. doi: 10.1039/C5TC01411E

Zhang, L., Tang, B., Wu, J., Li, R., and Wang, P. (2015a). Hydrophobic light-to-heat conversion membranes with self-healing ability for interfacial solar heating. *Adv. Mater.*27, 4889–4894. doi: 10.1002/adma.201502362

Zhang, W., Yue, L., Zhang, F., Zhang, Q., Gui, X., Guan, R., et al. (2015b). One-step *in situ* synthesis of ultrathin tungsten oxide@ carbon nanowire webs as an anode material for high performance. *J. Mater. Chem. A* 3, 6102–6109. doi: 10.1039/C4TA06262K

Zhang, Z., Jiang, X., Liu, B., Guo, L., Lu, N., Wang, L., et al. (2018). IR-driven ultrafast transfer of plasmonic hot electrons in non-metallic branched heterostructures for enhanced H_2 generation. *Adv. Mater.* 30**:**1705221. doi: 10.1002/adma.201705221

Zhao, Y., Tang, Q., Yang, P., and He, B. (2017). Robust electrocatalysts from metal doped $W_{18}O_{49}$ nanofibers for hydrogen evolution. *Chem. Commun.* 53, 4323–4326. doi: 10.1039/C7CC01249G

Zheng, J.Y., Haider, Z., Van, T.K., Pawar, A.U., Kang, M.J., Kim, C.W., et al. (2015). Tuning of the crystal engineering and photoelectrochemical properties of crystalline tungsten oxide for optoelectronic device applications. *CrystEngComm* 17, 6070–6093. doi: 10.1039/C5CE00900F

Zhenzhen, G., Xin, M., Gang, W., Baofei, H., Xinghang, L., Tao, M., et al. (2018). Super-hydrophilic copper sulfide films as light absorbers for efficient solar steam generation under one sun illumination. *Semicond. Sci. Technol.* 33**:**025008. doi: 10.1088/1361-6641/aaa323

Zhou, M., Zhang, R., Huang, M., Lu, W., Song, S., Melancon, M.P., et al. (2010). A chelator-free multifunctional [64Cu]CuS nanoparticle platform for simultaneous micro-PET/CT Imaging and photothermal ablation therapy. *J. Am. Chem. Soc.* 132, 15351–15358. doi: 10.1021/ja106855m

Zhou, Y., Ko, S., Lee, C.W., Pyo, S.G., Kim, S.-K., and Yoon, S. (2013). Enhanced charge storage by optimization of pore structure in nanocomposite between ordered mesoporous carbon and nanosized WO_{3-x}. *J. Pow. Sources* 244, 777–782. doi: 10.1016/j.jpowsour.2013.04.054

Zhu, Y.T., and Manthiram, A. (1994). New route for the synthesis of tungsten oxide bronzes. *J. Solid State Chem.* 110, 187–189. doi: 10.1006/jssc.1994.1156

Conflict of Interest Statement: The authors declare that the research was conducted in the absence of any commercial or financial relationships that could be construed as a potential conflict of interest.

Glass Science

Caio Bragatto

Caio Bragatto is an Assistant Professor of Physics at Coe College, Iowa, USA. Bragatto earned his BSc degree in Industrial Chemistry from the Universidade de São Paulo, São Paulo, Brasil, and his MSc and PhD degree in Materials Science and Engineering from the Universidade Federal de São Carlos, São Paulo, Brasil. Before being hired as an Assistant Professor, Bragatto worked as a research assistant at the Otto-Schott Institut für Materialwissenschaft in Thüringen, Germany. He specialized in ionic conductivity of glasses, focusing on unveiling the mechanisms behind the phenomena and working on a universal model to predict this property. Ionic conductive glasses are used mainly as electrolytes in solid-state batteries and sensors.

Courtney Calahoo

Courtney Calahoo currently holds a Post-Doctoral Fellowship from the Natural Sciences and Engineering Council of Canada (NSERC) at the Otto Schott Institute for Materials Research (OSIM) in Jena, Germany. Her PhD work at Dalhousie University, Nova Scotia focused on developing structure-property relationships in oxide glasses, specifically between molecular structure and mechanical and electrical properties. While there, she contributed to the NMR and EPS studies of glass chapter in the Springer Handbook of Glass. Since moving to Germany, she has been actively interested in extending current glass theory to different types of glass systems, including ionic glass and amorphous metal-organic frameworks. Recently, she was awarded funding from the Deutsche Forschungsgemainschaft (DFG) for her own research project; she looks forward to taking on a more supervisorial role. She also enjoys chemistry in the home: soap-making, pickling, canning and brewing all sorts of tasty, or otherwise, concoctions.

Saurabh Kapoor

Dr Saurabh Kapoor received his BS (Hons.) Physics in 2009 and MSc (Hons.) in Physics in 2011 from the Department of Physics, GNDU. He obtained his PhD in Materials Science and Engineering from the University of Aveiro, Portugal in 2014. At present he works as a Research Scientist – Optical fibers at Sterlite Technologies Ltd., Aurangabad, Maharashtra.

Prior to joining Sterlite Technologies Ltd, Dr Kapoor worked as a postdoctoral researcher at Aalborg University, Aalborg, Denmark and at Rutgers-The State University of New Jersey, New Jersey, USA. Dr Kapoor is an author of 21 research articles and one patent in the field of glass science. Dr Kapoor is also a member of TC-04 (Biomedical Glasses), a technical committee of the International Commission on Glass.

Stefan Karlsson

Stefan Karlsson is a scientist working at RISE Research Institutes of Sweden, the Glass unit (former Glafo) since 2012. He holds a BSc in Chemical Engineering (2006) and a PhD in Glass Technology (2012) from Linnaeus University, Sweden. He was awarded a Marie-Curie Fellowship in 2014 that was spent at Otto Schott Institute of Materials Research, University of Jena. He was the coordinator of the Solar-ERA.NET project LIMES – Light Innovative Materials for Enhanced Solar Efficiency from 2014 to 2017 and currently holds a three-year grant in the "Future Research Leader" program from the Swedish Research Council for Sustainable Development (FORMAS).

Bruno Poletto Rodrigues

Bruno Poletto Rodrigues was born in Belo Horizonte, Brazil on the 15th of April 1987. He was enrolled in the Federal University of São Carlos (UFSCar) in 2005 and concluded his BA in Materials Science and Engineering with an emphasis on Polymers in 2009. In 2012 he achieved the title of Master of Science in Materials Science with an emphasis on Ceramics, also at UFSCar. Between 2012 and 2018 he held a position of Research Associate at the Otto Schott Institute of Materials Research of the FSU Jena, and in 2016 he defended his PhD in Glass Chemistry. Since 2018 he holds a Postdoctoral Fellow position at the Institute of Photonics and Advanced Sensing at The University of Adelaide.

Jessica Rimsza

Dr Jessica Rimsza is a Senior Member of the Technical Staff at the Geochemistry Department of Sandia National Laboratories in Albuquerque NM. She received her BSc from the University of Arizona and a PhD from the University of North Texas, both in Materials Science and Engineering. Her research focuses on the computational modeling of the surface, degradation, and mechanical properties of ceramic and amorphous oxides including glasses, cement and concrete, carbides, and ionic solids. She joined Sandia National Laboratories in 2016 as a post-doc working on the chemical-mechanical fracture of geomaterials and became a permanent staff member in 2018. She was a National Science Foundation Graduate Research Fellow, the Chair of the American Ceramics Society President's Council of Student Advisors and has organized multiple symposia outside of Sandia focusing on bridging the gap between geo, materials, and planetary sciences.

frontiers in Materials

ORIGINAL RESEARCH
published: 31 May 2019
doi: 10.3389/fmats.2019.00121

Charge Carrier Mobility of Alkali Silicate Glasses Calculated by Molecular Dynamics

Rebecca S. Welch[1], *Collin James Wilkinson*[2], *John Christopher Mauro*[2] *and Caio Barca Bragatto*[1]*

[1] *Department of Physics, Coe College, Cedar Rapids, IA, United States,* [2] *Department of Materials Science and Engineering, The Pennsylvania State University, University Park, PA, United States*

Ionic conductivity is a property of rapidly increasing interest. Various models attempting to explain ionic conductivity of glass systems have shown limited agreement with experimental results; however, none have been comprehensive. By using molecular dynamics simulations, the diffusion of ion species through a network can be directly observed, providing insights into the mechanisms and their relation to ionic conductivity models. In this report, a method of utilizing molecular dynamics simulations is proposed for the study of the ionic mobility of Na, Li, and K ions in binary silicate glasses. Values found for glasses with $x = 0.1$, $x = 0.2$, and $x = 0.3$ alkali content are between 10^{-5} and 10^{-4} $cm^2 \cdot s^{-1} \cdot V^{-1}$ and did not change significantly with composition or temperature. This is in agreement with the interstitial pair and weak-electrolyte models used to explain ionic conductivity in glasses.

Keywords: glass, molecular dynamics, ionic conductivity, ionic mobility, ionic conductivity models

OPEN ACCESS

Edited by:
Lothar Wondraczek, Friedrich Schiller University Jena, Germany

Reviewed by:
Alfonso Pedone, University of Modena and Reggio Emilia, Italy
Donghui Zhao, Unifrax LLC, Tonawanda, United States

***Correspondence:**
Caio Barca Bragatto
cbragatto@coe.edu

Specialty section:
This article was submitted to Glass Science, a section of the journal Frontiers in Materials

Received: *02 January 2019*
Accepted: *10 May 2019*
Published: *31 May 2019*

Citation:
Welch RS, Wilkinson CJ, Mauro JC and Bragatto CB (2019) Charge Carrier Mobility of Alkali Silicate Glasses Calculated by Molecular Dynamics. Front. Mater. 6:121. doi: 10.3389/fmats.2019.00121

INTRODUCTION

In non-crystalline alkali silicate materials, alkalis are the most mobiles species; self-diffusion of alkali ions is generally understood as an exchange of cationic pairs between sites (Kahnt, 1991). If enough energy is applied to an ion to overcome a transition barrier to a new configuration, such as from an applied electric field, or thermal fluctuations, the atom can "hop" or "jump" to the next available site (Varshneya and Mauro, 2019). Since alkali ions are loosely associated and not strongly confined (when compared with the mostly rigid glass network), they can more easily jump between sites (Greaves et al., 1991). Certain glass compositions have been studied in literature due to their remarkably high ionic conductivity when compared to crystals (Minami et al., 1977), particularly phosphates doped with silver (Rodrigues et al., 2011), and lithium (Robert et al., 1981). In addition, increasing the conductivity of phosphate glasses by adding various modifiers has been of interest due to their already promising conductivity values (Martin and Angell, 1986; Martin, 1991).

In general, the electric conductivity, σ, can be defined as

$$\sigma = Ze\mu n, \tag{1}$$

Where Z is the valence number of the charge carrier, e is the charge of an electron, μ is the mobility of the charge carriers, and n is the concentration of the charge carriers. Further, μ can be understood from the random walk properties of mobile species and calculated using the Nernst-Einstein

equation (Murch, 1983) which relates the mobility of charge carriers to the diffusion coefficient:

$$\mu kT = ZeD, \tag{2}$$

Where k is the Boltzmann constant and T is the absolute temperature. D is the diffusion coefficient, which can be expressed using Boltzmann statistics dependent on the jump distance (d_j) of the mobile species, the geometrical factor (α) in which the diffusion hopping takes place, and the vibrational frequency (ν_0) of ions within the potential energy well of depth E_m (Tuller et al., 1980):

$$D = \alpha d_j^2 \nu_0 \exp\left(-\frac{E_m}{kT}\right). \tag{3}$$

The diffusion of ions can also be regarded more generally from the mean squared displacement (r^2) which is more commonly used in molecular dynamics (MD) simulations. First derived by Einstein (1906), the expression relates the diffusion coefficient to the mean squared displacement within a specified observational time according to

$$r^2 = \left\langle \Delta \vec{x}(t)^2 \right\rangle = \frac{1}{N} \sum_{i=1}^{N} (\vec{x}_i(t) - \vec{x}_i(0))^2, \tag{4}$$

where N is the number of averaged particles, $\vec{x}_i(0)$ is an initial reference position, $\vec{x}_i$ is the position with respect to time, and the related diffusion coefficient D is given by

$$D = \frac{r^2}{2n_d \Delta t}, \tag{5}$$

where Δt is the change in time over which diffusion is calculated, and n_d is the dimensionality in which the process occurs.

Such diffusion mechanisms in glasses have been widely studied with various models being developed in literature (Ingram, 1989; Martin, 1991; Bunde et al., 1994). However, there remains little consensus on which model is sufficient to explain the entirety of ionic conductivity in amorphous solids. Since the mobile species in an alkali silicate glass system are only monovalent ions, Z and e from equation (1) are constant, therefore making the conductivity proportional to only the mobility and concentration of charge carriers. The difficulty of accurately measuring μ and n separately with experimental techniques has led to a lack of agreement between various models (Dyre et al., 2009). Glasses are generally considered as either strong or weak electrolytes, with the notion that either all charge carriers are able to dissociate and move rapidly (as in strong electrolytes), or only a fraction of ions over a given time interval (weak electrolytes).

The strong electrolyte view comes from the model developed by Anderson and Stuart (Anderson and Stuart, 1954), which borrows principles from the Frenkel defect theory for crystalline materials (Frenkel, 1947). They theorize that ions must overcome two energy barriers: the amount of energy needed to break an ionic bond (electrostatic binding energy), and the energy needed to create a vacancy defect in the glass network for an occupying ion (strain energy). The main conclusion from this model is that all charge carriers instantaneously move through the network given enough supplied energy, and that the concentration of charge carriers is constant with temperature (McElfresh and Howitt, 1986), making the ionic mobility the limiting factor for conductivity.

In contrast, the Interstitial Pair model (Charles, 1961) and the Weak-Electrolyte (W-E) model (Ravaine and Souquet, 1976, 1977), suggest that the charge carrier concentration n from equation (1) is what limits the conductivity. By assuming that μ is constant for a specific time interval, the concentration of moving ions will therefore be the only determining factor. Since only a fraction of ions can move, the concentration of mobile species is low but with a higher constant mobility. Glasses are considered to behave as weak electrolytes due to the smaller fraction of available ions when compared to the overall concentration (Souquet et al., 2010).

Molecular dynamics simulations have been previously used in literature to study diffusion mechanisms in glassy systems (Soules and Busbey, 1981; Soules, 1982; Li and Garofalini, 2004) including some electronic properties (Tilocca and de Leeuw, 2006), and can be used as a tool for visualizing ion transport pathways (Cormack et al., 2002; Müller et al., 2007). Due to the availability of accurate potentials and the ability to have large enough systems that can capture the statistical nature of glass, MD enables observation of behaviors which are difficult to examine experimentally. In this report, a method for utilizing MD simulations to study the mobility of binary lithium, sodium, and potassium silicates is proposed. By applying an electric field to the simulated glasses, we can gain further insights on the mechanisms of ion transport and how they relate to the ionic conductivity models that currently exist.

METHODS

For an MD simulation, potentials define the inter-atomic interactions within the system and must be empirically fitted and optimized for a specific material property. In addition to potentials, the densities for each glass composition are also needed to specify the volume used in the canonical ensemble of the simulations presented. In our report, Large-scale Atomic/Molecular Massively Parallel Simulator (LAMMPS) molecular dynamics package was used to conduct all simulations. Lithium, sodium, and potassium oxide silicate glasses of the form x M_2O (1-x) SiO_2 were simulated for $x = 0.1$, $x = 0.2$, and $x = 0.3$. Pairwise potentials developed by Pedone et al. were used to describe the interactions between the species with the expression being (Pedone et al., 2006):

$$U(r) = \frac{Z_i Z_j e^2}{r} + D_{ij}[\{1 - e^{-a_{ij}(r-r_0)}\}^2 - 1] + \frac{C_{ij}}{r^{12}}, \tag{6}$$

where D_{ij} is the bond dissociation energy, a_{ij} is a function of the slope of the potential energy well, and r_0 is the equilibrium bond distance. The fitted parameters in **Table 1** were derived by Pedone et al. from binary oxide crystals. These potentials were chosen due to their widely reported accuracy for silicates and their known

TABLE 1 | Interatomic potential parameters used in binary silicates from Pedone et al., 2006.

	D_{ij} (eV)	a_{ij} (Å^{-2})	r_0 (Å)	C_{ij} (eV·Å^{12})
$Li^{0.6}$-$O^{-1.2}$	0.001114	3.429506	2.681360	1.0
$Na^{0.6}$-$O^{-1.2}$	0.023363	1.763867	3.006315	5.0
$K^{0.6}$-$O^{-1.2}$	0.011612	2.062605	3.305308	5.0
$Si^{2.4}$-$O^{-1.2}$	0.340554	2.006700	2.100000	1.0
$O^{-1.2}$-$O^{-1.2}$	0.042395	1.379316	3.618701	22.0

TABLE 2 | Densities (in g/cm^3) for corresponding x-values (converted from J values) used for simulations collected from Tischendorf et al., 1998.

x	J	Na	K	Li
0.1	0.0909	2.23	2.28	2.29
0.2	0.1667	2.25	2.32	2.34
0.3	0.2308	2.27	2.37	2.37

ability to reproduce mechanical properties (Prasada Rao et al., 2010; Xiang et al., 2013; Deng et al., 2015). Densities used were those collected by Tischendorf et al. and can be found in **Table 2** (Tischendorf et al., 1998).

For each composition, a timestep of 1 femtosecond (fs) was used and melting was simulated at 3,000 K. The system was then quenched and held for 1 ns at 2,000 K, 1,000 K, and 300 K in the NVT ensemble. For each sample, an electric field of $5{\cdot}10^5$ V/m across the x dimension (∼2 nm) was applied after the quenching process was complete. The voltage of the electric field was chosen based on experimental values used for typical Electrical Impedance Spectroscopy measurements in which a 5–10 mV electric field is applied to a 1–3 cm thickness sample (Park and Yoo, 2003). The system was heated from 300 K to 800 K with the electric field being applied simultaneously. During this process, the mean squared displacement (MSD) was calculated by equation (4) and was recorded every 100 timesteps (approximately every 5 K). The mobility was then calculated from the MSD values as a function of the temperature by first using equation (5) to calculate the diffusion co-efficient and then equation (2) to find the mobility. For each alkali the simulation and calculation were performed independently with 3000 atoms.

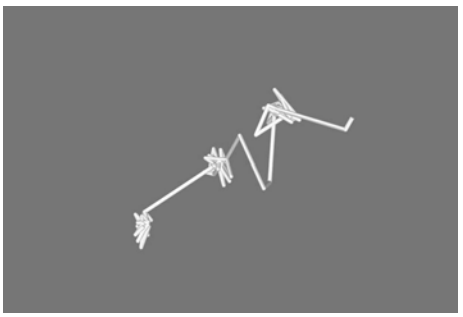

FIGURE 1 | Pathway for one single sodium ion during the simulation of the 0.3 Na_2O · 0.7 SiO_2 glass. It is possible to see how the ion has preferred sites and eventually jumps from one to the next.

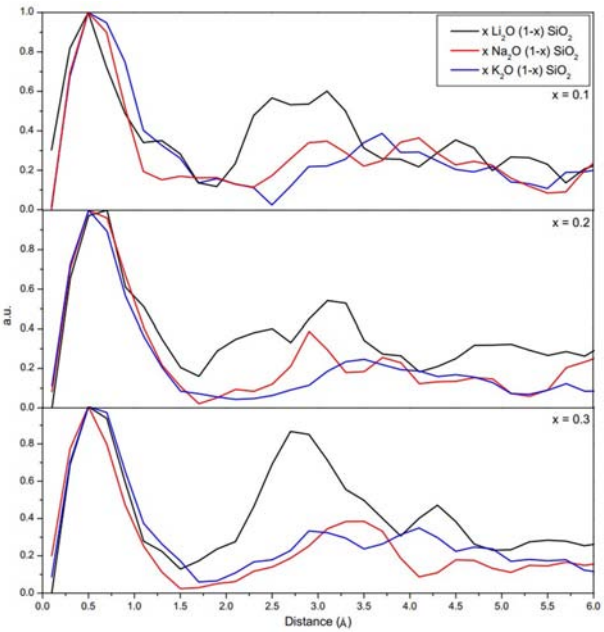

FIGURE 2 | Probability density function of the jump distance for the alkali ions. The jump distances can be estimated from the difference between two points in which the ions spent more time during the simulation.

RESULTS AND DISCUSSION

In **Figure 1**, the pathway for one single sodium ion is shown from the simulation of the $x = 0.1$ sodium silicate glass. It can be seen that the ion sits on specific sites before jumping to the next, where it vibrates until it can jump once more. Similar behavior has been observed in MD previously by Jund et al. (2001), where simulated sodium ions, not exposed to an electric field, showed a propensity to jump to new sites rather than returning to the previous one (Funke and Hoppe, 1990). This motion is predicted by both strong and weak electrolyte models. The specific behavior observed in **Figure 1** may be further explained as a Markovian chain process, suggesting that the motion of an ion depends only on its current environment, with no memory of its previous location (Landau and Binder, 2015).

Figure 2 shows the probability density function for the movement of alkali ions with varying alkali content. As shown in **Figure 2**, the jump distance appears to be ion-dependent, with shorter jump distances for Li, then Na, and lastly K. The average values for the jump distances are reported in **Table 3**. This can be attributed to the size of the ion, since a smaller ion will have a higher probability of finding a compatible site for it to move into.

Figure 3 shows the diffusion coefficient calculated using equation (5) as a function of $1000/T$ (in 1,000·K^{-1}). The diffusion follows an Arrhenius behavior for the process, as expected when comparing to experimental results (Varshneya

TABLE 3 | Average jump distance (in Å) for each composition obtained by peak fitting of the probability density function from **Figure 2**.

	x	Average jump distance (Å)
x Li_2O (1-*x*) SiO_2	0.1	0.49
	0.2	0.50
	0.3	0.50
x Na_2O (1-*x*) SiO_2	0.1	0.60
	0.2	0.59
	0.3	0.50
x K_2O (1-*x*) SiO_2	0.1	0.62
	0.2	0.59
	0.3	0.59

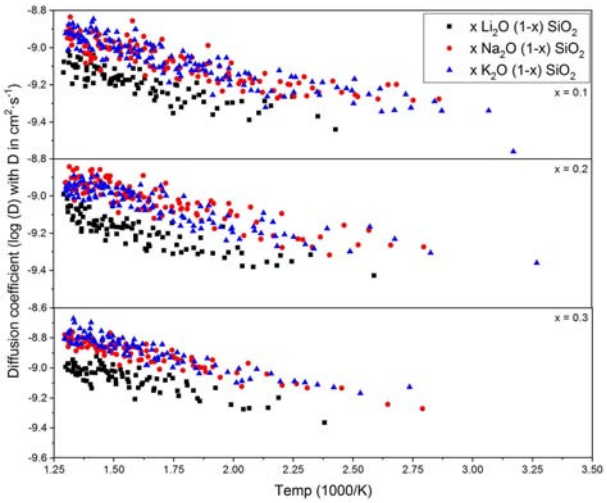

FIGURE 3 | Diffusion coefficient of the alkali ions calculated from equation (5) as a function of 1/T. The Arrhenius behavior is well-known for these glasses, being self-diffusion, or diffusion due to an external electric potential.

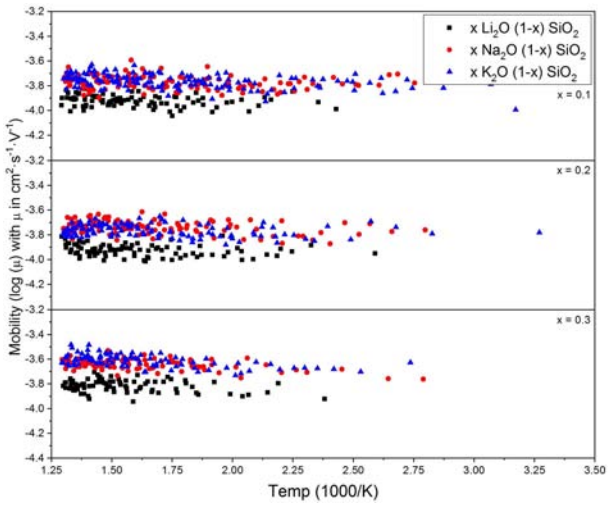

FIGURE 4 | Calculated alkali ion mobilities from equation (6) vs. temperature for three different compositions. The mobility does not change significantly with temperature or chemical composition, which is in agreement with the interstitial pair and weak-electrolyte models.

TABLE 4 | Intercept (log D_0, D_0 in $cm^2 \cdot s^{-1}$ and log μ_0, μ_0 in $cm^2 \cdot s^{-1} \cdot V$) and activation energy (E_D and E_μ, both in eV) for the diffusion process and the ionic mobility, respectively, calculated using the Arrhenius equation and the data from **Figure 2**.

	x	log D_0 (D_0 in $cm^2 \cdot s^{-1}$)	E_D (eV)	log μ_0 (μ_0 in $cm^2 \cdot s^{-1} \cdot V$)	E_μ (eV)
x Li_2O (1-*x*) SiO_2	0.1	−8.71	0.057	−3.84	0.009
	0.2	−8.69	0.061	−3.82	0.012
	0.3	−8.60	0.060	−3.73	0.010
x Na_2O (1-*x*) SiO_2	0.1	−8.65	0.047	−3.75	0.002
	0.2	−8.53	0.057	−3.65	0.011
	0.3	−8.42	0.059	−3.53	0.013
x K_2O (1-*x*) SiO_2	0.1	−8.58	0.054	−3.67	0.010
	0.2	−8.61	0.051	−3.71	0.006
	0.3	−8.38	0.061	−3.50	0.014

and Mauro, 2019). The ionic mobility, as well as the diffusion coefficient, was calculated using the MSD of the alkali ions that moved along the axis of the applied field with distances above the threshold of 3 Å. This threshold was chosen as a minimum jump distance from the probability density function of **Figure 2**. **Figure 4** show the temperature dependence of the ionic mobility of the simulated glasses at given temperatures. The diffusion and ionic mobility were fitted with an Arrhenius equation. The slopes, which correspond to the activation energy, and the intercept values can be seen in **Table 4**.

From **Figure 4** it is easy to see that the ionic mobility does not change significantly with either chemical composition or temperature, varying from $5 \cdot 10^{-5}$ to $5 \cdot 10^{-4}$ $cm^2 \cdot s^{-1} \cdot V^{-1}$. Thus, the diffusion process has a lower activation energy when compared to the activation energy needed for charge carrier formation or the energy required for the ionic conductivity process. This result is very close to the values found for $AgPO_3$-AgI conducted by Clément et al. from Hall effect measurements (Clément et al., 1988) and by Rodrigues who measured the enthalpy change for the glasses at temperatures above and below the glass transition temperature (Rodrigues et al., 2011). Diffusion of different alkali ions in water, both by physical experiments and by MD simulations, agree in order of magnitude (Lee and Rasaiah, 1994). This is in agreement with the weak-electrolyte model where the mobility is relatively constant (within one order of magnitude) and the number of effective charge carriers is largely responsible for whether a glass is more or less ionically conductive.

The ionic conductivity of these glasses may vary by orders of magnitude with temperature according to experimental results (Varshneya and Mauro, 2019). The results presented here which show a constant mobility with respect to temperature and composition, suggest that a change in the number of effective

charge carriers is what causes the increase in ionic conductivity in these alkali silicate glasses. Due to the non-crystalline nature of the glassy state and its complex energy landscape, the energy barriers for moving ions have a distribution. Thus, during a single ion's diffusion, it may either end up being "trapped" in a high-energy barrier site or stay for a comparably short time in a low-energy barrier one. Given enough time, however, all mobile ions should move and contribute equally to the ionic conductivity at non-zero temperatures, assuming that during this process each ion will jump through enough sites for an average energy to be observed. The problem resides in defining a sufficient time interval to wait before proceeding to calculations. This complicates the definitions of a charge carrier and its corresponding mobility, previously defined in equation (1), since the number of charge carriers can change depending on the time interval used (Dyre et al., 2009).

Physical experimental results in which the so-called DC ionic conductivity (Barsoukov and Macdonald, 2005) is observed, the data is normally obtained by AC impedance spectroscopy with frequencies varying from 10^4 to 10^2 Hz, i.e., the measurement takes from 10^8 to 10^{10} ps. This does not affect the mobility of the ions, but it does affect the number of effective charge carriers. With the simulated glasses, diffusion was observed for 5,000 ps at each temperature. Due to the difference in observation times, it is difficult to compare calculated ionic conductivity values obtained from these simulations with their physical counterparts. The only experimental data which exists was obtained by Clément using Hall Effect Measurement in silver phosphate glasses, and by indirect measurements by Rodrigues, also in silver phosphate glasses. The process of obtaining the ionic conductivity with these glasses in literature is by Electrical Impedance Spectroscopy measurements which are done in frequencies from 10^6 to 1 Hz, which is also not comparable to the nanosecond scales of molecular dynamics simulations.

It is also known that the ionic conductivity shows a dependence with the thermal history of the glass (Bragatto et al., 2016). Even though this dependency is small for physical experiments when compared to effects of temperature and chemical composition, the extreme cooling rates used in MD may have a larger impact on the results.

CONCLUSIONS

Lithium, sodium, and potassium silicates glasses were simulated using the LAMMPS molecular dynamics package with potential parameters from Pedone et al. while under an electric field. The mean squared displacement of the ions was used to calculate the jump distance between sites, the ionic diffusion, and the ionic mobility of the alkalis. In literature, models for ionic conductivity in glasses can be divided into two groups: one proposing that the ionic conductivity depends mainly on the ionic mobility of the glasses and one proposing that it depends on the dissociation equilibrium of the dopant salts in the glass. From our results, we conclude that the second is most likely to be true for alkali silicate glasses. The ionic mobility was found to be constant with temperature and independent of chemical composition. This is in agreement with predictions from the interstitial pair and the weak-electrolyte models, i.e., the ionic conductivity of glasses depends more strongly on the number of effective charge carriers than the mobility of the ions. The ionic conductivity itself was not accurately calculated due the short observational time intrinsic to MD experiments. MD has been shown to be a strong tool for observing many phenomena which would be impossible, costly, or labor-intensive, as in the present case for ionic diffusion due to electric fields in oxide glasses. The main objective of this study was to gain insight on the dependency of the ionic mobility with glass composition with the new technique of applying an electric field to simulated samples.

AUTHOR CONTRIBUTIONS

CB designed the research. RW, CW, and JM worked on the MD. RW and CW worked on the calculations and figures. All authors contributed to writing the article.

ACKNOWLEDGMENTS

The authors would like to acknowledge Penn State for the computational resources. The authors would also like to thank Dr. Steve Feller, Dr. Mario Affatigato, and Arron Potter for their comments and Dr. Lothar Wondraczek for the invitation to publish.

REFERENCES

Anderson, O. L., and Stuart, D. A. (1954). Calculation of activation energy of ionic conductivity in silica glasses by classical methods. *J. Am. Ceram. Soc.* 37, 573–580. doi: 10.1111/j.1151-2916.1954.tb13991.x

Barsoukov, E., and Macdonald, J. R. (2005). *Impedance Spectroscopy: Theory, Experiment, and Applications. 2nd Edn.* Somerset, NJ: John Wiley & Sons, Inc. doi: 10.1002/0471716243

Bragatto, C. B., Cassar, D. R., Peitl, O., Souquet, J.-L., and Rodrigues, A. C. M. (2016). Structural relaxation in AgPO3 glass followed by in situ ionic conductivity measurements. *J. Non Cryst. Solids* 437, 43–47. doi: 10.1016/j.jnoncrysol.2016.01.010

Bunde, A., Ingram, M. D., and Maass, P. (1994). The dynamic structure model for ion transport in glasses. *J. Non-Cryst. Solids* 172–174, 1222–1236. doi: 10.1016/0022-3093(94)90647-5

Charles, R. J. (1961). Polarization and diffusion in a silicate glass. *J. App. Phys.* 32, 1115–1126. doi: 10.1063/1.1736169

Clément, V., Ravaine, D., Déportes, C., and Billat, R. (1988). Measurement of hall mobilities in AgPO AgI glasses. *Solid State Ionics*. 28–30, 1572–1578. doi: 10.1016/0167-2738(88)90422-5

Cormack, A. N., Du, J., and Zeitler, T. R. (2002). Alkali ion migration mechanisms in silicate glasses probed by molecular dynamics simulations. *J. Phys. Chem. Chem. Phys.* 4, 3193–3197. doi: 10.1039/b201721k

Deng, Y., Eames, C., Chotard, J.-N., Lalère, F., Seznec, V., Emge, S., et al. (2015). Structural and mechanistic insights into fast lithium-ion conduction in Li4SiO4-Lo3PO4 solid electrolytes. *J. Am. Chem. Soc.* 137, 9136–9145. doi: 10.1021/jacs.5b04444

Dyre, J. C., Maass, P., Roling, B., and Sidebottom, D. L. (2009). Fundamental questions relating to ion conduction in disordered solids. *Rep. Prog. Phys.* 72:046501. doi: 10.1088/0034-4885/72/4/046501

Einstein, A. (1906). Investigations on the theory of the brownian movement (translated). *Ann. Phys*. 19:371. doi: 10.1002/andp.19063240208

Frenkel, J. (1947). *Kinetic Theory of Liquids*. New York, NY: Oxford University Press, 10-11, 544.

Funke, K., and Hoppe, R. (1990). Jump-relaxation model yields Kohlrausch-Williams-Watts behavior. *Solid State Ionics*. 40–41, 200–204. doi: 10.1016/0167-2738(90)90321-H

Greaves, G. N., Gurman, S. J., Catlow, R. A., Chadwick, A. V., Houde-Walter, S., Henderson, C. M. B., et al. (1991). A structural basis for ionic diffusion in oxide glasses. *Phil. Mag*. 64, 1059–1072. doi: 10.1080/01418619108204878

Ingram, M. D. (1989). Ionic conductivity and glass structure. *Phil. Mag. Part B*. 60, 729–740. doi: 10.1080/13642818908209739

Jund, P., Kob, W., and Jullien, R. (2001). Channel diffusion of sodium in a silicate glass. *Phys. Rev. B* 64, 1–5. doi: 10.1103/PhysRevB.64.134303

Kahnt, H. (1991). Ionic transport in oxide glasses and frequency dependence of conductivity. *Phys. Chem*. 95, 1021–1025. doi: 10.1002/bbpc.19910950913

Landau, D. P., and Binder, K. (2015). *A Guide to Monte Carlo Simulations in Statistical Physics. 4th Edn*. Cambridge, UK: Cambridge University Press, 33–35.

Lee, S. H., and Rasaiah, J. C. (1994). Molecular dynamics simulation of ionic mobility. I. Alkali metal cations in water at 25°C. *J. Chem. Phys*. 101, 6964–6974. doi: 10.1063/1.468323

Li, W., and Garofalini, S. H. (2004). Molecular dynamics simulation of lithium diffusion in Li2O-Al2O3-SiO2 glasses. *J. Solid State Ionics*. 166, 365–373. doi: 10.1016/j.ssi.2003.11.015

Martin, S. W. (1991). Ionic conduction in phosphate glasses. *J. Am. Ceram. Soc*. 74, 1767–1784. doi: 10.1111/j.1151-2916.1991.tb07788.x

Martin, S. W., and Angell, C. A. (1986). Dc and Ac conductivity in wide composition range Li2O P2O5 glasses. *J. Non-Crys. Sol*. 83, 185–207. doi: 10.1016/0022-3093(86)90067-0

McElfresh, D. K., and Howitt, D. G. (1986). Activation enthalpy for diffusion in glass. *J. Am. Ceram. Soc*. 69, C237–C238. doi: 10.1111/j.1151-2916.1986.tb07347.x

Minami, T., Nambu, H., and Tanaka, M. (1977). Comparison of ionic conductivity between glassy and crystalline solid electrolytes in the system AgI-Ag2O-MoO3. *J. Am. Ceram. Soc*. 60, 467–469. doi: 10.1111/j.1151-2916.1977.tb15539.x

Müller, C., Zienicke, E., Adams, S., Habasaki, J., and Maass, P. (2007). Comparison of ion sites and diffusion paths in glasses obtained by molecular dynamics simulations and bond valence analysis. *J. Phys. Rev. B* 75:014203. doi: 10.1103/PhysRevB.75.014203

Murch, G. E. (1983). The exact Nernst-Einstein equations and the interpretation of cross phenomenological coefficients in unary, binary, and ambipolar systems. *Radiat. Eff*. 73, 299–305. doi: 10.1080/00337578308220688

Park, S. M., and Yoo, J. S. (2003). Electrochemical Impedance Spectroscopy for Better Electrical Measurements. *Anal. Chem*. 75, 455–461. doi: 10.1021/ac0313973

Pedone, A., Malavasi, G., Menziani, C. M., Cormack, A. N., and Segre, U. (2006). A new self- consistent empirical interatomic potential model for oxides, silicates, and silica-based glasses. *J. Phys. Chem. B*. 110, 11780–11795. doi: 10.1021/jp0611018

Prasada Rao, R., Tho, T. D., and Adoms, S. (2010). Ion transport pathways in molecular dynamics simulated lithium silicate glasses. *Solid State Ionics* 181, 1–6. doi: 10.1016/j.ssi.2009.12.003

Ravaine, D., and Souquet, J.-L. (1977). A thermodynamic approach to ionic conductivity in oxide glasses. Part 2. A statistical model for the variations of the chemical potential of the constituents in binary alkali oxide glasses. *Phys. Chem. Glasses*. 19, 115–120.

Ravaine, D., and Souquet, J. L. (1976). A thermodynamic approach to ionic conductivity in oxide glasses. Part 1. Correlation of the ionic conductivity with the chemical potential of alkali oxide in oxide glasses. *Phys. Chem. Glasses*. 18, 27–31.

Robert, G., Malugani, J., and Saida, A. (1981). Fast ionic silver and lithium conduction in glasses. *Solid State Ionics* 3–4, 311–315. doi: 10.1016/0167-2738(81)90104-1

Rodrigues, A. C., Nascimento, M. L., Bragatto, C. B., and Souquet, J.-L. (2011). Charge carrier mobility and concentration as a function of composition in AgPO3-AgI glasses. *J. Chem. Phys*. 135:234504. doi: 10.1063/1.3666835

Soules, T. F. (1982). Molecular dynamic calculations of glass structure and diffusion in glass. *J. Non-Cryst. Solids*. 49, 29–52. doi: 10.1016/0022-3093(82)90107-7

Soules, T. F., and Busbey, R. F. (1981). Sodium diffusion in alkali silicate glass by molecular dynamics. *J. Chem. Phys*. 75, 969–975. doi: 10.1063/1.442097

Souquet, J.-L., Nascimento, M. L., and Rodrigues, A. C. (2010). Charge carrier concentration and mobility in alkali silicates. *J. Chem. Phys*. 132:034704. doi: 10.1063/1.3271154

Tilocca, A., and de Leeuw, N. H. (2006). Structural and electronic properties of modified sodium and soda-lime silicate glasses by Car-Parrinello molecular dynamics. *J. Mat. Chem*. 16, 1950–1955. doi: 10.1039/B517362K

Tischendorf, B., Ma, C., Hammersten, E., Venhuizen, P., Peters, M., Affatigato, M., and Feller, S. (1998). The density of alkali silicate glasses over wide compositional ranges. *J. Non-Cryst. Solids*. 239, 197–202. doi: 10.1016/S0022-3093(98)00740-6

Tuller, H. L., Button, D. P., and Uhlmann, D. R. (1980). Fast ion transport in oxide glasses. *J. Non-Cryst. Solids*. 40, 93–118. doi: 10.1016/0022-3093(80)90096-4

Varshneya, A. K., and Mauro, J. C. (2019). *Fundamentals of Inorganic Glasses. 3rd Edn*. Cambridge, MA: Elsevier. doi: 10.1016/B978-0-12-816225-5.00022-5

Xiang, Y., Du, J., Smedskjaer, M. M., and Mauro, J. C. (2013). Structure and properties of sodium aluminosilicate glasses from molecular dynamics simulations. *J. Chem. Phys*. 139:044507. doi: 10.1063/1.4816378

Conflict of Interest Statement: The authors declare that the research was conducted in the absence of any commercial or financial relationships that could be construed as a potential conflict of interest.

frontiers in Materials

ORIGINAL RESEARCH
published: 11 July 2019
doi: 10.3389/fmats.2019.00165

Structural Relaxation in Polyanionic Sodium Fluorophosphate Glasses

Courtney Calahoo[1], Jelena Petrovic[1], Quyen Huyen Le[1], Ulrike Werner-Zwanziger[2], Josef Zwanziger[2] and Lothar Wondraczek[1]**

[1] Otto Schott Institute of Materials Research, University of Jena, Jena, Germany, [2] Department of Chemistry, Dalhousie University, Halifax, NS, Canada

Structural heterogeneity is a common feature of all glasses, however, little is known about the underlying contributions of chemical fluctuations and modulations in free volume in concrete glass forming systems. In this investigation, we relate the dynamics of structural relaxation of (100-*x*)$NaPO_3$-*x*AlF_3 glasses to their heterogeneous structure as determined from multinuclear magnetic resonance spectroscopic analysis. For this, we evaluate differential scanning calorimetry (DSC) data using the integral isoconversional method to determine the variation in activation energy, E_a, of the glass transition as a function of temperature and conversion progress. Specific heat measurements from DSC allow for the determination of the effective size of the cooperatively rearranging region (CRR). From ^{31}P, ^{19}F, and ^{27}Al NMR, we observe that the introduction of AlF_3 into the $NaPO_3$ network increases the *average* connectivity (i.e., the number of heteronuclear Al—O—P bonds), rationalizing the higher E_a determined from the DSC measurements. We find highly constrained regions of $Al(OP)_4F_2$ with Al—F—Al cross-linking (high E_a) and, simultaneously, more flexible regions of phosphate chains containing P—F··$(Na^+)_n$ bonds (low E_a); this results in a topologically and dynamically heterogeneous structure as evidenced by the increased variability in E_a with higher AlF_3 content. The decreasing size of the CRR reflects the increased heterogeneity: at low AlF_3 the CRR is large, while at high AlF_3 (high heterogeneity), the CRR is significantly smaller (by a factor of 10^3). Finally, we relate the heterogeneity to other macroscopic properties, such as T_g and mechanical properties.

Keywords: structural relaxation, fluorophosphate glass, ionic glass, structural heterogeneity, thermal analysis, structure-property relationship, NMR spectroscopy, structural analysis

OPEN ACCESS

Edited by:
Randall Youngman, Corning Inc., United States

Reviewed by:
Yuanzheng Yue, Aalborg University, Denmark
Hellmut Eckert, Universidade de São Paulo São Carlos, Brazil

****Correspondence:***
Courtney Calahoo
courtney.calahoo@uni-jena.de
Lothar Wondraczek
lothar.wondraczek@uni-jena.de

Specialty section:
This article was submitted to Glass Science, a section of the journal Frontiers in Materials

Received: *19 March 2019*
Accepted: *24 June 2019*
Published: *11 July 2019*

Citation:
Calahoo C, Petrovic J, Le QH, Werner-Zwanziger U, Zwanziger J and Wondraczek L (2019) Structural Relaxation in Polyanionic Sodium Fluorophosphate Glasses. Front. Mater. 6:165. doi: 10.3389/fmats.2019.00165

INTRODUCTION

The non-equilibrium structure of glass becomes evident in the relaxation dynamics. Relaxation can occur while heating through the glass transition, or during annealing below the glass transition temperature (physical aging; Vyazovkin, 2015). Since the kinetics of structural relaxation are indicative of molecular mobility and therefore, glass stability, studying the dynamics near the glass transition is of importance for the characterization and fundamental understanding of physical and chemical properties (Greaves and Sen, 2007).

Since the glass is frozen dynamically, the transition preserves the heterogeneity of the liquid state, typically manifest in density fluctuations on the scale of a few nanometers (Ediger, 2000). Macroscopic consequences of structural heterogeneity are found in, e.g., ion mobility

(Greaves and Ngai, 1995), mechanical behavior (Benzine et al., 2018), crystallization (Moesgaard et al., 2010; Zhang et al., 2013), or Rayleigh scattering (Champagnon et al., 2009). During re-annealing of the glass, structural relaxation occurs toward a supercooled liquid via the cooperative motion of ions and molecules (Greaves and Sen, 2007). This process is typically known as α-relaxation; it is characterized by high activation energy (typically hundreds of kilojoules per mole) and stands in contrast to the movement of individual ions, atoms, or molecules (β relaxation). Molecules which are located in highly correlated regions can move only cooperatively, i.e., together with a large number of neighbors, while the molecules in less crowded areas are able to move in a less cooperative manner. The rearrangement of one molecule is only possible if a certain number (N_ξ) of neighbor molecules also move (Donth, 2001). According to Adam and Gibbs (Adam and Gibbs, 1965), a cooperatively rearranging region (CRR) is defined as a subsystem which, due to thermal fluctuations, can rearrange into another configuration independent of its environment. When the glass relaxes toward the liquid, the overall process generally occurs via convolution of multiple more or less cooperative reactions of structural rearrangement. However, one particular mechanism may dominate the relaxation, depending on temperature or relaxation progress (Vyazovkin, 2015). Near to the glass transition temperature (T_g), structural heterogeneity occurs on the order of a few nanometers in diameter (Duval et al., 2007).

According to the heterogeneous nature of the glass transition, the traditional concept of a constant activation energy [which has already been criticized from a physical point of view (Garn, 1990)] is ill-suited for glass transition kinetics: Garn (1990) has pointed out that a constant activation energy is strictly applicable only to reactions that take place in homogeneous media. In the case of an extremely heterogeneous, hyperquenched CaO-MgO-SiO_2 glass, DSC showed the existence of two separate sub-T_g relaxation peaks corresponding to two dynamically, structurally and energetically different domains (Zhang et al., 2013). However, even for a single-step reaction, the temperature dependence of the physical properties gives rise to variations in energy barrier height and, thus, the activation energy (Vyazovkin, 2016). As a consequence, the glass transition process is represented by a distribution of the activation energies (Moeller et al., 2006). For non-isothermal kinetic analyses, model-fits, and model-free methods are usually employed, whereby model fits are often ambiguous in terms of attributing a given reaction mechanism. For this reason, model-free evaluation routines can be used, such as the isoconversional method which allows for the determination of the effective activation energy as a function of conversion progress without assuming any particular form of the reaction mechanism (Vyazovkin, 2006).

The various isoconversional methods which are available for the evaluation of differential scanning calorimetric data can be distinguished into two groups: Differential isoconversional methods such as proposed by Friedman (2007) typically yield sufficiently accurate values of the effective activation energy, however, they are sensitive to noise in the raw data (Vyazovkin, 2016). Alternatively, integral isoconversional methods (Ozawa, 1965; Flynn and Wall, 1966; Vyazovkin, 2001, 2015) are significantly less sensitive to noise in the raw data; consequently, they are the most commonly used model-free methods for calculation of the variable activation energy. Common to both groups of methods, they do not yield the reaction model nor the pre-exponential factor. In order to interpret the obtained varying activation energy, a rational must be found from supporting mechanistic data.

Here, we report on the calorimetric investigation of the structural relaxation in fluoride-phosphate mixed-anion glasses of the type (100-x)$NaPO_3$ – $xAlF_3$ (NAPF) using the integral isoconversional method. In those glasses, large amounts of aluminum fluoride can be dissolved (Brow, 1992; Zhang et al., 2007; Le et al., 2017; Bradtmüller et al., 2018). The simultaneous formation of strong Al—O—P bonds *and* weaker terminal Al—F or P—F bonds reported (Brow, 1992) makes the NAPF system an interesting candidate for studying structural heterogeneity; there are highly constrained, strongly bonded regions (bridging O or F) interspersed among more flexible, less-constrained regions (NBOs or terminal F).

For rationalizing the observation of variable activation energy at the glass transition, we conduct complementary structural investigations of *both* glass former and anion mixing, using ^{31}P, ^{27}Al, and ^{19}F MAS NMR. From DSC analysis, we interpret the variations in activation energy in terms of chemical composition, i.e., changes in dominant intermolecular interactions. Assuming that the activation energy reflects the cooperative dynamics of the glass transition, we examine the activation energy variability as a function of CRR volume. Finally, we relate the distribution of activation energies and average CRR volume to the degree of structural heterogeneity within the glass as determined by NMR.

MATERIALS AND METHODS

In **Table 1** the melting conditions and nominal compositions of the fluorophosphate glasses of this study (NAPF: (100-x)$NaPO_3$ – $xAlF_3$) are given; glasses were prepared using optical-grade raw materials of $NaPO_3$ and AlF_3. We used platinum crucibles to melt batches of 100 g in a muffle furnace for 1.5 h at 850–1,000°C, followed by homogenization for 2 h at 1,000–1,100°C. Melts were cast into preheated graphite molds and annealed at T_g + 50° C for 4 h before cooling to room temperature at a rate of about 3–5 K/min. Due to planned NMR experiments, glasses were prepared with a small addition of CuO, 0.2 wt% (where CuO reduces relaxation times), and all types of measurements were made on these doped glasses. As has been thoroughly explored by Möncke et al. (2018), the loss of fluorine at high melting temperatures (> 850°C) is a common problem; as such, we expect that the actual fluorine content is significantly lower than the reported nominal values. All the same, in a binary series such as this, our current and past results indicate a step-wise increase in AlF_3 content (Le et al., 2017).

NMR Experiments

The ^{31}P NMR spectra were collected routinely and the experimental parameters are reported in our previous paper (Le et al., 2017). The ^{27}Al ssNMR experiments were conducted on a Bruker Avance NMR spectrometer with a 16.45 T magnet (182.46

TABLE 1 | Nominal compositions (mol %) and synthesis conditions for NAPF glass series.

Glass series		NAPF (100-x)$NaPO_3$ – $xAlF_3$				
	X	0	10	20	30	40
Synthesis condition	T [°C]	800	850	900	1,000	1,000
	T [h]	1.5	1.5	1.5	1.5	1.5

MHz ^{27}Al NMR Larmor frequency) using our H-F/C-P probe head for rotors of 2.5 mm diameter. The ^{27}Al NMR chemical shift scale was referenced externally against potassium alum at −0.033 ppm as a secondary reference. The ^{27}Al MAS NMR spectra were acquired after a single 0.31 μs pulse (10 degree pulse angle) at 25.00 kHz sample spinning with 0.2 s repetition times accumulating between 1,024 and 4,096 scans depending on the AlF_3 concentration. The short pulse was used to produce quantifiable spectra on quadrupolar nuclei. A spectrum of an empty rotor acquired under identical conditions but summing 18,000 scans characterized the ^{27}Al background signal. This spectrum was subtracted from the sample ^{27}Al NMR spectra after accounting for the different scan numbers accumulated. The chosen chemical shift ranges for integration of aluminum coordinations are the following: Al[4] (29–60 ppm); Al[5] (5–29 ppm); and Al[6] (−63 – 5 ppm).

The ^{19}F ssNMR experiments were acquired on a Bruker DSX Avance NMR spectrometer with a 9.4 T magnet (400 MHz ^{1}H, and 376.60 MHz ^{19}F NMR Larmor frequencies) using our H-F/C-P probe head for rotors of 2.5 mm diameter. The ^{19}F NMR chemical shift scale was referenced against Teflon at −123.2 ppm as a secondary reference relative to $CFCl_3$ (MacKenzie and Smith, 2002). The ^{19}F MAS NMR spectra were acquired with a Hahn-echo sequence ($\pi/2 - \tau - \pi$ – acquire) with π /2 and π pulse durations of 8.5 and 17 μs, respectively. The echo delay τ was synchronized to one spinner rotation at 25, 23 and 19 kHz MAS spinning frequency ($\tau = 40, 43, 52.6$ μs, respectively). Spin lattice relaxation times, T_1, were estimated from the 0-crossings of an inversion-recovery experiment with Hahn-Echo detection. The samples were acquired with recycle delays between 5 and 8.4 s equal to or exceeding five times the estimated spin lattice relaxation times, which were shortened by the copper doping. Between 16 and 256 scans were accumulated depending on the ^{19}F content. The absence of noteworthy background signal was confirmed on the ^{19}F MAS NMR spectrum of an empty rotor acquired under identical conditions.

Chemical Shielding Calculations

Calculations of the F-19 chemical shieldings were performed using the VASP code (Kresse and Furthmüller, 1996), an implementation of density functional theory using a plane wave basis, periodic boundary conditions, and the projector augmented wave formalism (PAW) (Kresse and Joubert, 1999). The PAW data sets used were those supplied with VASP as the 5.4 release, using the Perdew-Burke-Ernzerhof (PBE) exchange and correlation functional (Perdew et al., 1996). The valence spaces were as follows: F, $2s^22p^5$; Al, $3s^23p$; Na, $2s^22p^63s$; O, $2s^22p^4$; P, $3s^23p^3$. A 700 eV plane wave energy cut-off was used, and a k point mesh spacing of about 0.02 $Å^{-1}$. These values were found to be sufficient to converge the shieldings to better than 1 ppm, in these wide band-gap systems. The shieldings themselves were computed using the gauge-including PAW method (GIPAW, Pickard and Mauri, 2001) as implemented in VASP, in which the electron current due to an external magnetic field is computed to first order in density functional perturbation theory and then used to calculate the nuclear magnetic shieldings.

DSC Measurements

Both, specific heat capacity and non-isothermal DSC, measurements were conducted on a Netzsch STA 449 F3 Jupiter equipped with DSC sample holders. Samples were in a bulk form with mass of around 30 mg and one polished surface in order to ensure good contact with the bottom of the employed platinum crucibles and, hence, the thermal sensor. Each measurement was done in inert atmosphere of N_2 with a flow rate of 20 ml/min. Temperature and heat flow calibrations were done for all heating/cooling rates used in this investigation.

In order to erase the initial thermal history, each glass sample was first heated to a temperature of $T_g + 40$°C, held for 2 min and then cooled down to 60°C at a rate of 20 K/min. The actual DSC scan was subsequently conducted under constant heating rates of 5, 10, 15, and 20 K/min, respectively, up to a peak temperature of T_g + 60°C, followed by cooling back to room temperature at 20 K/min. Each full measurement consisted of two such runs under equivalent conditions. Thereby, the first run was a blank run, with both sample and reference crucibles empty, while the second run had the reference crucible empty and the glass sample in the sample crucible. The temperature program for each run consisted of two subsequent heating and cooling cycles with the same heating/cooling rates. This procedure resulted in four DSC curves per sample, recorded for four different heating rates (5, 10, 15, and 20 K/min).

Specific heat capacity measurements were done in accordance with previous studies (Wondraczek and Behrens, 2007; Wondraczek et al., 2007), using a sapphire crystal as bulk reference material. The specific program consisted of starting at room temperature, then heating up to 40°C, holding for 30 min to equalize the temperature on the samples and furnace, then heating up to $T_g + 60$°C with a heating rate of 20 K/min, holding at T_g + 60°C for another 30 min and finally cooling back to room temperature.

RESULTS

Structure Determination

In order to understand the thermal relaxation processes, the glass structure was analyzed by ^{31}P, ^{19}F, and ^{27}Al MAS NMR. Although the ^{31}P NMR spectra have partially been reported elsewhere (Le et al., 2017), we believe the analysis to be pertinent to the discussion here. As shown in **Figure 1**, the ^{31}P NMR spectrum of pure $NaPO_3$ is dominated by the expected single peak at ∼-20 ppm (assigned as Q^2_{0Al}) with a small contribution near −8 ppm (Q^1_{0Al}). Upon the introduction of 10 mol% AlF_3, two new peaks appear; a peak upfield of each the Q^1_{0Al} and Q^2_{0Al} peaks

at −14 and −26 ppm, respectively. Given that aluminum is an intermediate glass former and similar literature (Le et al., 2017), we assign these new peaks to $Q^1{}_{1Al}$ and $Q^2$1Al, respectively. In this paper, we follow the terminology used by Bradtmüller et al. (2018): $Q^n m$ notation is the typical Q^n notation, with n being the number of homonuclear phosphate bonds and m being the number of aluminum neighbors, whereas in the $P^q m$ notation, q refers to number of total bridging oxygens (P or Al). For the 10 and 20 mol% AlF_3, the peaks with one aluminum neighbor ($Q^1{}_{1Al}$ and $Q^2{}_{1Al}$) grow in at the expense of the $Q^1{}_{0Al}$ and $Q^2{}_{0Al}$ peaks, and commensurately with the amount of AlF_3 in the glass.

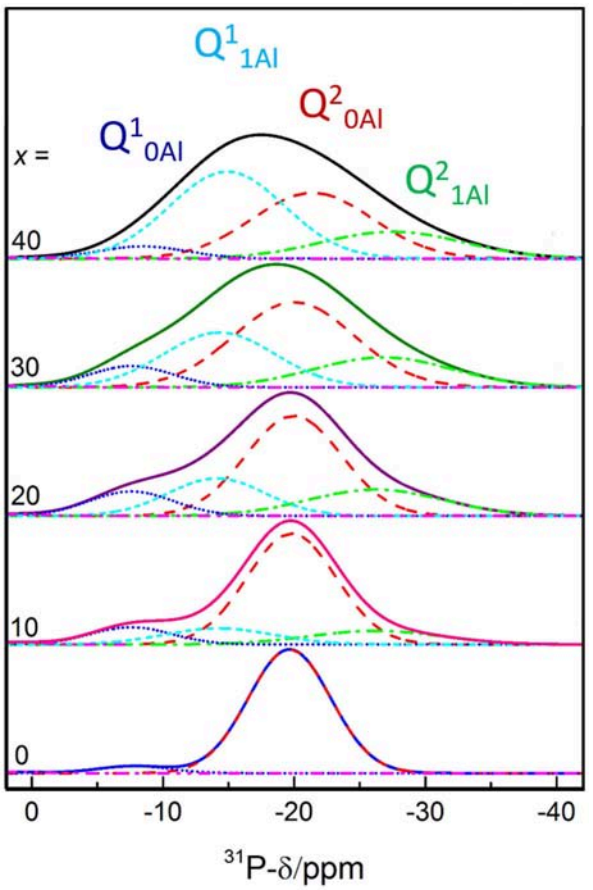

FIGURE 1 | ^{31}P MAS NMR spectra deconvolutions. Modified and reproduced from Le et al. (2017).

Figure 2 displays clearly the evolution of the Q^n_m species with increased AlF_3. For compositions with ≥ 30 mol% AlF_3, a structural change occurs, where now additional AlF_3 results in the formation of $Q^1{}_{1Al}$ species only, with $Q^2{}_{1Al}$ species remaining constant ($Q^1{}_{0Al}$ and $Q^2{}_{0Al}$ continue to decrease). Although the four peaks overlap, the area fractions show the expected monotonic exchange between the Q^n species with and without aluminum neighbors. Moreover, the trends match those of Bradtmüller et al. (2018) found for the same glass series, including the increase and then subsequent decrease of the $Q^1{}_{0Al}$ species. The exact fitting ^{31}P NMR parameters can be found in **Table 2**.

The major advantage of using the P^q_m(q refers to number of total bridging oxygens, P or Al) notation is that we can monitor the connectivity changes in the glass; we observe that although the homonuclear Q^n species, i.e., P—O—P bonds, are decreasing, they are being replaced with equal amounts of heteronuclear P—O—Al bonds. For example, when 10–20 mol% AlF_3 is present in the glass, $P^2{}_{0Al}$ is being replaced with roughly equal amounts of $P^1{}_{0Al}$, $P^2{}_{1Al}$, and $P^3{}_{1Al}$, summing to only small changes in the number of bridging oxygens connected to the phosphate network. For >30 mol% of AlF_3, $P^2{}_{0Al}$ tetrahedra are being replaced with more $P^3{}_{1Al}$ species than $P^1{}_{0Al}$ (we are ignoring the increase in $P^2{}_{1Al}$, since number of BO is the same). Consequently, the total number of bridging oxygens per phosphate tetrahedron is actually increasing for ≥ 30 mol% AlF_3.

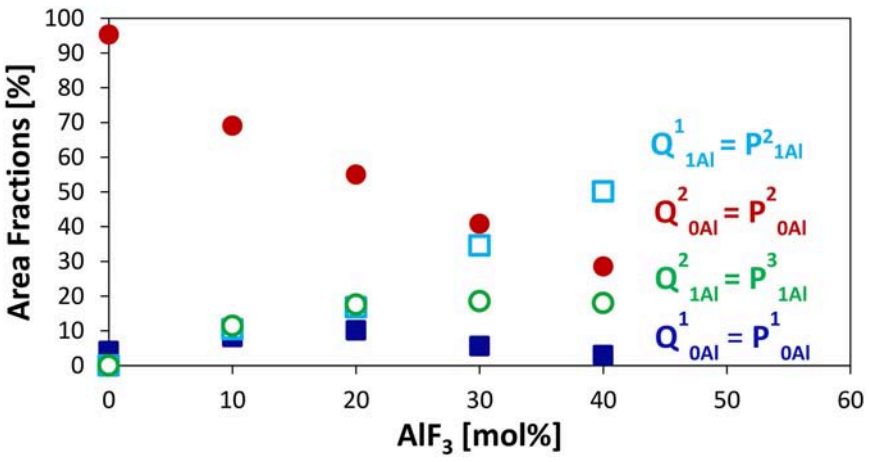

FIGURE 2 | Area Fractions of phosphate $Q^n m$ species (n = number of P neighbors, m = number of Al neighbors) or $P^q m$ (q refers to number of total bridging oxygens, P or Al) from ^{31}P MAS NMR.

TABLE 2 | ^{31}P NMR shifts NMR parameters of (100-x)$NaPO_3$ – xAlF_3 series.

	Q^0			$Q^1_{0Al} = P^1_{0Al}$			$Q^1_{1Al} = P^2_{1Al}$			$Q^2_{0Al} = P^2_{0Al}$			$Q^2_{1Al} = P^3_{1Al}$		
	δ	fwhm	Area	δ	fwhm	Area	δ	fwhm	Area	δ	fwhm	Area	δ	fwhm	Area
	[ppm]	[ppm]	[%]	[ppm]	[ppm]	[%]	[ppm]	[ppm]	[%]	[ppm]	[ppm]	[%]	[ppm]	[ppm]	[%]
X															
0	1.5	5	0.5	−7.8	6.5	4	–	–	–	−19.7	7.4	95	–	–	–
10	1.5	5	0.8	−7.6	7.3	8	−14.3	9.8	10	−19.8	8	69	−26.2	11.8	11
20	1.5	5	0.6	−7.6	7.5	10	−14.1	8.6	17	−20.0	8.7	55	−26.2	12.2	18
30	0.5	5.5	0.5	−7.6	8	6	−14.3	10.9	35	−20.5	10	41	−26.8	12.5	19
40	0	6	0.4	−7.6	9	3	−15.1	11.4	50	−21.6	11	29	−26.8	12.9	18

Modified and reproduced from Le et al. (2017).

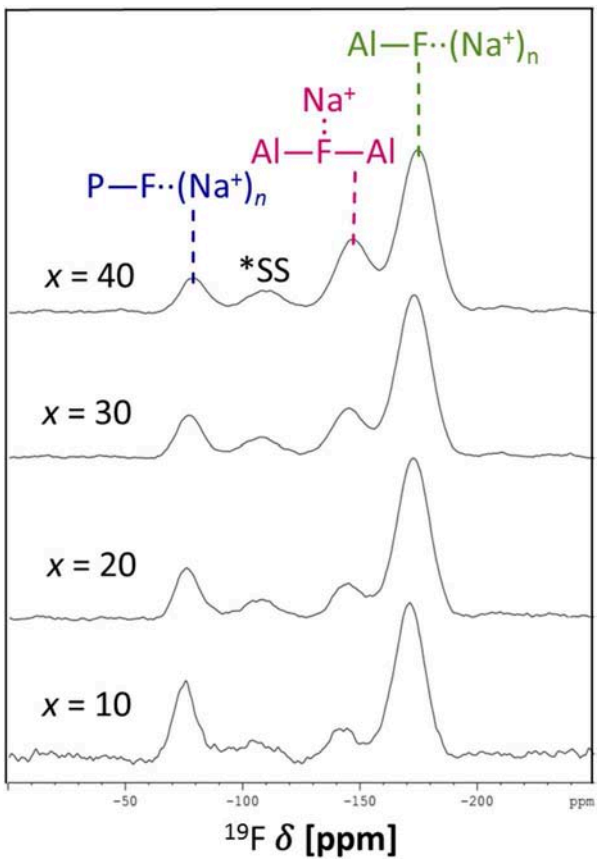

FIGURE 3 | ^{19}F MAS NMR of (100-x)$NaPO_3$ – xAlF_3 series.

The ^{19}F NMR spectra in **Figure 3** reveal three types of fluorine in the glass, i.e., terminal phosphorus-bound [P—F··$(Na^+)_n$], bridging Al—F—Al, and terminal aluminum-bound [Al—F··$(Na^+)_n$] found at −75, −148, and −172 ppm, respectively. The assignments are based on NMR studies of similar glass systems and double resonance NMR experiments, which showed a lack of Al—F—P bonds (Le et al., 2017; Bradtmüller et al., 2018). These assignments are validated further by calculated

TABLE 3 | Computed ^{19}F shifts in various crystal models.

Compound	Site	δ_{iso} [ppm]	Nearest Neighbors
AlF_3	F1	−172	2 Al
Na_3AlF_6	F1	−191	1 Al, 2 Na
	F2	−191	1 Al, 2 Na
	F3	−191	1 Al, 2 Na
$Na_5AlF_2(PO_4)_2$	F1	−170	1 Al, 4 Na
$NaAlFPO_4$	F1	−147	2 Al, 1 Na
Na_2PO_3F	F1	−68	1 P, 1 Na
	F2	−74	1 P, 1 Na

Shifts are referenced such that the computed of AlF_3 appears at −172 ppm, as it does experimentally when referenced to neat $CFCl_3$[1].

TABLE 4 | ^{19}F chemical shifts of (100-x)$NaPO_3$ – xAlF_3 series.

	Al—F··$(Na^+)_n$	Al—F—Al	P—F··$(Na^+)_n$
AlF_3	CS [ppm]	CS [ppm]	CS [ppm]
10	−171.4 ± 0.5	−148 ± 6	−74.7 ± 0.3
20	−172.7 ± 0.1	−146 ± 2	−75.6 ± 0.1
30	−173.1 ± 0.1	−147 ± 2	−76.7 ± 0.5
40	−174.5 ± 0.1	−147.2 ± 0.5	−78.2 ± 0.3

^{19}F NMR chemical shifts for various crystalline compounds (**Table 3**). These calculations reveal that *both* Na^+ neighbors and phosphate next-nearest neighbors change the ^{19}F chemical shifts of pure AlF_3 significantly: sodium coordination changes the ^{19}F chemical shift from −172 ppm (Al—F—Al) in crystalline AlF_3 to −191 ppm for terminal Al—F··$(Na^+)_2$, in Na_3AlF_6. Yet the further addition of phosphate moves the ^{19}F shift back to −170 ppm for terminal Al—F··$(Na^+)_4$ in $Na_5AlF_2(PO_4)_2$ and back to −147 ppm for bridging Al—F—Al with 1 Na^+ neighbor, in $NaAlFPO_4$. The lack of intensity in the ^{19}F spectra at −191 ppm, the computed chemical shift of Na_3AlF_6, indicates that no

[1]The near neighbors to fluorine were determined based on a cut-off of 2.35 Å, with the exception that the fourth Na in $Na_5AlF_2(PO_4)_2$ is slightly farther, at 2.45 Å.

TABLE 5 | ^{19}F intensities of (100-x)$NaPO_3$ – xAlF_3 series.

	Al—F··$(Na^+)_n$	Al—F—Al	P—F··$(Na^+)_n$
AlF_3	Int. [%]	Int. [%]	Int. [%]
10	68 ± 2	10 ± 4	22 ± 6
20	70 ± 2	16 ± 2	14 ± 3
30	67 ± 2	20 ± 3	13 ± 5
40	64 ± 2	29 ± 3	8 ± 2

"islands" of Al, F, and Na exist; the chemical shifts found in these glasses correspond to crystals containing phosphate. Also, these shifts indicate that fluorine is always associated with at least one sodium, even bridging fluorines, which may indicate a preference for F··$(Na^+)_n$ association.

^{19}F NMR spectra collected at three different MAS spinning speeds were fitted using the *dmfit* program (Massiot et al., 2002), accounting for the respective spinning sidebands and their results are given in **Tables 4**, **5**.

Figure 4 shows the progression of fluorine types with further addition of AlF_3 to $NaPO_3$. Within the uncertainty of the peak deconvolution, the relative concentration of Al—F··$(Na^+)_n$ stays constant, however, with increasing AlF_3 and correspondingly decreasing $NaPO_3$ content, P—F··$(Na^+)_n$ is replaced with bridging Al—F—Al (w/one Na^+ neighbor). This result indicates that as more aluminum is available connectivity increases between the aluminum atoms: at high AlF_3 content ($x = 30$, 40 mol%), there are significant amounts of bridging Al—F—Al bonds, ∼17% and ∼24%, respectively. The increase in bridging oxygens per phosphate and appearance of Al—F—Al bonds is likely caused by the decrease of sodium available; P and Al want to form four and six bonds, respectively, but are forced to bond to neighboring glass formers, rather than form non-bridging oxygens or terminal fluorines. It is also worth noting that initially when terminal P—F··$(Na^+)_n$ bonds are prevalent (high sodium), $P^1{}_{0Al}$ and P^3_{1Al} species increase (**Figure 2**), but at low $NaPO_3$ mol%, when P—F··$(Na^+)_n$ bonds are only a small structural contribution, $P^1{}_{0Al}$ and P^3_{1Al} peaks stop growing in; this similarity in trends demonstrates how aluminum fluorine initially adds to the phosphate backbone ($P^1{}_{0Al}$ and P^3_{1Al} species) *when sodium is present* until Al—F—Al bonds begin to dominate and only $P^2{}_{1Al}$ forms.

The ^{27}Al NMR spectra in **Figure 5** reveal that the aluminum site is to a high percentage octahedral (order of and larger than 90%), with a small variation between Al[5]- and Al[4]-fold sites. Given the low intensities of Al[5] and Al[4] coordinations, integration was fixed to a chemical shift range based on the 60$NaPO_3$-40AlF_3 sample, shown in **Figure 5**; our final values are given in **Table 6**. These values agree with the descriptions reported elsewhere on this same glass series: Bradtmüller et al. (2018) demonstrate that at low AlF_3 content, all the aluminum is 6-fold coordinated and only at high amounts of AlF_3 (40 mol%) are small amounts of 5-fold (8%) and 4-fold (1%) aluminum present. Similarly, Brow (Brow, 1992) observed only one central peak at −10 ppm in the ^{27}Al NMR spectra of this glass series, without any evidence for Al[4] or Al[5].

Bradtmüller et al. (2018) complete a comprehensive structural study giving many insights to the role of AlF_3 in these glasses. One major conclusion is that the fluorine is uniformly distributed throughout the glass structure, i.e., no AlF_3-like regions are formed. Using the 2nd moments from several nucleus pairs of double resonance NMR experiments, the authors determine that on average Al[6] is coordinated by four phosphorus and two fluorine atoms, $Al(OP)_4F_2$. Given the similarity in our NMR data as well as phase-pure XRD and optical microscopy results, we also conclude that our glasses contain $Al(OP)_4F_2$ and do not exhibit phase separation.

Brow et al. (1993) have measured and predicted the distribution of Al[4], Al[5], and Al[6] for a related glass system without fluoride, (1-x)$NaPO_3$ – xAl_2O_3. They found that the average Al coordination decreased from six to four as the Al/P ratio increased; specifically, only Al[6] was found at low Al/P, $\leq$ 0.3, while Al[4] dominates at higher Al/P, $\geq$ 0.6. The Al/P ratio of our glass series ranges from 0.1 to 0.7, yet no significant differences in Al-speciation are observed between samples, i.e., no dependence on amount of AlF_3 is found, indicating that fluorine is affecting the glass structure in a different way compared to oxygen.

The strong effect of fluoride addition upon Al coordination can be seen in **Figure 6**, where fluoride content clearly favors 6-fold aluminum at any Al/P ratio. Similar to our results, Zhang et al. (2007) found for sol-gel-derived glasses along the composition lines Na/Al/P/F 2:x:2:1, 2:2:x:1, 2:2:2:x, and x:2:2:x, respectively, that *both* low Al/P (< 1) and high F/Al (or F/P) ratio were associated with increased fraction of Al[6]. The Al/P ratio still plays a role: at lower Al/P ratio, less fluorine drastically increases the average Al coordination, which agrees well with our ^{27}Al NMR data. If we compare [F]/[Al+P] ratios for Zhang et al. (2007) and our glass system (indicated by degree of shading in **Figure 6**), all of our samples have higher [F]/[Al+P] ratios (and therefore higher proportion of Al[6], with the exception of the 90$NaPO_3$-10AlF_3 sample, which also has the lowest Al/P ratio). These two factors, Al/P ratio and fluorine content, are the reason we see nearly no variation in Al speciation, unlike the corresponding (1-x)$NaPO_3$ – xAl_2O_3 series.

The next several structural figures use valence unit [V.U.] theory (Bunker et al., 1991) to understand the driving forces behind the propensity of aluminum to form Al[6] in the presence of fluorine. Valence unit [V.U.] theory proposes that strong cations have V.U. equal to their valence which are shared by the number of bonds they form, i.e., tetrahedral P^{5+} has 5 V.U. shared among four bonds. Additionally, oxygen bonds must sum up to 2 V.U., while modifying ions are more fungible (0.1-−0.4 V.U. each). Due to the chemical complexity of our system, rather than finding crystals of corresponding composition, we have decided to focus on the fluoride bonding between aluminum and phosphorus. Brow et al. (1993) have used valence bond theory to explain the bonding in aluminophosphate glasses, specifically the equilibrium of Al[4] and Al[6] units as a function of Al/P. **Figure 7A** demonstrates that at low Al/P, $\leq$ 0.3, the fluoride bond in Al[4]—F—Al[4] is overbonded. Moreover, in

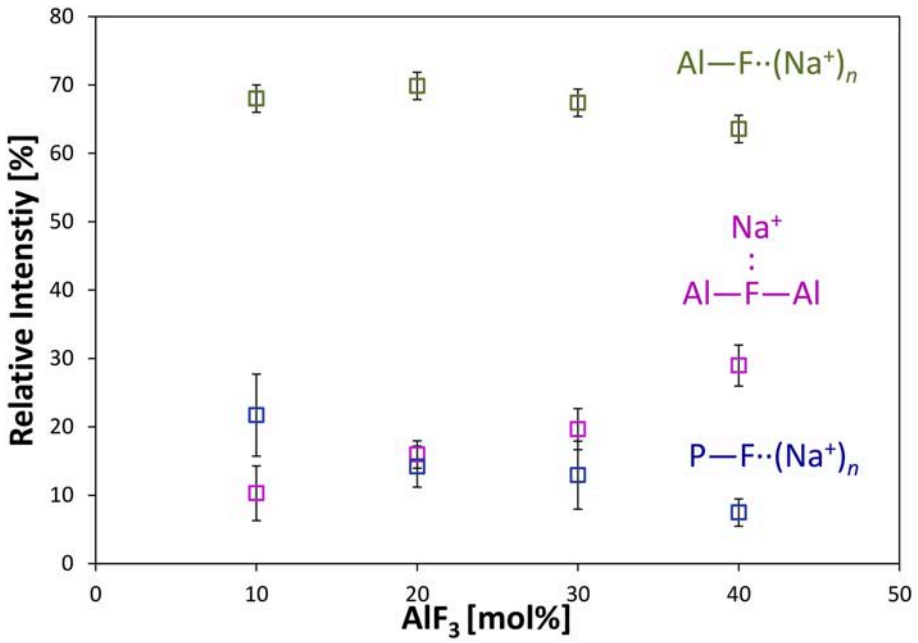

FIGURE 4 | Average area fractions (over different spinning speeds) from ^{19}F MAS NMR of different types of fluorine atoms: terminal P—F··$(Na^+)_n$, bridging Al—F—Al, and terminal Al—F··$(Na^+)_n$ bonds.

Figure 7B, we observe at the same low Al/P ratio, fluorine is overbonded in P—F—Al[4] and energetically unfavored (even when the NBO and terminal F possess maximum ionicity, *blue values*). In fact P—F··$(Na^+)_n$ bonds are much preferred and in agreement with the ^{19}F NMR results: at low Al/P, 10-−20 mol% AlF_3, P—F··$(Na^+)_n$ bonding is prevalent. Indeed, the experimental and calculated ^{19}F chemical shifts indicate that fluorine, even bridging Al—F—Al bonds have at least one coordinated Na^+, with terminal fluorines likely requiring more Na^+ partners; as such, we assume that every terminal fluorine has one Na^+ contributing 1/6 V.U.

On the one hand, **Figure 7C** clearly indicates the high stability of the bridging fluoride in Al[6]—F—Al[6], with it being preferred over P—F··$(Na^+)_n$ once sufficient aluminum is available at higher Al/P, 30-−40 mol% AlF_3 (^{19}F NMR). Yet we know that P—F—Al[6] is still not formed: **Figure 7D** proposes that the high electron density (1.8 V.U.) on two NBOs of the phosphate tetrahedra is unstable. In metaphosphate the maximum V.U. on the two NBOs is 1.5 (which can also be intraconverted into 2.0 and 1.0 VU or a double and single bond, respectively), thus there is likely a resonance stabilization which cannot be achieved in **Figure 7D**.

Finally, we find it interesting that at low phosphate content, the aluminum coordination is significantly less sensitive to fluorine content; even at the same [F]/[Al+P], the average aluminum coordination is five rather than six observed in Zhang's data (Zhang et al., 2007). **Figure 8** indicates that terminal fluorine have more flexibility in their valence (compared with bridging anions), therefore, they can compensate to ensure the bridging fluorine in Al—F—Al is not overbonded. There appears to be a large difference in Al/P of 0.67 and Al/P of 1.0, yet as it is always associated with terminal fluorines, the amount of sodium also plays a significant role; when an aluminum can have at least two terminal fluorines it can remain as Al[4] (right side), however, if two P—O—Al bonds are formed (low sodium), then the aluminum prefers Al[6] to accommodate more bridging oxygens (left side).

Thermal Analysis

Examples of endothermic peaks corresponding to the glass transition in NAPF glass ($x = 20$), using heating rates of 5, 10, 15, and 20 K/min, are shown in **Figure 9**. It is evident, from **Figure 9**, that the glass transition temperature (T_g) shifts to higher values with increasing heating rate, illustrating the kinetic nature of the glass transition.

In order to estimate the activation energy as a function of the extent of conversion (α), the integral isoconversional method proposed by Vyazovkin (2015) was applied to the non-isothermal DSC data. Here, variable activation energies (E_α) are calculated by minimizing the function:

$$\Phi\left(E_\alpha\right) = \sum_{i=1}^{n} \sum_{j \neq i}^{n} \frac{J[E_\alpha, T_i\left(t_\alpha\right)]}{J[E_\alpha,\ T_j\left(t_\alpha\right)]} \tag{1}$$

with the integral $J[E_\alpha,\ T\left(t_\alpha\right)]$

$$J[E_\alpha, T_i\left(t_\alpha\right)] \equiv \int_{t_\alpha - \Delta\alpha}^{t_\alpha} exp\left[\frac{-E_\alpha}{RT_i(t)}\right] dt \tag{2}$$

In Equation 2, $T_i(t)$, $i = 1 \ldots n$, is a set of arbitrary temperature programs and R is the universal gas constant. The method relies

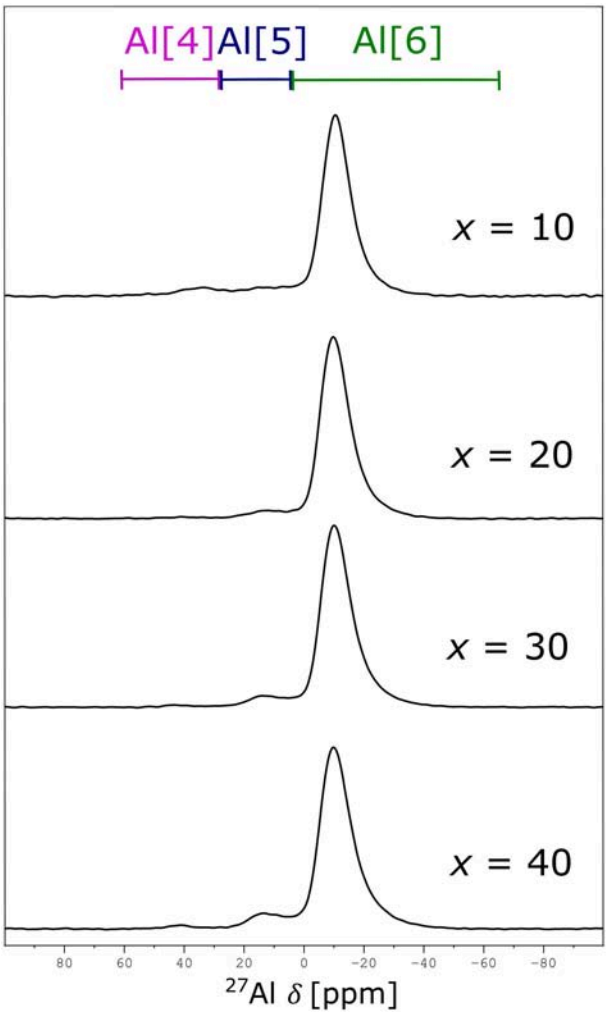

FIGURE 5 | ^{27}Al MAS NMR of (100-*x*)$NaPO_3$ – *x*AlF_3 series.

TABLE 6 | Chemical shift ranges and integration of (100-*x*)$NaPO_3$ – *x*AlF_3 series from ^{27}Al MAS NMR.

	Range Integrated Over [ppm]		
Start	60.2	29.4	5.1
End	29.4	5.1	−63.3
	Relative Intensity [%]		
%AlF_3	Al[4]	Al[5]	Al[6]
10	5	7	88
20	1	4	95
30	1	6	93
40	2	8	91

The uncertainties of all the relative intensities is ±2%.

on direct numerical integration without any approximations. In the next step, the progress of conversion is defined,

$$\alpha = \frac{(\Phi - \Phi_g)|_T}{(\Phi_l - \Phi_g)|_T} \quad (3)$$

where Φ is the heat flow at a given temperature T, and Φ_l and Φ_g represent heat flow values for the liquid and glass phases extrapolated to the same temperature T (inset of **Figure 9**).

The application of the aforementioned procedure results in α vs. Tcurves (**Figure 10**). The endothermic overshoot which is observed during heating gives rise to α-values which are formally higher than 1, however, the iso-conversional calculations for measurements performed on heating require only the ascending part of the α vs. Tcurves in the limit of $\alpha = 1$.

The activation energies as a function of both conversion extent and temperature are shown in **Figure 11**. The $E_\alpha$vs. α and E_α vs. T representations are linked to each other because they are two projections of the same line that cuts through the three-dimensional surface $E(\alpha, T)$. The line is determined by the α vs. T trace, which is simply a kinetic curve measured at a given heating rate (Vyazovkin, 2018). Based on the data presented in **Figure 11**, we find that the reduction of $NaPO_3/AlF_3$ ratio leads to an increase in E_α values, as well as an increase in the range of activation energies with conversion progress. Addition of 10 mol% AlF_3 causes a small but progressive change in E_α, but not in the range of activation energies. Activation energy in these glasses ($x = 0, 10$) can be considered as constant during the glass transition process, which according to Vyazovkin (2018) can be interpreted as an effectively single-mode relaxation, characterized by an almost constant degree of molecular cooperativity. The near-constant activation energy typically indicates that the rate of a multistep process is either limited or dominated by the rate of one step. When more AlF_3 is added, a distinct peak in E_a develops indicating a pronounced multi-mode relaxation process. The activation energy of the lowest process is equal to that at low AlF_3 content, yet the highest-energy step increases significantly, signifying that a different, higher-energy process is being introduced.

The characteristic volume of the cooperatively rearranging region (CRR) at the glass transition temperature (V_ξ) can be obtained from calorimetric data (Donth, 1982):

$$V_\xi = \xi^3 = \frac{k_B T_g^{\,2} \left(\frac{1}{c_V^{glass}} - \frac{1}{c_V^{liquid}} \right)}{\rho (\delta T)^2} \quad (4)$$

where, ξ represents characteristic length (size of CRR), T_g is the glass transition temperature, c_V is the specific heat at constant volume, ρ is density of the sample, k_B is the Boltzman constant and δT is the average temperature fluctuation of an average CRR. Specific heat capacity, c_V, is a function of the structure of the material itself and depends on the number of degrees of freedom of motion that are available; the larger the number of degrees of freedom available to the particles of the material, the larger the specific heat capacity of the material. Kinetic energy of the particles in the material, i.e., translation and rotation of polyatomic molecules, is only one of the many possible types of degrees of freedom which manifests as a temperature change; some thermal energy may also be stored as the potential energy

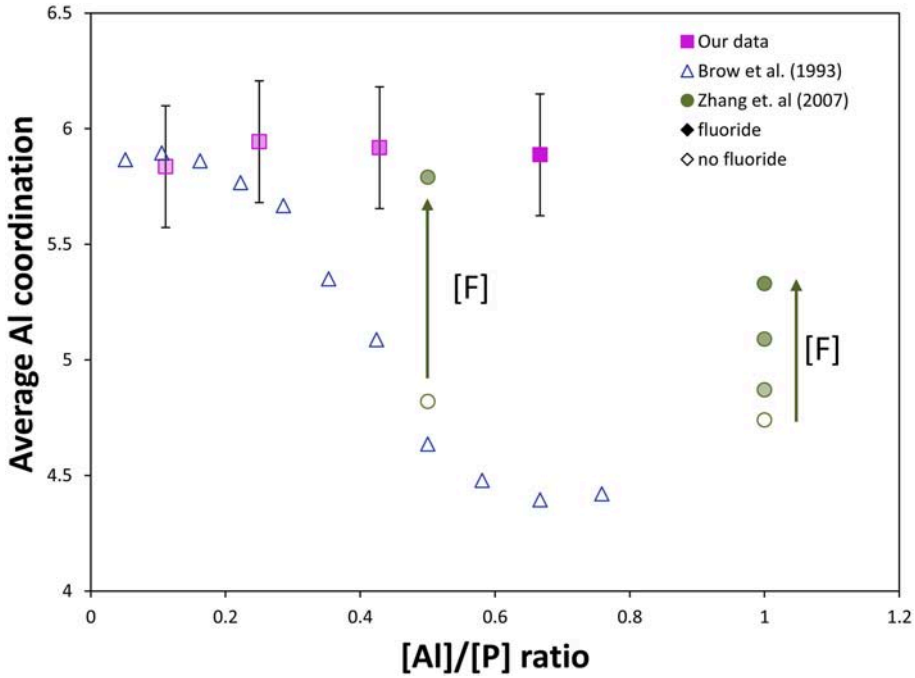

FIGURE 6 | Comparison of our NMR data to literature NMR data from Brow et al. (1993) and Zhang et al. (2007, 2013). Effect of [Al]/[P] ratio and fluorine content on the average Al coordination in aluminophosphate and fluoroaluminophosphate series (completely shaded markers have the most fluoride, [F]/[Al+P] = 1.2, and unshaded markers have no fluoride content, [F]/[Al+P] = 0). Without fluorine, substantial Al[6] only forms at very low [Al]/[P], ≤ 0.3. The effect of fluorine content on the Al coordination can be observed: addition of fluoride ([F]/[P] = 0.5) forces most Al content into Al[6] despite a much higher [Al]/[P] (∼0.5) compared with only aluminophosphate, while at sufficiently high [Al]/[P] (∼1), much more fluoride content can be added without forcing all aluminum into 6-fold coordination (some remains as Al[4] and Al[5]).

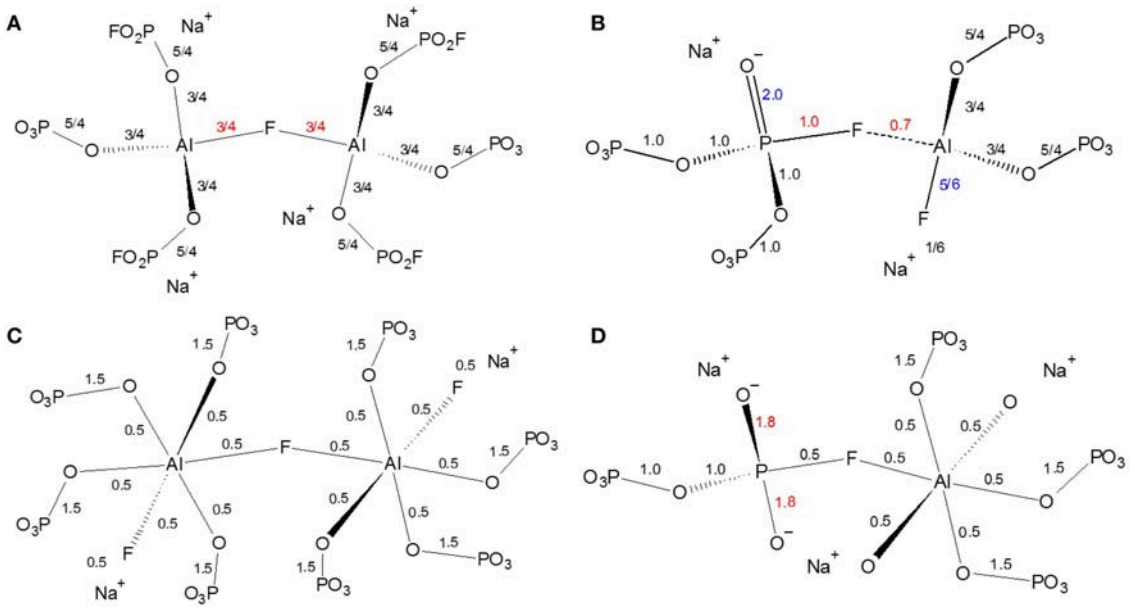

FIGURE 7 | Effect of fluoride in fluoroaluminophosphate glass in phosphate-rich (low Al/P ratio, 0.3) environment **(A)** instability of Al[4]—F—Al[4] bond; **(B)** Instability of P—F—Al[4] bond; **(C)** Al[6]—F—Al[6] bond; **(D)** Instability of P—F—Al[6] bond.

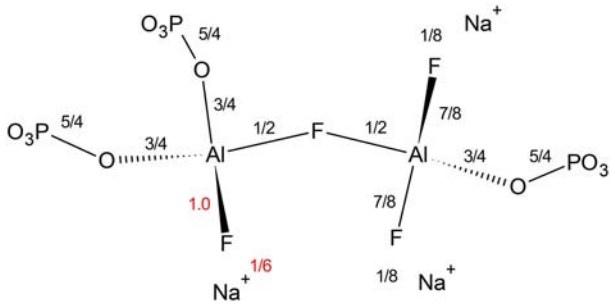

FIGURE 8 | Effect of increasing fluoride on Al[4]—F—Al[4] bond in Al/P ratios of 0.67 (right side) and 1.0 (left side) environment. We are assuming all terminal fluorines have one coordinated Na^+.

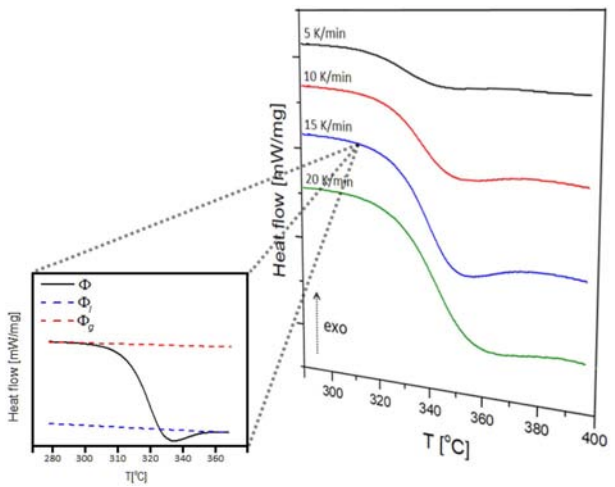

FIGURE 9 | Multiple heating rate DSC curves of $80NaPO_3 - 20AlF_3$ glass and determination of the extent of conversion at the heating rate of 15 K/min.

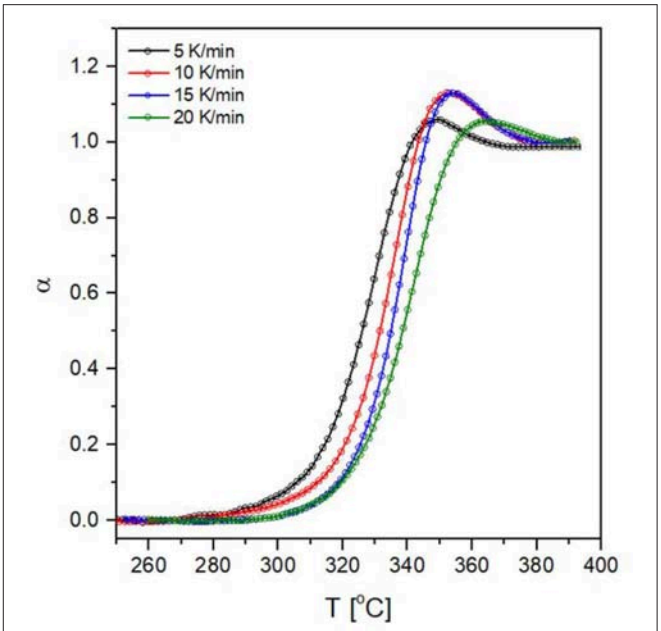

FIGURE 10 | Conversion against temperature curves for the glass transition of $80NaPO_3 - 20AlF_3$ glass at four heating rates.

associated with higher energy modes of vibration, often occurring in interatomic bonds in a glass. These two types of energy, kinetic and potential, represent the degrees of freedom of motion which classically contribute to the heat capacity of a thermodynamic system.

Reliable values of $\Delta 1/c_p$ and δT can be calculated according to Hempel et al. (2000) (**Figure 12**):

$$\Delta\,(1/c_v) = \left(\frac{1}{c_v}\right)^{glass} - \left(\frac{1}{c_v}\right)^{liquid} \approx \left(\Delta\frac{1}{c_p}\right) \approx \left(\frac{\Delta c_p}{c_p^{\,2}}\right)\left(1 + \left(\frac{1}{4}\right)\left(\frac{\Delta c_p}{c_p}\right)^2 + \ldots\right) \quad (5)$$

where c_p and c_v are specific heats (J/mol·K) at constant pressure and volume, respectively. δT represents the mean-square temperature fluctuation of one average CRR, and it is, in the case of specific heat measurements upon heating, calculated as Hempel et al. (2000):

$$\delta T = \frac{\Delta T}{2.5} \quad (6)$$

Since our specific heat measurements were done under constant pressure, the approximation $\Delta c_p \approx \Delta c_v$ was made in Equation 5 in order to calculate the characteristic volume of the CRR (Equation 4). Previously published Δc_p and Δc_v values (O'Reilly, 1977) were used to calculate a correction factor, S, determined from four small-molecule glass formers and 14 polymers (Hempel et al., 2000):

$$S \equiv \frac{\Delta(1/c_v)}{\Delta(1/c_p)} = 0.74 \pm 0.2 \quad (7)$$

where ± 0.22 is the standard deviation. All V_ξ values (**Figure 13**) are corrected by $S = 0.74$.

Taking the variability of activation energy as the difference between its minimum and maximum values, we find a relationship between activation energy variability and CRR volume (**Figure 13**): the activation energy variability decreases exponentially with increasing CRR volume.

DISCUSSION

To better visualize the changes in the phosphate network with increasing AlF_3 content, we begin with a schematic of pure $NaPO_3$ glass in **Figure 14A**. Although PO_4^{3-} are tetrahedra in the glass, we have chosen to represent them with triangles in 2d space. As in the glass, most phosphate tetrahedra

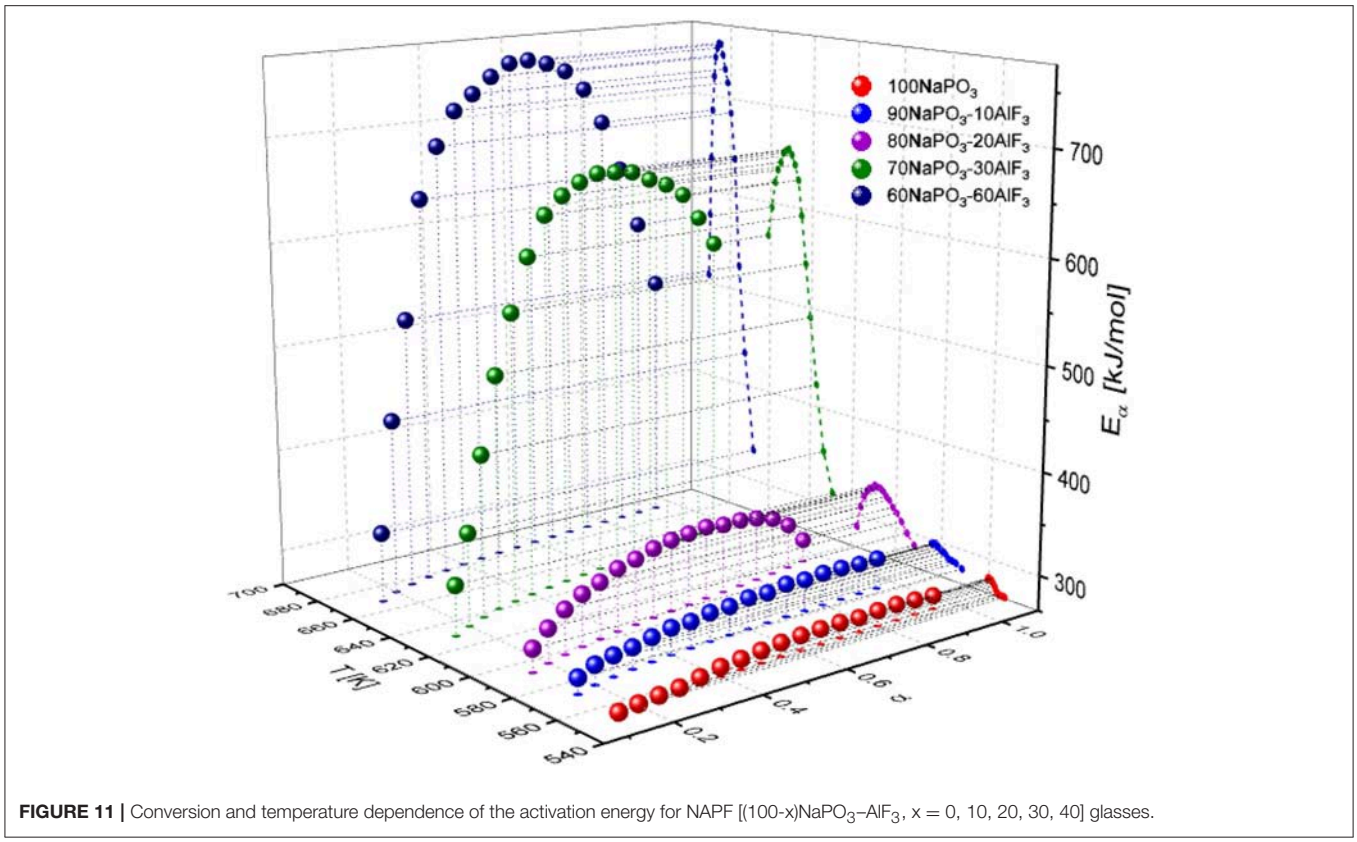

FIGURE 11 | Conversion and temperature dependence of the activation energy for NAPF [(100-x)$NaPO_3$–AlF_3, x = 0, 10, 20, 30, 40] glasses.

are $Q^2{}_{0Al}$ species and the average phosphate chain length is five tetrahedra (grouped in yellow). This is a relatively long chain length and represents a large cooperatively rearranging region (grouped in yellow), calculated to have volume of ∼70 nm^3 in **Figure 14Aa** (≈4 nm in effective diameter, or 10^3 phosphate tetrahedra, using molar volume Le et al., 2017). As CRR was defined earlier, we expect each phosphate chain to be able to rearrange independently of its environment. Despite some variation in chain length, the individual tetrahedra in the phosphate chains experience very similar bonding environments and the E_a required to plastically deform each chain is roughly equal. Consequently, the glass transition is dominated by one process with a relatively low E_a of 300 kJ/mol (**Figure 11**).

Addition of AlF_3 results in the formation of $Al(OP)_4F_2$ groups (Bradtmüller et al., 2018) causing a sufficient increase in the degree of molecular cooperativity to raise the activation energy barrier slightly, compared with sodium metaphosphate glass. Although the connectivity of the pure phosphate backbone is decreasing, the $P^2{}_{0Al-}$ are being replaced by $P^1{}_{0Al}$, $P^2{}_{1Al}$, and $P^3{}_{1Al}$ (**Figure 2**) maintaining the number of BOs per tetrahedra and bonding to Al, which in turn, is connected to four other phosphorus atoms through bridging oxygens (as $Al(OP)_4F_2$) (Bradtmüller et al., 2018). In terms of connectivity, $Al(OP)_4F_2$ may be considered as a Q^4 species, thus we argue that the introduction of AlF_3 increases the connectivity of the glass, which agrees with the higher activation energy observed for 10–20 mol% AlF_3 in **Figure 11**. Moreover,

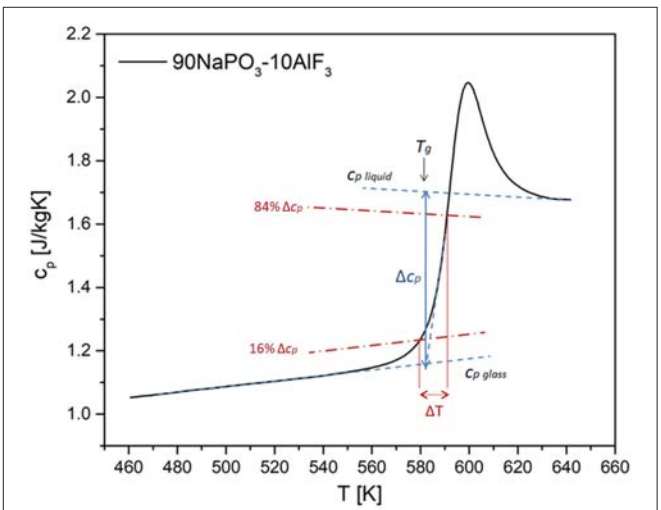

FIGURE 12 | Scheme for the determination of the quantities needed for the calculation of the CRR volume based on specific heat measurements using DSC.

there has been evidence that the introduction of halides encourages reforming of BOs from NBOs (Baasner et al., 2014); halides' bonding preference for modifiers is sufficiently strong so that the halides pull the modifiers from the phosphate backbone. In the case of $x = 20$, activation energy values

are a bit higher compared to that of $x = 10$, due to increased connectivity *via* more heteronuclear BOs between phosphate tetrahedra (Al—O—P), some bridging fluorines (Al—F—Al) and possibly some reformed P—O—P bonds as well.

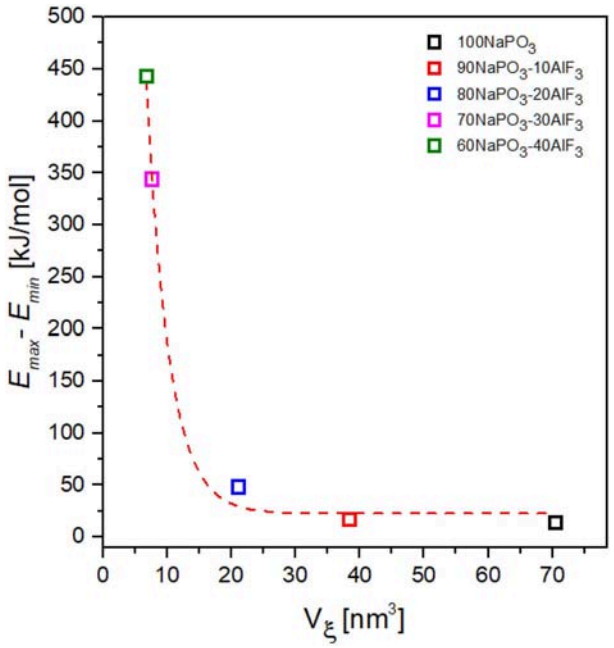

FIGURE 13 | Dependence of the activation energy variability on CRR volume for NAPF [(100-*x*)$NaPO_3$ – *x*AlF_3, $x = 0, 10, 20, 30, 40$] glasses.

In addition to increasing connectivity, $Al(OP)_4F_2$ is significantly more constrained than only Q^2 phosphate chains. The glass transition involves energy on the scale of plastic deformation and the $Al(OP)_4F_2$ octahedra can be thought as *pin* defects between phosphate chain segments. Nonetheless, the *average* phosphate chain length is much lower, 2.5 tetrahedra (grouped in yellow), making the calculated average CRR volume smaller as well (≈20–40 nm^3, corresponding to some 300–600 formula units of glass).

At the highest AlF_3 content, in **Figure 14C**, we introduce some bridging fluorines between $Al(OP)_4F_2$ octahedra. More AlF_3 results in further depolymerization of the phosphate backbone, but also the creation of more substantial grain-boundary-like AlF_3 chains. Here the CRRs (grouped in yellow) are very small (≈10 nm^3, < 200 formula units). The structural ensemble is becoming more heterogeneous in terms of the selective precipitation of super-structural units; the $Al(OP)_4F_2$ octahedra are significantly more constrained (more than four bridges to neighboring Al or P) than phosphate tetrahedra (less than two bridges to neighboring Al or P). This is similar to the structurally and dynamically heterogeneous domains found by Moesgaard et al. (2010) in calcium aluminosilicate: regions of highly constrained, alternating AlO_4 and SiO_4 tetrahedra located between more mobile, depolymerized calcium SiO_4 domains. As Brow (Brow, 1992) discusses, AlF_3 addition creates strong Al—O—P bonds, while simultaneously producing unconstrained terminal phosphorus-bound and aluminum-bound F-. As such, we expect that in contrast to highly constrained $Al(OP)_4F_2$ octahedra, there are also highly mobile phosphate regions with terminal fluorines.

A high AlF_3:$NaPO_3$ ratio ($x = 30, 40$) results in a large increase in activation energy (up to 700 kJ/mol) and a large

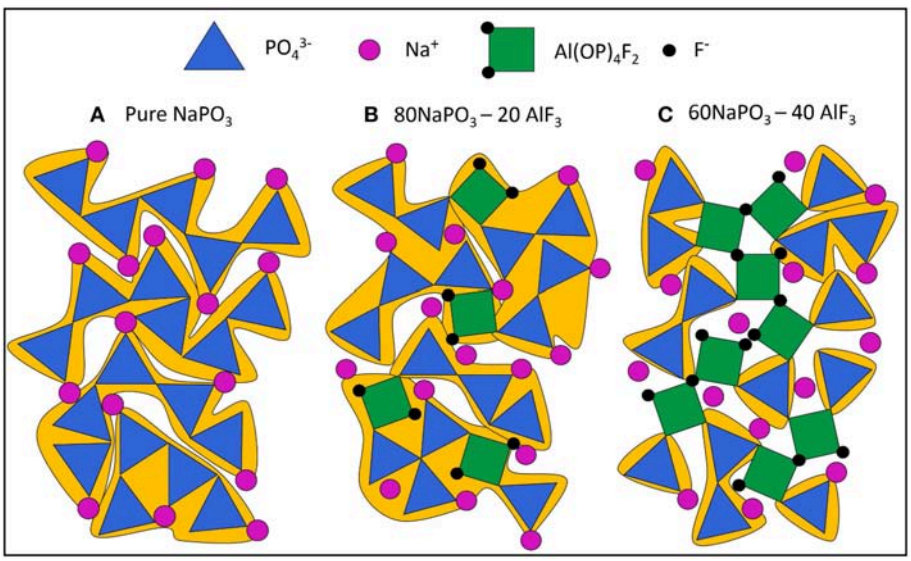

FIGURE 14 | Manually drawn schematic of **(A)** pure $NaPO_3$ glass, all Q^2 chains and an average chain length of 5 phosphate tetrahedra (large CRR, ≈ 70 nm^3, 10^3 phosphate tetrahedra for real system); **(B)** 80$NaPO_3$ – 20AlF_3, Q^1, and Q^2 species present and an average chain length of 2.5 phosphate tetrahedra (smaller CRR, ≈ 20 – 40 nm^3, 300 – 600 formula units in real system) and **(C)** 60$NaPO_3$ – 40AlF_3, Q^1, and Q^2 species present and an average chain length of 1 phosphate tetrahedra (smallest CRR, ≈ 10 nm^3, < 200 formula units in real system). Highlights the Al—F—Al bridges leading to high energy barrier for some CRR.

difference between the minimum and the maximum of the activation energy (450 kJ/mol). Interestingly, in **Figure 11** the activation energy minima remain relatively constant as AlF_3 is introduced (increasing from ∼275 to 325 kJ/mol), indicating that a similar relaxation process is present in all samples which involves the pure $NaPO_3$ component; when we assign the minimum E_a mode to $P^2{}_m$ phosphate chains, with or without Al or F^- neighbors, there appear to be only small differences based on the chemical identity of neighbors with number of constraints being the dominant factor.

At $x \geq 30$, a major structural change occurs; the aluminum-bound fluorine bridges (Al—F—Al) become more common than the phosphorus-bound terminal fluorines ($P—F\cdot\cdot(Na^+)_n$) and more BOs per phosphate tetrahedron are formed, leading to a sharp increase in the connectivity of the glass structure. According to the results shown in **Figure 11**, increase in temperature (conversion) up to around $\alpha = 0.5$ enhances molecular motion and increases the degree of molecular cooperativity leading to an increase in activation energy. Since the $Al(OP)_4F_2$ is highly constrained, all the neighboring phosphate chains need to be mobile before the $Al(OP)_4F_2$ participates cooperatively. As a result, the rearrangement of the regions involving $Al(OP)_4F_2$ lag behind those composed of mostly phosphate chains, but also have higher activation energies (stronger Al—O—P bonds). As α increases from 0.5 to 1, the free volume continues to increase and the bonds become weaker and longer, decreasing the activation energy of the relaxation processes as well as giving polyhedra more freedom of motion, resulting in higher probabilities of less cooperative motion.

The exact size or length of the two heterogeneous domains, $Al(OP)_4F_2$ octahedra and phosphate tetrahedra chains, is not known, however based on the ^{19}F, we expect mostly isolated $Al(OP)_4F_2$ octahedra at low AlF_3 and as more AlF_3 is introduced, $Al(OP)_4F_2$ octahedra form dimers, followed by longer $Al(OP)_4F_2$ octahedra "chains" (larger domain size). Consequently, at low AlF_3 content, the isolated $Al(OP)_4F_2$ octahedra domains are much shorter than the phosphate chains. Yet, at high AlF_3 content, half of the phosphate groups are no longer in chains, but are isolated pyrophosphate groups (Q^1, $P_2O_7^{4-}$). If we assume each $Al(OP)_4F_2$ octahedra has two F^- bonds and that no Al—O—Al bonds form, the ^{19}F NMR informs us that at high AlF_3 content, roughly half of the $Al(OP)_4F_2$ octahedra bond to another $Al(OP)_4F_2$ octahedron (dimers or longer "chains"); therefore, the sizes of the two domains [$Al(OP)_4F_2$ octahedra and phosphate tetrahedra] overlap and are much more comparable at high AlF_3 content. This similarity in domain size may be another reason for Al—F—Al bonding being such a crucial factor in determining the thermal relaxation behavior.

The structural schematics presented in **Figure 14** demonstrate clearly the decrease in CRR, however, they less accurately portray the structural relaxation with increasing temperature. Although $Al(OP)_4F_2$ octahedra separate the glass network into differently sized phosphate regions, when the glass relaxes, the phosphate regions do not relax completely, leaving frozen $Al(OP)_4F_2$ regions behind. We believe that this is more akin to lower aluminum-to-phosphorus regions cooperatively rearranging, followed by regions with higher aluminum-to-phosphorus ratios. This creates a topologically heterogeneous glass composed of faster (low E_a) and slower (high E_a) relaxing regions. We believe these higher E_a relaxation modes to govern macroscopic properties other than the T_g; shear and bulk modulus also increase non-linearly for samples with ≥ 30% AlF_3 content (without the commensurate non-linear increase in molar volume, packing density or volume density of bonding energy; Le et al., 2017).

CONCLUSION

^{31}P NMR indicated that the introduction of AlF_3 increases the average connectivity in the glass through heteronuclear Al—O—P bonding, i.e., replacement of $P^2{}_{0Al}$ with $P^2{}_{1Al}$ and formation of P^3_{1Al} at high AlF_3 content, and the forced association of Na^+ with terminal fluorines. ^{19}F NMR revealed that AlF_3 adds to the phosphate backbone mostly as $Al—F\cdot\cdot(Na^+)_n$, with initial AlF_3 addition creating $P—F\cdot\cdot(Na^+)_n$ bonds until the lack of sodium and availability of aluminum force Al—F—Al bonds to become more dominant at 30 mol% AlF_3. DFT calculations verified the ^{19}F assignments, lack of Al—F—P bonds and the strong coordination of Na^+ with *both* bridging and terminal fluorine. In agreement with other ^{27}Al NMR results, we found that low Al/P ratio or high fluorine content result in Al[6] sites being the dominant species negligible Al[5] and Al[4] sites at high AlF_3 content; based on Bradtmüller et al's. [15] investigation, we conclude that our system also contains octahedral $Al(OP)_4F_2$. Finally, we used Valence Unit theory to explain the instability of Al—F—P bonds, while demonstrating the preference for Al[6]—F—Al[6]; similarly, we used V.U. theory to discuss the role of sodium in the formation of $P—F\cdot\cdot(Na^+)_n$ and Al[4]—F—Al[4] bonds.

Multinuclear NMR analysis allowed us to produce structural schematics that demonstrate the structural and topological differences which occur as a function of AlF_3 and relate the trends to relaxation processes. Concurrent with the rise in maximum E_a, the variability of the E_a for the glass transition also increases with increasing AlF_3 content. We proposed that there are phosphate-rich regions which are more like $NaPO_3$ without many bridging bonds to Al, but at the same time, there are $Al(OP)_4F_2$-rich regions that are much more topologically constrained. As more AlF_3 is added, some glass regions become increasing constrained due to more Al—F—Al and Al—O—P cross-links, which increases further ΔE_a. At the same time, $P—F\cdot\cdot(Na^+)_n$ bonds create less constrained, flexible regions that have similarly low E_a as phosphate chains in pure $NaPO_3$. The large difference between minimum and maximum E_a indicates that the glass transition is composed of several different-energy structural relaxation processes and that the glass structure is heterogeneous on the length-scale of these processes.

Surprisingly, despite a higher maximum E_a for relaxation processes and a higher connectivity in the glass network at high AlF_3 content, an on average smaller volume of cooperatively rearranging regions is found for glasses with higher

fluorine content. The $Al(OP)_4F_2$ octahedra are significantly more topologically constrained and break up the phosphate network into smaller phosphate chains, similar to pin defects in granular materials. The observed decrease in the *average* CRR size agrees with the results from ^{31}P NMR: the average homonuclear phosphate chain length decreases with increasing AlF_3 content (mostly P^2_{1Al} at high AlF_3).

DATA AVAILABILITY

All datasets generated for this study are included in the manuscript and/or the supplementary files.

AUTHOR CONTRIBUTIONS

CC, LW, JP, and UW-Z conceived and planned the experiments. JP (thermal analysis) and UW-Z (NMR) performed the experiments, processed the experimental data and performed the analysis. JZ planned and carried out simulations. QL manufactured the samples. LW, CC, QL, UW-Z, JP, and JZ contributed to the interpretation of the results. CC took the lead in writing the discussion and manuscript with contributions from all authors. All authors provided critical feedback and helped shape the research, analysis and manuscript.

FUNDING

This project has received funding from the European Research Council (ERC) under the European Union's Horizon 2020 research and innovation program (ERC grant UTOPES, grant agreement no. 681652). CC is grateful to the Natural Sciences and Engineering Research Council of Canada (NSERC) for financial support.

REFERENCES

Adam, G., and Gibbs, J. H. (1965). On the temperature dependence of cooperative relaxation properties in glass-forming liquids. *J. Chem. Phys.* 43, 139–146. doi: 10.1063/1.1696442

Baasner, M., Hung, I., Kemp, T. F., Dupree, R., Schmidt, B. C., and Webb, S. L. (2014). Constraints on the incorporation mechanism of chlorine in peralkaline and peraluminous Na2O-CaO-Al2O3-SiO2 glasses. *Am. Mineral.* 99, 1713–1723. doi: 10.2138/am.2014.4717

Benzine, O., Bruns, S., Pan, Z., Durst, K., and Wondraczek, L. (2018). Local deformation of glasses is mediated by rigidity fluctuation on nanometer scale. *Adv. Sci.* 5:916. doi: 10.1002/advs.201800916

Bradtmüller, H., Zhang, L., de Araujo, C. C., Eckert, H., Möncke, D., and Ehrt, D. (2018). Structural studies of $NaPO_3$-AlF_3 glasses by high-resolution double-resonance NMR spectroscopy. *J. Phys. Chem. C* 122, 21579–21588. doi: 10.1021/acs.jpcc.8b06162

Brow, R. K. (1992). A multinuclear MAS NMR study of the short-range structure of fluorophosphate glass. *J. Mater. Res.* 7:1892. doi: 10.1557/JMR.1992.1892

Brow, R. K., Kirkpatrick, R. J., and Turner, G. L. (1993). Nature of alumina in phosphate glass: II, Structure of sodium aluminophosphate glass. *J. Am. Ceram. Soc.* 76, 919–928. doi: 10.1111/j.1151-2916.1993.tb05316.x

Bunker, B. C., Kirkpatrick, R. J., and Brow, R. K. (1991). Local structure of alkaline-earth boroaluminate crystals and glasses: I, Crystal chemical concepts—structural predictions and comparisons to known crystal structures. *J. Am. Ceram. Soc.* 29, 1425–1429. doi: 10.1111/j.1151-2916.1991.tb04123.x

Champagnon, B., Wondraczek, L., and Deschamps, T. (2009). Boson peak, structural inhomogeneity, light scattering and transparency of silicate glasses. *J. Non. Cryst. Solids* 355, 712–714. doi: 10.1016/j.jnoncrysol.2009.01.029

Donth, E. (1982). The size of cooperatively rearranging regions at the glass transition. *J. Non. Cryst. Solids* 53, 325–330. doi: 10.1016/0022-3093(82)90089-8

Donth, E.-J. (2001). *The Glass Transition: Relaxation Dynamics in Liquids and Disordered Materials*. Berlin: Springer-Verlag. doi: 10.1007/978-3-662-04365-3

Duval, E., Mermet, A., and Saviot, L. (2007). Boson peak and hybridization of acoustic modes with vibrations of nanometric heterogeneities in glasses. *Phys. Rev. B - Condens. Matter Mater. Phys.* 75, 1–9. doi: 10.1103/PhysRevB.75.024201

Ediger, M. D. (2000). Spatially heterogeneous dynamics in supercooled liquids. *Annu. Rev. Phys. Chem.* 51, 99–128. doi: 10.1146/annurev.physchem.51.1.99

Flynn, J. H., and Wall, L. A. (1966). A quick, direct method for the determination of activation energy from thermogravimetric data. *J. Polym. Sci. B Polym. Lett.* 4, 323–328. doi: 10.1002/pol.1966.110040504

Friedman, H. L. (2007). Kinetics of thermal degradation of char-forming plastics from thermogravimetry. Application to a phenolic plastic. *J. Polym. Sci. Part C Polym. Symp.* 6, 183–195. doi: 10.1002/polc.5070060121

Garn, P. D. (1990). Kinetics of thermal decomposition of the solid state. II. Delimiting the homogeneous-reaction model. *Thermochim. Acta* 160, 135–145. doi: 10.1016/0040-6031(90)80254-V

Greaves, G. N., and Ngai, K. L. (1995). Reconciling ionic-transport properties with atomic structure in oxide glasses. *Phys. Rev. B* 52, 6358–6380. doi: 10.1103/PhysRevB.52.6358

Greaves, G. N., and Sen, S. (2007). Inorganic glasses, glass-forming liquids and amorphizing solids. *Adv. Phys.* 56, 1–166. doi: 10.1080/00018730601147426

Hempel, E., Hempel, G., Hensel, A., Schick, C., and Donth, E. (2000). Characteristic length of dynamic glass transition near T_g for a wide assortment of glass-forming substances. *J. Phys. Chem. B* 104, 2460–2466. doi: 10.1021/jp991153f

Kresse, G., and Furthmüller, J. (1996). Efficient iterative schemes for ab initio total-energy calculations using a plane-wave basis set. *Phys. Rev. B* 54, 11169–11186. doi: 10.1103/PhysRevB.54.11169

Kresse, G., and Joubert, D. (1999). From ultrasoft pseudopotentials to the projector augmented-wave method. *Phys. Rev. B* 59, 1758–1775. doi: 10.1103/PhysRevB.59.1758

Le, Q. H., Palenta, T., Benzine, O., Griebenow, K., Limbach, R., Kamitsos, E. I., et al. (2017). Formation, structure and properties of fluoro-sulfo-phosphate poly-anionic glasses. *J. Non. Cryst. Solids* 477, 58–72. doi: 10.1016/j.jnoncrysol.2017.09.043

MacKenzie, K. J. D., and Smith, M. E. (2002). Multinuclear solid-state NMR of inorganic materials. *Pergamon Mater. Ser.* 6, 3–727. doi: 10.1016/j.jaap.2008.03.002

Massiot, D., Fayon, F., Capron, M., King, I., Le Calv,é, S., Alonso, B., et al. (2002). Modelling one- and two-dimensional solid-state NMR spectra. *Magn. Reson. Chem.* 40, 70–76. doi: 10.1002/mrc.984

Moeller, R. P., Gupta, P. K., Elterman, P. B., Moynihan, C. T., Sasabe, H., Macedo, P. B., et al. (2006). Structural relaxation in vitreous materials. *Ann. N. Y. Acad. Sci.* 279, 15–35. doi: 10.1111/j.1749-6632.1976.tb39688.x

Moesgaard, M., Keding, R., Skibsted, J., and Yue, Y. (2010). Evidence of intermediate-range order heterogeneity in calcium aluminosilicate glasses. *Chem. Mater.* 15, 4471–4483. doi: 10.1021/cm1011795

Möncke, D., da Neto, M. C. B., Bradtmüller, H., de Souza, G. B., Rodrigues, A. M., Elkholy, H. S., et al. (2018). $NaPO_3$-AlF_3 glasses: fluorine evaporation during melting and the resulting variations in structure and properties. *J. Chem. Technol. Metall.* 53, 1047–1060. Available online at: https://dl.uctm.edu/journal/web/j2018-6

O'Reilly, J. M. (1977). Conformational specific heat of polymers. *J. Appl. Phys.* 48, 4043–4048. doi: 10.1063/1.323444

Ozawa, T. (1965). A new method of analyzing thermogravimetric data. *Bull. Chem. Soc. Jpn.* 38, 1881–1886. doi: 10.1246/bcsj.38.1881

Perdew, J. P., Burke, K., and Ernzerhof, M. (1996). Generalized gradient approximation made simple. *Phys. Rev. Lett.* 77, 3865–3868. doi: 10.1103/PhysRevLett.77.3865

Pickard, C. J., and Mauri, F. (2001). All-electron magnetic response with pseudopotentials: NMR chemical shifts. *Phys. Rev. B* 63:245101. doi: 10.1103/PhysRevB.63.245101

Vyazovkin, S. (2001). Modification of the integral isoconversional method to account for 699 variation in the activation energy. *J. Comput. Chem* 22, 178–183. doi: 10.1002/1096-987X(20010130)22:2<178::AID-JCC5>3.0.CO;2-%23

Vyazovkin, S. (2006). Model-free kinetics: staying free of multiplying entities without necessity. *J. Therm. Anal. Calorim.* 83, 45–51. doi: 10.1007/s10973-005-7044-6

Vyazovkin, S. (2015). *Isoconversional Kinetics of Thermally Stimulated Processes*. London: Springer. doi: 10.1007/978-3-319-14175-6

Vyazovkin, S. (2016). A time to search: finding the meaning of variable activation energy. *Phys. Chem. Chem. Phys.* 18, 18643–18656. doi: 10.1039/C6CP02491B

Vyazovkin, S. (2018). "Chapter 4: Modern isoconversional kinetics," in *Handbook of Thermal Analysis and Calorimetry - Recent Advances, Techniques and Applications*, 2nd ed, eds S. Vyazovkin, N. Koga, and C. Schick (Amsterdam: Elsevier), 131–172.

Wondraczek, L., and Behrens, H. (2007). Molar volume, excess enthalpy, and Prigogine-Defay ratio of some silicate glasses with different (P,T) histories. *J. Chem. Phys.* 127:2794745. doi: 10.1063/1.2794745

Wondraczek, L., Behrens, H., Yue, Y., Deubener, J., and Scherer, G. W. (2007). Relaxation and glass transition in an isostatically compressed diopside glass. *J. Am. Ceram. Soc.* 90, 1556–1561. doi: 10.1111/j.1551-2916.2007.01566.x

Zhang, L., De Araujo, C. C., and Eckert, H. (2007). Structural role of fluoride in aluminophosphate sol-gel glasses: high-resolution double-resonance NMR studies. *J. Phys. Chem. B* 111, 10402–10412. doi: 10.1021/jp072725w

Zhang, Y., Yang, G., and Yue, Y. (2013). Calorimetric signature of structural heterogeneity in a ternary silicate glass. *J. Am. Ceram. Soc.* 96, 3035–3037. doi: 10.1111/jace.12562

Conflict of Interest Statement: The authors declare that the research was conducted in the absence of any commercial or financial relationships that could be construed as a potential conflict of interest.

frontiers in Materials

ORIGINAL RESEARCH
published: 18 April 2019
doi: 10.3389/fmats.2019.00063

Permanent Densification of Calcium Aluminophosphate Glasses

Saurabh Kapoor[1], Randall E. Youngman[2], Lina Ma[2], Nadja Lönnroth[2], Sylwester J. Rzoska[3], Michal Bockowski[3], Lars R. Jensen[4], Mathieu Bauchy[5] and Morten M. Smedskjaer[1]**

[1] Department of Chemistry and Bioscience, Aalborg University, Aalborg, Denmark, [2] Science and Technology Division, Corning Incorporated, Corning, NY, United States, [3] Institute of High-Pressure Physics, Polish Academy of Sciences, Warsaw, Poland, [4] Department of Materials and Production, Aalborg University, Aalborg, Denmark, [5] Department of Civil and Environmental Engineering, University of California, Los Angeles, Los Angeles, CA, United States

High-temperature densification of oxide glasses influences their interatomic distances and bonding patterns, resulting in changes in the mechanical and chemical properties. Most high-pressure investigations have focused on aluminosilicate and aluminoborosilicate based glasses, due to their relevance for the glass industry as well as the geological sciences. Relatively few studies have explored the pressure-induced changes in the structure and properties of phosphate-based glasses, although P_2O_5 is an important component in various multicomponent oxide glasses of industrial interest. In this work, we investigate the influence of permanent densification on the structure, mechanical properties (Vicker's hardness), and chemical durability (weight loss in water) of binary CaO-P_2O_5 and ternary CaO-Al_2O_3-P_2O_5 glasses. The densification of bulk glasses is obtained through isostatic compression (1–2 GPa) at the glass transition temperature. The binary CaO-P_2O_5 series is prepared with varying [CaO]/[P_2O_5] ratios to obtain glasses with different O/P ratios, while the ternary series CaO-Al_2O_3-P_2O_5 is prepared with a constant O/P ratio of 3 (metaphosphate) but with varying [CaO]/([CaO]+[Al_2O_3]) ratio. Using Raman and ^{31}P NMR spectroscopy, we observe minor, yet systematic and composition-dependent changes in the phosphate network connectivity upon compression. On the other hand, ^{27}Al NMR analysis of the compressed CaO-Al_2O_3-P_2O_5 glasses highlights an increase in the Al coordination number. We discuss these structural changes in relation to the pressure-induced increase in density, Vicker's hardness, and chemical durability.

Keywords: oxide glass, vickers micro hardness, hot compression, structure-property relationship, chemical durability

OPEN ACCESS

Edited by:
Lothar Wondraczek, Friedrich Schiller University Jena, Germany

Reviewed by:
Dominique De Ligny, University of Erlangen Nuremberg, Germany
Mouritz Nolsøe Svenson, Particle Analytical, Denmark

****Correspondence:***
Saurabh Kapoor
kapoor0588@gmail.com
Morten M. Smedskjaer
mos@bio.aau.dk

Specialty section:
This article was submitted to Glass Science, a section of the journal Frontiers in Materials

Received: *31 January 2019*
Accepted: *27 March 2019*
Published: *18 April 2019*

Citation:
Kapoor S, Youngman RE, Ma L, Lönnroth N, Rzoska SJ, Bockowski M, Jensen LR, Bauchy M and Smedskjaer MM (2019) Permanent Densification of Calcium Aluminophosphate Glasses. Front. Mater. 6:63. doi: 10.3389/fmats.2019.00063

INTRODUCTION

The application of pressure enables tuning of the interatomic distances and bonding patterns in glassy solids (Kapoor et al., 2017c), providing an additional degree of freedom for altering glass properties compared to varying composition or temperature alone. Understanding the gradual or abrupt densification mechanisms involving various structural transitions is thus an important task in glass science and engineering, but it is complicated by the intrinsic atomic-scale disorder in glasses and the experimental difficulties in undertaking *in situ* high-pressure characterization experiments (Huang and Kieffer, 2004). Permanent densification of bulk glasses can be achieved at

a modest pressure (∼1 GPa) by high-temperature compaction, enabling *ex situ* characterization and a controlled extent of densification by the choice of pressure and temperature treatment. Such hot compression treatments may be used as an effective post-treatment method (Kapoor et al., 2018). More generally, understanding the effect of densification on glass structure and properties is important for understanding the fracture mechanics of glasses at the atomic level (Januchta et al., 2017), since stresses in the GPa regime are easily reached during sharp contact deformation (e.g., Vickers indentation). Such deformation is a typical failure mode for, e.g., cover glass applications (Gross, 2012).

Aluminosilicate glasses are currently applied in various technological innovations, including chemically durable, scratch resistant, and high strength glasses for electronic and automobile industries (Ellison and Cornejo, 2010; Kafer et al., 2013). However, an ever-increasing demand for stronger, tougher, and more chemically durable glasses has led to the exploration of oxide glasses containing multiple network formers such as SiO_2, Al_2O_3, P_2O_5, and B_2O_3 (Ellison et al., 2014). The non-silicate network polyhedra interact, often in unpredictable ways, by forming a variety of structural associations, such as Al^{IV}-B^{III}, B^{III}-B^{IV}, Al^{V}, $AlPO_4$, and BPO_4 units (Gan et al., 1994; van Wüllen et al., 1996; Chan et al., 1998, 1999; Zuchner et al., 1998; Muñoz et al., 2006, 2007, 2008). These structural units result in a significant modification of the atomic network topology and related macroscopic properties. However, it is challenging to understand these interactions unambiguously in complex multicomponent oxide glasses. Furthermore, most of the high-pressure investigations have focused on aluminoborosilicate glasses with relevance for the geological sciences (Kapoor et al., 2017c), while only relatively few studies have explored the pressure-induced changes in structure and properties of P_2O_5-containing glasses (Hirao et al., 1991; Mosey et al., 2005; Gauvin et al., 2007, 2013; Yue et al., 2007; Brazhkin et al., 2011, 2014; Premila et al., 2012; Kapoor et al., 2017b; Shi et al., 2018). These previous studies reveal that the response of P_2O_5-based glasses toward high pressure treatment depends on the glass composition and the utilized compression route (e.g., cold vs. hot compression). We recently showed that hot compression of a binary ZnO-P_2O_5 at 1 GPa resulted in a decrease in the phosphate network polymerization degree, which was possibly compensated by an increase in Zn coordination number (Kapoor et al., 2017b). On the other hand, pressure quenched *v*-P_2O_5 did not show any clear evidence of polymerization changes at pressures <7 GPa (Brazhkin et al., 2011). Finally, we note that the recent inclusion of P_2O_5 as a network former in various compositions for damage resistant cover and display glasses (Aitken, 2008; Ellison et al., 2014; Siebers et al., 2014; Gross and Guo, 2015) further strengthens the need to understand the influence of densification on the structure and properties of P_2O_5-based glasses.

In this work, we investigate the structural and property changes upon densification of binary CaO-P_2O_5 and ternary CaO-Al_2O_3-P_2O_5 series of glasses. The former series is prepared with a varying $[CaO]/[P_2O_5]$ ratio to obtain glasses with different O/P ratios, while the latter is prepared with a constant O/P ratio of 3 (metaphosphate) but with a varying $[CaO]/([CaO]+[Al_2O_3])$ ratio. Permanent densification is achieved using an N_2 gas pressure chamber with a large inner volume, enabling the compression of bulk samples (mm to cm range) at high pressure (up to 2 GPa) and high temperature (in the range of the glass transition temperature, T_g). Permanent here refers to the finding that the glasses remain in their densified state unless they are heated to temperatures around T_g. Structural characterization was carried out using ^{31}P and ^{27}Al magic angle spinning (MAS) nuclear magnetic resonance (NMR) and Raman spectroscopy. To link the trends in atomic-scale structural changes with macroscopic properties, we also determined the density, hardness (through Vickers indentation), and chemical durability (through weight loss measurements in water).

EXPERIMENTAL SECTION

Sample Preparation

Binary CaO-P_2O_5 and ternary CaO-Al_2O_3-P_2O_5 series of glasses were batched from raw materials of phosphoric acid (VWR Scientific, 85–88%), alumina (Almatis, 99.78%), aluminum metaphosphate (BassTech International, >98%), calcium oxide (Avantor, 94.8%), and calcium pyrophosphate (Alfa Aesar, 96%). Batched raw materials were calcined at 400 °C for 12–16 h, then melted in a platinum crucible at 1,100–1,500°C for 2–4 h with an alumina cover. The glass melts were cast into stainless steel molds, and then annealed for 2 h at their estimated T_g. Samples with dimensions of about $10 \times 10 \times 3$ mm^3 were cut and the flats were optically polished. After cutting and grinding, the samples were then reannealed for 30 min at their measured T_g ($10^{12.2}$ Pa s isokom temperature as determined using beam bending viscosity method) to ensure uniform thermal history. The beam bending viscosity method measures the temperature dependence of viscosity in the range from 10^{11} to 10^{13} Pa s, conforming to ASTM C598 standard.

Ethanol was used for the initial stages of grinding and polishing, using silicon carbide papers of grit size up to 4,000. For the final steps of polishing, a water-free lubricant with diamond suspension (<6 μm) was used on a polishing cloth (Struers). The analyzed chemical compositions, by inductively coupled plasma optical emission spectroscopy (Perkin Elmer 7300V), and T_g are given in **Table 1**.

The glass samples were isostatically compressed at a raised temperature using two nitrogen gas pressure chambers: one vertically positioned with an internal diameter of 6 cm for compression at 1 GPa and the other horizontally positioned with an internal diameter of 3 cm for compression at 2 GPa. A multizone and single zone cylindrical graphite furnace was used for compression at 1 and 2 GPa, respectively. To monitor the temperature during the experiments, PtRh6%–PtRh30% thermocouples were used. They were arranged in the furnaces and coupled with the input power control electronic systems. In both cases, the pressure was measured by manganin gauges. The pressures and temperatures were stabilized with an accuracy of 1 MPa and 0.1 K, respectively. Glass samples were placed in an alumina crucible and then heated in the furnaces inside the high-pressure reactors with a constant heating rate of 600 K/h

TABLE 1 | Analyzed chemical compositions, glass transition temperature (T_g), density (ρ), atomic packing density (C_g), and molar volume (V_m) of the as-prepared glasses.

Glass ID	Analyzed composition (mol%)				(T_g) (°C)	C_g (-)	ρ (gcm^{-3})	V_m(cm^{3}mol^{-1})
	Al_2O_3	CaO	P_2O_5	O/P ratio				
P60	0	40.4	59.6	2.84	472	0.518	2.521	42.5
P50	0	49.9	50.1	3.00	514	0.533	2.654	37.3
P46	0	53.9	46.1	3.08	525	0.540	2.718	35.2
Al5	5.0	40.2	54.8	3.00	534	0.533	2.614	40.3
Al10	10.0	30.1	59.9	3.00	558	0.534	2.585	43.4
Al15	14.8	20.0	65.2	2.99	602	0.540	2.583	46.0

The errors in T_g, ρ, and C_g, do not exceed ±2°C, ±0.002 g/cm^3, and ±0.001. respectively.

to the ambient pressure T_g value of each glass. The systems were kept at these conditions under high nitrogen pressure (1 or 2 GPa) for 30 min. Afterward, the furnace was cooled down to room temperature at a constant rate of 60 K/h, followed by decompression at a rate of 30 MPa/min.

Structural Characterization

Raman spectroscopy measurements were performed at room temperature to obtain information about the structure of glasses at short- and intermediate-range length scales. This was done using a Renishaw Invia micro-Raman spectrometer with 532 nm laser in the range from 200 to 1,600 cm^{-1}. The measurements were conducted on as-prepared and compressed samples. All Raman data were subjected to intensity normalization by dividing the intensities by the maximum intensity of each spectrum.

Solid state NMR spectra of ^{31}P were obtained using a commercial magic-angle spinning (MAS) NMR probe (Agilent) and spectrometer (Agilent DD2), in combination with an 11.7 T superconducting magnet. All the glass samples (powder) were loaded into 3.2 mm zirconia rotors and spun with compressed nitrogen at 20 kHz. The resonance frequency of ^{31}P at this external field strength was 202.30 MHz. Spectra were acquired with a 1.2 μs pulse width, corresponding to a π/6 tip angle, using a delay time of 240 s and as a composite of 60 to 220 free induction decays. Spectra were processed without any additional apodization and referenced to 85% H_3PO_4 in water (0 ppm). The fitting of ^{31}P MAS NMR data was made using DMFit (Massiot et al., 2002), using a minimum number of Gaussian lineshapes to represent Q^n species, and with full consideration of spinning sidebands when determining site populations.

^{27}Al MAS NMR spectra were collected using a commercial MAS NMR probe (Agilent) and spectrometer (DD2), with a narrow-bore 16.4 T superconducting magnet and thus a resonance frequency of 182.34 MHz. Powdered glass samples were contained in low Al background zirconia rotors and spun at 22 kHz. The data were acquired with very short (0.6 μs) pulse widths (π/12 tip angle), recycle delays of 4 s and with signal averaging of typically 1,000 scans. ^{27}Al MAS NMR data were processed without extra line broadening and referenced to aqueous aluminum nitrate at 0.0 ppm. Fitting of ^{27}Al MAS NMR spectra was conducted with DMFit using the "CzSimple" model to accurately represent the 2nd-order quadrupolar broadened lineshapes belonging to various Al coordination environments.

Property Characterization

Density (ρ) was determined using the Archimedes method by first weighing the sample in air and then weighing it when suspended in ethanol at room temperature. This was repeated a minimum of ten times for each sample. The standard deviation of the reported density values did not exceed ±0.002 g cm^{-3}. The molar volume (V_m) was calculated as the ratio between the molar mass of the glass and its density. Furthermore, we calculated the atomic packing density (C_g) of the glasses to evaluate the differences in the free volume of the glasses. C_g is the ratio between the minimum theoretical volume occupied by the ions (assumed to be spherical) and the corresponding molar volume of the glass. The value of C_g is calculated using effective ionic radii to calculate the minimum theoretical volume occupied by the ions (Shannon, 1976), assuming 6-fold coordination for Ca, 2-fold coordination for O, 4-fold coordination for P, and coordination number for Al as obtained from the NMR results.

A Vickers micro-indenter (Duramin 5, Struers) was used to determine hardness (H_V). The measurements were performed in air at room temperature with a relative humidity of 50 ± 5%. At least 30 indents were performed at loads of 0.05 and 0.2 kgf for CaO-P_2O_5 and 0.05 and 0.1 kgf for CaO-Al_2O_3-P_2O_5 glasses with a dwell time of 15 s. H_V was calculated from the size of the imprint at respective load.

Glass chemical durability in an aqueous solution was measured for as-made annealed glasses and compressed glasses. Samples with dimensions of about 10 × 10 × 3 mm^3 were immersed into 200 ml deionized H_2O at 40 °C for different time durations up to 428 h. The water was not stirred and the samples were suspended by Teflon line in the solution. The weight loss of samples was regularly measured for different time intervals.

RESULTS AND DISCUSSION

^{31}P and ^{27}Al MAS NMR Spectroscopy: As-Made Glasses

Figure 1 shows the ^{31}P MAS NMR spectra of both as-made and compressed glasses. The center band intensities are isotropic resonances that can be assigned to Q^3, Q^2, and Q^1 units. We use the standard Q^n nomenclature for phosphorus speciation, in which the exponent (n) indicates the number of bridging oxygen (BO) per phosphorous atom. The experimental spectra were simulated using Gaussian line shapes for each Q^n site. The

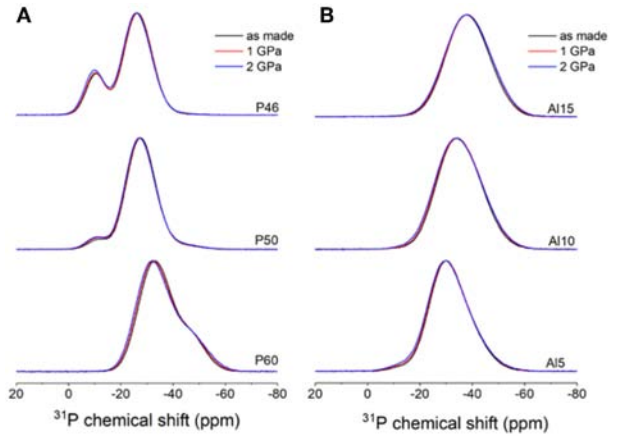

FIGURE 1 | ^{31}P MAS NMR spectra of the as-prepared glasses (black) and glasses hot compressed at 1 GPa (red) and 2 GPa (blue): **(A)** CaO-P_2O_5; **(B)** CaO-Al_2O_3-P_2O_5.

relative total area of each approximated isotropic peak and its associated sidebands was used as a measure of the respective site concentration. **Table 2** lists the isotropic chemical shifts (δ_{CS}) and the site concentrations determined for the phosphorous species in the present glasses.

First, we considered the as-made binary CaO-P_2O_5 glasses (**Figure 1A**). The ^{31}P spectrum of the ultraphosphate composition (P60, see **Table 1**) is dominated by isotropic peaks near −33 and −46 ppm, representing the Q^2 and Q^3 units, respectively (Brow, 2000). As expected, the spectrum of the metaphosphate composition (P50) is dominated by the Q^2 peak, but also contains small peaks for Q^1 and Q^3 tetrahedra. The relative peak areas for the different P polymerizations vary systematically with composition, i.e., with increasing CaO modifier content, the Q^3 peak decreases in intensity while that of Q^1 increases (**Table 2**). The observed P speciation is thus generally consistent with previous ^{31}P NMR results for Na- and Ca-phosphate glasses (Kirkpatrick and Brow, 1995; Brow, 1996). However, Na- and Ca-metaphosphate glasses exhibit different Q^n distribution, as the Na-metaphosphate glass contains predominantly Q^2 units, whereas the Ca-metaphosphate glass also features small but noticeable amounts of Q^1 and Q^3 units. The latter is due to the disproportionation reaction, i.e., $2Q^n \rightarrow \ Q^{n-1} + Q^{n+1}$, which is shifted to the right with increasing modifier field strength (charge-to-size ratio) (Fletcher et al., 1993). Furthermore, the chemical shift of the Q^2 peak shifts toward higher ppm values with increasing CaO content (**Table 2**). The change in the ^{31}P chemical shift with increasing CaO content in our glasses parallels the trend observed previously with increasing Na_2O content in Na_2O-P_2O_5 glasses (Kirkpatrick and Brow, 1995).

Next, we considered the as-made ternary CaO-Al_2O_3-P_2O_5 glasses (**Figure 1B**). The ^{31}P MAS NMR spectra contained several overlapping resonances that shows a progressive shift toward more negative ppm and a broadening with the increasing concentration of Al_2O_3. The observed results are similar to those observed in other alkali-alumino-metaphosphate glasses and have been attributed to the increasing formation of P-O-Al linkages in comparison to that of P-O-Ca (Schneider et al., 2003). Previous studies have reported similar shift in the positions of ^{31}P NMR peaks in alumino-metaphosphate glasses upon Al_2O_3 addition and have been correlated to general strengthening, or shortening, of the average P–O bonds related with the different metal polyhedra (Smith et al., 2014). Furthermore, it has been shown that the ^{31}P peak for a Q^2 unit connected to an alkali or alkaline earth ion will occur at a more positive chemical shift than the ^{31}P peak for a Q^2 unit connected to aluminum (Brow et al., 1993). Similar to the binary P50 composition, the ternary CaO-Al_2O_3-P_2O_5 metaphosphate glasses also feature small but non-negligible amounts of Q^3 and Q^1 units. The presence of Q^1 and concomitant Q^3 can also be explained by the disproportionation reaction. Furthermore, the deconvolution of the ternary glass spectra also indicates the presence of two distinct Q^2 units with resonances around −28 and −36 ppm, respectively. The former signal is attributed to Q^2 (0Al) units (where xAl represents the number of Al atoms as next nearest neighbor), while the latter is due to Q^2 (1Al) units as the formation of P-O-Al linkage leads to a shift of the ^{31}P resonance toward more negative ppm (i.e., shielded) by ∼7 to 8 ppm (Fletcher et al., 1993), consistent with the ∼8 ppm shift difference required to adequately fit the spectra (**Figure 2**).

Figure 3A shows the ^{27}Al MAS NMR spectra for the CaO-Al_2O_3-P_2O_5 glasses, with the site populations listed in **Table 3**. All three compositions yielded spectra with three peaks around 36, 6, and −17 ppm, which can be unambiguously assigned to Al^{IV}, Al^{V}, and Al^{VI} structural units, respectively (MacKenzie, 2002). The spectra show a decrease in the fraction of Al^{VI} species with increasing Al_2O_3 content, with Al^{VI} as the predominant species for all the compositions (**Figure 3B**). The results agree with previous investigations on aluminophosphate glasses, where Al predominantly exists in octahedral coordination within the metaphosphate (O/P ≈ 3) regime (Brow et al., 1990, 1993; Brow, 1993; Schneider et al., 2003). From the peak areas, the average coordination number (CN) of Al was calculated for the investigated glasses. The results are plotted in the inset of **Figure 3B**, showing a reduction of Al CN from 5.45 to approximately 5.28 with increasing Al_2O_3/CaO ratio. We also note that the present ^{27}Al NMR peak assignment is similar to that reported for Ca-aluminophosphate glasses with all Al bonded to P as next nearest neighbor (NNN) (Brow et al., 1990). On the other hand, the present glasses feature more shielded peaks relative to the ^{27}Al chemical shifts reported for aluminoborate and aluminosilicate glass (Bista et al., 2015). This shift upon introduction of phosphorus is likely due to the difference in electronegativity between phosphorus, silicon, and boron, which increases the shielding of the Al nucleus, resulting in a shift in these resonances by up to −25 ppm (MacKenzie, 2002).

^{31}P and ^{27}Al MAS NMR Spectroscopy: Densified Glasses

Structural changes in the P speciation upon hot compression have been found to be highly composition dependent, that

TABLE 2 | Phosphorus speciation obtained by deconvolution of ^{31}P MAS NMR spectra.

Glass ID	Q^1		Q^2		Q^3		*O/P ratio*
	Int (%)	δ_{CS} *(ppm)*	*Int (%)*	δ_{CS} *(ppm)*	*Int (%)*	δ_{CS} *(ppm)*	
P60	…	…	78.6	−32.9	21.4	−46.5	2.89
P60 (1 GPa)	…	…	74.6	−32.1	25.4	−45.9	2.87
P60 (2 GPa)	…	…	69.7	−31.5	30.3	−45.3	2.85
P50	4.1	−10.5	89.5	−27.7	6.4	−42.0	2.99
P50 (1 GPa)	4.5	−10.3	88.6	−27.4	6.9	−41.0	2.99
P50 (2 GPa)	4.9	−10.0	88.4	−27.2	6.8	−41.0	2.99
P46	18.3	−10.2	79.6	−26.5	2.1	−41.2	3.08
P46 (1 GPa)	18.5	−9.9	79.4	26.3	2.2	−41.2	3.08
P46 (2 GPa)	19.5	−9.7	78.4	−26.1	2.1	−41.2	3.09
Al5	1.6	−13.2	67.4	−28.9	5.0	−45.0	2.99
			25.9	−37.8			
Al5 (1 GPa)	2.4	−13.2	65.5	−28.7	7.0	−45.0	2.97
			25.0	−37.7			
Al5 (2 GPa)	3.1	−12.8	67.1	−28.6	5.3	−47.0	2.99
			24.5	−38.4			
Al10	1.2	−15.9	42.7	−30.0	14.2	−45.0	2.94
			41.9	−37.9			
Al10 (1 GPa)	1.4	−15.9	42.2	−29.7	16.9	−45.0	2.93
			39.5	−37.7			
Al10 (2 GPa)	1.6	−15.9	43.6	−29.5	18.6	−45.0	2.92
			36.1	−37.5			
Al15	0.2	−15.9	25.9	−32.6	19.7	−46.0	2.90
			54.1	−38.6			
Al15 (1 GPa)	0.3	−15.9	27.5	−32.2	25.9	−46.0	2.87
			46.3	−38.5			
Al15 (2 GPa)	0.4	−15.9	31.9	−31.9	28.5	−46.0	2.86
			39.2	−38.5			

Uncertainties in the Q^n populations and chemical shift (δ_{CS}) are ± 1% and ±1 ppm, respectively. (O/P ratio = (2.5[Q^3] + 3*[Q^2] + 3.5*[Q^1] + 4*[Q^0])/100, in which [Q^n] is the Int% by NMR deconvolution.)*

is, the phosphorus network undergoes depolymerization upon hot compression of (72-x)SiO_2-20B_2O_3-xP_2O_5-8Al_2O_3 glasses (Kapoor et al., 2017a), while in case of binary zinc phosphate and another SiO_2-B_2O_3-P_2O_5-Al_2O_3 glass, only minimal changes in the P network were observed (Kapoor et al., 2017b, 2018). In the present investigation, hot compression of the glasses results in insignificant changes in the ^{31}P chemical shifts and relative areas of the peaks corresponding to different Q^n phosphorous units (**Table 2**). Significant changes are only observed in the ultraphosphate glass (P60), where the pressure treatment at 2 GPa induces a 9% increase in the relative amount of Q^3 units at the expense of Q^2 units (**Table 2**). No significant changes are observed in the glasses with higher O/P ratio. The minimal changes in the P speciation upon compression agrees with the previous studies on pressure quenched ν-P_2O_5 by Brazhkin et al. using ^{31}P MAS NMR and X-ray diffraction studies (Brazhkin et al., 2011). Considering further the CaO-Al_2O_3-P_2O_5 glasses, compression induces even more subtle changes in the ^{31}P NMR spectra (**Figure 1**). **Table 2** shows that the quantitative changes upon compression are well within the uncertainty values expected in deconvolution.

As a glass is compressed, the ionic environments can change in different ways, including a coordination number increase, a change in bond distances, angles, and in the types and amounts of linkages present (e.g., P-O-Al, P-O-P). In the case of Al, the most obvious structural change is an increase in coordination number, as observed in various oxide glasses (Allwardt et al., 2004; Kapoor et al., 2017c). The comparative abundance of each aluminum species is proportional to the area under its peak and the fitted values are given in **Table 3**. The peak areas corresponding to Al^V and Al^{VI} are greater for the samples recovered from hot compression (1 and 2 GPa) in comparison to those at ambient pressure. The quantitative change in Al coordination per unit change in pressure increases with increasing [Al_2O_3]/[CaO] ratio (**Figure 3C**). It is noteworthy that compression at 1 GPa results in a relatively large change in the degree of polymerization of Al in comparison to that at 2 GPa, i.e., after increasing the pressure further to 2 GPa, relatively small changes are observed in the glass reticulation. The ^{27}Al NMR spectra (**Figure 3A**)

show a slight increase in the frequency of the Al^{VI} resonance and a decrease for Al^{IV} and Al^{V} peaks, upon compression. Analogous to aluminosilicates glasses, the high frequency shift in ^{27}Al spectra may be related to the decrease in bond angles, while the low frequency shift could be due to the development of links between high-coordinated Al sites (Kelsey et al., 2009). Further, in the case of phosphate and aluminophosphate glasses, network forming cations Al and P can both respond to pressure changes by changing their local environment. However, the observed structural changes for Al upon compression are more pronounced than those for P, suggesting that the threshold energy

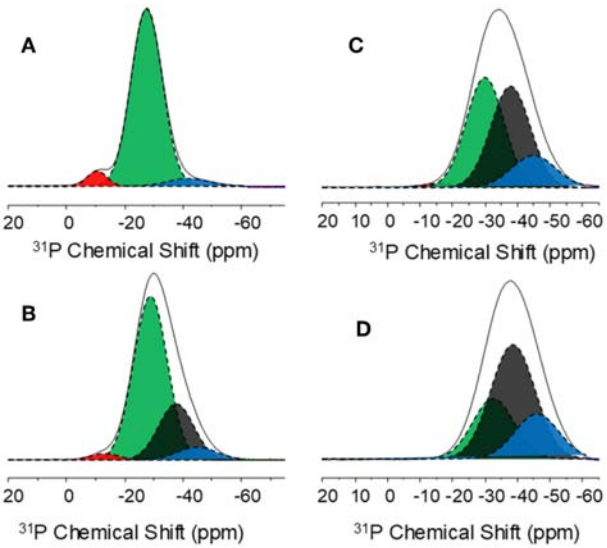

FIGURE 2 | Deconvolution of ^{31}P MAS NMR spectra for **(A)** P50, **(B)** Al5, **(C)** Al10, and **(D)** Al15 glasses. Q^1, Q^2 and Q^3 peaks are indicated by red, green, and blue curves. The black Gaussian peak represents the $Q^{2,1}$ peak formed in Al-containing glasses.

TABLE 3 | Aluminum speciation and associated NMR parameters obtained by deconvolution of ^{27}Al MAS NMR spectra.

Glass ID	Al^{IV}		Al^{V}		Al^{VI}	
	Int (%)	δ_{CS} (ppm)	Int (%)	δ_{CS} (ppm)	Int (%)	δ_{CS} (ppm)
Al5	8.6	35.3	38.2	5.9	53.2	−18.0
Al5 (1 GPa)	4.8	35.0	31.9	5.5	63.2	−18.2
Al5 (2 GPa)	3.5	34.8	27.9	4.9	68.8	−18.2
Al10	12.6	35.6	41.0	6.3	46.4	−17.3
Al10 (1 GPa	6.9	35.5	34.9	5.9	58.2	−17.5
Al10 (2 GPa)	4.3	35.3	30.5	5.7	65.2	−17.4
Al15	15.2	36.3	41.6	6.9	43.3	−16.4
Al15 (1 GPa	7.5	35.9	35.3	6.4	57.2	−16.6
Al15 (2 GPa)	4.4	35.6	30.3	6.1	65.3	−16.6

The uncertainties in intensity (Int) and isotropic chemical shift (δ_{CS}) are estimated to be 2%, and 1 ppm, respectively.

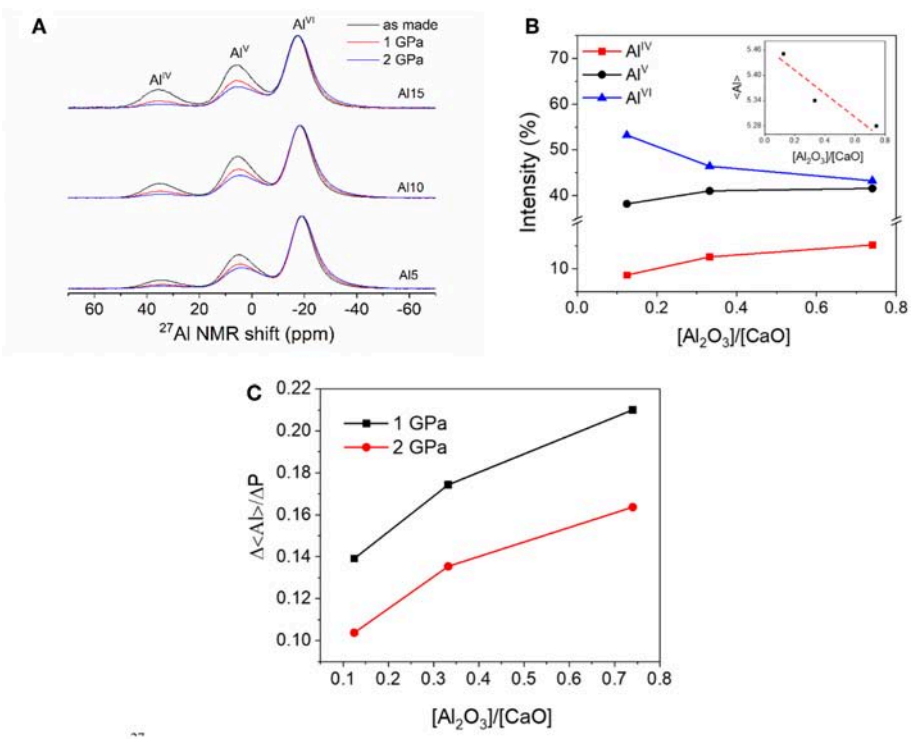

FIGURE 3 | (A) ^{27}Al MAS NMR spectra of as-prepared $CaO\text{-}Al_2O_3\text{-}P_2O_5$ glasses (black) and those hot compressed at 1 GPa (red) and 2 GPa (blue). **(B)** Intensities of each central ^{27}Al NMR line as a function of the glass composition. Inset: mean coordination number for Al calculated from the NMR intensities. **(C)** Composition dependence of the change in the mean Al coordination (<Al>) per unit change in pressure.

required for the structural changes upon compression in case of aluminophosphate glasses is higher for P compared to Al.

Raman Spectroscopy

We next considered the Raman spectra of the as-prepared and compressed $CaO\text{-}P_2O_5$ (**Figure 4A**) and $CaO\text{-}Al_2O_3\text{-}P_2O_5$ (**Figure 4B**) glasses between 200 and 1,500 cm^{-1}. In general, the Raman spectra are characterized by strong features in the mid-frequency (600–850 cm^{-1}) and high-frequency regions (950–1,400 cm^{-1}), with additional minor features in the low-frequency region (200–400 cm^{-1}).

The $CaO\text{-}P_2O_5$ glasses feature a broad band around 340 cm^{-1}, which has been attributed to vibrations of phosphate polyhedra (Meyer, 1998). In the mid-frequency region, the bands in the region from 650 to 850 cm^{-1} are attributed to stretching modes associated with BOs, linking two neighboring tetrahedra $(POP)_{sym}$ (Meyer, 1998). For the P60 glass, the band is centered around 666 cm^{-1} and assigned to the stretching modes associated with ν_s(P–O–P) (Meyer, 1998). The location of this band shifts toward higher frequency with increasing CaO content, as it is observed around 694 cm^{-1} for P50 and P46 glasses. As discussed above, the structure of the P60 glass primarily consists of Q^2 and Q^3 units, where Q^3 is primarily bonded to Q^2 units (Q^2-Q^3). That is, a cross-linked network dominated by Q^2-Q^3 and Q^2-Q^2 interactions, where Q^2-Q^2 chains dominate the glass network (**Table 2**). These chains are broken upon CaO addition, thus forming chain terminating Q^1 units attributed to the collective effect of modifier addition and disproportionation reactions (Fletcher et al., 1993). Therefore, the shifting of the Raman band (666 cm^{-1}) to higher frequency with increasing CaO content could be ascribed to the decrease in the average phosphate chain length when the NBO content increases (Brow, 2000).

The high-frequency region consists of bands associated with the symmetric and asymmetric stretching modes of NBOs on different P tetrahedra, along with the band due to stretching of $(P{=}O)_{sym}$ (Meyer, 1998). The P60 composition features two prominent bands in this region (**Figure 4A**). The band around 1174 cm^{-1} corresponds to $\nu(PO_2)_{sym}$, while that near 1,306 cm^{-1} is attributed to $(P{=}O)_{sym}$, and is consistent with the Q^3 environment identified in the ^{31}P MAS NMR spectra. The width of the $\nu(PO_2)_{sym}$ band is generally smaller than that of $(P{=}O)_{sym}$, indicating that the Q^3 tetrahedra exhibit wider bond angle distributions than the Q^2 tetrahedra. The relative intensity of the 1,174 cm^{-1} band increases upon CaO addition due to the increase in the number of NBOs. We also note that the addition of CaO results in disappearance of the band associated with $(P{=}O)_{sym}$, also similar to the reduction of Q^3 in the ^{31}P NMR data. This agrees with the findings of Hudgens et al. (1998), suggesting that modifier addition decreases the symmetry of $(P{=}O)_{sym}$ bond, resulting in an asymmetric bond which becomes indistinguishable from the $(PO_2)_{sym}$ mode of Q^2 tetrahedra. An additional weaker band at 1,018 cm^{-1} was observed in the P46 glass, which could be assigned to the symmetric stretching vibrations of the pyrophosphate Q^1 end-group units $\nu_s(PO_3^{2-})$ (Meyer, 1998).

Densification of the binary glasses at 1 and 2 GPa leads to changes in the Raman peak positions, with the most prominent changes in the mid-frequency region (**Figures 5A,B**) and minimal changes in the high-frequency region (**Figures 5A,B**). The changes in the mid-frequency region could be attributed to changes in the P-O-P bond angles. In the P60 and P50 glasses, the band corresponding to P-O-P shifts toward higher frequency upon hot compression, indicating a decrease in the P-O-P average bond angle (**Figure 5A**). This shift toward higher Raman band frequency upon compression has been observed for a wide range of vibrational modes and compositions, including silicates (Hemley et al., 1986; Mysen and Frantz, 1994), germanates (Le Parc et al., 2009), solid argon (Crawford et al., 1978; Watson and Daniels, 1988), and carbon-based solids (Boppart et al., 1985; Sandler et al., 2003). However, for the P46 glass, we observe a shift toward lower frequency upon compression (**Figure 5B**), which is analogous to the change observed in our recent high-pressure study on zinc phosphate glass with composition between meta- and pyro-phosphate regions (Kapoor et al., 2017b). Different responses to pressure exhibited by the high-P and low-P glasses here are indeed similar to how the P speciation as determined by ^{31}P MAS NMR is different for the P60 and P46 glasses (**Figure 1A**), confirming that the O/P ratio appears to dictate the network's response to compression.

The Raman spectra for the binary and ternary glasses are similar (**Figure 4**). This suggests that metaphosphate chains also dominate the structure in calcium aluminophosphate glasses, as indicated by the total Q^2 population determined for these glasses. With increasing aluminum content in these glasses, we observe a systematic change in the relative intensity and position of the bands, although the general pattern of the spectra remains similar (**Figure 5B**). This is consistent with spectroscopic studies of mixed alkali and alkaline earth metaphosphate glasses that reveal similar systematic changes in the nature of the phosphate network with modifier substitution (Rouse et al., 1978; Sato et al., 1992). Furthermore, addition of Al results in a shift of the high-frequency region band corresponding to P-NBO vibration from 1,188 to 1,220 cm^{-1}. The systematic changes in the Raman peaks agree with the peak shift observed in the ^{31}P NMR spectra where both spectral trends show a general strengthening, or shortening, of the average P–O bonds related with the different metal polyhedra (Smith et al., 2014). A previous study by Schneider et al. (2005) has correlated the positive shift in frequency with Al_2O_3 addition to two predominant factors: firstly to the increased interaction among the NBOs with the Al cation and secondly to the increased fraction of Al-O bonds, which exhibit larger bond strength than Ca-O. In addition, changes in the relative intensities of P-BO and P-NBO Raman peaks for metaphosphate glasses indicate that higher field strength cations produce stronger P–NBO bonds (Nelson and Exarhos, 1979). In contrast to the binary phosphate glasses, there are no systematic shifts in bands in the mid- and high-frequency regions upon compression of the ternary systems (**Figure 5B**).

Density, Molar Volume, Atomic Packing Density, and Plastic Compressibility

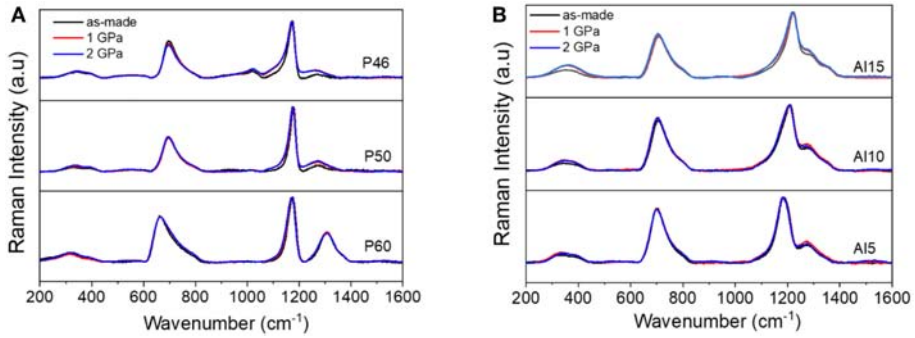

FIGURE 4 | Raman spectra of the as-prepared and compressed glasses: **(A)** $CaO\text{-}P_2O_5$ and **(B)** $CaO\text{-}Al_2O_3\text{-}P_2O_5$.

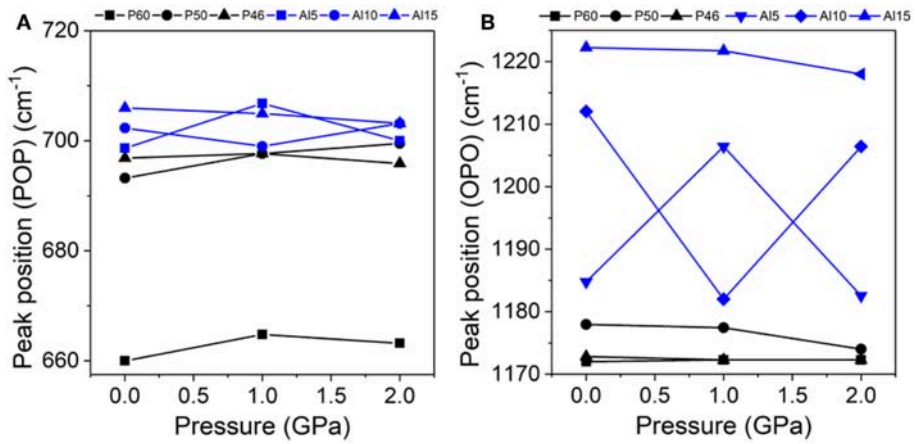

FIGURE 5 | Pressure dependence of the positions of the Raman bands corresponding to **(A)** P–O–P vibrations and **(B)** O–P–O vibrations for the binary and ternary phosphate glasses.

Figure 6 and **Table 1** show the variation of density (ρ), molar volume (V_m), and atomic packing density (C_g) with composition and pressure for the two series of glasses. For the as-prepared binary glasses, substitution of P_2O_5 by CaO results in an increase in density and a decrease in the molar volume (**Figure 6A**) accompanied by an increase in C_g of the glasses (**Table 1**). For the ternary glasses, addition of Al_2O_3 results in lower density in part due to the simultaneous reduction of CaO content (**Figure 6B**) and a concomitant increase in C_g (**Table 1**).

Following hot compression of the samples, the density of all glasses increases due to network compaction, in agreement with results for other oxide glasses in a similar pressure/temperature regime (Kapoor et al., 2017c). However, the magnitude of the pressure-induced change in density varies with composition, which can be evaluated by calculating the plastic compressibility (β), which is defined as the volume (V) change measured after decompression to ambient pressure, i.e., $-(1/V)(dV/dp)$ (Kapoor et al., 2017c). The plastic compressibility of binary phosphate decreases with the increase in CaO content, but it increases with increasing Al_2O_3/CaO ratio in the ternary glasses (**Figure 7**). We note that the plastic compressibility is negatively correlated to the C_g of the ambient condition glasses, suggesting that the free volume in the glasses accommodates the densification upon hot compression (inset of **Figure 7**) (Striepe et al., 2013). However, in the case of the aluminophosphate glasses, the volume densification is positively correlated to the C_g of the as-prepared glasses (inset of **Figure 7**) along with the change in mean alumina coordination number (**Figure 3C**). This apparent correlation could suggest that the Al CN change is an important densification mechanism for these ternary glasses.

Furthermore, and in agreement with previous studies, the β of the investigated glasses decreases with increasing pressure, i.e., a smaller observed increment in density when increasing the pressure from 1 to 2 GPa compared to that from ambient pressure to 1 GPa (**Figure 7**). The decrease in the plastic compressibility can be intuitively understood as initial compression first consumes the easiest available free volume and flexible structural units in the glass (Kapoor et al., 2017b). As discussed based on the Raman and NMR results above, the observed volume densification is mostly associated with changes in the inter-tetrahedral bond angles, and to the degree of polymerization of the glass network, as

well as changes in coordination number of Al in the ternary glasses (Kapoor et al., 2017c).

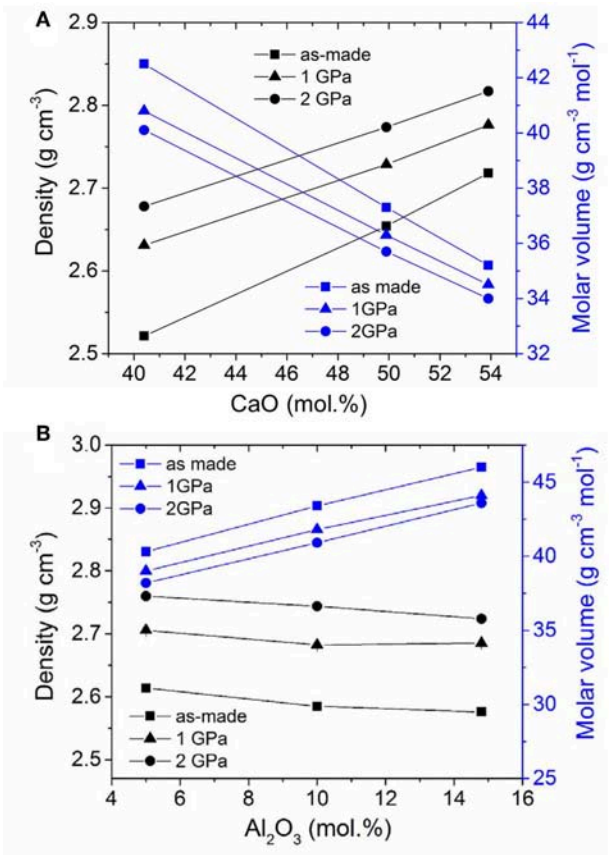

FIGURE 6 | Density and molar volume of as-prepared and hot compressed glasses as a function of the molar concentration of **(A)** CaO and **(B)** Al_2O_3 in $CaO\text{-}P_2O_5$ and $CaO\text{-}Al_2O_3\text{-}P_2O_5$ glasses, respectively. The errors associated with the density values are smaller than the size of the symbols.

Vickers Hardness

Indentation experiments on the $CaO\text{-}P_2O_5$ and $CaO\text{-}Al_2O_3\text{-}P_2O_5$ glasses provide insight into the resistance of glasses toward elastoplastic deformation, as quantified by Vickers hardness H_V (**Figure 8**). H_V of the calcium phosphate glasses increases with increasing CaO content (**Figure 8A**), indicating that the stacking of phosphate chains is more compact with an increase in the packing fraction of glasses (**Table 1**), as evident from the increase in molar volume and decrease of C_g with CaO addition. This space filling increases the number of bond constraints per volume, providing rigidity to the network, despite having a depolymerizing effect, and thus higher hardness for the high-CaO glasses. Previous studies indicate a similar increase in H_V of binary phosphate glasses with increasing CaO content (Rao and Shashikala, 2014). In the calcium aluminophosphate glasses, the addition of Al_2O_3 results in an increase in H_V (**Figure 8B**). This increase is attributed to the collective contribution from the increase in degree of network connectivity and average bond strength. The former is due to an increase in the Al_2O_3 concentration, which results in an increase in the average number of bond constraints per atom (Smedskjaer et al., 2010), while the latter is due to the higher field strength of the Al^{3+} cation. A similar trend is observed for T_g (**Table 1**), implying that both properties have similar structural origins, as also illustrated from the positive correlation between T_g and H_V (**Figure 9**) for a variety of different phosphate glasses.

Hot compression of the glasses results in an increase in H_V (**Figure 8**). This effect is qualitatively similar to previously investigated glass systems in the same pressure/temperature regimes (Kapoor et al., 2017b,c). However, consistent with the density results, we observe a larger increase in H_V from 0 to 1 GPa in comparison to that from 1 to 2 GPa, suggesting that the overall network densification is responsible for the increase in hardness. The volume densification facilitates a larger resistance to densification when subjected to sharp-contact loading at room temperature. It is worth noting that for the glasses compressed at 2 GPa, the H_V values remain similar despite the compositional differences.

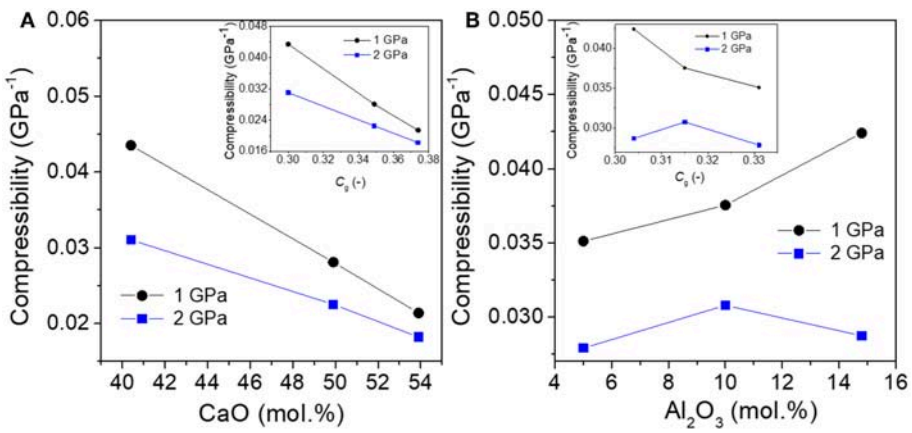

FIGURE 7 | Plastic compressibility (β) of compressed glasses as a function of the molar concentration and atomic packing density (C_g) (inset) of **(A)** CaO and **(B)** Al_2O_3 in $CaO\text{-}P_2O_5$ and $CaO\text{-}Al_2O_3\text{-}P_2O_5$ glasses, respectively.

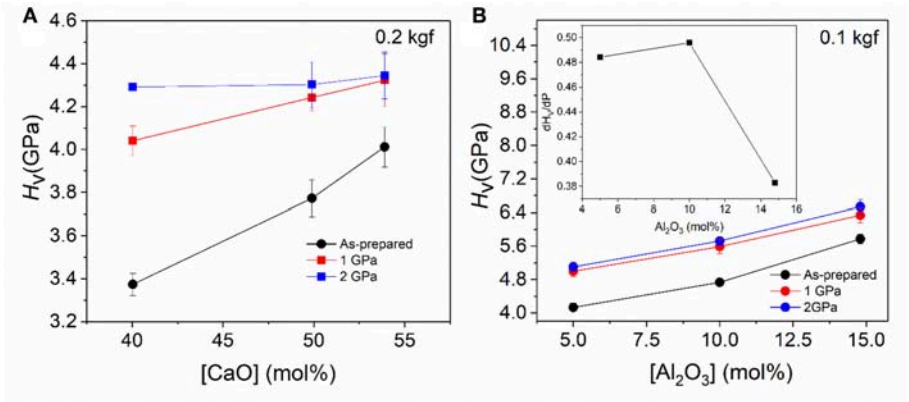

FIGURE 8 | Composition and pressure dependence of Vickers Hardness (H_V) of **(A)** CaO-P_2O_5 glasses and **(B)** CaO-Al_2O_3-P_2O_5 glasses. Inset in **(B)** shows dH_V/dP at 2 GPa, featuring similar trend as the plastic compressibility of the glasses at 2 GPa.

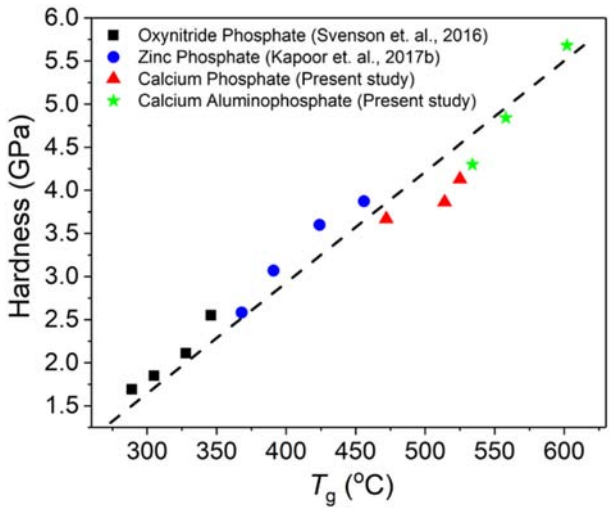

FIGURE 9 | Relationship between Vickers hardness (H_V) and T_g for various phosphate-based glasses (Svenson et al., 2016; Kapoor et al., 2017b). All the H_V values in the figure are obtained from tests conducted at 0.05 kgf load.

Chemical Durability

We investigated the chemical durability of selected as-made and compressed glasses (at 2 GPa) by measuring the weight loss in deionized water at 40°C (**Tables 4**, **5**). The weight loss is normalized by the initial surface area as a function of dissolution time. Aqueous corrosion of oxide glasses can generally occur through various processes, initially comprising hydration, ion exchange, and/or hydrolysis, depending on the glass composition and solution pH. Bunker et al. (1984) suggested that the dominating reaction in phosphate glass dissolution is the modifier–H^+ ion exchange reaction, dividing the dissolution process into two kinetic periods according to the profiles of dissolved amount (q) vs. time (t). That is, a decelerating dissolution period of $q \sim t^{1/2}$ and a uniform dissolution period of $q \sim t^1$. Furthermore, more recent studies

TABLE 4 | Mean weight loss (mg cm^{-2}) of CaO-P_2O_5 glasses after 24 h of immersion in deionized water at 40°C.

Glass ID	as-made	2 GPa
P60	0.98 ± 0.00	0.50 ± 0.05
P50	0.97 ± 0.11	0.79 ± 0.08
P46	0.77 ± 0.03	0.66 ± 0.03

propose that hydration and hydrolysis (breaking of P-O-P network bonds) play an interrelated role in glass dissolution, even proposing that hydrolysis reactions may dominate over hydration processes in metaphosphate glasses (Gao et al., 2004; Tošić et al., 2013). It is also possible that higher H^+ concentrations in acidic solutions may lead to elevated rates of hydration, thus accelerating the release rate of phosphate chains. On the other hand, in neutral–to–basic solutions (rich in H_2O or OH^-), where the degradation rate increases with pH, a hydrolysis-driven or alternate mechanism could be important, as H^+ is not readily available to hydrate non-bridging oxygens (NBOs) in the network (Tošić et al., 2013). However, some studies on binary Cu-phosphate glasses have reported that P-O-P bonds in linear phosphate chains are as resistant to hydrolysis as Si-O-Si bonds in neutral pH solutions, indicating that hydrolysis reactions may only be accelerated in acidic, but not in basic solutions.

Plots of weight loss in deionized water vs. time for the P50 glass are shown in **Figure 10**. The water-glass interaction gives rise to a general increase in weight loss within the time scale of the dissolution experiments. The chemical durability of the binary calcium phosphate glasses prepared at ambient conditions increases with increasing CaO content, as seen from a decrease in the weight loss from 0.97 to 0.77 gm cm^{-2} (**Table 4**). This increase in chemical durability has previously been attributed to the ability of Ca^{2+} to serve as ionic crosslinks between the NBOs of two different phosphate chains, thus increasing the chemical durability (Bunker et al., 1984). However, there is no further increase in chemical durability when the divalent

TABLE 5 | Mean weight loss (mg cm^{-2}) of $CaO\text{-}Al_2O_3\text{-}P_2O_5$ glasses after 428 h of immersion in deionized water at 40°C.

Glass ID	as-made	2 GPa
P50	14.61 ± 0.21	6.56 ± 0.68
Al5	0.45 ± 0.02	0.42 ± 0.07
Al10	0.13 ± 0.02	0.14 ± 0.03

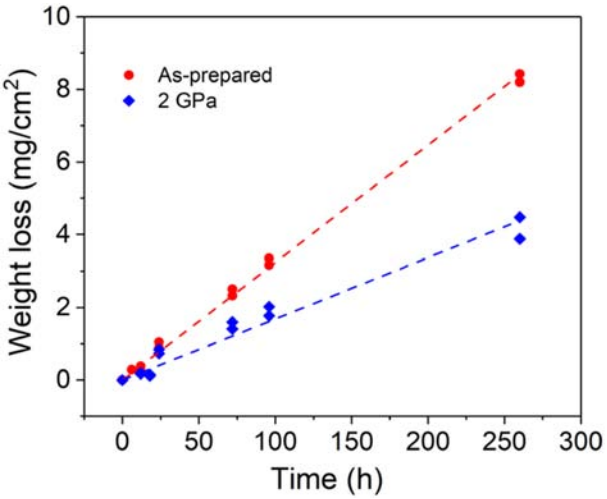

FIGURE 10 | Normalized weight loss (mg cm^{-2}) of the metaphosphate (P50) glass (as-prepared and compressed at 2 GPa) in deionized water as a function of dissolution time. The dashed lines represent linear fits to the data.

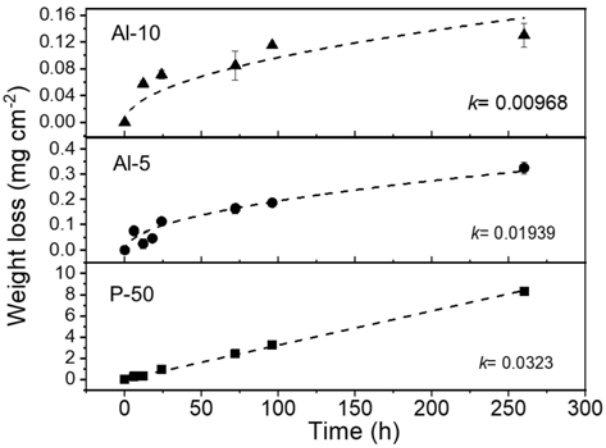

FIGURE 11 | Normalized weight loss (mg cm^{-2}) of the metaphosphate (P50) glass and $CaO\text{-}Al_2O_3\text{-}P_2O_5$ (Al5 and Al10) glass along with dissolution rate parameter (k) in deionized water as a function of time. The lines are drawn as guide for the eyes.

cation content reaches a certain point, because the polymer chains can only accommodate a limited number of chelate cross links (Bunker et al., 1984; Gao et al., 2004). Replacement of CaO by Al_2O_3 in calcium metaphosphate glasses (O/P = 3) improves the chemical durability by several orders of magnitude. While the binary phosphate glass experiments show a highly linear dependence of normalized weight loss (WL) on time ($WL = k \times t$), introduction of Al_2O_3 leads to half time dependence ($WL = k \times t^{1/2}$), as shown in **Figure 11**. After 428 h of dissolution, the metaphosphate glass (P50) exhibits ~14.6 g cm^{-2} of weight loss, while the Ca-Al-P glass with 10 mol% of Al_2O_3 has ~0.13 g cm^{-2} of weight loss (**Table 5**). Furthermore, the differences in WL vs. t curve shape as a function of Al_2O_3 content suggest a composition dependent shift in dissolution mechanism.

The effects of Al_2O_3 on the chemical durability and hardness of these calcium phosphate glasses are consistent with the widely reported structural role of Al_2O_3 in oxide glasses (Brow, 1993; Brow et al., 1993). Addition of Al_2O_3 strengthens the glass network by cross-linking phosphate chains, introducing relatively hydrolysis- and stress-resistant bonds into the phosphate network (i.e., Al-O-P and Al-O-Al), along with increasing the overall degree of network connectivity through formation of Al^V and Al^{VI} units. The resulting increase in structural polymerization degree is consistent with the increase in H_V, T_g, and chemical durability. Similar changes in chemical durability are also observed in silicate glasses, where the presence of Al_2O_3 impedes the molecular water from entering the glass network through the limited ability of H^+/H_3O^+ to ion-exchange for modifier ions and charge-compensate $[AlO_4]^-$ tetrahedra (Hamilton and Pantano, 1997). This makes it difficult to mobilize Na ions bonded to Al tetrahedra, resulting in enhanced chemical durability (Hamilton and Pantano, 1997).

Tables 4, **5** show the effect of densification on the chemical durability of the binary and ternary phosphate glasses. In general, we observe an enhancement of the corrosion resistance following permanent densification. This is likely due to an increase of C_g, because of the decline in the average bond angle and void volume, and a higher network connectivity. Previous studies on binary sodium silicate and borate glasses reported an increase in the chemical durability upon compression up to 5 GPa at T_g due to a decrease of the Na^+ release rate (Zhang et al., 1991a,b), which was in turn attributed to the decrease in void volume available for water migration into reactive sites (Mascaraque et al., 2017).

CONCLUSIONS

We investigated the influence of high-temperature densification on the structure, mechanical properties (Vicker's hardness), and chemical durability (weight loss in water) of binary $CaO\text{-}P_2O_5$ and ternary $CaO\text{-}Al_2O_3\text{-}P_2O_5$ glasses. We found that the changes in P speciation in P_2O_5-based glasses upon hot compression are generally small and highly composition dependent. In the $CaO\text{-}Al_2O_3\text{-}P_2O_5$ glasses, the compression induced an increase in the Al coordination number, the extent of which increases with an increasing $[Al_2O_3]/[CaO]$ ratio. The extent of volume densification upon hot compression also varies with composition, as the plastic compressibility of binary phosphate

decreases with the increase in CaO content, but increases with an increasing Al_2O_3/CaO ratio in ternary glasses. Furthermore, in the case of the aluminophosphate glasses, the observed extent of volume densification was positively correlated to the C_g and the change in the mean Al coordination number. In general, and as previously found for other oxide glasses, we observed an enhancement of hardness and corrosion resistance following permanent densification. This is likely due to an increased atomic packing density, because of the decrease in the average bond angle and free volume, and the increased network connectivity.

AUTHOR CONTRIBUTIONS

All authors listed have made a substantial, direct and intellectual contribution to the work, and approved it for publication.

FUNDING

This work was supported by the Independent Research Fund Denmark under Sapere Aude: DFF-Starting Grant (1335-00051A). MB acknowledges support from the National Science Foundation under Grants No. 1562066, 1762292, and 1826420.

REFERENCES

Aitken, B. G. (2008). *High Strain Point Glasses*. US20050142364A1.

Allwardt, J. R., Schmidt, B. C., and Stebbins, J. F. (2004). Structural mechanisms of compression and decompression in high-pressure $K_2Si_4O_9$ glasses: an investigation utilizing Raman and NMR spectroscopy of glasses and crystalline materials. *Chem. Geol.* 213, 137–151. doi: 10.1016/j.chemgeo.2004.08.038

Bista, S., Stebbins, J. F., Hankins, W. B., and Sisson, T. W. (2015). Aluminosilicate melts and glasses at 1 to 3 GPa: temperature and pressure effects on recovered structural and density changes. *Am. Mineral.* 100, 2298–2307. doi: 10.2138/am-2015-5258

Boppart, H., Straaten, J. V., and Silvera, I. F. (1985). Raman spectra of diamond at high pressures. *Phys. Rev. B*. 32, 1423–1425.h doi: 10.1103/PhysRevB.32.1423

Brazhkin, V. V., Akola, J., Katayama, Y., Kohara, S., Kondrin, M. V., Lyapin, A. G., et al. (2011). Densified low-hygroscopic form of P_2O_5 glass. *J. Mater. Chem.* 21, 10442–10447. doi: 10.1039/c1jm10889a

Brazhkin, V. V., Katayama, Y., Lyapin, A. G., and Saitoh, H. (2014). P-T phase diagram and structural transformations of molten P_2O_5 under pressure. *Phys. Rev. B* 89:104203. doi: 10.1103/PhysRevB.89.104203

Brow, R. K. (1993). Nature of alumina in phosphate glass: I, properties of sodium aluminophosphate glass. *J. Am. Cer. Soc.* 76, 913–918. doi: 10.1111/j.1151-2916.1993.tb05315.x

Brow, R. K. (1996). An XPS study of oxygen bonding in zinc phosphate and zinc borophosphate glasses. *J. Non Cryst Solids* 194, 267–273. doi: 10.1016/0022-3093(95)00500-5

Brow, R. K. (2000). The structure of simple phosphate glasses. *J. Non Cryst Solids* 263, 1–28. doi: 10.1016/S0022-3093(99)00620-1

Brow, R. K., Kirkpatrick, R. J., and Turner, G. L. (1990). Local structure of $xAl_2O_3 \cdot (1-x)NaPO_3$ glasses: an NMR and XPS study. *J. Am. Cer. Soc.* 73, 2293–2300. doi: 10.1111/j.1151-2916.1990.tb07591.x

Brow, R. K., Kirkpatrick, R. J., and Turner, G. L. (1993). Nature of alumina in phosphate glass: II, structure of sodium alurninophosphate glass. *J. Am. Ceram. Soc.* 76, 919–928. doi: 10.1111/j.1151-2916.1993.tb05316.x

Bunker, B. C., Arnold, G. W., and and Wilder, J. A. (1984). Phosphate-glass dissolution in aqueous-solutions. *J. Non Cryst. Solids* 64, 291–316. doi: 10.1016/0022-3093(84)90184-4

Chan, J. C. C., Bertmer, M., and Eckert, H. (1998). Double-quantum cross-polarization between half-integer quadrupolar spin systems: $^{11}B \leftrightarrow ^{23}Na$ and $^{11}B \leftrightarrow ^{27}Al$. *Chem. Phys. Let.* 292, 154–160. doi: 10.1016/S0009-2614(98)00660-5

Chan, J. C. C., Bertmer, M., and Eckert, H. (1999). Site connectivities in amorphous materials studied by double-resonance NMR of quadrupolar nuclei: high-resolution ^{11}B - ^{27}Al spectroscopy of aluminoborate glasses. *J. Am. Chem. Soc.* 121, 5238–5248. doi: 10.1021/ja983385i

Crawford, R. K., Bruns, D. G., Gallagher, D. A., and Klein, M. V. (1978). Raman scattering from condensed argon. *Phys. Rev. B* 17, 4871–4883. doi: 10.1103/PhysRevB.17.4871

Ellison, A., and Cornejo, I. A. (2010). Glass substrates for liquid crystal displays. *Int. J. Appl. Glass Sci.* 1, 87–103. doi: 10.1111/j.2041-1294.2010.00009.x

Ellison, A. J., Mauro, J. C., and Venkataraman, N. (2014). *Alkali-Free Phosphoborosilicate Glass*. WO2014182753A1.

Fletcher, J. P., Kirkpatrick, R. J., Howell, D., and Risbud, S. H. (1993). ^{31}P Magic-angle spinning nuclear magnetic resonance spectroscopy of calcium phosphate glasses. *J. Chem. Soc. Faraday Trans.* 89, 3297–3299. doi: 10.1039/ft9938903297

Gan, H., Hess, P. C., and Kirkpatrick, R. J. (1994). Phosphorus and boron speciation in K_2O-B_2O_3-SiO_2-P_2O_5 glasses. *Geochim. Cosmochim. Acta*, 58, 4633–4647. doi: 10.1016/0016-7037(94)90196-1

Gao, H. S., Tan, T. N., and Wang, D. H. (2004). Dissolution mechanism and release kinetics of phosphate controlled release glasses in aqueous medium. *J. Cont. Rel.* 96, 29–36. doi: 10.1016/j.jconrel.2003.12.031

Gauvin, M., Dassenoy, F., Minfray, C., Martin, J. M., Montagnac, G., and Reynard, B. (2007). Zinc phosphate chain length study under high hydrostatic pressure by Raman spectroscopy. *J. Appl Phys.* 101:063505. doi: 10.1063/1.2710431

Gauvin, M., Minfray, C., Belin, M., Aquilanti, G., Martin, J. M., and Dassenoy, F. (2013). Pressure-induced amorphization of zinc orthophosphate—Insight in the zinc coordination by XAS. *Tribology Int.* 67, 222–228. doi: 10.1016/j.triboint.2013.07.011

Gross, T. M. (2012). Deformation and cracking behavior of glasses indented with diamond tips of various sharpness. *J. Non Cryst. Solids* 358, 3445–3452. doi: 10.1016/j.jnoncrysol.2012.01.052

Gross, T. M., and Guo, X. (2015). *Damage Resistant Glass With High Coefficient of Thermal Expansion*. US9969644B2.

Hamilton, J. P., and Pantano, C. G. (1997). Effects of glass structure on the corrosion behavior of sodium-aluminosilicate glasses. *J. Non-Cryst. Solids* 222, 167–174. doi: 10.1016/S0022-3093(97)90110-1

Hemley, R. J., Mao, H. K., Bell, P. M., and Mysen, B. O. (1986). Raman spectroscopy of SiO_2 glass at high pressure. *Phys. Rev.Lett.* 57, 747–750. doi: 10.1103/PhysRevLett.57.747

Hirao, K., Yoshimoto, M., Soga, N., and Tanaka, K. (1991). Densification of magnesium and calcium metaphosphate glasses. *J. Non-Cryst. Solids* 130, 78–84. doi: 10.1016/0022-3093(91)90158-3

Huang, L., and Kieffer, J. (2004). Amorphous-amorphous transitions in silica glass. *I.* Reversible transitions and thermomechanical anomalies. *Phys. Rev. B* 69:224203. doi: 10.1103/PhysRevB.69.224203

Hudgens, J. J., Brow, R. K., Tallant, D. R., and Martin, S. W. (1998). Raman spectroscopy study of the structure of lithium and sodium ultraphosphate glasses. *J. Non Cryst. Solids* 223, 21–31. doi: 10.1016/S0022-3093(97)00347-5

Januchta, K., Youngman, R. E., Goel, A., Bauchy, M., Logunov, S. L., Rzoska, S. J., et al. (2017). Discovery of ultra-crack-resistant oxide glasses with adaptive networks. *Chem. Mater.* 29, 5865–5876. doi: 10.1021/acs.chemmater.7b00921

Kafer, D., He, M. Q., Li,J. F., Pambianchi, M. S., Feng, J. W., Mauro, J. C., and Bao, Z. N. (2013). Ultra-smooth and ultra-strong ion-exchanged glass as substrates for organic electronics. *Adv. Func. Mater.* 23, 3233–3238. doi: 10.1002/adfm.201202009

Kapoor, S., Guo, X., Youngman, R. E., Hogue, C. L., Mauro, J. C., Rzoska, S. J., et al. (2017a). Network glasses under pressure: permanent densification in modifier-free systems. *Phys. Rev. Appl.* 7:054011. doi: 10.1103/PhysRevApplied.7.054011

Kapoor, S., Januchta, K., Youngman, R. E., Guo, X., Mauro, J. C., Bauchy, M., et al. (2018). Combining high hardness and crack resistance in mixed network glasses through high-temperature densification. *Phys. Rev. Mater.* 2:063603. doi: 10.1103/PhysRevMaterials.2.063603

Kapoor, S., Lönnroth, N., Youngman, R. E., Rzoska, S. J., Bockowski, M., Jensen, L. R., et al. (2017b). Pressure-driven structural

depolymerization of zinc phosphate glass. *J. Non Cryst. Solids* 469, 31–38. doi: 10.1016/j.jnoncrysol.2017.04.011

Kapoor, S., Wondraczek, L., and Smedskjaer, M. M. (2017c). Pressure-induced densification of oxide glasses at the glass transition. *Front. Materials* 4:1. doi: 10.3389/fmats.2017.00001

Kelsey, K. E., Stebbins, J. F., Mosenfelder, J. L., and Asimow, P. D. (2009). Simultaneous aluminum, silicon, and sodium coordination changes in 6 GPa sodium aluminosilicate glasses. *Am. Miner.* 94, 1205–1215. doi: 10.2138/am.2009.3177

Kirkpatrick, R. J., and Brow, R. K. (1995). Nuclear-magnetic-resonance investigation of the structures of phosphate and phosphate-containing glasses - A review. *Solid State Nucl. Magn. Res.* 5, 9–21. doi: 10.1016/0926-2040(95)00042-O

Le Parc, R., Ranieri, V., Haines, J., Cambon, M., Cambon, O., Levelut, C., and Clément, S. (2009). *In situ* high pressure and high temperature Raman studies of (1– x)SiO_2.xGeO_2 glasses. *J. Phys. Condensed. Matter* 21:375109. doi: 10.1088/0953-8984/21/37/375109

MacKenzie, K. J. D. (2002). *Multinuclear Solid-State NMR of Inorganic Materials.* Amsterdam: Pergamon.

Mascaraque, N., Bauchy, M., Fierro, J. L. G., Rzoska, S. J., Bockowski, M., and Smedskjaer, M. M. (2017). Dissolution kinetics of hot compressed oxide glasses. *J. Phys. Chem. B* 121, 9063–9072. doi: 10.1021/acs.jpcb.7b04535

Massiot, D., Fayon, F., Capron, M., King, I., Le Calvé, S., Alonso, B., et al. (2002). Modelling one-and two-dimensional solid-state NMR spectra. *Magn. Res. Chem.* 40, 70–76. doi: 10.1002/mrc.984

Meyer, K. (1998). Characterisation of the structure of binary calcium ultraphosphate glasses by infrared and Raman spectroscopy. *Phys. Chem. Glasses* 39, 108–117.

Mosey, N. J., Muser, M. H., and Woo, T. K. (2005). Molecular mechanisms for the functionality of lubricant additives. *Science* 307, 1612–1615. doi: 10.1126/science.1107895

Muñoz, F., Montagne, L., and Delevoye, L. (2008). Influence of phosphorus speciation on the phase separation of Na_2O-B_2O_3-SiO_2 glasses. *Phys. Chem. Glasses* 49, 339–345.

Muñoz, F., Montagne, L., Delevoye, L., Durán, A., Pascual, L., Cristol, S., et al. (2006). Phosphate speciation in sodium borosilicate glasses studied by nuclear magnetic resonance. *J. Non Cryst. Solids* 352, 2958–2968. doi: 10.1016/j.jnoncrysol.2006.04.016

Muñoz, F., Pascual, L., Duran, A., Montagne, L., and Delevoye, L. (2007). Structure-property relationships in phase separated borosilicate glasses containing P_2O_5. *Phys. Chem. Glasses* 48, 296–301.

Mysen, B. O., and Frantz, J. D. (1994). Silicate melts at magmatic temperatures: *in-situ* structure determination to 1651°C and effect of temperature and bulk composition on the mixing behavior of structural units. *Contribut. Mineral. Petrol.* 117, 1–14. doi: 10.1007/BF00307725

Nelson, B., and Exarhos, G. J. (1979). Vibrational spectroscopy of cation-site interactions in phosphate glasses. *J. Chem. Phys.* 71, 2739–2747. doi: 10.1063/1.438679

Premila, M., Ravindran, T. R., Shekar, N. V. C., Abhaya, S., Rajaraman, R., Amarendra, G., et al. (2012). Effect of pressure on the structural stability of iron phosphate glass: role of trace water. *J. Non Cryst. Solids* 358, 2575–2580. doi: 10.1016/j.jnoncrysol.2012.06.005

Rao, G. V., and Shashikala, H. (2014). Optical and mechanical properties of calcium phosphate glasses. *Glass Phys. Chem.* 40, 303–309. doi: 10.1134/S1087659614030249

Rouse, G. B., Miller, P. J., and Risen, W. M. (1978). Mixed alkali glass spectra and structure. *J. Non Cryst. Solids* 28, 193–207. doi: 10.1016/0022-3093(78)90006-6

Sandler, J., Shaffer, M. S. P., Windle, A. H., Halsall, M. P., Montes-Morán, M. A., Cooper, C. A., et al. (2003). Variations in the Raman peak shift as a function of hydrostatic pressure for various carbon nanostructures: A simple geometric effect. *Phys. Rev. B* 67: 035417. doi: 10.1103/PhysRevB.67.035417

Sato, R. K., Kirkpatrick, R. J., and Brow, R. K. (1992). Structure of Li, Na metaphosphate glasses by ^{31}P and ^{23}Na MAS-NMR correlated with the mixed alkali effect. *J. Non Cryst. Solids* 143, 257–264. doi: 10.1016/S0022-3093(05)80575-7

Schneider, J., Oliveira, S. L., Nunes, L. A. O., Bonk, F., and Panepucci, H. (2005). Short-range structure and cation bonding in calcium–aluminum metaphosphate glasses. *Inorganic Chem.* 44, 423–430. doi: 10.1021/ic0499704

Schneider, J., Oliveira, S. L., Nunes, L. A. O., and Panepucci, H. (2003). Local structure of sodium aluminum metaphosphate glasses. *J. Am. Ceram. Soc.* 86, 317–324. doi: 10.1111/j.1151-2916.2003.tb00017.x

Shannon, R. D. (1976). Revised effective ionic radii and systematic studies of interatomic distances in halides and chalcogenides. *Acta Crystallogr. Sect. A.* 32, 751–767. doi: 10.1107/S0567739476001551

Shi, Y., Lonnroth, N. T., Youngman, R. E., Rzoska, S. J., Bockowski, M., and Smedskjaer, M. M. (2018). Pressure-induced structural changes in titanophosphate glasses studied by neutron and X-ray total scattering analyses. *J. Non Cryst. Solids* 483, 50–59. doi: 10.1016/j.jnoncrysol.2017.12.055

Siebers, F., Ruedinger, B., Langsdorf, A., and Heiss, M. (2014). *Glass Having Excellent Resistance Against Surface Damages and Method for the Production Thereof.* US8859079B2.

Smedskjaer, M. M., Mauro, J. C., and Yue, Y. Z. (2010). Prediction of glass hardness using temperature-dependent constraint theory. *Phys. Rev. Lett.* 105:115503. doi: 10.1103/PhysRevLett.105.115503

Smith, C. E., Brow, R. K., Montagne, L., and Revel, B. (2014). The structure and properties of zinc aluminophosphate glasses. *J. Non Cryst. Solids* 386, 105–114. doi: 10.1016/j.jnoncrysol.2013.11.042

Striepe, S., Smedskjaer, M. M., Deubener, J., Bauer, U., Behrens, H., Potuzak, M., et al. (2013). Elastic and micromechanical properties of isostatically compressed soda–lime–borate glasses. *J. Non Cryst. Solids* 364, 44–52. doi: 10.1016/j.jnoncrysol.2013.01.009

Svenson, M. N., Paraschiv, G. L., Muñoz, F., Yue, Y., Rzoska, S. J., Bockowski, M., et al. (2016). Pressure-induced structural transformations in phosphorus oxynitride glasses. *J. Non Cryst. Solids* 452, 153–160. doi: 10.1016/j.jnoncrysol.2016.08.039

Tošić, M., Nikolić, J., Grujić, S., Živanović, V., ZildŽović, S., Matijašević, S., et al. (2013). Dissolution behavior of a polyphosphate glass into an aqueous solution under static leaching conditions. *J. Non Cryst. Solids* 362, 185–194. doi: 10.1016/j.jnoncrysol.2012.11.024

van Wüllen, Züchner, L. L., Müller-Warmuth, W., and Eckert, H. (1996). $^{11}B\{^{27}Al\}$ and $^{27}Al\{^{11}B\}$ double resonance experiments on a glassy sodium aluminoborate. *Solid State Nucl. Magn. Res.* 6, 203–212.

Watson, G. H., and Daniels, W. B. (1988). Raman scattering from solid argon at high pressure. *Phys. Rev. B* 37, 2669–2673. doi: 10.1103/PhysRevB.37.2669

Yue, Y., Wondraczek, L., Behrens, H., and Deubener, J. (2007). Glass transition in an isostatically compressed calcium metaphosphate glass. *J. Chem. Phys.* 126:144902. doi: 10.1063/1.2719194

Zhang, Z., Hirao, K., and Soga, N. (1991b). Water corrosion behavior of densified glass. II. Borate glass. *J. Non-Cryst. Solids* 135, 62–66. doi: 10.1016/0022-3093(91)90443-A

Zhang, Z., Soga, N., and Hirao, K. (1991a). Water corrosion behavior of densified glass. I. Silicate glass. *J. Non-Cryst. Solids* 135, 55–61. doi: 10.1016/0022-3093(91)90442-9

Zuchner, L., Chan, J. C. C., Muller-Warmuth, W., and Eckert, H. (1998). Short-range order and site connectivities in sodium aluminoborate glasses: I. Quantification of local environments by high-resolution ^{11}B, ^{23}Na, and ^{27}Al solid-state NMR. *J. Phys. Chem. B* 102, 4495–4506. doi: 10.1021/jp980587s

Conflict of Interest Statement: RY, LM, and NL are employed by Corning Incorporated.

The reviewer MS declared a past collaboration with one of the authors MS to the handling editor.

The remaining authors declare that the research was conducted in the absence of any commercial or financial relationships that could be construed as a potential conflict of interest.

frontiers in Materials

ORIGINAL RESEARCH
published: 18 October 2019
doi: 10.3389/fmats.2019.00259

Transparent TiO_2 and ZnO Thin Films on Glass for UV Protection of PV Modules

*Wilhelm Johansson[1], Albert Peralta[2], Bo Jonson[1], Srinivasan Anand[2], Lars Österlund[3] and Stefan Karlsson[4]**

[1] LNU Glass Group, Department of Built Environment and Energy Technology, Faculty of Technology, Linnaeus University, Växjö, Sweden, [2] Department of Applied Physics, School of Engineering Sciences, KTH Royal Institute of Technology, Kista, Sweden, [3] The Ångström Laboratory, Department of Engineering Sciences, Uppsala University, Uppsala, Sweden, [4] RISE Glass, Built Environment Division, RISE Research Institutes of Sweden, Växjö, Sweden

Failure of PV modules frequently occurs as a result of degradation of their encapsulation material by destructive UV radiation. Both the life expectancy and efficiency of PV modules can be improved by reducing the transmittance of the destructive UV radiation through the cover glass without compromising the transmittance in the visible wavelength region. In addition, if the absorbed UV photons can be down-shifted to wavelengths that can be more efficiently converted to electrical energy, an additional increase of the PV efficiency could be achieved. In this study we have investigated transparent ZnO and TiO_2 thin films deposited by spray pyrolysis on soda lime silicate float glass as functional layers on PV cover glass. The optical bandgap, UV-cutoff, UV-Vis transmittance, reflectivity (total and diffuse) and photoluminescence have been determined. The ZnO coating shifted the optical bandgap to longer wavelengths, resulting in a reduction of the transmittance of destructive UV radiation by up to ~85%. Distinct photoluminescence peaks at 377 nm and at 640 nm were observed for one of the ZnO samples. The TiO_2 coated glasses also showed an increased UV cutoff, which resulted in a reduction of transmittance of destructive UV radiation by up to 75%. However, no photoluminescence peaks could be observed from the TiO_2 films with 325 nm excitation laser, which can be explained by the fact that only indirect interband transitions are accessible at this excitation wavelength. Deposition of both ZnO and TiO_2 coatings resulted in a reduction of the transmitted light convertible by PV modules, by up to 12.3 and 21.8%, respectively. The implication of the results is discussed in terms of lifetime expectancy and efficiency of PV modules.

Keywords: float glass, thin films, UV protection, photovoltaic modules, cover glass, transparent intelligence, solar energy materials, photoluminescence

OPEN ACCESS

Edited by:
Lothar Wondraczek, Friedrich Schiller University Jena, Germany

Reviewed by:
Martin Charles Wilding, Sheffield Hallam University, United Kingdom
Paul A. Bingham, Sheffield Hallam University, United Kingdom

***Correspondence:**
Stefan Karlsson
stefan.karlsson@ri.se

Specialty section:
This article was submitted to Glass Science, a section of the journal Frontiers in Materials

Received: *30 November 2018*
Accepted: *30 September 2019*
Published: *18 October 2019*

Citation:
Johansson W, Peralta A, Jonson B, Anand S, Österlund L and Karlsson S (2019) Transparent TiO_2 and ZnO Thin Films on Glass for UV Protection of PV Modules. Front. Mater. 6:259. doi: 10.3389/fmats.2019.00259

INTRODUCTION

To stabilize the global temperature and mitigate climate change, the emission of anthropogenic greenhouse gases will have to be greatly reduced. To make it possible, the energy sector will have to transfer from fossil energy to environmentally friendly and carbon neutral sources (IPCC, 2014). Solar energy exists in abundance. In roughly 90 min, the solar energy that reaches the earth equals the consumption of all human societies globally during one year (IEA, 2011). Only a fraction of this energy is captured today, and photovoltaic (PV)

modules account for a marginal part of the electricity production worldwide, around 1.8% at the end of 2016. In recent years, however, the sector has been growing exponentially at a rapid rate, which means that the ability to increase efficiency and lifespan of PV modules is interesting from an energy perspective (Masson et al., 2018). PV modules consist of a number of interconnected PV-cells, embedded in an encapsulant and a protective cover glass on the top. One of the issues facing the PV modules available today is the degradation of their encapsulant, which most often consists of EVA (ethylene vinyl acetate). It is damaged by UV radiation with wavelengths below 350 nm. The UV radiation makes the encapsulant degrade and acquire a yellow and eventually brown hue, which reduces the efficiency of the PV modules (Czanderna and Pern, 1996; Oliveira et al., 2018).

Developing the cover glass has become increasingly important as the share of cost for the cover glass is high (Burrows and Fthenakis, 2015). The cover glass (Brow and Schmitt, 2009; Deubener et al., 2009) has several important functionalities, e.g., providing optimal light capture, rigidity, mechanical protection, and chemical protection. Optimal light capture depends on the optical properties of the cover glass such as absorption and reflection. The latter comprises the largest part, about 8% for a typical flat glass, which can be minimized by employing antireflective coatings (Nielsen et al., 2014). Rigidity and mechanical protection are determined by the thickness, the elastic modulus and the strength of glass (Wondraczek et al., 2011), which for PV cover glass is conventionally thermally strengthened (Karlsson and Wondraczek, 2019). The strength of glass is lowered continuously in operation by handling, and it therefore also depends on the glass's scratch and crack resistance (Rouxel et al., 2014; Sundberg et al., 2019). The chemical protection is important and glass provides an excellent chemical protection where in principle the only weaknesses are the lamination (Kuitche et al., 2014) and the potential induced degradation (PID) (Oliveira et al., 2018).

The optical properties of flat glass (Bamford, 1982; Rubin, 1985) are affected by the presence of iron impurities in the glass melt as the iron in the glass increases the absorption of light in the glass in the UV-VIS region of the electromagnetic spectrum. Iron can be used as a colorant of glass, giving the glass a green tint (Volotinen et al., 2008). In some cases, this is a positive feature, e.g., when UV-protection is needed in beer and champagne bottles (Daneo et al., 2009). In other cases, as with PV-modules where transparency is coveted (Goodyear and Lindberg, 1980), the iron in the glass is considered as a contaminant. In these cases, low-iron glass, where measures have been taken to reduce the iron in the glass, is frequently used.

In the case of cover glass for PV modules, the trend has been to use low-iron glass to increase transmitted light (Deubener et al., 2009). A drawback to this type of glass is that a larger amount of high-energy UV radiation is transmitted, which is harmful to the encapsulation material EVA that is used in most PV modules today (Allsopp et al., 2018). When UV radiation below 350 nm reaches the PV module, both the semiconductor material (Osterwald et al., 2003) and the laminate (Kuitche et al., 2014; Oliveira et al., 2018) are degraded. The degradation of the EVA laminate is the major reason for the annual degradation of 0.6–2.5% (Jordan and Kurtz, 2013; Kuitche et al., 2014). As a result of the UV radiation, EVA degrades and loses some of its high transmissivity as it gets a yellow/brown hue and eventually starts to delaminate, letting moisture into the PV modules, which leads to failure of the PV module (Oliveira et al., 2018).

In the current study we have investigated float glass coated with ZnO and TiO_2 thin films by spray pyrolysis of organometallic compounds of zinc and titanium. We present a detailed characterization of their optical properties by means of UV-Vis and photoluminescence spectroscopy.

TABLE 1 | Composition of precursor solutions.

	Isopropanol (ml)	Zn $(acac)_2$ (g)	Ti-isopropoxide (ml)	Wt% metalorganic complex	Mol% metalorganic complex
Zn solution	150	0.62	–	0.5	0.12
Ti solution	100	–	2.5	3	0.64

TABLE 2 | Sample series, amount of solution sprayed in grams denoted according to this numbering Zn2, Zn3, … and Ti1, Ti2… etc.

Sample ID	1	2	3	4	5	6
Zn solution (g)	–	12	16	24	32	40
Ti solution (g)	2	4	6	8	12	18

MATERIALS AND METHODS

Thin film depositions were made by spray pyrolysis in a hot wall reactor employing the precursor solutions shown in **Table 1**. The solutions were heated to 70°C for 2 h. The thin films were deposited on the air surface of AGC Planibel Clearview float glass samples (size 50 mm × 50 mm × 3.89 mm), which is a conventional soda-lime silicate float glass. The samples were heated up to 500°C, after which they were sprayed with the metal organic solution using a Preval sprayer (paintbrush equipment driven by the carrier gases dimethyl ether, isobutene, and propane). The furnace hatch was temporarily opened, and the precursor was sprayed onto the glass surface, manually holding the sprayer about a decimeter from the substrate. Between each opening of the furnace hatch, the furnace temperature was set to 500°C, implying that all depositions were made between 485 and 515°C. After deposition, the temperature in the furnace was lowered in a controlled manner at a cooling rate of 0.5°C / min down to 300°C, after which the furnace was turned off and the samples were left to cool down to room temperature. A series of six coated glasses with different deposited quantities were produced. The amount of precursor solution sprayed onto every glass sample is shown in **Table 2**, and the denotation of each sample according to the numbering. We believe that the deposited coatings are thin (<100 nm), mostly amorphous for both ZnO (Kamata et al., 1994; Hosseinmardi et al., 2012; Villegas

et al., 2018) and TiO_2 (Okuya et al., 1999; Abou-Helal and Seeber, 2002). This will be discussed in section Change in Transmittance and Reflection and section Effect on Photoluminescence. The surface morphologies of the coatings were measured using a Dimension 3100 (Bruker) Atomic Force Microscopy (AFM) and the root-mean-square (RMS) roughness was determined.

UV-Vis Spectrophotometry

Transmittance, $T(\lambda)$, and reflectance, $R(\lambda)$, spectra were recorded in the wavelength range between 325 and 850 nm with a step resolution of 2.5 nm, employing a Lambda 950 double-beam UV/Vis/NIR spectrophotometer equipped with an integrating sphere and a Spectralon reflectance standard. Both total and diffuse reflectance, $R(\lambda)$, were measured with 8° incidence angle. The absorptance, $A(\lambda)$ is then obtained as

$$A(\lambda) = 1 - T(\lambda) - R(\lambda) \tag{1}$$

Instrument corrected values of $T(\lambda)$ and $R(\lambda)$ were used in Equation (1) (Roos, 1993). In order to estimate the fraction of blocked UV light and the solar spectrum weighted $T\%$ and $R\%$ data for given single values throughout the paper, we calculate a Figure of Merit (*FoM*). The solar spectrum AM 1.5 G-173 from NREL, $\phi_{AM\ 1.5\ G}(\lambda)$, is used as the solar light intensity distribution function, and the weighted average is between 320 and 350 nm for estimating UV blocking and between 350 and 1200 nm for estimating $T\%$ and $R\%$ as single values, according to

$$FoM \times 100(\%) = \frac{\int_{\lambda_0}^{\lambda} P(\lambda) \cdot \phi_{AM\ 1.5\ G}(\lambda) \cdot d\lambda}{\int_{\lambda_0}^{\lambda} \phi_{AM\ 1.5\ G}(\lambda) \cdot d\lambda} \tag{2}$$

where λ and λ_0 is the wavelength range that is evaluated and $P(\lambda)$ represents $T(\lambda)$ or $R(\lambda)$.

Photoluminescence

The photoluminescence of the ZnO- and TiO_2-coated samples was measured using a Renishaw Invia Raman microscope employing a 40× objective lens. The samples were irradiated with a He-Cd laser with a wavelength of 325 nm, and photoluminescence of wavelengths between 330 and 720 nm were recorded. The maximum effect of the laser was 6 mW, but 99 and 90% of the laser flux was filtered away for the ZnO and TiO_2 samples, respectively.

Energy calibration was performed by Raman spectroscopy on non-coated float glass with the same instrument settings. Prior to the measurements, the instrument was calibrated by measuring the 1,332 cm^{-1} peak of the diamond.

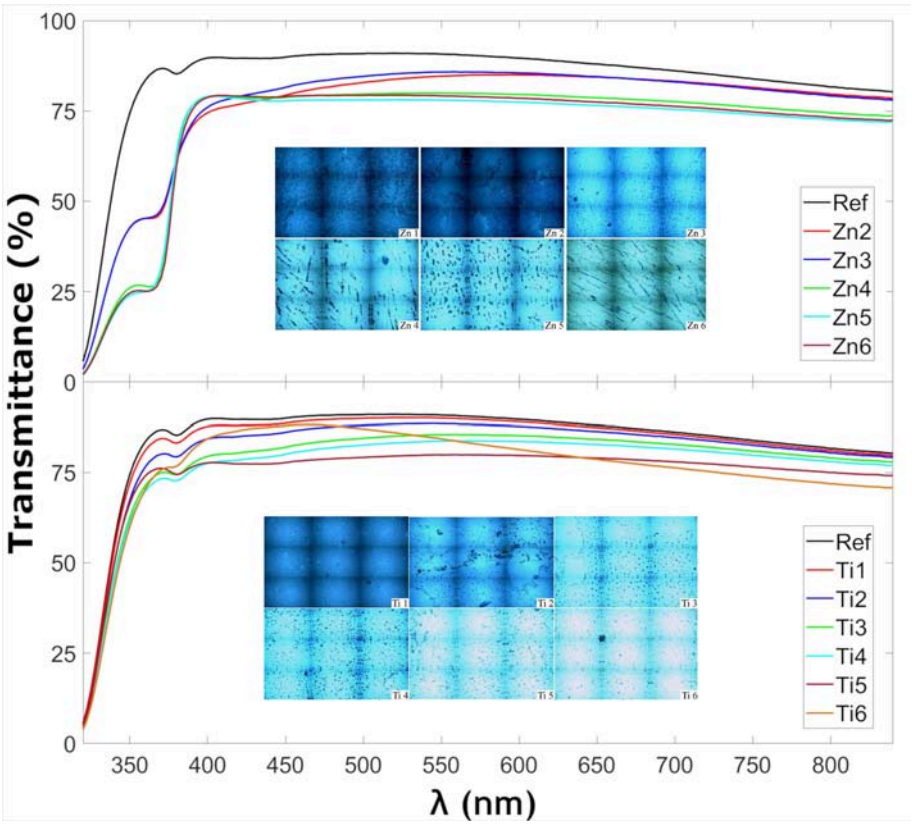

FIGURE 1 | Transmittance of thin film-coated glass samples at normal incidence as well as insets of microscope images of the samples taken from the Raman microscope.

TABLE 3 | Optical properties of coated glass samples, the fraction of the blocked UV light and the transmittance was calculated using (Equation 2).

Sample	Fraction of UV light blocked (%)[a]	Transmittance (%)[a]	Optical bandgap, E_g (eV)	UV cutoff wavelength (nm)[b]	RMS roughness (nm)
Estimated error	±2	±2	±0.01 (±2)	±2	±1
Reference	54.6	85.2	3.53 (351 nm)	322.7	0.5
Zn2	73.0	79.8	3.57 (347 nm)	325.6	31.0
Zn3	73.0	80.3	3.58 (346 nm)	325.6	4.2
Zn4	83.4	75.7	3.58 (346 nm)	329.6	8.4
Zn5	84.7	74.1	3.58 (346 nm)	330.0	8.0
Zn6	84.2	74.7	3.59 (345 nm)	330.4	8.0
Ti1	57.3	83.9	3.54 (350 nm)	323.0	2.0
Ti2	63.6	81.6	3.52 (352 nm)	323.6	2.7
Ti3	70.0	76.9	3.51 (353 nm)	324.1	5.4
Ti4	71.5	75.2	3.53 (351 nm)	324.2	4.4
Ti5	67.5	69.8	3.55 (349 nm)	323.6	11.6
Ti6	74.2	66.7	3.54 (350 nm)	324.8	4.8

Root-mean-square (RMS) data as determined from Atomic Force Microscopy (AFM).
[a] *Defined as given in section UV-Vis spectrophotometry.*
[b] *Defined as given in section optical bandgap and UV cutoff wavelength.*

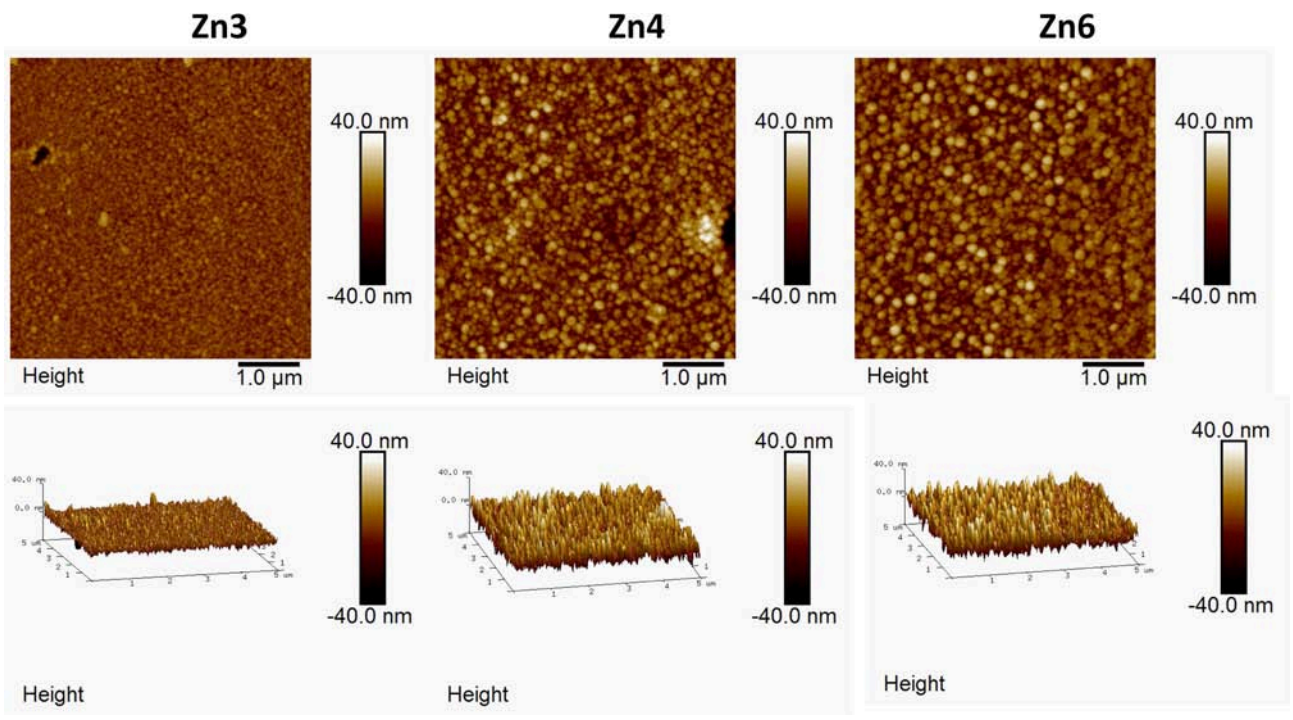

FIGURE 2 | 2D and 3D AFM images of selected ZnO-coated samples.

Optical Bandgap and UV Cutoff Wavelength

From the spectrophotometry data it is possible to estimate the optical bandgap, i.e., at which wavelength the coated glass starts to absorb most of the radiation acting as a short wavelength cutoff filter. In this study the cutoff wavelength was defined as the wavelength below which <10% of the incoming light is transmitted, i.e., at a somewhat larger wavelength compared to the optical bandgap.

The optical bandgap, E_g, of the coated glasses was analyzed according to a simplified demarcation point analysis which is very similar to the Tauc analysis (Tauc, 1968). The demarcation point can be graphically extracted from $A(\lambda)$ by approximating the bandgap region below E_g with a fairly horizontal straight line

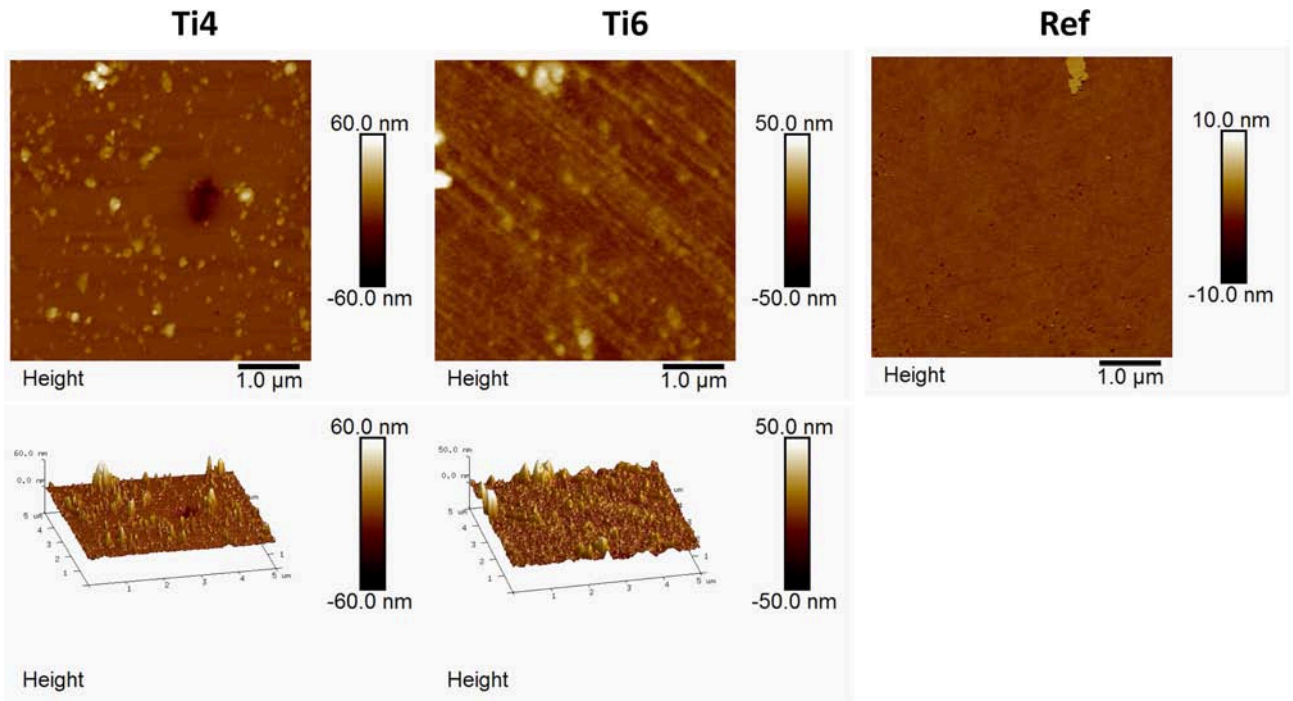

FIGURE 3 | 2D and 3D AFM images of selected TiO_2-coated samples.

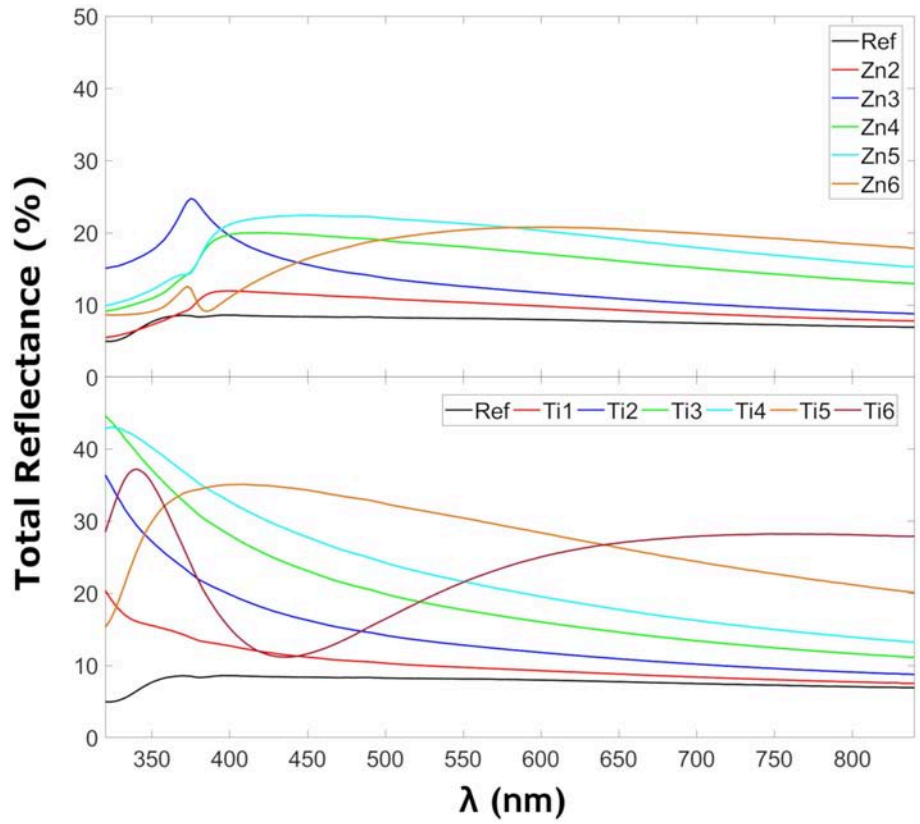

FIGURE 4 | Total reflectance of thin film-coated glass samples.

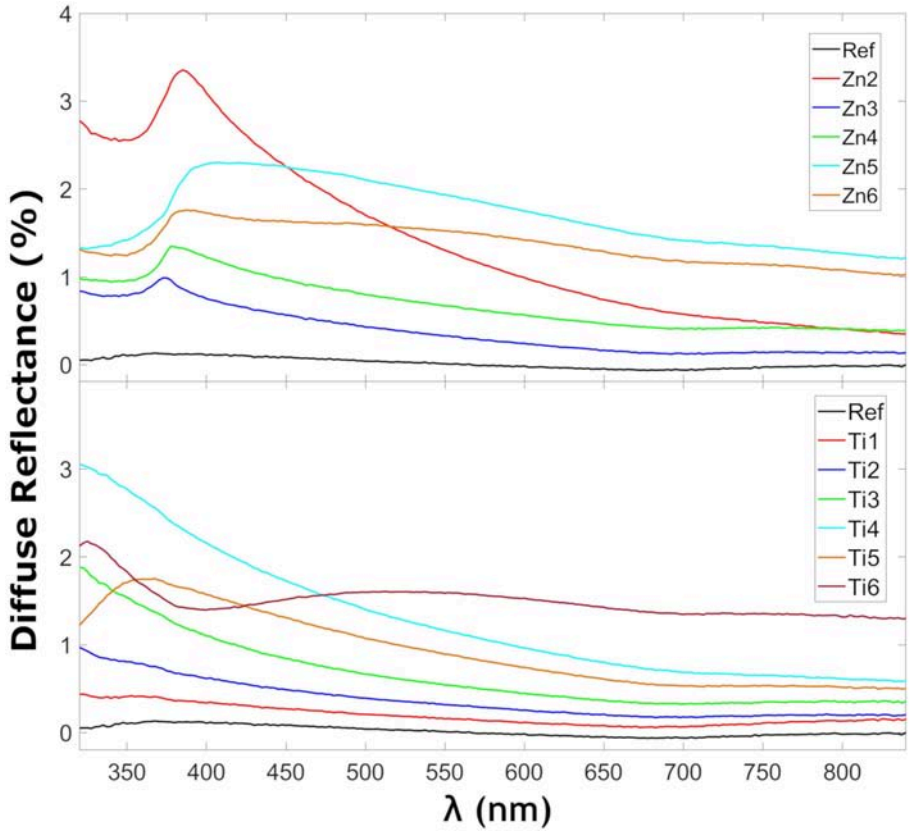

FIGURE 5 | Diffuse reflectance of thin film-coated glass samples.

and approximate the region above E_g (the actual UV-edge) with another straight line. The point where these two straight lines intersect is the demarcation point and is a good approximation of the E_g.

RESULTS

Change in Transmittance and Reflection

Figure 1 shows the transmittance at normal incidence for the glass samples coated with ZnO and TiO_2, respectively. The insets in **Figure 1** show optical microscopy images acquired with the Raman instrument, showing that the thin films consist of particulate features with a root-mean-square roughness of about 4–8 nm for the ZnO and 2–10 nm for the TiO_2 samples (see **Table 3**) which is quite common for the spray pyrolysis technique (Perednis and Gauckler, 2005). The ZnO coatings show the expected rough surface, see **Figure 2**. The highest roughness is for the thinnest layer, Zn2, while the others have comparable roughness values. In comparison, for the TiO_2 coated samples, see **Figure 3**, there are larger structures with peak to valley heights in the range 60–150 nm. Also, most samples show clear pits/openings in the film. The depths of these openings are in the range 10–40 nm. Both ZnO- and TiO_2-coated glass show a decrease of the transmittance compared to the uncoated reference sample. The ZnO-coated samples showed larger transmittance in the visible regime than the TiO_2-coated. While the sample coated with the largest amount of ZnO (sample Zn6) showed a transmittance of 74.7%, the transmittance for the sample coated with the largest amount of TiO_2 (sample Ti6) was 66.7%, see **Table 3**. Glass with ZnO coatings showed a decreased transmittance in the UV regime <350 nm, exhibiting a plateau between 320 and 370 nm. A small absorption peak can also be observed for the reference samples at 380 which can be denoted to tetrahedral configuration of Fe^{3+} (Volotinen et al., 2008). Therefore, we attribute the plateau between 320 and 370 nm for the ZnO-coated samples to be caused by Fe^{3+} but sensitized by the presence of ZnO thin film.

Figure 4 shows the reflectance in the glass samples coated with ZnO and TiO_2. The TiO_2 coated glasses show more reflection as expected due to a larger refractive index mismatch between the glass and the coating. The refractive index for TiO_2 is 2.65 for rutile-TiO_2 (Jellison et al., 1997) or 2.56 anatase-TiO_2 (Schröder, 1928) and for ZnO 2.0 (Jellison and Boatner, 1998), all reported at 589.3 nm as reported by Shannon et al. (2002). The peaks at 375 nm for the ZnO samples coincide with their observed absorption edge in **Figure 6** as expected for localized transitions, signaling the presence of defect states, possibly with contribution from Fe^{3+} charge transfer reactions, since the reference sample also exhibits small absorption in this region. It has only been

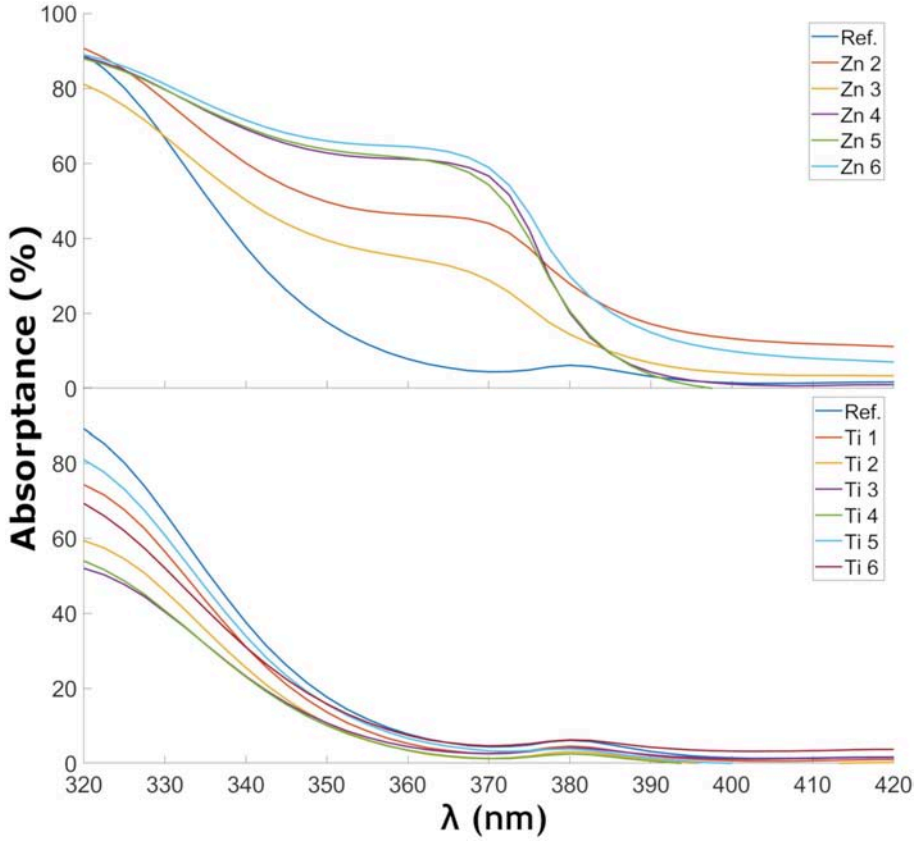

FIGURE 6 | Absorptance of ZnO- and TiO_2-coated glass samples in the wavelength range near the UV cutoff.

possible to find a zone without that reflection behavior for Zn5. That zone without the mentioned peak corresponded to a place which was far from the internal crack that the sample presented. It has been seen that the samples with that behavior show more spot to spot deviance in reflection measurements. **Figure 5** shows the diffuse reflection in the ZnO of the TiO_2-coated samples, respectively. The diffuse reflection of the coatings is <4% for both coatings. The low diffuse reflection is likely to be caused by non-uniform deposited thin films. This means that parts of the diffuse transmitted light that reaches the glass back end will be reflected back into the glass instead of being transmitted through it, similar to a conventional light trapping and back-reflecting cover glass structure (Deubener et al., 2009).

The measured transmittance/reflectance spectra do not exhibit any interference patterns as is expected for thin films with thicknesses >> 100 nm.

Change in UV-Cutoff and Optical Band Gap

Figure 6 shows the change in absorptance near the UV-cutoff in the glass samples coated with ZnO and TiO_2. A trend can be observed of a shift of the UV-cutoff to longer wavelength as more ZnO was deposited. This trend is less clear for TiO_2. The estimated optical bandgaps, using the demarcation point analysis, are shown in **Table 3**. In the ZnO spectra, two UV edges can be observed: one at about 330 to 340 nm and another one at 375 to 380 nm. The latter gave optical bandgap values in the range of 3.21–3.22, i.e., very similar to the wurtzite form of ZnO. The optical band gap of ZnO in wurtzite and zinc-blende form is 3.22 and 3.12 eV, respectively (Lee et al., 2002). The TiO_2-coated glasses also show a small absorption peak at 380 nm which is caused by the tetrahedral configuration of Fe^{3+} (Volotinen et al., 2008). TiO_2 in rutile, anatase, and brookite form has optical band gaps at 3.00, 3.21, and 3.13 eV, respectively (Dhar et al., 2013). The estimated optical bandgaps in **Table 3** are in the range around 3.55 eV, i.e., much influenced by the float glass and its conventional impurity Fe_2O_3. Fe_2O_3 has a considerable effect on the UV absorption and probably overshadows some of the effects that would otherwise be seen by our coatings (Volotinen et al., 2008). This is discussed more in section Discussion of the Effect for PV Modules.

UV-Blocking

Table 3 shows the UV-blocking characteristics as well as the transmittance of light convertible for Si-PV modules. The-ZnO coated samples show larger percentages of blocked UV light with larger transmission in the visible range compared with TiO_2 coatings. Compared to the reference float glass, the coatings show a relative increase of the *FoM* (c.f. Equation 2) up to 54.3 and 36.0% of UV-blocking characteristics and a relative decrease of the transmittance by up to 12.3 and 21.8% for ZnO and TiO_2 coatings, respectively.

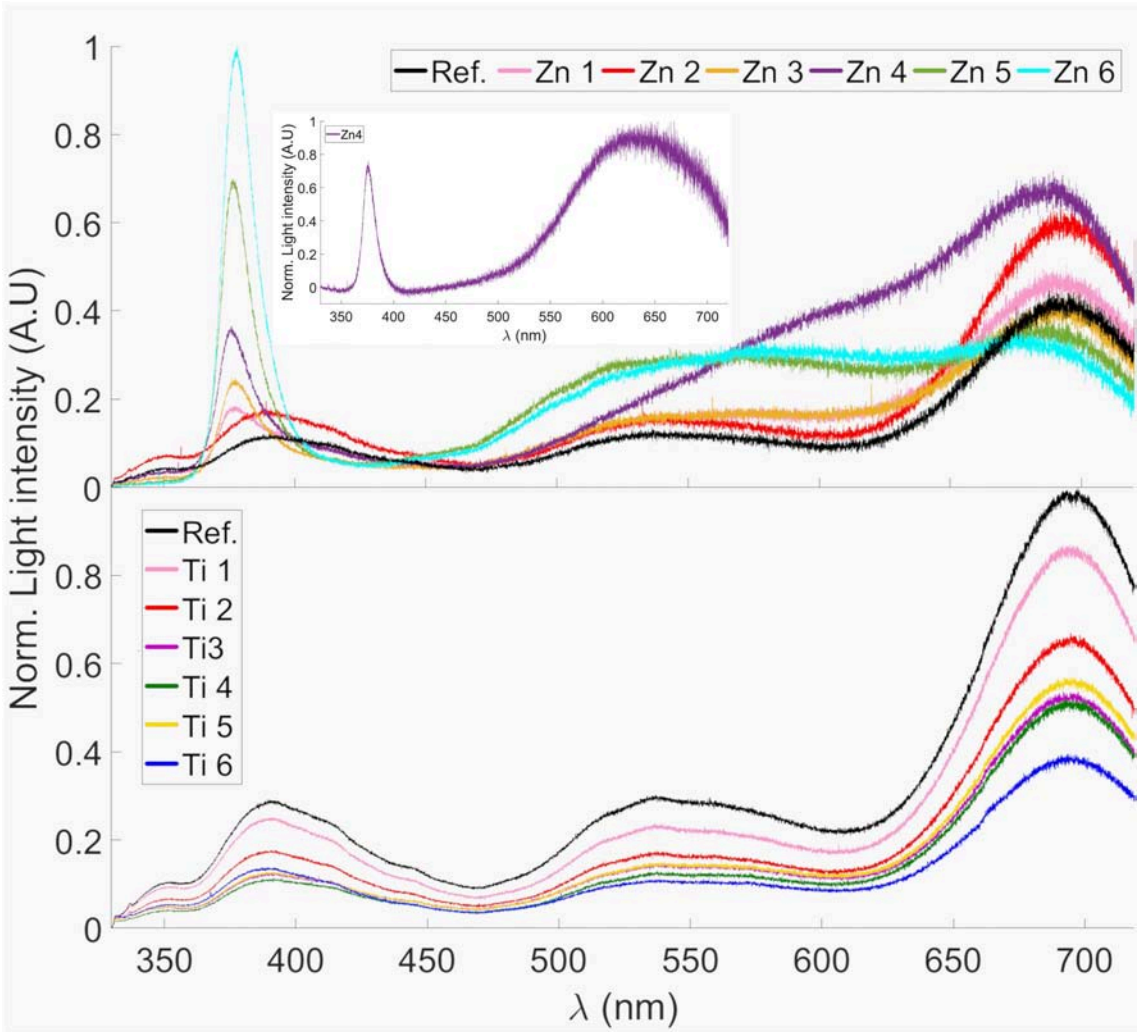

FIGURE 7 | Photoluminescence spectra of ZnO- and TiO_2-coated glass samples. The spectra were normalized to the highest peak. The inset shows the Zn4 photoluminescence spectra subtracted by the reference, clearly revealing the 640 nm emission peak.

Effect on Photoluminescence

Figure 7 shows the photoluminescence spectra between 330 and 720 nm of the ZnO- and TiO_2-coated glass substrates. All samples as well as the reference shows a distinct peak around 695 nm. This can probably be attributed to the Fe^{3+} present in the glass since it has shown a peak in photoluminescence at wavelengths around 700 nm when present in silicate glass (Bingham et al., 2007). The reference sample also shows a peak at 390 nm, this could be due to photoluminescence from SiO_2 (Nagata et al., 2004).

All Zn-samples, except Zn2, possess a strong narrow emission peak that can be observed at approximately 377 nm, which is not present in the reference sample. This corresponds well to the photoluminescence observed in ZnO nanorods by Wu et al. (2006) and which can be attributed to a common excitation recombination of ZnO (Studenikin et al., 1998; Kong et al., 2001). The 377 nm PL emission can be an explanation for the sensitization of Fe^{3+} absorption at 320–380 nm, c.f. **Figure 6**. Sample Zn4 shows a different pattern compared to the reference and the other coated samples in the wavelength interval 550–650 nm. When the photoluminescence from the reference sample was subtracted from sample 4, a peak at 640 nm could be distinguished; this is shown in the inset of **Figure 7**. This also corresponds well to the photoluminescence observed for ZnO nanorods (Wu et al., 2006), which was also observed by Studenikin et al. (1998) and has been attributed to oxygen interstitial defects in ZnO, i.e., over-stoichiometric ZnO. The opposite, under-stoichiometric ZnO, is indicated to give a green emission at about 510 nm.

The effect that our deposited ZnO and TiO_2 thin films have on the photoluminescence emission makes us confident that these thin films are mostly amorphous. The photoluminescent bands that we interpret as defects and the Fe^{3+} sensitization emissions for the samples are strong and dominate the photoluminescence spectra, see **Figure 7**. For the ZnO-coated samples it is despite that similar literature data, but with somewhat different experimental circumstances, refer to the ZnO films as mostly

crystalline (Kamata et al., 1994; Hosseinmardi et al., 2012; Villegas et al., 2018).

Discussion of the Effect for PV Modules

We have shown that UV blocking can be achieved with the cost of reducing the transmittance. Specifically, there was a 75.7% transmittance and a simultaneous reduction of 83.4% integrated transmittance for the sample Zn4, c.f. **Table 3**. This opens the possibility for maintaining UV protection and gaining useful energy for the PV by lowering the Fe_2O_3 content in the glass without compromising the service lifetime of the PV module. The energy balance for transmitted and useful light for PV modules will be possible to model and optimize in future studies based on information as for instance possible limits for Fe_2O_3 content, cost and efficiency. Furthermore, photon energy down-conversion, i.e., photoluminescence, can be an advantage and a route to utilizing UV light while still not exposing the PV cells to UV light. As for disadvantages, we can list higher reflectivity and scattering. If the surface coating is properly structured, it might not be a serious disadvantage or perhaps even an advantage (Brongersma et al., 2014), as the diffused light contains in fact more photons than the direct light of normal incidence. This is especially valid for façade-applied PV modules where there is in fact very little solar radiation of normal incidence. Another parameter not previously mentioned is the factor of heat. A photon's energy that is not converted into electricity is transformed into heat that in fact lowers the efficiency of the PV module. Beyond the scope of the current paper we would also like to draw the attention to making crystalline ZnO or TiO_2 coatings having similar beneficial properties but with the added value of photocatalysis (Gao and Nagai, 2006; He et al., 2012) and hydrophilic behavior with UV exposure (Watanabe et al., 1999; Sun et al., 2001), thereby giving PV-covered glasses reduced maintenance. Doped ZnO also offers another dimension as a transparent conductive coating offering possible IR reflection for wavelengths non-convertible to energy for PV modules (Deubener et al., 2009).

CONCLUSIONS

Glass coated with ZnO showed a trend to shift the UV-cutoff to longer wavelength as well as lowering the optical band gap of the coated glass sample. The major reason for this is likely to be caused by tetrahedrally coordinated Fe^{3+} having an absorption peak at about 380 nm but also being sensitized by the presence of the ZnO coating. Such a trend is less clear for the samples coated with TiO_2. Both sample series showed a significant increase in total reflection for the normal incident light due to the higher refractive index of the thin film oxide coatings. However, the increase in diffuse reflection was significantly lower, <4%; this is an advantage for application on the cover glass of PV-modules where most of the incoming light will be of diffuse character.

The coated glass showed a potential improvement in life expectancy of PV modules through a decrease of destructive UV-radiation transmission to the encapsulant up to a relative 36.0% and 54.3% for TiO_2 and ZnO, coatings, respectively. Additionally, although the coated samples have shown a relative transmission reduction at the useful spectral region up to 21.8 and 12.3% for TiO_2 and ZnO coatings, respectively, the transmissivity degradation of the encapsulant should be effectively prevented. For ZnO it is evident that the Fe^{3+} content plays an important role for the UV-blocking activity, which would be a tradeoff between limiting the glass's iron content while still having enough UV protection. Furthermore, ZnO-coated glass also showed potential regarding down conversion of UV light to visible wavelength with peaks at 377 and 640 nm. Thus, ZnO is feasible to be investigated for application as coating to cover glasses of PV modules but must be optimized as there is a tradeoff between UV-blocking and transmittance in the useful spectral region for PV modules.

AUTHOR CONTRIBUTIONS

SK perceived the idea of the paper. WJ performed the thin film deposition and photoluminescence measurements with the guidance of SK, BJ, and LÖ. AP performed the UV-VIS spectroscopy measurements with guidance from SA. SA performed the AFM measurements. WJ and AP evaluated the results of the measurements. WJ and SK wrote the draft of the paper. All authors were involved in the discussions and elaborating the final manuscript text.

ACKNOWLEDGMENTS

Jakob Thyr at the Ångström Laboratory, Uppsala University was greatly acknowledged for his supervision during the photoluminescence measurements.

REFERENCES

Abou-Helal, M. O., and Seeber, W. T. (2002). Preparation of TiO_2 thin films by spray pyrolysis to be used as a photocatalyst. *Appl. Surf. Sci.* 195, 53–62. doi: 10.1016/S0169-4332(02)00533-0

Allsopp, B. L., Christopoulou, G., Brookfield, A., Forder, S. D., and Bingham, P. A. (2018). Optical and structural properties of d^0 ion-doped silicate glasses for photovoltaic applications. *Phys. Chem. Glasses Euro. J. Glass Sci. Technol. B* 59, 193–202. doi: 10.13036/17533562.59.4.003

Bamford, C. R. (1982). Optical properties of flat glass. *J. Non Cryst. Solids* 47, 1–20. doi: 10.1016/0022-3093(82)90342-8

Bingham, P. A., Parker, J. M., Searle, T. M., and Smith, I. (2007). Local structure and medium range ordering of tetrahedrally coordinated Fe^{3+} ions in alkali–alkaline earth–silica glasses. *J. Non-Crystalline Solids* 353, 2479–2494. doi: 10.1016/j.jnoncrysol.2007.03.017

Brongersma, M. L., Cui, Y., and Fan, S. (2014). Light management for photovoltaics using high-index nanostructures. *Nat. Mater.* 13, 451–460. doi: 10.1038/nmat3921

Brow, R. K., and Schmitt, M. L. (2009). A survey of energy and environmental applications of glass. *J. Eur. Ceram. Soc.* 29, 1193–1201. doi: 10.1016/j.jeurceramsoc.2008.08.011

Burrows, K., and Fthenakis, V. (2015). Glass needs for a growing photovoltaics industry. *Solar Energy Mater. Solar Cells* 132, 455–459. doi: 10.1016/j.solmat.2014.09.028

Czanderna, A. W., and Pern, F. J. (1996). Encapsulation of PV modules using ethylene vinyl acetate copolymer as a pottant: a critical review.

Solar Energy Mater. Solar Cells 43, 101–181. doi: 10.1016/0927-0248(95)00150-6

Daneo, A. G., Falcone, R., and Hreglich, S. (2009). Effect of the redox state on container glass colour stability. *Glass Technol. Euro. J. Glass Sci. Technol. A* 50, 147–150. Available online at: https://www.ingentaconnect.com/content/sgt/gta/2009/00000050/00000003/art00004

Deubener, J., Helsch, G., Moiseev, A., and Bornhöft, H. (2009). Glasses for solar energy conversion systems. *J. Eur. Ceram. Soc.* 29, 1203–1210. doi: 10.1016/j.jeurceramsoc.2008.08.009

Dhar, S., Roy Barman, A., Rusydi, A., Gopinadhan, K., Feng, Y., Breese, M., et al. et al. (2013). "Effect of Ta alloying on the optical, electronic, and magnetic properties of TiO_2 thin films," in *Functional Metal Oxides: New Science and Novel Applications,* eds S. B. Ogale, T. V. Venkatesan, and M. G. Blamire (Weinheim: Wiley-VCH Verlag GmbH & Co), 133–162. doi: 10.1002/9783527654864.ch4

Gao, Y., and Nagai, M. (2006). Morphology evolution of ZnO thin films from aqueous solutions and their application to solar cells. *Langmuir* 22, 3936–3940. doi: 10.1021/la053042f

Goodyear, J. K., and Lindberg, V. L. (1980). Low absorption float glass for back surface solar reflectors. *Solar Energy Mater.* 3, 57–67. doi: 10.1016/0165-1633(80)90049-0

He, H., Liu, C., Dubois, K. D., Jin, T., Louis, M. E., and Li, G. (2012). Enhanced charge separation in nanostructured TiO_2 materials for photocatalytic and photovoltaic applications. *Ind. Eng. Chem. Res.* 51, 11841–11849. doi: 10.1021/ie300510n

Hosseinmardi, A., Shojaee, N., Keyanpour-Rad, M., and Ebadzadeh, T. (2012). A study on the photoluminescence properties of electrospray deposited amorphous and crystalline nanostructured ZnO thin films. *Ceramics Int.* 38, 1975–1980. doi: 10.1016/j.ceramint.2011.10.031

IEA (2011). *Solar Energy Perspectives.* Paris: International Energy Agency.

IPCC (2014). "Summary for policymakers," in *Climate Change 2014: Mitigation of Climate Change. Contribution of Working Group III to the Fifth Assessment Report of the Intergovernmental Panel on Climate Change,* eds O. Edenhofer, R. Pichs-Madruga, Y. Sokona, E. Farahani, S. Kadner, K. Seyboth, A. Adler, I. Baum, S. Brunner, P. Eickemeier, B. Kriemann, J. Savolainen, S. Schlömer, C. von Stechow, T. Zwickel, and J. C. Minx (Cambridge, UK; New York, NY: Cambridge University Press).

Jellison, G. E., and Boatner, L. A. (1998). Optical functions of uniaxial ZnO determined by generalized ellipsometry. *Phys. Rev. B* 58, 3586–3589. doi: 10.1103/PhysRevB.58.3586

Jellison, G. E., Modine, F. A., and Boatner, L. A. (1997). Measurement of the optical functions of uniaxial materials by two-modulator generalized ellipsometry: rutile (TiO_2). *Opt. Lett.* 22, 1808–1810. doi: 10.1364/OL.22.001808

Jordan, D. C., and Kurtz, S. R. (2013). Photovoltaic degradation rates—an analytical review. *Prog. Photovoltaics Res. Appl.* 21, 12–29. doi: 10.1002/pip.1182

Kamata, K., Nishino, J., Ohshio, S., Maruyama, K., and Ohtuki, M. (1994). Rapid formation of zinc oxide films by an atmospheric-pressure chemical vapor deposition method. *J. Am. Ceramic Soc.* 77, 505–508. doi: 10.1111/j.1151-2916.1994.tb07021.x

Karlsson, S., and Wondraczek, L. (2019). "Strengthening of Oxide Glasses," in *Encyclopedia for Glass Science, Technology, History and Culture*, ed P. Richet (Hoboken, NJ: John Wiley & Sons Inc.).

Kong, Y. C., Yu, D. P., Zhang, B., Fang, W., and Feng, S. Q. (2001). Ultraviolet-emitting ZnO nanowires synthesized by a physical vapor deposition approach. *Appl. Phys. Lett.* 78, 407–409. doi: 10.1063/1.1342050

Kuitche, J. M., Pan, R., and TamizhMani, G. (2014). Investigation of dominant failure mode(s) for field-aged crystalline silicon PV modules under desert climatic conditions. *IEEE J. Photovoltaics* 4, 814–826. doi: 10.1109/JPHOTOV.2014.2308720

Lee, G. H., Kawazoe, T., and Ohtsu, M. (2002). Difference in optical bandgap between zinc-blende and wurtzite ZnO structure formed on sapphire (0001) substrate. *Solid State Commun.* 124, 163–165. doi: 10.1016/S0038-1098(02)00537-9

Masson, G., Kaizuka, I., and Cambiè, C. (2018). *IEA Report PVPS: A Snapshot of Global PV (1992-2017).* International Energy Agency.

Nagata, S., Yamamoto, S., Toh, K., Tsuchiya, B., Ohtsu, N., Shikama, T., et al. (2004). Luminescence in SiO_2 induced by MeV energy proton irradiation. *J. Nuclear Mater.* 329–333, 1507–1510. doi: 10.1016/j.jnucmat.2004.04.242

Nielsen, K. H., Orzol, D. K., Koynov, S., Carney, S., Hultstein, E., and Wondraczek, L. (2014). Large area, low cost anti-reflective coating for solar glasses. *Solar Energy Mater. Solar Cells* 128, 283–288. doi: 10.1016/j.solmat.2014.05.034

Okuya, M., Prokudina, N. A., Mushika, K., and Kaneko, S. (1999). TiO_2 thin films synthesized by the spray pyrolysis deposition (SPD) technique. *J. Eur. Ceram. Soc.* 19, 903–906. doi: 10.1016/S0955-2219(98)00341-0

Oliveira, M. C. C. D., Diniz Cardoso, A. S. A., Viana, M. M., and Lins, V.,d.F.C. (2018). The causes and effects of degradation of encapsulant ethylene vinyl acetate copolymer (EVA) in crystalline silicon photovoltaic modules: A review. *Renew. Sust. Energy Rev.* 81, 2299–2317. doi: 10.1016/j.rser.2017.06.039

Osterwald, C. R., Benner, J. P., Pruett, J., Anderberg, A., Rummel, S., and Ottoson, L. (2003). "Degradation in weathered crystalline-silicon PV modules apparently caused by UV radiation," in *3rd World Conference on Photovoltaic Energy Conversion* (Osaka).

Perednis, D., and Gauckler, L. J. (2005). Thin film deposition using spray pyrolysis. *J. Electroceramics* 14, 103–111. doi: 10.1007/s10832-005-0870-x

Roos, A. (1993). Use of an integrating sphere in solar energy research. *Solar Energy Mater. Solar Cells* 30, 77–94. doi: 10.1016/0927-0248(93)90033-Y

Rouxel, T., Sellappan, P., Celarie, F., Houizot, P., and Sangleboeuf, J. C. (2014). Toward glasses with better indentation cracking resistance. *Cr Mecanique* 342, 46–51. doi: 10.1016/j.crme.2013.10.008

Rubin, M. (1985). Optical properties of soda lime silica glasses. *Solar Energy Mater.* 12, 275–288. doi: 10.1016/0165-1633(85)90052-8

Schröder, A. (1928). XXXV. Beiträge zur Kenntnis des Feinbaues des Brookits und des physikalischen Verhaltens sowie derZustandsänderungen der drei natürlichen Titandioxyde. *Z. Kristallograph.* 67:485. doi: 10.1524/zkri.1928.67.1.485

Shannon, R. D., Shannon, R. C., Medenbach, O., and Fischer, R. X. (2002). Refractive index and dispersion of fluorides and oxides. *J. Phys. Chem. Ref. Data* 31, 931–970. doi: 10.1063/1.1497384

Studenikin, S. A., Golego, N., and Cocivera, M. (1998). Fabrication of green and orange photoluminescent, undoped ZnO films using spray pyrolysis. *J. Appl. Phys.* 84, 2287–2294. doi: 10.1063/1.368295

Sun, R.-D., Nakajima, A., Fujishima, A., Watanabe, T., and Hashimoto, K. (2001). Photoinduced Surface Wettability Conversion of ZnO and TiO_2 Thin Films. *J. Phys. Chem. B* 105, 1984–1990. doi: 10.1021/jp002525j

Sundberg, P., Grund Bäck, L., Orman, R., Booth, J., and Karlsson, S. (2019). Simultaneous chemical vapor deposition and thermal strengthening of glass. *Thin Solid Films* 669, 487–493. doi: 10.1016/j.tsf.2018.11.028

Tauc, J. (1968). Optical properties and electronic structure of amorphous Ge and Si. *Mater. Res. Bull.* 3, 37–46. doi: 10.1016/0025-5408(68)90023-8

Villegas, E. A., Aldao, C. M., Savu, R., Ramajo, L. A., and Parra, R. (2018). Effects of grain size on the UV-photoresponse of zinc oxide thin films grown by spray-pyrolysis. *Phys. Status Solidi a* 215:1800107. doi: 10.1002/pssa.201800107

Volotinen, T. T., Parker, J. M., and Bingham, P. A. (2008). Concentrations and site partitioning of Fe^{2+} and Fe^{3+} ions in a soda-lime-silica glass obtained by optical absorbance spectroscopy. *Phys. Chem. Glasses Euro. J. Glass Sci. Technol. B* 49, 258–270. Available online at: https://www.ingentaconnect.com/content/sgt/ejgst/2008/00000049/00000005/art00004

Watanabe, T., Nakajima, A., Wang, R., Minabe, M., Koizumi, S., Fujishima, A., et al. (1999). Photocatalytic activity and photoinduced hydrophilicity of titanium dioxide coated glass. *Thin Solid Films* 351, 260–263. doi: 10.1016/S0040-6090(99)00205-9

Wondraczek, L., Mauro, J. C., Eckert, J., Kühn, U., Horbach, J., Deubener, J., et al. (2011). Towards ultrastrong glasses. *Adv. Mater.* 23, 4578–4586. doi: 10.1002/adma.201102795

Wu, L., Wu, Y., Pan, X., and Kong, F. (2006). Synthesis of ZnO nanorod and the annealing effect on its photoluminescence property. *Opt. Mater.* 28, 418–422. doi: 10.1016/j.optmat.2005.03.007

Conflict of Interest: The authors declare that the research was conducted in the absence of any commercial or financial relationships that could be construed as a potential conflict of interest.

frontiers in Materials

ORIGINAL RESEARCH
published: 04 June 2019
doi: 10.3389/fmats.2019.00128

Correlation Between Ionic Mobility and Plastic Flow Events in NaPO3-NaCl-Na2SO4 Glasses

Bruno Poletto Rodrigues[1,2]*, *Rene Limbach*[1], *Gabriel Buzatto de Souza*[3], *Heike Ebendorff-Heidepriem*[2] *and Lothar Wondraczek*[1,4]

[1] Otto Schott Institute of Materials Research, Friedrich Schiller University of Jena, Jena, Germany, [2] School of Physical Sciences, Institute of Photonics and Advanced Sensing, The University of Adelaide, Adelaide, SA, Australia, [3] Vitreous Materials Laboratory, Federal University of Sao Carlos, Sao Carlos, Brazil, [4] Center of Energy and Environmental Chemistry, Friedrich Schiller University of Jena, Jena, Germany

We report on the evolution of the mechanical and electrical properties of sodium metaphosphate glasses with addition of sodium sulfate or sodium chloride. The addition of these two sodium salts converts the medium-range order of our glasses from 2D phosphate chains to a mixed 1D + 2D network similar to ionic glasses, while the short-range order of the phosphate units remains unaffected. Replacing the phosphate units by chloride ion monotonically decreases the glass transition temperature, but enhances the Young's modulus and moderately increases the ionic conductivity. On the other hand, the sulfate group decreases the glass transition temperature as well, though the Young's modulus remains constant, while the ionic conductivity strongly increases. The changes in conductivity are related to the enhancement of the ionic mobility in these glasses, which in turn affect the size and distribution of the plastic events taking place during indentation-driven deformation.

Keywords: phosphate glasses, nanoindentation, shear transformation zones, impedance spectroscopy, ionic mobility

OPEN ACCESS

Edited by:
Takayuki Komatsu, Nagaoka University of Technology, Japan

Reviewed by:
Jean-Pierre Guin, University of Rennes 1, France
Hirokazu Masai, National Institute of Advanced Industrial Science and Technology (AIST), Japan

***Correspondence:**
Bruno Poletto Rodrigues
bruno.polettorodrigues@adelaide.edu.au

Specialty section:
This article was submitted to Glass Science, a section of the journal Frontiers in Materials

Received: *14 March 2019*
Accepted: *15 May 2019*
Published: *04 June 2019*

Citation:
Poletto Rodrigues B, Limbach R, Buzatto de Souza G, Ebendorff-Heidepriem H and Wondraczek L (2019) Correlation Between Ionic Mobility and Plastic Flow Events in NaPO3-NaCl-Na2SO4 Glasses. Front. Mater. 6:128. doi: 10.3389/fmats.2019.00128

INTRODUCTION

Unlike silicate and borosilicate glasses, phosphate glasses are mainly explored for specialty applications, such as laser gain media, hermetic seals, nuclear waste immobilization, and biomaterials (Brow, 2000). Another potential application is their use as solid electrolytes for ion-conducting solid state batteries (Jun et al., 1990; Kim et al., 2015) due to their high ionic conductivity at room temperature ranging from 10^{-5} to 10^{-3} S.cm^{-1} (Martin and Angell, 1986). For the latter, it has been observed that further significant enhancement can be achieved by the dissolution of ionic salts such as halides, sulfides, and sulfates into the glassy matrix (Martin, 1991). However, the mechanism of incorporation is not the same for all salts; usually sulfide and fluoride salts depolymerize the phosphate chain backbone by reacting with the bridging oxygens to form chain terminating P-F or P-S bonds (Brow et al., 1992; Cutroni et al., 1992; Saunders et al., 1996; Kartini et al., 2004), while the other halides and sulfates occupy the interstitial spaces in-between the phosphate chains, increasing the inter-chain spacing and keeping the short-range structure largely untouched (Malugani et al., 1982; Scotti et al., 1992; Kartini et al., 2002; Da et al., 2011; Sirotkin et al., 2012; Kabi and Ghosh, 2014; Möncke et al., 2014; Thieme et al., 2015; Le et al., 2017). Therefore, sulfate/halide-phosphate glassy systems are convenient model systems to study

how changes in the bonding and geometry of the first coordination shell of the modifier ions impact the ensemble's properties.

Selecting the $NaPO_3$-NaCl-Na_2SO_4 ternary system is convenient since both the Cl^- and SO_4^{2-} anions occupy the free volume available between the phosphate chains as they are incorporated into the glass network, while leaving the phosphate chains largely intact. These glasses also allow for a comparison between the behavior of Na^+ cations when only coordinated by non-bridging oxygens or when in a mixed halide and oxyanion environment, thus providing an interesting control group to whether the mechanical and electrical properties are more sensitive to changes in the overall packing density (where both the Cl^- and SO_4^{2-} should behave similarly, when taking their respective sizes into account) or to the chemistry of the anions coordinating the cationic modifier (where the $NaPO_3$ and the sulfate bearing glasses should be comparable, while the sodium chloride glasses should behave differently).

MATERIALS AND METHODS

Glasses with nominal compositions of (100–x)$NaPO_3$-xNaCl and (100–x)$NaPO_3$-(x/2)Na_2SO_4 with x = 0, 10, 20, 30, 40, 50 were prepared from mixtures of reagent grade $(NH_4)_2HPO_4$, $(NH_4)_2SO_4$, Na_2CO_3, and NaCl (Sigma Aldrich, purity > 99%) in the appropriate proportions. The powder mixtures were homogenized in a mortar and melted in Al_2O_3 crucibles for 1 h at 1,000 K. Melt droplets were splat-quenched between two stainless steel plates and several disks of about 1 mm thickness and 10 mm diameter were produced from each glass melt. The resulting quenched glasses were homogeneous, colorless, and transparent, with the exception of the 50$NaPO_3$-50NaCl sample, which fully crystallized during casting. The density ρ of the as-prepared glasses was determined by the Archimedes' method in distilled water and via He pycnometry (Quantachrome Ultrapyc 1200e, Anton Paar GmbH). The glass transition temperature T_g was determined from the onset of the endothermic event observed in the differential scanning calorimetry (DSC, Netzsch STA 499F1). All DSC measurements were performed in a flowing N_2 atmosphere at a constant heating rate of 20 K/min using powdered samples of 20 mg mounted in platinum crucibles. Except for the thermal analysis, all experiments were carried out in laboratory air under ambient conditions.

The elastic properties were analyzed using a piezoelectric transducer operating at frequencies of 8 to 12 MHz (Echometer 1077, Karl Deutsch GmbH & Co KG). Values of the longitudinal c_L and transversal c_T sound wave velocities were derived from the corresponding sound wave propagation times and the exact thickness of the co-planar, optically-polished glass plates. On that basis the shear G, bulk K, and Young's moduli E as well as the Poisson's ratio ν were calculated by means of the following equations:

$$G = \rho c_T^2 \tag{1}$$

$$K = \rho\left(c_L^2 - \frac{4}{3}c_T^2\right) \tag{2}$$

$$E = \rho\left[\frac{3c_L^2 - 4c_T^2}{(c_L/c_T)^2 - 1}\right] \tag{3}$$

$$\nu = \frac{c_L^2 - 2c_T^2}{2\left(c_L^2 - c_T^2\right)} \tag{4}$$

The mechanical properties were further analyzed through instrumented indentation testing using a nanoindenter (G200, Agilent Inc.), equipped with a three-sided Berkovich diamond indenter tip (Synton-MDP Inc.), and operating in the continuous stiffness measurement mode (CSM). The tip area function and instruments frame compliance were calibrated prior to the first experiments on a fused silica reference glass sample of known elastic properties (Corning Code 7980, Corning Inc.). On every glass specimen, 15 indentations with a maximum penetration depth of $h = 2\,\mu m$ were created at a constant strain-rate of $\dot{\varepsilon} = 0.05\ s^{-1}$ (defined as the loading rate dP/dt divided by the actual load P). The load-displacement curves recorded by the nanoindenter were subsequently analyzed following the method proposed by Oliver and Pharr (1992), where the hardness H is estimated from the load divided by the projected contact area of the indenter tip A_c:

$$H = \frac{P}{A_c} \tag{5}$$

and the values of E are derived from the combined elastic response of the diamond indenter used (E_i = 1,141 GPa, ν_i = 0.07) and the material tested (Johnson, 1985):

$$E = \left(1 - \nu^2\right)\left[\frac{1}{E_r} - \frac{1 - \nu_i^2}{E_i}\right]^{-1} \tag{6}$$

with the reduced elastic modulus E_r (Pharr et al., 1992):

$$E_r = \frac{S}{2}\sqrt{\frac{\pi}{A_c}} \tag{7}$$

Here, the parameter S denotes the contact stiffness as determined from the slope of the load-displacement curve at the onset of unloading. By operating in the CSM mode, the contact stiffness (or harmonic stiffness) can be recorded also during the monotonic load increase, which allows for the parallel determination of E and H as a function of the indenter displacement (Li and Bhushan, 2002; Pharr et al., 2009). For this purpose, the continuously increasing load-displacement signal was superimposed by a small oscillation of the indenter tip (f = 45 Hz, Δh = 2 nm). The values of E and H were finally averaged between the upper 10% and lower 20% of each indentation depth profile.

The strain-rate sensitivity m was analyzed in nanoindentation strain-rate jump test, as described in detail elsewhere (Limbach et al., 2014). On each glass specimen, ten strain-rate jump tests with strain-rates of 0.05; 0.007; and 0.001 s^{-1} (in descending order) were performed, and the values of m were derived from

the slope of the logarithmic plot of the hardness against the indentation strain-rate $\dot{\varepsilon}_i$ [defined as the displacement rate dh/dt divided by the total penetration depth (Shen et al., 2012)]:

$$m = \frac{\partial \ln H}{\partial \ln \dot{\varepsilon}_i} \tag{8}$$

where $\dot{\varepsilon}_i = \dot{\varepsilon}/2$ for materials with a depth-independent hardness value (Lucas and Oliver, 1999). The thermal drift rates are below 0.05 s^{-1} for the nanoindentation experiments. To avoid possible interactions between the residual stress fields, adjacent indentations were spaced by distances of 50 μm (Hay, 2009).

A structural analysis was carried out by Raman spectroscopy. Raman spectra were collected in the range of 150 to 1,300 cm^{-1}, using a 488 nm Ar-laser as excitation source (Renishaw in Via Raman microscope). Each spectra was averaged over 20 consecutive measurements, corrected for baseline and thermal population (Shuker and Gammon, 1970) and normalized by the intensity of the peak at ∼1,140 cm^{-1}.

The ionic conductivity was analyzed by impedance spectroscopy (Novocontrol Alpha-A analyzer and a Novotherm Temperature Control System), in the frequency range from 10^{-1} to 10^6 Hz and at temperatures between 303 and 423 K. A thin gold layer was deposited on the surface of each sample by means of a sputtering system (Anatech Hummer 10.2), operating for 300 s at an average current of 20 mA. In order to extract the glass properties from the experimental data, the setup was modeled with a single parallel RC element representing the bulk glass as an ideal solid electrolyte (Hodge et al., 1976; Almond and West, 1983) in series with a constant-phase element (CPE) representing the gold electrodes (Barsoukov and Macdonald, 2005). The total impedance of this circuit is given by Barsoukov and Macdonald (2005), Lvovich (2012):

$$\begin{aligned} Z^*(\omega) &= Z' + i \cdot Z'' \\ &= Z^*_{RC} + Z^*_{CPE} = \frac{R - i \cdot \omega \cdot R^2 \cdot C}{1 + (\omega \cdot R \cdot C)^2} + \frac{1}{Q \cdot (i \cdot \omega)^{\alpha}} \end{aligned} \tag{9}$$

where i is the imaginary number, $\omega = 2\pi f$ is the angular frequency, R and C are the parameters of the RC element, and Q and α are the CPE parameters. From Equation (9), the dc conductivity σ_{dc} of each sample can be evaluated by:

$$\sigma_{dc} = \frac{1}{R} \cdot \frac{l}{A} \tag{10}$$

where l and A are the sample thickness and area, respectively. The temperature dependence of the conductivity is given by the Arrhenius-scaling of both the number of effective charge carriers $n(T)$ and the frequency of successful atomic hops $\Gamma(T)$ (Tuller et al., 1980; Hairetdinov et al., 1994; Rodrigues et al., 2011):

$$\sigma_{dc} \cdot T = \sigma_0 \cdot exp\left(-\frac{E_\sigma}{RT}\right) \tag{11}$$

$$n(T) = n_c \cdot \exp\left(-\frac{E_n}{2 \cdot R \cdot T}\right) \tag{12}$$

$$\Gamma(T) = \Gamma_0 \cdot \exp\left(-\frac{E_m}{R \cdot T}\right) \tag{13}$$

where σ_0 is the conductivity pre-exponential term, n_c is the number density of ions, Γ_0 is the attempt frequency, R is the universal gas constant, and the parameters E_σ, E_n, and E_m are the activation energies of conductivity, charge carrier creation, and mobility, respectively. The activation energies are related via the following equation (Souquet, 1981; Ngai and Moynihan, 1998; Bandara and Mellander, 2011; Rodrigues et al., 2019):

$$E_\sigma = E_m + \frac{E_n}{2} \tag{14}$$

RESULTS

Raman Spectroscopy

Raman spectra of the $NaPO_3$-Na_2SO_4 and $NaPO_3$-NaCl glasses (**Figures 1**, **2**, respectively) show that the phosphate network is generally unaffected by the addition of NaCl and Na_2SO_4, as the main features at approximately 680 and 1,140 cm^{-1} [associated with the symmetric stretching modes ν_s(P-O-P) and $\nu_s(PO_2)$ of Q^2 species, respectively (Hudgens et al., 1998; Velli et al., 2005; Konidakis et al., 2011)], remain relatively unchanged. In the Raman spectra of the $NaPO_3$-Na_2SO_4 glasses in **Figure 1**, the appearance of a peak at ∼1,000 cm^{-1} is assigned to the symmetric stretching $\nu_s(SO_4^{2-})$ (Da et al., 2011; Thieme et al., 2015) and it increases in intensity with increasing Na_2SO_4 concentration. The spectra of the $NaPO_3$-NaCl glasses (**Figure 2**) are more complex. A slight shift of the $\nu_s(Q^2)$ to lower wavenumbers is observed with increasing NaCl content, in conjunction with the appearance of shoulders at ∼1,100 and ∼750 cm^{-1}, consistent with the phosphorus tetrahedron and bridging oxygen symmetric stretching vibrations of the Q^1 unit (Da et al., 2011; Thieme et al., 2015; Kapoor et al., 2017). The vibrations at ∼1,000 and 1,050 cm^{-1} can be assigned to chain-terminating Q^1 units (Brow et al., 1995; Brow, 2000; Da et al., 2011), while the broad envelope centered at around 340 cm^{-1} is due to network bending vibrations (Brow et al., 1995; Hudgens et al., 1998; Velli et al., 2005). These observations indicate that the addition of NaCl progressively depolymerizes the glass network, forming shorter phosphate chains, which is in accordance with previous observations from MD simulations of $LiPO_3$-LiCl glasses (Rao and Seshasayee, 2004). However, earlier studies have revealed that metaphosphate glasses are in general characterized by low degrees of network polymerization, with the reported average chain size of $NaPO_3$ glasses ranging from 3.5 to 9 phosphate units (Westman and Gartaganis, 1957; Brow, 2000). Considering that the $NaPO_3$ glass presently investigated already consists of relatively small chains, the effect of depolymerisation is assumed to be of secondary importance.

Thermal and Mechanical Characterization

Selected physical properties of the $NaPO_3$-Na_2SO_4 and $NaPO_3$-NaCl glasses examined in this study are listed in **Tables 1**, **2**,

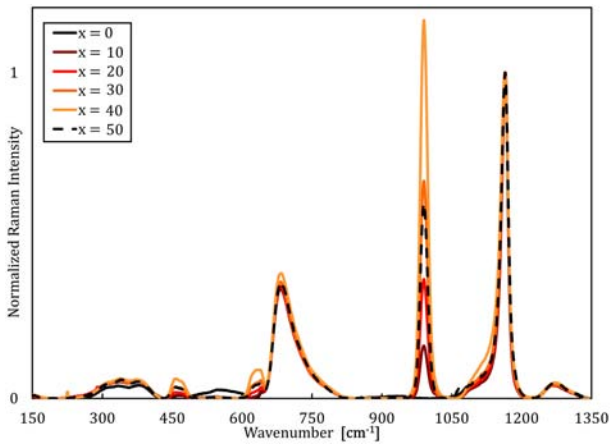

FIGURE 1 | Normalized Raman spectra for the (100–x)$NaPO_3$-(x/2)Na_2SO_4 glasses.

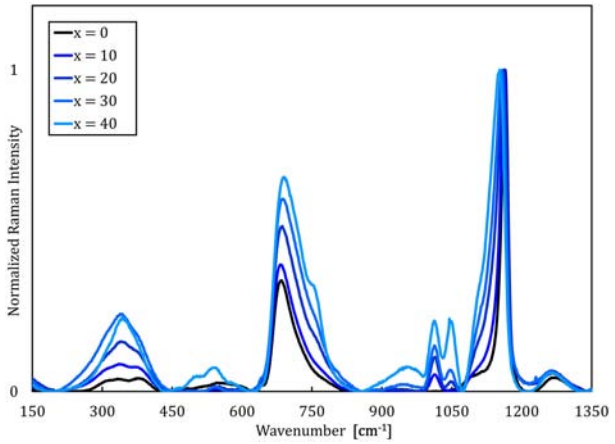

FIGURE 2 | Normalized Raman spectra for the (100–x)$NaPO_3$-xNaCl glasses.

respectively. As expected, the addition of Na_2SO_4 and NaCl leads to a decrease in both the glass transition temperature (**Figure 3**) and molar volume, illustrating the overall weakening of the glass network and the more efficient packing due to the presence of Cl^- and SO_4^{2-} groups occupying the interstitial spaces in-between the phosphate chains, similar to the effect of AgI in $AgPO_3$ glasses (Novita et al., 2009; Rodrigues and Wondraczek, 2013; Limbach et al., 2014). The mechanical properties show very different compositional trends (**Figures 4**, **5**): the addition of Na_2SO_4 leads to a slight decrease of the Young's modulus, while the strain-rate sensitivity and Poisson's ratio remain almost constant; on the other hand, the addition of NaCl induces a significant increase in the Young's modulus, while the strain-rate sensitivity decreases and the Poisson's ratio remains almost the same within the limits of error.

According to the elastic models of glass-forming liquids (Dyre, 2006), the instantaneous elastic properties measured at laboratory time-scales can be used as probes for the individual

TABLE 1 | Physical properties of the (100-x)$NaPO_3$- (x/2)Na_2SO_4 glasses.

Sample	T_g [K]	ρ [g.cm^{-3}]	V_m [cm^3.mol^{-1}]	G [GPa]	K [GPa]	ν	E [GPa][a]	E [GPa][b]	H [GPa]	m
$NaPO_3$	560 ± 3	2.52 ± 0.01[c]	40.5 ± 0.2	14.3 ± 0.1[d]	29.4 ± 0.5[d]	0.290 ± 0.007[d]	36.9 ± 0.7[d]	36.9 ± 0.4	2.25 ± 0.06	0.0400 ± 0.0001
90$NaPO_3$-5Na_2SO_4	551 ± 3	2.4853 ± 0.0005[e]	41.87 ± 0.01	13.7 ± 0.1	29.1 ± 0.5	0.296 ± 0.007	35.5 ± 0.6	36.6 ± 0.3	2.25 ± 0.03	0.0386 ± 0.0002
80$NaPO_3$-10Na_2SO_4	556 ± 3	2.4843 ± 0.0005[e]	42.83 ± 0.01	13.2 ± 0.1	28.7 ± 0.5	0.300 ± 0.007	34.4 ± 0.6	35.1 ± 0.3	2.11 ± 0.03	0.0397 ± 0.0005
70$NaPO_3$-15Na_2SO_4	549 ± 3	2.4842 ± 0.0005[e]	43.89 ± 0.01	13 ± 0.1[f]	28.2 ± 0.5[f]	–	–	33.8 ± 0.3	1.99 ± 0.03	0.0381 ± 0.0002
60$NaPO_3$-20Na_2SO_4	549 ± 3	2.5020 ± 0.0004[e]	44.76 ± 0.01	12.8 ± 0.1	29.1 ± 0.5	0.309 ± 0.007	33.5 ± 0.5	34.0 ± 0.3	2.04 ± 0.03	0.038 ± 0.001
50$NaPO_3$-25Na_2SO_4	546 ± 3	2.51 ± 0.01[c]	45.9 ± 0.2	13.5 ± 0.1	29.3 ± 0.4	0.299 ± 0.006	35.2 ± 0.5	33.9 ± 0.3	2.02 ± 0.03	0.03880 ± 0.00003

[a] *Values of E determined by ultrasonic echography.*

[b] *Values of E analyzed through nanoindentation. Note, that for the glasses where no Poisson's ratio could be detected by ultrasonic echography, a value of ν = 0.3 was used to calculate the Young's modulus from the reduced elastic modulus* $E_r = \left[\frac{1-\nu^2}{E} + \frac{1-\nu_i^2}{E_i}\right]^{-1}$, *where* E_i *= 1,141 GPa and* ν_i *= 0.07 are the elastic constants of the Berkovich diamond indenter tip used.*

[c] *Values of ρ as determined via the Archimedes method.*

[d] *Values of G, K, ν and E are taken from Le et al. (2017).*

[e] *Values of ρ as determined by means He pycnometry.*

[f] *Values of G and K are estimated from the values of E as determined by nanoindentation and* $\nu = 0.3$, *using the following relations:* $G = \frac{E}{[2(1+\nu)]}$ *and* $K = \frac{E}{[3(1-2\nu)]}$, *respectively.*

TABLE 2 | Physical properties of the (100–x)$NaPO_3$-x$NaPO_3$-xNaCl glasses.

Sample	T_g [K]	ρ [g.cm^{-3}]	V_m [cm^3.mol^{-1}]	G [GPa]	K [GPa]	ν	E [GPa][a]	E [GPa][b]	H [GPa]	m
$NaPO_3$	560 ± 3	2.52 ± 0.01[c]	40.5 ± 0.2	14.3 ± 0.1[d]	29.4 ± 0.5[d]	0.290 ± 0.007[d]	36.9 ± 0.7[d]	36.9 ± 0.4	2.25 ± 0.06	0.0400 ± 0.0001
90$NaPO_3$-10NaCl	562 ± 3	2.5045 ± 0.0005[e]	38.97 ± 0.01	15.0 ± 0.1[f]	32.4 ± 0.5[f]	–	–	38.9 ± 0.5	2.47 ± 0.06	0.0381 ± 0.0004
80$NaPO_3$-20NaCl	551 ± 3	2.5051 ± 0.0005[e]	37.23 ± 0.01	15.1 ± 0.1	31.9 ± 0.5	0.296 ± 0.007	39.1 ± 0.6	42.7 ± 0.5	2.90 ± 0.06	0.033 ± 0.001
70$NaPO_3$-30NaCl	537 ± 3	2.4967 ± 0.0005[e]	35.61 ± 0.01	16.2 ± 0.1	33.5 ± 0.6	0.286 ± 0.007	43.1 ± 0.8	45.5 ± 0.5	3.05 ± 0.06	0.029 ± 0.002
60$NaPO_3$-40NaCl	545 ± 3	2.4916 ± 0.0005[e]	33.94 ± 0.01	15.6 ± 0.1	33.5 ± 0.6	0.298 ± 0.008	40.6 ± 0.7	45.6 ± 0.5	3.06 ± 0.06	0.027 ± 0.002

[a] *Values of E determined by ultrasonic echography.*

[b] *Values of E analyzed through nanoindentation. Note, that for the glasses where no Poisson's ratio could be detected by ultrasonic echography, a value of ν = 0.3 was used to calculate the Young's modulus from the reduced elastic modulus* $E_r = \left[\frac{1-\nu^2}{E} + \frac{1-\nu_i^2}{E_i}\right]^{-1}$, *where* $E_i = 1{,}141$ *GPa and* $\nu_i = 0.07$ *are the elastic constants of the Berkovich diamond indenter tip used.*

[c] *Values of ρ as determined via the Archimedes method.*

[d] *Values of G, K, ν and E are taken from Le et al. (2017).*

[e] *Values of ρ as determined by means He pycnometry.*

[f] *Values of G and K are estimated from the values of E as determined by nanoindentation and ν = 0.3, using the following relations:* $G = \frac{E}{[2(1+\nu)]}$ *and* $K = \frac{E}{[3(1-2\nu)]}$, *respectively.*

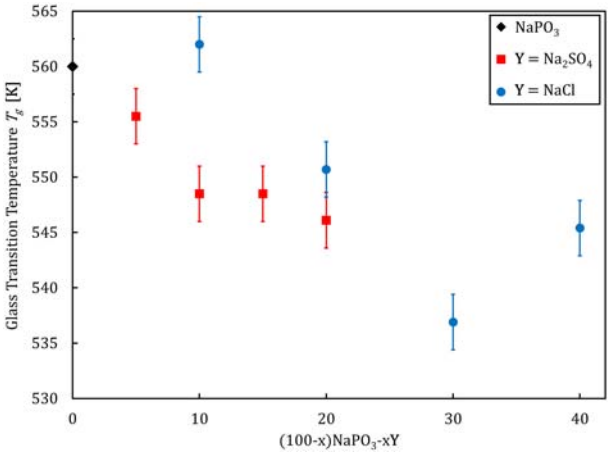

FIGURE 3 | Glass transition temperature as a function of composition for (100–x)$NaPO_3$-x**Y** (with **Y** = Na_2SO_4, NaCl) glasses.

"flow events" and molecular rearrangements which undergo some sort of transition through an energy barrier. The most classic of such relations is given by the Maxwell relation $\tau = \eta \cdot G$, which links the macroscopic shear modulus to the microscopic relaxation time τ through the shear viscosity η (Perez, 1994). In a more refined sense the same arguments are used when calculating the elastic constants in MD simulation boxes from the derivative of the energy landscape as a function of strain (Pedone et al., 2008a,b; Jabraoui et al., 2016). Drawing parallels between "traditional" glass systems and simple Lennard-Jones glass models, Heuer and Spiess argued that the glass transition should be given by:

$$T_g = k_g \cdot \bar{M}_e \cdot {c_a}^2 \tag{15}$$

where k_g is a constant (∼0.014 for glassy noble gases and ∼0.011 for "traditional" glassy systems), $\overline{M_e}$ is the average effective mass, and c_a is the acoustic sound velocity, defined as the square on the ratio between the bulk modulus and the density $c_a \equiv \sqrt{\frac{K}{\rho}}$ (Heuer and Spiess, 1994). With glass transition temperature and the acoustic sound velocity as easily accessible parameters, Equation (15) provides a convenient route to study the mechanism governing the glass transition. The proportionality constant includes information regarding the "elementary unit" undergoing an activated transition, which enables the whole system to evolve from a frozen-in state toward a supercooled liquid. **Figure 6** illustrates the compositional dependence of the calculated average effective mass, expressed as the factor $\left(T_g \cdot {c_a}^{-2}\right)$. The average effective mass remains upon the addition of Na_2SO_4, but it decreases when NaCl is added. This result suggests that the "elementary unit" in $NaPO_3$-Na_2SO_4 glasses remains largely unchanged when the phosphate groups are substituted by sulfate groups, as the molar mass of a PO_4^{3-} and a SO_4^{2-} tetrahedra are very similar (94.93 g.mol^{-1} as compared to 96.03 g.mol^{-1}). On the other hand, the average effective mass

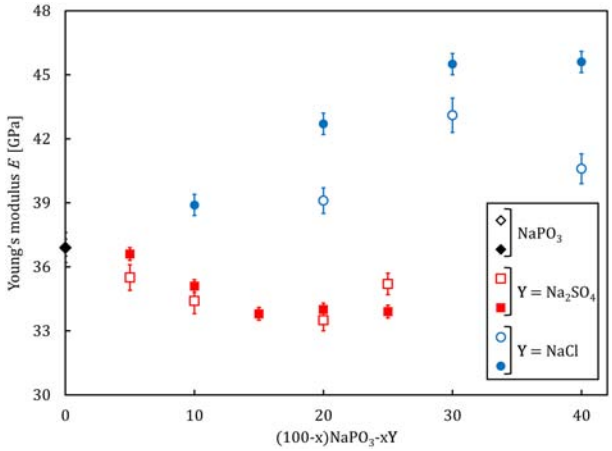

FIGURE 4 | Young's modulus, as determined by ultrasonic echography (empty symbols) and nanoindentation (filled symbols), respectively, as a function of composition for (100–x)$NaPO_3$-x**Y** (with **Y** = Na_2SO_4, NaCl) glasses.

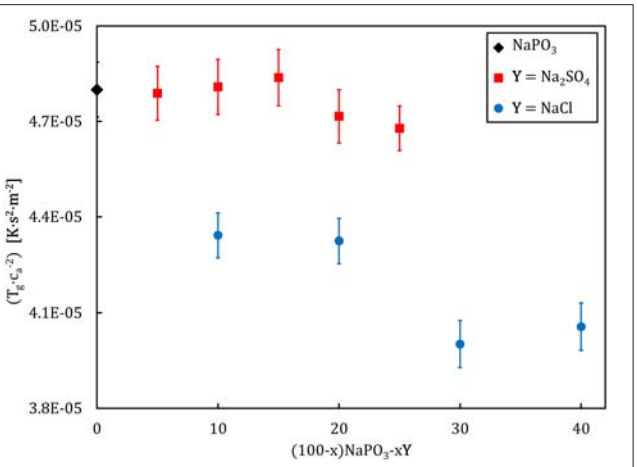

FIGURE 6 | Compositional dependence of the average effective mass, gauged by $\left(T_g \cdot c_a^{-2}\right)$, for (100–x)$NaPO_3$-x**Y** (with **Y** = Na_2SO_4, NaCl) glasses.

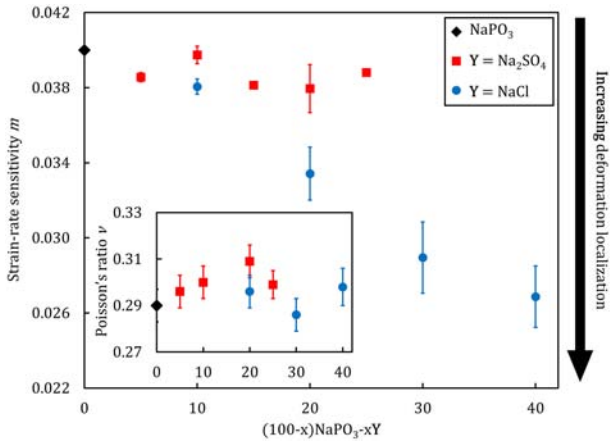

FIGURE 5 | Strain-rate sensitivity as a function of composition for (100–x)$NaPO_3$-x**Y** (with **Y** = Na_2SO_4, NaCl) glasses. The inset displays the compositional dependence of the Poisson's ratio.

decreases with NaCl addition due to the much smaller mass of the chloride ions (35.45 g.mol^{-1}).

The values of the Poisson's ratio and strain-rate sensitivity corroborate this interpretation. The Poisson's ratio, defined as the negative of the ratio between the transverse contraction strain and the longitudinal extension strain along the loading axis, is directly linked to the structural arrangements at short- and medium-range length scales in glasses, as evident from its interrelation to the packing density and network dimensionality (Rouxel, 2006, 2007; Rouxel et al., 2008a,b; Greaves et al., 2011). As our structural analysis have demonstrated, the phosphate network characteristic remains largely unchanged upon the addition of increasing amounts of Na_2SO_4 and NaCl salts. Accordingly, the overall network dimensionality also remains constant, as it is roughly composed of spherical elements (Na^+, SO_4^{2-}, Cl^- ions) packed around short phosphate chains. This is consistent with the observed relative invariance of the Poisson's ratio (**Figure 5**), where values of 0.3 are expected for glasses with a mixed 1D + 2D network structure (Rouxel, 2007). The slightly higher values of the Poisson's ratio which we observe for the sulfate-substituted glasses might originate from the significantly higher polarizability of the sulfate ion, leading to lower local order, and therefore, decreased structural dimensionality. For metallic glasses, the strain-rate sensitivity is an indicator for the tendency toward a localization of the plastic flow, and lower values are in general associated with more heterogeneous, localized plastic flow events (Spaepen, 1977; Limbach et al., 2017). This is consistent with the experimental data from **Figures 5**, **6**, demonstrating that the plastic flow event distribution and average effective mass remains constant for the $NaPO_3$-Na_2SO_4 glasses, while the incrementally lower average effective mass in the $NaPO_3$-NaCl glasses lead to a stronger localization of the plastic flow. Structural heterogeneities at short- and medium-range length scales are thought to be characteristic of the glassy state (Queiroz and Sestak, 2010; Hong et al., 2011), and their presence is an important factor controlling the mechanical properties of MD simulations (Tsamados et al., 2009; Rodney et al., 2011; Mantisi et al., 2012), colloidal glasses (Kawasaki et al., 2007; Schall et al., 2007; Rahmani et al., 2014; Varnik et al., 2014), metallic glasses (Fan et al., 2014; Hufnagel et al., 2016), and oxide glasses (Limbach et al., 2015; Benzine et al., 2018).

Impedance Spectroscopy

An example of the Nyquist plots graphed from the experimental impedance analysis of the 90$NaPO_3$-10NaCl glass is presented in **Figure 7**. The graph displays the temperature dependence of the semicircles, together with the fits from the model Equation (9). **Figure 8** shows the real part of the complex conductivity as a function of frequency for the $NaPO_3$ glass at four different

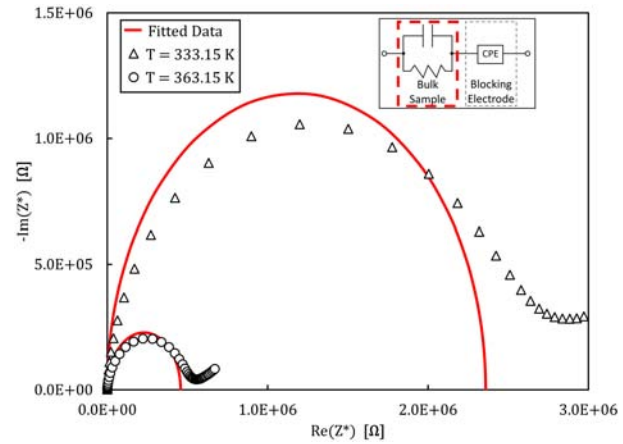

FIGURE 7 | Nyquist plot of the complex impedance measured for the $90NaPO_3$-10NaCl glass at different temperatures. The empty symbols show the experimental data and the continuous line is the fit to the equivalent circuit shown in the inset.

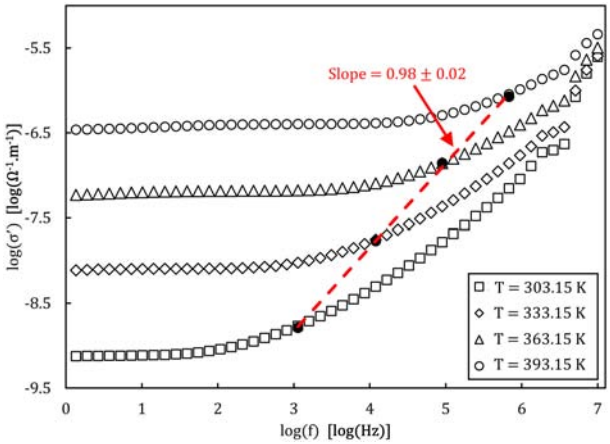

FIGURE 8 | Bode plot of the real part of the complex conductivity measured for the $NaPO_3$ glass at different temperatures. The empty symbols show the experimental data while the filled symbols represent the onset of AC conductivity $\sigma^*(f_H) = 2\sigma_{dc}$. The dashed line represents the linear fit of the onset frequencies.

temperatures. It also illustrates that our glasses obey the Nernst-Einstein relation (Sidebottom, 2009; Bandara and Mellander, 2011; Sangoro and Kremer, 2012):

$$\sigma_{dc} = \frac{n(T) \cdot \lambda^2 \cdot e^2 \cdot \Gamma(T)}{g' \cdot k \cdot H_R} \tag{16}$$

where λ is a characteristic length so that λ^2 is approximately equal to the mean square displamentent, e is the elementary charge (Bhattacharya and Ghosh, 2004), g' is a geometric factor, k is Boltzmann's constant, and $n(T)$ and $\Gamma(T)$ are given by Equations (12,13), respectively. Since f_H, as defined by the Jonscher power-law, $\sigma^*(f_H) = 2\sigma_{dc}$ (Almond et al., 1983, 1984; Popov et al., 2012; Singh et al., 2016), is directly related to the timescales of ionic hopping (Marple et al., 2018), $\Gamma(T)$ equals $f_H(T)$ and therefore Equation (16) can be rewritten as:

$$\log(\sigma_{dc}) = \log\left(\frac{n(T) \cdot \lambda^2 \cdot e^2}{g' \cdot k \cdot H_R}\right) + \log(f_H) \tag{17}$$

From which the linear relation between $\log(\sigma_{dc})$ and $\log(f_H)$ with a slope of unity is recovered.

Analysis of the activation energies show that for these glasses, $E_n \ll E_m < E_\sigma$ as can be seen in **Figure 9**, and thus the ionic conductivity is determined mainly by the ionic mobility. More specifically, the mobility of the sodium cation, as previous studies have shown that for sulfate- and chloride-containing alkali metaphosphate glasses the contributions of the anions is negligible (Sokolov et al., 2003; Bhide and Hariharan, 2007; Rao et al., 2009; Hraiech and Ferid, 2013). Despite that, charge carrier formation does play a non-negligible role in this glass system, as illustrated by the Walden plot of the conductivity data in **Figure 10**, where it is clear that the $NaPO_3$-NaCl-Na_2SO_4 glasses show a broad distribution, covering over two

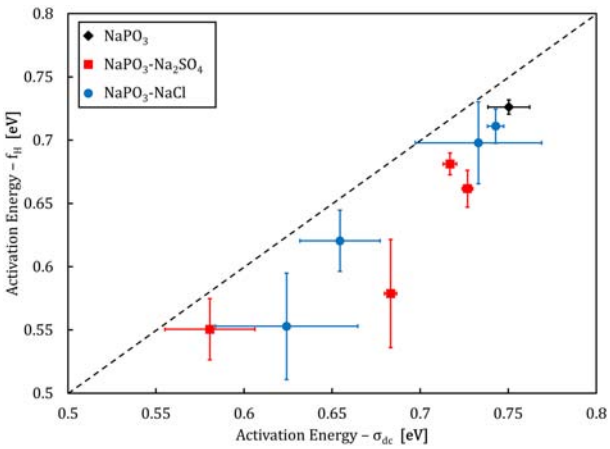

FIGURE 9 | Activation energy of the onset frequency f_H compared to the activation energy of dc conductivity σ_{dc}. The dashed line illustrates a 1:1 ratio.

orders of magnitude along the $\log(\sigma_{dc}.T)$ axis for each measured frequency, suggesting that the addition of sodium chloride and sodium sulfate enhances the number of effective charge carriers. However, calculation of the number of charge carriers $n(T)$ at 323 K from experimental activation energy values shows that both sodium salts seem to have the inverse effect: when considering the end-members of our compositions, the number density of charge carriers decreases non-linearly from 6.3×10^{21} ions.cm^{-3} for $NaPO_3$ to 5.0×10^{21} ions.cm^{-3} for $60NaPO_3$-40NaCl and to 4.6×10^{21} ions.cm^{-3} for $50NaPO_3$-$25Na_2SO_4$, respectively. Normalizing these numbers by the sodium number density derived from experimental density data, the ratio of charge carriers to the total sodium ion density decreases from 0.42 for $NaPO_3$ to 0.28 for $60NaPO_3$-40NaCl and to 0.34 for $50NaPO_3$-$25Na_2SO_4$, respectively. This result, in conjunction

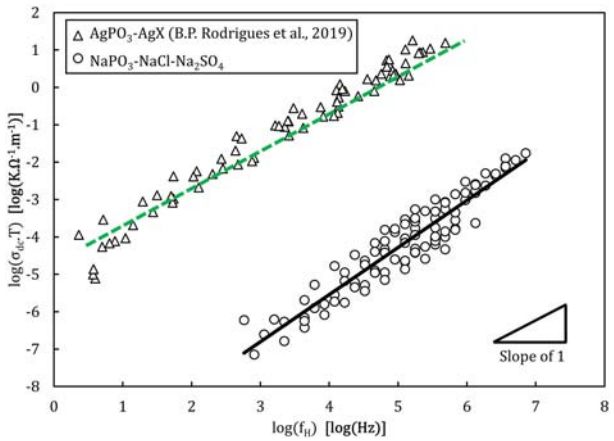

FIGURE 10 | Walden plot presenting the conductivity data of the $NaPO_3$-NaCl-Na_2SO_4 glasses in comparison with the $AgPO_3$-AgX glass system (Rodrigues et al., 2019). The lines show the linear regressions of the experimental data, with a slope of 1.2 ± 0.1 for the $NaPO_3$-NaCl-Na_2SO_4 glasses and of 1.08 ± 0.02 for $AgPO_3$-AgX glasses. The regression was performed between 10^4 and 10^6 Hz where experimental data is available for all samples, to avoid biasing the result.

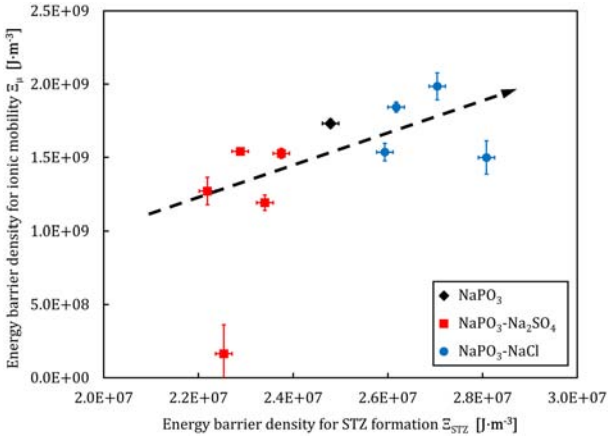

FIGURE 11 | Ionic mobility energy barrier density and the STZ formation energy barrier density derived from experimental data for the $NaPO_3$-NaCl-Na_2SO_4 glass system. The dashed line is a guide to the eye.

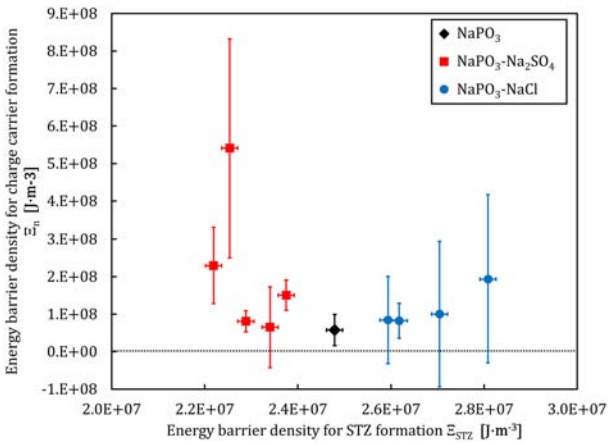

FIGURE 12 | Charge carrier formation energy barrier density and the STZ formation energy barrier density derived from experimental data for the $NaPO_3$-NaCl-Na_2SO_4 glass system.

with the fact that the linear regression of the $NaPO_3$-NaCl-Na_2SO_4 data in the Walden plot is significantly higher than one, indicates that both the average distance between ions and the Haven ratio (Rodrigues et al., 2019) exhibit non-trivial compositional and/or temperature dependences. Moreover, this also implies that the improved ionic conductivity is based on an even stronger increase in ionic mobility, as it has to compensate the parallel reduction in the number of charge carriers. Referring again to the end-members of the two glass series, the experimental data shows that the addition of NaCl causes an increase of about one order of magnitude in the ionic mobility, while the addition of Na_2SO_4 results in an enhancement of approximately three orders of magnitude (see inset in **Figure 14**).

DISCUSSION

Some of the terminology used to discuss the mechanical properties in this report originates from the concept of shear-transformation zones (STZ), i.e., the cooperative rearrangement of a group of atoms. While STZs are mostly used to describe the fundamental processes governing the plasticity of metallic glasses, the STZ theory has also been used to describe general glassy dynamics (Bouchbinder and Langer, 2009a,b,c, 2011). By definition, STZs are localized flow events marking the irreversible transition between the inherent structures of the energy landscape as the glassy system is subjected to mechanical stress or strain (Bouchbinder and Langer, 2011). Therefore, it is possible to draw a parallel between the atomic motion during plastic deformation and ionic conductivity, since both result from the activation of extremely localized, atomic-level rearrangements by external stimuli. While the atomic motion related to a STZ originates from the stress gradient and the strain bias, the ionic jumps which manifest in the electric conductivity are driven by the applied voltage.

The energy barrier density (in $J.m^{-3}$), which determines the STZ formation is given by Liu et al. (2010):

$$\Xi_{STZ} = \frac{8}{\pi^2} \cdot G \cdot \gamma_c^2 \cdot \xi \tag{18}$$

where $\gamma_c = 0.0267$ and $\xi = 3$ are constants from the cooperative shear model (Johnson and Samwer, 2005). The **Figures 11**, **12** show a comparison between the energy barrier density for STZ formation and the barrier densities for ionic mobility Ξ_μ and charge carrier formation Ξ_n, respectively. Interestingly, the energy barrier densities for mobility and STZ formation scale linearly for the $NaPO_3$-Na_2SO_4-NaCl system, while the relations

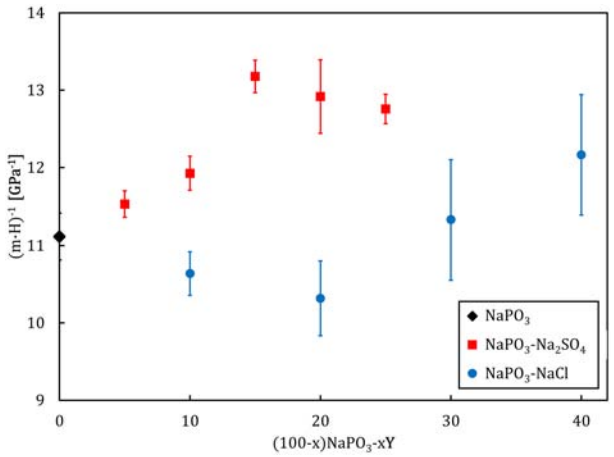

FIGURE 13 | Compositional dependence of the flow event volume, gauged by $(m \cdot H)^{-1}$, for the $NaPO_3$-NaCl-Na_2SO_4 glass system.

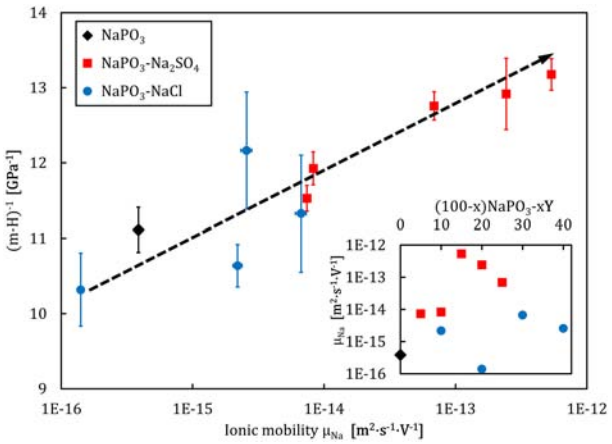

FIGURE 14 | Flow event volume, gauged by $(m \cdot H)^{-1}$, as a function of the logarithm of ionic mobility (at $T = 323$ K) for the $NaPO_3$-NaCl-Na_2SO_4 glass system. The dashed line is a guide to the eye. The inset shows the compositional dependence of the ionic mobility.

between the energy density barrier of charge carrier formation and STZ formation depend on the added salt: the $NaPO_3$-NaCl glasses follow a positive linear trend, while the $NaPO_3$-Na_2SO_4 glasses show a broad distribution of ionic mobility energy barriers within a somewhat narrow distribution of STZ energy barrier densities. These results suggest that the plastic deformation in $NaPO_3$-NaCl glasses is strongly coupled to the motion of the sodium cations, while the $NaPO_3$-Na_2SO_4 glasses deform in a more homogeneous way, requiring the rearrangement of the sulfate and phosphate groups that are part of the glass network. In conjunction with the data from **Figures 5**, **6**, we obtain a consistent picture of how the addition of NaCl shifts the structural units responsible for plastic deformation from the covalently-bonded phosphate network to the strongly ionic interchain Na^+-Cl^- "tissue." The addition of sodium sulfate, on the other hand, barely affects the average effective mass of the "elementary unit" (**Figure 6**) and its distribution (**Figure 5**). The strongly changing ionic mobility energy barrier density in relation to the relatively constant SZT formation energy barrier density suggests a larger degree of cooperative motion involved in the diffusion of sodium ions, which is consistent with our impedance measurements.

Considering the growing influence of the sodium cation and its environment on the mechanical properties, we arrive at the conclusion that ionic glasses with 1D + 2D mixed networks are created upon the progressive addition of Na_2SO_4 and NaCl, where the respective constituents can be approximated as quasi-spheres that interact mainly via electrostatic forces. As opposite to traditional oxide glasses with covalent network structures, these electrostatic forces are longer ranging and less directional. This in turn allows us to interpret the indentation deformation of the $NaPO_3$-Na_2SO_4-NaCl glasses in analogy to the mechanical behavior of metallic glasses and charged colloidal suspensions, which are characterized by spherical structural units, arranged as densely packed clusters bound via long-range, non-directional forces (Tokuyama, 1998; Pan et al., 2008; Varnik et al., 2014; Ma, 2015). The indentation deformation in such systems typically comprise the activation of flow units involving a collection of simultaneously operating STZs (Limbach et al., 2017). The volume of these flow units can be estimated by Pan et al. (2008):

$$\Omega = \frac{k \cdot T}{C' \cdot m \cdot H} \tag{19}$$

where C' is a constant related to the cooperative shear model (Johnson and Samwer, 2005). Since all experiments were performed under isothermal conditions, the factor $(k \cdot T)/C'$ is constant for all glasses and consequently, we can utilize the factor $(m \cdot H)^{-1}$ as a measure for the compositional dependence of the volume of the flow units (**Figure 13**). As Na_2SO_4 is added, an increase in $(m \cdot H)^{-1}$ is observed. On the other hand, NaCl incorporation initially results in a decrease of $(m \cdot H)^{-1}$ down to a minimum at x = 20. Further addition of NaCl causes $(m \cdot H)^{-1}$ to rapidly increase.

The effect of sulfate addition follows the slight decrease in the average effective mass of each "elementary unit" of plastic flow (**Figure 6**) as the deformation homogeneity remains constant, as reflected by the marginal changes in the strain-rate sensitivity of the $NaPO_3$-Na_2SO_4 glasses (**Figure 5**). However, the addition of NaCl illustrates the more complex scenario of the changing topological structures controlling the plastic deformation. Starting from $NaPO_3$, the addition of NaCl continuously increases the mobility of the phosphate chains. This is accompanied by a decreasing volume of the flow events and a lower strain-rate sensitivity, which indicates that the plastic deformation becomes more and more localized around the most mobile phosphate chains. At ~20 mol% NaCl, the interchain Na^+-Cl^- "tissue" reaches a critical threshold and starts to concentrate the flow events, causing the phosphate chains to stop being the controlling factor. Further, addition of NaCl continuously decreases the glass transition temperature and the

strain-rate sensitivity but increases the volume of the flow units since the fraction of the ionic interchain "tissue" also increases. Analogous behavior can be found on several physical properties of inorganic glass systems with marked compositional-dependent transitions in the glass topology (Vaills et al., 2005; Micoulaut and Phillips, 2007; Micoulaut, 2008), e.g., in (100–x)$AgPO_3$-xAgI system at x $\sim$ 20 (Micoulaut et al., 2009; Novita et al., 2009).

The dependence of the volume of flow events on interactions beyond the short-range scale is exemplified in the direct correlation to the effective ionic mobility (calculated for $T = 323$ K), illustrated in **Figure 14**. The ionic mobility contains information on the correlated motion of ions through the Haven ratio (Murch, 1982; Murch and Dyre, 1989), which the Impedance analysis suggests exhibits a non-trivial compositional dependence (**Figure 10**). These results relate back to the increased tendency for a localization of the plastic deformation upon the addition of NaCl (**Figure 5**), reflecting the smaller STZ volumes and lower ionic mobility in relation to the sodium metaphosphate. On the other hand, the addition of Na_2SO_4 strongly increases the ionic mobility, leading to larger STZ volumes but no change in the localization of deformation, also in line with recent results from Raman measurements of the Boson peak in indented SiO_2 (Benzine et al., 2018).

CONCLUSIONS

In this work we have shown an interesting correlation between the atomic motions governing the ionic conductivity and the plastic deformation in sodium metaphosphate glasses containing sodium sulfate and sodium chloride, respectively. In summary, the structure and physical properties of melt-quenched $NaPO_3$-NaCl-Na_2SO_4 glasses were characterized. The addition of sulfate and halide salts was found to maintain the phosphate network largely untouched, while the coordination sphere around the Na^+ cations changes, whereas the medium-range order evolves from 2D phosphate chains to a heterogeneous 1D + 2D mixed network. The addition of NaCl enhances the Young's modulus and results in a stronger localization of the plastic flow, while the addition of Na_2SO_4 on the other hand, keeps the Young's modulus and the homogeneity of the plastic flow events basically constant. Due to the similar atomic masses of the PO_4^{3-} and SO_4^{2-} tetrahedra, the average effective mass of the "elementary unit" remains constant as well. Impedance measurements show a moderate increase in ionic conductivity as a result of the enhanced mobility of the Na^+ cation, while the number density of charge carriers decreases with the addition of the two sodium salts. We observed a smaller STZ volume in glasses with less mobile ions and a more localized deformation, whereas higher ionic mobilities at similar localization degrees imply a larger STZ volume. This reflects in lower average effective masses for the elementary units of deformation, as the plastic flow events are concentrated in a smaller volume and become more dependent on the movement of the lighter ions. A higher Na^+ mobility increases the average displacement of the ions, leading to stronger cooperative motions, and a larger volume of the flow units.

DATA AVAILABILITY

The datasets generated for this study are available on request to the corresponding author.

AUTHOR CONTRIBUTIONS

All authors listed have made a substantial, direct and intellectual contribution to the work, and approved it for publication.

FUNDING

The financial support of the German Science Foundation through its priority program SPP 1594 (project number WO 1220/14-1), the European Research Council under the EU's Horizon 2020 research and innovation program (ERC grant UTOPES, grant agreement number 681652), and the Australian Research Council (grant number DP170104367) are gratefully acknowledged.

REFERENCES

Almond, D. P., Duncan, G. K., and West, A. R. (1983). The determination of hopping rates and carrier concentrations in ionic conductors by a new analysis of ac conductivity. *Solid State Ion.* 8, 159–164. doi: 10.1016/0167-2738(83)90079-6

Almond, D. P., Hunter, C. C., and West, A. R. (1984). The extraction of ionic conductivities and hopping rates from a.c. conductivity data. *J. Mater. Sci.* 19, 3236–3248. doi: 10.1007/BF00549810

Almond, D. P., and West, A. R. (1983). Impedance and modulus spectroscopy of "real" dispersive conductors. *Solid State Ion.* 11, 57–64. doi: 10.1016/0167-2738(83)90063-2

Bandara, T. M. W. J., and Mellander, B.-E. (2011). "Evaluation of mobility , diffusion coefficient and density of charge carriers in ionic liquids and novel electrolytes based on a new model for dielectric response," in *Ionic Liquids: Theory, Properties, New Approaches,* ed A. Kokorin (Rijeka: Intech), 384–407. doi: 10.5772/15183

Barsoukov, E., and Macdonald, J. R. (eds.). (2005). *Impedance Spectroscopy: Theory, Experiment, and Applications, 2nd Edn.* Hoboken, NJ: Wiley-Interscience. doi: 10.1002/0471716243

Benzine, O., Bruns, S., Pan, Z., Durst, K., and Wondraczek, L. (2018). Local deformation of glasses is mediated by rigidity fluctuation on nanometer scale. *Adv. Sci.* 5:1800916. doi: 10.1002/advs.201800916

Bhattacharya, S., and Ghosh, A. (2004). Conductivity spectra in fast ion conducting glasses: Mobile ions contributing to transport process. *Phys. Rev. B* 70:172203. doi: 10.1103/PhysRevB.70.172203

Bhide, A., and Hariharan, K. (2007). Sodium ion transport in $NaPO_3$-Na_2SO_4 glasses. *Mater. Chem. Phys.* 105, 213–221. doi: 10.1016/j.matchemphys.2007.04.044

Bouchbinder, E., and Langer, J. S. (2009a). Non-equilibrium thermodynamics of amorphous materials. *II*: effective-temperature theory. *Phys. Rev. E* 80:31132. doi: 10.1103/PhysRevE.80.031132

Bouchbinder, E., and Langer, J. S. (2009b). Non-equilibrium thermodynamics of driven amorphous materials. I. Internal degrees of freedom and volume deformation. *Phys. Rev. E* 80:31131. doi: 10.1103/PhysRevE.80.031131

Bouchbinder, E., and Langer, J. S. (2009c). Non-equilibrium thermodynamics of driven amorphous materials. III. Shear-transformation-zone plasticity. *Phys. Rev. E* 80:31133. doi: 10.1103/PhysRevE.80.031133

Bouchbinder, E., and Langer, J. S. (2011). Shear-transformation-zone theory of linear glassy dynamics. *Phy. Rev. E* 83:61503. doi: 10.1103/PhysRevE.83.061503

Brow, R. K. (2000). Review: the structure of simple phosphate glasses. *J. Non Cryst. Solids* 263–264, 1–28. doi: 10.1016/S0022-3093(99)00620-1

Brow, R. K., Osborne, Z. A., and Kirkpatrick, R. J. (1992). A multinuclear MAS NMR study of the short-range structure of fluorophosphate glass. *J. Mater. Res.* 7, 1892–1899. doi: 10.1557/JMR.1992.1892

Brow, R. K., Tallant, D. R., Myers, S. T., and Phifer, C. C. (1995). The short-range structure of zinc polyphosphate glass. *J. Non Cryst. Solids* 191, 45–55. doi: 10.1016/0022-3093(95)00289-8

Cutroni, M., Magistris, A., and Villa, M. (1992). Dynamics and structure of $(Ag_2S)x(AgPO_3)1\text{-}x$ glasses studied by ultrasounds and 31P NMR. *Solid State Ion. 53–56*, 1232–1236. doi: 10.1016/0167-2738(92)90318-J

Da, N., Grassme, O., Nielsen, K. H., Peters, G., and Wondraczek, L. (2011). Formation and structure of ionic (Na, Zn) sulfophosphate glasses. *J. Non Cryst. Solids* 357, 2202–2206. doi: 10.1016/j.jnoncrysol.2011.02.037

Dyre, J. C. (2006). The glass transition and elastic models of glass-forming liquids. *Rev. Mod. Phys.* 78, 953–972. doi: 10.1103/RevModPhys.78.953

Fan, Y., Iwashita, T., and Egami, T. (2014). How thermally activated deformation starts in metallic glass. *Nat. Commun.* 5:5083. doi: 10.1038/ncomms6083

Greaves, G. N., Greer, A. L., Lakes, R. S., and Rouxel, T. (2011). Poisson's ratio and modern materials. *Nat. Mater.* 10, 823–837. doi: 10.1038/nmat3134

Hairetdinov, E. F., Uvarov, N. F., Patel, H. K., and Martin, S. W. (1994). Estimation of the free-charge-carrier concentration in fast-ion conducting $Na_2S\text{-}B_2S_3$ glasses from an analysis of the frequency-dependent conductivity. *Phy. Rev. B* 50, 13259–13266. doi: 10.1103/PhysRevB.50.13259

Hay, J. (2009). Introduction to instrumented indentation testing. *Exp. Tech.* 33, 66–72. doi: 10.1111/j.1747-1567.2009.00541.x

Heuer, A., and Spiess, H. W. (1994). Universality of the glass transition temperature. *J. Non Cryst. Solids* 176, 294–298. doi: 10.1016/0022-3093(94)90090-6

Hodge, I. M., Ingram, M. D., and West, A. R. (1976). Impedance and modulus spectroscopy of polycrystalline solid electrolytes. *J. Electroanal. Chem.* 74, 125–143. doi: 10.1016/S0022-0728(76)80229-X

Hong, L., Novikov, V. N., and Sokolov, A. P. (2011). Is there a connection between fragility of glass forming systems and dynamic heterogeneity/cooperativity? *J. Non Cryst. Solids* 357, 351–356. doi: 10.1016/j.jnoncrysol.2010.06.071

Hraiech, S., and Ferid, M. (2013). Synthesis, electrical and dielectric properties of $(Na_2O)_{0.5}\text{-}(P_2O_5)_{0.5}$ glass. *J. Alloys Compd.* 577, 543–549. doi: 10.1016/j.jallcom.2013.06.168

Hudgens, J. J., Brow, R. K., Tallant, D. R., and Martin, S. W. (1998). Raman spectroscopy study of the structure of lithium and sodium ultraphosphate glasses. *J. Non Cryst. Solids* 223, 21–31. doi: 10.1016/S0022-3093(97)00347-5

Hufnagel, T. C., Schuh, C. A., and Falk, M. L. (2016). Deformation of metallic glasses: recent developments in theory, simulations, and experiments. *Acta Mater.* 109, 375–393. doi: 10.1016/j.actamat.2016.01.049

Jabraoui, H., Vaills, Y., Hasnaoui, A., Badawi, M., and Ouaskit, S. (2016). Effect of sodium oxide modifier on structural and elastic properties of silicate glass. *J. Phys. Chem. B* 120, 13193–13205. doi: 10.1021/acs.jpcb.6b09664

Johnson, K. L. (1985). *Contact Mechanics*. Cambridge: Cambridge University Press. doi: 10.1017/CBO9781139171731

Johnson, W. L., and Samwer, K. (2005). A universal criterion for plastic yielding of metallic glasses with a $(T/Tg)^{2/3}$ temperature dependence. *Phys. Rev. Lett.* 95:195501. doi: 10.1103/PhysRevLett.95.195501

Jun, L., Portier, J., Tanguy, B., Videau, J. J., Allal, M. A., Morcos, J., et al. (1990). Application of silver conducting glasses to solid state batteries and sensors. *Active Passive Electr. Comp.* 14, 81–94. doi: 10.1155/1990/82403

Kabi, S., and Ghosh, A. (2014). Ion dynamics in glassy ionic conductors: scaling of mean square displacement of mobile ions. *Europhys. Lett.* 108:36002. doi: 10.1209/0295-5075/108/36002

Kapoor, S., Loennroth, N., Youngman, R. E., Rzoska, S. J., Bockowski, M., Jensen, L. R., et al. (2017). Pressure-driven structural depolymerization of zinc phosphate glass. *J. Non Cryst. Solids* 469, 31–38. doi: 10.1016/j.jnoncrysol.2017.04.011

Kartini, E., Kennedy, S. J., Itoh, K., Kamiyama, T., Collins, M. F., and Suminta, S. (2004). Anion effect on the structure of $Ag_2S\text{-}AgPO_3$ superionic glasses. *Solid State Ion.* 167, 65–71. doi: 10.1016/j.ssi.2003.12.021

Kartini, E., Kennedy, S. J., Sakuma, T., Itoh, K., Fukunaga, T., Collins, M. F., et al. (2002). Structural , thermal and electrical properties of $AgI\text{-}Ag_2S\text{-}AgPO_3$ superionic glasses. *J. Non Cryst. Solids* 312–314, 628–632. doi: 10.1016/S0022-3093(02)01782-9

Kawasaki, T., Araki, T., and Tanaka, H. (2007). Correlation between dynamic heterogeneity and medium-range order in two-dimensional glass-forming liquids. *Phys. Rev. Lett.* 99:215701. doi: 10.1103/PhysRevLett.99.215701

Kim, J. G., Son, B., Mukherjee, S., Schuppert, N., Bates, A., Kwon, O., et al. (2015). A review of lithium and non-lithium based solid state batteries. *J. Power Sources* 282, 299–322. doi: 10.1016/j.jpowsour.2015.02.054

Konidakis, I., Varsamis, C. P. E., and Kamitsos, E. I. (2011). Effect of synthesis method on the structure and properties of $AgPO_3$-based glasses. *J. Non Cryst. Solids* 357, 2684–2689. doi: 10.1016/j.jnoncrysol.2011.03.013

Le, Q. H., Palenta, T., Benzine, O., Griebenow, K., Limbach, R., Kamitsos, E. I., et al. (2017). Formation, structure and properties of fluoro-sulfo-phosphate poly-anionic glasses. *J. Non Cryst. Solids* 477, 58–72. doi: 10.1016/j.jnoncrysol.2017.09.043

Li, X., and Bhushan, B. (2002). A review of nanoindentation continuous stiffness measurement technique and its applications. *Mater. Char.* 48, 11–36. doi: 10.1016/S1044-5803(02)00192-4

Limbach, R., Kosiba, K., Pauly, S., Kuehn, U., and Wondraczek, L. (2017). Serrated flow of CuZr-based bulk metallic glasses probed by nanoindentation: role of the activation barrier, size and distribution of shear transformation zones. *J. Non Cryst. Solids* 459, 130–141. doi: 10.1016/j.jnoncrysol.2017.01.015

Limbach, R., Rodrigues, B. P., Moencke, D., and Wondraczek, L. (2015). Elasticity, deformation and fracture of mixed fluoride-phosphate glasses. *J. Non Cryst. Solids* 430, 99–107. doi: 10.1016/j.jnoncrysol.2015.09.025

Limbach, R., Rodrigues, B. P., and Wondraczek, L. (2014). Strain-rate sensitivity of glasses. *J. Non Cryst. Solids* 404, 124–134. doi: 10.1016/j.jnoncrysol.2014.08.023

Liu, Y. H., Wang, K., Inoue, A., Sakurai, T., and Chen, M. W. (2010). Energetic criterion on the intrinsic ductility of bulk metallic glasses. *Scr. Mater.* 62, 586–589. doi: 10.1016/j.scriptamat.2009.12.042

Lucas, B. N., and Oliver, W. C. (1999). Indentation power-law creep of high-purity indium. *Metal. Mater. Transact. A* 30, 601–610. doi: 10.1007/s11661-999-0051-7

Lvovich, V. F. (2012). *Impedance Spectroscopy–Applications to Electrochemical and Dielectric Phenomena*. Hoboken, NJ: John Wiley & Sons. doi: 10.1002/9781118164075

Ma, E. (2015). Tuning order in disorder. *Nat. Mater.* 14, 547–552. doi: 10.1038/nmat4300

Malugani, J. P., Mercier, R., Fahys, B., and Robert, G. (1982). Ionic conductivity of and Raman spectroscopy investigation binary oxosalts $(1\text{-}x)AgPO_3\text{-}xAg_2SO_4$ glasses. *J. Solid State Chem.* 45, 309–316. doi: 10.1016/0022-4596(82)90176-1

Mantisi, B., Tanguy, A., Kermouche, G., and Barthel, E. (2012). Atomistic response of a model silica glass under shear and pressure. *Eur. Phys. J. B* 85:304. doi: 10.1140/epjb/e2012-30317-6

Marple, M. A. T., Avila-Paredes, H., Kim, S., and Sen, S. (2018). Atomistic interpretation of the ac-dc crossover frequency in crystalline and glassy ionic conductors. *J. Chem. Phys.* 148:204507. doi: 10.1063/1.5026685

Martin, S. W. (1991). Ionic conduction in phosphate glasses. *J. Am. Ceramic Soc.* 74, 1767–1784. doi: 10.1111/j.1151-2916.1991.tb07788.x

Martin, S. W., and Angell, C. A. (1986). DC and AC conductivity in wide composition range $Li_2O\text{-}P_2O_5$ glasses. *J. Non Cryst. Solids* 83, 185–207. doi: 10.1016/0022-3093(86)90067-0

Micoulaut, M. (2008). Constrained interactions, rigidity, adaptative networks, and their role for the description of silicates. *Am. Mineral.* 93, 1732–1748. doi: 10.2138/am.2008.2903

Micoulaut, M., Malki, M., Novita, D. I., and Boolchand, P. (2009). Fast-ion conduction and flexibility and rigidity of solid electrolyte glasses. *Phys. Rev. B* 80:184205. doi: 10.1103/PhysRevB.80.184205

Micoulaut, M., and Phillips, J. C. (2007). Onset of rigidity in glasses: from random to self-organized networks. *J. Non Cryst. Solids* 353, 1732–1740. doi: 10.1016/j.jnoncrysol.2007.01.078

Möncke, D., Sirotkin, S., Stavrou, E., Kamitsos, E. I., and Wondraczek, L. (2014). Partitioning and structural role of Mn and Fe ions in ionic sulfophosphate glasses. *J. Chem. Phys.* 141:224509. doi: 10.1063/1.4903191

Murch, G. E. (1982). The Nernst-Einstein equation in high-defect-content solids. *Philos. Magazine A* 45, 685–692. doi: 10.1080/01418618208236198

Murch, G. E., and Dyre, J. C. (1989). Correlation effects in ionic conductivity. *Crit. Rev. Solid State Mater. Sci.* 15, 345–365. doi: 10.1080/10408438908243739

Ngai, K. L., and Moynihan, C. T. (1998). The dynamics of mobile ions in ionically conducting glasses and other materials. *Mater. Res. Soc. Bull.* 23, 51–56. doi: 10.1557/S0883769400031006

Novita, D. I., Boolchand, P., Malki, M., and Micoulaut, M. (2009). Elastic flexibility, fast-ion conduction, boson and floppy modes in $AgPO_3$-AgI glasses examined in Raman scattering, infrared reflectance, modulated differential scanning calorimetry, ac electrical conductivity and molar volume experiments. *J. Phys.Condensed Matter.* 21:205106. doi: 10.1088/0953-8984/21/20/205106

Oliver, W. C., and Pharr, G. M. (1992). An improved technique for determining hardness and elastic modulus using load and displacement sensing indentation experiments. *J. Mater. Res.* 7, 1564–1583. doi: 10.1557/JMR.1992.1564

Pan, D., Inoue, A., Sakurai, T., and Chen, M. W. (2008). Experimental characterization of shear transformation zones for plastic flow of bulk metallic glasses. *Proc. Natl. Acad. Sci. U.S.A.* 105, 14769–14772. doi: 10.1073/pnas.0806051105

Pedone, A., Malavasi, G., Cormack, A. N., Segre, U., and Menziani, M. C. (2008a). Elastic and dynamical properties of alkali-silicate glasses from computer simulations techniques. *Theor. Chem. Acc.* 120, 557–564. doi: 10.1007/s00214-008-0434-7

Pedone, A., Malavasi, G., Menziani, M. C., Segre, U., and Cormack, A. N. (2008b). Role of magnesium in soda-lime glasses: insight into structural, transport, and mechanical properties through computer simulations. *J. Phys. Chem. C* 112, 11034–11041. doi: 10.1021/jp8016776

Perez, J. (1994). Theories of liquid-glass transition. *J. Food Eng.* 22, 89–114. doi: 10.1016/0260-8774(94)90027-2

Pharr, G. M., Oliver, W. C., and Brotzen, F. R. (1992). On the generality of the relationship among contact stiffness, contact area and elastic modulus during indentation. *J. Mater. Res.* 7, 613–617. doi: 10.1557/JMR.1992.0613

Pharr, G. M., Strader, J. H., and Oliver, W. C. (2009). Critical issues in making small-depth mechanical property measurements by nanoindentation with continuous stiffness measurement. *J. Mater. Res.* 24, 653–666. doi: 10.1557/jmr.2009.0096

Popov, I. I., Nigmatullin, R. R., Khamzin, A. A., and Lounev, I. V. (2012). Conductivity in disordered structures: verification of the generalized Jonscher's law on experimental data. *J. Phys.* 394:12026. doi: 10.1088/1742-6596/394/1/012026

Queiroz, C. A., and Sestak, J. (2010). Aspects of the non-crystalline state. *Phys. Chem. Glasses* 51, 165–172.

Rahmani, Y., Koopman, R., Denisov, D., and Schall, P. (2014). Visualizing the strain evolution during the indentation of colloidal glasses. *Phys. Rev. E* 89:12304. doi: 10.1103/PhysRevE.89.012304

Rao, R. P., and Seshasayee, M. (2004). Molecular dynamics simulation of ternary glasses Li_2O-P_2O_5-LiCl. *Solid State Commun.* 131, 537–542. doi: 10.1016/j.ssc.2004.06.019

Rao, R. P., Tho, T. D., and Adams, S. (2009). Lithium ion transport pathways in xLiCl-(1-x)($0.6Li_2O$-$0.4P_2O_5$) glasses. *J. Power Sources* 189, 385–390. doi: 10.1016/j.jpowsour.2008.07.089

Rodney, D., Tanguy, A., and Vandembroucq, D. (2011). Modeling the mechanics of amorphous solids at different length scale and time scale. *Model. Simul. Mater. Sci. Eng.* 19:83001. doi: 10.1088/0965-0393/19/8/083001

Rodrigues, A. C., Nascimento, M. L., Bragatto, C. B., and Souquet, J. L. (2011). Charge carrier mobility and concentration as a function of composition in $AgPO_3$-AgI glasses. *J. Chem. Phys.* 135:234504. doi: 10.1063/1.3666835

Rodrigues, B. P., Ebendorff-Heidepriem, H., and Wondraczek, L. (2019). Decoupling mobility and charge carrier concentration in AgR-$AgPO_3$ glasses (R = Cl, Br, I). *Solid State Ion.* 334, 99–104. doi: 10.1016/j.ssi.2019.02.009

Rodrigues, B. P., and Wondraczek, L. (2013). Medium-range topological constraints in binary phosphate glasses. *J. Chem. Phys.* 138:244507. doi: 10.1063/1.4810868

Rouxel, T. (2006). Elastic properties of glasses: a multiscale approach. *Comptes Rendus Mecanique* 334, 743–753. doi: 10.1016/j.crme.2006.08.001

Rouxel, T. (2007). Elastic properties and short-to medium-range order in glasses. *J. Am. Ceramic Soc.* 90, 3019–3039. doi: 10.1111/j.1551-2916.2007.01945.x

Rouxel, T., Ji, H., Hammouda, T., and Moréac, A. (2008a). Poisson's ratio and the densification of glass under high pressure. *Phys. Rev. Lett.* 100:225501. doi: 10.1103/PhysRevLett.100.225501

Rouxel, T., Ji, H., Keryvin, V., Hammouda, T., and Yoshida, S. (2008b). Poisson's ratio and the glass network topology–relevance to high pressure densification and indentation behavior. *Adv. Mater. Res.* 39–40, 137–146. doi: 10.4028/www.scientific.net/AMR.39-40.137

Sangoro, J. R., and Kremer, F. (2012). Charge transport and glassy dynamics in ionic liquids. *Acc. Chem. Res.* 45, 525–532. doi: 10.1021/ar2001809

Saunders, G. A., Metcalfe, R. D., Cutroni, M., Federico, M., and Piccolo, A. (1996). Elastic and anelastic properties, vibrational anharmonicity, and fractal bond connectivity of superionic glasses. *Phys. Rev. B* 53, 5287–5300. doi: 10.1103/PhysRevB.53.5287

Schall, P., Weitz, D. A., and Spaepen, F. (2007). Structural rearrangements that govern flow in colloidal glasses. *Science* 318, 1895–1899. doi: 10.1126/science.1149308

Scotti, S., Villa, M., Mustarelli, P., and Cutroni, M. (1992). Structure, conductivity and acoustic attenuation in $(Ag_2SO_4)x(AgPO_3)1$-x. *Solid State Ion. 53–56*, 1237–1244. doi: 10.1016/0167-2738(92)90319-K

Shen, L., Cheong, W. C. D., Foo, Y. L., and Chen, Z. (2012). Nanoindentation creep of tin and aluminium: a comparative study between constant load and constant strain rate methods. *Mater. Sci. Eng. A* 532, 505–510. doi: 10.1016/j.msea.2011.11.016

Shuker, R., and Gammon, R. W. (1970). Raman-scattering selection-rule breaking and the density of states in amorphous materials. *Phys. Rev. Lett.* 25, 222–225. doi: 10.1103/PhysRevLett.25.222

Sidebottom, D. L. (2009). Understanding ion motion in disordered solids from impedance spectroscopy scaling. *Rev. Mod. Phys.* 81, 999–1014. doi: 10.1103/RevModPhys.81.999

Singh, D. P., Shahi, K., and Kar, K. K. (2016). Superlinear frequency dependence of AC conductivity and its scaling behavior in xAgI-(1-x)$AgPO_3$ glass superionic conductors. *Solid State Ion.* 287, 89–96. doi: 10.1016/j.ssi.2016.01.048

Sirotkin, S., Meszaros, R., and Wondraczek, L. (2012). Chemical stability of ZnO-Na2O-SO_3-P_2O_5 glasses. *Int. J. Appl. Glass Sci.* 3, 44–52. doi: 10.1111/j.2041-1294.2011.00076.x

Sokolov, I. A., Valova, N. A., Tarlakov, Y. P., and Pronkin, A. A. (2003). Electrical properties and the structure of glasses in the Li_2SO_4-$LiPO_3$ system. *Glass Phys. Chem.* 29, 548–554. doi: 10.1023/B:GPAC.0000007930.11101.ee

Souquet, J. L. (1981). Electrochemical properties of ionically conductive glasses. *Solid State Ion.* 5, 77–82. doi: 10.1016/0167-2738(81)90198-3

Spaepen, F. (1977). A microscopic mechanism for steady state inhomogeneous flow in metallic glasses. *Acta Metal.* 25, 407–415. doi: 10.1016/0001-6160(77)90232-2

Thieme, A., Moencke, D., Limbach, R., Fuhrmann, S., Kamitsos, E. I., and Wondraczek, L. (2015). Structure and properties of alkali and silver sulfophosphate glasses. *J. Non Cryst. Solids* 410, 142–150. doi: 10.1016/j.jnoncrysol.2014.11.029

Tokuyama, M. (1998). Theory of slow dynamics in highly charged colloidal suspensions. *Phys. Rev. E* 58, R2729–R2732. doi: 10.1103/PhysRevE.58.R2729

Tsamados, M., Tanguy, A., Goldenberg, C., and Barrat, J. L. (2009). Local elasticity map and plasticity in a model Lennard-Jones glass. *Phys. Rev. E* 80:26112. doi: 10.1103/PhysRevE.80.026112

Tuller, H. L., Button, D. P., and Uhlmann, D. R. (1980). Fast ion transport in oxide glasses. *J. Non Cryst. Solids* 40, 93–118. doi: 10.1016/0022-3093(80)90096-4

Vaills, Y., Qu, T., Micoulaut, M., Chaimbault, F., and Boolchand, P. (2005). Direct evidence of rigidity loss and self-organization in silicate glasses. *J. Phys.* 17, 4889–4896. doi: 10.1088/0953-8984/17/32/003

Varnik, F., Mandal, S., Chikkadi, V., Denisov, D., Olsson, P., Vågberg, D., et al. (2014). Correlations of plasticity in sheared glasses. *Phys. Rev. E* 89:40301. doi: 10.1103/PhysRevE.89.040301

Velli, L. L., Varsamis, C. P. E., Kamitsos, E. I., Moencke, D., and Ehrt, D. (2005). Structural investigation of metaphosphate glasses. *Phys. Chem. Glasses* 46, 178–181.

Westman, A. E. R., and Gartaganis, P. A. (1957). Constitution of sodium, potassium, and lithium phosphate glasses. *J. Am. Ceramic Soc.* 40, 293–299. doi: 10.1111/j.1151-2916.1957.tb12625.x

Conflict of Interest Statement: The authors declare that the research was conducted in the absence of any commercial or financial relationships that could be construed as a potential conflict of interest.

frontiers in Materials

ORIGINAL RESEARCH
published: 24 April 2019
doi: 10.3389/fmats.2019.00079

Mechanisms of Silica Fracture in Aqueous Electrolyte Solutions

Jessica M. Rimsza[1]*, *Reese E. Jones*[2] and *Louise J. Criscenti*[1]

[1] Sandia National Laboratories, Geochemistry Department, Albuquerque, NM, United States, [2] Sandia National Laboratories, Mechanics of Materials Department, Livermore, CA, United States

Glassy silicates are substantially weaker when in contact with aqueous electrolyte solutions than in vacuum due to chemical interactions with preexisting cracks. To investigate this silicate weakening phenomenon, classical molecular dynamics (MD) simulations of silica fracture were performed using the bond-order based, reactive force field ReaxFF. Four different environmental conditions were investigated: vacuum, water, and two salt solutions (1M NaCl, 1M NaOH) that form relatively acidic and basic solutions, respectively. Any aqueous environment weakens the silica, with NaOH additions resulting in the largest decreases in the effective fracture toughness (eK_{IC}) of silica or the loading rate at which the fracture begins to propagate. The basic solution leads to higher surface deprotonation, narrower radius of curvature of the crack tip, and greater weakening of the silica, compared with the more acidic environment. The results from the two different electrolyte solutions correspond to phenomena observed in experiments and provide a unique atomistic insight into how anions alter the chemical-mechanical fracture response of silica.

Keywords: fracture, silica, molecular dynamics simulation, dissolution, electrolytes

OPEN ACCESS

Edited by:
Lothar Wondraczek, Friedrich Schiller University Jena, Germany

Reviewed by:
Joachim Deubener, Clausthal University of Technology, Germany
Mathieu Bauchy, University of California, Los Angeles, United States

***Correspondence:**
Jessica M. Rimsza
jrimsza@sandia.gov

Specialty section:
This article was submitted to Glass Science, a section of the journal Frontiers in Materials

Received: *26 November 2018*
Accepted: *05 April 2019*
Published: *24 April 2019*

Citation:
Rimsza JM, Jones RE and Criscenti LJ (2019) Mechanisms of Silica Fracture in Aqueous Electrolyte Solutions. Front. Mater. 6:79. doi: 10.3389/fmats.2019.00079

INTRODUCTION

The environmental impact of salt solutions on fracture has been well-established in both crystalline (Atkinson and Meredith, 1981; Dove, 1995) and glassy materials (Wiederhorn and Johnson, 1973). The subcritical fracture velocity in silicate glasses increases when in contact with both high and low pH solutions, with acidic conditions resulting in less extreme changes (Wiederhorn and Johnson, 1973). This has been attributed to two different mechanisms that cause subcritical fracture growth, as outlined by Dove (1995). The first reaction mechanism is facilitated by a water molecule, which forms a temporary hydrogen bond with the siloxane (Si-O-Si) oxygen and weakens the Si-O linkage until the bond is broken (Equation 1). This is often referred to as the acidic site, because an hydrogen from the water molecule is transferred to the oxygen in the siloxane bond during rupture (White et al., 1987). The result is the formation of two surface silanol groups through consumption of a water molecule:

$$> Si - O - Si < + H_2O = 2 > Si - OH \quad (1)$$

where $>$ and $<$ indicate surface bound species. The second pathway is facilitated by an OH^- ion that forms a temporary over-coordinated silicon until the Si-O bond is sufficiently stretched for Si-O bond breakage (Equation 2). This allows for the electrons to transfer from the siloxane to an

adjacent oxygen, weakening the siloxane bond (White et al., 1987).

$$> Si - O - Si < + OH^- = > Si - OH + > Si - O^- \quad (2)$$

The result is the formation of one neutral (Si-OH) and one deprotonated (Si-O^-) silanol group. Computationally, significant research has been performed to distinguish different mechanisms for silanol bond breakage in the presence of water (Rimola and Ugliengo, 2008; Morrow et al., 2009; Kubicki et al., 2012; Zapol et al., 2013; Kagan et al., 2014; Lowe et al., 2015; Rimsza and Du, 2015; Rimsza J. M. et al., 2016). The exact intermediates and their relative stabilities are still under debate, offering the explanation that both mechanisms may be occurring or, more generally, that a variety of reaction pathways are available (Du and Rimsza, 2017).

In both experimental (Wiederhorn and Johnson, 1973) and computational (Zapol et al., 2013) studies the response of silica to electrolytes is pH dependent. Reactions between the glass and water at the crack tip can result in localized pH's in the fracture volume, due to hydroxyl (-OH) exchange between the solution and the glass (Wiederhorn and Johnson, 1973). Therefore, when comparing different solutions, the concentration of OH^- needs to be considered. Dove hypothesized, in the context of transition state theory, that the increased crack velocity in basic conditions is due to increased attempt frequency facilitated by the ability of the OH^- ion to diffuse to the crack tip (Dove, 1995). This effect is assumed to dominate the small change in reaction enthalpy for the water-mediated (Dove, 1995; Equation 1) vs. the hydroxide-mediated (Dove, 1995; Equation 2) reaction. Additionally, White et al. (1987) hypothesized that the cations with OH^- in their first solvation shell could keep OH^- from accessing the crack tip, thereby altering the fracture mechanism. The confined geometry of a crack tip is also unusual, with the water or electrolyte solution becoming increasingly confined as the solution enters the wedge-like fracture volume. This causes challenges in analysis, since crack tips represent a small percent of the total volume of a system, and are distinctly different from more traditionally studied confined geometries, such as slit pores (Bonnaud et al., 2010; Ho et al., 2011; Bourg and Steefel, 2012).

Because crack tips are a small fraction of macroscopic systems and are difficult to analyze experimentally, simulations have been used to investigate fracture properties of silica in the presence of water. Until recently, the application of molecular dynamics (MD) simulations has been limited because few force fields have the functionality to simulate proton transport in water (Mahadevan and Garofalini, 2007) and even fewer have relevant functionality with electrolyte solutions. At the same time, applications of more accurate electronic structure methods such as density functional theory (DFT) have had difficulty simulating the large number of atoms required to encompass the farther reaching effects of fracture, such as the nanometer sized process zone (Célarié et al., 2007; Rimsza et al., 2017b). Recently, the development and subsequent parameterization of the bond order, reactive force field ReaxFF (Fogarty et al., 2010; van Duin et al., 2013; Yeon and van Duin, 2015) has allowed for investigations of electrolyte-silica interactions. Building from recent work on simulation of sodium hydroxide adsorption on silica surfaces (Rimsza et al., 2018b), as well as silica fracture in vacuum (Rimsza et al., 2017b) and in the presence of water (Rimsza et al., 2018a), we are now able to investigate how electrolyte solutions impact silica fracture with sufficient accuracy to make mechanistic statements on the role of different salt solutions. This is, to the best of our knowledge, the first study to investigate the impact of coupled stress and chemical reactivity on silica fracture in an electrolyte solution using reactive MD simulations. This closes a critical gap in our understanding of silica fracture mechanisms, that until now was beyond the scope of both experimental and computational methods.

Here, simulations of silica fracture are performed with four different environmental conditions: vacuum, water, and two different electrolyte solutions (1M NaCl, 1M NaOH). The systems are analyzed for structural features, including surface configurations, solution composition, and connectivity, as well as mechanical properties such as effective fracture toughness (eK_{IC}). This provides evidence for differences in fracture mechanisms between NaCl and NaOH solutions, and how anions alter chemical-mechanical fracture of silicates.

METHODS

Reactive Molecular Dynamic Force Field (ReaxFF)

Investigating the chemical-mechanical of silica requires a force field which both correctly estimates the mechanical properties of silica and the water/electrolyte interaction with the surface. Very few MD force fields exhibit both capabilities. These include one (Mahadevan and Garofalini, 2007) which is an adaptation of a dissociative water force field (Guillot and Guissani, 2001) and the other, a bond-order based force field (ReaxFF) (Van Duin et al., 2003; Fogarty et al., 2010; Pitman and Van Duin, 2012; Yeon and van Duin, 2015). ReaxFF allows for the dissociation and creation of chemical bonds and redistribution of charges through environmentally dependent charge equilibrium methods. Previous studies have used the Yeon (Yeon and van Duin, 2015) and the Pitman (Pitman and Van Duin, 2012) parametrizations of ReaxFF to investigate silica surface energies (Rimsza et al., 2017a; Yu et al., 2018) and the Fogarty (Fogarty et al., 2010) parameterization to calculate mechanical properties (Yu et al., 2016). For this work, the Yeon version of ReaxFF was selected because it is a reparametrization of the Fogarty version that improves the energetics of water-surface interactions (Rimsza J. M. et al., 2016), which are critical to chemical-mechanical fracture. Additionally, our previous investigations of silica fracture toughness (K_{IC}) process zone size, and radius of curvature (Rimsza et al., 2017b) have been consistent with experiment. Some concerns have been raised surrounding the over estimation of bulk modulus of α-quartz, reported as 602 GPa by Yu et al. (2018). Elastic constants for the Yeon ReaxFF parametrization were calculated as $E = 76.1 \pm 0.3$ GPa, $K = 55.2 \pm 5.2$ GPa, $\mu = 21.8 \pm 0.8$ GPa, and $\nu = 0.32 \pm 0.02$ for the elastic modulus, bulk modulus, shear modulus, and Poisson's ratio, respectively. Reported error is from variation in strain rates.

These values do not compare exactly with experimental results (E = 73.1 GPa, K = 36.7 GPa, μ = 31.2 GPa, and ν = 0.17) (Varshneya, 2013) but are within an order of magnitude. The elastic constant that is of primary concern is E, since the loading methodology (discussed below) is focused on mode I or pure tension. The overestimation of G in the Yeon parametrization (55.2 ± 5.2 GPa from simulation and 36.7 GPa from experiment) would be a larger concern for studies which focused on the analysis of silica in shear and compression. All simulations were performed using the LAMMPS MD code with the USER-REAXC package with the Yeon and van Duin Si/O/H ReaxFF parameterization (Aktulga et al., 2012; Yeon and van Duin, 2015) as the force field (included in **Supporting Information**).

Silica Structure Model

To investigate crack propagation in silica, thin, quasi-2D simulation cells (140 × 140 × 28 Å) were created through a melt-and-quench procedure. Three replicas of the silica glass were generated to enable statistical averaging. The initial cristobalite configurations contained 38,400 atoms in a 2:1 oxygen to silicon ratio. These systems were heated to 4,000 K, then held for 100 ps to melt the crystal structure under periodic boundary conditions. They were then cooled from 4,000 to 300 K at a rate of 5 K/ps, which is reported to accurately replicate bond distance and angles in glassy silica (Lane, 2015). Densities were controlled during cooling at the measured density of silica, 2.2 g/cm^3 (Mozzi and Warren, 1969), through a canonical (NVT) ensemble which controls the number (*N*) of atoms, volume (V), and temperature (T) of the simulation with a damping coefficient of 100 time steps and a time-step of 0.5 fs. After the systems had reached 300 K, the density fluctuated in simulations that alternated isothermal-isobaric dynamics with energy minimization to achieve low energy configurations. Final silica structures had a density of 2.187 ± 0.001 g/cm^3.

First a slit crack has been introduced into the silica on a half-plane by deleting bonds between atoms on opposite sides of the half-plane, then the crack was mechanically loaded by displacement of far-field atoms in a region outside a cylinder centered on the crack tip (**Figure 1**). This displacement field was taken from the linear elastic fracture mechanics (LEFM) continuum solution for a semi-infinite slit crack in mode I (tension) loading that is spatially varying and parameterized by K_I (Lawn and Wilshaw, 1993, Equation 2.11). Prior to loading, the in-plane (x and y) boundary conditions were changed to non-periodic since periodicity is lost during loading of the system (**Figure 1**). Via the prescribed displacement field, a pre-existing slit crack on a halfplane was first opened to a K_I of 0.05 MPa$\sqrt{}$m. Alternating minimizations and low temperature NVT relaxations were then performed to reach an equilibrium structure. Subsequently, the systems were loaded by incrementally increasing K_I by 0.071 MPa$\sqrt{}$m. While holding the periphery fixed to enforce the prescribed mode I displacement, the interior region of atoms was integrated at 300 K with a 0.1 fs time step for 5 ps with NVT dynamics at each mechanical loading step. The effect of different relaxation times between each loading step was previously tested for values of 2.5, 5, and 10 ps (Rimsza et al., 2018a). It was found that changing the relaxation time did not significantly alter the eK_{IC} values. Therefore, it appears that variation in the glassy silica structure has a greater impact on the mechanical response than the relaxation time used between loading steps. Through 100 loading steps the system was fractured with a final loading state of K_I = 0.65 MPa$\sqrt{}$m. During loading, four different chemical environments (vacuum, water, 1M NaCl, and 1M NaOH) were introduced in separate simulations to investigate the role of different aqueous solution compositions on fracture properties.

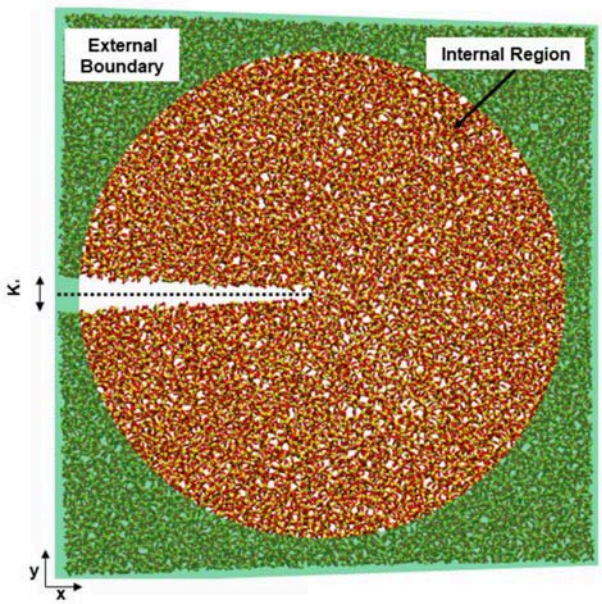

FIGURE 1 | Schematic of the quasi-2D silica system with a slit crack, oxygen atoms are red and silicon atoms are yellow. The half plane where bonds are severed to form a slit crack is denoted by a dashed line. The boundary region (radius 3.2 nm), where the motion of the atoms is prescribed, is shaded green. In the internal cylindrical region, the atoms are free to relax to a minimum energy configuration while atoms in the boundary are fixed to the displacement prescribed by the mode I loading. The axis of the cylinder is out-of-plane and the thickness of the system is 2.8 nm.

We use effective fracture toughness (eK_{IC}) in this paper, which is different than the K_{IC} used in classical fracture mechanics. Classically, the K_{IC} is the point at which a pre-existing fracture converts from subcritical to critical behavior. Due to our small system size, a single fracture event, in which a few bonds break at the fracture tip, results in fracture velocities on the order of 10 m/s. These high fracture velocities are indicative of a critical behavior, but several subsequent events would need to occur to produce an experimentally measurable change in fracture length. Therefore, we are defining the loading at which the first fracture event occurs as eK_{IC} to highlight that it is (1) defined differently than the K_{IC} in classical mechanics and (2) is likely to be an underestimation of the experimentally-derived K_{IC} values, which do not have the atomistic level accuracy exhibited in these simulations. Also, as we will see, eK_{IC} is impacted by the chemical environment unlike the strict definition of K_{IC} defined as an intrinsic material property in fracture mechanics text books (Lawn and Wilshaw, 1993).

For the vacuum systems, no water was introduced, and the internal surfaces stay unhydroxylated during the simulation. When aqueous solutions (water, 1M NaCl, 1M NaOH) are introduced it is necessary to add water to the fracture volume as the crack opens, so that water is available to wet the surface as the system is loaded. A grand canonical Monte Carlo (GCMC) method was used to add water into the crack during the simulation. The GCMC input used a chemical potential of −250 kcal/mol, corresponding to a target density of liquid water, and 10,000 attempts were made to insert water molecules at the beginning of every loading step. To avoid inserting water directly into the glass matrix, a modified GCMC method was used that limited insertion to within 3 Å of an existing water molecule. To maintain stable NaCl and NaOH concentrations, one NaCl or NaOH was added following the addition of water. Each NaCl or NaOH was added as a molecule at the widest point of the fracture, rather than inserted near the crack tip, to emulate the diffusion of ions from the bulk fluid. A reflective wall at the crack opening was used to keep the solution inside the fracture without adding external pressure.

After insertion of the water and NaCl/NaOH molecules, 5 ps of NVT dynamics at 300 K was performed to allow for equilibration of the system. The relaxation time for water-silica interactions was investigated by performing several fracture simulations with shorter (2.5 ps) and longer (10 ps) periods between loading steps. Previous studies have found that a range of relaxation times resulted in overlapping silica energy curves and minimal differences in the results (Rimsza et al., 2018a), indicating that variation in glass structure dominate differences in fracture due to simulated relaxation times.

Due to the high variation in the glassy silica structure, we used 12 replicas of the pre-cracked systems in each of the four loading conditions (48 simulations in total). These 12 replicas were constructed by rotating the three original silica systems by 0, 90,180, and 270° in plane and then introducing slit cracks on the -x half-plane. The results from these 12 systems are reported as the average and standard error unless otherwise noted.

As part of the analysis of the systems, the radius of curvature of the crack tip was calculated by fitting the locations of the surface atoms to a second order polynomial ($y = f(x) = ax^2 + bx + c$) and then obtaining the crack tip radius (ρ) from the formula (Howard, 1988):

$$\rho = \left. \frac{\left(1 + f'(x)^2\right)^{\frac{3}{2}}}{f''(x)} \right|_{x=0, b\approx 0} = \frac{1}{2a} \quad (3)$$

The radius of curvature has been previously calculated for silica fracture in MD simulations using this method (Rimsza et al., 2017b).

The coordination environment of the Na^+ ion was analyzed to identify how the salt solution was altering the silica surface. The coordination was calculated by using interatomic distances with cut-offs: Si-O (2.3 Å), H-O (1.25 Å), Na-O (2.20 Å), O-O (1.5 Å), and H-H (1.0Å). Cut-off values were selected based on previous investigations of Na^+ adsorption on silica surfaces from NaOH solutions using the ReaxFF force fields (Rimsza et al., 2018b). See

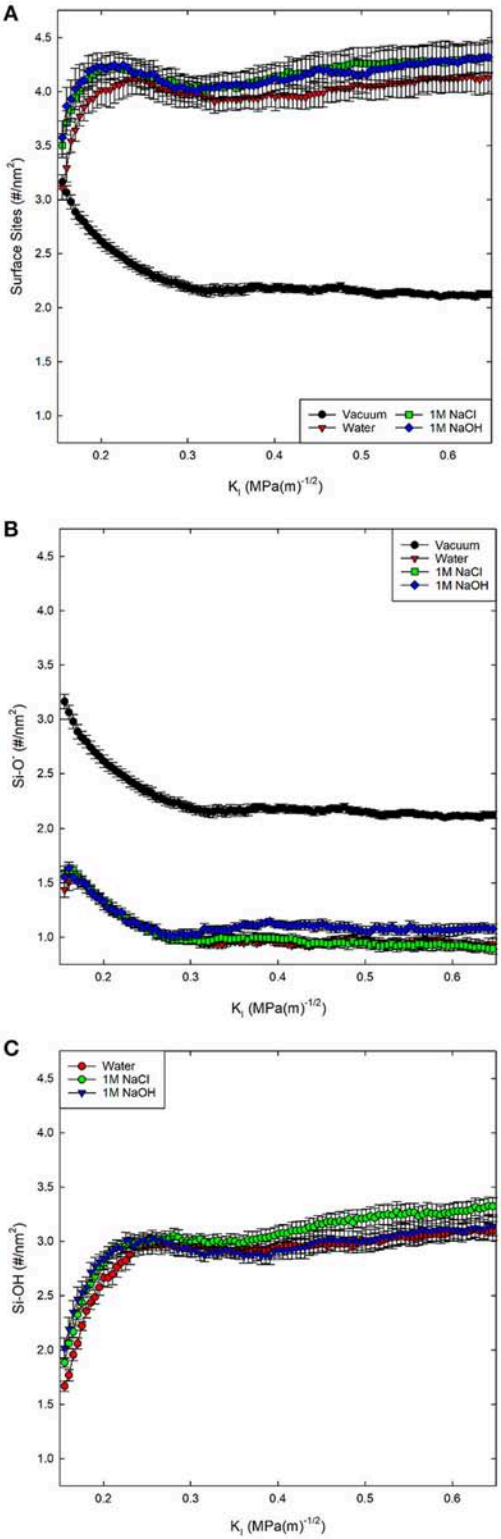

FIGURE 2 | Total concentration of **(A)** surface sites (Si-OH, Si-O^-, Si-OH_2) on the fracture surfaces of silica in four environmental conditions, **(B)** the concentration of Si-O^-, and **(C)** Si-OH on the surface. No Si-OH sites are present under vacuum conditions. K_I indexes the far-field mechanical loading and fracture occurs at a K_I of ∼0.25 MPa-$m^{-1/2}$.

Rimsza et al. (2018b) for the pair distribution functions used for cut-off selection and further discussion.

RESULTS

Solution and Surface Chemistry

During fracture the energy balance is controlled by the energetic cost associated with creating new surfaces, namely the surface energy, as described through the Griffith criterion (Lawn and Wilshaw, 1993). Therefore, a detailed understanding of the surface chemistry as the fluid infiltrates the fracture and reacts with freshly fractured surface is critical to identify the mechanisms that are responsible for environmentally-assisted fracture. Previous work has been done on the interactions between electrolyte solutions and silica surfaces (Ho et al., 2011; DelloStritto et al., 2016; Pfeiffer-Laplaud and Gaigeot, 2016); however, these have not typically included the application of external loading. A stress field can alter the structure of the silica by introducing voids, stretching bonds and ring structures (Muralidharan et al., 2005), and generally increasing the reactivity of the silica matrix (Rimsza J. M. et al., 2016).

Here we identify four different surface species. The most dominant surface species when the surface is contact with an aqueous solution is a silanol group, with a dangling bond terminated by one hydrogen (Si-OH). Several other surface species are present including protonated silanols ($Si\text{-}OH_2$), deprotonated silanols ($Si\text{-}O^-$), and protonated siloxane oxygen atoms (Si-OH-Si). In this work the crack surface is dominated by either Si-OH or $Si\text{-}O^-$, with concentrations of $Si\text{-}OH_2$ and Si-OH-Si being <0.06 #/nm^2.

The concentration of silanol groups on silica surfaces varies, but is reported as 4.0–5.0 #/nm^2 (Zhuravlev, 2000) and represents the total number of surface sites including neutral, deprotonated, and protonated silanol groups. We analyze all the available surface sites for protonation to determine how the silica surface has relaxed in the presence of the different solution compositions. Fewer surface sites would suggest that more silanol groups have recombined, forming Si-O-Si from Si-OH and $Si\text{-}O^-$ sites. In our simulated silica, the initial concentration of available sites for formation of Si-OH groups is ~3.05–3.5 #/nm^2 (**Figure 2A**). The slight differences in surface site concentrate at 0.15 MPa$\sqrt{}$m is due to initial relaxation of the system before loading is applied. The silica surfaces exposed to salt solutions exhibit more sites (Si-OH, $Si\text{-}O^-$) than those in pure water, suggesting that these surfaces have higher concentrations of broken Si-O bonds.

By separating the types of sites (**Figures 2B,C**), it becomes apparent that the surface species formed in 1M NaCl solution are more likely to be Si-OH in contrast to those formed in the 1M NaOH solution. The concentration of surface sites ($Si\text{-}O^-$, Si-OH, $Si\text{-}OH_2$) and level of relaxation has been explicitly tied to the K_{IC} of the material (Lawn and Wilshaw, 1993) through the surface energy and elastic modulus.

The surface structure is therefore influenced by solution composition. These variations can be simulated when a reactive force field is used (compared with traditional MD force fields that do not allow for molecular disassociation). In these simulations the bonding states of atoms can change and the introduction of a NaOH or NaCl molecule into solution does not guarantee that the molecules will remain intact as the simulation evolves. Investigations of NaOH solution wetting a silica surface with a reactive force field (Rimsza et al., 2018b) noted the development of many different aqueous species including OH^-, H_3O^+, H_2, and O_2. Here, the solution composition is tracked over time to look at the development of these species.

In other work, the steric effects of solution infiltration in fractures focused on what, if any, impact occurred with changing crack tip accessibility (Jones et al., 2018), identifying that the size of the molecules was less important than the reactivity in

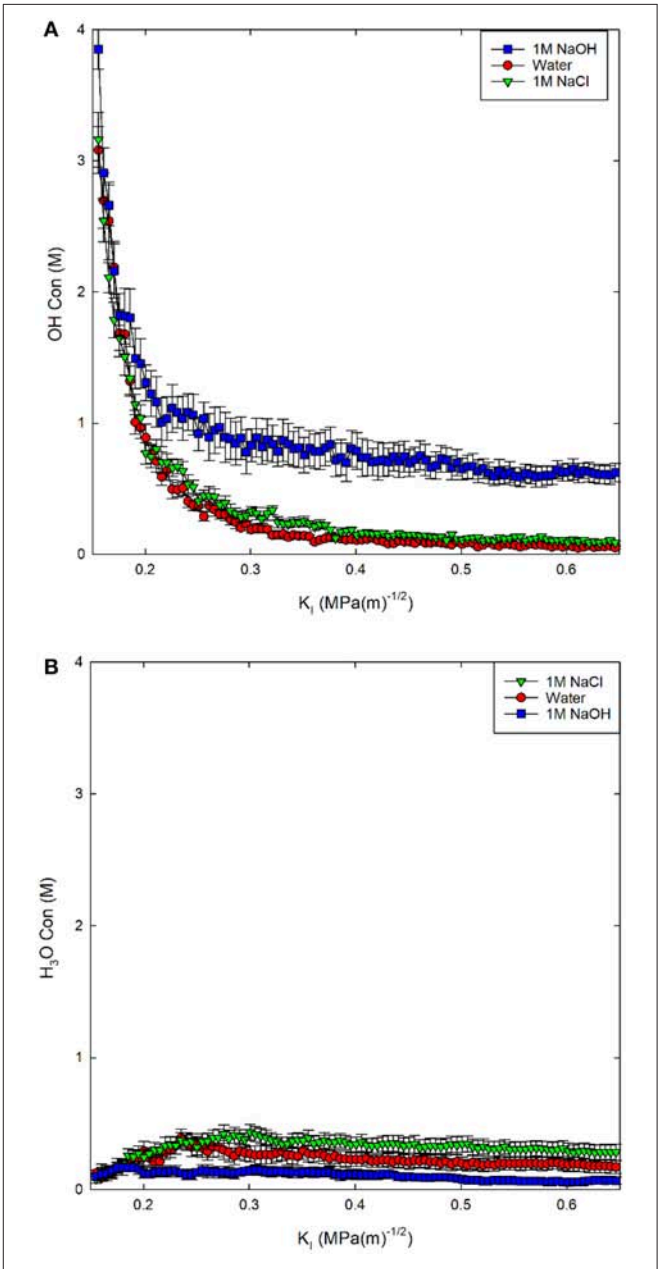

FIGURE 3 | (A) OH^- concentration in solution and **(B)** H_3O^+ concentration in solution reported as a molarity (M) for three environmental conditions.

altering the fracture properties of the material. Salt solutions are known to alter the silica surface due to adsorption (Dove and Craven, 2005). In the present context, the addition of OH^- creates a basic solution that increases the dissolution rates of glass (Du and Rimsza, 2017), while the addition of Cl^- has a less significant effect on the pH of the solution. Studies of the dissolution rate of glasses have shown the rate increases in both acidic and basic conditions, but is slower in acidic conditions (Alexander et al., 1954). In **Figure 3**, the OH^- and H_3O^+ concentrations influencing pH in the simulations are reported as molar concentrations based on the number of water molecules in the fracture volume. Clearly, the most rapid change occurs during

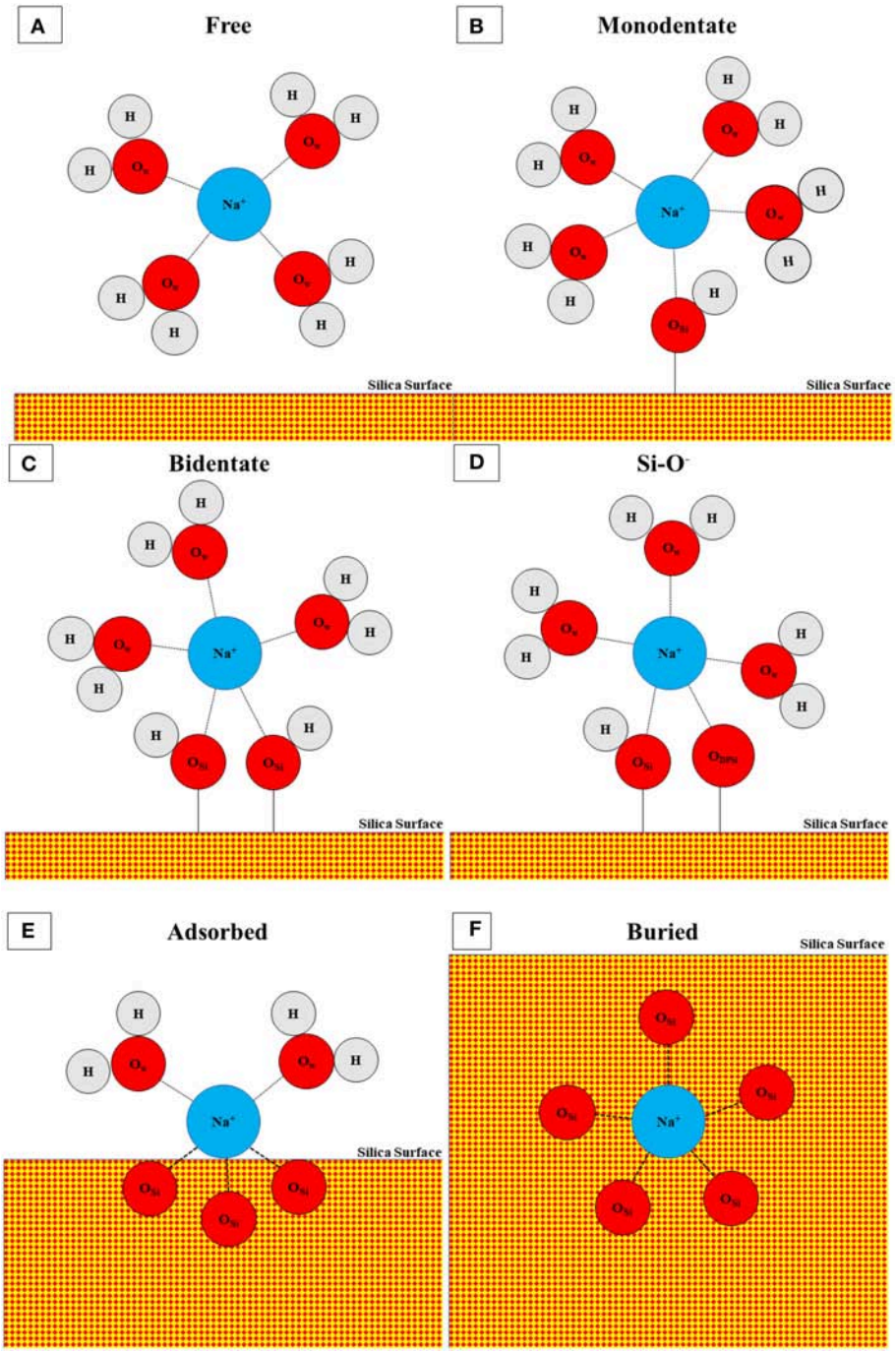

FIGURE 4 | Schematic of coordination structures for Na^+ including **(A)** free, **(B)** monodentate, **(C)** bidentate, **(D)** Si-O^-, **(E)** adsorbed, and **(F)** buried. Tridentate and mixed configurations are not pictured. Atoms are represented with circles and bonds by connecting lines. Oxygen in water (O_W), oxygen in silicon (O_{Si}), and oxygen in deprotonated silanol (O_{DPSi}) are distinguished by subscript and silica is denoted with red-yellow checks. Not to scale.

TABLE 1 | Distribution (%) of Na^+ coordination environments in 1M NaCl and 1M NaOH solutions.

	Free	Dentates			Buried	Adsorbed	Mixed	Si-O^-
		Mono	Bi	Tri				
1M NaCl	74.23 ± 1.13	4.70 ± 0.43	1.87 ± 0.25	0.78 ± 0.29	3.74 ± 0.55	4.79 ± 0.72	8.39 ± 0.80	1.50 ± 0.30
1M NaOH	61.49 ± 1.12	6.85 ± 0.76	3.02 ± 0.41	1.00 ± 0.30	3.40 ± 0.55	7.45 ± 1.06	13.61 ± 0.74	3.10 ± 0.50

the initial loading, before the crack propagates, where OH^- decreases rapidly and H_3O^+ increases slightly. The formation of a steady-state concentration occurs at ∼0.25–0.3 MPa$\sqrt{m}$, due to a balance of the rate of water infiltration and addition of NaCl or NaOH molecules as the fracture is loaded.

The addition of the NaOH molecules results in a relatively steady OH^- concentration of 1M (**Figure 3A**). The concentration of OH^- drops more dramatically to <0.25 M for both the 1M NaCl and pure water solutions. The addition of NaCl molecules results in a higher concentration of both OH^- and H_3O^+ in solution compared to pure water; however, both solutions become slightly acidic, with higher concentrations of H_3O^+ than OH^-. The concentration of H_3O^+ increases with decreasing pH: 1M NaOH < water < 1M NaCl, as expected. The deviation from neutral pH indicates that in both salt solutions, silica dissolution should be higher than in pure water, increasing the chemical impact on chemical-mechanical subcritical fracture growth.

Electrolyte Chemistry and Adsorption

For the salt solutions, the silica surface interacts not just with water, but also with dissolved Na^+ and either Cl^- (1M NaCl) or OH^- (1M NaOH) ions. Both salt solutions change the concentrations of surface species (Si-O^-, Si-OH, Si-OH_2) when compared with water; this can be partially attributed to adsorption of Na^+ to maintain local charge balance. In a previous study, we used ReaxFF (Rimsza et al., 2018b) to investigate Na^+ adsorption environments with OH^- counter ions and identified several adsorption structures with Na^+ ions coordinated by a mixture of water, silanols, and siloxane oxygen atoms. In this work, eight distinct Na^+ structures are found in the NaCl and NaOH solutions. Different Na^+ structures are identified by the coordinating oxygen species, which include the oxygen atoms in water molecules, silanol groups, and siloxane groups. The most common species is a free Na^+ ion coordinated exclusively by water molecules (**Figure 4A**). These cations have at least one water molecule between them and the silica surface, and account for ∼75% of the Na^+ ions in the 1M NaCl simulations compared to only 61.5% in the 1M NaOH simulations (**Table 1**). The next three structures are inner-sphere monodentate (**Figure 4B**), bidentante (**Figure 4C**), and tridentate (not pictured), which include Na^+ coordinated by water molecules and by one, two, or three Si-OH groups, respectively. These types of configurations (including the tridentate) were also observed on flat surfaces at 1M NaOH concentrations (Rimsza et al., 2018b). In contrast, the coordination of Na^+ by Si-O^- species did not occur on flat surfaces at the same NaOH concentration, where Si-O^- was more commonly coordinated with either neighboring silanol groups or water (Rimsza et al., 2018b). However, in the fracture simulations, coordination of Na^+ by Si-O^- does occur and is more common than the tridentate species (**Table 1**). We hypothesize that the confining conditions at the crack tip results in increased Si-O^- interactions with Na^+ (**Figure 4D**) compared with flat surfaces. The final three configurations include Na^+ that is at least partially coordinated by siloxane oxygen species. The first is a buried species (**Figure 4F**), which is a Na^+ coordinated only by siloxane oxygen and indicates the Na^+ has been entirely incorporated into the silica structure. Na^+ diffusing into bulk silica occurs readily due to the open structure of the silica and Na^+ is a common component of industrial glasses (Smit et al., 1978; Varshneya, 2013). The next is an adsorbed species (**Figure 4E**), defined as a Na^+ ion coordinated by siloxane and water oxygen, but no silanol. Finally, there is a mixed coordination structure at the surface with Na^+ ions coordinated by water, silanol, and siloxane oxygen atoms. Overall, the higher free and lower adsorbed Na^+ ion concentrations in the 1M NaCl simulations may be leading to the higher Si-OH surface concentration and the lower deprotonation that is seen on the surface.

In addition to the coordination environment, the location of the Na^+ ions can vary inside the fracture geometry. Several hypotheses on the role of pH on the fracture of silica suggest that the accessibility of the crack tip by OH^- is the primary means of enhancing fracture in basic solutions (White et al., 1987); therefore, understanding how the confined geometry of the crack tip alters the fracture properties is critical. Snapshots of the fracture geometry and the infiltrating fluid (**Figure 5**) provide some geometric insight into the crack tip accessibility by solution species. For silica fracture in water, the crack tip is primarily filled with complete water molecules along with a few H_3O^+; the OH^- ions present do not migrate to the crack tip, in contrast to those in NaOH and NaCl solutions. In the NaCl solution, the fracture volume is filled with both Na^+ and Cl^- ions, along with some OH^- and H_3O^+ ions. Therefore, it appears that the presence of Na^+ with a Cl^- counter ion may allow for easier migration toward the crack tip. In the breakdown of the different coordination environments (Supporting Information, **Table S2**) there is some limited coordination of the Na^+ ion by Cl^-, with an average of 0.52 ± 0.02 Cl^- ions coordinating each free Na^+ ion in the first solvation shell. In the NaOH system, the Na^+ ions have limited diffusion into the fracture volume, so that most of the aqueous species near the crack tip are either surface coordinated OH^- or free H_3O^+ molecules. NaCl and

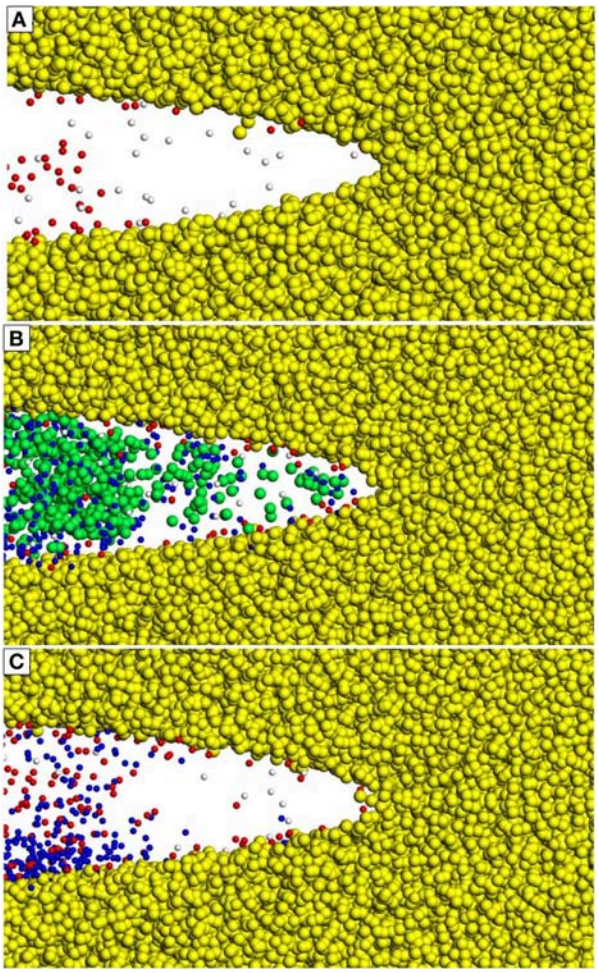

FIGURE 5 | Atomic positions of Na^+, Cl^-, OH^-, and H_3O^+ molecules inside the crack tip for three different solutions **(A)** water, **(B)**, 1M NaCl, and **(C)** 1M NaOH. Water is not shown for clarity. All 12 replicates are overlaid to sample the variety of atomic positions and are at a constant loading of 0.2 MPa$\sqrt{m}$. Atom types: Si (yellow), Na^+ (blue), Cl^- (green), OH^- (red), H_3O^+ (white).

NaOH solutions result in different fracture properties (discussed below), which is unexpected considering that both are promoting the diffusion of OH^- to the crack tip and potentially encouraging the hydroxide–mediated reaction (Equation 2). It is hypothesized that the hydration shells of the Na^+ and Cl^- ions are affecting the $OH^-/H_3O^+/H_2O$-silica interactions, altering the energy barriers or the frequency of interactions (White et al., 1987) and the presence of different counter ions at the crack tip alters the activity of the OH^-.

Material Chemistry

Siloxane bond strength in the glass structure varies with the number of oxygen bonds connecting two silica tetrahedra. Previous MD (Mahadevan and Garofalini, 2008) and DFT (Criscenti et al., 2006) simulations have been used to investigate the relative Si-O bond strength of different linkages to elucidate glass dissolution mechanisms as a function of glass composition. Here, the Q_n (n = 0–4) descriptor is used to distinguish silicon species, where n is the number of siloxane oxygen atoms attached to a silicon. A perfectly coordinated silicon atom is bonded to exactly four siloxane oxygen atoms and, hence, is a Q_4 species. Surfaces, defects, and network modifiers (e.g., Na^+, Li^+, Ca^{2+}) can disrupt the glass structure, introducing silicon with lower concentrations of siloxane bonds and therefore lower Q_n species. Occasionally Q_5 species can also be formed, typically in low concentrations (<3%); this is a known defect in silica glass simulated with ReaxFF that has been previously reported for different silica systems (Rimsza J. et al., 2016; Rimsza and Du, 2018). Q_5 species have been identified by both MD simulations (Rimsza J. et al., 2016) and nuclear magnetic resonance (NMR) characterization (Zotov and Keppler, 1998), but at lower concentrations. By looking at the change in Q_n species in the structure, we can compare the relative strength of the siloxane bonds that link Q_n species in the glass.

The change in Q_n species from the first to the last loading step (0.15 MPa$\sqrt{m}$ to 0.65 MPa$\sqrt{m}$) is provided in **Figure 6** and generally, we expect higher Q_n species to transition to lower Q_n species during dissolution ($Q_4 \rightarrow Q_3 \rightarrow Q_2 \rightarrow Q_1 \rightarrow Q_0$). Regardless of environment, our simulations show that there is a decrease in Q_4 species. This is balanced by an increase in Q_3, Q_2, and Q_1 species. Interestingly, a water environment results in a decrease in the Q_0 species during loading, suggesting that the few Q_0 species that are formed reprecipitate in pure water. Previous computational results showed that during dissolution without mechanical stress, the $Q_1 \rightarrow Q_0$ conversion has the lowest activation energy (Mahadevan and Garofalini, 2008). Therefore, when dissolution occurs we would expect a decrease in Q_1 species and an increase in Q_0. In contrast, the $Q_4 \rightarrow Q_3$ and $Q_3 \rightarrow Q_2$ transitions have higher activation energies and, hence, these species should be maintained in the system under dissolution-only conditions. As **Figure 6** demonstrates, Q_3 and Q_2 concentrations are also maintained in these chemo-mechanical fracture simulations. When water is present, Q_3 and Q_2 appear to be more stable than in dry conditions, consistent with predictions from dissolution-only studies.

The impact of solution composition is most apparent when examining the Q_1 species data. Generally, there is an increase in Q_1 from vacuum to water to 1M NaOH to 1M NaCl. The only simulations that exhibit silica monomers released from the surface are those with a 1M NaCl solution, and the Q_0 is still in very low concentrations. In contrast, bulk glass dissolution is expected to occur most readily for the 1M NaOH solution (due to the higher pH). In the 1M NaCl solution the ∼33% increase seen in **Figure 6** is an average increase of total Q_0 speciation of ∼0.5 silicon atoms, which is large only with respect to the low initial concentration in the replica systems. Despite the low change, several previous investigations have not seen spontaneous dissolution (Dove, 1999; Kubicki et al., 2012; Zapol et al., 2013; Rimsza and Du, 2017, 2018).

Material Mechanics

It is well-established that the strength of the silica decreases in the presence of an aqueous environment, which is typically attributed to dissolution inside the fracture volume and around

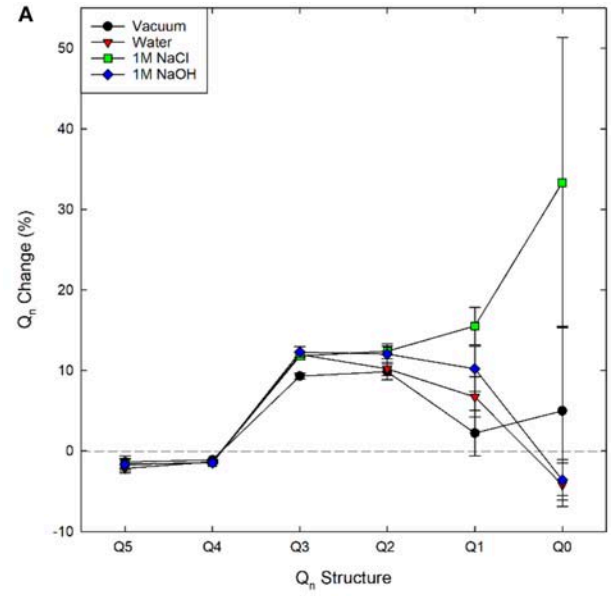

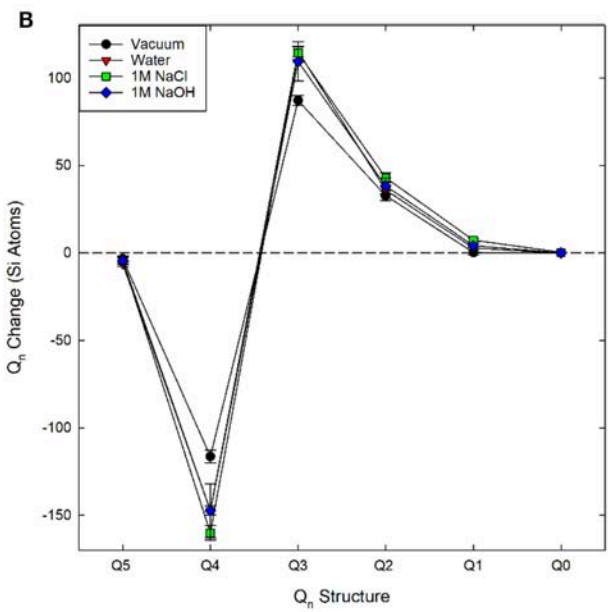

FIGURE 6 | Change in **(A)** percent and **(B)** total Q_n speciation as a function of solution chemistry over the loading range 0.5 MPa$\sqrt{}$m to 0.65 MPa$\sqrt{}$m.

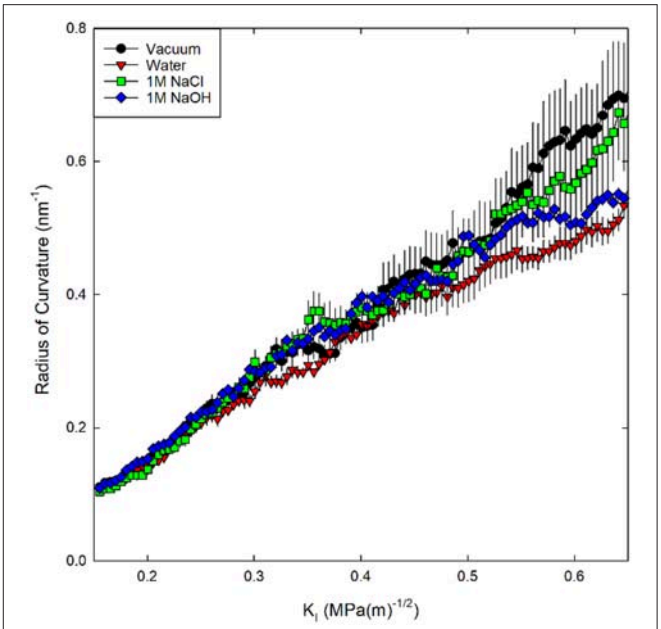

FIGURE 7 | Radius of curvature for silica systems in four chemical environments.

the crack tip. The radius of curvature of the crack is a structural parameter that is connected to the amount of local inelasticity in a brittle material, with a blunter tip being associated with more inelasticity. It has also been investigated (Rimsza et al., 2017b) for its role in identifying the level of dissolution in the fracture volume, and how this impacts the chemical-mechanical fracture. Previous work (Rimsza et al., 2018a) noted that, in the presence of water, the radius of curvature decreased, resulting in a narrow crack tip, suggesting a higher stress concentration and a lower threshold for fracture propagation. Interestingly, the simulations with a 1M NaCl solution exhibit fractures with a larger radius of curvature than those with a 1M NaOH solution or pure water (**Figure 7**), and are the simulations that exhibit the highest increase in Q_1 species, and the only formation of simulations in which Q_0 species. Based on these results, we hypothesize that the presence of a highly reactive fluid like the NaCl solution under confinement may cause rapid increases in dissolution and in the radius of a crack tip, even within the picosecond timeframe in these MD simulations.

Due to the metastable nature of glass, the silica network within the bulk material is somewhat inelastic and is modified when an external stress is applied. The energy associated with the structural changes in the bulk material is described by the energy dissipation (G_{diss}) term in the well-known strain energy release rate (G_{IC}) equation:

$$G_{IC} = G_{diss} + 2\gamma_s \tag{4}$$

which accounts for the energetic cost of fracture propagation in terms of the surface energy ($2\gamma_s$) associated with new surfaces and a non-conservative process to create them (i.e., irreversible changes in bulk silica structure quantified by G_{diss}). The G_{diss} term is extracted from the atomistic simulations through the change in internal energy of the silica (dU) and the added surface area (dA) (Rimsza et al., 2017b).

$$G_{diss} = \frac{dU}{dA} \tag{5}$$

A derivation for Equation (5) is included in **Appendix I**. Here, surface area was calculated through construction of a surface mesh along the crack face with a spherical probe molecule with a radius of 4.5 Å as implemented in the Ovito Visualization Tool (Stukowski, 2009). In previous investigations, the energy

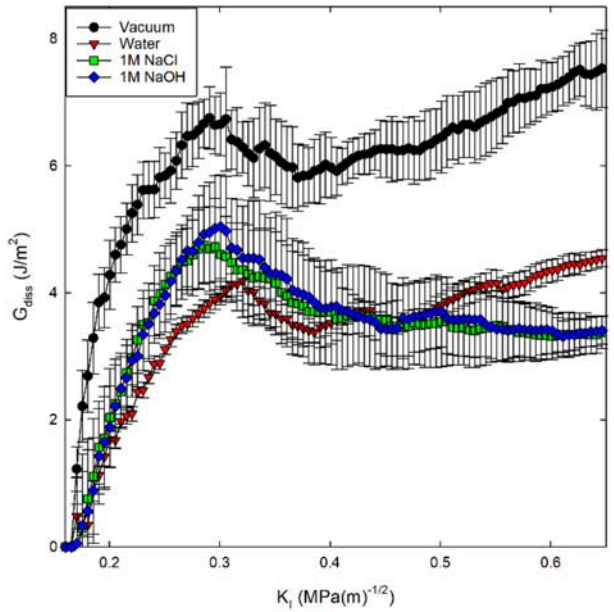

FIGURE 8 | Energy dissipation (G_{diss}) during crack loading and subsequent crack propagation for silica systems in four environmental conditions. G_{diss} is calculated from Equation (5).

dissipation has been associated with the amount of inelasticity occurring around the crack tip (Rimsza et al., 2017b, 2018a). Using this description, the following trend in inelastic energy generation was calculated for the four fracture environments considered: vacuum > 1M NaOH solution > 1M NaCl solution > pure water (**Figure 8**). The higher G_{diss} value for the 1M NaOH solution compared with the other aqueous solutions suggests that there is more unrecoverable inelastic strain in the region surrounding the crack tip.

Identification of eK_{IC} values for the four silica systems was based on step-wise changes in the potential energy of the silica during loading, as outlined in previous studies of silica fracture (Rimsza et al., 2017b). A sudden change in energy is accompanied by bond breakage, indicating a crack propagation event. The loading at which these crack propagation events occur are averaged over multiple simulations to estimate the eK_{IC} for the system. The results identify that the silica systems fractured in vacuum exhibit the highest eK_{IC} value, the fewest fracture events, and the highest G_{IC} value (**Table 2**). This is consistent with experimental observations that silica is stronger in a non-reactive or dry environment (Rimsza et al., 2018a). Experiments have shown that the addition of any electrolytes that perturb the pH of the solution make the system fracture at lower loads than in neutral water (Dove, 1995). From the simulation data reported here, the eK_{IC} values overlap, but it appears that the silica in 1M NaCl solution has a slightly higher eK_{IC} than that in water or a 1M NaOH solution. It is hypothesized that a broader crack tip radius (**Figure 7**) reduces the drive for fracture propagation at these time scales.

DISCUSSION

The differences in solution composition and the unique confined geometry of the crack tip generate unusual chemical environments that impact the fracture properties of silica. In this work, the confined 1M NaCl aqueous solution is slightly acidic, and the confined 1M NaOH solution is alkaline (**Figure 3**). The elevated OH^- concentration leads to an increased number of Si-O^- surface sites, which allows for the formation of Na^+ adsorption complexes in the confined space that are not seen on flat surfaces (Rimsza et al., 2018b). These complexes include Na^+ coordinated by Si-O^- surface species and Na^+ coordinated by siloxane oxygen and water molecules only (**Table 1**). With increasing confinement of the aqueous solution as the molecules approach the crack tip, more interactions between the Na^+ ions and the surface occur, possibly made more energetically favorable due to increased surface deprotonation.

Snapshots of the fracture geometry also indicate that the solution composition influences the diffusion of electrolyte ions into the crack tip. For example, in the 1M NaCl solution the Na^+ ions infiltrate the crack tip much farther than in the 1M NaOH solution (**Figure 5**). This observation supports the hypothesis that changing the composition of the hydration shells of Na^+ and Cl^- ions may alter the accessibility of the crack tip and the reactivity of the infiltrating fluid (White et al., 1987). This finding also highlights the importance of understanding how aqueous electrolyte solutions are interacting with surfaces in confined geometries, which appear to be where most critical surface reactions and stress concentrators occur.

Increased radius of curvature of the crack tip in the salt solutions provides further evidence that the crack morphology is impacted by the infiltrating fluid. The increase in the radius of the crack tip has been proposed to be a function of dissolution events (Freiman et al., 2009). This chemo-mechanical effect is apparently related to the fracture properties of silica, with the 1M NaCl solution resulting in a higher eK_{IC} for the silica than in the 1M NaOH solution of pure water. We hypothesize that the increase in formation of Q_1 and Q_0 species in the 1M NaCl solution (**Figure 6**) is resulting in crack tip blunting (**Figure 7**) that dissipates energy through mechanisms other than fracture propagation. Additionally, the interaction between the Na^+/Cl^- ions and the aqueous OH^- may be limiting the ability of the OH^- to interact with the crack tip, resulting in a larger eK_{IC} (see **Figure 5** and related discussion).

Interactions between electrolyte solutions and the surface impact the formation of Q_1 and Q_0 species, which are a critical components of glass degradation (Guin et al., 2005; Wiederhorn et al., 2011). Dissolution has been difficult to investigate with atomistic simulations, because of the pico- or nanosecond time frames accessible by MD simulations. In this study, we used a Q_n distribution analysis to determine if any of the aqueous solutions were causing local dissolution. The 1M NaCl solution caused the most dissolution events in the simulations, demonstrated by increased concentrations of Q_1 and Q_0 species (**Figure 6**). Most atomistic simulations to date have not generated Q_0 species (without positioning atoms to facilitate a $Q_1 \rightarrow Q_0$ conversion)

TABLE 2 | Fracture properties of silica in four different environmental conditions (vacuum, water, 1M NaCl, 1M NaOH) as the average and standard deviation of twelve unique simulations.

	eK_{IC} (MPa$\sqrt{m}$)		Fracture Events (#)	G_{IC} (J/m^2)	G_{diss} (J/m^2)	Si-OH (#/nm^2)	γ (J/m^2)
	First	Average					
Vacuum	0.34 ± 0.04	0.43 ± 0.04	3.67 ± 1.18	7.91	6.78	0.00	1.13
Water	0.20 ± 0.06	0.37 ± 0.05	4.33 ± 1.03	4.59	4.21	3.10	0.38
1M NaCl	0.28 ± 0.09	0.41 ± 0.05	5.42 ± 1.66	5.14	4.75	3.04	0.39
1M NaOH	0.19 ± 0.05	0.37 ± 0.05	6.00 ± 1.41	5.47	5.06	2.95	0.41

TABLE 3 | Ranking of factors that influence environmentally assisted fracture from highest (1) to lowest (4).

Environment	eK^*_{IC}	Fracture events	Dissolution$^+$	Si-O$^-$ surface concentration	Crack tip accessibility$^\circ$	Radius of curvature
Vacuum	1	4	4	1	–	1
Water	3	3	3	4	3	4
1M NaCl	2	2	1	3	1	2
1M NaOH	4	1	2	2	2	3

**Average loading at first fracture, $^+$Increasing Q_0 and Q_1 concentration, $^\circ$Concentration of OH^-, H_3O^+, Na^+, or Cl^- in the fracture volume.*

(Kagan et al., 2014; Rimsza and Du, 2017, 2018). The Q_n distribution analysis leads us to conclude that the silica dissolves most readily in the 1M NaCl solution. This conclusion is at odds with experimental observations that bulk glass dissolution occurs most readily in basic solutions (Alexander et al., 1954). However, previous atomistic *ab initio* DFT studies of reaction barrier heights have reported that the Si-O-Si bond is more easily broken with an adsorbed proton on the bridging oxygen, which would be expected to occur more readily in acidic conditions, than when one of the terminating Si has a deprotonated oxygen (Nangia and Garrison, 2008; Zapol et al., 2013); these results are also inconsistent with experimental observations on bulk glass dissolution.

This coupled chemical-mechanical fracture study from atomistic methods has highlighted several factors influencing the weakening of silica that appear to be at odds with accepted theory or chemical intuition. A ranking of proposed factors for environmentally assisted fracture is included in **Table 3**. From this data we can see that the environment which results in the highest number of fracture events and lowest eK_{IC} (NaOH) does not exhibit the fastest dissolution as evidenced by the formation of Q_1 and Q_0 species. There does not appear to be a direct correlation between the factors: dissolution, Si-O$^-$ concentration, crack tip accessibility, or radius of curvature, and the fracture properties: eK_{IC} or the number of fracture events. Generally, our simulations show a pure aqueous environment decreases the radius of curvature and the eK_{IC}. Furthermore, the inclusion of either NaOH or NaCl increases the number of fracture events, silica dissolution, and the crack tip accessibility; however, separating out the impact of the two electrolytes is more complicated. We hypothesize that both the geometry of the fracture and composition of the fluid alter the reactivity of the system through:

1. Compared with flat surfaces, the nanoconfined crack tip favors different adsorbed species and concentrations and limits diffusion thereby increasing the residence time of reactive species and altering the chemical gradients in solution.
2. The presence of Na^+, Cl^-, or OH^- ions impacts the reaction frequency between the surface and water molecules, affects the protonation and deprotonation of the surface, and exposes strained and unstrained bonds along the fracture surface and at the crack tip to the solution.

Therefore, dissolution and reaction rates inside the fracture are distinct from those observed in bulk or equilibrium systems. These hypotheses will be explored through a targeted study of the details of the crack geometry. In conclusion, we propose that this investigation demonstrates that the geometry of the fracture is impacting the water and ion accessibility at the crack tip, the kinetics, and the reactions occurring at the fracture surfaces, and, results in behavior unique to fracture conditions on the nanoscale.

CONCLUSION

To investigate weakening of silica in contact with aqueous electrolyte solutions, classical MD simulations of silica fracture were performed using the bond-order based, reactive force field ReaxFF. Four different environmental conditions were investigated, including vacuum, water, and two salt solutions (1M NaCl, 1M NaOH). The highlights of our findings are:

- Any aqueous condition weakens the silica, with the addition of basic NaOH further encouraging fractures to propagate, possibly due to increased interactions between ions and the silica surface.

- The 1M NaCl solution generates increased Q_1 and Q_0 species compared with 1M NaOH and water, altering the geometry of the crack tip and the fracture properties of the silica, in contrast to bulk glass dissolution. Additionally, the observed formation of Q_0 silicon in solution is a rarely identified dissolution event in atomistic simulations and may be a function of nanoconfinement, mechanical stress, or both.
- The nanoconfinement of the crack tip alters Na^+ adsorption and surface properties compared with flat surfaces, and its role in chemical-mechanical fracture should be explored further.

Overall, reactive classical MD study provides unique insight into how anions alter the chemical-mechanical fracture response of silica and indicate that critical factors for fracture at the nanoscale may differ from those that are seen in bulk systems over long time scales.

In summary, this work provides a mechanistic investigation of chemo-mechanical fracture in silica in several different aqueous solutions. By using atomistic simulations, we have shown that we can identify factors that are unique to the nanoscale environment and are difficult or impossible to separate out through current experimental techniques. This is, to the best of our knowledge, the first study of its kind to consider the mechanical and chemical impact on silica fracture in an electrolyte solution from a reactive MD simulation, which includes the formation and breakage of bonds. This study builds upon an expertise in hydroxylation (Rimsza et al., 2017a) and sodium adsorption (Rimsza et al., 2018b) on silica surfaces, atomistic mechanisms of silica fracture in vacuum (Rimsza et al., 2017b) and in aqueous environments (Rimsza et al., 2018a) and adds the complexity of electrolyte solutions. This work provides a unique atomistic perspective on chemically assisted silica fracture which has thus far been too complex to be investigated with a molecular level of detail and indicates that similar investigations of multicomponent glass compositions can be undertaken in the future as suitable potentials become available.

AUTHOR CONTRIBUTIONS

JR performed the simulations, analyzed the data, and wrote the manuscript. LC and RJ helped design the simulations and all authors edited and discussed the manuscript prior to submission.

ACKNOWLEDGMENTS

Mark Wilson (Sandia National Laboratories) is acknowledged for his technical support in the development of the grand canonical Monte Carlo (GCMC) methods used in the manuscript. This work was fully supported by the Laboratory Directed Research and Development (LDRD) program of Sandia National Laboratories. Sandia National Laboratories is a multi-mission laboratory managed and operated by National Technology and Engineering Solutions of Sandia, LLC., a wholly owned subsidiary of Honeywell International, Inc., for the U.S. Department of Energy's National Nuclear Security Administration under contract DE-NA0003525. This paper describes objective technical results and analysis. Any subjective views or opinions that might be expressed in the paper do not necessarily represent the views of the U.S. Department of Energy or the United States Government.

SUPPLEMENTARY MATERIAL

The Supplementary Material for this article can be found online at: https://www.frontiersin.org/articles/10.3389/fmats.2019.00079/full#supplementary-material

Supporting information includes the ReaxFF force field used in this manuscript as a pdf file.

REFERENCES

Aktulga, H. M., Fogarty, J. C., Pandit, S. A., and Grama, A. Y. (2012). Parallel reactive molecular dynamics: Numerical methods and algorithmic techniques. *Parall. Comput.* 38, 245–259. doi: 10.1016/j.parco.2011.08.005

Alexander, G. B., Heston, W., and Iler, R. K. (1954). The solubility of amorphous silica in water. *J. Phys. Chem.* 58, 453–455. doi: 10.1021/j150516a002

Atkinson, B. K., and Meredith, P. G. (1981). Stress corrosion cracking of quartz: a note on the influence of chemical environment. *Tectonophysics* 77, T1–T11. doi: 10.1016/0040-1951(81)90157-8

Bonnaud, P., Coasne, B., and Pellenq, R. J. (2010). Molecular simulation of water confined in nanoporous silica. *J. Phys.* 22:284110. doi: 10.1088/0953-8984/22/28/284110

Bourg, I. C., and Steefel, C. I. (2012). Molecular dynamics simulations of water structure and diffusion in silica nanopores. *J. Phys. Chem. C* 116, 11556–11564. doi: 10.1021/jp301299a

Célarié, F., Ciccotti, M., and Marliere, C. (2007). Stress-enhanced ion diffusion at the vicinity of a crack tip as evidenced by atomic force microscopy in silicate glasses. *J. Non Crystall. Solids* 353, 51–68. doi: 10.1016/j.jnoncrysol.2006.09.034

Criscenti, L. J., Kubicki, J. D., and Brantley, S. L. (2006). Silicate glass and mineral dissolution: calculated reaction paths and activation energies for hydrolysis of a Q3 Si by H3O+ using ab initio methods. *J. Phys. Chem. A* 110, 198–206. doi: 10.1021/jp044360a

DelloStritto, M. J., Kubicki, J. D., and Sofo, J. O. (2016). Effect of Ions on H-bond structure and dynamics at the quartz (101)–water interface. *Langmuir* 32, 11353–11365. doi: 10.1021/acs.langmuir.6b01719

Dove, P. M. (1995). Geochemical controls on the kinetics of quartz fracture at subcritical tensile stresses. *J. Geophys. Res. Solid Earth* 100, 22349–22359. doi: 10.1029/95JB02155

Dove, P. M. (1999). The dissolution kinetics of quartz in aqueous mixed cation solutions. *Geochim. Cosmochim. Acta* 63, 3715–3727. doi: 10.1016/S0016-7037(99)00218-5

Dove, P. M., and Craven, C. M. (2005). Surface charge density on silica in alkali and alkaline earth chloride electrolyte solutions. *Geochim. Cosmochim. Acta* 69, 4963–4970. doi: 10.1016/j.gca.2005.05.006

Du, J., and Rimsza, J. M. (2017). Atomistic computer simulations of water interactions and dissolution of inorganic glasses. *NPJ Mater. Degrad.* 1:16. doi: 10.1038/s41529-017-0017-y

Fogarty, J. C., Aktulga, H. M., Grama, A. Y., Van Duin, A. C, and Pandit, S. A. (2010). A reactive molecular dynamics simulation of the silica-water interface. *J. Chem. Phys.* 132:174704. doi: 10.1063/1.3407433

Freiman, S. W., Wiederhorn, S. M., and Mecholsky J. J. Jr. (2009). Environmentally enhanced fracture of glass: a historical perspective. *J. Am. Ceramic Soc.* 92, 1371–1382. doi: 10.1111/j.1551-2916.2009.03097.x

Guillot, B., and Guissani, Y. (2001). How to build a better pair potential for water. *J. Chem. Phys.* 114, 6720–6733. doi: 10.1063/1.1356002

Guin, J. P., Wiederhorn, S. M., and Fett, T. (2005). Crack-tip structure in soda–lime–silicate glass. *J. Am. Ceramic Soc.* 88, 652–659. doi: 10.1111/j.1551-2916.2005.00108.x

Ho, T. A., Argyris, D., Cole, D., and Striolo, A. (2011). Aqueous NaCl and CsCl solutions confined in crystalline slit-shaped silica nanopores of varying degree of protonation. *Langmuir* 28, 1256–1266. doi: 10.1021/la2036086

Howard, A. (1988). *Calculus: With Analytic Geometry*. New York, NY: John Wiley.
Jones, R., Tucker, W. C., Rimsza, J., and Crisenti, L. (2018). Atomic-scale interaction of a crack and an infiltrating fluid. *Chem. Phys. Lett. X* 1:100005. doi: 10.1016/j.cpletx.2018.100005
Kagan, M., Lockwood, G. K., and Garofalini, S. H. (2014). Reactive simulations of the activation barrier to dissolution of amorphous silica in water. *Phys. Chem. Chem. Phys.* 16, 9294–9301. doi: 10.1039/C4CP00030G
Kubicki, J. D., Sofo, J. O., Skelton, A. A., and Bandura, A. V. (2012). A new hypothesis for the dissolution mechanism of silicates. *J. Phys. Chem. C* 116, 17479–17491. doi: 10.1021/jp300623v
Lane, J. M. D. (2015). Cooling rate and stress relaxation in silica melts and glasses via microsecond molecular dynamics. *Phys. Rev. E* 92:012320. doi: 10.1103/PhysRevE.92.012320
Lawn, B., and Wilshaw, T. R. (1993). *Fracture of Brittle Solids*. New York, NY: Cambridge University Press. doi: 10.1017/CBO9780511623127
Lowe, B. M., Skylaris, C. -K., and Green, N. G. (2015). Acid-base dissociation mechanisms and energetics at the silica–water interface: an activationless process. *J. Colloid Interface Sci.* 451, 231–244. doi: 10.1016/j.jcis.2015.01.094
Mahadevan, T., and Garofalini, S. (2007). Dissociative water potential for molecular dynamics simulations. *J. Phys. Chem. B* 111, 8919–8927. doi: 10.1021/jp072530o
Mahadevan, T., and Garofalini, S. (2008). Dissociative chemisorption of water onto silica surfaces and formation of hydronium ions. *J. Phys. Chem. C* 112, 1507–1515. doi: 10.1021/jp076936c
Morrow, C. P., Nangia, S., and Garrison, B. J. (2009). Ab initio investigation of dissolution mechanisms in aluminosilicate minerals. *J. Phys. Chem. A* 113, 1343–1352. doi: 10.1021/jp8079099
Mozzi, R., and Warren, B. (1969). The structure of vitreous silica. *J. Appl. Crystallogr.* 2, 164–172. doi: 10.1107/S0021889869006868
Muralidharan, K., Simmons, J., Deymier, P., and Runge, K. (2005). Molecular dynamics studies of brittle fracture in vitreous silica: review and recent progress. *J. Non Crystall. Solids* 351, 1532–1542. doi: 10.1016/j.jnoncrysol.2005.03.026
Nangia, S., and Garrison, B. J. (2008). Reaction rates and dissolution mechanisms of quartz as a function of pH. *J. Phys. Chem. A* 112, 2027–2033. doi: 10.1021/jp076243w
Pfeiffer-Laplaud, M., and Gaigeot, M. -P. (2016). Adsorption of singly charged ions at the hydroxylated (0001) α-quartz/water interface. *J. Phys. Chem. C* 120, 4866–4880. doi: 10.1021/acs.jpcc.5b10947
Pitman, M. C., and Van Duin, A. C. (2012). Dynamics of confined reactive water in smectite clay–zeolite composites. *J. Am. Chem. Soc.* 134, 3042–3053. doi: 10.1021/ja208894m
Rimola, A., and Ugliengo, P. (2008). A quantum mechanical study of the reactivity of (SiO) 2-defective silica surfaces. *J. Chem. Phys.* 128:204702. doi: 10.1063/1.2929827
Rimsza, J., Deng, L., and Du, J. (2016). Molecular dynamics simulations of nanoporous organosilicate glasses using Reactive Force Field (ReaxFF). *J. Non Crystall. Solids* 431, 103–111. doi: 10.1016/j.jnoncrysol.2015.04.031
Rimsza, J., and Du, J. (2015). Ab initio molecular dynamics simulations of the hydroxylation of nanoporous silica. *J. Am. Ceramic Soc.* 98, 3748–3757. doi: 10.1111/jace.13731
Rimsza, J., and Du, J. (2017). Interfacial structure and evolution of the water–silica gel system by reactive force-field-based molecular dynamics simulations. *J. Phys. Chem. C* 121, 11534–11543. doi: 10.1021/acs.jpcc.7b02734
Rimsza, J., and Du, J. (2018). Nanoporous silica gel structures and evolution from reactive force field-based molecular dynamics simulations. *NPJ Mater. Degrad.* 2:18. doi: 10.1038/s41529-018-0039-0
Rimsza, J., Jones, R., and Criscenti, L. (2017a). Surface structure and stability of partially hydroxylated silica surfaces. *Langmuir* 33, 3882–3891. doi: 10.1021/acs.langmuir.7b00041
Rimsza, J., Jones, R. E., and Criscenti, L. J. (2017b). Crack propagation in silica from reactive classical molecular dynamics simulations. *J. Am. Ceramic Soc.* 101, 1488–1499. doi: 10.1111/jace.15292
Rimsza, J. M., Jones, R. E., and Criscenti, L. J. (2018a). Chemical effects on subcritical fracture in silica from molecular dynamics simulations. *J. Geophys. Res. Solid Earth* 123, 9341–9354. doi: 10.1029/2018JB016120
Rimsza, J. M., Jones, R. E., and Criscenti, L. J. (2018b). Interaction of NaOH solutions with silica surfaces. *J. Colloid Interface Sci.* 516, 128–137. doi: 10.1016/j.jcis.2018.01.049
Rimsza, J. M., Yeon, J., van Duin, A. C., and Du, J. (2016). Water interactions with nanoporous silica: comparison of ReaxFF and ab Initio based molecular dynamics simulations. *J. Phys. Chem. C* 120, 24803–24816. doi: 10.1021/acs.jpcc.6b07939
Smit, W., Holten, C., Stein, H., De Goeij, J., and Theelen, H. (1978). A radiotracer determination of the adsorption of sodium ion in the compact part of the double layer of vitreous silica. *J. Colloid Interface Sci.* 63, 120–128. doi: 10.1016/0021-9797(78)90042-5
Stukowski, A. (2009). Visualization and analysis of atomistic simulation data with OVITO–the Open Visualization Tool. *Model. Simulat. Mater. Sci. Eng.* 18:015012. doi: 10.1088/0965-0393/18/1/015012
Van Duin, A. C., Strachan, A., Stewman, S., Zhang, Q., Xu, X., and Goddard, W. A. (2003). ReaxFFSiO reactive force field for silicon and silicon oxide systems. *J. Phys. Chem. A* 107, 3803–3811. doi: 10.1021/jp0276303
van Duin, A. C., Zou, C., Joshi, K., Bryantsev, V., and Goddard, W. A. (2013). A ReaxFF reactive force-field for proton transfer reactions in bulk water and its applications to heterogeneous catalysis. *Computat. Catal.* 14, 223–243. doi: 10.1039/9781849734905-00223
Varshneya, A. K. (2013), *Fundamentals of Inorganic Glasses*. San Diego, CA: Elsevier.
White, G. S., Freiman, S. W., Wiederhorn, S. M., and Coyle, T. D. (1987). Effects of counterions on crack growth in vitreous silica. *J. Am. Ceramic Soc.* 70, 891–895. doi: 10.1111/j.1151-2916.1987.tb04912.x
Wiederhorn, S., and Johnson, H. (1973). Effect of electrolyte pH on crack propagation in glass. *J. Am. Ceramic Soc.* 56, 192–197. doi: 10.1111/j.1151-2916.1973.tb12454.x
Wiederhorn, S. M., Guin, J.-P., and Fett, T. (2011). The use of atomic force microscopy to study crack tips in glass. *Metallurg. Mater. Trans. A* 42, 267–278. doi: 10.1007/s11661-010-0411-3
Yeon, J., and van Duin, A. C. (2015). ReaxFF molecular dynamics simulations of hydroxylation kinetics for amorphous and nano-silica structure, and its relations with atomic strain energy. *J. Phys. Chem. C* 120, 305–317. doi: 10.1021/acs.jpcc.5b09784
Yu, Y., Krishnan, N. A., Smedskjaer, M. M., Sant, G., and Bauchy, M. (2018). The hydrophilic-to-hydrophobic transition in glassy silica is driven by the atomic topology of its surface. *J. Chem. Phys.* 148:074503. doi: 10.1063/1.5010934
Yu, Y., Wang, B., Wang, M., Sant, G., and Bauchy, M. (2016). Revisiting silica with ReaxFF: Towards improved predictions of glass structure and properties via reactive molecular dynamics. *J. Non Crystall. Solids* 443, 148–154. doi: 10.1016/j.jnoncrysol.2016.03.026
Zapol, P., He, H., Kwon, K. D., and Criscenti, L. J. (2013). First-principles study of hydrolysis reaction barriers in a sodium borosilicate glass. *Int. J. Appl. Glass Sci.* 4, 395–407. doi: 10.1111/ijag.12052
Zhuravlev, L. (2000). The surface chemistry of amorphous silica. *Zhuravlev Model Colloids Surfaces A Physicochem. Eng. Aspects* 173, 1–38. doi: 10.1016/S0927-7757(00)00556-2
Zotov, N., and Keppler, H. (1998). The structure of sodium tetrasilicate glass from neutron diffraction, reverse Monte Carlo simulations and Raman spectroscopy. *Phys. Chem. Min.* 25, 259–267. doi: 10.1007/s002690050112

Conflict of Interest Statement: The authors declare that the research was conducted in the absence of any commercial or financial relationships that could be construed as a potential conflict of interest.

APPENDIX 1

The Griffiths strain energy release rate (G) for a crack in an elastic material is given by

$$G = -d\left(U_E - W_L\right)/dA \tag{A1}$$

where U_E is the elastic potential energy, W_L is the external work, and A the fracture surface area. In this case the fracture toughness is associated with the critical value of G, $G_{IC} = 2\gamma_S$, which is equal to the energetic cost of creating new surfaces, i.e., twice the surface energy γ_S. To account for energy dissipated during fracture, a dissipation energy term (G_{diss}) is typically added:

$$G_{IC} = G_{diss} + 2\gamma_s \tag{A2}$$

Using that the internal energy of the system (U) is the elastic potential energy (U_E) minus the external work due to loading (W_L) plus the surface energy (U_S):

$$U = \left(U_E - W_L\right) + U_S \tag{A3}$$

and assuming G_{diss} and γ_s are constant, we arrive at

$$d(U_E - W_L) = d(U - U_s) = -(G_{diss} + 2\gamma_s)dA \tag{A4}$$

After equating the change of surface energy $dU_s = 2\gamma_s dA$, we obtain

$$G_{diss} = \frac{dU}{dA} \tag{A5}$$

Mechanics of Materials

Ettore Barbieri

Ettore Barbieri is a Senior Scientist at the Japan Agency for Marine-Earth Science and Technology (JAMSTEC) at the Center for Mathematical Science and Advanced Technology. He holds a PhD in Mechanical Engineering from the University of Bath (UK). Subsequently, he spent 3 years as a postdoctoral researcher at the University of Oxford, at the Department of Engineering Science under the mentoring of Prof. Nik Petrinic and Dr Vito Tagarielli. In 2013, he obtained his first academic post as Lecturer (equivalent to Assistant Professor) at the Queen Mary University of London. In 2017 he joined JAMSTEC as a Scientist and was then promoted to Senior Scientist the following year.

His research interests lie in theoretical and computational mechanobiology, specifically in the fundamental nonlinear mechanisms behind the mechanical behaviour of biological soft and hard tissues. Examples of mechanisms include hierarchy, large deformations, fracture, viscoelasticity, hysteresis, plasticity, and folding.

Lorenzo Botto

Lorenzo Botto is an Assistant Professor at the Process & Energy Department, TU Delft, the Netherlands. His research focuses on the flow microphysics of particulate suspensions, the micro/nanomechanics of interfaces, and the coupling of flow, transport and mechanics in materials science problems. He obtained his PhD degree at Johns Hopkins University (USA) in 2009, followed by postdoctoral appointments at the University of Pennsylvania and Imperial College London, from 2009 to 201), and a Lecturer/Senior lecturer position in Fluid Mechanics at Queen Mary University of London. In 2017, he was awarded an ERC Starting Grant to study the hydrodynamics of 2D nanomaterials.

Sinan Keten

Sinan Keten is an Associate Professor of Civil & Environmental Engineering and Mechanical Engineering at Northwestern University. He joined the Northwestern University faculty in 2010 after obtaining his PhD from MIT. His research expertise focuses on computational materials design and mechanics with an emphasis on polymer nanocomposites and biomolecular materials. He has over 100 publications in this field and has received several honors including the SES Young Investigator Award, the ASCE Huber Prize, the ASME Sia-Nemat Nasser Award, the Presidential Early Career Award for Scientists and Engineers (PECASE), the Office of Naval Research (ONR) Young Investigator Program (YIP) Award, the JMBBM Early Career Award, and the ASME Haythornthwaite Award. He is also a Fellow of the American Physical Society.

Anastasiia Krushynska

Dr Anastasiia O. Krushynska is an Assistant Professor at the Engineering and Technology Institute Groningen, University of Groningen, the Netherlands. With a PhD degree in Mechanics of Deformable Solids (2008, Ukraine), she worked as a Post-Doctoral Researcher in Ukraine from 2008 to 2010, in the Netherlands from 2013 to 2015, and as a Marie Sklodowska-Curie Research Fellow in Italy from 2016 to 2017. Her background is in the field of wave dynamics and vibrations of solids, acoustics and piezoelectricity, with a focus on phononic and acoustic metamaterials. She published about 35 papers in leading peer-reviewed journals, including Physical Review Letters, Applied Physics Letters, Journal of Mechanics and Physics of Solids, New Journals of Physics, etc. Her research is distinguished by individual research grants and young researcher awards. Dr Krushynska serves as a review associate editor in *Frontiers in Materials*, is a reviewer for 23 international peer-reviewed journals and several international conferences, and as an external evaluator of the European Commission projects.

Marco Miniaci

Dr Marco Miniaci obtained his doctorate in Civil & Environmental Engineering in 2014 at the ALMA MATER STUDIOURUM of Bologna, Italy, defending a thesis on the propagation of elastic waves in ordinary structures and metamaterials.

In 2013, he was awarded a regional fellowship promoting international mobility, which brought him to the Institute of Fluid-Flow Machinery - Polish Academy of Science, Gdansk, Poland, where he specialized in Lamb wave measurements via SLDV.

After a 1-year post-doc at the University of Torino, he joined the French CNRS (UMR 6294 of Le Havre) in 2015 in the framework of an Individual Marie-Skłodowska Curie Action, working on periodic structures. He then moved to the United States, to the Georgia Institute of Technology, where he worked on topological protection in elasto-dynamic systems. His current position is again a Marie-Skłodowska Curie fellow at the Swiss Federal Laboratories for Materials Science and Technology, in Switzerland.

His major research interests are periodic structures (phononic crystals and metamaterials), wave propagation, topological protection, non-destructive evaluation, finite element methods, and time reversal.

Diego Misseroni

Diego Misseroni is an Assistant Professor of Solid and Structural Mechanics at the University of Trento, Italy. He earned his PhD in 'Engineering of Civil and Mechanical Structural Systems' from the University of Trento in 2013. He was a Marie Curie experienced researcher at the Department of Mathematical Sciences, University of Liverpool, UK, in 2014. In 2017, he was awarded the 'AIMETA Junior Prize' in Solid and Structural Mechanics by the Italian Association of Theoretical and Applied Mechanics. His research interests are in the field of the Mechanics of Solids and Structures and include fracture mechanics, buckling and instabilities of structures undergoing large deformations, contact mechanics, wave propagation and metamaterials, elasto-plastic modelling, and mechanical characterization of traditional and advanced ceramics. The peculiarity of his approach to research is the employment of a broad vision of mechanics based on a combination of mechanical modeling, numerical simulation and experimental validation.

Maria Pantano

Maria F. Pantano is an Assistant Professor of Solid and Structural Mechanics at the University of Trento, Italy, at the Department of Civil, Environmental and Mechanical Engineering. She received her BA degree in 2007 and MSc degree in 2009 in Mechanical Engineering from the University of Calabria, Italy. She obtained her PhD in Mechanical Engineering in 2013 from the same Institution, under the supervision of Prof. Leonardo Pagnotta. During her graduate studies, she was a visiting scholar from 2010 to 2012 in the Micro and Nanomechanics Laboratory of Prof. Horacio D. Espinosa at Northwestern University in Evanston, IL, USA. In 2013, she was a post-doctoral fellow (supervisor: Prof. Nicola M. Pugno) at the University of Trento, where she was appointed as Assistant Professor in 2014.

Her research activities focus on the mechanical characterization and modeling of micro/nanoscale materials and structures, design and application of microelectromechanical systems (MEMS), and bio-inspired strategies for enhancing the mechanical properties of materials.

Seunghwa Ryu

Seunghwa Ryu is an Associate Professor of mechanical engineering at Korea Advanced Institute of Science and Technology (KAIST). He received his PhD at Stanford in 2011, and a BSc degree in physics from KAIST in 2004. Prof. Ryu's research interests lie in predicting mechanical properties through theory and computer simulations of microstructures across multiple scales. In particular, his recent research subjects include nanoscale fracture and plasticity by advanced atomistic simulation techniques such as autonomous basin climb method, bio-inspired surface and composite designs based on fundamental theory and simulations, and the application of micromechanics-based homogenization theory to technologically important problems. He has published 60 papers in international journals and serves as an associate editor in Frontiers in Materials, Mechanics of Materials, and is an editorial board member of Scientific Reports (Springer Nature) and Material Design & Processing Communications (Wiley).∞

frontiers in Materials

ORIGINAL RESEARCH
published: 19 March 2019
doi: 10.3389/fmats.2019.00041

Curvature Tuning in Folded Strips Through Hyperstatic Applied Rotations

*Ettore Barbieri**

Japan Agency for Marine-Earth Science and Technology, Department of Mathematical Science and Advanced Technology, Yokohama Institute for Earth Sciences, Yokohama, Japan

Folding a strip of paper generates extremely localized plastic strains. The relaxation of the residual stresses results in a ridge that joins two flat faces at an angle known as the *dihedral* angle. When constrained isostatically, the strip will be at its undeformed roof-like state. Instead, if confined hyperstatically, the flat faces will undergo bending. We demonstrate that the generated curvatures can change their sign with appropriate rotations applied at the ends. We use Euler's theory of the *Elastica* and a shooting method to match the applied rotations at the boundaries. We also consider a constitutive model for the discontinuous rotation that takes into account the initial dihedral angle and the rotational stiffness of the fold. We show that the curvatures on the left and the right of the fold change according to a law also confirmed by the Euler-Bernoulli beam theory for small displacements and rotations. For opposite applied rotations, the fold disappears in the limit of zero rotational stiffness; instead, for applied rotations of the same sign, there exists a theoretical non-zero critical rotational stiffness that neutralizes the fold. Below such critical value, the fold can mutate, for example, from a mountain to a valley fold.

Keywords: fold, crease, ridge, *Elastica*, discontinuous rotations

OPEN ACCESS

Edited by:
Nicola Maria Pugno, University of Trento, Italy

Reviewed by:
Lorenzo Bardella, Universitá degli Studi di Brescia, Italy
Stefano Vidoli, Sapienza University of Rome, Italy

***Correspondence:**
Ettore Barbieri
e.barbieri@jamstec.go.jp

Specialty section:
This article was submitted to Mechanics of Materials, a section of the journal Frontiers in Materials

Received: *18 December 2018*
Accepted: *22 February 2019*
Published: *19 March 2019*

Citation:
Barbieri E (2019) Curvature Tuning in Folded Strips Through Hyperstatic Applied Rotations. Front. Mater. 6:41. doi: 10.3389/fmats.2019.00041

1. INTRODUCTION

Folds in thin strips are extremely localized curvatures that occur over a small length-scale. In the limit of such length to zero, the shape of the strip transforms into one with a sharp corner (Lechenault et al., 2014). Such mechanical instabilities in thin strips are often the consequence of an over-constraining environment and material mismatch (Tanaka et al., 1987; Bowden et al., 1998), such as films on foundations.

Examples of patterns generated in confined conditions (Wang and Zhao, 2015) include wrinkles (Huang et al., 2004, 2005; Guvendiren et al., 2010), creases (Hong et al., 2009; Lechenault et al., 2014), blisters, folds (Conti and Maggi, 2007; Pocivavsek et al., 2008; Bayart et al., 2014), crumples (Vliegenthart and Gompper, 2006; Deboeuf et al., 2013), and ridges (Lobkovsky et al., 1995; Lobkovsky, 1996; Lobkovsky and Witten, 1997; Audoly and Pomeau, 2010). The transitions from one to the other manifest as a consequence of the change in the boundary conditions (Holmes and Crosby, 2010; Jin et al., 2015).

Several researchers explored the mechanical snap-back and snap-through instabilities of thin structures constrained by controlled boundary conditions, both on displacements and rotations.

In Beharic et al. (2014), the authors examined the bi-stable snap-through behavior of a beam with both positive and negative curvatures. To achieve such configuration, they confined the beam

with applied symmetrical rotations at both ends and end-to-end horizontal span smaller than the arc-length. By deriving a strain energy landscape, they were able to determine a critical angle at which the deformation becomes mono-stable. Such critical angle depends monotonically only on the (compression) ratio between the arc-length and the horizontal span and not on the material or thickness, (Gomez et al., 2017) by studying a very similar system, demonstrated that the speed of the snapping is lower than the prediction based on the speed of sound; in fact, even without dissipation, they discovered the existence of a slow-down near criticality.

Cazzolli and Dal Corso (2018) studied the snapping mechanisms for elastic strips without folds, generalizing the work of Beharic et al. (2014). They derived an energy release map of all the possible rotations (symmetrical and non-symmetrical) for which the strip exhibits a snap mechanism. Other recent works on snapping in over-confined thin strips include (Yu and Hanna, 2019), where they used the Kirchhoff equations for anisotropic rods to explain the stability under compression, shear, and symmetric clamping: they revealed a series of boundary conditions that can generate stable configurations. Sano and Wada (2018) instead explored a range of controlled asymmetrical boundary conditions (hinged-clamped) that generate snapping.

From the literature survey, there appears to be a considerable amount of research in confined thin sheets, especially in determining their stability. Very little yet exists on confined folded sheet. By fold, in this paper, we mean a sharp corner in the deformation (Lobkovsky, 1996; Lechenault et al., 2014).

Despite the abundance of solutions of the Euler's *Elastica* (Bigoni, 2012; Manning, 2014), there seems to be a lack of closed-form (or even numerical) solutions of the *Elastica* containing folds as we intend in this paper. Related works are (Dado et al., 2004) and (Phungpaingam and Chucheepsakul, 2018), where they studied the post-buckling response of a cantilevered column (fixed-free ends) with a rotational spring in the middle, subjected to a concentrated horizontal force at the free end. However, there is no specific connection to folds, nor the spring contains a residual dihedral angle.

A sharp corner translates into a discontinuity of the rotation of the strip. Using a numerical meshfree method initially developed for cracks, our recently published work (Barbieri et al., 2019) presented a discretization method to model thick plates with multiple folds with infinite rotational stiffness.

In this paper, we are particularly interested in how constraining a thin strip with a fold with finite rotational stiffness leads to non-zero curvatures. Also, we study how such curvatures can be tuned by modifying the applied rotations at the boundaries (**Figure 1**). The question of whether such shapes are stable or unstable remains a topic that requires further investigation.

2. NUMERICAL MODEL USING CLOSED-FORM SOLUTIONS OF THE *ELASTICA*

To examine which boundary conditions create curvatures in folded strips, we carried out semi-analytical simulations. Assuming invariance in the width, we modeled the strip as a plate under cylindrical bending. Therefore, instead of the Föppl-von Kármán equations, we modeled the strip as a planar, linearly elastic, unshearable, and inextensible rod, according to the Euler's theory of the *Elastica*.

The equilibrium equations for the *Elastica* are (Landau and Lifshitz, 1959; Frisch-Fay, 1962)

$$\mu' + \frac{H_0}{B}\sin\theta - \frac{V_0}{B}\cos\theta = 0 \tag{1a}$$

$$\theta' = \mu \tag{1b}$$

$$x' = \cos\theta \tag{1c}$$

$$y' = \sin\theta \tag{1d}$$

with boundary conditions

$$\mu(0) = \frac{M_0}{B} \tag{2a}$$

$$\theta(0) = \theta_0 \tag{2b}$$

$$x(0) = x_0 \tag{2c}$$

$$y(0) = y_0 \tag{2d}$$

where $(\cdot)' = \mathrm{d}/\mathrm{d}S$, with $0 \leq S \leq L$ being the curvilinear coordinate, μ is the curvature, θ is the rotation, x and y the Cartesian coordinates of the deformation, L the length of the rod, $B = EI/(1-\nu^2)$ the bending stiffness, E the Young modulus, I the second moment of area of the cross-section, ν the Poisson ratio, H_0 the applied horizontal force at $S = 0$, V_0 the applied vertical force at $S = 0$, M_0 the bending moment at $S = 0$, and θ_0 the rotation at $S = 0$, with positions x_0, y_0 at $S = 0$ (**Figure 2A**).

We pass to the dimensionless form using the following normalizations:

$$\bar{S} = \frac{S}{L} \qquad \bar{\mu} = \mu L \qquad \bar{x} = \frac{x}{L} \qquad \bar{y} = \frac{y}{L} \tag{3}$$

resulting in

$$\bar{H_0} = \frac{H_0 L^2}{B} \qquad \bar{V_0} = \frac{V_0 L^2}{B} \qquad \bar{M_0} = \frac{M_0 L}{B} \tag{4}$$

and the following system of non-linear ordinary differential equations [the $\bar{(\cdot)}$ is removed for ease of notation]

$$\mu' + H_0\sin\theta - V_0\cos\theta = 0 \tag{5a}$$

$$\theta' = \mu \tag{5b}$$

$$x' = \cos\theta \tag{5c}$$

$$y' = \sin\theta \tag{5d}$$

with boundary conditions

$$\mu(0) = M_0 \tag{6a}$$

$$\theta(0) = \theta_0 \tag{6b}$$

$$x(0) = x_0 \tag{6c}$$

$$y(0) = y_0 \tag{6d}$$

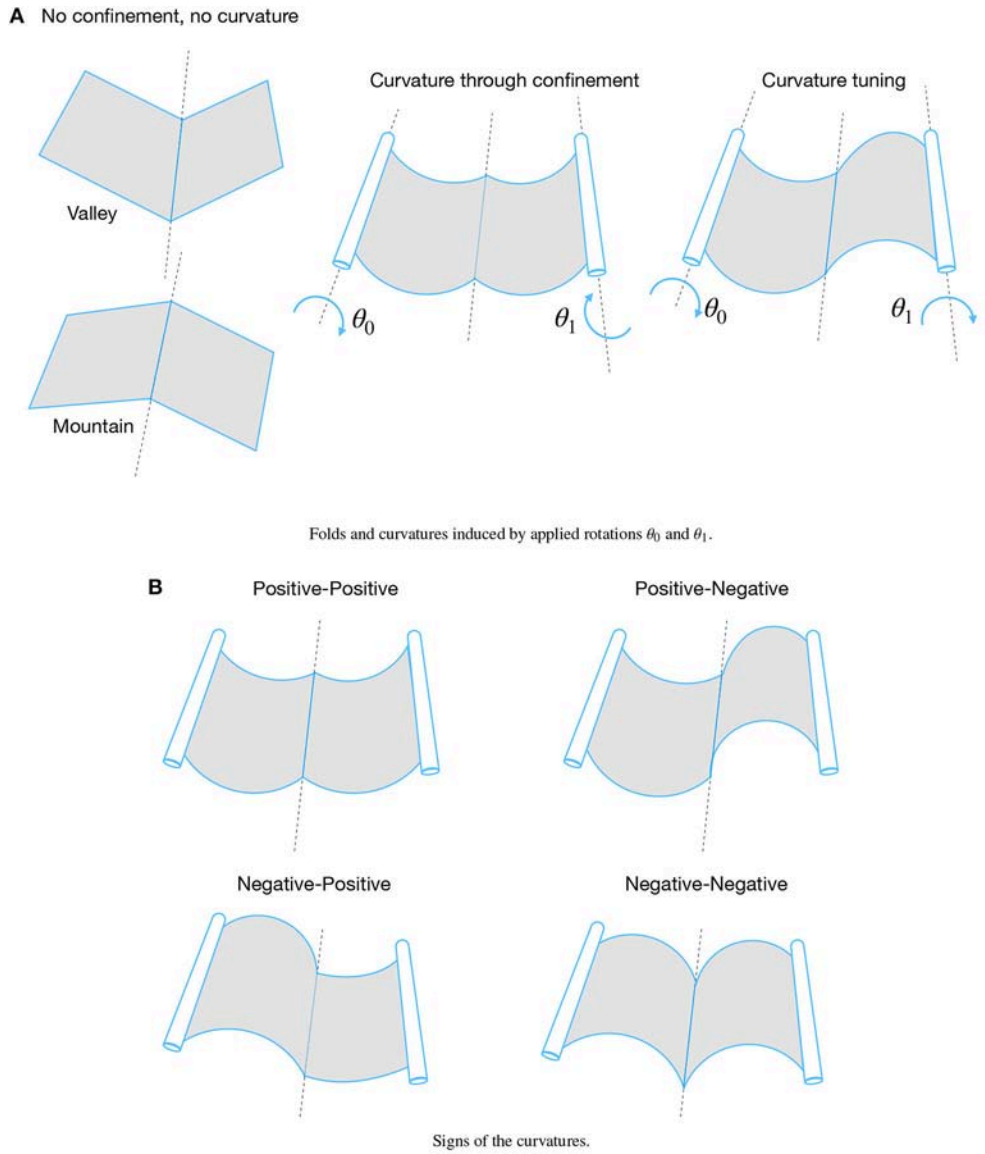

FIGURE 1 | Curvature induced by hyperstatic confinement, and change in curvature (tuning) through applied rotations. **(A)** Folds and curvatures induced by applied rotations θ_0 and θ_1. **(B)** Signs of the curvatures.

where $(\cdot)' = \mathrm{d}/\mathrm{d}\bar{S}$, with $0 \leq \bar{S} \leq 1$. Following standard techniques (Bigoni, 2012) of solution for Equation (5), we get

$$\theta(S) = \theta_{F_0} + 2\,\phi(S) \tag{7}$$

with θ_{F_0} such that

$$H_0 = F_0\,\cos\theta_{F_0} \tag{8a}$$

$$V_0 = F_0\,\sin\theta_{F_0} \tag{8b}$$

$$F_0 = \sqrt{{H_0}^2 + {V_0}^2} > 0 \tag{8c}$$

and

$$\phi(S) = \mathrm{sign}\,(M_0)\;\mathrm{am}\left(\alpha(S)\middle|k^2\right) \tag{9}$$

where am is the *Jacobi amplitude function* and

$$\alpha(S) = \mathrm{sign}\,(M_0)\,M_c\,S + f_0 \tag{10}$$

with

$$f_0 = F\left(\phi_0\middle|k^2\right) \tag{11}$$

with F is the *elliptic integral of the first kind* and

$$\phi_0 = \frac{\theta_0 - \theta_{F_0}}{2} \tag{12}$$

$${M_c}^2 = \frac{{M_0}^2 + 2\,F_0\,(1 - \cos 2\,\phi_0)}{4} \tag{13}$$

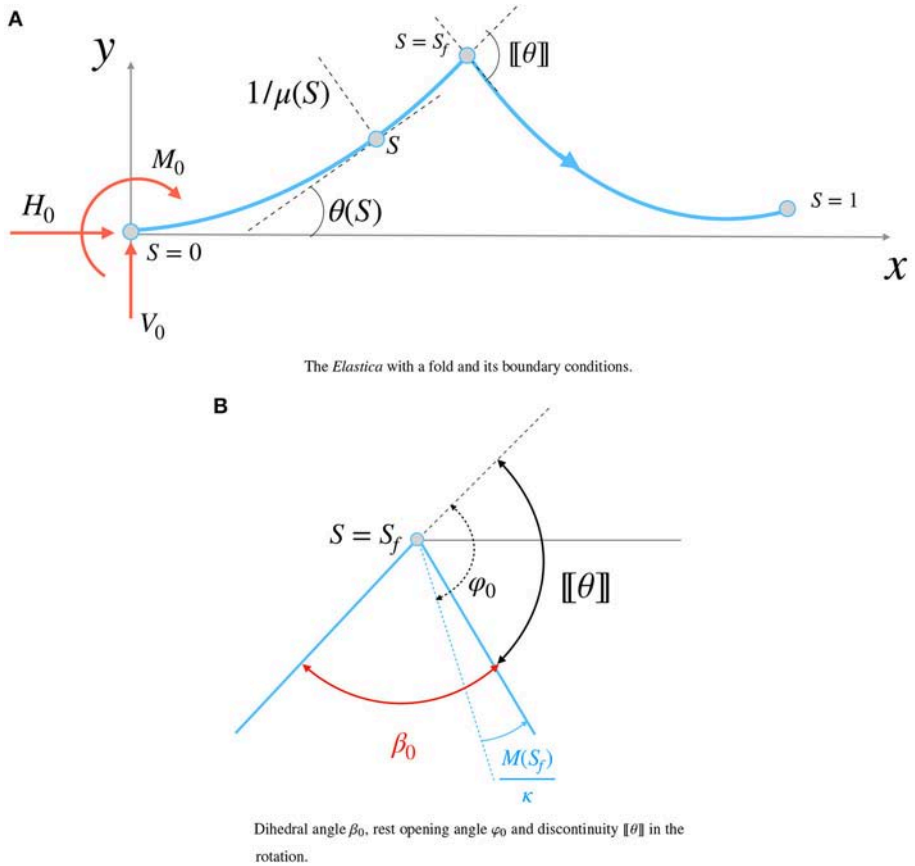

FIGURE 2 | The *Elastica* with a fold at $S = S_f$. **(A)** The *Elastica* with a fold and its boundary conditions. **(B)** Dihedral angle β_0, rest opening angle φ_0 and discontinuity $[\![\theta]\!]$ in the rotation.

$$k^2 = \frac{F_0}{{M_c}^2} \tag{14}$$

The Cartesian coordinates of the deformation are

$$x(S) = x_0 + \cos\theta_{F_0}\, C_\phi(S) - \sin\theta_{F_0}\, S_\phi(S) \tag{15}$$

$$y(S) = y_0 + \sin\theta_{F_0}\, C_\phi(S) + \cos\theta_{F_0}\, S_\phi(S) \tag{16}$$

with

$$S_\phi(S) = \int_0^S \sin\left(2\,\phi(S)\right) \mathrm{d}S = \frac{2}{M_c\, k^2}\left(\mathrm{dn}\left(\alpha(S)\middle|k^2\right) - \mathrm{dn}\left(f_0\middle|k^2\right)\right) \tag{17}$$

where dn is the *Jacobi dn function*

$$C_\phi(S) = \int_0^S \cos\left(2\,\phi(S)\right) \mathrm{d}S = S - \frac{2}{M_c}\Big(\mathrm{sign}\,\phi'\, I(\phi) - \mathrm{sign}\,\phi_0'\, I(\phi_0) + 2\, I_{\max}\, n_{\phi'\uparrow\downarrow}(S)\Big) \tag{18}$$

where

$$I(\phi) = \frac{1}{k^2}\left(F(\phi|k^2) - E(\phi|k^2)\right) \tag{19}$$

where E is the *elliptic integral of the second kind*, $I_{\max} = I(\phi_{\max})$ and $n_{\phi'\uparrow\downarrow}$ is the number of times from 0 to S when ϕ' changes sign. Furthermore,

$$\phi_{\max} = \arcsin\left(\frac{1}{k}\right) \tag{20}$$

$$\phi'(S) = \mathrm{sign}\,(M_0)\, M_c\ \mathrm{dn}\left(\alpha(S)\middle|k^2\right) \tag{21}$$

and

$$\mu(S) = 2\,\phi'(S) \tag{22}$$

The strain energy of the rod is

$$U = \frac{1}{2}\int_0^1 \mu^2\,\mathrm{d}S = 2\int_0^1 \phi'(S)^2\,\mathrm{d}S = 2\,M_c^2 - 2\,F_0\int_0^1 \sin^2\phi\,\mathrm{d}S = 2\,M_c^2 - F_0\,\left(1 - C_\phi(1)\right) \tag{23}$$

Let us now assume that a fold exists at $0 < S_f < 1$. The fold is a discontinuity $[\![\cdot]\!]$ on the rotation, with the following constitutive model (Lechenault et al., 2014)

$$[\![\theta]\!] = \theta(S_f^+) - \theta(S_f^-) = \frac{M(S_f)}{\kappa} + \varphi_0 \tag{24}$$

with S_f^+ the curvilinear coordinate immediately to the right of S_f and S_f^- the one immediately on the left (**Figure 2B**). The quantity $\kappa > 0$ is the rotational stiffness of the fold, and $M(S_f)$ is the bending moment, assumed continuous in the absence of concentrated moments applied at S_f. The angle φ_0 is the *rest opening angle*. When $\varphi_0 = 0$, there is no fold; when $\varphi_0 < 0$ the fold is called a *mountain* and when $\varphi_0 > 0$ the fold is called a *valley* (**Figure 1**). The linear relationship between bending moment and dihedral angle was showed experimentally in Lechenault et al. (2014) and Jules et al. (2019) to hold for a wide range of dihedral angles. In their experiments, Lechenault and co-workers used the setup in **Figure 3**. The sample is clamped at one end, with a dynamometer attached to the other end. Both ends lie in the same plane. The right end can translate as the force pulls the specimen. The sample is illuminated by a laser, and the successive deformations are captured by a digital camera. In this way, it is possible to measure the dihedral angle β_0. The moment at the fold is calculated as the product of the force measured by the dynamometer and the maximum height of the profile $y(S_f)$.

The geometrical meaning of φ_0 is shown in **Figure 2B**. The rest opening angle is related to the dihedral angle β_0 by the simple relation

$$\beta_0 = \pi - \left(\varphi_0 + \frac{M(S_f)}{\kappa}\right) \tag{25}$$

The rest opening angle is a mechanical property related to the yield stress of the material of the strip (Lechenault et al., 2014): to create a sharp fold, one needs to apply an extreme deformation that generates localized and irreversible strains. Such strains, in turn, lead to high stress concentrations beyond the yield stress of the material. An estimate of the dihedral angle is (Lechenault et al., 2014)

$$\varphi_0 \sim \epsilon_p \sim \frac{\sigma_Y}{E} \tag{26}$$

where ϵ_p is the plastic strain, σ_Y the yield stress and E the Young modulus of the material composing the strip. In addition, φ_0 appears to be independent from the thickness of the strip (Lechenault et al., 2014).

To tune the curvatures, we will further assume that at least one of the following quantities is assigned:

$$\theta(0) = \theta_0 \qquad \theta(1) = \theta_1 \qquad x(1) = x_1 \qquad y(1) = y_1 \tag{27}$$

which renders one or all of H_0, V_0, M_0 unknowns to be determined. The procedure to compute such unknowns is a *shooting* method (Press et al., 2007). Firstly, the solutions (7), (15), (16), and (22) are applied from $0 \le S \le S_f$: let us call this solution μ^-, θ^-, x^-, and y^-. Then, the values $\theta(1)$, $x(1)$, and $y(1)$ are computed by applying the solution (7), (15), and (16) with the following boundary conditions:

$$\theta(S_f) = \theta^-(S_f) + \left(\varphi_0 + \frac{\mu^-(S_f)}{\kappa}\right) \tag{28a}$$

$$\mu(S_f) = \mu^-(S_f) \tag{28b}$$

$$x(S_f) = x^-(S_f) \tag{28c}$$

$$y(S_f) = y^-(S_f) \tag{28d}$$

the procedure is iterated with a non-linear solver until $\theta(1)$, $x(1)$, and $y(1)$ computed in this way match the conditions (27), within a certain tolerance.

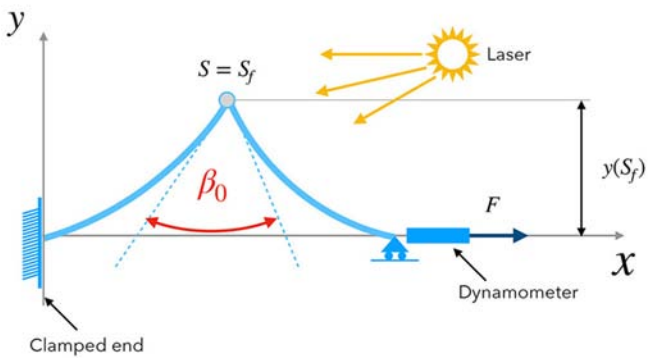

FIGURE 3 | Experimental setup used in Lechenault et al. (2014) for the characterization of the rotational stiffness of the fold (adapted).

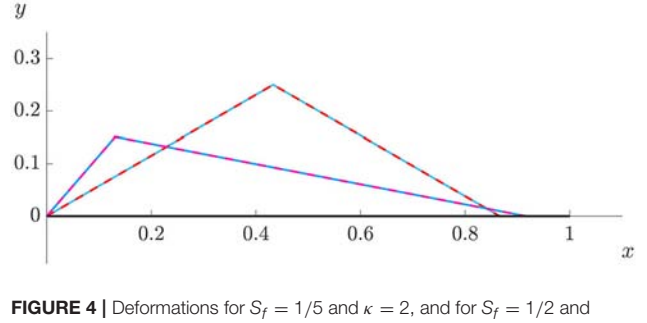

FIGURE 4 | Deformations for $S_f = 1/5$ and $\kappa = 2$, and for $S_f = 1/2$ and $\kappa = \infty$, both with rest opening angle $\varphi = -60°$ with $y_1 = 0$ (isostatic confinement). Blue continuous line: *Elastica*, red dashed line: Euler-Bernoulli (Equations 34).

3. RESULTS

In this section we report the results of the *Elastica* model for strips containing folds. We examine both isostatic and hyperstatic boundary conditions. In all the numerical calculations, we set the origin of the Cartesian system to the origin of the rod, therefore $x_0 = y_0 = 0$.

3.1. Isostatic Boundary Conditions: no Curvature

Let us examine the case where only $y(1)$ is assigned

$$y(1) = y_1 \tag{29}$$

Therefore

$$H_0 = 0 \qquad M_0 = 0 \qquad V_0 = 0 \qquad \theta_0 = \text{unknown} \tag{30}$$

Figure 4 shows that no curvature is generated under conditions (30), regardless of the position of the fold and rotational stiffness. This configuration corresponds to the undeformed state of the folded strip when is at rest. This undeformed state depends only on the position of the fold S_f and the rest opening angle φ_0.

3.2. Hyperstatic Boundary Conditions

In addition to condition (29), we consider cases where the boundary conditions are provided by a couple of rotations applied respectively at the start and the end of the strip:

$$y(1) = y_1 = 0 \qquad \theta(0) = \theta_0 \qquad \theta(1) = \theta_1 \tag{31}$$

We also impose that the end lies in the same plane as the start of the strip, therefore $y_1 = 0$. Under boundary conditions (31),

$$H_0 = 0 \qquad M_0 = \text{unknown} \qquad V_0 = \text{unknown} \tag{32}$$

Firstly, we consider the case of a fold with infinite rotational stiffness. By changing the applied rotations, we investigate the changes in sign of the curvatures at both sides of the fold (**Figure 1B**). Secondly, we repeat the same calculations for a finite rotational stiffness.

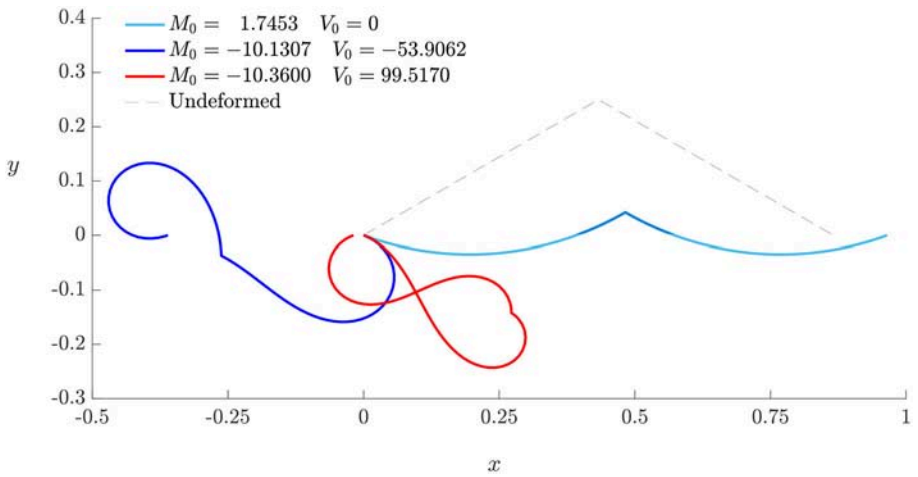

FIGURE 5 | Non-uniqueness of the deformation for a sheet with an infinitely stiff fold positioned at $S_f = 0.5$, with rest angle $\varphi_0 = -60°$ and applied rotations $\theta_0 = 20°$, $\theta_1 = -20°$.

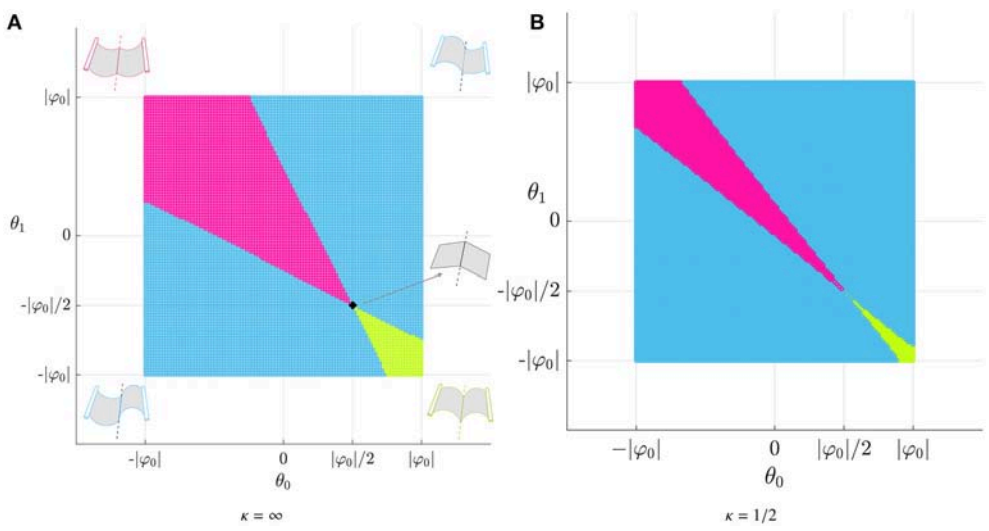

FIGURE 6 | Signs of the curvatures at the left $M_0 = \mu(0)$ and at the right $\mu(1)$ of the fold. The rest angle is $\varphi_0 = -60°$ and the position is $S_f = 1/2$. **(A)** Infinite rotational stiffness ($\kappa = \infty$). **(B)** Finite rotational stiffness ($\kappa = 1/2$).

Thirdly, we isolate the effect of the rotational stiffness by varying κ for different strips under the strips under the same couple of applied rotations and the same position of the fold. We consider anti-symmetrical applied rotations.

3.2.1. Variable Applied Rotations and Rotational Stiffness

Figure 5 shows the deformations for a sheet under the same applied rotation, infinite rotational stiffness, same fold position and same rest angle.

There exist multiple solutions, depending on the initial moment M_0 and shear force V_0. This non-uniqueness is a consequence of the non-linearity of the *Elastica*: in fact, the solutions (15) and (16) are periodic in space, with the period depending on M_0, H_0 and V_0 (Equation 13).

In the proceeding of the paper, we will always refer to the solution with the lowest strain energy. In fact, Equation (23) states that for the same θ_0 and θ_1, the strain energy grows with M_0 and F_0

$$U \sim {M_c}^2 \sim {M_0}^2 + F_0 \tag{33}$$

Having resolved this disambiguation, we now examine the changes in sign of the curvatures (**Figure 1B**). **Figure 6A** shows the curvatures at both sides of the fold for varying applied rotations at both ends. We considered θ_0 and θ_1 ranging from $-|\varphi_0|$ to $|\varphi_0|$, with an increment of 1°. The fold has position $S_0 = 1/2$ and infinite rotational stiffness. With respect to the signs of the curvatures, there exist three regions: one where both curvatures are positive, one where both are negative and one where the curvatures have different signs.

Figure 6B shows a map of the signs of the curvatures for the same strip with reduced rotational stiffness $\kappa = 1/2$. We can still identify three domains, as in **Figure 6A**, except that the domains with the same curvatures have decreased, while the sub-regions with opposite curvature have increased. Regardless of the rotational stiffness, the three regions meet at the same point, which corresponds to the isostatic boundary conditions.

Figures 7A,B show instead the dimensionless shear force at $S = 0$. Both graphs are identical, with the zero shear force line being straight with equation $\theta_1 = -\theta_0$.

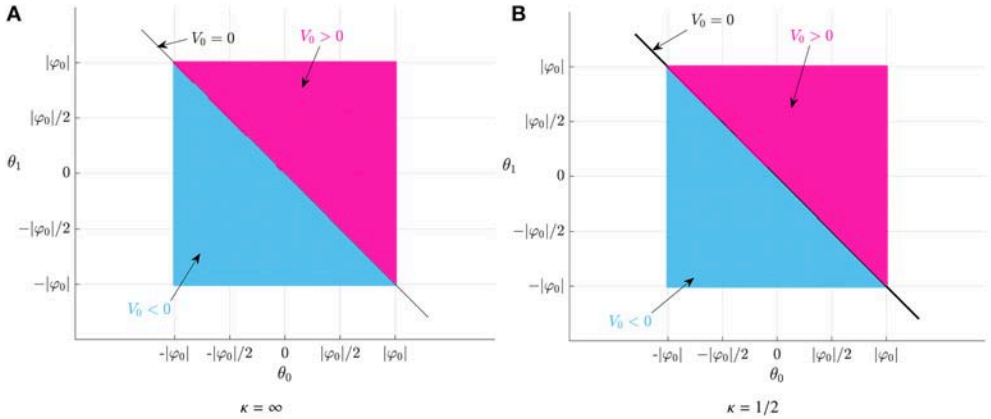

FIGURE 7 | Sign of the shear force V_0 for a fold with rest angle $\varphi = -60°$ and position $S_f = 1/2$. **(A)** Infinite rotational stiffness ($\kappa = \infty$). **(B)** Finite rotational stiffness ($\kappa = 1/2$).

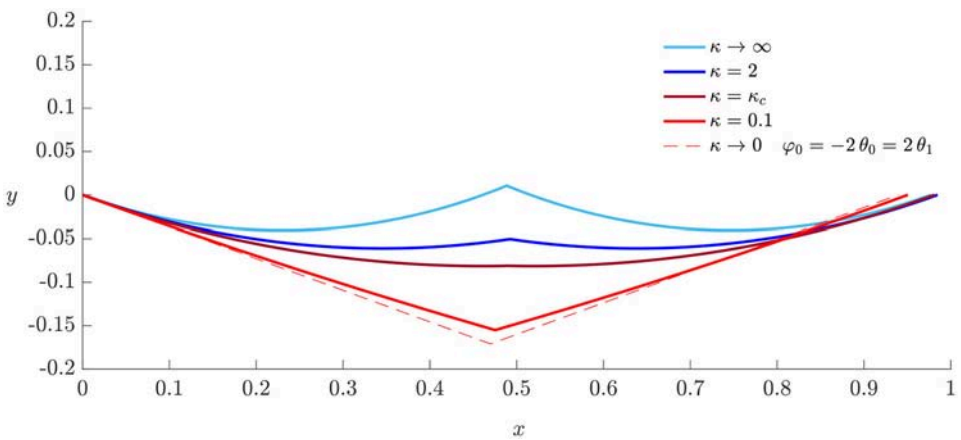

FIGURE 8 | Deformations for variable rotational stiffness for symmetrical applied rotations $\theta_0 = -\theta_1 = -20°$, with rest angle $\varphi_0 = -45°$.

3.2.2. Variable Rotational Stiffness for Symmetrical and Anti-symmetrical Applied Rotations

Figure 8 shows the deformations for a strip with a fold at $S_f = 1/2$, rest angle $\varphi_0 = -45^\circ$ and variable rotational stiffness κ. The boundary conditions are given by a fixed y-coordinate at the end $y_1 = 0$ and symmetrical applied rotations $\theta_0 = -\theta_1 = -20^\circ$. The curvature $\mu(S)$ is uniform throughout the rod, and decreases with the decrease in κ. As expected, the dihedral angle β_0 increases as κ decreases. When κ reaches a critical value κ_c, the discontinuity on the rotation disappears; below κ_c, the fold transitions from a mountain into a valley. In the limit of zero rotational stiffness, the fold becomes a

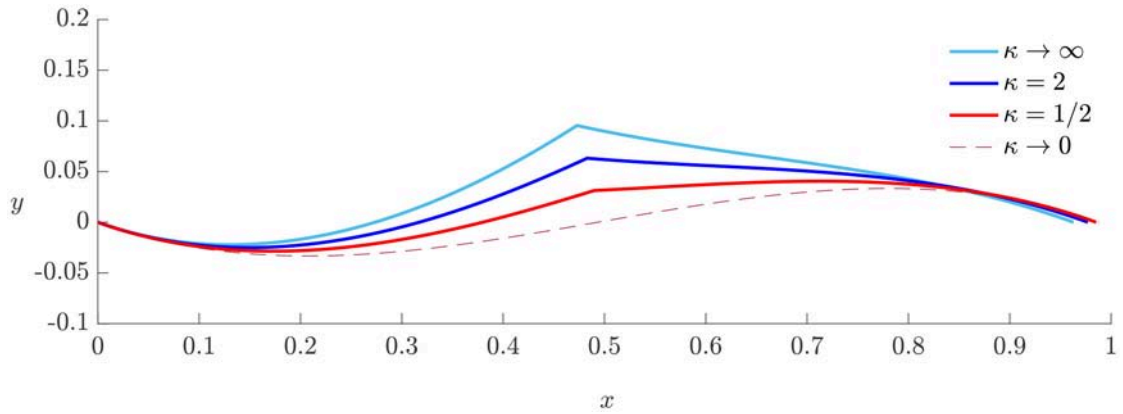

FIGURE 9 | Deformations for variable rotational stiffness for anti-symmetrical applied rotations $\theta_0 = \theta_1 = -20^\circ$, with rest angle $\varphi_0 = -45^\circ$.

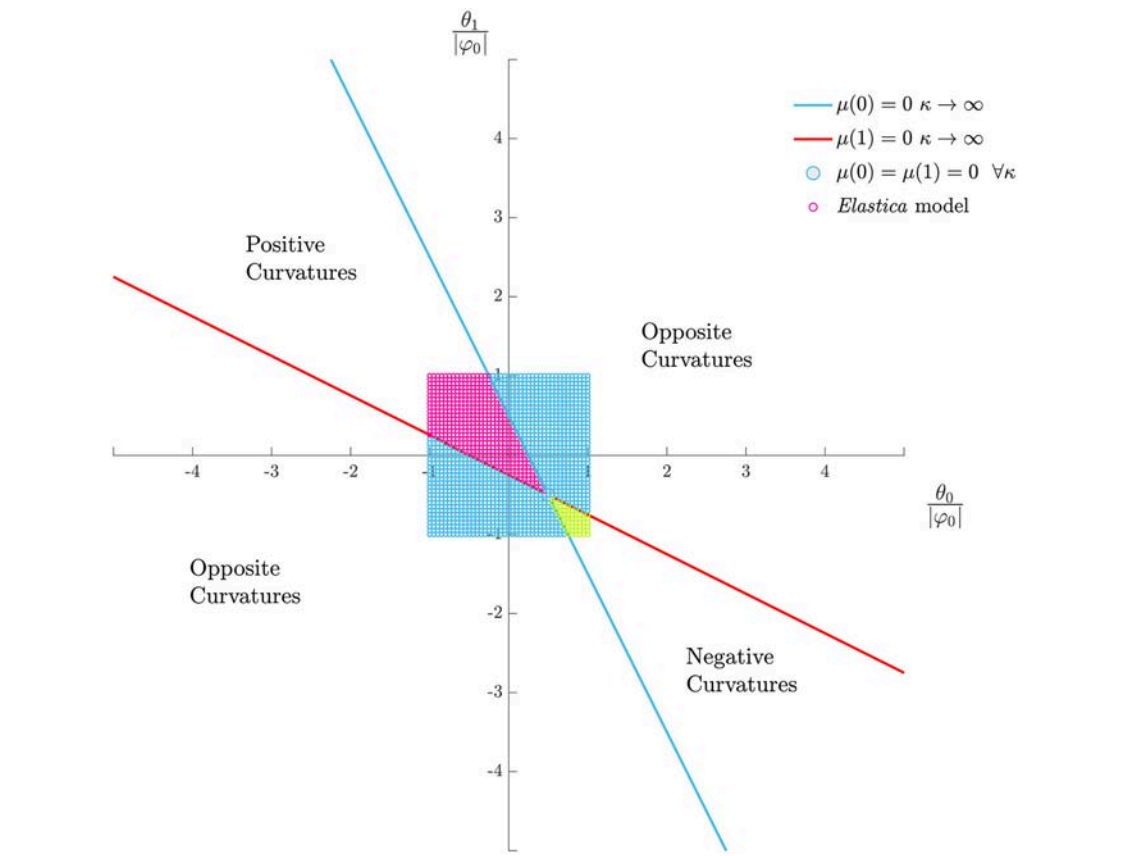

FIGURE 10 | Curvature signs due to hyperstatic confinement through applied rotations. The fold has infinite rotational stiffness. Comparison between the *Elastica* model (dots) and *Euler-Bernoulli* beam (continuous straight lines). Pink dots: positive curvatures; green dots: negative curvatures; blue dots: opposite curvatures.

perfect hinge: the deformation is equivalent to one of a flat rod, under isostatic boundary conditions, containing a fold with a rest opening angle equal to twice the applied rotation at the end.

Instead, when the applied rotations are equal (anti-symmetrical rotations), the limit configuration for zero rotational stiffness is the solution of the *Elastica* with no folds (**Figure 9**).

4. DISCUSSION

In this section, we derive a simplified analytical model to explain the numerical results obtained in section 3.

4.1. Influence of the Isostatic Confinement

In this case, the solution of the system (5) is

$$\mu(S) = \varphi_0\,\delta(S - S_f) \tag{34a}$$

$$\theta(S) = \theta_0 + \varphi_0\,\mathcal{H}(S - S_f) \tag{34b}$$

$$x(S) = \cos\theta_0\,S - \Big(\cos\theta_0 - \cos(\theta_0 + \varphi_0)\Big)\,\langle S - S_f\rangle \tag{34c}$$

$$y(S) = \sin\theta_0\,S - \Big(\sin\theta_0 - \sin(\theta_0 + \varphi_0)\Big)\,\langle S - S_f\rangle \tag{34d}$$

with δ being the *Dirac delta* function, $\mathcal{H}$ the *Heaviside* function and

$$\langle S\rangle = \frac{S + |S|}{2} \tag{35}$$

is the *ramp* function. The solutions in Equation (34) correspond to a piece-wise roof-like deformation, where each side of the fold is flat.

The angle θ_0 is given by

$$\theta_0 = \text{atan2}\left(-\frac{(1 - S_f)\,\sin\varphi_0}{S_f + \cos\varphi_0\,(1 - S_f)}\right) \tag{36}$$

meaning that the deformation depends only upon the position of the fold S_f and the rest angle φ_0, as anticipated in **Figure 4**.

4.2. Influence of the Applied Rotations

For simplicity, we will also assume x_1 unassigned, making $H_0 = 0$. In addition, we will assume, in first instance, that the fold is infinitely stiff, meaning $\kappa \to \infty$. In this case, the *Elastica* coincides with the classic *Euler-Bernoulli* beam equation:

$$\mu' = V_0^\infty \tag{37}$$

and the solutions for the beam are

$$\mu(S) = M_0^\infty + V_0^\infty\,S + \varphi_0\,\delta(S - S_f) \tag{38a}$$

$$\theta(S) = \theta_0 + M_0^\infty\,S + V_0^\infty\,\frac{S^2}{2} + \varphi_0\,\mathcal{H}(S - S_f) \tag{38b}$$

$$x(S) = S \tag{38c}$$

$$y(S) = \theta_0\,S + M_0^\infty\,\frac{S^2}{2} + V_0^\infty\,\frac{S^3}{3} + \varphi_0\,\langle S - S_f\rangle \tag{38d}$$

Assigning the following boundary conditions

$$\theta(0) = \theta_0 \qquad \theta(1) = \theta_1 \qquad y(1) = y_1 = 0 \tag{39}$$

the two unknowns V_0 and M_0 are given by

$$V_0^\infty = 6\left(\theta_0 + \theta_1 + \varphi_0(1 - 2\,S_f)\right) \tag{40a}$$

$$M_0^\infty = -4\left(\theta_0 + \frac{\theta_1}{2} + \varphi_0\left(1 - \frac{3}{2}\,S_f\right)\right) \tag{40b}$$

For $S_f = 1/2$, the curvature will be uniform ($V_0 = 0$) if

$$\theta_0 = -\theta_1 \tag{41}$$

regardless of the rest angle of the fold. Such straight line in Equation (41) is observable in both **Figures 7A,B**.

Therefore, the curvature will be identically zero if both $V_0 = M_0 = 0$, which happens for

$$\theta_0 = \varphi_0\,(1 - S_f) \qquad \theta_1 = -\varphi_0\,S_f \tag{42}$$

The curvature in Equation (38a) is a linear function in S. Therefore, by inspecting the signs of the values at $S = 0$ and $S = 1$, it is possible to discern whether the beam has the same curvature (either positive or negative) or opposite curvatures:

$$\mu(0) > 0 \quad \mu(1) > 0 \qquad \text{same positive curvature} \tag{43a}$$

$$\mu(0) < 0 \quad \mu(1) < 0 \qquad \text{same negative curvature} \tag{43b}$$

$$\mu(0)\,\mu(1) < 0 \qquad \text{opposite curvatures} \tag{43c}$$

The values of $\mu(0)$ and $\mu(1)$ are

$$\mu(0) = {M_0}^\infty \tag{44a}$$

$$\mu(1) = {M_0}^\infty + {V_0}^\infty \tag{44b}$$

Figure 10 shows the presence of the three regions for the signs of the curvatures, as observed in **Figure 6**; also, there is agreement between the *Euler-Bernoulli* theory and the *Elastica* model.

4.3. Influence of the Rotational Stiffness

Interestingly, the values in Equation (42) hold also for folds with finite rotational stiffness. In fact, when κ is finite, the solutions are

$$\mu(S) = M_0^\kappa + V_0^\kappa\,S + \left(\varphi_0 + \frac{M_0^\kappa + V_0^\kappa\,S_f}{\kappa}\right)\,\delta(S - S_f) \tag{45a}$$

$$\theta(S) = \theta_0 + M_0^\kappa\,S + V_0^\kappa\,\frac{S^2}{2} + \left(\varphi_0 + \frac{M_0^\kappa + V_0^\kappa\,S_f}{\kappa}\right)\,\mathcal{H}(S - S_f) \tag{45b}$$

$$x(S) = S \tag{45c}$$

$$y(S) = \theta_0\,S + M_0^\kappa\,\frac{S^2}{2} + V_0^\kappa\,\frac{S^3}{3} + \left(\varphi_0 + \frac{M_0^\kappa + V_0^\kappa\,S_f}{\kappa}\right)\,\langle S - S_f\rangle \tag{45d}$$

where

$$V_0{}^{\kappa} = \frac{V_0{}^{\infty}}{1+\frac{4}{\kappa}\left(1-3\,S_f+3\,{S_f}^2\right)} + 12\,\frac{\theta_1+S_f\,(\theta_0-\theta_1)}{1+\frac{4}{\kappa}\left(1-3\,S_f+3\,{S_f}^2\right)} \tag{46a}$$

$$M_0{}^{\kappa} = \frac{M_0{}^{\infty}}{1+\frac{4}{\kappa}\left(1-3\,S_f+3\,{S_f}^2\right)} + 12\,S_f\,\frac{\theta_1+S_f\,(\theta_0-\theta_1)}{1+\frac{4}{\kappa}\left(1-3\,S_f+3\,{S_f}^2\right)} \tag{46b}$$

with $V_0{}^{\infty}$ given by Equation (40a) and $M_0{}^{\infty}$ by Equation (40b). By substituting Equations (42) into (46), the values of $V_0{}^{\kappa}$ and $M_0{}^{\kappa}$ also become zero.

In addition, for $S_f = 1/2$, $\theta_0 = -\theta_1$, also $V_0{}^{\kappa} = 0$, which means that for opposite applied rotations, the curvature will be uniform also for folds with finite rotational stiffness.

The *Euler-Bernoulli* theory for soft folds in Equation (46) confirms the shrinkage of the domains with same-sign curvatures, as showed in **Figure 11**.

The denominator in Equation (46) is always positive

$$\kappa + 12\,{S_f}^2 - 12\,S_f + 4 > 0 \qquad 0 < S_f < 1 \quad \kappa > 0 \tag{47}$$

preventing the appearance of any singularities.

The discontinuity in rotation at the fold is given by

$$[\![\theta]\!]^{\kappa} = \theta(S_f^{+}) - \theta(S_f^{-}) = \frac{M(S_f)}{\kappa} + \varphi_0 = \frac{\varphi_0\,\kappa + \theta_0\,\left(6\,S_f-4\right) + \theta_1\,\left(6\,S_f-2\right)}{\kappa + 12\,{S_f}^2 - 12\,S_f + 4} \tag{48}$$

and is showed in **Figure 12** for $\theta_0 = -\theta_1 = 20^{\circ}$ and $\varphi_0 = -45^{\circ}$.

The discontinuity becomes zero for

$$\kappa_c = 4\,\frac{\theta_0}{\varphi_0}\left(1-\frac{3}{2}\,S_f\right) + 2\,\frac{\theta_1}{\varphi_0}\,\left(1-3\,S_f\right) \tag{49}$$

For $S_f = 1/2$:

$$\kappa_c = \frac{\theta_0}{\varphi_0} - \frac{\theta_1}{\varphi_0} \tag{50}$$

therefore, when the applied rotations are equal, then the critical rotational stiffness is zero, as in **Figures 9**, **12**, when the applied

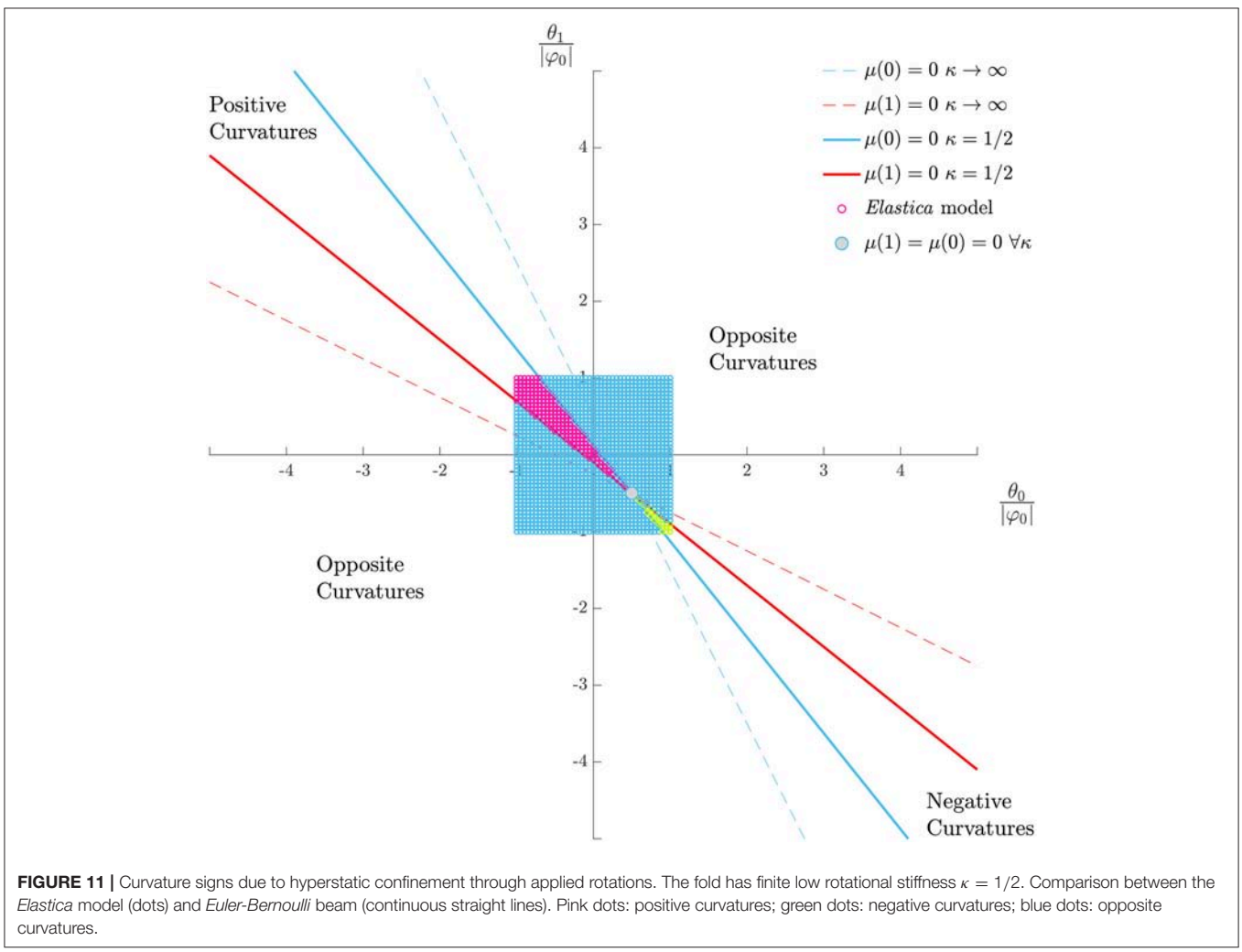

FIGURE 11 | Curvature signs due to hyperstatic confinement through applied rotations. The fold has finite low rotational stiffness $\kappa = 1/2$. Comparison between the *Elastica* model (dots) and *Euler-Bernoulli* beam (continuous straight lines). Pink dots: positive curvatures; green dots: negative curvatures; blue dots: opposite curvatures.

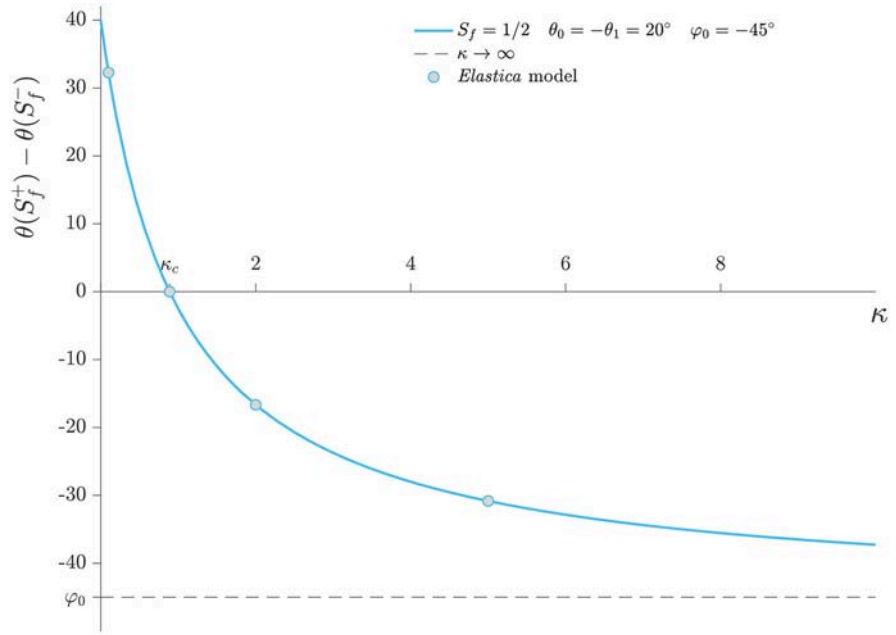

FIGURE 12 | Discontinuity on the rotation at the fold for variable rotational stiffness. Comparison between values from **Figure 8** and Equation (48).

rotations are opposite, then

$$\kappa_c = 2\,\frac{\theta_0}{\varphi_0} \tag{51}$$

When θ_0 is of the same sign of φ_0, then $k_c > 0$ as in **Figures 8**, **13** and there exist a physical critical value of the rotational stiffness. Otherwise, for $\theta_0 = -\theta_1$ and φ_0 of the opposite sign, then there is no critical value, and the solution is an undeformed roof-like deformation, as determined by Equation (42).

It must be remarked, however, that even though a critical rotational stiffness for fold disappearance exists, the linear relationship in (24) might not hold for small rotational stiffness.

5. CONCLUSIONS

A thin sheet containing a fold assumes a roof-like undeformed state when confined isostatically. Instead, if confined hyperstatically, it will possess one or more curvatures. Such curvatures change according to the rotations applied at the ends of the sheet. Using the Euler's *Elastica* theory, we calculated the values of the applied rotations corresponding to a switch in the curvatures' signs.

We considered a fold as a discontinuity in the rotations, equal to the supplementary angle to its dihedral angle. The mechanical behavior of the fold depends upon two material properties: the rest opening angle and the rotational stiffness. The rest opening angle is a material property closely related to the yield stress; the rotational stiffness contributes to increasing the dihedral angle of the fold when subjected to a bending moment.

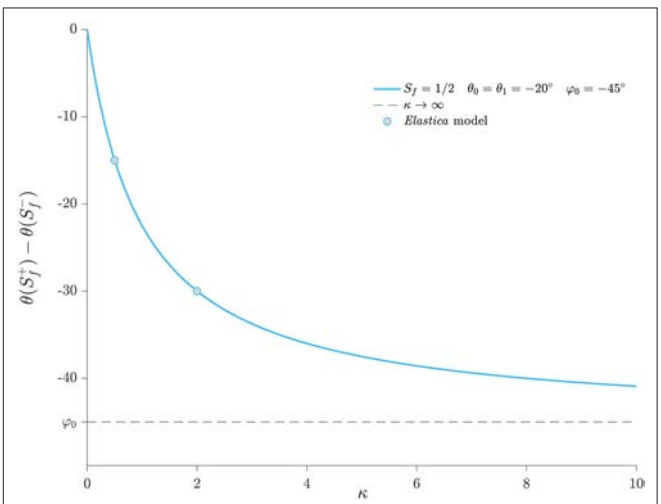

FIGURE 13 | Discontinuity on the rotation at the fold for variable rotational stiffness. Comparison between values from **Figure 9** and Equation (48).

For infinite rotational stiffness, the dihedral angle depends only on the rest opening angle. For the signs of the curvatures before and after the fold, we can identify three regions: one where both curvatures are positive, one where they are both negative and one when they are opposite in sign. We presented a map of such occurrences according to the applied rotations; for small rotations and displacements, the numerical results agree with a simplified model based on the *Euler-Bernoulli* beam. Also, this map confirmed the presence of values of applied rotations for which the curvature is uniform throughout the sheet; in

particular, there is one couple of applied rotations when such uniform curvature is zero. These rotations correspond to the isostatic confinement.

For folds with finite rotational stiffness, the two regions with same-sign curvatures shrink. Interestingly, there exists a critical value of the rotational stiffness when the fold disappears, meaning that the discontinuity on the rotation becomes zero. In particular, when the applied rotations are opposite in signs and the fold is a mountain, the critical value of the rotational stiffness is different from zero, and represents a transition from mountain to valley. In the limit of zero rotational stiffness, the sheet transforms into an undeformed valley with rest angle equal to twice the applied rotation at the end.

DATA AVAILABILITY

All datasets generated for this study are included in the manuscript and/or the supplementary files.

AUTHOR CONTRIBUTIONS

EB designed the research, conducted the analysis, and wrote the manuscript.

FUNDING

EB's work was supported by the Japan Society for the Promotion of Science JSPS KAKENHI Grant Number JP18K18065.

REFERENCES

Audoly, B., and Pomeau, Y. (2010). *Elasticity and Geometry: From Hair Curls to the Non-linear Response of Shells*. Oxford: Oxford University Press.

Barbieri, E., Ventura, L., Grignoli, D., and Bilotti, E. (2019). A meshless method for the nonlinear von Kármán plate with multiple folds of complex shape - a bridge between cracks and folds. *Comput. Mech.* 1–19. doi: 10.1007/s00466-019-01671-w

Bayart, E., Boudaoud, A., and Adda-Bedia, M. (2014). Tuning the ordered states of folded rods by isotropic confinement. *Phys. Rev. E* 89:012407. doi: 10.1103/PhysRevE.89.012407

Beharic, J., Lucas, T. M., and Harnett, C. K. (2014). Analysis of a compressed bistable buckled beam on a flexible support. *J. Appl. Mech.* 81:081011. doi: 10.1115/1.4027463

Bigoni, D. (2012). *Nonlinear Solid Mechanics: Bifurcation Theory and Material Instability*. Cambridge: Cambridge University Press.

Bowden, N., Brittain, S., Evans, A. G., Hutchinson, J. W., and Whitesides, G. M. (1998). Spontaneous formation of ordered structures in thin films of metals supported on an elastomeric polymer. *Nature* 393, 146. doi: 10.1038/30193

Cazzolli, A., and Dal Corso, F. (2018). Snapping of elastic strips with controlled ends. *Int. J. Solids Struct.* 162, 285–303. doi: 10.1016/j.ijsolstr.2018.12.005

Conti, S., and Maggi, F. (2007). Confining thin elastic sheets and folding paper. *Arch. Ration. Mech. Anal.* 187, 1–48. doi: 10.1007/s00205-007-0076-2

Dado, M., Al-Sadder, S., and Abuzeid, O. (2004). Post-buckling behavior of two elastica columns linked with a rotational spring. *Int. J. Nonlinear Mech.* 39, 1579–1587. doi: 10.1016/j.ijnonlinmec.2004.01.003

Deboeuf, S., Katzav, E., Boudaoud, A., Bonn, D., and Adda-Bedia, M. (2013). Comparative study of crumpling and folding of thin sheets. *Phys. Rev. Lett.* 110:104301. doi: 10.1103/PhysRevLett.110.104301

Frisch-Fay, R. (1962). *Flexible Bars*. London: Butterworths.

Gomez, M., Moulton, D. E., and Vella, D. (2017). Critical slowing down in purely elastic snap-through instabilities. *Nat. Phys.* 13, 142–145. doi: 10.1038/nphys3915

Guvendiren, M., Burdick, J. A., and Yang, S. (2010). Solvent induced transition from wrinkles to creases in thin film gels with depth-wise crosslinking gradients. *Soft Matter* 6:5795. doi: 10.1039/c0sm00317d

Holmes, D., and Crosby, A. J. (2010). Draping films: a wrinkle to fold transition. *Phys. Rev. Lett.* 105:038303. doi: 10.1103/PhysRevLett.105.038303

Hong, W., Zhao, X., and Suo, Z. (2009). Formation of creases on the surfaces of elastomers and gels. *Appl. Phys. Lett.* 95:111901. doi: 10.1063/1.3211917

Huang, Z., Hong, W., and Suo, Z. (2004). Evolution of wrinkles in hard films on soft substrates. *Phys. Rev. E* 70:030601. doi: 10.1103/PhysRevE.70.030601

Huang, Z., Hong, W., and Suo, Z. (2005). Nonlinear analyses of wrinkles in a film bonded to a compliant substrate. *J. Mech. Phys. Solids* 53, 2101–2118. doi: 10.1016/j.jmps.2005.03.007

Jin, L., Takei, A., and Hutchinson, J. W. (2015). Mechanics of wrinkle/ridge transitions in thin film/substrate systems. *J. Mech. Phys. Solids* 81, 22–40. doi: 10.1016/j.jmps.2015.04.016

Jules, T., Lechenault, F., and Adda-Bedia, M. (2019). Local mechanical description of an elastic fold. *Soft Matter*. 15, 1619–1626. doi: 10.1039/C8SM01791C

Landau, L. D., and Lifshitz, E. M. (1959). *Course of Theoretical Physics Vol 7: Theory and Elasticity*. London: Pergamon Press.

Lechenault, F., Thiria, B., and Adda-Bedia, M. (2014). Mechanical response of a creased sheet. *Phys. Rev. Lett.* 112:244301. doi: 10.1103/PhysRevLett.112.244301

Lobkovsky, A., Gentges, S., Li, H., Morse, D., and Witten, T. A. (1995). Scaling properties of stretching ridges in a crumpled elastic sheet. *Science* 270, 1482–1485.

Lobkovsky, A. E. (1996). Boundary layer analysis of the ridge singularity in a thin plate. *Phys. Rev. E* 53:3750. doi: 10.1103/PhysRevE.53.3750

Lobkovsky, A. E., and Witten, T. (1997). Properties of ridges in elastic membranes. *Phys. Rev. E* 55:1577. doi: 10.1103/PhysRevE.55.1577

Manning, R. S. (2014). A catalogue of stable equilibria of planar extensible or inextensible elastic rods for all possible dirichlet boundary conditions. *J. Elasticity* 115, 105–130. doi: 10.1007/s10659-013-9449-y

Phungpaingam, B., and Chucheepsakul, S. (2018). Postbuckling behavior of variable-arc-length elastica connected with a rotational spring joint including the effect of configurational force. *Meccanica* 53, 2619–2636. doi: 10.1007/s11012-018-0847-x

Pocivavsek, L., Dellsy, R., Kern, A., Johnson, S., Lin, B., Lee, K. Y., et al. (2008). Stress and fold localization in thin elastic membranes. *Science* 320, 912–916. doi: 10.1126/science.1154069

Press, W. H., Teukolsky, S. A., Vetterling, W. T., and Flannery, B. P. (2007). *Numerical Recipes 3rd Edition: The Art of Scientific Computing*. Cambridge: Cambridge university press.

Sano, T. G., and Wada, H. (2018). Snap-buckling in asymmetrically constrained elastic strips. *Phys. Rev. E* 97:013002. doi: 10.1103/PhysRevE.97.013002

Tanaka, T., Sun, S.-T., Hirokawa, Y., Katayama, S., Kucera, J., Hirose, Y., et al. (1987). Mechanical instability of gels at the phase transition. *Nature* 325:796. doi: 10.1038/325796a0

Vliegenthart, G. A., and Gompper, G. (2006). Forced crumpling of self-avoiding elastic sheets. *Nat. Mater.* 5:216. doi: 10.1038/nmat1581

Wang, Q., and Zhao, X. (2015). A three-dimensional phase diagram of growth-induced surface instabilities. *Sci. Rep.* 5:8887. doi: 10.1038/srep08887

Yu, T., and Hanna, J. (2019). Bifurcations of buckled, clamped anisotropic rods and thin bands under lateral end translations. *J. Mech. Phys. Solids* 122, 657–685. doi: 10.1016/j.jmps.2018.01.015

Conflict of Interest Statement: The author declares that the research was conducted in the absence of any commercial or financial relationships that could be construed as a potential conflict of interest.

frontiers in Materials

ORIGINAL RESEARCH
published: 27 November 2019
doi: 10.3389/fmats.2019.00302

Toward Nanomechanical Models of Liquid-Phase Exfoliation of Layered 2D Nanomaterials: Analysis of a π – *peel* Model

Lorenzo Botto [1,2]*

[1] School of Engineering and Materials Science, Queen Mary University of London, London, United Kingdom, [2] Process & Energy Department, TU Delft, Delft, Netherlands

In liquid-phase exfoliation for the production of 2D nanomaterials fluid forces are used to gently overcome adhesive interlayer forces, leading to single- or few-layer 2D nanomaterials. Predicting accurately the critical fluid shear rate for exfoliation is a crucial challenge. By combining notions of fluid mechanics and fracture mechanics, we analyze a mathematical model of exfoliation, focusing on the π – *peel* regime in which bending forces are much smaller than the applied hydrodynamic forces. We find that in this regime the shear rate is approximately proportional to the adhesion energy, independent of the bending rigidity of the exfoliated sheet, and inversely proportional to the size a of a (assumed pre-existing) material flaw. The model appears to give values comparable to those obtained in wet ball milling, but to overestimate the shear rate values reported for turbulent exfoliation (by rotor mixing or microfluidization). We suggest that for turbulent exfoliation a "cleavage model" may be more appropriate, as it gives a stronger dependence on a and smaller critical shear rates.

Keywords: graphene, liquid-phase exfoliation, mechanics, fracture, theoretical modeling

OPEN ACCESS

Edited by:
Nicola Maria Pugno, University of Trento, Italy

Reviewed by:
Enrico Radi, University of Modena and Reggio Emilia, Italy
Massimiliano Gei, Cardiff University, United Kingdom

***Correspondence:**
Lorenzo Botto
l.botto@tudelft.nl

Specialty section:
This article was submitted to Mechanics of Materials, a section of the journal Frontiers in Materials

Received: *14 January 2019*
Accepted: *13 November 2019*
Published: *27 November 2019*

Citation:
Botto L (2019) Toward Nanomechanical Models of Liquid-Phase Exfoliation of Layered 2D Nanomaterials: Analysis of a π – peel Model. Front. Mater. 6:302. doi: 10.3389/fmats.2019.00302

INTRODUCTION

Graphene and other 2D nanomaterials in the form of atomically thin nanosheets promise unexpected performance in many applications. The nanosheets can be embedded in nanocomposites to make them conductive (Santagiuliana et al., 2018), improve barrier properties or increasing strength and toughness (Rafiee et al., 2010). Or they can be suspended in liquid solvents to produce conductive inks for printed electronics and high-performance coatings (Torrisi and Carey, 2018). While these applications are currently tested in small scale applications, to reach true market impact it is paramount to produce large quantities of 2D nanosheets cheaply, and with control over thickness, lateral area and amount of defects (Ferrari et al., 2015).

A very promising technique for the large-scale production of 2D nanosheets is liquid-phase exfoliation (Hernandez et al., 2008; Coleman, 2009; Yi and Shen, 2015). This technique is relatively simple. It consists in subjecting microparticles of layered 2D nanomaterial (each microparticle being composed of hundreds or thousands of layers) to large mechanical forces that detach the layers. Several different variants of the technique exist, the main ones being turbulent exfoliation (e.g., in rotor-stator mixers, Paton et al., 2014 or microfluidisation devices, Paton et al., 2017), wet ball milling (Knieke et al., 2010; Zhao et al., 2010), and sonication (Alaferdov et al., 2014). These techniques have in common the fact that the microparticles are initially suspended in a liquid (in wet ball milling the particles are wet by a liquid, but a thin layer of liquid is still present). In

addition to transmit mechanical stresses, the liquid enables to reduce the adhesion between the layers, prevent reaggregation, and make the mechanical action less aggressive (Shen et al., 2015). Bottom-up synthesis methods, such as Chemical Vapor Deposition in its different variants (Aïssa et al., 2015), are promising for producing high-quality 2D nanomaterials particularly suitable for devices. However, to produce 2D nanomaterials very cheaply for large-scale applications such as nanocomposites, inks or coatings, liquid-phase exfoliation is difficult to beat.

Optimizing liquid-exfoliation processes requires addressing a delicate balance: the mechanical stresses applied to the particles by the fluid must be sufficiently high to delaminate the particles, but not much higher. Excessive stresses can fragment the nanosheets, producing small area sheets of low intrinsic value, or damage the sheets (Johnson et al., 2015). Reaching the right stress level is thus paramount. However, particle-level stresses cannot be controlled directly. What can be controlled are large scale flow variables, such as the mixing power or, equivalently, the average shear rate the suspension is subject to. These are the macroscopic variables that can be controlled by the user in the production process. It would be highly valuable if analytical formulas relating these macroscopic variables to microscopic exfoliation thresholds and time scales were available. Developing these formulas requires an understanding of the flow physics and deformation mechanics at the particle level (**Figure 1**).

Quite surprisingly, despite the growing importance of liquid-phase processing in the production of graphene and other 2D nanomaterials, the development of theoretical models for liquid-phase exfoliation is at its infancy. Two theoretical models have appeared recently which seem to be relevant. An exfoliation model based on a sliding deformation was proposed by Chen et al. (2012), and later extended by Paton et al. (2014). In this model, the shear forces exerted by the fluid are assumed to balance the rate at which the total surface energy (including solid-solid, solid-liquid, and liquid-liquid interaction energy) changes with respect to the sliding distance. The model was used to describe the dependence of the critical shear rate for exfoliation on the size of the suspended plate-like particles, the viscosity of the fluid, and the energy of adhesion. Chen-Paton's model is insensitive to the mechanical property of the particle: the bending rigidity or young Modulus of the particles do not appear in the model. The assumptions of this model were not stated with sufficient clarity to rigorously assess its validity from a nanomechanical perspective. Prior to the work of Chen, in 2009, a model of exfoliation was developed by Borse and Kamal (2009) to model the exfoliation of multilayer clay particles in polymers. Unlike Chen/Paton's model, Borse's model is sensitive to the mechanical properties of the particle. The formulation of Borse's model is based on Kendall's theory for peeling of elastomers (Kendall, 1975). Borse correctly identified that because the area of contact between the sheets is large, a simple balance between adhesive forces and shear forces gives values of the shear stress too high to be realistic. As a consequence, one must hypothesize that the debonding of the layers is due to stress concentration at the microscopic crack tip of a pre-existing flaw in the inter-layer interface.

Borse's model includes in the fracture mechanics formulation the work done by the fluid forces, the stretching energy associated to the extension of each layer, and the adhesion energy associated to the van der Waals forces between the layers. For the case of constant edge load (identical to the one analyzed by Kendall), Borse and collaborators analyzed the values of the critical shear stress as a function of the peeling angle and the Young modulus of the exfoliated sheet.

We adopt a view similar to that of Borse, and consider exfoliation due to extension of an initial flaw in the inter-layer interface. The extension is caused by a peeling process, whereby the forces driving peeling are hydrodynamic in nature. We envision that the fluid opens a pre-existing crack of length a. The opening angle will depend on the ratio of hydrodynamic and bending forces. If this ratio is small, the opening angle will be small. If this ratio is much larger than one, the flap will turn by 180, and the direction of pulling will be parallel to the direction of propagation of the crack, as illustrated in **Figure 2b**. This configuration is analogous to the one considered in the "$\pi - peel$" mechanical test to measure adhesion (Lin et al., 2002). For brevity, in the current paper, we refer to this configuration as "π-peel" configuration.

In this paper we analyze in detail a mathematical model of exfoliation for this "π-peel" configuration**,** by rigorously justifying the fluid and solid mechanics aspects of the problem. Particularly, we discuss the parameter values for which this configuration may be observed. In contrast to the model by Borse et al., we assume that each layer is perfectly inextensible. Our work takes inspiration from the work on the "inextensible fabric" approximation discussed in Roman (2013), but we recast our results in the context of 2D nanomaterials processing, so that a direct comparison with experimental data from the literature can be made.

The problem we are tackling is one of the first explorations in terms of mechanics of a very complex fluid-structure interaction problem, which needs to be analyzed from different perspectives to be fully understood. Rather than analyzing in depth a sophisticated model, our aim with the paper is to test the prediction of simple models which will enable us to identify the theoretical directions that could bring us close, in terms of orders of magnitude, to the published experimental data for the critical shear rates.

DIMENSIONAL ANALYSIS OF THE EXFOLIATION PROBLEM

Before considering a particular exfoliation configuration, let us first analyze the general problem of exfoliation from the point of view of dimensional analysis. The critical shear rate for exfoliation, $\dot{\gamma}$, depends on the properties of the fluid (density ρ, viscosity μ, and wetting properties), the mechanical and geometrical properties of the layered micro-particle (particle length L, particle width W, Young modulus of each layer E, bending rigidity of each layer D_0, total number of layers N, flaw

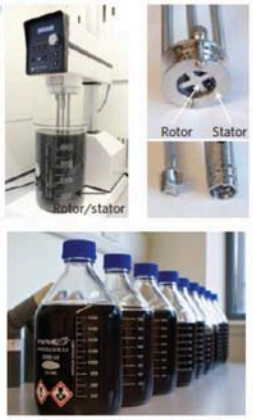

Large-scale flow variables
(average shear rate, mixing power)

Microscale exfoliation mechanics
(threshold for inter-layer debonding, time-scales of microscopic exfoliation)

FIGURE 1 | Optimizing liquid-phase exfoliation processes (left, reproduced with permission from Paton et al., 2014) requires models to link large-scale flow variables to the micromechanics of exfoliation.

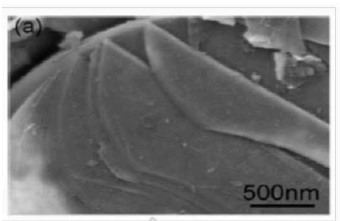

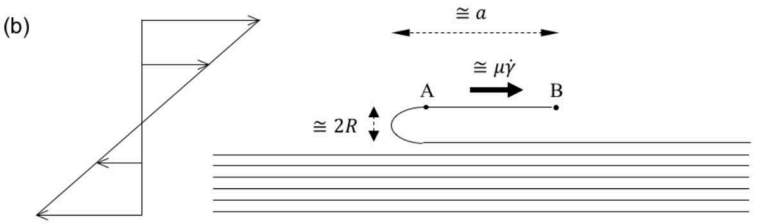

FIGURE 2 | (a) Peeling deformation of Boron Nitride following wet ball milling; Scanning Electron Microscopy image reproduced with permission from Li et al. (2011). **(b)** Schematic of the "π-peel" configuration. We assume that the inter-layer interface is debonded over a length $a - 2R \approx a$, where R is the radius of curvature of the fold. The local shear flow, whose linear profile is illustrated in the sketch, produces a tangential stress on the flap of order $\mu\dot{\gamma}$.

size a), and the mechanical and geometrical properties of each inter-layer interface (adhesion energy Γ, area of contact, presence of flaws, etc.).

In exfoliation problems, the particle Reynolds number is typically small, $Re = \rho\dot{\gamma}L^2/\mu \ll 1$, so ρ is not an important parameter. Among the mechanical properties, the adhesive properties of each inter-layer, parameterized by Γ and the bending rigidity of each layer D_0 are likely to be dominant controlling parameters. The Young modulus of graphene is huge ($E \sim 1TPa$, Lee et al., 2008) while its bending rigidity is low ($D_0 \sim$7eV, Lindahl et al., 2012), so we may regard graphene as an inextensible membrane of finite bending rigidity.

The above parameters suggest a functional relationship of the form

$$\dot{\gamma} = f\left(\Gamma, D_0, N,\ n, \mu, a,\ L,\ W\right) \tag{1}$$

Some simplifications are possible, under the following hypotheses and observations:

- In the zero Reynolds number limit appropriate for colloidal particles, the pressure and viscous stresses scale as $\mu\dot{\gamma}$, so the viscosity enters into the problem only multiplied by the shear rate;
- It can be assumed that the forces induced by the fluid scale proportionally to W. This is not strictly true unless $W \gg L$, while typically $W \sim L$. However, if edge effects are neglected this is a reasonable approximation if the goal is to obtain order of magnitude estimates;
- The direct dependence on n can be neglected if one assumes $\frac{n}{N} \ll 1$. The indirect dependence of the problem on n is still present, because the bending rigidity of the flap depends on n. The bending rigidity of multilayer graphene scales roughly as n^3 for $n \geq 3$, so for multilayers we can write $D(n) \cong D_0 n^3$, where $D_0 \cong 20eV$ is the extrapolated value of the single graphene sheet (Sen et al., 2010);
- The dependence on L can be ignored, at least as a first approximation, because the applied hydrodynamic forces on the flap and the "resistive" forces due to elasticity and adhesion depend primarily on a.

Under the hypotheses above, using a and D to make the other parameters dimensionless, Equation (1) can be written as

$$\frac{\dot{\gamma}\mu a^3}{D} = f_1\left(\frac{\Gamma a^2}{D}\right) \tag{2}$$

where f_1 is a non-dimensional function of its argument. Equation (2) shows that the *non-dimensional critical shear rate*, $\frac{\dot{\gamma}\mu a^3}{D}$, is a unique function of the *non-dimensional adhesion energy*, $\frac{\Gamma a^2}{D}$.

To discuss the comparison of analytical and experimental results, it is useful to assume for f_1 a power-law relationship, for which Equation (2) becomes

$$\frac{\dot{\gamma}\mu a^3}{D} \sim \left(\frac{\Gamma a^2}{D}\right)^{\xi} \tag{3}$$

The values the exponent ξ can attain are constrained by physical consideration. It is expected that an increase in flaw size will make the material weaker, so $\dot{\gamma}$ must decrease with increasing a. This requires $\xi < 3/2$. In addition, an increase in adhesion energy must translate into a larger fluid shear stress. This is only possible if $\xi > 0$.

An interesting possibility is the case $\xi = 1$. For this choice of the exponent, the bending rigidity becomes an irrelevant parameter. A complete independence on the bending rigidity can only be plausible if the bending rigidity is so low, that its precise value does not matter (or nearly so).

EXFOLIATION IN THE "π-PEEL" CONFIGURATION

Figure 2a, from Li et al. (2011), shows the surface of a nanomaterials after wet ball milling. Flexible layers of nanomaterials have been partially peeled off due to strong shear forces, leaving a fold of very small radius of curvature. A model for this situation can be developed by considering a continuum sheet partially detached from a rigid "mother particle" (**Figure 2b**). We assume that all the sheets have the same length L. The total thickness of the microparticle is $h \ll L$. The geometry of the peeled flap is composed of a curved fold, of radius of curvature R, and a flat portion (from point A to point B in the schematic). The flat portion is subject to a tangential shear stress $\mu\dot{\gamma}$.

In the case of ball milling, the shear stress is created by a relative velocity U between the milling balls acting on a small gap d between the balls, leading to a shear rate $\dot{\gamma} \cong U/d$. In the case of a multilayer particle suspended in a turbulent flow, the ambient shear rate instantaneously "seen" by the particle is the result of the work done by the largest turbulence structures on the smallest, dissipative Kolmogorov eddies (Tennekes and Lumley, 1972). For microparticles smaller than the Kolmogorov scale, equilibrium between the energy rate input P (e.g., the mixing power) and the viscous dissipation occurring at the scale of the particles gives $\dot{\gamma} \cong \sqrt{P/(V\mu)}$, where V is the liquid volume (see, e.g., Varrla et al., 2014 for an application to graphene).

The length of the detached layer is a. Because $R \ll a$, the flap length is also approximately equal to a. The tangential force per unit width acting on the flap is $\mu\dot{\gamma}a$.

We need to better specify certain fluid mechanics assumptions. First of all, the model assumes that the particle is aligned with the flow. In fact, plate-like particles rotate when suspended in a shear flow. However, the rotation is very slow when the plate-like particle is nearly aligned with the flow and the aspect ratio is large, with a rate of rotation of the order of $h/L\dot{\gamma}$ (Jeffery, 1922). For most of its rotation period, a plate-like particle of large aspect ratio such as a multilayer microparticle can be considered to be aligned with the flow. A second aspect not included in the model above is the effect of normal hydrodynamic stresses. For a plate-like particle aligned with the flow, normal stresses of the order of $\left(\frac{h}{L}\right)\mu\dot{\gamma}$ act on the surfaces of the particle parallel to the flow direction (e.g., on the flap surface between A and B) (Singh et al., 2014). Because $\frac{h}{L} \ll 1$, along the surface of the flap these stresses are subdominant with respect to the tangential stresses and are thus neglected in the current model. The normal stresses acting on the curved fold, in the direction of the flow, are instead of $O(\mu\dot{\gamma})$. The effect of normal stresses on the model predictions will be considered in section Normal Load on the Curved Fold. We assume that L is smaller than any scale of the flow, so that the flow field around the particle is smooth. For particles in turbulence, this requirement translates to $L \ll \eta_K$, where η_K is the Kolmogorov scale (Landau and Lifshitz, 1986).

The critical value of $\dot{\gamma}$ for exfoliation can be calculated by considering the instantaneous equilibrium between the external work, the change in adhesion energy and the change in bending energy for an inextensible sheet. The analysis is similar to that in Roman (2013), but now the external force is not constant. The velocity of point A (or B) is twice the velocity of the advancing peeling front. As a consequence, as the peeling front moves by an amount da the work done by the external force is $(W\mu\dot{\gamma}a)\,2da$, where W is the width. The change in adhesion energy is $W\Gamma da$, where Γ is the adhesion energy per unit area (also called work of separation). Calling $dE(\dot{\gamma})$ the infinitesimal change in adhesion energy corresponding to da, the critical value of $\dot{\gamma}$ for crack initiation satisfies:

$$dE(\dot{\gamma}) + W\Gamma da = 2W\mu\dot{\gamma}ada \tag{4}$$

The bending energy is denoted $E(\dot{\gamma})$ to highlight that this quantity is a function of the shear rate. Considering a curvilinear coordinate s with origin at the crack tip, the bending energy is $E = \frac{1}{2}DW\int_0^a(\dot{\theta})^2 ds$, where $\theta(s)$ is the rotation angle at s and $\dot{\theta} = \frac{d\theta}{ds}$ is the local curvature. The bending energy integral is dominated by the curvature $1/R$ at the crack tip, which has an extent of the order of $2R$. Thus, the order of magnitude of the bending energy is $W\frac{D}{R}$. The function $\theta(s)$ can be calculated by considering the equation for the Elastica (Audoly and Pomeau, 2010) for a fixed value of a, which in our case reads

$$\ddot{\theta} + \frac{\mu\dot{\gamma}a}{D}\sin(\theta) = 0 \tag{5}$$

Here D is the bending rigidity of the elastic element. Equation (5) is obtained from the equation of equilibrium to rotation for an infinitesimal element of flap, $\frac{dM}{ds} = (\boldsymbol{F}(s) \times \boldsymbol{t}) \cdot \boldsymbol{e}_z$ (Landau and Lifshitz, 1986). In this expression, $M = D\dot{\theta}$ is the moment of the internal stresses, $\boldsymbol{F}$ is the internal force per unit width, $\boldsymbol{t}$ is the local tangent vector, and $\boldsymbol{e}_z$ is the unit vector oriented along the width direction. We have assumed that the only external (hydrodynamic) forces act from point A to point B. Hence, in the curved portion of the flap, the equation of equilibrium to translation $\frac{d\mathbf{F}}{ds} = 0$ requires that $\boldsymbol{F}$ is a constant vector (Landau and Lifshitz, 1986). Such constant vector can be easily calculated

by noting that point A the force per unit width $\boldsymbol{F}$ is equal to the tension $\cong\mu\dot{\gamma}a\mathbf{e}_x$ (the unit vector $\mathbf{e}_x$ being parallel to the flow and pointing in the flow direction). As a consequence, $\boldsymbol{F}(s)\cong\mu\dot{\gamma}a\boldsymbol{e}_x$ and $(\boldsymbol{F}(s)\times\boldsymbol{t})\cdot\boldsymbol{e}_z\cong\mu\dot{\gamma}a\sin\theta$. Inserting this last expression into the equation of equilibrium to rotation gives (5).

The parameter $\frac{\mu\dot{\gamma}a}{D}$ appearing in Equation (5) has the dimensions of the square of a reciprocal length. Because there are no other characteristic lengths in the problem, we anticipate that the curvature of the fold R scales as $\left(\frac{D}{\mu\dot{\gamma}a}\right)^{1/2}$.

A solvable first-order non-linear equation can be obtained by multiplying Equation (5) by $\dot{\theta}$, and integrating with respect to s. The result is $\frac{1}{2}\left(\dot{\theta}\right)^2-\frac{\mu\dot{\gamma}a}{D}\cos(\theta)=c_1$, where c_1 is a constant. For values of s corresponding to the region from point A to point B, the rotation angle is constant and equal to $\theta=\pi$. Hence, $c_1=\frac{\mu\dot{\gamma}a}{D}$. Using this value and the trigonometric identity $(1+cos\theta)=2\cos^2\theta/2$, we obtain $\dot{\theta}=2\sqrt{\frac{\mu\dot{\gamma}a}{D}}\cos(\frac{\theta}{2})$. This is a separable equation whose solution is $\theta\left(s'\right)=2\arcsin(\tanh s')$, where $s'=s/\sqrt{\frac{D}{\mu\dot{\gamma}a}}$. The corresponding bending energy is

$$E=2W\sqrt{\mu\dot{\gamma}aD} \tag{6}$$

For $s\ll\sqrt{\frac{D}{\mu\dot{\gamma}a}}$ we have $\theta(s)\cong 2s/\sqrt{\frac{D}{\mu\dot{\gamma}a}}$. Hence, the radius of curvature near the crack tip is of the order of $\left(\frac{D}{\mu\dot{\gamma}a}\right)^{1/2}$, as anticipated.

Inserting expression (6) into the energy balance (4) gives

$$a^{-1/2}\sqrt{\mu\dot{\gamma}D}+\Gamma=2\mu\dot{\gamma}a \tag{7}$$

This expression yields the critical shear rate as a function of the parameters a, D and μ.

It is convenient to recast Equation (7) in terms of the non-dimensional shear rate $\frac{\dot{\gamma}\mu a^3}{D}$ and non-dimensional adhesion energy $\frac{\Gamma a^2}{2D}$ (introduced in section Dimensional Analysis of the Exfoliation Problem):

$$\frac{\Gamma a^2}{2D}=\frac{\dot{\gamma}\mu a^3}{D}-\frac{1}{2}\sqrt{\frac{\dot{\gamma}\mu a^3}{D}} \tag{8}$$

In contrast to the constant edge force case (Roman, 2013), in our case the bending energy depends on a and the term dE is not zero, giving rise to the square root term on the right-hand side of Equation (8).

From Equation (8), and comparing with Equation (3), the limit $\frac{\mu\dot{\gamma}a^3}{D}\to\infty$ gives a power-law exponent $\xi=1$, exactly. The effect of the bending energy term is to increase the critical exfoliation value obtained in this asymptotic limit by an amount that depends on the square-root of the shear rate.

Conditions for "π-peel"

For the analytical solution (8) to be valid, the flap length must be long in comparison to the radius of curvature of the fold (Roman, 2013). The condition $R\ll a$ gives $\frac{\mu\dot{\gamma}a^3}{D}\gg 1$. Equation (9) also requires the flap geometry at equilibrium to assume a shape similar to that in **Figure 2**. For the flap to bend to such an extent the ratio of viscous forces ($\sim\mu\dot{\gamma}Wa$) to bending forces ($\sim DW/a^2$) must be large. This, again, gives $\frac{\mu\dot{\gamma}a^3}{D}\gg 1$. Hence, the condition $\frac{\mu\dot{\gamma}a^3}{D}\gg 1$ simultaneously ensures a good separation of scale between the fold and the flap, and that the assumption of nearly tangential viscous force on the flap is valid.

Figure 3 illustrates how the radius of curvature of the fold, estimated as $R\cong\frac{1}{2}\left(\frac{D}{\mu\dot{\gamma}a}\right)^{1/2}$, varies with the length of the flap, for three typical shear rates. Rather than plotting R we plot $2R$, which gives a measure of the maximum height of the folded region. The bending rigidity is set to $D=10^{-18}J$, close to that of single-layer graphene (Lindahl et al., 2012). In **Figure 3A**, a dynamic viscosity $\mu=0.001\ Pa\cdot s$ is assumed, typical of aqueous solvents and NMP (Paton et al., 2014). In **Figure 3B**, the viscosity is increased to $\mu=1\ Pa\cdot s$. For $\mu=0.001\ Pa\cdot s$, a good separation of scales between R and a occurs if the shear rate is at least $\dot{\gamma}=10^6s^{-1}$. As the viscosity increases to $\mu=1\ Pa\cdot s$, the *"π-peel"* configuration regime occurs for smaller values of shear rate (**Figure 3B**).

The radius of curvature of the flap increases strongly with the number of layers n. Assuming a cubic relation $D=D_0n^3$ yields the results shown in **Figure 4**. For this figure, $a=200\ nm$ and $\dot{\gamma}=10^6s^{-1}$; results are shown for three different viscosities. Even considering relatively few layers, for R to be sufficiently small in comparison to a, either the viscosity must be relatively large or, if the viscosity is comparable to that of water, the shear rate must be larger than 10^6s^{-1}.

We can call *strongly-stressed* nanosheets, 2D material nanosheets for which the scale separation between R and a is complete, and *mildly-stressed* nanosheets, nanosheets for which R is larger than a, but not by a very large factor. Correspondingly we have two approximations for the critical shear rate. For strongly stressed nanosheets the bending rigidity contribution is negligible and

$$\dot{\gamma}\approx\frac{\Gamma}{2\mu a} \tag{9}$$

This equation is, strictly speaking, a good approximation when $\frac{\mu\dot{\gamma}a^3}{D}\to\infty$ (which is equivalent to $\Gamma a^2/D\to\infty$). For mildly stressed sheets, solving Equation (8) for $\dot{\gamma}$ yields

$$\frac{\dot{\gamma}\mu a^3}{D}=\frac{\Gamma a^2}{2D}\left(1+\frac{1}{4(\Gamma a^2/D)}+\frac{\sqrt{1+\frac{8\Gamma a^2}{D}}}{\frac{4\Gamma a^2}{D}}\right) \tag{10}$$

This approximation is more accurate than (9) when $\frac{\Gamma a^2}{D}$ (or equivantly $\frac{\mu\dot{\gamma}a^3}{D}$) is large but finite. For order of magnitude estimates, both (9) and (10) are acceptable. Note that Γ is the work required to separate two surfaces, so $\Gamma/2$ is equal to the surface tension of the solid.

Equation (9) is consistent with Kendall's theory for peeling of an extensible thin sheet [Borse's model for exfoliation of clays

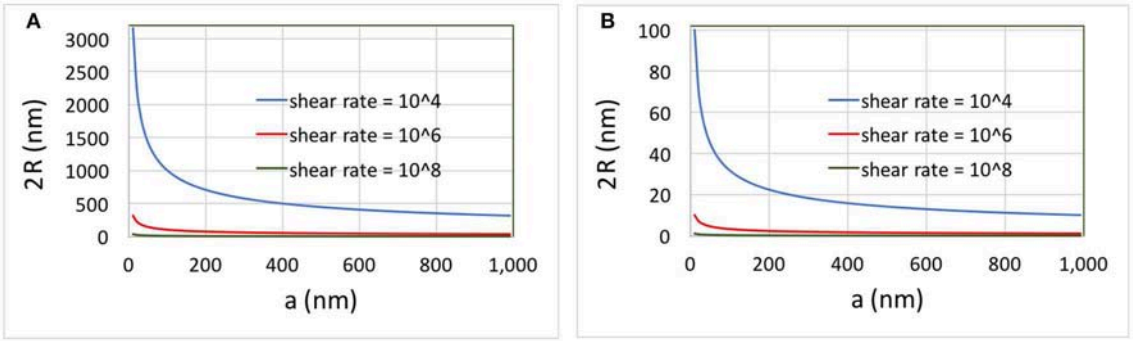

FIGURE 3 | Two times the radius of curvature of the fold vs. length of the flap for **(A)** $\mu = 0.001\ Pa \cdot s$ *and* **(B)** $\mu = 1\ Pa \cdot s$. The bending ridigity is assumed to be $D = 10^{-18}J$, corresponding to ∼6eV. The quantity 2R corresponds approximately to the maximum height of the fold.

(Borse and Kamal, 2009) is based on Kendall's theory, so it reaches the same conclusions]. In the case of a constant edge load F applied at an angle ϕ, Kendall calculated that the peeling force for an elastic film of thickness d and Young's modulus E satisfies $\left(\frac{F}{W}\right)^2 \frac{1}{2dE} + \left(\frac{F}{W}\right)(1 - cos\phi) = \Gamma$. For $E \to \infty$ (inextensible sheet) and $\phi = \pi$, this equation recovers Equation (9) when $F = \mu aW$. Incidentally, the order of magnitude scaling suggested by Equation 9 is identical to that obtained by Paton et al. (2014) for sliding of parallel, rigid platelets, although their configuration is different. In Paton's formulation, the energy term is given by the change in surface energy corresponding to a change in overlap length x between the platelets. Paton's argument for obtaining the critical sliding force is that the overlap area is Wx, and the corresponding surface energy is ΓWx (apart from constant energy terms that do not affect the force). Thus, the sliding force $d/dx(\Gamma x)$ per unit width is constant, and equal to Γ. This results seems to contradict Kendall's theory, which shows that for $\phi = 0$ (as in a lap shear joint configuration) F is proportional to $\sqrt{\Gamma}$, not Γ. A possible explanation for the discrepancy is the neglect in Paton's model of the straining of molecular bonds as two rigid sheets slide by a distance comparable to the crystal lattice (Xu et al., 2011) and the disregard of non-uniformities in the interfacial stress (Pugno, 2010).

Normal Load on the Curved Fold

Models (9) and (10) neglect the normal force on the curved fold acting in the direction of the flow. This distributed force pushes the fold in the same direction as the tangential force pulling the flap, so we expect a reduction in the critical shear rate. We can better quantify this statement. The normal force on the flap f can be estimated to be of the order of $\mu\dot{\gamma}RW$. Without attempting to solve Equation (5) exactly by including a distributed force, we can approximate the problem by assuming that f is concentrated in the mid-point of the fold, $s \cong R/2$. At this location the internal force $\boldsymbol{F}(s)$ will have a discontinuity: for $s > R/2$, $\boldsymbol{F} \approx \mu\dot{\gamma}a\boldsymbol{e}_x$ as before; for $s < R/2$, $\boldsymbol{F}$ will increase to $\approx \mu\dot{\gamma}(a + R)\boldsymbol{e}_x$.

The equation for the flap shape for $s \leq R/2$ is thus identical to Equation (5), except that in this case $(a + R)$ replaces a. In terms

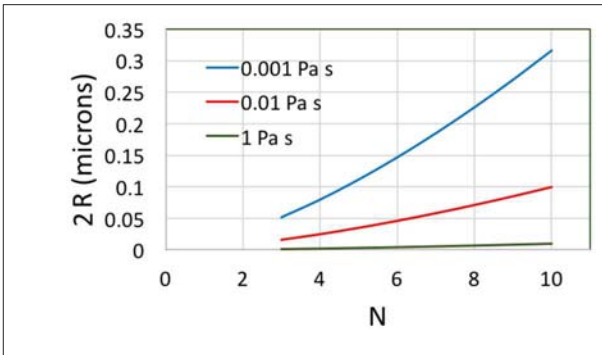

FIGURE 4 | Two times the radius of curvature of the fold *vs. number of layers* for a = 200 nm, $\dot{\gamma} = 10^6 s^{-1}$ and $D = 10^{-18}J$.

of the non-dimensional curvilinear coordinate $S = s\sqrt{\mu\dot{\gamma}a/D}$, the system to be solved is thus:

$$\frac{d^2\theta}{dS^2} + \left(1 + \frac{R}{a}\right)\sin(\theta) = 0 \ \ for\ S \leq \frac{1}{2} \tag{11a}$$

$$\frac{d^2\theta}{dS^2} + \sin(\theta) = 0 \ \ for\ S > \frac{1}{2} \tag{11b}$$

Figure 5 illustrates a numerical solution of the system above, comparing the rotation angle $\theta(S)$ obtained for $f = 0$ with the corresponding value obtained for $f = \mu\dot{\gamma}RW$. A relatively large ratio $\frac{R}{a} = 0.7$ is chosen to make the effect of f clearer on the graph. The deviation in $\theta(S)$ due to f is small, and decays as S increases. Because of this small deviation, it is useful to decompose θ as $\theta = \theta_0 + \theta'$ where θ_0 is the unperturbed solution. **Figure 6A** illustrates how θ' varies with S for $\frac{R}{a} = 0.5$. The perturbation has a maximum near $S = 1$, and decays to negligible values for $S \cong 6$. **Figure 6B** shows how the maximum value of θ' changes with R/a. This figure shows that $\theta' \propto R/a$ when R/a is sufficiently small. The numerical data suggests

$$\theta'(S) = \frac{kR}{a}g(S) \tag{12}$$

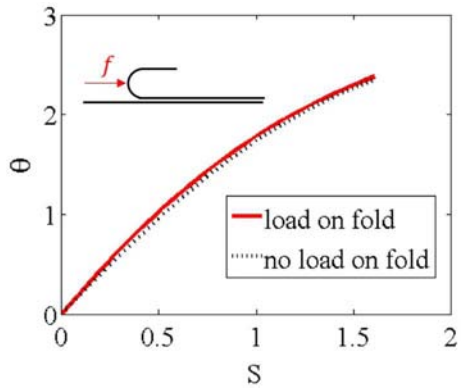

FIGURE 5 | Effect of a point load of magnitude $f = \mu R\dot{\gamma}W$ acting on a fold of radius R for R/a = 0.7.

where $k \approx 0.07$ and g is a non-dimensional function whose maximum is 1. Up to first order in θ' the bending energy can be written as

$$E \cong \frac{1}{2}D\frac{W}{R}\int_0^\infty \left(\frac{d\theta_0}{dS}\right)^2 dS + D\frac{W}{R}\int_0^\infty \left(\frac{d\theta_0}{dS}\right)\left(\frac{d\theta'}{dS}\right) dS \quad (13)$$

The first integral is the bending energy contribution appearing in Equation 8. The second integral is, to leading order, the change in E due to f. By observing that that the integral from 0 to ∞ converges for values of S of order 1, the order of magnitude of this second term can be estimated as

$$D\frac{W}{R}\int_0^\infty \left(\frac{d\theta_0}{dS}\right)\left(\frac{d\theta'}{dS}\right) dS \sim D\frac{W}{R}k\left(\frac{R}{a}\right) \quad (14)$$

This expression shows that the bending energy contribution originating from the normal load on the fold is, to leading order, independent of R and $\dot{\gamma}$.

Using Equation (14), Equation (7) can be written as

$$a^{-1/2}\sqrt{\mu\dot{\gamma}D} + \left(\Gamma - c_L k\frac{D}{a^2}\right) = 2\mu\dot{\gamma}a \quad (15)$$

where the constant c_L is a numerical prefactor. By comparing Equations (15) and (7), we can see that the leading-order effect of f is to reduce the critical shear rate. The net effect is analogous to reducing Γ, by an amount that depends on D and a.

The second-order term neglected in Equation (13), together with the corresponding external work done by f, would give rise to a bending energy contribution scaling as DWk^2R/a. This correction would translate to a term $O\left(\frac{k^2}{\sqrt{\frac{\dot{\gamma}\mu a^3}{D}}}\right)$ in Equation 10, much smaller than the retained bending energy terms.

We have initially assumed that the normal force on the fold is $\mu\dot{\gamma}RW$. The correct prefactor, and thus c_L, will depend on the detailed fluid dynamics of the problem. The drag force per unit width on a cylinder of radius R attached to a wall in shear flow is $4\pi\mu\dot{\gamma}R$ (Davis and O'Neill, 1977). If the drag on the fold is assumed to be half that on a cylinder, then $f = 2\pi\mu\dot{\gamma}RW$. Based on this estimate, the numerical prefactors should be 2π larger than assumed so far.

The effect of the normal force on the fold is typically small, because $R \ll a$. However, it could become important if the tangential force on the flap is reduced. Carbon 2D nanomaterials in contact with water exhibit relatively large slip velocities [with slip lengths in the range 10–80 nm (Thomas and McGaughey, 2008; Falk et al., 2010)], meaning that the no-slip condition at the solid-liquid interface is not satisfied identically. If a large velocity slip is present, the tangential stress on the flap will be reduced from the value $\dot{\gamma}\mu$ assumed in our model. On the other hand, the value of f–being related to a normal force—should not depend strongly on the slip length (a finite normal force on the fold is expected even for infinite slip lengths). In this situation, the effect of the normal force on the fold could become significant.

Modeling the force using a constant distributed force in the horizontal direction, rather than a point force, does not change the order of magnitude of the estimate presented in the current section. Indeed, in this case $\frac{d\boldsymbol{F}}{ds} = -\mu\dot{\gamma}\boldsymbol{e}_x$, which integrated gives $\boldsymbol{F} = \mu\dot{\gamma}(s^* + a - s)\boldsymbol{e}_x$, where $s^* \cong 2R$ is the location where the flap starts becoming horizontal. Inserting into the equation for the moment and normalizing gives $\frac{d^2\theta}{dS^2} + \left(1 + \frac{s^*}{a} - \frac{s}{a}\right)\sin(\theta) = 0$ for $s < s^*$. The essential difference with Equation (11a) is the term containing $\sin\theta$ multiplied by s; this difference makes the equation not easily solvable by direct integration (Rohde, 1953). However, because the term in parenthesis is smaller than $\left(1 + \frac{s^*}{a}\right)$, and $s^* \cong 2R$, the equation is bound from above by Equation (11a), if we choose $f = 2\mu\dot{\gamma}RW$ instead of $f = \mu\dot{\gamma}RW$. Differences between the point force and distributed force prediction are thus within the uncertainties, which we have discussed above, in the value of the drag force f.

Effect of the Solvent on Adhesion Strength

The parameter Γ is the energy of adhesion per unit area of contact. In vacuum or in an inert gas, the work to separate the surfaces is twice the surface tension of the solid, $\Gamma = 2\gamma_{so}$ (Lawn, 1993).

It is well-known that the presence of a liquid can reduce adhesion. Johnson et al. (1971) carried out lubricated adhesion experiments with rubber spheres, both in air and in liquids. They found that immersion of the surfaces in water reduced the adhesion between the spheres. When the contact was immersed in a 0.01 molar solution of sodium dodecyl sulfate (SDS) the results closely agreed with the Hertz theory down to the lowest loads measured, indicating that adhesion was practically suppressed. Haidara et al. (1995) studied the adhesion of semi spherical PDMS lenses on flat PDMS surfaces. They also found that the presence of surfactants reduced the size of the contact region. The deformations resulting on contacting small (1–2 mm) semispherical lenses of elastomeric poly-(dimethylsiloxane) (PDMS) with the flat sheets of this material were measured in air and in mixtures of water and methanol by Chaudhury and Whitesides (1991). They found that the adhesion between PDMS surfaces was strongest in water, and

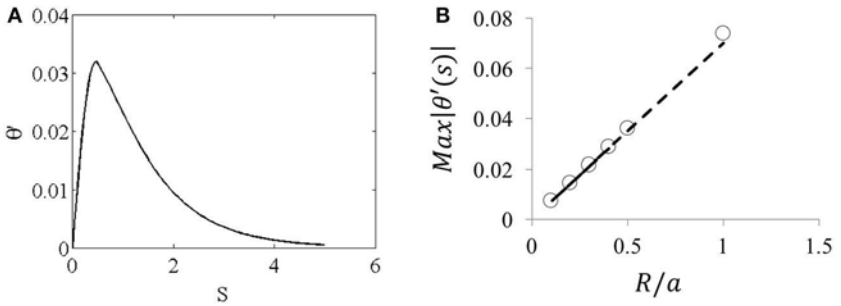

FIGURE 6 | (A) Perturbation in the local angle due to the point load for R/a = 0.5. **(B)** Maximum value of $|\theta'(S)|$ vs. R/a'. The dashed line is $|\theta'(S)| = 0.07R/a$.

decreased as the hydrophobicity of the medium decreased. van Engers et al. (2017) using a method conceptually similar to that of Johnson, Kendall and Roberts measured experimentally the graphene-graphene interfacial energy γ_{so}, obtaining 115 mN/m in inert gas, 83 in water, 29 in sodium cholate, a surfactant. The value obtained for graphene in an inert gas is close to the value 110 mN/m previously reported for graphene-graphite interaction by Wang et al. (2016). Shih et al. (2010) carried out molecular dynamics of the interaction between rigid graphene sheets in a variety of solvents, and obtained a minimum in the interaction energy of 250 $kJmol^{-1}nm^{-2}$ for water and around 100 $kJmol^{-1}nm^{-2}$ for N-methylpyrrolidone (NMP). Because the reduction in cohesive stresses can be related to a reduction in the depth of the potential energy well for the molecular bonds near the crack tip (Stoloff and Johnston, 1963; Lawn, 1993), this last data suggests that the values of the surface tension for water and NMP are of comparable order of magnitude (despite the fact that NMP is considered a much better solvent for graphene than water!).

From the data above there is evidence to suggest that: (i) the intrinsic value of Γ corresponding to vacuum or an inert gas is in the range 0.20–0.25 N/m; (ii) "good" solvents can reduce Γ, but probably not by several orders of magnitude. To compare with experimental data we will assume that Γ in typical liquid solvents ranges from 0.01 N/m to 0.1 N/m, with the lower value being characteristic of a good solvent.

Critical Shear Rate: Comparison With Experimental Data

We have seen that if the microscopic peeling configuration is as in **Figure 2** the order of magnitude of the critical shear rate is given by $\dot{\gamma} \approx \frac{\Gamma}{2\mu a}$, i.e., Equation 3 with $\xi = 1$. **Figure 7A** compares $\dot{\gamma} = \frac{\Gamma}{2\mu a}$ curves against experimental data for $\mu = 10^{-3} Pa \cdot s$ and two surface energy values: $\Gamma = 0.1 N/m$ and $\Gamma = 0.01 N/m$. Each experimental case is denoted by a horizontal row of symbols corresponding to several values of *a*. This was done because the value of *a* in experiments is unknown. Experimental cases correspond to turbulent exfoliation in a rotor-stator mixer (Paton et al., 2014), turbulent exfoliation in microfluidization (Karagiannidis et al., 2017; Paton et al., 2017) and wet ball milling (Knieke et al., 2010). In the case of wet ball milling, a typical stress energy SE∼0.134 μJ was reported for ball diameter $d_{gm} = 100\ \mu$m and rotation rate 1,500 rpm. The critical stress energy can be converted to a stress τ of the order of $10^5 Pa$ assuming that SE is dissipated within a contact region of volume $\sim d_{gm}^3$. With $\tau = \mu\dot{\gamma}$ and viscosity $\mu = 10^{-3} Pa \cdot s$, a stress of $10^5 Pa$ corresponds to an equivalent critical shear rate value of $10^8 s^{-1}$. This is the estimated value reported in **Figure 7A**.

The graph shows that for realistic values of Γ and for a range of plausible values of flaw size (we can estimate that for particles of length $L = 1\mu$m the flaw size ranges roughly from 50 nm to 500 nm) the expression $\dot{\gamma} \approx \frac{\Gamma}{2\mu a}$ largely overestimates the experimental data for turbulent exfoliation (i.e., exfoliation in rotor-stator mixers or microfluidisation). Even for $\Gamma = 0.01$ N/m, which is smaller than any measured value for the adhesion energy of graphene (see discussion in section Effect of the Solvent on Adhesion Strength), the critical shear rate is much larger than what reported for rotating mixer and microfluidization. Instead, the values predicted by $\dot{\gamma} \approx \frac{\Gamma}{2\mu a}$ are reasonably close to those estimated for ball milling, a technique that allows large stresses to be produced.

An Alternative Model: Flow-Induced Cleavage (for Small Opening Angles)

From **Figure 7A** it can be seen that if an exponent $\xi = 1/2$ is assumed, a much closer agreement with the experimental data for rotating mixer and microfluidisation approaches is achieved. An exponent of 1/2 can be obtained if we assume that the bending of the flap is caused by a *normal* stress on the flap of order of $\mu\dot{\gamma}$, as in the "cleavage" configuration illustrated in **Figure 7B**. In this case the flap would be subject to a force $\sim \mu\dot{\gamma} aW$ acting on a lever arm $\sim a$. Equating the corresponding external moment $\sim \mu\dot{\gamma} a^2 W$ to the bending moment $DW\sqrt{\Gamma/D}$ required for fracture initiation (Obreimoff, 1930) leads to $\frac{\mu\dot{\gamma} a^3}{D} \sim \left(\Gamma a^2/D\right)^{1/2}$. The same result can be obtained by considering the analytical solution for the displacement of a cantilever beam of length *a* subject to a constant normal load $\mu\dot{\gamma}$ (Timošenko, 1940):

$$w = \frac{\mu\dot{\gamma}}{24D}(x-a)^2\left(x^2 + 2ax + 3a^2\right) \tag{16}$$

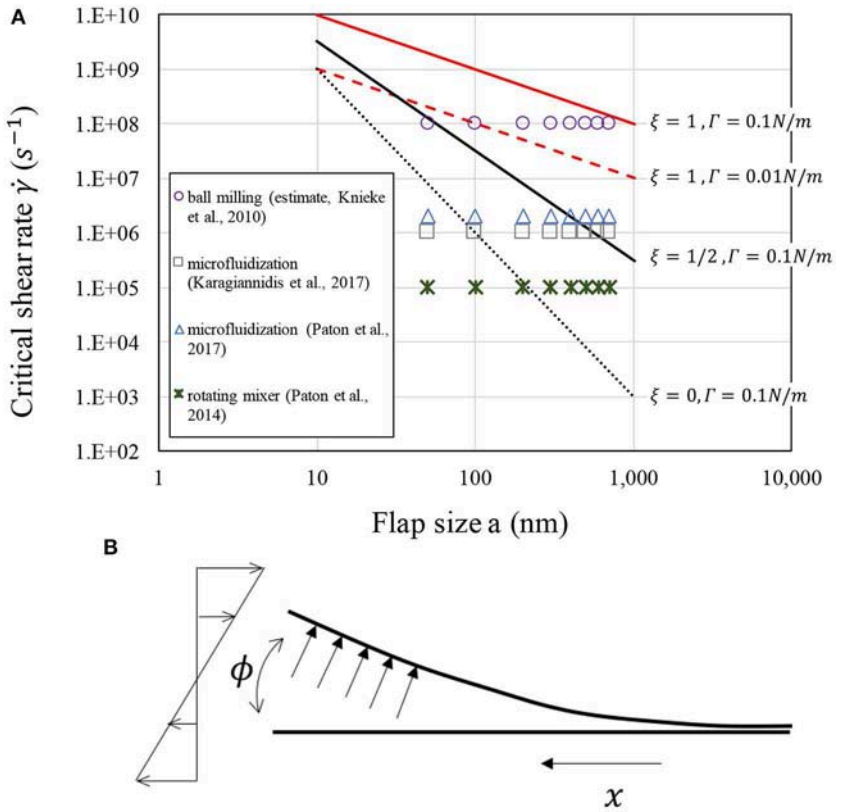

FIGURE 7 | (A) Critical shear rate for exfoliation as a function of flaw size (in nanometers) for different scaling exponents, assuming $D = 10^{-18}J$. Experimental references: Knieke et al. (2010), Paton et al. (2014, 2017), and Karagiannidis et al. (2017). **(B)** In the "cleavage" configuration the fluid stresses act normal to the flap, and the opening angle ϕ is small.

The bending energy per unit width $U = \frac{D}{2}\int\left(\frac{d^2w}{dx^2}\right)^2 dx$ is quadratic in $\mu\dot{\gamma}$. The strain energy release rate $G = \frac{dU}{da}$, with units of energy per unit area, is proportional to $\frac{(\mu\dot{\gamma})^2 a^4}{D}$. Equating the strain energy release rate to Γ (Griffith's criterion, Lawn, 1993) gives again the scaling

$$\frac{\mu\dot{\gamma}a^3}{D} \sim \left(\Gamma a^2/D\right)^{1/2} \tag{17a}$$

An intuitive explanation for why the critical shear rate in the "cleavage" configuration is smaller than in the "π -peel" configuration is that even if the forces applied to the flap are the same in both cases, the lever arm in the "π -peel" configuration is of $O\left(\frac{R}{a}\right)$ smaller than in the "cleavage" configuration. For a given value of a, reaching the critical bending moment in the "cleavage" configuration therefore requires as smaller value of $\dot{\gamma}$.

Equation (17a) is valid provided that the displacement of the flap is small. For larger displacements, one needs to account for two factors, which are extensively discussed in a recent paper by the author (Salussolia, 2019): (i) even in the case of uniform pressure applied to the flap, the direction of load depends on the normal to the flap, which itself depends on the shape of the flap (i.e., the load is follower); (ii) as the flap displacement increases, the pressure on the flap increases, essentially because more area of the flap is exposed to flow. Factor (ii) makes the dependence on $\Gamma a^2/D$ weaker, reducing effectively the power-law exponent significantly below 1/2. The inclusion of large-deformation effects does not change this conclusion, although it changes somewhat the value of the critical shear rate (without a change in order of magnitude of this quantity).

Time Scales of Microstructural Rearrangement: Toward Exfoliation Kinetics

Once the critical shear rate is reached, the fracture will propagate and exfoliation will occur. But exfoliation is not an instantaneous event. If this was the case, at a critical shear rate one would obtain complete exfoliation of all the microplates. This is not observed in practice. For instance, Paton and co-workers found that the concentration of exfoliated material follows a rather slow kinetics, apparently governed by a power-law of time (Paton et al., 2014). While explaining the emergence of this power-law requires tools that go beyond simple micromechanics, it is instructive to consider examples of dissipation processes occurring in the vicinity of the crack tip that could make the exfoliation mechanics depend on time.

An important dissipative process is due to the viscosity of the solvent. As the crack of the interlayer interface propagates, fluid must be drawn in from the surroundings toward the crack tip. Because the gap distance between the layers is small in the crack region, the viscous dissipation can be substantial (Rieutord et al., 2005; Lister et al., 2013). The rate of dissipation per unit volume of fluid is

$$\varepsilon \sim \mu \left(\frac{U(x)}{h(x)} \right)^2 \tag{17b}$$

where $h(x)$ is the gap height at a position x, and $U(x)$ is the characteristic fluid velocity at x (Eggers and Fontelos, 2015). The total power per unit width dissipated in the fluid can be estimated to be of the order of (Rieutord et al., 2005).

$$\frac{P_d}{W} = \int_{x_{\min}}^{x_{\max}} \int_0^h \varepsilon dx dy \sim \mu \frac{V^2}{H^2} (H \ell_D) \tag{18}$$

where V is the crack tip speed. Here H and ℓ_D are the characteristic height and length of the wedge-like region in the vicinity of the crack tip where the bulk of the viscous dissipation occurs. The high-dissipation region is limited by the coordinates $x_{\min}$ and $x_{\max}$. If there is no external force applied to the flap, the power to drive the crack motion against the viscous dissipation is provided by the adhesion force, $\frac{P_d}{W} = \Gamma V$, leading to (Rieutord et al., 2005)

$$V \sim \frac{\Gamma}{\mu} \frac{H}{\ell_D} \tag{19}$$

In the "π -peel" case examined in the current paper, an external force per unit width $\mu \dot{\gamma} a$ is applied to the flap and the corresponding driving power is $\frac{P_d}{W} = (2\mu \dot{\gamma} a - \Gamma) V$. Hence, the crack velocity, for the case in which viscous dissipation is the only effect resisting the motion of the crack, can be estimated to be of the order of

$$V_{viscous} \sim \frac{(2\mu \dot{\gamma} a - \Gamma)}{\mu} \frac{H}{\ell_D} \tag{20}$$

The inverse of the geometrical ratio $\frac{H}{\ell_D}$ is equal to the integral of $h(x)$ from $x_{\min}$ to $x_{\max}$ (Rieutord et al., 2005). Because the region near the crack tip is thin and slender, we have $\frac{H}{\ell_D} \ll 1$. Thus, $V_{viscous} \ll \frac{(2\mu \dot{\gamma} a - \Gamma)}{\mu}$.

A second important dissipative process is caused by the time-dependent rupture of the molecular bonds in the adhesion zone. A model for such process assumes that the rupture rate is governed by Maxwell-Boltzmann statistics. For small deviations from Griffith's condition, this model gives an exponential dependence of the crack velocity on the difference between the strain energy release rate G and the energy of adhesion per unit area of contact $2\gamma_{so}$ (Lawn, 1993):

$$V = 2 v_0 a_0 \exp\left(-\frac{U^\circ}{kT} \right) \sinh\left(\alpha \frac{G - 2\gamma_{so}}{kT} \right) \tag{21}$$

Here, a_0 is the characteristic lattice dimension, v_0 is a molecular frequency (typically a few THz), α is an activation area, kT is the thermal energy, γ_{so} is the surface tension of the solid (section Effect of the Solvent on Adhesion Strength) and ΔU° is a quiescent activation energy. In the "π -peel" configuration, the external work $2\mu \dot{\gamma} a$ takes the place of G. Using the definition $\Gamma = 2\gamma_{so}$the following expression crack velocity expression is obtained:

$$V_{br} \sim V_{br,0} \sinh\left(\alpha \frac{2\mu \dot{\gamma} a - \Gamma}{kT} \right) \tag{22}$$

where

$$V_{br,0} = 2 v_0 a_0 \exp\left(-\frac{\Delta U^\circ}{kT} \right) \tag{23}$$

The molecular velocity $v_0 a_0$ is of the order of 100 m/s−1 km/s, i.e., sonic velocities. The energy barrier ΔU° is typically taken to be of the order of $10kT$ (Brochard-Wyart and de Gennes, 2003). Setting $\Delta U^\circ = 25$ kT, gives values of $V_{br,0}$ in the range 1−10 nm/s. The effect of the solvent (through chemically-assisted bond rupture) can be accounted for through the dependence of Γ on the solvent, and by appropriately modifying the activation terms (Stoloff and Johnston, 1963; Lawn, 1993).

We can use Equations (20) and (22) to make some considerations regarding the relative importance of viscous dissipation and dissipation due to bond rupture. Let us assume that we are carrying out exfoliation using a shear rate of the order of the critical one, a situation that is expected to hold in practice. Because $\frac{2\mu \dot{\gamma} a}{\Gamma} = O(1)$ and $\frac{H}{\ell_D} < 1$, an upper bound for $V_{viscous}$ is the "capillary velocity" $\frac{\Gamma}{\mu}$. This quantity is ∼100 m/s for solvents having the viscosity of water (using a reference value $\Gamma = 0.1$ N/m). The velocity due to (interlayer) molecular bond rupture can be estimated to be, typically, larger than this value. This is because for a_0 in the nanoscopic range the energy scale $\Gamma\alpha$ is typically larger than the energy barrier ΔU° (taking $\alpha = 1nm^2$ and $\Gamma = 0.1$ N/m, we get $\Gamma\alpha \approx 250kT$). As a result, the growing hyperbolic sine term is much larger than the decaying term $exp\left(-\frac{\Delta U^\circ}{kT} \right)$. Noting that the "capillary velocity" $\frac{\Gamma}{\mu}$ is roughly comparable in magnitude to $v_0 a_0$, we have $V_{viscous} \ll V_{br}$.

Thus, viscous dissipation can be very important. The relative importance with respect to dissipation due to bond rupture (which we estimate to be subdominant) will depend on the very specific values of α and ΔU°. Recent measurements of self-tearing and peeling of graphene sheets from solid substrates suggest a method to calculate these parameters (Annett and Graham, 2016).

In the regime of viscous dominated dissipation, the characteristic time required to complete peeling of a flap from a particle of lateral size L is

$$T_v = \frac{L}{V_{viscous}} \sim \frac{\mu}{(2\mu \dot{\gamma} L - \Gamma)} \frac{\ell_D}{H} \tag{24}$$

For values of the applied shear rate much larger than the critical one the viscous peeling time scales proportionally to the inverse shear rate, $T_v \sim \dot{\gamma}^{-1} \frac{\ell_D}{2H}$. This time scale depends on the viscosity only through the dependence of the ratio $\frac{\ell_D}{2H}$ on hydrodynamics.

Because $\frac{\ell_D}{H} \gg 1$ we expect $T_v \gg \dot{\gamma}^{-1}$. The viscous peeling time scale is proportional to the local shear rate, with a large numerical prefactor.

In this section, we have focused on the "π -peel" configuration. The arguments proposed can be extended to the "cleavage' configuration by replacing the work of the external force per unit width with the strain energy release rate.

CONCLUSIONS: FRONTIERS IN THE HYDRODYNAMICS OF 2D NANOMATERIALS

We have analyzed theoretically a simple model of hydrodynamic peeling, by focusing mostly on the "π - peel" configuration (**Figure 2**). Based on our analysis, the shear rates that one needs to apply to the fluid for this configuration to result in exfoliation are rather large, of the order of $10^8 - 10^9 s^{-1}$. These large shear rates are available in exfoliation methods that produce large stresses on the particle, such as ball milling, but not in most published exfoliation approaches in which the shear rate is produced by conventional turbulence (as in rotor-stator shear mixing or microfluidisation approaches). The fact that in rotor-stator or microfluidisation approaches exfoliation is observed for shear rates in the range $10^4 - 10^6 s^{-1}$ suggests that alternative microscale exfoliation configurations are likely to dominate the exfoliation micromechanics in these approaches, at least in the initial stages of exfoliation.

We suggest that, due to its stronger dependence on the flaw size a, a "cleavage" configuration (**Figure 7B**) can yield critical shear rate values much smaller than those predicted for "π - peel," closer to the values observed experimentally. While for "π - peel" the critical shear rate decays as $\frac{1}{a}$ (Equation 9), for cleavage under a constant pressure $\mu\dot{\gamma}$ the critical shear rate decays as $\frac{1}{a^2}$ (Equation 17a). We anticipate that if the pressure is not constant, but depends on the configuration of the wedge creating the fracture, the dependence on a can be even stronger. This effect results in even lower values of the critical shear rate. The analysis of this case is the subject of a separate paper (Salussolia, 2019).

This initial study on the hydrodynamics of 2D materials exfoliation only begins to uncover the complexity of the exfoliation process as seen at the scale of each particle. To better understand the micromechanics of liquid-phase exfoliation, future computational investigations must consider the fully coupled fluid-structure interaction problem and include atomistic details. In the wedge region, near the crack tip, the liquid is strongly confined, with gaps of nanometric dimensions. Hence the problem severely challenges the use of continuum approaches. For carbon nanomaterials in contact with water, hydrodynamic slip characterizes the flow behavior at the solid-liquid surface (Tocci et al., 2014; Striolo et al., 2016), with slip lengths of the order of a few tens of nanometers (Thomas and McGaughey, 2008; Falk et al., 2010). Our work provides estimates for geometric quantities—such as the shear rate dependent radius of curvature of the fold R–that are obtained neglecting molecular effects. These quantities can be used as a reference to evaluate the limitations of continuum treatments. Molecular dynamics studies for the configurations investigated in the current paper could provide insights into the general process of liquid intercalation under flow, a topic that could lead to the design of improved solvents for the exfoliation of 2D nanomaterials.

Another important topic is the prediction of the kinetics of exfoliation. We have estimated that the time scale for microscopic peeling can in many cases be controlled by viscous dissipation. For "π -peel" at shear rates largely exceeding the critical one, the time scale for viscous peeling has been found to scale proportionally to $\dot{\gamma}^{-1}$ (with a large prefactor, $\frac{\ell_D}{H} \gg 1$, see Equation 24). This time scale has to be compared to two dynamic time scale: the time scale of particle rotation (of the order of $\dot{\gamma}^{-1}\Lambda$, where Λ is the aspect ratio, Challabotla et al., 2015), and the time scale of permanence in a turbulent structure (which can be estimated to be of the order of $\dot{\gamma}^{-1}$, Babler et al., 2012). The inter-play of these different time scales should give rise to a rich phase diagram. Uncovering the features of this diagram, through a comparison of multi-particle simulations and experiments (Voth, 2015), should be of interest for researchers investigating the statistical physics of complex systems, and is a necessary step toward predicting the yield of industrial-scale exfoliation processes.

Theoretical modeling of exfoliation processes in sheared liquids is an important and currently largely unexplored frontier in carbon nanomaterials research. Understanding how graphene "breaks" under the action of fluid dynamic forces has implications not only for large-scale graphene production but also for quantifying the time-evolving size and thickness distribution of graphene (or any other 2D material) *during* its transport. In industrial liquids such as lubricants and paints, the performance of a graphene additive whose size depends on time—because of fragmentation or exfoliation—will also depend on time. Size and shape are dominant variables affecting how a nanoparticle interacts with a biological cell, and the prediction of these variables during flow is thus essential to evaluate toxicological effects on human health or the environment (Wick et al., 2014). Our work on the modeling of graphene hydrodynamics, funded by the European Research Council, lays basic theoretical building blocks that are necessary to develop the next generation of predictive multiscale software for fragmentation, exfoliation and liquid processing of 2D nanomaterials.

AUTHOR CONTRIBUTIONS

LB designed the research, carried out the analysis, and wrote the paper.

ACKNOWLEDGMENTS

Funding from ERC Starting Grant FLEXNANOFLOW (no. 715475) is gratefully acknowledged. The author would like to thank Dr. E. Barbieri, and G. Salussolia for useful scientific discussions.

REFERENCES

Aïssa, B., Memon, N. K., Ali, A., and Khraisheh, M. K. (2015). Khraisheh recent progress in the growth and applications of graphene as a smart material: a review. *Front. Mater*. 2:58. doi: 10.3389/fmats.2015.00058

Alaferdov, A. V., Gholamipour-Shirazi, A., Canesqui, M. A., Yu Danilov, A., and Moshkalev, S. A. (2014). Size-controlled synthesis of graphite nanoflakes and multi-layer graphene by liquid phase exfoliation of natural graphite. *Carbon* 69, 525–535. doi: 10.1016/j.carbon.2013.12.062

Annett, J., and Graham, L. W. (2016). Cross Self-assembly of graphene ribbons by spontaneous self-tearing and peeling from a substrate. *Nature* 535, 271–275. doi: 10.1038/nature18304

Audoly, B., and Pomeau, Y. (2010). *Elasticity and Geometry: From Hair Curls to the Non-linear Response of Shells*. Oxford, UK: Oxford University Press

Babler, M. U., Biferale, L., and Lanotte, A. S. (2012). Lanotte. Breakup of small aggregates driven by turbulent hydrodynamical stress. *Phys. Rev*. 85:025301. doi: 10.1103/PhysRevE.85.025301

Borse, N. K., and Kamal, M. R. (2009). Estimation of stresses required for exfoliation of clay particles in polymer nanocomposites. *Polymer Eng. Sci*. 49, 641–650. doi: 10.1002/pen.21211

Brochard-Wyart, F., and de Gennes, P.-G. (2003). Unbinding of adhesive vesicles. *Comp. Rendus Phys*. 4, 281–287. doi: 10.1016/S1631-0705(03)00048-3

Challabotla, N. R., Zhao, L., and Andersson, H. I. (2015). Orientation and rotation of inertial disk particles in wall turbulence. *J. Fluid Mech.* 766:R2. doi: 10.1017/jfm.2015.38

Chaudhury, M. K., and Whitesides, G. M. (1991). Direct measurement of interfacial interactions between semispherical lenses and flat sheets of poly (dimethylsiloxane) and their chemical derivatives. *Langmuir* 7, 1013–1025. doi: 10.1021/la00053a033

Chen, X., Dobson, J. F., and Raston, C. L. (2012). Vortex fluidic exfoliation of graphite and boron nitride. *Chem. Commun*. 48, 3703–3705. doi: 10.1039/c2cc17611d

Coleman, J. N. (2009). Liquid-phase exfoliation of nanotubes and graphene. *Adv. Funct. Mater*. 19, 3680–3695. doi: 10.1002/adfm.200901640

Davis, A. M. J., and O'Neill, M. E. (1977). Separation in a slow linear shear flow past a cylinder and a plane. *J. Fluid Mech.* 81, 551–564. doi: 10.1017/S0022112077002225

Eggers, J., and Fontelos, M. A. (2015). *Singularities: Formation, Structure, and Propagation*. Cambridge: Cambridge University Press.

Falk, K., Sedlmeier, F., Joly, L., Netz, R. R., and Bocquet, L. (2010). Molecular origin of fast water transport in carbon nanotube membranes: superlubricity versus curvature dependent friction. *Nano Lett.* 10, 4067–4073. doi: 10.1021/nl1021046

Ferrari, A. C., Bonaccorso, F., Fal'ko, V., Novoselov, K. S., Roche, S., Bøggild, P., et al. (2015). Technology roadmap for graphene, related two-dimensional crystals, and hybrid systems. *Nanoscale* 7, 4598–4810. doi: 10.1039/C4NR01600A

Haidara, H., Chaudhury, M. K., and Owen, M. J. (1995). A direct method of studying adsorption of a surfactant at solid-liquid interfaces. *J. Phys. Chem*. 21, 8681–8683. doi: 10.1021/j100021a037

Hernandez, Y., Nicolosi, V., Lotya, M., Blighe, F. M., Sun, Z., De, S., et al. (2008). High-yield production of graphene by liquid-phase exfoliation of graphite. *Nat. Nanotechnol.* 3:563. doi: 10.1038/nnano.2008.215

Jeffery, G. B. (1922). The motion of ellipsoidal particles immersed in a viscous fluid. *Proc. R. Soc. Lond. A*. 102, 161–179. doi: 10.1098/rspa.1922.0078

Johnson, D. W., Dobson, B. P., and Coleman, K. S. (2015). A manufacturing perspective on graphene dispersions. *Curr. Opin. Colloid Interface Sci*. 20, 367–382. doi: 10.1016/j.cocis.2015.11.004

Johnson, K. L., Kendall, K., and Roberts, A. D. (1971). Surface energy and the contact of elastic solids. *Proc. R. Soc. Lond. A* 20, 301–313. doi: 10.1098/rspa.1971.0141

Karagiannidis, P. G., Hodge, S. A., Lombardi, L., Tomarchio, F., Decorde, N., Milana, S., et al. (2017). Microfluidization of graphite and formulation of graphene-based conductive inks. *ACS Nano*. 11, 2742–2755. doi: 10.1021/acsnano.6b07735

Kendall, K. (1975). Thin-film peeling - the elastic term. *J. Phys. D Appl. Phys.* 8:1449. doi: 10.1088/0022-3727/8/13/005

Knieke, C., Berger, A., Voigt, M., Taylor, R. N. K., Röhrl, J., and Peukert, W. (2010). Scalable production of graphene sheets by mechanical delamination. *Carbon* 48, 3196–3204. doi: 10.1016/j.carbon.2010.05.003

Landau, L. D., and Lifshitz, E. M. (1986). *Theory of Elasticity*. Amsterdam: Elsevier, 7.

Lawn, B. R. (1993). *Fracture of Brittle Solids*. Cambridge: Cambridge University Press.

Lee, C., Wei, X., Kysar, J. W., and Hone, J. (2008). Measurement of the elastic properties and intrinsic strength of monolayer graphene. *Science* 321, 385–388. doi: 10.1126/science.1157996

Li, L. H., Chen, Y., Behan, G., Zhang, H., Petravic, M., and Glushenkov, A. M. (2011). Large-scale mechanical peeling of boron nitride nanosheets by low-energy ball milling. *J. Mater. Chem.* 21, 11862–11866. doi: 10.1039/c1jm11192b

Lin, Y. Y., Hui, C. Y., and Wang, Y. C. (2002). Modeling the failure of an adhesive layer in a peel test. *J. Polymer Sci. Part B Polym. Phys*. 40, 2277–2291. doi: 10.1002/polb.10289

Lindahl, N., Midtvedt, D., Svensson, J., Nerushev, O. A., Lindvall, N., Isacsson, A., et al. (2012). Determination of the bending rigidity of graphene via electrostatic actuation of buckled membranes. *Nano Lett.* 12, 3526–3531. doi: 10.1021/nl301080v

Lister, J. R., Peng, G. G., and Neufeld, J. A. (2013). Viscous control of peeling an elastic sheet by bending and pulling. *Phys. Rev. Lett.* 111:154501. doi: 10.1103/PhysRevLett.111.154501

Obreimoff, J. W. (1930). The splitting strength of mica. *Proc. R. Soc. Lond. Ser. A* 127:290. doi: 10.1098/rspa.1930.0058

Paton, K. R., Anderson, J., Pollard, A. J., and Sainsbury, T. (2017). Production of few-layer graphene by microfluidization. *Mater. Res. Exp*. 4:025604. doi: 10.1088/2053-1591/aa5b24

Paton, K. R., Varrla, E., Backes, C., Smith, R. J., Khan, U., O'Neill, A. Paton, K. R., et al. (2014). Scalable production of large quantities of defect-free few-layer graphene by shear exfoliation in liquids. *Nat. Mater*. 13:624. doi: 10.1038/nmat3944

Pugno, N. M. (2010). The design of self-collapsed super-strong nanotube bundles. *J. Mech. Phys. Solids*. 58, 1397–1410. doi: 10.1016/j.jmps.2010.05.007

Rafiee, M. A., Rafiee, J., Srivastava, I., Wang, Z., Song, H., Yu, Z. Z., et al. (2010). Fracture and fatigue in graphene nanocomposites. *Small* 6, 179–183. doi: 10.1002/smll.200901480

Rieutord, F., Bataillou, B., and Moriceau, H. (2005). Dynamics of a bonding front. *Phys. Rev. Lett.*. 94:236101. doi: 10.1103/PhysRevLett.94.236101

Rohde, F. (1953). Large deflections of a cantilever beam with uniformly distributed load. *Q. Appl. Math*. 11, 337–338. doi: 10.1090/qam/56438

Roman, B. (2013). Fracture path in brittle thin sheets: a unifying review on tearing. *Int. J. Fract*. 182, 209–237. doi: 10.1007/s10704-013-9869-5

Salussolia, G. (2019). Micromechanics of liquid-phase exfoliation of a layered 2D material: a hydrodynamic peeling model. *J. Mech. Phys. Solid*s. 134:103764. doi: 10.1016/j.jmps.2019.103764

Santagiuliana, G., Picot, O. T., Crespo, M., Porwal, H., Zhang, H., Li, Y., et al. (2018). Breaking the nanoparticle loading–dispersion dichotomy in polymer nanocomposites with the art of croissant-making. *ACS Nano*. 12, 9040–9050. doi: 10.1021/acsnano.8b02877

Sen, D., Novoselov, K. S., Reis, P. M., and Buehler, M. J. (2010). Tearing graphene sheets from adhesive substrates produces tapered nanoribbons. *Small* 6, 1108–1116. doi: 10.1002/smll.201000097

Shen, J., He, Y., Wu, J., Gao, C., Keyshar, K., Zhang, X., et al. (2015). Liquid phase exfoliation of two-dimensional materials by directly probing and matching surface tension components. *Nano Lett*. 15, 5449–5454. doi: 10.1021/acs.nanolett.5b01842

Shih, C. J., Lin, S., Strano, M. S., and Blankschtein, D. (2010). Understanding the stabilization of liquid-phase-exfoliated graphene in polar solvents: molecular dynamics simulations and kinetic theory of colloid aggregation. *J. Am. Chem. Soc.* 132, 14638–14648. doi: 10.1021/ja1064284

Singh, V., Koch, D. L., Subramanian, G., and Stroock, A. D. (2014). Rotational motion of a thin axisymmetric disk in a low Reynolds number linear flow. *Phys. Fluids* 26:033303. doi: 10.1063/1.4868520

Stoloff, N. S., and Johnston, T. L. (1963). Crack propagation in a liquid metal environment. *Acta Metallurg.* 11, 251–256. doi: 10.1016/0001-6160(63)90180-9

Striolo, A., Michaelides, A., and Joly, L. (2016). The carbon-water interface: modeling challenges and opportunities for the water-energy nexus. *Annu. Rev. Chem. Biomol. Eng.* 7, 533–556. doi: 10.1146/annurev-chembioeng-080615-034455

Tennekes, H., and Lumley, J. L. (1972). *A First Course in Turbulence*. Massachusetts: MIT press.

Thomas, J. A., and McGaughey, A. J. H. (2008). Reassessing fast water transport through carbon nanotubes. *Nano Lett.* 8, 2788–2793. doi: 10.1021/nl80 13617

Timošenko, S. P. (1940). *Strength of Materials: Elementary Theory and Problems*. New York, NY: D. Van Nostrand Company.

Tocci, G., Joly, L., and Michaelides, A. (2014). Friction of water on graphene and hexagonal boron nitride from ab initio methods: very different slippage despite very similar interface structures. *Nano Lett.* 12, 6872–6877. doi: 10.1021/nl502837d

Torrisi, F., and Carey, T. (2018). "Printing 2D materials," in *Flexible Carbon-Based Electronics*, eds P. Palermo and V. Samorí (Hoboken, NJ: John Wiley and Sons), 131–184.

van Engers, C. D., Cousens, N. E., Babenko, V., Britton, J., Zappone, B., Grobert, N., et al. (2017). Direct measurement of the surface energy of graphene. *Nano Lett.* 6, 3815–3821. doi: 10.1021/acs.nanolett.7b01181

Varrla, E., Paton, K. R., Backes, C., Harvey, A., Smith, R. J., McCauley, J., et al. (2014). Turbulence-assisted shear exfoliation of graphene using household detergent and a kitchen blender. *Nanoscale* 6, 11810–11819. doi: 10.1039/C4NR03560G

Voth G. A. (2015). Disks aligned in a turbulent channel. *J. Fluid Mech.* 772, 1–4. doi: 10.1017/jfm.2015.144

Wang, J., Sorescu, D. C., Jeon, S., Belianinov, A., Kalinin, S. V., Baddorf, A. P., et al. (2016). Atomic intercalation to measure adhesion of graphene on graphite. *Nat. Commun.* 7:13263. doi: 10.1038/ncomms13263

Wick, P., Louw-Gaume, A. E., Kucki, M., Krug, H. F., Kostarelos, K., Fadeel, B., et al. (2014). Classification framework for graphene-based materials. *Angew. Chem.* 53, 7714–7718. doi: 10.1002/anie.201403335

Xu, L., Ma, T. B., Hu, Y. Z., and Wang, H. (2011). Vanishing stick–slip friction in few-layer graphenes: the thickness effect. *Nanotechnology* 22:285708. doi: 10.1088/0957-4484/22/28/285708

Yi, M., and Shen, Z. (2015). A review on mechanical exfoliation for the scalable production of graphene. *J. Mater. Chem.* 3, 11700–11715. doi: 10.1039/C5TA00252D

Zhao, W., Wu, F., Wu, H., and Chen, G. (2010). Preparation of colloidal dispersions of graphene sheets in organic solvents by using ball milling. *J. Nanomater.* 2010:528235. doi: 10.1155/2010/5 28235

Conflict of Interest: The author declares that the research was conducted in the absence of any commercial or financial relationships that could be construed as a potential conflict of interest.

frontiers in Materials

ORIGINAL RESEARCH
published: 19 July 2019
doi: 10.3389/fmats.2019.00174

Microstructure and Size Effects on the Mechanics of Two Dimensional, High Aspect Ratio Nanoparticle Assemblies

Benjamin C. Marchi[1] *and Sinan Keten*[1,2]*

[1] Department of Mechanical Engineering, Northwestern University, Evanston, IL, United States, [2] Department of Civil and Environmental Engineering, Northwestern University, Evanston, IL, United States

Uniaxially arranged nanocomposite structures are common across biological materials. Through efficient structural ordering and hierarchies, these materials exhibit stiffnesses and strengths comparable to the better of their constituents. While much is known regarding the mechanical properties of materials with explicit stiff and compliant phases, substantially less is understood about neat (matrix-free) materials composed from high aspect ratio particles. A promising example of nanoparticle assemblies are cellulose nanocrystal (CNC) thin films, which display desirable elastic and failure properties. Despite the exceptional properties of CNC films, accurately linking their nanoscopic properties to macroscale performance remains a challenge. Therefore, this work assesses the effects of fiber geometry and in-plane topology on the elastic and failure behaviors of neat CNC thin films using an atomistically informed coarse-grained molecular dynamics model. Short fiber films show a greater dependence on their specific in-plane ordering compared to longer fiber films. Furthermore, aligned, brick, and mortar type CNC films exhibit a remarkable resiliency to random structural perturbations, particularly for films built from long fibers. Finally, simulation size is shown to affect the apparent failure properties of CNC films, with no meaningful impact on elastic property predictions. The relationships between structure and fiber length, as well as the sensitivities to structural randomness and simulation size, elucidated herein provide a comprehensive overview of the expected mechanics of high aspect ratio nanoparticle assemblies.

Keywords: bioinspired nanocomposites, CNC film, coarse-grained molecular dynamics, size effect, staggered composites

OPEN ACCESS

Edited by:
Nicola Maria Pugno, University of Trento, Italy

Reviewed by:
Dongchan Jang, Korea Advanced Institute of Science and Technology (KAIST), South Korea
Guy M. Genin, Washington University in St. Louis, United States

***Correspondence:**
Sinan Keten
s-keten@northwestern.edu

Specialty section:
This article was submitted to Mechanics of Materials, a section of the journal Frontiers in Materials

Received: *14 January 2019*
Accepted: *08 July 2019*
Published: *19 July 2019*

Citation:
Marchi BC and Keten S (2019) Microstructure and Size Effects on the Mechanics of Two Dimensional, High Aspect Ratio Nanoparticle Assemblies. Front. Mater. 6:174. doi: 10.3389/fmats.2019.00174

INTRODUCTION

Nature achieves impressive mechanical properties in its uniaxial nanocomposite structures through highly regular ordering of hard and soft phases. Many biological systems exhibit high stiffness, strength, and toughness with their compliant matrices only occupying ∼5% of the total material volume (Jackson et al., 1988). These structures are common across biology, from nacre in sea shells (Wang et al., 2012) to bone (Jäger and Fratzl, 2000). They possess stiffnesses and strengths on the order of their hard constituents, while, at the same time, displaying ductilities and fracture toughnesses several orders of magnitude higher than would be expected from pure hard constituent materials (Jackson et al., 1988; Jäger and Fratzl, 2000; Kamat et al., 2000; Menig et al., 2000). The

small strain, elastic mechanical responses of these materials with high mechanical mismatches between phases are primarily governed by the shear deformation of the matrix phase, which is initiated by the stiff constituents sliding relative to each other during deformation. While significantly contributing to small strain behaviors, these interfaces also provide robust toughening mechanisms through stable energy dissipation (Mayer, 2005; Barthelat et al., 2012). The multiple hierarchical levels found in many biological composites further improve their mechanical responses and failure properties (Zhang Z. et al., 2010; Wei et al., 2015; Gao et al., 2016; Henry and Pimenta, 2018). It has been shown that hierarchal microstructures provide improved resiliency to stress concentrations near inclusions (Gorbatikh et al., 2010) and enhanced damage dispersion (Ritchie, 2011; Dutta and Tekalur, 2014; Mirzaeifar et al., 2015; Henry and Pimenta, 2018). These observations are part of a large and ever growing body of work establishing that staggered microstructures tend to be the most favorable architectures for simultaneously producing stiffness, strength, and toughness in thin, macroscopic materials (Espinosa et al., 2009; Zhang Z. Q. et al., 2010; Barthelat and Zhu, 2011; Dutta et al., 2013; Barthelat, 2014; Ni et al., 2015; Pro et al., 2015; Qwamizadeh et al., 2015, 2017a,b; Abid et al., 2018).

The outstanding mechanical properties of natural uniaxial nanocomposites have inspired the use of staggered architectures in engineered materials. These materials have been fabricated using techniques like freeze casting (Munch et al., 2008), coextrusion (Wilkerson et al., 2018), rapid prototyping (Gu et al., 2016), and laser cutting (Henry and Pimenta, 2018). While these synthetic materials have shown impressive combinations of stiffness, strength, and toughness (Podsiadlo et al., 2007; Bonderer et al., 2008; Wang et al., 2012; de Obaldia et al., 2015; Valashani and Barthelat, 2015; Zhang et al., 2015; Gu et al., 2017; Kim et al., 2018), attempts at reconstructing the mechanical properties of natural materials often fall short of theoretical predictions (Espinosa et al., 2009; Wei et al., 2012). This deficiency has spurred myriad studies hoping to inform the design of optimal nanocomposites built from ordered, uniaxial members embedded in relatively compliant matrices. While there have been many efforts to investigate the mechanics of these brick and mortar systems in two dimensions, they often rely on continuum (Arzt et al., 2003; Ji and Gao, 2004; Zhang Z. Q. et al., 2010; Dutta et al., 2013; Barthelat, 2014; Sakhavand and Shahsavari, 2015; Zhang et al., 2015; Ghazlan et al., 2018; Henry and Pimenta, 2018) or micromechanical (Begley et al., 2012; Abid et al., 2018; Chandler and Cheng, 2018) descriptions. Despite these constitutive and microstructural simplifications, these theoretical works have helped to elucidate many important deformation mechanisms in staggered composites. In particular, how they can achieve simultaneously high strength and toughness through features like crack bridging and deflection (Jackson et al., 1988; Shao et al., 2012; Dutta and Tekalur, 2014; Gu et al., 2017).

Understanding and designing materials adopted from Nature is further complicated by the fact that Nature is not perfect. Nearly all naturally occurring brick and mortar materials exhibit some degree of randomness in their microstructures (Barthelat et al., 2007), as do their synthetic counterparts (Bonderer et al., 2008; Munch et al., 2008; Wilkerson et al., 2018). In particular, the staggered arrangement of hard phase particles may not be adequately represented by idealization of a perfect brick wall, where the overlap between each brick relative to its neighbors is specified. The length scales over which this randomness occurs is important for determining the elastic response of these materials, as well as how efficiently energy is dissipated during yield and failure. This is especially true if matrix shear is the primary mechanism of load transfer (Zhang Z. Q. et al., 2010). Theoretical studies have indicated that randomness in the overlaps between adjacent stiff bricks can substantially and simultaneously decrease the stiffnesses, strengths, and toughnesses of brick and mortar materials (Zhang Z. Q. et al., 2010; Barthelat, 2014; Ni et al., 2015; Pro et al., 2015; Abid et al., 2018). However, boundary cases, like staggered microstructures with relatively strong matrix phases and relatively long, stiff members much greater than the critical length for shear load transfer, have yet to be fully explored.

In addition to the potential challenges manifesting from the constitutive and structural representations of materials with staggered microstructures in predictive material design, a systematic evaluation of the size scaling behaviors of these materials is severely lacking. What limited information exists on the subject is primarily used as validation of model convergence (Abid et al., 2018). However, quasibrittle materials, like many natural and synthetic microstructurally staggered materials, exhibit strong size effects, which are both statistical and deterministic (Bažant et al., 2009; Luo and Bažant, 2017a). This means that test specimen size can have a tremendous effect on the apparent mechanical properties of a material, particularly as the length scale of the material changes by orders of magnitude (Chen et al., 2006; Mathur and Erlebacher, 2007).

Previous studies have also pre-dominately focused on ordered structures with two distinct material phases; however, neat films are another important class of materials that display hierarchical ordering. One such example of this type of material is cellulose nanopaper. Cellulose nanopapers, derived from cellulose nanocrystals (CNCs), have emerged as a promising candidate for applying the outstanding properties of CNCs at the macroscale (Henriksson et al., 2008; Eichhorn, 2011; Dumanli et al., 2014; Natarajan et al., 2018). CNCs are an abundant and renewable material that can be extracted from many biological sources, including plants, bacteria, and tunicates (Moon et al., 2011; Sinko et al., 2015), as well as the by-products of the timber, paper, and pulp industries (Fratzl and Weinkamer, 2007). CNCs also readily self-assemble chiral nematic thin films with emergent photonic features (Lagerwall et al., 2014) and highly modifiable surface chemistries (Habibi et al., 2010; Moon et al., 2011; Wei et al., 2018).

Despite the successes of materials like cellulose nanopapers, much regarding the relationship between constituent structure and macroscale mechanical properties in neat, ordered uniaxial nanocomposites remains elusive. While continuum models have been useful in predicting optimal mechanical properties in matrix containing, ordered uniaxial composites, they may lack the necessary nanoscopic details required to accurately

predict the mechanical performance of neat films. They tend to rely on phenomenological descriptions of deformation and interfacial physics, which is why molecular dynamics (MD) simulations have proved useful in establishing structure-property relationships for many topological and composite materials (Ostanin et al., 2013; Koh et al., 2015; Hansoge et al., 2018). In particular, MD simulations have been used in a number of recent studies to describe deformation non-uniformity and discrete failure in both stiff and soft domains of staggered, two dimensional nanocomposite materials (Mathiazhagan and Anup, 2016a,b,c, 2018). However, MD simulations, particularly at the atomic scale, are computationally expensive, minimizing their capacity as predictive material design tools for large scale materials. Between atomistic MD and continuum models lie mesoscopic, or coarse-gained (CG), MD models. These models have been highly successful at describing the mechanical properties of all CNC materials, both during quasi-static (Qin et al., 2017; Natarajan et al., 2018) and dynamic (Qin et al., 2019) deformation processes. Furthermore, MD simulations do not require explicit failure criteria and can capture discrete and non-affine deformation events, like bond breakage and molecular sliding.

The goal of this work is to analyze the effects of system size and microstructural randomness on mechanical properties of staggered, high aspect ratio nanoparticle assemblies, taking CNCs as a model structural building block. Specifically, an atomistically-informed CG MD model of CNCs is used to explore the effects of fiber geometry, arrangement, and system size on the mesoscopic mechanical properties of thin and neat, two dimensional CNC nanopapers. First, the mechanical properties of neat CNC films with various fiber lengths and regular structures (i.e., no randomness) are investigated and compared to established brick and mortar theories. Next, randomness is introduced in the ordering of CNC films to assess the resiliency of their mechanical properties to misalignment. Finally, the sizes of simulated CNC assemblies are systemically increased to evaluate the relationship between system size and observed mechanics.

METHODS

The two dimensional, neat CNC films used in this study were constructed using a previously validated CG model (Qin et al., 2017). Briefly, this CG framework is a bead-spring, mesoscopic model of CNCs that is characteristic of cellulose I with a Iβ crystal structure. Each bead in the CG model represents all 4,536 atoms contained within three repeat-units of a CNC with a 36 chain internal structure and exposing (110) surfaces. Detailed atomistic mechanical assessments (uniaxial extension, three point bending, etc.) were performed to inform the CG force field parameters following the strain energy conservation principle (Qin et al., 2017). Intra-CNC bonds with local strains >5% engineering strain were deemed failed and removed from the simulation (Wu et al., 2014; Qin et al., 2017). More information on the specifics of the CG model form, its validation, or potential applications can be found in previous work (Qin et al., 2017, 2019; Natarajan et al., 2018).

Individual CNCs were assembled into close packed configurations to investigate the effects of CNC fiber length (L) and in-plane ordering on the mechanical properties of neat, thin films. **Figure 1** shows representative CNC films with various in-plane orderings. The blue beads in **Figure 1** represent the starts, or first CG bead, in a given CNC fiber, with the subsequent gray beads corresponding to the remainder of the fiber. This means that the total fiber length (L) is equivalent to the spacing between axially adjacent blue CG beads. Fiber in-plane orderings or arrangements refer to the spatial distribution of chain starts, which are represented by blue CG beads throughout this work. In particular, both regular (**Figures 1A,B**) and staggered (**Figure 1C**) orderings were considered for $L = 50$, 100, 150, 220, and 300 nm.

All CG MD simulations were conducted using LAMMPS (Plimpton, 1995), with all visualizations completed using VMD (Humphrey et al., 1996). Uniaxial tensile tests were used to determine the Young's modulus, failure strength, and toughness of each film; each uniaxial tensile test followed the same procedure. The Young's modulus was defined as the slope of the linear region (up to 0.125% nominal strain) of the stress-strain response of each CNC film. Strength was assumed to be the maximum stress supported by each CNC film prior to failure, and film toughness was calculated by directly integrating the corresponding stress-strain responses from the unloaded configuration until macroscopic film failure. Films were determined to have failed when a significant reduction (>30 MPa over a 0.00125% strain increment) in stress was observed—typically, the stress-strain responses of CNC films abruptly shifted from a loaded state to one where no effective load was measured.

Prior to each uniaxial simulation, the total energy of each CNC film was minimized using a conjugate gradient procedure until the relative difference in total energy between steps was sufficiently small ($<10^{-10}$). Next, the energy minimized films were equilibrated at 300 K under an NVT ensemble for 20 ns. This was followed by another 50 ns of equilibration, again at 300 K, under an NPT ensemble with traction-free boundaries. Simulations were assumed to be periodic in direction of loading, as well as in the in-plane normal direction. Two dimensionality was strictly enforced by zeroing out-of-plane velocities and forces on a per atom basis. All non-bonded interactions between CG beads located at the starts and ends of individual CNCs were ignored to minimize any artificial confinement effects. After each film was equilibrated, uniaxial tension tests were conducted by deforming the simulation domain along the axial CNC direction with a constant engineering strain rate of 5×10^{-10} 1/fs. This strain rate was selected due to negligible strain rate and inertial effects around the specified rate (see **Supplemental Material**). During each uniaxial tension simulation, the total pressure acting normal and in-plane to the direction of loading was specified to be stress-free using a Berendsen barostat, while the tensile stress was assumed to be the global stress tensor, normalized by the film thickness, in the direction of loading (shown with red arrows in **Figure 1**). For each CNC film structure and fiber length, multiple tensile simulations were conducted to assess the expected ranges of the mechanical characterization data. Differences between

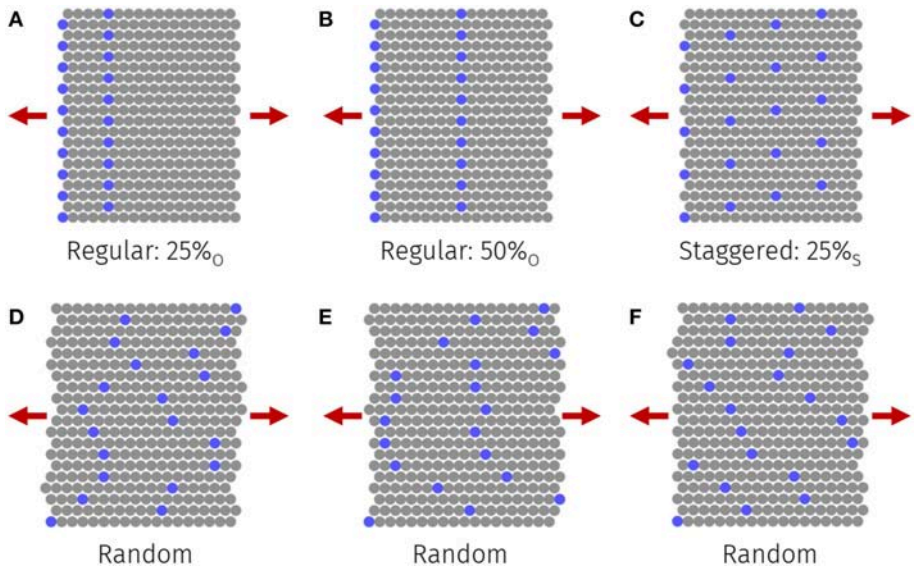

FIGURE 1 | CNC nanopapers ($L = 50$ nm) with **(A)** 25%$_O$ and **(B)** 50%$_O$ regular and **(C)** 25%$_S$ staggered offset between neighboring fibers. x%$_O$ and x%$_S$ refer to regular and staggered offset structures with x% offset between neighboring fibers, respectively. **(D–F)** Three representative realizations of CNC films ($L = 50$ nm) with random ordering. Red arrows indicate direction of applied load.

mechanical responses of structurally similar films were driven by variations in the initial positions and velocities of the individual CNC atoms. All statistical comparisons between two groups of data tested a null hypothesis that there did not exist a difference between the group medians, with an alternative hypothesis of a difference between group medians using a Mann–Whitney U-test (Mann and Whitney, 1947). Statistical comparisons between groups of three or more data used a Kruskal–Wallis H-test to test a null hypothesis that all the group medians were equal, with an alternative hypothesis that at least one of the medians was different (Kruskal and Wallis, 1952).

Randomness in the structure of CNC films was introduced to determine the sensitivities of their uniaxial mechanical properties to specified in-plane ordering schemes. **Figures 1D–F** provides examples of three realizations of CNC films with structural randomness. In this work, film randomness was controlled by specifying the distribution of allowable offsets relative to a perfectly aligned CNC film with 50% regular offsets between neighboring fibers (see **Figure 1B** for an example of this baseline structure type). Uniform (U) and normal (N) offset distributions of mean 50% were considered. For each of the ranges and standard deviations of the uniform and normal distributions, respectively, specified, 16 unique CNC films were constructed. In addition to quantifying the sensitivities of films to random fiber offsets, the size scaling behavior of CNC film mechanical properties were evaluated. **Figure 2** provides an illustration of how size scaling was introduced for a CNC film with $L = 50$ nm. Neat films with between 1 and 512 serial CNC fibers in each periodic image were simulated. The total length of the simulation box (l) depends on the number of axial fibers, as well as the individual fiber length (L).

RESULTS

Both fiber length and the specific ordering of CNC films affected their observed mechanical properties. **Figure 3** shows representative stress-strain responses of individual CNC films subjected to uniaxial tension. At short fiber lengths, the elastic responses of CNC films are highly non-linear (**Figure 3A**). This is particularly true as the films approach failure. No difference between the responses of films with $L = 50$ nm and 10 and 12.5% regular offset structures was observed because, at this fiber length, their close packed structures were identical; this is a topological limitation of the CNC bead-spring model. As the lengths of CNC fibers increases, the extent of non-linearity in the mechanical responses of the corresponding films decreases (**Figures 3B,C**). Additionally, the uniaxial responses of long fiber length CNC films appear more qualitatively similar compared to the responses of short fiber CNC films (**Figure 3**), particularly with respect to their small strain behaviors.

In all cases, significant drops in stress are observed at the transition between elasticity and failure. While short fiber films exhibited responses indicative of ductile, yield-like behavior (**Figure 3A**), longer fiber length films failed in a brittle manner (**Figure 3C**). These two distinct failure behaviors manifest from differences in the types motion present between individual CNC fibers. There exists a transition between CNC sliding (short fiber lengths) and CNC rupture (long fiber lengths), which is controlled by the critical length for shear transfer (Zhang Z. Q. et al., 2010; Wei et al., 2012; Xia et al., 2016; Qin et al., 2017). Below this critical value, individual CNC fibers freely slide during externally applied axial loads, meaning that the corresponding deformed structures do not exhibit any evidence of intra-CNC bond rupture (**Figures 4A,B**). Independent from

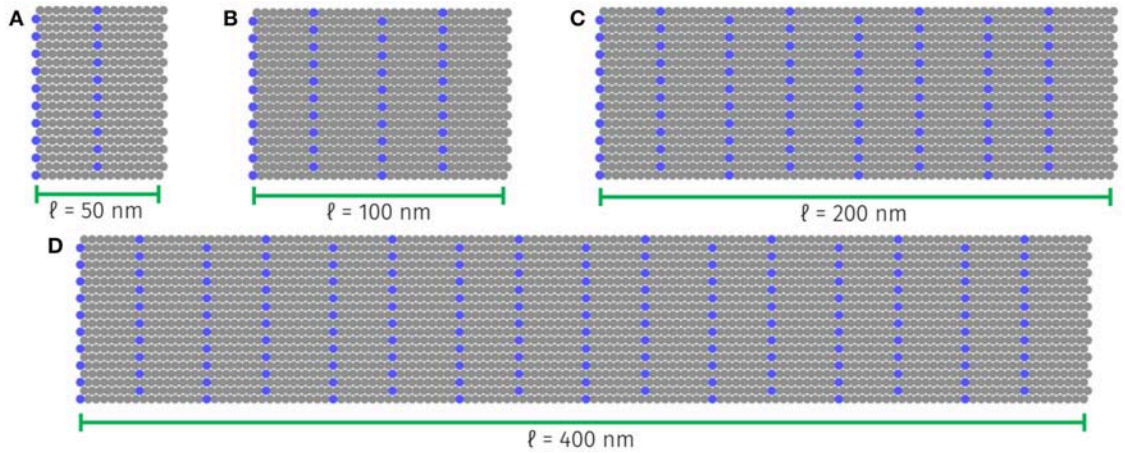

FIGURE 2 | Size scaled initial configurations of CNC films with **(A)** one, **(B)** two, **(C)** four, and **(D)** eight serial fibers in each periodic image. In each case, the individual fibers are equally sized ($L = 50$ nm), but the overall simulation axial length (l) is variable.

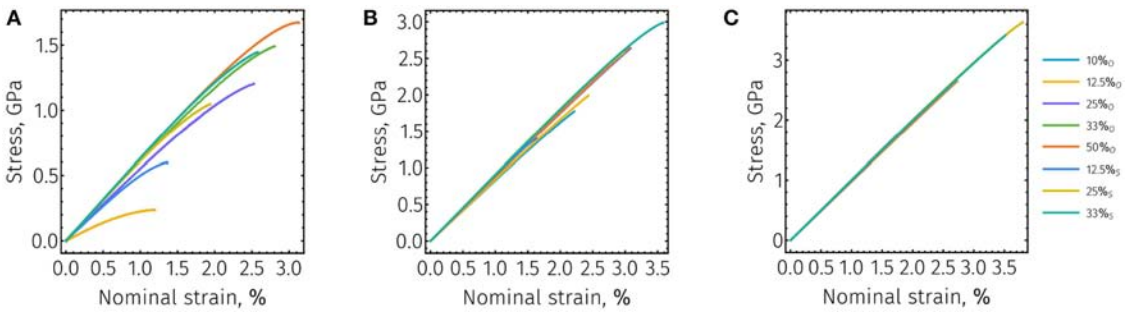

FIGURE 3 | Stress strain responses of CNC films with approximate base fiber lengths **(A)** $L = 50$ nm, **(B)** $L = 150$ nm, and **(C)** $L = 300$ nm. Colors in each plot correspond to various fiber ordering schemes. $x\%_O$ and $x\%_S$ refer to regular and staggered offset structures with $x\%$ offset between neighboring fibers, respectively.

their specific internal structure, all short fiber CNC films ($L = 50$ and $L = 100$ nm) failed without bond rupture. For CNC films with longer fibers (e.g., $L = 300$ nm), film failure occurs via catastrophic fiber failure (**Figures 4E,F**). For CNC films with regular offsets, this failure results from fiber rupture at the axial position of fiber junctions (**Figure 4E**). For staggered structures, long fiber films similarly failed by fiber rupture, except with more spatial variation (even among individual replicates of the same film structure) between their ruptures (**Figure 4F**). At the transition between fiber sliding and rupture, CNC films failed through a combination of the two modes (**Figures 4C,D**).

A more quantitative comparison between structure and fiber length can be accomplished by taking a closer look at the distributions of mechanical properties of these neat, two dimensional CNC films. **Figures 5A–C** show box-whisker plots of the initial, or Young's, modulus of CNC films with $L = 50$, 150, and 300 nm, respectively. For each specified fiber arrangement and length, 20 independent simulations were conducted to assess the expected group variation. For all fiber lengths examined, significant differences were observed among the initial moduli of the various in-plane ordering schemes (**Figure 5**; Kruskal–Wallis $P < 0.001$). For short fiber films ($L = 50$ nm), a substantial increase in the median initial modulus is observed as the amount of regular and staggered overlapping increases (**Figure 5A**). This translates to CNC films with 50% regular offsets exhibiting the highest initial modulus for $L = 50$ nm. In the intermediate fiber length range ($L = 150$ nm), increasing the shortest overlap between adjacent fibers similarly results in an increase in initial moduli (**Figure 5B**). However, for films of this fiber length, staggered structures tend to have higher median initial moduli compared to those with regular offsets. As the fiber length increases to $L = 300$ nm, the amount of variation between the initial moduli of individual film structures decreases substantially (**Figure 5C**). As with $L = 150$ nm films, $L = 300$ nm films with staggered structures tend to outperform regularly offset structures (**Figure 5C**; Mann–Whitney U between all regular and staggered structures; $P < 0.001$).

Much like the small strain behavior of neat, two dimensional CNC films is coupled to the specifics of their structure, so too are their failure properties. Across fiber lengths and in-plane orderings, CNC film strength distributions display substantially

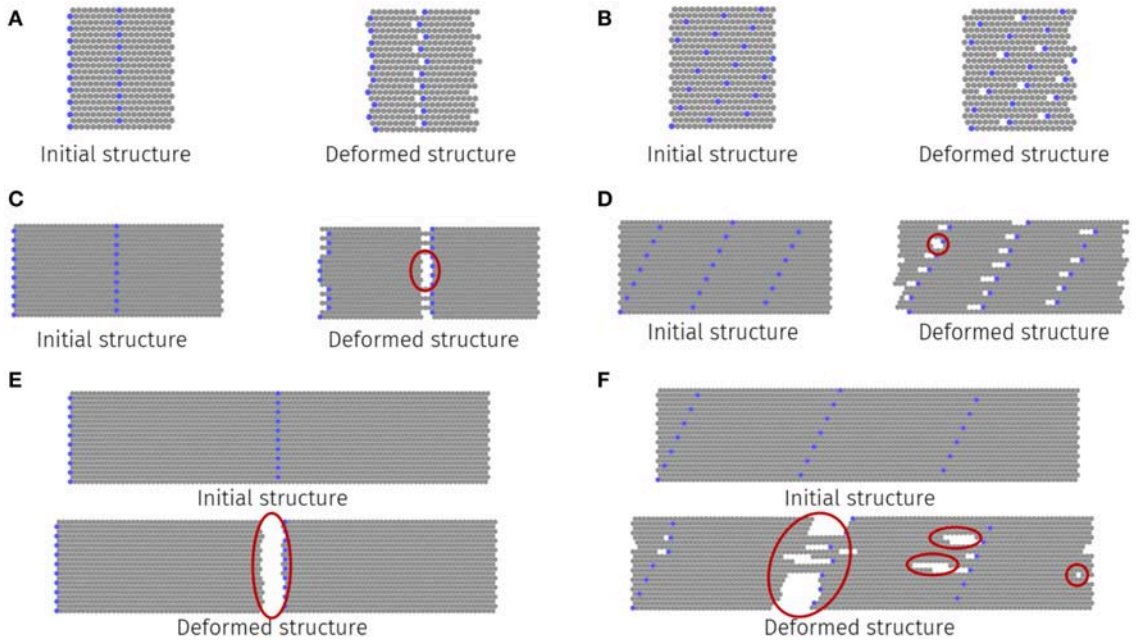

FIGURE 4 | Initial and deformed configurations of various sized [**(A,B)** $L = 50$ nm, **(C,D)** $L = 150$ nm, and **(E,F)** $L = 300$ nm] and arranged [**(A,C,E)** 50% regular and **(B,D,F)** 33% staggered offset between neighboring fibers] two dimensional CNC films. Locations of chain rupture are indicated by red circles in deformed structures.

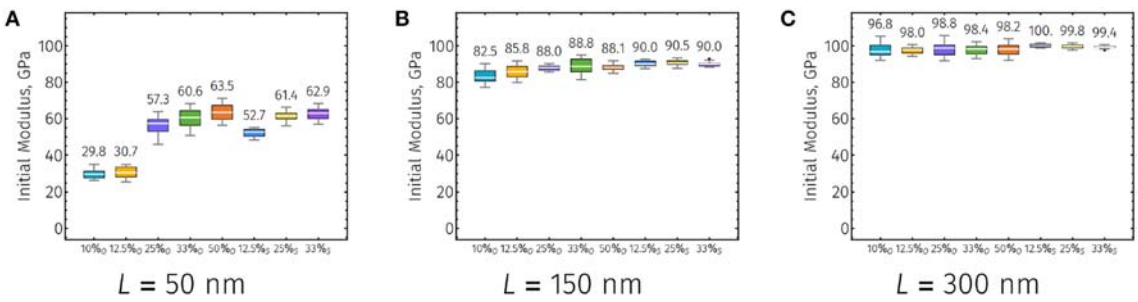

FIGURE 5 | Initial modulus box-whisker plots (20 independent simulations for each structure) of CNC films with approximate base fiber lengths **(A)** $L = 50$ nm, **(B)** $L = 150$ nm, and **(C)** $L = 300$ nm. Colors in each plot correspond to various fiber ordering schemes. White horizontal lines, colored box, gray vertical lines, and black dots indicate the median, interquantile range (IQR) between 3rd and 1st quantiles, range (of all data within $\pm 1.5 \times$ IQR), and outliers (points outside the range), respectively. Numeric values of the distribution medians are listed above their respective box plots.

less relative variation between replicates compared to initial moduli distributions (**Figures 5**, **6**). With short fibers, the trend between the strengths of CNC film structures is similar to that of initial moduli, with 50% regularly offset films demonstrating the highest strengths (**Figures 5A**, **6A**). However, as fiber length increases, the apparent strengths of neat CNC films with regular offsets become invariant to structure and saturates (**Figures 6B,C**). This strength plateau is present for films with fibers longer than the critical length for shear load transfer and regular in-plane ordering, where failure occurs via fiber rupture at a particular axial location normal to the direction of loading (**Figures 4C,E**). For intermediate and long length fibers, the structures with the highest strengths have staggered internal orderings (**Figures 6B,C** and **Supplemental Information**). Given the nearly linear uniaxial responses of neat CNC films with fibers of these lengths (**Figures 3B,C**), the effect of in-plane structure on toughnesses largely follows that of strengths (see **Supplemental Information**). This is especially true for long fiber length films that experience purely brittle failures.

The sensitivities of neat films to small variations in their internal ordering was measured by introducing increasing levels of structural randomness. Using 50% regular offset structures as baselines, normal, and uniform distributions of offsets, centered about the corresponding baseline configurations, were used to uncover any specific effects related to the particular form of the randomness within CNC films of various fiber lengths. **Figures 7A,B** show the distributions of expected initial moduli and strengths of neat CNC films, respectively. Each

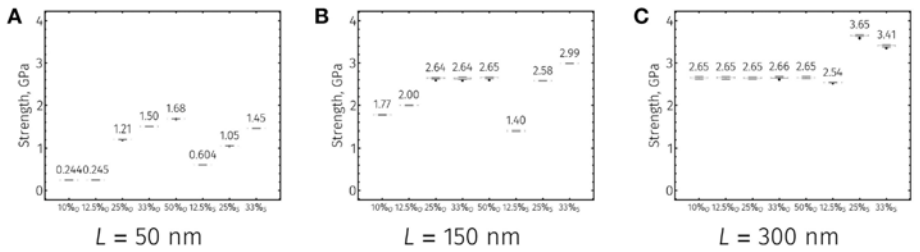

FIGURE 6 | Strength box-whisker plots (20 independent simulations for each structure) of CNC films with approximate base fiber lengths **(A)** $L = 50$ nm, **(B)** $L = 150$ nm, and **(C)** $L = 300$ nm. Colors in each plot correspond to various fiber ordering schemes. $x\%_O$ and $x\%_S$ refer to regular and staggered offset structures with $x\%$ offset between neighboring fibers, respectively. White horizontal lines, colored box, gray vertical lines, and black dots indicate the median, interquantile range (IQR) between 3rd and 1st quantiles, range (of all data within $\pm 1.5 \times$ IQR), and outliers (points outside the range), respectively. Numeric values of the distribution medians are listed above their respective box plots.

random distribution includes 16 distinct structural realizations, each with 20 independent simulations (320 simulations total). Insufficient evidence was found to reject the null hypotheses of significant differences between the initial moduli medians of ordered and random CNC films with $L = 50$ and $L = 100$ nm (**Figure 7A**; Kruskal–Wallis $P > 0.05$); however, a significant, but not substantial, difference between the initial moduli medians of ordered and random films with $L = 300$ nm (**Figure 7A**; Kruskal–Wallis $P < 0.001$). In terms of film strengths, there was sufficient evidence to reject the null hypotheses of no significant difference between the medians of strengths for each fiber length (**Figure 7B**; Kruskal–Wallis $P < 0.001$). Interestingly, for $L = 300$ nm films with $N_{5\%}$ random fiber offsetting, the median film strength is higher than the corresponding film with regular offsetting (**Figure 7B**). Similarly, the median strength of the $U_{55\%}$ random distribution with $L = 150$ nm is greater than, but not meaningfully different from, the median strength of the regularly offset structure (**Figure 7B**). For each fiber length, the distributions in film toughnesses followed the trends in film strengths (**Figure 7B** and **Supplemental Information**). Qualitatively, films with random offset distributions tend to have more variation in their observed mechanics, both in their elastic (**Figure 7A**) and failure (**Figure 7B** and **Supplemental Information**) behaviors. Specifically, CNC films with normal random offsets displayed the most variance among replicates in their mechanical properties (**Figure 7** and **Supplemental Information**).

In addition to assessing the sensitivity of CNC films to varying degrees of in-plane ordering randomness, the effect of system size on their observed mechanical properties was also investigated. **Figure 8** shows the distributions of initial moduli for CNC films of various fiber lengths. The data in **Figure 8** are equally spaced along the abscissa of their respective plots; therefore, each plot should be viewed as logarithmically transformed about system size. Independent from fiber length, the predicted initial moduli medians of neat CNC films are not significantly affected by the number of serial fibers in each periodic image (**Figure 8** and **Supplemental Information**; Kruskal–Wallis $P > 0.05$). However, as the number of fibers in the simulation domain increases, the variance of the distributions of initial moduli decreases dramatically. This means that it is possible to achieve a realistic estimate of the true initial modulus median of a neat CNC film with a relatively small number of replicates if the system is sufficiently large. However, while the distribution variance does decrease with simulation size, there still exists an unavoidable statistical effect even for arbitrarily large systems.

While system size did not significantly affect the small strain behaviors of neat CNC films, a pronounced effect on their failure behaviors was observed. **Figures 9**, **10** show the relationships between system size (number of serial fibers in each periodic images) and the predicted strength and toughness of neat CNC films of varying fiber lengths, respectively. Like **Figures 8**–**10** are logarithmically transformed along their abscissa. Given the relatively small nominal differences between the minimum and maximum strengths of CNC films of a particular fiber length, **Figure 9** may be equivalently viewed as either linearly or logarithmically transformed with respect to strength; this is also true, to a large extent, for the toughness plots shown in **Figure 10**. For all fiber lengths, the predicted strength and toughness medians of neat CNC films are significantly affected by the number of serial fibers in each periodic image (**Figures 9**, **10** and **Supplemental Information**; Kruskal–Wallis $P < 0.001$). Short fiber films (e.g., $L = 50$ nm) display a strongly non-linear relationship between strength and simulation size in log-log space (**Figure 9A**). Within the range of system sizes investigated, the effect of size on film strength for $L = 50$ nm films appears to essentially saturate for sufficiently large systems. This behavior is qualitatively different from that observed for intermediate ($L = 150$ nm) and long ($L = 300$ nm) fiber films, where strongly linear relationships between system size and strength in log-log space can be seen (**Figures 9B,C**, respectively). Moreover, the rates at which strength is affected by system size for neat CNC films with $L = 150$ nm and $L = 300$ nm are similar (i.e., the slopes of the best fit lines in log-log space between the median strengths and system sizes). The variance of predicted strengths tends to decrease with increase system size for short fiber neat CNC films (**Figure 9A**); however, the variance of intermediate and long fiber films is mostly invariant to system size (**Figures 9B,C**, respectively).

The effects of system size on predicted toughness were even more noticeable than those on strength. For short fiber

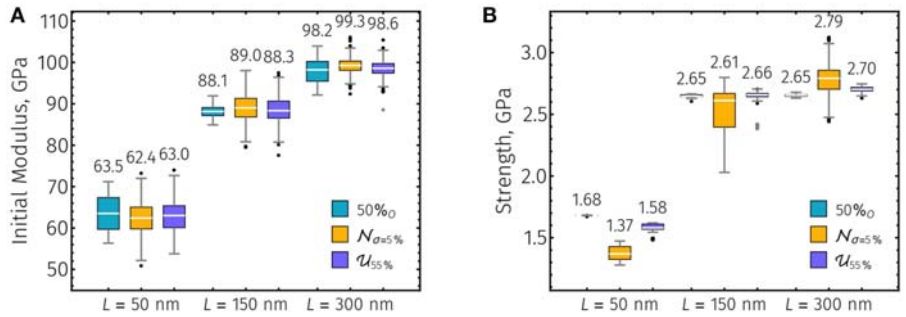

FIGURE 7 | Box-whisker plots of **(A)** initial moduli and **(B)** strengths of CNC films with 50% regular and random orderings for $L = 50$, 150, and 300 nm. Random offset distributions are either normal ($N_{x\%}$) or uniform ($U_{x\%}$) with mean 50%, where x% indicates standard deviations and maxima of the normal and uniform distributions, respectively. The box-whisker plots for each ordered structure contains 20 independent simulations. White horizontal lines, colored box, gray vertical lines, and black dots indicate the median, interquantile range (IQR) between 3rd and 1st quantiles, range (of all data within $\pm 1.5 \times$ IQR), and outliers (points outside the range), respectively. Numeric values of the distribution medians are listed above their respective box-whisker plots.

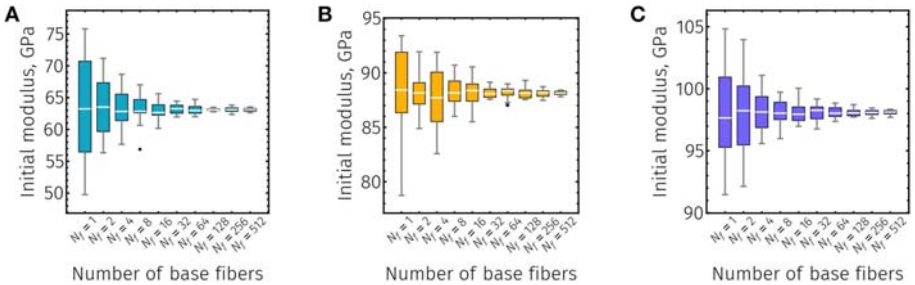

FIGURE 8 | Initial modulus box-whisker plots (20 independent simulations for each structure size) of CNC films with approximate base fiber lengths **(A)** $L = 50$ nm, **(B)** $L = 150$ nm, and **(C)** $L = 300$ nm. Number of fibers (N_f) refers to number of CNC fibers in series within the simulation volume and scales linearly with simulation size along the direction of loading. White horizontal lines, colored box, gray vertical lines, and black dots indicate the median, interquantile range (IQR) between 3rd and 1st quantiles, range (of all data within $\pm 1.5 \times$ IQR), and outliers (points outside the range), respectively.

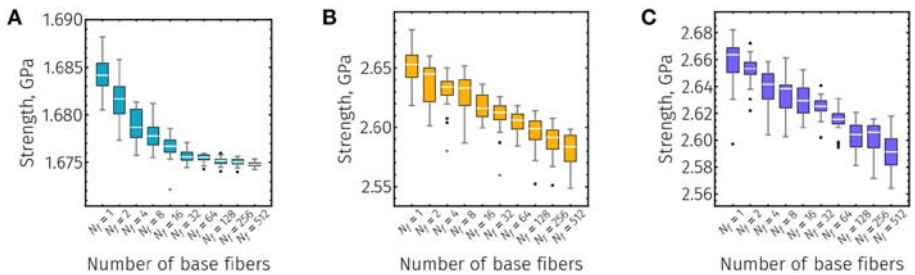

FIGURE 9 | Strength box-whisker plots (20 independent simulations for each structure size) of CNC films with approximate base fiber lengths **(A)** $L = 50$ nm, **(B)** $L = 150$ nm, and **(C)** $L = 300$ nm. Number of fibers (N_f) refers to number of CNC fibers in series within the simulation volume and scales linearly with simulation size along the direction of loading. White horizontal lines, colored box, gray vertical lines, and black dots indicate the median, interquantile range (IQR) between 3rd and 1st quantiles, range (of all data within $\pm 1.5 \times$ IQR), and outliers (points outside the range), respectively.

CNC films, a qualitatively similar, non-linear relationship exists between toughness and system size (**Figure 10A**). While this effect appeared to saturate with respect to strength (**Figure 9A**), no such convergent behavior for toughness is present (**Figure 10A**). Additionally, across fiber lengths and contrary to the distributions of film strengths (**Figure 9**), there does not appear to be any substantial relationships between the variance of the toughness distribution and the system size (**Figure 10**). Linear relationships between toughness and system size are similarly observed for both intermediate and long fiber CNC films (**Figures 10B,C**, respectively), with the rates at which the median toughnesses decrease with system size being approximately equal. Compared to the size scaling behaviors of film strength, system size has a considerably larger

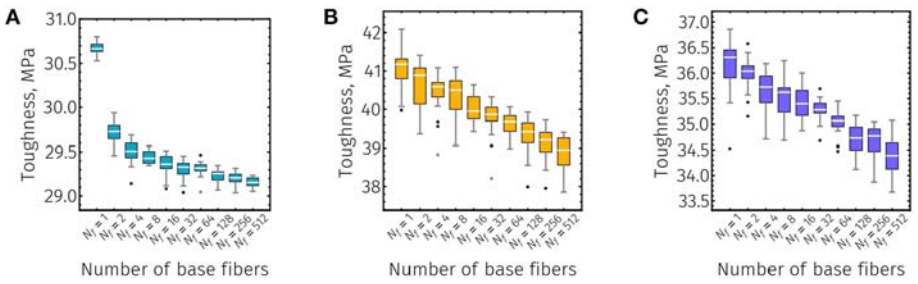

FIGURE 10 | Toughness box-whisker plots (20 independent simulations for each structure size) of CNC films with approximate base fiber lengths **(A)** $L = 50$ nm, **(B)** $L = 150$ nm, and **(C)** $L = 300$ nm. Number of fibers (N_f) refers to number of CNC fibers in series within the simulation volume and scales linearly with simulation size along the direction of loading. White horizontal lines, colored box, gray vertical lines, and black dots indicate the median, interquantile range (IQR) between 3rd and 1st quantiles, range (of all data within $\pm 1.5 \times$ IQR), and outliers (points outside the range), respectively.

nominal effect with respect to toughness. The predicted median toughness of a neat CNC film with $L = 50$ nm and 512 serial fibers was roughly 95% of the single fiber film (**Figure 10A**), while the median strength only decreased by 0.5% over the same system size range (**Figure 9A**). Similarly, over the size interval from 1 to 512 serial fibers, decreases of over 5% in film toughness can be observed for of both intermediate and long fiber length CNC films (**Figures 10B,C**). However, compared to short fiber films, intermediate, and long fiber films did display more consequential decreases in strength with increased system size on the order of 2.5% with respect to films with a single serial fiber (**Figures 9B,C**).

In addition to the quantitative effects of system size on the distributions of predicted mechanical properties, increasing the size of the simulated domain fundamentally alters the initiation and failure topologies of neat CNC films. Representative examples of neat films following failure are shown in **Figure 11**. Compared to films with a single CNC fiber in each periodic image (**Figure 4**), many-fibered films undergo more diffuse failure (**Figure 11**). This diffusive behavior can be readily seen in short fiber films that fail without fiber rupture (**Figures 11A,B**). Not only is the coordination of inter-fiber sliding and eventual surface creation of these films significantly more complex than their single fiber counterparts, there also exists evidence of heterogeneous damage far field from the primary damage site (**Figures 11A,B**). While long fiber films still tend to fail in a pre-dominately brittle fashion, the axial locations of the failure initiation are non-unique (**Figures 11E,F**). Finally, for films with intermediate length fibers, there is evidence of a combination of both brittle intra-CNC rupture and sliding events in the failed structures with many serial fibers (**Figure 11D**). This combination of failure modes, which is not necessarily present in every case of material failure (**Figure 11C**), underscores the importance of understanding how material performance may be tied to the size of the system simulated.

DISCUSSION

Understanding how Nature efficiently uses structural ordering in its composite materials has been the driving force behind countless theoretical and experimental investigations aimed at adopting its designs to engineered material systems (Zhang Z. Q. et al., 2010; Shao et al., 2012; Dutta et al., 2013; Barthelat, 2014; Ni et al., 2015; Wei et al., 2015; Qwamizadeh et al., 2017a; Henry and Pimenta, 2018). Yet, Nature consistently outperforms manufactured composites composed from stiff and aligned fibers embedded in low, or non-existent, volume fractions of compliant matrix material (Espinosa et al., 2009; Wei et al., 2012; Gu et al., 2016). Despite a strong theoretical understanding of how these structured materials behave, it is clear that much still remains unknown about their mechanics. In this work, many of the lessons learned from matrix-containing nanocomposites with high aspect ratio, stiff elements were put to the test in the context of quantifying the mechanical properties of neat, two-dimensional CNC films. Specifically, the initial moduli, strengths, and toughnesses of neat films of various fiber lengths and in-plane orderings were determined. The expected mechanical properties of neat film were found to be, in most cases, closely tied to their structure; therefore, the sensitivities of these mechanical property predictions were assessed to better understand the distribution of performances that might be observed for real materials that contain topological defects. Finally, simulations are often limited by their accessible length and time scales. In many situations, the size of the physical structures are orders of magnitude greater than the simulated domains. This inconsistency between the simulated and physical can have significant effects of the expected mechanics, with the neat CNC films investigated in this work showing substantial mechanical and structural effects related to simulated system size.

Structural and Fiber Length Effects

For the fiber lengths investigated in this work, the corresponding neat films exhibited, to varying degrees, non-linearity in their uniaxial stress-strain responses, and this non-linearity persisted across in-plane orderings (**Figure 3**). The existence of non-linearity is typically ignored in theoretical analyses of brick and mortar systems since brittle failure is assumed (Zhang Z. et al., 2010; Zhang Z. Q. et al., 2010; Dutta et al., 2013; Barthelat, 2014); however, given the apparent strain softening of these films (**Figure 3**), failure to consider non-linearity can potentially lead

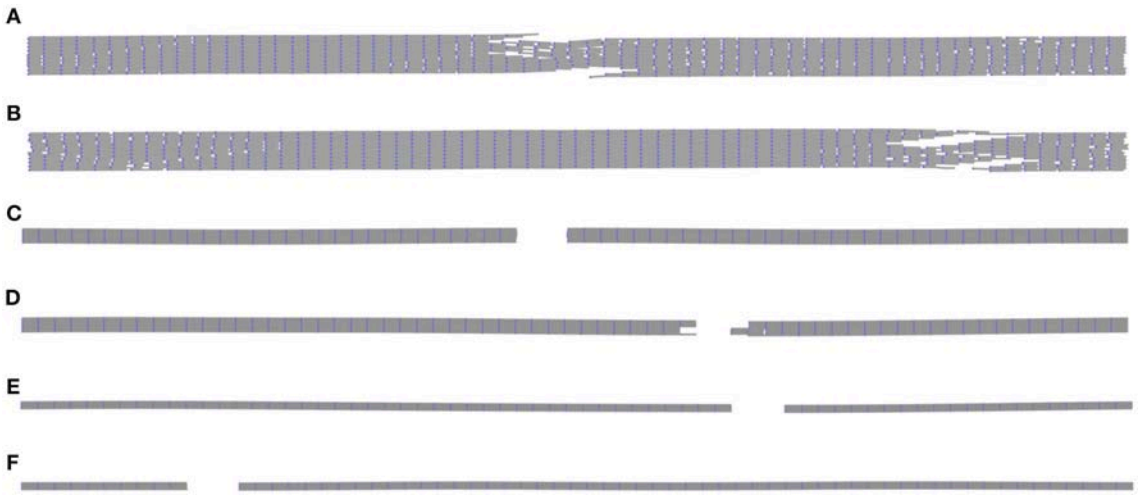

FIGURE 11 | Deformed configurations of **(A,B)** $L = 50$ nm, **(C,D)** $L = 150$ nm, and **(E,F)** $L = 300$ nm size scaled CNC films with 32 CNC fibers in series.

to overestimating film toughness. In short fiber length films (e.g., $L = 50$ nm) that tended to show the most non-linearity in their uniaxial response, assuming a linear elastic response can result in errors of over 20% compared to the true toughness (**Figure 3**). Errors in toughnesses calculated with the assumption of linear elasticity are less evident in films that exhibit brittle failure, with errors of <5% for intermediate and long fiber length films.

It is possible to compare many of the elastic predictions of neat CNC films to established continuum theories constructed to describe the mechanics of two phase, brick and mortar material systems. This can be accomplished by assuming the space between CG CNC fibers corresponds to the theoretical matrix material, with its mechanical properties govern by the non-bonded interactions between fibers (see **Supplemental Information** for details regarding the comparison of neat films to established continuum theories). Continuum theories have been successfully used to derive bounds for the initial elastic response of brick and mortar materials (Zhang Z. Q. et al., 2010; Lei et al., 2013; Qwamizadeh et al., 2017a). While short fiber CNC films qualitatively follow expected trends from relevant continuum theories (Zhang Z. Q. et al., 2010; Qwamizadeh et al., 2017a), the initial moduli of neat CNC films are consistently lower than predicted ranges (see **Supplemental Information**). This discrepancy may be attributed to a number of factors. First, many theories ignore the normal elastic contribution of the matrix between axial elements and its role in load transfer (Kim et al., 2018). However, accounting for the presence of pseudo-matrix material in the axial spaces between fibers of neat CNC films has only a negligible effect on the predicted initial moduli and, for the ranges of material parameters relevant to the films investigated herein, are not substantial enough to drive predictions outside the bounding cases. Another possible explanation for the discrepancy between the initial moduli of neat films and two phase continuum predictions is that continuum theories tend to assume the matrix material only supports shear loads (Ji and Gao, 2004; Zhang Z. Q. et al., 2010; Dutta et al., 2013; Lei et al., 2013; Ni et al., 2015; Wei et al., 2015; Henry and Pimenta, 2017, 2018; Qwamizadeh et al., 2017a; Abid et al., 2018; Kim et al., 2018). However, for neat films, substantial lateral expansion occurs during uniaxial extension due to the topological constraints of the CG bead-spring model. Additionally, uniformity is often assumed in the distributions of stress within both the matrix and stiff constituents, but recent simulations have suggested that the actual distributions of deformation within these domains are much more complex (Mathiazhagan and Anup, 2016c). Finally, in the context of CG bead-spring systems, as the fibers slide out of their close packed configuration during the initial film stretching, the directions of the frictional forces between fibers (the interactions that provide the effective matrix shear modulus) are not aligned with the axial fiber direction. This feature may affect the shear modulus of the region between fibers in a close packed system, as well as contribute to increased fiber deformation due topological constraints.

As fiber lengths increase, neat film initial moduli predictions start to fall within continuum ranges. With $L = 150$ nm and regular offsets, the initial moduli of CG MD simulations of neat CNC films are within continuum theory ranges (Zhang Z. Q. et al., 2010; Qwamizadeh et al., 2017a); however, the CG MD results of small overlap, staggered structures are more compliant than predicted by continuum theory (see **Supplemental Information**). The initial moduli predictions of long fiber, neat films all lie within expected ranges derived from continuum theories (see **Supplemental Information**). The convergent behavior between neat film and continuum theory predictions is motivated by the increased uniformity of axial stresses in stiff nanocomposite elements as their length increases (Mathiazhagan and Anup, 2016c).

Sensitivity to Structural Randomness

The sensitivities of neat CNC films to perturbations in their in-plane orderings were assessed by mechanically

characterizing many independent structural replicates with different distributions of randomness. The introduction of randomness did not significantly affect the median initial moduli of neat films (**Figure 7A**). This result is contrary to previous work on two phase brick and mortar systems that has suggested structural randomness leads to decreased initial modulus independent from fiber geometry and mechanics (Zhang Z. Q. et al., 2010; Ni et al., 2015; Abid et al., 2018). The insensitivity to randomness in the small strain behavior of neat CNC films in this work is likely driven by the topological constraints of the CNC bead-spring model. For small deformations, it is energetically favorable for the CNC bead-spring chains to maintain their close packing. In the complimentary continuum brick and mortar theories (Zhang Z. Q. et al., 2010), this constrain is not present and the initial deformation is primarily dictated by the overlapping between neighboring stiff elements.

The strengths of brick and mortar films have also been shown to be susceptible to structural randomness, with as much as 50% reduced strength compared to pristinely ordered systems (Zhang Z. Q. et al., 2010; Ni et al., 2015; Abid et al., 2018). For many of the fiber lengths and distributions of randomness tested herein, some significant differences in strength were indeed observed. In particular, randomness reduced strength in films with short fibers ($L = 50$ nm; **Figure 7B**). This observation can be explained by the high sensitivity of short fiber length films to their structure (**Figure 6A**). In randomly ordered short fiber films, there exists a distribution of local, fiber-to-fiber interactions with failure behaviors that are similar to staggered films with that ordering. This means that, as films with random orderings approach failure, the local fiber-to-fiber interaction with the lowest strength will fail and, for these neat films, cause total film failure. However, as the lengths of the fibers increases, the sensitivity to structural randomness decreases and, in some cases, results in higher median film strength (**Figure 7B**). Looking at the distributions of film strengths for systems with intermediate fibers (**Figure 6B**), there is also almost no variation in strength between structures. Therefore, the presence of a distribution of local fiber-to-fiber overlaps does not tend to lead to a substantial sensitivity to randomness (**Figure 7B**). In the case of long fibers, there are staggered configurations that exhibit superior strengths relative to the baseline 50% regular structure (**Figure 6C**). This allows for certain random structural realizations of $L = 300$ nm films to withstand higher peak loads compared to films with a 50% regular structure. The improved strengths of long fiber films may also be aided by the admissibility of bending within and rotation about their stiff elements. Continuum theories of often neglect this contribution (Zhang Z. Q. et al., 2010; Lei et al., 2013; Qwamizadeh et al., 2017a), but it may be significant in brick and mortar systems with non-regular orderings and long fibers (Mathiazhagan and Anup, 2016c).

Size Scaling Mechanical Behavior

The small strain behavior of neat CNC films appear insensitive to simulation size. In nanoscopic materials there has been some evidence of a size dependence on the elastic properties of thin films (Miller and Shenoy, 2000; Chen et al., 2006; Mathur and Erlebacher, 2007), but also evidence that suggests minimal size influence after a critical size threshold is met (Sharpe et al., 2001). In general, the neat films studied herein are not susceptible to external factors (e.g., free surface effects, material defects, etc.) that may contribute differences in apparent initial moduli of variously sized films. As the number of serial fibers increases within the simulated domain, the variance of the initial moduli distribution decreases (**Figure 8**). This phenomenon may be attributed to the increased number of degrees of freedom in the system with increased system size. As the number of degrees of freedom increases, the specific mechanical outcome of the particular realization of a film tends toward the mean behavior. This central tendency is especially meaningful in the context of the random thermal motion of individual CG beads (i.e., there is a higher probability of consequential and coordinated thermal motions in smaller simulations).

While no significant variation in small strain elastic behaviors were observed for neat films of increasing system size, there were significant relationships between simulation size and failure properties. Specifically, regardless of the fiber length, as the number of serial fibers in the simulation domain increases, the measured median strength and toughness decrease (**Figures 9**, **10**, respectively). Long fiber neat films with regular ordering tend to fail brittly via intra-CNC rupture independent from system size (**Figures 4E**, **11E,F**). Consequently, the relationships between their failure properties (i.e., strength and toughness) are mostly linear in log-log space with respect to system size (**Figures 9B,C**, **10B,C**). This type of behavior closely matches the size effect curve of a two dimensional material with a Weibull distribution of strengths (Bažant and Le, 2017). The modulus of a Weibull distribution of strengths can be estimated directly from the slopes of the size scaling curves in log-log space (Bažant and Le, 2017; Luo and Bažant, 2017a). Therefore, given the similarities between the slopes of the size scaling relationships for $L = 150$ nm and $L = 300$ nm films (**Figures 9B,C**), there is evidence to suggest that an intrinsic failure property of CNCs dictates the distribution of failure behaviors for neat films. This feature means that uniformity should be expected among the distributions of strengths of CNCs with fibers longer than the critical length for shear load transfer.

In the case of short fibers, non-linear relationships were observed in the size scaling behaviors of strength and toughness (**Figures 9A**, **10A**, respectively). Introducing more unique opportunities for strain localization also leads to more spatially diffuse failure modes in multi-fiber short films (**Figures 11A,B**). These deformed configurations, in combination with the non-linear size scaling relationships (**Figures 9A**, **10A**), are indicative of quasibrittle materials (Luo and Bažant, 2017a,b). In these types of materials, it is possible for multiple local failure events to occur prior to total material failure, providing enhanced fracture toughness and resiliency to defects. This size dependent behavior is independent from previous efforts that describe a transition from ductile to brittle failure mechanisms in nanowires with increasing length, but constant cross-sectional area (Wu et al., 2012). Future work involves extending these distributional observations of material performance to three dimensions, as well as analytic investigations to build statistical theories capable

of capturing the transition between quasibrittle and brittle failure regimes of neat CNC films.

CONCLUSION

Taken together, the results presented herein provide reasonable evidence to suggest that many of the conclusions from matrix-containing, uniaxial nanocomposites can be applied to neat films with high aspect ratio particle assembles. Specifically, the non-bonded interactions between adjacent fibers in neat films can be well-approximated by the matrix phase of standard brick and mortar continuum theories. That being said, some important differences between two phase and neat films were observed. Namely, short fiber neat films tended to be more compliant than expected given the properties of their constituents, and this trend was consistent independent from the particular in-plane fiber arrangement. Moreover, for short fibers, CNC films with regular overlaps exhibited higher initial moduli compared to those with staggered microstructures. The differences between the initial moduli of CNC films with regular and staggered arrangements becomes less pronounced as the fiber lengths exceed the critical length for shear load transfer. However, a similar saturation trend in both strength and toughness was not observed with increasing fiber length, with staggered architectures outperforming those with regular overlaps. Additionally, neat films showed a meaningful insensitivity to randomness with respect to their in-plane fiber arrangements during elastic deformations, as well as during failure for films with sufficiently long fibers. While in-plane ordering randomness of fibers did not significantly or substantially affect the median film elastic or failure responses, a widening of the property distributions was observed. Finally, the size scaling behavior of these neat films exhibited a readily identifiable transition between quasibrittle and brittle failure modes, but an insensitivity to system size during elastic deformation.

AUTHOR CONTRIBUTIONS

BM conducted the computation simulations and data analysis, as well as designed the statistical analyses. BM and SK contributed to the manuscript preparation and study design.

FUNDING

BM and SK would like to acknowledge funding from the Army Research Office (award #W911NF1710430), Office of Naval Research (PECASE Award, grant number N00014-16-1-3175), the Center for Hierarchical Materials Design (CHiMaD) funded by National Institute of Standards and Technology (award #70NANB14H012), and the Northwestern University High Performance Computing Center.

SUPPLEMENTARY MATERIAL

The Supplementary Material for this article can be found online at: https://www.frontiersin.org/articles/10.3389/fmats.2019.00174/full#supplementary-material

REFERENCES

Abid, N., Mirkhalaf, M., and Barthelat, F. (2018). Discrete-element modeling of nacre-like materials : Effects of random microstructures on strain localization and mechanical performance. *J. Mech. Phys. Solids* 112, 385–402. doi: 10.1016/j.jmps.2017.11.003

Arzt, E., Fratzl, P., Gao, H., Ji, B., and Ja, I. L. (2003). Materials become insensitive to flaws at nanoscale. *Proc. Natl. Acad. Sci. U.S.A.* 100, 5597–5600. doi: 10.1073/pnas.0631609100

Barthelat, F. (2014). Designing nacre-like materials for simultaneous stiffness, strength and toughness: optimum materials, composition, microstructure and size. *J. Mech. Phys. Solids* 73, 22–37. doi: 10.1016/j.jmps.2014.08.008

Barthelat, F., Rabiei, R., and Dastjerdi, A. K. (2012). Toughness amplification in natural composites. *Mater. Res. Soc. Symp. Proc.* 1420, 61–66. doi: 10.1557/opl.2012.714

Barthelat, F., Tang, H., Zavattieri, P. D., Li, C. M., and Espinosa, H. D. (2007). On the mechanics of mother-of-pearl: a key feature in the material hierarchical structure. *J. Mech. Phys. Solids* 55, 306–337. doi: 10.1016/j.jmps.2006.07.007

Barthelat, F., and Zhu, D. (2011). A novel biomimetic material duplicating the structure and mechanics of natural nacre. *J. Mater. Res.* 26, 1203–1215. doi: 10.1557/jmr.2011.65

Bažant, Z. P., Le, J., and Bažant, M. Z. (2009). Scaling of strength and lifetime probability distributions of quasibrittle structures based on atomistic fracture mechanics. *Proc. Natl. Acad. Sci.* U. S. A. 106, 11484–11489. doi: 10.1115/IMECE2009-11824

Bažant, Z. P., and Le, J.-L. (2017). *Probabilistic Mechanics of Quasibrittle Structures: Strength, Lifetime, and Size Effect*, Cambridge: Cambridge University Press.

Begley, M. R., Philips, N. R., Compton, B. G., Wilbrink, D. V., Ritchie, R. O., and Utz, M. (2012). Micromechanical models to guide the development of synthetic 'brick and mortar' composites. *J. Mech. Phys. Solids* 60, 1545–1560. doi: 10.1016/j.jmps.2012.03.002

Bonderer, L. J., Studart, A. R., and Gauckler, L. J. (2008). Bioinspired design and assembly of platelet reinforced polymer films. *Science* 319, 1069–1074. doi: 10.1126/science.1148726

Chandler, M. Q., and Cheng, J. R. C. (2018). Discrete element modeling of microstructure of nacre. *Comput. Part. Mech.* 5, 191–201. doi: 10.1007/s40571-017-0162-7

Chen, C. Q., Shi, Y., Zhang, Y. S., Zhu, J., and Yan, Y. J. (2006). Size dependence of Young's modulus in ZnO nanowires. *Phys. Rev. Lett.* 96, 1–4. doi: 10.1103/PhysRevLett.96.075505

de Obaldia, E. E., Jeong, C., Grunenfelder, L. K., Kisailus, D., and Zavattieri, P. (2015). Analysis of the mechanical response of biomimetic materials with highly oriented microstructures through 3D printing, mechanical testing and modeling. *J. Mech. Behav. Biomed. Mater.* 48, 70–85. doi: 10.1016/j.jmbbm.2015.03.026

Dumanli, A. G., Van Der Kooij, H. M., Kamita, G., Reisner, E., Baumberg, J. J., Steiner, U., et al. (2014). Digital color in cellulose nanocrystal films. *ACS Appl. Mater. Interfaces* 6, 12302–12306. doi: 10.1021/am501995e

Dutta, A., Arjun, S., and Miklavcic, M. (2013). Optimal overlap length in staggered architecture composites under dynamic loading conditions. *J. Mech. Phys. Solids* 61, 145–160. doi: 10.1016/j.jmps.2012.08.005

Dutta, A., and Tekalur, S. A. (2014). Crack tortuousity in the nacreous layer–Topological dependence and biomimetic design guideline. *Int. J. Solids Struct.* 51, 325–335. doi: 10.1016/j.ijsolstr.2013.10.006

Eichhorn, S. J. (2011). Cellulose nanowhiskers: promising materials for advanced applications. *Soft Matter* 7, 303–315. doi: 10.1039/C0SM00142B

Espinosa, H. D., Rim, J. E., Barthelat, F., and Buehler, M. J. (2009). Merger of structure and material in nacre and bone – Perspectives on de novo biomimetic materials. *Prog. Mater. Sci.* 54, 1059–1100. doi: 10.1016/j.pmatsci.2009.05.001

Fratzl, P., and Weinkamer, R. (2007). Nature's hierarchical materials. *Prog. Mater. Sci*. 52, 1263–1334. doi: 10.1016/j.pmatsci.2007.06.001

Gao, L., Nie, G., and Zhang, T. (2016). A study of hierarchical biological composite structures via a coarse-grained molecular dynamics simulation approach. *Int. J. Appl. Mech*. 8:1650084. doi: 10.1142/S1758825116500848

Ghazlan, A., Ngo, T. D., and Tran, P. (2018). Influence of geometric and material parameters on the behavior of nacreous composites under quasi-static loading. *Compos. Struct*. 183, 457–482. doi: 10.1016/j.compstruct.2017.05.015

Gorbatikh, L., Lomov, S. V., and Verpoest, I. (2010). Original mechanism of failure initiation revealed through modelling of naturally occurring microstructures. *J. Mech. Phys. Solids* 58, 735–750. doi: 10.1016/j.jmps.2010.02.007

Gu, G. X., Libonati, F., Wettermark, S. D., and Buehler, M. J. (2017). Printing nature: unraveling the role of nacre's mineral bridges. *J. Mech. Behav. Biomed. Mater*. 76, 135–144. doi: 10.1016/j.jmbbm.2017.05.007

Gu, G. X., Su, I., Sharma, S., Voros, J. L., Qin, Z., and Buehler, M. J. (2016). Three-dimensional-printing of bio-inspired composites. *J. Biomech. Eng*. 138:021006. doi: 10.1115/1.4032423

Habibi, Y., Lucia, L. A., and Rojas, O. J. (2010). Cellulose nanocrystals: chemistry, self-assembly, and applications. *Chem. Rev*. 110, 3479–3500. doi: 10.1021/cr900339w

Hansoge, N. K., Huang, T., Sinko, R., Xia, W., Chen, W., and Keten, S. (2018). Materials by design for stiff and tough hairy nanoparticle assemblies. *ACS Nano*. 12, 7946–7958. doi: 10.1021/acsnano.8b02454

Henriksson, M., Berglund, L. A., Isaksson, P., and Lindstro, T. (2008). Cellulose nanopaper structures of high toughness. *Biomacromolecules* 9, 1579–1585. doi: 10.1021/bm800038n

Henry, J., and Pimenta, S. (2017). Semi-analytical simulation of aligned discontinuous composites. *Compos. Sci. Technol*. 144, 230–244. doi: 10.1016/j.compscitech.2017.01.027

Henry, J., and Pimenta, S. (2018). Increasing damage tolerance in composites using hierarchical brick-and-mortar microstructures. *J. Mech. Phys. Solids* 118, 322–340. doi: 10.1016/j.jmps.2018.06.003

Humphrey, W., Dalke, A., and Schulten, K. (1996). VMD: visual molecular dynamics. *J. Mol. Graph*. 14, 33–38. doi: 10.1016/0263-7855(96)00018-5

Jackson, A. P., Vincent, J. F. V., and Turner, R. M. (1988). The mechanical design of nacre. *Proc. R. Soc. B*. 234, 415–440. doi: 10.1098/rspb.1988.0056

Jäger, I., and Fratzl, P. (2000). Mineralized collagen fibrils: A mechanical model with a staggered arrangement of mineral particles. *Biophys. J*. 79, 1737–1746. doi: 10.1016/S0006-3495(00)76426-5

Ji, B., and Gao, H. (2004). Mechanical properties of nanostructure of biological materials. *J. Mech. Phys. Solids* 52, 1963–1990. doi: 10.1016/j.jmps.2004.03.006

Kamat, S., Su, X., Ballarini, R., and Heuer, A. (2000). Structural basis for the fracture toughness of the shell of the conch Strombus gigas. *Nature* 405, 1036–1040. doi: 10.1038/35016535

Kim, Y., Kim, Y., Lee, T. I., Kim, T. S., and Ryu, S. (2018). An extended analytic model for the elastic properties of platelet-staggered composites and its application to 3D printed structures. *Compos. Struct*. 189, 27–36. doi: 10.1016/j.compstruct.2018.01.038

Koh, L. D., Cheng, Y., Teng, C. P., Khin, Y. W., Loh, X. J., Tee, S. Y., et al. (2015). Structures, mechanical properties and applications of silk fibroin materials. *Prog. Polym. Sci*. 46, 86–110. doi: 10.1016/j.progpolymsci.2015.02.001

Kruskal, W. H., and Wallis, W. A. (1952). Use of ranks in one-criterion variance analysis. *J. Am. Stat. Assoc*. 47, 583–621. doi: 10.1080/01621459.1952.10483441

Lagerwall, J. P. F., Schutz, C., Salajkova, M., Noh, J., Park, J. H., Scalia, G., et al. (2014). Cellulose nanocrystal-based materials : from liquid crystal self-assembly and glass formation to multifunctional thin films. *NPG Asia Mater*. 6, 1–12. doi: 10.1038/am.2013.69

Lei, H. J., Zhang, Z. Q., Han, F., Liu, B., and Gao, H. J. (2013). Elastic bounds of bioinspired nanocomposites. *J. Appl. Mech*. 80:1017. doi: 10.1115/1.4023976

Luo, W., and Bažant, Z. P. (2017a). Fishnet statistics for probabilistic strength and scaling of nacreous imbricated lamellar materials. *J. Mech. Phys. Solids* 109, 264–287. doi: 10.1016/j.jmps.2017.07.023

Luo, W., and Bažant, Z. P. (2017b). Fishnet model for failure probability tail of nacre-like imbricated lamellar materials. *Proc. Natl. Acad. Sci. U. S. A*. 114:201714103. doi: 10.1073/pnas.1714103114

Mann, H. B., and Whitney, D. R. (1947). On a test of whether one of two random variables is stochastically larger than the other. *Ann. Math. Stat*. 18, 50–60. doi: 10.1214/aoms/1177730491

Mathiazhagan, S., and Anup, S. (2016a). Mechanical behaviour of bio-inspired brittle-matrix nanocomposites under different strain rates using molecular dynamics. *Mol. Simul*. 42, 1490–1501. doi: 10.1080/08927022.2016.1205192

Mathiazhagan, S., and Anup, S. (2016b). Investigation of deformation mechanisms of staggered nanocomposites using molecular dynamics. *Phys. Lett. A* 380, 2849–2853. doi: 10.1016/j.physleta.2016.06.046

Mathiazhagan, S., and Anup, S. (2016c). Influence of platelet aspect ratio on the mechanical behaviour of bio-inspired nanocomposites using molecular dynamics. *J. Mech. Behav. Biomed*. 59, 21–40. doi: 10.1016/j.jmbbm.2015.12.008

Mathiazhagan, S., and Anup, S. (2018). Atomistic simulations of length-scale effect of bioinspired brittle-matrix nanocomposite models. *J. Eng. Mech*. 144, 1–9. doi: 10.1061/(ASCE)EM.1943-7889.0001533

Mathur, A., and Erlebacher, J. (2007). Size dependence of effective Young's modulus of nanoporous gold. *Appl. Phys. Lett*. 90, 2005–2008. doi: 10.1063/1.2436718

Mayer, G. (2005). Rigid biological systems as models for synthetic composites. *Science*. 310, 1144–1147. doi: 10.1126/science.1116994

Menig, R., Meyers, M. H., Meyers, M. A., and Vecchio, K. S. (2000). Quasi-static and dynamic mechanical response of *Haliotis rufescens* (abalone) shells. *Acta Mater*. 48, 2383–2398. doi: 10.1016/S1359-6454(99)00443-7

Miller, R. E., and Shenoy, V. B. (2000). Size-dependent elastic properties of nanosized structural elements. *Nanotechnology* 11, 139–147. doi: 10.1088/0957-4484/11/3/301

Mirzaeifar, R., Dimas, L. S., Qin, Z., and Buehler, M. J. (2015). Defect-tolerant bioinspired hierarchical composites: simulation and experiment. *ACS Biomater. Sci. Eng*. 1, 295–304. doi: 10.1021/ab500120f

Moon, R. J., Martini, A., Nairn, J., Youngblood, J., Martini, A., and Nairn, J. (2011). Cellulose nanomaterials review: structure, properties and nanocomposites. *Chem. Soc. Rev*. 40, 3941–3994. doi: 10.1039/c0cs00108b

Munch, E., Launey, M. E., Alsem, D. H., Saiz, E., Tomsia, A. P., and Ritchie, R. O. (2008). Tough, bio-inspired hybrid materials. *Science* 322, 1516–1521. doi: 10.1126/science.1164865

Natarajan, B., Krishnamurthy, A., Qin, X., Emiroglu, C. D., Forster, A., Foster, E. J., et al. (2018). Binary cellulose nanocrystal blends for bioinspired damage tolerant photonic films. *Adv. Funct. Mater*. 28, 1–11. doi: 10.1002/adfm.201800032

Ni, Y., Song, Z., Jiang, H., Yu, S., and He, L. (2015). Optimization design of strong and tough nacreous nano- composites through tuning characteristic lengths. *J. Mech. Phys. Solids* 81, 41–57. doi: 10.1016/j.jmps.2015.04.013

Ostanin, I., Ballarini, R., Potyondy, D., and Dumitric,ă, T. (2013). A distinct element method for large scale simulations of carbon nanotube assemblies. *J. Mech. Phys. Solids* 61, 762–782. doi: 10.1016/j.jmps.2012.10.016

Plimpton, S. (1995). Fast parallel algorithms for short-range molecular dynamics. *J. Comput. Phys*. 117, 1–19. doi: 10.1006/jcph.1995.1039

Podsiadlo, P., Kaushik, A. K., Arruda, E. M., Waas, A. M., Shim, B. S., Xu, J., et al. (2007). Ultrastrong and stiff layered polymer nanocomposites. *Science* 318, 1–4. doi: 10.1126/science.1143176

Pro, J. W., Kwei, R., Petzold, L. R., Utz, M., and Begley, M. R. (2015). The impact of stochastic microstructures on the macroscopic fracture properties of brick and mortar composites. *Extrem. Mech. Lett*. 5, 1–9. doi: 10.1016/j.eml.2015.09.001

Qin, X., Feng, S., Meng, Z., and Keten, S. (2017). Optimizing the mechanical properties of cellulose nanopaper through surface energy and critical length scale considerations. *Cellulose* 24, 3289–3299. doi: 10.1007/s10570-017-1367-x

Qin, X., Marchi, B. C., Meng, Z., and Keten, S. (2019). Impact resistance of nanocellulose films with bioinspired Bouligand microstructures. *Nanoscale Adv*. 1:1351. doi: 10.1039/C8NA00232K

Qwamizadeh, M., Lin, M., Zhang, Z., Zhou, K., and Wei, Y. (2017a). Bounds for the dynamic modulus of unidirectional composites with bioinspired staggered distributions of platelets. *Compos. Struct*. 167, 152–165. doi: 10.1016/j.compstruct.2017.01.077

Qwamizadeh, M., Zhang, Z., Zhou, K., and Wei, Y. (2015). On the relationship between the dynamic behavior and nanoscale staggered structure of the bone whole bone. *J. Mech. Phys. Solids* 78, 17–31. doi: 10.1016/j.jmps.2015.01.009

Qwamizadeh, M., Zhou, K., and Zhang, Y. W. (2017b). Damping behavior investigation and optimization of the structural layout of load-bearing biological materials. *Int. J. Mech. Sci*. 120, 263–275. doi: 10.1016/j.ijmecsci.2016.12.003

Ritchie, R. O. (2011). The conflicts between strength and toughness. *Nat. Mater.* 10, 817–822. doi: 10.1038/nmat3115

Sakhavand, N., and Shahsavari, R. (2015). Universal composition-structure-property maps for natural and biomimetic platelet-matrix composites and stacked heterostructures. *Nat. Commun*. 6:6523. doi: 10.1038/ncomms7523

Shao, Y., Zhao, H., Feng, X., and Gao, H. (2012). Discontinuous crack-bridging model for fracture toughness analysis of nacre. *J. Mech. Phys. Solids* 60, 1400–1419. doi: 10.1016/j.jmps.2012.04.011

Sharpe, W. N., Jackson, K. M., Hemker, K. J., and Xie, Z. (2001). Effect of specimen size on young's modulus and fracture strength of polysilicon. *J. Microelectromechanical Syst.* 10, 317–326. doi: 10.1109/84.946774

Sinko, R., Qin, X., and Keten, S. (2015). Interfacial mechanics of cellulose nanocrystals. *MRS Bull.* 40, 340–348. doi: 10.1557/mrs.2015.67

Valashani, S. M. M., and Barthelat, F. (2015). A laser-engraved glass duplicating the structure, mechanics and performance of natural nacre. *Bioinspir. Biomim.* 10:026005. doi: 10.1088/1748-3190/10/2/026005

Wang, J., Cheng, Q., and Tang, Z. (2012). Layered nanocomposites inspired by the structure and mechanical properties of nacre. *Chem. Soc. Rev.* 41, 1111–1129. doi: 10.1039/C1CS15106A

Wei, X., Filleter, T., and Espinosa, H. D. (2015). Statistical shear lag model–unraveling the size effect in hierarchical composites. *Acta Biomater.* 18, 206–212. doi: 10.1016/j.actbio.2015.01.040

Wei, X., Naraghi, M., and Espinosa, H. D. (2012). Optimal length scales emerging from shear load transfer in natural materials: application to carbon-based nanocomposite design. *ACS Nano* 6, 2333–2344. doi: 10.1021/nn204506d

Wei, Z., Sinko, R., Keten, S., and Luijten, E. (2018). Effect of surface modification on water adsorption and interfacial mechanics of cellulose nanocrystals. *ACS Appl. Mater. Interfaces* 10, 8349–8358. doi: 10.1021/acsami.7b18803

Wilkerson, R. P., Gludovatz, B., Watts, J., Tomsia, A. P., Hilmas, G. E., and Ritchie, R. O. (2018). A study of size effects in bioinspired,"nacre-like", metal-compliant- phase (nickel-alumina) coextruded ceramics. *Acta Mater.* 148, 147–155. doi: 10.1016/j.actamat.2018.01.046

Wu, X., Moon, R. J., and Martini, A. (2014). Tensile strength of I b crystalline cellulose predicted by molecular dynamics simulation. *Cellulose* 21, 2233–2245. doi: 10.1007/s10570-014-0325-0

Wu, Z., Zhang, Y., Jhon, M. H., Gao, H., and Srolovitz, D. J. (2012). Nanowire failure: long = brittle and short = ductile. *Nano Lett.* 12, 10–14. doi: 10.1021/nl203980u

Xia, W., Ruiz, L., Pugno, N. M., and Keten, S. (2016). Critical length scales and strain localization govern the mechanical performance of multi-layer graphene assemblies. *Nanoscale* 8, 6456–6462. doi: 10.1039/C5NR08488A

Zhang, P., Heyne, M. A., and To, A. C. (2015). Biomimetic staggered composites with highly enhanced energy dissipation : modeling, 3D printing, and testing. *J. Mech. Phys. Solids* 83, 285–300. doi: 10.1016/j.jmps.2015.06.015

Zhang, Z., Zhang, Y., and Gao, H. (2010). On optimal hierarchy of load-bearing biological materials. *Proc. R. Soc. B.* 278, 519–525. doi: 10.1098/rspb.2010.1093

Zhang, Z. Q., Liu, B., Huang, Y., Hwang, K. C., and Gao, H. (2010). Mechanical properties of unidirectional nanocomposites with non-uniformly or randomly staggered platelet distribution. *J. Mech. Phys. Solids* 58, 1646–1660. doi: 10.1016/j.jmps.2010.07.004

Conflict of Interest Statement: The authors declare that the research was conducted in the absence of any commercial or financial relationships that could be construed as a potential conflict of interest.

frontiers in Materials

ORIGINAL RESEARCH
published: 13 August 2019
doi: 10.3389/fmats.2019.00182

Between Science and Art: Thin Sound Absorbers Inspired by Slavic Ornaments

*Anastasiia O. Krushynska**

Faculty of Science and Engineering, ENTEG-Engineering and Technology Institute Groningen, University of Groningen, Groningen, Netherlands

Acoustic metamaterials have opened fascinating opportunities for manipulation of low-frequency sound and development of compact structures with broadband acoustic performance for noise mitigation applications, room and architectural acoustics. So far, several mechanisms have been studied to achieve perfect sound absorption at subwavelength frequencies, when structural dimensions are much smaller than the wavelength of incident waves. Here, we analyze two alternative approaches based on the use of interacting and coupled resonators in absorbing panels with the aim to reduce the panel thickness. We numerically demonstrate that proper designs of interacting resonators allow extending a single-peak absorption to broadband frequencies, while the use of coupled resonators enables broadband absorption at several frequency ranges. The proposed configurations are inspired by ancient Slavic folk patterns with delicate ligature, multi-layered structure, and concealed meaning. Our results open new possibilities for creating acoustic metamaterials with added art effects, which individualize occupied space and make absorbing panels more appealing for various applications.

Keywords: wave dynamics, acoustic metamaterial, Helmholtz resonator, sound absorption, dispersion, Slavic ornament

OPEN ACCESS

Edited by:
Asa Barber,
London South Bank University,
United Kingdom

Reviewed by:
Ettore Barbieri,
Japan Agency for Marine-Earth Science and Technology, Japan
Domenico De Tommasi,
Politecnico di Bari, Italy

***Correspondence:**
Anastasiia O. Krushynska
a.o.krushynska@rug.nl

Specialty section:
This article was submitted to Mechanics of Materials, a section of the journal Frontiers in Materials

Received: *27 November 2018*
Accepted: *10 July 2019*
Published: *13 August 2019*

Citation:
Krushynska AO (2019) Between Science and Art: Thin Sound Absorbers Inspired by Slavic Ornaments. Front. Mater. 6:182. doi: 10.3389/fmats.2019.00182

1. INTRODUCTION

Manipulation of low-frequency sound is a challenge due to the limited acoustic performance of conventional materials (Allard and Atalla, 2009). Recently developed acoustic metamaterials (Liu et al., 2000; Deymier, 2013; Brunet et al., 2015) and metasurfaces (Holloway et al., 2012; Liang and Li, 2012) have enabled advanced control of sound waves due to unusual functionalities, including negative refraction (Fang et al., 2006; Kaina et al., 2015; Krushynska et al., 2017), sound focusing (Guenneau et al., 2007; Li et al., 2009), acoustic cloaking (Li and Pendry, 2008; Kan et al., 2016), and one-way propagation (Liang et al., 2010; Fleury et al., 2014) (see also the excellent reviews of Craster and Guenneau, 2012; Cummer et al., 2016; Liang et al., 2018; Wu et al., 2018 for additional references). These fascinating properties have opened the way to the development of compact sound absorbing materials. For example, membrane-type (Yang et al., 2008, 2015; Park et al., 2011; Mei et al., 2012; Lu et al., 2016; Gao et al., 2017) or scape-coiling (Liang and Li, 2012; Li et al., 2012, 2013, 2014, 2015; Xie et al., 2013, 2014; Molerón et al., 2016; Krushynska et al., 2018) metamaterials are capable of totally absorbing sound at frequencies, when the corresponding wavelength is up to two orders of magnitude larger than their thickness. Rigidly-backed structures with Helmholtz resonators (HRs) (Jiménez et al., 2016, 2017a) also act as perfect absorbers, if the critical coupling conditions are satisfied (Theocharis et al., 2014; Merkel et al., 2015; Groby et al., 2016). However, the resonant nature of the dispersion manipulation mechanisms results in narrowband performance that substantially limits application possibilities of meta-structures.

A common approach to broaden the bandwidth is the use of multiple detuned resonating units with absorption peaks at different frequencies. These can be optimally designed panels with graded sets of quarter-wavelength resonators (Jiang et al., 2014; Groby et al., 2016), series of detuned HRs (Groby et al., 2015; Jiménez et al., 2016, 2017b), space-coiled channels (Zhang and Hu, 2016; Tang et al., 2017; Jia et al., 2018) or poroelastic plates in rigidly-backed waveguides (Romero-García et al., 2016). Other solutions include membranes (Mei et al., 2012) or plate-type (Ma et al., 2017, 2018) structures decorated by multiple masses. The use of optimized coiled-up Fabry-Perot channels even enables to achieve a minimum sample thickness imposed by causality (Yang et al., 2017).

This work investigates two alternative approaches to extend the absorption performance of acoustic metamaterials with internal HRs under restriction on structural thickness. The *first approach* relies on synergetic interactions of detuned HRs resulting in merging of isolated absorption peaks and, thus, broadband absorption. An important feature is that the HRs are equidistant from the sound source, in contrast to widely analyzed "in-series" arrangement (Jiménez et al., 2016, 2017a,b,c; Romero-García et al., 2016), that largely reduces the system thickness. To decrease the lateral dimensions, we adopt the space-coiling mechanism for the HR cavities. The *second approach* introduces the concept of coupled HRs when an HR cavity is separated into two (or several) parts joint by the supplementary neck(s). We show that a coupled resonator preserves the first-order absorption peak originating from the initial configuration and exhibits additional absorption peak(s) at subwavelength frequencies. This characteristic enables broadband sound absorption at several frequency ranges, without introducing additional HRs or a noticeable increase in the system dimensions. The developed approaches are illustrated by the examples of acoustic absorbers inspired by ancient Slavic ornaments.

The choice of ornamental designs is not by chance. Common applications of sound absorbers are in the areas of architectural acoustics, room acoustics and noise insulation, including sound mitigation in public buildings (hotels, offices, schools, stations, shopping malls, etc.), target acoustics of theaters, attenuation of air- or structure-borne noise, etc. Given the advanced functionalities of acoustic metamaterials, one may think of fascinating effects of variable audible space, in contrast to its fixed physical dimensions, that is of importance for modern cinemas and concert halls. These applications obviously imply high visibility of meta-structures suggesting that they should not only be functional and optimized but also give meaning to the occupied space. Moreover, since even the thinnest absorbers reduce available space, they can be designed in a creative way, playing the role of artwork, in addition to tailored audible performance. This can be achieved by incorporating ornamental designs of acoustic metamaterials, i.e., balancing the relationship between voids and solids, with the aim to improve visual experience and personalize the environment targeted at a specific audience.

The paper is organized as follows. After the introduction, section 2 provides basic information about the peculiarities of Slavic ornaments. In section 3, we introduce a general model of the proposed sound absorbers and describe the numerical approach to analyze their absorption capability. Section 4 discusses the properties of absorbers with folded HRs sharing the spatial location. Section 5 presents the concept of coupled resonators and the design of an acoustic absorber with broadband quasi-perfect ($\geq$95%) sound absorption at low frequencies. Finally, section 6 summarizes the main findings of the paper and illustrates how the proposed designs can be integrated in a room interior.

2. SLAVIC ORNAMENTS

Slavic ornaments are decorative elements in architecture, weaving, and fancywork of Slavs native to Central, Eastern, and Southeastern Europe. They resemble holographic pictures that should be viewed with defocused eyes (to create a stereoscopic 3D effect) by switching attention between dark and light patterns, which have a different meaning. The interpretation of patterns varies depending on their location at a piece of clothing or an object. The basic constituent elements range from simple geometric forms to complex images of plants, animals, geometric forms, etc.

Antique ornaments are characterized by isometric areas of a background and a pattern so that intervals between the patterns also have a symbolic meaning (Kachaeva, 2008). This resulted that ornaments were typically entitled according to the shape of unfilled area, rather than to a pattern itself. Some traditional symbols of Slavic patterns are shown in **Figure 1A**.

The weaving technique of symbolic ornaments governs not only the strict geometry and proportions of patterns, but also their high density. In addition, it influences the sequence of ornamental patterns based on the symmetry of different orders (Nekrasova, 1983). Strong traditions of periodic repetitions of symbols resulted that separate symbols, unlike letters, have no meaning, but altogether, in combinations with other symbols, translate a comprehensive mythological figure or character (**Figure 1B**).

Surprisingly, Slavic ornamental patterns are not unique, and have close counterparts around the world. Except some differences in graphics and colors, similar meaning, rhythm, and temper are recognizable in Scandinavian, Arabic, Brazilian, and other ornaments (Nekrasova, 1983; Kachaeva, 2008). Rich history of Slavic ornaments together with examples of multiple patterns from different centuries and comprehensive interpretation of their meaning can be found elsewhere (see e.g., the excellent surveys of Nekrasova, 1983; Kachaeva, 2008, and the references therein).

The preservation of the ancient art of folk ornaments is a vital problem of significant cultural and societal importance. One of the possible solutions can be the use of ornamental patterns in the design of functional acoustic devices proposed in sections 4 and 5.

3. MODELS AND METHODS

In this work, we numerically analyze the absorption of air-borne sound in acoustic metamaterials with Helmholtz

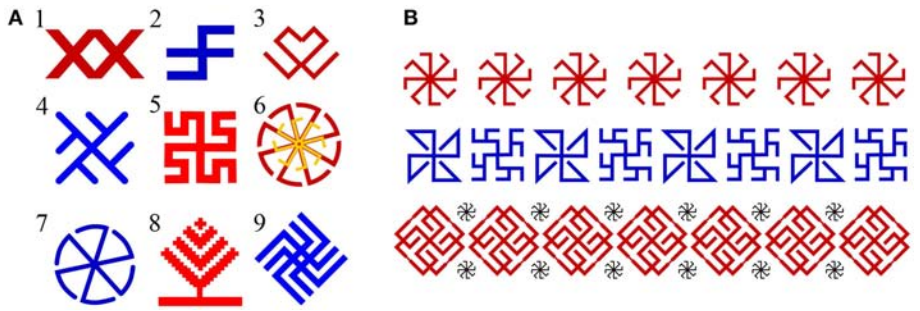

FIGURE 1 | (A) Some symbols in geometric Slavic ornaments and their Slavic names (with English translations, if possible): 1—"*vodyanoj*" (*the water sprite*); 2—"*slavez*"; 3—"*kryuchki*" (*hooks*); 4—"*kolard*"; 5—"*bogovnik*"; 6—"*svetoch*" (*cresset*); 7—"*grozovik*" (*the spirit of thunderstorm*); 8—"*derevo*" (*tree*); 9—"*vepr' nebesnyj*" (*the sky wild boar*). **(B)** Top: a row of the symbols "*kolyadnik*" (*a kind of Christmas carol*); middle: alternations of the symbols "*solon'*" and "*the fern flower*"; bottom: rows of the symbols "*skarozhych*" and "*kolyadnik*".

resonators (HRs) using the concepts of slow sound and critical coupling (Theocharis et al., 2014; Groby et al., 2015; Jiménez et al., 2017a). The designed systems are thin rigidly-backed panels with periodic sets of perforated cylindrical holes of length L loaded by N resonators and arranged in a rectangular lattice with pitches L_x, L_y in the Oxy plane (**Figure 2A**). An HR is composed of a cylindrical neck of radius $R_n^{(k)}$ and length $L_n^{(k)}$ and a cylindrical cavity of radius $R_c^{(k)}$ and length $L_c^{(k)}$, where the superscript k indicates the HR number (**Figure 2B**). In the analyzed frequency ranges, the wavelength of sound waves is larger than the HR dimensions, and thus, the holes loaded by the HRs (**Figure 2C**) act as asymmetric Fabry-Perót cavities with N point-like resonant scatterers and the rigid backing, playing the role of a mirror (Romero-García et al., 2016; Jiménez et al., 2017a).

As the perforations are periodic, the panel dynamics is analyzed by considering an elementary building block. Periodic boundary conditions are applied at the lateral boundaries of the block, normal to the x and y axes, which are reduced to symmetric boundary conditions for normally incident waves. The system absorption $\alpha = 1 - |R|^2$ with the complex reflection coefficient R evaluated numerically. A finite-element model is developed by using the Pressure Acoustic module of the COMSOL Multiphysics v.5.2 (the Comsol files are available in Krushynska, 2019). The model includes the air confined in the panel and surrounding free air with mass density $\rho^{air} = 1.21$ kg/m^3, sound speed $c_0 = 343$ m/s and dynamic viscosity $\eta = 1.8 \times 10^{-5}$ Pa·s at $T = 293$ K. For the air inside the HRs and the Fabry-Perót cavities, the visco-thermal losses are taken into account by means of effective complex-valued bulk modulus K^{eff} and mass density ρ^{eff} (Groby et al., 2015):

$$K^{\text{eff}} = \frac{\gamma P_0}{1 + 2(\gamma - 1)/\sqrt{\text{Pr}\zeta}\, J_1\left(r\sqrt{\text{Pr}\zeta}\right)/rJ_0\left(r\sqrt{\text{Pr}\zeta}\right)}, \quad (1)$$

$$\rho^{\text{eff}} = \frac{\rho^{air}}{1 - 2/\sqrt{\zeta}\, J_1\left(r\sqrt{\zeta}\right)/rJ_0\left(r\sqrt{\zeta}\right)}, \quad \zeta = -i\rho^{air}\omega/\eta. \quad (2)$$

Here $P_0 = 1$ atm is the atmospheric pressure; $\gamma = 1.4$ and Pr are the specific heat ratio and the Prandtl number; J_0 and J_1 are the standard Bessel's functions of the first kind; r is the radius of a cylinder. Harmonic plane waves of a unit amplitude and frequency ω are normally incident on the panel surface along the negative direction of the z axis (the red arrow in **Figure 2C**). Due to a large impedance mismatch, the sound hard boundary conditions are imposed at the interfaces of the air and solid elements. The reflection coefficient is calculated by evaluating the acoustic pressure p_1 and p_2 at two acquisition points:

$$R = \frac{H_{12} - e^{-ikd}}{e^{ikd} - H_{12}} e^{-2ikz} \quad (3)$$

where $H_{12} = p_1/p2$, d is the distance between the points, $k = \omega/c_0$ is the wavenumber. More details on the numerical implementation can be found in **Appendix**.

4. FOLDED INTERACTING RESONATORS FOR BROADBAND ABSORPTION

In this section, we design and analyze acoustic absorbers with HRs sharing spatial location, i.e., having identical z coordinates. We demonstrate that such an arrangement allows not only reducing the thickness of a panel, but also improves its absorption performance. We first consider a panel with six detuned HRs arranged "in-series" on a tube of radius $R_t = 7$ mm, with the center-to-center distance $a = L/6 = 15$ mm. The radii of the neck $R_n = 2.5$ mm and the HR cavity $R_r = 5$ mm are identical for all the HRs. The lengths of the HR necks are $L_n^{(1)} = 5$ mm, $L_n^{(2)} = 10$ mm, $L_n^{(3)} = 15$ mm, $L_n^{(4)} = 25$ mm, $L_n^{(5)} = 35$ mm, and $L_n^{(6)} = 45$ mm. For the identical total length of every HR $L_{HR} = L_r + L_n^{(k)}$ equal to 11.92 cm, the resonator eigenfrequencies are $f_{HR}^{(1)} = 1$ kHz, $f_{HR}^{(2)} = 770$ Hz, $f_{HR}^{(3)} = 658$ Hz, $f_{HR}^{(4)} = 546$ Hz, $f_{HR}^{(5)} = 492$ Hz, and $f_{HR}^{(6)} = 464$ Hz.

We start from the evaluation of wave dispersion by applying the Floquet-Bloch conditions at the tube ends (Krushynska et al., 2018), imitating an infinite sequence of the HRs, and by neglecting any losses in the system. **Figure 3A** shows the

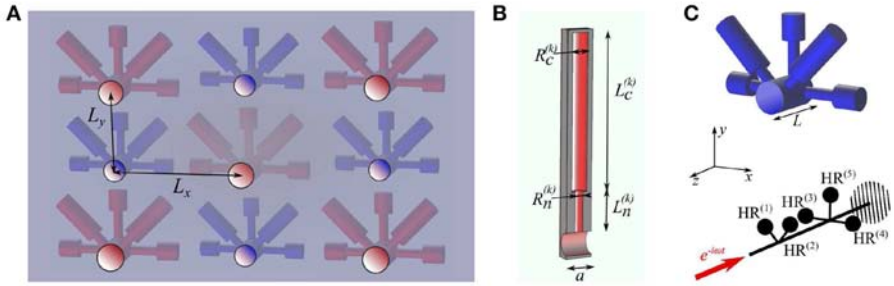

FIGURE 2 | (A) Sketch of a rigidly-backed transparent panel with cylindrical perforated cavities arranged in a rectangular lattice and loaded by five colored HRs. **(B)** The dimensions of a Helmholtz resonator. **(C)** Top: the geometry of a cavity loaded by five HRs; bottom: schematic diagram of the corresponding 1D analog with the red arrow indicating the direction of incident sound.

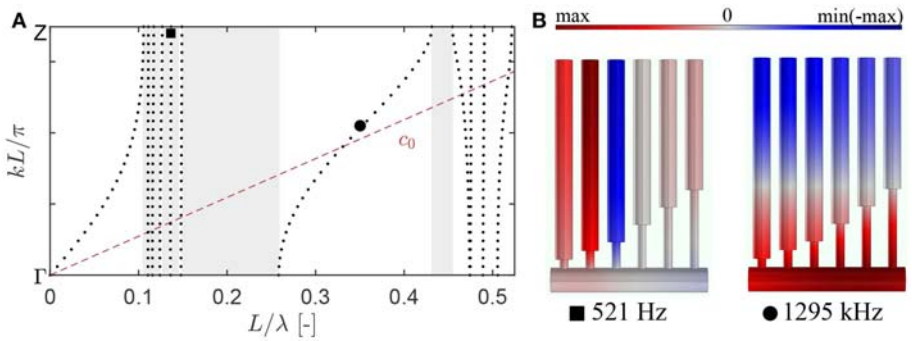

FIGURE 3 | (A) The dispersion relation for a periodic arrangement of the six detuned HRs on a tube. The shaded regions indicate band gaps with inhibited wave propagation. The dashed line c_0 describes a propagating band of sound waves in free air. **(B)** The pressure distribution at frequencies indicated in **(A)**.

corresponding dispersion relation with the band gaps shaded in gray. The lowest pass band is strongly dispersive with the phase velocity ω/k lower than c_0 (cf. the pass band c_0 for a sound wave in free air shown by the dashed red line), indicating the activation of slow sound conditions at these frequencies (Theocharis et al., 2014; Jiménez et al., 2017a). At the cut-off frequency of the first pass band ($L/\lambda = Lf/c_0 = 0.105$), the phase velocity is zero, and the corresponding mode shape has maximum acoustic pressure in the cavities of the fifth and sixth HRs (with the longest necks) and close-to-zero pressure level in the other four HRs. The simultaneous excitation of the two HRs explains a lower cut-off frequency, 402 Hz, as compared to individual eigenfrequencies of the excited HRs. Above the cut-off, one observes a small band gap with an upper bound formed by an almost flat band, which, in turn, is a low bound of an adjacent band gap. Altogether, there are five small band gaps separated by (almost) flat bands. The separating pass bands correspond to modes localized in the HRs and have similar vibration patterns: two HRs with strong out-of-phase pressure levels and one weakly excited HR (e.g., **Figure 3B**, on the left). The simultaneous activation of several HRs explains lower frequencies of the localized modes relative to $f_{HR}^{(k)}$. The fifth flat band forms a lower bound of a large band gap centered around $L/\lambda = 0.2$. This and the next large band gaps are separated by a mode with the pressure distribution shown in **Figure 3B** on the right.

The discussed dispersion properties reveal that the panel can manipulate sound waves at subwavelength frequencies since the characteristic system size L is smaller than the wavelength of an incident sound wave λ.

Next, we analyze the sound absorption for a finite-size tube with the six HRs. If the HRs with the longer necks are placed close to the air domain (**Figure 4A**), the absorption coefficient of the panel has three non-zero peaks below 1.5 kHz ($L/\lambda < 0.5$). At the first peak, 328 Hz ($\alpha = 0.78$), the HRs and the cavity act as rigid scatterers for an incident wave and are characterized by a uniform pressure distribution. At the second peak, 407 Hz, only the HR with the longest neck (the sixth HR) is activated. It has the lowest eigenfrequency $f_{HR}^{(6)}$, and thus, the resonant frequencies of the other HRs fall in the band gap. In other words, at frequencies above $f_{HR}^{(6)}$, sound waves are strongly reflected, and only a small amount of energy propagates further in the cavity, which is insufficient to activate the other HRs. Since the geometry of the excited HR is not optimized to critically couple the system with the exterior medium, it results in a low absorption $\alpha = 0.08$. Instead, if sound waves incident on a panel with on opposite order of the HRs (**Figure 4B**), the activation of each HRs becomes possible, and the absorption coefficient has seven peaks below the second large band gap. In the absence of losses, the peaks of Re(R) (the dotted line) match the frequencies of the localized modes in the dispersion relation (**Figure 3A**). In the lossy case

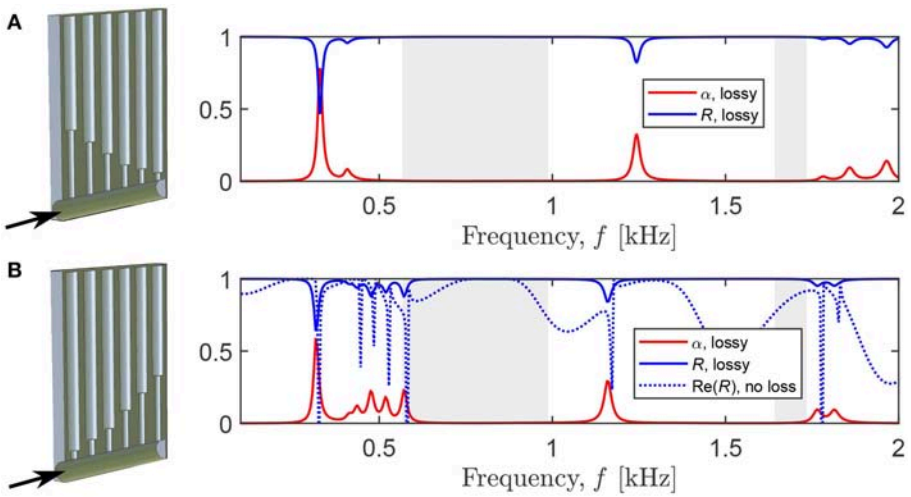

FIGURE 4 | The reflection (blue) and absorption (red) coefficients for the panels with periodically arranged rigidly-backed cavities loaded by six detuned HRs. The black arrow indicates the direction of incident sound. Shaded regions indicate the band gaps evaluated by the dispersion analysis (only the two wide band gaps are presented). The arrangement of the HRs with gradually **(A)** decreasing and **(B)** increasing length of a neck.

(the solid lines), the reflection and absorption peaks are shifted to slightly lower frequencies (Molerón et al., 2016). Note that the first absorption peak occurs at a similar frequency, 316 Hz with α = 0.58, as in **Figure 4A**, and has the same pressure distribution.

The obtained results show that the absorption of a panel with detuned HRs strongly depends on the arrangement of the HRs—the property first discussed for the transmission problem in Jiménez et al. (2017b). One can maximize the panel absorption by optimizing the HR geometries in order to satisfy the critical coupling conditions (Jiménez et al., 2017a,b).

Alternatively, the absorption can be increased by varying the positions of the HRs along the cavity. To this end, we consider the system with the gradually increasing HR necks toward the closed end of the tube (**Figure 4B**). We fold the HR cavities by curving the parts of length 5.42 cm from the top and rotating them 90° to the remaining parts (**Figure 5A**). This transformation should preserve the HR eigenfrequencies and the absorption coefficient of the panel as proven experimentally elsewhere (Jiménez et al., 2017a; Yang et al., 2017). The simulations show that it is indeed the case, except for the first absorption peak that is reduced by 10%. This decrease can be explained by the use of Equations (1) and (2), which are, strictly speaking, not applicable for non-uniform cross-sections of the HR cavities. However, the insertion of the losses by means of the effective parameters (1) and (2) leads to a computationally cheaper problem as compared to the direct incorporation of thermal and viscous boundary layers into a finite-element model (Krushynska et al., 2018). Since the inaccuracy concerns only the first absorption peak, and the goal of this work is not the demonstration of some quantitative results, but understanding the physical mechanisms of the sound absorption, we proceed further by using the effective parameters for the folded HR cavities.

Next, we rotate the folded HRs by 60° relative to each other (**Figure 5B**). Since the resonators act as point-like scatterers (**Figure 1C**), the panel absorption is again preserved as confirmed by the simulations.

Finally, the HRs are shifted toward the air domain, so that they have an identical z coordinate. Note that this transformation replaces the non-symmetric HR configuration by symmetric, since the order of the HRs becomes irrelevant. The simulations show that the system with the shifted HRs has a better absorption (the red curve in **Figure 6**). Namely, at the first five peaks, the absorption (frequency) increases by 20% (26%), 380% (0%), 195% (2%), 91% (4%), 28% (2%), and only at the sixth peak α decreases by 38%, while the corresponding frequency increases by 2%. Since the frequency of the first peak approaches the higher peaks, all the peaks are merged and form a continuous frequency range with non-zero absorption. The occurrence of a broadband absorption can be explained by interactions of the HRs sharing the spatial location, as compared to the "in-series" configuration. **Figure 7** shows that every shifted HR is activated at each resonant peak, and thus, every HR contributes to the sound attenuation. In contrast, the "in-series" HRs are simultaneously excited only at the first peak, while at the higher-frequency peaks at least one HR is "switched off." If the length of the cavity is reduced to $L/6 = 15$ mm (**Figure 5C**), the absorption has slightly lower values (the blue dashed line in **Figure 6**), but the panel thickness becomes 6 times smaller. Therefore, the arrangement of the HRs at the same spatial location appears to be an efficient means to increase the sound absorption, if the structural thickness should be minimized. We emphasize that several HRs with the same z coordinate are not equivalent to a single HR since the induced absorption is broadband in contrast to the individual peak of a single resonator.

Apart from the HR resonances, there is an additional absorption peak at 937 Hz, corresponding to the cavity resonance $f_t = c_0/4L$. It is characterized by a maximum pressure concentrated in the closed end of the cavity. This resonance can

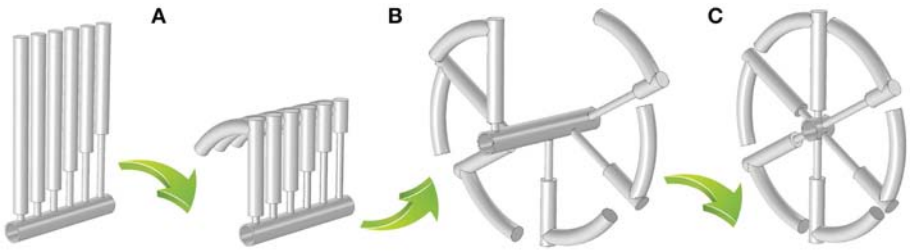

FIGURE 5 | Transformation steps to replicate the "*grozovik*"-inspired design (see the symbol 7 in **Figure 1A**), including **(A)** coiling the HR cavities, **(B)** rotation of the HRs along the central axis of the tube, **(C)** shift of the HRs toward an open end of the tube.

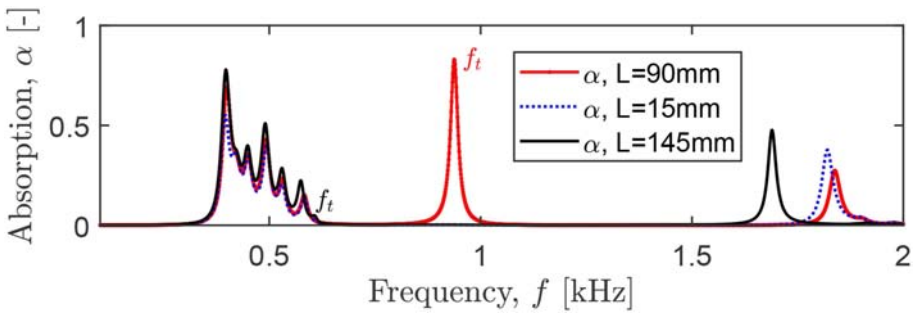

FIGURE 6 | The absorption of a panel with folded HRs (with an identical *z* coordinate) placed close to an open end of the tube of varying length *L*. The f_t indicates the cavity resonance at $c_0/4L$.

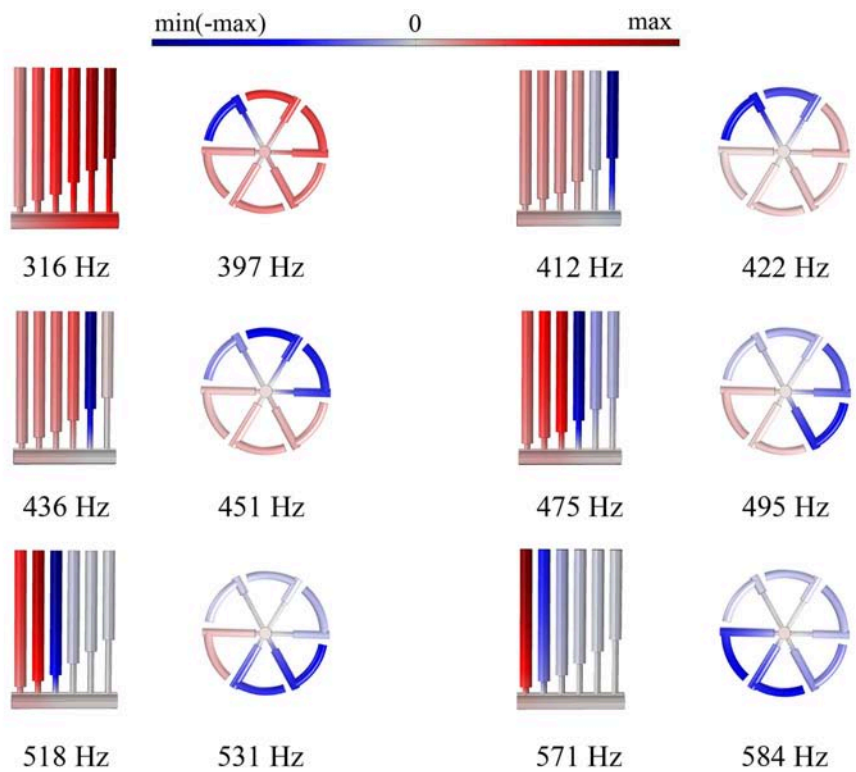

FIGURE 7 | The pressure distributions at the absorption peaks shown in **Figure 4**, bottom and **Figure 6**.

be used to improve the overall panel absorption by matching the frequency f_t to the HR peaks (Jiménez et al., 2017b) and simultaneously folding the excessive length of the cavity in order to minimize the panel thickness. Indeed, for $L = 145$ mm, $f_t = 592$ Hz that is close to the frequency of the sixth localized mode 583 Hz. The corresponding absorption (the black curve in **Figure 6**) is higher at the HR peaks, as compared to the configurations with the other L (the red and blue curves in **Figure 6**). However, the closer f_t to the HR peaks, the smaller the absorption peak associated with f_t: it almost disappears for $L = 145$ mm, since the energy of the cavity resonance is used to intensify the HR resonances.

We have shown that the use of interacting HRs sharing the spatial location allows substantially reducing the panel thickness, while the lateral sizes remain large. Such configurations can comply with the requirements for a wide range of engineering applications in room acoustics and noise reduction when the restrictions on the absorber thickness are severe. The lateral dimensions of the HRs can be further reduced. The presented configuration replicates the shape of the "*grozovik*" symbol (N. 7 in **Figure 1A**), while one can develop more compact designs, e.g., by folding the HR cavities into spirals as in Jiménez et al. (2017a).

The absorption ability of the panel can be further improved by periodically replicating the HRs along the z-axis direction (Jiménez et al., 2017a) or by superimposing the HRs of different dimensions (e.g., by imitating the structure of the symbol 6 in **Figure 1A**). Another approach implies a systematic optimization of the resonator geometry (Jiménez et al., 2016, 2017b), taking into account the coupling between the HRs. Since the number of HRs is not fixed and can be arbitrary, it opens many possibilities for various complex configurations with a sufficient amount of geometric parameters to increase the absorption to a desired level.

5. COUPLED RESONATORS FOR BROADBAND ABSORPTION AT DIFFERENT FREQUENCY RANGES

In this section, we design and analyze absorbing panels with coupled HRs. A simple coupled resonator is obtained through the partition of the HR cavity by a supplementary neck. A peculiar property of a coupled HR is the presence of an absorption peak at subwavelength frequencies in addition to the peak originating from the first-order resonance of an unpartitioned HR.

As an illustrative example, we consider a cylindrical cavity loaded by a single HR (**Figure 8A**). The length of the cavity is $L_t = 2$ cm, and its radius is $R_t = 7$ mm. The lattice pitches are $L_x = 10.9$ cm and $L_y = 15.1$ cm (**Figure 2A**). The HR parameters $L_{r1} = 12$ cm, $R_{r1} = 7.4$ mm, $L_{n1} = 5$ mm, and $R_{n1} = 6.75$ mm are chosen to achieve a quasi-perfect absorption at the first resonant peak $f_1 = 589$ Hz, $\alpha_1 = 0.983$ (the red line in **Figure 8C**). If the HR cavity is partitioned into two equal parts by a neck of length $L_{n2} = 1$ mm and radius $R_{n2} = 2.75$ mm (**Figure 8B**), there appears an additional peak at $f_2 = 1557$ Hz with $\alpha_2 = 0.885$, while the first peak is shifted to a slightly lower frequency $f_1 = 553$ Hz, $\alpha_1 = 0.951$ (the blue line in **Figure 8C**). The second peak originates from the second-order HR resonance shifted to lower frequencies due to added losses in the supplementary neck. Therefore, by varying the level of losses in the neck, one can tune the frequency f_2 and absorption α_2 to desired values. This feature enables the design of compact systems capable of absorbing sound at several frequency scales at the cost of a negligible increase of the HR length.

To understand the influence of the neck geometry on the system absorption, we perform parametric studies for the panel with the coupled HR described above and the neck of $R_{n2} = 3.75$ mm and $L_{n2} = 1$ mm, if other values are not indicated. First, we vary the radius of the neck R_{n2}. **Figure 9A** shows that the smaller R_{n2}, the larger the shift of both absorption peaks to lower frequencies. Note that the corresponding absorption drastically decreases. Instead, for increasing R_{n2}, the first absorption peak closely approaches the values of f_1 and α_1 for the unpartitioned HR, while the second peak is shifted to higher frequencies with an unchanged absorption level. This behavior can be expected, as for large R_{n2} the dynamics of the coupled HR becomes indistinguishable from that of the unpartitioned HR. Next, we change the position of the neck within the HR cavity. **Figure 9B** shows the first and second absorption peaks for the indicated length of the upper HR cavity L_{r2}. One can see that the location of the neck does not influence the absorption coefficient of the first resonance peak, while the corresponding frequency monotonically decreases with the increase of L_{r2}. For the second peak, the dependence is non-monotonic with the initial decrease of f_2 and α_2 for $L_{r2} < 6$ cm and the subsequent increase for $L_{r2} > 6$ cm. The observed dependence can be easily understood taking into account the pressure distribution at f_1 and f_2. Since for f_1, the HR cavity is excited as a whole, with an equal maximum level of pressure along the cavity, the position of the supplementary neck cannot change this resonance significantly. For f_2, the pressure has maximum out-of-phase values at the top and bottom of the HR cavity and close to zero levels in the middle. Thus, the location of the neck close to the top or bottom of the HR cavity results in larger absorption and higher resonant frequency. For further simulations, we choose $L_{r1} = 7$ cm, $L_{r2} = 5$ cm and analyze the influence of the length of the neck L_{n2}. For both peaks, the long necks result in lower frequencies of the absorption peaks and the slightly decreasing absorption level (**Figure 9C**). Obviously, longer necks increase the HR size and the cavity volume that leads to lower f_1 and f_2 and decreasing absorption. Finally, we estimate the influence of the position of the upper HR cavity on the system absorbing capability. We rotate the upper part of the HR by 90°and shift it along the cavity of the lower part. The distance between the upper end of the lower cavity and the central axis of the rotated part is designated as d (**Figure 10A**, left). The absorption graphs in **Figure 10A** show that if d increases, the values of f_1 and α_1 also increase, and one can even achieve perfect absorption, $\alpha_1 = 1$ when the upper cavity is close to the HR neck. Instead, for larger d, the absorption α_2 decreases significantly, and f_2 is shifted to lower values. The parametric studies reveal that the length of the supplementary neck L_{n2} and the position of the upper HR cavity have a larger influence on the absorption than the other analyzed parameters.

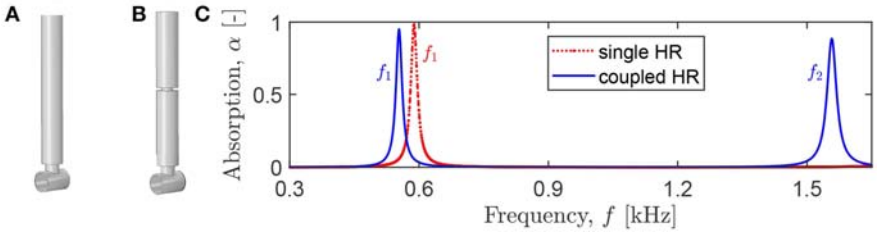

FIGURE 8 | Rigidly backed cavity loaded by **(A)** a single HR (an initial configuration) and **(B)** a coupled HR. **(C)** The absorption coefficient for a panel with a rectangular lattice of cavities loaded by a single or a coupled HR.

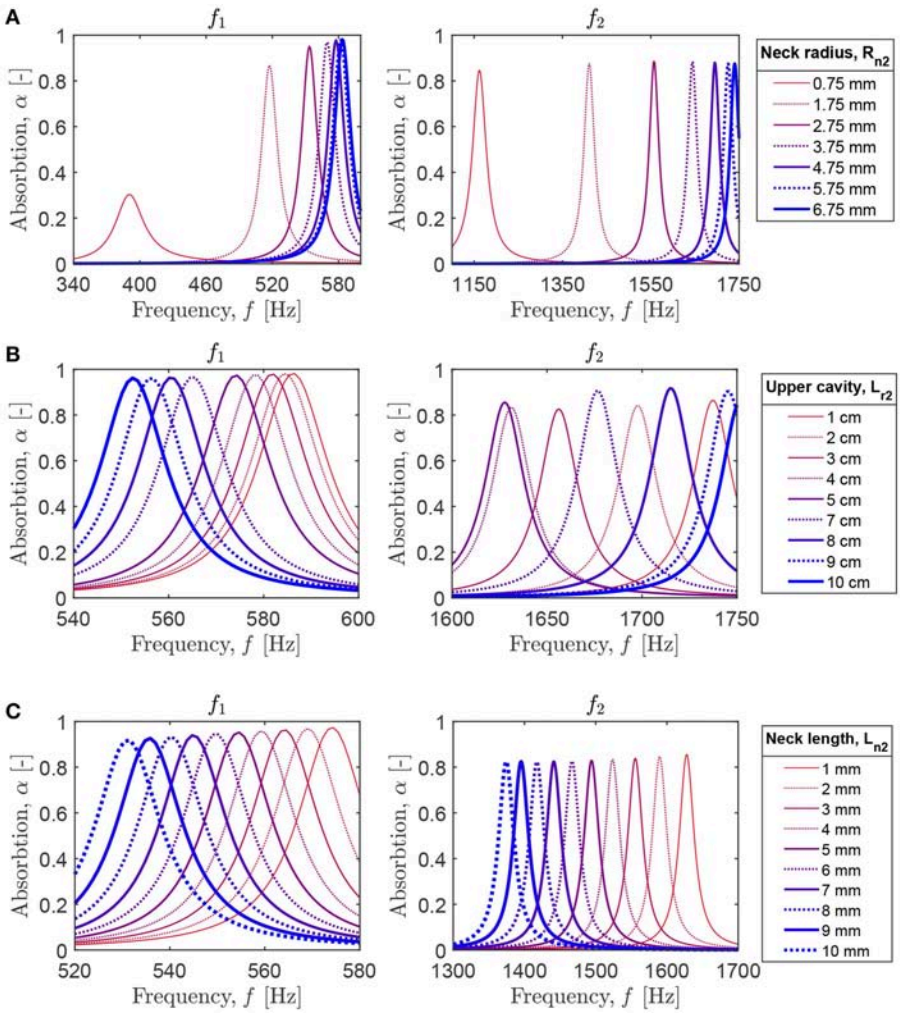

FIGURE 9 | Parametric analysis of the geometry and position of the supplementary neck on the absorption of the panel with the coupled HR: the first (left) and second (right) absorption peaks for the varying **(A)** radius of the neck; **(B)** length of the upper HR cavity; **(C)** length of the neck.

This can be exploited to design broadband absorbers working at several frequency ranges.

For instance, we use four coupled resonators loading four identical cavities (**Figure 10B**). The geometric parameters for the cavities and the HRs are the same as described above. The only difference between the coupled HR is in the length of the supplementary neck: $L_{n2}^{(1)} = 2$ mm, $L_{n2}^{(2)} = 3$ mm, $L_{n2}^{(3)} = 5$ mm, and $L_{n2}^{(4)} = 7$ mm. The center-to-center distance between the adjacent cavities is R_t. When the upper HR cavities are shifted at $d = 4$ cm, so that the designed

structure (**Figure 10B**, on the left) resembles the symbol "*kolard*" (the symbol 4 in **Figure 1A**), the corresponding system exhibits broadband 90% absorption at 625–655 Hz, and four additional absorption peaks at 1,345, 1,430, 1,478, and 1,567 Hz. For $d = 0$ cm, the absorption is almost quasi-perfect, exceeding 95%, between 542 and 562 Hz, and, in addition, there occurs a broadband range with absorption exceeding 25% between 1400 Hz-1590 Hz. Obviously, one can further optimize the system geometry to achieve perfect absorption or to broaden the absorption frequency ranges. However, this example already reveals important advantages of the coupled HRs: the negligible increase of the HR size due to the insertion of a supplementary neck allows to achieve *broadband* sound absorption at *several* frequency ranges in contrast to a single frequency range typical for unpartitioned HRs (Jiménez et al., 2017a,b).

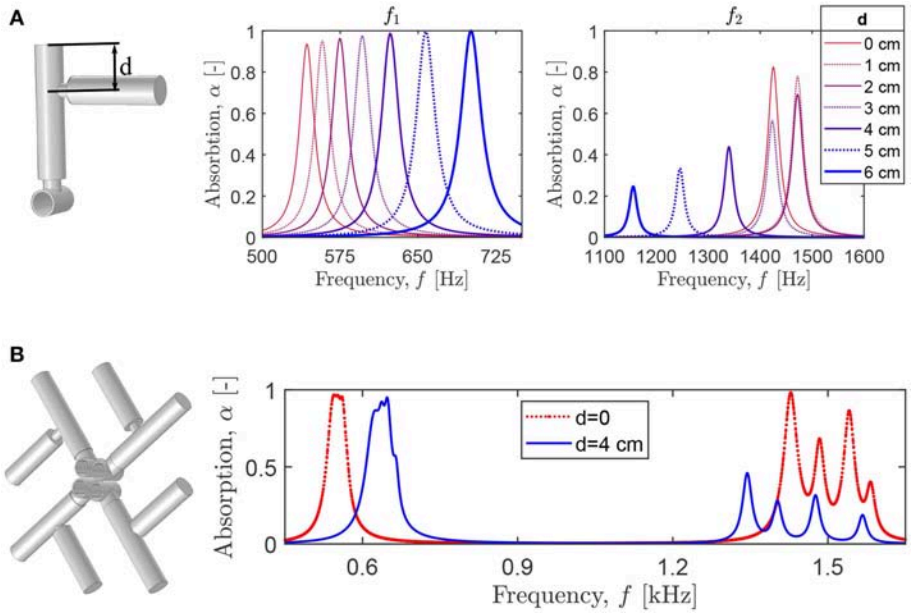

FIGURE 10 | (A) The absorption peaks for the varying position of the upper part of the coupled HR relative to the lower part. **(B)** The absorption coefficient of a configuration with four coupled HRs of identical geometry, except the length of the supplementary neck: $L_{n2}^{(1)} = 2$ mm, $L_{n2}^{(2)} = 3$ mm, $L_{n2}^{(3)} = 5$ mm, and $L_{n2}^{(4)} = 7$ mm.

FIGURE 11 | An example of the metamaterial panel in a room (thanks to "https://pixnio.com" for an original image).

6. CONCLUSIONS

In this work, we numerically investigated two approaches for broadening the sound absorption of acoustic metamaterial panels with incorporated HRs. The first approach relies on interactions of the HRs sharing a spatial locationthat result in merging of isolated absorption peaks. The second approach exploits the concept of coupled resonators with a supplementary neck introduced in the HR cavity. We show that the panels with coupled HRs can attenuate broadband sound at several subwavelength frequency ranges. The considered design approaches are suitable for panels with severe restrictions on the structural thickness, while lateral dimensions can be large.

We propose to exploit the plane geometry of a panel (normal to the thickness direction) for decorative purposes, in addition to its acoustic functionality. Specifically, we analyzed the panels with the HR appearance replicating ancient Slavic patterns composed of periodic repetitions of traditional symbols. The modern manufacturing techniques allow easy and inexpensive implementation of these designs in practical configurations. **Figure 11** shows an example of a panel with the Slavic-inspired HRs in a room interior. In this design, the combination of the "*grozovik*" and "*yashur*" symbols implements the discussed concepts of interacting and coupled HRs. (The middle row in the panel of **Figure 11** is obtained by the superposition of the "*yashur*" symbol and its mirror-reflected counterpart.) The panel is made of a transparent material (e.g., polylactic acid) with a red background, while the perforated cavities and HR interiors are colored in black and metallic white. Given an almost unlimited choice of symbolic and other designs, numerous panel configurations are possible, in which the HR geometries and form can be adjusted to working frequency ranges and target environment. In this way, decorated absorbing panels can not only control acoustic properties of a surrounding environment but also inspire the creativity of designers, who actively work on creating functional artworks.

We finally note that the ideas of combining smart materials, art and advanced functionalities are central to the modern architecture and interior design. Recent examples include sun-shade screens of Al-Bahar towers in Abu-Dhabi, the Hapra concert hall in Reykjavik with a lattice-type exterior harnessing the sunlight, and a renovated concert hall of Tokyo National University of Fine Art and Music with the ceiling decoration working as an acoustic system. We hope that the proposed Slavic-inspired designs of acoustic absorbers will contribute to a wider practical implementation of the metamaterial-based systems.

AUTHOR CONTRIBUTIONS

AK designed the research, conducted the analysis, and wrote the manuscript.

FUNDING

The support of COST Action DENORMS CA15125 funded by COST (European Cooperation in Science and Technology), grant No. 40013 was appreciated.

ACKNOWLEDGMENTS

The author gratefully acknowledges the support of the Laboratoire de l'Université du Mans (France) with the simulations and inspiring discussions with Dr. J.-P. Groby and Dr. V. Romero-García from the same university.

REFERENCES

Allard, J., and Atalla, N. (2009). *Propagation of Sound in Porous Media: Modelling Sound Absorbing Materials*. Chichester, UK: Willey.

Brunet, T., Merlin, A., Mascaro, V., Zimny, K., Leng, J., Poncelet, O., et al. (2015). Soft 3D acoustic metamaterial with negative index. *Nat. Mater.* 14:384. doi: 10.1038/nmat4164

Craster, R. V., and Guenneau, S. (2012). *Acoustic Metamaterials: Negative Refraction, Imaging, Lensing and Cloaking*. Heidelberg: Springer.

Cummer, S. A., Christensen, J., and Alu, A. (2016). Controlling sound with acoustic metamaterials. *Nat. Rev. Mater.* 1:16001. doi: 10.1038/natrevmats.2016.1

Deymier, P. A. (Ed). (2013). *Acoustic Metamaterials and Phononic Crystals*. Berlin; Heidelberg: Springer.

Fang, N., Xi, D., Xu, J., Ambati, M., Srituravanich, W., Sun, C., et al. (2006). Ultrasonic metamaterials with negative modulus. *Nat. Mater.* 5, 452–456. doi: 10.1038/nmat1644

Fleury, R., Sounas, D. L., Sieck, C. F., Haberman, M. R., and Alu, A. (2014). Sound isolation and giant linear nonreciprocity in a compact acoustic circulator. *Science* 343, 516–519. doi: 10.1126/science.1246957

Gao, N., Wu, J. H., Hou, H., and Yu, L. (2017). Excellent low-frequency sound absorption of radial membrane acoustic metamaterial. *Int. J. Mod. Phys. B* 30:1750011. doi: 10.1142/S0217979217500114

Groby, J.-P., Lagarrigue, C., Brouard, B., Dazel, O., and Tournat, V. (2015). Enhancing the absorption properties of acoustic porous plates by periodically embedding Helmholtz resonators. *J. Acoust. Soc. Am.* 137, 273–280. doi: 10.1121/1.4904534

Groby, J.-P., Pommier, R., and Aurégan, Y. (2016). Use of slow sound to design perfect and broadband passive sound absorbing materials. *J. Acoust. Soc. Am.* 139, 1660–1667. doi: 10.1121/1.4945101

Guenneau, S., Movchan, A., Pétursson, G., and Ramakrishna, S. A. (2007). Acoustic metamaterials for sound focusing and confinement. *New J. Phys.* 9:399. doi: 10.1088/1367-2630/9/11/399

Holloway, C. L., Kuester, E. F., Gordon, J. A., O'Hara, J., Booth, J., and Smith, D. R. (2012). An overview of the theory and applications of metasurfaces: the two-dimensional equivalents of metamaterials. *IEEE Antenn. Propag.* M54, 10–35. doi: 10.1109/MAP.2012.6230714

Jia, Z., Li, J., Shen, C., Xie, Y., and Cummer, S. A. (2018). Systematic design of broadband path-coiling acoustic metamaterials. *J. Appl. Phys.* 123:025101. doi: 10.1063/1.5009488

Jiang, X., Liang, B., Li, R.-Q., Zhou, X.-Y., Yin, L.-L., and Cheng, J.-C. (2014). Ultra-broadband absorption by acoustic metamaterials. *Appl. Phys. Lett.* 105:243505. doi: 10.1063/1.4904887

Jiménez, N., Cox, T. J., Romero-García, V., and Groby, J.-P. (2017c). Metadiffusers: deep-subwavelength sound diffusers. *Sci. Rep.* 7:5389. doi: 10.1038/s41598-017-05710-5

Jiménez, N., Huang, W., Romero-García, V., Pagneux, V., and Groby, J.-P. (2016). Ultra-thin metamaterial for perfect and quasi-omnidirectional sound absorption. *Appl. Phys. Lett.* 109:121902. doi: 10.1063/1.4962328

Jiménez, N., Romero-García, V., Pagneux, V., and Groby, J.-P. (2017a). Quasiperfect absorption by subwavelength acoustic panels in transmission using accumulation of resonances due to slow sound. *Phys. Rev. B* 95:014205. doi: 10.1103/PhysRevB.95.014205

Jiménez, N., Romero-García, V., Pagneux, V., and Groby, J. P. (2017b). Rainbow-trapping absorbers: broadband, perfect and asymmetric sound absorption by subwavelength panels for transmission problems. *Sci. Rep.* 7:13595. doi: 10.1038/s41598-017-13706-4

Kachaeva, M. (2008). *Treasures of the Russian Ornament*. Moscow: Belye Alvy.

Kaina, N., Lemoult, F., Fink, M., and Lerosey, G. (2015). Negative refractive index and acoustic superlens from multiple scattering in single negative metamaterials. *Nature* 525:77. doi: 10.1038/nature14678

Kan, W., Liang, B., Li, R., Jiang, X., Zou, X., Yin, L., et al. (2016). Three-dimensional broadband acoustic illusion cloak for sound-hard boundaries of curved geometries. *Sci. Rep.* 6:36936. doi: 10.1038/srep36936

Krushynska, A. O. (2019). *COMSOL Dataset for the Paper "Between Science and Art: Thin Sound Absorbers Inspired by Slavic Ornaments" by A. O. Krushynska*. DataverseNL, V1. Available online at: https://hdl.handle.net/10411/L5G6K0 (accessed July 8, 2019).

Krushynska, A. O., Bosia, F., Miniaci, M., and Pugno, N. M. (2017). Spider web-structured labyrinthine acoustic metamaterials for low-frequency sound control. *New J. Phys.* 19:105001. doi: 10.1088/1367-2630/aa83f3

Krushynska, A. O., Bosia, F., and Pugno, N. M. (2018). Labyrinthine acoustic metamaterials with space-coiling channels for low-frequency sound control. *Acta Acust. United With Acust.* 104, 200–210. doi: 10.3813/AAA.919161

Li, J. S., Fok, L., Yin, X. B., Bartal, G., and Zhang X. (2009). Experimental demonstration of an acoustic magnifying hyperlens. *Nat. Mater.* 8, 931–934. doi: 10.1038/nmat2561

Li, J. S., and Pendry, J. B. (2008). Hiding under the carpet: a new strategy for cloaking. *Phys. Rev. Lett.* 101:203901. doi: 10.1103/PhysRevLett.101.203901

Li, Y., Jiang, X., Li, R. Q., Liang, B., Zou, X. Y., Yin, L. L., et al. (2014). Experimental realization of full control of reflected waves with subwavelength acoustic metasurfaces. *Phys. Rev. Appl.* 2, 1–11. doi: 10.1103/PhysRevApplied.2.064002

Li, Y., Jiang, X., Liang, B., Cheng, J. C., and Zhang, L. (2015). Metascreen-based acoustic passive phased array. *Phys. Rev. Appl.* 4:024003. doi: 10.1103/PhysRevApplied.4.024003

Li, Y., Liang, B., Gu, Z. M., Zou, X. Y., and Cheng, J. C. (2013). Reflected wavefront manipulation based on ultrathin planar acoustic metasurfaces. *Sci. Rep.* 3:2546. doi: 10.1038/srep02546

Li, Y., Liang, B., Tao, X., Zhu, X. F., Zou, X. Y., and Cheng, J. C. (2012). Acoustic focusing by coiling up space. *Appl. Phys. Lett.* 101:233508. doi: 10.1063/1.4769984

Liang, B., Cheng, J.-C., and Qui, C.-W. (2018). Wavefront manipulation by acoustic metasurfaces: from physics and applications. *Nanophotonics* 7, 1191–1205. doi: 10.1515/nanoph-2017-0122

Liang, B., Guo, X. S., Tu, J., Zhang, D., and Cheng, J. C. (2010). An acoustic rectifier. *Nat. Mater.* 9, 989–992. doi: 10.1038/nmat2881

Liang, Z., and Li, J. (2012). Extreme acoustic metamaterial by coiling up space. *Phys. Rev. Lett.* 108:114301. doi: 10.1103/PhysRevLett.108.114301

Liu, Z., Zhang, X., Mao, Y., Zhu, Y.-Y., Yang, Z., Chan, C.-T., et al. (2000). Locally resonant sonic materials. *Science* 289, 1734–1736. doi: 10.1126/science.289.5485.1734

Lu, K., Wu, J. H., Guan, D., Gao, N., and Li, J. (2016). A lightweight low-frequency sound insulation membrane-type acoustic metamaterial. *AIP Adv.* 6:025116. doi: 10.1063/1.4942513

Ma, F., Huang, M., and Wu, J. H. (2017). Acoustic metamaterials with synergetic coupling. *J. Appl. Phys.* 122:215102. doi: 10.1063/1.5003276

Ma, F., Huang, M., Xu, Y., and Wu, J. H. (2018). Bilayer synergetic coupling double negative acoustic metasurface and cloak. *Sci. Rep.* 8, 1–12. doi: 10.1038/s41598-018-24231-3

Mei, J., Ma, G., Yang, M., Yang, Z., Wen, W., and Sheng, P. (2012). Dark acoustic metamaterials as super absorbers for low-frequency sound. *Nat. Commun.* 3:756. doi: 10.1038/ncomms1758

Merkel, A., Theocharis, G., Richoux, O., Romero-García, V., and Pagneux, V. (2015). Control of acoustic absorption in one-dimensional scattering by resonant scatterers. *Appl. Phys. Lett.* 107:244102. doi: 10.1063/1.4938121

Molerón, M., Serra-García, M., and Daraio, C. (2016). Visco-thermal effects in acoustic metamaterials: from total transmission to total reflection and high absorption. *New J. Phys.* 18:033003. doi: 10.1088/1367-2630/18/3/033003

Nekrasova, M. (1983). *Russian Folk Art*. Moscow.

Park, C. M., Park, J. J., Lee, S. H., Seo, Y. M., Kim, C. K., and Lee, S. H. (2011). Amplification of acoustic evanescent waves using metamaterial slabs. *Phys. Rev. Lett.* 107:194301. doi: 10.1103/PhysRevLett.107.194301

Romero-García, V., Theocharis, G., Richoux, O., Merkel, A., Tournat, V., and Pagneux, V. (2016). Perfect and broadband acoustic absorption by critically coupled sub-wavelength resonators. *Sci. Rep.* 6:19519. doi: 10.1038/srep19519

Tang, Y., Ren, S., Meng, H., Xin, F., Huang, L., Chen, T., et al. (2017). Hybrid acoustic metamaterial as super absorber for broadband low-frequency sound. *Sci. Rep.* 7:43340. doi: 10.1038/srep43340

Theocharis, G., Richoux, O., Romero-García, V., Merkel, A., and Tournat, V. (2014). Limits of slow sound propagation and transparency in lossy, locally resonant periodic structures. *New J. Phys.* 16:093017. doi: 10.1088/1367-2630/16/9/093017

Wu, Y., Yang, M., and Sheng, P. (2018). Perspective: acoustic metamaterials in transition. *J. Appl. Phys.* 123:090901. doi: 10.1063/1.5007682

Xie, Y., Popa, B.-I., Zigoneanu, L., and Cummer, S. (2013). Measurement of a broadband negative index with space-coiling acoustic metamaterials. *Phys. Rev. Lett.* 110:175501. doi: 10.1103/PhysRevLett.110.175501

Xie, Y., Wang, W., Chen, H., Konneker, A., Popa, B. I., and Cummer, S. A. (2014). Wavefront modulation and subwavelength diffractive acoustics with an acoustic metasurface. *Nat. Commun.* 5:5553. doi: 10.1038/ncomms6553

Yang, M., Chen, S., Fu, C., and Sheng, P. (2017). Optimal sound-absorbing structures. *Mater. Horizons* 4, 673–680. doi: 10.1039/C7MH00129K

Yang, M., Meng, C., Fu, C., Li, Y., Yang, Z., and Sheng, P. (2015). Subwavelength total acoustic absorption with degenerate resonators. *Appl. Phys. Lett.* 107:104104. doi: 10.1063/1.4930944

Yang, Z., Mei, J., Yang, M., Chan, N. H., and Sheng, P. (2008). Membrane-type acoustic metamaterial with negative dynamic mass. *Phys. Rev. Lett.* 101:204301. doi: 10.1103/PhysRevLett.101.204301

Zhang, C., and Hu, X. (2016). Three-dimensional single-port labyrinthine acoustic metamaterial: perfect absorption with large bandwidth and tunability. *Phys. Rev. Appl.* 6:064025. doi: 10.1103/PhysRevApplied.6.064025

Conflict of Interest Statement: The author declares that the research was conducted in the absence of any commercial or financial relationships that could be construed as a potential conflict of interest.

APPENDIX: NUMERICAL ANALYSIS

The dispersion and transmission analyses are performed by means of eigenfrequency and frequency domain studies in the Acoustic Pressure module in COMSOL Multiphysics. The models are represented by discretized geometries of the panel cavities and outside air, while the presence of panels is replicated by the sound hard boundary conditions. The outside-air domain has the width L_x, the height L_y, and the depth $L_z = 3 * \max\{L_x, L_y\}$, where the latter is chosen to exclude from the consideration near-field effects. Incident waves are represented by a background plane-wave field of a unit amplitude within all the domains. At the side of the outside-air domain opposite to the panel, plane-wave radiation conditions are applied. The air inside the cavities and HRs is discretized by means of free-mesh tetrahedral elements; for outside air, the swept mesh is used.

The dispersion analysis is done by a parametric sweep from 0 to π/L_t with 15 values. The transmission simulations are performed within specified frequency ranges by solving the frequency-domain problem at 2,000 intermediate frequencies. The transmitted pressure field is extracted at two domain point probes with coordinates $(0, 0, L_z)$ and $(0, 0, L_z - 0.01)$ that allows evaluation the reflection coefficient by means of Equation (3).

frontiers in Materials

ORIGINAL RESEARCH
published: 24 April 2019
doi: 10.3389/fmats.2019.00074

Modeling Bloch Waves in Prestressed Phononic Crystal Plates

Matteo Mazzotti[1], *Ivan Bartoli*[1] *and Marco Miniaci*[2]*

[1] Civil, Architectural and Environmental Engineering Department, Drexel University, Philadelphia, PA, United States,
[2] Laboratory of Acoustics and Noise Control, Swiss Federal Laboratories for Materials Science and Technology (EMPA), Dübendorf, Switzerland

The study aims at investigating the effect of a generic state of prestress on the passbands and bandgaps of a phononic crystal plate. To this end, an Updated Lagrangian scheme is developed, consisting in a two-step procedure: first, a static geometrically nonlinear analysis of a representative unit cell undergoing the action of an applied external load is conducted and then the Floquet-Bloch decomposition is applied to the linearized equations of the acousto-elasticity for the unit cell in the deformed configuration. In addition, a formula for the calculation of the energy velocity is proposed. In the case of an epoxy plate with cylindrical steel inclusions, it is shown that, even in the presence of prestress inducing full reversible deformation state, the bandgap experiences a shift towards higher frequencies when the cell is subjected to a compressive prestress, whereas a frequency downshift is registered when the cell is subjected to traction. In particular, it is demonstrated that the frequency downshift of the bandgap for the phononic plate undergoing a tensile prestress is approximately 3.5% with respect to the case of the phononic plate under compression. The results presented herein provide insights in the behavior of phononic crystal plates with tunable dispersive properties, and suggest new leverages for wave manipulation valuable in many application fields such as wave filters, waveguiding and beam splitting, sensing devices, and vibration shielding.

Keywords: phononic crystals, prestress, Floquet-Bloch, energy velocity, acousto-elasticity, Comsol

OPEN ACCESS

Edited by:
Nicola Maria Pugno,
University of Trento, Italy

Reviewed by:
Paolo S. Valvo,
University of Pisa, Italy
Enrico Babilio,
University of Naples Federico II, Italy

***Correspondence:**
Marco Miniaci
marco.miniaci@gmail.com

Specialty section:
This article was submitted to Mechanics of Materials, a section of the journal Frontiers in Materials

Received: *13 January 2019*
Accepted: *05 April 2019*
Published: *24 April 2019*

Citation:
Mazzotti M, Bartoli I and Miniaci M (2019) Modeling Bloch Waves in Prestressed Phononic Crystal Plates. Front. Mater. 6:74. doi: 10.3389/fmats.2019.00074

1. INTRODUCTION

The propagation of elastic waves in periodic structures is governed by the elastomorphic and material parameters of its unit cell (Kushwaha and Halevi, 1994; Sainidou et al., 2005). Properly conceiving their design in terms of size, shape, and arrangement, as well as choosing their density and elastic properties demonstrated great potential for attaining exceptional dynamic behavior, such as frequency bandgaps (Kushwaha and Halevi, 1994; Mártinez-Sala et al., 1995; Liu et al., 2000; Miniaci et al., 2018a), negative refraction (Morvan et al., 2010; Zhu et al., 2014; Zhu and Semperlotti, 2016), topological protection (Mousavi et al., 2015; Süsstrunk and Huber, 2015; Pal et al., 2016; Miniaci et al., 2018b), etc. This opened up new perspectives in many fields, ranging from microelectromechanical systems to nondestructive evaluation (Pennec et al., 2010; Craster and Guenneau, 2012; Deymier, 2013), including but not limited to wave filters, waveguiding and beam splitting, sensing devices, wave splitters, vibration shielding, subwavelength imaging (Sukhovich et al., 2009; Li et al., 2015; Trainiti et al., 2015; Colombi et al., 2016; Miniaci et al., 2016, 2017; Su et al., 2016; Miniaci et al., 2019).

However, most of the configurations proposed so far are limited by the fact that their unconventional dynamic properties are accessible to specific frequencies only, once the unit cell design is conceived, being its geometrical and mechanical properties constant with respect to time. To overcome this limitation, periodic systems with adaptive elastic properties have received great attention in the recent years. Indeed, introducing an additional degree of freedom, enables the reversible tailoring of the dispersive diagram of the structure, considerably enhancing their functionality and technological applications. To achieve this goal, several approaches have been proposed and explored so far. They include active systems, such as piezoelectric materials (Casadei et al., 2010; Bergamini et al., 2014; Kherraz et al., 2016), temperature (Jim et al., 2009; Airoldi et al., 2011; Cheng et al., 2011; Wu et al., 2018) and magneto-based techniques (Robillard et al., 2009; Matar et al., 2012; Guo and Wei, 2016; Zhang et al., 2017), actuated polymers via electromagnetic waves (Walker et al., 2014, 2017) as well as the application of an external mechanical load. Among them, the latter has shown to be particularly promising to achieve tunable dispersive properties. Bigoni et al. (2008) formulated a theoretical model for an orthotropic, prestressed (compressible) elastic layer vibrating on an elastic half space assuming long-wave asymptotics for the solution. It was found that the influence of the prestress over bandgaps and passbands, so that it could be exploited as a tuning parameter to shift the dispersion curves of the system. A modeling tool for the prediction of controlled bandgap structures responding to flexural vibrations was provided by Gei et al. (2009), also relaxing the hypothesis of perfect periodicity, allowing thus to consider quasi-periodic structures (Gei, 2010). Wang and Bertoldi (2012) showed how mechanical deformations enabled the tuning of the phononic bandgaps in 3D periodic elastomeric structures. The ability of the elastomers to undergo small as well as large strain deformations guaranteed the reversibility and repeatability of the process. Both the linear and nonlinear regimes of elastic deformation were explored, including different geometrical topology for triggering mechanical instability. Galich et al. (2016) showed how local deformations experienced by a composite structure can bring to local stiffening influencing the instability-induced interfaces on elastic wave propagation in finitely deformed layered materials. Finally, Norris and Parnell (2012) tried to exploit the effects of the prestress to theoretically show the feasibility of a hyperelastic cloaking via transformation elasticity.

In this paper, the effects of an applied mechanical load on the dispersive diagram for phononic crystal plates is investigated in the case of elastic deformations, so to have a complete reversibility of the phenomena. The paper is organized as follows: section 2 provides the description of an Updated Lagrangian scheme, in which a representative unit cell of the phononic crystal plate is studied in its static and dynamic deformed configurations. In section 3, the procedure to extract the band diagrams and in particular the energy velocity using the equations described in section 2 is detailed. Finally, section 4 investigates the effect of a reversible compressive and tensile state of prestress on an epoxy plate with cylindrical inclusions.

2. FLOQUET-BLOCH ANALYSIS OF A PRESTRESSED PHONONIC CRYSTAL

2.1. Static Analysis

In what follows, the equations of static and dynamic equilibrium are derived with reference to the generic infinite phononic crystal (PC) shown in **Figure 1**, where C_0 indicates the static undeformed configuration, C the static configuration resulting from the application of an external load, and C' the dynamic configuration undergoing a harmonic motion. The so called Updated Lagrangian (UL) scheme is employed to analyze the PC in the three different equilibrium configurations. The UL approach consists of two steps: in the first step, C_0 is used as the reference configuration to calculate the displacement and stress fields relative to the configuration C, while in the second step, C is used as the new reference configuration to evaluate the dynamic equilibrium of the unit cell in the configuration C'.

Due to the periodicity of the system under consideration, in the undeformed configuration C_0 any scalar, vector or tensor function ϕ satisfies the condition $\phi(\mathbf{x}_0 + \mathbf{r}_0\mathbf{m}) = \phi(\mathbf{x}_0)$, where $\mathbf{m} \in \mathbb{Z}^2$ and $\mathbf{r}_0 = [\mathbf{r}_{01}, \mathbf{r}_{02}]$ is the matrix of lattice vectors. This allows to restrict the computational domain to a unit cell of domain Ω_0 and boundary $\partial\Omega_0$ (Collet et al., 2011; Mazzotti et al., 2017). Similarly, the unit cell in the configuration C satisfies the periodic condition $\phi(\mathbf{x} + \mathbf{rm}) = \phi(\mathbf{x})$, with $\mathbf{r} = [\mathbf{r}_1, \mathbf{r}_2]$. For this cell, the mapping between the coordinates $\mathbf{x}_0 = \{x_{01}, x_{02}, x_{03}\}^{\mathrm{T}}$ of a material point in C_0 and the coordinates $\mathbf{x} = \{x_1, x_2, x_3\}^{\mathrm{T}}$ of the same point in C is established by the deformation gradient $\mathbf{F}(\mathbf{x}_0) = \nabla_0\mathbf{x} = \mathbf{I} + \nabla_0\mathbf{u}_0$, where ∇_0 denotes the gradient operator defined with respect to C_0, $\mathbf{u}_0$ is the pseudo-static displacement resulting from the application of external, Ω_0-periodic, volume ($\mathbf{f}_V$) and surface ($\mathbf{t}_S$) loads. Following Zhang and Parnell (2017), the deformation gradient can be decomposed as $\mathbf{F}(\mathbf{x}_0) = \mathbf{F}_L(\mathbf{x}_0)\mathbf{F}_P(\mathbf{x}_0)$, where $\mathbf{F}_L$ indicates the affine deformation gradient of the lattice points such that $\mathbf{r} = \mathbf{F}_L\mathbf{r}_0$, while $\mathbf{F}_P$ denotes a periodic non-affine deformation.

The specific material density of the unit cell in C_0 is $\rho_0(\mathbf{x}_0)$, while, assuming a hyperelastic material behavior described by the Murnaghan's model (Murnaghan et al., 1937; Pau and Lanza di Scalea, 2015; Dubuc et al., 2017, 2018), the tensor of tangential elastic moduli with respect to C_0 is expressed by $\mathbf{D}_0 = 4\partial^2\Psi/(\partial\mathbf{C}\partial\mathbf{C})$, where the elastic energy density Ψ has the form

$$\Psi = \frac{1}{2}(\lambda + 2\mu) I_1^2(\mathbf{E}) - 2\mu I_2(\mathbf{E}) + \frac{1}{3}(l + 2m) I_1^3(\mathbf{E}) - 2mI_1(\mathbf{E})I_2(\mathbf{E}) + nI_3(\mathbf{E}), \quad (1)$$

in which λ and μ denote the first and second Lamé parameters, respectively, (l, m, n) the third order Murnaghan parameters, $\mathbf{C} = \mathbf{F}^{\mathrm{T}}\mathbf{F}$ the right Cauchy-Green deformation tensor, $\mathbf{E} = \frac{1}{2}(\mathbf{F}^{\mathrm{T}}\mathbf{F} - \mathbf{I})$ the Green-Lagrange strain tensor and $I_1(\mathbf{E})$, $I_2(\mathbf{E})$, and $I_3(\mathbf{E})$ its first, second and third invariants, respectively.

Finding the coordinates of the deformed configuration C and the associated stress fields requires the solution of a variational

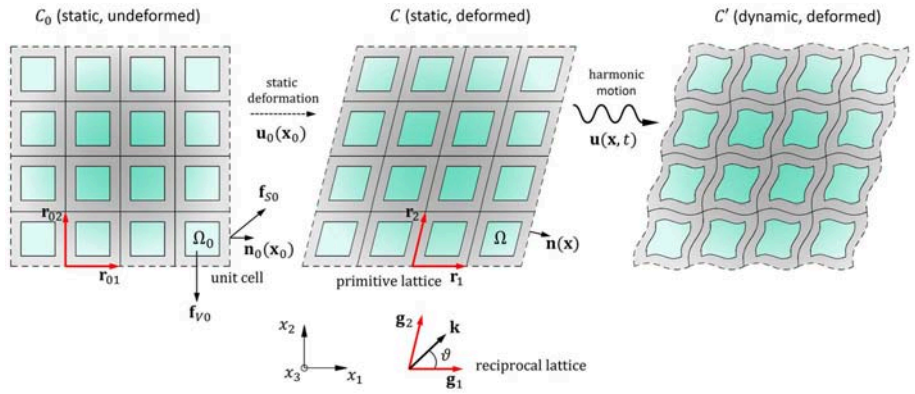

FIGURE 1 | Schematic representation of the Updated Lagrangian (UL) scheme for the infinite phononic crystal (PC) plate.

functional of the form (Bonet and Wood, 2008)

$$\int_\Omega \mathbf{S}(\mathbf{x}) : \delta\mathbf{E}(\mathbf{x})\mathrm{d}\Omega = \int_\Omega \mathbf{f}_{V0}(\mathbf{x}) \cdot \delta\mathbf{u}_0 \mathrm{d}\Omega + \int_{\partial\Omega} \mathbf{t}_{S0}(\mathbf{x}) \cdot \delta\mathbf{u}_0 \mathrm{d}(\partial\Omega), \tag{2}$$

subjected to the Dirichlet boundary conditions

$$\mathbf{u}_0(\mathbf{x} + \mathbf{r}\mathbf{n}(\mathbf{x})) = \mathbf{u}_0(\mathbf{x}) \quad \text{on } \partial\Omega, \tag{3}$$

in which $\delta\mathbf{u}_0$ is an arbitrary admissible kinematic variation of $\mathbf{u}_0(\mathbf{x}_0)$, $\mathbf{S} = \mathbf{D}_0 : \mathbf{E}$ the second Piola-Kirchhoff stress tensor and $\mathbf{n}(\mathbf{x}_0)$ the outward pointing normal at $\mathbf{x}_0 \in \partial\Omega_0$. The application of a standard Galerkin approach to Equation (2) results in the generalized system of equations

$$\left[\mathbf{\Gamma}_0^{\mathrm{T}} \mathbf{K}(\mathbf{Q}_0) \mathbf{\Gamma}_0\right] \mathbf{Q}_0(\mathbf{X}) = \mathbf{P}_0(\mathbf{X}), \tag{4}$$

where $\mathbf{K}(\mathbf{Q}_0)$ is a static stiffness matrix, $\mathbf{P}_0$ represents the global vector of nodal forces, $\mathbf{Q}_0$ denotes a global vector of independent nodal displacements and $\mathbf{\Gamma}_0$ is a mapping operator resulting from Equation (3) and realizing the condition $\mathbf{U}_0 = \mathbf{\Gamma}_0\mathbf{Q}_0$, in which $\mathbf{U}_0$ indicates the full vector of nodal displacements. In this work, the solution of Equation (4) is carried out using the weak form module implemented in Comsol Multiphysics 5.3 (Comsol, 2017).

2.2. Geometry and Mechanical Properties Updating

Once the set of independent static displacements $\mathbf{Q}_0$ is obtained, the reference configuration is updated from C_0 to C by calculating the corresponding nodal coordinates $\mathbf{x} = \mathbf{x}_0 + \mathbf{\Gamma}_0\mathbf{Q}_0(\mathbf{x}_0)$. The updated material properties in C are given by $\rho = \rho_0(\det\mathbf{F})^{-1}$ and $D_{ijkl} = (\det\mathbf{F})^{-1}F_{iI}F_{jJ}F_{kK}F_{lL}(D_0)_{IJKL}$, while the Cauchy stress tensor is obtained from the relation $\boldsymbol{\sigma} = (\det\mathbf{F})^{-1}\mathbf{F}\mathbf{S}\mathbf{F}^{\mathrm{T}}$. The geometry of the unit cell in the configuration C is then re-meshed and used as the basis for the linear dynamic analysis presented in the next section.

2.3. Dynamic Analysis Using the Floquet-Bloch Decomposition

Assuming C as the new reference configuration, the position vector for the unit cell in the dynamic deformed configuration C' is given by $\mathbf{x}' = \mathbf{x} + \mathbf{u}(\mathbf{x}, t)$, where $\mathbf{u}(\mathbf{x}, t) = \mathbf{u}(\mathbf{x})\exp(-\mathrm{i}\omega t)$ is a time-harmonic perturbation superimposed on C, being t the time and ω the angular frequency. In the rest of the paper, the time-dependence $\exp(-\mathrm{i}\omega t)$ is dropped for conciseness. According to the small-on-large displacement hypotheses usually assumed in acousto-elasticity (Mazzotti et al., 2012; Pau and Lanza di Scalea, 2015; Shim et al., 2015), only small perturbations $\mathbf{u}(\mathbf{x}, t)$ are considered. In this case, the approximations $\mathbf{x}' \approx \mathbf{x}$ and $C' \approx C$ hold and any displacement-dependent vector and tensor field can be obtained in a linearized incremental form. Following this procedure, the stress tensor is linearized in the direction of $\mathbf{u}(\mathbf{x}, t)$ by applying a first order Taylor series expansion of $\boldsymbol{\sigma}(\mathbf{x})$ about $\mathbf{x}$, resulting in (Mazzotti et al., 2012)

$$\mathscr{D}_\mathbf{u}\boldsymbol{\sigma}(\mathbf{x}) = \boldsymbol{\sigma}_0(\mathbf{x}) \otimes \nabla\mathbf{u}(\mathbf{x}) + \mathbf{D}(\mathbf{x}) : \mathbf{e}(\mathbf{x}), \tag{5}$$

where $\mathbf{e}(\mathbf{x}) = \frac{1}{2}[\nabla\mathbf{u}(\mathbf{x}) + (\nabla\mathbf{u}(\mathbf{x}))^{\mathrm{T}}]$ denotes the linearized Green-Lagrange strain tensor.

From the application of the Floquet-Bloch theorem, any small harmonic perturbation $\mathbf{u}(\mathbf{x})$ can be expressed in the form (Collet et al., 2011)

$$\mathbf{u}(\mathbf{x}) = \tilde{\mathbf{u}}(\mathbf{x})\exp(\mathrm{i}\mathbf{k} \cdot \mathbf{x}), \tag{6}$$

in which $\tilde{\mathbf{u}}(\mathbf{x})$ is a Ω-periodic displacement amplitude and $\mathbf{k} \in \Lambda$ is the Bloch wavenumber vector, being Λ the reciprocal unit cell defined in C by the reciprocal lattice vector basis $\mathbf{g}_j$, $j = 1, 2$, satisfying the condition $\mathbf{r}_i \cdot \mathbf{g}_j = 2\pi\delta_{ij}$, where δ_{ij} is the Kronecker delta. These are related to the reciprocal lattice vector basis $\mathbf{g}_{0j}$ in C_0 by $\mathbf{g}_j = \mathbf{F}_L^{-\mathrm{T}}\mathbf{g}_{0j}$, $j = 1, 2$ (Zhang and Parnell, 2017). In the reciprocal lattice domain, the Bloch wavenumber vector is described in terms of its orientation angle ϑ as $\mathbf{k}(\vartheta) = k\Phi(\vartheta)$, where ϑ is defined with respect to $\mathbf{g}_1$, $k = \|\mathbf{k}(\vartheta)\|_2$ and $\Phi(\vartheta) =$

$\{\cos\vartheta, \sin\vartheta, 0\}^{\mathrm{T}}$. The relation between the orientation vector in C_0 and C writes $\Phi = \mathbf{F}_L^{-\mathrm{T}}\Phi_0$.

From Equation (6), and by defining the k-shifted gradient of a generic Ω-periodic vector field $\tilde{\phi}(\mathbf{x}) \in \mathbb{C}^3$ as

$$\nabla_{\mathbf{k}}\tilde{\phi}(\mathbf{x},\vartheta) = \nabla_{\mathbf{x}}\tilde{\phi}(\mathbf{x}) + \mathrm{i}k\tilde{\phi}(\mathbf{x}) \otimes \Phi(\vartheta), \tag{7}$$

the solution of the elastodynamic problem for free vibrations of the unit cell in C subjected to an initial stress $\boldsymbol{\sigma}_0$ can be obtained from the variational statement

$$\begin{aligned} -\omega^2 &\int_\Omega \rho(\mathbf{x})\delta\tilde{\mathbf{u}}^*(\mathbf{x}) \cdot \tilde{\mathbf{u}}(\mathbf{x})\mathrm{d}\Omega \\ &+ \int_\Omega \delta\tilde{\mathbf{e}}_{\mathbf{k}}^*(\mathbf{x},\vartheta) : \mathbf{D}(\mathbf{x}) : \tilde{\mathbf{e}}_{\mathbf{k}}(\mathbf{x},\vartheta)\mathrm{d}\Omega, \\ &+ \int_\Omega \boldsymbol{\sigma}_0(\mathbf{x}) : \left[\left(\nabla_{\mathbf{k}}\delta\tilde{\mathbf{u}}^*(\mathbf{x})\right)^{\mathrm{T}} \nabla_{\mathbf{k}}\tilde{\mathbf{u}}(\mathbf{x})\right]\mathrm{d}\Omega = 0, \end{aligned} \tag{8}$$

subjected to the Dirichlet boundary condition

$$\tilde{\mathbf{u}}(\mathbf{x} + \mathbf{r}\mathbf{n}(\mathbf{x})) = \tilde{\mathbf{u}}(\mathbf{x}) \quad \text{on } \partial\Omega, \tag{9}$$

in which $(\cdot)^*$ stands for the conjugate of a complex vector or tensor field, $\tilde{\mathbf{e}}_{\mathbf{k}}(\mathbf{x},\vartheta) = \frac{1}{2}[\nabla_{\mathbf{k}}\tilde{\mathbf{u}}(\mathbf{x}) + (\nabla_{\mathbf{k}}\tilde{\mathbf{u}}(\mathbf{x}))^{\mathrm{T}}]$ follows from Equation (7) and $\mathbf{n}(\mathbf{x})$ represents the outpointing surface normal at $\mathbf{x} \in \partial\Omega$. After the application of a Galerkin discretization scheme, Equations (8) and (9) lead to the following generalized linear eigenvalue problem

$$\left\{\boldsymbol{\Gamma}^{\mathrm{T}}\left[k^2\mathbf{K}_3(\vartheta) + \mathrm{i}k\left(\mathbf{K}_2(\vartheta) - \mathbf{K}_2^{\mathrm{T}}(\vartheta)\right) + \mathbf{K}_1 - \omega^2\mathbf{M}\right]\boldsymbol{\Gamma}\right\}\tilde{\mathbf{Q}}(\omega,\vartheta) = \mathbf{0}, \tag{10}$$

which forms the basis of the band structure analysis for the prestressed PC. In Equation (10), $\boldsymbol{\Gamma}$ is a mapping operator implementing the Dirichlet boundary condition in Equation (9) such that $\tilde{\mathbf{U}}(\vartheta) = \boldsymbol{\Gamma}\tilde{\mathbf{Q}}(\vartheta)$ is verified, where $\tilde{\mathbf{U}}(\vartheta)$ is the global vector of nodal displacement amplitudes and $\mathbf{Q}(\tilde{\vartheta})$ a subvector of $\tilde{\mathbf{U}}(\vartheta)$ collecting only its independent components. The mass operator $\mathbf{M}$ and the stiffness operators $\mathbf{K}_1$, $\mathbf{K}_2$, and $\mathbf{K}_3$ are given by

$$\mathbf{M} = \bigcup_e \int_{\Omega^{(e)}} \mathbf{N}^{\mathrm{T}}(\mathbf{x})\rho(\mathbf{x})\mathbf{N}(\mathbf{x})\mathrm{d}\Omega, \tag{11}$$

$$\mathbf{K}_1 = \bigcup_e \int_{\Omega^{(e)}} \mathbf{N}^{\mathrm{T}}(\mathbf{x})\left[\mathbf{B}^{\mathrm{T}}\mathbf{D}(\mathbf{x})\mathbf{B} + \mathbf{B}_0^{\mathrm{T}}\boldsymbol{\Sigma}_0(\mathbf{x})\mathbf{B}_0\right]\mathbf{N}(\mathbf{x})\mathrm{d}\Omega \tag{12}$$

$$\mathbf{K}_2(\vartheta) = \bigcup_e \int_{\Omega^{(e)}} \mathbf{N}^{\mathrm{T}}(\mathbf{x})\left[\mathbf{B}^{\mathrm{T}}\mathbf{D}(\mathbf{x})\mathbf{H}(\vartheta) + \mathbf{B}_0^{\mathrm{T}}\boldsymbol{\Sigma}_0(\mathbf{x})\mathbf{H}_0(\vartheta)\right]\mathbf{N}(\mathbf{x})\mathrm{d}\Omega, \tag{13}$$

$$\mathbf{K}_3(\vartheta) = \bigcup_e \int_{\Omega^{(e)}} \mathbf{N}^{\mathrm{T}}(\mathbf{x})\left[\mathbf{H}^{\mathrm{T}}(\vartheta)\mathbf{D}(\mathbf{x})\mathbf{H}(\vartheta) + \mathbf{H}_0^{\mathrm{T}}(\vartheta)\boldsymbol{\Sigma}_0(\mathbf{x})\mathbf{H}_0(\vartheta)\right]\mathbf{N}(\mathbf{x})\mathrm{d}\Omega, \tag{14}$$

where $\Omega^{(e)}$ denotes the domain of the e-th finite element of the mesh, $\bigcup_e(\cdot)$ stands for the standard direct stiffness assembling procedure, $\mathbf{N}(\mathbf{x})$ is a matrix of shape functions for the e-th element, $\boldsymbol{\Sigma}_0(\mathbf{x})$ is a block-diagonal matrix of the form

$$\boldsymbol{\Sigma}_0(\mathbf{x}) = \begin{bmatrix} \boldsymbol{\sigma}_0(\mathbf{x}) & \mathbf{0} & \mathbf{0} \\ \mathbf{0} & \boldsymbol{\sigma}_0(\mathbf{x}) & \mathbf{0} \\ \mathbf{0} & \mathbf{0} & \boldsymbol{\sigma}_0(\mathbf{x}) \end{bmatrix}, \tag{15}$$

while the different compatibility operators are expressed as

$$\mathbf{B} = \sum_{i=1}^{3} \frac{\partial}{\partial x_i}\mathbf{L}_i, \quad \mathbf{H}(\vartheta) = \sum_{i=1}^{3}\left(\mathbf{z}_i^{\mathrm{T}}\boldsymbol{\Phi}(\vartheta)\right)\mathbf{L}_i, \tag{16}$$

$$\mathbf{B}_0 = \sum_{i=1}^{3} \frac{\partial}{\partial x_i}\mathbf{L}_{0i}, \quad \mathbf{H}_0(\vartheta) = \sum_{i=1}^{3}\left(\mathbf{z}_i^{\mathrm{T}}\boldsymbol{\Phi}(\vartheta)\right)\mathbf{L}_{0i}, \tag{17}$$

being $\mathbf{z}_i$ a unit vector identifying the i-th coordinate in the Cartesian frame of reference. The operators $\mathbf{L}_i$ and $\mathbf{L}_{0i}$ are given in the Appendix. It should be noted that, since the mass and stiffness matrices in Equations (11)–(14) are evaluated with respect to the deformed configuration C, a new mesh for the deformed geometry of the unit cell needs to be generated after the static analysis described in section 2.1 has been completed and before the eigenvalue analysis is carried out.

3. BAND STRUCTURE ANALYSIS AND ENERGY VELOCITY EXTRACTION

The homogeneous problem in Equation (10) can be solved in the wavenumber $k(\vartheta,\omega)$ and corresponding Floquet eigenvectors $\tilde{\mathbf{Q}}(\vartheta,\omega)$ for any fixed direction ϑ and circular frequency $\omega \in \mathbb{R}$, $\omega > 0$, from which the band structures of the propagation and attenuation constants of a specific mode m are obtained by taking the real and imaginary components of the corresponding wavenumber $k_m(\vartheta,\omega)$, respectively. For the particular case of a lossless structure ($\mathrm{Im}(\mathbf{D}) = 0$) immersed in vacuum, the modes supported by the crystal can be either propagative ($\mathrm{Im}(k) = 0$) or evanescent ($\mathrm{Re}(k) = 0$), the latter belonging to the so called deaf frequency range (bandgap).

In addition to the Bloch wavenumber $k(\vartheta,\omega)$, from the computed set of solutions $(k_m(\vartheta,\omega), \mathbf{Q}_m(\vartheta,\omega))$ it is possible to extract the band structure of the energy velocity, which corresponds to the velocity of propagation of packets of waves having close central frequency (Brillouin, 1953; Mazzotti et al., 2012). The energy velocity of a specific Bloch mode can be found as the ratio between the time-averaged energy flux in the direction ϑ over one period $T = 2\pi/\omega$ and the time-averaged total mechanical energy over the same period, i.e.

$$c_e(\vartheta,\omega) = \frac{\langle\mathscr{I}(\vartheta,\omega)\rangle}{\langle\mathscr{K}(\vartheta,\omega)\rangle + \langle\mathscr{W}(\vartheta,\omega)\rangle + \langle\mathscr{W}_{\sigma_0}(\vartheta,\omega)\rangle}, \tag{18}$$

where $\langle\phi\rangle = \frac{\omega}{2\pi}\int_t^{t+2\pi/\omega}\phi\mathrm{d}t$ denotes the time-averaging operation, $\mathscr{I}(\vartheta,\omega)$ denotes the total energy flux along the orientation ϑ of the Bloch wavenumber k, $\mathscr{K}(\vartheta,\omega)$ indicates the total kinetic energy while $\mathscr{W}(\vartheta,\omega)$ and $\mathscr{W}_{\sigma_0}(\vartheta,\omega)$ represent the total stored elastic energy related to the harmonic motion and prestress, respectively. The time-averaged expressions for these quantities are given by

$$\langle\mathscr{I}(\vartheta,\omega)\rangle = \frac{\omega}{2}\mathrm{Im}\left\{\int_\Omega\left[\left(\mathscr{D}_{\mathbf{u}}\tilde{\boldsymbol{\sigma}}(\mathbf{x},\vartheta,\omega)\tilde{\mathbf{u}}^*(\mathbf{x},\vartheta,\omega)\right)\cdot\Phi(\vartheta)\right]\mathrm{d}\Omega\right\}, \tag{19}$$

$$\langle\mathscr{K}(\vartheta,\omega)\rangle = \frac{\omega^2}{4}\mathrm{Re}\left\{\int_\Omega \tilde{\mathbf{u}}^*(\mathbf{x},\vartheta,\omega)\cdot\rho(\mathbf{x})\tilde{\mathbf{u}}(\mathbf{x},\vartheta,\omega)\mathrm{d}\Omega\right\}, \tag{20}$$

$$\langle \mathscr{W}(\vartheta,\omega)\rangle = \frac{1}{4}\mathrm{Re}\left\{\int_\Omega \left[\tilde{\mathbf{e}}^*_{\mathbf{k}}(\mathbf{x},\vartheta,\omega):\mathbf{D}(\mathbf{x}):\tilde{\mathbf{e}}_{\mathbf{k}}(\mathbf{x},\vartheta,\omega)\right]\mathrm{d}\Omega\right\}, \tag{21}$$

$$\langle \mathscr{W}_{\sigma_0}(\vartheta,\omega)\rangle = \frac{1}{4}\mathrm{Re}\left\{\int_\Omega \left[\left(\left(\nabla_{\mathbf{k}}\tilde{\mathbf{u}}(\mathbf{x},\vartheta,\omega)\right)^{\mathrm{T}}\nabla_{\mathbf{k}}\tilde{\mathbf{u}}(\mathbf{x},\vartheta,\omega)\right)^*:\boldsymbol{\sigma}_0(\mathbf{x})\right]\mathrm{d}\Omega\right\}. \tag{22}$$

Equation (18) can be evaluated at any given solution $k_m(\vartheta,\omega)$ by means of a Gauss quadrature scheme over the finite element mesh of the unit cell in the configuration C, in which the displacement, strain and stress fields can be post-processed from $\mathbf{Q}_m(\vartheta,\omega)$ using nodal interpolations.

4. NUMERICAL APPLICATIONS: EPOXY PLATE WITH CYLINDRICAL STEEL INCLUSIONS

The numerical method presented in the previous section is here applied to study a PC plate made of steel cylinders embedded in an epoxy matrix. In the undeformed configuration, the plate is 2.5 mm thick, while the cylindrical inclusions have a radius of 3.0 mm and are arranged in a square lattice of 10.0 mm side length, as shown in **Figure 2A**. The material properties for the steel and the epoxy are reported in **Table 1**.

To study how an initial state of stress affects the passbands and bandgaps of the PC plate, two different deformed configuration are considered. In the first configuration, the plate is subjected to a state of compressive stress representative of a normal displacement $\mathbf{u}_0(\mathbf{x}_0)\cdot\mathbf{n}_0(\mathbf{x}_0) = -0.025$ mm applied at each point $\mathbf{x}_0$ belonging to a lateral face of the unit cell. In the second case, a generic tensile state is applied by assuming a normal displacement $\mathbf{u}_0(\mathbf{x}_0)\cdot\mathbf{n}_0(\mathbf{x}_0) = 0.025$ mm for each point $\mathbf{x}_0$ belonging to a lateral face of the unit cell. **Figures 2B,C** report the von Mises stress consequent to the compression and tension prestress condition, respectively. It is worth noticing that the maximum magnitude of the applied prestretch has been limited to the typical strength at yield of both epoxy and steel in order to ensure the elastic behavior of the materials. This choice enables a full reversibility of the undeformed configuration, and thus of the dispersive behavior of the PC plate, once the load is removed, which is of more practical interest with respect to the case of a permanently induced deformation.

The band diagrams in terms of wavenumber k and energy velocity c_e versus frequency are shown in **Figure 3**. In these diagrams, the blue and red dots denote the dispersion curves relative to the unit cell subjected to the compressive stress and tensile stress shown in **Figures 2B**,**C**, respectively. It should be noted that, since the deformation due to prestress applied to each face of the cell is isotropic in the xy-plane in both cases, the deformation gradient $\mathbf{F}$ and its affine component $\mathbf{F}_L$ are diagonal and, as a consequence, the orientation of the reciprocal lattice vectors $\mathbf{g}_j$ in the deformed configurations does not change with respect to that in the deformed configuration. This implies that the orientation angle θ of the Bloch wavevector also remains unchanged between the undeformed and deformed configurations. The results presented in **Figure 3** have been obtained for an angle $\theta = 0$ measured with respect to $\mathbf{g}_{01}$ and $\mathbf{g}_1$. In classical Bloch analysis, this angle corresponds to the $\Gamma - X$ direction of the irreducible Brillouin zone.

From the dispersion analysis of the undeformed unit cell, it can be found that, at frequencies below 110 kHz, only one bandgap is present along the direction $\vartheta = 0$, which is located in the [68.3–88.6] kHz frequency range (see **Figure A1** in Appendix B). This result, which has not been reported in the **Figure 3** for the sake of clarity, can be readily obtained by carrying out the analysis of sections 2.3 and 3 on the undeformed geometry and by setting $\boldsymbol{\sigma}_0 = \mathbf{0}$ in Equation (15). However, when the cell is subjected to a compressive stress as shown in **Figure 2B**, the bandgap experiences a shift towards higher frequencies, being it located, in this case, in the [70.7 − 87.3] kHz frequency range. On the other hand, when the cell is subjected to traction, the lower bound of the bandgap is observed at 68.3 kHz while its upper bound at 84.3 kHz, which corresponds to a frequency downshift of approximately 3.5% of the bandgap with respect to the case of the PC plate under compression. These results suggest that, even in the elastic regime, a deformation due to prestress can lead to significant changes in the passband and bandgap behavior.

Furthermore, looking at the behavior of the energy velocity for the two deformed configurations, it is possible to infer that, similarly to the case of homogeneous plates (Pau and Lanza di Scalea, 2015), a generic state of compression leads to an increase of the energy velocity, whereas a state of traction leads, in general, to its decrease. This situation can be readily deduced from the inspection of the energy velocity band diagrams in **Figure 3**, from which it can be noted that the largest variations take place in proximity of the cutoff frequencies. Moreover, in the case of prestressed homogeneous plates (Dubuc et al., 2017), characteristic spikes in the energy velocity dispersion curves appear due to mode coupling. This behavior can also be observed for the third fundamental mode at around 36 kHz when the PC plate is subjected to a compression.

Finally, in the case of the PC plate under compression, it is possible to observe the presence of a cutoff wavenumber for the first fundamental mode at about 108 rad/m and null frequency. This value can be derived by solving the eigenvalue problem reported in Equation (10) in $k(\vartheta)$ by imposing $\omega = 0$. In this case, the eigenvalue problem corresponds to that of the buckling load and, consequently, the lowest eigenvalue (the cutoff wavenumber) corresponds to a bifurcation point that indicates the onset of buckling for the infinite PC plate. It should be noted that the specific value of the cutoff wavenumber depends on the magnitude and distribution of the compressive stress in the PC.

5. CONCLUSIONS

An Updated Lagrangian computational scheme has been presented for the calculation of the band diagrams of phononic crystal plates subjected to a generic state of prestress. The scheme involves the solution of a geometrically nonlinear static problem for a representative unit cell and the application of the Floquet-Bloch theorem to the linearized equations of acousto-elasticity on the deformed configuration of the unit cell undergoing the static load. For the case of an epoxy plate with cylindrical steel

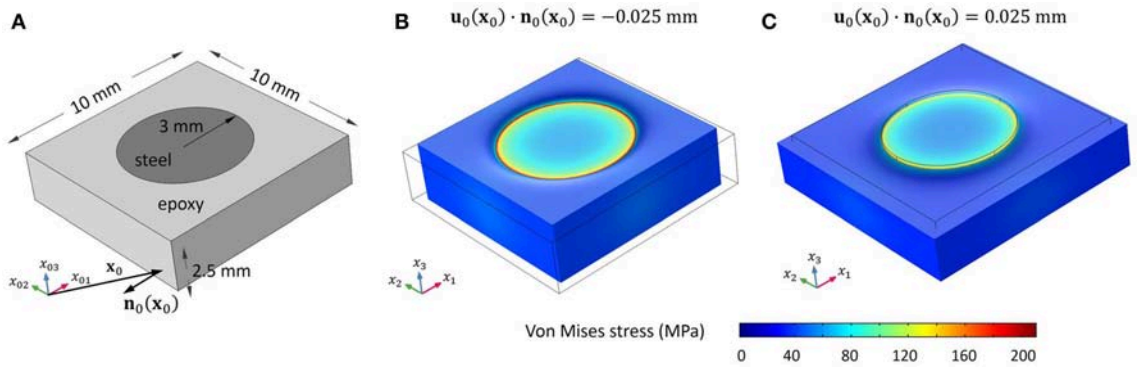

FIGURE 2 | Unit cell of steel cylinders embedded in an epoxy matrix: undeformed geometry **(A)** and deformed geometry corresponding to isotropic traction **(B)** and compression **(C)**. The deformation scale is amplified of 20 times.

TABLE 1 | Material constants for the steel and the epoxy.

	ρ_0 [kg/m^3]	λ [Gpa]	μ [Gpa]	l [Gpa]	m [Gpa]	n [Gpa]
Steel, Zhu et al., 2014	7,700	153.66	79.16	−248	−623	−714
Epoxy, Cattani and Rushchitsky, 2007	1,540	2.59	1.34	−18.94	−13.36	−9.81

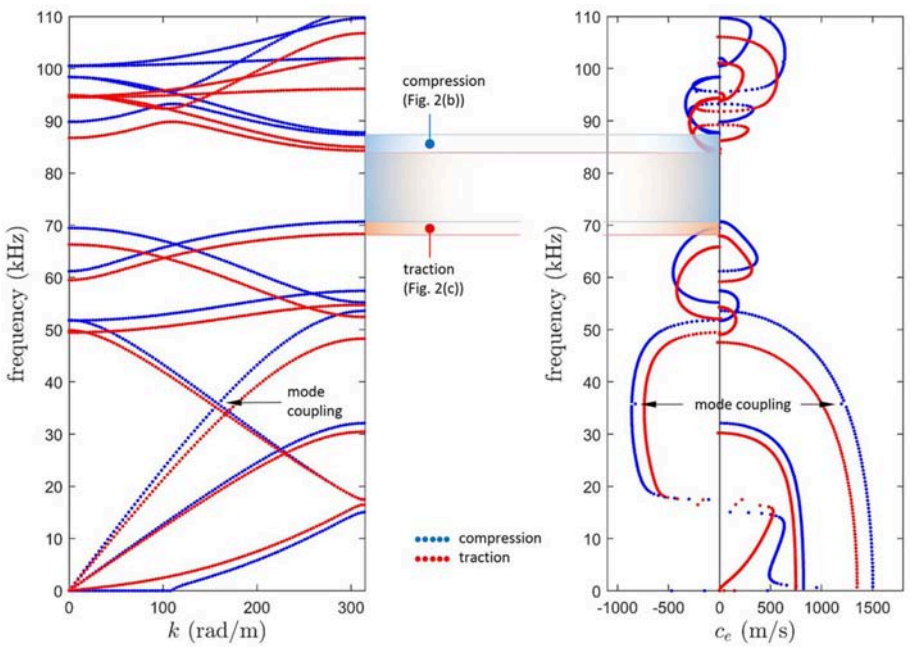

FIGURE 3 | Band diagrams of the wavenumber k **(Left)** and energy velocity c_e **(Right)** versus frequency for the PC plate under isotropic compression and isotropic traction reported in **Figures 2B,C**, respectively.

inclusions, it has been demonstrated that the existence of a prestress state of compression or tension can lead to significant changes in the passbands and bandgaps of a phononic crystal plate, even in the case of prestress inducing full reversible deformation state, which is of more practical interest with respect to the case of a permanently induced deformation. It has been observed that when the cell is subjected to a compressive stress, the bandgap experiences a shift toward higher frequencies, whereas when the cell is subjected to traction, we observe a frequency downshift of approximately the 3.5% of the bandgap with respect to the case of the phononic plate under compression. Similarly to the case of homogeneous plates, a generic state of compression leads to an increase of the energy velocity, whereas a state of traction tends to lower its value. The largest variations

have been observed in proximity of the cutoff frequencies. Characteristic spikes in the energy velocity dispersion curves appear due to mode coupling for the third fundamental mode at around 36 kHz when the phononic plate is subjected to a compression.

The results presented herein provide insights in the behavior of phononic crystal plates with tunable dispersive properties, and suggest new leverages for wave manipulation valuable in many application fields such as wave filters, waveguiding and beam splitting, sensing devices, and vibration shielding.

AUTHOR CONTRIBUTIONS

MMa and MMi conceived the idea and wrote the first draft of the paper. MMa performed numerical calculations. All the authors discussed the manuscript.

ACKNOWLEDGMENTS

MMi has received funding from the European Union's Horizon 2020 research and innovation programme under the Marie Skłodowska-Curie grant agreement N. 754364.

REFERENCES

Airoldi, L., and Ruzzene, M. (2011). Design of tunable acoustic metamaterials through periodic arrays of resonant shunted piezos. *New J. Phys.* 13:113010. doi: 10.1088/1367-2630/13/11/113010

Bergamini, A., Delpero, T., De Simoni, L., Di Lillo, L., Ruzzene, M., and Ermanni, P. (2014). Phononic crystal with adaptive connectivity. *Adv. Mater.* 26, 1343–1347. doi: 10.1002/adma.201305280

Bigoni, D., Gei, M., and Movchan, A. (2008). Dynamics of a prestressed stiff layer on an elastic half space: filtering and band gap characteristics of periodic structural models derived from long-wave asymptotics. *J. Mech. Phys. Solids* 56, 2494–2520. doi: 10.1016/j.jmps.2008.02.007

Bonet, J., and Wood, R. D. (2008). *Nonlinear Continuum Mechanics for Finite Element Analysis*. New York, NY: Cambridge University Press.

Brillouin, L. (1953). *Wave Propagation in Periodic Structures: Electric Filters and Crystal Lattices, 2nd Edn*. New York, NY: Dover Publications (1953).

Casadei, F., Ruzzene, M., Dozio, L., and Cunefare, K. A. (2010). Broadband vibration control through periodic arrays of resonant shunts: experimental investigation on plates. *Smart Mater. Struct.* 19:015002. doi: 10.1088/0964-1726/19/1/015002

Cattani, C., and Rushchitsky, J. (2007). *Wavelet and Wave Analysis as Applied to Materials with Micro or Nanostructure*. Singapore: World Scientific.

Cheng, Y., Liu, X. J., and Wu, D. J. (2011). Temperature effects on the band gaps of lamb waves in a one-dimensional phononic-crystal plate (l). *J. Acoust. Soc. Am.* 129, 1157–1160. doi: 10.1121/1.3543970

Collet, M., Ouisse, M., Ruzzene, M., and Ichchou, M. (2011). Floquet-bloch decomposition for the computation of dispersion of two-dimensional periodic, damped mechanical systems. *Int. J. Solids Struct.* 48, 2837–2848. doi: 10.1016/j.ijsolstr.2011.06.002

Colombi, A., Colquitt, D., Roux, P., Guenneau, S., and Craster, R. V. (2016). A seismic metamaterial: the resonant metawedge. *Sci. Rep.* 6:27717. doi: 10.1038/srep27717

Comsol (2017). *Comsol Multiphysics 5.3*. Available online at: https://www.comsol.com/

Craster, R. V., and Guenneau, S. (2012). *Acoustic Metamaterials: Negative Refraction, Imaging, Lensing and Cloaking*. Springer Series in Materials Science. London: Springer (2012).

Deymier, P. A. (2013). *Acoustic Metamaterials and Phononic Crystals, Springer Series in Solid-State Sciences*. Berlin; Heidelberg: Springer (2013).

Dubuc, B., Ebrahimkhanlou, A., and Salamone, S. (2017). The effect of applied stress on the phase and group velocity of guided waves in anisotropic plates. *J. Acoust. Soc. Am.* 142, 3553–3563. doi: 10.1121/1.5016969

Dubuc, B., Ebrahimkhanlou, A., and Salamone, S. (2018). Higher order longitudinal guided wave modes in axially stressed seven-wire strands. *Ultrasonics* 84, 382–391. doi: 10.1016/j.ultras.2017.12.003

Galich, P., Slesarenko, V., and Rudykh, S. (2016). Elastic wave propagation in soft microstructured composites undergoing finite deformations. *PAMM* 16, 627–628. doi: 10.1002/pamm.201610302

Gei, M. (2010). Wave propagation in quasiperiodic structures: stop/pass band distribution and prestress effects. *Int. J. Solids Struct.* 47, 3067–3075. doi: 10.1016/j.ijsolstr.2010.07.008

Gei, M., Movchan, A., and Bigoni, D. (2009). Band-gap shift and defect-induced annihilation in prestressed elastic structures. *J. Appl. Phys.* 105:063507. doi: 10.1063/1.3093694

Guo, X., and Wei, P. (2016). Dispersion relations of elastic waves in one-dimensional piezoelectric/piezomagnetic phononic crystal with initial stresses. *Ultrasonics* 66, 72–85. doi: 10.1016/j.ultras.2015.11.008

Jim, K. L., Leung, C. W., Lau, S. T., Choy, S. H., and Chan, H. L. W. (2009). Thermal tuning of phononic bandstructure in ferroelectric ceramic/epoxy phononic crystal. *Appl. Phys. Lett.* 94:193501. doi: 10.1063/1.3136752

Kherraz, N., Haumesser, L., Levassort, F., Benard, P., and Morvan, B. (2016). Controlling bragg gaps induced by electric boundary conditions in phononic piezoelectric plates. *Appl. Phys. Lett.* 108:093503. doi: 10.1063/1.4943138

Kushwaha, M. S., and Halevi, P. (1994). Band gap engineering in periodic elastic composites. *Appl. Phys. Lett.* 64, 1085–1087. doi: 10.1063/1.110940

Li, J., Wu, F., Zhong, H., Yao, Y., and Zhang, X. (2015). Acoustic beam splitting in two-dimensional phononic crystals using self-collimation effect. *J. Appl. Phys.* 118:144903. doi: 10.1063/1.4932138

Liu, Z., Zhang, X., Mao, Y., Zhu, Y. Y., Yang, Z., Chan, C. T., et al. (2000). Locally resonant sonic materials. *Science* 289, 1734–1736. doi: 10.1126/science.289.5485.1734

Mártinez-Sala, R., Sancho, J., Sánchez, J. V., Gomez, V., Llinares, J., and Meseguer, F. (1995). Sound attenuation by sculpture. *Nature* 378:241. doi: 10.1038/378241a0

Matar, O. B., Robillard, J. F., Vasseur, J. O., Hladky-Hennion, A.-C., Deymier, P. A., Pernod, P., et al. (2012). Band gap tunability of magneto-elastic phononic crystal. *J. Appl. Phys.* 111:054901. doi: 10.1063/1.3687928

Mazzotti, M., Marzani, A., Bartoli, I., and Viola, E. (2012). Guided waves dispersion analysis for prestressed viscoelastic waveguides by means of the safe method. *Int. J. Solids Struct.* 49, 2359–2372. doi: 10.1016/j.ijsolstr.2012.04.041

Mazzotti, M., Miniaci, M., and Bartoli, I. (2017). Band structure analysis of leaky bloch waves in 2d phononic crystal plates. *Ultrasonics* 74, 140–143. doi: 10.1016/j.ultras.2016.10.006

Miniaci, M., Gliozzi, A. S., Morvan, B., Krushynska, A., Bosia, F., Scalerandi, M., et al. (2017). Proof of concept for an ultrasensitive technique to detect and localize sources of elastic nonlinearity using phononic crystals. *Phys. Rev. Lett.* 118:214301. doi: 10.1103/PhysRevLett.118.214301

Miniaci, M., Krushynska, A., Bosia, F., and Pugno, N. M. (2016). Large scale mechanical metamaterials as seismic shields. *N. J. Phys.* 18:083041. doi: 10.1088/1367-2630/18/8/083041

Miniaci, M., Mazzotti, M., Radzieski, M., Kherraz, N., Kudela, P., Ostachowicz, W., et al. (2018a). Experimental observation of a large low-frequency band gap in a polymer waveguide. *Front. Mater.* 5:8. doi: 10.3389/fmats.2018.00008

Miniaci, M., Pal, R. K., Manna, R., and Ruzzene, M. (2019). Valley based splitting of topologically protected helical waves in elastic plates. *arXiv 1811.04814*.

Miniaci, M., Pal, R. K., Morvan, B., and Ruzzene, M. (2018b). Experimental observation of topologically protected helical edge modes in patterned elastic plates. *Phys. Rev. X* 8:031074. doi: 10.1103/PhysRevX.8.031074

Morvan, B., Tinel, A., Hladky-Hennion, A.-C., Vasseur, J., and Dubus, B. (2010). Experimental demonstration of the negative refraction of a transverse elastic

wave in a two-dimensional solid phononic crystal. Appl. Phys. Lett. 96:101905. doi: 10.1063/1.3302456

Mousavi, S. H., Khanikaev, A. B., and Wang, Z. (2015). Topologically protected elastic waves in phononic metamaterials. *Nat. Comm.* 6:8682. doi: 10.1038/ncomms9682

Murnaghan, F. D. (1937). Finite deformations of an elastic solid. *Amer. J. Math.* 59, 235–260. doi: 10.2307/2371405

Norris, A. N., and Parnell, W. J. (2012). Hyperelastic cloaking theory: transformation elasticity with pre-stressed solids. *Proc. R. Soc. Lond. A* 468, 2881–2903. doi: 10.1098/rspa.2012.0123

Pal, R. K., Schaeffer, M., and Ruzzene, M. (2016). Helical edge states and topological phase transitions in phononic systems using bi-layered lattices. *J. Appl. Phys.* 119:084305. doi: 10.1063/1.4942357

Pau, A., and Lanza di Scalea, F. (2015). Nonlinear guided wave propagation in prestressed plates. *J. Acoust. Soc. Am.* 137, 1529–1540. doi: 10.1121/1.4908237

Pennec, Y., Vasseur, J. O., Djafari-Rouhani, B., Dobrzyński, L., Deymier, P. A. (2010). Two-dimensional phononic crystals: examples and applications. *Surf. Sci. Rep.* 65, 229–291. doi: 10.1016/j.surfrep.2010.08.002

Robillard, J.-F., Matar, O. B., Vasseur, J. O., Deymier, P. A., Stippinger, M., Hladky-Hennion, A.-C., et al. (2009). Tunable magnetoelastic phononic crystals. *Appl. Phys. Lett.* 95:124104. doi: 10.1063/1.3236537

Sainidou, R., Stefanou, N., Psarobas, I., and Modinos, A. (2005). A layer-multiple-scattering method for phononic crystals and heterostructures of such. *Comput. Phys. Commun.* 166, 197–240. doi: 10.1016/j.cpc.2004.11.004

Shim, J., Wang, P., and Bertoldi, K. (2015). Harnessing instability-induced pattern transformation to design tunable phononic crystals. *Int. J. Solids Struct.* 58, 52–61. doi: 10.1016/j.ijsolstr.2014.12.018

Su, X., and Norris, A. N. (2016). Focusing, refraction, and asymmetric transmission of elastic waves in solid metamaterials with aligned parallel gaps. *J. Acoust. Soc. Am.* 139, 3386–3394. doi: 10.1121/1.4950770

Sukhovich, A., Merheb, B., Muralidharan, K., Vasseur, J. O., Pennec, Y., Deymier, P. A., et al. (2009). Experimental and theoretical evidence for subwavelength imaging in phononic crystals. *Phys. Rev. Lett.* 102:154301. doi: 10.1103/PhysRevLett.102.154301

Süsstrunk, R., Huber, S. D. (2015). Observation of phononic helical edge states in a mechanical topological insulator. *Science* 349, 47–50. doi: 10.1126/science.aab0239

Trainiti, G., Rimoli, J. J., and Ruzzene, M. (2015). Wave propagation in periodically undulated beams and plates. *Int. J. Solids Struct.* 75–76, 260–276. doi: 10.1016/j.ijsolstr.2015.08.019

Walker, E., Reyes, D., Rojas, M. M., Krokhin, A., Wang, Z., and Neogi, A. (2014). Tunable ultrasonic phononic crystal controlled by infrared radiation. *Appl. Phys. Lett.* 105:143503. doi: 10.1063/1.4894489

Walker, E. L., Wang, Z., and Neogi, A. (2017). Radio-frequency actuated polymer-based phononic meta-materials for control of ultrasonic waves. *NPG Asia Mater.* 9:e350. doi: 10.1038/am.2016.209

Wang, L., and Bertoldi, K. (2012). Mechanically tunable phononic band gaps in three-dimensional periodic elastomeric structures. *Int. J. Solids Struct.* 49, 2881–2885. doi: 10.1016/j.ijsolstr.2012.05.008

Wu, Y., Yu, K., Yang, L., Zhao, R., Shi, X., and Tian, K. (2018). Effect of thermal stresses on frequency band structures of elastic metamaterial plates. *J. Sound Vibrat.* 413, 101–119. doi: 10.1016/j.jsv.2017.10.014

Zhang, P., and Parnell, W. J. (2017). Soft phononic crystals with deformation-independent band gaps. *Proc. R. Soc. A Math. Phys. Eng. Sci.* 473:20160865. doi: 10.1098/rspa.2016.0865

Zhang, S., Shi, Y., and Gao, Y. (2017). Tunability of band structures in a two-dimensional magnetostrictive phononic crystal plate with stress and magnetic loadings. *Phys. Lett. A* 381, 1055–1066. doi: 10.1016/j.physleta.2017.01.044

Zhu, H., Semperlotti, F. (2016). Anomalous refraction of acoustic guided waves in solids with geometrically tapered metasurfaces. *Phys. Rev. Lett.* 117:034302. doi: 10.1103/PhysRevLett.117.034302

Zhu, Q., Burtin, C., and Binetruy, C. (2014). Acoustoelastic effect in polyamide 6: linear and nonlinear behaviour. *Polym. Testing* 40, 178–186. doi: 10.1016/j.polymertesting.2014.09.007

Zhu, R., Liu, X. N., Hu, G. K., Sun, C. T., and Huang, G. L. (2014). Negative refraction of elastic waves at the deep-subwavelength scale in a single-phase metamaterial. *Nat. Commun.* 5, 241–241. doi: 10.1038/ncomms6510

Conflict of Interest Statement: The authors declare that the research was conducted in the absence of any commercial or financial relationships that could be construed as a potential conflict of interest.

The handling editor declared a past co-authorship with MMa.

APPENDIX A

The operators $\mathbf{L}_i$ and $\mathbf{L}_{0i}$ are expressed as

$$\mathbf{L}_1 = \begin{bmatrix} 1&0&0\\0&0&0\\0&0&0\\0&0&0\\0&0&1\\0&1&0 \end{bmatrix}, \quad \mathbf{L}_2 = \begin{bmatrix} 0&0&0\\0&1&0\\0&0&0\\0&0&1\\0&0&0\\1&0&0 \end{bmatrix}, \quad \mathbf{L}_3 = \begin{bmatrix} 0&0&0\\0&0&0\\0&0&1\\0&1&0\\1&0&0\\0&0&0 \end{bmatrix}, \tag{23}$$

$$\mathbf{L}_{01} = \begin{bmatrix} 1&0&0\\0&0&0\\0&0&0\\0&1&0\\0&0&0\\0&0&0\\0&0&1\\0&0&0\\0&0&0 \end{bmatrix}, \quad \mathbf{L}_{02} = \begin{bmatrix} 0&0&0\\1&0&0\\0&0&0\\0&0&0\\0&1&0\\0&0&0\\0&0&0\\0&0&1\\0&0&0 \end{bmatrix}, \quad \mathbf{L}_{03} = \begin{bmatrix} 0&0&0\\0&0&0\\1&0&0\\0&0&0\\0&0&0\\0&1&0\\0&0&0\\0&0&0\\0&0&1 \end{bmatrix}. \tag{24}$$

APPENDIX B

The band diagram in terms of wavenumber k and energy velocity c_e for the undeformed unit cell of **Figure 2** at $\vartheta = 0$ is reported in **Figure A1**.

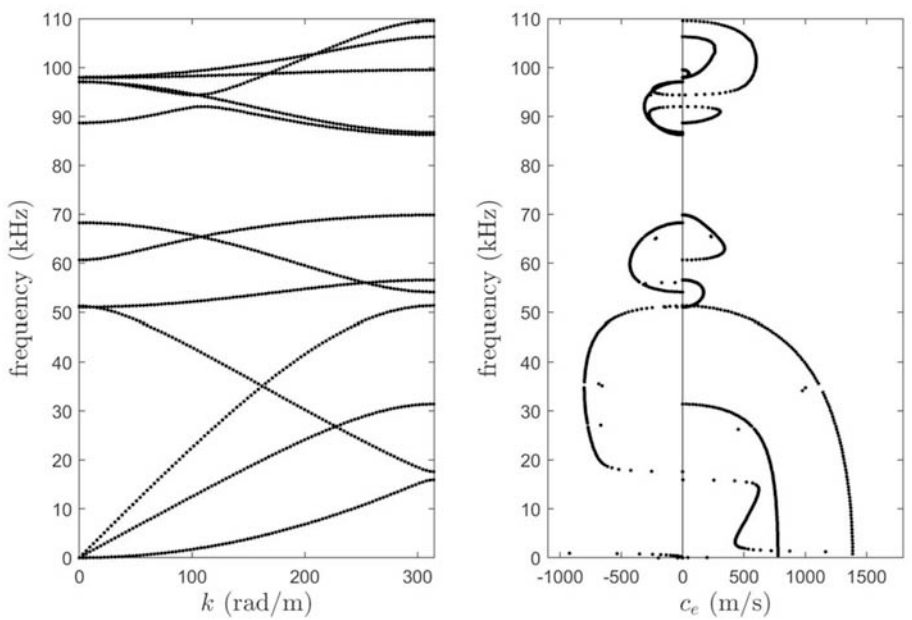

Figure A 1 | Band diagrams of the wavenumber k **(Left)** and energy velocity c_e **(Right)** vs. frequency for the PC plate in the undeformed configuration reported in **Figure 2A**.

frontiers in Materials

ORIGINAL RESEARCH
published: 31 July 2019
doi: 10.3389/fmats.2019.00169

Compressive Response of Non-slender Octet Carbon Microlattices

Akira Kudo[1], *Diego Misseroni*[2]*, *Yuchen Wei*[1] *and Federico Bosi*[3]

[1] Division of Engineering and Applied Science, California Institute of Technology, Pasadena, CA, United States, [2] Department of Civil, Environmental and Mechanical Engineering, University of Trento, Trento, Italy, [3] Department of Mechanical Engineering, University College London, London, United Kingdom

Lattices are periodic three-dimensional architected solids designed at the micro and nano-scale to achieve unique properties not attainable by their constituent materials. The design of lightweight and strong structured solids by additive manufacturing requires the use of high-strength constituent materials and non-slender geometries to prevent strut elastic instabilities. Low slenderness carbon octet microlattices are obtained through pyrolysis of polymeric architectures manufactured with stereolithography technique. Their compressive behavior is numerically and experimentally investigated when the relative density $\bar{\rho}$ ranges between 10 and 50%, with specific stiffness and strength approaching the limit of existing micro and nanoarchitectures. It is shown that additive manufacturing can introduce imperfections such as increased nodal volume, non-cubic unit cell, and orientation-dependent beam slenderness, all of which deeply affect the mechanical response of the lattice material. An accurate numerical modeling of non-slender octet lattices with significant nodal volumes is demonstrated to overcome the limitations of classical analytical methods based on beam theory for the prediction of the lattice stiffness, strength and scaling laws. The presented numerical results and experimental methods provide new insights for the design of structural carbon architected materials toward ultra-strong and lightweight solids.

Keywords: architected materials, additive manufacturing, structural metamaterials, pyrolyzed lattices, mechanics

OPEN ACCESS

Edited by:
Seunghwa Ryu,
Korea Advanced Institute of Science and Technology (KAIST), South Korea

Reviewed by:
Dongchan Jang,
Korea Advanced Institute of Science and Technology (KAIST), South Korea
Anastasiia O. Krushynska,
University of Groningen, Netherlands

***Correspondence:**
Diego Misseroni
diego.misseroni@unitn.it

Specialty section:
This article was submitted to Mechanics of Materials, a section of the journal Frontiers in Materials

Received: *14 January 2019*
Accepted: *01 July 2019*
Published: *31 July 2019*

Citation:
Kudo A, Misseroni D, Wei Y and Bosi F (2019) Compressive Response of Non-slender Octet Carbon Microlattices. Front. Mater. 6:169. doi: 10.3389/fmats.2019.00169

1. INTRODUCTION

Additive manufacturing has become one of the most promising technique to fabricate advanced materials and microstructures that exhibit properties unattained by homogeneous solids or conventionally manufactured architectures. The available 3D printing techniques have recently grown and comprise fused deposition modeling (FDM), direct ink writing (DIW), selective laser sintering (SLS), stereolithography (SLA), etc. Similarly, the selection of materials compatible with these processes has expanded and include thermoelastic polymers (Carneiro et al., 2015), transparent glasses (Nguyen et al., 2017), oxide ceramics (Wilkes et al., 2013), metallic alloys (Schwab et al., 2016), and composites (Spierings et al., 2015; Ni et al., 2018; Quintanilla et al., 2018). The precise micro- and nano-scale topology control achievable through additive manufacturing has allowed the development of unique functionalities to catalysis (Essa et al., 2017), batteries (Xia et al., 2016; Li et al., 2017), scaffolds (Maggi et al., 2017), biomedical implants (Murr et al., 2010), and

metamaterials (Hengsbach and Lantada, 2014; Misseroni et al., 2016; Bertoldi et al., 2017; Bilal et al., 2017). In particular, the field of architected material has benefited from the advancement of small-scale manufacturing that enables the design of multistable solids for energy storage (Shan et al., 2015), the evolution of phononic bandgap behavior (Sugino et al., 2015; Amendola et al., 2018) and the exploration of previously inaccessible mechanical property combinations (Bauer et al., 2016). Examples include structural metamaterials designed to achieve extremely lightweight and strong solids through a hierarchical design (Meza et al., 2015) or novel highly deformable and recoverable nanolattices made up of brittle materials (Meza et al., 2014).

Structured solids can be classified as rigid or non-rigid architectures depending on their nodal connectivity, states of self stress, and mechanisms (Pellegrino and Calladine, 1986). The former includes octet lattices and shows a stretching dominated behavior, while the latter mostly presents a bending dominated response as demonstrated by pyramidal lattices. The response of architected materials has been extensively analyzed through the investigation of their constituent unit cells using beam theory to obtain the lattice effective stiffness and strength scaling laws (Gibson and Ashby, 1997; Deshpande et al., 2001). These analytical tools have been proven to well predict the mechanical response of several lattices when the relative density $\bar{\rho}$ is lower than 0.1 and the strut slenderness ratio r/l does not exceed 0.06 (Meza et al., 2017). However, some computational and experimental studies (Schaedler et al., 2011; Meza et al., 2015; Bauer et al., 2016) have recently reported deviations from the classical scaling laws due to non-slender struts and the influence of the node geometry (Portela et al., 2018), thus proposing different scaling laws. The difficult micro- and nano-scale fabrication of slender structured solids that obey to classical scaling laws motivates the investigation of non-slender architectures with pronounced nodal volume caused by an imperfect 3D printing. Therefore, the study of their mechanical properties is fundamental for the design of stronger lattices that do not suffer from strut elastic instabilities.

One of the most promising materials to fabricate extremely lightweight and resistant architected solids is carbon, which has recently become compatible with additive manufacturing processes. Direct ink writing (DIW) with printable inks that contain graphene, carbon nanotube, and graphene oxide (Fu et al., 2017) has been employed for the realization of flexible, conductive, and chemically stable prototypes (Sun et al., 2013; Zhu et al., 2015; Yao et al., 2016; Zhang et al., 2016), while 3D-printed carbon fiber reinforced composites have been manufactured by means of FDM (Lewicki et al., 2017; Anwer and Naguib, 2018). Carbon nano- and micro-lattices are another form of 3D printed carbon which have demonstrated elevated structural performances. Architected carbon materials are obtained by pyrolyzing 3D-printed precursor, especially polymer lattices prepared by photocuring techniques. Carbon nanolattices fabricated through two-photon lithography have shown a strength comparable with the theoretical strength of flaw insensitive glassy carbon (Bauer et al., 2016). This printing technique solidifies the polymeric precursor solution point-by-point at a submicron scale in a prolonged process, thus preventing the production of micro- and nano-architectures at a large scale. Carbon microlattices produced by self-propagating photopolymer waveguides (Jacobsen et al., 2011) and stereolithography (SLA) (Chen et al., 2017) overcome the scalability difficulties toward faster manufacturing of larger scale lattices. However, their mechanical performances are still limited, and the development of enhanced architected solids demands further understanding of the influence of the manufacturing-induced imperfection on the mechanics of 3D-printed carbon lattices.

The aim of this work is to manufacture stiff and strong non-slender octet carbon microlattices through digital light processing stereolithography (DLP-SLA), and to analytically, computationally, and experimentally investigate their compressive mechanical properties and scaling laws. We show that DLP-SLA 3D printing and pyrolysis techniques can affect the designed lattice architecture introducing undesired features as increased nodal volume, non-cubic unit cell and different strut slenderness depending on the beam orientation with respect to the printing direction. We investigate the influence of these factors on the compressive stiffness and strength of non-slender lattices with relative density $\bar{\rho}$ that ranges between 10 and 50%. We prove the inappropriateness of classical analytical tools based on beam theory and the derived expressions for non-slender architectures with negligible effective Poisson's ratio, due to the topological features that are not accounted for in these formulations. We develop computational models that faithfully predicts the experimental lattice response by reproducing the manufactured geometry and we demonstrate that an accurate numerical modeling of non-slender octet lattices with significant nodal volumes allows to identify the deviation from classical scaling laws and enables a proper design of advanced structural DLP-SLA 3D printed carbon architectures.

2. MATERIALS AND METHODS

2.1. Sample Fabrication

Three sets (A, B, and C) of carbon octet microlattices were manufactured by pyrolyzing polymeric lattices fabricated with a DLP-SLA Autodesk Ember 3D printer that employs a PR-48 transparent photoresist resin. The periodic polymeric 3D printed specimens consisted of a 10 × 3 × 6 (length × width × height) tassellation of 900 μm octet unit cell with three different strut radii of $r_A = 52.8$ μm, $r_B = 71.4$ μm, and $r_C = 90.0$ μm (**Figure 1**). The microlattices presented a theoretical relative density $\bar{\rho}_A = 0.16$, $\bar{\rho}_B = 0.27$, $\bar{\rho}_C = 0.40$, and a beam slenderness ratio of $(r/l)_A = 0.08$, $(r/l)_B = 0.11$, $(r/l)_C = 0.14$. The DLP-SLA layers were deposited along the height direction and the bottom-most anchoring layer was designed to be thicker in order to sustain the microlattice. Prior to pyrolysis, the anchoring layer of each microstructure was removed using a razor blade to prevent lattice distortion, thus resulting in a 10 × 3 × 5 tassellation. The polymeric lattices were inserted in a fused quartz tube set on a Lindberg tube furnace (model 54357) and pyrolyzed under vacuum. During pyrolysis, the furnace temperature was first raised to 300°C and held constant for 4 h, then increased to 400°C and maintained for 1 h, and finally elevated to 1,000°C

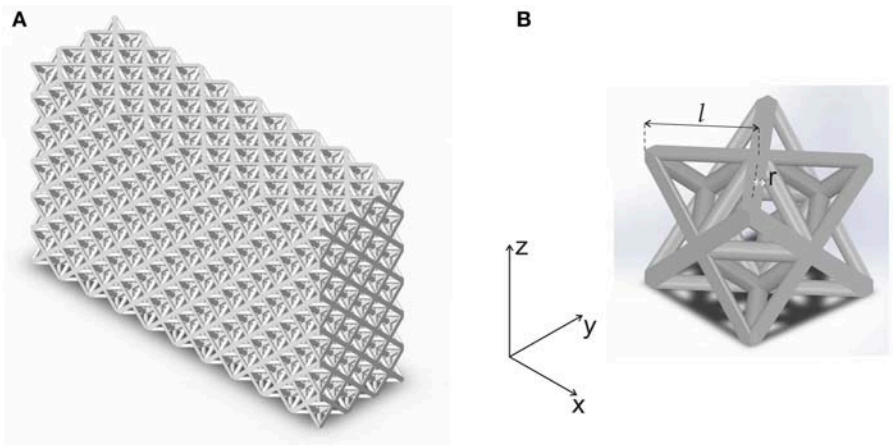

FIGURE 1 | (A) CAD of the microlattice constructed through a three-dimensional tasselation of octet unit cells. **(B)** A cubic octet unit cell with its geometric parameters *l* (strut length) and *r* (strut radius).

and kept constant for 4 h. This procedure, with all heating rates carried out at 10°C/min, led to fully dense microlattices without gasified components and preserved the 3D printed topology.

2.2. Microstructural Characterization

The polymeric and carbon microlattices obtained after 3D printing and pyrolysis were investigated using a Thermo-Fisher Versa 3D DualBeam Scanning Electron Microscopy (SEM). Specimen sizes, unit cell radii and strut diameters were measured to assess any imperfection and anisotropy introduced during fabrication. The compressive tests on the carbon microlattices were performed using an Instron 5569 electromechanical machine. The load P was applied by imposing a constant displacement rate of 2.5 μm/s on the 5 × 10 unit cells sample surface and was measured with an Instron 2525-804 load cell (R.C. 10 kN). The compressive displacement Δy was evaluated with an LE-01 (Electronic Instrument Research) laser extensometer interfaced with the electromechanical testing frame for data synchronization. Five samples for each set of octet density were characterized and tested along the y-direction. The nominal lattice stress σ was obtained dividing the applied load P by the specimen footprint area, whereas the nominal strain ϵ was calculated from the initial sample height H as $\epsilon = \Delta y/H$.

2.3. Finite Element Analysis

Full three-dimensional finite element analyses were performed in ABAQUS Standard 2018 in order to simulate the compressive behavior of the microlattices. Numerical simulations were carried out on representative octet unit cells loaded in the y-direction and constrained with boundary conditions that reproduce the response of the unit cell within the lattice. The three-dimensional unit cells were parametrically designed in SolidWorks to reproduce the measured geometrical parameters such as node and beam radii, unit cell height and width, and fillet junction radii between nodes and struts. In addition to the unit cells representative of the fabricated microlattices, other unit cells with different relative density were modeled to investigate the stiffness and strength scaling laws. The microlattices were discretized with linear elastic second-order tetrahedral elements (C3D10) with Young's modulus E = 25.38 GPa (Kudo et.al., in preparation) and Poisson coefficient ν = 0.21 (Price and Kaae, 1969). Compressive forces were applied at the top nodes of the unit cell, with F acting on the central node and $F/4$ on the lateral nodes shared with four adjacent unit cells. The effective lattice Young's modulus $E_y^* = E_x^*$ in the y-direction was calculated as the ratio between the average compressive stress on the unit cell $\sigma_y^{\text{avg}} = 2F/wh$ and the average compressive strain $\epsilon_y^{\text{avg}} = \delta_y/w$, where δ_y represents the displacement in the y-direction, w and h are the width and height of the unit cell (**Figure 2**). Similarly, the effective Young's modulus E_z^* in the z-direction was obtained as the ratio between the average compressive stress $\sigma_z^{\text{avg}} = 2F/w^2$ and the average compressive strain $\epsilon_z^{\text{avg}} = \delta_z/h$, where δ_z represents the displacement in the z-direction. Furthermore, a linear perturbation buckling analysis was conducted on each unit cell to assess the microlattices critical buckling strength.

3. RESULTS AND DISCUSSION

3.1. Manufacturing

The geometrical features of the three sets of non-slender 3D-printed polymeric microlattices were investigated by using the SEM. From the images in **Figure 3**, it was observed that the additive manufacturing technique introduced undesirable lattice imperfections not present in the original computer-aided design (CAD) input files, where the lattices were constituted of cubic octet unit cells with strut radius r and length l. In particular, the height h of the unit cell resulted smaller than the width w, leading to a non-cubic unit cell. Therefore, the length l_1 of the struts deposited along the width direction (x–y plane) was greater than the length l_2 of the inclined struts 3D-printed along the height direction (z-direction). Similarly, the in-plane strut radius r_1 resulted bigger than the out-of-plane beam radius r_2. Moreover,

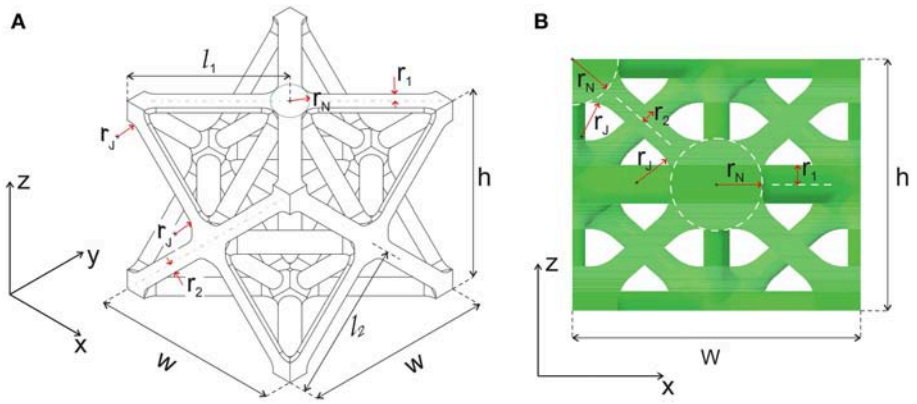

FIGURE 2 | CAD isometric **(A)** and lateral **(B)** views of a representative 3D printed and pyrolyzed non-slender octet unit cell as modeled for the finite element analysis. The x-y in-plane beams present radius r_1 and length l_1, while the out-of-plane struts have radius r_2 and length l_2. The struts junction is characterized by the node radius r_N and junction radius r_j.

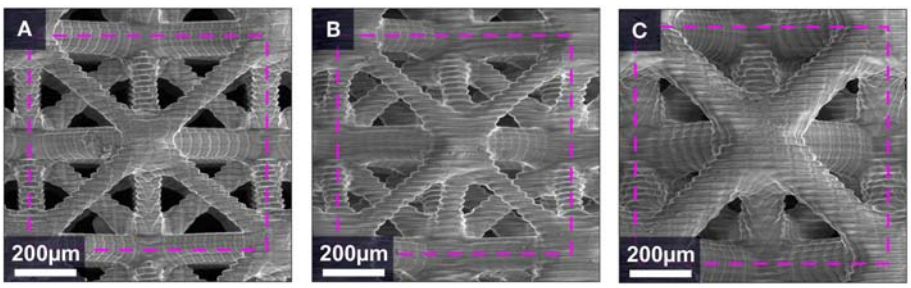

FIGURE 3 | SEM images of the DLP-SLA manufactured polymeric microlattices *A* **(A)**, *B* **(B)**, and *C* **(C)** observed from the x-z plane. The imperfections introduced by additive manufacturing, visible in all the samples, are orientation dependent strut slenderness, increased nodal volume, and corrugation on the beam surface.

the intersection of twelve struts in a single point produced quasi-spherical nodes with radius r_N and the microlattices presented unsought corrugated surfaces (**Figure 3**). The deviations from the originally designed lattices were caused by the DLP-SLA 3D printer, whose resolution was limited to 50 μm in the x-y plane and the layer thickness was 25 μm. For these reasons, stereolithography appears inadequate to precisely manufacture features as small as a few tens of microns, which would require other 3D printing techniques as two-photon lithography (Meza et al., 2014; Bauer et al., 2016). The average strut slenderness for the polymeric lattices was $\left(r_1/l_1\right)_A^{p,xy} = 0.10$, $\left(r_1/l_1\right)_B^{p,xy} = 0.12$, and $\left(r_1/l_1\right)_C^{p,xy} = 0.15$ for the struts deposited in x-y plane, and for the inclined struts printed along the z-direction $\left(r_2/l_2\right)_A^{p,z} = 0.07$, $\left(r_2/l_2\right)_B^{p,z} = 0.09$, and $\left(r_2/l_2\right)_C^{p,z} = 0.12$. By comparing the designed struts (from the CAD input files) and the beams of the manufactured lattices, we observed a decrease in the in-plane struts slenderness and an increase in the out-of-plane beam slenderness. This discrepancy is caused by the stereolithography 3D printing.

The polymeric lattices were subjected to pyrolysis that led to a $\sim$ 70% linear shrinkage and produced pyrolytic carbon microlattices (Chen et al., 2017) (**Figure 4**, left). The three sets of pyrolyzed lattices were examined with SEM and their averaged geometrical parameters were used to define the octet unit cell CAD geometry employed in the numerical simulations (**Table 1**). **Figure 4** shows progressive magnification images which testify that the features present in the original polymeric lattices were preserved throughout the heat treatment for all lattices. It was observed that the strut slenderness after pyrolysis slightly decreased with respect to the polymeric lattices values (maximum deviation was $\approx$ 10%), hence the heat treatment did not significantly modify the lattice geometry. The average ratio between the unit cell height and width was measured as $(h/w)_A = 0.87$ and $(h/w)_{B,C} = 0.97$, thus showing a quasi-cubic architecture for lattices *B* and *C*. The ratio between the out-of-plane and in-plane strut radii was $r_2/r_1 \simeq 0.8$ and the quasi-spherical nodes presented a radius $r_N \simeq 2r_1$. The highest magnification images report the lateral view of the octet unit cell and are paired with the CAD geometry, showing an excellent agreement between the manufactured and simulated unit cells (**Figure 4**, right). The only feature not reproduced in the CAD, and therefore not accounted for in the finite element analysis, was the strut corrugation.

3.2. Relative Density

The relative density of the polymeric lattices was measured before pyrolysis as $\bar{\rho}_A^p = 0.17$, $\bar{\rho}_B^p = 0.27$, and $\bar{\rho}_C^p = 0.39$, thus proving that 3D printing did not alter the desired relative density. After

TABLE 1 | SEM measured geometrical parameters of the octet unit cell for the manufactured carbon microlattices.

Unit cell	w [μm]	h [μm]	r_1 [μm]	r_2 [μm]	r_N [μm]	r_j [μm]	$\bar{\rho}$ [-]	$\bar{\rho}^{CAD}$ [-]	$\bar{\rho}^t$ [-]
A	230.35	200.78	15.02	11.33	32.00	26.27	0.16	0.17	0.16
B	241.68	233.72	18.38	15.15	40.53	30.79	0.23	0.23	0.23
C	251.02	244.61	24.60	19.88	46.19	33.14	0.34	0.32	0.32

The experimental relative density $\bar{\rho}$ is reported together with the relative density $\bar{\rho}^{CAD}$ obtained from the CAD and the relative density $\bar{\rho}^t$ calculated through the analytical expression (1).

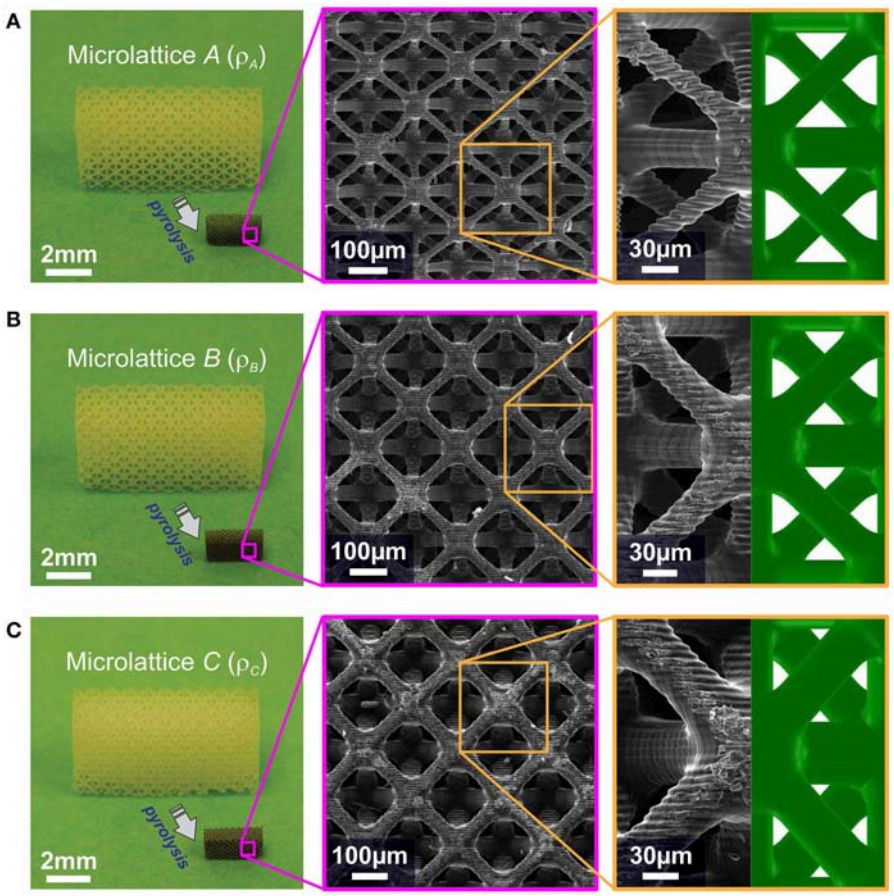

FIGURE 4 | Optical microscopy (left), SEM characterization (center), and CAD model (right) of the manufactured microlattices *A* **(A)**, *B* **(B)**, and *C* **(C)** before and after pyrolysis. Progressive magnification images show that pyrolysis preserved the features of the polymeric lattices. The comparison between the fabricated carbon unit cell and the CAD model employed for computational analysis highlights the accuracy of the reproduced architectures.

pyrolysis, the density ρ of the carbon microlattices was measured as $\rho_A = 0.29 \pm 0.02$ g/cm^3, $\rho_B = 0.43 \pm 0.02$ g/cm^3, and $\rho_C = 0.62 \pm 0.03$ g/cm^3 for the three sets of manufactured microlattices. Considering the density of pyrolytic carbon $\rho_c = 1.85$ g/cm^3 (Kudo et.al., in preparation), their relative densities were $\bar{\rho}_A = 0.16 \pm 0.01$, $\bar{\rho}_B = 0.23 \pm 0.01$, and $\bar{\rho}_C = 0.34 \pm 0.02$. The relative density of the carbon microlattices slightly decreased with respect to the polymeric lattices, as an effect of the pyrolysis. The theoretical expression for the relative density of a non-cubic octet unit cell in which in-plane cylindrical struts of radius r_1 and length l_1 and out-of-plane cylindrical beams of radius r_2 and length l_2 converge into spherical nodes of radius r_N can be written as

$$\bar{\rho}^t = \frac{2\sqrt{2}\pi\left(r_1^2(l_1 - 2r_N) + 2r_2^2(l_2 - 2r_N)\right)}{l_1^2 l_2} + \frac{5\sqrt{2}}{3}\pi\frac{r_N^3}{l_1^2 l_2}, \quad (1)$$

where the first term accounts for the struts volume while the second term considers the nodal volume. Although the previous relation neglects the node-strut junctions and the beam corrugations, it well approximates the experimental relative density, with a maximum error of 4% over the three sets

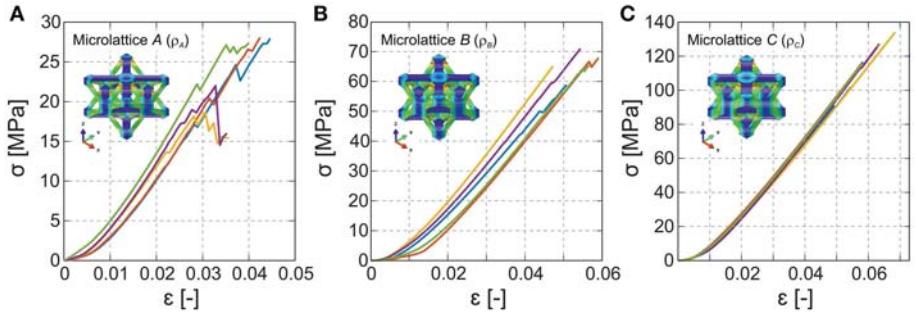

FIGURE 5 | Experimental stress-strain curves for the three sets of microlattices considered: *A* **(A)**, *B* **(B)**, and *C* **(C)**. Five samples were tested for each relative density considered. The insets show the modeled unit cells and their stress distribution during compression.

of microlattices (**Table 1**). The same table reports the relative density $\bar{\rho}^{\mathrm{CAD}}$ extrapolated from the unit cell drawing developed with the measured geometrical parameters. The CAD relative density resulted in excellent agreement with the measured relative density even if it does not consider strut corrugation.

3.3. Stiffness

The effective Young's modulus E^* of an ideal octet-truss lattice with beam radius r and length l was first examined by Deshpande et al. (2001) as a stretching dominated solid with pin-jointed struts. Later, several authors investigated the octet lattice as a frame architecture and demonstrated that the assumption of negligible bending effects is valid for a relative density $\bar{\rho}$ lower than 0.1 and strut slenderness r/l lower than 0.06 (Dong et al., 2015; He et al., 2017). From the analysis of the octet unit cell free to deform laterally due to Poisson effect, the lattice stiffness is

$$E^* = \frac{2\sqrt{2}\pi}{3} E \left(\frac{r}{l}\right)^2 K_b, \tag{2}$$

where E is the constituent material Young's modulus, and K_b is a coefficient that accounts for bending effects. In particular, for truss architectures with pin-joined struts $K_b = 1$, while frame lattices that show bending effects have nodal rigidity $K_b > 1$, and K_b can be written as

$$K_b = \frac{1 + 15\left(\frac{r}{l}\right)^2 + 36\left(\frac{r}{l}\right)^4}{1 + 7\left(\frac{r}{l}\right)^2}. \tag{3}$$

These expressions obtained by means of the beam theory predict that the effective Poisson's ratio ν^* is independent of the relative density and equal to 0.33. However, numerical simulations have proven that both rigid (Tancogne-Dejean et al., 2016) and non-rigid (Thiyagasundaram et al., 2010) architectures experience a decrease of ν with an increase of $\bar{\rho}$. Lattices with high relative density behave as bending-dominated structures with irrotational nodes and show limited lateral expansion when compressed. Similarly, the microlattices studied in this work presented a relative density $\bar{\rho}_j$ greater than 0.1 and non-slender struts $(r_i/l_i)_j > 0.06$ for $i = 1, 2$ and $j = A, B, C$. These features contribute to limit the lateral displacement of the microlattices, which experimentally showed a negligible effective Poisson's ratio ν^*. Therefore, the effective Young's modulus of non-slender cubic lattices can be obtained by considering the bending effects of a laterally constrained frame unit cell. Through this approximation, equivalent to a null effective Poisson's ratio, the unit cell effective Young's modulus E^* can be written as

$$E^* = \sqrt{2}\pi E \left(\frac{r}{l}\right)^2 \left(1 + 3\left(\frac{r}{l}\right)^2\right). \tag{4}$$

It should be noticed that the derived formulation (4) predicts the effective stiffness for non-slender lattices with negligible effective Poisson's ratio more accurately than the classical expression (2). However, it can be further improved by considering the manufacturing-induced imperfections as non-cubic unit cells, orientation-dependent beam slenderness, and increased nodal volume, in order to readily provide insights on the influence of each one of these features on the lattice behavior. Therefore, the effective stiffness E^* predicted through Equation (4) is expected to underestimate the experimental microlattice effective Young's modulus as obtained from uniaxial compression tests, testifying the inaccuracy of currently available analytical techniques and justifying the use of numerical tools for the mechanical characterization of the manufactured lattices.

Figure 5 reports the stress-strain curves of the three sets of fabricated carbon microlattices, with five specimens compressed for each relative density considered. It is observed that all samples showed a brittle linear elastic response after an initial toe region. An increase of the relative density yields an higher maximum stress and strain and a lower variability of the results. The effective Young's modulus E_y^* resulted $E_{y,A}^* = 877.90 \pm 48.57$ MPa for *A*, $E_{y,B}^* = 1565.43 \pm 66.99$ MPa for *B*, and $E_{y,C}^* = 2464.81 \pm 129.53$ MPa for *C*. Although the achieved stiffnesses do not represent the highest specific stiffness (stiffness to density ratio) ever recorded, they exceed the majority of natural materials and approach the values obtained for nanolattices (Zhang et al., 2019). **Figure 6A** shows the measured compressive stiffness as a function of the lattice relative density $\bar{\rho}$. The same figure reports the microlattice stiffness obtained from finite element analyses performed on representative octet unit cells with the geometrical

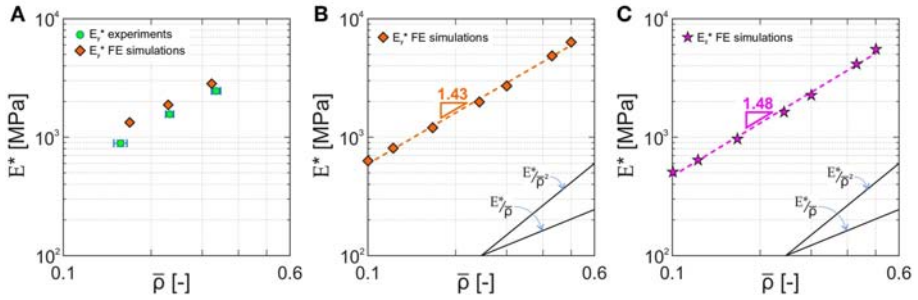

FIGURE 6 | Effective Young's modulus E^* of non-slender carbon microlattices reported as a function of the octet unit cell relative density $\bar{\rho}$. **(A)** Comparison between the stiffness measured from experiments (green/dot markers) and values predicted from finite element simulations (orange/diamond markers). Effective Young's modulus E_y^* **(B)** and E_z^* **(C)** scaling laws obtained from numerical simulations for relative density that ranges between 10 and 50%.

TABLE 2 | Geometrical parameters of the octet unit cell employed in the numerical simulations.

Microlattice	w [μm]	h [μm]	r_1 [μm]	r_2 [μm]	r_N [μm]	r_j [μm]	$\bar{\rho}^{CAD}$ [-]	$\bar{\rho}^t$ [-]
01	240.42	240.42	12.50	10.00	25.00	17.00	0.10	0.10
02	240.42	240.42	14.00	11.00	28.00	18.70	0.12	0.13
03	240.42	240.42	16.50	13.00	33.00	22.10	0.17	0.17
04	240.42	240.42	20.00	16.00	40.00	27.20	0.24	0.24
05	240.42	240.42	22.50	18.00	45.00	30.60	0.30	0.30
06	240.42	240.42	27.50	22.00	55.00	37.40	0.43	0.44
07	240.42	240.42	30.00	24.00	60.00	40.80	0.50	0.51

The relative density $\bar{\rho}^{CAD}$ obtained from the modeled geometry is reported together with the density $\bar{\rho}^t$ calculated through the analytical expression (1).

parameters measured from SEM (**Table 1**). The computational effective Young's modulus for the three investigated geometry resulted $E^*_{y,A} = 1334.74$ MPa, $E^*_{y,B} = 1876.18$ MPa, and $E^*_{y,C} = 2849.78$ MPa. The predicted values are in fair agreement with experimental measurements, with 33.5, 16.6, and 13.5% relative errors for the three sets of microlattices A, B, and C. The discrepancy between numerical predictions and measurements decreases with an increase of the sample relative density $\bar{\rho}$. This is primarily attributed to the manufacturing induced corrugation that were not modeled in the computational analysis and were less pronounced as the beam diameter and relative density increase. In particular, the average corrugation amplitude was measured as 18.4% of the off-plane beam diameter for the microlattice A, while it was limited to 11.2 and 8.7% for lattices B and C, respectively. The influence of each one of the manufacturing-induced imperfections on the lattice effective stiffness was not considered because these features are inherently related, however, it is believed that the non-cubic unit cell had the most pronounced effect for the microlattice A, while the nodal geometry had a significant role for microlattices B and C, where the deviation from cubic unit cell is small.

In order to investigate the effective stiffness scaling law, we performed other numerical simulations on non-slender octet unit cells with relative density $\bar{\rho}$ that varied between 0.10 and 0.50 (**Table 2**). Similarly to the manufactured microlattices, we modeled cubic unit cells with node radius $r_N = 2r_1$, junction radius $r_j = 1.7r_2$, and that contain struts with different in-plane and out-of-plane diameters, with $r_2 = 0.8r_1$. The obtained stiffness in the y and z directions are reported as a function of the relative density in **Figures 6B,C**. The effective Young's modulus of the considered non-slender octet lattices scales as $E^*_y \propto \bar{\rho}^{1.43}$ and $E^*_z \propto \bar{\rho}^{1.48}$ for the y and z directions respectively, whereas classical scaling law for stretching dominated octet-truss lattices predicts a scaling exponent equal to one (Fleck et al., 2010). Deviations from classical theory were also observed for different rigid architectures when the strut slenderness ratio r/l was larger than 0.07, as a result of nodal contribution on the effective lattice stiffness (Portela et al., 2018). The microlattices manufactured and analyzed in this work present beam slenderness that ranges between 0.065 and 0.17, pronounced nodal volumes and edge effects caused by a limited number of unit cells along the height and width (Christodoulou, 2017). Therefore a scaling exponent $m_E > 1$ testifies that the lattices experience significant bending during compression.

3.4. Strength

The compressive strength of an octet-truss lattice material was determined considering the two possible failure mechanisms of elastic buckling or plastic yielding (Deshpande et al., 2001). The analysis of an octet-truss unit cell constituted of cylindrical beams reveals that the strut axial compressive stress σ_a is related to the vertical stress applied to the unit cell σ_v through the relation

$$\sigma_v = 2\sqrt{2}\pi \left(\frac{r}{l}\right)^2 \sigma_a. \tag{5}$$

If the lattice presents a low relative density, elastic buckling will be responsible of the octet-truss structural collapse when the axial stress σ_a reaches the Euler critical value

$$\sigma_b = \frac{n^2\pi^2 E}{4}\left(\frac{r}{l}\right)^2, \tag{6}$$

where n depends on the strut boundary conditions, with $n = 1$ for a pin-joined strut and $n = 2$ for a doubly clamped beam.

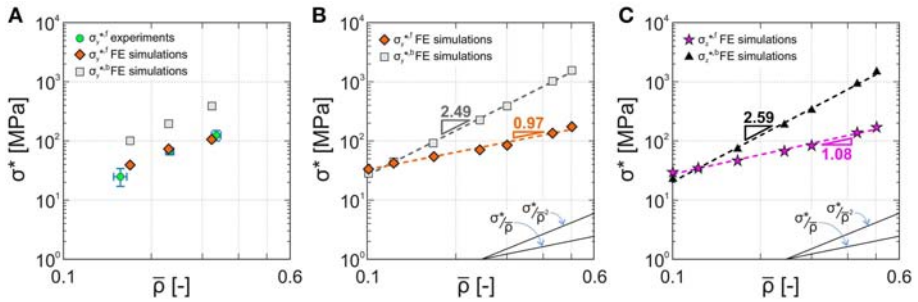

FIGURE 7 | Compressive strength σ^* of non-slender carbon microlattices reported as a function of the octet unit cell relative density $\bar{\rho}$. **(A)** Comparison between the strength measured from experiments (green/dot markers) and predicted failure $\sigma_y^{*,f}$ (orange/diamond markers) and buckling $\sigma_y^{*,b}$ (gray/square markers) strengths from finite element simulations. Fracture and buckling strengths scaling laws along the y-direction **(B)** and z-direction **(C)** obtained from numerical simulations for a relative density that ranges between 10 and 50%.

When the strut slenderness increases, buckling is preceded by strut failure (yielding) as the stress reaches the material failure (yield) strength σ_f. Therefore, the compressive strength for an octet-truss material can be expressed as Deshpande et al. (2001)

$$\sigma^* = \min\left\{\frac{\sqrt{2}\pi^3 n^2 E}{2}\left(\frac{r}{l}\right)^4;\ 2\sqrt{2}\pi\left(\frac{r}{l}\right)^2\sigma_f\right\}. \tag{7}$$

The extension of the expression (7) to non-slender cubic frame lattices was obtained through the analysis of an octet unit cell constrained to deform laterally. Considering bending effects, the relationship (5) between the strut axial stress σ_a and the vertical stress σ_v applied to the unit cell becomes

$$\sigma_v = 2\sqrt{2}\pi\left(\frac{r}{l}\right)^2\left(1+3\left(\frac{r}{l}\right)^2\right)\sigma_a, \tag{8}$$

while the dependence of σ_v on the maximum normal stress σ_m at the edges of the strut was obtained considering a combination of the bending moment and axial force effects

$$\sigma_z = 2\sqrt{2}\pi\left(\frac{r}{l}\right)^2\frac{1+3\left(\frac{r}{l}\right)^2}{1+6\left(\frac{r}{l}\right)^2}\sigma_m. \tag{9}$$

The octet-frame buckling strength was calculated by inserting Equation (6) into Equation (8), while the lattice failure (yield) strength is achieved when $\sigma_m = \sigma_f$. Hence, the compressive strength for a cubic octet-frame lattice material writes as

$$\sigma^* = \min\left\{\frac{\sqrt{2}\pi^3 n^2 E}{2}\left(\frac{r}{l}\right)^4\left(1+3\left(\frac{r}{l}\right)^2\right);\ 2\sqrt{2}\pi\left(\frac{r}{l}\right)^2\frac{1+3\left(\frac{r}{l}\right)^2}{1+6\left(\frac{r}{l}\right)^2}\sigma_f\right\}. \tag{10}$$

As observed for the stiffness calculation, simplified analytical expressions fail to capture the complex mechanical response of non-slender architectures as the orientation-dependent slenderness, non cubic unit cell and the nodal contribution are not accounted for Portela et al. (2018). Even though Equation (10) provides an improved strength estimation of octet lattices with negligible effective Poisson's ratio compared to Equation (7), the effects of the manufacturing-induced imperfections are not fully reflected, and they were considered through numerical analyses. Therefore, more comprehensive analytical formulations need to be developed in order to assess the mechanics of imperfect lattices. The experimental strength of the octet microlattices σ_y^* increased with the relative density as shown in **Figure 7A**, where $\sigma_{y,A}^* = 24.80 \pm 4.26$ MPa, $\sigma_{y,B}^* = 65.68 \pm 4.45$ MPa, and $\sigma_{y,C}^* = 122.74 \pm 12.28$ MPa refer to the three sets of lattices. It should be noticed that the attained specific strengths (strength to density ratio) exceed most of natural materials and approach the values obtained by carbon nanolattices (Bauer et al., 2016; Zhang et al., 2019), which represent the strongest architected materials ever realized. The achievement of strengths comparable to those of nanolattices testifies that through the current manufacturing technique is possible to realize large-scale ultra-strong materials, overcoming the current scalability disadvantages of two-photon lithography nanofabrication.

Considering the limitations of the analytical formulations, the complex microlattice stress distribution was assessed through numerical simulations, from which the maximum equivalent stress was obtained and was compared with the strength of the constituent material. The bulk strength of pyrolytic carbon has been shown to be dependent on the specimen length-scale (Bullock and Kaae, 1979), with an increase as specimens dimensions decrease. This behavior depends on the probability of finding large critical flaws within the materials, which decreases when the sample dimensions reduce. In brittle materials, the failure strength σ_f is inversely proportional to the square root of the pre-existing flaw size

$$\sigma_f = \frac{YK_{Ic}}{\sqrt{\pi a_c}}, \tag{11}$$

where $K_{Ic} = 0.91$ MPa$\sqrt{\text{m}}$ is the fracture toughness (Zhao et al., 1985; Brezny and Green, 1990), $Y = 1$ is a non-dimensional geometrical parameter for a semi-elliptical surface flaw loaded in tension or bending (Bauer et al., 2016), and a_c represents the

critical flaw size. The strength of glassy carbon fibers of 5 μm diameter made by carbonization of organic polymer reached 2 GPa, corresponding to a flaw size of 66 nm (Kawamura and Jenkins, 1970). Since the strut diameters of the manufactured microlattices range between 20 and 50 μm, we assume that a material strength $\sigma_f = 1.5$ GPa can be reached, equivalent to a flaw size of 0.12 μm. From the results of numerical simulations, it is possible to obtain the octet compressive stress along the y-direction that produces a critical equivalent stress within the unit cell. The numerical lattice failure strengths were found $\sigma^{*,f}_{y,A} = 39.31$ MPa, $\sigma^{*,f}_{y,B} = 73.17$ MPa, and $\sigma^{*,f}_{y,C} = 102.83$ MPa for the three sets of carbon microlattices and they are reported in **Figure 7A** together with the experimental data. Considering the uncertainties in the determination of the material failure strength σ_f and the lack of beam corrugation modeling in the finite element analysis, these results are in fair agreement with the measured values, with a maximum relative error of 36.9%. Furthermore, it should be noted that the numerical simulations were performed on a unit cell level, thus neglecting the edge effects that a finite lattice experience.

Since the struts of the studied microlattices are non-slender, buckling is unlikely to cause failure before the onset of fracture. Numerical buckling analyses on the three octet unit cells confirmed that the fracture strength was achieved before elastic buckling of the out-of-plane beams. The compressive stresses $\sigma^{*,b}_y$ that trigger elastic instabilities were numerically found, with $\sigma^{*,b}_{y,A} = 100.88$ MPa, $\sigma^{*,b}_{y,B} = 196.07$ MPa and $\sigma^{*,b}_{y,C} = 389.57$ MPa. It can be seen that the numerical buckling strength $\sigma^{*,b}_{y,j}$ is always greater than the fracture strength $\sigma^{*,f}_{y,j}$ for the three microlattices $j = A, B, C$, thus excluding strut instability mechanisms.

The computational analyses on non-slender octet unit cells performed to investigate the effective stiffness scaling laws were employed to calculate the fracture and buckling strengths and their scaling laws. **Figures 7B,C** shows that for the y loading direction the fracture strength scales as $\sigma^{*,f}_y \propto \bar{\rho}^{0.97}$, and the buckling strength scales as $\sigma^{*,b}_y \propto \bar{\rho}^{2.49}$, while in the z-direction $\sigma^{*,f}_z \propto \bar{\rho}^{1.08}$ and $\sigma^{*,b}_z \propto \bar{\rho}^{2.59}$. As already noticed for the effective stiffness behavior, the fracture and buckling strengths scaling laws deviate from the classical analysis of octet-truss architectures, where the scaling exponents are $m_f = 1$ for fracture and $m_b = 2$ for buckling (Deshpande et al., 2001). The different scaling exponents obtained from the numerical

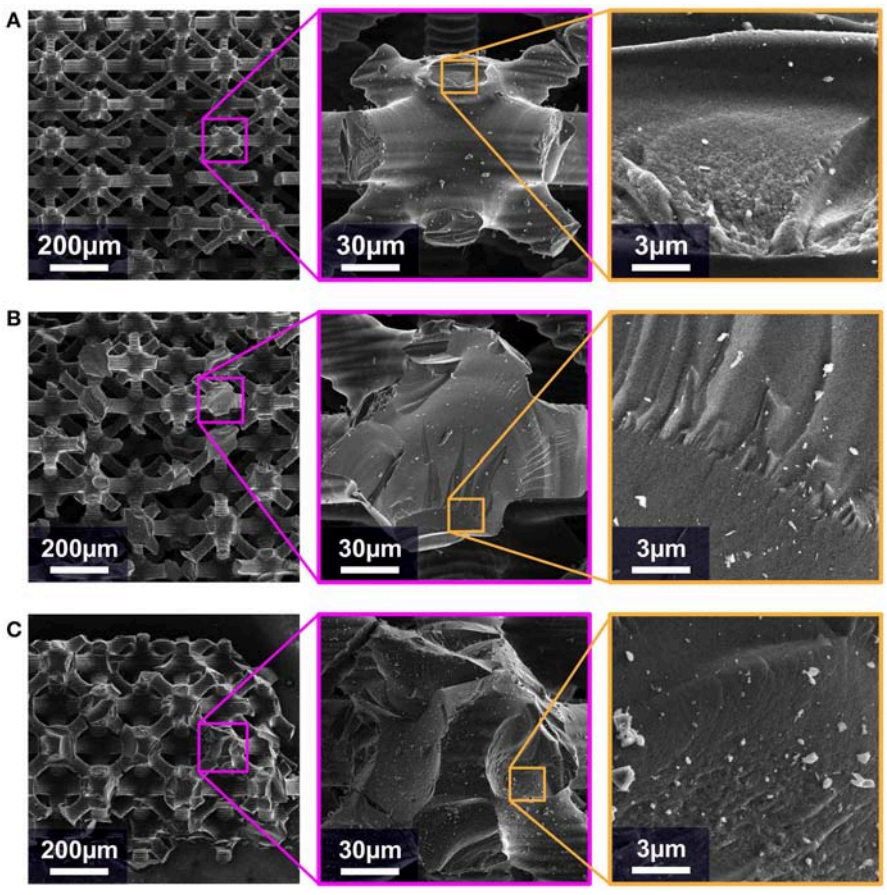

FIGURE 8 | SEM fractography of the three sets of manufactures microlattices *A* **(A)**, *B* **(B)**, and *C* **(C)** after catastrophic mechanical compression tests. Progressive magnification images highlight the brittle fracture surfaces.

simulations depend on the non-slender architecture and the pronounced nodal volume, and will help the evaluation of the mechanical properties prediction of any lattice with the same ratios between geometrical parameters. Lastly, it should be noted that the results of computational analysis on non-slender cubic octet unit cells with $r_2 = 0.8r_1$, $r_N = 2r_2$, and $r_j = 1.7r_2$ predict that failure due to elastic instability occurs when the relative density $\bar{\rho}$ is lower than 0.12, corresponding to an out-of-plane strut slenderness $r_2/l_2 = 0.065$.

Similarly to the results reported by Portela et al. (2018), from finite element analyses it was also observed that strain energy concentrates in the nodes and the stress concentration migrates toward the nodes as the relative density increases and beam slenderness decreases. **Figure 8**, left shows the SEM images of the three sets of manufactured microlattices after catastrophic compression tests, highlighting the failed components and the brittle fracture surfaces. As numerically predicted, the experimental fractographic examination proved that in the lighter microlattice *A* the nodes remained undamaged and only struts fractured (**Figure 8A**), while as density increases in lattices *B* and *C* node failures were observed (**Figures 8B,C**). Furthermore, it was commonly noticed among the three sets of samples that fracture within the struts did not follow the stereolithography induced corrugations.

4. CONCLUSION

In the present work, we have investigated the compressive behavior of stiff and strong non-slender octet carbon microlattices obtained by pyrolyzing 3D-printed polymer architectures fabricated through stereolithography. We have shown that additive manufacturing can lead to imperfect lattices with significant nodal volumes and strut slenderness dependent on the beam inclination with respect to the 3D-printing direction. The effects of these features on the lattice structural response have been numerically and experimentally studied considering carbon microlattices with a relative density higher than 10%. The manufactured microarchitectures have achieved superior relative stiffness and strength that approach those of carbon nanolattices. Therefore, we have demonstrated that the employed manufacturing technique can lead a fast realization of large scale strong materials, currently not achievable through nanofabrication. We have extended the classical analytical tools based on beam theory to include non-slender cubic architectures that show a negligible effective Poisson's ratio. These formulations can be adopted for octet lattices constituted of any materials with negligible nonlinearities and viscoelastic effects, independently of the manufacturing process. Although more accurate than classical octet-truss formulations when bending effects are pronounced, the developed analytical construction remains inadequate for the prediction of the effective stiffness and strength of the manufactured non-slender lattices, thus identifying the needs for future analytical investigations of structured solids with orientation dependent geometrical features and pronounced nodal connections, in order to develop optimized materials and assess the influence of these parameters on the lattice mechanical response. To overcome the identified limitations of the analytical tools, we have developed computational models that reproduce the unit cell geometry and capture the mechanical properties of the tested architectures. The numerical investigation has revealed the mechanics of low slenderness microlattices through the prediction of compressive stiffness, failure and buckling strengths, and their scaling laws, which provide a reliable method to estimate the mechanical properties of imperfectly manufactured octet lattices featuring the investigated topology. The presented manufacturing process and numerical methods represent tools to enhance the design of carbon architected materials toward strong and lightweight solids.

AUTHOR CONTRIBUTIONS

AK, DM, and FB designed the research, discussed the results, and wrote the paper. DM and FB carried out the analytical and numerical analyses. AK manufactured the specimens. AK and YW performed the experiments. All authors reviewed the paper and gave final approval for publication.

FUNDING

Vannevar-Bush Faculty Fellowship of the US Department of Defense. The Resnick Sustainability Institute Postdoctoral Fellowship of Caltech. Financial support from National Group of Mathematical Physics (GNFM-INdAM).

ACKNOWLEDGMENTS

AK gratefully acknowledges the financial support from the Resnick Sustainability Institute at the California Institute of Technology and from Prof. Julia R. Greer (Caltech) through the Vannevar-Bush Faculty Fellowship of the US Department of Defense. The authors thank Prof. Julia R. Greer's research group (Caltech) and Prof. Sergio Pellegrino (Caltech) for their support in conducting experiments in their laboratories.

REFERENCES

Amendola, A., Krushynska, A., Daraio, C., Pugno, N., and Fraternali, F. (2018). Tuning frequency band gaps of tensegrity metamaterials with local and global prestress. *arXiv preprint arXiv:1803.03472*. doi: 10.1016/j.ijsolstr.2018.07.002

Anwer, A., and Naguib, H. (2018). Multi-functional flexible carbon fiber composites with controlled fiber alignment using additive manufacturing. *Addit. Manuf.* 22, 360–367. doi: 10.1016/j.addma.2018.05.013

Bauer, J., Schroer, A., Schwaiger, R., and Kraft, O. (2016). Approaching theoretical strength in glassy carbon nanolattices. *Nat. Mater.* 15, 438–443. doi: 10.1038/nmat4561

Bertoldi, K., Vitelli, V., Christensen, J., and van Hecke, M. (2017). Flexible mechanical metamaterials. *Nat. Rev. Mat.* 2:17066. doi: 10.1038/natrevmats.2017.66

Bilal, O. R., Foehr, A., and Daraio, C. (2017). Bistable metamaterial for switching and cascading elastic vibrations. *Proc. Natl. Acad. Sci. U.S.A.* 114, 4603–4606. doi: 10.1073/pnas.1618314114

Brezny, R., and Green, D. (1990). The effect of cell size on the mechanical behavior of cellular materials. *Acta Metall. Mater.* 38, 2517–2526. doi: 10.1016/0956-7151(90)90263-G

Bullock, R., and Kaae, J. (1979). Size effect on the strength of glassy carbon. *J. Mater. Sci.* 14, 920–930. doi: 10.1007/BF00550723

Carneiro, O., Silva, A., and Gomes, R. (2015). Fused deposition modeling with polypropylene. *Mater. Des.* 83, 768–776. doi: 10.1016/j.matdes.2015.06.053

Chen, X., Zhao, G., Wu, Y., Huang, Y., Liu, Y., He, J., et al. (2017). Cellular carbon microstructures developed by using stereolithography. *Carbon* 123, 34–44. doi: 10.1016/j.carbon.2017.07.043

Christodoulou, I. (2017). *Mechanical properties of micro-architectured lattices: edge effects, fatigue and fracture* (Ph.D. thesis). University College London, London, United Kingdom.

Deshpande, V., Fleck, N., and Ashby, M. (2001). Effective properties of the octet-truss lattice material. *J. Mech. Phys. Solids* 49, 1747–1769. doi: 10.1016/S0022-5096(01)00010-2

Dong, L., Deshpande, V., and Wadley, H. (2015). Mechanical response of t-6al-4v octet-truss lattice structures. *Int. J. Solids Struct.* 60–61, 107–124. doi: 10.1016/j.ijsolstr.2015.02.020

Essa, K., Hassanin, H., Attallah, M., Adkins, N. J., Musker, A., Roberts, G., et al. (2017). Development and testing of an additive manufactured monolithic catalyst bed for htp thruster applications. *Appl. Catal. Gen.* 542, 125–135. doi: 10.1016/j.apcata.2017.05.019

Fleck, N., Deshpande, V., and Ashby, M. (2010). Micro-architectured materials: past, present and future. *Proc. R. Soc. Lond. Math. Phys. Eng. Sci.* 466, 2495–2516. doi: 10.1098/rspa.2010.0215

Fu, K., Yao, Y., Dai, J., and Hu, L. (2017). Progress in 3d printing of carbon materials for energy-related applications. *Adv. Mater.* 29:1603486. doi: 10.1002/adma.201603486

Gibson, L., and Ashby, M. (1997). *Cellular Solids: Structures and Properties*. Cambridge: Cambridge University Press.

He, Z., Wang, F., Zhu, Y., Wu, H., and Park, H. (2017). Mechanical properties of copper octet-truss nanolattices. *J. Mech. Phys. Solids* 101, 133–149. doi: 10.1016/j.jmps.2017.01.019

Hengsbach, S., and Lantada, A. (2014). Direct laser writing of auxetic structures: present capabilities and challenges. *Smart Mater. Struct.* 23.8:085033. doi: 10.1088/0964-1726/23/8/085033

Jacobsen, A., Mahoney, S., and Carter, S. N. (2011). Vitreous carbon micro-lattice structures. *Carbon* 49, 1025–1032. doi: 10.1016/j.carbon.2010.10.059

Kawamura, K., and Jenkins, G. (1970). A new glassy carbon fibre. *J. Mater. Sci.* 5, 262–267. doi: 10.1007/BF00551003

Lewicki, J. P., Rodriguez, J. N., Zhu, C., Worsley, M. A., Wu, A. S., Kanarska, Y., et al. (2017). 3d-printing of meso-structurally ordered carbon fiber/polymer composites with unprecedented orthotropic physical properties. *Sci. Rep.* 7:43401. doi: 10.1038/srep43401

Li, J., Leu, M., Panat, R., and Park, J. (2017). A hybrid three-dimensionally structured electrode for lithium-ion batteries via 3D printing. *Mater. Des.* 119, 417–424. doi: 10.1016/j.matdes.2017.01.088

Maggi, A., Li, H., and Greer, J. (2017). Three-dimensional nano-architected scaffolds with tunable stiffness for efficient bone tissue growth. *Acta Biomater.* 63, 294–305. doi: 10.1016/j.actbio.2017.09.007

Meza, L., Phlipot, G., Portela, C., Maggi, A., Montemayor, L., Comella, A., et al. (2017). Reexamining the mechanical property space of three-dimensional lattice architectures. *Acta Mater.* 140, 424–432. doi: 10.1016/j.actamat.2017.08.052

Meza, L. R., Das, S., and Greer, J. R. (2014). Strong, lightweight, and recoverable three-dimensional ceramic nanolattices. *Science* 345, 1322–1326. doi: 10.1126/science.1255908

Meza, L. R., Zelhofer, A. J., Clarke, N., Mateos, A. J., Kochmann, D. M., and Greer, J. R. (2015). Resilient 3D hierarchical architected metamaterials. *Proc. Nat. Acad. Sci. U.S.A.* 112, 11502–11507. doi: 10.1073/pnas.1509120112

Misseroni, D., Colquitt, D. J., Movchan, A. B., Movchan, N. V., and Jones, I. S. (2016). Cymatics for the cloaking of flexural vibrations in a structured plate. *Sci. Rep.* 6:23929. doi: 10.1038/srep23929

Murr, L. E., Gaytan, S. M., Medina, F., Lopez, H., Martinez, E., Machado, B. I., et al. (2010). Next-generation biomedical implants using additive manufacturing of complex, cellular and functional mesh arrays. *Philos. Trans. R. Soc. Lond. Math. Phys. Eng. Sci.* 368, 1999–2032. doi: 10.1098/rsta.2010.0010

Nguyen, D. T., Meyers, C., Yee, T. D., Dudukovic, N. A., Destino, J. F., Zhu, C., et al. (2017). 3D-printed transparent glass. *Adv. Mater.* 29. doi: 10.1002/adma.201701181

Ni, R., Qian, B., Liu, C., Liu, X., and Qiu, J. (2018). Three-dimensional printing of hybrid organic/inorganic composites with long persistence luminescence. *Opt. Mater. Express* 8, 2823–2831. doi: 10.1364/OME.8.002823

Pellegrino, S., and Calladine, C. (1986). Matrix analysis of statically and kinematically indeterminate frameworks. *Int. J. Solids Struct.* 22, 409–428. doi: 10.1016/0020-7683(86)90014-4

Portela, C., Greer, J., and Kochmann, D. (2018). Impact of node geometry on the effective stiffness of non-slender three-dimensional truss lattice architectures. *Extreme Mech. Lett.* 22, 138–148. doi: 10.1016/j.eml.2018.06.004

Price, R., and Kaae, J. (1969). Poisson's ratio of pyrolytic carbon. *Carbon* 7, 706–708. doi: 10.1016/0008-6223(69)90529-6

Quintanilla, A., Casas, J., Miranzo, P., Osendi, M., and Belmonte, M. (2018). 3D-printed fe-doped silicon carbide monolithic catalysts for wet peroxide oxidation processes. *Appl. Catal. B Environ.* 235, 246–255. doi: 10.1016/j.apcatb.2018.04.066

Schaedler, T. A., Jacobsen, A. J., Torrents, A., Sorensen, A. E., Lian, J., Greer, J. R., et al. (2011). Ultralight metallic microlattices. *Science* 334, 962–965. doi: 10.1126/science.1211649

Schwab, H., Palm, F., Kühn, U., and Eckert, J. (2016). Microstructure and mechanical properties of the near-beta titanium alloy ti-5553 processed by selective laser melting. *Mater. Des.* 105, 75–80. doi: 10.1016/j.matdes.2016.04.103

Shan, S., Kang, S. H., Raney, J. R., Wang, P., Fang, I., candido, F., et al. (2015). Multistable architected materials for trapping elastic strain energy. *Adv. Mater.* 27, 4296–4301. doi: 10.1002/adma.201501708

Spierings, A., Wegener, K., Kenel, C., and Leinenbach, C. (2015). Processing of metal-diamond-composites using selective laser melting. *Rapid Prototyp. J.* 21, 130–136. doi: 10.1108/RPJ-11-2014-0156

Sugino, C., Leadenham, S., Ruzzene, M., and Erturk, A. (2015). On the mechanism of bandgap formation in locally resonant finite elastic metamaterials. *J. Appl. Phys.* 120:134501. doi: 10.1063/1.4963648

Sun, K., Wei, T. S., Ahn, B. Y., Seo, J. Y., Dillon, S. G., and Lewis, J. A. (2013). 3D printing of interdigitated Li-ion microbattery architectures. *Adv. Mater.* 25, 4539–4543. doi: 10.1002/adma.201301036

Tancogne-Dejean, T., Spierings, A., and Mohr, D. (2016). Additively-manufactured metallic micro-lattice materials for high specific energy absorption under static and dynamic loading. *Acta Mater.* 116, 14–28. doi: 10.1016/j.actamat.2016.05.054

Thiyagasundaram, P., Sankar, B., and Arakere, N. (2010). Elastic properties of open-cell foams with tetrakaidecahedral cells using finite element analysis. *AIAA J.* 48:818. doi: 10.2514/1.J050022

Wilkes, J., Hagedorn, Y., Meiners, W., and Wissenbach, K. (2013). Additive manufacturing of zro2-al2o3ceramic components by selective laser melting. *Rapid Prototyp. J.* 19, 51–57. doi: 10.1108/13552541311292736

Xia, X., Leo, C. D., Gu, X., and Greer, J. (2016). *In situ* lithiation–delithiation of mechanically robust cu-si core-shell nanolattices in a scanning electron microscope. *ACS Energy Lett.* 1, 492–499. doi: 10.1021/acsenergylett.6b00256

Yao, Y., Fu, K. K., Yan, C., Dai, J., Chen, Y., Wang, Y., et al. (2016). Three-dimensional printable high-temperature and high-rate heaters. *ACS Nano* 10, 5272–5279. doi: 10.1021/acsnano.6b01059

Zhang, Q., Zhang, F., Medarametla, S., Li, H., Zhou, C., and Lin, D. (2016). 3D printing of graphene aerogels. *Small* 12, 1702–1708. doi: 10.1002/smll.201503524

Zhang, X., Vyatskikh, A., Gao, H., Greer, J. R., and Li, X. (2019). Lightweight, flaw-tolerant, and ultrastrong nanoarchitected carbon. *Proc. Natl. Acad. Sci. U.S.A.* 116, 6665–6672. doi: 10.1073/pnas.1817309116

Zhao, J., Bradt, R., and Walker, P. L. Jr. (1985). The fracture toughness of glassy carbons at elevated temperatures. *Carbon* 23, 15–18. doi: 10.1016/0008-6223(85)90190-3

Zhu, C., Han, T. Y., Duoss, E. B., Golobic, A. M., Kuntz, J. D., Spadaccini, C. M., et al. (2015). Highly compressible 3D periodic graphene aerogel microlattices. *Nat. Commun.* 6:6962. doi: 10.1038/ncomms7962

Conflict of Interest Statement: The authors declare that the research was conducted in the absence of any commercial or financial relationships that could be construed as a potential conflict of interest.

frontiers in Materials

ORIGINAL RESEARCH
published: 17 July 2019
doi: 10.3389/fmats.2019.00161

Load Sensor Instability and Optimization of MEMS-based Tensile Testing Devices

Maria F. Pantano [1], Benedetta Calusi [1,2], Barbara Mazzolai [2], Horacio D. Espinosa [3] and Nicola M. Pugno [1,4,5]*

[1] Laboratory of Bio-inspired and Graphene Nanomechanics, Department of Civil, Environmental and Mechanical Engineering, University of Trento, Trento, Italy, [2] Center for Micro-BioRobotics, Istituto Italiano di Tecnologia, Pontedera, Italy, [3] Department of Mechanical Engineering, Northwestern University, Evanston, IL, United States, [4] Ket-Lab, Fondazione E. Amaldi, Rome, Italy, [5] School of Engineering and Materials Science, Queen Mary University of London, London, United Kingdom

MEMS-based tensile testing platforms are very powerful tools for the mechanical characterization of nanoscale materials, as they allow for testing of micro/nano-sized components *in situ* electron microscopes. In a typical configuration, they consist of an actuator, to deliver force/displacement, and a load sensor, which is connected to the sample like springs in series. Such configuration, while providing a high resolution force measurement, can cause the onset of instability phenomena, which can later compromise the test validity. In the present paper such phenomena are quantitatively discussed through the development of an analytical model, which allows to find a relationship between the rise of instability and the sensor stiffness, which is the key parameter to be optimized.

Keywords: MEMS, mechanical testing, SEM/TEM, instability, nanomaterials

OPEN ACCESS

Edited by:
Alberto Corigliano, Politecnico di Milano, Italy

Reviewed by:
Shangchao Lin, Florida State University, United States
Dongchan Jang, Korea Advanced Institute of Science & Technology (KAIST), South Korea

****Correspondence:***
Maria F. Pantano
maria.pantano@unitn.it

Specialty section:
This article was submitted to Mechanics of Materials, a section of the journal Frontiers in Materials

Received: *13 January 2019*
Accepted: *24 June 2019*
Published: *17 July 2019*

Citation:
Pantano MF, Calusi B, Mazzolai B, Espinosa HD and Pugno NM (2019) Load Sensor Instability and Optimization of MEMS-based Tensile Testing Devices. Front. Mater. 6:161. doi: 10.3389/fmats.2019.00161

INTRODUCTION

Mechanical characterization of materials at the micro/nanoscale has gained increasing attention during the last two decades, as acknowledged by the dramatic increase in number of correlated studies (Pantano et al., 2012). Such trend can be explained by two main reasons. First, the further scaling down of electronic devices, like micro/nanoelectromechanical systems (MEMS/NEMS), is shrinking the size of their structural components to the micro/nanometer scale. Second, experiments carried out on micro/nanostructures, like nanotubes and nanowires, revealed an extraordinary behavior (Wang and Song, 2006; Lee et al., 2008), not known at the macroscale, which can be exploited for a new generation of devices and materials (Ke et al., 2005; Pugno et al., 2005).

For the mechanical characterization of micro/nano-samples, MEMS-based tensile testing devices were shown to be very powerful tools (Zhu and Chang, 2015). In fact, because of their unique compatibility with scanning/transmission electron microscopes (SEM/TEM), they allow tests to be performed under real-time imaging of the sample deformation.

In a typical configuration, the sample to be tested is positioned between an actuator (to apply loads/displacements) and a flexible structure with load sensing function (Haque and Saif, 2002; Espinosa et al., 2007) (i.e., load sensor).

During a test, the actuator pulls the specimen, and this, in turn, transfers part of the delivered displacement to the load sensor, which, as a consequence, undergoes a deformation. This can be measured either electronically (Zhang et al., 2010) or from the analysis of successive pictures taken during the test (Brown et al., 2009), and can then be converted into force if multiplied by the sensor spring constant, known by design.

The choice of the sensor spring constant is not a trivial task. In fact, smaller its value higher the sensitivity of the load measurement. However, if the sensor stiffness is too low compared to that of the specimen, then most of the displacement delivered by the actuator is transferred to the sensor, causing a small deformation of the specimen itself. More critically, a low sensor stiffness may promote the onset of instability phenomena. In fact, when the load sensor moves along with the sample, it accumulates elastic energy. When the force transmitted by the sample to the load sensor decreases after a certain strain has been applied, the elastic energy stored up to that point is released. This means that the load sensor moves back, pulling the end of the specimen attached to it (Agrawal et al., 2009). In such a situation, the displacement-control condition of the sample may no longer be guaranteed, triggering its dynamic failure. Thus, in the case of softening, the testing system may not be able to follow the sample characteristic curve after stress relaxation, even though this could be very interesting to explore.

The influence of the machine stiffness on the mechanical properties and instability phenomena occurring during macroscopic mechanical tests has been pointed out in different studies (Chilver, 1955; Johnston, 1962; Hudson et al., 1972; Han et al., 2009, 2010). In general, it is well-known that a machine with high stiffness should be chosen in order to avoid instability issues in tensile tests. However, while in macroscopic tests, the machine stiffness can be set much bigger than that of the specimen, at the microscale, the metrological strategies adopted for load measurement in MEMS devices make it not possible. The maximum sample deformation which can be achieved before instability occurs can be quantitatively evaluated from the analytical model shown in the following sections.

ANALYTICAL MODELING OF MEMS-BASED TENSILE TESTING DEVICES

In most of MEMS tensile testing devices, the load sensor and the sample to be tested are connected like springs in series, as in the lumped parameters model reported in **Figure 1A**. This is a 2-degrees-of-freedom system, where the sample is represented as a spring with a generic characteristic (its mass is negligible with respect to that of the load sensor), while the load sensor is modeled through a mass (M_{LS}) connected to the substrate through a damper (with damping constant D) and a spring (with spring constant k_{LS}). The sample undergoes a displacement x_S, as a consequence of the actuator movement, whereas x_{LS} is the load sensor's displacement.

For simplicity, let us first neglect both the damping and inertial contribution, and let us evaluate the global quasi-static force-displacement relationship characterizing the system comprising the load sensor and sample springs (**Figure 1B**).

Global System Behavior

The overall deformation undergone by the system is $x_S = x_{LS} + (x_S - x_{LS})$, where $(x_S - x_{LS})$ is the sample elongation. If infinitely small displacements are considered, the overall system elongation becomes:

$$dx_S = dx_{LS} + d(x_S - x_{LS}) \tag{1}$$

Since k_{LS} is the load sensor spring constant, then $dx_{LS} = dF/k_{LS}$. If a general characteristic is assumed for the sample, it follows that $d(x_S - x_{LS}) = \partial(x_S - x_{LS})/\partial F dF$, where dF is the force acting on the system, which is the same on both the sample and load sensor (since they are connected in series). Thus, Equation (1) can be rewritten as:

$$dx_S = \frac{dF}{k_{LS}} + \frac{\partial(x_S - x_{LS})}{\partial F} dF, \tag{2}$$

or,

$$\frac{dx_S}{dF} = \frac{1}{k_{LS}} + \frac{\partial(x_S - x_{LS})}{\partial F}. \tag{3}$$

At the beginning, the sample characteristic has a linear increasing trend [e.g., $\partial(x_S - x_{LS})/\partial F$ or $\partial F/\partial(x_S - x_{LS})$ are constant, and the sample can be modeled like a linear spring], and the slope of the system characteristic ($\partial F/\partial x_S$) is equal to the equivalent stiffness of the sample and load sensor spring constants. Then, the system characteristic may either increase or decrease with increasing x_S, depending on the sample's behavior. In particular, either of the following cases may occur (**Figure 1B**):

(a) Overall system hardening as a consequence of sample hardening, i.e., if $\partial(x_S - x_{LS})/\partial F > 0$;

(b) Overall softening with negative slope, if the sample exhibits softening (i.e., $\partial F/\partial(x_S - x_{LS}) < 0$) and its slope in modulus is smaller than the load sensor spring constant. In fact, from Equation (3):

$$\frac{dx_S}{dF} < 0 \Leftrightarrow \frac{1}{k_{LS}} + \frac{\partial(x_S - x_{LS})}{\partial F} < 0, \tag{4}$$

which is equivalent to

$$k_{LS} > \left| \frac{\partial F}{\partial (x_S - x_{LS})} \right|. \tag{5}$$

(c) Overall softening with positive slope, if the sample exhibits softening (e.g., $\partial F/\partial(x_S - x_{LS}) < 0$) and its slope in modulus is bigger than the load sensor spring constant. In fact, from Equation (3):

$$\frac{dx_S}{dF} > 0 \Leftrightarrow \frac{1}{k_{LS}} + \frac{\partial(x_S - x_{LS})}{\partial F} > 0, \tag{6}$$

which is equivalent to

$$k_{LS} < \left| \frac{\partial F}{\partial (x_S - x_{LS})} \right|. \tag{7}$$

Thus, in this latter case, the system would tend to come back to smaller values of x_S, displaying a snap-back

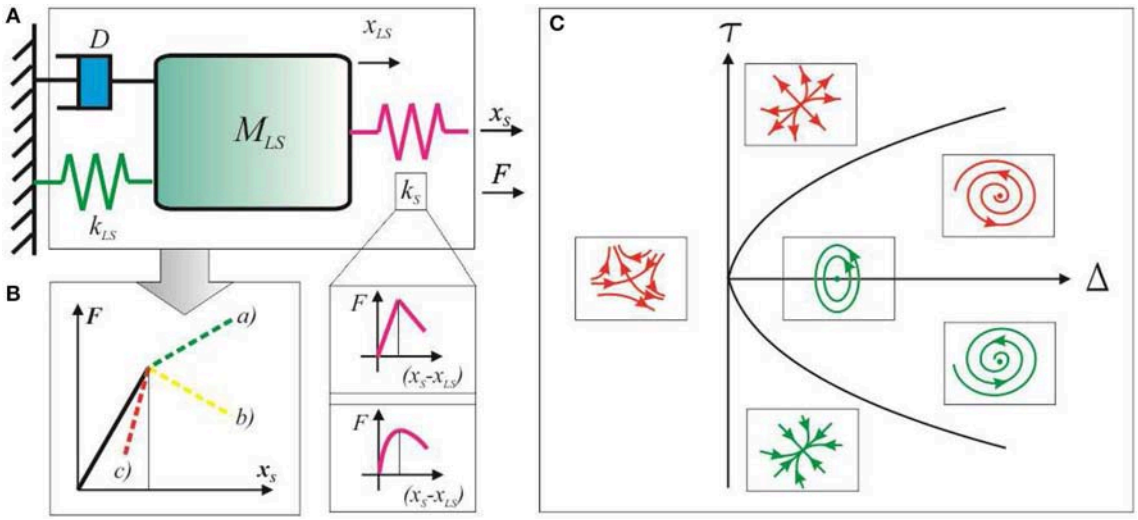

FIGURE 1 | (A) Lumped parameters model of a typical tensile testing device, where the sample can be modeled like a spring whose characteristic shows a softening branch; **(B)** Global behavior of the system consisting of both the load sensor and the sample, showing the relationship between the force (F) corresponding to the applied displacement (x_S). When the sample enters the softening regime, F may increase (line a) or decrease (either line b or c) with x_S, depending on the magnitude of the slope of the sample characteristic, $\partial F/\partial(x_S\text{-}x_{LS})$, compared to the load sensor stiffness, k_{LS}. In particular, line (b) corresponds to $\partial F/\partial(x_S\text{-}x_{LS})<0$ and $k_{LS}>|\partial F/\partial(x_S\text{-}x_{LS})|$, whereas c) to $\partial F/\partial(x_S\text{-}x_{LS})<0$ and $k_{LS}<|\partial F/\partial(x_S\text{-}x_{LS})|$. In order to evaluate the stability of the equilibrium position of the load sensor, its dynamic behavior can be linearized and modeled around such position through a Jacobian matrix. **(C)** The sign of the trace, τ, and the determinant, Δ, of the Jacobian matrix determine the stability of the equilibrium point.

instability with positive slope. However, since in a typical tensile test, x_S is progressively increased, the sample is broken without the possibility to follow the snap-back instability and, thus, the corresponding region of the sample characteristic. As a consequence, the optimal design value for the load sensor stiffness depends on the steepest point of interest to be expected during softening regime in the sample characteristic curve. Thus, as a compromise between high resolution during the elastic regime and stability requirement, we can define an optimal load sensor stiffness as

$$k_{LS,\,opt} = \eta \left| \frac{\partial F}{\partial\,(x_S - x_{LS})} \right|_{MAX}$$

where η is a safety factor for stability, which could be set for example equal to 10%.

Load Sensor Stability

It is now interesting to study what happens to the load sensor when its stiffness is smaller than the sample characteristic slope during softening. To this aim, it is convenient to refer to the model depicted in **Figure 1A** and write the load sensor's equilibrium equation:

$$M_{LS}\frac{d^2x_{LS}}{dt'^2} = \sum_i F_i, \tag{8}$$

where F_i is the i-th force acting on the load sensor. In this case, three forces have to be considered:

$$F_S = F\,(x_S - x_{LS})\,, \tag{9}$$

$$F_{LS} = -k_{LS}x_{LS}\,, \tag{10}$$

$$F_D = -D\frac{dx_{LS}}{dt'}, \tag{11}$$

where F_S is the force transmitted to the load sensor by the sample and depends on the actual sample elongation $(x_S\text{-}x_{LS})$, F_{LS} is the elastic force exerted by the load sensor spring, and F_D the damping force. Thus, considering the (9)–(11), Equation (8) can be rewritten as:

$$M_{LS}\frac{d^2x_{LS}}{dt'^2} = -D\frac{dx_{LS}}{dt'} - k_{LS}x_{LS} + F\,(x_S - x_{LS})\,. \tag{12}$$

In steady-state condition, the equilibrium points of Equation (12) are given by the roots of $f\,(x_{LS}) = -k_{LS}x_{LS} + F\,(x_S - x_{LS})$. In order to infer about the stability of a load sensor equilibrium point, x^*_{LS} (solution of Equation 12), it is convenient to linearize $f(x_{LS})$ through Taylor expansion as $f\,(x_{LS}) \approx f'\left(x^*_{LS}\right)\left(x_{LS} - x^*_{LS}\right)$, where $f'\left(x^*_{LS}\right) = \left(-k_{LS} - \frac{dF}{d(x_S - x_{LS})}\right)\Big|_{x^*_{LS}}$ (Pelesko and Bernstein, 2003). From this, it follows that the sign of the slope of function $f\,(x_{LS})$ depends on the magnitude of the slope of $F\,(x_S - x_{LS})$ compared to k_{LS}, providing two possible cases:

$$1)\quad f'\left(x^*_{LS}\right) > 0 \;\Leftrightarrow\; \dot{F}\left(x_S - x^*_{LS}\right) < -\,k_{LS},$$
$$2)\quad f'\left(x^*_{LS}\right) < 0 \;\Leftrightarrow\; \dot{F}\left(x_S - x^*_{LS}\right) > -\,k_{LS}.$$

It is now convenient to rewrite Equation (12) through the following system

$$\begin{cases} \frac{dx_{LS}}{dt'} = v, \\ \frac{dv}{dt'} = -\frac{D}{M_{LS}}v + \frac{f(x_{LS})}{M_{LS}}, \end{cases}$$

that we can linearize near the equilibrium point, x^*_{LS}, as $\frac{d\mathbf{u}}{dt'} = J\,\mathbf{u}$, with

$$J = \left.\begin{pmatrix} 0 & 1 \\ \frac{f'}{M_{LS}} & -\frac{D}{M_{LS}} \end{pmatrix}\right|_{x^*_{LS}}, \mathbf{u} = \begin{pmatrix} x_{LS} - x^*_{LS} \\ v \end{pmatrix}.$$

The stability of the solution, x^*_{LS}, depends on the trace and determinant of the Jacobian matrix (Strogatz, 2000; Pelesko and Bernstein, 2003), $\tau = tr(J), \Delta = det(J)$, respectively, that on turn depend on f'. In particular, in our system $\tau = -D/M_{LS} < 0$, whereas $\Delta = -f'/M_{LS}$. Therefore, when $f' > 0$ (previous case 1) $\Delta < 0$, meaning that the equilibrium point is unstable (saddle point from **Figure 1C**). On the contrary, when $f' < 0$ (previous case 2), $\Delta > 0$, always corresponding to stable equilibrium points (**Figure 1C**). As a conclusion, when the sample characteristic slope is negative (e.g., softening in the sample) and its modulus is smaller than k_{LS}, stable equilibrium points are allowed to the load sensor (case 2); while instead the sample characteristic slope is negative and its modulus is bigger than k_{LS}, no stable equilibrium points are possible (case 1). Indeed, in such case, as shown in the previous section, the system of the sample and load sensor springs show a snap-back instability with a positive slope, which cannot be followed during the tensile test.

In some simple cases, the previous generic (Equation 12) can be solved analytically. As an example, let us consider a piecewise linear expression of $F(x_S\text{-}x_{LS})$, which is characterized by an initial region, where the force increases with the deformation, followed by a second region with a decreasing trend (softening region), that can be defined as (**Figure 1A**):

$$F(x_S - x_{LS}) = \begin{cases} k_0 (x_S - x_{LS}), & \text{if } x_S - x_{LS} < x^*, \\ k_0 x^* - k_1 (x_S - x_{LS} - x^*), & \text{if } x_S - x_{LS} > x^*. \end{cases} \quad (13)$$

Its first region defines the sample elastic regime, while the second one corresponds to the softening region. In order to study what happens to the sensor as soon as the sample enters the softening regime, we substitute the second of Equations (13) in Equation (12), which then becomes:

$$M_{LS}\frac{d^2x_{LS}}{dt'^2} = -D\frac{dx_{LS}}{dt'} - k_{LS}x_{LS} + k_0x^* - k_1\left(x_S - x_{LS} - x^*\right). \quad (14)$$

It is convenient to rewrite Equation (14) in dimensionless form. To this aim, we introduce the dimensionless time, $t = t'\sqrt{\frac{|k_1 - k_{LS}|}{M_{LS}}}$, and length, $y = x_{LS}/l$, being l the sample gage length and $k_1 \neq k_{LS}$. With these positions, Equation (14) can be rewritten as:

$$\frac{d^2y}{dt^2} = -\alpha\frac{dy}{dt} + sgn\left(k_1 - k_{LS}\right)y + \frac{x^*\left(k_0 + k_1\right) - k_1x_S}{l\left|k_1 - k_{LS}\right|}, \quad (15)$$

where $\alpha = \frac{D}{\sqrt{M_{LS}|k_1 - k_{LS}|}}$ is a corrected quality factor, which takes into account the presence of the sample through the term k_1.

Considering a typical MEMS testing platform, like that one reported in Pantano et al. (2015), the damping contribution can be neglected with respect to the inertial effects (see the **Appendix** for further details), meaning that $\alpha << 1$. Thus, in the inertia-dominated regime, Equation (15) simplifies as:

$$\frac{d^2y}{dt^2} = sgn\left(k_1 - k_{LS}\right)y + \frac{x^*\left(k_0 + k_1\right) - k_1x_S}{l\left|k_1 - k_{LS}\right|}. \quad (16)$$

In general, $x_S = x_S(t)$, but in the hypothesis of a negligible variation of x_S with time, Equation (16) can be solved analytically depending on the positive (a) or negative (b) sign of $(k_1\text{-}k_{LS})$.

(a) If $k_1 > k_{LS}$, the general solution of Equation (16) is:

$$y = Ae^t + Be^{-t} - \frac{x^*\left(k_0 + k_1\right) - k_1x_S}{l\left(k_1 - k_{LS}\right)}, \quad (17)$$

(b) If $k_1 < k_{LS}$, the general solution of Equation (16) is instead:

$$y = A\cos t + B\sin t - \frac{x^*\left(k_0 + k_1\right) - k_1x_S}{l\left(k_1 - k_{LS}\right)}, \quad (18)$$

A, B are constants depending on the initial conditions.

In order to infer about the stability of the load sensor equilibrium positions defined by Equations (17) and (18), it is useful to write the second-order differential equation (16) as a non-homogeneous linear system:

$$\begin{cases} \frac{dy_1}{dt} = y_2, \\ \frac{dy_2}{dt} = sgn\left(k_1 - k_{LS}\right)y_1 + \frac{x^*(k_0+k_1) - k_1x_S}{l|k_1 - k_{LS}|}. \end{cases}$$

This latter can be turned in a homogeneous system, by introducing the translations $\chi_1 = y_1 - \frac{x^*(k_0+k_1) - k_1x_S}{l(k_1 - k_{LS})}$, $\chi_2 = y_2$, i.e.,

$$\begin{cases} \frac{d\chi_1}{dt} = \chi_2, \\ \frac{d\chi_2}{dt} = sgn\left(k_1 - k_{LS}\right)\chi_1. \end{cases}$$

The above homogeneous linear system has a fixed point, χ^*, at $\chi_1 = 0$, $\chi_2 = 0$, i.e., the origin corresponds to the equilibrium position of the system. Repeating the same logic as before, the trace, τ, and the determinant, Δ, of the Jacobian matrix associated to the linear system provides the stability of the fixed point. In this case, $\tau = 0$, while $\Delta = -sgn(k_1\text{-}k_{Ls})$. Thus, with reference to **Figure 1C**,

(a) If $k_1 > k_{LS}$, $\Delta < 0$, thus the equilibrium point, χ^*, is a saddle point, i.e., unstable.
(b) If $k_1 < k_{LS}$, $\Delta > 0$, the equilibrium point, χ^*, is a center, i.e., neutrally stable.

Since $\frac{dF}{d(x_S - x_{LS})} = k_1$ and k_1 represents the slope of the decreasing branch of the sample characteristic, the results found now match the conclusions derived previously in case of a sample with a generic characteristic.

ANALYSIS OF RESULTS AND DISCUSSION

From the analytical models presented above, two main conclusions can be derived. First, the range of possible deformation which can be applied to the specimen is limited by the value of the load sensor spring constant. In particular, higher the sensor spring constant, higher the displacement which can be delivered by the actuator (x_S), without compromising the load sensor stability. Second, when the sample characteristic becomes negative and its slope overcomes the load sensor spring constant (in absolute value), the system comprising both the sample and load sensor springs shows a snap-back instability with a positive slope, which cannot be followed during a conventional tensile test, where the end of the sample connected to the actuator is not allowed to come back to decreasing values. From the load sensor's point of view, this translates into unavailability of stable equilibrium positions.

Our result about the occurrence of instability in the case of sample softening with a slope bigger than the sensor stiffness agrees well with similar conclusions drawn in the past, through an energetic approach, from macroscopic compression tests on rocks (Salamon, 1970), as well as with previous hypotheses adduced to explain divergences of the experimental behavior of ZnO nanowires from numerical simulations (Agrawal et al., 2009). As a matter of fact, it is rare to find in the literature experimental stress-strain curves of nanoscale materials showing a steep softening branch. One example can be found in Pantano et al. (2018), where the stress-strain curve of a poly(methyl methacrylate) (PMMA) film with about 100 nm thickness shows a final softening region with negative slope of ∼-736 N/m. This value approaches (yet is still below) the limit of the load sensor stability region, whose upper bound corresponds to the load sensor stiffness (831 N/m in this case). Hence, as a design rule, in order to mitigate the instability issues of typical MEMS-based tensile testing configurations, the load sensor stiffness should be chosen according to the optimal value definition reported above. Then, in order to be able to follow the complete stress-strain curve of micro/nano-samples with any kind of softening, alternative designs should be considered. The first solution is to choose a sensor with infinite spring constant. This, in practice, would correspond to fix one end of the specimen, thus preventing any displacement of the sensor itself. In such case, the sensor would lose its sensing function and other metrological strategies than those based on its deformation should be considered for the force measurement. In this regard, a feedback-control strategy could be implemented, as in Pantano et al. (2015). Here, the load sensor is kept fixed at its initial position through the implementation of a position feedback-control, which also provides an electrical load measurement, based on the electrostatic force that has to be applied to keep the sensor at rest (**Figure 2**).

In this case, it is possible to provide the load sensor with a significantly small stiffness (55 N/m by design), which could guarantee high resolution in the displacement measurement. However, in case of softening, if no feedback control is implemented, according to the model presented in the previous section, the maximum slope which can be detected before instability is:

$$\left|\frac{\partial F}{\partial\,(x_S - x_{LS})}\right|_{max} = k_{LS} = 55\ \mathrm{N/m}.$$

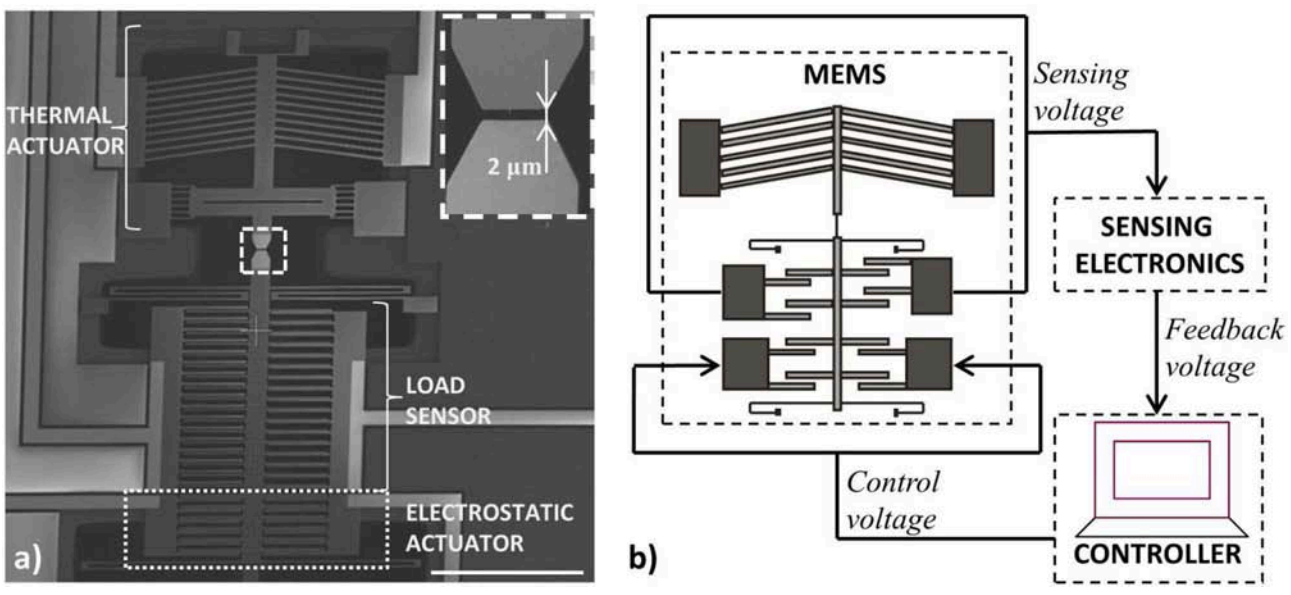

FIGURE 2 | (a) SEM picture of the tensile testing device proposed in Pantano et al. (2015) provided with load sensor feedback control. It consists of a thermal actuator, a capacitive load sensor, and an electrostatic actuator. The thermal actuator and the load sensor are separated by a 2 μm gap for accommodation of the sample to be tested (zoomed view on top); **(b)** Implementation of the feedback voltage control scheme for keeping the load sensor at rest during test on a sample. Scale bar: 500 μm.

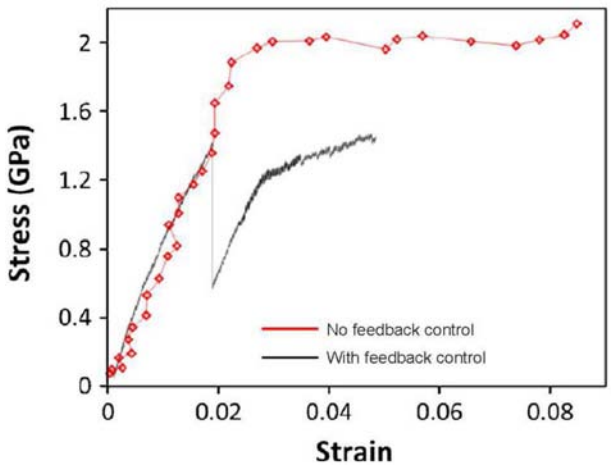

FIGURE 3 | Stress-strain curves derived from tensile tests on silver nanowires of 118 nm diameter. The red curve is referred to a test where the load sensor is allowed to move, while the black curve was derived during a test where a displacement feedback control of the load sensor was implemented. Reprinted with permission from Pantano et al. (2015). Copyright 2015, Springer.

With reference to a typical nanowire with gage length of 4 μm and diameter of about 120 nm, this corresponds to a maximum detectable negative slope in the stress-strain curve of about 20 GPa, which is one fourth of the Young modulus of bulk silver (Wu et al., 2006; Gao et al., 2012) [that represents a lower bound value for the Young modulus of silver nanowires as this increases with size reduction (Sun and Li, 2005)]. This relatively low value would not allow to record the steep load drop at yield of a silver nanowire (118 nm diameter), which can instead be measured if feedback control is implemented in the load sensor operation mode (**Figure 3**).

The second possibility for limiting instability issues is a tuning of the load sensor stiffness during the test. In particular, the load sensor stiffness should be relatively low at small sample displacement (in order to guarantee sufficient force resolution) and increase at high sample displacement, when softening is expected. This tunable stiffness ability would be a sort of bio-inspired solution, as examples of stiffness modulation can be found in nature, and, in particular in the behavior of humans, when they have to move in unstable dynamic environments. In fact, in these cases, the central neural system is able to control the muscles stiffness in order to overcome the instability of their movements (Burdet et al., 2001). In the case of MEMS devices, such ability can be readily available if the sensor geometry can change significantly during the tensile test. For example, sensors with a v-shaped geometry, like the amplifier reported in Pantano and Pugno (2014), have a stiffness depending on the length and inclination angle of their chevron beams. In particular, as the test proceeds and this kind of sensor is deformed, both the length and inclination angle of chevron beams change with a consequent stiffness increase. Currently, stiffness tuning finds application in many systems, like atomic force microscopy (AFM) (Mueller-Falcke et al., 2004) and, above all, microresonators (Kozinsky et al., 2006) and the strategies adopted in those cases can be borrowed and transferred to the context of tensile testing devices, too. In particular, among the broad range of available options, solutions based on either an electrostatic or a mechanical working principle are the most interesting, since they allow for the highest stiffness increase (de Laat et al., 2016). In the first case, a voltage is applied between moving and fixed electrodes in order to produce an electrostatic force that causes an increase or reduction of the overall system stiffness, depending on the system design (de Laat et al., 2016). In the second case, the overall system stiffness can be increased by causing the moving shuttle to engage more flexural elements. Such engagement can be induced by applying a critical voltage causing the pull-in of the moving shuttle to the additional springs (de Laat et al., 2016).

CONCLUSIONS

The sensor stiffness was shown to play a major role on the efficacy of MEMS tensile testing devices. In fact, if on one hand, it defines the resolution of the force measurement, on the other hand, it can affect the stability of the whole testing system, especially when the sample characteristic starts decreasing after a certain strain has been applied, as a consequence of plasticity or necking, for example.

The development of an analytical model allowed to find a relationship between the sensor stiffness and the rise of instability. In particular, it was shown that instability occurs when the slope of the sample characteristic is negative and its modulus exceeds the sensor stiffness. Thus, in order to prevent load sensor from instability, two possible solutions can be followed with the implementation of either a feedback control to keep the load sensor constantly at rest or a bio-inspired design, where the load sensor's stiffness can be modulated (i.e., increased when instability issues may arise).

AUTHOR CONTRIBUTIONS

MP conceived the study, developed the analytical models, and wrote the manuscript. BC contributed to the development of the analytical model related to the load sensor. All the authors discussed the results and approved the manuscript.

FUNDING

NP was supported by the European Commission H2020 under the Graphene Flagship Core 2 No. 785219 (WP14 Composites) and FET Proactive Neurofibres Grant No. 732344 as well as by the Italian Ministry of Education, University and Research (MIUR) under the Departments of Excellence grant L.232/2016 and ARS01-01384-PROSCAN.

REFERENCES

Agrawal, R., Peng, B., and Espinosa, H. D. (2009). Experimental-computational investigation of ZnO nanowires strength and fracture. *Nanoletters* 9, 4177–4183. doi: 10.1021/nl9023885

Bao, M., and Yang, H. (2007). Squeeze film air damping in MEMS. *Sensors Actuators A* 137, 3–27. doi: 10.1016/j.sna.2007.01.008

Brown, J. J., Suk, J. W., Singh, G., Baca, A. I., Dikin, D. A., Ruoff, R. S., et al. (2009). Microsystem for nanofiber electromechanical measurements. *Sensors Actuators A* 155, 1–7. doi: 10.1016/j.sna.2008.11.001

Burdet, E., Osu, R., Franklin, D. W., Milner, T. E., and Kawato, M. (2001). The central nervous system stabilizes unstable dynamics by learning optimal impedance. *Nature.* 414, 446–449. doi: 10.1038/35106566

Chilver, A. H. (1955). The instability of testing machines. *Proc. Inst. Mech. Eng.* 169, 407–418. doi: 10.1243/PIME_PROC_1955_169_053_02

de Laat, M. L. C., Pérez Garza, H. H., Herder, J. L., and Ghatkesar, M. K. (2016). A review on in situ stiffness adjustment methods in MEMS. *J. Micromech. Microeng.* 26:063001. doi: 10.1088/0960-1317/26/6/063001

Espinosa, H. D., Zhu, Y., and Moldovan, N. (2007). Design and operation of a MEMS-based material testing system for nanomechanical characterization. *J. Microelectromech. Syst.* 16, 1219–1231. doi: 10.1109/JMEMS.2007.905739

Gao, Y., Fu, Y., Sun, W., Sun, Y., Wang, H., Wang, F., et al. (2012). Investigation on the mechanical behavior of fivefold twinned silver nanowires. *Comput. Mater. Sci.* 55, 322–328. doi: 10.1016/j.commatsci.2011.11.005

Han, Z., Li, Y., and Gao, H. J. (2010). Effect of frame stiffness on the deformation behavior of bulk metallic glass. *J. Mater. Res.* 25, 1958–1962. doi: 10.1557/JMR.2010.0256

Han, Z., Wu, W. F., Li, Y., Wei, Y. J., and Gao, H. J. (2009). An instability index of shear band for plasticity in metallic glasses. *Acta Mater.* 57, 1367–1372. doi: 10.1016/j.actamat.2008.11.018

Haque, M. A., and Saif, M. T. A. (2002). *In-situ* tensile testing of nanoscale specimens in SEM and TEM. *Exp. Mech.* 42, 123–128. doi: 10.1007/BF02411059

Hudson, J. A., Crouch, S. L., and Fairhurst, C. (1972). Soft, stiff and servo-controlled testing machines: a review with reference to rock failure. *Eng. Geol.* 6, 155–189. doi: 10.1016/0013-7952(72)90001-4

Johnston, W. G. (1962). Yield points and delay times in single crystals. *J. Appl. Phys.* 33, 2716–2730. doi: 10.1063/1.1702538

Ke, C.-H., Pugno, N., Peng, B., and Espinosa, H. D. (2005). Experiments and modeling of carbon nanotube-based NEMS devices. *J. Mech. Phys. Solids* 53, 1314–1333. doi: 10.1016/j.jmps.2005.01.007

Kozinsky, I., Postma, H., and Bargatin, W. C. I., Roukes, M. L. (2006). Tuning nonlinearity, dynamic range, and frequency of nanomechanical resonators. *Appl. Phys. Lett.* 88:253101. doi: 10.1063/1.2209211

Lee, C., Wei, X., Kysar, J. W., and Hone, J. (2008). Measurement of elastic properties and intrinsic strength of monolayer graphene. *Science.* 321, 385–388. doi: 10.1126/science.1157996

Mueller-Falcke, C., Song, Y. A., and Kim, S. G. (2004). Tunable stiffness scanning microscope probe optomechatronic micro/nano components. devices, and systems. *Proc. SPIE.* 5604, 31–37. doi: 10.1117/12.571273

Pantano, M. F., Bernal, R. A., Pagnotta, L., and Espinosa, H. D. (2015). Multiphysics design and implementation of a microsystem for displacement-controlled tensile testing of nanomaterials. *Meccanica.* 50, 549–560. doi: 10.1007/s11012-014-9950-9

Pantano, M. F., Espinosa, H. D., and Pagnotta, L. (2012). Mechanical characterization of materials at small length scales. *J. Mech. Sci. Technol.* 26, 545–561. doi: 10.1007/s12206-011-1214-1

Pantano, M. F., and Pugno, N. M. (2014). Design of a bent beam electrothermal actuator for in situ tensile testing of ceramic nanostructures. *J. Eur. Ceram. Soc.* 34, 2767–2773. doi: 10.1016/j.jeurceramsoc.2013.12.001

Pantano, M. F., Speranza, G., Galiotis, C., and Pugno, N. M. (2018). A mechanical system for tensile testing of supported films at the nanoscale. *Nanotechnology.* 29, 395707. doi: 10.1088/1361-6528/aacf50

Pelesko, J. A., and Bernstein, D. H. (2003). *Modeling MEMS and NEMS*. Boca Raton, FL: Chapman & Hall/CRC. doi: 10.1201/9781420035292

Pugno, N., Ke, C.-H., and Espinosa, H. D. (2005). Analysis of doubly-clamped nanotube devices in finite deformation regime. *J. Appl. Mech.* 72, 445–449. doi: 10.1115/1.1875452

Salamon, M. D. G. (1970). Stability, instability and design of pillar workings. *Int. J. Rock Mech. Mining Sci. Geomech. Abstracts.* 7, 613–631. doi: 10.1016/0148-9062(70)90022-7

Strogatz, S. H. (2000). *Nonlinear Dynamics and Chaos: With Applications to Physics, Biology, Chemistry, and Engineering*. Boulder, CO: Westview Press, a member of the Perseus Books Group.

Sun, X., and Li, Y. (2005). Cylindrical silver nanowires: preparation. structure, and optical properties. *Adv. Mater.* 17, 2626–2630. doi: 10.1002/adma.200500957

Wang, Z. L., and Song, J. (2006). Piezoelectric nanogenerators based on zinc oxide nanowire arrays. *Science* 312, 242–246. doi: 10.1126/science.1124005

Wu, B., Heidelberg, A., Boland, J. J., Sader, J. E., Sun, X., and Li, Y. (2006). Microstructure-hardened silver nanowires. *Nanoletters* 6, 468–472. doi: 10.1021/nl052427f

Zhang, D., Breguet, J. M., Clavel, R., Sivakov, V., Christiansen, S., and Michler, J. (2010). *In situ* electron microscopy mechanical testing of silicon nanowires using electrostatically actuated tensile stages. *J. Microelectromech. Syst.* 19, 663–674. doi: 10.1109/JMEMS.2010.2044746

Zhu, Y., and Chang, T. (2015). A review of microelectromechanical systems for nanoscale mechanical characterization. *J. Micromech. Microeng.* 25:093001. doi: 10.1088/0960-1317/25/9/093001

Conflict of Interest Statement: The authors declare that the research was conducted in the absence of any commercial or financial relationships that could be construed as a potential conflict of interest.

The handling editor declared a past co-authorship with one of the authors HE.

APPENDIX

With reference to the MEMS device reported in Pantano et al. (2015), the load sensor mass is about 10^{-10} kg, k_{LS}=55 N/m, the damping coefficient, D, can be evaluated as due to the squeezing of air trapped between its comb-drive pairs. Considering the classical formula (Bao and Yang, 2007) that describes the squeeze-film air damping between two rectangular plates:

$$D = N\mu \frac{Lw^3}{h^3},$$

where N is the number of comb-drive finger pairs, μ is the air viscosity, h is the thickness of the air gap, L and w are the larger and the smaller side of the plate, D results to be about 10^{-4} Ns/m at atmospheric pressure. In this condition, for almost all values of k_1, $\alpha = \frac{D}{\sqrt{M_{LS}|k_1 - k_{LS}|}} < 1$. Furthermore, since these kinds of MEMS devices work in vacuum, D is expected to be much smaller when air is rarefied, causing α to be much smaller than 1 as well, as assumed in section Load Sensor Stability.

frontiers in Materials

REVIEW
published: 01 March 2019
doi: 10.3389/fmats.2019.00021

Micromechanics-Based Homogenization of the Effective Physical Properties of Composites With an Anisotropic Matrix and Interfacial Imperfections

Seunghwa Ryu[1*†], *Sangryun Lee*[1†], *Jiyoung Jung*[1], *Jinyeop Lee*[2] *and Youngsoo Kim*[1]

[1] Department of Mechanical Engineering, Korea Advanced Institute of Science and Technology (KAIST), Daejeon, South Korea, [2] Department of Mathematical Sciences, Korea Advanced Institute of Science and Technology (KAIST), Daejeon, South Korea

Micromechanics-based homogenization has been employed extensively to predict the effective properties of technologically important composites. In this review article, we address its application to various physical phenomena, including elasticity, thermal and electrical conduction, electric, and magnetic polarization, as well as multi-physics phenomena governed by coupled equations such as piezoelectricity and thermoelectricity. Especially, for this special issue, we introduce several research works published recently from our research group that consider the anisotropy of the matrix and interfacial imperfections in obtaining various effective physical properties. We begin with a brief review of the concept of the Eshelby tensor with regard to the elasticity and mean-field homogenization of the effective stiffness tensor of a composite with a perfect interface between the matrix and inclusions. We then discuss the extension of the theory in two aspects. First, we discuss the mathematical analogy among steady-state equations describing the aforementioned physical phenomena and explain how the Eshelby tensor can be used to obtain various effective properties. Afterwards, we describe how the anisotropy of the matrix and interfacial imperfections, which exist in actual composites, can be accounted for. In the last section, we provide a summary and outlook considering future challenges.

Keywords: homogenization, micromechanics, anisotropy, interfacial imperfection, effective properties

OPEN ACCESS

Edited by:
Nicola Maria Pugno,
University of Trento, Italy

Reviewed by:
Pasquale Vena,
Polytechnic University of Milan, Italy
Stefano Mariani,
Polytechnic University of Milan, Italy

****Correspondence:***
Seunghwa Ryu
ryush@kaist.ac.kr

[†]These authors have contributed equally to this work

Specialty section:
This article was submitted to Mechanics of Materials, a section of the journal Frontiers in Materials

Received: *30 November 2018*
Accepted: *04 February 2019*
Published: *01 March 2019*

Citation:
Ryu S, Lee S, Jung J, Lee J and Kim Y (2019) Micromechanics-Based Homogenization of the Effective Physical Properties of Composites With an Anisotropic Matrix and Interfacial Imperfections. Front. Mater. 6:21. doi: 10.3389/fmats.2019.00021

INTRODUCTION

Composites, typically referred to materials consisting of reinforcements and a matrix, offer many advantages that cannot be gained solely with only one of its constituents to improve various materials properties, such as resistance to chemicals (Jawaid et al., 2011; Taurino et al., 2016), a high strength-to-weight ratio (Walther et al., 2010), electrical (Allaoui et al., 2002; Gojny et al., 2005; Tuncer et al., 2007) or thermal insulation properties (Wei et al., 2011; Li et al., 2016), and/or combinations of these properties (Flahaut et al., 2000; Park et al., 2012). Most advanced materials in many engineering applications are composites, such as anti-corrosion composites in the marine industry (Mouritz et al., 2001), lightweight structural carbon composites in the car

(Obradovic et al., 2012; Friedrich and Almajid, 2013) and airplane industries (Immarigeon et al., 1995; EL-Dessouky and Lawrence, 2013), and electric or thermal shielding composites (Imai et al., 2006; Zheng et al., 2009) as used in relation to electric wire and heat pipe technology.

In addition to manmade synthetic composites, nature has exploited the advantages of composites to meet certain requirements related to survival and sustained living conditions, even with the limited resources and building blocks available in nature (Gibson et al., 1995; Wegst and Ashby, 2004; Launey et al., 2009; Sen and Buehler, 2011). For example, the combined high toughness and high strength levels of nacre, bone, and cone shells are attributed to their unique hierarchical composite structures ranging from the nano to macro scale, and significant effort has been expended to understand and mimic the natural composites (Tang et al., 2003; Ji and Gao, 2004; Li et al., 2012; Hu et al., 2013; Das et al., 2015; Shao and Keten, 2015; Gao et al., 2017). For the facile design and application of various composites, it is of paramount importance to understand and predict the effective properties of composites as a function of their shape, volume fraction, and spatial distribution of the reinforcements used in them.

Numerical modeling based on finite element analyses has been widely used to predict the effective properties of composites, including the mechanical, thermal, electrical, piezoelectric, thermoelectric properties (Pan et al., 2008; Wang et al., 2011; Miled et al., 2013; Lu et al., 2014; Doghri et al., 2016; Lee et al., 2018a, 2019). However, to obtain statistically meaningful results, finite element analyses require multiple evaluations of large simulation cells involving a large number of fillers, thus necessitating a much fine mesh near the boundary to serve as representative volumes and leading to the requirement of computationally expensive and time-consuming calculations (Xu and Yagi, 2004; Marcos-Gomez et al., 2010; Lee et al., 2018a, 2019). Such extensive numerical calculations are feasible for predictions of the effective properties of systems in the linear response regime. However, it becomes a formidable task numerically to predict the behavior of composites in the nonlinear response regime, where multiple linearization and convergence tasks are required (Miled et al., 2013; Doghri et al., 2016).

When composites have relatively periodic and regular arrangements, they can be modeled reasonably well by an analytic model focusing on the load transfer mechanism of a unit cell. Typical examples include synthetic composites with very long fiber reinforcements (Suh, 2005) and natural staggered platelet structures (Gao, 2006; Kim et al., 2018). In contrast, composites involving random arrangements of short-fiber fillers or spherical reinforcements must be studied via homogenization schemes, as it is infeasible directly to model the interaction among randomly/aperiodically distributed reinforcements and load transfer mechanisms in detail.

The mechanical properties of such short-fiber-reinforced composites and multicomponent alloys can be deduced by computing the strain fields in the reinforcements and the matrix (Mura, 1982). Especially for composites including well-dispersed low-volume-fraction reinforcements (below 20%), the influence of other reinforcements can be taken into account via a mean-field approach by approximating the surrounding area of each reinforcement as the matrix subjected to local strain that is identical to the average strain of the matrix within the entire specimen (Benveniste, 1987) (Mori-Tanaka method) or using a medium with the effective stiffness of the composite (Hill, 1965) (self-consistent method). In this regime, where mean-field approximation is valid, a solution to the single-inhomogeneity problem can be applied to model the effective properties while taking into account multiple reinforcements. Once such homogenization scheme has been established for the linear response regime, and it can be extended to model the non-linear response of composites based on various linear approximation schemes such as the incremental tangent method (Castaneda and Tiberio, 2000; Idiart et al., 2006; Doghri et al., 2016), the incremental secant method (Wu et al., 2013), variational approaches (Castaneda, 1991; Lahellec and Suquet, 2007a; Brassart et al., 2011), and others (Nemat-Nasser, 1999; Lahellec and Suquet, 2007b).

Although extensive efforts have been devoted to determine various effective properties of composites, relatively less attention has been paid to the modeling of the effects of imperfect matrix-reinforcement interfaces and anisotropic matrices. Moreover, while the governing equations of various phenomena are mathematically analogous, the connections among them have not been discussed in detail in the literature. Hence, in this paper, we present research which considers interfacial imperfections and anisotropy effects for the predictions of various effective physical properties and suggest a universal formalism and numerical recipe based on a mathematical analogy. Especially, for this special issue, we introduce several papers published recently from our group on this issue.

The paper is structured as follows. In section Eshelby tensor and its application to effective stiffness calculations in elasticity, we provide a brief overview on the concept of the Eshelby tensor of isotropic materials in elasticity and its application to the computation of the effective stiffness of composites. In section Mathematical analogy between governing equations in various physical phenomena, we discuss the mathematical analogy among the steady-state equations governing various physical phenomena and how the Eshelby tensor and homogenization concept can be applied to predict various effective physical properties. Section Interfacial imperfections and anisotropy of the matrix describes how anisotropy of the matrix and interfacial imperfections, present in most realistic composites, can be accounted for. In the last section, we summarize the discussion and provide our perspective on future challenges.

ESHELBY TENSOR AND ITS APPLICATION TO EFFECTIVE STIFFNESS CALCULATIONS IN ELASTICITY

Single Inclusion Problem

We can deduce the mechanical properties of fiber-reinforced composites by considering the strain field in inclusions and in inhomogeneities. An inclusion refers to an embedded material

with an elastic stiffness tensor L_{pqrs} identical to that of the matrix, while an inhomogeneity refers to an embedded material with a different stiffness L'_{pqrs}. Eshelby showed that the strain field inside an ellipsoidal inclusion embedded in an infinite matrix is uniform when the inclusion is subject to uniform eigenstrain (Eshelby, 1957, 1959). Eigenstrain indicates the stress-free deformation strain associated with thermal expansion (Jun and Korsunsky, 2010), initial strain (Chiu, 1977), or phase transformation (George and Dvorak, 1992; Tirry and Schryvers, 2009). The Eshelby tensor is defined as the fourth-order tensor S_{ijrs} which links the constrained strain within the inclusion ε^c_{ij} to the eigenstrain ε^*_{rs}, as $\varepsilon^c_{ij} = S_{ijrs}\varepsilon^*_{rs}$ (Eshelby, 1957; Mura, 1982). In this section, we discuss (i) the key concept of the Eshelby tensor, (ii) how an ellipsoidal inhomogeneity subjected to an external load can be transformed into the equivalent Eshelby inclusion problem, and (iii) the mean-field method used to predict the effective stiffness of a composite based on the average theorem, considering an isotropic matrix in the absence of interfacial damage.

We begin the discussion by introducing the governing equation for Green's function $G_{ij}(\boldsymbol{x}-\boldsymbol{y})$ in elastostatics, which indicates the displacement in the i^{th} direction at point $\boldsymbol{x}$ by the unit body force in the j^{th} direction at point $\boldsymbol{y}$, in an infinite elastic medium:

$$L_{ijkl}G_{kp,lj}(\boldsymbol{x}-\boldsymbol{y}) + \delta_{ip}\delta(\boldsymbol{x}-\boldsymbol{y}) = 0 \tag{1}$$

Here, L_{ijkl} is the fourth-order elastic stiffness tensor, and the repeated indices represent the summation over all values from 1 to 3. For an isotropic material, L_{ijkl} can be represented by two independent elastic constants (Section Interfacial imperfections and anisotropy of the matrix includes a discussion of anisotropy). Green's function for the isotropic material is available in a closed form (Mura, 1982), as follows,

$$G_{ij}(\boldsymbol{x}-\boldsymbol{y}) = \frac{1}{16\pi\mu(1-\nu)|\boldsymbol{x}-\boldsymbol{y}|} \times \left[(3-4\nu)\delta_{ij} + \frac{(x_i-y_i)(x_j-y_j)}{|\boldsymbol{x}-\boldsymbol{y}|^2}\right] \tag{2}$$

where μ and ν are the shear modulus and the Poisson's ratio of the material, respectively, and $|\boldsymbol{x}-\boldsymbol{y}|$ denotes the standard norm of vector $\boldsymbol{x}-\boldsymbol{y}$.

The schematic for the single inclusion problem is depicted in **Figure 1**, which is solved with a four-step procedure. We assume that the inclusion can deform by the eigenstrain ε^* when there is no external displacement or load (step 1). In order to maintain the original shape, the load $\boldsymbol{T}$ is applied to the inclusion (step 2). The inclusion is then plugged into a hole having the original shape and size within an infinite matrix (step 3). After removing the applied load ($\boldsymbol{T}$), the inclusion exerts traction of $\boldsymbol{F} = -\boldsymbol{T}$ on the matrix (step 4). Due to the constraining effect of the matrix, the inclusion deforms by the constrained strain ε^c, which is different from the eigenstrain ε^*. The constrained strain field

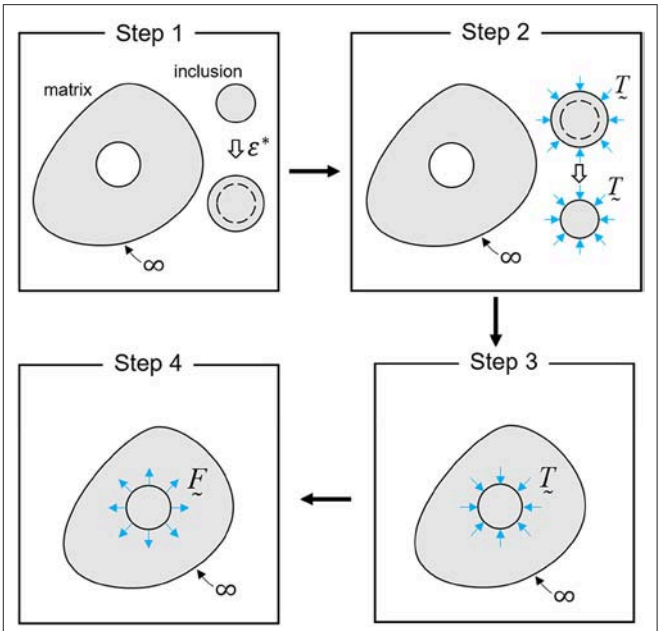

FIGURE 1 | Schematic of the single inclusion problem in elasticity.

can be expressed by employing Green's function, as follows:

$$\varepsilon^c_{ij} = S_{ijrs}\varepsilon^*_{rs},$$
$$\text{where } S_{ijrs} = \frac{1}{2}\int_\Omega L_{pqrs}\left\{\frac{\partial^2 G_{ip}(\boldsymbol{x}-\boldsymbol{y})}{\partial x_j \partial y_q} + \frac{\partial^2 G_{jp}(\boldsymbol{x}-\boldsymbol{y})}{\partial x_i \partial y_q}\right\} d\boldsymbol{y}. \tag{3}$$

Because the eigenstrain and constrained strain are symmetric, the Eshelby tensor has minor symmetry ($S_{ijkl} = S_{jikl} = S_{ijlk}$) but no major symmetry ($S_{ijkl} \neq S_{klij}$). In an isotropic medium, for an ellipsoidal inclusion with three different semi-axes a_1, a_2, *and* a_3, the expression is given in terms of standard elliptic integrals (Mura, 1982; Qu and Cherkaoui, 2007). For isotropic material having an axi-symmetric ellipsoidal inclusion ($a_1 \neq a_2 = a_3$), all components of the Eshelby tensor can be obtained in a closed form, as shown in **Appendix A** (Mura, 1982; Lee and Ryu, 2018). The orientation average of a randomly distributed ellipsoidal inclusion was considered in one of our studies (Lee and Ryu, 2018). For a spherical inclusion, the Eshelby tensor can be compactly expressed as

$$S_{ijkl} = \frac{5\nu-1}{15(1-\nu)}\delta_{ij}\delta_{kl} + \frac{4-5\nu}{15(1-\nu)}\left(\delta_{ik}\delta_{jl} + \delta_{il}\delta_{jk}\right). \tag{4}$$

We note that the Eshelby tensor for the spherical inclusion does not depend on the radius. In general, the Eshelby tensor does not depend on the absolute size of the inclusion because there is no characteristic length scale in elasticity. In contrast, in the presence of an interfacial imperfection, the modified Eshelby tensor depends on the absolute size of the inclusion, which will be discussed in Section Interfacial imperfections and anisotropy of the matrix. We will also describe the Eshelby tensor for an anisotropic medium in Section Interfacial imperfections and anisotropy of the matrix.

Single Inhomogeneity Problem

Having introduced the concept of the Eshelby tensor, we discuss how an ellipsoidal inhomogeneity subjected to a uniform external load (external strain ε_{kl}^{A} for the following example) can be transformed into the equivalent Eshelby inclusion problem. In the presence of a uniform external load (either stress or strain), the total strain field of the aforementioned Eshelby inclusion problem becomes $\varepsilon_{kl}^{t} = \varepsilon_{kl}^{A} + \varepsilon_{kl}^{c}$, and the stress field becomes $\sigma_{ij}^{I} = L_{ijkl}\left(\varepsilon_{kl}^{t} - \varepsilon_{kl}^{*,\mathrm{Eq}}\right)$. When the total strain field $\varepsilon_{kl}^{t\prime} = \varepsilon_{kl}^{A} + \varepsilon_{kl}^{c\prime}$ and stress field $\sigma_{ij}^{I\prime} = L'_{ijkl}\epsilon_{kl}^{t\prime}$ of an inhomogeneity subjected to an identical applied load are identical to those of the Eshelby inclusion, $\varepsilon_{kl}^{*,\mathrm{Eq}}$ is referred to as an equivalent eigenstrain. Therefore, from the total strain and stress equality conditions, or equivalently $\varepsilon_{kl}^{A} + \varepsilon_{kl}^{c\prime} = \varepsilon_{kl}^{A} + \varepsilon_{kl}^{c}$ and $L'_{ijkl}\left(\varepsilon_{kl}^{A} + \varepsilon_{kl}^{c\prime}\right) = L_{ijkl}\left(\varepsilon_{kl}^{A} + \varepsilon_{kl}^{c} - \varepsilon_{kl}^{*,\mathrm{Eq}}\right)$, we obtain the following expression for the equivalent eigenstrain:

$$\left[\left(L'_{ijkl} - L_{ijkl}\right) S_{klmn} + L_{ijmn}\right] \varepsilon_{mn}^{*,\mathrm{Eq}} = \left(L'_{ijkl} - L_{ijkl}\right) \varepsilon_{kl}^{A}. \quad (5)$$

In a tensor expression,

$$\varepsilon^{*,\mathrm{Eq}} = \left[\left(\boldsymbol{L}' - \boldsymbol{L}\right) : \boldsymbol{S} + \boldsymbol{L}\right]^{-1} : \left(\boldsymbol{L} - \boldsymbol{L}'\right) : \varepsilon^{A} \quad (6)$$

where : and $[\,]^{-1}$ refer to the double contraction and inverse operator, respectively. The double contraction and inverse operation of fourth-order tensors can be facilitated by adopting the Mandel notation (Helnwein, 2001), which converts all tensor operations into conventional 6 × 6 matrix operations (Lee et al., 2018b, 2019).

In the Mandel notation, the strain vector $\overrightarrow{\sigma}$, stress vector $\overrightarrow{\varepsilon}$, stiffness matrix $\langle \boldsymbol{L} \rangle$, and Eshelby matrix $\langle \boldsymbol{S} \rangle$ are defined as follows:

$$\overrightarrow{\sigma} := \begin{bmatrix} \sigma_{11} \\ \sigma_{22} \\ \sigma_{33} \\ \sqrt{2}\sigma_{23} \\ \sqrt{2}\sigma_{31} \\ \sqrt{2}\sigma_{12} \end{bmatrix}, \qquad \overrightarrow{\varepsilon} := \begin{bmatrix} \varepsilon_{11} \\ \varepsilon_{22} \\ \varepsilon_{33} \\ \sqrt{2}\varepsilon_{23} \\ \sqrt{2}\varepsilon_{31} \\ \sqrt{2}\varepsilon_{12} \end{bmatrix}, \quad (7)$$

$$\langle \boldsymbol{L} \rangle := \begin{bmatrix} L_{1111} & L_{1122} & L_{1133} & \sqrt{2}L_{1123} & \sqrt{2}L_{1131} & \sqrt{2}L_{1112} \\ L_{1122} & L_{2222} & L_{2233} & \sqrt{2}L_{2223} & \sqrt{2}L_{2231} & \sqrt{2}L_{2212} \\ L_{1133} & L_{2233} & L_{3333} & \sqrt{2}L_{3323} & \sqrt{2}L_{3331} & \sqrt{2}L_{3312} \\ \sqrt{2}L_{1123} & \sqrt{2}L_{2223} & \sqrt{2}L_{3323} & 2L_{2323} & 2L_{2331} & 2L_{2312} \\ \sqrt{2}L_{1131} & \sqrt{2}L_{2231} & \sqrt{2}L_{3331} & 2L_{2331} & 2L_{3131} & 2L_{3112} \\ \sqrt{2}L_{1112} & \sqrt{2}L_{2212} & \sqrt{2}L_{3312} & 2L_{2312} & 2L_{3112} & 2L_{1212} \end{bmatrix}$$

$$\langle \boldsymbol{S} \rangle := \begin{bmatrix} S_{1111} & S_{1122} & S_{1133} & \sqrt{2}S_{1123} & \sqrt{2}S_{1131} & \sqrt{2}S_{1112} \\ S_{2211} & S_{2222} & S_{2233} & \sqrt{2}S_{2223} & \sqrt{2}S_{2231} & \sqrt{2}S_{2212} \\ S_{3311} & S_{3322} & S_{3333} & \sqrt{2}S_{3323} & \sqrt{2}S_{3331} & \sqrt{2}S_{3312} \\ \sqrt{2}S_{2311} & \sqrt{2}S_{2322} & \sqrt{2}S_{2333} & 2S_{2323} & 2S_{2331} & 2S_{2312} \\ \sqrt{2}S_{3111} & \sqrt{2}S_{3122} & \sqrt{2}S_{3133} & 2S_{3123} & 2S_{3131} & 2S_{3112} \\ \sqrt{2}S_{1211} & \sqrt{2}S_{1222} & \sqrt{2}S_{1233} & 2S_{1223} & 2S_{1231} & 2S_{1212} \end{bmatrix}$$

The prefactors $\sqrt{2}$ and 2 ensure that the matrix-matrix product and the inverse coincide with the double contraction and the inverse of the fourth-order tensors, respectively. Hence, if $\boldsymbol{A}, \boldsymbol{B}$ denote a fourth-order tensor with minor symmetry ($A_{ijkl} = A_{jikl} = A_{ijlk}$), and $\langle \boldsymbol{A} \rangle$, $\langle \boldsymbol{B} \rangle$ represent the corresponding 6 × 6 matrix following the Mandel notation, we can calculate the double contraction and inverse from the 6 × 6 matrix multiplication and inverse, respectively, as

$$\langle \boldsymbol{A} : \boldsymbol{B} \rangle = \langle \boldsymbol{A} \rangle \langle \boldsymbol{B} \rangle, \qquad \left\langle \boldsymbol{A}^{-1} \right\rangle = \langle \boldsymbol{A} \rangle^{-1}. \quad (8)$$

Mean-Field Homogenization of the Effective Stiffness

For the problem involving multiple inhomogeneities, the Mori-Tanaka method has been widely used for predicting the effective stiffness by considering the interaction among the inhomogeneities (see **Figure 2**). Each inhomogeneity is assumed to be embedded effectively in the matrix subjected to a spatial average strain of the matrix over the entire specimen, which is why the technique is referred to as the mean-field homogenisation method. Because the interaction between the inhomogeneities becomes intense at a high volume fraction of inhomogeneities, the Mori–Tanaka method is known to be reliable at a relatively low volume fraction of inhomogeneities (<20%). In this mean-field homogenization scheme, the average strain fields in the matrix, inhomogeneity, and composite ($\overline{\varepsilon_0}$, $\overline{\varepsilon_I} (\approx \overline{\varepsilon_0} + \boldsymbol{S} : \varepsilon^{*,\mathrm{Eq}})$, and $\overline{\varepsilon} (= \varepsilon^{A})$, respectively) are related as follows:

$$\overline{\varepsilon_I} = \boldsymbol{T}\overline{\varepsilon_0} = \boldsymbol{T} : (c_0\boldsymbol{I} + c_1\boldsymbol{T})^{-1}\overline{\varepsilon} = \boldsymbol{A} : \overline{\varepsilon}, \quad (9)$$

where $\boldsymbol{A} = \boldsymbol{T} : (c_0\boldsymbol{I} + c_1\boldsymbol{T})^{-1}$ (where $\boldsymbol{T} = [\boldsymbol{I} + \boldsymbol{S} : \boldsymbol{L_0^{-1}} : (\boldsymbol{L_1} - \boldsymbol{L_0})]^{-1}$) is the strain concentration tensor for the Mori-Tanaka method. $\boldsymbol{A}$ converges to the strain concentration tensor for the

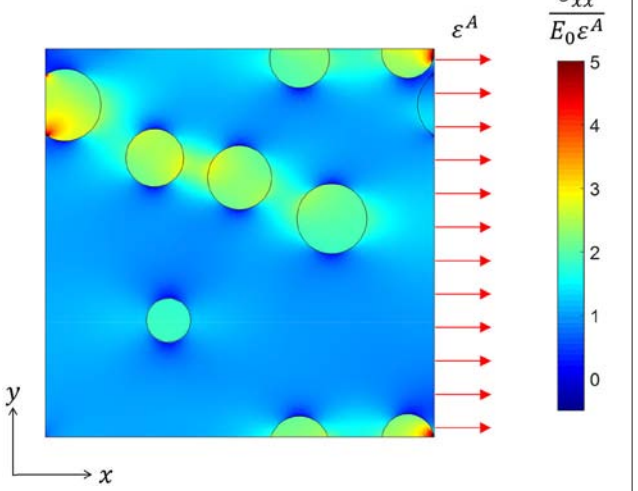

FIGURE 2 | Non-uniform σ_{xx} field under uniform applied strain in the x direction within a cross-section in a three-dimensional volume simulation. The material properties used for this figure are $E_1 = 10E_0$ *and* $\nu_1 = \nu_0 = 0.25$ and the volume fraction is 10%.

TABLE 1 | Interpretation of conductivity/dielectric-related equations under a steady state, as governed by a single class of PDE.

Problem	*j*	*e*	*K*
Electrical conduction	Electricalcurrent J^E	Electricalfield E	Electricalconductivity σ_e
Dielectrics	Displacementfield D	Electricalfield E	Dielectricpermittivity ϵ
Magnetism	Magneticinduction b	Magneticfield h	Magneticpermittivity μ_m
Thermal conduction	Heat flux q	Temperaturegradient $-\nabla T$	Thermalconductivity κ
Diffusion	Particle current j^N	Concentrationgradient $-\nabla c$	Diffusivity D_f
Flow inporous media	Weighted fluidvelocity $\eta v j^f$	Pressuregradient ∇P	Fluid permeability k

single inhomogeneity problem, $\boldsymbol{T}$, in the limit of very small inhomogeneity volume fraction, c_1. The effective stiffness can be obtained from the relationship between the volume-averaged stress and strain within the composite ($\overline{\sigma} = c_0\overline{\sigma_0} + c_1\overline{\sigma_1} = c_0\boldsymbol{L}_0 : \overline{\varepsilon_0} + c_1\boldsymbol{L}_1 : \overline{\varepsilon_1}$ and $\overline{\varepsilon} = c_0\overline{\varepsilon_0} + c_1\overline{\varepsilon_1}$, respectively) as follows:

$$\overline{\sigma} = \boldsymbol{L}_{eff} : \overline{\varepsilon} \qquad \boldsymbol{L}_{eff} = (c_0\boldsymbol{L}_0 + c_1\boldsymbol{L}_1 : \boldsymbol{T}) : (c_0\boldsymbol{I} + c_1\boldsymbol{T})^{-1} \quad (10)$$

There is another class of homogenization method called the self-consistent method, where the surrounding area is approximated as a medium with the effective stiffness of the composite. However, we omit the discussion of the self-consistent method here because the effective stiffness cannot be solved explicitly (Hill, 1965; Qu and Cherkaoui, 2007). Instead, it requires an iterative numerical solution.

MATHEMATICAL ANALOGY BETWEEN GOVERNING EQUATIONS IN VARIOUS PHYSICAL PHENOMENA

Mathematical Analogy Discussion

Having introduced the key concepts of the Eshelby tensor and the mean-field homogenization scheme, we turn our attention to the predictions of various physical phenomena via a mathematical analogy. We consider two representative classes of steady-state equations governing different physics: conduction/dielectric-related equations and coupled multi-physics equations. An extensive discussion can be found in the literature (Milton, 2002).

For the first class of the equations, referred to as conductivity/dielectric-related equations, the governing equation under a steady state at any point $\boldsymbol{x}$ in a medium in the absence of an internal source can be written using the following equations,

$$\boldsymbol{j}(\boldsymbol{x}) = \boldsymbol{K}(\boldsymbol{x}) \cdot \boldsymbol{e}(\boldsymbol{x}), \quad \nabla \cdot \boldsymbol{j} = 0, \quad \nabla \times \boldsymbol{e} = \boldsymbol{0}, \qquad (11)$$

which appear in physical problems concerning the conductivity of dielectrics, such as those linked to the concepts of electrical conductivity, dielectric phenomena, magnetism, thermal conduction, diffusion, and flows in porous media. In each field, the vector fields $\boldsymbol{j}(\boldsymbol{x})$, $\boldsymbol{e}(\boldsymbol{x})$ and, the second-order tensor $\boldsymbol{K}(\boldsymbol{x})$ have the physical interpretations given in **Table 1**. We note that the governing equations for these phenomena in a dynamic regime differ from each other; equations pertaining to dissipative transport phenomena use a first-order derivative with respect to time, leading to a homogeneous distribution of the temperature or concentration in an infinite time limit if an external driving force is not present, whereas equations pertaining to non-dissipative transport phenomena use a second-order derivative with respect to time, leading to electro-magnetic or acoustic wave propagation (Kreyszig, 1972). Because the steady-state equations are identical in terms of their mathematical descriptions, the homogenization scheme obtained for one of these equations can be applied directly to any of the other equations in **Table 1** to obtain the effective electrical and thermal conductivities, the effective dielectric and magnetic permittivities, the effective diffusivity, and the effective fluid permeability.

As examples of the second class of equations, we consider piezoelectric and thermoelectric equations. The aforementioned conductivity/dielectric-related equations describe idealized cases. In practice, lattice distortion can cause electric polarization in some classes of anisotropic materials, and vice versa (Fu and Cohen, 2000). Moreover, conducting electrons can carry some heat with them and thus causes coupling between thermal and electric phenomena (Zhao et al., 2014). The former is referred to as piezoelectricity and the latter is termed thermoelectricity.

The constitutive equations of piezoelectricity are given as

$$\begin{aligned} \sigma_{ij} &= L_{ijmn}\varepsilon_{mn} + d_{nij}(-E_n) \\ D_i &= d_{imn}\varepsilon_{mn} - \epsilon_{in}(-E_n), \end{aligned} \qquad (12)$$

where D_i is the electrical displacement vector, E_n is the electric field vector, $\epsilon_{mk} = \left(\frac{\partial D_m}{\partial E_k}\right)_\varepsilon$ is the second rank tensor of the dielectric permittivity constants under constant strain with $\epsilon_{mk} = \epsilon_{km}$, and $-d_{ijm} = \left(\frac{\partial \sigma_{ij}}{\partial E_m}\right)_\varepsilon = -\left(\frac{\partial D_m}{\partial \epsilon_{ij}}\right)_E$ is the third rank tensor of the piezoelectric constants under constant stress σ_{ij} with $d_{kij} = d_{kji}$. We can express Equation (12) as a simplified form of a linear equation, similar to the constitutive equations of elasticity, thermal conduction and electrical conduction using the notation introduced by Barnett and Lothe (1975). This notation is identical to the conventional notation, except that the repeated capital index implies summation from 1 to 4. With this notation, we can express the elastic strain and electric field as

$$Z_{Mn} = \begin{cases} \varepsilon_{mn} & M = 1, 2, 3 \\ -E_n & M = 4 \end{cases}, \qquad (13)$$

where Z_{Mn} is obtained by the differentiate U_M, which is given by

$$U_M = \begin{cases} u_m & M = 1,2,3 \\ V & M = 4 \end{cases}. \tag{14}$$

In a similar manner, we can simplify the stress and electric displacement to one matrix using the notation

$$\Sigma_{iJ} = \begin{cases} \sigma_{ij} & J = 1,2,3 \\ D_i & J = 4 \end{cases}. \tag{15}$$

Then, the electroelastic moduli and constitutive equation are obtained using the equations below.

$$C_{iJMn} = \begin{cases} L_{ijmn} & J,M = 1,2,3 \\ d_{nij} & J = 1,2,3,\ M = 4 \\ d_{imn} & J = 4,\ M = 1,2,3 \\ -\epsilon_{in} & J,M = 4 \end{cases} \tag{16}$$

$$\Sigma_{iJ} = C_{iJMn} Z_{Mn}$$

On the other hand, for a thermoelectric material, similarly, the constitutive equation is arranged in tensor form, as follows:

$$\begin{bmatrix} \boldsymbol{J_E} \\ \boldsymbol{J_S} \end{bmatrix} = \begin{bmatrix} \sigma & \alpha \cdot \sigma \\ \alpha \cdot \sigma \& \gamma/T & \end{bmatrix} \begin{bmatrix} \boldsymbol{E} \\ \boldsymbol{e} \end{bmatrix} \tag{17}$$

By using the notation introduced for a piezoelectric material (Jung et al., 2018), the expression is as follows,

$$J_{Ji} = P_{JiMn} Q_{Mn} \tag{18}$$

where

$$J_{Ji} = \begin{Bmatrix} J_i^E & J = 1 \\ J_i^S & J = 2 \end{Bmatrix}, \tag{19}$$

$$Q_{Mn} = \begin{Bmatrix} E_n & M = 1 \\ e_n & M = 2 \end{Bmatrix}, \tag{20}$$

$$P_{JiMn} = \begin{Bmatrix} (\sigma_{\boldsymbol{e}})_{in} & J = 1,\ M = 1 \\ (\sigma_{\boldsymbol{e}} \cdot \alpha)_{in} & J = 1,\ M = 2 \\ (\alpha \cdot \sigma_{\boldsymbol{e}})_{in} & J = 2,\ M = 1 \\ \gamma_{in}/T & J = 2,\ M = 2 \end{Bmatrix}. \tag{21}$$

Here, $\boldsymbol{J^E}$ is the electrical current density, $\boldsymbol{J^S}(= \boldsymbol{q}/T)$ is the entropy flux, $\boldsymbol{q}$ is the heat flux, T is the temperature, $\sigma_{\boldsymbol{e}}$ is the electrical conductivity, α is the Seebeck coefficient, $\gamma(= \kappa + T\alpha \cdot \sigma_{\boldsymbol{e}} \cdot \alpha)$ is the heat conductivity under a zero electric field, and κ is the heat conductivity at zero current. As shown in Equation (21), P_{JiMn} contains T, which depends on the position $\boldsymbol{x}$ and therefore does not have mathematical similarity with other physics in general. For a small temperature difference across the hot and cool sides ($T_H - T_L = \Delta T \approx 0$), we can assume that the temperature variable T in the constitutive equation is a constant average temperature $T_{avg}\left(= \frac{T_H + T_L}{2}\right)$, allowing us to obtain a linear constitutive equation. The validity of this assumption has been studied for wide range of ΔT by comparing theoretical predictions with finite element analysis outcomes (Jung et al., 2018).

Eshelby Tensor for Various Physical Phenomena

Due to the mathematical analogy, the Eshelby tensor can be expressed in a similar form. In the most general case of a medium with arbitrary anisotropy and an ellipsoidal inclusion with three different semi-axes a_1, a_2, *and* a_3, by simplifying Equation (3), the elastic Eshelby tensor can be expressed as Mura (1982),

$$S_{ijrs} = \frac{1}{8\pi} L_{pqrs} \int_{-1}^{1} \int_{0}^{2\pi} \left\{ g_{ipjq}\left(\overline{\xi}\right) + g_{jpiq}\left(\overline{\xi}\right) \right\} d\theta d\overline{\zeta_3}, \tag{22}$$

where $g_{ijkl}\left(\overline{\xi}\right) = \overline{\xi}_k \overline{\xi}_l Z_{ij}\left(\overline{\xi}\right)$. Here, $\boldsymbol{Z}(\xi) = [(\boldsymbol{L} \cdot \xi) \cdot \xi]^{-1}$ and ξ are Green's function and a vector in the Fourier space, respectively. Because $Z_{ij}(\xi)$ is a homogeneous function of degree -2, $\xi_k \xi_l Z_{ij}(\xi)$ is identical to $\overline{\xi}_k \overline{\xi}_l Z_{ij}\left(\overline{\xi}\right)$, where $\overline{\xi}$ is a normalized vector. Equation (22) can be evaluated by using the integral variables $\overline{\zeta_3}$ and θ; thus, $\overline{\xi}_1 = \frac{1}{a_1}\sqrt{1 - \overline{\zeta_3}^2}\cos\theta$, $\overline{\xi}_2 = \frac{1}{a_2}\sqrt{1 - \overline{\zeta_3}^2}\sin\theta$, *and* $\overline{\xi}_3 = \frac{1}{a_3}\overline{\zeta_3}$ given the semi-axes of an ellipsoidal inclusion (a_i). Similarly, by adding three more degrees of freedom from electric polarization and its coupling with lattice distortion, the pizeoelectric Eshelby tensor is derived as follows (Dunn and Taya, 1993),

$$S_{MnAb} = \begin{cases} \frac{1}{8\pi} C_{iJAb} \int_{-1}^{1} \int_{0}^{2\pi} \left[h_{MJin} + h_{nJiM} \right] d\theta d\overline{\zeta_3}, & M = 1,2,3 \\ \frac{1}{4\pi} C_{iJAb} \int_{-1}^{1} \int_{0}^{2\pi} h_{4Jin} d\theta d\overline{\zeta_3}. & M = 4 \end{cases} \tag{23}$$

Here, $h_{MJkl}\left(\overline{\xi}\right) = \overline{\xi}_k \overline{\xi}_l \left(\boldsymbol{Y}^{-1}\right)_{MJ}$ where $Y_{MJ}\left(\overline{\xi}\right) = \overline{\xi}_s \overline{\xi}_t C_{sMJt}$. Because the piezoelectric coefficients are zero for all centrosymmetric crystals, the piezoelectric Eshelby tensor for an isotropic medium does not exist.

For the conduction or dielectric phenomena described by Equation (11) and physical property tensor $\boldsymbol{K}$ in **Table 1**, the Eshelby tensor is obtained from

$$S_{ik}(\boldsymbol{x}) = \frac{\partial}{\partial x_i} \int_{\Omega} \frac{\partial G(\boldsymbol{x} - \boldsymbol{y})}{\partial y_j} d\boldsymbol{y} K_{jk}. \tag{24}$$

Unlike the Green's function in elasticity, the Green's function in the conduction or dielectric phenomena for a medium with arbitrary symmetry has been derived in a closed form as follows:

$$G\left(\boldsymbol{x} - \boldsymbol{y}\right) = \frac{1}{4\pi\sqrt{\det\left(\boldsymbol{K}\right)\left[\left(\boldsymbol{x} - \boldsymbol{y}\right)^T \boldsymbol{K}^T \left(\boldsymbol{x} - \boldsymbol{y}\right)\right]}}. \tag{25}$$

The second-order Eshelby tensor can be further simplified for an arbitrary ellipsoidal inclusion as an integral having one variable (Giordano and Palla, 2008; Lee et al., 2018a):

$$\boldsymbol{S} = \frac{\det(\boldsymbol{a})}{2}\int_0^\infty \frac{\left(\boldsymbol{a}^2 + s\boldsymbol{K}\right)^{-1}\cdot\boldsymbol{K}}{\sqrt{\det\left(\boldsymbol{a}^2 + s\boldsymbol{K}\right)}}ds \text{ where } \boldsymbol{a} = \begin{bmatrix} a_1 & 0 & 0 \\ 0 & a_2 & 0 \\ 0 & 0 & a_3 \end{bmatrix}, \tag{26}$$

Or it can be written in an integral involving two variables:

$$S_{ik} = \frac{1}{4\pi}K_{ij}\int_{-1}^{1}\int_0^{2\pi}\overline{\xi}_j\overline{\xi}_k H^{-1}d\theta d\overline{\zeta_3} \tag{27}$$

where $H = \overline{\xi}_p\overline{\xi}_q K_{pq}$. For a spherical inclusion in an isotropic matrix, the Eshelby tensor can be simplified as $S_{ik} = \frac{1}{3}\delta_{ik}$. For a thermoelectric material, with the coupling of electrical and heat conduction, the Eshelby tensor can be written as follows Jung et al. (2018),

$$S_{MnAb} = \frac{1}{4\pi}P_{PiAb}\int_{-1}^{1}\int_0^{2\pi}\overline{\xi}_i\overline{\xi}_n\left(\boldsymbol{W}^{-1}\right)_{MP}d\theta d\overline{\zeta_3} \tag{28}$$

where $W_{MP} = \overline{\xi}_a\overline{\xi}_t P_{MsPt}$. The Eshelby tensor for a spherical inclusion in an isotropic matrix becomes $S_{MnAb} = \frac{1}{3}\delta_{MA}\delta_{nb}$. We note that the Eshelby tensor expressions for the conduction/dielectric and thermoelectric phenomena are simpler than those for elasticity and piezoelectricity, because the Green's functions for the latter consider a vector field (displacement) whereas the Green's functions for the former only involve scalar fields (such as temperature and electrical potential).

Examples of Numerical Calculations and FEA Validation

We now turn our attention to predict the effective properties of composites based on a mathematically analogous formula. In Mandel notation represented by $\boldsymbol{p} = \boldsymbol{X}\boldsymbol{q}$, where $\boldsymbol{X}$ is a $N \times N$ matrix and the input (output) field $\boldsymbol{q}$ ($\boldsymbol{p}$) has N components, the linear operator in elasticity L_{ijmn}, conduction (or dielectric) κ_{in}, piezoelectricity C_{iJMn}, and thermoelectricity P_{JiMn} become 6×6, 3×3, 9×9, and 6×6 symmetric matrices, respectively. Although most existing studies (Dunn and Taya, 1993; Huang and Kuo, 1996; Odegard, 2004; Duschlbauer et al., 2006; Martinez-Ayuso et al., 2017) utilize the Voigt notation, we adapt the Mandel notation here. For example, if we use the Voigt notation for a piezoelectric case, the linear operator matrix (which corresponds to the material properties) and the Eshelby matrix can be expressed as Equations (29, 30), respectively:

$$\begin{bmatrix} \sigma_{11} \\ \sigma_{22} \\ \sigma_{33} \\ \sigma_{23} \\ \sigma_{31} \\ \sigma_{12} \\ D_1 \\ D_2 \\ D_3 \end{bmatrix} = \begin{bmatrix} C_{1111} & C_{1122} & C_{1133} & C_{1123} & C_{1131} & C_{1112} & C_{1141} & C_{1142} & C_{1143} \\ C_{2211} & C_{2222} & C_{2233} & C_{2223} & C_{2231} & C_{2212} & C_{2241} & C_{2242} & C_{2243} \\ C_{3311} & C_{3322} & C_{3333} & C_{3323} & C_{3331} & C_{3312} & C_{3341} & C_{3342} & C_{3343} \\ C_{2311} & C_{2322} & C_{2333} & C_{2323} & C_{2331} & C_{2312} & C_{2341} & C_{2342} & C_{2343} \\ C_{3111} & C_{3122} & C_{3133} & C_{3123} & C_{3131} & C_{3112} & C_{3141} & C_{3142} & C_{3143} \\ C_{1211} & C_{1222} & C_{1233} & C_{1223} & C_{1231} & C_{1212} & C_{1241} & C_{1242} & C_{1243} \\ C_{1411} & C_{1422} & C_{1433} & C_{1423} & C_{1431} & C_{1412} & C_{1441} & C_{1442} & C_{1443} \\ C_{2411} & C_{2422} & C_{2433} & C_{2423} & C_{2431} & C_{2412} & C_{2441} & C_{2442} & C_{2443} \\ C_{3411} & C_{3422} & C_{3433} & C_{3423} & C_{3431} & C_{3412} & C_{3441} & C_{3442} & C_{3443} \end{bmatrix} \begin{bmatrix} \varepsilon_{11} \\ \varepsilon_{22} \\ \varepsilon_{33} \\ 2\varepsilon_{23} \\ 2\varepsilon_{31} \\ 2\varepsilon_{12} \\ -E_1 \\ -E_2 \\ -E_3 \end{bmatrix} \tag{29}$$

$$\begin{bmatrix} \varepsilon_{11} \\ \varepsilon_{22} \\ \varepsilon_{33} \\ 2\varepsilon_{23} \\ 2\varepsilon_{31} \\ 2\varepsilon_{12} \\ -E_1 \\ -E_2 \\ -E_3 \end{bmatrix} = \begin{bmatrix} S_{1111} & S_{1122} & S_{1133} & S_{1123} & S_{1131} & S_{1112} & S_{1141} & S_{1142} & S_{1143} \\ S_{2211} & S_{2222} & S_{2233} & S_{2223} & S_{2231} & S_{2212} & S_{2241} & S_{2242} & S_{2243} \\ S_{3311} & S_{3322} & S_{3333} & S_{3323} & S_{3331} & S_{3312} & S_{3341} & S_{3342} & S_{3343} \\ 2S_{2311} & 2S_{2322} & 2S_{2333} & 2S_{2323} & 2S_{2331} & 2S_{2312} & 2S_{2341} & 2S_{2342} & 2S_{2343} \\ 2S_{3111} & 2S_{3122} & 2S_{3133} & 2S_{3123} & 2S_{3131} & 2S_{3112} & 2S_{3141} & 2S_{3142} & 2S_{3143} \\ 2S_{1211} & 2S_{1222} & 2S_{1233} & 2S_{1223} & 2S_{1231} & 2S_{1212} & 2S_{1241} & 2S_{1242} & 2S_{1243} \\ S_{4111} & S_{4122} & S_{4133} & S_{4123} & S_{4131} & S_{4112} & S_{4141} & S_{4142} & S_{4143} \\ S_{4211} & S_{4222} & S_{4233} & S_{4223} & S_{4231} & S_{4212} & S_{4241} & S_{4242} & S_{4243} \\ S_{4311} & S_{4322} & S_{4333} & S_{4323} & S_{4331} & S_{4312} & S_{4341} & S_{4342} & S_{4343} \end{bmatrix} \begin{bmatrix} \varepsilon^*_{11} \\ \varepsilon^*_{22} \\ \varepsilon^*_{33} \\ 2\varepsilon^*_{23} \\ 2\varepsilon^*_{31} \\ 2\varepsilon^*_{12} \\ -E^*_1 \\ -E^*_2 \\ -E^*_3 \end{bmatrix} \tag{30}$$

As shown by Equations (29, 30), the coefficients in the transformed matrix are different for the two set of matrices. In contrast, with the Mandel notation, the two matrices can be expressed as

$$\begin{bmatrix} \sigma_{11} \\ \sigma_{22} \\ \sigma_{33} \\ \sqrt{2}\sigma_{23} \\ \sqrt{2}\sigma_{31} \\ \sqrt{2}\sigma_{12} \\ D_1 \\ D_2 \\ D_3 \end{bmatrix} = \begin{bmatrix} C_{1111} & C_{1122} & C_{1133} & \sqrt{2}C_{1123} & \sqrt{2}C_{1131} & \sqrt{2}C_{1112} & C_{1141} & C_{1142} & C_{1143} \\ C_{2211} & C_{2222} & C_{2233} & \sqrt{2}C_{2223} & \sqrt{2}C_{2231} & \sqrt{2}C_{2212} & C_{2241} & C_{2242} & C_{2243} \\ C_{3311} & C_{3322} & C_{3333} & \sqrt{2}C_{3323} & \sqrt{2}C_{3331} & \sqrt{2}C_{3312} & C_{3341} & C_{3342} & C_{3343} \\ \sqrt{2}C_{2311} & \sqrt{2}C_{2322} & \sqrt{2}C_{2333} & 2C_{2323} & 2C_{2331} & 2C_{2312} & \sqrt{2}C_{2341} & \sqrt{2}C_{2342} & \sqrt{2}C_{2343} \\ \sqrt{2}C_{3111} & \sqrt{2}C_{3122} & \sqrt{2}C_{3133} & 2C_{3123} & 2C_{3131} & 2C_{3112} & \sqrt{2}C_{3141} & \sqrt{2}C_{3142} & \sqrt{2}C_{3143} \\ \sqrt{2}C_{1211} & \sqrt{2}C_{1222} & \sqrt{2}C_{1233} & 2C_{1223} & 2C_{1231} & 2C_{1212} & \sqrt{2}C_{1241} & \sqrt{2}C_{1242} & \sqrt{2}C_{1243} \\ C_{1411} & C_{1422} & C_{1433} & \sqrt{2}C_{1423} & \sqrt{2}C_{1431} & \sqrt{2}C_{1412} & C_{1441} & C_{1442} & C_{1443} \\ C_{2411} & C_{2422} & C_{2433} & \sqrt{2}C_{2423} & \sqrt{2}C_{2431} & \sqrt{2}C_{2412} & C_{2441} & C_{2442} & C_{2443} \\ C_{3411} & C_{3422} & C_{3433} & \sqrt{2}C_{3423} & \sqrt{2}C_{3431} & \sqrt{2}C_{3412} & C_{3441} & C_{3442} & C_{3443} \end{bmatrix} \begin{bmatrix} \varepsilon_{11} \\ \varepsilon_{22} \\ \varepsilon_{33} \\ \sqrt{2}\varepsilon_{23} \\ \sqrt{2}\varepsilon_{31} \\ \sqrt{2}\varepsilon_{12} \\ -E_1 \\ -E_2 \\ -E_3 \end{bmatrix} \tag{31}$$

and

$$\begin{bmatrix} \varepsilon_{11} \\ \varepsilon_{22} \\ \varepsilon_{33} \\ \sqrt{2}\varepsilon_{23} \\ \sqrt{2}\varepsilon_{31} \\ \sqrt{2}\varepsilon_{12} \\ -E_1 \\ -E_2 \\ -E_3 \end{bmatrix} = \begin{bmatrix} S_{1111} & S_{1122} & S_{1133} & \sqrt{2}S_{1123} & \sqrt{2}S_{1131} & \sqrt{2}S_{1112} & S_{1141} & S_{1142} & S_{1143} \\ S_{2211} & S_{2222} & S_{2233} & \sqrt{2}S_{2223} & \sqrt{2}S_{2231} & \sqrt{2}S_{2212} & S_{2241} & S_{2242} & S_{2243} \\ S_{3311} & S_{3322} & S_{3333} & \sqrt{2}S_{3323} & \sqrt{2}S_{3331} & \sqrt{2}S_{3312} & S_{3341} & S_{3342} & S_{3343} \\ \sqrt{2}S_{2311} & \sqrt{2}S_{2322} & \sqrt{2}S_{2333} & 2S_{2323} & 2S_{2331} & 2S_{2312} & \sqrt{2}S_{2341} & \sqrt{2}S_{2342} & \sqrt{2}S_{2343} \\ \sqrt{2}S_{3111} & \sqrt{2}S_{3122} & \sqrt{2}S_{3133} & 2S_{3123} & 2S_{3131} & 2S_{3112} & \sqrt{2}S_{3141} & \sqrt{2}S_{3142} & \sqrt{2}S_{3143} \\ \sqrt{2}S_{1211} & \sqrt{2}S_{1222} & \sqrt{2}S_{1233} & 2S_{1223} & 2S_{1231} & 2S_{1212} & \sqrt{2}S_{1241} & \sqrt{2}S_{1242} & \sqrt{2}S_{1243} \\ S_{4111} & S_{4122} & S_{4133} & \sqrt{2}S_{4123} & \sqrt{2}S_{4131} & \sqrt{2}S_{4112} & S_{4141} & S_{4142} & S_{4143} \\ S_{4211} & S_{4222} & S_{4233} & \sqrt{2}S_{4223} & \sqrt{2}S_{4231} & \sqrt{2}S_{4212} & S_{4241} & S_{4242} & S_{4243} \\ S_{4311} & S_{4322} & S_{4333} & \sqrt{2}S_{4323} & \sqrt{2}S_{4331} & \sqrt{2}S_{4312} & S_{4341} & S_{4342} & S_{4343} \end{bmatrix} \begin{bmatrix} \varepsilon_{11}^* \\ \varepsilon_{22}^* \\ \varepsilon_{33}^* \\ \sqrt{2}\varepsilon_{23}^* \\ \sqrt{2}\varepsilon_{31}^* \\ \sqrt{2}\varepsilon_{12}^* \\ -E_1^* \\ -E_2^* \\ -E_3^* \end{bmatrix}, \quad (32)$$

where the same coefficients are multiplied in the two matrixes. It is important to note that the Eshelby matrix of a piezoelectric and thermoelectric material has dimensions with N/C and V/K in the coupling term. In a piezoelectric material, instead of using SI units for all physical parameters, we can use $1\text{nC} = 10^{-9}\text{C}$ for the charge to avoid numerical problems due to the very large order of the magnitude difference between the elastic constant ($\sim 10^9 \text{N/m}^2$) and the coupling constant (~C/N).

For the physical phenomena represented by matrix equation $p = Xq$ in the Mandel notion, the effective property can be obtained by $X^{\text{Eff}} = (c_0 X_0 + c_1 X_1 T)(c_0 I + c_1 T)^{-1}$, where $T = \left[I + S X_0^{-1}(X_1 - X_0)\right]^{-1}$ and S is the $N \times N$ matrix representation of the corresponding Eshelby tensor. We then compare the effective property prediction based on the Mori-Tanaka method with a FEA analysis for the simple case involving spherical inhomogeneities embedded in a transversely isotropic medium for piezoelectric and isotropic media for others, as shown in **Figure 3**.

INTERFACIAL IMPERFECTIONS AND ANISOTROPY OF THE MATRIX

Effects of Anisotropy of the Matrix in Various Physical Problems

As mentioned in the previous chapters, we can obtain the effective properties from the Mori-Tanaka method because the expression $X^{\text{Eff}} = (c_0 X_0 + c_1 X_1 T)(c_0 I + c_1 T)^{-1}$ is applicable to any arbitrarily anisotropic matrix if the Eshelby tensor is known. The Eshelby tensor for anisotropic medium in various physical problems has been extensively studied in the literature (Mura, 1982; Yu et al., 1994; Huang and Kuo, 1996; Dunn and Wienecke, 1997; Qu and Cherkaoui, 2007; Quang et al., 2011; Martinez-Ayuso et al., 2017; Lee et al., 2018b) and the Eshelby tensors for an ellipsoidal inclusion embedded in an arbitrarily anisotropic medium for elasticity, piezoelectricity, conduction/dielectric phenomena, and thermoelectricity can be obtained numerically from Equations (22, 23, 27, 28), respectively.

Although the Eshelby tensor can be obtained numerically, significant efforts have been devoted to derive the explicit expressions (either closed-form or analytical expression) for the facile application of the homogenization method and to provide better insight into the nature of the tensor. In elasticity, analytic expressions for ellipsoidal shape given in terms of a few integrals are available for spheroidal inclusion in transversely isotropic solids involving five independent elastic constants (or any medium with higher symmetry, i.e., less number of independent elastic constants) (Mura, 1982; Yu et al., 1994). In conduction/dielectric phenomena, analytic solutions have been derived for spheroidal inclusion in isotropic material (Hatta and Taya, 1986) and spherical inclusion in orthotropic and transversely isotropic material (Lee et al., 2018a). For piezoelectricity, Huang and Kuo (1996) suggested the Eshelby tensor expression of spheroidal inclusion in transversely isotropic material with a few integrals. However, for thermoelectricity, to the best of our knowledge, analytic solutions have not been obtained for an anisotropic medium.

Definition of Interfacial Imperfections

In actual composites, the interface between the matrix and an inclusion often has imperfections originating from the manufacturing process or from an inherent lattice mismatch (People and Bean, 1985; Habas et al., 2007). An interfacial imperfection in elasticity refers to debonding or slippage, i.e., a displacement jump (Qu, 1993; Lee and Ryu, 2018; Lee et al., 2018b, 2019), and an interfacial imperfection under thermal conduction (or Kapitza resistance) refers to an abrupt change in the temperature, i.e., a temperature jump (Quang et al., 2011; Lee et al., 2018a). An interfacial imperfection in electrical conduction (i.e., the electrical contact resistance) refers to an abrupt change in the electrical voltage across the interface (Giordano and Palla, 2008). The interfacial imperfection in piezoelectricity considers both displacement jump and the electric potential jump (Wang et al., 2014a,b). Similarly, the interfacial imperfection in thermoelectricity considers the abrupt discontinuities of both temperature and electric potential (Jung et al., 2018).

Out of a few characteristic methods used to describe an interfacial imperfection in elasticity (Qiu and Weng, 1991; Duan et al., 2005), in this work, we consider the interfacial spring model (Qu, 1993) owing to its (i) mathematical simplicity and (ii) mathematical analogy with the interfacial thermal (electrical) resistance in thermal (electrical) conduction. As will be shown later, due to the mathematical similarity, the expressions of the effective stiffness and effective conductivity in the presence of an interfacial imperfection are nearly identical to each other.

It is noteworthy that the interfacial imperfection can be well-treated only for a spherical inclusion, because an ellipsoidal inclusion (even with slight deviation from a sphere) introduces significantly non-uniform interior field (Qu, 1993; Qu and Cherkaoui, 2007; Lee et al., 2018a,b, 2019). In problems involving

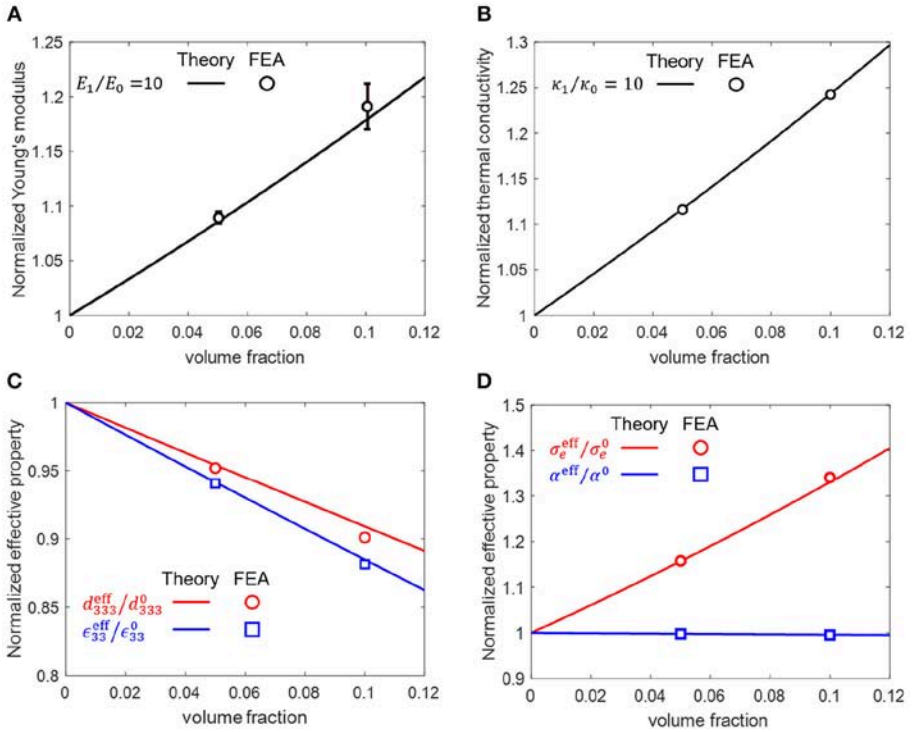

FIGURE 3 | (A) Normalized Young's modulus of a particle-reinforced composite. The Poisson's ratios (ν) of two phases are identical at 0.25. **(B)** Effective heat conductivity of the composite. **(C)** Normalized effective piezoelectric properties of composites. The matrix and reinforcement are PZT-7A and SiC particles, respectively. **(D)** The effective thermoelectric properties of a Cu-reinforced Bi_2Te_3 composite at 300 K. All properties are normalized with respect to the properties of the matrix. We use the material properties for the piezoelectricity (Odegard, 2004) and the thermoelectricity (Jung et al., 2018) presented in the literature.

the elastic deformation, the equality between the normal and tangential interfacial compliances is additionally required to ensure the uniform field inside the inclusion (which is critical for the applicability of the Eshelby tensor and the mean field homogenization). Unfortunately, there exist several studies employing the Mori-Tanaka method to obtain effective physical properties of a composite involving ellipsoidal inhomogeneities in the presence of different normal and tangential compliances (Yang et al., 2013b; Wang et al., 2014a,b; Lee and Ryu, 2018).

Another common mistake in mean-field homogenization studies considering the interfacial damage is the application of the effective physical property expression $X^{\mathrm{Eff}} = (c_0X_0 + c_1X_1T)\,(c_0I + c_1T)^{-1}$ and $T = \left[I + SX_0^{-1}\,(X_1 - X_0)\right]^{-1}$ by simply replacing the Eshelby tensor S with a modified Eshelby tensor S^M accounting for the interfacial imperfection (Qu, 1993; Barai and Weng, 2011; Yanase and Ju, 2012; Pan et al., 2013; Wang et al., 2014a,b; Shokrieh et al., 2016; Lee and Ryu, 2018). However, in addition to the Eshelby tensor, different expressions for X^{Eff} and T should be used because the derivation in Section Single inhomogeneity problem and Mean-field homogenization of the effective stiffness (where the problem is solved with the superposition of two sub-problems involving applied and constrained fields, respectively) does not account for the additional contribution from the interface imperfection. We will discuss these issues in detail in the next section.

Prediction of Effective Physical Properties in the Presence of Interfacial Imperfections

We adopt the interface spring model to consider the interfacial damage, as depicted in **Figure 4**. A displacement jump occurs at the interface due to the spring layer having a vanishing thickness between the infinite matrix and the single inclusion. The spring compliance(η) is represented by α and β for the tangential and normal directions, respectively, and is expressed by Equation (33) in the form of a second-order tensor, as follows:

$$\eta_{ij} = \alpha\delta_{ij} + (\beta - \alpha)\, n_i n_j. \tag{33}$$

The constitutive equations and traction(t_i) equilibrium equation at the interface are expressed as follows,

$$\begin{aligned} \Delta t_i &= \Delta\sigma_{ij}n_j = \left[\sigma_{ij}\left(\partial\Omega^+\right) - \sigma_{ij}\left(\partial\Omega^-\right)\right] n_j = 0 \\ \Delta u_i &= \left[u_i\left(\partial\Omega^+\right) - u_i\left(\partial\Omega^-\right)\right] = \eta_{ij}\sigma_{jk}n_k \end{aligned} \tag{34}$$

where $\left(\partial\Omega^+\right)$ and $\left(\partial\Omega^-\right)$ denote the interface on the matrix and the inclusion side, respectively. Formulating the Eshelby inclusion problem by adopting the interfacial condition in Equation (34), the constrained strain is

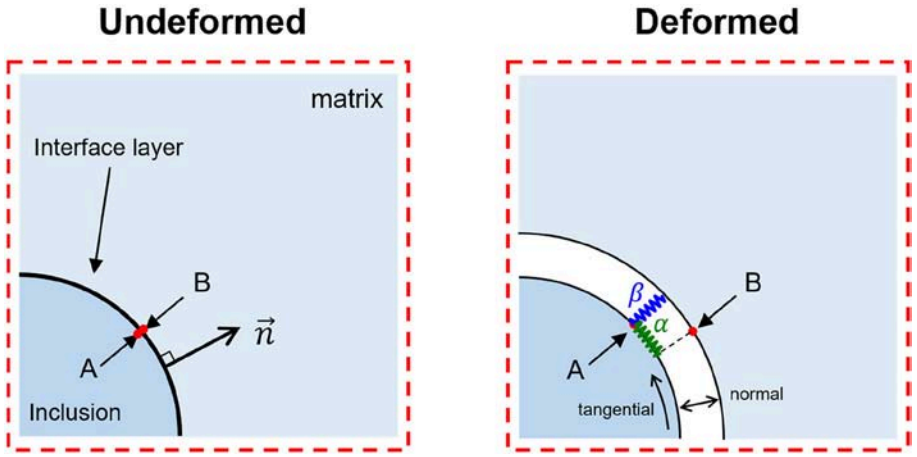

FIGURE 4 | Schematic of an interface spring model in elasticity. To visualize the interface spring in two directions, we compare undeformed and deformed states.

written as Othmani et al. (2011) and Lee et al. (2018b, 2019)

$$\varepsilon_{ij}^{c} = S_{ijrs}\varepsilon_{rs}^{*} + \frac{1}{2}L_{klmn}L_{pqrs}\int_{\partial\Omega}\eta_{kp}\left\{\frac{\partial^2 G_{im}(x-y)}{\partial x_j \partial y_n} + \frac{\partial^2 G_{jm}(x-y)}{\partial x_i \partial y_n}\right\} n_q(y)\, n_l(y)\left(\varepsilon_{rs}^{c}(y) - \varepsilon_{rs}^{*}\right) dy. \quad (35)$$

Equation (35) is shown to reproduce the perfect interface case with zero spring compliance; i.e., $\eta_{ij} = 0$.

Because Equation (35) is an implicit integral equation involving the constrained strain ε_{ij}^{c}, it is difficult to determine the relationship between ε_{ij}^{c} and ε_{rs}^{*}, i.e., the modified Eshelby tensor. Zhong and Meguid (1997) showed that, when $\alpha = \beta \equiv \gamma_s$ and the inclusion shape is a perfect sphere, the strain field inside the spherical inclusion is uniform, as in the case of a perfect interface. Hence, for this special case, the integral equation can be decomposed as follows,

$$\varepsilon_{ij}^{c} = S_{ijrs}\varepsilon_{rs}^{*} - \Gamma_{ijrs}\left(\varepsilon_{rs}^{c} - \varepsilon_{rs}^{*}\right) \quad (36)$$

where the fourth-order tensor Γ_{ijkl} in Equation (36) is defined by

$$\Gamma_{ijpq} \equiv -\frac{1}{2}\gamma_s L_{plmn}L_{pqrs}\int_{\partial\Omega}\left\{\frac{\partial^2 G_{im}(x-y)}{\partial x_j \partial y_n} + \frac{\partial^2 G_{jm}(x-y)}{\partial x_i \partial y_n}\right\} \times n_q(y)\, n_l(y)\, dy. \quad (37)$$

The constrained strain field then can be expressed by a tensor algebraic equation as follows Othmani et al. (2011) and Lee et al. (2018b),

$$\varepsilon^{c} = (I+\Gamma)^{-1} : (S+\Gamma) : \varepsilon^{*} = S^{M} : \varepsilon^{*} \quad (38)$$

where S^M is the modified Eshelby tensor. Related to this, in an earlier work by the authors, we proved that for materials with an arbitrary elastic anisotropy, the Γ tensor can be written in terms of the Eshelby tensor for a perfect interface and an elastic stiffness tensor as Lee et al. (2018b)

$$\Gamma_{ijpq} = \frac{\gamma_s}{R}\left(I_{ijpq} - S_{ijpq}\right) L_{pqrs} \quad (39)$$

where R is the radius of the inclusion. Therefore, it is proven that the modified Eshelby The tensor S^M can be written as follows:

$$S^{M} = \left[I + \frac{\gamma_s}{R}(I-S) : L\right]^{-1} : \left[S + \frac{\gamma_s}{R}(I-S) : L\right]. \quad (40)$$

The numerical validation against a finite element analysis on a triclinic single crystal material ($NaAlSi_3O_8$) with 21 independent elastic constants (and 36 independent Eshelby tensor components) is presented in **Figure 5**. This leads to the simplified expression of the modified T tensor $\left(T^{M}\right)$ in the Mori-Tanaka method when the matrix modulus is L_0 and the inhomogeneity modulus is L_1:

$$T^{M} = \left(I + S : L_0^{-1} : (L_1 - L_0) + \frac{\gamma_s}{R}(I-S) : L_1\right)^{-1} \quad (41)$$

We derive the effective modulus $\left(L^{\mathrm{Eff}}\right)$ of the composite as follows Lee et al. (2019):

$$L^{\mathrm{Eff}} = \left(c_0 L_0 + c_1 L_1 : T^{\mathrm{M}}\right) : \left(c_0 I + c_1 T^{\mathrm{M}} + c_1 \frac{\gamma_s}{R} L_1 : T^{\mathrm{M}}\right)^{-1}. \quad (42)$$

To confirm the validity of Equation (42), we compare the theoretical prediction with the effective Young's modulus of a composite for a wide range of interface damage as obtained by a FEA (See **Figure 6**). The equation can also be formulated in terms of the effective inclusion, and we concisely summarize the formulation in **Appendix B**. We note that many previous studies (Qu, 1993; Barai and Weng, 2011; Yanase and Ju, 2012; Yang et al., 2012; Pan et al., 2013; Shokrieh et al., 2016; Lee and Ryu, 2018) employing the effective stiffness equation in the presence of an interfacial imperfection employ a few incorrect

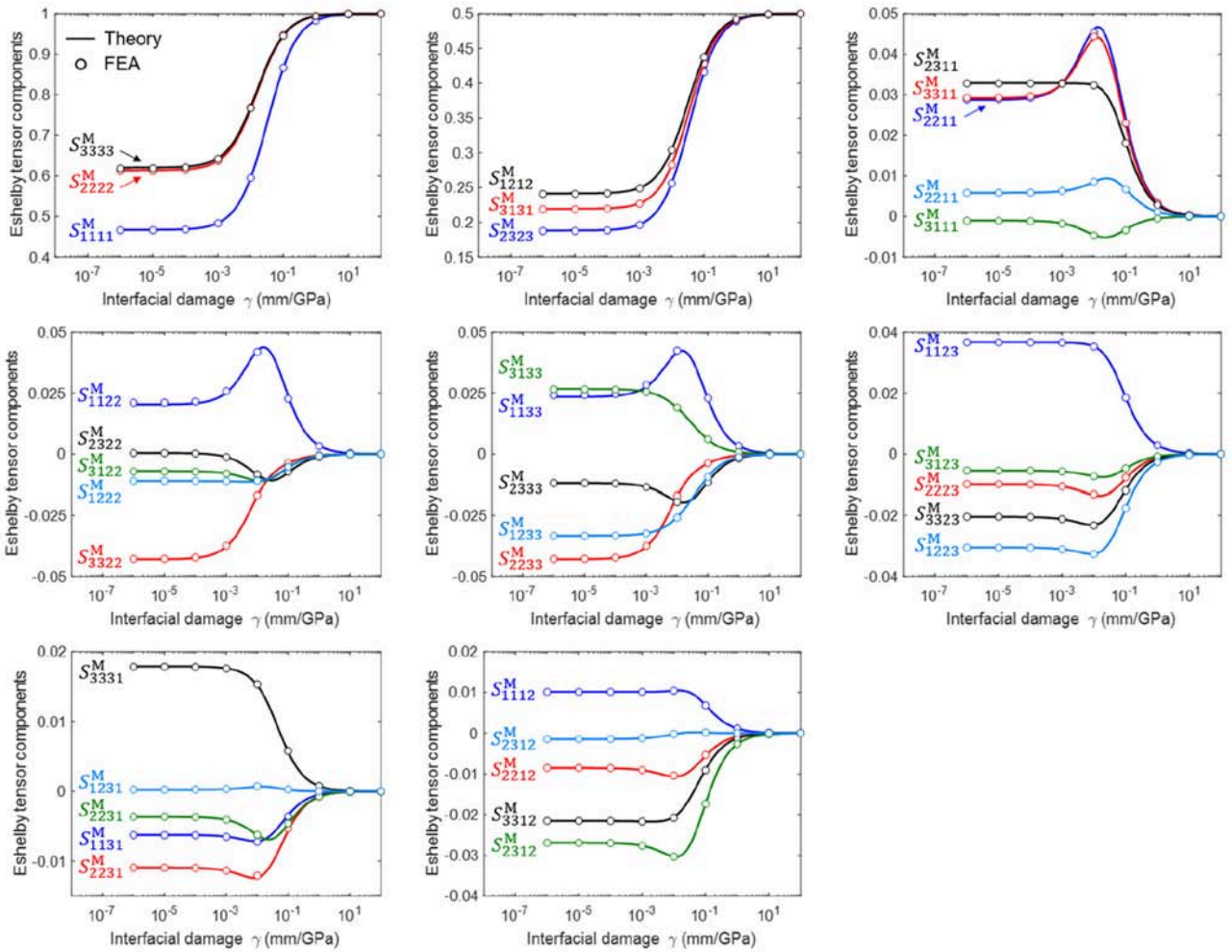

FIGURE 5 | Thirty-six independent components of a modified Eshelby tensor for a wide range of interfacial damage. The triclinic material used for this calculation is $NaAlSi_3O_8$ (Lee et al., 2018b).

expressions derived by violating Fubini's theorem and relying on inappropriate superposition. A detailed discussion of this issue can be found in work by Dogri's group (Othmani et al., 2011) and by our group (Lee et al., 2018b).

We now turn our attention to other physical phenomena where interfacial imperfections play an important role, specifically the conduction problem. The interfacial thermal resistance α_K (or the Kapitza resistance) is defined as Kapitza (1941) and Quang et al. (2011)

$$T^{\text{out}} - T^{\text{in}} = -\alpha_K q \cdot n, \tag{43}$$

where T^{out} and T^{in} refer to the temperatures on the outer and inner surfaces of the interface, respectively, and q is the heat flux at the interface (see **Figure 7**). The SI unit of the interfacial thermal resistance α_K is $[m^2K/W]$. The interfacial resistance augments an additional surface integration term in the eigen-intensity problem (which corresponds to the eigenstrain problem in elasticity), as follows Quang et al. (2011) and Lee et al. (2018a),

$$e_m(x) = \frac{\partial}{\partial x_m}\int_V \frac{\partial G(x-y)}{\partial y_i} dy \kappa_{0ij} e_j^* + \frac{\partial}{\partial x_m}\alpha_K \kappa_{0ij}\kappa_{0sr} \int_{\partial V} \frac{\partial G(x-y)}{\partial y_j} n_i(y)\, n_s(y)\left(e_r(y) - e_r^*(y)\right) dy. \tag{44}$$

It has been found that the heat flux within a spherical inclusion is uniform in the presence of interfacial thermal resistance. In an earlier work of ours, we proved that the modified Eshelby tensor for a matrix with arbitrary anisotropy can be written as follows Lee et al. (2018a),

$$S^M = \left(I + \frac{\alpha_K}{R}(I-S)\kappa_0\right)^{-1}\left(S + \frac{\alpha_K}{R}(I-S)\kappa_0\right), \tag{45}$$

which is similar to the modified Eshelby tensor in elasticity except that the double contraction for the fourth-order tensor is replaced

with matrix multiplication for the second-order tensor. Here, I is the second-order identity tensor and S is the Eshelby tensor for the thermal conduction problem. This leads to the simplified expression of the modified concentration tensor (subjected to the constant temperature boundary condition) in the Mori-Tanaka method when the matrix and inhomogeneity thermal conductivity tensors are given as κ_0 and κ_1, respectively:

$$T^M = \left(I + S\kappa_0^{-1}(\kappa_1 - \kappa_0) + \frac{\alpha_K}{R}(I - S)\kappa_1\right)^{-1}. \quad (46)$$

We can also obtain the modified localization tensor (subjected to the constant flux boundary condition (q_0)) as

$$q_1 = B^M q_0, \quad (47)$$

where q_1 is the heat flux within a single inhomogeneity and $B^M = \kappa_1 T^M \kappa_0^{-1}$; subsequently, we compare the equation with the FEA results for the anisotropic matrix case (see **Figure 8**; the FEA with the flux boundary condition is more convenient to perform). Based on the modified concentration tensor, we derive

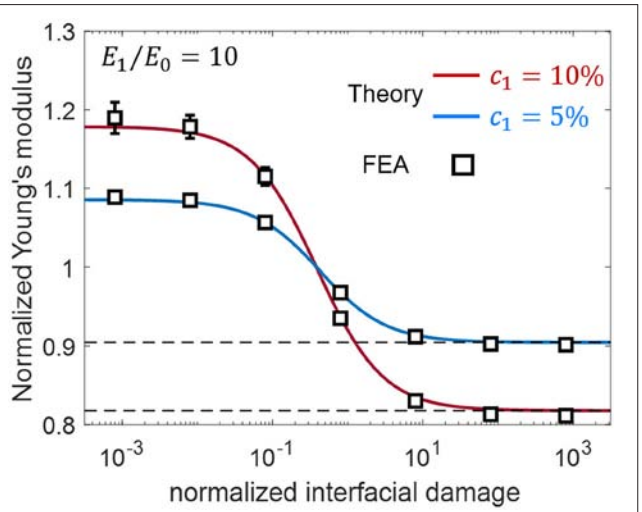

FIGURE 6 | Effective Young's modulus of a composite with respect to the normalized interface damage parameter $(\mu_0\gamma/R)$. The Poisson's ratio of the two phases is 0.25 (Lee et al., 2019).

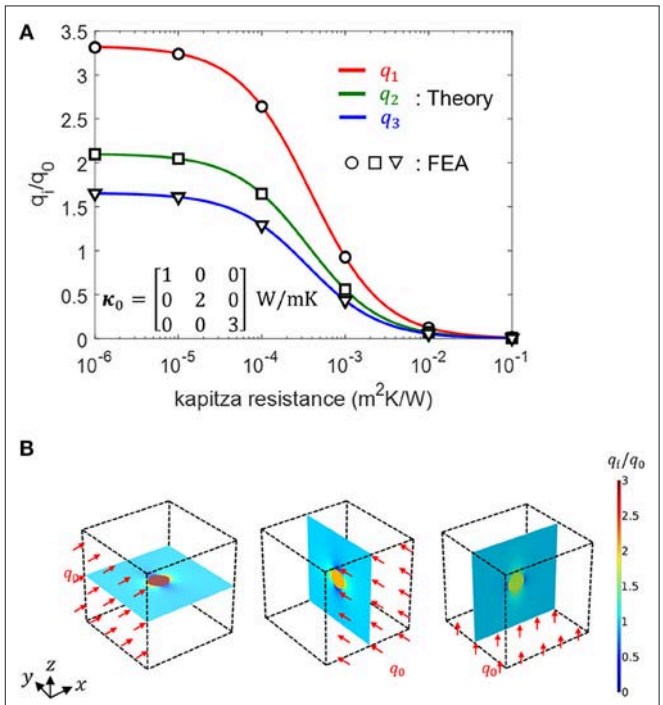

FIGURE 8 | (A) Normalized heat flux within an inhomogeneity with respect to the interfacial thermal resistance in a single inhomogeneity problem. The inhomogeneity is an isotropic material for which $\kappa_1 = \begin{bmatrix}10&&\\&10&\\&&10\end{bmatrix}$ W/mK. **(B)** Heat flux distribution within a matrix and an inhomogeneity on the *x*, *y*, and *z* planes for three different heat flux directions (Lee et al., 2018a).

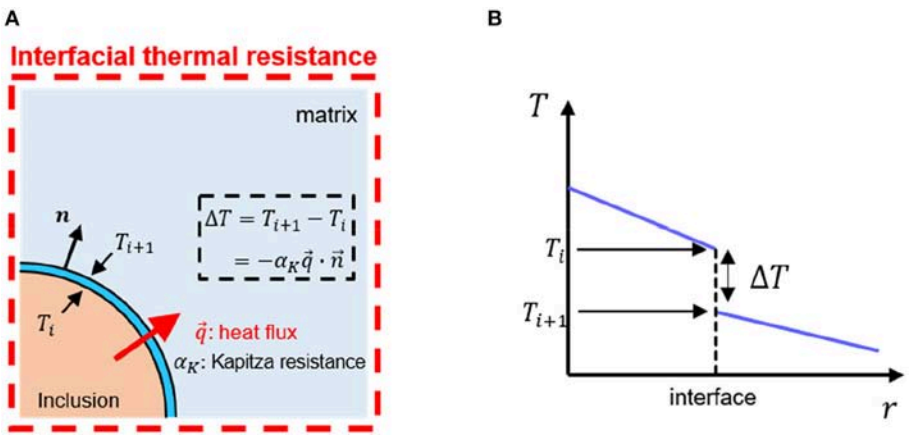

FIGURE 7 | (A) Schematic of the Kapitza resistance at the interface, and **(B)** temperature jump across the interface.

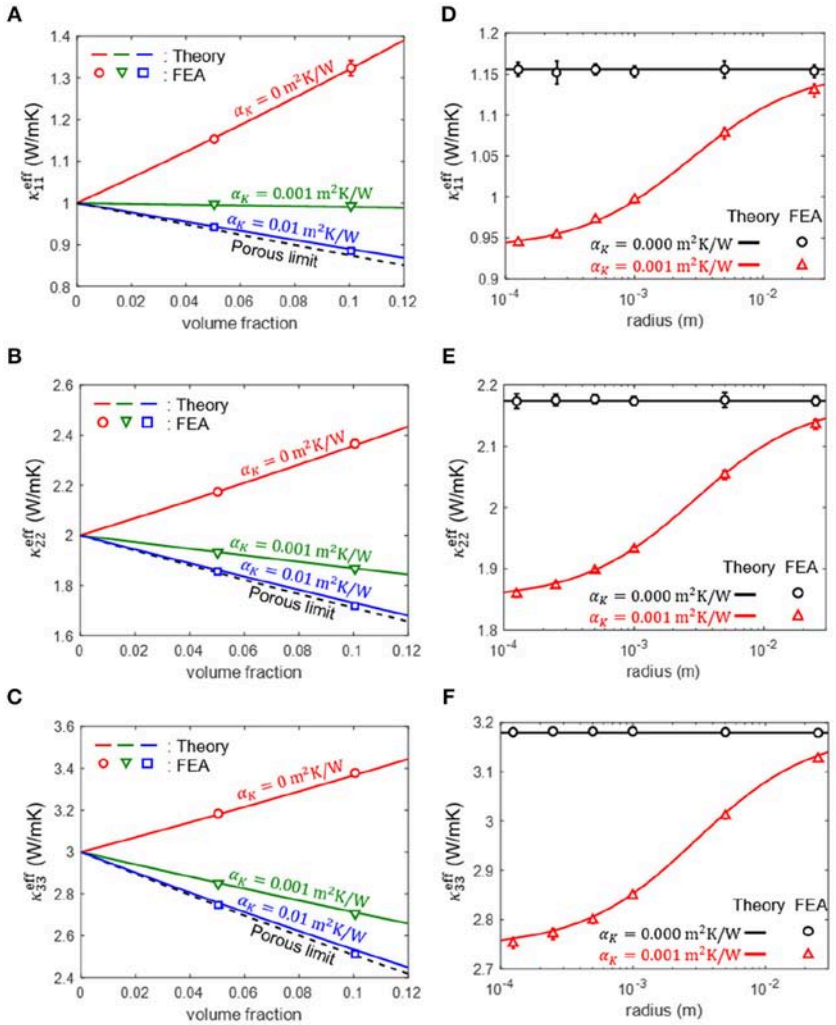

FIGURE 9 | Effective thermal conductivity values [**(A)**κ_{11}^{eff}, **(B)**κ_{22}^{eff}, and **(C)**κ_{33}^{eff}] of a particle-reinforced composite with different interfacial thermal resistances. The material properties of the matrix and particle are $\kappa_0 = \begin{bmatrix} 1 & & \\ & 2 & \\ & & 3 \end{bmatrix}$ and $\kappa_1 = \begin{bmatrix} 10 & & \\ & 10 & \\ & & 10 \end{bmatrix}$ (W/mK), respectively. The radius of the particle used in **(A–C)** is 1 (mm). The effective thermal conductivity [**(D)**κ_{11}^{eff}, **(E)**κ_{22}^{eff}, and **(F)**κ_{33}^{eff}] as a function of the radius of the particle under a fixed volume fraction of 5% is also shown (Lee et al., 2018a).

the effective conductivity $\left(\kappa^{\text{eff}}\right)$ of the composite as follows Quang et al. (2011) and Lee et al. (2018a),

$$\kappa^{\text{Eff}} = \left(c_0\kappa_0 + c_1\kappa_1 T^{\text{M}}\right)\left(c_0 I + c_1 T^{\text{M}} + c_1 \frac{\alpha_K}{R}\kappa_1 T^{\text{M}}\right)^{-1}, \quad (48)$$

and the theoretical predictions are well-matched with the FEA results (see **Figure 9**).

For a thermoelectric composite, we refer to our work on micromechanics homogenization considering both the interfacial thermal and electrical resistance (Jung et al., 2018) where mathematical solutions were obtained for the modified Eshelby tensor, the modified concentration tensor, and the effective thermoelectric properties. Our homogenization study provides new insight on the effect of interfacial thermal and electrical resistance on the thermoelectric properties. In piezoelectricity, the modified Eshelby tensor has been derived by violating the Fubini's theorem by changing integral order (Wang et al., 2014a,b). Hence, the effective piezoelectric property has not been obtained correctly in the presence of interfacial imperfections considering both displacement jump and electric potential jump. With the adaptation of Mandel notation and the careful mathematical derivation, the expression for the effective piezoelectric property is expected to be similar to that of the effective thermoelectric property (Jung et al., 2018). We close the section by providing numerically obtained interior field inside ellipsoidal reinforcement (**Figure 10**), which clearly demonstrate the limited applicability of the homogenization method in the presence of interfacial imperfection.

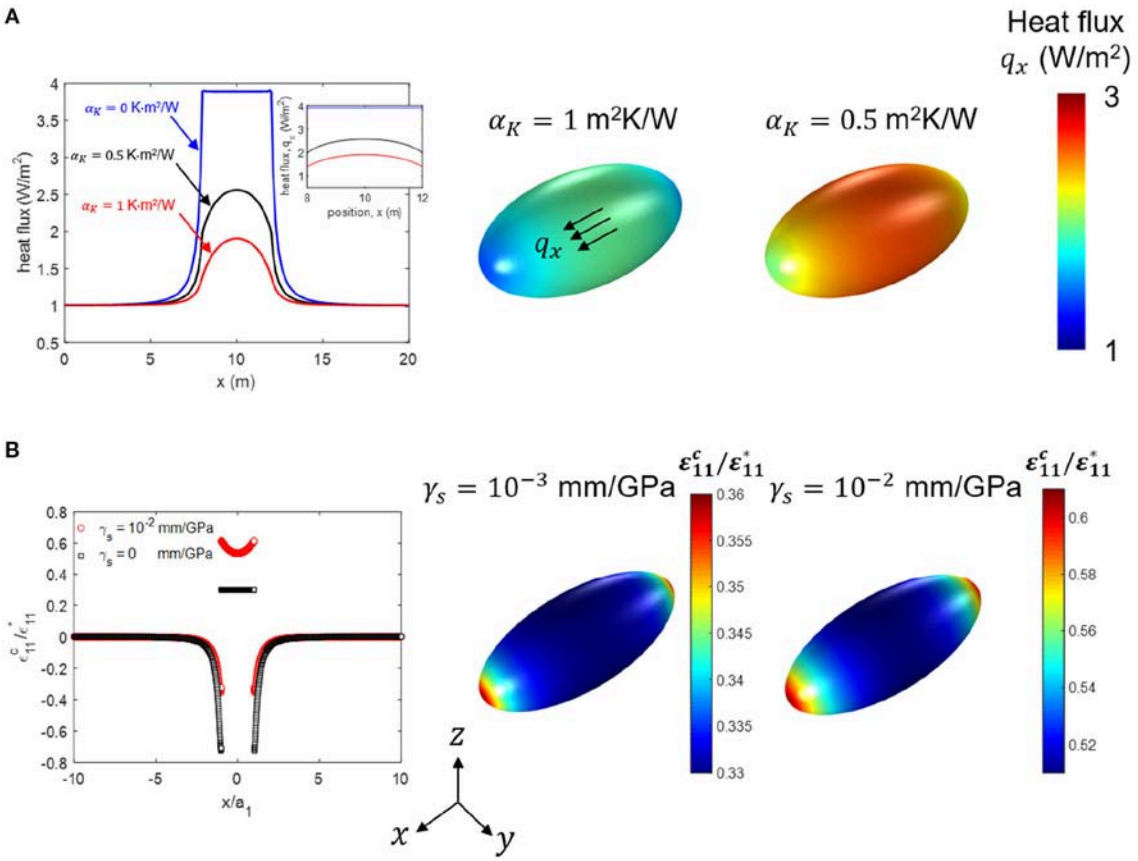

FIGURE 10 | (A) Heat flux within an ellipsoidal inhomogeneity and **(B)** strain field within an ellipsoidal inclusion ($a_x/a_y = a_x/a_z = 2$). The material properties used for the calculations are **(A)** $\kappa_0 = 1$, $\kappa_1 = 10$ (W/mK) (Lee et al., 2018a), and **(B)** $E_0 = 200$GPa, $\nu_0 = 0.25$ (Lee et al., 2018b).

SUMMARY AND OUTLOOK

In this paper, we introduce a series of recent studies which attempted to obtain the effective physical properties of composites by taking into account the interfacial damage and anisotropy of the matrix, providing a universal formulation for different physical phenomena based on their mathematical analogies. First, with the specific example of elasticity, we introduced the concept of the Eshelby tensor and discussed a how single-inclusion problem can be related to a single inhomogeneity problem, which ultimately is applied to mean-field homogenization to predict the effective properties of composites. Second, based on a mathematical analogy, we show that mean-field homogenization equations for different physical phenomena can be represented by linear equations involving symmetric matrices with different dimensions by adapting Mandel's notation. Third, we extend our discussion by taking into account two common issues in realistic applications: imperfections in a matrix-inhomogeneity interface and anisotropy of the matrix.

Although we have discussed the homogenization method while covering a wide range of issues, there remain a few issues requiring further developments. We categorize the advanced issues of homogenization theory into the six problems of (i) various physical phenomena, (ii) anisotropy of the matrix, (iii) matrix-filler interfacial imperfections, (iv) nonlinear responses, (v) time-dependent responses, and (vi) high volume fractions of reinforcements. Although issues (i)-(iii) have been investigated extensively, we nonetheless cannot take into account important non-spherical reinforcement materials (including ellipsoidal types) such as carbon nanotubes and graphene in the presence of interfacial imperfections due to the non-uniform interior field. Although there have been many scaling up attempts to couple micro/nanoscale simulations and homogenization theory to predict the properties of nanocomposites (Yang et al., 2012, 2013a, 2014; Pan et al., 2013; Shin et al., 2013; Shokrieh et al., 2016), they either rely on an incorrect solution stemming from effective stiffness expressions derived from a few problematic bases, such as violations of Fubini's theorem or inappropriate superpositions, or do not recognize the non-uniform interior field (Barai and Weng, 2011; Yang et al., 2012, 2013b; Pan et al., 2013; Shokrieh et al., 2016). There are a few studies of composites showing highly nonlinear (such as hyperelastic) and time-dependent (such as viscoelastic) responses (Friebel et al., 2006; Miled et al., 2011, 2013; Brassart et al., 2012; Doghri et al., 2016), but most lack consideration of interfacial imperfections, which can play an important role on the macroscale composites during repeated cyclic loading

and/or in nanocomposites including nanoscale reinforcements with large interfacial fractions. Lastly, to account for the high reinforcement volume fraction regime where the interaction among reinforcements becomes important, several heuristic methods have been developed, such as differential schemes (Hashin, 1988) and/or matrix-filler inversion schemes (Friebel et al., 2006) as well as studies of the lower and upper bounds of the effective properties (Hashin and Shtrikman, 1961), leaving room, however, for further improvements. Studies to overcome aforementioned challenges are underway in our research group with the formation of an international collaborative research network.

AUTHOR CONTRIBUTIONS

SR designed the structure of the review paper. SR and SL wrote the manuscript. SR and SL. contributed the sections on the micromechanics review and the treatment of anisotropy and interfacial imperfections. SR, SL, and JJ contributed to the summary of theoretical derivations, prepared figures, and discussed the mathematical analogy among different physical problems. JL contributed the theoretical derivations. YK contributed the effective inclusion method section.

FUNDING

This work is supported by the National Research Foundation of Korea (NRF) funded by the Ministry of Science and ICT (2016M3D1A1900038, 2016R1C1B2011979, and 2018K2A9A2A12000223).

SUPPLEMENTARY MATERIAL

The Supplementary Material for this article can be found online at: https://www.frontiersin.org/articles/10.3389/fmats.2019.00021/full#supplementary-material

REFERENCES

Allaoui, A., Bai, S., Cheng, H. M., and Bai, J. B. (2002). Mechanical and electrical properties of a MWNT/epoxy composite. *Composites Sci. Technol.* 62, 1993–1998. doi: 10.1016/S0266-3538(02)00129-X

Barai, P., and Weng, G. J. (2011). A theory of plasticity for carbon nanotube reinforced composites. *Int. J. Plast.* 27, 539–559. doi: 10.1016/j.ijplas.2010.08.006

Barnett, D. M., and Lothe, J. (1975). Dislocations and line charges in anisotropic piezoelectric insulators. *Physica Status Solidi* 67, 105–111. doi: 10.1002/pssb.2220670108

Benveniste, Y. (1987). A new approach to the application of mori-tanaka theory in composite-materials. *Mech. Mater.*6, 147–157. doi: 10.1016/0167-6636(87)90005-6

Brassart, L., Stainier, L., Doghri, I., and Delannay, L. (2011). A variational formulation for the incremental homogenization of elasto-plastic composites. *J. Mech. Phys. Solids* 59, 2455–2475. doi: 10.1016/j.jmps.2011.09.004

Brassart, L., Stainier, L., Doghri, I., and Delannay, L. (2012). Homogenization of elasto-(visco) plastic composites based on an incremental variational principle. *Int. J. Plast.* 36, 86–112. doi: 10.1016/j.ijplas.2012.03.010

Castaneda, P. P. (1991). The effective mechanical-properties of nonlinear isotropic composites. *J. Mech. Phys. Solids* 39, 45–71. doi: 10.1016/0022-5096(91)90030-R

Castaneda, P. P., and Tiberio, E. (2000). A second-order homogenization method in finite elasticity and applications to black-filled elastomers. *J. Mech. Phys. Solids* 48, 1389–1411. doi: 10.1016/S0022-5096(99)00087-3

Chiu, Y. P. (1977). On the stress field due to initial strains in a cuboid surrounded by an infinite elastic space. *J. Appl. Mech.* 44, 587–590. doi: 10.1115/1.3424140

Das, P., Malho, J. M., Rahimi, K., Schacher, F. H., Wang, B. C., Demco, D. E., et al. (2015). Nacre-mimetics with synthetic nanoclays up to ultrahigh aspect ratios. *Nat. Commun.*6:6967. doi: 10.1038/ncomms6967

Doghri, I., El Ghezal, M. I., and Adam, L. (2016). Finite strain mean-field homogenization of composite materials with hyperelastic-plastic constituents. *Int. J. Plast.* 81, 40–62. doi: 10.1016/j.ijplas.2016.01.009

Duan, H. L., Wang, J., Huang, Z. P., and Luo, Z. Y. (2005). Stress concentration tensors of inhomogeneities with interface effects. *Mech. Mater.* 37, 723–736. doi: 10.1016/j.mechmat.2004.07.004

Dunn, M. L., and Taya, M. (1993). Micromechanics predictions of the effective electroelastic moduli of piezoelectric composites. *Int. J. Solids Struct.* 30, 161–175. doi: 10.1016/0020-7683(93)90058-F

Dunn, M. L., and Wienecke, H. A. (1997). Inclusions and inhomogeneities in transversely isotropic piezoelectric solids. *Int. J. Solids Struct.* 34, 3571–3582. doi: 10.1016/S0020-7683(96)00209-0

Duschlbauer, D., Bohm, H. J., and Pettermann, H. E. (2006). Computational simulation of composites reinforced by planar random fibers: homogenization and localization by unit cell and mean field approaches. *J. Compos. Mater.* 40, 2217–2234. doi: 10.1177/,0021998306062317

EL-Dessouky, H. M., and Lawrence, C. A. (2013). Ultra-lightweight carbon fibre/thermoplastic composite material using spread tow technology. *Compos. Part B Eng.* 50, 91–97. doi: 10.1016/j.compositesb.2013.01.026

Eshelby, J. D. (1957). The determination of the elastic field of an ellipsoidal inclusion, and related problems. *Proc. R. Soc. Lond. A* 241, 376–396. doi: 10.1098/rspa.1957.0133

Eshelby, J. D. (1959). The elastic field outside an ellipsoidal inclusion. *Proc. R. Soc. Lond. A* 252, 561–569. doi: 10.1098/rspa.1959.0173

Flahaut, E., Peigney, A., Laurent, C., Marliere, C., Chastel, F., and Rousset, A. (2000). Carbon nanotube-metal-oxide nanocomposites: microstructure, electrical conductivity and mechanical properties. *Acta Mater.* 48, 3803–3812. doi: 10.1016/S1359-6454(00)00147-6

Friebel, C., Doghri, I., and Legat, V. (2006). General mean-field homogenization schemes for viscoelastic composites containing multiple phases of coated inclusions. *Int. J. Solids Struct.* 43, 2513–2541. doi: 10.1016/j.ijsolstr.2005.06.035

Friedrich, K., and Almajid, A. A. (2013). Manufacturing aspects of advanced polymer composites for automotive applications. *Appl. Compos. Mater.* 20, 107–128. doi: 10.1007/s10443-012-9258-7

Fu, H., and Cohen, R. E. (2000). Polarization rotation mechanism for ultrahigh electromechanical response in single-crystal piezoelectrics. *Nature* 403, 281–283. doi: 10.1038/35002022

Gao, H. J. (2006). Application of fracture mechanics concepts to hierarchical biomechanics of bone and bone-like materials. *Int. J. Fracture* 138, 101–137. doi: 10.1007/s10704-006-7156-4

Gao, H. L., Chen, S. M., Mao, L. B., Song, Z. Q., Yao, H. B., Cölfen, H., et al. (2017). Mass production of bulk artificial nacre with excellent mechanical properties. *Nat. Commun.* 8:287. doi: 10.1038/s41467-017-00392-z

George, J., and Dvorak, Y. B. (1992). On transformation strains and uniform fields in multiphase elastic media. *Proc. R. Soc. Lond. Ser. A Math. Phys. Sci.* 437:291. doi: 10.1098/rspa.1992.0062

Gibson, L. J., Ashby, M. F., Karam, G. N., Wegst, U., and Shercliff, H. R. (1995). The mechanical-properties of natural materials.2. *Microstructures for mechanical efficiency. Proc. R. Soc. Math. Phys. Sci.* 450, 141–162. doi: 10.1098/rspa.1995.0076

Giordano, S., and Palla, P. L. (2008). Dielectric behavior of anisotropic inhomogeneities: interior and exterior point Eshelby tensors. *J. Phys. A Math. Theor.* 41:415205. doi: 10.1088/1751-8113/41/41/415205

Gojny, F. H., Wichmann, M. H. G., Fiedler, B., Bauhofer, W., and Schulte, K. (2005). Influence of nano-modification on the mechanical and electrical properties of conventional fibre-reinforced composites. *Compos. Part A Appl. Sci. Manuf.* 36, 1525–1535. doi: 10.1016/j.compositesa.2005.02.007

Habas, S. E., Lee, H., Radmilovic, V., Somorjai, G. A., and Yang, P. (2007). Shaping binary metal nanocrystals through epitaxial seeded growth. *Nat. Mater.* 6, 692–697. doi: 10.1038/nmat1957

Hashin, Z. (1988). The differential scheme and its application to cracked materials. *J. Mech. Phys. Solids* 36, 719–734. doi: 10.1016/0022-5096(88)90005-1

Hashin, Z., and Shtrikman, S. (1961). Note on a variational approach to the theory of composite elastic materials. *J. Franklin Inst.* 271, 336–341. doi: 10.1016/0016-0032(61)90032-1

Hatta, H., and Taya, M. (1986). Equivalent inclusion method for steady-state heat-conduction in composites. *Int. J. Eng. Sci.* 24, 1159–1172. doi: 10.1016/0020-7225(86)90011-X

Helnwein, P. (2001). Some remarks on the compressed matrix representation of symmetric second-order and fourth-order tensors. *Comput. Methods Appl. Mech. Eng.* 190, 2753–2770. doi: 10.1016/S0045-7825(00)00263-2

Hill, R. (1965). A self-consistent mechanics of composite materials. *J. Mech. Phys. Solids* 13, 213–222. doi: 10.1016/0022-5096(65)90010-4

Hu, X., Xu, Z., Liu, Z., and Gao, C. (2013). Liquid crystal self-templating approach to ultrastrong and tough biomimic composites. *Sci. Rep.* 3:02374. doi: 10.1038/srep02374

Huang, J. H., and Kuo, W. S. (1996). Micromechanics determination of the effective properties of piezoelectric composites containing spatially oriented short fibers. *Acta Mater.* 44, 4889–4898. doi: 10.1016/S1359-6454(96)00090-0

Idiart, M. I., Danas, K., and Castaneda, P. P. (2006). Second-order theory for nonlinear composites and application to isotropic constituents. *Comptes Rendus Mecanique* 334, 575–581. doi: 10.1016/j.crme.2006.06.006

Imai, T., Sawa, F., Nakano, T., Ozaki, T., Shimizu, T., Kozako, M., et al. (2006). Effects of nano- and micro-filler mixture on electrical insulation properties of epoxy based composites. *IEEE Trans. Dielectr. Electr. Insulat.* 13, 319–326. doi: 10.1109/TDEI.2006.1624276

Immarigeon, J. P., Holt, R. T., Koul, A. K., Zhao, L., Wallace, W., and Beddoes, J. C. (1995). Lightweight materials for aircraft applications. *Mater. Chara.* 35, 41–67. doi: 10.1016/1044-5803(95)00066-6

Jawaid, M., Khalil, H. P. S. A., Abu Bakar, A., and Khanam, P. N. (2011). Chemical resistance, void content and tensile properties of oil palm/jute fibre reinforced polymer hybrid composites. *Mater. Des.* 32, 1014–1019. doi: 10.1016/j.matdes.2010.07.033

Ji, B. H., and Gao, H. J. (2004). Mechanical properties of nanostructure of biological materials. *J. Mech. Phys. Solids* 52, 1963–1990. doi: 10.1016/j.jmps.2004.03.006

Jun, T. S., and Korsunsky, A. M. (2010). Evaluation of residual stresses and strains using the Eigenstrain Reconstruction Method. *Int. J. Solids Struct.* 47, 1678–1686. doi: 10.1016/j.ijsolstr.2010.03.002

Jung, J., Lee, S., Ryu, B., and Ryu, S. (2018). Effective thermoelectric properties of a composite with interfacial resistance using a micromechanics-based homogenization. *eprint* arXiv:1811.11340.

Kapitza, P. L. (1941). Heat transfer and superfluidity of helium II. *Phys. Rev.* 60, 354–355. doi: 10.1103/PhysRev.60.354

Kim, Y., Kim, Y., Lee, T. I., Kim, T. S., and Ryu, S. (2018). An extended analytic model for the elastic properties of platelet-staggered composites and its application to 3D printed structures. *Compos. Struct.* 189, 27–36. doi: 10.1016/j.compstruct.2018.01.038

Kreyszig, E. (1972). *Advanced Engineering Mathematics*. London: John Whiley and Sons.

Lahellec, N., and Suquet, P. (2007a). On the effective behavior of nonlinear inelastic composites: I. *Incremental variational principles. J. Mech. Phys. Solids* 55, 1932–1963. doi: 10.1016/j.jmps.2007.02.003

Lahellec, N., and Suquet, P. (2007b). On the effective behavior of nonlinear inelastic composites: II - a second-order procedure. *J. Mech. Phys. Solids* 55, 1964–1992. doi: 10.1016/j.jmps.2007.02.004

Launey, M. E., Munch, E., Alsem, D. H., Barth, H. B., Saiz, E., Tomsia, A. P., et al. (2009). Designing highly toughened hybrid composites through nature-inspired hierarchical complexity. *Acta Mater.* 57, 2919–2932. doi: 10.1016/j.actamat.2009.03.003

Lee, S., Kim, Y., Lee, J., and Ryu, S. (2019). Applicability of the interface spring model for micromechanical analyses with interfacial imperfections to predict the modified exterior Eshelby tensor and effective modulus. *eprint arXiv:1811.03411*. doi: 10.1177/1081286519826343

Lee, S., Lee, J., Ryu, B., and Ryu, S. (2018a). A micromechanics-based analytical solution for the effective thermal conductivity of composites with orthotropic matrices and interfacial thermal resistance. *Sci. Rep.* 8:7266. doi: 10.1038/s41598-018-25379-8

Lee, S., Lee, J., and Ryu, S. (2018b). Modified Eshelby tensor for an anisotropic matrix with interfacial damage. *Math. Mech. Solids*. doi: 10.1177/1081286518805521

Lee, S., and Ryu, S. (2018). Theoretical study of the effective modulus of a composite considering the orientation distribution of the fillers and the interfacial damage. *Euro. J. Mech. a-Solids* 72, 79–87. doi: 10.1016/j.euromechsol.2018.02.008

Li, T., Zhu, M. W., Yang, Z., Song, J. W., Dai, J. Q., Yao, Y. G., et al. (2016). Wood composite as an energy efficient building material: guided sunlight transmittance and effective thermal insulation. *Adv. Energy Mater.* 6:1601122. doi: 10.1002/aenm.201601122

Li, Y. Q., Yu, T., Yang, T. Y., Zheng, L. X., and Liao, K. (2012). Bio-inspired nacre-like composite films based on graphene with superior mechanical, electrical, and biocompatible properties. *Adv. Mater.* 24, 3426–3431. doi: 10.1002/adma.201200452

Lu, Z. X., Yuan, Z. S., and Liu, Q. (2014). 3D numerical simulation for the elastic properties of random fiber composites with a wide range of fiber aspect ratios. *Comput. Mater. Sci.* 90, 123–129. doi: 10.1016/j.commatsci.2014.04.007

Marcos-Gomez, D., Ching-Lloyd, J., Elizalde, M. R., Clegg, W. J., and Molina-Aldareguia, J. M. (2010). Predicting the thermal conductivity of composite materials with imperfect interfaces. *Compos. Sci. Technol.* 70, 2276–2283. doi: 10.1016/j.compscitech.2010.05.027

Martinez-Ayuso, G., Friswell, M. I., Adhikari, S., Khodaparast, H. H., and Berger, H. (2017). Homogenization of porous piezoelectric materials. *Int. J. Solids Struct.* 113, 218–229. doi: 10.1016/j.ijsolstr.2017.03.003

Miled, B., Doghri, I., Brassart, L., and Delannay, L. (2013). Micromechanical modeling of coupled viscoelastic-viscoplastic composites based on an incrementally affine formulation. *Int. J. Solids Struct.* 50, 1755–1769. doi: 10.1016/j.ijsolstr.2013.02.004

Miled, B., Doghri, I., and Delannay, L. (2011). Coupled viscoelastic-viscoplastic modeling of homogeneous and isotropic polymers: numerical algorithm and analytical solutions. *Comput. Methods Appl. Mech. Eng.* 200, 3381–3394. doi: 10.1016/j.cma.2011.08.015

Milton, G. W. (2002). *The theory of composites. The Theory of Composites, by Graeme W. Milton.* Cambridge, UK: Cambridge University Press, 748. doi: 10.1017/CBO9780511613357

Mouritz, A. P., Gellert, E., Burchill, P., and Challis, K. (2001). Review of advanced composite structures for naval ships and submarines. *Compos. Struct.* 53, 21–41. doi: 10.1016/S0263-8223(00)00175-6

Mura, T. (1982). Micromechanics of Defects in Solids. *Netherlands: Kluwer Academic Publishers*. doi: 10.1007/978-94-011-9306-1

Nemat-Nasser, S. (1999). Averaging theorems in finite deformation plasticity. *Mech. Mater.* 31, 493–523. doi: 10.1016/S0167-6636(98)00073-8

Obradovic, J., Boria, S., and Belingardi, G. (2012). Lightweight design and crash analysis of composite frontal impact energy absorbing structures. *Compos. Struct.* 94, 423–430. doi: 10.1016/j.compstruct.2011.08.005

Odegard, G. M. (2004). Constitutive modeling of piezoelectric polymer composites. *Acta Mater.* 52, 5315–5330. doi: 10.1016/j.actamat.2004.07.037

Othmani, Y., Delannay, L., and Doghri, I. (2011). Equivalent inclusion solution adapted to particle debonding with a non-linear cohesive law. *Int. J. Solids Struct.* 48, 3326–3335. doi: 10.1016/j.ijsolstr.2011.08.002

Pan, Y., Iorga, L., and Pelegri, A. A. (2008). Numerical generation of a random chopped fiber composite RVE and its elastic properties. *Compos. Sci. Technol.* 68, 2792–2798. doi: 10.1016/j.compscitech.2008.06.007

Pan, Y., Weng, G. J., Meguid, S. A., Bao, W. S., Zhu, Z. H., and Hamouda, A. M. S. (2013). Interface effects on the viscoelastic characteristics of

carbon nanotube polymer matrix composites. *Mech. Mater.* 58, 1–11. doi: 10.1016/j.mechmat.2012.10.015

Park, M., Im, J., Shin, M., Min, Y., Park, J., Cho, H., et al. (2012). Highly stretchable electric circuits from a composite material of silver nanoparticles and elastomeric fibres. *Nat. Nanotechnol.* 7, 803–809. doi: 10.1038/nnano.2012.206

People, R., and Bean, J. C. (1985). Calculation of critical layer thickness versus lattice mismatch for Gexsi1-X/Si strained-layer heterostructures. *Appl. Phys. Lett.* 47, 322–324. doi: 10.1063/1.96206

Qiu, Y. P., and Weng, G. J. (1991). Elastic-moduli of thickly coated particle and fiber-reinforced composites. *J. Appl. Mech. Trans. Asme* 58, 388–398. doi: 10.1115/1.2897198

Qu, J., and Cherkaoui, M. (2007). *Fundamentals of Micromechanics of Solidss.* Hoboken, NJ: John Wiley and Sons, Inc.

Qu, J. M. (1993). The effect of slightly weakened interfaces on the overall elastic properties of composite-materials. *Mech. Mater.* 14, 269–281. doi: 10.1016/0167-6636(93)90082-3

Quang, H. L., He, Q. C., and Bonnet, G. (2011). Eshelby's tensor fields and effective conductivity of composites made of anisotropic phases with Kapitza's interface thermal resistance. *Philos. Mag.* 91, 3358–3392. doi: 10.1080/14786435.2011.580286

Sen, D., and Buehler, M. J. (2011). Structural hierarchies define toughness and defect-tolerance despite simple and mechanically inferior brittle building blocks. *Sci. Rep.* 1:35. doi: 10.1038/srep00035

Shao, C., and Keten, S. (2015). Stiffness enhancement in nacre-inspired nanocomposites due to nanoconfinement. *Sci. Rep.* 5:16452. doi: 10.1038/srep16452

Shin, H., Yang, S., Chang, S., Yu, S., and Cho, M. (2013). Multiscale homogenization modeling for thermal transport properties of polymer nanocomposites with Kapitza thermal resistance. *Polymer* 54, 1543–1554. doi: 10.1016/j.polymer.2013.01.020

Shokrieh, M. M., Ghajar, R., and Shajari, A. R. (2016). The effect of time-dependent slightly weakened interface on the viscoelastic properties of CNT/polymer nanocomposites. *Compos. Struct.* 146, 122–131. doi: 10.1016/j.compstruct.2016.03.022

Suh, N. P. (2005). *Axiomatic Design and Fabrication of Composite Structures: Applications in Robots, Machine Tools, and Automobiles.* New York, NY: Oxford University Press.

Tang, Z., Kotov, N. A., Magonov, S., and Ozturk, B. (2003). Nanostructured artificial nacre. *Nat. Mater.* 2, 413–U418. doi: 10.1038/nmat906

Taurino, R., Lancellotti, I., Tatano, F., Carchesio, M., and Pozzi, P. (2016). Mechanical and chemical resistance of composite materials with addition of anaerobic digestate. *Compos. Part B Eng.* 92, 259–264. doi: 10.1016/j.compositesb.2016.02.012

Tirry, W., and Schryvers, D. (2009). Linking a completely three-dimensional nanostrain to a structural transformation eigenstrain. *Nat. Mater.* 8, 752–757. doi: 10.1038/nmat2488

Tuncer, E., Sauers, I., James, D. R., Ellis, A. R., Paranthaman, M. P., Aytug, T., et al. (2007). Electrical properties of epoxy resin based nano-composites. *Nanotechnology* 18:025703. doi: 10.1088/0957-4484/18/2/025703

Walther, A., Bjurhager, I., Malho, J. M., Pere, J., Ruokolainen, J., Berglund, L. A., et al. (2010). Large-area, lightweight and thick biomimetic composites with superior material properties via fast, economic, and green pathways. *Nano Lett.* 10, 2742–2748. doi: 10.1021/nl1003224

Wang, H. W., Zhou, H. W., Peng, R. D., and Mishnaevsky, L. (2011). Nanoreinforced polymer composites: 3D FEM modeling with effective interface concept. *Compos. Sci. Technol.* 71, 980–988. doi: 10.1016/j.compscitech.2011.03.003

Wang, Z., Zhu, J., Chen, W. Q., Jin, X. Y., and Zhang, C. Z. (2014a). Modified Eshelby tensor for an ellipsoidal inclusion imperfectly embedded in an infinite piezoelectric medium. *Mech. Mater.* 74, 56–66. doi: 10.1016/j.mechmat.2014.03.005

Wang, Z., Zhu, J., Jin, X. Y., Chen, W. Q., and Zhang, C. (2014b). Effective moduli of ellipsoidal particle reinforced piezoelectric composites with imperfect interfaces. *J. Mech. Phys. Solids* 65, 138–156. doi: 10.1016/j.jmps.2013.12.007

Wegst, U. G. K., and Ashby, M. F. (2004). The mechanical efficiency of natural materials. *Philos. Mag.* 84, 2167–2181. doi: 10.1080/14786430410001680935

Wei, G. S., Liu, Y. S., Zhang, X. X., Yu, F., and Du, X. Z. (2011). Thermal conductivities study on silica aerogel and its composite insulation materials. *Int. J. Heat Mass Transf.* 54, 2355–2366. doi: 10.1016/j.ijheatmasstransfer.2011.02.026

Wu, L., Noels, L., Adam, L., and Doghri, I. (2013). A combined incremental-secant mean-field homogenization scheme with per-phase residual strains for elasto-plastic composites. *Int. J. Plast.* 51, 80–102. doi: 10.1016/j.ijplas.2013.06.006

Xu, Y. B., and Yagi, K. (2004). Automatic FEM model generation for evaluating thermal conductivity of composite with random materials arrangement. *Comput. Mater. Sci.* 30, 242–250. doi: 10.1016/j.commatsci.2004.03.011

Yanase, K., and Ju, J. W. (2012). Effective elastic moduli of spherical particle reinforced composites containing imperfect interfaces. *Int. J. Damage Mech.* 21, 97–127. doi: 10.1177/1056789510397076

Yang, B. J., Shin, H., Kim, H., and Lee, H. K. (2014). Strain rate and adhesive energy dependent viscoplastic damage modeling for nanoparticulate composites: Molecular dynamics and micromechanical simulations. *Appl. Phys. Lett.* 104, 101901–101904. doi: 10.1063/1.4868034

Yang, B. J., Shin, H., Lee, H. K., and Kim, H. (2013a). A combined molecular dynamics/micromechanics/finite element approach for multiscale constitutive modeling of nanocomposites with interface effects. *Appl. Phys. Lett.* 103:241903. doi: 10.1063/1.4819383

Yang, S., Yu, S., Kyoung, W., Han, D. S., and Cho, M. (2012). Multiscale modeling of size-dependent elastic properties of carbon nanotube/polymer nanocomposites with interfacial imperfections. *Polymer (Guildf).* 53, 623–633. doi: 10.1016/j.polymer.2011.11.052

Yang, S., Yu, S., Ryu, J., Cho, J. M., Kyoung, W., Han, D. S., et al. (2013b). Nonlinear multiscale modeling approach to characterize elastoplastic behavior of CNT/polymer nanocomposites considering the interphase and interfacial imperfection. *Int. J. Plast.* 41, 124–146. doi: 10.1016/j.ijplas.2012.09.010

Yu, H. Y., Sanday, S. C., and Chang, C. I. (1994). Elastic inclusions and inhomogeneities in transversely isotropic solids. *Proc. R. Soc. Math. Phys. Sci.* 444, 239–252. doi: 10.1098/rspa.1994.0014

Zhao, L. D., Lo, S. H., Zhang, Y., Sun, H., Tan, G. J., Uher, C., et al. (2014). Ultralow thermal conductivity and high thermoelectric figure of merit in SnSe crystals. *Nature* 508, 373-+. doi: 10.1038/nature13184

Zheng, Y., Chonung, K., Wang, G. L., Wei, P., and Jiang, P. K. (2009). Epoxy/nano-silica composites: curing kinetics, glass transition temperatures, dielectric, and thermal-mechanical performances. *J. Appl. Polym. Sci.* 111, 917–927. doi: 10.1002/app.28875

Zhong, Z., and Meguid, S. A. (1997). On the elastic field of a spherical inhomogeneity with an imperfectly bonded interface. *J. Elast.* 46, 91–113. doi: 10.1023/A:1007342605107

Conflict of Interest Statement: The authors declare that the research was conducted in the absence of any commercial or financial relationships that could be construed as a potential conflict of interest.

Polymeric and Composite Materials

Federico Carosio

Federico Carosio obtained his PhD in 2012 in Materials Science and Technology at Politecnico di Torino with a thesis titled: "*Layer by Layer assembly of nanostructured coatings for flame retardancy and barrier properties*". At present he is a senior researcher at the Department of Applied Science and Technology of Politecnico di Torino, Italy. His research focuses on polymers and nanostructures, smart fibers and textiles and nanocellulose-based materials with particular attention on their flame retardancy properties achieved through the Layer by Layer deposition technique. He has coauthored more than 70 scientific papers (total citations: 3161, H-index 30, source google scholar) published in international peer reviewed journals and has attended several national and international congresses and workshops.

Andrea Dorigato

Andrea Dorigato is an Assistant Professor (RTDB) at the Department of Industrial Engineering at the University of Trento, Italy since 2016. His research activity focuses on the development of multifunctional polymer micro- and nanocomposites, with attention to the investigation of innovative materials for the sustainable development. His most significant research topics are related to the investigation of the viscoelastic and fracture behaviour of polymer nanocomposites and of electro-active multiscale polymer composites. His research also focuses on the development of innovative polymeric materials obtained from renewable resources and recycled materials with low environmental impact, of nanostructured foams for the thermal insulation and energy saving, and of phase transition materials for the thermal energy storage/release. The study of the Life Cycle Assessment (LCA) of engineering materials is also included in his research fields.

Gianmarco Griffini

Gianmarco Griffini is currently an Assistant Professor (tenure-track) of Science and Technology of Materials at the Department of Chemistry, Materials and Chemical Engineering "Giulio Natta" of Politecnico di Milano, Italy. He received his PhD degree in Materials Engineering in 2012, from Politecnico di Milano. Since 2014 he serves as a lecturer in the School of Industrial and Information Engineering (MSc and BSc degrees in Materials Engineering and Nanotechnology) and in the School of Design (MSc degree in Design & Engineering and MSc degree in Product Design for Innovation) at Politecnico di Milano. His current research interests are mainly related to the field of science and technology of materials and are focuses particularly on the development and characterization of polymeric materials and on the study of their structure-property relationships.

frontiers in Materials

ORIGINAL RESEARCH
published: 27 February 2019
doi: 10.3389/fmats.2019.00020

Three Organic/Inorganic Nanolayers on Flexible Foam Allow Retaining Superior Flame Retardancy Performance Upon Mechanical Compression Cycles

Federico Carosio and Alberto Fina*

Dipartimento di Scienza Applicata e Tecnologia, Politecnico di Torino, Alessandria Campus, Alessandria, Italy

The water-based deposition of flame retardant coatings on flexible polyurethane foams has attracted great interest among the scientific community due to the great performances associated with this technology. Unfortunately, this approach results inefficient as it requires a high number of steps in order to achieve the desired properties. In this paper, we report the production of flame-retardant foams by means of the simple deposition of only three nanoparticles containing layers. The composition and order of the deposited layer has been designed in order to provide specific flame retardant actions, targeting the delayed release of polymer decomposition products to the gas phase, the dilution of these flammable products with water, and the intumescent barrier formation. The morphology of the coated foams after the adsorption of each layer has been investigated by scanning electron microscopy, demonstrating the ability of each adsorbed layer to completely wrap the complex 3D structure of the foam. This three layers-based coating produces a protective exoskeleton that is capable of self-extinguishing the flame in standard flammability tests, leaving the foam almost unaffected (final residue 98%). In forced combustion tests by cone calorimetry, treated foams showed considerably reduced combustion rates, with reduced peak of heat release rate (−50%) as well as consistent reduction in the smoke optical density (−51%) and the total smoke release (−34%). In addition, treated foams have been demonstrated to maintain the ability to self-extinguish the flame as well as reduced combustion rates and smoke production even after being subjected to 100 compression cycles.

Keywords: layer-by-layer, flexible polyurethane foams, boehmite, montmorillonite, ammonium polyphosphate, flame retardancy

OPEN ACCESS

Edited by:
Alessandro Pegoretti, University of Trento, Italy

Reviewed by:
José-Marie Lopez-Cuesta, Institut Mines -Télécom Mines Alès, France
Mustapha Kaci, University of Béjaïa, Algeria

****Correspondence:***
Federico Carosio
federico.carosio@polito.it

Specialty section:
This article was submitted to Polymeric and Composite Materials, a section of the journal Frontiers in Materials

Received: *30 November 2018*
Accepted: *04 February 2019*
Published: *27 February 2019*

Citation:
Carosio F and Fina A (2019) Three Organic/Inorganic Nanolayers on Flexible Foam Allow Retaining Superior Flame Retardancy Performance Upon Mechanical Compression Cycles. Front. Mater. 6:20. doi: 10.3389/fmats.2019.00020

INTRODUCTION

Recent trends in materials science have clearly pointed toward the production of green and environmentally friendly material concepts capable of improving sustainability while also delivering optimized and competitive performances. To this aim, research has been focused on the exploitation of natural resources (e.g., nanocellulose, natural fibers etc.) and water-based processes in different application fields (Mohanty et al., 2002; Klemm et al., 2011). The fire safety of polymeric materials represents an area of concern; indeed, due to their organic nature, polymers can easily ignite after accidental exposure to small flames or irradiation at high heat

fluxes, leading to catastrophic fire events. Current concerns about the toxicity of some commonly used flame retardant (FR) chemicals (halogen-based) (Stapleton et al., 2011), coupled with recent tragic events involving flammability of non-flame retarded polymer foams (Rawlinson et al., 2017), have been presented to broad audiences of non-experts. This clearly increased societal awareness on the problem of halogen-based FR and the need for safer and better performing alternatives. A possible solution is represented by the exploitation of a nanotechnological approach in which the surface of flammable items (i.e., fabrics and open cell polyurethane foams, PU), is modified with nanostructured coatings deposited by means of green water-based deposition processes (Malucelli et al., 2014; Alongi et al., 2016). Among the possible different approaches, the Layer-by-Layer (LbL) deposition technique represents one of the most widely employed surface modification tool to achieve flame retardancy properties (Holder et al., 2017). Nanostructured coatings are LbL-assembled on the surface following the alternate adsorption of oppositely charged species from aqueous based solutions/suspensions (Decher and Schlenoff, 2012). One of the key advantages of LbL is certainly its versatility in both the components selection and deposition parameters. Indeed, for virtually any combination of water-soluble polyelectrolytes and water-stable nanoparticles, it is possible to find suitable deposition conditions (e.g., time, temperature, concentration, pH) that allow for a steady coating buildup (Hammond, 2004). Thanks to its versatility, the LbL deposition has been applied to various substrates, including textiles, foams and thin films, and the effects of pH, ionic strength and molecular weight on the achieved FR properties have also been investigated (Laufer et al., 2012; Carosio et al., 2015c, 2018a). Although the concept of LbL-assembled FR coatings was first validated on fabrics, open cell foams have recently attracted great interest as a substrate to protect due to their inherently high flammability, which makes them one of the first items to be ignited during a fire (Ahrens, 2008). Different coating compositions and FR strategies have been investigated, mainly targeting the deposition of nanoparticles-rich coatings characterized by brick and mortar structures or the assembly of organic polyelectrolytes with intumescence-like behavior (Carosio et al., 2014b, 2018c; Smith et al., 2017). These two FR concepts have also been combined together using nanoparticles as reinforcing agents either within the intumescent coating or below it in stacked configurations (Cain et al., 2013; Holder et al., 2015). Treated foams usually achieve considerably reduced combustion rates and, in some cases, the ability to stop flame spread during flammability tests. Self-extinguishing typically requires a high number of deposition steps (usually >10), which is currently preventing the scale-up and large scale industrial exploitation of the LbL approach (Richardson et al., 2015; Carosio and Alongi, 2016). In addition, the durability of the LbL coating during repeated foam deformation has never been properly addressed. This represents another strong limitation of the state of the art, as one of the main applications of soft open cell PU foams is in upholstered furniture for buildings and transportations. In the present paper, we aim at the design of a coating composition and its assembly onto a soft PU foam in order to obtain highly performing and durable FR coatings, with only three depositions steps. To this aim, open cell PU foams have been treated, following the procedure schematized in **Figure 1**.

Each deposition step deposits a nanoparticle/polyelectrolyte layer with specific FR characteristics. The hypothesis is that the first layer made of polyacrylic acid and montmorillonite may produce a "brick and mortar" structure to reduce volatile feed to the gas phase, while providing stability to the remaining portion of the coating (Carosio et al., 2015a). In the second layer, boehmite (BOH) nanoparticles deposited within a poly(diallyldimethylammonium chloride) (PDAC) may release water during combustion (with volatile dilution and cooling effects) while also leaving an inorganic protective layer made of aluminum oxide (Rothon and Hornsby, 2014). The outermost layer made of ammonium polyphosphate (APP) and montmorillonite (MMT) acts as inorganic intumescent layer producing an expanded silicoalluminophosphate barrier (Alongi and Carosio, 2016). The resulting coating morphology has been evaluated by scanning electron microscopy while the resulting FR properties have been assessed by horizontal flammability and cone calorimetry tests. Furthermore, in an effort to evaluate the coating durability, treated foams have been subjected to deformation cycles evaluating the effects on coating morphology and FR properties.

MATERIALS AND METHODS

Materials

Open cell polyurethane foams (PU) with a density of 18 g/dm^3 and thickness of 18 mm were purchased from a local warehouse. The as received foams were washed by dipping and vigorous squeezing in deionized water in order to remove dust and processing residues and then dried in a ventilated oven at the temperature of 70°C. Poly(diallyldimethylammonium choride) (PDAC, average Mw 400,000–500,000, 20% wt in H_2O), polyacrylic acid (PAA, solution average Mw ∼100,000, 35% wt. in H_2O), Sigma-Aldrich. The sodium montmorillonite (MMT) was purchased from Southern Clays. Ammonium polyphosphate (PHOS-CHEK® P30) was purchased from ICL Performance Products, Inc. Bohemite nanoparticles (Dispal 10F4) with average dispersed size 240 nm (as declared by the producer) have been supplied by Sasol. Ultrapure water (18.2 MΩ) supplied by a Q20 Millipore system was employed for the preparation of the solutions and suspensions employed in this work. Both PAA/MMT and PDAC/BOH have been employed to prepare a 3% wt suspension with 1:2 polyelectrolyte/nanoparticle ratio. The suspension was prepared by firstly diluting the polyelectrolyte solution and then adding the required amount of nanoparticles. APP and MMT have been employed with a 2:1 polyelectrolyte/nanoparticle ratio for the preparation of a 3% wt water suspension.

Layer-by-Layer Deposition

The prewashed PU foam has been treated with a three-step deposition process as schematized in **Figure 1**. First the foam was dipped in the PAA/MMT bath (negative suspension), then

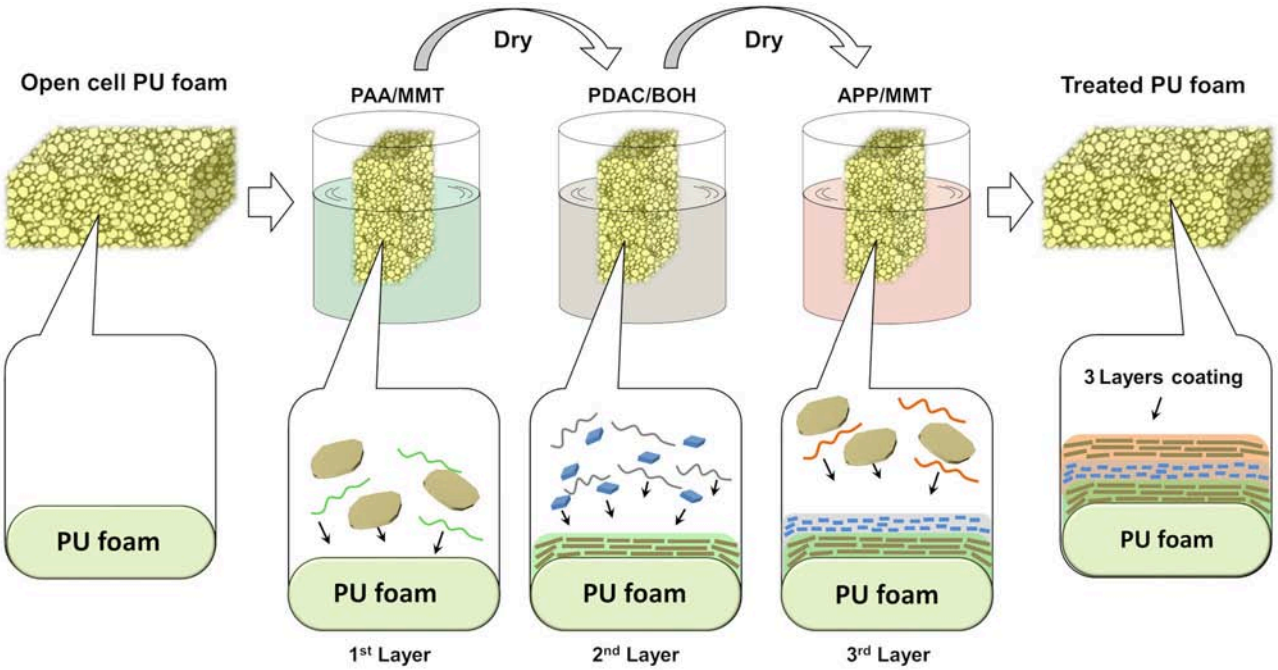

FIGURE 1 | Schematization of the coating procedure employed in this study. PU foams are dipped in three different baths following the order: polyacrylic acid/montmorillonite (PAA/MMT) suspension, poly(diallyldimethylammonium chloride)/boehmite (PDAC/BOH), and ammonium polyphosphate/montmorillonite (APP/MMT). This process deposits a three-layer coating.

in the PDAC/BOH bath (positive suspension) and eventually in the APP/MMT bath (negative suspension). During each deposition step, the foam is dipped in the bath and vigorously squeezed in order to fill its internal structure with the suspension. After an immersion time of 10 min, the wet foam was removed from the bath, squeezed to remove the excess of suspension and dried in a ventilated oven at 70°C. The process as shown in **Figure 1** deposits a three layer coating (PAA/MMT)/(PDAC/BOH)/(APP/MMT) on the PU structure. The mass gain, evaluated by weighting the samples before and after the LbL deposition, was 37 ± 3%. In the following, a sample coated with three layers is denoted as PU-3 L.

Characterization

The morphology of untreated and treated PU foams was investigated using a LEO^{-1}450VP Scanning Electron Microscope (SEM) operating at 5 kV. Small pieces (∼10 × 10 × 5 mm^3) of PU foams were positioned on conductive adhesive tape and gold coated prior to observation. Fourier Transformed-Infrared spectra in attenuated total reflectance (FT-IR ATR) were collected at room temperature in the range of 4,000–700 cm^{-1} (16 scans and 4 cm^{-1} resolution) using a Perkin Elmer Frontier spectrometer equipped with a diamond crystal. In order to preliminarily evaluate the coating durability during foam deformation, simple compression cycles have been performed on coated PU samples as schematized in **Supplementary Figure 1**. During the test the foam is placed between two 1 mm thick aluminum plates and then manually compressed by the action of a weight placed on top of the plate resulting in 16 kPa pressure[1]. The compression is maintained for 5 s after which the weight is removed in order to let the foam recover its original shape. Then, after 10 s the weight is applied again in order to perform a second compression cycle. This cycle has been repeated 50 and 100 times. In the followings, samples coded as PU-3 L @50 c and PU-3 L @100 c refer to a coated foam subjected to 50 and 100 compression cycles, respectively.

Flammability tests were performed in horizontal configuration. 50 × 150 × 15 mm^3 specimens positioned on a metallic grid were ignited by applying a 20 mm blue methane flame on the short side of the sample. The flame was applied for 6 s. During the test, the formation of incandescent droplets of molten polymer (melt dripping) was evaluated by placing dry cotton underneath the sample. The time, in seconds, a flame persisted on the sample after the igniting source has been removed was recorded as flaming time. The percentage of mass left at the end of the test is reported as final residue and was evaluated by weighting the sample before and after the test. Three different samples were tested for each formulation. Forced combustion tests were performed by cone calorimetry (Fire Testing Technology). 50 × 50 ×18 mm^3 specimens were exposed to a 35 k W/m^2 radiative heat flux. Average values concerning Time To

[1](i.e., ∼163 g/cm^2, roughly simulating the weight of a person, despite a full mechanical deformation study would require a more complex setup, well beyond the scope of this study).

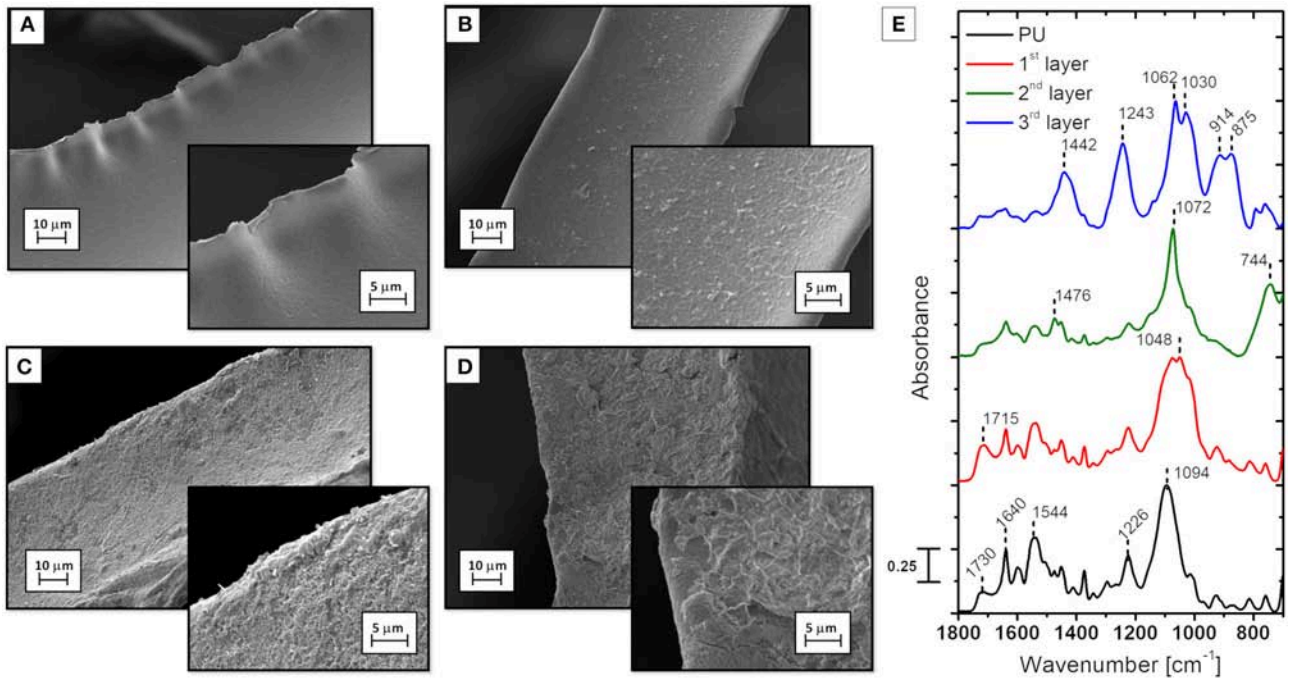

FIGURE 2 | SEM micrograph of untreated and treated PU foam (main: 1000X, inlet: 2500X): **(A)** neat PU, **(B)** 1st layer, **(C)** 2nd layer, **(D)** 3rd layer, and **(E)** ATR spectra of neat PU and PU coated with 1, 2, and 3 layers.

Ignition (TTI), peak of Heat Release Rate (pkHRR), Total Heat Release (THR), average Specific Extintion Area (SEA), Total smoke release (TSR) and final residue were evaluated and are presented with their experimental deviations. Measurements were performed four times for each formulation. Prior to flammability and forced combustion tests, all specimens were conditioned in a climatic chamber (23 ± 1°C 50% R.H) for 48 h.

RESULTS AND DISCUSSION

Coating Morphology

The changes in surface morphology and chemical composition of small samples of PU foam after each deposition step have been investigated by SEM and ATR spectroscopy. **Figure 2** reports collected micrographs and IR spectra. In **Figure 2** a sample coded as PU 1st layer denotes the deposition of only the (PAA/MMT) layer, PU 2nd layer denotes the deposition of the (PAA/MMT)/(PDAC/BOH) layers and PU 3rd layer denotes the deposition of the (PAA/MMT)/(PDAC/BOH)/(APP/MMT) layers (i.e. the complete coating structure).

The unmodified PU shows a typical open cell structure where cell walls generated during the foaming process are characterized by a smooth and even morphology (**Figure 2A**). The deposition of the PAA/MMT layer (8 ± 1% add-on) completely changes the foam walls morphology. Indeed, the formation of a thin and homogeneous coating containing MMT nanoplatelets embedded within a PAA matrix can be easily observed in **Figure 2B**. This is in agreement with previously reported LbL assemblies comprising polyelectrolytes and MMT (Carosio et al., 2014a). The deposition of the second PDAC/BOH layer (20 ± 3% total add-on) provides an additional change, and BOH nanoparticles are evenly distributed on every surface available producing a granular morphology as reported in high magnification micrographs in **Figure 2C**. The final deposition step adds the APP/MMT layer (37 ± 3% total add-on) and this corresponds to another change in surface morphology that appears to have higher rugosity (**Figure 2D**). It is worth observing that, starting from the first deposition step, the PAA/MMT coating completely covers all the surfaces available without displaying an island growth that is typical of LbL assemblies at early deposition steps. This can be ascribed to the good affinity between the PAA and the PU surface, where extensive hydrogen bonding between the urethane bonds and undissociated carboxylic acids of PAA may occur (Laufer et al., 2013). The stability and homogeneity of this first adsorbed layer is fundamental for the proper depositions of the subsequent layers. The resulting coating creates a complete protective exoskeleton that completely wraps the 3D structure of the foam without altering its open cell nature as reported in low magnification micrographs collected in **Supplementary Figure 2**. ATR spectroscopy has been also employed to evaluate the change in surface chemistry after each adsorption step (**Figure 2E**). Neat PU shows characteristic signals associated to C=O vibrations related to the urethane (broad peak centered at 1,730 cm^{-1}), urea group (1,640 cm^{-1}), N–H and C–N vibrations of the urethane and urea groups (band centered at 1,544 cm^{-1}) and C–O–C asymmetric and

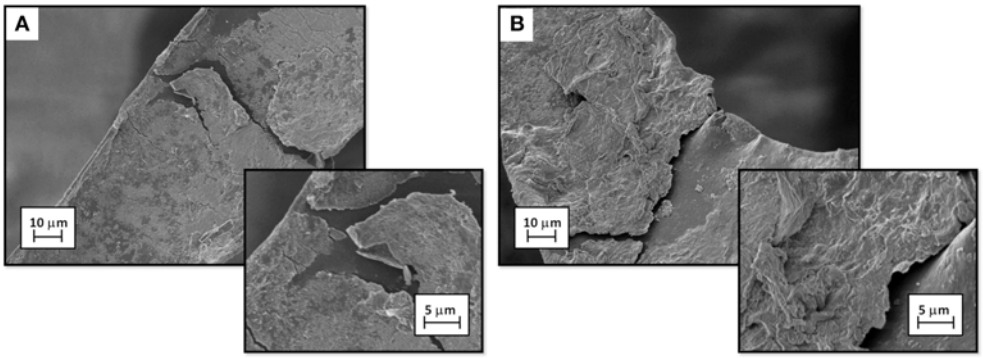

FIGURE 3 | SEM micrographs (main: 1000X, inlet: 2500X) of PU-3 L foam after 50 **(A)** and 100 **(B)** compression cycles.

symmetric vibrations (1,226 and 1,094 cm^{-1}, respectively) (Gómez-Fernández et al., 2016). The neat coating constituents have been also analyzed, and collected spectra are reported in **Supplementary Figure 3**. Pure PAA shows characteristic C=O and C-O-C signals at 1,700 and 1,164 cm^{-1}, respectively (Dong et al., 1997). MMT displays the strongest peak centered at 1,000 cm^{-1} and ascribed to Si-O vibrations (Madejová, 2003). PDAC shows the main characteristic bands associated to C-H bonds in CH_2 (1,470 cm^{-1}) and N-C bonds (1,122 cm^{-1}) (Sun et al., 2008). BOH asymmetric and symmetric Al-OH vibrations are found at 1,153 and 1,075 cm^{-1}, respectively (Haghnazari et al., 2014). This latter peak also accounts for Al-O vibrations while OH groups are evidenced by the peak at 738 cm^{-1} (Guido et al., 2013). APP shows characteristic peaks associated to P=O (1,245 cm^{-1}), P-O (1,062 and 1,022 cm^{-1}), P-O^- (880 cm^{-1}), and N-H of ammonium ions (1,423 cm^{-1}) (Socrates, 2006). When the first PAA/MMT layer is deposited on PU foams, the characteristic peaks of the substrate change consistently, evidencing the formation of new peaks at 1,715 and 1,048 cm^{-1} ascribed to C=O stretching in PAA and Si-O-Si vibrations in MMT, respectively. The deposition of the second layer results in the appearance of signals associated to CH_2 vibration (1,476 cm^{-1}) in PDAC as well as Al-O/Al-OH (1,072 cm^{-1}) and O-H vibration (744 cm^{-1}) in BOH. The presence of the last layer is evidenced by signals mainly associated to APP such as P=O (1,243 cm^{-1}), P-O (1,062 cm^{-1}), P-O^- (914 and 875 cm^{-1}) and N-H (1442 cm^{-1}), while MMT contributes with the signal at 1,030 cm^{-1}. It is worth mentioning that in the assembled layers many signals associated to polar functional groups of adsorbed species are shifted to different wavenumbers with respect to the neat products. The most apparent is the P-O- signal of APP that appears with two distinct peaks at 914 and 875 cm^{-1}, likely ascribed to P-O- interactions with PDAC and ammonium ions, respectively. The Si-O signal of MMT appears at higher wavenumbers as a consequence of hydrogen bond interactions with the co-adsorbed polyelectrolytes (i.e., PAA and APP; Chen and Zhang, 2006). In order to evaluate the durability of the coating, the foams treated with three layers have been subjected to repeated compression tests as described in the Materials and Methods section.

The morphology of the coating after 50 and 100 compression cycles has been evaluated by SEM, see **Figure 3** for collected micrographs. The deformation cycles impart strong deformations to the deposited coating that must comply to the change in shape of the substrate. Due to the ionic bonds in between the adsorbed layers and the nanoparticle-based structure, the deposited coating is inevitably rigid and the cyclic deformation results in the formation of cracks where portion of the assembly are partially detached from the substrate (**Figures 3A,B**). Interestingly, no visible differences in terms of damage extent can be appreciated when comparing the coating morphologies after 50 and 100 deformation cycles. This suggests that the cracks that are clearly visible in **Figures 3A,B** are generated during the first compression cycles in order to allow the foam walls to completely collapse upon compression. SEM investigations performed on PU-3 L samples after the first compression cycle support this as reported in **Supplementary Figure 4** where low magnification micrographs clearly show extensive cracks formation with minimal detachment of the coating. This is also confirmed by practical observations of the coated foams that are firmer after the deposition of the coating, but after few deformation cycles no significant qualitative differences can be observed when compared to the untreated foam. Such behavior is in agreement with previously reported literature (Li et al., 2013) where LbL-treated foams partially recovered the original stress/strain curve after few compression cycles. This is particularly important for the application in upholstered furniture and seats, allowing to preserve the comfort feeling for which the pristine foam was designed.

Flammability

Since PU foams represent one of the first items to be ignited during the start of a fire, it is mandatory to evaluate the flammability properties by means of horizontal flame spread tests. This test simulates the accidental exposure of the foam to a small flame thus allowing for the evaluation of the potential fire starting capability associated with the sample. **Figure 4** summarizes collected flammability parameters as well as snapshots of neat and coated foams during the test. Numerical

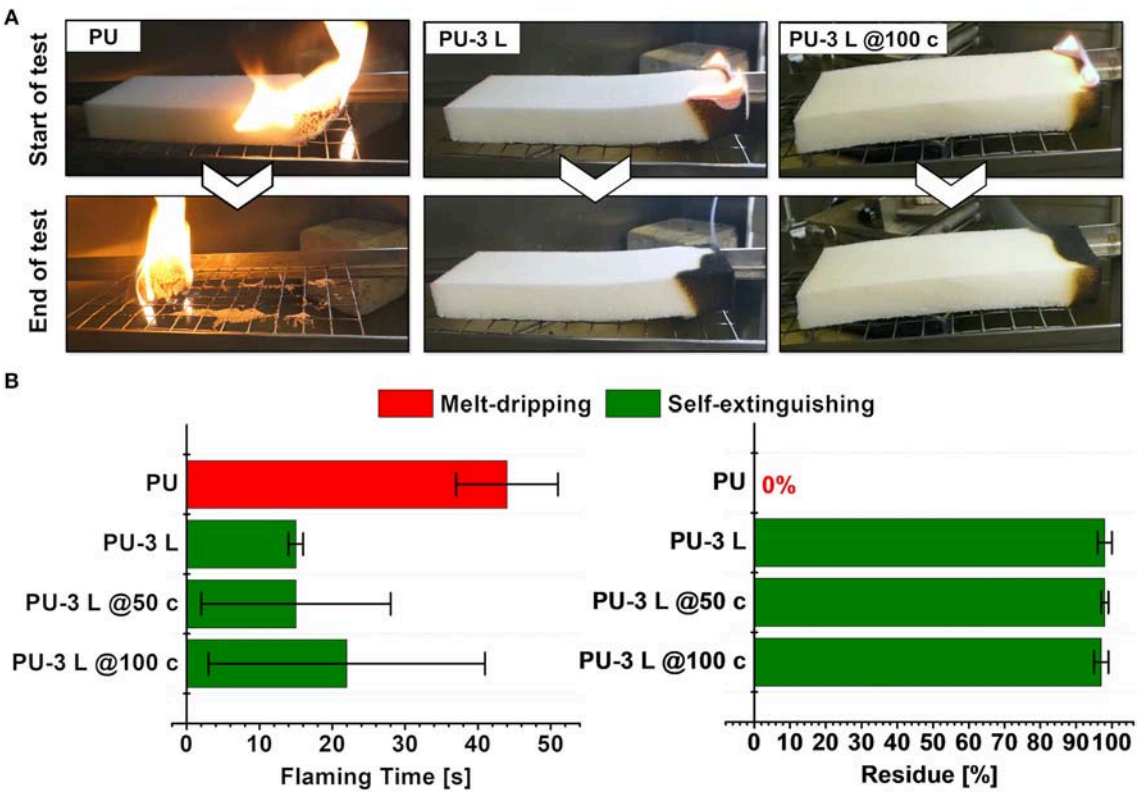

FIGURE 4 | Flammability tests performed on neat PU, treated PU, and treated PU foams after compression cycles; **(A)** snapshot of samples during the test, **(B)** flaming time and final residue.

parameters with their standard deviation are reported in **Supplementary Table 1**.

The uncoated PU foam can be easily ignited by the methane flame. When the ignition source is removed, the flames grow in size and rapidly spread to the entire length of the sample, completely consuming it (**Figure 4A**). During combustion, a vigorous melt dripping ignites the dry cotton placed underneath the sample. This phenomenon is typical of flexible PU foam and is related to the formation of flaming droplets of molten polymer that pose additional fire risks as not only the foam can be quickly ignited, but also the melt dripping can easily spread the fire to other ignitable materials. The presence of the three-layer coating completely changes this burning behavior. Indeed, upon removal of the ignition source, only a small flame remains confined in the first 2 cm of the foam, constantly reducing in size until it extinguishes within few seconds. No melt dripping is observed, and the residue collected at the end of the test accounts for 98% of the original mass. A nearly identical behavior is observed in coated foams subjected to 50 and 100 deformation cycles. Only a slight increase in the average flaming time was observed for compressed foams, meaning that self-extinguishing takes slightly longer to occur, but the deviation of burning times obtained for different specimens is considerably increased, suggesting a dependency on local density of defects. Nevertheless, all coated foams are capable of stopping flame spread and suppress the melt dripping phenomenon, yielding final residues within 97–98%. These results clearly point out the improved fire safety achieved by the deposited coatings. Indeed, thanks to the engineered structure of the three layers, the protective exoskeleton is able to prevent foam melting and collapsing while at the same time considerably reducing the release of volatile gasses that feed and sustain the flame. The resulting FR action is very efficient as self-extinguishing behavior is achieved with only three deposition steps. In addition, it seems that the formation of cracks during deformation cycles had rather limited effects on the FR performances of the coated foam.

Cone Calorimetry

Cone calorimetry tests allow to evaluate the reaction of untreated and treated foams when exposed to heat fluxes typically obtained in developing fires, thus assessing the contribution of the samples to fire growth and spread. During the test, samples are exposed to 35 kW/m^2 (i.e., heat flux related to early stages of a developing fire; Schartel and Hull, 2007), which triggers thermal degradation processes and the subsequent release of flammable volatiles that, when the proper concentration is reached, can be ignited by a spark igniter leading to flaming combustion. The instrument measures parameters associated to heat and smoke release. **Figure 5** collects HRR plots and histograms of the main parameters evaluated during the test

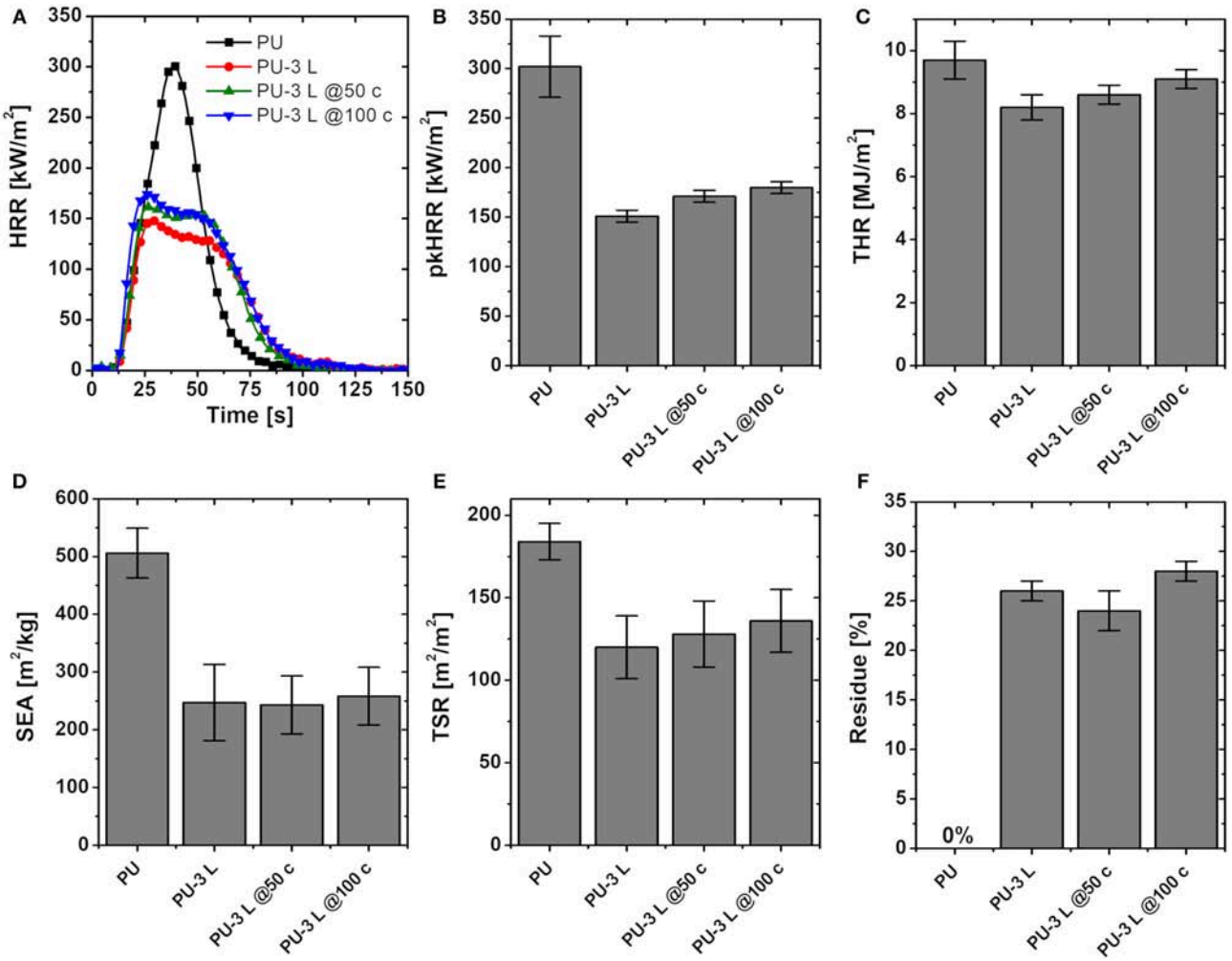

FIGURE 5 | Cone calorimetry parameters neat PU, treated PU, and treated PU foams after compression cycles: **(A)** HRR vs. time plot, **(B)** peak of heat release rate (pkHRR), **(C)** total heat release (THR), **(D)** average specific extinction area (SEA), **(E)** total smoke release (TSR), and **(F)** final residue.

while numerical values with their standard deviation are reported in **Supplementary Table 2**.

Upon exposure to the cone calorimetry heat flux, the neat PU foams show a quick ignition (TTI=2 s) followed by the foam structural collapse and the formation of a molten pool of a low viscosity liquid. This latter step produces a steeply increase in heat release rate that reaches the maximum value of about 300 kW/m^2 (**Figure 5A**, HRR vs. time plots). The behavior of flexible PU foam during cone testing is well documented and the collapsing and melting stages are normally associated to increased fire spreading risks (Kramer et al., 2010). The presence of the three-layers coating completely changes the burning behavior of coated PU foams. Indeed, upon ignition no structural collapse is observed and the foams maintain their original shape at the end of the test (see **Supplementary Figure 5**). Heat release rates are considerably reduced as demonstrated by a −50% in pkHRR value (**Figure 5B**, pkHRR histograms); on the other hand, the effect on THR values is rather limited, suggesting combustion of the PU is complete, yet delayed in time. Interestingly, a positive effect on smoke related parameters is also observed. Indeed, smoke optical density (SEA) and total smoke produced (TSR) are considerably reduced: −50 and −34%, respectively (**Figures 5D,E**). The final residue is increased to 25% of the starting mass. These results point out that the presence of the coating not only can efficiently reduce the rate of combustion and potential fire spread risk, but can also influence the production of smoke. Such observation is of crucial importance since it is reported that people are normally confronted with smoke and its effects during evacuation (Frantzich, 1994). The presence of dense smoke considerably increases escaping times while also causing loss of ability to react, unconsciousness, slower walking speed and long-term damage such as lung cancer (Gann, 2004). For these reasons, smoke-related effects represent an important cause of fire fatalities. Furthermore, coated foams subjected to 50 and 100 deformation cycles maintain performances similar to the

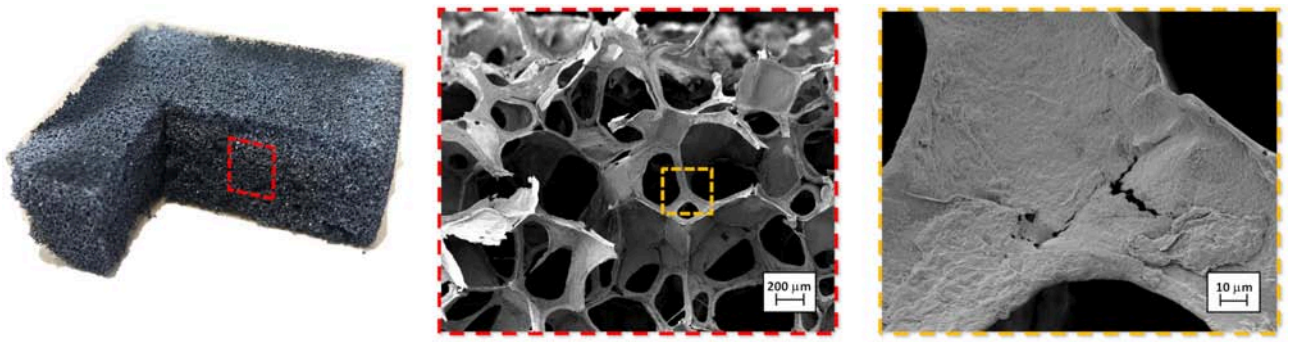

FIGURE 6 | SEM analysis (50X and 1000X) performed on the residue PU-3 L collected after cone calorimetry test.

non-compressed PU-3 L. Despite a slight detrimental effect, proportional to the number of deformation cycles observed, pkHRR values still maintain a reduction ≥40% while average smoke parameters remain within the experimental error of the PU-3 L. It seems that the cracks produced during deformation can affect the efficiency of the coating in reducing volatile release while the smoke diluting action exerted by BOH nanoparticles is mostly unaffected.

The residues collected after cone calorimetry tests have been observed by SEM (**Figure 6**). Low magnification micrographs suggest that the original 3D structure of the PU foam is left almost undamaged (compare **Figure 6** with **Supplementary Figure 2**). By increasing the magnification it is possible to reveal the real structure of the residue that mostly comprises a hollow protective exoskeleton resulting from the deposited coating. The morphology has clearly changed during combustion due to the different processes occurring within the coating (i.e., PAA degradation, BOH water release and APP decomposition) resulting in the formation of a compact barrier. The presence of cracks on the surface can be related to the release of volatiles produced by the PU that is almost completely consumed during combustion as demonstrated by the negligible change in THR values. The achieved results have been compared with other FR systems deposited on open-cell flexible PU foams by the LbL deposition of inorganic nanoparticles, natural polysaccharides or carbon nanotubes, as presented in **Figure 7**, where the best reduction in heat release rate peak achievable with each coating composition is plotted as function of the number of deposited layers (Laufer et al., 2012; Carosio et al., 2014b, 2015b, 2018b; Wang et al., 2014; Haile et al., 2016; Holder et al., 2016; Mu et al., 2017; Smith et al., 2017; Lazar et al., 2018). Red or green symbols refer to flammability and account for the ability to self-extinguish the flame and prevent its spread to the entire surface of the sample.

It can be easily appreciated that most LbL coatings can achieve substantial reductions in pkHRR (in the 40–70% range) regardless of the deposited layer number. However, in order to grant self-extinguishing behavior during flammability tests, a minimum number of 10 deposited layers is needed. This considerably reduces the efficiency of the deposited

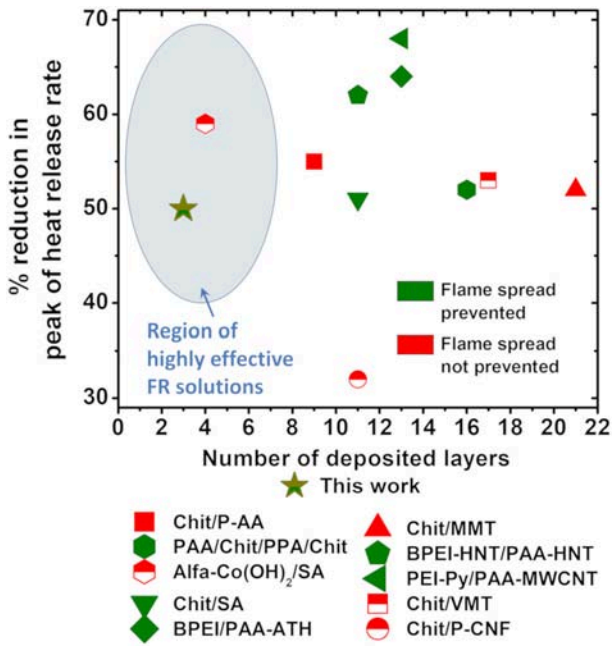

FIGURE 7 | Comparison of the flame-retardant performance in terms of peak of heat release reduction during cone calorimetry tests (35 kW/m^2). In the legend, Chit, chitosan; P-AA, phosphonated allylamine; PAA, poly(acrylic acid); PPA, poly(phosphoric acid); SA, sodium alginate; BPEI, branched polyethyleneimine; ATH, aluminum trihydroxide; MMT, montmorillonite; HNT, halloysite nanotubes; PEI-Py, pyrene functionalized polyethyleneimine; MWCNT, multi wall carbon nanotubes; VMT, vermiculite; P-CNF, phosphorylated cellulose nanofibrils.

LbL coatings and their potential applicability. On the other hand, in this paper we demonstrate that the proper design of the layer composition and the coating structure allows to achieve substantial reductions in pkHRR values (50–40%) while also obtaining self-extinguishing behavior. In addition, these characteristics are maintained after 100 deformation cycles thus confirming the potentialities of the developed solutions.

CONCLUSIONS

In this manuscript, we reported the preparation of efficient and durable layer-by-layer coatings based on the deposition of only three layers of nanoparticles containing polyelectrolytes. The deposition procedure produces a protective exoskeleton that completely covers the complex 3D geometry of the foam. The layer constituents and position have been selected on the basis of the desired flame retardant mechanism. The first layer that comprises PAA and MMT nanoplatelets produces a first barrier to volatile release. BOH nanoparticles contained in the second layer can release water with gas phase diluting and cooling effects while leaving a thermally insulating layer made of Al oxide. This latter effect is further enhanced by the third layer where APP and MMT can react together in order to produce an inorganic intumescent layer. The joint action of these three layers can stop flame spread during horizontal flammability tests leaving most of the foam undamaged (final residue up to 98% of the initial mass). Combustion rates are considerably lowered as demonstrated by a 50% reduction in pkHRR during cone calorimetry tests. Smoke production is also efficiently addressed with coated foams showing reduced smoke optical density and total smoke released. This latter aspect can prove fundamental during the evacuation of buildings in case of fire. The durability of the achieved FR performances has been evaluated by means of compression cycles. To this aim, treated foams were compressed cyclically to maximum deformation for 50 and 100 times and then their FR properties have been evaluated again. Only minor differences have been observed for the compressed foams that still exhibited excellent FR properties thus confirming the great efficiency and potential durability of the proposed coating solution. In summary, thanks to an efficient coating composition and by relying on a simple water-based approach it is possible to prepare foams capable of improving the fire safety in several applications where flexible polyurethane foams are used, including upholstered furniture and seats for households, transports, public buildings, theaters/cinemas etc.).

AUTHOR CONTRIBUTIONS

FC conceived the experiments, carried out the LbL deposition and the characterization. AF contributed to the interpretation of results and the revision of the manuscript. The manuscript was mainly written by FC.

SUPPLEMENTARY MATERIAL

The Supplementary Material for this article can be found online at: https://www.frontiersin.org/articles/10.3389/fmats.2019.00020/full#supplementary-material

REFERENCES

Ahrens, M. (2008). *Home fires that began with upholstered furniture.* Quincy, MA: National Fire Protection Association Quincy.

Alongi, J., and Carosio, F. (2016). All-inorganic intumescent nanocoating containing montmorillonite nanoplatelets in ammonium polyphosphate matrix capable of preventing cotton ignition. *Polymers* 8:430. doi: 10.3390/polym8120430

Alongi, J., Carosio, F., and Kiekens, P. (2016). Recent advances in the design of water based-flame retardant coatings for polyester and polyester-cotton blends. *Polymers* 8:357. doi: 10.3390/polym8100357

Cain, A. A., Nolen, C. R., Li, Y. C., Davis, R., and Grunlan, J. C. (2013). Phosphorous-filled nanobrick wall multilayer thin film eliminates polyurethane melt dripping and reduces heat release associated with fire. *Polym. Degrad. Stab.* 98, 2645–2652. doi: 10.1016/j.polymdegradstab.2013.09.028

Carosio, F., and Alongi, J. (2016). Ultra-fast layer-by-layer approach for depositing flame retardant coatings on flexible pu foams within seconds. *ACS Appl. Mater. Interfaces* 8, 6315–6319. doi: 10.1021/acsami.6b00598

Carosio, F., Colonna, S., Fina, A., Rydzek, G., Hemmerle, J., Jierry, L., et al. (2014a). Efficient gas and water vapor barrier properties of thin poly(lactic acid) packaging films: functionalization with moisture resistant nafion and clay multilayers. *Chem. Mater.* 26, 5459–5466. doi: 10.1021/cm501359e

Carosio, F., Di Blasio, A., Cuttica, F., Alongi, J., and Malucelli, G. (2014b). Self-assembled hybrid nanoarchitectures deposited on poly(urethane) foams capable of chemically adapting to extreme heat. *RSC Adv.* 4, 16674–16680. doi: 10.1039/C4RA01343C

Carosio, F., Di Pierro, A., Alongi, J., Fina, A., and Saracco, G. (2018a). Controlling the melt dripping of polyester fabrics by tuning the ionic strength of polyhedral oligomeric silsesquioxane and sodium montmorillonite coatings assembled through Layer by Layer. *J. Colloid Interface Sci.* 510, 142–151. doi: 10.1016/j.jcis.2017.09.059

Carosio, F., Ghanadpour, M., Alongi, J., and Wågberg, L. (2018b). Layer-by-layer-assembled chitosan/phosphorylated cellulose nanofibrils as a bio-based and flame protecting nano-exoskeleton on PU foams. *Carbohydr. Polym.* 202, 479–487. doi: 10.1016/j.carbpol.2018.09.005

Carosio, F., Kochumalayil, J., Cuttica, F., Camino, G., and Berglund, L. (2015a). Oriented clay nanopaper from biobased components–mechanisms for superior fire protection properties. *ACS Appl. Mater. Interfaces* 7, 5847–5856. doi: 10.1021/am509058h

Carosio, F., Maddalena, L., Gomez, J., Saracco, G., and Fina, A. (2018c). Graphene oxide exoskeleton to produce self-extinguishing, nonignitable, and flame resistant flexible foams: a mechanically tough alternative to inorganic aerogels. *Adv. Mater. Interfaces*. 5:1801288. doi: 10.1002/admi.201801288

Carosio, F., Negrell-Guirao, C., Alongi, J., David, G., and Camino, G. (2015b). All-polymer layer by layer coating as efficient solution to polyurethane foam flame retardancy. *Eur. Polym. J.* 70, 94–103. doi: 10.1016/j.eurpolymj.2015.07.001

Carosio, F., Negrell-Guirao, C., Di Blasio, A., Alongi, J., David, G., and Camino, G. (2015c). Tunable thermal and flame response of phosphonated oligoallylamines layer by layer assemblies on cotton. *Carbohydr. Polym.* 115, 752–759. doi: 10.1016/j.carbpol.2014.06.066

Chen, P., and Zhang, L. (2006). Interaction and properties of highly exfoliated soy protein/montmorillonite nanocomposites. *Biomacromolecules* 7, 1700–1706. doi: 10.1021/bm050924k

Decher, G., and Schlenoff, J. B. (eds.). (2012). *Multilayer Thin Films: Sequential Assembly of Nanocomposite Materials, 2nd Edn.* Weinheim: Wiley-VCH.

Dong, J., Ozaki, Y., and Nakashima, K. (1997). Infrared, Raman, and near-infrared spectroscopic evidence for the coexistence of various hydrogen-bond forms in poly (acrylic acid). *Macromolecules* 30, 1111–1117. doi: 10.1021/ma960693x

Frantzich, H. (1994). *A Model for Performance-Based Design of Escape Routes.* Department of Fire Engineering, Lund Institute of Technology, Lund University.

Gann, R. G. (2004). Estimating data for incapacitation of people by fire smoke. *Fire Technol.* 40, 201–207. doi: 10.1023/B:FIRE.0000016843.38848.37

Gómez-Fernández, S., Ugarte, L., Peña-Rodriguez, C., Zubitur, M., Corcuera, M. Á., and Eceiza, A. (2016). Flexible polyurethane foam nanocomposites with modified layered double hydroxides. *Appl. Clay Sci.* 123, 109–120. doi: 10.1016/j.clay.2016.01.015

Guido, E., Alongi, J., Colleoni, C., Di Blasio, A., Carosio, F., Verelst, M., et al. (2013). Thermal stability and flame retardancy of polyester fabrics sol-gel

treated in the presence of boehmite nanoparticles. *Polym. Degrad. Stab.* 98, 1609–1616. doi: 10.1016/j.polymdegradstab.2013.06.021

Haghnazari, N., Abdollahifar, M., and Jahani, F. (2014). The effect of NaOH and KOH on the characterization of mesoporous AlOOH nanostructures in the hydrothermal route. *J. Mexican Chem. Soc.* 58, 95–98. doi: 10.29356/jmcs.v58i2.163

Haile, M., Fomete, S., Lopez, I. D., and Grunlan, J. C. (2016). Aluminum hydroxide multilayer assembly capable of extinguishing flame on polyurethane foam. *J. Mater. Sci.* 51, 375–381. doi: 10.1007/s10853-015-9258-8

Hammond, P. T. (2004). Form and function in multilayer assembly: new applications at the nanoscale. *Adv. Mater.* 16, 1271–1293. doi: 10.1002/adma.200400760

Holder, K. M., Cain, A. A., Plummer, M. G., Stevens, B. E., Odenborg, P. K., Morgan, A. B., et al. (2016). Carbon nanotube multilayer nanocoatings prevent flame spread on flexible polyurethane foam. *Macromol. Mater. Eng.* 301, 665–673. doi: 10.1002/mame.201500327

Holder, K. M., Huff, M. E., Cosio, M. N., and Grunlan, J. C. (2015). Intumescing multilayer thin film deposited on clay-based nanobrick wall to produce self-extinguishing flame retardant polyurethane. *J. Mater. Sci.* 50, 2451–2458. doi: 10.1007/s10853-014-8800-4

Holder, K. M., Smith, R. J., and Grunlan, J. C. (2017). A review of flame retardant nanocoatings prepared using layer-by-layer assembly of polyelectrolytes. *J. Mater. Sci.* 52, 12923–12959. doi: 10.1007/s10853-017-1390-1

Klemm, D., Kramer, F., Moritz, S., Lindström, T., Ankerfors, M., Gray, D., et al. (2011). Nanocelluloses: a new family of nature-based materials. *Angew. Chem. Int. Ed Engl.* 50, 5438–5466. doi: 10.1002/anie.201001273

Kramer, R. H., Zammarano, M., Linteris, G. T., Gedde, U. W., and Gilman, J. W. (2010). Heat release and structural collapse of flexible polyurethane foam. *Polym. Degrad. Stab.* 95, 1115–1122. doi: 10.1016/j.polymdegradstab.2010.02.019

Laufer, G., Kirkland, C., Cain, A. A., and Grunlan, J. C. (2012). Clay-chitosan nanobrick walls: completely renewable gas barrier and flame-retardant nanocoatings. *Acs Appl. Mater. Interfaces* 4, 1643–1649. doi: 10.1021/am2017915

Laufer, G., Kirkland, C., Morgan, A. B., and Grunlan, J. C. (2013). Exceptionally flame retardant sulfur-based multilayer nanocoating for polyurethane prepared from aqueous polyelectrolyte solutions. *ACS Macro Lett.* 2, 361–365. doi: 10.1021/mz400105e

Lazar, S., Carosio, F., Davesne, A. L., Jimenez, M., Bourbigot, S., and Grunlan, J. (2018). Extreme heat shielding of clay/chitosan nanobrick wall on flexible foam. *ACS Appl. Mater. Interfaces* 10, 31686–31696. doi: 10.1021/acsami.8b10227

Li, Y. C., Kim, Y. S., Shields, J., and Davis, R. (2013). Controlling polyurethane foam flammability and mechanical behaviour by tailoring the composition of clay-based multilayer nanocoatings. *J. Mater. Chem. A* 1, 12987–12997. doi: 10.1039/c3ta11936j

Madejová, J. (2003). FTIR techniques in clay mineral studies. *Vib. Spectrosc.* 31, 1–10. doi: 10.1016/S0924-2031(02)00065-6

Malucelli, G., Carosio, F., Alongi, J., Fina, A., Frache, A., and Camino, G. (2014). Materials engineering for surface-confined flame retardancy. *Mater. Sci. Eng. R-Rep.* 84, 1–20. doi: 10.1016/j.mser.2014.08.001

Mohanty, A. K., Misra, M., and Drzal, L. (2002). Sustainable bio-composites from renewable resources: opportunities and challenges in the green materials world. *J. Polym. Environ.* 10, 19–26. doi: 10.1023/A:1021013921916

Mu, X., Yuan, B., Pan, Y., Feng, X., Duan, L., Zong, R., et al. (2017). A single α-cobalt hydroxide/sodium alginate bilayer layer-by-layer assembly for conferring flame retardancy to flexible polyurethane foams. *Mater. Chem. Phys.* 191, 52–61. doi: 10.1016/j.matchemphys.2017.01.023

Rawlinson, K., Dodd, V., and Sherwood, H. (2017). *Grenfell Tower Final Death Toll: Police Say 71 Lives Lost as Result of Fire*. The Guardian.

Richardson, J. J., Björnmalm, M., and Caruso, F. (2015). Technology-driven layer-by-layer assembly of nanofilms. *Science* 348, aaa2491. doi: 10.1126/science.aaa2491

Rothon, R., and Hornsby, P. (2014). "Fire retardant fillers for polymers," in *Polymer Green Flame Retardants*, eds C. Papaspyrides and P. Kiliaris (Amsterdam: Elsevier), 289–321. doi: 10.1016/B978-0-444-53808-6.00009-3

Schartel, B., and Hull, T. R. (2007). Development of fire-retarded materials—Interpretation of cone calorimeter data. *Fire Mater.* 31, 327–354. doi: 10.1002/fam.949

Smith, R. J., Holder, K. M., Ruiz, S., Hahn, W., Song, Y., Lvov, Y. M., et al. (2017). Environmentally benign halloysite nanotube multilayer assembly significantly reduces polyurethane flammability. *Adv. Funct. Mater.* 28:1703289. doi: 10.1002/adfm.201703289

Socrates, G. (2006). *Infrared and Raman Characteristic Group Frequencies - Table and Charts*. Weinheim: Wiley.

Stapleton, H. M., Klosterhaus, S., Keller, A., Ferguson, P. L., Van Bergen, S., Cooper, E., et al. (2011). Identification of flame retardants in polyurethane foam collected from baby products. *Env. Sci. Technol.* 45, 5323–5331. doi: 10.1021/es2007462

Sun, W., Liu, W.-L., and Hu, Y.-H. (2008). FTIR analysis of adsorption of poly diallyl-dimethyl-ammonium chloride on kaolinite. *J. Central South Univer. Technol.* 15, 373–377. doi: 10.1007/s11771-008-0070-3

Wang, X., Pan, Y.-T., Wan, J.-T., and Wang, D.-Y. (2014). An eco-friendly way to fire retardant flexible polyurethane foam: layer-by-layer assembly of fully bio-based substances. *RSC Adv.* 4, 46164–46169. doi: 10.1039/C4RA07972H

Conflict of Interest Statement: The authors declare that the research was conducted in the absence of any commercial or financial relationships that could be construed as a potential conflict of interest.

frontiers in Materials

ORIGINAL RESEARCH
published: 26 April 2019
doi: 10.3389/fmats.2019.00076

Thermo-Mechanical Behavior of Novel Wood Laminae-Thermoplastic Starch Biodegradable Composites With Thermal Energy Storage/Release Capability

Andrea Dorigato, Giulia Fredi and Alessandro Pegoretti*

Department of Industrial Engineering and INSTM Research Unit, University of Trento, Trento, Italy

For the first time, multifunctional fully biodegradable composites combining structural and thermal energy storage/release capabilities were prepared and thermo-mechanically characterized. Within this scope, thin beech laminae impregnated with a phase change material (PCM) represented by poly(ethylene glycol) (PEG) were interleaved with thin foils of thermoplastic starch (TPS) and consolidated by hot pressing. From scanning electron microscopy, it was observed that a certain amount of PEG (about 11 wt% of the total laminate) remained entrapped within the wood pores, negatively affecting the interfacial adhesion between wood laminae and TPS foils. The presence of PEG stabilized in the wood laminae was confirmed by differential scanning calorimetry tests, in which a specific melting enthalpy of 27.4 J/g was detected with a melting peak at 55°C. Wood permeation with PEG was responsible for an increase of the dynamic moduli E' and E'', as well as of the tensile and Charpy impact strength of the laminates. Therefore, this paper highlighted the possibility of developing multifunctional fully biodegradable composites capable of combining structural and thermal energy storage properties, in which the selected PCM positively contributed to the mechanical behavior of the laminates.

Keywords: starch, ultrathin wood laminae, composites, poly(ethylene glycol), energy storage

OPEN ACCESS

Edited by:
Luca Valentini,
University of Perugia, Italy

Reviewed by:
Debora Puglia,
University of Perugia, Italy
Loris Giorgini,
University of Bologna, Italy

****Correspondence:***
Andrea Dorigato
andrea.dorigato@unitn.it

Specialty section:
This article was submitted to Polymeric and Composite Materials, a section of the journal Frontiers in Materials

Received: *30 November 2018*
Accepted: *05 April 2019*
Published: *26 April 2019*

Citation:
Dorigato A, Fredi G and Pegoretti A (2019) Thermo-Mechanical Behavior of Novel Wood Laminae-Thermoplastic Starch Biodegradable Composites With Thermal Energy Storage/Release Capability. Front. Mater. 6:76. doi: 10.3389/fmats.2019.00076

INTRODUCTION

It is well-known that interest in fiber reinforced polymers (FRPs) has noticeably grown over the last decades (Gay et al., 2003), mostly because of their elevated specific mechanical performance, easy processability and corrosion resistance. On the other hand, various environmental concerns have arisen regarding the use of traditional reinforcing fibers (such as glass, carbon and aramid) in FRPs (Pegoretti, 2007) as life cycle assessments on these materials have evidenced their limits in terms of recyclability and final disposal operations (Dorigato and Pegoretti, 2012). A partial solution to these concerns could be represented by the use of natural fibers (i.e., kenaf, hemp, flax, cellulose, etc.) as reinforcement of both thermoplastic and thermosetting matrices (Wu, 2009). However, even though with these fibers it is possible to reach most of the physical properties of conventional laminates (García et al., 2008; Iwatake et al., 2008; Kunanopparat et al., 2008), it is very difficult from a technological point of view to perform efficient thermo-mechanical recycling of these materials because of the limited thermal degradation resistance of natural reinforcements

(Houshyar and Shanks, 2003). In this sense, a possible solution to these environmental issues could be represented by the development of fully biodegradable composites, in which both the constituents (i.e., the matrix and the reinforcing phase) can be degraded under certain environmental conditions.

Among the natural reinforcements that can be used for the production of fully biodegradable composites, wood fibers represent one of the most interesting options (Bledzki et al., 2002). Wood is mainly constituted by carbon, hydrogen and oxygen in the form of cellulose (40–50 wt%), hemicellulose (20 wt%), lignin (about 35 wt%) and pectic substances in limited concentrations (Core et al., 1979). From a mechanical point of view, wood behaves like a heterogeneous anisotropic material. Moreover, in the low deformation regime it can be considered as an orthotropic material (Green et al., 1999), and its mechanical performance is strongly influenced by the presence of nodes and microstructural defects. Moreover, considering that wood can absorb up to 25–30 wt% of water, the environmental conditions strongly affect the mechanical response of wood-based materials.

From a microstructural point of view, the cross section of wood-based materials is formed by a regular distribution of cellular lumen with isolated and clustered pores and thick-walled fibers. In the case of beech, large parenchymal rays are generally distended along growth ring boundaries, while the concentration of gum inclusions, salt crystals or lattices is rather limited (Giordano, 1981). In the last years, particular scientific and technological attention was given to wood plastic composites (WPCs), constituted by wood fibers or wood flour compounded with thermoplastic matrices, such as polypropylene (PP), polyethylene (PE), and polyvinylchloride (PVC) (Oksman and Sain, 2008). These materials can be processed through the traditional technologies of thermoplastics (i.e., extrusion, injection molding). However, the mechanical properties of WPCs are generally considerably poorer than those of structural wood components, even at elevated filler amounts, especially under severe environmental conditions (Srimalanon et al., 2016). Quite surprisingly, the possibility to utilize thin wood laminae to develop novel thermoplastic wood composites laminates did not receive much attention in the open literature.

Among biodegradable matrices that could be potentially applied in fully biodegradable composite laminates, thermoplastic starch (TPS) has recently drawn considerable attention. From the chemical point of view, starch is a polysaccharide with a semicrystalline structure, composed by linear amylose and highly branched amylopectin (Bogracheva et al., 2002), and it can be processed through extrusion and injection molding. In order to overcome the problems related to its elevated hydrophilicity, some attempts were made to modify the TPS chemical structure through acetylation (Chi et al., 2008; Ayucitra, 2012) or upon blending with other biopolymers, such as polycaprolactone (PCL) and polyhydroxybutyrate-co-valerate (PHBV) (Averous et al., 2000), or with synthetic plastics, like polyethylene. The most widespread TPS-based products are commercially known as Mater-Bi® (Novamont, Italy) (Bastioli, 1997) and Bioplast® (Biotec, Germany) (Lorcks, 1998).

Two examples of biodegradable laminates have been recently developed by our group. In the first case, polyvinyl alcohol (PVOH)-based composites were prepared by a hand lay-up procedure, impregnating ultrathin beech laminae with an aqueous solution of PVOH (Dorigato et al., 2018b), while in a second paper thermoplastic composites reinforced with wood laminae were produced through a hot-pressing process by using thermoplastic starch foils (Dorigato et al., 2018a). In both of these papers, it was found that the resulting materials were characterized by a peculiar microstructure, in which the porosity of the beech laminae was occluded by the polymer matrix. The consequence of the matrix permeation within the wood pores was that the resulting laminates showed higher elastic modulus and tensile strength with respect to their constituents.

It is challenging to impart also multifunctional properties to fully biodegradable composites. In fact, the scientific and industrial interest toward materials able to combine different properties (structural, electrical, magnetic, thermal, etc.) has strongly increased in the latest years (Gibson, 2010). In this scenario, polymer–matrix composites are particularly suitable to be designed as multifunctional materials (Salonitis et al., 2010) because they combine the peculiar properties of polymers, such as the low density, good processability and cheapness, with the elevated stiffness and strength of the reinforcing fibers (Mallick, 2007). According to the authors' opinion, one of the most interesting options could be to prepare fully biodegradable laminates with thermal energy storage (TES) capability. In fact, TES technology is based on the storage of heat and its release when needed, thus reducing the gap between thermal energy availability and request (Pielichowska and Pielichowski, 2014). Therefore, TES systems can be utilized to accumulate excess or waste heat, like in solar thermal power plants, to recover waste industrial heat (Khadiran et al., 2015), to control the temperature inside the buildings (Onder et al., 2008), in smart textiles for body temperature regulation (Sobolciak et al., 2016), or in the cooling systems for electronic devices (Luyt and Krupa, 2009). Multifunctional composites combining good mechanical properties and TES capability could thus be applied were weight and volume saving requirements should be coupled with energy storage capability and/or temperature control operations (Rigotti et al., 2018). TES systems are generally classified depending on the underlying process in sensible, thermochemical, or latent heat-storage systems. Among them, phase change materials (PCMs) undergo an endo/exo-thermic solid-solid or solid-liquid transition, and can be classified as organic, inorganic or eutectic (Sari et al., 2005). Thanks to their elevated specific phase change enthalpy, narrow transition temperature interval, limited supercooling, lightness and cheapness, organic PCMs, i.e., paraffins, poly(ethylene glycol) (PEG) and fatty acids, are probably the most widely diffused (Dorigato et al., 2017; Fredi et al., 2017). In particular, PEG is a versatile and biodegradable PCM with elevated melting enthalpy, tunable transition temperature range, elevated thermal stability, good biocompatibility, non-toxicity and non-corrosiveness (Sundararajan et al., 2016; Kou et al., 2019). Because of these peculiar properties, researchers have recently put much efforts to synthesize novel PCMs based on PEG, trying to

physically blend PEG with other supporting materials, to perform chemical modifications to prepare PEG based solid/solid PCMs or to impregnate PEG in porous materials (Wang et al., 2016; Yang et al., 2016; Zhou et al., 2018). Nowadays, most of the studies on PEG-based PCMs are focused on the preparation of novel PCMs with improved thermal energy storage capability. The problems associated with the poor thermal conductivity of organic PCMs and their need to be confined to limit their leakage at the molten state (Kastiukas et al., 2016) could be partially solved through their encapsulation in organic or inorganic shells (Ozaki et al., 2008), or upon the shape stabilization in a polymer matrix (Yoo et al., 2016), in a layered/porous structure or in a nanostructured filler (Alexandre et al., 2009). Moreover, the use of a conductive nanofiller could also improve the thermal conductivity of the resulting systems. Due to its porous microstructure, it is possible to hypothesize that wood could also be an interesting candidate for the shape stabilization of organic PCMs at the molten state.

Quite interestingly, only a few investigations have been performed on the possibility of preparing multifunctional PMCs combining TES and structural features. For example, our group recently developed novel epoxy/carbon fiber composites containing carbon nanotube (CNT)-stabilized paraffinic wax (Fredi et al., 2017, 2018a), epoxy/discontinuos carbon fibers with microencapsulated paraffin (Dorigato et al., 2019), thermoplastic polyamide 12 (PA12)/glass fiber composites containing both microencapsulated and shape stabilized PCMs, reinforced with long glass fibers (Fredi et al., 2018a) or with discontinuous carbon fibers (Dorigato et al., 2018c; Fredi et al., 2019), or thermoplastic acrylic Elium®/carbon fiber laminates containing microencapsulated paraffin (Fredi et al., in preparation). However, no papers on the production of fully biodegradable composites with good mechanical properties and TES capability can be found in the open literature. On the basis of these considerations, the aim of the present paper is to develop for the first time multifunctional fully biodegradable composite laminates, constituted by a thermoplastic starch matrix reinforced with thin wood laminae, in which the thermal energy storage function can be obtained by impregnating wood laminae with PEG in the molten state. The microstructural, thermal and mechanical behavior of the resulting laminates was investigated, considering also the effect of the orientation of the reinforcing phase within the composites. The properties of the resulting laminates were also compared with those of their constituents.

EXPERIMENTAL

Materials

Thermoplastic starch MaterBi® EF51V was supplied by Novamont Spa (Novara, Italy) in the form of foils with a thickness of 100 μm. This TPS grade is characterized by a density of 1.2 g/cm^3, a MFI of 4 g/10 min (190°C, 2.16 kg) and a melting temperature of 167°C.

The employed poly(ethylene glycol) was PEG 2000 purchased by Alfa Aesar (Karlsruhe, Germany). It has a molecular weight of 1,800–2,200 g/mol and a melting temperature of 51–55°C, according to the producer's datasheet.

For the preparation of the thin wood laminae (**Figure 1A**), a beech plant with a density of about 0.73 g/cm^3 if conditioned at 23°C and a relative humidity of 50% was selected. The selection of this wood species is motivated by its regular morphology and anatomical structure, as described in the Introduction. Thin wood laminae, with a thickness of about 320 μm, were kindly provided by the CNR Ivalsa Institute (San Michele all' Adige,

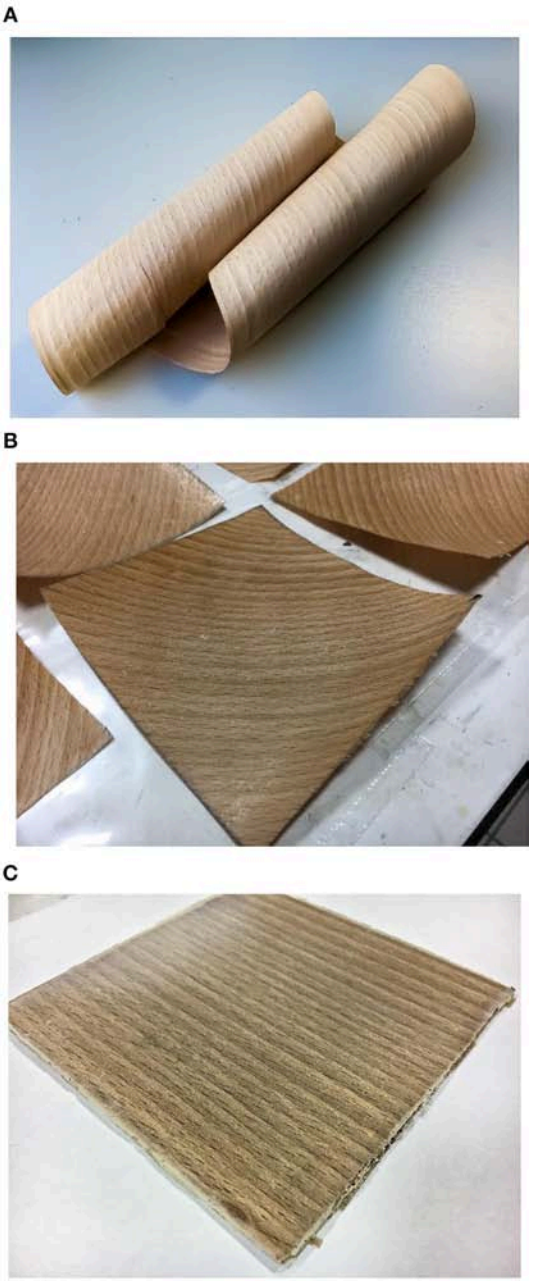

FIGURE 1 | Representative images of **(A)** neat wood lamina; **(B)** wood laminae after PEG impregnation; **(C)** wood/PEG/starch laminate.

Italy). The laminae were obtained through a Marunaka Super Meca-s planer (Marunaka Tekkosho Inc., Shizuoka, Japan) from beech boards, conditioned at a temperature of 23°C and a relative humidity of 50%. Although this machine allows the production of even thinner laminae, the choice of the thickness was motivated by the need to reach a compromise between the flexibility of the thinner laminae and their PEG storage capability.

Preparation of the Samples

Wood laminae were cut in square sheets of 120 × 120 mm^2, with the wood fibers oriented either parallel or at 45° with respect to the square edge. The sheets were immersed in the molten PEG at 70°C for 5 min, then taken out and immediately gently blotted with absorbent paper to remove excess molten PEG from the surface (**Figure 1B**). Each wood lamina was weighed before and after immersion in liquid PEG in order to measure the weight fraction of absorbed PEG. Preliminary experiments had shown that a soaking time of 5 min was enough to reach the maximum weight increase due to PEG absorption, as a longer soaking time (up to 24 h) did not result in a greater weight increase. The wood/PEG laminae were interleaved with starch foils of 120 × 120 mm^2 and compacted in a hot-plate press at 170°C for 7 min, with an applied pressure of 1 MPa. Each laminate (**Figure 1C**) consisted of 5 wood/PEG laminae interleaved with 6 starch sheets. The samples were produced following two stacking sequences, i.e., $[0_5]$ (unidirectional) and [+45/−45/+45/−45/+45] (angle ply). Laminates with virgin wood laminae (without PEG impregnation) were also prepared for comparison. Moreover, the mass of each constituent of each laminate was measured before the hot-pressing stage and compared to the final mass of the prepared laminates to study the PEG leakage during the laminate preparation. Specimens with different orientations were cut out of the prepared laminates for the subsequent characterization. The characterization was performed also on the constituents, i.e., the starch foils, the virgin wood laminae and the PEG-impregnated laminae. The list of the prepared samples is reported in **Table 1**. All the composite laminates with their relative constituents were stored at 23°C with a relative humidity of 50%. It was decided to condition both the constituents and the laminates at this temperature and humidity level because these are the typical hygrothermal conditions of the laboratory. In this way, the influence of the temperature and of the moisture absorption during the lab tests could be minimized. It could be also interesting to point out that this production process, which consists of embedding the PCM directly in the reinforcing phase and employing matrix foils, allows the preparation of thermoplastic laminates without a melt compounding step, which could partially degrade the PCM (Fredi et al., 2018a). Therefore, the pristine thermal energy storage properties of PEG should be retained.

TABLE 1 | List of the prepared samples.

Sample acronym	Description of the constituents	Wood fiber orientation
F-L	Single wood lamina	Longitudinal
F-T	Single wood lamina	Transversal
PEG	Poly(ethylene glycol)	–
A	Single starch foil	–
FP-L	Single wood lamina impregnated with PEG	Longitudinal
FP-T	Single wood lamina impregnated with PEG	Transversal
FA-L	5 wood laminae and 6 starch foils	Unidirectional (long.)
FA-T	5 wood laminae and 6 starch foils	Unidirectional (transv.)
FA-O	5 wood laminae and 6 starch foils	Angle ply
LAM-L	5 wood laminae impregnated with PEG and 6 starch foils	Unidirectional (long.)
LAM-T	5 wood laminae impregnated with PEG and 6 starch foils	Unidirectional (transv.)
LAM-O	5 wood laminae impregnated with PEG and 6 starch foils	Angle ply

Experimental Techniques

The microstructural features of the prepared samples were investigated through a scanning electron microscope (SEM) Jeol IT300, operating at an acceleration voltage of 15 kV. The samples F, FP, FA, and LAM were cryofractured in liquid nitrogen, and the fracture surface was analyzed after Pt-Pd sputtering.

Thermogravimetric analysis (TGA) was performed through a TA Q5000 IR thermobalance. The test was performed on the constituents (A, F and PEG), on the PEG-impregnated wood lamina (FP) and on both the prepared laminate types (FA and LAM). Specimens of ∼20 mg were cut out of all the prepared samples and tested at 10°C/min up to 700°C, under a nitrogen flow of 150 ml/min. These tests allowed the measurement of the temperatures corresponding to a mass loss of 1 wt% ($T_{1\%}$) and 5 wt% ($T_{5\%}$), the temperature corresponding to the initial stages of degradation (T_{onset}), determined with the tangent method, the peak temperature of the mass loss derivative (T_d), indicating the maximum degradation kinetics, the initial mass loss before T_{onset} (m_i) and the residual mass after the test (m_r).

Differential scanning calorimetry (DSC) was performed with a Mettler DSC30 instrument. The test was performed on the constituents (A, F, and PEG), on the PEG-impregnated wood lamina (FP) and on both the prepared laminate types (FA and LAM). Specimens of ∼10 mg were cut out of all the prepared samples and tested at 10°C/min in the temperature interval between −20 and 100°C, under a nitrogen flow of 100 ml/min. All the specimens were subjected to a first heating scan, a cooling scan and a second heating scan. In this way, the melting and crystallization temperatures (T_m, T_c) and enthalpy (ΔH_m, ΔH_c) of the PEG and of the starch phases were determined. An effective weight fraction of PEG inside the laminates was then calculated from the measured phase change enthalpy. The test also evidenced the presence of irreversible phenomena, such as the evaporation of the absorbed water.

The viscoelastic properties of the samples were investigated through dynamic-mechanical analysis (DMA), by using a DMAQ800 machine, provided by TA Instruments (New Castle, DE, USA). The test was performed in tensile mode, between 0 and 150°C at 3°C/min, with a maximum deformation of 0.05% applied at a frequency of 1 Hz. The test was performed on the

TABLE 2 | Mass and weight fraction of the constituents of the sample FP and the two laminates (FA and LAM).

Sample	Constituent	Mass (g)	Nominal weight fraction (%)	Experimental total weight (g)
FP	F (wood)	2.9 ± 0.1	53 ± 6	5.4 ± 0.5
	PEG	2.5 ± 0.4	46 ± 11	
FA	A (starch)	10.1 ± 0.3	41 ± 2	24.3 ± 0.9
	F (wood)	14.6 ± 0.6	59 ± 3	
LAM	A (starch)	10.1 ± 0.3	27 ± 2	28.2 ± 0.8
	F (wood)	14.6 ± 0.6	39 ± 3	
	PEG	12 ± 2	34 ± 5	

samples F, A, FP, FA and LAM, in the L and T directions (where applicable), on rectangular specimens with dimension of 25 × 5 mm^2, while the thickness was that of each sample.

Quasi-static tensile tests were performed with a universal dynamometer Instron 5969, equipped with a 50 kN load cell, according to ISO 527 standard. Rectangular specimens with in-plane dimensions of 120 × 10 mm^2 were cut from the samples F, A, FP, FA, and LAM and tested at 5 mm/min until failure. The samples FA and LAM were tested in L, T and O directions, while the samples F and FP were tested in the L and T directions. Five specimens were tested for each sample and for each considered direction. The stress-strain curves allowed the determination of the tensile strength (σ_b), and of the strain at break (ε_b). While testing the wood laminae with and without PEG (samples F and FP), small plywood blocks were interposed between the specimen and the grips to avoid damaging the sample due to the contact with the hard steel grips. For the samples LAM and FA, five additional specimens for each of the considered directions (L, T, O) were tested at 0.25 mm/min for the measurement of the elastic modulus by using a resistance extensometer Instron 2620 with a gauge length of 12.5 mm. The elastic modulus was measured as the secant modulus of the stress/strain curves between the strain values of 0.05% and 0.25%. The elastic modulus was calculated in the same way also on the stress-strain curve of the other specimens.

Finally, Charpy impact tests were performed on the samples FA and LAM in the L and T directions, by using a Ceast 6549 impactor equipped with a hammer with an arm length of about 25 cm and a mass of 0.48 kg, positioned at a starting angle of 150°. In this way, the tests were performed at an impact speed of 2.9 m/s, with a maximum impact energy of 2 J. A thin plasticine layer was used to damp the vibrations to avoid the inertial peak in the force-displacement signal. Tests were performed on rectangular specimens having nominal dimensions of 120 × 10 × 2 mm^3, with a span length of 40 mm. At least five specimens were tested for each sample. In this way, the values of maximum force (F_b) and of the specific energy absorbed under impact conditions (U_{sp}) were determined.

RESULTS AND DISCUSSION

Table 2 reports the weight composition of a single wood lamina impregnated with PEG (FP) as well as the nominal mass of each component before the hot-pressing step and the nominal weight composition for each laminate (FA and LAM). It can be observed that the quantity of PEG absorbed by a single lamina is ∼86 wt% of its initial mass. On the other hand, if five of these laminae are alternated to 6 starch foils, the experimental mass of the laminate obtained through hot-pressing (LAM) is ∼25 wt% lower than the sum of its components. This mass loss can be almost entirely attributed to the leakage of PEG out of the wood laminae, as the mass loss of the laminate without PEG (FA) is almost negligible. Therefore, the effective PEG weight fraction in the laminate is ∼11 wt%. This leakage suggests that a considerable fraction of the absorbed PEG has just solidified on the surface of the laminae and is not properly confined in the wood porosity, and the gentle blotting is not sufficient to remove excess PEG. However, the major part of PEG was successfully stabilized into the wood laminae.

Figures 2A–F shows the SEM micrographs of the cryofracture surface of the prepared samples. Since the cross section was investigated with this technique, in the samples with longitudinal fibers (L) the wood fibers are perpendicular to the fracture plane, while they are parallel in the samples with transversal fibers (T). In **Figures 2A,B** FESEM micrographs of the wood laminae cut in the transversal and in the longitudinal direction are respectively reported. As already shown in our previous papers on ultra-thin wood laminae impregnated with poly(vinyl alcohol) (Dorigato et al., 2018b), in the longitudinal direction the peculiar structure of the wood can be appreciated, with tracheids, wood fibers and vessels, while the parenchymal cells are less clearly visible. Tracheids and wood fibers are characterized by a mean diameter of about 10 μm, while wood vessels present an average size of 40 μm. The presence of some tracheids in radial direction can be appreciated in the transversal section. From the micrographs of the laminae impregnated with PEG (**Figures 2C,D**), it can be observed that PEG partially fills the wood porosity. This could be explained by assuming that the volume fraction of the closed porosity is not negligible. Moreover, the viscosity of the molten PEG is too high to allow the smallest pores to be filled in the time window of the impregnation process (up to 24 h). Moreover, the surface of the lamina hosts a considerable amount of PEG, as suggested by the smoothness of the surfaces of the laminae containing PEG (indicated by arrows), if compared to the remarkably rough surfaces of the neat wood laminae. This may complicate the adhesion between the wood laminae and the starch matrix, an issue partially visible from the fracture surface of the two laminates

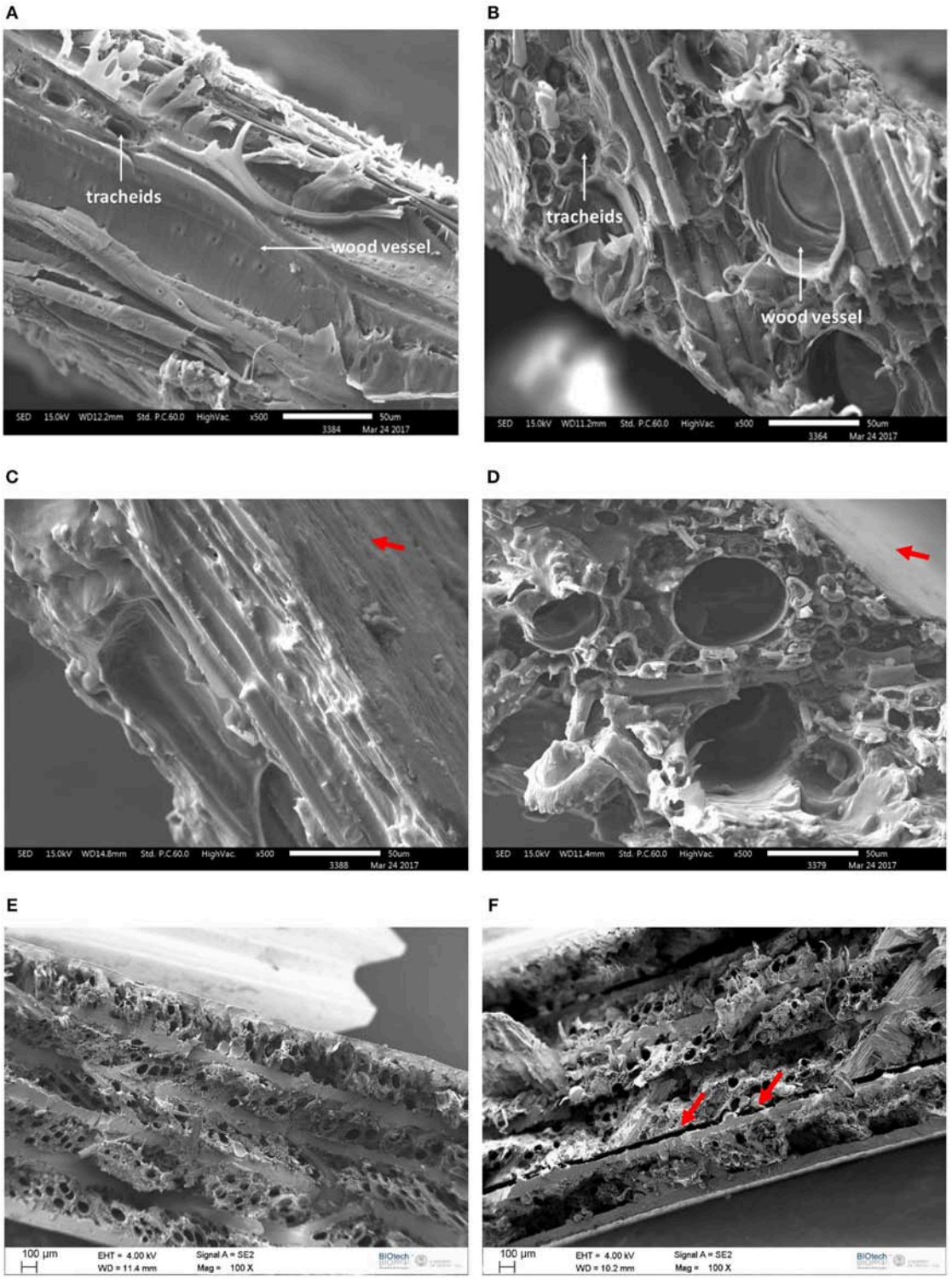

FIGURE 2 | SEM micrographs of the cryofracture surface (cross-section) of the prepared samples. **(A)** F-T; **(B)** F-L; **(C)** FP-T; **(D)** FP-L; **(E)** FA-T; **(F)** LAM-T.

(**Figures 2E,F**). In the laminate containing PEG (**Figure 2F**) the interlaminar adhesion seems worse than that of the neat laminate, as the cryofracturing operations caused delamination (indicated by the arrow), which is not observed in the neat laminate. However, this apparent worsening in the interlaminar adhesion due to the PCM does not negatively affect the mechanical

TABLE 3 | Results of the TGA tests on the prepared samples.

Sample	$T_{1\%}$ (°C)	$T_{5\%}$ (°C)	T_d (°C)	T_{onset} (°C)	m_i (%)	m_r (%)
F	53.0	241.3	345.0	263.0	5.76	0.38
PEG	208.4	274.5	396.9	352.4	0.00	0.00
A	281.3	316.0	400.0	316.8	0.00	0.00
FP	89.3	265.4	405.1	317.8	2.01	0.04
LAM	29.4	260.7	365.5	293.5	2.04	0.27

$T_{1\%}$, $T_{5\%}$ = temperature corresponding to a mass loss of 1 and 5 wt%.
T_d = temperature corresponding to the maximum degradation rate (peak of the mass loss derivative signal).
T_{onset} = temperature corresponding to the initial stages of degradation, after the water evaporation.
m_i = initial mass loss before T_{onset}.
m_r = residual mass after the test.

and impact properties, as reported hereafter. In future works on these systems it could be important to perform a detailed characterization of the interlaminar adhesion conditions of the prepared composites, as the interlaminar fracture toughness is one of the key aspects in the assessment of the mechanical behavior of composite materials.

TGA analysis was performed to evaluate the resistance to the thermal degradation of the laminates and of each constituent. **Figure 3** shows the TGA thermograms (with the residual mass and the derivative of the mass loss) of the sample LAM and of its three constituents, i.e., PEG, F, and A, while **Table 3** reports also the results on the sample FP. For the sample F, the initial mass loss (m_i) of ∼5.8% is imputable to the absorbed water. This behavior is also observed in the samples FP and LAM, but to a lesser extent, as for these samples the wood laminae are only a fraction of the total mass. After water evaporation, the thermal degradation of the wood phase becomes appreciable above 250°C and occurs in two main steps. Conversely, no water was detected on the samples A and PEG, which indicates that the total water fraction of the composites is entirely absorbed by the wooden phase. The thermal degradation of these two polymer phases starts to be evident at 320–350°C and reaches the maximum rate at ∼400°C. From these results, it can be concluded that the thermal stability of all the constituents is sufficient to withstand the processing temperature of 170°C. Moreover, as expected, the degradation thermogram of the sample FP lies between those of its constituents, i.e., F and PEG. Also, the thermal degradation of the sample LAM shows all the degradation steps of its constituents, as it can be better appreciated from the mass loss derivative signal. From TGA/DTG thermograms reported in **Figure 3**, it is also evident that the degradation of PEG and A samples is almost complete at 500°C, while the F and LAM samples present a last degradation step between 500 and 550°C, probably due to the degradation of some wood constituents in inert atmosphere. A detailed analysis of this degradation stage, which occurs far above the application temperature interval of the prepared laminates, is out of the scope of this work, and it could be better investigated in the future developments of this work. However, as reported in **Table 3**, the residual mass values at 700°C (m_r) are below 0.4% for all the samples, meaning that all the tested

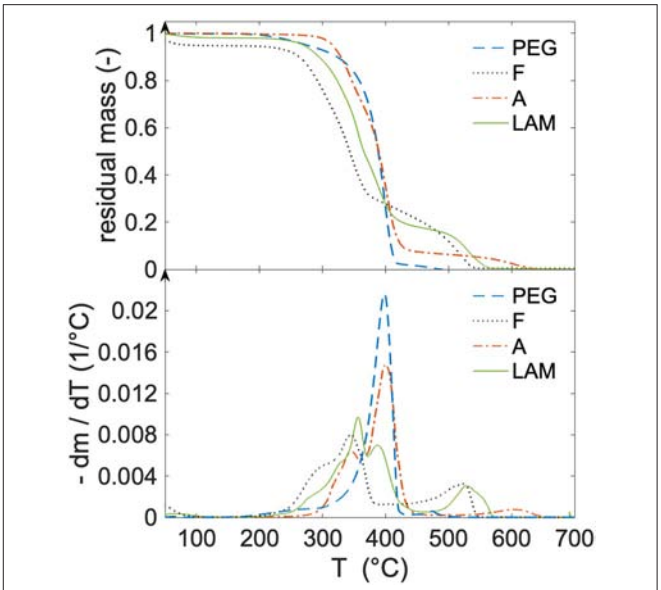

FIGURE 3 | Results of the TGA tests on the samples F, A, PEG, and LAM: residual mass and mass loss derivative as a function of temperature.

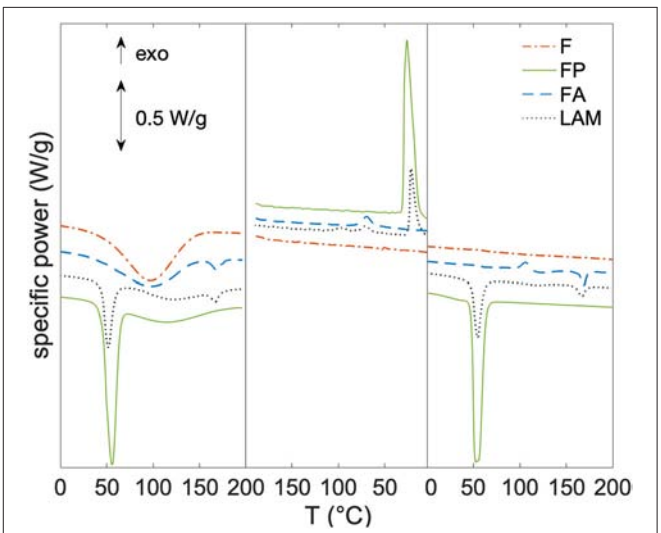

FIGURE 4 | DSC thermograms of the prepared laminates, showing the three scans (first heating, cooling, second heating). Samples F, FP, FA, and LAM.

materials underwent a complete thermal degradation even in inert atmosphere.

The DSC tests were performed to investigate the thermal transitions of the constituents and to assess the thermal energy storage capability of the PEG within the laminates. In fact, as reported in many papers in the literature, DSC is the most useful technique to assess the TES capability of these materials (Pielichowska and Pielichowski, 2014). In the present paper, this test allowed the determination of the melting (and crystallization) enthalpy values of the PEG phase within the laminates. The DSC thermograms of the prepared samples are reported in **Figure 4**,

TABLE 4 | Results of the DSC tests on the prepared samples (first heating scan and cooling scan).

Sample	T_m^{PEG} (°C)	ΔH_m^{PEG} (J/g)	T_c^{PEG} (°C)	ΔH_c^{PEG} (J/g)	T_m^A (°C)	ΔH_m^A (J/g)	T_c^A (°C)	ΔH_c^A (J/g)
PEG	52.6	168.9	30.9	155.3	–	–	–	–
A	–	–	–	–	168.1	9.8	71.1	10.1
FP	56.1	88.5	25.8	86.7	–	–	–	–
FA	–	–	–	–	168.7	4.6	70.9	5.1
LAM	54.7	27.4	21.5	24.1	166.8	4.4	71.8	4.8

T_m^{PEG}, T_c^{PEG} = *melting and crystallization temperatures of PEG.*
ΔH_m^{PEG}, ΔH_c^{PEG} = *melting and crystallization enthalpy values of PEG.*
T_m^A, T_c^A = *melting and crystallization temperatures of thermoplastic starch.*
ΔH_m^A, ΔH_c^A = *melting and crystallization enthalpy values of thermoplastic starch.*

while the most important results are collected in **Table 4**. The DSC thermogram of the neat starch (A) was not reported here for the sake of brevity, but this test was performed as a preliminary experiment to find a suitable hot-pressing temperature of the laminates (however, the results of this test are reported in **Table 4**). The thermogram of the neat beech (F) shows a broad endothermic peak on the heating scan that is not present in the cooling and second heating scans. This peak, associated with water evaporation, has an enthalpy of 161.5 J/g. Considering that the latent evaporation heat of water is 2,272 J/g, the water present in the neat beech can be estimated at ∼7.1 wt%, which is in good agreement with the mass losses observed by TGA in the low temperature region. The other DSC signals of this sample, such as those associated with the glass transitions of the amorphous wood components, are not clearly visible in this plot, but they have been thoroughly described in a recent work of our group on wood/starch composite laminates (Dorigato et al., 2018a). The signal of water evaporation is partially visible also in the first heating scan on the sample FP, which also presents the signals of the melting and crystallization transitions of PEG, through the presence of narrow peaks at 55 and 25°C, respectively. The phase change enthalpy measured in the first heating scan is 88.5 J/g. Assuming that the phase change performance and the crystallization behavior of the PEG embedded in the wood are not different from those of the virgin PEG, the total PEG weight fraction in the sample FP can be calculated from the phase change enthalpy of the neat PEG (169 J/g), with the result being 52.4 wt%, in good agreement with the nominal PEG content (see **Table 2**). The peak of water evaporation is also present in the thermograms of the two prepared laminates. The sample FA also clearly shows all the thermal transitions of the starch phase, which are visible in the second heating scan, i.e., a glass transition at ∼60°C, post-crystallization at 110°C and a melting peak at 168°C. The thermal transitions of the starch phase are also visible in the thermogram of the sample LAM (except for the post-crystallization in the second heating scan), although the most intense signal is represented by the phase change transitions of the PEG, whose enthalpy is 27.4 J/g (first heating scan). From this signal, the effective PEG weight fraction in the LAM is 16.2 wt%, slightly higher than that calculated from the masses of the laminates, but in the same order of magnitude. This DSC signal clearly demonstrates that the prepared composites could be potentially applied for TES applications.

Figures 5A,B, **6A,B** report the thermograms obtained from DMA on the tested materials, performed to investigate their viscoelastic response below and above the PCM melting temperature. **Figures 5A,B** show the thermograms of the samples A, F, and FP. The latter two samples have been tested with the wood fibers oriented parallel (L) and perpendicular (T) to the applied load. The thermogram of the neat starch (A) has been reported together with the samples in the T directions (for a better comprehension of the plots). The starch phase (A) exhibits a storage modulus at 0°C of ∼250 MPa, and it shows a considerable drop at ∼60°C in correspondence of the glass transition, in good agreement with the DSC results. The same phenomenon is detectable through peaks in the E'' and tanδ thermograms. For the neat wood lamina (F), the value of E' in the L direction is one order of magnitude higher than that in the T direction, and in both cases it shows a slight decrease at ∼50°C because of the amorphous fraction in the wood (i.e., lignin) (Kelley et al., 1987). From a comparison between the signals of the neat wood (F) and the PEG-impregnated wood (FP) laminae, it is immediately evident that the presence of PEG significantly contributes to increase the storage modulus of the wood laminae in both directions, probably due to a partial filling of the wood porosity. The major signals in the FP thermograms are those related to the PEG phase transition, as E' shows a step, while peaks are visible in both the E'' and tanδ signals, which are evident mostly in the L direction (**Figure 5A**). The positive contribution of PEG in increasing E' is also transferred to the laminates (**Figures 6A,B**), even though this is accomplished to a lesser extent. Also in this case, the thermograms present all the signals related to the thermal transitions of the PEG and starch phases. For example, the PEG melting is clearly detectable through the DMA thermograms. This effect, which evidences the interesting and unusual possibility to study a melting event through DMA, was also observed by our group in other works related to polymer matrix composites containing a PCM (Fredi et al., 2017, 2018a). Further efforts will be performed in the future to better characterize the PCM melting signals through DMA analysis.

Finally, two tests were performed to investigate the effect of PEG on the mechanical properties of the wood laminae and of

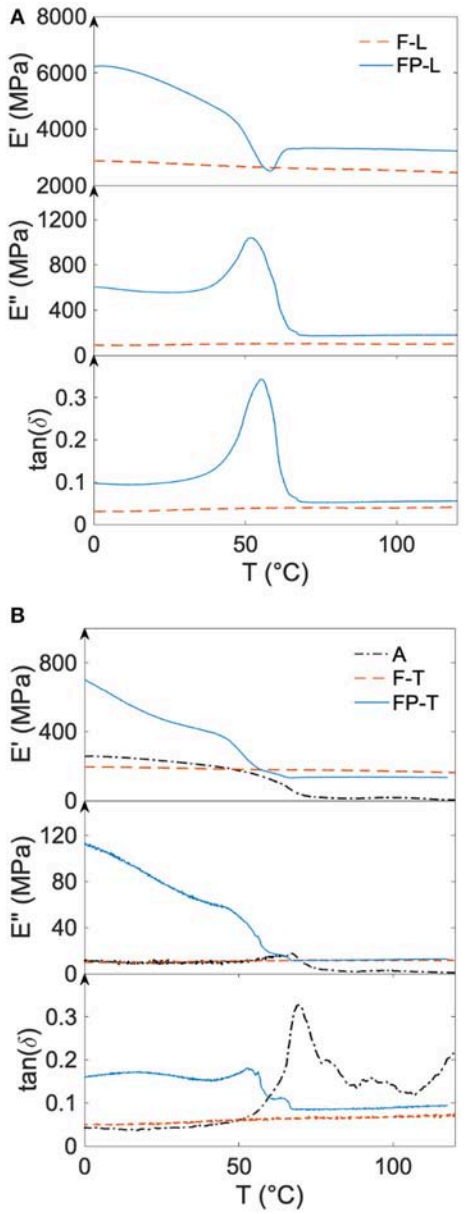

FIGURE 5 | DMA thermograms of the constituents, showing the storage modulus E′, the loss modulus E", and the loss factor tanδ. **(A)** Samples F and FP (longitudinal direction); **(B)** samples F, FP (transversal direction), and A.

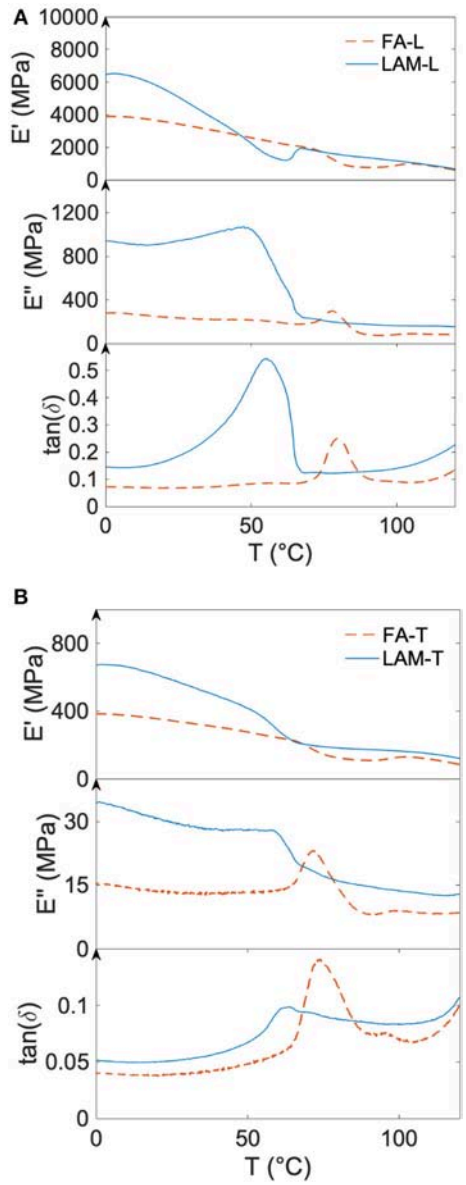

FIGURE 6 | DMA thermograms of the laminates, showing the storage modulus (E′), the loss modulus (E"), and the loss factor (tanδ). **(A)** Samples FA and LAM (longitudinal direction); **(B)** samples FA and LAM (transversal direction).

the relative laminates, i.e., quasi-static tensile tests and Charpy impact tests. For the tensile tests, representative stress-strain curves of the sample FA in all the three considered directions are reported in **Figure 7** (the curves for the other samples are not reported for the sake of brevity), while **Figure 8** shows the trends of the elastic modulus and of the tensile strength, respectively. The sample F has a linear stress-strain curve until failure in both the L and T directions, with a rather low strain at break (∼1%). PEG-impregnated laminae (FP) show an initial linear behavior, followed by a region in which the slope decreases until failure. This test also evidences the positive contribution of PEG on the tensile properties of the wood laminae, especially in the T direction, as the average elastic modulus increases from 120 to 310 MPa and the tensile strength from 60 to 170 MPa, while the properties in the L direction of the two samples are not significantly different from each other. The mechanical properties measured on these thin laminae are remarkably lower than those reported for bulk beech, which exhibits a flexural elastic modulus of 14.5 GPa and a flexural strength of 120 MPa (Giordano, 1981). This effect, already observed in previous works of our group (Dorigato et al., 2018b), is attributable to the considerable destroying of the pristine cellular morphology

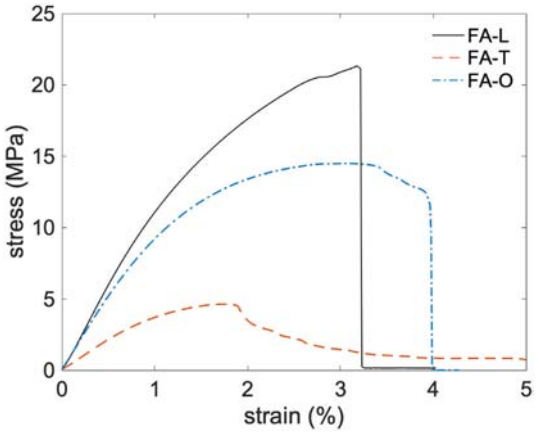

FIGURE 7 | Representative stress-strain curves from quasi-static tensile tests of the sample FA (all the three considered directions).

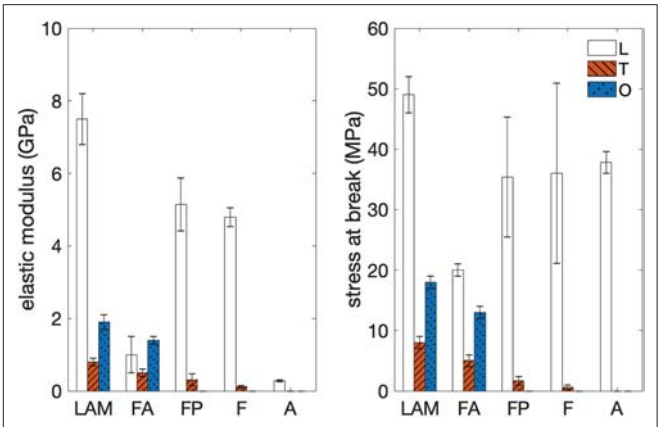

FIGURE 8 | Results of quasi-static tensile tests on the prepared samples. Elastic modulus and stress at break.

to which the ultrathin laminae are subjected during cutting. The stress-strain curve of A is typical of a thermoplastic, highly ductile polymer; the initial linear region terminates with a relative maximum, conventionally regarded as the yield point, followed by a strain-hardening region until failure, which happens at high strain values (i.e., 450%). The properties measured on this starch film are consistent with those reported in the literature for similar materials (Bastioli, 1997; Mark, 1999). From **Figure 7** it is immediate to observe that, as expected, the mechanical properties of the angle ply (O) laminates are intermediate in respect to those of the samples L and T. From the results reported in **Figure 8**, it is also evident that the properties measured on the laminates are considerably higher than those expected from the traditional rule of mixture, largely used to predict the performance of composites. This effect, already observed in previous works (Dorigato et al., 2018a; Fredi et al., 2018b), stems from the partial filling of the wood porosity by the interpenetrated matrix, which reduces the total pore volume fraction. As reported before for the single laminae, this porosity filling effect is also the reason of the enhanced tensile stiffness and strength of the sample LAM compared to FA, in all the considered directions. Considering the elastic modulus results reported in **Figure 8**, it should be pointed out that the laminates (i.e., FA and LAM) and the constituents (i.e., FP, F, and A) were not tested at the same speed. However, elastic modulus results of the laminates and of their constituents could be directly compared, at least from a qualitative point of view. It must also be considered that the most important comparison in the mechanical properties should be performed between the FA and LAM samples in different orientations, which were tested at the same speed.

Similar conclusions can be drawn by analyzing the results of the Charpy impact tests, summarized in **Table 5** (representative force-time curves were not reported for the sake of brevity). The maximum force measured during the test is considerably higher for the LAM samples, and so is the absorbed specific energy, for all the considered fiber orientations. It can be therefore concluded that, contrarily to what has been reported

TABLE 5 | Results of Charpy impact tests on the two prepared laminates, performed in different orientations.

Sample	F_b (N)	U_{sp} (J/m^2)
FA-L	24	1.2
FA-T	11	0.6
FA-O	18	1.0
LAM-L	138	23.7
LAM-T	52	7.5
LAM-O	95	14.8

F_b = maximum value of force reached during the test.
U_{sp} = specific energy absorbed under impact conditions.

up to now by our group for PCM-containing polymer composites (Fredi et al., 2017, 2018a), in this case the PCM contributes positively to the mechanical properties of the host composite, and the mechanical and TES properties can be considered as synergistic and not parasitic. This is remarkably important in the perspective of developing multifunctional materials combining structural and thermal management functions.

CONCLUSIONS

This work aimed at developing novel multifunctional fully biodegradable composite laminates with thermal energy storage/release capability. With this aim, thin wood beech laminates were impregnated with PEG at the molten state, and the resulting reinforcements were interleaved to foils of thermoplastic starch through hot compaction. The microstructural and thermo-mechanical behavior of the resulting laminates was thoroughly investigated and compared with that of the relative constituents.

Even though not all the PEG introduced in the samples is effectively confined within the wood pores, a PEG fraction of about 11 wt% of the whole laminate remained entrapped within wood laminae. From SEM micrographs it was found that PEG is able to partially fill the wood porosity, but

the presence of PEG on the surface of wood laminae could negatively affect the adhesion and the compenetration between the wood laminae and the starch matrix, thereby worsening the delamination resistance of the resulting composites. From DSC tests it was evident that the stabilization of PEG within the wood pores was responsible for the presence of an endothermic signal at 55°C, with a specific melting enthalpy of 27.4 J/g. DMA analysis revealed that the presence of PEG significantly contributed to increasing the dynamic moduli of the laminates because of the partial filling of the wood porosity. For the same reason, the quasi-static properties (stiffness and strength) measured on the laminates were considerably higher than those expected from the traditional rule of mixture, and Charpy tests also showed that the impact resistance of the composites was systematically higher than that of their constituents and of the neat wood/starch laminate.

This work demonstrated the possibility to prepare fully biodegradable multifunctional materials by combining structural and thermal management functions, in which the insertion of a biodegradable PCM had a positive effect on the mechanical performance of the host composite.

AUTHOR CONTRIBUTIONS

AD performed part of the experimental work and performed the editing of the manuscript. GF performed part of the experimental work and performed the editing of the manuscript. AP coordinated the editing of the manuscript.

ACKNOWLEDGMENTS

Mr. Federico Vespa is gratefully acknowledged for his support to the experimental work.

REFERENCES

Alexandre, B., Langevin, D., Mederic, P., Aubry, T., Couderc, H., Nguyen, Q. T., et al. (2009). Water barrier properties of polyamide 12/montmorillonite nanocomposite membranes: structure and volume fraction effects. *J. Memb. Sci.* 328, 186–204. doi: 10.1016/j.memsci.2008.12.004

Averous, L., Fauconnier, N., Moro, L., and Fringant, C. (2000). Blends of thermoplastic starch and polyesteramide: processing and properties. *J. Appl. Polym. Sci.* 76, 1117–1128. doi: 10.1002/(SICI)1097-4628(20000516)76:7<1117::AID-APP16>3.0.CO;2-W

Ayucitra, A. (2012). Preparation and characterisation of acetylated corn starches. *Int. J. Chem. Eng. Appl.* 3, 156–159. doi: 10.7763/IJCEA.2012.V3.178

Bastioli, C. (1997). Properties and applications of Mater-Bi starch-based materials. *Polym. Degrad. Stab.* 59, 263–272. doi: 10.1016/S0141-3910(97)00156-0

Bledzki, A., Sperber, V., and Faruk, O. (2002). *Natural and Wood Fibre Reinforcements in Polymers*. Schrewsbury: Rapra Technology Limited.

Bogracheva, T. Y., Wang, Y. L., Wang, T. L., and Hedley, C. L. (2002). Structural studies of starches with different water contents. *Biopolymers.* 64, 268–281. doi: 10.1002/bip.10190

Chi, H., Xu, K., Wua, X., Chen, Q., Xue, D., Song, C., et al. (2008). Effect of acetylation on the properties of corn starch. *Food Chem.* 106, 923–928. doi: 10.1016/j.foodchem.2007.07.002

Core, H. A., Coté, W. A., and Day, A. C. (1979). *Wood: Structure and Identification. 2nd Edn.* Syracuse, NY: Syracuse University Press.

Dorigato, A., Ciampolillo, M. V., Cataldi, A., Bersani, M., and Pegoretti, A. (2017). Polyethylene wax/EPDM blends as shape-stabilized phase change materials for thermal energy storage. *Rubber Chem. Technol.* 90, 575–584. doi: 10.5254/rct.82.83719

Dorigato, A., Fredi, G., and Pegoretti, A. (2018c). "Novel phase change materials using thermoplastic composites," in *9th International Conference on Times of Polymers and Composites, AIP Conference Proceedings*, 020044-1–020044-4. doi: 10.1063/1.5045906

Dorigato, A., Fredi, G., and Pegoretti, A. (2019). Application of the thermal energy storage concept to novel epoxy/short carbon fiber composites. *J. Appl. Pol. Sci.* 136:47434. doi: 10.1002/APP.47434

Dorigato, A., Negri, M., and Pegoretti, A. (2018a). Ultrathin wood laminae-thermoplastic starch biodegradable composites. *J. Renew. Mater.* 6, 493–503. doi: 10.7569/JRM.2017.634177

Dorigato, A., Negri, M., and Pegoretti, A. (2018b). Ultrathin wood laminae-polyvinyl alcohol biodegradable composites. *Polym. Compos.* 39, 1116–1124. doi: 10.1002/pc.24040

Dorigato, A., and Pegoretti, A. (2012). Biodegradable single polymer composites from polyvinylalcohol. *Colloid Polym. Sci.* 290, 359–370. doi: 10.1007/s00396-011-2556-z

Fredi, G., Dorigato, A., Artuso, N., and Pegoretti, A. (2019). Discontinuous carbon fiber/polyamide composites with microencapsulated paraffin for thermal energy storage. *J. Appl. Polym. Sci.* 136:47408. doi: 10.1002/app.47408

Fredi, G., Dorigato, A., Fambri, L., and Pegoretti, A. (2017). Wax confinement with carbon nanotubes for phase changing epoxy blends. *Polymers.* 9, 405–420. doi: 10.3390/polym9090405

Fredi, G., Dorigato, A., Fambri, L., and Pegoretti, A. (2018a). Multifunctional epoxy/carbon fiber laminates for thermal energy storage and release. *Compos. Sci. Technol.* 158, 101–111. doi: 10.1016/j.compscitech.2018.02.005.

Fredi, G., Dorigato, A., and Pegoretti, A. (2018b). Multifunctional glass fiber/polyamide composites with thermal energy storage/release capability. *Express Polym. Lett.* 12, 349–364. doi: 10.3144/expresspolymlett.2018.30

Fredi, G., Dorigato, A., and Pegoretti, A. (2019). Novel reactive thermoplastic resin as a matrix for laminates containing phase change microcapsules. *Pol. Compos.* doi: 10.1002/pc.25233

García, M., Garmendia, I., and García, J. (2008). Influence of natural fiber type in eco-composites. *J. Appl. Polym. Sci.* 107, 2994–3004. doi: 10.1002/app.27519

Gay, D., Hoa, S. V., and Tsai, S. W. (2003). *Composite Materials. Design and Applications*. Boca Raton, FL: CRC Press.

Gibson, R. F. (2010). A review of recent research on mechanics of multifunctional composite materials and structures. *Compos. Struct.* 92, 2793–2810. doi: 10.1016/j.compstruct.2010.05.003

Giordano, G. (1981). *Tecnologia del legno. La materia prima.* Vol. 1. Torino: UTET.

Green, D. W., Winandy, J. E., and Kretschmann, D. E. (1999). "Mechanical properties of wood," in *Wood Handbook—Wood as an Engineering Material*, ed. F. P. Laboratory (Madison, WI: U.S. Department of Agriculture, Forest Service, Forest Products Laboratory).

Houshyar, S., and Shanks, R. A. (2003). Morphology, thermal and mechanical properties of poly(propylene) fibre-matrix composites. *Macromol. Mater. Eng.* 288, 599–606. doi: 10.1002/mame.200300023

Iwatake, A., Nogi, M., and Yano, H. (2008). Cellulose nanofiber-reinforced polylactic acid. *Compos. Sci. Technol.* 68, 2103–2106. doi: 10.1016/j.compscitech.2008.03.006

Kastiukas, G., Zhou, X. M., and Castro-Gomes, J. (2016). Development and optimisation of phase change material-impregnated lightweight aggregates for geopolymer composites made from aluminosilicate rich mud and milled glass powder. *Constr. Build. Mater.* 110, 201–210. doi: 10.1016/j.conbuildmat.2016.02.029

Kelley, S. S., Rials, T. G., and Glasser, W. G. (1987). Relaxation behaviour of the amorphous components of wood. *J. Mater. Sci.* 22, 617–624. doi: 10.1007/BF01160778

Khadiran, T., Hussein, M. Z., Zainal, Z., and Rusli, R. (2015). Encapsulation techniques for organic phase change materials as thermal energy

storage medium: a review. *Solar Energy Mater. Solar Cells.* 143, 78–98. doi: 10.1016/j.solmat.2015.06.039

Kou, Y., Wang, S., Luo, J., Sun, K., Zhang, J., Tan, Z., et al. (2019). Thermal analysis and heat capacity study of polyethylene glycol (PEG) phase change materials for thermal energy storage applications. *J. Chem. Thermodyn.* 128, 259–274. doi: 10.1016/j.jct.2018.08.031

Kunanopparat, T., Menut, P., Morel, M., and Guilbert, S. (2008). Reinforcement of plasticized wheat gluten with natural fibers: from mechanical improvement to deplasticizing effect. *Compos. Appl. Sci. Manufac.* 39, 777–785. doi: 10.1016/j.compositesa.2008.02.001

Lorcks, J. (1998). Properties and applications of compostable starch-based plastic material. *Polym. Degrad. Stab.* 59, 245–249. doi: 10.1016/S0141-3910(97)00168-7

Luyt, A. S., and Krupa, I. (2009). Phase change materials formed by uv curable epoxy matrix and Fischer–Tropsch paraffin wax. *Energy Conv. Manage.* 50, 57–61. doi: 10.1016/j.enconman.2008.08.026

Mallick, P. K. (2007). *Fiber Reinforced Composites. Materials, Manufacturing, and Design*. Boca Raton, FL: Taylor & Francis Group, LLC.

Mark, J. E. (1999). *Polymer Data Handbook*. Oxford: Oxford University Press.

Oksman, K., and Sain, M. (2008). *Wood-Polymer Composites*. Cambridge: Woodhead Publishing Materials.

Onder, E., Sarier, N., and Cimen, E. (2008). Encapsulation of phase change materials by complex coacervation to improve thermal performances of woven fabrics. *Thermochim. Acta.* 467, 63–72. doi: 10.1007/s12221-016-5113-z

Ozaki, T., Takeya, H., Kume, M., and Sekine, K. (2008). Multifunctional composite structures for space satellites. *Sampe J.* 44, 6–11.

Pegoretti, A. (2007). Trends in composite materials: the challenge of single-polymer composites. *Express Polym. Lett.* 1, 710. doi: 10.3144/expresspolymlett.2007.97

Pielichowska, K., and Pielichowski, K. (2014). Phase change materials for thermal energy storage. *Prog. Mater. Sci.* 65, 67. doi: 10.1016/j.pmatsci.2014.03.005

Rigotti, D., Dorigato, A., and Pegoretti, A. (2018). 3D printable thermoplastic polyurethane blends with thermal energy storage/release capabilities. *Mater. Today Commun.* 15, 228–235. doi: 10.1016/j.mtcomm.2018.03.009

Salonitis, K., Pandremenos, J., Paralikas, J., and Chryssolouris, G. (2010). Multifunctional materials: engineering applications and processing challenges. *Int. J. Adv. Manufac. Technol.* 49:803. doi: 10.1007/s00170-009-2428-6

Sari, A., Akcay, M., Soylak, M., and Onal, A. (2005). Polymer-stearic acid blends as form-stable phase change material for thermal energy storage. *J. Sci. Ind. Res.* 64, 991–996. Available online at: http://hdl.handle.net/123456789/5380

Sobolciak, P., Karkri, M., Al-Maaded, M. A., and Krupa, I. (2016). Thermal characterization of phase change materials based on linear low-density polyethylene, paraffin wax and expanded graphite. *Renew. Energy.* 88:372. doi: 10.1016/j.renene.2015.11.056

Srimalanon, P., Yamsaengsung, W., Kositchaiyong, A., Wimolmala, E., Isarangkura, K., and Sombatsompop, N. (2016). Effects of UV-accelerated weathering and natural weathering conditions on anti-fungal efficacy of wood/PVC composites doped with propylene glycol-based HPQM. *Express Polym. Lett.* 10, 289–301. doi: 10.3144/expresspolymlett.2016.27

Sundararajan, S., Samui, A. B., and Kulkarni, P. S. (2016). Interpenetrating phase change polymer networks based on crosslinked polyethylene glycol and poly(hydroxylethyl methacrylate). *Solar Energy Mater. Solar Cells.* 149, 266–274. doi: 10.1016/j.solmat.2015.12.040

Wang, J. J., Yang, M., Lu, Y. F., Jin, Z. K., Tan, L., Gao, H. Y., et al. (2016). Surface functionalization engineering driven crystallization behavior of polyethylene glycol confined in mesoporous silica for shape-stabilized phase change materials. *Nano Energy.* 19, 78–87. doi: 10.1016/j.nanoen.2015.11.001

Wu, C.-S. (2009). Renewable resource-based composites of recycled natural fibers and maleated polylactide bioplastic: characterization and biodegradability. *Polym. Degrad. Stab.* 94, 1076–1084. doi: 10.1016/j.polymdegradstab.2009.04.002

Yang, J., Zhang, E., Li, X., Zhang, Y., Qu, J., and Yu, Z. (2016). Cellulose/graphene aerogel supported phase change composites with high thermal conductivity and good shape stability for thermal energy storage. *Carbon.* 98, 50–57. doi: 10.1016/j.carbon.2015.10.082

Yoo, S., Kandare, E., Shanks, R., Al-Maadeed, M. A., and Afaghi Khatibi, A. (2016). Thermophysical properties of multifunctional glass fibre reinforced polymer composites incorporating phase change materials. *Thermochim. Acta.* 642, 25–31. doi: 10.1016/j.tca.2016.09.003

Zhou, Y., Sheng, D. K., Liu, X. D., Lin, C. H., Ji, F. C., Dong, L., et al. (2018). Synthesis and properties of crosslinking halloysite nanotubes/polyurethane based solid-solid phase change materials. *Sol. Energy Mater. Sol. Cells.* 174, 84–93. doi: 10.1016/j.solmat.2017.08.031

Conflict of Interest Statement: The authors declare that the research was conducted in the absence of any commercial or financial relationships that could be construed as a potential conflict of interest.

frontiers in Materials

MINI REVIEW
published: 04 March 2019
doi: 10.3389/fmats.2019.00029

Host Matrix Materials for Luminescent Solar Concentrators: Recent Achievements and Forthcoming Challenges

*Gianmarco Griffini**

Department of Chemistry, Materials and Chemical Engineering "Giulio Natta", Politecnico di Milano, Milan, Italy

Luminescent solar concentrators (LSCs) have attracted increasing attention in the past few years as appealing solar energy technology for the seamless integration of photovoltaic (PV) systems into the built environment. Traditionally, research in this field has focused on two main aspects: the optimization of the device assembly, in the quest for more efficient architectures to maximize collection, transport, and conversion of photons into usable electrical energy; the development of novel, highly emissive luminescent species, to ensure broad light collection and efficient photon emission. Only recently, the attention has also been directed toward the selection and development of suitable host matrix/waveguide materials with appropriate optical properties, sufficient chemical compatibility with the guest luminescent species, good processability for easy device fabrication and prolonged durability in outdoor operation. In addition to consolidated polymeric systems based on polyacrylates or polycarbonates, in recent years different examples of alternative host matrix systems have been proposed, characterized by peculiar chemical, physical and optical characteristics specifically designed to meet the stringent requirements of the LSC technology. This mini-review will focus on recent developments in the design of new host matrix materials for LSC applications. An overview of the most recent examples of novel LSC host matrices will be provided here, mainly focusing on new polymers, polymer-based organic-inorganic hybrids and multifunctional organic systems. Finally, opportunities and challenges in the field will be considered in view of the effective exploitation of the LSC technology in real application scenarios.

Keywords: luminescent solar concentrator (LSC), photovoltaic (PV), solar cells (SC), waveguide (WG), polymer, organic-inorganic hybrid, multifunctional devices

OPEN ACCESS

Edited by:
Alessandro Pegoretti, University of Trento, Italy

Reviewed by:
Luca Beverina, Università Degli Studi di Milano Bicocca, Italy
Rodrigo Cercená, Universidade do Extremo Sul Catarinense, Brazil

***Correspondence:**
Gianmarco Griffini
gianmarco.griffini@polimi.it

Specialty section:
This article was submitted to Polymeric and Composite Materials, a section of the journal Frontiers in Materials

Received: *13 January 2019*
Accepted: *12 February 2019*
Published: *04 March 2019*

Citation:
Griffini G (2019) Host Matrix Materials for Luminescent Solar Concentrators: Recent Achievements and Forthcoming Challenges. Front. Mater. 6:29. doi: 10.3389/fmats.2019.00029

INTRODUCTION

Luminescent solar concentrators (LSCs) have been regarded as a promising, accessible solar energy technology for reducing architectural barriers to the integration of photovoltaic (PV) systems into the built environment (Meinardi et al., 2017).

Originally proposed in the late 70's (Weber and Lambe, 1976; Goetzberger and Greube, 1977), LSC systems typically consist in bulk slabs or thin films/coatings of a transparent host matrix material embedding luminescent species that act as light-harvesting and spectral-conversion

centers of the incident light. Upon light absorption, photons are re-emitted *via* radiative decay by these luminophores and a fraction of the downshifted light is confined within the host matrix as a result of the difference in refractive indexes between the LSC material and the surrounding (air) medium. Total internal reflection (TIR) allows such trapped photons to be conveyed in waveguide mode toward the edges of the LSC device, where they become concentrated and can be collected by small-area optically-coupled solar cells for photon-to-electron conversion

In the past decade, research has pushed forward the performance of LSCs making them closer to practical deployability on the market.

In this mini-review, the focus will be on recent developments in the design of new host/waveguide materials for LSC applications. This discussion will include new polymers, polymer-based organic-inorganic hybrids and multifunctional systems. Opportunities and challenges in the field will also be considered in view of the effective exploitation of the LSC technology in real-life scenarios.

LSC OPERATION AND HOST MATERIAL REQUIREMENTS

In general terms, the performance of LSC systems can be quantified based on the so-called optical efficiency of the LSC η_{opt}, which is a measure of the optical power effectively delivered at the edges of the LSC (P_{out}^{opt}) with respect to the optical power incident on its top surface (P_{in}^{opt}):

$$\eta_{opt} = P_{out}^{opt}/P_{in}^{opt} \quad (1)$$

This parameter provides a direct estimation of the fundamental properties of a LSC (i.e., to collect and concentrate incident light) as it is directly influenced by all intrinsic loss mechanisms occurring to photons prior to being successfully collected at the edges of the waveguide (Debije and Verbunt, 2012; Moraitis et al., 2018). To tackle some of these loss mechanisms, research in the field of LSCs has been traditionally driven by the development of highly emissive luminescent species and by the engineering of more efficient device assemblies, as recently summarized in some excellent review articles (Debije and Verbunt, 2012; McKenna and Evans, 2017; Mazzaro and Vomiero, 2018; Pucci, 2018).

The choice of the host/waveguide material employed for the LSC assembly has also a direct effect on efficiency as it can greatly impact the processes of photon harvesting (reflection and scattering losses are matrix-dependent), absorption/emission (photoluminescence quantum yield (PLQY) of the luminophore can be affected by its solubility in the host matrix material), waveguiding/collection at the LSC perimeter (TIR and parasitic absorption by the host matrix are determined by its optical properties) (Kastelijn et al., 2009). Host materials for LSC applications should be designed so as to provide simultaneously a number of desirable features (Zettl et al., 2017), including: suitable refractive index; high transmittance in the visible and near-infrared range; high thermodynamic solubility for the embedded luminescent species; suitable thermal properties (namely, thermo-oxidative stability, and glass transition temperature T_g) compatible with the conditions used for materials processing and with the target application; long-term durability in outdoor contexts.

Glass was originally considered a reference material for LSCs due to its excellent optical properties as well as unbeatable chemical, photochemical, and environmental stability. However, the high processing temperatures needed for the production of conventional glass together with its high specific weight have shifted the attention toward polymeric systems. In this area, commodity polymers such as poly(methyl methacrylate) (PMMA) or polycarbonate (PC) have been traditionally employed as inexpensive host waveguide materials in bulk LSCs or as easily processable host carriers in thin-film LSCs. To overcome some of the limitations of these conventional systems and to provide additional functionalities to the resulting LSC system, in recent years a surge of new alternative matrix systems has been proposed with chemical, physical, and optical characteristics appropriately designed to meet the specific requirements of the LSC technology, as will be discussed in the next sections.

POLYMERIC MATRICES

PMMA is by far the most widely employed host polymer for LSCs because of its excellent transparency to visible light and its suitable refractive index ($n \approx 1.5$) (Li et al., 2019). Recently, its use as host matrix material in bulk LSCs was benchmarked against other commodity thermoplastics with similarly suitable thermal characteristics [polystyrene (PS), styrene-acrylonitrile (SAN) and different classes of PC] in terms of optical properties, compatibility with the target luminescent species (Lumogen F 305 Red by BASF, LF305 from here on) and resulting optical efficiency (Zettl et al., 2017). It was found that PMMA and PC (compact-disc grade) displayed the highest output irradiance level from the LSC edges, in both cases yielding η_{opt} values of 8.9% with dye doping concentration of 500 ppm. This result was correlated with the high internal transmittance of these matrices, which enables strong absorption of incoming photons by the embedded fluorescent dye.

However, PMMA usefulness is limited by the poor solubility that efficient luminophores feature in such a matrix (Al-Kaysi et al., 2006; Colby et al., 2010; Yoo et al., 2010), as well as by its limited photostability, especially toward high energy UV light (Kaczmarek et al., 2000; Griffini et al., 2013a). Improving the stability of PMMA as host polymeric matrix for LSCs has been a key focus for many research groups in the last few years. In an early study (Mansour et al., 2005), a copolymer made of methyl methacrylate and styrene [poly(STY-co-MMA)] doped with three different organic dyes was developed and its photodegradative response was benchmarked against PMMA. It was shown that all tested copolymer/dye systems displayed much enhanced stability compared with PMMA homopolymer,

irrespectively from the type of dye employed, due to more favorable dye/matrix interactions.

More recently, crosslinked systems based on partially fluorinated polymers were presented as potential alternative host matrix materials for the fabrication of durable polymer-based LSC devices (Griffini et al., 2013b). The new host matrix systems were obtained by thermally crosslinking a functional chloro-trifluoro-ethylenevinyl-ether (CTFE–VE) copolymer with different types of aliphatic polyisocyanates. The resulting LSCs in thin-film configuration (with LF305 as fluorophore) were shown to yield superior long-term operational stability compared to PMMA-based devices without compromising the efficiency. Further work by the same group demonstrated that different crosslinking agents (isocyanate *vs.* melamine) play a role in the evolution of chemical, physical, and morphological properties of the CTFE–VE-based LSC coatings during weathering (Griffini et al., 2014).

In the field of cross-linked systems, an unsaturated polyester (UP) resin (a mixture of UP and STY with methyl ethyl ketone peroxide as thermal initiator) was proposed as a possible alternative LSC host material to more conventional PMMA (Lim et al., 2012). To enhance the optical properties of the host matrix, a blend between UP and MMA was proposed, embedding coumarin 6 as luminescent species and resulting in satisfactory absorption and emission response.

A different, interesting approach for the development of novel polymeric host matrix systems was recently proposed based on the use of poly(p-xylylene) (or parylene) (Maggioni et al., 2013). By employing a suitably developed vacuum-based co-sublimation process, the parylene-based host material and

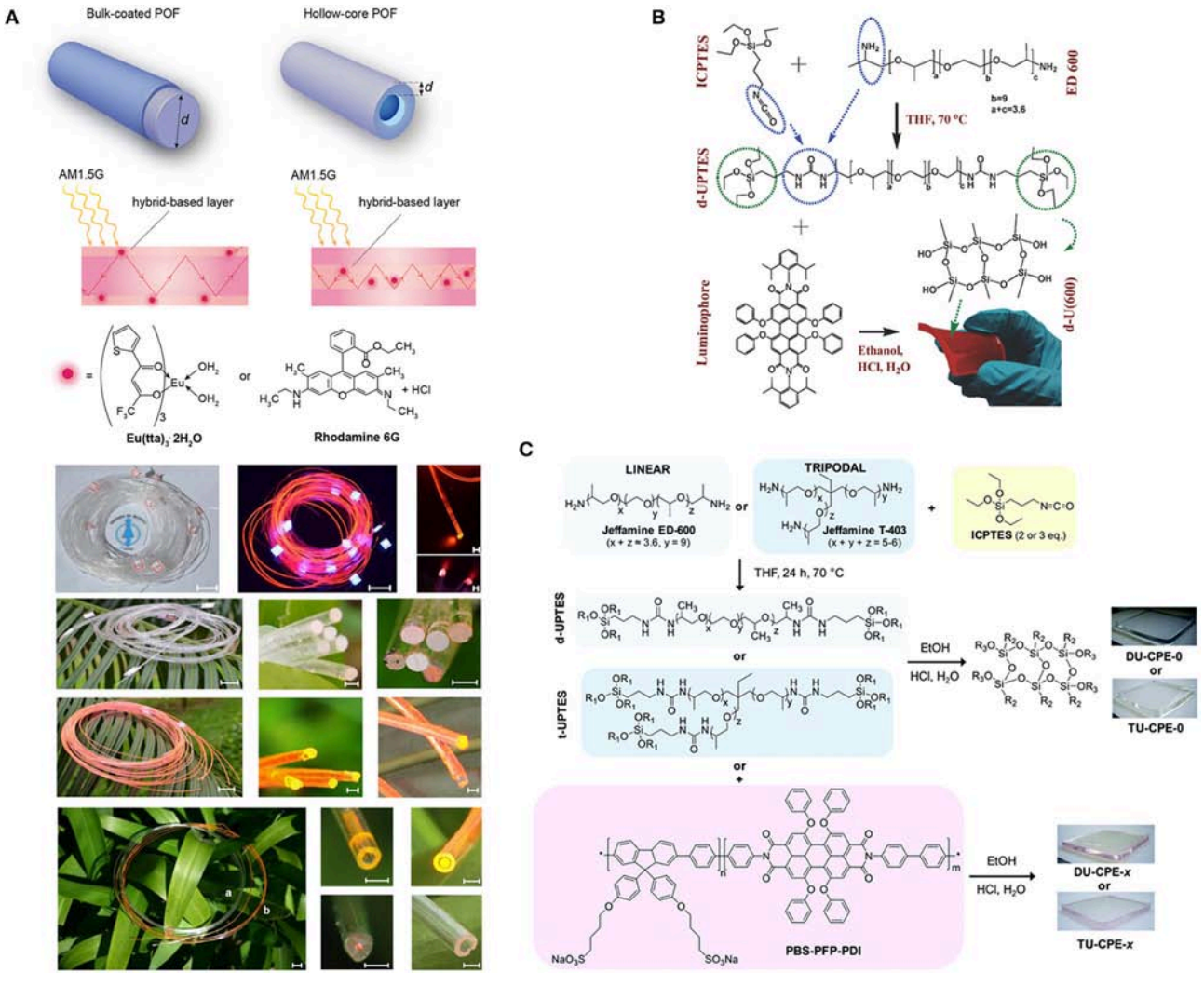

FIGURE 1 | (A) Schematic representation of optical fiber LSCs with the used luminescent active layers and corresponding photographs of the obtained demonstrators. Adapted with permission from Correia et al. (2016). Copyright 2016, John and Wiley and Sons. **(B)** Schematic representation of the chemical mechanism for the formation of planar di-ureasil LSCs doped with LR305. Reproduced with permission from Kaniyoor et al. (2016). Copyright 2015, WILEY–VCH Verlag GmbH & Co. KGaA. **(C)** Synthetic route for the preparation of ureasil-based LSCs embedding a conjugated polyelectrolyte as luminophore. Reproduced with permission from Meazzini et al. (2017). Copyright 2017, The Royal Society of Chemistry.

the guest fluorophore (LR305) were deposited simultaneously from the solid state on the target substrate (glass or PMMA), thereby allowing the *in-situ* formation of a parylene polymeric film embedding a fine dispersion of the dye within the matrix, while maintaining its surface roughness in the nanometer range. Tests on LSCs obtained by depositing fluorescent parylene films on glass and polymer waveguides showed a maximum η_{opt} as high as 22.6%. Further studies by the same group focused on widening the applicability of vacuum-deposited parylene-based matrices in combination with another luminescent species based on the rare-earth complex tris(2-thenoyl trifluoroacetone) mono (1,10-phenantroline) europium (III) ($Eu(tta)_3phen$) (Tonezzer et al., 2015).

The increasing demand for environmentally-friendly materials has recently led to the development of novel bio-based polymeric host matrices that may offer some ecological advantages compared with conventional oil-based systems. Within this framework, a poly-L-lactic acid (PLA) matrix was proposed as an environmentally friendly alternative to PMMA in LSC applications (Fattori et al., 2011). The smaller index of refraction of PLA *vs.* PMMA led to a minor reduction in maximum light trapped. On the other hand, when a luminescent species was added to the PLA matrix, the PLQY resulted to be higher than in PMMA at similar loading. Further studies from the same research group reported on another class of biopolymer-based eco-friendly matrix from silk fibroin (SF) (Melucci et al., 2012), with promising optical properties.

Another potential source of useful bio-based materials is represented by lignocellulosic biomass, in which cellulose is present as major constituent (Tuck et al., 2012). The possibility to exploit cellulose nanocrystals (CNCs) as host matrix in thin-film LSCs was recently assessed in comparison to a more conventional

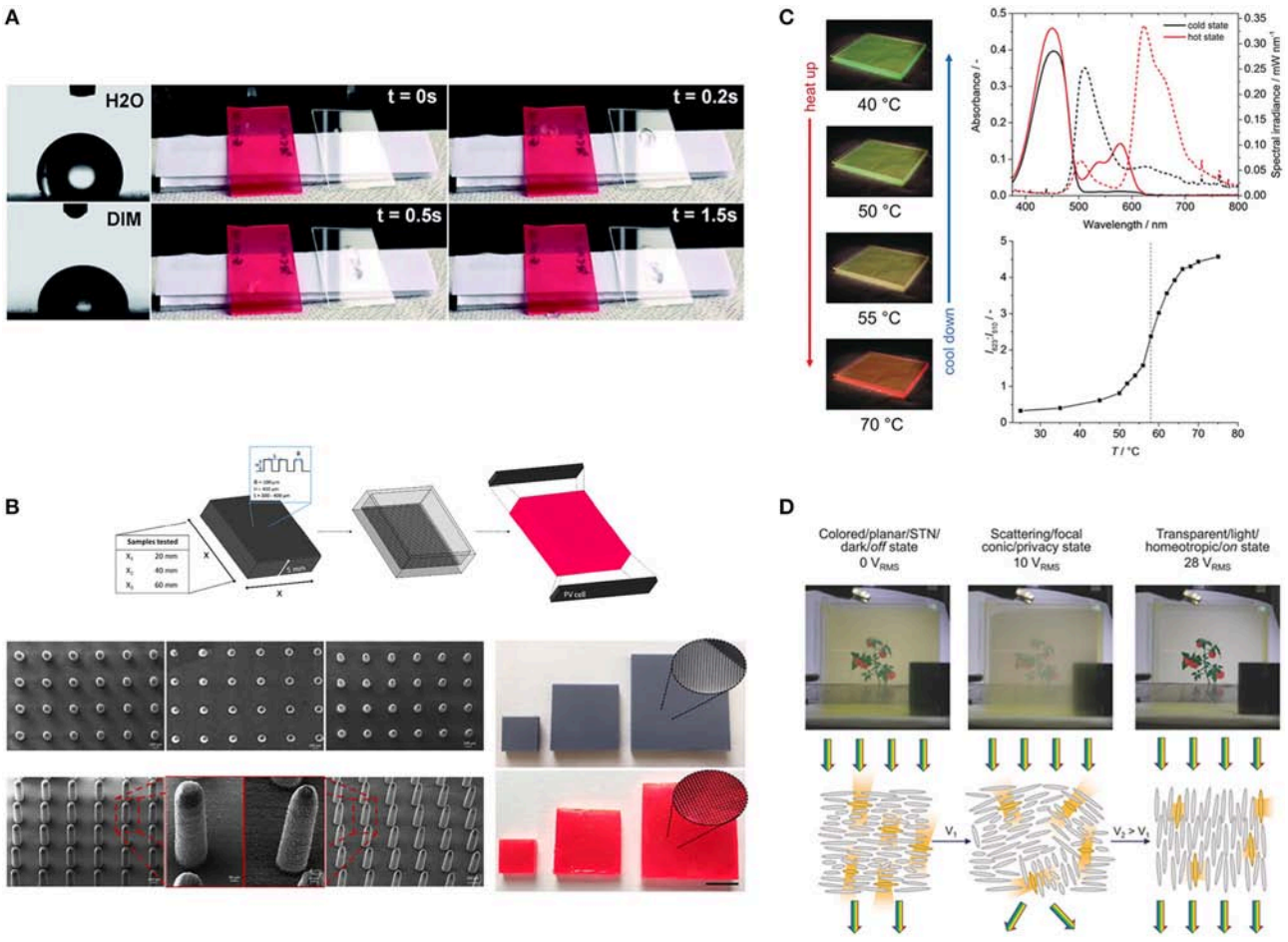

FIGURE 2 | (A) Surface wettability behavior of fluorinated LSCs compared with bare glass as observed from movie stills depicting water droplets falling at increasing times. Adapted with permission from Pintossi et al. (2017). Copyright 2017, The Royal Society of Chemistry. **(B)** Scheme illustrating the fabrication process to realize superhydrophobic LSCs, SEM images of the obtained surface features and photographs of 3D-printed templates (Upper) with corresponding LSCs devices (Lower) obtained by replica molding. Adapted with permission from Credi et al. (2017). Copyright 2017, Elsevier. **(C)** Photographs of a thermo-responsive LSC demonstrating the color change as the surrounding temperature is increased from 40 to 70°C, with changes in the optical response measured in terms of absorbance spectrum, edge emission spectrum, and ratio between edge emission intensities at 623 and 510 nm. Adapted with permission from Sol et al. (2018a) under the terms of the CC BY-NC license. **(D)** Photographs of the smart LSC window at increasing bias with a schematic representation of LCs and dyes alignment, and the emission direction. Adapted with permission from Sol et al. (2018b). Copyright 2018, WILEY-VCH Verlag GmbH & Co. KGaA.

acrylic polymer emulsion, in both cases using rhodamine 6G as fluorescent doping species (Chowdhury et al., 2017). It was shown that the CNC matrix may be considered suitable as host matrix material because of the enhanced absorption properties compared to the acrylic polymer emulsion. However, the latter behaved better as waveguide maintaining high efficiency also for long light propagating distances.

Very recently (Geervliet et al., 2018), two different types of renewable polyesters obtained *via* a catalyzed two-step melt-polycondensation reaction (a homopolymer of diethyl 2,3:4,5-di-*O*-methylene galactarate (GxMe) and isosorbide and a random copolymer of GxMe with 1,3-propanediol and dimethyl terephthalate) were proposed as host matrix materials in thin film LSCs. The spectroscopic characterization and the η_{opt} of resulting LSCs (embedding LR305 or an aggregation-induced emission molecule as guest luminophores) evidenced a performance similar or superior to that of reference LSC thin films based on PMMA/LR305, thus further indicating the potential of bio-based polymers as valuable renewable matrices for high-performance LSCs.

ORGANIC-INORGANIC HYBRID MATRICES

In addition to purely polymeric materials, also hybrid organic-inorganic systems have been thoroughly investigated as viable option for LSC host matrices. In these materials the high refractive index and enhanced stability typical of inorganic glasses are combined with the good processability and accessible chemical functionality characteristic of polymers (Pandey and Mishra, 2011; Reisfeld et al., 2011).

An interesting demonstration of LSCs based on a hybrid system employed a polysiloxane-rubber waveguide as flexible host material for LSC applications doped with LR305 (Buffa et al., 2012). It was shown that for low dye concentrations efficiencies comparable to those obtained by using conventional PC waveguides could be achieved, as a result of the good dispersibility of the fluorophore in these conditions. On the contrary, at higher concentrations luminescence quenching was observed, associated to the lower solubility of the luminophore in an apolar environment. LSC devices obtained by coupling this doped polysiloxane rubber with Si or GaAs PV cells demonstrated the viability of this material as flexible host matrix system for LSCs.

In the field of glassy hybrids, bridged silsesquioxanes containing europium(III) salts and 2-thenoyltrifluoroacetone were more recently proposed as integrated host-guest system for LSC device applications (Freitas et al., 2015). It was shown that high η_{opt} could be reached due to the peculiar optical properties resulting from the combination of the Eu^{3+} complex and the hybrid matrix. This allowed the easy fabrication of free-standing thick films (440 μm) and highly luminescent coatings (200–400 nm) on glass substrates exhibiting acceptable PLQY (∼60%). Further studies concentrated on the use of different functional bridged silsesquioxanes in combination with various trivalent lanthanide ions (Ln^{3+}), demonstrating the high versatility of these systems for the production of defect- and crack-free films with controlled nanostructure *via* the sol-gel chemistry (Graffion et al., 2011, 2012).

Another important class of sol-gel-based hybrid materials widely investigated as host matrices for LSCs is that of ureasil systems. These compounds are generally prepared from the reaction between a commercially available polyetheramine and an organo-silica precursor, followed by hydrolysis and condensation of the silica network using sol-gel chemistry (McKenna and Evans, 2017). One interesting application based on such ureasil matrices is their use to fabricate cylindrical LSCs. In a first proof of concept study, a commercial PMMA optical fiber was coated with an organic-inorganic ureasil hybrid layer doped with a Eu^{3+} complex as luminescent species (Correia et al., 2015). Optimized fiber-based LSC devices could attain $\eta_{opt} > 20\%$, calculated in the absorption spectral region of the luminescent material (300–380 nm). Using an optical-fiber drawing facility, the same group extended their previous studies by scaling up large-area LSCs (up to 2.5 m) based on bulk and hollow-core optical fibers (**Figure 1A**), using rhodamine 6G- or Eu^{3+}-doped hybrids based on two different matrices, namely a di-ureasil and a tripodal tri-ureasil system (Correia et al., 2016). Efforts on the use of tri- and di-ureasil compounds as host matrices in LSCs have also focused on their combination with different doping species in planar devices (Nolasco et al., 2013; Rondão et al., 2017; Frias et al., 2018).

The ureasil family was recently further exploited as precursor for the formation of host matrix systems for planar LSC devices in bulk configuration and embedding LR305 as luminescent species (Kaniyoor et al., 2016). The host matrix was obtained by the reaction between a polyetheramine of the Jeffamine family and an isocyanate-functionalized organo-silane with the formation of urea bonds (**Figure 1B**). From the optical analysis it was found that this material exhibits enhanced transmittance in the whole UV-visible range, with optical clarity (and refractive index) comparable to glass or PMMA. Förster resonance energy transfer (FRET) was demonstrated between the matrix and the organic dye, which enabled an extension of the light-harvesting window of the LSC device. For optimized devices, $\eta_{opt} = 14.5\%$ (emission: 300–800 nm, $G = 3.3$) was reported. In a later work (Meazzini et al., 2017), the same class of host matrix system was tested in the presence of a poly(fluorene-*alt*-phenylene) copolymer containing on-chain perylenediimide chromophore units as the luminophore (**Figure 1C**), further confirming the key role played by the interplay between host matrix material and guest luminescent species in determining the optical performance of the resulting LSC.

MULTIFUNCTIONAL MATRICES

Recent efforts in the field of LSCs have been addressed to the development of multifunctional systems in which the matrix material not only acts as host environment for the luminophore, but also displays added functionalities such as extended photochemical durability, peculiar surface properties and/or stimuli-responsiveness. Within this context

(Pintossi et al., 2017), a novel photopolymeric matrix for thin-film LSCs was recently developed for higher outdoor durability but also displaying a highly hydrophobic and oleophobic surface character (**Figure 2A**). Such system was based on a blend of three different UV-curable fluorinated oligomers to be co-reacted upon UV-light exposure with a suitably functionalized perylene-based organic luminophore bearing lateral carbon double bonds, to yield a solid crosslinked LSC thin film. The long-term stability of such photocurable LSC system was demonstrated by full retention of its initial performance, as opposed to the decline observed in reference host/guest luminescent systems. The highly hydrophobic character (water contact angle $\sim$120°) and moderate oleophobicity (mineral-oil contact angle $>$ 90°) resulting from the highly perfluorinated nature of the polymeric matrix was shown to impart easy cleanability to the LSC coating. In a successive work by the same group, superhydrophobicity of the LSC surface could be achieved by combining a soft-lithographic process together with an additive manufacturing approach based on stereolithography (Credi et al., 2017). Surface-microstructured superhydrophobic LSCs could be obtained using a suitably developed UV-curable formulation incorporating perfluorinated monomers doped with LR305 (**Figure 2B**), leading to water contact angles $>$160°.

Another interesting approach to multifunctionality in LSCs is focused on providing the host matrix with thermo-responsive properties. In this respect, the possibility to have liquid crystals (LC) as host matrix was recently explored, with the incorporation of donor–acceptor fluorescent dye pairs which could yield fluorescence through a FRET mechanism (Sol et al., 2018a). In particular, at low temperature one of the two dyes is in its aggregated form, preventing any type of fluorescence, while the second is emitting in the green region of the electromagnetic spectrum. Upon increasing temperature, the solubility of both dyes in the LC matrix increases and FRET phenomena are allowed to occur, shifting the emission of the device from green toward red. This system (**Figure 2C**) offers the opportunity to tune both absorption and emission colors, which may be a particularly interesting esthetic feature with great potential for LSCs and smart windows in general. Furthermore, positive and negative dichroic dyes can be exploited to change the appearance of a window as a function of applied voltage (**Figure 2D**) (Verbunt et al., 2009; Debije et al., 2014; Khandelwal et al., 2015; Sol et al., 2018b).

CONCLUSIONS AND PERSPECTIVES

The importance of the selection of appropriate host matrix materials for LSCs has driven research to the development of novel systems working alongside more conventional host matrix platforms such as glass or commodity polymers. Within this framework, the extensive array of properties achievable by the use of polymers has made them the most widely exploited class of materials for use in LSC devices. Together with polymers, research has also focused on the development of hybrid systems to simultaneously exploit the beneficial properties of both the glassy inorganic phase (chemical inertness, optical clarity) and the organic phase (chemical tunability, light-weight). Only recently, the attention has been also shifted toward matrix materials capable of imparting added functionalities to the LSC ensemble. In this respect, examples of (super)hydrophobic, oleophobic, or stimuli (thermally, electrically) responsive host matrices have been proposed and successfully demonstrated.

Considering that research on alternative matrix materials for LSCs has been addressed in detail only in recent years, the examples presented in this mini-review clearly demonstrate that there are enormous opportunities for enhanced LSC performance by developing suitably tailored host materials. In addition, the development of multifunctional matrix systems will be expected to pave the path to novel and truly smart devices with potential application in a variety of fields, thus anticipating a wider permeation of the LSC technology into the market.

AUTHOR CONTRIBUTIONS

The author confirms being the sole contributor of this work and has approved it for publication.

REFERENCES

Al-Kaysi, R. O., Ahn, T. S., Muller, A. M., and Bardeen, C. J. (2006). The photophysical properties of chromophores at high (100 mM and above) concentrations in polymers and as neat solids. *Phys. Chem. Chem. Phys.* 8, 3453–3459. doi: 10.1039/b605925b

Buffa, M., Carturan, S., Debije, M. G., Quaranta, A., and Maggioni, G. (2012). Dye-doped polysiloxane rubbers for luminescent solar concentrator systems. *Solar Energy Mater. Solar Cells* 103, 114–118. doi: 10.1016/j.solmat.2012.04.019

Chowdhury, F. I., Dick, C., Meng, L., Mahpeykar, S. M., Ahvazi, B., and Wang, X. (2017). Cellulose nanocrystals as host matrix and waveguide materials for recyclable luminescent solar concentrators. *RSC Adv.* 7, 32436–32441. doi: 10.1039/C7RA04344A

Colby, K. A., Burdett, J. J., Frisbee, R. F., Zhu, L., Dillon, R. J., and Bardeen, C. J. (2010). Electronic energy migration on different time scales: concentration dependence of the time-resolved anisotropy and fluorescence quenching of lumogen red in poly(methyl methacrylate). *J. Phys. Chem. A* 114, 3471–3482. doi: 10.1021/jp910277j

Correia, S. F. H., Lima, P. P., André, P. S., Ferreira, M. R. S., and Carlos, L. A. D. (2015). High-efficiency luminescent solar concentrators for flexible waveguiding photovoltaics. *Solar Energy Mater. Solar Cells* 138, 51–57. doi: 10.1016/j.solmat.2015.02.032

Correia, S. F. H., Lima, P. P., Pecoraro, E., Ribeiro, S. J. L., André, P. S., Ferreira, R. A. S., et al. (2016). Scale up the collection area of luminescent solar concentrators towards metre-length flexible waveguiding photovoltaics. *Progress Photovolt.* 24, 1178–1193. doi: 10.1002/pip.2772

Credi, C., Pintossi, D., Bianchi, C. L., Levi, M., Griffini, G., and Turri, S. (2017). Combining stereolithography and replica molding: on the way to superhydrophobic polymeric devices for photovoltaics. *Mater. Des.* 133, 143–153. doi: 10.1016/j.matdes.2017.07.068

Debije, M. G., Menelaou, C., Herz, L. M., and Schenning, A. P. H. J. (2014). Combining positive and negative dichroic fluorophores for advanced light management in luminescent solar concentrators. *Adv. Optical Mater.* 2, 687–693. doi: 10.1002/adom.201400132

Debije, M. G., and Verbunt, P. P. C. (2012). Thirty years of luminescent solar concentrator research: solar energy for the built environment. *Adv. Energy Mater.* 2, 12–35. doi: 10.1002/aenm.201100554

Fattori, V., Melucci, M., Ferrante, L., Zambianchi, M., Manet, I., Oberhauser, W., et al. (2011). Poly(lactic acid) as a transparent matrix for luminescent solar concentrators: a renewable material for a renewable energy technology. *Energy Environ. Sci.* 4, 2849–2853. doi: 10.1039/C1EE01391B

Freitas, V. T., Fu, L., Cojocariu, A. M., Cattoën, X., Bartlett, J. R., Le Parc, R., et al. (2015). Eu3+-based bridged silsesquioxanes for transparent luminescent solar concentrators. *ACS Appl. Mater. Interfaces* 7, 8770–8778. doi: 10.1021/acsami.5b01281

Frias, A. R., Pecoraro, E., Correia, S. F. H., Minas, L. M. G., Bastos, A. R., García-Revilla, S., et al. (2018). Sustainable luminescent solar concentrators based on organic–inorganic hybrids modified with chlorophyll. *J. Mater. Chem. A* 6, 8712–8723. doi: 10.1039/C8TA01712C

Geervliet, T. A., Gavrila, I., Iasilli, G., Picchioni, F., and Pucci, A. (2018). Luminescent solar concentrators based on renewable polyester matrices. *Chem. Asian J.* doi: 10.1002/asia.201801690. [Epub ahead of print].

Goetzberger, A., and Greube, W. (1977). Solar energy conversion with fluorescent collectors. *Appl. Phys.* 14, 123–139. doi: 10.1007/BF00883080

Graffion, J., Cattoën, X., Wong Chi Man, M., Fernandes, V. R., André, P. S., Ferreira, R. A. S., et al. (2011). Modulating the photoluminescence of bridged silsesquioxanes incorporating Eu3+-complexed n,n′-Diureido-2,2′-bipyridine isomers: application for luminescent solar concentrators. *Chem. Mater.* 23, 4773–4782. doi: 10.1021/cm2019026

Graffion, J., Cojocariu, A. M., Cattoën, X., Ferreira, R. A. S., Fernandes, V. R., André, P. S., et al. (2012). Luminescent coatings from bipyridine-based bridged silsesquioxanes containing Eu3+ and Tb3+ salts. *J. Mater. Chem.* 22, 13279–13285. doi: 10.1039/C2JM31289A

Griffini, G., Brambilla, L., Levi, M., Del Zoppo, M., and Turri, S. (2013a). Photo-degradation of a perylene-based organic luminescent solar concentrator: molecular aspects and device implications. *Solar Energy Mater. Solar Cells* 111, 41–48. doi: 10.1016/j.solmat.2012.12.021

Griffini, G., Levi, M., and Turri, S. (2013b). Novel crosslinked host matrices based on fluorinated polymers for long-term durability in thin-film luminescent solar concentrators. *Solar Energy Mater. Solar Cells* 118, 36–42. doi: 10.1016/j.solmat.2013.05.041

Griffini, G., Levi, M., and Turri, S. (2014). Novel high-durability luminescent solar concentrators based on fluoropolymer coatings. *Progress Organic Coat.* 77, 528–536. doi: 10.1016/j.porgcoat.2013.11.016

Kaczmarek, H., Kaminska, A., and van Herk, A. (2000). Photooxidative degradation of poly(alkyl methacrylate)s. *Eur. Polym. J.* 36, 767–777. doi: 10.1016/S0014-3057(99)00125-1

Kaniyoor, A., McKenna, B., Comby, S., and Evans, R. C. (2016). Design and response of high-efficiency, planar, doped luminescent solar concentrators using organic–inorganic di-ureasil waveguides. *Adv. Opt. Mater.* 4, 444–456. doi: 10.1002/adom.201500412

Kastelijn, M. J., Bastiaansen, C. W. M., and Debije, M. G. (2009). Influence of waveguide material on light emission in luminescent solar concentrators. *Opt. Mater.* 31, 1720–1722. doi: 10.1016/j.optmat.2009.05.003

Khandelwal, H., Loonen, R. C. G. M., Hensen, J. L. M., Debije, M. G., and Schenning, A. P. H. J. (2015). Electrically switchable polymer stabilised broadband infrared reflectors and their potential as smart windows for energy saving in buildings. *Sci. Rep.* 5:11773. doi: 10.1038/srep11773

Li, Y., Zhang, X., Zhang, Y., Dong, R., and Luscombe, C. K. (2019). Review on the role of polymers in luminescent solar concentrators. *J. Polym. Sci Part A* 57, 201–215. doi: 10.1002/pola.29192

Lim, Y. S., Lo, C. K., and Teh, G. B. (2012). Unsaturated polyester resin blended with MMA as potential host matrix for luminescent solar concentrator. *Renew. Energy* 45, 156–162. doi: 10.1016/j.renene.2012.02.025

Maggioni, G., Campagnaro, A., Carturan, S., and Quaranta, A. (2013). Dye-doped parylene-based thin film materials: application to luminescent solar concentrators. *Solar Energy Mater. Solar Cells* 108, 27–37. doi: 10.1016/j.solmat.2012.08.009

Mansour, A. F., Killa, H. M. A., Abd El-Wanees, S., and El-Sayed, M. Y. (2005). Laser dyes doped with poly(ST-Co-MMA) as fluorescent solar collectors and their field performance. *Polym. Test.* 24, 519–525. doi: 10.1016/j.polymertesting.2004.11.014

Mazzaro, R., and Vomiero, A. (2018). The renaissance of luminescent solar concentrators: the role of inorganic nanomaterials. *Adv. Energy Mater.* 8:1801903. doi: 10.1002/aenm.201801903

McKenna, B., and Evans, R. C. (2017). Towards efficient spectral converters through materials design for luminescent solar devices. *Adv. Mater.* 29:1606491. doi: 10.1002/adma.201606491

Meazzini, I., Blayo, C., Arlt, J., Marques, A.-T., Scherf, U., Burrows, H. D., et al. (2017). Ureasil organic–inorganic hybrids as photoactive waveguides for conjugated polyelectrolyte luminescent solar concentrators. *Mater. Chem. Front.* 1, 2271–2282. doi: 10.1039/C7QM00264E

Meinardi, F., Bruni, F., and Brovelli, S. (2017). Luminescent solar concentrators for building-integrated photovoltaics. *Nat. Rev.s Mater.* 2:17072. doi: 10.1038/natrevmats.2017.72

Melucci, M., Durso, M., Favaretto, L., Capobianco, M. L., Benfenati, V., Sagnella, A., et al. (2012). Silk doped with a bio-modified dye as a viable platform for eco-friendly luminescent solar concentrators. *RSC Adv.* 2, 8610–8613. doi: 10.1039/C2RA21568C

Moraitis, P., Schropp, R. E. I., and van Sark, W. G. J. H. M. (2018). Nanoparticles for luminescent solar concentrators–a review. *Opt. Mater.* 84, 636–645. doi: 10.1016/j.optmat.2018.07.034

Nolasco, M. M., Vaz, P. M., Freitas, V. T., Lima, P. P., Andr,é, P. S., Ferreira, R. A. S., et al. (2013). Engineering highly efficient Eu(iii)-based tri-ureasil hybrids toward luminescent solar concentrators. *J. Mater. Chem. A* 1, 7339–7350. doi: 10.1039/C3TA11463E

Pandey, S., and Mishra, S. B. (2011). Sol–gel derived organic–inorganic hybrid materials: synthesis, characterizations and applications. *J. Sol Gel Sci. Technol.* 59, 73–94. doi: 10.1007/s10971-011-2465-0

Pintossi, D., Colombo, A., Levi, M., Dragonetti, C., Turri, S., and Griffini, G. (2017). UV-curable fluoropolymers crosslinked with functional fluorescent dyes: the way to multifunctional thin-film luminescent solar concentrators. *J. Mater. Chem. A* 5, 9067–9075. doi: 10.1039/C7TA01692A

Pucci, A. (2018). Luminescent solar concentrators based on aggregation induced emission. *Israel J. Chem.* 58, 837–844. doi: 10.1002/ijch.201800028

Reisfeld, R., Levchenko, V., and Saraidarov, T. (2011). Interaction of luminescent dyes with noble metal nanoparticles in organic–inorganic glasses for future luminescent materials. *Polym. Adv. Technol.* 22, 60–64. doi: 10.1002/pat.1842

Rondão, R., Frias, A. R., Correia, S. F. H., Fu, L., de Zea Bermudez, V., André, P. S., et al. (2017). High-performance near-infrared luminescent solar concentrators. *ACS Appl. Mater. Interfaces* 9, 12540–12546. doi: 10.1021/acsami.7b02700

Sol, J. A. H. P., Dehm, V., Hecht, R., Würthner, F., Schenning, A. P. H. J., and Debije, M. G. (2018a). Temperature-responsive luminescent solar concentrators: tuning energy transfer in a liquid crystalline matrix. *Angew. Chem. Int. Ed.* 57, 1030–1033. doi: 10.1002/anie.201710487

Sol, J. A. H. P., Timmermans, G. H., van Breugel, A. J., Schenning, A. P. H. J., and Debije, M. G. (2018b). Multistate luminescent solar concentrator "Smart" windows. *Adv. Energy Mater.* 8:1702922. doi: 10.1002/aenm.201702922

Tonezzer, M., Maggioni, G., Campagnaro, A., Carturan, S., Quaranta, A., della Pirriera, M., et al. (2015). Luminescent solar concentrators employing new Eu(TTA)3phen-containing parylene films. *Progress Photovolt.* 23, 1037–1044. doi: 10.1002/pip.2524

Tuck, C. O., Pérez, E., Horváth, I. T., Sheldon, R. A., and Poliakoff, M. (2012). Valorization of biomass: deriving more value from waste. *Science* 337, 695–699. doi: 10.1126/science.1218930

Verbunt, P. P. C., Kaiser, A., Hermans, K., Bastiaansen, C. W. M., Broer, D. J., and Debije, M. G. (2009). Controlling light emission in luminescent solar concentrators through use of dye molecules aligned in a planar manner by liquid crystals. *Adv. Funct. Mater.* 19, 2714–2719. doi: 10.1002/adfm.200900542

Weber, W. H., and Lambe, J. (1976). Luminescent greenhouse collector for solar radiation. *Appl. Opt.* 15, 2299–2300. doi: 10.1364/AO.15.002299

Yoo, H., Yang, J., Yousef, A., Wasielewski, M. R., and Kim, D. (2010). Excimer formation dynamics of intramolecular π-stacked perylenediimides probed by single-molecule fluorescence spectroscopy. *J. Am. Chem. Soc.* 132, 3939–3944. doi: 10.1021/ja910724x

Zettl, M., Mayer, O., Klampaftis, E., and Richards, B. S. (2017). Investigation of host polymers for luminescent solar concentrators. *Energy Technol.* 5, 1037–1044. doi: 10.1002/ente.201600498

Conflict of Interest Statement: The author declares that the research was conducted in the absence of any commercial or financial relationships that could be construed as a potential conflict of interest.

Smart Materials

Xian-Xu 'Frank' Bai

Dr Bai received a PhD degree in Instrument Science and Technology from Chongqing University in 2013. He joined the Hefei University of Technology in 2013 and founded the Laboratory for Adaptive Structures and Intelligent Systems (LASIS) in 2016. His research interests are focused in two areas. (i) Design, optimization, dynamics, and control of smart structures based on smart materials, including magnetorheological fluids/elastomers and magnetostrictive materials, applied to automotive and aerospace systems, and (ii) New mechatronics-based vehicle dynamics and control with an emphasis on intelligent/unmanned vehicles. Dr Bai has authored over 50 international journal and conference articles. He is an inventor on 16 issued Chinese patents and two PCT US patents (pending). Currently, Dr Bai serves as an Associate Editor of the Journal of Intelligent Material Systems and Structures. He is a Committee Member of the Adaptive Structures and Materials System Branch of the Aerospace Division of ASME. He is a peer reviewer of over 30 internal journals. Dr Bai is a member of ASME (S'09, M'12), SAE-China (M'16) and IEEE (M'17).

Ali El Wahed

Ali K. El Wahed was awarded a PhD degree in Mechanical Engineering by the University of Liverpool in 1991. He has been active in various areas of research, especially in Smart Materials and in Applied Electrostatics. He is currently a Reader in Mechanical Engineering, University of Dundee where he leads the Smart Materials Group. He has published over 60 papers in technical literature.

Yancheng Li

Dr Yancheng Li obtained his PhD degree from Nanjing University of Science and Technology in 2007, majoring in Mechanical Engineering. After graduating, he joined the School of Civil and Environmental Engineering at the University of Technology Sydney in 2008 and has been working at the university as a Postdoctoral Research Associate, Chancellor's Research Fellow, Lecturer, and Senior Lecturer. He has been a Professor in Structural Dynamics at the College of Civil Engineering, Nanjing Tech University since 2018. His research interest include to innovatively explore the applications of various smart materials into building protection of civil structures, including magnetorheological materials (fluids, elastomer, gel and grease) and piezoelectric materials. Dr Li has published around 100 peer-reviewed journal and conference papers on the topic of smart materials and structures.

Jong-Seok Oh°

Jong-Seok Oh received a BSc degree, MSc degree, and PhD degree in Mechanical Engineering from Inha University in 2009, 2011, and 2015, respectively. He is currently an Assistant Professor at Kongju National University. His research interests include robust controller design and the control of various systems using smart actuators such as magnetorheological (MR), electrorheological (ER) fluids, and piezo actuators.

Ubaid Ubaidillah

Ubaidillah currently works at the Mechanical Engineering Department, Faculty of Engineering, at the Universitas Sebelas Maret. He obtained a PhD degree in 2016 from the Universiti Teknologi Malaysia; a MSc degree in 2010 from the Universiti Teknikal Malaysia Melaka; and a B.Eng. degree in 2007 from the Institut Teknologi Sepuluh Nopember (ITS). His research interest include smart materials development and actuators based on smart materials. He started to do research in magnetorheology in 2007 and has published more than 30 ISI papers. He has also started to produce an MR damper for lateral damper, seismic damper, and a secondary suspension for train etc. Some types of MR brakes were fabricated for ankle foot orthoses braking systems. In addition to MR based actuators, he has also been continuously developing MR materials such as MR elastomers, MR foam, MR grease, and MR fluids.

frontiers in Materials

ORIGINAL RESEARCH
published: 12 March 2019
doi: 10.3389/fmats.2019.00036

On the Hysteresis Mechanism of Magnetorheological Fluids

Xian-Xu Bai[1]* *and Peng Chen*[1,2]

[1] *Laboratory for Adaptive Structures and Intelligent Systems, Department of Vehicle Engineering, Hefei University of Technology, Hefei, China,* [2] *GAC Automotive Research and Development Center, Guangzhou Automobile Group Co., Ltd., Guangzhou, China*

In this paper, hysteresis of magnetorheological (MR) fluids is identified from experimental tests following the mechanism of rate-independence and further studied to explore the hysteresis mechanism. The theoretical analysis based on the dipole model is provided to reveal the hysteresis mechanism of MR fluids. Specifically, the performance tests of a self-developed double-rod MR damper under different excitations show that instead of the typical force-velocity plot, the relationship between the force and displacement meets the requirements of rate-independence of the hysteresis well. A critical concept of "yield displacement" is defined and analyzed in the force-displacement plot to illustrate the hysteresis characteristics. In addition, the relationship of the normalized restoring force vs. strain is derived for a single chain from the dipole model. Then a stress-strain curve is developed for the multi-chain structure with an assumption of the dynamic equilibrium between the rupture and reconstruction of the chains. Sequentially, the hysteresis mechanism is established based on the force-displacement characteristics under reciprocating excitations. The consistency between the yield displacement in experiment and yield strain in theory verifies the effectiveness of the hypothetical hysteresis mechanism. The analysis results provide a guideline for the structural design of MR devices to enhance/reduce the hysteresis effect. The hysteresis mechanism-based further extension for the stress-strain properties of MR elastomers and the response time of MR fluids are provided as well.

Keywords: hysteresis, magnetorheological (MR) fluids, force-displacement characteristics, yield displacement, dipole model, yield strain

OPEN ACCESS

Edited by:
Seung-Bok Choi,
Inha University, South Korea

Reviewed by:
Yang Yu,
University of Technology Sydney, Australia
Xuan Shouhu,
University of Science and Technology of China, China
U. Ubaidillah,
Sebelas Maret University, Indonesia
Fitrian Imaduddin,
Faculty of Engineering, Sebelas Maret University, Indonesia

***Correspondence:**
Xian-Xu Bai
bai@hfut.edu.cn;
www.lasiser.com

Specialty section:
This article was submitted to Smart Materials, a section of the journal Frontiers in Materials

Received: *11 January 2019*
Accepted: *18 February 2019*
Published: *12 March 2019*

Citation:
Bai X-X and Chen P (2019) On the Hysteresis Mechanism of Magnetorheological Fluids. Front. Mater. 6:36. doi: 10.3389/fmats.2019.00036

INTRODUCTION

Magnetorheological (MR) fluids are a smart material with magnetic field-dependent rheological properties (De Vicente et al., 2011). Hysteresis is an inherent property of MR fluids and MR fluid-based actuators. Such hysteretic non-linearity increases the control complexity of MR actuators, which in turn limits the MR applications. Understanding the working mechanism of the hysteresis characteristics of MR fluids is significant for studying the hysteresis characteristics of MR actuators and implementing high-efficiency control for MR semi-active systems.

At present, the research on MR hysteresis characteristics mainly focuses on the mechanical properties of MR actuators (Wang and Liao, 2011; Bai et al., 2013, 2015; Sapinski et al., 2017; Yu et al., 2017; Chen et al., 2018; Shou et al., 2018), such as MR dampers and MR clutches/brakes. Experimental tests of MR dampers in valve or shear mode show that the hysteresis only occurs around the direction-change points under sinusoidal displacement excitations

(Wang and Liao, 2011; Bai et al., 2015). Coincidentally, the associated velocities in this area are relatively small, and the hysteresis displays more distinctly in the force-velocity plot. However, from a view of rate-independence of hysteresis (Visintin, 2013; Chen et al., 2018), the experimental results (Wang and Liao, 2011; Bai et al., 2015; Sapinski et al., 2017; Yu et al., 2017; Shou et al., 2018) show that the hysteresis behaviors of MR fluids occur in force-displacement plot while not in the typical force-velocity plot. The "rate-independence" concept is defined by the path of the couple [with the input $z(t)$ and the output $F(t)$ of the system] that is invariant with respect to any increasing time, i.e., the output is not dependent on the derivative of the input z (Visintin, 2013). It should be noted that the hysteresis loops are not regarded as an essential feature of hysteresis (Visintin, 2013). The rate-independence, as the critical property of the hysteresis, provides an index to identify the input/output in any hysteresis phenomenon. In addition, the modeling analysis of MR fluids operated in squeeze mode indicates that the hysteresis in squeeze mode cannot be described by the normal force-velocity plot-based hysteresis models, but can be well-described by the force-displacement relation-based model–Bouc-Wen model (Chen et al., 2017a) and resistor-capacitor (RC) operator-based models (Chen et al., 2018; Bai et al., 2019). Similarly, as a derivative of MR fluids, the macroscopic mechanical properties of MR elastomers can also be modeled by the Bouc-Wen model or RC operator-based models. It indicates that MR fluids have the similar hysteresis characteristics to MR elastomers (Behrooz et al., 2014). Based on the rate-independence property of hysteresis, the macroscopic mechanical properties of MR actuators are actually a coupling of Duhem-type hysteresis and viscous properties which is rate-dependent (Visintin, 2013; Chen et al., 2018).

Compared with the experimental investigations of the hysteresis characteristics of MR actuators, the research on its working mechanism is rare to be found. Theoretical and experimental studies show that the compressibility of MR fluids and the compressibility of the accumulator (if exists) can be effectively used to establish the mechanical model of the hysteresis characteristics of MR dampers in valve mode (Wang and Gordaninejad, 2007; Guo et al., 2014). However, the compressibility of MR fluids fails to explain the inherent hysteresis of MR fluid- and elastomer-based actuators (Weber, 2013; Behrooz et al., 2014) working in shear mode.

Dipole model can be used to theoretically explain the working mechanism of the controllable mechanical properties of MR fluids and MR elastomers from the microscopic level. Based on the simply dipole model, researchers have deduced the enhanced dipole model considering the magnetic interaction, the local magnetic field interaction and the magnetic chain interaction in the whole chain (Jolly et al., 1996; Furst and Gast, 2000; Xu et al., 2016). A corresponding stress-strain curve is derived under the assumption that all chains maintain consistent deformation.

The main contribution and work of this paper is to theoretically analyze the experimental performance of MR dampers and explain the hysteresis mechanism of MR fluids. In order to avoid the influence of the compressibility of the accumulator and viscous damping on the hysteresis characteristics, a self-developed double-rod MR damper will be tested under triangle displacement excitations. Applying normalization method, the expression of hysteresis of MR fluids in force-displacement plot is studied. Yield displacement concept is proposed to quantitatively analyze the experimental results. Theoretically, using the dipole model, under the assumption of the dynamic equilibrium between the rupture and reconstruction, the expression of hysteresis of MR fluids via the stress-strain curve will be derived.

EXPERIMENTAL TESTS OF HYSTERESIS CHARACTERISTICS OF MR FLUIDS

The hysteresis characteristics of MR fluids are tested on a self-developed double-rod MR damper (Bai et al., 2013, 2018a,b), as shown in **Figure 1A**, using the servo-hydraulic testing system (Type: LFH-LFV3068, SAGINOMIYA Inc.), as shown in **Figure 1B**. Observing **Figure 1B**, the experimental setup is composed of the servo-hydraulic testing system, the MR damper, and a power supply (Type: IT6861A, from ITECH Company). The servo-hydraulic testing system is integrated with a shaker actuator driven by a servo-hydraulic system, data acquisition and processing system with force sensors and displacement sensors, and a controller (i.e., a host computer, not shown in the figure). In order to avoid the influence from viscosity characteristics under different excitation velocities, the mechanical behaviors of the MR damper are tested under triangle displacement excitations provided by the servo-hydraulic testing system. The force and displacement signals are acquired by the data acquisition and processing system with a sample rate of 1 kHz. The geometrical dimensions and parameters of the self-developed double-rod MR damper are listed in **Table 1**. Such specifically developed double-rod MR damper will effectively eliminate the influence from the compressibility of the accumulator. As a reference, the experimental results of a commercial MR damper with an accumulator are provided in **Appendix A**.

Figure 2 presents the test results of the MR damper under a triangle displacement excitation with a frequency of 1 Hz and an amplitude of 25 mm. As shown in the figure, the damping force of the MR damper changes rapidly and converges to a stable value in a region where the excitation direction changes and the excitation velocity is constant. Moreover, the tendency of the damping forces under different currents shows a good consistency in this region.

Figure 3 presents the force-displacement plot of the MR damper under different excitation frequencies to further verify the rate-independence of the hysteresis characteristics. As seen from **Figure 3**, the force-displacement plots also show a very good consistency. Combining **Figures 2**, **3**, the force-displacement hysteresis characteristics of the MR damper/fluids are verified. Such phenomenon of the hysteresis being presented by the force-displacement plot is also consistent with the pre-yield and post-yield definitions of the stress-strain curve of MR fluids (De Vicente et al., 2011). Sequentially, the pre-yield and post-yield regions are defined in **Figures 2**, **3**. As known, the unavoidable friction for the MR damper shown

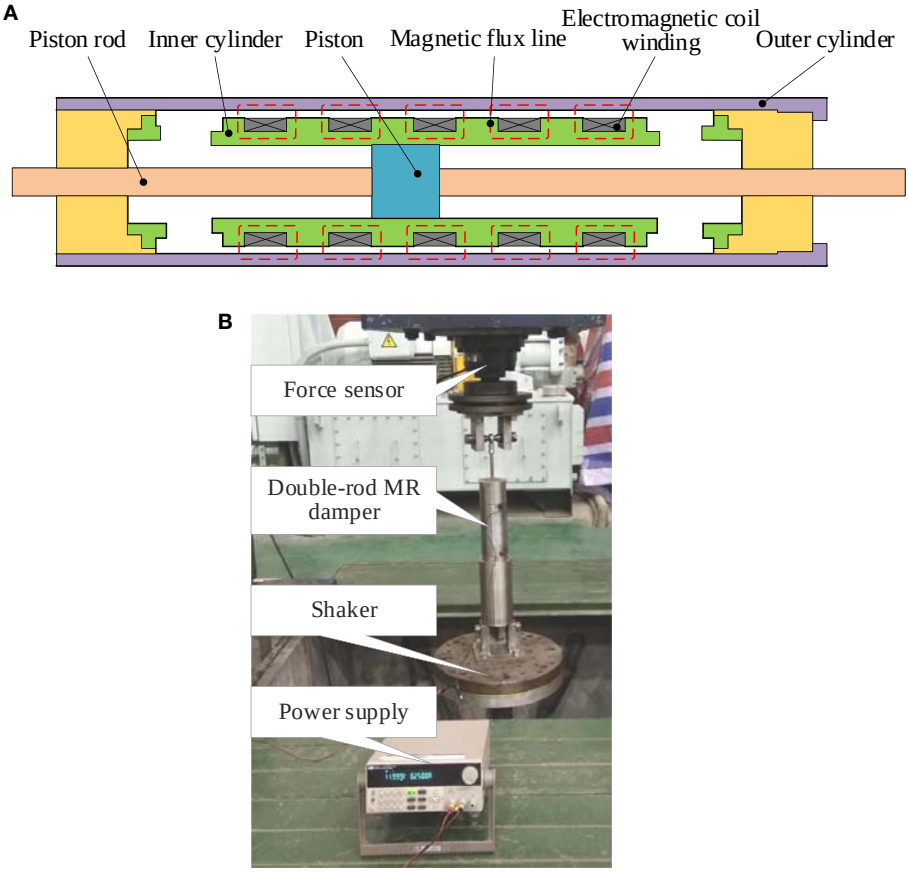

FIGURE 1 | The self-developed double-rod MR damper: **(A)** schematic and **(B)** experimental setup.

in **Figure 1** also behaves as a kind of Duhem hysteresis. The macroscopic mechanical characteristics of MR damper are the coupling of the hysteresis characteristics of the MR fluids and the hysteresis characteristics of friction. As seen from **Figure 2**, in field-off state (i.e., 0 A, where only the friction shows the hysteresis characteristics), the length of pre-yield is significantly different from that in field-on states. It indicates that the hysteresis characteristics of MR fluids is an important factor for the hysteresis of the MR damper, while not the friction. In addition, in **Figures 2**, **3**, the consistence of the pre-yield lengths under different currents provides a clue for the study of the hysteresis mechanism.

To study the hysteresis characteristics of MR fluids, a concept of normalized damping force is defined as

$$\hat{F}_{I,i} = \frac{F_{I,i} - F_{0,i}}{F_{I,0} - F_{0,0}} \tag{1}$$

where $F_{I,i}$ is the damping force of the MR damper with current of I at displacement i when under triangle displacement excitation; $F_{I,0}$ is the damping force when under forward excitation and the displacement excitation at position zero; $F_{0,i}$ and $F_{0,0}$ are the damping force of the MR damper with no current at displacement i and the damping force of the MR damper with no current at the position zero, respectively; $\hat{F}_{I,i}$ is the normalized damping force.

On one hand, the influence of the friction on the hysteresis characteristics of the MR damper (i.e., $F_{I,i} - F_{0,i}$) can be effectively excluded by using the normalization concept. On the other hand, it is convenient to study the commonality of the hysteresis characteristics of MR fluids with different currents (magnetic fields). **Figure 4** presents the normalized force-displacement plot of the MR damper with different currents under triangle displacement excitation with a frequency of 1 Hz and an amplitude of 25 mm. As seen from **Figure 4**, the normalized force-displacement plots under different currents show a very good consistence. The distance from the displacement turning point to the convergence point of the damping force is defined as the yield displacement in this study. The yield displacements of the MR damper are nearly equal to each other under different currents, as seen from **Figure 4**. The yield displacement increases little with the increase of the current, due to the compressibility of the MR fluids. In other words, the compressibility of the MR fluids is not the essential factor for the hysteresis characteristics of MR actuators/fluids.

TABLE 1 | Geometries and parameters of the self-developed double-rod MR damper.

Specification	Value/type
Piston radius	15×10^{-3} m
Piston-rod radius	5×10^{-3} m
Active length of a stage	15×10^{-3} m
Length of MR fluid flow gap	0.175 m
Outer radius of inner cylinder	24.8×10^{-3} m
Inner radius of outer cylinder	25.8×10^{-3} m
Inductance of electromagnetic coil windings	21.9 mH
Resistance of electromagnetic coil windings	6.6 Ω
Number of turns of electromagnetic coil winding	150
Relative roughness of pipe wall	1.6×10^{-6} m
MR fluid (from Chongqing instrument material research institute)	MRF-G28 (Density = 2,720 kg/m^3; Field-off viscosity at 10 s^{-1} = 1.1 Pa s; Operational temperature: −40 to 130°C)

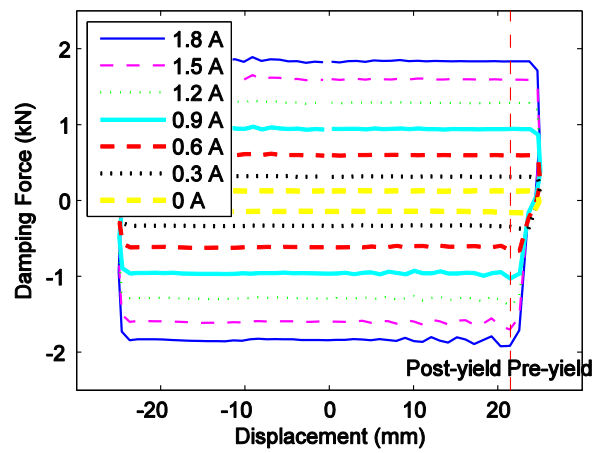

FIGURE 2 | Mechanical behavior of the MR damper with different currents under triangle displacement excitation with a frequency of 1 Hz and an amplitude of 25 mm.

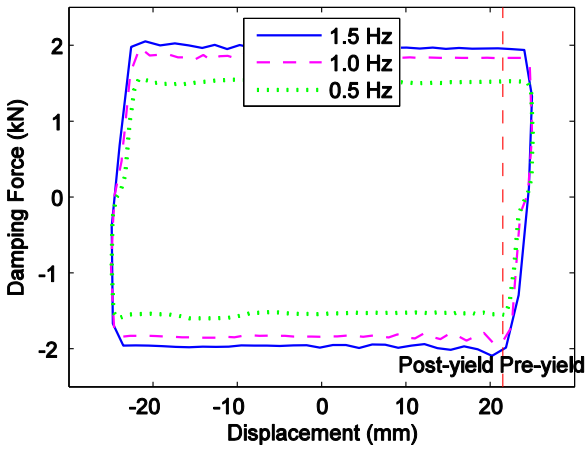

FIGURE 3 | Mechanical behavior of the MR damper with 1.8 A current under triangle displacement excitations with different frequencies and an amplitude of 25 mm.

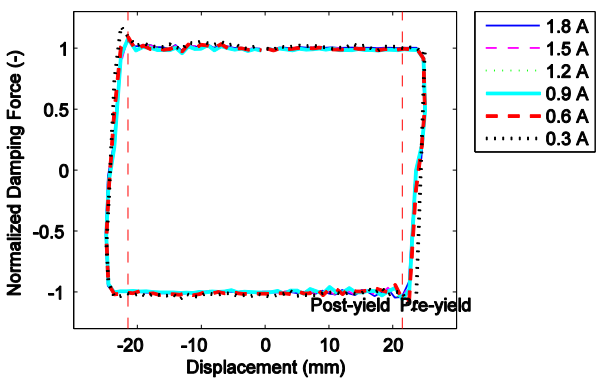

FIGURE 4 | Normalized force-displacement plot of the MR damper with different currents under triangle displacement excitation with a frequency of 1 Hz and an amplitude of 25 mm.

THEORETICAL ANALYSIS OF HYSTERESIS CHARACTERISTICS OF MR FLUIDS

Test results and analysis have shown that the friction is only a very limited part of the hysteresis characteristics of the MR damper, and the compressibility of the MR fluids cannot fully explain the hysteresis characteristics of the MR damper. We will try to theoretically explain the hysteresis characteristics of MR damper/fluids via a theoretical perspective with the magnetic interaction of ferromagnetic particles.

Structural Evolution of Chain Clusters of MR Fluids

Dipole model can be used to essentially explain the MR effect in microscopic point. Based on the dipole model, the deformation of the chains or columns of MR fluids leads to the restoring force in the presence of the magnetic field. Further, the expression of the restoring force between two particles is derived with relation to the particle distance and the polar angle between the line of centers and the direction of the magnetic field (Klingenberg et al., 1990). This model can be applied to analyze the yield stress of MR fluids in shear mode (Bossis and Lemaire, 1991; Jolly et al., 1996). Following this idea, modified dipole models that account for the particle interaction along a single chain have been proposed (Furst and Gast, 2000; Tao, 2001; Si et al., 2008). In such models, the chains are assumed to deform in shear mode, Chen et al. proved that the restoring force would be varied with different kinds of structural evolution and the deformation of the chains would be affected by the hydraulic inaction when under valve or squeeze mode (Chen et al., 2017b).

The deformation of chains in shear mode is the focus of this study, so the hydraulic interaction is neglected. A schematic of the deformation of a single chain is presented in **Figure 5**. With the magnetic field, the identical spherical particles dispersed in

the carrier oil align themselves in the direction of the magnetic field. According to the minimum energy principle, the field energy would be minimized when $d = 2R$, where d is the vertical distance between the centers of the adjacent particles and R is the radius of the particle. We assume that there is no relative motion between the particles and the carrier oil, and then the chain would be stretched and deviates an angle θ from the direction of the magnetic field. Meanwhile, the minimum energy principle would allow a uniform distance between the two adjacent particles. Under magnetic field, only the interaction between the two adjacent particles would be considered, and then the restoring force F^H induced by the deformation of a chain can be calculated by taking the derivative of the energy with respect to the displacement. It can be expressed as

$$F^H = \frac{A}{2d}\frac{2\gamma\left(\gamma^2+1\right)-5\gamma(\gamma^2-2)}{(\gamma^2+1)^{3.5}} \tag{2a}$$

$$A = \frac{m^2}{4\pi\mu_f\mu_0 d^3} \tag{2b}$$

$$\gamma = \tan\theta \tag{2c}$$

$$\hat{F}^H = \frac{2dF^H}{A} \tag{2d}$$

where $m = |\boldsymbol{m}|$ and $\boldsymbol{m}$ $(= 3\mu_f\mu_0\beta V\boldsymbol{H}_0)$ is the dipole moment when a particle is placed in the magnetic field $\boldsymbol{H}_0$. $\beta = \frac{(\mu_p-\mu_f)}{(\mu_p+2\mu_f)}$, μ_p and μ_f are the relative permeabilities of the particles and medium, respectively, μ_0 is the vacuum permeability, V $(= \frac{4}{3}\pi R^3)$ is the volume of a particle and γ is the shear strain. $\hat{F}^H$ is defined as the normalized restoring force to study the relationship between the chain restoring force and shear strain under different magnetic fields.

Figure 6 shows the relationship between the normalized restoring force $\hat{F}^H$ and shear strain of a single chain of MR fluids. As seen from the figure, in the initial deformation stage, as the strain increases, $\hat{F}^H$ quickly reaches the peak. The corresponding strain is defined as the yield strain. $\hat{F}^H$ gradually decreases to zero after the yield strain. It should be noted that the yield strain is a constant value independent of the magnetic field.

In addition, **Figure 6** presents the schematic of the test results of the restoring force vs. strain of a single chain (Furst and Gast, 2000). It is seen from **Figure 6**, the yield strain based on the magnetic dipole model is in good agreement with the test results, but after the yield strain, the chain of the MR fluids ruptures and the corresponding restoring force drops to zero sharply. Therefore, it is unreasonable to derive the yield stress of MR fluids based on the assumption of consistent deformation of the chain clusters (i.e., the deformation of all chains of MR fluids is consistent). The yield strain in the dipole model is derived from the derivation of the yield stress. The relationship between the restoring force and strain before the yield strain provides clues for the deformation of the chain clusters.

An assumption is made here during the expansion of a single chain to the entire chain clusters: under magnetic fields, the structural evolution of the chain clusters of MR fluids in the shearing motion is in dynamic equilibrium state from the micro deformation of chain to rupture and reconstruction. Specifically, as seen from the structural evolution of the chain clusters in **Figure 7**, the ferromagnetic particles are polarized into chains in a static state, and the chains of MR fluids are not in an absolute parallel with the magnetic field direction. There are slight differences between the chains. As seen from **Figure 7**, under the shearing motion, the inclination angle of the chains gradually increases, and due to the difference of the initial inclination angle, part of the chains reach the yield strain and then rupture occurs. As the shearing motion advances, more chains rupture to yield stress and the previously ruptured chains reconstruct and form new chains with the adjacent broken chains. The rupture and reconstruction of the chains reach a dynamic equilibrium under the steady-state conditions. In other words, the number of chains ruptured at a certain instant is equal to the amount of chains reconstructed. Thus, it exhibits a stable mechanical property. The non-absolute parallel hypothesis in the static state is verified with the results of MR fluids under electron microscope (De Vicente et al., 2011). Also, the shear tests of a single chain of MR fluids show that the restoring force of the MR fluids abruptly decreases to zero (Furst and Gast, 2000), which

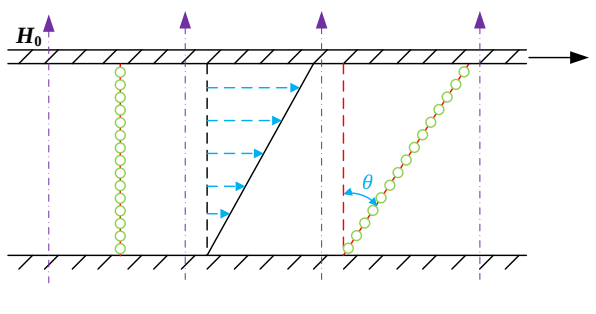

FIGURE 5 | Schematic of the deformation of a single chain of MR fluids in shear mode under magnetic field.

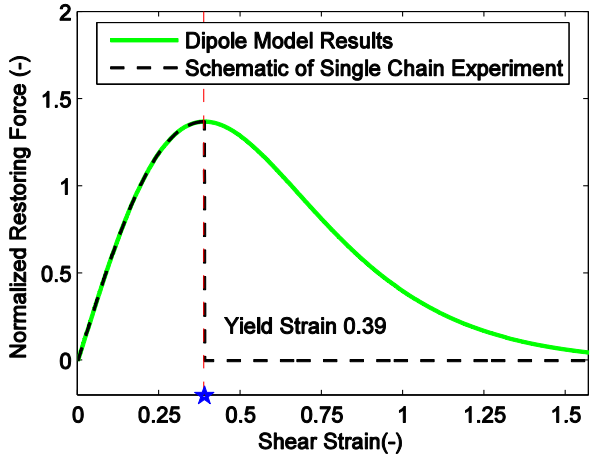

FIGURE 6 | Response of the normalized restoring force vs. shear strain for a single chain of MR fluids.

indicates that the structural evolution of the chain clusters of MR fluids is not consistent. Therefore, the assumption of a dynamic equilibrium of the chain clusters of MR fluids is reasonable. Based on such assumption and the dipole model of the single chain of MR fluids [i.e., equation (2)], **Figure 8** shows the stress-strain relationship of MR fluids under shearing motion. As seen from **Figure 8**, before the yield strain, the stress increases rapidly to the peak with the increase of the overall strain of the chain clusters. When reaches the dynamic equilibrium of the rupture and reconstruction, MR fluids exhibit stable stress characteristics. Consistent with the normalized restoring force-strain plot of a single chain of MR fluids, the yield stress under the evolution of the chain clusters structure is also a magnetic field-independent constant. It should be noted that the yield stress and also the corresponding yield strain of MR fluids and the stable stress are not consistent in numerical values.

Hysteresis Mechanism of MR Fluids Under Reciprocating Displacement Excitation

Based on the stress-strain plot of the chain clusters of MR fluids obtained in **Figure 8**, under the reciprocating displacement excitations, the MR fluids stress increases rapidly and gradually reaches the stable. When the displacement excitation direction changes, the transient shear rate of the MR fluids can be seen as zero. Then the chain ruptured at the previous moment maintains the trend to the parallel direction of the magnetic field, while the unruptured chains maintain the previous shear strain. Therefore, when a new shearing motion starts (i.e., the shear direction changes), the restoring force of part of the chains is opposite to the shear rate, and part of the chains begin to undergo new deformation. Thus, the overall stress direction is opposite to the shear rate. As the shearing motion progresses, the stress of MR fluids gradually approaches a new stability until the new shear strain direction-change point.

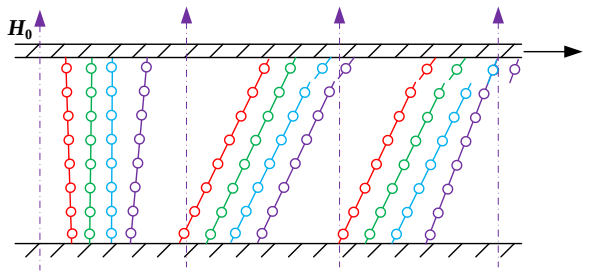

FIGURE 7 | Structural evolution of the multi-chain of MR fluids under magnetic field.

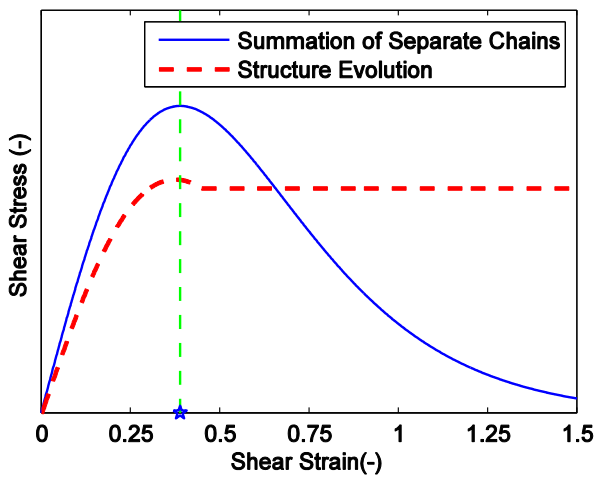

FIGURE 8 | Schematic of the stress vs. strain for multi-chain of MR fluids under dynamic equilibrium state.

Figures 9A,B provide the dipole model-based hysteresis characteristics of MR fluids under reciprocating displacement excitations with large and small amplitudes, respectively. As shown in **Figure 9A**, the simulation results with coupled viscous properties of MR fluids are also provided for comparison. Consistent with **Figures 6**, **8**, the distance from the strain direction-change point to the stress stable point is a magnetic field-independent quantification. It is numerically twice of the yield strain. This agrees with the test results of the hysteresis of MR fluids. However, in the hysteresis characteristics tests of MR fluids, the macroscopic mechanical performance is affected by the friction and compressibility of MR fluids. The yield strain converted from yield displacement is not identical with the theoretical value.

As seen from **Figure 9B**, when the excitation amplitude is small, the excitation strain is insufficient to reach the yield strain, and majority of the chains of MR fluids are not ruptured. The stress generated by the MR effect maintains good coincidence during the reciprocating processes, and its energy consuming characteristics are mainly reflected by the viscosity characteristics of MR fluids. This phenomenon is in good agreement with the results of MR elastomers tests. Under low shear strain amplitudes, the influence of MR effect on the macroscopic properties of MR elastomers is mainly manifested in the stiffness characteristics (Li et al., 2013). The energy consumption characteristics is influence by the MR effect (Lopez-Lopez et al., 2016), so the damping characteristics of MR elastomers is also affected by the excitation amplitudes.

FURTHER EXTENSIONS

Hysteresis in MR Elastomers

The experimental tests and macroscopic modeling analysis indicate that the hysteresis also happened in MR elastomers where the corresponding strain is very small (Tian et al., 2011; Li et al., 2013) and it can be effectively modeled by Bouc-Wen model (Yang et al., 2013; Behrooz et al., 2014). Fortunately, the particles in MR elastomers are fixed in the rubber matrix, and especially for the anisotropic one, the deformation of the chains can be reasonably predicted. Then two properties of the proposed theoretical model can be experimentally verified: (i) the similarity in **Figure 9B** would be checked under quasi-static tests, and (ii) as shown in **Figure 10**, the yield strain can be directly measured in MR elastomers (Tian et al., 2011). Then the comparison of the yield strain would be done between experiment and theory. In MR fluids, it is not easy to measure the yield strain. The yield

displacement is a vague value in the force-displacement plot, and the mixed air or the machining error would be amplified on the value of the yield strain.

Response Time of MR Fluids

Researchers believe that the response time of MR actuators has three main sources: response time of MR fluids, inductance of coil, and eddy current in the coil bobbin (Bai et al., 2018b). Under a fixed applied current, the response time from inductance of MR damper coil and eddy current in the coil bobbin would be a constant value regardless of the excitation velocity. The measured results of response time vs. excitation velocity (Koo et al., 2006) shown in **Figure 11** indicate that with increasing velocity, the response time sharply decreases before the convergence. If we take the stable value as the constant value from inductance of MR actuator coil and eddy current in the coil bobbin, the response time from MR fluids seems to be inverse proportion to the excitation velocity. Hence, we can make a conjecture that instead of the response time, the response displacement is more suitable to interpret the zero-stare response of MR actuators and it would be a constant value. This conjecture is consistent with the constant yield displacement or strain in the hysteresis, which also provides another way to the measurement of the yield strain.

Yield Strain in Theory of Dipole Model

The yield strain in shear mode is derived with the simple dipole model, and it should be noted that the yield strain would be different if another dipole model is used. **Figure 12** presents the comparison of the normalized restoring force response between simple dipole model and local field dipole model (Zhang et al., 2004). Ignoring the difference of the maximum restoring force, the corresponding yield strain is different. In addition, the yield strain is also different related with the working mode (Chen et al., 2017b). The comparison/difference between shear mode and valve mode is presented in **Figure 13**.

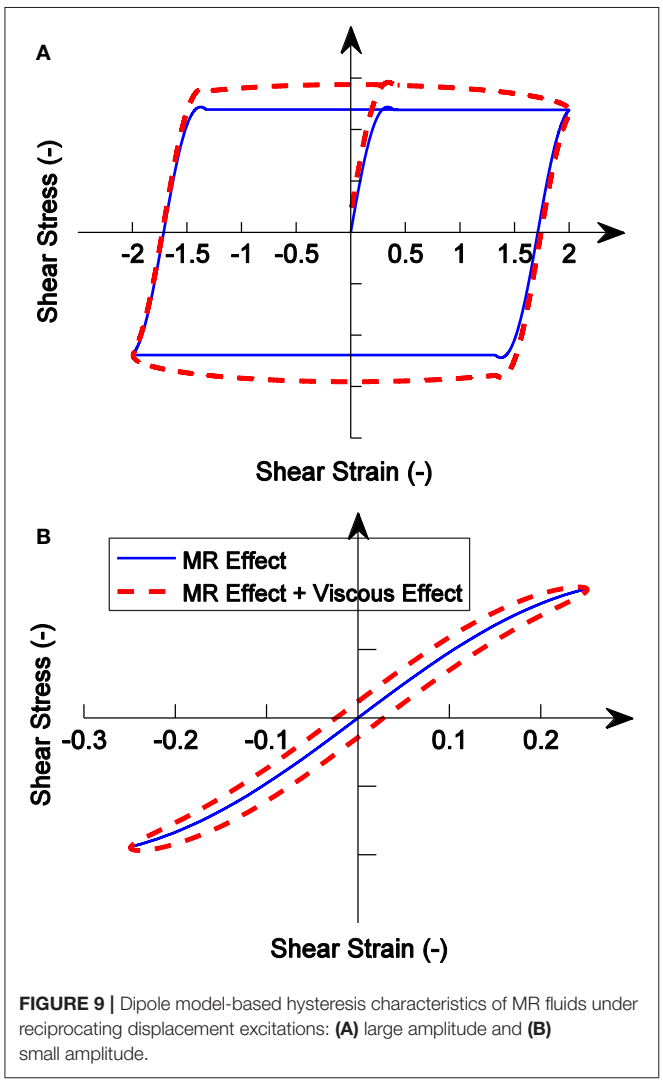

FIGURE 9 | Dipole model-based hysteresis characteristics of MR fluids under reciprocating displacement excitations: **(A)** large amplitude and **(B)** small amplitude.

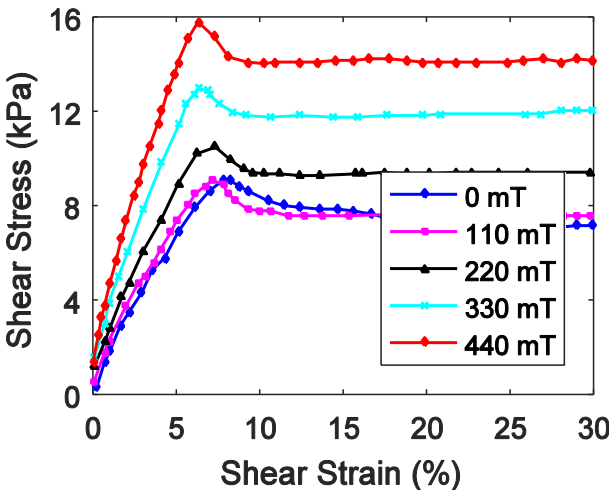

FIGURE 10 | Measured stress-strain curve of MR elastomers (Tian et al., 2011).

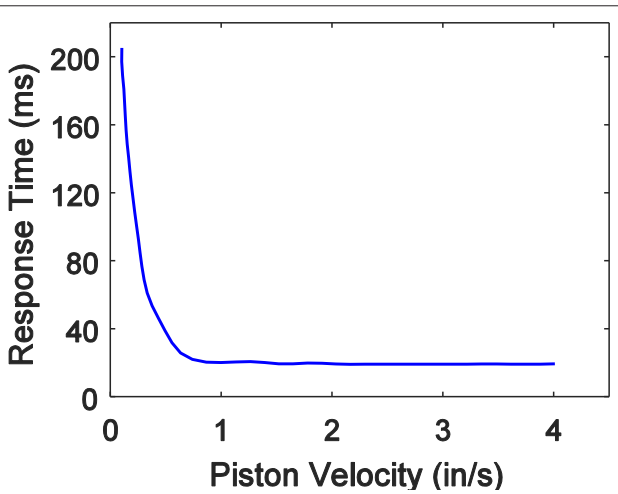

FIGURE 11 | Response time of MR damper in field-on state as a function of piston velocity (Koo et al., 2006).

Discussion

The comparison between the experimental tests (refer to **Figures 2–4** and Figures A1,A2 in **Appendix A**) and the theoretical results (**Figure 9A**) indicates that the hysteresis in force-displacement plot is consistent with each other and satisfies the requirement of rate-independence of hysteresis and the invariance of the experimental yield displacements under different currents and theoretical yield strain under different fields. It is also noted that (i) in the case of the double-rod MR damper, the yield displacement is almost current-dependent, and (ii) in theory, the distance between the direction-change point and yield point is approximately twice of yield strain. Hence, the tested yield displacement can be easily converted to a sort of strain, and the direct comparison of its value with the yield strain from theory would strongly prove the proposed theory. In addition, the tested stable damping force would be converted to a kind of stress, and the comparison with stable stress would provide a clue to the dynamic equilibrium of multi-chain structural evolution. We can realize the precise prediction of the hysteresis of MR fluids and MR fluid-based actuators before experimental tests, as long as we figure out the above.

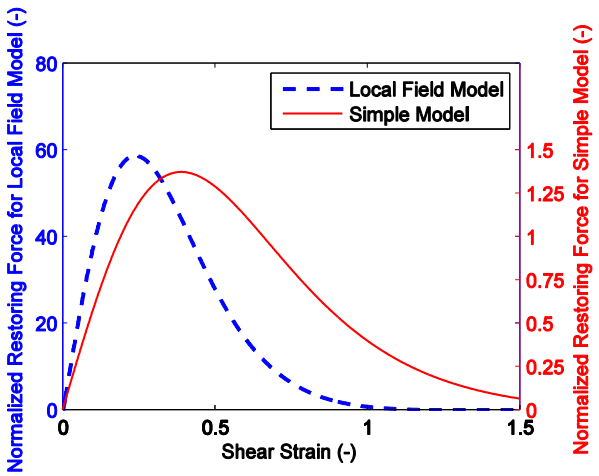

FIGURE 12 | Comparison of normalized restoring force response between simple dipole model and local field dipole model.

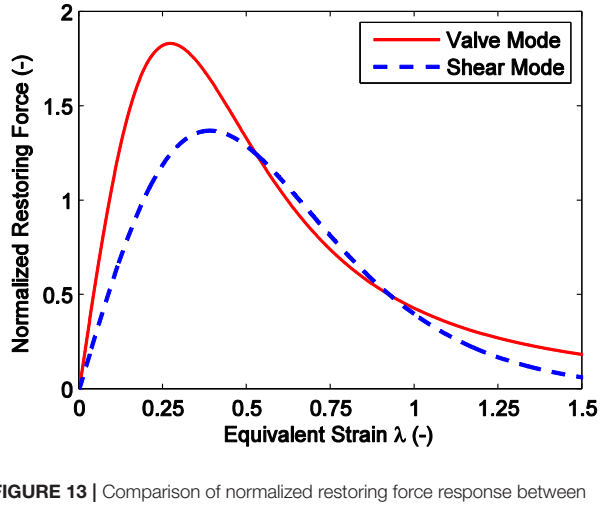

FIGURE 13 | Comparison of normalized restoring force response between shear mode and valve mode (Chen et al., 2017b).

CONCLUSIONS

Aiming at understanding the hysteresis mechanism of MR fluids, a self-developed double-rod MR damper was tested and the hysteresis mechanism of MR fluids using a dipole model was theoretically analyzed and explained. The double-rod MR damper under triangle displacement excitations were tested and a normalization concept was applied, to eliminate the compressibility of the accumulator and the influence of the viscous damping on macroscopic hysteresis characteristics. Test results, especially the uniformity of yield displacements under different excitation conditions, indicate that the hysteresis characteristics of MR fluids are mainly reflected in the force-displacement plot. Based on the theory of the dipole model and the dynamic equilibrium hypothesis of chain clusters rupture and reconstruction, the hysteresis mechanism of MR fluids under different excitation amplitudes was derived. Consistent with the experimental results, the theoretically derived yield strain is also independent of the excitation conditions. The theoretically derived yield strain shows difference in the magnitude of the strain corresponding to the yield displacement, due to the influence of other factors in the tests of the hysteresis characteristics of MR fluids. But the consistent rate-independence characteristics provide fundamentals for the further work on the MR effect mechanism. The reasonable deductions on the response time of MR fluids as well as the stress-strain properties of MR elastomers are helpful for the related research or applications.

From the view of future research on the MR effect mechanism, three significant issues are worthy of in-depth study. (i) Detailed physical process for portraying and explaining the MR effect mechanism should be mathematically formulated to in full-scale verify the deduction of this work, which was using only a preliminary analytical model. (ii) Tests of the yield displacements of MR fluids when filled in gaps with different widths but an identical cross-sectional area can be conducted to verify the deduction of this work: smaller gap width, smaller yield displacement. (iii) Tests of the yield strain of MR elastomers, especially the anisotropic ones, can be done to verify the deduction on the MR elastomers in this work.

DATA AVAILABILITY

The datasets generated for this study are available on request to the corresponding author.

AUTHOR CONTRIBUTIONS

X-XB conceived the conception, investigated the technical background, and coordinated the study, and revised the manuscript. PC carried out the modeling and computation work, and drafted the manuscript.

ACKNOWLEDGMENTS

The authors wish to acknowledge the Key Research and Development Projects of Anhui Province (Grant No. 1704E1002211) for its support of this research.

SUPPLEMENTARY MATERIAL

The Supplementary Material for this article can be found online at: https://www.frontiersin.org/articles/10.3389/fmats.2019.00036/full#supplementary-material

REFERENCES

Bai, X. X., Cai, F. L., and Chen, P. (2019). Resistor-capacitor (RC) operator-based hysteresis model for magnetorheological (MR) dampers. *Mech. Syst. Signal Process.* 117, 157–169. doi: 10.1016/j.ymssp.2018.07.050

Bai, X. X., Chen, P., and Qian, L. J. (2015). Principle and validation of modified hysteretic models for magnetorheological dampers. *Smart Mater. Struct.* 24:085014. doi: 10.1088/0964-1726/24/8/085014

Bai, X. X., Deng, X. C., and Shen, S. (2018b). Controllability of magnetorheological shock absorber: II. Testing and analysis. *Smart Mater. Struct.* 28:015023. doi: 10.1088/1361-665X/aaf099

Bai, X. X., Hu, W., and Wereley, N. M. (2013). Magnetorheological damper utilizing an inner bypass for ground vehicle suspensions. *IEEE Trans. Magn.* 49, 3422–3425. doi: 10.1109/TMAG.2013.2241402

Bai, X. X., Shen, S., Wereley, N. M., and Wang, D. H. (2018a). Controllability of magnetorheological shock absorber: I. insights, modeling and simulation. *Smart Mater. Struct.* 28:015022. doi: 10.1088/1361-665X/aaf072

Behrooz, M., Wang, X., and Gordaninejad, F. (2014). Modeling of a new semi-active/passive magnetorheological elastomer isolator. *Smart Mater. Struct.* 23:045013. doi: 10.1088/0964-1726/23/4/045013

Bossis, G., and Lemaire, E. (1991). Yield stresses in magnetic suspensions. *J. Rheol.* 35, 1345–1354. doi: 10.1122/1.550234

Chen, P., Bai, X. X., Qian, L. J., and Choi, S. B. (2017a). A new hysteresis model based on force–displacement characteristics of magnetorheological fluid actuators subjected to squeeze mode operation. *Smart Mater. Struct. 26*:06LT01. doi: 10.1088/1361-665X/aa6ec8

Chen, P., Bai, X. X., Qian, L. J., and Choi, S. B. (2018). An approach for hysteresis modeling based on shape function and memory mechanism. *IEEE/ASME Trans. Mechatr.* 23, 1270–1278. doi: 10.1109/TMECH.2018.2833459

Chen, P., Qian, L. J., Bai, X. X., and Choi, S. B. (2017b). Velocity-dependent characteristics of magnetorheological fluids in squeeze mode considering the hydrodynamic and the magnetic field interactions. *J. Rheol.* 61, 455–465. doi: 10.1122/1.4978594

De Vicente, J., Klingenberg, D. J., and Hidalgo-Alvarez, R. (2011). Magnetorheological fluids: a review. *Soft Matter* 7, 3701–3710. doi: 10.1039/c0sm01221a

Furst, E. M., and Gast, A. P. (2000). Micromechanics of magnetorheological suspensions. *Phys. Rev. E* 61, 6732–6739. doi: 10.1103/PhysRevE.61.6732

Guo, P., Guan, X., and Ou, J. (2014). Physical modeling and design method of the hysteretic behavior of magnetorheological dampers. *J. Intell. Mater. Syst. Struct.* 25, 680–696. doi: 10.1177/1045389X13500576

Jolly, M. R., Carlson, J. D., and Munoz, B. C. (1996). A model of the behaviour of magnetorheological materials. *Smart Mater. Struct.* 5:607. doi: 10.1088/0964-1726/5/5/009

Klingenberg, D. J., and Zukoski, I. V., C. F. (1990). Studies on the steady-shear behavior of electrorheological suspensions. *Langmuir* 6, 15–24. doi: 10.1021/la00091a003

Koo, J. H., Goncalves, F. D., and Ahmadian, M. (2006). A comprehensive analysis of the response time of MR dampers. *Smart Mater. Struct.* 15:351. doi: 10.1088/0964-1726/15/2/015

Li, Y., Li, J., Li, W., and Samali, B. (2013). Development and characterization of a magnetorheological elastomer based adaptive seismic isolator. *Smart Mater. Struct.* 22:035005. doi: 10.1088/0964-1726/22/3/035005

Lopez-Lopez, M. T., Rodriguez-Arco, L., Zubarev, A., Kuzhir, P., Iskakova, L., and Gonzalez-Caballero, F. (2016). N-like rheograms of concentrated suspensions of magnetic particles. *J. Rheol.* 60, 267–274. doi: 10.1122/1.4942232

Sapinski, B., Rosół, M., Jastrzebski, Ł., and Gołdasz, J. (2017). Outlook on the dynamic behavior of an magnetorheological squeeze-mode damper prototype. *J. Intell. Mater. Syst. Struct.* 28, 3025–3038. doi: 10.1177/1045389X17704919

Shou, M., Liao, C., Zhang, H., Li, Z., and Xie, L. (2018). Modeling and testing of magnetorheological energy absorbers considering inertia effect with non-averaged acceleration under impact conditions. *Smart Mater. Struct.* 27:115028. doi: 10.1088/1361-665X/aae6a0

Si, H., Peng, X., and Li, X. (2008). A micromechanical model for magnetorheological fluids. *J. Intell. Mater. Syst. Struct.* 19, 19–23. doi: 10.1177/1045389X06072488

Tao, R. (2001). Super-strong magnetorheological fluids. *J. Phys.* 13:R979. doi: 10.1088/0953-8984/13/50/202

Tian, T. F., Li, W. H., Alici, G., Du, H., and Deng, Y. M. (2011). Microstructure and magnetorheology of graphite-based MR elastomers. *Rheol. Acta* 50, 825–836. doi: 10.1007/s00397-011-0567-9

Visintin, A. (2013). *Differential Models of Hysteresis (Vol. 111).* Berlin: Springer Science & Business Media.

Wang, D. H., and Liao, W. H. (2011). Magnetorheological fluid dampers: a review of parametric modelling. *Smart Mater. Struct.* 20:023001. doi: 10.1088/0964-1726/20/2/023001

Wang, X., and Gordaninejad, F. (2007). Flow analysis and modeling of field-controllable, electro-and magneto-rheological fluid dampers. *J. Appl. Mech.* 74, 13–22. doi: 10.1115/1.2166649

Weber, F. (2013). Bouc–Wen model-based real-time force tracking scheme for MR dampers. *Smart Mater. Struct.* 22:045012. doi: 10.1088/0964-1726/22/4/045012

Xu, F. H., Xu, Z. D., Zhang, X. C., Guo, Y. Q., and Lu, Y. (2016). A compact experimentally validated model of magnetorheological fluids. *J. Vib. Acoust.* 138:011017. doi: 10.1115/1.4031757

Yang, J., Du, H., Li, W., Li, Y., Li, J., Sun, S., et al. (2013). Experimental study and modeling of a novel magnetorheological elastomer isolator. *Smart Mater. Struct.* 22:117001. doi: 10.1088/0964-1726/22/11/117001

Yu, J., Dong, X., and Zhang, Z. (2017). A novel model of magnetorheological damper with hysteresis division. *Smart Mater. Struct.* 26:105042. doi: 10.1088/1361-665X/aa87d6

Zhang, X. Z., Gong, X. L., Zhang, P. Q., and Wang, Q. M. (2004). Study on the mechanism of the squeeze-strengthen effect in magnetorheological fluids. *J. Appl. Phys.* 96, 2359–2364. doi: 10.1063/1.1773379

Conflict of Interest Statement: PC is employed by the company Guangzhou Automobile Group, China.

The remaining author declares that the research was conducted in the absence of any commercial or financial relationships that could be construed as a potential conflict of interest.

frontiers in Materials

ORIGINAL RESEARCH
published: 28 February 2019
doi: 10.3389/fmats.2019.00027

Performance Evaluation of a Magnetorheological Fluid Damper Using Numerical and Theoretical Methods With Experimental Validation

Ali K. El Wahed and Hao Chen Wang*

Mechanical Engineering, University of Dundee, Dundee, United Kingdom

Magnetorheological (MR) fluids which can exhibit substantial reversible rheological changes under the excitation of external magnetic fields, have enabled the construction of many novel and robust electromechanical devices in recent years. Generally, Bingham plastic model is utilized for the estimation of the characteristics of MR fluids. However, when the geometry and design of the MR device as well as the rheological conditions of the fluid itself become complicated due to the engineering application requirements, the accuracy of Bingham plastic model, which simplifies the relation between the fluid shear stress, and shear rate into a linear function, is degraded. In this paper, a multi-degree-of-freedom (MDOF) magnetorheological fluid damper with a novel ball-and-socket structure was developed, which was aimed to enhance the human shoulder rehabilitation treatment. The performance of the proposed smart device with its complex design was estimated numerically using a finite element method (FEM) with a Herschel-Bulkley model and theoretically with a model that is based on a Bingham plastic fluid characteristics. The performance of the developed damper was validated experimentally using a dedicated testing facility for various input conditions. It was found that the FEM simulations with the Herschel-Bulkley model showed a better agreement with the experimental results in comparison with the theoretical predictions which were somewhat degraded with the employed Bingham plastic model.

Keywords: MDOF smart damper, magnetorheological fluids, Herschel-Bulkley model, Bingham plastic model, finite element modeling

OPEN ACCESS

Edited by:
Seung-Bok Choi,
Inha University, South Korea

Reviewed by:
Tianhong Yan,
China Jiliang University, China
Jianbo Yin,
Northwestern Polytechnical University, China

****Correspondence:***
Ali K. El Wahed
a.elwahed@dundee.ac.uk

Specialty section:
This article was submitted to Smart Materials, a section of the journal Frontiers in Materials

Received: *05 December 2018*
Accepted: *08 February 2019*
Published: *28 February 2019*

Citation:
El Wahed AK and Wang HC (2019) Performance Evaluation of a Magnetorheological Fluid Damper Using Numerical and Theoretical Methods With Experimental Validation. Front. Mater. 6:27. doi: 10.3389/fmats.2019.00027

INTRODUCTION

Magnetorheological (MR) fluids belong to the general area of smart materials, which consists of micron-size magnetisable particles suspended in non-magnetic oil based liquid carrier. When the magnetic field is applied, the suspended particles become magnetically polarized, and align themselves into chains, which increases the apparent viscosity and yields stress of the MR fluid. This fast and reversable MR fluid rheological changes can be controlled by the applied magnetic field intensity and therefore, a continuously variable fluid characteristics could be realized. As a result, these smart properties have enabled MR fluids to be utilized in the construction of various novel electromechanical devices (El Wahed and McEwan, 2011).

MR fluids have been utilized into different modes of operation, which are shear (Wereley et al., 2007), flow (Wang and Gordaninejad, 2000), or squeeze (El Wahed and Balkhoyor, 2015) modes.

More recently, two new modes have been reported which are the pinch (Goncalves and Carlson, 2009) and mixed (El Wahed and Balkhoyor, 2016) modes of operation. The most successful exploitation of the MR fluids has been realized in the area of vibration control (Chrzan and Carlson, 2001) with a specific successful commercialization in the automotive and structural industries when some passenger cars and buildings are now equipped with smart shock absorbing systems (Nguyen and Choi, 2009) and large seismic dampers (Dyke et al., 1998), respectively. In addition, rotary smart fluid devices, such as clutches or brakes, have been developed (Olabi and Grunwald, 2007). Currently, rotary MR fluid devices exist primarily in two different configurations, namely, disc type and cylindrical type, which permit one degree-of-freedom (DOF) movements. As a result, these devices are not useful if they are proposed to control the joints of an upper limb rehabilitation training machines, since the human arm is capable of handling multi degrees-of freedom (MDOF) motions along a multiple-axis system as it benefits from a flexibility offered by the natural arm joints with a ball-and-socket structure. For example, the arm could be raised above the head, lowered beside the body, extended from the body or moved forward across the body. In addition, the arm rotates in a 360-degree circle when held to the side. Consequently, any developed orthotic device aimed for the rehabilitation of human upper limbs should have similar flexibility at its joints. Accordingly, a ball-and-socket configuration was chosen by the authors to design a novel type of a smart MR damper (El Wahed and Balkhoyor, 2018), **Figure 1A**, which should allow movements that are similar to those offered by the human shoulder joint, **Figure 1B**. Accordingly, the controllable rheological properties of the MR fluid that fills the gap between the ball and socket components should enable the smart damper to offer the pre-defined kinematics and force constraints required at the joints of the upper-limb rehabilitation orthosis. Therefore, this novel damper design, which is proposed to be incorporated at the joints of the rehabilitation device, should maximize the working function and reduce the overall size of current rehabilitation training systems.

The comparative performance of the ball-and-socket damper using numerical, theoretical, and experimental procedures is reported in this article. In order to estimate the characteristics of the MR fluid in the developed device, a proper relation between the shear stress and shear rate of the MR fluid should be addressed. This relation is assumed to be linear by the Bingham plastic model which has widely been used in recent years by numerous research teams for the theoretical modeling of magnetorheological fluids (Ghaffari et al., 2014). However, the shear thinning or shear thickening characteristics of MR fluids are poorly modeled by the Bingham plastic model (Wang and Liao, 2011). One major reason for this modeling shortage is that the Bingham plastic model only includes two parameters which assumes a linear fluid shear stress/shear rate relation, while the experimental results indicate that the slope of the fluid characteristics curve changes with the variation of the shear rate (Zubieta et al., 2009). Consequently, when the MR device design and the rheological conditions of the MR fluid become complicated due to the requirements of the engineering application, the Bingham plastic model was deemed to be insufficient to accurately predict the performance of the MR fluid (Zhu et al., 2012). As a result, other fluid models, such as the bi-viscous model (El Wahed, 2011), were utilized for the efficient modeling of smart fluids characteristics.

In this study, the resistive torque of the ball-and-socket damper was first estimated using a theoretical model based on the assumption of a Bingham plastic fluid characteristics for different input velocity inputs. Subsequently the device torque performance was numerically investigated using finite element analyses, which were performed using Ansys Fluent computer code with a Herschel-Bulkley fluid model. Furthermore, a dedicated experimental facility was then utilized to validate the device performance under the same sets of input conditions.

BALL-AND-SOCKET DAMPER PERFORMANCE EVALUATION PROCEDURES

The new smart ball-and-socket damper was designed with an opening angle (from one socket edge to another) of 126°. The MR fluid is proposed to fill the gap between the ball and socket components to control the impedance of the damper, which is proportional to the electromagnetic field intensity generated by the electromagnetic coil element that is imbedded inside the socket component, as shown in **Figure 2**. The overall size of the device was designed to be ∼150 mm in diameter. Due to the compact size of the electromagnetic circuit of the smart damper, which was designed and optimized using electromagnetic finite element methods, the electromagnetic coil element only requires few volts to generate the magnetic field required for the excitation of the MR fluid and therefore, the smart device is considered to be electrically safe in the normal rehabilitation training environment.

In the authors' previous study (Wang and El Wahed, 2018), it was found that the early design of the ball-and-socket damper was capable to deliver a maximum torque output of about 26 Nm using Lord Corporation commercial MR fluid, type MRF122-2ED under a magnetic flux density excitation of about 1.1 Tesla and an input angular velocity of about 1 rad/s. Accordingly, this fluid was employed in the current investigation.

In the present theoretical model, the total damping torque T_t delivered by the smart ball-and-socket damper was assumed to consist of three components, which are the controllable field-dependent torque, the viscous friction torque and the mechanical friction torque (El Wahed and Balkhoyor, 2018). The shear stress, τ of the MR fluid in the present model was accounted for using the Bingham plastic fluid model which is given by:

$$\tau = \tau_y(H) + \eta\gamma \tag{1}$$

where η and γ are the fluid dynamic viscosity and shear rate, respectively whilst $\tau_y(H)$ is the fluid yield stress which depends on the magnetic field intensity H. Accordingly, the total damping

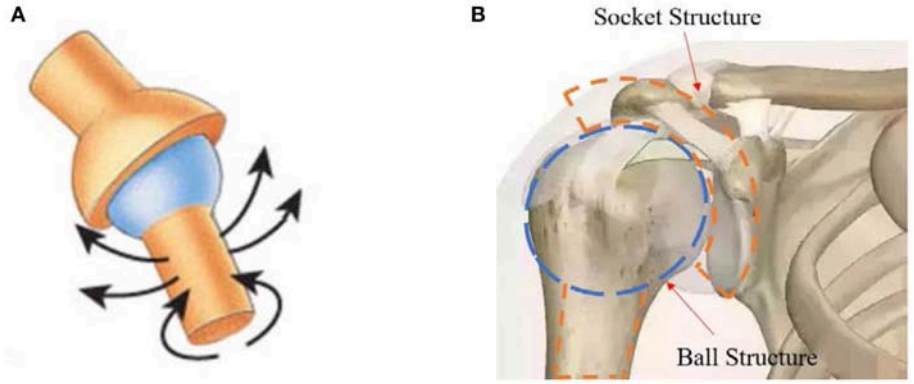

FIGURE 1 | Ball-and-socket damper **(A)** and human shoulder joint **(B)**.

torque of the device was derived into the following equation:

$$T_t = \pi r^3 \tau_y(H)(\varphi - \sin\varphi\cos\varphi) + \frac{8\eta\pi r^4\omega}{3h}\sin^4\left(\frac{\varphi}{2}\right)(\cos\varphi + 2) + T_f \quad (2)$$

where r, ω, and h are the ball radius, input angular velocity and MR fluid gap size, respectively whilst φ is the socket angle which is measured from the lower end (6 o'clock) to one of the socket ends. T_f is the mechanical frictional torque, which was measured experimentally in this study and will be detailed at the end of this section. The fluid temperature was assumed to be maintained at 40°C whilst the density and viscosity of the employed fluid, which are required to complete the theoretical modeling as well as the FEM simulations of the new damper, were provided as 2,380 kg/m^3 and 70 mPa.s, respectively (Adhesives Coatings Vibration Motion Control Sensing Magnetically Responsive Technologies, 2018). The yield stress of the adopted MR fluid as a function of the magnetic flux density is presented in **Figure 3** (Adhesives Coatings Vibration Motion Control Sensing Magnetically Responsive Technologies, 2018). Using the estimated yield stress values (**Figure 3**) and Equation (2) together with the measured mechanical frictional torque, T_f, the total damping torque of the damper was then estimated theoretically for a range of magnetic flux densities of up to 0.7 Tesla and for a ball angular speed of 10 RPM.

A numerical technique was then developed to estimate the performance of the developed ball-and-socket damper, which was based on finite element methods (FEM) that were performed using Ansys Fluent computer code. A model representing the fluid volume filling the gap between the ball and socket components of the damper was first created using SolidWorks CAD software, and was then exported into the Ansys Fluent environment. The magnetic flux density is assumed to be uniformly distributed along the fluid gap whilst the yield stress of the MR fluid required for the FEM simulations was again derived from the results presented in **Figure 3**. The fluid volume was meshed with a minimum element size of 3.5×10^{-4} m. As part of the boundary conditions set up for these simulations, the fluid volume that is adjacent to the ball component was assumed to move at the ball angular speed (sliding motion), while the surface which is in contact with the socket is assumed to be stationary (no-slip condition). The top horizontal surface of the fluid at the socket opening was also considered as a stationary wall since it is in contact with a large lip-seal that is designed to seal the fluid gap between the ball and socket. In the current FEM settings, the stationary wall boundary condition was realized when its velocity is set to zero along the three coordinates, while the moving wall condition was achieved when the applied angular speed was set in the direction along which the torque is estimated. Since the applied angular speed is low, the MR fluid flow inside the gap initiated by the ball motion was assumed to be steady, laminar, and incompressible. In addition, thermal interaction inside the MR fluid was ignored and therefore, the flow was assumed to be under adiabatic condition. The minimum pressure magnitude was also assumed to be above the fluid vapor pressure so that any cavitation was excluded from the analysis.

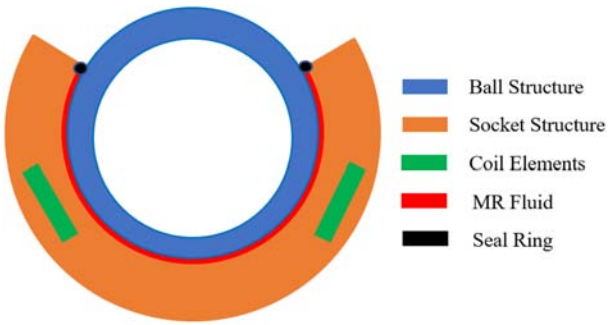

FIGURE 2 | Section view showing the main elements of the new smart damper.

The MR fluid behavior was characterized using the Ansys built-in Herschel-Bulkley model which is represented by the following shear stress equation (Zubieta et al., 2009):

$$\tau = \tau_y(H) + k\gamma^n \quad (3)$$

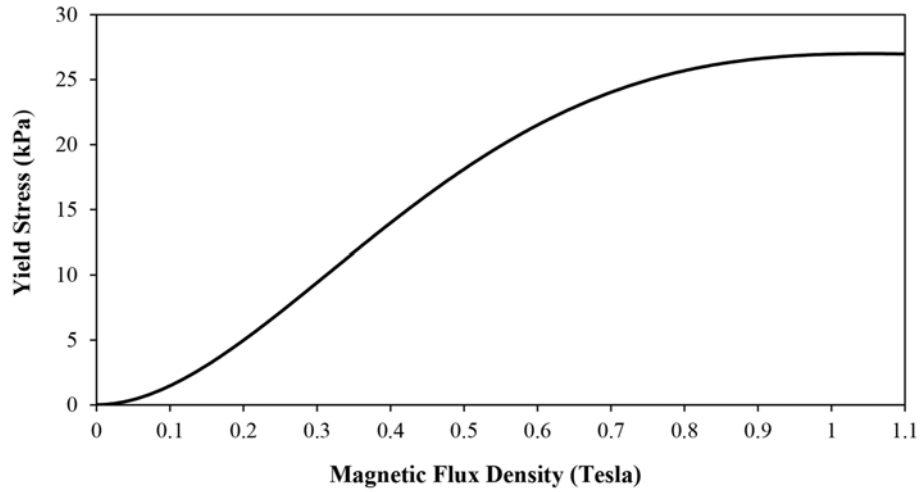

FIGURE 3 | Yield stress vs. magnetic field density for Lord Corp MRF122-2ED fluid.

where k is referred to as the consistency index and n is the pseudoplastic index. The relationship between the shear stress and shear rate estimated by the Bingham plastic model is shown in **Figure 4** for a magnetic flux density of 0.5 Tesla. It can be seen that the changes in the shear stress values over the shear rate range were small. This is ascribed to the fact that the fluid viscosity of 70 mPa.s, which was assumed in this model, was small and therefore, the resulting shear stress does not see dramatic changes when the shear rate changes. The lack of response in the fluid shear stress to variations in the shear rate usually affect the accuracy of the simulated performance of the MR fluid device and hence, degrade its agreement with the experimental results. However, unlike the Bingham plastic model, the shear stress-shear rate dependency is represented more accurately by the Herschel-Bulkley model through the added pseudoplastic and consistency indexes which are used to describe the shear thinning/shear thickening effects of the MR fluid. In this study, the well-recognized analysis (Zubieta et al., 2009), which was done on the same MR fluid employed in the current investigation (MRF122-2ED), was utilized for the quotation of the n and k indexes under different operation conditions. This enabled the estimation of the shear stress-shear rate characteristics of the employed MR fluid using the Herschel-Bulkley model, which are also presented in **Figure 4** and compared with those estimated using the Bingham plastic model for an applied magnetic flux density of 0.5 Tesla.

In order to experimentally verify the performance of the smart damper, a dedicated testing facility was designed and built, which comprises an AC motor with its associated speed controller type IMO Jaguar, model CUB8A-1 to supply the input rotational motion to the damper, TorqueSense Technology, model RWT320 speed and torque transducers and a magnetic particle brake type Warner Electric, model MPB240M-24-24 to apply and simulate resistive torques at the output of the smart damper, as shown in **Figure 5**.

In addition, a National Instruments analog-to-digital converter, model NI9205 in conjunction with a cDAQ-9172 CompactDAQ USB chassis capable of simultaneous sampling, which was controlled by a National Instruments data acquisition software, type LabVIEW running on an IBM compatible personal computer, was used to collect and record the data from the sensors and power supplies used to energize the smart damper and the magnetic particle brake. In order to allow a continuous supply of power to the electromagnetic coil of the smart damper while it is under a rotational input operation, a special arrangement was designed which consists of a plastic disc to which two copper rings were attached. The two copper rings were electrically insulated from each other and the electrical resistance between them was measured using a digital multimeter, which was found to be in access of 5 kOhm. This resistance was deemed to be high enough to prevent any charge leakage between the two copper electrodes across the plastic shank of the disc. The plastic disc was fixed on the rotating shaft just upstream the smart damper, **Figure 5**, and the damper's coil wires were soldered to the two copper rings. The connection of the power supply to the copper rings was achieved using two carbon brush mechanisms which were equipped with tensioning springs to ensure a continues contact with the copper rings.

The output speed and torque of the smart damper are expected to change in response to both the level of the electrical current supplied to the electromagnetic coil element of the damper and the magnitude of the resistance applied by the magnetic particle brake. In order to allow a direct comparison between the braking torque results measured experimentally and those estimated theoretically and numerically using Equation (2) and the FEM procedure, respectively the relationship between the magnetic field density generated by the damper's magnetic circuit and its coil energizing current was first established using a 3-D finite element electromagnetic approach that was executed using Ansys Workbench software. In these simulations, coil energizing currents similar to those used in the experimental assessments of the smart damper were assumed and the corresponding average magnetic field

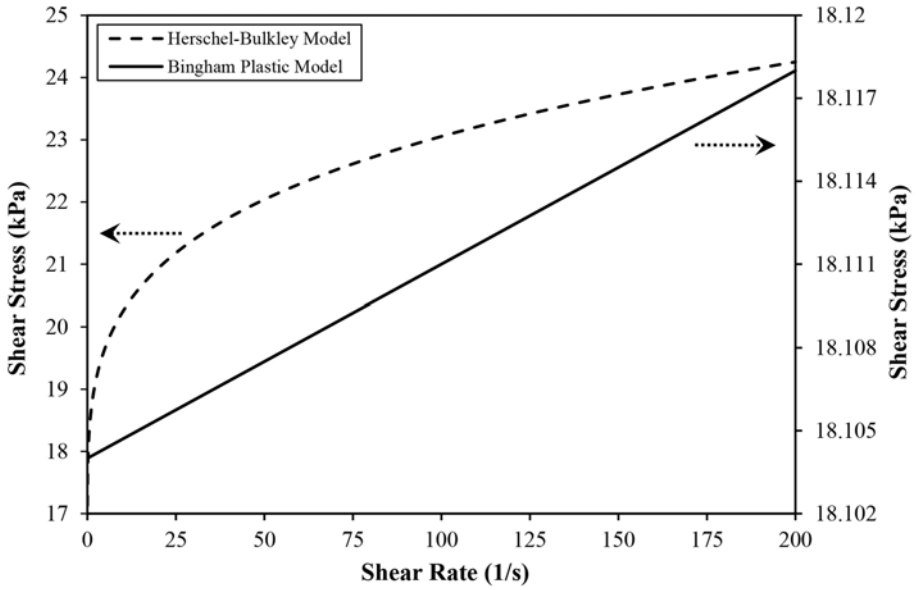

FIGURE 4 | Shear stress vs. shear rate of MR fluid type MRF122-2ED based on Bingham Plastic and Herschel-Bulkley models for a magnetic flux density of 0.5 Tesla.

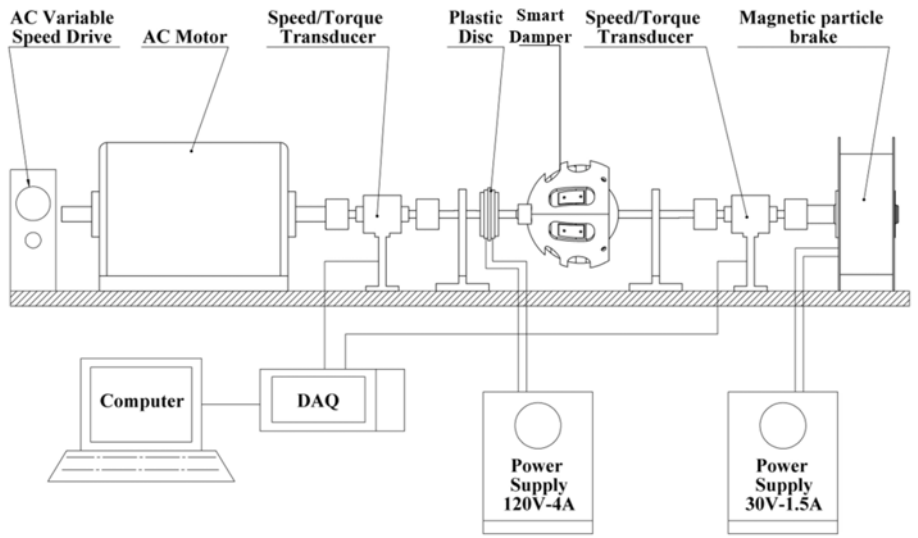

FIGURE 5 | Schematic diagram of the experimental testing rig.

density values along an imaginary path spanning the MR fluid gap from one socket end to the other were estimated. **Figure 6** shows the magnetic field density distribution along this imaginary median path inside the MR fluid gap of the ball-and-socket damper for a coil energizing current value of 1.0 A.

Figure 7 shows the variation of the average magnetic field density simulated inside the MR fluid gap of the smart damper as a function of the damper's coil energizing current in the range between 0.25 and 2.1 A. It can be seen that a maximum energizing current of 2.1 A supplied to the electromagnetic coil of the smart damper produced an average magnetic field density in the MR fluid gap of about 1 Tesla, which is the magnetic excitation level under which the employed MR fluid becomes saturated (Adhesives Coatings Vibration Motion Control Sensing Magnetically Responsive Technologies, 2018).

The simulated data presented in **Figure 7** enabled the application of coil energizing currents at the required magnetic field densities and the corresponding braking torque values of the smart ball-and-socket damper were measured for an input speed of 10 RPM. The measured torque was limited to a maximum of 20 Nm which is the maximum range of the employed torque

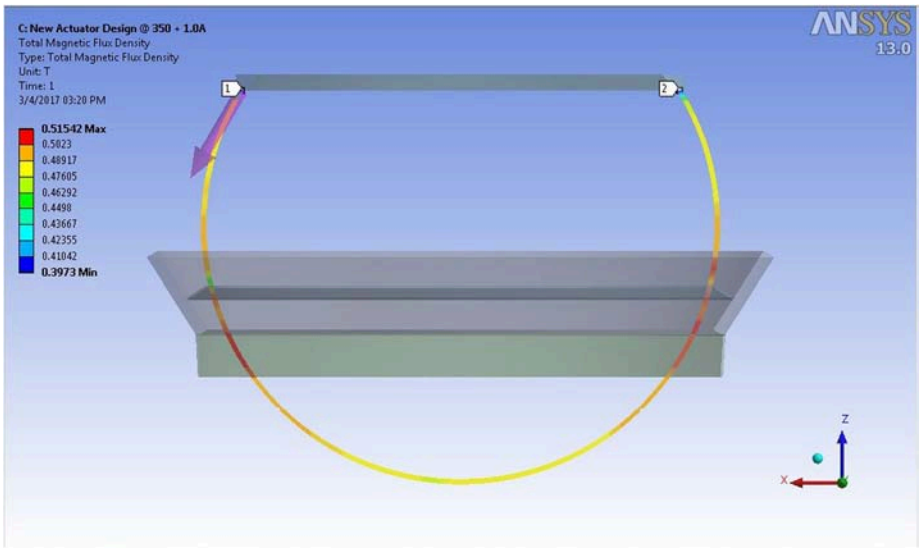

FIGURE 6 | Magnetic field density distribution along an imaginary median path inside the MR fluid gap of the ball-and-socket damper for a coil current of 1.0 A.

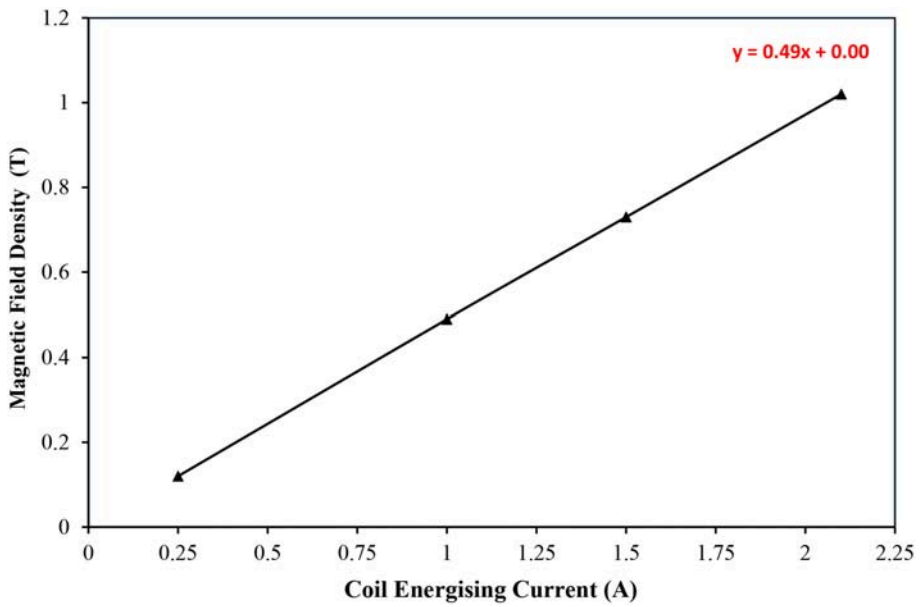

FIGURE 7 | Variation of average magnetic field density simulated inside the MR fluid gap of the smart damper as a function of damper's coil energizing current.

transducers. This equipment limitation made it difficult to extend the tests beyond magnetic flux densities of about 0.6 Tesla otherwise the measured torques become higher than the maximum capability of the employed torque transducers. In addition, it is worth mentioning that velocities around 10 RPM did not produce any real difference in the measured torque values, which is expected under such low velocity range that is typical of the aimed rehabilitation application of the developed smart device. However, it was thought that despite the above hardware limitation, the reported results would still provide a useful insight into the performance of the developed device and its aimed rehabilitation application.

Finally, the mechanical friction torque, T_f, which is mainly caused by the friction between the ball and the lip-seal components of the smart damper, was measured experimentally. In this test, the socket component was fixed to a sturdy bench while a metallic shaft was attached to the center of the ball component and set at a horizontal position using a spirit level tool. Whilst the smart damper is not energized, the ball shaft was gradually loaded with static weights, **Figure 8**, until the ball

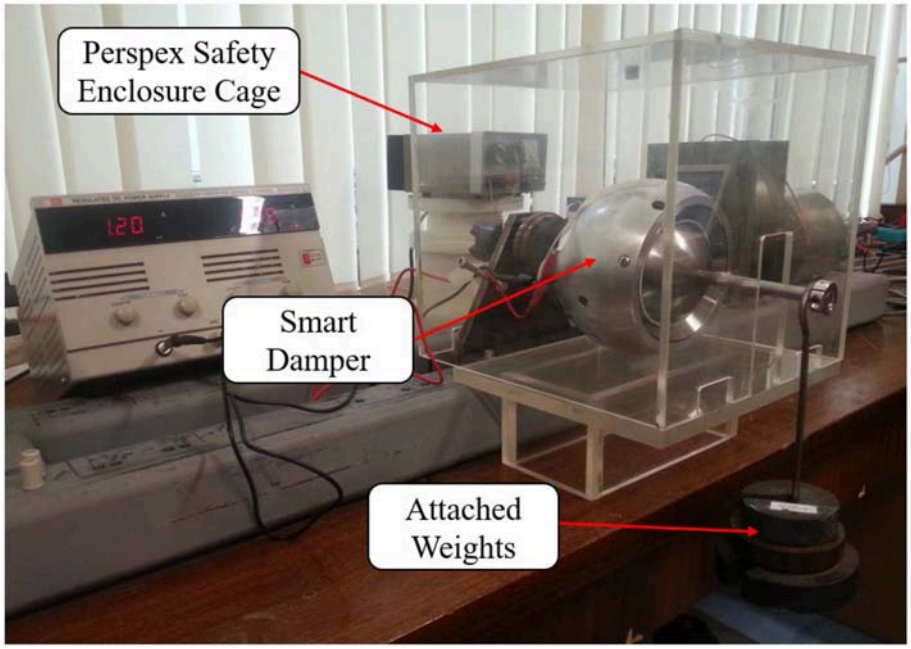

FIGURE 8 | Test set-up for the evaluation of the mechanical friction torque.

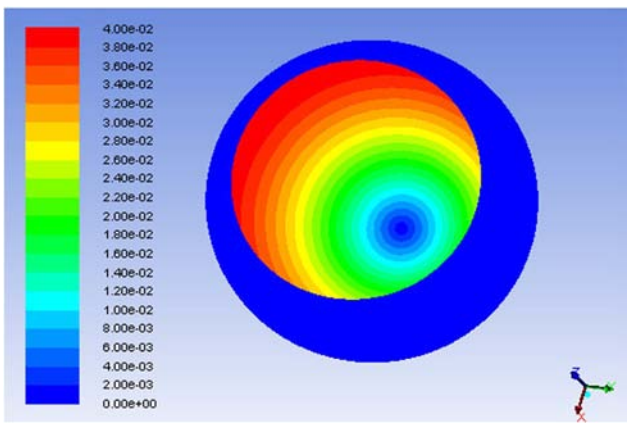

FIGURE 9 | Isometric view of the velocity contour throughout the MR fluid volume for 0.3 Tesla fluid magnetic excitation and 10 RPM ball angular velocity.

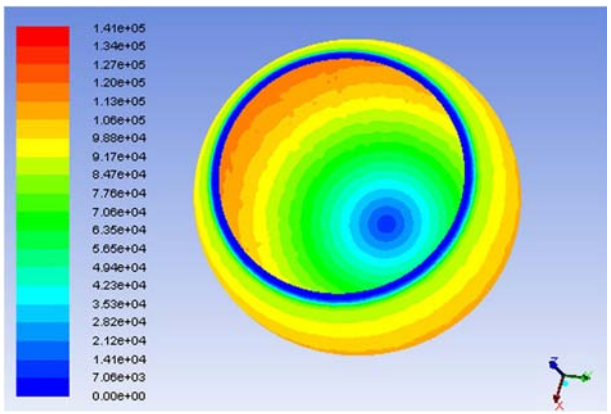

FIGURE 10 | Shear stress distribution along the MR fluid volume for 0.3 Tesla fluid magnetic excitation and 10 RPM ball angular velocity.

rotates, indicating that the damper's mechanical resistance is breached. This test was repeated several times and the weight that caused the ball rotation was used to estimate the damper's mechanical torque which was found to be about 1.16 Nm. This mechanical torque value was added to the total damping torques estimated theoretically (Equation 2) and also to those simulated numerically (FEM model).

RESULTS AND DISCUSSION

The theoretical, numerical, and experimental procedures were then executed for the intended yield stresses which are related to the magnetic field density levels through their relationship presented in **Figure 3**. **Figure 9** shows an isometric view of the velocity contour simulated in the fluid gap under a magnetic excitation of 0.3 Tesla when the ball was allowed to rotate with an angular speed of 10 RPM about its z axis. It can be seen that the fluid velocity varies from zero on the socket side to its maximum value on the ball side. In addition, the velocity appears to increase from the center of the socket where the fluid appears to be stationary to its maximum nearby the socket opening.

For the same magnetic field excitation and input velocity conditions, the shear stress distribution was simulated along the

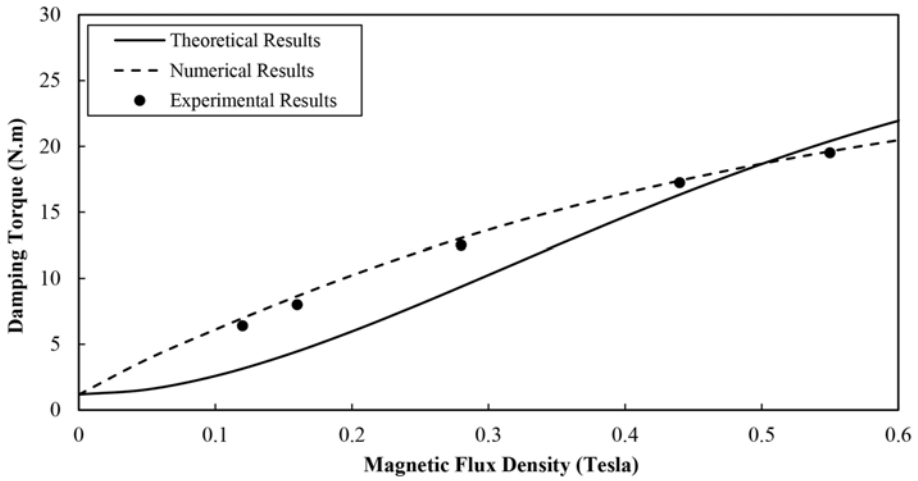

FIGURE 11 | Damping torque vs. magnetic field density of the smart damper for angular speed of 10 RPM.

fluid volume, which is shown in **Figure 10**. The wall shear stress appears to increase from its minimum magnitude, which occurs at the bottom end of the socket, to a maximum magnitude that occurs in areas close to the socket opening. This shear stress pattern is attributed to the fact that the fluid shearing force becomes larger with increasing angle of the socket opening, which changes from zero at the bottom of the socket to 90 degrees nearby the socket opening.

The damping torque of the smart damper as a function of the magnetic flux density was estimated using the three employed techniques for a rotational speed of 10 RPM and the results are shown in **Figure 11**.

It can be seen that higher magnetic flux densities and hence larger fluid yield strengths caused the smart damper to produce higher damping torques. The damping torques appeared to increase almost linearly with the magnetic flux density particularly the current range of the fluid magnetic excitation is far from those magnetic field levels that cause fluid saturation. However, the simulated damping torque results seem to be closer to those obtained experimentally in comparison with the theoretical results. This is ascribed to the fact that the numerical approach with its employed Herschel-Bulkley model contributed to a more accurate estimation of the fluid shear stress in comparison with those produced theoretically in association with the Bingham plastic model (**Figure 4**). It could also be seen in this figure that when the magnetic field density is <0.4 Tesla, the theoretical results with their assumed Bingham plastic fluid characteristics seem to depart further from the experimental results. This might be caused by the fact that the shear thinning effect of the MR fluid is more obvious when the applied magnetic field is weak, which is not accounted for by the utilized Bingham plastic model unlike the Herschel-Bulkley model which takes care of this effect.

Furthermore, a deviation of 5–7% was observed between the experimental and numerical results which could be ascribed to the fact that although the electromagnetic circuit of the smart damper was designed through the electromagnetic FEM to generate a uniform magnetic field along the fluid gap, the prototype smart damper, due to various experimental deviations, may not exactly maintain this field uniformity. Overall, and according to the three assessment approaches, the smart damper appears to deliver a damping torque of about 22 Nm under a magnetic excitation of about 0.6 Tesla.

CONCLUSION

In this study, theoretical, numerical, and experimental approaches were developed to assess the performance of a novel smart MR fluid damper which was designed with a ball and socket structure to enable a multi-degrees-of-freedom device output. The theoretical model assumed a Bingham plastic fluid characteristics whilst the numerical technique employed the Herschel-Bulkley model which resulted in a more accurate fluid shear stress estimation. The mechanical torque of the device, which was caused by the friction between the ball and lip-seal components, was also measured experimentally, and was added to the theoretical and numerical torque results. A dedicated testing facility was utilized to verify the performance of the smart damper, which was found to be in a good agreement with the simulated device performance in comparison with that estimated theoretically.

AUTHOR CONTRIBUTIONS

All authors listed have made a substantial, direct and intellectual contribution to the work, and approved it for publication.

REFERENCES

Adhesives Coatings Vibration and Motion Control Sensing and Magnetically Responsive Technologies (2018). *LORD Corp, Lord.com*, [Online]. Available online at: https://www.lord.com/ (Accessed February 05 2018).

Chrzan, M., and Carlson, J. (2001). MR fluid sponge devices and their use in vibration control of washing machines. *Smart Struct. Mater*. 4331, 370–379. doi: 10.1117/12.432719

Dyke, S., Spencer, B., Sain, M., and Carlson, J. (1998). An experimental study of MR dampers for seismic protection. *Smart Mater. Struct*. 7, 693–703. doi: 10.1088/0964-1726/7/5/012

El Wahed, A. (2011). The influence of solid-phase concentration on the performance of electrorheological fluids in dynamic squeeze flow. *Mater. Design* 32, 1420–1426. doi: 10.1016/j.matdes.2010.09.003

El Wahed, A., and Balkhoyor, L. (2015). Magnetorheological fluids subjected to tension, compression, and oscillatory squeeze input. *Smart Struct. Syst*. 16, 961–980. doi: 10.12989/sss.2015.16.5.961

El Wahed, A., and Balkhoyor, L. (2016). Characteristics of magnetorheological fluids under single and mixed modes. *Proc. Institut. Mech. Eng. C* 231, 3798–3809. doi: 10.1177/0954406216653621

El Wahed, A., and Balkhoyor, L. (2018). The performance of a smart ball-and-socket actuator applied to upper limb rehabilitation. *J. Intell. Mater. Syst. Struct*. 29, 2811–2822. doi: 10.1177/1045389X18780349

El Wahed, A., and McEwan, C. (2011). Design and performance evaluation of magnetorheological fluids under single and mixed modes. *J. Intell. Mater. Syst. Struct*. 22, 631–643. doi: 10.1177/1045389X11404453

Ghaffari, A., Hashemabadi, S., and Ashtiani, M. (2014). A review on the simulation and modeling of magnetorheological fluids. *J. Intell. Mater. Syst. Struct*. 26, 881–904. doi: 10.1177/1045389X14546650

Goncalves, F., and Carlson, J. (2009). An alternate operation mode for MR fluids—magnetic gradient pinch. *J. Phys.* 149:012050. doi: 10.1088/1742-6596/149/1/012050

Nguyen, Q., and Choi, S. (2009). Optimal design of MR shock absorber and application to vehicle suspension. *Smart Mater. Struct*. 18:035012. doi: 10.1088/0964-1726/18/3/035012

Olabi, A., and Grunwald, A. (2007). Design and application of magneto-rheological fluid. *Mater. Design* 28, 2658–2664. doi: 10.1016/j.matdes.2006.10.009

Wang, D., and Liao, W. (2011). Magnetorheological fluid dampers: a review of parametric modeling. *Smart Mater. Struct.* 20:023001. doi: 10.1088/0964-1726/20/2/023001

Wang, H., and El Wahed, A. (2018). "CFD simulation of a smart magnetorheological fluid actuator,"in *ACTUATOR 2018-16th International Conference on New Actuators*, Bremen.

Wang, X., and Gordaninejad, F. (2000). Field-controllable electro- and magneto-rheological fluid dampers in flow mode using Herschel-Bulkley theory. *Smart Struct. Mater.* 3989, 232–244. doi: 10.1117/12.384564

Wereley, N., Cho, J., Choi, Y., and Choi, S. B. (2007). Magnetorheological dampers in shear mode. *Smart Mater. Struct.* 17:015022. doi: 10.1088/0964-1726/17/01/015022t

Zhu, X., Jing, X., and Cheng, L. (2012). Magnetorheological fluid dampers: a review on structure design and analysis. *J. Intell. Mater. Syst. Struct*. 23, 839–873. doi: 10.1177/1045389X12436735

Zubieta, M., Eceolaza, S., Elejabarrieta, M., and Bou-Ali, M. (2009). Magnetorheological fluids: characterization and modeling of magnetization. *Smart Mater. Struct.* 18:095019. doi: 10.1088/0964-1726/18/9/095019

Conflict of Interest Statement: The authors declare that the research was conducted in the absence of any commercial or financial relationships that could be construed as a potential conflict of interest.

frontiers in Materials

ORIGINAL RESEARCH
published: 10 April 2019
doi: 10.3389/fmats.2019.00056

Rheological Properties of Polyurethane-Based Magnetorheological Gels

Guang Zhang[1], *Yancheng Li*[2,3]*, *Huixing Wang*[1] and *Jiong Wang*[1]*

[1] School of Mechanical Engineering, Nanjing University of Science and Technology, Nanjing, China, [2] College of Civil Engineering, Nanjing Tech University, Nanjing, China, [3] School of Civil and Environmental Engineering, University of Technology Sydney, Ultimo, NSW, Australia

The paper tests the influence of mass fractions of carbonyl iron particles (CIPs) on the rheological properties of magnetorheological (MR) gels. Polyurethane-based MR gels with different weight fraction of CIPs, i.e., 40, 60, and 80%, were firstly prepared by mechanical mixing, respectively. The changes of shear stress and viscosity with shear rate under different magnetic flux density were tested and analyzed. It was found that the shear stress increases with mass fraction under magnetic flux density. The viscoelastic properties of MRGs were achieved by oscillatory shear measure. The effects of strain amplitude and frequency on viscoelastic of MRGs under different magnetic flux density were measured and analyzed. The study results shown that the elastic characteristics become more obvious with the increase of CIPs mass fraction. However, it has opposite effect on the viscous properties of materials.

Keywords: magnetorheological gel, rotation shear, oscillatory shear, Payne effect, loss factor, linear viscoelasticity

OPEN ACCESS

Edited by:
Miao Yu,
Chongqing University, China

Reviewed by:
Luwei Zhou,
Fudan University, China
Xianzhou Zhang,
Independent Researcher, Tomago, NSW, Australia

***Correspondence:**
Yancheng Li
yli@njtech.edu.cn;
yancheng.li@uts.edu.au
Jiong Wang
wjiongz@njust.edu.cn

Specialty section:
This article was submitted to Smart Materials, a section of the journal Frontiers in Materials

Received: *26 November 2018*
Accepted: *20 March 2019*
Published: *10 April 2019*

Citation:
Zhang G, Li Y, Wang H and Wang J (2019) Rheological Properties of Polyurethane-Based Magnetorheological Gels. Front. Mater. 6:56. doi: 10.3389/fmats.2019.00056

INTRODUCTION

MRG is a new generation of MR smart materials with soft magnetic particles uniformly suspending in non-magnetic carriers. Fast and reversible magnetorheological effect will occur under the applied of magnetic field (Gan et al., 2017). It was more than two decades when Shiga et al. first reported silicone-based MR gel for solving the problem of particle settling in 1995 by dispersing the CIPs into silicone polymer colloid uniformly and since then MR gel has been considered as a momentous member of MR intelligent materials (Shiga et al., 1995). MR gels bring out larger MR effect than MR elastomer while overcoming the sedimentation issue associated with MR fluids, which can be regarded as an intermediate product between MR fluid and MR elastomer (Wilson et al., 2002; Wei et al., 2010; Zhang et al., 2010; Xu et al., 2013; Miao et al., 2014). MR gel is normally composed of micron or submicron soft magnetic particles (such as CIPs and pure iron powders), crosslink polymer liquid (such silicone resin and polyurethane), and additives (Ju et al., 2013). Notably, the MR gel shows a colloidal with a certain shear yield stress without magnetic field due to its matrix. Once the magnetic field is applied, the MR gel will transform into a solid state in a very short time (within milliseconds) and will exhibit a higher degree of shear yield stress. This process has a continuous and reversible characteristic (Hu et al., 2010; An et al., 2012). The above characteristics indicate that MR gel carries the basic rheological properties of the MR material and has larger magnetorheological effect and better settlement resistance, which offers a reliable and simple solution to design brakes (Wilson et al., 2002), dampers (Yang et al., 2015), and isolators

(Xu et al., 2013). However, the research on MR gel-like material is still in its early stage and much work are to be conducted. The researchers in the field were initially from chemistry with focus on heat flow and conversion of the polymeric matrix, and it is now gradually shifting to the stage with more engineers involved. From an application point of view, the mechanical properties of the material under influence of magnetic field, such as shear yield stress, viscosity, storage modulus, loss factor and MR effect, are of great interest and hence should be carefully investigated.

Owing to its great potentials, understanding its rheological properties holds the key to unlock reliable and efficient usage in engineering applications. Among the main composition, the soft magnetic particles play the key role to activate the MR effect and hence their impact should be carefully investigated. The influences of CIP contents on magneto-mechanical performances of MR materials have been tested by different researchers. Fuchs et al. prepared two silicone-based MR gel samples with different CIP contents. Variable magneto-induced features were examined by rheometer sweeping of shear rate from 20 to 6,000 s^{-1}. It was found that the silicone-based MR gel with 84.5 wt% CIPs has a stable shear yield stress over a wide range of shear rate (Fuchs et al., 2004). Xu et al. prepared several MR gels consisting plastic polyurethane matrix swollen by non-volatile solvent in different weight fractions of CIPs and their MR properties (both shear yield stress and modulus) were tested and analyzed. It was shown that the carrier has little effect on the linear viscoelastic (LVE) region of MRGs, though the magnitude the storage modulus G' can be greatly changed by the solvent content (Xu et al., 2013). The dynamic magneto-induced properties of the shear-stiffening gel under compression was measured by Wang et al. It was found that CIP contents have great influences on dynamic properties (Wang et al., 2016). Xu et al. developed MR gels with different weight fractions and the stress evolution characteristics of MRGs under stepwise shear loading are tested. It was found that the mass fraction of CIPs has a significant effect on the rheological properties of prepared materials. The dynamic modulus and the plain modulus increase along with CIPs weight fraction (Xu et al., 2017). These results indicate that the CIP weight fraction has a significant impact on the magneto-mechanical features of MR materials.

In addition, the basic carrier has a great impact on the rheological properties of MR materials (Xu et al., 2011). Mitsumata et al. firstly prepared carrageenan/iron oxide MR gels and the reversible rheological properties were tested. It was found that great variety of the storage modulus was almost not exhibited when the carrageenan concentration was 2 wt%; however, the MR effect appeared on reduced concentration. The limit variation in the relative storage modulus was 24 when the carrageenan concentration was 0.6 wt% (Mitsumata and Abe, 2011). Zhang et al. developed silicone-based MR gels by with 30, 50, and 70 wt% CIPs and the rheological properties were systematically tested, respectively. It was found that the content of silicone has a great influence on the zero-field viscosity, shear stress and response rate, and MR gel with 30 wt% silicone has the best MR effect (Zhang et al., 2018). Wilson et al. self-developed series of PUs and silicones matrix by controlling the weight of reactants and the content of modifier (reacting or non-reacting) and then developed PU-based and silicone-based MR gels, respectively. It was found that rheological property can be qualitatively controlled of as-developed MR products by adjusting the ratio of reactants and diluents. The PU and silicone polymers have three existing states, that is solid, gel, and liquid forms, according to the crosslinking and dilution (Wilson et al., 2002). Xu et al. developed a novel high-performance PU-based MR material. The dynamic properties of the MR material were systematically measured and the influences of the PU contents were analyzed. It was found that the material with 20% PU matrix weight fraction shows a high dynamic property (Xu et al., 2011). Fuchs et al. developed polyurethane (PU)-based and silicone-based MR gels, respectively. In this work, tunable rheological properties and settling rate were investigated. The results show that PU-based has the better particle settling resistance and has a high shear yield stress (23 kPa at 350 mT). Both dynamic and static shear stress values of the samples were found to be similar in magnitude: the dynamic and static shear stress of both PU and silicone-based produces with 84.5% weight mass CIPs under 120 mT range from 5 to 8 kPa (Fuchs et al., 2004). PU have attracted the attention of researchers among the various polymer matrixes due to better degradation stability than natural rubber and superior mechanical properties compared with silicone rubber. Interestingly, it is found that PU can be tuned from flow-able liquid to semi solid (gel like) depending upon the degree of crosslinking (Mordina et al., 2016). Accordingly, an appropriate carrier should be selected to prepare stable MR gels for obtaining a suitable modulus and wider magnetorheological effect. In addition, MRG based on PU has better sedimentation resistance and particle aggregation resistance (Wilson et al., 2002; Yang et al., 2015). The above characteristics can greatly simplify the sealing structure in the device structure design with MRG as the medium, thus reducing the cost, and is of certain significance to improve the stability of the device.

To this point, this research is to investigate the influence of the CIP fractions on their rheological properties with commercially available PU matrix. PU-based MR gels with CIP mass fractions of 40, 60, and 80% are freshly developed and the magnetic properties and microstructure were tested and analyzed accordingly. Then the magneto-mechanical features of MR gel under continuous shear with different CIP weight fractions are measured and discussed. Finally, the viscoelastic properties of MRGs were achieved by oscillatory shear measure. The effects of magnetic flux density, shear rate, strain amplitude and driving frequency on the dynamic properties of MR gel with different CIP weight fractions were discussed comprehensively.

MR GELS PREPARATION

In this study, the synthesis of the MR gels was carried out by mixing CIPs (type: JCF2-2, JiLin Jien Nickel Industry Co., Ltd, China, with an average particle size of about 5 μm) into a commercial PU (Shanghai mile Chemical Technology Co., Ltd, China). The several important physical properties of PU employed in the study are exhibited in **Table 1**. The CIPs mass fraction of MR gels are selected as 40, 60, and 80%, respectively.

TABLE 1 | Properties of the PU used in this paper.

Technical name	Technical property
State	Solution-colloid
Appearance	Transparent
Viscosity (room temperature: 25°C)	5000 ± 100 mpa.s
Solid content	100%
Particle size (μ m)	<0.001

There are three-prongs in the development of MR gels. Firstly, weighing the exact quantity of the PU and CIPs. Placing PU matrix into three 250 ml beakers. Secondly, the carrier (PU) was mechanically stirred at 400 rpm for 30 min in the environment of a constant temperature (65°C) in order to make the CIPs dispersed more uniformly. Finally, the CIPs with 40, 60, and 80% weight fractions were added into the accommodating matrix and were stirred at 750 rmp until the PU matrix and CIPs were fully and evenly mixed. In this paper, the three MRG samples were named as MRG-40, MRG-60, and MRG-80, respectively.

PROPERTIES CHARACTERIZATION

The magnetic hysteresis characteristic of CIP and MR gels with CIPs weight fraction of 40, 60, and 80 % were measured by using the vibrating sample magnetometer (VSM, Lake Shore 7407, USA) at the temperature of 25°C. A commercial rheometer (Physica MCR 302, Anton Paar Co., Austria) with plate (the diameter is 20 mm) was employed to measure the magnetic-induced mechanical properties of MR gels by continuous shear and oscillatory shear tests. The magnetic field generated by the coil can be controlled by regulating the current through the coil. The gap between the plate and the base was maintained at 1 mm so as to emerge symmetrical magnetic flux density range from 0 to 1,200 mT through the samples by adjusting the current in the coil from 0 to 5 A.

Rotational and oscillatory shear test are the most frequently used testing methods to investigate the rheological properties of materials. Scanning test of magnetic flux density (changing from 0 to 1,200 mT) was carried out under a constant shear rate of 50 s^{-1} during shear rotation test. The shear stress and viscosity of the products were tested under different magnetic flux densities (0, 240, 480, 720, and 960 mT), with shear rate from 1 to 100 s^{-1}. The dynamic properties of samples were captured by mean of oscillation shear. The amplitude changes from 0.01 to 10% under the strain amplitude sweeping at a constant frequency of 5 Hz. The oscillation frequency changes from 5 to 100 Hz for scanning of frequency measurements at a constant strain amplitude of 0.01%. Both the scanning measurements of strain amplitude and frequency were carried out under the four magnetic flux densities, which are 240, 480, 720, and 960 mT. In order to ensure the comparability of the test data, the pre-shearing process with a shear rate of 50 s^{-1} for 3 min was carried out before each step was measured.

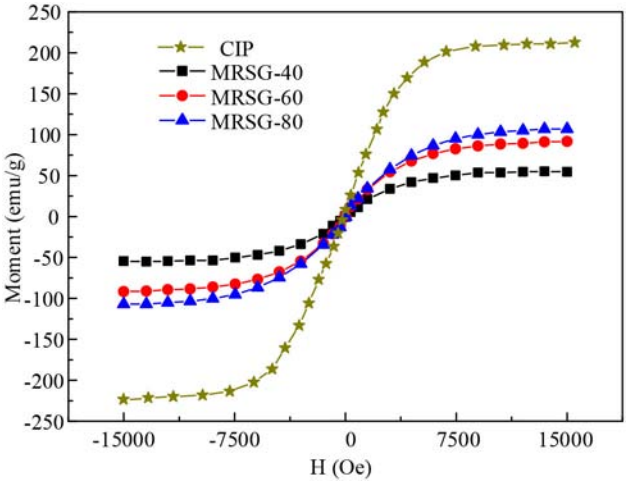

FIGURE 1 | Magnetization curve of MR gels and CIP at room temperature.

RESULTS AND DISCUSSION

Magnetic Properties

The magnetic hysteresis properties of pure CIP and MR gels with different CIP content, i.e., 40, 60, and 80 wt%, were investigated by VSM. **Figure 1** display the magnetic properties of as-developed MR gels with various weight fraction of CIPs, which indicated that the samples exhibits obvious soft magnetic property. The moment increases linearly with the increase of magnetic field and then goes to saturation value. For CIP, the yielding starts around 5,000 Oe and when the external magnetic field strength increases to 8,000 Oe, CIP reaches a magnetic saturation state with a saturation moment of 206 emu/g. For MR gels, the CIPs weight fraction has great influence on saturation moment. MR gel with higher CIP weight fraction have higher saturated moment, i.e., about 54 emu/g for MRG-40, 91 emu/g for MRG-60, and 107 emu/g for MRG-80.

Magnetic Field Sweep

The magnetic flux density dependence of shear stress for different samples in small strain (linear viscoelastic range) was shown in **Figure 2**. The magnetic flux density has a significant influence on the mechanical properties of samples. Shear stress increases with the enhancement of the magnetic flux density under the constant shear rate. When the magnetic flux density is very small, i.e., $B < 100$ mT, the shear stress of the samples changes slightly. With the increase of the magnetic flux density, the shear stress of the materials changes approximately linear at moderate magnetic field. When the magnetic flux densities are 700 and 900 mT, the shear stresses of MRG-40 and MRG-60 reach saturation value, 8 and 20 kPa, respectively; however, when the magnetic flux density increases to 1,200 mT, the shear stress of MRG-80 does not reach the saturation value, but its growth rate decreases obviously.

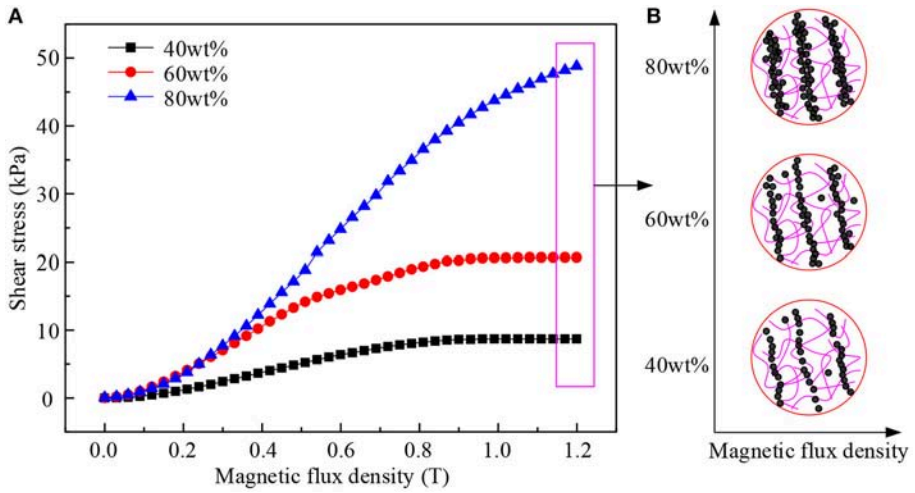

FIGURE 2 | (A) Shear stress as a function of magnetic flux density at $\dot{\gamma} = 50\ s^{-1}$ for samples; **(B)** microscopic chain structure (red solid line represents polyurethane polymer, and solid small circle represents CIPs).

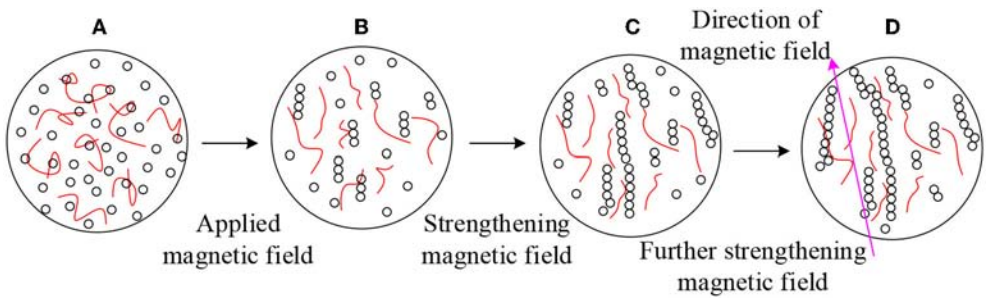

FIGURE 3 | Internal chain forming process (red solid line represents polyurethane polymer, and hollow small circle represents CIPs). **(A)** no magnetic field; **(B)** applying a weak magnetic field; **(C)** magnetic field enhancement and **(D)** further strengthening of magnetic field.

Therefore, the change is roughly divided into three kinds of growth: the initial growth (from **Figures 3A,B**), the linear growth (from **Figures 3B,C**), and the saturate tendency (from **Figures 3C,D**). The change of magnetic-induced micro-structure of samples can be interpolated as the process that the CIPs inside material attempt to overcome the internal friction resistance (mainly the resistance of the polymer matrix). At the initial stage, the intertwined polymer chains are flexible along the moving direction under the drive of particles, and the damping force to restrict particles motion weakens slightly. Therefore, the chain forming process is also slow, and the change of microstructure is as shown from **Figures 3A,B**. With the increase of magnetic flux density, the particle chain presents a linear growth process in the flexible polymer chain environment as shown from **Figures 3B,C**. Further enhancing the magnetic field, the free particles combine into chains and become scarce as shown from **Figures 3C,D**, which leads to the saturated shear stress with the increasing of magnetic flux density. This phenomenon coincide with the hysteresis curve of samples in **Figure 1**.

Rheology Properties in Rotational Shear

The shear stress and viscosity curves along shear rate of MR gels with various CIP weight fractions under different magnetic flux densities are exhibited in **Figures 4**, **5**, respectively. As shown in **Figure 4A**, in the absence of an external magnetic field, the shear stress increases linearly along with shear rate, which shows Newtonian fluid characteristics. With the influence of the magnetic flux density, the MR gel behaves as non-Newtonian fluid which needs to overcome a certain amount of the stress (named as yield stress) to become fluidic state, i.e., Bingham plastic behavior. It is shown that the yield stress increases with weight fraction at a given magnetic flux density. The magnetic flux density has a great impact on the yield stress of prepared MR materials, which changes from 2 to 10 kPa for 40 wt% MR gel and from 5.6 to 45 kPa for 80 wt% MR gel sample. This is due to the stronger interaction in chain-like structure at higher magnetic flux density level. After the yield stress, the shear stress has a slight increase along shear rate for the magnetic flux density below saturated magnetic flux density, which should be below 960 mT as under such conditions the MR gel has distinct saturation

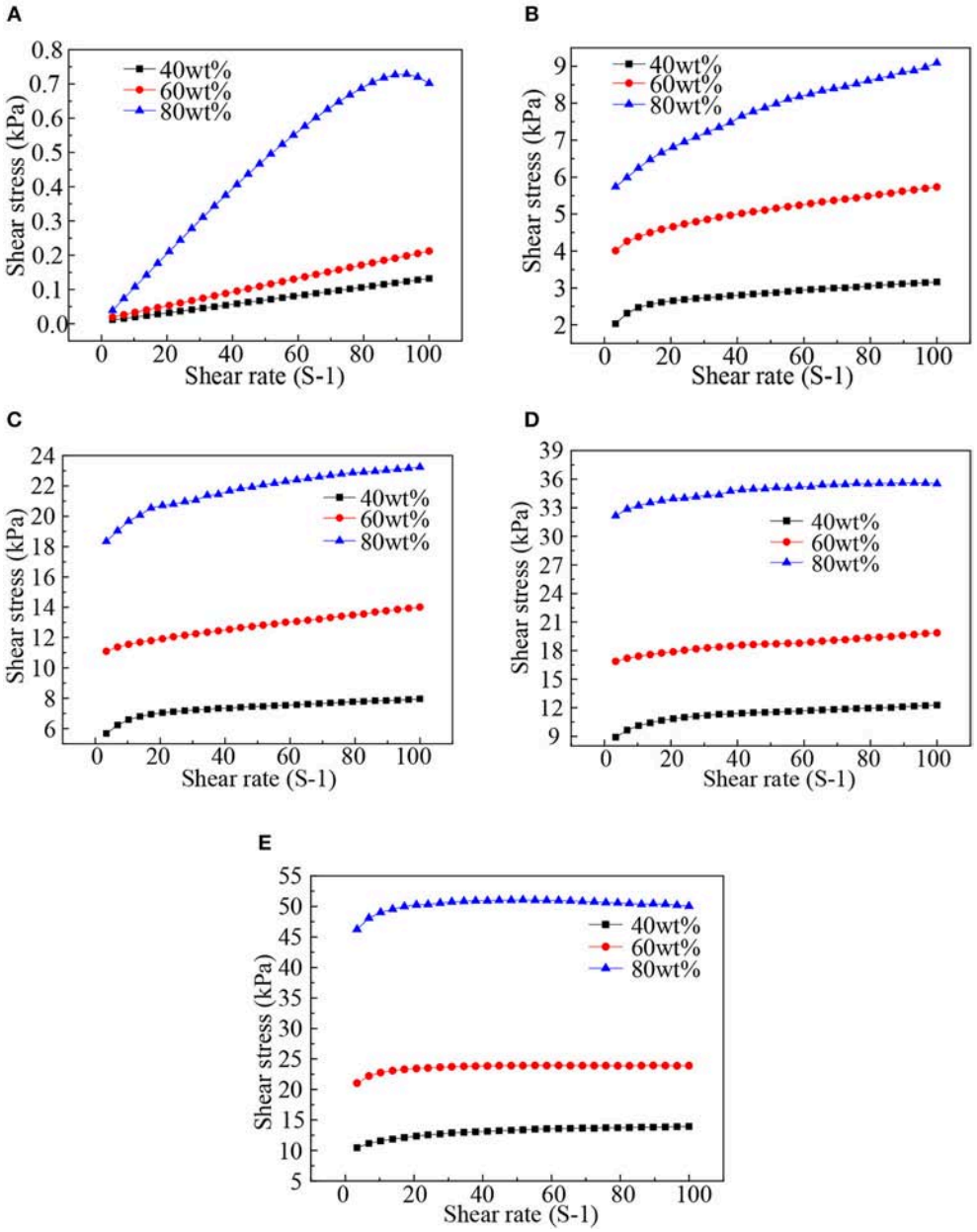

FIGURE 4 | Shear stress vs. shear rate under different magnetic flux densities (**A**: B = 0 mT; **B**: B = 240 mT; **C**: B = 480 mT; **D**: B = 720 mT; **E**: B = 960 mT).

yield stress. It implies that the better damping property at lower magnetic flux density levels. Under the magnetic flux density of 960 mT, the MR gel presents a slight shear thinning behavior, especially for 80 wt% sample, which has slight decreasing shear stress against shear rate.

The viscosity of the MR gel decreases along shear rate at low shear rate level, i.e., below 20 s^{-1}, shown in **Figure 5**. Such behavior is more distinct under the influence of the magnetic flux density. The CIP content has considerable impact on the viscosity of the MR gel with and without magnetic flux density. For example, at the magnetic flux density of 960 mT, the MRG-80 has a viscosity of 503 Pa.s at the shear rate of 100 s^{-1}; with lower fraction of CIPs as 40 wt% the viscosity of the sample has significant reduction to 139 Pa.s.

Rheological Properties Under Oscillatory Shear

Storage modulus and loss modulus are the key mechanical parameters used to reveal the dynamic properties of materials (Xu et al., 2013). Among them, the storage modulus is an important parameter to characterize the elastic properties of

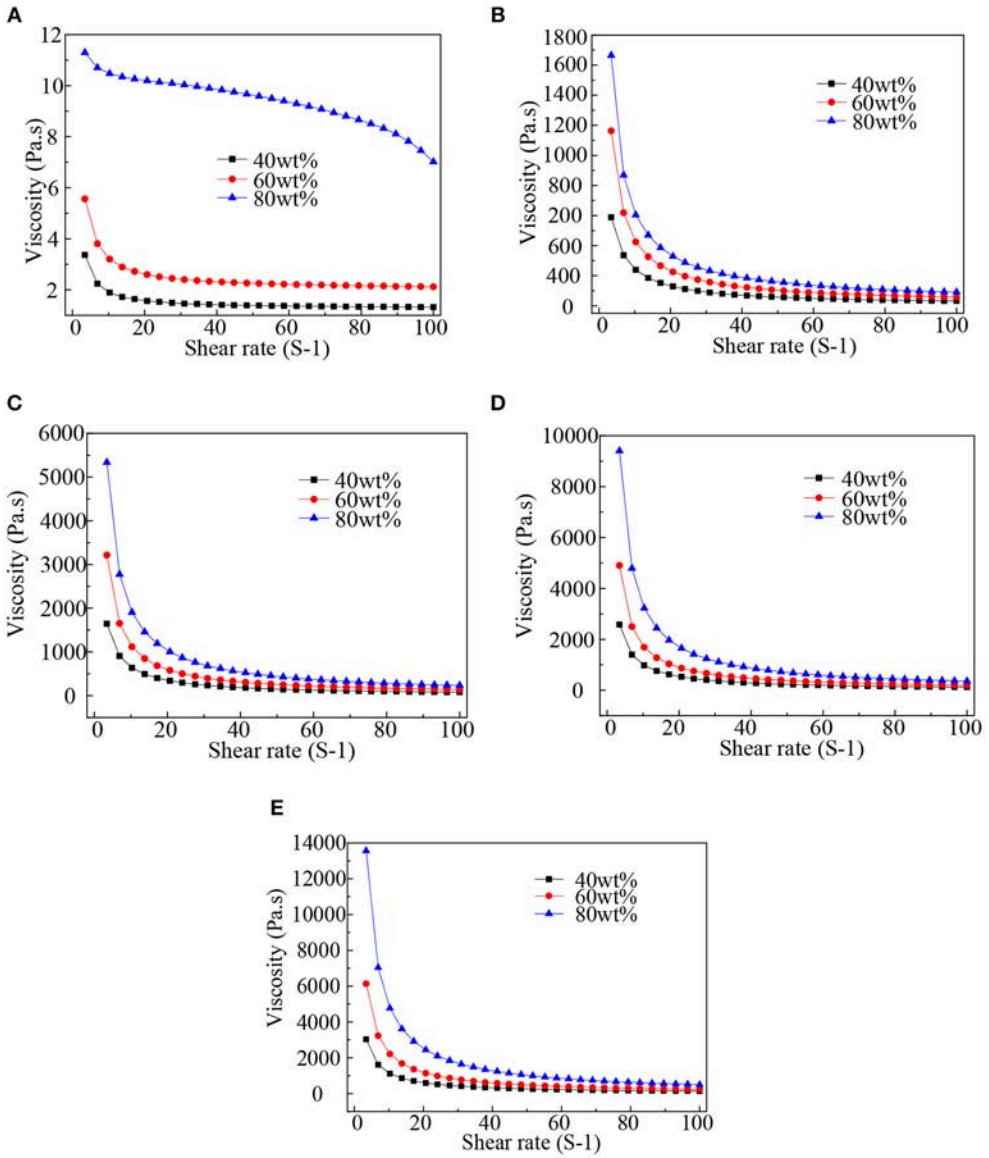

FIGURE 5 | Viscosity vs. shear rate under different magnetic flux densities (**A**: B = 0 mT; **B**: B = 240 mT; **C**: B = 480 mT; **D**: B = 720 mT; **E**: B = 960 mT).

materials, which can show the ability of materials to store energy (have the feature that all the energy completely available after the external load is removed) after shear deformation (Zhang et al., 2011). The storage modulus of the samples was studied by scanning shear strain amplitude change from 0.01 to 10% under the condition of constant strain frequency of 5 Hz at different constant magnetic flux density of 0, 240, 480, 720, and 960 mT, respectively. The results are shown in **Figure 6**.

As shown in **Figure 6A**, in the absence of an external magnetic flux density, storage modulus decreases rapidly along shear strain amplitude and then tends to stabilize beyond certain strain. It can be concluded that the ability of energy storage for PU matrix decreases with the increase of shear strain amplitude. With the influence of the magnetic flux density, as can be seen in **Figures 6B–E**, MR gels exhibit obvious linear viscoelastic region at the small strain range, which was the same as the dynamic properties of MR grease (Wang et al., 2019). It should be noted that the data is plotted with logarithmic horizontal axis to clear present the linear region. The shear strain amplitude has great impact on the storage modulus of samples. Firstly, the storage modulus of the material does not change with the increase of strain amplitude at small shear strain, indicating the linear viscoelasticity (LVE). Further increasing with the strain amplitude, the storage modulus decreases with the strain amplitude, which is called Payne effect (Arief and Mukhopadhyay, 2015), i.e., the impact of the applied strain amplitude on the storage modulus. Above an approximately 0.1% strain, the storage modulus decrease rapidly along with applied

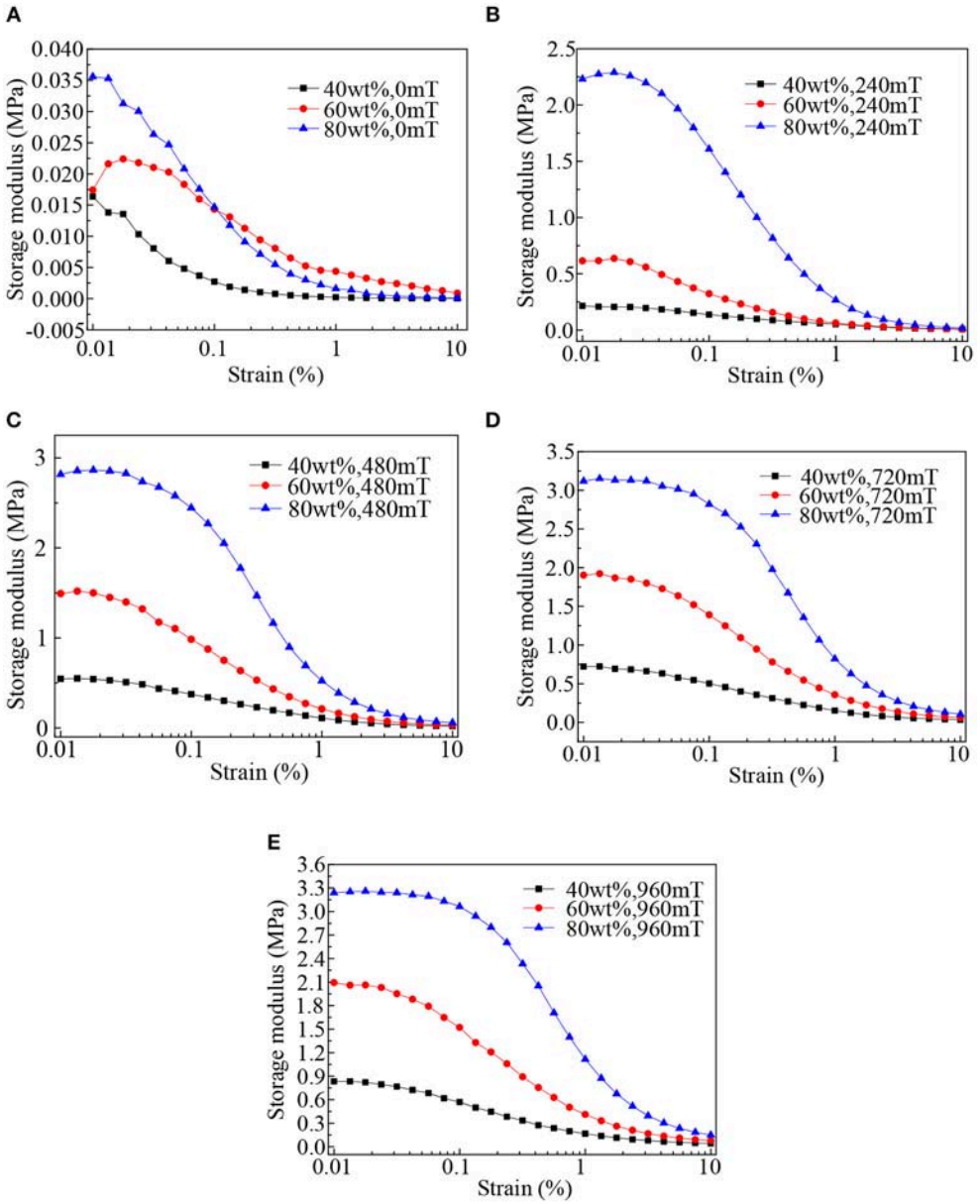

FIGURE 6 | Storage modulus of samples as a function of strain under different magnetic flux densities. (**A**: B = 0mT; **B**: B = 240mT; **C**: B = 480mT; **E**: B = 720mT; **E**: B = 960mT).

strain amplitude. This threshold strain is called the critical strain amplitude of the material and is dependent on the fillers of the content in the matrix. The critical strain increases along with magnetic flux density and mass fraction of the CIP content for MRG and the critical strain values of samples under different magnetic flux density is shown in **Table 2**.

The linear viscoelastic properties of the MR gels have special physical meaning: in the linear viscoelastic region, the internal structure of the material is elastic deformation under shear strain. Once withdrawn, the structure is restored to its original shape, and the change has a continuous and reversible property.

Another important measure of the MR material is the MR effect. The MR effect is related to the zero field storage modulus and magneto-induced storage modulus at the same time. It increases with the increase of magneto-induced storage modulus and decreases with the increase of zero-field modulus. The specific expressions are as follows (Xu et al. 2011):

$$MR\ effect(\%) = \frac{G'_B - G'_{B=0}}{G'_{B=0}} \times 100,$$

where G'_B is storage modulus under magnetic field, $G'_{B=0}x$ is the storage modulus without applied magnetic field, $G'_B - G'_{B=0}$ is magneto-induced storage modulus.

The magnetic flux density dependence of storage modulus for the materials is shown in **Figure 7**. It is found that the storage

TABLE 2 | The critical strain amplitude of samples under different field.

Samples	240 mT (%)	480 mT (%)	720 mT (%)	960 mT (%)
MRG-40	0.0238	0.0422	0.0471	0.0564
MRG-60	0.0316	0.0512	0.0981	0.1127
MRG-80	0.1012	0.1102	0.1287	0.1341

moduli of materials increase with the increase of CIP content under the same magnetic flux density. Interestingly, the MR effect of the 60 wt% MR gel is higher than that of 80 wt% MR gel (as shown in **Figure 8**). The MR effect of the samples with different mass concentrations of CIPs under different magnetic flux densities are shown in **Figure 8**. It should be noted that the MR effect was calculated based on the storage moduli measured at maximum strain value of linear viscoelastic range at saturated magnetic field flux density 960 mT and zero magnetic field. As indicated in **Figure 6** and **Table 2**, the strain value used for MR effect calculation is 0.02% below which is the strain to define linear viscoelastic range of the MR gel for all magnetic field levels. Each measurement was repeated five times to ensure accuracy of data and then the average values and standard error were taken. Among three samples, the 60 wt% MR gel has demonstrated the highest MR effect. In addition, it was shown that the MR effect does not increase along with the CIPs content. For instance, for MRG-60 and MRG-80, the MR effect at the magnetic flux density of 240, 480, 720, and 960 mT decreases as shown in **Figure 8**. Such behavior attributes to the off-state modulus of the samples, with MRG-80 has highest off-state modulus (Xu et al., 2011). The MR effect is determined by two factors in the LVE region, which are (i) the induced storage modulus of MR samples under magnetic field due to inter-action between the CIP particles, and (ii) the off-state storage modulus of the samples. Higher CIP content may increase the formation of the chain structure in the sample and lead to higher storage modulus. However, the high off-state shear modulus due to the high particle concentration compromises the relative increase of the modulus.

The storage properties and loss behavior of the samples were studied by scanning strain frequency from 5 to 100 Hz under different magnetic field at shear strain amplitude of 0.01%, which is within the linear viscoelastic range for all samples. The results are shown in **Figures 9**, **10**, respectively.

Figure 9 shows the characteristic curves of storage modulus-frequency of the samples under different magnetic flux densities. At low frequency (<10 Hz), the shear frequency has a great influence on the storage modulus and increases with the increase of the storage modulus. However, the frequency dependence of storage modulus disappears when the frequency is beyond 10 Hz. This interesting phenomenon may be caused by changes in the internal microstructures of PU-based MR gels: PU-based matrix polymers in MR gels intertwined with each other initially. The orientation of these polymer chains distributes along the shear direction under the action of shear oscillation (Zhang et al., 2018). Therefore, the resistance of particles moving in the matrix decreases under the application of magnetic flux density, which makes the storage modulus of MR gels increase

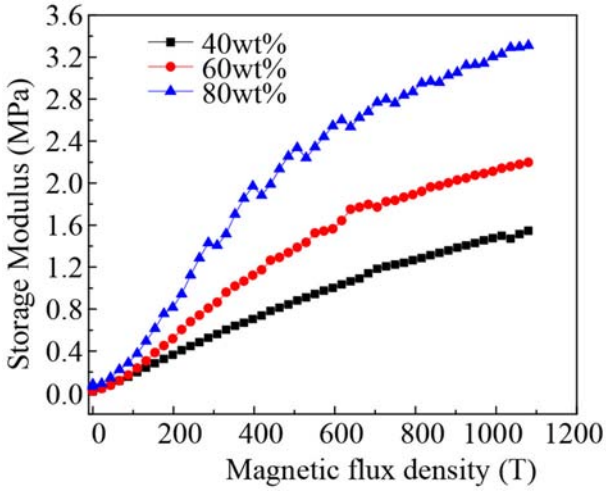

FIGURE 7 | The magnetic flux density dependence of storage modulus for the samples with different mass concentration of CIPs.

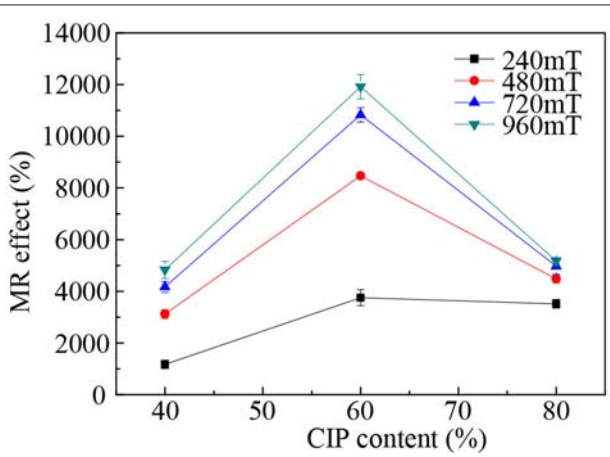

FIGURE 8 | The MR effect of the samples with different mass concentration of CIPs under different magnetic flux density.

firstly. This phenomenon is more obvious at the higher magnetic flux density. However, further increasing the shear frequency, the storage modulus no long changes, which indicates that the weakening of the storage modulus caused by molecular chain winding is compensated under low shear frequency. From **Figure 9**, in addition, it was shown that elastic performance (storage modulus) is also strongly dependent on CIPs mass fraction, which increases along CIPs mass fraction under the magnetic field.

The loss factor is an important parameter that was determined by both the storage and loss modulus of materials. The specific influence mechanism is explained by the following definition: the loss factor can be defined as the ratio of loss modulus to storage modulus. Therefore, the loss factor characterizes the damping performance of materials (Chandra et al., 1999).

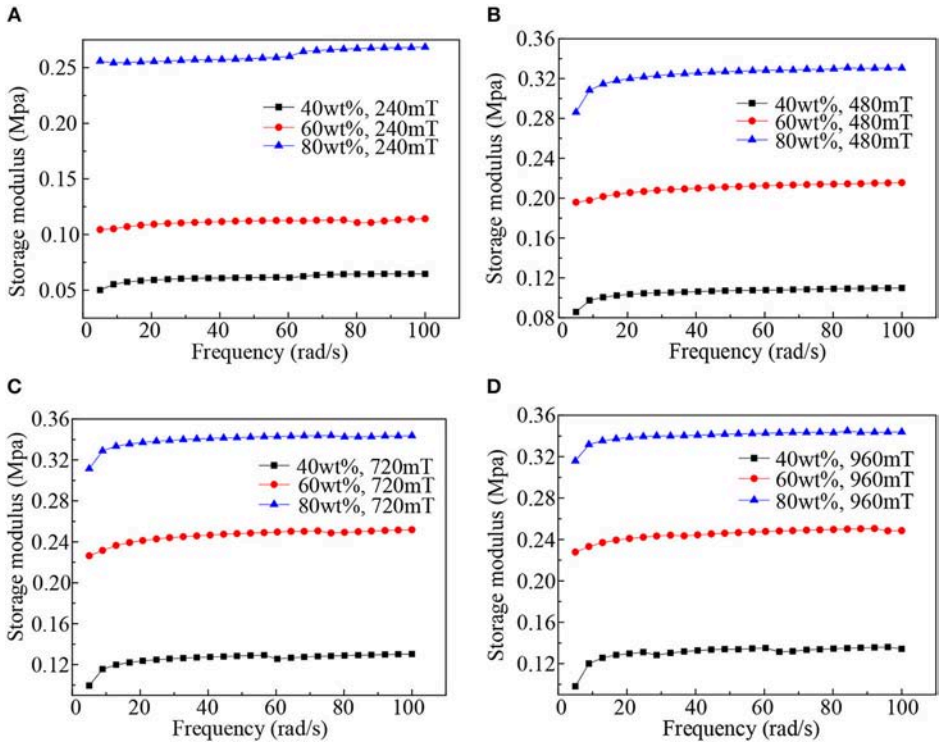

FIGURE 9 | Storage modulus as a function of angular frequency. (**A**: B = 240mT; **B**: B = 480mT; **C**: B = 720mT; **D**: B = 960mT).

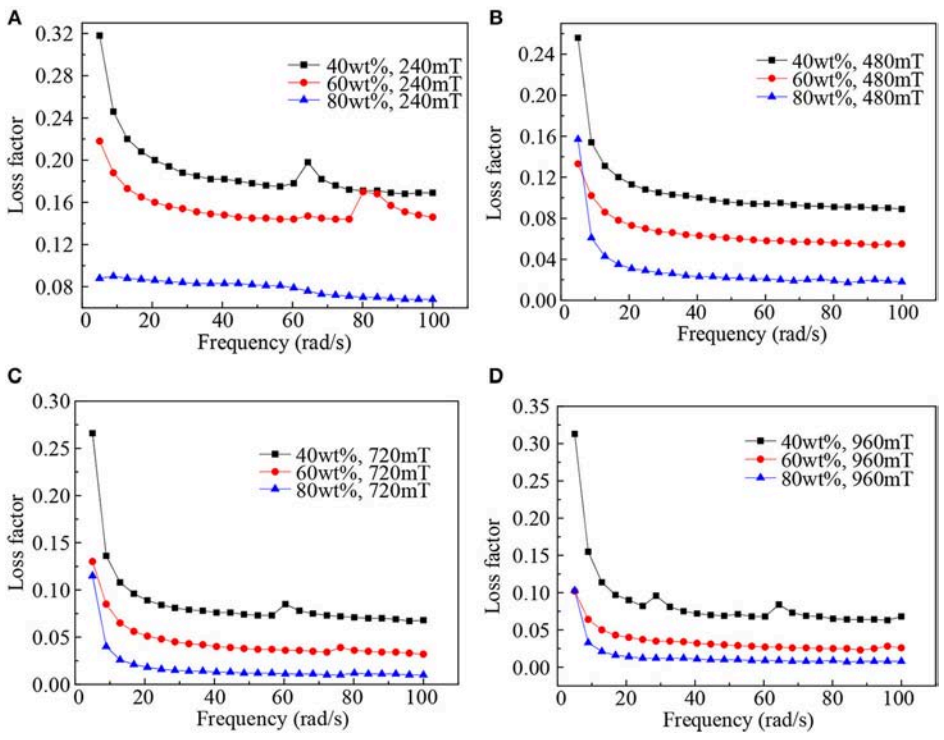

FIGURE 10 | Loss factor as a function of angular frequency. (**A**: B = 240mT; **B**: B = 480mT; **C**: B = 720mT; **D**: B = 960mT).

When the frequency is <20 Hz, loss factor of samples shows a downward trend along with strain frequency. However, when the frequency is higher than 20 Hz, the frequency dependence of loss factor nearly disappears for both samples under the magnetic flux density. As we all know, the loss factor has something to do with the ability of energy dissipation for the material. This is mainly due to the interaction of different structures within the materials. That is to say the energy dissipation of as-prepared MR gels primarily determined by the interaction between CIPs and PU-based matrix. The position of CIPs changes under low frequency shear. During this process, the movement of CIPs are hindered by PU-based polymer chains and energy dissipation occurs. However, when the frequency increases to the threshold, the segment with strong partial bound has not yet been cut off, so the loss factor decreases along with applied shear frequency and finally tends to a stable state.

CONCLUSIONS

Three PU-based MRGs with a CIPs mass fraction of 40, 60, and 80% were prepared and named MRG-40, MRG-60, and MRG-80, respectively. The static and dynamic tests of the materials were carried out. The conclusions are as follows: the influence of magnetic flux density on the mechanical properties of samples is remarkable, and its tendency with magnetic flux density can be divided into the initial growth, the linear growth and the saturate tendency. In the absence of an external magnetic flux density, the shear stress increases linearly with the increase of the shear rate, which showing Newtonian fluid characteristics. The shear stress of the samples increases with the increment of the CIPs percentage. The shear strain amplitude has different influence on the storage modulus of the materials under different magnetic flux density, and the amplitude of LVE critical strain increases with the increase of magnetic flux density and CIPs mass fraction. It was found that the relative MR effect does not increase with the increasing of CIPs content. Storage modulus is also strongly dependent on CIPs mass fraction, which increases along CIPs mass fraction under the magnetic flux density while loss factor has the opposite trend.

AUTHOR CONTRIBUTIONS

GZ conducted the research and wrote the paper. HW assisted the research. YL and JW supervised the research. YL edited the paper.

FUNDING

This work is supported by the National Natural Science Foundation of China (No.51675280, No.51805209, and No.51705467) and the Postgraduate Scientific Innovation Research Foundation of Jiangsu Province (NO. KYCX18_0457).

REFERENCES

An, H. N., Picken, S. J., and Mendes, E. (2012). Direct observation of particle rearrangement during cyclic stress hardening of magnetorheological gels. *Soft Matter* 8, 11995–12001. doi: 10.1039/c2sm26587

Arief, I., and Mukhopadhyay, P. K. (2015). Magnetorheological Payne effect in bidisperse MR fluids containing Fe nanorods and Fe_3O_4, nanospheres: a dynamic rheological study. *J. Alloys Comp*. 696, 1053–1058. doi: 10.1016/j.jallcom.2016.12.039

Chandra, R., Singh, S. P., and Gupta, K. (1999). Damping studies in fiber-reinforced composites-a review. *Compos. Struct*. 46, 41–51. doi: 10.1016/S0263-8223(99)00041-0

Fuchs, A., Xin, M., Gordaninejad, F., Wang, X., Hitchcook, G. H., Gecol, H., et al. (2004). Development and characterization of hydrocarbon polyol polyurethane and silicone magnetorheological polymeric gels. *J. Appl. Polym. Sci.* 92, 1176–1182. doi: 10.1002/app.13434

Gan, J., He, X., Zhang, G., Zhou, C., Zheng, Q., Gao, C., et al. (2017). Study on off-state characteristics of polyurethane based magnetorheological gels. *Mater. Sci. Eng. R.* 231:012168. doi: 10.1088/1757-899X/231/1/012168

Hu, B., Fuchs, A., Huseyin, S., Gordaninejad, F., and Evrensel, C. (2010). Supramolecular magnetorheological polymer gels. *J. Appl. Polym. Sci.* 100, 2464–2479. doi: 10.1002/app.23578

Ju, B., Yu, M., Fu, J., Zheng, X., and Liu, S. (2013). Magnetic field-dependent normal force of magnetorheological gel. *Ind. Eng. Chem. Res*. 52, 11583–11589. doi: 10.1021/ie4013419

Miao, Y., Ju, B., Jie, F., Liu, S., and Choi, S. B. (2014). Magnetoresistance characteristics of magnetorheological gel under a magnetic field. *Ind. Eng. Chem. Res*. 53, 4704–4710. doi: 10.1021/ie4040237

Mitsumata, T., and Abe, N. (2011). Giant and reversible magnetorheology of carrageenan/iron oxide magnetic gels. *Smart Mater. Struct*. 20:124003. doi: 10.1088/0964-1726/20/12/124003

Mordina, B., Tiwari, R. K., Setua, D. K., and Sharma, A. (2016). Impact of graphene oxide on the magnetorheological behaviour of $BaFe_{12}O_{19}$, nanoparticles filled polyacrylamide hydrogel. *Polymer* 97, 258–272. doi: 10.1016/j.polymer.2016.05.026

Shiga, T., Okada, A., and Kurauchi, T. (1995). Magnetroviscoelastic behavior of composite gels. *J. Appl. Polym. Sci*. 58, 787–792. doi: 10.1002/app.1995.070580411

Wang, H., Li, Y., Zhang, G., and Wang, J. (2019). Effect of temperature on rheological properties of lithium-based magnetorheological grease. *Smart Mater. Struct*. 28:035002. doi: 10.1088/1361-665X/aaf32b

Wang, Y., Wang, S., Xu, C., Xuan, S., Jiang, W., Gong, X., et al. (2016). Dynamic behavior of magnetically responsive shear-stiffening gel under high strain rate. *Compos. Sci. Technol*. 127, 169–176. doi: 10.1016/j.compscitech.2016.03.009

Wei, B., Gong, X., Jiang, W., Qin, L., and Fan, Y. (2010). Study on the properties of magnetorheological gel based on polyurethane. *J. Appl. Polym. Sci*. 118, 2765–2771. doi: 10.1002/app.32688

Wilson, M. J., Fuchs, A., and Gordaninejad, F. (2002). Characterization of magnetorheological polymer gels. *J. Appl. Polym. Sci*. 84, 2733–2742. doi: 10.1002/app.10525

Xu, Y., Gong, X., and Xuan, S. (2013). Soft magnetorheological polymer gels with controllable rheological properties. *Smart Mater. Struct*. 22:075029. doi: 10.1088/0964-1726/22/7/075029

Xu, Y., Gong, X., Xuan, S., Zhang, W., and Fan, Y. (2011). A high-performance magnetorheological material: preparation, characterization and magnetic-mechanic coupling properties. *Soft Matter* 7, 5246–5254. doi: 10.1039/c1sm05301a

Xu, Y., Liu, T., Liao, G. J., and Lubineau, G. (2017). Magneto-dependent stress relaxation of magnetorheological gels. *Smart Mater. Struct*. 26:115005. doi: 10.1088/1361-665X/aa89ac

Yang, P., Yu, M., Fu, J., Liu, S., Qi, S., and Zhu, M. (2015). The damping behavior of magnetorheological gel based on polyurethane matrix. *Polym. Compos*. 38, 1248–1258. doi: 10.1002/pc.23689

Zhang, G., Wang, H. X., Ouyang, Q., Wang, J., and Zhen, J. (2018). Study on the rheological properties of magnetorheological gel based on silicone and Herschel-Bulkley model parameter identification. *J. Hunan Univ*. 45, 62–71. doi: 10.16339/j.cnki.hdxbzkb.2018.06.010

Zhang, W., Gong, X., Xuan, S., and Jiang, W. (2011). Temperature-dependent mechanical properties and model of magnetorheological elastomers. *Ind. Eng. Chem. Res*. 50, 6704–6712. doi: 10.1021/ie200386x

Zhang, W., Gong, X. L., Xuan, S. H., and Xu, Y. (2010). High-performance hybrid magnetorheological materials: preparation and mechanical properties. *Ind. Eng. Chem. Res*. 49, 12471–12476. doi: 10.1021/ie101904f

Conflict of Interest Statement: The authors declare that the research was conducted in the absence of any commercial or financial relationships that could be construed as a potential conflict of interest.

frontiers in Materials

ORIGINAL RESEARCH
published: 04 February 2019
doi: 10.3389/fmats.2019.00008

Ride Quality Control of a Full Vehicle Suspension System Featuring Magnetorheological Dampers With Multiple Orifice Holes

Jong-Seok Oh[1]* *and Seung-Bok Choi*[2]*

[1] Division of Mechanical & Automotive Engineering, Kongju National University, Cheonan-Si, South Korea, [2] Smart Structures and Systems Laboratory, Department of Mechanical Engineering, Inha University, Incheon, South Korea

This study proposes a relationship between the ride comfort of passenger vehicles and two different types of magnetorheological (MR) dampers, with and without orifice holes in the piston. To achieve superior ride comfort, two cylindrical-type MR dampers with identical dimensions (piston radius, pole lengths, and the distance between two poles) are proposed. One of the MR dampers adds the orifice holes in the piston bobbin to obtain a relatively low damping force slope in the low piston velocity region. To enhance the ride quality of a passenger vehicle, the damping force slope of the rear damper should be more gradual than that of the front damper. Thus, it can be inferred that identical semi-active vehicle systems require normal MR dampers in the front and MR dampers with orifice holes in the rear, with proper control strategies. To evaluate ride performance, a robust sliding mode controller was designed. It is demonstrated through simulation that the proposed vehicle system produces better ride comfort than vehicle systems equipped with only one type of MR damper.

Keywords: magnetorheological fluid, MR damper with orifice hole (OMRD), ride quality, damping force, sliding mode controller, passenger vehicle

OPEN ACCESS

Edited by:
Ilkwon Oh,
Korea Advanced Institute of Science & Technology (KAIST), South Korea

Reviewed by:
Hargsoon Yoon,
Norfolk State University, United States
Youngjae Chun,
University of Pittsburgh, United States
Taihong Cheng,
Wenzhou University, China

***Correspondence:**
Jong-Seok Oh
jongseok@kongju.ac.kr
Seung-Bok Choi
seungbok@inha.ac.kr

Specialty section:
This article was submitted to Smart Materials, a section of the journal Frontiers in Materials

Received: *30 November 2018*
Accepted: *15 January 2019*
Published: *04 February 2019*

Citation:
Oh J-S and Choi S-B (2019) Ride Quality Control of a Full Vehicle Suspension System Featuring Magnetorheological Dampers With Multiple Orifice Holes. Front. Mater. 6:8. doi: 10.3389/fmats.2019.00008

INTRODUCTION

Magnetorheological (MR) fluid is considered a smart material because its rheological properties can be controlled by the application of magnetic fields. Specifically, the yield shear stress of MR fluid is easily controlled by the intensity of the magnetic field. Owing to this salient feature, numerous studies have been conducted on the development of new application devices and systems using this material, and continuous advancements are being made. Among its numerous applications, MR dampers for vehicle suspension systems have been commercialized and installed in numerous vehicles of different types, such as passenger vehicles and sport utility vehicles, for the improvement of the ride quality by controlling unwanted vibrations. Conventionally, the primary design parameters of MR dampers for vehicle suspension applications are: the magnetic gap in which MR fluids flow between the upper and lower chambers, the radius of the piston, and the bobbin structures with coil turns. By appropriately selecting these primary design parameters, successful vibration control performance can be obtained. Furthermore, when a control device malfunctions during the operation of an MR suspension system, it can still provide vibration control because of the viscosity of the MR fluid serving as its carrier liquid. Active suspension systems of vehicles also provide excellent vibration control capability during normal operation.

However, vibration control stability of an active suspension system could be lost because of a malfunction of the numerous sensors and actuators that require a sophisticated control logic and are significantly costly (Sunwoo et al., 1991).

The benefits of a semi-active MR damper are fast response time, easy controllability, and a simple structure. Dyke et al. researched an MR damper for absorbing seismic vibrations and verified the validity of a proposed analytical model of the MR damper (Dyke et al., 1996). Carson et al. researched an MR damper for vehicle suspension systems and applied a sky-hook controller to evaluate vibration control performance (Carlson et al., 1996). Choi et al. proposed a novel controller to improve the ride quality of a vehicle using the MR damper (Choi et al., 2009; Sung and Choi, 2012). In addition to the above studies, a number of studies have been conducted on the vibration control performance of passenger vehicles using electrorheological (ER) or MR dampers (Ahmadian and Pare, 2000; Choi et al., 2001; Yao et al., 2002; Poussot-Vassal et al., 2006; Brigley et al., 2008; Choi and Sung, 2008; Sung et al., 2013). All MR dampers used in these previous studies were cylindrical types in which MR fluid flows only through the magnetic gap (or orifice). This type of MR damper exhibits a steep slope of the field-dependent damping force in the low range of piston velocities, which could degrade the smooth motion of the vehicle body at low speeds. Therefore, a number of researches have proposed an MR damper which has orifice holes to allow increased MR fluid flow without any magnetic effect like in the passive viscose-resistance holes (Hong et al., 2007; Bai et al., 2013; Sohn et al., 2015; Park et al., 2016). Hong et al. researched a hydro-mechanical model to analyze the field-dependent damping force of an MR damper with orifice holes (Hong et al., 2007). Bai et al. researched an MR damper featuring inner orifice holes for increased MR fluid flow and applied it to land-vehicle suspensions for vibration control (Bai et al., 2013). Sohn et al. researched an MR damper with orifice holes in the piston and investigated its field-dependent damping force characteristics (Sohn et al., 2015). Recently, Park et al. reported that an MR damper with orifice holes exhibited a relatively lower damping force slope than an MR damper without orifice holes (Park et al., 2016).

Different ride frequencies and damping ratios are experienced by a vehicle as the front and rear wheels experience different static loads because of the weight distribution. Therefore, a difference in optimum values between the front and rear damping should be anticipated (Georgiou and Natsiavas, 2009; Albinsson and Routledge, 2019). Typically, the slope of the damping force of the front damper is high because of the mass of the engine, as shown in **Figure 1**. Therefore, in this study, MR dampers with (or without) orifice holes were used as rear or front dampers. The ride quality of the total vehicle system is then evaluated. Despite the number of studies on MR dampers with orifice holes, the relationship between the ride comfort of a vehicle and the effect of using different types of front/rear MR dampers has not yet been reported on.

The originality of this study lies in demonstrating the superior ride quality achieved by using two different types of MR dampers as opposed to one. To achieve this aim, two MR dampers, applicable to middle-sized passenger cars, are considered based on a mathematical model. Prior to investigating the ride comfort, the field-dependent damping force characteristics of two MR dampers were evaluated via simulation, and a full car mathematical model was derived. A sliding mode controller was then designed. Vibration control performance and ride quality were then investigated and evaluated under two different road profiles: bumps, and random road excitations. The reductions in both body displacements and body accelerations in the ride comfort of a vehicle equipped with two different types of MR dampers is significantly improved compared to with one using the same type of MR dampers.

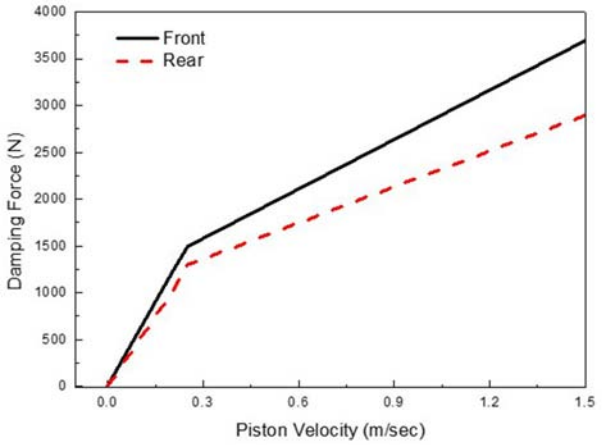

FIGURE 1 | Required damping force characteristics of passenger vehicle.

MR DAMPER

MR Damper Without Orifice Holes

Figure 2 shows the configuration of a cylindrical-type MR damper. The MR damper can be divided into upper and lower chambers, and it is filled with MR fluid. The MR fluid flows from one chamber to the other through the orifice. The gas chamber acts as an accumulator for absorbing sudden pressure variations in the lower chamber of the MR damper induced by the fast motion of the piston. By neglecting frictional forces, the damping force of the MR damper can be written as follows:

$$F_{d\_MRD} = k_e x_p + F_v + F_{MR}\,\mathrm{sgn}\left(\dot{x}_p\right) \tag{1}$$

where x_p and $\dot{x}_p$ are the piston displacement and velocity, respectively.

The first term in Equation (1) represents the spring force from the gas compliance, and the spring constant of the air chamber can be expressed as follows (Choi and Han, 2012):

$$k_e = \frac{{A_r}^2}{C_g} = \frac{P_0\kappa}{V_0}{A_r}^2 \tag{2}$$

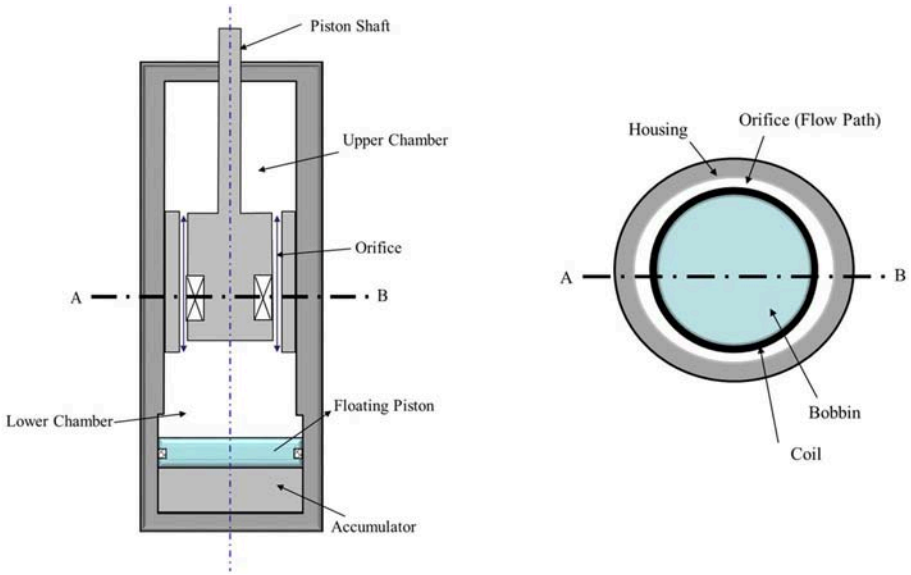

FIGURE 2 | Schematic configuration of conventional MR damper.

where A_r is the piston-rod area; P_0 and V_0 are the initial volume and pressure of the gas chamber, respectively; C_g is the gas compliance in the gas chamber;κ is the specific heat ratio.

The second term in Equation (1) represents the damping force due to the viscosity of the MR fluid. The viscous damping force of the damper is as follows:

$$\begin{aligned} F_v &= \Delta P\left(A_p - A_r\right) \\ \Delta P &= \rho g h_f \end{aligned} \tag{3}$$

where A_p and A_r are the cross-sectional areas of the piston and piston head, respectively; ΔP is the pressure difference between the upper and lower chambers; h_f is the head loss induced by the viscous friction force. As mentioned earlier, the MR fluid flows through the gap and the orifice holes. Therefore, the head loss for the annular duct and orifice holes should be derived. Initially, the annular duct flow is assumed as the flow of a duct between two parallel plates (Choi and Han, 2012). This assumption is valid because the radius of the duct is greater than the radius of the gap. From this assumption, the head loss for the annular duct is as follows:

$$\begin{aligned} h_{duct} &= f_{duct}\frac{L_{duct}}{D_{duct}}\frac{V_{duct}}{2g} = \frac{96\eta V_{duct}L_{duct}}{2g\rho {D_{duct}}^2} \\ D_{duct} &= \frac{4Wd}{2d+2W} = \lim_{W\to\infty}\frac{4Wd}{2d+2W} \cong 2d \end{aligned} \tag{4}$$

where f_{duct}, D_{duct}, and L_{duct} are the friction coefficient, the diameter, and the length of the duct, respectively; V_{duct} is the flow velocity through the duct; η is the viscosity constant of the MR fluid. As the total flow rate is identical to the flow rate at the orifice, the velocity of the duct and the viscous damping force can be obtained as follows:

$$\begin{aligned} \dot{x}_p\left(A_p - A_r\right) &= V_{duct}A_{duct} \\ F_{v\_MRD} = \rho g h_f\left(A_p - A_r\right) &= \frac{12\eta L_{duct}}{d^2}\frac{\left(A_p - A_r\right)^2}{A_{duct}}\dot{x} \end{aligned} \tag{5}$$

The third term in Equation (1) is deduced from the yield stress of the MR fluid, which can be controlled by the magnitude of the magnetic field. This phenomenon is due to the polarization induced in the particles by applying a magnetic field. The induced dipoles cause the particles to form columnar structures parallel to the applied magnetic field. This phenomenon increases the restriction in the flow direction. To describe the rheological behaviors of MR fluids, the Bingham model is adopted as follows:

$$\begin{aligned} \tau_y(B) &= A_0 + A_1B + A_2B^2 + A_3B^3 + A_4B^4 + A_5B^5 + A_6B^6 \\ B &= a_0 + a_1H + a_2H^2 + a_3H^3 + a_4H^4 + a_5H^5 + a_6H^6 \end{aligned} \tag{6}$$

where $\tau_y(B)$ is the yield shear stress and is a function of the magnetic flux density, B. This function can be expressed by the polynomial function of magnetic intensity, H. It is known that $[a_0, a_1, a_2, a_3, a_4, a_5, a_6] = [-155.548\ \ 328630593\ \ -277283388\ \ 119373779\ \ -27459273\ \ 3198253\ \ -146313.95]$. In this study, the commercial MR fluid (RMS Corp., MRF 500CP) was used. Based on the Bingham model, the controllable damping force induced from the yield stress of the MR fluid can be represented as follows:

$$F_{MR} = \left(A_p - A_r\right)\frac{cL_m}{h_m}\tau_y(B) \tag{7}$$

where L_m is the length of the magnetic pole; h_m is the gap between the magnetic poles; c is the coefficient dependent on the flow velocity profile and has a value of 2.0–3.0.

MR Damper With Orifice Holes

The schematic configuration of the proposed MR damper utilizing an orifice hole is shown in **Figure 3**. The piston head comprises a bobbin, orifice holes, and a coil. The MR fluid flows through the orifice hole and the gap between the bobbin and the outer housing of the piston head. As the orifice hole is closer to the center of the non-magnetic hollow cylinder than the coil, the magnetic flux induced from the coil is mainly applied to gap. Since the magnetic field has little effect on orifice hole, the viscous damping force model of OMRD is different with that of MRD. More information related to magnetic analysis can be found in our previous study (Sohn et al., 2015; Park et al., 2016). Since the MR fluid of the OMRD flows through the annular duct and orifice holes, the head loss for the orifice hole is represented as follows:

$$h_{by} = f_{by}\frac{L_{by}}{D_{by}}\frac{V_{by}^2}{2g} = \frac{64\eta V_{by}L_{by}}{2g\rho {D_{by}}^2} \tag{8}$$

where f_{by}, D_{by}, and L_{by} are the friction coefficient, the diameter, and the length of the orifice hole, respectively. Particularly, the other components of damping force model are identical to Equation (1). As the inlet and outlet for the annular duct and orifice hole are identical, the velocities of the annular duct (V_{duct}) and the orifice hole (V_{by}) are obtained as follows:

$$\begin{aligned} V_{by} &= \dot{x}_p\frac{(A_p - A_r)}{\left(A_{by} + \frac{2L_{by}}{3{D_{by}}^2}\frac{{D_{duct}}^2}{L_{duct}}A_{duct}\right)}, \\ V_{duct} &= \dot{x}_p\frac{(A_p - A_r)}{\left(A_{duct} + \frac{3L_{duct}}{2{D_{duct}}^2}\frac{{D_{by}}^2}{L_{by}}A_{by}\right)} \end{aligned} \tag{9}$$

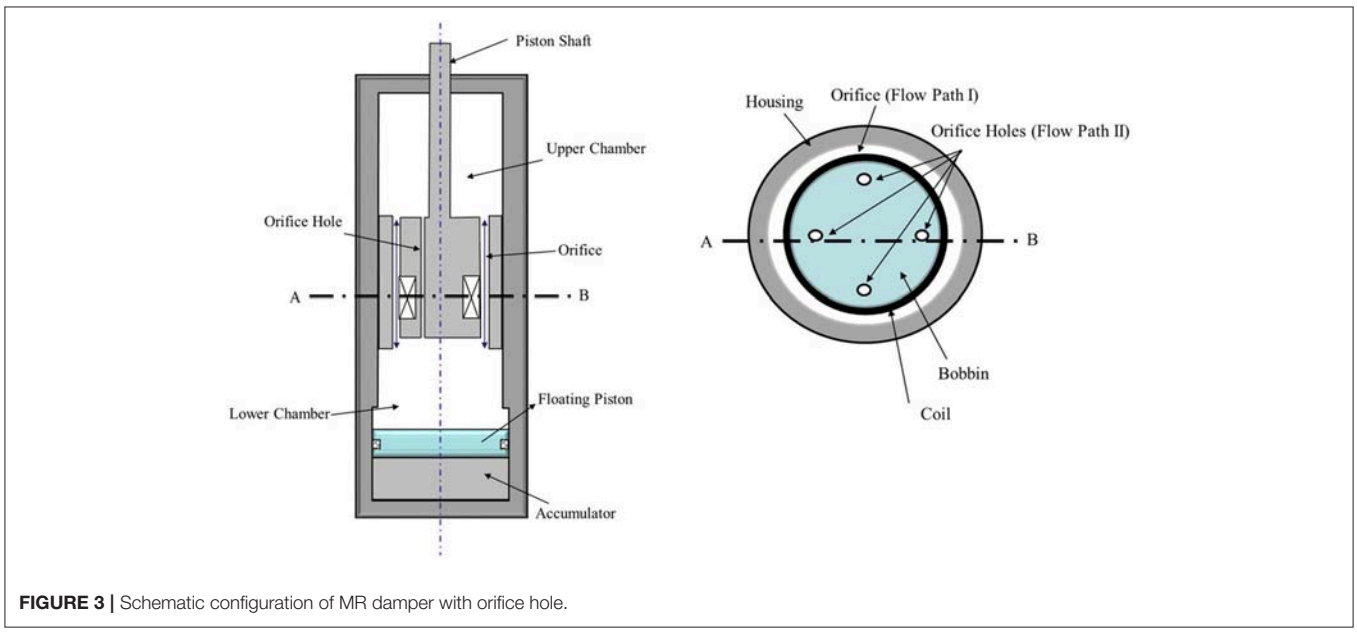

FIGURE 3 | Schematic configuration of MR damper with orifice hole.

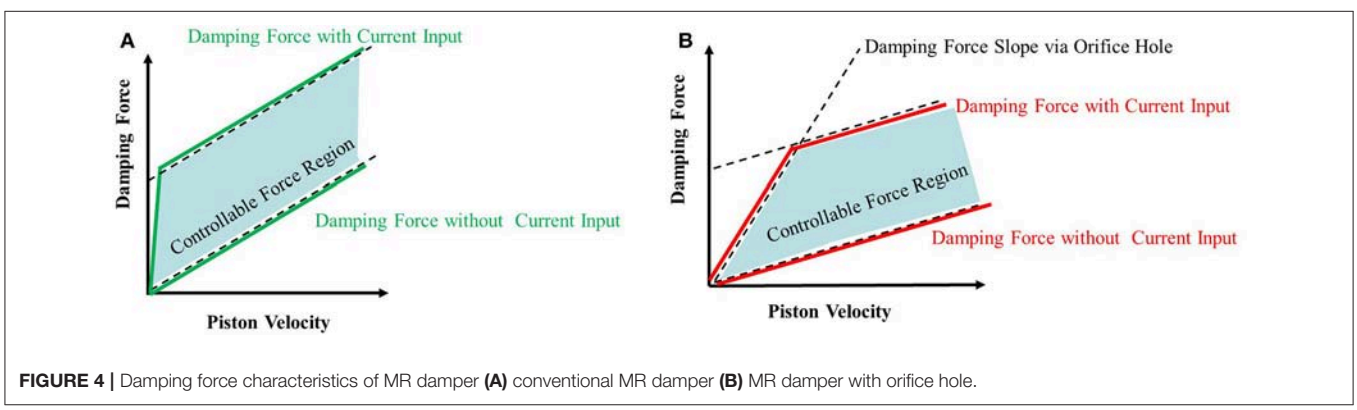

FIGURE 4 | Damping force characteristics of MR damper **(A)** conventional MR damper **(B)** MR damper with orifice hole.

By substituting Equations (8, 9) into Equation (3), the damping force induced by the viscous friction force is represented as follows:

$$F_{v\_OMRD} = \rho g h_f \left(A_p - A_r\right) = \frac{32\eta L_{by}}{{D_{by}}^2} \frac{\left(A_p - A_r\right)^2}{\left(A_{by} + \frac{2L_{by}}{3{D_{by}}^2} \frac{{D_{duct}}^2}{L_{duct}} A_{duct}\right)} \dot{x}_p$$
$$= \frac{12\eta L_{duct}}{d^2} \frac{\left(A_p - A_r\right)^2}{\left(A_{duct} + \frac{3L_{duct}}{2{D_{duct}}^2} \frac{{D_{by}}^2}{L_{by}} A_{by}\right)} \dot{x}_p \quad (10)$$

From the obtained viscous damping force model in Equations (5, 10), it is observed that the obtained viscous damping force of the OMRD is smaller than that of the MRD. In addition, when magnetic input is applied to the coil, and the damper is moved at a low piston velocity, it is difficult for the MR fluid to flow in the annular duct. The viscous damping force in the orifice hole is expressed as follows:

$$F_{v\_orifice} = \rho g h_f \left(A_p - A_r\right) = \frac{32\eta L_{by}}{{D_{by}}^2} \frac{\left(A_p - A_r\right)^2}{A_{by}} \dot{x}_p \quad (11)$$

The orifice holes are located close to the center of the bobbin to avoid the MR fluid effect on the flow motion through the orifice hole. When magnetic input is applied to the MR damper, fluid friction induced from yield stress makes the MR fluid flow via only the orifice hole. However, at high piston velocity, the viscous damping force in the orifice hole is larger than the viscous and the controllable damping force in the orifice, as shown in **Figure 4**.

TABLE 1 | Design parameters of MR dampers.

	Specification	Value	Specification	Value
Conventional MR Damper	Gap size of orifice [mm]	0.7	Length of Orifice [mm]	35
	Diameter of bobbin [mm]	37.5	Height of Coil [mm]	8.5
	Diameter of Coil [mm]	0.49	Number of Coil Turns	100
MR Damper with Orifice Hole	Number of Orifice Hole [EA]	4	Diameter of Orifice Hole [mm]	1.9

Therefore, the total damping force of the (OMRD) is expressed as follows:

$$F_{d\_OMRD} = \min\left(F_{v\_orifice}, F_{v\_OMRD} + F_{MR}\,\mathrm{sgn}\left(\dot{x}_p\right)\right) + k_e x_p \quad (12)$$

where min () means the minimum value between two damping forces. More information regarding this can be found in our previous study (Sohn et al., 2015; Park et al., 2016).

Characteristics of Damping Force

From the damping force models in Equations (1, 12), analytical calculations were implemented on a personal computer for MRD and OMRD. Appropriate design parameters were obtained to generate a maximum damping force of 4,000 N, which is the required damping force for a middle-sized passenger car. Design parameters were selected based on an input current of 3 A. The properties of the MR fluid and the design specifications of MR dampers are presented in **Table 1**. To reasonably compare the ride comfort of the vehicle under the different conditions, all design parameters of the two dampers were identical, except for the orifice holes. The number of orifice hole is 4, and the diameter of the orifice hole is 2.5 mm.

Figures 5A–C shows the calculated damping force curves. Firstly, under the same input current, the maximum damping force of the OMRD is lower than that of the MRD. The maximum damping forces of each damper are 4,238 N, 3,890 N, and 3,657 N, respectively. Additionally, the damping force gradients at 0 A are 1,534 $N \cdot s/m$, 1,303.5 $N \cdot s/m$, and 1,148 $N \cdot s/m$, respectively. This is the result of the additional flow rate via the orifice holes, which are not affected by the input current, reducing the damping force. It can be inferred from these results that the orifice hole limits the maximum damping force. However, this does not imply that the damping force can be controlled by orifice holes. Secondly, parameter study of MR damper with orifice hole had been conducted and the results can be found in our previous study (Sohn et al., 2015). From previous study results, the number of orifice holes is considered as dominant factor among many design parameters. From **Figure 5**, it is known that the damping force of OMRD is smaller than that of MRD. Also, the low damping characteristic is generally known as essential for superior ride quality (Els et al., 2007). So, it can be expected that MR damper with many orifice hole ensure

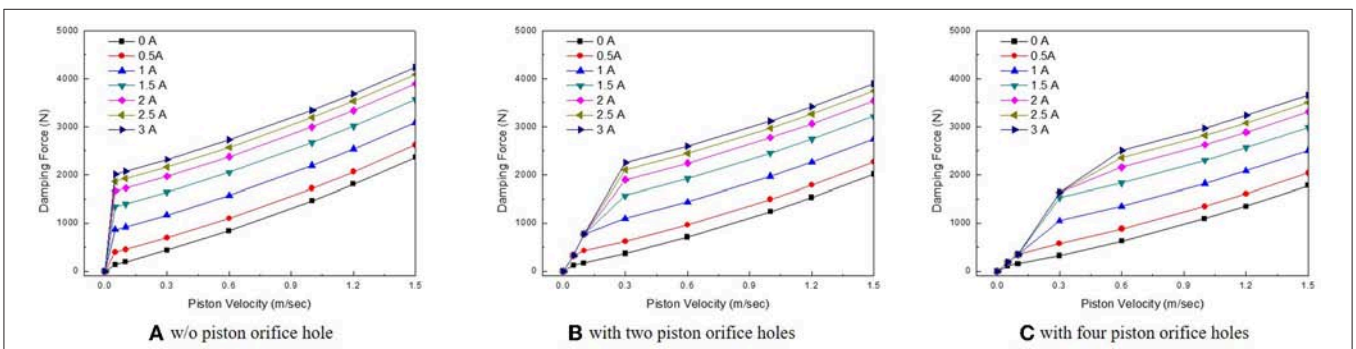

FIGURE 5 | Simulated field-dependent damping force **(A)** w/o piston orifice hoel **(B)** with two piston orifice holes **(C)** with four piston orifice holes.

good ride quality. Although the main objective of this work is to evaluate the ride quality of MRD and OMRD, optimal design of MR damper related to damping capability also very important for commercialization so it will be conducted as a future study. Thirdly, **Figures 5B,C** show that the orifice holes reduce the occurrence of sudden increases in the field-dependent damping force at low piston velocities. In other words, the damping force with 4 orifice holes is smaller than that with 2 orifice holes. The maximum difference in damping force is 1831.5 N at low velocity (approximately 0.05 m/sec) at 3 A. This difference in the trend of damping force controllability by the magnitude of the current will result in different ride qualities for the vehicles. Accordingly, in order to compare the performance in ride quality, MRD and OMRD with 4 orifice holes will be considered at next chapter.

Performance Evaluation of Ride Comfort

As discussed earlier, as the front and rear wheels experience different static loads because of weight distribution, different values are applied. Therefore, it is anticipated that the required damping force characteristics of the front or rear suspension are in agreement with those of the MRD or OMRD. To investigate this, different vehicle case studies were conducted:

Vehicle I: Four identical MRDs are installed for the front and rear suspension.
Vehicle II: Two MRDs (or two OMRDs) are installed for the front (or rear) suspension.

In addition, a robust sliding mode controller was designed and applied identically to all vehicles. By comparing the control performance, we aim to demonstrate the effectiveness of the proposed method.

Vehicle Suspension System

The mathematical model of the full car system with four MR shock absorbers is constructed as shown in **Figure 6**. The vehicle body (sprung mass) is assumed to be rigid and has three degrees of freedom (vertical, pitch, and roll directions). The sprung mass is connected to four unsprung masses that have a vertical degree of freedom. The full car model includes body bounce (z_g), body roll (φ), body pitch (θ), wheel hop (z_1, z_2, z_3, and z_4), and independent road excitations (r_1, r_2, r_3, and r_4). The ride comfort of a passenger could be significantly affected because of the vibrations in the bounce, pitch, and roll directions. Therefore, in this study, the design configuration of the proposed MR damper and controllers was simulated to consider these multiple vibration modes. From **Figure 6**, the governing equations of motion are derived as follows (Jazar, 2017):

$$
\begin{aligned}
M\ddot{x} &= -c_f\left(\dot{x}-\dot{x}_1+b_1\dot{\phi}-a_1\dot{\theta}\right)-c_f\left(\dot{x}-\dot{x}_2-b_2\dot{\phi}-a_1\dot{\theta}\right)\\
&\quad - c_r\left(\dot{x}-\dot{x}_3-b_2\dot{\phi}+a_2\dot{\theta}\right)-c_r\left(\dot{x}-\dot{x}_4+b_1\dot{\phi}+a_2\dot{\theta}\right)\\
&\quad - k_f(x-x_1+b_1\phi-a_1\theta)-k_f(x-x_2-b_2\phi-a_1\theta)\\
&\quad - k_r(x-x_3-b_2\phi+a_2\theta)-k_r(x-x_4+b_1\phi+a_2\theta)\\
&\quad + F_{MR1}+F_{MR2}+F_{MR3}+F_{MR4}\\
I_x\ddot{\phi} &= -b_1c_f(\dot{x}-\dot{x}_1+b_1\dot{\phi}-a_1\dot{\theta})+b_2c_f(\dot{x}-\dot{x}_2-b_2\dot{\phi}-a_1\dot{\theta})\\
&\quad + b_2c_r(\dot{x}-\dot{x}_3-b_2\dot{\phi}+a_2\dot{\theta})-b_1c_r(\dot{x}-\dot{x}_4+b_1\dot{\phi}+a_2\dot{\theta})\\
&\quad - b_1k_f(x-x_1+b_1\phi-a_1\theta)+b_2k_f(x-x_2-b_2\phi-a_1\theta)\\
&\quad + b_2k_r(x-x_3-b_2\phi+a_2\theta)-b_1k_r(x-x_4+b_1\phi+a_2\theta)\\
&\quad + b_1F_{MR1}-b_2F_{MR2}-b_2F_{MR3}+b_1F_{MR4}\\
I_y\ddot{\theta} &= a_1c_f(\dot{x}-\dot{x}_1+b_1\dot{\phi}-a_1\dot{\theta})+a_1c_f(\dot{x}-\dot{x}_2-b_2\dot{\phi}-a_1\dot{\theta})\\
&\quad - a_2c_r(\dot{x}-\dot{x}_3-b_2\dot{\phi}+a_2\dot{\theta})-a_2c_r(\dot{x}-\dot{x}_4+b_1\dot{\phi}+a_2\dot{\theta})\\
&\quad + a_1k_f(x-x_1+b_1\phi-a_1\theta)+a_1k_f(x-x_2-b_2\phi-a_1\theta)\\
&\quad - a_2k_r(x-x_3-b_2\phi+a_2\theta)-a_2k_r(x-x_4+b_1\phi+a_2\theta)\\
&\quad - a_1F_{MR1}-a_1F_{MR2}+a_2F_{MR3}+a_2F_{MR4}\\
m_f\ddot{x}_1 &= c_f(\dot{x}-\dot{x}_1+b_1\dot{\phi}-a_1\dot{\theta})+k_f(x-x_1+b_1\phi-a_1\theta)\\
&\quad - k_{tf}(x_1-y_1)-F_{MR1}\\
m_f\ddot{x}_2 &= c_f(\dot{x}-\dot{x}_2-b_2\dot{\phi}-a_1\dot{\theta})+k_f(x-x_2-b_2\phi-a_1\theta)\\
&\quad - k_{tf}(x_2-y_2)-F_{MR2}\\
m_r\ddot{x}_3 &= c_r(\dot{x}-\dot{x}_3-b_2\dot{\phi}+a_2\dot{\theta})+k_r(x-x_3-b_2\phi+a_2\theta)
\end{aligned}
$$

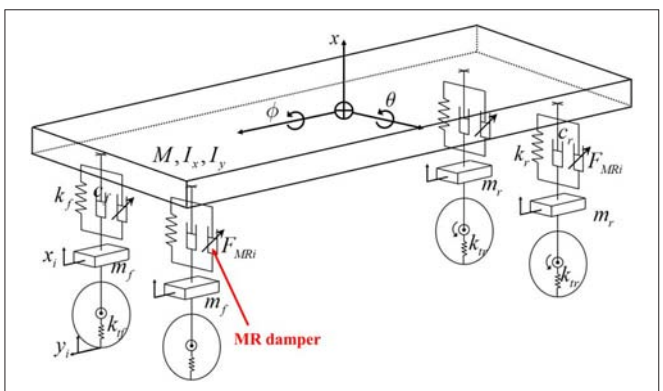

FIGURE 6 | Mechanical model of a full passenger vehicle system with MR dampers.

TABLE 2 | Parameters of passenger vehicle system.

	Specification	Value	Specification	Value
Vehicle I (with same MRD)	Sprung mass [kg]	1,370	Unsprung mass [kg]	80
	Longitudinal mass moments of inertia [kg·m^2]	356.3	Lateral mass moments of inertia [kg·m^2]	1,159.6
	Front suspension stiffness constant [N/m]	153,000	Rear suspension stiffness constant [N/m]	82,000
	Tire stiffness constant [N/m]	230,000	Damping coefficient [N·sec/m]	1,534
	Distance from C.G. to front suspensions [m]	1.11	Distance from C.G. to rear suspensions [m]	1.1666
	Distance from C.G. to left suspensions [m]	0.335	Distance from C.G. to right suspensions [m]	0.335
MR damper with orifice hole	Front damping coefficient [N·sec/m]	1,534	rear damping coefficient [N·sec/m]	1,148

$$
\begin{aligned}
&- k_{tr}(x_3 - y_3) - F_{MR3} \\
m_r\ddot{x}_4 &= c_r(\dot{x} - \dot{x}_4 + b_1\dot{\phi} + a_2\dot{\theta}) + k_r(x - x_4 + b_1\phi + a_2\theta) \\
&- k_{tr}(x_4 - y_4) - F_{MR4}
\end{aligned} \tag{13}
$$

where M is the sprung mass; m_f and m_r are the front and rear unsprung masses, respectively; I_x and I_y are the longitudinal and lateral mass moments of inertia, respectively; k_f and k_r are the front and rear suspension stiffness constant, respectively; k_t is the tire stiffness; c_f and c_r are the front and rear suspension damping coefficients, respectively; and a_1, a_2, b_1, and b_2 are the distances from the center of gravity to each sprung mass and shock absorber.

By defining the state vector of the vehicle dynamic system as $\mathbf{X} = \left[x\ \dot{x}\ \phi\ \dot{\phi}\ \theta\ \dot{\theta}\ x_1\ \dot{x}_1\ x_2\ \dot{x}_2\ x_3\ \dot{x}_3\ x_4\ \dot{x}_4\right]^T$, the state space model for the vehicle dynamic system can be rewritten as follows:

$$
\begin{aligned}
\dot{\mathbf{X}} &= \mathbf{AX} + \mathbf{BU} + \Gamma\mathbf{D} \\
\mathbf{Y} &= \mathbf{CX}
\end{aligned} \tag{14}
$$

Where **A**, **B**, Γ, **C**, **U**, and **D**are defined in **Appendix 1**. **Y**is the piston velocity matrix of each damper. **Table 2** presents the mechanical properties of the vehicle system, and in it the spring and damping properties of the front and rear suspensions are different.

Controller Design

To evaluate the control performance, a sliding mode controller (SMC), which has an inherent robustness against system uncertainties and disturbances (Edwards and Spurgeon, 1998; Utkin et al., 1999), was designed. Before designing the SMC, multiple inputs of the vehicle system in Equation (13) are transformed as follows:

$$
\begin{bmatrix} u_1 \\ u_2 \\ u_3 \\ u_4 \end{bmatrix} = T \begin{bmatrix} F_{MR1} \\ F_{MR2} \\ F_{MR3} \\ F_{MR4} \end{bmatrix} = \begin{bmatrix} 1 & 1 & 1 & 1 \\ b_1 & -b_2 & -b_2 & b_1 \\ -a_1 & -a_1 & a_2 & a_2 \\ -1 & 0 & 0 & 0 \end{bmatrix} \begin{bmatrix} F_{MR1} \\ F_{MR2} \\ F_{MR3} \\ F_{MR4} \end{bmatrix} \tag{15}
$$

To regulate the generalized inputs, the sliding surfaces are designed as follows:

$$
\begin{aligned}
\mathrm{s}_1 &= \mathbf{G}_1\mathbf{X} = c_1 x + \dot{x} \\
\mathrm{s}_2 &= \mathbf{G}_2\mathbf{X} = c_2\phi + \dot{\phi} \\
\mathrm{s}_3 &= \mathbf{G}_3\mathbf{X} = c_3\theta + \dot{\theta} \\
\mathrm{s}_4 &= \mathbf{G}_4\mathbf{X} = c_4 x_1 + \dot{x}_1
\end{aligned} \tag{16}
$$

A control law must be selected to drive the system state to the sliding surface $\mathrm{s} = 0$, in which the following reachability condition is satisfied:

$$
s_i\dot{s}_i \le -\eta\left|s_i(t)\right|,\ i = 1, 2, 3, 4 \tag{17}
$$

where η is a strictly positive constant. To satisfy the reachability condition in Equation (17), the control input is determined as follows:

$$
u_i = -(\mathbf{G}_i\mathbf{B}_i)^{-1}\left[\mathbf{G}_i\mathbf{AX}(t) + k_i \cdot \mathrm{sgn}(s_i(t))\right] \tag{18}
$$

where $\mathrm{sgn}(\cdot)$ is a signum function andk_i is the discontinuous gain which is designed to overcome the uncertainty of the passenger vehicle system. The left side of Equation (16) is expressed as follows:

$$
\begin{aligned}
\mathrm{s}\dot{\mathrm{s}} &= s_i\mathbf{G}_i\dot{\mathbf{x}} \\
&= \mathrm{s}_i\left[\mathbf{G}_i\mathbf{AX} + \mathbf{G}_i\mathbf{B}_i\mathbf{U} + \mathbf{G}_i\Gamma\mathbf{D}\right] \\
&= \mathrm{s}_i\left[\mathbf{G}_i\mathbf{AX} - \left[\mathbf{G}_i\mathbf{AX} + k_i \cdot \mathrm{sgn}(s(t))\right] + \mathbf{G}_i\Gamma\mathbf{D}\right] \\
&= \mathrm{s}_i\left[-k_i \cdot \mathrm{sgn}(s(t)) + \mathbf{G}_i\Gamma\mathbf{D}\right] \\
&\le |\mathrm{s}_i|\left(-k_i\right)
\end{aligned} \tag{19}
$$

Therefore, to ensure that the condition (17) holds, the discontinuous control gain in Equation (18) is chosen as follows:

$$
k_i > |\mathbf{G}_i\Gamma\mathbf{D}| \tag{20}
$$

Moreover, the signum function is switched with a saturation function to avoid the problem of chattering:

$$
sat(s_i(t)) = \begin{cases} \frac{s_i(t)}{\varepsilon}, & |s(t)| \le \varepsilon \\ \mathrm{sgn}(s_i(t)), & |s(t)| > \varepsilon \end{cases} \tag{21}
$$

where ε is the boundary layer width of the saturation function. Finally, the control input voltage is determined as follows:

$$
u_i = -(\mathbf{G}_i\mathbf{B}_i)^{-1}\left[\mathbf{G}_i\mathbf{AX} + k_i \cdot sat(\mathrm{s}_i(t))\right] \tag{22}
$$

Then the generalized inputs are transformed to original inputs of the vehicle system via the inverse matrix of T.

The block diagram of the control strategy is shown in **Figure 7**, from which the minimum and maximum damping forces are calculated based on the damping force model and piston velocity. When the desired damping force is obtained from the sliding mode controller in Equation (22), the final damping force is determined by comparing the minimum and maximum values.

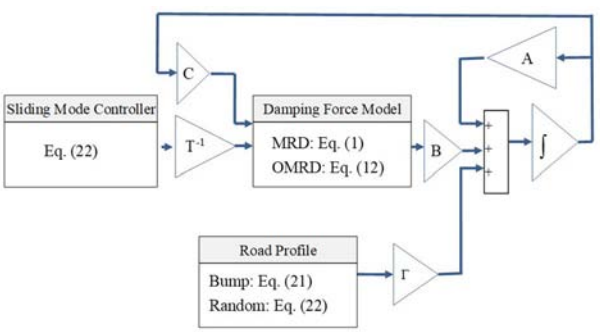

FIGURE 7 | Block diagram of semi-active vehicle system.

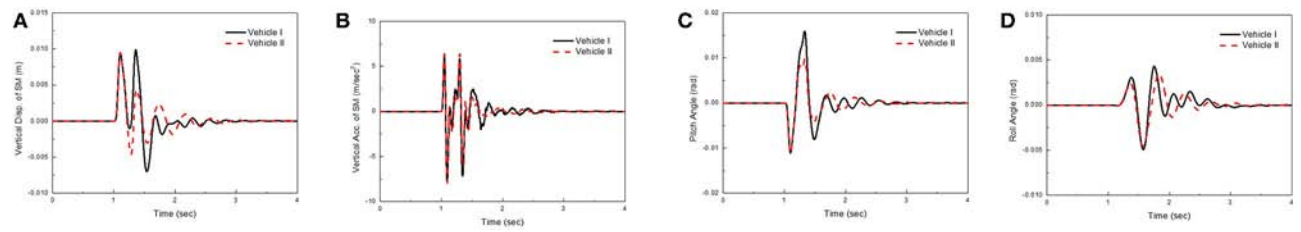

FIGURE 8 | Bump road responses at 40 km/h **(A)** vertical displacement **(B)** vertical acceleration **(C)** pitch angle **(D)** roll angle.

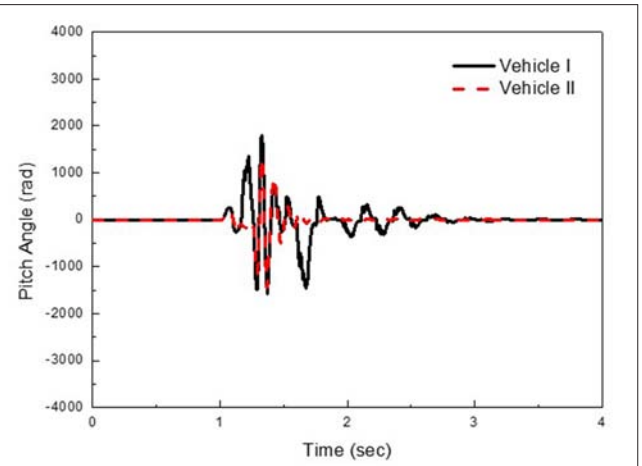

FIGURE 9 | Applied total damping force of rear right damper for bump road responses.

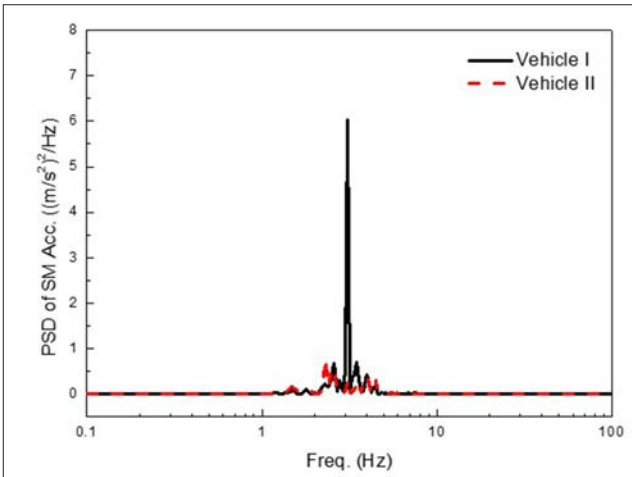

FIGURE 10 | Random road responses at 72 km/h.

RESULTS AND DISCUSSIONS

The MR suspension system should be installed on an actual vehicle and its effectiveness for ride comfort should be evaluated under various road conditions. However, it is expensive to manufacture a full vehicle system from scratch with hardware. Therefore, the ride quality performance and MR dampers are evaluated by computer simulation. A number of previous studies have reported that simulation results are in relatively good agreement with field test results (Seong et al., 2011, 2012; Park et al., 2016).

In this study, suspension control performance was evaluated under two types of road conditions. The first excitation, which is typically used to reveal the transient response characteristics, is a bump described by:

$$y_i = z_b\left(1 - \cos\left(\frac{2\pi V}{D}t\right)\right), \quad i = 1, 2, 3, 4 \tag{23}$$

where z_b is half of the bump height (0.035 m), and D is the width of the bump (0.8 m). In the bump excitation, the vehicle crosses the bump at a constant vehicle velocity of 40 km/h (11.12 m/s). The second type of road excitation is a stationary random process with zero mean, described by White (1994):

$$\dot{y}_i + \rho_r V y_i = W_n, \quad i = 1, 2, 3, 4 \tag{24}$$

where W_n is the white noise with intensity $2\sigma^2\rho_r V$; ρ_r is the road roughness parameter, 0.45 m^{-1}; σ^2 is the covariance of white noise, 300 mm^2. For random excitations, the road irregularity values were chosen by supposing that the vehicle drives on a paved road at a constant velocity of 72 km/h (20 m/s).

Figures 8, **9** show road bump responses under road bump excitation. It is typically accepted that the acceleration of the sprung mass is used to evaluate ride comfort. As seen in **Figure 8**, unwanted vibrations induced from the bump excitations have been significantly reduced by adopting the different damper combinations. It was also observed from the vertical displacement of the sprung mass, vertical acceleration of the sprung mass, pitch angle, and roll angle that the ride comfort of **Vehicle II** is superior to that of **Vehicle I**.

Figure 10 shows random road responses at a constant vehicle velocity of 72 km/h (20 m/s). The power spectral density (PSD) of the vertical acceleration is plotted against frequency. As anticipated, the PSDs for the vertical acceleration of **Vehicle II** are significantly decreased compared to those of **Vehicle I,** from 2.62 to 0.1364 $(m/s^2)^2$/Hz at 3.1 Hz. The suspension control performances shown in **Figures 8–10** indicates that the ride comfort of the vehicle can be simultaneously improved by employing two front MRDs and two rear OMRDs.

CONCLUSION

In this study, the ride comfort of passenger vehicles equipped with different combinations of front/rear suspension systems featuring two different types of MR dampers, with and without orifice holes, were compared. To achieve this aim, the damping force model of the two different MR dampers were analyzed. It was observed that the OMRD exhibited a smaller damping force than the MRD. To evaluate the ride quality, a robust sliding mode controller was designed. It was demonstrated that displacement, acceleration of the vehicle body, and pitch angle could be significantly reduced by activating the MR dampers under two road conditions: bumps, and random roads. In particular, it was shown that the ride quality performance of the vehicle with different damper combinations was superior to that of a vehicle with the same type of MR dampers. This was because of the small damping force in the low piston velocity range. In other words, by eliminating sudden increases in the field-dependent damping force, smooth and comfortable vehicle motions are obtained. In the second phase of this study, two semi-active MR dampers will be manufactured, and the ride comfort of both will be tested under various road conditions.

AUTHOR CONTRIBUTIONS

All authors listed have made a substantial, direct and intellectual contribution to the work, and approved it for publication.

ACKNOWLEDGMENTS

This work was supported by the Technology Innovation Program (Intelligent landing gear with variable damping force for 1500lb class) (10073291) funded by the Ministry of Trade, Industry & Energy (MOTIE, Korea).

REFERENCES

Ahmadian, M., and Pare, C. A. (2000). A quarter-car experimental analysis of alternative semiactive control methods. *J. Intell. Matreial Syst. Struct.* 11, 604–612. doi: 10.1106/MR3W-5D8W-0LPL-WGUQ

Albinsson, A., and Routledge, C. (2019). *The Damper Levels Influence on Vehicle Roll, Pitch, Bounce and Cornering Behaviour of Passenger Vehicles*. Master's thesis in automotive engineering, Department of Applied Mechanics, Division of Vehicle Engineering and Autonomous Systems, Chalmers University of Technology, Sweden.

Bai, X., Hu, W., and Wereley, N. M. (2013). Magnetorheological damper utilizing an inner bypass for ground vehicle suspensions. *IEEE Trans. Magnetics* 49, 3422–3425. doi: 10.1109/TMAG.2013.2241402

Brigley, M., Choi, Y. T., and Wereley, N. M. (2008). Experimental and theoretical development of multiple fluid mode magnetorheological isolators. *J. Guidance Control Dyn.* 31, 449–459. doi: 10.2514/1.32969

Carlson, J. D., Cantanzarite, D. M., and St. Clair, K. A. (1996). Commercial magneto-rheological fluid devices. *Int. J. Modern Phys. B.* 10, 2857–2865. doi: 10.1142/S0217979296001306

Choi, S. B., and Han, Y. M. (2012). *Magnetorheological Fluid Technology Applications in Vehicle Systems.* Padstow: CRC Press Taylor and Francis Group.

Choi, S. B., Lee, H., K., and Chang, E. G. (2001). Field test results of a semi-active ER suspension systems associated with skyhook controller. *Mechatronics* 11, 345–353. doi: 10.1016/S0957-4158(00)00022-2

Choi, S. B., Seong, M. S., and Ha, S. H. (2009). Vibration control of an MR vehicle suspension system considering both hysteretic behavior and parameter variation. *Smart Mater. Struct.* 18:125010. doi: 10.1088/0964-1726/18/12/125010

Choi, S. B., and Sung, K. G. (2008). Vibration control of magnetorheological damper system subjected to parameter variations. *Int. J. Vehicle Design* 45, 94–110. doi: 10.1504/IJVD.2008.017071

Dyke, S. J., Spencer, B. F., Sain, M. K. S., and Carlson, J. D. (1996). "A new semi-active control device for seismic response reduction,"in *Proceeding of 11th ASCE Engrg. Mech. Spec. Conf. ASCE* (Fort Lauderdale, UL), 886–889.

Edwards, C., and Spurgeon, S. (1998). *Sliding Mode Control*. London: CRC Press.

Els, P. S., Theron, N. J., Uys, P. E., and Thoresson, M. J. (2007). The ride comfort vs. handling compromise for off-road vehicles. *J. Terramech.* 44, 303–317. doi: 10.1016/j.jterra.2007.05.001

Georgiou, G., and Natsiavas, S. (2009). Optimal selection of suspension parameters in large scale vehicle models. *Vehicle Syst. Dyn.* 47, 1147–1166. doi: 10.1080/00423110802531075

Hong, S. R., Wang, G., Hu, W., Wereley, N. M., and Choi, S. B. (2007). "Hydro-mechanical Analysis of a Magnetorheological Bypass Damper," *Proceedings of the 10th International Conference on Electrorheological Fluids and Magnetorheological Suspensions*. (Singapore, World Scientific Publishing Company). 438–444.

Jazar, R. N. (2017). *Vehicle Dynamics: Theory and Application*. Berlin: Springer

Park, J. H., Kim, W. H., Shin, C. S., and Choi, S. B. (2016). A comparative work on vibration control of a quarter car suspension system with two different magneto-rheological dampers. *Smart Mater. Struct.* 26:015009. doi: 10.1088/1361-665X/26/1/015009

Poussot-Vassal, C., Sename, O., Dugard, L., Ramirez-Mendoza, R., and Flores, L. (2006). Optimal skyhook control for semiactive suspensions. *IFAC Proc.* 39, 608–613. doi: 10.3182/20060912-3-DE-2911.00106

Seong, M. S., Choi, S. B., and Kim, C. H. (2011). Design and performance evaluation of MR damper for integrated isolation mount. *J. Intell. Mater. Syst. Struct.* 22, 1729–1738. doi: 10.1177/1045389X11421820

Seong, M. S., Choi, S. B., and Lee, Y. S. (2012). Vibration control of quarter vehicle magnetorheological suspension using preisach hysteretic compensator. *Adv. Sci. Lett.* 13, 540–546. doi: 10.1166/asl.2012.3883

Sohn, J. W., Oh, J. S., and Choi, S. B. (2015). Design and novel type of a magnetorheological damper featuring piston bypass hole. *Smart Mater. Struct.* 24:035013. doi: 10.1088/0964-1726/24/3/035013

Sung, K. G., and Choi, S. B. (2012). Magnetorheological fluid shock absorber for electronic control suspension of a passenger vehicle. *Adv. Sci. Lett.* 14, 495–498. doi: 10.1166/asl.2012.3982

Sung, K. G., Seong, M. S., and Choi, S. B. (2013). Performance evaluation of electronic control suspension featuring vehicle ER dampers. *Meccanica* 48, 121–134. doi: 10.1007/s11012-012-9588-4

Sunwoo, M. H., Cheok, K. C., and Huang, N. J. (1991). Model reference adaptive control for vehicle active suspension system. *IEEE Trans. Industr. Electr.* 38, 217–222. doi: 10.1109/41.87590

Utkin, V., Guldner, J., and Shi, J. (1999). *Sliding Mode Control in Electromechanical Systems*. London; Boca Raton, FL: CRC Press.

White, F. M. (1994). *Fluid Mechanics, 5th Edn*. New York: McGraw-Hill.

Yao, G. Z., Yap, F., Chen, G., Li, W. H., and Yeo, S. H. (2002). MR damper and its application for semi-active control vehicle suspension system *Mechatronics* 12, 963–973. doi: 10.1016/S0957-4158(01)00032-0

Conflict of Interest Statement: The authors declare that the research was conducted in the absence of any commercial or financial relationships that could be construed as a potential conflict of interest.

APPENDIX I

$$\mathbf{A} = \begin{bmatrix}
0 & 1 & 0 & 0 & 0 & 0 & 0 & 0 & 0 & 0 & 0 & 0 \\
\frac{-2k_f-2k_r}{M} & \frac{-2c_f-2c_r}{M} & \frac{-b_1k_f+b_2k_f+b_2k_r-b_1k_r}{M} & \frac{-b_1c_f+b_2c_f+b_2c_r-b_1c_r}{M} & \frac{2a_1k_f-2a_2k_r}{M} & \frac{2a_1c_f-2a_2c_r}{M} & \frac{k_f}{M} & \frac{c_f}{M} & \frac{k_f}{M} & \frac{c_f}{M} & \frac{k_r}{M} & \frac{c_r}{M} \\
0 & 0 & 0 & 1 & 0 & 0 & 0 & 0 & 0 & 0 & 0 & 0 \\
\frac{-b_1k_f+b_2k_f+b_2k_r-b_1k_r}{I_z} & \frac{-b_1c_f+b_2c_f+b_2c_r-b_1c_r}{I_z} & \frac{-b_1{}^2k_f-b_2^2k_f-b_2^2k_r-b_1^2k_r}{I_z} & \frac{-b_1^2c_f-b_2{}^2c_f-b_2^2c_r-b_1^2c_r}{I_z} & \frac{a_1b_1k_f-a_1b_2k_f+a_2b_2k_r-a_2b_1k_r}{I_z} & \frac{a_1b_1c_f-a_1b_2c_f+a_2b_2c_r-a_2b_1c_r}{I_z} & \frac{b_1k_f}{I_z} & \frac{b_1c_f}{I_z} & \frac{-b_2k_f}{I_z} & \frac{-b_2c_f}{I_z} & \frac{-b_2k_r}{I_z} & \frac{-b_2c_r}{I_z} & \frac{b_1k_r}{I_z} & \frac{b_1c_r}{I_z} \\
0 & 0 & 0 & 0 & 0 & 1 & 0 & 0 & 0 & 0 & 0 & 0 \\
\frac{2a_1k_f-2a_2k_r}{I_y} & \frac{2a_1c_f-2a_2c_r}{I_y} & \frac{a_1b_1k_f-a_1b_2k_f+a_2b_2k_r-a_2b_1k_r}{I_y} & \frac{a_1b_1c_f-a_1b_2c_f+a_2b_2c_r-a_2b_1c_r}{I_y} & \frac{-2a_1^2k_f-2a_2^2k_r}{I_y} & \frac{-2a_1^2c_f-2a_2{}^2c_r}{I_y} & \frac{-a_1k_f}{I_y} & \frac{-a_1c_f}{I_y} & \frac{-a_1k_f}{I_y} & \frac{-a_1c_f}{I_y} & \frac{a_2k_r}{I_y} & \frac{a_2c_r}{I_y} & \frac{a_2k_r}{I_y} & \frac{a_2c_r}{I_y} \\
0 & 0 & 0 & 0 & 0 & 0 & 0 & 1 & 0 & 0 & 0 & 0 \\
\frac{k_f}{m_f} & \frac{c_f}{m_f} & \frac{b_1k_f}{m_f} & \frac{b_1c_f}{m_f} & \frac{-a_1k_f}{m_f} & \frac{-a_1c_f}{m_f} & \frac{-k_f-k_f}{m_f} & \frac{-c_f}{m_f} & 0 & 0 & 0 & 0 \\
0 & 0 & 0 & 0 & 0 & 0 & 0 & 0 & 0 & 1 & 0 & 0 \\
\frac{k_f}{m_f} & \frac{c_f}{m_f} & \frac{-b_2k_f}{m_f} & \frac{-b_2c_f}{m_f} & \frac{-a_1k_f}{m_f} & \frac{-a_1c_f}{m_f} & 0 & 0 & \frac{-k_{tf}-k_f}{m_f} & \frac{-c_f}{m_f} & 0 & 0 \\
0 & 0 & 0 & 0 & 0 & 0 & 0 & 0 & 0 & 0 & 1 & 0 \\
\frac{k_r}{m_r} & \frac{c_r}{m_r} & \frac{-b_2k_r}{m_r} & \frac{-b_2c_r}{m_r} & \frac{a_2k_r}{m_r} & \frac{a_2c_r}{m_r} & 0 & 0 & 0 & 0 & \frac{-k_{tr}-k_r}{m_r} & \frac{-c_r}{m_r} \\
0 & 0 & 0 & 0 & 0 & 0 & 0 & 0 & 0 & 0 & 0 & 1 \\
\frac{k_r}{m_r} & \frac{c_r}{m_r} & \frac{b_1k_r}{m_r} & \frac{b_1c_r}{m_r} & \frac{a_2k_r}{m_r} & \frac{a_2c_r}{m_r} & 0 & 0 & 0 & 0 & 0 & 0 & \frac{-k_{tr}-k_r}{m_r} & \frac{-c_r}{m_r}
\end{bmatrix}$$

$$\mathbf{B} = \begin{bmatrix}
0 & 0 & 0 & 0 \\
\frac{1}{M} & \frac{1}{M} & \frac{1}{M} & \frac{1}{M} \\
0 & 0 & 0 & 0 \\
\frac{b_1}{I_z} & \frac{-b_2}{I_z} & \frac{-b_2}{I_z} & \frac{b_1}{I_z} \\
0 & 0 & 0 & 0 \\
\frac{-a_1}{I_y} & \frac{-a_1}{I_y} & \frac{a_2}{I_y} & \frac{a_2}{I_y} \\
0 & 0 & 0 & 0 \\
\frac{-1}{m_f} & 0 & 0 & 0 \\
0 & 0 & 0 & 0 \\
0 & \frac{-1}{m_f} & 0 & 0 \\
0 & 0 & 0 & 0 \\
0 & 0 & \frac{-1}{m_r} & 0 \\
0 & 0 & 0 & 0 \\
0 & 0 & 0 & \frac{-1}{m_r}
\end{bmatrix}, \quad \Gamma = \begin{bmatrix}
0 & 0 & 0 & 0 \\
0 & 0 & 0 & 0 \\
0 & 0 & 0 & 0 \\
0 & 0 & 0 & 0 \\
0 & 0 & 0 & 0 \\
0 & 0 & 0 & 0 \\
\frac{k_{tf}}{m_f} & 0 & 0 & 0 \\
0 & 0 & 0 & 0 \\
0 & \frac{k_{tf}}{m_f} & 0 & 0 \\
0 & 0 & 0 & 0 \\
0 & 0 & \frac{k_{tr}}{m_r} & 0 \\
0 & 0 & 0 & 0 \\
0 & 0 & 0 & \frac{k_{tr}}{m_r}
\end{bmatrix}, \quad \mathbf{C} = \begin{bmatrix}
0 & 1 & 0 & b_1 & 0 & -a_1 & 0 & -1 & 0 & 0 & 0 & 0 & 0 & 0 \\
0 & 1 & 0 & -b_2 & 0 & -a_1 & 0 & 0 & 0 & -1 & 0 & 0 & 0 & 0 \\
0 & 1 & 0 & -b_2 & 0 & a_2 & 0 & 0 & 0 & 0 & 0 & -1 & 0 & 0 \\
0 & 1 & 0 & b_1 & 0 & a_2 & 0 & 0 & 0 & 0 & 0 & 0 & 0 & -1
\end{bmatrix}$$

frontiers in Materials

ORIGINAL RESEARCH
published: 26 March 2019
doi: 10.3389/fmats.2019.00047

Swelling, Thermal, and Shear Properties of a Waste Tire Rubber Based Magnetorheological Elastomer

Ubaidillah[1], Endra Dwi Purnomo[1], Hanafi Ismail[2], Seung-Bok Choi[3]*, Aishah Abdul Aziz[4] and Saiful Amri Mazlan[4]**

[1] *Fungsional Materials and Actuators Laboratory, Mechanical Engineering Department, Universitas Sebelas Maret, Surakarta, Indonesia,* [2] *School of Materials and Mineral Resources Engineering, USM Engineering, Nibong Tebal, Malaysia,* [3] *Department of Mechanical Engineering, Inha University, Incheon, South Korea,* [4] *Engineering Materials and Structures (eMast) iKohza, Malaysia Japan International Institute of Technology (MJIIT), Universiti Teknologi Malaysia, Kuala Lumpur, Malaysia*

In this study, the achievement of revulcanization, thermal stability, and rheological behaviors of waste tire rubber (WTR), based magnetorheological elastomers (MREs), were evaluated to convince their applicability as one of smart material possessing the field-dependent tuning capability of material characteristics such as complex modulus. The cross-linking density of the MREs was assessed through the swelling test to ratify the degree of reclaiming. The behavior of MREs to the temperature enhancement was evaluated via thermogravimetric analysis and thermomechanical analysis. Meanwhile, the alteration of shear stress depending on the magnetic fields was investigated at both steady and oscillatory states, measured using a rheometer. It has been shown that the increment of shear stress is proportional to the increment of the magnetic field. More specifically, it has been found that the WTR based MRE can achieve the maximum static stress ranging from 9 to 13 kPa (at 656 mT) with a linear viscoelastic (LVE) region above 3% strain amplitude. In addition, from the oscillatory test it has been determined that the highest MR effect of 24.71% can be achieved, which directly indicates the augmentation of both storage and loss moduli under ramped frequency and strain. Finally, it has been shown that the highest degree of reclamation based on swelling test can be achieved up to 54%, confirming the occurrence of the crosslinking during the reclamation process.

Keywords: waste tire rubber, magnetorheological elastomer, thermal analysis, swelling test, MR effect

OPEN ACCESS

Edited by:
Miao Yu,
Chongqing University, China

Reviewed by:
Rongjia Tao,
Temple University, United States
Jie Zhang,
Chongqing University, China

****Correspondence:***
Ubaidillah
ubaidillah_ft@staff.uns.ac.id
Seung-Bok Choi
seungbok@inha.ac.kr
Saiful Amri Mazlan
amri.kl@utm.my

Specialty section:
This article was submitted to Smart Materials, a section of the journal Frontiers in Materials

Received: *27 November 2018*
Accepted: *27 February 2019*
Published: *26 March 2019*

Citation:
Ubaidillah, Purnomo ED, Ismail H, Choi S-B, Aziz AA and Mazlan SA (2019) Swelling, Thermal, and Shear Properties of a Waste Tire Rubber Based Magnetorheological Elastomer. Front. Mater. 6:47. doi: 10.3389/fmats.2019.00047

INTRODUCTION

Reclaiming waste tire is usually performed by blending waste tire rubber (WTR) to the virgin rubber or revulcanization the inert rubber by treating them in physical and chemical ways. Reclamation of rubber is mainly scission or cleavage of sulfur-sulfur, carbon-sulfur, or carbon-carbon to break down three-dimensional network structures from the vulcanization process. At the same time, the division bonds are reformed through a revulcanization mechanism obtaining new rubber products. Application of temperature, shear force and chemical agents could facilitate such physical processes (Tripathy et al., 2002) including screw extruder (Formela et al., 2014; Piszczyk et al., 2014), roll mill-compression molding (De et al., 2013), internal mixer [5, 6, 7], and high-pressure high-temperature (HPHT) sintering reclamation techniques (Morin et al., 2002; Tripathy et al., 2002).

So far, recycled rubber-based products exhibit non-tunable mechanical properties. The WTR reclamation would draw attentions when the reclaimed articles have smart material characteristics. Here, smart features refers to the capability of goods reacting to the external condition in which smart materials only own the behavior. Such capability could enhance the economic value of the recycled product. According to the advancement of rubber reclaiming technologies, waste tire rubber has the potential to be reclaimed as smart materials, namely, magnetorheological elastomers (MREs). MREs have taken a prominent position in actively tunable vibration devices such as automotive bushing, rotating machine mounting and a seismic damper, due to their tunable properties by the intensity of the magnetic fields (Li et al., 2014; Ubaidillah et al., 2015). MREs are also compatible with the sensory application and morphing structure devices (Ottaviani et al., 2005; Li et al., 2009; Ghafoorianfar et al., 2013; Ausanio et al., 2014; Bica et al., 2014).

Based on the survey provided by Ubaidillah et al. (2015), all scientific reports published since the 1990s proposed MREs using virgin elastomers in which the vulcanization mechanism did not become the main issue. And so far, most of the research interests have been addressed on the enhancing rheological properties such as MR effect, storing, and dissipating energy performances. Some efforts were carried out for enhancing MREs properties such as; (a) manipulating the matrix, either by using single type matrix or mixed matrix, (b) controlling the particle types, size, morphology, and composition, and (c) manipulating cross-link density through operating additives and processing condition. The latest research relating to the vulcanizing issue was undertaken by considering self-cross-linking between two different compounds. Wang et al. (2015) fabricated new class MREs by blending polychloroprene rubber with epoxidized natural rubber, without curing agents that the so-called self-cross-linking MREs. This work indeed provided a breakthrough for the MREs preparation since there was no additive involvement in the vulcanization process. Again, the self-cross-linked MREs preparation incorporated virgin rubber. Therefore, the MREs fabrication based on waste tire rubber would be a fascinating exploration of some aspects in terms of manufacturing and performance.

Regarding to the challenges, Ubaidillah et al. (2016a,b,c) have successfully reclaimed WTR as the primary matrix of MREs. First, Ubaidillah et al. (2016c) fabricated MREs utilizing WTR as the matrix as well as Fe3O4 (magnetite) powders obtained from electronic wastes. In this work, the specimen's physicochemical properties and stress-strain behaviors were evaluated through the static compression test. Pursuing the complete investigation on dynamic compression properties, the magneto-induced rheological properties of the samples were determined as can be found in Ubaidillah et al. (2016b). It became evident that the MR effect of WTR based MREs featuring magnetite achieved about 15% MR effect under dynamic compression loadings. To enhance the magnetic properties, the magnetite powders were then replaced with carbonyl iron (CI) particles. As reported by Ubaidillah et al. (2016a), WTR based MREs were examined for their physicochemical and rheological properties under dynamic shear loadings. The MREs achieved a higher MR effect that was about 24.71%. As surveyed from the literatures Ubaidillah et al. (2016a,b,c), both swelling problem and thermal analysis have not yet been treated, even though these are important issues to be addressed in order to ensure high stability and reliability of the field-dependent rheological properties of the WTR based MREs.

Consequently, the technical originality of this work was to investigate the swelling, thermal, steady state, and dynamic properties of the WTR based MREs. This study is important as

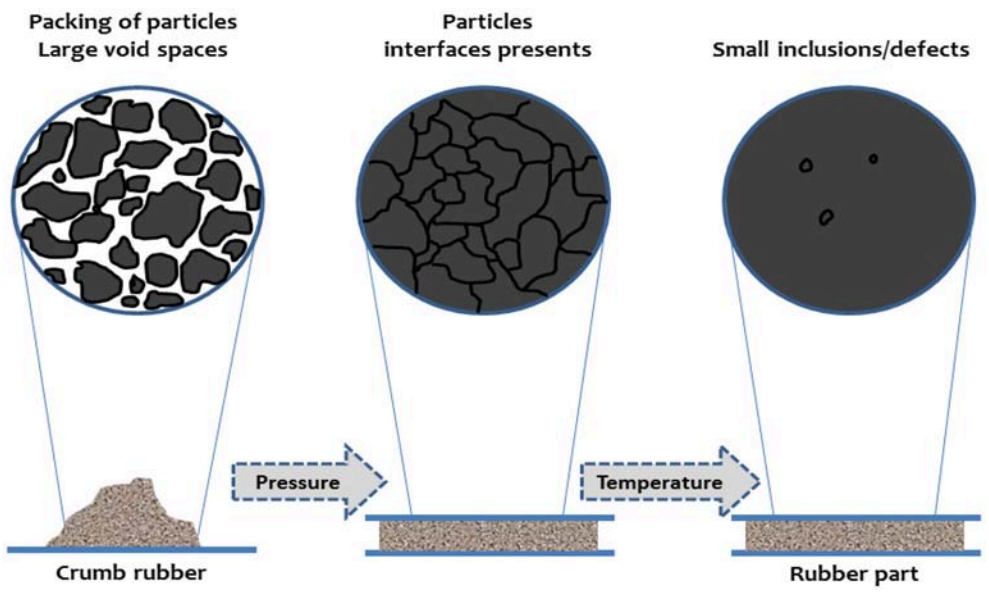

FIGURE 1 | HPHT mechanism (Morin et al., 2002).

it is necessary to determine why the hesitation on the reliability issue, since it is known that the waste rubber is hard to be reclaimed without incorporating virgin rubber. Swelling tests are first conducted to ensure the revulcanization process within MREs based on the obtained swelling parameters. Thermal analyzes are provided to study the stability of the synthesized samples. The properties, such as the dependence magnetic fields, are explored through the rheological test in both absence and presence of magnetic fields in the shear direction. The steady state loading reveals the stress-strain properties of waste tire based MREs including understanding in the linear viscoelastic region. Authors believe that the utilization of the WTR for raw materials of the MREs is a useful idea for waste tire management and a clean environment.

MATERIALS AND RECLAMATION PROCESS

The company of PT Bengawan Sumber Baru, Indonesia, provided the WTR with the average size of ≈2.8 mm. It was obtained from discarded tires (passenger and commercial vehicles) which were ground mechanically and free from metals and textiles. Screening was then carried out to get the uniform size of WTR (about mesh 60). The additives employed were chosen based on the typical rubber reclamation process such as stearic acid (98%, Justus Kimia Raya, Indonesia), zinc oxide (99%, $<1\,\mu$m, Bratachem, Indonesia), sulfur (Bratachem, Indonesia). The magnetizable particles were carbonyl iron (CI) particles, having an average size of 6 μm, type CN supplied by BASF, Germany. The additional latex solution was used as first raw material bonding between CI particles and WTR.

The HPHT sintering method implements the same principle concepts with the mechanical approach in that they both apply high temperature and high pressure. **Figure 1** depicts the schematic mechanism of the HPHT sintering process. The HPHT is conducted using simultaneous high temperature (between 200 and 240°C) and high-pressure compaction (above 20 MPa) on the ground tire rubber in a mold for a specified duration. Therefore, the process does not involve the twin screw extruder or roll mill that operates through shearing the waste rubber at a temperature of ±180°C. In this process, the cleavage and reforming of the rubber vulcanizates happen in a single step process. According to the working principle of the HPHT sintering process, the recycling procedure is simpler than that of the common mechanical approach.

The MRE samples were prepared through two major steps: mixing and reclamation. First, the WTR (100 phr) and additives (1.5 phr stearic acid, 5 phr ZnO, and 2 phr sulfur) were mixed in a laboratory mechanical stirrer at 250 rpm until the mixture was visually homogenous. Unlike the virgin rubber-based MREs that require a roll mill for compounding, homogenous mixtures were easily achieved since all raw materials were in powdered form except the latex solutions. The CI particles in contents of 10, 20, 30, and 40 wt% were then mixed homogeneously with the WTR mixtures using a mechanical stirrer. Hereafter, the 10 phr latex solution was added to the mixed raw materials and then further assorted until well blended. The formulation of WTR based MRE was detailed in **Table 1**.

Second, the reclamation process was conducted using the laboratory HPHT sintering device which could exert 20 tons of hydraulic pressure (Krisbow, Indonesia) and was equipped with a heat controller. The molding kit was fabricated using the conventional machine and was made of mild steels. The thickness could be adjusted based on the amount of molded mixtures. Two heater cartridges were equipped with the mold having heat power of 150 W each. Heater controller was constructed of current driver, display monitor, K-type thermocouple, and circuit breaker. The samples were fabricated in a mold with a bore diameter of 30 mm. The final mixtures were placed in the cavity, and the hydraulic pressure of 25 MPa was applied at a temperature of 200°C for 1 h to accomplish revulcanization. This procedure adopted the reclamation technique by Morin et al. (2002) and Tripathy et al. (2002). The heating rate from ambient to a steady temperature was 10°C/min. Following the revulcanization process, the heater controller was turned off, and the mold was then allowed to cool until reaching ambient temperature.

CHARACTERIZATION

Morphological Examination

Field emission scanning electron microscopy (FESEM), SUPRATM 35SV, ZEISS, USA, was utilized for capturing the morphology of CI particles and their distribution within the MRE matrix. The device was operated at an accelerating voltage of 10 kV. During observation, the MRE samples were

TABLE 1 | Formulation of WTR based MRE.

Compounding ingredients	Batch weights			
	MRE 10 wt% CI particle	MRE 20 wt% CI particle	MRE 30 wt% CI particle	MRE 40 wt% CI particle
WTR (phr)	100	100	100	100
Zinc oxide (phr)	5	5	5	5
Stearic acid (phr)	1.5	1.5	1.5	1.5
Sulfur (phr)	2	2	2	2
Latex (phr)	10	10	10	10
CI particle (wt%)	10	20	30	40

TABLE 2 | Apparent flux densities corresponding to the applied current.

MREs	Flux density (T)				
(CI Particle wt%)	0 A	1 A	2 A	3 A	4 A
10	0	0.158	0.313	0.474	0.617
20	0	0.162	0.320	0.485	0.633
30	0	0.165	0.331	0.496	0.645
40	0	0.169	0.337	0.505	0.656

crushed using a hammer after immersion in liquid nitrogen. The observed surfaces were coated with a thin layer of gold.

Swelling Test

The swelling test was conducted to examine the degree of revulcanization process of the MREs. The synthesized sample was subjected to an equilibrium swelling in toluene at ambient temperature. Small sliced MREs were initially weighed (m_1) and then immersed in 100 ml toluene and allowed to swell for 72 h. The sample was then wiped to remove the toluene on its surfaces and quickly weighed to measure the swollen weight (m^2). The step was followed by drying in an oven at 80°C to remove small molecular weight substance until reaching same dried weight (m_3).

The swelling parameters such as soluble fraction, swelling degree, cross-link density, and the degree of reclaiming were determined based on the recorded weight. The following relation (Equation 1) is useful for determining soluble fraction (SF),

$$SF = \frac{m_1 - m_3}{m_1} x100\% \tag{1}$$

The swelling degree (Q) was calculated in accordance with Equation (2) as follows,

$$Q = \frac{m_2 - m_1}{m_1} x100\% \tag{2}$$

Meanwhile, the cross-link density of the MREs was determined based on ASTM D 6,814 that according to the Flory-Rehner formula (Flory and Rehner, 1943) without Kraus correction (Equation 3),

$$v = \frac{-\left[ln\left(1 - V_r\right) + V_r + \chi V_r{}^2\right]}{\left[\frac{V_1\left(V_r{}^{\frac{1}{3}} - V_r\right)}{2}\right]} \tag{3}$$

where: v -cross-link density, mol/cm^3; V_r-represents volume fraction in the swollen sample; V_1-molar volume of toluene (106.2 cm^3/mol) (Yazdani et al., 2011); χ-parameter of rubber-solvent interaction (in calculation, it was assumed to be 0.391; Formela et al., 2014).

The volume fraction of rubber was calculated according to Equation (4),

$$V_r = \frac{\frac{m_e}{\rho_e}}{\frac{m_e}{\rho_e} + \frac{m_t}{\rho_t}} \tag{4}$$

where: m_e-mass of dry MREs in *gram* (g); ρ_e-density of dry MREs in $\frac{g}{cm^3}$; m_t-mass of absorbed toluene by MREs in *gram* (g); ρ_t-density of toluene in $\frac{g}{cm^3}$.

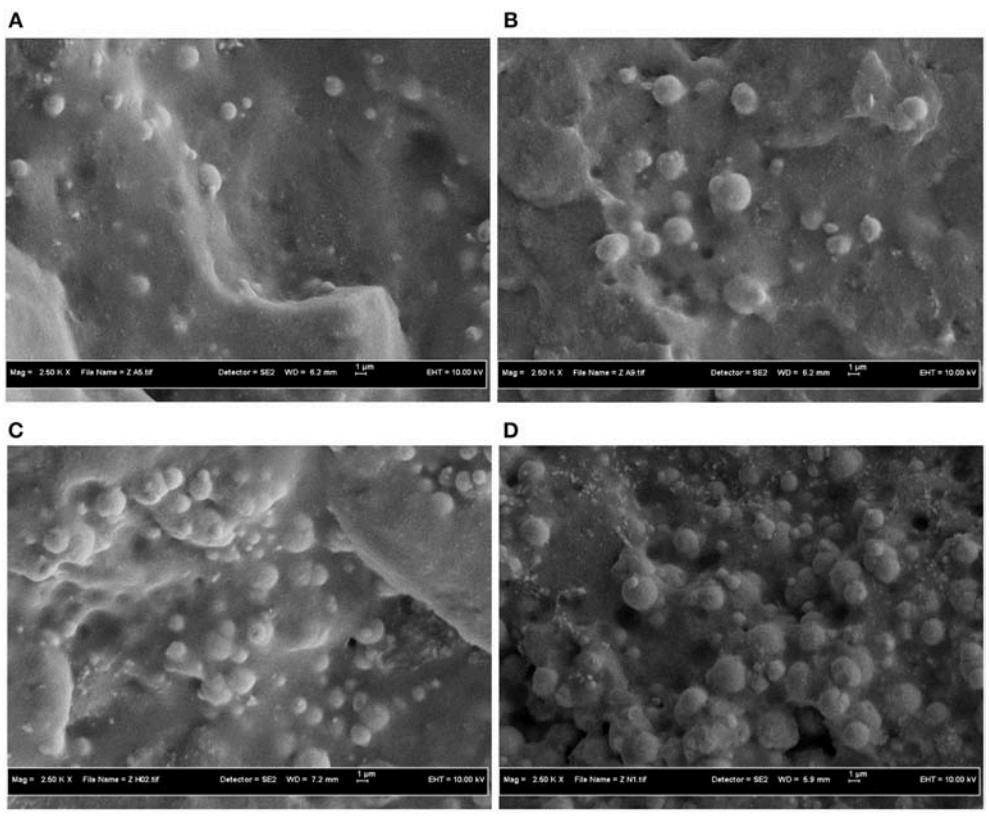

FIGURE 2 | SEM micrograph of the WTR based MRE with CI particles: **(A)** 10 wt%, **(B)** 20 wt%, **(C)** 30 wt%, and **(D)** 40 wt%.

The achievement of revulcanization process through HPHT sintering was determined on the basis of alteration in the cross-linking density of the reclaimed MREs (v_1) relative to the ground tire rubber without reclamation (v_0), regarding Equation 5 as follows,

$$Degree\ of\ reclaiming = \frac{v_0 - v_1}{v_0} x100\% \quad (5)$$

Thermal Test

The thermogravimetric tests were undertaken using TGA Q50, TA Instruments (US). The test samples had masses of 5–10 mg, and the temperature was varied from 30 to 600°C. The heating rate was 20°C/min under a nitrogen gas environment (100 ml/min flow rate). The thermal expansion of MREs was evaluated using TMA Q400 TA Instruments (US). An expansion probe was equipped to measure the dimension change of an MRE sample that measured 5 × 5 × 10 mm. Data were collected at a heating rate of 10°C/min from an ambient temperature of 150°C while the initial load was set to 0.05 N.

Rheological Test

Viscoelastic properties of the WTR based MREs were witnessed in a rotational shear mode using the parallel-plate rheometer (model Physica MCR 302, Anton Paar, Austria) equipped with a magnetorheological device MRD 70/1T. The diameter of parallel plate disk was 20 mm (PP20/MRD/T1/P2). A temperature control Viscotherm VT2, Anton Paar was also utilized for maintaining the desired testing temperature of 25°C. The rheological measurement system with parallel-plate is described in standards ISO 6721-10 and DIN 53019-1 (Sorokin et al., 2015). An electromagnet unit in MRD 70/1T can generate a homogeneous magnetic field perpendicular to the sample and non-magnetic measurement plate. The variation of magnetic flux could be from 0 until 690 mT by applying current from 0 to 4 A. **Table 2** exhibits how the flux density alters with the current which means the flux density across the MREs samples would be different as the consequences of CI particles fraction.

Under steady condition test, the MREs sample was sheared at a constant shear rate of 100 s^{-1} at a zero magnetic field for 30 s. The pre-conditioning was objected to making a uniform distribution of particle within the sample. The step was also aimed at releasing the possible stored residual stress. Then, it was followed by preliminary magnetic energizing for 30 s to make a homogeneous static attraction between iron particles within the sample. After running the preconditioning step, the sequence of steady testing was allowed to proceed. The steady-state measurement was then applied by twisting the sample in a constant strain swept with a very low strain rate. The treatment was nearly similar to a static shear test.

The magneto-induced dynamic properties of the samples were evaluated through the oscillatory test. The storage modulus changes which can be represented by the effect of ramped magnetic flux was assessed under strain amplitude of 1%, and excitation frequency of 1 Hz. The ramp magnetic flux was realized by driving an electric current from 0 to 5 A in a linear fashion. Moreover, the frequency swept tests from 0.1 to 100 Hz were carried out under a constant strain amplitude of 1%. Meanwhile, the strain amplitude was set from 0.01 to 10% ramped logarithmically and the excitation frequency was fixed at 1 Hz. During both frequency and strain swept tests, the samples were energized by different magnetic fields of 0, 1A, 2A, 3A, and 4 A, respectively.

RESULTS AND DISCUSSION

Morphological Appearances

The morphologies of the cross-sectional MREs with a different weight fraction of CI particles are depicted in **Figure 2**. A random dispersion of CI particles within the MREs matrix is the primary requirement of the consistent performance in their functional

TABLE 3 | Swelling properties of WTR based MRE.

Sample	Soluble fraction (%)	Swelling degree (%)	Crosslink density (10^{-4} mol/cm^3)	Degree of reclaiming (%)
Reclaimed WTR	7.967	195.330	8.390	54.007
MREs 10 wt% CIP	6.060	165.343	8.770	51.922
MREs 20 wt% CIP	5.677	135.998	8.780	56.916
MREs 30 wt% CIP	5.238	117.043	8.810	52.143
MREs 40 wt% CIP	4.901	97.962	9.040	50.478
THE PREVIOUS STUDY BENCHMARKING				
Formela et al., 2014	7.4–9.6	NA	3.76–7.94	41–52
Yazdani et al., 2011	NA	NA	1.3–6.98	NA

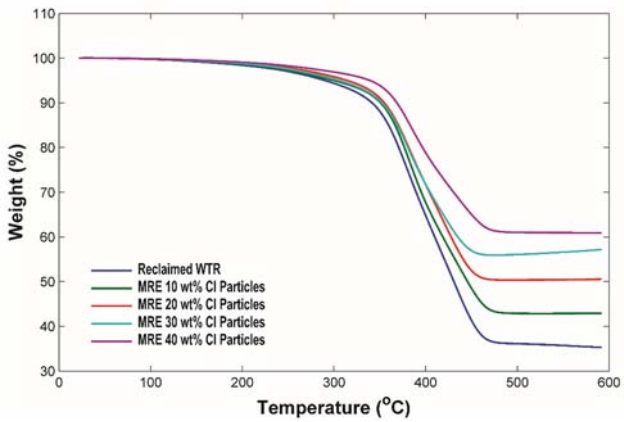

FIGURE 3 | Thermogravimetric curves of WTR based MREs.

TABLE 4 | Residual mass of decomposed WTR based MREs.

Sample	Residue (%)
MREs 10 wt% CI particle	61.08
MREs 20 wt% CI particle	55.95
MREs 30 wt% CI particle	50.46
MREs 40 wt% CI particle	42.93
Reclaimed WTR	36.23

behavior. A random distribution will ensure the magnetic flux to flow uniformly through the MREs. The dispersion of particles can be clearly observed in the SEM micrograph shown in **Figure 2**. The random distribution type of the MREs is confirmed by non-aligned dispersion of particles in the observed area. It can be seen that the CI particles adhere completely in the matrix. The weight percentage of each sample can be visually differentiated from the micrographs. The MREs with higher weight fraction of CI particles seem to be a closer distance and tend to agglomerate.

According to **Figure 2**, the micrograph of WTR based MRE confirmed that the fractured samples show well-blended rubber matrix. This fact indicates that the WTR has mixed thoroughly with each other as the results of high-pressure and high-temperature treatment. The blending of WTR can be considered as the occurrence of the revulcanization process. If the WTR only adhered to each other without curing, the matrix appearance of the fractured sample would exhibit different patterns. It would definitely show the WTR borders as the effect of non-blended WTR. Besides, the cryogenic effect during sample preparation would easily break the WTR interfaces when the rubber was not cured. The curing reaction during the reclamation process does not leave any particle boundaries among WTR.

Swelling Properties

A common issue that occurs in WTR reclamation is a revulcanization (crosslinking) achievement because the WTR belongs to inert materials. Therefore, the swelling test is often used to facilitate the evaluation of crosslinking of waste rubber reclamation. In this study, the degree of vulcanization of the MRE samples was also assessed by a swelling test to confirm the success of the revulcanization. The swelling properties including the soluble fraction, the swelling degree, the crosslinking density, and the degree of reclamation are listed in **Table 3**. Based on the calculation, the values are comparable to that of waste rubber reclamation through either a twin extruder or roll mills (Yazdani et al., 2011; Formela et al., 2014). For comparison purposes, **Table 3** also provides the summary data of swelling properties obtained from the previous work. The values of the soluble fraction and the swelling degree were decreased with the increase of CI particles. Moreover, the revulcanized MREs consists of crosslinked and free-chain portions. The immersion in toluene extracted the free chains. Meanwhile, the crosslinked sections were insoluble and swollen. The crosslink density values and degree of reclamation are in agreement with previous research reported by Formela et al. (2014). The degree of reclamation data was calculated and compared with the WTR without CI particles, and the results confirmed that the revulcanization was positive for the inert rubber during the thermomechanical reclamation.

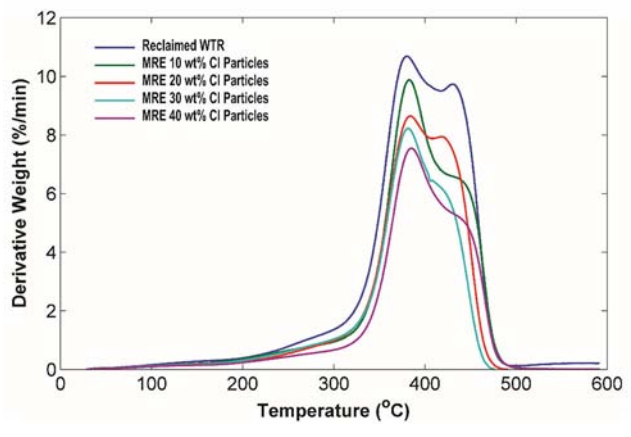

FIGURE 4 | DTG curves for pure reclaimed WTR and MREs.

A physical explanation of the successful mechanism of revulcanization can refer to some existing theories that has been proven through experimental works. Tobolsky et al. (1944), MacKnight et al. (1965) and Kende et al. (1965) initially discussed the theory of rubber reclamation. They found that the sulfur-sulfur bonds were the weakest chemical bonds with bond energies as follows: monosulfide crosslink (50–60 kcal/mol), disulfide crosslink (35 kcal/mol), and polysulfide crosslink (27 kcal/mol). Employing heat and pressure in certain degrees cleaved the sulfide linkages in the vulcanized rubber *in situ* during molding (Tripathy et al., 2002). Furthermore, Tobolsky (1960a,b) stated that when the polymers were protected from oxygen and other compounds at elevated temperatures, the rates of bond scission and reformation were principally equivalent. Tamura et al. (1983) also found that the secondary carbon atoms adjacent to the cross-linked moiety can be degraded when the isoprene rubber is heated beyond 200°C. Therefore, based on the aforementioned reclamation theory, it is expected that the HPHT sintering would be sufficient for the second vulcanization of dead (?) rubber. During the fabrication of the MREs, the mixture of WTR, additives, and CI particles was compressed under high pressure. The high pressure could assist the removal of excessive voids. The absence of void during application of high pressure was confirmed by Tripathy et al. (2002) and Morin et al. (2002) who have implemented the HPHT reclamation technique for waste tire rubber.

Thermal Analysis

Thermogravimetric Analysis

Boczkowska et al. (2006) have initially carried out thermogravimetric analysis on MREs. The thermogravimetric test as part of thermal analysis can provide important material properties related to the stability of MREs against external temperature by identifying the thermal stability, oxidative mass reduction, and their decomposition performance. Boczkowska et al. (2006) reported that the additional iron particles to the elastomeric matrix would augment the thermal stability indicated from the lower oxidative mass loss at about 600°C. The higher magnetizable particles within MRE samples, which consequently increase the thermal conductivity would have a better thermal conductivity. This is because the closer inter-particle distance is achieved as the higher fraction of magnetizable particles. For that reason, the MREs elements with a higher amount of iron particles would ease thermal energy flows across the samples.

MREs that use WTRs as the primary matrix would be facing issues related to thermal stability, which is critical to durability and age resistance. Thermogravimetric Analysis (TGA) can

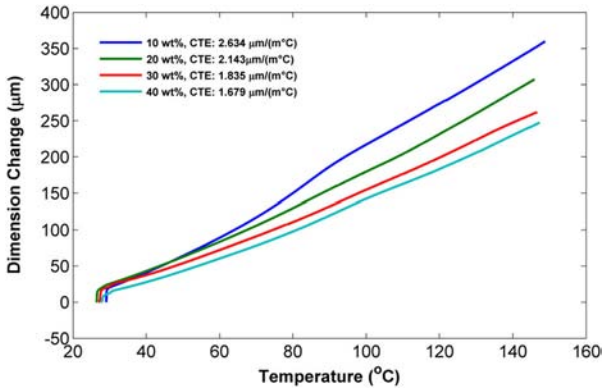

FIGURE 5 | Coefficient of thermal expansion curves of WTR based MREs.

be used to evaluate the thermal stability of a polymer. It can also be used to observe the content of compounds such as carbon black and ash in rubber. **Figures 2**, **3** show the TGA thermogram and corresponding derivative plots (DTG) of reclaimed WTR and MRE samples, respectively. As shown in **Figure 3**, the rubber content of all samples was entirely decomposed. The onset temperature of the volatile compounds released in all samples was >200°C. The volatile contents of the samples were determined at about from 5.15 to 9.85%. The temperature, at which 5% (T5) mass loss happen, increases from 288.6°C (reclaimed WTR) to 341.9°C (MRE 40 wt% CI particle). After that, the second transformation occurred involving the decomposition of rubber content that was releasing hydrocarbon compounds. During second transformation, there were changing slope values at temperature ranges of 379 to 385°C. Furthermore, the second transformation has been stopped at a temperature that is higher than 450°C. The final curves were maintained at the same weight until the next transformations. The changes of carbon content and CI particles occurred at temperatures higher than 600°C. A weight reduction would either confirm the substance of the rubber or reflect the composition of CI particles carried by the rubber. A lower content of CI particles implies a higher weight reduction of the samples. In this study, the weight reductions of each sample until the end of the second transformation were evaluated by 33.77, 36.88, 41.31, 47.99, and 53.92 percent for MRE with 40, 30, 20, 10, and 0 (pure rubber) wt% of CI particles, respectively. The residual elements (at 600°C) as detailed in **Table 4** were carbon black and CI particles. Wang et al. (2006) found the same patterns in different CI particle compositions in MREs and concluded that the MRE with higher CI particle content exhibits better thermal stability.

At the second transformation, there was a slightly different slope that indicated the existence of overlapping thermal degradations. The different slope was also marked by the appearance of two peaks shown in the DTG curves in **Figure 4**. All samples shared a trend wherein the peaks were related to the maximum rate of thermal degradation temperature. The first peak was well identified and narrower than the second one. The sharp peak (first) indicated a deterioration of the natural

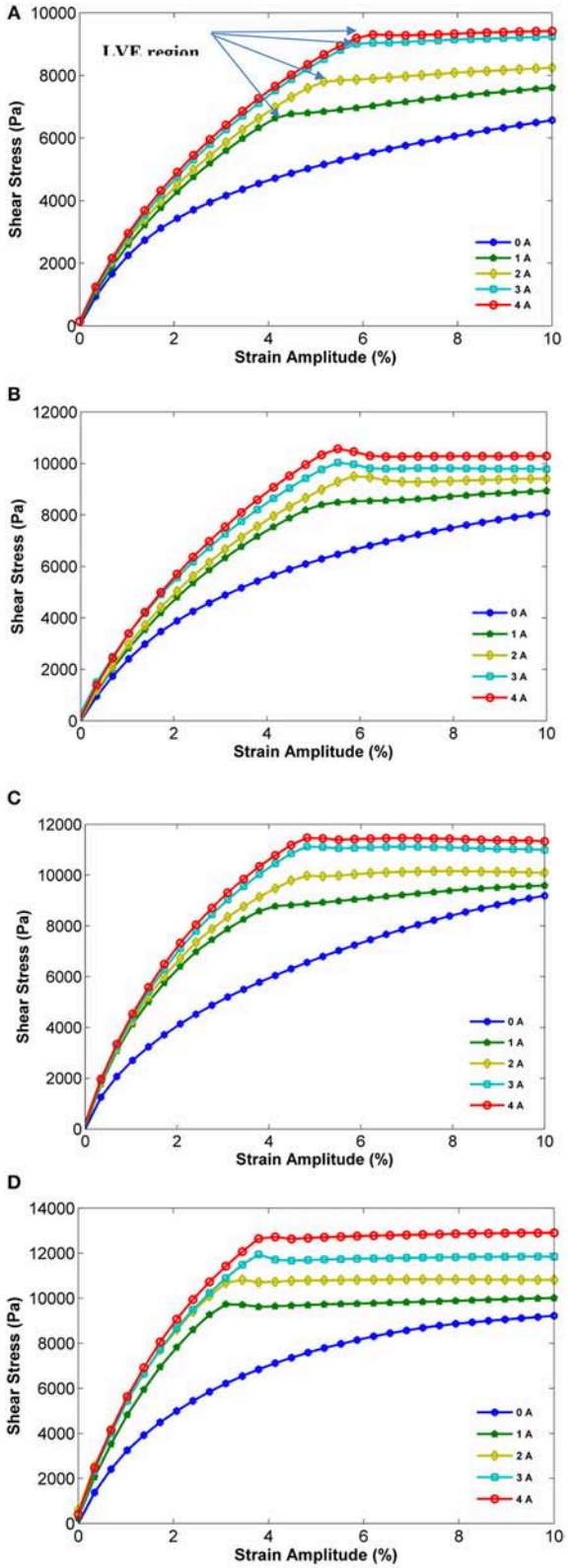

FIGURE 6 | Stress-strain curves of the MREs: **(A)** 10 wt%, **(B)** 20 wt%, **(C)** 30 wt%, and **(D)** 40 wt%.

rubber (NR) at temperatures that ranged from 379.7 to 384.8°C. By comparison, the temperature range for the broad peak was in between 418.6 and 449.3°C. The temperature range for the second peak designated a synthetic rubber, which was styrene-butadiene rubber (SBR) (De and De, 2011). The mass loss rate decreased with an increase of CI particle content within the MREs. The values of peak mass loss rate at a temperature range of 379.7 to 384.8°C decreased from 10.68%/min (reclaimed WTR) to 7.54%/min (MRE 40 wt% CI particle). Comparing the decomposition results with other studies, different authors (Kim et al., 1995; Gisbert et al., 2007) have reported similar results. Gisbert et al. (2007) found that the range of temperature for the decomposition of natural rubber was between 325.27 and 376.06°C, while Kim et al. (1995) discovered the first peak at 377°C. Moreover, the second broad peaks were reported to be in the range between 461.6 and 463.9°C by Gisbert et al. (2007), and 444°C by Kim et al. (1995). Based on the reported data, the TG/DTG results agreed with the fact that the tire rubber was a blend of various types of rubbers including both natural and synthetic rubbers.

Thermogravimetric Analysis

Thermal expansion is an important property for composite materials, particularly MREs. The test can reveal the behavior of material expansion during temperature alterations. For instance, the further application of MREs is common as a vibration insulator. The MREs must be bound well to a mounting bracket that is usually made of metals. When the mounted MREs work at engine temperature, a micro-scale expansion occurs at the mounting interface (between MREs and the mounting bracket). Since the coefficient of thermal expansion of the MREs portion is different from that of the steel bracket, thermal stress can occur at the MREs-steel bonding interface. Therefore, characterization of thermal expansion characteristic on MREs is often important to prevent product malfunction. The CTE evaluation of MREs is seldom reported. As far as could be ascertained, the thermal expansion of MREs has been reported by Nayak et al. (2015), which delivered the CTE of MREs based on silicon RTV.

Figure 5 depicts the dimension change of the MRE samples with increases in temperature. The expansion data of the MREs were taken under off-state conditions (no magnetic fields). The MRE samples changed their dimensions (micron size) in a positive slope, which resulted in an enlarged sample. The slopes decrease from 2.634 to 1.679 μm/(m°C) for MRE 10 to 40 wt% CI particle. Apparently, the higher slope was represented by the lower CI particle fraction contained in the MRE matrix. The smaller quantity of the slope implied that the sample with the higher content of CI particles has the lower expansion rate at an increase in temperature. This phenomenon is caused by the CTE of the CI particles, which is much lower than that of the rubber. The CTE of MR reported in Ubaidillah et al. (2016a) also depends on the state of the matrix. A softer matrix, such as silicon-based MREs, could produce a higher CTE, as reported by Nayak et al. (2015).

TABLE 5 | Linear viscoelastic region limit.

MREs sample	Strain (%)				
	0 A	1 A	2 A	3 A	4 A
MRE 10 wt% CI particle	>>10	4.48	5.17	5.86	6.21
MRE 20 wt% CI particle	>>10	5.17	5.86	5.52	5.52
MRE 30 wt% CI particle	>>10	4.14	4.83	4.83	4.83
MRE 40 wt% CI particle	>>10	3.1	3.45	3.79	3.79

Steady State Properties

MREs have been acknowledged for their tuning capability of viscoelastic properties under external magnetic fields treatment. The rheological property such as shear modulus has a directly proportional correlation with the flux density. Therefore, the magnetic field dependent properties are a most important parameter of MREs. The stress-strain relationship of the waste tire based MREs was evaluated under steady state rotary shear at elevated current from 0 to 4 A sequentially and fix ambient temperature. This kind of test was relatively less studied since only minor information could be revealed such as shear modulus and the linear region at the very low strain. Previous publications on shear steady state properties of MREs can be found elsewhere (Tian et al., 2011; Qiao et al., 2012; Li and Nakano, 2013; Zhu et al., 2013; Mordina et al., 2014).

Figure 6 show the stress strain relationship under various magnetic fields. The shear rate was set to be 5 rad/s from 0 to 10% ramp linear strain. In off state condition, the stress grew up slowly until nearly reaching a constant value at >10% strain. The curves exhibit different trends with on state condition. The stress growth in the presence of magnetic fields was faster than before and had slight overshoot before reaching steady stress. Based on the figures, all MREs types express an appreciable response to the presence of magnetic fields. The behaviors reflect the shear modulus enhancement when the magnetic fields increase from 0 to 3 A. The increment of shear modulus appears as a steep rise at the current elevation, while, the increment upper than 3 A applied current is relatively small. The responsiveness of the MREs to the presence of magnetic fields increases from the lower iron particle fraction to the higher one. The almost linear increment of stress growth under magnetic fields confirmed the particle attraction. With these interactions, MREs behave as a solid material under a small strain. MREs exhibit a linear dependence on strain elevation until a specified strain limit is reached. Therefore, the region in which the shear modulus behaves in a linear condition is often referred to as the LVE region. Under a larger strain, the magnetized MREs exhibit a highly non-linear plastic flow in which the rigid chain-like structure of CI particles experience slippages between the particles and the reclaimed rubber matrix. At this stage, the stress overshoot appears to be significantly influenced by the shear orientation of the attracting particles. Another point of view about overshoot at the yield point is that the static friction caused by the surface roughness of MRE samples and a moving plate, which is a normal force, may contribute to the ultimate yield stress (Mordina et al., 2014).

The LVE regions of MRE based on **Figure 6**, under different magnetic fields regarding strain percentage, are detailed in

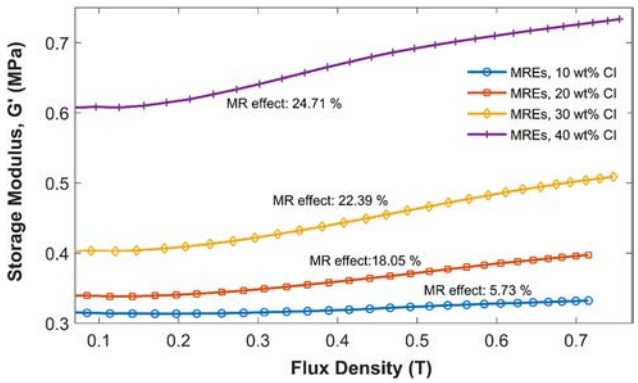

FIGURE 7 | Storage modulus under increment of magnetic fields.

Table 5. The limits of the linear region under magnetized conditions were influenced by CI particles composition and magnetic field density. Based on the stress-strain relationship, there was no agreement that either CI particles composition or magnetic field density have a dominant influence on the limit of LVE region. Based on **Table 5** as well as **Figure 6**, the higher CI particle content was followed by the smaller LVE region except for MRE 20 wt% at 1 and 2 A tests. These 2 points were considered as data uncertainties since the other test condition showed normal trends. Moreover, the higher field density also slightly changed the LVE region. As a highlight, the attractive force among particles was one of the determining factors of the LVE region, and was greatly influenced by both the CI particles fraction and the magnetic field density.

Dynamic Properties

Figure 7 portrays the change of storage modulus in each sample as a function of the magnetic flux. While the magnetic flux is raised up, all specimens exhibit the augmentations of storage modulus in different quantities. The MREs with small contents of CI particles exhibit a slight modulus growth associated with those having the big fraction. The magnetic fields cause an inter-particle attraction forming a strong magnetic reinforcement. The elevated modulus is an implication of the aforementioned phenomenon. The fractional difference called MR effect between on state (5 A) and off state (0 A) is also shown in **Figure 7**. The highest MR effect was achieved by the sample with 40 wt% CI particles that is 24.71%.

Furthermore, this sample was tested to achieve dynamic properties under increment of excitation frequency and strain amplitude. **Figures 8A–C** display the trends of respective storage modulus, loss modulus, and loss factor under increment of excitation frequency. Both storage and loss moduli demonstrated the same behavior: this being augmentation of each value when the magnetic flux was amplified. The phenomenon of increased storage modulus as an effect of frequency suggests that at a higher excitation frequency, the MR elastomer samples have a larger storage modulus. When the different current was applied, it also affected the increment of the storage modulus at a certain frequency. Moreover, the magneto-induced loss

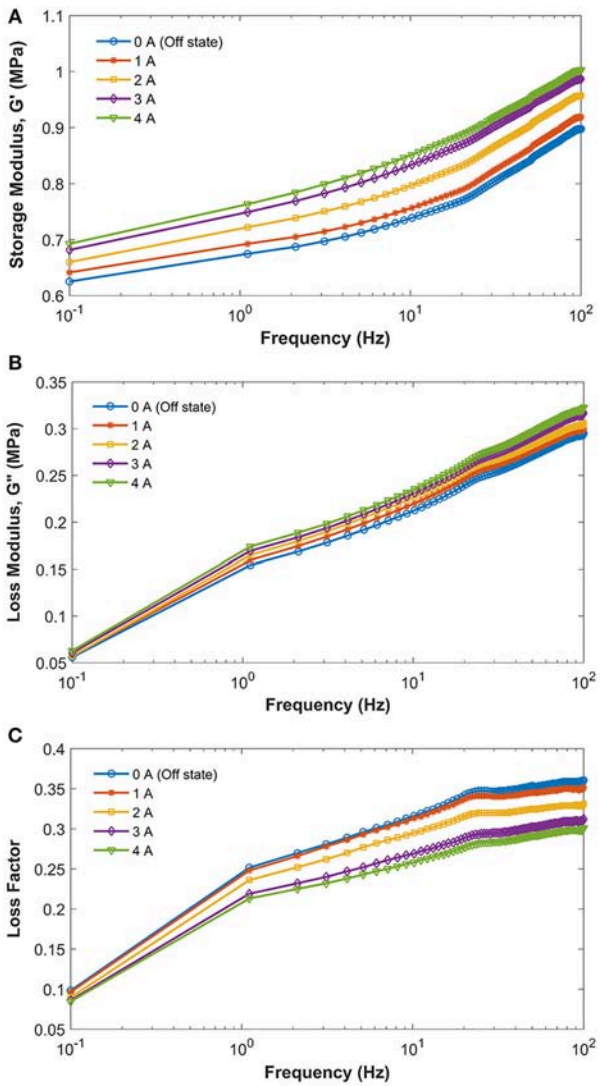

FIGURE 8 | Dynamic properties of WTR based MREs with 40 wt% CIP under frequency domain. **(A)** Storage Modulus, **(B)** Loss Modulus, and **(C)** Loss Factor.

modulus was increased monotonically with the frequency for all measured variants in both off- and on-states. In the off-state, the filler particles of both iron particles and carbon black served to strengthen the matrix when subjected to a higher frequency. The enhancement of the loss modulus reflected how the MR elastomer materials dissipate more energy at higher frequencies. Different to storage and loss moduli, the loss factor which represents phase-lag between stress and strain, exhibits a decrement value when the sample was subjected to the increase of magnetic flux. The magnetic flux strongly affects the inter-particle attraction forces. Thus, the relative motion between CI particles is clogged resulting in the reduction of slipping displacement of the other fillers such as carbon black.

Figures 9A–C show the behavior of WTR based MREs under ramped strain amplitude. The storage moduli diminished in the initial regions and underwent drastic drops up to a 10%

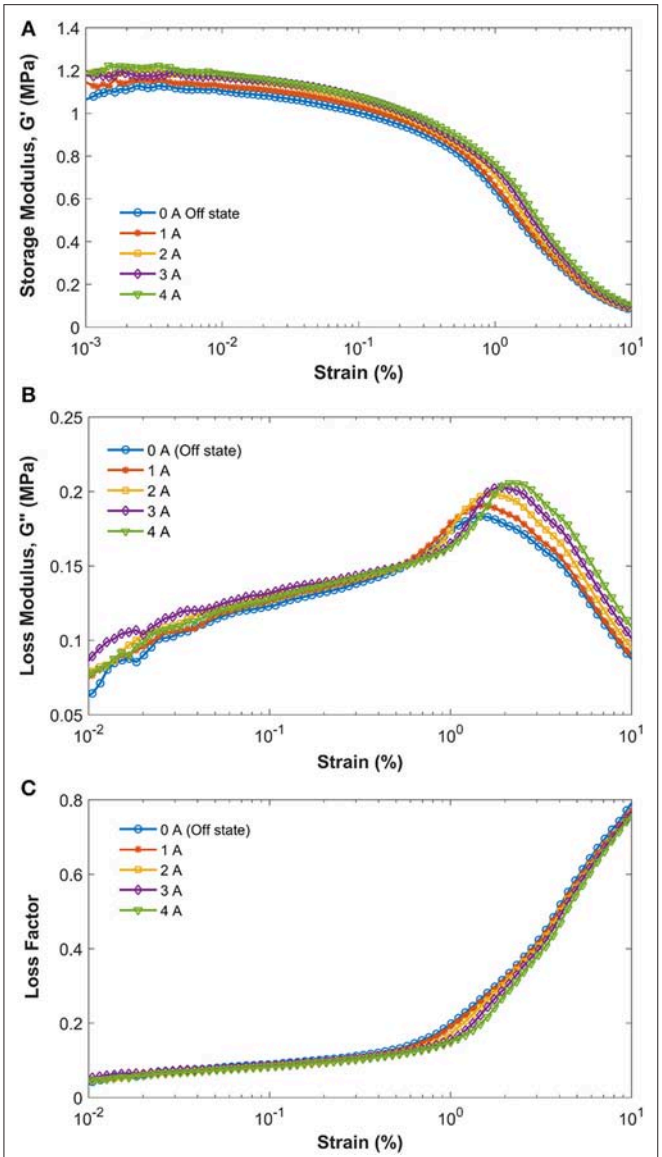

FIGURE 9 | Dynamic properties of WTR based MREs with 40 wt% CIP under strain domain: **(A)** Storage modulus, **(B)** Loss modulus, and **(C)** Loss factor.

strain amplitude. As can be seen in **Figure 9A**, the Payne effect appears in both on and off states. The strain dependence modulus in the off-state is purely influenced by filler—filler and filler—matrix interactions. Meanwhile, during on state situation the magnetic attraction strengthens the filler—filler—matrix interactions. Therefore, the magnetic attraction between CI particles escalates the storage modulus as the increase of magnetic flux. The same trends went to the strain dependence loss modulus as depicted in **Figure 9B**. The increase of magnetic fields also augmented the loss modulus values. However, the alteration was not clearly indicated at a lower strain amplitude. At the strain where the storage modulus dropped caused by Payne Effect, the loss modulus also exhibited the same situation. The loss modulus increased from low to medium strain followed by dramatic drops at the corresponding strain until 10%. As stated previously, the increase of magnetic flux reduced the phase-lag between stress and strain. Therefore, the loss factor also diminished at the time increasing magnetic flux and strain amplitude as can be seen in **Figure 9C**. However, the decrement of loss factor under ramped strain was not clearly determined compared to those under ramped frequency (refer to **Figure 8C**).

CONCLUSION

In this work, the morphology, swelling properties, thermal analysis, and rheological tests of the WTR based MREs have been investigated to ensure the reclamation achievement and thermal stability. The three-dimensional cross-link of inert rubber has been successfully reformed for the MREs matrix through HPHT sintering process. This phenomenon was confirmed by the swelling tests for the MREs, in which the degree of reclaiming achieved was higher than 54%. The weight reduction trends have exhibited that a logical pattern is proven in which the lower filler content was accompanied by a higher weight reduction percentage compared to the high iron particle fraction. The TMA results confirmed that the lower rubber content led to the lower coefficient of thermal expansion. The steady state test confirmed that the linear viscoelastic were about 3% to 6.5% strain in on state condition. The dynamic tests of the samples were also studied to justify rheological behavior under oscillating loads. Under increment of the magnetic flux, the storage moduli were augmented and showed the maximum MR effect of 24.71%. It is finally remarked that the results presented in this work can be referred as useful data to demonstrate high performance of smart MREs based on the waste tire rubber.

DATA AVAILABILITY

The datasets generated for this study are available on request to the corresponding author.

AUTHOR CONTRIBUTIONS

U: experiment, writing, and formatting; EP: writing and formatting; HI, S-BC, AA, and SM: writing and editing.

FUNDING

This research has been supported by Mandatory Research Grant, 2019, UNS and USAID through Sustainable Higher Education Research Alliances (SHERA) Program—Centre for Collaborative (CCR) National Center for Sustainable Transportation Technology (NCSTT) with Contract No. IIE00000078-ITB-1.

ACKNOWLEDGMENTS

This work is supported by Universitas Sebelas Maret through Mandatory Research Grants 2019. Authors thank to Universiti Teknologi Malaysia (UTM) for research facilities.

REFERENCES

Ausanio, G., Iannotti, V., and Ricciardi, E. (2014). Magneto-piezoresistance in Magnetorheological elastomers for magnetic induction gradient or position sensors. *Sensors Actuators A: Phys*. 205, 235–239. doi: 10.1016/j.sna.2013.10.009

Bica, I., Anitas, E. M., and Bunoiu, M. (2014). Hybrid magnetorheological elastomer: influence of magnetic field and compression pressure on its electrical conductivity. *J Indus Eng Chem*. 20, 3994–3999. doi: 10.1016/j.jiec.2013.12.102

Boczkowska, A., Awietjan, S. F., and Babski, K. (2006). "Effect of the processing conditions on the microstructure of urethane magnetorheological elastomers," in *Smart Structures and Materials: Active Materials: Behavior and Mechanics.* ed W. D. Armstrong (San Diego, CA: SPIE Digital Library), 61700R−61700R11. doi: 10.1117/12.651668

De, D., and De, D. (2011). Processing and material characteristics of a reclaimed ground rubber tire reinforced styrene butadiene rubber. *Mater. Sci. Appl.* 2, 486–495. doi: 10.4236/msa.2011.25066

De, D., Panda, P. K., and Roy, M. (2013). Reinforcing effect of reclaim rubber on natural rubber/polybutadiene rubber blends. *Mater. Design* 46, 142–150. doi: 10.1016/j.matdes.2012.10.014

Flory, P. J., and Rehner, J. (1943). Statistical mechanics of cross-linked polymer networks I. Swelling. *J. Chem. Phys.* 11:521. doi: 10.1063/1.1723792

Formela, K., Cysewska, M., and Haponiuk, J. (2014). The influence of screw configuration and screw speed of co-rotating twin screw extruder on the properties of products obtained by thermomechanical reclaiming of ground tire rubber. *Polimery* 59, 170–177. doi: 10.14314/polimery.2014.170

Ghafoorianfar, N., Wang, X. J., and Gordaninejad, F. (2013). "On the sensing of magnetorheological elastomers," in *Sensors and Smart Structures Technologies for Civil, Mechanical and Aerospace System.* eds J. P. Lynch, C.-B. Yun, and K.-W. Wang, 869214-1-869214–10. doi: 10.1117/12.2009944

Gisbert, A. N., Crespo, A. J. E., and López, M. J. (2007). Study of thermal degradation kinetics of elastomeric powder (ground tire rubber). *Polym. Plast. Technol. Eng.* 47, 36–39. doi: 10.1080/03602550701580870

Kende, I., Pickering, T. L., and Tobolsky, A. V. (1965). The dissociation energy of the tetrasulfide linkage. *J. Am. Chem. Soc.* 87, 5582–5586. doi: 10.1021/ja00952a012

Kim, S., Park, J. K., and Chun, H. D. (1995). Pyrolysis kinetics of scrap tire rubbers. I: using DTG and TGA. *J. Env. Eng.* 121, 507–514. doi: 10.1061/(ASCE)0733-9372(1995)121:7(507)

Li, W. H., Kostidis, K., and Zhou, Y. (2009). "Development of a force sensor working with MR elastomers," in *International Conference on Advanced Intelligent Mechatronics* (Singapore: IEEE), 233–238. doi: 10.1109/AIM.2009.5230010

Li, W. H., and Nakano, M. (2013). Fabrication and characterization of PDMS based magnetorheological elastomers. *Smart Mater. Struct.* 22:55035. doi: 10.1088/0964-1726/22/5/055035

Li, Y. C., Li, J. C., and Li, W. H. (2014). A state-of-the-art review on magnetorheological elastomer devices. *Smart Mater. Struct.* 23:123001. doi: 10.1088/0964-1726/23/12/123001

MacKnight, W. J., Leroi, G. E., and Tobolsky, A. V. (1965). Physical chemistry of crosslinked polysulfide elastomers. *J. Chem. Educ.* 42, 1–7. doi: 10.1021/ed042p4

Mordina, B., Tiwari, R. K. R. K., and Setua, D. K. D. K. (2014). Magnetorheology of polydimethylsiloxane elastomer/FeCo 3 nanocomposite. *J. Phys. Chem. C* 118, 25684–25703. doi: 10.1021/jp507005s

Morin, J. E., Williams, D. E., and Farris, R. J. (2002). A novel method to recycle scrap tires: high-pressure high-temperature sintering. *Rubber Chem. Technol.* 75, 955–968. doi: 10.5254/1.3547695

Nayak, B., Dwivedy, S. K. K., and Murthy, K. S. S. (2015). Fabrication and characterization of magnetorheological elastomer with carbon black. *J. Intell. Mater. Syst. Struct.* 26, 830–839. doi: 10.1177/1045389X14535011

Ottaviani, R. A., Ulincy, J. C., and Golden, M. A. (2005). *Magnetorheological Nanocomposite Elastomer for Releasable Attachment Applications.*

Piszczyk, Ł., Hejna, A., and Formela, K. (2014). Effect of ground tire rubber on structural, mechanical and thermal properties of flexible polyurethane foams. *Iranian Polymer J.* 24, 75–84. doi: 10.1007/s13726-014-0301-4

Qiao, X. Y., Lu, X. S., and Li, W. H. (2012). Microstructure and magnetorheological properties of the thermoplastic magnetorheological elastomer composites containing modified carbonyl iron particles and poly(styrene- b -ethylene-ethylenepropylene- b -styrene) matrix. *Smart Mater. Struct.* 21:115028. doi: 10.1088/0964-1726/21/11/115028

Sorokin, V. V., Stepanov, G. V., and Shamonin, M. (2015). Hysteresis of the viscoelastic properties and the normal force in magnetically and mechanically soft magnetoactive elastomers: effects of filler composition, strain amplitude and magnetic field. *Polymer.* 76, 191–202. doi: 10.1016/j.polymer.2015.08.040

Tamura, S., Murakami, K., and Kuwazoe, H. (1983). Isothermal degradation of cis-1,4-polyisoprene vulcanizates. *J. Appl. Polymer Sci.* 28, 3467–3484. doi: 10.1002/app.1983.070281112

Tian, T. F., Li, W. H., and Alici, G. (2011). Microstructure and magnetorheology of graphite-based MR elastomers. *Rheologica Acta* 50, 825–836. doi: 10.1007/s00397-011-0567-9

Tobolsky, A. V. (1960a). *Polymer Science and Materials*. New York, NY: Interscience.

Tobolsky, A. V. (1960b). *Properties and Structures of Polymers*. New York, NY: John Wiley and Sons, Inc.

Tobolsky, A. V., Prettyman, I. B., and Dillon, J. H. (1944). Stress relaxation of natural and synthetic rubber stocks. *J. Appl. Phys.* 15:380. doi: 10.1063/1.1707442

Tripathy, A. R., Morin, J. E., and Williams, D. E. (2002). A novel approach to improving the mechanical properties in recycled vulcanized natural rubber and its mechanism. *Macromolecules* 35, 4616–4627. doi: 10.1021/ma012110b

Ubaidillah, C., Jin Choi, H., Amri Mazlan, S., and Imaduddin, F. (2016a). Fabrication and viscoelastic characteristics of waste tire rubber based magnetorheological elastomer. *Smart Mater. Struct.* 25, 1–14. doi: 10.1088/0964-1726/25/11/115026

Ubaidillah, S., Amri Mazlan, S., Sutrisno, J., and Yahya, I. (2016c). Physicochemical properties and stress-strain compression behaviors of a ground tire rubber based magnetorheological elastomers. *Scientia Iranica, Trans. C: Chem. Chem. Eng.* 23, 1144–1159. doi: 10.24200/sci.2016.3885

Ubaidillah, S., Imaduddin, F., Li, S., and Amri Mazlan, S. (2016b). A new class of magnetorheological elastomers based on waste tire rubber and the characterization of their properties. *Smart Mater. Struct.* 25, 1–15. doi: 10.1088/0964-1726/25/11/115002

Ubaidillah, S. J., Purwanto, A., and Amri Mazlan, S. (2015). Recent progress on magnetorheological solids: materials, fabrication, testing, and applications. *Adv. Eng. Mater.* 17, 563–597. doi: 10.1002/adem.201400258

Wang, Y. H., Zhang, X. R., and Oh, J. E. (2015). Fabrication and properties of magnetorheological elastomers based on CR/ENR self-crosslinking blends. *Smart Mater. Struct.* 24:95006. doi: 10.1088/0964-1726/24/9/095006

Wang, Y. L., Hu, Y., and Deng, H. X. (2006). Magnetorheological elastomers based on isobutylene–isoprene rubber. *Polymer Eng. Sci.* 46, 264–268. doi: 10.1002/pen.20462

Yazdani, H., Karrabi, M., and Ghasmi, I. (2011). Devulcanization of waste tires using a twin-screw extruder: the effects of processing conditions. *J. Vinyl Addit. Technol.* 17, 64–69. doi: 10.1002/vnl.20257

Zhu, J. T., Xu, Z. D., and Guo, Y. Q. (2013). Experimental and modeling study on magnetorheological elastomers with different matrices. *J. Mater. Civil Eng.* 25, 1762–1771. doi: 10.1061/(ASCE)MT.1943-5533.0000727

Conflict of Interest Statement: The authors declare that the research was conducted in the absence of any commercial or financial relationships that could be construed as a potential conflict of interest.

Structural Materials

Paulo Borges

Dr Paulo H. R. Borges holds a BSc in Civil Engineering (1997) and a MSc (2002) in Engineering Materials from the Federal University of Minas Gerais, Brazil, as well as a PhD (2007) in Engineering Materials from The University of Sheffield, UK. Dr Borges has academic and industry experience (Technical services, Research and Development) related to ceramics and construction materials. He is currently an Associate Professor at the Federal Centre for Technological Education of Minas Gerais (CEFET-MG), Brazil, where his current research and special interests focuses on the development of high performance composites, fiber reinforced concrete, sustainable mortars and concretes, alternative binders to Portland cement, fresh behaviour and particle packing methods applied to ceramic / cementitious materials, microstructural characterization and durability testing of construction materials, reuse and recycling in construction and sustainability applied to construction materials.

Dimitri Feys°

Dimitri Feys obtained his combined BSc and MSc degree in Civil Engineering in 2004 from Ghent University, Belgium. Five years later, he obtained his Ph-D degree from the same institute focusing on the interactions between rheology and pumping of self-compacting concrete. He continued his academic career with a post-doc position at the Universite de Sherbrooke, QC, Canada before joining the Missouri University of Science and Technology, United States, as an Assistant Professor in January of 2013. His research focuses on rheology and placement of cement-based materials, with specific focus on the influence of mix design, performing and interpreting measurements, the interactions between rheology and placement (including pumping), and how placement affects the final properties of the material. He is active in RILEM, ACI, and ACerS and is a member of different technical committees within those organizations. He serves as the deputy chair for RILEM TC-266: Measuring rheology of cement-based materials and is also secretary of the ACI Missouri local chapter. In 2018, he received the ACI Young Member Award for Professional Achievement.

Márlon Longhi

Márlon Longhi is a civil engineer with a MSc degree in engineering from the Universidade Federal do Rio Grande do Sul (UFRGS) Brazil, and is currently a PhD student at UFRGS, with part of the PhD being completed at the University of Southern Queensland (USQ). During the last years he also worked in the construction industry and was a former Professor at the Universidade de Caxias do Sul (UCS) and the Universidade do Vale do Taquari (Univates).

His main research topics are related to the development, optimization, and use of alternative cement with low CO2 emissions, especially geopolymer, the use of industrial waste, and the development of high-performance concrete.

Hongyan Ma

Dr °Hongyan Ma° is an Assistant Professor of civil engineering at the Missouri University of Science and Technology (S&T). He obtained his PhD in civil engineering from the Hong Kong University of Science and Technology (HKUST) in 2013, and then worked as a postdoctoral fellow developing functional composites in HKUST before joining Missouri S&T in 2015. Dr Ma has 14 years of experience in R&D of cement-based materials, and his current research interests include multi-scale modeling, biological materials, R&D of traditional and innovative cements based on performance targets, as well as new sensing/monitoring technologies. He has published over 60 peer-reviewed journal papers in the field of civil engineering and materials science. Dr Ma was an ASCE Excellence in Civil Engineering Education Fellow in 2017 and a recipient of the Missouri S&T Joseph H. Senne Jr. Academy of Civil Engineers Faculty Scholarly Achievement Award in 2019.

Michele V. Manuel

Michele Manuel is the Department Chair of the Department of Materials Science and Engineering at the University of Florida. She received her PhD in Materials Science and Engineering at Northwestern University in 2007 and her BS in Materials Science and Engineering at the University of Florida. She is and ASM Fellow and the recipient of the Presidential Early Career Award for Scientists and Engineers (PECASE), NSF CAREER, NASA Early Career Faculty, ASM Bradley Stoughton Award for Young Teachers, AVS Recognition for Excellence in Leadership, TMS Early Career Faculty, TMS Young Leaders Professional Development, and TMS/JIM International Scholar Awards. Her research lies in the basic understanding of the relationship between processing, structure, properties and performance. She uses a systems-based materials design approach that couples experimental research with theory and mechanistic modeling for the accelerated development of materials. Her current research focuses on the use of systems-level design methods to advance the development of new materials through microstructure optimization. Of specific interest are lightweight alloys, self-healing metals, computational thermodynamics and kinetics, shape memory alloys, and materials in extreme environments – specifically under high magnetic fields or under irradiation.

Behzad Nematollahi

Dr Nematollahi is an ARC DECRA Fellow at the Center for Smart Infrastructure and Digital Construction. He is also Deputy Director of the Smart Structures Laboratory.

Dr Nematollahi received an Australian Research Council (ARC) Discovery Early Career Researcher Award (DECRA) for his 3-year project which started in January 2018. The project aims to develop a 3D printable fiber-reinforced geopolymer/Portland cement concrete for digital construction. DECRA is a Fellowship Program for Early Career Researchers and forms part of the ARC National Competitive Grants Program, which is an incredibly competitive process with a success rate of 16%.

Dr Nematollahi's research interest include 3D Concrete Printing, Geopolymer Concrete, Strain-Hardening Cementitious Composites (SHCC) and Ultra-High Performance Concrete (UHPC).

Dr Nematollahi received his PhD from Swinburne University of Technology. The topic of his PhD thesis was "Investigation of Geopolymer as a Sustainable Alternative Binder for Fiber-Reinforced Strain-Hardening Composites" under the supervision of Prof. Jay Sanjayan.

Didier Snoeck

Dr Ir. Didier Snoeck is a postdoctoral research Fellow of the Research Foundation Flanders (FWO) at the Magnel Laboratory for Concrete Research of Ghent University, Belgium. He is a member of RILEM, is active in several technical committees and was awarded the RILEM Gustavo Colonnetti Medal. His main topics of research focus on concrete technology, durability, nano- and microstructural properties, superabsorbent polymers, self-sealing and self-healing of cementitious materials.

frontiers in Materials

ORIGINAL RESEARCH
published: 07 May 2019
doi: 10.3389/fmats.2019.00077

Silica Fume as Precursor in the Development of Sustainable and High-Performance MK-Based Alkali-Activated Materials Reinforced With Short PVA Fibers

Raquel P. Batista[1], *Ana Carolina C. Trindade*[2], *Paulo H. R. Borges*[1]* *and Flávio de A. Silva*[2]

[1] Department of Civil Engineering, Centro Federal de Educação Tecnológica de Minas Gerais (CEFET-MG), Belo Horizonte, Brazil, [2] Department of Civil and Environmental Engineering, Pontifical Catholic University of Rio de Janeiro (PUC-RIO), Rio de Janeiro, Brazil

OPEN ACCESS

Edited by:
John L. Provis,
University of Sheffield,
United Kingdom

Reviewed by:
Ali Behnood,
Purdue University, United States
Dimitri Feys,
Missouri University of Science and Technology, United States

***Correspondence:**
Paulo H. R. Borges
Paulo.borges@cefetmg.br

Specialty section:
This article was submitted to Structural Materials, a section of the journal Frontiers in Materials

Received: 01 December 2018
Accepted: 05 April 2019
Published: 07 May 2019

Citation:
Batista RP, Trindade ACC, Borges PHR and Silva FA (2019) Silica Fume as Precursor in the Development of Sustainable and High-Performance MK-Based Alkali-Activated Materials Reinforced With Short PVA Fibers. Front. Mater. 6:77. doi: 10.3389/fmats.2019.00077

Alkali-activated materials (AAM) are currently the subject of increasing interest and research, mainly due to the possibility of reducing the carbon dioxide (CO_2) emissions in their production when compared to Portland cement (PC) and still achieve superior performance in many aspects when compared to traditional PC-based products. However, the use of sodium silicate (SS) as an alkaline activator in AAM is controversial when the aim is to reduce the environmental impact, as the production of the first also releases significant amount of CO_2 per ton of activator produced. Therefore, a demand has emerged for alternative silica-rich materials that could effectively reduce the demand for SS without compromising the mechanical behavior of the matrices and consequently the performance of fiber reinforced AAM. This paper investigates the gradual replacement (0–18% wt.) of metakaolin (MK) with silica fume (SF) in PVA-reinforced AAM, allowing the reduction of SS in the activator, also containing NaOH. Matrices with different composition were studied, i.e., with $[SiO_2]/[Al_2O_3]$ molar ratios of 3.0 and 3.8. All formulations were reinforced with 2% vol. of PVA fibers. The mechanical properties investigated were compressive strength, modulus of elasticity, flexural strength, and toughness. Apparent dry density, water absorption, and porosity of the composites were also assessed to give an indication of their durability. Single fiber pullout, fracture toughness, and direct tensile tests were also carried out in order to understand the deformation capability of the composites. Results indicated that the employment of SF may effectively reduce the demand for SS in the alkaline activators, in order to produce alkali-activated composites with lower environmental impact (reduced CO_2 emissions). Adjustments in the formulations may improve toughness in flexion in 170% with 30 wt.% reduction of SS in the activator, as well as improvements in deformation capability in tension. The development of strain-hardening MK-based AAM, however, has some challenging aspects that are also discussed.

Keywords: alkali-activated materials, geopolymers, activators, PVA fibers, metakaolin, silica fume

INTRODUCTION

The intense energy consumption and the wide emission of carbon dioxide (CO_2) involved in the production of Portland cement (PC) led to the development of several alternative cements, also known as "green" cements, that have emerged in the last two decades. These binders have been studied with the aim of developing products that require less energy to be produced, release less CO_2 into the atmosphere, and that have similar or improved structural properties than those presented by PC products (Stavrinides, 2010; Komnitsas, 2011).

Alkali-activated materials (AAM) are alternative binders to PC that result from reactions between alkaline solution and precursor materials rich in silica and alumina (Lloyd and Rangan, 2010; Van Deventer et al., 2010). In terms of sustainability, the AAM production generate, in average, 0.18 tons of CO_2 per ton of binder, which corresponds to a reduction of about 80% in CO_2 emissions when compared to the production of ordinary Portland cement (Stavrinides, 2010; Juenger et al., 2011).

Besides the environmental factor, AAM present several other advantages in comparison to PC-based mortars and concretes, such as fast development of mechanical strength (Duxson et al., 2007), reduced expansion by alkali-aggregate reaction (Davidovits, 1994), higher durability in aggressive environment (Bakharev et al., 2001a,b, 2002, 2003) and higher resistance to elevated temperatures (Kong et al., 2007; Kong and Sanjayan, 2008).

Alkaline activation is a complex process, consisting of several steps that involve a series of dissolution, reorientation, and solidification reactions (Provis et al., 2005). One of the most important factors related to alkali-activated systems is the availability of soluble silica, as it affects workability, hardening and the development of mechanical strength, as well as the modification of the gel composition and the microstructure of the produced material (Garcia-Lodeiro et al., 2015). The soluble silica is only detrimental when employed in high concentrations, with consequent reductions in pH and an increase in the viscosity of the activating solution, leading to a reduction in the raw material's reaction rate (Duxson et al., 2005).

In this sense, the use of controlled amount of sodium silicate (SS) as an alkaline activator ensures high mechanical strength and low permeability of AAM, since it accelerates the activation reactions by providing silica readily available to react with the precursors. However, the employment of SS has become an issue in the production of AAM due to (i) its high cost in some countries and (ii) the fact that its production cannot be considered environmentally friendly (Bernal et al., 2012; Borges et al., 2014). In fact, the production process of SS involves the calcination of sodium carbonate (Na_2CO_3) with quartz sand (SiO_2) at temperatures between 1,400 and 1,500°C; this process generates CO_2 and other emissions related to the fuels used during calcination (Bernal et al., 2012). Thus, a demand has emerged for alternative alkaline activators or silica-rich precursors that could effectively reduce the demand of SS in AAM.

Several studies have shown that amorphous silica-rich materials may be used as alternative alkaline activators to produce AAM (Bernal et al., 2012), such as silica fume (Rouseková et al., 1997; Bajza et al., 1998; Živica, 1999, 2004, 2006; Bernal et al., 2012; Rodríguez et al., 2013), rice husk ash (Bernal et al., 2012; Kamseu et al., 2017), and waste glass (Puertas and Torres-Carrasco, 2014; Torres-Carrasco and Puertas, 2015; Tchakouté et al., 2016; Vafaei and Allahverdi, 2017). Those materials may be both economically and environmentally advantageous when compared to commercially available SS solutions.

However, sustainability involves not only the quantification of the environmental impact but also the assurance of high durability and consequently long service life of the structures. The durability of cementitious materials is, among other factors, limited by its inherent brittleness, which leads to cracking of the matrix and facilitates the penetration of deleterious agents. Like PC matrices, AAM are brittle materials that may require fibers to improve the ductile character, which ultimately affects their durability (Sakulich, 2011; Bernal et al., 2014; Komljenović, 2015).

Several types of fibers have already been employed in reinforced AAM. Poly vinyl alcohol (PVA) fibers stand out because of their high stability in alkaline environments and because they are currently employed in the development of high-performance cementitious composites. Recent researches have shown that these fibers may also improve the performance of AAM (Li et al., 2005; Lee et al., 2012; Shaikh, 2013; Nematollahi et al., 2014). Further studies (Bhutta et al., 2016; Borges et al., 2017) indicate that the toughness of PVA reinforced AAM may be a function of the amount of soluble silica in the system. However, this relationship is still not completely understood.

Micromechanical models based on concepts of fracture mechanics and materials deformation mechanisms were created to allow the understanding of the deformation capability mechanism of cementitious composites. Those models meet the increasing demand for materials with higher mechanical performance; they describe the deformation behavior of fiber-reinforced cementitious composites by the combination of properties presented by the matrix, the fibers and the fiber-matrix interface. According to Li and Leung (1992), two conditions must be fulfilled for the strain-hardening behavior to occur:

(i) Energy criterion: The maximum complementary energy of the composite ($J_b^{'}$) [J/m^2], must be greater than the crack tip toughness of the matrix (J_{tip}) [J/m^2], that is, $J_{tip} \leq J_b^{'}$.

$$J_{tip} = \frac{{K_m}^2}{E_m} \quad (1)$$

where K_m is the matrix fracture toughness [MPa.$\sqrt{}$m] and E_m is the matrix Young's modulus [GPa] (Li and Leung, 1992).

(ii) Tension criterion: The matrix resistance to the first crack (σ_{cc}) [MPa] cannot exceed the maximum bond stress (σ_o) [MPa] that prevents cracking (i.e., $\sigma_{cc} \leq \sigma_o$).

Based on these criteria, the use of two performance indexes (Pseudo Strain-Hardening index–PSH), related to energy (PSH_{energy}) and tension ($PSH_{tension}$), has been suggested by Kanda and Li (2006) to measure the performance of the composites.

This paper investigates the effects of the source of soluble silica on the mechanical performance and deformation capability of different formulations of alkali-activated mortars reinforced with short PVA fibers. The matrix composition varied due to the replacement of metakaolin (MK) with silica fume (SF), with consequent reduction of the amount of sodium silicate (SS) used in the activator. The results help understand the factors affecting the mechanical performance and the development of high-performance alkali-activated composites.

MATERIALS AND METHODS

Materials

MK was supplied by Metacaulim do Brasil ltda.; this was the main precursor material employed in the production of the AAM. The AAM produced with 100% MK was then used as reference. Other matrices were produced by partially replacing MK with small quantities of SF, the latter supplied by Tecnosil ltda., Brazil. Differently from MK (SiO_2 = 43.55%; Al_2O_3 = 37.00% calculated by XRF), SF (SiO_2 = 93.40%; Al_2O_3 = 0.75%) contains negligible amounts of Al_2O_3 and it is mainly composed of SiO_2. Therefore, the addition of SF makes it possible (i) to increase the $[SiO_2]/[Al_2O_3]$ molar ratio of the matrices without the need to considerably increase the amount of SS in the activator or (ii) to maintain the $[SiO_2]/[Al_2O_3]$ molar ratio and reduce the SS from the activating solution.

The particle size distribution of the precursor materials was determined using a CILAS 1090 laser diffraction particle size analyser; the mean particle size was 0.37 μm for SF and 2.12 μm for MK. This difference in particle size may affect the workability of the produced mortars, i.e., possible reduction of the consistency with the increase of the SF content in the mortars. However, it should be noted that consistency was not fixed for mortars produced in this work; in contrary, the decision was to keep the H_2O/Na_2O molar ratio constant with a value equal to 12.8 in order to ensure that the total amount of water was the same for all formulations. Therefore, the fineness of the particles is not the only parameter that can influence the workability of the studied mortars.

The alkaline activator is composed of sodium hydroxide (NaOH) solution (50% vol.), sodium silicate (SS) (31.79% SiO_2; 15.00% Na_2O; 53.21% H_2O) and extra water.

Fine sands are regarded as suitable aggregates for the development of high-performance cementitious composites (Li et al., 2001). Therefore, fine quartz sand (passing 0.6 mm, fineness modulus of 1.03) was used as aggregate.

The matrices were reinforced with REC15 PVA fibers supplied by Kuraray Co. Ltd; these fibers have a diameter of 40 μm, length of 8.0 mm, tensile strength = 1,600 MPa and an elongation of 6% and modulus of Young of 41 GPa.

Methods

Seven different mortar formulations were studied, three with a $[SiO_2]/[Al_2O_3]$ molar ratio equal to 3.0 and four with this molar ratio equal to 3.8. The formulations, their mix design and the respective activation parameters are shown in **Table 1**. The formulation code describes the matrix $[SiO_2]/[Al_2O_3]$ molar ratio (3.0 or 3.8), as well as the mass ratio between each precursor (MK and SF) used.

The amount of sodium hydroxide and sodium silicate used in each formulation varied to ensure that the total $[SiO_2]/[Al_2O_3]$ molar ratio of each system is equal to 3.0 or 3.8. $[Na_2O]/[SiO_2]$ and $[H_2O]/[Na_2O]$ molar ratios were held constant for all formulations with values equal to 0.26 and 12.80, respectively. By fixing these parameters, $[Na_2O]/[Al_2O_3]$ molar ratio has values of 0.78 or 0.99 for mortars with $[SiO_2]/[Al_2O_3]$ ratio equal to 3.0 or 3.8, respectively.

An aggregate to binder (MK and SF) mass ratio equal to 1 was used for all formulations. This value was determined in preliminary tests; molding fiber-reinforced AAM becomes impracticable when higher aggregate to binder ratios are used. All mortars were reinforced with 2% vol. content of fibers, as used in other studies (Li et al., 2001; Lee et al., 2012; Nematollahi et al., 2014; Borges et al., 2017).

The addition of PVA fibers significantly alters the workability of the mortars; therefore, the amount of water (which determines the $[H_2O]/[Na_2O]$ molar ratio) employed in each formulation was experimentally determined and later on fixed to enable the mixing and compaction of all mortars. In other words, although the solution to binder ratios varied between 0.91 and 1.23 for the composites (**Table 1**), this variation occurs due to the increase of soluble silica in the activator, rather than an increase in the amounts of H_2O or Na_2O.

SF was supplied in powder; however, to ensure full dissolution, it was dissolved in the NaOH solution 24 h prior to mixing, as recommended by Bernal et al. (2012). In the following day, extra water and the SS solution were added to the activator (initially composed of NaOH + SF), resulting in the activating solution used in each formulation.

For each activating solution produced it is possible to calculate (i) the silica concentration provided by the SS as a function of the Na_2O concentration and (ii) the total soluble silica concentration (provided by the SS and the dissolved SF) as a function of Na_2O concentration. Those parameters are presented in the last two columns of **Table 1**. **Table 1** shows that the overall $[SiO_2]/[Na_2O]$ ratio in the activator is always equal to 1.29 or 1.83 for mortars with $[SiO_2]/[Al_2O_3]$ ratio equal to 3.0 or 3.8, respectively. However, the $[SiO_2]_{SS}/[Na_2O]_{sol.}$ ratio gradually decreases from 1.40 to 0.88 as SF replaces MK in the mortars.

The mixing procedure started by mixing MK with the activating solution in a mortar mixer at low speed, until the paste was homogeneous. The aggregates were slowly added and the mixing continued at high speed until fully homogenization of the mortar. The mixer was set again to low speed while the PVA fibers were added. The composites were cast and cured at ambient temperature (∼ 28°C). After 24 h they were demoulded and kept in plastic bags until the testing age (28 days), in order to avoid water loss and possible cracking.

Mortar Characterization

The consistency of the composites was determined by the flow table test, carried out according to the Brazilian standards NBR

TABLE 1 | Mix design and activation parameters for the produced mortars.

Formulation	$[SiO_2]/[Al_2O_3]$	MK:SF (wt.)	Solution to binder (wt.)	Sodium silicate/ solution mass ratio	$[SiO_2]_{SS}/[Na_2O]_{sol.}$	$[SiO_2]/[Na_2O]$ in the activator	$[H_2O]$
3.0 100MK-00SF	3.00	100:00	1.05	0.66	1.29	1.29	18.12
3.0 96MK-04SF	3.00	96:04	0.97	0.56	1.06	1.29	17.41
3.0 93MK-07SF	3.00	93:07	0.91	0.48	0.88	1.29	16.87
3.8 91MK-09SF	3.80	91:09	1.23	0.70	1.40	1.83	20.92
3.8 88MK-12SF	3.80	88:12	1.16	0.64	1.24	1.83	20.25
3.8 85MK-15SF	3.80	85:15	1.09	0.57	1.07	1.83	19.57
3.8 82MK-18SF	3.80	82:18	1.02	0.48	0.89	1.83	18.90

7215 (Associação Brasileira de Normas Técnicas, 1996) and NBR 13276 (Associação Brasileira De Normas Técnicas, 2016). This test was not carried out for unreinforced mortars, as they were extremely fluid.

Compressive strength and static modulus of elasticity tests were carried out at 28 days of ambient curing according to the standard NBR 7215 (Associação Brasileira de Normas Técnicas, 1996) and NBR 8522 (Associação Brasileira de Normas Técnicas, 2017) respectively; four cylindrical specimens (50 × 100) mm of each formulation were tested using an EMIC DL 30000 universal equipment, with load cell with 300 KN capacity. For the modulus of elasticity, the deformations of the specimens were measured by an electronic strain gauge with maximum measurable deformation of 2.5 mm and 0.0001 mm accuracy.

Three-point bending tests were performed as described in ASTM C 293 standard (American Society For Testing Materials, 2002). Four prismatic specimens (160 × 40 × 40 mm; spam = 120 mm) were tested for each mortar formulation, at a loading rate equal to (1.0 ± 0.1) MPa/min. The electronic deflectometer used to measure the specimen's displacement during the test has 0.001 mm of resolution and maximum measurable deflection of 12.5 mm. The first crack strength and peak strength (modulus of rupture–MOR) were determined.

The mortar's water absorption was determined by immersion in water under vacuum (RILEM, 1984) for four specimens of each of the formulations.

Deformation Capability Parameters

In a second stage of this work, it was decided to reduce the number of formulations to two matrices with different SiO_2/Al_2O_3 ratios; the first with $[SiO_2]/[Al_2O_3]$ ratio equal to 3.0 and neat MK (3.0 100MK-00SF) and the other one with $[SiO_2]/[Al_2O_3]$ equal to 3.8 and maximum amount of SF (3.8 82MK-18SF). Those extremes in the formulation envelope represented the largest reduction in the amount of SS used in the matrix composition and, therefore, the biggest environmental appeal. Direct tensile test, single fiber pullout test and matrix fracture toughness test were carried out for these two mortars, in order to better understand the deformation capability of those materials.

The single fiber pullout test is a commonly used technique to investigate the interface properties between fiber and matrix, where physical and chemical interactions occur. Those interactions can be quantified from the load and displacement values obtained in the test, by means of properties like the adhesional stress (τ_a), the frictional stress at the beginning of fiber slip (τ_b), the maximum shear stress (τ_{max}) and chemical bond (G_d) between fiber and matrix. The stress to which the fiber is subjected (τ) [MPa] can be calculated from the Equation 2 (Redon et al., 2001):

$$\tau = \frac{P}{\pi d_f L_e} \tag{2}$$

where P is the applied load [N]; d_f is the fiber diameter [mm] and L_e is the fiber embedment length [mm] in the matrix.

Equation 3 can be applied to estimate the superficial stress due to the chemical bonding (G_d) [N/mm] between fiber and matrix, based on the maximum load [N] supported until the loss of bond (P_a) and the initial friction loading [N] in the sliding step (P_b) (Redon et al., 2001):

$$G_d = \frac{2(P_a - P_b)^2}{\pi^2 E_f d_f^3} \tag{3}$$

where E_f is the modulus of elasticity of the fiber [N/mm^2].

The crack opening δ_0 [mm] that corresponds to the maximum bond stress (σ_o) [MPa] that prevents crack propagation, can be calculated with Equation 4 (Wang and Li, 2007):

$$\delta_0 = \frac{\tau_0 L_e^2}{d_{fE_f}} - \frac{2G_d}{\tau_0} \tag{4}$$

Equation 5 gives the maximum bond strength corresponding to δ_0 (Wang and Li, 2007):

$$\sigma(\delta) = \begin{cases} 2V_f\sqrt{(2G_d + \tau_0\delta)\frac{E_f}{d_f}} - \frac{V_f E_f \delta}{L_e} & \delta \le \delta_c \\ \frac{4V_f\tau_0}{L_e d_f}\left(\frac{L_e}{2} - \delta\right)^2 & \delta_c < \delta \le \frac{L_e}{2} \end{cases} \tag{5}$$

where δ_c corresponds to the critical crack opening [mm] in which the fibers lose adhesion with the matrix and V_f is the volume of fibers [%].

For the specimens casting, a single short PVA fiber was inserted into the end of a hollow cannula. Each of the fibers was attached to the cannula with wax in a way to ensure a 4 mm embedment length in the matrix. **Figure 1** shows the mold used in the preparation of the specimens for the single fiber pullout test and the detail of fiber positioning in the cannula. The produced specimens have cylindrical geometry (2.5 cm diameter × 2.5 cm height).

The single fiber pullout tests were carried out in an MTS model 810 universal test equipment with 250 kN load capacity and 100 N load transducer. The displacement rate employed was 0.02 mm/min. Six specimens from each formulation were tested at the age of 28 days. The displacement was measured by the actuator displacement. **Figure 2** shows the assembly of the test and the detail shows how the fibers were fixed to a metal plate coupled to the load cell, using a universal instant adhesive.

The fracture toughness corresponds to the measure of the magnitude of the existing concentration of tension when a crack begins to propagate. Three-point bending tests on notched prismatic specimens are usually carried out to evaluate properties related to the matrix fracture, including modulus of elasticity (E_m) [N/m^2], matrix fracture toughness (K_m) [N.m$^{3/2}$], and effective critical depth of crack opening (a_c) [m]. According to RILEM TC 89-FMT recommendation (RILEM, 1990), parameters related to matrix fracture can be calculated according to Equations 6–8:

$$E_m = \frac{6Sa_0V_1(\alpha)}{C_i d^2 b} \quad (6)$$

$$V_1(\alpha) = 0.76 - 2.28\alpha + 3.87\alpha^2 - 2.04\alpha^3 + \frac{0.66}{(1-\alpha)^2} \quad (7)$$

$$\alpha = \frac{a_0 + HO}{d + HO} \quad (8)$$

where E_m is the material modulus of elasticity; S is the adopted spacing between supports [m]; a_0 is the initial notch depth [m]; C_i is the initial compliance [m.N^{-1}] calculated from the initial slope of the load × crack mouth opening displacement (CMOD) curve; d is the specimen height [m]; b is the specimen width [m]; and HO is the thickness [m] of the metal sheet that supports the clip gauge.

From the modulus of elasticity (E_m) calculated by the Equation 6, the effective critical crack depth (a_c) can be obtained by means of an interactive process to satisfy Equation 9 (RILEM, 1990):

$$E_m = \frac{6Sa_cV_1(\alpha)}{C_u d^2 b} \quad (9)$$

where C_u is the compliance [m.N^{-1}] when a discharge corresponding to 95% of the maximum load is reached, calculated from the slope of the load × CMOD curve.

The matrix fracture toughness (K_m) [N.m$^{3/2}$] can be calculated from Equations 10–13 (RILEM, 1990):

$$K_m = 3(P_{max} + 0.5W)\frac{S(\pi a_c)^{\frac{1}{2}}F(\alpha)}{2d^2 b} \quad (10)$$

$$F(\alpha) = \frac{1.99 - \alpha(1-\alpha)(2.15 - 3.93\alpha + 2.7\alpha^2)}{\sqrt{\pi}(1+2\alpha)(1-\alpha)^{\frac{3}{2}}} \quad (11)$$

$$\alpha = \frac{a_c}{d} \quad (12)$$

$$W = \frac{W_0 S}{L} \quad (13)$$

where P_{max} is the maximum load [N] measured in the test; S is the adopted spacing between supports [m]; W_0 is the weight of the specimen [N]; and L is the length of the specimen [m].

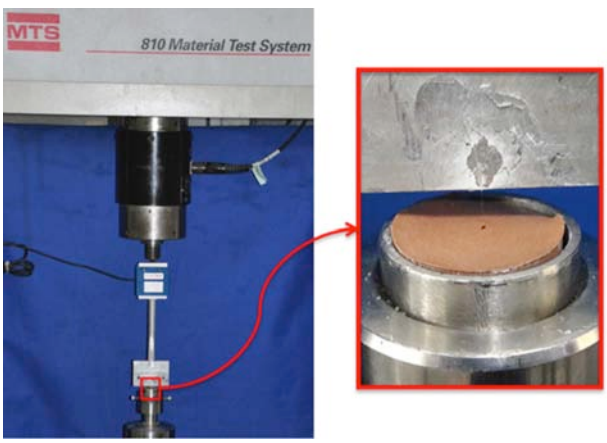

FIGURE 2 | Assembly of the single fiber pullout test and detail showing the fixation of the fiber to the equipment with Super Bonder type adhesive.

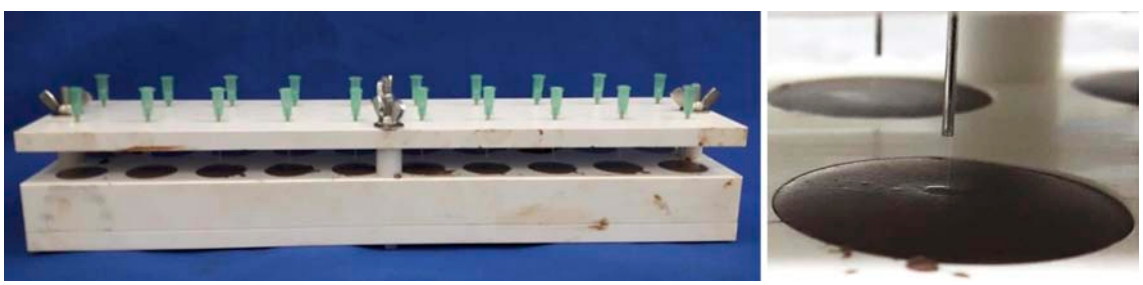

FIGURE 1 | Mold used to produce the specimens for the single fiber pullout test and detail of the fiber positioning in the cannula.

Ten prismatic (160 × 40 × 40) mm specimens were tested for each of the two investigated formulations (3.0 100MK-00SF and 3.8 82MK-18SF), with a 1.5 mm thickness by 12 mm height notch.

The fracture toughness tests were performed in an MTS model 204.63 reaction frame with a servo-hydraulic actuator, with 100 kN load capacity. The distance between the supports was set at 120 mm and the loading rate used was equal to 0.008 mm/min. The crack mouth opening displacement (CMOD) was measured by a clip gauge attached to two metal plates and positioned in the center of the notch. The metallic plates were previously fixed to the specimens with adhesive plastic mass. The thickness (HO) of the metal plates is equal to 2 mm.

The direct tensile test gives the fracture process of the studied composites, allowing the identification of strain-hardening or strain-softening behavior; it also provides one of the parameters required by the micromechanical model to describe the materials' behavior. The first crack stress and deformation values were determined, as well as the maximum strength and deformation capability presented by the material after the initial cracking. It is important to note the complexity of this test, considering that the sample misalignment in relation to the axis of load application can generate undesired torsion or bending stresses, which may lead to premature failure of the specimens. The tests were performed at the age of 28 days, using four dumbbell specimens (24 mm × 40 mm central section and 250 mm length), as adopted by Mechtcherine et al. (2011), for each formulation. The tests were performed in an MTS model 810 universal test equipment with 250 kN load capacity. The loading rate employed is equal to 0.06 mm/min and the displacements were measured by two linear variable displacement transducers (LVDT), positioned on the specimen's sides, with a measurement length equal to 100 mm. The assembling of the direct tensile test is shown in **Figure 3**.

With the capability parameters presented above, it was possible to use the two PSH indexes (Equations 14, 15) to evaluate the deformation performance of the composites (Kanda and Li, 2006):

$$PSH_{energy} = \frac{J_b'}{J_{tip}} \quad (14)$$

$$PSH_{tension} = \frac{\sigma_0}{\sigma_{cc}} \quad (15)$$

FIGURE 3 | Assembling the tensile strength test and fractured specimen.

RESULTS AND DISCUSSION

Flow Table Test

Figure 4 shows the flow table test results (spreading in mm) for the fiber-reinforced mortars, as well as the solution/binder ratio adopted for each formulation and the SS/solution mass ratio (y-axis).

It can be noticed that the increase in the amount of SF in the formulations does not seem to negatively affect the workability of the AAM. SF particles are thinner than MK ones, but they are also spherical; therefore, their incorporation in AAM may lead to a lower solution demand to maintain the same workability, as already verified by Rodríguez et al. (2013).

Figure 4 shows a slight increase in the consistency (measured by the flow table test) of the mortars with $[SiO_2]/[Al_2O_3]$ ratio equal to 3.8 when compared to those with this ratio equal to 3.0. This behavior is probably related to the solution/binder ratio employed (black dotted curve in **Figure 4**): 0.92–1.92 for mortars with $[SiO_2]/[Al_2O_3] = 3.0$ against 0.94–2.37 for those with $[SiO_2]/[Al_2O_3] = 3.8$. However, this relationship is not linear. For example, the formulation 3.0 100MK-00SF has solution/binder ratio equal to 1.05 and a flow table = 190 mm; the formulation 3.8 82MK-18SF has lower solution/binder ratio (1.02) and higher flow table (235 mm). The same trend is found for the SS/solution ratio (gray dotted curve in **Figure 4**). Therefore, in general the variation of the solution/solids ratio or the SS/solution mass ratio did not influence the mortar's consistency for both series with the same $[SiO_2]/[Al_2O_3]$ ratio.

Compressive Strength and Modulus of Elasticity

Figure 5 shows the results of compressive strength, corresponding to the average of four specimens for each mortar. It is possible to see that the compressive strength significantly vary neither with the change in the $[SiO_2]/[Al_2O_3]$ molar ratio nor with the increase of the SF percentage in the system (i.e., with a reduction in the $[SiO_2]_{SS}/[Na_2O]_{sol.}$ ratio in the activating solutions). These results indicate that the SF is effectively reacting and may reduce the demand for SS in AAM without any significant impact on the compressive strength of these composites.

It could be expected that fiber-reinforced composites would have slightly lower compressive strength than non-reinforced composites. The fiber addition usually reduces the compressive strength of cementitious composites, as a consequence of the interface between fiber and matrix, with possible sites for the formation and propagation of cracks and material failure at lower loadings (Bentur and Mindess, 2007). However, in general, there

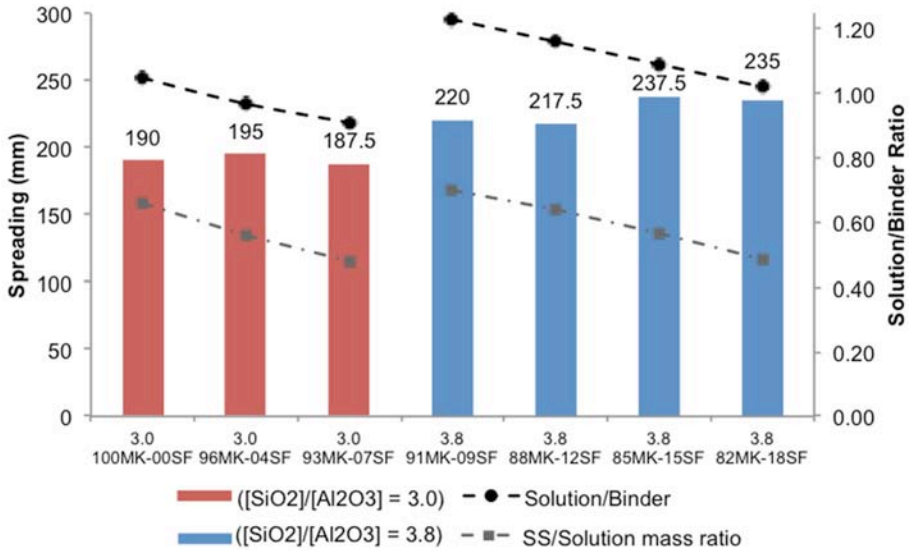

FIGURE 4 | Flow table test results for the fiber-reinforced mortars.

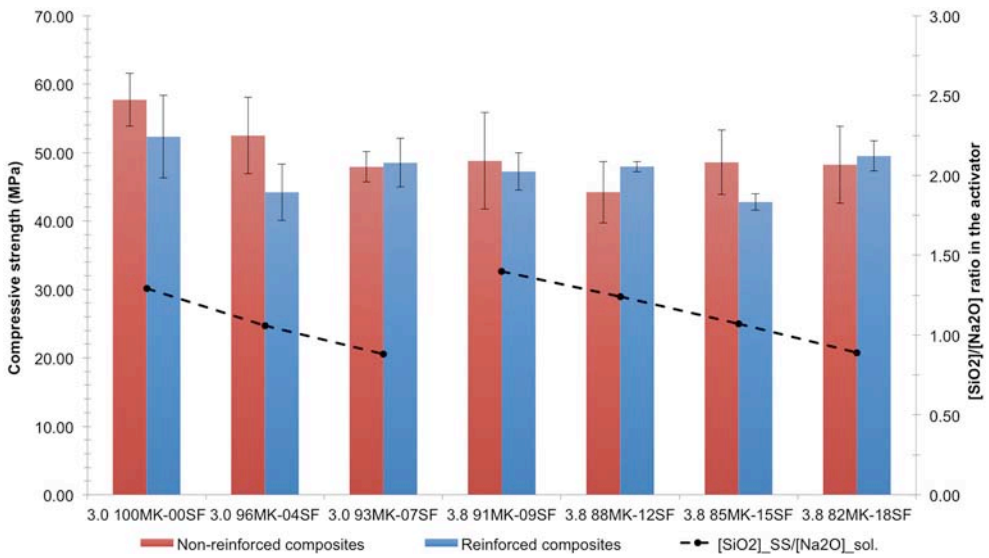

FIGURE 5 | Compressive strength (28 days).

are no statistical variations in strength (marked by the error bars) for plain and reinforced composites. Therefore, for the MK-based AAM studied, the compressive strength is not significantly affected by the fiber addition.

It should be noted that the high standard deviations in the compressive strength for almost all formulations seem to be inherent to AAM, as previously reported in the literature (Provis et al., 2009). In addition, Bernal et al. (2012) reported that the replacement of SS with SF-based activators in the preparation of AAM seems to lead to higher variability in compressive strength results.

The results of the modulus of elasticity are shown in **Figure 6**. The presented values correspond to the average of four specimens for each formulation. In general, reference formulations (without fibers, red bars) have higher modulus of elasticity than those reinforced with fibers, but the difference is not significant. This behavior agrees with the results reported by Puertas et al. (2003) for the incorporation of polypropylene fibers in alkali-activated mortars, which led to a slight reduction in the modulus of elasticity in comparison to non-reinforced composites.

Figure 6 also shows an overall reduction in the modulus of elasticity for AAM with $SiO_2/Al_2O_3 = 3.8$; within each of these

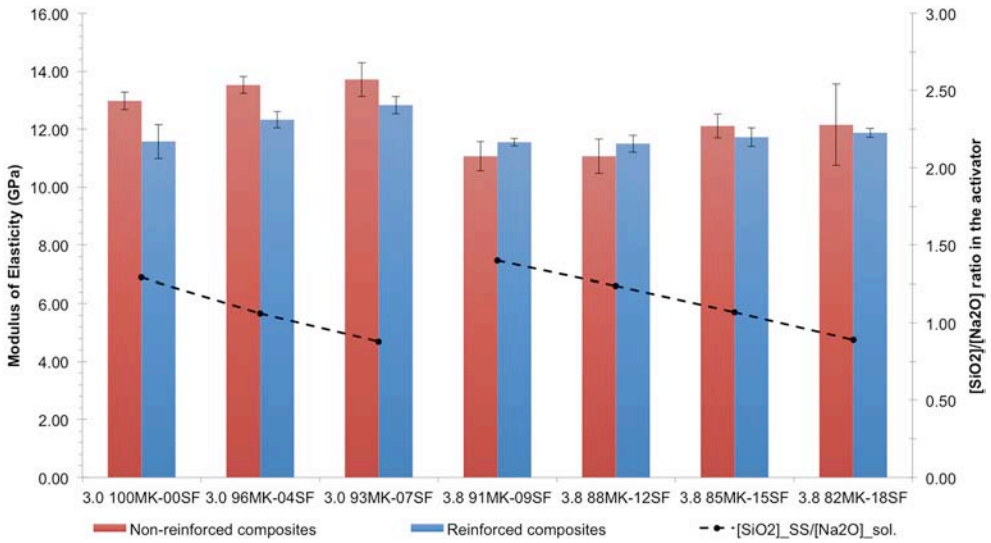

FIGURE 6 | Modulus of elasticity results.

series (3.0 or 3.8) the mean value of the modulus of elasticity appears to increase for higher amounts of SF.

Obonyo et al. (2011) stated that the modulus of elasticity is in the range of 4–35 GPa for geopolymers and other AAM. Němeček et al. (2011) argue that AAM have an inherent modulus of elasticity in a range between 17 and 18 GPa and that this property appears to be, for a given formulation, independent of the precursor material or the type of curing regime employed. Ye et al. (2017) produced blast furnace slag based AAM with modulus of elasticity varying between 13.25 and 20.71 GPa.

Therefore, the modulus of elasticity of the studied composites seems to be slightly lower than those reported in the literature for AAM. However, as stated by Provis et al. (2014), research is still needed to establish the interrelationships between the binder structure and its elastic properties.

In addition, Bondar et al. (2010) argued that the development of the modulus of elasticity is directly related to the curing temperature; its increase is limited by the water/fine materials ratio, i.e., by the amount of water available to evaporate during the activation process (Bondar et al., 2010). The curing regime used in this paper (ambient temperature) is probably responsible for slightly lower results for the modulus of elasticity.

No clear relationship between the modulus of elasticity and the compressive strength was found for the studied AAM. This behavior is corroborated by the literature, which states that the modulus of elasticity of alkali-activated binders presents little variation with the increase in compressive strength (Pacheco-Torgal et al., 2009).

Flexural Strength and Toughness

Figures 7A,B shows the Load (N) × Deflection (mm) curves, for the series produced with $[SiO_2]/[Al_2O_3]$ ratio equal to 3.0 and 3.8, respectively, obtained for four specimens of each composite, as well as the distribution of the cracks in one of the specimens after the three-point bending tests. It is possible to notice that all the composites present deflection-hardening behavior, with increased strength capacity after the first crack. After the initial matrix cracking, mortars with $[SiO_2]/[Al_2O_3]$ molar ratio equal to 3.0 had an average increase of 44% in flexural strength, against 47% in mortars with $[SiO_2]/[Al_2O_3]$ molar ratio equal to 3.8. It is worth to note that until the first crack, the fibers basically do not work, i.e., the load is supported mainly by the matrix until cracking (Bentur and Mindess, 2007).

The data provided by the Load (N) × Deflection (mm) curves (**Figure 7**) shows that there is a subtle reduction of flexural strength with the increase of $[SiO_2]/[Al_2O_3]$ molar ratio from 3.0 to 3.8, although these parameters may be considered the same when the standard deviation is taken into account. However, toughness of the reinforced mortars with $[SiO_2]/[Al_2O_3]$ molar ratio equal to 3.8 is higher than that of the materials with this ratio equal to 3.0, which had already been described by Borges et al. (2017).

Figure 8 shows the toughness in flexion of the composites as a function of the amount of SF employed, $[SiO_2]_{SS}/[Na_2O]_{sol.}$ and solution/binder ratio. At first, **Figure 8A** appears to indicate that the toughness of the composites increases with the SF addition. However, one may note that the toughness is roughly the same for composites with up to 7% SF. Similarly, the toughness does not vary when SF content changes from 9 to 18%. **Figure 8B** shows that the $[SiO_2]_{SS}/[Na_2O]_{sol.}$ molar ratio also does not play an important role in the toughness, which is roughly the same when the first is reduced from 1.40 to 0.89 for formulations with $[SiO_2]/[Al_2O_3] = 3.8$ or from 1.29 to 0.88 for formulations with $[SiO_2]/[Al_2O_3] = 3.0$. In that sense, SS may be successfully removed from the mixes without jeopardizing the toughness of MK-based alkali-activated composites. The solution/solids ratio did not determine the toughness behavior either. **Figure 8C** shows that the formulation 3.8 82MK-18SF

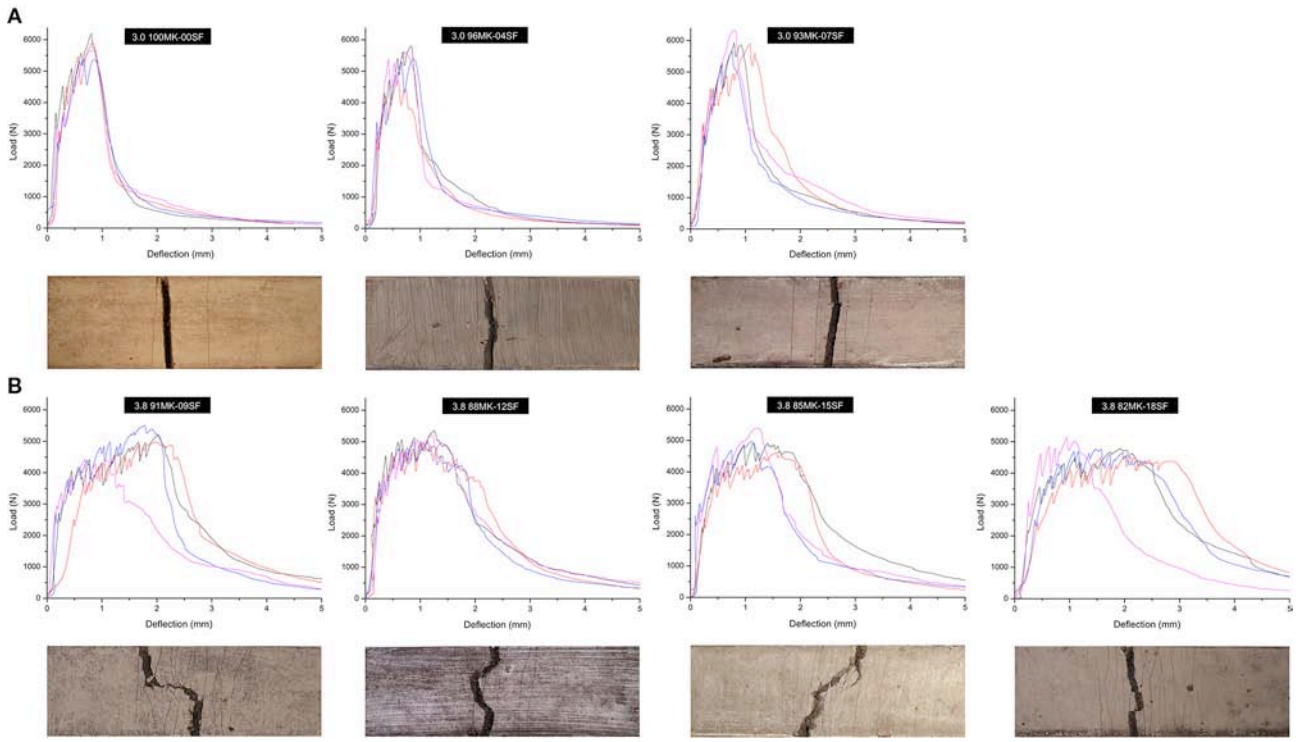

FIGURE 7 | Load (N) × Deflection (mm) curves and cracked specimens of mortars with $[SiO_2]/[Al_2O_3]$ ratio equal to **(A)** 3.0 and **(B)** 3.8.

with solution/binder ratio of 1.02 has double the toughness of 3.0 100MK-00SF, the latter with solution/binder of 1.05.

In all three **Figures 8A–C** the toughness is affected by the $[SiO_2]/[Al_2O_3]$ ratio, i.e., formulations with $[SiO_2]/[Al_2O_3] = 3.8$ have higher toughness than those with $[SiO_2]/[Al_2O_3] = 3.0$, as already seen in **Table 5**. Nevertheless, higher toughness in **Figure 8** (6.37–8.38 J) corresponds to formulations with the overall $[SiO_2]/[Na_2O]$ ratio in the activator equal to 1.83, whereas the lower values of toughness (2.69–3.41) are found for those composites with this ratio equal to 1.29, irrespective of changes in other activating parameters. In other words, the toughness of alkali-activated composites remains unaffected even when other significant changes in their composition take place, such as (i) the replacement of MK with SF; (ii) reduction of SS; and (iii) variation of solution/binder ratio.

Apparent Dry Density, Porosity, and Water Absorption

Apparent dry density (g/cm^3), water absorption (%), and apparent porosity (%) values were calculated from data of the water absorption test; the mean value and the standard deviation (in parentheses) are presented in **Table 2**.

There was no significant variation of the apparent dry density, water absorption or apparent porosity between all the formulations, or between fiber-reinforced composites and those without reinforcement. This indicates that the reduction of SS in the activator (by replacing MK with SF) will not jeopardize the durability of the composites, as long as the $[H_2O]/[Na_2O]$ molar ration is kept constant.

It is important to remember that apparent dry density is also a function of the specific gravity of the precursors. The specific gravity is 2.22 g/cm^3 for SF and 2.56 g/cm^3 for MK. Thus, it makes sense that the apparent dry density of the produced composites decreases with the increase of the SF content, and consequently, with the reduction of MK amount in the composites. However, this is not a linear correlation, since other parameters change for different formulations, e.g., solution/solids ratio and SS/NaOH mass ratio. Thus, the employment of SF in MK-based AAM could also contribute in the design of lighter structures, when compared to neat MK AAM.

Single Fiber Pullout Test

Figure 9 shows the pullout force (N) × slipping (mm) curves obtained in the PVA fiber pullout test, with 4 mm embedment length in the matrices 3.0 100MK-00SF and 3.8 82MK-18SF. Six specimens were tested for each of the matrices.

There is a large variation in the results of the pullout test for different samples of the same matrix; however, in general a slightly greater slip of the fibers is observed in the matrix 3.0 100MK-00SF, when compared to the matrix 3.8 82-MK-18SF. Nevertheless, the pullout forces observed for the two matrices have similar values, way below the fibers tensile strength (1,600 MPa, which corresponds to a 2N loading).

Table 3 summarizes the main parameters related to the fiber-matrix interface, calculated from the average of six tests, with standard deviation presented in parentheses.

It can be noticed that the design parameters related to the fiber-matrix interface can be considered essentially the same for

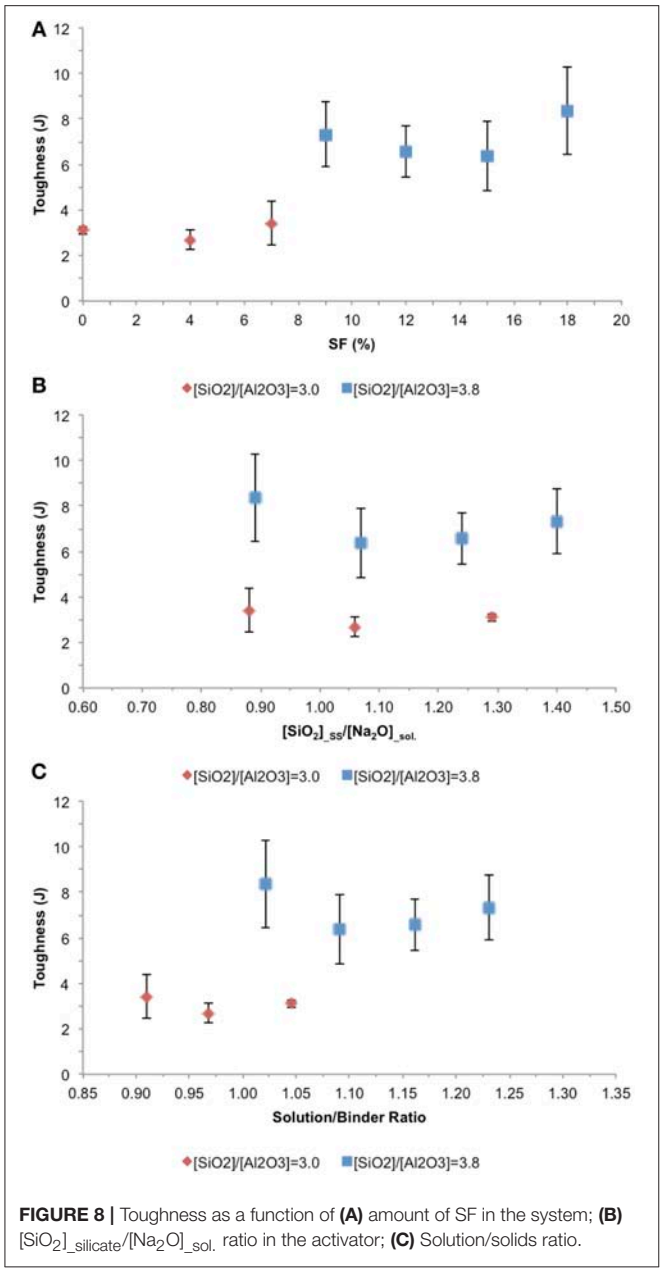

FIGURE 8 | Toughness as a function of **(A)** amount of SF in the system; **(B)** $[SiO_2]_{silicate}/[Na_2O]_{sol.}$ ratio in the activator; **(C)** Solution/solids ratio.

TABLE 2 | Mortars apparent specific dry density, water absorption, and apparent porosity.

Formulation		Apparent dry density (g/cm^3)	Water absorption (%)	Apparent porosity (%)
Non-reinforced composites	3.0 100MK-00SF	1.687 (0.004)	16.61 (0.05)	28.02 (0.13)
	3.0 96MK-04SF	1.673 (0.005)	16.97 (0.07)	28.40 (0.12)
	3.0 93MK-07SF	1.668 (0.007)	17.26 (0.03)	28.80 (0.13)
	3.8 91MK-09SF	1.634 (0.005)	17.95 (0.14)	29.33 (0.27)
	3.8 88MK-12SF	1.627 (0.005)	18.40 (0.16)	29.95 (0.23)
	3.8 85MK-15SF	1.621 (0.005)	18.58 (0.08)	30.12 (0.10)
	3.8 82MK-18SF	1.612 (0.012)	18.81 (0.07)	30.33 (0.26)
Reinforced composites	3.0 100MK-00SF	1.678 (0.004)	16.36 (0.08)	27.46 (0.12)
	3.0 96MK-04SF	1.662 (0.007)	16.68 (0.14)	27.72 (0.24)
	3.0 93MK-07SF	1.685 (0.007)	17.18 (0.40)	28.96 (0.57)
	3.8 91MK-09SF	1.647 (0.010)	17.34 (0.28)	28.57 (0.39)
	3.8 88MK-12SF	1.641 (0.011)	17.56 (0.26)	28.80 (0.35)
	3.8 85MK-15SF	1.609 (0.006)	18.47 (0.32)	29.72 (0.54)
	3.8 82MK-18SF	1.612 (0.007)	18.38 (0.14)	29.63 (0.15)

the two studied formulations. This behavior indicates once again that the SF incorporated into the matrix is effectively reacting and that the interface properties are not affected by the reduction of SS in the matrices. Comparing the mean values obtained for the two different formulations, results indicate that the chemical bond between fiber and matrix (G_d), the required tension for adhesion loss (σ_a) and the frictional tension at the beginning of pullout (τ_0) are not significantly affected by the increase of the SiO_2/Al_2O_3 ratio.

The comparison of these values with results described in the literature (Li et al., 2002; Oliveira, 2015; Nematollahi et al., 2017) indicates that the adhesion of PVA fibers to metakaolin-based alkali-activated matrixes is lower than that observed for fly ash-based AAM or for Portland cement matrices, behavior that may be related to both fiber embedment length in the matrix and to chemical properties of the matrices. The chemical bonding energy (G_d) and the frictional tension at the beginning of the pullout (τ_0) have significantly lower values for the metakaolin-based AAM studied in this paper than those described in the literature. Therefore, it can be inferred that the fibers properties are not exploited to their full potential in this case, since sliding of fibers occurs without considerable resistance at the interface.

Matrix Fracture Toughness

Table 4 shows the parameters found in the fracture toughness test for the mortars 3.0 100MK-00SF and 3.8 82MK-18SF. The mean values, obtained for 10 specimens of each formulation, are followed by the standard deviation in parentheses.

The modulus of elasticity (E_m) found for the two composites agree with the values described in the literature. In addition, the matrices of both formulations present higher values of fracture toughness (K_m) than those reported in the literature (Nematollahi et al., 2015). These high K_m values result in high matrix crack tip toughness (J_{tip}), which may negatively influence the deformation capability of the composites when subjected to direct tensile stresses.

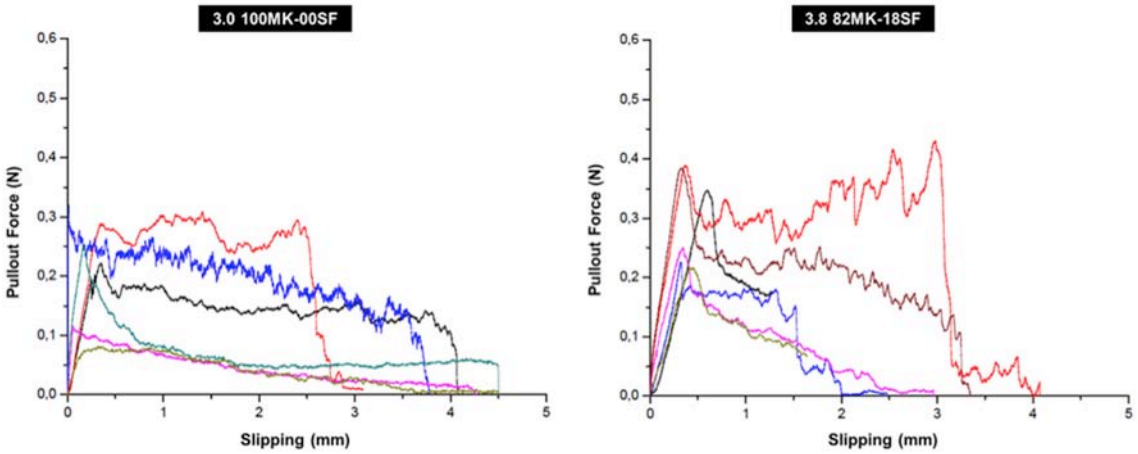

FIGURE 9 | Pullout curves for PVA fibers embedded (Le = 4 mm) in two alkali-activated matrices with different SiO_2/Al_2O_3 ratios.

TABLE 3 | Main parameters obtained in the single fiber pullout test for two alkali-activated matrices with different SiO_2/Al_2O_3 ratios.

Formulation	P_a (N)	P_b (N)	$P_{máx}$ (N)	σ_a (MPa)	σ_b or τ_0 (MPa)	$\sigma_{máx}$ (MPa)	G_d (J/m^2)
3.0 100MK-00SF	0.24 (0.07)	0.19 (0.08)	0.29 (0.13)	0.48 (0.15)	0.39 (0.16)	0.57 (0.25)	0.36 (0.62)
3.8 82MK-18SF	0.30 (0.08)	0.24 (0.09)	0.31 (0.09)	0.60 (0.16)	0.48 (0.19)	0.61 (0.18)	0.34 (0.28)

TABLE 4 | Matrix fracture toughness related properties.

Formulation	$P_{máx}$ (N)	E_m (GPa)	K_m (MPa.$\sqrt{m}$)	J_{tip} (J/m^2)
3.0 100MK-00SF	709.51 (28.17)	12.34 (0.87)	0.62 (0.02)	31.04 (2.38)
3.8 82MK-18SF	663.86 (64.33)	9.22 (1.65)	0.54 (0.07)	31.73 (3.94)

Behavior in Direct Tensile Test

Figure 10 shows the stress (MPa) × strain (%) curves corresponding to the tensile tests performed for the two matrices. These results correspond to the mean value obtained for four specimens, with standard deviation presented in parentheses. The measured values of deformation correspond to the average of the readings of the two LVDT.

These curves show that both composites present a slight increase in strength after the initial cracking of the matrix; the formation of multiple cracks, however, occurs in reduced quantity. It is also noticeable that the first peak strength is quite high and very close to the maximum composite strength, characterizing the strain-softening behavior in tension, with little deformation until failure.

Like the flexural strength test (section Flexural Strength and Toughness), an increasing number of cracks is associated with a higher $[SiO_2]/[Al_2O_3]$, i.e., equal to 3.8. However, this behavior is less pronounced in the direct tension test.

The analysis of the results indicates that the first crack strength of the matrices should be reduced in order to increase the deformation capability of the composites. In fact, very high σ_{cc} values (3.78 MPa for 3.0 100MK-00SF and 4.22 MPa for 3.8 82MK-18SF) lead to a reduction in the tension performance index ($PSH_{tension} = \sigma_0/\sigma_{cc}$). This will be further discussed in section $PSH_{tension}$ and PSH_{energy}.

It was observed the formation of about 2 to 5 cracks and deformation capability of 0.20–0.30% for the studied composites. The literature (Ohno and Li, 2014; Nematollahi et al., 2017) describes AAM with similar fracture toughness (K_m) and modulus of elasticity (E_m) but with deformation capability of around 4% and with the development of an elevated number of cracks in the axial tensile test, although the maximum tensile strengths described are similar to the formulations produced in this study. Nevertheless, the comparison of the obtained results with the data found in the literature (Li et al., 2002; Ohno and Li, 2014; Nematollahi et al., 2015) demonstrates the feasibility of optimizing the matrix and interface properties to obtain high ductility AAM reinforced with PVA fibers. This is discussed in the following section.

$PSH_{tension}$ and PSH_{energy}

Parameters related to the micromechanical modeling criteria were calculated for the studied composites with the aim of describing their deformation capability (**Table 5**). Both $PSH_{tension}$ and PSH_{energy} indexes have values lower than 1 for both composites. Therefore, the studied composites do not fit any of the two design criteria established for SHCC, considering those indexes. As previously discussed, they do not present the strain-hardening behavior, despite the formation of multiple cracks.

The comparison between the obtained values and results described in the literature may indicate which parameters should be optimized for the production of strain-hardening AAM. According to Nematollahi et al. (2017), in order to obtain AAM with strain-hardening behavior and saturation in the number

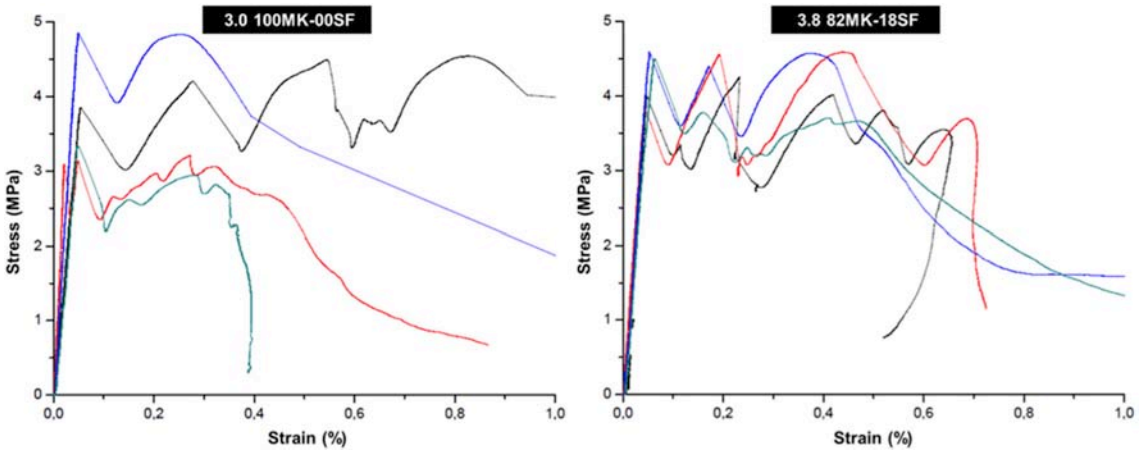

FIGURE 10 | Stress (MPa) × Strain (%) curves obtain in direct tension tests for composites with different SiO_2/Al_2O_3 ratios.

TABLE 5 | Design parameters related to the micromechanical modeling criteria.

Formulation	σ_0 (MPa)	σ_{cc} (MPa)	J_b' (J/m^2)	J_{tip} (J/m^2)	$PSH_{tension}$ (σ_0/σ_{cc})	PSH_{energy} (J_b'/J_{tip})
3.0 100MK-00SF	1.88 (0.68)	3.78 (0.78)	5.31 (3.85)	31.04 (2.38)	0.50	0.17
3.8 82MK-18SF	2.14 (0.67)	4.22 (0.38)	9.67 (6.67)	31.73 (3.94)	0.51	0.30

of cracks (in that case values of $PSH_{energy} = J_b'/J_{tip} > 2.7$ and $PSH_{tension} = \sigma_0/\sigma_{cc} > 1.3$ were used), the critical fiber volume (V_f) to be used decreases with the increase of the frictional stress (τ_0). However, when this tension is too high, fiber breaking prevails over slipping, which is a not desired condition. On the other hand, low τ_0 values are usually associated with low values of adhesional tension between fiber and matrix, causing a decrease in complementary energy (J_b'). Therefore, in order to meet both performance indexes ($PSH_{tension}$ and PSH_{energy}) requirements, it would be necessary to increase the volume of fibers to about 9%.

The employment of such high fiber volume is both economically and experimentally infeasible; therefore, another possible approach is to adjust the matrix properties. In this case, it is possible to reduce the fracture toughness of the matrix or to previously induce defects in the composite to control the distribution of cracks. The first scenario is easily executable by increasing the amount of water or adjusting the amount of aggregates used in the composite production. The second alternative requires the introduction of artificial defects in the matrix with a previously defined and controlled distribution, which is more difficult to achieve in practice (Nematollahi et al., 2017). In fact, some strain-hardening AAM related in the literature (Ohno and Li, 2014; Nematollahi et al., 2015) were produced with higher amount of water than the one employed in the AAM produced for this paper; consequently, these composites have lower values of J_{tip} than those obtained herein (31.04 and 31.73 J/m^2). In addition, those researches tend to use lower aggregate to binder content (0.3:1) than those employed in this paper (1:1), or even suppress the use of aggregates (studies with alkali-activated pastes), which implies in the reduction of K_m and, consequently, of J_{tip}. Nevertheless, at this point it is important to note that this is not an economically feasible approach when it comes to engineering materials.

TABLE 6 | Amount of silicate used and toughness obtained in each formulation.

Formulation	Mass of sodium silicate/volume of AAM [kg/m^3]	Toughness (J)
3.0 100MK-00SF	446.51	3.11
3.0 96MK-04SF	361.48	2.69
3.0 93MK-07SF	295.11	3.41
3.8 91MK-09SF	519.12	7.32
3.8 88MK-12SF	453.75	6.57
3.8 85MK-15SF	385.74	6.37
3.8 82MK-18SF	314.91	8.38

Thus, the simplest strategies to try to adapt the studied composites to SHCC design criteria would be to increase the $[H_2O]/[Na_2O]$ molar ratio adopted. However, this approach only impacts the value of PSH_{energy}, and it is necessary to adopt some other strategy to optimize $PSH_{tension}$. An increase in the $[H_2O]/[Na_2O]$ molar option is also undesirable with regards to durability aspects.

In this case, increasing the fiber embedment length in the matrix, with the use of fibers with a longer length (e.g., 12 mm), could contribute to the increase of τ_0 and δ_0, representing a feasible approach to increase the values of J_b' and of σ_0, in order to obtain higher values for the PSH_{energy} and $PSH_{tension}$ indexes.

Moreover, the values of $[SiO_2]/[Al_2O_3]$ molar ratios adopted by the studies described in the literature corroborate the finding that higher ratios are preferred when the production

of composites with higher deformation capability is desired. It is well known that one of the ways to reduce the matrix fracture toughness is by reducing its mechanical strength and, as pointed out in this research, the mechanical strength of the metakaolin based AAM seems to be strongly related to the $[SiO_2]/[Al_2O_3]$ ratio.

Thus, another possible approach to optimize the properties of the matrix would be to increase even more the $[SiO_2]/[Al_2O_3]$ ratio of the studied composites (higher than 3.8), thus reducing their mechanical strength and the σ_{cc} values and increasing the $PSH_{tension}$ value. Alternatively, it is also possible to evaluate composites activated with alkaline solution composed only of NaOH, considering that this activator produce AAM with lower mechanical performance but with better workability; this option would reduce σ_{cc} and still make it possible to improve the fiber dispersion capability and the incorporation of larger fiber volume, if desired. NaOH-based AAM cured at ambient temperature, however, are very prone to surface efflorescence (formation of Na_2CO_3), which is also undesirable. Therefore, the production of MK-based SHCC appear to be quite challenging since it will imply on the reduction of the aggregates to binder ratio (higher costs) and/or lower durability (increase in water content).

Environmental Analysis

Regarding the development of environmentally-friendly composites, **Table 6** presents the amount of SS employed in each formulation (in kg of SS/m^3 of AAM) and the corresponding toughness in flexion, in Joules. When comparing composites 3.0 100MK-00SF and 82MK-18SF, it is possible to notice that even with a reduction of 131.60 kg of SS per m^3 of AAM, toughness of the composite is improved by 5.27 J (i.e., 29.47% less SS is used and a gain of 169.68% in the toughness performance of the material is observed).

For a fixed $[SiO_2]/[Al_2O_3]$ it is still possible to reduce SS and improve the toughness: 33.91% less SS with corresponding 9.66% rise in toughness for $[SiO_2]/[Al_2O_3] = 3.0$; 39.34% less SS with an increase of 14.45% in toughness for $[SiO_2]/[Al_2O_3] = 3.8$.

CONCLUDING REMARKS

The employment of SF in the alkali-activated composites does not seem to affect their consistency. What appears to be governing the consistency is the value of the $[SiO_2]/[Al_2O_3]$ molar ratio of the matrix, with the highest indices (spreading) observed for mortars with $[SiO_2]/[Al_2O_3] = 3.8$.

In terms of mechanical performance, the compressive strength, flexural strength, and modulus of elasticity of the AAM significantly change neither with the alteration of the $[SiO_2]/[Al_2O_3]$ molar ratio nor with the increase of the percentage of SF present in the system, i.e., with consequent reduction of the $[SiO_2]_{SS}/[Na_2O]_{sol.}$ in the activating solutions. It can be inferred, therefore, that SF is effectively reacting in these systems; its employment satisfactorily reduce the demand of SS as source of SiO_2 without jeopardizing the mechanical performance.

All the produced mortars present deflection-hardening behavior in flexion. However, the deflection capacity is higher for composites with $[SiO_2]/[Al_2O_3]$ molar ratio equal to 3.8, compared to those with $[SiO_2]/[Al_2O_3] = 3.0$. Neither the amount of SF employed nor the $[SiO_2]_{SS}/[Na_2O]_{sol.}$ molar ratio or the solution to binder ratio seems to affect the toughness behavior of the composites. The parameter that appears to be governing toughness is the overall $[SiO_2]/[Na_2O]$ ratio in the activator, regardless of the soluble silica source (SF or SS). Therefore, the employment of SF as precursor is not detrimental to the toughness performance of MK-based alkali-activated composites.

There was no significant variation in apparent dry density, water absorption or apparent porosity between all composites, and this implies that the durability properties will not be affected if less SS is employed in the design of fiber-reinforced alkali-activated composites, as long as the water content is kept constant (herein in terms of $[H_2O]/[Na_2O]$ molar ratio). The composites developed in this study did not present the strain-hardening behavior, but rather deflection-hardening properties with multi cracking development in flexion. All results presented in the paper indicate that the employment of SF as an alternative precursor can provide MK-based alkali-activated composites with satisfactory physical, mechanical and durability properties, as well as enable the development of binders with lower environmental impact (lower SS demand). The cost reduction (not assessed here) will depend on local availability and costs of the main raw materials, i.e., MK, SF and SS and may vary from one country to another.

AUTHOR CONTRIBUTIONS

RB, PB, and FS conceived and designed the analysis. RB and AT collected the data. RB performed the analysis and wrote the paper.

ACKNOWLEDGMENTS

The authors would like to thank CNPq, CAPES, FAPEMIG, and CEFET-MG for supporting this research, as well as the companies Kuraray Co. Ltd. (Japan), Metacaulim do Brasil Ltda. (Brazil), Moinhos Gerais Ltda. (Brazil) and Tecnosil Construction Materials (Brazil), which donated raw materials to the research group.

REFERENCES

American Society For Testing Materials (2002). *ASTM C293 - 02*. Standard Test Method for Flexural Strength of Concrete (Using Simple Beam With Center-Point Loading.

Associação Brasileira de Normas Técnicas (1996). *NBR 7215 - Cimento Portland - Determinação da Resistência à Compressão*. 1–8.

Associação Brasileira De Normas Técnicas (2016). *NBR 13276 - Argamassa Para Assentamento e Revestimento de Paredes e Tetos - Determinação do Índice de Consistência*.

Associação Brasileira de Normas Técnicas (2017). *NBR 8522 - Concreto - Determinação dos Módulos Estáticos de Elasticidade e de Deformação à Compressão*.

Bajza, A., Rouseková, I., and Živica, V. (1998). Silica fume-sodium hydroxide binding systems. *Cem. Concr. Res.* 28, 13–18. doi: 10.1016/S0008-8846(97)00192-0

Bakharev, T., Sanjayan, J., and Cheng, Y.-B. (2003). Resistance of alkali-activated slag concrete to acid attack. *Cem. Concr. Res.* 33, 1607–1611. doi: 10.1016/S0008-8846(03)00125-X

Bakharev, T., Sanjayan, J. G., and Cheng, Y.-B. (2001a). Resistance of alkali-activated slag concrete to alkali–aggregate reaction. *Cem. Concr. Res.* 31, 331–334. doi: 10.1016/S0008-8846(00)00483-X

Bakharev, T., Sanjayan, J. G., and Cheng, Y.-B. (2001b). Resistance of alkali-activated slag concrete to carbonation. *Cem. Concr. Res.* 31, 1277–1283. doi: 10.1016/S0008-8846(01)00574-9

Bakharev, T., Sanjayan, J. G., and Cheng, Y.-B. (2002). Sulfate attack on alkali-activated slag concrete. *Cem. Concr. Res.* 32, 211–216. doi: 10.1016/S0008-8846(01)00659-7

Bentur, A., and Mindess, S. (2007). *Fibre Reinforced Cementitious Composites. 2nd Edn*. London: CRC Press; Taylor and Francis.

Bernal, S. A., Krivenko, P. V., Provis, J. L., Puertas, F., Rickard, W. D. A., Shi, C., et al. (2014) "Other potential applications for alkali-activated materials," in *Alkali Activated Materials. RILEM State-of-the-Art Reports*, Vol. 13. eds J. Provis and J. van Deventer (Dordrecht: Springer), 339–379. doi: 10.1007/978-94-007-7672-2_12

Bernal, S. A., Rodríguez, E. D., Mejia de Gutiérrez, R., Provis, J. L., and Delvasto, S. (2012). Activation of metakaolin/slag blends using alkaline solutions based on chemically modified silica fume and rice husk ash. *Waste Biomass Valorization* 3, 99–108. doi: 10.1007/s12649-011-9093-3

Bhutta, A., Borges, P. H. R., and Banthia, N. (2016). "Mechanical properties Mk-based geopolymer composites reinforced with," in *Proceedings of the 9th Rilem International Symposium on Fiber Reinforced Concrete (BEFIB 2016)* (Vancouver, BC).

Bondar, D., Lynsdale, C. J., Milestone, N. B., Hassani, N., and Ramezanianpour, A. A. (2010). "Engineering properties of alkali activated natural pozzolan concrete," in *Proceedings of the Second International Conference on Sustainable Construction Materials and Technologies*, eds J. Zachar, P. Claisse, T. R. Naik, and E. Ganjian (Ancona: Università Politecnica delle Marche), 1093–1102. Available online at: http://www.claisse.info/2010%20papers/m42.pdf

Borges, P. H. R., Bhutta, A., Bavuzo, L. T., and Banthia, N. (2017). Effect of SiO2/Al2O3 molar ratio on mechanical behavior and capillary sorption of MK-based alkali-activated composites reinforced with PVA fibers. *Mater. Struct.* 50, 1–12. doi: 10.1617/s11527-017-1021-y

Borges, P. H. R., de Lourenço, T. M. F., Foureaux, A. F. S., and Pacheco, L. S. (2014). Estudo comparativo da análise de ciclo de vida de concretos geopoliméricos e de concretos à base de cimento Portland composto (CP II). *Ambient. Construído* 14, 153–168. doi: 10.1590/S1678-86212014000200011

Davidovits, J. (1994). "Properties of geopolymer cements," in *Proceedings of the First international Conference on Alkaline Cements and Concretes* (Kiev: Scientific Research Institute on Binders and Materials), 131–149.

Duxson, P., Fernández-Jiménez, A., Provis, J. L., Lukey, G. C., Palomo, A., and Van Deventer, J. S. J. (2007). Geopolymer technology: the current state of the art. *J. Mater. Sci.* 42, 2917–2933. doi: 10.1007/s10853-006-0637-z

Duxson, P., Lukey, G. C., Separovic, F., and Van Deventer, J. S. J. (2005). Effect of alkali cations on aluminum incorporation in geopolymeric gels. *Ind. Eng. Chem. Res.* 44, 832–839. doi: 10.1021/ie0494216

Garcia-Lodeiro, I., Palomo, A., and Fernández-Jiménez, A. (2015). "Crucial insights on the mix design of alkali-activated cement-based binders," in *Handbook of Alkali-Activated Cements, Mortars and Concretes*, eds F. Pacheco-Torgal, J. A. Labrincha, C. Leonelli, A. Palomo, and P. Chindaprasirt (Oxford: Woodhead Publishing), 49–73. doi: 10.1533/9781782422884.1.49

Juenger, M. C. G., Winnefeld, F., Provis, J. L., and Ideker, J. H. (2011). Advances in alternative cementitious binders. *Cem. Concr. Res.* 41, 1232–1243. doi: 10.1016/j.cemconres.2010.11.012

Kamseu, E., Beleukà Moungam, L. M., Cannio, M., Billong, N., Chaysuwan, D., Melo, U. C., et al. (2017). Substitution of sodium silicate with rice husk ash-NaOH solution in metakaolin based geopolymer cement concerning reduction in global warming. *J. Clean. Prod.* 142, 3050–3060. doi: 10.1016/j.jclepro.2016.10.164

Kanda, T., and Li, V. C. (2006). Practical design criteria for saturated pseudo strain hardening behavior in ECC. *J. Adv. Concr. Technol.* 4, 59–72. doi: 10.3151/jact.4.59

Komljenović, M. (2015). "Mechanical strength and Young's modulus of alkali-activated cement-based binders," in *Handbook of Alkali-Activated Cements, Mortars and Concretes*, eds F. Pacheco-Torgal, J. A. Labrincha, C. Leonelli, A. Palomo, and P. Chindaprasirt (Oxford: Woodhead Publishing), 171–215. doi: 10.1533/9781782422884.2.171

Komnitsas, K. A. (2011). Potential of geopolymer technology towards green buildings and sustainable cities. *Proced. Eng.* 21, 1023–1032. doi: 10.1016/j.proeng.2011.11.2108

Kong, D. L. Y., and Sanjayan, J. G. (2008). Damage behavior of geopolymer composites exposed to elevated temperatures. *Cem. Concr. Compos.* 30, 986–991. doi: 10.1016/j.cemconcomp.2008.08.001

Kong, D. L. Y., Sanjayan, J. G., and Sagoe-Crentsil, K. (2007). Comparative performance of geopolymers made with metakaolin and fly ash after exposure to elevated temperatures. *Cem. Concr. Res.* 37, 1583–1589. doi: 10.1016/j.cemconres.2007.08.021

Lee, B. Y., Cho, C.-G., Lim, H.-J., Song, J.-K., Yang, K.-H., and Li, V. C. (2012). Strain hardening fiber reinforced alkali-activated mortar – A feasibility study. *Constr. Build. Mater.* 37, 15–20. doi: 10.1016/j.conbuildmat.2012.06.007

Li, V. C., and Leung, C. K. Y. (1992). Steady-state and multiple cracking of short random fiber composites. *J. Eng. Mech.* 118, 2246–2264. doi: 10.1061/(ASCE)0733-9399(1992)118:11(2246)

Li, V. C., Wang, S., and Wu, C. (2001). Tensile strain-hardening behavior of polyvinyl alcohol engineered cementitious composite (PVA-ECC). *ACI Mater. J.* 98, 233–268. doi: 10.14359/10851

Li, V. C., Wu, C., Wang, S., Ogawa, A., and Saito, T. (2002). Interface tailoring for strain-hardening Polyvinyl Alcohol-engineered cementitious composite (PVA-ECC). *ACI Mater. J.* 99, 463–472. doi: 10.14359/12325

Li, Z., Zhang, Y., and Zhou, X. (2005). Short fiber reinforced geopolymer composites manufactured by extrusion. *J. Mater. Civ. Eng.* 17, 624–631. doi: 10.1061/(ASCE)0899-1561(2005)17:6(624)

Lloyd, N. A., and Rangan, B. V. (2010). "Geopolymer concrete: a review of development and opportunities," in *Proceedings of the 35th Conference on Our World in Concrete and Structures* (Singapore: CI-Premier PTE LTD). Available online at: https://pdfs.semanticscholar.org/1049/5b9901443d533445ddd6e5adcab449597742.pdf (accessed on December 01, 2017).

Mechtcherine, V., Silva, F., de, A., Butler, M., Zhu, D., Mobasher, B., et al. (2011). Behaviour of strain-hardening cement-based composites under high strain rates. *J. Adv. Concr. Technol.* 9, 51–62. doi: 10.3151/jact.9.51

Nematollahi, B., Qiu, J., Yang, E.-H., and Sanjayan, J. (2017). Micromechanics constitutive modelling and optimization of strain hardening geopolymer composite. *Ceram. Int.* 43, 5999–6007. doi: 10.1016/j.ceramint.2017.01.138

Nematollahi, B., Sanjayan, J., and Shaikh, F. U. A. (2014). Comparative deflection hardening behavior of short fiber reinforced geopolymer composites. *Constr. Build. Mater.* 70, 54–64. doi: 10.1016/j.conbuildmat.2014.07.085

Nematollahi, B., Sanjayan, J., and Shaikh, F. U. A. (2015). Tensile strain hardening behavior of PVA fiber-reinforced engineered geopolymer composite. *J. Mater. Civ. Eng.* 27, 1–12. doi: 10.1061/(ASCE)MT.1943-5533.0001242

Němeček, J., Šmilauer, V., and Kopecký, L. (2011). Nanoindentation characteristics of alkali-activated aluminosilicate materials. *Cem. Concr. Compos.* 33, 163–170. doi: 10.1016/j.cemconcomp.2010.10.005

Obonyo, E., Kamseu, E., Melo, U. C., and Leonelli, C. (2011). Advancing the use of secondary inputs in geopolymer binders for sustainable cementitious composites: a review. *Sustainability* 3, 410–423. doi: 10.3390/su3020410

Ohno, M., and Li, V. C. (2014). A feasibility study of strain hardening fiber reinforced fly ash-based geopolymer composites. *Constr. Build. Mater.* 57, 163–168. doi: 10.1016/j.conbuildmat.2014.02.005

Oliveira, A. M. (2015). *Fluência a Altas Temperaturas, Aderência Fibra-Matriz E Comportamento Mecânico Sob Ações Higrotérmicas De Compósitos Cimentícios Reforçados Com Fibras De Pva*. Available online at: http://www.coc.ufrj.br/pt/teses-de-doutorado/390-2015/4605-andrielli-morais-de-oliveira

Pacheco-Torgal, F., Jalali, S., and Castro Gomes, J. P. (2009). "Utilization of mining wastes to produce geopolymer binders," in *Geopolymers: Structure,*

Processing, Properties and Industrial Applications, eds J. L. Provis and J. S. J. Van Deventer (Cambridge: Woodhead Publishing Limited), 267–293. doi: 10.1533/9781845696382.2.267

Provis, J. L., Bílek, V., Buchwald, A., Dombrowski-Daube, K., and Varela, B. (2014). "Durability and testing-physical processes," in *Alkali Activated Materials. RILEM State-of-the-Art Reports*, Vol. 13. eds J. Provis and J. van Deventer (Dordrecht: Springer), 277–307. doi: 10.1007/978-94-007-7672-2_10

Provis, J. L., Duxson, P., Van Deventer, J. S. J., and Lukey, G. C. (2005). The role of mathematical modelling and gel chemistry in advancing geopolymer technology. *Chem. Eng. Res. Des.* 83, 853–860. doi: 10.1205/cherd.04329

Provis, J. L., Yong, S. L., and Duxson, P. (2009). "Nanostructure/microstructure of metakaolin geopolymers," in *Geopolymers: Structure, Processing, Properties and Industrial Applications*, eds J. L. Provis and J. S. J. Van Deventer (Cambridge: Woodhead Publishing Limited), 72–88. doi: 10.1533/9781845696382.1.72

Puertas, F., Amat, T., Fernández-Jiménez, A., and Vázquez, T. (2003). Mechanical and durable behaviour of alkaline cement mortars reinforced with polypropylene fibres. *Cem. Concr. Res.* 33, 2031–2036. doi: 10.1016/S0008-8846(03)00222-9

Puertas, F., and Torres-Carrasco, M. (2014). Use of glass waste as an activator in the preparation of alkali-activated slag. Mechanical strength and paste characterisation. *Cem. Concr. Res.* 57, 95–104. doi: 10.1016/j.cemconres.2013.12.005

Redon, C., Li, V. C., Wu, C., Hoshiro, H., Saito, T., and Ogawa, A. (2001). Measuring and modifying interface properties of PVA fibers in ECC matrix. *J. Mater. Civil Eng.* 13, 399–406. doi: 10.1061/(asce)0899-1561(2001)13:6(399)

RILEM (1984). CPC 11.3. Absorption d'eau par immersion sous vide [Absorption of water by immersion under vacuum]. *Matér. Constr.* 17, 391–394. doi: 10.1007/BF02478713

RILEM (1990). RILEM Draft Recommendation TC 89-FMT (Fracture Mechanics of Concrete - Test Methods): determination of fracture parameters of plain concrete using three-point bend tests. *Mater. Struct.* 23, 457–460. doi: 10.1007/B. F.02472029

Rodríguez, E. D., Bernal, S. A., Provis, J. L., Paya, J., Monzo, J. M., and Borrachero, M. V. (2013). Effect of nanosilica-based activators on the performance of an alkali-activated fly ash binder. *Cem. Concr. Compos.* 35, 1–11. doi: 10.1016/j.cemconcomp.2012.08.025

Rouseková, I., Bajza, A., and Živica, V. (1997). Silica fume-basic blast furnace slag systems activated by an alkali silica fume activator. *Cem. Concr. Res.* 27, 1825–1828. doi: 10.1016/S0008-8846(97)00191-9

Sakulich, A. R. (2011). Reinforced geopolymer composites for enhanced material greenness and durability. *Sustain. Cities Soc.* 1, 195–210. doi: 10.1016/j.scs.2011.07.009

Shaikh, F. U. A. (2013). Deflection hardening behaviour of short fibre reinforced fly ash based geopolymer composites. *Mater. Des.* 50, 674–682. doi: 10.1016/j.matdes.2013.03.063

Stavrinides, G. (2010). *Alternative Cements in Concrete Construction: Assessment, Prospects and Commercialisation Strategies*. MSc. Thesis, University College London (London).

Tchakouté, H. K., Rüscher, C. H., Kong, S., Kamseu, E., and Leonelli, C. (2016). Geopolymer binders from metakaolin using sodium waterglass from waste glass and rice husk ash as alternative activators: a comparative study. *Constr. Build. Mater.* 114, 276–289. doi: 10.1016/j.conbuildmat.2016.03.184

Torres-Carrasco, M., and Puertas, F. (2015). Waste glass in the geopolymer preparation. Mechanical and microstructural characterisation. *J. Clean. Prod.* 90, 397–408. doi: 10.1016/j.jclepro.2014.11.074

Vafaei, M., and Allahverdi, A. (2017). High strength geopolymer binder based on waste-glass powder. *Adv. Powder Technol.* 28, 215–222. doi: 10.1016/j.apt.2016.09.034

Van Deventer, J. S. J., Provis, J. L., Duxson, P., and Brice, D. G. (2010). Chemical research and climate change as drivers in the commercial adoption of alkali activated materials. *Waste Biomass Valorization* 1, 145–155. doi: 10.1007/s12649-010-9015-9

Wang, S., and Li, V. C. (2007). Engineered cementitious composites with high-volume fly ash. *ACI Mater. J.* 104, 233–241. doi: 10.14359/18668

Ye, H., Cartwright, C., Rajabipour, F., and Radlinska, A. (2017). Understanding the drying shrinkage performance of alkali-activated slag mortars. *Cem. Concr. Compos.* 76, 13–24. doi: 10.1016/j.cemconcomp.2016.11.010

Živica, V. (1999). Possibilities of a novel use of silica fume in mineral binding systems. *Constr. Build. Mater.* 13, 271–277. doi: 10.1016/S0950-0618(99)00028-8

Živica, V. (2004). High effective silica fume alkali activator. *Bull. Mater. Sci.* 27, 179–182. doi: 10.1007/BF02708502

Živica, V. (2006). Effectiveness of new silica fume alkali activator. *Cem. Concr. Compos.* 28, 21–25. doi: 10.1016/j.cemconcomp.2005.07.004

Conflict of Interest Statement: The authors declare that the research was conducted in the absence of any commercial or financial relationships that could be construed as a potential conflict of interest.

frontiers in Materials

ORIGINAL RESEARCH
published: 25 April 2019
doi: 10.3389/fmats.2019.00073

Characterization of Air Dissolution and Reappearance Under Pressure in Cement Pastes by Means of Rheology

Daniel Gálvez-Moreno[1], *Dimitri Feys*[1]* *and Kyle Riding*[2]

[1] *Department of Civil, Architectural and Environmental Engineering, Missouri University of Science and Technology, Rolla, MO, United States,* [2] *Department of Civil and Coastal Engineering, University of Florida, Gainesville, FL, United States*

Concrete pumping is the most used technique to transfer concrete from the mixer truck to the formwork. Numerous studies have been performed on the flow behavior of concrete in pipes, as well as the consequences of pumping on fluid and hardened concrete properties. One of the negative consequences of pumping concrete is a decrease in freeze-thaw resistance. This is caused by a decrease in air content and an increase in air bubble size, due to dissolution and reappearance of air and air bubble coalescence under pressure. This paper investigates the capability of rheology to understand air dissolution and reappearance in cement paste under combined action of pressure and flow. A majority of the air bubbles in the cement pastes show low capillary-numbers, indicating the applied stress is insufficient to overcome the surface tension. Removing air causes a decrease in viscosity (or shear stress), up to a certain threshold pressure sufficient for full dissolution of the air. For mixtures with small air bubbles, the sudden application of pressure causes an immediate decrease in viscosity or shear stress. Mixtures with larger bubbles display a more gradual decrease in viscosity with the application of pressure. At depressurization, the viscosity of the sample is recovered almost instantly, although in some cases the viscosity is not fully recovered. This can be attributed to either an immediate air loss or to a coarsening of the air-void system, resulting in less non-deformable air bubbles in the paste.

Keywords: cement paste, rheology, pressure, air-entrained, dissolution, reappearance

OPEN ACCESS

Edited by:
John L. Provis,
University of Sheffield,
United Kingdom

Reviewed by:
Jian Ouyang,
Dalian University of Technology (DUT),
China
Kenan Song,
Massachusetts Institute of Technology, United States

***Correspondence:**
Dimitri Feys
feysd@mst.edu

Specialty section:
This article was submitted to Structural Materials, a section of the journal Frontiers in Materials

Received: *15 January 2019*
Accepted: *04 April 2019*
Published: *25 April 2019*

Citation:
Gálvez-Moreno D, Feys D and Riding K (2019) Characterization of Air Dissolution and Reappearance Under Pressure in Cement Pastes by Means of Rheology. Front. Mater. 6:73. doi: 10.3389/fmats.2019.00073

INTRODUCTION

Concrete is the most popular construction material worldwide due to the global availability of its components at a relatively low cost, and suitable mechanical properties for most structural purposes (Aïtcin, 2014). The construction industry constantly challenges concrete producers to develop more complex mixture designs that are able to fulfill the mechanical and durability requirements of modern construction paired with demanding placement schedules and complex jobsite conditions. Concrete pumps have been used for over 80 years to place concrete and meet these conditions (Ball, 1935). Nowadays, pumping concrete is one of the most used practices to deliver concrete from mixer trucks directly to the casting place (ACI 304.2R-17, 2017). Many scientific studies have been performed to understand the flow of concrete through pipes and the influence of the mixture

design and pumping parameters on the fresh properties of concrete after pumping (Jacobsen et al., 2008; Jolin et al., 2009; Choi et al., 2013; Kwon et al., 2013a,b; Feys et al., 2016a,b; Riding et al., 2016; Secrieru et al., 2017, 2018).

Typically, air-entrained concrete shows lower viscosity than non-air-entrained concrete with the same water-to-cement ratio (w/c) (Wallevik and Wallevik, 2011), but this is not necessarily true under pumping conditions. The role of entrained air on the rheological properties is one of the hardest to elucidate because when concrete flows under pressure, the air bubbles are prone to be dissolved in the water and reappear when pressure is removed, altering air bubble volume and size distribution (Elkey et al., 1994; Pleau et al., 1995). An adequate air-void system, with small air bubbles and low spacing factors, is essential for the freeze-thaw durability of permeable concrete (Pleau and Pigeon, 2014). Experiments and experiences show typically an increase in spacing factor due to pumping operations, which may negatively affect freeze-thaw resistance (Elkey et al., 1994; Pleau et al., 1995; Hover and Phares, 1996; Pleau and Pigeon, 2014).

The physical background for air dissolution and reappearance is covered by Henry's law (Equation 1) which states that, in steady-state conditions and at constant temperature, the concentration of gas that can be dissolved in a liquid is proportional to the partial pressure of that gas in that liquid (Elkey et al., 1994):

$$p = kC \tag{1}$$

Where p is the partial pressure, k is Henry's law constant and C is the concentration of the dissolved gas in solution at equilibrium (Wang et al., 2010). Therefore, as the pressure increases, the capacity of water to carry dissolved air increases proportionally. In addition, if a fluid is under shearing conditions, dissolution is expected to happen faster (Favelukis et al., 1995). The air can be dissolved partially or totally depending on: the air content of concrete, the water availability, the pressure exerted by the pump (Macha et al., 1994), the portion of concrete sheared inside the pipe, degree of equilibrium between the air-water interface achieved during the pressurization time, filling coefficient of the pump pistons (Kaplan et al., 2005), and the permeability of the air-entraining admixture bubble film.

To add further complexity, bubbles in fluids act as soft particles susceptible to be deformed by the shearing forces acting on its surface. This shape distortion is described in literature by the capillary number (Equation 2) and it expresses the ratio between viscous forces and surface tension as follows:

$$Ca = \frac{\dot{\gamma}\eta a}{\Gamma} \tag{2}$$

Where Ca is the capillary number (-), $\dot{\gamma}$ is the shear rate in s^{-1}, η is the apparent viscosity of the suspending medium (Pa s), a is the bubble diameter (m) and Γ is the surface tension at the water-air interface (N/m). When $Ca \gg 1$, the shearing forces on the bubble surface are sufficiently high to overcome the surface tension, the bubble elongates and reduces the apparent viscosity of the fluid (Rust and Manga, 2002; Feys et al., 2016b). At $Ca \ll 1$ the surface tension is strong enough to keep the bubbles spherical and amplify the overall rheological properties (Rust and Manga, 2002; Feys et al., 2009). With so many factors that affect the rheological properties of air entrained concrete during pumping, and possible interactions among them, the evaluation of the rheological properties under pressure would be more representative for the behavior during pumping.

MATERIALS AND METHODS

Materials and Mixture Design

The cement pastes used in this study were produced using ordinary Portland cement (PC), ASTM C494 type F polycarboxylate ether (PCE) superplasticizer (SP) (C494/C494M-17, 2017), ASTM C494 Type B retarder (C494/C494M-17, 2017), air-entraining admixture (AEA), and tap water at water-to-cement ratios (w/c) of 0.35 and 0.45 (by mass). The retarder was added to minimize the effect of hydration during the rheological tests. In order to keep constant w/c regardless of the dosage of the AEA, the solid residue of the admixtures was determined by oven-drying as specified in ASTM C494-17 and the resulting mass loss was assumed to be water, which later was subtracted from the mixing water. The solid residues for the AEA, SP, and retarder were found to be 6, 25, and 13%, respectively.

The mixture proportions are shown in **Table 1**. Every mixture made had a replicate that was tested without pressurization (see further). The code name of the non-pressurized samples starts with "NP". The solubility coefficient of air in water at 1.01 bar (atmospheric pressure) and 20°C is 1.85%v/v (% volume of gas/volume of water) (Krofta and Wang, 2000). As the solubility coefficient varies linearly with barometric conditions (Wang et al., 2010), 1.84%v/v was used to compensate for the local altitude and calculate the theoretical minimum required pressure (Equation 3) to fully dissolve the air bubbles into the liquid phase of the paste. It should however be noted that in the evaluated cement pastes, the amount of water was sufficient to dissolve all air, a condition which may not be valid for concrete.

$$P_2 = \frac{P_1 C_2}{C_1} \tag{3}$$

Where P_2 (bar) is the pressure required to achieve a solubility C_2 (%v/v), and C_1 (%v/v) is the solubility of air in water at atmospheric pressure P_1 (bar). For example, the mixture P035-A3 requires a pressure, $P_2 = 7.2$ bar to reach a solubility of 13.36% v/v (67.9 ml of air/508.2 ml of water * 100), parting from the atmospheric pressure $P_1 = 0.99$ bar and an air solubility in water of 1.84%v/v at 20°C.

Two different mixing procedures and high doses (1.6–16 g/kg of cement) of AEA had to be used in order to achieve different volumes of entrained air. The main mixing procedure, using a small Hobart N50 mixer, consisted of first adding the water and the AEA to the mixing bowl, followed by the cement. Next, the mixer was started at speed 1 (139 rev/min) and the materials were mixed for 1 min. Then, the mixer was stopped for 30 s, the mixing bowl was scraped and the SP was added. Immediately after, the mixer was turned on at either speed 2 (285 rev/min) for mixtures P035-A2 and P035-A3 or speed 1 for all others. After 1 min, the

TABLE 1 | Mixture proportions and measured air contents (units in g/l, unless indicated otherwise).

Material	Mixture					
	P045-A1	P045-A2	P045-A3	P035-A1	P035-A2	P035-A3
w/c (by mass)	0.45	0.45	0.45	0.35	0.35	0.35
Water	561.5	557.6	553.7	490.2	490.2	479.0
Cement	1264.5	1264.2	1264.0	1452.9	1452.9	1452.1
AEA	2.023	6.068	10.112	11.624	11.624	23.233
SP	1.644	1.644	1.643	3.196	3.196	3.195
Retarder	5.058	5.057	5.056	5.812	5.812	5.808
Air (%)	4.6	5.9	7.5	4.1	5.9	6.8
Air (ml)	46.4	58.8	75.0	41.2	59.3	67.9
Overall water (ml)	569.0	568.9	568.8	508.5	508.5	508.2
Pressure for complete air dissolution (bar/10^5 Pa)	4.4	5.6	7.1	4.4	6.3	7.2

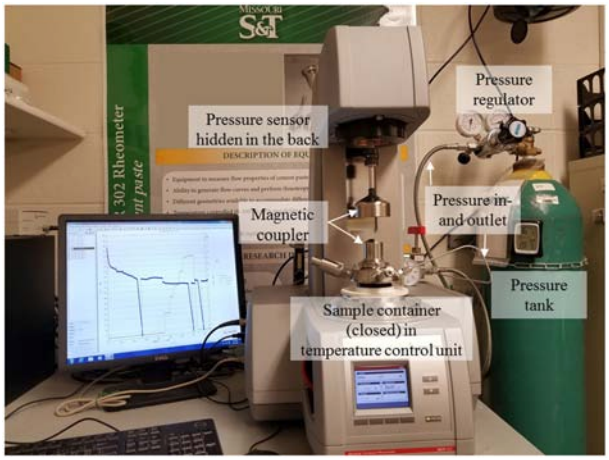

FIGURE 1 | Set-up of rheometer with pressure system in Anton Paar MCR 302.

retarder was incorporated to the mixture without stopping the mixer and the paste was mixed for an additional minute.

Testing Procedures

Self-consolidating consistency was desired to avoid: slippage between the wall of the inner cylinder of the rheometer and the sample, plug-flow, and entrapment of unquantified air in the rheometer cup when the samples were poured. Immediately after mixing, the air content was estimated using the procedure specified in ASTM C185-15a with the exception that the samples were not placed in layers inside the calibrated measure nor tamped. Two other samples were collected, one for rheological analysis and another for the estimation of the air-void size distribution using the AVA-3000 apparatus (Petersen, 2009). The rheometer used was an Anton Paar MCR-302 equipped with a cylindrical pressure cell that encapsulated the inner cylinder (**Figure 1**). The rotation of the inner cylinder was driven by a magnetic coupler attached to the rheometer transducer. The pressure was supplied by a gas tank filled with common air and controlled manually by an ordinary pressure regulator. The volume of the sample inside the rheometer cup was 22 ml, which ensured that the inner cylinder wall was always covered even when pressure was applied. The Peltier control unit kept temperature constant at 20°C throughout the experiment.

Two testing procedures were used for this project, and are denominated as "A" and "B" (**Figures 2**, **3**). The main objective of procedure "A" was to assess the changes in the rheological properties caused by modifications in applied pressure, while procedure "B" evaluated the influence of a single pressure step on the rate of air dissolution and reappearance. Procedure "A" was using a set of prolonged shearing stages at a fixed shear rate of 100 s^{-1} combined with 3 flow curves. Apparent viscosity during the prolonged shearing steps was calculated by dividing the shear stress by the shear rate. The pressure was supplied in stepwise fashion, starting from atmospheric conditions to ∼12 bar. Although the pressure regulator was adjusted manually, care was taken regarding supplying the pressure as consistently as possible across all tests. The flow curves were defined by linearly decreasing the shear rate from 100 to 10 s^{-1} in 25 s followed by a logarithmic decrease in shear rate from 10 to 0.01 s^{-1} during 5 s to obtain a better approximation of the yield stress. A 6th order polynomial was fitted to the whole data set conforming each flow curve and differentiated to the shear rate in order to define the differential viscosity at 50 s^{-1} (Feys and Asghari, 2019). The flow curves captured the rheological properties of the cement paste at the beginning of the test after structural breakdown (FC-1), under pressure (FC-2), and right after depressurization (FC-3).

Procedure "B" (**Figure 3**) was applied only on replicates of mixture P035-A3, and it imposes uninterrupted shearing at 100, 50, 20, and 10 s^{-1}. Since every shear rate requires different stabilization times to reach shear stress equilibrium (Feys and Asghari, 2019), pressurization was not performed unless the shear stress was considered, visually, sufficiently stable. The pressure was supplied by opening the inlet valve of the pressure chamber in a single and fast maneuver exposing the sample from atmospheric conditions to ∼4 bar during 2 min. Although the pressure regulator was set up to the desired pressure previously to loading the sample in the pressure chamber, the way pressure built up over time changed randomly between samples from a single sudden increase to the desired pressure, or a combination of a sudden increase with a slight further increase in pressure over time. However, there was not an evident change in the rheometer output attributable to this artifact.

RESULTS AND DISCUSSION

Capillary Number

Table 2 shows that most of the air bubbles of the pressurized samples were <500 μm. Considering a constant shear rate of 100 s^{-1}, an apparent viscosity of the suspending medium as $\eta = 0.15$ Pa s for w/c = 0.45 and $\eta = 0.52$ Pa s for w/c = 0.35, and assuming the surface tension of a combination of water-SP-AEA to be 0.040 N/m (Szwabowski and Lazniewska-Piekarczyk, 2009), the capillary number (Ca) would be <0.19

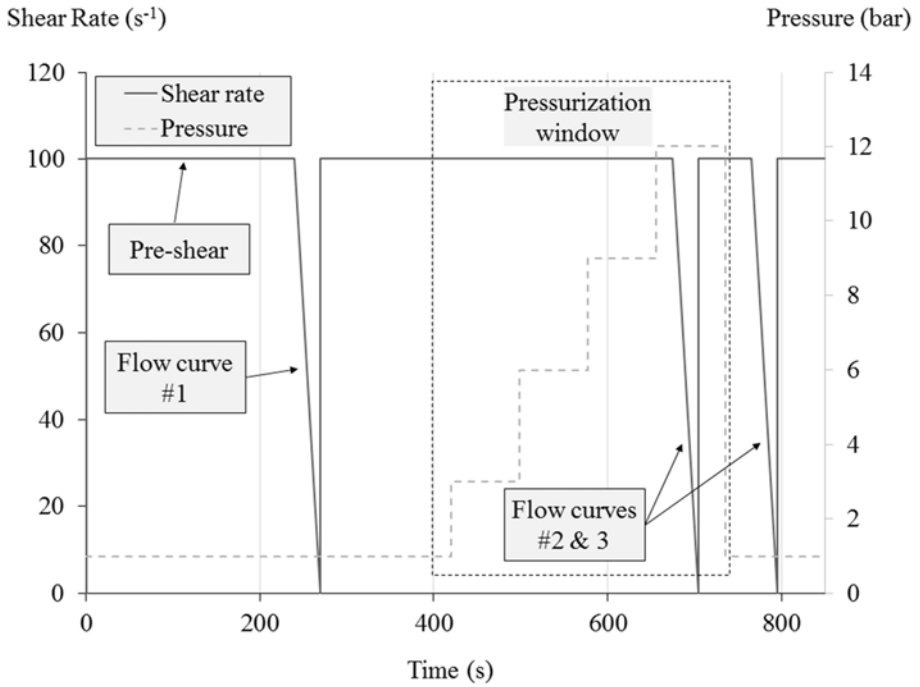

FIGURE 2 | Procedure A contained a constant shear at 100 s^{-1}, with flow curves being determined before, during and after pressure. Pressure was applied in several stepwise increments during the pressurization window.

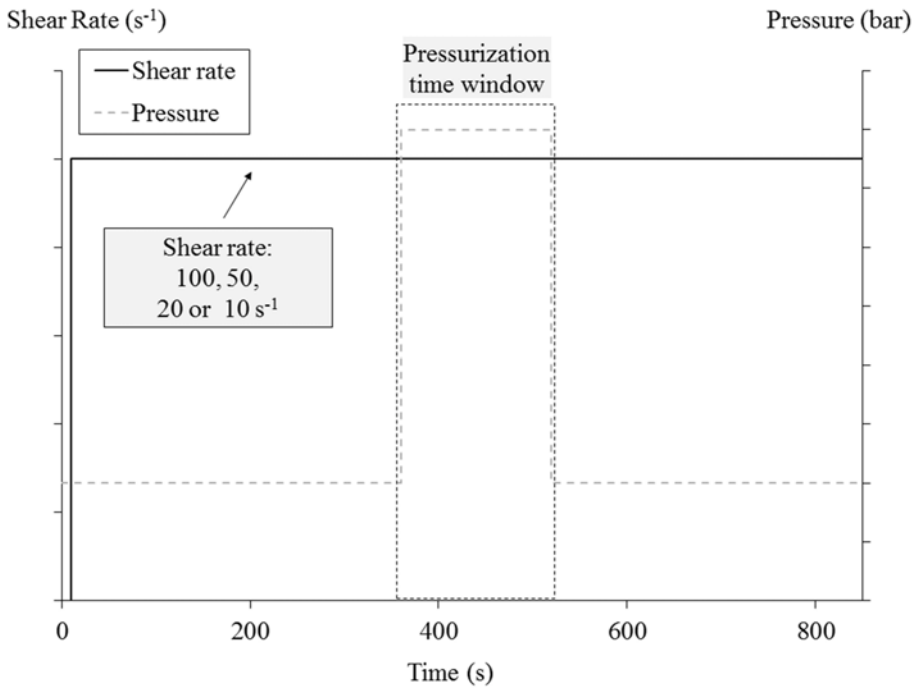

FIGURE 3 | Procedure B imposed a constant shear rate during the test. Different tests had different constant values of shear rate. Pressure was applied in one single step during pressurization window.

and 0.645, respectively, for bubbles sizes <500 μm. Therefore, a large majority of the air bubbles behaved mostly as solid particles and had the tendency to amplify the rheological properties, similar to solid particles amplifying the rheology of suspensions (Krieger, 1972). One caution about the results is that the AVA-3000 software is not designed to measure the air-void distribution

of cement paste as it is programed to stop the measurement automatically after 3 min of not recording significant changes in the recorded data. As consequence, the smaller bubble size fractions may be underestimated, however those bubbles are also less susceptible to being deformed.

The set of 6 mixtures and their corresponding non-pressurized replicates were tested using procedure "A". **Table 3** shows a summary of the apparent viscosity recorded at specific points of procedure "A" for w/c = 0.35 and 0.45. The column "Pressure" shows the pressure recorded after which the apparent viscosity no longer changed. As it was expected, the larger the volume of entrained air, the larger the pressure required to achieve full air dissolution in the liquid phase (see **Table 1**) (Elkey et al., 1994; Wang et al., 2010) and the larger the reduction of the rheological properties (Krieger, 1972). However, the experimental pressure values for which the rheological properties stabilized are higher than the theoretical ones required to achieve full dissolution. The w/c = 0.35 mixtures did not fully recover the apparent viscosity recorded right before the pressurization contrary to the mixtures with w/c = 0.45, suggesting changes in either air volume or distribution, which is discussed further.

Figure 4 depicts the typical rheometer output for a pressurized and non-pressurized sample in terms of relative shear stress vs. time for the w/c = 0.45 mixtures. The relative shear stress is defined as "*the shear stress at any time t divided by the average shear stress recorded 10 to 0 s before the pressurization step.*" The effect of pressure can be clearly seen after $t = 450$ s. When the sample is suddenly pressurized to ∼2.8 bar, a gradual reduction in the shear stress was experienced and was briefly stabilized for few seconds. When the next pressure step increment was supplied (4.8 bar), a gradual reduction on the shear stress was recorded once more. Further pressure additions did not provide significant changes in the rheometer output. The non-pressurized sample did not show any changes in rheological behavior during the same time period, indicating that the changes in rheology of the pressurized sample is solely caused by the pressure.

It is well known that the reduction of the (non-deformable) particle concentration of a suspension leads to a decrease in its rheological properties (Krieger, 1972). Since the only highly compressible phase present in the sample was air, the reduction in size and its eventual dissolution into the liquid phase due the pressure increase created a reduction in the bubble concentration and viscosity decreases. **Figure 4** shows that when pressure was released at $t = 736$ s, the shear stress or viscosity was recovered to levels close to where it was before pressurization, as can also be seen in **Table 3**. Once the cement paste was exposed again to atmospheric conditions, the air-dissolving capacity of the water was restored to its original level and the dissolved air nucleated back almost instantly. The dynamic conditions of the sample during depressurization may accelerate this effect. The performed experiments cannot tell if the subsequent air nucleation created similar bubble size distributions or where the air reappeared. However, it is suggested by Dyer (1991) that dissolved air will preferentially reappear in already formed bubbles since it is thermodynamically less energy consuming than forming a new bubble. As a consequence, a coarser air-void system is expected to occur after depressurization (Elkey et al., 1994; Macha et al., 1994). At the end of the experiment, a thick layer of coarse foam was always observed on top of the inner cylinder, but only for the pressurized samples (**Figure 5**), suggesting that once pressure was released, air bubbles were formed somewhere in the rheometer cup, expanded due to the pressure decrease, and traveled to the surface due to buoyancy.

Figure 6 illustrates the response to pressurization/depressurization of mixture P035-A3. This mixture showed that at $t = 450$ s, the pressure was increased from atmospheric conditions to 3.9 bar leading to a sudden drop, followed by a gradual reduction of the rheological properties until equilibrium was reached. At $t = 510$ s the pressure was increased to 6.5 bar and a new (but smaller) drop in the shear stress was recorded. **Figure 7** shows that the sudden drop of rheological properties was only observed in the mixtures P035-A2 and P035-A3 and such effect can be related to their finer bubble size distribution (see **Table 2**). Part of the mixing process of P035-A2 and P035-A3 was performed at a higher mixing speed than the other samples. This change in the mixing energy produced a more refined bubble size distribution. On the other hand, P035-A1 was mixed using the same procedure as all w/c = 0.45 mixtures. The reduced amount of water combined with relatively low mixing energy did not permit the incorporation of high volumes of air and resulted in the coarser bubble size distribution of all the mixtures tested. Since for mixtures P035-A2 and P035-A3, the concentration of small bubbles was larger than in the others, a small increase in pressure leads to the rapid dissolution of an important fraction

TABLE 2 | Bubble size distribution (expressed as % passing) for the w/c = 0.35 and 0.45 mixtures, obtained from the AVA 3000.

Size (μm)	Mixture					
	P045-A1	P045-A2	P045-A3	P035-A1	P035-A2	P035-A3
1,000	100	100	100	100	100	100
500	74	72	70	57	79	89
300	56	46	41	33	39	69
200	37	32	30	22	22	49
150	25	19	18	12	9	20
125	14	13	12	0	3	11
100	0	0	4	0	0	0

Bulk response of the rheological properties to pressure.

TABLE 3 | Summary of apparent viscosity changes due to pressurization.

Mixture	Apparent viscosity, η (Pa s)			Pressure (bar)
	Pressurization			
	Before	During	After	
P045-A1	0.172	0.159	0.173	7.8
P045-A2	0.176	0.162	0.188	8.7
P045-A3	0.166	0.135	0.165	7.9
P035-A1	0.567	0.534	0.522	8.8
P035-A2	0.549	0.518	0.517	9.4
P035-A3	0.563	0.495	0.520	12.8

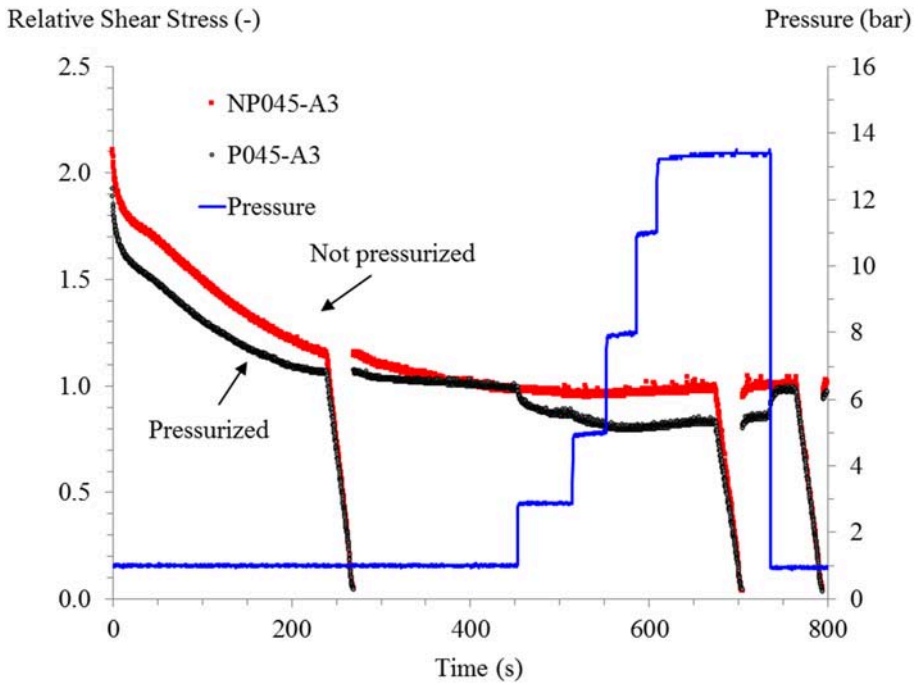

FIGURE 4 | Rheological testing procedure "A" applied on mixture P045-A3. The relative shear stress equals 1 just before the application of pressure.

FIGURE 5 | The pressurization/depressurization of the samples yielded a substantial volume of foam on top of the inner cylinder of the pressure cell. Picture taken after removing the inner cylinder from the pressure cell.

of the air-void system. The internal air pressure due to surface tension is inversely proportional to the diameter of the bubble (Elkey et al., 1994; Macha et al., 1994; Wang et al., 2010). The solubility of air depends on the partial pressure surrounding the bubble, the small bubbles are the first ones to dissolve because their internal pressure is higher and any further increase in pressure will increase the degree of air under-saturation of water, promoting air diffusion from the bubbles (Macha et al., 1994). In addition, small bubbles have larger specific surface, which accelerates the dissolution process (Pleau et al., 1995). Therefore, the rheological properties decrease consistently with the principle of particle concentration of suspensions as the air dissolves (Krieger, 1972). **Figure 6** also shows that once the pressure was released, the rheological properties were not fully restored as was the case of the w/c = 0.45 mixtures, at least not within the remaining part of the test. This behavior was observed in all pressurized w/c = 0.35 samples. The lack of reestablishment of the rheological properties suggests a change in air volume and/or distribution.

Flow Curves

Since every mixture design tested was different in terms of AEA dose and air content, small changes in workability were observed between samples. Therefore, the pre-shear performed during the first 240 s of the testing procedure "A" was insufficient to achieve shear stress equilibrium. Nevertheless, the pressurization of the samples was performed under equilibrium conditions ensuring that any major change in the rheometer output was induced by pressure changes only. The changes in yield stress were too small to derive any conclusions. **Figure 8** depicts the behavior

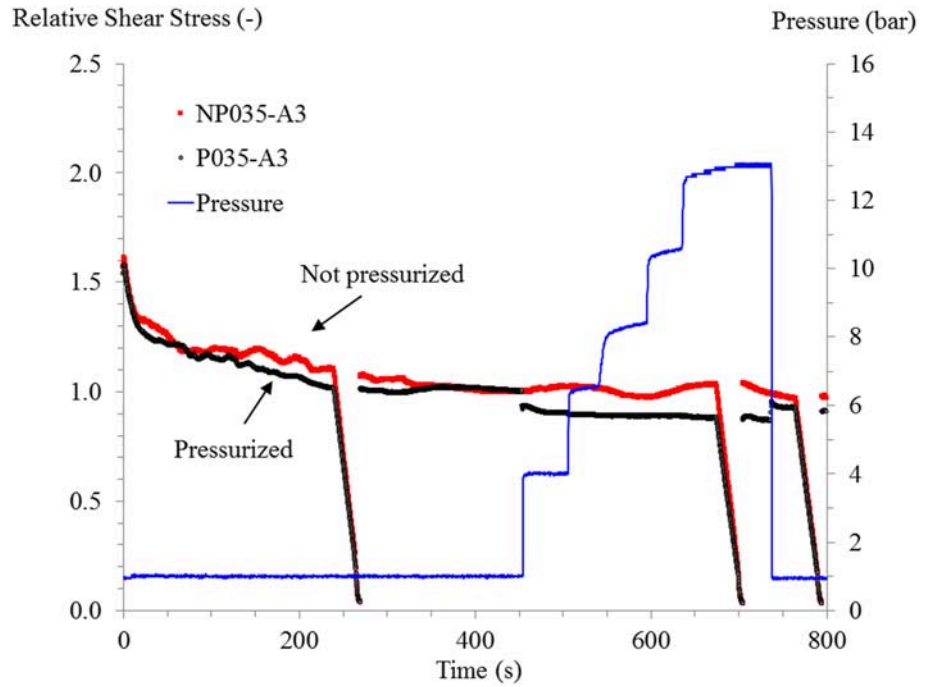

FIGURE 6 | Rheological testing procedure "A" applied on mixture P035-A3.

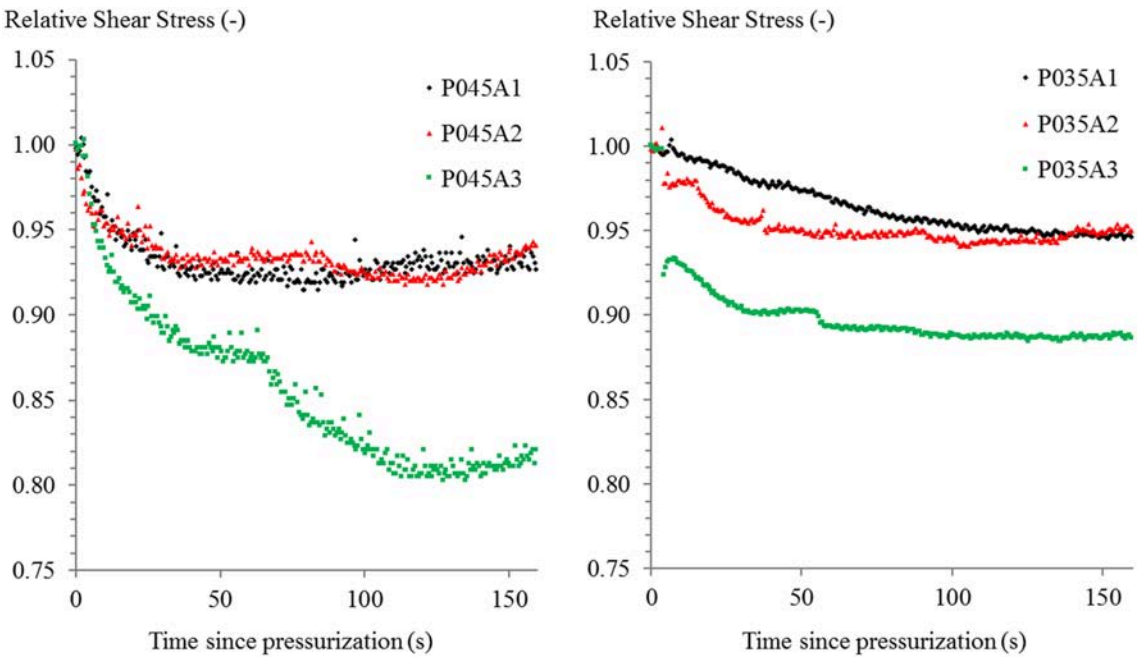

FIGURE 7 | Comparison of the relative shear stress response to pressurization over time of w/c = 0.45 **(left)** and w/c = 0.35 **(right)** mixtures. Pressure steps are not shown.

of the differential viscosity of the flow curves. When w/c = 0.45 mixtures were pressurized, the reduction in differential viscosity was increased with a higher initial air content, and the viscosity fully recovered once the pressure was released. The case of the mixtures prepared with w/c = 0.35 followed a similar trend but the differential viscosity was not fully recovered after subjecting

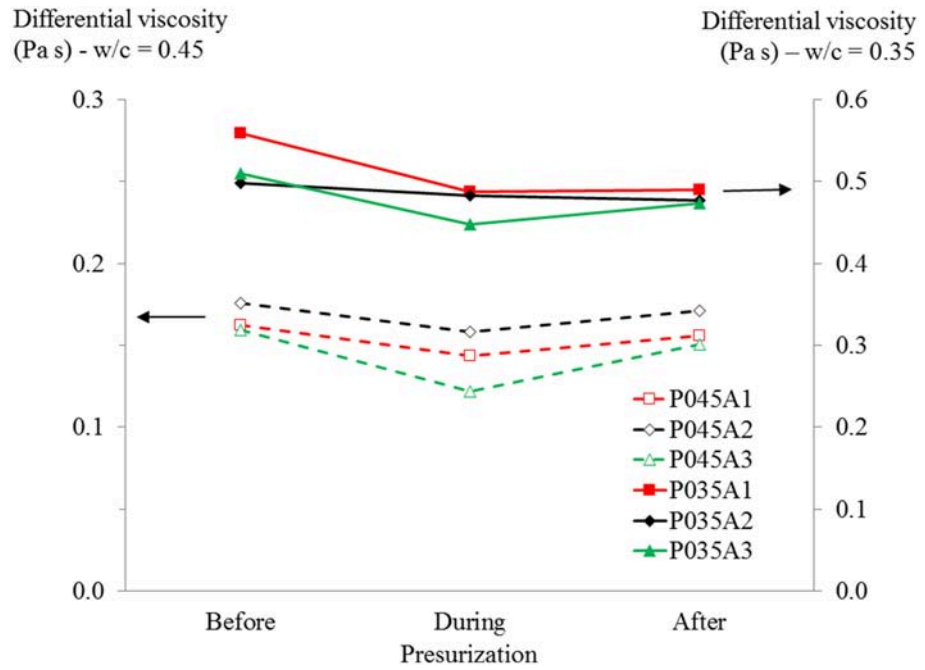

FIGURE 8 | Differential viscosity at 50 s^{-1}. Mixtures with w/c = 0.45 are plotted on the left axis, those with w/c = 0.35 on the right axis.

the system to atmospheric conditions. The results on differential viscosity followed the observations for the apparent viscosity.

Rate of Air Dissolution and Reappearance

For this testing series, replicates of mixture P0.35-A3, all containing ∼7% air by volume, were evaluated according to procedure B. The samples were exposed to a constant shear rate (100, 50, 20 or 10 s^{-1}), and were subjected to a sudden increase in pressure of ∼4 bar, which was maintained for 2 min. A pre-shear period was applied on all samples in an attempt to reach equilibrium. Although visually, the shear stress appeared to be in equilibrium during the tests, analysis has shown this was not the case. As such, to eliminate the effect of structural breakdown, the shear stress-time curve before pressurization was fitted with a double exponentially decreasing function (Equation 4), adequately capturing the behavior (**Figure 9**).

$$\tau = A * e^{(-Bt)} + C * e^{(-Dt)} + E \quad (4)$$

Where τ is shear stress (Pa), t is time (s) and, A, B, C, D, and E are fitting constants. Then, the data of the pressurization stage at each shear rate were normalized point by point using the extrapolated fitted function. **Figures 10–13** show the influence of the shear rate on the shear stress response caused by air dissolution at 100, 50, 20 and 10 s^{-1}. At 100 s^{-1} the changes in the rheological properties of the sample occur immediately and a small recovery hump followed again by a slight reduction and further stabilization of the rheological properties can be seen during the pressurization stage. When pressure is relieved, the rheological properties are partially restored after 6 s. At 50 s^{-1}, the same behavior can be seen but this time the instantaneous reduction on the shear stress was higher than the observed at 100 s^{-1} and, once the mixture got depressurized the shear stress partially recovered in ∼2 s and stayed relatively constant for the rest of the test. At 20 and 10 s^{-1}, there is an abrupt drop in the rheological properties as well, with the main difference that the recovery hump that happens immediately after pressurizing the system is broader and takes ∼40 s to get stable. Once that the pressure is released, it takes only a few seconds to fully recover the initial relative shear stress but immediately after this it starts decreasing again.

From the results in **Figures 10–13**, it can be concluded that air is dissolved almost instantaneously after application of the pressure, regardless of the applied shear rate. However, as the evolution over time of rheological properties due to pressure application was different for mixtures P0.35-A2 and P0.35-A3 compared to the others (compare **Figures 4**, **6**), it is believed that bubble size and shear rate will play an important role on air dissolution. This is also clear in **Figure 7**, as only P0.35-A2 and A3 showed a sudden decrease in relative shear stress, while all others showed a gradual decrease with time. As mentioned before, smaller air bubbles dissolve quickly, regardless of the applied shear rate. The larger air bubbles dissolve more slowly, and that process may be influenced by the applied shear rate. An explanation for the recovery of relative shear stress under pressure has not been found yet.

For the mixtures in **Figures 10–13**, the recovery of relative shear stress is immediate after depressurization, and for the low shear rates (20 and 10 s^{-1}), the relative shear stress is fully recovered. At higher shear rates, the relative shear stress is not

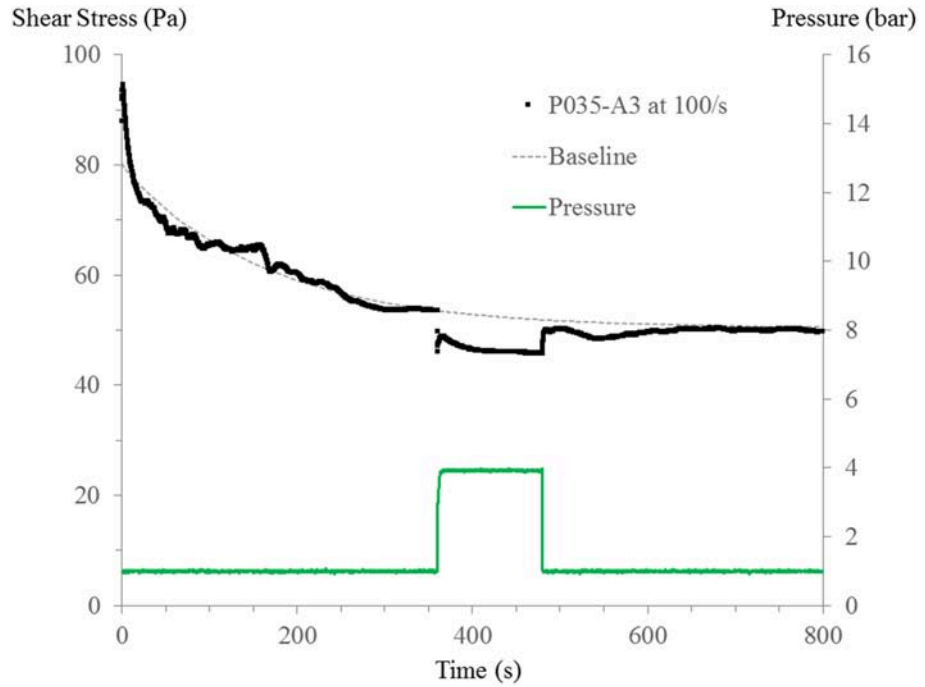

FIGURE 9 | A double exponential approach based on data prior to pressurization was implemented to define a baseline for normalization.

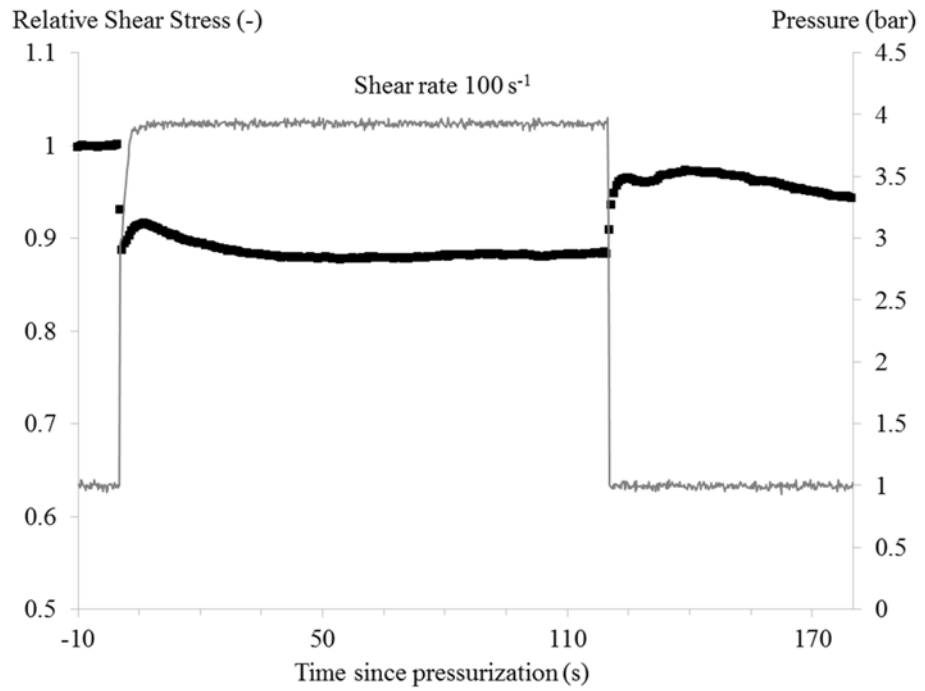

FIGURE 10 | Rate of air dissolution and reappearance at a shear rate of 100 s^{-1}.

equal to 1 after depressurization, which may have several causes. This could indicate (1) an immediate air loss, (2) part of the air remains dissolved, or (3) the air-void system coarsens, creating larger air bubbles. The first hypothesis cannot be excluded. The second hypothesis seems unlikely, as at low shear, all air reappears. There are no physical reasons why all air would not

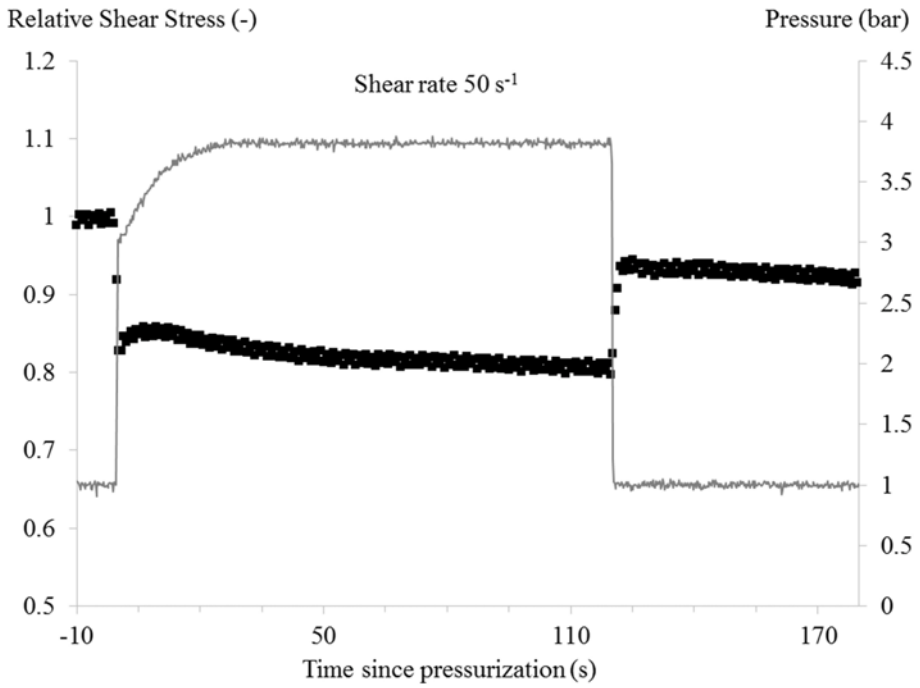

FIGURE 11 | Rate of air dissolution and reappearance at a shear rate of 50 s^{-1}.

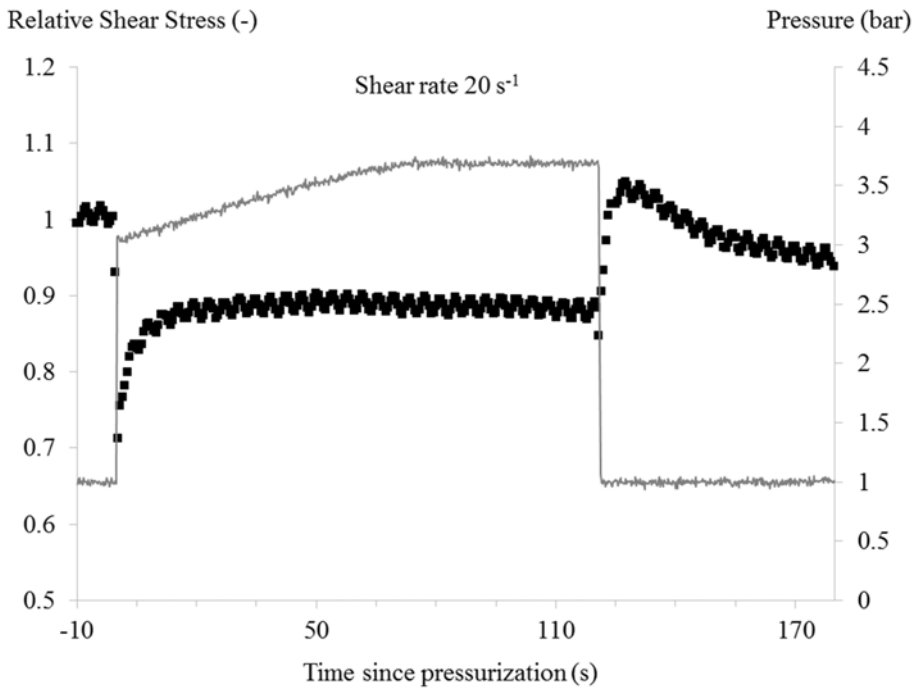

FIGURE 12 | Rate of air dissolution and reappearance at a shear rate of 20 s^{-1}.

reappear at higher shear rate, as on the contrary, increasing the shear rate should accelerate air reappearance. Hypothesis 3 is also possible. For the mixtures with w/c = 0.35, *Ca* starts to be close to 1, especially for the larger bubbles. This means that the deformation behavior of the air bubbles is uncertain (Rust and Manga, 2002). However, as air is assumed to reappear in existing bubbles at depressurization, the average bubble size increases, increasing the average *Ca*. As *Ca* is also proportional to the

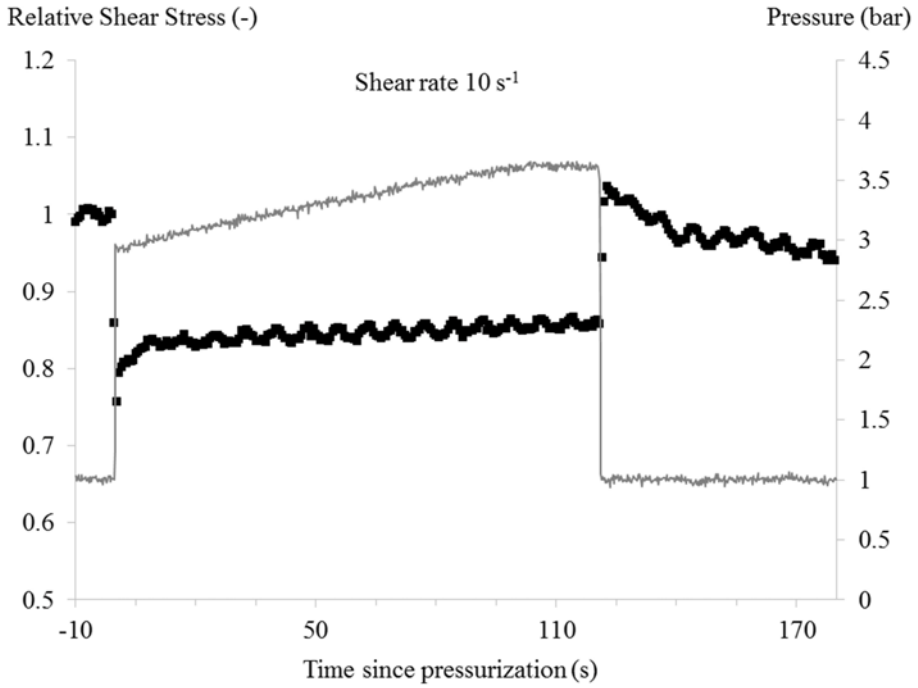

FIGURE 13 | Rate of air dissolution and reappearance at a shear rate of 10 s^{-1}.

applied shear rate, increasing the bubble size could yield a lower amount of non-deformable air bubbles at high shear rates (50 and 100 s^{-1}), while this would not be observed at low shear rates (10 and 20 s^{-1}). More research is needed to verify these hypotheses. Furthermore, all samples show a lower relative shear stress at and beyond 30 s after depressurization, indicating that air is escaping from the sample (see **Figure 5**).

CONCLUSIONS

Applying pressure on air-entrained cement paste samples causes the shear stress or apparent viscosity at fixed shear rate to decrease. This decrease is attributed to the decrease in entrained air, which, based on the low capillary number, mainly remains non-deformed during the executed tests. Similarly, the differential viscosity of flow curves determined during pressurization decreases compared to the flow curves determined before the pressure step.

Increases in pressure beyond the initial pressure step cause a further decrease in viscosity, until a threshold pressure, above which all air is assumed to be dissolved in the water of the cement paste. This threshold pressure is dependent on the amount of air in the sample, according to Henry's law.

The shear stress or apparent viscosity of a mixture decreases either gradually or suddenly when applying the pressure. This difference in behavior is attributed to the size distribution of the air bubbles, as the mixtures with smaller air bubbles showed a sudden decrease in viscosity, while those with larger bubbles showed a more gradual decrease. The sudden decrease in viscosity seems to be independent of the applied shear rate.

At low shear rate, the shear stress is fully recovered in a short time after releasing the pressure, indicating that all air has reappeared almost instantly. At higher shear rates, the shear stress is not fully recovered at depressurization, which can be either attributed to an immediate loss of air, or to a coarsening of the air-void system, rendering less air bubbles non-deformable at the applied shear rates. With further shearing after depressurization, the shear stress decreases with time, which is assumed to be caused by a loss of air bubbles.

AUTHOR CONTRIBUTIONS

DG-M is a Ph.D student who has executed all experimental work and analyses, under the supervision of DF and KR. DF is PI on the ACI and RE-CAST projects and KR is Co-PI on the ACI project. Several in-person meetings have been held, either at conferences or in Rolla. MO, to discuss the results, analyses, work plan, etc. with all authors.

ACKNOWLEDGMENTS

The authors would like to acknowledge the American Concrete Institute's Concrete Research Council and the US Department of Transportation Tier-1 UTC (RE-CAST) (grant DTRT13-G-UTC45) at Missouri S&T for the financial support, the center for infrastructure engineering studies at Missouri S&T for the use of the equipment, and the staff of the Civil, Architectural and Environmental Engineering Department for the technical assistance in setting up the pressure system.

REFERENCES

ACI 304.2R-17 (2017). *Placing Concrete by Pumping Methods*. Farmington Hills, MI: American Concrete Institute.

Aïtcin, P. C. (2014). *Binders for Durable and Sustainable Concrete*. London: CRC Press.

Ball, C. F. (1935). U.S. Patent No. 2,012,944. Washington, DC: US. Patent and Trademark Office.

C494/C494M-17 (2017). *Standard Specification for Chemical Admixtures for Concrete*. West Conshohocken, PA: ASTM International.

Choi, M., Roussel, N., Kim, Y., and Kim, J. (2013). Lubrication layer properties during concrete pumping. *Cement Concrete Res.* 45, 69–78. doi: 10.1016/j.cemconres.2012.11.001

Dyer, R. M. (1991). *An Investigation of Concrete Pumping Pressure and the Effects of Pressure on the Air-Void System of Concrete.* Master Thesis, University of Washington.

Elkey, W., Janssen, D. J., and Hover, K. C. (1994). Concrete Pumping Effects on Entrained Air-Voids. Washington State Department of Transportation, Washington State Transportation Commission, Transit, Research, and Intermodal Planning (TRIP) Division, Seattle, WA. Available online at: http://www.wsdot.wa.gov/research/reports/fullreports/313.1.pdf

Favelukis, M., Tadmor, Z., and Talmon, Y. (1995). Bubble dissolution viscous liquids in simple shear flow. *AIChE J.* 41, 2637–2641. doi: 10.1002/aic.690411213

Feys, D., and Asghari, A. (2019). Influence of maximum applied shear rate on the measured rheological properties of flowable cement pastes. *Cement Concr. Res.* 117, 69–81. doi: 10.1016/j.cemconres.2018.12.003

Feys, D., De Schutter, G., Khayat, K. H., and Verhoeven, R. (2016b). Changes in rheology of self-consolidating concrete induced by pumping. *Mater. Struct.* 49, 4657–4677. doi: 10.1617/s11527-016-0815-7

Feys, D., Khayat, K. H., and Khatib, R. (2016a). How do concrete rheology, tribology, flow rate and pipe radius influence pumping pressure? *Cement Concrete Comp.* 66, 38–46. doi: 10.1016/j.cemconcomp.2015.11.002

Feys, D., Roussel, N., Verhoeven, R., and De Schutter, G. (2009). "Influence of air bubbles size and volume fraction on rheological properties of fresh self-compacting concrete," in *3rd International RILEM Symposium on Rheology of Cement Suspensions Such as Fresh Concrete* (Reykjavik).

Hover, K. C., and Phares, R. J. (1996). Impact of concrete placing method on air content, air-void system parameters, and freeze-thaw durability. *Transport. Res. Record* 1532, 1–8. doi: 10.1177/0361198196153200101

Jacobsen, S., Mork, J. H., Lee, S. F., and Haugan, L. (2008). *Pumping of Concrete and Mortar-State of the Art.* COIN Project Report, SINTEF Building and Infrastructure.

Jolin, M., Burns, D., Bissonnette, B., Gagnon, F., and Bolduc, L.-S. (2009). "Understanding the pumpability of concrete," in *Proceedings of the 11th Conference on Shotcrete for Underground Support* (Davos).

Kaplan, D., De Larrard, F., and Sedran, T. (2005). Avoidance of blockages in concrete pumping process. *ACI Mater. J.* 102, 183–191. doi: 10.14359/14446

Krieger, I. M. (1972). Rheology of monodisperse latices. *Adv. Colloid Interface Sci.* 3, 111–136. doi: 10.1016/0001-8686(72)80001-0

Krofta, M., and Wang, L. K. (2000). *Flotation Engineering*. Technical Manual No. Lenox/01–05–2000/368, 1st Edition. Lenox, MA: Lenox Institute of Water Technology, 255.

Kwon, S. H., Park, C. K., Jeong, J. H., Jo, S. D., and Lee, S. H. (2013a). Prediction of concrete pumping: part I–development of new tribometer for analysis of lubricating layer. *ACI Mater. J.* 110,647–656. doi: 10.14359/51686332

Kwon, S. H., Park, C. K., Jeong, J. H., Jo, S. D., and Lee, S. H. (2013b). Prediction of concrete pumping: part II-analytical prediction and experimental verification. *ACI Materials J.* 110, 657–668. doi: 10.14359/51686333

Macha, R. K., Zollinger, D. G., and Szecsy, R. (1994). *Examination of Air Entrainment Stability Factors of Pumped Concrete*. College Station, TX: Texas Transportation Institute, Texas A & M University System.

Petersen, C. G. (2009). "Air void analyzer (AVA) for fresh concrete, latest advances," in *Ninth ACI International Conference on Superplasticizers and Other Chemical Admixtures in Concrete* (Sevilla).

Pleau, R., and Pigeon, M. (2014). *Durability of Concrete in Cold Climates*. London: CRC Press.

Pleau, R., Pigeon, M., Lamontagne, A., and Lessard, M. (1995). Influence of pumping on characteristics of air-void system of high-performance concrete. *Transport. Res. Record* 1478, 30–36.

Riding, K., Vosahlik, J., Feys, D., Malone, T. R., and Lindquist, W. (2016). *Best Practices for Concrete Pumping (No. K-TRAN: KSU-14-2).* Topeka, KS: Kansas Department of Transportation.

Rust, A. C., and Manga, M. (2002). Effects of bubble deformation on the viscosity of dilute suspensions. *J. Non Newton. Fluid Mech.* 104, 53–63. doi: 10.1016/S0377-0257(02)00013-7

Secrieru, E., Cotardo, D., Mechtcherine, V., Lohaus, L., Schröfl, C., and Begemann, C. (2018). Changes in concrete properties during pumping and formation of lubricating material under pressure. *Cement Concrete Res.* 108, 129–139. doi: 10.1016/j.cemconres.2018.03.018

Secrieru, E., Fataei, S., Schröfl, C., and Mechtcherine, V. (2017). Study on concrete pumpability combining different laboratory tools and linkage to rheology. *Construct. Build. Mater.* 144, 451–461. doi: 10.1016/j.conbuildmat.2017.03.199

Szwabowski, J., and Lazniewska-Piekarczyk, B. (2009). Air-entrainment problem in self-compacting concrete. *J. Civil Eng. Manage.* 15, 137–147. doi: 10.3846/1392-3730.2009.15.137-147

Wallevik, O. H., and Wallevik, J. E. (2011). Rheology as a tool in concrete science: the use of rheographs and workability boxes. *Cement Concrete Res.* 41, 1279–1288. doi: 10.1016/j.cemconres.2011.01.009

Wang, L. K., Shammas, N. K., Selke, W. A., and Aulenbach, D. B. (2010). Gas dissolution, release, and bubble formation in flotation systems. *Flotation Technol.* 12, 49–83. doi: 10.1007/978-1-60327-133-2_2

Conflict of Interest Statement: This research work is sponsored by ACI and the US DOT.

The authors declare that the research was conducted in the absence of any commercial or financial relationships that could be construed as a potential conflict of interest.

frontiers in Materials

HYPOTHESIS AND THEORY
published: 30 April 2019
doi: 10.3389/fmats.2019.00089

Efflorescence of Alkali-Activated Cements (Geopolymers) and the Impacts on Material Structures: A Critical Analysis

Márlon A. Longhi[1,2], *Zuhua Zhang*[1,3]*, *Erich D. Rodríguez*[4], *Ana Paula Kirchheim*[2] and *Hao Wang*[1]

[1] Centre for Future Materials, University of Southern Queensland, Toowoomba, QLD, Australia, [2] Building Innovation Research Unit, Federal University of Rio Grande do Sul (NORIE/UFRGS), Porto Alegre, Brazil, [3] Key Laboratory for Green & Advanced Civil Engineering Materials and Application Technology of Hunan Province, College of Civil Engineering, Hunan University, Changsha, China, [4] Department of Structural and Civil Construction, Technological Centre, Federal University of Santa Maria, Santa Maria, Brazil

Even with the rapid development of the alkali-activated cement (AAC) technology in the past few years, some phenomena still needs to be better understood, that may alter the durability of the material. In many industrial uses and laboratory researches the formation of the salts on the surface alkali-activated type cements was observed, which was identified as efflorescence. This occurs due to the presence of an alkali transported in contact with the humidity and CO_2 environment. It may present externally from the formation of salts on the surface and internally with the carbonation of the alkalis in capillary pores. The effects of efflorescence on the material in use, as well as all factors that can influence its formation are not yet fully understood or reported. The search for papers was conducted using the search words efflorescence and geopolymer/alkali-activated, combined in the electronic data base. Due to the limited quantity of papers published related to efflorescence in geopolymers, the review was complemented using papers that discuss this behavior in Portland cement (PC) and based on the main properties that can influence the formation of efflorescence. In this paper, to understand the nature of efflorescence, upon which proper methods of minimizing of this issue can be based, the following aspects are discussed and re-examined: (1) the development of efflorescence's in PC concrete, (2) the role of alkalis in AACs, (3) efflorescence in AACs, and (4) effect from a physical and microstructural point of view of efflorescence's on the ACCs. This paper highlights that the nature of the pore structure and the design parameters (such as alkali concentration, presence of soluble silicates, and water content in the activator) are the two most important factors that control efflorescence rate and changes in mechanical behavior. However, the stability of the alkalis and their relationship with the formed gel, which are determining factors in the formation of efflorescence, remain not completely understood. In the same way, the effect of efflorescence in tensile strength and shrinkage needs to be evaluated.

Keywords: alkali-activated cement (AAC), geopolymer, fly ash, metakaolin, efflorescence, carbonation, durability

OPEN ACCESS

Edited by:
Andrew C. Heath,
University of Bath, United Kingdom

Reviewed by:
Mauricio Lopez,
Pontificia Universidad Católica de Chile, Chile
Jinrui Zhang,
Tianjin University, China

***Correspondence:**
Zuhua Zhang
Zuhua.Zhang@usq.edu.au

Specialty section:
This article was submitted to Structural Materials, a section of the journal Frontiers in Materials

Received: *18 November 2018*
Accepted: *09 April 2019*
Published: *30 April 2019*

Citation:
Longhi MA, Zhang Z, Rodríguez ED, Kirchheim AP and Wang H (2019) Efflorescence of Alkali-Activated Cements (Geopolymers) and the Impacts on Material Structures: A Critical Analysis. Front. Mater. 6:89. doi: 10.3389/fmats.2019.00089

INTRODUCTION

Alkali-activated cements (AACs), also broadly termed as geopolymers (mainly for those systems with low content of calcium), have been extensively studied in the past 40 years, due to the potential in the development of "green alternatives" to Portland cement (PC). The formation of geopolymers uses alkalis such as sodium hydroxide, silicate, and/or carbonate to activate aluminosilicates precursors usually heated clays, fly ash and slag, at room or elevated temperatures. The environmental benefit of applying AAC technology mainly lies in the reduction of CO_2 emissions and energy consumption, which are issues of wide concern for the sustainable development of the present cement and concrete industries (Damtoft et al., 2008). McLellan et al. (2011) pointed out that the unit emissions of greenhouse gas in making a geopolymer binder depend on the location of source materials, the energy source and the mode of transport. The counting of the four mixtures using typical Australian fly ashes indicated the potential for a 44–64% reduction in greenhouse gas emissions. Heath et al. (2014) showed that geopolymer manufacture can reduce CO_2 emissions by about 40% when clay minerals are used to replace fly, ash, and slag. In terms of weight, the manufacture of 1 m^3 of C25 (compressive strength of 25 MPa at 28 days) geopolymer concrete can reduce 154 kg of CO_2 emissions compared to using PC. This reduction will increase at a higher strength design (40 MPa geopolymer concrete reduces 220 kg of CO_2). The increase in the environmental impact can be related to the composition of the alkali-activator, where soluble silicate (such as sodium silicate) is the highest contributor. More recently, Passuelo et al. (2017), using a Brazilian calcined clay as precursor and a rice husk ash as part of the activator, reported that, per unit of compressive strength, the right design of material can provide a 50–75% reduction of CO_2 emissions. These have been one of the main forces driving the current research and industrial development of geopolymers.

Although the total volume of geopolymer concretes is negligible compared to OPC concretes, there has been rapid growth in the construction of demonstrative structures and buildings in the past decade because of increasing scientific research and environmental driving (Provis and Bernal, 2014). Notable examples are the 33 full-scale geopolymer concrete beams installed in the Global Change Institute building at the University of Queensland and the flooring of 40,000 m^3geopolymer concrete at Wellcamp airport, Queensland, Australia. From the challenges in supplying consistent raw materials and the cost issues, there are still a variety of technical and political barriers remaining, either unclear, or un-solved (Van Deventer et al., 2006, 2012). Efflorescence is one such problem which has been raised as a concern in some AAC formulations and this has been discussed briefly by Bernal et al. (2014), systematically investigated by Zhang et al. (2014c) and Zhang et al. (2018).

Looking back to efflorescence occurring in OPC based masonry and concrete, the most common phenomenon is related to the formation of calcium carbonate ($CaCO_3$) on the surface (Dow and Glasser, 2003). To avoid and mitigate efflorescence, the first principle is to reduce the alkali concentration of cements and also to reduce the solubility and absorption rate of CO_2 from the ambient environment (Dow and Glasser, 2003). However, in AAC systems, the concentrations of Na and K in pore solution usually contain much higher soluble alkali metal concentrations than conventional OPC based materials. Burciaga-Díaz et al. (2010) mentioned that alkali-activated slag based materials show significant efflorescence and some have also shown negative impacts on the mechanical properties. It must be noted that alkali-activated slag contains a higher concentration of calcium than alkali-activated metakaolin and fly ash systems, and this may lead to certain differences in the specific effects in the development of efflorescence. Škvára et al. (2012) assessed a set of fly ash-based geopolymers, where the acceptable workability and compressive strength above 40 MPa were achieved at a thermal curing (>50°C) and an alkali content of 30–150 g/kg, expressed as Na_2O to total mass of paste. These values are up to 42 times higher than in Portland cement paste (assuming 0.5% Na_2O in cement and w/c = 0.4 for paste). Therefore, this raises attention to the efflorescence issue in the application of AAC.

In literature and in the previous research done by these authors, a set of AAC mixtures developed efflorescence rapidly on drying surfaces when samples were in contact with water and under highly humid atmosphere conditions. A number of factors have been reported to affect the extent of efflorescence in AAC: alkali metal type (Škvára et al., 2009, 2012), raw materials (Temuujin et al., 2011; Kani et al., 2012; Bernal, 2016; Zhang et al., 2018), and reaction conditions (Burciaga-Díaz et al., 2010; Kani et al., 2012; Zhang et al., 2014c). However, there is still a lack of consensus relating to the mechanisms of reaction and formation, relationship between activator and reactivity, micro- and macro-structural impact of efflorescence and effective ways to mitigate.

Thus, the aim of this paper is to re-examine the results found in literature and complement the literature analysis with some ongoing experiments. The role of alkalis in AAC (low calcium systems) and the effect of alkali concentration on efflorescence are discussed. Particular interests are given to the different efflorescence behaviors of AACs that were prepared with fly ashes derived from different power stations, as well as calcined rich kaolinite clays. The importance of this issue is highlighted by the observations of the microstructural and mechanical properties of AACs that are subjected to efflorescence. The analyses and suggestions made here are based on the understanding of the effect of the curing scheme, design parameters, and reaction process of ACC, which is further related to reactivity.

EFFLORESCENCE IN PC CONCRETE

In Portland cement hydration process, the main constituents, the silicates C_2S (belite) and C_3S (alite) react with water to form the calcium silicate hydrates (C-S-H) and calcium hydroxide (CH, also named as portlandite). The CH is responsible for maintaining the high pH of concrete, which plays an important role in the compatibility between concrete and steel for reinforced concrete structures (Gallucci and Scrivener, 2007). The alkalis in PC concrete are generated into the system by the

hydration reaction of anhydrous components, including clinkers and supplementary cementitious materials (SCMs). SCMs are normally used as addition or substitution of cement (or clinker) to consume the content of $Ca(OH)_2$ and produce C-S-H via a pozzolanic reaction. On the other hand, the presence of CH within the concrete can promote its leaching, where part of this compound migrates to the surface and precipitates in contact with CO_2, forming a carbonate product as efflorescence. Other phenomena that can be developed is the internal crystallization due to the migration of soluble CO_2 from the environment into the matrix. The reaction of CO_2 with CH starts instantly and leads to formation of calcium carbonate (Cizer et al., 2012; Zhang et al., 2017). Further, other calcium phases are susceptible to carbonation (Garcia-González et al., 2006; Gallucci and Scrivener, 2007).

To understand the process related to the formation of whitish products, mainly efflorescence products, a model was proposed for Dow and Glasser (2003). According to the authors, efflorescence involves six basic and synergetic stages: dissolution of CO_2 (g) in H_2O at air-water interface on the surface of products, conversion of CO_2 to aqueous species, release of alkali(s), dissolution of $Ca(OH)_2$, diffusion of reactants through solution and precipitation of calcium carbonate, as shown in **Figure 1**.

According to the authors, in the first and second stages, the presence of another source of alkali such as NaOH or KOH may increase the dissolution of CO_2 and its absorption in the sample. It is related to the abundance of OH^- group in a high pH solution, which increases the reaction to form H_2CO_3. On the other hand, dissolved $Ca(OH)_2$ cannot increase the solubility, due to the insolubility of $CaCO_3$. In the third and fourth stages, the leaching of alkalis occurs, of which the main source is the cement itself. The content of $Ca(OH)_2$ is dependent on other factors as the type of cement, the use of SCMs, as well as the time of curing. Porosity is an important factor, according to Zhang et al. (2014a); while the reaction processes, the transport paths become longer if the matrix becomes more porous. The fifth stage is related to the diffusion, which is dependent on factors such as the pH of the pore solution, and the speciation of CO_2 adjusts to a new equilibrium amongst $(CO)_2$ (aqueous), H_2CO_3 and CO_3^{2-} and is then incorporated to the stages 1 and 2 and dissolved Ca^+ species. The final stage is related to the precipitation of $CaCO_3$ species.

The efflorescence in PC is usually observed in recent constructions and is not normally damaging, but, aesthetically undesirable (Dow and Glasser, 2003). However, it is necessary to evaluate the effect by the leaching process and the pore structure of the material, because this process can increase the porosity and accelerate the leaching. As efflorescence is a natural process, the material is exposed to evaporation. According to Dow and Glasser (2003), the efflorescence cycle can be interrupted by loss of liquid film by evaporation, perhaps combined with suction into porous material. During evaporation, the storage capacity of pure water for CO_2 is sufficiently low and the formation of efflorescence by complete evaporation makes a negligible contribution to efflorescence, relative to steady-state transportation. However, the concentrations of NaOH or KOH can increase the storage of CO_2. With this, even with evaporation, the content of CO_2 can increase during the wet/dry cycles. The efflorescence cycle can restart by reestablishment of a water film. The precipitated products may, depending on permeability and content of leachable alkalis, affect the reaction kinetics.

On the other hand, internal carbonation also induces a neutralizing effect to the highly alkaline environment provided by PC hydration (which in healthy/normal conditions shows a pH above 13 in pore solution), thereby increasing the vulnerability of embedded reinforcing steel to corrosion (Zhang et al., 2017). Internally, the effect is relative to crystallization process. According to Šavija and Lukovic (2016), there are two types of the carbonation process, (1) passive process when the carbonation causes unwanted and unplanned changes in the surface layer of a concrete structure or an element when exposed to the environment as pH drop, porosity changes, mechanical changes and cracking. However, (2) active carbonation assumes controlled exposure of cementitious materials to elevated CO_2 concentrations for certain periods of time, resulting in benefits in terms of mechanical performance or environmental impact of the material. The first one is attributed to deterioration and the second one to utilization. With this, it is evident that the process of carbonation and efflorescence is a complex subject even for PC-based materials, which have a great deal of related research. In fact, besides the reaction between CO_2, water, calcium and alkalis, efflorescence may also involve the reaction with cations sucked from the base of concrete embedded in saline soils and environment. This is a broad issue that occurs in many aging constructions.

ROLE OF ALKALIS IN AACs

When related to PC, ACCs present some peculiarities and differences in production process, raw material and reactions. AAC formation is a reaction between two parts of materials: reactive aluminossilicate powder (precursor) with a high alkaline solution (activator). The precursor presents negligible or no reactivity with water, and therefore it makes it necessary to introduce an alkali material to "activate" the precursor. It means that, the alkali placed in the system is necessary. The main reaction product of AAC is a disordered and highly reticulate structure named M-A-S-(H) gel (where M represents the alkali type, usually Na^+ or K^+) (Provis et al., 2005). The chemical process is well-known as alkali activation for CaO-rich systems or geopolymerization for CaO-free systems. This gel is a three-dimensional alumino-silicate network configurated of SiO_4 and AlO_4 tetrahedrons by oxygen bridges with positive alkali ions to compensate the negative balance of Al in a Q^4 molecular coordination (Provis et al., 2005; Fernández-Jimenez et al., 2006). However, just part of the alkali is bounded to the structure, the other part remains in pores (Provis and Bernal, 2014; San Nicolas and Provis, 2015), as proposed by the model of Rowles et al. (2007). According to the model, in a situation where there is sufficient amount of OH^-, Na^+ is bound superficially to the aluminate (**Figure 2A**). In situations where OH^- is not directly involved or accessible, Na^+ may associate with part of the silicon

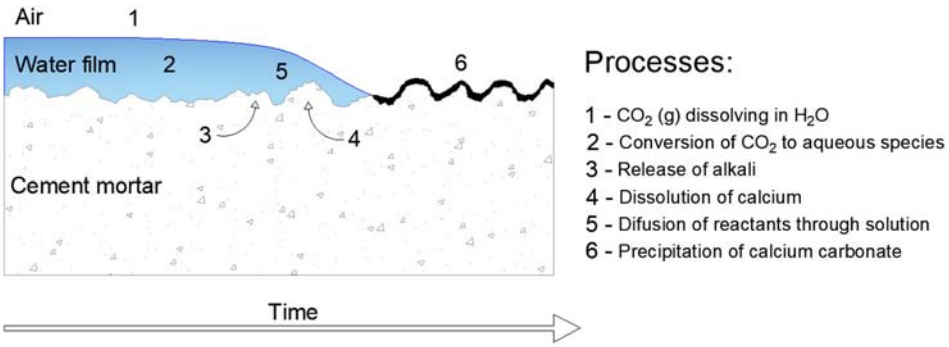

FIGURE 1 | Schematic process diagram for the formation of efflorescence of Portland cement concrete. Adapted from Dow and Glasser (2003).

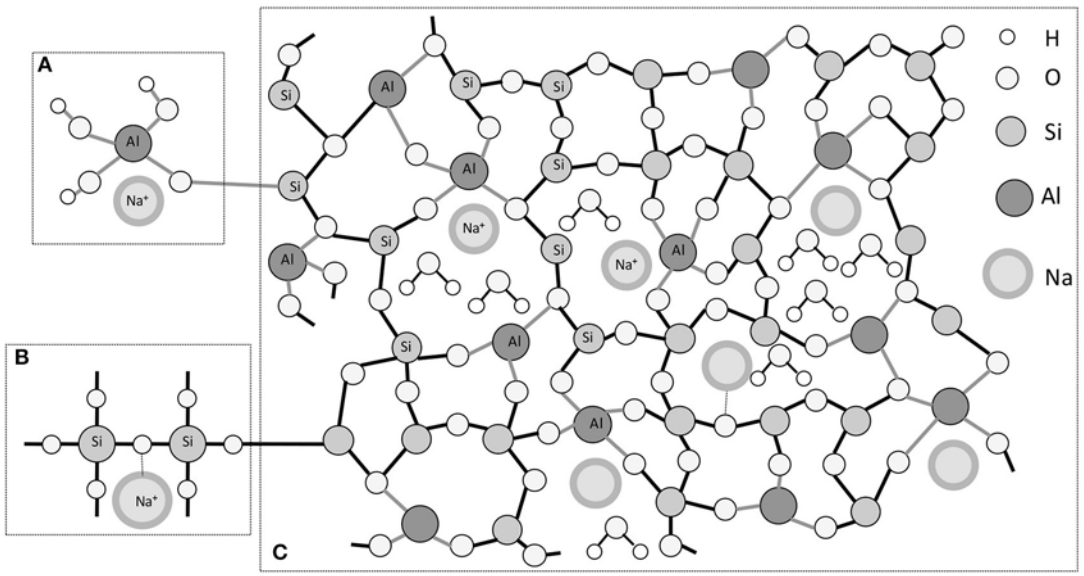

FIGURE 2 | Schematical model for aluminosilicates inorganic polymers adapted from Rowles et al. (2007). **(A)** Location of the charge-balancing Na^+ in form of a semiattached Na Aluminate species. **(B)** Location of the charge-balancing Na^+ cation in form of a modified brinding network. **(C)** Proposed schematic model for aluminosilicate inorganic polymers structure.

in the SiO-(Na^+)-Si^- form. In this situation, the negative charge of the AlO_4 tetrahedron can be located on the bridge with the oxygen atom, where Si-O-Si consequently generates the ionic bond with Na^+ (**Figure 2B**). In **Figure 2C** the model is fully represented, where in some points the ionic bonding with Na^+ occurs, but the other part of this element remains free in the pores of the structure.

According to Duxson et al. (2005), sodium can be linked with aluminum inside the gel structure, located within the pore solutions, neutralizing the charge of $Al(OH)_4^-$ group. Thus, sodium can be partially in the Na-O-Al(Si) form in the gel structure, with a relatively stronger Na-O bond, and partially in the form $Na(H_2O)_n^+$, with a weakly Na^+ associated with molecular water. This is aligned with the leaching result and deconvolution of ^{23}Na MAS NMR spectra for alkali-activated fly ash, assessed by Fernández-Jimenez et al. (2006). If it is assumed that the Na-O in gel structure is relatively more stable than in hydration conditions (contact with water molecules), similar to the Na-O in dehydrated zeolite, the soluble sodium must be limited, i.e., a certain fraction of sodium ions are not readily leached. Kani et al. (2012) grounded hardened AAC pastes and used stable leaching method at water to solid ratio of 20:1 to evaluate the leaching process. It was reported that after 24 h the leached alkalis were 1–7%, depending on the overall Si/Na and Na/Al molar ratios. Also, Zhang et al. (2014c) crushed hardened alkali-activated fly ash pastes (after 28 days of curing) into 1.25–1.5 mm particles. The authors used the stable leaching method at water/solid ratio of 25:1 and found that after 24 h the leached sodium was 12–16%, depending on the activator type, curing temperature, and amount of slag (added as a substitute for fly ash). These results are in agreement with the above hypothesis.

Škvára et al. (2012) crushed hardened AAC pastes after 28 days of curing and obtained particles under the size of 0.5 mm and used the dynamic leaching method (regularly change leaching

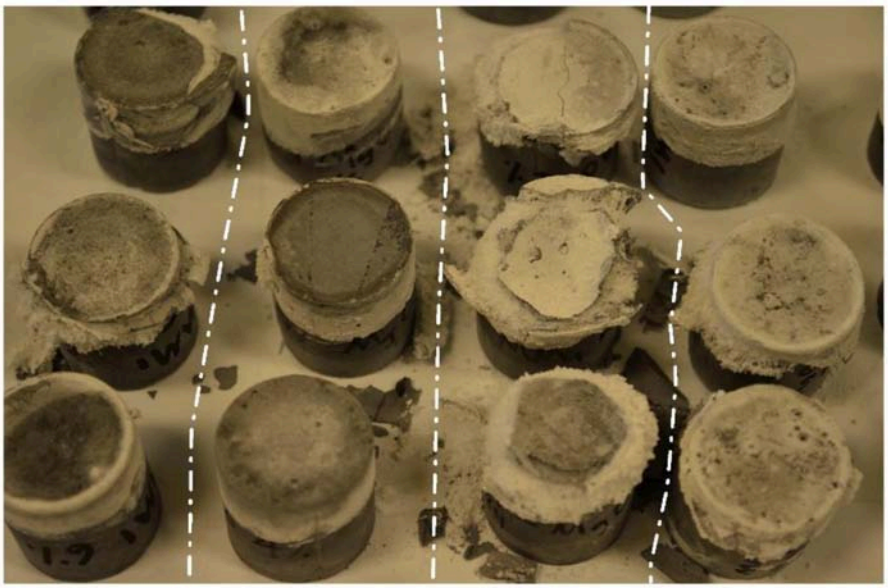

Mix design:
FA-6%MgO = Addition of 6% of MgO
FA-4%MgO = Addition of 4% of MgO
FA-2%MgO = Addition of 2% of MgO
FA-0%MgO = Addition of 2% of MgO

Production: Mixed 6 minutes at medium speed

Curing condition: 1 day sealed at RH = 90% ± 10% and 65 ± 1°C
27 days sealed at RH = 90% ± 10% and 25 ± 1°C

FIGURE 3 | Efflorescence formation in fly ash AAC with different contents of external MgO.

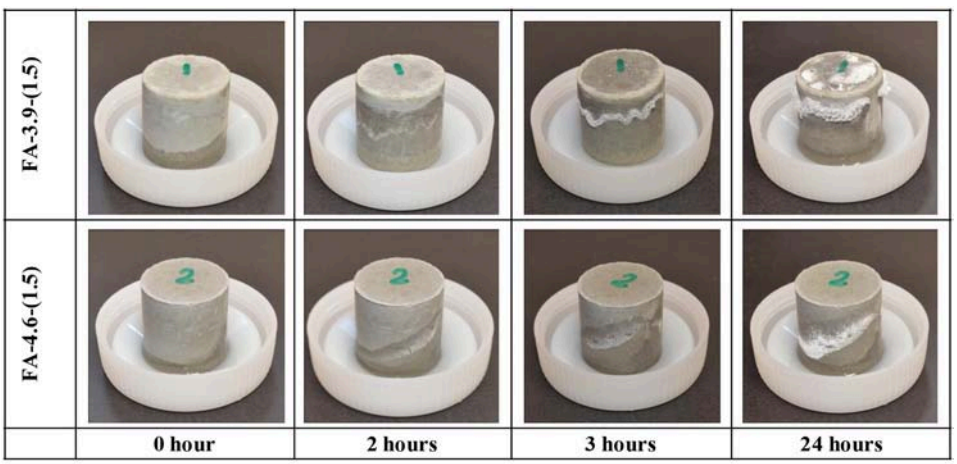

Mix design:
FA-3.9-(1.5) = 3.9% of Na_2O and MS content of 1.5
FA-4.6-(1.5) = 4.6% of Na_2O and MS content of 1.5

Production: Mixed 6 minutes at medium speed

Curing condition: 1 day sealed at RH = 90% ± 10% and 25 ± 1°C
12 hours sealed at RH = 90% ± 10% and 75 ± 1°C
5.5 days sealed at RH = 90% ± 10% and 25 ± 1°C

FIGURE 4 | Efflorescence of hardened alkali-activated fly ash pastes in contact with water. FA-4.6-(1.5).

solution with fresh water) and found that the alkalis can be almost completely leached from the binder after 150 days. In comparison with zeolite leaching behavior (usually extremely slow in water content), it was concluded that the alkalis (Na^+ and K^+) were only weakly bonded in the form of $Na(H_2O)n^+$.

However, some controversy about the leaching process was reported. Lloyd et al. (2010) measured the alkali concentration in the extracted pore solutions of typical ACC with 7% of Na_2O provided from activator. If it is assumed that all of the sodium presents in the form of $Na(H_2O)_n^+$ in pore solution, therefore, the followed analyses can be deduced: assuming 100 g of binder, the pore water (free water) is 10 g and the structural water is 5 g, and the sodium concentration is estimated to be higher than 20,000 mM. This value is far from the content identified by Lloyd et al. (2010), which were between 600 to 1,600 mM for alkali-activated fly ash systems. In fact, it is well-known that the alkalis bound in zeolite frame structure may have different states, and each state has its own ion exchange capacity. Therefore, a new hypothesis is proposed here: the alkalis in AAC have different states (maybe more than the two as was discussed above), and each state has its own leaching rate. If the alkali is available in pores of the material or it is weakly bounded, and the pores allow the movement of those alkalis, depending on the intensity and direction of this movement, different phenomena may occur, and will alter the integrity of the material.

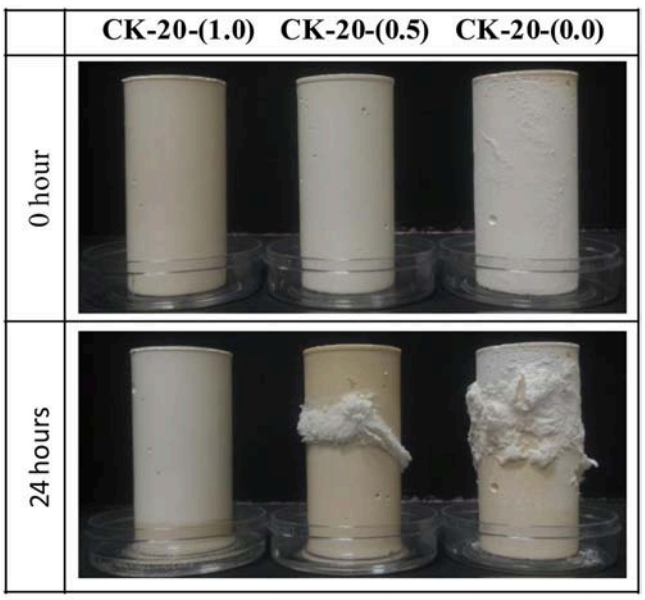

FIGURE 5 | Efflorescence of hardened alkali-activated calcined kaolin pastes in contact with water. CK-20-(1.0) means 20% Na_2O in terms of mass ratio to calcined kaolin, and MS is 1.0.

EFFLORESCENCE OF AACs

During the last few years of rapid development and application of AAC technology, the formation of depositions of material was observed on the surface of the samples. This was initially observed in laboratory conditions and later began to receive attention (Škvára et al., 2009; Kani et al., 2012; Bernal et al., 2014; Zhang et al., 2014c, 2018; Yao et al., 2015). This phenomenon is the result of a chemical reaction between free leached alkalis in porous structure with CO_2 in the aqueous form, where alkalis are the result of a physical leaching process, i.e., this only happens when alkalis are free to transport. With this, alkali leaching is relative to the amount of free cations and movement facility within the porous structure. These factors are dependent from synthesis conditions and the reacted products formed after the alkali-activation.

The Relation Between Alkali Leaching, Design Parameters, and Activation Products

The first design parameter is related to precursor. The most used are fly ash, metakaolin, and ground granulated blast-furnace slag (GGBFS). All of them have a specific chemical composition, with different oxides content, particle size and geometry, which changes the properties and features of the final reacted product. The reactivity has a wide behavior due to an internal factor of the material that depends on its generation process. In this regard, particle size has an important function, since smaller particles have a larger specific surface area and consequently a higher initial reactivity. A more reactive material can usually provide a denser matrix, with less porosity. Systems with fly ash and metakaolin are known as low calcium, while granulated blast furnace slag is known as high calcium precursor. In low calcium systems, the molar ratio SiO_2/Al_2O_3 is an important indicator of the initial reactivity and microstructural features of the gel formed. According to Criado et al. (2007), the Si-O bond is stronger than the Al-O bond, and this influences the precursor dissolution process, which result in an easier dissolution to precursor with higher content of Al_2O_3. This relation also alters the final product, that is Q^4 linked with different degrees of Al substitution (Duxson et al., 2005). Relating this to the Rowles et al. (2007) model, more Al content is believed to result in the higher imprisonment of Na^+.

Precursor with high calcium content exhibits a different behavior. Usually, this material needs less content of alkalis for its dissolution. Also, the gels formed are different from low calcium gels. While low calcium presents the M-A-S-(H), high calcium systems presents gels calcium aluminosilicate hydrate (C-A-S-H). According to Provis and Bernal (2014), this type of product possesses a disordered tobermorite structure in layers of coordinated silicon tetrahedral, where the interlayer region contains Ca^{2+} cations, alkalis, and the water chemically incorporated into their molecular structure. This is important for the alkali leaching because cations incorporated into the gel are less leachable in a system where water is also attached to the structure and does not work as a transport agent. Zhang

et al. (2014c) assessed the efflorescence in geopolymeric systems (free calcium AAC) activated by the use of NaOH and sodium silicate as activators, where a significant reduction of the means particle size and porosity with GGBFS addition was observed, reducing the susceptibility of efflorescence development. When slag is introduced in metakaolin or fly ash systems, the products may contain hydrotalcite-like phases, which have been proven to have ion binding properties. However, there is no report on this aspect, which deserves future insight study.

Besides the addition of slag, a certain amount of MgO in alkali-activated metakaolin-based geopolymers (Zhang et al., 2012) and slag/fly ash-based geopolymers (Shen et al., 2011) have shown benefits of reducing autogenous shrinkage and drying shrinkage. An experiment of adding MgO in ambient cured sodium silicate-activated fly ash-based geopolymers has been conducted to examine its effect on efflorescence. **Figure 3** shows the appearance of sodium silicate-activated fly ash ACCs with different amounts of MgO. When MgO is used between 2 and 6%, the efflorescence behavior does not show a consistent trend. After 2 weeks in contact with 2 mm-deep water at bottom and naturally drying at the ambient conditions (20 ± 10°C, RH = 50 ± 20%), the control samples without MgO have sever efflorescence products formed on the surface, while the samples with 2 and 6% MgO show more severe efflorescence, and the products formed under surface lead to enough crystallization stress to break the top surface of the sample. Interestingly, the sample with 4% MgO addition have slower and much less severe efflorescence. This behavior indicates that efflorescence is a complex function of the raw materials, the minerals and the microstructure of the products. The risk of adding MgO in low calcium geopolymers must be considered.

About the activators, the most usual are sodium and potassium in the form of hydroxide and silicate. Commonly both materials are used combined and the addition of silicates increases the content of soluble silica in the activator, which enhances the compactness of matrix (Zhang et al., 2013; Longhi et al., 2016). As molar ratio is used to characterize the activation content, M_2O/Al_2O_3 represents the fraction between the activator oxide and the Al_2O_3 content of the precursor. This relationship is determined by the stoichiometric equilibrium, where in a fully reacted precursor, each Na^+ can connect with an $[AlO_4]^{5-}$, establishing an ionic bond (Rowles and O'Connor, 2003; Duxson et al., 2007). In an ideal system, the unit value indicates the consumption of all Na^+ cations. According to Zhang et al. (2013), when Na_2O/Al_2O_3 <1, the increase in NaOH concentration is effective in increasing the extent of the reaction, however, values higher than 1 indicate excess of Na^+, which will not establish connections and will be free in the structure. This part is prone to form efflorescence. However, the results reported by Kani et al. (2012) showed that the extent of leaching alkalis improved with Na/Al increasing from 0.61 to 1.23, and the susceptibility in the development of efflorescence of dry samples after immersion. Although, for this relationship to be chemically possible, during the design process it is important to consider the reactive (or reacted) part of precursor, because other fractions will just work as inert filler. In the same way, a different activation design will provide different values of dissolution and reaction, with changes in the effective content of oxides in the geopolymer gel. The relation between design parameters, amount of gel formed, and alkali stability is an important topic to be approached and better understood, and is directly associated with efflorescence formation.

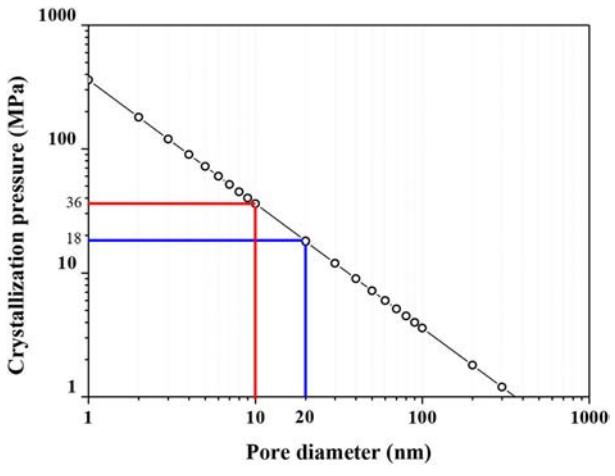

FIGURE 6 | Crystallization pressure as a function of the diameter of a cylindrical pore.

Another important factor is related to the curing process. The increase in the temperature promotes the reaction and dissolution of oxides and the acceleration of the kinetics of geopolymerization reactions (Granizo et al., 2014). This factor was also evaluated for the formation of efflorescence. Kani et al. (2012) observed that the curing temperatures higher than 65°C provided a significant effect in efflorescence reduction and also higher compressive strength using natural pozzolan. This behavior was also verified by Zhang et al. (2014c) from the use of fly ash as precursor and then cured at temperatures between 25° and 80°C. The use of thermal curing is effective to precursors with low reactivity and its effect can be attributed to a higher amount of gel formed with associated higher density and higher amount of imprisoned Na^+.

The information discussed above has shown that activator type and curing conditions are likely to be the critical aspects in the development of efflorescence, and this has been backed up by experimental data. **Figure 4** shows experiments where the rate of efflorescence development was assessed using fly ash-based as precursor [FA-**3.9**-(1.5) and FA-**4.6**-(1.5)] and **Figure 5** shows experiments using calcined kaolin [CK-20-(**1.0**), CK-20-(**0.5**) and CK-20-(**0.0**)]. The fly ash-based geopolymers were prepared by the activation of sodium silicate (SS) solution at different dosages: FA-**3.9**-(1.5) contained 3.9% Na_2O (expressed as Na_2O to fly ash mass ratio, excluding the Na_2O originating from fly ash) and Ms value of 1.5 (molar SiO_2/Na_2O ratio in the activator), while FA-**4.6**-(1.5) contained 4.6% Na_2O and Ms values of 1.5. The fly ash samples were cured in sealed molds for initial 24 h at RH = 90 ± 10%, 25 ± 1°C, followed by 12 h curing at 75 ± 1°C and naturally cooled down to 25 ± 1°C and allowed further 7 days of aging. Specimens were removed from molds and put in ambient air with the bottom immersed

in water at a depth of 0.5–1 mm. The efflorescence occurs on the surface of FA-**3.9**-(1.5) more rapidly: tiny white products are observable after 1.5 h (not presented here), and after only 2 h, evident efflorescence products can be seen on its surface above the wet line. In comparison, FA-**4.6**-(1.5) starts to exhibit visible efflorescence after 2 h. The leaching analysis of the crushed samples, as a quantitative method of assessing efflorescence potential (Zhang et al., 2014c), shows that the two AACs have very close sodium releasing rate and fraction (not shown). It means that FA-**4.6**-(1.5) has higher efflorescence potential as the absolute amount of leached alkali is higher. This result indicates that lowering the alkali concentration in an AAC by reducing the amount of sodium silicate activator may not be a good practical method to mitigate efflorescence. In fact, other factors, such as gel

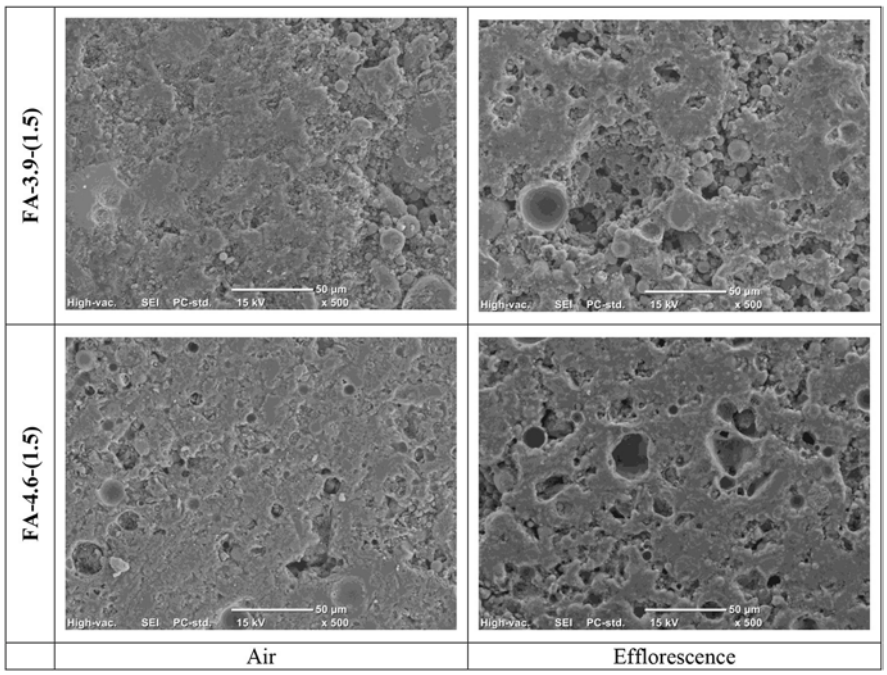

FIGURE 7 | Scanning electron micrographs of AACs after 28 days of aging under ambient air and accelerating efflorescence conditions.

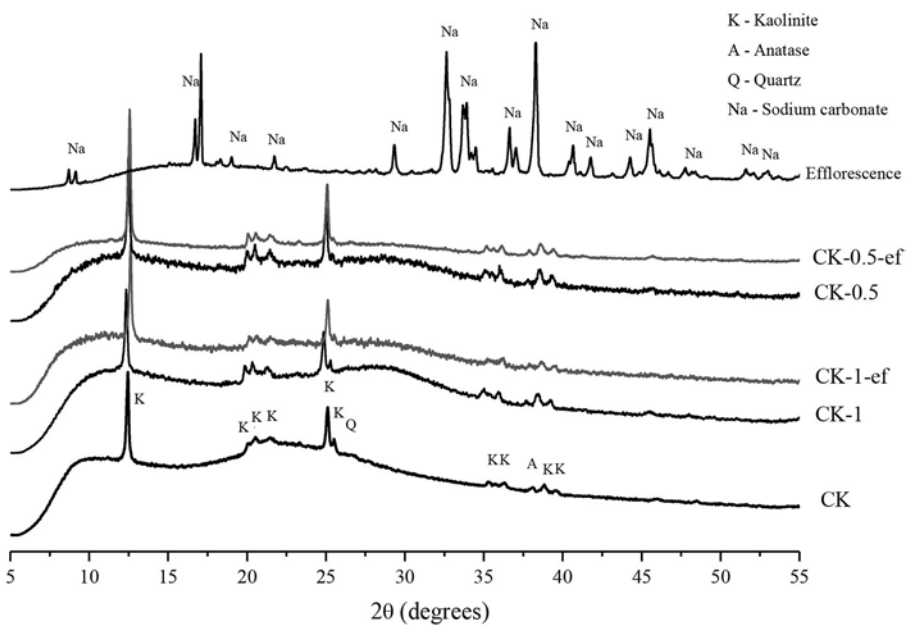

FIGURE 8 | XRD analysis of precursor, CK-bases geopolymers before and after efflorescence formation and efflorescence product.

composition (as a result of varied reaction extent of fly ash due to the change of activation conditions) and the pore features (size and volume), can also influence the efflorescence rate.

Figure 5 shows experiments on calcined kaolin-based geopolymers (CK). This material was activated with sodium silicate and NaOH, with fixed 20% of Na_2O and different MS values: CK-20-(**1.0**) with MS = 1.0, CK-20-(**0.5**) with MS = 0.5 and CK-20-(**0.0**) with MS = 0.0 (NaOH-based geopolymer without any soluble silicate in the activator). The CK samples were cured for 28 days at RH = 90 ± 10% and 25 ± 1°C in a sealed plastic container. Specimens were removed from molds and partially immersed in distilled water (at a depth of 5 mm). The system with MS = 1 did not show efflorescence even after 28 days of assessment (not shown here). With MS = 0.5 after 1 day, it was able to clearly identify a layer of efflorescence from the middle of the sample. For the system with MS = 0, the efflorescence was observed even before contact with water, where the leaching was observed due to the internal moisture of the test specimen. After the immersion, an increase in the formation of efflorescence was rapidly identified. This makes it evident that the effectiveness of silicate is soluble when used as activator. In this sense, the system that did not show efflorescence also presented higher mechanical (∼52 MPa at 28 days) behavior. Another factor to be considered when comparing with fly ash systems is that the amount of activator required for calcined clay-based geopolymers is usually two to three times higher.

The Difference and Similarities Between Efflorescence and Subflorescence

Crystallization process is the opposite to the solubilisation of a solid. In a solution when saturation is exceeded, part of solute will be separated from the solution and precipitates as solid crystals to keep the solution saturated. As shown previously, after the leaching process, the alkalis are brought to the surface and are crystallized by the carbonation process, generating efflorescence. However, according to Scherer (2004), porous material can be damaged when crystal precipitate from the liquid in their pores. The size of the pores and the magnitude of the repulsive force between the salt and the confining pore surfaces are also important factors. In turn, supersaturation is dependent on the nature of the salt, the rate of the supply of the solution and the evaporation of water (Scherer, 2004). In this way, the crystallization can occur in two ways: efflorescence, when the internal alkalis are carried toward the surface, providing Na^+ for the precipitation of sodium carbonates, until an equilibrium (saturation) condition between the pore solution and the crystals is reached (Zhang et al., 2018); or subflorescence, when the crystallization occurs within pores (Dow and Glasser, 2003), in a depth sufficient to allow the absorption of dissolved CO_2. According to Zhang et al. (2018), efflorescence and subflorescence are both related to the carbonation process, however, the material properties, exposition, and environment can determine what will be formed.

Regarding porosity, in a porous material, water is draw up by capillary pressure, which is dependent on the pore size distribution. The flux ($J = -\kappa.\Delta\rho/\eta$) into the porous material is given by Darcy's law, and is dependent on permeability (κ), viscosity (η), and pressure (ρ). To balance the system, water raises between the pores until an equilibrium height is achieved. In the evaporation process, the internal water of pores is brought to surface and reduces the height of equilibrium. When there is the presence of dissolved salts, as water evaporates, the concentration of salt in the liquid rises and the salt concentration at the drying surface until the supersaturation are high enough to cause the salt precipitation (Scherer, 2004). Summarizing this, the water will be transported into the material by capillary pressure. With the evaporation process, the transported salts are precipitated in a spatial sequence according to the ion activities of the salt phases in the system (Arnold and Zehnder, 1989). However, above the evaporation region, as well as throughout the inner part, due to the presence of remaining soluble salts, is the subflorescence zone. In AACs, if a soluble carbonate is available, it can be transported to the inside and enable the crystallization of the salt, which in this case is a carbonate, and the resulting crystallization pressure may exceed the tensile strength of the material (Scherer, 2004).

In the crystallization process, every salt has an equilibrium relative humidity, which is also relevant to the ambient humidity and temperature. If the relative air humidity is lower than the equilibrium humidity of the salt (RH < Hr eq), the salt will

FIGURE 9 | Sample with calcined kaolin as precursor and activated with 10% of Na_2O from NaOH with visible surface deterioration.

crystallize. Correlating this with AACs, when RH is low, with the availability of a hydrated carbonate provides a movement to inside structure, which may crystallize internally with the contact with free alkali. If the relative air humidity is higher than the equilibrium humidity of the salt (RH > Hr eq), the salt dissolves and can be brought to the surface by a transport agent. This means that the relative humidity of the environment and salt crystallization will define whether there will be efflorescence or internal crystallization (subflorescence). The equilibrium humidity of a specific salt is not always available or has never been evaluated; however, the carbonate Na_2CO_3:$10H_2O$, at 25°C, presents Hr eq of 88.2% (38). In the same way, the capillarity will determine the rate of water movement and aqueous CO_2 movement and consequently the depth of subflorescence.

In literature that evaluated the formation of efflorescence in AACs, the main products formed are sodium carbonates. The formation of a hydrated carbonate ($Na_2CO_3.7H_2O$) was observed by Škvára et al. (2009) and Zhang et al. (2014c), sodium bicarbonate ($NaHCO_3$) by Kani et al. (2012) and natrite (Na_2CO_3) by Burciaga-Díaz et al. (2010). In a system with potassium as activator, it is possible to form potassium carbonate (K_2CO_3) or hydrated potassium carbonate phases, however, this last one does not give rise to visible hydrates as postulated by Škvára et al. (2009), and for this reason, the use of potassium could be indicated for the reduction of efflorescence (or efflorescence visibility). Even without visible efflorescence formation in geopolymers based on potassium as main activator, the leaching process of this element can allow the removal of alkalis and cause microstructural damages.

In short, efflorescence is the crystallization process of alkalis leached from the AAC matrix in contact with aqueous carbonate solution in a reaction format as follows Zhang et al. (2014c).

$$CO_2(g) + 2OH^-(aq) \rightarrow CO_3^{2-}(aq) + H_2O$$
$$2Na^+(aq) + CO_3^{2-}(aq) + 7H_2O \rightarrow Na_2CO_3.7H_2O(s)$$

According to Zhang et al. (2014c), this is therefore a partial neutralization for alkaline geopolymers under natural carbonation conditions, as dissolved CO_2 acts as an acid and consumes hydroxides. The main reason for efflorescence in these materials is the availability of mobile Na^+ and OH^-, which are related to the material permeability. In a situation with very aggressive leaching, it can also remove the equilibrium cation (Na^+) and destabilize the aluminum tetrahedral, which may damage the matrix structure. This mechanism, however, has not been solidly verified nor highlighted to date.

Internally, the carbonation process may follow the same reactions, but its effect could be different. The formed crystal can be expansive which induces internal stresses. The stress in the megapascal range is only expected in nanometric pores, and lower pressure in larger pores. This pressure can be mechanically damaging depending on the pore structure. According to Scherer theory (Scherer, 2004), the supersaturation of salts can result from capillary rise and evaporation, or from cycles of wetting and drying. In contact with water, the humidity in the pores is expected to be very high, which support the formation of $Na_2CO_3{\cdot}7H_2O$ as detected by Zhang et al. (2014c).

To predict the relation between crystallization pressure and pore diameter, using the estimated liquid interfacial free energy ($\gamma_{CL} = 0.09$ N/m) of $Na_2CO_3{\cdot}10H_2O$ (Rijniers et al., 2005) and Equation 1 that describes the pressure in a confined spherical crystal with radius of r as proposed by Scherer (2004), it is possible to estimate the crystallization pressure in a cylindrical. The relation between crystallization pressure and pore diameter is shown in the **Figure 6**.

$$p = 2\gamma_{CL}/r \quad (1)$$

As reported in some previous papers (Škvára et al., 2006; Van Deventer et al., 2006; Zhang and Wang, 2016), the pore sizes in geopolymers determined by mercury intrusion are at a range of several nanometres to 2,000 nm. In an experiment conducted using different contents of fly ash and metakaolin, (Zhang et al., 2014b,c) observed the concentration of 80–90% of the pores smaller than 20 nm. The crystallization process inside a pore of 20 nm can generate a pressure of 18 MPa and 36 MPa for 10 nm pores. The pressure increases in an exponential relation to the pore diameter. Large pores can permit the growing of crystal with a low crystallization pressure, however, the crystal formation in small pores can generate a high pressure (Longhi et al., 2016). The impact on the integrity of the samples, and particularly whether the process will be harmful or harmless, depends on the magnitude of the crystallization pressure compared to the tensile strength of the geopolymer matrix (Zhang et al., 2018).

IMPACTS OF EFFLORESCENCE ON AACs

Microstructural Impacts

So far, there has been very limited structural analysis reported in literature related to the formation of efflorescence in ACC. Zhang et al. (2014c) analyzed the pore structure by scanning electron microscopy (SEM), and made some important considerations. The leaching process is related to the pore size distribution where a large pore induces a faster alkali leaching.

The effect of efflorescence on the microstructure of the same material showed in **Figure 7**, FA-**3.9**-(1.5) and FA-**4.6**-(1.5), is

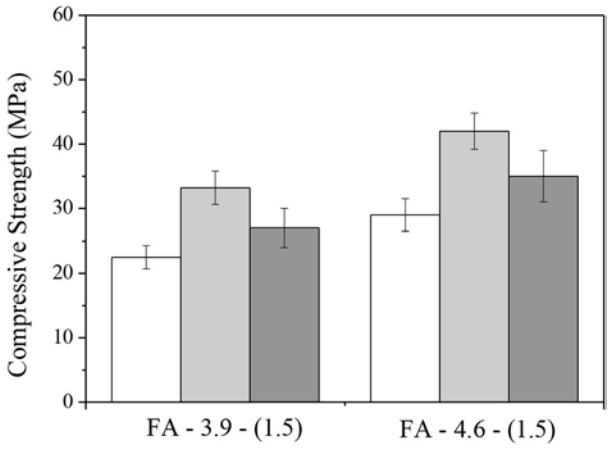

FIGURE 10 | Compressive strengths of well-matured fly ash AACs after demoulding, air-aging and accelerating efflorescence for 28 days.

shown in **Figure 7**. The images correspond to the surface parts of each sample after 28 days of ambient aging (in the air) and accelerating efflorescence (with bottom immersed in water as described above). The crushed particles near surface were solidified using resin, polished, and washed in acetone using an ultrasonic washer to remove loose particles.

After the accelerating the efflorescence procedure, FA-**3.9**-(1.5) becomes more porous when compared to the corresponding samples. The same polishing and washing procedures were used for all samples; the porous microstructure in cross-section implies that the binder may be softer or less strong as a consequence of the development of efflorescence. The cross-section of FA-**4.6**-(1.5) after the accelerating efflorescence program shows the same microstructural feature. Zhang et al. (2018) implied that one of the reasons for the increase in large pores is that the later reaction was affected in the specimens with efflorescence, due the consumptions of alkalis to form de $Na_2CO_3 \cdot nH_2O$, reducing the ongoing reaction of gel.

Trying to understand the microstructural effect of efflorescence, Zhang et al. (2018) evaluated the T-O (T = Al or Si) bonding environments by FTIR spectroscopy in systems with intense efflorescence in contact with water. The authors observed a shift of the main band as well as a lower intensity in the systems in contact with water when compared with those samples in air. The author also indicated that efflorescence in geopolymers does not change the main mineralogical composition of the binder, however, it restricts the later reactions, which is expected to be harmful to the strength development. Unfortunately, the actual mechanical testing on tensile strength change was not reported in the previous study.

Figure 8 shows XRD results of the CK-based geopolymers as presented in **Figure 5**. The first diffractogram represents the precursor, a calcined kaolin (CK), which shows the presence of kaolinite, anatase, and quartz. The hump between 19 and 28 degrees is attributed to the amorphous feature of metakaolin. After the geopolimerization process, another hump is visible between 26 and 34, and attributed to the gel formation. After the efflorescence process, it is able to identify a hydrate sodium carbonate ($CaCO_3.nH_2O$). The formation of such carbonate may be from the carbonation of calcium solution as the calcined kaolin contains a certain amount of CaO as impurity, which becomes available after alkali-activation. The system CK-20-(1.0) shows 34.8% of crystalline content, and after the efflorescence process it becomes 41.4%. The system CK-20-(0.5) presents 39.7% before and 49.7% after efflorescence. This degree of crystallinity was obtained by mathematical peak deconvolution. This increase is visible by the reduction of the main hump near to 28° in 2θ. This means that there is a reduction in the material amorphic structure after the efflorescence.

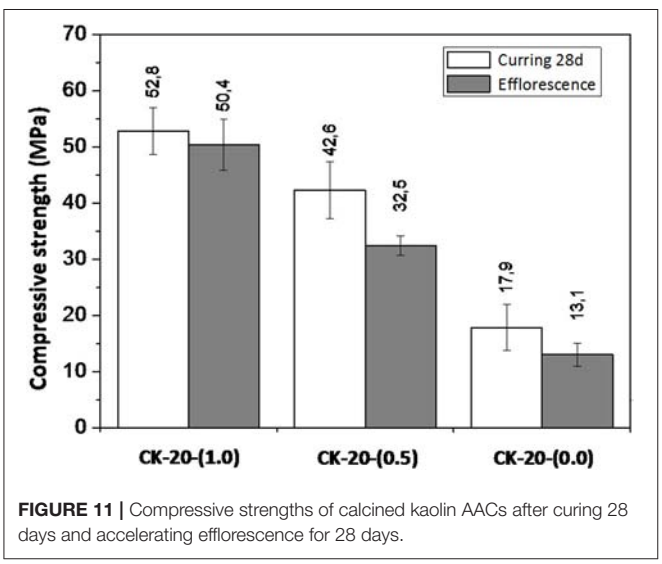

FIGURE 11 | Compressive strengths of calcined kaolin AACs after curing 28 days and accelerating efflorescence for 28 days.

Due to the formation of the carbonate crystal, microstructural changes become visible in sample integrity. In some systems, after wetting and drying cycles, the process of dissolving alkalis is followed by evaporation of the water, which allows the movement to surface, and it causes severe deterioration. **Figure 9** shows a sample produced with the CK subjected to contact with water at the bottom in an environment with ∼50% RH, so that the movement of water and alkalis by evaporation was forced. The excess of leaching or/and the crystallization in superficial pores may cause this deterioration.

Mechanical Impacts

Burciaga-Díaz et al. (2010) evaluated how different formulations affected the development of compressive strength, and found that in slag-based AAC, the addition of more than 5% of Na_2O decreased the compressive strength. This effect was attributed to the excess of alkalis and the consequent efflorescence formation, which was visually observed. In the same work, however, when MK was added as a precursor, it required a larger amount of Na_2O (15%), while no reduction in the mechanical properties was observed, nor any efflorescence.

In a long-term exposure for a fly ash-based AAC, Škvára et al. (2012) observed reduction in compressive strength for the water immersed samples when compared with those exposed to air. However, this reduction was attributed to the higher cohesion forces between the gel particles in the dry concrete. To the same authors, as it was found that Na^+ was replaced by H_3O^+, Škvára et al. (2009) argued that a large part of Na are bounded in the form of $Na(H_2O)_n^+$, rather than ironic bonds -O-Na^+. It should be noted that in this specific case, the immersed sample only lost the alkalis by leaching, and no crystallization process occurred.

The mechanical properties of fly ash-based geopolymers by different periods of curing, and types of exposure were evaluated by Yao et al. (2015). By comparing the compressive strength results, it was found that the immersed samples and those submitted to bottom contact with water (accelerating efflorescence) presented lower values compared to the control samples that were left in air. The time of exposure also contributed to the strength reduction. The negative effect of immersion was attributed to the instability of sodium aluminosilicate gel in water. For the samples with bottom contacting water, the formation of carbonate crystal and microstructure damage was believed to be the main factor to the reduction of mechanical behavior. In terms of linear shrinkage, the shrinkage of the samples immersed was smaller than that of

efflorescence samples due to the availability to free water in the binder under the immersion condition.

As observed by Yao et al. (2015), the environment of exposure is an import factor that affect carbonation process. A direct comparison by measuring the specimens after demoulding, air-aging, and accelerating efflorescence were recently made by the authors. **Figure 10** shows the compressive strengths of the fly ash-based AACs, the same as presented in **Figure 2**. After 28 days of aging, the compressive strengths of the pastes in air showed an increase by 20–35% compared with that at demoulding age, while the efflorescence samples showed smaller increase.

Calcined clays-based AACs were also evaluated by compressive strength (**Figure 11**). The samples identified as CK-20-(**1.0**), CK-20-(0.5), and CK-20-(0.0) were the same as presented in **Figure 3**. After 28 days of curing in a sealed plastic container at RH = 90 ± 10% and 25 ± 1°C, followed by 28 days more in contact with water to accelerate efflorescence formation, it was found that the first system [CK-20-(**1.0**)] showed less susceptibility of efflorescence, and this behavior is attributed to the denser and stronger structure which provides a lower water absorption, and consequently a lower movement of alkalis to the surface. The other systems presented strength reductions of ∼25% and extensive effloresce formation. Thus, it is able to confirm that the mechanical behavior and its susceptibility to efflorescence formation in these systems are related to the design parameters.

Therefore, it is evident that the efflorescence has a negative influence on the strength development. When an AAC paste is placed in accelerating efflorescence conditions, water can be drawn into the pores of the solid matrix by capillary suction and evaporate from the sample surface. The internal alkalis are able to diffuse toward the surface, providing Na^+ for the precipitation of sodium carbonates, until an equilibrium (saturation) condition between the pore solution and the crystals is reached. The reduced alkali concentration in the matrix, due to diffusion, will affect, or suppress the later activation of residual precursors. In addition, the crystallization pressure due to the precipitation of sodium carbonates in the pores of binder may also introduce inner stress, which consequently affects the mechanical properties of AACs.

CONCLUSIONS

Even with the recent advances in AAC technology, the understanding of the efflorescence phenomenon is still a knowledge gap and is distinct from that which occurs in PC-based materials. Some progress has been made to understand these efflorescence mechanisms and the factors that influence them, but some topics need to be better clarified. Based on the previous researches and some experimental results, the importance of: the effect of soluble silicates as an activator, the hydrothermal curing and the use of slag to reduce the efflorescence rate, is evident when used with the correct design parameters. However, it is necessary to identify the micro and nanostructural effect of the materials and the mechanisms, the relationship between design parameter and gel formed and the alkalis stability. It is also necessary to understand the carbonation process, how the pore network structure is related to external or internal crystallization, how the humidity is connected to the process and how all of these could be associated to the performance of the material in service. The effect of efflorescence formation on mechanical properties, including compressive strength, tensile strength, and linear deformation requires a greater understanding. The use of this material in civil construction requires the understanding of this phenomenon to avoid durability problems.

AUTHOR CONTRIBUTIONS

The first version of this review paper has been drafted by ZZ, and enriched by ML in 2018. ML and ZZ did all the experimental part and data analysis (collection). In the discussion part, ER and AK provided a lot of insight comments and improvements, and HW finalized the whole presentation and format of this paper. The greatest contribution of content is ML and ZZ and the rest three authors contributed equally.

ACKNOWLEDGMENTS

Funding from Australian Research Council through Discovery project (DP160104149) and DECRA (DE170101070) project are acknowledged. ML thanked the financial support of CAPES and of SWE 203750/2017-9. The participation of Brazilian authors was sponsored CNPq (Brazilian National Council for Scientific and Technological Development) through the research project UNIVERSAL grant number 458597/2014-7, as well as the research fellowships PQ2017 303753/2017-0 and 305530/2017-8. We would like to thanks the previous paper presented at the conference of the Second International Conference on Performance-based and Life-cycle Structural Engineering (PLSE 2015).

REFERENCES

Arnold, A., and Zehnder, E. K. (1989). "Salt weathering on monuments," in *I' Simposio Internazionale Bari*.

Bernal, S. A. (2016). Microstructural changes induced by CO_2 exposure in alkali-activated slag/metakaolin pastes. *Front. Mater.* 3:43. doi: 10.3389/fmats.2016.00043

Bernal, S. A., Bílek, V., and Criado, M. (2014). "Durability and testing - degradation via mass transport," in *Alkali Activated Materials: State of the Art Report*, eds por J. L. Provis and J. S. J Van Deventer (Dordrecht: Springer), 223–276.

Burciaga-Díaz, O., Escalante-Garcia, J. I., Arellano-Aguilar, R., and Gorokhovsky, A. (2010). Statistical analysis of strength development as a function of varios parameters on activated metakaolin/slag cements. *J. Am. Ceram. Soc.* 93, 541–547. doi: 10.1111/j.1551-2916.2009.03414.x

Cizer, Ö., Van Balen, K., Elsen, J., and Van Gemert, D. (2012). Real-time investigation of reaction rate and mineral phase modifications. *Constr. Build. Mater.* 35, 741–751. doi: 10.1016/j.conbuildmat.2012.04.036

Criado, M., Fernandez-Jiménez, A., and Palomo, A. (2007). Alkali activation of fly ash: effect of the SiO2/Na2O ratio. *Mocropor. Mesopor. Mater.* 106, 180–191. doi: 10.1016/j.micromeso.2007.02.055

Damtoft, J. S., Lukasik, J., Herfort, D., Sorrentino, D., and Gartner, E. M. (2008). Sustainable development and climate change initiatives. *Cement Concrete Res.* 38, 115–127. doi: 10.1016/j.cemconres.2007.09.008

Dow, C., and Glasser, F. P. (2003). Calcium carbonate efflorescence on Portland cement and building materials. *Cement Concrete Res.* 33, 147–154. doi: 10.1016/S0008-8846(02)00937-7

Duxson, P., Lukey, G. C., Separovic, F., and Deventer, J. S. J. (2005). Effect of alkali cations on aluminus incorporation in geopolymeric gels. *Ind. Eng. Chem. Res.* 44, 832–839. doi: 10.1021/ie0494216

Duxson, P., Mallicoat, S. W., Lukey, G. C., Kriven, W. M., and Van Deventer, J. S. J. (2007). The effect of alkali and Si/Al ratio on the development of mechanical properties of metakaolin-based geopolymers. *Colloids Surf.* 292, 8–20. doi: 10.1016/j.colsurfa.2006.05.044

Fernández-Jimenez, A., Palomo, A., Sobrados, I., and Sanz, J. (2006). The role played by the reactive alumina content in the alkaline activation of fly ashes. *Micropor. Mesopor. Mater.* 91, 111–119. doi: 10.1016/j.micromeso.2005.11.015

Gallucci, E., and Scrivener, K. (2007). Crystallisation of calcium hydroxide in early age model and ordinary cementitious systems. *Cement Concrete Res.* 37, 492–501. doi: 10.1016/j.cemconres.2007.01.001

Garcia-González, C. A., Hidalgo, A., Andrade, C., Alonso, M. C., Fraile, J., López-Periago, A. M., et al. (2006). Modification of composition and microstructure of Portland cement pastes as a result of natural and supercritical carbonation procedures. *Ind. Eng. Chem. Res.* 45, 4985–4992. doi: 10.1021/ie0603363

Granizo, N., Palomo, A., and Fernandez-Jiménez, A. (2014). Effect of temperature and alkaline concentration on metakaolin leaching kinetics. *Ceramics Int.* 40, 8975–8985. doi: 10.1016/j.ceramint.2014.02.071

Heath, A., Paine, K., and McManus, M. (2014). Minimising the global warming potential of clay based geopolymers. *J. Clean. Prod.* 78, 75–83. doi: 10.1016/j.jclepro.2014.04.046

Kani, E. N., Allahverdi, E. A., and Provis, J. L. (2012). Efflorescence control in geopolymers binders based on natural pozzolan. *Cement Concrete Composites* 34, 25–33. doi: 10.1016/j.cemconcomp.2011.07.007

Lloyd, R. R., Provis, J. L., and Van Deventer, J. S. J. (2010). Pore solution composition and alkali diffusion in inorganic polymer cement. *Cement Concrete Res.* 40, 1386–1392. doi: 10.1016/j.cemconres.2010.04.008

Longhi, M. A., Rodríguez, E. D., Bernal, S. A., Provis, J. L., and Kirchheim, A. P. (2016). Valorisation of a kaolin mining waste for the production of geopolymers. *J. Clean. Produc.* 115, 265–272. doi: 10.1016/j.jclepro.2015.12.011

McLellan, B. C., Williams, R. P., Lay, J., Riessen, A. V., and Corder, G. D. (2011). Costs and carbon emissions for geopolymers pastes im comparison to ordinary portland cement. *J. Clean. Prod.* 19, 1080–1090. doi: 10.1016/j.jclepro.2011.02.010

Passuelo, A., Rodríguez, E. D., Hirt, E., Longhi, M., Bernl, S. A., Provis, J. L., et al. (2017). Evaluation og the potential improvement in the environmental footprint of geopolymers using waste-derived activators. *J. Clean. Prod.* 166, 680–689. doi: 10.1016/j.jclepro.2017.08.007

Provis, J. L., and Bernal, S. A. (2014). Geopolymers and related alkali-activated material. *Ann. Rev. Mater. Res.* 44, 299–327. doi: 10.1146/annurev-matsci-070813-113515

Provis, J. L., Lukey, G. C., and Van Deventer, J. S. J. (2005). Do geopolymers actually contain nanocrystalline zeolites: a reexamination of existing results. *Chem. Mater.* 17, 3075–3085. doi: 10.1021/cm050230i

Rijniers, L. A., Huinink, H. P., Pel, L., and Kopinga, K. (2005). Experimental evidence of crystallization pressure inside porous media. *Phys. Rev. Lett.* 94, 75503–75507. doi: 10.1103/PhysRevLett.94.075503

Rowles, M. R., Hanna, J. V., Pike, K. J., Smith, M. E., and Connor, B. H. (2007). 9Si, 27Al, 1H and 23Na MAS NMR study of the bonding character in aluminosilicate inorganic polymers. *Appl. Magnet. Ressonance* 32, 663–687. doi: 10.1007/s00723-007-0043-y

Rowles, M. R., and O'Connor, B. (2003). Chemical optimisation of the compressive strength of aluminosilicate geopolymers synthesised by sodium silicate activation of metakaolinite. *J. Mater. Chem.* 13, 1161–1165. doi: 10.1039/b212629j

San Nicolas, R., and Provis, J. L. (2015). The interfacial transition zone in alkali-activated slag mortars. *Front. Mater.* 2:70. doi: 10.3389/fmats.2015.00070

Šavija, B., and Lukovic, M. (2016). Carbonation of cement paste: understanding, challenge and opportunities. *Construc. Build. Mater.* 117, 285–301. doi: 10.1016/j.conbuildmat.2016.04.138

Scherer, G. W. (2004). Stress from crystallization of salt. *Cement Concrete Res.* 34, 1613–1624. doi: 10.1016/j.cemconres.2003.12.034

Shen, W., Wang, Y., Zhang, T., Zhou, M., Li, J., and Cui, X. (2011). Magnesia modification of alkali-activated slag fly ash cement. *J. Wuhan Univer. Tech. Mater.* 26, 121–125. doi: 10.1007/s11595-011-0182-8

Škvára, F., Kopecký, L., Mysková, L., Smilauer, V., Alberovská, L., and Vinsová, L. (2009). Aluminosilicate polymers - influence of elevated temperatures, efflorescence. *Ceram. Silikáty* 53, 276–282.

Škvára, F., Kopecký, L., Nemecek, J., and Bittnar, Z. (2006). Microstructure of geopolymer materials based on fly ash. *Ceram. Silikaty* 50, 208–215.

Škvára, F., Šmilauer, V., Hlavácek, P., Kopecky, L., and Cilová, Z. (2012). A weak alkali bond in (N, K)-A-S-H gels: evidende from leaching and modeling. *Ceram. Silikáty* 56, 374–382.

Temuujin, J., Minjigmaa, A., Lee, M., Chen-Tan, N., and van Riessen, A. (2011). Characterization of glass F fly ash geopolymer pastes immersed in acid and alkali solutions. *Cement Concrete Composites* 33, 1086–1091. doi: 10.1016/j.cemconcomp.2011.08.008

Van Deventer, J. S. J., Lukey, G. C., and Xu, H. (2006). Effect of curing temperature and silicate concentration on fly-ash-based geopolymerization. *Ind. Eng. Chem. Res.* 45, 3559–3568. doi: 10.1021/ie051251p

Van Deventer, J. S. J., Provis, J. L., and Duxson, P. (2012). Technical and commercial progress in the adoption of geopolymer cement. *Miner. Eng.* 29, 89–104. doi: 10.1016/j.mineng.2011.09.009

Yao, X., Yang, T., and Zhang, Z. (2015). Compressive strength development and shrinkage of alkali-activated fly ash-slag blends associated with efflorescence. *Mater. Struct.* 49, 2907–2918. doi: 10.1617/s11527-015-0694-3

Zhang, D., Ghouleh, Z., and Shao, Y. (2017). Review on carbonation curing of cement-bases materials. *J. CO_2 Utilizat.* 21, 119–131. doi: 10.1016/j.jcou.2017.07.003

Zhang, X., Glasser, F. P., and Scrivener, K. L. (2014a). Reaction kinetics of dolomite and portlandite. *Cement Concrete Res.* 66, 11–18. doi: 10.1016/j.cemconres.2014.07.017

Zhang, Z., Provis, J. L., Ma, X., Reid, A., and Wang, H. (2018). Efflorescence and subflorescence induced microstructural and mechanical evolution in fly ash-based geopolymers. *Cement Concrete Composit.* 92, 165–177. doi: 10.1016/j.cemconcomp.2018.06.010

Zhang, Z., Provis, J. L., Reid, A., and Wang, H. (2014c). Fly Ash-based geopolymers: the relation between composition, pore structure ans eflforescence. *Cement Concrete Res.* 64, 30–41. doi: 10.1016/j.cemconres.2014.06.004

Zhang, Z., Provis, J. L., Wang, H., Bullen, F., and Reid, A. (2013). Quantitative kinetic and structural analysis of geopolymers. Part 2. Thermodynamics of sodium silicate activation of metakaolin. *Thermochim. Acta* 565, 163–171. doi: 10.1016/j.tca.2013.01.040

Zhang, Z., and Wang, H. (2016). The pore characteristics of geopolymer foam concrete and their impact on the compressive strength and modulus. *Front. Mater.* 3:38. doi: 10.3389/fmats.2016.00038

Zhang, Z., Wang, H., Zhu, Y., Reid, A., and Provis, J. L. (2014b). Using fly ash to partially substitute metakaolin in geopolymer synthesis. *Appl. Clay Sci.* 88–89, 194–201. doi: 10.1016/j.clay.2013.12.025

Zhang, Z., Yao, X., and Zhu, H. (2012). Potential application of geopolymers as protection coatings for marine concrete III. Field experiment. *Appl. Clay Sci.* 67–68, 57–60. doi: 10.1016/j.clay.2012.05.008

Conflict of Interest Statement: The authors declare that the research was conducted in the absence of any commercial or financial relationships that could be construed as a potential conflict of interest.

frontiers in Materials

ORIGINAL RESEARCH
published: 24 April 2019
doi: 10.3389/fmats.2019.00078

Hydration of Binary Portland Cement Blends Containing Silica Fume: A Decoupling Method to Estimate Degrees of Hydration and Pozzolanic Reaction

*Wenyu Liao[1], Xiao Sun[2,1], Aditya Kumar[3], Hongfang Sun[4] and Hongyan Ma[1]**

[1] Department of Civil, Architectural and Environmental Engineering, Missouri University of Science and Technology, Rolla, MO, United States, [2] College of Water Conservancy and Hydropower Engineering, Hohai University, Nanjing, China, [3] Department of Materials Science and Engineering, Missouri University of Science and Technology, Rolla, MO, United States, [4] Guangdong Province Key Laboratory of Durability for Marine Civil Engineering, School of Civil Engineering, Shenzhen University, Shenzhen, China

OPEN ACCESS

Edited by:
John L. Provis, University of Sheffield, United Kingdom

Reviewed by:
Guang Ye, Delft University of Technology, Netherlands
M. Iqbal Khan, King Saud University, Saudi Arabia

***Correspondence:**
Hongyan Ma
mahon@mst.edu;
mhy1103@gmail.com

Specialty section:
This article was submitted to Structural Materials, a section of the journal Frontiers in Materials

Received: *30 November 2018*
Accepted: *05 April 2019*
Published: *24 April 2019*

Citation:
Liao W, Sun X, Kumar A, Sun H and Ma H (2019) Hydration of Binary Portland Cement Blends Containing Silica Fume: A Decoupling Method to Estimate Degrees of Hydration and Pozzolanic Reaction. Front. Mater. 6:78. doi: 10.3389/fmats.2019.00078

Determination of degrees of hydration/reaction of components of blended cementitious systems (i. e., cement and SCMs: supplementary cementitious materials) is essential to estimate the systems' properties. Although the best methods for determining degrees of reaction of different SCMs have been recommended by RILEM TC238, they rely on either expensive equipment (e.g., nuclear magnetic resonance) or time-consuming sample preparation and data processing (e.g., backscattered electron image analysis). Furthermore, these methods cannot simultaneously characterize degree of hydration of cement and degree of reaction of SCMs. A novel decoupling method, which can simultaneously estimate the degree of hydration of cement and the degree of reaction of silica fume in binary cementitious materials, is proposed in this study. Based on experimentally determined and theoretically validated stoichiometric parameters of cement hydration and pozzolanic reaction, the contents of calcium hydroxide and hydrate water in pastes are expressed as functions of degree of hydration of cement and degree of reaction of silica fume. With the two contents determined by thermogravimetric analysis, the two degrees can be solved mathematically. It is found that in binary binders the incorporation of silica fume affects hydration kinetics of cement, leading to lower ultimate degree of hydration, shorter dormant stage, and faster hydration in the acceleration stage. As a result, the degree of hydration of cement in blended paste is higher at early ages (e.g., 3 days) but lower at later ages (e.g., 120 days) than that in plain cement paste. In a given blended paste, the degree of reaction of silica fume can be tied to the degree of hydration of cement. The decoupling method is promising for rapid estimations of degrees of hydration/reaction of cementitious materials in a blended system, since it does not require expensive characterization tools or complex data processing methods.

Keywords: silica fume, blended cement, degree of hydration, pozzolanic reaction, thermogravimetric analysis, decoupling

INTRODUCTION

Supplementary cementitious materials (SCMs), such as silica fume (SF), fly ash (FA), ground granulated blast-furnace slag (GGBFS) and limestone (LS) powder, have been widely used in concrete because of their environmental and performance merits (Juenger and Siddique, 2015). On the one hand, SCMs can minimize energy consumption and CO_2 emission associated with portland cement production (Damtoft et al., 2008; Schneider et al., 2011; Gruyaert et al., 2012; Wang et al., 2017). On the other hand, after short or long hydration times, SCMs incorporated concrete can achieve similar or better mechanical properties, as well as improved durability with respect to various deterioration mechanisms, such as sulfate attack and chloride penetration, compared with plain portland cement concrete (Lee et al., 2016; Yoo and Kwon, 2016). Regardless of the type of cementitious materials used, the temporal evolutions of degree of hydration and assemblage of hydration products have direct and significant impact on mechanical and transport properties of concrete. Therefore, hydration kinetics of cementitious materials and microstructure development of the paste are crucial to evaluate and/or predict the serviceability and durability of concrete.

Several well-established methods for studying hydration kinetics and microstructure evolution of plain portland cement have been developed. The degree of hydration can be routinely monitored/determined using one, or a combination, of several experimental approaches, such as measurement of heat of hydration (Wadsö, 2015; Lapeyre and Kumar, 2018), quantification of non-evaporable water and calcium hydroxide (CH) contents with thermogravimetric analysis (TGA) (Powers and Brownyard, 1946; Fagerlund, 2009; Ma and Li, 2013; Lothenbach et al., 2015), quantitative phase analysis with powder x-ray diffraction (XRD) (Snellings, 2015), and backscattered electron (BSE) image analysis (Scrivener et al., 2016). The microstructure and phase assemblage of hardened pastes can be characterized using mercury intrusion porosimetry (MIP) (Ma, 2014), nitrogen adsorption (Escalante-Garcia, 2003), BSE image analysis (Scrivener et al., 2016), etc. Based on experimental results and/or theoretical hydration kinetics, computer models, such as HYMOSTRUC (van Breugel, 1995a,b), the multi-component model (Kishi and Maekawa, 1996), CEMHYD3D (Bentz et al., 1998), and μic (Bishnoi and Scrivener, 2009; Kumar et al., 2012), have been developed to describe the hydration process of cement and/or microstructural development of cement paste. However, when these methods are employed in SCMs incorporated cementitious materials, one may encounter problems due to complexities of SCMs and the multi-component pastes (Fanghui et al., 2015). Although thermodynamic models, for example, GEMS (Gibbs free energy minimization software), have been used to resolve such complexities, they necessitate specific inputs of degrees of hydration of each reactant at a target point (De Weerdt et al., 2011; Schöler et al., 2015; Fernández et al., 2018). Computer-based microstructure models also need explicit information pertaining to degree of reaction of each component and/or kinetic (e.g., C-S-H nucleation and growth) parameters to simulate microstructure development in multi-phase cement paste (Ma, 2013). How to determine degrees of hydration/reaction of various components in a blended cementitious material is thus an essential research topic.

Since hydration of cement and pozzolanic reactions of SCMs are exothermic processes, several models based on direct calorimetry measurements have been developed to describe the hydration of blended cementitious materials (De Schutter and Taerwe, 1995; Swaddiwudhipong et al., 2003; Riding et al., 2013). They are useful in predicting the heat of hydration and semi-adiabatic temperature rise in mass concrete, and can be used to broadly estimate the overall degree of hydration of blended cementitious materials (Fanghui et al., 2016; Qiang et al., 2016; Zhang et al., 2016). However, the interactions between cement hydration and pozzolanic reaction of SCMs (with portlandite) are not explicitly considered by these models. To better describe the hydration behavior of multi-component cementitious materials, quantitative methods that can simultaneously determine the degree of hydration of cement and the degrees of pozzolanic reaction of SCMs are needed.

It is generally accepted that the reactions of SCMs (amorphous silica and alumina) consume CH from hydration of cement, leading to formation of secondary (i.e., pozzolanic) C-S-H and other phases (e.g., calcium aluminate hydrates). Assuming that the degree of hydration of cement is not affected by SCMs, one can determine the degree of pozzolanic reaction of SCMs incorporated in the same paste based on experimentally determined reduction in CH content and reasonably formulated stoichiometry of pozzolanic reactions (Shi and Day, 2000; Pane and Hansen, 2005; Neithalath et al., 2009; Rodríguez et al., 2012). However, this assumption, albeit basic, is invalid due to the filler effect, dilution effect, as well as pozzolanic effect of SCMs. Similarly, calculating degree of hydration of blended cementitious materials directly from non-evaporable water content may also be problematic, because the influence of SCMs on the non-evaporable water content of the paste is not explicitly known (Weng et al., 1997; Escalante-Garcia, 2003). Some researchers proposed to determine the degree of reaction of SCMs first, and then to calculate the degree of hydration of cement mathematically. Lam et al. (2000) proposed a method which uses the degree of reaction of FA as a "cementing efficient factor" to calculate the effective water-to-cement ratio, based on which the degree of hydration of cement is estimated. Li et al. (Xiang et al., 2009) experimentally determined the degree of reaction of FA and the overall content of CH, from which the hydration degree of cement in the blended cement paste was derived based on the stoichiometric relationships proposed by Papadakis (1999). The accuracy of this type of method depends on the stoichiometric relationships used to describe the pozzolanic reactions and the experimental methods employed to characterize the degree of pozzolanic reaction. The degrees of reaction of SCMs are often determined by measuring the amount of unreacted SCMs using selective dissolution methods (Li et al., 1985; Ohsawa et al., 1985; Lam et al., 2000; Poon et al., 2001; Haha et al., 2010; Narmluk and Nawa, 2011). However, in some instances, the selective dissolution method may not be reliable. For instance, Haha et al. (2010) demonstrated that the EDTA-based selective dissolution methods underestimate the degree of reaction of FA due to the presence of amorphous phases.

Similarly other solvents-based selective dissolution methods cannot completely dissolve the hydrates and unreacted OPC phases, and thus lead to unpredictable errors. Image analysis methods (Haha et al., 2010; Deschner et al., 2013) have been also proposed for such estimations. These methods, which rely on analyses of BSE images, are not perfect, but considered to be more reliable than selective dissolution methods (Scrivener et al., 2015). Kocaba et al. (2012) showed that selective dissolution methods are also unreliable when used to determine the degree of reaction of GGBFS, and suggested an image analysis method to produce relatively more accurate estimates. BSE image analysis was also recommended as the best method to characterize the degree of reaction of GGBFS in a blended paste, because unreacted GGBFS particles have a unique gray level range in BSE images, thus making it easier to distinguish them from unhydrated cement and hydrates (Scrivener et al., 2015). In spite of these merits, BSE image analysis fails to characterize degree of reaction of SF, since SF particles can be smaller than the pixel size of a BSE image. In such cases, researchers have recommended using nuclear magnetic resonance (NMR) (Scrivener et al., 2015). However, NMR is not a widely and routinely available characterization tool in most of research institutes. BSE image analysis has another drawback, that is, it requires tedious and time consuming procedure to prepare samples and a large number of images to perform statistical analysis. Therefore, this method is more suitable for validation of other methods, rather than being used as the primary method for characterization of degree of reaction of SCMs (Scrivener et al., 2016).

Another class of methods used to characterize the hydration of binary blended cementitious materials can be called decoupling methods. These methods require only basic material characterization equipment (e.g., TGA and calorimetry) that are cost-efficient and widely available. They need neither time-consuming sample preparation nor complicated data interpretation. The obtained experimental results can be analyzed mathematically, based on theoretically-derived stoichiometric relations, to estimate degree of hydration of cement and degree of reaction of SCMs in a single step. Wang et al. (2004) assumed that the volumetric expansion coefficients of pozzolanic reaction products are equal to that of hydration products and established a set of functions to describe the reduction of porosity. The porosity and the CH content in the hardened blended cement paste were experimentally quantified, and the equations were solved to estimate both degree of hydration of cement and the degree of pozzolanic reaction of FA. A similar method was employed to study SF-cement system (Atlassi, 1995). These methods are straightforward and easy to use, thus are worthy to be further tested and refined.

Inspired by prior decoupling methods, this study proposes a novel decoupling method to simultaneously estimate the degree of hydration of cement and the degree of reaction of the SCM in binary pastes. SF, which is a relatively pure and homogeneous compound (amorphous silica content >90%), is selected as a representative example of SCM to demonstrate fundamental aspects of this decoupling method. The proposed method does not require determination of the degree of reaction of SF through selective dissolution or NMR. Instead, the hydrate (chemically bonded) water and CH contents of SF-cement pastes are expressed as functions of the degree of hydration of cement (α) and the degree of reaction of SF (α_{SF}), using well-established and validated stoichiometric relations. Since the aforementioned pair of contents can be determined using TGA, α, and α_{SF} can be estimated by solving an equation set (two equations of two unknowns). Validation of the method is provided using a separate and indirect porosity-based method.

EXPERIMENTS

Materials

Cement that satisfies the requirements of ASTM C150 for Type I portland cement was used in this study. Its engineering properties can be expressed by the initial setting time of 150 min, the final setting time of 180 min, 7 days compressive strength of 41 MPa and 28 days compressive strength of 57 MPa. The chemical composition of the cement, as expressed by percentages of oxides, is listed in **Table 1**. The mineral composition, in percentages of the four basic mineral phases and gypsum, calculated from modified Bogue calculations (Standard US., 2018) is listed in **Table 2**. Besides, Blain surface area of the irregularly shaped cement particles is 360 m^2/kg, and its density is 3.15 g/cm^3. Condensed SF, of which 93% is amorphous silica, was used in this study. Its chemical composition is shown in **Table 1**. The mean single particle diameter of the SF is 0.1 μm and the average density is 2.2 g/cm^3.

Sample Preparation

Plain cement pastes were prepared with water-to-cement ratios (*w/c*) of 0.3, 0.4, and 0.5. In binary cementitious materials, weight-based substitution levels of cement by SF were 5 and 10%, respectively. In blended pastes, the water-to-binder ratio (*w/b*) was kept constant at 0.4. The six pastes were named PC03, PC04, PC05, SF00 (identical to PC04), SF05, and SF10, respectively. To prepare the pastes, raw materials were mixed using a vertical-axis pot mixer. Water was poured into the pot, then cementitious materials were added slowly while the blades were rotating. In the case of blended pastes, SF was added first, followed by cement. The subsequent mixing process consisted of a 3-min low speed mixing, a half-minute pause, and a 2-min high-speed mixing. After mixed, fresh mixtures were cast into ϕ15 mm plastic tubes, and two ends of the tubes were sealed to prevent moisture exchange and carbonation. Sealed specimens were stored at 23 ± 2°C until specific ages for characterization. Concerned ages included 1, 3, 7, 28, 60, and 120 days.

Thermogravimetric Analysis

Thermogravimetric analysis (TGA) was used to determine the contents of hydrate water and CH in the plain and blended cement pastes. At specific ages, small pieces were firstly sawed off from the paste specimens, and then ground into fine particles (<63 μm) in a CO_2-free chamber. Hydration was arrested using isopropanol [solvent exchange (Winnefeld et al., 2016)] for 15 min followed by ether flushing. After drying, about 40 mg of the resulting powder sample was analyzed by recording the weight while heating the sample up from room temperature

TABLE 1 | Chemical composition of the ordinary portland cement (%).

	CaO	SiO_2	Al_2O_3	Fe_2O_3	SO_3	MgO	Equivalent Na_2O	Free CaO	LOI
Cement	64.05	20.37	5.37	3.18	2.09	2.35	0.52	1	1.05
SF	0.42	93.02	0.69	1.07	0.41	1.21	0.65	-	1.03

TABLE 2 | Mineral composition of the ordinary portland cement (%).

C_3S	C_2S	C_3A	C_4AF	$C\bar{S}H_2$
54.49	17.30	8.85	9.68	5.05

to 1,000°C at 10°C/min, in a TGA 5500 (TA Instruments). Nitrogen gas was chosen to maintain an inert atmosphere, and corundum was selected as the reference material. Contents of hydrate water and CH were calculated from the weight loss in the ranges of <550°C and 450–550°C, respectively (De Weerdt et al., 2011; Schöler et al., 2015; Adu-Amankwah et al., 2017). Hydrate water content is normalized by dehydrated sample weight at 550°C, to obtain the hydrate water amount per gram of binder (w_H). In plain cement paste, w_H is used to calculate the degree of hydration of cement (α), that is, $\alpha = w_H/0.23$. CH content is normalized by the dried sample weight before TGA, to calculate m_{CH}, that is, weight percentage of CH in dry paste sample (anhydrous binder and hydration products). Note that the abovementioned temperature ranges are rough descriptions, and the exact temperature boundaries for temperature intervals were determined by the tangent method from the corresponding derivative thermogravimetric (DTG) curve. The standard deviations of five independent TGA analyses at all tested ages were not larger than 0.15% for m_H and 0.2% for m_{CH}. It is also worth noting that the adopted drying method may lead to overestimation of hydrate water content, and, thus, degree of hydration. However, this method is consistent with current practice of characterization (Scrivener et al., 2016), and has high enough reliability for the purpose of estimating, rather than accurately determining, the degree of hydration of cement and the degree of reaction of silica fume in a blended cement paste.

Mercury Intrusion Porosimetry

Mercury intrusion porosimetry (MIP) was employed to determine the capillary porosity (ϕ), pore size distribution (PSD) curves, and skeletal density ($\rho_p^{skeletal}$, g/cm^3) of hydrated pastes, for parameter derivation and validation of the decoupling method. At all concerned ages, cuboid samples with the smallest dimension smaller than 5 mm were sawed off from the specimen. Hydration suspension and drying were performed according to the solvent replacement drying procedure suggested by Aligizaki (2005). For pore size calculations based on Washburn equation (Washburn, 1921), the contact angle between mercury and hardened cement paste was chosen as 130° and the mercury surface tension of 480 mN/m was used. The abovementioned critical specimen size, drying method, and theoretical parameters, as well as other operational parameters, were all selected based on a general discussion on utilization of MIP in concrete technology (Ma, 2014). A Micromeritics AutoPore IV 9500 was used for MIP measurements. The instrument has a maximum applicable pressure of 210 MPa, which corresponds to a minimum detectable pore diameter of approximately 6 nm, when the selected contact angle and surface tension are used for pore size calculation. It is worth noting that, although MIP is an inappropriate method for determining the pore size distribution of cement-based materials because of the well-known ink-bottle effect (Moro and Böhni, 2002), it is useful to provide threshold diameters, intrudable pore volume measurements, as well as overall comparisons of pore structures (finer or coarser) (Diamond, 2000). Only physically meaningful parameters from MIP were used for derivations and validations in this study.

RESULTS AND ANALYSIS

Parameters Related to Cement Hydration

Since pozzolanic reaction of SF consumes CH from cement hydration to form secondary reaction product, it is essential to know how CH is formed and consumed. Cement hydration is so complex that no agreement on how it takes place has been reached. Therefore, in this study, CH formation during cement hydration is estimated from experimental results. Another key parameter, volume of hydrates generated when one unit volume of cement is completely hydrated (κ_h), is also derived from experimental results. Derivations of these two parameters from TGA and MIP results are presented in this section. TGA results (i.e., α and m_{CH}) and MIP results (i.e., ϕ and $\rho_p^{skeletal}$) of the three plain cement pastes at different ages—used for the derivations—are shown in **Table 3**. **Figure 1** shows a comparison of α characterized in this study and those predicted (at 23°C, consistent with the curing temperature in this study) by a model developed by Riding et al. (2013). Riding's model was developed through regression on degrees of hydration of 7 types of portland cements in various pastes (various *w/c* ratios at 18 different ages), and, thus, captures the effects of cement composition, fineness, and *w/c* on hydration kinetics. This comparison, to a large extent, shows the reliability of the TGA method used in this study in estimating the degree of hydration of cement.

m_{CH} and $\rho_p^{skeletal}$ take only solid phases (anhydrous cement and hydration products) into account, and the fractions of anhydrous cement and hydration products in the solid phases are determined by α (regardless of *w/c*). Therefore, both m_{CH} and $\rho_p^{skeletal}$ should be functions of α. In **Figures 2**, **3**, m_{CH} and $\rho_p^{skeletal}$ are plotted against α. Two curves/lines are added to mark the global and high degree of hydration range trends. In **Figure 2**, it can be seen that m_{CH} slightly increases in the low-α range,

TABLE 3 | Experimental results of plain cement pastes.

Age (days)		1	3	7	28	60	120
PC03	α	0.28	0.43	0.52	0.61	0.65	0.68
	m_{CH}	0.149	0.165	0.188	0.205	0.217	0.227
	ϕ	0.261	0.198	0.184	0.142	0.122	0.114
	$\rho_p^{skeletal}$	2.464	2.355	2.308	2.255	2.206	2.219
PC04	α	0.33	0.51	0.63	0.7	0.72	0.75
	m_{CH}	0.196	0.208	0.217	0.236	0.245	0.250
	ϕ	0.337	0.283	0.251	0.202	0.182	0.158
	$\rho_p^{skeletal}$	2.448	2.304	2.275	2.219	2.136	2.092
PC05	α	0.36	0.56	0.67	0.73	0.79	0.81
	m_{CH}	0.203	0.215	0.227	0.239	0.249	0.258
	ϕ	0.386	0.329	0.301	0.238	0.212	0.176
	$\rho_p^{skeletal}$	2.454	2.301	2.241	2.081	2.087	2.082

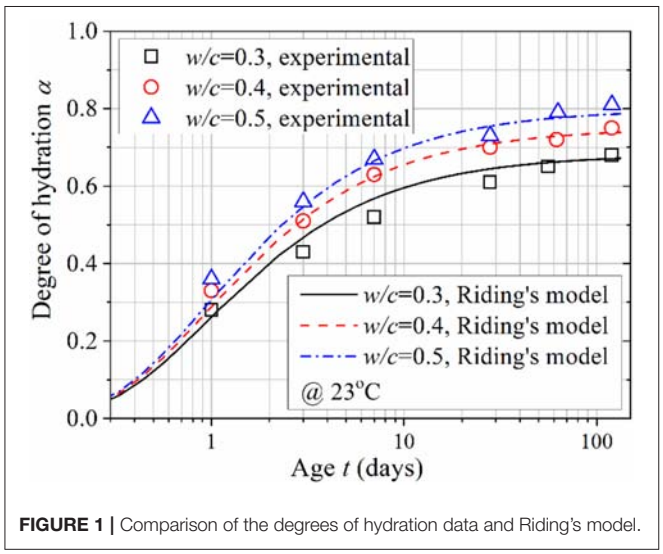

FIGURE 1 | Comparison of the degrees of hydration data and Riding's model.

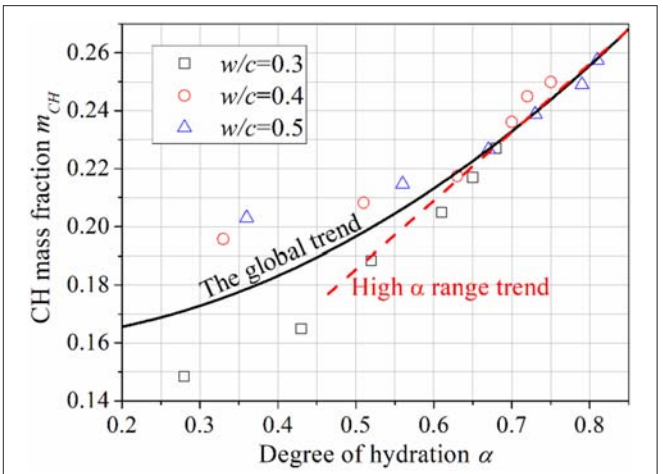

FIGURE 2 | Evolution of CH mass fraction following degree of hydration.

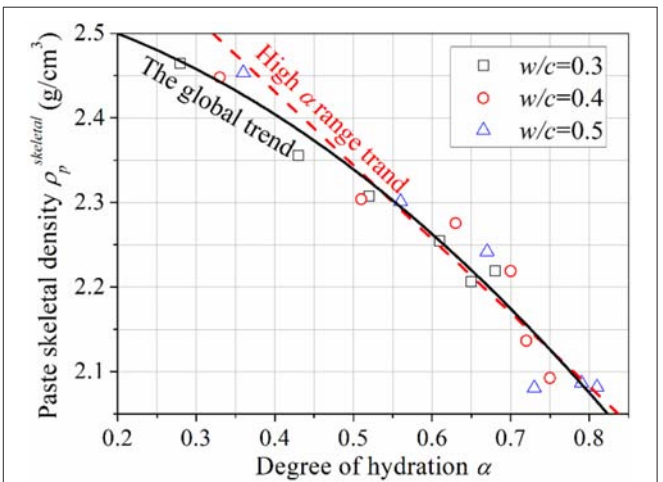

FIGURE 3 | Evolution of paste skeletal density following degree of hydration.

while gradually merging with the high-α range trend line—which shows a directly proportional relation between m_{CH} and α. As seen in **Figure 3**, the evolution of $\rho_p^{skeletal}$ has a similar trend: it decreases, slightly, with respect to α in low-α range, and then merges into a line where there is a negative constant ratio between these two parameters. The authors acknowledge that early age (or low-α range) data are affected by the rapid hydration of C_3A, so only data of age >3 days (or $\alpha > 0.5$) are selected for further analysis. It also implies that the method developed in this study is applicable for cementitious materials at later ages as opposed to early ages.

Provided 1 cm^3 (unit volume) of cement, and ignoring shrinkage, the volume of cement paste prepared with a specific w/c is

$$V_p = 1 + \rho_{cem} \cdot w/c \tag{1}$$

where ρ_{cem} is the density of cement. At a specific degree of hydration, α, the volume of anhydrous cement is

$$V_{anhydrous} = 1 - \alpha \tag{2}$$

The total volume of solid phases including anhydrous cement and hydrates can be calculated as

$$V_s = V_p \cdot (1 - \phi) \tag{3}$$

in which the volume of hydrates is

$$V_h = V_s - V_{anhydrous} \tag{4}$$

From m_{CH}, the volume fraction of CH in the solid phases can be calculated as

$$v_{CH}^s = m_{CH} \cdot \frac{\rho_p^{skeletal}}{\rho_{CH}} \tag{5}$$

where density of CH, $\rho_{CH} = 2.24$ g/cm^3. Thus, the volume of CH can be obtained as

$$V_{CH} = v_{CH}^s \cdot V_s \tag{6}$$

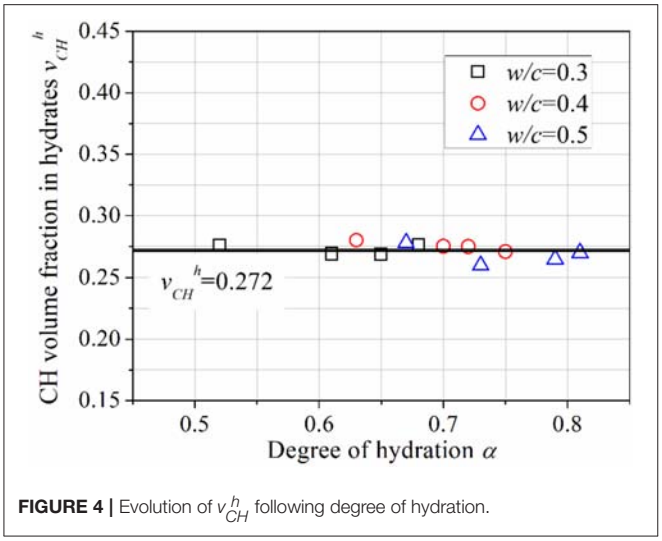

FIGURE 4 | Evolution of v_{CH}^h following degree of hydration.

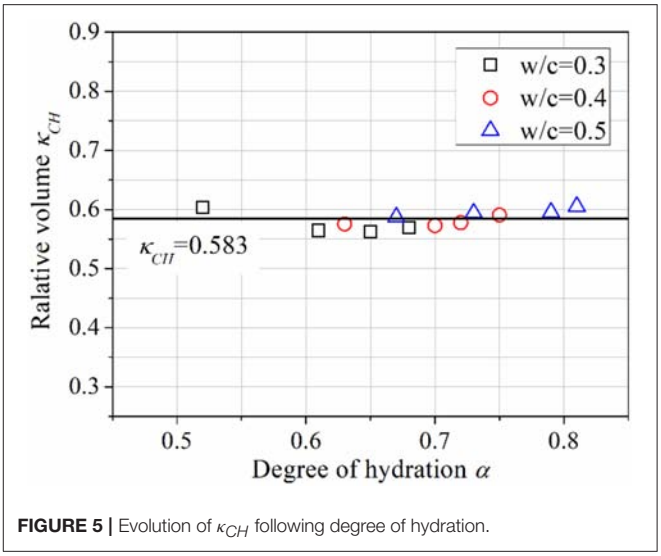

FIGURE 5 | Evolution of κ_{CH} following degree of hydration.

Based on V_{CH}, the volume fraction of CH in hydrates is calculated as

$$v_{CH}^h = \frac{V_{CH}}{V_h} \tag{7}$$

and the volume of CH generated when this unit volume of cement is completely hydrated can be determined as

$$\kappa_{CH} = \frac{V_{CH}}{\alpha} \tag{8}$$

To sum up, the above two parameters can be expressed as

$$v_{CH}^h = \frac{m_{CH} \cdot \rho_p^{skeletal}}{\rho_{CH}} \cdot \frac{(1-\phi)(1+\rho_{cem} \cdot w/c)}{(1-\phi)(1+\rho_{cem} \cdot w/c) - (1-\alpha)} \tag{9}$$

$$\kappa_{CH} = \frac{m_{CH} \cdot \rho_p^{skeletal} \cdot (1-\phi)(1+\rho_{cem} \cdot w/c)}{\rho_{CH} \cdot \alpha} \tag{10}$$

Using TGA and MIP results included in **Table 3**, v_{CH}^h and κ_{CH} are calculated, and plotted against α in **Figures 4, 5**, respectively. It can be seen that, in the high-α range, both v_{CH}^h and κ_{CH} are constants. After averaging, these two parameters are derived as $v_{CH}^h = 0.272$ and $\kappa_{CH} = 0.583$, respectively.

Given these two constants, the volume of hydrates when one unit volume of cement is completely hydrated, κ_h, can be obtained as $\kappa_h = \kappa_{CH}/v_{CH}^h = 0.583/0.272 = 2.14$. This deduced value of κ_h is consistent with the value used for developing the well-known Powers' model, that is, 2.13 (Sanahuja et al., 2007).

Reaction of SF in Binary Paste

In this study, it is assumed that the pozzolanic reaction of SF takes place according to Equation (11). This assumption has been adopted successfully in many simulations and calculations involving SF (Bentz, 2000; Bentz et al., 2000; Swaddiwudhipong et al., 2003; Yajun and Cahyadi, 2004).

$$S + 1.1\text{CH} + 2.8\text{H} \rightarrow \text{C}_{1.1}\text{SH}_{3.9} \tag{11}$$

According to Equation (11), when 1 g of amorphous silica is reacted, the mass of pozzolanic C-S-H produced is

$$\kappa_{r,S}^m = M_{PC-S-H}/M_S \tag{12}$$

where M_i represents the molecular weight of i in g/mol. Given that molecular weight of pozzolanic C-S-H $M_{PC-S-H} = 191.8$ g/mol (based on C-S-H stoichiometry shown in Equation 11) and that of silica $M_S = 60$ g/mol, $\kappa_{r,S}^m$ =191.8/60= 3.20 g/g reacted silica. The masses of consumed CH and water are $1.1M_{CH}/M_S = 1.36$ g/g reacted silica and $2.8M_H/M_S = 0.84$ g/g reacted silica, respectively. In the SF incorporated system, the increase in hydrate water equals the amount of water consumed, that is, 0.84 g/g reacted silica. When the reactant is SF rather than silica, the amounts of CH and H consumption should be multiplied by the glass phase content, GC_{SF}, while the total amount of solid products generated when 1 g of SF is totally reacted reads

$$\kappa_{r,SF}^m = \kappa_{r,S}^m \cdot GC_{SF} + (1 - GC_{SF}) \tag{13}$$

For the SF used in this study, $GC_{SF} = 93\%$, thus, $\kappa_{r,SF}^m$ = 3.20×0.93+(1–0.93) = 3.04 g/g reacted SF. One of the reactants in Equation (11), CH, is formed in cement hydration. Therefore, the net mass increase of reaction products when 1 g of SF is totally reacted can be calculated by subtracting the mass of consumed CH, i.e.,1.36 g/g reacted silica, from $\kappa_{r,SF}^m$, that is

$$\kappa_{r,SF}^{m\,\prime} = \kappa_{r,SF}^m - 1.36\,GC_{SF} \tag{14}$$

Substituting GC_{SF} into Equation (14), the calculations lead to $\kappa_{r,SF}^{m\,\prime}$ =1.78 g/g reacted SF, in which the increase in chemically bound hydrate water and gel water totals 0.78 g/g reacted SF. It should be noted that this describes the "undersaturated" state. If the reaction products are dried under 11%RH, gel water will evaporate, and $\text{C}_{1.1}\text{SH}_{3.9}$ transforms into $\text{C}_{1.1}\text{SH}_{2.0}$ (Bentz, 2000). Under such dry conditions, $\kappa_{r,S}^m$ =2.63 g/g reacted silica, and the consumed water is $0.9M_H/M_S$ =0.27 g/g reacted silica. Through

Equations (13, 14), the value of $\kappa_{r,SF}^{m\prime}$ =1.25 g/g reacted SF, in which the chemically bound water is 0.25 g/g reacted SF. To sum up, the complete reaction of 1 g SF (used in this study) under saturated condition needs 0.78 g water, in which 0.25 g transforms to chemically bound water, while 0.53 g to gel water or physically bound water.

When 1 cm^3 (unit volume) of silica is totally reacted, the volume of pozzolanic C-S-H is

$$\kappa_{r,S}^{v} = \frac{V_{PC-S-H}}{V_S} \tag{15}$$

where V_i represents the molar volume of i in cm^3/mol. Given that V_{PC-S-H} = 101.81 cm^3/mol, V_S = 27.27 cm^3/mol, V_{CH} = 33.1 cm^3/mol and V_H = 33.1 cm^3/mol, it can be calculated that $\kappa_{r,S}^{v}$ =101.81/27.27 = 3.73 cm^3/cm^3 reacted silica. The volume of consumed CH and water are $1.1V_{CH}/V_S$ = 1.34 cm^3/cm^3 reacted silica and 2.8 V_H/V_S = 1.85 cm^3/cm^3 reacted silica, respectively. When the reactant is SF rather than silica, calculations can be carried out in a similar way with that in mass calculations above. Thus, when 1 cm^3 (unit volume) of SF is totally reacted, the total volume of reaction products (including the inert residue and assuming that the residue has the same density as that of amorphous silica) is

$$\kappa_{r,SF}^{v} = \kappa_{r,S}^{v} \cdot GC_{SF} + (1 - GC_{SF}) \tag{16}$$

The net volume increase of reaction products, with respect to the volume of cement hydrates, is

$$\kappa_{r,SF}^{v\prime} = \kappa_{r,SF}^{v} - 1.34\, GC_{SF} \tag{17}$$

Substituting GC_{SF} = 93% into Equations (16, 17), it can be deduced that $\kappa_{r,SF}^{v}$ =3.54 cm^3/cm^3 reacted SF and $\kappa_{r,SF}^{v\prime}$ =2.29 cm^3/cm^3 reacted SF. The parameter $\kappa_{r,SF}^{v\prime}$ is higher than κ_h (2.14 cm^3/cm^3 hydrated cement), which implies that SF is more effective in filling capillary pores than cement at the same degree of hydration/reaction.

Decoupling Cement Hydration and SF Reaction

In section Parameters related to Cement Hydration, κ_{CH} has been deduced to be 0.583 cm^3/cm^3 hydrated cement. When 1 g of cement is totally hydrated, the mass of CH formed can be calculated as $\kappa_{CH}^{m} = \kappa_{CH} \cdot \rho_{CH}/\rho_{cem}$ = 0.415 g. Considering that 1 g of blended binder consists of m_{cem} g of cement and m_{SF} g of SF, and it is hydrated to a specific degree, in which the degree of hydration of cement is α and the reaction degree of SF is α_{SF}, the mass fraction of CH in dried solid phase (dried according to section Thermogravimetric Analysis) can be calculated as

$$m_{CH} = \frac{\kappa_{CH}^{m} m_{cem}\alpha - 1.36GC_{SF}m_{SF}\alpha_{SF}}{m_{cem}(1 + 0.23\alpha) + m_{SF}(1 + 0.27GC_{SF}\alpha_{SF})} \tag{18}$$

while the amount of hydrate water is

$$w_H = 0.23\alpha m_{cem} + 0.27GC_{SF}\alpha_{SF}m_{SF} \tag{19}$$

TABLE 4 | Results of TGA for SF blended pastes (w/b = 0.4).

Age (days)	SF replacement level					
	0 (SF00)		0.05 (SF05)		0.1 (SF10)	
	m_{CH}	w_H	m_{CH}	w_H	m_{CH}	w_H
1	0.155	0.090	0.141	0.085	0.139	0.086
3	0.198	0.126	0.180	0.123	0.168	0.126
7	0.218	0.141	0.189	0.142	0.175	0.142
28	0.230	0.158	0.199	0.158	0.182	0.148
120	0.260	0.169	0.218	0.172	0.202	0.160

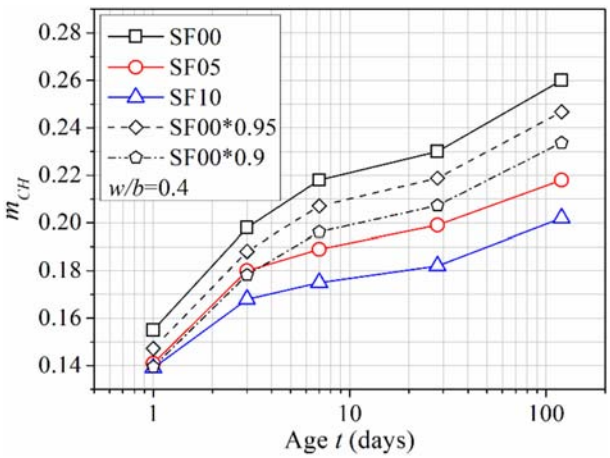

FIGURE 6 | Evolution and comparison of m_{CH} in SF blended pastes.

The two parameters, m_{CH} and w_H, of blended pastes at different ages were determined by TGA. The results are shown in **Table 4**. Note that SF00 here and PC04 in section Parameters Related to Cement Hydration are the same pastes (same cement and same w/c). However, they were prepared in two different batches—the first batch (PC04) for parameters derivation while the second batch (SF00) for comparison with SF blended pastes. The m_{CH} and w_H (or α) of SF00 in **Table 4** deviate more or less from that of PC04 in **Table 3** at the same ages. These limited derivations are attributed to variations in the actual curing conditions (i.e., temperature and humidity in the curing room). The evolution of m_{CH} is plotted in **Figure 6**. It can be seen that, the higher the SF replacement, the lower the m_{CH} at the same age. Even after considering the dilution effect resulted from the incorporation of SF, the m_{CH} in blended cement paste is still lower than that of reference plain cement paste. This should certainly be attributed to the consumption of CH in the pozzolanic reaction of SF.

Substituting m_{CH}, w_H (**Table 4**), m_{cem} (0.95 in SF05 and 0.90 in SF10) and m_{SF} (0.05 in SF05 and 0.10 in SF10) into Equations (18, 19), there are only two unknowns left in these two equations, i.e., the degree of hydration of cement, α, and the degree of reaction of SF, α_{SF}. Solving this equation set, α and α_{SF} can be determined simultaneously. The results have been plotted in **Figure 7**. It can be seen from **Figure 7** that the

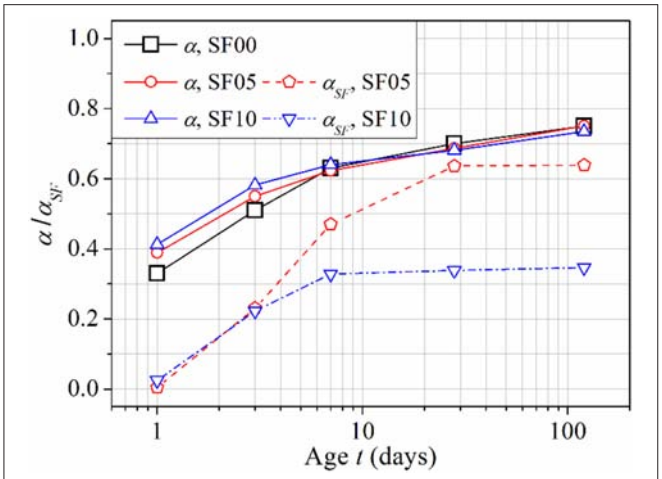

FIGURE 7 | Evolutions of α and α_{SF} in cement-SF blended pastes.

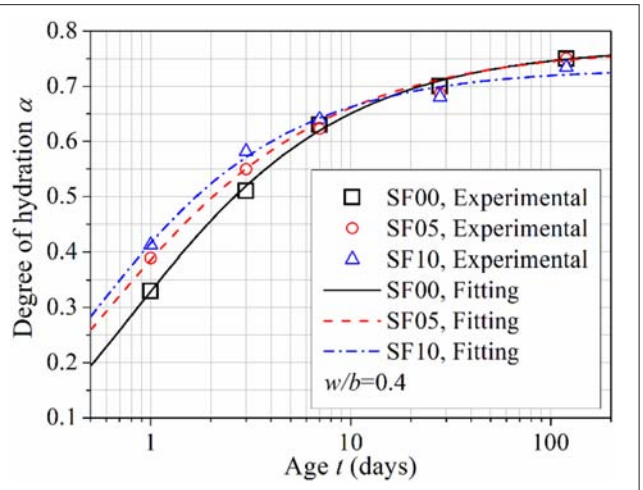

FIGURE 8 | Nonlinear fitting of hydration degree of cement (α) in blended pastes.

inclusion of SF accelerates hydration of cement at early ages, but suppresses cement hydration slightly at later ages. The higher the replacement ratio is, the more significant the effect will be. The early age acceleration can be explained by the dilution effect (constant *w/b* increases effective *w/c*) and the filler effect (fine SF particles increase nucleation sites for precipitation of hydration products), and the latter effect should be dominant. SF is beneficial to the early development of hydration and strength, and leads to the formation of denser microstructure as compared with that of plain cement paste. However, the dense microstructure may make it difficult for water to penetrate toward the unhydrated remnants of cement, which suppresses the late age hydration of cement (Neville, 1995). This dense microstructure formed through early ages could also hinder the reaction of agglomerated SF particles at later ages. This explains why α_{SF} almost stops increasing after 28 days, as shown in **Figure 7**.

Hydration Kinetics of Cement-SF Binary Pastes

In this study, the model developed by Riding et al. (2013) is adopted to describe the hydration kinetics of cement in plain cement paste. This model is expressed by Equation (20)

$$\alpha\,(t) = \alpha_u \cdot e^{-\left(\frac{\tau}{24\cdot t}\right)^{\beta}} \tag{20}$$

in which α_u is a physically meaningful parameter—ultimate degree of hydration, τ is the hydration time parameter in hours related to the induction period, β is the hydration slope parameter in the acceleration period, and t represents age of paste in days. In blended pastes, the overall degree of hydration of binder has two components, i.e., the degree of hydration of cement, α, and the degree of reaction of SF,α_{SF}. It is assumed that the degree of hydration of cement in the blended binder can also be described by the Riding's model. Equation (20) was used to fit the data points in **Figure 7**, as shown in **Figure 8**, and the obtained kinetic parameters are listed in **Table 5**. It is seen

TABLE 5 | Kinetic parameters in Equation (20) obtained from non-linear fitting.

Parameters	α_u	τ (hours)	β	R^2
SF00	0.7721	19.08	0.6561	0.9975
SF05	0.7701	13.66	0.6965	0.9949
SF10	0.7324	11.23	0.7503	0.9912

that the incorporation of SF tends to shorten the dormant stage (smaller τ) and further accelerate the acceleration stage (larger β), both of which imply accelerated hydration of cement at early ages. However, the long-term/ultimate degree of hydration of cement is suppressed (slightly smaller α_u).

To express hydration kinetics of the blended binders, the reaction kinetics of SF also need to be known. Rather than through separated fittings, the degree of reaction of SF (α_{SF}) is tied to the degree of hydration of cement (α) in the same blended paste through a reasonably established relation, shown in Equation (21), which is modified from Swaddiwudhipong et al.'s work (Swaddiwudhipong et al., 2003). It is assumed that, in a specific cement-SF binary paste at a particular status (or age), the amount of SF that can be reacted depends on the content of CH available for pozzolanic reaction. A parameter, μ_{CH}, is proposed to denote the ratio of reacted CH in pozzolanic reaction to total amount of CH form due to hydration of cement. The relation between α_{SF} and α can thus be expressed as

$$\alpha_{SF} = \frac{0.74\mu_{CH}\kappa_{CH}^{m}m_{cem}\alpha}{GC_{SF}m_{SF}} \tag{21}$$

where the constant 0.74 is the weight (g) of amorphous silica reacted with 1 g of CH during the pozzolanic reaction described by Equation (11). Theoretically, the parameter μ_{CH} should not be a constant, but a function of the total amount of CH generated by cement hydration (i.e., $\kappa_{CH}^{m}m_{cem}\alpha$) and the total amount

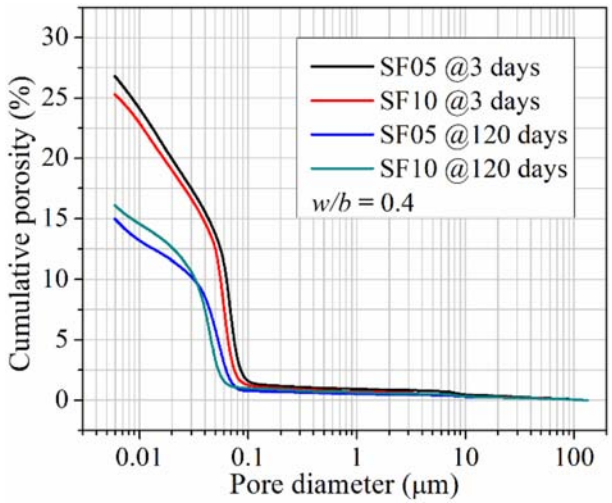

FIGURE 9 | Comparison of pore structure of SF incorporated cement pastes at early and late ages.

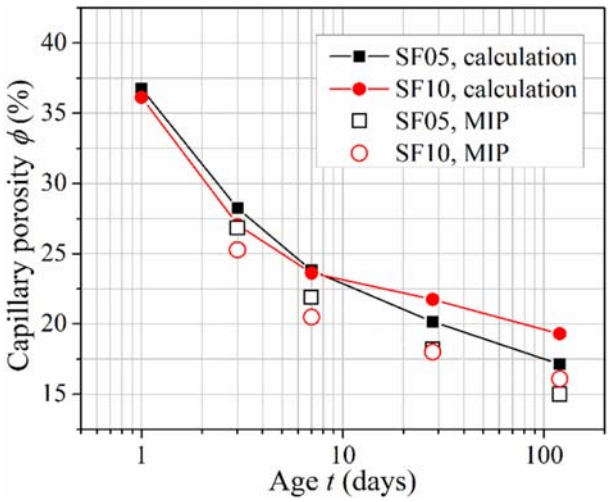

FIGURE 10 | Comparison of calculated and measured capillary porosity.

of amorphous silica (i.e., $GC_{SF}m_{SF}$). This function has been deduced empirically through surface fitting on experimental data (in **Figure 7**), as shown in Equation (22),

$$\mu_{CH} = 2.445 - 34.54m'_{CH} - 12.34m'_S + 152.7{m'_{CH}}^2 + 103.1m'_{CH}m'_S - 209.3{m'_{CH}}^3 - 307.6{m'_{CH}}^2m'_S \quad (22)$$

where $m'_{CH} = \kappa^m_{CH}\, m_{cem}\alpha$, $m'_S = GC_{SF}m_{SF}$, and $R^2 = 0.9966$ for the surface fitting. It is worth noting that Equation (22) is only valid for the specific case in this study, as μ_{CH} should also depends on the mean diameter and degree of agglomeration of SF particles.

Validation

Since no precise method has been available to simultaneously estimate the degree of hydration of cement (α) and degree of reaction of SF (α_{SF}) in a binary paste, an indirect method is employed to preliminarily validate the decoupling approach developed in this study. To do this, capillary porosity calculated from a modified Powers' model, based on the estimated α and α_{SF}, is compared with capillary porosity determined by MIP. Assuming paste volume equals summation of volumes of water, cement, and SF, and pore volume decreases due to expansions of solid hydration/reaction products of cement and SF, the modified Powers' model is derived as

$$\phi = \frac{w/b - \frac{\kappa_h - 1}{\rho_{cem}} \cdot m_{cem}\alpha - \frac{\kappa^v_{r,SF}{}' - 1}{\rho_{SF}} m_{SF}\alpha_{SF}}{w/b + \frac{m_{cem}}{\rho_{cem}} + \frac{m_{SF}}{\rho_{SF}}} \quad (23)$$

Substituting $\kappa_h = 2.14$, $\kappa^v_{r,SF}{}' = 2.29$, $\rho_{cem} = 3.15$ g/cm^3 and $\rho_{SF} = 2.2$ g/cm^3 into Equation (22), the modified Powers' model can be re-written as

$$\phi = \frac{w/b - 0.36m_{cem}\alpha - 0.59m_{SF}\alpha_{SF}}{w/b + 0.32m_{cem} + 0.45m_{SF}} \quad (24)$$

Chemical shrinkage is ignored in this derivation.

Pore structure of SF incorporated cement pastes, SF05 and SF10, are characterized by MIP. Their cumulative porosity curves at ages of 3 days and 120 days are shown in **Figure 9**. It can be seen that at both ages SF10 shows a finer pore structure, represented by smaller threshold pore diameter. At early ages (e.g., 3 days), higher SF content facilitates hydration of cement and results in lower porosity; while at later ages (e.g., 120 days), higher SF content suppresses further hydration of cement and leads to higher porosity. These findings of pore structure are consistent with the revealed degrees of hydration/reaction shown in **Figure 7**. Capillary porosities calculated from Equation (24) and measured by MIP are compared in **Figure 10**. The trends of evolution of porosities as well as the comparative relations between SF05 and SF10 revealed by calculations and measurements are consistent to each other, but the results of calculations are consistently higher than MIP results. On the one hand, Equation (24) ignores chemical shrinkage, which can lead to errors in capillary porosity calculation. On the other hand, MIP tends to underestimate, more or less, the capillary porosity due to limited maximum pressure and the existence of pores isolated from the interconnected capillary network (Ma and Li, 2013; Ma et al., 2014, 2015). Considering these two points, the deviation of calculated capillary porosities from MIP results seems to be reasonable.

DISCUSSION

A decoupling method which can simultaneously estimate the degree of hydration of cement and the degree of reaction of SF of a cement-SF binary cementitious material in a

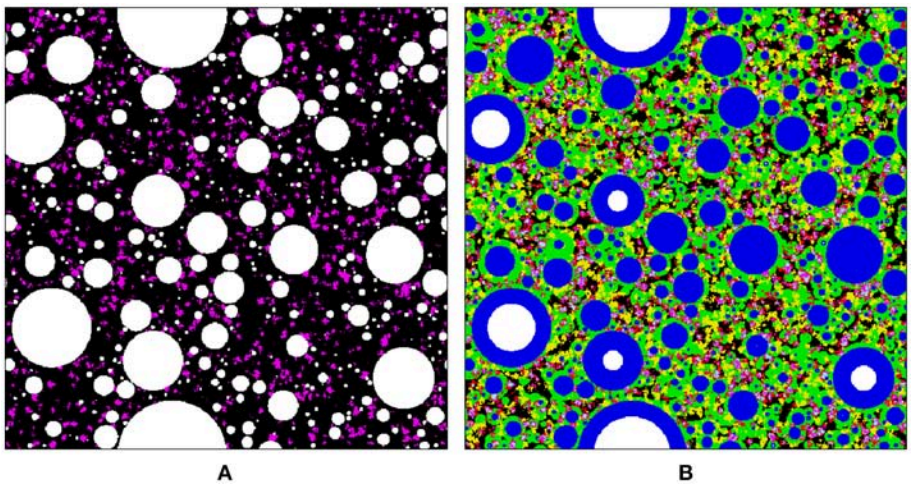

FIGURE 11 | Sketch of the microstructure of SF incorporated cement paste: **(A)** initial status; **(B)** mature paste. In the images, colors represent specific phases: white, anhydrous cement; blue, inner hydration products; green, outer C-S-H layer; yellow, crystalline hydrate (including CH); magenta, agglomerated SF particles; cyan/red, secondary C-S-H formed in pozzolanic reaction of SF.

blended paste is presented in section Results and Analysis. This method has been preliminarily and indirectly validated through comparison of capillary porosities calculated from the estimated degrees of hydration/reaction and those measured by MIP. A direct validation is desired in future study, through comparison of the estimated degree of reaction of SF with that characterized by NMR, according to the RILEM TC 238 report (Scrivener et al., 2015), as well as a comparison of the estimated degree of hydration of cement with that characterized by quantitative XRD and/or BSE image analysis. Once validated, this decoupling method will be a promising method for prompt estimations of degrees of hydration/reaction of blended cementitious materials, since it requires only widely available and inexpensive characterization tools (i.e., TGA and MIP) and simple data processing. It must be noted that the accuracy of this method is limited by the stoichiometric parameters of cement hydration, which are derived roughly from experimental results in this study, and the assumed pozzolanic reaction, that is, Equation (11). However, since the viability of the decoupling method has been proven, stoichiometric parameters of cement hydration and pozzolanic reaction derived from more reliable methods, for example, thermodynamic simulation and advanced characterizations, can be substituted into this model to improve its accuracy. Furthermore, this decoupling method can be readily extended to estimate the degree of reaction of other SCMs, for example, FA and GGBFS, provided the stoichiometric parameters of their pozzolanic reactions can be determined reliably.

The reaction kinetics of SF and the effect of SF on hydration of cement depend on the degree of agglomeration of SF particles (Meng et al., 2016) (out of other factors like mean particle size and mass percentage of silica). This is because SF particles can rarely be perfectly dispersed in cement paste; instead they form flocs as sketched in **Figure 11A.** If SF can be perfectly dispersed, its influence on cement hydration can be enhanced, and the degree of hydration of cement can be improved. The authors posit that it is reasonable to use Equations (20, 21) to describe the hydration of cement in cement-SF blended paste, and the relation between degree of hydration of SF and degree of hydration of cement, respectively. However, it is clarified that Equation (22) and the kinetic parameters listed in **Table 5** are only valid under the specific conditions of this study. Nevertheless, no regardless of how SF particles are distributed in cement paste, they can block the interconnected capillary network due to their small particle size/large surface area and high reactivity, leading to finer pore structures as sketched in **Figure 11B** and illustrated by the MIP results in **Figure 9**.

CONCLUSIONS

Widely available and inexpensive experimental methods, that is, TGA and MIP, are used to derive important stoichiometric parameters of cement hydration and to characterize the porosity, skeletal density, hydrate water, and CH contents of plain and blended cement pastes. Based on the experimental results, a decoupling method is developed to estimate the degree of hydration of cement and degree of reaction of SF in a cement-SF blended cement paste, using only TGA. A modified Powers' model is derived to calculate capillary porosities of blended pastes from the degrees of hydration/reaction of the pastes' components. The calculated porosities are compared to MIP results to validate the decoupling method, albeit indirectly. In addition to the development and validation of the decoupling method, the following conclusions can be drawn from this study:

(1) The incorporation of SF affects the hydration kinetics of cement in the binary binder, leading to lower ultimate degree of hydration, shorter dormant stage, and faster reaction in the acceleration stage. As a result, the degree

of hydration of cement in a blended paste is higher at early ages (e.g., 3 days) but lower at later ages (e.g., 120 days) than that in the reference plain cement paste. In the tested range of substitution levels of cement by SF (i.e., 5 and 10%), the higher the substitution level of SF, the more significant the effects on cement hydration kinetics.

(2) In a given blended paste, the degree of reaction of SF can be tied to the degree of hydration of cement through a secondary parameter. The parameter describes the rate of CH consumption in pozzolanic reaction. The higher the substitution level, the lower the degree of reaction of SF at a given age.

(3) A higher substitution level of SF, in a blended paste, results in lower porosity, and smaller threshold pore diameter at early ages (e.g., 3 days), but higher porosity at later ages (e.g., 120 days).

The decoupling method developed in this study is based on widely available characterization tools and simple data analysis, and does not necessitate the use of expensive instrumentation or time-consuming data-processing protocols. It is thus a promising method for prompt and convenient estimations of degrees of hydration/reaction of blended cementitious materials, especially when accurate estimates are not required. Methods recommended by RILEM TC 238 should be used for more accurate estimations. For future work, the degree of hydration of cement and the degree of reaction of SF, in relation to various processing parameters—for example, water-to-binder ratio, substitution level of SF, chemical composition and fineness of cement and SF, and curing temperature—will be characterized by validated and reliable methods. Based on collected datasets, advanced approaches, for example, machine learning, will be used to model and predict the hydration kinetics of blended cements.

AUTHOR CONTRIBUTIONS

All authors listed have made a substantial, direct and intellectual contribution to the work, and approved it for publication.

FUNDING

Financial support from National Science Foundation under 1761697 and 1661609 and from the Advanced Materials for Sustainable Infrastructure seed funding at Missouri University of Science and Technology is gratefully acknowledged. HS would also like to acknowledge the support from National Natural Science Foundation of China under 51520105012 and 51408365.

ACKNOWLEDGMENTS

Technical support from the Materials Research Center and the Center for Infrastructure Engineering Studies at Missouri University of Science and Technology is also acknowledged.

REFERENCES

Adu-Amankwah, S., Zajac, M., Stabler, C., Lothenbach, B., and Black, L. (2017). Influence of limestone on the hydration of ternary slag cements. *Cement Concrete Res.* 100, 96–109. doi: 10.1016/j.cemconres.2017.05.013

Aligizaki, K. K. (2005). *Pore Structure of Cement-Based Materials: Testing, Interpretation and Requirements*. Boca Raton, FL: CRC Press.

Atlassi, E. H. (1995). Nonevaporable water and degree of cement hydration in silica fume-cement systems. *Special Publication*. 153, 703–718.

Bentz, D. P. (2000). Influence of silica fume on diffusivity in cement-based materials: II. Multi-scale modeling of concrete diffusivity. *Cement Concrete Res.* 30, 1121–1129. doi: 10.1016/S0008-8846(00)00263-5

Bentz, D. P., Jensen, O. M., Coats, A. M., and Glasser, F. P. (2000). Influence of silica fume on diffusivity in cement-based materials: experimental, I., and computer modeling studies on cement pastes. *Cement Concrete Res.* 30, 953–962. doi: 10.1016/S0008-8846(00)00264-7

Bentz, D. P., Waller, V., and de Larrard, F. (1998). Prediction of adiabatic temperature rise in conventional and high-performance concretes using a 3-D microstructural model. *Cement Concrete Res.* 28, 285–297. doi: 10.1016/S0008-8846(97)00264-0

Bishnoi, S., and Scrivener, K. L. (2009). μic: a new platform for modelling the hydration of cements. *Cement Concrete Res.* 39, 266–274. doi: 10.1016/j.cemconres.2008.12.002

Damtoft, J. S., Lukasik, J., Herfort, D., Sorrentino, D., and Gartner, E. M. (2008). Sustainable development and climate change initiatives. *Cement Concrete Res.* 38, 115–127. doi: 10.1016/j.cemconres.2007.09.008

De Schutter, G., and Taerwe, L. (1995). General hydration model for Portland cement and blast furnace slag cement. *Cement Concrete Res.* 25, 593–604. doi: 10.1016/0008-8846(95)00048-H

De Weerdt, K., Been Haha, M., Le Saout, G., Kjellsen, K. O., Justnes, H., and Lothenbach, B. (2011). Hydration mechanisms of ternary Portland cements containing limestone powder and fly ash. *Cement Concrete Res.* 41, 279–291. doi: 10.1016/j.cemconres.2010.11.014

Deschner, F., Münch, B., Winnefeld, F., and Lothenbach, B. (2013). Quantification of fly ash in hydrated, blended Portland cement pastes by backscattered electron imaging. *J. Microsc.* 251, 188–204. doi: 10.1111/jmi.12061

Diamond, S. (2000). Mercury porosimetry: an inappropriate method for the measurement of pore size distributions in cement-based materials. *Cement Concrete Res.* 30, 1517–1525. doi: 10.1016/S0008-8846(00)00370-7

Escalante-Garcia, J. (2003). Nonevaporable water from neat OPC and replacement materials in composite cements hydrated at different temperatures. *Cement Concrete Res.* 33, 1883–1888. doi: 10.1016/S0008-8846(03)00208-4

Fagerlund, G. (2009). *Chemically Bound Water as Measure of Degree of Hydration: Method and Potential Errors: Division of Building Materials*. Lund Institute of Technology.

Fanghui, H., Qiang, W., and Jingjing, F. (2015). The differences among the roles of ground fly ash in the paste, mortar and concrete. *Construction Building Mater.* 93, 172–179. doi: 10.1016/j.conbuildmat.2015.05.117

Fanghui, H., Qiang, W., Mutian, L., and Mutian, M. (2016). Early hydration properties of composite binder containing limestone powder with different finenesses. *J. Thermal Analysis Calorimetry* 123, 1141–1151. doi: 10.1007/s10973-015-5088-9

Fernández, Á., Lothenbach, B., Cruz Alonso, M., and García Calvo, J. L., (2018). Thermodynamic modelling of short and long term hydration of ternary binders. Influence of Portland cement composition and blast furnace slag content. *Construc. Build. Mater.* 166, 510–521. doi: 10.1016/j.conbuildmat.2018.02.007

Gruyaert, E., Van den Heede, P., Maes, M., and De Belie, N. (2012). Investigation of the influence of blast-furnace slag on the resistance of concrete against organic acid or sulphate attack by means of accelerated degradation tests. *Cement Concrete Res.* 42, 173–185. doi: 10.1016/j.cemconres.2011.09.009

Haha, M. B., De Weerdt, K., and Lothenbach, B. (2010). Quantification of the degree of reaction of fly ash. *Cement Concrete Res.* 40, 1620–1629. doi: 10.1016/j.cemconres.2010.07.004

Juenger, M. C., and Siddique, R. (2015). Recent advances in understanding the role of supplementary cementitious materials in concrete. *Cement Concrete Res.* 78, 71–80. doi: 10.1016/j.cemconres.2015.03.018

Kishi, T., and Maekawa, K. (1996). Multi-component model for hydration heating of Portland cement. *Concrete Library JSCE* 28, 97–115.

Kocaba, V., Gallucci, E., and Scrivener, K. L. (2012). Methods for determination of degree of reaction of slag in blended cement pastes. *Cement Concrete Res.* 42, 511–525. doi: 10.1016/j.cemconres.2011.11.010

Kumar, A., Bishnoi, S., and Scrivener, K. L. (2012). Modelling early age hydration kinetics of alite. *Cement Concrete Res.* 42, 903–918. doi: 10.1016/j.cemconres.2012.03.003

Lam, L., Wong, Y., and Poon, C. (2000). Degree of hydration and gel/space ratio of high-volume fly ash/cement systems. *Cement Concrete Res.* 30, 747–756. doi: 10.1016/S0008-8846(00)00213-1

Lapeyre, J., and Kumar, A. (2018). Influence of pozzolanic additives on hydration mechanisms of tricalcium silicate. *J. Am. Ceramic Soc.* 101, 3557–3574. doi: 10.1111/jace.15518

Lee, B., Kim, G., Nam, J., Cho, B., Hama, Y., and Kim, R. (2016). Compressive strength, resistance to chloride-ion penetration and freezing/thawing of slag-replaced concrete and cementless slag concrete containing desulfurization slag activator. *Construct. Build. Mater.* 128, 341–348. doi: 10.1016/j.conbuildmat.2016.10.075

Li, S., Roy, D. M., and Kumar, A. (1985). Quantatative determination of pozzolanas in hydrated systems of cement or Ca(OH)2 with fly ash or silica fume. *Cement Concrete Res.* 15, 1079–1086. doi: 10.1016/0008-8846(85)90100-0

Lothenbach, B., Durdzinski, P., and De Weerdt, K. (2015). Thermogravimetric analysis, in *A Practical Guide to Microstructural Analysis of Cementitious Materials*, eds K. Scrivener, R. Snellings, and B. Lothenbach (Boca Raton, FL: CRC Press). doi: 10.1201/b19074-6

Ma, H. (2013). *Multi-Scale Modeling of the Microstructure and Transport Properties of Contemporary Concrete.* Doctoral dissertation, the Hong Kong University of Science and Technology.

Ma, H. (2014). Mercury intrusion porosimetry in concrete technology: tips in measurement, pore structure parameter acquisition and application. *J. Porous Mater.* 21, 207–215. doi: 10.1007/s10934-013-9765-4

Ma, H., Hou, D., and Li, Z. (2015). Two-scale modeling of transport properties of cement paste: Formation factor, electrical conductivity and chloride diffusivity. *Comp. Mater. Sci.* 110, 270–280. doi: 10.1016/j.commatsci.2015.08.048

Ma, H., Hou, D., Lu, Y., and Li, Z. (2014). Two-scale modeling of the capillary network in hydrated cement paste. *Construct. Build. Mater.* 64, 11–21. doi: 10.1016/j.conbuildmat.2014.04.005

Ma, H., and Li, Z. (2013). Realistic pore structure of Portland cement paste: experimental study and numerical simulation. *Comput. Concr.* 11, 317–336. doi: 10.12989/cac.2013.11.4.317

Meng, W., Lunkad, P., Kumar, K., and Khayat, K. (2016). Influence of silica fume and polycarboxylate ether dispersant on hydration mechanisms of cement. *J. Phys. Chem. C* 120, 26814–26823. doi: 10.1021/acs.jpcc.6b08121

Moro, F., and Böhni, H. (2002). Ink-bottle effect in mercury intrusion porosimetry of cement-based materials. *J. Colloid Interface Sci.* 246, 135–149. doi: 10.1006/jcis.2001.7962

Narmluk, M., and Nawa, T. (2011). Effect of fly ash on the kinetics of Portland cement hydration at different curing temperatures. *Cement Concrete Res.* 41, 579–589. doi: 10.1016/j.cemconres.2011.02.005

Neithalath, N., Persun, J., and Hossain, A. (2009). Hydration in high-performance cementitious systems containing vitreous calcium aluminosilicate or silica fume. *Cement Concrete Res.* 39, 473–481. doi: 10.1016/j.cemconres.2009.03.006

Neville, A. M. (1995). *Properties of Concrete: Fourth and final Edition.* London: Pearson Education Limited.

Ohsawa, S., Goto, A. S., and Daimon, M. (1985). Quantitative determination of fly ash in the hydrated fly ash - CaSO4●2H2O●Ca(OH)2 system. *Cement Concrete Res.* 15, 357–366. doi: 10.1016/0008-8846(85)90047-X

Pane, I., and Hansen, W. (2005). Investigation of blended cement hydration by isothermal calorimetry and thermal analysis. *Cement Concrete Res.* 35, 1155–1164. doi: 10.1016/j.cemconres.2004.10.027

Papadakis, V. G. (1999). Effect of fly ash on Portland cement systems: Part, I. Low-calcium fly ash. *Cement Concrete Res.* 29, 1727–1736. doi: 10.1016/S0008-8846(99)00153-2

Poon, C. S., Kou, S. C., Wong, Y. L., and Wong, R. (2001). Rate of pozzolanic reaction of metakaolin in high-performance cement pastes. *Cement Concrete Res.* 31, 1301–1306. doi: 10.1016/S0008-8846(01)00581-6

Powers, T. C., and Brownyard, T. L. (1946). "Studies of the physical properties of hardened portland cement paste," in *American Concrete Institute Journal Proceedings*, 43, 101–132.

Qiang, W., Mengxiao, S., and Dengquan, W. (2016). Contributions of fly ash and ground granulated blast-furnace slag to the early hydration heat of composite binder at different curing temperatures. *Adv. Cement Res.* 28, 320–327. doi: 10.1680/jadcr.15.00077

Riding, K. A., Poole, J. L., Folliard, K. J., Juenger, M. C. G., and Schindler, A. K. (2013). Modeling hydration of cementitious systems. *ACI Mater. J.* 109, 225–234. doi: 10.14359/51683709

Rodríguez, E. D., Bernal, S. A., Provis, J. L., and Pay,á, J. (2012). Structure of Portland cement pastes blended with sonicated silica fume. *J. Mater. Civil Eng.* 24, 1295–1304. doi: 10.1061/(ASCE)MT.1943-5533.0000502

Sanahuja, J., Dormieux, L., and Chanvillard, G. (2007). Modelling elasticity of a hydrating cement paste. *Cement Concrete Res.* 37, 1427–1439. doi: 10.1016/j.cemconres.2007.07.003

Schneider, M., Romer, M., Tschudin, M., and Bolio, H. (2011). Sustainable cement production—present and future. *Cement Concrete Res.* 41, 642–650. doi: 10.1016/j.cemconres.2011.03.019

Schöler, A., Lothenbach, B., Winnefeld, F., and Zajac, M. (2015). Hydration of quaternary Portland cement blends containing blast-furnace slag, siliceous fly ash and limestone powder. *Cement Concrete Composites* 55, 374–382. doi: 10.1016/j.cemconcomp.2014.10.001

Scrivener, K., Snellings, R., and Lothenbach, B. (2016). "Electron microscopy," *in A Practical Guide to Microstructural Analysis of Cementitious Materials,* eds K. Scrivener, R. Snellings, and B. Lothenbach (Boca Raton, FL: CRC Press), 351–418.

Scrivener, K. L., Lothenbach, B., De Belie, N., Gruyaert, E., Skibsted, J., Snellings, R., et al. (2015). TC 238-SCM: hydration and microstructure of concrete with SCMs - State of the art on methods to determine degree of reaction of SCMs. *Mater. Struct.* 48, 835–862. doi: 10.1617/s11527-015-0527-4

Shi, C., and Day, R. L. (2000). Pozzolanic reaction in the presence of chemical activators: Part, I. Reaction kinetics. *Cement Concrete Res.* 30, 51–58. doi: 10.1016/S0008-8846(99)00205-7

Snellings, R. (2015). "X-ray powder diffraction applied to cement," in *A Practical Guide to Microstructural Analysis of Cementitious Materials*, eds K. Scrivener, R. Snellings, and B. Lothenbach (Boca Raton, FL: CRC Press), 107–176. doi: 10.1201/b19074-5

Standard US. (2018). *ASTM C150/ C150M-18 Standard Specification for Portland Cement.* West Conshohocken, PA: ASTM International. Available online at: www.astm.org

Swaddiwudhipong, S., Wu, H., and Zhang, M. (2003). Numerical simulation of temperature rise of high-strength concrete incorporating silica fume and superplasticiser. *Adv. Cement Res.* 15, 161–169. doi: 10.1680/adcr.2003.15.4.161

van Breugel, K. (1995a). Numerical simulation of hydration and microstructural development in hardening cement-based materials: (I) theory. *Cement Concrete Res.* 25, 319–331. doi: 10.1016/0008-8846(95)00017-8

van Breugel, K. (1995b). Numerical simulation of hydration and microstructural development in hardening cement-based materials: (II) applications. *Cement Concrete Res.* 25, 522–530. doi: 10.1016/0008-8846(95)00041-A

Wadsö, L., Winnefeld, F., Riding, K. A., Sandberg, P. (2015). "Calorimetry," in *A Practical Guide to Microstructural Analysis of Cementitious Materials*, eds K. Scrivener, R. Snellings, and B. Lothenbach (Boca Raton, FL: CRC Press), 37–74. doi: 10.1201/b19074-3

Wang, A., Zhang, C., and Sun, W. (2004). Fly ash effects: II. The active effect of fly ash. *Cement Concrete Res.* 34, 2057–2060. doi: 10.1016/j.cemconres.2003.03.001

Wang, D., Zhou, X., Meng, Y., and Chen, Z. (2017). Durability of concrete containing fly ash and silica fume against combined freezing-thawing and sulfate attack. *Construct. Build. Mater*. 147, 398–406. doi: 10.1016/j.conbuildmat.2017.04.172

Washburn, E. W. (1921). The dynamics of capillary flow. *Phys. Rev*. 17, 273–283. doi: 10.1103/PhysRev.17.273

Weng, J. K., Langan, B., and Ward, M. (1997). Pozzolanic reaction in Portland cement, silica fume, and fly ash mixtures. *Can. J. Civil Eng.* 24, 754–760. doi: 10.1139/l97-025

Winnefeld, F., Scholer, A., and Lothenbach, B. (2016). "Sample Preparation," in *A Practical Guide to Microstructural Analysis of Cementitious Materials,* eds K. Scrivener, R. Snellings, and B. Lothenbach (Boca Raton, FL: CRC Press), 1–36.

Xiang, L., Peiyu, Y., and Aruhan. (2009). Assessment method of hydarion degree of cement in complex binder based on the calcium hydroxide content. *J. Chinese Ceramic Soc*. 37, 1–5.

Yajun, J., and Cahyadi, J. (2004). Simulation of silica fume blended cement hydration. *Mater. Struct*. 37, 397–404. doi: 10.1007/BF02479636

Yoo, S.-W., and Kwon, S.-J. (2016). Effects of cold joint and loading conditions on chloride diffusion in concrete containing GGBFConstruction, S., and Building *Materials*. 115, 247–255.

Zhang, Z., Wang, Q., and Chen, H. (2016). Properties of high-volume limestone powder concrete under standard curing and steam-curing conditions. *Powder Technol*. 301, 16–25. doi: 10.1016/j.powtec.2016.05.054

Conflict of Interest Statement: The authors declare that the research was conducted in the absence of any commercial or financial relationships that could be construed as a potential conflict of interest.

frontiers in Materials

ORIGINAL RESEARCH
published: 29 August 2019
doi: 10.3389/fmats.2019.00210

A Reactive Element Approach to Improve Fracture Healing in Metallic Systems

*Charles R. Fisher[1], John J. Mecholsky Jr.[2], Hunter B. Henderson[3], Michael S. Kesler[3] and Michele V. Manuel[2]**

[1] Naval Surface Warfare Center - Carderock Division, West Bethesda, MD, United States, [2] Department of Materials Science & Engineering, University of Florida, Gainesville, FL, United States, [3] Oak Ridge National Laboratory, Oak Ridge, TN, United States

Self-healing materials demonstrate the ability to close fractures and regain mechanical integrity after a catastrophic failure. However, self-healing in metals can be inhibited by the natural tendency for technologically-relevant metallic systems to oxidize on the crack surface. This study seeks to provide a thermodynamically-based mechanism to enhance healing capability at a solid/liquid interface through alloys designed with a reactive element alloying addition possessing a lower free energy of oxide formation than the parent element. In this study, model Sb-Cu and Sb-Zn systems enable comparisons between mechanistic behaviors based only on thermodynamic reactivity. Mechanical and microstructural investigation demonstrated that the more reactive alloying addition resulted in more effective bonding through increasing bond area and load-bearing capacity of the system. The improved bonding was attributed to improved wetting and reduction of the passivating surface oxide across an interface. The work has potential to advance self-healing capabilities in metallic systems through more appropriate alloy selection to enable improved healing.

Keywords: interfacial bonding, thermodynamic, chevron notch, liquid phase, self-healing

OPEN ACCESS

Edited by:
John L. Provis, University of Sheffield, United Kingdom

Reviewed by:
Amit Bandyopadhyay, Washington State University, United States
Amy Sarah Gandy, University of Sheffield, United Kingdom

***Correspondence:**
Michele V. Manuel
mmanuel@mse.ufl.edu

Specialty section:
This article was submitted to Structural Materials, a section of the journal Frontiers in Materials

Received: *22 November 2018*
Accepted: *14 August 2019*
Published: *29 August 2019*

Citation:
Fisher CR, Mecholsky JJ Jr, Henderson HB, Kesler MS and Manuel MV (2019) A Reactive Element Approach to Improve Fracture Healing in Metallic Systems. Front. Mater. 6:210. doi: 10.3389/fmats.2019.00210

INTRODUCTION

Engineered materials have suffered from the lack of healing or self-repair capabilities. However, material systems with intentionally designed self-healing characteristics have been developed (Wool, 2008; Ghosh, 2009; Zwaag et al., 2009). This design strategy has been employed most successfully in polymeric materials, where a variety of chemical pathways enable crack closure and bonding (White et al., 2001; Wu et al., 2008). For metallic systems, differences in thermodynamic forces compared to polymeric materials has required researchers to focus analysis on non-autonomous self-healing, typically through the introduction of thermal energy to enable the healing of the metallic system (Hager et al., 2010). A primary objective in this field has been to fabricate structural materials with self-repair capabilities. One example of healing in an aluminum-based, metal-matrix composite system was first described by Fisher et al. (2018). Using this technique, cracks are healed by a thermal treatment that creates a partially liquefied (specifically 20% liquid, 80% solid) matrix alloy. This elevated temperature also activates the shape memory behavior in the nickel-titanium (NiTi) shape-memory alloy (SMA) reinforcement, resulting a compressive force along the crack line during the healing phase. The compressive force across the crack surface, coupled with increased diffusion rates from the liquefied matrix, produces consolidation and

healing in the composite structure. Upon cooling, self-healed specimens were shown to result in a > 90% retention of strength (compared to the original) for an aluminum-copper (Al-Cu) based matrix longitudinally reinforced with continuous NiTi SMA wires (Fisher et al., 2018).

However, one significant obstacle to self-healing in metallic systems is the formation an oxide layer on free surfaces, inhibiting full crack bonding. The focus of this work is a thermodynamic-based mechanism to enable oxide dissolution for potential usage in liquid-assisted self-healing metals. This oxide dissolution process employs a reactive element alloying addition that possesses a more negative free energy of oxide formation than the base metal. When molten, this reactive element reduces the native oxide on the free surface at the crack, thus forming a strong chemical bond. **Figure 1** shows a schematic of this process, with predicted outcomes based on reactivity of the alloying element.

The approach of using a more reactive element in a liquid phase has been used in joining technologies such as liquid phase sintering (LPS) (Kingery, 1959; German et al., 2009) and transient liquid phase bonding (TLP) (Gale and Butts, 2004; Cook and Sorensen, 2011). Additionally, investigations into lead-free solders with rare-earth element additions to increase bond strength between metals and oxides have yielded positive results (Mavoori et al., 2002; Wu, 2004; Dong et al., 2008). The improvement in bond strength is attributed to a strong chemical bond created at the solid/liquid interface through reduction of the metal oxide by the rare-earth element addition, which possess a highly negative free energy of formation (Mavoori et al., 2002; Ramirez et al., 2002; Wu and Wong, 2006). Thus, the increase in interface strength is not the result of oxide prevention, but of a reduction of the surface oxide enabling chemical bonding at the interface.

With the goal of incorporating these technologies into a self-healing metallic system, this study seeks to prove this phenomenon in a model system to ensure scientific rigor before shifting the technique to structural self-healing systems. Two similar alloys are investigated, one with an alloying element more reactive than the base metal and one with an alloying element less reactive. A Chevron Notched Short Bar Sample (CNSB) sample geometry enables quantification of the strength of bonded and monolithic material (Mecholsky and Barker, 1984; O'Dowd et al., 1992). Additionally, analysis using metallography and fractography techniques will be used connect thermodynamic parameters to mechanical properties.

EXPERIMENTAL

Alloy Design

To evaluate the difference in the bonding behavior between a reactive and non-reactive element in a healing cycle, two binary alloy systems of the same base metal were selected which displayed the following three characteristics: (1) each system exhibited a low temperature eutectic phase transformation with similar eutectic temperatures and compositions, (2) each system had limited solubility of the reactive or non-reactive species (i.e., translating to the additive element strongly partitioning to the liquid phase during heat treatment), and (3) one binary should possess an alloying element with a higher free energy of oxide formation than the base element, while the other binary should possess an alloying element with a lower free energy of oxide formation than the base element. These criteria ensured that the alloys are microstructurally and mechanically similar, with variable alloying element reactivity.

After a thorough search of thermodynamic data and phase diagrams, antimony-copper (Sb-Cu) and antimony-zinc (Sb-Zn) were chosen as the model system to test the reactive element hypothesis as shown in **Figure 2**. For this study, Sb serves as the base element, while Cu is the thermodynamically less reactive and Zn is the more reactive addition based on the Gibbs energy change for the respective reaction as shown in **Figure 3A**.

The 4at% alloying element composition was selected by plotting the percent liquid and percent solute in liquid vs. temperature for a wide range of compositions, as shown in **Figure 3B** (ASM, 2012). The 4at% composition ensured there would be sufficient alloying element in the liquid phase during heat treatment while still maintaining a robust heat treatment temperature. Using the results of **Figure 3B**, each alloy's heat treatment temperature was chosen to be that which yielded 20% liquid and 80% solid to minimize liquid continuity and thus ensure structural stability during the healing cycle (Manuel, 2007). The desired intersections translate to heat treatment temperatures of 555°C for Sb-Zn and 574°C for Sb-Cu as shown in **Figure 3B**, and labeled on the phase diagrams in **Figure 2**. Alloys of each eutectic composition, Sb-37at% Cu and Sb-33at% Zn, were also prepared for testing to quantify the strength of the solidified liquid phase for comparative purposes.

Figure 4 shows the free energies of reaction for the three possible reactions of Zn or Cu with Sb_2O_3 on a per-mole oxygen basis at the calculated heat treatment temperatures (Reed, 1971). The ΔG_0 values, as opposed to those used for the Ellingham diagram in **Figure 3A**, are adjusted to account for activity of the reactants since the compounds are assumed to be not in their standard states. Reactions with negative free energy are favorable, while those with positive energy are unfavorable. Thus, Zn should reduce Sb_2O_3 (to Sb metal and ZnO) at the heat treatment temperature and Cu should not, confirming the basis for choosing the alloys as the model system. This confirms the results from the original Ellingham diagram comparison of the relative reactivity of Zn, Sb, and Cu.

Experimental Procedure

A methodology based on interfacial plane-strain fracture toughness testing via the chevron-notch short bar (CNSB) technique (Chizhi et al., 1984; Mecholsky and Barker, 1984; Newman, 1984) was used to evaluate bonding effectiveness for each of the bonded and monolithic specimens. Fatigue pre-cracking was not necessary due to the brittle nature of the interface causing a sharp crack to be initiated at the tip of the chevron-shaped notch. A schematic of a representative CNSB specimen is found in **Figure 5A**. This geometry of the CNSB specimen fabricated a B/W ratio of 1.45 and an a_0/W ratio of 0.4.

The alloys were prepared by placing appropriate amounts of antimony (99.999% shot, Alfa Aesar) and copper (99.9% shot,

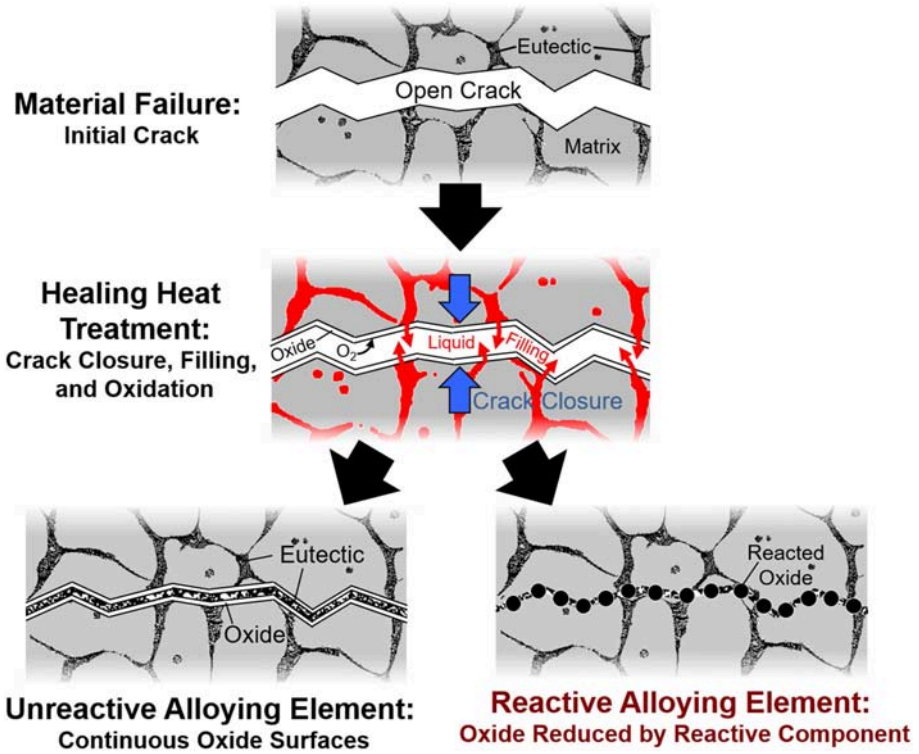

FIGURE 1 | Schematic of crack healing in alloy systems with reactive vs. non-reactive element additions. An alloying element more reactive than the base metal will reduce oxides at the interface, thus creating a strong, thermodynamically-favorable bond.

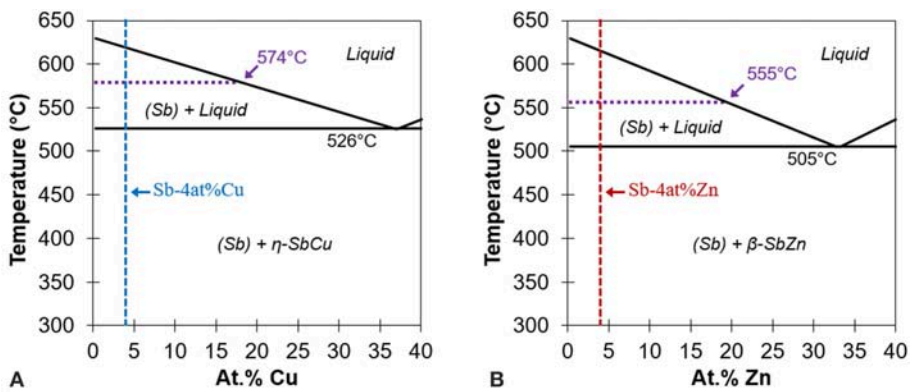

FIGURE 2 | Partial binary phase diagrams for **(A)** Sb-Cu and **(B)** Sb-Zn highlighting the high Sb region. Note the similarities between the two eutectic reactions. Adapted from ASM (2012).

Alfa Aesar) or zinc (99.99% shot, Alfa Aesar,) in boron nitride-coated graphite crucibles at 750°C until a liquid solution formed. Each alloy was cast into a coated graphite bar mold and allowed to air cool.

The eutectic composition alloys, Sb-37Cu and Sb-33Zn, were heat-treated at 400°C in air for 24 h to homogenize the as-cast microstructure before machining. The Sb-4Zn and Sb-4Cu alloys were heat-treated in air for 24 h at 555 and 574°C, respectively, to stabilize the microstructure and then subsequently air-cooled. All specimens were machined to a nominal size of 10 mm × 10 mm × 14 mm and ground to a 320-grit surface finish to reduce the possibility of surface cracks skewing results.

To evaluate bonding characteristics, a set of the Sb-4Zn and Sb-4Cu alloys were longitudinally cut in half and polished to a 4,000-grit finish on the cut surfaces. The polished surfaces of each half were pressed together and placed into a steel clamp covered with carbon paper to prevent any chemical reaction between the steel and the specimen during heat treatment as shown

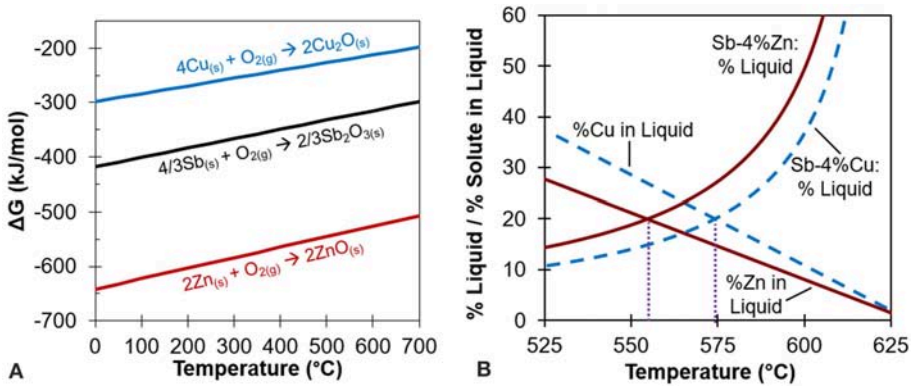

FIGURE 3 | (A) Ellingham diagram of oxides showing Cu, Sb, and Zn. Note how oxide formation of ZnO would preferentially occur over Sb_2O_3, but not Cu_2O over Sb_2O_3. Adapted from Reed (1971). **(B)** Percent liquid and percent solute in liquid at different temperatures for Sb-4at% Zn and Sb-4at% Cu. The crossing point for each alloy yields the healing temperature, 555°C for Sb-4Zn and 574°C for Sb-4Cu, as also shown in **Figure 2**. Adapted from ASM (2012).

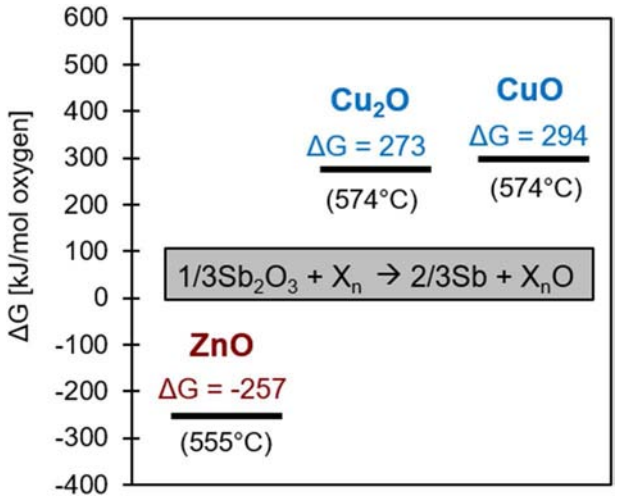

FIGURE 4 | Free energy diagram of the three possible ways Zn or Cu can reduce Sb_2O_3. The adjustment of ΔG_0, the reference free energy for each specific oxide of Cu or Zn, to ΔG considers thermodynamic activity for the 4 at% alloys at the healing temperature.

in **Figure 5B**. These specimens underwent the identical heat treatment as their monolithic counterparts (Sb-4Zn and Sb-4Cu alloys heat-treated in air for 24 h at 555 and 574°C, respectively) in order to compare bonded and monolithic specimens with the same microstructure as confirmed through optical microscopy.

After heat treatment, a chevron notch was machined into all Sb-Zn and Sb-Cu specimens as per ASTM Standard E-1304 (ASTM, 2008). For the bonded specimens, the notch was located along the bonded interface. During testing, it was found that a portion of the bonded samples did not have full connectivity in the chevron notch region, making the test inappropriate for true K_{1c} testing. However, the test is still useful for determining how well samples bonded and comparing to unbonded monolithic samples, thus maximum load during the test is used for comparison purposes. CNSB samples were tested on a TerraTek Model 4400A Fractometer. After testing, the specimens were also examined using optical microscopy (OM), scanning electron microscopy (SEM), and energy dispersive spectroscopy (EDS).

RESULTS

The experimental data from the fracture toughness testing, in terms of maximum load, is summarized in **Table 1**. For each specimen type the average with one standard deviation values are shown. Comparing the bonded samples to each other, the difference in normalized maximum bond strength is statistically significant to $p < 0.005$. The maximum load of the bonded specimens, normalized to the monolithic of their sample type, is shown in the bar chart in **Figure 6**.

Representative images of the fracture surfaces for both Sb-4Cu and Sb-4Zn bonded alloys are shown in **Figure 7**. The dashed lines show the location of the chevron notch, whereas the solid line represents the end of the bonded area over which the fracture occurred. For the Sb-4Cu alloys, the remaining, non-bonded, area is coated in a layer of Sb_2O_3 (as confirmed through EDS analysis) from the oxidation of Sb during heat treatment. It was noted that the Sb-Zn specimens bonded over a larger area than Sb-Cu specimens, as shown on the right axis of the chart in **Figure 6**.

Representative micrographs of Sb-4Cu and Sb-4Zn in **Figure 8** show that all alloys exhibit coarse microstructures; on average, the Sb-4Cu grains were approximately 500 μm and Sb-4Zn grains were approximately 700 μm. The coarseness of the microstructure likely contributes to the spread in bonding strength. The phases present at the grain boundaries of all the Sb-4Cu and Sb-4Zn monolithic and bond specimens was determined to be eutectic in nature based on the dual-phase morphology. As seen in **Figure 8**, the eutectic phases can be observed near the interface in both the Sb-Cu and Sb-Zn bond specimens. EDS analysis also revealed the presence of Zn and O at the bond interface, likely in the form of ZnO. Copper oxide was not found along the Sb-Cu bonded interface; instead, a Sb_2O_3 phase was found on the outer perimeter of the specimens.

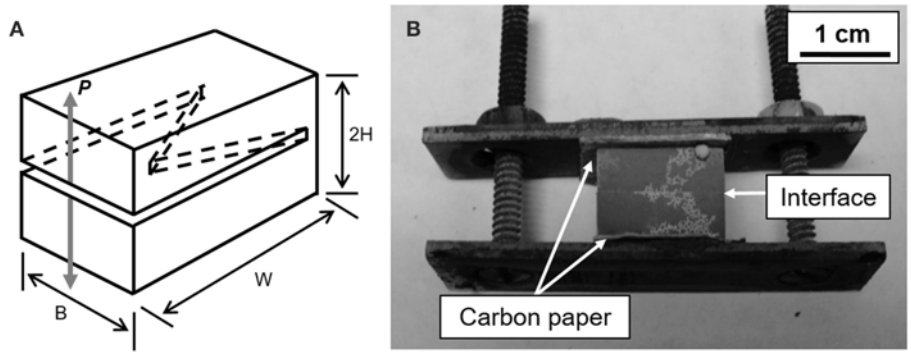

FIGURE 5 | (A) Schematic of chevron notch short bar specimen (CNSB). Adapted from Newman (1984). **(B)** Representative image of a Sb-4Zn bonded specimen showing the configuration after heat treatment.

TABLE 1 | Fracture toughness values of Sb-Cu and Sb-Zn chevron-notch short bar specimens.

Alloy	Short bar fracture toughness test maximum load [N]		
	Monolithic	Bond	Eutectic
Sb-Cu	133.5 ± 22.6	102.5 ± 25.3	124.1 ± 14.1
Sb-Zn	60.1 ± 14.8	70.6 ± 7.9	32.1 ± 14.1

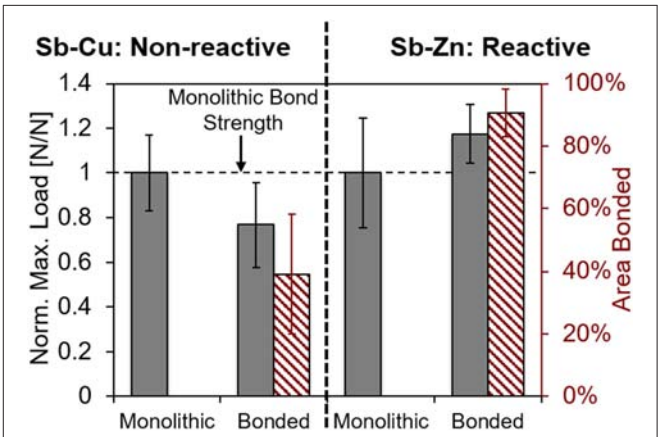

FIGURE 6 | Results of chevron notch testing showing maximum load of bonded Sb-Cu and Sb-Zn normalized to their respective monolithic maximum loads.

DISCUSSION

The behavior of bonded alloys Sb-4Cu and Sb-4Zn in the chevron notch testing is different in three important ways. First, during healing, the bond area reliably bonded to a much greater degree in the Sb-Zn samples as highlighted by the chart in **Figure 6** and the representative images in **Figure 7**. Second, the bonded Sb-Zn samples became stronger than their monolithic counterparts, whereas the bonded Sb-Cu samples became weaker after healing than their monolithic counterparts as shown by the chart in **Figure 6**. Finally, the crack propagation pathway through the specimen was distinct between the alloy types. For Sb-4Cu, the crack in the bonded specimens moved along the bond line, whereas for Sb-4Zn, the strong bond along the interface causes crack deflection away from the bonded interface and along the grain boundaries as shown in **Figure 8C**. A detailed description of the thermodynamic driving force to explain the crack deflection in Sb-4Zn follows. These interconnected effects are attributed to the thermodynamic driving force for oxide formation in the liquid phase during the bonding heat treatment.

Thermodynamic Driving Force

During the bonding heat treatment for the Sb-4Zn and Sb-4Cu alloys, the eutectic constituents (Sb + β-SbZn or Sb + η-SbCu) and a portion of primary Sb liquefied as the temperature was raised above the eutectic temperature. The main half-reactions of Sb, Zn and Cu with O_2 at the processing temperatures are shown in **Table 2**. Since Sb is known to oxidize readily at elevated temperatures, especially above 500°C (Russell and Lee, 2005), the newly liquefied eutectic phases in the Sb-Cu and Sb-Zn alloys would immediately begin to form Sb_2O_3 on the exposed surfaces, including the cut and polished interface in accordance with the Sb + O_2 half reaction shown in **Table 2**.

Figure 5B shows the small spheres of excess Sb_2O_3 formed on the outside of each specimen. These features were found on all of the bonded specimens after heat treatment. The presence of this surface oxide was noted on every Sb alloy and verified through EDS analysis.

To analyze the propensity for each reaction to occur, activities of each component in the reaction were considered by the following method. For Equation (1) below, in which two reactants (i and j) react to form two products (k and l), w, x, y and z are the coefficients. For this reaction, the free energy of formation can be calculated by Equation (2), in which ΔG_0 is the standard free energy of formation at temperature T, R is the gas constant, and a_w to a_z are the activities of each reaction component raised to their coefficients. Given this relationship and the relevant half-reactions, the free energies $Zn_{(l)}$ and $Cu_{(l)}$ reacting with Sb_2O_3 to form their oxides are calculated in **Table 3**. Activities of Zn and Cu with Sb are provided from literature

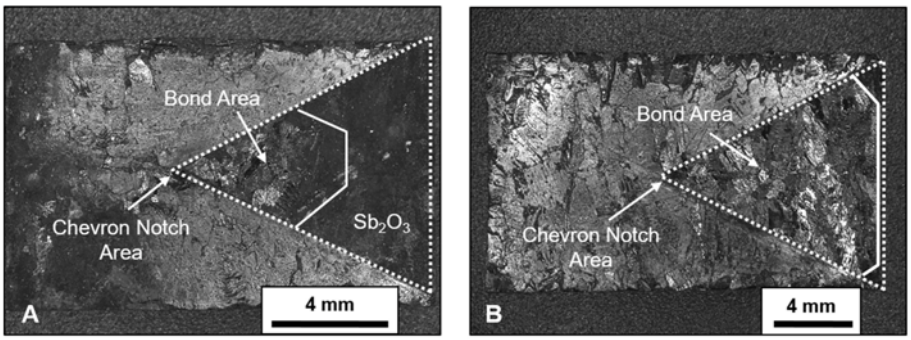

FIGURE 7 | Images of **(A)** Sb-Cu and **(B)** Sb-Zn showing top view the chevron notch fracture surface after bonding heat treatment and subsequent fracture toughness testing. The dashed lines show the entire area of the chevron notch, whereas the solid white line shows the end of the bond, and hence fracture, area.

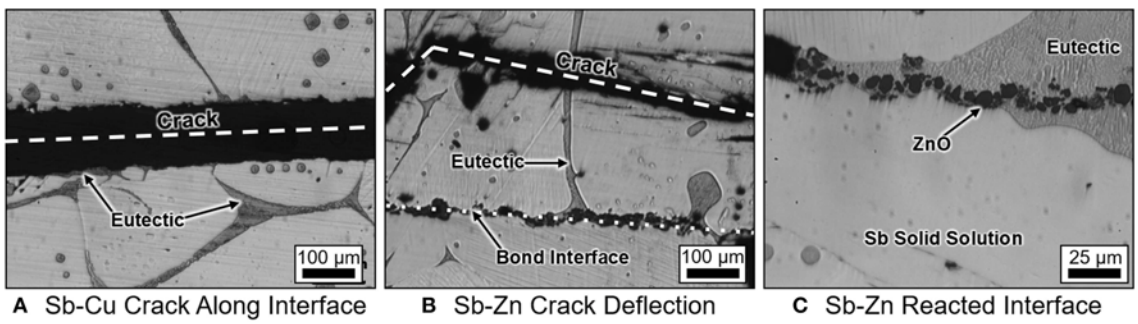

FIGURE 8 | Representative micrographs of **(A)** Sb-4at% Cu and **(B)** Sb-4at% Zn showing fracture line after bonding. Note that the Sb-Zn alloys had fractures occur away from the bonded interface. **(C)** Image of the Sb-4at% Zn bonded microstructure highlighting ZnO along the bond interface formed by the reduction of Sb_2O_3 by Zn.

TABLE 2 | Thermodynamic half-reactions of Sb, Zn, and Cu at relevant heat treatment temperatures.

Half reaction	Temp [K]	ΔG_0 [kJ/mol O_2]
$4/3Sb + O_2 \rightarrow 2/3Sb_2O_3$	828	−317
	847	−322
$2Zn + O_2 \rightarrow 2ZnO$	828	−531
$4Cu + O_2 \rightarrow 2Cu_2O$	847	−211
$2Cu + O_2 \rightarrow 2CuO$	847	−159

TABLE 3 | Free energies for the reaction of Sb_2O_3 with Zn and Cu at 555 and 574°C, respectively, according to Equation (2).

Reaction	ΔG_0 [kJ/mol]	Activity	ΔG [kJ/mol]
$Sb_2O_3 + 3Zn \rightarrow 3ZnO + 2Sb$	−314	$Zn_{(l)}$: 0.056	−257
		$Sb_{(l)}$: 0.8	
$Sb_2O_3 + 6Cu \rightarrow 3Cu_2O + 2Sb$	160	$Cu_{(l)}$: 0.063	274
		$Sb_{(l)}$: 0.8	
$Sb_2O_3 + 3Cu \rightarrow 3CuO + 2Sb$	238	$Zn_{(l)}$: 0.063	294
		$Sb_{(l)}$: 0.8	

(Li et al., 2007; Gierlotka and Jendrzejczyk-Handzlik, 2009). Activities for the oxides are assumed to be 1.

$$wi + xj \rightarrow yk + zl \tag{1}$$

$$\Delta G = \Delta G_0 + RT \ln \left(\frac{a_i^w a_j^x}{a_k^y a_l^z} \right) \tag{2}$$

Bonding Behavior

The ability to bond the separated halves of material was found to be dependent on the ability of the alloying element to reduce Sb_2O_3 at the interface. At the heat treatment temperatures (555°C for Sb-4Zn and 574°C for Sb-4Cu), the alloys have a liquid phase with 20at% solute available to react with oxygen. As seen in **Table 3**, $Zn_{(l)}$ is expected to react with Sb_2O_3 to form ZnO, as the reaction has a significantly negative free energy (Reed, 1971). However, since both Cu_2O and CuO possesses a greater Gibbs free energy of formation than Sb_2O_3, it is not thermodynamically favorable for Cu to reduce the Sb_2O_3 formed along the interface during heat treatment, as indicated by the positive free energy of formation.

This formation of ZnO creates a chemical bond, essentially welding the two halves of the specimen together during the heat treatment. Additionally, Zn reduces the Sb_2O_3 that normally would not melt at 555°C and thus inhibit bonding. Although it

was anticipated that the Sb-4Zn alloys would display an increase in interfacial fracture toughness over the monolithic value due to its increased propensity of forming a strong bond the interface, it was noted that the bonded samples did not deviate significantly from monolithic. Close inspection of the crack path in **Figure 8B** shows that the crack progressed through the bulk of the specimen as opposed to the strongly bonded interface. The low fracture toughness of the bulk facilitated this failure mechanism as it represented the "weakest link." It was also noted that often the crack path followed the eutectic constituent network, which was the least fracture resistant component of the system. The crack had to follow a more tortuous path not along the main bond line, possibly accounting for the slightly elevated maximum load.

There was also no physical evidence of Cu_2O bonding the halves together as there was ZnO in the Sb-4Zn alloys. The Sb_2O_3 in Sb-Cu bonded specimen passivated the crack surface, thereby preventing efficient bonding by the liquefied eutectic constituent. **Figure 7** shows the reduction of bonded surface area at the interface, which is quantified in **Figure 6**. It is suspected that the Sb_2O_3 would start forming at the exterior edges of the interface first and continue inward to the center of the specimen. Therefore, the bonded area of the interface would have only been in the center of each specimen where the Sb_2O_3 was not able to form. As the chevron notch was cut after the heat-treatment was completed, the bonded area was near the tip of the chevron notch, locating the crack front at the center of the specimen. This unexpected processing condition would explain why the fracture area for the Sb-Cu alloys was at the interior of each of the chevron notch specimens. The reduction in bond area could account for the lowered maximum load shown in **Figure 6**.

Another possible explanation for differences in bond area is a change in wettability. This phenomenon would correlate with previous studies in which a reactive element increased liquid metal wettability on metal oxide (Humenik and Kingery, 1954; Naidich, 1981; Peden et al., 1991; Finnis, 1996). This increase in wettability and bonding was also similar to results found by several groups working on lead-free solders (Mavoori et al., 2002; Ramirez et al., 2002; Wu and Wong, 2006; Dong et al., 2008). These groups have shown that small additions of rare-earth elements to lead-free solders enables interfacial bonding to several classes of materials including steels, oxides and carbides.

CONCLUSION

This paper illustrates how a reactive element alloying addition possessing a lower free energy of oxide formation than the base element can improve self-healing capability in a metallic system. Results from a model system showed an improvement in bonded area across a bonded interface, compared to non-reactive control, as well as crack deflection away from the healed crack. The improved bonding was attributed to the formation of stable oxides formed at the interface through the reduction of the passivate parent metal surface oxide, resulting in a strong chemical bond across the interface.

The results from the model Sb-Cu/Zn system show promise for using the reactive element technique within self-healing in structural metallic systems, especially for healing in an oxygen-containing environment. Additionally, this work could benefit powder additive manufacturing of metals, in which oxygen incorporation reduces toughness dramatically. However, there is a need for further investigation to better understand the effect of solute and liquid volume fractions on the process, as only 4% solute, 20% liquid, and 24 h heat treatment schedules were investigated. Additionally, this methodology must be demonstrated in more industrially relevant systems like Al and Mg with the addition of reactive alloying elements to find industrial application.

AUTHOR CONTRIBUTIONS

CF performed the majority of the material testing and manuscript writing. JM assisted with test program design and manuscript revision. HH and MK assisted with manuscript revisions and figure development. MM served as advisor to CF, HH, and MK in addition to project design and manuscript revision.

ACKNOWLEDGMENTS

The authors would like to gratefully acknowledge the support of the NASA Space Technology Research Opportunities for Early Career Faculty under grant number NNX12AQ42G and the Department of Defense and the Office of the Navy for their financial support through the Science, Mathematics, and Research for Transformation (SMART) Scholarship, a part of the National Defense Education Program.

REFERENCES

ASM (2012). *Alloy Phase Diagrams in ASM Handbook, Vol. 3*. Materials Park, OH: ASM International.

ASTM (2008). "Standard E 1304 - 97 (Reapproved 2008)," in Standard Test Method for Plane-Strain (Chevron-Notch) Fracture Toughness of Metallic Materials, eds. H. Okamoto, M. E. Schlesinger, and E. M. Mueller (West Conshohocken, PA: ASTM International), 585–590.

Chizhi, W., Maochan, Y., and Tzeguang, C. (1984). "An investigation on the method for determination of fracture toughness K_{Ic} of metallic materials with chevron-notched short-rod and short-bar specimens," in *Chevron-Notched Specimens: Testing and Stress Analysis, ASTM STP 855,* eds. J. H. Underwood, S. W. Freiman., and F. I. Baratta (Philidelphia, PA: American Society for Testing and Materials), 193–204. doi: 10.1520/STP32730S

Cook, G. O., and Sorensen, C. D. (2011). Overview of transient liquid phase and partial transient liquid phase bonding. *J. Mater. Sci.* 46, 5305—5323. doi: 10.1007/s10853-011-5561-1

Dong, W., Shi, Y., Xia, Z., Lei, Y., and Guo, F. (2008). Effects of trace amounts of rare earth additions on microstructure and properties of Sn-Bi-based solder alloy. *J. Electron. Mater.* 37, 982–991. doi: 10.1007/s11664-008-0458-8

Finnis, M. W. (1996). The theory of metal-ceramic interfaces. *J. Phy. Condensed Matter* 8, 5811–5836. doi: 10.1088/0953-8984/8/32/003

Fisher, C. R., Henderson, H. B., Kesler, M. S., Zhu, P., Bean, G. E., Wright, M. C., et al. (2018). Repairing large cracks and reversing fatigue damage in

structural metals. *Appl. Mater. Today* 13, 64–68. doi: 10.1016/j.apmt.2018.07.003

Gale, W. F., and Butts, D. A. (2004). Transient liquid phase bonding. *Sci. Technol. Weld. Join.* 9, 283–300. doi: 10.1179/136217104225021724

German, R. M., Suri, P., and Park, S. J. (2009). Review: liquid phase sintering. *J. Mater. Sci.* 44, 1–39. doi: 10.1007/s10853-008-3008-0

Ghosh, S. K. (2009). *Self-Healing Materials: Fundamentals, Design Strategies, and Applications*. Hoboken, NJ: Wiley-VCH. doi: 10.1002/9783527625376

Gierlotka, W., and Jendrzejczyk-Handzlik, D. (2009). Thermodynamic description of the Cu–Sb binary system. *J. Alloys Comp.* 484, 172–176. doi: 10.1016/j.jallcom.2009.05.056

Hager, M. D., Greil, P., Leyens, C., Zwaag, S. V. D., and Schubert, U. S. (2010). Self-healing materials. *Adv. Mater.* 22, 5424–5430. doi: 10.1002/adma.201003036

Humenik, J. M., and Kingery, W. D. (1954). Metal-ceramic interactions: III, surface tension and wettability of metal-ceramic systems. *J. Am. Ceram. Soc.* 37, 18–23. doi: 10.1111/j.1151-2916.1954.tb13972.x

Kingery, W. D. (1959). Densification during sintering in the presence of a liquid phase - 1. theory. *J. Appl. Phy.* 30:301 doi: 10.1063/1.1735155

Li, J.-B., Record, M.-C., and Tedenac, J.-C. (2007). A thermodynamic assessment of the Sb–Zn system. *J. Alloys Comp.* 438, 171–177. doi: 10.1016/j.jallcom.2006.08.035

Manuel, M. V. (2007). *Design of a biomimetic self-healing alloy composite* (Ph.D), Evanston, IL: Northwestern University.

Mavoori, H., Ramirez, A. G., and Jin, S. (2002). Lead-free universal solders for optical and electronic devices. *J. Electron. Mater.* 31, 1160–1165 doi: 10.1007/s11664-002-0005-y

Mecholsky, J. J., and Barker, L. M. (1984). "A chevron-notched specimen for fracture toughness measurements of ceramic-metal interfaces," in *Chevron-Notched Specimens: Testing and Stress Analysis, ASTM STP 855,* eds. J. H. Underwood, S. W. Freiman & F. I. Baratta (Philadelphia: American Society for Testing and Materials), 324–336. doi: 10.1520/STP32738S

Naidich, J. V. (1981). The wettability of solids by liquid metals. progress in surface and membrane science. *Prog. Surf. Membr. Sci.* 14, 353–484. doi: 10.1016/B978-0-12-571814-1.50011-7

Newman, J. C. Jr. (1984). "A review of chevron-notched fracture specimens," in *Chevron-Notched Specimens: Testing and Stress Analysis, ASTM STP* 855, eds. J. H. Underwood, S. W. Freiman and F. I. Baratta. (Philadelphia: American Society for Testing and Materials), 5–31. doi: 10.1520/STP32719S

O'Dowd, N. P., Stout, M. G., and Shih, C. F. (1992). Fracture toughness of alumina-niobium interfaces: experiments and analyses. *Philos. Mag. A* 66, 1037–1064. doi: 10.1080/01418619208248005

Peden, C. H. F., Kidd, K. B., and Shinn, N. D. (1991). Metal/metal-oxide interfaces: a surface science approach to the study of adhesion. *J. Vacuum Sci. Technol. A* 9:1518. doi: 10.1116/1.577656

Ramirez, A. G., Mavoori, H., and Jin, S. (2002). Bonding nature of rare-earth containing lead-free solders. *Appl. Phy. Lett.* 80, 398–400. doi: 10.1063/1.1435075

Reed, T. B. (1971). *Free Energy of Formation of Binary Compounds: An Atlas of Charts for High Temperature Chemical Calculations*. Cambridge, MA: MIT Press. doi: 10.1149/1.2404111

Russell, A. M., and Lee, K. L. (2005). *Structure-Property Relations in Nonferrous Metals.* Hoboken, NJ: John Wiley and Sons, Inc. doi: 10.1002/0471708542

White, S. R., Sottos, N. R., Geubelle, P. H., Moore, J. S., Kessler, M. R.S., Viswanathan. R., et al. (2001). Automatic healing of polymer composites. *Nature* 409, 794–797. doi: 10.1038/35057232

Wool, R. P. (2008). Self-healing materials: a review. *Soft Matter* 4:400. doi: 10.1039/b711716g

Wu, C. (2004). Properties of lead-free solder alloys with rare earth element additions. *Mater. Sci. Eng. R Rep.* 44, 1–44. doi: 10.1016/j.mser.2004.01.001

Wu, C. M. L., and Wong, Y. W. (2006). Rare-earth additions to lead-free electronic solders. *J. Mater. Sci. Mater. Electron.* 18, 77–91. doi: 10.1007/s10854-006-9022-6

Wu, D. Y., Meure, S., and Solomon, D. (2008). Self-healing polymeric materials: a review of recent developments. *Prog. Poly. Sci.* 33, 479–522. doi: 10.1016/j.progpolymsci.2008.02.001

Zwaag, S. V. D., Dijk, N. H.,V., Jonkers, H. M., Mookhoek, S. D., and Sloof, W. G. (2009). Self-healing behaviour in man-made engineering materials: bioinspired but taking into account their intrinsic character. *Philos. Trans. R. Soc. A* 367, 1689–1704. doi: 10.1098/rsta.2009.0020

Conflict of Interest Statement: The authors declare that the research was conducted in the absence of any commercial or financial relationships that could be construed as a potential conflict of interest.

frontiers in Materials

ORIGINAL RESEARCH
published: 04 July 2019
doi: 10.3389/fmats.2019.00160

Post-processing Methods to Improve Strength of Particle-Bed 3D Printed Geopolymer for Digital Construction Applications

Behzad Nematollahi, Ming Xia* and Jay Sanjayan*

Centre for Smart Infrastructure and Digital Construction, Faculty of Science, Engineering and Technology, Swinburne University of Technology, Hawthorn, VIC, Australia

The strength of powder-based 3D printed geopolymer samples immediately after the de-powdering process ("green" strength) is inherently very low. Therefore, different post-processing techniques have been explored in the previous study of the authors to enhance the "green" strength of the printed geopolymer. The highest strength of around 30 MPa was achieved for the printed slag-based geopolymer sample cured in an alkaline solution for 7 days at 60°C. Although this strength is sufficient for a wide range of construction applications, the necessity for the heat curing procedure, which requires a significant amount of energy, can compromise the sustainability credentials of the developed powder-based 3D printed geopolymer and limit its commercial viability and large-scale applications in the construction industry. To tackle this issue, this study aims to develop a new post-processing method which eliminates the necessity for the heat curing. The influences of type of curing medium, duration and temperature of curing, and testing direction on the compressive strength of the printed geopolymer were investigated. The "green" printed geopolymer samples were immersed in four different curing mediums, including two sodium (Na)-based, and two potassium (K)-based activators with different alkali modulus (SiO_2/M_2O where M = Na or K), and cured at two different curing temperatures (ambient temperature (23°C) vs. 60°C) for 7 and 28 days. The compressive strength of the "post-processed" printed geopolymer specimens was measured in two different testing directions, namely the binder jetting direction and layer stacking direction. The results showed that the 28-day compressive strength of the ambient temperature cured printed geopolymer sample was comparable to the 7-day compressive strength of the corresponding heat cured sample. Therefore, the feasibility of enhancing the strength of printed geopolymer by curing in an alkaline solution at ambient temperature was established. This developed post-processing method based on the ambient temperature curing is more viable and less energy-intensive, yet provides comparable strength, as compared to the previously developed post-processing method based on the heat curing. The results also showed that the strength of the printed geopolymer samples cured in the K-based activators was lower than that of the specimens cured in the Na-based activators.

Keywords: geopolymer, 3D concrete printing, digital construction, post-processing, powder-based 3D printing

OPEN ACCESS

Edited by:
John L. Provis, University of Sheffield, United Kingdom

Reviewed by:
Jadambaa Temuujin, Mongolian Academy of Sciences (MAS), Mongolia
Alastair T. M. Marsh, University of Leeds, United Kingdom

****Correspondence:***
Behzad Nematollahi
bnematollahi@swin.edu.au
Ming Xia
mxia@swin.edu.au

Specialty section:
This article was submitted to Structural Materials, a section of the journal Frontiers in Materials

Received: *05 February 2019*
Accepted: *21 June 2019*
Published: *04 July 2019*

Citation:
Nematollahi B, Xia M and Sanjayan J (2019) Post-processing Methods to Improve Strength of Particle-Bed 3D Printed Geopolymer for Digital Construction Applications. Front. Mater. 6:160. doi: 10.3389/fmats.2019.00160

INTRODUCTION

3D Concrete Printing (3DCP), a digitally layer-by-layer manufacturing process, has recently begun to draw significant attention in the construction industry (Wu et al., 2016; Nematollahi et al., 2017c). As an emerging field of additive manufacturing, 3DCP has the potential to revolutionize the construction industry (Wangler et al., 2016). This technology can bring significant benefits to the current construction industry such as increasing geometrical flexibility, adding multi-functionalities, eliminating the use of formwork, and a considerable reduction in construction cost and time (Wangler et al., 2016). Although this technology is still in its infant stages of realization in the construction industry, numerous studies have been conducted on the related areas for better utilization in the future.

Two common 3DCP techniques are used in the current construction industry, namely extrusion-based 3DCP and powder-based 3DCP (also known as particle-bed 3DCP). The extrusion-based 3DCP is a selective material deposition technique aimed for on-site concrete construction. In this technique, the cementitious material is extruded by a digitally controlled extruder to manufacture the component layer-by-layer [e.g., Contour Crafting (Khoshnevis, 2004), Concrete Printing (Le et al., 2012a,b)]. In this process, the material must be fluid enough during the transferring in the pumping system and must have sufficient viscosity and yield stress to keep the shape after being extruded out. Not only large-scale buildings, such as houses, could be built using this method, but also this could be achieved without any formwork. Formwork is the temporary structure and mold for pouring wet concrete, typically built with timber. The cost of formwork is estimated to be between 35 and 60% of the overall cost of concrete construction (Lloret et al., 2015). Besides, formwork represents a source of waste, as all formwork made of timber is discarded sooner or later, contributing to a generally increasing amount of waste in the world (De Schutter et al., 2018; Sanjayan and Nematollahi, 2019).

In the powder-based 3DCP technique a liquid binder (or "Ink") is selectively deposited onto the powder surface to bind the powder particles (e.g., D-Shape (Cesaretti et al., 2014), Emerging Objects (Rael and San Fratello, 2011) which enables the production of complex structures with subtle details and intricate shapes. This technique which is aimed for off-site construction is highly suitable for the manufacture of small-scale building components such as panels, permanent formworks and interior structures that then can later be assembled on site. One of the important advantages of the powder-based 3DCP technique, as compared to the extrusion-based technique, is that structures with overhang parts can be printed without the necessity of having a support structure, because unbound powder particles can support the printed parts.

In general in 3DCP process, due to the layer-by-layer production process, the deposited layers should gain adequate green strength to support the upper layers without significant deformation or collapsing. In the extrusion-based 3DCP process, the ability of the deposited layer to sustain its own weight and to support the upper layers is linked to its rheology and more particularly to its yield stress (Roussel, 2018) With regards to the powder-based 3DCP process, according to Shanjani and Toyserkani (2008), the maximum compact pressure occurred in the narrowest gap between the roller and the underneath powder layer was < 0.9 Pa. In other words, the green strength of each printed layer should be more than 0.9 Pa to prevent any deformation during the printing process.

Although the powder-based 3DCP technique can offer numerous advantages in the construction industry, there are several challenges which should be overcome before the technique is fully utilized. One of the main challenges is the severely limited range of printing materials that are suitable for construction applications. It is worth noting that some printing materials have been developed and used in commercial powder-based 3D printers for different applications in other industries. For instance, biocompatible materials including hydroxyapatite (Zhou et al., 2014), tricalcium phosphate (Al-Sanabani et al., 2013; Zhou et al., 2014), calcium sulfate hemihydrate (Asadi-Eydivand et al., 2016) have been used for biomedical applications. Ceramic materials such as barium titanate (Gaytan et al., 2015) and silicon carbide (Moon et al., 2001) have been used for manufacture of electrical components. Inconel 718 (Nandwana et al., 2017) and copper powder (Bai and Williams, 2015) have been used for fabricating metal components. Fine silica sand is used for fabrication of sand molds and cores (ExOne, 2015; Voxeljet, 2016). However, these printing materials are not suitable for construction applications. Therefore, it is urgently needed to develop new printing materials which can be used in the commercially available powder-based 3D printers for construction applications.

Conventional Portland cement has been considered as the master construction material for its high strength and stability, as well as its low cost for over 100 years and will probably be produced and used for at least the next 100 years (Biernacki et al., 2017). However, the slow setting time of Portland cement may limit its use for the powder-based 3DCP process. Few studies have reported the use of other types of cementitious materials. For instance, magnesium oxychloride cement (also known as Sorel cement) (Cesaretti et al., 2014) and fiber reinforced cement polymer (Rael and San Fratello, 2011) were used in D-shape and Emerging Objects, respectively. In addition, Gibbons et al. (Gibbons et al., 2010) conducted a preliminary study to investigate the feasibility of using a mixture of polyvinyl alcohol and rapid hardening Portland cement (RHPC) for the powder-based 3DCP process for the manufacture of biomedical implants. The printed specimens exhibited a maximum modulus of rupture of 2.4 MPa after 26-day water immersion at ambient temperature. The low strength of the developed RHPC powder may limit its use for construction applications. Maier et al. (2011) investigated a mixture of flash-setting calcium aluminate cement (CAC) for powder-based 3D printing to fabricate a bone regeneration scaffold. A compressive strength of up to 20 MPa was reported for the printed specimen after 3-day water immersion.

It is well established that the production of ordinary Portland cement (OPC) is highly energy- and emissions-intensive. As a rule of thumb, production of each ton of OPC would emit about one ton of carbon dioxide (Mccaffrey, 2002). The emissions due

to the manufacture of OPC are the fourth largest source of carbon emissions after petroleum, coal, and natural gas and are estimated to account for 5–7% of all anthropogenic emissions (Huntzinger and Eatmon, 2009). Therefore, it is essential to develop alternative OPC-less binders which would be suitable for the powder-based 3DCP process. To tackle this limitation, the authors of this study have been working on developing innovative methodologies for formulating geopolymer-based materials which can be used in the commercially available powder-based 3D printers for construction applications.

Geopolymer can be manufactured by alkaline activation of industrial by-products such as fly ash and slag. (Nematollahi et al., 2015b). The production of fly ash-based geopolymer can emit up to 80% less carbon dioxide (Duxson et al., 2007) and can consume up to 60% less energy than the production of OPC (Li et al., 2004). It should be pointed out that the environmental impact (i.e., carbon emission and embodied energy) of geopolymer is highly dependent on the specific precursor, and moreover, on the activator used. Apart from the potential environmental benefits of geopolymer as compared to OPC, the authors believe that geopolymer is a highly suitable material for the layer-by-layer build-up process in the powder-based 3DCP technique. This is because geopolymer, as compared to OPC, has more flexibly adjustable setting characteristics and is capable of developing higher strengths in a short period of time (Nematollahi et al., 2015a, 2017b). Many characteristics of geopolymer such as its setting time and strength development can be controlled by manipulating the activation and curing techniques, which can eliminate the necessity for using admixtures for development of 3D printable geopolymers. However, Portland cement is manufactured to comply with strict specifications with regards to setting time, strength development, etc. Therefore, different admixtures are required for the development of 3D printable OPC-based mixtures. The use of admixtures may not only increase the cost but can also have possible side effects and incompatibilities (Marchon et al., 2018).

Several geopolymer-based formulations using slag/fly ash have been developed by the authors which are suitable for the powder-based 3DCP applications (Xia and Sanjayan, 2016, 2018; Xia et al., 2018a,b). The 3D printed samples using the developed geopolymer-based powders are presented in **Figure 1**. It should be noted that in this paper, the term geopolymer is used in its broad meaning to represent alkali-activated cements, although it is understood that some can be alkali-activated slag or fly ash, especially those cured with relatively low alkalinity. This is justified since the term "geopolymer" has become a common-usage-term for alkali-activated cements in the literature (Duxson et al., 2006).

The strength of powder-based 3D printed geopolymer specimens immediately after completion of the de-powdering process often referred to as "green" strength, is typically very low due to the inherently high porosity of the powder bed. Therefore, further post-processing methods are required to increase the strength of the 3D printed geopolymer specimens to be adequate for construction applications. In the authors' previous study (Xia and Sanjayan, 2018), different post-processing procedures have been explored to increase the "green" strength of the powder-based 3D printed geopolymers. According to the results, immersing the printed "green" samples in a combination of sodium silicate solution with SiO_2/Na_2O of 3.22 and 8.0 M sodium hydroxide solutions for 7 days at 60°C resulted in the highest compressive strength of 30 MPa, which is sufficient for a wide range of construction applications (Xia and Sanjayan, 2018).

Although the authors' previously developed post-processing procedure based on the heat curing (Xia and Sanjayan, 2018) significantly improved the final mechanical properties of the 3D printed geopolymer samples, the necessity for the heat curing procedure not only limits the commercial viability and large-scale applications of the developed powder-based 3D printed geopolymers in the construction industry, but also can compromise the sustainability credentials of 3D printed geopolymers. Therefore, the first objective of this study is to investigate the feasibility of developing a new post-processing procedure based on the ambient temperature curing, which eliminates the necessity for heat curing. In this regard, the effect of curing temperature (heat curing vs. ambient temperature curing) on the compressive strength of the powder-based 3D printed geopolymers were investigated.

All alkaline solutions (i.e., curing mediums) used for the post-processing procedure developed in the previous study of the authors (Xia and Sanjayan, 2018) were sodium (Na)-based. The effect of potassium (K)-based curing mediums has not yet been investigated. Therefore, the second objective of this study is to investigate the effect of type of curing medium (Na-based vs. K-based) and alkali modulus (SiO_2/M_2O where M = Na or K) of sodium silicate (Na_2SiO_3) and potassium silicate (K_2SiO_3) solutions on the compressive strength of the powder-based 3D printed geopolymers.

MATERIALS AND EXPERIMENTAL PROCEDURES

Raw Materials

Printable Geopolymer Powder

A printable geopolymer powder previously developed by the authors (Xia and Sanjayan, 2016) was used in this study. **Figure 2** shows the particle size distribution of the printable geopolymer powder obtained using CILAS 1190 laser diffraction particle analyzer.

The printable geopolymer powder was a mixture of slag, ground anhydrous sodium metasilicate powder and fine silica sand. The slag supplied from Independent Cement, Australia was used as the aluminosilicate source material. The chemical composition and loss on ignition (LOI) of the slag was determined by X-ray Fluorescence (XRF), on an ignited mass basis (LOI: 0.09 wt %), as CaO (44.64 wt%) SiO_2 (32.76 wt %), Al_2O_3 (12.37 wt %), MgO (5.15 wt %), SO_3 (4.26 wt %), and others (0.73 wt%). **Figure 3** shows the X-ray diffraction pattern and crystalline phases of slag used in this study. The XRD analysis of slag was carried out using a Bruker D8 Advance X-ray diffractometer (Bruker, Germany). Scans were collected between 5 and 70° (2θ) with a step size of 0.02° and a scan rate of 5s

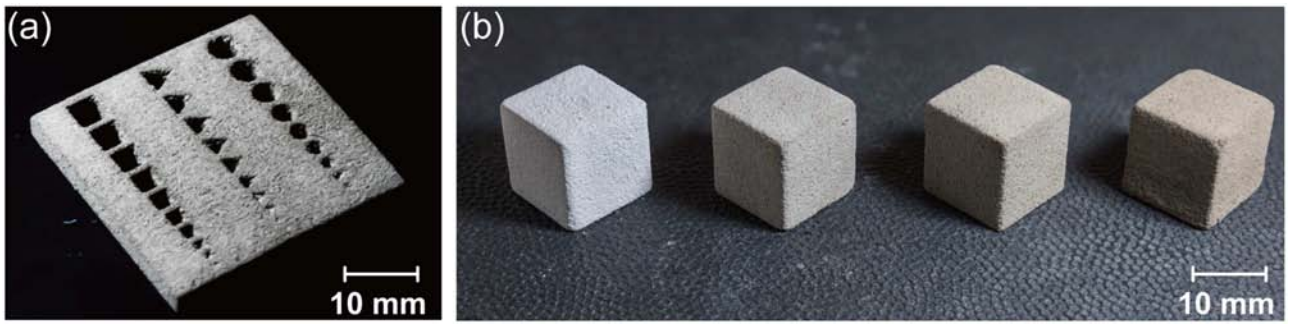

FIGURE 1 | 3D printed samples using the authors' developed geopolymer-based powder. **(a)** 40.4 × 40.4 × 5 mm plate structure with different holes. **(b)** 20 × 20 × 20 mm cubic samples. [Reprinted from Xia and Sanjayan (2016); Xia et al. (2018b) with permissions].

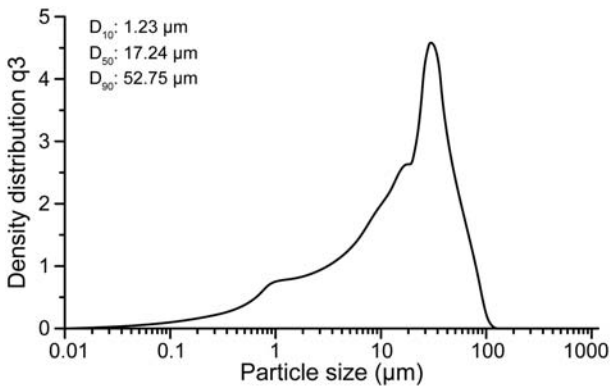

FIGURE 2 | Particle size distributions of the authors' developed 3D printable geopolymer powder.

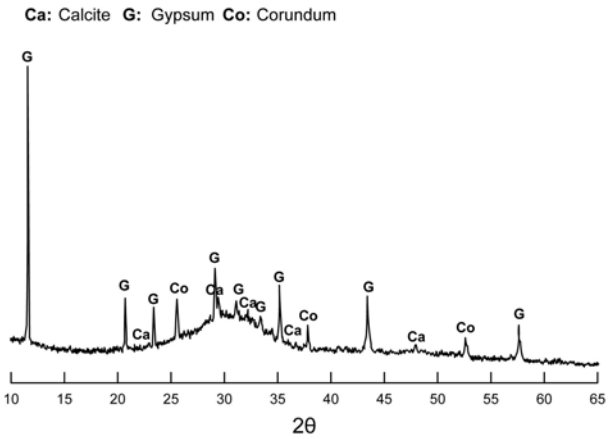

FIGURE 3 | X-ray diffraction analysis of slag. (Note: The corundum was added as internal standard for quantitative analysis).

per step. An internal standard (10 wt % corundum, Al_2O_3) was added to the raw slag to allow quantitative analysis using Rietveld refinement. As can be seen in **Figure 3**, a significant hump is shown between 25 and 35°. Calcite and gypsum crystalline phases are observed. The mineralogical phase percentages determined by using the Rietveld method are calcite (6.22%), gypsum (7.42%), and amorphous phase (86.36%).

Anhydrous sodium metasilicate powder (in the form of bead) supplied by Redox, Australia with the chemical composition of 50.66 wt Na_2O, 47.00 wt SiO_2 and 2.34 wt% H_2O was used as the alkaline activator. The alkaline activator beads were firstly ground for 5 min using a ball mill (Matest Jar Mill A091-10, MATEST system, Italy). The ceramic milling pot has a capacity of 300 cc and the ceramic ball has a diameter of 25 mm. For each batch, 150 grams of anhydrous sodium silicate beads were milled for 5 min at 400 RPM with powder/ball mass ratio of 0.3. A high purity silica sand with a median size of 184 µm supplied by TGS Industrial Sand Ltd., Australia was also used in this study.

Curing Mediums

Sodium hydroxide (NaOH) solution and potassium hydroxide (KOH) solution with 8.0 M concentration were prepared by dissolving NaOH and KOH flakes, respectively in tap water. The aim of using tap water, instead of distilled water, was to simulate the "real" condition at large-scale applications of the 3D printed geoplymers, in which condition it may not be easy and cost-effective to use distilled water. The NaOH and KOH flakes with a purity of 97% were both supplied by Sigma Aldrich Pty Ltd., Australia.

Two types of sodium silicate (Na_2SiO_3) solutions and two types of potassium silicate (K_2SiO_3) solutions were used in this study. All silicate solutions were supplied by PQ Australia Pty Ltd. The specifications of the silicate solutions are presented in **Table 1**.

Four different curing mediums, including two sodium (Na)-based alkaline solutions and two potassium (K)-based alkaline solutions were prepared as follows:

1. Na-based solution I (denoted as "Na-I"): composed of Na_2SiO_3- Grade D solution (71.4% w/w) and NaOH solution (28.6% w/w).
2. Na-based solution II (denoted as "Na-II"): composed of Na_2SiO_3-Grade N solution (71.4% w/w) and NaOH solution (28.6% w/w).

TABLE 1 | Specifications of the silicate solutions.

Silicate solutions	SiO_2^a (wt.%)	$M_2O^{a,b}$ (wt.%)	H_2O^a (wt.%)	Modulus^a (SiO_2/ M_2O^b)	Viscosity at 20°C (cps)^a
Na_2SiO_3-Grade D	29.4	14.7	55.9	2.00	250-450
Na_2SiO_3-Grade N	28.7	8.9	62.4	3.22	100-300
K_2SiO_3-Grade KASIL 1552	32.0	21.2	60.0	1.51	300-600
K_2SiO_3-Grade KASIL 2236	24.5	11.0	64.5	2.22	80-120

[a] *Average wt.% reported by the supplier.*
[b] *M in M_2O refers to Na or K.*

3. K-based solution I (denoted as "K-I"): composed of K_2SiO_3-Grade KASIL 1552 solution (71.4% w/w) and NaOH solution (28.6% w/w).
4. K-based solution II (denoted as "K-II"): composed of K_2SiO_3-Grade KASIL 2236 (71.4% w/w) and NaOH solution (28.6% w/w).

The alkali content (in terms of Na_2O or K_2O) and modulus of the four curing mediums used in this study are listed in **Table 2**. It should be noted that the selection of the type of NaOH and KOH solutions and Na_2SiO_3 and K_2SiO_3 solutions and the specific formulations of the curing mediums used in this study were based on the numerous research studies (e.g., Hardjito et al., 2004; Wallah and Rangan, 2006; Kong and Sanjayan, 2010; Nematollahi et al., 2014, 2017a,b) conducted by the authors and other researchers around the world on the production of geopolymer paste, mortar and concrete for "civil engineering" applications.

According to the alkali content and modulus listed in **Table 2** and the viscosity charts provided in Provis (2009) and PQ Corporation (2004), it can be inferred that the Na-I solution has higher viscosity than the Na-II solution at 20°C. Same trend is also true for the K-I and K-II solutions. According to Yang et al. (2008), the viscosity of sodium silicate solution decreases significantly with increasing temperature. The potassium silicate solutions also follow a similar trend (PQ Corporation, 2004). Therefore, based on the previous published data, it is assumed that the Na-II and K-II solutions have lower viscosity than that of the Na-I and K-I solutions. This is true regardless of the temperature.

3D Printing of Geopolymer Specimens

In this study, 20 mm cubic geopolymer specimens were printed using Zprinter® 150. The Zprinter® 150 is a commercial powder-based 3D printer manufactured by Z-Corp, USA with a specific resolution of 300 × 450 dpi, a build volume of 182 × 236 × 132 mm, and a build speed of 2–4 layers/min. It should be pointed out that at a resolution of 300 × 450 dpi, the minimum point size is 0.06 mm, which is much bigger than the median size of the printable powder (which is 17.24 μm as shown in **Figure 2**). The limiting factor on the resolution comes from the printer.

During the printing process, the binder liquid is jetted by HP11 print head, which requires a surface tension of approximately 45 dyn/cm and a viscosity of approximately 1.35 cP to function properly. An aqueous solvent (Zb® 63, Z-Corp, USA) was used as the binder during the printing process. The Zb® 63 binder was an aqueous commercial clear solution, composed of mainly water with 2-Pyrrolidone (Asadi-Eydivand et al., 2016), with the viscosity similar to pure water which does not react with the geopolymer powder.

TABLE 2 | The alkali content and modulus of the four curing mediums.

Curing mediums	M_2O^a (wt.%)	Modulus ($nSiO_2$/ nM_2O^a)
Na-I	17.4	1.47
Na-II	12.7	1.62
K-I	23.3	1.50
K-II	16.0	1.67

[a] *M in M_2O refers to Na or K.*

Figure 4 schematically illustrates the powder-based 3DCP process. First, a thin layer of powder is spread over the powder bed surface. Subsequently, binder droplets are selectively applied on the powder layer by a print-head, causing powder particles to bind to each other. The built part is completed by repeating the described steps and then is removed after certain drying time.

After the printing process completed, the samples were left undisturbed within the powder bed of the printer at room temperature for 6 h and then unbound powder was removed by using compressed air.

Post-processing and Testing Methods

After the de-powdering process, the printed cubes were divided into two groups denoted as "heat curing" and "ambient temperature curing".

For the "heat curing" group, the printed samples were immersed in each of the four curing mediums inside separate containers. The containers were sealed and placed in an oven at 60 ± 3°C for 7 days. After completion of the heat curing period, the containers were removed from the oven, and the heat cured samples were taken out from the curing mediums and kept undisturbed at ambient temperature (23 ± 3°C) and RH of 65% until the day of testing.

For the "ambient temperature curing" group, the printed samples were similarly immersed in each of the four curing mediums inside separate containers, but the sealed containers were kept at ambient temperature (23 ± 3°C) for 7 and 28 days. At the end of the curing period, the ambient temperature cured samples were taken out from the curing mediums and kept undisturbed until the day of testing. It should be pointed out

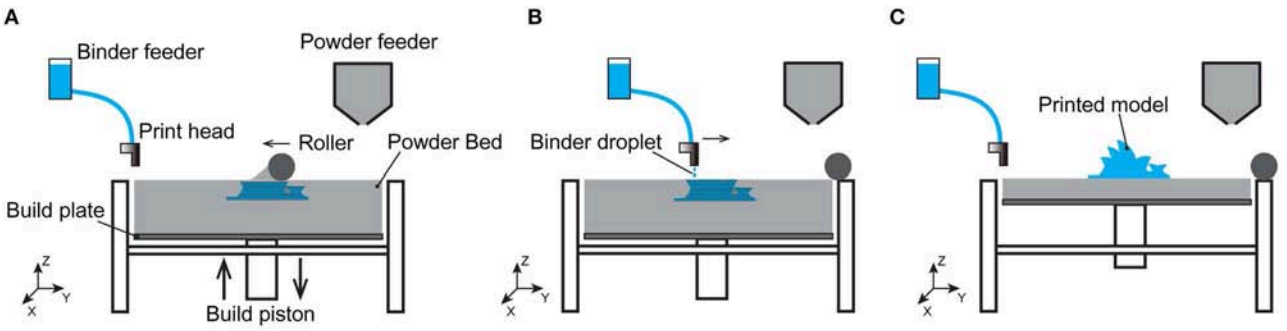

FIGURE 4 | Schematic illustration of the powder-based 3DCP process. **(A)** Powder spreading, **(B)** binder droplet deposition, **(C)** finished "green" sample.

that according to the authors' previous studies (Xia and Sanjayan, 2016, 2018), no dissolution of the "green" samples happened after being immersed in the curing mediums and subjected to heat/ambient temperature curing.

The heat cured specimens were tested at 7 days, while the ambient temperature cured samples were tested at 7 and 28 days. A population of 10 samples for each curing medium was used.

The apparent porosity of the printed cubic structures was measured based on Australian Standard AS 1774.5:2014. First of all, the samples were weighed in a dry state (M_{dry}) using a precision balance with an accuracy of 0.001 g, and then submerged in an immersion liquid for 30 min. Then, the weight of the samples suspended in the immersion liquid (M_{susp}) was measured. Subsequently, each sample was taken out from the immersion liquid and dabbed with a wet cloth to remove the excess immersion liquid and then was weighed to determine the wet weight (M_{wet}). The immersion liquid used in this study was ethanol (Reagent grade with 98% purity supplied by Sigma Aldrich Pty Ltd., Australia). The apparent porosity (P_{cube}) was calculated based on the following equations. A population of 10 samples for each curing medium was used.

$$\rho_{bulk.cube} = \rho_{liquid} \times \frac{M_{dry}}{M_{wet} - M_{susp}} \quad (1)$$

$$\rho_{cube} = 1 - \frac{\rho_{bulk.cube}}{\rho_{true.powder}} \times 100\% \quad (2)$$

The compressive strengths in both X-direction (i.e., the binder jetting direction) and Z-direction (i.e., layer stacking direction) were measured by an automated compressive strength testing machine (Technotest, Italy) under load control at the rate of 0.33 MPa/s. A population of 10 samples for each testing direction and curing medium was used.

RESULTS AND DISCUSSIONS

Heat Curing Group

Figure 5 shows the 7-day compressive strength of the heat cured 3D printed samples in two loading directions. In both directions, the compressive strength of the heat cured samples was significantly higher than that of the "green" strength. This

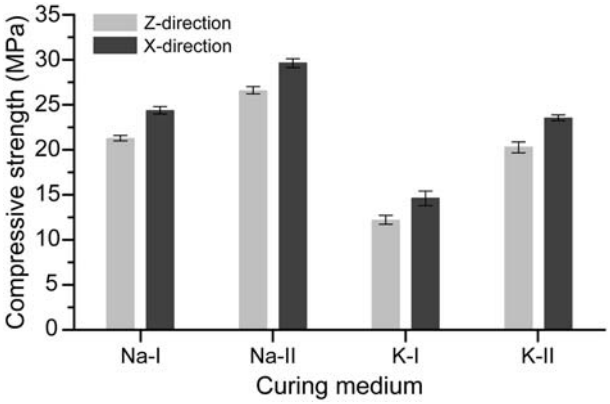

FIGURE 5 | Seven-day compressive strength of the heat cured 3D printed geopolymers. Note: The test result for the Na-II curing medium in the X-direction adopted from Xia and Sanjayan (2018). The error bars are calculated by standard deviation.

is true regardless of the type of curing medium. According to the authors' previous study (Xia and Sanjayan, 2016), the "green" strength of the printed sample is 0.76 ± 0.10 MPa in Z-direction and 0.91 ± 0.03 MPa in X-direction. The possible reason for the significantly higher compressive strength of the heat cured samples can be explained as follows:

Before the post-processing treatment, it is hypothesized that the "green" strength may come from the formation of calcium silicate hydrate due to the reaction among slag, sodium metasilicate powder and the liquid binder. However, during the post-processing treatment, when the green samples are immersed in the alkaline solutions, it is hypothesized that polymerization occurred within the sodium/potassium silicate solution, resulted in formation and development of geopolymeric products, which in turn led to the densification of porous structures of the "green" samples. As can be seen in **Table 3**, the apparent porosity of the heat-cured samples is far less than that of the "green" samples, which confirms the densification of the porous structure of the "green" samples. The exact reaction mechanism of these systems should be investigated in the future.

As can be seen in **Figure 5**, in both directions the 7-day compressive strength of the heat cured specimens immersed in the K-based solutions was lower than that of the specimens immersed in the Na-based solutions. This is attributed to the larger size of K^+ ion than Na^+ ion. According to Fernández-Jiménez et al. (2006), K^+ ion induces a lower crystallization speed of zeolites and slower development of pre-zeolitic gel due to its larger ion size, leading to lower compressive strength gain of the specimens immersed in the K-based solutions than the samples immersed in the Na-based solutions. It is worth to note that the Na-based liquid activators are generally cheaper than the K-based alkaline solutions (Nematollahi et al., 2015a, 2017a). Thereby, it can be concluded that for curing of "green" printed geopolymer samples, use of the Na-based alkaline solutions is highly beneficial in terms of lower cost and higher compressive strength gain, as compared to the K-based activators.

Among the Na-based solutions, according to **Figure 5**, the compressive strength of the heat cured samples immersed in the Na-II solution was 21–28% higher than that of the samples immersed in the Na-I solution, depending on the loading direction. The possible reasons for this result can be explained as follows:

As mentioned in Section Curing mediums, based on the previously published data, it is assumed that the viscosity of the Na-I solution is lower than that of the Na-II solution; thereby it is hypothesized that it can be relatively easier for the Na-II solution to penetrate into the "green" sample during the curing process, which favors the rate of geopolymerization reaction and compressive strength gain. The exact mechanism should be investigated in the future. In addition, the higher compressive strength of the heat cured samples immersed in the Na-II solution can also be due to the higher modulus of the Na-II solution than that of the Na-I solution (**Table 2**), which provides a higher amount of soluble silica in the Na-II solution. According to Xu and Van Deventer (2000), it is hypothesized that the higher amount of soluble silica in the Na-II solution accelerates the rate of geopolymerization reaction, thereby improves the compressive strength. Alshaaer (2013) has reported a similar curing method for kaolinite-based geopolymers by immersing them in an alkaline solution. The results of his study showed that secondary treatment (immersion in 6M NaOH solution at 80°C) led to an increase in the compressive strength and water resistance and a decrease in shrinkage of the samples.

For the heat-cured samples immersed in the K-based solutions, a similar trend was observed. The compressive strength of the heat cured samples immersed in K-II solution was about 61–66% higher than that of the specimens immersed in K-I solution, depending on the loading direction. Similar to the above discussion, this is due to the significantly lower viscosity and higher modulus of K-II solution than that of K-I solution.

As shown in **Figure 5**, an anisotropic phenomenon was observed in the compressive strength of the heat cured geopolymers depending on the loading directions. The compressive strength was always higher in the X-direction than in the Z-direction, regardless of the type of the curing medium. The ratios of the compressive strength in the X-direction to that in Z-direction (f_{c-x}/f_{c-z}) were listed in **Table 4**. The f_{c-x}/f_{c-z} of the samples immersed in the Na-II solution was higher than that of the Na-I solution. Similarly, the f_{c-x}/f_{c-z} of the samples immersed in the K-II solution was higher than that of the K-I solution. The higher f_{c-x}/f_{c-z} of the samples cured in the Na-II and K-II solutions might be related to the enhanced interlayer bond. According to Lowke et al. (2018), in powder-based 3D printed samples the water content significantly oscillates in accordance with a higher water content in the top region of the layer and a significantly lower content in the bottom region. In other words, the interlayer regions are more porous than other regions. Therefore, due to relatively lower viscosity of the Na-II and K-II solutions than the Na-I and K-I solutions (see Section Curing mediums), it is hypothesized that it is relatively easier for the Na-II and K-II solutions to transport to the pores in the interlayer regions and enhance the interlayer bond.

TABLE 3 | The apparent porosities of the green and 7-day heat-cured samples.

Samples	"Green"	Curing mediums			
		Na-I	Na-II	K-I	K-II
Apparent porosity (%)	57.4 ± 0.8	15.3 ± 0.7	13.6 ± 0.5	18.5 ± 1.1	15.6 ± 0.9

Each value is presented as mean ± standard deviation.

TABLE 4 | Anisotropy in the compressive strength of the heat cured 3D printed geopolymers.

Curing mediums	Na-I	Na-II	K-I	K-II
f_{c-x}/f_{c-z}	1.06	1.12	1.17	1.24

Ambient Temperature Curing Group

Figure 6 shows the 7-day and 28-day compressive strengths of the ambient temperature cured 3D printed samples in two loading directions. The 28-day compressive strength of the ambient temperature cured printed samples was higher than the 7-day compressive strength. This is true regardless of the testing direction and type of curing medium. This significant increase can be attributed to the continued geopolymerization process in the presence of alkaline solution, resulting in lower porosity of the samples cured for 28 days as compared to those cured for 7 days, as can be seen from **Table 5**. A similar result was reported for the conventionally mold-casting geopolymers, where the longer curing time increased the compressive strength (Nematollahi et al., 2015b; Wongsa et al., 2018).

According to **Figure 6**, the compressive strength of the ambient temperature cured printed specimens immersed in the K-based solutions was generally lower than that of the specimens immersed in the Na-based solutions. This is true regardless of the age of curing. As discussed in Section Heat curing group, a similar trend was also observed for the heat cured printed specimens (**Figure 5**). The reason for the lower strength of the specimens immersed in the K-based solutions than that of the specimens

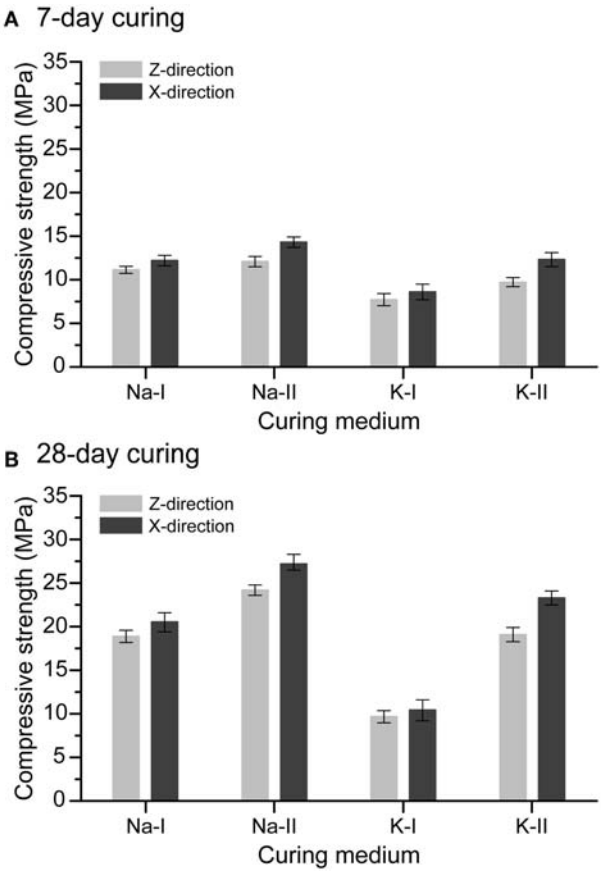

FIGURE 6 | Compressive strength of the ambient temperature cured 3D printed geopolymers at **(A)** 7 days and **(B)** 28 days. The error bars are calculated by standard deviation.

TABLE 5 | The apparent porosities of the 7- and 28-day ambient temperature cured samples.

Curing mediums	Apparent porosities (%)	
	7-day	28-day
Na-I	21.2 ± 0.9	15.5 ± 1.3
Na-II	19.5 ± 1.3	13.2 ± 0.9
K-I	27.6 ±1.4	22.5 ± 1.5
K-II	23.6 ± 0.6	20.2 ± 0.7

Each value is presented as mean ± standard deviation.

immersed in the Na-based solutions is explained in Section Heat curing group.

As can be seen in **Figure 6**, the compressive strength of the ambient temperature cured printed samples immersed in the Na-II solution was higher than that of the specimens immersed in the Na-I solution. In addition, the compressive strength of the ambient temperature cured printed samples immersed in the K-II solution was higher than that of the specimens immersed in the K-I solution. These are true regardless of testing direction and age of curing. As discussed in Section Heat curing group,

TABLE 6 | Anisotropy in the compressive strength of the ambient temperature cured 3D printed geopolymers.

	Curing mediums			
	Na-I	Na-II	K-I	K-II
f_{c-x}/f_{c-z} at 7 days	1.09	1.18	1.11	1.27
f_{c-x}/f_{c-z} at 28 days	1.08	1.13	1.07	1.22

a similar trend was also observed for the heat cured printed specimens (**Figure 5**). The reason for the higher strength of the specimens immersed in the Na-II or K-II solutions than that of the specimens immersed in the Na-I or K-I solutions is explained in Section Heat curing group.

Similar to the heat cured specimens (**Figure 5**), the compressive strength of the ambient temperature cured printed specimens also exhibited similar anisotropic behavior, depending on the loading direction. The compressive strength was always higher in the X-direction than in the Z-direction, regardless of the type of curing medium and age of curing. The f_{c-x}/f_{c-z} ratios were listed in **Table 6**. The f_{c-x}/f_{c-z} of the Na-II solution cured samples was higher than that of the Na-I solution cured samples. In addition, the f_{c-x}/f_{c-z} of the K-II solution cured samples was higher than that of the K-I solution cured samples. These trends are true regardless of the age of curing. As discussed in Section Heat curing group, a similar trend was also observed for the heat cured printed specimens (**Figure 5**). The reason for the higher f_{c-x}/f_{c-z} of the samples cured in the Na-II and K-II solutions is explained in Section Heat curing group. It is worth noting that the increase in age of curing (from 7 days to 28 days) slightly reduced the observed anisotropic behavior in the compressive strength results.

Among the curing mediums investigated, according to **Figures 5**, **6**, the printed samples immersed in the K-I solution exhibited the lowest compressive strength. This is true regardless of the type and age of curing, as well as the testing direction. This is because of the very high viscosity and the low modulus of the K_2SiO_3-Grade KASIL 1552 solution used to prepare the K-I solution, which makes this solution not as effective as the other curing mediums.

Comparison between **Figures 5**, **6B** showed that, except for the samples immersed in the K-I solution, the 28-day compressive strength of the ambient temperature cured printed samples was only up to 8% lower than the 7-day compressive strength of the corresponding heat cured printed samples. Therefore, the feasibility of the developed post-processing method based on the ambient temperature curing for enhancing the strength of powder-based 3D printed geopolymers is established, which requires less energy, yet provides comparable strength as compared to the previously developed post-processing method based on the heat curing. At the same time, eliminating the necessity for the heat curing reduces the complexity (and therefore likely cost) of the production process, and therefore enhances the commercial viability of the developed powder-based 3D printed geopolymers in the construction industry.

CONCLUSIONS

This study focused on the post-processing (i.e., curing) techniques to improve the compressive strength of the geopolymers made by the powder-based 3D printing process for construction applications. The effects of type of curing medium, curing temperature, duration of curing, and loading direction on the compressive strength of the powder-based 3D printed geopolymers were experimentally evaluated. The following conclusions are drawn:

1) The compressive strength of the printed geopolymer sample cured at ambient temperature (23°C) for 28 days was comparable to that of the sample cured at elevated temperature (60°C) for 7 days. This is true regardless of the type of curing medium, and testing direction. Achieving the comparable strength without the necessity for heat curing reduces the complexity (and therefore likely cost) of the production process, and therefore enhances the commercial viability of the developed powder-based 3D printed geopolymers in the construction industry.
2) For post-processing of the "green" samples under the heat curing condition, the Na-based activators were highly beneficial in terms of higher compressive strength gain and lower cost as compared to the K-based activators. This is true regardless of the testing direction and modulus of the activator solution.
3) Among the Na-based curing mediums, the Na-II activator containing the Na_2SiO_3 solution with a higher alkali modulus of 3.22 and a lower viscosity (N Grade) was the most effective in increasing the compressive strength of the printed geopolymers, as compared to the Na-I activator containing the Na2SiO3 solution with a lower alkali modulus of 2.00 and a higher viscosity (D Grade). This is true regardless of the duration and temperature of curing, and testing direction.
4) Among the K-based curing mediums, the K-II activator containing the K_2SiO_3 solution with a higher alkali modulus of 2.22 and a lower viscosity (KASIL 2236 Grade) was the most effective in increasing the compressive strength of the printed geopolymers, as compared to the K-I activator containing the K_2SiO_3 solution with a lower alkali modulus of 1.51 and a higher viscosity (KASIL 1552 Grade). This is true irrespective of the duration and temperature of curing, and testing direction.
5) The compressive strength of the printed geopolymers exhibited an anisotropic behavior, depending on the testing direction. The compressive strength was always higher in the binder jetting direction (X-direction) than in the layer stacking direction (Z-direction). This is true irrespective of the type of the curing medium, and duration and temperature of curing.
6) The 28-day compressive strength of the ambient temperature cured printed geopolymer samples was considerably higher than the 7-day compressive strength. This is true regardless of the testing direction and type of curing medium. This result is consistent with that reported in the literature for conventionally mold-cast geopolymer where the longer curing period results in higher compressive strength.

AUTHOR CONTRIBUTIONS

BN and JS jointly secured the grants and designed the research project. BN designed the experimental plan of this paper. MX performed the experimental work. MX and BN jointly interpreted the results and wrote the draft of the paper. JS reviewed and edited the paper.

ACKNOWLEDGMENTS

Authors acknowledge the support by the Australian Research Council Discovery Grant DP170103521 and Linkage Infrastructure Grant LE170100168 and Discovery Early Career Researcher Award DE180101587.

REFERENCES

Al-Sanabani, J. S., Madfa, A. A., and Al-Sanabani, F. A. (2013). Application of calcium phosphate materials in dentistry. *Int. J. Biomater.* 2013:876132. doi: 10.1155/2013/876132

Alshaaer, M. (2013). Two-phase geopolymerization of kaolinite-based geopolymers. *Appl. Clay Sci.* 86, 162–168. doi: 10.1016/j.clay.2013.10.004

Asadi-Eydivand, M., Solati-Hashjin, M., Shafiei, S. S., Mohammadi, S., Hafezi, M., and Osman, N. A. A. (2016). Structure, properties, and *In Vitro* behavior of heat-treated calcium sulfate scaffolds fabricated by 3D printing. *PloS ONE* 11:e0151216. doi: 10.1371/journal.pone.0151216

Bai, Y., and Williams, C. B. (2015). An exploration of binder jetting of copper. *Rapid Prototyping J.* 21, 177–185. doi: 10.1108/RPJ-12-2014-0180

Biernacki, J. J., Bullard, J. W., Sant, G., Brown, K., Glasser, F. P., Jones, S., et al. (2017). Cements in the 21st century: challenges, perspectives, and opportunities. *J. Am. Ceram. Soc.* 100, 2746–2773. doi: 10.1111/jace.14948

Cesaretti, G., Dini, E., De Kestelier, X., Colla, V., and Pambaguian, L. (2014). Building components for an outpost on the lunar soil by means of a novel 3D printing technology. *Acta Astronaut.* 93, 430–450. doi: 10.1016/j.actaastro.2013.07.034

De Schutter, G., Lesage, K., Mechtcherine, V., Nerella, V. N., Habert, G., and Agusti-Juan, I. (2018). Vision of 3D printing with concrete—technical, economic and environmental potentials. *Cement Concrete Res.* 112, 25–36. doi: 10.1016/j.cemconres.2018.06.001

Duxson, P., Fernández-Jiménez, A., Provis, J. L., Lukey, G. C., Palomo, A., and Deventer, J. S. J. (2006). Geopolymer technology: the current state of the art. *J. Mater. Sci.* 42, 2917–2933. doi: 10.1007/s10853-006-0637-z

Duxson, P., Provis, J. L., Lukey, G. C., and Van Deventer, J. S. (2007). The role of inorganic polymer technology in the development of 'green concrete'. *Cement Concrete Res.* 37, 1590–1597. doi: 10.1016/j.cemconres.2007.08.018

ExOne (2015). *Exerial Industrial Production 3D Printer*. Available online at: https://www.exone.com/Systems/Production-Printers/-Exerial (accessed June 12, 2019).

Fernández-Jiménez, A., Palomo, A., and Criado, M. (2006). Alkali activated fly ash binders. a comparative study between sodium and potassium activators. *Mater Construcción* 56, 51–65. doi: 10.3989/mc.2006.v56.i281.92

Gaytan, S., Cadena, M., Karim, H., Delfin, D., Lin, Y., Espalin, D., et al. (2015). Fabrication of barium titanate by binder jetting additive manufacturing technology. *Ceram. Int.* 41, 6610–6619. doi: 10.1016/j.ceramint.2015.01.108

Gibbons, G. J., Williams, R., Purnell, P., and Farahi, E. (2010). 3D Printing of cement composites. *Adv. Appl. Ceram.* 109, 287–290. doi: 10.1179/174367509X12472364600878

Hardjito, D., Wallah, S. E., Sumajouw, D. M. J., and Rangana, B. V. (2004). On the development of fly ash-based geopolymer concrete. *Aci. Mater. J.* 101, 467–472. doi: 10.14359/13485

Huntzinger, D. N., and Eatmon, T. D. (2009). A life-cycle assessment of portland cement manufacturing: comparing the traditional process with alternative technologies. *J. Clean Prod.* 17, 668–675. doi: 10.1016/j.jclepro.2008.04.007

Khoshnevis, B. (2004). Automated construction by contour crafting—related robotics and information technologies. *Automat. Constr.* 13, 5–19. doi: 10.1016/j.autcon.2003.08.012

Kong, D. L., and Sanjayan, J. G. (2010). Effect of elevated temperatures on geopolymer paste, mortar and concrete. *Cement Concrete Res.* 40, 334–339. doi: 10.1016/j.cemconres.2009.10.017

Le, T. T., Austin, S. A., Lim, S., Buswell, R. A., Gibb, A. G. F., and Thorpe, T. (2012a). Mix design and fresh properties for high-performance printing concrete. *Mater. Struct.* 45, 1221–1232. doi: 10.1617/s11527-012-9828-z

Le, T. T., Austin, S. A., Lim, S., Buswell, R. A., Law, R., Gibb, A. G. F., et al. (2012b). Hardened properties of high-performance printing concrete. *Cement Concrete Res.* 42, 558–566. doi: 10.1016/j.cemconres.2011.12.003

Li, Z., Ding, Z., and Zhang, Y. (2004). "Development of sustainable cementitious materials," in: *Proceedings of International Workshop on Sustainable Development and Concrete Technology*. (Beijing). Available online at: http://publications.iowa.gov/2941/1/SustainableConcreteWorkshop.pdf#page=66 (accessed June 5, 2019).

Lloret, E., Shahab, A. R., Linus, M., Flatt, R. J., Gramazio, F., Kohler, M., et al. (2015). Complex concrete structures: merging existing casting techniques with digital fabrication. *Comput. Aided Desig.* 60, 40–49. doi: 10.1016/j.cad.2014.02.011

Lowke, D., Dini, E., Perrot, A., Weger, D., Gehlen, C., and Dillenburger, B. (2018). Particle-bed 3D printing in concrete construction–possibilities and challenges. *Cement Concrete Res.* 112, 50–65. doi: 10.1016/j.cemconres.2018.05.018

Maier, A. K., Dezmirean, L., Will, J., and Greil, P. (2011). Three-dimensional printing of flash-setting calcium aluminate cement. *J. Mater. Sci.* 46, 2947–2954. doi: 10.1007/s10853-010-5170-4

Marchon, D., Kawashima, S., Bessaies-Bey, H., Mantellato, S., and Ng, S. (2018). Hydration and rheology control of concrete for digital fabrication: potential admixtures and cement chemistry. *Cement Concrete Res.* 112, 96–110. doi: 10.1016/j.cemconres.2018.05.014

Mccaffrey, R. (2002). Climate change and the cement industry. *Glob. Cem. Lime. Mag.* 15–19.

Moon, J., Caballero, A. C., Hozer, L., Chiang, Y.-M., and Cima, M. J. (2001). Fabrication of functionally graded reaction infiltrated SiC–Si composite by three-dimensional printing (3DP^{TM}) process. *Mater. Sci. Eng. A.* 298, 110–119. doi: 10.1016/S0921-5093(00)01282-X

Nandwana, P., Elliott, A. M., Siddel, D., Merriman, A., Peter, W. H., and Babu, S. S. (2017). Powder bed binder jet 3D printing of Inconel 718: Densification, microstructural evolution and challenges. *Curr. Opin. Solid St. M.* 21, 207–218. doi: 10.1016/j.cossms.2016.12.002

Nematollahi, B., Qiu, J., Yang, E.-H., and Sanjayan, J. (2017a). Micromechanics constitutive modelling and optimization of strain hardening geopolymer composite. *Ceram Int.* 43, 5999–6007. doi: 10.1016/j.ceramint.2017.01.138

Nematollahi, B., Qiu, J., Yang, E.-H., and Sanjayan, J. (2017b). Microscale investigation of fiber-matrix interface properties of strain-hardening geopolymer composite. *Ceram Int.* 43, 15616–15625. doi: 10.1016/j.ceramint.2017.08.118

Nematollahi, B., Sanjayan, J., and Ahmed Shaikh, F. U. (2015a). Tensile strain hardening behavior of PVA fiber-reinforced engineered geopolymer composite. *J. Mater. Civil. Eng.* 27:04015001. doi: 10.1061/(ASCE)MT.1943-5533.0001242

Nematollahi, B., Sanjayan, J., and Shaikh, F. U. A. (2014). Comparative deflection hardening behavior of short fiber reinforced geopolymer composites. *Constr. Build. Mater.* 70, 54–64. doi: 10.1016/j.conbuildmat.2014.07.085

Nematollahi, B., Sanjayan, J., and Shaikh, F. U. A. (2015b). Synthesis of heat and ambient cured one-part geopolymer mixes with different grades of sodium silicate. *Ceram Int.* 41, 5696–5704. doi: 10.1016/j.ceramint.2014.12.154

Nematollahi, B., Xia, M., and Sanjayan, J. (2017c). "Current progress of 3D concrete printing technologies," in: *ISARC Proceedings of the International Symposium on Automation and Robotics in Construction*. (Taipei: Vilnius Gediminas Technical University, Department of Construction Economics & Property).

PQ Corporation (2004). *Sodium and Potassium Silicates*. Available online at: https://www.pqcorp.com/docs/default-source/recommended-literature/pq-corporation/lithium-silicate/sodium-and-potassium-silicates-brochure-eng-oct-2004.pdf?sfvrsn=d22426fb_3 (accessed June 5, 2019).

Provis, J. L. (2009). "Activating solution chemistry for geopolymers," in *Geopolymers Structures, Processing, Properties and Industrial Applications*. Series in Civil and Structural Engineering, eds J. L. Provis and J. S. J. van Deventer (Woodhead Publishing), 50–71. doi: 10.1533/9781845696382.frontmatter

Rael, R., and San Fratello, V. (2011). "Developing concrete polymer building components for 3D printing," in: *ACADIA. 31st Annual Conference of the Association for Computer Aided Design in Architecture*. (Banff). Available online at: http://www.rael-sanfratello.com/media/emerging_objects/papers/243.pdf (accessed June 5, 2019).

Roussel, N. (2018). Rheological requirements for printable concretes. *Cement Concrete Res.* 112, 76–85. doi: 10.1016/j.cemconres.2018.04.005

Sanjayan, J. G., and Nematollahi, B. (2019). "3D concrete printing for construction applications," in *3D Concrete Printing Technology*. Melbourne, VIC: Elsevier, 1–11.

Shanjani, Y., and Toyserkani, E. (2008). "Material spreading and compaction in powder-based solid freeform fabrication methods: Mathematical modeling," in: *19th Annual International Solid Freeform Fabrication Symposium, SFF 2008*), 399–410. Available online at: http://edge.rit.edu/edge/P10551/public/SFF/SFF%202008%20Proceedings/Manuscripts/2008-36-Shanjani.pdf (accessed June 5, 2019).

Voxeljet (2016). *Largest Industrial 3D Sand Printing System in the World: The VX4000*. Available online at: https://www.voxeljet.com/3d-printing-systems/vx4000/ (accessed 12, June 2019).

Wallah, S., and Rangan, B. V. (2006). *Low-Calcium Fly Ash-Based Geopolymer Concrete: Long-Term Properties*. Available online at: https://www.geopolymer.org/fichiers_pdf/curtin_flyash_GC-2.pdf (accessed June 5, 2019).

Wangler, T., Lloret, E., Reiter, L., Hack, N., Gramazio, F., Kohler, M., et al. (2016). Digital concrete: opportunities and challenges. *RILEM Tech. Lett.* 1, 67–75. doi: 10.21809/rilemtechlett.2016.16

Wongsa, A., Sata, V., Nematollahi, B., Sanjayan, J., and Chindaprasirt, P. (2018). Mechanical and thermal properties of lightweight geopolymer mortar incorporating crumb rubber. *J. Clean Prod.* 195, 1069–1080. doi: 10.1016/j.jclepro.2018.06.003

Wu, P., Wang, J., and Wang, X. (2016). A critical review of the use of 3-D printing in the construction industry. *Automat. Constr.* 68, 21–31. doi: 10.1016/j.autcon.2016.04.005

Xia, M., Nematollahi, B., and Sanjayan, J. (2018a). Influence of binder saturation level on compressive strength and dimensional accuracy of powder-based 3D printed geopolymer. *Mater. Sci. Forum.* 939, 177–183. doi: 10.4028/www.scientific.net/MSF.939.177

Xia, M., Nematollahi, B., and Sanjayan, J. (2018b). Printability, accuracy and strength of geopolymer made using powder-based 3D printing for construction applications. *Automat. Constr.* 101, 179–189. doi: 10.1016/j.autcon.2019.01.013

Xia, M., and Sanjayan, J. (2016). Method of formulating geopolymer for 3D printing for construction applications. *Mater. Design* 110, 382–390. doi: 10.1016/j.matdes.2016.07.136

Xia, M., and Sanjayan, J. (2018). Methods of enhancing strength of geopolymer produced from powder-based 3D printing process. *Mater. Lett.* 227, 281–283. doi: 10.1016/j.matlet.2018.05.100

Xu, H., and Van Deventer, J. S. J. (2000). The geopolymerisation of alumino-silicate minerals. *Int. J. Miner. Process* 59, 247–266. doi: 10.1016/S0301-7516(99)00074-5

Yang, X., Zhu, W., and Yang, Q. (2008). The viscosity properties of sodium silicate solutions. *J. Solution Chem.* 37, 73–83. doi: 10.1007/s10953-007-9214-6

Zhou, Z., Buchanan, F., Mitchell, C., and Dunne, N. (2014). Printability of calcium phosphate: calcium sulfate powders for the application of tissue engineered bone scaffolds using the 3D printing technique. *Mater. Sci. Eng. C.* 38, 1–10. doi: 10.1016/j.msec.2014.01.027

Conflict of Interest Statement: The authors declare that the research was conducted in the absence of any commercial or financial relationships that could be construed as a potential conflict of interest.

frontiers in Materials

ORIGINAL RESEARCH
published: 26 March 2019
doi: 10.3389/fmats.2019.00048

Autogenous Healing in Strain-Hardening Cementitious Materials With and Without Superabsorbent Polymers: An 8-Year Study

Didier Snoeck and Nele De Belie†*

Magnel Laboratory for Concrete Research, Department of Structural Engineering, Faculty of Engineering and Architecture, Ghent University, Ghent, Belgium

OPEN ACCESS

Edited by:
John L. Provis, University of Sheffield, United Kingdom

Reviewed by:
Antonis Kanellopoulos, University of Hertfordshire, United Kingdom
Aaron Richard Sakulich, Worcester Polytechnic Institute, United States

***Correspondence:**
Didier Snoeck
didier.snoeck@UGent.be
orcid.org/0000-0001-9427-6312

†*Nele De Belie*
orcid.org/0000-0002-0851-6242

Specialty section:
This article was submitted to Structural Materials, a section of the journal Frontiers in Materials

Received: *07 November 2018*
Accepted: *27 February 2019*
Published: *26 March 2019*

Citation:
Snoeck D and De Belie N (2019) Autogenous Healing in Strain-Hardening Cementitious Materials With and Without Superabsorbent Polymers: An 8-Year Study. Front. Mater. 6:48. doi: 10.3389/fmats.2019.00048

To obtain a more sustainable concrete, occurring cracks should be repaired. However, as manual repair is time-consuming and expensive, self-healing may provide a proper solution. Autogenous healing is an already a present feature in cementitious materials, but it is an inferior mechanism as it can only completely heal cracks up to 30 μm in the presence of water. Therefore, a cementitious material with synthetic microfibers to limit the crack widths and superabsorbent polymers (SAPs) to provide the necessary water was proposed. However, due to ongoing hydration, autogenous healing based on further hydration of unhydrated cement may be less efficient in time. In this study, the ability of autogenous healing in time (on specimens with an age of 7 days, 28 days, 3 months, 1 year, 3 years, and 8 years) is investigated by comparing the mechanical characteristics after performing four-point-bending tests. The specimens were first loaded to 1% strain at their respective age, stored in a specific healing condition (a relative humidity of 60%, more than 90% and wet/dry cycles) for 28 days and were subsequently reloaded. The results show that, with increasing age, the mean crack width decreases. All specimens can partially heal and regain some of the mechanical properties after being preloaded and re-cracked under four-point-bending. If SAPs are added, there is partial healing in an environment without liquid water (more than 90% RH). At an early age, the healing is governed by further hydration and calcium carbonate crystallization. From 3 months onwards, the main autogenous healing mechanism is calcium carbonate crystallization. Overall, mixtures with SAPs generally showed more self-healing and are thus a promising material to be used in future building applications.

Keywords: age, self-healing, SHCC, hydrogels, fiber reinforcement

INTRODUCTION

Concrete is one of the most-used construction materials in the world and has left an undeniable mark on society. Dating back to the classical and Roman era, concrete was used to construct domes—such as on the Pantheon –, aqueducts and bridges, amongst others. Almost 200 years ago, the modern cementitious material was re-designed by Joseph Aspdin. Now, structures such as

the Hoover Dam and the Burj Khalifa are shaping the view of the world. The gray material is all around us, but it has one major downside. Even at low tensile stress, (micro-)cracks can easily originate resulting in ingress of potentially harmful substances which deteriorate reinforced concrete from the inside. Costly maintenance is required which is not always successful, therefore, opportunities are studied to tackle this problem. A possible durable and sustainable solution is the use of a concrete with self-healing capacity mimicking the human body.

Concrete possesses a passive healing of its own, called autogenous healing (Snoeck and De Belie, 2015a). Other healing mechanisms include the use of protected bacteria (Wang et al., 2014, 2015), encapsulated polyurethanes (Van Tittelboom et al., 2011, 2012b), microcapsules containing healing agents (Kanellopoulos et al., 2016; Van Tittelboom et al., 2016), other minerals (Sisomphon et al., 2012; Roig-Flores et al., 2015), and a porous vascular system to introduce healing agents (Sangadji and Schlangen, 2012), amongst others (Van Tittelboom and De Belie, 2013; Snoeck et al., 2018b). Generally, autogenous healing is considered to be the combination of further hydration of unhydrated cement and pozzolanic materials, the precipitation of calcium carbonate, the expansion of calcium-silicate-hydrate phases and the closing of cracks to the blockage by loose particles and impurities (Edvardsen, 1999; ter Heide, 2005; Granger et al., 2007; Homma et al., 2009).

The autogenous healing can be improved by considering three influencing factors. These are the presence of sufficient building blocks (Ca^{2+}, CO_2, unhydrated cement, pozzolanic materials, etc.) to sustain healing, the restriction of occurring cracks to healable widths and the provision of water to trigger the healing mechanisms. Cracks in reinforced cementitious materials need to be narrow enough to be completely healable. If not, the constituents available in the cementitious mix are consumed before the crack is effectively closed. A typical boundary is 30–50 μm when water is present. From 150 μm onwards, almost no closing of the crack is expected (Yang, 2008; Yang et al., 2009; Snoeck et al., 2014b; Snoeck, 2015; Snoeck and De Belie, 2015b). A thorough material design can improve the autogenous healing capacity by influencing the three above-mentioned features. By changing the mixture design, adding synthetic microfibers and superabsorbent polymers, all criteria are met to have a proper self-healing cementitious material. This cementitious material containing microfibers and superabsorbent polymers is investigated in this study.

The inclusion of poly(vinyl alcohol) (PVA) microfibers to obtain a fiber-reinforced material with a high tensile ductility leads to a strain-hardening behavior achieved by matrix multiple cracking (Li et al., 1988; Li, 2008). Due to the use of microfibers, the crack widths are within the healable range. This healing can occur in tensile cracks (Li, 2008), bending cracks (Yang et al., 2009; Snoeck et al., 2014b) and impact cracks (Snoeck et al., 2018a), showing the same behavior. As liquid water needs to be present, the healing is limited and needs to be promoted. The material does not show any form of healing when placed in a humid environment (Yang et al., 2009).

To include water, one way is through the use of superabsorbent polymers (SAPs). These materials are able to absorb a significant amount of fluid from the surrounding environment (up to 1,000 times their own weight) and to retain the fluid without dissolving (Mignon et al., 2017). SAP particles absorb mixing water during the mixing process and shrink to their dry size during hardening of the cementitious material, forming air-filled macro pores (Yao et al., 2011; Snoeck et al., 2014a). These macro pores act as crack initiators and thus promote multiple cracking (Yao et al., 2011; Snoeck et al., 2014a). Furthermore, SAP particles absorb water during wet periods and slowly release this water during dry periods to further improve the autogenous healing (Snoeck, 2015, 2018). Upon crack formation and water ingress, SAP particles along the crack faces will swell and cause a physical blockage of the crack (Snoeck et al., 2012). In this way SAPs will initially seal the crack from intruding fluids, increasing the durability (Lee et al., 2010, 2016; Snoeck et al., 2012, 2018d). Other applications of SAPs include mitigation of autogenous shrinkage (Jensen and Hansen, 2001, 2002; Snoeck et al., 2015a, 2017) and plastic shrinkage (Snoeck et al., 2018c), increased freeze-thaw resistance (Mechtcherine et al., 2017), and change in rheology (Mechtcherine et al., 2015), amongst others (Mechtcherine and Reinhardt, 2012).

The aim of this paper is to report on how SAPs promote autogenous healing in microfiber-reinforced cementitious materials when performing wet-dry cycles, and in air with a certain relative humidity. This will be monitored as a function of time up to a total age of 8 years. As the building blocks in cementitious materials are consumed over time due to ongoing hydration, the material may behave differently upon loading and healing at different ages. In literature, a recent study showed that autogenous healing is still present in 1-year old specimens (Yıldırım et al., 2018). However, in this research, specimens with an age up to 8 years are studied.

MATERIALS AND METHODS

Materials

The studied cementitious mixtures are composed of ordinary Portland cement (C) (CEM I 52.5 N, Holcim, Belgium), fly ash (FA) (Class F, OBBC, Belgium), fine quartz sand M34 (S) (D50 = 170 μm, Silbelco, Belgium), water (W), and a polycarboxylate superplasticizer (Spl) (Glenium 51, conc. 35%, BASF, Belgium). Multiple cracks needed to be created and an amount of 2 v% (volume percent) of polyvinyl alcohol fibers (PVA, 15 dtex; 8 mm cutting length; 12 cN/dtex tenacity, Kuraray, Japan) is sufficient to show a pronounced amount of multiple cracking and strain-hardening. Additionally, a varying amount of SAP (0/0.5/1 m% mass-percentage of cement weight) was added on top of the reference mixture without SAPs. Two different types of SAP were used. These include SAP A (a copolymer of acrylamide and sodium acrylate with a particle size of 100.0 ± 21.5 μm, BASF, Germany) and SAP B (a cross-linked potassium salt polyacrylate having a particle size of 477 ± 53 μm, BASF, Germany). Both SAPs are bulk-polymerized and consist of irregular crushed particles. Additional water was used to compensate for the loss in workability. This additional water is stored in the SAPs during hydration, resulting in a cement paste with the same effective water-to-binder ratio and free water content as the

TABLE 1 | Mortar composition of the studied mixture [kg/m^3].

[kg/m^3]	C	FA	S	W + W_{add}	Spl	PVA	SAP A	SAP B
REF	608	608	426	365 + 0	11.8	–	–	–
0.5A	554	554	388	332 + 85	10.7	26	2.77	–
0.5B	590	590	413	354 + 26	11.4	26	–	2.95
1B	572	572	400	343 + 51	11.1	26	–	5.72

C stands for cement, and FA, S, W, Spl, and PVA for fly ash, sand, water, superplasticizer, and PVA fibers, respectively. The water content is divided to show the amount of additional water W_{add}.

reference without SAPs. The reference mixture had a sand-to-binder (S/B) ratio of 0.35, a superplasticizer content (Spl/B) of 0.0097, a fly-ash-to-cement (FA/C) ratio of 1 and a water-to-binder (W/B) factor of 0.30 (Snoeck, 2015). The compositions (with superabsorbent polymers where applicable) are shown in **Table 1**. "REF" states a mixture without SAPs, "0.5A/0.5B/1B" a mixture with 0.5 m% SAP A and SAP B and 1 m% of SAP B, respectively.

The mixing procedure started with dry mixing of cement, fly ash and where appropriate SAPs (depending on the mixture composition) with a standard mortar mixer for 30 s until they were equally distributed. The total amount of water and superplasticizer were added to the dry constituents (mixing during 30 s at 140 rpm) and fine silica sand was added (additional mixing during 30 s at 140 rpm and at increased speed during 30 s at 285 rpm). The edges of the bowl were scraped for 30 s and the mixture was able to rest during 60 s. The synthetic microfibers were slowly added (mixing during 30 s at 140 rpm), followed by mixing for 60 s at 285 rpm. The molds (160 × 40 × 10 mm^3 samples) were subsequently filled and the specimens were demoulded after 24 h. Afterwards, the specimens were stored at a relative humidity of 95 ± 5% and a temperature of 20 ± 2°C until an age of 7 days, 28 days, 3 months, 1 year, 3 years, and 8 years. Series used within this study consisted of minimally three samples per tested age.

Four-Point-Bending Test

A four-point-bending test (Walter+Bai DB 250/15) was used to study the multiple-cracking behavior of the fiber-reinforced composites at the respective age. The first-cracking-strength was measured as the first kink in the stress-strain curve prior to strain-hardening. The ductility was measured as the strain at the lower side of the sample starting at the first-cracking-strength until the point the material showed the highest stress due to strain hardening. Strain-softening was thus not considered as this would imply a previously formed crack to widen. The cracking occurred under standard laboratory conditions at a temperature of 20 ± 2°C. The displacement was increased until 1% strain at the bottom of the specimen. This strain was calculated from the vertical displacement (0.0015 mm/s to imitate a quasi-static load) during four-point-loading using trigonometry (Snoeck, 2015).

After cracking, the samples were placed for 28 days under three conditions:

i) at a relative humidity of 60 ± 5% and 20 ± 2°C in a climate-controlled room.
ii) at a relative humidity of more than 90% (95 ± 5%) and 20 ± 2°C in a climate-controlled room, and;
iii) wet/dry cycles in which samples are stored alternately for 1 h in water and 23 h in the first mentioned curing condition of 60% relative humidity;

The specimens were reloaded in four-point-bending after the healing period until complete failure and the mechanical properties (first-cracking-strength) obtained during the first (loading prior to healing) and the second (loading after healing) cycle were compared. The self-healing capacity was calculated as the regain of the first-cracking-strength. Before and after healing, the crack widths were microscopically measured and the closing percentage was calculated.

Additional reference samples and SAP samples containing 1 m% SAP B were cracked until failure at an age of 28 days and healed for a subsequent 28 days in the above-mentioned healing conditions. In this way, different crack widths could be studied as strain softening already occurred, opening previously formed cracks. This leads to complete curves to determine the average observed closure as the range of studied crack widths is expanded.

RESULTS AND DISCUSSION

Study on the Autogenous Healing of Reference Cementitious Composites

All results of the measured crack widths, maximum crack widths, number of cracks and ductility can be found in **Table 2**. The crack widths were measured on specimens loaded until 1% strain, not reaching the maximal ductility. The ductility itself was determined on specimens loaded until failure. With increasing age, the crack width decreases in all mixtures. This is due to the stronger cementitious matrix with time due to hardening and thus the higher fiber-pull-out force needed, leading to the smaller pull-out length of the separate fibers and thus lower crack width. This was also found in literature (Yang et al., 2011; Kan and Shi, 2012). Generally, the crack widths are lower than in literature [16 cracks with average crack width of 39 μm and maximum of 60 μm at an age of 3 days (Yang et al., 2011) and average crack widths of 29–35, 24–31, and 15–17 μm after 3 days, 28 days, and 3 months, respectively (Yang et al., 2007; Kan and Shi, 2012)] due to a different mixture composition, the use of different raw materials and possible differences in age and curing conditions. The same conclusions can be drawn about the largest crack width.

The number of cracks and the strain in the cracked zone are closely related when specimens are loaded to complete failure.

TABLE 2 | Mean values and standard deviations for the crack width [μm] when loaded till 1% strain, the maximal crack width [μm] when loaded till 1% strain, the number of cracks [#] when loaded to complete failure, and the multiple cracking amount as measure for the ductility [%] when loaded to complete failure with their respective standard deviations on single results ($n = 3$).

		Crack width [μm]*	Maximum crack width [μm]*	Number of cracks [#]**	Multiple cracking amount [%]**
REF	7 days	24 ± 12	49	24–30	5.4 ± 0.6
	28 days	20 ± 11	42	10–18	2.9 ± 0.6
	3 months	16 ± 10	35	8–12	2.4 ± 0.4
	1 year	11 ± 7	30	6–12	1.8 ± 0.5
	3 years	10 ± 8	24	4–10	1.4 ± 0.5
	8 years	9 ± 6	20	4–8	1.2 ± 0.3
0.5A	7 days	23 ± 10	51	20–30	5.1 ± 1.2
	28 days	18 ± 10	40	7–18	3.5 ± 0.4
	3 months	16 ± 9	32	6–14	2.6 ± 0.4
	1 year	10 ± 6	28	8–15	2.2 ± 1.0
	3 years	9 ± 7	24	6–12	1.8 ± 0.6
	8 years	8 ± 6	20	6–11	1.6 ± 0.6
0.5B	7 days	22 ± 10	50	13–19	4.9 ± 0.2
	28 days	19 ± 11	41	8–18	3.5 ± 0.3
	3 months	17 ± 9	34	7–16	2.8 ± 0.4
	1 year	11 ± 8	28	8–16	2.5 ± 0.3
	3 years	10 ± 8	26	6–14	2.1 ± 0.6
	8 years	9 ± 8	22	5–12	1.9 ± 0.6
1B	7 days	21 ± 9	46	20–30	5.5 ± 0.1
	28 days	21 ± 10	42	14–24	3.8 ± 0.4
	3 months	13 ± 10	30	10–25	3.1 ± 0.2
	1 year	12 ± 6	28	8–21	2.6 ± 0.6
	3 years	10 ± 8	24	8–15	2.2 ± 0.7
	8 years	9 ± 6	20	6–14	2.0 ± 0.6

*When loaded to 1% strain.
**When loaded to complete failure.

The highest ductility is found when cracking the specimens at an age of 7 days and decreases with increasing age. This is due to the hardening of the cementitious matrix in time, reducing the ductile capacity. This is mainly due to the stronger matrix, influencing the crack-tip and strength criterion to obtain strain-hardening cementitious materials (Li et al., 2002). Thus, due to the stronger bond of the microfibers with the matrix in time and the stronger cementitious matrix, the overall ductility decreases. Even though the ductility decreases, the crack widths decrease, leading to a better opportunity to show healing. This is also due to the stronger bond of the microfibers with the matrix. But, as hydration continues, the available building blocks may be less present.

In specimens loaded until total failure, sometimes more than 15–20 cracks were formed, showing the high ductility. This is an inherent feature of the pronounced strain-hardening found when using synthetic microfibers. All cracks were through-going, which is typical for steady-state cracks formed when performing four-point-bending tests on mixtures with incorporated synthetic microfibers (Li, 2008). The crack width as determined by microscopic analysis did not vary significantly over the total crack length and all microscopic properties were similar. Most important is the range of crack widths (mean value) and the largest fracture. The latter is important, as the width is mostly the limiting factor for the regain in mechanical properties. If there is one large crack compared to the others, this larger one will preferentially open even if the other cracks are perfectly sealed and healed by healing products.

The influence of the age on the strength criterion to obtain a strain-hardening cementitious material is also reflected in the value of the first-cracking-strength, as shown in **Table 3**. The strength increases in time during hardening, which is logical. All strength values are within the same range irrespective of the SAP addition and are typical values for strain-hardening cementitious materials (Yang et al., 2007, 2009; Li, 2008; Yang, 2008). The regain in first-cracking-strength in the three different storage conditions is also shown in **Table 3**. The three storage conditions are storage in wet/dry cycles (1 h in water and 23 h in standard laboratory conditions), at a relative humidity of more than 90% and at a relative humidity of 60%. The temperature was always 20 ± 2°C and the healing period was 28 days.

To study the regain in mechanical properties, specimens were used with a strain at the bottom limited to 1%. The crack width was hereby always limited to 30 μm in all specimens, which is ideal for autogenous healing. Not only are cracks able to visually close, the composite is able to regain some of its mechanical properties. The regain in mechanical properties—in this case the first-cracking-strength—when storing specimens in wet/dry

TABLE 3 | Mean values and standard deviations for the first-cracking-strength [MPa], and the regain in first-cracking-strength [%] with their respective standard deviations on single results ($n = 3$).

		First-cracking-strength [MPa]	Regain in first-cracking-strength [%]		
			wet/dry cycles	RH>90%	RH = 60%
REF	7 days	4.5 ± 0.3	59 ± 9	7 ± 2	1 ± 1
	28 days	4.8 ± 0.6	45 ± 7	7 ± 1	1 ± 1
	3 months	5.4 ± 0.5	42 ± 5	7 ± 1	1 ± 1
	1 year	6.0 ± 0.5	35 ± 6	6 ± 1	0 ± 1
	3 years	6.3 ± 0.6	25 ± 8	5 ± 1	1 ± 1
	8 years	6.4 ± 0.6	18 ± 7	6 ± 1	0 ± 1
0.5A	7 days	4.9 ± 0.4	74 ± 9	49 ± 7	27 ± 6
	28 days	4.9 ± 1.5	65 ± 2	51 ± 3	29 ± 9
	3 months	5.3 ± 2.2	59 ± 2	46 ± 2	28 ± 9
	1 year	5.6 ± 2.0	45 ± 1	33 ± 3	19 ± 4
	3 years	5.9 ± 1.8	36 ± 4	22 ± 4	12 ± 3
	8 years	6.1 ± 2.1	24 ± 5	16 ± 5	4 ± 5
0.5B	7 days	4.6 ± 0.5	72 ± 4	58 ± 5	33 ± 2
	28 days	5.1 ± 1.1	69 ± 3	54 ± 3	35 ± 7
	3 months	5.2 ± 1.0	65 ± 6	44 ± 2	26 ± 2
	1 year	5.5 ± 2.0	53 ± 2	44 ± 5	21 ± 4
	3 years	5.8 ± 1.2	44 ± 5	31 ± 6	14 ± 5
	8 years	6.0 ± 1.2	30 ± 3	22 ± 6	8 ± 4
1B	7 days	4.7 ± 0.4	87 ± 6	61 ± 4	45 ± 8
	28 days	4.9 ± 0.9	86 ± 8	64 ± 8	44 ± 2
	3 months	5.3 ± 1.8	81 ± 8	62 ± 9	43 ± 3
	1 year	5.5 ± 1.3	65 ± 5	54 ± 3	32 ± 2
	3 years	5.7 ± 1.2	52 ± 6	36 ± 6	18 ± 4
	8 years	5.9 ± 1.5	41 ± 6	23 ± 5	8 ± 4

cycles is dependent on the age of the specimen. The older the specimen, the lower the regain in mechanical properties. This is due to the further hydration and stiffening of the cementitious matrix in time. This leads to a lower amount of available building blocks for the autogenous-healing mechanisms, even though a low water-to-binder ratio is used. The pozzolanic reaction by the fly ash [and even a latent-hydraulic reaction of blast-furnace slag as shown in previous research (Snoeck, 2015)] is promising for the autogenous healing. Fly ash continues to hydrate after 28 days, and the hydrated products may heal the cracks, increasing the self-healing ability. This was also found by (Jacobsen et al., 1995; Termkhajornkit et al., 2009; Zhou et al., 2011). In the long term, $Ca(OH)_2$ may not exist anymore due to the well-progressed pozzolanic reaction and carbonation, explaining the lower regain in mechanical properties at later ages as the pozzolanic reaction slows down.

At an early age, there is further hydration combined with calcium-carbonate crystallization and from 3 months onwards, the main healing mechanism is the precipitation of $CaCO_3$. This was visually monitored as the white $CaCO_3$ could be distinguished. The results are comparable to literature (Van Tittelboom et al., 2012a). A remark can be made. The matrix is composed out of C-S-H, CH (amongst others) and alkali oxides are found in the pore solution. If more C-S-H from the fly-ash reaction is formed, the pH value is expected to decrease, especially when high amounts of fly ash are available in the composite and $Ca(OH)_2$ is consumed. The formation of $CaCO_3$ could hereby be limited (due to the reduced pH level and availability of $Ca(OH)_2$). This was not the case in the studied reference mixture in this research. The pH value of the intruding fluid inside a crack is dependent on the fluid composition itself rather than the mixture composition. In time, the leaching of products from the cementitious matrix may change the pH-value of the fluid in the crack. Some examples of the (partial) healing through further hydration, calcium carbonate crystallization and their combined effect are shown in **Figure 1**. Even though the substantial loading was observed, the multiple small cracks were able to close completely. Instead of the need to close a wide crack—which is impossible—the smaller cracks were all closed, showing the potential of the material. Overall, $CaCO_3$ crystallization was found as the main healing mechanism, as confirmed by means of thermogravimetric analysis (Snoeck et al., 2014b; Snoeck and De Belie, 2015b). In the interior of the crack, possible further hydration would lead to the increase in mechanical properties. Furthermore, in the interior of the crack, less healing products are present (Snoeck et al., 2016) and the material is able to regain the mechanical properties to some

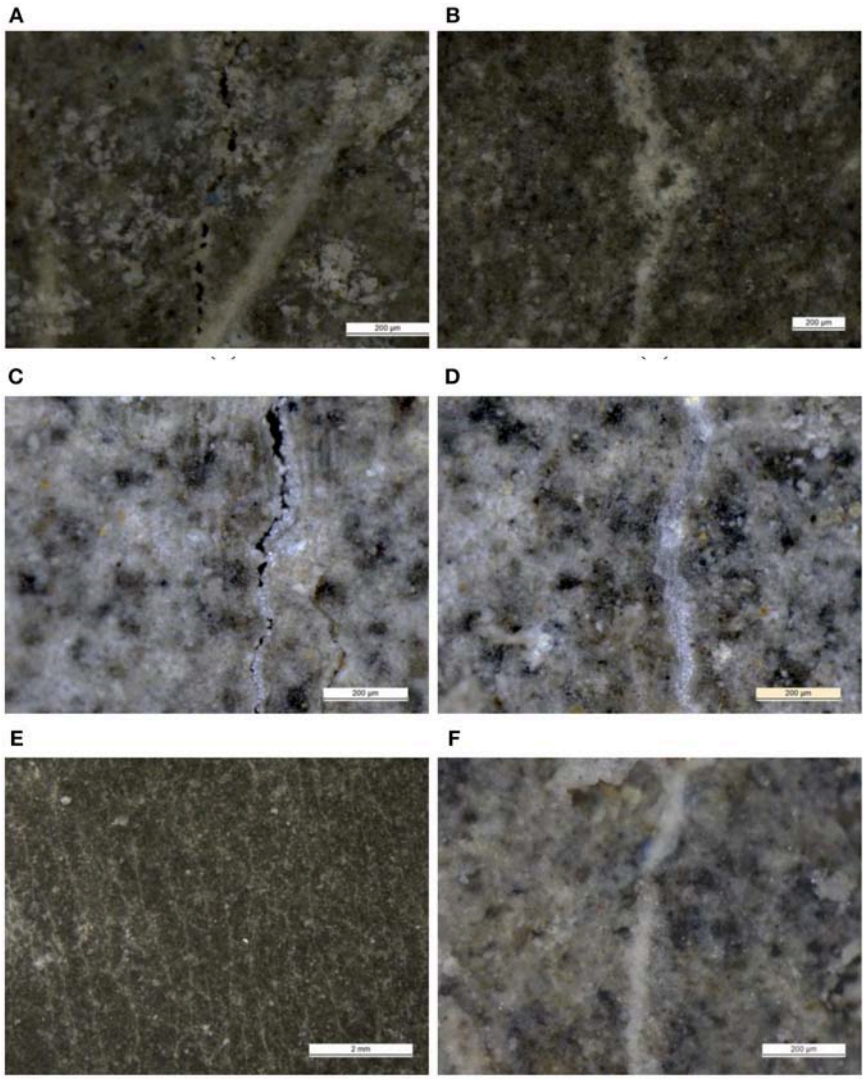

FIGURE 1 | Autogenous healing mechanisms showing partial **(A)** and further hydration **(B)** partial **(C)** and full calcium carbonate crystallization **(D)** and the combination of both in a number of cracks **(E)** and close-up **(F)**. The scale bars amount to 200 μm **(A–D,F)** and 2 mm **(E)**.

extent for subsequent healing periods after being re-damaged (Snoeck and De Belie, 2015b).

Inclusion of SAPs to Further Promote Autogenous Healing

Superabsorbent polymers were also included, and their effects were studied in great detail. This information is new to literature, especially for ages up to 8 years. Important properties are the strength and the regain in strength of the cementitious materials with and without superabsorbent polymers, which will be tackled at the end of this section. First, the microscopic analysis will be discussed, mainly at the age of 28 days, as more specimens were studied at that age, giving more information about the healing over a broad crack width range in different storage conditions.

All cracks were microscopically studied and recorded. The microscopic visual crack closure of reference specimens without SAPs in wet/dry cycles, at a relative humidity of more than 90% and at a relative humidity of 60%, is shown in **Figure 2** for the testing age of 28 days and different times of measuring the crack widths while healing. **Figure 3** gives the results for specimens containing superabsorbent polymers (1 m% of SAP B) stored in the same healing conditions. In the left part of the figures, the crack widths of the respective cracks after a certain healing period are compared to the width of the initially unhealed crack. If the crack visually closed, the data point shifts downwards compared to the bisector. The right-hand side of the figures shows the percentage of closure of the investigated crack.

Cracks in specimens without SAPs heal completely up to 30 μm and heal partly up to 150 μm when subjected to 28 wet/dry cycles. The cracks steadily close in time. Also Li et al. proved this, but their limit was 50 μm instead of 30 μm (Li,

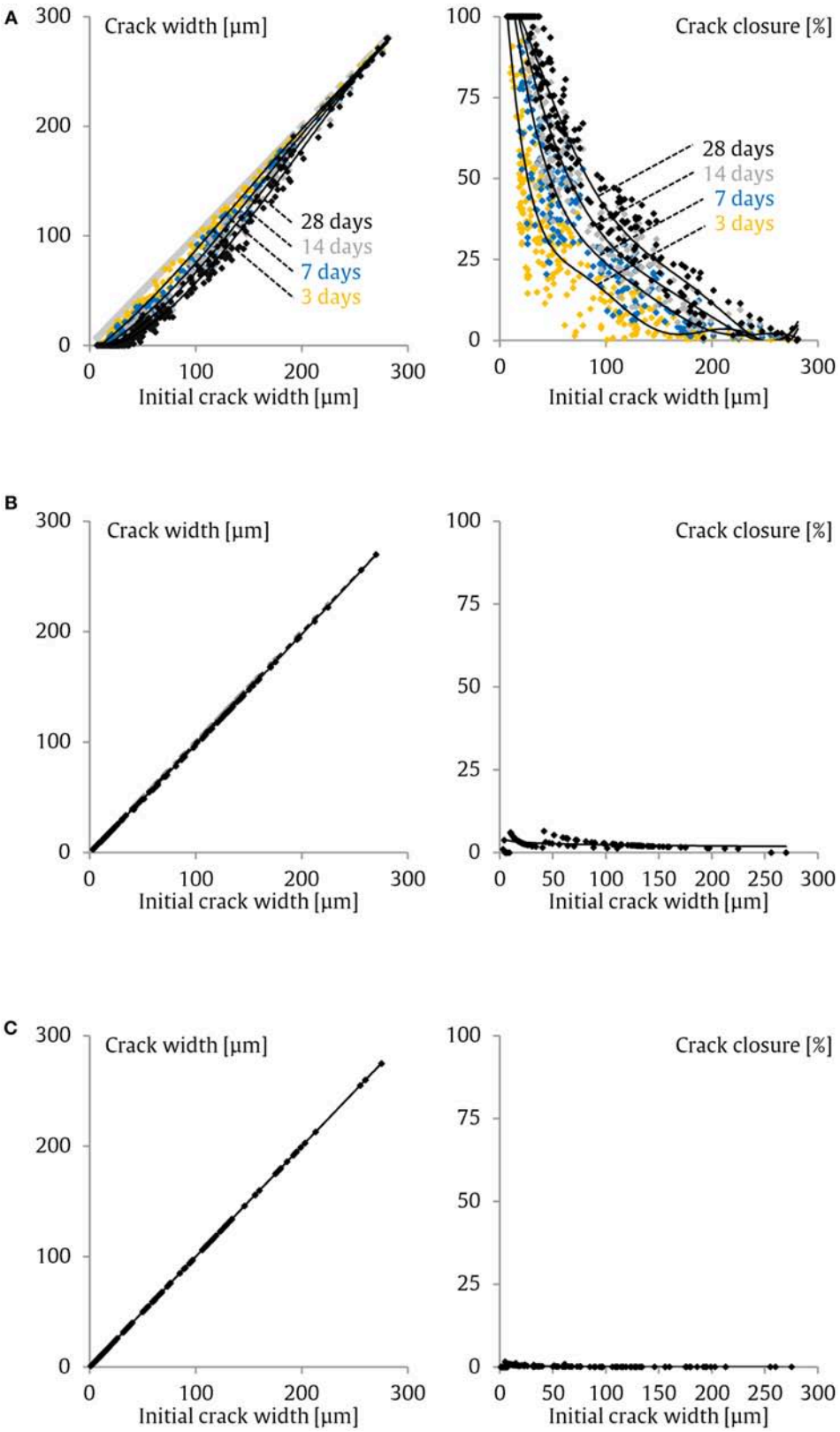

FIGURE 2 | Specimens without SAPs healed in wet/dry cycles (after 3, 7, 14, and 28 cycles) **(A)**, at a relative humidity of more than 90% (28 days) **(B)**, and at 60% (28 days) **(C)**, showing the crack closure as a function of the initial crack width.

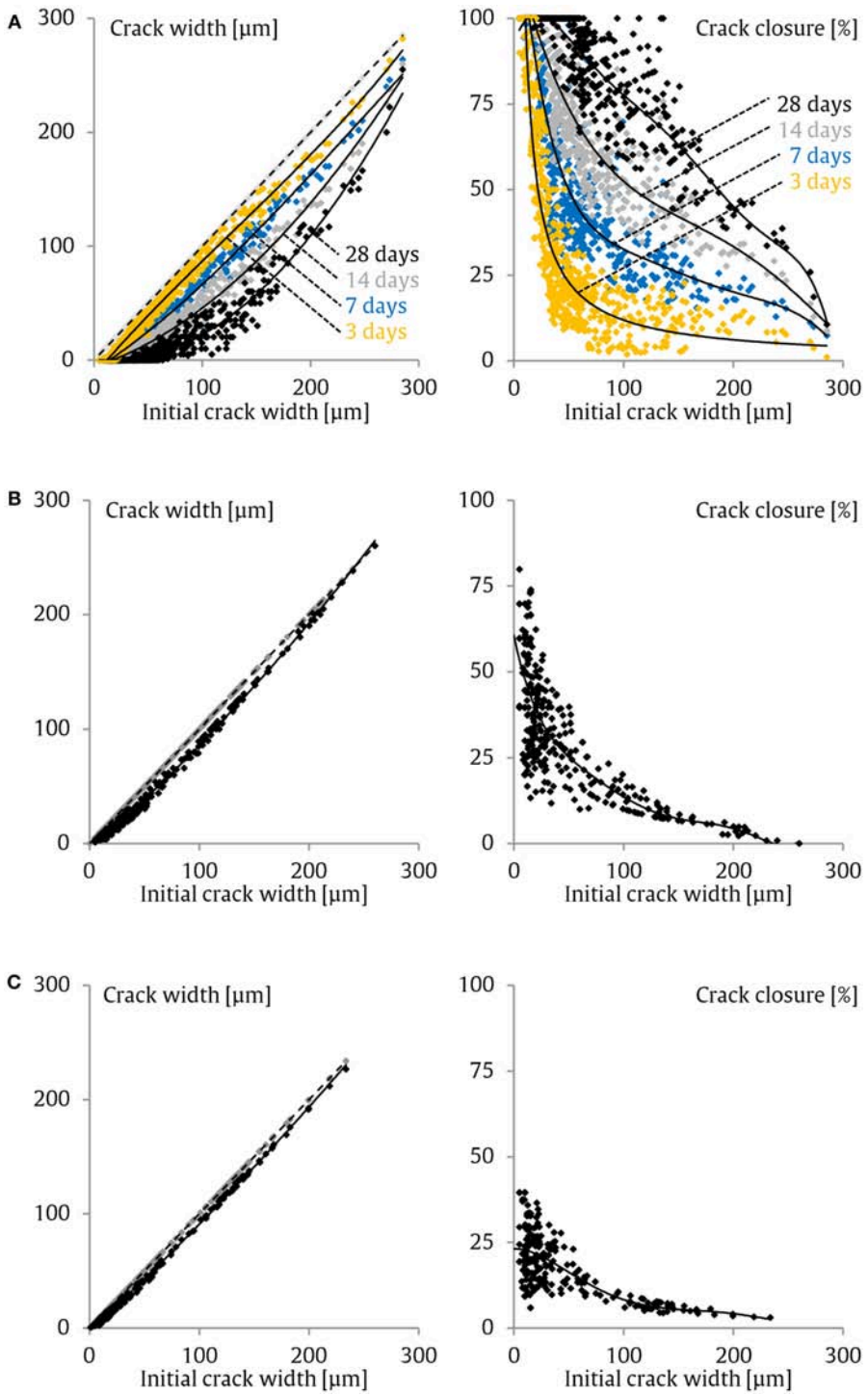

FIGURE 3 | Specimens with 1 m% SAP B healed in wet/dry cycles (after 3, 7, 14, and 28 cycles) **(A)**, at a relative humidity of more than 90% (28 days) **(B)**, and at 60% (28 days) **(C)**, showing the crack closure as a function of the initial crack width.

2008; Yang, 2008; şahmaran et al., 2013). They also showed that, in the presence of air (without any water available), samples cannot heal. **Figure 2** shows that at a relative humidity of more than 90%, there is only partial and minor healing. At 60% RH, the formation of healing products in a crack is non-existing.

In specimens with SAPs, however, some healing occurred at 60% and at more than 90% relative humidity as crack

closure was noticed visually. This means that SAPs are capable of providing liquid water toward the cementitious matrix for improved autogenous healing. SAPs are thus able to fulfill the criterion for exposure to environmental conditions and provide water as they are to adsorb four times their weight in moisture from the environment (Snoeck et al., 2015b). This adsorbed water can be given to the cementitious matrix and causes autogenous healing to occur in the form of further hydration of unhydrated cement grains (Snoeck et al., 2016). Storing pure cement in humid conditions of more than 90% RH and at a temperature of 20 ± 2°C for 1 month only partially ages the cement (Dubina and Plank, 2013). The cement paste was placed in an open cup and had a thickness of ∼1 mm. When SAPs are added as well, some hard-hydrated parts in the vicinity of the SAPs are found and thus visually more hydration occurred. This led to the conclusion that SAPs are able to provide water toward the cementitious matrix due to possible small changes in relative humidity.

Cracks smaller than 30 μm healed completely both with and without SAPs after being exposed to wet/dry cycles. Cracks ranging from 50 to 150 μm only healed partly in samples without SAP but sometimes showed complete closure in specimens containing SAPs after performing 28 wet/dry cycles (**Figure 3**). With superabsorbent polymers, there is a higher amount of formed healing products in a crack. So, not only narrow cracks up to 30 to 50 μm are able to heal, but also cracks up to 130 μm and larger. Cracks larger than 200 μm showed a reduced visual closure. The microfibers act as a nucleation site for $CaCO_3$ crystals and thus promote autogenous healing as well, as also seen by (Homma et al., 2009).

The crack width, maximum crack width, the number of cracks, and the amount of multiple cracking as a measure of the ductility of the specimens used to study the effect of the age are shown in **Table 2**. The mean crack widths are not statistically significantly different between the different mixtures and they decrease with age. This is due to the hardening of the cementitious matrix as explained before. Superabsorbent polymers do not have an influence on the properties of the cementitious matrix when additional water is used; they only facilitate multiple cracking and the cracks formed are alike. The microstructure is similar as well (Snoeck et al., 2014a, 2015b). This is a positive influence to obtain a high regain in mechanical properties and this is even further improved by using SAPs. Air voids—and thus also SAP macro pores—act as crack initiators, so the crack path likely follows the position of macro pores. The SAPs are thus available for swelling upon crack formation as the crack runs through the formed macro pore. There is no significant difference at an age of 7 days, but from 28 days onwards, the amount of multiple cracking is increased in specimens containing SAPs. This is reflected at an age of 8 years where the reference samples show 4–8 cracks and a ductility of 1.2 ± 0.3% while SAP specimens show 5–14 cracks and a ductility of 1.6–2.0%. This is mainly due to the observed facilitation due to macro pore formation. The crack widths have, as mentioned, the same order of magnitude around 10 μm.

With increasing age, the building blocks will become exhausted. This will also lead to a lower amount of autogenous healing as the healing relies on the amount of unhydrated cement particles, $Ca(OH)_2$, unhydrated parts of the pozzolanic fly ash and the amount of leachable Ca^{2+} ions present in the matrix. As already found previously, the healing mechanism changes in time due to the changing availability of building blocks. At early age, a greater degree of further hydration will occur but later on, the calcium-carbonate crystallization will govern the overall healing. At an age of 7 days and 28 days of healing, the self-healing mechanism is mostly the stitching of the crack by further hydration and calcium carbonate around SAPs. In samples with an age of 28 days, there is a little bit more whitish $CaCO_3$ in the crack. With a sample age of 3 months onwards, there is mainly the white $CaCO_3$ on the crack faces, also for the samples which are 8 years old.

The first-cracking-strength of the different test series cracked at 7 days and stored at different healing conditions for 28 days can be compared. No significant differences exist between the stress values measured for samples with and without SAPs. SAPs have a dual effect on the strength (Hasholt et al., 2012; Snoeck et al., 2014a). On one hand, they will increase the strength due to the further hydration by the release of mixing water in time during hardening of the cementitious matrix (i.e., due to internal curing). However, on the other hand, they will decrease the strength due to the formation of macro pores. Both influences combined leads in this case to an equivalent first-cracking-strength in these strain-hardening mixtures with a low water-to-binder ratio. Overall, the strength is not significantly different between all studied samples. However, in specimens with an age of 8 years, the difference is slightly larger. The amounts of SAPs were limited to 0.5 m% and 1 m% in the case of SAP A and SAP B, respectively. These amounts did not induce a decrease in mechanical properties. Higher amounts of SAPs would result in a decrease in initial mechanical properties. The used amount of superabsorbent polymers is rather high compared to literature for other applications, as only 0.3–0.6 m% SAP (Jensen and Hansen, 2002) or 0.4 m% SAP (Brüdern and Mechtcherine, 2010) is used to reduce the shrinkage by internal curing (also see Chapter 3). In this research, the amount of SAP (up to 1 m%) was substantially higher, in order to investigate the healing efficiency. The beneficial amount for internal curing is 0.22 m% for SAP A and 0.45 m% for SAP B (Snoeck et al., 2017).

The regain in mechanical properties is certainly noticed in wet/dry cycles where abundant water is available for the autogenous healing mechanisms of further hydration and calcium-carbonate crystallization. When stored at a high relative humidity (more than 90%), partial visual closure was found in SAP samples. The adsorbed moisture by the SAPs is responsible for this closure and the subsequent observed regain in mechanical properties (Snoeck et al., 2014b). At lower relative humidity (of ∼60%) only minor healing is observed in specimens containing SAPs, leading to a regain in first-cracking-strength. Again, this is due to the release of adsorbed water as if the SAPs are

acting as an internal curing agent. The reference samples without superabsorbent polymers are expected to show no regain in mechanical properties in a moist environment as no water will be present to induce autogenous healing.

At an age of 28 days, reference samples in wet/dry cycles show a regain of about 45%, which is comparable to values found in literature of 40% (Yang et al., 2009) and 42% (Yang, 2008). SAPs, however, promote self-healing at a relative humidity of more than 90%. The moisture uptake by SAPs (up to four times their own weight in moisture (Snoeck et al., 2015b) seems to be sufficient to promote a certain degree of autogenous healing, especially in the interior of the crack in the form of further hydration. In the relative humidity condition of more than 90%, the material with 1 m% SAP B shows a strength regain of 60%. In those specimens, further hydration occurred, leading to the regain in mechanical properties. At the crack mouth, the crack was still clearly open and only at some distinct places, there was some bridging of a crack by healing products (Snoeck et al., 2016). At reloading, previously created cracks re-opened and no new cracks were formed until all cracks reopened. Newly formed cracks were only seen when the specimens were stored in wet/dry cycles.

A higher number of SAPs, without decreasing the strength, leads to a higher amount of promoted autogenous healing due to an increase in steadily available water in time. Using 1 m% SAP B leads to a regain of 80–90% in wet/dry cycles and sometimes, a new crack is formed instead of the reopening of a healed crack, which shows a total regain of the mechanical properties at that distinct place. In the interior, mostly further hydration occurred and more pronounced $CaCO_3$ crystals mixed together with hydration products were formed at the crack mouth. Most regain in mechanical properties in all curing conditions is obtained by using 1 m% SAP B. An even higher amount of SAP B would be detrimental in terms of the mechanical properties.

At an age of 8 years, the healing in wet/dry cycles is reduced with a factor 3 in reference samples compared to an age of 7 days. This is approximately the same in SAP specimens, but the regain in mechanical properties is still pronounced. This is possibly due to the release during wet/dry cycling of stored water absorbed during dry periods by the SAPs. Reference samples do not show (or a limited 6%) healing in relative humidity conditions. SAP samples, however, still show around 16–23% healing in a relative humidity condition of more than 90%. In a relative humidity condition of 60%, this healing is 4–8%. Overall, the healing and regain in mechanical properties decrease over time.

An issue which may be important is the possible degradation of a SAP in time, especially in the harsh alkaline environment such as pore solution or the cementitious matrix (Vandenhaute et al., 2017). Also, the exposure to UV light may be detrimental for the use of SAPs in time, as their swelling capacity may decrease over time and may completely dissolve or carbonate (Mechtcherine et al., 2018). With the polymers used in this research, no degradation was found. The swelling was still the same after being stored in dry conditions without direct contact of UV light for a period of up to 8 years' time. Even after heating up to 75°C and freezing to −15°C, the polymer was still able to swell to full extent. In 8-year old specimens, the SAPs were still able to swell when they were exposed to water. The polymers are thus stable over time. However, when using another type of SAP which can degrade (Vandenhaute et al., 2017), one should verify the degradation phenomena in time.

CONCLUSIONS

Based on the findings on the healing capacity as a function of time for cementitious materials with and without SAPs, the following conclusions can be drawn:

- The highest number of cracks and ductility are found in younger specimens. Smaller average cracks are found in older specimens due to the further hydration and change in bond strength of the microfibers.
- SAPs improve the overall ductility due to their crack initiator capability and the subsequent formation of macro pores. This feature is more significant at later ages. At an age of 8 years, the reference samples show 4–8 cracks and a ductility of 1.2 ± 0.3%, while SAP specimens show 5–14 cracks and a ductility of 1.6–2.0% showing the same order of magnitude of crack widths around 10 μm. This higher ductility can be interesting in construction areas where high strains are expected.
- At an early age (7 days), the main healing mechanism is the stitching of a crack by further hydration. After an age of 28 days more calcium carbonate is seen, and after 3 months of age (and even up to 8 years of age), this calcium carbonate crystallization is the main healing mechanism.
- Superabsorbent polymers are beneficial as they can promote autogenous healing in wet/dry cycling and at high relative humidity (more than 90%) by the release of their adsorbed and absorbed water upon crack formation. They promote further hydration and calcium carbonate crystallization. In SAP specimens compared to reference samples, larger crack widths show complete healing.
- The healing and regain in mechanical properties decrease over time. Being cracked at an age of 8 years, the healing in reference samples is only a third of the healing when specimens are cracked at an age of 7 days. This is the same order of magnitude as for the SAP samples, but the latter specimens still show a pronounced healing, mainly due to the calcium carbonate crystallization.
- SAPs in a cementitious matrix seem to be stable up to a period of 8 years showing almost no degradation. This is important as they may be effective for sealing and healing purposes up to a minimum of 8 years of construction service life, showing an increased healing capacity compared to a reference sample without SAPs.

DATA AVAILABILITY

The datasets generated for this study are available on request to the corresponding author.

AUTHOR CONTRIBUTIONS

DS was involved in work conception, experimental design, experimental work, data analysis, manuscript writing and revision, and final manuscript approval. NDB was involved in work conception, critical manuscript revision, and final manuscript approval. All authors agree for work accountability.

ACKNOWLEDGMENTS

As a Postdoctoral Research Fellow of the Research Foundation-Flanders (FWO-Vlaanderen), DS would like to thank the foundation for the financial support (12J3617N). The authors want to thank Dr. A. Assmann and Dr. G. Herth from BASF for providing SAP A and SAP B.

REFERENCES

Brüdern, A. E., and Mechtcherine, V. (2010). "Multifunctional use of SAP in strain-hardening Cement-based Composites," in *International RILEM Conference on Use of Superabsorbent Polymers and Other New Additives in Concrete*. eds O. M. Jensen, M. T. Hasholt, and S. Laustsen (Lyngby: RILEM Publications, S.A.R.L), 11–22.

Dubina, E., and Plank, J. (2013). "Influence of moisture- and CO_2-induced ageing of cement on the performance of chemical admixtures used in concrete and mortar," in *8th International Symposium on Cement & Concrete*. ed W. Zhang (Nanjing), 1–8.

Edvardsen, C. (1999). Water permeability and autogenous healing of cracks in concrete. *ACI Mater. J.* 96, 448–454.

Granger, S., Loukili, A., Pijaudier-Cabot, G., and Chanvillard, G. (2007). Experimental characterization of the self-healing of cracks in an ultra high performance cementitious material: mechanical tests and acoustic emission analysis. *Cement Concr. Res.* 37, 519–527. doi: 10.1016/j.cemconres.2006.12.005

Hasholt, M. T., Jensen, O. M., Kovler, K., and Zhutovsky, S. (2012). Can superabsorbent polymers mitigate autogenous shrinkage of internally cured concrete without compromising the strength? *Constr. Build. Mater.* 31, 226–230. doi: 10.1016/j.conbuildmat.2011.12.062

Homma, D., Mihashi, H., and Nishiwaki, T. (2009). Self-healing capability of fibre reinforced cementitious composites. *Adv. Concr. Technol.* 7, 217–228. doi: 10.3151/jact.7.217

Jacobsen, S., Marchand, J., and Hornain, H. (1995). SEM observations of the microstructure of frost deteriorated and self-healed concrete. *Cement Concr. Res.* 25, 55–62. doi: 10.1016/0008-8846(95)00174-3

Jensen, O. M., and Hansen, P. F. (2001). Water-entrained cement-based materials I. Principles and theoretical background. *Cement Concr. Res.* 31, 647–654. doi: 10.1016/S0008-8846(01)00463-X

Jensen, O. M., and Hansen, P. F. (2002). Water-entrained cement-based materials II. Experimental observations. *Cement Concr. Res.* 32, 973–978. doi: 10.1016/S0008-8846(02)00737-8

Kan, L., and Shi, H. (2012). Investigation of self-healing behavior of Engineered Cementitious Composites (ECC) materials. *Constr. Buil. Mater.* 29, 348–356. doi: 10.1016/j.conbuildmat.2011.10.051

Kanellopoulos, A., Giannaros, P., and Al-Tabbaa, A. (2016). The effect of varying volume fraction of microcapsules on fresh, mechanical and self-healing properties of mortars. *Constr. Build. Mater.* 122, 577–593. doi: 10.1016/j.conbuildmat.2016.06.119

Lee, H. X. D., Wong, H. S., and Buenfeld, N. R. (2010). Potential of superabsorbent polymer for self-sealing cracks in concrete. *Adv. Appl. Ceramics* 109, 296–302. doi: 10.1179/174367609X459559

Lee, H. X. D., Wong, H. S., and Buenfeld, N. R. (2016). Self-sealing of cracks in concrete using superabsorbent polymers. *Cement Concr. Res.* 79, 194–208. doi: 10.1016/j.cemconres.2015.09.008

Li, V. C. (2008). "Engineered Cementitious Composites (ECC) – Material, Structural, and Durability Performance," in *Concrete Construction Engineering Handbook*. ed E. Nawy (Boca Raton, FL: CRC Press), 78.

Li, V. C., Lim, Y. M., and Chan, Y. W. (1988). Feasibility study of a passive smart self-healing cementitious composite. *Composites Part B* 29, 819–827. doi: 10.1016/S1359-8368(98)00034-1

Li, V. C., Wu, C., Wang, S., Ogawa, A., and Saito, T. (2002). Interface tailoring for strain-hardening Polyvinyl Alcohol - Engineered Cementitious Composites (PVA-ECC). *ACI Mater. J.* 99, 463–472. doi: 10.14359/12325

Mechtcherine, V., and Reinhardt, H. W. (eds.). (2012). *Application of Super Absorbent Polymers (SAP) in Concrete Construction*. Dordrecht; Heidelberg; London; New York, NY: Springer. doi: 10.1007/978-94-007-2733-5

Mechtcherine, V., Schröfl, C., Wyrzykowski, M., Gorges, M., Cusson, D., Margeson, J., et al. (2017). Effect of superabsorbent polymers (SAP) on the freeze-thaw resistance of concrete: results of a RILEM interlaboratory test. *Mater. Struct.* 50, 1–19. doi: 10.1617/s11527-016-0868-7

Mechtcherine, V., Secrieru, E., and Schröfl, C. (2015). Effect of superabsorbent polymers (SAPs) on rheological properties of fresh cement-based mortars – development of yield stress and plastic viscosity over time. *Cement Concr. Res.* 67, 52–65. doi: 10.1016/j.cemconres.2014.07.003

Mechtcherine, V., Snoeck, D., Schröfl, C., De Belie, N., Klemm, A. J., Ichimiya, K., et al. (2018). Testing superabsorbent polymer (SAP) sorption properties prior to implementation in concrete: results of a RILEM Round-Robin Test. *Mater Struct.* 51:28. doi: 10.1617/s11527-018-1149-4

Mignon, A., Snoeck, D., Dubruel, P., Van Vlierberghe, S., and De Belie, N. (2017). Crack mitigation in concrete: superabsorbent polymers as key to success? *Materials* 10, 1–25. doi: 10.3390/ma10030237

Roig-Flores, M., Moscato, S., Serna, P., and Ferrara, L. (2015). Self-healing capability of concrete with crystalline admixtures in different environments. *Constr. Build. Mater.* 86, 1–11. doi: 10.1016/j.conbuildmat.2015.03.091

şahmaran, M., Yildirim, G., and Erdem, T. K. (2013). Self-healing capability of cementitious composites incorporating different supplementary cementitious materials. *Cement Concr. Composites* 35, 89–101. doi: 10.1016/j.cemconcomp.2012.08.013

Sangadji, S., and Schlangen, E. (2012). Self healing of concrete structures - novel approach using porous network concrete. *J Adv Concr Technol.* 10, 185–194. doi: 10.3151/jact.10.185

Sisomphon, K., Çopuroğlu, O., and Koenders, E. A. B. (2012). Self-healing of surface cracks in mortars with expansive additive and crystalline additive. *Cement Concr. Composites* 34, 566–574. doi: 10.1016/j.cemconcomp.2012.01.005

Snoeck, D. (2015). *Self-Healing and Microstructure of Cementitious Materials with Microfibres and Superabsorbent Polymers*. Doctor in Civil Engineering: Construction Design, Ghent University.

Snoeck, D. (2018). Superabsorbent polymers to seal and heal cracks in cementitious materials. *RILEM Tech. Lett.* 3, 32–38. doi: 10.21809/rilemtechlett.2018.64

Snoeck, D., and De Belie, N. (2015a). From straw in bricks to modern use of microfibres in cementitious composites for improved autogenous healing – a review. *Constr. Build. Mater.* 95, 774–787. doi: 10.1016/j.conbuildmat.2015.07.018

Snoeck, D., and De Belie, N. (2015b). Repeated autogenous healing in strain-hardening cementitious composites by using superabsorbent polymers. *J. Mater. Civil Eng.* 04015086, 1–11. doi: 10.1061/(ASCE)MT.1943-5533.0001360

Snoeck, D., De Schryver, T., and De Belie, N. (2018a). Enhanced impact energy absorption in self-healing strain-hardening cementitious materials with superabsorbent polymers. *Constr. Build. Mater.* 191, 13–22. doi: 10.1016/j.conbuildmat.2018.10.015

Snoeck, D., Dewanckele, J., Cnudde, V., and De Belie, N. (2016). X-ray computed microtomography to study autogenous healing of cementitious materials promoted by superabsorbent polymers. *Cement Concr Composites* 65, 83–93. doi: 10.1016/j.cemconcomp.2015.10.016

Snoeck, D., Jensen, O. M., and De Belie, N. (2015a). The influence of superabsorbent polymers on the autogenous shrinkage properties of cement pastes with supplementary cementitious materials. *Cement Concr Res.* 74, 59–67. doi: 10.1016/j.cemconres.2015.03.020

Snoeck, D., Malm, F., Cnudde, V., Grosse, C. U., and Van Tittelboom, K. (2018b). Validation of self-healing properties of construction materials through non-destructive and minimal invasive testing. *Adv. Mater. Int.* 5:1800179. doi: 10.1002/admi.201800179

Snoeck, D., Pel, L., and De Belie, N. (2017). The water kinetics of superabsorbent polymers during cement hydration and internal curing visualized and studied by NMR. *Sci. Rep.* 7, 1–14. doi: 10.1038/s41598-017-10306-0

Snoeck, D., Pel, L., and De Belie, N. (2018c). Superabsorbent polymers to mitigate plastic drying shrinkage in a cement paste as studied by NMR. *Cement Concr. Composites* 93, 54–62. doi: 10.1016/j.cemconcomp.2018.06.019

Snoeck, D., Schaubroeck, D., Dubruel, P., and De Belie, N. (2014a). Effect of high amounts of superabsorbent polymers and additional water on the workability, microstructure and strength of mortars with a water-to-cement ratio of 0.50. *Constr. Build. Mater.* 72, 148–157. doi: 10.1016/j.conbuildmat.2014.09.012

Snoeck, D., Steuperaert, S., Van Tittelboom, K., Dubruel, P., and De Belie, N. (2012). Visualization of water penetration in cementitious materials with superabsorbent polymers by means of neutron radiography. *Cement Concr. Res.* 42, 1113–1121. doi: 10.1016/j.cemconres.2012.05.005

Snoeck, D., Van den Heede, P., Van Mullem, T., and De Belie, N. (2018d). Water penetration through cracks in self-healing cementitious materials with superabsorbent polymers studied by neutron radiography. *Cement Concr. Res.* 113, 86–98. doi: 10.1016/j.cemconres.2018.07.002

Snoeck, D., Van Tittelboom, K., Steuperaert, S., Dubruel, P., and De Belie, N. (2014b). Self-healing cementitious materials by the combination of microfibres and superabsorbent polymers. *J. Intell. Mater. Syst. Struct.* 25, 13–24. doi: 10.1177/1045389X12438623

Snoeck, D., Velasco, L. F., Mignon, A., Van Vlierberghe, S., Dubruel, P., Lodewyckx, P., et al. (2015b). The effects of superabsorbent polymers on the microstructure of cementitious materials studied by means of sorption experiments. *Cement Concr. Res.* 77, 26–35. doi: 10.1016/j.cemconres.2015.06.013

ter Heide, N. (2005). *Crack Healing in Hydrating Concrete*. Delft University of Technology.

Termkhajornkit, P., Nawa, T., Yamashiro, Y., and Saito, T. (2009). Self-healing ability of fly ash-cement systems. *Cement Concr Composites* 31, 195–203. doi: 10.1016/j.cemconcomp.2008.12.009

Van Tittelboom, K., and De Belie, N. (2013). Self-healing in cementitious materials - a review. *Materials* 6, 2182–2217. doi: 10.3390/ma6062182

Van Tittelboom, K., De Belie, N., Van Loo, D., and Jacobs, P. (2011). Self-healing efficiency of cementitious materials containing tubular capsules filled with healing agent. *Cement Concr. Composites* 33, 497–505. doi: 10.1016/j.cemconcomp.2011.01.004

Van Tittelboom, K., Gruyaert, E., Rahier, H., and De Belie, N. (2012a). Influence of mix composition on the extent of autogenous crack healing by continued hydration or calcium carbonate formation. *Constr. Build. Mater.* 37, 349–359. doi: 10.1016/j.conbuildmat.2012.07.026

Van Tittelboom, K., Snoeck, D., Vontobel, P., Wittmann, F. H., and De Belie, N. (2012b). Use of neutron radiography and tomography to visualize the autonomous crack sealing efficiency in cementitious materials. *Mater. Struct.* 46, 105–121. doi: 10.1617/s11527-012-9887-1

Van Tittelboom, K., Wang, J., Gomes De Araújo, M. A., Snoeck, D., Gruyaert, E., Debbaut, B., et al. (2016). Comparison of different approaches for self-healing concrete in a large-scale lab test. *Constr. Build. Mater.* 108, 125–137. doi: 10.1016/j.conbuildmat.2015.12.186

Vandenhaute, M., Snoeck, D., Vanderleyden, E., De Belie, N., Van Vlierberghe, S., and Dubruel, P. (2017). Stability of Pluronic® F127 bismethacrylate hydrogels: Reality or utopia? *Polymer Degrad. Stabil.* 146, 201–211. doi: 10.1016/j.polymdegradstab.2017.10.003

Wang, J., Mignon, A., Snoeck, D., Wiktor, V., Boon, N., and De Belie, N. (2015). Application of modified-alginate encapsulated carbonate producing bacteria in concrete: a promising strategy for crack self-healing. *Front. Microbiol.* 6:1088. doi: 10.3389/fmicb.2015.01088

Wang, J., Snoeck, D., Van Vlierberghe, S., Verstraete, W., and De Belie, N. (2014). Application of hydrogel encapsulated carbonate precipitating bacteria for approaching a realistic self-healing in concrete. *Constr. Build. Mater.* 68, 110–119. doi: 10.1016/j.conbuildmat.2014.06.018

Yang, E.-H. (2008). *Designing Added Functions in Engineered Cementitious Composites*. University of Michigan.

Yang, E.-H., Yang, Y., and Li, V. C. (2007). Use of high volumes of fly ash to improve ECC mechanical properties and material greenness. *ACI Mater. J.* 104, 303–311. doi: 10.14359/18966

Yang, Y., Lepech, M. D., Yang, E.-H., and Li, V. C. (2009). Autogenous healing of engineered cementitious composites under wet-dry cycles. *Cement Concr Res.* 39, 382–390. doi: 10.1016/j.cemconres.2009.01.013

Yang, Y., Yang, E.-H., and Li, V. C. (2011). Autogenous healing of engineered cementitious composites at early age. *Cement Concr Res.* 41, 176–183. doi: 10.1016/j.cemconres.2010.11.002

Yao, Y., Zhu, Y., and Yang, Y. (2011). Incorporation of SAP particles as controlling pre-existing flaws to improve the performance of ECC. *Constr. Build. Mater.* 28, 139–145. doi: 10.1016/j.conbuildmat.2011.08.032

Yıldırım, G., Khiavi, A. H., Yeşilmen, S., and şahmaran, M. (2018). Self-healing performance of aged cementitious composites. *Cement Concr. Composites* 87, 172–186. doi: 10.1016/j.cemconcomp.2018.01.004

Zhou, Z. H., Li, Z. Q., Xu, D. Y., and Yu, J. H. (2011). Influence of slag and fly ash on the self-healing ability of concrete. *Adv. Mater. Res.* 306–307, 1020–1023. doi: 10.4028/www.scientific.net/AMR.306-307.1020

Conflict of Interest Statement: The authors declare that the research was conducted in the absence of any commercial or financial relationships that could be construed as a potential conflict of interest.

Translational Materials Science

Yang Bai

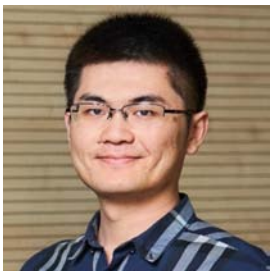

Dr Yang Bai is a tenure track Assistant Professor for the Small-power Self-sufficient Sensor System in the Microelectronics Research Unit, University of Oulu, Finland. He obtained his BA degree in Materials Science and Engineering in 2011 from Tianjin University, China, and his PhD degree in Metallurgy and Materials in 2015 from the University of Birmingham, UK. In 2016, he was granted a Marie Sklodowska-Curie Individual Fellowship under the European Union's Horizon 2020 research and innovation program. He is also an elected committee member of the IOP (Institute of Physics) Energy Group, UK. His research interests include multi-functional perovskites, photo-ferroelectrics, ferroelectric and piezoelectric materials for smart sensing, and energy harvesting technologies.

Jyri-Pekka Mikkola

Dr Mikkola received a MSc in Chemical Engineering from Åbo Akademi University, Åbo-Turku, Finland in 1992. After spending a few years in the industry he returned to the academia to complete his PhD at Åbo Akademi University in 1999. Since 2008 he is a Professor of Sustainable Chemical Technology at both Umeå University, Sweden and Åbo Akademi, Finland.

He has co-authored more than 300 scientific articles and holds a number of patents. The principal areas of interest are green chemistry, heterogeneous catalysis, ionic liquid technologies, chemical kinetics, and novel materials. He is also involved in two start-up companies, namely ECO-OIL AB and SPINCHEM AB. In 2004 he was appointed as an Academy Research Fellow and received 'The Incentive Award' by the Academy of Finland in 2006. In 2009 he received the Umeå University 'Young scientist Award' and in 2018 the Umeå University's Baltics price for entrepreneurship.

Mikko Nelo

Mikko Nelo performed his MSc studies in Organic chemistry at the University of Oulu with a thesis on "Development of pine-oil based wood preservatives and their oxidative polymerization catalysts" He then worked as a project researcher at the University of Oulu and Kemira Inc. working on wastewater purification research and wood preservatives development among others. He obtained his doctorate degree in the Microelectronics research unit, at the University of Oulu with a thesis on "Inks based on inorganic nanomaterials for printed electronics applications."

He is currently a Post-doctoral research fellow at Microelectronics research unit, University of Oulu. His current research topics include Ultra-low manufacturing temperature electroceramics, 3D-printing of ultra-low permittivity materials, and utilizing biomaterials in electronics applications.

Kristiina Oksman

Dr Oksman obtained her PhD from Luleå University of Technology, in Sweden in 1997 on wood thermoplastic composites. After a period as project leader at SICOMP (Swedish Institute of Composites) in Piteå, Sweden she was appointed as Professor of Polymers and polymer-based composites at NTNU 2001 and is now an Adjunct Professor at the University of Toronto's Faculty of Forestry. She has collaborated with the Forest Products Laboratory in Madison, USA since 1994 as a visiting scientist on wood thermoplastic composites and is also working on organizing a committee for the Wood Fiber Thermoplastic Composite Conference, held every second year in Madison. Her most important collaboration partners include the University of Toronto, Centre for Biocomposites and Biomaterials Processing in Toronto, Canada, Chalmers Technical University, Biopolymer Technology, in Gothenburg, Sweden, Helsinki University, Department of Applied Chemistry and Microbiology in Helsinki, Finland, and the Forest Products Laboratory in Madison, USA focused on wood thermoplastic composites and bio-nanocomposites.

Ming-Chung Wu

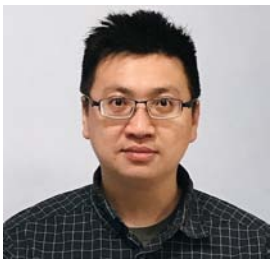

Prof. Ming-Chung Wu's research group at Chang Gung University develops innovative nanomaterials for various applications including photocatalysis, volatile organic compounds sensing devices, antimicrobial technology, flexible electronics, and perovskite solar cells. For perovskite solar cells (PSCs), he concentrates on developing a lead-reduced perovskite active layer, novel electron transport layer, interface modification, and the PSCs sub-module. For nanomaterials, Prof. Wu is working on the synthesis of TiO2 nanofibers, nanoscale photocatalysts, cellulose nanofibers, and their corresponding material properties analysis. For biomedical materials, he focuses on developing antibacterial materials and biocompatibility materials used in medical practices. For the advanced process, he is working on 3D printing technique, electrospinning method, and plasma technologies. Prof. Wu has published nearly 70 peer-reviewed journal papers in several leading materials journals including ACS Nano, the Journal of Materials Chemistry A, ACS Applied Materials& Interface, Nanoscale, etc. His publications have been cited over 1,200 times with and he has an H index of 20.

frontiers in Materials

MINI REVIEW
published: 13 November 2018
doi: 10.3389/fmats.2018.00065

Hybrid, Multi-Source, and Integrated Energy Harvesters

Yang Bai, Heli Jantunen and Jari Juuti*

Microelectronics Research Unit, Faculty of Information Technology and Electrical Engineering, University of Oulu, Oulu, Finland

Energy harvesting is one of the most rapidly growing of the emerging technologies. This field has arrived at the hybrid and multi-source era, where hybrid structures and novel materials are able to boost the energy conversion efficiency and/or make the harvesters capable of benefitting from multiple energy sources simultaneously. Such hybrid and multi-source energy harvesters have not frequently been reviewed in the past, potentially because of the small number of publications compared to that of their single-source and individual counterparts. However, as their number is becoming larger, it is now necessary to give sufficient and frequent reviews of developments in the field. Furthermore, an increasing number of developed energy harvesters are moving out of the laboratory into industrial markets. In practice, energy harvesters need to be integrated with energy storage and/or end users such as sensors and wireless sensor networks. Therefore, the harvester-storage and harvester-sensor integration systems also need to be reviewed frequently. This mini review includes works reported in the first half of 2018 and provides a timely update to the published review. It focuses on the above-mentioned hybrid and multi-source energy harvesters as well as on integrated harvesters, energy storage systems and end users (e.g., sensors), including CMOS (complementary metal-oxide-semiconductor) technology-based harvesters and systems.

Keywords: energy harvesting, hybrid, multi-source, integration, energy storage, piezoelectric, triboelectric, photovoltaic

OPEN ACCESS

Edited by:
Michael P. M. Jank, Fraunhofer Institut für Integrierte Systeme und Bauelementetechnologie IISB, Germany

Reviewed by:
Romana Schirhagl, University Medical Center Groningen, Netherlands
Hien Duy Tong, Nanosens BV, Netherlands

****Correspondence:***
Yang Bai
yang.bai@oulu.fi

Specialty section:
This article was submitted to Translational Materials Science, a section of the journal Frontiers in Materials

Received: *10 July 2018*
Accepted: *23 October 2018*
Published: *13 November 2018*

Citation:
Bai Y, Jantunen H and Juuti J (2018) Hybrid, Multi-Source, and Integrated Energy Harvesters. Front. Mater. 5:65. doi: 10.3389/fmats.2018.00065

INTRODUCTION

Energy harvesting technology covers the conversion of solar/light, vibration/kinetic, wind/fluidic, magnetic, and thermal energies into electricity, via various mechanisms such as the photovoltaic, piezoelectric, electromagnetic, electrostatic, triboelectric, magnetostrictive, thermoelectric, and pyroelectric effects. Recently, a comprehensive review of energy harvesting research has been published (Bai et al., 2018). It summarizes single-source energy harvesters and focuses on hybrid and multi-source energy harvesters with novel materials and structures. In addition, the latest comprehensive reviews on piezoelectric energy harvesters, where the majority of energy harvesting research is relevant, have now been published (Uchino, 2018; Yang et al., 2018c).

This mini review focuses on hybrid and multi-source energy harvesters as well as those integrated with energy storage and/or sensors. Works reported in the first half of 2018 are included and it is recommended to be read together with the reference (Bai et al., 2018) as this review provides a timely update. Hybrid, single-source energy harvesters contains recent work on hybrid, single-source energy harvesters. Hybrid, multi-source energy harvesters involves the work on hybrid, multi-source energy harvesters. Energy harvesters integrated with energy

storage and/or end users introduces the work on the integration of energy harvesters with energy storage or sensors, including CMOS (complementary metal-oxide-semiconductor) technology-based harvesters and systems. In certain situations, energy storage systems can act simultaneously as harvesters and these works are also included in Energy harvesters integrated with energy storage and/or end users. Conclusions and perspectives concludes this mini review and provides perspectives for further research.

HYBRID, SINGLE-SOURCE ENERGY HARVESTERS

Kinetic energy harvesters have the largest number of available energy conversion mechanisms among all the harvesters, however each has its own advantages and disadvantages. The piezoelectric effect can generate only moderate output voltage and power density with a large matched resistive load (up to the MΩ level), but has the advantage of ease of miniaturization. The triboelectric effect can provide very high output voltage, high peak power density and flexibility, and this makes triboelectric harvesters considerably attractive for wearable applications. However, the matched resistive load for the maximum output power is usually also very large (tens of MΩ). This challenges the regulator designs in interface circuits (ICs). Also, triboelectric harvesters are mostly made with polymers which cannot endure the high or low temperatures which may be generated by combustion engines/electric motors or the ambient conditions in the polar winter, respectively. Electrostatic and electrostrictive effects can also provide solutions for flexibility or miniaturization but an external voltage source is needed in most cases. The electromagnetic effect is able to offer large output power if space is not limited but, otherwise, miniaturization and low power density will be the main issues. The magnetostrictive effect requires the presence of both piezoelectric materials and permanent magnets in order to harvest kinetic energy. On the other hand, this enables structural hybridization, thus allowing multiple sources (i.e., kinetic energy and magnetic field) to be harvested simultaneously.

Because of energy losses, each of the above-mentioned effects has a limit on the harvestable kinetic energy and extractable electricity and hence a limit on the energy conversion efficiency. Therefore, the hybridization of several kinetic energy harvesting effects into the same harvester not only complements each other's disadvantages but also helps to increase the overall efficiency. Hybrid harvesters for kinetic energy are the most common single-source harvesters.

A bi-directional, piezoelectric-electromagnetic hybrid harvester built around a tube-shaped frame, combining two piezoelectric cantilevers with cuboidal magnets as tip masses, a suspended cylindrical magnet and a set of coils, has been reported (Fan et al., 2018a). The two cantilevers were attached at both ends of the tube frame. The cylindrical magnet was suspended in the tube. The coils were wound around the wall of the tube. The harvester could be excited in two directions, i.e., along the tube length and thus driving the suspended magnet to move in the tube, or perpendicular to the tube length and thus bending the cantilevers. In the former scenario, the moving magnet passes through the coil, harvesting the kinetic energy via the electromagnetic effect. It also couples with the two magnets on the cantilever tips, forcing the cantilevers to bend and thus harvesting the energy via the piezoelectric effect simultaneously. In such a working mode, the harvester could be driven at an ultra-low frequency (<10 Hz). In a capacitor charging test, this hybrid harvester showed an efficiency increase of up to 49 and 14% compared to its electromagnetic and piezoelectric individual counterparts, respectively (Fan et al., 2018a).

Another piezoelectric-electromagnetic hybrid harvester has been designed for higher operating frequencies (60–120 Hz) (Li et al., 2018a). A piezoelectric beam was fixed at both ends, with a magnet attached at the center of the beam. A set of coils was placed under the magnet with an adjustable gap. When the beam was excited by vibration, the energy was harvested via both piezoelectric and electromagnetic effects. Although the data for efficiency calculation were not fully given, the output power of the hybrid harvester was shown to be up to 40 and 130% higher than those of its piezoelectric and electromagnetic counterparts, respectively (Li et al., 2018a). In addition, a couple of recently published patents reveal two-dimensional (or two-degree-of-freedom) piezoelectric-electromagnetic hybrid harvesters (Fan et al., 2018b,c). Such harvesters comprised a U-shaped piezoelectric cantilever or two-stage piezoelectric cantilevers, magnets, coils, springs, and other supportive structures. These harvesters, as claimed in the patent descriptions, featured compact design, high energy conversion efficiency, and low cost (Fan et al., 2018b,c).

Biomechanical energy (e.g., human body movement) is another important kinetic energy source which is attractive in the application of wearable electronics. An electromagnetic-triboelectric hybrid harvester has been designed and fabricated for the energy generated from the swinging behavior of human arms during locomotion (Maharjan et al., 2018). An ABS (acrylonitrile butadiene styrene) ring tube was fabricated by 3D printing and a 50 μm PTFE (polytetrafluoroethylene) film with a nanowire-like surface was fabricated and then attached on the inner wall of the ABS tube. Inter-digitated Al electrodes and Cu coils were wrapped around the tube and the Al and Cu layers were separated by Kapton tape. Meanwhile, an NdFeB magnetic ball was placed in the tube. Such a harvester can be worn on the wrist, thus harvesting the human arm swinging motion during walking or running. The Al electrodes and nanowire-like surface of the PTFE acted as the triboelectric harvester, whilst the magnet and Cu coils acted as the electromagnetic harvester. In a capacitor charging test this hybrid harvester showed efficiency increases of 9 and 300% at the early stage of the charging compared to its electromagnetic and triboelectric individual counterparts, respectively. At the later stage of the charging, the increases were 36 and 25%, respectively. With a 5 s charging, the harvested energy was able to power a wristwatch to operate for 410 s. This harvester could also power a heart-rate sensor and monitor real-time signals of the wearer's heart rates.

Another electromagnetic-triboelectric hybrid harvester has been created for oceanic energy harvesting (Feng et al., 2018).

Figure 1A explains the structure of this harvester. Seven Al electrodes covered by PTFE were fixed on an acrylic substrate. The electrodes were made into three groups, forming a honeycomb-like three electrode structure, as marked by different colors in the figure. A magnet was suspended above the substrate via three springs while the bottom of the magnet was covered by another Al electrode, thus acting as the triboelectric harvester in cooperation with the PTFE and other electrodes. The triboelectric harvester could work in both in-plane sliding mode and vertical contact-separation mode. Seven sets of Cu coils were attached on the back of the substrate, acting as the electromagnetic harvester together with the magnet. In a capacitor charging test, the hybrid harvester achieved 54 and 150% efficiency increases compared to those of its electromagnetic and triboelectric individual counterparts (Feng et al., 2018). **Table 1** summarizes the hybrid, single-source energy harvesters reviewed in this paper.

HYBRID, MULTI-SOURCE ENERGY HARVESTERS

Magnetic and Kinetic Energy

In practice, a single energy source may not always be powerful and stable enough for a harvester to generate sufficient electricity for the end usage. Multi-source energy harvesting through structural hybridization or multi-functional materials addresses this issue. By employing magnetostrictive and piezoelectric materials at the same time, ambient magnetic waves dissipated from electric devices and power transmission lines can be

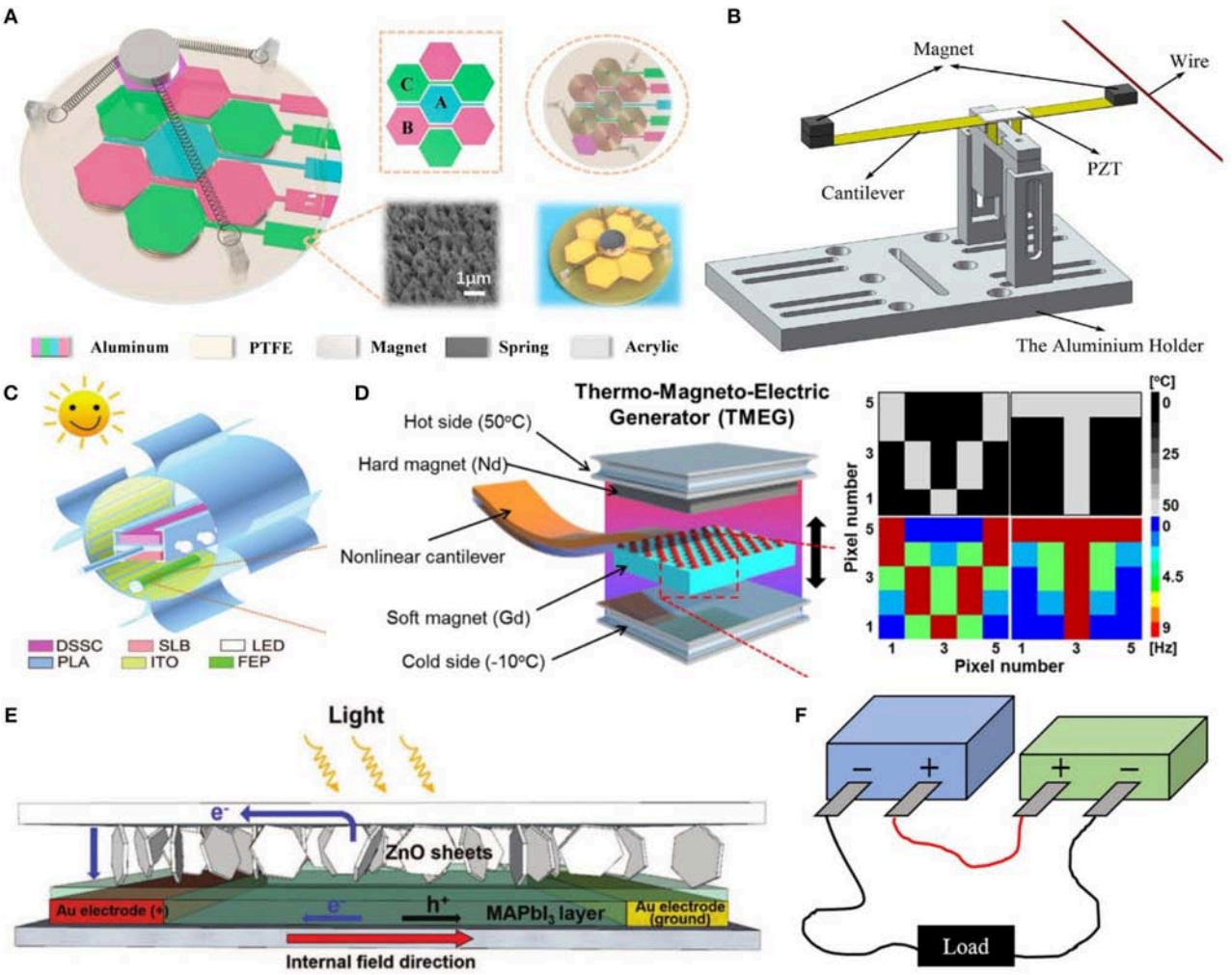

FIGURE 1 | (A) Schematic of a honeycomb-like, three-electrode and triboelectric-electromagnetic hybrid energy harvester for ocean waves. Reproduced with permission (Feng et al., 2018). Copyright 2018, Elsevier. **(B)** Schematic of a hybrid harvester for vibrational and magnetic energy. Reproduced under the terms of the Creative Commons Attribution (CC BY) license (Hu et al., 2018). Copyright 2018, AIP Publishing. **(C)** Schematic of a triboelectric-photovoltaic hybrid energy harvester for self-powered lighting. Reproduced with permission (Cao et al., 2018). Copyright 2018, John Wiley and Sons. **(D)** Schematic of a thermoelectric energy harvester employing piezoelectric effect (left) and its demonstration of surface temperature mapping function (right). Reproduced with permission (Chun et al., 2018). Copyright 2018, American Chemical Society. **(E)** Schematic and working principle of a monolithic, solar-powered tactile sensor. Reproduced with permission (Saraf et al., 2018). Copyright 2018, John and Wiley and Sons. **(F)** Schematic of the Li-ion batteries working as a kinetic energy harvester simultaneously. Reproduced with permission (Schiffer and Arnold, 2018). Copyright 2017, Springer Nature.

TABLE 1 | Summary of the hybrid energy harvesters and integrated harvester-storage/harvester-end user systems.

Input energy source	Energy conversion principle	Materials/configuration	Output power or efficiency	Increase of output	End user	Reference
Vibration (<10 Hz), sinusoidal excitation, 1.5 g acceleration	Piezoelectric + Electromagnetic	Piezoelectric cantilever coupled with suspended magnet	1.41 mW	14–49% (efficiency)	–	Fan et al., 2018a
Vibration (60–120 Hz resonant frequencies)	Piezoelectric + Electromagnetic	PZT on stainless steel beam, NdFeB magnet	150 μW	40–130% (power)	–	Li et al., 2018a
Vibration	Piezoelectric + Electromagnetic	U-shaped piezoelectric cantilever or two-stage piezoelectric cantilevers, magnets, coils, springs, frames, cylinders, and fixed/detachable fixtures or fixed clamp	–	–	–	(Fan et al., 2018b,c)
Biomechanical (human arm motion)	Electromagnetic + Triboelectric	PTFE film with nanowire-like surface, NdFeB magnet, Al, and Cu electrodes	25 μW (calculated from capacitor charging test)	9–300% (efficiency)	Wristwatch (5 s charging−410 s operation); Heart-rate sensor	Maharjan et al., 2018
Oceanic wave	Electromagnetic + Triboelectric	PTFE film, magnet, Al electrodes, Cu coils	0.47 μW (calculated from capacitor charging test)	54–150% (efficiency)	–	Feng et al., 2018
Magnetic wave (50–60 Hz, <1 mT)	Magnetostrictive + Piezoelectric	PMN-PZT single crystal macro-fiber composite, textured Fe-Ga alloy	3.8 mW or 3.22 mW/cm^3	An order of magnitude compared to piezoelectric kinetic energy harvesting (power density)	Wireless sensor networks for IoT	Annapureddy et al., 2018
Magnetic wave (50 Hz) + vibration (<10 Hz)	Electromagnetic induction + Piezoelectric	PZT, $Nd_2Fe_{14}B$ magnets, beryllium bronze beam	200 μW	up to 300% (power)	–	Hu et al., 2018
Wind and solar energy	Triboelectric + photovoltaic	FEP film, ITO electrodes, DSSC	–	33–100% (efficiency)	SLB and LED	Cao et al., 2018
Raindrops and solar energy	Triboelectric + photovoltaic	Si, PEDOT:PSS, Ag, and Al electrodes, PDMS	13.6% (solar part, measured) 1.74 mW/m^2 (triboelectric part simulated)	–	–	Liu et al., 2018d
Kinetic energy (with the potential of harvesting solar energy)	Piezoelectric (potentially with photovoltaic)	PVDF, ZnO nanowires	–	300% compared to that of sole PVDF (voltage)	–	Ma et al., 2018
Wind/weak airflow (and potentially kinetic)	Pyroelectric (potentially with piezoelectric)	PVDF, vortex generator	2.82 μW/cm^2	–	–	Raouadi and Touayar, 2018
Solar, kinetic (wind, raindrops, and impact) and RF energy	Photovoltaic, piezoelectric, electromagnetic, and RF energy harvesting circuit	Polymer solar cell, PVDF, magnet, coils, RF energy harvesting circuit, and other supportive structures	–	–	Energy harvesting umbrella, portable charging station, rechargeable battery	Lu et al., 2018
Forced vibration on pipes	Piezoelectric	Piezoelectric patch	μW level	–	Damage detector and indicator for control	Cahill et al., 2018
Low-frequency human body motion	Piezoelectric	Impact-based piezoelectric harvester	122 μW	–	Neural activity monitor	Kim et al., 2018
Thermal energy (temperature gradient)	Piezoelectric	Trapezoidal stainless steel cantilever, PVDF, macro-fiber composite, Nd, and Gd magnets, Ag nanoparticles	80 μW	2200% (power)	Temperature-mapping sensors	Chun et al., 2018

(Continued)

TABLE 1 | Continued

Input energy source	Energy conversion principle	Materials/configuration	Output power or efficiency	Increase of output	End user	Reference
Vehicle exhaust flow	Triboelectric	PTFE, Al electrode, NO_2 sensor, LED	~ 90 μW	–	Exhaust detector	Shen et al., 2018
Rotation	Triboelectric + electromagnetic	Acrylic, steel bar, spring, nylon screw, Cu coil, Cu, PTFE film, magnets	30 μW (calculated from capacitor charging test) or 150 μW/cm^2	70–300% (efficiency)	Rotation speed and displacement sensor	Yang et al., 2018a
Solar and thermal (temperature gradient) energy	Photovoltaic + thermoelectric	Sensor, computational module, communication module, energy harvesting system, and battery	349 mW (photovoltaic) 18 mW (thermoelectric)	–	Floating wireless sensor node	Lee et al., 2018
Solar (light) energy	Photovoltaic	$MAPbI_3$ film, Au electrodes, ZnO nanosheets	–	–	Tactile sensor	Saraf et al., 2018
Solar (light) energy	Photovoltaic	2D perovskite, glass, Al, stainless steel, Li, whatman borosilicate paper soaked with $LiPF_6$, Cu, FTO	39 μW (calculated form the charging test)	–	Li-ion photobattery	Ahmad et al., 2018
Kinetic energy (compression)	Piezoelectrochemical	Pouch cells containing LCO and graphite electrodes	0.012%	–	Li–ion battery	Schiffer and Arnold, 2018
Kinetic energy (pressure)	Piezoelectrochemical	CNT/Ti mesh electrodes, Al_2O_3 membrane	0.03–0.1%	–	Supercapacitor	Yang et al., 2018b
Solar and kinetic energy	Photovoltaic and piezoelectric	CMOS−130 nm technology-based interface circuit including dual-mode DC-DC converter, programmable switch, MPPT, and supercapacitor	0.5–2.7 mW 61–90.5% (efficiency of the circuit, not the harvesters)	–	IoT	Elhebeary et al., 2018
Thermal (temperature gradient) and vibration energy	Thermoelectric, electromagnetic and piezoelectric	CMOS−180 nm technology-based interface circuit including cross-coupled charge pump, low drop-out AC-DC doubler, negative voltage converter, synchronous power extraction, DC-DC conversion, external inductor, and Schottky diode	110 μW	360% (power)	Wearable devices	Ulusan et al., 2018
RF energy (−15 dBm, 900 MHz)	Antenna and RF-DC converter	CMOS-180 nm technology, RF-DC converter, MPPT	11 μW 39.3%	–	–	Khan et al., 2018
RF energy (−16 dBm, 915 MHz)	Antenna and RF-DC converter	CMOS-130 nm technology, RF-DC converter, voltage limiter, level shifter, buffer, back scattering switch, temperature sensor (consisting of voltage regulator and subthreshold ring oscillator)	17.63% (back scattering switch deactivated) 7.67% (loaded with wireless sensor and back scattering switch activated)	–	Temperature sensor	Saffari et al., 2018
Solar energy	Photovoltaic	Standard CMOS process, vertical $P+$-N_{well}-P_{sub} junctions, imaging with holes as charge carriers	30 μW 998 pW/klux/mm^2	15–1100% (compared to literature)	Image sensor	Park et al., 2018

harvested. For instance, a magneto-mechano-electric generator consisting of a highly textured Fe-Ga alloy (magnetostrictive) and a $Pb(Mg_{1/3}Nb_{2/3})O_3$-$Pb(Zr,Ti)O_3$ (PMN-PZT) single crystal macro-fiber composite (piezoelectric) has been reported to achieve an output power density of 3.22 mW/cm^3 with <1 mT magnetic input energy. This power density was an order of magnitude higher than that using piezoelectric cantilevers to harvest kinetic energy (Annapureddy et al., 2018). A wireless sensor network for the IoT (Internet of Things) could be powered by such harvested energy for timing and sensing (pressure and temperature) functions. Although simultaneously harvesting kinetic energy via the piezoelectric effect was not realized in this work, it is definitely an option for such a hybrid structure.

A specially designed piezoelectric cantilever with magnets as tip masses has also been reported to simultaneously harvest magnetic and vibrational energy (Hu et al., 2018). **Figure 1B** shows the configuration. A beryllium bronze beam was fabricated with a special curve which was fixed with an Al holder and a PZT ($Pb(Zr,Ti)O_3$) piezoelectric transducer was attached above the curve and bridged the two parts of the beam. Two magnets were embedded on both tips of the beam. The hybrid harvester was placed close to a wire emitting a magnetic field and subject to a vibration. An output power increase of up to 300% was achieved when simultaneously harvesting both energy sources compared to that of harvesting either single source (Hu et al., 2018).

Kinetic and Solar Energy

Kinetic and solar energy can be considered the most pervasive and commonly co-existing ambient energy sources, where harvesting of both simultaneously can be significantly beneficial. A self-powered lantern based on a triboelectric-photovoltaic hybrid structure has been built for harvesting wind and light energy (Cao et al., 2018). **Figure 1C** shows the schematic of the configuration. A transparent PLA (polylactic acid) tube was connected to a central axis rod via bearings and transparent, inter-digitated ITO electrodes were coated on the inner wall of the tube. A rod coated with a layer of FEP (fluorinated ethylene propylene) film was placed on top of the ITO electrodes. A DSSC (dye-sensitized solar cell) was also mounted in the tube as shown in the figure. In addition, a SLB (soft lithium battery) and 10 LEDs (light-emitting diodes) were connected. The PLA tube rotated when driven by the wind, and the freely moving FEP rod generated friction with the ITO electrodes, thus harvesting the wind energy through the triboelectric effect. Meanwhile, solar energy was harvested by the DSSC. The harvested energy was stored in the SLB and used for lighting the LEDs. Being charged for 0.88 h, the SLB could be discharged for 4.12 h with 10 μA current (Cao et al., 2018). This performance was equivalent to 100 and 33% efficiency increases compared to those of the individual triboelectric generator and solar cell, respectively.

A lamination of Al, Si, PEDOT:PSS (poly(3,4-ethylenedioxythiophene):poly(styrenesulfonate)), Ag finger electrode and PDMS (polydimethylsiloxane) from bottom to top has been proposed to harvest solar energy and raindrops (Liu et al., 2018d). The novelty of this hybrid harvester is that the PEDOT:PSS layer acted not only as an anti-reflection layer for the Si solar cell but also as the mutual electrode for the triboelectric component (PDMS). The raindrops hit the PDMS layer and thus electricity was generated via the triboelectric effect which complemented the efficiency decrease of the solar cell on rainy days. The efficiency of the solar cell was measured to be 13.6% under a standard AM 1.5G solar spectrum and the output power density of the triboelectric component was simulated to be 1.74 mW/m^2 (Liu et al., 2018d).

Apart from structural hybridization as introduced above, multi-source energy harvesters can also be realized with multi-functional materials. Details have been given in the reference (Bai et al., 2018). Recently, a PVDF (polyvinylidene fluoride)-ZnO composite has been reported (Ma et al., 2018). The composite consisting of 33 wt% ZnO nanowires and PVDF polymer helped to increase the output voltage by over 300% compared to that using PVDF only. Although ZnO has a wide band gap and cannot absorb the visible range of the solar spectrum, such a composite does provide a potential method of making multi-functional materials by replacing the ZnO filler with some narrow band gap materials. In this case the PVDF matrix can perform as a piezoelectric harvester and the filler as a photovoltaic harvester.

Wind and Thermal Energy

The pyroelectric effect is known for the energy harvesting from temperature fluctuations. A pyroelectric harvester has been reported to utilize a vortex to generate the temperature fluctuation and thus harvest wind energy via the pyroelectric effect (Raouadi and Touayar, 2018). The vortex generator was a right-angled substrate on which a PVDF film was deposited on the horizontal part. The wind flowed along the horizontal direction and when it collided with the vertical part of the substrate, a vortex and thus a temperature fluctuation was generated and applied to the PVDF film. An output power density of 2.82 $\mu W/cm^2$ was obtained. The main advantage of this harvester was that it was able to capture energy even with a very weak air flow (down to 1 m/s velocity) (Raouadi and Touayar, 2018). Although the piezoelectric effect was not mentioned, PVDF is also ferroelectric and well known for its co-exhibition of piezoelectric and pyroelectric effects. Therefore, this structure could naturally become a multi-source harvester by employing the piezoelectric effect at the same time. Stronger ferroelectric materials e.g., PZT ($Pb(Zr,Ti)O_3$), PMN-PT ($Pb(Mg_{1/3}Nb_{2/3})O_3$-$PbTiO_3$), Mn-doped BNT-BT ($(Bi_{0.5}Na_{0.5})TiO_3$-$BaTiO_3$), and $Sr_{0.5}Ba_{0.5}NbO_3$ (Bowen et al., 2014a,b) could also replace the PVDF in order to improve the piezoelectric and pyroelectric performance.

Solar, Kinetic, and Radio Frequency Energy

A recently published patent has released the design of an umbrella apparatus which managed to incorporate photovoltaic, piezoelectric, electromagnetic, and radio frequency (RF) energy harvesters into different parts of an umbrella (Lu et al., 2018). The canopy of the umbrella was replaced by a multi-layer lamination combining photovoltaic and piezoelectric energy harvesters. The lamination consisted of an inverted polymer solar cell layer (He et al., 2012), a PVDF piezoelectric layer, electrode layers, and other supportive layers. When the energy harvesting canopy was open, solar and kinetic (i.e., wind and raindrops) energy

could be harvested. Meanwhile, the open canopy could spin when subjected to wind force, thus driving a miniature windmill (electromagnetic energy harvester) embedded in the shaft of the umbrella. In addition, the shaft of the umbrella could act as a monopole antenna and an RF energy harvesting circuit could be installed in the shaft in order to harvest RF energy. Furthermore, the shaft, in conjunction with a movable ferrule, contained a magnet and coils. When the canopy was closed, the umbrella could used as a cane. By striking the ferrule on the ground while walking, the magnet would be forced to move through the coils, forming another electromagnetic harvester. Apart from these energy harvesting components, the necessary DC-DC converters, switches, conductive leads and a rechargeable battery were also installed in the umbrella (Lu et al., 2018). Personal electronic devices could be charged through a port of the umbrella so that the entire umbrella became a self-powered, portable charging station. Hybrid, multi-source energy harvesters in this paper are also summarized in **Table 1**.

ENERGY HARVESTERS INTEGRATED WITH ENERGY STORAGE AND/OR END USERS

Harvester-Sensor Integrations

The IoT is undoubtedly where energy harvesting technology is aiming to have a significant impact. As the IoT requires an extensive number of sensors and wireless sensor networks, energy harvesters need to show their compatibility when integrated or utilized in different cases rather than only giving consideration to their output performance. As energy harvesters as individual components are becoming mature, there is an increasing number of publications demonstrating the feasibility of integrated energy harvesters with sensors or electricity consuming devices.

Piezoelectric energy harvesters have been integrated with structural health monitoring sensors for various constructions and bio-activity monitoring circuits used in implantable biomedical devices. In the former case piezoelectric patches were attached on a pipe which was undergoing forced vibrations, for the purposes of damage detection and indicators for control (Cahill et al., 2018). In the latter case, a self-powered neural activity monitor consisting of an impact-based piezoelectric harvester, a power transfer circuit, and a neural signal monitoring circuit was proposed (Kim et al., 2018). Both of them successfully demonstrated enough energy generated by the harvesters to power all the devices, as well as the feasibility and reliability of these methods.

A thermo-magneto-piezoelectric generator made with a non-linear piezoelectric cantilever, a hard magnet (Nd) and a soft magnet (Gd) has been reported (Chun et al., 2018). **Figure 1D** (left) shows the configuration of the harvester. The soft magnet was attached to the tip of the piezoelectric cantilever and the hard magnet was placed on the hot side. As the soft magnet was ferroelectric, it was attracted by the hard magnet but when they touched each other the temperature of the soft magnet became higher than the Curie temperature and it thus became paramagnetic (losing its permanent magnetic properties momentarily). The soft magnet was then released, driving the cantilever to oscillate and harvest the vibration energy. When the soft magnet cooled down and returned to the ferromagnetic state, a new cycle started. With this method, thermal energy (temperature gradient) was harvested via the piezoelectric effect. By applying Ag nanoparticles on the surface of the soft magnet, thermal transport was enhanced. This, together with the non-linearity of the cantilever, induced a 2200% higher output power compared to that of the linear counterpart (Chun et al., 2018). Such a harvester was used to power temperature-mapping sensors, thus monitoring the surface thermal variations, as shown in **Figure 1D** (right).

A self-powered chemical sensing system has been built by connecting a resistance-type gas (NO_2) sensor with a contact-separate mode triboelectric harvester in series and an LED in parallel (Shen et al., 2018). The system worked as a vehicle exhaust detector, where the triboelectric harvester was driven by the motor vehicle exhaust flow, thus powering the gas sensor and giving an alarm via the LED. The system provided an independent operation regardless of the working frequency of the harvester.

An electromagnetic-triboelectric hybrid harvester-sensor integration has been reported to be able to harvest the kinetic energy of vehicular wheel rotation and act as a rotation speed and displacement sensor simultaneously (Yang et al., 2018a). With the hybrid harvesting working principle, an efficiency increase of 70–300% was achieved. The sensing data could be transmitted wirelessly, which provided a potential application for self-powered rotating mobile devices used in a remote environment (e.g., a moon car).

A floating wireless sensor node has been reported to be powered by solar and thermal energy via photovoltaic and thermoelectric harvesters, respectively. On a sunny day, the sensor node could operate self-sufficiently on the water, enabling long-range wireless communication between the sensor node and a gateway. The sensor node consumed 6.6 Wh energy per day (equivalent to 275 mW power), whilst the solar panels and thermoelectric generator could provide 349 and 18 mW power, respectively (Lee et al., 2018).

Some organic-halide perovskites, e.g., $(CH_3NH_3)PbI_3$ ($MAPbI_3$), are known for the co-existence of their ferroelectric and photovoltaic properties (Bai et al., 2018). Based on this unique feature, a self-powered tactile sensor has been fabricated using ZnO nanosheets and $MAPbI_3$ film (Saraf et al., 2018). The schematic and working principle of the configuration is shown in **Figure 1E**. The $MAPbI_3$ film was poled laterally, with the ZnO nanosheets aligned approximately perpendicular to the film. The ZnO acted as a pressure-sensitive drain. This means that when a pressure was applied, the ZnO nanosheets were forced to bend, thus increasing their interfacing area with the $MAPbI_3$ film. Under illumination, this resulted in a higher charge collection and a pressure-sensitive modulation of the photocurrent. Such a solar-powered tactile sensor could be functional for more than 72 h after a 5 min poling process which required a 55 $\mu W/h{\cdot}cm^2$ energy budget (Saraf et al., 2018).

Harvester-Storage Integrations

In practice, it is common to connect a solar cell with a Li-ion battery for simultaneous energy harvesting and storage. However, a monolithic photo-battery has been invented to substitute this two-component solar cell-battery combination (Ahmad et al., 2018). A highly photoactive 2D perovskite, $((C_6H_9C_2H_4NH_3)_2PbX_4$ (X = I or Br), was used for both photo-charging and Li-ion storage. The photo-battery was a lamination of glass, Al, stainless steel, metal Li, Whatman borosilicate paper soaked with $LiPF_6$, 2D perovskite, Cu and FTO (fluorine-doped SnO_2) layers, from bottom to top. The efficiency and capacity (up to 100 mAh/g) similar to that of individual photovoltaic materials and batteries, respectively, were retained.

Apart from their electrochemical properties, Li-ion intercalation materials are also mechanically active. When a stress is applied, they can exhibit a mechanical-electrochemical coupling that increases the voltage of the battery (Schiffer and Arnold, 2018). Therefore, a study into using Li-ion batteries to simultaneously harvest energy has been carried out (Schiffer and Arnold, 2018). Two 170 mAh pouch cells containing LCO (lithium cobalt oxide) and graphite electrodes were connected together as shown in **Figure 1F**. The green cell was compressed as the harvester and the blue one was the reference and reservoir. The efficiency of this harvester-storage integration was only 0.012%, much smaller than that of conventional kinetic energy harvesters such as piezoelectric, electromagnetic, and triboelectric systems (Bai et al., 2018). The theoretical efficiency was predicted to be 2.9%. A supercapacitor has been reported for the same purpose of simultaneously harvesting and storing energy (Yang et al., 2018b). A piece of anodic Al_2O_3 membrane with nanochannels was sandwiched between two layers of CNT (carbon nanotube)/Ti mesh electrodes. The electrolyte started to flow when subjected to pressure, causing the electrokinetic supercapacitor to operate in both harvesting and storage modes. The efficiency could reach 0.03–0.1% under one bar pressure or regulated external load.

CMOS Technology-Based Harvesters and Systems

As sensors (especially large sensors for the IoT) are made with CMOS technology, work focusing on the full integration of energy harvesters (and/or storage), interface circuits and sensors based on CMOS technology are also reviewed here. CMOS technology provides an approach to integrating all micro-scale components on one chip. Therefore, a number of CMOS-based power conditioning circuits (e.g., converters, rectifiers, etc.) for energy harvesting have been reported, including those allowing multiple energy sources as the input (Camarda et al., 2018; Katic et al., 2018; Li et al., 2018b; Liu et al., 2018a,b,c; Luo et al., 2018; McCullagh, 2018; Shi et al., 2018; Taghadosi et al., 2018; Wang et al., 2018; Yi et al., 2018a,b; Yoon et al., 2018).

A low-power battery-less energy harvesting system implemented in a CMOS−130 nm technology for IoT applications used a dual-mode DC-DC converter to harvest solar and kinetic energy via photovoltaic and piezoelectric transducers, respectively (Elhebeary et al., 2018). A supercapacitor was used as the storage. On-chip, there were also a programmable switch to optimize the efficiency of the system and a maximum power point tracking circuit (MPPT). This circuit realized self-starting and a peak efficiency of 90.5% (the ratio of rectified energy to harvested energy) (Elhebeary et al., 2018). Meanwhile, a triple-source hybrid circuit implemented in a CMOS−180 nm technology managed simultaneously to extract thermal energy via a thermoelectric harvester and vibration via electromagnetic and piezoelectric harvesters, and then deliver a single DC output (Ulusan et al., 2018). The system included an on-chip cross-coupled charge pump to boost the thermoelectric voltage, a low drop-out AC-DC doubler to rectify the electromagnetic output, and a combination of negative voltage converter, synchronous power extraction, DC-DC converter and external inductor for the piezoelectric signal. Tested with an electromagnetic harvester worn on the wrist of a jogger, a commercial low volume PZT-based harvester and a thermoelectric generator, the system provided up to 110 μW output power in the simultaneous multi-mode operation, equivalent to 460% of the power delivered by a stand-alone circuit (Ulusan et al., 2018).

Beside CMOS-based power conditioning circuitry, full integrations involving energy harvesters have also been reported. For instance, RF energy harvesters were integrated with a power management circuit, temperature sensor or image sensor on the same chip (Khan et al., 2018; Park et al., 2018; Saffari et al., 2018). The RF-DC converter using internal threshold voltage cancellation with an auxiliary transistor block was implemented in a CMOS−180 nm technology together with a MPPT (Khan et al., 2018). This RF harvesting system delivered nearly 11 μW output power and 39.3% power conversion efficiency with −15 dBm, 900 MHz input (Khan et al., 2018).

On the other hand, implemented in a CMOS−130 nm technology, a fully integrated RF-powered temperature sensor managed to operate non-intermittently with 1.05 μW power consumption and −16 dBm, 915 MHz input (Saffari et al., 2018). As distinct from other works, this RF harvester-temperature sensor system eliminated the power management circuit for a minimalistic design. To achieve this, a subthreshold ring oscillator was used in order to produce a highly temperature-dependent oscillation frequency, thus acting as a temperature-frequency converter. The frequency-modulated signal was then transferred to an external reader using back scattering (Saffari et al., 2018).

A multifunctional CMOS active pixel which could simultaneously complete the tasks of imaging and energy harvesting has been reported (Park et al., 2018). In contrast to conventional CMOS electron-based imaging pixels, this work adopted a hole-based imaging method, being able to self-power the image capturing function at 15 fps with the energy harvested from >60 klux illumination. The output power density of 998 pW/klux/mm^2 was the highest among all counterparts of its kind (Park et al., 2018). A summary of the integrated energy harvesters introduced in this paper is given in **Table 1**.

Others

Other relevant circuit designs for ultra-low power management used in energy harvesting powered IoT systems, with a special

focus on multiple energy sources, have recently been reviewed (Estrada–Lopez et al., 2018).

CONCLUSIONS AND PERSPECTIVES

Recent works on hybrid single-source and multi-source energy harvesters have been reviewed. Although the number of investigations is not large, recent works on harvester-sensor and harvester-storage integrations, including those energy stores operating simultaneously as harvesters, have also been reviewed. As individual energy harvesters become mature, hybridization of different energy harvesting mechanisms is one of the directions of future research. The hybridization is not only limited to the configurations combining different energy conversion mechanisms via complex structures. Multi-source energy harvesting with a single-piece of multi-functional material, either composite or novel monolithic material, should particularly receive attention. Research on such a topic is relatively lacking. However, some organic-halide perovskites (e.g., $(CH_3NH_3)PbI_3$) (Rakita et al., 2017) and narrow band gap photo-ferroelectric thin-films (e.g., BFCO (Bi_2FeCrO_6)) (Nechache et al., 2015) and ceramics (e.g., KBNNO ($(K,Ba)(Ni,Nb)O_{3-\delta}$), KNBNNO ($(K,Na,Ba)(Ni,Nb)O_{3-\delta}$)) (Bai et al., 2017a,b), have been proved to have both visible-range photovoltaic effect and recognizable/strong ferroelectricity. Novel multi-source energy harvesters can be developed based on such materials, where photovoltaic, piezoelectric, and pyroelectric effects can be exhibited simultaneously to harvest solar, kinetic and thermal energy with only one material. In addition, in order better to support industrial applications, more self-powered sensing systems or self-charging energy stores need to be developed. The feasibility of these devices will be significantly improved when employing hybrid or multi-source energy harvesters to increase their efficiency.

AUTHOR CONTRIBUTIONS

All authors listed have made a substantial, direct and intellectual contribution to the work, and approved it for publication.

ACKNOWLEDGMENTS

JJ acknowledges the funding of the Academy of Finland (project numbers 267573 and 298409).

REFERENCES

Ahmad, S., George, C., Beesley, D. J., Baumberg, J. J., and De Volder, M. (2018). Photo–rechargeable organo–halide perovskite batteries. *Nano Lett.* 18, 1856–1862. doi: 10.1021/acs.nanolett.7b05153

Annapureddy, V., Na, S., Hwang, G., Kang, M. G., Sriramdas, R., Palneedi, H., et al. (2018). Exceeding milli–watt powering magneto–mechano–electric generator for standalone–powered electronics. *Energy Environ. Sci.* 11, 818–829. doi: 10.1039/C7EE03429F

Bai, Y., Jantunen, H., and Juuti, J. (2018). Energy harvesting research: the road from single source to multisource. *Adv. Mater.* 30:1707271. doi: 10.1002/adma.201707271

Bai, Y., Siponkoski, T., Perantie, J., Jantunen, H., and Juuti, J. (2017a). Ferroelectric, pyroelectric, and piezoelectric properties of a photovoltaic perovskite oxide. *Appl. Phys. Lett.* 110:063903. doi: 10.1063/1.4974735

Bai, Y., Tofel, P., Palosaari, J., Jantunen, H., and Juuti, J. (2017b). A game changer: a multifunctional perovskite exhibiting giant ferroelectricity and narrow bandgap with potential application in a truly monolithic multienergy harvester or sensor. *Adv. Mater.* 29:1700767. doi: 10.1002/adma.201700767

Bowen, C. R., Kim, H. A., Weaver, P. M., and Dunn, S. (2014a). Piezoelectric and ferroelectric materials and structures for energy harvesting applications. *Energy Environ. Sci.* 7, 25–44. doi: 10.1039/C3EE42454E

Bowen, C. R., Taylor, J., LeBoulbar, E., Zabek, D., Chauhan, A., and Vaish, R. (2014b). Pyroelectric materials and devices for energy harvesting applications. *Energy Environ. Sci.* 7, 3836–3856. doi: 10.1039/C4EE01759E

Cahill, P., Pakrashi, V., Sun, P., Mathewson, A., and Nagarajaiah, S. (2018). Energy harvesting techniques for health monitoring and indicators for control of a damaged pipe structure. *Smart. Struct. Syst.* 21, 287–303. doi: 10.12989/sss.2018.21.3.000

Camarda, A., Tartagni, M., and Romani, A. (2018). A−8 mV/+15 mV double polarity piezoelectric transformer–based step–up oscillator for energy harvesting applications. *IEEE Trans. Circuits Syst. I Regul. Papers* 65, 1454–1467. doi: 10.1109/TCSI.2017.2741779

Cao, R., Wang, J., Xing, Y., Song, W., Li, N., Zhao, S., et al. (2018). A self–powered lantern based on a triboelectric–photovoltaic hybrid nanogenerator. *Adv. Mater. Technol.* 3:1700371. doi: 10.1002/admt.201700371

Chun, J., Kishore, R. A., Kumar, P., Kang, M., Kang, H. B., Sanghadasa, M., et al. (2018). Self–powered temperature–mapping sensors based on thermo–magneto–electric generator. *ACS Appl. Mater. Interfaces* 10, 10796–10803. doi: 10.1021/acsami.7b17686

Elhebeary, M. R., Ibrahim, M. A. A., Aboudina, M. M., and Mohieldin, A. N. (2018). Dual–source self–start high–efficiency microscale smart energy harvesting system for IoT. *IEEE Trans. Ind. Electron.* 65, 342–351. doi: 10.1109/TIE.2017.2714119

Estrada–Lopez, J. J., Abuellil, A., Zeng, Z., and Sanchez–Sinencio, E. (2018). Multiple input energy harvesting systems for autonomous IoT end–nodes. *J. Low Power Electron. Appl.* 8:6. doi: 10.3390/jlpea8010006

Fan, K., Liu, S., Liu, H., Zhu, Y., Wang, W., and Zhang, D. (2018a). Scavenging energy from ultra–low frequency mechanical excitations through a bi–directional hybrid energy harvester. *Appl. Energy* 216, 8–20. doi: 10.1016/j.apenergy.2018.02.086

Fan, K., Ren, H., Zhu, Y., Wang, W., and Zhang, D. (2018b). "Two–degree–of–freedom piezoelectric electromagnetic hybrid energy harvester," Patent No CN107733284(A) (Xi'an).

Fan, K., Zhu, Y., Wang, W., and Zhang, D. (2018c). "Two–dimensional piezoelectric electromagnetic hybrid energy harvester," Patent No CN107834902(A) (Xi'an).

Feng, L., Liu, G., Guo, H., Tang, Q., Pu, X., Chen, J., et al. (2018). Hybridized nanogenerator based on honeycomb–like three electrodes for efficient ocean wave energy harvesting. *Nano Energy* 47, 217–223. doi: 10.1016/j.nanoen.2018.02.042

He, Z., Zhong, C., Su, S., Xu, M., Wu, H., and Cao, Y. (2012). Enhanced power–conversion efficiency in polymer solar cells using an inverted device structure. *Nat. Photonics* 6, 591–595. doi: 10.1038/nphoton.2012.190

Hu, Z., Qiu, J., Wang, X., Gao, Y., Liu, X., Chang, Q., et al. (2018). An integrated multi-source energy harvester based on vibration and magnetic field energy. *AIP Adv.* 8:056623. doi: 10.1063/1.5006614

Katic, J., Rodriguez, S., and Rusu, A. (2018). A high–efficiency energy harvesting interface for implanted biofuel cell and thermal harvesters. *IEEE Trans. Power Electr.* 33, 4125–4134. doi: 10.1109/TPEL.2017.2712668

Khan, D., Abbasizadeh, H., Kim, S., Khan, Z. H. N., Shah, S. A. A., Pu, Y. G., et al. (2018). A design of ambient RF energy harvester with sensitivity of−21 dBm and power efficiency of a 39.3% using internal threshold voltage compensation. *Energies* 11:1258. doi: 10.3390/en11051258

Kim, S., Ju, S., and Ji, C. (2018). Impact–based piezoelectric energy harvester as a power source for a neural activity monitoring circuit. *Int. J. Grid Distrib. Comput.* 11, 51–62. doi: 10.14257/ijgdc.2018.11.3.05

Lee, W., Schubert, M. J. W., Ooi, B., and Ho, S. J. (2018). Multi-source energy harvesting and storage for floating wireless sensor network nodes with long range communication capability. *IEEE Trans. Ind. Appl.* 54, 2606–2615. doi: 10.1109/TIA.2018.2799158

Li, P., Gao, S., and Cong, B. (2018a). Theoretical modeling, simulation and experimental study of hybrid piezoelectric and electromagnetic energy harvester. *AIP Adv.* 8, 035017. doi: 10.1063/1.5018836

Li, Y., Tang, Z., Zhu, Z., and Yang, Y. (2018b). A novel MPPT circuit with 99.1% tracking accuracy for energy harvesting. *Analog Integr. Cir. Signal Proc.* 94, 105–115. doi: 10.1007/s10470–017–1079–z

Liu, J., Li, Q., Liu, X., Li, Z., Liu, Y., Lin, Z., et al. (2018a). Picowatt 0.5 V supply with 3 ppm/degrees C CMOS voltage reference for energy harvesting system. *IEICE Electr. Exp.* 15:20180372. doi: 10.1587/elex.15.20180372

Liu, L., Pang, Y., Liao, X., Zhu, Z., and Yang, Y. (2018b). A power–enhanced active rectifier with offset–controlled comparator for self–powered PEH systems. *J. Circuits Syst. Comput.* 27:1850079. doi: 10.1142/S0218126618500792

Liu, L., Pang, Y., Yuan, W., Zhu, Z., and Yang, Y. (2018c). A self–powered piezoelectric energy harvesting interface circuit with efficiency–enhanced P–SSHI rectifier. *J. Semiconduct.* 394:045002. doi: 10.1088/1674–4926/39/4/045002

Liu, Y., Sun, N., Liu, J., Wen, Z., Sun, X., Lee, S., et al. (2018d). Integrating a silicon solar cell with a triboelectric nanogenerator via a mutual electrode for harvesting energy from sunlight and raindrops. *ACS Nano* 12, 2893–2899. doi: 10.1021/acsnano.8b00416

Lu, R. P., Ramirez, A. D., and Pascoguin, B. M. L. (2018). Multi-source energy harvesting device. Patent No US20180069405A1: United States of America as represented by Secretary of the Navy (San Diego, CA).

Luo, Z., Zeng, L., Lau, B., Lian, Y., and Heng, C. (2018). A Sub−10 mV power converter with fully integrated self–start, MPPT, and ZCS control for thermoelectric energy harvesting. *IEEE Trans. Circuits Syst. I Regul. Papers* 65, 1744–1757. doi: 10.1109/TCSI.2017.2757505

Ma, J., Zhang, Q., Lin, K., Zhou, L., and Ni, Z. (2018). Piezoelectric and optoelectronic properties of electrospinning hybrid PVDF and ZnO nanofibers. *Mater. Res. Exp.* 5:035057. doi: 10.1088/2053–1591/aab747

Maharjan, P., Toyabur, R. M., and Park, J. Y. (2018). A human locomotion inspired hybrid nanogenerator for wrist–wearable electronic device and sensor applications. *Nano Energy* 46, 383–395. doi: 10.1016/j.nanoen.2018.02.033

McCullagh, J. (2018). An active diode full–wave charge pump for low acceleration infrastructure–based non–periodic vibration energy harvesting. *IEEE Trans. Circuits Syst. I Regul. Papers* 65, 1758–1770. doi: 10.1109/TCSI.2017.27 64878

Nechache, R., Harnagea, C., Li, S., Cardenas, L., Huang, W., Chakrabartty, J., et al. (2015). Bandgap tuning of multiferroic oxide solar cells. *Nat. Photonics* 9, 61–67. doi: 10.1038/nphoton.2014.255

Park, S., Lee, K., Song, H., and Yoon, E. (2018). Simultaneous imaging and energy harvesting in CMOS image sensor pixels. *IEEE Electron Device Lett.* 39, 532–535. doi: 10.1109/LED.2018.2811342

Rakita, Y., Bar–Elli, O., Meirzadeh, E., Kaslasi, H., Peleg, Y., Hodes, G., et al. (2017). Tetragonal CH3NH3PbI3 is ferroelectric. *Proc. Natl. Acad. Sci. U. S. A.* 114, E5504–E5512. doi: 10.1073/pnas.1702429114

Raouadi, M. H., and Touayar, O. (2018). Harvesting wind energy with pyroelectric nanogenerator PNG using the vortex generator mechanism. *Sens. Actuator A Phys.* 273, 42–48. doi: 10.1016/j.sna.2018.02.009

Saffari, P., Basaligheh, A., Sieben, V. J., and Moez, K. (2018). An RF–powered wireless temperature sensor for harsh environment monitoring with non–intermittent operation. *IEEE Trans. Circuits Syst. I Regul. Papers* 655, 1529–1542. doi: 10.1109/TCSI.2017.2758327

Saraf, R., Pu, L., and Maheshwari, V. (2018). A light harvesting, self–powered monolith tactile sensor based on electric field induced effects in MAPbI perovskite. *Adv. Mater.* 30:1705778. doi: 10.1002/adma.201705778

Schiffer, Z. J., and Arnold, C. B. (2018). Characterization and model of piezoelectrochemical energy harvesting using lithium ion batteries. *Exp. Mech.* 58, 605–611. doi: 10.1007/s11340–017–0291–1

Shen, Q., Xie, X., Peng, M., Sun, N., Shao, H., Zheng, H., et al. (2018). Self–powered vehicle emission testing system based on coupling of triboelectric and chemoresistive effects. *Adv. Funct. Mater.* 28:1703420. doi: 10.1002/adfm.201703420

Shi, G., Xia, Y., Wang, X., Qian, L., Ye, Y., and Li, Q. (2018). An efficient self–powered piezoelectric energy harvesting CMOS interface circuit based on synchronous charge extraction technique. *IEEE Trans. Circuits Syst. I Regul. Papers* 65, 804–817. doi: 10.1109/TCSI.2017.2731795

Taghadosi, M., Albasha, L., Quadir, N. A., Rahama, Y. A., and Qaddoumi, N. (2018). High efficiency energy harvesters in 65nm CMOS process for autonomous IoT sensor applications. *IEEE Access* 6, 2397–2409. doi: 10.1109/ACCESS.2017.2783045

Uchino, K. (2018). Piezoelectric energy harvesting systems–essentials to successful developments. *Energy Technol.* 6, 829–848. doi: 10.1002/ente.201700785

Ulusan, H., Chamanian, S., Pathirana, W. P. M. R., Zorlu, O., Muhtaroglu, A., and Kulah, H. (2018). A triple hybrid micropower generator with simultaneous multi–mode energy harvesting. *Smart Mater. Struct.* 27:014002. doi: 10.1088/1361–665X/aa8a09

Wang, S., Ke, Y., Huang, P., and Hsieh, P. (2018). Electromagnetic energy harvester interface design for wearable applications. *IEEE Trans. Circuits Syst. Ii Exp. Briefs* 65, 667–671. doi: 10.1109/TCSII.2018.2820158

Yang, H., Liu, W., Xi, Y., Lai, M., Guo, H., Liu, G., et al. (2018a). Rolling friction contact–separation mode hybrid triboelectric nanogenerator for mechanical energy harvesting and self–powered multifunctional sensors. *Nano Energy* 47, 539–546. doi: 10.1016/j.nanoen.2018.03.028

Yang, P., Qu, X., Liu, K., Duan, J., Li, J., Chen, Q., et al. (2018b). Electrokinetic supercapacitor for simultaneous harvesting and storage of mechanical energy. *ACS Appl. Mater. Interfaces* 10, 8010–8015. doi: 10.1021/acsami.7b18640

Yang, Z., Zhou, S., Zu, J., and Inman, D. (2018c). High–performance piezoelectric energy harvesters and their applications. *Joule* 2, 642–697. doi: 10.1016/j.joule.2018.03.011

Yi, H., Yin, J., Mak, P., and Martins, R. P. (2018a). A 0.032–mm 0.15–V three–stage charge–pump scheme using a differential bootstrapped ring–VCO for energy–harvesting applications. *IEEE Trans. Circuits Syst. Ii Exp. Briefs* 65, 146–150. doi: 10.1109/TCSII.2017.2676159

Yi, H., Yu, W., Mak, P., Yin, J., and Martins, R. P. (2018b). A 0.18–V 382–mu W bluetooth low–energy receiver front–end with 1.33–nW sleep power for energy–harvesting applications in 28–nm CMOS. *IEEE J Solid State Circuits* 53, 1618–1627. doi: 10.1109/JSSC.2018.2815987

Yoon, E., Park, J., and Yu, C. (2018). Thermal energy harvesting circuit with maximum power point tracking control for self–powered sensor node applications. *Front. Inform. Technol. Electron Eng.* 19, 285–296. doi: 10.1631/FITEE.1601181

Conflict of Interest Statement: The authors declare that the research was conducted in the absence of any commercial or financial relationships that could be construed as a potential conflict of interest.

frontiers in Materials

REVIEW
published: 22 March 2019
doi: 10.3389/fmats.2019.00042

Ionic Liquids: Potential Materials for Carbon Dioxide Capture and Utilization

Shashi Kant Shukla[1]*, *Santosh G. Khokarale*[1], *Thai Q. Bui*[1] and *Jyri-Pekka T. Mikkola*[1,2]*

[1] Technical Chemistry, Department of Chemistry, Chemical-Biological Centre, Umeå University, Umeå, Sweden, [2] Industrial Chemistry and Reaction Engineering, Department of Chemical Engineering, Johan Gadolin Process Chemistry Centre, Åbo Akademi University, Åbo-Turku, Finland

The non-volatility, structure-tunability, and high CO_2 uptake capacity render ionic liquids (ILs) the most exciting materials for the carbon dioxide (CO_2) capture and fixation to value-added chemicals. The aim of this mini-review is to give a brief idea about the development of the potential ILs for CO_2 capture, the mechanism involved in the CO_2 binding and the application of ILs in the conversion of CO_2 to useful chemicals. The mechanisms and nature of interactions in between IL-CO_2 have been discussed in terms of the nature of cation, anion, presence of functional group, and the extent of interaction between the components of ILs. The fixation of CO_2 to linear and cyclic carbonates and electroreduction of CO_2 to carbon-rich fuels in ILs has been accounted in detail. At the end, future challenges in terms of commercializing the ILs for CO_2 capture and utilization technology are discussed.

Keywords: ionic liquid (IL), CO_2 capture, mechanism of CO_2-IL interaction, electrochemical reduction, dimethyl carbonate and faradaic efficiency

OPEN ACCESS

Edited by:
Krisztian Kordas,
University of Oulu, Finland

Reviewed by:
Sápi András,
University of Szeged, Hungary
Janos Kiss,
University of Szeged, Hungary

***Correspondence:**
Shashi Kant Shukla
shashi.kant.shukla@umu.se
Jyri-Pekka T. Mikkola
jyri-pekka.mikkola@umu.se

Specialty section:
This article was submitted to Translational Materials Science, a section of the journal Frontiers in Materials

Received: *30 November 2018*
Accepted: *22 February 2019*
Published: *22 March 2019*

Citation:
Shukla SK, Khokarale SG, Bui TQ and Mikkola J-PT (2019) Ionic Liquids: Potential Materials for Carbon Dioxide Capture and Utilization. Front. Mater. 6:42. doi: 10.3389/fmats.2019.00042

INTRODUCTION

Carbon dioxide (CO_2) emissions to the atmosphere give rise to negative environmental impacts as the release of it causes greenhouse effect leading to global warming (Ben-Mansour et al., 2016; Sanz-Perez et al., 2016). Apart from the anthropogenic activities, which account for the major release of the CO_2 into the environment, the energy gas resources, like natural or shale gas, syngas, and biogas, also contain a significant fraction of CO_2 lowering the heating value of gases, causing corrosion of equipment and demanding high energy cost during conversion and transportation (Huang et al., 2014; George et al., 2016). Therefore, developing technologies that can capture CO_2 have been of prime importance. One such technology is carbon dioxide capture and sequestration (CCS) where aqueous amine [typically monoethanolamine (MEA) and methyldiethylamine (MDEA)] are used as scavengers in CO_2 capture (Thitakamol et al., 2007). These solvents have several disadvantages such as high volatility, high cost, substantial energy consumption and corrosiveness and, therefore, designing new solvents is of prime importance (Shao and Stangeland, 2009). Ionic liquids (ILs) possess unique characteristics over the volatile organic compounds (VOCs) and have been explored in various chemical and biological applications (Steinruck and Wasserscheid, 2015). In the past decade, they were extensively studied as scrubbers of greenhouse gases (Zeng et al., 2017). The initial interests in these solvents emerged because of their negligible vapor pressure, high thermal stability, wide liquidus range, relative non-flammability, designability, and recyclability. The designability gives an extra edge to ILs over conventional scrubbers like MEA and MDEA and large number of potential ILs have been designed to achieve optimum CO_2 solubility. Of these,

the representative class consists of imidazolium, pyridinium, pyrrolidinium, guanidinium and amine cations, and organic/inorganic (carboxylate, azolate, phenoxide, prolinate, thionate, halide, tetrafluoroborate, hexafluorophosphate, anion, etc (Zhang Y. Q. et al., 2009; Goodrich et al., 2011; Niedermaier et al., 2014). Contrary to the cation, the basicity of the anion was noted to influence more the CO_2 uptake in ILs. Process simulations showed that use of ILs in place of well-known MDEA can bring down the total electrical and thermal energy by 42.8 and 66.04%, respectively (Liu et al., 2016). The regeneration energy demand also decreased by 15% when IL (1-butylpyridinium tetrafluoroborate) was used in place of MEA (Mumford et al., 2015).

The major drawback of ILs as a scrubbing agent arises from their high viscosity which further increases upon CO_2 capture. For example, the viscosity of 3-aminopropyl tributylphosphoniumamino acid ($[aP_{4443}][AA]$) and trihexyl(tetradecyl)-phosphonium isoleucinate ($[P_{66614}][Iso]$) increased 3- and 200-fold, respectively, upon CO_2 capture (Liu et al., 2009; Gurkan et al., 2010a). However, the high viscosity of ILs can be lowered by incorporating ether functionality, imidazolate anion, addition of molecular solvents, and incorporating them on polymer membrane. The viscosity of trihexyl-(tetradecyl)phosphonium imidazolate ($[P_{66614}][Im]$) was lowered upon CO_2 capture from 810.4 to 648.7 mPa.s because of the combined effect of physisorption and chemisorption (Wang et al., 2011). Similarly, the addition of ether functionality in ILs lowered the viscosity by 43% compared to non-functionalized ILs (Zeng et al., 2015). The addition of amine-based solvent in ILs also decreases viscosity exponentially without affecting the CO_2 uptake (Zhao et al., 2011).

The Carbon Capture Storage and Utilization (CCSU), which comprises all the efforts taken to reduce the CO_2 release in environment and its conversion to value-added products, has been worldwide accepted as the strategy to reduce the negative environmental effects of CO_2. Due to their dual nature, both as catalyst and solvent, ILs have been utilized in the conversion of CO_2 to useful organic moieties like, linear and cyclic carbonates, carbonmonooxide, methanol, formic acid/formates etc (Alvarez-Guerra et al., 2015). The electrochemical reduction of CO_2 is interesting as it operates at low temperatures and pressures. The electro-reduction of CO_2 requires an aqueous electrolyte medium which can absorb CO_2 and decrease the over-potential required to give rise to the $CO_2^{-\cdot}$ radical anion in the presence of a metal cathode (Ag, Au, Pt, etc.) (Oh and Hu, 2013). Similarly, CO_2 can yield linear and cyclic carbonates at elevated temperatures and pressures. Thus, ILs serve the purpose because of the high CO_2 uptake efficiency (Xu et al., 2015).

Ionic Liquids in Carbon Dioxide Capture

The pioneering work of Blanchard et al. showed for the first time that IL (1-butyl-3-methylimidazolium hexafluorophosphate, $[BmIm][PF_6]$) can be employed in CO_2 capture. Since then, plethora of research unraveling the mode and mechanism of CO_2 capture in conventional and functionalized ILs have been reported. In conventional ILs, the cation plays a minor role and the basicity of the anion is observed to affect the CO_2 adsorption. Higher CO_2 uptake was attained in task-specific ILs despite their high viscosity. In this regard, superbase-derived ILs were tested for the optimum CO_2 uptake (Rebecca et al., 2015). Bates et al. (2002) reported semimolar CO_2 absorption in amino-functionalized ILs under ambient conditions. Gurkan et al. (2010b) succeeded in the equimolar absorption with amino acid-based ILs containing prolinate and methioninate anions with phosphonium cation. Later, Wang et al. (2011) achieved equimolar absorption in ILs comprised of pyrazolate, imidazolate, triazolate, tetrazolate, indolate, and oxalate anion and phosphonium cation thus obtaining a linear correlation between the CO_2 capacity and basicity (pK_a) of ILs in DMSO. Multimolar CO_2 absorption ($1.69\ mol.mol^{-1}$) was observed during the activation of carboxylic group in amino-functionalized ILs (Chen et al., 2016). The carboxylate group in the vicinity of NH- moiety stabilizes the CO_2 at the carbamic acid stage, thereby promoting the multimolar absorption. Similarly, a combined experimental and theoretical study on hydroxyl IL with phenolate anion showed 1.5 equivalent CO_2 uptake as both hydroxyl and phenoxide groups participated in the absorption (Vafaeezadeh et al., 2015).

MECHANISMS OF CARBON DIOXIDE CAPTURE IN ILS

Besides the CO_2 uptake efficiency and selectivity, the mode of IL-CO_2 interaction also reveals important information in terms of selection of components and functionality for designing potential ILs. In $[BF_4]$- and $[PF_6]$-based ILs, an acid-base interaction was observed operating between the acetate anion and CO_2 (ATR-IR spectroscopy, Raman spectroscopy and DFT calculations) (Kazarian et al., 2000; Cabaco et al., 2011). Though acid-base interaction shed light on the interaction mechanism, it is not the sole reason for CO_2 uptake as the uptake efficiency doesn't follow the basicity order (Lei et al., 2014). The shortcomings of acid-base theory were later explained by the amount of free-volume in the IL system (Aki et al., 2004). The longer alkyl chain on cation and high anion fluorination increase the extent of free-volume and hence increase CO_2 solubility (Muldoon et al., 2007; Almantariotis et al., 2010). For example, 1-hexyl-3-methylimidazoliumtris(pentafluoroethyl) trifluorophosphate ([HmIm][FEP]) showed 70% higher CO_2 solubility than $[HmIm][PF_6]$ because of the presence of six CF_2/CF_3 in [FEP] than $[PF_6]$ and hence leads to larger free-volume (obtained by Monte Carlo and MD simulations) (Zhang X. C. et al., 2009). Apart from these, weak interactions such as hydrogen and halogen bonding were shown to affect the CO_2 uptake (Palomar et al., 2011; Zhu et al., 2011). The CO_2 capture mechanism in $[HmIm][PF_6]$ and [FEP] showed the importance of electrostatic interaction in the CO_2 uptake in smaller and symmetrical $[PF_6]$ anion whereas the van der Waals interaction has a key role in large and asymmetrical [FEP] anion (Zhang X. C. et al., 2009). In case of gas-[BmIm] cation complex, CO_2 interacts with cation by the formation of hydrogen bond on the C2 carbon (Zhao et al., 2015).

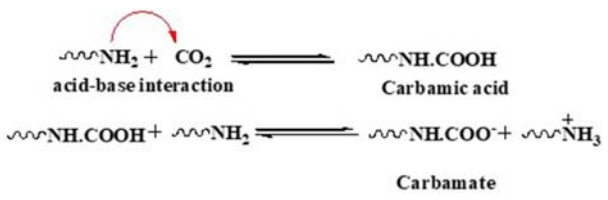

SCHEME 1 | A representative CO_2 capture mechanism in amine-functionalized ILs.

The amine-CO_2 interaction in ILs follows two mechanisms, namely semimolar and equimolar, depending on the presence of amine moiety on cation or anion in ILs (Bates et al., 2002). It is noted that ILs cation tethered with amine moiety follows semimolar mechanism while an equimolar mechanism operates if the amine is a part of the anion (Cao et al., 2016). A molar uptake plot clearly reveals the type of operative mechanism in a medium. In semimolar mechanism, CO_2 first reacts with amine moiety to form carbamic acid which further reacts with another molecule of amine to yield ammonium carbamate as the final product (**Scheme 1**). Thus, for one mole of CO_2, two moles of amine are required.

In equimolar mechanism, one mole of amine captures one mole of CO_2 and stabilizes the product as carbamic acid (Kasahara et al., 2016). Various studies have claimed multimolar absorption in ILs because of the presence of stabilizing group in the vicinity of NH_2- moiety of the amine (Luo et al., 2014).

Though amine-functionalized ILs improves CO_2 solubility in ILs, high viscosity and regeneration of ILs remain as challenges. To address these problems Wang et al. (2010) proposed non-amine functionalized superbase-derived protic ILs for equimolar CO_2 capture. Later, phenolic ILs were prepared from the phosphonium hydroxide and substituted phenols whereupon the effect of position and nature of substituents on the anion were correlated with the physicochemical properties and CO_2 uptake efficiency (Wang et al., 2012). Thus, cation-anion interaction strength affects the CO_2 uptake in phenolic ILs (Lee et al., 2016).

APPLICATIONS OF IONIC LIQUIDS IN CONVERSION OF CARBON DIOXIDE TO VALUE-ADDED PRODUCTS

IL-mediated conversion of CO_2 to value added products has been achieved through chemical, thermochemical, photochemical, biochemical, and electrochemical reduction methods (Barton et al., 2008; Chueh et al., 2010; Rosen et al., 2011; Chen et al., 2012; Costentin et al., 2012). Out of these methods, chemical and electrochemical reduction of CO_2 are the most attractive methods. In the chemical conversion method, epoxides and methanol were employed to convert CO_2 to cyclic and linear carbonates, respectively, via cycloaddition reactions. The electrochemical reduction of CO_2 is highly popular because of its higher conversion efficiency, product selectivity and its potential to store electrical energy from renewable energy sources like the sun (Spinner et al., 2012).

Conversion of CO_2 to Organic Carbonates

Organic carbonates have many industrial applications as green aprotic polar solvents, electrolytes for lithium-ion batteries as well as intermediates upon production of pharmaceuticals and polymers (Chaugule et al., 2017). This mini-review highlights recent findings in catalysis converting CO_2 to organic carbonates based on ILs under mild conditions (low temperature and pressure).

Five-Membered Ring Cyclic Carbonate

Traditional ILs-based catalysis for cyclic carbonates synthesis from CO_2 was reported first time in 2001 (Peng and Deng, 2001). In this study, a series of RTILs based on cations ($BmIm^+$, BPy^+) and anions (Cl^-, BF_4^-, PF_6^-) acted as recyclable catalysts to produce propylene carbonate from propylene oxide and CO_2 in the absence of a solvent. Among them, [Bmim][BF_4] showed the highest catalyst activity with 100% yield under optimal conditions (110°C, 6 h, 2.5 MPa of CO_2, 2.5 mmol of [BmIm][BF_4] per 100 mmol of epoxide). Until now, numerous other ILs including new generations such as task-specific ILs were investigated for improving the production of cyclic carbonates under different experimental conditions (Chaugule et al., 2017).

Recently, a dual-IL system as a recyclable, efficient catalyst for cyclic carbonate synthesis under mild, solvent-free conditions was developed (Hu et al., 2018). In this study, $[TMGH^+][^-O_2MMIm^+]Br^-$ showed the best catalytic performance with 84% yield under optimal conditions (30°C, 12 h, 0.1 MPa of CO_2, 0.5 mmol of IL per 2 mmol of epichlorohydrin). The mechanism was also suggested, wherein a synergistic catalytic effect among carboxylate anion, bromide anion and the N-H bond of the iminium ion results in the cycloaddition of CO_2 and epoxide.

Moreover, to render the catalyst separation and reusability issues easier and practical in industry, the immobilization of ILs-based catalysts on recyclable solid supports has been widely studied (Chaugule et al., 2017). Several ILs such as [BmIm][X] (where X = Cl, Br, I) and [EpIm][X] were immobilized on commercial SiO_2 (pore size 6 nm, 35–70 μm) to yield efficient catalysts to produce cyclic carbonates under mild conditions (Martínez-Ferraté et al., 2018). Silica-supported [EpIm]Br was the best system reaching 99% conversion in just 30 min under optimal conditions (80°C, 5 bar of CO_2, 1.67 mmol of IL per 3.34 mmol of propylene oxide). This catalyst system was still active (79% conversion) when using a model gas mixture from an industrial exhaust (15% CO_2) instead of synthetic CO_2.

Dimethyl Carbonate

Recently, in the presence of different organic and inorganic bases, several imidazolium hydrogen carbonate ILs ([CnCmIm][HCO_3]) were used (recyclable catalyst and dehydrant) upon straightforward synthesis of dimethyl carbonate from CH_3OH and CO_2, at room temperature and 1 MPa of CO_2 (Zhao et al., 2017). Under optimal conditions, a combination between [BmIm][HCO_3] and Cs_2CO_3 in the presence of CH_2Br_2 solvent showed the highest conversion of CH_3OH (74%) and was easily reused.

Electrochemical Fixation of CO_2 in ILs

CO_2 is an abundantly available renewable C1 feedstock from various emission sources such as coal fired power plants, bio-refineries, crude oil processing industries etc (Friedlingstein et al., 2011). In the view of the negative impact of CO_2 on environment, its conversion to fuels and fine chemicals could be a way to eliminate the harmful effects of this greenhouse gas (Ansari and Park, 2012). The electrochemical and photochemical approaches were undertaken to convert CO_2 into useful chemicals such as methanol, carbon monoxide, ethylene, formic acid/formate, higher alcohols, alkanes etc. as well as important building blocks to synthesize various platform chemicals as well as polymers (Xiaoding and Moulijn, 1996). The electrochemical process involves cathodic reduction of CO_2 and anodic oxidation of solvent.

The centrosymmetric structure makes CO_2 electrically neutral though it has a bond dipole. **Scheme 2** shows steps through which CO_2 is reduced to various useful products, at different standard potentials (E^0). The hydrogen formed in these reactions is an undesired major byproduct and should be avoided (Feng et al., 2018a). To eliminate H_2 from the process, a non-aqueous medium is required and room temperature ionic liquids (RTIL) are ideal in this regard.

Electrochemical Conversion of CO_2 to CO

RTILs as a dual medium were extensively explored in the electrochemical conversion of CO_2 to CO during the last decade. Rosen et al. (2011) studied electrochemical reduction of CO_2 to CO in 18% aqueous 1-ethyl-3-methylimidazolium tetrafluoroborate ([Emim][BF_4]) and observed high Faradaic efficiency (96% for 7 h) with extremely low potential. The RTIL cation was noted to reduce the H_2 generation thereby assisting in the reduction of CO_2 to CO. Later, several ILs comprised of imidazolium, pyrrolidinium, ammonium, phosphonium cation and (bis(trifluoromethylsulfonyl)imide ([NTf_2]), tris(pentafluoroethyl)trifluorophosphate ([FAP]), and tetrafluoroborate [BF_4]) anion and role of substituents on the cationic core was investigated in the reduction of CO_2 to CO (Alvarez-Guerra et al., 2015; Lim and Kim, 2017). In all these studies Au, Ag, Pt, and glassy carbon-based cathodes were used as electro-catalysts (Alvarez-Guerra et al., 2015). During the reduction, the IL cation coordinates with CO_2 molecule and forms $CO_2^{\cdot -}$ radicals under negative electrode potential which subsequently form CO (Sun et al., 2014; Feng et al., 2018b).

In other words, as shown in **Figure 1**, the electrochemical reduction of CO_2 to CO follow alternative path where the conversion proceeds with low overpotential compared with the case when there is an IL involved in the process. In reality, IL activates CO_2 molecule via formation of "cation-CO_2" intermediate through which the formation energy of $CO_2^{-\cdot}$ radical anion decreases.

Alternatively, as shown in **Figures 2**, **3**, Sun et al. (2014) proposed a mechanism for the electrochemical reduction of CO_2 to CO in the absence and presence of an IL at the Pd electrode in acetonitrile. In this case, based on the experimental evidence, the author proposed that the precense of an IL switches the course of electrochemical reduction of CO_2 where the IL favors the CO formation pathway instead of the undesirable oxalate anion formation.

As shown in **Figure 2**, the *in-situ* formed $CO_2^{-\cdot}$ radical anion formed over the Pd electrode further dimerizes to an oxalate anion in the absence of an IL. On the other hand, as shown in **Figure 3**, the IL stabilizes $CO_2^{-\cdot}$ and prevents its dimerization whereupon this stabilized $CO_2^{-\cdot}$ further converts to CO molecule.

Additionally, it was also observed that along with CO formation, the imidazolium carboxylate formation pathway also exists (**Figure 4**). An earlier theoretical as well as experimental studies study performed by Zhao et al. (2016) claims that the formation of this carboxylate species deactivates the active sites on the imidazolium cation. However, these active imidazolium sites can be recovered by an addition of a proton source such as water.

Further, based on the density functional theory (DFT) as well as Raman and NMR spectroscopic techniques, Wang et al. (2015) also represented another alternative mechanism

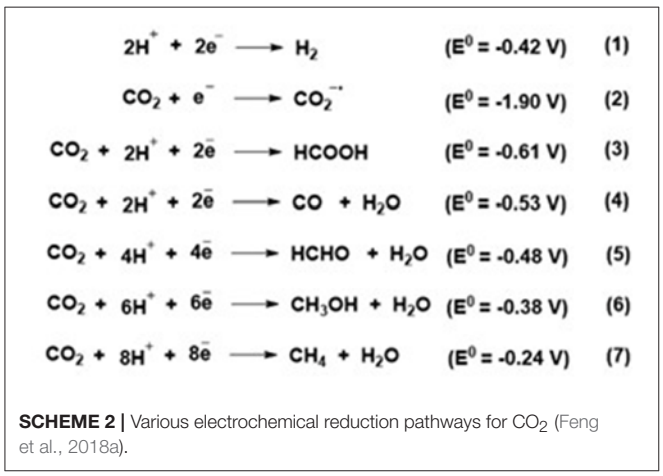

SCHEME 2 | Various electrochemical reduction pathways for CO_2 (Feng et al., 2018a).

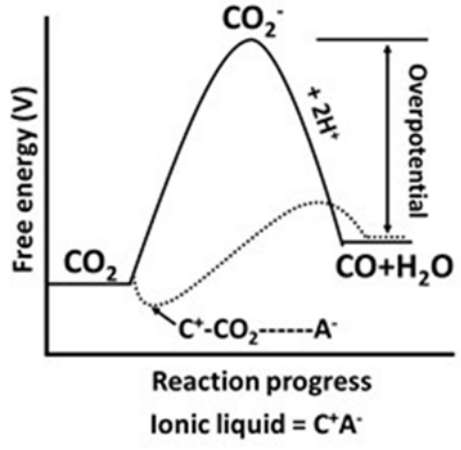

FIGURE 1 | Schematic representation for free energy change for electrochemical conversion of CO_2 to CO in water (solid line) or ionic liquid (dotted line). Adopted from Li et al. (2013).

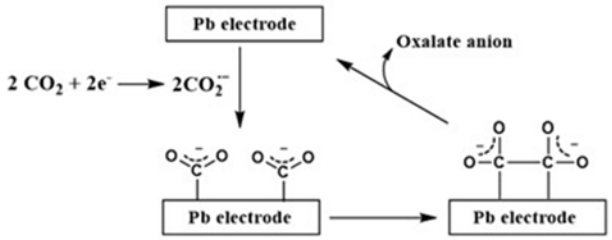

FIGURE 2 | The electrochemical reduction pathway for CO_2 to CO at Pd electrode in acetonitrile. Adopted from Sun et al. (2014).

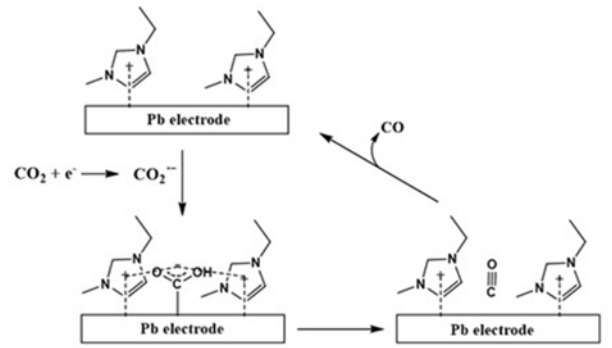

FIGURE 3 | The electrochemical reduction pathway for CO_2 to CO at Pd electrode in [emim][Tf_2N]/acetonitrile (CO formation). Adopted from Sun et al. (2014).

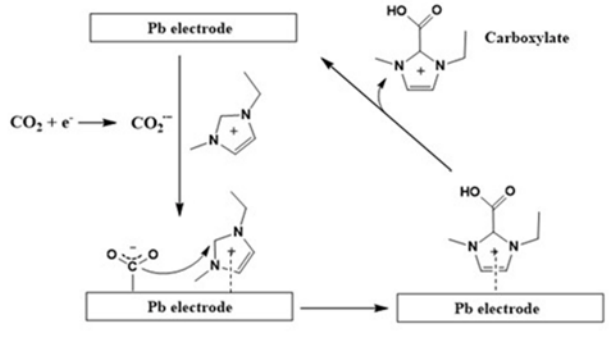

FIGURE 4 | The electrochemical reduction pathway for CO_2 to CO at the Pd electrode in [emim][Tf_2N]/acetonitrile (imidazolium carboxylate formation). Adopted from Sun et al. (2014).

for the formation of CO through electrochemical reduction of CO_2. The author proposed that in the presence of a proton source such as water, the *in-situ* formed carboxylate species can decompose into CO and the active imidazolium cation can be recovered (**Scheme 3**). In this case, the author reported that the imidazolium cation served as a co-catalyst as it provides its own acidic proton in the CO formation process. However, the role of this co-catalysis is limited to the having a proton source in the reaction medium to recover the imidazolium cation in the catalytic cycle.

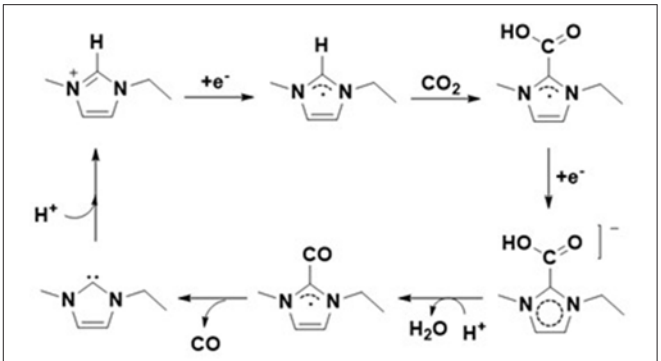

SCHEME 3 | Electrochemical reduction CO_2 to CO through imidazolium carboxylate species. Adopted from Zhao et al. (2016).

Hence, even though the formation of CO can be explained based on different mechanistic approaches, these studies indicate that ILs are playing an important role upon electrochemical reduction of CO_2 to CO.

Electrochemical Conversion of CO_2 to Formic Acid/Formate

The electrochemical conversion of CO_2 to formic acid was also undertaken by several workers. Watkins and Bocarsly (2014) used 1-ethyl-3-methylimidazolium trifluoroacetate ([Emim][TFA]) along with various metals as co-catalysts in the electrochemical conversion of CO_2 to HCOOH and found that iridium is an efficient catalyst. Hollingsworth et al. (2015) performed selective conversion of CO_2 to formate and syngas by an anion assisted electrochemical process. The IL consisting of tetraalkylphosphonium cation and 1,2,4-triazolate anion [P_{66614}][1,2,4Triz] absorbed equimolar amount of CO_2 and assisted in the selective conversion of CO_2 to formate under extremely low applied electrode potential (−0.7 V vs. Ag^+/Ag).

In a detailed study based on cyclic volumetric measurements for two different ILs, [P_{66614}][1,2,4Triz] and [P_{66614}][NTf_2], the author observed that the [1,2,4Triz]$^-$ anion comprising IL were found more efficient compared to their [NTf_2]$^-$ anion containing analogs upon electrochemical reaction of CO_2 to CO. In this case, in addition to physical interactions of the [P_{66614}]$^+$ cation with CO_2 (i.e., formation of [CO_2]$^-$[P_{66614}]$^+$), the chemical interactions of the [1,2,4Triz]$^-$ anion with CO_2 allowed for low-energy electrochemical reaction of CO_2 to CO (**Scheme 4**) compared to the case when the [P_{66614}][NTf_2] IL was employed.

Zhang et al. (2017) studied CO_2 to formic acid conversion in the aqueous solution of 1-ethyl-3-methylimidazolium dicyanamide ([Emim][$N(CN)_2$]) using Sn powder electrode and noted that IL assisted in the electrochemical activation and conversion of CO_2 to HCOOH but also increased the solubility of CO_2 in the electrolyte system for maximum output. The 81.9% of Faradaic efficiency was achieved with 0.5 M [Emim][$N(CN)_2$] in water, under the potential of −1.2V vs. reversible hydrogen electrode (RHE). Lu et al. (2017) first time introduced photo-electrochemical conversion of CO_2 to

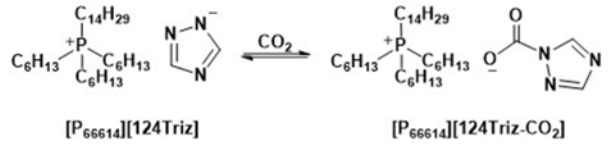

SCHEME 4 | Chemical interactions of $[P_{66614}][124Triz]$ IL with CO_2. Adopted from Wang et al. (2015).

HCOOH using functionalized IL such as 1-aminopropyl-3-methylimidazolium bromide ($[NH_2C_3mim]Br$) and the 94.1% faradaic efficiency was obtained for HCOOH conversion. The author claimed that the effective interaction of CO_2 with the IL cation facilitated the conversion of CO_2 to HCOOH. Recently, Huan et al. (2017) observed a cost-effective electro-reduction of CO_2 to HCOOH in $[EMIM][BF_4]$ using a copper-based electrocatalyst as cathode achieving high Faradaic efficiency (87% for 8 h). Compared to the electrochemical reduction of CO_2 to CO, the electrochemical transformation of CO_2 to HCOOH or formate is still in its infancy in ILs and further addressing is required to understand the phenomena in detail.

Electrochemical Conversion of CO_2 to CH_3OH

Similar to electrochemical conversion of CO_2 to CO and HCOOH, formation of methanol by electrochemical conversion of CO_2 is another anticipated application and has been investigated extensively in ILs. Transformation of CO_2 to methanol via electrochemical activation of CO_2 has been performed recently by Han and coworkers (Sun et al., 2016). They used various bimetallic catalysts such as Mo-Bi, Mo-Ag, and Mo-Cu in $[BmIm][BF_4]$/acetonitrile solution. The synergic effect of Mo and Bi metals as bimetallic catalyst upon electrochemical CO_2-activation in 0.5 M solution of IL in acetonitrile gave 71.2% Faradaic efficiency in methanol formation. In bimetal Mo-Bi catalyst, Mo facilitates conversion of CO_2 to CO while Bi assists in the formation of H_2 and adsorption of *in-situ* formed CO and, therefore, increases the possibility of hydrogenation of CO_2 to CH_3OH.

Hence, RTILs play an important role in the electrochemical conversion of CO_2 to various value-added and industrially important products such as CO, HCOOH, and CH_3OH. Though several hypotheses have been introduced to investigate the role of RTILs in the electrochemical reduction of CO_2, none of them provide satisfactory information regarding the process. This could more be due to the complex structural and electronic nature of ILs at the IL-electrode interface than that of water. However, last but not least, ILs are proposed as a sustainable and green approach to activate and reduce the CO_2 to essential chemical moieties with minimum energy consumption rather than the existing thermochemical approach.

CONCLUSIONS AND OUTLOOK

The remarkable properties of ILs over the conventional volatile solvents, such as non-volatility and structure-tunability, make them suitable for applications involving CO_2 capture and fixation. The mini-review highlights the development in the CO_2 uptake since the inception of ILs in this area and further development in the last decade. The effects of cations, anions, and functional groups on the physicochemical properties and their impact on CO_2 uptake were reviewed, in both conventional and functionalized ILs. The forces involved in the CO_2 capture and mechanism were discussed in various types of ILs. Despite the exciting response, the lack of inexpensive and diverse ILs poses a problem in applying them on large scale. Moreover, the impact of ILs on environment, corrosion, toxicity, and long-term stability need to be addressed.

DATA AVAILABILITY

All datasets generated for this study are included in the manuscript and the supplementary files.

AUTHOR CONTRIBUTIONS

All authors listed have made a substantial, direct and intellectual contribution to the work, and approved it for publication.

ACKNOWLEDGMENTS

We are thankful to the Wallenberg Wood Science Center (WWSC), Kempe Foundations, the Swedish Research Council, the Swedish Energy Agency, and the Bio4energy programme. This work is also part of the activities of the Johan Gadolin Process Chemistry Center at Åbo Akademi University.

REFERENCES

Aki, S., Mellein, B. R., Saurer, E. M., and Brennecke, J. F. (2004). High pressure phase behavior of carbon dioxide with imidazolium-based ionic liquids. *J. Phys. Chem. B* 108, 20355–20365. doi: 10.1021/jp046895+

Almantariotis, D., Gefflaut, T., Padua, A. A. H., Coxam, J. Y., and Costa Gomes, M. F. (2010). Effect of fluorination and size of the alkyl side-chain on the solubility of carbon dioxide in 1-alkyl-3-methylimidazolium bis(trifluoromethylsulfonyl)amide ionic liquids. *J. Phys. Chem. B* 114, 3608–3617. doi: 10.1021/jp912176n

Alvarez-Guerra, M., Albo, J., Alvarez-Guerra, E., and Irabien, A. (2015). Ionic liquids in the electrochemical valorisation of CO_2. *Energy Environ. Sci.* 8, 2574–2599. doi: 10.1039/C5EE01486G

Ansari, M. B., and Park, S.-E. (2012). Carbon dioxide utilization as a soft oxidant and promoter in catalysis. *Energy Environ. Sci.* 5, 9419–9437. doi: 10.1039/C2EE22409G

Barton, E. E., Rampulla, D. M., and Bocarsly, A. B. (2008). Selective solar-driven reduction of CO_2 to methanol using a catalyzed p-GaP based photoelectrochemical cell. *J. Am. Chem. Soc.* 130, 6342–6344. doi: 10.1021/ja0776327

Bates, E. D., Mayton, R. D., Ntai, I., and Davis, J. H. (2002). CO_2 capture by a task-specific ionic liquid. *J. Am. Chem. Soc.* 124, 926–927. doi: 10.1021/ja017593d

Ben-Mansour, R., Habib, M. A., Bamidele, O. E., Basha, M., Qasem, N. A. A., Peedikakkal, A., et al. (2016). Carbon capture by physical adsorption: materials, experimental investigations and numerical modeling and simulations—A review. *Appl. Energy* 161, 225–255. doi: 10.1016/j.apenergy.2015.10.011

Cabaco, M. I., Besnard, M., Danten, Y., and Coutinho, J. A. P. (2011). Solubility of CO_2 in 1-butyl-3-methyl-imidazolium-trifluoro acetate ionic liquid studied by raman spectroscopy and DFT investigations. *J. Phys. Chem. B* 115, 3538–3550. doi: 10.1021/jp111453a

Cao, B. B., Du, J. Y., Liu, S. Y., Zhu, X., Sun, X. J., Sun, H. T., et al. (2016). Carbon dioxide capture by amino-functionalized ionic liquids: DFT based theoretical analysis substantiated by FT-IR investigation. *RSC Adv.* 6, 10462–10470. doi: 10.1039/C5RA23959A

Chaugule, A. A., Tamboli, A. H., and Kim, H. (2017). Ionic liquid as a catalyst for utilization of carbon dioxide to production of linear and cyclic carbonate. *Fuel* 200, 316–332. doi: 10.1016/j.fuel.2017.03.077

Chen, F.-F., Huang, K., Zhou, Y., Tian, Z.-Q., Zhu, X., Tao, D.-J., et al. (2016). Multi-molar absorption of CO_2 by the activation of carboxylate groups in amino acid ionic liquids. *Angew. Chem. Int. Ed.* 55, 7166–7170. doi: 10.1002/anie.201602919

Chen, Y., Li, C. W., and Kanan, M. W. (2012). Aqueous CO_2 reduction at very low overpotential on oxide-derived Au nanoparticles. *J. Am. Chem. Soc.* 134, 19969–19972. doi: 10.1021/ja309317u

Chueh, W. C., Falter, C., Abbott, M., Scipio, D., Furler, P., Haile, S. M., et al. (2010). High-flux solar-driven thermochemical dissociation of CO_2 and H_2O using nonstoichiometric ceria. *Science* 330, 1797–1801. doi: 10.1126/science.1197834

Costentin, C., Drouet, S., Robert, M., and Saveant, J.-M. (2012). A local proton source enhances CO_2 electroreduction to CO by a molecular Fe catalyst. *Science* 338, 90–94. doi: 10.1126/science.1224581

Feng, J., Zeng, S., Feng, J., Dong, H., and Zhang, X. (2018a). CO_2 electroreduction in ionic liquids: a review. *Chin. J. Chem.* 36, 961–970. doi: 10.1002/cjoc.201800252

Feng, J., Zeng, S., Liu, H., Feng, J., Gao, H., Bai, L., et al. (2018b). Insights into carbon dioxide electroreduction in ionic liquids: carbon dioxide activation and selectivity tailored by ionic microhabitat. *ChemSusChem* 11, 3191–3197. doi: 10.1002/cssc.201801373

Friedlingstein, P., Solomon, S., Plattner, G.-K., Knutti, R., Ciais, P., and Raupach, M. R. (2011). Long-term climate implications of twenty-first century options for carbon dioxide emission mitigation. *Nat. Clim. Change* 1, 457–461. doi: 10.1038/nclimate1302

George, G., Bhoria, N., AlHallaq, S., Abdala, A., and Mittal, V. (2016). Polymer membranes for acid gas removal from natural gas. *Sep. Purif. Technol.* 158, 333–356. doi: 10.1016/j.seppur.2015.12.033

Goodrich, B. F., de la Fuente, J. C., Gurkan, B. E., Zadigian, D. J., Price, E. A., Huang, Y., et al. (2011). Experimental measurements of amine-functionalized anion-tethered ionic liquids with carbon dioxide. *Ind. Eng. Chem. Res.* 50, 111–118. doi: 10.1021/ie101688a

Gurkan, B. E., de la Fuente, J. C., Mindrup, E. M., Ficke, L. E., Goodrich, B. F., Price, E. A., et al. (2010b). Equimolar CO_2 absorption by anion-functionalized ionic liquids. *J. Am. Chem. Soc.* 132, 2116–2117. doi: 10.1021/ja909305t

Gurkan, B. E., Goodrich, B. F., Mindrup, E. M., Ficke, L. E., Massel, M., Seo, S., et al. (2010a). Molecular design of high capacity, low viscosity, chemically tunable ionic liquids for CO_2 capture. *J. Phys. Chem. Lett.* 1, 3494–3499. doi: 10.1021/jz101533k

Hollingsworth, N., Taylor, S. F. R., Galante, M. T., Jacquemin, J., Longo, C., Holt, K. B., et al. (2015). Reduction of carbon dioxide to formate at low overpotential using a superbase ionic liquid. *Angew. Chem. Int. Ed.* 54, 14164–14168. doi: 10.1002/anie.201507629

Hu, J., Ma, J., Liu, H., Qian, Q., Xie, C., and Han, B. (2018). Dual-ionic liquid system: an efficient catalyst for chemical fixation of CO_2 to cyclic carbonates under mild conditions. *Green Chem.* 20, 2990–2994. doi: 10.1039/C8GC01129J

Huan, T. N., Simon, P., Rousse, G., Genois, I., Artero, V., and Fontecave, M. M. (2017). Porous dendritic copper: an electrocatalyst for highly selective CO_2 reduction to formate in water/ionic liquid electrolyte. *Chem. Sci.* 8, 742–747. doi: 10.1039/C6SC03194C

Huang, K., Zhang, X. M., Xu, Y., Wu, Y. T., Hu, X. B., and Xu, Y. (2014). Protic ionic liquids for the selective absorption of H_2S from CO_2: thermodynamic analysis. *AIChE J.* 60, 4232–4240. doi: 10.1002/aic.14634

Kasahara, S., Kamio, E., Shaikh, A. R., Matsuki, T.;, and Matsuyama, H. (2016). Effect of the amino-group densities of functionalized ionic liquids on the facilitated transport properties for CO_2 separation. *J. Membr. Sci.* 503, 148–157. doi: 10.1016/j.memsci.2016.01.007

Kazarian, S. G., Briscoe, B. J., and Welton, T. (2000). Combining ionic liquids and supercritical fluids: *in situ* ATR-IR study of CO_2 dissolved in two ionic liquids at high pressures. *Chem. Commun.* 20, 2047–2048. doi: 10.1039/B005514J

Lee, T. B., Oh, S., Gohndrone, T. R., Morales-Collazo, O., Seo, S., Brennecke, J. F., et al. (2016). CO_2 chemistry of phenolate-based ionic liquids. *J. Phys. Chem. B* 120, 1509–1517. doi: 10.1021/acs.jpcb.5b06934

Lei, Z. G., Dai, C. N., and Chen, B. H. (2014). Gas solubility in ionic liquids. *Chem. Rev.* 114, 1289–1326. doi: 10.1021/cr300497a

Li, Z., Wang, Q., Liu, D., Yang, B., Zhang, X., and Lei, L. (2013). Ionic liquid-mediated electrochemical CO_2 reduction in a microbial electrolysis cell. *Electrochem. Commun.* 35, 91–93. doi: 10.1016/j.elecom.2013.08.002

Lim, H.-K., and Kim, H. (2017). The mechanism of room-temperature ionic-liquid-based electrochemical CO_2 reduction: a review. *Molecules* 22, 536–541. doi: 10.3390/molecules22040536

Liu, X. M., Zhou, G. H., Zhang, S. J., and Yao, X. Q. (2009). Molecular dynamics simulation of dual amino-functionalized imidazolium-based ionic liquids. *Fluid Phase Equilib.* 284, 44–49. doi: 10.1016/j.fluid.2009.06.004

Liu, X. Y., Huang, Y., Zhao, Y. S., Gani, R., Zhang, X. P., and Zhang, S. J. (2016). Ionic liquid design and process simulation for decarbonization of shale gas. *Ind. Eng. Chem. Res.* 55, 5931–5944. doi: 10.1021/acs.iecr.6b00029

Lu, W., Jia, B., Cui, B., Zhang, Y., Yao, K., Zhao, Y., et al. (2017). Efficient photoelectrochemical reduction of carbon dioxide to formic acid: a functionalized ionic liquid as an absorbent and electrolyte. *Angew. Chem. Int. Ed.* 56, 11851–11854. doi: 10.1002/anie.201703977

Luo, X. Y., Guo, Y., Ding, F., Zhao, H. Q., Cui, G. K., Li, H. R., et al. (2014). Significant improvements in CO_2 capture by pyridine-containing anion-functionalized ionic liquids through multiple-site cooperative interactions. *Angew. Chem. Int. Ed.* 53, 7053–7057. doi: 10.1002/anie.201400957

Martínez-Ferraté, O., Chacón, G., Bernardi, F., Grehl, T., Brüner, P., and Dupont, J. (2018). Cycloaddition of carbon dioxide to epoxides catalysed by supported ionic liquids. *Catal. Sci. Technol.* 8, 3081–3089. doi: 10.1039/C8CY00749G

Muldoon, M. J., Aki, S. N. V. K., Anderson, J. L., Dixon, J. K., and Brennecke, J. F. (2007). Improving carbon dioxide solubility in ionic liquids. *J. Phys. Chem. B* 111, 9001–9009. doi: 10.1021/jp071897q

Mumford, K. A., Wu, Y., Smith, K. H., and Stevens, G. W. (2015). Review of solvent based carbon-dioxide capture technologies. *Front. Chem. Sci. Eng.* 9, 125–141. doi: 10.1007/s11705-015-1514-6

Niedermaier, I., Bahlmann, M., Papp, C., Kolbeck, C., Wei, W., Calderon, S. K., et al. (2014). Carbon dioxide capture by an amine functionalized ionic liquid: fundamental differences of surface and bulk behavior. *J. Am. Chem. Soc.* 136, 436–441. doi: 10.1021/ja410745a

Oh, Y., and Hu, X. (2013). Organic molecules as mediators and catalysts for photocatalytic and electrocatalytic CO_2 reduction. *Chem. Soc. Rev.* 42, 2253–2261. doi: 10.1039/C2CS35276A

Palomar, J., Gonzalez-Miquel, M., Polo, A., and Rodriguez, F. (2011). Understanding the physical absorption of CO_2 in ionic liquids using the COSMO-RS method. *Ind. Eng. Chem. Res.* 50, 3452–3463. doi: 10.1021/ie101572m

Peng, J., and Deng, Y. (2001). Cycloaddition of carbon dioxide to propylene oxide catalyzed by ionic liquids. *New J. Chem.* 25, 639–641. doi: 10.1039/B008923K

Rebecca, S. F., McCrellis, T. C., McStay, C., Jacquemin, J., Hardacre, C., Mercy, M., et al. (2015). CO_2 capture in wet and dry superbase ionic liquids. *J Solution Chem.* 44, 511–527. doi: 10.1007/s10953-015-0319-z

Rosen, B. A., Salehi-Khojin, A., Thorson, M. R., Zhu, W., Whipple, D. T., Kenis, P. J. A., et al. (2011). Ionic liquid–mediated selective conversion of CO_2 to CO at low overpotentials. *Science* 334, 642–643. doi: 10.1126/science

Sanz-Perez, E. S., Murdock, C. R., Didas, S. A., and Jones, C. W. (2016). Direct capture of CO_2 from ambient air. *Chem. Rev.* 116, 11840–11876. doi: 10.1021/acs.chemrev.6b00173

Shao, R., and Stangeland, A. (2009). *Amines Used in CO_2 Capture–Health and Environmental Impacts*. Oslo: The Bellona Foundation.

Spinner, N. S., Vega, J. A., and Mustain, W. E. (2012). Recent progress in the electrochemical conversion and utilization of CO_2. *Catal. Sci. Technol.* 2, 19–28. doi: 10.1039/C1CY00314C

Steinruck, H.-P., and Wasserscheid, P. (2015). Ionic liquids in catalysis. *Catal. Lett.* 145, 380–397. doi: 10.1007/s10562-014-1435-x

Sun, L., Ramesha, G. K., Kamat, P. V., and Brennecke, J. F. (2014). Switching the reaction course of electrochemical CO_2 reduction with ionic liquids. *Langmuir* 30, 6302–6308. doi: 10.1021/la5009076

Sun, X., Zhu, Q., Kang, X., Liu, H., Qian, Q., Zhang, Z., et al. (2016). Molybdenum–bismuth bimetallic chalcogenide nanosheets for highly efficient electrocatalytic reduction of carbon dioxide to methanol. *Angew. Chem. Int. Ed.* 55, 6771–6775. doi: 10.1002/anie.201603034

Thitakamol, B., Veawab, A., and Aroonwilas, A. (2007). Environmental impacts of absorption-based CO_2 capture unit for post-combustion treatment of flue gas from coal-fired power plant. *Int. J. Greenhousen Gas Control* 1, 318–342. doi: 10.1016/S1750-5836(07)00042-4

Vafaeezadeh, M., Aboudi, J., and Hashemi, M. M. (2015). A novel phenolic ionic liquid for 1.5 molar CO_2 capture: combined experimental and DFT studies. *RSC Adv.* 5, 58005–58009. doi: 10.1039/C5RA09845A

Wang, C. M., Luo, H. M., Jiang, D. E., Li, H. R., and Dai, S. (2010). Carbon dioxide capture by superbase-derived protic ionic liquids. *Angew. Chem. Int. Ed.* 49, 5978–5981. doi: 10.1002/anie.201002641

Wang, C. M., Luo, H. M., Li, H. R., Zhu, X., Yu, B., and Dai, S. (2012). Tuning the physicochemical properties of diverse phenolic ionic liquids for equimolar CO_2 capture by the substituent on the anion. *Chem. Eur. J.* 18, 2153–2160. doi: 10.1002/chem.201103092

Wang, C. M., Luo, X. Y., Luo, H. M., Jiang, D. E., Li, H. R., and Dai, S. (2011). Tuning the basicity of ionic liquids for equimolar CO_2 capture. *Angew. Chem. Int. Ed.* 50, 4918–4922. doi: 10.1002/anie.201008151

Wang, Y., Hatakeyama, M., Ogata, K., Wakabayashi, M., Jinb, F., and Nakamura, S. (2015). Activation of CO_2 by ionic liquid EMIM–BF_4 in the electrochemical system: a theoretical study. *Phys. Chem. Chem. Phys.* 17, 23521–23531. doi: 10.1039/C5CP02008E

Watkins, J. D., and Bocarsly, A. B. (2014). Direct reduction of carbon dioxide to formate in high-gas-capacity ionic liquids at post-transition-metal electrodes. *ChemSusChem* 7, 284–290. doi: 10.1002/cssc.201300659

Xiaoding, X., and Moulijn, J. A. (1996). Mitigation of CO_2 by chemical conversion: plausible chemical reactions and promising products. *Energy Fuels* 10, 305–325. doi: 10.1021/ef9501511

Xu, B.-H., Wang, J.-Q., Sun, J., Huang, Y., Zhang, J.-P., Zhang, X.-P., et al. (2015). Fixation of CO_2 into cyclic carbonates catalyzed by ionic liquids: a multi-scale approach. *Green Chem.*17, 108–122. doi: 10.1039/C4GC01754D

Zeng, S., Zhang, X., Bai, L., Zhang, X., Wang, H., Wang, J., et al. (2017). Ionic-liquid-based CO_2 capture systems: structure, interaction and process. *Chem. Rev.* 117, 9625–9673. doi: 10.1021/acs.chemrev.7b00072

Zeng, S. J., Wang, J., Bai, L., Wang, B. Q., Gao, H. S., Shang, D. W., et al. (2015). Highly selective capture of CO_2 by ether-functionalized pyridinium ionic liquids with low viscosity. *Energy Fuels* 29, 6039–6048. doi: 10.1021/acs.energyfuels.5b01274

Zhang, X., Zhao, Y., Hu, S., Gliege, M. E., Liu, Y., Liu, R., et al. (2017). Electrochemical reduction of carbon dioxide to formic acid in ionic liquid [EmIm][$N(CN)_2$]/water system. *Electrochim. Acta* 247, 281–287. doi: 10.1016/j.electacta.2017.06.112

Zhang, X. C., Huo, F., Liu, Z. P., Wang, W. C., Shi, W., and Maginn, E. J. (2009). Absorption of CO_2 in the ionic liquid 1-n-hexyl-3- methylimidazolium tris(pentafluoroethyl)trifluorophosphate ([hmim][FEP]): a molecular view by computer simulations. *J. Phys. Chem. B* 113, 7591–7598. doi: 10.1021/jp900403q

Zhang, Y. Q., Zhang, S. J., Lu, X. M., Zhou, Q., Fan, W., and Zhang, X. P. (2009). Dual amino-functionalised phosphonium ionic liquids for CO_2 capture. *Chem. Eur. J.* 15, 3003–3011. doi: 10.1002/chem.200801184

Zhao, S., Tian, X. Z., Liu, J. N., Ren, Y. L., and Wang, J. J. (2015). A theoretical investigation on the adsorption of CO_2, N_2, O_2 and H_2 in 1-buty-3-methylimidazolium heptafluorobutyrate ionic liquid. *Comput. Theor. Chem.* 1052, 12–16. doi: 10.1021/jp205830d

Zhao, S.-F., Horne, M., Bond, A. M., and Zhang, J. (2016). Is the imidazolium cation a unique promoter for electrocatalytic reduction of carbon dioxide? *J. Phys. Chem. C* 120, 23989–24001. doi: 10.1021/acs.jpcc.6b08182

Zhao, T., Hu, X., Wu, D., Li, R., Yang, G., and Wu, Y. (2017). Direct synthesis of dimethyl carbonate from carbon dioxide and methanol at room temperature using imidazolium hydrogen carbonate ionic liquid as a recyclable catalyst and dehydrant. *ChemSusChem* 10, 2046–2052. doi: 10.1002/cssc.201700128

Zhao, Y. S., Zhang, X. P., Zhen, Y. P., Dong, H. F., Zhao, G. Y., Zeng, S. J., et al. (2011). Novel alcamines ionic liquids based solvents: preparation, characterization and applications in carbon dioxide capture. *Int. J. Greenhouse Gas Control* 5, 367–373. doi: 10.1016/j.ijggc.2010.09.010

Zhu, X., Lu, Y. X., Peng, C. J., Hu, J., Liu, H. L., and Hu, Y. (2011). Halogen bonding interactions between brominated ion pairs and CO_2 molecules: implications for design of new and efficient ionic liquids for CO_2 absorption. *J. Phys. Chem. B* 115, 3949–3958. doi: 10.1021/jp111194k

Conflict of Interest Statement: The authors declare that the research was conducted in the absence of any commercial or financial relationships that could be construed as a potential conflict of interest.

frontiers in Materials

ORIGINAL RESEARCH
published: 03 May 2019
doi: 10.3389/fmats.2019.00094

Solid Air—Low Temperature Manufacturing of Ultra-Low Permittivity Composite Materials for Future Telecommunication Systems

Mikko Nelo[1], Henrikki Liimatainen[2], Maria Väätäjä[1], Jonne Ukkola[2], Jari Juuti[1] and Heli Jantunen[1]*

[1] *Microelectronics Research Unit, University of Oulu, Oulu, Finland,* [2] *Fiber and Particle Engineering, University of Oulu, Oulu, Finland*

The frequency spectrum to be used by future wireless telecommunication systems such as 5G and beyond requires novel materials which are environment-friendly, are low cost and, most importantly, have low dielectric loss and permittivity when approaching higher frequencies. In this work, the development of all-inorganic composites with a relative permittivity of ∼1.2 and loss tangents in the range of 10^{-3} is presented. The composites were fabricated at the exceptionally low temperature of 120°C and were based on lithium molybdate (Li_2MoO_4) ceramic as a water-soluble binder reinforced by quartz fibers. The relative permittivity was further decreased by the addition of hollow micron-sized glass spheres having very low dielectric loss. A simple manufacturing method through filtration, stencil printing and drying is presented. The microstructure of the composites was investigated with FESEM microscopy and the dielectric properties by SPDR. Printing tests were carried out in order to evaluate the possibility of using the proposed composites in, for example, printed antenna applications.

Keywords: low permittivity, ceramic composites, nanocellulose, low temperature, GHz antenna application, electroceramic composites, electronics substrate

OPEN ACCESS

Edited by:
Michael P. M. Jank, Fraunhofer Institut für Integrierte Systeme und Bauelementetechnologie IISB, Germany

Reviewed by:
Janos Kiss, University of Szeged, Hungary
Ari Alastalo, VTT Technical Research Centre of Finland Ltd., Finland

****Correspondence:***
Mikko Nelo
mikko.nelo@oulu.fi

Specialty section:
This article was submitted to Translational Materials Science, a section of the journal Frontiers in Materials

Received: *06 December 2018*
Accepted: *15 April 2019*
Published: *03 May 2019*

Citation:
Nelo M, Liimatainen H, Väätäjä M, Ukkola J, Juuti J and Jantunen H (2019) Solid Air—Low Temperature Manufacturing of Ultra-Low Permittivity Composite Materials for Future Telecommunication Systems. Front. Mater. 6:94. doi: 10.3389/fmats.2019.00094

INTRODUCTION

The future telecommunication systems such as 5G will lead to new challenges to be solved: the increasingly high frequencies will increase the parasitic capacitances between the metal interconnects, the line-to-line crosstalk noise, the resistance—capacitance delay on the signal and the increased power dissipation (Maex et al., 2003; Shamiryan et al., 2004; Zhao et al., 2018). The use of low relative permittivity (ε_r) and low dielectric loss (tan δ) materials would minimize the parasitic capacitances, thus decreasing signal latency and allowing higher signal speeds and improved efficiency (Farrell et al., 2011). Low ε_r dielectric materials have been utilized in improving semiconductor packaging and integrated circuit performance as well as in high frequency, low-loss circuit boards (Shamiryan et al., 2004; Lee et al., 2005; Farrell et al., 2011). In polymeric materials both the use of porosity (Rathore et al., 2008; Joseph et al., 2015; Zhao et al., 2018) and low permittivity functional groups (Yuan et al., 2013; Liu et al., 2015; Lei et al., 2016) have been employed. Permittivity values as low as 1.05 with excellent dielectric losses have been achieved with porous polymeric materials such as the polyurethane and polyethylene foams as used in radomes (Eccostock product data sheet, 2018; General Plastics product data sheet, 2018).

Hollow glass microspheres (HGMS) offer an inexpensive solution to reducing the dielectric permittivity and losses of circuit boards or thick film devices (Kellerman, 1988; Chellis et al., 1992). Recently, coated glass microspheres have also been utilized in EM-shielding (Fu et al., 2007; Wang et al., 2016). Traditional solutions for making HGMS composites include a polymeric binder phase, although in this case the temperature stability is again a challenge.

Ceramic composite materials offer good stability at higher temperatures and their permittivity has been successfully reduced by introducing porosity (Bittner and Schmid, 2010; Sobocinski et al., 2015; Synkiewicz et al., 2017). Their downside has been the high manufacturing temperature resulting in high energy consumption and increased production costs. With the recent invention of a room temperature fabrication method (RTF), a water-based suspension of lithium molybdenum oxide (LMO), has been used to produce bulk dielectric samples and composites (Kähäri et al., 2014, 2015; Väätäjä et al., 2017). Using LMO enables a new approach to the manufacture of low ε_r ceramic materials at very low temperature due to its ability to form solid structures with 3D printing utilizing a low external pressure (Väätäjä et al., 2018). This enables the use of HGMS as a porosity-adding material without the risk of crushing them during molding. In this work, with the combination of the RTF method with its low pressure approach, a further development step is taken to achieve extremely low ε_r ceramic based composite materials.

EXPERIMENTAL

HGMS were purchased from Kevra Oy (Finland). According to the datasheet from the manufacturer, the spheres were C-type glass with 50–75% SiO_2 and had an average particle size of 40–80 μm, a volumetric density of 0.1–0.15 g/cm^3 and a temperature resistance of up to 650°C. Saturated Li_2MoO_4 (LMO) solution was made by mixing 80.0 g of LMO powder (>99%; Alfa Aesar, USA) in 100.0 g of deionized water overnight. The resulting saturated clear solution was collected and used in the experiments. The quartz fibers used were purchased from Robson Scientific (UK). According to the manufacturer, the fibers were quartz wool with a fiber diameter range of 5–30 μm, a purity of 99.995% SiO_2 and a temperature resistance of up to 1,000°C.

Cellulose nanofibers (CNF) were synthesized from bleached birch-wood pulp (Betula Pendula) using a non-derivatizing urea-choline chloride deep eutectic solvent (DES) pre-treatment (Sirviö et al., 2015). First, the DES system was formed by heating 107.5 g choline chloride and 92.5 g urea in a round-bottom flask at 100°C in an oil bath to obtain a clear, colorless liquid, after which the cellulose fibers (2.0 g of dry sheets) were introduced into the liquid at 100°C for 2 h. After the DES pre-treatment, 200 ml of deionized water was added while mixing and the cellulose fibers were filtered (Whatman 413) and washed with deionized water (2,000 ml). The pretreated sample was further individualized into cellulose nanofibers using a microfluidizer (Microfluidics M-110EH-30, USA). The sample was diluted in a low concentration (0.5%) before microfluidization, and was then passed five times through 400 and 200 μm chambers at a pressure of 1,000 bar. The obtained viscous cellulose nanofiber suspension was stored in a cold environment (+4°C).

The samples were fabricated by the following method, inspired by the paper making process, but instead of cellulose fibers, 100 mg of quartz fibers were used to provide mechanical strength for the samples. The fibers were placed in a square format on a filter sheet using a 200 μm thick 60 × 60 mm stencil as a guide. They were moistened with deionized water to temporary bind them together. Two Hundred milligram of HGMS were mixed with 1.0 g of deionized water and 1.0 g of saturated LMO solution to form a paste. This paste was applied on top of the quartz fibers using a 100 μm thick, 50 × 50 mm sized stencil and a blade. The resulting sandwich-like structure was lifted from the filter and placed on a release film with the LMO-HGMS paste downwards, thus achieving a smooth surface. The second layer of LMO-HGMS paste was printed through the 100 μm stencil as in the previous step, resulting in samples with LMO-HGMS paste layers on both sides. A perforated plastic film was placed on top of the samples, followed by four layers of suction paper to absorb the excess LMO solution. Finally, the samples, release films and papers were placed between two aluminum plates, pressed using 2 kPa pressure and dried in an oven for 18 h at 110°C. The aluminum plates and additional pressure were used to avoid warping during drying. The resultant samples were treated with an additional 2 h of drying without the plates and pressure to ensure that all the water was evaporated.

The dimensions and weight of samples were measured after drying. Since the amounts of glass spheres and quartz wool were precisely known, the LMO content could be calculated from the weight of the samples. After the weighing, the samples were cut into 52 × 52 mm squares for density and dielectric measurements. Post-treatments for surface smoothening with CNF suspension or LMO solution were carried out after the first measurements. On post-treatment with CNF, 1.0 ml of 0.49 wt.% CNF suspension was spread on each side of the samples using a doctoring blade, and on post-treatment with LMO, 0.50 g of saturated solution and 0.5 g of deionized water was applied to both sides of the samples. Moistened samples were handled as in the original preparation step by drying them between smooth and perforated release films, suction papers, aluminum plates, and pressure for 18 h at 110°C followed by additional drying of 2 h freely at 110°C.

The printing tests of the conductive patterns were done by manually screen printing DuPont 5064H (DuPont Ltd, UK) silver ink through a 180 mesh nylon screen with 16 μm thick emulsion and 500 μm wide lines. The printed patterns were dried for 30 min at 120°C. The flow of the sample manufacturing process with a schematic drawing of the sample structure is presented in **Figure 1**.

The dielectric measurements were carried out with a vector network analyzer (VNA) (Rhodes and Schwarz ZVB20, Germany) with split-post dielectric resonators (SPDR) (QWED, Poland) with nominal resonances at 2,475 and 5,180 MHz. The measurement results were calculated using QWED analysis software developed for the resonators. The resistance of the printed conductive lines was measured using a four-point measurement carried out in a probe station (Wentworth

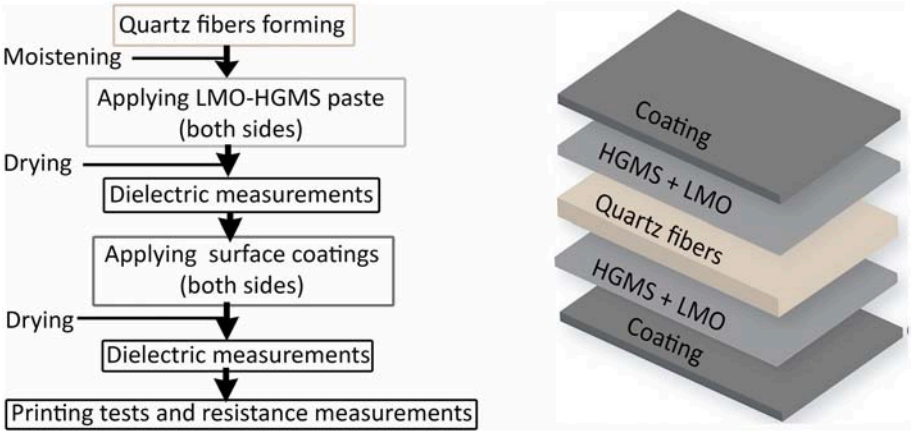

FIGURE 1 | (Left) Flow diagram of sample preparation process. **(Right)** Structural layers of the samples.

Laboratories, USA) connected to a multimeter (Agilent Technologies 34401A, USA). The surface quality after different treatments and elemental composition was investigated with field emission scanning electron microscopy (FESEM-EDS) analysis (Carl Zeiss Ultra Plus, Germany). Finally, the surface roughness analysis was done with a 3D laser scanning microscope (Keyence VK-X200, USA).

RESULTS AND DISCUSSION

The dielectric values for the coated samples are shown in **Table 1**. Untreated LMO-HGMS samples were measured before and after two different coatings. A total of six samples were measured in each case and the standard deviations calculated. The uncoated samples had an average relative permittivity of 1.19 and a loss tangent of 1.6–1.7 $\times$ 10^{-3} at both measurement frequencies, whereas the CNF coated samples had a permittivity of 1.19 with an increased loss tangent of 2.5–2.7 $\times$ 10^{-3}. The small influence of the CNF coating on the permittivity was estimated to be caused by the small quantity of CNF needed to achieve a smooth surface; typically 10 mg per sample. However, the increased losses were probably caused by polar functional groups in the CNF coating. The LMO coated samples remained similar in their dielectric properties with only minor changes in both relative permittivity and loss tangent. This result is due to the low dielectric loss of LMO, thus leading to very small changes in dielectric properties.

FESEM analysis was used to assess the surface quality of the samples. On uncoated samples (**Figure 2a**), it was noted that despite the gentle manufacturing process (maximum of 2 kPa pressure) some of the HGMS on the surface were cracked. This could be further improved by selecting smaller HGMS. Some quartz fibers were also visible on the surface. These caused some problems later in the printing experiments. Although the LMO was observed to bind most of the particles together, some porosity was observed on the sample surfaces. LMO and CNF coated samples (**Figures 2b,c**) had clearly reduced porosity, the latter being the least porous. CNF coating resulted in the smoothest surface, whereas LMO coating appeared to form crystals during the precipitation of LMO from the coating solution. EDS analysis (**Figure 2d**) was carried out on an uncoated sample to determine the SiO_2 content of the HGMS beads. After reduction of LMO from the result, the HGMS contained 72 wt.% SiO_2, 14 wt.% Na_2O, and 14 wt.% CaO. Using reduced alkali HGMS could possibly further reduce the dielectric losses of the composite samples.

The roughness after different surface treatments was studied with 3D laser scanning microscope using 3 $\times$ 3 mm^2 area of each sample. In addition, a common printing paper (Xerox, 80 g/m^2), a sintered ceramic substrate (DuPont 951) and a PET sheet for printed electronics (Melinex 339 PET) were analyzed to compare the surface quality of the produced samples. The results collected in **Figure 3** show that whereas LMO coating has a small effect, the utilization of CNF greatly reduces surface roughness. With further optimization, even smoother surface should be achievable.

The conductive lines were fabricated by screen printing. The high viscosity of the printing ink was considered to be beneficial when printing on a porous surface, while low viscosity inks could easily be completely absorbed into the samples. The printing proved to be challenging due to the contact that the printing screen made with the substrate despite the offset of the screen. In the untreated samples, loosely attached HGMS or quartz fibers adhered to the screen's surface. The same tendency was observed with the loose crystals on the LMO coated samples. This contaminated the printing surface of the screen and caused damage to the printed lines, as shown in **Figures 4a,b**. These problems were not present with CNF coated samples (**Figure 4c**), which resulted in more uniform printed patterns.

The resistance values of the 4.0 mm long and 0.5 mm wide printed lines as determined by four-point measurement were compared with those of the patterns printed on PET sheet. Six parallel lines were measured and their resistance values and standard deviations are shown in **Table 2**. The results showed that the lines printed on CNF coated samples gave lower resistance values than those measured from uncoated and LMO

TABLE 1 | Dielectric properties with standard deviation of samples at 2.5 and 5 GHz.

Sample treatment	2.5 GHz				5 GHz			
	ε_r	σ	tan δ, E-3	σ, E-3	ε_r	σ	tan δ, E-3	σ, E-3
Untreated	1.19	0.02	1.63	0.1	1.19	0.03	1.70	0.2
LMO coating	1.24	0.03	1.86	0.1	1.18	0.02	1.94	0.2
CNF coating	1.19	0.02	2.50	0.5	1.19	0.02	2.66	0.4

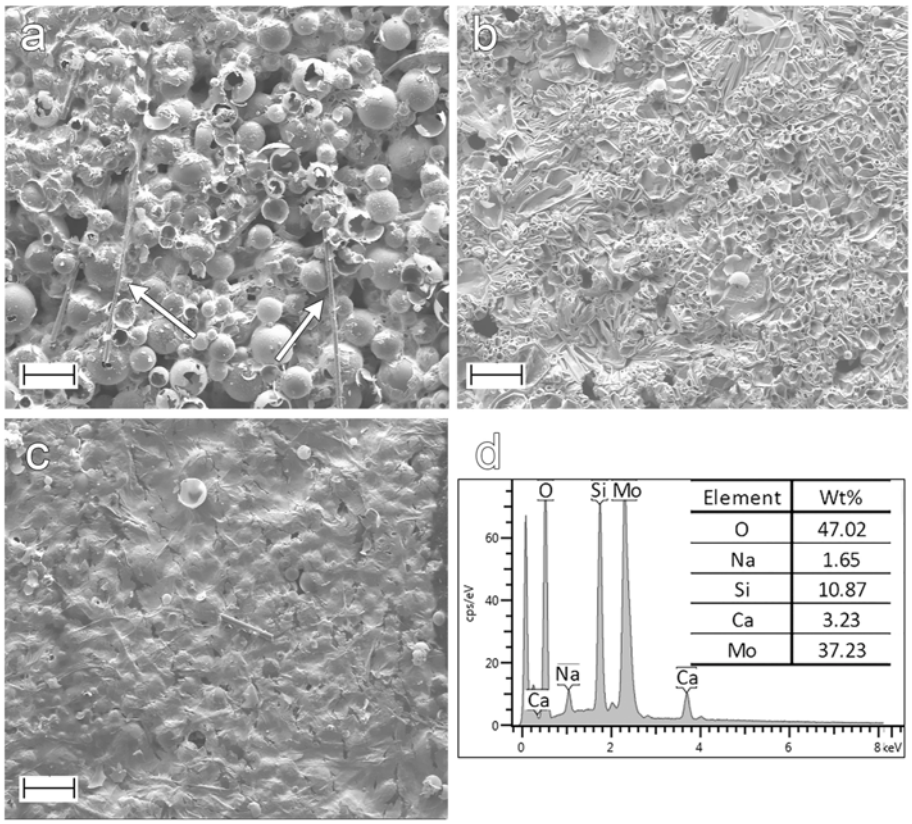

FIGURE 2 | (a) Uncoated sample. The surface consisted of LMO- bound HGMS showing porosity and some quartz fibers (white arrows). **(b)** LMO-coating reduced the surface porosity and submerged fibers. The LMO was observed to form hexagonal patterns on the sample surface. **(c)** CNF coated sample showed the smoothest surface with only a minor amount of porosity visible. All scale bars 100 μm. **(d)** EDS analysis of uncoated sample surface showing molybdate and oxygen from the LMO and the other elements from the HGMS.

coated samples. Moreover, these CNF coated samples exhibited very similar resistance values to those of the lines printed on the PET sheet. The feasibility of the silver ink used here has been earlier demonstrated for antenna operating at ∼ 4 GHz (Kähäri et al., 2016).

CONCLUSIONS AND PERSPECTIVES

A simple method of manufacturing extremely low ε_r ceramic based composite materials at very low temperature is presented. The composites showed low losses at high frequencies. In addition to this, a surface coating method was developed by utilizing LMO solution and CNF suspension for resulting in improved surface smoothness which enabled printing of conductive lines with low resistance. The composite with CNF coating exhibited ε_r and tan δ values of 1.19 and 0.0027 at 5 GHz, respectively. The lines printed on this composite showed a resistance of 0.29 Ω, similar to those printed on PET. The performance of the composite can be even further optimized in the future with lower alkali content or reduced size of HGMS, and different methods of surface coatings, such as applying sol-gel film on top of the samples.

The proposed method provides a simple approach to fabricate ceramic-based low ε_r substrates with only five processing steps starting from raw powder materials. The method is also environmentally friendly due to its low energy consumption achieved by low fabrication temperature (120°C) compared to the one commonly used for ceramics (>850°C). Moreover, since

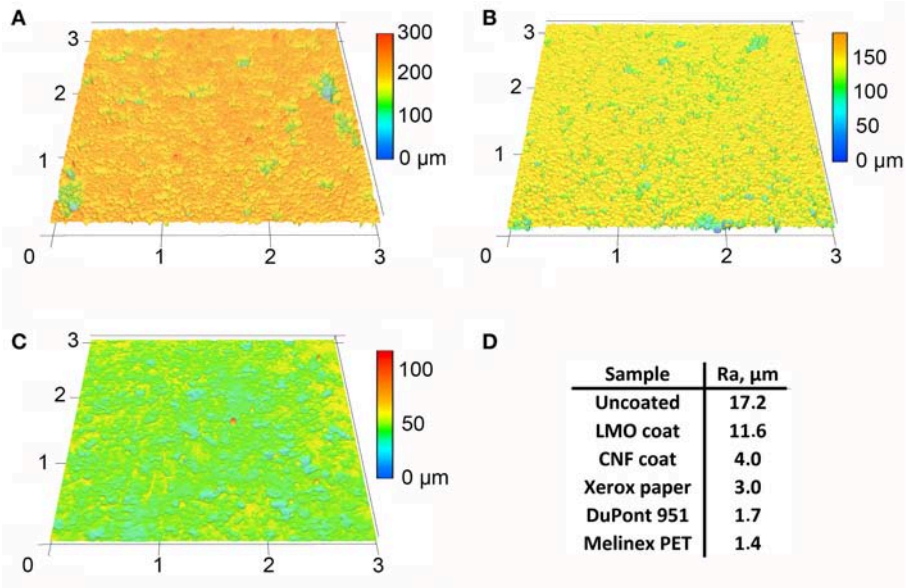

FIGURE 3 | Surface profiles and roughness values for different samples. Zero height is set as the lowest point for each sample. **(A)** Uncoated sample with the highest roughness. **(B)** Sample with LMO-coating with lower roughness. **(C)** CNF coated sample with the smoothest surface of HGMS composites. **(D)** Surface roughness measured for the HGMS composite samples, printing paper, sintered ceramic substrate, and PET sheet.

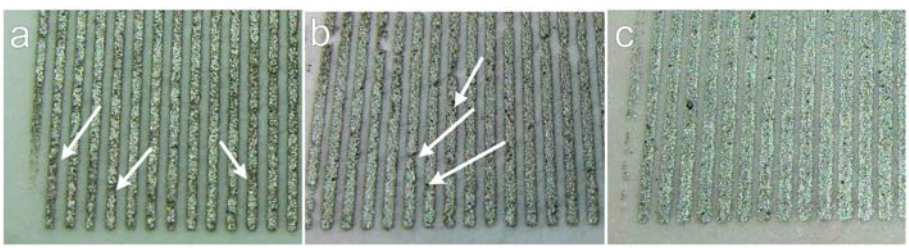

FIGURE 4 | (a–c) Printed 500 µm wide test lines. **(a)** Sample with untreated surface, **(b)** sample with LMO coating, **(c)** sample with CNF coating. Damage (white arrows) on lines was observed in untreated and LMO coated samples.

TABLE 2 | Resistance of 4.0 × 0.5 mm^2 printed lines.

	PET sheet	Untreated	LMO coating	CNF coating
R, Ω	0.28	0.56	0.41	0.29
σ	0.02	0.09	0.04	0.05

only low fabrication temperature and pressure are used, no special devices with high investment costs are required.

AUTHOR CONTRIBUTIONS

MN produced and measured all the samples, obtained the used materials and developed the filtration-based manufacturing method. HL and JU prepared the nanocellulose used in surface treatments of the samples. MV operated the laser scanning microscope and assisted on measurement data processing. HJ and JJ formulated the original hypotheses and discussed the dielectric results and printing experiments of the study. All authors contributed to the writing of the manuscript and evaluation of the results.

ACKNOWLEDGMENTS

The work leading to these results has received funding from the European Research Council (ERC) under the ERC POC grant agreement No. 812837. This work was supported in part by the Academy of Finland 6 Genesis Flagship (grant no. 318927) and by the Academy of Finland Printed Intelligence Infrastructure, PII (grant no. 320020).

REFERENCES

Bittner, A., and Schmid, U. (2010). Permittivity of LTCC substrates porousified with a wet chemical etching process. *Proce Eng.* 5, 327–330. doi: 10.1016/j.proeng.2010.09.114

Chellis, L. N., Japp, R. M., Summa, W. J., Rudik, W. J., and Wang, D. W. (1992). *Flame Retardant, Low Dielectric Constant Microsphere Filled Laminate.* New York, NY: International Business Machines Corporation. Patent, US5126192A

Eccostock product data sheet (2018) Available online at: http://www.eccosorb.com/Collateral/Documents/English-US/RFP-DS-PP%20112515.pdf (accessed April 25, 2019).

Farrell, R., Goshal, T., Cvelbar, U., Petkov, N., and Morris, M.A. (2011). Advances in ultra low dielectric constant ordered porous materials. *Electrochem. Soc. Interface Winter* 20, 39–46. doi: 10.1149/2.F04114if

Fu, W., Liu, S., Fan, W., Yang, H., Pang, X., Xu, J., et al. (2007). Hollow glass microspheres coated with CoFe2O4 and its microwave absorption property. *J. Magn. Magn. Mater*. 316, 54–58. doi: 10.1016/j.jmmm.2007.03.201

General Plastics product data sheet (2018) https://www.generalplastics.com/wp-content/uploads/2016/11/White-Paper-PU-Foam-Dielectric-Materials-for-Use-in-Radomes-and-Other_Applications.pdf (accessed April 25, 2019).

Joseph, A. M., Nagendra, B., Surendran, K. P., and Gowd, E. B. (2015). Syndiotactic polystyrene/hybrid silica spheres of POSS siloxane composites exhibiting ultralow dielectric constant. *ACS Appl. Mater. Interfaces* 7, 19474–19483. doi: 10.1021/acsami.5b05933

Kähäri, H., Ramachandran, P., Juuti, J., and Jantunen, H. (2016). Room-temperature-densified Li_2MoO_4 ceramic patch antenna and the effect of humidity. *Int. J. Appl. Ceram. Technol*. 14, 50–55. doi: 10.1111/ijac.12615

Kähäri, H., Teirikangas, M., Juuti, J., and Jantunen, H. (2014). Dielectric properties of lithium molybdate ceramic fabricated at room temperature. *J. Am. Ceram. Soc*. 97, 3378–3379. doi: 10.1111/jace.13277

Kähäri, H., Teirikangas, M., Juuti, J., and Jantunen, H. (2015). Improvements and modifications to room-temperature fabrication method for dielectric Li2MoO4 ceramics. *J. Am. Ceram. Soc*. 98, 687–689. doi: 10.1111/jace.13471

Kellerman, D. (1988). *Micro-Electronics Devices and Methods of Manufacturing Same.* Maynard, MA: Digital Equipment Corporation. Patent US4781968A.

Lee, B., Park, Y.-H., Hwang, Y.-T., Oh, W., Yoon, J., and Ree, M. (2005). Ultralow-k nanoporous organosilicate dielectric fi lms imprinted with dendritic spheres. *Nat. Mater*. 4, 147–150. doi: 10.1038/nmat1291

Lei, X., Qiao, M., Tian, L., Chen, Y., and Zhang, Q. (2016). Tunable permittivity in high-performance hyperbranched polyimide films by adjusting backbone Rigidity. *J. Phys. Chem. C* 120, 2548–2561. doi: 10.1021/acs.jpcc.5b11667

Liu, Y., Qian, C., Qu, L., Wu, Y., Zhang, Y., Wu, X., et al. (2015). A bulk dielectric polymer film with intrinsic ultralow dielectric constant and outstanding comprehensive properties. *Chem. Mater*. 27, 6543–6549. doi: 10.1021/acs.chemmater.5b01798

Maex, K., Baklanov, M. R., Shamiryan, D., Iacopi, F., Brongersma, S. H., and Yanovitskaya, Z. S. (2003). Low dielectric constant materials for microelectronics. *J. Appl. Phys*. 93, 8793–8841. doi: 10.1063/1.1567460

Rathore, J. S., Interrante, L. V., and Dubois, G. (2008). Ultra Low-k Films Derived from Hyperbranched Polycarbosilanes (HBPCS). *Adv. Funct. Mater*. 18, 4022–4028. doi: 10.1002/adfm.200801197

Shamiryan, D., Abell, T., Iacopi, F., and Maex, K. (2004). Low-k dielectric materials. *Mater. Today* 7, 34–39. doi: 10.1016/S1369-7021(04)00053-7

Sirviö, J. A., Visanko, M., and Liimatainen, H. (2015). Deep eutectic solvent system based on choline chloride-urea as a pre-treatment for nanofibrillation of wood cellulose. *Green Chem.* 17, 3401–3406. doi: 10.1039/C5GC00398A

Sobocinski, M., Teirikangas, M., Peräntie, J., Vahera, T., Nelo, M., Juuti, J., et al. (2015). Decreasing the relative permittivity of LTCC by porosification with poly(methyl methacrylate) microspheres. *Ceram. Int*. 41, 10871–10877. doi: 10.1016/j.ceramint.2015.05.028

Synkiewicz, B., Szwagierczak, D., and Kulawik, J. (2017). Multilayer LTCC structures based on glass-cordierite layers with different porosity. *Microelectron* 34, 110–115. doi: 10.1108/MI-12-2016-0084

Väätäjä, M., Kähäri, H., Juuti, J., and Jantunen, H. (2017). Li2MoO4 -based composite ceramics fabricated from temperature- and atmosphere-sensitive MnZn ferrite at room temperature. *J. Am. Ceram. Soc*. 100, 3626–3635. doi: 10.1111/jace.14914

Väätäjä, M., Kähäri H., Ohenoja, K., Sobocinski, M., Juuti, J., and Jantunen, H. (2018). 3D printed dielectric ceramic without a sintering stage. *Sci. Rep.* 8:15955. doi: 10.1038/s41598-018-34408-5

Wang, J., Wang, J., Zhang, B., Sun, Y., Chen, W., and Wang, T. (2016). Combined use of lightweight magnetic Fe_3O_4-coated hollow glass spheres and electrically conductive reduced graphene oxide in an epoxy matrix for microwave absorption. *J. Magn. Magn. Mater*. 401, 209–216. doi: 10.1016/j.jmmm.2015.10.001

Yuan, C., Jin, K., Li, K., Diao, S., Tong, J., and Fang, Q. (2013). Non-porous low- k dielectric films based on a new structural amorphous fluoropolymer. *Adv. Mater*. 25, 4875–4878. doi: 10.1002/adma.201302021

Zhao, B., Zhao, C., Wang, C., and Park, C.B. (2018). Poly(vinylidene fluoride) foams: a promising low-k dielectric and heat-insulating material. *J. Mater. Chem. C* 6, 3065–3073. doi: 10.1039/c8tc00547h

Conflict of Interest Statement: The authors declare that the research was conducted in the absence of any commercial or financial relationships that could be construed as a potential conflict of interest.

frontiers in Materials

MINI REVIEW
published: 12 April 2019
doi: 10.3389/fmats.2019.00062

Lignin-Based Electrospun Carbon Nanofibers

Manish Kumar[1], *Maiju Hietala*[1] *and Kristiina Oksman*[1,2]*

[1] *Fibre and Particle Engineering Research Unit, University of Oulu, Oulu, Finland,* [2] *Division of Materials Science, Luleå University of Technology, Luleå, Sweden*

The article summarizes the scientific progress that has occurred in the past several years in regard to the preparation of carbon nanofibers from lignin as a low-cost environmentally-friendly raw material using electrospinning. It presents an overview of using lignin, electrospinning, and carbonization to convert lignin to carbon nanofibers. Lignin is a renewable source for carbon material, and it is very abundant in nature. It is mostly produced as a byproduct from the paper industry and biomass fractionation. Despite its extensive availability and beneficial properties, only a few studies have reported on its use in electronic applications. Lignin-based carbon nanofibers have a high surface area, high porosity, and good electrical conductivity; thus, it is proposed that they are suitable for future energy storage applications.

Keywords: lignin, electrospinning, carbonization, carbon nanofibers, energy storage

OPEN ACCESS

Edited by:
Zoltán Kónya,
University of Szeged, Hungary

Reviewed by:
Sápi András,
University of Szeged, Hungary
Istvan Palinko,
University of Szeged, Hungary
Yejun Qiu,
Harbin Institute of Technology, Shenzhen, China

***Correspondence:**
Kristiina Oksman
kristiina.oksman@ltu.se

Specialty section:
This article was submitted to Translational Materials Science, a section of the journal Frontiers in Materials

Received: *18 January 2019*
Accepted: *26 March 2019*
Published: *12 April 2019*

Citation:
Kumar M, Hietala M and Oksman K (2019) Lignin-Based Electrospun Carbon Nanofibers. Front. Mater. 6:62. doi: 10.3389/fmats.2019.00062

INTRODUCTION

Electrospun carbon nanofibers (ECNFs) are part of a technological revolution due to their operational simplicity and extraordinary properties, such as being lightweight, having a high surface area, and exhibiting good thermal and electrical conductivity (Lallave et al., 2007). ECNFs have a wide range of applications in areas such as energy conversion and storage (Peng et al., 2016), sensing and diagnostics (Huang et al., 2010), aerospace (Wu et al., 2013), and micro/nano electromechanical systems (Arshad et al., 2011). However, the widespread use of ECNFs is limited due to the high cost of the precursor material and the low yield. Currently, polyacrylonitrile (PAN), produced from depleting petroleum resources, is the prevalent precursor material used to produce ECNFs (Inagaki et al., 2012). The solvents required to convert electrospun nanofibers from the PAN precursor polymer, i.e., dimethylformamide (DMF), are toxic. Therefore, it is essential to develop an alternative, greener precursor material based on renewable plant-based materials.

Lignin, a natural polymer present in lignocellulosic plants, is one of the best substitute materials for producing carbon nanofibers (Baker and Rials, 2013). According to a recent research report, the lignin market is growing at a compound annual growth rate (CAGR) of 2.2%, and it is estimated to generate revenues of 913.1 million USD by 2025 (Grand View Research Inc., 2017). Using the electrospinning method, dissolved lignin suspensions can be processed into submicron and nanoscale fibers. After Lallave et al. (2007) reported the use of electrospinning for fabricating lignin-based carbon fibers, the number of studies related to converting lignin into carbon nanofibers has steadily grown. The recent progress in lignin-based carbon nanofibers has substantially increased the intention of using them for technical applications, such as energy storage (dye-sensitized solar cells [DSCC], batteries, capacitors, and supercapacitors) (Fang et al., 2017). An ISI Web of Science literature search showed that, currently, only 61 research papers have been published on lignin, electrospinning, and carbon fibers. Researchers in Republic of China, the United States, and Canada have been most active in this field.

This literature review focuses on the preparation of lignin-based carbon nanofibers using electrospinning for electronic applications. The lignin-based carbon nanofibers have unique properties that could be used for developing value-added applications, such as a low-cost, "green" carbon material for energy storage.

LIGNIN

Lignin is a natural biopolymer that mainly consists of three common monomeric units: coniferyl alcohol, p-coumaryl alcohol, and sinapyl alcohol. Lignin provides structure and strength, and it has antioxidative and antimicrobial properties; it also stores energy in a plant (Boerjan et al., 2003). Lignin is very promising as a low-cost carbon precursor material (Rosas et al., 2014); it is a renewable resource and it has a carbon-rich phenolic chemical structure (Boudet et al., 2003). While lignin is produced in large quantities as a byproduct in the paper industry and in biomass fractionation (Kadla et al., 2002), it has few applications other than energy recovery. All lignocellulosic plants contain lignin, making it one of the most common biopolymers on earth. Typically, lignin is separated from wood, which contains ∼30% lignin. The Kraft and Organosolv processes are the most common delignification methods for lignin isolation (Shi et al., 2018). The Kraft process uses sodium hydroxide and sodium sulfide to extract lignin; the Organosolv process uses organic solvents, such as methanol, ethanol, and acetic acid, or their aqueous solutions, for extraction. Additionally, large amounts of lignin are generated in bioethanol production (Matsushita et al., 2009).

SPINNING SOLUTION FOR ELECTROSPINNING

A suitable spinning solution is essential for the electrospinning of nanofibers. The most important properties of the spinning solution that affect the quality of the electrospun fibers are its electrical conductivity, surface tension, and viscosity (Ramakrishna, 2005). Lower or higher viscosity than is required results in the formation of beads or no fibers at all. In the first publication on the electrospinning of lignin, Lallave et al. (2007) used a lignin:ethanol solution at a w/w ratio of 1:1 with a viscosity range between 350 and 400 cPs to fabricate lignin fibers without any additional polymer. The addition of phosphoric acid, H_3PO_4, into a similar lignin:ethanol solution (H_3PO_4:lignin:ethanol–weight ratio: 0.3:1:1) resulted in more curly fibers with a diameter $\leq 1\,\mu m$ (García-Mateos et al., 2018). García-Mateos et al. (2018) suggested that H_3PO_4 is the reason for the curly fibers because of the increased viscosity of 450 cPs and the increased electrical conductivity of the spinning solution. Polymers are more commonly used as processing aids to achieve the necessary chain entanglement for electrospinning of nanofibers. In order to produce "green" nanofibers, water soluble polymers, such as polyethylene oxide (PEO) and polyvinyl alcohol (PVA), are preferred for the preparation of the lignin-based carbon nanofibers (Poursorkhabi et al., 2015). In addition to water soluble polymers, lignin-PAN solutions with DMF as a solvent have been used in electrospinning (Seo et al., 2011). Seo et al. (2011) observed that increasing the lignin content from 50 to 80 wt% decreased the viscosity and conductivity of the solution, leading to beads and thicker fibers in electrospinning.

ELECTROSPINNING

Electrospinning is a simple, productive technique used to fabricate highly functional micro- and nanometer scale (0.01–10 μm) fibers. These fibers have significant advantages: they are extremely lightweight, their fabrication cost is low, and they have a large aspect ratio, reduced defects (small diameter), high molecular orientation, and high flexibility in surface functionality. When a high-voltage electric field is applied to a polymer solution, fibers are initiated at the tip of a "Taylor cone." In the beginning, the fiber path is almost straight (a stable region). After a specific distance, the fiber path becomes complex (a bending instability region) (Yarin et al., 2001). A significant decrease in the fiber diameter occurs in the instability region (Reneker and Yarin, 2008). The reasons for this bending instability are explained by Earnshaw's theorem. **Figure 1A** shows the basic principle of the electrospinning process, and **Figures 1B–D** shows the electrospun lignin/PVA nanofiber mat at different post-processing stages.

Adjusting the electrospinning processing parameters, such as the voltage, feed rate, needle type, and the tip-to-collector distance, affects the properties of electrospun lignin nanofibers. Using a co-axial and tri-axial spinneret, solid, and hollow nanofibers from the lignin:ethanol solution were prepared using a tip-to-collector distance of 20–25 cm, a potential difference of 12 kV, and variable feed rates (Lallave et al., 2007). Similar processing conditions (12 kV potential difference, 20–25 cm tip-to-collector distance, and feed rates of 0.06 and 0.8 mL/h) were used to prepare nanofibers from a platinum (Pt)-doped lignin:ethanol solution (Ruiz-Rosas et al., 2010). Dallmeyer et al. (2010) found that the addition of PEO could result in the transition from the electrospray of lignin to the formation of uniform fibers. They used the operating tip-to-collector distance of 14–20 cm, a potential difference of 9–14 kV, and a feed rate of 0.03 mL/min.

STABILIZATION AND CARBONIZATION OF LIGNIN FIBER MATS

Stabilization is an intermediate step in the conversion of lignin-based ECNFs. In this step, the electrospun fibrous mat undergoes cyclization, oxidation, and dehydrogenation. Consequently, the intermolecular atomic bonding pattern is rearranged and the lignin transforms from a thermoplastic into a thermoset-type material at temperature range of about 200–300°C (Dallmeyer et al., 2014). Moreover, the volatile byproduct, is removed. A lower heating ramp of 0.05–5°C min^{-1} is preferred in the stabilization condition to achieve complete oxidation of the fibrous mat (Huang, 2009). If the stabilization condition is not properly maintained, the fibers could melt during the carbonization procedure (Seo et al., 2011). For safe handling,

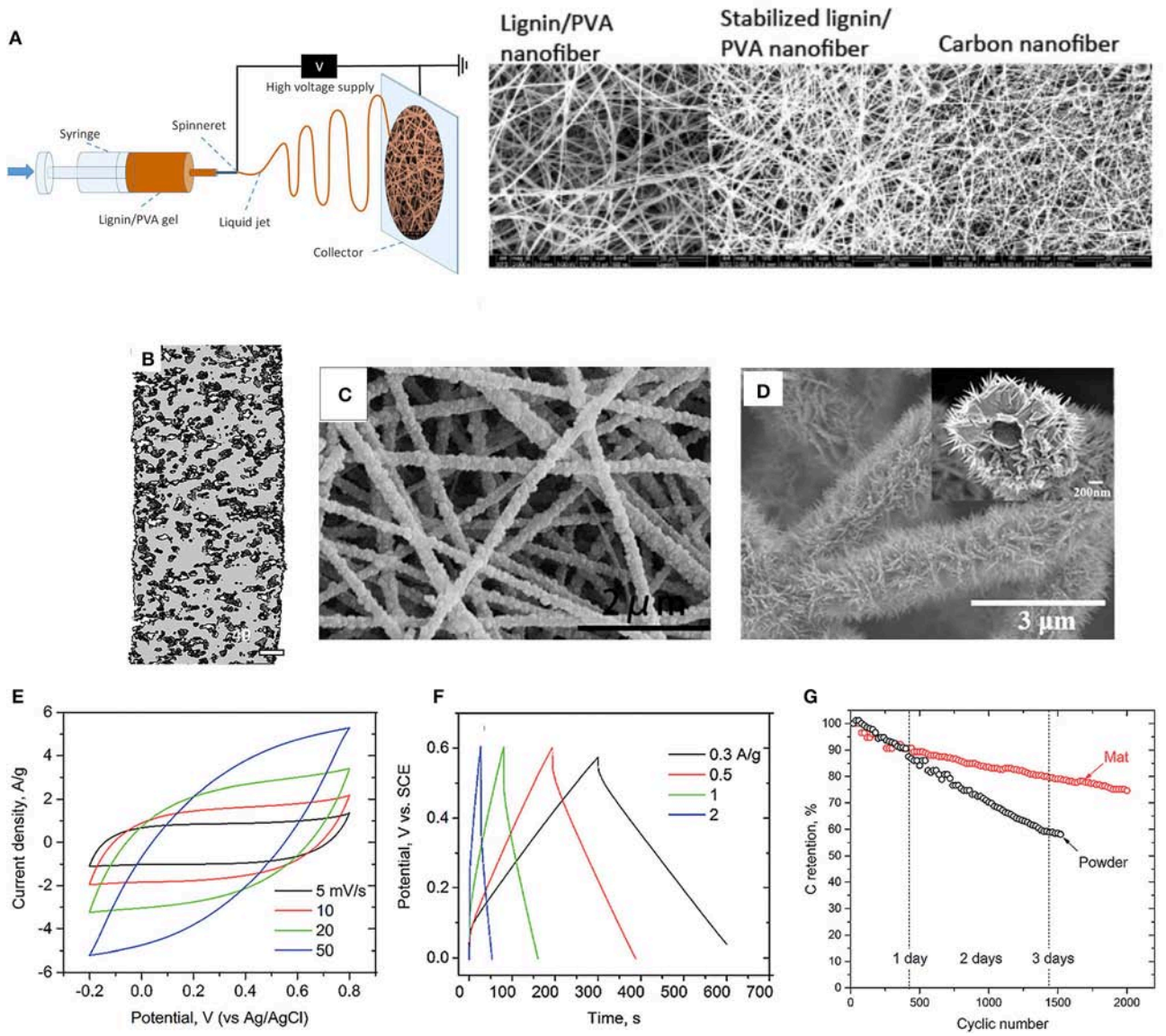

FIGURE 1 | Preparation of lignin-based electrospun carbon nanofibers (ECNFs), their structure and electrochemical properties. **(A)** Schematic of electrospinning of the lignin/PVA suspension (75/25) and electrospun lignin/PVA nanofibers before post-processing, after stabilization, and after carbonization; **(B–D)** methods which are used to reach very high specific surface area on the carbon fibers: **(B)** KOH treatment prior the carbonization process resulting in a mesoporous carbon nanofiber by Ago et al. (2016) reproduced under the terms of the Creative Commons Attribution (CC BY 3.0) license, **(C)** magnesium nitrate treated ECNFs resulting in carbon nanofibers with improved porosity, surface area and electrochemical performance by Ma et al. (2018) with permission from Elsevier, **(D)** nickel cobaltite ($NiCo_2O_4$) decorated ECNFs which resulted in high specific surface area and high specific capacitance by Lei et al. (2017) with permission from Elsevier; **(E–G)** electrochemical characterization of lignin-based ECNFs as electrode material using three-electrode cell configuration in 0.5 M Na_2SO_4 electrolyte by Ago et al. (2016) reproduced under the terms of the Creative Commons Attribution (CC BY 3.0) license: **(E)** cyclic voltammograms at varying scan rates; **(F)** galvanostatic charge/discharge curve at varying current densities, **(G)** cycling stability of ECNFs and powder at 10 mV s^{-1}.

slow heating and a long duration are recommended during the stabilization procedure. As an outcome of the stabilization procedure, the size of the fibrous mat shrinks and the color slightly darkens. For example, Lallave et al. (2007) stabilized the fiber mat in air at 0.25°C min^{-1} from room temperature to 200°C for 24 h. Lignin was oxidized and the fiber weight was reduced (81 wt%) due to the release of water. No fusion of the fibers was obtained after stabilization, and the fiber size (diameter) in the resulting product was similar to the size of the original mat. You et al. (2015) shortened the stabilization time from 38 to 3 h using hexamethylenetetramine. According to Yen and Chang (2016), stabilization is a crucial step because it prevents fiber fusion and rupture in the subsequent carbonization step. In contrast, Cho et al. (2018) reported that it is possible to obtain uniform

lignin-based carbon nanofibers without the thermal stabilization step by adding small amounts of nanocrystalline cellulose.

Carbonization is the final step in the conversion of lignin-based ECNFs. Here, the carbon atoms are cross-linked at temperature ranging from 600 to 1,500°C in an inert atmosphere. The non-carbon elements evaporate as a mixture of different gases in the applied high temperature range. The remaining mat is nearly 100% pure ECNFs. As an outcome of the carbonization procedure, the size of the fibrous mat shrinks more and the color becomes black. Moreover, a decrease in the fiber diameter has been observed as the carbonization temperature increases (Ruiz-Rosas et al., 2010). A higher carbonization temperature has been found to result in a higher degree of structural ordering in carbon (Rodríguez-Mirasol et al., 1996), and lignin-based carbon fibers with higher electrical conductivity were obtained by increasing the carbonization temperature from 600 to 900°C (Aslanzadeh et al., 2017).

GREEN CARBON FIBERS FOR ENERGY STORAGE APPLICATIONS

Lignin-based carbonized carbon fibers have been reported to have a high specific surface area, high porosity, high electrical conductivity, good mechanical properties, high oxidation resistance, and superior thermal stability. These unique properties of lignin-based ECNFs make them ideal resources for low-cost energy storage applications, especially as green electrode materials for supercapacitors. Supercapacitors are considered to be very promising devices for energy storage due to their high power density, long cycling stability/durability, short charging times, and environmental friendliness (Ma et al., 2018). **Table 1** summarizes recent studies on the use of lignin-based ECNFs in energy storage applications showing the material combination used for the electrospinning, the carbonization temperatures, the surface activating agents that were used, the surface area measured by the Brunauer-Emmett-Teller (BET) method, the electrolyte used, and the specific capacitance for energy storage applications.

Lai et al. (2014b) reported on the properties of ECNFs from a lignin–PVA nanofiber mat followed by stabilization and carbonization to be used in supercapacitors. The carbonized mat was found to be highly effective as binder-free electrodes. The gravimetric capacitance of 64 Fg^{-1} was achieved at a current density of 400 mAg^{-1} and 50 Fg^{-1} at 2,000 mAg^{-1}. The membrane showed a capacitance retention of 10% after 6,000 cycles of charge/discharge. Ago et al. (2016) reported on the conversion of lignin-PVA fiber mats into a mesoporous carbon fiber mat for supercapacitor electrode. The fiber mat was stabilized at 250°C; it was then impregnated with potassium hydroxide (KOH), and then carbonized at 900°C. The resulting fiber mat exhibited a high surface area, up to 2005 m^2g^{-1}, and a large pore volume, 0.7 cm^3g^{-1} with 70% mesoporosity, which greatly improved the material's electrochemical performance (**Figures 1B,E,F**). The specific capacitance of 205 Fg^{-1} was measured, and 83% of the capacity could be maintained after 1,500 cycles and **Figure 1G**).

Ma et al. (2016) applied manganese (IV) dioxide (MnO_2) nanowhiskers for the decoration of carbonized ECNFs from the lignin–PVA mat, and then tested this material as an electrode material for supercapacitors. The small fiber diameters of 200 nm and the high surface area of 583 m^2g^{-1} exhibited superior supercapacitor performance with a high gravimetric capacitance of 83.3 Fg^{-1}, as well as an energy density of 84.3 $WhKg^{-1}$ and a power density of 5.72 $kWkg^{-1}$, making the material suitable for application in a high-performance supercapacitor. The improved supercapacitor performances were explained by the MnO_2 surface coating, which provided high specific/gravimetric capacitance and a large reaction surface area, resulting in fast reaction kinetics. Same authors, Ma et al. (2018) used magnesium nitrate hexahydrate ($Mg(NO_3)\cdot 6H_2O$) as an additive in lignin-polyvinylpyrrolidone (PVP)-based carbon nanofibers resulting in a carbon nanofiber mat with a specific surface area of 1,140 m^2g^{-1}, increased mesoporosity (2–4 nm pore size) (shown in **Figure 1C**), and specific capacitance of 248 F/g^{-1} at a current density of 0.2 Ag^{-1}. They also reported a good cycling stability of 97% capacitance retention after 1,000 cycles.

Deposition of silver (Ag) nanoparticles to lignin-PVA derived ECNFs was reported as a cost-effective and highly efficient electrocatalyst in alkaline fuel cells; the suitable activating agent can provide additional functionality as well as higher crystallinity due to the particle size growth (Lai et al., 2014a). That study observed the electrochemical activity of Ag/ECNFs electrocatalyst systems toward oxygen reduction reaction; they found that the mass activity of 15 wt% Ag/ECNFs system was 119 $mAmg^{-1}$. You et al. (2015) reported the fabrication of lignin-based activated carbon fibers (ACFs), without using an additional polymer, followed by stabilization, carbonization, and steam activation for electric double layer capacitor application. The nitrous oxide (N_2) adsorption and desorption measurement indicated that the ACFs had a high specific surface area of 2,185 m^2g^{-1} and large pores (0.5–1.3 nm range). These favored the good electrical capacitance of 133.3 Fg^{-1} at a current density of 1 Ag^{-1}. Wang et al. (2017) used iron oxide (Fe_2O_3 and Fe_3O_4) particles to decorate acetic acid lignin–PEO based carbon nanofibers, and then used the carbon nanofibers as an electrode material for a pseudocapacitor. The iron oxide-lignin based composite ECNF showed excellent electrochemical performance due to the reversible multi-electron redox faradaic reactions. The specific capacitance of 72.1 Fg^{-1} at a constant current density of 500 mAg^{-1} was achieved. Hu et al. (2014) used a KOH solution to activate lignin-PEO–based carbon fibers as the electrode material for a supercapacitor. The prepared ACFs showed a high microporosity (0.75 nm pore size) and high specific capacitance (344 Fg^{-1}) at a low electrode mass of 1.8 mg and a scan rate of 10 mVs^{-1}. ACFs also showed a low equivalent series resistance (ESR) of 1.71 Ω and outstanding cycling stability. Recently, Lei et al. (2017) decorated nickel cobaltite ($NiCo_2O_4$) on carbon nanofibers of lignin-PAN blend solution using the hydrothermal method, and then utilized the material as a flexible electrode for an asymmetric supercapacitor (**Figure 1D**). They obtained the following electrochemical properties: a specific capacitance of 1,757 Fg^{-1} at 2 $mAcm^{-2}$ and an excellent cycling stability with

TABLE 1 | Electrospun carbon fibers tested in energy storage applications.

References	Material combination	Carbonization (°C)	Surface activation	BET (m^2g^{-1})	Electrolyte	Spec. cap. (Fg^{-1})
Lai et al., 2014b	Kraft lignin:PVA (70:30)	1,200	No	–		64
You et al., 2015	Hexamine:Acetic acid lignin (10:90)	1,000	900°C steam	2185	1 M $TEMABF_4$/PC	133
Ago et al., 2016	Kraft lignin:PVA (75:25)	900	KOH prior carbonization	2005	0.5 M Na_2SO_4	205
Ma et al., 2016	Lignin:PVA	1,200	MnO_2	583	1.0 M LiPF6	83.3
Wang et al., 2017	Acetic acid lignin:PEO (30:70)	900	$Fe(acac)_3$	–	1 M Na_2SO_3	72.1
Ma et al., 2018	Kraft lignin:PVP (1:2)	800	$Mg(NO_3)\cdot 6H_2O$	1140	6 M KOH	248
Lei et al., 2017	Kraft lignin:PAN (50:50)	1000	$NiCo_2O_4$	–	2 M KOH	1757
Hu et al., 2014	Lignin:PEO (9:1)	850	KOH	–	6 M KOH	344
Kim et al., 2007	PAN:$ZnCl_2$	800	No	550	6 M KOH	130
Niu et al., 2011	PAN:PVP	970	CO_2	531	1 M H_2SO_4	221
Lai and Lo, 2015	PAN:PMMA (50:50)	800	No	248	2 M KOH	195

∼138% capacitance retention after 5,000 cycles at 7 $mAcm^{-2}$. Comparing these numbers with PAN-based carbon nanofibers in **Table 1** the lignin based carbon fibers show promising electrochemical performance.

Zhao et al. (2018) prepared a flexible carbon nanofiber mat from a lignin-PVA solution and used it as a binder-free counter electrode for DSCC, instead of supercapacitors. The mat was carbonized at 1,500°C, and it was reported to have a relatively high specific surface area of 941 m^2g^{-1}; it also provided a maximum photoelectric conversion efficiency of up to 7.6% due to its high specific surface area and low charge transfer resistance, which is of the same magnitude as the conventional and expensive Pt material used for DSSC.

CONCLUSIONS

Developments in the manufacture and properties of lignin-based carbon nanofibers has significantly increased the intention of their use for technical applications, such as green electrode materials for energy storage applications. Green carbon nanofibers prepared using the electrospinning technique have been shown to have a high surface area, high porosity, high electrical conductivity, and superior graphite content. This brief literature review provides a step-by-step understanding of the lignin material, the preparation of the spinning solution, the electrospinning parameters, and the conversion process involved in the preparation of green carbon nanofibers. It also includes a concise summary of the recent electrochemical studies on lignin-based carbon nanofibers for energy storage applications. In the near future, a more detailed study about electrospinning of native lignin-based carbon nanofibers needed in order to implement for an exciting possibility as a "greener" electrode material.

AUTHOR CONTRIBUTIONS

All authors listed have made a substantial, direct and intellectual contribution to the work, and approved it for publication.

ACKNOWLEDGMENTS

The authors gratefully acknowledge Business Finland for the financial support it provided through the Grelectronics research project. The Swedish partners thank Bio4Energy, a Swedish strategic research program, and the Swedish Research Council (VR) for their financial support.

REFERENCES

Ago, M., Borghei, M., Haataja, J. S., and Rojas, O. J. (2016). Mesoporous carbon soft-templated from lignin nanofiber networks: microphase separation boosts supercapacitance in conductive electrodes. *RSC Adv.* 6, 85802–10. doi: 10.1039/C6RA17536H

Arshad, S. N., Naraghi, M., and Chasiotis, I. (2011). Strong carbon nanofibers from electrospun polyacrylonitrile. *Carbon* 49, 1710–19. doi: 10.1016/j.carbon.2010.12.056

Aslanzadeh, S., Ahvazi, B., Boluk, Y., and Ayranci, C. (2017). Carbon fiber production from electrospun sulfur free softwood lignin precursors. *J. Eng. Fibers Fabrics* 12, 33–43. doi: 10.1177/155892501701200405

Baker, D. A., and Rials, T. G. (2013). Recent advances in low-cost carbon fiber manufacture from lignin. *J. Appl. Poly. Sci.* 130, 713–28. doi: 10.1002/app.39273

Boerjan, W., Ralph, J., and Baucher, M. (2003). Lignin biosynthesis. *Annu. Rev. Plant Biol.* 54, 519–46. doi: 10.1146/annurev.arplant.54.031902.134938

Boudet, A. M., Kajita, S., Grima-pettenati, J., and Goffner, D. (2003). Lignins and lignocellulosics : a better control of synthesis for new and improved uses. *Trends Plant Sci.* 8, 576–81. doi: 10.1016/j.tplants.2003.10.001

Cho, M., Karaaslan, M., Chowdhury, S., Ko, F., and Renneckar, S. (2018). Skipping oxidative thermal stabilization for lignin-based carbon nanofibers. *ACS Sustain. Chem. Eng.* 6, 6434–44. doi: 10.1021/acssuschemeng.8b00209

Dallmeyer, I., Ko, F., and Kadla, J. F. (2010). Electrospinning of technical lignins for the production of fibrous networks. *J.*

Wood Chem. Technol. 30, 315–29. doi: 10.1080/02773813.2010.527782

Dallmeyer, I., Lin, L. T., Li, Y., Ko, F., and Kadla, J. F. (2014). Preparation and characterization of interconnected, kraft lignin-based carbon fibrous materials by electrospinning. *Macromol. Mater. Eng.* 299, 540–51. doi: 10.1002/mame.201300148

Fang, W., Yang, S., Wang, X.-L., Yuan, T.-Q., and Sun, R.-C. (2017). Manufacture and application of lignin-based carbon fibers (LCFs) and lignin-based carbon nanofibers (LCNFs). *Green Chem.* 19, 1794–1827. doi: 10.1039/C6GC03206K

García-Mateos, F. J., Berenguer, R., Valero-Romero, M. J., Rodríguez-Mirasol, J., and Cordero, T. (2018). Phosphorus functionalization for the rapid preparation of highly nanoporous submicron-diameter carbon fibers by electrospinning of lignin solutions. *J. Mater. Chem. A* 6, 1219–33. doi: 10.1039/C7TA08788H

Grand View Research Inc. (2017). *Lignin Market Analysis By Product (Ligno-Sulphonates, Kraft Lignin, Organosolv Lignin) By Application (Macromolecules, Aromatics), By Region (North America, Europe, Asia Pacific, Central & South America, MEA), And Segment Forecasts, 2018 - 2025.* Available online at: https://www.grandviewresearch.com/press-release/global-lignin-market (accessed September 21, 2018).

Hu, S., Zhang, S., Pan, N., and Hsieh, Y.-L. (2014). High energy density supercapacitors from lignin derived submicron activated carbon fibers in aqueous electrolytes. *J. Power Sources* 270 , 106–12. doi: 10.1016/j.jpowsour.2014.07.063

Huang, J., Liu, Y., and You, T. (2010). Carbon nanofiber based electrochemical biosensors: a review. *Anal. Methods* 2, 202–11. doi: 10.1039/b9ay00312f

Huang, X. (2009). Fabrication and properties of carbon fibers. *Materials* 2, 2369–2403. doi: 10.3390/ma2042369

Inagaki, M., Yang, Y., and Kang, F. (2012). Carbon nanofibers prepared via electrospinning. *Adv. Mater.* 24, 2547–66. doi: 10.1002/adma.201104940

Kadla, J. F., Kubo, S., Venditti, R. A., Gilbert, R. D., Compere, A. L., and Griffith, W. (2002). Lignin-based carbon fibers for composite fiber applications. *Carbon* 40, 2913–20. doi: 10.1016/S0008-6223(02)00248-8

Kim, C., Ngoc, B. T. N., Yang, K. S., Kojima, M., Kim, Y. A., Kim, Y. J., et al. (2007). Self-sustained thin webs consisting of porous carbon nanofibers for supercapacitors via the electrospinning of polyacrylonitrile solutions containing zinc chloride. *Adv. Mater.* 19, 2341–46. doi: 10.1002/adma.200602184

Lai, C., Kolla, P., Zhao, Y., Fong, H., and Smirnova, A. L. (2014a). Lignin-derived electrospun carbon nanofiber mats with supercritically deposited ag nanoparticles for oxygen reduction reaction in alkaline fuel cells. *Electrochim. Acta* 130, 431–38. doi: 10.1016/j.electacta.2014.03.006

Lai, C., Zhou, Z., Zhang, L., Wang, X., Zhou, Q., Zhao, Y., et al. (2014b). Free-standing and mechanically flexible mats consisting of electrospun carbon nanofibers made from a natural product of alkali lignin as binder-free electrodes for high-performance supercapacitors. *J. Power Sources* 247, 134–41. doi: 10.1016/j.jpowsour.2013.08.082

Lai, C.-C., and Lo, C.-T. (2015). Preparation of nanostructural carbon nano fi bers and their electrochemical performance for supercapacitors. *Electrochim. Acta* 183, 85–93. doi: 10.1016/j.electacta.2015.02.143

Lallave, M., Bedia, J., Ruiz-Rosas, R., Rodríguez-Mirasol, J., Cordero, T., Otero, J. C., et al. (2007). Filled and hollow carbon nanofibers by coaxial electrospinning of alcell lignin without binder polymers. *Adv. Mater.* 19, 4292–96. doi: 10.1002/adma.200700963

Lei, D., Li, X.-D., Seo, M. K., Khil, M.-S., Kim, H.-Y., and Kim, B.-S. (2017). NiCo2O4 nanostructure-decorated PAN/lignin based carbon nanofiber electrodes with excellent cyclability for flexible hybrid supercapacitors. *Polymer* 132, 31–40. doi: 10.1016/j.polymer.2017.10.051

Ma, C., Li, Z., Li, J., Fan, Q., Wu, L., Shi, J., et al. (2018). Lignin-based hierarchical porous carbon nanofiber films with superior performance in supercapacitors. *Appli. Surf. Sci.* 456, 568–76. doi: 10.1016/j.apsusc.2018.06.189

Ma, X., Kolla, P., Zhao, Y., Smirnova, A. L., and Fong, H. (2016). Electrospun lignin-derived carbon nanofiber mats surface-decorated with MnO2 nanowhiskers as binder-free supercapacitor electrodes with high performance. *J. Power Sources* 325, 541–48. doi: 10.1016/j.jpowsour.2016.06.073

Matsushita, Y., Inomata, T., Hasegawa, T., and Fukushima, K. (2009). Solubilization and functionalization of sulfuric acid lignin generated during bioethanol production from woody biomass. *Bioresource Technol.* 100, 1024–26. doi: 10.1016/j.biortech.2008.07.026

Niu, H., Zhang, J., Xie, Z., Wang, X., and Lin, T. (2011). Preparation, structure and supercapacitance of bonded carbon nanofiber electrode materials. *Carbon* 49, 2380–88. doi: 10.1016/j.carbon.2011.02.005

Peng, S., Li, L., Lee, J. K. Y., Tian, L., Srinivasan, M., Adams, S., et al. (2016). Electrospun carbon nanofibers and their hybrid composites as advanced materials for energy conversion and storage. *Nano Energy* 22, 361–95. doi: 10.1016/j.nanoen.2016.02.001

Poursorkhabi, V., Mohanty, A. K., and Misra, M. (2015). Electrospinning of aqueous lignin/poly(Ethylene Oxide) complexes. *J. Appli. Polym. Sci.* 132:41260. doi: 10.1002/app.41260

Ramakrishna, S. (2005). *An Introduction to Electrospinning and Nanofibers*. World Scientific Publishing. 396. doi: 10.1142/5894

Reneker, D. H., and Yarin, A. L. (2008). Electrospinning jets and polymer nanofibers. *Polymer* 49, 2387–2425. doi: 10.1016/j.polymer.2008.02.002

Rodríguez-Mirasol, J., Cordero, T., and Rodríguez, J. J. (1996). High-temperature carbons from kraft lignin. *Carbon* 34, 43–52. doi: 10.1016/0008-6223(95)00133-6

Rosas, J. M., Berenguer, R., Valero-Romero, M. J., Rodriguez-Mirasol, J., and Cordero, T. (2014). Preparation of different carbon materials by thermochemical conversion of lignin. *Front. Mater.* 1:29. doi: 10.3389/fmats.2014.00029

Ruiz-Rosas, R., Bedia, J., Lallave, M., Loscertales, I. G., Barrero, A., Rodríguez-Mirasol, J., et al. (2010). The production of submicron diameter carbon fibers by the electrospinning of lignin. *Carbon* 48, 696–705. doi: 10.1016/j.carbon.2009.10.014

Seo, D. K., Jeun, J. P., Kim, H. B., and Kang, P. H. (2011). Preparation and characterization of the carbon nanofiber mat produced from electrospun PAN/lignin precursors by electron beam irradiation. *Rev. Adv. Mater. Sci.* 28, 31–34. Available online at: www-proxy.ipme.ru/e-journals/RAMS/no_12811/08_paper.pdf

Shi, X., Wang, X., Tang, B., Dai, Z., Chen, K., and Zhou, J. (2018). Impact of lignin extraction methods on microstructure and mechanical properties of lignin-based carbon fibers. *J. Appl. Polym. Sci.* 135. doi: 10.1002/app.45580

Wang, L., Aorigele, and Sun, Y. (2017). Preparation of iron oxide particle-decorated lignin-based carbon nanofibers as electrode material for pseudocapacitor. *J. Wood Chem. Technol.* 37, 423–32. doi: 10.1080/02773813.2017.1310900

Wu, X.-F., Rahman, A., Zhou, Z., Pelot, D. D., Sinha-Ray, S., Chen, B., et al. (2013). Electrospinning core-shell nanofibers for interfacial toughening and self-healing of carbon-fiber/epoxy composites. *J. Appl. Polym. Sci.* 129, 1383–93. doi: 10.1002/app.38838

Yarin, A. L., Koombhongse, S., and Reneker, D. H. (2001). Bending instability in electrospinning of nanofibers bending instability in electrospinning of nanofibers. *J. Appli. Phys.* 89, 3018–26. doi: 10.1063/1.1333035

Yen, S.-H., and Chang, F.-C. (2016). Effects of fiber processing conditions on the yield, carbon content, and diameter of lignosulfonate-based carbon fibers. *BioResources* 11, 10158–72. doi: 10.15376/biores.11.4.10158-10172

You, X., Koda, K., Yamada, T., and Uraki, Y. (2015). Preparation of electrode for electric double layer capacitor from electrospun lignin fibers. *Holzforschung* 69, 1097–1106. doi: 10.1515/hf-2014-0262

Zhao, Y., Liu, Y., Tong, C., Ru, J., Geng, B., Ma, Z., et al. (2018). Flexible lignin-derived electrospun carbon nanofiber mats as a highly efficient and binder-free counter electrode for dye-sensitized solar cells. *J. Mater. Sci.* 53, 7637–47. doi: 10.1007/s10853-018-2059-0

Conflict of Interest Statement: The authors declare that the research was conducted in the absence of any commercial or financial relationships that could be construed as a potential conflict of interest.

frontiers in Materials

MINI REVIEW
published: 12 April 2019
doi: 10.3389/fmats.2019.00057

High-Performance Perovskite Solar Cells Based on Low-Temperature Processed Electron Extraction Layer

Shun-Hsiang Chan[1], *Yin-Hsuan Chang*[1] *and Ming-Chung Wu*[1,2,3]*

[1] Department of Chemical and Materials Engineering, Chang Gung University, Taoyuan, Taiwan, [2] Green Technology Research Center, Chang Gung University, Taoyuan, Taiwan, [3] Division of Neonatology, Department of Pediatrics, Chang Gung Memorial Hospital, Taoyuan, Taiwan

Organic-inorganic perovskite solar cells (PSCs) is considered one of the most promising energy harvesting technologies due to its high power conversion efficiency (PCE). The T. Miyasaka group first reported the methylammonium lead halide ($CH_3NH_3PbX_3$) as a light absorber of dye-sensitized solar cells with a PCE of 3.8% in 2009. Over the past decade, many research groups have been dedicated to constructing high-performance PSCs and have obtained fantastic progress. Before commercialization, many issues have to be overcome. To extend the application of PSCs, flexible PSCs are seen as the preferred choice. However, the conventional process requires high-temperature procedures that are incompatible with the production of flexible PSCs. Here, we specifically focus on the recent developments of the low-temperature process strategies for fabricating high-performance PSCs. This mini-review briefly discusses the development in low-temperature processed metal oxide and carbon-based electron extraction layer (EEL). The approaches for low-temperature solution-processed PSCs are introduced and then the various PSCs with distinctive EEL are discussed. Overall, this mini-review contributes to a better understanding of the low-temperature processed electron extraction layer. Strategies and perspectives are also provided for further high-performance PSCs.

Keywords: perovskite solar cell, low-temperature process, electron extraction layer, metal oxide, power conversion efficiency

OPEN ACCESS

Edited by:
Liming Dai,
Case Western Reserve University,
United States

Reviewed by:
Lola González-García,
Leibniz Institut für Neue Materialien (LG), Germany
Josep Albero,
Instituto de Tecnología Química (ITQ), Spain

***Correspondence:**
Ming-Chung Wu
mingchungwu@cgu.edu.tw

Specialty section:
This article was submitted to Translational Materials Science, a section of the journal Frontiers in Materials

Received: *06 December 2018*
Accepted: *20 March 2019*
Published: *12 April 2019*

Citation:
Chan S-H, Chang Y-H and Wu M-C (2019) High-Performance Perovskite Solar Cells Based on Low-Temperature Processed Electron Extraction Layer. Front. Mater. 6:57. doi: 10.3389/fmats.2019.00057

INTRODUCTION

The issue of energy crisis has received increasing attention in recent years. Researchers from all over the world have been focusing on the development of renewable energy, such as wind, geothermal, biomass, and solar energy, etc. Solar energy is less costly among renewable energy, it is predictable compared with wind energy, and is less site-dependent. Hence, solar energy technology has flourished in recent years. From first-generation poly/monocrystalline silicon solar cell, second-generation thin-film solar cell to third-generation solution-processed solar cell, the manufacturing cost has been significantly reduced. Third-generation solution-processed solar cells include organic photovoltaic (OPV), dye-sensitized solar cell (DSSC), and perovskite solar cell (PSC). Currently, PSC exhibits a power conversion efficiency (PCE) of as high as 23.7% in 2019. The typical perovskite structure is ABX_3, where A is a monovalent cation [e.g., methylammonium (MA), formamidinium (FA), cesium (Cs), and rubidium (Rb)], B is a divalent cation [e.g., lead (Pb) and tin (Sn)], and X is a halide [e.g., chlorine (Cl), bromine (Br), and iodine (I)] (Liu et al., 2016; Saliba et al., 2016a,b).

Furthermore, the structure is based on A-site cation occupying a cuboctahedral site with BX_6 octahedra. The octahedron will connect with each other, and the center of each octahedron is the location of A cation. The PSC structure can be divided into two types, including p-i-n and n-i-p structures (**Figures 1A,B**). The p-i-n structured PSC is based on the organic solar cells having ITO/p-type material (HTL)/perovskite/n-type material (EEL)/metal electrode (Heo et al., 2015; Fan et al., 2018; Mali et al., 2018). In contrast, n-i-p structured PSC is adopted to construct DSSC with structure FTO/n-type material (EEL)/perovskite/p-type material (HTL)/metal electrode (Chan et al., 2017; Wu et al., 2018a). Many n-type materials, including TiO_2, Al_2O_3, ZnO, ZrO_2, and SnO_2, are often used as electron extraction layer (EEL) for PSC due to the appropriate energy band alignment with perovskite absorber (Anaraki et al., 2016; Che et al., 2016; Zhang et al., 2017, 2018; Wu et al., 2018a). However, the synthesis of metal oxides often requires high-temperature treatment to increase the crystallinity. Therefore, developing metal oxides for EEL through the low-temperature process is imperative. For the flexible PSC, the processing temperature is usually lower than 150°C. The low-temperature process can effectively reduce production cost and increase the feasibility of mass-production (e.g., roll-to-roll manufacturing) (Dou et al., 2018). The photovoltaic characteristic of PSC based on various EELs prepared by the low-temperature process are shown in **Table 1**. In this mini-review, we briefly introduce the development of the low-temperature processed metal oxide and carbon-based EEL for state-of-the-art PSC. Moreover, we also compared the PSC made by the high-temperature process to the ones made by the low-temperature process.

LOW-TEMPERATURE TiO_2 ELECTRON EXTRACTION LAYER

For n-i-p structured perovskite device, TiO_2 is often used as EEL due to the chemical stability, low-cost, and high charge transportability (**Figure 1C**). The minimum conduction band of TiO_2 is lower than that of perovskite absorber, so that the electron can be effectively transported from perovskite absorber to TiO_2 EEL. Moreover, the maximum valence band of TiO_2 is also lower than that of perovskite absorber, resulting in the excellent hole blocking capability (Wu et al., 2016). For the TiO_2-based EEL, it can be classified into two types, mesoporous-structured TiO_2 layer and TiO_2 compact layer (Wu et al., 2018b; Chen et al., 2019). The mesoporous-structured TiO_2 layer must be calcined at above 400°C to remove the organic binder (e.g., ethyl cellulose) and form the porous structure (Wu et al., 2018a). However, the high-temperature calcination leads to cost increment and energy consumption, and it is not conducive to the low-temperature process. Therefore, the low-temperature process to prepare the nanostructure TiO_2 layer has been regarded as a breakthrough. The low-temperature processed TiO_2 as the EEL of PSC can be prepared by pulsed laser deposition. A laser beam was used to sublime a TiO_2 target. Subsequently, the sublimed TiO_2 films were deposited onto an ITO substrate at 300°C. The hierarchical TiO_2 nanostructures can effectively increase the contact area with perovskite absorber. Therefore, the interface between hierarchical TiO_2 EEL/perovskite absorber exhibits high electron-hole pair separation and electron extraction behavior. The PSC based on hierarchical TiO_2 EEL has demonstrated a PCE of 14.1% (Yang et al., 2016).

The low-temperature processed 3D flower-like TiO_2 array is also an alternative EEL for high-performance PSC. The TiO_2 array layer was deposited on an FTO substrate by chemical bath deposition method. In this process, the FTO glass was immersed in an 80°C $TiCl_3$/HCl solution for 4 to 10 h in a furnace. Subsequently, the TiO_2 array layer was washed and dried at 100°C for 2 h. The light-harvesting efficiency of the perovskite-coated TiO_2 array increases with increasing chemical bath deposition reaction time of the 3D flower-like TiO_2 array EEL. This is beneficial for obtaining a full coverage of the perovskite absorber layer. The flower-like TiO_2 nanorods is anatase phase, and it shows the high light-harvesting and low recombination rate. The PSCs based on flower-like TiO_2 nanorods EEL has shown a PCE of 15.7% with high reproducibility and less hysteresis (**Supplementary Figure 1A**) (Chen et al., 2016).

The pin-hole free compact TiO_2 can be coated on FTO substrate with high coverage by the vacuum electron beam evaporation technique. For the mesoporous TiO_2 layer, it was fabricated by spin-coating method, followed by a UV treatment for 200 min. UV irradiation is used to remove the organic binders to form mesoporous scaffold. This work uses a full low-temperature process to prepare compact TiO_2 and mesoporous TiO_2 layer. For J-V curve measurement, the champion device reached a stabilized efficiency of 18.2% under AM 1.5G solar simulator light (**Supplementary Figure 1A**). This research has carried all requirements for high-efficiency perovskite/silicon tandem cell with the full low-temperature process (Schulze et al., 2017).

The planar PSC fabricated by the low-temperature process can reach a PCE >20%. The deep trap states present at the perovskite absorber/EEL interface can hinder the photovoltaic performance. Many literatures have indicated that passivating the perovskite absorber/EEL interface can efficiently suppress deep trap states. Chlorine-capped TiO_2 EEL is able to reduce interface recombination at TiO_2/perovskite absorber interface. Chlorine-capped TiO_2 nanocrystals was fabricated by the modified non-hydrolytic sol-gel method. The precursor solution was spin-coated on FTO glass, then annealed in 150°C ambient air for 30 min. The chloride added into perovskite absorber can enhance grain boundary passivation in perovskite device. This type of planar PSC has exhibited a high PCE of 20.1% without J-V hysteresis (**Supplementary Figure 1A**) (Tan et al., 2017).

LOW-TEMPERATURE ZnO ELECTRON EXTRACTION LAYER

ZnO is a low-cost n-type semiconductor having a bandgap of 3.3 eV (Gaspar et al., 2017). ZnO can replace TiO_2 as an EEL for PSC due to its higher electron mobility and suitable energy structure. Also, ZnO has a beneficial conduction band position at 4.4 eV, which is lower than LUMO of perovskite absorber.

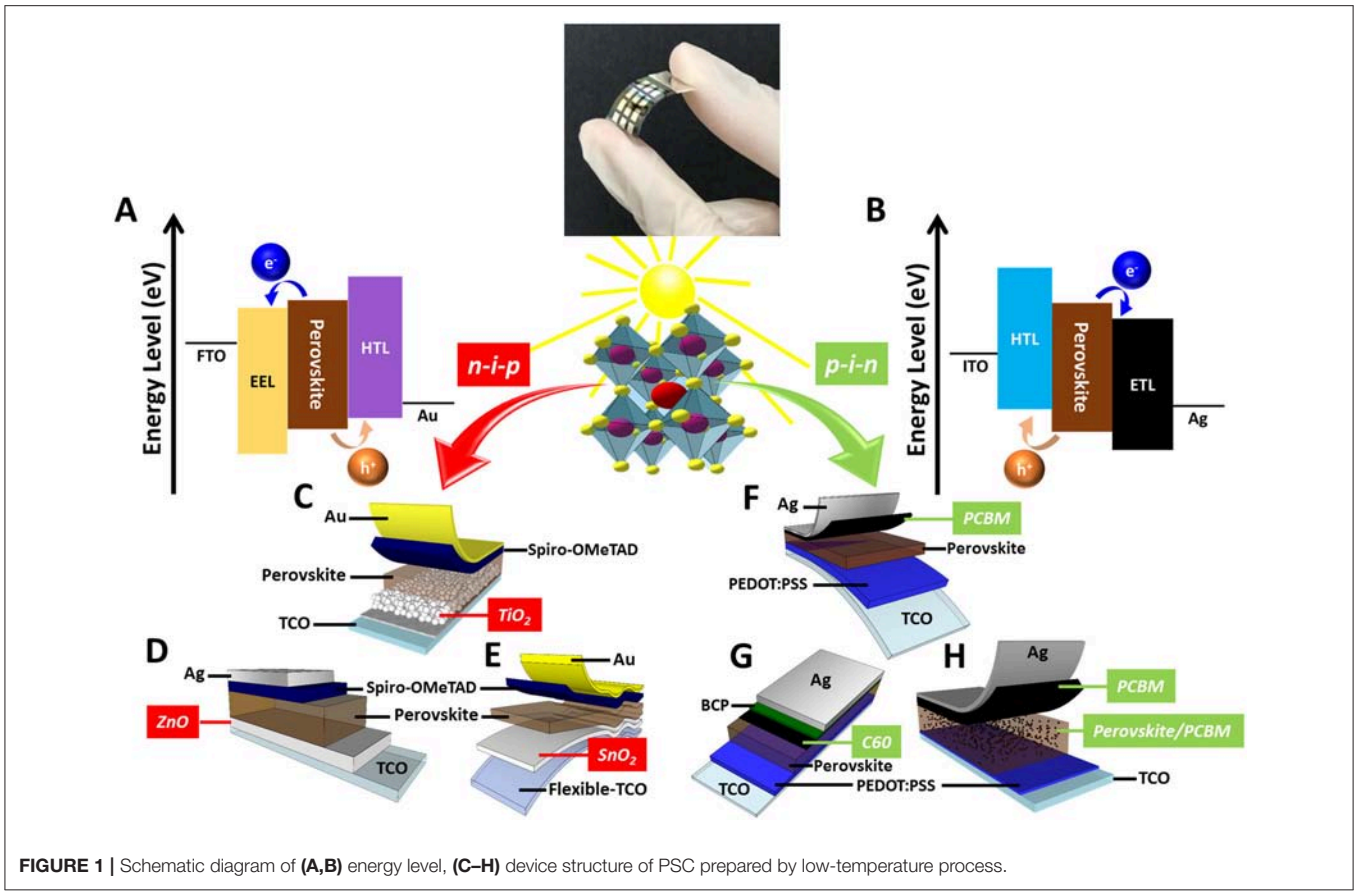

FIGURE 1 | Schematic diagram of **(A,B)** energy level, **(C–H)** device structure of PSC prepared by low-temperature process.

Therefore, ZnO has shown to play a critical role in improving the performance of PSC (Song et al., 2017). Especially, the fabricating temperature of ZnO film as EEL has been reduced to below 150°C (**Figure 1D**). The sol-gel ZnO was spin coated on ITO substrate, then annealed at 140°C. The optical property, surface morphology, and crystal structure of ZnO film can be tuned by adjusting thickness. The results have shown that the multi-layer ZnO film with high optical transmittance can increase the light absorption in perovskite absorber. After the thickness optimization of ZnO film, ZnO exhibits homogeneous surface morphology for the increment of perovskite crystal growth and suppression of deep trap states at the ZnO film/perovskite absorber interface. The PCE of PSC with ZnO film has reached 8.8% (**Supplementary Figure 1B**) (Mahmud et al., 2017).

To reduce the surface defects of the ZnO, chemical alkali-metal (Li, Na, and K) doping method has been adopted to passivate surface defect resulting in electron mobility enhancement and in raising the Fermi level. Doping metal ion into the semiconductor has been regarded as an effective strategy for electronic structure change. The alkali-metal doped ZnO EEL was prepared by dipping ZnO films into various 100°C alkali-metal hydroxide solutions for 10 min. Successfully doping alkali-metal ion into the low-temperature processed ZnO can simultaneously passivate surface defects. The performance of PSC with various alkali-metal doped ZnO EEL has shown to be higher than that with non-doped ZnO EEL. The PSC with K-doped ZnO EEL has achieved a PCE of 19.9% without significant J-V hysteresis (**Supplementary Figure 1B**) (Azmi et al., 2018).

LOW-TEMPERATURE SnO_2 ELECTRON EXTRACTION LAYER

J-V hysteresis in n-i-p planar PSC remains a challenge for the advancement of such material. The hysteresis can lead to misjudgment of photovoltaic performance because the forward and reverse scans show different results. Recently, SnO_2 has been reported as EEL of perovskite device that could eliminate J-V hysteresis in planar structure PSC due to its large bandgap (3.6 eV), higher electron mobility, optimal band alignment with perovskite absorber, and excellent electron extraction capability (Chen et al., 2018). SnO_2 has shown high conductivity without high-temperature calcination treatment, thus beneficial for the preparation of flexible PSC (**Figure 1E**).

For the band structure of SnO_2, it shows a lower conduction band and higher electron mobility compared to TiO_2 EEL. Tuning the band alignment between SnO_2 and perovskite absorber can facilitate charge transfer from perovskite absorber to SnO_2 EEL and reduce charge accumulation. Applying the low-temperature solution-processed SnO_2 as EEL can maintain high-performance for PSC. The SnO_2 precursor solution was prepared

TABLE 1 | List of state-of-the-art PSC based on EEL prepared by the low-temperature process.

Device structure	EEL	Processing temp. (°C)	Fabrication method	J_{SC} (mA/cm^2)	V_{OC} (volts)	FF (%)	PCE (%)	References
n-i-p	TiO_2	80	Chemical bath deposition	22.0	0.99	72.0	15.7	Chen et al., 2016
		120	Evaporation/UV Treatment	21.3	1.07	84.0	19.1	Schulze et al., 2017
		150	Spin-Coating	22.3	1.19	80.6	21.4	Tan et al., 2017
		300	Pulsed laser deposition	20.1	1.01	69.0	14.1	Yang et al., 2016
	ZnO	140	Spin-Coating	14.9	0.93	62.7	8.8	Mahmud et al., 2017
		130	Spin-Coating	23.0	1.13	77.1	19.9	Azmi et al., 2018
		150	Spin-Coating	22.6	1.11	75.3	18.9	Song et al., 2017
	SnO_2	150	Spin-Coating	24.9	1.09	75.7	20.5	Jiang et al., 2016
		≈RT	Spin-Coating /N_2 Plasma treatment	21.8	1.12	83.0	20.3	Subbiah et al., 2018
		180	Spin-Coating	21.9	1.13	78.0	19.4	Bu et al., 2018
		200	Atomic layer deposition	22.1	1.08	75.0	17.8	Kuang et al., 2018
	WO_x	150	Spin-Coating	21.8	0.71	58.0	9.0	Wang et al., 2015
	CeO_x	150	Spin-Coating	23.3	1.06	69.1	17.0	Wang et al., 2017b
	Nb_2O_5	≈RT	RF Magnetron sputtering technique	22.9	1.04	72.0	17.1	Ling et al., 2017
p-i-n	PCBM	100	Spin-Coating	21.8	1.04	78.0	17.8	Zhou et al., 2018
	PCBM (BHJ)	100	Spin-Coating	21.8	1.00	73.3	16.2	Chang et al., 2018
		100	Spin-Coating	20.2	0.97	82.0	16.0	Chiang and Wu, 2016
	C60	≈RT	Thermal evaporation	22.3	1.08	75.9	18.2	Liu et al., 2018

RT, room temperature; BHJ, bulk heterojunction; RF, radio frequency.

by diluting SnO_2 aqueous solution. The precursor solution was spin coated onto ITO substrates, then annealed on a 150°C hot plate for 30 min. SnO_2 EEL has been further constructed with the perovskite absorber by introducing an excess PbI_2 phase, passivating the traps in perovskite. This has achieved the best PCE of 20.5% without J-V hysteresis (**Supplementary Figure 1C**) (Jiang et al., 2016).

The low power nitrogen plasma treatment has been used to fabricate the low-temperature processed SnO_2 EEL. The SnO_2 precursor solution was prepared by dissolving $SnCl_4.5H_2O$ in IPA followed by continuous stirring for 2 h. The precursor solution was spin coated on rigid FTO or PET-ITO. Then, the samples were treated by low power RF plasma under nitrogen gas flow. Nitrogen plasma induces the initial cleavage of metal alkoxy and hydroxyl groups, resulting in the formation of the Sn-O-Sn framework. The PCE of PSC based on nitrogen plasma threated SnO_2 EEL has achieved 20.3% for rigid FTO substrates and 18.1% for flexible PSC (**Supplementary Figure 1C**) (Subbiah et al., 2018).

Atomic layer deposition is a deposition technique for high-quality film fabrication. Highly transparent amorphous SnO_2 was manufactured in atomic layer deposition reactor by low-temperature process (<200°C). The high-quality SnO_2 film exhibited high electron mobility (36 cm^2/V•s). The PCE of PSC with deposition temperature of 50 and 200°C SnO_2 has reached 17.5 and 17.8%, respectively (Kuang et al., 2018).

The PSC modules based on the low-temperature synthesized crystalline SnO_2 have been studied. The electron transport resistance of SnO_2 and charge recombination at EEL/perovskite absorber interface have been significantly decreased by thermal and UV-ozone treatments. The reported optimal thermal temperature for rigid PSC is 180°C, and can be decreased to 120°C for flexible PSC. The PCE of rigid PSC, flexible PSC, and 5 × 5 cm^2 flexible module have achieved 19.4, 16.5, and 12.4%, respectively (**Supplementary Figure 1C**) (Bu et al., 2018).

OTHER METAL OXIDE ELECTRON EXTRACTION LAYER

Tungsten oxide (WO_x) is n-type semiconductors with wide bandgap (2.0–3.0 eV) and high electron mobility (10–20 cm^2/V•s). These excellent properties make WO_x suitable as an EEL for perovskites photovoltaics. For the preparation of WO_x solution, tungsten hexachloride and n-propanol were mixed together, then the WO_x solution was spin coated on FTO. The amorphous WO_x EEL prepared by low-temperature solution process (150°C) shows higher electrical conductivity compared to TiO_2. Moreover, the excited electrons in perovskite absorber have shown to transfer more efficiently from perovskite absorber to WO_x EEL. Therefore, the short-circuit current density of PSC with WO_x EEL has shown to be higher than that of PSC with TiO_2 EEL. The PSC with WO_x EEL has shown an average PCE of 9.0% (**Supplementary Figure 1D**) (Wang et al., 2015).

Niobium oxide (Nb_2O_5) exhibits high electronic properties and high chemical stability. Therefore, Nb_2O_5 has also been seen as a candidate material for EEL. The amorphous Nb_2O_5 was fabricated at room temperature by a facile radio frequency magnetron sputtering technique on a Nb_2O_5 target in an argon atmosphere. The room-temperature sputtered Nb_2O_5 was successfully used as the EEL for planar PSC. The amorphous Nb_2O_5 film is highly transparent under visible region. As a

results, the PSC with the amorphous Nb_2O_5 EEL has exhibited a PCE of 17.2% (**Supplementary Figure 1D**) (Ling et al., 2017).

Cerium oxide (CeO_x) demonstrates wide bandgap, good transparency, large dielectric constant, and high chemical stability. CeO_x film was fabricated by sol-gel and spin-coating method at low temperature (150°C). The PSCs with CeO_x film showed high performance and high stability. Then the PCE of PSC with CeO_x film increased from 14.32 to 17.04% by [6,6]-phenyl C61 butyric acid methyl ester (PCBM) insertion (**Supplementary Figure 1D**) (Wang et al., 2017b).

FULLERENE COMPOUNDS ELECTRON EXTRACTION LAYER

The p-i-n structured PSC usually shows no hysteresis and is easier to prepare a flexible device. The p-i-n structured PSC has used [6,6]-phenyl C61 butyric acid methyl ester (PCBM) (**Supplementary Figure 2A**) (**Figure 1F**) and C60 (**Figure 1G**) as n-type EEL owing to its high electron mobility (Kuang et al., 2015). In order to further improve the PCE of the p-i-n structured PSC, the perovskite/PCBM heterojunction solar cell can be fabricated by a solvent engineering method (**Figure 1H**). The perovskite precursor solution contained PbI_2, $PbCl_2$, and CH_3NH_3I in DMSO/GBL solvent. PCBM solution was dissolved in chlorobenzene with various concentrations. After the perovskite precursor solution was spin coated on the substrate, the PCBM solution was injected on the perovskite film. The perovskite/PCBM films were annealed at 100°C for 20 min. The perovskite/PCBM heterojunction can improve the perovskite absorber quality and can increase charge extraction. Notably, adding PCBM during the baking procedure for perovskite absorber can form two separated EELs simultaneously, which effectively reduces the processing time. The champion device has exhibited a PCE of 17.8%, which is higher than that of the reference device (13.7%) (Zhou et al., 2018).

On the other hand, owing to the poor solubility of PCBM in DMF solvents, PCBM modification by fluorination can increase the solubility in the perovskite precursor. For the perovskite/fluorinated PCBM precursor solution, the fluorinated PCBM was directly added into the perovskite precursor solution. The perovskite/fluorinated PCBM precursor solution was spin coated on PEDOT:PSS film. The perovskite/fluorinated PCBM film was annealed at 100°C for 3 min to form the bulk heterojunction active layer. The fluorinated PCBM has shown to reduce the surface defects and to enhance the current density of PSC. The bulk heterojunction device with fluorinated PCBM has achieved a PCE of 16.2% with long-term stability (**Supplementary Figure 2B**) (Chang et al., 2018).

In order to enhance the fill factor of PSC, the perovskite-PCBM bulk heterojunction PSC has been fabricated by a low-temperature two-step spin-coating method. PCBM has been used as an acceptor to fill the vacancies and grain boundaries of the perovskite absorber. The product has demonstrated high current density, high fill factor, and high PCE because of high conductivity, high mobility, and long diffusion length of charge carriers. The bulk heterojunction PSC has achieved a PCE of 16.0%, fill factor of 82%, and without J-V hysteresis (Chiang and Wu, 2016).

Although fullerene compounds have been commonly used in p-i-n structured PSC, C60 has also been used as an EEL for p-i-n structured PSC recently. The C60 EEL with various thickness was deposited by vapor deposition in the evaporation chamber. Fluorescence microscopy and impedance spectroscopy have been used to investigate electron extraction behavior. The role of the C60 EEL can support electron extraction and collection. The PCE of PSC with 1 nm C60 EEL has achieved 18.0%. J-V hysteresis has also been significantly eliminated due to reduced space charge accumulation at the interface (**Supplementary Figure 2C**) (Liu et al., 2018).

ADVANTAGES AND DISADVANTAGES OF THE DIFFERENT APPROACHES

As mentioned above, most of the EEL is prepared by spin coating method due to easy fabrication, low-cost, and solution process. However, the spin coating method is very difficult when preparing a large-area film as the non-uniform film can directly affect device performance. The advantages of chemical bath deposition are a simple experimental setup and good reproducibility. But chemical bath deposition often requires a large amount of solution. Although evaporation and sputtering technique can produce large-area and uniform film, such methods require high vacuum and expensive equipment. Pulsed laser deposition can deposit many materials with the same composition as the target materials. Nevertheless, the coverage of the films is difficult to control by pulsed laser deposition. Atomic layer deposition can grow different multilayer structures with high sensitivity and precision. However, the disadvantages of atomic layer deposition are a longer process time for film fabrication and expensive setup. This summary also shows that the advantages and disadvantages of various methods should be considered for EEL fabrication.

CURRENT ISSUES AND FUTURE CHALLENGES FOR ELECTRON EXTRACTION LAYER

For the traditional high-temperature process, the EEL exhibits uniform mesoporous structure and high crystallinity. Comparing to the high-temperature process, the low-temperature process shows many fascinating advantages. The photovoltaic performance of PSC with the low-temperature process can still maintain high efficiency due to (1) passivation of the perovskite absorber/EEL interface, (2) high conductivity of EEL, and (3) application of UV or plasma treatment for EEL coalescence. Furthermore, the low-temperature processed EEL has shown to eliminate the hysteresis (Wojciechowski et al., 2014; Hou et al., 2015; Jeong et al., 2016; Tan et al., 2017; Wang et al., 2017a). When selecting EEL, several essential properties should be considered: (1) good electron mobility, (2) wide bandgap, and (3) band alignment with perovskite absorber. EEL with good electron mobility can facilitate the electron collection. For n-i-p

structured PSC, the wide bandgap EEL is selected to facilitate the absorption behavior of perovskite absorber. With the proper band alignment, it can promote electron transfer from perovskite active layer to EEL and can block holes to avoid recombination. If the above issues can all be satisfied and the existence of J-V hysteresis be eliminated, PSC with low-temperature process EEL can achieve a breakthrough in solar energy technology and realize commercialization.

CONCLUSIONS

In this mini-review, we summarized the metal oxide-based and fullerene compound-based EEL for PSC. Many n-type materials used for EEL, including TiO_2, ZnO, SnO_2, WO_x, CeO_x, Nb_2O_5, PCBM, and C60 have been thoroughly introduced. In addition, all these alternative materials for EEL can be fabricated under low-temperature process and can achieve PCE of over 20%. Using a low-temperature process to produce high-performance PSC is a major breakthrough. However, there are two issues that must be overcome before commercialization. The first one is the fast degradation phenomenon under humidity or constant irradiation, and the second is the hysteresis phenomena that can cause inaccurate estimation of PCE. The low-temperature process can effectively reduce production costs and energy waste. After addressing these issues, the commercialization of the low cost and flexible PSC is just around the corner.

AUTHOR CONTRIBUTIONS

S-HC wrote the submitted this mini-review. Y-HC revised and communicated the manuscript. M-CW supervised and wrote the manuscript.

ACKNOWLEDGMENTS

Financial support was obtained from Ministry of Science and Technology of Taiwan (Project Nos. 106-2221-E-182-057-MY3 and 107-2119-M-002-012), Chang Gung University (QZRPD181), and Chang Gung Memorial Hospital, Linkou (CMRPD2H0171 and BMRPC74) are highly appreciated.

SUPPLEMENTARY MATERIAL

The Supplementary Material for this article can be found online at: https://www.frontiersin.org/articles/10.3389/fmats.2019.00057/full#supplementary-material

REFERENCES

Anaraki, E. H., Kermanpur, A., Steier, L., Domanski, K., Matsui, T., Tress, W., et al. (2016). Highly efficient and stable planar perovskite solar cells by solution-processed tin oxide. *Energy Environ. Sci.* 9, 3128–3134. doi: 10.1039/C6EE02390H

Azmi, R., Hwang, S., Yin, W., Kim, T.-W., Ahn, T. K., and Jang, S.-Y. (2018). High efficiency low-temperature processed perovskite solar cells integrated with alkali metal doped ZnO electron transport layers. *ACS Energy Lett.* 3, 1241–1246. doi: 10.1021/acsenergylett.8b00493

Bu, T., Shi, S., Li, J., Liu, Y., Shi, J., Chen, L., et al. (2018). Low-temperature presynthesized crystalline tin oxide for efficient flexible perovskite solar cells and modules. *ACS Appl. Mater. Interfaces* 10, 14922–14929. doi: 10.1021/acsami.8b02624

Chan, S.-H., Wu, M.-C., Lee, K.-M., Chen, W.-C., Lin, T.-H., and Su, W.-F. (2017). Enhancing perovskite solar cell performance and stability by doping barium in methylammonium lead halide. *J. Mater. Chem. A* 5, 18044–18052. doi: 10.1039/C7TA05720B

Chang, C.-Y., Wang, C.-P., Raja, R., Wang, L., Tsao, C.-S., and Su, W.-F. (2018). High-efficiency bulk heterojunction perovskite solar cell fabricated by one-step solution process using single solvent: synthesis and characterization of material and film formation mechanism. *J. Mater. Chem. A* 6, 4179–4188. doi: 10.1039/C7TA07939G

Che, M., Zhu, L., Zhao, Y. L., Yao, D. S., Gu, X. Q., Song, J., et al. (2016). Enhancing current density of perovskite solar cells using TiO_2-ZrO_2 composite scaffold layer. *Mater. Sci. Semicond. Process.* 56, 29–36. doi: 10.1016/j.mssp.2016.07.003

Chen, S.-H., Chan, S.-H., Lin, Y.-T., and Wu, M.-C. (2019). Enhanced power conversion efficiency of perovskite solar cells based on mesoscopic Ag-doped TiO_2 electron transport layer. *Appl. Surf. Sci.* 469, 18–26. doi: 10.1016/j.apsusc.2018.10.256

Chen, X., Tang, L. J., Yang, S., Hou, Y., and Yang, H. G. (2016). A low-temperature processed flower-like TiO_2 array as an electron transport layer for high-performance perovskite solar cells. *J. Mater. Chem. A* 4, 6521–6526. doi: 10.1039/C6TA00893C

Chen, Y., Meng, Q., Zhang, L., Han, C., Gao, H., Zhang, Y., et al. (2018). SnO_2-based electron transporting layer materials for perovskite solar cells: a review of recent progress. *J. Energy Chem.* 35, 144–167. doi: 10.1016/j.jechem.2018.11.011

Chiang, C.-H., and Wu, C.-G. (2016). Bulk heterojunction perovskite-PCBM solar cells with high fill factor. *Nat. Photonics* 10, 196–200. doi: 10.1038/nphoton.2016.3

Dou, B., Whitaker, J. B., Bruening, K., Moore, D. T., Wheeler, L. M., Ryter, J., et al. (2018). Roll-to-roll printing of perovskite solar cells. *ACS Energy Lett.* 3, 2558–2565. doi: 10.1021/acsenergylett.8b01556

Fan, P., Zheng, D., Zheng, Y., and Yu, J. (2018). Efficient and stable planar p-i-n perovskite solar cells by doping tungsten compound into PEDOT:PSS to facilitate perovskite crystalline. *Electrochim. Acta* 283, 922–930. doi: 10.1016/j.electacta.2018.07.029

Gaspar, D., Pereira, L., Gehrke, K., Galler, B., Fortunato, E., and Martins, R. (2017). High mobility hydrogenated zinc oxide thin films. *Sol. Energy Mater. Sol. Cells* 163, 255–262. doi: 10.1016/j.solmat.2017.01.030

Heo, J. H., Han, H. J., Kim, D., Ahn, T. K., and Im, S. H. (2015). Hysteresis-less inverted $CH_3NH_3PbI_3$ planar perovskite hybrid solar cells with 18.1% power conversion efficiency. *Energy Environ. Sci.* 8, 1602–1608. doi: 10.1039/C5EE00120J

Hou, Y., Quiroz, C. O. R., Scheiner, S., Chen, W., Stubhan, T., Hirsch, A., et al. (2015). Low-temperature and hysteresis-free electron-transporting layers for efficient, regular, and planar structure perovskite solar cells. *Adv. Energy Mater.* 5:1501056. doi: 10.1002/aenm.201501056

Jeong, I., Jung, H., Park, M., Park, J. S., Son, H. J., Joo, J., et al. (2016). A tailored TiO_2 electron selective layer for high-performance flexible perovskite solar cells via low temperature UV process. *Nano Energy* 28, 380–389. doi: 10.1016/j.nanoen.2016.09.004

Jiang, Q., Zhang, L., Wang, H., Yang, X., Meng, J., Liu, H., et al. (2016). Enhanced electron extraction using SnO_2 for high-efficiency planar-structure $HC(NH_2)_2PbI_3$-based perovskite solar cells. *Nat. Energy* 2:16177. doi: 10.1038/nenergy.2016.177

Kuang, C., Tang, G., Jiu, T., Yang, H., Liu, H., Li, B., et al. (2015). Highly efficient electron transport obtained by doping PCBM with graphdiyne in planar-heterojunction perovskite solar cells. *Nano Lett.* 15, 2756–2762. doi: 10.1021/acs.nanolett.5b00787

Kuang, Y., Zardetto, V., Van Gils, R., Karwal, S., Koushik, D., Verheijen, M. A., et al. (2018). Low-temperature plasma-assisted atomic-layer-deposited SnO_2 as

an electron transport layer in planar perovskite solar cells. *ACS Appl. Mater. Interfaces* 10, 30367–30378. doi: 10.1021/acsami.8b09515

Ling, X., Yuan, J., Liu, D., Wang, Y., Zhang, Y., Chen, S., et al. (2017). Room-temperature processed Nb_2O_5 as the electron-transporting layer for efficient planar perovskite solar cells. *ACS Appl. Mater. Interfaces* 9, 23181–23188. doi: 10.1021/acsami.7b05113

Liu, D., Wang, Q., Traverse, C. J., Yang, C., Young, M., Kuttipillai, P. S., et al. (2018). Impact of ultrathin C60 on perovskite photovoltaic devices. *ACS Nano* 12, 876–883. doi: 10.1021/acsnano.7b08561

Liu, X., Yang, Z., Chueh, C.-C., Rajagopal, A., Williams, S. T., Sun, Y., et al. (2016). Improved efficiency and stability of Pb-Sn binary perovskite solar cells by Cs substitution. *J. Mater. Chem. A* 4, 17939–17945. doi: 10.1039/C6TA07712A

Mahmud, M. A., Elumalai, N. K., Upama, M. B., Wang, D., Chan, K. H., Wright, M., et al. (2017). Low temperature processed ZnO thin film as electron transport layer for efficient perovskite solar cells. *Sol. Energy Mater. Sol. Cells* 159, 251–264. doi: 10.1016/j.solmat.2016.09.014

Mali, S. S., Kim, H., Kim, H. H., Shim, S. E., and Hong, C. K. (2018). Nanoporous p-type NiOx electrode for p-i-n inverted perovskite solar cell toward air stability. *Mater. Today* 21, 483–500. doi: 10.1016/j.mattod.2017.12.002

Saliba, M., Matsui, T., Domanski, K., Seo, J.-Y., Ummadisingu, A., Zakeeruddin, S. M., et al. (2016a). Incorporation of rubidium cations into perovskite solar cells improves photovoltaic performance. *Science*. 354, 206–209. doi: 10.1126/science.aah5557

Saliba, M., Matsui, T., Seo, J.-Y., Domanski, K., Correa-Baena, J.-P., Nazeeruddin, M. K., et al. (2016b). Cesium-containing triple cation perovskite solar cells: improved stability, reproducibility and high efficiency. *Energy Environ. Sci.* 9, 1989–1997. doi: 10.1039/c5ee03874j

Schulze, P. S. C., Bett, A. J., Winkler, K., Hinsch, A., Lee, S., Mastroianni, S., et al. (2017). Novel low-temperature process for perovskite solar cells with a mesoporous TiO_2 scaffold. *ACS Appl. Mater. Interfaces* 9, 30567–30574. doi: 10.1021/acsami.7b05718

Song, J., Liu, L., Wang, X.-F., Chen, G., Tian, W., and Miyasaka, T. (2017). Highly efficient and stable low-temperature processed ZnO solar cells with triple cation perovskite absorber. *J. Mater. Chem. A* 5, 13439–13447. doi: 10.1039/C7TA03331A

Subbiah, A. S., Mathews, N., Mhaisalkar, S., and Sarkar, S. K. (2018). Novel plasma-assisted low-temperature-processed SnO_2 thin films for efficient flexible perovskite photovoltaics. *ACS Energy Lett.* 3, 1482–1491. doi: 10.1021/acsenergylett.8b00692

Tan, H., Jain, A., Voznyy, O., Lan, X., García De Arquer, F. P., Fan, J. Z., et al. (2017). Efficient and stable solution-processed planar perovskite solar cells via contact passivation. *Science* 355, 722–726. doi: 10.1126/science.aai9081

Wang, K., Shi, Y., Dong, Q., Li, Y., Wang, S., Yu, X., et al. (2015). Low-temperature and solution-processed amorphous WO_X as electron-selective layer for perovskite solar cells. *J. Phys. Chem. Lett.* 6, 755–759. doi: 10.1021/acs.jpclett.5b00010

Wang, L., Liu, F., Liu, T., Cai, X., Wang, G., Ma, T., et al. (2017a). Low-temperature processed compact layer for perovskite solar cells with negligible hysteresis. *Electrochim. Acta* 235, 640–645. doi: 10.1016/j.electacta.2017.03.145

Wang, X., Deng, L.-L., Wang, L.-Y., Dai, S.-M., Xing, Z., Zhan, X.-X., et al. (2017b). Cerium oxide standing out as an electron transport layer for efficient and stable perovskite solar cells processed at low temperature. *J. Mater. Chem. A* 5, 1706–1712. doi: 10.1039/C6TA07541J

Wojciechowski, K., Saliba, M., Leijtens, T., Abate, A., and Snaith, H. J. (2014). Sub-150°C processed meso-superstructured perovskite solar cells with enhanced efficiency. *Energy Environ. Sci.* 7, 1142–1147. doi: 10.1039/C3EE43707H

Wu, M.-C., Chan, S.-H., Jao, M.-H., and Su, W.-F. (2016). Enhanced short-circuit current density of perovskite solar cells using Zn-doped TiO_2 as electron transport layer. *Sol. Energy Mater. Sol. Cells* 157, 447–453. doi: 10.1016/j.solmat.2016.07.003

Wu, M.-C., Chan, S.-H., Lee, K.-M., Chen, S.-H., Jao, M.-H., Chen, Y.-F., et al. (2018a). Enhancing the efficiency of perovskite solar cells using mesoscopic zinc-doped TiO_2 as the electron extraction layer through band alignment. *J. Mater. Chem. A* 6, 16920–16931. doi: 10.1039/C8TA05291C

Wu, M.-C., Liao, Y.-H., Chan, S.-H., Lu, C.-F., and Su, W.-F. (2018b). Enhancing organolead halide perovskite solar cells performance through interfacial engineering using Ag-doped TiO_2 hole blocking layer. *Solar RRL* 2:1800072. doi: 10.1002/solr.201800072

Yang, B., Mahjouri-Samani, M., Rouleau, C. M., Geohegan, D. B., and Xiao, K. (2016). Low temperature synthesis of hierarchical TiO_2 nanostructures for high performance perovskite solar cells by pulsed laser deposition. *Phys. Chem. Chem. Phys.* 18, 27067–27072. doi: 10.1039/C6CP02896A

Zhang, J., Hultqvist, A., Zhang, T., Jiang, L., Ruan, C., Yang, L., et al. (2017). Al_2O_3 underlayer prepared by atomic layer deposition for efficient perovskite solar cells. *ChemSusChem* 10, 3810–3817. doi: 10.1002/cssc.201701160

Zhang, P., Wu, J., Zhang, T., Wang, Y., Liu, D., Chen, H., et al. (2018). Perovskite solar cells with ZnO electron-transporting materials. *Adv. Mater.* 30:1703737. doi: 10.1002/adma.201703737

Zhou, L., Chang, J., Liu, Z., Sun, X., Lin, Z., Chen, D., et al. (2018). Enhanced planar perovskite solar cell efficiency and stability using a perovskite/PCBM heterojunction formed in one step. *Nanoscale* 10, 3053–3059. doi: 10.1039/C7NR07753J

Conflict of Interest Statement: The authors declare that the research was conducted in the absence of any commercial or financial relationships that could be construed as a potential conflict of interest.

Advantages of publishing in Frontiers

OPEN ACCESS
Articles are free to read for greatest visibility and readership

FAST PUBLICATION
Around 90 days from submission to decision

HIGH QUALITY PEER-REVIEW
Rigorous, collaborative, and constructive peer-review

TRANSPARENT PEER-REVIEW
Editors and reviewers acknowledged by name on published articles

Frontiers
Avenue du Tribunal-Fédéral 34
1005 Lausanne | Switzerland

Visit us: www.frontiersin.org
Contact us: info@frontiersin.org | +41 21 510 17 00

REPRODUCIBILITY OF RESEARCH
Support open data and methods to enhance research reproducibility

DIGITAL PUBLISHING
Articles designed for optimal readership across devices

FOLLOW US
@frontiersin

IMPACT METRICS
Advanced article metrics track visibility across digital media

EXTENSIVE PROMOTION
Marketing and promotion of impactful research

LOOP RESEARCH NETWORK
Our network increases your article's readership